JOURNAL
OF THE
PHYSICAL SOCIETY
OF JAPAN

Volume 16

1961

PT-1

Published by the
PHYSICAL SOCIETY OF JAPAN

Digitized by the Internet Archive
in 2024

https://archive.org/details/physical-society-of-japan-journal_january-june-1961_16_part-1-1-6

Journal of the Physical Society of Japan, Vol. 16, No. 1, January, 1961

Study on Spark Counters of the Rosenblum Type for Counting α Particles and Neutrons

By Suekichi KAWATA

Department of Physics, Kōnan University, Kōbe

(Received March 23, 1960)

Characteristics of the Rosenblum type spark counters were studied experimentally. In the case of a single-wire counter, number of count was investigated when the α-particle source was moved parallel to the cathode plate, and in relation to voltage applied to the anode wire and also when the source was moved perpendicularly to the cathode plate. Especially effects of temperature, pressure and humidity of the surrounding air on counts were investigated, and the efficiency of counting of α particles was estimated. Experiments were also carried out for a multiple-wire counter. A counter with 14 anode wires was constructed, and it was found that uniformity of counting through the whole acting region might be greatly improved by inserting a high resistance in series with each wire. A neutron detector was constructed by putting a boron-coated glass plate above the multiple wires and surrounding the counter with paraffin.

§ 1. Introduction

The Chang-Rosenblum type spark counter[1] for α-particle detection has several attracting features: (1) it is insensitive to low specific ionization radiation; (2) it has a rapid rise-time of pulse; (3) it operates in the open air; (4) it is of very simple construction; (5) it does not need special amplifiers; and (6) it can get easily a wide plateau for applied voltage. Many workers have offered various reports[1)–16)] about its characteristics and applications, but their experimental results are not always consistent among themselves. Sometimes the experimental conditions are not made clear. The present writer has investigated the counter to make its characteristics clearer and also to make contributions from the point of practical uses.

§ 2. Single-wire Counter

A counter was constructed with a tungsten wire 0.1 mm thick and 40 mm long (anode) and a flat plate of stainless steel of 60×60 mm (cathode), the wire having been stretched on a frame made of acryl-resin and placed at a distance of about 1.2 mm above the plate separated by two narrow spacers of glass. The cathode plate was put on an ebonite plate placed on a horizontal stage of a travelling-microscope. Two modes of irradiation by α particles from Po^{210} were used. Firstly, an old deposit of Po on a silver foil prepared 2–3 years ago was used, and secondly a newly prepared deposit was used after the most part of the experiment had been performed with the first source. The α particles were passed through a circular hole of 2 mm in diameter and 5.5 mm in length in the first case, and through a hole of 0.8 mm in diameter and 11 mm in length in the second case. The second source was found to be much more homogeneous with respect to the energy when it was examined by a scintillation spectrometer with a CsI(Tl) crystal of 1/16″ thick, and was far stronger than the first source. The sources with the slits were attached to the microscope holder projected horizontally from the vertical support. Generally the whole apparatus was placed in a thermostat of 40×40 ×60 cm which communicated slightly with outer air. The counter was operated by a circuit as shown in Fig. 1.

The voltage pulses of sparks caused by the passage of α particles are of nearly uniform shape and magnitude, when examined with an oscilloscope and a synchroscope. The rise time and the recovery time were estimated to be of the order of 10^{-7} sec and a few hundred μsec respectively.

(1) After preliminary experiments the old Po source was placed at about 28.0 mm above the cathode plate, and the counter was ope-

63/ 0 neu

rated by applying 3.70 kV to the anode wire. Throughout the experiment the irradiation was always end-on. Curve (A) in Fig. 2 shows variation of count of the spark when the first source was moved perpendicularly to the anode wire. The situation of the source giving the maximum count at about 28.0 mm from the plate was taken as the normal position for the measurement. Curve (B) is the corresponding one with the new Po-α source.

(2) Fig. 3 illustrates curves of count *versus* applied voltage of the anode wire, not the potential difference between the anode and the cathode, the Po source being at the normal position, under three different conditions of the air. Corona current is given in the curve II′ corresponding to the curve II. The voltage characteristics depend naturally on resistances inserted in the circuit. In the present example it has a very wide plateau.

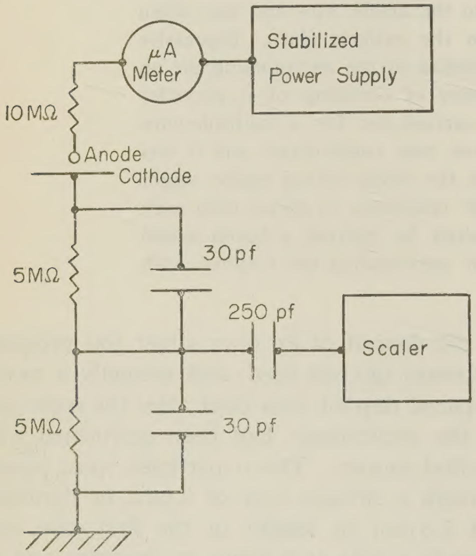

Fig. 1. Operating circuit of the spark counter.

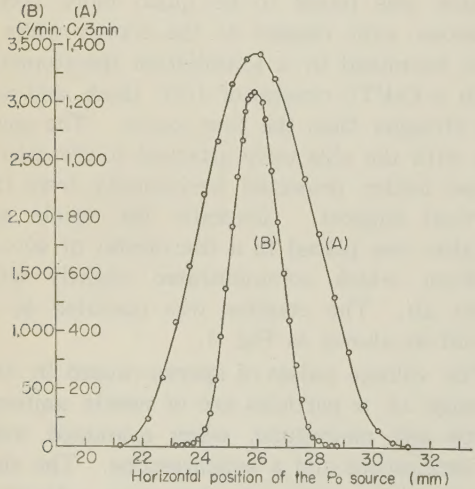

Fig. 2. Relation between count and displacement of the Po source perpendicular to the anode wire, (A) when α particles from the old source were passed through a hole of 2×5.5 mm, and (B) when α particles from the new source were passed through a hole of 0.8×11 mm.

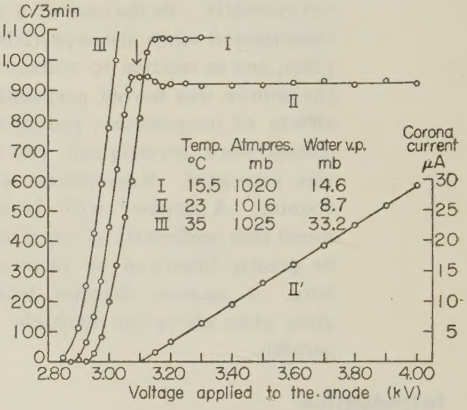

Fig. 3. Relation between count of spark and voltage applied to the anode wire, under three different conditions of air (curves I, II and III). The curve II′ showing corona current *versus* applied voltage corresponds to the curve II. (The old source was used.)

Various workers have shown that such humps as marked by a vertical arrow to the curve II were observed generally, and sometimes very markedly in such characteristic curves, but others have not observed them, and an opinion was presented by the latters to attribute their appearance to the different collimation of α particles. In the present experiment, however, such humps appeared rather markedly in some cases, but not in other cases notwithstanding that the geometry of irradiation was the same. Again, the appearance was not much more marked with the well-collimated beam of α particles from the second source. Also it is not clear that whether conditions of temperature or humidity may affect their appearance or not.

(3) Fig. 4 shows a diagram obtained when the old Po source was moved vertically, i.e. perpendicularly to the cathode plate, from the normal position indicated by a vertical arrow. Since the ordinate indicates count of spark, this diagram is different from the ordinary Bragg curve obtained for the ionization cur-

rent in a shallow chamber. In the present case it may be remarked that the count will depend upon the number of incident particles and also upon specific ionization, angular spread of particles and directional sensitivity of the counter. In this figure, (a) indicates the position of the source about 7 mm from the cathode plate. Then there is a region of rapid increase of count as indicated by (b), arriving at a maximum (c), and next there comes a somewhat gradual decrease (d) followed by a plateau (e) of about 10 mm, and lastly a steep fall (f) appears which is familiar in the Bragg curve near the end of the range.

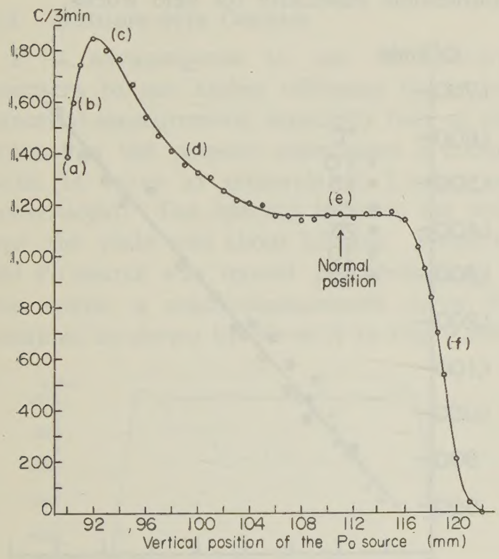

Fig. 4. Variation of count when the Po source was moved vertically to the cathode plate. (The old source was used.)

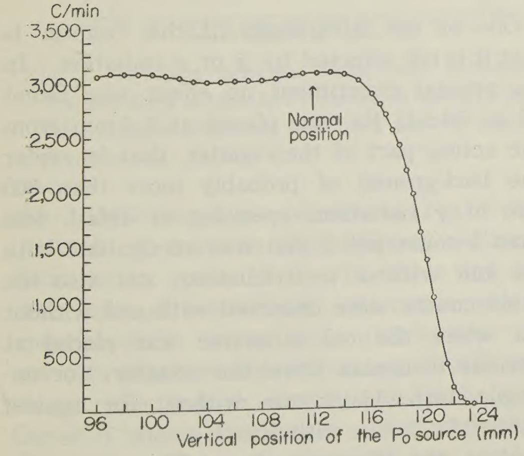

Fig. 5. Variation of count when the new Po source was moved vertically to the cathode plate.

Fig. 5 shows the similar curve obtained with the second source. In this curve the regions corresponding to (c) and (d) in Fig. 4 are not observed.

(4) Effects of temperature and humidity. As to the effect of temperature Saha and Nath[11] indicated a shift of the count *versus* source-distance curve at 20°C and 49°C (humidity having not been indicated), and as to the effect of humidity Andreschev and Isaev[9] showed a nearly linear increase of count with vapour pressure in 5–28 mb, and very recently Daddi and Franceschi[14] gave results obtained for water vapour of 27 and 112 mm Hg in broadside irradiation and remarked that the counting efficiency depended upon the air condition and particularly upon humidity, and in the case of completely dry air the efficiency was practically zero for broadside irradiation.

In order to obtain various conditions of temperature and humidity we used saturated solutions of various salts in the thermostat at different temperatures, and stirred the air violently with a fan. Both the temperature and the humidity were measured by use of a small resistance-type hygrometer devised by K. Shiba.

As illustrated in Fig. 3 the count *versus* applied voltage curve alters with different conditions of the air. Fig. 6 shows curves similar

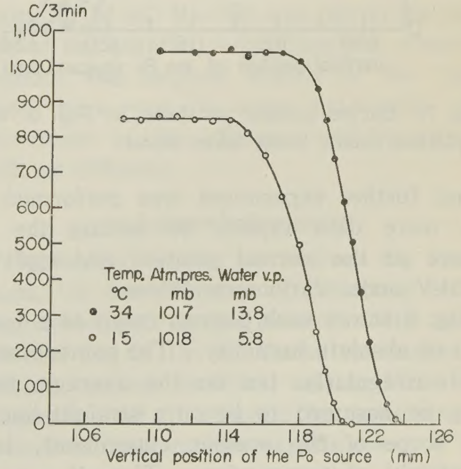

Fig. 6. Two curves similar to the curve in Fig. 4 near the end of the range of α particles under different conditions of temperature, atmospheric pressure and water vapour pressure.

to the curve in Fig. 4, which was obtained by applying 3.70 kV to the anode and moving the old Po source vertically under two different conditions of temperature and humidity. It was found that the curves move not only horizontally as shown by Saha and Nath[11)], but also vertically. In order to clarify the matter, curves were drawn again with two additional ones by taking the plateau counts to be equal. The results are shown in Fig. 7. It will be seen that the normalized curves undergo displacement approximately due to the density variation of the air in the path of α particles from the source to the counter, and that the displacement along the horizontal axis will not be intrinsic to the counter, whereas the displacement along the vertical axis seems to be due al most to humidity.

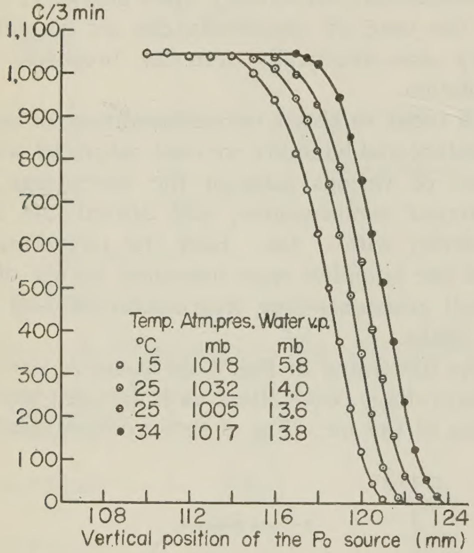

Fig. 7. Curves similar to those in Fig. 6, the plateau counts being taken equal.

Thus, further experiment was performed to get more data rapidly by setting the Po source at the normal position and applying 3.70 kV under various conditions.

Fig. 8 shows such plateau count as a function of absolute humidity. The points scatter fairly irregularly, but on the average, they may be assumed to lie on a straight line in the scope of the present experiment, irrespectively of temperature. Thus it may be concluded that temperature has only minute effect upon the counting efficiency, but humidity influences remarkably. Dependence of the applied voltage-count curve upon temperature and humidity will be seen again in Fig. 3. It seems that the curves undergo displacement towards lower voltage side with the rise of temperature and towards higher voltage side with increase of absolute humidity, and count increases with absolute humidity. The effect of humidity seems to be an interesting problem for the understanding of the mechanism of the counter, yet in order to avoid this effect the counter will have to be put in an enclosed vessel or corrections will have to be made by preliminary experiment, and from the point of practical use, the effect will be troublesome especially for field works.

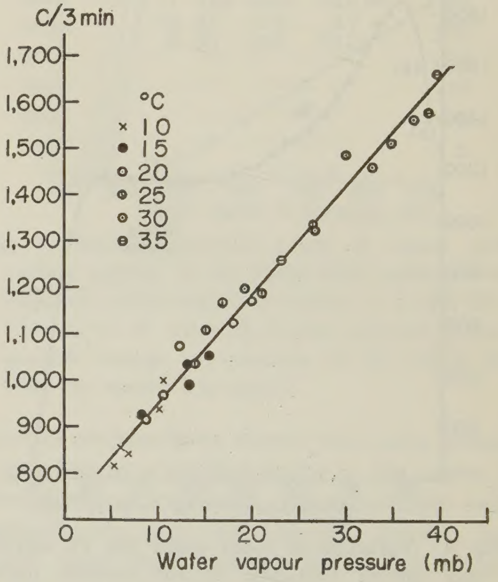

Fig. 8. Relation between plateau count and absolute humidity.

One of the advantages of this counter is that it is not affected by β or γ radiation. In the present experiment no effect was found when 50 mC Ra was placed at 5–6 mm from the acting part of the counter, that is, under the background of probably more than 600 r/hr of γ radiation, speaking in detail, less than 1 count per 5 min was recognized with Ra and without α irradiation, and also the same counts were observed with and without Ra when the old α source was placed at various distances from the counter, for example 1476±15 c/3 min without Ra against 1491±15 c/3 min with Ra.

Next, the efficiency of counting α particles with the counter was studied. For this purpose, count was taken, in one hand, with the counter by placing the new source at about 28.0 mm directly above the anode wire, and passing α rays through the narrow slit, and in the other hand, with the scintillation counter by placing the source with the same slit at as possibly equal distance as 28.0 mm above the CsI(Tl) crystal. The count ratio was ~3090 c/min for 23°C and 18.8 mb water vapour and ~3610 c/min for 25.4°C and 28.8 mb water vapour against ~7720 c/min, that is, ~40% and ~47% respectively, by assuming the CsI(Tl) scintillation count as 100%, under the indicated conditions of geometry.

§ 3. Multiple-wire Counter

It is advantageous to use multiple-wire counters to get higher efficiency for various practical measurement, especially that of neutrons. In the present experiment a counter with 14 wires at intervals of 2.5 mm was constructed. The spacing between the wires and the plate was about 1.3 mm. When the old Po source was moved perpendicularly to the wires, a count-displacement curve was obtained as shown by curve A in Fig. 9 when the 10 MΩ resistance shown in Fig. 1 was omitted. It may be that different nature of each acting space of the 14 wires and also their mutual interactions will cause such an unsatisfactory non-uniform distribution. In order to eliminate the interaction 10 MΩ resistance was put in series with each wire. Curve B shows the result. The uniformity of counting shown in curve B was not obtained without adding such a high resistance to each wire, for example with a resistance of 1 MΩ to each wire or with one resistance of 10 MΩ in series with a parallel connection of the 14 wires. Fig. 10 shows a voltage-count curve obtained by putting the α source at about 27 mm above the central part of the wires. It shows also a very wide plateau.

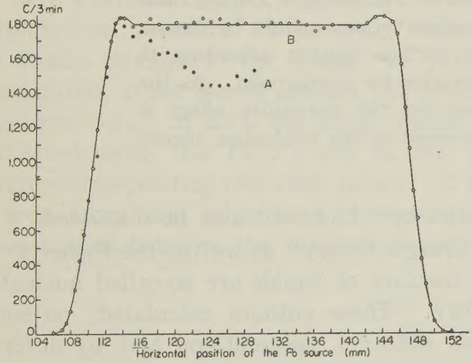

Fig. 9. Relation between count and horizontal displacement of the old Po source in the multiple-wire counter similar to the curve for the single-wire counter in Fig. 2.

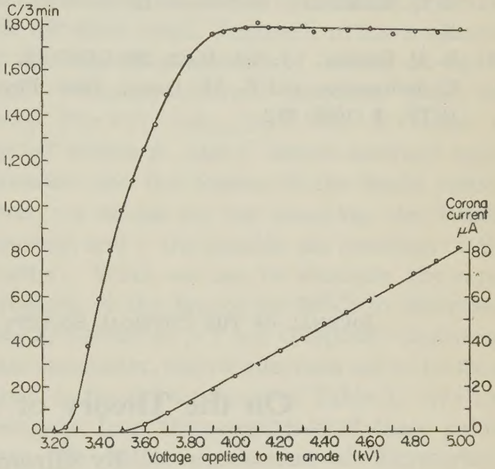

Fig. 10. Relation between count and applied voltage to the anode wires in the multiple-wire counter, similar to the curve for the single-wire counter as shown in Fig. 3.

Next, an apparatus for measuring neutrons was constructed by making use of the 14-wires counter. A glass plate coated with natural boron powder mixed with styrol over the area of 3×3 cm was put above 1.5 mm from the wires and the assembly was covered with paraffin 4 cm thick. When a neutron source of 50 mC Ra+Be was put on the upper side of the paraffin, ~70 c/min was observed. Without the neutron source or the boron plate there was no count practically. Improvement of the efficiency will be achieved without difficulty.

Acknowledgements

The writer wishes to express his cordial thanks to the Ministry of Education for the financial support to this research. His thanks are also due to Dr. K. Yuasa for kindly affording various facilities, and to Messrs. T. Watanabe and T. Aragaki for their kind assistance throughout the experiment.

References

1) W. Y. Chang and S. Rosenblum: Phys. Rev. **67** (1945) 222.

2) R. D. Connor: Nature **163** (1949) 540.
3) R. M. Payne: J. Sci. Instr. **26** (1949) 321.
4) R. Ricamo: Nuovo Cimento, Ser. 9, **7** (1950) 49.
5) R. D. Connor: Proc. Phys. Soc. London **B 64** (1951) 30.
6) M. P. Savel: Compt. Rend. **234** (1952) 2596; **235** (1952) 156.
7) G. G. Eichholtz: Nucleonics **10** (1952) No. 10, 46.
8) R. D. Connor: J. Sci. Instr. **29** (1952) 12.
9) E. Andreschev and B. M. Isaev: Sov. Phys. JETP. **1** (1955) 212.
10) M. J. Swetnick and N. G. Anton: Nucleonics **15** (1957) No. 6, 93.
11) N. K. Saha and Narendra Nath: Nucleonics **15** (1957) No. 6, 94.
12) E. Leisk: Nucleonics **16** (1958) No. 7, 95.
13) L. Daddi and L. de Franceschi: Nuovo Cimento **7** (1958) 895.
14) L. Daddi and L. de Franceschi: Rev. Sci. Instr. **30** (1959) 419.
15) C. W. Peters and F. E. Jablonski: Rev. Sci. Instr. **30** (1959) 728.
16) A. El-Nadi and F. M. Aly: J. Sci. Instr. **36** (1959) 434.

JOURNAL OF THE PHYSICAL SOCIETY OF JAPAN, Vol. 16, No. 1, JANUARY, 1961

On the Theory of the Fracture of Liquids

By Hiromu WAKESHIMA

The Kobe University of Mercantile Marine

(Received April 25, 1960)

The theories of fracture of liquids, those of Temperley's, Döring's and Fisher's are criticized in comparison with observations mainly by Lyman J. Briggs. The effect of bubble size on surface tension according to Tolman's theory is also taken into consideration for comparison. As the result is not satisfactory, a new hypothesis for the curvature effect is proposed, which brings about a better agreement of the nucleation theory with Briggs' data.

§ 1. Introduction

As is well known, there are different theories of the fracture of liquids at present. Temperley[1] put forward an idea that the pressure at the minimum on van der Waals' isothermals corresponds to the tensile strength of the liquid. The temperature at which the minimum of the pressure is practically zero, i.e. the limit of superheating of the liquid according to this theory, is, as is shown by Temperley, in general accord with the observed limits given by Kenrick, Gilbert and Wismer[2]. But, as far as the author is aware, there seems to be no published comparison of his theoretical results with the recent experimental data obtained by Lyman J. Briggs[3], applying centrifugal forces to liquids in a rotating tube. Moreover, there are other ways than that given by Temperley, of computing the pressure corresponding to the minimum on van der Waals' isothermals, the results by which will also be discussed.

Döring's theory[4] as well as the Fisher's[5], of the fracture of liquids are so-called nucleation theory. These authors calculated, on somewhat different assumptions and by different technique of derivation, the rate of formation by thermal fluctuation, of critical nuclear bubbles for the rupture in homogeneous liquids under tensile stress. The ultimate strengths of liquids according to these two theories show considerable discrepancies; the limiting negative pressures from Döring's theory come out to be larger than those from the Fisher's. It will be shown that this is mainly due to an unrealistic assumption upon which Döring's theory is based. The tensile strength of liquids, when calculated by Döring's method, but modified so as to give more reasonable foundation, is essentially the same as that by Fisher's formula, as it is the case for the limit of superheat. Both of these theories give tensile strengths of right order of magnitude in many cases, but agreement with the experiment is still unsatisfactory. It will be shown that the agreement is much deteriorated when we take into consideration the effect of curvature on surface tension, which is to be expected from Tolman's theory[6]. To improve the accordance the author has made a new approach to the problem of the effect of curvature on surface tension, the result of which seems to be promising.

§ 2. Temperley's Theory and Its Implications

A simple treatment of the problem of tensile strength of liquids by Temperley[1], in a slightly modified form, is as follows: The limit of stable region of the state of liquid corresponds to the minimum on van der Waals' isothermal. Therefore, eliminating V numerically from the equation

$$(\boldsymbol{P}+3/V^2)(V-1/3)=8/3\cdot \boldsymbol{T}, \tag{1}$$

expressed with corresponding variables, and the relation

$$(\partial \boldsymbol{P}/\partial V)_T=0, \quad \text{or} \quad \boldsymbol{P}-3/V^2+2/V^3=0 \tag{2}$$

we have a relation $\boldsymbol{P}_m(\boldsymbol{T})$, from which we can compute the pressure $\boldsymbol{P}_m\cdot p_c=p_{\min}$, meaning the tensile strength of the liquid. In Table I is tabulated, in the second column, the limiting pressures $-p_{\min}$ at 20°C for some liquids, as calculated using this $\boldsymbol{P}_m(\boldsymbol{T})$, and in the last column corresponding observed values. It will be seen from this table that in most cases discrepancies between the theoretical and the observed tensile strengths are not so large. But this does not necessarily mean the correctness of Temperley's stand point, because it would obviously be an over-simplification to use van der Waals' relation of the form Eq.(1) as the equation of state throughout the liquid state and to correlate the limiting tensile strength with $\boldsymbol{P}_m$ times the critical pressure. On the other hand, Tolman[8], in his treatment of the superficial density of matter at liquid-vapor boundary, derived formulas which express $p_v/\gamma'rT$, $-p_{\min}/\gamma'rT$ etc. in terms of $a\gamma'/rT$ where p_v, and γ' denote ordinary vapor pressure and the density of the liquid respectively; a stands for the usual van der Waals' constant and r the specific gas constant of the matter. When we use, for example, the vapor pressure of the liquids (at 20°C) to determine the parameter $a\gamma'/rT$ and compute $-p_{\min}$ using this parameter, the results turn out to be those given in the third column of Table I. We can recognize from the comparison of these values that the better agreement of Temperley's results with the observation is rather a fortunate coincidence.

Formally we can determine in other ways the parameter $a\gamma'/rT$, e.g. from a relation including the bulk modulus κ of the liquid as follows: As the van der Waals' equation using density, instead of volume, is

$$p=\gamma rT/(1-\gamma/\gamma_\infty)-a\gamma^2 \tag{3}$$

(here $1/\gamma_\infty$ stands for the usual van der Waals' constant b), for the compressibility

$$\kappa=\gamma(\partial p/\partial\gamma)_T \tag{4}$$

Table I. Limitting Pressures
(at 20°C, in Atm. P.)

Liquid	from Crit. Const.	from Vap. Pres.	from Compr.	Döring	Döring Mod.	Fisher	Tolman	Curve III		
								from Vap. Pres.	from Comp.	Obs.
Water	1,000	6,840	1,390	1,400	1,320	1,380	4,030	1,330	750	270
Ethyl Alcohol	177	1,550	545	538	248	243	523	241	199	39*
Ethyl Ether	71	446	320	268	161	158	1,110	137	125	72*
Chloroform	167	814	554	636	324	318	2,530	269	238	290
Benzene	166	846	564	750	358	352	2,960	292	252	150
Acetic Acid	225	1,940	643	678	331	325	753	322	256	288
Aniline	274		979		636	625			441	280
Carbon Tetra-Chloride	153	731	511	656	321	315	2,720	259	227	275
Mercury	12,400	20,100	9,270	80,900	23,500	23.100	162,000	11,400	6,250	425

* Those marked with asterisk are data given by J. Meyer[7].

we have

$$\kappa/\gamma rT=(a\gamma/rT+p/\gamma rT)^2-2a\gamma/rT \qquad (5)$$

If we denote $\kappa=\kappa_0$ for $p=0$, then

$$a\gamma'/rT=1+\sqrt{1+\kappa_0/\gamma' rT} \qquad (6)$$

Now the parameter $a\gamma'/rT$ from κ_0 give the tensile strengths given in the fourth column of Table I. These values come closer to the observation than those in the third column do, but it is doubtful whether we have come to the reality more closely. A direct estimation of the limiting negative pressures from extrapolation of the observed pressure-compressibility relations give results which do not agree with these values, though they do not differ in the order of magnitude.

§ 3. Döring's Theory in Comparison with the Fisher's

Döring imagines that, by thermal fluctuation, there appears in meta-stable liquids a series of embryonic bubbles, in mechanical equilibrium with the surrounding liquids; the vapor in the bubbles is assumed to obey the perfect gas law:

$$p_\nu'=p+2\sigma/r_\nu;\ p_\nu'\cdot 4/3\cdot\pi r_\nu^3=\nu kT \qquad (7)$$

Here p_ν' denotes the vapor pressure in a bubble with ν molecules, r_ν the radius of the bubble, p the ambient pressure σ, the surface tension of the liquid and k Boltzmann constant. Note that p_ν' is not the vapor pressure p_n of vapor in thermodynamical equilibrium with the liquid in question. Now from the equation of state above, it follows that, with p negative, ν as a function of r_ν, has a maximum at a radius $r_{\nu m}=4\sigma/(-3p)$, which is smaller than $2\sigma/(p_n-p)$ if $p<-2p_n$: A bubble which happens to grow larger than this critical size, will continue to develope spontaneously, resulting in a rupture of the liquid. Döring calculated, from a kinetic consideration, the number J, of such critical bubbles appearing in a stationary state, per unit volume of the liquid per unit time, the result being

$$J=B\cdot\exp(-A) \qquad (8)$$

where

$$A=\frac{64\,\pi\sigma^3}{27\,kT(-p)^2}\{1+2/3\cdot\log(-p/2p_n)\}$$

The factor before the exponential term in the above expression is taken by Döring to be roughly equal to the molecular collision frequency, times the number density of molecules, times the fraction of molecules having an energy larger or at least equal to that required to remove a molecule from the interior of the liquid, i.e. twice the heat of vaporization per molecule $2\varepsilon_0$, namely

$$B\doteq(1/\rho\cdot\sqrt{3kT/m})\cdot\gamma'/m\cdot(\sqrt{2\varepsilon_0/kT})$$
$$\exp(-2\varepsilon_0/kT) \qquad (9)$$

Here ρ and m denote the average distance between molecules and the mass of molecule respectively. As the value of p satisfying Eq.(8) does not vary much when J is multiplied by a factor of a few powers of ten, the tensile strength of liquids can be computed approximately by putting $J=1$* in Eq.(8) and solving for $(-p)$ which are tabulated in the fifth column of Table I.

Now there are some points in Döring's theory which have no physically plausible basis. First, Döring assumes the perfect gas law for the vapor in embryonic bubbles supposed in mechanical equilibrium with the ambient liquid (see Eq. (7)). Even at the critical bubble with a radius $4\sigma/(-3p)$, where the vapor pressure in the bubble is just half the magnitude of the tensile strength of the liquid, one will be convinced from Table I that he has assumed the perfect gas law quite improperly for the vapor in question. A more serious objection to Döring's theory can be raised against his basic idea that only embryonic bubbles in mechanical equilibrium (but not in thermodynamical equilibrium, as noted previously) with the ambient liquid, are needed for consideration in the nucleation problem of this kind. But before going into details of the discussion on this point, Fisher's theory[5] of the fracture of liquids will be reviewed briefly.

According to Fisher, the rate of formation of nuclei for the rupture of liquids can be approximated by a statistical population in equilibrium of the critical hole in meta-stable liquids, $n\cdot\exp(-\Delta\psi^*/kT)$, (here $n=\gamma'/m$), times a factor expressing the time rate at which a critical hole passes to a larger bubble capable of growing spontaneously. $\Delta\psi$ for the critical hole, $\Delta\psi^*$, corresponds to the maximum free energy of formation of a hole in the liquid; i.e. to $\partial\Delta\psi/\partial r=0$, where

$$\Delta\psi=4\,\pi r^2\sigma+4/3\cdot\pi r^3 p\ ,$$

therefore

---

* c.f., e.g. J.C. Fisher: J. Appl. Phys. 19 (1948) 1063.

$$\Delta\psi^* = 4\pi r^{*2}\sigma/3 \qquad (10)$$

Here r^* means the radius of the critical hole. The kinetic factor derived from the theory of absolute reaction rates by Turnbull and Fisher[9] is to the order of magnitude, $kT/h \cdot \exp(-\Delta f^*/kT)$, where h is Planck's constant and Δf^* the free energy of activation for the motion of a molecule, at the boundary of the critical hole, into or away from the hole. Therefore

$$J = nkT/h \cdot \exp\{-(\Delta\psi^* + \Delta f^*)/kT\} = B' \exp(-A')$$
$$A' = 16\pi\sigma^3/3kTp^2, \quad B' = nkT/h \cdot \exp(-\Delta f^*/kT) \qquad (11)$$

Fisher thinks Δf^* to be less than 10 Kcal/mol in most cases. If we assume with Fisher that $\Delta f^* = 0$, then the tensile strengths of liquids, as listed in the seventh column of Table I will be obtained. Evidently these values correspond to the lowest possible strengths from Fisher's theory and when, for example, the value of 10 Kcal/mol is assumed for Δf^*, some thirteen percent increase of these values results.

Discrepancies between the tensile strengths from Döring's theory and those according to Fisher's are primarily due to the exponential factors in Eq.(8) and in Eq.(11), specifically to the difference in magnitude of A and A'. Now A can be interpreted as the work, necessary to generate a Döring's critical bubble, divided by kT, just as $A'kT$ is the free energy of formation of a Fisher's critical hole. Let W_1 be the work necessary to expand a spherical surface against the surface tension σ from radius 0 to a radius $r_{\nu m} = 4\sigma/(-3p)$, with a constant inner pressure $(-p/2)$ and under an ambient pressure $(-p)$. We have

$$W_1 = \int_0^{r_{\nu m}} 4\pi r^2 \left\{ p + \frac{2\sigma}{r} - (-p/2) \right\} dr = \frac{64\pi\sigma^3}{27p^2} \qquad (12)$$

Further, let W_2 be the work of transformation of ν_m molecules satisfying

$$4/3 \cdot \pi r_{\nu m}^3 (-p/2) = \nu_m kT$$

from the liquid state to the vapor state of presure $(-p/2)$. We have

$$W_2 = \nu_m kT \log \frac{-p/2}{p_n} = \frac{2}{3} \times \frac{64\pi\sigma^3}{27p^2} \log \frac{-p}{2p_n} \qquad (13)$$

Therefore

$$(W_1 + W_2)/kT$$
$$= \frac{64\pi\sigma^3}{27p^2kT}\{1 + 2/3 \cdot \log(-p/2p_n)\} = A \qquad (14)$$

We now see that Döring's critical bubble is less likely formed by thermal fluctuation than Fisher's critical hole, as $A > A'$. Though the Döring's critical bubble is smaller in size than Fisher's, Döring obtains larger tensile strengths as Döring's embryos are of rarer occurrence than the Fisher's. Fisher's treatment, however, has weakness too. Because, here the population factor for the critical holes is that in thermodynamical equilibrium and so discrepancies therefrom is more or less to be expected in the stationary state of nucleation. Moreover, a rational evaluation of the quantity Δf^* would be difficult. Therefore it may be of interest to modify Döring's theory so as to consider embryonic bubbles of other category than those treated by him. When we assume the vapor in embryonic bubbles to have a constant pressure p_n, instead of the pressure given by Eq.(7), and follow the similar approach of the problem as made by Döring, it is easy to obtain the rate of nucleation J,

$$J = n \cdot \exp(-\Delta\psi_{\nu c}/kT) \cdot \sqrt{2\sigma/\pi m} \qquad (15)$$

Here $\Delta\psi_{\nu c}$ denotes the work to be done to form the critical embryonic bubble. The tensile strengths of liquids as computed using this formula, are listed in the sixth column of Table I. It will be seen that the values are essentially the same as obtained by Fisher's formula.

When these theoretical values are compared with the observed ones, we see that in many cases they are not different as far as the order of magnitude is concerned, but generally speaking the theoretical threshold pressures are larger than the observed and notably in cases of water and mercury. But before going into the discussion of a detailed comparison, we must first inquire into the factor assumed in the theory, which has possibly a large influence upon the values mentioned above, i.e. the problem of using macroscopic surface tensions in the above theory.

§ 4. Tolman's Theory of Surface Tension and the Fracture of Liquids

Even if we leave the question unanswered, whether the term surface tension has any meaning when applied to small clusters of molecules[10], there is a serious problem about the dependence of surface tension on the size of bubbles. Various authors has discussed a possible effect in question[11], but only Tolman could afford a general formula[6] readily comparable with experimental results, though his stand point has some theoretical weaknesses[11]. Tolman argued that droplet size has a considerable effect on surface tension when it is under, e.g. 10^{-6} cm in radius. Similar effect should exist for embryonic bubbles for the rupture of liquids, according to his theory, and not in a slight degree. A conspicuous influence is expected to appear on the rate of nucleation, as the latter is sensitive to the change in surface tension. Therefore a brief discussion of the possible influences will be made.

Tolman derived in a detailed thermodynamical treatment of surface tension a formula of the change in surface tension of a spherical boundary of radius r:

$$\frac{1}{\sigma}\frac{d\sigma}{dr}=\left(\frac{2}{r^2}\frac{\Gamma}{\gamma'-\gamma''}\right)\Big/\left(1+\frac{2}{r}\frac{\Gamma}{\gamma'-\gamma''}\right) \tag{16}$$

where γ', γ'' denote densities of the fluid on the concave side as well as on the convex side of the boundary respectively, and Γ Gibbs' superficial density with reference to his surface of tension. Further Tolman showed that between $\Gamma/(\gamma'-\gamma'')$ and a quantity δ, which means the distance from the surface of tension to the dividing surface with respect to which superficial density vanishes, the following relation holds:

$$\Gamma/(\gamma'-\gamma'')=\delta\{1+(\delta/r)+1/3\cdot(\delta^2/r^2)\} \tag{17}$$

For a nearly plane surface with the liquid on the concave side, i.e. for a large droplet, δ is approximately the superficial density Γ, divided by the difference in densities of homogeneous portion of fluids on both sides of the boundary, whereas for a large bubble the sign of δ must be reversed though the magnitude is unaltered, as will be seen from Eq.(17). Therefore, following Tolman's calculation we obtain a formula for the corrected surface tension σ of a bubble of radius r,

$$\begin{aligned}\sigma(r)&=\sigma_0\phi(z)\\&=\sigma_0\exp\int_0^z\{(1-z+z^2/3)/[1-2z(1-z+z^2/3)]\}dz\\&\qquad z=\delta/r\end{aligned} \tag{18}$$

An explicit expression can be obtained for the integral on the right side of this equation, but the result is so complicated that it cannot be used conveniently for further computation of, e.g. the critical radius or the rate of nucleation. The following results were all obtained by numerical calculations.

Fig. 1 gives the change in surface tension with the radius of bubble (Curve I). Corresponding change with the radius of droplet is shown for comparison (Curve II). We see from these graphs that the change is, not only reversed, but more conspicuous for embryonic bubbles than for droplets according to his theory, and that application to the limiting pressure for liquids would possibly throw much light upon the validity of Tolman's theory.

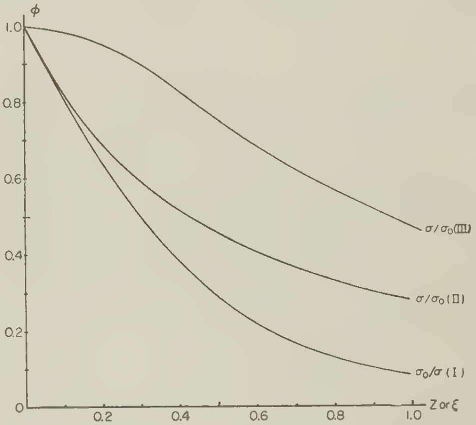

Fig. 1. Change of Surface Tension with the Size of Bubbles or Drops
$\phi(z)$ is given by Eq. (18); $z=\delta/r$
$\phi(\xi)$ is given by Eq. (32), Eq. (33); $\xi=c\lambda$

Now in the computation of the rate of nucleation when the surface tension changes with the size of embryonic bubbles, we are not allowed, simply to replace the ordinary surface tension σ in the factor A' in Eq.(11) or in the corresponding factor $\Delta\psi_{vc}/kT$ in Eq.(15), with the one given by Eq.(18). Because with the change in surface tension the radius of critical bubbles also changes. As an approximate evaluation of the corrected threshold pressures, we shall make use of the fact that the magnitude of the rate of nucleation is primarily determined by the factor A'/kT in Eq.(11) or $\Delta\psi_{vc}$ in Eq.(15), expressing the work of formation of a critical bubble in the meta-stable liquid, and proceeded as follows: The rate of nucleation is the same approximately for the corrected surface tension and at the corrected threshold pressures p_c, as the rate for the ordinary surface tension σ_0 and at the uncorrected threshold pressure p. Therefore, from Eq.(10) we have

$$4/3\cdot\pi r^{*2}\sigma_0=4/3\cdot\pi r_c{}^{*3}p_c+8\pi\int_0^{r_c^*}r\sigma(r)dr \tag{19}$$

where $r_c{}^*$ denotes the corrected critical radius, satisfying

$$-p_c=2\sigma(r_c{}^*)/r_c{}^* \tag{20}$$

Changing the variable from r to $z=\delta/r$, we get the relation,

$$1/2\cdot z^{*2}=-\phi(z_c{}^*)/z_c{}^{*2}+3\int_1^{z_c^*}\phi(z)/z^3\cdot dz \tag{21}$$

the lower limit for the integral above is set unity, meaning in effect that the work needed to form a cavity of the size δ is neglisible compared with the total work necessary for the formation of a critical bubble. The right hand side of Eq.(21) was numerically computed, from which we obtained the corrected critical radii $r_c{}^*=\delta/z_c{}^*$ or the corresponding threshold pressures p_c which satisfy

$$p_c/p=z_c{}^*\phi(z_c{}^*)/z^* \tag{22}$$

The results are summarized in the eighth column of Table I. We see from this table that accordance with the observed data is much deteriorated by taking into consideration the change of surface tension with radius of bubbles as derived from Tolman's theory.

Now, as is well known, Tolman's theory of the effect of droplet size on surface tension is based upon the relation6)

$$d\sigma=-\Gamma d\mu \tag{23}$$

where μ is the Gibbs' potential for the fluid in the homogeneous portions of either of vapor and liquid phases. In calculating Γ Tolman first introduces approximate expressions giving fluid pressure as a function of position within the transition layer on the boundary, (see the next paragraph) and determines a parameter giving the rate of change of pressure in the layer, by comparing the conclusion therefrom with the fact for a plane boundary. Then, making use of van der Waals' equation, he transforms his expressions for fluid pressure into expressions for fluid density within the transition layer, with which Γ is expressed. Finally this Γ is used for the computation of δ which is assumed to be approximately constant in the integration of Eq.(18). It cannot be justified, however, that van der Waals' equation even with the choice of parameters adopted by him, give a plausible representation of the succession of fluid states in the heterogeneous and minute layer in the transition region. The large discrepancy between the experimental fact and the theory mentioned above seems to show that his assumption is impermissible even in approximation.

§ 5. A New Approach to the Problem of Surface Tension of Embryonic Bubbles

To improve Tolman's theory, we shall try to avoid using Eq.(23) and van der Waals' equation in the way followed by Tolman, i.e. to connect fluid pressure and density in the transition layer: Instead, we shall use the relations

$$\sigma=\int_{-a}^{0}(p'-p)(1+cx)^2dx+\int_0^b(p''-p)(1+cx)^2dx \tag{24}$$

$$0=\int_{-a}^{0}(p'-p)(1+cx)xdx+\int_0^b(p''-p)(1+cx)xdx \tag{25}$$

first derived by Tolman12) thermodynamically and interpreted on a molecular theoretical bases by Buff10) afterward. Here x means the distance of a point in the transition layer, measured from the surface of tension along its normal, in the direction from concave side to convex side of the boundary with a curvature c. The first of these equations gives the surface tension σ in terms of distribution of liquid pressures p', and p'' in the homogeneous portion of the two phases and p in the transition layer respectively.* The second prescribes a specific location for the surface of tension within the transition layer. We shall further retain formally the parameter expressions for the stress factors in the transition layer ($p'-p$ or $p''-p$), adopted by Tolman in his theory;

$$p'-p=(p'-p_{\mathrm{max}})e^{y/\lambda_v} \tag{26}$$

$$p''-p=(p''-p_{\mathrm{min}})e^{-y/\lambda_l} \tag{27}$$

each holding over the range of vapor states from $y=-\infty$ to $y=0$, and over the range of liquid state from $y=0$ to $y=\infty$ respectively. Here a variable y designates distance along axis normal to the dividing surface between phases and has the value zero at the point of abrupt change in stress, increasing in the same direction as x increases, therefore $x=y-y_t$, where y_t denotes the distance of surface of tension from the point of abrupt change in stress. p_{max} and p_{min} are tentatively assumed to be equal in magnitude to the maxium and minimum possible pressures from van der Waals' equation. λ_v and λ_l are parameters expressing the rates with which stresses in the transition region on each side of the discontinuous dividing surface change. Now, combining Eqs. (24) and (25) we have the relation

---

* p means the stress tangential to the transition layer in the statistical-mechanical treatment10).

$$\sigma=\int_{-a}^{0}(p'-p)(1+cx)dx+\int_{0}^{b}(p''-p)(1+cx)dx \tag{28}$$

Therefore, making use of Eqs.(26) and (27) we get ($c\ll 1$)

$$\sigma=(p'-p_{\max})\lambda_v(1-cy_t-c\lambda_v)+(p'-p'')(y_t-1/2\cdot cy_t^2)+(p''-p_{\min})\lambda_l(1-cy_t+c\lambda_l) \tag{29}$$

The first term can be neglected compared with the rest on the right hand side of this equation, as it is expected that $p_{\max}\ll|p_{\min}|$ and $\lambda_v\approx\lambda_l$. Kelvin's relation is available when σ is defined with reference to the surface of tension, as proved by Tolman[8], therefore $p'-p''=2c\sigma$; further, $p'\ll|p''|$ for minute bubbles. Using these relations a formula for σ is obtained:

$$\sigma=\frac{-p_{\min}\lambda(1-cy_t+c\lambda)}{1-2cy_t(1-1/2\cdot cy_t)+2c\lambda(1-cy_t+c\lambda)} \tag{30}$$

Here we dropped the suffix of λ_l. On the other hand, eliminating p' by the use Eq.(25) a similar equation for σ can be easily derived:

$$\sigma=\frac{-p_{\min}\lambda\{(1-cy_t)cy_t-c\lambda(1-2cy_t)-2c^2\lambda^2\}}{-[c^2y_t^2(1-2/3\cdot cy_t)-2c\lambda\{(1-cy_t)cy_t-c\lambda(1-2cy_t)-2c^2\lambda^2\}]} \tag{31}$$

In order that σ remains finite, y_t must be equal to λ when $c=0$. Either of the above equations for σ give the same surface tension $\sigma_0=-p_{\min}\lambda$ for $c=0$, the result already obtained by Tolman. Now, in order that Eq.(30) and Eq.(31) are compatible with each other, $cy_t\equiv\eta$ must be a function of $c\lambda\equiv\xi$. This relation between η and ξ can be obtained by comparing the factors σ/σ_0 from Eq. (28) and that from Eq.(29). i.e.

$$\begin{aligned}\Phi_1&=\frac{1-\eta+\xi}{1-2\eta(1-1/2\cdot\eta)+2\xi(1-\eta+\xi)}\\ \Phi_2&=\frac{2\xi^2+\xi(1-2\eta)-\eta(1-\eta)}{\eta^2(1-2/3\cdot\eta)+2\xi\{2\xi^2+\xi(1-2\eta)-\eta(1-\eta)\}}\end{aligned} \tag{32}$$

In order that $\Phi_1=\Phi_2$, the following relation must hold,

$$(1-\eta)^2/(1-\eta+\xi)=\eta^2(1-2/3\cdot\eta)/\{2\xi^2+\xi(1-2\eta)-\eta(1-\eta)\}$$

From this equation, ξ can be expressed as a function of η

$$\xi=-F_1+\sqrt{F_1^2+F_2}$$

where

$$F_1=\{(1-2\eta)^2-4/3\cdot\eta^3\}/4(1-\eta)^2;\qquad F_2=\eta(1-\eta+1/3\cdot\eta^2)/2(1-\eta) \tag{33}$$

We can compute numerically an inverse expression, η as a function of ξ and thus compute $\Phi=\Phi_1=\Phi_2$ as a function of ξ. The curve III in Fig. 1 shows this in comparison with Tolman's surface tension, though the relation between radius of bubble and y_t or λ is not given yet. Now assumptions Eq.(26) and Eq.(27) imply that pressure and density distribution near the surface $y=0$ would be essentially the same down to very minute bubbles, so far as the material and the temperature remains unaltered. Then it seems natural to assume that parameter λ can be regarded as approximately independent of radius of bubbles, in view of the circumstance λ is presumably a function of molecular force and the local density distribution. If this is the case, we can see from the curve III how surface tension changes with the size of bubbles. It should be remarked that surface tension diminishes as radius of bubbles decreases, contrary to the result from Tolman's theory. Second, the change in surface tension with the size of bubble is not so conspicuous in magnitude, as compared with Tolman's case.

A similar treatment as described in the preceding paragraph derives the threshold pressures for the fracture of liquids, as listed in the ninth column of Table I. Here $-p_{\min}$, listed in the third column of the same table, are used for computation of $\lambda(=\sigma_0/-p_{\min})$. When the values of $-p_{\min}$ as given in the fourth column of Table I are used, the threshold pressures in the column the last but one of the table will be obtained. We notice from this table that agreement with experimental fact is somewhat improved, instead of getting worse as in the former case, when the surface tension for embryonic bubbles is given by the relation Eq. (18) shown previously.

§ 6. Concluding Remarks

Generally speaking, the discrepancy between the theoretical threshold pressures and the observed ones shown in the table are not so large as it is sometimes believed to be. Larger disagreement for water, alcohol, ether and mercury may primarily be due to different causes. In cases of alcohol and ether, observational errors which probably have accompanied Meyer's old experiment[7)] may be responsible for the discord, while in the case of mercury the discrepancy can essentially be explained by the assumption that observed rupture took place at the mercury-glass boundary, instead of occurring in the body of the liquid. When contact angle of, e.g. 140° is assumed as a condition at the boundary, it is expected from the theory of nucleation[5)] that the threshold pressure for the rupture at a plane boundary will be reduced almost to one quarter of those for the rupture in the body of mercury. Moreover, there is no reason to believe that only plane boundary is concerned, as minute portions of a boundary, almost of molecular dimensions are in question here. As discussed, for example by Fisher, we can expect small fraction of this threshold pressure, by assuming the existence of a suitable cavity at the boundary. Further, inapplicability, for the metalic mercury, of van der Waals' equation to compute $-p_{\min}$ may be responsible for the discord. Whether the discrepancy between the theoretical and the observed values of the threshold pressure for water is to be attributed to a similar situation due to heterogeneous nucleation, or to any other peculiarity of this common but special material, is not clear at present.

As for the constancy of parameter λ assumed in our theory of the size effect of surface tension, it has evidently to be confirmed by statistical-mechanical treatment of the problem, though it is recalled that Tolman had also to assume a similar relation, the constancy of parameter δ, in addition to the validity of van der Waals' equation to describe the fluid state in the transition region between phases. Actually, as will be seen from Table II, δ and λ or y_t for plane surfaces are most likely related quantities, presumably closely connected with intermolecular distances in the fluid. Further, it may be necessary to add that assumption of the constancy of y_t, instead of λ, leads to an improbable consequence that λ becomes unreasonably large as radius of bubbles diminishes.

Table II. Various Constants
(Unit 10^{-8} cm)

Liquid	r^*	δ	λ	λ/δ
Water	10.3	0.988	1.05	1.06
Ethyl Alcohol	18.1	1.35	1.47	1.09
Ethyl Ether	20.8	3.44	3.82	1.11
Chloroform	16.5	3.04	3.34	1.10
Benzene	16.0	3.15	3.43	1.09
Acetic Acid	16.5	1.31	1.42	1.08
Aniline	13.2**	1.68**		
Carbon Tetra-Chloride	16.6	3.37	3.69	1.09
Mercury	4.00	2.27	2.37	1.04

** The values for Aniline, marked with asterisks, are computed, using an extra-polation for the vapor pressure and are less reliable.

The preceding arguments are based upon the premise of correctness of the experimental fact. In this respect it seems that there remain much to be done to expand the scope of observation and to increase the reliability of the values of tensile strength of liquids.

In conclusion, the author wishes to express his gratitude to Professor Akira Harashima of the International Christian University, Professor Ituro Uhara of Kobe University and Professor Ichiro Shoji of Marine Technical College for their kind discussions.

References

1) H. N. V. Temperley: Proc. Phys. Soc. London. **59** (1947) 119.
2) F. B. Kenrick, C. S. Gilbert and K. L. Wismer: J. Phys. Chem. **28** (1924) 1297.
3) L. J. Briggs: J. Appl. Phys. **21** (1950) 721; Science **112** (1950) 427; Ibid. **113** (1951) 483; J. Chem. Phys. **19** (1951); 970; J. Appl. Phys. **24** (1953) 488.
4) W. Döring: Z. Phys. Chem. Ab. **B 36** (1937) 371; Ibid. **38** (1938) 292.
5) J. C. Fisher: J. Appl. Phys. **19** (1948) 1062.
6) R. C. Tolman: J. Chem. Phys. **17** (1949) 333.
7) J. Meyer: Abh. Bunsenges. VI (1911).
8) R. C. Tolman: J. Chem. Phys. **17** (1949) 118.
9) D. Turnbull and J. C. Fisher: J. Chem. Phys. **17** (1949) 71.
10) H. Reiss: J. Chem. Phys. **20** (1952) 1216; Ind. Eng. Chem. **44** (1952) 1284: S. G. Reed: J. Chem. Phys. **20** (1952) 208.
11) J. G. Kirkwood and F. P. Buff: J. Chem. Phys. **17** (1949) 338: F. P. Buff: Ibid. **19** (1951) 1591; Ibid. **23** (1955) 419; F. O. König: J. Chem. Phys. **18** (1950) 449: T. L. Hill: J. Chem. Phys. **20** (1952) 141.
12) R. C. Tolman: J. Chem. Phys. **16** (1948) 758.

JOURNAL OF THE PHYSICAL SOCIETY OF JAPAN, Vol. 16, No. 1, JANUARY, 1961

On the Irreversible Behavior of Coupled Oscillators with Application to Time of Flight

By Youzou KOGURE

Department of Physics, Faculty of Science
Tokyo University of Education

(Received September 3, 1960)

The irreversible behavior of simple systems is studied. An example is a system composed of coupled many harmonic oscillators. It is shown that the amplitude of a specified oscillator under appropriate initial condition, and the response function vanish after a long time, as the number of oscillators tends to infinity. Another example is a system of gaseous particle which is subject to collisions due to fixed scattering centers. It is shown that if there is only one scatterer the occupation number for the initial state changes periodically, and if there are many scatterers the occupation number exhibits exponential decay.

§ 1. Introduction

One of the basic problems of statistical mechanics is to account for the irreversibility which takes place generally in physical phenomena.

Since the day of Maxwell and Boltzmann, this problem has been extensively studied. General approaches to irreversible statistical mechanics has been developed. A remarkable progress in this field is due to Van Hove[1], R. Kubo[2] has afforded the theory of linear response in which relation between physical quantities are derived in elegant forms.

In this paper, however, we shall pay special attention to irreversible behavior of simple systems which can be treated more or less rigorously. As the complete dynamics of a set of coupled harmonic oscillators can be treated in a simple mathematical way, it is convenient to calculate its physical quantities with reference to irreversible processes.

There are a number of irrestigations of this sort. Recently, taking an assembly of harmonic oscillators coupled in periodic array, P. Mazur and E. Montroll[3] have shown that the irreversibility is a consequence of the vanishing of the correlation coefficients as the recurrence time becomes infinite M. Toda[4] has treated the Brownian motion of a harmonic oscillator coupled with thermostat which is composed of a great number of harmonic oscillators, and has derived the damping equation and the Langevin equation.

On the other hand, we may cite other attempts dealing with special phenomena. V. E. Derr[5] has investigated the irreversibility of quantum mechanical systems perturbed by random forces using phenomenological equation derived from Schrödinger equation. M. Lax[6] has shown in his theory of mobility of electrons that the response function vanishes after a sufficiently long time if one takes into account the effect of the surrounding heat reservoir in a rather conventional way.

Moreover N. Saito[7] has pointed out that the transfer function, the Laplace transformation of the response function with respect to time, has poles on the imaginary axis. In the limit of infinitely large system, the distribution of these poles becomes continuous, which might be replaced by some poles on the left half of the complex plane, just like image charges in electrostatistics. If this is the case, the response function will really vanish after a long time.

In § 2, of this paper we shall study general dynamics of systems to harmonic oscillator with a specified one, with special reference to the subsequent development and especially to the relations of transformation coefficients or the direction cosines between the particle coordinates and the normal coordinates. Taking a special example in § 3, the amplitude of an excited oscillator is shown to diminish after a time under an appropriate condition. In § 4, we evaluate the response function classically, and quantum mechanically. It is shown that the response function really vanishes after sufficiently long time. In § 5, we shall be concerned with application of § 3 to the calculation of time of flight of a particle subject to fixed scattering counters. § 6 and § 7, are devoted to conjectures and discussions.

§ 2. General Theory

Let us consider a simple system which is composed of a great number of harmonic oscillators. The interaction energy between each pair of oscillators is assumed to be proportional to the product of the displacements from their equilibrium positions.

In unperturbed state, the set of equations which determine the frequencies Ω of the normal modes is given by

$$m_j(\omega_j^2-\Omega^2)x_j+\sum_{k=1}^{N}{}' \lambda_{jk}x_k=0\,, \qquad (j=1,2,\cdots,N). \tag{2.1}$$

where x_j is the displacement, m_j the mass and ω_j the frequency of the j-th oscillator, $\sum'$ represents the sum over oscillators excluding the specified oscillator and λ_{jk} is the coupling constant between the j-th and the k-th oscillator.

Denoting $y_s=\sqrt{m_s}\,x_s$, $y_j=\sqrt{m_j}\,x_j$ and $\Lambda_{jk}=\lambda_{jk}/\sqrt{m_jm_k}$, we rewrite Eq. (2.1) as

$$(\omega_j^2-\Omega^2)y_j+\sum_{k=1}^{N}{}' \Lambda_{jk}y_k=0\,. \tag{2.2}$$

It is convenient to write the coordinates $\{y_j\}$ in terms of the normal coordinates $\{Q_j\}$ by the orthogonal transformation

$$Q_n=\sum_{j=1}^{N}(c^{-1})_{nj}y_j\,, \qquad y_j=\sum_{n=1}^{N}c_{jn}Q_n\,. \tag{2.3}$$

From Eqs. (2.2) and (2.3) we see that the characteristic frequency Ω_n of the n-th mode is given by one of the characteristic roots of $N\times N$ matrix whose elements satisfy the relation

$$\sum_{k,l=1}^{N}(c^{-1})_{nk}(\omega^2+\Lambda)_{kl}c_{ln}$$
$$=\sum_{k=1}^{N}\omega_k^2|c_{kn}|^2+\sum_{k,l=1}^{N}\Lambda_{kl}c_{kn}^{*}c_{ln}=\Omega_n^2\,. \tag{2.4}$$

In virture of Eq. (2.4) we have $\sum\omega_k^2=\sum\Omega_n^2$, that is, trace is invariant. Differentiating both sides of Eq. (2.4) with respect to ω_j^2, we obtain

$$c_{kn}^2=\partial\Omega_n^2/\partial\omega_k^2\,. \tag{2.5}$$

On the other hand, Ω_n^2 is defined as the n-th eigenvalue of Ω^2 which approaches to ω_n^2 of the n-th oscillator when all the coupling constants Λ_{jk} tend to zero.

With the matrix $c=(c_{jk})$ satisfying

$$\sum_j c_{jk}c_{jl}=\delta_{kl}\,, \quad \sum_k c_{jk}c_{lk}=\delta_{jk}\,,$$
$$(c^{-1})_{kj}=c_{jk}\,. \tag{2.6}$$

We note that the transformation coefficient c_{jn} is the direction cosine between the coordinate y_j and the normal coordinate Q_n. As an example we shall assume first that the oscillator s is interacting with the surrounding oscillators, but the latter are not interacting among themselves. Then Eq. (2.2) can be rewritten as

$$(\omega_s^2-\Omega^2)y_s+\sum_{j=1}^{N}{}' \Lambda_{sj}y_j=0\,, \tag{2.7}$$

$$(\omega_j^2-\Omega^2)y_j+\Lambda_{sj}y_s=0\,. \tag{2.7$'$}$$

Eliminating y_s and y_j from Eqs. (2.7) and (2.7)′, we get the equation for Ω_n

$$\omega_s^2-\Omega_n^2=\sum_{j=1}^{N}\frac{\Lambda_{sj}\Lambda_{js}}{\omega_j^2-\Omega_n^2}\,. \tag{2.8}$$

Differentiation of Eq. (2.8) with respect to ω_s^2 and ω_j^2 leads to

$$\left.\begin{aligned} c_{sn}^2&=\frac{\partial\Omega_n^2}{\partial\omega_s^2}=\frac{1}{1+\sum_{k=1}^{N}{}'\{\Lambda_{sk}^2/(\omega_k^2-\Omega_n^2)^2\}}\,,\\ c_{jn}^2&=\frac{\partial\Omega_n^2}{\partial\omega_j^2}=-\frac{\Lambda_{sj}^2/(\omega_j^2-\Omega_n^2)^2}{1+\sum_{k=1}^{N}{}'\{\Lambda_{sk}^2/(\omega_k^2-\Omega_n^2)^2\}}\,.\end{aligned}\right\} \tag{2.9}$$

Thus we get the relation

$$c_{sn}^2+\sum_{j=1}^{N}{}'\,c_{jn}^2=1\,. \tag{2.10}$$

Differentiating both sides of $\sum\omega^2=\sum\Omega_n^2$ with respect to ω_j^2, and using (2.3), we obtain

$$\sum_{n=1}^{N}c_{jn}^2=1\,. \tag{2.11}$$

Another example for which Eq. (2.2) can be solved explicitly is the case when all the coupling constants are equal and is Λ, Eqs. (2.10) and (2.11) are easily verified with the same method as in the previous case. The set of equations which corresponds to Eq. (2.2) is given by

$$(\omega_j^2-\Omega^2)y_j+\Lambda\sum_{k=1}^{N}{}'\,y_k=0\,. \tag{2.12}$$

Eliminating the coordinates $\{y_j\}$ from Eq. (2.12), we obtain the equation for Ω_n,

$$\sum_{j=1}^{N}{}'\frac{\Lambda}{\omega_j^2-\Lambda-\Omega_n^2}=-1\,, \tag{2.13}$$

and the direction cosines

$$c_{jn}^2=\frac{1/(\omega_j^2-\Lambda-\Omega_n^2)^2}{\sum_{k=1}^{N}\{1/(\omega_k^2-\Lambda-\Omega_n^1)^2\}}\,. \tag{2.14}$$

§ 3. Special Example

In this section, we examine a system composed of N harmonic oscillators which have the special frequency spectrum given by

$$\omega_j^2=\omega_s^2+(j-s)\Delta^2\,,$$
$$j=s\pm1,\ s\pm2,\ \cdots,\ s\pm N/2\,. \tag{3.1}$$

As is well known, a condition that has proved vital in all works in statistical mechanics of irreversible processes is the largeness of the system. In this section, this manifests itself in the fact that the spectrum of frequencies ω_j becomes dense as $N\to\infty$.

We shall take the first model in the previous section, and assume that all coupling constants Λ_{sk} do not depend on the k-th oscillator, that is, $\Lambda_{sk}=\Lambda$.

We can easily calculate Eq. (2.8) in the limit of infinite N:

$$\omega_s^2-\Omega_n^2=\frac{\pi\Lambda^2}{\Delta^2}\cot\frac{\pi}{\Delta^2}(\omega_s^2-\Omega_n^2)-\frac{\Lambda^2}{\omega_s^2-\Omega_n^2}\,. \tag{3.2}$$

From Eq. (2.9) we obtain

$$\begin{aligned} c_{sn}^2&=\left\{1+\sum_{j=1}^{N}{}'\frac{\Lambda^2}{(\omega_j^2-\Omega_n^2)^2}\right\}^{-1}\\ &=\left\{1+\frac{\pi^2\Lambda^2}{\Delta^4}\operatorname{cosec}^2\frac{\pi(\omega_s^2-\Omega_n^2)}{\Delta^2}-\frac{\Lambda^4}{(\omega_s^2-\Omega_n^2)^2}\right\}^{-1}.\end{aligned} \tag{3.3}$$

With use of Eq. (3.2), the above equation can be written as

$$\begin{aligned} c_{sn}^2&=\frac{\Lambda^2}{3\Lambda^2+(\pi^2\Lambda^4/\Delta^4)+(\omega_s^2-\Omega_n^2)^2}\\ &\approx\frac{\Delta^2}{\pi}\cdot\frac{\alpha}{\alpha+(\omega_s^2-\Omega^2)^2}\,,\\ \alpha&=\pi\Lambda^2/\Delta^2\,.\end{aligned} \tag{3.4}$$

Λ and Δ^2 being assumed to be constants of the order $\sqrt{N}$ and N^{-1} respectively. We have therefore neglected $3\Lambda^2$ in the denominator, which is valid for large N.

c_{sn} becomes continuous with respect to Ω_n in the limit of large N and small Δ^2. $N\Delta^2$ approaches to a constant of the order 1 in this limit. And α in Eq. (3.4) approaches to a constant of the order 1 in the same limit.

A state of motion can be generally represented by a superposition of eigen-vibrations. By an eigen-vibration we mean a synchronous oscillation of all particles with eigenfrequency Ω_n and amplitude a_n. The displacement of the j-th oscillator can be described by

$$y_j=\sum_n c_{jn}(a_n\cos\Omega_n t+b_n\sin\Omega_n t)\,. \tag{3.5}$$

We impose the initial condition that, at $t=0$, all the oscillators, except a specified oscillator s, are at rest in their equilibrium position, and this oscillator is displaced by unit distance with vanishing velocity. To satisfy the initial condition, we take

$$a_n = c_{sn}\,, \qquad b_n = 0\,,$$

and then

$$y_j = \sum_n c_{sn} c_{jn} \cos \Omega_n t\,. \tag{3.6}$$

We can see that the amplitude of the oscillator s is continuously damped down with time from Eqs. (3.4) and (3.6). y_s can be represented as

$$y_s = \sum_n c_{sn}^2 \cos \Omega_n t = \frac{\Delta^2}{\pi} \sum_n \frac{\alpha}{\alpha^2 + (\omega_s{}^2 - \Omega_n{}^2)^2} \cos \Omega_n t\,. \tag{3.7}$$

Since the spectrum of frequencies $\omega_j{}^2$ becomes dense about ω_s as remarked before, the normal mode frequencies Ω_n distributed about ω_s as $N \to \infty$.

In Eq. (3.7), the factor $\alpha/(\alpha^2 + (\omega_s{}^2 - \Omega_n{}^2)^2)$ has a sharp maximum around $\Omega_n \sim \omega_s$. Consequently, $\Omega_n{}^2 - \omega_s{}^2$ can be substituted by $2\omega_s(\Omega_n - \omega_s)$, neglecting the second power of $\Omega_n - \omega_s$. It is noted that there is a solution $\Omega_n{}^2$ of the transcendental equation (3.2), in each interval $[\omega_s{}^2 + (n-s)\Delta^2,\ \omega_s{}^2 + (n-1-s)\Delta^2]$ for $n-s = 0, \pm 1, \pm 2, \cdots$. Hence we may use the approximation that, for $\Omega \sim \omega_s$, there are $g(\Omega)d\Omega = (2\omega_s/\Delta^2)d\Omega$ oscillators with frequency between Ω and $\Omega + d\Omega$. Therefore the sum is reduced to the integral

$$\begin{aligned} y_s &= \frac{\Delta^2}{2\pi\omega_s} \sum_n \frac{\beta}{\beta^2 + (\omega_s - \Omega_n)^2} \cos \Omega_n t \\ &= \frac{1}{\pi} \int_{-\infty}^{\infty} \frac{\beta}{\beta^2 + (\omega_s - \Omega)^2} \cos \Omega t \cdot d\Omega \\ &= e^{-\beta|t|} \cos \omega_s t\,. \end{aligned} \tag{3.8}$$

where

$$\beta = \alpha/2\omega_s\,.$$

Thus, we see that the amplitude of the excited oscillator s diminishes to zero after a sufficiently long time, and initial situation will never return.

§ 4. The Response Function

We consider the system with Hamiltonian $\mathscr{H}$, which is composed of two parts; the unperturbed part $\mathscr{H}_0$ which described the natural motion of the systems considered in the previous section, and the external perturbation on the oscillator s: $\mathscr{H}' = -x_s f(t)$, where $f(t)$ is the applied force.

The system is assumed to be in a certain distribution $\rho(\mathscr{H}_0)$ at time $t=0$ in the phase space Γ. We confine ourselves to weak perturbation, for which the linear response is observed through the change of $\Delta\dot{\boldsymbol{x}}_s$, where $\dot{\boldsymbol{x}}(t)$ is the velocity given by $\boldsymbol{x}_s = \boldsymbol{p}_s/m_s$.

We may write the change in $\Delta\dot{x}(t)$ as

$$\begin{aligned} \Delta\dot{\boldsymbol{x}}_s &= -\int d\Gamma \int_{-\infty}^{t} (\boldsymbol{x}_s,\ f)\dot{\boldsymbol{x}}_s(t-t')f(t')dt' \\ &= \int_{-\infty}^{t}\int e^{-i(t-t')\boldsymbol{L}} \dot{\boldsymbol{x}}(f,\ \boldsymbol{x}_s)f(t')dt'd\Gamma\,. \end{aligned} \tag{4.1}$$

where the bracket means the Poisson bracket, and $\boldsymbol{L}$ is the self-adjoint operator introduced by Kirkwood[8)], defined by $i\boldsymbol{L}g = (\mathscr{H}_0,\ g)$. Thus $\dot{\boldsymbol{x}}(t)$ is given by

$$\dot{\boldsymbol{x}}_s(t) = e^{-i\boldsymbol{L}t}\dot{\boldsymbol{x}}_s(0)\,. \tag{4.2}$$

The response $\Delta\dot{\boldsymbol{x}}_s(t)$ may be written as

$$\Delta\dot{\boldsymbol{x}}_s = \int^{t} \phi_{\dot{\boldsymbol{x}}_s \boldsymbol{x}_s}(t-t')f(t')dt'\,. \tag{4.3}$$

The response function is defined, comparing Eq. (4.3), with Eq. (4.1), by

$$\phi_{\dot{\boldsymbol{x}}_s \boldsymbol{x}_s}(t) = -\int d\Gamma(\boldsymbol{x}_s,\ f)\dot{\boldsymbol{x}}_s(t)\,. \tag{4.4}$$

By the use of normal coordinates in the previous section, unperturbed Hamiltonian $\mathscr{H}_0$ is given by

$$\mathscr{H}_0 = \sum_n \{\tfrac{1}{2}P_n{}^2 + \Omega_n{}^2 Q_n{}^2\}\,. \tag{4.5}$$

In terms of the normal coordinates we have

$$x_s = \frac{1}{\sqrt{m_s}} \sum_{n=1}^{N} c_{sn} Q_n\,, \qquad \dot{x}_s = \sqrt{m_s} \sum_{n=1}^{N} c_{sn} P_n\,. \tag{4.6}$$

Thus we obtain

$$\begin{aligned} \phi(t) &= -\sum_{n=1}^{N} \sum_{m=1}^{N} \int c_{sn} c_{sm} P_n P_m (\partial\rho_0/\partial\mathscr{H}_0) \cos \Omega_m t\, d\Gamma \\ &= \sum_{n=1}^{N} c_{sn}^2 \cos \Omega_n t\,. \end{aligned} \tag{4.7}$$

in which we have used the relation

$$\int P_n P_m (\partial\rho_0/\partial\mathscr{H}_0) d\Gamma = -\delta_{nm}\,,$$

and

$$\sum_m c_{sm} e^{-i\boldsymbol{L}t} P_m = \sum_m c_{sm} P_m \cos \Omega_m t\,. \tag{4.8}$$

Since Eq. (4.7) agrees with the right hand side of Eq. (3.7), the response function $\phi(t)$ is given by Eq. (3.8), that is,

$$\phi(t) = e^{-\beta t} \cos \omega_s t\,, \qquad t > 0\,. \tag{4.9}$$

Thus we see that though the response function is a sum of terms periodic in time, it vanishes after a sufficiently long time. The transfer function is defined by

$$\Psi(z) = \int_0^{\infty} e^{-zt} \phi(t) dt\,.$$

Except unimportant factor, we can easily evaluate $\Psi(z)$ from Eq. (4.9) to obtain

$$\Psi(z)=\frac{1}{z+\beta+i\omega_s}+\frac{1}{z-\beta-i\omega_s} .$$

$\Psi(z)$ has pole at $z=-\beta-i\omega_s$ and $-\beta+i\omega_s$ on the left half of the complex z-plane. The poles are equivalent to position of time image charges for induced charge on the surface of the conductor. This fact satisfies the condition which has been proposed by Saito[7]. Now we shall treat the problem quantum-mechanically by a method which is analogous to that of classical mechanics.

The similar expression for the response function can be derived in this case. Poisson bracket are to be replaced by commutators and the distribution function $\rho_0(\mathscr{H}_0)$ is to be replaced by the density matrix. We have

$$\phi_{\dot{x}_s x_s}(t)=\frac{1}{i\hbar}\sum_{k,l}[\rho_0,\, x_s]_{kl}(\dot{x}_s)_{lk}e^{-i(\varepsilon_k-\varepsilon_l)t/\hbar} . \quad (4\ 12)$$

By the use of the same transformation as in the classical case, we obtain Hamiltonian as a sum of those for harmonic oscillators whose eigenfrequencies are given by Ω_n as before. It is easily proved the matrix **C** of the transformation coefficients has the same elements as for the classical mechanics in virtue of the properties of harmonic oscillators.

We take the representation which make $\mathscr{H}_0$ diagonal,

$$\left.\begin{aligned}\mathscr{H}_0&=\sum_k \hbar\Omega_n\left(k+\frac{1}{2}\right),\\ x_s&=\frac{1}{\sqrt{m_s}}\sum c_{sn}Q_n ,\\ \dot{x}_s&=\sqrt{m_s}\sum_n c_{sn}P_n .\end{aligned}\right\} \quad (4.13)$$

In this case we shall assume that the system is initially in the state of thermal equilibrium with temperature T, that is, we assume that

$$\rho_0(\mathscr{H}_0)=\exp\{\beta(F-\mathscr{H}_0)\} .$$

where $\beta=1/kT$, and F is Helmholtz free energy of the system.

By the use of Eqs. (4.12), (4.13) and (4.14), $\phi(t)$ can be written as

$$\begin{aligned}\phi(t)=&\frac{1}{i\hbar}\sum_{n=1}^{N}c_{sn}^2\sum_{k,l}e^{\beta F_n}\\ &\times\{e^{-\hbar\beta\Omega_n(k+(1/2))}-e^{-\hbar\beta\Omega_n(l+(1/2))}\}\\ &\times(k|Q_n|l)(l|P_n|k)e^{-i(k-l)\Omega_n t} .\end{aligned} \quad (4.15)$$

where

$$e^{-\beta F_n}=\sum_{k=0}^{\infty}e^{-\beta\hbar\Omega_n(k+(1/2))}=e^{-\hbar\beta\Omega_n/2}(1-e^{-\hbar\beta\Omega_n})^{-1} .$$

Making use of the relations

$$\left.\begin{aligned}(k|Q_n|k+1)&=\left(\frac{\hbar}{2\Omega_n}\right)^{1/2}\left(k+\frac{1}{2}\right)^{1/2},\\ (k|Q_n|k-1)&=\left(\frac{\hbar}{2\Omega_n}\right)^{1/2}k^{1/2} ,\\ (k|P_n|k+1)&=-\frac{1}{i}\left(\frac{\hbar\Omega_n}{2}\right)^{1/2}k^{1/2} ,\\ (k|P_n|k-1)&=\frac{1}{i}\left(\frac{\hbar\Omega_n}{2}\right)^{1/2}(k+1)^{1/2} .\end{aligned}\right\} \quad (4.16)$$

we sum up over l, and then over k and n

$$\begin{aligned}\phi(t)=&\sum_{n=1}^{N}c_{sn}^2\sum_{k=0}^{\infty}\sqrt{k(k+1)}\\ &\times e^{\beta F_n}e^{-\beta\hbar\Omega_n(k+(1/2))}(1-e^{-\hbar\beta\Omega_n})\cos\Omega_n t .\end{aligned} \quad (4.17)$$

Eq. (4.17) can not be calculated exactly as the factor $\sqrt{k(k+1)}$ induces complicate calculations.

Since except for very low temperature, the main contribution to Eq. (4.17) may arise from the terms of large k values, $\sqrt{k(k+1)}$ can be replaced by $k+\frac{1}{2}$ in Eq. (4.17). We have then

$$\phi(t)=\sum_{n=1}^{N}c_{sn}^2\,\frac{1+e^{-\beta\hbar\Omega_n}}{2}\cos\Omega_n t . \quad (4.18)$$

in which we have used the relations

$$e^{\beta F_n}\sum_{k=0}^{\infty}\left(k+\frac{1}{2}\right)e^{-\beta\hbar\Omega_n(k+(1/2))}=\frac{1}{2}+\frac{1}{e^{\beta\hbar\Omega_n}-1} ,$$

$$\left(\frac{1}{2}+\frac{1}{e^{\beta\hbar\Omega_n}-1}\right)(1-e^{-\hbar\beta\Omega_n})=\frac{1}{2}(1+e^{-\beta\hbar\Omega_n}) .$$

Replacing the sum over n by integration as we have done in the previous section, we obtain

$$\phi(t)=\frac{1}{2\pi}\int_0^{\infty}\frac{\beta}{\beta^2+(\omega_s-\Omega)^2}\cos\Omega t(1+e^{-\hbar\beta\Omega})d\Omega . \quad (4.19)$$

For small coupling constants we get finally for

$$\phi(t)\cong\phi_{\text{class}}\left(\frac{1+e^{-\hbar\beta\omega_s}}{2}\right)$$

This expression is valid only if $\beta\hbar\omega_s\ll 1$. The classical limit can be obtained formally taking the limit $\hbar\to 0$. As in the classical case, the response function for large t really vanishes in the limit of large system.

§ 5. Application to the Calculation of Time of Flight

We shall be concerned here with an application of the method shown in the previous sections. As an application it is of some interest to consider the problem of time of flight of gaseous particle scattered elastically by fixed scattering centers, the number of the incident particles is expected to diminish continuously.

Let us start with the Hamiltonian in momentum representation

$$\mathscr{H}=\sum_{\boldsymbol{k}} \varepsilon_k a_{\boldsymbol{k}}^* a_{\boldsymbol{k}}+\sum_{\boldsymbol{k},\boldsymbol{l}} V_{\boldsymbol{k}\boldsymbol{l}} a_{\boldsymbol{k}}^* a_{\boldsymbol{l}} \, . \tag{5.1}$$

The equation of motion, in Heisenberg representation, for the operator $a_{\boldsymbol{k}}$ is

$$\hbar a_{\boldsymbol{k}}=i[\mathscr{H}, a_{\boldsymbol{k}}]=-i\varepsilon_{\boldsymbol{k}} a_{\boldsymbol{k}}-i \sum_{\boldsymbol{k},\boldsymbol{l}} V_{\boldsymbol{k}\boldsymbol{l}} a_{\boldsymbol{l}} \, . \tag{5.2}$$

$$a_{\boldsymbol{k}}=\sum_n c_{kn} A_{\boldsymbol{n}} e^{-iE_n t/\hbar} \, . \tag{5.3}$$

$$\sum_n c_{ln}^* c_{kn}=\delta_{lk} \, . \tag{5.4}$$

where n stands for the eigen-state which reduces, when interaction vanishes, to the unperturbed level with the wave vector $\boldsymbol{n}$. We have written c_{kn} for $c_{\boldsymbol{k}\boldsymbol{n}}$ and $\delta_{l,k}$ for $\delta_{\boldsymbol{l},\boldsymbol{k}}$. Annihilation and creation operators A_n and A_m^*, for eigenstates satisfy the same commutation relations as $a_{\boldsymbol{k}}$ and a_k^*.

From Eqs. (5.2), (5.3) and (5.4) we obtain

$$(\varepsilon_k-E_n)c_{kn}+\sum_l V_{\boldsymbol{k}l} c_{ln}=0 \, . \tag{5.5}$$

The occupation number $n_k(t)$ in the state k can be written as

$$n_k=(t)\langle a_{\boldsymbol{k}}^* a_{\boldsymbol{k}}\rangle=\mathrm{Tr}\,(a_{\boldsymbol{k}}^* a_{\boldsymbol{k}}\rho) \, . \tag{5.6}$$

where ρ is the density matrix which characterizes the total system.

Inserting Eq. (5.3) to Eq. (5.6), we get

$$n_k(t)=\sum_n \sum_m e^{-i(E_n-E_m)t/\hbar} c_{kn}^* c_{km} \langle A_m^* A_n\rangle \, . \tag{5.7}$$

We have to note the fact that in Heisenberg representation ρ do not depend upon time, but A_n depends upon time.

Now we assume that at t=0, an incident particle was found in the state s, that is, $n_k(0)=0$ $(k\neq s)$, $n_s(0)=1$. To satisfy this initial condition, we shall take $\langle A_m^* A_n\rangle$ equal to $c_{sn}^{*\prime} c_{sm}^*$. Then we obtain

$$n_s(t)=|S|^2 \, , \qquad S=\sum_n |c_{sn}|^2 e^{-i(E_n-E_0)t/\hbar} \, . \tag{5.8}$$

where E_0 is an arbitary constant which can be chosen appropriately so as to facilitate the calculation.

First we shall assume a scattering center at the position $\boldsymbol{R}$, and further that its size is very small compared with the wave length in question, that is, the wave length of the order of the incident particle. If we denote by $v(\boldsymbol{r}-\boldsymbol{R})$ the potential of the scatterer, we have

$$v_{\boldsymbol{k}\boldsymbol{l}}=\lambda e^{-i(\boldsymbol{k}-\boldsymbol{l})\cdot\boldsymbol{R}} \, ,$$

with

$$\lambda=\frac{1}{V}\int v(\boldsymbol{r})d\boldsymbol{r} \, . \tag{5.9}$$

when the scatterer is very small in size. Eq. (5.5) reduces to

$$(\varepsilon_k-E_n)c_{kn}'+\lambda \sum c_{ln}'=0 \, , \qquad c_{kn}'=c_{kn}\cdot e^{i\boldsymbol{k}\cdot\boldsymbol{R}} \, . \tag{5.10}$$

we have therefore the equation determining E_n:

$$\sum_k \frac{1}{\varepsilon_k-E_n}=-\frac{1}{\lambda} \, . \tag{5.11}$$

and, normalizing c_{kn}' by Eq. (5.4), we have

$$c_{kn}'=\frac{c_n}{(\varepsilon_k-E_n)} \, , \qquad c_n^2=\frac{1}{\sum_k \{1/(\varepsilon_k-E_n)^2\}} \, . \tag{5.12}$$

To solve Eq. (5.11) in a closed from we shall simplify the structure of the unperturbed energy levels. This simplification ought to be legitimate. Usually we assume the system which is a regular cube in form. In this case each level is generally three-fold degenerate because of symmetry. The degeneracy, however, can be removed by a slight change in the form of system. We see that we may assume non-degenerate energy scheme. Then it is permitted to set numbering $k=\cdots 1, 2, \cdots$ for the levels, in such a way that the energy of the level with smaller k is lower than that with larger k value. The number k thus defined is to be distinguished with causion from the wave number $|\boldsymbol{k}|$.

An incident particle initially in the level $k=s$ will be shifted to another level by collision with the scattering center. Since the unperturbed level ε_s is not an eigenstate of the total system, the incident particle is scattered to another level with slightly different energy.

Thus it seems legitimate to approximate the unperturbed energy levels near the energy ε_s of the incident particle by levels equidistantly placed. That is

$$\varepsilon_k=\varepsilon_s+(k-s)\varepsilon \, . \tag{5.13}$$

where k runs from $-\infty$ to ∞, and the level distance $\mathcal{E}$ is equal to the inverse of the level density.

By the use of Eqs. (5.11) and (5.13), we get the equation which the eigenvalues E_n satisfy:

$$\frac{\pi\lambda}{\mathcal{E}} \cot \frac{\pi}{\mathcal{E}} E_n = 1 . \tag{5.14}$$

Since this equation is of the same from as Eq. (3.17), we can easily obtain the following results.

$$\left.\begin{aligned} E_n &= E_s + (n-s)\mathcal{E} , \\ E_s &= \frac{\mathcal{E}}{\pi} \operatorname{Tag}^{-1} \frac{\pi\lambda}{\mathcal{E}} + \mathcal{E}_s , \\ c_{sn}' &= \frac{C}{\mathcal{E}[a-(n-s)]} . \end{aligned}\right\} \tag{5.15}$$

where

$$C^2 = \left(\frac{1}{\mathcal{E}^2} \sum_{k=-\infty}^{\infty} \frac{1}{\{k-((\lambda+E_n)/\mathcal{E})\}^2} \right)^{-1} = \frac{\lambda^2}{1+\pi\lambda^2/\mathcal{E}^2} ,$$

and

$$a = -\frac{1}{\pi} \operatorname{Tag}^{-1} \frac{\pi\lambda}{\mathcal{E}} .$$

Now, at $t=0$ there is a incident particle in the level s. At later instant the expectation value of the number of particle in this state is $n_s(t) = |S|^2$ as is given by Eq. (5.8).

Taking the arbitary constant in Eq. (5.8) to $E_s - s\mathcal{E}$, by the use of Eq. (5.15) we get the result

$$\begin{aligned} S &= \sum_{n=-\infty}^{\infty} \frac{C^2 e^{i[a-(n-s)]\mathcal{E}t/\hbar}}{\mathcal{E}^2[a-(n-s)]^2} \\ &= \frac{C^2}{\mathcal{E}^2} \left\{ \pi^2 \operatorname{cosec}^2(\pi a) + \pi[it \cot(\pi u) - |t|] \frac{\mathcal{E}}{\hbar} \right\} , \\ & \qquad 0 < \frac{\mathcal{E}|t|}{\hbar} < 2\pi . \end{aligned} \tag{5.16}$$

In virtue of Eq. (5.15) we obtain from Eq. (5.13)

$$\begin{aligned} n_s(t) &= 1 - \frac{\lambda^2}{\mathcal{E}^2 + \pi^2\lambda^2} \left\{ 2\pi \frac{\mathcal{E}|t|}{\hbar} - \left(\frac{\mathcal{E}t}{\hbar} \right)^2 \right\} , \\ & \qquad 0 \leq \frac{\mathcal{E}|t|}{\hbar} \leq 2\pi . \end{aligned} \tag{5.17}$$

$n_s(t)$ is seen to be a periodic function of $\mathcal{E}t/\hbar$ with period 2π. This strict recurrence is, of course, due to the approximation of equidistant levels given by Eq. (5.13).

Here we have to estimate the order of magnitude of $\lambda/\mathcal{E}$. λ is inversely proportional to the volume V as is seen from Eq. (5.9). $\mathcal{E}$, the inverse of the level density, is also inversely proportional to the volume. If the scattering center has radius δ and potential depth U_0,

$$\lambda = \frac{4\pi}{3} \frac{U_0 \delta^3}{V_0} . \qquad (|\boldsymbol{k}|\delta \ll 1) .$$

If the mass of the incident particle is m, the total cross section is[9]

$$\sigma = 16\pi(mU_0\delta^3/3\hbar^2)^2 .$$

On the other hand, the level density $g(\mathcal{E}_s)$ is given by

$$\frac{1}{\mathcal{E}} = g(\mathcal{E}_s) = V \frac{4\pi}{(2\pi)^3} |\boldsymbol{k}|^2 d|\boldsymbol{k}|/d\mathcal{E}_s .$$

where $\mathcal{E}_s = \hbar^2|\boldsymbol{k}|^2/2m$. Therefore in the order of magnitude

$$\frac{\lambda}{\mathcal{E}} \sim \frac{U_0}{\mathcal{E}_s} (|\boldsymbol{k}|\delta)^3 \sim \sigma^{1/2} |\boldsymbol{k}| .$$

Since δ is assume so small as $|\boldsymbol{k}|\delta \ll 1$, except for very strong scattering center we way assume that

$$|\lambda/\mathcal{E}| \ll 1 .$$

For instance, the wave number of electrons in solid is of the order of the atomic spacing, and we may expect this criterion to be valid for usual disturbing potential in solid.

From Eq. (5.17), the change in $n_s(t)$ with time is primarily governed by the constant

$$\beta = 2\pi \frac{\lambda^2}{\mathcal{E}\hbar} .$$

The time of flight or the life time is β^{-1}, which is of the order

$$\beta^{-1} \sim \frac{V/\sigma}{v} .$$

where $v = \hbar|\boldsymbol{k}|/m$ is the velocity of incidence. Under these circumstances, if these is only one scatterer, the life time is very long. Usual decay can be expected when there are many scattering centers randomly distributed.

Finally we shall assume N scattering centers fixed randomly at $\boldsymbol{R}_1$, $\boldsymbol{R}_2$, $\cdots$, $\boldsymbol{R}_N$. In this case, instead of Eq. (5.9) we have

$$\hbar \dot{a}_{\boldsymbol{k}} = -i\mathcal{E}_k a_{\boldsymbol{k}} - i\lambda \sum_{\mu=1}^{N} \sum_{l} e^{i(\boldsymbol{l}-\boldsymbol{k})\cdot\boldsymbol{R}_\mu} a_{\boldsymbol{l}} .$$

Taking the eigenstates n as before, we write

$$a_{\boldsymbol{k}} = \sum_n D_{kn} A_{\boldsymbol{n}} e^{-iE_n t/\hbar} .$$

Then we obtain

$$\begin{aligned} (\mathcal{E}_k - E_n) D_{kn} = -\lambda \{ & e^{-i\boldsymbol{k}\cdot\boldsymbol{R}_1} \sum_l e^{i\boldsymbol{l}\cdot\boldsymbol{R}_1} D_{ln} \\ & + e^{-i\boldsymbol{k}\cdot\boldsymbol{R}_2} \sum_l e^{i\boldsymbol{l}\cdot\boldsymbol{R}_2} D_{ln} + \cdots \\ & + e^{-i\boldsymbol{k}\cdot\boldsymbol{R}_N} \sum_l e^{i\boldsymbol{l}\cdot\boldsymbol{R}_N} D_{ln} \} . \end{aligned} \tag{5.18}$$

The way to solve this equation is to decompose the orthogonal transformation, represented by D_{kn}, into N step rotations; the first rotation to eliminate the first term in the right hand side of Eq. (5.18), the second rotation to eliminate the second term and so on. Let

$$D_{kn}=D^{(1)}_{kn}e^{-i\boldsymbol{k}\cdot\boldsymbol{R}_1}\ . \tag{5.18$'$}$$

We have

$$(\mathcal{E}_k-E_n)D^{(1)}_{kn}+\lambda\sum D^{(1)}_{ln}$$
$$=-\lambda\{\sum_{\mu\geq 2}{}' e^{-i\boldsymbol{k}\cdot(\boldsymbol{R}_\mu-\boldsymbol{R}_1)}\sum_l e^{i\boldsymbol{l}\cdot(\boldsymbol{R}_\mu-\boldsymbol{R}_1)}D^{(1)}_{ln}\ .\} \tag{5.19}$$

Therefore we shall proceed to the second rotation by putting

$$D^{(1)}_{kn}=\sum_m C^{(1)}_{km}D^{(2)}_{mn}e^{-i\boldsymbol{k}\cdot(\boldsymbol{R}_2-\boldsymbol{R}_1)}\ . \tag{5.19$'$}$$

where $C^{(1)}_{km}$ is the coefficient C'_{km} given by Eq. (5.10), i.e.

$$C^{(1)}_{kn}=\frac{C_m{}^{(1)}}{\mathcal{E}_k-E_m{}^{(1)}}\ . \tag{5.20}$$

with the roots $E_m{}^{(1)}$ of the equation

$$\sum_k\frac{1}{\mathcal{E}_k-E_m{}^{(1)}}=-\frac{1}{\lambda}\ . \tag{5.20$'$}$$

and $C^{(1)}_{kn}$ is determined by the condition of ortho-normality.

$$\sum_k C^{(1)*}_{kn}C^{(1)}_{km}=\delta_{n,m}\ . \tag{5.20$''$}$$

Inserting Eq. (5.19′) into Eq. (5.19) we get

$$\sum_m(E_n{}^{(1)}-E_n)C^{(1)}_{km}D^{(2)}_{mn}$$
$$+\lambda\sum_{n\geq 2}{}' e^{-i\boldsymbol{k}\cdot(\boldsymbol{R}_\mu-\boldsymbol{R}_2)}\sum_l\sum_{m'} e^{i\boldsymbol{l}\cdot(\boldsymbol{R}_\mu-\boldsymbol{R}_2)}C^{(1)}_{lm'}D^{(2)}_{mn'}=0\ . \tag{5.21}$$

After multiplying (5.21) by $C^{(1)*}_{km'}$ and suming over k, we get, in virtue of Eq. (5.20)″, the result

$$(E_m{}^{(1)}-E_n)D^{(2)}_{mn}+\lambda\sum_{\mu\geq 2,}{}'\sum_k e^{-i\boldsymbol{k}\cdot(\boldsymbol{R}_\mu-\boldsymbol{R}_2)}C^{(1)*}_{km}$$
$$\times\sum_{m'}\sum_l e^{i\boldsymbol{l}_1\cdot(\boldsymbol{R}_\mu-\boldsymbol{R}_2)}C^{(1)}_{lm'}D^{(2)}_{m'n}=0\ . \tag{5.22}$$

where we have interchanged the roles of m and m'

We have therefore to calculate the sums oven $\boldsymbol{k}$ and $\boldsymbol{l}$ in second term of Eq. (5.22). For $\mu=2$ we get immediately, by Eq. (5.22)′

$$\sum_k C^{(1)*}_{km}=\frac{1}{\lambda}C_m{}^{(1)*}\ ,\qquad \sum_l C^{(1)}_{lm'}=\frac{1}{\lambda}C^{(1)}_{m'}\ . \tag{5.23}$$

To get through the calculation we shall here adopt the approximation of equidistant levels given by Eq. (5.8).

Then by Eq. (5.10)

$$C_m{}^{(1)}=\frac{\lambda}{\sqrt{1+\pi^2\lambda^2/\mathcal{E}^2}}\simeq\lambda\ . \tag{5.24}$$

For $\mu\neq 2$ we have

$$\sum_l\frac{e^{-i\boldsymbol{k}\cdot(\boldsymbol{R}_\mu-\boldsymbol{R}_2)}}{\mathcal{E}_l-E_m{}^{(1)}}C_m{}^{(1)*}\simeq\frac{e^{-i\boldsymbol{m}\cdot(\boldsymbol{R}_\mu-\boldsymbol{R}_2)}}{\mathcal{E}_m-E_m{}^{(1)}}C_m{}^{(1)*}$$
$$=\frac{1}{2}C_m{}^{(1)*}e^{-i\boldsymbol{m}\cdot(\boldsymbol{R}_\mu-\boldsymbol{R}_2)}\ . \tag{5.25}$$

where we have assumed λ small and have taken out the largest contribution. A similar equation holds for the sum over l and hence Eq. (5.22) turns out to be

$$(E_m{}^{(1)}-E_n)D^{(2)}_{mn}+\lambda\sum_{m'}D^{(2)}_{mn'}$$
$$+\lambda\sum_{\mu 23}{}'' e^{-i\boldsymbol{m}\cdot(\boldsymbol{R}_\mu-\boldsymbol{R}_2)}\sum_{m'}e^{-i\boldsymbol{m}'\cdot(\boldsymbol{R}_\mu-\boldsymbol{R}_2)}D^{(2)}_{m'n}=0\ . \tag{5.26}$$

This equation for $D^{(2)}_{mn}$ has the same form as Eq. (5.18) for $D^{(1)}_{ln}$, and so we can proceed in the same way. We put

$$D^{(2)}_{mn}=\sum_{m'}C^{(2)}_{mm'}D^{(3)}_{m'n}e^{-i\boldsymbol{m}\cdot(\boldsymbol{R}_3-\boldsymbol{R}_2)}\ . \tag{5.26$'$}$$

and eliminate the term $\mu=3$ in the last equation. Then we get an equation for $D^{(3)}_{m'n}$ which is the same in form as Eqs. (5.19) or (5.26).

Thus we can repeat the same procedure and get finally the result

$$D_{kn}=e^{-i\boldsymbol{k}\cdot\boldsymbol{R}_1}\sum_{m'}\sum_{m''}\cdots\sum_{m^{(N-1)}}C^{(1)}_{km'}C^{(2)}_{m'm''}C^{(3)}_{m''m'''}\cdots$$
$$C^{(N)}_{m^{(N-1)}n}\cdot e^{-i\boldsymbol{k}\cdot(\boldsymbol{R}_2-\boldsymbol{R}_1)}\cdot e^{-i\boldsymbol{m}'\cdot(\boldsymbol{R}_3-\boldsymbol{R}_2)}\cdots$$
$$\cdot e^{-i\boldsymbol{m}(N-1)\cdot\boldsymbol{R}_N}\ . \tag{5.27}$$

which expresses N step rotations to bring the states to coincide the eigen-states. For each rotation $C^{(u)}_{mm'}$ is given by an equation analogous to Eq. (5.15). As we are assuming λ small,

$$C^{(u)}_{mm'}=-\lambda/[\lambda+(m'-m)\mathcal{E}]$$
$$E^{(u)}_{m'}-E^{(u-1)}_{m}=\lambda+(m'-m)\mathcal{E}$$
$$E_n=\mathcal{E}_s+N\lambda+(n-s)\mathcal{E}$$

These equations hold for small λ.

We impose the same initial condition as before. That is, at $t=0$, $n_s(0)=1$, $n_k(0)=0$ $(k\neq s)$. This is satisfied by choosing the state $\langle A_m{}^*A_n\rangle=D_{sm}{}^*D_{sn}$. We have

$$n_s(t)=|S|^2\ ,\quad S=\sum_n|D_{sn}|^2e^{-i(E_n-E_0)t/\hbar}\ . \tag{5.29}$$

where E_0 is a constant which can be chosen appropriately.

Under the supperposition that the scatterers are distributed randomly, the equation

$$\sum_{n=-\infty}^{\infty} \frac{e^{i\{\lambda/\varepsilon+(n-m)\}x}}{\{\lambda/\mathcal{E}+(n-m_1)\}\{\lambda/\mathcal{E}+(n-m)\}} e^{-i(\boldsymbol{m}-\boldsymbol{m}_1)\cdot\boldsymbol{R}_\mu}$$

can be replaced by

$$\delta_{m_1,m}\{\pi^2 \operatorname{cosec}^2(\pi\lambda/\mathcal{E})+\pi(-|x|+ix\cot(\pi\lambda/\mathcal{E})\} ,$$
$$0\leq|x|<2\pi . \tag{5.30}$$

where x stands for $\mathcal{E}t/\hbar$; m_1 and m stand for $m^{(N-1)}$ and a similar suffix in $|D_{sn}|^2$. We first sum up over $n-m^{(N-1)}$, next over $m^{(N-1)}-m^{(N-2)}$ and so on. We then split E_n-E_0 as

$$(E_n-E_0)/\mathcal{E}=\{\lambda/\mathcal{E}+(n-m^{(N-1)})\}$$
$$+\{\lambda/\mathcal{E}+(m^{(N-1)}-m^{(N-2)})\}+\cdots$$
$$+\{\lambda/\mathcal{E}+(m'-s)\} .$$

By the repeated use of Eq. (5.30), we obtain finally

$$n_s(t)=\left[1-\frac{\lambda^2}{\mathcal{E}^2}\left\{2\pi\frac{\mathcal{E}|t|}{\hbar}-\left(\frac{\mathcal{E}t}{\hbar}\right)^2\right\}\right]^N .$$

As $\mathcal{E}$ is taken very small, for large N, we get exponential decay of the incident beam;

$$n_s(t)=e^{-\beta|t|} . \tag{5.32}$$

with the decay constant

$$\beta=2\pi\frac{\lambda^2 N}{\mathcal{E}\hbar} .$$

This result agrees with that obtained by usual perturbation treatment. That is, the transition probability from the level l to k is given by

$$p=\frac{2\pi}{\hbar}|V_{kl}|^2 g(\mathcal{E}_k)=\frac{2\pi}{\hbar}\cdot\frac{\lambda^2}{\mathcal{E}} .$$

Hence, one should expect the equation

$$\frac{dn_s}{dt}=-Npn_s .$$

which after integration, gives Eq. (5.32) for $t\geq0$.

§ 6. Concluding Remarks and Acknowledgements

For small system with finite degrees of freedom, the initial state will be reproduced by any desired degree of accuracy. This follows from the general theorem in dynamics due to Poincaré. For large system, however, we may expect, in general, no recurrence in a finite time interval. In fact irreversibility is a very general phenomena common to physical systems. We have confined ourselves to simple systems to clarify irreversibility. However, for the purpose of dealing with more general cases the following way of approximation will be of some value.

To find the approximate expression for c_{sn}, for the first model system of § 2, we may take only the main term of Eq. (2.8) and neglect other terms in which ω_j is far from Ω_n. That is

$$\omega_s{}^2-\Omega_n{}^2\simeq\Lambda_{sn}^2/(\omega_n{}^2-\Omega_n{}^2) ,$$
$$c_{sn}^2\simeq\frac{1}{\Lambda_{ns}^2}(\omega_n{}^2-\Omega_n{}^2)^2\simeq\frac{\Lambda_{ns}^2}{(\omega_s{}^2-\Omega_n{}^2)^2} .$$
$$n\neq s \tag{6.1}$$

However, c_{sn} is to be normalized in such a way that

$$1=\sum_n c_{sn}^2\simeq\int c^2(\Omega)d\Omega . \tag{6.2}$$

The summation over n has be replaced by integration over as N tends to infinity. However, we have to notice the fact that the expression Eq. (6.1) for c_{sn}^2 fails when n is too close to s. Eq. (6.1) means that except for the immediate neighbourhood of ω_s, the number of oscillators in the range $d\Omega$ is

$$c^2(\Omega)d\Omega\simeq g(\Omega)d\Omega\frac{\lambda^2(\Omega)}{(\omega_s{}^2-\Omega^2)^2}\simeq g(\Omega)d\Omega\frac{\lambda^2(\Omega)/4\omega_s{}^2}{(\omega_s-\Omega)^2} . \tag{6.3}$$

For $\Omega\sim\omega_s$ Eq. (6.3) should be modified. The simplest way to satisfy normalization condition Eq. (6.2), is to modify Eq. (6.3) as

$$c^2(\Omega)d\Omega=\frac{1}{\pi}\frac{\beta}{\beta^2+(\omega_s-\Omega)^2}d\Omega , \tag{6.4}$$

where

$$\beta=\frac{\pi}{4}\frac{g(\Omega)}{\omega_s{}^2}\lambda^2(\Omega)$$

Since Eq. (6.4) is equivalent to Eq. (3.9), this sort of way of approximation seems to apply to many cases where exact calculation is not capable.

The author wishes to express his hearty thanks to Prof. Toda of Tokyo University of Education for extremely helpful discussions throughout the entire course of the work.

References

1) L. Van Hove: Physica **21** (1955) 517.
2) R. Kubo: J. Phys. Soc. Japan **12** (1957) 570.
3) P. Mazur and E. Montroll: J. Math. Phys. **1** (1960) 70.
4) M. Toda: J. Phys. Soc. Japan **13** (1958) 1266; **14** (1959) 722.

5) V. E. Derr: Phys. Rev. **117** (1960) 1421.
6) M. Lax: Phys. Rev. **109** (1958) 1921.
7) N. Saito: Phys. Rev. **117** (1960) 1163.
8) J. G. Kirkwood: J. Chem. Phys. **14** (1946) 180.
9) L. I. Schiff: *Quantum Mechanics* (McGrew-Hill Book Comp. Inc. New York. 1949.) p. 167.

JOURNAL OF THE PHYSICAL SOCIETY OF JAPAN, Vol. 16, No. 1, JANUARY, 1961

A New Picture of the Vibration of Linear Lattices

By Jun-ichi HORI

Department of Physics, Hokkaido University, Sapporo

(Received September 9, 1960)

A new version of the method of transfer matrix is presented, which largely simplifies the derivation of eigenfrequency equation, on the one hand, and gives rise to a very simple and vivid picture (vector picture), on the other hand, of the normal vibration for the linear isotopic lattices. By using this version and the vector picture, the wave forms of the extra- and in-band vibrations of the lattices containing a small amount of impurity and the eigenfrequency spectrum of generalized diatomic lattices are discussed, obtaining some interesting conclusions.

§ 1. Introduction

Some years ago the author devised a simple and effective method of treating the problem of vibration of linear lattices (method of transfer matrix), and treated several cases of regular and disordered lattices, obtaining some interesting results[1),2)]. In the present paper, a more effective version of the transfer-matrix method is presented, and some further results obtained by this new version concerning the frequency spectrum of generalized diatomic lattices and the impurity modes of disordered lattice are reported.

In § 2, we first show that, if we use a new representation (vector representation) of the transfer matrices, we can visualize very vividly the vibration of linear lattice as successive regular or random transformations of a complex vector on the complex plane. We shall call such a visualization " vector picture ". It is the main object of the paper to demonstrate how the vector representation and vector picture shed new light on the understanding of linear-lattice vibration.

In § 3, we illustrate by a simple example that the vector picture enables us to derive the eigenfrequency equation in a very simple way and to give a remarkably intuitive explanation for the shift of eigenfrequencies due to impurities.

In § 4, the eigenfrequency equation for the lattice of the type

$$mm\cdots mMM\cdots M$$

and the lattice which contains the above lattice as its unit cell (so-called generalized diatomic lattice) are derived by using the vector representation. It is shown that there is an intimate connection between these two equations.

The vector picture leads to a simple graphical method of calculating the wave forms of normal vibrations. In § 5, we first calculate the wave forms of the impurity vibration and an in-band vibration of the lattice with a single impurity, and compare them with each other. It becomes clear that the former is localized whereas the latter is not. Next the spectra of a lattice with two impurities are calculated for the cases in which the distance between the impurities is maximum and minimum. In contrast to the former case where two impurity frequencies appear, there appears in the latter only one impurity mode: one of the two has got into the band. By calculating as an example the wave form of one of the in-band vibrations, it is shown that all the in-band vibrations have essentially simple harmonic character and are not localized, whether they may be proper in-band vibrations or " got-in " extra-band ones.

In § 6 we enter into discussion on the basis of the equation derived in § 4 of the band structure of generalized diatomic lattices. In addition to the results which prove to be the same as those obtained by Maradudin and Weiss[3)], we get some new results, for example, concerning the wave form of the vibrations corresponding to the frequencies at the boundaries of each band. It is also shown that the existence of forbidden bands can be explained very vividly by vector picture.

For random lattices, the successive transformations of the complex vector become a kind of two-dimensional random walk which forms a Markov process. In view of mathematical difficulties, we leave the analysis of this process for future investigations, and confine ourselves to some comments on the general feature of the process (§ 7). It is also shown that the fact discovered by Dean[4)] that the spectra of disordered diatomic lattices have extremely fine structure, which seems rather strange as judged from the hitherto supported general view that the spectra of disordered lattice have only moderate number of rounded peaks, can be explained very naturally on the analogy of generalized diatomic lattice.

§ 2. Polar Decomposition of the Transfer Matrices and the Vector Picture of Lattice Vibration

An arbitrary finite-dimensional matrix A can be represented as the product of a unitary matrix Z and a non-negative Hermite matrix P (polar decomposition):

$$A=ZP\,, \tag{2.1}$$

where P and Z are given by $(A^*A)^{1/2}$ and AP^{-1}, respectively[5)].

We consider in this paper only the linear lattice containing isotopic atoms. Out of the isotopes composing the lattice we choose a " basic isotope " at our convenience, and use its mass m to define β:

$$\omega^2=(4\lambda/m)\sin^2\beta\,, \tag{2.2}$$

where ω is the frequency and λ is the force constant. Then, according to I*, the transfer matrix corresponding to the atom belonging to this isotope (basic atom) is

$$1+\Lambda=\begin{pmatrix}\exp(2i\beta) & 0\\ 0 & \exp(-2i\beta)\end{pmatrix}, \tag{2.3}$$

and the transfer matrix for other atoms (non-basic atoms) has the form

$$Q=\begin{pmatrix}\exp(2i\beta)(1+i\mathcal{E}\tan\beta) & i\mathcal{E}\tan\beta\exp(-2i\beta)\\ -i\mathcal{E}\tan\beta\exp(2i\beta) & \exp(-2i\beta)(1-i\mathcal{E}\tan\beta)\end{pmatrix}, \tag{2.4}$$

where $\mathcal{E}=M/m-1$, M being the mass of the non-basic atom.**

Let us seek the polar decomposition of Q. Putting

$$\mathcal{E}\tan\beta=\tan\gamma\,, \tag{2.5}$$

the eigenvalues of the matrix Q^*Q come out to be

$$\mu_\pm=(\sec\gamma\pm\tan\gamma)^2\,. \tag{2.6}$$

Therefore the eigenvalues of $P=(Q^*Q)^{1/2}$ are given by

$$\mu_\pm{}^{1/2}=\sec\gamma\pm\tan\gamma\,. \tag{2.7}$$

---

* The author's first paper cited above will be referred to as I in the following.

** Since we treat in this paper only diatomic case, it is unnecessary to use the suffix to distinguish between different non-basic isotopes.

In I, Q was called impurity matrix. Here we avoid this terminology for two reasons. Firstly, in the general diatomic lattice it is meaningless to call one isotope regular and the other impurity. Secondly, even in the case in which one isotope may properly be called impurity, it is often convenient, as will be seen later, to take the impurity atom as the basic one. Then the name " impurity matrix " will give rise to confusion.

We shall always use the letter m for the mass of basic atom, and M for that of non-basic one.

The diagonalization matrix $\boldsymbol{V}$ and $\boldsymbol{V}^{-1}$ of $\boldsymbol{P}$ are easily obtained as

$$\boldsymbol{V}=\begin{pmatrix}\exp(-2i\beta)i(1-i\tan\gamma) & \exp(-2i\beta)i(1-i\tan\gamma)\\ \exp(2i\beta)\sec\gamma & -\exp(2i\beta)\sec\gamma\end{pmatrix} \tag{2.8}$$

and

$$\boldsymbol{V}^{-1}=(i/2\sec\gamma(1-i\tan\gamma))\begin{pmatrix}-\exp(2i\beta)\sec\gamma & -\exp(-2i\beta)i(1-i\tan\gamma)\\ -\exp(2i\beta)\sec\gamma & \exp(-2i\beta)i(1-i\tan\gamma)\end{pmatrix}. \tag{2.9}$$

We get therefrom

$$\boldsymbol{P}=\boldsymbol{V}\operatorname{diag}(\mu_+^{1/2},\mu_-^{1/2})\boldsymbol{V}^{-1}=\begin{pmatrix}\sec\gamma & -i\exp(-4i\beta)\tan\gamma\exp(-i\gamma)\\ i\exp(4i\beta)\tan\gamma\exp(i\gamma) & \sec\gamma\end{pmatrix}, \tag{2.10}$$

and

$$\boldsymbol{Z}=\boldsymbol{Q}\boldsymbol{P}^{-1}=\begin{pmatrix}\exp[i(2\beta+\gamma)] & 0\\ 0 & \exp[-i(2\beta+\gamma)]\end{pmatrix}. \tag{2.11}$$

In the representation in which $\boldsymbol{P}$ is diagonalized, $\boldsymbol{Z}$ becomes

$$\boldsymbol{V}^{-1}\boldsymbol{Z}\boldsymbol{V}=\begin{pmatrix}\cos(\gamma+2\beta) & i\sin(\gamma+2\beta)\\ i\sin(\gamma+2\beta) & \cos(\gamma+2\beta)\end{pmatrix}, \tag{2.12}$$

and consequently $\boldsymbol{1}+\boldsymbol{\Lambda}$ becomes

$$\boldsymbol{V}^{-1}(\boldsymbol{1}+\boldsymbol{\Lambda})\boldsymbol{V}=\begin{pmatrix}\cos(2\beta) & i\sin(2\beta)\\ i\sin(2\beta) & \cos(2\beta)\end{pmatrix}. \tag{2.13}$$

In what follows we shall use this representation throughout, unless otherwise stated, and call it "(complex) vector representation", for the reason which will become clear below. Moreover, we shall denote matrices in this representation by the same letters as has hitherto been used, i. e., by $\boldsymbol{Z}$, $\boldsymbol{P}$, $\boldsymbol{Q}$ and $\boldsymbol{1}+\boldsymbol{\Lambda}$.

Let us use the complex representation for the vector representing the state of each atom, and denote it by $\boldsymbol{x}=x+iy$ or $\boldsymbol{x}=(x,iy)^T$. Then $\boldsymbol{P}$ represents the operation of multiplying the real component x of $\boldsymbol{x}$ by $\sec\gamma+\tan\gamma$ and the imaginary component y by $\sec\gamma-\tan\gamma$ ($\boldsymbol{P}$-transformation). If we operate $\boldsymbol{Z}$ on $\boldsymbol{x}$, the resulting vector $\boldsymbol{x}'$ is, putting $\alpha=2\beta+\gamma$,

$$\boldsymbol{x}'=\begin{pmatrix}x'\\ iy'\end{pmatrix}=\begin{pmatrix}\cos\alpha & i\sin\alpha\\ i\sin\alpha & \cos\alpha\end{pmatrix}\begin{pmatrix}x\\ iy\end{pmatrix}=\begin{pmatrix}x\cos\alpha+iiy\sin\alpha\\ xi\sin\alpha+iy\cos\alpha\end{pmatrix},$$

or

$$\boldsymbol{x}'=(x+iy)\exp(i\alpha)=\boldsymbol{x}\exp(i\alpha). \tag{2.14}$$

This means that $\boldsymbol{Z}$ rotates an arbitrary complex vector $\boldsymbol{x}$ by an angle $2\beta+\gamma$ ($\boldsymbol{Z}$-rotation). Similarly $\boldsymbol{1}+\boldsymbol{\Lambda}$ rotates $\boldsymbol{x}$ by an angle 2β.

The vibration of linear lattice can thus be visualized as successive transformations of a complex vector on the complex plane: At basic atoms, the state vector $\boldsymbol{x}$ is merely rotated by the angle 2β. At non-basic atoms, $\boldsymbol{x}$ is subjected to a stretch (contraction) of its real component by the factor $\sec\gamma+\tan\gamma$ and a contraction (stretch) of its imaginary component by the factor $\sec\gamma-\tan\gamma$, and a following rotation by the angle $2\beta+\gamma$. We shall call this visualization the "vector picture".

§ 3. Vector Picture for the Regular Monatomic Lattice and the Lattice with one Impurity

Consider the linear lattice composed of N isotopic atoms. We adopt as before the cyclic boundary condition. Then if for some β there exist vectors which return to their initial position after N successive transformations as described in § 2, this gives an eigenfrequency according to (2.4). When the number of such vectors is finite, the phase of the vibration with this eigenfrequency is not arbitrary, but is determined uniquely or restricted to those which correspond to these "recurrent" vectors. If every vector is recurrent, the phase of the vibration is arbitrary.

It is well known that the eigenfrequencies of a regular monatomic lattice is given by

$$\beta = n\pi/N\,, \qquad n = 1, 2, \cdots, N/2 \ \text{ or } \ (N-1)/2\,. \tag{3.1}$$

In I it was shown that the phase of vibration is arbitrary except for the vibration at the band-edge. This corresponds to the fact that for regular lattices every transformation of the vector is a simple rotation by the constant angle 2β, and consequently, if $\beta = n\pi/N$, arbitrary vector is recurrent. At the band-edge, the absolute values of the displacements of neighboring two atoms are the same, so that the phase should be considered unique.

Next consider the lattice with one impurity. It we take the regular atom as the basic one, the state vector is subject to $\boldsymbol{P}$-transformation with following $\boldsymbol{Z}$-rotation only once. When the impurity is heavier than the regular atom, $\boldsymbol{P}$-transformation consists of a stretch of the real component and a contraction of the imaginary component, since then $\mathcal{E}>0$ and consequently $\gamma>0$. Fig. 1 shows successive transformations of the vector for this case, from which it is readily seen that in any normal vibration the phase cannot be arbitrary, in harmony with the result obtained in I.

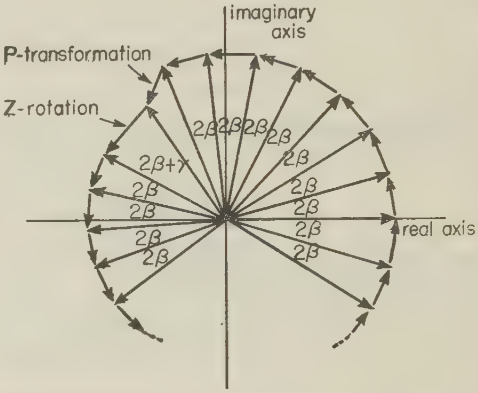

Fig. 1.

If we take the state vector of the atom just before the impurity as the initial vector $\boldsymbol{x}_0 \equiv (x_0 + iy_0)$, the eigenfrequencies are determined by the condition that $\boldsymbol{x}_0$ returns to itself after a $\boldsymbol{P}$-transformation with the following $\boldsymbol{Z}$-rotation and succeeding $N-1$ simple rotations by angle 2β, i.e., by the equation

$$\{x_0(\sec\gamma+\tan\gamma)+iy_0(\sec\gamma-\tan\gamma)\}\exp[i(2\beta+\gamma)]\exp[2i(N-1)\beta] = x_0+iy_0 \tag{3.2}$$

or

$$\left.\begin{aligned} x_0\{(\sec\gamma+\tan\gamma)\cos(2N\beta+\gamma)-1\}-y_0(\sec\gamma-\tan\gamma)\sin(2N\beta+\gamma)=0 \\ x_0(\sec\gamma+\tan\gamma)\sin(2N\beta+\gamma)+y_0\{(\sec\gamma-\tan\gamma)\cos(2N\beta+\gamma)-1\}=0 \end{aligned}\right\}. \tag{3.3}$$

These equations have non-trivial solution only if

$$\cos(2N\beta)-\mathcal{E}\tan\beta\sin(2N\beta)=1\,. \tag{3.4}$$

This is just the eigenfrequency equation derived in I.

From (3.4) we have the relations

$$\tan\gamma=(\cos(2N\beta)-1)/\sin(2N\beta)=-2\sin^2(N\beta)/2\sin(N\beta)\cos(N\beta)=-\tan(N\beta)\,, \tag{3.5a}$$

or

$$\sec\gamma=(N\beta)\,,\quad \cos\gamma=\cos(N\beta)\,,\quad \sin\gamma=-\sin(N\beta)\,,\quad \exp(2Ni\beta)=\exp(-2i\gamma)\,. \tag{3.5b}$$

For the solutions $\beta=n\pi/N$ of (3.4), however, these relations are not valid, for $\sin(2N\beta)=0$. Then (3.5b) should be replaced by

$$\cos(2N\beta+\gamma)=\cos\gamma\,,\qquad \sin(2N\beta+\gamma)=\sin\gamma\,,\qquad \exp(2Ni\beta)=1\,. \tag{3.6}$$

From (3.3) we obtain

$$x_0/y_0=[(\sec\gamma-\tan\gamma)\sin(2N\beta+\gamma)]/[(\sec\gamma+\tan\gamma)\cos(2N\beta+\gamma)-1]$$
$$=[(\sec\gamma-\tan\gamma)\cos(2N\beta+\gamma)-1]/[-(\sec\gamma+\tan\gamma)\sin(2N\beta+\gamma)]\ , \tag{3.7}$$

which becomes

$$x_0/y_0=(\sin\gamma-1)/\cos\gamma=-\cos\gamma/(1+\sin\gamma)\ , \tag{3.8}$$

for the case of (3.5) and

$$x_0/y_0=(1-\sin\gamma)/\cos\gamma=\cos\gamma/(1+\sin\gamma)\ , \tag{3.9}$$

for the case of (3.6).

When we return to the old representation in which Z and $1+\varLambda$ are diagonalized, we get, for the ratio of two components of the vector $\boldsymbol{x}_0$

$$\exp(-4i\beta-2i\gamma)=\exp(-4i\beta-2Ni\beta) \tag{3.10}$$

or

$$-\exp(-4i\beta)\ , \tag{3.11}$$

according as (3.5) or (3.6) is valid. These results are in accord with those obtained in I.

In the present case, the $\boldsymbol{P}$-transformation must be reduced to a simple rotation for $\boldsymbol{x}_0$ to return to itself after N transformations. (3.7) can be regarded as the solutions of this condition. In fact, the condition that $\boldsymbol{P}$-transformation conserves the length of $\boldsymbol{x}_0$ is

$$(\sec\gamma+\tan\gamma)^2x_0^2/y_0^2+(\sec\gamma-\tan\gamma)^2=x_0^2/y_0^2+1\ , \tag{3.12}$$

from which we get

$$x_0^2/y_0^2=[1-(\sec\gamma-\tan\gamma)^2]/[(\sec\gamma+\tan\gamma)^2-1]=(1-\sin\gamma)/(1+\sin\gamma) \tag{3.13}$$

which gives the same ratio x_0/y_0 as is obtained from (3.8) or (3.9).

The angle of rotation by $\boldsymbol{P}$-transformation must be γ for the case of (3.5) and $-\gamma$ for the case of (3.6). This can also be verified by the fact that the equation $\boldsymbol{P}\boldsymbol{x}_0=\exp(i\xi)\boldsymbol{x}_0$, or

$$\pm(\sec\gamma+\tan\gamma)(1-\sin\gamma)+i(\sec\gamma-\tan\gamma)\cos\gamma=\exp(i\xi)(\pm(1-\sin\gamma)+i\cos\gamma) \tag{3.14}$$

is satisfied by $\xi=\pm\gamma$.

In the case of (3.5), every eigenfrequency is smaller than the corresponding one for the regular lattice, since the vector is subjected to an excessive rotation by the angle 2γ, while in the case of (3.6), there are no shifts of eigenfrequencies since the vector is not subjected to any excessive rotation. This result is also in harmony with that attained in I. We thus see that the variation of the eigenfrequencies can be explained very intuitively by the vector picture.

The case of light impurity, i.e., the case $\varepsilon<0$ and $\gamma<0$ can also be discussed in a similar manner. Here, however, it should be remarked that, in order to visualize the operation of transfer matrices as the transformation of the complex vector, it is necessary for the matrix elements of $\boldsymbol{P}$ to be real and for the matrix $\boldsymbol{Z}$ to have the form (2.14), so that $\boldsymbol{Z}$ transforms the vector in such a way that the real component remains real and the imaginary component remains imaginary. For the extra-band frequencies which appear when $\varepsilon<0$, β and consequently γ becomes complex, which invalidates this condition. We should, therefore, take the lightest atom as the basic one, if we wish to use the vector picture also for the extra-band frequencies.

§ 4. The Eigenfrequency Equations for the Lattices of $mm\cdots mMM\cdots M$-type and the generalized diatomic lattice

Consider the lattice of the type

$$\underbrace{mmm\cdots m}_{q}\underbrace{MMM\cdots M}_{p} \tag{4.1}$$

The product of all the transfer matrices (total transfer matrix) $\boldsymbol{h}$ is then

$$\boldsymbol{h}=(\boldsymbol{1}+\boldsymbol{\Lambda})^q\boldsymbol{Q}^p\ . \tag{4.2}$$

Let us calculate $\mathrm{Tr}\,\boldsymbol{h}$. Putting

$$\mathrm{Tr}\,\boldsymbol{Q}=2\cos(2\beta+\gamma)\sec\gamma=2\cos\tau\ , \tag{4.3}$$

we obtain for the eigenvalues of $\boldsymbol{Q}$

$$\rho_\pm=\exp(\pm i\tau)\ , \tag{4.4}$$

and for the diagonalizing matrices

$$\boldsymbol{W}=\begin{pmatrix} -i(\sec\gamma-\tan\gamma)\sin(2\beta+\gamma) & -i(\sec\gamma-\tan\gamma)\sin(2\beta+\gamma) \\ (\sec\gamma+\tan\gamma)\cos(2\beta+\gamma)-\exp(i\tau) & (\sec\gamma+\tan\gamma)\cos(2\beta+\gamma)-\exp(-i\tau) \end{pmatrix}. \tag{4.5a}$$

and

$$\begin{aligned} \boldsymbol{W}^{-1}&=1/[2\sin\tau\sin(2\beta+\gamma)(\sec\gamma-\tan\gamma)] \\ &\times\begin{pmatrix} (\sec\gamma+\tan\gamma)\cos(2\beta+\gamma)-\exp(-i\tau) & i(\sec\gamma-\tan\gamma)\sin(2\beta+\gamma) \\ -(\sec\gamma+\tan\gamma)\cos(2\beta+\gamma)+\exp(i\tau) & -i(\sec\gamma-\tan\gamma)\sin(2\beta+\gamma) \end{pmatrix}. \end{aligned} \tag{4.5b}$$

The we have, putting $2\beta+\gamma\equiv\alpha$,

$$\begin{aligned} (\boldsymbol{1}+\boldsymbol{\Lambda})^q\boldsymbol{Q}^p&=(\boldsymbol{1}+\boldsymbol{\Lambda})^q\boldsymbol{W}\,\mathrm{diag}\,(\exp(ip\tau),\exp(-ip\tau))\,\boldsymbol{W}^{-1}=(1/\sin\tau) \\ &\times\begin{pmatrix} \begin{array}{l} (\sec\gamma+\tan\gamma)\cos\alpha\cos 2q\beta\sin p\tau \\ -\sin[(p-1)\tau]\cos 2q\beta \\ -(\sec\gamma+\tan\gamma)\sin 2q\beta\sin\alpha\sin p\tau \end{array} & \begin{array}{l} i(\sec\gamma-\tan\gamma)\sin\alpha\cos 2q\beta\sin p\tau \\ -i(\sec\gamma+\tan\gamma)\cos\alpha\sin 2q\beta\sin p\tau \\ +i\sin 2q\beta\sin[(p+1)\tau] \end{array} \\ \begin{array}{l} i(\sec\gamma+\tan\gamma)\cos\alpha\sin 2q\beta\sin p\tau \\ -i\sin 2q\beta\sin[(p-1)\tau] \\ +i(\sec\gamma+\tan\gamma)\sin\alpha\cos 2q\beta\sin p\tau \end{array} & \begin{array}{l} -(\sec\gamma-\tan\gamma)\sin\alpha\sin 2q\beta\sin p\tau \\ -(\sec\gamma+\tan\gamma)\cos\alpha\cos 2q\beta\sin p\tau \\ +\cos 2q\beta\sin[(p+1)\tau] \end{array} \end{pmatrix} \end{aligned} \tag{4.6}$$

and

$$\mathrm{Tr}\,\boldsymbol{h}=2\cos 2q\beta\cos p\tau-2\sin 2q\beta\sin p\tau\tan\alpha\cot\tau\ . \tag{4.7}$$

The eigenfrequency equation for the lattice of the type (4.1) is, therefore,

$$F(\beta)\equiv\mathrm{Tr}\,\boldsymbol{h}/2\equiv\cos 2q\beta\cos p\tau-\sin 2q\beta\sin p\tau\tan\alpha\cot\tau=1\ . \tag{4.8}$$

To get the eigenfrequencies, we have only to plot the function $F(\beta)$ and locate the crossings of it with the line representing the constant 1.

In the case of $m<M$, there is no real τ for the values of β near $\pi/2$ (band-edge), since $|\mathrm{Tr}\,\boldsymbol{Q}|$ becomes here larger than 2. We have to put $\tau=\pi+i\tau'$ in such a region to obtain the curve $F(\beta)$ for the whole region of β. As will be seen below (at the end of this section), the point at which the value of $|\mathrm{Tr}\,\boldsymbol{Q}|$ becomes larger than 2 gives the maximum eigenfrequency of the regular lattice composed only of non-basic atoms (M-lattice). The region of complex τ corresponds therefore to the extra-band region of M-lattice. It is of course possible for F(β) to become less than or equal to 1 also in this region.

When $m>M$, τ does not become complex within the band. In this case, however, $F(\beta)$ can be smaller than or equal to 1 for complex β, corresponding to the existence of extra-band frequencies. We should then put $\beta=\pi/2+i\zeta$ in order to obtain the complete frequency spectrum.

We next consider the lattice composed of L lattices of the type considered above, that is, the lattice which has the unit cells of the type (4.1) (the so-called generalized diatomic lattice). Its total transfer matrix $\boldsymbol{H}$ is given by

$$\boldsymbol{H}=\boldsymbol{h}^L . \tag{4.9}$$

Putting

$$F(\beta)=\cos 2q\beta \cos p\tau-\sin 2q\beta \sin p\tau \tan \alpha \cot \tau=\sec \delta , \qquad |F(\beta)|>1 , \tag{4.10a}$$

$$=\cos \sigma , \qquad |F(\beta)|\leqslant 1 , \tag{4.10b}$$

we obtain as the eigenvalues of $\boldsymbol{h}$:

$$\eta_{\pm}=\begin{cases}\sec \delta \pm \tan \delta , & |F(\beta)|>1 , \quad (4.11a)\\ \cos \sigma \pm i \sin \sigma=\exp (i\sigma) , & |F(\beta)|\leqslant 1 . \quad (4.11b)\end{cases}$$

Hence the eigenfrequency equation of the generalized diatomic lattice is

$$\mathrm{Tr}\, \boldsymbol{H}=\eta_+{}^L+\eta_-{}^L=2 . \tag{4.12}$$

In the case of (4.11b), the eigenfrequencies are given by

$$\sigma=2\pi n/L \qquad (n: \quad \text{integer}) , \tag{4.13}$$

since

$$\eta_+{}^L+\eta_-{}^L=2 \cos L\sigma . \tag{4.14}$$

In the case of (4.11a), on the contrary, there are no eigenfrequencies, inasmuch as (4.12) then becomes

$$(1+\sin \delta)^L+(1-\sin \delta)^L=2 \cos^L \delta , \tag{4.15}$$

the left-hand side of which is always larger than unity. We thus see that only the β-values for which $|F(\beta)|\leqslant 1$ can give rise to the eigenfrequencies. In other words, the intervals of β in which the curve $F(\beta)$ lies between $+1$ and -1 give the allowed bands of the frequency spectrum of generalized diatomic lattice. Other intervals correspond to the forbidden bands.

To sum up, the problem of obtaining the eigenfrequencies of the lattice of the type (4.1) and that of obtaining the frequency spectrum of generalized diatomic lattice whose unit cell is of the type (4.1) are reduced to one and the same problem of plotting the curve $F(\beta)$.

It is easy to get the eigenfrequency distribution within each allowed band. We have only to locate the points at which $F(\beta)$ crosses the lines representing the constant values $\cos [2\pi n/L]$ $(n=0, 1, 2, \cdots L/2$ or $(L-1)/2)$. Therefore, if L is even, the β-values for which $F(\beta)=\pm 1$ give the edges of allowed bands. Since the equation $F(\beta)=\pm 1$ or $\mathrm{Tr}\, \boldsymbol{h}=\pm 2$ expresses the condition that the corresponding atoms in the neighboring two unit cells have the same or opposite state vectors, the cyclic boundary condition here adopted for the whole lattice is obviously satisfied when $F(\beta)=\pm 1$, as long as L is even. When L is odd, one edge of each allowed band is given by $F(\beta)=\cos [(L-1)\pi/L]$. Since, however, for large L the value of the right-hand side is almost equal to unity, we may consider that for long lattices both edges of the allowed band are given by $F(\beta)=\pm 1$ whether L may be even or odd.

The fact explained just above means that, in the normal vibrations corresponding to the frequencies at the edges of the allowed band, the atoms at the corresponding positions of the two neighboring unit cells vibrate in the same or opposite directions. For ordinary diatomic lattices this fact is already well known. It will be shown in § 6 that the solutions of $F(\beta)$ $=\pm 1$ in fact give the well-known frequencies at the edges of acoustical and optical branches.

It is to be noted that, for the special case of $L=2$, the eigenfrequency equation is given by $F(\beta)=\pm 1$.

For M-lattice with even N, the equation which gives the eigenfrequencies corresponding to the edges of the band is $\mathrm{Tr}\, \boldsymbol{Q}=\pm 2$, since the total transfer matrix of the unit cell $\boldsymbol{h}$ is now reduced to $\boldsymbol{Q}$. In this case, however, there is only one allowed band, so that $\mathrm{Tr}\, \boldsymbol{Q}=2$

gives the minimum eigenfrequency, i. e., zero, and Tr $\boldsymbol{Q}=-2$ gives the maximum eigenfrequency. If N is odd, the latter is given by Tr $\boldsymbol{Q}=[\cos(N-1)\pi/N]$.

§ 5. Wave Forms of Impurity Vibrations

(i) One light impurity.

As was already noted, we have to take the impurity as the basic atom, in order to use the vector picture for the impurity vibration. This implies that we should consider the case $q=1$ of (4.1). In this case we have

$$F(\beta)=\cos 2\beta \cos p\tau-\sin 2\beta \sin p\tau \tan \alpha \cot \tau \ . \tag{5.1}$$

Fig. 2 shows the curve $F(\beta)$ for the case $p=6$ and $\mathcal{E}=1/2$. In general, if p is odd, the curve first descends to take large negative value as we get into the region $|\mathrm{Tr}\, Q|>2$, but soon begins to ascend rapidly without sloping down again. For even p the behavior is just opposite to the above. In either case, $F(\beta)$ takes the value 1 once and only once in the extra-band region of M-lattice (in this case, the regular lattice), which means that there is only one impurity vibration.

Let us calculate the wave form of this impurity vibration. To begin with, we consider the general lattice of the type (4.1). As the initial vector $\boldsymbol{x}_0$ take the state vector of the last (the leftmost) basic atom. Then $\boldsymbol{x}_0$ is the solution of

$$\boldsymbol{h}\boldsymbol{x}_0=(1+\boldsymbol{\Lambda})^q\boldsymbol{Q}^p\boldsymbol{x}_0=\boldsymbol{x}_0 \ . \tag{5.2}$$

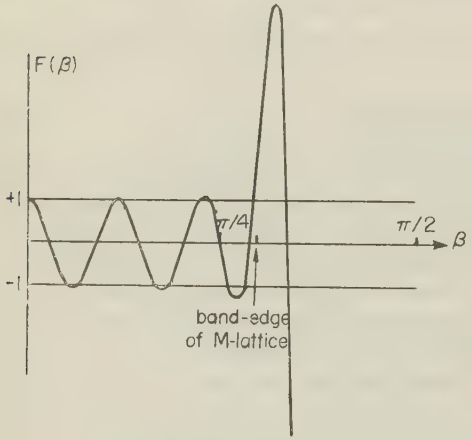

Fig. 2.

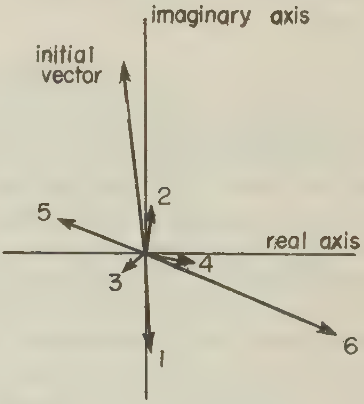

Fig. 3.

The ratio of the two components of $\boldsymbol{x}_0$ can be calculated by using (4.6), with the result that

$$\frac{x_0}{y_0}=\frac{\sin p\tau[\sec\gamma \sin(\alpha-2q\beta)-\tan\gamma \sin(\alpha+2q\beta)]+\sin 2q\beta \sin[(p+1)\tau]}{(\sin\gamma+\tan\gamma)\sin p\tau \cos(\alpha+2q\beta)-\sin[(p-1)\tau]\cos 2q\beta-\sin\tau} \tag{5.3a}$$

$$=\frac{\sin\tau+\sin p\tau[\sec\gamma \cos(\alpha-2q\beta)+\tan\gamma \cos(\alpha+2q\beta)]-\cos 2q\beta \sin[(p+1)\tau]}{(\sec\gamma+\tan\gamma)\sin p\tau \sin(\alpha+2q\beta)-\sin 2q\beta \sin[(p-1)\tau]} \ . \tag{5.3b}$$

The eigenfrequency equation (4.8) is none other than the condition that (5.3a) and (5.3b) should coincide with each other.

Putting $q=1$ in (5.3a) or (5.3b), and giving β the value corresponding to the impurity frequency, the initial vector $\boldsymbol{x}_0$ for the present case is obtained. Fig. 3 shows $\boldsymbol{x}_0$ and its successive transformations for the case $p=6$, $\mathcal{E}=1/2$. It is seen that $\boldsymbol{x}_0$ returns to itself after seven successive transformations, as it should be. It is also seen that the length of the vector at first diminishes rapidly, and afterwards increases rapidly again to return to its initial value. This clearly illustrates the localized property of the impurity vibration.

The localized property can be demonstrated much more concretely if we return to the original representation in which the two components of the state vector represent the displacement of the atom and the difference in displacement of the neighboring atoms. The matrix which transforms the present representation to the original one is, according to (I, 2.5) and (2.11a),

$$UV=\begin{pmatrix} \exp(-2i\beta)i(1-i\tan\gamma)+\exp(2i\beta)\sec\gamma & \exp(-2i\beta)i(1-i\tan\gamma)-\exp(2i\beta)\sec\gamma \\ i(1-i\tan\gamma)-\exp(-2i\beta)i(1-i\tan\gamma) & i(1-i\tan\gamma)-\exp(-2i\beta)i(1-i\tan\gamma) \\ +\sec\gamma-\exp(2i\beta)\sec\gamma & -\sec\gamma+\exp(2i\beta)\sec\gamma \end{pmatrix}. \tag{5.4}$$

Hence the displacement of the atom is given by

$$x'=(\sec\gamma+\sin 4\beta+\tan\gamma\cos 4\beta)x+(\tan\gamma\sin 4\beta-\cos 4\beta)y \tag{5.5}$$

in terms of the real and imaginary component in the vector representation. Fig. 4 shows the actual wave form obtained from Fig. 3 by aid of (5.5).

The in-band vibrations have, on the contrary, no such localized property. Figs. 5 and 6 show the successive transformations of the vector and the wave form, respectively, for the second inband frequency from the band-edge. It is seen that the wave form is nearly simple harmonic and not localized.

For the in-band frequencies we can construct the vector picture also when the regular atom is used as the basic one. The picture becomes even simpler, inasmuch as now all the transformations are simple rotations except the one at the impurity atom, where the vector is transformed by $\boldsymbol{P}$ and $\boldsymbol{Z}$. From this one can see that, for all the in-band frequencies, the amplitudes of successive regular atoms are just equal to the values of a sine-function at regularly spaced points. This is actually the case, as seen in Fig. 6.

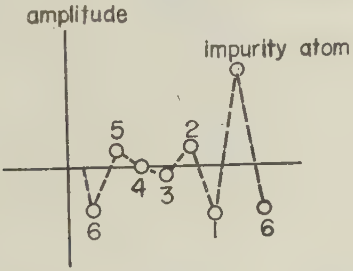

Fig. 4.

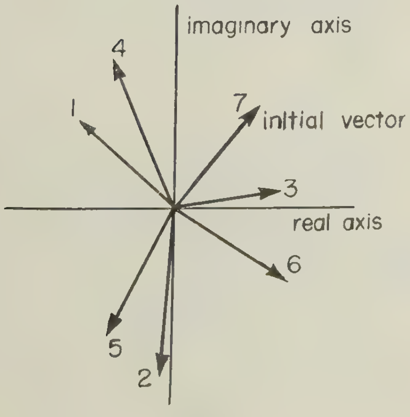

Fig. 5.

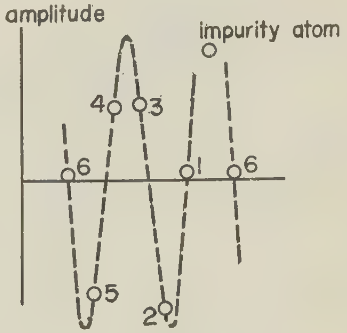

Fig. 6.

(ii) Two light impurities.

Consider first a lattice composed of 14 atoms, of which two are light impurities located at the largest possible distance from each other, i. e., with 6 regular atoms between them. Since such a lattice is a repetition of the lattice of the type considered in (i), the eigenfrequency equation is given by the expression (5.1) put equal to ±1, provided the impurity atom is taken as the basic one. The eigenfrequencies for the case $\varepsilon=1/2$ are given therefore by the points where the curve $F(\beta)$ of Fig. 2 crosses the lines representing ±1. It is seen that two impurity modes now make their appearance. Moreover, the upper mode is antisymmetric and the lower one is symmetric, according to the result obtained in § 4.

Next let us consider the case where the impurities are at the least distance from each other, i. e., they form a couple of the nearest neighbors. Since such a lattice is obtained by putting $q=2$ and $p=12$ in (4.1), the eigen-frequency equation is

$$F(\beta)=\cos 4\beta \cos 12\tau-\sin 4\beta\, 12\tau \tan \alpha \cos \tau=1\ . \tag{5.6}$$

Fig. 7 shows the curve $F(\beta)$, which indicates that an excess in-band frequency appears near the band-edge, whereas one of the two impurity frequencies disappear and the other is shifted to a remarkably higher position. This can be interpreted as that, owing to the mutual interaction of the impurity atoms, two impurity frequencies have been largely separated, and the lower one has got into the band.

From the statement made at the end of (i), it is almost clear that all the in-band vibrations are essentially simple harmonic and not localized, whether they may be proper in-band

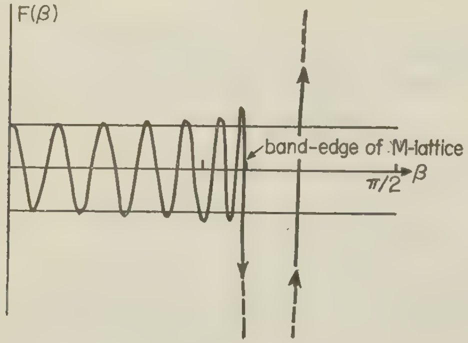

Fig. 7.

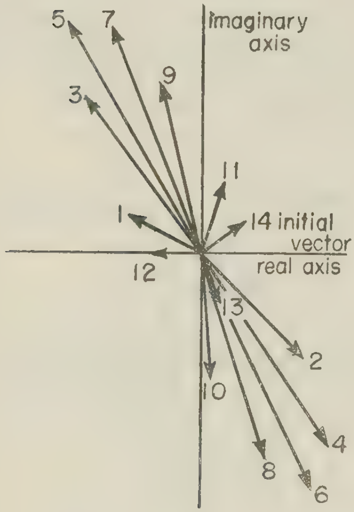

Fig. 8.

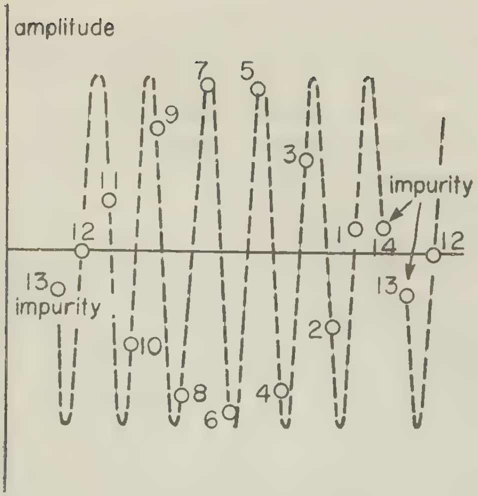

Fig. 9.

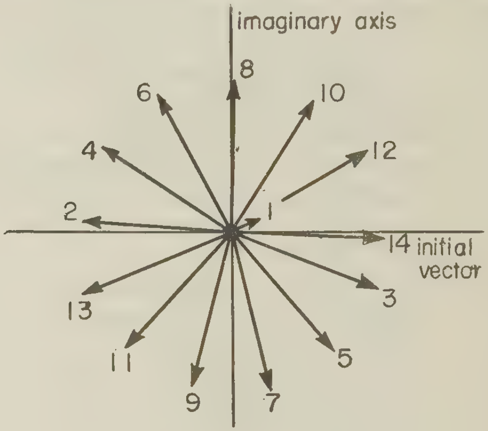

Fig. 10.

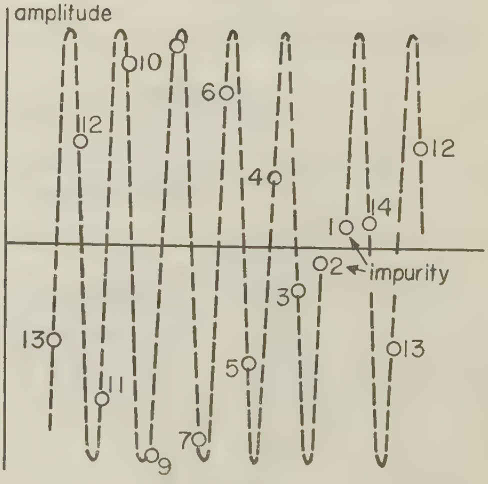

Fig. 11.

vibrations or "got-in" extra-band ones. As an example, Figs. 8 and 9 show the transformations of the vector and the wave form, respectively, for the uppermost in-band vibration, obtained by the same method as described above. They show very vividly that this vibration is no more localized, but has essentially the same character as a simple harmonic wave. This can be seen more clearly if we take the regular atom as the basic one. Figs. 10 and 11 show the vector picture and the wave form, respectively, so obtained.

§ 6. Frequency Spectrum of Generalized Diatomic Lattice

In § 4 is was shown that the frequency spectrum of the generalized diatomic lattice and that of its unit cell is obtained from one and the same curve $F(\beta)$. Therefore, for example, the allowed bands of the lattice in which the mass of every seventh atom is two-thirds of that of host atom, and those of the lattice in which two light atoms appear in pairs in every 13th and 14th positions, are given by the intervals in which each of the curves in Fig. 2 and Fig. 7 lies between $+1$ and -1. The number of allowed bands is thus equal to the number of atoms in the unit cell.

In general, the allowed bands become wider, and the forbidden bands narrower, as the frequency becomes higher. When in particular the basic atom is lighter and fewer than non-basic atoms, the curve $F(\beta)$ falls or rises very rapidly and only once in the extra-band region of M-lattice, the gradient of fall or rise becoming extremely steep as the unit cell becomes longer. The allowed band which originates from this last fall or rise corresponds precisely to the so-called impurity band, which therefore becomes rapidly narrower when the impurities (light atoms) become fewer, and the frequencies therein contained become almost equal to that of the impurity frequency of the unit cell.

Let us now turn to the simplest case of ordinary diatomic lattice, i. e., the case $q=p=1$. In this case we have

$$F(\beta)=\cos 4\beta-\mathcal{E}\tan\beta\sin 4\beta\,, \qquad (6.1)$$

which is plotted in Fig. 12 for the case $\mathcal{E}=1/2$. The figure clearly demonstrates the separation of two branches—optical and acoustical. Edges of each band are given, as already shown, by $F(\beta)=\pm 1$. Corresponding frequencies are calculated to be

$$\left.\begin{array}{lll}
F(\beta)=1, & \sin^2\beta=0, & \omega^2=0: \\
\multicolumn{3}{l}{\quad\text{lower edge of acoustical branch,}} \\
F(\beta)=-1, & \sin^2\beta=1/2(1+\mathcal{E}), & \omega^2=2\lambda/M: \\
\multicolumn{3}{l}{\quad\text{upper edge of acoustical branch,}} \\
F(\beta)=-1, & \sin^2\beta=1/2, & \omega^2=2\lambda/m: \\
\multicolumn{3}{l}{\quad\text{lower edge of optical branch,}} \\
F(\beta)=1, & \sin^2\beta=(\mathcal{E}+2)/2(1+\mathcal{E}), & \\
 & \omega^2=2(M+m)\lambda/Mm: & \\
\multicolumn{3}{l}{\quad\text{upper edge of optical branch,}}
\end{array}\right\}\quad(6.2)$$

in harmony with the well-known result. That also the wave forms of the corresponding vibrations come out to be the same as the old results was already shown in § 4. In the forbidden bands, no initial vector x_0 can return to itself, however often it may be transformed by $\boldsymbol{h}$. Since in the present case $\boldsymbol{h}=(\boldsymbol{1}+\boldsymbol{\Lambda})\boldsymbol{ZP}$, $\boldsymbol{h}$ stretches the real component of the vector by the factor $\sec\gamma+\tan\gamma$ and contracts the imaginary component by $\sec\gamma-\tan\gamma$, and then rotates it by the angle $4\beta+\gamma$. Therefore, at the β a little smaller then $\pi/4$, the vector

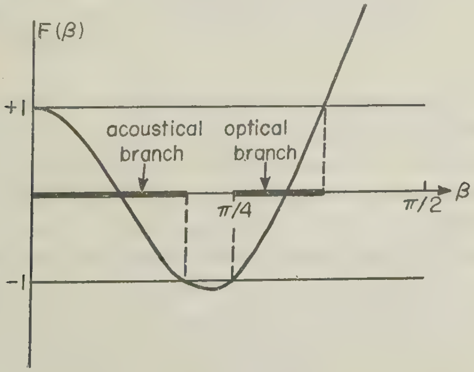

Fig. 12.

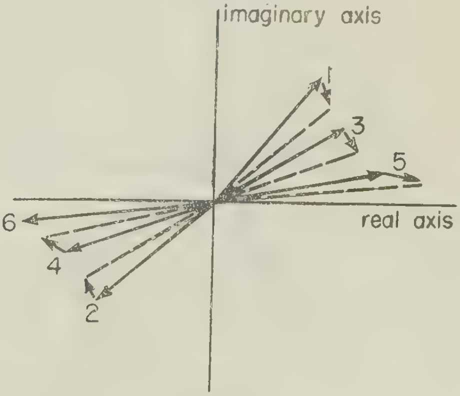

Fig. 13.

picture will become such as shown in Fig. 13. It vividly shows that every initial vector approaches the real axis while it is rapidly elongated, and never returns to its initial position.

Similar explanation applies also to more complicated cases. Consider for example the case $q=1$, $p=2$, $\varepsilon>0$, which is less simple than ordinary diatomic lattice. Now the vector is subjected to the $\boldsymbol{P}$-transformations with succeeding $\boldsymbol{Z}$-rotations repeated twice, and then to the rotation by $\mathbf{1}+\boldsymbol{\Lambda}$. Hence it is expected from the vector picture that the forbidden bands appear at about $\beta=\pi/6$ and $\beta=\pi/3$. In fact the curve $F(\beta)$ is now of the form illustrated in Fig. 14, which shows the appearance of forbidden bands nearly at the predicted positions. Since, however, in the present case $\boldsymbol{P}$-transformation has a larger effect because of its repetition, the forbidden band corresponding to $\beta=\pi/3$ appears at the position somewhat shifted to the smaller β-value. Near $\beta=\pi/4$ there appears no forbidden band, inasmuch as the vector is transformed here in such a way as is shown in Fig. 15, and may be recurrent.

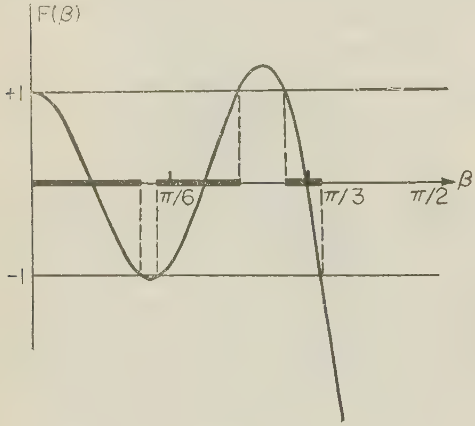

Fig. 14.

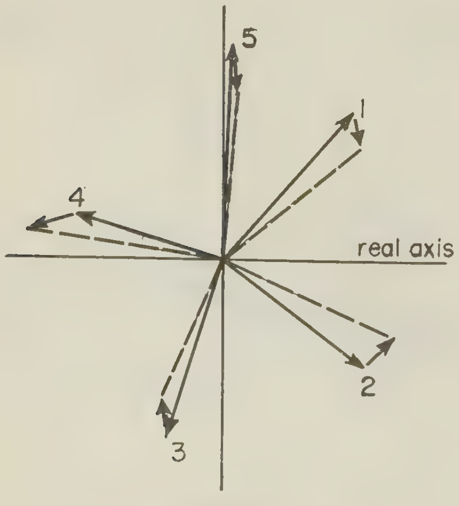

Fig. 15.

For larger p's, however, the transformations of the vector will become more complicated and the condition that no vector should be recurrent will become more subtle. It may be difficult in such a case to predict the band structure merely from the qualitative considerations based on the vector picture.

§ 7. Some Speculations for Random Lattice

In the case of random lattices, the vector is transformed fortuitously, sometimes by $\boldsymbol{Q}=\boldsymbol{ZP}$ and sometimes by $\mathbf{1}+\boldsymbol{\Lambda}$. Only the probability of occurrence of each transformation is known. The series of transformations of the vector becomes therefore a kind of random walk on the complex plane, which forms mathematically a Markov process. It the limiting distribution of this process be obtained for each β-value, it would become possible to calculate the probability of recurrence of any arbitrary initial vector, and hence the frequency spectrum. Unfortunately, there have been only very few investigations on such a process which is discrete in time and continuous in space, except for a general mathematical argument which is too abstract and vague from the view-point of physical application[6). Moreover, in our case, the limiting distribution will become very singular because of the singularity of transition probabilities. Such a situation, which was already encountered by Schmidt[7) in his treatment of lattice vibration by the method of transfer matrices, makes the problem all the more difficult. We therefore leave the analysis of our Markov process for future investigations and restrict here only to some remarks of extremely general nature.

If for some β the process has ergodic or periodic sets, this β-value will give an eigenfrequency at least with some probability, for any vector belonging to these sets will be recurrent with finite probability. If, on the contrary, the process for this β-value has only transient sets, as was the case in the forbidden band of the diatomic latice (Fig. 13), this β will never give an eigenfrequency. The sets of β-values with the former and the latter properties will form the allowed and forbidden bands, respectively. An argument of such a kind is of little use, however, in view of the above-mentioned difficulty of the analysis and consequently of obtaining the concrete ergodic structure of our process.

We can, however, on the analogy of the generalized diatomic lattices, well expect that the frequency spectrum of the random lattice may have an extremely fine structure. For, since the unit cell of the random lattice is the whole lattice itself, the total transfer matrix $\boldsymbol{H}=\boldsymbol{h}$ should turn out a very intricate product of randomly arranged $\boldsymbol{Q}$'s and $(1+\boldsymbol{\Lambda})$'s. The function $F(\beta)$ will then oscillate very rapidly, especially for large β. The set of β-values for which $|F(\beta)|>1$ will then form an assembly of dispersed narrow intervals. The result obtained by Dean[4], that the spectra of disordered diatomic lattice have astonishingly fine structures, can thus be explained in a reasonable way.

References

1) J. Hori and T. Asahi: Prog. Theor. Phys. **17** (1957) 523.
2) J. Hori: Prog. Theor. Phys. **18** (1957) 367.
3) A. Maradudin and G. H. Weiss: J. Chem. Phys. **29** (1958) 631.
4) P. Dean: Proc. Roy. Soc. **254** (1960) 507.
5) P. R. Halmos: *Finite-Dimensional Vector Spaces* (Van Nostrand Co., Inc., Princeton, 1958) 169.
6) J. L. Doob: *Stochastic Processes* (John Wiley and Sons, Inc., 1953) 190.
7) H. Schmidt: Phys. Rev. **105** (1957) 425.

JOURNAL OF THE PHYSICAL SOCIETY OF JAPAN, Vol. 16, No. 1, JANUARY, 1961

Crystal Distortion in Copper Ferrite-Chromite Series

By Haruyuki OHNISHI and Teruo TERANISHI

Department of Physics, Faculty of Science,
Hokkaido University, Sapporo, Japan

(Received March 25, 1960)

The cation distributions in copper ferrite-chromite series and the copper ferrite quenched from high temperatures are measured by X-ray diffraction method. The lattice parameters are also measured as a function of chromium ion content and of temperature. The critical fractions of copper ions on 16d and 8a sites for the occurrence of bulk crystal distortion from cubic to tetragonal symmetry are determined. The critical temperature for the distortion of copper ferrite is 360°C. This crystal distortion depends only upon the copper ion distribution. The abrupt appearance of distortion and coexistence of two phases, cubic and tetragonal, near the critical fraction and the critical temperature suggest that this distortion is of the first order as predicted by the statistical theory. From the aging of the distortion, the activation energy for copper ion to migrate from 16d site to 8a site is obtained. From the comparison of the critical fraction of copper ion in this series with those in other mixed spinels, the origin of this crystal distortion is discussed.

§1. Introduction

It has been known that some spinel-type oxides have lower symmetry than cubic below some critical temperatures. Snoek[1] and Bertaut[2] reported that copper ferrite is cubic above 760°C and is tetragonal with the axial ratio c/a>1 below this temperature. On the other hand some investigators observed anomalous behaviours in magnetization[3], initial permeability[4] and specific heat[5] at about 360° C. The detailed study on the meaning of these temperature values has not yet been given. Copper chromite ($CuCr_2O_4$) is also known to be tetragonal at room temperature with the axial ratio less than one.

The origin of the crystal distortion in certain compounds containing transition metal ions was discussed already by several investigators. Goodenough and Loeb[6] examined the role of covalency of the transition metal ions, and explained that the origin of the distortion of copper ferrite was square covalent bond of copper ions at octahedral sites. Dunitz and Orgel[7] discussed the distortion from the point of view of the crystalline field theory. According to their theory the Jahn-Teller effect in the ligation of some transition metal ions gives rise to the lattice distortion. Since the cupric ion is expected to have Jahn-Teller effect in both tetrahedral and octahedral ligand, the tetragonal distortions of copper ferrite and chromite are explained directly from their theory, and the difference in axial ratio is ascribed to the difference of the ligand of the cupric ion in the two spinels. (Copper ferrite has an inverse spinel structure, while copper chromite has a normal spinel structure.)

Statistical problem of the temperature dependence of the distortion relating with the distribution of transition metal ions was treated by Finch et al.[8] Wojtowicz[9] investigated this problem in detail and refined the theory. Kanamori[10] wrote down the microscopic Hamiltonian as a sum of the interaction energy relating to the distortion and the electronic state of cations. He explained the distortion at 0°K and also its temperature dependence.

In the present paper the results of a detailed experimental study of the distortion in the copper ferrite-chromite series are given. Their cation distributions were determined by means of the intensity measurement of X-ray diffraction lines. Variation of c/a was observed as a function of temperature and also of the ratio of copper ions distributed in the two sites of spinel lattice. Kinetic study of the distortion was also made by annealing the quenched specimen at various temperatures. From the present study it was concluded that the lattice distortion is a cooperative phenomenon. The meaning of the two critical temperatures (360°C and 760°C) was also given clearly. Moreover, the origin of distortion was discussed, comparing the critical cation distribution for the occurrence of distortion of this series with those of other series.

§ 2. Preparation of Specimens

All specimens are prepared by usual ceramic technique. CuO is obtained from copper carbonate by calcination, Fe_2O_3 from iron oxalate and Cr_2O_3 from ammonium dichromate. These oxides are mixed in a desired proportion and fired at 900°C in the air for two weeks and then cooled down to room temperature at the rate of 0.5°C/min. This rather low firing temperature prevents eventual reduction of cupric ion.

Specimens which contain more chromium ions than 50 at. % are fired at 700°C for several weeks in order to eliminate the formation of $CuCrO_2$ phase which has been observed after the firing at 900°C. Chemical analysis assures that the metal compositions of all specimens are correct within 3 wt. %. According to X-ray diffraction all specimens include no other phase than spinel and hausmannite phases.

§ 3. Experimental Procedure

For the determination of lattice parameter and cation distribution, "Norelco" and "Geigerflex" X-ray diffractometers are used. Their temperature variations are determined by using high and low temperature attachments.

The intensity of the X-ray diffraction line is expressed as

$$I=\gamma\cdot p\cdot L(\theta)\cdot|F|^2\cdot A(\theta)\cdot T(\theta)\ ,$$

where γ is a constant, p multiplicity of plane (hkl), $L(\theta)$ Lorentz and polarization factor, $|F|$ structure factor, $A(\theta)$ absorption factor and $T(\theta)$ is a temperature factor.

In the geometry of the diffractometers used, the absorption factor can be put as constant[11]. The temperature factor is also constant, since the relevant correction to the intensity ratio is considered to be less than 3%.*

In determining the cation distribution, we

---

* Bacon and Roberts obtain 500°K as the Debye temperature of magnesium ferrite[12]. Assuming the same Debye temperature for copper ferrite, the ratio of the temperature factors of two lines does not change so much from 300°K to 700°K.

ratio of T / temperature	$\frac{T(220)}{T(400)}$	$\frac{T(422)}{T(400)}$
300°K	1.026	0.987
700°K	1.030	0.976

assume that chromium ions occupy mainly octahedral sites. This assumption is very reasonable when we consider the experimentally determined cation distributions of other chromites[13] and the preference energy of chromic ion for octahedral site[14]. Therefore, the cation distribution of the copper ferrite-chromite series is expressed by the formula

$$(Cu_xFe_{1-x})[Cu_{1-x}Fe_{1+x-t}Cr_t]O_4 ,$$

where ( ) and [ ] mean tetrahedral and octahedral sites, respectively.* For copper chromite itself, we consider that some amount of chromium ion situates on tetrahedral sites and so the formula is

$$(Cu_xCr_{1-x})[Cu_{1-x}Cr_{1+x}]O_4 .$$

We measured intensities of (111), (220), (440) and (422) lines. Intensity ratios $I(111)/I(400)$, $I(220)/I(400)$ and $I(422)/I(400)$ are considered to be most sensitive to the cation distribution parameter x[15].

It is not allowed to ignore the oxygen parameter, u, for the calculation of structure factor. Especially u has a large effect on the ratio $I(220)/I(400)$ because with increasing of u $I(400)$ decreases while $I(220)$ increases[16]. The change in u of about 0.4% corresponds to the change in x of about 10% for copper ferrite. We determined u-values experimentally only for two end members of the series, $CuFe_2O_4$ and $CuCr_2O_4$, and for other specimens we assumed that u varies linearly from $CuFe_2O_4$ to $CuCr_2O_4$.

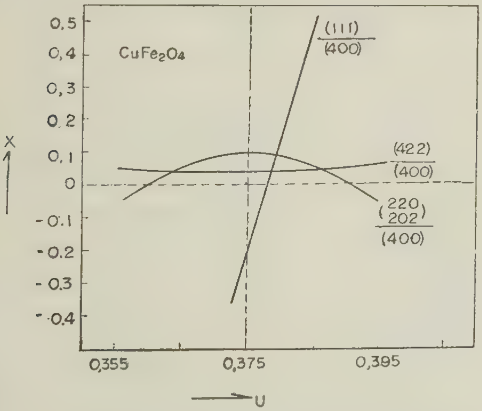

Fig. 1. The curves of cation distribution parameter versus oxygen parameter for $CuFe_2O_4$.

$CoK\alpha$ radiation is used for iron rich specimens and $CuK\alpha$ radiation for chromium rich specimens. As the atomic scattering factors we used the values calculated by Dascola and von Nagy[17]. Corrections due to the anomalous depression of scattering near the absorption edge were also made for atomic scattering factors[18].

In the diffractometers used, the particle size of specimen affects largely the intensity of diffraction line. The particle size of our specimens spreads over from 100μ to 2μ just after the firing, but it is reduced to within 10μ~2μ by a few hour's grinding. This particle size will produce only a few percent deviation of intensity[11].

§4. Experimental Results

1. *Cation distribution and Crystal structure of* $CuFe_{2-t}Cr_tO_4$ *at room temperature*

Fig. 1 and Fig. 2 indicate the relation between u and x obtained for three intensity ratios of slowly cooled $CuFe_2O_4$ and $CuCr_2O_4$,

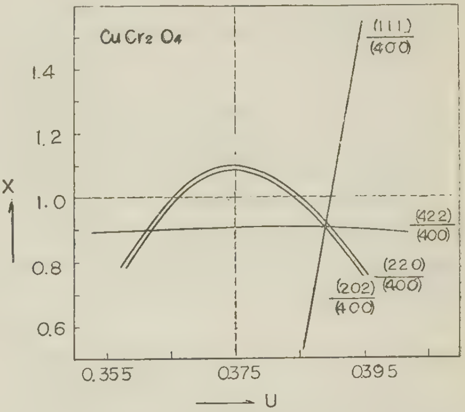

Fig. 2. The curves of cation distribution parameter versus oxygen parameter for $CuCr_2O_4$.

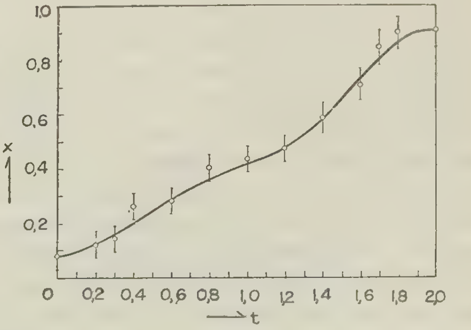

Fig. 3. The relation between the cation distribution parameter and the chromium content.

---

* The geometry of the spinel lattice has been described in detail by E. W. Gorter, Philips Res. Rep. **9** (1954) 295.

respectively. From these diagrams, $x=0.08\pm0.05$, $u=0.380\pm0.003$ for $CuFe_2O_4$ and $x=0.90\pm0.06$, $u=0.389\pm0.003$ for $CuCr_2O_4$ are obtained as the most appropriate values. These x values are in good agreement with those obtained by Bertaut[2)] and by Bertaut and Delorme[19)].

In Fig. 3 the fraction of cupric ion in 8a site, x, changing with chromic ion content, t, are illustrated. x values of mixed compositions are corrected by assuming that u changes linearly from $CuFe_2O_4$ to $CuCr_2O_4$. These x values agree well with values[20)] obtained previously by microphotometric method. For the specimen $CuFe_{0.8}Cr_{1.2}O_4$ intensity measurement was carried out by using two radiations, CoKα and CuKα, and there is no great difference between x values obtained from both radiations. This will prove the correctness of the procedure used.

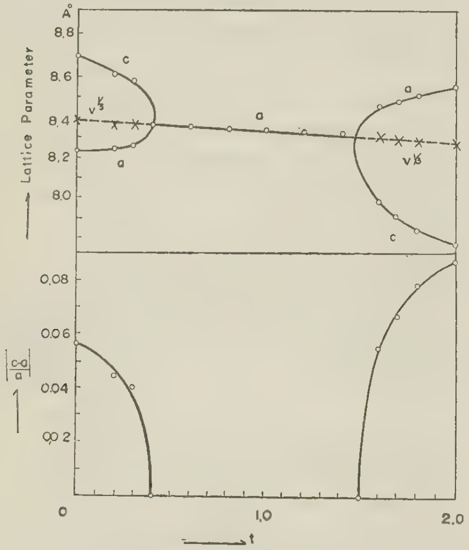

Fig. 4. The lattice parameter and the tetragonality versus chromium content.

Lattice parameters and axial ratio c/a of the series at room temperature are illustrated in Fig. 4. The series has a tetragonal structure with c/a>1 in the range $0\leq t\leq0.3$ and that with c/a<1 in the range $1.6\leq t\leq2.0$. In the range $0.4<t<1.4$, cubic structure is realized and the lattice parameter decreases linearly with increasing t just as expected by Vegard's law. As is shown, cube root of the unit cell volume in the two tetragonal ranges can be plotted on the same straight line with the lattice parameter in the cubic range. Therefore it will be seen that no volume change is present as a result of the distortion. It is noticed that in the sample $t=1.6$ additional weak lines of cubic spinel structure were also observed.

2. *Temperature dependence of crystal structure of* $CuFe_{2-t}Cr_tO_4$

In Figs. 5 and 6 are shown the temperature dependence of lattice parameters of $CuFe_2O_4$ and $CuCr_2O_4$. Temperature dependence of axial ratio is also plotted in Figs. 7 and 8. As is shown, slowly cooled $CuFe_2O_4$ transforms from cubic to tetragonal structure at 360°C[21)]. This critical temperature is quite different from that given by Bertaut (760°C). The origin of this discrepancy will be made clear in the later sections. As illustrated in Figs. 7 and 8 the axial ratio decreases rather sharply at the critical temperature and two phases, cubic and tetragonal, are usually ob-

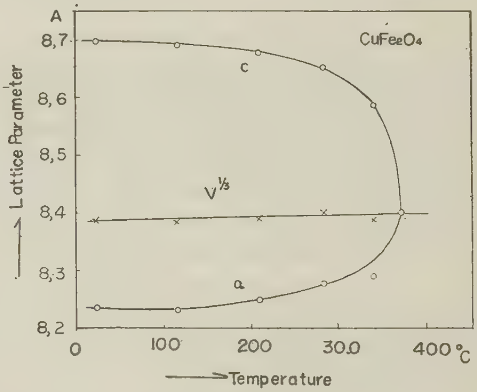

Fig. 5. The temperature variation of lattice parameter for $CuFe_2O_4$.

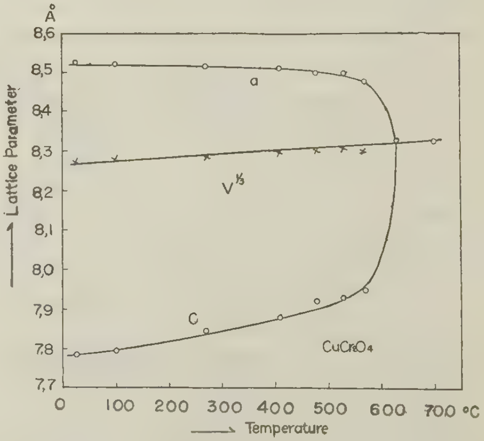

Fig. 6. The temperature variation of lattice parameter for $CuCr_2O_4$.

served at the critical temperature. Although there is a possibility that the temperature is not uniform in the sample in case of X-ray measurement, we believe that the appearance of two phases is essential. It is noticed that a rather large thermal hysteresis of transformation (from 20°C to 50°C) was observed at the critical temperature.

The cation distribution at high temperature was not determined definitely because of the insufficient accuracy of the intensity measurement.

Being cooled to liquid nitrogen temperature, more three samples, $CuFe_2O_4$ quenched from 810°C, $CuFe_{0.4}Cr_{1.6}O_4$ and $CuFe_{0.6}Cr_{1.4}O_4$ were found to undergo distortion. In all cases, however, they do not exhibit a single phase but two phases, cubic and tetragonal, down to liquid nitrogen temperature. As the temperature is lowered, intensities of cubic phase lines decrease while those of tetragonal phase lines increase. But relative intensities of tetragonal phase lines remain unchanged.

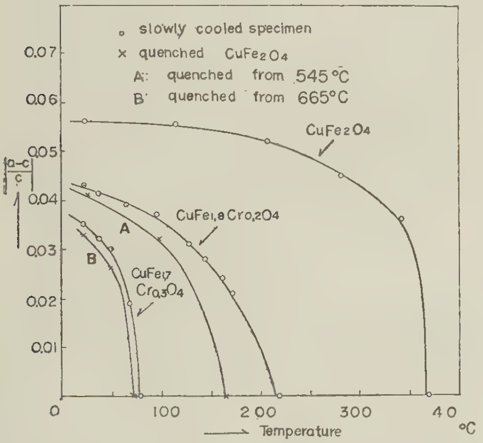

Fig. 7. The temperature variation of tetragonality for iron rich copper ferrite-chromite and quenched copper ferrite.

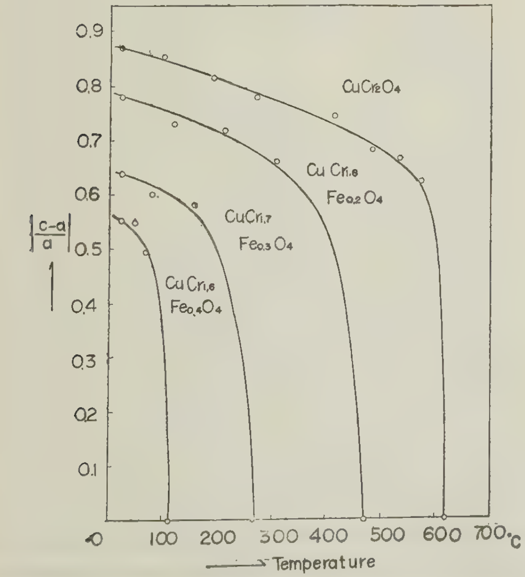

Fig. 8. The temperature variation of tetragonality for chromium rich copper ferrite-chromite.

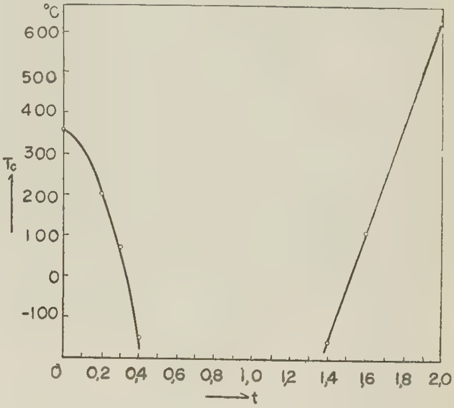

Fig. 9. The critical temperature versus chromium content.

The critical temperatures are plotted against the chromium content in Fig. 9. The critical temperature was defined as such a temperature below which two phases emerge into a single cubic phase. Over the range $0.6<t<1.2$ there appears no structural change in the temperature range down to the liquid nitrogen temperature.

3. *Cation distribution and structure of quenched* $CuFe_2O_4$

We examined crystal structures of $CuFe_2O_4$ quenched from various temperatures in order

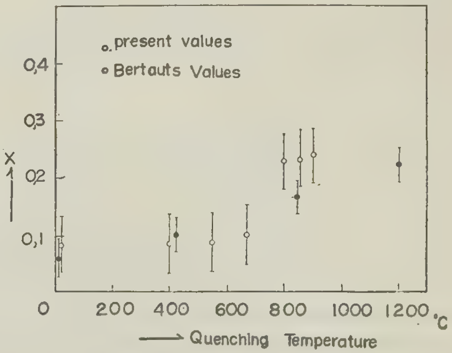

Fig. 10. The cation distribution parameter versus quenching temperature for $CuFe_2O_4$.

to clarify the meaning of the critical temperature 760°C which had been presented by Bertaut as the transition temperature from cubic to tetragonal. In Figs. 10 and 11, cation distribution parameter x and lattice parameters are plotted against the temperature from which the samples are quenched. In Fig. 10, the result obtained previously by Bertaut is also plotted. There is no appreciable discrepancy between Bertaut's values and ours. It should be noted that the parameter x increases sharply from 0.1 to about 0.2 at about 750°C. For samples quenched from 720°C and 740°C we observed the diffraction lines of both tetragonal and cubic structures and the intensity ratios of tetragonal phase-lines to cubic phase-lines depend on the quenching method. There is no appreciable volume change for all specimens in accordance with the result of Fig. 4.

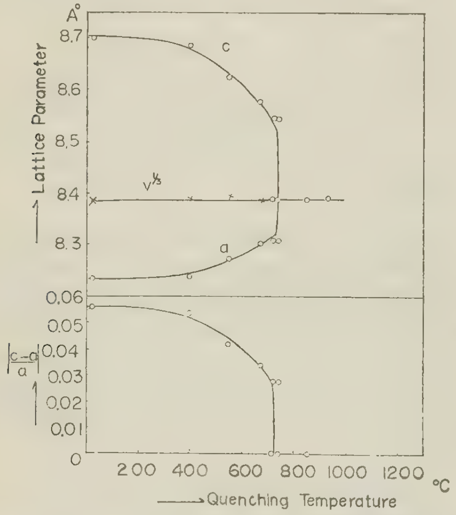

Fig. 11. The lattice parameter and the tetragonality versus quenching temperature for $CuFe_2O_4$.

Although the study of the quenching effect is not in detail for samples with chromium ion, it is certain that no change of crystal structure takes place for the samples that have tetragonal structure with $c/a<1$.

4. *Temperature dependence of crystal structure of quenched* $CuFe_2O_4$

We have measured the temperature dependence of lattice parameter of $CuFe_2O_4$ that had been quenched from various temperatures. Results are already shown in Fig. 7 by curves A and B. The figure illustrates that the quenching gives the same effect on the distortion as the addition of chromium ion.

The critical temperatures of quenched samples are plotted against the quenching temperature in Fig. 12. The sample quencned from 720°C has the critical temperature which is equal to room temperature.

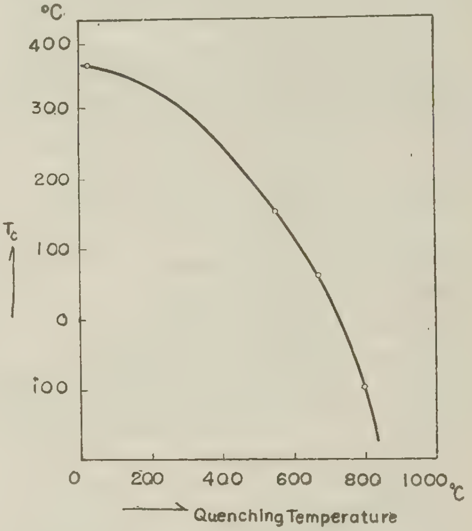

Fig. 12. The critical temperature versus quenching temperature for quenched $CuFe_2O_4$.

5. *Time variation of crystal structure of* $CuFe_2O_4$

The lattice parameters of quenched $CuFe_2O_4$ exhibit a time variation in isothermal annealing at the intermediate temperature range. This phenomenon was observed by the following procedure. Copper ferrite specimens are first quenched from 805°C. They are cubic at room temperature. These samples are inserted at a desired temperature and after the isothermal annealing of a desired time one of these samples is quenched to room temperature and then lattice parameter is observed. This procedure is repeated with changing the temperature of anneal and also the time of anneal. The results are shown in Fig. 13 in which axial ratios are plotted against the annealing time. Although the sample annealed at 450°C transforms into tetragonal structure only after 5 minutes, the sample annealed at 320°C remains cubic even after 80 hours. It means cations commence to migrate easily at about 360°C. Thus for the slowly cooled copper ferrite, cupric ions will commence to migrate nearly at the critical temperature on heating. However, this fact will not produce a large effect upon the observed behaviour of the temperature variation of lattice parameters because it requires at most two hours in order to make all measurements of the diffraction lines from room temperature to 360°C.

The slowly cooled specimen becomes two phases, cubic and tetragonal, after two hours' annealing at 360°C.

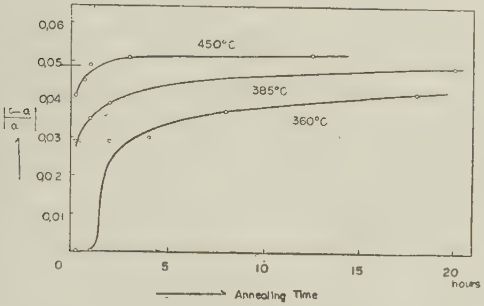

Fig. 13. The variation of tetragonality with annealing time for quenched $CuFe_2O_4$.

§ 5. Discussion

1. *Crystal distortion and cation distribution*

In view of our results on the temperature variation of lattice parameter of copper ferrite the above mentioned magnetic and thermal anomalies occurring at 360°C are definitely due to the structural change from tetragonal to cubic, and the temperature 760°C is only the quenching temperature which provides such a cation distribution that the room temperature is the critical temperature. Some investigators[22] have obtained the activation energy which is required for cupric ion to migrate from 16d site to 8a site on the basis of thermodynamical theory. This activation energy, however, is obtained from the cation distribution which is determined from the magnetic measurement, assuming the Néel theory of ferrimagnetism. Now, we can similarly obtain the activation energy from the aging of lattice parameter of the quenched copper ferrite, assuming that the lattice parameter and the lattice distortion depend upon the copper ion content on the 16d site.

By assuming a simple relaxation process, we can get from the experiment in Fig. 13 the relaxation times of 600 sec. and 60 sec. for the annealing at 385°C and 430°C, respectively. These values give the activation energy of $\Theta=1300$°K, being in good agreement with those of the other authors.

2. *Origin of the lattice distortion*

Now for the iron rich samples we plott the axial ratio and the critical temperature against the parameter x in Figs. 14 and 15, respectively. It is evident from Fig. 14 that the axial ratio depends only upon x, the fraction of copper ion on 8a site, no large difference being recognized between samples containing chromic ion and those quenched from high temperatures. The critical temperature also depends only upon the parameter x and it decreases linearly with increasing x. In Figs. 16 and 17 axial ratio and the critical temperature are plotted against the parameter x for the chromium rich samples. Their behaviours are just the same as those of the iron rich samples, except the fact that the axial ratio

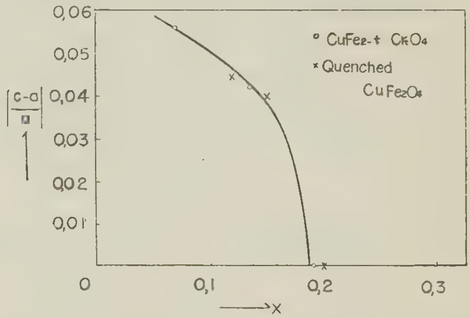

Fig. 14. The variation of tetragonality with cation distribution parameter for iron rich copper ferrite-chromite and quenched copper ferrite.

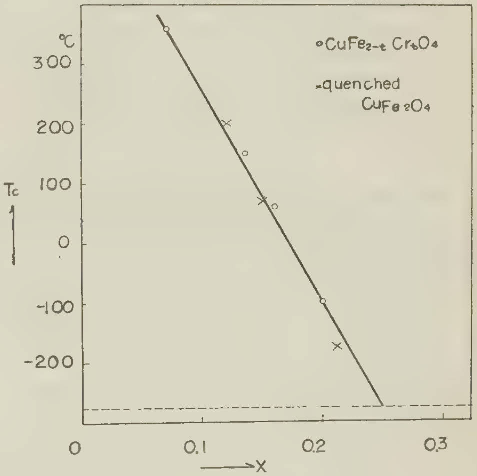

Fig. 15. The variation of critical temperature with cation distribution parameter for iron rich copper ferrite-chromite and quenched copper ferrite.

is less than one in this case. According to Dunitz and Orgel[7] copper ions on 8a site cause such distortion that the axial ratio is less than one. Therefore the distortion in the chromium rich specimen will be due to copper ions on 8a site.

From Figs. 14 and 16 it is obvious that there is no distortion with $c/a>1$ for $x>0.2$ and no distortion with $c/a<1$ for $x<0.65$. That is to say, for the bulk distortion with $c/a>1$ it is required that 16d site is occupied by copper ions more than 0.8. On the other hand for the distortion with $c/a<1$ it is required that 8a site is occupied by copper ions more than 0.65.

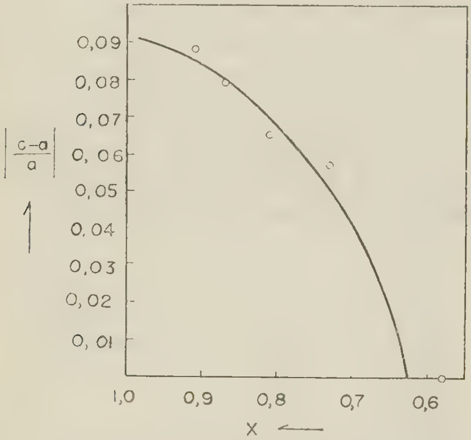

Fig. 16. The variation of tetragonality with cation distribution parameter for chromium rich copper ferrite-chromite.

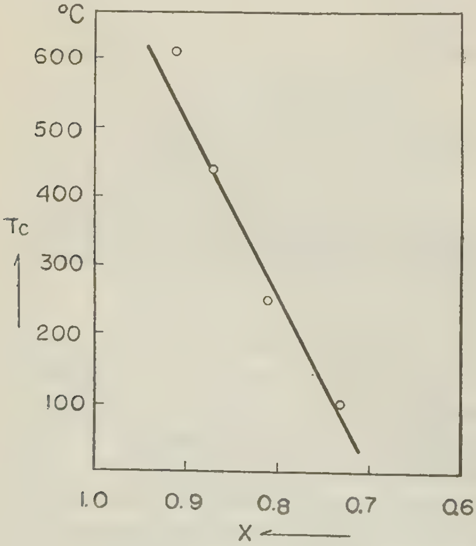

Fig. 17. The variation of critical temperature with cation distribution parameter for chromium rich copper ferrite-chromite.

Delorme[24] examined in detail lattice distortions of the series A) $Cu_{1-x}Ni_xFe_2O_4$, B) $Cu_{1-x}Mg_xFe_2O_4$, C) $Cu_{1-x}Co_xFe_2O_4$ and D) $Cu_xZn_{1-x}Cr_2O_4$. According to his experiment maximum values of x above which distortion with $c/a>1$ no longer takes place are 0.35, 0.275 and 0.25 for the series A), B) and C), respectively. For the series D) minimum value of x below which distortion with $c/a<1$ no longer takes place is 0.55. He did not determined the copper ion distribution in all these series. From the consideration of crystal energy and experimental results it will be able to consider that almost all copper ions situate on 16d site for the series A), B) and C); and on 8a site for the series D)[23]. Comparing our results with those by Delorme, minimum values for the distortion of the copper ion fraction on 16d site and 8a site obtained from the series $CuFe_{2-t}Cr_tO_4$ are greater than those obtained from the series A), B), C) and D). This means that in the present series, $CuFe_{2-t}Cr_tO_4$, more large amount of copper ions on either site, 16d and 8a, is required than in the series A), B), C) and D) for the occurrence of the distortion. According to Dunitz and Orgel the directions of distortion by copper ions on 8a and 16d sites are opposite and therefore these distortions will be partly compensated. In the series $CuFe_{2-t}Cr_tO_4$ copper ions occupy both sites, 8a and 16d, and this compensation effect will be realized to a certain degree. Therefore, in order that the distortion takes place, larger amount of copper ions is necessary to situate on a specific site for the series $CuFe_{2-t}Cr_tO_4$ than for the series where copper ions situate only in either site, 8a or 16d.

Similarly, the smaller values of x for the series B) and C) than those for the series A) will also be explained by the fact that some fraction of cupric ions is situated on 8a site, and the compensation takes place in the two former series.

3. *Co-operative phenomenon*

In the preceding chapter it is shown that the origin of the lattice distortion in the series $CuFe_{2-t}Cr_tO_4$ will be the Jahn-Teller effect of cupric ion Cu^{2+} as suggested by Dunitz and Orgel[7]. In order to explain the observed bulk distortion some statistical treatments are required. Finch, Sinha and Sinha[8] have investigated this problem and found that the temperature and composition dependences of the lattice distortion are just like as the order-disorder problem of binary alloy. Wojtowicz[9] and Kanamori[10] examined this problem in detail and predicted that this transformation is thermodynamically of the first order.

It is noteworthy to mention that axial ratio drops off with temperature rather sharply at the critical temperature for $CuFe_2O_4$ (Fig. 8), and two phases, tetragonal and cubic structure, are simultaneously found in some cases. Although the detailed discussion of the cooperative mechanism of distortion has not been given here, these facts will support that the transformation is of the first order.

§ 6. Acknowledgements

The authors wish to express their hearty thanks to Prof. Miyahara for continuous encouragement and valuable discussions. They are also much indebted to Dr. Yamadaya for his suggestion about the first order transition and to Dr. Wojtowicz and Dr. Kanamori for sending us their manuscripts prior to publication.

References

1) J. L. Snoek: Rev. Techn. Philips **8** (1946) 359.
2) E. F. Bertaut: J. Phys. et radium **12** (1951) 252.
3) T. Takei: J. Inst. Elect. Eng. Japan **59** (1939) 274.
4) K. Stierstadt: Z. f. Phys. **146** (1956) 169.
5) Ohta, Sakamoto and Miyahara: read at the meeting of the Physical Society of Japan, April 1951. T. Inoue and S. Iida: J. Phys. Soc. Japan **13** (1958) 656.
6) J. B. Goodenough and A. L. Loeb: Phys. Rev. **98** (1953) 391.
7) J. D. Dunitz and L. E. Orgel: J. Phys. Chem. Solids **3** (1957) 20.
8) G. I. Finch, A. P. B. Sinha and K. P. Sinha: Proc. Roy. Soc. Ser. **A 242** (1957) 28.
9) P. J. Wojtowicz: Phys. Rev. **116** (1960) 32.
10) J. Kanamori: (Private Communication.)
11) H. P. Klug and L. E. Alexander: *X-ray Diffraction Procedures*, John Wiley and Sons, New York, 1954.
12) C. E. Bacon and F. F. Roberts: Act. Cryst. **6** (1953) 57.
13) F. C. Romeijn: Philips Res. Rep. **8** (1953) 304. C. R. Delorme: Compt. rend. **241** (1955) 1588. P. L. Edwards: Bull. Amer. Phys. Soc. **3** (1958) 43.
14) D. S. McClure: J. Phys. Chem. Solids **3** (1957) 311. J. D. Dunitz and L. E. Orgel: ibid. **3** (1957) 318.
15) E. F. Bertaut: Compt. rend. **230** (1950) 213.
16) L. P. Skolnick, S. Kondo and L. R. Lavine: J. Appl. Phys. **29** (1958) 198.
17) G. Dascola: Z. Krist. **100** (1939) 538. B. von Nagy: Z. Phys. **91** (1935) 229.
18) L. G. Paratt and C. F. Hempstead: Phys. Rev. **94** (1954) 1593. C. H. Dauben and D. H. Templeton: Act. Cryst. **8** (1955) 841. D. H. Templeton: Act. Cryst. **8** (1955) 842.
19) E. F. Bertaut et C. Delorme: Compt. rend. **239** (1954) 505.
20) S. Miyahara and H. Ohnishi: J. Phys. Soc. Japan **11** (1956) 1256.
21) H. Ohnishi, T. Teranishi and S. Miyahara: J. Phys. Soc. Japan **14** (1959) 106.
22) L. Néel: Compt. rend. **230** (1950) 190. R. Pauthenet et L. Bochirol: J. Phys. et radium **12** (1951) 249. H. H. Callen, S. E. Harrison and C. J. Kriessman: Phys. Rev. **103** (1956) 861.
23) H. Ohnishi: J. of Faculty of Science, Hokkaido Univ. Ser. II **5** (1959) 187.
24) C. Delorme: Thesis, Grenoble, 1956.

JOURNAL OF THE PHYSICAL SOCIETY OF JAPAN, Vol. 16, No. 1, JANUARY, 1961

Distribution of Interstitials and Vacancies Produced by an Incident Fast Neutron

By Masayuki YOSHIDA

*Japan Atomic Energy Research Institute, Tokaimura, Nakagun, Ibarakien, Japan**

(Received August 11, 1960)

The distribution of the interstitial-vacancy (I–V) pairs produced in such a substance as germanium by successive knock-on is discussed. Calculation of the distribution is performed basing on the formula proposed by Bohr and Seitz and Koehler and applying the Monte-Carlo Method. Ratio of the close I–V pairs to the total I–V pairs produced by an 10^4 eV first knocked-on atom is about 60%. Taking into account the replacement collision, decrease of about 40% in the total number of the I–V pairs is obtained and the ratio becomes 30%. The decrease in the total number reduces the difference between the total number deduced from calculation and that obtained by experiment. The following results are also obtained. The interstitials and vacancies are distributed in several groups. They exist in the region enveloped by a sphere of about from 50 to 100 atomic distances of diameter. There is no tendency that the concentrated damaged region spreads in the incident direction of the first knocked-on atom and that the interstitials distribute in the outer part of the concentrated damaged region.

§ 1. Introduction

By the high energy particle irradiation on solid, atoms are displaced from their normal lattice sites and the physical properties of the solid change. The mechanism of displacement of atoms has been discussed by many researchers and a several kinds of models have been proposed. Interstitial-vacancy pair production, thermal spike¹⁾ and displacement spike²⁾ are representative ones. Not only the thermal spike and displacement spike may bring the concentrated damaged region in solid, but also the I–V pair production would bear a similar region if an incident particle is massive. That is, a first knocked-on atom by an incident fast neutron can have sufficiently large energy to knock-on succesively other stationary atoms and these knocked-on atoms may form the concentrated damaged region. On the other hand, a first knocked-on atom by electron or γ-ray can not have so large energy as to knock-on successively other stationary atoms and the concentration of knocked-on atoms will not occur. The idea of concentrated damaged region has been supported by the experimental results that there are differences in annealing behaviours between neutron- and electron-irradiated copper³⁾,⁴⁾ and of resistivity change of germanium by neutron and γ-ray irradiation⁵⁾,⁶⁾. The concentrated damaged region has also been suggested for deuteron bombardment on gallium-antimonide⁷⁾ and germanium⁸⁾.

Among the above models, assumption for the I–V pair production model is the most reasonable and the model shows straightforwardly the displacement of atoms. If the transfered energy to an atom by an incident particle is so small that, at the most, only one or two atoms are influenced, the I–V pair production model can be applied for it. This may be the case for an electron or γ-ray irradiation. In order to compare the effect of a neutron and an electron irradiation, we had, therefore, better assume the model even for a neutron irradiation.

Here we discuss the distribution of the I–V pairs produced in such a substance as germanium by successive konck-ons, which is calculated basing on the formulas proposed by Bohr⁹⁾ and Seitz and Koehler¹⁰⁾ and applying the Monte-Carlo Method¹¹⁾.

---

* On leave from Ibaraki Branch of Electrical Communication Laboratory, Tokaimura, Nakagun, Ibarakiken, Japan.

§ 2. Assumptions for Calculations

The energy of a primary knocked-on atom produced by a neutron of 2 MeV, which is the average energy of fast neutrons in an atomic reactor, distributes from zero to 10^5 eV.

This energy is consumed by exciting electrons until it decreases to I_c given by[12)]

$$I_c = \frac{M}{m} \frac{I_t}{8}$$

where M and m are mass of an moving atom and an electron respectively and I_t is excitation energy of a valence electron to the conduction band. I_c is then about 1.2×10^4 eV for germanium. Therefore, we may put 10^4 eV for the energy of the first knocked-on atom in the successive collisions.

We assume that the screened interaction potential is expressed by

$$\frac{Z^2 e^2}{r} \exp(-r/a)$$

where Z is the atomic number of the nucleus, e is the electronic charge, r is the distance of the moving and the stationary atom and a is screening constant given by $a_h/Z^{1/3}$ in which a_h is the Bohr radius of the hydrogen atom.

If the screening constant a is larger than the de Broglie's wave length $\lambdabar$ of the moving atom but is smaller than the classical distance of closest approach b in Coulomb interaction, the collision can be treated by hard sphere collision in classical mechanical method. b and $\lambdabar$ are given by

$$\frac{(Ze)^2}{b} = \frac{\mu V^2}{2}$$

and

$$\lambdabar = \hbar/\mu V$$

respectively where μ is the reduced mass of the two particles, V is the relative velocity before collision and $\hbar$ is the Plank's constant devided by 2π. a, b and $\lambdabar$ for a moving germanium atom with an energy of 10^4 eV are $a = 0.17$ Å, $b = 3.0$ Å and $\lambdabar = 0.0001$ Å. Thus the conditions for hard sphere collision

$$a > \lambdabar$$
$$b > a$$

are satisfied. Even if the energy of the moving atom decreases to 10 eV the above conditions are satisfied. We can, therefore, treat all of the collisions following the primary knock-on as the hard sphere collision which gives isotropic scattering in the center of gravity system.

We assume in addition that the atoms in a solid in question distribute randomly. We shall take no account of crystal structure of the solid. The assumption may be correct as the approximation. Then, the free path of the moving atom in the solid can be given by exponential distribution.

Threshold energy E_d for displacement of atoms from normal lattice sites by collision has been measured and calculated by many researchers[13)] for germanium, silicon and copper. We adopt $E_d = 25$ eV and assume that the probability of the displacement changes abruptly from zero to unity as the energy received by the struck atom passes through the value E_d. Influence of the relation between the probability and the received energy upon total displacement cross section has been discussed by Corbett et al.[4)], and they concluded that it is not so large. The above assumption for the threshold energy means that there is a cylindrical potential well around the collision site, depth of which is E_d. The energy E_d of the total energy received by the struck atom must be consumed by climbing up the well and the rest will become the kinetic energy of the struck atom, which we use to calculate the mean free path. If the received energy is smaller than E_d, the struck atom will suffer several times of collision at the bottom of the well and will return to the original site. After the atom climbs up the well, it never falls down to the original site. Although the radius of the cylinder is not certain, it may be two or three atomic distances. It is neglected in the calculation of free path.

§ 3. Calculations

In the following section, suffix i indicates the value after the ith collision and a prime indicates the value for the struck atom. $i=1$ corresponds to the first knocked-on by a fast neutron. ξ is a uniformly distributing random number from zero to unity and adopted from the IBM library[14)].

In Fig. 1 a vector $\vec{l_i}$ corresponds to a free path between ith and $i+1$th collision. Components $x_{i,i-1}$, $y_{i,i-1}$ and $z_{i,i-1}$ of the vector $\vec{l_i}$ in the Cartesian co-ordinates X_{i-1}, Y_{i-1} and

Z_{i-1} are shown, where Z_{i-1} axis consists with incident direction of a moving atom, or $\vec{l}_{i-1}$, and X_{i-1} and Y_{i-1} axes are decided from $i=2$ collision as shown later. The components in the spherical co-ordinates l_i, θ_i and φ_i are also shown. The components $x_{i,i}$, $y_{i,i}$ and $z_{i,i}$ of $\vec{l}_i$ in the Cartesian co-ordinates X_i, Y_i and Z_i, where Z_i axis consists with $\vec{l}_i$ and Z_{i-1}, Z_i and Y_i axes are in the same plane, are $(0\ 0\ l_i)$.

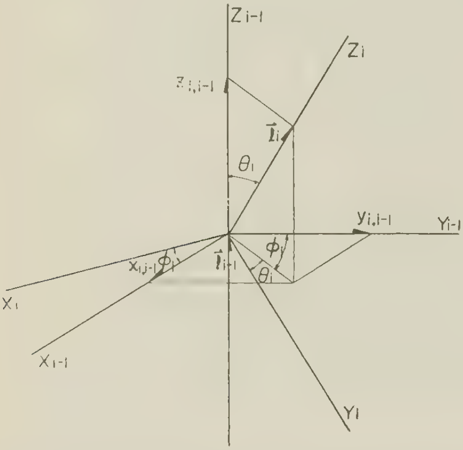

Fig. 1. Vectors $\vec{l}_{i-1}$ and $\vec{l}_i$, the directions and magnitudes of the moving atom before and after collision, in the Cartesian co-ordinates.

As the collision can be regarded as isotropic, the probability that the energy of a moving atom after ith collision is in the range of E_i and E_i+dE_i is given by

$$f(E_i)dE_i=dE_i/E_{i-1}\ .$$

Then E_i is given by

$$E_i=\xi E_{i-1}\ .$$

As the free paths have an exponential distribution, the probability that free path of a moving atom with energy E_i is in the range of l_i and l_i+dl_i is given by

$$f(l_i)dl_i=\frac{1}{\lambda_i}\exp(-l_i/\lambda_i)dl_i\ .$$

Then l_i is given by[11]

$$l_i=-\lambda_i\log\xi\ ,$$

where λ_i is the mean free path and given by

$$\lambda_i=1/n_0\pi R_i^2$$

and

$$E_i=\frac{(Ze)^2}{R_i}\exp(-R_i/a) \qquad (1)$$

in which n_0 is the number of atoms in unit volume.

For a struck atom the energy after displacement from normal lattice site must be $E_i'-E_d$ and this value is used instead of E_i in (1).

As the energy and momentum are conserved, the deflection angle θ_i and θ_i' of the moving and struck atoms after ith collision from the incident direction of the moving atoms are given by

$$\theta_i=\mathrm{Cos}^{-1}\sqrt{E_i/E_{i-1}}$$

and

$$\theta_i'=-\mathrm{Cos}^{-1}\sqrt{E_i'/E_{i-1}}\ .$$

Minus sign in θ_i' corresponds to the fact that θ_i and θ_i' are in the opposite directions with regards to Z_{i-1} axis taking $\varphi_i=\varphi_i'$.

As φ_i is an optional value from zero to 2π, it is given by

$$\varphi_i=2\pi\xi\ .$$

In the above calculations, l_i, θ_i, ϕ_i and their primed values are given.

In the next calculations there are no differences in the primed and non-primed values. The relation between $x_{i,i-1}$, $y_{i,i-1}$, $z_{i,i-1}$ and l_i, θ_i, φ_i is given by

$$\begin{bmatrix} x_{i,i-1} \\ y_{i,i-1} \\ z_{i,i-1} \end{bmatrix}=\begin{bmatrix} \cos\varphi_i & \cos\theta_i\sin\varphi_i & \sin\theta_i\sin\varphi_i \\ -\sin\varphi_i & \cos\theta_i\cos\varphi_i & \sin\theta_i\cos\varphi_i \\ 0 & -\sin\theta_i & \cos\theta_i \end{bmatrix}\begin{bmatrix} 0 \\ 0 \\ l_i \end{bmatrix}$$

$$=[A_i]\begin{bmatrix} 0 \\ 0 \\ l_i \end{bmatrix}.$$

If the relation between $x_{i,i-1}$, $y_{i,i-1}$, $z_{i,i-1}$ and $x_{i,1}$, $y_{i,1}$, $z_{i,1}$, the components of $\vec{l}_i$ in the basic Cartesian co-ordinates, is given by

$$\begin{bmatrix} x_{i,1} \\ y_{i,1} \\ z_{i,1} \end{bmatrix}=[B_{i-1}]\begin{bmatrix} x_{i,i-1} \\ y_{i,i-1} \\ z_{i,i-1} \end{bmatrix},$$

the vector $\vec{l_i}$ is expressed in the basic Cartesian co-ordinates by

$$\begin{bmatrix} x_{i,1} \\ y_{i,1} \\ z_{i,1} \end{bmatrix} = [B_{i-1}][A_i]\begin{bmatrix} 0 \\ 0 \\ l_i \end{bmatrix} . \qquad (2)$$

By putting

$$[B_i]=[B_{i-1}][A_i] \, , \qquad (3)$$

(2) becomes

$$\begin{bmatrix} x_{i,1} \\ y_{i,1} \\ z_{i,1} \end{bmatrix} = [B_i]\begin{bmatrix} 0 \\ 0 \\ l_i \end{bmatrix} .$$

As we choose the Cartesian co-ordinates X_1, Y_1 and Z_1, where Z_1 axis consists with the direction of $\vec{l_1}$, to be the basic Cartesian co-ordinates, $[B_1]$ is given by

$$[B_1]=\begin{bmatrix} 1 & 0 & 0 \\ 0 & 1 & 0 \\ 0 & 0 & 1 \end{bmatrix} .$$

And we can find successively $[B_i]$ by (3). As X_1 and Y_1 axes of the basic Cartesian co-ordinates are optional, it is convenient to choose the direction decided by φ_2 to be X_1 and Y_1 axes.

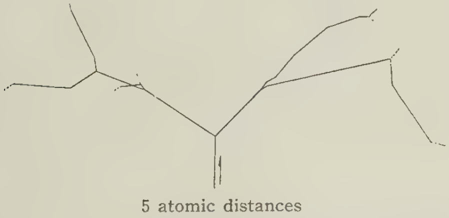

Fig. 2. Y–Z components of 480 eV branch of 10^4 eV first knocked-on atom. Tracks of knocked-on atoms are shown by full lines. Dotted lines correspond to interstitials and their directions and magnitudes are optional. The cross points of full and dotted lines indicate vacancies.

By the above method, $x_{i,1}$, $y_{i,1}$ and $z_{i,1}$ are calculated until E_i becomes smaller than E_d. All of the calculations were performed by IBM 650 at the Japan Atomic Energy Research Institute. 480 eV branch of a 10^4 eV primary knocked-on atom is shown in Fig. 2. If the energy of a moving atom is smaller than E_d, (1) does not give a good approximation and the moving atom can not knock-on the stationary atom any more. Its mean free path is smaller than 2 atomic distances according to (1). It collides with stationary atoms several times then it rests there as an interstitial atom. Tracks of interstitial atoms are shown by dotted lines in Fig. 2. The direction and length of dotted lines are optional. In other words, a dotted line shows that there must be an interstitial atom in one or two atomic distances from the cross point of dotted and full line.

§ 4. Discussion

We practiced the above calculations 6 times for the first knocked-on atom of the energy of 10^4 eV. Two typical distributions of the interstitials and the vacancies are shown in Figs. 3 to 6 for X–Z and Y–Z components. In order to emphasize the interstitials and the vacancies, they are expressed by the white and black spots of a diameter of about one atomic distance and are pictured so as to avoid overlapping. Therefore, the positions of the spots do not necessarily indicate the exactly calculated positions and some of the tracks of moving atoms are omitted.

Taking into account of the statistical characteristics of the calculations, the more the number of times of the calculations, the better the result. In our calculations the numbers of collision for one time are 231, 226, 216, 227, 230 and 214 respectively. Snyder and Neufeld[15] have calculated the number of collision for isotropic collision. The number is 225 according to their result if E_1 and E_d are taken to be 10^4 and 25 eV. The results of our practical and their theoretical calculations are in fairly good agreement. We think, therefore, that there is not large error in discussing general situation of the defects produced by the collision from our calculations.

There are four types of collisions near the threshold energy, which include replacement collision[16]. First; The energy of the moving atom after collision is still large and it progresses forward further. The stationary atom receives larger energy than the threshold energy and is displaced from its original lattice site but its kinetic energy after diplacement is smaller than the threshold energy and it can knock-on other stationary atom no further. In this case, one vacancy and one interstitial, or close I–V pair, are produced. Second; The energy of the moving atom becomes smaller than the threshold energy after collision and it can knock-on other atom no further. On the other hand, the stationary atom receives large energy and it can knock-on other stationary atom further after displaced from its original lattice site. The mean free path of the moving atom with energy below 25 eV is below 2 atomic distances as is given by (1) and it is not clear whether the moving atom becomes the interstitial or drops back to the vacant lattice site. In this case one vacancy and one interstitial, or close I–V pair, are produced or only the replacement of the moving and the knocked-on atoms occures. Third; It is the combination of First and Second. Both of the moving and the struck atom can knock-on other atoms no further. Close I–V pair and one interstitial or one interstitial are produced. Fourth; Even if the energy of the moving atom is larger than E_a, it can happen that it does not give a sufficient value of energy to the stationory atom

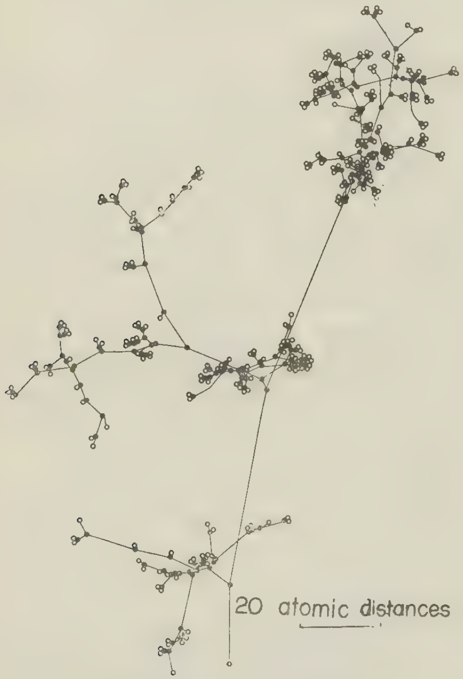

X-Z components of 1st calculation

Fig. 3.

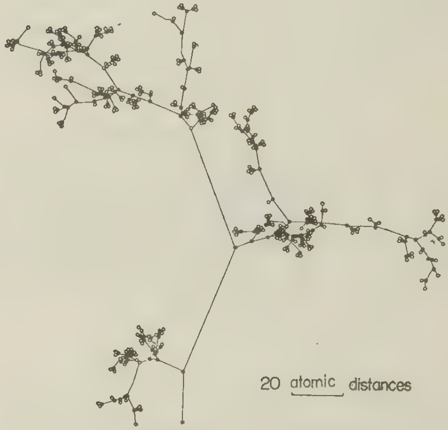

Y-Z components of 1st calculation

Fig. 4.

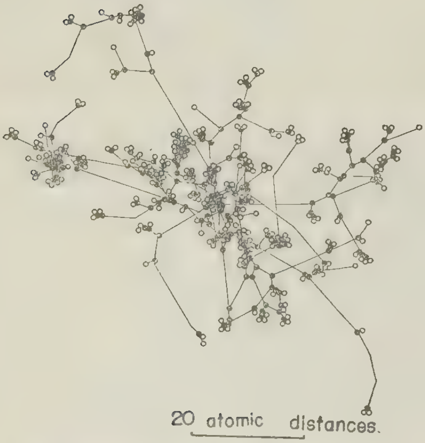

X-Z components of 4th calculation

Fig. 5.

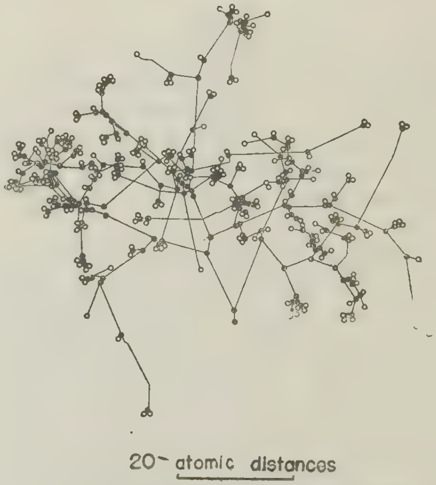

Y-Z components of 4th calculation

Fig. 6.

Figs. 3-6. X-Z and Y-Z components of two typical distributions of interstitials and vacancies are shown. A black spot is a vacancy and a white spot is an interstitial.

Table I.

Time of calculation	1st	2nd	3rd	4th	5th	6th	total	Notice
First Ⅰ	41	43	46	33	35	39	237	close I–V pair
Second Ⅱ	31	39	34	37	47	38	226	close I–V pair or nothing
Third Ⅲ	58	42	43	52	51	44	290	close I–V pair and free I or free I
Fourth Ⅳ	43	60	50	53	46	49	301	free I
A	231	226	216	227	230	214	1344	Ⅰ+Ⅱ+2Ⅲ+Ⅳ
B	130	124	123	122	133	121	753	Ⅰ+Ⅱ+Ⅲ
C	0.56	0.55	0.57	0.54	0.58	0.57	0.56	B/A
D	142	145	139	138	132	132	828	Ⅰ+Ⅲ+Ⅳ
E	41	43	46	33	35	39	237	Ⅰ
F	0.28	0.30	0.33	0.24	0.27	0.30	0.29	E/D
G							0.62	D/A

Notice

A: Total number of the I–V pairs assuming all of the moving atoms with energies below 25 eV after collision become interstitials.

B: Number of the close I–V pairs of A.

D: Total number of the I–V pairs assuming all of the moving atoms with energies below 25 eV after collision can not become interstitials.

E: Number of the close I–V pairs of D.

and after a several times of such a collision, it losses most of the energy and becomes the interstitial. In this case the distance of the interstitial and the vacancy is larger as compared with the former three cases. These four cases are listed in Table I. In the above classification we consider the two extreme cases that the close I–V pair is produced and not in Second and Third. We will call them Case 1 and Case 2. The ratios of the number of the close I–V pairs to that of the total I–V pairs are listed in lines C and F in Table I.

Since all of the calculations hitherto proceeded are idealized ones and other process such as annealing are never considered, the results must be compared with irradiation experiments done at liquid helium temperature, where all of the I–V pairs produced by irradiation will be conserved without annealing. The Oak Ridge group find[3] that in copper and aluminium about 40 and 50% of the damage anneal below 60°K respectively. Our calculation is done for germanium but we have not any special consideration upon crystal structure. Our results, therefore, can be applied to copper and aluminium. By our results the ratios of the close I–V pairs to the total I–V pairs are about 60 and 30% for Case 1 and Case 2 respectively.

The method by Snyder and Neufeld has been used to calculate the number of defects produced by irradiation of high energy particles. And it has been found that the calculated number is larger than the experimental number[17]. The number of the I–V pairs in Case 1 corresponds to the above method. There are several reasons that the calculated number is larger than the experimental number. For instance behaviour of the moving atom with energy below 25 eV after collision must be taken into accounts. The decrease of about 40% in the total number of the I–V pairs is seen in Case 2.

Considering the number of the I–V pairs, Case 2 is better than Case 1. The ratio of the close I–V pairs to the total I–V pairs is about 30% in Case 2 and it is 10 and 20% smaller than the annealing ratio of the damage below 60°K for copper and aluminium respectively. The annealing of the damage below 60°K is caused mainly by the close I–V pairs. Discrepancy of 10 and 20% shown above must be caused by the assumptions in § 2 and the fact that the values calculated for germanium are used for other substances.

The following results can be known from Figs. 3 to 6. The interstitials and the vacancies are distributed in several groups. They exist in the concentrated damaged region which is enveloped by a sphere of about from 50 to 100 atomic distances of diameter. There is no tendency that the concentrated damaged region spreads in the incident direction of the first knocked-on atom and that the interstitials distribute in the outer part of the concentrated damaged region.

The concentrated damaged region in germanium may cause energy levels of electrons and holes in a forbidden band due to defects to have band structure. We found⁶⁾ that the energy level of neutron-irradiated germanium has band structure and that of γ-ray irradiated germanium is fairly discrete. The experimental results agree with the idea of the concentrated damaged region.

§ 5. Acknowledgements

The author gratefully acknowledges the discussion with Dr. E. Fujita, Dr. H. Suzuki and Dr. Y. Takagi for his work. The help of IBM group of J. A. E. R. I. for the calculations is also gratefully acknowledged.

References

1) F. Seitz and J. S. Koehler: Solid State Physics Vol. 2, ed. by F. Seitz and D. Turnbull.
2) J. A. Brinkman: J. Appl. Phys. **25** (1954) 961.
3) T. H. Blewitt et al.: J. Appl. Phys. **28** (1957) 639.
4) J. W. Corbett et al.: Phys. Rev. **108** (1957) 954.
5) J. H. Crawford and J. W. Cleland: J. Appl. Phys. **30** (1959) 1204.
6) M. Yoshida: J. Phys. Soc. Japan to be published.
7) U. Gonser and B. Okkerse: Phys. Rev. **109** (1958) 663.
8) F. E. Fujita and U. Gonser: J. Phys. Soc. Japan **13** (1958) 1068.
9) N. Bohr: K. Danske Vidensk. Selsk. Mat. Fys. Medd. **18** (1948) 8.
10) See reference 1.
11) E. Goto and H. Yamada: Nihon Butsurigakkai Shi **9** (1954) 163.
12) G. H. Kinchin and R. S. Pease: Rep. Prog. Phys. **18** (1955) 1.
13) D. T. Eggen and M. J. Laubenstein: Phys. Rev. **91** (1953) 238. J. M. Denney: Phys. Rev. **92** (1953) 531. H. B. Huntington: Phys. Rev. **93** (1954) 1414. W. Kohn: Phys. Rev. **94** (1954) 1409. J. J. Loferski and P. Rappaport: Phys. Rev. **98** (1955) 1861. P. Rappaport and J. J. Loferski: Phys. Rev. **100** (1955) 1261.
14) G. E. Haynam: IBM 650 Library Program, File No. 6-0-017.
15) W. S. Snyder and J. Neufeld: Phys. Rev. **97** (1955) 1636. Also see Reference 1 p. 381.
16) J. Neufeld and W. S. Snyder: Phys. Rev. **99** (1955) 1326.
17) J. S. Koehler, F. Seitz and R. O. Simmons: AEC Report, Tech. Rep. No. 13 AT (11-1)-182 p. 5. Also see Reference 16.

JOURNAL OF THE PHYSICAL SOCIETY OF JAPAN, Vol. 16, JANUARY, 1961

On the Electron Emission From Oxide Coated Cathode Subject to Strong Electric Field

By Chokichiro SHIBATA
Research Division, Nihon Musen, Mitaka, Tokyo

(Received August 12, 1960)

The electron emission from the oxide coated cathode was measured in a wide range of electric field intensity, where a deviation from Shottky effect appears.

The phenomena could be explained by considering the emission increase by avalanche effect in the oxide layer. The calculation of the enhanced emmission current was performed and compared with the measured results.

§ 1. Introduction

When the anode voltage is sufficiently higher than the voltage just enough to draw the thermal saturation current from the cathode, we have the so-called Schottky current given by the following formula[1],

$$i_0 = i_s \exp\left(e^{3/2}\sqrt{E}\,/\kappa T\right), \qquad (1)$$

where e is the electronic charge, E the field intensity and i_s is the thermal saturation current given by Richardson's formula[2]. In the Schottky region, the $\log i_0$ *vs.* $\sqrt{E}$ curve should show a straight line and its gradient gives $e^{3/2}/\kappa T$. It is known that for the oxide coated cathode the gradient is several times larger than the Schottky's theoretical value, but the relation between $\log i_0$ and $\sqrt{E}$ remains to be a straight line[3),4)].

The author has found the fact that, in a very strong electric field such as is encountered in high power magnetrons and klystrons, the electron emission from the oxide coated cathode differs from the formula (1). It was also found that the phenomena is highly dependent upon the structure of the oxide matrix[5].

In this paper, the data measured by the author are presented, which can not be explained by the existing theories. Further, a theoretical formula is derived by considering the avalanche effect in the oxide matrix in order to clarify the mechanism of the anomalous emission.

Measurements of both the resistance of the oxide layer and the electron mean free path in the matrix are described and the results were used for the evaluation of the theoretical formula. The measured values are compared with the calculation from the formula. Both show a fair agreement in tendency.

§ 2. Electron Emission in Strong Electric Field

2.1 *Measuring method and apparatus*

Test tubes were small gap diodes as shown in Fig. 1. The anode consisted of a single tungsten rod 4 mm in diameter to which a radiator was attached for cooling. The cathode was made of a nickel disc 6 mm in diameter.

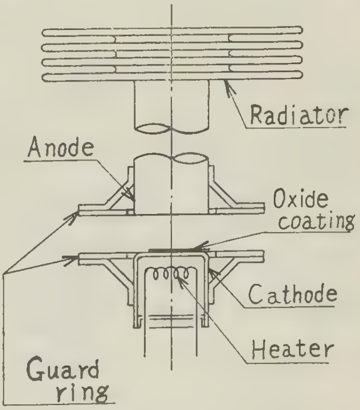

Fig. 1. The construction of the test diode.

In order to reduce the anode loss, the area of the oxide coating was limited to 2 mm in diameter. Guard rings were attached to both the anode and the cathode for making the field uniform. Tubes of the first kind (abridged No. 1) had cathodes of SrBa $(CO_3)_2$ coating, about 50 μ in thickness. Tubes of the second kind (abridged No. 2) were prepared by making treatment on tubes No. 1 after completing all the measurement with them, as follows. Wet hydrogen gas was injected into a tube

No. 1 and the cathode heated in that atomosphere, and then the tube was exhausted and treated in the ordinary ways. After these treatments, the No. 2 cathode is considered to be more sintered and far less porous than the No. 1 cathode. Table I shows an example on the shrinkage of the cathode matrix. The anode currents i were measured for No. 1 and No. 2 cathodes at various temperatures and anode voltages. The measuring circuit is shown in Fig. 2. To avoid the overheating of the anode and the destruction of the cathode matrix by high current, the pulsed measurements were adopted in the high voltage region, while the DC measurements were performed at low voltages (below about 2,000 V), because the pulse modulator was unstable at such low voltages. The pulse width was 1 μs, pulse repetition rate 500 p.p.s. and the duty cycle 5/10000.

Table I.

Sprayed thickness of $BaSr(Co_3)_2$	No. 1 after exhausting treatment	No. 2 after exhausting treatment
100 μ	70 μ	40 μ

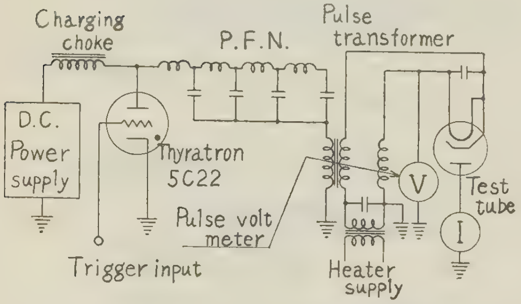

Fig. 2. The circuit for pulse measurement.

2.2 *Experimental results and discussions*

The currents measured at various temperatures for various anode voltages are plotted versus the square root of the field intensity in Fig. 3 and Fig. 4 for No. 1 and No. 2 cathodes respectively. According to the Schottky formula, $\log i$ *vs.* $\sqrt{E}$ curves should show straight lines. However, noticeable deviations are clearly seen in Fig. 3, while the deviations are rather less noticeable for No. 2 cathode as shown in Fig. 4, but in the low field region where DC measurements were carried out, the linearity is well kept excepting in the space charge limited region, as shown in Fig. 5. The dependence of $\log i/T^2$ upon $1/T$ is shown in Fig. 6. As to the Schottky current, this relation should show a straight line, but it seems to be correct only in the low voltage region (DC measurement) as seen in Fig. 6. The gradient of the Schottky line is given by

$$d\log i_0/d\sqrt{E} = e^{3/2}/\kappa T\ . \qquad (2)$$

The measured and computed values of the gradient $d\log i/d\sqrt{E}$ are plotted against $1/T$ in Fig. 7. The lines for DC measurements (weak field) using both No. 1 and No. 2, and for pulsed measurements (strong field) using No. 2 are parallel with the Schottky-theoretical

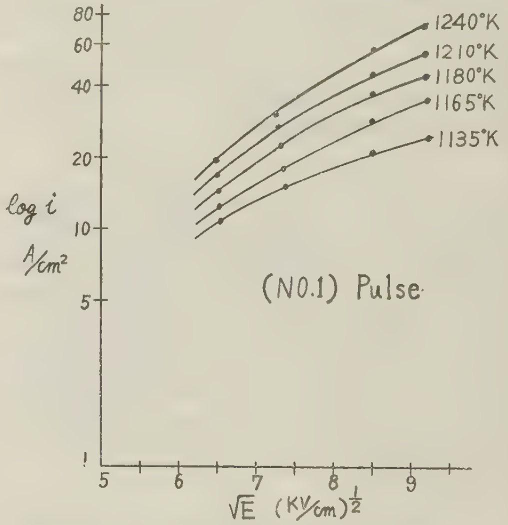

Fig. 3. $\log i$ *vs.* $\sqrt{E}$ for No. 1 cathode.

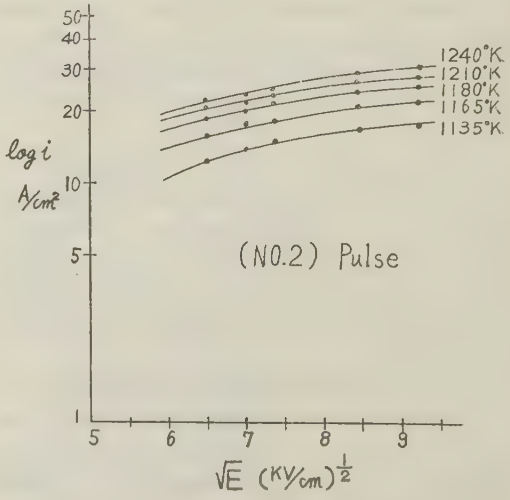

Fig. 4. $\log i$ *vs.* $\sqrt{E}$ for No. 2 cathode.

line, but the line for pulsed emission from No. 1 cathode is far from parallel. From these results, we can see that under very strong field such as of a few ten thousands volts per centimeter, the mechanism of the high emission current from oxide coated cathode differs from the Schottky effect.

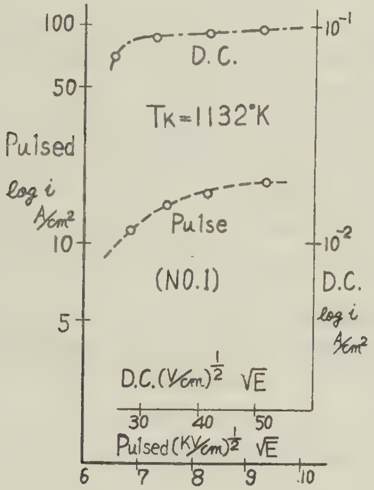

Fig. 5. Comparison between $\log i$ *vs.* $\sqrt{E}$ relations for No. 1 cathode in pulse and *DC* measurements.

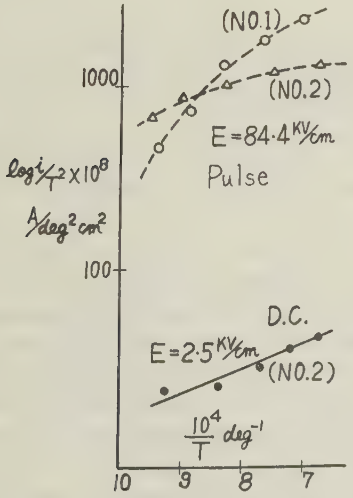

Fig. 6. The temperature dependence of $\log i/T^2$ for No. 1 and No. 2 cathodes.

2.3 *Discussion on the existing theories of the anomalous emission from oxide coated cathode*

There have been published several studies about the anomalous emission from oxide cathode, which deviates from the Schottky effect.

The first is that the deviation has been attributed to the nonuniformity of the electric field at the surface of the cathode caused by the inhomogeneity of the work function of the surface[6]. However, since the partial difference of work function between patches on the cathode surface is no more than a few volts, it will contribute to deviation from a straight line only in the low voltage region. So, it may be put out of consideration in such a very strong field as is associated with our present problem. The second is that the deviation is due to the local high field on the oxide surface, resulting from the ruggedness of the cathode surface[3),4)]. Even if this effect is taken into consideration, since the structure of the cathode surface does not be changed with the temperature the dependency of $\log i/T^2$ upon $1/T$ must remain a straight line.

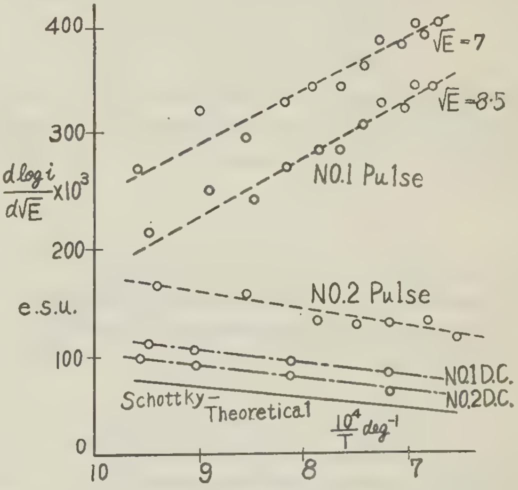

Fig. 7. The temperature dependence of the gradient $d \log i/d\sqrt{E}$.

In the low voltage region this relation seems to be correct, but in the high voltage region and especially in the case of No. 1 cathode, the deviation from a straight line is clearly seen in Fig. 6, and besides, in Fig. 7 the gradient becomes opposite to the Schottky-theoretical line in some cases. Thus, the existing theories do not seem to be able to explain the deviation from the Schottky formula. The author has succeeded in explaining the deviation by considering the electron multiplication in the oxide matrix.

§ 3. Electron Multiplication due to Secondary Emission

3.1 *Possibility of avalanche in the oxide matrix*

Metson has shown that the whole cathode current is thermionically emitted at the cathode core surface and passes vacuum-wise through the pores of the matrix in the temperature range higher than 900°K[7]. An electron which has travelled through the pores without impact and gained a sufficient velocity to emit secondary electrons, will cause secondary electrons at an impact with an oxide particle. The circumstances are very similar to the electron moving between gas molecules, which after travelling some distance makes an impact with gas molecules, ionizes them, and increases the number of electrons[8].

Let n_0 be the initial number of electrons and L the mean free path. The number n which made first impacts between $x=a$ and $x=b$ $(b>a)$ is expressed by

$$n=\int_a^b \frac{n_0}{L}\exp\left(-\frac{x}{L}\right)dx \tag{3}$$

and the number n_1 which make first impacts between $x=a$ and $x=b$ and then travel until $x=d$ $(d>b)$ without impacts is given by

$$n_1=\int_a^b \frac{n_0}{L}\exp\left(-\frac{d}{L}\right)dx\ . \tag{4}$$

In this paper, the theory is constructed in a similar manner to the electron discharge in gas on the basis of the following assumptions in which the author's fundamental concepts are included.

(i) The number of primary electrons emitted at the cathode core is determined by the Schottky current according to the formula (1), depending on the temperature and the field intensity there.

(ii) The electron motion is only in the direction towards the anode.

(iii) The coefficient of secondary electron gain α should vary with the primary electron velocity, but for the simplicity we assume in the following that the gain in zero below a certain value (V_c) of the accelerating voltage and becomes a constant value α when the voltage has reached V_c and remains it afterwards.

(iv) We assume that the electric field in the matrix is uniform, so the field intensity in the matrix is given by

$$E=\frac{V_l}{l}\ ,$$

where l is the thickness of the matrix layer and V_l is the potential of the oxide surface.

(v) The path L_c through which the electron must travel to obtain the accelerating voltage V_c is

$$L_c=\frac{V_c}{V_l}l \tag{5}$$

and the electron velocity corresponding to V_c is given by

$$v_c=\sqrt{\frac{2l}{m}V_c}\ .$$

Electron that makes impact after travelling a path less than L_c is assumed to start from there with zero velocity, without being multiplied.

The electron that has travelled more than L_c will produce α secondary electrons at an impact, which start from there with zero velocity.

3.2 *Enhanced current in the case of* $2L_c>l\geq L_c$

In the case of $L_c>l$ or $V_c>V_l$, the formula (1) can be applied. In this section, the simplest case, when $2L_c>l\geq L_c$ is considered.

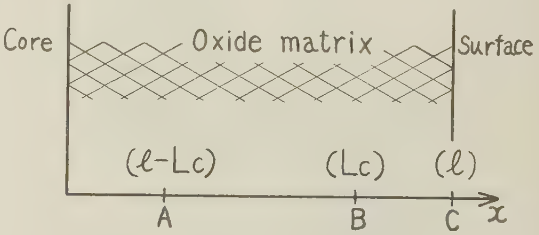

Fig. 8. The section of the cathode.

In Fig. 8, the surface of core metal is denoted by 0 and the surface of oxide matrix by C. Electron can be multiplied by α times at an impact if it is accelerated to more than V_c. After m times repetition of these impacts, the number of electrons will be multiplied by α^m. In the general case, $nL_c>l\geq(n-1)L_c$, m takes values, $1, 2, 3, \cdots (n-1)$. When $n=2$ as in the present case, we have only to consider the case of $m=1$.

Referring to Fig. 8, only the following two groups of electrons are considered for the calculation of α time multiplication.

(a) Electrons which make the first impacts between B and C.

(b) Electrons which make impacts between 0 and A, and next impacts between B and C after having travelled L_c or more.

The currents of electrons of groups (a) and (b) are given by the following formulas

$$i_1=\int_{L_c}^{l}\frac{i_0}{L}\exp\left(-\frac{x_1}{L}\right)dx_1=i_0\left\{\exp\left(-\frac{L_c}{L}\right)-\exp\left(-\frac{l}{L}\right)\right\} \tag{6}$$

and

$$i_2=\int_0^{l-L_c}dx_2\int_{x_2+L_c}^{l}\frac{i_0}{L^2}\exp\left(-\frac{x_1}{L}\right)dx_1=i_0\left\{\exp\left(-\frac{L_c}{L}\right)-\frac{l+L-L_c}{L}\exp\left(-\frac{l}{L}\right)\right\}, \tag{7}$$

where i_0 is the primary current starting from the core surface and is determined by the formula (1). Let the current of the other electrons which can not cause secondary electrons be denoted by i_3. Then we have

$$i_0=i_1+i_2+i_3\ .$$

The observed emission current i_0' is given by

$$i_0'=\alpha(i_1+i_2)+i_3=i_0+(\alpha-1)(i_1+i_2)\ . \tag{8}$$

Using (6) and (7) we get

$$i_0'=i_0[1+(\alpha-1)\{2\exp(-A)-\exp(-B)(2+B-A)\}] \tag{9}$$

where $A=\frac{L_c}{L}=\frac{V_c}{V_l}\frac{l}{L}$, and $B=\frac{l}{L}$.

Substituting $p=\frac{V_c}{V_l}$, we obtain

$$A=pB \qquad \text{or} \qquad p=\frac{L_c}{l} \tag{10}$$

and

$$i_0'=i_0\{1+(\alpha-1)[2\exp(-pB)-\exp(-B)\{2+B(1-p)\}]\}\ . \tag{11}$$

The condition for l is expressed by

$$2>\frac{1}{p}\geq 1\ . \tag{12}$$

3.3 *Theoretical formula of the general case*

The method described in 3.2, can be extended to the general case of $nL_c>l\geq(n-1)L_c$. Substituting $f(x)=\exp(-x/L)$, the current i_m of the electrons which cause α^m time multiplications is given by the expression:

$$i_m=i_0[\textstyle\sum_1(\phi_1(l)+\phi_2(l)+\phi_3(l)+\phi_4(l))+\sum_2(\phi_1(x_1)+\phi_2(x_1)+\phi_3(x_1)+\phi_4(x_1))]\ , \tag{13}$$

where

$$\textstyle\sum_1=\sum_{j_m=1}^{n-m-1}\ \sum_{j_{m-1}=1}^{(n-2)-j_m}\ \sum_{j_{m-2}=1}^{(n-2)-j_{m-1}}\cdots\sum_{j_h=1}^{(n-2)-j_{h+1}}\cdots\sum_{j_1=1}^{(n-2)-j_2}\ , \tag{14}$$

$$\textstyle\sum_2=\sum_{j_m=1}^{(n-m)-(m-1)}\ \sum_{j_{m-1}=1}^{(n-m)-(m-2)-j_m}\ \sum_{j_{m-2}=1}^{(n-m)-(m-3)-(j_m+j_{m-1})}\cdots\sum_{j_h=1}^{(n-m)-(h-1)-\sum_{k=h+1}^{m}j_k}\cdots\sum_{j_1=1}^{(n-m)-\sum_{k=2}^{m}j_k}\ , \tag{15}$$

and

$$\phi_1(x_1)=\int_{j_m L_c}^{l-[(n-1)-j_m]L_c} dx_m \int_{x_m+j_{m-1}L_c}^{l-[(n-1)-(j_m+j_{m-1})]L_c} dx_{m-1}\cdots\int_{x_{h+1}+j_h L_c}^{l-[(n-1)-\sum\limits_{k=h}^{m} j_k]L_c} dx_h\cdots$$
$$\times\int_{x_2+j_1L_c}^{l-[(n-1)-\sum\limits_{k=1}^{m} j_k]L_c}\frac{f(x_1)}{L^m}dx_1\ , \qquad (16)$$

$$\phi_2(x_1)=\int_{0}^{l-(n-1)L_c} dx_{m+1}\int_{x_{m+1}+j_m L_c}^{l-[(n-1)-j_m]L_c} dx_m\cdots\int_{x_{h+1}+j_h L_c}^{l-[(n-1)-\sum\limits_{k=h}^{m} j_k]L_c} dx_h\cdots$$
$$\times\int_{x_2+j_1L_c}^{l-[(n-1)-\sum\limits_{k=1}^{m} j_k]L_c}\frac{f(x_1)}{L^{m+1}}dx_1\ , \qquad (17)$$

$$\phi_3(x_1)=\int_{l-(n-1)L_c+j_mL_c}^{(1+j_m)L_c} dx_m\int_{x_m+j_{m-1}L_c}^{(1+j_m+j_{m-1})L_c} dx_{m-1}\cdots\int_{x_{h+1}+j_hL_c}^{\left(1+\sum\limits_{k=h}^{m} j_k\right)L_c} dx_h\cdots$$
$$\times\int_{x_2+j_1L_c}^{\left(1+\sum\limits_{k=1}^{m} j_k\right)L_c}\frac{f(x_1)}{L^m}dx_1\ , \qquad (18)$$

and

$$\phi_4(x_1)=\int_{l-(n-1)L_c}^{L_c} dx_{m+1}\int_{x_{m+1}+j_mL_c}^{(1+j_m)L_c} dx_m\cdots\int_{x_{h+1}+j_hL_c}^{\left(1+\sum\limits_{k=h}^{m} j_k\right)L_c} dx_h\cdots\int_{x_2+j_1L_c}^{\left(1+\sum\limits_{k=1}^{m} j_k\right)L_c}\frac{f(x_1)}{L^{m+1}}dx_1\ . \qquad (19)$$

$\phi_1(l)$, $\phi_2(l)$, $\phi_3(l)$ and $\phi_4(l)$ in (13) are given by substituting $f(l)$ for $f(x_1)$ in the formulas (16), (17), (18) and (19) respectively.

Using (13), the enhanced current to be observed is given by the formula:

$$i_0'=\sum_{m=1}^{n-1}[i_0+(\alpha^m-1)i_m]\ . \qquad (20)$$

---

§ 4. Measurement of Resistance of Oxide Layer and Estimation of V_l

It is very difficult to directly measure the surface potential V_l of the matrix when a heavy current is passing through it. So we shall attempt to determine the value of V_l at each temperature of the cathode as the product of the resistance and the current passing through the matrix given in Fig. 3 and Fig. 4.

4.1 *Method of measuring resistance*

The measurement of the cathode layer resistance was performed in a similar way to Metson's[8] but the prove was not inserted in the matrix. The construction of the experimental tube is shown in Fig. 9 and the circuital arrangement for measurement of the potential and the current between base cores is shown in Fig. 10. Each heating current was adjusted so as to maintain the temperature of each core at the desired value. First the potential difference V_0 between both cores was observed when no voltage was applied on the oxide layer. Then applying the volt-

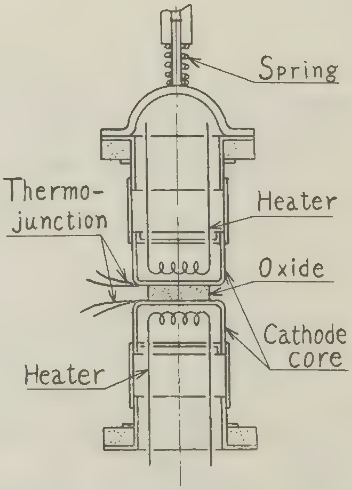

Fig. 9. The construction of the test tube for measuring oxide layer resistance.

age between cores the current was fixed at some value I_1 and the potential difference V_1 between cores was again observed. In measuring the potential difference, attention was paid not to pick up currents through the circuit for measuring the potential difference. The zero method was adopted by making use of potentiometer.

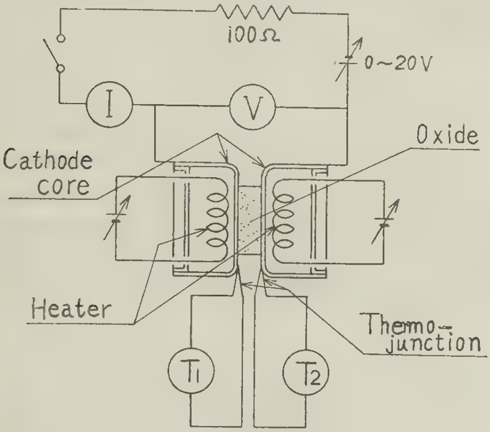

Fig. 10. The circuit for resistance measurement.

The resistance of the oxide layer is then given as follows:

$$R=\frac{1}{I_1}(V_1-V_0)\,. \tag{21}$$

4.2 *Results of measurement*

The value of the oxide layer resistance thus obtained is plotted as a function of $1/T$ as shown in Fig. 11. Using the values of resistance in Fig. 11 and the values of current in Fig. 3 and Fig. 4, the surface potential V_l is estimated as shown in Fig. 12 and Fig. 13. It is seen that V_l is higher than 100 volts in almost the whole range of measurement for No. 1 cathode while it is below 100 volts for No. 2 cathode.

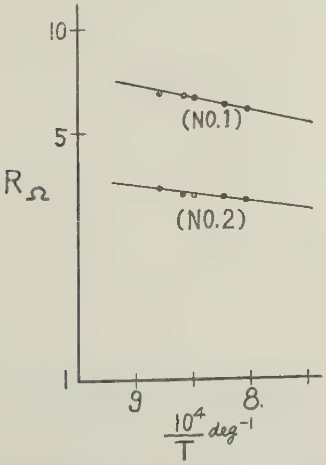

Fig. 11. The temperature dependence of the oxide layer resistance.

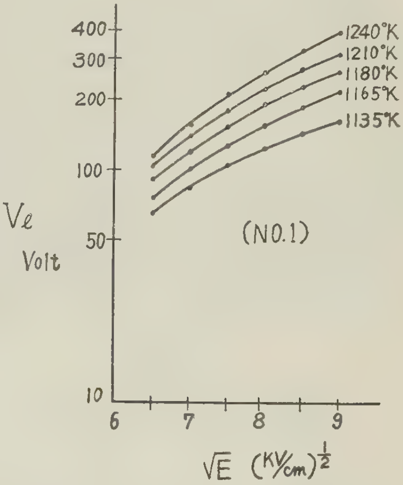

Fig. 12. The temperature dependence of the surface potential for No. 1 cathode.

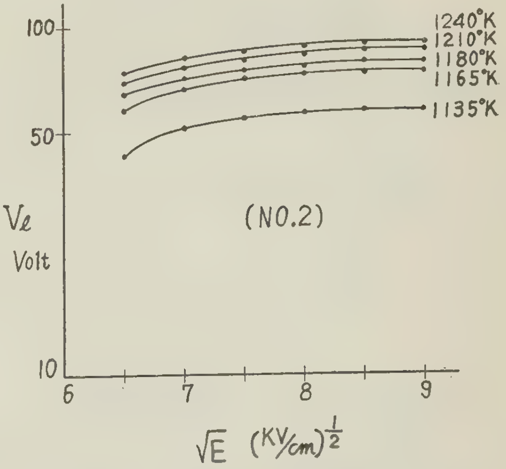

Fig. 13. The temperature dependence of the surface potential for No. 2 cathode.

§ 5. Mean Free Path of Electron in the Oxide Matrix

5.1 *Principle of measurement*

The measurement of the mean free path of electron in the oxide matrix was performed according to the following principle. In Fig. 14, let n_0 be the number of electrons incident on the oxide matrix, then the number of electrons which have passed through the matrix without impacts is given by:

$$n_1 = n_0 \exp\left(-\frac{l}{L}\right).$$

Let the incident electrons have an uniform velocity $v_0 = \sqrt{\frac{2e}{m} V_0}$ and the cathode core be at the potential V_0. If the potential drop of the matrix surface against the core is ΔV_0, the electrons produced at impacts should have velocities less than $\Delta v_0 = \sqrt{\frac{2e}{m} \Delta V_0}$ at the core surface. On the other hand, the electrons which arrive at the base core without impacts should have the velocity v_0. Thus the velocity distribution of electrons at the base core must be as shown in Fig. 15. If a retarding potential is applied to the base core, only those electrons which have velocities sufficient to overcome the retarding potential can arrive at the core. Thus the current versus retarding potential can be represented by a curve as shown in Fig. 16. The current at the zero retarding potential is given by incident electrons corresponding to n_0 and the current at higher voltages near $-V_0$ is equal to i_1 corresponding to n_1. Thus the mean free path L is given by the formula:

$$L = -l \Big/ \log \frac{i_1}{i_0}. \qquad (22)$$

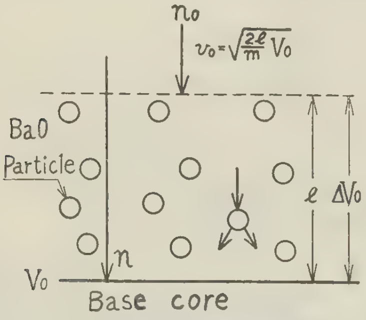

Fig. 14. A schematic representation of electron behaviour in the oxide matrix.

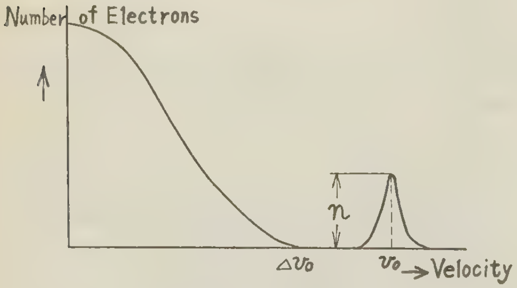

Fig. 15. The velocity distribution of electrons at the core surface.

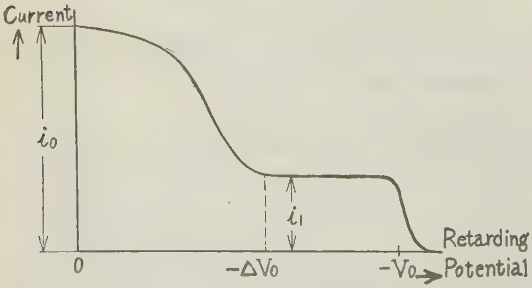

Fig. 16. The current *vs.* retarding potential on the core.

5.2 *Experimental procedure and results*

The measuring arrangement is shown in Fig. 17, where K_1 is the cathode which supplies the primary electrons, A the accelerating grid, B the shielding plate, C the Faraday cage for suppressing stray electrons and K_2 is the cathode on which the oxide matrix to be measured is coated. In Fig. 17, V_0 is fixed at a predetermined value (200 V) and by varying V_1, the potential of K_2 is adjusted to be negative against A. The measured value of the current passing through the matrix is

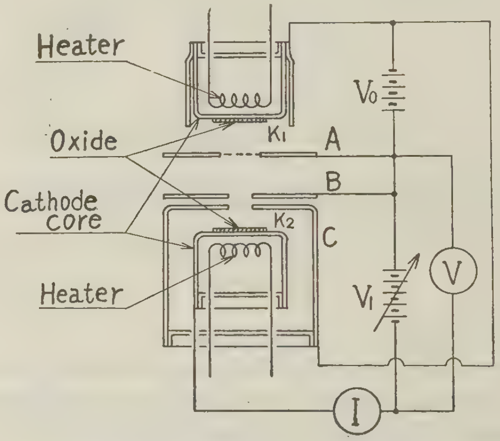

Fig. 17. The construction of the test tube and the arrangement for mean free path measurement.

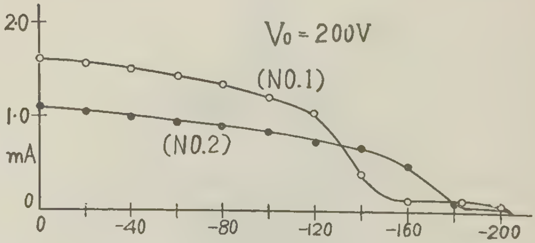

Fig. 18. Measured currents *vs.* retarding potential on the core.

shown in Fig. 18. Using the formula (22) and the values of current in Fig. 18, the values of the mean free path are obtained as shown in Table II.

Though precise reports on the measurement of the mean free path of electron in the oxide matrix have not been reported, it is generally believed that the mean free path is of the order of the size of oxide particles and pores, which is about a few microns. The measured values in Table II seem to be somewhat larger. The reason for it is not clear but the following circumstances must be considered.

Table II.

Cathode	i_1	i_0	$\log i_0/i_1$	l	L
No. 1	0.11mA	1.6mA	3,314	56 μ	20.9 μ
No. 2	0.04mA	1.1mA	2,677	32 μ	9.65 μ

In our measurement, the electrons which make elastic impacts with oxide particles are equivalent to the electrons which make no impacts. So, the mean free path we obtained might have resulted in the larger value. However, such values just fit the fundamental concepts, since the elastic impacts are regarded ineffective.

§ 6. Comparison between Numerical and Experimental Results

Bruining has measured the variation in the coefficient of secondary emission gain α of BaO with the incident electron voltage V_p, which is shown by the solid line in Fig. 19. In order to simplify the calculation, we assume that α is zero under a certain value of V_p (that is, V_c) and is a constant value at and beyond V_c, as approximated by the broken line taking $V_c=100$ volts and $\alpha=4$ in the mean.

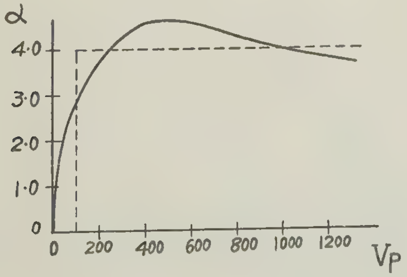

Fig. 19. The secondary emission coefficient *vs.* accelerating voltage.

It can be seen at once from this value of V_c and the values of V_l in Fig. 13 why the avalanche effect is not remarkable for No. 2 cathode. As is seen in Fig. 12, V_l for No. 1 cathode ranges from less than 100 volts to more than 100 volts, but as an approximation the formula (11) is used here for No. 1. First, DC measurements were performed at various cathode temperatures to obtain the thermal saturation currents i_s, which were reduced to the zero field. The i_s *vs.* T curve is shown in Fig. 20. Using the values of i_0 which are obtained by applying the i_s on the formula (1), the enhanced currents i_0' are derived from the formula (11). The curves in Fig. 21 which show the relation between i_0' and $\sqrt{E}$ at various cathode temperatures have a very

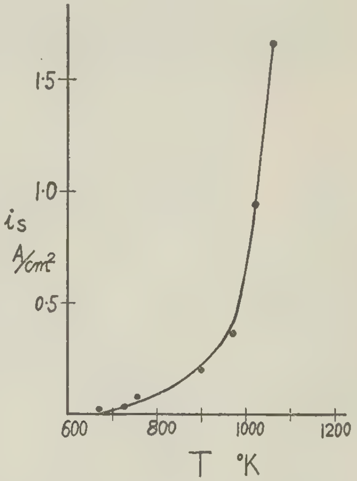

Fig. 20. The temperature dependence of the thermal saturation current.

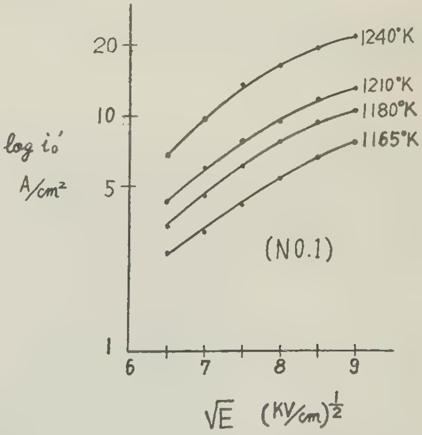

Fig. 21. Computed curves for $\log i_0'$ *vs.* $\sqrt{E}$ for No. 1 cathode.

similar tendency to the curves in Fig. 3. Numerical discrepancies are thought to be due chiefly to the following reasons. First, some approximation procedures were taken in the calculation. Secondly, DC measurements were performed to determine the values of i_s. It is well known that the values by pulsed measurements are often several times larger than the values by DC measurements because of the initial decay of the emission, especially when a pulse of short width is used[4]. The gradient of the curves in Fig. 21, that is $d \log i_0'/d\sqrt{E}$, has been calculated as shown in Fig. 22. These gradients are opposite to the Schottky-theoretical one, and they agree in tendency with the experimental curves for No. 1 in Fig. 7. In the case of No. 2 cathode, since it is so much sintered that the surface potential is very low and the mean free path is also small, the multiplication does not occur and the gradient is similar to the Schottky line.

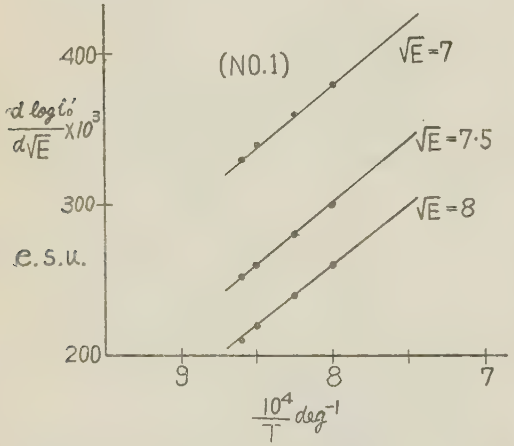

Fig. 22. Computed curves from Fig. 21 for the gradients $d \log i_0'/d\sqrt{E}$ *vs.* $1/T$.

§7. Conclusion

It has been shown that the electron emission current from the oxide coated cathode in the very strong field is enhanced beyond the Schottky effect by the avalanche effect in the oxide matrix. In the temperature range of our measurements, the behaviours of electrons in the oxide matrix are considered as follows.

(i) The primary electrons starting from the core surface are the thermal saturation currents or Schottky currents corresponding to the temperature and the field intensity at that place.

(ii) The electrons moving vacuumwise in the oxide matrix are classified as follows:

(a) The electrons which pass through without impacts or make impacts with oxide particles with velocities less than a critical velocity v_c. These electrons after impacts will start with zero velocity from the positions of impact in the matrix.

(b) The electrons which make impacts after having been accelerated in the matrix to the velocity higher than v_c in the matrix. These electrons will be multiplied α times at each impact, and then they start with zero velocity from the positions of impact.

(iii) The electrons transfered from solid n-type semi-conduction will act to keep the potential constant at each part of the matrix in spite of the electron multiplication. The measured emission current i_0' is the summation of the currents caused by the electrons belonging to (ii)-(a) and (ii)-(b). Since the result of calculation from formula (11) is in fair agreement in tendency with the experimental result, it seems that the above described model can explain the mechanism of the emission in the very strong field.

Acknowledgement

The author wishes to express sincere thanks to Prof. I. Takahashi of Kyoto University, Prof. H. Kawamura of Tokyo University and Prof. S. Mito of Osaka City University for their guidances and discussions. His thanks are also due to Dr. S. Fukagawa, director of our company and Dr. Y. Yasuoka of our laboratory for their encouragements to this work. He is also indebted to Mr. Y. Araki and Mr. H. Okano for their assistances in the measurements.

References

1) W. Schottky: Phys. Z. S. **15** (1914) 872.
2) W. O. Richardson: Proc. Camb. Phil. Soc. **11** (1901) 286.
3) H. Y. Fan: J. App. Phys. **14** (1943) 552.
4) R. L. Sproul: Phys. Rev. **67** (1945) 166.
5) C. Shibata: J. Phys. Soc. Japan **15** (1960) 1124.
6) H. Kawamura, et al.: *Denshi-Hosha to Handotai* (*Electron Emission and Semiconductors*) (Sangyo Tosho Press, Tokyo, 1950).
7) G. H. Metson: I. E. E. No. **239R** (part C) Feb. (1958) 374.
8) L. B. Loeb: *Fundamental Processes of Elec-*

tron Discharge in Gases (John Wiley & Sons. Ins., N. Y., 1939).
9) G. H. Metson: I. E. E. No. **221R** (part C) Feb. (1957) 316.
10) H. Bruinings: *Die Sekundaeremission Fester Koerper* (J. Springer, Berlin, 1941).

JOURNAL OF THE PHYSICAL SOCIETY OF JAPAN Vol. 16, No. 1, JANUARY, 1961

Resistivity Striations in Germanium Single Crystals

By Hiroshi UEDA*
Musashi Works, Hitachi Ltd. Kodaira-machi, Tokyo

(Received August 25, 1960)

Resistivity striations resulting from periodic distribution of impurities have been observed in single crystals of germanium grown horizontally. The period of the striations ranges from 0.1 to 0.6 mm, depending upon growth conditions. It is proportional to the average growth rate and inversely proportional to the temperature gradient within the crystal near the solid-liquid interface. This relation can be explained by assuming the supercooled state in the course of germanium crystal growth by the zone leveling technique. By the repeated supercooling and recovery from it, the crystalization proceeds periodically, resulting in the periodic change of the transient growth rate and the periodic segregation of impurities.

§ 1. Introduction

Periodic resistivity variations have been observed in germanium crystals grown horizontally. Two methods of detecting minute resistivity variations were developed. One is selective electrolytic etching and the other is micro potential scanning. The two methods, when properly correlated, can yield full information about the resistivity variations both qualitatively and quantitatively.

The period of the resistivity striation ranged from 0.1 mm to 0.6 mm, and 30 to 50 per cent resistivity variations are observed. In the case of the vertically pulled crystals this effect was very small.

At first we attributed this effect to outer conditions[1),2)] of crystal growth such as a temperature controller, furnace pulling mechanism, line voltage fluctuations, etc. But the period resulting from these fluctuations do not coincide with that of resistivity striations. Furthermore, we used high power batteries as the power source of the furnace, eliminated the temperature controller, and took special care to get smooth furnace movement. But in spite of these, resistivity striations were still present. So, it was concluded that the cause of these phenomena was purely internal.

Definite relation was shown to exist between the period of the striations, the growth rate and the temperature gradient near the solid-liquid interface. In this paper we show that this relation can be explained by assuming the existence of supercooled state in the crystalizing solid-liquid interface of germanium.

§ 2. Preparation of Samples and Observation of Striations

Germanium single crystals were grown by the zone leveling technique, using intrinsic zone-refined polycrystals and intrinsic seed crystals. For n type, antimony was doped to control the resistivity, ranging from 0.1 to 20 Ω cm. The test bars were cut from zone leveled crystals to include two end surfaces perpendicular to the growth direction, the other surfaces being parallel to the growth direction. All surfaces were lapped by #4,000 carborandum, and a lead wire was soldered,

---

* Present address: Central Research Laboratory, Hitachi, Ltd. Kokubunji, Tokyo, Japan.

Samples were electrolytically etched in 10% KOH solution anodically. The conditions for current density are not critical, 0.1 to 0.3 A/cm², and can be determined by preliminary tests. Etching time ranges from 1 to 2 minutes, and the temperature of electrolyte is about 70°C. An example thus treated is shown in Fig. 1. From Fig. 1 we see that the side surfaces during crystal growth have curved surface. The latter was confirmed as follows. A p-n junction was made by proper doping in the course of crystal growth. In Fig. 2 a p-n boundary is revealed and striation patterns run parallel to the p-n boundary. Fig. 3 shows the interface between the seed crystal and the grown crystal. As in Fig. 2, striations run parallel to the boundary. In this case the seed crystal was made by the Czochralski method, and did not exhibit striations.

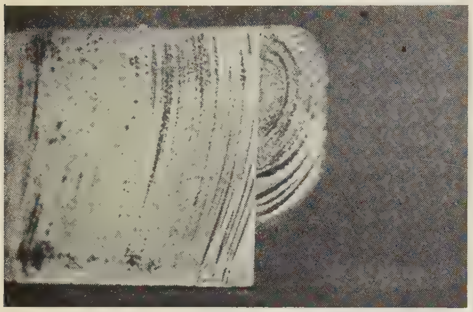

Fig. 1. An *n*-type Ge sample anodically etched in the 10% KOH solution.

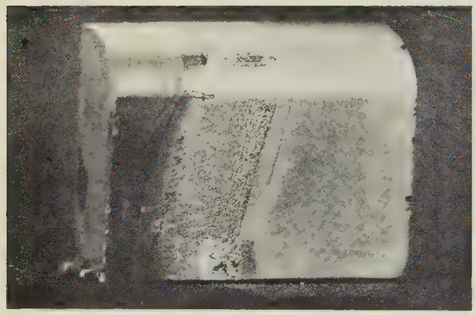

Fig. 2. A *p-n* junction and striations shown by electrolytic etching.

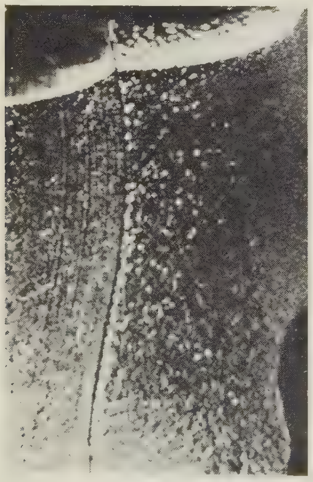

Fig. 3. A solidification line of a zone leveled crystal.

§ 3. The Measurement of Resistivity Striations

Measurements of resistivity of semiconductor are usually carried out by the four probe method[3]. But this method is not adequate to determine the minute resistivity variations in a localized small portion. We used one probe potential scanning method. D. C. voltage was applied across the sample and potential profile was taken by scanning the tungsten probe along the sample, using the micromanipulator. The sample should be in a form of rectangular bar. The bar should be cut so that the long dimension in the direction of scanning should be perpendicular to the equiresistivity planes. These planes can be marked with this electrolytic etching. From the derivatives of the potential profile resistivity can be estimated. Fig. 4 shows an example of resistivity variations in a zone leveled single crystal. In Fig. 4, the arrows indicate the deep etched portions of the same sample. Comparing the period of etched striations with that of resistivity striations, the agreement is very satisfactory.

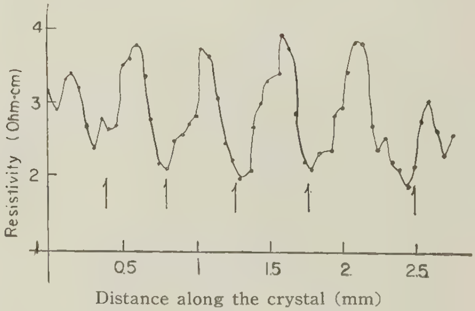

Fig. 4. Resistivity plotted by micro potential scanning. Arrows indicate deep etched portion of the same sample.

§ 4. Resistivity Variations and Growing Conditions

4.1 *Czochralski method versus horizontal zone leveling*

Using the above mentioned two methods, a comparison was made between variations in Czochralski crystals and horizontally grown crystals. It was found that vertically grown crystals showed very small resistivity variations, but in some samples of horizontally pulled crystals variations over 50 per cent were found. A typical result is shown in Fig. 5. As shown in Fig. 3. the Czochralski crystal showed no etched striation pattern.

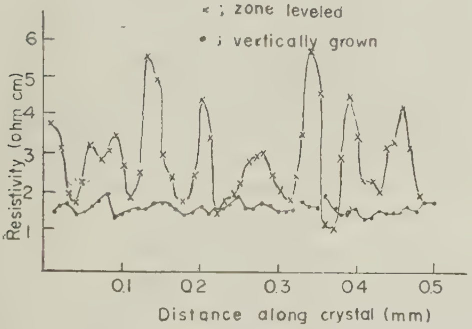

Fig. 5. Resistivity plots, taken from zone leveled germanium and vertically grown crystal.

4.2 *Annealing effects*

If a crystal which has resistivity striations were subjected to heat treatment, a diffusion process would take place and striations would disappear. To confirm this effect, a sample of *n* type 2Ω cm horizontal crystal was annealed at 910°C for 10 hours. The sample which showed about 50% variations at first showed variations much less than 10% after heat treatment.

4.3 *Striations and outer growing conditions*

We thought at first that the striation should be attributed to the fluctuations of the growing conditions such as furnace temperature, rate of pulling, gas atmosphere. We checked carefully above conditions. For instance, we used a high power battery to heat the furnace to eliminate the effect of line voltage fluctuation. Various pulling mechanisms were used, but the striations appeared. To eliminate the effect of atmosphere fluctuation, some crystals were pulled in vacuum. But the striations still appeared.

§ 5. The Period of Resistivity Striations

In the next step, we tried to vary the period of the resistivity striations by changing the growing conditions.

First, we changed the pulling speed of furnace. To drive the zone-leveling furnace, a synchronous motor and oscillator with variable frequency were used. The result is shown in Fig. 6 that the period of the resistivity varies linearly to the pulling speed.

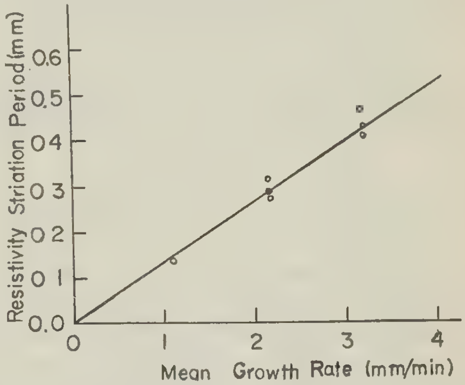

Fig. 6. Relation between striation period and mean growth rate.

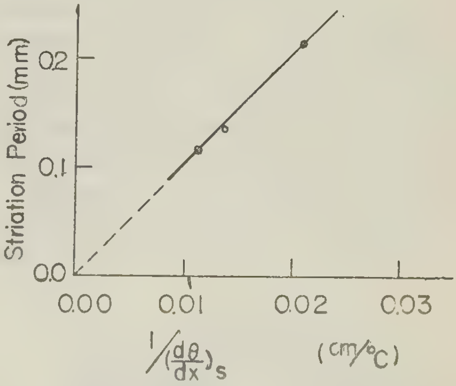

Fig. 7. Relation between striation period and temperature gradient.

Next, we tried to find the relations between the striation period and temperature gradient in the crystal near the solid-liquid interface. The temperature gradient of the furnace was varied by adding either after-heater furnace or after-cooling tube to the main furnace. Three conditions were established which correspond to temperature gradient respectively 47°C/cm, 73°C/cm and 90°C/cm. Striation observations on the crystals thus obtained showed that the periods of the striations are inversely proportional to the temperature gradient. In Fig. 7, a typical result is shown for mean growth rate, $R=1$ mm per minute. Results of the above mentioned two experiments are summarized in the following relation.

$$d=c\frac{R}{(d\theta/dx)_s}\,, \tag{5.1}$$

were

d: period of the resistivity striations (mm)
R: mean growth rate (mm/min)
$(d\theta/dx)_s$: temperature gradient (°C/mm)
c: constant

By selecting units as described, the numerical value of c was about one in our experiments.

§ 6. Discussions

6.1 *Discussion on the causes of the resistivity striations*

As to the possible cause of the resistivity striations we considered that the growth rate of germanium crystal is not uniform, but changes periodically even though the furnace pulling was smooth and uniform.

It is well known that the segregation coefficient between solid and liquid varies with the variation of the growth speed of crystals[4]. So, if there exists a periodic variation of crystal growth speed, there appears a periodic variation in the apparent segregation coefficient, and thus, periodic impurity distribution may result. To explain why periodic variation in growth speed occurs, we considered the effect of supercooling. As will be shown in the next section, definite supercooling degree ΔT°C exists in crystallization of germanium. If germanium melt is cooled slowly enough, it does'nt solidify at its melting point θ_m°C, but supercooling of ΔT°C is required to start solidification. Once solidification begins, the latent heat of fusion is produced and the temperature of melt rises ΔT°C. After reaching the melting point, solidification stops.

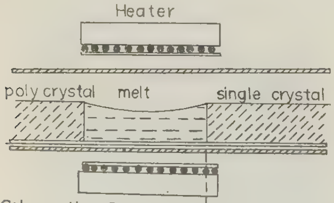

(a) Schematic Configuration

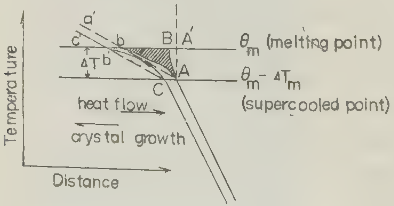

(b) Temperature distribution

Fig. 8. Temperature distributions near the solid-liquid interface in horizontal growing crystal.

Fig. 8(a) and (b) show schematically the single crystal growing in the zone-leveling furnace and the temperature distribution near the solid-liquid interface respectively. In Fig. 8(b), the direction of heat flow is indicated. Temperature distribution a'Aa shows the state in which supercooling reaches its maximum value ΔT_m°C. As the furnace moves to the left, the temperature of the solid-liquid interface falls under this threshold $\theta_m-\Delta T_m$°C, and solidification begins suddenly to the left over the AA' surface and the position of interface moves to the left. The latent heat of fusion being produced, the temperature near the interface rises rapidly and the temperature gradient in the melt decreases. While the temperature of interface reaches the melting point θ_m and the crystal growth stops, heat is accumulated in the melt in front of the solid-liquid interface, and its temperature distribution becomes as shown in a'bBAa in Fig. 8(b). Then the position of the interface is indicated as B of the same figure. This process (recovery from supercooling) is completed in relatively short time, and so the movement of the furnace can be neglected. When the crystal growth stops, the latent heat of fusion is no longer produced, and the heat accumulated in the melt flows to the right through the solid-liquid interface. During this process, the temperature of solid-liquid interface falls gradually, keeping the supercooling state. When the temperature of the interface reaches its limit $\theta_m-\Delta T_m$, the furnace is located to the left by the amount of $AC(=A'B)$. Temperature fall of the interface is mainly caused by the thermal conduction in the ingot and not by the temperature gradient of the furnace. This can be shown by the measured value of the temperature gradient and the growth rate. At the end of this process, the temperature distribution becomes c'Cc as shown in the figure. It is similar to the initial temperature distribution a'Aa. Thus, the same process is repeated periodically and the crystal grows periodically with the period AC.

According to the above consideration, the experimental formula (5.1) can be derived as follows:

$$Q = T\cdot\left(\frac{d\theta}{dx}\right)_s\cdot\kappa\ .$$

Where Q is the heat to be carried away to the solid through the interface,

$(d\theta/dx)_s$ is the temperature gradient in the solid near the interface,

T is the time necessary for the process $\overrightarrow{BC}$,

κ is the thermal conductivity in the solid.

In this expression T means the time necessary for the process $\overrightarrow{BC}$, but process $\overrightarrow{AB}$ is assumed to be very short, so T can be thought to be equal to the time interval of the whole process. As the crystal is growing at the mean speed R, the period of striation is represented by the following relation.

$$d = RT = \frac{QR}{\kappa(d\theta/dx)_s}\ .$$

Thus we obtained the same relation as (5.1). To compare this formula with experiments, the numerical value of Q must be estimated. Q can be considered approximately as the heat accumulated in the volume ΔABb (Fig. 8).

$$Q \doteqdot \rho\cdot C_p\cdot\Delta T/2\cdot\overline{bB}\ .$$

Where ρ is the density

C_p is the specific heat.

As the excess temperature we take the half of the supercooling T and as the bB we take the half of the melt zone length. In our experiment zone length is 4 cm, and ΔT is 30°C as shown in next section. We get

$$Q = 5.5\times0.09\times30/2\times2.0 = 15\ \text{cal/cm}^2\ .$$

The value of κ can be taken as 0.1 watts/cm. deg. near the melting point[5], so we get

$$Q/\kappa = 1.0\ \text{degree min/mm}\ .$$

The agreement with our experiment is very satisfactory.

6.2 *Supercooling of germanium*

To examine the supercooling character of germanium, the following experiments were made. Zone refined germanium was melted in the quartz crucible and cooling curve was determined. Typical curve was shown in Fig. 9. ΔT of this figure is called the supercooling degree. Supercooling degree was measured at the various cooling rate. Fig. 10 shows the relation between ΔT and the cooling rate. In our ordinary zone leveling experiments ΔT can be taken as constant, that is about 30°C.

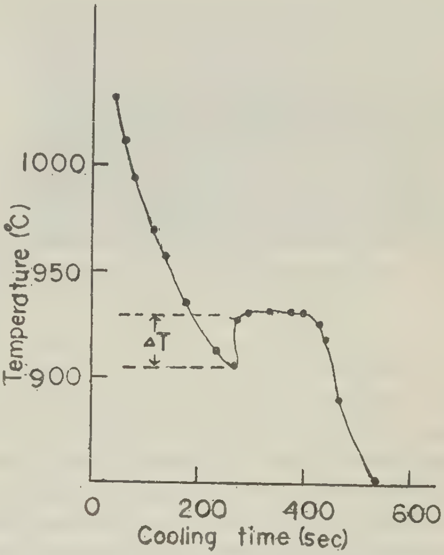

Fig. 9. Typical cooling curve of germanium.

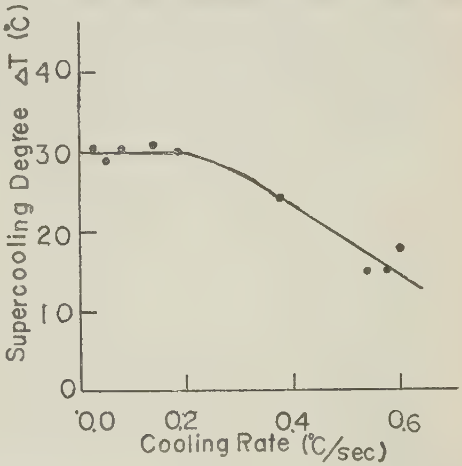

Fig. 10. Supercooling degree and cooling rate.

6.3 *Periodic variation of the melt temperature*

According to the above mentioned mechanism of crystal growth, periodic variation of the melt temperature should exist in the melt in front of the interface. Measurements were made by a temperature recorder of 0.05°C sensitivity[6].

The periodic temperature is shown in Fig. 11. The period of variation coincides with the value determined from the resistivity striations, so this periodic temperature variation can be considered to have the same origin as that of striations.

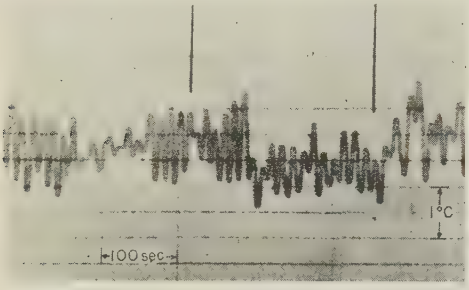

Fig. 11. Temperature variation in the melt during crystalization.

§ 7. Conclusions

Resistivity striations were observed in germanium single crystal grown horizontally. All possible outer fluctuations which should affect the growth conditions were eliminated, but the striations still remained and we attributed the cause of striations to internal phenomena. We tried some experiments to change the period of striations and obtained an experimental formula concerning to the striation period and growing conditions.

As mentioned in the previous sections, the cause of periodic resistivity variations can be explained by assuming that the supercooled state plays an important role in crystal growth, and we derived an equation relating to striation period and growing conditions. We evaluated its numerical value and obtained a good agreement with experimental formula.

§ 8. Acknowledgement

The author wishes to express his sincere thanks to Dr. T. Kikuta and Dr. S. Miyagi for continual encouragement and helpful discussions on the subjects. Thanks are also due to Mr. M. Tomono for suggestions and criticism and to Mr. M. Shoji for many stimulating arguments and several experiments.

References

1) H. E. Bridges, J. H. Scaff, and J. N. Shive: Transistor Technology (D. van Nostrand, 1958) 113.
2) P. R. Camp: J. Appl. Phys. **25** (1954) 459.
3) Reference 1; 265.
4) R. N. Hall: Phys. Rev. **88** (1952) 139.
5) J. Pankove: Rev. Sci. Instr. **30** (1959) 495.
6) Z. Abe, H. Ueda et al: J. Inst. Elect. Eng. Japan **78** (1958) 1064. (in Japanese)

JOURNAL OF THE PHYSICAL SOCIETY OF JAPAN, Vol. 16, No. 1, JANUARY, 1961

X-ray Studies on Precipitation of Metastable Centers in Mixed Crystals $NaCl$-$CdCl_2$

By Kazuo SUZUKI*

Radiation Laboratory, the Electrical Communication Laboratory, Nippon Telegraph and Telephone Public Corporation, Tokai, Ibaraki

(Received August 6, 1960)

Mixed crystals $NaCl$-$CdCl_2$ containing a few mole per cent of $CdCl_2$ were examined by X-ray method. By a certain heat treatment, precipitates of a structure having f.c.c. lattice with lattice constant twice as that of the matrix are formed within the matrix. By another heat treatment, there appear diffuse spots corresponding to the intensity distribution of rods extended to the directions of $<100>$ at odd-order reciprocal-lattice points of the above mentioned structure. Crystal structure of the precipitates, which is identified to be $CdCl_2\cdot 6NaCl$, are determined, and at the same time, main features of the diffuse reflexions are explained on the basis of the structure.

§ 1. Introduction

Preston[1] and Guinier[2], and afterwards many authors[3],[4], reported on characteristic diffuse reflexions in X-ray photographs from single crystals of age-hardening alloys at different stages of the hardening. Some of these reflexions are interpreted in terms of rod-like distributions of intensity weight in reciprocal space, and are ascribed to Guinier-Preston zones, or thin plate-like regions, formed in the matrix by segregation of solute atoms.

In previous X-ray studies of mixed crystals of $NaCl_2$ and $CaCl_2$[5],[6],[7],[8], the present author found that the solid solutions containing a few mole per cent of $CaCl_2$ give diffuse diffraction patterns similar to those observed in certain kinds of age-hardening alloys. The observed patterns could be explained by assuming the formation of plate-like regions in the matrix, into which Ca^{++} ions, Cl^- ions and vacancies segregate in an atomic arrangement similar to the crystal structure of $CaCl_2$.

In the present investigation the mixed crystals $NaCl$-$CdCl_2$ are dealt with by the X-ray method, and in particular, diffuse reflexions similar to those found in the case of $NaCl$-$CaCl_2$ are studied. It is revealed that these diffuse reflexions are due to the precipitation of a compound $CdCl_2\cdot 6NaCl$.

§ 2. Phase Diagram for the $NaCl$-$CdCl_2$ System

Phase diagram for the system $NaCl$-$CdCl_2$ was given by Brand[9] by means of thermal analysis (Fig. 1). In drawing the phase boundaries, he presumed the existence of the compound $CdCl_2\cdot 2NaCl$ from the fact that the mixed crystals containing 33.3 mole per cent of $CdCl_2$ showed the longest plateau in cooling curves. It is to be noticed, however, that the

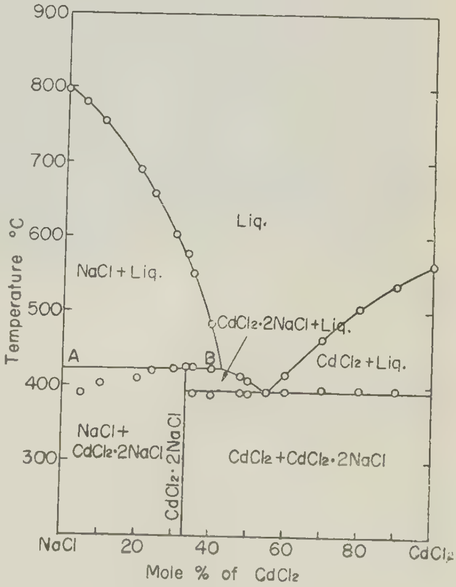

Fig. 1. Phase diagram for $NaCl$-$CdCl_2$ system. (H. Brand)

experimental points indicated by circles in Fig. 1 show a marked deviation from a horizontal boundary *AB* at lower concentrations of $CdCl_2$.

---

* This work was done when the author was in Tokyo Institute of Technology, Oh-Okayama, Meguro, Tokyo.

The present author repeated the cooling-curve measurement for powder mixtures containing 1, 2, 3, 5, 10, 15, 20 and 33.3 mole per cent of $CdCl_2$. Results were in good accordance with those of Brand so far as the measured range of concentrations is concerned, and confirmed again the deviation of the solidus from the horizontal line.

Table I. Intensity change of powder lines in X-ray photographs from mixed crystals $NaCl$-$CdCl_2$ with different concentrations of $CdCl_2$. Indices *hkl* are referred to superstructure, *hk·l* are referred to $CdCl_2 \cdot 2NaCl$.

Mole % of $CdCl_2$	111	800	52·0 43·1	Intensity ratios of 33·0 to 400
1	trace	s	—	0
2	distinct	s	vw	⩽1
3	distinct	s	w	<1
5	distinct	m	m	<1
10	distinct	w	m	~1
15	trace	vw	s	>1
20	trace	vvw	s	>1
33.3	—	—	s	∞

Debye-Scherrer photographs were also taken on the specimens used for the thermal analyses. The photographs are shown in Fig. 2, in which it is seen that two kinds of extra lines gradually appear with increase of the $CdCl_2$ content.

The first kind of extra lines begin to appear from 1 mole per cent concentration of $CdCl_2$, and become most distinct in the region of 2~10 mole per cent concentration of $CdCl_2$, and vanish at near 20 mole per cent $CdCl_2$. The change of the intensity of these lines with the $CdCl_2$ content according to a visual estimation is shown in Fig. 3 (*b*) in an arbitrary scale, and are also listed in Table I. These extra lines can be indexed by half integers such as 1/2, 1/2, 1/2; 3/2, 1/2, 1/2; 5/2, 3/2, 1/2; etc., indicating the fact that they are due to a structure having a superstructre unit

Table II. Lattice spacings of $CdCl_2 \cdot 2NaCl$. Indices are referred to hexagonal lattice.

(*hk·l*)	cal. (Å)	obs. (Å)	(*hk·l*)	cal. (Å)	obs. (Å)
(11·0)	8.5	8.5	(10 1·0) (83·1) (10 0·1)	1.401 1.400 1.382	1.389
(22·0)	4.26	4.33	(84·1) (00·3) (85·0) (81·2)	1.314 1.310 1.299 1.297	1.308
(21·1)	3.21	3.27	(64·2)	1.283	1.281
(33·0) (31·1)	2.84 2.84	2.84	(10 2·1)	1.256	1.251
(32·1)	2.57	2.52	(12 0·0)	1.230	1.232
(52·0) (50·1)	2.36 2.36	2.36	(91·2) (65·2)	1.216	1.217
(43·1)	2.06	2.08	(10 3·1) (83·2)	1.193 1.192	1.199
(71·0) (61·1)	1.955 1.953	1.957	(10 0·2)	1.180	1.175
(20·2)	1.899	1.914	(86·1)	1.159	1.158
(62·1)	1.815	1.791	(84·2)	1.137	1.136
(55·0) (54·1)	1.704 1.703	1.737	(96·0)	1.129	1.127
(80·1)	1.670	1.684	(76·2) (71·3) (12 2·1)	1.090 1.088 1.082	1.088
(82·0) (42·2)	1.610 1.606	1.618	(11 4·1) (10 3·2)	1.057 1.056	1.059
(43·2)	1.527	1.512	(11 5·0)	1.041	1.044
(61·2)	1.480	1.482	(15 0·0) (14 1·1)	0.9838 0.9836	0.9843
(91·1) (65·1)	1.439	1.463			
(66·0) (62·2)	1.420 1.417	1.429			

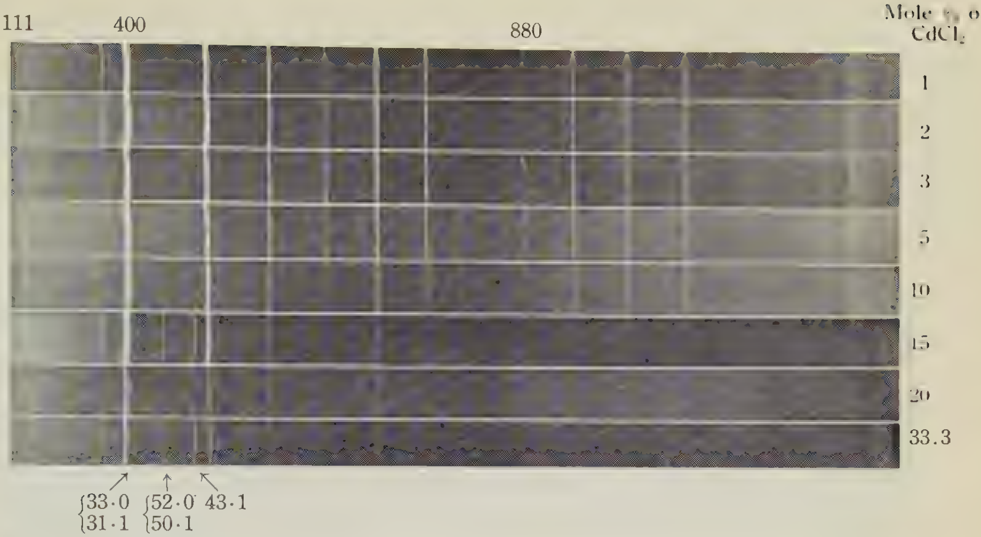

Fig. 2. Series of powder photographs for mixed crystals NaCl-CdCl$_2$ with different contents of CdCl$_2$, which have been cooled slowly to room temperature from the melts. Filtered Cu radiation, 30 kV, 15 mA, 0.5~1 h. Camera radius 5.74 cm.

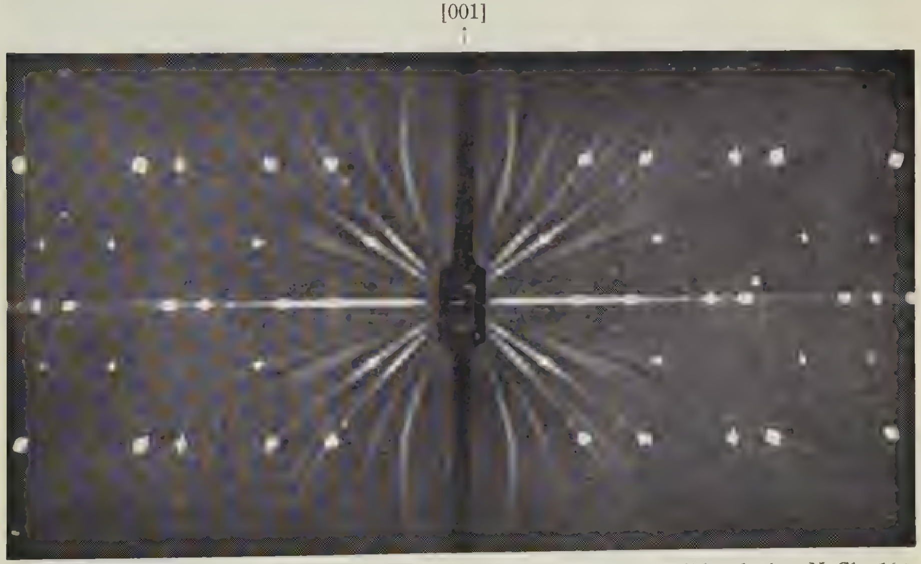

Fig. 4. Rotating-crystal X-ray photograph for a single crystal of solid solution NaCl+1% CdCl$_2$ which has been cooled very slowly to room temperature from 500°C. [001] axis rotation. Filtered Cu radiation, 40 kV, 10 mA, 6 h. Cylindrical film.

cell which is twice as that of NaCl matrix in linear dimension. We shall see later, that these lines are ascribed to the formation of the compound CdCl$_2$·6NaCl, and that this composition is chemically justified.

The second kind of extra lines begin to appear from 2 mole per cent of CdCl$_2$, and become stronger with increase of the CdCl$_2$ content. For 33.3 mole per cent CdCl$_2$, which corresponds to the composition CdCl$_2$:2NaCl, the pattern becomes exclusively composed of this type of lines. Thus, we can presume that the second kind of extra lines are due to the CdCl$_2$·2NaCl compound. These lines can be indexed by assuming a rhombohedral unit cell of dimension $a_0=9.92$Å, $\alpha=118°\ 18'$.* In Table II, the calculated lattice spacings are compared with those observed. The number, n, of chemical units contained in the unit cell can be estimated from the relation $n=\rho v_0/M$, where ρ is the density of the crystal, M the mass of the chemical unit, and v_0 the unit cell volume. For $CdCl_2 \cdot 2NaCl$ samples, ρ is measured to be 3.03, $M(CdCl_2 \cdot 2NaCl)=4.951 \times 10^{-22}$ g and $v_0=3.275\times 10^{-22}$ cm^3. The value of n is then found to be equal to 2.005, which is very close to 2.

---

* By using hexagonal unit cell, the dimension is given by $a_0=17.04$Å, $c_0=3.93$Å, $c_0/a_0=0.231$.

As revealed by the above X-ray studies, we are encountered with the fact contradicting the phase diagram shown in Fig. 1, that three kinds of phases, namely the α-phase or the

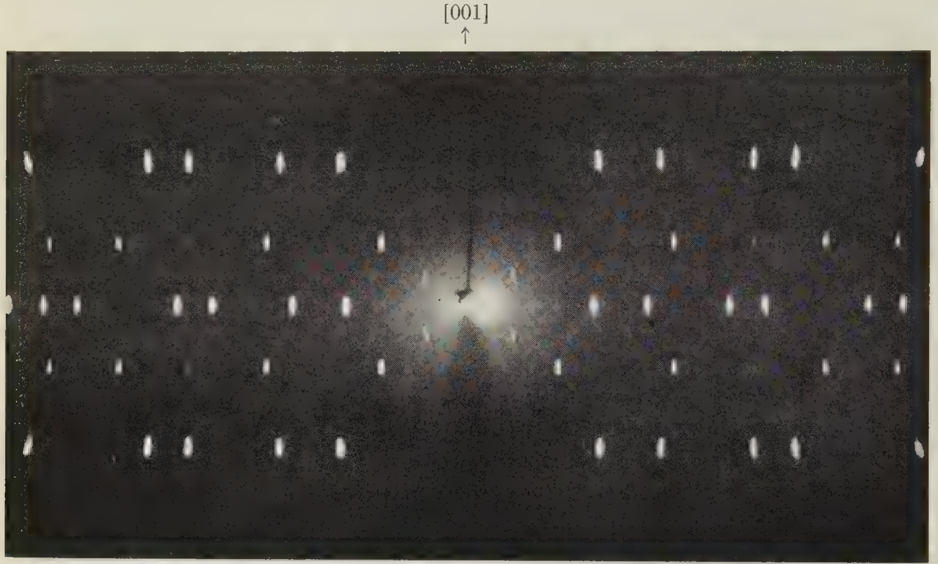

Fig. 5. Rotating-crystal X-ray photograph for a single crystal of solid solution NaCl+1% $CdCl_2$ which has been cooled very slowly to room temperature from 500°C. [001] axis rotation. Monochromatic Cu $K\alpha$ radiation reflected from a LiF single crystal monochromator, 36 kV 15 mA, 30 h. Cylindrical film.

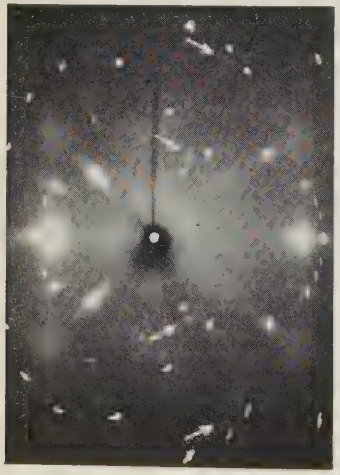

Fig. 6. Stationary-crystal X-ray photograph for a single crystal of solid solution NaCl+1% $CdCl_2$ which has been kept at room temperature for several months after being subjected to heat treatment. [001] axis vertical. $\varphi=19°$. Unfiltered Cu radiation, 36 kV, 15 mA, 5 h. Cylindrical film. Diffuse spots are indicated by arrows.

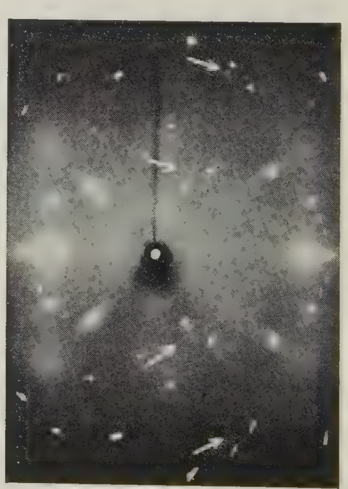

Fig. 7. Stationary-crystal X-ray photograph for a single crystal of solid solution NaCl+1% $CdCl_2$ which has been quenched from 200°C. [001] axis vertical. $\varphi=19°$. Unfiltered Cu radiation, 36 kV, 15 mA, 5 n. Cylindrical film. Diffuse reflexions are indicated by arrows.

NaCl matrix, the $CdCl_2 \cdot 2NaCl$ compound, and the $CdCl_2 \cdot 6NaCl$ compound having superstructure, co-exist at room temperature in the region of the $CdCl_2$ concentration from 2 to 20 mole per cent. This contradiction can, however, be removed by assuming a metastable phase diagram for the formation of $CdCl_2 \cdot 6NaCl$. Fig. 3 (*a*) shows schematically the phase boundaries for the range of low $CdCl_2$ concentrations, by superposing those corresponding to the presumed metastable phase diagram related to the formation of $CdCl_2 \cdot 6NaCl$ on to those of the stable phase diagram related to the formation of $CdCl_2 \cdot 2NaCl$.

If the formation of $CdCl_2 \cdot 2NaCl$ and $CdCl_2 \cdot 6NaCl$ takes place simultaneously by two independent processes according to both of the phase diagrams, the co-existence of the three

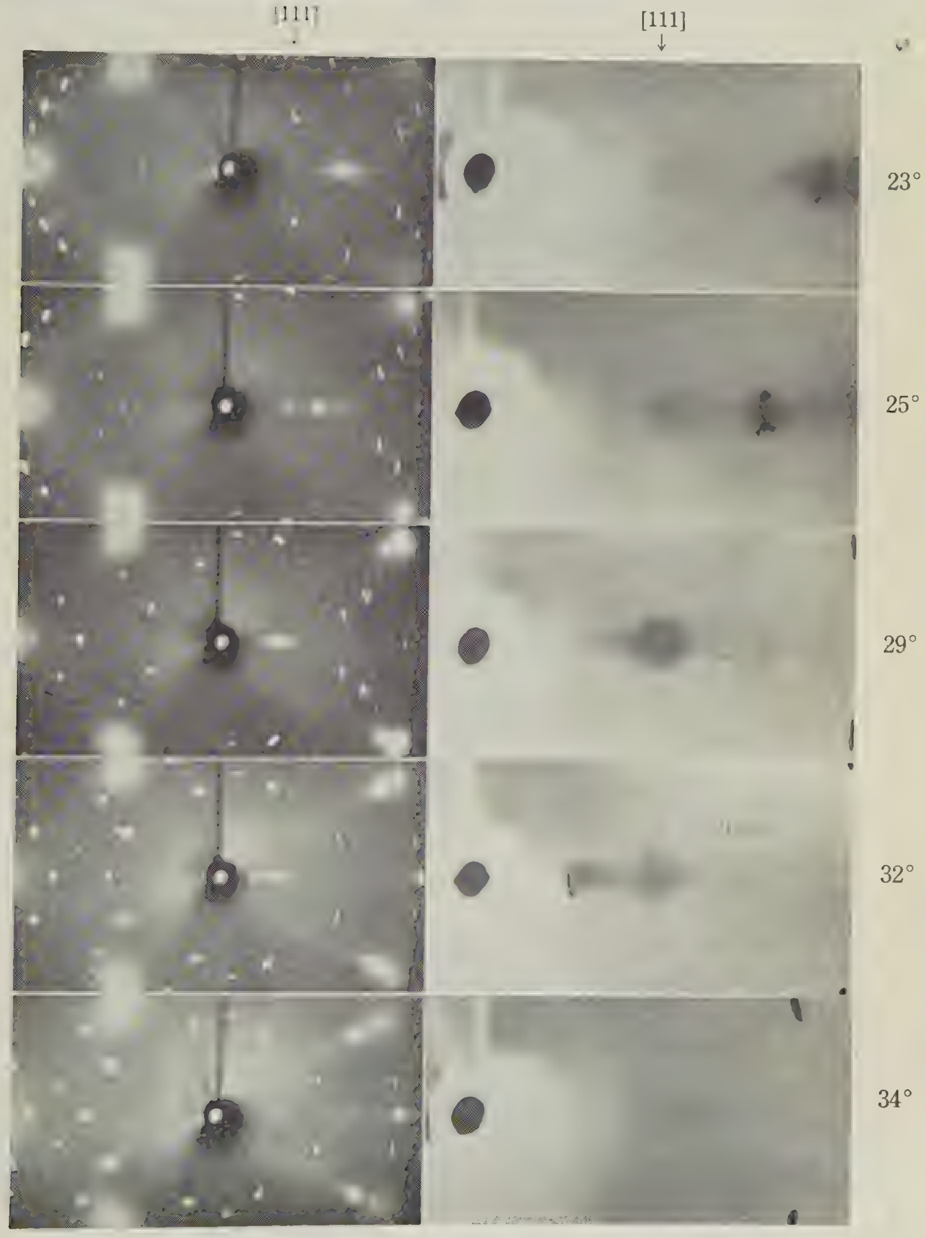

Fig. 8. (*a*) Series of stationary-crystal X-ray photographs for a single crystal of solid solution NaCl+1% $CdCl_2$ which has been quenched from 200°C. Crystal was rotated around [101]. Cylindrical films. (*b*) Negative prints of (*a*), being enlarged from the parts containing diffuse spots.

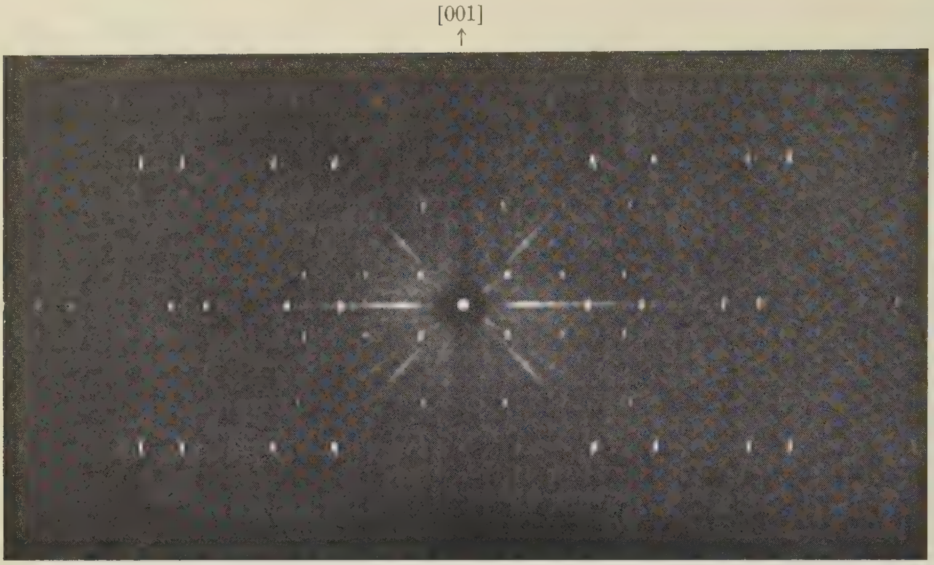

Fig. 9. Rotating-crystal X-ray photograph from $CdCl_2 \cdot 6NaCl$. [001] axis rotation. Filtered Cu radiation, 35 kV, 10 mA, 1 h. Cylindrical film.

kinds of phases may be explained. Further, if we assume that the solidus for the metastable phase diagram lies at lower temperature than that for the stable one, as shown in Fig. 3 (*a*), the observed deviation of the solidius from the horizontal line may be qualitatively understood.

The existence of the phase boundary between α and $\alpha + CdCl_2 \cdot 6NaCl$ is confirmed by the X-ray observations on single crystals described in the next section.

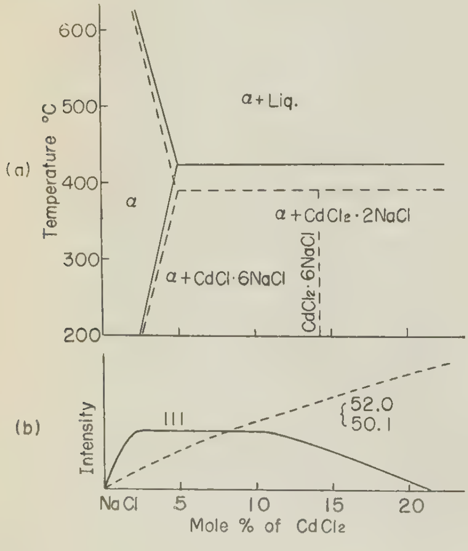

Fig. 3. (*a*) Phase diagram for NaCl-$CdCl_2$ system at lower $CdCl_2$ compositions. (*b*) Relative intensities of powder lines. Intensity is given in arbitrary scale.

§ 3. X-ray Observations on Single Crystals of the Solid Solutions NaCl-$CdCl_2$

a) *Experimentals*

Single crystals of solid solutions NaCl-$CdCl_2$ were prepared from pulverized mixtures of NaCl and $CdCl_2 \cdot 2\frac{1}{2}H_2O$. The molten mixture in a ceramic crucible was kept in an electric furnace at a temperature slightly higher than the melting point for about 1 hour, and then was solidified gradually by moving the crucible to cooler portions in the furnace with a constant velocity (*ca.* 3 mm/h). Single crystals of the size of about 1 cm^3 were easily obtained in this way.

The crystals were transparent when $CdCl_2$ content is less than 1∼2 mole per cent.* The crystals were shaped for X-ray examination by cutting by a razor brade and etching in water.

Heating and quenching of specimens were performed in a small vessel made of thin nickel foil (0.07 mm thickness). The quenching to room temperature after heating at a desired temperature for a desired duration was done by drawing out the vessel from the furnace and placing it immediately on a copper plate at room temperature.

---

* Implication of the percentage is the same as in the case of the mixed crystals NaCl-$CaCl_2$[6].

Stationary-crystal and rotating-crystal X-ray photographs were taken at room temperature, using either unfiltered or nickel filtered Cu radiations, or crystal-monochromated Cu radiations by a LiF single crystal.

b) Precipitation of the CdCl$_2$·6NaCl phase

The diffraction patterns from the single crystal samples change with the heat treatment. In what follows, the observation for the [001] rotation photographs obtained from the solid solution NaCl-CdCl$_2$ containing 1 mole per cent CdCl$_2$ is described for an example.

When the crystal is kept at 500°C and then cooled very slowly to room temperature, weak extra Bragg reflexions appear superposing on the reflexions due to the NaCl matrix, indicating that the precipitation of a new phase has occurred within the matrix at temperatures lower than 500°C. The extra reflexions lie on layer lines intermediate between those due to the NaCl matrix (Fig. 4). By the use of monochromated radiation it was confirmed that the extra reflexions are present also on equatorial, 2nd and 4th layer lines of the NaCl matrix (Fig. 5). All of these reflexions could be indexed by assuming the face-centred cubic lattice with the lattice constant twice as that of the matrix, and it is clear that these superstructure reflexions and the superstructure lines found in Debye-Scherrer photographs (§ 2) are due to the same crystal structure.

When this sample was kept at 500°C for 1 hour and was then quenched to room temperatures, all the extra superstructure reflexions disappeared. When the same sample was reheated at 200°C for 1 hour and was then quenched to room temperatures, the extra superstructure reflexions appeared again, though the superstructure spots were weak and rather diffusive.

Since, as already quoted, the structure giving rise to the superstructure reflexions is identified to be the CdCl$_2$·6NaCl compound, the above observations show the fact that there exists the α-phase, or the uniform solid solution of NaCl-CdCl$_2$, in the range of low CdCl$_2$ concentrations, and that the boundary between the α-phase and the mixed phase of α+CdCl·6NaCl lies between 200°∼500°C for 1 mole per cent concentration of CdCl$_2$. The position of the boundary between α and α+CdCl$_2$·6NaCl is roughly drawn in Fig. 3 (*a*) by considering this experimental result.

c) Diffuse reflexions

In order to study the initial stage of precipitation of the CdCl$_2$·6NaCl phase, stationary-crystal X-ray photographs were taken with unfiltered Cu radiations. Either [001] or [101] axis of the crystal was set vertically, and the angle φ between the horizontal [0$\bar{1}$0] axis and the direction of incident beam was successively changed.

When the sample, having the structure of the homogeneous α-phase formed by a suitable heat treatment, was kept at room temperature for several months, there appear extra superstructure reflexions as shown in Fig. 6. These spots are weak and not well defined, indicating that the sizes of the precipitates are very small.

When this sample is re-heated at 200°C for 1 hour and then quenched to room temperature, the broad reflexions are separated into groups of spots (Fig. 7). This phenomenon is analogous to that occurred in the case of NaCl-CaCl$_2$ mixed crystals[5),6)]. Fig. 8 shows the cases in in which the sphere of reflexion passes near the (111) point.* For $\varphi=23°$, in which the (111) point is inside of the sphere of reflexion, the diffuse spots form a triangle with the apex located at the nearer side of the direct spot, while for $\varphi=34°$, in which the (111) point lies outside of the sphere of reflexion, the apex of the triangle is at the farther side of the direct spot. From the change of the shape of the diffuse spot with φ, the distribution of weights in the reciprocal-lattice space could be determined as follows:

(i) All the odd-order super-reciprocal-lattice points are accompanied with $\langle 100\rangle_r$ rods;**

(ii) Neither even-order super-reciprocal-lattice points, nor main reciprocal-lattice points due to the NaCl matrix, are accompanied with the rods.

The fact (i) shows that, in the matrix, vacancies as well as Cd^{++} ions segregate parallel to {100}, forming thin {100} platelets. The characteristic (ii) will be discussed in § 5.

§ 4. Crystal Structure of CdCl$_2$·6NaCl

The structure determination of the crystal having super unit cell revealed by the above mentioned X-ray observations could be performed on single crystal samples composed of this substance only, which were fortunately obtained as follows.

---

* Indices are referred to super-reciprocal-lattice points.

** As to the meaning of the suffix r, see ref. 6), p. 705.

When the mixture of NaCl containing about 33 mole per cent of $CdCl_2$ was melt in a plutinum crucible and crystallized by the same procedure as described in § 2, almost all parts of the products obtained were polycrystals, but sometimes a few specks of transparent single crystals distinguished by orthorhombic forms of the size of the about $1 \times 1 \times 1\,mm^3$ were found distributing in the polycrystalline parts. It was confirmed by the Laue method, that these single crystals have cubic symmetry. The reflexions in the rotating-crystal X-ray photograph (Fig. 9) could be indexed by assuming f.c.c. lattice with the lattice constant twice as that of NaCl crystal.* The comparison of over-all features of Fig. 9 and Fig. 4 or 5 shows that the single crystals thus obtained and the precipitates in the homogeneous α-phase as described in § 3 are of the same structure.

In taking X-ray photographs, samples were made as thin as possible (*ca.* 0.2 mm in diameter), because of a large absorption of the specimen.* The intensity of the Bragg reflexions was measured using a microphotometer.

By chemical analysis performed on a collected mass (*ca.* 8 mg) of single crystals, it was found that molar concentration of $CdCl_2$ in these single crystals is 13.9 per cent. This value is nearly equal to 14.3 mole per cent, which corresponds to the compound having the composition $CdCl_2 \cdot 6NaCl$.

As the structure of $CdCl_2 \cdot 6NaCl$ has a super unit cell of the NaCl matrix, it is supposed that the main framework of the NaCl matrix is succeeded by the structure of $CdCl_2 \cdot 6NaCl$. It should, however, be assumed for the formation of $CdCl_2 \cdot 6NaCl$ that, when a Na^+ ion in the NaCl matrix is replaced by a divalent Cd^{++} ion, another Na^+ ion should be correspondingly removed from a lattice site, leaving a positive ion vacancy in the matrix, so as to maintain the electrical neutrality of the structure. It is reasonable to assume that the original unit cell volume of NaCl lattice can contain exactly one half the $CdCl_2 \cdot 6NaCl$ chemical unit, when the volumes of each kind of ions and also of the positive ion vacancies are taken into account. As the volume of the super unit cell is eight times as that of the NaCl matrix, it is concluded that the number, n, of the chemical unit $CdCl_2 \cdot 6NaCl$ in the unit cell is four, namely the unit cell in the $CdCl_2 \cdot 6NaCl$ structure must contain 24 Na^+ ions, 4 Cd^{++} ions, 32 Cl^- ions and, besides, 4 positive ion vacancies.

Since the extinction rule of reflexions other than that characteristic of the face-centred cubic lattice has not been observed, the possible space groups are T^2-F23, T_h^3-Fm3, T_d^2-F43m, O^3-F43 and O_h^5-Fm3m. T_d^2-F43m may, however, be discarded because it is hard to find probable positions of 24 Na^+ ions by this space group. The other space groups are identical regarding the positions for which the number of equivalent positions are small, as is expected to be the case for atoms in the present structure. Thus, we can assume without losing generality that the structure of $CdCl_2 \cdot 6NaCl$ belongs to the holohedral cubic space group O_h^5 as similarly as the case of NaCl.

Then, possible positions for the ions in $CdCl_2 \cdot 6NaCl$ are assumed in the following way: Four Cd^{++} ions occupy the sites (4*a*). For 24 Na^+ ions, there are two possibilities, either (24*d*) or (24*e*). However, (24*e*) should be discarded in connection with the positions of Cd^{++} ions. Positions of 32 Cl^- ions are placed at (8*c*) and (24*e*), considering the framework of the NaCl matrix. The positions of vacancies are then determined as (4*b*). Thus, the positions of ions (including those of vacancies) are written as follows:*

$(0, 0, 0;\ 0, \frac{1}{2}, \frac{1}{2};\ \frac{1}{2}, 0, \frac{1}{2};\ \frac{1}{2}, \frac{1}{2}, 0)+$
Cd^{++} : (4*a*) $0, 0, 0;$
vacancy: (4*b*) $\frac{1}{2}, \frac{1}{2}, \frac{1}{2};$
Na^+ : (24*d*) $0, 1/4, 1/4;\ 1/4, 0, 1/4;\ 1/4, 1/4, 0;\ 0, 1/4, 3/4;\ 3/4, 0, 1/4;\ 1/4, 3/4, 0;$
Cl^- : (8*c*), (24*e*) $1/4, 1/4, 1/4;\ 3/4, 3/4, 3/4;\ x, 0, 0;\ 0, x, 0;\ 0, 0, x;\ \bar{x}, 0, 0;\ 0, \bar{x}, 0;\ 0, 0, \bar{x}.$

---

* Some of the low-order reflexions such as 111, 311 etc. show splitted structures due to strong absorption of the sample containing the heavy Cd^{++} ions.

* The sites of vacancies are described here in order to indicate explicitly what Na^+ ions have been removed from the matrix.

Fig. 10 shows the arrangement of ions in the (100) plane of the proposed unit cell, in which the dashed lines indicate the unit cells of the original NaCl matrix. In this structure, Na^+ ions at the centers of the faces of the original NaCl matrix lattice are retained, and Na^+ ions at the corners of the original cells are replaced by Cd^{++} ions and vacancies alternately, forming a face-centred cubic lattice with the unit cell edge, a_0, twice that of the NaCl lattice. All the Cl^- ions are also retained except for small displacements. It is convenient to use in place of x the parameter δ defined by $x=1/4-\delta$, representing the displacement of each Cl^- ion towards the nearest Cd^{++} ion from the original position as illustrated by arrows in Fig. 10.

The intensities, J, of the reflexions of the rotation photograph are given by the following formulae:

$$J=I_0\cdot Q\cdot j\cdot A\cdot V\,, \tag{1}$$

$$Q=C\cdot P\cdot L\cdot|F(hkl)|^2\cdot\exp(-2\mathrm{M})\cdot 1/v_0{}^2\,, \tag{2}$$

$$\begin{aligned}F(hkl)=&\{1+\exp\pi i(h+k)+\exp\pi i(k+l)\\&+\exp\pi i(l+h)\}\times[f_{\mathrm{Cd}}+2f_{\mathrm{Na}}(\exp\tfrac{1}{2}\pi ih\cdot\cos\tfrac{1}{2}\pi k\\&+\exp\tfrac{1}{2}\pi ik\cdot\cos\tfrac{1}{2}\pi l+\exp\tfrac{1}{2}il\cdot\cos\tfrac{1}{2}\pi h)\\&+2f_{\mathrm{Cl}}\{\cos\tfrac{1}{2}\pi(h+k+l)+\cos2\pi hx+\cos2\pi kx\\&+\cos2\pi lx\}]\,.\end{aligned} \tag{3}$$

I_0 is the intensity of the incident X-ray beam, j the multiplicity, A the absorption factor, V the volume of the specimen immersed in the incident beam, C square of the classical e-

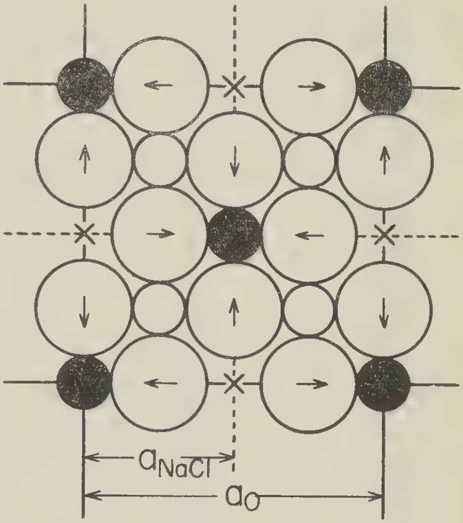

Fig. 10. Arrangement of ions in the (100) plane of the proposed unit cell of $CdCl_2\cdot6NaCl$. Small solid circles are Cd^{++} ions, small open circles Na^+ ions, and large open circles Cl^- ions. Vacancies are shown by crosses. Arrows indicate the displacement of Cl^- ions.

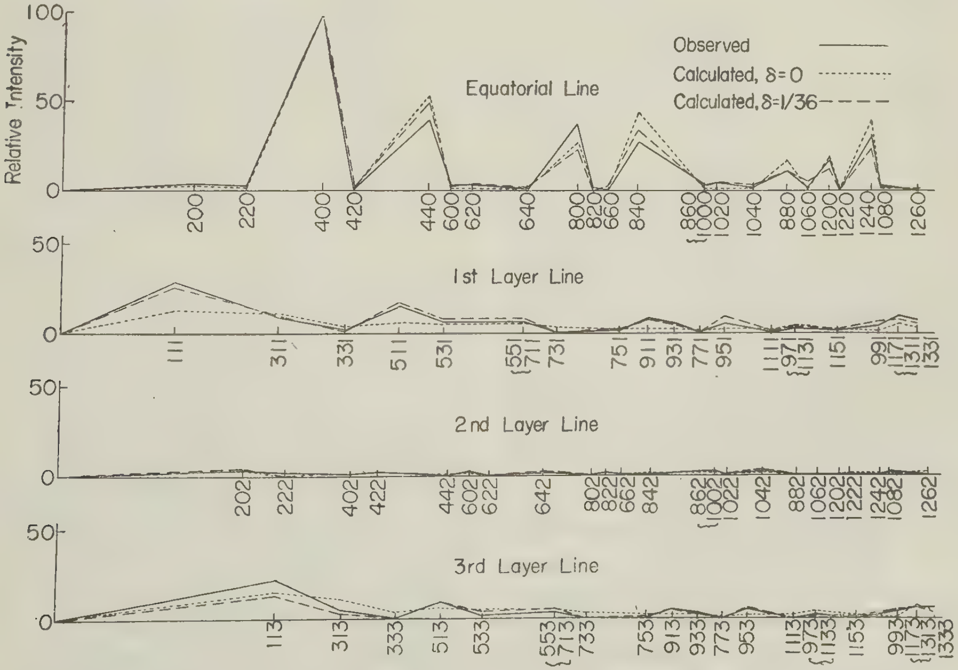

Fig. 11. Comparison of calculated and observed intensities of Bragg reflexions from $CdCl_2\cdot6NaCl$. Intensities are normalized to 400 reflexion.

Table III. Calculated and observed relative intensities of Bragg reflexions from $CdCl_2 \cdot 6NaCl$. Intensities are normalized to 400 reflexion. The asterisks, *, show the reflexions which are coincide with those from NaCl.

hkl	$\delta=0$	$\delta=1/36$	obs.	*hkl*	$\delta=0$	$\delta=1/36$	obs.
200	3	4	4	202	3	4	3
220	2	3	3	222*	0	0	2
400*	100	100	100	402	1	1	1
420	2	2	1	422	2	2	2
440*	53	50	40	442	1	0	0
600	1	2	3	602	1	2	2
620	1	4	3	622*	0	0	0
640	1	2	1	642	1	2	1
800*	27	23	38	802	0	0	0
820	1	0	1	822	1	0	1
660	0	2	0	662*	0	0	0
840*	44	34	27	842	1	0	0
860 1000	1	2	3	862 1002	1	2	2
1020	1	4	4	1022*	0	0	0
1040	1	3	2	1042	1	3	2
880*	17	11	11	882	0	0	0
1060	1	5	2	1062*	0	0	0
1200*	18	12	17	1202	0	0	0
1220	1	0	0	1222	1	0	0
1240*	40	24	31	1242	1	0	0
1080	1	2	3	1082	1	1	2
1260	1	0	0	1262	2	0	0
111	13	26	29	113	15	13	22
311	11	10	9	313	11	3	5
331	4	1	2	333	4	0	0
511	6	17	15	513	6	9	9
531	5	8	6	533	5	4	2
551 711	5	8	6	553 713	5	5	3
731	3	0	0	733	3	0	0
751	2	2	1	753	2	1	0
911	2	7	8	913	2	5	5
931	2	4	5	933	2	2	3
771	1	0	0	773	1	0	0
951	2	9	5	953	2	6	5
1111	2	1	0	1113	2	0	0
971 1131	4	3	2	973 1133	4	1	2
1151	2	2	1	1153	2	1	0
991	1	6	4	993	1	5	4
1171 1311	5	7	9	1173 1313	7	6	6
1331	3	5	7	1333	4	3	6

lectronic radius, P and L the polarization and the Lorentz factors respectively, $\exp(-2M)$ the Debye-Waller temperature factor, v_0 the unit cell volume, and f_{Cd}, f_{Na} and f_{Cl} are the atomic structure factors for Cd^{++}, Na^{+} and Cl^{-} ions, respectively. The absorption factor was obtained from the International Tables[10] by assuming the cylindrical form for the specimen, with $\mu r \sim 3.0$, where μ is the linear absorption coefficient and r the radius of the specimen. The tabulated values of the absorption factors can be applied approximately also to layer lines other than the equator by replacing r by the value $r(1+\sec\psi_n)/2$, where ψ_n is the angle given by the relation $\tan\psi_n = x_n/R$, x_n being the distance from the n-th layer line to the equatorial line, and R the radius of the cylindrical film. Actually, however, the factor $(1+\sec\psi_n)/2$ is almost equal to unity for the 1st, the 2nd and the 3rd layer lines of the present rotation photograph. The factor $\exp(-2M)=\exp\{-2B(\sin\theta/\lambda)^2\}$ was roughly estimated by assuming the characteristic temperature equal to that of pure NaCl, i.e., $\Theta=281°\mathrm{K}$, and the average atomic weight $(CdCl_2 \cdot 6NaCl)/15=35.6$. B thus calculated is 1.23×10^{-16} at room temperature.

Calculated intensities for $\delta=0$ are listed in Table III. In this Table and also in Fig. 11, we can see a fairly good agreement between observed and calculated intensities, although there are a few exceptions, for instance the observed intensities of 511, 911 are too strong, and those of 331, 333 are too weak.

Agreement between the observed and calculated intensities can be improved by assuming a finite value of δ. For example, calculated intensities for $\delta=1/36$ are listed in Table III, and are also shown in Fig. 11. However, the further refinement of the perameter δ is postponed, because of lack of the accuracy of the observed intensities, owing to the large absorption of the samples.

§ 5. Discussions

As is confirmed in the above section, the main skeleton of the NaCl structure is retained in the structure of $CdCl_2 \cdot 6NaCl$ fairly well, being accompanied only with very small displacements of Cl^- ion sites, even though there take place the replacement of Na^+ ions by Cd^{++} ions and the formation of positive ion vacancies. This result suggests that the precipitation of $CdCl_2 \cdot 6NaCl$ may take place in the NaCl matrix with very small activation energy, without producing long range disturbances in the NaCl matrix lattice.

With the knowledge of the unit cell structure of $CdCl_2 \cdot 6NaCl$, we can explain the characteristic features of the $\langle 100 \rangle_r$ rods mentioned in § 3 (*c*), that they appear only at odd-order indices of the super-reciprocal-lattice points, but not at even-order reciprocal-lattice points.

At the early stage of the precipitation, Cd^{++} ions are assumed to segregate in thin plate-like regions, or platelets, parallel to {100} of the matrix lattice, forming there complete or incomplete $CdCl_2 \cdot 6NaCl$ structure.

The structure amplitude, F', due to a platelet contributing to the diffuse scattering is expressed by[6)]

$$F' = S \cdot f', \tag{4}$$

$$f' = -\sum_{\text{cell}} + \sum_{\text{cell}}', \tag{5}$$

$$\sum_{\text{cell}} = \sum_{n} f_n \exp(2\pi i \boldsymbol{h} \cdot \boldsymbol{r}_n),$$

$$\sum_{\text{cell}}' = \sum_{N} f_N' \exp(2\pi i \boldsymbol{h} \cdot \boldsymbol{r}_N), \tag{6}$$

where S is the shape function for the platelet concerned, i.e., it is the sum over all the representative points of the unit cells of the precipitates contained in the platelet. The summations $\sum_{n}$ and $\sum_{N}$ are taken over the lattice points within a unit cell of the precipitates, f_n and $\boldsymbol{r}_n$ are the scattering factor and position vector of the n-th atom in the original matrix lattice respectively, and f_N' and $\boldsymbol{r}_N$ those of the N-th atom in the structure of the precipitate respectively, and $\boldsymbol{h}=(\boldsymbol{s}-\boldsymbol{s}_0)/\lambda$, where $\boldsymbol{s}_0$ and $\boldsymbol{s}$ are the unit vectors of the directions of incident and scattered X-rays respectively, and λ the wave-length of X-rays.

When the unit cell structure of the platelet is assumed to be that of $CdCl_2 \cdot 6NaCl$, (5) is written as

$$\begin{aligned} f' = &\{1+\exp\pi i(h+k)+\exp\pi i(k+l)+\exp\pi i(l+h)\} \\ &\times[-f_{Na}\{1+\exp\pi i(h+k+l)\}+f_{Cd} \\ &+2f_{Cl}\{\cos\tfrac{1}{2}\pi h(1-\cos 2\pi h\delta)+\sin\tfrac{1}{2}\pi h\cdot\sin 2\pi\delta \\ &\quad +\cos\tfrac{1}{2}\pi k(1-\cos 2\pi k\delta)+\sin\tfrac{1}{2}\pi k\cdot\sin 2\pi\delta \\ &\quad +\cos\tfrac{1}{2}\pi l(1-\cos 2\pi l\delta)+\sin\tfrac{1}{2}\pi l\cdot\sin 2\pi\delta\}], \end{aligned} \tag{7}$$

where δ is the same as what appeared in § 4. As was stated in § 4 (Table III, Fig. 11), main features of the structure of $CdCl_2 \cdot 6NaCl$ are represented fairly well by the case of $\delta=0$. Then, (7) reduces simply to

$$\begin{aligned} f' = &\{1+\exp\pi i(h+k)+\exp\pi i(k+l)+\exp\pi i(l+h)\} \\ &\times[-f_{Na}\{1+\exp\pi i(h+k+l)\}+f_{Cd}]. \end{aligned} \tag{8}$$

This expression results in the following relations:

(i) $f'_{odd}=4f_{Cd}$ for odd-order super-reciprocal-lattice points;

(ii) $f'_{even}=4(-2f_{Na}+f_{Cd})$ for even-order reciprocal-lattice points (including both super-reciprocal-lattice points and main reciprocal-lattice points).

Then, we have the relation $f'_{odd} \gg f'_{even}$. The shape function S, which is mainly responsible for the rod-like intensity weight of the diffuse reflexions, is common to all the reciprocal-lattice points, while the intensities of these reflexions near reciprocal-lattice points are mainly determined by the value of f'. Then, by the relation $f'_{odd} \gg f'_{even}$, the observed relative intensities of the $\langle 100 \rangle_r$ rods at reciprocal-

Table IV. Comparison of characteristic features of rods for the mixed crystals NaCl-CdCl$_2$ and NaCl-CaCl$_2$.

Mixed crystals	Types of rods	Reciprocal-lattice points about which rods appear	Symmetry about reciprocal-lattice points
NaCl-CdCl$_2$	$<100>_r$	Superlattice points	Symmetric
NaCl-CaCl$_2$	$<111>_r$ $<310>_r$	Matrix points	Asymmetric

lattice points of odd and even indices can be understood well.

It is interesting to compare the present results concerning the diffuse reflexions with the case of the mixed crystals $NaCl_2$-$CaCl_2$, for which $\langle 111 \rangle_r$ and $\langle 310 \rangle_r$ rods were observed in reciprocal space at an early stage of precipitation. Main features of the rods for these two kinds of mixed crystals are listed in Table IV.

1) From the mixed crystals NaCl-$CdCl_2$, the rods appeared only at super-reciprocal-lattice points and not at the matrix points, while, from NaCl-$CaCl_2$ the rods appeared only at reciprocal-lattice points for the matrix and not at super-reciprocal-lattice points. As has been shown above, the former case is readily explained by the unit cell structure of $CdCl_2 \cdot 6NaCl$. On the other hand, the latter could not be explained by unit cell structure only, and it was necessary to assume the formation of anti-phased platelets in thin regions called the plate-zones[5),6)].

2) The rods in reciprocal space are extended symmetrically about each reciprocal-lattice point in the case of NaCl-$CdCl_2$, and asymmetrically in the case of NaCl-$CaCl_2$. As the asymmetry of rods may be caused by the modulation of lattice spacings in the regions of platelets, the modulation of the spacings in the directions perpendicular to the platelets seems to be more conspicuous in the case of NaCl-$CaCl_2$ than in NaCl-$CdCl_2$. Such a difference may be explained in the following way. In the case of NaCl-$CdCl_2$, the platelets are the products in the initial stage of precipitation of the compound $CdCl_2 \cdot 6NaCl$ which have accidentally the same lattice spacings as NaCl. On the other hand, in the case of NaCl-$CaCl_2$,—especially for the $\langle 310 \rangle_r$ rods,—the platelets are the intermediate products which have grown up in the process of the precipitation of $CaCl_2$ crystal having different crystal structure, and therefore different lattice spacings from the NaCl matrix.

In conclusion, the author wishes to express his sincere thanks to Prof. S. Miyake for his kind guidance and encouragement throughout this work.

References

1) G. D. Preston: Proc. Roy. Soc. **A167** (1938) 526.
2) A. Guinier: Compt. rend. **206** (1938) 1641.
3) C. S. Barrett and A. H. Geisler: J. Appl. Phys. **11** (1940) 733.
4) A. H. Geisler and J. K. Hill: Acta Cryst. **1** (1948) 238.
5) S. Miyake and K. Suzuki: Acta Cryst. **7** (1954) 514.
6) S. Miyake and K. Suzuki: J. Phys. Soc. Japan **9** (1954) 702.
7) K. Suzuki: J. Phys. Soc. Japan **10** (1955) 794.
8) K. Suzuki: J. Phys. Soc. Japan **13** (1958) 179.
9) H. Brand: Neues Jahrb. Min. **32** (1911) 627.
10) *International Tables for the Determination of Crystal Structures*, Volume II (G. Bell and Sons, London, 1938) 584 p.

JOURNAL OF THE PHYSICAL SOCIETY OF JAPAN, Vol. 16, No. 1, JANUARY, 1961

Theory of Ferro- and Antiferromagnetic Resonance Absorption

By Takehiko OGUCHI and Akio HONMA
Department of Physics, Tokyo University of Education
Otsuka-kubo-machi, Tokyo

(Received August 3, 1960)

The resonance conditions in ferro- and antiferromagnetic resonance absorptions are obtained by the spin-wave theory. According to the usual free spin-wave theory, the resonance frequency is independent of temperature and has only the value at 0°K. The spin-wave interactions give the correct temperature dependence for the resonance frequency. As the results of including these interactions, the ferromagnetic resonance condition taken account of the anisotropy energy agrees with the Kittel's formula. For the cases of the ferromagnetic resonance including the demagnetizing effect, and the antiferromagnetic resonance, however, the resonance conditions obtained at high temperatures agree with the formulae of Kittel and Nagamiya, Keffer-Kittel respectively, but at low temperatures our conditions show the different temperature dependence from their formulae. However, this new theoretical result is not in agreement with the experimental data in MnF_2 by Jaccarino-Shulman and Johnson-Nethercot.

§1. Introduction

Ferromagnetic resonance was discovered first in experiments by Griffiths[1]. In the experiments, however, it is found that the apparent g values are often very much larger than the free electron g value when the results are interpreted in terms of the paramagnetic resonance relation. It has been shown by Kittel[2], when all demagnetizing effects are included, resonance condition is modified and g factor obtained becomes reasonable value.

Kittel's theory is based on the equation of motion for the macroscopic magnetization vector consisting of the total spin of the entire saturated ferromagnet as quantized in the large magnetic field, which includes not only static magnetic field but also demagnetizing field and effective anisotropy field.

In antiferromagnetic resonance absorption, the situation is similar to ferromagnetic case, that is, the theory[3] is based on the equations of motion for the sublattice magnetization vector, although they are more complicated than the ferromagnetic one, because the former has interactions between sublattice magnetization.

So far as the magnetization vector M, the demagnetizing field (which related to M) and the anisotropy field (which related to the anisotropy constant K) are defined correctly, the theories mentioned above are valid. Therefore it has been believed that even at arbitrary temperatures the theories can be applied if M and K are replced by $M(T)$ and $K(T)$ at its temperature. In fact, basing upon this idea, a number of experimental data for the ferro- and antiferromagnetic resonance absorptions have been analysed.

From the theoretically rigorous point of view, however, $M(T)$ and $K(T)$ are not the quantities which are given from the the beginning, but they should be derived from the interactions in a system—in language of quantum mechanics, from the Hamiltonian—and also the resonance frequency itself must be obtained from the same Hamiltonian. When the resonance frequency at arbitrary temperatures is calculated by this way, it will become clear whether the naive idea stating the replacement of M and K by $M(T)$ and $K(T)$ is right.

In this paper we treat the magnetic system by the spin-wave theory. As is well known, the free spin-wave theory neglecting the spin-wave interactions was given first by Bloch[4]. The same result was obtained by the first approximation of the Holstein-Primakoff's theory[5] which uses the creation and annihilation operators of spin waves. According to the selection rule, the microwave field absorbs or emits the spin waves with wave number

$k=0$, so that the resonance frequency ω is equal to the energy of spin wave of $k=0$. Since the spin-wave energy of $k=0$ in the free spin-wave theory is constant, the resonance frequency obtained is independent of temperature. If the spin-wave interactions are taken into account, the spin wave of $k=0$ feels the Hartree field made by the other spin waves, therefore, its energy depends upon the occupation number of spin waves. As the occupation number obeys the Bose distribution and hence depends on temperature, the resonance frequency obtained shows consequently the temperature dependence. Following such an idea, the resonance frequency in the case of free spin-wave theory corresponds to no occupation of spin waves, so that it has only the value at 0°K, $\omega(0)$. If the spin-wave interactions are treated carelessly in the Holstein-Primakoff's method, there arises the discrepancy[6] with the result by Dyson[7] who has studied rigorously these interactions. Recently one of the authors[8] has shown that the perturbational method to treat the spin-wave interactions in the Holstein-Primakoff theory is essentially in agreement with the Dyson's theory. His method is very favourable, because it can be applied easily to the Kubo's theory[9] which is antiferromagnetic analog of the Holstein-Primakoff's theory.

Though the problem of the width in ferromagnetic resonance absorption line had been thought to be one of the difficult problems, and a clue of the solution was given by Clogston et al.[10] In our theory it seems also to be capable to treat the problems of absorption line width. They will be discussed in the subsequent paper.

§ 2. Ferromagnetic Resonance Absorption, Anisotropy Energy Effect

A portion of the energy in ferromagnetic single crystals depends on the direction of the magnetization relative to the crystalline axis. This part of energy is called the anisotropy energy. In this section we confine ourselves to a spherical specimen, so that the effect of the demagnetizing field (dipolar interaction) on the resonance frequency may be neglected.

We consider first the ferromagnetic crystal with the uniaxial anisotropy energy. The principal axis is taken as the z axis and the x and y axes are taken to the prependicular to it. The nearest neighbour exchange interaction model of the ferromagnet, with the static magnetic field $\boldsymbol{H}$ along the z axis, is described by the following Hamiltonian,

$$\mathscr{H}=-2J\sum_{\langle j,l\rangle}\boldsymbol{S}_j\cdot\boldsymbol{S}_l + g\mu\boldsymbol{H}\sum_{j=1}^{N}\boldsymbol{S}_j^z-\kappa\sum_{j=1}^{N}S_j^{z2}\ . \tag{2.1}$$

Here J is the exchange integral, $\boldsymbol{S}_j$ the spin operator at the j-th atom, g the spectroscopic splitting factor, μ the Bohr magneton, the summation $\sum_{\langle j,l\rangle}$ is taken over all nearest neighbour pairs, N the total number of atoms and κ is a constant proportional to the anisotropy energy at 0°K. The last term in (2.1) is the simplest Hamiltonian representing the uniaxial anisotropy energy and the spin quantum number S of each atom must be greater than unity. We take the ζ axis as the axis of quantization of spins, perpendicular to which the ξ and η axes are defined. In the present case the static magnetic field is along the z axis, so that the ζ axis agrees with the $-z$ one and the ξ and η axes are equal to the $-x$ and $+y$ ones respectively.

Following Holstein-Primakoff we express the spin operators in the forms;

$$\begin{aligned} S_j^+&=S_j^\xi+iS_j^\eta=\sqrt{2S}\,f_j(S)a_j\ ,\\ S_j^-&=S_j^\xi-iS_j^\eta=\sqrt{2S}\,a_j^*f_j(S)\ ,\\ S_j^\zeta&=S-n_j\ . \end{aligned} \tag{2.2}$$

where

$$f_j(S)=\left(1-\frac{n_j}{2S}\right)^{1/2}\doteqdot 1-\frac{n_j}{4S}+\cdots \tag{2.3}$$

and the operator $a_j^*a_j=n_j$ is called the spin deviation operator, and a_j^* and a_j are to be regarded as the creation and annihilation operators of the spin deviation and they satisfy the commutation rule

$$a_ja_l^*-a_j^*a_l=\delta_{jl}\ . \tag{2.4}$$

Using these operators the Hamiltonian (2.1) can be written as follows;

$$\begin{aligned} \mathscr{H}=&-N(zJS^2+g\mu SH+\kappa S^2)\\ &-2J\sum_{\langle j,l\rangle}[2Sa_j^*f_j(S)f_l(S)a_l-2Sa_j^*a_j+a_j^*a_ja_l^*a_l]\\ &+Hg\mu\sum_j a_j^*a_j+\kappa\sum_j(2Sa_j^*a_j-a_j^*a_ja_j^*a_j) \end{aligned} \tag{2.5}$$

We introduce the Fourier transforms of a_j and a_j^*,

$$a_k=\frac{1}{\sqrt{N}}\sum_j e^{-ikj}a_j\,,\qquad a_k^*=\frac{1}{\sqrt{N}}\sum_j e^{ikj}a_j^*\,,\tag{2.6}$$

which satisfy the commutation relation

$$a_k a_{k'}^*-a_{k'}^*a_k=\delta_{kk'}\,,\tag{2.7}$$

and $a_k^*a_k=n_k$ is the number of spin wave with wave number k. Then using (2.3), we obtain

$$\begin{aligned}\mathscr{H}=&-N(zJS^2+g\mu SH+\kappa S^2)\\&+\sum_k\left\{2SzJ(1-\gamma_k)+g\mu H+2S\kappa\left(1-\frac{1}{2S}\right)\right\}n_k\\&+\sum_{k_1,\cdots,k_4}\delta(k_1+k_2-k_3-k_4)\frac{1}{N}\left\{\frac{zJ}{2}(\gamma_1+\gamma_4-2\gamma_{2-4})-\kappa\right\}a_1^*a_2^*a_3a_4\,,\end{aligned}\tag{2.8}$$

where we have picked up all terms proportional to S^0, S and S^2, and we have defined

$$\gamma_k=\sum_\rho e^{ik\rho}/z\tag{2.9}$$

with ρ denoting the vectors to the nearest neighbor atoms, and z the number of them. We have used the notation a_1, γ_1, etc. instead of a_{k1}, γ_{k1}, etc., and later we will use n_1 etc. instead of n_{k1}.

Though the last term in (2.8) contains the non-diagonal terms in the representation of diagonalizing n_k, we shall neglect them because they give a negligibly small contribution to the resonance frequency. Then (2.8) is written in the following form.

$$\mathscr{H}=A+\sum_k B_k n_k+\frac{1}{2}\sum_{k,k'}C_{kk'}n_k n_{k'}\,,\tag{2.10}$$

where

$$A=-N(zJS^2+g\mu SH+\kappa S^2)\,,\tag{2.11}$$

$$B_k=2SzJ(1-\gamma_k)+g\mu H+2S\kappa\left(1-\frac{1}{2S}\right),\tag{2.12}$$

$$C_{kk'}=C_{k'k}=\frac{4}{N}\left\{\frac{zJ}{2}(\gamma_1+\gamma_2-1-\gamma_{1-2})-\kappa\right\}.\tag{2.13}$$

According to Kubo and Tomita[11], the imaginary part of the frequency dependent susceptibility $\chi''(\omega)$ is proportional to the following quantity,

$$\chi''(\omega)\propto\int_{-\infty}^{\infty}\langle e^{it\mathscr{H}/\hbar}M_\xi e^{-it\mathscr{H}/\hbar}M_\xi\rangle e^{i\omega t}dt\,,\tag{2.14}$$

where the average $\langle\ \rangle$ is defined by

$$\langle A\rangle=\mathrm{Tr}\,e^{-\mathscr{H}/k_0T}A/\mathrm{Tr}\,e^{-\mathscr{H}/k_0T}\,,\tag{2.15}$$

k_0 is the Boltzmann's constant and M_ξ is the magnetization component along the ξ axis,

$$M_\xi=\sqrt{\frac{SN}{2}}(a_0+a_0^*)-\frac{1}{4S}\sqrt{\frac{S}{2N}}\sum_{k,k'}(a_k^*a_{k'}a_{k-k'}+\mathrm{c.c})+\cdots.\tag{2.16}$$

Inserting only the first term of the right hand side in (2.16) into (2.14), (2.14) becomes

$$\frac{SN}{2}\int_{-\infty}^{\infty}\langle e^{it\mathscr{H}/\hbar}(a_0+a_0^*)e^{-it\mathscr{H}/\hbar}(a_0+a_0^*)\rangle e^{i\omega t}dt$$

$$=\frac{SN}{2}\int_{-\infty}^{\infty}\langle(n_0+1)e^{-it(B_0+\Sigma C_{0k}n_k)/\hbar}+n_0e^{it(B_0+\Sigma C_{0k}n_k)/\hbar}\rangle e^{i\omega t}\,dt\,. \tag{2.17}$$

The integral in (2.17) can be calculated as follows:

$$\int_{-\infty}^{\infty}\langle e^{-it(B_0+\Sigma C_{0k}n_k)/\hbar}\rangle e^{i\omega t}\,dt$$

$$\doteqdot\int_{-\infty}^{\infty}e^{i(\omega-B_0/\hbar)t}e^{-it\sum_k C_{0k}\langle n_k\rangle/\hbar-t^2\{\langle(\Sigma C_{0k}n_k)^2\rangle-\langle\Sigma C_{0k}n_k\rangle^2\}/2\hbar^2}\,dt$$

$$=\left\{\frac{2\hbar^2\pi}{\sum C_{0k}^2(\langle n_k^2\rangle-\langle n_k\rangle^2)}\right\}^{1/2}\exp\left\{-\frac{\hbar^2}{2}\frac{\left(\omega-\dfrac{B_0+\sum C_{0k}\langle n_k\rangle}{\hbar}\right)^2}{\sum C_{0k}^2(\langle n_k^2\rangle-\langle n_k\rangle^2)}\right\}. \tag{2.18}$$

According to (2.14), (2.17) and (2.18), $\chi''(\omega)$ has a maximum value at

$$\hbar\omega=B_0+\sum C_{0k}\langle n_k\rangle \tag{2.19}$$

and has the following line width

$$\hbar\Delta\omega=\{\sum C_{0k}^2(\langle n_k^2\rangle-\langle n_k\rangle^2)\}^{1/2}\,. \tag{2.20}$$

This width arises from the fluctuation of spin waves with wave number k, depends strongly on temperature and vanishes at 0°K. Since this width, however, suffers the narrowing by the motion of spin waves, it is not the true origin of the width in ferromagnetic resonance curve. The discussions about the width will be performed in the subsequent paper. For the present we neglect this width, i.e. fluctuation. Then the effective Hamiltonian for the spin wave of $\boldsymbol{k}=0$ is given from (2.10) by

$$\mathscr{H}_0=B_0n_0+\sum_k C_{0k}n_0\langle n_k\rangle\,. \tag{2.21}$$

Using the selection rule of microwave $\Delta n_0=\pm1$, Eq. (2.19) as the resonance frequency can be obtained directly, that is, $\chi''(\omega)$ is represented by the δ function which has a center at (2.19).

The second term in (2.16) leads the smaller term than (2.18) by the factor $\sum\langle n_k\rangle/N$. Therefore, we leave them out of consideration.

Eq. (2.19) is the resonance frequency at the temperature T. Using (2.12) and (2.13), and omitting the terms of order $1/S$, we have

$$\omega=\frac{g\gamma}{2}\left[H+\frac{2S\kappa\left(1-\dfrac{1}{2S}\right)\left(1-\dfrac{2}{NS}\sum_k\langle n_k\rangle\right)}{g\mu}\right]. \tag{2.22}$$

When the axis of quantization of spins ζ is inclined by angle θ from the $-z$ axis (the magnetization vector being inclined by θ from the z axis), the anisotropy energy is given by the following canonical average,

$$\langle\mathscr{H}_{an}\rangle=-\kappa\sum_j\left\langle\frac{1}{2}(S^2-S_{j\zeta}^2)-\frac{1}{2}(S^2-3S_{j\zeta}^2)\cos^2\theta\right\rangle. \tag{2.23}$$

In (2.23), the portion proportional to $\cos^2\theta$ is the anisotropy constant $K(T)$, that is

$$K(T)=K(0)\left\{1-\frac{3}{NS}\sum_k\langle n_k\rangle\right\}, \tag{2.24}$$

$$K(0)=\kappa NS^2\left(1-\frac{1}{2S}\right). \tag{2.25}$$

On the other hand, the magnetization is written as

$$M(T)=g\mu\sum_j S_j{}^{\zeta}=M(0)\left(1-\frac{1}{NS}\sum_k\langle n_k\rangle\right), \tag{2.26}$$

$$M(0)=g\mu NS. \tag{2.27}$$

Using (2.22), (2.24) and (2.26), we have as the resonance frequency at temperature T

$$\omega(T)=\frac{g\gamma}{2}\left[H+\frac{2K(T)}{M(T)}\right], \tag{2.28}$$

which is perfectly in agreement with the Kittel's formula.

Next we shall consider the case of ferromagnetic specimen with the cubic anisotropy energy. The Hamiltonian of the anisotropy energy in this case is written as, provided that the non-commutative relations of spin operators are disregarded;

$$\mathcal{H}_{an}=\frac{\kappa}{S^2}\sum_j(S_j{}^{x^2}S_j{}^{y^2}+S_j{}^{y^2}S_j{}^{z^2}+S_j{}^{z^2}S_j{}^{x^2}). \tag{2.29}$$

We take the axis of quantization of spins as ζ and define S_ξ, S_η, S_ζ as follows:

$$\begin{aligned}
S_x&=\cos\theta\cos\varphi S_\xi-\sin\varphi S_\eta+\sin\theta\cos\varphi S_\zeta,\\
S_y&=\cos\theta\sin\varphi S_\xi+\cos\varphi S_\eta+\sin\theta\sin\varphi S_\zeta,\\
S_z&=-\sin\theta\, S_\xi+\cos\theta\, S_\zeta.
\end{aligned} \tag{2.30}$$

Inserting (2.30) to (2.29), we have

$$\begin{aligned}
\mathcal{H}_{an}=\frac{\kappa}{S^2}\sum_j[&S_j{}^{\xi^2}S_j{}^{\eta^2}+S_j{}^{\eta^2}S_j{}^{\zeta^2}+S_j{}^{\zeta^2}S_j{}^{\xi^2}\\
&+(\sin^4\theta\sin^2\varphi\cos^2\varphi+\sin^2\theta\cos^2\theta)(S_j{}^{\xi^4}+S_j{}^{\zeta^4}-6S_j{}^{\xi^2}S_j{}^{\zeta^2})\\
&+\sin^2\varphi\cos^2\varphi\{(1-2\sin^2\theta)S_j{}^{\xi^4}+S_j{}^{\eta^4}-6\cos^2\theta S_j{}^{\xi^2}S_j{}^{\eta^2}\\
&\qquad+6\sin^2\theta(S_j{}^{\xi^2}S_j{}^{\zeta^2}-S_j{}^{\eta^2}S_j{}^{\zeta^2})\}].
\end{aligned} \tag{2.31}$$

When the static magnetic field $\boldsymbol{H}$ is strong enough, the magnetization points parallel to $\boldsymbol{H}$[12]. In the case of the magnetic field $\boldsymbol{H}$ along the [001] direction, we can put $\theta=\pi$ and $\varphi=0$. Then (2.31) becomes

$$\begin{aligned}
\mathcal{H}_{an}&=\frac{\kappa}{S^2}\sum_j(S_j{}^{\xi^2}S_j{}^{\eta^2}+S_j{}^{\eta^2}S_j{}^{\zeta^2}+S_j{}^{\zeta^2}S_j{}^{\xi^2})\\
&=\kappa\left\{2S\sum_k n_k-\frac{9}{N}\sum_{k,k'}n_k n_{k'}\right\}.
\end{aligned} \tag{2.32}$$

By the similar method as previous one, we obtain the resonance frequency as follows;

$$\omega(T)=\frac{g}{2}\gamma\left[H+\frac{2\kappa S\left(1-\dfrac{9}{NS}\sum_k\langle n_k\rangle\right)}{g\mu}\right]. \tag{2.33}$$

Next we consider the magnetic field along the $[\bar{1}\bar{1}\bar{1}]$ direction. In this case $\cos\theta$ and $\cos\varphi$ are equal to $1/\sqrt{3}$ and $1/\sqrt{2}$ respectively, so that (2.31) can be written as

$$\begin{aligned}
\mathcal{H}_{an}&=\frac{\kappa}{S^2}\sum_j\left[\frac{1}{4}S_j{}^{\xi^4}+\frac{1}{4}S_j{}^{\eta^4}+\frac{1}{3}S_j{}^{\zeta^4}+\frac{1}{2}S_j{}^{\xi^2}S_j{}^{\eta^2}\right]\\
&=\frac{1}{3}\kappa NS^2-\frac{4}{3}\kappa S\sum_k n_k+\frac{6}{N}\kappa\sum_{k,k'}n_k n_{k'}.
\end{aligned} \tag{2.34}$$

Therefore the resonance frequency is given by

$$\omega(T)=\frac{g\gamma}{2}\left[H-\frac{\frac{4}{3}\kappa S\left(1-\frac{9}{NS}\sum_k\langle n_k\rangle\right)}{g\mu}\right]. \tag{2.35}$$

Now we take the average of (2.31) by multiplying the density matrix, considering the following relations from the symmetry;

$$\begin{gathered}\langle S_\xi{}^4\rangle=\langle S_\eta{}^4\rangle=\frac{1}{3}\langle S_\xi{}^2S_\eta{}^2\rangle\,,\\ \langle S_\xi{}^2S_\zeta{}^2\rangle=\langle S_\eta{}^2S_\zeta{}^2\rangle\,.\end{gathered} \tag{2.36}$$

Then, we have

$$\begin{aligned}\langle\mathscr{H}_{an}\rangle=\frac{\kappa}{S^2}\sum_j\langle&(S_{j\xi}{}^2S_{j\eta}{}^2+S_{j\eta}{}^2S_{j\zeta}{}^2+S_{j\zeta}{}^2S_{j\xi}{}^2)\\&+(\sin^4\theta\sin^2\varphi\cos^2\varphi+\sin^2\theta\cos^2\theta)(S_{j\xi}{}^4+S_{j\zeta}{}^4-6S_{j\xi}{}^2S_{j\zeta}{}^2)\rangle\,.\end{aligned} \tag{2.37}$$

Since the second term of Eq. (2.37) shows the angular dependence of cubic symmetry, its coefficient equals to the anisotropy constant $K_1(T)$, that is,

$$\begin{aligned}K_1(T)&=\frac{\kappa}{S^2}\sum_j\langle S_{j\xi}{}^4+S_{j\zeta}{}^4-6S_{j\xi}{}^2S_{j\zeta}{}^2\rangle\\&=K_1(0)\left(1-\frac{10}{SN}\sum_k\langle n_k\rangle\right).\end{aligned} \tag{2.38}$$

$$K_1(0)=\kappa NS^2\,. \tag{2.39}$$

From (2.26) and (2.38), we have the following relation[13)]

$$\frac{K_1(T)}{K_1(0)}=\left\{\frac{M(T)}{M(0)}\right\}^{10}. \tag{2.40}$$

Using (2.26) and (2.38), Eqs. (2.33) and (2.35) reduce to

$$\omega(T)=\frac{g\gamma}{2}\left[H+\frac{2K_1(T)}{M(T)}\right] \tag{2.41}$$

and

$$\omega(T)=\frac{g\gamma}{2}\left[H-\frac{4}{3}\frac{K_1(T)}{M(T)}\right] \tag{2.42}$$

respectively, which are perfectly in agreement with the Kittel's formulae.

§ 3. Ferromagnetic Resonance Absorption, Demagnetizing Effect

In this section we investigate the effect of the demagnetizing field on ferromagnetic resonance absorption. For this purpose we consider the non-spherical specimen and omit, for the sake of simplicity, the one atomic anisotropy energy treated in the preceding section. The Hamiltonian is

$$\mathscr{H}=\mathscr{H}_{ex}+\mathscr{H}_{f}+\mathscr{H}_{\rm dip} \tag{3.1}$$

where $\mathscr{H}_{ex}$ and $\mathscr{H}_{f}$ represent the first and second terms of (2.1) respectively and $\mathscr{H}_{\rm dip}$ is the magnetic dipolar interactions written as

$$\mathscr{H}_{\rm dip}=\sum_{j>l}D_{jl}[\boldsymbol{S}_j\cdot\boldsymbol{S}_l-3(\boldsymbol{r}_{jl}\cdot\boldsymbol{S}_j)(\boldsymbol{r}_{jl}\cdot\boldsymbol{S}_l)]\,, \tag{3.2}$$

$$D_{jl}=(g\mu)^2/R_{jl}{}^3\,. \tag{3.3}$$

Here R_{jl} and r_{jl} are the distance connecting the j-th atom and the l-th one, and the unit vector along its direction respectively. Taking the axis of quantization of spins as the z axis ($\xi=x$, $\eta=y$, $\zeta=z$, i.e., the static magnetic field is applied along the $-z$ direction), and using the procedures below (2.2), (3.2) is rewritten as

$$\begin{aligned}\mathscr{H}_{\mathrm{dip}}=\sum_h D_h\Big[&\frac{N}{2}S^2(1-3z_h^2)\\&-S\sum_k\left\{(1-3z_h^2)\left(1+\frac{1}{2}e^{iR_hk}\right)a_k^*a_k+\frac{3}{4}(r_h^{+2}e^{iR_hk}a_k^*a_{-k}^*+r_h^{-2}e^{-iR_hk}a_ka_{-k})\right\}\\&+\frac{3}{2}\sqrt{\frac{2S}{N}}\sum_{k_1,k_2,k_3}\delta(k_1+k_2-k_3)(z_hr_h^+e^{iR_hk_1}a_1^*a_2^*a_3+z_hr_h^-e^{-iR_hk_1}a_3^*a_2a_1)\\&+\frac{1}{2N}\sum_{k_1,\cdots,k_4}\Big\{\delta(k_1+k_2-k_3-k_4)\left[(1-3z_h^2)e^{i(k_1-k_3)R_h}+\frac{1}{4}(e^{iR_hk_1}+e^{-iR_hk_4})\right]a_1^*a_2^*a_3a_4\\&\qquad+\frac{3}{4}\delta(k_1+k_2+k_3-k_4)[r_h^{+2}e^{iR_hk_1}a_1^*a_2^*a_3^*a_4+r_h^{-2}e^{-iR_hk_1}a_4^*a_3a_2a_1]\Big\}\Big]\end{aligned}\tag{3.4}$$

where

$$r_h^{\pm}=x_h\pm iy_h\,,\tag{3.5}$$

with x_h, y_h and z_h describing the direction cosines of lattice vector R_h. In order to simplify the calculations without destroying the essence of the problem, let the ferromagnetic specimen be a spheroid of revolution about the z axis. Then taking account of the symmetry, (3.1) is written by

$$\mathscr{H}=\mathscr{H}_0+\mathscr{H}_2+\mathscr{H}_3+\mathscr{H}_4\,.\tag{3.6}$$

Here $\mathscr{H}_0$ is independent of operators and $\mathscr{H}_2$ is given by

$$\mathscr{H}_2=A_0a_0^*a_0+\sum_{k\neq0}\left\{A_ka_k^*a_k+\frac{1}{2}B_ka_ka_{-k}+\frac{1}{2}B_k^*a_k^*a_{-k}^*\right\},\tag{3.7}$$

where

$$A_0=g\mu\{H+(N_T-N_z)M(0)\}\,,\tag{3.8}$$

$$A_{\pm k}=2zJS(1-\gamma_k)+g\mu\{H-N_zM(0)+2\pi M(0)\sin^2\Theta_k\}\,,\tag{3.9}$$

$$B_{\pm k}=2\pi g\mu M(0)\sin^2\Theta_k\,e^{-2i\Phi_k}\,,\tag{3.10}$$

$$N_z=\frac{1}{N}\sum_h\frac{1}{R_h^3}(1-3z_h^2)+\frac{4\pi}{3}\,.\tag{3.11}$$

$$N_T=N_x=N_y=\frac{1}{N}\sum_h\frac{1}{R_h^3}(1-3x_h^2)+\frac{4\pi}{3}\,.\tag{3.12}$$

N_x, N_y and N_z are the demagnetization factors and Θ_k and Φ_k are the polar angles of $\boldsymbol{k}$. We have used the method by Cohen and Keffer[14] to evaluate A_0, $A_{\pm k}$ and $B_{\pm k}$.

In (3.6), $\mathscr{H}_3$ and $\mathscr{H}_4$ are the terms of 3rd and 4th orders of spin-wave operators respectively. These are very important in the relaxation problem[10),15)]. In our case, however, we need only terms which are diagonal and involve $a_0^*a_0$ in the final expression. Therefore $\mathscr{H}_3$ does not contribute* and $\mathscr{H}_4$ is

---

* By the 2nd order perturbation, it contributes to the terms like $\frac{1}{N}\sum_k\langle b_0^*b_0\rangle\langle b_k^*b_k\rangle$ and $\frac{1}{N}\sum_{k,k'}\langle b_0^*b_0\rangle\cdot\langle b_k^*b_k\rangle\langle b_{k'}^*b_{k'}\rangle$ using the transformation (3.15), but the former is negligible by the factor $1/N$ compared with the other terms and the latter can be neglected for it expresses three spin-wave interaction.

$$\mathscr{H}_4 = \sum_{k\neq 0} \frac{3}{2N} \sum_h D_h \Big[(1-3z_h^2)(1+e^{ikR_h}) a_k^* a_k a_0^* a_0 + \frac{1}{2}(r_h^{-2} e^{-ikR_h} a_k a_{-k} + r_h^{+2} e^{ikR_h} a_k^* a_{-k}^*) a_0^* a_0 \Big] \tag{3.13}$$

$$= \frac{g\mu}{NS} M(0) \sum_{k\neq 0} [\{(N_T - N_z) + 3(N_z - 2\pi \sin^2 \Theta_k)\} a_k^* a_k a_0^* a_0 - \pi \sin^2 \Theta_k (e^{-2i\Phi_k} a_k a_{-k} + e^{2i\Phi_k} a_k^* a_{-k}^*) a_0^* a_0] . \tag{3.14}$$

We first diagonalize (3.7) by means of the following transformation,

$$\begin{aligned} a_0 &= b_0 \\ a_k &= \frac{1}{\sqrt{2}} \{\cosh \theta_k (b_k + b_{-k}) + \sinh \theta_k (b_k^* - b_{-k}^*)\} e^{i\Phi_k} \qquad (k\neq 0) \\ a_{-k} &= \frac{1}{\sqrt{2}} \{\cosh \theta_k (b_k - b_{-k}) + \sinh \theta_k (b_k^* + b_{-k}^*)\} e^{i\Phi_k} \qquad (k\neq 0) \end{aligned} \tag{3.15}$$

and

$$\tanh 2\theta_k = -|B_k|/A_k . \tag{3.16}$$

Then we get

$$\langle \mathscr{H}_2 \rangle = \text{const.} + g\mu\{H + (N^T - N_z) M(0)\} \langle b_0^* b_0 \rangle + \sum_{k\neq 0} g\mu \Big[\Big\{ \frac{2zJS}{g\mu}(1-\gamma_k) + H - N_z M(0) + 4\pi M(0) \sin^2 \Theta_k \Big\} \times \Big\{ \frac{2zJS}{g\mu}(1-\gamma_k) + H - N_z M(0) \Big\} \Big]^{1/2} \langle b_k^* b_k \rangle . \tag{3.17}$$

This result was obtained already by the group in Bell Telephone Laboratories[10),15)]. The energy spectrum given in (3.17) is not correct in the region of $k < k_{\min}$ except $k=0$, where $k_{\min}$ is about equal to ten times the reciprocal sample dimensions. In this region, we must replace (3.17) by Walker's modes[16)] which are taken account of boundary condition at the sample-air interface. But Walker's mode is so complicated that we will use the spin-wave expression (3.17) even for $k < k_{\min}$. This assumption may be justified from the fact that Suhl's result[15)] based on the same assumption is in good agreement with the experiment. By means of the transformation (3.15), we obtain

$$\langle \mathscr{H}_4 \rangle = \frac{g\mu}{NS} M(0) \sum_{k\neq 0} \Big[\{(N_T - N_z) + 3(N_z - 2\pi \sin^2 \Theta_k)\} \times (\cosh 2\theta_k \langle b_k^* b_k \rangle + \sinh^2 \theta_k) - 2\pi \sin^2 \Theta_k \sinh 2\theta_k \Big(\langle b_k^* b_k \rangle + \frac{1}{2} \Big) \Big] \langle b_0^* b_0 \rangle . \tag{3.18}$$

The magnetization is given by

$$M(T) = M(0) \Big[1 - \frac{1}{NS} \{ b_0^* b_0 + \sum_{k\neq 0} (\cosh 2\theta_k \langle b_k^* b_k \rangle + \sinh^2 \theta_k) \} \Big] . \tag{3.19}$$

When the temperature is sufficiently low, an overwhelmingly numerous number of spin waves with small energy is excited. These spin waves are those which are $k \approx 0$ and $\Theta_{k\simeq 0} \approx 0$. (These are not important in the mechanism of subsidiary absorption treated by Suhl[15)]. However, it is the case of high signal power.) Thus we may be allowed to replace the coefficients of $\langle b_k^* b_k \rangle$ in (3.18) and (3.19) by their values at $k \approx 0$ and $\Theta_{k\simeq 0} = 0$. $\Theta_{k\simeq 0} = 0$ means $\theta_{k\simeq 0} = 0$ by (3.9), (3.10) and (3.16). Then from (3.18) and (3.19) we obtain

$$\langle \mathscr{H}_4 \rangle = \frac{g\mu}{NS} M(0) \sum_k (N_T + 2N_z) \langle b_k^* b_k \rangle \langle b_0^* b_0 \rangle , \tag{3.20}$$

$$M(T)=M(0)\left[1-\frac{1}{NS}\sum_k\langle b_k{}^*b_k\rangle\right]. \tag{3.21}$$

The resonance frequency is the coefficient of $\langle b_0{}^*b_0\rangle$ in (3.17) and (3.20), as follows,

$$\begin{aligned}\omega(T)&=\frac{g}{2}\gamma\left[H+(N_T-N_z)M(0)-M(0)\{2(N_T-N_z)-3N_T\}\frac{1}{NS}\sum_k\langle b_k{}^*b_k\rangle\right]\\&=\frac{g}{2}\gamma\left[H+(N_T-N_z)M(0)\left\{\frac{M(T)}{M(0)}\right\}^2+3N_T\{M(0)-M(T)\}\right].\end{aligned} \tag{3.22}$$

This result differs from the Kittel's formula.

On the other hand, when the temperature is considerably high and a number of spin waves with large k are uniformly excited, and hence $a_k{}^*a_k$ does not depend strongly on k, we may eliminate the terms involve $\exp(\pm i\boldsymbol{kR})$ in (3.13). In this case we have

$$\langle\mathscr{H}_4\rangle=-g\mu M(0)(N_T-N_z)\frac{1}{NS}\sum_k\langle a_k{}^*a_k\rangle\langle a_0{}^*a_0\rangle\,, \tag{3.23}$$

$$M(T)=M(0)\left\{1-\frac{1}{NS}\sum_k\langle a_k{}^*a_k\rangle\right\}. \tag{3.24}$$

By the same way, the resonance frequency is

$$\omega(T)=\frac{g}{2}\gamma\{H+(N_T-N_z)M(T)\}\,, \tag{3.25}$$

which is agreement with the Kittel's formula. It is concluded that the Kittel's formula in this case, is correct at 0°K, but at low temperatures it does not give the correct dependence of the temperature and at considerably high temperatures it has again the correct dependence. The fact that the temperature dependence changes as the temperature is increased is somewhat similar to the case of the anisotropy constant. In that case (2.40) holds at low temperatures, but the power changes to 6 instead of 10 as the temperature is increased[13].

Though a number of experimental data in ferromagnetic resonance absorption have entirely been analysed by the Kittel's formula, it is not proper at low temperatures. Thus the g-factor obtained by such an analysis, especially its temperature dependence, is not correct.

§ 4. Antiferromagnetic Resonance Absorption

The theories of antiferromagnetic resonance absorption were treated classically by Nagamiya and Keffer-Kittel (abbreviated as NKK)[3] in the same method as in ferromagnetic resonance absorption, while by Nakamura and Ziman by means of the spin-wave method (free spin-wave theory)[17]. We shall derive the correct temperature dependence of resonance absorption frequency, by including the interactions between spin waves as in the previous sections.

For the sake of simplicity let the antiferromagnetic crystal have the uniaxial anisotropy energy represented by the one atomic spin. Therefore the atomic spin S must be greater than unity. First in the case of the static magnetic field along the principal axis (taken as the $-z$ axis), the Hamiltonian can be written as

$$\mathscr{H}=2|J|\sum_{\langle l,m\rangle}\boldsymbol{S}_l\cdot\boldsymbol{S}_m-g\mu H\Big(\sum_l S_l{}^z+\sum_m S_m{}^z\Big)-\kappa\sum_l S_l{}^{z2}-\kappa\sum_m S_m{}^{z2}\,. \tag{4.1}$$

According to Kubo[9] we have to introduce two different definitions of creation and anninhilation operators of the spin deviation. These are

$$\begin{aligned}S_l{}^+&=\sqrt{2S}\,f_l(S)a_l\,,\\S_l{}^-&=\sqrt{2S}\,a_l{}^*f_l(S)\,,\\S_l{}^z&=S-a_l{}^*a_l\end{aligned} \tag{4.2}$$

for an "up" spin on the l sublattice, and

$$\begin{aligned} S_m^+ &= \sqrt{2S}\, b_m^* f_m(S)\,, \\ S_m^- &= \sqrt{2S}\, f_m(S) b_m\,, \\ S_m^z &= -S + b_m^* b_m \end{aligned} \tag{4.3}$$

for a "down" spin on the m sublattice. The operators b and b^* are defined in the same way as a and a^*, and satisfy the equations,

$$\begin{aligned} b_m^* b_m &= n_m'\,, \\ b_m b_{m'}^* - b_{m'}^* b_m &= \delta_{mm'}\,. \end{aligned} \tag{4.4}$$

We introduce the Fourier transforms of a_l, a_l^* and b_m, b_m^*:

$$\begin{aligned} a_k &= \sqrt{2/N} \sum_l e^{ikl} a_l\,, & a_k^* &= \sqrt{2/N} \sum_l e^{-ikl} a_l^*\,, \\ b_k &= \sqrt{2/N} \sum_m e^{-ikm} b_m\,, & b_k^* &= \sqrt{2/N} \sum_m e^{ikm} b_m^*\,, \end{aligned} \tag{4.5}$$

where N is the total number of atoms. Furthermore, we use the new operators α_k, α_k^* and β_k, β_k^* defined by

$$\begin{aligned} a_k &= \alpha_k \cosh\theta_k - \beta_k^* \sinh\theta_k\,, & a_k^* &= \alpha_k^* \cosh\theta_k - \beta_k \sinh\theta_k\,, \\ b_k &= -\alpha_k^* \sinh\theta_k + \beta_k \cosh\theta_k\,, & b_k^* &= -\alpha_k \sinh\theta_k + \beta_k^* \cosh\theta_k\,, \end{aligned} \tag{4.6}$$

where

$$\tanh 2\theta_k = \frac{\gamma_k}{1+\tilde{\kappa}}\,, \tag{4.7}$$

$$\tilde{\kappa} = \frac{2S\left(1-\dfrac{1}{2S}\right)\kappa}{2z|J|S}\,. \tag{4.8}$$

Then the Hamiltonian (4.1) can be written as (only the main terms)

$$\begin{aligned} \frac{\mathscr{H}}{2z|J|S} = \sum_k \big[&\{(1+\tilde{\kappa})\cosh 2\theta_k - \gamma_k \sinh 2\theta_k + \tilde{H}\} n_k + \{(1+\tilde{\kappa})\cosh 2\theta_k - \gamma_k \sinh 2\theta_k - \tilde{H}\} n_k'\big] \\ + \sum_{k,k'} \Big[&-\frac{2}{SN}\Big\{(1+2\tilde{\kappa})\cosh 2\theta_1 \sinh^2\theta_2 + \frac{1}{2}\sinh 2\theta_1 \sinh 2\theta_2\, \gamma_{1-2} \\ &\qquad -\frac{1}{2}\cosh 2\theta_1 \sinh 2\theta_2 \gamma_2 - \sinh 2\theta_1 \sinh^2\theta_2 \gamma_1\Big\}(n_1+n_1') \\ &-\frac{2}{SN}\Big\{\cosh^2\theta_1 \sinh^2\theta_2 + \frac{1}{4}\sinh 2\theta_1 \sinh 2\theta_2 \gamma_{1-2} - \frac{1}{2}\sinh 2\theta_1 \cosh 2\theta_2 \gamma_1 \\ &\qquad + \tilde{\kappa}(\cosh^2\theta_1 \cosh^2\theta_2 + \sinh^2\theta_1 \sinh^2\theta_2)\Big\}(n_1 n_2 + n_1' n_2') \\ &-\frac{2}{SN}\Big\{\cosh^2\theta_1 \cosh^2\theta_2 + \sinh^2\theta_1 \sinh^2\theta_2 + \frac{1}{2}\sinh 2\theta_1 \sinh 2\theta_2 \gamma_{1-2} - \frac{1}{2}\sinh 2\theta_1 \cosh 2\theta_2 \gamma_1 \\ &\qquad -\frac{1}{2}\cosh 2\theta_1 \sinh 2\theta_2 \gamma_2 + 2\tilde{\kappa}(\sinh^2\theta_1 \cosh^2\theta_2 + \cosh^2\theta_1 \sinh^2\theta_2)\Big\} n_1 n_2' \Big]\,. \end{aligned} \tag{4.9}$$

with

$$n_k = \alpha_k^* \alpha_k\,, \qquad n_k' = \beta_k^* \beta_k\,, \tag{4.10}$$

$$\tilde{H} = g\mu H / 2z|J|S \tag{4.11}$$

In (4.9) $\tilde{\kappa}$ which is included in the coefficients of the quadratic terms of spin deviation operators is that replaced by 1 instead of $1-1/2S$ in the definition (4.8). There are two modes in the antiferromagnetic spin wave and the selection rules of microwave for these modes are represented by $\varDelta n_0=\pm 1$ and $\varDelta n_0'=\pm 1$ respectively. Therefore the antiferromagnetic resonance absorption can be obtained by the canonical average of the coefficients of n_0 and n_0' in (4.9). Denoting the two resonance absorption frequencies by ω_+ and ω_- respectively, we have

$$\frac{\hbar\omega_\pm}{2z|J|S}=\sqrt{2\tilde{\kappa}}\pm\tilde{H}-\frac{2}{SN}\sum_k\frac{\sqrt{2\tilde{\kappa}}}{4}\left(\frac{3-\gamma_k^2}{\sqrt{(1+\tilde{\kappa})^2-\gamma_k^2}}-3\right)$$
$$-\frac{2}{SN}\sum_k\frac{\sqrt{2\tilde{\kappa}}}{4}\frac{3-\gamma_k^2}{\sqrt{(1+\tilde{\kappa})^2-\gamma_k^2}}\langle n_k+n_k'\rangle\mp\frac{1}{SN}\sum_k(1-2\tilde{\kappa})\langle n_k-n_k'\rangle\,. \tag{4.12}$$

The average magnetization along the z axis is

$$\sum_l M_l^z(T)+\sum_m M_m^z(T)=g\mu\langle\sum_l S_l^z+\sum_m S_m^z\rangle=-g\mu\sum_k\langle n_k-n_k'\rangle\,. \tag{4.13}$$

Eq. (4.13) is connected by the following relation with the parallel susceptibility

$$\sum_k\langle n_k'-n_k\rangle=\frac{\chi_{||}}{g\mu}H=\frac{1}{2}NS\,\tilde{H}\frac{\chi_{||}}{\chi_\perp}\,, \tag{4.14}$$

where

$$\chi_\perp=N(g\mu)^2/4z|J|\,. \tag{4.15}$$

Eq. (4.15) is the perpendicular susceptibility obtained by the molecular field theory. $\chi_\perp$ obtained by the spin-wave theory has small corrections of (4.15) and furthermore includes the temperature dependent terms, too. Using (4.14), (4.12) is written as

$$\omega_\pm(T)=\frac{g\gamma}{2}\left[\left\{\frac{8z|J|S^2\left(1-\frac{1}{2S}\right)\kappa}{(g\mu)^2}\right\}^{1/2}\left\{1-\frac{1}{2SN}\sum_k\left(\frac{3-\gamma_k^2}{\sqrt{(1+\tilde{\kappa})^2-\gamma_k^2}}-3\right)\right.\right.$$
$$\left.\left.-\frac{1}{2SN}\sum_k\frac{3--\gamma_k^2}{\sqrt{(1+\kappa)^2-\gamma_k^2}}\langle n_k+\langle n_k'\rangle\right\}\pm H\left(1-\frac{1}{2}\frac{\chi_{||}}{\chi_\perp}\right)\right]. \tag{4.16}$$

The anisotropy constant $K(T)$ is given by, in the same form as (2.23),

$$K(T)=-\frac{1}{2}\kappa(\sum_l\langle S^2-3S_l^{z\,2}\rangle+\sum_m\langle S^2-3S_m^{z\,2}\rangle)$$
$$=K(0)\left[1-\frac{3}{NS}\sum_k\left(\frac{1}{\sqrt{(1+\tilde{\kappa})^2-\gamma_k^2}}-1\right)-\frac{3}{NS}\sum_k\frac{1}{\sqrt{(1+\tilde{\kappa})^2-\gamma_k^2}}\langle n_k+n_k'\rangle\right], \tag{4.17}$$

$$K(0)=\kappa NS^2\left(1-\frac{1}{2S}\right). \tag{4.18}$$

Let us now introduce two approximations; (1) in the terms which do not contain $\langle n_k+n_k'\rangle$ in (4.16) and (4.17), the corrections of order $1/S$ are omitted with S^0. (2) as in the ferromagnetic case at considerably high temperatures $\langle n_k+n_k'\rangle$ can be placed outside the summation over $\boldsymbol{k}$, because the spin waves with large $\boldsymbol{k}$ are also excited uniformly. Then $\sum_k\gamma_k^2$ can be neglected compared with unity. Accordingly (4.16) and (4.17) can be written as follows,

$$\omega_\pm(T)=\frac{g\gamma}{2}\left[\left\{\frac{8z|J|K(0)}{N(g\mu)^2}\right\}^{1/2}\left\{1-\frac{1}{2NS}\frac{3}{1+\tilde{\kappa}}\sum_k\langle n_k+n_k'\rangle\right\}\pm H\left(1-\frac{1}{2}\frac{\chi_{||}}{\chi_\perp}\right)\right], \tag{4.19}$$

$$K(T)=K(0)\left[1-\frac{3}{NS}\frac{1}{1+\tilde{\kappa}}\sum_k\langle n_k+n_k'\rangle\right]. \tag{4.20}$$

Using (4.19) and (4.20), we have

$$\omega_\pm = \frac{g\gamma}{2}\left[\left\{\frac{8z|J|K(0)}{N(g\mu)^2}\right\}^{1/2}\left\{\frac{K(T)}{K(0)}\right\}^{1/2} \pm H\left(1-\frac{1}{2}\frac{\chi_{||}}{\chi_\perp}\right)\right]$$
$$= \frac{g\gamma}{2}\left[\left\{\frac{8z|J|K(T)}{N(g\mu)^2}\right\}^{1/2} \pm H\left(1-\frac{1}{2}\frac{\chi_{||}}{\chi_\perp}\right)\right]. \tag{4.21}$$

On the other hand the antiferromagnetic resonance absorption frequency obtained by NKK is expressed by

$$\omega_\pm = \frac{g\gamma}{2}\left[\left\{\frac{8z|J|K(T)}{N(g\mu)^2} + \left(\frac{1}{2}\frac{\chi_{||}}{\chi_\perp}H\right)^2\right\}^{1/2} \pm H\left(1-\frac{1}{2}\frac{\chi_{||}}{\chi_\perp}\right)\right]. \tag{4.22}$$

We take up MnF_2 as the numerical example. Since at low temperatures $8z|J|K(T)/N(g\mu)^2 \simeq 10^{10}\ (\mathrm{Oe})^2$ and $(1/2\cdot\chi_{||}/\chi_\perp\cdot H)^2 < 10^5\ (\mathrm{Oe})^2$ for $H=5000$ Oe, the latter in (4.22) can be entirely omitted. Therefore (4.21) agrees with the NKK's formula. In order to obtain the omitted term $(1/2\cdot\chi_{||}/\chi_\perp\cdot H)^2$ in our theory, it is necessary to calculate the 6-th order terms of annihilation and creation operators.

Next we leave alone the first approximation mentioned above and discard the second approximation in order to consider the case of low temperature. As at low temperatures there are an overwhelming number of spin waves with small $\boldsymbol{k}$, the coefficients of n_k and n_k' may be replaced by their values at $\boldsymbol{k}=0$. In this case, therefore, γ_k is equal to unity. Accordingly (4.16) and (4.17) are written as

$$\omega_\pm(T) = \frac{g\gamma}{2}\left[\left\{\frac{8z|J|K(0)}{N(g\mu)^2}\right\}^{1/2}\left\{1-\frac{1}{SN}\frac{1}{\sqrt{2\tilde{\kappa}}}\sum_k\langle n_k+n_k'\rangle\right\} \pm H\left(1-\frac{1}{2}\frac{\chi_{||}}{\chi_\perp}\right)\right], \tag{4.23}$$

$$K(T) = K(0)\left[1-\frac{3}{NS}\frac{1}{\sqrt{2\tilde{\kappa}}}\sum_k\langle n_k+n_k'\rangle\right]. \tag{4.24}$$

respectively and combining (4.23) with (4.24) we have

$$\omega_\pm(T) = \frac{g\gamma}{2}\left[\left\{\frac{8z|J|K(0)}{N(g\mu)^2}\right\}^{1/2}\left\{\frac{K(T)}{K(0)}\right\}^{1/3} \pm H\left(1-\frac{1}{2}\frac{\chi_{||}}{\chi_\perp}\right)\right]. \tag{4.25}$$

On the one hand the sublattice magnetization $M(T)$ at low temperatures is given by

$$M(T) = g\mu\sum_m S_m{}^z = M(0)\left\{1-\frac{1}{NS}\frac{1}{\sqrt{2\tilde{\kappa}}}\sum_k\langle n_k+n_k'\rangle\right], \tag{4.26}$$

$$M(0) = g\mu NS/2\ , \tag{4.27}$$

so that we have another form of (4.25) as follows

$$\omega_\pm(T) = \frac{g\gamma}{2}\left[\left\{\frac{8z|J|K(T)}{N(g\mu)^2}\right\}^{1/2}\left\{\frac{M(0)}{M(T)}\right\}^{1/2} \pm H\left(1-\frac{1}{2}\frac{\chi_{||}}{\chi_\perp}\right)\right]. \tag{4.28}$$

Thus at low temperatures it is concluded that the NKK's formula gives the incorrect temperature dependence.

Furthermore we attempt to calculate accurately the resonance frequency without the approximations stated above. Using the numerical evaluations of Anderson[18] and Kubo[9], the correction terms in (4.16) and (4.17) are given by

$$-\frac{1}{2SN}\sum_k\left(\frac{3-\gamma_k^2}{\sqrt{1-\gamma_k^2}}-3\right) = \begin{cases}-0.054/S & \text{for NaCl type}\\ -0.057/S & \text{for CsCl type}\end{cases} \tag{4.29}$$

and

$$-\frac{3}{NS}\sum_k\left(\frac{1}{\sqrt{1-\gamma_k^2}}-1\right) = \begin{cases}-0.234/S & \text{for NaCl type}\\ -0.225/S & \text{for CsCl type}\end{cases} \tag{4.30}$$

respectively. $\tilde{\kappa}$ in the denominator of the left hand side of (4.29) or (4.30) was neglected, since it is much smaller than 1 and the term $k=0$ does not contribute to the summation. The factors proportional to $\langle n_k+n_k'\rangle$ in (4.16) and (4.17) can be calculated by applying the Eisele-Keffer's method[19] as follows;

$$\frac{1}{2SN}\sum_{k}\frac{3-\gamma_k^2}{\sqrt{(1+\tilde{\kappa})^2-\gamma_k^2}}\langle n_k+n_k'\rangle=\frac{4}{S\pi^2}\sum_{n=1}^{\infty}\cosh\left(n\frac{2z|J|S}{k_0T}\tilde{H}\right)\left\{\varDelta\frac{K_1(x)}{x}+\frac{3}{2}\varDelta^2\frac{K_2(x)}{x^2}\right\}, \tag{4.31}$$

where

$$\varDelta=\tilde{\kappa}(2+\tilde{\kappa}), \tag{4.32}$$

$$x=nT_{AB}/T, \tag{4.33}$$

$$k_0T_{AB}=2z|J|S\sqrt{\varDelta}. \tag{4.34}$$

Here K_1 and K_2 are the real Hankel functions of degree one and two respectively. In the same way, we have

$$\frac{3}{NS}\sum_{k}\frac{\langle n_k+n_k'\rangle}{\sqrt{(1+\tilde{\kappa})^2-\gamma_k^2}}=\frac{12}{S\pi^2}\sum_{n=1}^{\infty}\cosh\left(n\frac{2z|J|S}{k_0T}\tilde{H}\right)\varDelta\frac{K_1(x)}{x}. \tag{4.35}$$

Let us carry out the numerical evaluations of (4.31) and (4.35), by assuming $T_{AB}=15$°K, $S=5/2$ (values of MnF_2) and $H=0$. Using these values we have from (4.16), (4.17), (4.31) and (4.35)

$$\frac{\omega(T)}{\omega(0)}=0.98\left\{\frac{K(T)}{0.91K(0)}\right\}^{A}. \tag{4.36}$$

Values of A are shown in the following table.

T°K	5	10	15	20	25	30
A	1/3.14	1/3.00	1/2.82	1/2.61	1/2.42	1/2.22

According to this table, as was anticipated in the beginning, at low temperatures A lies near 1/3 and approaches to 1/2 as the temperature increases. The facts that A at low temperatures differs from 1/3 and the numerical coefficient in (4.36) is different from unity are due to the $1/S$ correction.

Finally we consider the case where the static magnetic field is applied along the direction perpendicular to the preferred axis. This situation is more complicated than the previous one, so that we shall not describe the detailed calculations. The essential point is that we include the terms of 3rd and 4th orders of spin-wave operators. If we neglect the $1/S$ corrections, the resonance frequencies at 0°K are

$$\omega_1(0)=\frac{g\gamma}{2}\left\{\frac{8z|J|K(0)}{N(g\mu)^2}\right\}^{1/2}, \tag{4.37}$$

$$\omega_2(0)=\frac{g\gamma}{2}\left\{\frac{8z|J|K(0)}{N(g\mu)^2}+H^2\right\}^{1/2} \tag{4.38}$$

which are in agreement with the NKK's formulae. In the spin-wave calculations by Nakamura[17], the terms of 3rd and 4th orders of operators were not included and he could not obtain the field dependence of resonance frequency (4.38). On the other hand, Kanamori and Yosida[20] have obtained the same results as NKK's, in consideration of the deviation of spin equilibrium directions from the z axis due to the external magnetic field. As was already pointed out in their paper, our treatment in the case of perpendicular field is equivalent to theirs.

§ 5. Considerations on Experiments of Antiferromagnetic Resonance Absorption in MnF_2

Though there are observations of antiferromagnetic resonance absorptions for several substances, we consider here the experimental results of antiferromagnetic resonance absorption in MnF_2 especially.

The antiferromagnetic resonance absorption of MnF_2 was observed first by Johnson and Nethercot[21]. Afterwards Foner[22] observed it in the temperature range from low temperatures to the Néel point, by means of pulsed field and millimeter waves (wave length being 8 mm and 4 mm). Furthermore Johnson and Nethercot[23] had the very accurate measurements of antiferromagnetic resonance absorption over the wide range of temperature making use of the oscillating field with shorter wave length (3 mm and 1 mm). When their experimental data were analysed, they used the NKK's formula. Accordingly in the case of zero static field, the resonance frequency is expressed by (4.22), that is,

$$\frac{\omega(T)}{\omega(0)}=\left\{\frac{K(T)}{K(0)}\right\}^{1/2}. \tag{5.1}$$

As easily seen from (4.24) and (4.26), we have

$$\frac{K(T)}{K(0)}=\left\{\frac{M(T)}{M(0)}\right\}^{3}. \tag{5.2}$$

The more detailed calculation including the $1/S$ correction and the anisotropy energy coming from the dipolar interaction states that the power of the right hand side of (5.2) become 2.9[24].

On the other hand Jaccarino and Shulman[25] observed the nuclear magnetic resonance of F^{19} in MnF_2 in the antiferromagnetic range. The resonance frequency shifts considerably from the predicted nuclear resonance frequency. According to the theory by Shulman and Jaccarino[26] its shift $\Delta\omega$ is given by

$$\Delta\omega(T)=\frac{1}{\hbar}(2A_z^{I}-A_z^{II})\left(\frac{5}{2}-\alpha\right)\frac{M(T)}{M(0)}, \tag{5.3}$$

where A_z^I and A_z^{II} are the elements of effective hyperfine coupling tensor regarded as constants here and α is the deviation of the expectation value of Mn spin at 0°K (5/2). (5.3) means

$$\frac{\Delta\omega(T)}{\Delta\omega(0)}=\frac{M(T)}{M(0)}. \tag{5.4}$$

From (5.1), (5.2) and (5.4)

$$\frac{\omega(T)}{\omega(0)}=\left\{\frac{\Delta\omega(T)}{\Delta\omega(0)}\right\}^{1.45} \tag{5.5}$$

should be satisfied. In fact Johnson and Nethercot, by using their observed values and Jaccarino and Shulman's, showed that (5.5) is satisfied very well at low temperatures.

At low temperatures, however, we pointed out the replacement of NKK's formula (4.22) by (4.25). Accordingly

$$\frac{\omega(T)}{\omega(0)}=\frac{M(T)}{M(0)}=\frac{\Delta\omega(T)}{\Delta\omega(0)}, \tag{5.6}$$

must be held due to (5.2). According to Johnson and Nethercot, (5.6) is, however, rather valid at high temperatures and deviates at low temperatures. One question arises about the cause of the temperature variation in ω or $\Delta\omega$, because we assumed it came chiefly through the temperature dependence of $K(T)$ and $M(T)$ and regarded the exchange integral J and effective hyperfine coupling constant independent of temperature. In reality these quantities have the temperature dependence through the thermal expansion, so that we shall attempt to estimate these indirect effect on the temperature dependence of ω or $\Delta\omega$. We examine here the hyperfine coupling constant on which we have a number of data. The data obtained by Benedek and Kushida[27] are used, but the following method of estimation is different from theirs. (5.3) is written as

$$\Delta\omega(T)=AM(T) \tag{5.7}$$

or

$$\log \Delta\omega=\log A+\log M \tag{5.8}$$

where we call temporarily A "the hyperfine coupling constant". Differentiating (5.8) with respect to temperature under the constant pressure p, we have

$$\frac{1}{\Delta\omega}\left(\frac{\partial\Delta\omega}{\partial T}\right)_p=\left(\frac{\partial\log A}{\partial V}+\frac{\partial\log M}{\partial V}\right)_T\left(\frac{\partial V}{\partial T}\right)_p+\left(\frac{\partial\log M}{\partial T}\right)_V . \tag{5.9}$$

Here the first term of (5.9) is the correction due to the temperature variation of A and M (being the functions of distance between nearest neighbours) through the thermal expansion of specimen, that is, A arises chiefly from the overlaps of electrons belonging to the nearest neighbour ions[28] and M is the quantity determined by the exchange integral. Next we differentiate (5.8) with respect to p under constant T, resulting in

$$\frac{1}{\Delta\omega}\left(\frac{\partial\Delta\omega}{\partial p}\right)_T=\left(\frac{\partial\log A}{\partial V}+\frac{\partial\log M}{\partial V}\right)_T\left(\frac{\partial V}{\partial p}\right)_T . \tag{5.10}$$

According to Benedeck and Kushida, the observed values of the left hand side of (5.10) are 1.9×10^{-6}, 2.2×10^{-6} and 3.2×10^{-6} $(\mathrm{kg/cm^2})^{-1}$ at 4.2°, 20.4° and 35.7° respectively. For the sake of simple estimation we adopt the average value of them, 2×10^{-6} $(\mathrm{kg/cm^2})^{-1}$. Denoting the lattice constants of $\mathrm{MnF_2}$ perpendicular and parallel to the antiferromagnetic axis by a and c respectively, we have

$$\left(\frac{\partial V}{\partial p}\right)_T=\left(\frac{\partial(a^2c)}{\partial p}\right)_T=V\left\{\frac{2}{a}\left(\frac{\partial a}{\partial p}\right)_T+\frac{1}{c}\left(\frac{\partial c}{\partial p}\right)_T\right\} . \tag{5.11}$$

The measured values of the right hand side of (5.11) compressibility, at 20°C are $1/a\cdot(\partial a/\partial p)_T=-0.45\times10^{-6}$ $(\mathrm{kg/cm^2})^{-1}$, $1/c\cdot(\partial c/\partial p)_T=-0.31\times10^{-6}$ $(\mathrm{kg/cm})^{-1}$. We do not have low temperature values, but assume them to be valid even at low temperatures. Then $1/V\cdot(\partial V/\partial p)_T=-1.2\times10^{-6}$ $(\mathrm{kg/cm^2})^{-1}$ and from (5.10) we obtain

$$\left(\frac{\partial\log A}{\partial V}+\frac{\partial\log M}{\partial V}\right)_T=\frac{\dfrac{1}{\Delta\omega}\left(\dfrac{\partial\Delta\omega}{\partial p}\right)_T}{\left(\dfrac{\partial V}{\partial p}\right)_T}=-\frac{1.7}{V} . \tag{5.12}$$

Inserting (5.12) into (5.9)

$$\frac{1}{\Delta\omega}\left(\frac{\partial\Delta\omega}{\partial T}\right)_p=-\frac{1.7}{V}\left(\frac{\partial V}{\partial T}\right)_p+\left(\frac{\partial\log M}{\partial T}\right)_V . \tag{5.13}$$

The coefficient of linear expansion was measured by Gibbons.[29] Since the coefficient of linear expansion along the a axis is negligibly small at low temperatures, we may put

$$\frac{1}{V}\left(\frac{\partial V}{\partial T}\right)_p=\frac{1}{c}\left(\frac{\partial c}{\partial T}\right)_p . \tag{5.14}$$

The values of $1/c\cdot(\partial c/\partial T)_p$ at 15°, 20° and 30°K are 3.25, 6.40 and 10.33×10^{-6} $(\mathrm{deg})^{-1}$ respectively and at 4°K smaller than 10^{-6}. According to Benedeck and Kushida, on the other hand, the values of the left hand side of (5.13) are -0.075, -3.2 and -8.5×10^{-3}

(deg)$^{-1}$ at 4.2°, 20.4° and 35.7°K respectively. Therefore the first term of the right hand side of (5.13) is negligible. As a result of this estimation we must conclude that the temperature dependence of $\Delta\omega$ is chiefly determined from the explicit temperature dependence of M, and that A can be regarded as a constant. It could be also said that the exchange integral is constant.

Our result (5.6) seems to be theoretically correct. As both the experiments of Jaccarino and Shulman, and Johnson and Nethercot are very accurate, there is no room to doubt about their experimental results. It looks as though we are between Scylla and Charybdis.

The authors wish to express their sincere thanks to Professor R. Kubo for his kind discussions, and also their sincere appreciations to Professor M. Toda for his encouragements and advices.

References

1) J.H.E. Griffiths: Nature **158** (1946) 670.
2) C. Kittel: Phys. Rev. **73** (1948) 155. J. H. Van Vleck: Phys. Rev. **78** (1950) 266.
3) T. Nagamiya: Prog. Theoret. Phys. **6** (1951) 350. C. Kittel: Phys. Rev. **82** (1951) 565. F. Keffer and C. Kittel: Phys. Rev. **85** (1952) 329.
4) F. Bloch: Zeits. f. Phys. **61** (1930) 206.
5) T. Holstein and H. Primakoff: Phys. Rev. **58** (1940) 1908.
6) M. R. Schafroth: Proc. Phys. Soc. **A67** (1954) 33.
7) F. J. Dyson: Phys. Rev. **102** (1956) 1217, 1230.
8) T. Oguchi: Phys. Rev. **117** (1960) 117.
9) R. Kubo: Phys. Rev. **87** (1952) 568.
10) A.M. Clogston, H. Suhl, L. Walker and P.W. Anderson: J. Phys. Chem. Solids, **1** (1956) 129.
11) R. Kubo and K. Tomita: J. Phys. Soc. Japan **9** (1960) 888.
12) T. Oguchi: Prog. Theoret. Phys. **17** (1957) 659.
13) F. Keffer: Phys. Rev. **100** (1955) 1692.
14) M. H. Cohen and F. Keffer: Phys Rev. **99** (1955) 1128, 1135.
15) H. Suhl: J. Phys. Chem. Solids. **1** (1957) 209.
16) L. K. Walker: Phys. Rev. **105** (1957) 390.
17) T. Nakamura: Prog. Theoret. Phys. **7** (1952) 539. J. M. Ziman: Prog. Phys. Soc. **65** (1952) 540.
18) P. W. Anderson: Phys. Rev. **86** (1952) 694.
19) J. A. Eisele and F. Keffer: Phys. Rev. **96** (1954) 929.
20) J. Kanamori and K. Yosida: Prog. Theoret. Phys. **14** (1955) 423.
21) F. M. Johnson and A. H. Nethercot Jr.: Phys. Rev. **104** (1956) 847.
22) S. Foner: Phys. Rev. **107** (1957) 683.
23) F.M. Johnson and A.H. Nethercot Jr.: Phys. Rev. **114** (1959) 705.
24) T. Oguchi: Phys. Rev. **111** (1958) 1063.
25) V. Jaccarino and R. G. Shulman: Phys. Rev. **107** (1957) 1196.
26) R. G. Shulman and V. Jaccarino: Phys. Rev. **108** (1957) 1219.
27) G. B. Benedeck and T. Kushida: Phy. Rev. **118** (1960) 46.
28) F. Keffer. T. Oguchi. W. O'Sullivan and J. Yamashita: Phys. Rev. **115** (1959) 1553.
29) D. F. Gibbons: Phys. Rev. **115** (1959) 1194.

JOURNAL OF THE PHYSICAL SOCIETY OF JAPAN, Vol. 16, No. 1, JANUARY, 1961

A Method for Measuring High Electron Densities in Plasmas

By Susumu TAKEDA and Michel ROUX

Nagoya University, Nagoya, Japan University of Illinois,
Urbana, Illinois, U.S.A.

(Received September 21, 1960)

It is proposed that high electron densities in plasmas can be determined from the complex reflection coefficient of a plane microwave at the plasma boundary. The coefficient which is related to the electron density and the collision frequency in plasmas is measured from the standing wave pattern produced by the incident and reflected wave at the boundary. As a result of the calculation, for a microwave frequency of 9000 MC, electron densities of 10^{14} and 10^{16} cm^{-3} are determinable respectively from the measurement of 11 and 1.1 degree in the phase angle of the complex reflection coefficient.

§1. Introduction

Recently, the measurement of high electron densities in plasmas has become increasingly important for researches in high temperature plasma physics. An approach to this problem, using microwave techniques, has been reported,[1] in which a TE_{011} mode cavity has been used; but such cavity techniques are not adapted to plasmas contained in large discharge chambers. When probing techniques in such plasmas are based on microwaves, usually the transmitted waves through the plasma have been considered; however, the reflection of an electromagnetic wave by the plasma limits the measurable density to its upper value of 10^{14} cm^{-3}, even in the case of 4 mm wave length. Thus, the measurement of densities higher than 10^{15} cm^{-3}, requires other techniques, such as spectroscopy.

This article proposes a new microwave method, able to extend the measurable density range by a factor of 10^4 above that by the propagation method previously used. This means that densities up to 10^{16} and 10^{18} cm^{-3} can be measured by waves of 9 KMC and 75 KMC respectively.

The well known method for measuring the electron density by means of an electromagnetic wave is based on the fact that the complex conductivity of the medium to be measured depends on the electron density and the collision frequency. When the frequency of the electromagnetic wave is much lower than the plasma frequency, most of the energy of the incident wave is reflected at the discontinuity surface and does not penetrate deeply into the plasma. However, the reflection at the surface of a high electron density plasma is a little different from that at the perfect conductor.

In the complex reflection coefficient given by $|R|e^{j\theta}$, a perfect conductor gives $|R|=1$ and $\theta=180°$. Therefore, in principle the measurement of the small deviations, $1-|R|$ and $180°-\theta=\phi$ should allow the determination of electron densities corresponding to plasma frequencies much higher than the wave frequency.

§2. Formulas for the reflection coefficient

A plane electromagnetic wave, propagating through a plasma with a complex conductivity σ, takes the form $\exp j(\omega t-kz)$ where k, the propagation constant in the medium, is given by the expression

$$k=\alpha-j\beta=k_0\left(1-j\frac{\sigma}{\omega\mathcal{E}}\right)^{1/2} \tag{1}$$

k_0 is the phase constant in vacuum; the complex conductivity of the plasma is, as well known,

$$\sigma=\frac{ne^2}{m}\,\frac{1}{\nu+j\omega} \tag{2}$$

From Eqs. (1) and (2), and making use of the relation $ne^2/m\mathcal{E}=\omega_p{}^2$, one obtains

$$\alpha^2=\frac{k_0{}^2}{2}\left[\left\{1-\frac{(\omega_p/\omega)^2}{1+(\nu/\omega)^2}\right\}+\left\{\left(1-\frac{(\omega_p/\omega)^2}{1+(\nu/\omega)^2}\right)^2+(\nu/\omega)^2\,\frac{(\omega_p/\omega)^4}{(1+(\nu/\omega)^2)^2}\right\}^{1/2}\right] \tag{3a}$$

$$\beta^2=\frac{k_0{}^2}{2}\left[-\left\{1-\frac{(\omega_p/\omega)^2}{1+(\nu/\omega)^2}\right\}+\left\{\left(1-\frac{(\omega_p/\omega)^2}{1+(\nu/\omega)^2}\right)^2+(\nu/\omega)^2\,\frac{(\omega_p/\omega)^4}{(1+(\nu/\omega)^2)^2}\right\}^{1/2}\right] \tag{3b}$$

The absolute value of the reflection coefficient $|R|$ and its phase angle θ are given as

$$|R| = \left|\frac{k_0-k}{k_0+k}\right| = \frac{\{(k_0-\alpha^2-\beta^2)^2+4k_0^2\beta^2\}^{1/2}}{(k_0+\alpha)^2+\beta^2} \qquad (4a)$$

$$\tan\theta \equiv -\tan\phi = \frac{2k_0\beta}{k_0^2-\alpha^2-\beta^2} \qquad (4b)$$

When $\nu/\omega=0$ and $\omega_p^2/\omega^2>1$,

$$\tan\phi = \frac{2\sqrt{(\omega_p/\omega)^2-1}}{(\omega_p/\omega)^2-2}, \qquad |R|=1 \qquad (4b)'$$

When $(\omega_p/\omega)^2/1+(\nu/\omega)^2 \gg 1$, α and β in (3a) and (3b) simplify to:

$$\alpha^2 = \frac{k_0^2}{2}\frac{(\omega_p/\omega)^2}{1+(\nu/\omega)^2}[\{1+(\nu/\omega)^2\}^{1/2}-1] \qquad (3c)$$

$$\beta^2 = \frac{k_0^2}{2}\frac{(\omega_p/\omega)^2}{1+(\nu/\omega)^2}[\{1+(\nu/\omega)^2\}^{1/2}+1] \qquad (3d)$$

Eqs. (4a) and (4b) can be rewritten as

$$1-|R| = 1-\frac{\{(1-C)^2+B^2\}^{1/2}}{1+A+C} \doteqdot A-\frac{B^2}{2}+2C \qquad (4c)$$

$$\tan\phi = \frac{B}{1-C} \qquad (4d)$$

where

$$A = \frac{2\alpha k_0}{\alpha^2+\beta^2} = \frac{\sqrt{2}\,[\{1+(\nu/\omega)^2\}^{1/2}-1]^{1/2}}{\omega_p\omega}$$

$$B = \frac{2\beta k_0}{\alpha^2+\beta^2} = \frac{\sqrt{2}\,[\{1+(\nu/\omega)^2\}^{1/2}+1]^{1/2}}{\omega_p/\omega}$$

$$C = \frac{k_0^2}{\alpha^2+\beta^2} = \frac{\{1+(\nu/\omega)^2\}^{1/2}}{\omega_p/\omega}$$

Again, when $(\omega_p/\omega)^2/1+(\nu/\omega)^2 \gg 1$, (4c) and (4d) simplify to

$$1-|R| \doteqdot A = \frac{\sqrt{2}}{\omega_p/\omega}[\{1+(\nu/\omega)^2\}^{1/2}-1]^{1/2} \qquad (4e)$$

$$\tan\phi \doteqdot B = \frac{\sqrt{2}}{\omega_p/\omega}[\{1+(\nu/\omega)^2\}^{1/2}+1]^{1/2} \qquad (4f)$$

The values of $\tan\phi$, and $1-|R|$ versus $(\omega_p/\omega)^2$ are shown in Figs. 1 and 2 for different parameters of ν/ω. For $\omega_p^2/\omega^2 \gg 2$ the value of $\tan\phi$ for $\nu/\omega<1$ does not differ too much from its value for $\nu/\omega=0$.

Solving Eqs. (4e) and (4f) for ω_p^2/ω^2 and $(\nu/\omega)^2$

$$(\omega_p/\omega)^2 = \frac{4}{\tan^2\phi-(1-|R|)^2} \qquad (5a)$$

$$(\nu/\omega)^2 = \left[\frac{1+\dfrac{\{1-|R|\}^2}{\tan^2\phi}}{1-\dfrac{\{1-|R|\}^2}{\tan^2\phi}}\right]^2-1 \qquad (5b)$$

When ν/ω is small,

$$1-|R| \doteqdot 0 \qquad (5c)$$

and

$$(\omega_p/\omega)^2 = \frac{4}{\tan^2\phi} \qquad (5d)$$

It may be worthwhile to note that $\phi=11°$ at $(\omega_p/\omega)^2=10^2$ for $\nu/\omega=0$. This means that $n=10^{14}\,\text{cm}^{-3}$ will be very easily measured by using a wave of 9000 MC.

The electromagnetic wave is very rapidly attenuated in plasmas, where ω_p^2/ω^2 is greater than one. The attenuation distant d is defined[2] by

$$d=1/\beta \qquad (6)$$

The ratio of the attenuation distance to the free space wave length d/λ is shown in Fig. 3 for different ν/ω. From (3b) it is simplified for $\nu/\omega=0$, as

$$\frac{d}{\lambda} = \frac{1}{2\pi}\frac{1}{\{(\omega_p/\omega)^2-1\}^{1/2}} \qquad (7)$$

Except at the low value of ω_p/ω, the ratio is very small. A plasma which has a thickness larger than this value is considered to be infinite. In other words, the effect of another surface can be neglected. The electron density in the vicinity of the wall is not uniform, but changes rapidly within a distance which is the order of the Debye length. The latter is much smaller than the attenuation

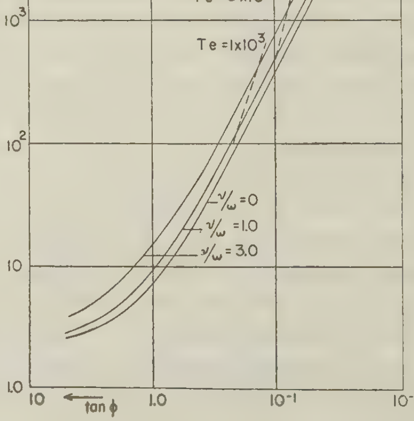

Fig. 1. Normalized electron density versus phase angle of the complex reflection coefficient for different values of ν/ω and T_e.

distance. Therefore, this non-uniformity close to the wall may be neglected.

If the gas is perfectly ionized, ν is a function of the electron temperature T_e and the electron density n as

$$\nu=3.6nT_e^{-3/2}\log\left(1.25\times10^4\frac{T_e^{3/2}}{n^{1/2}}\right) \qquad (8)$$

This equation is obtained from the collision characteristic time[3] between ions and electrons. In Figs. 1, and 2, the dotted lines correspond to the constant electron temperature for 9300 MC.

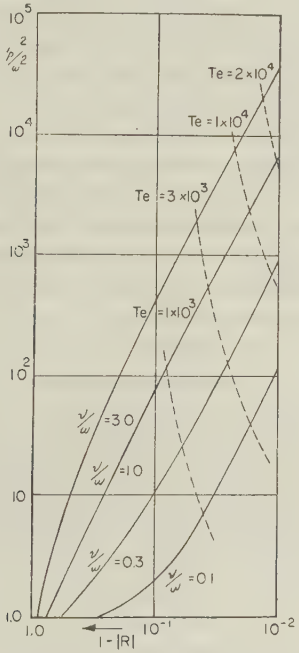

Fig. 2. Normalized electron density versus absolute value of the complex reflection coefficient for different values of ν/ω and T_e.

Thus, the electron density can be found from $1-|R|$ or $\tan\phi$, if the electron temperature is known, or both of the electron density and the collision frequency can be calculated from Eqs. (5a) and (5b) for $\omega_p^2/\omega^2\gg1$. Then the electron temperature can also be estimated from these values and Eq. (8).

§ 3. Principle of the measurement

The next problem is the measurement of the small values of $1-|R|$ and $\tan\phi$. If the plasma is a steady state or repeated one, the standard techniques of the impedance measurement (standing wave or interferometer method) can determine the complex reflection coefficient. However, for non-reproducible and transcient plasmas, the following improvement is here developed.

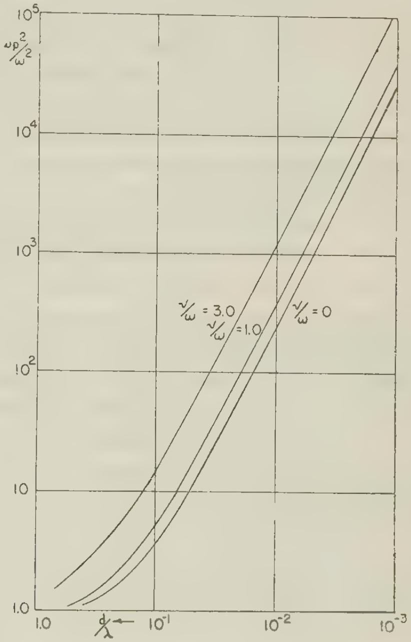

Fig. 3. Normalized electron density versus ratio of attenuation constant in plasmas to the free space wave length.

The standing wave pattern due to the reflection at a plane plasma surface and at a metal surface are shown by solid and dotted lines in Fig. 4. The signal heights h_1 and h_2, which are functions of the electric field at these points are related to $|R|$ and ϕ by means of the equations,

$$h_1=\frac{1}{4}\left|1-|R|e^{j\phi}\right|^2=\frac{1}{4}\{(1-|R|\cos\phi)^2+|R|^2\sin^2\phi\} \qquad (9a)$$

$$h_2=\frac{1}{4}\left|1+|R|e^{i\phi}\right|^2=\frac{1}{4}\{(1+|R|\cos\phi)^2+|R|^2\sin^2\phi\} \qquad (9b)$$

where a square characteristic of the crystal detectors is assumed, and h_1 and h_2 are normalized to have their maximum value 1. By solving Eqs. (9a) and (9b),

$$|R|=\frac{h_2-h_1}{\cos\phi}=\{2(h_1+h_2)-1\}^{1/2} \qquad (10a)$$

$$\sin\phi=\left\{1-\frac{(h_2-h_1)^2}{2(h_1+h_2)-1}\right\}^{1/2} \qquad (10b)$$

The small changes ΔR and $\Delta\phi$ in $|R|$ and ϕ cause the small deviation Δh_1 and Δh_2 in h_1

and h_2; they are deduced from (10a).

$$\Delta R=\frac{\Delta h_2-h_1\Delta}{|R|}=\frac{\Delta h_1+\Delta h_2-|R|\sin\phi\Delta\phi}{\cos\phi} \tag{11a}$$

$$\Delta\phi=\frac{\Delta h_1+\Delta h_2-\cos\phi\cdot\Delta R}{|R\ \sin\phi} \tag{11b}$$

The two time varying signals of h_1 and h_2 are displayed simaltaneously on a dual trace oscilloscope, where the continuous microwave is used. Two probe detectors, movable along the slotted sections of the wave-guide pick up the signals h_1 and h_2 and are fixed at such positions that one is at the minimum, and the other is at the maximum amplitude of a perfect standing wave pattern built by a metal plate, which shorts the open end of the waveguide. The correction of the formulas in the wave guide propagation is not serious except small ω_p^2/ω^2. The movable shorting plate slipped between the end of the waveguide and the plasma acts to show a standing wave as a reference. A thin mica plate is used to minimanize the wall effect between the plasma and the space in the waveguide. The maximum value of the detector signals, h_m, which is necessary to normalize h_1 and h_2 can be known from the maximum height of h_2, where a pulse modulated microwave should be used

As is seen in Fig. 4, better sensibility in h_1 and h_2 with respect to the small change of ϕ is expected at some value of ϕ other than $\phi=0$. Therefore, the probe detectors are better to be shifted out of their initial minimum or maximum amplitude positions to new positions to have a bigger slope, $\Delta h_1/\Delta\phi$. The normalized value, $\Delta h_1=0.01$ (1 mm for $h_m=100$ mm) yields a 1° change in the phase angle for $\phi=90°$, if ΔR is neglected. (refer (11b)), This phase angle change corresponds to $n=1\times10^{16}\,\mathrm{cm}^{-3}$ at a frequency of 9000 MC.

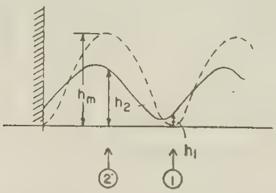

Fig. 4. Standing wave patterns due to the reflection at the plasma surface and the perfect conductor.

The application of this method to shock wave produced plasmas is now undertaken and the results will be reported with the experimental procedures. The measurement method here developed is also useful in other time varying complex values, such as impedances or propagation constants.

Although the calculation of the complex reflection coefficient described here assumes a free space propagation of the wave, a sharp discontinuity in the electron density at the plane boundary, and plasmas without magnetic field, the idea could be extended to more complicate conditions.

Acknowledgment

The authors greatly appreciate Professor L. Goldstein who gave us the opportunity to start the experiment. They also thank to Prof. R. John who kindly send them an unofficial report on the wave propagation.

References

1) S. J. Buchsbaum and S. C. Brown: Phys. Rev. **106** 196 (1957).
2) L. Spitzer: "Physics of Fully Ionized Gases" p. 50 Eq. (4-4).
3) ,, ,, ,, ,, p. 80 Eq. (5-31).

JOURNAL OF THE PHYSICAL SOCIETY OF JAPAN, Vol. 16, No. 1, JANUARY, 1961

Energy Spectrum of Mn^{++} Ion in Calcium Fluorophosphate I

By Koziro NARITA

Hitachi Central Research Laboratory, Kokubunji, Tokyo

(Received July 6, 1960)

In order to find the effect of the change in the lattice constants of the host crystal upon the energy levels of the activator ion, calculations were performed for the particular case of calcium fluorophosphate activated by Mn^{++}. The wave functions of the d^5 configuration in excited states are formed by the method of Condon and Shortley, and the matrix elements of the crystalline field potential at the Mn^{++} ion were calculated. The Hamiltonian matrix thus obtained was diagonalized by a computer to derive the eigenvalues. On the assumption that the emission of this fluorescent body is due to the transition of Mn^{++} ions from the lowest excited state to the ground state, the calculation leads to a shift of the emission peak by about 200Å to the longer wave length side caused by 1% decrease in the lattice constant.

§ 1. Introduction

The position of the emission peak varies when the composition of the basic compound is changed, even under activation by the same element. For example, in the system of MVO_3 activated by manganese, where M stands for alkaline metals Na, K, Rb or Cs, the position of the emission peak moves to the shorter wave length side with increasing order of ionic radii of the alkaline metal ions involved.[1] But in the case of barium strontium orthophosphate phosphors the emission peak shifts toward the shorter wave length side, when a part of barium ions is replaced by strontium ions having smaller ionic radii than barium.[2]

These emissions are considered to be due to the transition of the activator ion from an excited state to the ground state. The excited state from which the transition takes place is the lowest state among those arising from the 1st excited state of the free ion by the crystal field splitting. When we replace a part of ions by the ions of smaller ionic radii, the crystal field at the position of the activator ion is strengthened due to the contraction of the crystal lattice. Therefore the experimental results mentioned above for the system of MVO_3 can be reasonably understood with this view point.

From these consideration G.R. Fonda[3] speculated that the main cause of these variation of the position of spectral emission would be the variation of crystal field strength due to the change in lattice constant, and that in the case of alkaline earth orthophosphate phosphors other factor such as polarization of ions might become important.

Recently, M. Emoto[4] found the similar phenomena. Namely, when a part of the calcium ions in $\beta-Ca_3(PO_4)_2$ is replaced by magnesium or barium, the emission peak shifts towards the shorter wave length side, while a similar replacement by strontium causes the shift toward the longer wave length side. He also found that in the case of calcium fluorophospate, the emission peak shifts towards the longer wave length side when a part of the calcium ions is replaced by cadmium. The change in lattice constant resulting from the replacement of ions in these crystals is measured by T. Mitsuishi[5] using X-ray method.

In investigating the causes of such emission peak shift, one of the most important points is to examine the effect of the change in lattice constant of the host crystals upon the energy levels of the activator ion.

Systematic calculation of the crystal field for the case of $\beta-Ca_3(PO_4)_2$ and MVO_3 would be very interesting to compare with the experimental results. Unfortunately we have no information about the crystal structure or the change in lattice constant due to the replacement of ions.

In this report, therefore, the author decided to calculate the energy levels of the activating Mn^{++} ion in calcium fluorophosphate, and compare with the available experimental results.

The energy levels of the d^5 configuration have been calculated by Orgel[6] for the case of cubic crystalline field, and the result is given against the parameter Dq corresponding to the cubic field strength. Calcium fluorophosphate, however, has more complex crystal structure and one of the sites of the activating manganese ions possesses a 3-fold symmetry axis parallel to the z-axis, and it needs four parameters to describe the crystalline field potential at this point.

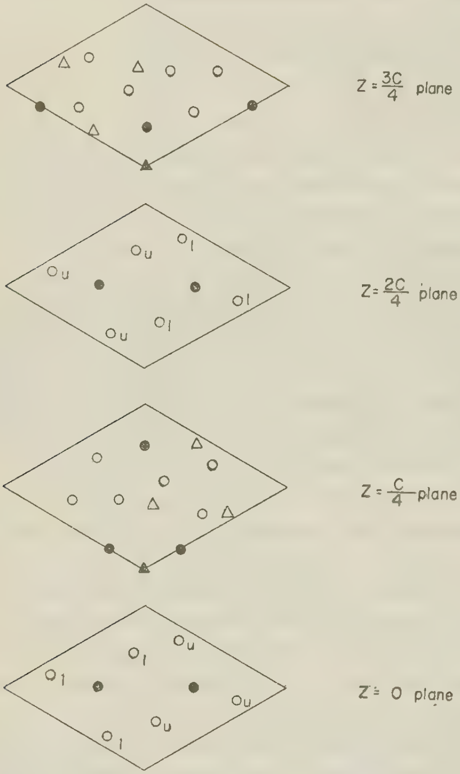

Fig. 1. Crystal Structure of Calcium Fluorophosphate.

lattice constant $a = 9.37$ Å and $c = 6.88$ Å

○ Oxygen ion, ● Calcium ion

△ Phosphorus ion, ▲ Fluorin ion

The suffix u or l indicates whether so-indicated oxygen is $c/16$ above or below the plane

We, therefore, calculate these parameters, regarding the ions surrounding the activator ion as point charges, and investigate the order of magnitude of the shift of these energy levels caused by the change in lattice constant.

§ 2. Crystal Structure[7]

A unit cell of the calcium fluorophosphate crystal comprises 4 layers and possesses 42 ions as illustrated in Fig. 1. The suffices u and l on O (oxygen) in Fig. 1 indicate that the relevant oxygen are located at $c/16$ above or below the plane respectively.

Each of the Ca^{++} ions lying in the $z=0$ and $z=2c/4$ planes possesses a 3-fold symmetry axis parallel to the z axis, but those in the $z=c/4$ and $z=3c/4$ planes have no such symmetry axis. It is not known which of these sites are occupied by the Ca^{++} ions replaced by Mn^{++}, but it is believed that, when considering only the dependence of the energy level on the change in lattice constant, there would be no great variance due to the difference in site. Therefore we shall carry out the calculation on the assumption that the Ca^{++} ions in the $z=0$ plane are replaced by Mn^{++}. The Mn^{++} ion in this case is in a crystalline field having a 3-fold symmetry axis.

§ 3. Wave Function

The ground state of Mn^{++} ion is ${}^6S$. The excited state of $3d^5$ configuration are ${}^4G$, ${}^4P$, ${}^4D$ and ${}^4F$[8]. The wave functions of these excited states can be derived by the method of Condon and Shortley[9]. Namely, the wave function of ${}^4G$ state having maximum M_L is given by

$$({}^4G4) = (2^+2^-1^+0^+-1^+)$$

where the last index on the left side of above equation gives the values of M_L and notation such as $(2^+\ 2^-\ 1^+\ 0^+-1^+)$ stands for a determinantal wave function in which one electron has $m_l=2$ and spin up, while the 2nd has $m_l=1$ and spin down, and so on.

Operation of $L^- \equiv L_x - iL_y$ upon the state (${}^4G$ 4) gives (${}^4G$ 3) as a linear combination of certain determinantal functions. The state (${}^4F$ 3) can be expressed as the linear combination of the same component functions orthogonalized to (${}^4G$ 3). In this way, we can obtain the whole wave functions of $3d^5$ configuration.

§ 4. Matrix Elements of Crystalline Field

The potential of the crystalline fields possessing a 3-fold symmetry around the z-axis can generally be given by the following expression.[10)]

$$V=\sum_i \{C_2{}^0 r_i{}^2 P_2{}^0(\cos\theta_i)+C_4{}^0 r_i{}^4 P_4{}^0(\cos\theta_i)+C_4{}^3 r_i{}^4 P_4{}^3(\cos\theta_i)\cos 3\varphi_i+d_4{}^3 r^4{}_i P_4{}^3(\cos\theta_i)\times\sin 3\varphi_i\}, \tag{1}$$

and if we regard the ions surrounding to the activator ion as point charges,[11)]

$$\begin{aligned} C_l{}^0&=\sum_j \frac{e\ e_j}{R_j{}^{l+1}}\quad P_l(\cos\Theta_j)\\ C_l{}^m&=2\frac{(l-m)!}{(l+m)!}\sum_j \frac{e\ e_j}{R_j{}^{l+1}}\quad P_l{}^m(\cos\Theta_j)\cos m\Phi_j\\ d_l{}^m&=2\frac{(l-m)!}{(l+m)!}\sum_j \frac{e\ e_j}{R_j{}^{l+1}}\quad P_l{}^m(\cos\Theta_j)\sin m\Phi_j, \end{aligned} \tag{2}$$

where r_i, θ_i and φ_i are the coordinates of the ith electron in the activator ion under consideration, while R_j, Θ_j and Φ_j give the coordinates of the jth ion measured from the center of this ion. The charge of the electron and of the jth ion are denoted by e and e_j respectively. Since the potential of the crystalline field is of the form of $\sum v_i$, its matrix elements $(L, M\,|V|\,L', M')$ can be expressed in terms of the matrix elements $(m\ |v|\ m')$ of a single electron. Also, on account of the fact that the matrix element $(L, M\,|V|\,L', M')$ has a non-zero element only when $M'=M$ and $M'=M\pm3$, total 24×24 matrix can be factorized into three 8×8 matrices. In the rest of this article we shall use symbols ***A***, ***B***, and ***C*** to represent these matrices. The states involved in these matrices are listed in Table I.

Table I. The states involved in matrices ***A***, ***B*** and ***C***.

Matrix	States contained in the Matrix							
A	$(^4G4)$,	$(^4G1)$,	$(^4G{-2})$,	$(^4F1)$,	$(^4F{-2})$,	$(^4D1)$,	$(^4D{-2})$,	$(^4P1)$
B	$(^4G3)$,	$(^4G0)$,	$(^4G{-3})$,	$(^4F3)$,	$(^4F\ 0)$,	$(^4F{-3})$,	$(^4D\ 0)$,	$(^4P0)$
C	$(^4G2)$,	$(^4G{-1})$,	$(^4G{-4})$,	$(^4F2)$,	$(^4F{-1})$,	$(^4D2)$,	$(^4D{-1})$,	$(^4P{-1})$

Of the matrix elements of the crystal field potential thus obtained only the following elements have non-zero values. (Owing to the Hermitian character of these matrices, it is only necessary to write half of the off-diagonal elements above the diagonal.)

Matrix ***A***

$$(4, 4\,|V|\,3, 1)=-2\frac{\sqrt{3}}{\sqrt{10}}(2\,|v|-1)$$

$$(4, 4\,|V|\,1, 1)=-2\frac{\sqrt{2}}{\sqrt{10}}(2\,|v|-1)$$

$$(4, 1\,|V|\,3, 1)=\frac{\sqrt{3}}{\sqrt{140}}\times[2(2|v|2)+2(1|v|1)-4(0|v|0)]$$

$$(4, 1\,|V|\,3, -2)=\frac{2\sqrt{6}}{\sqrt{28}}(2\,|v|-1)$$

$$(4, 1\,|V|\,1, 1)=\frac{2\sqrt{2}}{\sqrt{140}}\times[(2|v|2)-4(1|v|1)+3(0|v|0)]$$

$$(4,-2\,|V|\,3,1)=\frac{4\sqrt{3}}{\sqrt{280}}(-1|v|2)$$

$$(4,-2\,|V|\,3,-2)\frac{-2\sqrt{6}}{\sqrt{56}}[(2|v|2)-(0|v|0)]$$

$$(4,-2\,|V|\,1, 1)=\frac{14\sqrt{2}}{\sqrt{280}}(-1|v|2)$$

$$(3, 1\,|V|\,2, 1)=\frac{2\sqrt{2}}{\sqrt{140}}\times[3(2|v|2)-4(1|v|1)+(0|v|0)]$$

$$(3, 1\,|V|\,2,-2)=-\frac{10\sqrt{2}}{\sqrt{140}}(2|v|-1)$$

$$(3,-2\,|V|\,2, 1)=-\frac{2}{\sqrt{28}}(-1|v|2)$$

$$(3,-2\,|V|\,2, -2)=-\frac{4}{\sqrt{28}}[(2|v|2)-(0|v|0)]$$

$$(2, 1\,|V|\,1, 1)=\frac{2\sqrt{3}}{\sqrt{140}}\times[2(2|v|2)-(1|v|1)-(0|v|0)].$$

Matrix ***B***

$$(4, 3\,|V|\,3, 3)=[(2|v|2)-(1|v|1)]$$

$$(4, 3\,|V|\,3, 0)=-\frac{2}{\sqrt{20}}(2|v|-1)$$

$$(4, 3\,|V|\,1, 0)=\frac{6}{\sqrt{20}}(2|v|-1)$$

$$(4, 0\,|V|\,3, 3)=\frac{10}{\sqrt{140}}(-1|v|2)$$

$$(4, 0\,|V|\,3, -3)=\frac{10}{\sqrt{140}}(2|v|-1)$$

$$(4,-3\,|V|\,3,0)=-\frac{2}{\sqrt{20}}(-1|v|2)$$

$$(4,-3\,|V|\,3,-3)=-[(2|v|2)-(1|v|1)] \tag{4}$$

$$(4,-3\,|V|\,1,0)=\frac{6}{\sqrt{20}}(-1|v|2)$$

$$(3,3\,|V|\,2,0)=\frac{6}{\sqrt{28}}(2|v|-1)$$

$$(3,-3\,|V|\,2,0)=\frac{6}{\sqrt{28}}(-1|v|2).$$

Matrix ***C***

$$(4,2\,|V|\,3,2)=\frac{2\sqrt{6}}{\sqrt{56}}[(2|v|2)-(0|v|0)]$$

$$(4,2\,|V|\,3,-1)=\frac{4\sqrt{3}}{\sqrt{280}}(2|v|-1)$$

$$(4,2\,|V|\,1,-1)=\frac{14\sqrt{2}}{\sqrt{280}}(2|v|-1)$$

$$(4,-1\,|V|\,3,2)=\frac{2\sqrt{6}}{\sqrt{28}}(-1|v|2)$$

$$(4,-1\,|V|\,3,-1)=-\frac{\sqrt{3}}{\sqrt{140}}\times[2(2|v|2)+2(1|v|1)-4(0|v|0)]$$

$$(4,-1\,|V|\,1,-1)=-\frac{2\sqrt{2}}{\sqrt{140}}[2(2|v|2)-4(1|v|1)+3(0|v|0)]$$

$$(4,-4\,|V|\,3,-1)=-\frac{2\sqrt{3}}{\sqrt{10}}(-1|v|2)$$

$$(4,-4\,|V|\,1,-1)=-\frac{2\sqrt{2}}{\sqrt{10}}(-1|v|2)$$

$$(3,2\,|V|\,2,2)=\frac{4}{\sqrt{28}}[(2|v|2)-(0|v|0)] \tag{5}$$

$$(3,2\,|V|\,2,-1)=-\frac{2}{\sqrt{28}}(2|v|-1)$$

$$(3,-1\,|V|\,2,2)=-\frac{10\sqrt{2}}{\sqrt{140}}(-1|v|2)$$

$$(3,-1\,|V|\,2,-1)=-\frac{2\sqrt{2}}{\sqrt{140}}\times[3(2|v|2)-4(1|v|1)+(0|v|0)]$$

$$(2,-1\,|V|\,1,-1)=-\frac{2\sqrt{3}}{\sqrt{140}}[2(2|v|2)-(1|v|1)-(0|v|0)].$$

One electron matrix element $(m|v|m')$ can be calculated by Stevens' method.[12]

$$\begin{aligned}(m|v|m')=&\frac{1}{2}C_2^0\alpha\overline{r^2}(3m^2-6)\delta_{mm'}\\&+\frac{1}{8}C_4^0\beta\overline{r^4}(35m^4-155m^2+72)\delta_{mm'}\\&+315(C_4^3+id_4^3)\beta\overline{r^4}(2m-3)\delta_{m,m'+3}\\&+315(C_4^3-id_4^3)\beta\overline{r^4}(2m+3)\delta_{m,m'-3}\end{aligned} \tag{6}$$

Here, α and β are constants and their values for the single d-electron are

$$\alpha=-\frac{2}{21} \qquad \beta=\frac{2}{63} \tag{7}$$

$\overline{r^2}$ and $\overline{r^4}$ are the average values of r^2 and r^4 respectively, and they can be estimated by assuming the wave function of d-electron in the following form with the value of Z_{eff} determined by Slater's rule[13].

$$\psi_m=N_m r^2\exp\left(-\frac{Z_{eff}}{3a_H}r\right)P_2^{|m|}(\cos\theta)\exp(im\varphi). \tag{8}$$

With $Z_{eff}=5.6$ for 3d-electron, we obtain

$$\overline{r^2}=8\cdot7\cdot\left(\frac{3a_H}{2Z_{eff}}\right)^2.$$

$$\text{and}\quad \overline{r^4}=10\cdot9\cdot8\cdot7\cdot\left(\frac{3a_H}{2Z_{eff}}\right)^4. \tag{9}$$

Here a_H is the Bohr radius.

In order to obtain the coefficients, C_2^0, C_4^0, C_4^3 and d_4^3, we calculate the sum of equation (2) for the eight unit cells around Mn^{++}. We use $+2e$ and $-e$ for the charges of Ca and F ion respectively. Considering the fact that a P ion is surrounded nearly tetrahedrally by four O ions, we assume the charges of P and O ions to be $+e$ and $-e$, although the bonding character between P and O ions in this crystal is not clear. The values of the coefficients for the ordinary lattice constant of calcium fluorophosphate in C.G.S. units are as follows

$$\begin{aligned}&C_2^0=0.4311\times10^4\\&C_4^0=-0.6450\times10^{20}\\&C_4^3=0{,}005543\times10^{20}\\&d_4^3=-0.005216\times10^{20}\end{aligned} \tag{10}$$

The change in lattice constant due to the replacement of ions is not always isotropic. For example, when the Ca^{++} ion in calcium fluorophosphate is replaced by Cd^{++}, the change in lattice constant has been found to be anisotropic as referred later. In this article, however, we shall carry out our calculation assuming, for simplicity, a uniform lattice contraction. Under this assumption, the crystalline field potential for the case of, say, 2% decrease of the lattice constant can be obtained by multiplying C_2^0 by 0.98^{-3} and C_4^0, C_4^3 and d_4^3 by 0.98^{-5} in equation (10).

By using equations (3)∼(10), we can obtain the numerical values of the matrix elements. Non-vanishing elements of the matrices $\boldsymbol{A}$, $\boldsymbol{B}$, and $\boldsymbol{C}$ obtained in this manner are listed in Tables II∼IV. In these Tables, $R=R^0$ and $R=0.98R^0$ indicate, respectively, the case of normal lattice constant and the case where the lattice constant decreases by 2% from the normal values.

Table II. Non-zero elements of matrix $\boldsymbol{A}$

elements	values for $R=R^0$	values for $R=0.98R^0$
$(4, 4 \|V\|3,1)$	$621.3+584.6i$	$687.2+646.7i$
$(4, 4 \|V\|1,1)$	$507.3+477.3i$	$561.2+528.0i$
$(4, 1 \|V\|3,1)$	869.6	984.2
$(4, 1 \|V\|3,-2)$	$-525.1-494.1i$	$-580.9-546.6i$
$(4, 1 \|V\|1,1)$	-2629.3	-2908.6
$(4,-2\|V\|3,1)$	$-234.8+221.0i$	$-259.8+244.4i$
$(4,-2\|V\|3,-2)$	-115.4	-167.5
$(4,-2\|V\|1,1)$	$-671.1+631.5i$	$-742.3+698.5i$
$(3, 1 \|V\|2,1)$	-2545.0	-2786
$(3, 1 \|V\|2,-2)$	$677.9+637.9i$	$749.9+705.6i$
$(3,-2\|V\|2,1)$	$214.4-201.7i$	$237.1-223.1i$
$(3,-2\|V\|2,-2)$	-133.3	-193.4
$(2, 1 \|V\|1,1)$	-714.7	-759.5

Table III. Non-zero elements of matrix $\boldsymbol{B}$

elements	values for $R=R^0$	values for $R=0.98R^0$
$(4, 3 \|V\|3,3)$	-2617.6	-2850.0
$(4, 3 \|V\|3.0)$	$253.6+238.7i$	$280.6+264.0i$
$(4, 3 \|V\|1.0)$	$-761.0-716.0i$	$-841.7-792.0i$
$(4, 0 \|V\|3,3)$	$-479.4+451.0i$	$-530.2+498.9i$
$(4\ \ 0 \|V\|3,-3)$	$-479.4-451.0$	$-530.2-498.9i$
$(4,-3\|V\|3,0)$	$253.7+238.7i$	$280.6+264.0i$
$(4,-3\|V\|3,-3)$	2617.6	2850.0
$(4,-3\|V\|1,0)$	$-761.0-716.0i$	$-841.7-792.0i$
$(3, 3 \|V\|2,0)$	$-643.1-605.2i$	$-711.4-669.4i$
$(3,-3\|V\|2,0)$	$-643.1+605.2i$	$-711.4+669.4i$

Table IV. Non-zero elements of matrix $\boldsymbol{C}$

elements	values for $R=R^0$	values for $R=0.98R^0$
$(4, 2 \|V\|3,2)$	115.4	167.5
$(4, 2 \|V\|3,-1)$	$-234.8-221.0i$	$-259.8-244.4i$
$(4, 2 \|V\|1.-1)$	$-671.1-631.5i$	$-742.3-698.5i$
$(4,-1\|V\|3,2)$	$-525.1+494.1i$	$-580.9+546.6i$
$(4,-1\|V\|3,-1)$	-869.6	-984.2
$(4,-1\|V\|1,-1)$	2629.3	2908.6
$(4,-4\|V\|3,-1)$	$621.3-584.6i$	$687.2-646.7i$
$(4,-4\|V\|1,-1)$	$507.3-477.3i$	$561.2-528.0i$
$(3, 2 \|V\|2,2)$	136.7	193.4
$(3, 2 \|V\|2,-1)$	$214.4+201.7i$	$237.1+223.1i$
$(3,-1\|V\|2,2)$	$677.9-637.0i$	$749.9-705.6i$
$(3,-1\|V\|2,-1)$	2545.0	2786.2
$(2,-1\|V\|1,-1)$	714.7	759.5

§ 5. Results and Discussion

The Hamiltonian matrix is completed by placing the following spectral values of the free Mn^{++} ion which come from the free ion part of the total Hamiltonian, in the diagonal part of the matrix obtained above.

$$^4G=26800 \qquad {}^4P=29200$$
$$^4D=32300 \qquad {}^4F=43600\ \mathrm{cm}^{-1}.$$

This matrix was then diagonalized by using I.B.M. 650 computer to obtain the energy levels of Mn^{++} in the calcium fluorophosphate crystal. By multiplying the perturbation matrix elements by $\mathcal{E}$ and taking the limit of $\mathcal{E}\to 0$, it is possible to find out the free ion state corresponding to each of the perturbed levels. Also, from the degeneracy of the free ion states and the fact that the trace of a matrix is invariant under the unitary transformation, we could derive the degeneracy of the perturbed energy levels obtained above.

The energy levels thus obtained are shown in Fig. 2. The symbols G, P, D, and F in Fig. 2 indicate the free ion state to which the levels converge at the limiting case of $\mathcal{E}\to 0$, while the numerals indicate the degeneracy of that level. Group theoretical consideration shows that the C_3 symmetry should remove all the degeneracies involved in this problem. However, two levels which are close enough to fall within the range of resolution of our machine computation can not be discriminated as such in our calculation. Therefore the degeneracies shown here are those of accidental type and not substantial.

According to these results, the lowest excited state appears near 24500 cm^{-1}. And a decrease by 2% in the lattice constant will cause a shift of approximately 300 cm^{-1} to the lower energy side. The magnitude of this shift corresponds to about 13% of the energy depression due to the perturbation of the crystalline field of the original lattice constant.

The absorption spectra of Mn^{++} ion in calcium fluorophosphate has not been measured yet. The emission spectrum has a peak near 17300 cm^{-1}. We have assumed that the Mn^{++} ion is imbedded in the crystalline field created by the surrounding ions and calculated its energy levels treating the crystalline field as a perturbation. It is not known how closely this crystal field model approximates our particular problem. Also, when Mn^{++} is excited, there should be a change in the configuration of the surrounding ions and hence a further decrease in the energy of the ion corresponding to the Stokes shift. Therefore, it may not be appropriate to use the results of the above calculation to determine quantitatively the shift of the emission peak near $17300\,cm^{-1}$ due to the change in lattice constant. We should, however, be able to deduce the order of magnitude of the shift from our calculation. Let us assume that even for the actual state giving the emission peak at $17300\,cm^{-1}$, 2% decrease in the lattice constant gives rise to a further shift of 13% of that due to the perturbation of the crystalline field at the original lattice constant. Then there should be a shift of about $1200\,cm^{-1}$ to the lower energy side when there is a lattice contraction by 2%.

Experimentally it has been found that the peak shifts by about $100\,cm^{-1}$ to the longer wave side when one Ca in each calcium fluorophosphate $Ca_{10}(PO_4)_6F_2$ is replaced by Cd. The changes in lattice constant for this particular case are anisotropic and are decrease by 0.042% and 0.35% along *a*-axis and *c*-axis respectively.5)

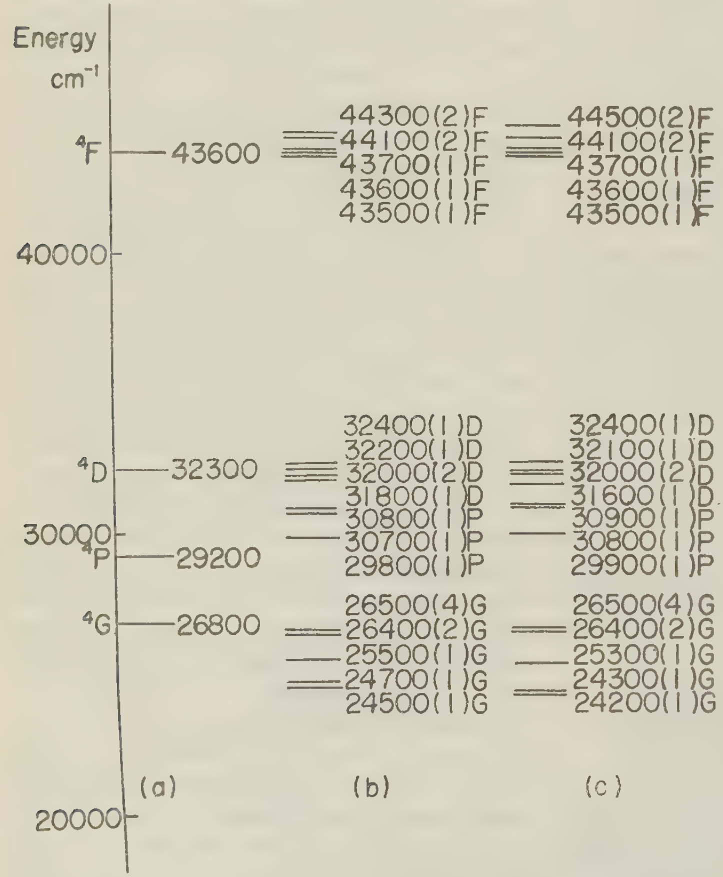

Fig. 2. Energy levels of Mn^{++} ion in free state and in the calcium fluorophosphate crystal. Energies are given in the unit of cm^{-1}

(a) Energy levels of free Mn^{++} ion from spectroscopic data.
(b) Calculated energy levels of Mn^{++} ion in the calcium fluorophosphate crystal having ordinary lattice oonstant.
(c) Calculated energy levels of Mn^{++} ion in the crystal of calcium fluorophosphate contracted by 2%.

Since our calculations are made on the assumption of isotropical decrease in the lattice constant, direct comparison can not be made. If, however, we were to replace the above mentioned anisotropic contraction with an isotropic contraction with the identical volume reduction, we would get a decrease by 0.14% in the lattice constant. Therefore, together with the above estimate of the energy shift per 2% decrease in the lattice constant, one would expect a shift by $85\,cm^{-1}$ to the longer wave side when one mole of Ca^{++} ions is replaced by Cd^{++} ions in each calcium fluorophosphate.

In calculating the crystalline potential around the Mn^{++} ion, we assume the charge $+e$ and $-e$ for P and O ion respectively. However, the validity of this assumption is not so clear, and ionicity of these ions will have considerable influence on the energy levels of Mn^{++} ion. Furthermore the oxygen ions near the Mn^{++} ion may be polarized, and if so, one must add the field from the electric dipole moments of the oxygen ions. These effect will be investigated in the forthcoming paper.

Because of the rough approximation employed in our calculation the value obtained here should not be taken too quantitatively but should be regarded as a measure of the order of the energy level shift due to the change in the crystalline field potential.

In regard to what other mechanism contribute to the energy level shift, the author is planning to carry on the similar study after obtaining the results of the experiments in which Ca is replaced by various divalent metals other than Cd in a systematic manner.

Acknowledgement

The author wishes to express his cordial thanks to Mr. M. Emoto for offering his experimental data, and to Mr. T. Mitsuishi and Dr. P. H. Kasai for their continual and hearty guidance and encouragement.

References

1) H. Gobrecht & G. Heinsohn: Z. f. Phys. **147** (1957) 350.
2) K. H. Butler: J. Electrochem. Soc. **100** (1953) 250.
3) G. R. Fonda: J. Opt. Soc. Am. **47** (1957) 877.
4) M. Emoto: Private communication (unpublished).
5) T. Mitsuishi: Private communication (unpublished).
6) L. E. Orgel: J. Chem. Phys. **23** (1955) 1004.
7) Strukur Berichte II 99–102 (1928–1932).
8) C. E. Moore: Atomic Energy Levels (National Bureau of Standard).
9) E.U. Condon and G.H. Shortley: The Theory of Atomic Spectra (Cambridge University Press).
10) B. Bleaney and K. W. H. Stevens: Repts. Prog. Phys. **16** (1953) 108.
11) J. Kanamori, T. Moriya, K. Motizuki and T. Nagamiya: J. Phys. Soc. Japan **10** (1955) 93.
12) K. W. H. Stevens: Proc. Phys. Soc. **A 65** (1952) 209.
13) J. C. Slater: Phys. Rev. **36** (1930) 57.

JOURNAL OF THE PHYSICAL SOCIETY OF JAPAN, Vol. 16, No. 1, JANUARY, 1961

The Wavelength Dependence of Quantum Efficiency and Absorption Coefficient of ZnSiO₃/Mn Powder Phosphor

By Isoo MASUDA

Matsuda Research Laboratory,
Tokyo Shibaura Electric Co., Ltd.

(Received June 9, 1960)

In this paper, the relation between the wavelength dependence of the absorption coefficient of $ZnSiO_3$/Mn powder phosphor and that of the quantum efficiency of fluorescence as well as the relation between the latter and the activator concentration were studied. It was found out that the peak of the quantum efficiency was always at the longer wavelength side than that of the absorption coefficient, and that with decrease of manganese concentration, the quantum efficiency becomes larger, and its curve sharper. A simple theory was presented to explain these facts.

§1. Introduction

We have already reported on the measuring technique of the absorption coefficient of the powdered material following the theory of Kubelka.[1] According to our method, the absorption coefficient (α) can be estimated roughly from the following formula,

$$\alpha(cm^{-1})=210(1-R)^2/2R$$

under the resonable assumption that the scattering constant σ is always taken as 210 cm^{-1} irrespectively of wavelength. Here, R is the reflectivity of the powdered sample which has a sufficiently large thickness, and can be determined in comparison with the spectral reflectivity of the smoked magnesium oxide plate calibrated beforehand.

We have also reported the method of measuring the fluorescent intensity of these powdered material, and of obtaining the quantum efficiency of fluorescence. We found that the quantum efficiency in many cases was enormously varied with the wavelength of the exciting light. This fact was confirmed even when the absorption other than the characteristic absorption was eliminated and the emission was caused only by the characteristic absorption. Though the reason was briefly explained already,[2] it will be accounted for in detail in the present paper, taking $ZnSiO_3/Mn$ of low Mn concentration as an example and referring to the measured result of absorption coefficient.

The quantum efficiency η is defined as

$$\eta = \frac{\textit{number of emitted quanta}}{\textit{number of absorbed quanta}} = \frac{F \cdot \lambda_F}{J \cdot \lambda_J \cdot A_J}$$

where, A_J is the absorption factor for the exciting light, J the excitation intensity, λ_J the exciting wavelength, F the fluorescent intensity and λ_F the mean wavelength of the fluorescence. When the absorption of the host crystal became is of considerable amount, we subtracted it from the absorption of the sample containing the activator.

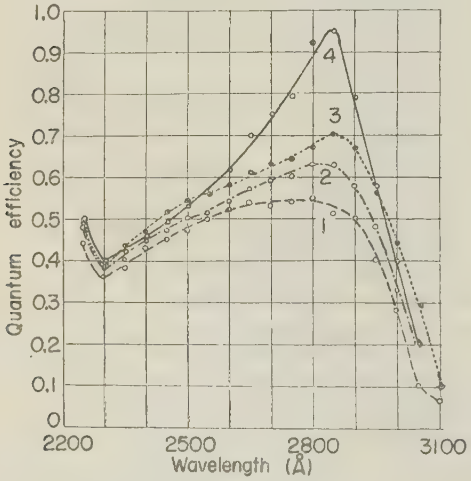

Fig. 1. Quantum efficiency curve of $ZnSiO_3/Mn$ Phosphor

① 10×10^{-2} mole Mn ② 4×10^{-2} mole Mn

③ $3\times10_{-}^{2}$ mole Mn ④ 2×10^{-2} mole Mn

§ 2. Experimental results

Fig. 1 shows curves of quantum efficiency of four kinds of $ZnSiO_3/Mn$ different in activator concentration. As activator concentration decreases, the quantum efficiency increases, especially at 2850Å. Consequently the curve shape becomes sharp with decrease of concentration. This effect will probably due to the fact that the concentration quenching effect becomes smaller with decrease of concentration.

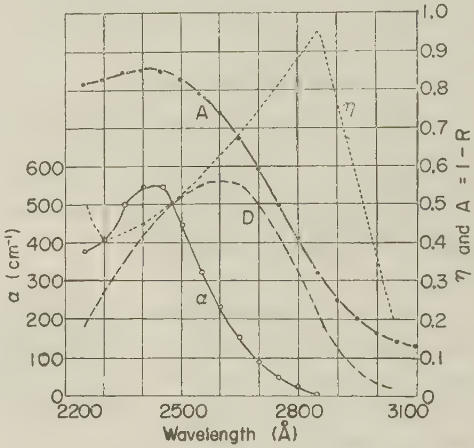

Fig. 2. Quantum efficiency (η), Absorption coefficient (α), Absorption (A) and Excitation (D–arbitraly unit) of $ZnSiO_3/Mn$ (2×10^{-2} mole) powder phosphor.

Fig. 2 shows the curve of absorption coefficient α, that of quantum efficiency η and excitation spectrum ($D=F/J$, in an arbitrary scale) of the material, in the case where manganese concentration is 2×10^{-2} mole. In this figure, it is observed that the quantum efficiency decreases with steep slant in the region shorter than 2300Å with increases wavelength, then begines to increase with gentle slant up to 2850Å, and after passing a maximum it decreases again with steep slant with increasing wavelength. There is a peak of absorption coefficient near 2450Å and its cauve is likely to be the bell shape. In the range shorter than 2300Å, there will probably be another characteristic absorption band. The absorption coefficient at 2850Å is about 10cm^{-1}. This value is the critical one which could be estimated by the mentioned method[1] and is about 1/60 times of the value at 2450Å.

§ 3. Discussion

Let us consider the relation between the curve of absorption coefficient and that of quantum efficiency shown in Fig. 2, in which the concentration quenching effect seems to be the smallest.

The absorption peak corresponding to the photon energy shown as AA′ in Fig. 3, lies at 2450Å in this material. This shown that most of the activation centers absorb photons of this energy and are excited, but the broad shape of the absorption band shows that an appreciable fraction of the activation centers are excited with photons of another energy. When the center absorbs minimum energy needed for excitation, the difference between the energy of the electron and the energy corresponding to the point *F* in the figure should be maximum, and the probability of radiative transition is to be maximum.[3] If the absorption curve is bell shape, this minimum energy will not be that which is equivalent to *AA′* in Fig. 3, but correspond to minimum energy component of bell shape distribution. So, in the characteristic absorption band, the quantum efficiency of fluorescence will increase monotonously from the shorter wavelength side towards the longer wavelength side. Indeed, Fig. 2 shows this tendency until 2850Å, which is the longest wavelength that we can distinguish the characteristic absorption from the background. Perhaps, the fact that the steep slant decrease in the longer wavelength region than 2850Å will be explained by the appearance of the weak absorption, the large part of which are the inactive absorption caused by other kinds of defects.

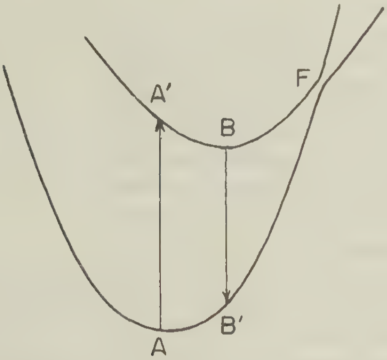

Fig. 3. Configrational coordinate Model of luminescent center.

C. K. Lui stated that the speak of characteristic absorption ought to correspond to that of excitation spectrum,[4] but, because quantum efficiency is not constant, D-curve is displaced to the longer wavelength side as shown in Fig. 2.

Pringsheim[5)] predicted that "So called specific excitation spectra are, in general, nothing but the characteristic absorption spectra of the photoluminescent substance", but at least in the case of inorganic crystal phosphor, D-curve does not correspond to the curve of characteristic absorption.

If we assume the specific excitation spectrum to be equal to the K-curve defined by Vavilov[6)], the following formula can be obtained by neglecting the quantum energy difference of exciting radiation;

$$K=D/A_J=\eta\cdot A_J/A_J=\eta.$$

Accordingly the specific excitation spectrum corresponds to the quantum efficiency spectrum, but not to the characteristic absorption spectrum. It has been reported that for solutions such as eosin, rhodamin or fluorescein, the quantum efficiency of fluorescence does not depend upon exciting wavelength. In the case of inorganic crystal phosphor, however, it is likely that the quantum efficiency of fluorescence depends upon the exciting wavelength and is similar to the excitation function of gaseous discharge.

Acknowledgement

I have much pleasure in acknowledging my indebtedness to Dr. Tsuneo Harada, Dr. Yasuo Uehara, Mr. Keiji Maeda of our laboratory, and Dr. Shoji Makishima, professor of Tokyo University, for their kind encouragement and helpful discussions, and also to Mr. Yoshimasa Kobuke, who helped me in preparing materials, and Mr. Minoru Yamanaka, who assisted me in this experiment.

Reference

1. Isoo Masuda; Oyobutsuri, **28**, 147 (1959).
2. Y. Uehara, I. Masuda and Y. Kobuke; J. Electrochem. Soc. **107**, 1 (1960).
3. N. F. Mott and R. W. Gurney; Electronic Processes in Ionic Crystals, p. 221 (the Clarendon Press 1950)
4. C. K. Lui; J. Opt. Soc. Amer.; **35**, 492 (1945).
5. P. Pringsheim and M. Vogel, Luminescence P. 18 (1946).
6. S. I. Vavilov; Phyl. Mag., **43**, 307 (1922).

JOURNAL OF THE PHYSICAL SOCIETY OF JAPAN, Vol. 16, No. 1, JANUARY, 1961

Radiation Induced Optical Absorptions in Crystalline Quartz and Fused Silica

By Kazuko KUBO

Japan Atomic Energy Research Institute
Tokai Research Establishment
Tokai-mura, Ibaraki-ken, Japan

(Received September 8, 1960)

The optical absorption of γ- and fast neutron-irradiated crystalline quartz and fused silica was measured from 186 mμ to 2.6 μ. Dichroism of the A-band was confirmed. The phenomenon of radiation bleaching of the B_1-band and a remarkable movement of the C-band were found. The irradiation and optical bleaching experiments showed that only the C-band is essential due to radiation, and this was considered to be caused by an absorption center similar to the F-center which changes F′- or colloidal-center with subsequent irradiation.

§ 1. Introduction

Physical property changes in quartz and fused silica exposed to various radiations have been studied for many years, and reports published in this connection have been listed in a bibliography by Bechman.[1] Above all, optical absorption has been actively investigated by many authors who placed the absorption peaks in positions differing fairly markedly from author to author. The present author tabulated the hitherto reported data on the absorption bands according to the kind of radiation, that is, X-rays, γ-rays and neutrons, and found that (1) the principal absorption bands in the region from about 200 mμ to 2.6 μ are A-, B- and C-bands, so named by Mitchell and Paige, while the remaining bands are not important, and result from particular chemical impurities; and (2) except for the C-band, little discrepancy is found between the results obtained by irradiation with different sources. The disagreement of data mentioned above can be the result of differences in the conditions of irradiation and of measurement, and this has been partly proved by the present experiment: Firstly, the A-band of irradiated crystalline quartz shows anisotropy which caused peak deviation when measured from absorption with unpolarized light. It should be noted that there is a difference between the spectral polarizability curves of the A-band induced by γ-rays and those induced by neutrons. Secondly, there was found the most interesting fact that the C-band of irradiated fused silica moves from around 200 mμ to 215 mμ with increase of absorption coefficient after subsequent irradiation, and this displacement is reversed by annealing: This effect spread the peak of the C-band within a range whose upper limit varied from 200 mμ to 215 mμ depending on the exposure dose. The absorption bands are nearly stable and scarcely fade even at room temperature with the return of the C-band to shorter wavelength.

The experiments on optical bleaching with a 2536Å light revealed discrepancies between the bleaching behavior of A-, B- and C-bands. A- and B-band behavior appears to be attributable to defects existing in the crystal lattice of quartz or in the network of the fused silica existing before irradiation, while on the other hand the effect on the C-band appears to be essentially due to radiation, as affected by radiation-induced defects. The E-band observed by Mitchell and Paige in the vacuum ultraviolet region is considered very probably to be a complementary of the C-band to be the result of electron-trapping by an anion vacancy or corresponding broken bond in the fused silica network, similarly to the case of the *F*-center in alkali halides. This model of the absorption center is more apt to explain the C-band behavior.

§ 2. Irradiations and Measurements

The specimens were prepared as thin plates of fused silica and crystalline quartz with planparallel optically polished surfaces on both faces. The crystalline plates were cut from a natural Brazilian single crystal of optical grade and from synthetic quartz made at the Yamanashi University, which kindly donated the material to the author. Several kinds of fused silica were used.

The specimens were placed in some instances in the vertical beam hole of the JRR–1 (water boiler type reactor), where fast neutron irradiation of 2×10^{15} n/cm^2 is performed in a day, and in other instances in the 10000 Curie Co^{60} γ-irradiation facility, in a rotating cylinder 3 cm from the source.

The measurements of optical absorption, from 186 mμ to 2.6 μ, were made with a Cary spectrophotometer Model 14.

All irradiations and measurements were made at the ambient temperature (<50°C) since it was believed by many authors that radiation-induced absorption in this material was very stable at the room temperature.

§ 3. Radiation-Induced Absorption Bands

The absorption bands were induced by radiation in the vicinity of the following wavelengths:

Table I (in mμ)

Crystalline quartz	A$_1$(600)	A$_2$(⊥ to c-axis 440 ∥ to c-axis 380)		C(215)
Fused silica	A (540)	B$_1$(300)	B$_2$(240)	C(215)

where the designation of the absorption bands A, B and C corresponds to that of Mitchell and Paige. The above results represent the mean positions determined by averaging the values obtained from many measurements. The A$_1$–, A$_2$–, and A–bands spread over a wide range, since these bands are very broad; the A$_2$–band in particular had an anisotropy resulting in a broadening into the absorption spectrum when measured with unpolarized light, and which caused the peak position to spread over a rather wide ranges.

Absorption bands induced by radiations of different kinds generally have a bell-shaped appearance of very similar form and position. It is not wise, however, to conclude from appearances that the absorption center is analogous to the typical color center in alkali halides. Some specimens cut from natural crystal showed a striped pattern which appeared to have some relation to crystal growth, while some fused silica showed colored speckles after irradiation. Both examples indicate that the visible coloring has close connection with chemical impurities. Spectroscopic analysis indicated that all the specimens contained more or less Al and Mg, while the natural and synthetic crystal contained Cu and Fe respectively. The relation between chemical impurities and radiation-induced absorption bands is however not clear.

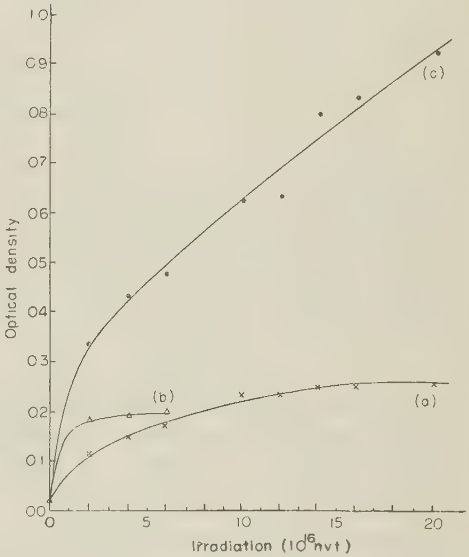

Fig. 1. Growth of optical absorption bands in fused silica of 3 mm thickness upon successive irradiations.
(a) A-band (b) B$_1$-band (C) C-band

The increase of absorption in the 2 mm thick plates of fused silica and crystalline quartz after successive irradiation in the reactor is shown in Figs. 1 and 2 respectively. The letters X, Y and Z in Fig. 2 indicate the directions of cut of the quartz plate. The B$_1$–band saturates first followed by that in the A–band, but the C–band continues to increase almost linearly after the change of growth rate. The difference in the characteristic forms of A–, B– and C–bands are clearly discernible. Further details of each band are as follows.

1) A-band. Ditchburn et al[2] have concluded that the A$_1$– and A$_2$–bands were caused by a hole trapped in the Al^{3+}-ion substituted for the Si^{4+}-ion in the crystal lattice with the optical and e.s.r. methods. Cohen and Smith[3] have also reported the anisotropy of the A$_1$–

and A_2–bands. This is confirmed by the present author with the neutron- and γ-irradiated specimens. The A_2–band measured with light polarized in a plane perpendicular to the *c*-axis forms a fine bell shape in contrast to the flat curve with ambiguous maximum point when measured with light polarized in the plane parallel to the *c*-axis.

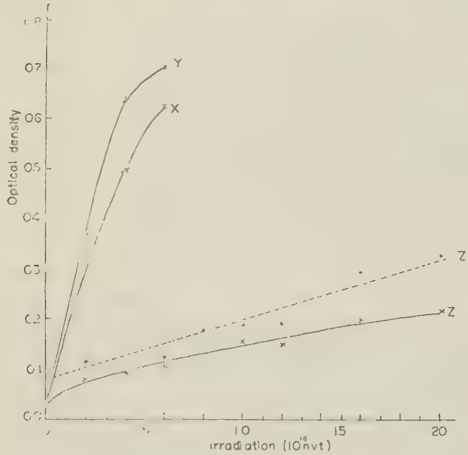

Fig. 2. Growth of optical absorption bands in crystalline quartz of 2 mm thickness upon successive irradiations. X, Y and Z indicate cut direction of crystal.

On the whole, scattering of the A–band position in crystalline quartz is due to the above-described dichroism, and Ditchburn's model of the A–center agrees with respect to the chemical impurity Al found in the present specimens and the saturation tendency of the A–band growth curve.

(2) B–band. This band is observed solely in irradiated fused silica. The B_1–band appears at rather low irradiation levels and rises to a maximum, after which the effect of bleaching by radiation makes itself felt. This behavior is shown in Fig. 3. The second increase after 5×10^{16} nvt represents masking by another absorption band. The present experiment has yielded little data about the B_1–band. Many authors have thought the B_2–band to be the result of various chemical impurities, but disagreement between the authors on the impurities suggested to be the cause would appear to indicate that the B_2–band is not due to any particular impurity other than the simple excess of Si or O. Yokota[4] found the B_2–band in a specimen prepared in a reducing environment and he concluded that it was due to interstitial Si or SiO. The data of Arnold and Compton[5] appear to support the idea of excess Si. They observed a 257 mμ band in an OH^--free specimen irradiated with electrons at 77°K, but did not discern this band in the OH^--bearing specimen under similar treatment. It can thus be inferred that OH^--ions fill the excess bonds of Si or SiO in the SiO_2 network, which correspond to the cation interstitial or to the anion vacancy in the ionic crystal if the 257 mμ band and the B_2–band are one and the same. The B–band is probably due to defects in fused silica network, broken bonds etc.

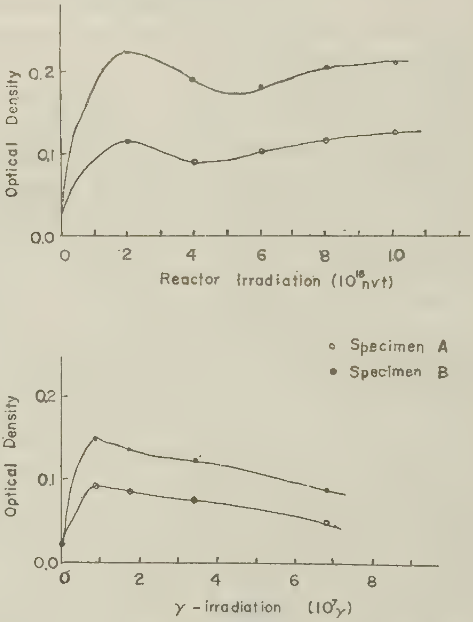

Fig. 3. Radiation bleaching effect on B_1–band.

(3) C–band. Nelson and Crawford[6] have reported that the C–band appeared in crystalline quartz only after a heavy neutron irradiation that could produce local disordered regions in the crystal, and they have suggested the C–center to be the resulting broken bonds or local strains with trapped electrons or holes.

In the present experiment, a prominent C–band was observed in every irradiated specimen of fused silica, as well as in some of the neutron-irradiated crystalline quartz, including the synthetic quartz in which the optical density of the A–band was very low, after irradiation with fast neutrons of an integrated flux of 8×10^{16} nvt.

The C-bank in fused silica has the remarkable behavior of moving towards the longer wavelengths with increasing exposure. This is shown in Fig. 4 in which the abscissa represents the exposure to γ-rays in log scale while the ordinate represents the wavelengths of the C-band maxima. The peak maximum moves from below 200 mμ to 215 mμ and it does not appear to move further. While Nelson and Crawford consider the C-center to be analogous to a center like the F-center in the alkali halides, the author judges that the behavior can be better explained if it is represented as the formation with radiation of an F′-band or a colloidal band at 215 mμ.

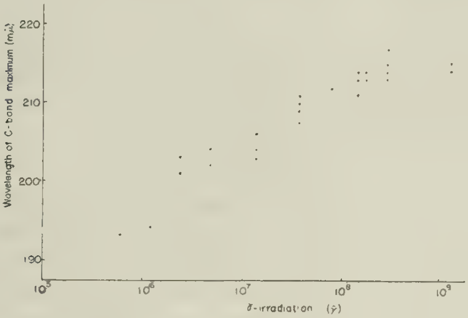

Fig. 4. Movement of C-band towards longer wavelength with increasing irradiation.

The C-band is positively due to radiation and not to chemical impurities because the absorption band is observed even with the most purified fused silica (Corning 7940 and 7943).

It might be said that the irradiation dose of 10^{17} nvt was too low to produce the C-band in the crystalline quartz, assuming the crystal to be perfect and the disorder to be the result only of radiation. Actually however, an as-grown crystal is never absolutely free of local disordered regions, and it may therefore be considered quite natural to find the C-band even after such slight irradiation.

§4. Optical Bleaching

The bleaching experiment was made with 2536 Å light from a high pressure mercury lamp with glass filter by Toshiba (UV-D 25). The absorption spectrum bleaches evenly under exposure to 2536 Å light as is shown in Fig. 5. The bleaching rate of each band is shown in Fig. 6. The B_1-band, unsubjected to radiation bleaching, rapidly bleaches, followed by the A-band. The A-band does not bleach with visible A-light, evidencing that the A-band is not due to an absorption center such as the F-center. The C-band is fairly stable but is bleached by C-light, and the peak moves back towards the shorter wavelength during bleaching. The bleaching is the reverse of that of ionizing radiation. The electrons must be released from the C-center by exposure to light and should recombine with the holes released from the A-center (or E-center).

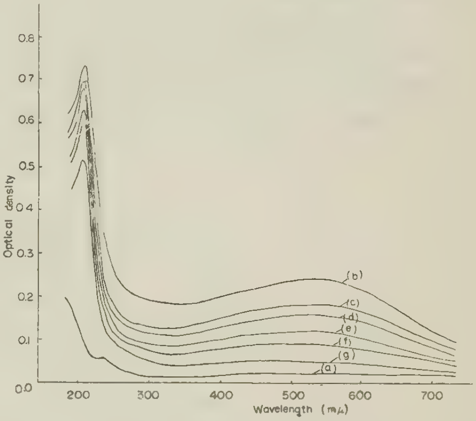

Fig. 5. Optical bleaching of γ-irradiated fused silica under illumination of 2536 A light.

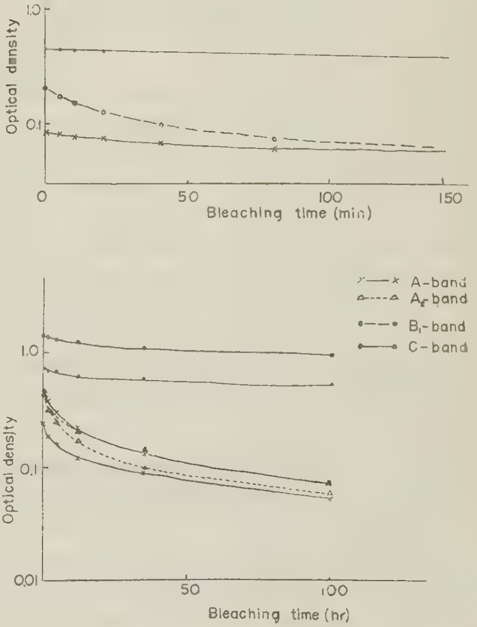

Fig. 6. Optical bleaching behavior of each absorption band in irradiated crystallide quartz and fused silica.

It is an interesting fact that the electron trapping cross section of the absorption center increased after bleaching, as is seen in Figs. 7 and 8. These figures respectively show the absorption behavior of a neutron-irradiated crystalline quartz and a γ-irradiated fused silica after bleaching and re-irradiation. After bleaching, much lighter irradiation than that previously received by specimen before bleaching is enough to restore the absorption to the previous value. In other words, the amount of absorption bleached by the light is recovered by slight radiation.

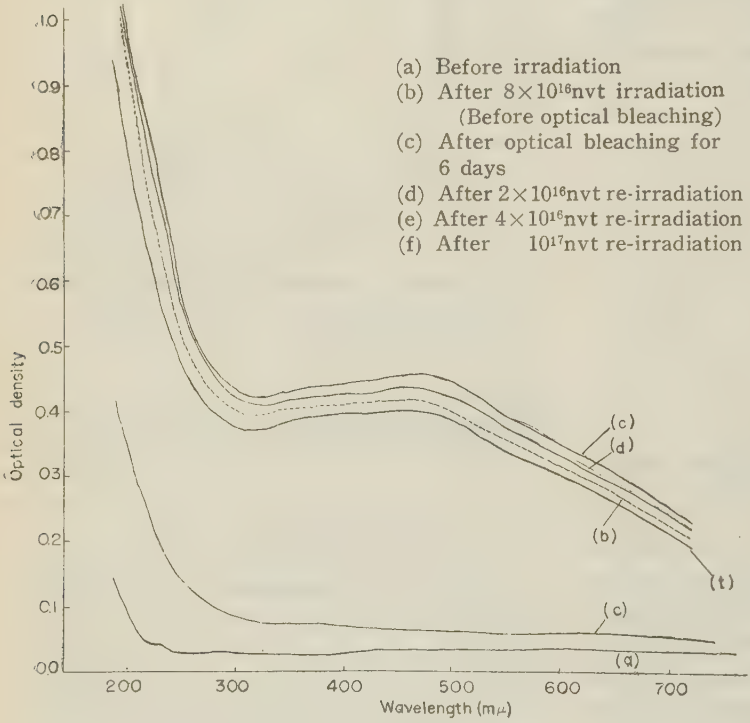

Fig. 7. Effect of optical bleaching on restoring of optical absorption in crystalline quartz upon re-irradiation.

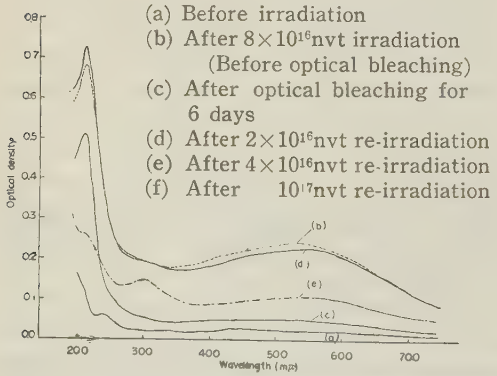

Fig. 8. Effect of optical bleaching on restoring of optical absorption in fused silica upon re-irradiation.

§ 5. Summary

The absorption spectrum of crystalline quartz and fused silica irradiated in reactor or with γ-rays was measured from 186 mμ to 2.6 μ.

The behavior of the absorption band during irradiation and during optical bleaching was investigated. Dichroism of the A–band in the crystalline quartz reported by Cohen and Smith was confirmed, and radiation bleaching of the B_1–band was found. These occurrences are clearly the cause of displacement of the absorption peak, and result in the disagreement found between the data reported hitherto.

The experimental results would lead us to conclude that the A–band and B–band are not important, and that it is the C–band that is essential from the point of view of radiation effect. The C–band is the result of a center like the F–center changing to F′–center or colloidal center with subsequent radiation. This explanation however does not for the moment represent more than a supposition. More effective measurements are required before conclusive confirmation can be offered.

The author wishes to express her gratitude to the JRR–1 Operations Section and Co⁶⁰ Irradiation Laboratory for their help in the irradiating work. Appreciation is also due to Mr. S. Taki of the Yamanashi University for his generous offer of the synthetic quartz crystal prepared by him.

References

1. R. Bechmann: Nucleonics **16** (1958) 122.
2. R. W. Ditchburn, E. W. J. Mitchell, E. G. S. Paige, J. F. Custers, H. B. Dyer and C. D. Clark: Defects in Crystalline Solids, (1955) 92.
3. A. J. Cohen and H. L. Smith: J. Chem. Phys. **28** (1958) 401.

4. R. Yokota: J. Phys. Soc. Japan **7** (1952) 222.
5. G.W. Arnold and W.D. Compton: Phys. Rev. **116** (1959) 802.
6. C. M. Nelson and J. H. Crawford, Jr.: Symposium of Defect Structure of Quartz and Glassy Silica. (1957).

Journal of the Physical Society of Japan, Vol. 16, No. 1, January, 1961

Propagation of Ultrasonics in Triethylamine-water Mixture

By Seiken Shimakawa

Department of Precision Mechanics Eng., Faculty of Eng., University of Tokyo

(Received April 5, 1960)

Velocity and attenuation of ultrasonic waves in a binary mixture of Triethylamine-water were measured at different temperatures by using a pulse method at 1.5 and 2.5 Mc/s.

Assuming a Gaussian distribution of relaxation times centering on the main relaxation frequency, calculation showed that this main·frequency lies in a range of approximately 1 to 6 Mc/s and diminishes with increasing liquid temperature below the critical solution point. Tne prominent change of sound attenuation near the critical solution temperature depends mainly on the main relaxation frequency which varies with the liquid temperature.

§1. Introduction

The object of this work was to study the propagation of ultrasonic pulses in a mixture of triethylamine and water at different temperatures.

§2. Experimental Apparatus

The apparatus used in this work was similar to that which Brown⁽¹⁾ used for the measurement of ultrasonic propagation in an aniline-cyclohexane system in this laboratory.

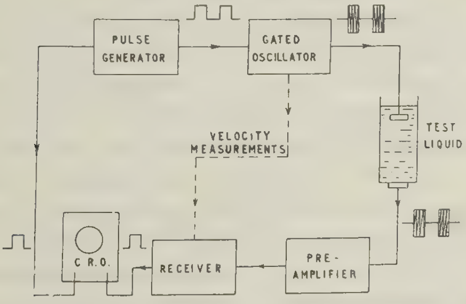

Fig. 1. Block diagram of the apparatus.

A block diagram of the mechanical and electrical apparatus is given in Fig. 1. The pulse generator gives 250 volt pulses of any width from 10 to 200 microseconds. In the present experiment an electrical pulse of some 40 microseconds was applied to the gating valve of the gated oscillator and switched on the oscillator at a repetition frequency of 200 per second. The resulting signal gave rise to a series of short pulses of R.F. voltage, which were amplified and fed to a piezoelectric transducer. The generated sound travelled through a liquid, triethylamine-water system, and was picked up by the second transducer, the receiver. The electrical pulses of R.F. oscillation, having an amplitude proportional to that of the incident sound, were amplified and detected, and the resulting signal was exhibited on a cathode-ray oscillograph, the time base of which was triggered by the pulse generator.

The transmitting crystal parallel to the receiving crystal was carried on a movable piston. As the distance between the crystals was increased, the attenuation due to the passage of the sound through the liquid became larger and the displayed signal decreased in amplitude. The amplitude absorption coefficient α' (db/cm) or α (neper/cm) can be obtained from the following relations,

---

* Present address: Dept. of Physics, King's College, University of Durham, Newcastle upon Tyne, England.

$$\alpha' = 20 \log_{10} \frac{A_0}{A} \Big/ x = 8{\cdot}686\alpha$$

where A_0 and A are the amplitudes of the received signal when the separation of the transmitting and received crystals are d and $d+x$ cms. respectively.

A cross-sectional view of the mechanical apparatus is given in Fig. 2. The receiving crystal was fixed and held in the upper crystal holder attached to the piston. This piston could be moved up and down by a micrometer screw of 20 threads per inch, and was prevented from rotating by three steel guiderods sliding in bushes in the upper plate, which carried a revolution counter and index mark for the micrometer head. The vessel containing the experimental liquid was of glass, 2″ in diameter and some 6½″ long.

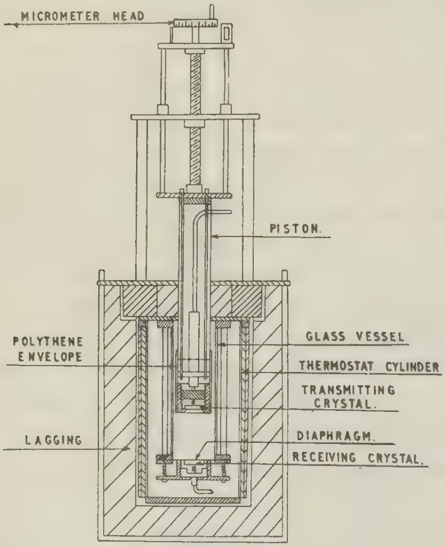

Fig 2. Cross-sectional view of the mechanical apparatus.

The transducers were conventional X-cut quartz of 1″ diameter and fundamental frequency 500 kc/s. A pair of these crystals was employed for work at 1.5 and 2.5 Mc/s., working at their 3rd and 5th harmonics respectively. One face of each crystal was exposed to air so that more energy could be radiated into the liquid from the transmitting crystal and that a larger amplitude of signal could be received by the receiving crystal. Both faces of the crystals were silver-plated. A thin aluminium foil was inserted between the near face of each transducer and a wire spring connected to the coaxial lead. This was to prevent the plating of the crystals from coming off which may have caused poor electrical contact.

Special care was taken to align the crystals parallel to one another so that unnecessary errors were not introduced into the results. As it was observed that the triethylamine-water mixture quickly attacked brass and aluminium, the bottom of the vessel which contained the experimental liquid was closed by a 0.005″ thick "Fluon" diaphram against which the lower crystal, the receiver, was pressed, acoustic contact being secured by a film of castor oil. A polythene envelope was used to insulate the upper crystal, the transmitter, in order to avoid any trouble caused by an electric current which could flow as a result of the electrolytic property of the triethylamine-water system.

In order to keep the liquid temperature below room temperature, say to about 5°C, double cylinders made of brass having 1.5 cm. clearance surrounded by felt lagging and glass wool in a wooden box were used. The glass vessel containing the test liquid was inserted inside the inner cylinder, a mixture of ice and calcium chloride being packed into the clearance between the cylinders. A thermostatically controlled heating coil was used to keep the test liquid above room temperature. A brass cylinder 8″ long and 4″ in diameter was used to enclose the glass vessel containing the test liquid. A pair of temperature control coils, one of copper and the other of constantan, were wound on the outside of the cylinder and formed two arms of a Wheatstone bridge circuit. Since the temperature coefficient of resistance of copper is 43×10^{-4} per degree C. whilst that of constantan is some 100 times smaller, the bridge is balanced at a certain temperature, the value of which is decided by the setting of the balance arms. The heating coil was wound on the outside of the control coils and connected to a relay mechanism. The relay was operated by the amplified voltage from the Wheatstone bridge circuit when the latter was out of balance. The temperature was kept constant to within 0.01°C between 20°C and 30°C. To measure the liquid temperature a copper constantan thermocouple was immersed in the liquid in the experimental vessel, the cold junction being maintained at 0°C in melting ice. The current flowing in the circuit was indicated by a Tinsley galvanometer with lamp and scale, and the temperature could be read significantly to 0.01°C. To enable the thermal equilibrium to be attained quickly, a manual stirrer formed of a loop of nichrome wire was also contained in the liquid vessel. A series of velocity and attenuation readings could be taken, the temperature remaining sufficiently steady during the short time required—perhaps 5 minutes.

In the measurement of velocity, the continuous electrical oscillation was fed directly into the receiving system. As the acoustic path changed, the phase difference between the received pulse, which had passed through the liquid, and the original oscillation varied. This was exhibited on an oscilloscope as the fluctuation of the received pulse every wavelength. In this experiment, the micrometer reading was taken every five or ten fluctuations. The velocity was then calculated from this wavelength and the frequency measured using a wave-meter.

The triethylamine-water system was used in the present work, because the sound absorption near the critical solution temperature is extremely large and also this temperature is close to room temperature, enabling the experiment to be carried out easily and with good accuracy. Commercially pure triethylamine and distilled water were used. When a series of experiments was finished, the triethylamine and water used were replaced by a new sample and the two crystals were carefully aligned before starting the next work. The test liquid was composed of 33.5 c.c. of triethylamine and 74.5 c.c. of water, i.e., 25% by weight of amine.

§ 3. Experimental Results

Previous experiments showed that the critical solution temperature for the triethylamine-water system occurred at 17.9°C(2) for a 44.6% mixture by weight of amine and 19.5°C(3) for a 34% mixture respectively. In the present test this temperature was 18.2°C for a mixture 25% by weight of amine. The measurements of velocity and absorption as a function of temperature for the above concentration at frequencies of 1.5 Mc/s. and 2.5 Mc/s. are given in Figs. 3 6.

The measurements of both absorption and velocity were first made while the temperature decreased from room temperature down

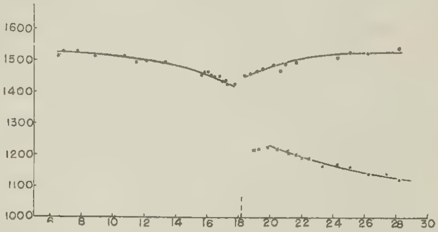

Fig. 3. Velocity vs temperature in Triethylamine-water system at 1.5 Mc/s.

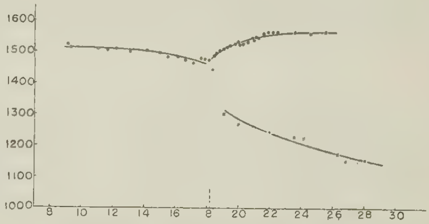

Fig. 4 Velocity vs temperature in Triethylamine-water system at 2.5 Mc/s.

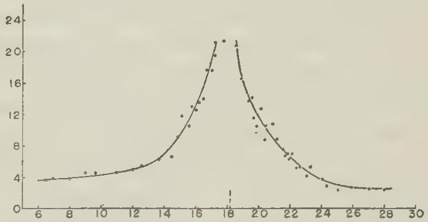

Fig. 5. Absorption vs temperature in Triethylamine-water system at 1.5 Mc/s.

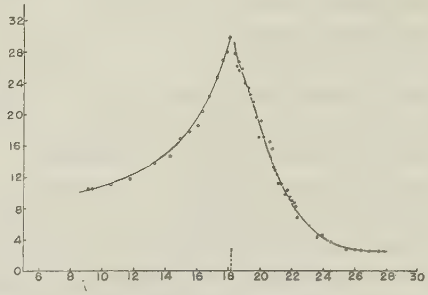

Fig. 6. Absorption vs temperature in Triethylamine-water system at 2.5 Mc/s.

to about 5°C and then the same measurements were carried out while the temperature increased. No effects of hysteresis were observed between these two series of measurements within the accuracy of experiment. The measurements in the temperature range from room temperature (about 20°C) up to about 28°C were made only as the temperature increased. The same measurements were checked three or four times keeping the temperature constant within the accuracy of ±0.05°C and the mean values of the absorption and velocity were plotted against the temperature.

For the "triethylamine-rich" layer, the received signal slightly above the critical temperature was so small because much of the sound energy was absorbed during the transmission through the "water-rich" layer that the measurement of absorption in it was made difficult, especially at 2.5 Mc/s.

§ 4. Discussion

The thermodynamic behaviour of triethylamine-water systems has been investigated by earlier workers[4) 5)], and it was noticed that the system has a minimum critical temperature of 18.4°C. By the Schlieren method used in the present work, it was observed that the liquid was not homogeneous especially above 13°C, and the density fluctuation of part of the liquid was evident. This phenomenon was very clear near the critical temperature and large clusters of greater density were observed to precipitate in various string-like shapes. Figs. 5 and 6 show the curves of absorption in db/cm. plotted against the temperature. These results give similar values of the velocity and absorption to those of previous workers[2) 3) 6)] and it is evident that the sound absorption increases rapidly with increasing temperature below the critical solution temperature.

In order to make clear the actual mechanism of absorption in binary liquid systems, some calculations have been done in terms of clusters associated with two components.

It can be assumed that the molecules of the two components combine to form clusters of various sizes and of various compositions in the critical region and they are in equilibrium giving rise to inhomogeneous density in the system. Lucas[7)] developed Stokes' theory of viscosity loss due to the inhomogeneity of the liquid, and then Sette calculated its value with certain assumptions. According to his estimate, it is found that the viscosity absorption as a consequence of heterogeneity of the liquid in the critical region can have a certain importance at low frequencies, but is far too small to explain the observed absorption, at least at frequencies higher than a few megacycles.

The scattering loss α_{sc} due to the inhomogeneity of density in the liquid can be calculated from the difference between the compressibilities of the clusters and the mother phase. An approximate calculation indicated that α_{sc}/f^2 should increase in proportion to f^2. The experiments, however, show α_{sc}/f^2 decreasing with the increasing of frequency and hence a large absorption due to scattering appears improbable. Therefore, it is most plausible to ascribe the anomalous high absorption to the relaxation phenomena predicted by earlier workers.

In a relaxation phenomenon occurring with only two equilibrium states, the amplitude absorption coefficient α is given by the following expression,[8)]

$$\alpha = Af^2 \frac{1}{1+(f/f_m)^2}\ , \tag{1}$$

where f and f_m are the frequencies of the ultrasonic waves and the relaxation phenomenon respectively. A is a parameter which depends on the temperature of the liquid but does not change with the ultrasonic frequency. Equation (1) can be written as follows,

$$\frac{\alpha}{f^2} = -\frac{1}{f_m^{\,2}}\alpha + A \tag{2}$$

which shows that the relationship between α/f^2 and α should give a straight line of slope $-1/f_m^2$. f_m can be estimated by this method. Sette estimated that the relaxation frequency in the triethylamine-water system lies in the range 2.5 to 30 Mc/s. at 15°C by this method.

Table I gives the relaxation frequencies calculated from curves in Figs. 5 and 6. These values are shown in Fig. 7 in relation to the liquid temperature. From this, although only two ultrasonic frequencies were used in the present work, the relaxation frequency in triethylamine-water was found to lie in the range 1 to 6 Mc/s. The relaxation frequency decreases with increasing liquid temperature

Table I.
Relaxation frequencies in triethylamine-water system.
(25% by weight of amine)

Temperature °C	$\alpha/f^2 \times 10^{14}$ (cm^{-1}sec^2) at 1.5 Mc/s.	$\alpha/f^2 \times 10^{14}$ (cm^{-1}sec^2) at 2.5 Mc/s.	f_m(Mc/s)
9	21.0	18.7	5.5
10	22.0	19.7	5.6
11	23.6	21.0	5.5
12	25.6	22.7	5.4
13	29.2	24.5	4.3
14	35.3	27.2	3.4
15	48.4	30.7	2.2
16	67.5	35.7	1.5
17	96.9	42.7	0.95

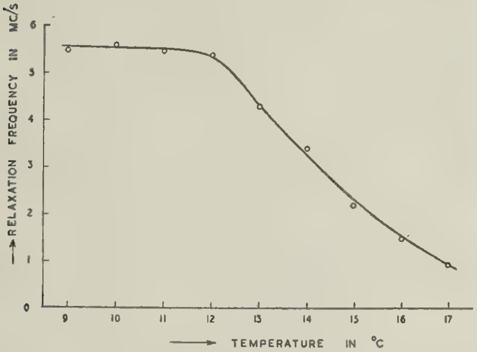

Fig. 7. The variation of the relaxation frequency with temperature in the Triethylamine-water system.

below the critical solution temperature.

The above result was obtained using the assumption that a single relaxation frequency exists for the liquid. In the present experiment, however, the relaxation phenomenon is unlikely to occur with a single relaxation time because of the existence of various associations of the components, or of clusters of various sizes and compositions. It may be that clusters of many different sizes co-exist and therefore the relaxation times are assumed to be distributed about the main relaxation time. In these mixtures, the total absorption by relaxation phenomena is given by summing up the absorptions over all relaxation frequencies. When the distribution band of relaxation times is narrow, a simple calculation assuming a Gaussian distribution of relaxation times shows that the value of α/f^2 is given by the same equation as equation (1) which involves only one single relaxation time. It may be considered that the distribution of relaxation times will change with changing liquid temperature and that the large absorption observed near the critical solution temperature depends mainly on the main relaxation frequency which depends on the liquid temperature.

The author wishes to thank the British Council for the award of a scholarship enabling him to carry out this research and Professor E. G. Richardson for suggesting the problem.

References

1) A. E. Brown and E. G. Richardson: Phil. Mag. **4** (1959) 705.
2) A. G. Chynoweth and W. G. Schneider: J. Chem. Phys. **19** (1951).
3) G. F. Alfrey and W. G. Schneider: Faraday Soc. Discussion **15** (1953) 218.
4) L. D. Roberts and J. E. Mayer: J. Chem. Phys. **9** (1941) 852.
5) J. L. Copp and D. H. Everett: Trans. Faraday Soc. **53** (1957).
6) D. Sette: Nuovo Cimento **1** (1955) 800.
7) R. Lucas: J. Phys. et Red. **8** (1937) 41.
8) H. O. Kneser: Ann. Phys. Lpz. **32** (1938) 277.

Short Notes

This section is intended to secure prompt publication of important discoveries in physics. The reports should not exceed 800 words in length. A figure of size 7 cm×7 cm will be counted as 150 words.

J. Phys. Soc. Japan **16** (1961) 118

Paramagnetic Resonance Study in Some Copper Salts

By Hidetaro Abe and Hiroko Shirai
The Institute for Solid State Physics,
University of Tokyo,
Azabu, Minato-ku, Tokyo, Japan

(Received November 5, 1960)

As the continuation of the work on copper propionate monohydrate[1)], single crystals of copper-*n*-butyrate monohydrate, copper monochloroacetate monohydrate, and copper trichloroacetate monohydrate are examined by the method of electron paramagnetic resonance (EPR), at about 24 Gc/sec. and at room temperature.

It was checked by the chemical analysis of Cu and H_2O that these crystals have formulas $Cu(CH_3CH_2CH_2COO)_2 \cdot H_2O$, $Cu(CH_2ClCOO)_2 \cdot H_2O$, and $Cu(CCl_3COO)_2 \cdot H_2O$, respectively.

(a) *Copper-n-butyrate monohydrate*

This crystal grows in the monoclinic system and in a colour of dark green. The unit-cell dimensions were determined by Iball[2)] as $a=25.12\,kx$, $b=14.65\,kx$, $c=26.79\,kx$ and $\beta=109.7°$. Different crystals used for our investigation gave the same results within the experimental errors.

The EPR showed that there exist seven independent magnetic units in this crystal. Spectrum of each unit is described by a spin-Hamiltonian

$$\mathscr{H}=\tilde{g}\beta\vec{H}\vec{S}+D\{S_z^2-\tfrac{1}{3}S(S+1)\} \qquad (1)$$

with the effective spin $S=1$. The parameters for the seven units are almost the same and given by $g_{\parallel}=2.40$, $g_{\perp}=2.04\sim2.10$, and $D=0.34\,\mathrm{cm}^{-1}$. From this result of $S=1$, it is deduced that the magnetic unit in this crystal consists of a pair of Cu^{++} ions, namely of two formula units described as $Cu_2(CH_3CH_2CH_2COO)_4 \cdot 2H_2O$. Such constitution has been first discovered in copper acetate monohydrate[3)]. Afterwards, it was deduced in copper propionate monohydrate[1)]. It was found that one of the seven units has its principal axis within the *ac*-plane and other six units reduce to three independent units having three units in their mirror positions with the *ac*-plane. Therefore, it was concluded, so far as the EPR spectra are concerned, there exist 16 independent Cu^{++} ions per unit cell. On the other hand, Iball concluded from his data of unit-cell dimensions that the unit cell contains 32 formula units. These two results, however, are not contradictory, when it is taken into account that the crystallographically independent ions are not necessarily independent in magnetic behaviours. Similar situation occurs in copper acetate whose unit cell was determined by x-ray analysis to contain eight ions, while it was shown by EPR that only four of them are independent in magnetic behaviours.

(b) *Copper monochloroacetate monohydrate*

This crystal grows in shape of monoclinic system, though some possibilities of twinning are remained. Its colour is dark green. The examined crystals seem to have two independent Cu^{++} pairs, with other two in the mirror positions with the *ac*-plane. The EPR spectra are well explained by Eq. (1) with $g_{\parallel}=2.38$, $g_{\perp}=2.13$, and $D=0.35_0\,\mathrm{cm}^{-1}$.

(c) *Copper trichloroacetate monohydrate*

This crystal also grows in the monoclinic system and in a colour of light blue, as that of the copper sulfate pentahydrate. The dimensions of unit cell are $a=22.5\,\text{Å}$, $b=6.21\,\text{Å}$, $c=9.8\,\text{Å}$ and $\beta=90°\pm1°$ (C_s^4 or C_{2h}^6). The EPR spectrum shows only one resonance line at every direction of static magnetic field, which is well described by

$$\mathscr{H}=\tilde{g}\beta\vec{H}\vec{S} \qquad (2)$$

with $S=\frac{1}{2}$ and $g(2.44_1,\ 2.10$ and $2.05)$. The direction giving the maximum g-value coincides with the b-axis. The half width of the resonance line is about 60 oer. independently of direction. From the results of the paramagnetic resonance, it is deduced, in this crystal, that one copper ion has no other copper ions in its nearest neighbours but only diamagnetic ions such as O^{--} or Cl^-, as in the ordinary copper salts.

More detailed reports will appear in this Journal. We wish to thank Drs. H. Iwasaki and S. Tamura for the x-ray and chemical analysis.

References

1) H. Abe: J. Phys. Soc. Japan **13** (1958) 987.
2) J. Iball: Nature **159** (1947) 95.
3) J. N. van Nieckerk and F. R. L. Schoening: Acta Cryst. **6** (1953) 227.

J. PHYS. SOC. JAPAN **16** (1961) 119

Magnetic and Crystallographical Properties of Hexagonal Barium Mono-Ferrite, $BaO \cdot Fe_2O_3$

By Chisato OKAZAKI, Saburo MORI and
Research Department, Wireless Division,
Matsushita Electric Industrial Co.,
Ltd. Osaka, Japan
Fumikazu KANAMARU
Institute of Scientific and Industrial
Research, Osaka University

(Received October 10, 1960)

Among the mixed oxides belonging to the barium-iron oxide system, it was found that one new stable compound appeared as a single phase having the chemical composition of $BaO \cdot Fe_2O_3$, which had already been suggested in our previous report1). Here, we should like to report on the preliminary investigation on its magnetic and crystallographic properties.

Magnetic measurements of this compound were carried out using an automatic recording magnetic balance. The paramagnetic susceptibility of this crystal at room temperature was

$$\chi_{RT} = 7.6 \times 10^{-6} \text{ e.m.u./gr} .$$

where an aqueous solution of $NiCl_2$ was used as a reference. The results obtained from thermomagnetic measurements are shown in Fig. 1. In the high temperature range, the $1/\chi$-T curve is well described by the Curie-Weiss law, $\chi = C/(T+\theta)$, where $C = 3.75 \times 10^{-3}$ emu/gr-deg., $\theta = 200°$K. It may be concluded that this compound, $BaO \cdot Fe_2O_3$, is anti-ferromagnetic. To confirm it more definitely, it is desirable to consider the arrangement of the magnetic ions in this crystal.

It is reported that this compound may have a tetragonal lattice1),2) by means of the indexing for its Debye-Scherrer patterns: the lattice constants calculated are $a \sim 6.0$Å, $c \sim 9.4$Å. If each unit cell contains four chemical formula units, the calculated density of this crystal may be about 6.0 $\text{gr} \cdot \text{cm}^{-3}$. On the other hand, the measured density was estimated as 4.70 $\text{gr} \cdot \text{cm}^{-3}$. This disagreement is so large that, it is impossible to give a reasonable explanation. Therefore, more precise study is needed.

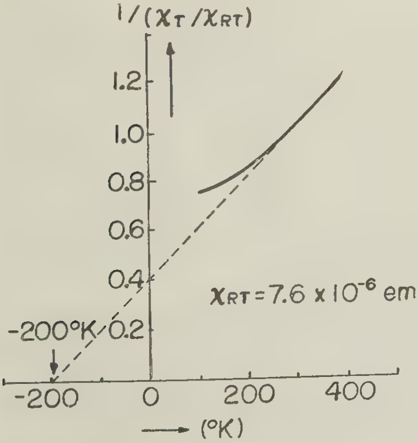

Fig. 1. Curve of inverse susceptibility versus temperature for $BaO \cdot Fe_2O_3$.

Fortunately, this compound has a rather low melting point (about 1450°C)2). So, we were able to prepare a small flake of single crystal by slow cooling from the molten phase. Laue photographs of this crystal did not show tetragonal symmetry but showed hexagonal holo-hedral symmetry, D_{6h}. Oscillation photographs and powder patterns were prepared using Fe-$K\alpha$ and Co-$K\alpha$ radiations. They indicated for the hexagonal sub-unit cell dimensions of this crystal,

$$a = 5.51\text{Å}(\times n) , \quad c = 8.44\text{Å} ,$$

where n is an integer and may be 2 in the real lattice. There are 2 formula units in each sub-unit. The calculated density is 4.78 $\text{gr} \cdot \text{cm}^{-3}$. If it is assumed that both barium and oxygen ions occupy the special positions in the lattice, the possible space group of this sub-unit cell is considered to be $D_{6h}^4 - P6_3/mmc$.

If the lattice has a usual hexagonal close-packed skeleton with respect to large barium and oxygen ions, the lattice dimension along the a axis must be about 5.88Å3), therefore, this crystal, $BaO \cdot Fe_2O_3$, may have a non close-packed Ba−O skeleton system and may be of a new type. It may be considered that this crystal has a modified type of $KFe_{11}O_{17}$ which is known already as a anti-ferromagnetic substance4), with respect to the ionic packing and magnetic coupling.

In order to confirm the above speculative consideration, further systematic investigations on the crystal structure are now in progress and the results will be published later.

References

1) C. Okazaki, T. Kubota and S. Mori: National Tech. Rep. **1** (1955) 23. (in Japanese),
2) Y. Goto and T. Takada: J. Amer. Ceram. Soc. **43** (1960) 150.
3) For example, P. B. Braun: Philips Res. Rep. **12** (1957) 491.
4) J. J. Went, G. W. Rathenau, E. W. Gorter and G. W. van Oosterhaut: Philips Tech. Rev. **13** (1952) 192.

J. Phys. Soc. Japan **16** (1961) 120

Electron Linear Accelerator as a Source of Intense Secondary Particle Beams

By Kazuto OKAMOTO*

Department of Physics, Tohoku University, Sendai

(Received October 10, 1960)

An electron linear accelerator produces a very intense electron beam. If this electron beam is used to produce secondary particles, their intensities are expected to be very high. In this note we investigate the efficiency of π meson production. We assume $E_0=760$ MeV, $I_e=100\mu A$ (average).

The electron beam must be converted into γ rays. Therefore knowledge of the thickness dependence of the γ yield is necessary. Energy loss of electrons passing through the target can be calculated by Heitler's straggling theory[1]. One can then calculate the numbers of photons at varions thicknesses using Schiff's bermsstrahlung spectrum multiplied by the photon decay factor. The results for Pt are that the maximum appears at around 1.5 mm. Hence we assume this thickness.

Production of π mesons is calculated as follows. The yield produced in the π converter of thickness dx due to a certain energy interval of bremsstrahlung, $d\phi/dk$, is denoted as dY/dk. Then

$$dY/dk=N(d\phi/dk)\sigma dx\ , \qquad (1)$$

were N is the number of atoms per cm³ and σ is a (γ, π) cross section.

Assuming $\phi=\phi_0(k)\exp(-x/X)$ and intergrating eq. (1) we obtain

$$\begin{aligned} Y&=N\int_0^l \exp(-x/X)\,dx \int_{140}^{760} \frac{d\phi_0(k)}{dk}\,\sigma dk \\ &\simeq NX[1-\exp(-l/X)]\sum_{k=140}^{760} \frac{\Delta\phi_0(k)}{\Delta k}\,\sigma\Delta k\ . \qquad (2) \end{aligned}$$

In the last equation we replaced the integral by the sum for convenience of numerical calculation. Eq. (2) can easily be evaluated if one uses the table of bremsstrahlung spectrum[2]. We assume that a π converter is Be of thickness 2 cm. Assuming also that $\sigma(\gamma, \pi)$ for Be is about 2.5 times that for H and that $\pi^-/\pi^+=1.5$, and inserting necessary values, we get

$$Y(\pi^+)=2\sim3\times10^{10}\pi^+/\text{sec}\ , \qquad (3)$$

$$Y(\pi^-)=3\sim5\times10^{10}\pi^-/\text{sec}\ . \qquad (3')$$

If these mesons are analysed by a magnetic analyser which has a solid angle of 0.1%, we get differential π yields at the target for experiment.

$$6\times10^5\pi^+/\text{sec} \qquad (4)$$

$$1\times10^6\pi^-/\text{sec} \qquad (T_\pi=80\pm3\ \text{MeV})\ , \qquad (4')$$

They agree fairly well with the experimental data[3]. If the area of the target is several tens of cm², these values correspond to about $\gtrsim10^4$ mesons/sec/cm², which is an order of magnitude higher than the present meson beams from synchrocyclotrons.

If microwave of about 1300 MC is used for the electron linear accelerator, the average beam intensity could be increased up to 500μA$\sim$1 mA. Such an electron linear accelerator would produce π meson beams which are two orders of magnitude stronger than the strongest π meson beams at present.

Very recently the Stanford group carried out similar calculations for an electron linear accelerator of 25 Bev, 60μA[4],[5],[6]. Their conclusions are also that the linac can produce substantially high yields of π, K, μ and $\bar{p}$. Although the energies are quite different, that the two independent calculations agree very well shows that an electron linear accelerator will be a powerful machine for producing very intense beams of secondary particles.

The background of the beams thus obtained is probably not large at large angles, so that for slow pions it is not serious. For fast pions emitted at forward angles it is serious, but can be eliminated by an RF mass separator. It shoud be pointed out here that a beam from a linac is sharply bunched into small groups, which greatly facilitates mass separation[7] or time of flight technique[8].

The author expresses his gratitude to Prof. M. Kimura for his hospitality during his stay at Tohoku University. He is also indebted to Dr. Kitagaki and Dr. Torizuka for valuable discussions. He is especially grateful to Prof. W. K. H. Panofsky of Stanford University for kindness in sending him the results of recent calculations of Stanford. Finally he would like to thank the Japan Society for the Promotion of Science for the financial help.

References

1) W. Heitler: *Quantum Theory of Radiation*, 3rd Edition (Clarendon Press, 1954) 377.
2) Y. Ohnuki: *Bremsstrahlung Spectrum* TUHEL-No. 3 (1960) unpublished.
3) J. R. Walers: Phys. Rev. **113** (1959) 1133.
4) S. D. Drell: Hansen Laboratories Report M-200-7 Revision A (1960) unpublished.
5) S. D. Drell: Pays. Rev. Letter **5** (1960) 278.
6) J. Ballam: Hansen Laboratories Report M-200-8 (1960) unpublished.
7) J. P. Blewett: *International Conference on High Energy Accelerators and Instrumentation*, CERN 1959, 422.
8) V. T. Cocconi et al.: Phys. Rev. Letter **5** (1960) 19.

---

* Visiting research associate of the Japan Society for the Promotion of Science.

J. PHYS. SOC. JAPAN **16** (1961) 121∼122

A-Centers in Potassium Chloride Crystals

By Kazuko KOJIMA and Noriko NISHIMAKI
Osaka Women's University, Osaka

(Received October 24, 1960)

Recently, the *A*-center in alkali halide crystals, which has not been received much attention since the first discovery by Petroff[1], has become an object of active investigation[2,3,4]. We also report here some new experimental results on this center in KCl crystals. Single crystals used for experiments were grown out of reagent grade KCl by Kyropoulos method. Absorption measurements and optical bleaching were carried out with a Hitachi EPU-2 Spectrophotometer. The wavelength of *F*-light used for optical bleaching was chosen to be somewhat shorter than the peak wavelength of the *F*-band (520±5 mμ at −70°C, for example), because the *A*-band overlaps with the long-wavelength side of the *F*-band.

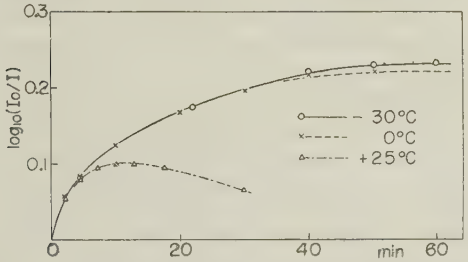

Fig. 1. Temperature dependency of the growth-rate of the *A*-band during irradiation with *F*-light.

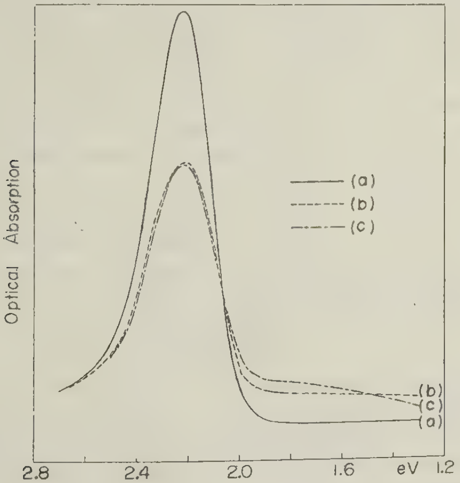

Fig. 2. Formation of the A'-band due to irradiation with *F*-light: (*a*) immediately after additive coloration, (*b*) after 10 min irradiation with λ=520 mμ at −70°C, (*c*) after additional 1.5 hrs irradiation. All measurements were made at −70°C.

Near room temperature, the *A*-band grows fairly rapidly with irradiation in the *F*-band. Its initial rate of growth, however, was almost the same at −30°C, 0°C, and +25°C (Fig. 1), and was about 1/10 as that for the typical $F \to F'$ conversion. This fact may be contrasted with the case of *M*-centers whose growth-rate is very sensitive to temperature[1]. Prolonged irradiation at +25°C causes the rise of the *M*-band and reduces again the *A*-band, while at −30°C the concentration of *A*-centers saturates and no *M*-centers appear at least within a time about three times as long as needed for the saturation of *A*-centers.

Near −70°C, at the beginning of irradiation with *F*-light, *F*-centers go over preferentially to F'-centers because the electron trapping cross section of an *F*-center is presumably larger than that of an *A*-center. Prolonged irradiation, however, seems to yield new centers which are supposed to be A'-centers from the following experiments: When a sample containing only *F*-centers is irradiated with *F*-light about 10 minutes at −70°C, no centers appear other than F'-centers (this can be confirmed by a recovery of the *F*-band upon warming to room temperature) (Fig. 2, curve *b*). However, further irradiation in the *F*-band more than 1.5 hours at −70°C changes the shape of the long-wavelength side of the F'-band as shown in curve *c* of Fig. 2, without any observable change in the peak-height of the *F*-band. The *A*-band appears on warming this sample to room temperature. When a crystal corresponding to curve *c* is irradiated with light in the vicinity of 850 mμ, it seems that the F'-band decreases and another broad band appears which is extensively superposed on the F'-band. We observed also that when a crystal in the state *c* is left in the dark at −70°C, the F'-band decreases gradually (whose half life time is about 1000 seconds at −70°C in accordance with Pick's data[5]), whereas the other centers are relatively stable and do not become unstable until −40°C. In addition, when a sample containing a large amount of *A*-centers is irradiated with *F*-light at −70°C, the F'-band develops only weakly and the new band grows within 5 minutes at the expense of the *A*-band. These experiments suggest that the new center may be an *A*-center captured another surplus electron, which we may term the A'-center. It should also be noted that *A*-centers decrease when the *M*-band is irradiated at room temperature in a sample containing a considerable amount of *M*-centers, and that scarcely no *A*-centers restore when we repeat irradiation in the *F*-band after most of the *M*-centers has been optically destroyed.

Judging from the above experimental facts, we may conclude that the A-center is a center produced by trapping an electron at a certain lattice defect existing originally without involving diffusion of ions, unlike the case of M-centers which is now commonly believed to accompany diffusion of vacancies in their formation. Moreover, if the existence of A'-centers is the truth, the assumptions would become irrelevant such that the A-center may be a paired vacancy carrying an electron[3], or a vacancy near a dislocation which has trapped an electron[6]. Thus it seems more reasonable to assume that a sort of impurities existing from the first in crystals is responsible for the A-centers.

References

1) St. Petroff: Z. Phys. **127** (1950) 443.
2) H. Okura: J. Phys. Soc. Japan **15** (1960) 1349.
3) F. Lüty: Naturwiss. (in press).
4) M. Hirai: J. Phys. Soc. Japan **14** (1959) 1400.
   T. Tomiki: J. Phys. Soc. Japan **15** (1960) 488.
5) H. Pick: Ann. Physik **31** (1938) 365.
6) T. Kojima: Busseiron Kenkyu (in Japanese) **52** (1952) 64.

J. PHYS. SOC. JAPAN **16** (1961) 122

Vibrational Effect on the Nuclear Quadrupole Coupling in ND_3

By Yoshifumi KATO

Osaka Municipal Technical Research Institute, Kita-ku, Osaka, Japan

(Received October 25, 1960)

The nuclear quadrupole coupling constant eQq ($=-4.10$ Mc/sec)[1] at the position of the nitrogen nucleus in ND_3 is nearly equal to the eQq ($=-4.0842$ Mc/sec)[2] in NH_3. When the electric field gradient q at the nitrogen nucleus is evaluated without respect to the effect of nuclear vibrations, field gradients in the two molecules have to take the same value. It may be obvious that the slight difference between the values of eQq is attributed to the effect of nuclear vibrations on the field gradient.

Now, the total field gradient q in ND_3 is divided into two parts, $q=q_n+q_e$, where q_n and q_e respectively mean the contributions to the field gradient from the nuclei and the electrons. However, it may be very difficult to take the effect of nuclear vibrations on q_e into account. Here the vibrational average has been evaluated only for q_n, on the assumption that the electron distribution near the nitrogen nucleus do not vary by small vibrations of the nuclei. In such a case, q_e in ND_3 would be equal to that in NH_3.

In the same way as the previous evaluation of the field gradient in NH_3[3], two approximate averages have been taken for q_n. One is the average over the simple harmonic oscillation by using the following normal coodinates on the symmetric bending mode $\nu_2(a_1)$ ($=749\,\mathrm{cm}^{-1}$),

$$Q_2=0.00402S_1+0.80996S_2\,,$$

where S_1 and S_2 respectively express normalized stretching and bending symmetry coordinates (assuming the anharmonicity factor $\chi=0.0867$, so that the harmonic frequency $\omega=814\,\mathrm{cm}^{-1}$). The other is the average over the inversion doubling by using the results of Manning on ND_3[4], as previously shown in NH_3[3] (assuming $\lambda=-0.26$).

Table I. Calculated values of the nuclear part q_n of the electric field gradient in ND_3 and the nuclear quadrupole moment $Q(N^{14})$.

	(I)*	(II)**
q_n (in au)	$-0.24492e$***	$-0.25173e$
$Q(N^{14})$ (in $10^{-26}\,\mathrm{cm}^2$)	0.941	0.938

* The value averaged over the simple harmonic oscillation.

** The value averaged over the inversion doubling.

*** e is the protonic charge ($=4.8022\times10^{-10}$ esu).

The results obtained are given in Table I. Here, for the value of q_e, the previous estimate by Kaplan's wave function with configuration interactions among 13 states has been used ($=-1.60973e$ au: e is the protonic charge)[3]. As seen in Table I, the value of the nuclear quadrupole moment $Q(N^{14})$ obtained from ND_3 is consistent with that obtained from NH_3 ($=0.94\times10^{-26}\,\mathrm{cm}^2$)[3]. This fact shows that the difference of eQq between ND_3 and NH_3 can be explained sufficiently by the above approximate calculation of the effect of nuclear vibrations. The value of $Q(N^{14})$ obtained above seems also to be supported by the value ($\sim1\times10^{-26}\,\mathrm{cm}^2$) calculated from nuclear shell model under the L-S coupling, while a recent direct experimental value gives $(1.6\pm0.7)\times10^{-26}\,\mathrm{cm}^2$[5].

The author wishes to express his appreciation to Prof. H. Narumi who suggested this problem and made helpful discussions.

References

1) M. T. Weiss and W. P. Strandberg: Phys. Rev. **83** (1951) 567.
2) G. R. Gunther-Mohr, R. L. White, A. L. Shawlow, W. E. Good and D. K. Coles: Phys. Rev. **94** (1954) 1184.
3) Y. Kato: J. Chem. Phys. (to be published).
4) M. F. Manning: J. Chem. Phys. **3** (1935) 136.
5) C. C. Lin: Phys. Rev. **119** (1960) 1027.

J. PHYS. SOC. JAPAN **16** (1961) 123~124

Proton Resonance and Spin Quenching Effect in $NiSO_4\cdot 7H_2O$

By Hiroshi NAGASAWA and Yuzo TOMONO
Department of Physics, University of Tokyo

(Received November 18, 1960)

In some paramagnetic salts, all the degeneracies in the spin state of a paramagnetic ion, which has even number of unpaired electrons, are completely lifted by the combined action of spin orbit coupling and crystalline electric field. The static susceptibility of these salts above room temperature is well described by Curie-Weiss law. But as far as the line width of nuclear magnetic resonance is concerned, the polarization of the "quenched spin" plays an important role as a function of the applied magnetic field. Such an effect was generally studied by T. Moriya and Y. Obata[1]. According to their theory, the line width of the nuclear resonance is expected to be proportional to $H_0^2+H_i^2$ so long as the separation of initial splitting is larger than Zeeman energy, where H_0 and H_i mean the external magnetic field and the low frequency part of the spin-spin interaction respectively.

In this study the field dependence of second moment of proton resonance was observed on powdered $NiSO_4\cdot 7H_2O$ at room temperature. For a single crystal, paramagnetic resonance was observed by K. Ohno[2]. It has been found that the effect of paramagnetic ion on protons is comparatively smaller than that of the dipolar interaction between protons of the water molecules, which can be estimated by utilizing the line of $ZnSO_4\cdot 7H_2O$ as a reference substance, because it is nearly identical in structure to $NiSO_4\cdot 7H_2O$. Their lattice parameter are shown in Table I.

Table I.[3]

	a	b	c
$NiSO_4\cdot 7H_2O$	11.86 A	12.08	6.81
$ZnSO_4\cdot 7H_2O$	11.85	12.09	6.83

Here it is assumed that the effect of paramagnetic ions is a small perturbation and the unperturbed line shape is equal to that of zinc complex. According to this assumption, the absorption line of nickel complex is constructed from the line of zinc complex, of which each line element is broadened by the effect of the paramagnetic ions. So the shape function is written as follows,

$$G_{NiSO_4\cdot 7H_2O}(H-H_0)$$
$$=\int G_{ZnSO_4\cdot 7H_2O}(H'-H_0)\cdot f_{para}(H-H')dH' .$$

From this convolution, it is easily found that

$$\langle(\Delta H)^2_{NiSO_4\cdot 7H_2O}\rangle=\langle(\Delta H)^2_{ZnSO_4\cdot 7H_2O}\rangle+\langle(\Delta H)^2_{para}\rangle ,$$

where G_A is the shape function of A, f_{para} is the influence function of paramagnetic ion which, according to Moriya and Obata, is expected to be of Lorentzian type as a result of exchange narrowing. Strictly speaking the second moment is not affected by the exchange narrowing[4], and is not expected to have the field dependence of $(H_0^2+H_i^2)^2$, but it is impossible to know the exact second moment from the observed derivative curve because of the finite range of the magnetic field. Therefore it is estimated that the square root of the second moment should be proportional to $H_0^2+H_i^2$.

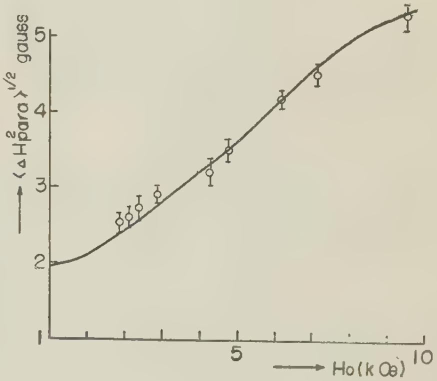

Fig. 1. The field dependence of the effective line width, which is obtained from the difference of the observed second moments of Ni and Zn complexes.

The experimental result is shown in Fig. 1. The field dependence of the effective line width shown in the figure does not always agree to $H_0^2+H_i^2$. But this discrepancy can be understood by taking into account that the Zeeman energy becomes comparable with the magnitude of initial splitting, and spin level separation varies appreciably from the initial value. This correction becomes important when external field is more than three thousands gauss. The solid curve shown in the figure is the result of the calculation considering this effect.

The unexpected result from experiment is the order of magnitude in the internal field H_i. The cause of the internal field discussed in the theory quoted above is the dipolar interaction between paramagnetic ions, but experimental result is about several ten times larger than the predicted value. The reason of this disagreement is not so certain, but it is expected that a sort of exchange interaction such as Moriya-Dzialoshinski term contributes to the internal field. The contribution can be evaluated, according to Moriya's mechanism[5], by utilising the value of isotropic exchange interaction which is estimated from the observed susceptibility by T. Watanabe[6]. The result seems to be consistent with the observed value.

References

1) T. Moriya and Y. Obata: J. Phys. Soc. Japan **13** (1958) 1333.
2) K. Ohno: J. Phys. Soc. Japon **8** (1953) 802.
3) C. A. Beevers and C. M. Schwartz: Z. Krist. **A, 91** (1935) 157. Wyckoff: Crystal Structure Vol. 3.
4) R. Kubo and K. Tomita: J. Phys. Soc. Japan **9** (1954) 888.
5) T. Moriya: Phys. Rev. Letters **4** (1960) 228.
6) T. Watanabe: to be published.

J. PHYS. SOC. JAPAN **16** (1961) 124

Electrical Properties of Sb-Doped *n*-Type SnSe

By Jun-ichi UMEDA

Department of Physics, Faculty of Science, Kyushu University, Fukuoka, Japan

(Received November 4, 1960)

The electrical resistivity ρ and Hall coefficient R_H of Sb-doped n-type SnSe single crystals were measured in the temperature range between 100°K and 700°K, and the effects of some heat-treatments on them were also investigated.

Recently, Asanabe1) published a detailed report on the electrical properties of p-type SnSe single crystals, especially on the effects of heat-treatment on them. In his report the hole concentrations of those crystals at room temperature were increased by quenching from above 200°C and were decreased by annealing at below 200°C, whereas the Hall mobilities showed little change. He showed also that these behaviours could be explained if some acceptor levels were generated at high temperature and were frozen by the quenching, whereas they were annihilated at relatively low annealing temperature. It may be interesting to compare these behaviours with those of n-type SnSe.

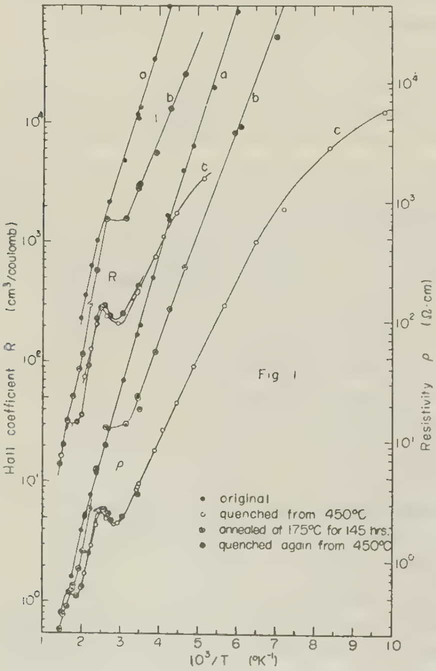

Fig. 1.

Single crystals of n-type specimens were obtained from the reaction $Sn_{0.98}+Se+Sb_{0.02}$* in an evacuated sealed quartz glass tube in the same method as described elsewhere1). The samples were cut in the rectangular form; their largest dimensions lay in c-plane.

The measured Hall coefficient and resistivity of one of these n-type specimens are shown in Fig. 1, in the three cases of heat treatment, i.e. a) original, b) annealed and c) quenched. Slopes of the curves of the Hall coefficient versus $1/T$ show the existence of two impurity levels below the conduction band by 0.16 eV and 0.20 eV. The effect of heat-treatment is found; that is, the carrier concentration increases by the quenching and decreases by the annealing. This behaviour is different from that expected from the results on p-type SnSe, and it is hardly understood on the model of the generation or annihilation of acceptors only. The similar behaviours have been reported on InAs, but they are different from those of SnSe, as the effect of the annealing on the carrier concentration of the InAs is reversed when n-type material is converted to p-type one2).

These electrical behaviours of SnSe suggest that donor levels made by Sb-doping are annihilated by the annealing and are generated by the quenching in the same way as the acceptor levels in p-type SnSe. But this is inconsistent with the fact that mobility of Sb-doped p-type SnSe is decreased by the annealing. No consistent explanation on this point has been obtained. It is conceivable, however, that some electrical properties of p- and n-type Sb-doped SnSe single crystals may be explained qualitatively by assuming simultaneous annihilation or generation of both acceptors and donors.

The author should like to express his sincere thanks to the late Prof. A. Okazaki for kind guidance. He is also indebted to Mr. K. Hashimoto for valuable advices.

---

* Sn; Johnson Matthey and Co.. Se; American Smelting and Refining Co.. Sb; Yokosawa Pure Chemical Co..

References

1) S. Asanabe: J. Phys. Soc. Japan **14** (1959) 281.
2) J. R. Dixon: J. Appl. Phys. **30** (1959) 753.

J. PHYS. SOC. JAPAN **16** (1961) 125~126

Change of Surface state of Ge by Electron Bomberdment

By Kiichi KOMATSUBARA

Hitachi Central Reserch Laboratory, Tokyo

(Received November 16, 1960)

Change of surface state of germanium by electron bombardment has been studied by measuring the reverse current of a field effect change of *p-n* junction.

An alloy type *p-n* junction was prepared with 30 ohm. c.m. N type Ge. The change curves of ths reverse current, *Is*, by the application of an electric field, *E*, verfical to the opposide surface of the alloying surface has been pictured on the oscilloscope[1].

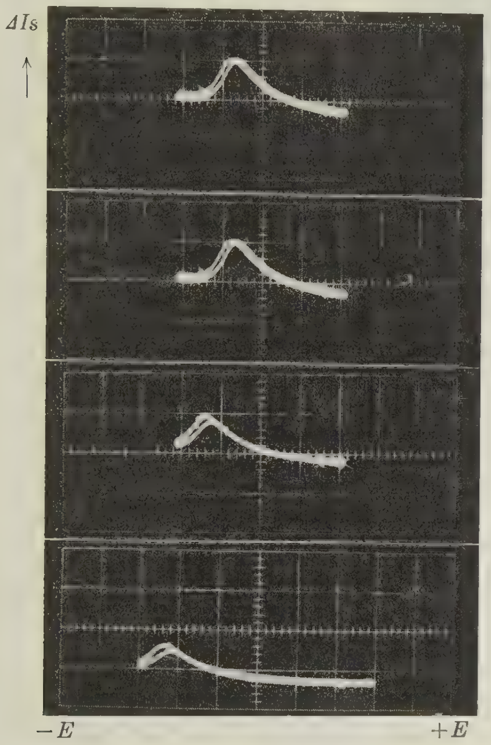

before bombardment

Is 48 μA

after bombardment of 0.42×10^{15} electrons/c.m.^{2}

Is 35 μA

1.76×10^{15} electrons/c.m.^{2}

Is 110 μA

4.2×10^{15} electrons/c.m.^{2}

Is 162 μA

V-scale 10 μA/div. H-scale 100 V/div.

Fig. 1. The change of *ΔIs*~*E* curve due to the electron bombardment.
electron energy; 0.8 MeV current density; 0.2 μA/c.m.^{2}

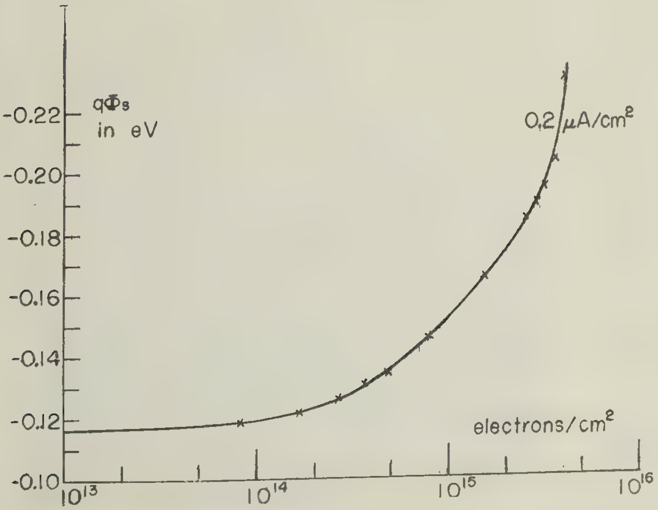

Fig. 2. The changes of surface potential by the electron irradiation of 0.8 MeV from the electrostatic accelerator.
sample: about 30 ohm. c.m. N type Ge.
current density of irradiation.

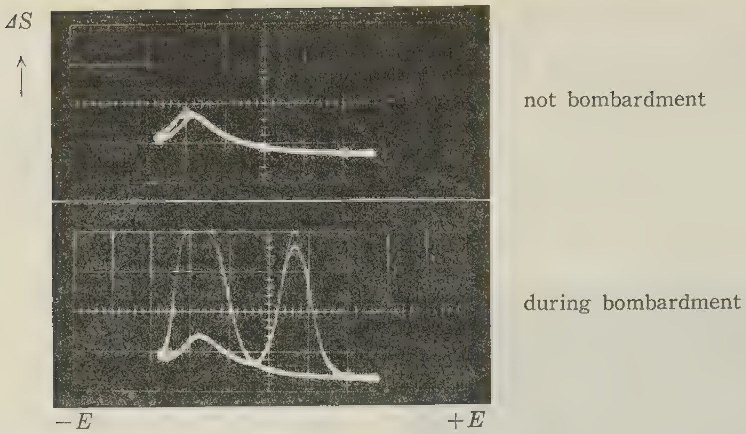

V-scale 10 μA/div. H-scale 100 V/div.

Fig. 3. The variation of a S E curve during the electron bombardment.

The p-n junction was sealed in to a glass tube at 10^{-4} mm Hg vacuum, and the Ge surface on the other side of the p-n junction was mounted on a Ni electrode with a 0.1 mm mica spacer placed in between. The germanium was bombarded through the nickel electrode with an electron beam of energy about 0.8 MeV and current density 0.2 μA after passing through the electrode.

50 c/s A.C. voltage was applied on the nickel electrode for observing, then Is the changes in Is by the change of surface potential.

In this case the contributing factor to the reverse current here is the generation recombination mechanism of charged caraier on Ge surface[2]. With the dimension and the concentration of impurities of present sample, the following relationship exists between the variation of Is and that of surface recombination velocity, S:[3]

$$dS/S=1.3dIs/Is\ .$$

Therefore the variation in reverse current, Is, can be used as the measure of the variation in surface recombination velocity, s.

As the total dosage of electron was increased, the value of E corresponding to the maximum value of S shifted toward more negative direction as shown in Fig. 1.

From the value of E and of the capacity between the electrode and the Ge surface, the surface charge Qs was computed, and from this the surface potential, $\emptyset s$ have been obtained. The relation between the total dosage of bombarding electrons and the surface potential $\emptyset s$ in the absence of external electric field is shown in Fig. 2.

During the bombardment the S-E cvrve displayed curious phenomena which was shown in Fig. 3.

References

1) Geoge C. Dousmanis: Phys. Rev. **112** (1953) 369.
2) W. M. Webster: Proc. I. R. E. **43** (1955) 277.
3) J. E. Thomas jr and R. H. Rediker: Phys. Rev. **101** (1956) 984.

J. Phys. Soc. Japan **16** (1961) 126~127

Antiferromagnetic Magnetostriction in CoO and NiO Single Crystals

By Takurô NAKAMICHI and Mikio YAMAMOTO

Research Institute for Iron, Steel and Other Metals, Tôhoku University, Sendai

(Received September, 1960)

In connection with the origin of the lattice deformation accompanied with the magnetic transformation in antiferromagnets, it may be important to investigate the nature and behavior of magnetostriction in those substances. Recently, Belov and Levitin[1] reported briefly some magnetostrictive behavior of NiO polycrystals measured in magnetic field up to 14,000 Oe. We have made preliminary measurements on the antiferromagnetic magnetostriction of single crystals of CoO and NiO and obtained some interesting results.

The crystal specimens employed are rounded square plates, 3 mm thick and 13 mm wide, with plate surfaces coinciding with the (100) plane, which were cut out, making use of the cleavage, from large crystals grown by Mr. Y. Nakazumi of Fuji Titanium Industrial Co. using the Verneuil method. They were submitted to the measurements without any treatment. Magnetostriction measurements by the strain gauge technique[2] were performed at room and liquid air temperatures in magnetic field up to 11,000 Oe applied parallel to the (100) plate surface.

The results obtained are summarized as follows:

(1) The longitudinal and transverse magnetostrictions along the [100] and [110] directions vary monotonously with increasing field (Fig. 1). It seems that the measured magnetostrictions are proportinal to the square of the intensity of magnetic field, as contrasted to a linear increase of the magnetostriction beyond a distinct critical field as claimed by Belov and Levitin[1] with NiO polycrystals. (2) The magnitude of longitudinal magnetostriction is twice as large as that of the transverse one, and they have different signs, except the magnetostrictions along the [110] direction in CoO, for which the signs of longitudinal and transverse magnetostrictions are the same. (3) The magnetostriction along the [100] direction is larger than that along the [110] direction. (4) The dependency of the magnetostriction on the direction of an applied field is of the $\cos 2\phi$ type, where ϕ is the angle between the direction of the magnetostriction measurement and that of an applied field (Fig. 2). (5) The magnitude of the magnetostriction observed in the maximum applied field is of the order of 10^{-6} (Fig. 1 and 2). (6) For CoO single crystal, of which the Néel temperature is 279°K, the magnetostriction could not be observed at room temperature, showing that the magnetostriction observed here is certainly originated from antiferromagnetism. (7) The magnetostrictions along the [100] and [110] directions in CoO single crystal as well as those along the [100] direction in NiO single crystal are larger at the liquid air temperature than at room temperature, but the magnetostriction along the [110] direction in NiO single crystal is reverse in this respect. These are to be compared with Belov and Levitin's[1] finding that the magnetostriction in NiO polycrystal decreases monotonously with raising temperature. (8) Small hysteresis of magnetostriction was observed when an applied field was decreased in magnitude or reversed in direction, which seems to be originated from an accidental thermal expansion.

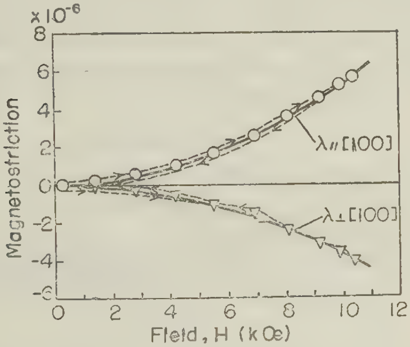

Fig. 1. Longitudinal and transverse magnetostrictions measured along the [100] direction in CoO single crystal at the liquid air temperature. Dashed lines follow the measured points in increasing and decreasing magnetic field and ○ and ▽ show the mean values of longitudinal and of transverse magnetostriction, respectively. Thick lines express the relation $\lambda \propto H^2$.

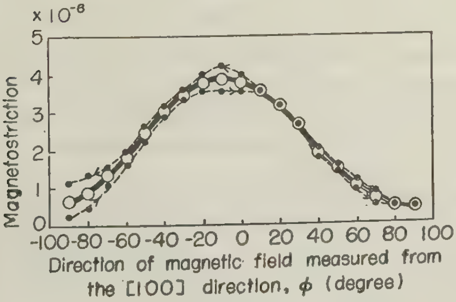

Fig. 2. Magnetostriction along the [100] direction as dependent on the direction, ϕ, of magnetic field of 10,200 Oe applied parallel to the (001) plane in NiO single crystal at the liquid air temperature. The measured points for the clockwise and anti-clockwise rotation of the field and their mean values are connected by dashed and thick lines, respectively.

We may conclude from these measured results that the magnetostriction observed here is originated from antiferromagnetism and make its appearance as a result of displacements of antiferromagnetic domain walls. Notably, the above mentioned experimental facts (1)～(4), can be interpreted in terms of the concept of the antiferromagnetic domain wall displacements proposed by Néel[3].

References

1) K. P. Belov and R. Z. Levitin: Sov. Phys. (JETP), **10** (1960) 400.
2) M. Yamamoto and T. Nakamichi: J. Phys. Soc. Japan, **13** (1958), 288; Sci. Rep. RITU, **A11** (1959), 168.
3) L. Néel: Proc. Internat. Conf. Theor. Phys. (Kyôto-Tôkyo), (1953), 701.

J. PHYS. SOC. JAPAN **16** (1961) 128

The Purification of KCl by the Zone Refining Method

By Morio INOUE and Hiroyuki MIZUNO
Matsushita Electronics Corporation, Takatsuki

(Received November 12, 1960)

The zone melting method has proved to be an effective technique for the purifying and growing of single crystals of non-polar semi-conductors.

Recently Gründig[1], by applying this method for the purification of alkali halides, could give an estimation of the binding energies of some divalent metal ions with positive ion vacancies in KCl and KBr. So far, however, the method has not been in common practice.

This report is the first of a series concerning the behaviour of impurities in KCl when the KCl is subjected to the purifying zone melting process.

The interior of the carbon boat containing KCl material was completely covered with thin platinum foil of 0.05 mm thickness in order to prevent adhesion of the KCl to the boat. The boat was moved with a speed of 1 to 100 mm/hour in the atmosphere of nitrogen through a furnace having a temperature distribution with a peak at its center.

In the zone refining method an impurity distribution is given by[2]

$$C_s=C_0\left[1-(1-K)\exp\left(-K\frac{x}{l}\right)\right], \qquad (1)$$

where C_0 is the initial concentration of an impurity, C_s is the concentration at a distance x from the starting point of the melting zone, K is the effective distribution coefficient and l is the zone length. Fig. 1 show the distributions of Br ions in a KCl crystal after zone refining is repeated n times. The moving speed of the zone is 42 mm/hour. The solid curve for $n=1$ in Fig. 1 is a theoretical curve given by Eq. (1). The value of K is chosen to be 0.75 to give the best fit to the experimental data for $n=2$ and $n=3$. Following the same procedures the effective distribution coefficient of Na ions in KCl was also measured and found to be 0.1 for the zone speed of 42 mm/hour. The concentration of Br ions was analysed[3] by the colorimetric method and that of Na ions by a spectroscopic method both with the probable error of ±5%. The distribution coefficient is expected to depend to a considerable extent on the speed of the zone and therefore closer examination of the relation between the distribution coefficient and the zone speed should be desirable. Moreover a similar study on the other impurities in a KCl single crystal is under investigation. The authors wish to thank the staff of the analysis section in their laboratory for the impurity analysis.

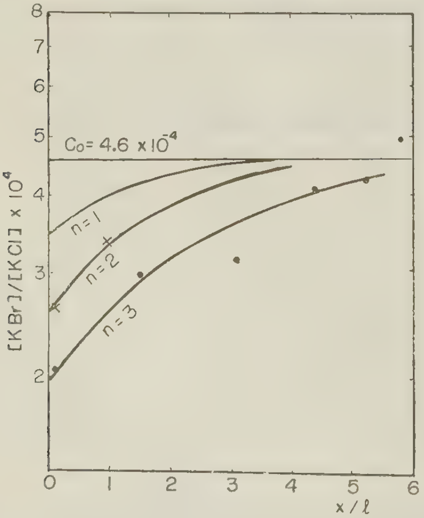

Fig. 1. The distribution of Br⁻ in KCl with the zone speed of 42 mm/hour.

References

1) H. Gründig: Z. Phys. **138** (1960) 577.
2) W. G. Pfann: Zone Melting (John Wiley and Sons, New York, 1958).
3) D. F. Boltz: Colorimetric Determination of Nonmetals (Interscience Publishers, New York).

J. PHYS. SOC. JAPAN **16** (1961) 128~129

Heat Capacities of Two Manganese Salts*

H. FORSTAT and G. O. TAYLOR
Department of Physics and Astronomy Michigan State University, East Lansing, Michigan, U.S.A.

(Received August 31, 1960)

During the course of some work on the antiferromagnetic behavior of single crystals, heat capacity studies have been made on $MnSO_4 \cdot 4H_2O$ and $MnHPO_4 \cdot 3H_2O$. These single crystals were grown from aqueous solutions at room temperature and they weighed approximately 2 grams. The sulfate crystals were monoclinic while the phosphate crystals were rhombic. The heat capacity measurements were made in an adiabatic calorimeter using carbon resistance thermometry[1].

Fig. 1 shows the results of these experiments. The data for $MnHPO_4 \cdot 3H_2O$ shows no magnetic ordering process usually associated with an antiferromagnetic-paramagnetic transition. Proton resonance data[2] on this crystal did not indicate an antiferromagnetic state. These heat capacity measurements indicate a Debye temperature of 28°K. In the case of the manganese sulphate crystal, the heat capacity curve shows a slight rise at the lowest temperature. Whether this represents the beginning of a magnetic transition or a Schottky type anomaly is difficult to say, since our experiment could not be performed below 1.3°K. Preliminary proton resonance work²⁾ shows no evidence of a magnetic ordering process, but a more detailed examination in the low temperature region is in progress.

---

* Supported by the Office of Ordnance Research, U. S. Army.

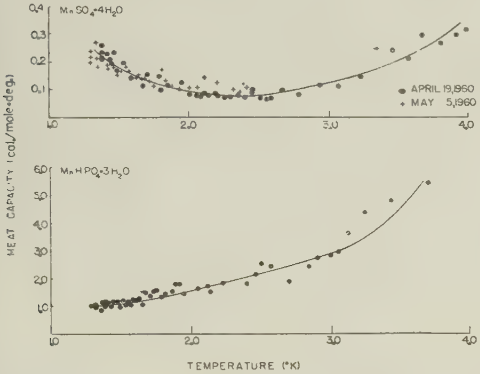

Fig. 1. Heat Capacities of $MnSO_4 \cdot 4H_2O$ and $MnHPO_4 \cdot 3H_2O$.

References

1) Forstat, Taylor, King: J. Chem. Phys. **31** (1959) 929.
2) R. D. Spence: private communication.

J. Phys. Soc. Japan **16** (1961) 129

Excitation Function for the Reaction $O^{16}(\alpha, pn)F^{18}$

By Michiaki FURUKAWA and Shigeo TANAKA

Institute for Nuclear Study,
University of Tokyo,
Tanashi-Machi, Tokyo

(Received November 2, 1960)

The energy dependence of cross sections for the reaction $O^{16}(\alpha, pn)F^{18}$ has been determined for the alpha-particle energies up to 40 MeV. The bombardments were performed with the external alpha-particle beam from the 160 cm INSJ variable energy cyclotron by means of a stacked-foil technique. The values of energy loss in target and in aluminum absorber were taken from the compilation of Sternheimer (Phys. Rev. **115** (1959) 137). The beam was collected in a Faraday cup and the total charge of the beam was measured by a 100% feed-back type current integrator. In different experiments, the initial alpha-particle energies were 40.0 and 31.3 MeV. Sodium carbonate (about 4 mg/cm²) was used as an oxygen target. Sodium carbonate powder suspended in acetone containing a trace of polyvinylacetate (binder) was deposited onto a thin aluminum backing-foil by slow evaporation of acetone. And the target was dehydrated by heating in an oven before use. After the bombardment, the target foil was sandwiched by two brass plates of sufficient thickness to stop the positrons, and the two 0.51 MeV γ-rays were detected in coincidence with two ($1\frac{1}{2}$ in. dia. × 1 in. high) NaI scintillation counters positioned 180° from each other with respect to the source. After shorter-lived activities including C^{11} had decayed out, the decay was followed for about 12 hours. The half-life showed the literature value (112 min.) of F^{18}. The counting efficiency of the instrument was calibrated by an Na^{22} standard source.

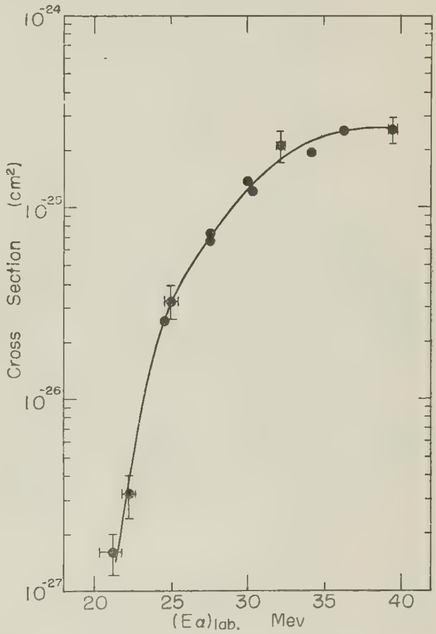

Fig. 1. Excitation function for the reaction $O^{16}(\alpha, pn)F^{18}$.

The result is shown in Fig. 1, together with the energy spread in target foil and with the estimated error of the magnitude of cross section for some experimental points. The error in the magnitude of cross section is mainly due to inhomogeneity of target foil. It can be seen that F^{18} is produced even below the threshould energy (23.2 MeV) of the (α, pn) reaction. This is not due to impuritie in target. It is thought that the deuteron emission is very important in this case. The threshold energy of the (α, d) reaction is 20.4 MeV. Further, the present result may give some informations about the interference of F^{18} towards the activation studies in which oxide targets are used.

J. PHYS. SOC. JAPAN **16** (1961) 130

Mass Spectra of Baryons

By Seitaro NAKAMURA and
Ken KAWARABAYASHI
Department of Physics, Facult of Science,
University of Tokyo, Tokyo, Japan

(Received December 3, 1960)

Recently, one of the present authors (S.N.)[1)-2)] constructed a Hamiltonian for the strong interaction between baryons and mesons with the spin 0. All baryons are here considered to represent different states of one particle, and among them a number of the Yukawa processes mediated by sixteen kinds of mesons (kaons, pions and D-mesons) are assumed. In order to specify baryons and mesons a new quantum number κ charge is introduced. ($Q_\kappa=+1$ for nucleons and Ξ-particles, $Q_\kappa=0$ for Σ and Λ-particles, $Q_\kappa=\pm1$ for kaons, and $Q_\kappa=0$ for pions and D-mesons.) The concept of strangeness and hypercharge are not used. We use two orthogonal Euclidian spaces; one is the three dimentional κ-charge space, and the other the three dimensional electric charge space, called N-space, which is identical with the M-space[3)] except its hypercharge assignment. The interaction Hamiltonian is assumed to be completely symmetric in these speculated charge spaces; $|\kappa|$, κ_3 and $|N|$, n_3 are conserved. In terms of such Hamiltonian (9)-12) in the reference 1)), we would expect the same number of the mass correction terms for all baryons. By means of a perturbation calculation to the lowest order, we obtain the following relations:

$$M_\Xi=M_0+g^2\left\{3I_{L\Sigma}+I_{L\Lambda}+I_{D^\pm}+\frac{1}{2}I_{D0}+\frac{1}{2}I_{D^{0\prime}}\right\}+\frac{g'^2}{2}\{3I_\pi+I_{\pi^{0\prime}}\}\,,$$
$$M_N=M_0+g^2\left\{3I_{K\Sigma}+I_{K\Lambda}+I_{D^\pm}+\frac{1}{2}I_{D^0}+\frac{1}{2}I_{D^{0\prime}}\right\}+\frac{g'^2}{2}\{3I_\pi+I_{\pi^{0\prime}}\}\,,$$
$$M_\Sigma=M_0+g^2\left\{2I_{KN}+2I_{L\Xi}+I_{\Sigma D}+\frac{1}{2}I_{\Lambda D}+\frac{1}{2}I_{D^{0\prime}}\right\}+\frac{g'^2}{2}\{2I_{\Sigma\pi}+I_{\Lambda\pi}+I_{\Sigma\pi^{0\prime}}\}\,,$$
$$M_\Lambda=M_0+g^2\left\{2I_{KN}+2I_{L\Xi}+\frac{3}{2}I_{\Sigma D}+\frac{1}{2}I_{D^{0\prime}}\right\}+\frac{g'^2}{2}\{3I_{\Sigma\pi}+I_{\Lambda\pi^{0\prime}}\}\,. \qquad (1)$$

Where $I_{L\Sigma}$ etc. in the expressions for M_Ξ etc. are the self energy terms of the lowest order derived from the respective channels $\Xi\rightarrow\Sigma+L\rightarrow\Xi$. (1) is independent of the cut-off which we resort to in order to get a finite result. It is clear that the sign of the integrals $I_{L\Sigma}$ etc. depends on their coupling types. To know their gross behaviors, however, we have only to make clear the sign of the leading terms in the finite self energy terms which are obtained by means of the Feynman cut (λ).

For scalar mesons,

$$\delta M=-f_1^2/4\pi\cdot3/8\pi\cdot M_0\log\lambda^2/M_0^2:\qquad(s-s)$$
$$\delta M=+f_2^2/4\pi\cdot M_0\cdot(M_0/\kappa)^2\cdot1/8\pi\cdot\lambda^2/M_0^2:\qquad(v-v)\,,\quad(2)$$

and for pseudoscalar mesons,

$$\delta M=g_1^2/4\pi\cdot M_0\cdot1/8\pi\log\lambda^2/M_0^2:\qquad(ps-ps)$$
$$\delta M=-g_2^2/4\pi\cdot M_0\cdot3/8\pi\cdot(M_0/\kappa)^2\cdot\lambda^2/M_0^2:\qquad(pv-pv)$$
$$\delta M=-g_1g_2^2/4\pi\cdot M_0\cdot(M_0/\kappa)\cdot1/2\pi\cdot\lambda^2/M_0^2:\qquad(ps-pv)\quad(3)$$

Here the interaction Lagrangians are taken as follows:

$$L_s=f_1\bar{\psi}\psi\varphi+i(f_2/\kappa)\bar{\psi}\gamma_\mu\partial_\mu\varphi$$
$$L_{ps}=ig_1\bar{\psi}\gamma_5\psi\varphi+i(g_2/\kappa)\bar{\psi}\gamma_5\gamma_\mu\psi\partial_\mu\varphi\,.$$

If we assume that the parity of K-kaons and that of L-kaons are of the opposite sign, we could predict the mass splitting for baryons into the three groups Ξ—$\Sigma\Lambda$—N. In fact, if we take $\Omega_{K\Sigma N.K\Lambda N}=i\gamma_5\gamma_\mu$ or 1, $\Omega_{L\Sigma\Xi.L\Lambda\Xi}=i\gamma_\mu$ or γ_5, then we obtain $M_\Xi>M_\Sigma=M_\Lambda>M_N$. In this case, the mass difference between the Σ and the Λ particles can not be explained.

If we take into account the hermiticity, either S or PS coupling will be cancelled in (12)-(13)[1)], so that only V–A couplings are preferred.

Lastly we mention that the mass splitting derived from the present considerations is of the right order of magnitude if we assume that $M_0\approx1000$ MeV, $g^2/4\pi\sim1$ and with the reasonable order of the cut-off.

References

1) S. Nakamura: J. Phys. Soc. Japan **15** (1960) 2122.
2) S. Nakamura: J. Phys. Soc. Japan **15** (1960) 2108.
3) G. Takeda: Prog. Theor. Phys. **19** (1958) 361.
B. d'Espagnat, J. Prentki and A. Salam: Nuclear Phys. **5** 447 (1958) 447.

J. PHYS. SOC. JAPAN **16** (1961) 131

Preferential Plastic Deformation in the Surface Region of Al and α-Fe Single Crystals

By Kôji SUMINO and Mikio YAMAMOTO

Research Institute for Iron, Steel and Other Metals, Tôhoku University, Sendai

(Received November 11, 1960)

Although there are many evidences on the start of plastic deformation from the crystal surface[1)] and on the higher density of dislocations near the surface than that in the interior of deformed crystal[2)], very few evidences[1a)] are available on the difference in the proceeding of work-hardening in the surface region and in the interior, which has an important bearing on the theory of work-hardening of crystals.

We have pursued this problem with aluminium single crystals. As shown in Fig. 1, the value of flow stress at any stage of deformation is lowered by electrolytic polishing out of the surface region. It has been confirmed that the value of $(\sigma_2-\sigma_0)/(\sigma_1-\sigma_0)$ (σ_0 is the critical shear stress, and σ_1 and σ_2 are the flow stresses before and after the polishing out of the surface layer, respectively) decreases with an increase of the thickness of the polished-out surface layer, Δd, and attains to a smallest value of 0.5 at $\Delta d = 150-200\,\mu$ for a relatively small deformation, while the $(\sigma_2-\sigma_0)/(\sigma_1-\sigma_0)$ value shifts to a larger value for larger deformation (its orientation dependence is not yet clear). These results indicate the advance of work-hardening in the surface region more than in the interior. This effect seems to be interpreted in terms of the easiness of the operation of the dislocation sources in the surface region, although a part of the effect may be attributed to the hindrance action of the surface film against the escape of dislocations to the surface.

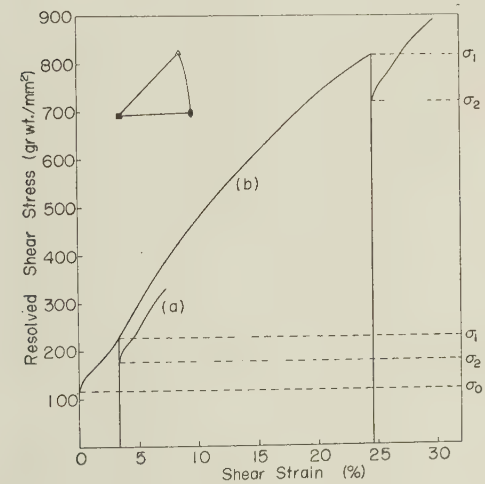

Fig. 1. Stress-strain curves of an aluminium single crystal. In curves (a) and (b) the surface layers of 190 μ and of 150 μ in thickness were removed after the deformation of 3.38% and of 24.6% shear strain, respectively.

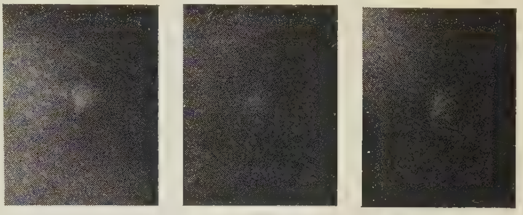
(a) (b) (c)

Photo. 1. (111) Laue back-reflection spots taken from the same portion of α-Fe single crystal (a) before and (b) after deformation of 7.6% elongation, and (c) on removing the surface layer of 260 μ in thickness after the deformation.

Furthermore, by observing the change in appearance of the back-reflection Laue spots with deformed α-iron single crystals (containing less than 0.01% C), we have obtained an evidence for the fact that the dislocation density is higher in the surface region more than in the interior upon the deformation. As is well known, in α-iron, there are strong interactions between dislocations and various impurity atoms resulting a high critical shear stress, so that the influence of surface oxide film may be very little. Photo. 1 shows that (111) back-reflection Laue spot of the same portion of a specimen changes from a spotty appearance to a very diffused one upon the deformation, but its spotty appearance comes back by removing the surface layer by electrolytic polishing.

A theoretical explanation of such a preferential plastic deformation in the surface region of crystals will be presented elsewhere in the near furture.

The authors thank to Prof. T. Suzuki for his suggestion of the present work and to Mr. K. Nakajima for his help in X-ray observations.

References

1) T. Suzuki: *Dislocations and Mechanical Properties of Crystals* (John Wiley and Sons (1957)), 116. J. J. Gilman and W. G. Johnston: *ibid.*, 215. M. A. Adams: Acta Met. **6** (1958) 327.
2) F. E. Fujita, D. Watanabe, M. Yamamoto and S. Ogawa: J. Phys. Soc. Japan **11** (1956) 502. S. Karashima, H. Fujiwara and K. Kojima: Proc. 1st Japan Cong. on Testing Materials (1958) 59. S. Karashima, H. Fujiwara and Y. Nakamura: Mem. Inst. Sci. Ind. Res. **16** (1959) 55. K. Nakajima: Sci. Rep. RITU **A, 12** (1960) 324.

Errata

Study on the Ordered Phases with Long Period in the Gold-Zinc Alloy System

I. Survey of Crystal Structures and Calorimetric Measurement

By Hiroshi IWASAKI, Makoto HIRABAYASHI, Kunio FUJIWARA,
Denjiro WATANABE and Shiro OGAWA

J. Phys. Soc. Japan **15** (1960) 1771

Page	Column	Line		Should be read
1777		Table I	$\sqrt[3]{a_f{}^2 2c_f}$	$\sqrt[3]{a_f{}^2 c_f}$
1779		Table II	$\sqrt[3]{a_f{}^2 2c_f}$	$\sqrt[3]{a_f{}^2 c_f}$
1782	left	4 (from the bottom)	A_3uZn[H]	Au$_3$Zn[H]

Anisotropic Hall Coefficients in *n*-Type Germanium

By Hisao MIYAZAWA and Hajime MAEDA

J. Phys. Soc. Japan **15** (1960) 1924

Page	Column	Line	Wrong	Corrected
1926	right	4 from the bottom	bv	by
1931		4th of Eq.'s (4.14)	$\beta^* = \sum_{n=0}^{\infty}(-1)^n \beta_n p^n, \cdots$	$\beta^* = \sum_{n=0}^{\infty}(-1)^n \beta_n{}^* p^n, \cdots$
1932		Table III.	$\begin{array}{c\|c\|c} \cdots & \cdots\cdots & \cdots \\ \hline \delta & (4/3\sqrt{\pi})\beta_1 \ (s=1/6) & \\ \hline \cdots & \cdots\cdots & \cdots \\ \cdots & \cdots\cdots & \cdots \\ 0.8 & 0.102215 & \cdots \\ \cdots & \cdots\cdots & \cdots \\ \cdots & \cdots\cdots & \cdots \end{array}$	$\begin{array}{c\|c\|c} \cdots & \cdots\cdots & \cdots \\ \hline \delta & (4/3\sqrt{\pi})\beta_1 \ (s=1/6) & \\ \hline \cdots & \cdots\cdots & \cdots \\ \cdots & \cdots\cdots & \cdots \\ 0.8 & 0.10225 & \cdots \\ \cdots & \cdots\cdots & \cdots \\ \cdots & \cdots\cdots & \cdots \end{array}$
1932		1st of Eq.'s (4.16)	$S \equiv \frac{2K}{K+2}\left(\frac{K\beta_0 + 2\beta_0{}^*}{2K\alpha_0 + \alpha_0{}^*}\right)^2$	$S \equiv \frac{3K}{K+2}\left(\frac{K\beta_0 + 2\beta_0{}^*}{2K\alpha_0 + \alpha_0{}^*}\right)^2$
1935	left	9 from the bottom	was	as
1935	right	3 from the bottom	phenon	phonon
1936	left	12	bee	been

1937 Equations (A.4) should be read as follows:

$$S_{11} = u\sum_{i=1}^{4}[(1/3)\{2K\alpha(p^{(i)}, s^{(i)}) + \alpha^*(p^{(i)}, s^{(i)})\} + v^2K^2H_1{}^2\gamma(p^{(i)})]$$

$$S_{12} = u\sum_{i=1}^{4}[(-1)^i(1/3)\{K\alpha(p^{(i)}, s^{(i)}) - \alpha^*(p^{(i)}, s^{(i)})\}$$
$$-(1/3)vK\{Kq^{(i)}\beta(p^{(i)}, s^{(i)}) + q^{*(i)}\beta^*(p^{(i)}, s^{(i)})\} + v^2K^2H_1H_2\gamma(p^{(i)}, s^{(i)})]$$

$$S_{12} = (\boldsymbol{H}) = S_{21}(-\boldsymbol{H}) .$$

Page	Line	Wrong	Corrected
1939	Eq. (A.20)	$\varphi \equiv p/\delta < 0.2$.	$\varphi \equiv p/\delta < 2.0$.
1939	Reference 12)	W. Shockleye	W. Shockley

Seiji Nakamura

(1869—1960)

OBITUARY NOTICE OF PROFESSOR SEIJI NAKAMURA

Professor Seiji Nakamura, Honorary member of the Society, Emeritus Professor of the University of Tokyo and Member of the Japan Academy died in Tokyo on 18th July, 1960 at the age of ninety. By his death Japan has lost one of the great scholars who have made physics in Japan as it is today.

He was born at Sabae-machi in Fukui Prefecture on 24th September, 1869 as the fourth son of Masanori Nakamura and in his childhood he came up to Tokyo with his parents. In 1892, he was graduated from the College of Science of Tokyo Imperial University (now University of Tokyo) majoring in physics, after he had his preparatory education in the First Higher School. In 1895, he was appointed a Professor of the First Higher School, and in 1900 he was appointed an Assistant Professor in the College of Science of Tokyo Imperial University, his Alma Mater, where he conducted his researches under Professor Dr. Tanakadate.

In 1903, he visited Europe to study optics and crystallography, and made an intensive research under Professor Dr. Voigt at the University of Göttingen, Germany. In 1907, he was awarded a Doctor of Science by his thesis on Optics, and was promoted to professorship in Tokyo Imperial University in 1912. In 1925, he was elected a member of the Japan Academy, and also acted as Dean of the Faculty of Science of the University for three years beginning in 1926, contributing much to the administration of the institution. At his retirement in 1930, he was awarded an honorary title of Professor Emeritus. In the Academy, he also contributed to the promotion of science in Japan by issuing many papers at its regular meetings, and at the same time, he devoted his time to edit the History of Japanese Science before the Meiji Era which was one of the projects of the Academy.

He is an experimental physicist, especially excellent in experimental technique, obtained from his own abundant experiences. We can easily see his excellence in experiment by some of the remarks he made in his class at Tokyo Imperial University. Two examples of his hortative sayings are given here: "Don't carry a microscope as you swing a cat by the scruff of the neck." "In experiment an iron bank is not an iron bank; mind that it is like a jelly."

He had a special interest in the field of optical instruments, and endeavored to train the technical specialists in this field. It is not too much to say that all of the leading technicians of the optical instrument makers in Japan are educated by him directly or indirectly. His research fields extended also to geophysics in general, but specially in geomagnetism, geodesy and seiches of Japanese lakes. And he had a very deep interest in such curious phenomena related to optics and to acoustics known from the olden times in Japan as, for example, mysterious lights on the seas (Shiranuhi) in Kyushu, Singing Dragon in Toshogu Shrine in Nikko, Magic Mirror, and the musical scales in Japan and China.

His major achievements are his efforts in publishing great many books and articles and in promoting the education of physics in Japan. Furthermore, he was the foremost scholar who popularized the study of natural science for the younger people by devising new methods for it. Because of his contribution in education, he was awarded a national commendation as one of the Persons of Cultural Merits in 1953.

He was lucid and illumitable by his character, and he had not only a profound ability for scholarship in Japanese, Chinese and European languages, but also wide interest in most of all the fields of art and natural sciences. He was very fond of journey, and after his retirement, he especially enjoyed his trips which covered every nook and corner of Japan. He loved Japan as he loved his own family, and desired the advent of the eternal peace on this world.

He was survived by a son and a daughter.

——(*K. T.*)——

JOURNAL OF THE PHYSICAL SOCIETY OF JAPAN, Vol. 16, No. 2, FEBRUARY, 1961

Elastic and Inelastic Scattering of Protons from Carbon Nucleus from 6.5 to 16 Mev

By Yukio NAGAHARA

Physics Department, Yokohama National University, Minami-ku, Yokohama

(Received May 11, 1960)

Angular distributions and excitation functions of C^{12} (p, p) C^{12} $(Q=0)$ and C^{12} (p, p') C^{12*} $(Q=-4.43$ Mev) reactions were investigated with the bombarding energy from 6.5 to 16 Mev and from 9.5 to 16 Mev, respectively, by the INS variable energy cyclotron. Though the angular distributions were found to vary gradually with energy, several distinct anomalies were observed. Especially, at $T_p=9.1$ Mev, very sharp anomaly was found for the elastic scattering. Around $T_p=10.5$ Mev, large anomaly of composite nature was found (which had been reported by Braid and Yntema), where the angular distributions of the elastic and inelastic scattering varied violently. Rather strong correlations were observed between the elastic and inelastic $(Q=-4.43$ Mev) scattering. Observed anomalies were found to be closely related to the levels of the compound nucleus N^{13}.

§ 1. Introduction

Up to now, many investigations, both theoretical and experimental, have been performed with regard to the elastic and inelastic scattering of nucleons from various nuclei. We will hereafter restrict our subjects to 1) the medium low energy region, e.g., from several Mev to about 20 Mev, and 2) the elastic scattering and the inelastic scattering leaving the target nucleus to the well resolved excited states.

In the case of the medium weight nuclei, the elastic scattering shows the typical diffraction pattern and also shows the remarkably systematic transient change, in the absolute values and in the angular distribution, from nucleus to nucleus[1]. These are considered to be the very feature of the optical model. As to the inelastic scattering, at least for the even-even nucleus and in the higher energy region (say, higher than 10 Mev), the angular distributions are shown to be well-fitted with the simple Born approximation calculation based on the surface direct process[1,)2]. In several Mev region, the angular distributions are shown to become more flat and are believed to suggest the increase of the importance of the contribution via the compound process[3]. Also, the results of the angular correlation measurements are thought to be the support to these interpretation[3].

On the contrary to these comparatively clear situations, the scattering of nucleons from lighter nuclei have shown some complexity. At first, the elastic scattering showed the typical diffraction pattern, which would lead us to the understanding that the optical model had its validity. But, at the same time, it has been shown that the systematic regularities from nucleus to nucleus were not so distinct and also the energy dependence of the angular distribution was rather violent[4].

For the inelastic scattering, the situation is more complicated[4,5,5,7]. For example in Ne^{20} (p, p') Ne^{20*} $(Q=-1.63$ Mev), the experimental studies by K. Matsuda et al. have shown that the formerly obtained good fit of the theoretical result based on the surface direct process had to be thought as accidental. Here, it must be noted that for lighter nuclei, these energy regions may be the transient region from the resonance to the continum region and also the wave length of the incident nucleon is of the same order as the radius of the target nucleus.

Many refined direct precess theories have been presented about the inelastic scattering of nucleons from nuclei[8)-15]. The proton-carbon system is treated as their examples most frequently. But, we can say that the scarcity of the experimental materials[16)-23] is fatal in order to clarify the situation. The object of our experimental study is to make a " map ", though rather crude, on the elastic and the inelastic scattering of protons from carbon nuclei.

§ 2. Apparatus

The general feature of the experimental arrangement is shown in Fig. 1, schematically.

1) *Beam*

The 160 cm synchro- and variable energy ordinary cyclotron of the Institute for the Nuclear Study (University of Tokyo) was used in the latter operation condition. Detailes of the design, construction and operation have been published elsewhere[33], so they will not be repeated here.

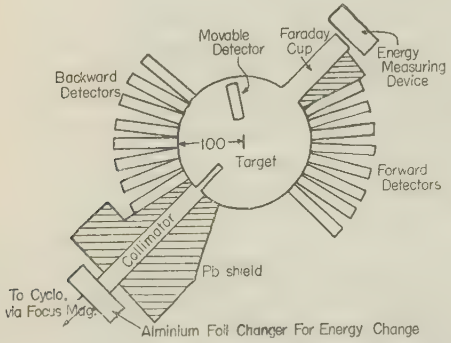

Fig. 1. Schematic view of the experimental arrangement.

Beam energy was varied with the interval of about 500 Kev by adjusting the machine parameters. Aluminium absorber foils were inserted between the focus magnet and the collimator, and then we could attain the fine variation of the beam energy.

After passing through the target, beam was collected in the Faraday cup and the collected charge was measured by the precision current integrator.

Beam energy was measured by the range measuring device outside the scattering chamber which comprised of an aluminium foil changer sandwitched between two ionization chambers.

2) *Scattering chamber*

The large scattering chamber, 100 cm in diameter and 40 cm in height, was used. As described in reference[24], this chamber has thirty-three ports on its side wall to which many detectors can be attached simultaneously.

3) *Target*

From 9.5 to 16 Mev, thin CH_2 foil was used. Its mean thickness was estimated to be 2.88 mg/cm^2 by weighing. Because of the degration of the foil caused by the proton irradiation, CH_4 gas target was used in the later stage (from 6.5 to 9.7 Mev and at two energy in the higher energy region for the calibration of the absolute value). CH_4 gas of 99.9% purity was filled in a gas target chamber, which was a brass cylinder of 90 mm in diameter and had two side slits of about 20 mm in breadth which were sealed by 20 micron aluminium foils.

4) *Detectors and Electronics*

The scattered protons were detected by NaI (Tl) crystals of about 20×20×1.5 mms, which were slightly thicker than the maximum range of protons, to minimize the gamma-ray background. As we have used so many detectors simultaneously, we were obliged to abandon to attach any gamma-ray removing devices (for example, proportional counters).

In the case of CH_2 foil target, sixteen detectors were mounted to the ports of the scattering chamber. The forward angle detectors (from 20° to 90°) were arranged with the interval of 10° on the beam transmitting side and the backward ones were arranged also with the interval of 10° (from 95° to 165°) on the beam reflecting side. One detector was mounted on the turntable of the scattering chamber and was able to be rotate around the target freely. Its aim was to make up for the defects which might be caused by the fixedness of the main detectors.

In the case of the gas target, fifteen detectors were mounted on one side of the scattering chamber with the interval of 10° ranging from 20° to 160°. The defining slits of rectangular shape (5 mm in width and 20 mm in height) spaced 34 cm apart were attached to the ports of the scattering chamber.

The signal pulses were fed to the plugboard in the counting room, where five of them were picked up and fed to five amplifier and pulse height analyzer systems, respectively. So, we could get the full angular distribution by changing the plug connection only four times, which economized the measuring time considerably and reduced the relative errors. All of these electronic equipments were designed and constructed in the Electronics Division of INS.

The diameters of the circular apertures of these detectors were 3 mm for 20° detector, 5 mm for 30° to 50° detectors and 10 mm for others. The aim of this design was to compensate the steep increase of the yields of the elastically scattered protons at forward angles and then to generally equalize the load to the succeeding stages.

§ 3. Experimental Procedures

The detectors were grouped into four sets, taking account of the yields and other measuring conditions. Each set included the 90° detector which served also as the monitor.

A particular set of 30°, 60°, 90, 125°, (120° for gas target) and 155° (150° for gas target) detectors was extensively used for the investigation of the excitation functions. By inspecting the obtained excitation functions, when some interesting features would be expected, then full observation for all angles was carried out. When the 90° detector's counts showed differences larger than the statistical error from those of the other run at the same energy, that run was deserted and repeated again. In fact, this has seldom occurerd.

The energy measurements were carried out when the coarse variation of beam energy had done. For the fine variation, only the thickness of the absorber foils used was recorded.

§ 4. Possible Errors and Corrections

1) *Energy*

The INS cyclotron has an excellent beam energy stability. Moreover, the measuring time required was rather short. So, the fluctuation of beam energy might be very small.

For the determination of the beam energy, the results of Bichsel, Mozley and Aron[25] were used. As we have used the same apparatus and the same procedure at each time, the relative value of T_p (the proton energy at the center of the target) was expected to be accurate within ±30 Kev. But, the absolute value of T_p was estimated to be accurate within about ±100 Kev. It has been reported that the energy spread at the half-maximum was about 0.5% at the outlet of the focus magnet[24]. So, at the center of the target, the energy spread might be 1% or less. (It is expected to be somewhat larger when the aluminium absorber foils are used to lower the beam energy).

2) *Angle*

Accuracy of the angular position of the port of the scattering chamber is very good[24], and the misalignment of the scattering chamber to the beam collimator is +0.01° or less. Considering the possible incorrectness in mounting the defining slit, the inaccuracy in angle was estimated to be at most ±0.1° for the foil target, and ±0.3° for the gas target. The other resposible factor to this inaccuracy was the one originated from the effectiveness of the collimator which was estimated to be ±0.05°.

3) *Current*

The accuracy of the current integrator used was estimated to be 1.5% or less, including both the zero-point drift and the relative fluctuation. But, when using the gas target, multiple scattering correction for the escape of the beam out of the Faraday cup was estimated by the theory of Bethe[26]. Aluminium foils which sealed the gas target chamber were most responsible. They were only appreciable in the energy region lower than 10 Mev and estimated to 8% at the lowest energy investigated. This correction might introduce about 2 to 3% error to the absolute value of the cross-section.

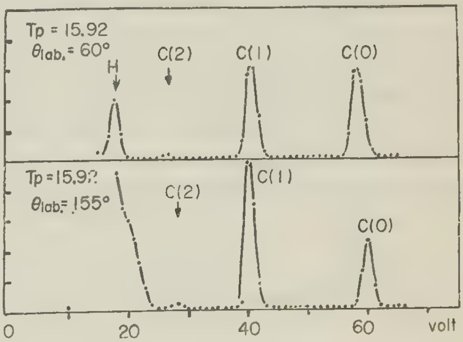

Fig. 2. Examples of the publse height spectrum of the emitted particles.

4) *Backround subtraction*

As is shown in Fig. 2, in almost all the cases, background subtraction did not introduce any disturbing errors. The maximum and minimum background spectrums were assumed by extraporating from both sides and subtraction was performed. When the subtraction error was larger than 15%, that data was deserted.

5) *Yield* (*CH_4 gas target*)

The gas pressure was pressure by Hg manometer and found to be substantially constant throughout (386 mm Hg). The temperature was also constant (20.0°C). The inaccuracy of the target density was estimated to be less than ±1%.

As for the G-factor, it was proved that all the higher order terms and also the effect of the finite beam width could be neglected[27]. Multiple scattering corrections on the G-factor were estimated and it was proved that they had some influences on the elastic scattering at forward angles for the lower energy region. Because of the difficulty in precise determination of this correction factor, estimated factors were treated as errors. (This correction should not be neglected in the sharp cusp of the elastic scattering angular distribution. But, we had no way of correction owing to the coarseness of the measuring angles).

6) *Yield (CH_2 foil target)*

In this case, the nonuniformity and the irradiation degradation of the target foil would have larger effects. So, to check the foil experiments, we measured the differential cross-sections of elastic and inelastic scattering by using CH_4 gas target at $T_p=15.50$ Mev, and 13.64 Mev, where both scatterings were expected to have the gradually varying features with energy. At both energies, it was found that the foil results would coincide to the gas results within at most ±5% by multiplying a factor of 1.06, the origin of which might be attributed to the nonuniformity and the possible inadequate mounting of the target foil.

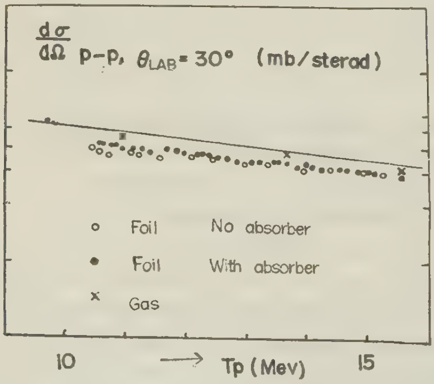

Fig. 3. Differential cross-sections of proton-hydrogen scattering at $\theta_{lab}=30°$.

On the other hand, the effects of the degradation of the target were of more complex nature. In Fig. 3, the proton-hydrogen differential cross-sections at $\theta_{Lab}=30°$ obtained by our experiments are plotted, which show small but regular bumps. (We have carried out our experiments from the higher energy side). It was found that these bumps corresponded to the presence of the absorber foils for lowering the beam energy. The origin of this phenomena might be attributed to the beam diverging effect of the absorber foils. By proton irradiation, the hydrogen atoms in the beam spot would be struck out or evaporated, the rate of which would be larger than for carbon atoms owing to their smaller mass. So, on the presence of the foils, diverged beam would strike the wider (that is, newer) region and then result in the formation of the abovestated bumps. On the other hand, we could not find any correlation between the proton-carbon scattering yields and the bumps of the proton-hydrogen scattering yields. So, we concluded that the degradation effects would have not introduced serious error.

Consequently, we have multiplied the results of the foil target experiment by a factor of 1.06 throughout. The accompanied error were assumed to be ±2% in the higher energy region, and ±3% in the lower energy region.

7) *Absolute value of the cross-section*

In Fig. 3, the full line shows the straight line interpolation curve joining between the proton-proton scattering data at $T_p=9.7$ Mev, 9.85 Mev[28] and 18.2 Mev[29] at $\theta_{Lab}=30°$. Our values obtained by gas target are slightly smaller, but it can be said that good agreement exsists.

8) *Grouping of the errors*

Above mentioned errors were grouped into two.

δ_1 is the error which may distort the shapes of the angular distribution. It is the combination of the statistical error, background subtraction error, errors from the inaccuracy in angle and G-factor.

δ_2 is the error which, after combined with δ_1, forms the error that may affects the shapes of the excitation function and the absolute value of the individual cross-section. It is the combination of the error in charge collection and its measurement and errors from the fluctuation in the properties of the target.

§ 5. Results

1) *Representation in tables and graphs*

Absolute values (in the center of mass system) of the differential cross-section of the elastic scattering are tabulated in Table I, and those of the inelastic scattering are tabulated in Table II.

Over-all view of the angular distributions are shown in Fig. 4a (elastic) and Fig. 4b (inelastic), where some of our results are omitted in order to make the figures clear-cut.

Excitation functions at five angles are shown in Fig. 5 to 9 and in Fig. 11, including other author's results.

The integrated partial cross-section of the inelastic scattering are plotted in Fig. 10.

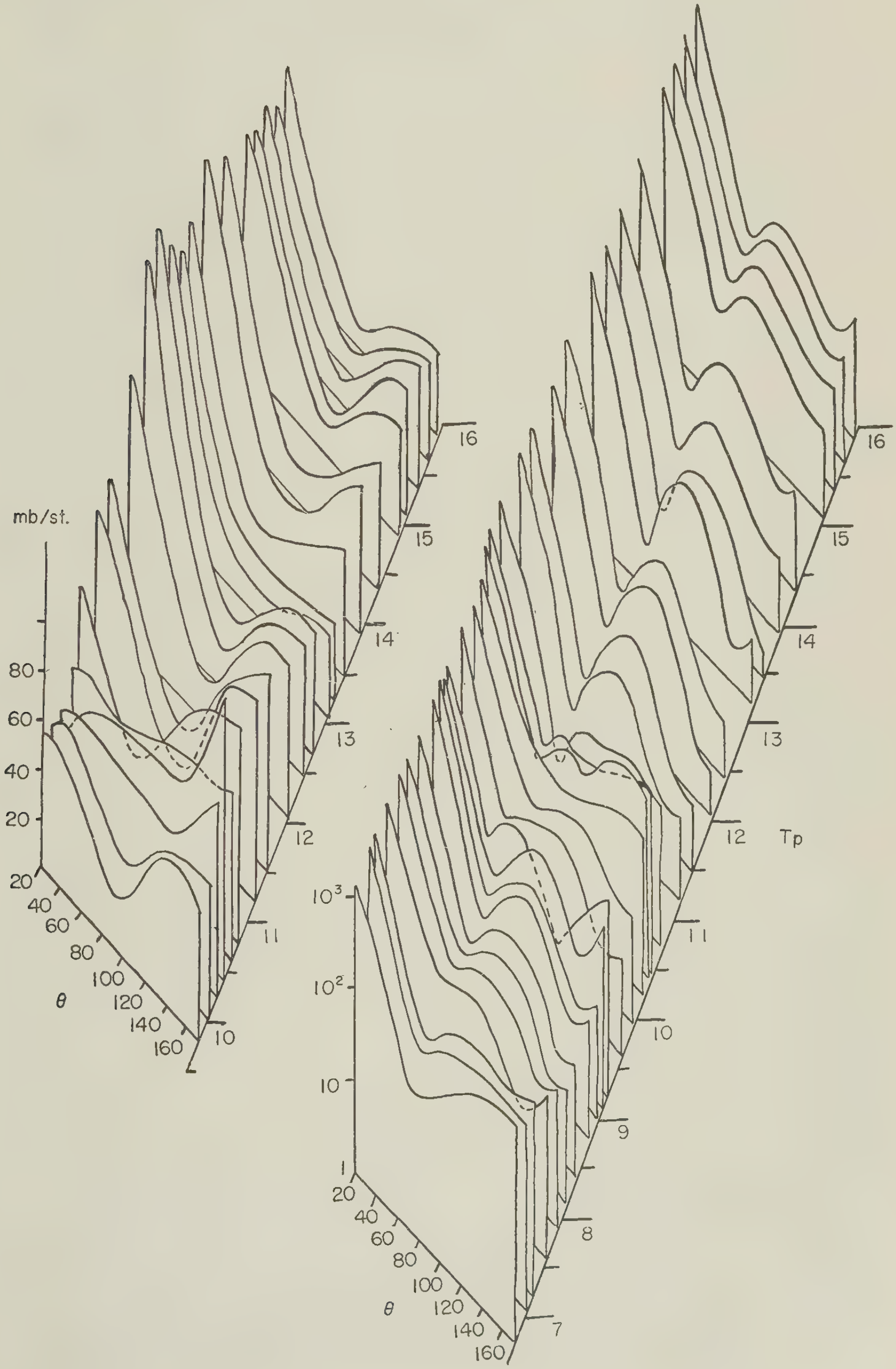

Fig. 4. Angular distributions of the elastic and inelastic ($Q=-4.43$ Mev) scattering.

Table Ia. Differential cross-section: $C^{12}(p, p)C^{12}$.

Run	T_p θ	21.8	32.4	43.0	53.7	64.1	74.4	84.7	94.8	99.7	109.6	119.3	128.9	138.4	147.7	157.0	166.2	δ_2
1	15.92		265	118	39.1	12.3	12.4	20.9	27.4	28.5	29.2	24.0	17.8	12.2	9.30	9.36	11.8	2.5
12	15.79	514	268	117	37.9	11.9	12.0	20.6	26.6	27.9	28.4	24.1	18.0	12.1	8.80	9.00	10.6	2.5
16	15.66	503	275	120	37.9	11.6	12.2	20.2	27.4	28.4	30.3	24.1	18.1	12.9	9.46	9.07	10.6	2.5
23	15.37	547	285	119	37.8	10.8	12.8	21.7	27.6	28.6	30.1	26.6	19.1	14.8	10.6	9.21	10.2	2.5
29	15.11	572	290	113	33.3	9.57	11.9	20.7	26.4	27.6	29.0	25.0	18.8	14.8	11.6	10.3	10.0	2.5
35	14.94	563	296	123	36.6	10.7	12.7	22.9	29.0	29.5	29.8	25.6	19.6	14.3	9.90	6.58	5.57	2.5
43	14.36	560	288	126	40.8	12.0	12.0	20.6	28.7	30.7	33.4	29.7	21.8	14.6	9.55	8.05	9.14	2.5
51	13.92	524	279	127	44.2	11.5	6.97	13.4	21.0	23.3	26.1	23.8	18.4	12.9	8.73	6.94	6.47	2.5
59	13.48	508	261	117	40.9	9.50	4.62	11.6	20.5	23.8	28.1	27.1	21.6	14.7	8.95	4.60	2.16	3.0
64	13.35	519	251	115	37.8	7.80	3.79	12.1	23.2	26.3	31.8	29.1	21.4	14.0	6.96	3.10	1.66	3.0
65	13.21		264	117	36.6	4.96	4.22	17.0	30.6	33.7	37.7	30.5	19.0	9.25	3.64	2.20	3.76	3.0
66	13.06		294	129	39.1	5.98	8.50	24.8	37.8	40.0	41.6	31.6	18.5	8.77	4.94	5.51	9.53	3.0
81	12.67	559	270	122	40.3	7.43	6.14	18.4	30.6	33.8	37.4	32.1	22.1	13.6	7.54	4.85	4.02	3.0
86	12.43	566	261	116	49.5	7.13	6.60	19.5	31.6	34.3	36.7	31.1	22.0	13.5	7.61	4.93	4.16	3.0
88	12.25		269	115	36.3	7.22	8.14	21.3	32.7	35.3	36.7	31.0	22.0	14.3	8.40	5.40	3.93	3.0
97	12.07	653	288	123	38.3	7.31	9.00	23.3	34.9	37.0	38.9	32.6	24.1	16.0	9.45	5.55	3.56	3.0
105	11.51	677	297	135	46.0	8.06	6.56	22.3	39.1	44.2	49.5	43.3	30.8	19.2	10.2	5.73	4.35	3.0
117	11.19	855	358	155	45.6	6.96	8.91	25.2	38.3		39.8	30.6	21.1	12.2	7.08	5.64	6.53	3.0
124	10.72	950	472	213	71.7	13.7	7.22	18.9	27.3	29.0	30.6	31.6	35.2	39.4	39.8	33.8	25.5	3.5
138	10.60	955	475	220	76.6	19.1	11.4	16.7	19.3	19.4	22.8	33.8	50.6	65.7	65.7	54.2	34.8	3.5
130	10.44	920	454	183	47.5	15.7	22.4	29.4	26.4	24.0	25.9	40.5	60.4	82.4	89.5	86.6	68.5	3.5
134	10.39	663	375	164	46.0	15.0	21.6	33.1	36.5	37.7	40.0	46.5	54.8	65.5	79.6	90.0	117	3.5
142	10.23	368	200	114	57.3	28.4	16.7	16.2	17.5	18.8	26.1	34.4	41.2	49.3	52.1	56.4	64.3	3.5
146	9.95	374	152	86.5	51.7	30.3	21.3	18.8	23.4	26.4	32.8	35.0	32.8	28.8	21.4	17.1	16.8	3.5
150	9.80	443	170	88.1	47.6	28.6	22.5	24.8	32.6	33.4	39.3	40.7	32.7	22.5	18.6	10.6	12.8	3.5
	δ_1	1	1	1	1	1	1	1	1	1	1	1	1	1	1	1	1	

Table Ib. Differential cross-sections $C^{12}(p, p)C^{12}$

θ T_p	21.8	32.4	43.0	53.7	64.1	69.2	74.4	84.7	94.8	104.7	114.4	124.1	133.6	143.0	152.4	161.6	δ_2
15.50	530(2)	286(2)	124(2)	37.1	11.8		12.1	21.4	27.7	31.6	28.8	22.0	16.1	11.2	9.8	10.4	2
13.64	500	251	120	38.7	10.1	5.0	4.9	11.2	19.0	25.2	26.3	21.2	16.8	11.5	6.7	4.7	2
9.65	570	194	90	39.1	20.1		20.6	31.1	40.1	45	42	33.4	23.3	13.7	8.3	8.2	2
9.29	810	256	98	35.6	21.5		29.5	41.6	47	45	36.5	28.1	20.6	17.1	15.1	18.9	2
9.27	840	264	98	36.1	23.3		36.7	48	46	37.8	25.4	22.4	17.2	20.2	20.8	29.0	2
9.21		340	87	21.5	39.2	54	67	74	53	30.3	19.1	19.1	24.8	37.4	57	89	2.5
9.14	730	429	86	21.8	49		73		69			28.4	41		75		2.5
9.08	730	287	114	41	16.8		23.4	43.2	72	98	102	82	51	28.2	32.0	55	2.5
8.98	690	268	131	55	14.5		17.3	32.0	58	78	77	61	36.8	16.4	9.1	16.4	2.5
8.80	730	263	125	50	16.3	12.5	16.4	35.5	59	74	73	56	35.8	17.1	9.0	12.0	2.5
8.40	820(3)	290(3)	132(3)	54	21.9	17.1	21.7	39.8	59	72	70	54	34.4	19.2	11.4	12.1	2.5
8.15	870	314	159	71	32.6	27.4	29.0	44	63	72	71	54	34.4	20.2	12.2	13.9	2.5
7.88	990	350	157	73	42	35.3	40.7	56	70	76	69	55	34.7	19.8	17.0	18.1	2.5
7.57	920	326	163	87	57	53	58	70	79	83	66	45	29.4	21.0	19.5	34.5	2.5
7.26	1010	315	128	48	23.2	19.9	33.2	58	75	86	82	72	69	66	72	84	3
7.21	1150	371	149	59	28.8	27.6	34.8	57	77	90	87	83	75	76	81	92	3
7.19	1140(4)	350(4)	155(4)	60	29.2	27.9	33.6	55	73	84	86	81	76	75	78	91	3
7.19	1190	380	160	66	34.0	29.0	35.7	54	73	85	85	79	79	78	82	94	3
7.04	1260	420	190	86	41	35	39	56	73	85	94	91	93	96	100	116	3
6.74	1280(5)	450(5)	230(5)	120(4)	58	42	39	43	57	79	101	119	150	152	165	177	3
δ_1	( )	( )	( )	2	2	2	2	2	2	2	2	2	2	2	2	2	

T_p (Mev)—Proton energy at the center of the target; relative error ~±30 kev; absolute error ~±100 kev. All in lab system.
Cross-section (mb/sterad)—In the center of mass system.
δ_1 in the lowest column and also in parenthesis; δ_2 in the last column. Both in %.
θ (degree)—Scattering angle in the center of mass system.

Table II. Differential cross-sections C^{12} (p, p') C^{12*}

T_p θ	22.3	32.9	43.6	54.4	64.9	75.4	85.6	95.8	100.4	110.6	120.2	129.4	139.0	148.3	157.6	166.5	δ_2
15.92	38(3)		23.9(3)	17.7(3)	12.3(3)	8.1(3)	5.7(3)	5.4(3)	5.3(3)	6.8(3)	8.4(3)	10.8(3)	12.1(3)	14.2(3)	15.2(3)	16.4(3)	2.5
15.79	42		23.1	17.8	11.6	8.1	6.1	5.4	5.3	6.7	8.1	10.5	12.1	14.0	15.3	16.2	2.5
15.66	35	33(9)	24.4	17.3	12.9	8.7	6.4	5.5	5.3	6.8	9.0	10.9	13.2	15.5	16.7	17.2	2.5
15.37	42	33(6)	25.3	18.5	13.1	9.6	7.4	6.5	6.4	7.5	9.5	12.4	15.8	18.9	21.2	23.2	2.5
15.11	42	35	25.6	19.2	14.3	10.8	7.9	6.1	5.6	6.0	8.4	11.7	16.6	21.5	22.8	24.6	2.5
14.94	43	39(4)	30.2	23.2	15.6	10.5	7.5	5.6	5.2	6.5	9.0	12.6	15.8	17.6	18.1	18.6	2.5
T_p θ	22.3	32.9	43.7	54.5	65.0	75.5	85.7	95.9	100.5	110.7	120.3	129.5	139.1	148.4	157.6	166.5	
14.36	51	44(3)	33	23.1	15.4	10.2	7.8	7.3	7.3	8.6	10.3	12.3	15.4	18.2	21.0	23.4	2.5
13.92	58	51	39	28.6	19.8	14.7	10.8	10.6	10.2	10.9	12.0	14.0	17.6	22.7	26.5	32.2	2.5
T_p θ	22.3	33.0	43.8	54.6	65.1	75.6	85.8	96.0	100.6	110.8	120.4	129.6	139.2	148.5	157.7	166.5	
13.48	54	49	35 (5)	27.6	19.1	14.1	11.8	11.9	11.4	12.9	14.5	16.1	17.7	19.7	22.2	22.7	3
13.35	53	45	34 (9)	24.6	17.3	13.6	11.9	11.1	10.7	12.3	13.1	14.1	15.5	15.9	16.8	17.1	3
13.21	54	49		22.6	16.7	13.4	11.6	11.1	10.6	11.2	11.7	11.8	13.0	13.1	13.1	12.9	3
13.06	59	47		23.8	17.4	14.7	12.7	11.1	10.6	11.2	11.7	11.8	13.0	14.6	14.9	15.2	3
T_p θ	22.3	33.0	43.8	54.6	65.2	75.7	86.0	96.1	100.7	110.9	120.4	129.7	139.3	148.5	157.7	166.6	
12.67	67	57		28.6	20.3	15.4	12.5	10.9	10.5	12.6	15.7	18.6	22.3	23.2	24.1	23.8	3
12.43	66	53		28.2	19.6	14.1	10.0	10.3	10.3	12.7	16.6	20.4	23.5	24.6	25.1	25.0	3
T_p θ	22.3	33.0		54.7	65.3	75.8	86.1	96.2	100.8	111.0	120.5	129.7	139.3	148.5	157.7	166.6	
12.25	54	45		22.9	16.5	9.9	9.4	9.8	9.7	12.8	17.7	21.8	26.2	27.1	27.6	29.9	3
12.07	52	44		22.7	17.5	13.3	10.8	10.2	10.2	13.2	17.7	22.3(4)	26.6(4)	28.8(4)	29 (4)	29 (4)	3
T_p θ	22.3	33.1		54.8	65.4	75.9	86.2	96.3	100.9	111.1	120.6	129.8	139.4	148.6	157.7	166.6	
11.51	43	34		22.0	16.1	13.0	11.3	10.6	10.9	14.5	18.5	24	29	33	35	38	3.5
11.19	43(4)	39		28.0	21.1	17.6	11.8	9.0		10.8	18.0	26	36	37	38	39	3.5

θ T_p	22.3	33.2		54.9	65.5	76.0	86.3	96.4	101.0	111.2	120.7	129.9	139.5	148.7	157.8	166.6	
10.72	38	31.3		20.7	17.4	16.8	18.4	21.7	23 (4)	29	34	37	40	41 (5)	41 (6)	43 (6)	3.5
10.60	24	25.5		21.4	21.9	23.6	25.2	26.6	28	29	31 (4)	32 (5)	32 (5)	29 (4)	31 (4)		3.5
θ T_p	22.4	33.2		55.0	65.6	76.1	86.3	96.5	101.1	110.3	120.8	130.1	139.6	148.7	157.8	166.6	
10.44	16.6	20.7		27.6	29.4	30.8	31.1	31.1	31 (5)	32 (4)	29	28	29	33	40	33 (4)	3.5
10.39	15.3	21.1		26.4	26.8	29.7	29.0	29.4		30	29	29 (4)	33 (4)	39	46	46 (8)	3.5
θ T_p	22.4	33.2		55.0	65.6	76.1	86.4	96.6	102.2	110.4	120.8	130.1	139.6	148.7	157.8	166.6	
10.23	22	23 (4)		25 (4)	24 (4)	25 (4)	24 (4)	23 (4)		22	22	23	25 (5)	29 (5)	32 (5)	53 (6)	3.5
θ T_p	22.4	33.2		55.1	65.7	76.2	86.5	96.7	101.3	110.5	120.9	130.2	139.6	148.7	157.8	166.6	
9.95	25	26		23	19.1	15.7	13.8	13.2		16.9	19.3	23	25	26	28	36	3.5
9.80	28	27		22	17.1	12.0	11 (5)	10 (6)		15.8	22 (7)	27 (7)		28 (8)	27 (8)		3.5

T_p (Mev)—Proton energy at the center of the target; relative error ~±30 kev; absolute error ~±30 kev. All in lab. system.
Cross-section (mb/sterab)—In the center of the system.
δ_1 in parenthesis; δ_2 in the last column. Both in %.
θ (degree)—Scattering angle in the center of mass system.

2) *Self-consistency of our results*

The first check is done on the reproducibility of our results. The energy region ranging from 11.25 Mev to 10.60 Mev was doubly scanned in different days and both results were found to be quite consistent.

The second check is on the smooth joining of CH_2 foil results and CH_4 gas results. As is shown in Fig. 5 to 9, it is quite apparent that the excitation functions join together smoothly (for $\theta_{\mathrm{Lab}}=125°$ and $155°$, it must be take into consideration that the gas results are $120°$ and $150°$, respectively).

After all, we can conclude that our results are self-consistent.

3) *Comparison with other experiments*

Referring to Fig. 5 to 10, it is quite obvious that our results are in good agreement with those of Peelle ($T_p=14.0$, 14.7, 15.2 and 15.6 Mev) and of Conzett ($T_p=12$ Mev) in both the elastic and inelastic scattering[16), 17)].

Fisher's results ($T_p=9.94$ Mev) have no

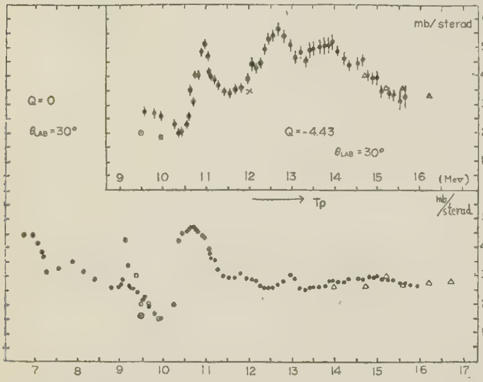

Fig. 5. Excitation functions of the elastic and inelastic scattering ($Q=-4.43$ Mev) at $\theta_{\mathrm{lab}}=30°$. Notations; ● present results, △ Peele, ○ Gibson et al., × Conzett, ⊙ Burcham et al., ⊡ Fisher.

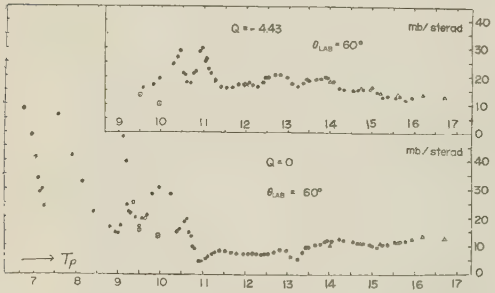

Fig. 6. Excitation functions of the elastic and inelastic scattering ($Q=-4.43$ Mev) at $\theta_{\mathrm{lab}}=60°$. Notations; see Fig. 5.

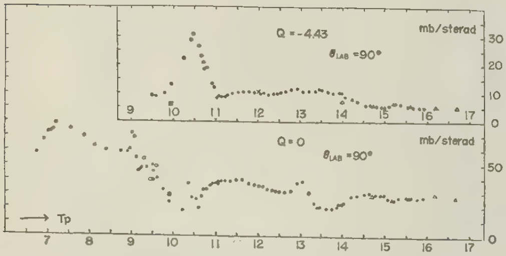

Fig. 7. Excitation functions of the elastic and inelastic scattering ($Q=-4.43$ Mev) at $\theta_{\mathrm{lab}}=90°$. Notations; see Fig. 5.

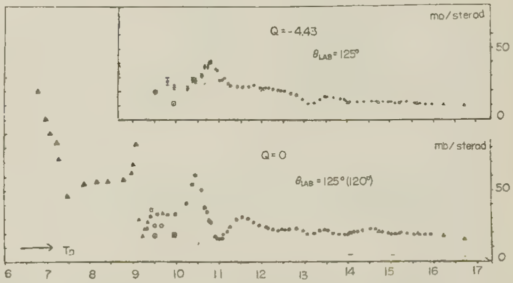

Fig. 8. Excitation functions of the elastic and inelastic scattering ($Q=-4.43$ Mev) at $\theta_{\mathrm{lab}}=125°$ for $T_p>9.80$ Mev and at 120° for $T_p<9.65$ Mev. Notations; see Fig. 5.

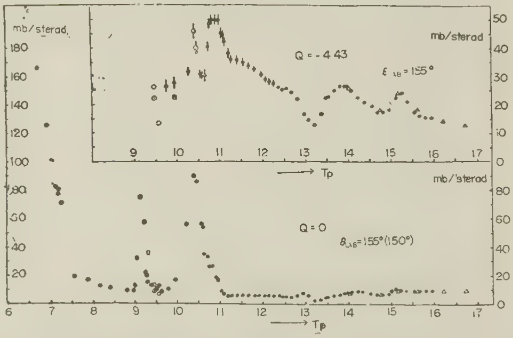

Fig. 9. Excitation functions of the elastic and inelastic scattering ($Q=-4.43$ Mev) at $\theta_{\mathrm{lab}}=155°$ for $T_p>9.80$ Mev and at 150° for $T_p<9.65$ Mev. Notations; see Fig. 5.

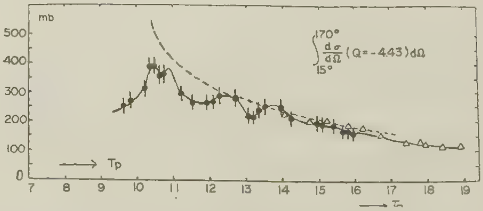

Fig. 10. Integrated partial cross-sections $\int_{15}^{170}\frac{d\sigma}{d\sigma}\cdot d\sigma$ for the inelastic scattering ($Q=-4.43$ Mev). Notations; see Fig. 5.

counterpart in ours[18]. For elastic scattering, his results most resembles to our 9.80 Mev run. As to the inelastic scattering, his angular distribution shape is quite similar to ours but the absolute values amount to only 0.6 times of ours.

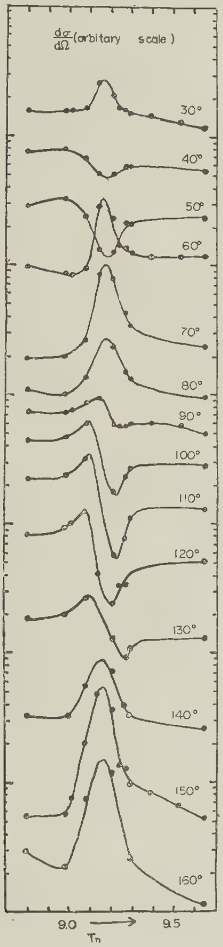

Fig. 11. Behavior of the elastic scattering around $T_p=9.1$ Mev.

The angular distribution of the elastically scattered protons by Burcham et al. at $T_p=9.5$ Mev[21], shows rather good agreement with our $T_p=9.5$ Mev run, but their absolute values are larger than ours about a factor of 1.2.

The results of the elastic scattering by Greenlees et al. at $T_p=9.37$ Mev[30] fall between our 9.29 Mev run and 9.26 Mev run.

The results by Gibson et al. for the elastic scattering at $T_p=9.58$, 9.49 and 9.45 Mev[20] are in good fit with ours. The inelastic scattering at $T_p=9.58$ Mev, however, shows rather large difference at backward angles.

As to the above-mentioned three cases, if we take into account of the uncertaintly involved both in beam energy and absolute value, we can say that good agreement exists.

Braid and Yntema[23] reported the existence of the large anomaly around $T_p=10.8$ Mev which occurs in our results around $T_p=10.5$ Mev. As the detailed report has not yet been available, further comparison will be postponed.

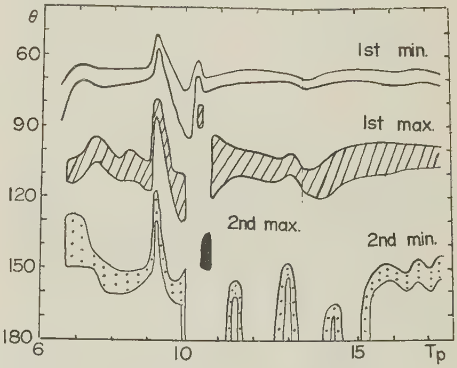

Fig. 12. Variation of the angular distribution shape of the elastic scattering with the proton energy. For detailes, see the top of paragraph 4) of § V.

4) *Qualtative description of the results*

To clarify the variation of the angular distribution of the elastic scattering with energy, in Fig. 12, the angular band, where the differential cross-sections differ by less than some percent (say, 5%) from those at the 1st minimum, 1st maximum, 2nd minimum and 2nd miximum in the angular distribution curve, are drawn against T_p, including those obtained by Peelle. From this figure, it seems reasonable to divide the whole energy region investigated into following four; $T_p>11.2$, $11.2>T_p>10$, $10>T_p>7$ and $T_p<7$ Mev.

a) $T_p>11.2$ Mev

For elastic scattering, the angular distribution is of diffraction type and the positions of the 1st minimum and 1st maximum are roughly constant. This means that the main feature of the elastic scattering is determined by the "shape" of the nucleus. Moreover, the presence of the 2nd minimum seems to become stable for $T_p>15$ Mev, but intermittent for $T_p<15$ Mev. This may suggest that some partial wave (e.g. $l=3$) becomes to participate to the reaction constantly for $T_p>15$ Mev, which may reflect the level structure of the compound nucleus N^{13}. Excitation function show small anomaly around 15.1 Mev.

The inelastic scattering for $T_p>15$ Mev has a smooth U-type angular distribution with forward-backward asymmetry which was first discovered by Peelle. σ_t (integrated partial cross-section) shows a small stagnation around 15.1 Mev and monotone decrease with increasing energy.

For $T_p<15$ Mev, several anomalies are observed around 13 Mev. For $14.2>T_p>13.5$, the positions of the 1st minimum and maximum shift backward and the width of the angular band becomes broader. The excitation functions of the elastic scattering show small depression and, on the other hand, those of the inelastic scattering show small bump. Rather clear bump is seen in σ_t. As will be seen later, this mutual compensating behavior of the elastic and inelastic scattering holds in every anomalous region.

For $13.5>T_p>12.7$, the diffraction pattern shifts forward and the excitation functions show rather sharp peak, for elastic scattering. On the other hand, the angular distribution of the inelastic scattering exhibits a strong forward-backward asymmetry; e.g., at $T_p=13.21$ Mev, the angular distribution is substantially flat for $\theta>90°$.

Fairly distinct anomaly accurs around 12.5 Mev, where the inelastic scattering becomes large. Its angular distribution gradually recovers from the above-mentioned strong forward-backward asymmetry.

For $12.0>T_p>11.2$, the most remarkable feature is that the variations are fairly gradual. The inelastic scattering continues to go on towards the 90° symmetry shape and between 11.8 Mev and 11.2 Mev, approximate 90° symmetry is established.

b) $11.2>T_p>10$

Drastic variations occur. With decreasing energy, the diffraction pattern disappears, and the angular distribution of the inelastic scattering varies violently (Fig. 4a and 4b). σ_t becomes very large (about 380 mb) and has some structures.

c) $10>T_p>7$

At about 10 Mev, elastic scattering recovers the diffraction pattern and the inelastic scattering establishes another stable 90° symmetrical shape, which was first observed by Gove and Stoddard at $T_p=7.26$ Mev[19] and later by Fisher[18], Burcham et al.[21] and Gibson et al.[20].

Around $T_p=9.1$ Mev, the elastic scattering shows very sharp anomaly. Its angular distribution shifts strongly forward and gives typical resonance-like excitation functions (see Fig. 11).

For $8.9>T_p>7.0$, the elastic scattering varies slowly. Here, it must be noted that the behavior of the excitation functions strikingly resembles to those in the region above the 10.5 Mev large anomaly at each angle.

d) $T_p<7$

This region is the higher energy side tail of 6.65 Mev broad anomaly which corresponds to the 8.08 Mev broad level of N^{13}. Here, it must also be noted that the behavior is quite similar to 10.5 Mev large anomaly.

§ 6. Qualitative Discussions

1) *Correlation between elastic and inelastic scattering*

As is clear from the foregoing descriptions, there exist remarkable correlations between elastic and inelastic scattering.

As already pointed out, the excitation functions of the inelastic scattering behave in compensating manner to those of the elastic scattering. This is one of the most striking features in the proton-carbon reaction in the energy region here investigated. In fact, in the similar experiments on $O^{16}+p$[6], $Ne^{20}+p$[6] and $Mg^{24}+p$ reactions[7] carried on at INS in the same energy region, no such marked correlations have not been found. The existence of this correlation may be attributed to the non-existence of the other open channel of large yield.

Next, when the inelastic scattering cross-section shows a bump, the diffraction pattern of the elastic scattering shifts backward and grows shallower, as is most obviouse around $T_p=13$ Mev. This feature would lead us to remember the optical model interpretation in which the optical potential varies with proton energy. But, as will be seen in the next paragraph, this energy region rather belongs to the resonance region and also the obtained cross-sections are not the averaged ones. So, we cannot literally adopt the optical potential interpretation.

Table III. Resonance levels of the compound nucleus N^{13}

C^{13}			N^{13}			
E_x (Mev)	Γ (kev)	Decay	T_p (Mev)	E_x (Mev)	Γ (kev)	Decay
(8.33)	1000	n	(6.65)	(8.08)		
10.76						
10.94			9.1*	10.4*	150	(*p*, *p*)
11.97	70					
12.21	140		10.5*	11.6*	700	(*p*, *p*) and (*p*, *p*) group of 3(?) levels
12.24	140					
13.41	50		12.5*	13.5*	500	$(p, p) < (p, p')$
13.77	280		13.2*	14.2*	500	$(p, p) > (p, p')$
14.1	210		13.7*	14.6*	500	$(p, p) < (p, p')$
16.1			15.1*	15.9*		(*p*, *p*) and (*p*, *p'*)

*s denote the new levels proposed by us. For other levels, see Ref. 31).

2) *Comparison with $C^{12}+n$ system*

In Fig. 13, the excitation functions of the related reactions are drawn against the excitation energy of the compound nucleus C^{13} and N^{13} [31].

Striking similarity is found between curve d) and e), though d) is of σ_t and e) is of excitation functions at some angle. Moreover, curves e) and f) also correspond each other, and further, all the anomalies which were discovered in our experiment have their corresponding part in the reactions which pass through C^{13}. Also, it is noted that the excitation function of pure reaction $Be^9(\alpha, n)C^{12}$ shows the corresponding anomalies.

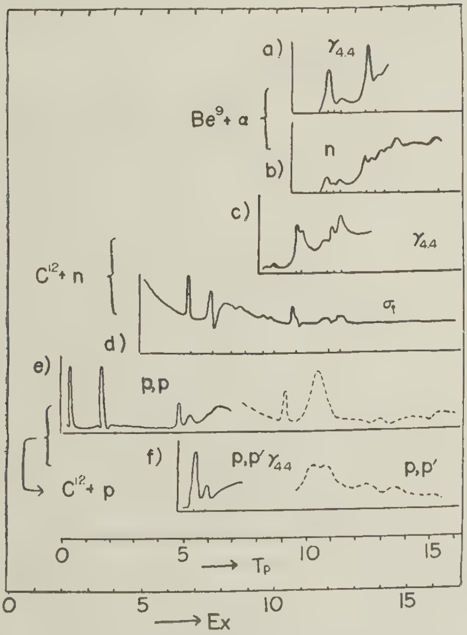

Fig. 13. Excitation functions of the related reactions via the compound nucleus N^{13} and C^{13}. Dotted lines—our results. Full lines—reproduced from reference 31).

Consequently, we can conclude that the discovered anomalies in $C^{12}+p$ reaction are in close relation to the resonance levels of the compound nucleus N^{13}. Table III tabulates the newly found levels. But, as the beam energy resolution is of order of 1% ($\sim\pm100$ Kev) and also as any detailed analysis has not been made, the tabulated figures should not be considered to be decisive.

3) *Qualitative comparison with theory*

a) Inelastic scattering

It may be a very interesting matter to investigate how the various mechanisms of the direct process can explain the experimental evidences, especially in the energy regions which lie between the anomalies where the direct process could be expected to be predominant.

For $T_p > 11$ Mev, the results obtained by Levinson and Banerjee (shell model, volume direct)[14], Glendinning (shell model, surface direct)[15] and Hayakawa and Yoshida (collective model, surface direct)[9] can be compared with our results. They all show roughly good, though qualitative, agreement. Whether they can also explain the gradual variation with energy of the angular distribution or not, is one of the remaining problems. As to the total cross-section, the result of Levinson and Banerjee only is now available, which excellently reproduces the general trend of the experimental σ_t. (See Fig. 10).

As to the other stable pattern of Fisher type ($T_p < 10$ Mev), Fujimoto and Sasagawa[32] has tried to realize it theoretically. More extensive studies are desired.

Braid and Yntema[23] investigated (p', γ) angular correlation around the 10.5 Mev large anomaly and found that the symmetrical axis shifted away largely from the recoil nucleus direction, which might suggest either the predominancy of the compound process or the strong distortion of the proton wave in the direct process. Angular correlation measurements are now in progress at INS in several energy regions selected by the inspection of our results.

b) Elastic scattering

Many calculations have been performed on the elastic scattering of nucleons from light potential nuclei using the optical of various type. The common features are as follows; 1) they cannot obtain good fit for the backward angular distribution, 2) the imaginary part is large (say, 4 Mev for carbon).

Now, in spite of the fact that our energy region is surely included in the resonance region, the averaged feature of the angular distribution roughly exhibits the diffraction type pattern (Fig. 12). This is the evidence advantageous to the optical model. The approximate constancy of the positions of the 1st minimum and maximum against the energy, may be attributed either to the long wavelength of the incident protons, or to the large diffuseness of the carbon nucleus.

At the same time, however, it is to be noted that the individual angular distribution (that is, not averaged) has the diffraction type only in the off-anomaly regions. This fact suggest that the diffraction type elastic scattering, in the energy region here considered, may have its origin in the potential scattering in the old resonance theory.

As to the large imaginary part, there seems to exist the possibility that it may be the reflection of the out-of-step application of the optical potential analysis on the individual angular distribution. Or, it may be the true reflection of the large yield of the inelastic scattering.

c) Concluding remarks

Almost all of the theories ever presented treat the elastic and the inelastic scattering separately. In other words, the reaction from the inelastic events on the elastic scattering is not explicitly formulated in them.

A. Bohr and Mottelson[33] solved the elastic scattering of nucleon by properly taking account of the reaction from the collective mode excitation, and Yoshida has succeeded to give general and compact formalism for the unified treatment of the elastic and inelastic events[10),13)]. He showed that 1) the reaction yield was distributed among the elastic and inelastic events according to the degree of the matching of the wave functions of the various channels, 2) giant anomaly could occur which was interpreted as the virtual trap of the incident nucleon in the surface interaction potential, 3) the perturbation treatment was not a good approximation to the exact solution. So, his theory has many promising characters for the explanation of our results, where the large yield suggests that the 1st excited state of C^{12} is of collective nature*.

If this theory can explain the experimental evidences, the level structure of the compound nucleus (C^{13} or N^{13}) will also have the possibility to be interpreted based upon the picture in which the excited states are formed by the C^{12} core excitation and the single particle excitation of the extra nucleon in the potential formed by C^{12} core or its excited states**. This possibility has already been proposed by Reich et al. for the 6.4 and 6.9 Mev levels of N^{13} as a doublet[34].

§ 7. Acknowledgements

We wish to express deep thanks to Prof. I. Nonaka and the members of the Low Energy Group of the Institute for Nuclear Study for their hospitality and many valuable discussions. Deepest thanks must be expressed to Drs. K. Matsuda and S. Kobayashi for their kind guidance and support without which this study could not be performed. Thanks are also given to Prof. Y. Oda and Mr. N. Yamamuro for their active participation in obtaining data and their kind help. Our thanks have to be given to the members of the Electronics Division of INS for their kind co-operation. We are very glad to express our deep thanks to the INS cyclotron crew for their excellent operation and their contact co-operation throughout this study.

---

* We owe much to Profs. S. Yoshida and T. Tamura for their kindly pointing out the importance of Yoshida's theory.

** We owe to prof. Morinaga for his encouraging discussions on this point.

We wish to express our thanks to Profs. H. Shimazu and T. Tamura for their elucidating discussions in the theoretical field. Our thanks are also given to Prof. M. Takeuchi for his continuous encouragement on this study.

References

1) K. Kikuchi, S. Kobayashi and K. Matsuda: J. Phys. Soc. Japan **14**, 121 (1959). C. Hu, K. Kikuchi, S. Kobayashi, K. Matsuda, Y. Nagahara, Y. Oda, N. Takano, M. Takeda and T. Yamazaki: J. Phys. Soc. Japan **14**, 861 (1959).
2) M. Austern, S. T. Butler and H. McManus: Phys. Rev. **92**, 350 (1953).
3) F. D. Seward: Phys. Rev. **114**, 514 (1959).
4) Y. Oda, M. Takeda, N. Takano, T. Yamazaki, C. Hu, K. Kikuchi, S. Kobayashi, K. Matsuda and Y. Nagahara: J. Phys. Soc. Japan **15**, 760 (1960).
5) R. G. Freemantle, D. J. Prowse and J. Rotblat: Phys. Rev. **96**, 1268 (1954).
6) S. Kobayashi: To be published.
7) S. Kobayashi, K. Matsuda, Y. Nagahara, Y. Oda and N. Yamamuro: To be published.
8) D. M. Brink: Proc. Phys. Soc. **A68**, 994 (1955).
9) S. Hayakawa and S. Yoshida: Proc. Phys. Soc. **A68**, 656 (1955); Prog. Theor. Phys. **14**, 1 (1955).
10) S. Yoshida: Proc. Phys. Soc. **A69**, 668 (1959).
11) J. A. Lamarsh and H. Feshbach: Phys. Rev. **104**, 1633 (1959).
12) H. Ui: Prog. Theor. Phys. **18**, 163 (1967).
13) S. Yoshida: Prog. Theor. Phys. **19**, 169 (1958).
14) C. A. Levinson and M. K. Banerjee: Annals of Physics **3**, 670 (1958).
15) N. K. Glendinning: Phys. Rev. **114**, 1297 (1959).
16) R. W. Peelle: Phys. Rev. **105**, 1311 (1957).
17) H. E. Conzett: Phys. Rev. **105**, 1324 (1957).
18) G. E. Fisher: Phys. Rev. **96**, 704 (1954).
19) H. E. Gove and H. F. Stoddart: Phys. Rev. **86**, 572 (1952).
20) W. M. Gibson, D. J. Prowse and J. Rotblat: Proc. Roy. Soc. **243**, 237 (1957).
21) W. E. Burcham, W. M. Gibson, A. H. Hossain and J. Rotblat: Phys. Rev. **92**, 1266 (1953).
22) C. P. Browne and J. R. Lamarsh: Phys. Rev. **104**, 1099 (1956).
23) S. T. Braid and J. L. Yntema: Bull. Am. Phys. Soc. Ser II, **3**, 188 (1958); ibid. Ser II, **4**, 17 (1959)
24) S. Kikuchi et al.: J. Phys. Soc. Japan **15**, 41 (1960).
25) H. Bichsel, R. F. Mozley and W. A. Aron: Phys. Rev. **105**, 1788 (1957).
26) H. A. Bethe: Phys. Rev. **89**, 1256 (1953).
27) E. A. Silverstein: Nuclear Instruments and Methods **4**, 53 (1959).
28) B. Cork and W. Hartsough: Phys. Rev. **94**, 1300 (1954).
29) J. L. Yntema and M. G. White: Phys. Rev. **95**, 1266 (1954).
30) G. W. Greenlees, L. G. Kuo and M. Petravic: Proc. Roy. Soc. **243**, 206 (1957).
31) F. Ajzenberg-Selove and T. Lauritsen: Nuclear Physics **11**, 1 (1959).
32) Y. Fujimoto and T. Sasagawa: Genshikaku Kenkyu **2**, Special issue, (1956). (in Japanese)
33) A. Bohr and B. R. Mottelson: Kgl. Danske Videnskab. Selskab. Mat-fys. Medd. **29**, No. 16 (1953).
34) C. W. Reich, G. C. Phillips and J. L. Russel: Phys. Rev. **104**, (1956).

JOURNAL OF THE PHYSICAL SOCIETY OF JAPAN, Vol. 16, No. 2, FEBRUARY, 1961

Short-lived Activity of Ag^{106}

By Mitsuo SAKAI, Hidetsugu IKEGAMI and Toshimitsu YAMAZAKI

Institute for Nuclear Study, University of Tokyo, Tokyo, Japan

(Received June 25, 1960)

24-min Ag^{106} was produced by (n, 2n) reaction. New gamma rays of 295, 450, 625, 883, 1045, 1190, 1398, 1525, 1730, 1880 and 2170 KeV were observed with scintillation gamma-ray spectrometer. These gamma rays were compared with those appearing in the decay of Rh^{106}, Rh^{106m} and Ag^{106m}. The beta transition to the second excited level was discussed in light of the new beta-decay selection rule.

§ 1. Introduction

24-min Ag^{106} has been known[1] to emit two components of positrons and one gamma ray. Recently the spin of this isotope was measured[2] by atomic-beam methods and found to be $I=1$. The excited levels of the daughter nucleus Pd^{106} have been well investigated from the decay of 30-sec Rh^{106} which is produced by the decay of parent 1.0-year Ru^{106}[3] and also from the decay of 130-min Rh^{106m}[4] and 8.3-day Ag^{106m}[5]. The spins of the low excited levels were measured by gamma-gamma angular correlation measurement[6] and Coulomb excitation experiment[7]. The decay scheme proposed from these informations is shown in Fig. 1.[8] Since 24-min. Ag^{106} is now found to have the same spin as that of Rh^{106}, of which the decay involves many gamma rays as shown in Fig. 1, a rather complicated decay scheme could be expected also for 24-min. Ag^{106}. The simple decay scheme known up to the present is contrary to this prediction. Therefore, it was thought worth while to undertake once again study of this isotope by using the scintillation techniques developed since the previous publication[1] appeared in 1953.

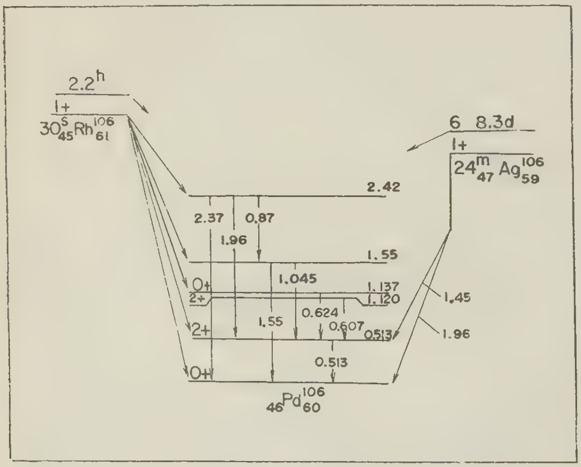
2.2^h
1+
$30^s_{45}\mathrm{Rh}^{106}_{61}$
6 8.3d
1+
$24^m_{47}\mathrm{Ag}^{106}_{59}$
2.42
2.37
0.87
1.96
1.55
1.045
1.137
1.120
0+
2+
2+
0+
1.55
0.624
0.607
0.513
0.513
1.45
1.96
$_{46}\mathrm{Pd}^{106}_{60}$

Fig. 1. Decay scheme for mass number 106 taken from Ref. 8)

§ 2. Source Preparation

24-min Ag^{106} was induced by bombarding silver metal with fast neutrons in the INS cyclotron which were produced by the bombardment of a carbon target with 22-MeV deuteron beam. The silver metal was inserted behind the carbon piece. Hence, the reaction utilized was Ag^{107}(n, 2n)Ag^{106}. Since the bombardment may induce also 8.3-day Ag^{106m}, 2.3-min Ag^{108}, 24.2-sec Ag^{110} and 270-day Ag^{110m}, the bombardment was done for twenty minutes and the measurement started ten minutes after the end of the bombardment.

§ 3. Gamma-Ray Scintillation Spectrometry

The gamma-ray spectrum was measured by means of three scintillation spectrometers. The first consisted of a cylindrical NaI(Tl) crystal, 2-in. long and 1^3/$_4$-in. in diameter, coupled to an RCA 6342 photomultiplier, the second of a cylindrical NaI(Tl) crystal, 3-in. long and 3-in. in diameter, coupled to a Dumont 6363 photomultiplier and the third of a cylindrical NaI(Tl) crystal, 4-in. long and 4-in. in diameter, coupled to a Dumont 6364 photomultiplier.

3.1 *Single Spectrum*

Fig. 2 shows the single spectrum taken by a gamma-ray scintillation spectrometer with 4-in. NaI(Tl) crystal. In this case, the source was placed 10 cm in distance from the front of the scintillation crystal, and the gamma rays were collimated by a Pb shield with a hole of 20-mm diameter. From this spectrum gamma rays of 295, 450, 510, 625, 883, 1045, 1190, 1398, 1525, 1730, 1880 and 2170 KeV were noticed. Some of these peaks may be composite peaks. These gamma rays were compared with those appearing in the decay of Rh^{106}, Rh^{106m} and Ag^{106m} (see Table I). The radiation caused by the annihilation of positrons in flight[9] may contribute to the pulse height distribution above 0.51 MeV. However, this effect was not found to change the main feature of the spectrum.

The decay of each peak was followed and found to have the same half-life of 24 min. within the experimental error, except 625 KeV peak. The latter peak had a fast component due to Ag^{108}. Decay curves were presented in Fig. 3.

In order to check the possibility of the sum peak or the pile-up peak, a Pb absorber of 12.5 mm thickness was placed between the source and the crystal. The counting rates N_a and N_i with and without the absorber were

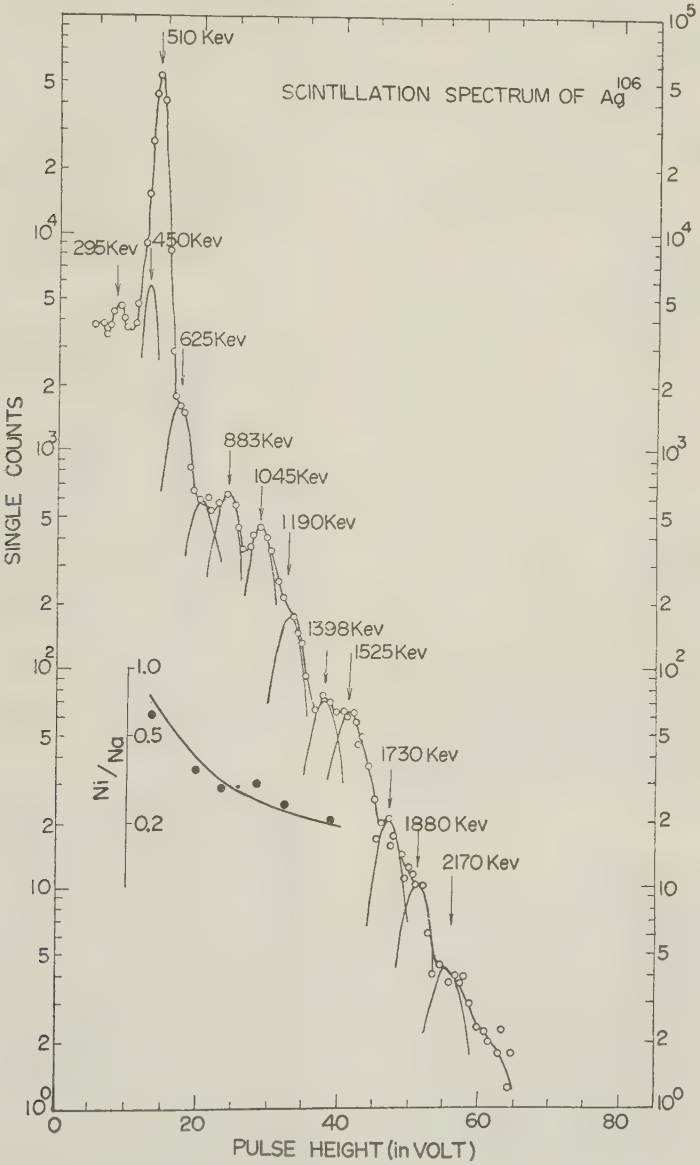

Fig. 2. Single gamma-ray scintillation spectrum taken by 4-in. diameter 4-in. long NaI(Tl) crystal. The full line in the under part of the figure shows a theoretical absorption ratio N_i/N_a with a Pb absorber of 12.5 mm thickness where N_a and N_i are the counting rates with and without the absorber, respectively. The circles are the experi-mental ratio N_i/N_a.

measured and the ratio N_i/N_a was compared with the theoretical absorption curve. The comparison was shown in Fig. 2. Although we could notice a slight contribution of sum peak about at 1.05 MeV resulting from the strong 0.51 MeV peak, it was concluded that the spectrum was caused by genuin gamma rays.

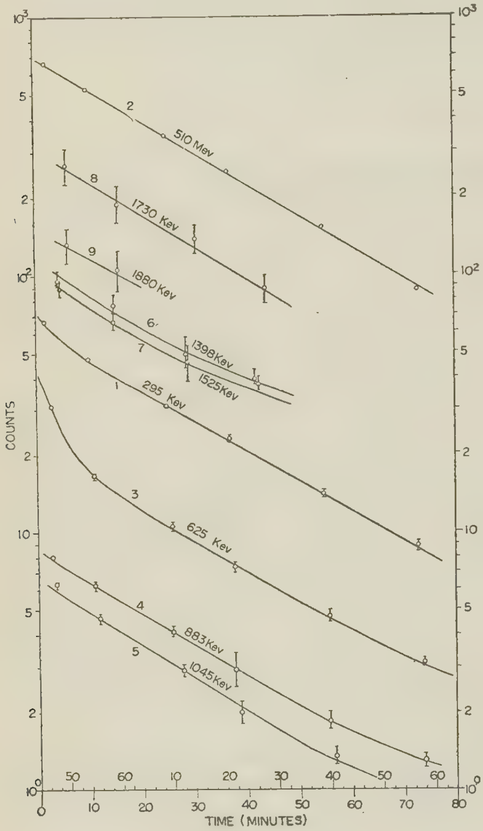

Fig. 3. Decay of scintillation spectrum.
Each curve concerns the decay of pulse height indicated in Fig. 2.

3.2 *Coincidence Spectrum*

For the coincidence experiment a conventional slow coincidence circuit of $2\tau=1.1\,\mu$s was used. The main and gate system used were a $1^3/_4$-in. diameter 2-in. long NaI(Tl) crystal with an RCA 6342 photomultiplier and a 3-in. diameter 3-in. long NaI(Tl) crystal with a Dumont 6363 photomultiplier, respectively. Fig. 4 shows the coincidence spectrum with the reference gate set at 0.51 MeV gamma ray which presents both of the annihilation radiation and the 0.51 MeV gamma ray. The ratio of the true coincidence rate N_{tr} to the accidental coincidence rate N_{ac} is also plotted in Fig. 4. A nearly constant ratio was obtained above 0.6 MeV. This fact means that the gamma rays of the energy higher than 0.6 MeV has about the same genetic relation with that of the 0.51 MeV.

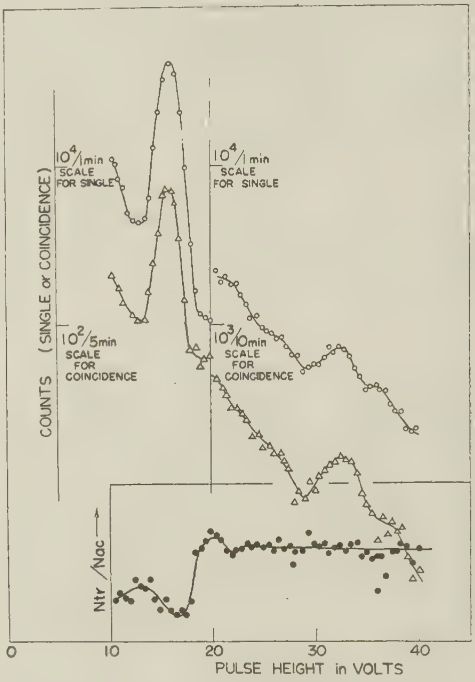

Fig. 4. Coincidence spectrum (—△—△—) with the reference gate set at 0·51 MeV peak. The spectrum in the right-hand side has an experimental set-up with a larger solid angle than that in the spectrum of the left hand-side. The in-set in the under-part is the ratio N_{tr}/N_{ac}, where N_{tr} and N_{ac} are the counting rate of the true coincidence and the accidental coincidence, respectively.

§ 4. Discussion and Conclusion

As we can see in Table I, the gamma radiations which have been expected from the decay of Rh^{106}, Rh^{106m} and Ag^{106m} were also found in the decay of Ag^{106}, so that the contradiction mentioned in § 1 disappears.

In the recent study[10] we had a new selection rule on the beta transition from odd-odd nuclei which can be described as follows: In general, nuclei having the spin and parity of 1+, 2+ or 3+ is hindered to decay to the second 2+ level, while the decay to the first 2+ and to the first or second 0+ level is allowed. Therefore, it is very interesting to study intensity relation of the beta transitions to 0+ and 2+ doublet at about 1.1 MeV excitation energy.

In the present case, the problem can be reduced partly to the determination of the intensity of 625 KeV and 607 KeV gamma rays, which are emitted by $0+\rightarrow 2+$ and $2+\rightarrow 2+$ transitions.

Table I. Gamma Rays in De-excitation of Pd^{106}

Parent Nucleus	Rh^{106}	Rh^{106m}	Ag^{106m}	Ag^{106}
Half Life	30s.	130 min	8.3d	24 min
Spin and Parity	1+	—	6	1+
Reference	3)	4)	5)	Present Work
Gamma-Ray Energy (KeV)				
1		220	227	
2				295
3		435	408	450
4	513	515	513	510
5	619	610	624	625
6		735	720	
7		820	805	
8	870			883
9		940		
10	1040	1070	1045	1045
11	1131		1131	1190
12	1205	1225	1205	
13		1380	1225 1388	1398
14	1540	1550	1530	1525
15	1760	1760	1720	1730
16		1860	1850	1880
17	1960			2170
18	2100	2090	2100	
19	2370	2260		
20	2660		2630	

Therefore, the pulse-height spectrum in the region of 510 KeV peak was carefully analysed. First, the Compton tail resulted from the gamma rays of higher energy than 625 KeV was subtracted. Then, the remained spectrum which is presented in Fig. 5 was compared with the 510 KeV anihilation peak of Na^{22} which was obtained by the subtraction of Compton tail of 1.28 MeV gamma ray. We can see clearly both of 450 KeV and 625 KeV peaks. The expected peak position of 607 KeV gamma ray was indicated by the arrow. From this analysis, we were lead to conclude that, if 607 KeV gamma ray exists, its intensity is weaker than that of 625 KeV gamma ray. This fact may suggest that the third beta component mainly consists of the decay to the 0+ level. It is consistent with the new beta-decay selection rule.

The author's thanks are due to Drs. H. Morinaga and K. Sugiyama for the kindful collaboration for the bombardment of fast neutrons.

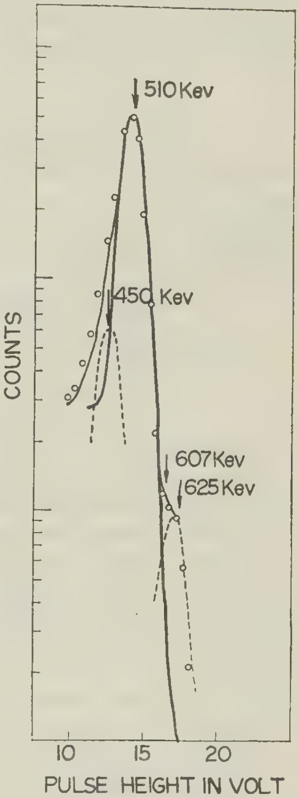

Fig. 5. Analysis of the pulse-height spectrum in the region of 510 KeV peak.

Open circles are the experimental points. The broad line is the pulse height spectrum of 510 KeV annihilation radiation of Na^{22} obtained by subtracting the tail of 1.28 MeV gamma ray. The expected peak position of 607 KeV gamma ray is indicated by the arrow.

References

1) W. L. Bendel, F. J. Shore, H. N. Brown and R. A. Becker: Phys. Rev. **90** (1953) 888.

2) J. B. Reynolds, R. L. Christensen, D. R. Hamilton, W. M. Hooke and H. H. Stroke: Phys. Rev. **109** (1958) 465. W. B. Ewbank, L. L. Marino, W. A. Nierenberg, H. A. Shugart and H. B. Silsbee: Phys. Rev. **115** (1959) 614.

3) D. E. Alburger and B. J. Toppel: Phys. Rev. **100** (1955) 1357. B. Kahn and W. S. Lyon: Phys. Rev. **92** (1953) 902.

4) S. Mayo and S. J. Nassiff: Phys. Rev. **111** (1958) 1140.

5) D. E. Alburger and B. J. Toppel: Phys. Rev. **100** (1955) 1357.

6) E. D. Klema and F. K. McGrown: Phys. Rev. **92** (1953) 1469.
7) F. K. McGowan: Proceeding of the Paris Conference 225, Dunod, Paris, 1959.
8) K. Way et al.: Nuclear Data Cards (National Research Council).
9) J. B. Gerhart, B. C. Carlson and R. Sherr: Phys. Rev. **94** (1954) 917.
10) M. Sakai: Report of the Institute for Nuclear Study INSJ-19 July 1, 1959.

JOURNAL OF THE PHYSICAL SOCIETY OF JAPAN, Vol. 16, No. 2, FEBRUARY, 1961

Counting Efficiency of Gamma Rays in Counter Tubes

By Tatsusaburo SUZUKI and Jiro YUHARA

First Research and Development Center Technical Research and Development H. Q., Japan Defense Agency, Tokyo

(Received September 6, 1960)

The counting efficiency of gamma rays in cylindrical counters and end-window counters is examined by means of a very thin sheet and a collimated fine pencil beam of gamma rays. The distribution of the number of gamma rays emitted from the thin slit is measured by means of a end-window counter or by the effect of the fine anode wire of the cylindrical counter. When the plane of thin sheet of gamma rays reaching from side to a cylindrical counter is parallel to the axis, the counting efficiency registers a maximum value at the position where the sheet of gamma rays is in contact with the inner surface of the counter, and a smaller value near the central wire, but when the pencil beam of gamma rays is parallel to the anode wire and the gamma rays entering the counter through the end-window plate, the counting efficiency gives a maximum value at the anode wire and the inner surface of the counter. An average efficiency for a sheet of gamma rays which are in a plane perpendicular to the counter axis is also investigated.

§ 1. Introduction

Investigations have been performed on the counting efficiency near the ends of the counter[1),2)]. In the present work the collimated gamma rays (energy 0.662 MeV) are used to study the efficiency of the central portion of cylindrical counters and the variation of efficiency with distance from the anode wire in the end-window counters.

Because the range of the Compton-electrons or photo-electrons emitted by the interaction of 0.662 MeV gamma ray is greater than that by soft X-rays, many electrons from counter wall and anode wire can enter the counter. Therefore, the counting efficiency mainly depends upon the number of Compton-electrons or photoelectrons emitted from the counter wall. A sheet of gamma rays emitted from a slit, 0.25 mm wide and 8 mm long, and a fine pencil beam (1 mm × 1 mm) of gamma rays are used to study the variation of the efficiency with the distance between the gamma sheet the anode wire and or the distance between the anode wire and the fine gamma pencil beam. Using this method, the efficiency of the Geiger counter was compared with that of the proportional counter.

§ 2. Experimental Arrangements and Procedures

This experiment was counducted by using a stainless steel flow counter (radius of the anode wire $r_w=0.025$ mm, external radius $r_e=30$ mm, internal radius $r_c=25$ mm) and end-window counters (TGC-2 type $r_e=18.5$ mm, $r_c=16.5$ mm, TEN GM 132 type $r_e=22.7$ mm, $r_c=10$ mm and halogen quenched philips 18514 type $r_e=15.1$ mm, $r_c=13.0$ mm) as shown Fig. 1.

A Cs^{137} source which emits homogeneous gamma rays (energy 0.662 MeV) was used, the intensity being 2 curie. The CsCl gamma source is put into the cylindrical container 4 mm in diameter and 4 mm in length. The source is embedded in a lead collimating arrangement as shown in Fig. 2a and 2b.

The radiation from the source passes through an opening 8 mm in diameter and 200 mm in depth and a narrow channel (0.25 mm wide, 8 mm long and 100 mm deep) or a fine hole (1 mm × 1 mm and 100 mm deep). Thus homogeneous gamma rays parallel or perpendicular to the axis of the counter pass through the counter. The counter can be displaced accurately by the screw shown in Fig. 2a and we can measure the counting efficiency and the distribution of the number of gamma rays. The counting rate is measured at each position of the counter with a standard deviation less than a few percent.

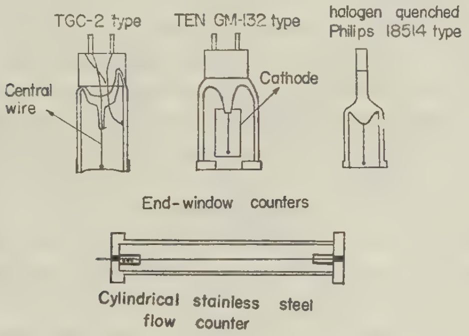
TGC-2 type
TEN GM-132 type
halogen quenched Philips 18514 type
Central wire
Cathode
End-window counters
Cylindrical stainless steel flow counter

Fig. 1. Counters.

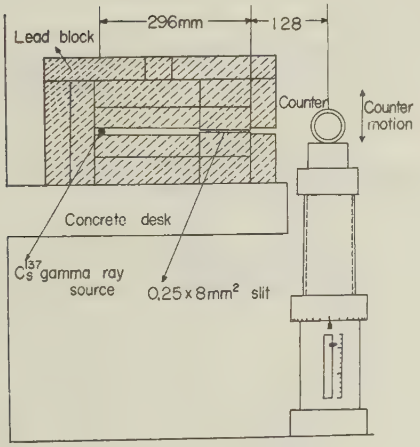

Fig. 2a. Experimental arrangement for collimated gamma rays.

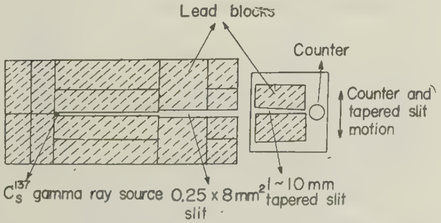

Fig. 2b. Experimental arrangement for measuring distribution of gamma rays from slit along its 8 mm length.

§ 3. Experimental Results

For the purpose of measuring the intrinsic efficiency of the central portion of the cylindrical proportional counter for 0.662 MeV gamma

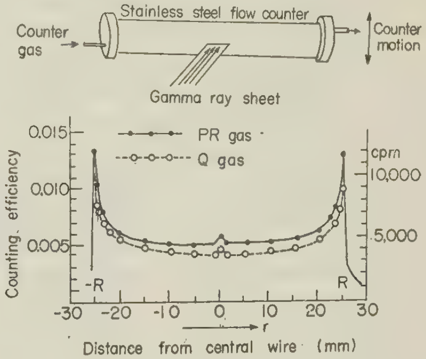

Fig. 3a. Variation of counting efficiency and counting rate with distance between central wire and gamma ray sheet. (Stainless steel flow counter)

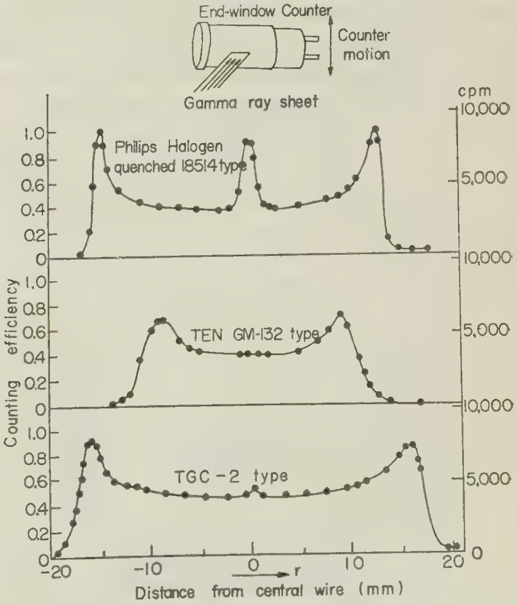

Fig. 3b. Variations of counting efficiency and counting rate with distance between central wire and gamma ray sheet. (End-window counters)

rays, the counting rates for gamma rays emitted from a 1 mc standard gamma source and enter the cylindrical counter through a lead hole (20 mm × 20 mm or 20 mm × 40 mm) are measured. The counting rates for 7.08×10^4 and 1.416×10^5 gamma ray quanta per minute which enter the counter are 358.7 and 702.6 cpm respectively. Thus the intrinsic counting efficiency of the central portion of the counter for 0.662 MeV gamma ray is 0.0050. The total number of gamma rays emitted from the thin slit per unit time is determined from the counting efficiency and the counting rate near the anode wire. The total number of gamma rays thus obtained is 9.12×10^5 gamma photons per minute.

The variation of counting rate with distance between the anode wire and the sheet of gamma rays is measured as shown in Fig. 2a. In this experiment, PR gas (90% argon and 10% methane) and *Q* gas (99% helium and 1% isobutane) were used in the same stainless steel flow counter. The experimental data for stainless steel flow counter is as shown in Fig. 3a, and those for end-window counters are as shown in Fig. 3b. Since the number of gamma rays crossing the counter per unit time is obtained as described above, the counting efficiency of gamma rays at each position is determined from the counting rate and the number of gamma rays passing through the counter per unit time. The counting efficiencies thus determined are also shown in Fig. 3a and Fig. 3b (left scale).

In this case the counting efficiency mainly depends on the number of Compton-electrons and photoelectrons emitted into the counter gas from the wall material per unit time. The smaller the angle between the inner surface of the counter and the sheet of gamma rays, more electrons are emitted into the counter. Thus each counting efficiency curve gives two maximum values at the position where the sheet of gamma rays is in contact with the inner surface of the counter. The increased counting efficiency due to the anode wire in efficiency curve in Fig. 3a is shown in Fig. 4. This curve can show the distribution of gamma rays along 0.25 mm width. When the stainless steel counter is used as a flow counter, the counting efficiency of gamma rays depends on the atomic number of the gas, in view of their absorption coefficient. The difference of counting efficiency in proportional and Geiger counters at the same position depends on the traveling distance of the gamma rays in the counter gas. This gives maximum values at the central wire, and almost zero at the position where the sheet of gamma rays comes in contact with the inner surface of the counter as shown in Fig. 3a.

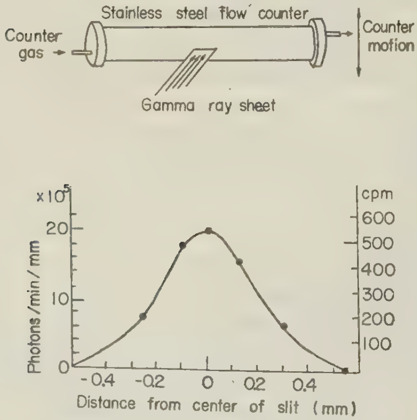

Fig. 4. Counting rate due to the electrons emitted from central wire which can show the distribution of number of gamma rays along 0.25 mm slit width.

When a fine pencil beam of gamma rays is parallel to the axis of an end window counter

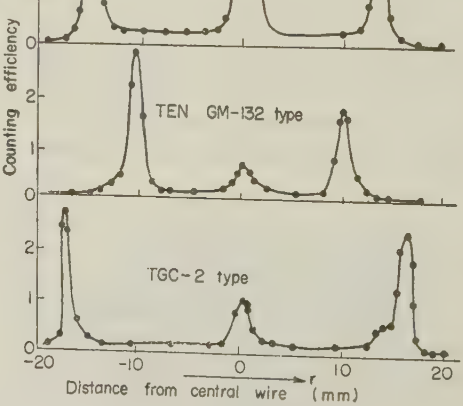

Fig. 5. Variations of counting efficiency with distance between central wire and center of gamma ray pencil beam. (End-window counter)

the efficiency gives three maximum values as shown in Fig. 5. In this case the counting efficiency registers a large value at the central wire of the counter because the fine beam is parallel to the anode wire and a great number of Compton-electrons and photoelectrons are emitted from both anode wire and the glass bead attached to the end of the wire.

For the purpose of measuring the counting efficiency for collimated gamma ray sheet end-window Geiger counters along their axes, the counters are moved in a direction of their axes as is shown in Fig. 6. The experimental results are as shown in Fig. 6.

The distribution of the number of gamma ray sheet from the slit along its 8 mm length is determined from the number of gamma rays per unit time and the counting rate which is measured as shown in Fig. 2b. The experimental data obtained is as shown in Fig. 7.

To measure the average counting efficiency or the counting rate for gamma rays whose distribution is as shown in Fig. 7., the counter is moved in the plane of gamma ray sheet. This arrangement is shown in Fig. 8. Fig. 8 also shows the observed counting rate (scale

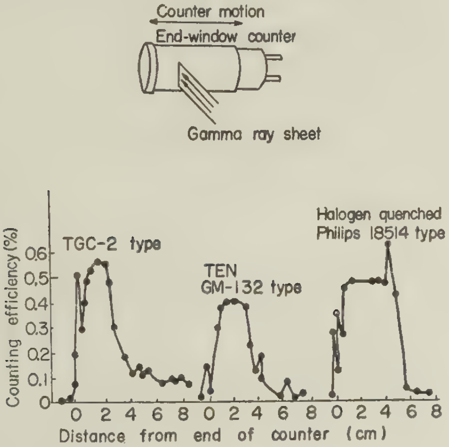

Fig. 6. Counting efficiency for collimated gamma ray sheet moved parallel to the axis of end window counter.

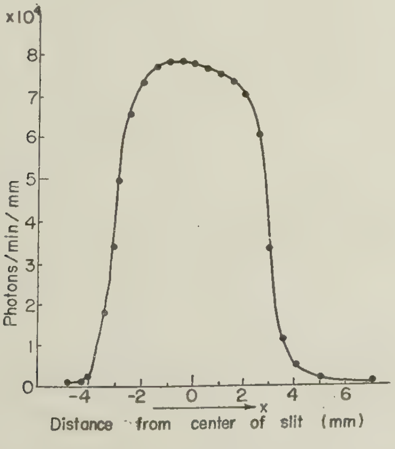

Fig. 7. Distribution of number of gamma rays emitted from slit along its 8 mm length.

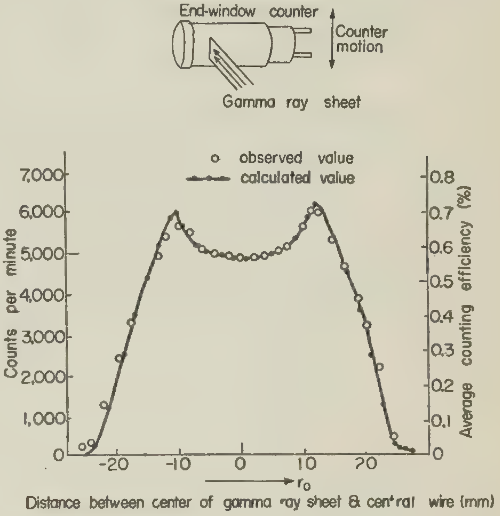

Fig. 8. Variation of counting rate or average counting efficiency for collimated gamma ray sheet whose distribution is shown in Fig. 7. (TGC-2 type counter)

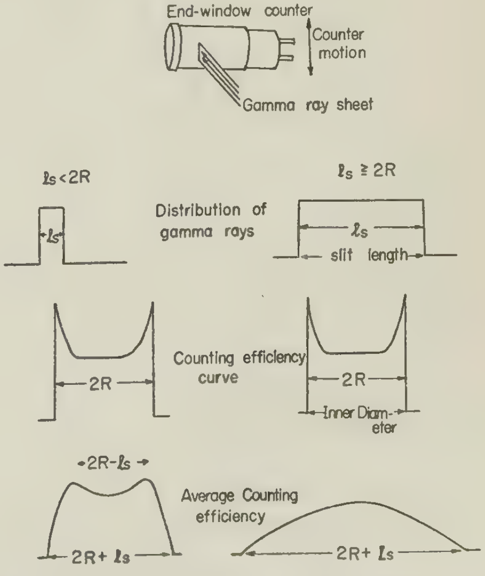

Fig. 9. Relation of average counting efficiency and slit length.

left) or the average counting efficiency (scale right). This result can be also obtained from the counting efficiency shown in Fig. 3b and the distribution of number of gamma rays in Fig. 7. If the counting efficiency shown in Fig. 3b is represented by $E(r)$ and photons per unit length per unit time shown in Fig. 7 is represented by $D(x)$, where r is the distance from the central wire and x is the distance from the center of the slit, the counting rate $C(r_0)$ at r_0 can be formularized as

$$C(r_0)=\int_{-\infty}^{\infty} D(x)E(r_0+x)dx\ .$$

The numerical integration is calculated from Fig. 3b and Fig. 7, and is compared with the observed counting rate as shown in Fig. 8.

When the distribution of the number of gamma rays is uniform as shown in Fig. 9, the average efficiency has two maximum values at the positions separated at $2R-l_s$ distance if the length of slit l_s is shorter than the inner diameter $2R$ of the counter, but the average efficiency gives only one maximum value at the center as shown in Fig. 9 if the length of slit is equal or larger than the inner diameter.

§ 4. Conclusion

It is important to know that the counting efficiency gives variation to positions when counters are used to measure gamma rays, and especially when they are collimated. The distribution of the number of gamma rays emitted from a thin slit can be measured by means of the increased local counting efficiency due to the anode wire of the counter.

References

1) A. Cockroft and S. Curran: Rev. Sci. Instr., 22, 37 (1951).

2) T. Suzuki and J. Yuhara: J. Appl. Phys. Japan, 29, 540 (1960).

JOURNAL OF THE PHYSICAL SOCIETY OF JAPAN, Vol. 16, No. 2, FEBRUARY, 1961

On the Protons from the $N^{14}(d, p)N^{15}$ Reaction

By Nawoyuki KAWAI*

Department of Physics, Kyushu University, Fukuoka, Japan

(Received October 6, 1960)

Angular distributions for the $N^{14}(d, p)N^{15}$ reaction were investigated at nine deuteron energies ranging from 1.5 to 3.2 MeV. Measurements were carried out in the angular range from 0 to 165 degrees at intervals of 15 degrees. The results for the $N^{14}(d, p)N^{15}$ ground state reaction showed generally a forward peak, as was expected from deuteron stripping, and a considerable rise in backward directions. These experimental data were analyzed with the heavy particle stripping theory and parameters adjusted to get a best fit were obtained.

With the exception at forward directions, the main feature of angular distributions was found to be very similar to that for the $N^{14}(d, n)O^{15}$ ground state reaction, which is the mirror reaction, at the same deuteron energies. At forward directions proton yields from the $N^{14}(d, p)N^{15}$ reaction were substantially larger than neutron yields from the $N^{14}(d, n)O^{15}$ reaction.

Angular distributions for the first excited doublet state reaction were found to be nearly isotropic, but a slight peak was observed at about 60 degrees similarly at all deuteron energies.

Total cross sections for both state reactions were also estimated. Excitation functions for the $N^{14}(d, p)N^{15}$ and $N^{14}(d, n)O^{15}$ ground state reactions showed similar behavior, having some resonance-like structures.

§1. Introduction

In our previous work[1], angular distributions and absolute cross sections for the $N^{14}(d, n)O^{15}$ ground state reaction have been investigated at seven deuteron energies from 1.5 to 2.9 MeV. It has been found that the main feature of the angular distributions is a strong forward peak attributed to deuteron stripping with $l_p=1$ and a remarkable rise in backward directions. The neutron yields at backward directions varied considerably with the deuteron energy and at 1.96 MeV it reached the value of almost three times as that of the forward maximum. Retz-Schmidt and Weil[2] have made the same measurements at the energy range of deuterons from 0.91 to 5.27 MeV with larger energy intervals and obtained the similar results. It is considered, therefore, to be worthwhile to investigate the angular distributions for the $N^{14}(d, p)N^{15}$ reaction and to compare them with these for the $N^{14}(d, n)O^{15}$ reaction, which is the mirror reaction to the former, at the same bombarding energies. Such comparison will be useful for the investigation of reaction mechanisms of deuteron induced reactions in this energy region. The present investigation was undertaken to measure total cross sections and angular distributions for the $N^{14}(d, p)N^{15}$ ground state and first excited 5.28 and 5.31 MeV doublet state reactions at nine deuteron energies ranging from 1.5 to 3.2 MeV.

Up to present, the angular distributions for this reaction have been investigated by many authors at deuteron energies from 5 to 20 MeV, that is, by Gibson and Thomas at 7.89 MeV[3], Eby at 11.9 MeV[4], Green and Middleton at 9 MeV[5], Warburton and McGruer at 14.8 MeV[6], and Morita *et al.* at 16 MeV[7]. The results for the $N^{14}(d, p)N^{15}$ ground state and 6.33 MeV state reactions which were obtained by these authors could be fitted qualitatively by means of deuteron stripping with $l_n=1$. As for the 5.28 and 5.31 MeV doublet state reaction, the obtained results are contradictory to each other. Gibson and Thomas have obtained the roughly isotropic distribution indicating that the deuteron stripping did not contribute to any appreciable extent, while Eby has reported the anisotropic distribution showing a forward maximum. Unlike to their results, the angular distribution obtained by Green and Middleton had a broad maximum at about 50 degrees in consistent with the fact that one of the doublet was formed by deuteron stripping with $l_n=2$ and the other was probably isotropic.

---

* Now at Nippon Atomic Industry Group Co., Ltd., Chiyoda-ku, Tokyo, Japan.

Many measurements have also been accumulated at deuteron energies below one MeV. At 400, 500 and 600 keV, Jongerius *et al.*[8] have observed angular distributions for the ground state reaction which have appreciable forward maximum and a slight backward rise. Then, they have concluded that deuteron stripping seems to take place considerably in addition to compound nucleus formation at such lower deuteron energies as mentioned above. Booth *et al.*[9] have made the same investigations at 595, 805 and 990 keV and found the angular distributions, contradicting to those of Jongerius *et al.*, which were rather symmetrical about 90 degrees. It will be noted that in the energy region below one MeV, angular distributions for the ground state reaction become more symmetrical with increasing deuteron energy. For the 5.28 and 5.31 MeV doublet state reaction, Sjögren and Ahnlund[10] have observed the angular distributions for these state separately with a double-focusing heavy particle spectrometer. At 800 keV, their results revealed the distribution for the 5.276 MeV state reaction to have a broad maximum at about 100 degrees and that for the 5.305 MeV state reaction to have a characteristic minimum at about 80 degrees. Stanley[11] has measured the angular correlation between protons and gamma-rays emitted from the 5.28 and 5.31 MeV doublet state at the deuteron energy of 630 keV.

In the energy region of several MeV, very few investigations on the angular distributions for this reaction have been done. Wyly[12] has measured them at five different deuteron energies only in the angular range from 15 to 135 degrees. The angular distributions obtained by him for the 5.28 and 5.31 MeV doublet state reaction were essentially isotropic at every deuteron energy, while those for the ground state reaction were found generally to have a forward maximum.

§ 2. Experimental Arrangements and Procedures

Arrangements of a scattering chamber and detector are shown schematically in Fig. 1. The scattering chamber used in this experiment is 23 cm in its inner diameter and 10 cm in height. On one side of its side wall with respect to the incident beam, eleven apertures of 6 mm in diameter were bored at intervals of 15 degrees in the angular range from 15 to 165 degrees and on the other side, ten apertures with the same intervals from 22.5 to 157.5 degrees. These apertures, to which a detector system was attached directly, were sealed with 20 microns thick aluminum foils for vacuum tight. A insulated Faraday cup was mounted to measure the deuteron beam and secondary electrons were suppressed by magnetic field produced by two pieces of Ferrite. In the case of the measurement of protons emitted to zero degree, the detector system was mounted instead of the Faraday cup. In this case a silver absorber of 23 mg/cm² thick was inserted before the aluminum foil to cut off the deuteron beam.

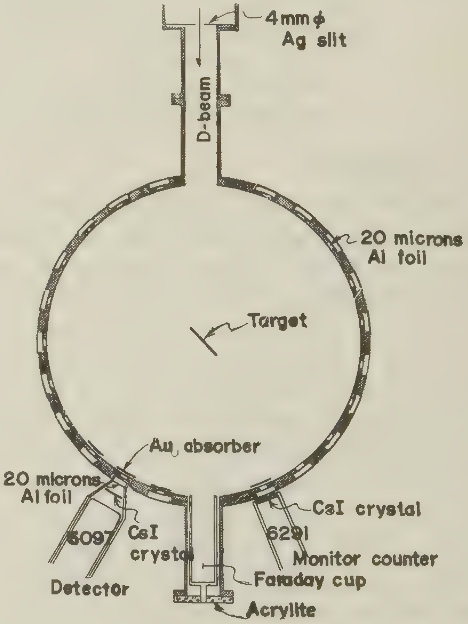

Fig. 1. Arrangements of the scattering chamber and the detector system.

As a nitrogen target, melamine ($C_3H_6N_6$) evaporated on a silver backing was used. Three targets of different thickness of melamine were prepared and these thickness were determined by weighing to be 0.30, 0.42 and 0.48 mg/cm².

Measurements were made at nine deuteron energies from 1.5 to 3.2 MeV, five of which were chosen to be almost same as those used in the previous investigation on the $N^{14}(d,$

$n)O^{15}$ reaction. The deuteron beam from the electrostatic generator at Kyushu University was magnetically analyzed and led into the scattering chamber after through a defining silver slit of 4 mm in diameter. The target was placed at the centre of the scattering chamber to make 45 degrees to the deuteron beam. The incident deuteron energy which was expected to have an uncertainly of less than 0.5 per cent was corrected for the energy loss in traversing one-half of effective target thickness. Finally, the deuteron beam was collected with the Faraday cup and was measured to be from 0.05 to 0.5 microamperes.

In order to evaluate the absolute cross sections, the excitation function for the $N^{14}(d, p)N^{15}$ reaction was measured at 15 degrees. In such case, a gas target was used instead of the melamine target. This target chamber was made of brass cylinder of 2 cm long and 2 cm in diameter and was supported with a brass pipe which served also for gas inlet. It has three windows sealed with 1.09 mg/cm² thick nickel foils, through which the deuteron beam and emitted protons pass. The mixed gas of 92.0 per cent nitrogen and 8.0 per cent deuterium was introduced into the target chamber up to 20 cm Hg pressure. Protons from these two elements are detected simultaneously. It is, then, possible to evaluate absolute differential cross sections for the $N^{14}(d, p)N^{15}$ reaction by refering to the proton yield from the $D(d, p)T$ reaction[13].

The proton detector is made of an one mm thick CsI(Tl) crystal and an EMI 6097 photomultiplier. The thickness of the CsI(Tl) crystal was chosen to be 1.0 mm so as to stop all emitted protons completely. At several angles in forward directions gold absorbers of suitable thickness are inserted, if necessary, in front of the detector to stop the elastically scattered deuterons. Output pulses from the detector were amplified and fed to a twenty channel pulse height analyzer. At 22.5 degrees, a monitor counter consisted of a 2 mm thick CsI(Tl) crystal and a Dumont 6291 photo-multiplier was mounted and its discriminator level was set in such a way that only the protons from the $N^{14}(d, p)N^{15}$ ground state reaction were detected.

§ 3. Experimental Results

Complete pulse height spectra were taken at each angle and each bombarding energy. Typical spectra of measured protons are shown in Fig. 2, (A) and (B), which were taken with the melamine and the gas target, respectively. Errors indicated in figures are those due to counting statistics only. In each spectrum a well separated group of protons of the highest energy, designated by p_0, is the one from the $N^{14}(d, p)N^{15}$ ground state reaction. p_1 corresponds to the group from the 5.28 and 5.31 MeV doublet state reaction. Because of the small difference in energy by only about 25 keV, it is not possible to distinguish separately the protons corresponding to this doublet state reaction. The group of protons emitted from the 6.33 MeV state reaction, p_2, was also clearly separated from other groups in the case of the gas target. In the case of the melamine target, however, this group is obscured by that from the $C^{12}(d, p)C^{13}$ ground state reaction and is hardly resolved. Moreover, the group of alpha-particles from the $N^{14}(d, \alpha)C^{12}$ ground state reaction was observed at forward directions. At the angles larger than 105 degrees, this group of alpha-particles overlapped on or smeared out into the groups of protons from

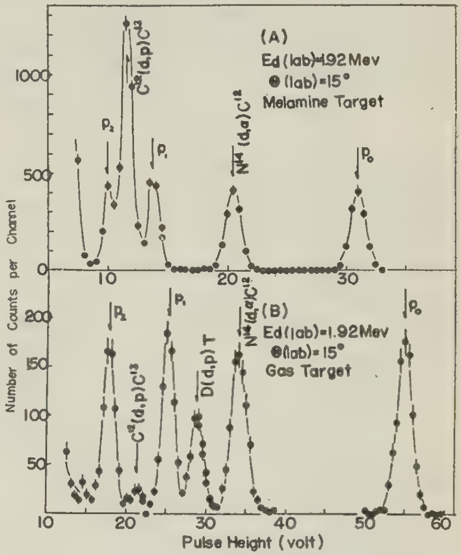

Fig. 2. Pulse height spectra of protons and alpha-particles. (A) and (B) were obtained using the melamine and the gas target, respectively. p_0, p_1 and p_2 indicate the groups of the protons from the $N^{14}(d, p)N^{15}$ ground state, 5.28 and 5.31 MeV doublet state and 6.33 MeV state reactions, respectively.

the $N^{14}(d, p)N^{15}$ and $C^{12}(d, p)C^{13}$ reactions. In such case in order to detect the protons from the $N^{14}(d, p)N^{15}$ 5.28 and 5.31 MeV doublet state reaction only, a 20 microns thick aluminum absorber was attached in front of the detector to discriminate those alpha-particles. Background protons were measured using the silver backing without melamine and it was confirmed that those having the energy in question were not observed to any appreciable extent.

From these pulse height spectra obtained at each angle, angular distributions for the $N^{14}(d, p)N^{15}$ ground state and first excited doublet state reactions are obtained. In Figs. 3 and 4, these results are shown with solid

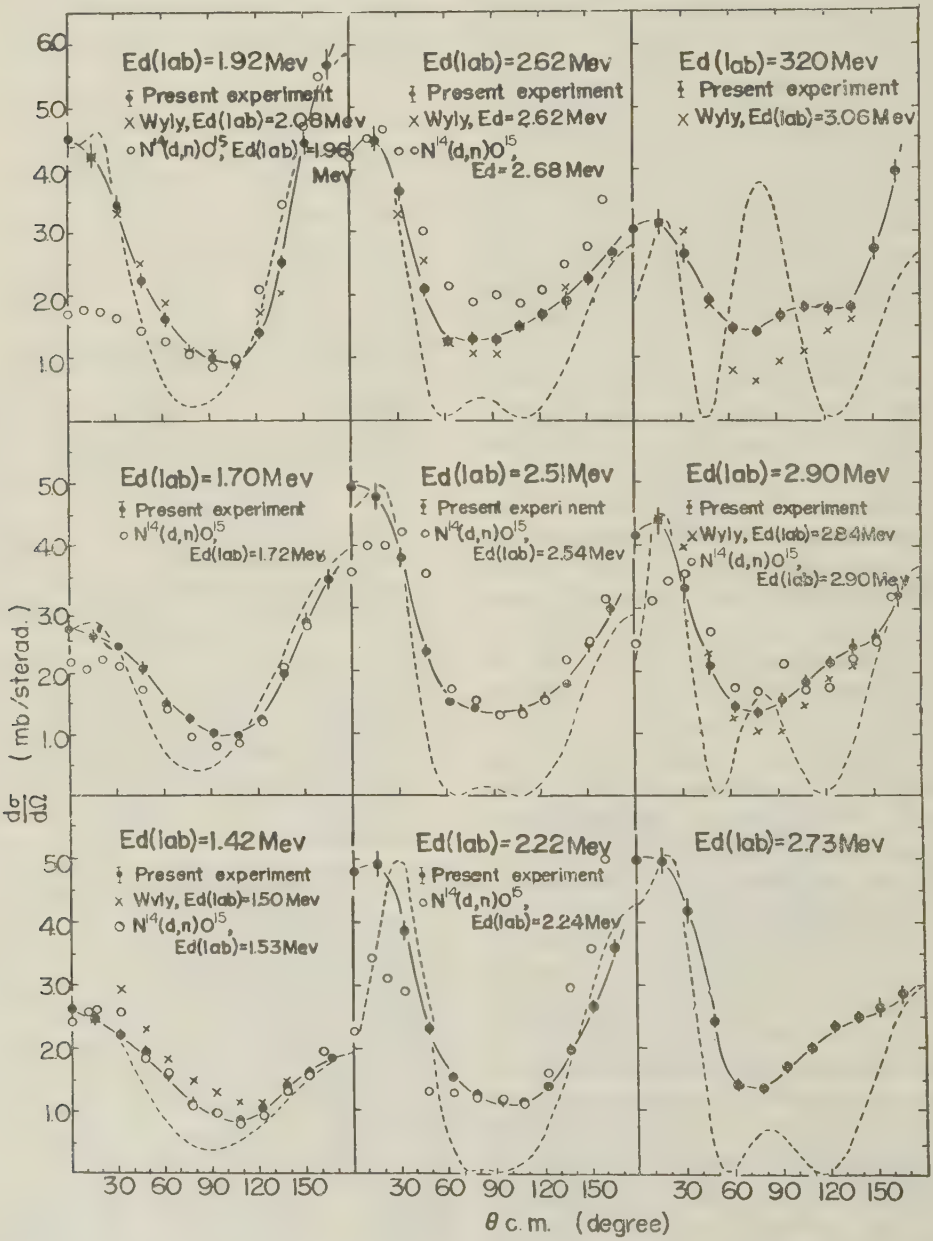

Fig. 3. Angular distributions for the $N^{14}(d, p)N^{15}$ ground state reaction. Dotted curves were calculated using the heavy particle stripping formula of Owen and Madansky. Open circles and crosses are results for the $N^{14}(d, n)O^{15}$ ground state reaction obtained in our previous work and the $N^{14}(d, p)N^{15}$ ground state reaction by Wyly, respectively.

lines. The relative errors indicated in figures include the ambiguities of the separation of overlapped proton groups and the statistical ones due to counting. Absolute values of differential cross sections were evaluated from the mixing ratio of target gases and the known value of cross sections for the $D(d, p)T$ reaction[13]. Uncertainties in the absolute scale of angular distribution for each deuteron energy, thus determined, are considered to amount to 15 per cent at maximum. As shown in Fig. 3, nine angular distributions for the ground state reaction are found to have a similar characteristic in shape which is a pronounced forward maximum and a remarkable backward rise. However, the absolute values of differential cross sections, in particular in backward directions, vary slowly with the deuteron energy. The position of minimum at medium angles also moves to smaller angles with the increasing deuteron energy from 100 degrees at 1.42 MeV to 70 degrees at 3.20 MeV, respectively. In Fig. 3, Wyly's results which were normalized to the present ones at 15 degrees were also presented. Satisfactory agreements can be seen between the present results and Wyly's ones, considering the difference of deuteron energies. For the comparison with the mirror reaction, the angular distributions for the $N^{14}(d, n)O^{15}$ ground state reaction were also plotted in Fig. 3. At every seven bombarding energies, the backward yields of emitted particles from both reactions show the striking agreements. It will be noted that with the exception at 1.42 MeV the proton yields from the $N^{14}(d, p)N^{15}$ reaction at forward directions are considerably larger than the neutron yields from the $N^{14}(d, n)O^{15}$ reaction.

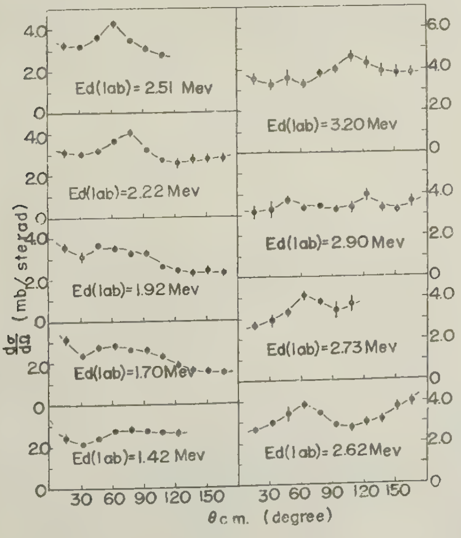

Fig. 4. Angular distributions for the $N^{14}(d, p)N^{15}$ 5.28 and 5.31 MeV doublet state reaction.

Fig. 4 shows angular distributions for the 5.28 and 5.31 MeV doublet state reaction. Their patterns are found to be essentially isotropic and to agree with the results obtained by Wyly. Considering in more detail, however, a broad maximum at about 60 degrees, though is not so remarkable, is observed similarly at every bombarding energy and a second slight maximum seems to take place at about 120 degrees in the case of 3.20 and probably of 2.90 MeV.

Total cross sections estimated by integrating the angular distributions are plotted in Fig. 5. Both yield curves for the $N^{14}(d, p)N^{15}$ ground state and first excited doublet state reactions increase rapidly with the increasing deuteron energy up to 1.92 MeV. Beyond 1.92 MeV, the yield curve for the ground state reaction is nearly constant, while that for the

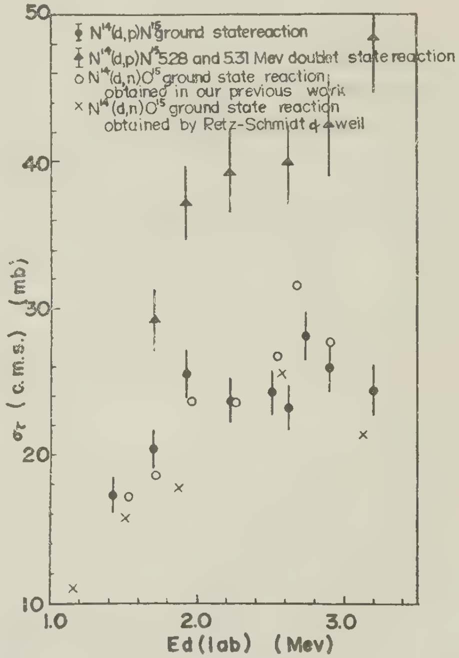

Fig. 5. Excitation curves for the $N^{14}(d, p)N^{15}$ ground state and 5.28 and 5.31 MeV doublet state reactions. Open circles and crosses are results for the $N^{14}(d, n)O^{15}$ ground state reaction obtained in our previous work and by Retz-Schmidt and Weil, respectively.

5.28 and 5.31 MeV doublet state reaction still increases gradually. Absolute cross sections for the doublet state reaction are generally larger by a factor of 1.5 than that for the ground state reaction over the whole range of deuteron energies investigated. It must be noted that at 1.92 and 2.73 MeV, slight maxima for the ground state reaction and sharp knicks for the doublet state reaction are observed, respectively. For comparison, total cross sections for the $N^{14}(d, n)O^{15}$ ground state reaction are also presented in Fig. 5 together with that obtained by Retz-Schmidt and Weil. The yield curves for these two reactions are all found to be very similar both in shape and in absolute value.

§ 4. Discussions

The $N^{14}(d, p)N^{15}$ ground state reaction

In the energy region of a few MeV, deuteron induced reactions are usually considered to proceed through a mixture of compound nucleus formation and deuteron stripping with comparable importance. Moreover, in deuteron stripping the distortion of wave function by the Coulomb and nuclear forces may not be neglected. Accordingly, it is not certain that the pure stripping theory will give a good fit to the present data obtained at such a energy region of deuterons as mentioned above. As shown in Fig. 3, however, nine angular distributions have a striking similarity in shape, namely the characteristic forward peak and the remarkable backward rise. This similarity of patterns over the entire energy range and the pronounced forward peak immediately suggest that deuteron stripping contributes appreciably to this reaction. The backward rise will be also interpreted in terms of heavy particle stripping. Angular distributions, then, have been attempted to analyze using the deuteron and heavy particle stripping theory of Owen and Madansky[14]. In spite of some inconsistency of its derivation as was pointed out by Hasegawa and Ichikawa[15], the formula of Owen and Madansky was used because of its simplicity and was considered enough to see the qualitative agreement.

The values of orbital angular momenta of captured particles which appear in the theoretical formula were estimated as follows. The l_n- value for a captured neutron was decided to be 1 by refering to the shape of angular distributions and also by the values of spins and parities of N^{14} and N^{15} nuclei. Secondly, the orbital angular momentum of a captured C^{13} core is limited by the conservation of parity and angular momentum. The ground state of N^{15} nucleus is known to have odd parity and spin 1/2. The deuteron has even parity and spin 1 and the C^{13} core has odd parity. Accordingly, the l_c-value of the captured C^{13} core must be even and is limited to 0 or 2. Since $j_2(k_2R_2)$ approches zero at backward angles and d-wave penetrability is much less than that for the s-wave, the $l_c=2$ term would be possibly neglected. The formula for the differential cross section at a given deuteron energy, following the notation of Owen and Madansky, is

$$d\sigma/d\omega=\text{const.}|G_D(K_1)j_1(k_1R_1)+(\lambda_2/\lambda_1)G_H(K_2)j_0(k_2R_2)|^2 ,$$

where

$$G_D(K_1)=1/(K_1^2+\alpha_D^2)$$

and

$$G_H(K_2)=[1/(\alpha_N^2-K_2^2)+1/(\beta_N^2+K_2^2)][K_2r_Nj_1(\alpha_Nr_N)j_0(K_2r_N)-\alpha_Nr_Nj_0(\alpha_Nr_N)j_1(K_2r_N)] .$$

are momentum distribution functions for deuteron and heavy particle stripping, respectively. λ_2/λ_1 is the ratio of amplitudes for heavy particle stripping to deuteron stripping. A radius and depth of the potential well used to determine the neutron wave function for the calculation of $G_H(K_2)$ were chosen to be 3.37×10^{-13} cm and 40 MeV, respectively. The parameters that are adjustable to get a fit to experimental data are the interaction radii, R_1 and R_2, and the ratio of two stripping amplitudes, λ_2/λ_1. The value of interaction radius R_1 was chosen to be 7.0×10^{-13} cm constantly for every deuteron energy. With this value of R_1, the experimental angular distributions at forward directions could be all fitted satisfactorily by pure deuteron stripping. For simplicity, constant value of 7.0×10^{-13} cm was also chosen for the interaction radius R_2, being the same as that for R_1. The interaction radii, R_1 and R_2, in themselves, should be adjusted to get the best fit to experimental data independently to each other and to the deuteron energy. Owen and Madansky pointed out that these two parameters should not necessarily be a constant over the entire energy range, since they represent phenomenological expressions for the behavior of the incoming rather complicated wave functions in the interior of the nucleus. In the case of the $B^{11}(d, n)C^{12}$ reaction, Owen and Madansky have chosen the value of R_1 and R_2 to be both constant, while Weil and Jones[16)] have obtained the energy dependent ones in the analysis of $N^{15}(d, n)O^{16}$ ground state reaction.

The dotted curves in Fig. 3 are theoretical ones thus calculated. With the exception of the curve at 3.20 MeV the agreement with experimental angular distributions is satisfactory, considering the crude choise of parameters. At 3.20 MeV, it was impossible to obtain a good fit for any value of the amplitude ratio, λ_2/λ_1, because the calculated interference term between both amplitudes of deuteron and heavy particle stripping resulted to be abnormaly large. Such interference is in itself one of the important features of the formula obtained by Owen and Madansky and was evaluated to be appreciable even at other lower bombarding energies. But it was not so unreasonably large value. On the other hand, some of the experimental angular distributions show also rather considerable humps at medium angles that would be attributed, at least partially, to the interference effect. In the formula obtained by Hasegawa and Ichikawa, another parameter was introduced in the interference term between the both stripping processes. With the suitable choise of parameters as a function of the deuteron energy and also using the formula of Hasegawa and Ichikawa, it would be sure that much better fits to experimental data could be obtained.

The values of amplitude ratio, λ_2/λ_1, adopted in the calculation of theoretical curves in Fig. 3, were plotted in Fig. 6 together with that for the $N^{14}(d, n)O^{15}$ ground state reaction. It was found that the amplitude ratio, λ_2/λ_1, for the $N^{14}(d, p)N^{15}$ ground state reaction remained fairly constant with the increasing deuteron energy, while this ratio for the $N^{14}(d, n)O^{15}$ ground state reaction showed a sharp maximum and a slight rise at 1.96 and 2.90 MeV, respectively. In the case of the $B^{11}(d, n)C^{12}$ and $N^{15}(d, n)O^{16}$ ground state reactions, these amplitude ratios increased gradually up to the deuteron energy corresponding to the Coulomb barrier and then became nearly flat. Owen and Madansky have pointed out, as the possible explanation for the behavior of the amplitude ratio for the $B^{11}(d, n)C^{12}$ reaction, that a reduction of the heavy particle stripping amplitude relative to the deuteron stripping amplitude would be expected at lower deuteron energies than that of the Coulomb barrier. However, the amplitude ratio for the $N^{14}(d, p)N^{15}$ reaction does not exhibit such reduction even at lower deuteron energies. On the other hand, the emitted particle yields in forward directions from the $N^{14}(d, n)O^{15}$ reaction was found to be considerably smaller than that from the $N^{14}(d, p)N^{15}$ reaction, especially at 1.96 and 2.90 MeV, as was shown in Fig. 3. This evidence seems to imply that the deuteron stripping amplitude would rather decrease considerably. It is interesting to notice that the amplitude ratios for the three (d, n) reactions, described above, have abnormally sharp maximum or minimum at the deuteron energy corresponding to the Coulomb barrier, while that for the $N^{14}(d, p)N^{15}$ reaction has not any such anomaly.

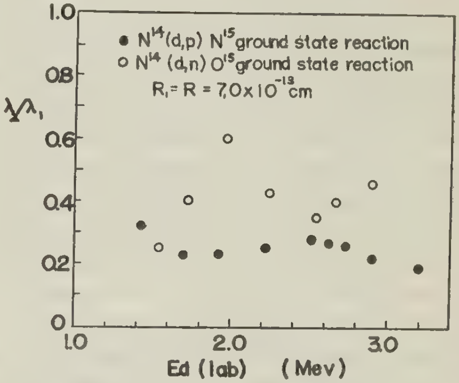

Fig. 6. The experimental ratio of the heavy particle stripping amplitude to the deuteron stripping amplitude, λ_2/λ_1, for $R_1=R_2=7.0\times10^{-13}$ cm. Those for the $N^{14}(d, n)O^{15}$ ground state reaction obtained in our previous work are also shown with open circles.

Comparison of yield curves for the $N^{14}(d, p)N^{15}$ and $N^{14}(d, n)O^{15}$ ground state reactions is also expected to give some informations on the reaction mechanism. As shown in Fig. 5, the yield curves for both reactions rise gradually up to 1.9 MeV with a shape that will be fitted by the deuteron penetrability through the Coulomb barrier. At the bombarding energies of 1.92 and 2.73 MeV, there can be seen slight resonance-like maxima. Moreover, absolute values of yield curves for both reactions are roughly equal over the whole range of deuteron energy investigated. It can not be decided yet whether these maxima are due to the distortion effect of wave function in the stripping process or to compound nucleus formation. In the usual derivation of the stripping formula, the incoming deuteron and the outgoing particle are represented by plane waves. A more exact formulation taking into account the distortion of these waves by the Coulomb and nuclear forces has been investigated by several authors17). It may be possible that the use of distorted waves would explain those resonance-like structures of the yield curves. However, it will be more reasonable to consider that those evidences would show both reactions to proceed appreciably through compound nucleus formation in these lower energy range of deuterons. In the present experiment the compound nucleus O^{16} is formed in the excitation approximately by 22 MeV. The level structure of O^{16} nucleus at this region of excitation has been investigated with photo-disintegration reactions18). In particular, Penfold and Spicer have found ten levels, widths of which are less than 40 keV. The above described resonance-like maxima are certainly considered to correspond to 22.4 and 23.1 MeV excited levels of O^{16} nucleus which were well confirmed by other reactions. Other levels observed in the photo-disintegration reactions, however, were not found in the present yield curves. This situation would be understood by the isotopic spin selection rule, assuming that this reaction proceeds through compound nucleus formation. As the isotopic spins of N^{14} nucleus and deuteron are both zero, the levels of the compound nucleus O^{16} formed by the $N^{14}+d$ reaction must have the isotopic spin of zero. The gamma-ray absorption in the 20 MeV region of excitation will be mainly electric dipole, which requires the difference of isotopic spin to be 1. The levels of O^{16} nucleus excited by gamma-ray will have, then, the isotopic spin 1. It must be pointed out, of cource, that data points did not space closely enough to detect the narrow levels and so some resonance structure might be missed in the present experiment.

The yield curves and angular distributions show two rather conflicting evidences about the mechanism by which these reactions take place. Considering the angular distribution alone, the mechanism would appear to be the stripping reaction. But if that is the case, then it is difficult to explain the resonance-like structure in the yield curve. This double-faced behavior was also observed in the $C^{12}(d, p)C^{13}$ reaction19),20). Bonner *et al.* took a viewpoint in their analysis on this reaction that a small amount of compound nucleus formation could interfer with the stripping reaction and cause the resonant behavior of the yield curve, almost not affecting the shape of the angular distribution.

The $N^{14}(d, p)N^{15}$ 5.28 and 5.31 MeV doublet state reaction

The close doublet structure of the first excited 5.28 and 5.31 MeV states of N^{15} nucleus complicates the interpretation of the present results. Fig. 4 shows that the angular distributions for the $N^{14}(d, p)N^{15}$ 5.28 and 5.31 MeV doublet state reaction are roughly spherical symmetric. Such results have been obtained also by Gibson and Thomas and by Wyly. These distributions seem to infer that stripping process does not take place to any appreciable extent. The angular distributions for the $C^{14}(d, n)N^{15}$ reaction leading to this doublet state were measured by R. Chiba21) and found to have a remarkable forward peak attributed to deuteron stripping with $l_p=0$. This results requires that the spin of at least one of the doublet states should be 1/2 and even parity. Halbert and French22) have predicted on the basis of the single particle model that the 5.31 MeV state has spin 1/2 and even parity and belongs to $s^4p^{10}s^1$ configuration of N^{15} nucleus. The internal conversion coefficient of the 5.299 MeV gamma-ray from N^{15} nucleus following the beta-decay of C^{15} nucleus has been observed by Alburger *et al.*23) to be E1-transition. They have, then, concluded that this evidence is consistent with spin 1/2 and even parity for the 5.31 MeV state of N^{15} nucleus. If that is the case, it is implausible that the $N^{14}(d, p)N^{15}$ reaction leading to this state would proceeds through the stripping process appreciably. The reason is that the stripping process should be followed with the rearrangement of nucleons in the residual nucleus to lead to this state and such mechanism would not take place to any appreciable extent.

On the other hand, it cannot be overlooked that a broad maximum at about 60 degrees is observed, though is not so intense, commonly in every angular distribution. If it can be approved that those maxima show the contribution of deuteron stripping, the reaction corresponding to at least one of the doublet states, probably 5.27 MeV state, is considered to proceed through this process with $l_n=2$. The contribution of deuteron stripping with $l_n=2$ has also observed by Green and Middleton and by Sjögren and Ahnlund. In particular, the latter authors have reported the angular distribution for the 5.276 MeV state reaction showing that this reaction proceeds through deuteron stripping with $l_n=2$ undoubtedly. It is interesting to notice that the 5.31 MeV state of N^{15} nucleus is likely to be led through the (d, n) stripping process alone, while the 5.27 MeV state through the (d, p) stripping process. Of course, more precise investigation is required to obtain the definite conclusion.

In conclusion, the deuteron induced reactions in the present energy region do not appear to take place through any one pure reaction mechanism. It may be natural that such reactions are not able to be explained by one of the pure reaction mechanisms which based on particular approximation.

The author wishes to express his cordial thanks to Prof. I. Nonaka, Prof. S. Morita and all other staffs of the nuclear laboratory of Kyushu University for their support and discussions throughout this work. This work has been supported by the Scientific Research Expenditure of the Ministry of Education.

References

1) M. Morita, K. Kawai, Y. Gotō, T. Maki and M. Mukae: to be published in J. Phys. Soc. Japan.
2) T. Retz-Schmidt and J. L. Weil: private communication.
3) W. M. Gibson and E. E. Thomas: Proc. Roy. Soc. **A, 210** (1951) 543.
4) F. S. Eby: Phys. Rev. **96** (1954) 1355.
5) T. S. Green and R. Middleton: Proc. Phys. Soc. London **A, 69** (1956) 28.
6) E. K. Warburton and J. N. McGruer: Phys. Rev. **105** (1957) 639.
7) S. Morita, N. Kawai, N. Takano, Y. Gotō, R. Hanada, Y. Nakajima, S. Takemoto and Y. Yaegashi: J. Phys. Soc. Japan **15** (1960) 361.
8) H. M. Jongerius, F. P. G. Valckx and P. M. Endt: Physica **20** (1954) 29.
9) D. L. Booth, F. V. Price, D. Roaf and G. L. Salmon: Proc. Phys. Soc. London **A, 71** (1958) 325.
10) B. Sjögren and K. Ahnlung: Arkiv Fysik **12** (1957) 547.
11) A. G. Stanley: Phil. Mag. **45** (1954) 807.
12) L. D. Wyly: Phys. Rev. **76** (1949) 104.
13) J. M. Blair, G. Freier, E. Lampi, W. Sleator and J. H. Williams: Phys. Rev. **74** (1948) 1599.
14) G. E. Owen and L. Madansky: Phys. Rev. **105** (1957) 1766.
15) K. Hasegawa and H. Ichikawa: Progr. Theor. Phys. **21** (1959) 569.
16) J. L. Weil and K. W. Jones: Phys. Rev. **112** (1958) 1975.
17) J. Horowitz and A. L. M. Messiah: J. phys. radium **14** (1953) 695. W. Tobocman and M. H. Kalos: Phys. Rev. **97** (1955) 132. I. P. Grant: Proc. Phys. Soc. London **A, 68** (1955) 244.
18) L. Katz, R. N. Haslam, R. J. Horsley, A. G. W. Cameron and R. Montalbetti: Phys. Rev. **95** (1954) 464. B. M. Penfold and A. S. Spicer: Phys. Rev. **100** (1955) 1377. L. Cohen, A. K. Mann, B. J. Patton, K. Reibel, W. E. Stephens and E. J. Winhold: Phys. Rev. **104** (1956) 108. D. L. Liversey: Can. J. Phys. **34** (1956) 1022. F. K. Goward and J. J. Wilkins: Proc. Phys. Soc. London **A, 65** (1952) 671.
19) T. W. Bonner, J. T. Eisinger, A. A. Kraus, Jr. and J. B. Marion: Phys. Rev. **101** (1956) 209.
20) M. T. McEllistrem, K. W. Jones, R. Chiba, R. A. Douglas, D. F. Herring and E. A. Silverstein: Phys. Rev. **104** (1956) 1008.
21) R. Chiba: to be published.
22) E. C. Halbert and J. B. French: Phys. Rev. **105** (1957) 1563.
23) D. E. Alburger, D. H. Wilkinson and A. Gallmann: Bull. Amer. Phys. Soc. **4** (1959) 56. F. Ajzenberg-Selove and T. Lauritsen: Nuclear Physics **11** (1959) 1.

JOURNAL OF THE PHYSICAL SOCIETY OF JAPAN, Vol. 16, No. 2, FEBRUARY, 1961

Inelastic Scattering of Neutrons by the Time-of-Flight Method

By Kineo TSUKADA, Shigeya TANAKA and Michio MARUYAMA

Japan Atomic Energy Research Institute, Tokai-mura, Ibaraki-ken

(Received October, 20, 1960)

Neutrons scattered by Ti, Fe, Zn and Se have been observed by the time-of-flight technique in the energy range of 3.4 to 4.6 MeV. The inelastic scattering cross sections for the excitations of the 1st, 2nd and 3rd levels of these elements except Se, were obtained. The excitation functions of these levels were compared with those calculated with a formula which was made by modifying Hauser-Feshbach's formula so as to be used without detailed knowledge about the levels of high excitation.

Agreement was fairly well except for the case of the 2nd and 3rd levels of Zn, where calculated values were about twice as large as experimental values. Thus it has been concluded that the compound-formation process is considered to predominate over the direct process in these energy and mass regions.

§ 1. Introduction

According to the current theory of nuclear reaction, scattering of fast neutrons proceeds partly through compound-formation process and partly through direct process. Although quite a lot of theoretical works have been published by various authors[1),2)], the mechanism of the reaction is not yet known definitely. From the standpoint that much more experimental data are required to improve the theory, it will be worth while to measure the energy and angular dependence of the cross sections of scattering leading to definite levels of the residual nucleus.

It is not so easy to observe the energy spectrum of the scattered neutrons with good accuracy and resolution. Experimental data[3),4)] available at present are rather few. Of the various methods of measuring neutron energies: the nuclear emulsion[5)], the proton-recoil proportional counter[6)], the He^3 counter[7)] the counter telescope[8)], the time-of-flight method[3),9),10)], etc. the time-of-flight method is the most promising in the energy range of several MeV.

In the present investigations, it has been tried to observe the energy spectra of the neutrons scattered inelastically from several medium-weight nuclei, Ti, Fe, Zn and Se (in Sec. 2) and to obtain the differential cross sections at 90° direction for the excitation of several low-lying levels as the functions of the incident-neutron energy in a range of 3.4 to 4.6 MeV (in Sec. 3). Cross sections observed were then compared with those calculated using a formula, which was made by modifying Hauser-Feshbach's formula so as to be applied to the cases where levels in the residual nucleus were not known definitely except the lowest-lying levels (in Sec. 4).

§ 2. Experimental

The neutrons were generated from the $D(d, n)He^3$ reaction by using a 2-MV Van de Graaff accelerator, and energy spectra of inelastically scattered neutrons were measured by the pulsed-beam time-of-flight method which had been developed by Cranberg et al[11)].

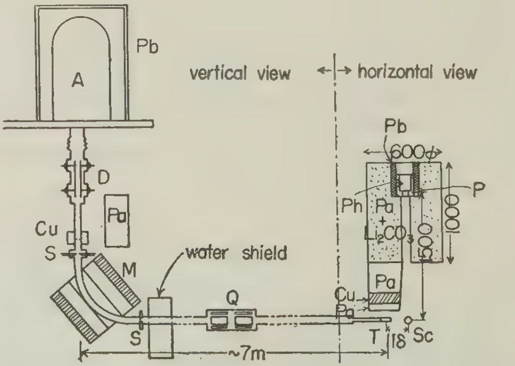

Fig. 1. Schematic diagram of the experimental arrangement. A: 2-MV Van de Graaff accelerator. D: Rf deflector for pulse operation. S: Slit. M: Beam-analysing magnet. Q: A couple of electrostatic quadrupole lenses. T: Gas target. Sc: Scatterer. P: Plastic scintillator. Ph: Photomultiplier. Pa, Pb and Cu: Paraffin, lead and copper shields, respectively.

A. *Arrangement*

As shown in Fig. 1 the continuous deuteron beam from the 2-MV Van de Graaff accelerator is chopped by a 3.7-Mc rf deflector which makes the beam sweep a slit with a width of 1.5 mm. The duration of the ion-beam pulse was calculated to be about 4 mμ sec by a calculation, and was checked by measuring the total- and the pulsed-beam current.

The pulsed ion beam is deflected by an analysing magnet and then focused on a gas target[12], which is located about 7 m distant from the magnet by means of a couple of electrostatic quadrupole lenses. The chamber of the gas target has a diameter of 1 cm and is 3 cm long. Deuterium is stored in a uranium oven attached to the chamber. The entrance window of the chamber is covered with a nickel foil with a thickness of 0.00005 in. In the present experiments the pressure of the deuterium was 50 cm Hg. But only in the case of a low neutron energy of 3.4 MeV, the gas pressure was decreased to 25 cm Hg in order to prevent the increase of the spread of neutron energy. The spread of the neutron energy was estimated to be 350 keV and 280 keV at neutron energies of 3.8 MeV and 4.6 MeV, respectively.

The scatterers were placed at 0° with respect to the direction of the deuteron beam and 11 cm distant from the gas target. The dimensions of the Fe and Zn scatterers were 5 cm long and 2.5 cm in diameter, and those of the Se scatterer were 6.5 cm and 2.5 cm respectively. As the Ti sample was granular, it was packed in a 5 cm × 5 cmϕ vessel made of polyethylene. The correction for multiple scattering was estimated not to be serious in the present experiments.

The neutron detector was placed at 90° with respect to the direction of the incident neutrons and at 150 cm distant from the scatterer.

B. *Background and shielding*

The background radiation is composed of the natural radiation, the room-scattered radiation, the machine background (the radiation from the accelerator, the ion-beam chopper and the analysing magnet) and the radiation which enters the detector from the gas target directly. In the case of deuteron acceleration, the machine background is serious and it is necessary to shield the detector especially from this background.

The measurement was carried out at the middle of a large room (24.2 m × 13 m) which had a pit of 2.5 m in depth in order to decrease the effect of neutrons scattered from the walls and the ground. The Van de Graaff accelerator was covered with a box made of lead 6 m thick, which served as a shield against the X rays generated in the accelerator, and other sources of machine background was also shielded properly, but the machine background was most effectively reduced by setting the target far away from the accelerator by means of electrostatic quadrupole lenses. As shown in Fig. 1, the detector was surrounded by a lead collar 6.5 cm thick and a shield tank 100 cm in length and 60 cm in diameter which was filled with a mixture of paraffin and lithium carbonate (mixing ratio 3 : 1 by weight). In order to shield the neutrons which entered the detector directly, paraffin blocks 10 cm thick and copper blocks 20 cm thick were placed between the gas target and the shield tank.

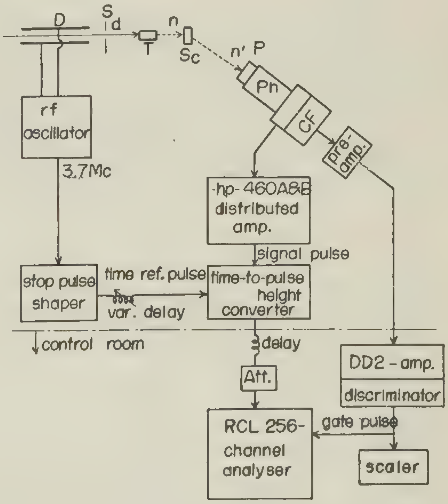

Fig. 2. Block diagram of the detector system. D: Rf deflector. S. Slit. T: Gas target. Sc. Scatterer. P: 2″×2″ϕ plastic scintillator. Ph: RCL 6342 photomultiplier. Cf: Cathode follower. Att: Attenuator.

The block diagram of the neutron-detecting system is shown in Fig. 2. A 2″×2″ϕ plastic scintillator and an RCA 6342 photomultiplier composed the neutron detector. The fast-rise single pulses delivered from the detector were amplified by Hewlett-Packard 460A and 460B distributed amplifiers and then brought to a time-to-pulse height converter[11]. The output of the converter was next fed to an RCL 256-channel pulse-height analyser. A side channel composed of a nonoverloading amplifier and a discriminator was used to open the gate of the pulse-height analyser. This side channel cut off small pulses and reduced the time jittering due to the variation of the pulse height. The discrimination level for the side channel was 2 to 3 times higher than that for the time-to-pulse height converter.

The linearity of the time-to-pulse height conversion was checked by using a double-pulse generator having calibrated delay intervals between pulses. The deviation from the linearity was smaller than ±1 mμsec in the whole time range. The time interval per channel was estimated to be 0.98 mμsec.

A current integrator was used to measure the deuteron beam entering the gas target and to estimate the neutron yield. The yield was also monitored by a Hanson-and-McKibben long counter.

C. *Time spectra*

Fig. 3 shows a typical time spectrum of the neutrons scattered from Fe. In this figure, time increases to the left, i.e. from the right to the left there appear several peaks corresponding to the gamma rays (γ) which are produced in the scatterer at the moment of the inelastic scattering, elastically scattered neutrons (n) and inelastically scattered neutrons (n', n'', n''', $\cdots$) corresponding to the excitation of the low-lying levels of the residual nuclei of the scatterer. Since two neutron bursts were generated every time-reference pulse, two similar patterns appear in the time spectrum. The peaks corresponding to the gamma rays were used as the fiducial points to determine the flight time of the scattered neutrons. It took 1.5 to 2 hours to accumulate counts as are shown in this figure. In the present experiments, the pulsed beam entering the gas target was 0.2 to 0.4 μA in the average. The dashed line in Fig. 3 represents the background obtained in the absence of the scatterer.

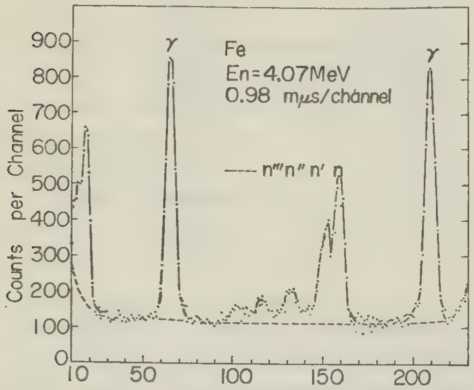

Fig. 3. Time spectrum obtained at 90° for neutron scattering at 4.07 MeV from Fe. The dashed line under the spectrum is the background obtained in the absence of the scatterer. Peaks corresponding to gamma rays, elastically scattered neutrons and inelastically scattered neutrons are marked with γ, n and n', n'', $\cdots$, respectively.

D. *Efficiency*

The efficiency of the neutron detector was determined as a function of the energy by calculating the yield[13] of neutrons at the target.

The measurements of the efficiency were made several times during the experiment. The efficiency was estimated to be 0.25±0.05 in the range of 2 to 4.5 MeV, where the error gives the maximum deviation from the mean of the measured values. For neutron energies less than 2 MeV, the efficiency decreases gradually and becomes zero at 0.7 MeV. These observed values are in good agreement with those calculated by using the neutron cross section of hydrogen in the plastic scintillator and taking account of the discrimination of neutrons below 0.7 MeV by the side channel.

E. *Resolution*

There are several reasons why the peaks in the time spectrum have finite widths. The gamma-ray peak has a half-width of about 6 mμsec, which is due to the following three effects: (1) the time jittering in the time-analyser system, (2) the finite duration of the deuteron pulse (~4 mμsec), and (3) the variation in the paths of the neutron in the gas target and the scatterer (~2.7 mμsec for 4-MeV neutrons). For the width of the neutron peak, the following effects are to be added: (4) the spread of the neutron energies due to the energy loss of the deuterons in the gas target and, also, due to the large solid angle subtended by the scatterer at the target (~2 mμsec for 4-MeV neutron energy) and (5) the spread in the flight-path lengths of the scattered neutrons ($\sim$2 mμsec for 4-MeV neutron energy). The energy of the deuterons incident to the target was homogeneous enough to have negligible effect on the width of the peak. The half-width for the elastically scattered neutrons of 4-MeV was observed to be 6 to 7 mμsec.

From the observed half-width of the gamma-ray peak and the time spreads of (2) and (3) stated above, the jittering in the time-analyser system was estimated to be less than 3.5 mμsec. Since the rise time of the signal pulse from the neutron detector was about 5 mμsec, this estimation will be reasonable, if one takes into consideration a fact that the small signal pulses were cut off by the discriminator in the side channel.

The half-width of the neutron peaks was calculated to be 6.5 mμsec by adding the time spread of (4) and (5) to the observed half-width of the gamma-ray peaks, assuming that all of the time spreads were also of Gaussian forms.

§ 3. Results

Figs. 4, 5, 6 and 7 show the energy spectra of neutrons scattered by Ti, Fe, Zn and Se, respectively. The energies of the incident neutrons are 3.44, 3.83, 4.07, 4.30 and 4.61 MeV. In these figures, the abscissas are expressed in the energy scale. The excitation energies of the residual nuclei increase to the left, and the peaks at the right-most are due to the elastic scattering. The ordinates give

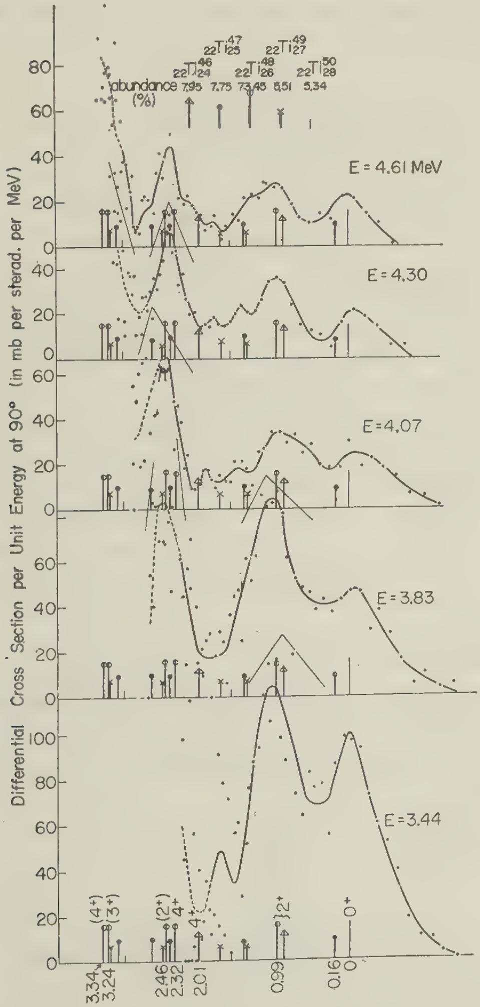

Fig. 4. Energy spectra for Ti. The vertical lines under the spectra show the positions of levels. Isotopes are specified by the marks as shown at the top of the figure.

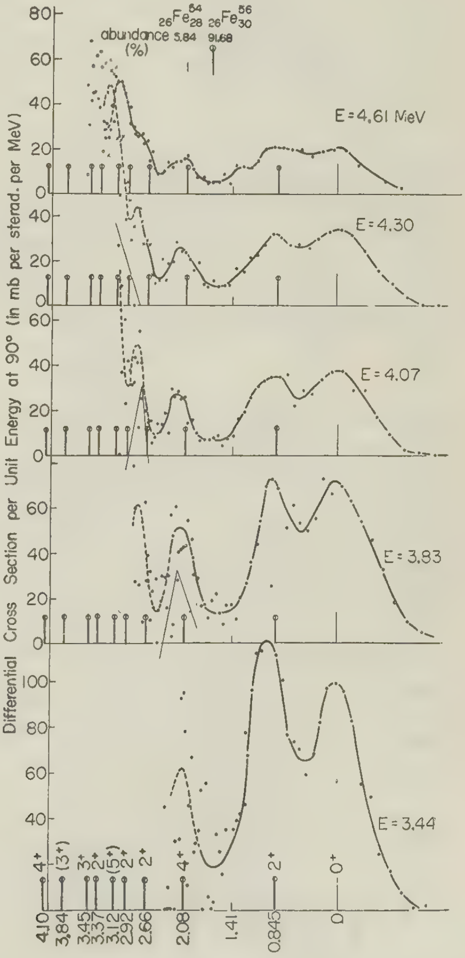

Fig. 5. Energy spectra for Fe.

the differential cross sections in mb per steradian per MeV of the energy of the scattered neutrons measured at 90° with respect to the direction of the incident neutrons. Those parts of the spectra which are shown by dashed curves have large errors, because, in those parts (1 to 2 MeV), determination of the efficiency of the detector suffers rather large uncertainty.

In the present investigations, the absolute value of the cross section has a large systematic error which is derived from the measurement, of the efficiency of the detector (±20%). But, as far as the relative magnitudes of peaks are concerned, the error from this origin is canceled out, because the variation of the efficiency was small in a series of measurements.

These figures show that the differential cross section of the inelastic scattering at 90° is comparable with that of the elastic scattering at the same direction. Generally speaking, the cross sections corresponding to the excitation of higher levels in the residual nuclei are smaller, and the level density increases with the excitation energy, so that the neutron groups corresponding to the excitation of the higher levels are not resolved. In the case of Se (and Ge also, which is not presented in this paper), even the peaks corresponding to the excitation of low-lying levels are not resolved as shown in Fig. 7.

The differential cross sections of the elastic scattering and of the inelastic scattering corresponding to the excitation of lowlying levels for Ti, Fe and Zn are shown in Fig. 8 as as functions of neutron energies. The peeling-

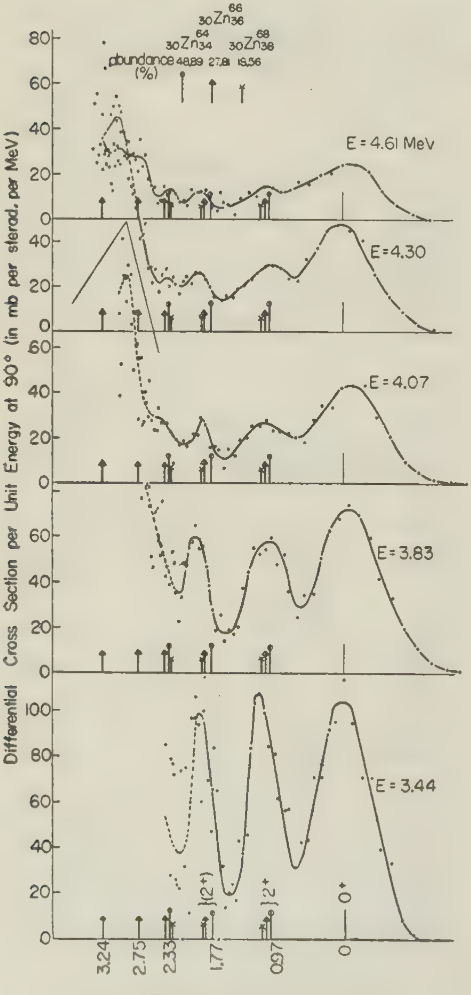

Fig. 6. Energy spectra for Zn.

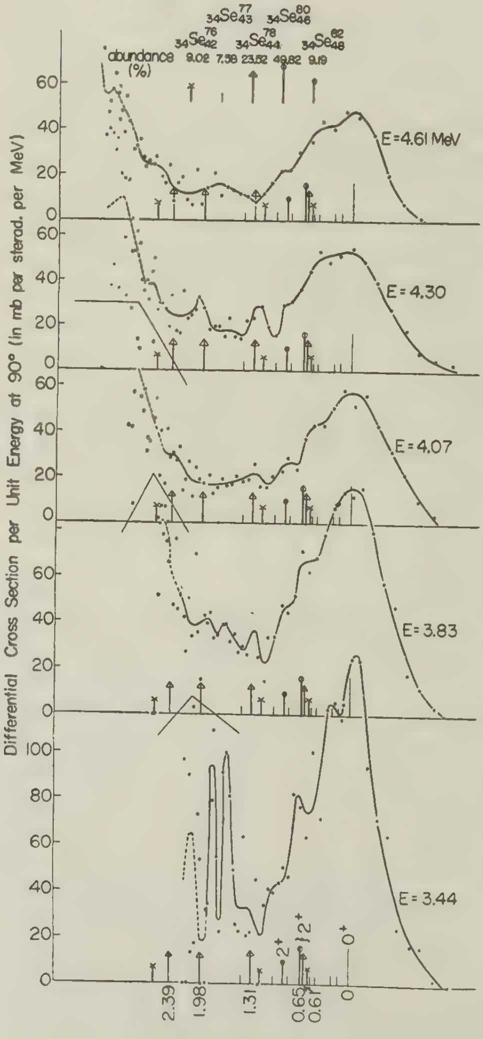

Fig. 7. Energy spectra for Se.

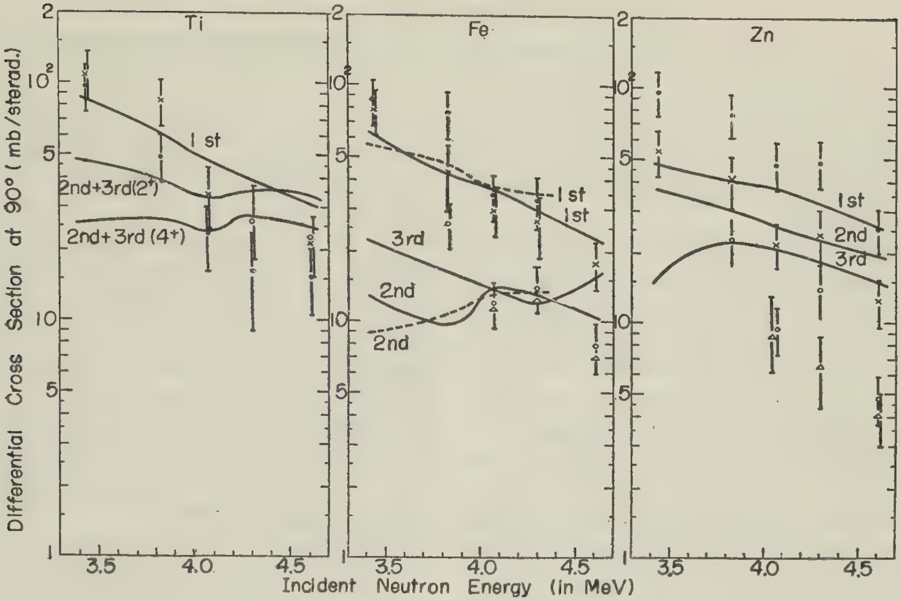

Fig. 8. Differential cross sections of Ti, Fe and Zn at 90°. The points shown by closed circles represent the data of the elastic scattering, and those shown by the crosses, open circles and triangles represent the data of the inelastic scattering corresponding to the excitation of the 1st, 2nd and 3rd levels in each residual nucleus, respectively. The dashed curves represent the theoretical calculations by Hauser-Feshbach's formula and the full curves by the modified Hauser-Feshbach formula.

off method was used to separate the peaks overlapping partially with each other, and the errors due to this procedure were estimated to be 10 to 15% of the differential cross sections. For Se, this procedure was not applied. In these figures, it is shown that all of the excitation functions decrease rapidly with the increase of the energy of the incident neutrons.

§ 4. Discussion

In order to investigate which process, the compound-formation process or the direct process, will be predominant in the inelastic scattering in the energy and mass regions of the present work, the total cross sections of the inelastic scattering through the compound-formation process were calculated by using Hauser-Feshbach's formula[1] on the following assumptions.

Assumption 1: The levels of the compound nucleus are so dense that the statistical treatment can be allowed for these levels.

Assumption 2: The angular distribution of the inelastically scattered neutrons is nearly isotropic.

According to Hauser and Feshbach, the total cross section for the inelastic scattering with respect to the transition from the initial nucleus with spin i to the final nucleus with spin i' is given by

$$\sigma(i/i')=\frac{\pi\bar{\lambda}^2}{2(2i+1)}\sum_{l}\mathrm{T}_l(E)\sum_{J}\frac{\mathcal{E}_{jl}{}^{J}(2J+1)\sum_{l'j'}\mathcal{E}_{l'j'}{}^{J}\mathcal{E}_{l'j'}{}^{J}\mathrm{T}_{l'}(E')}{\sum_{l''j''E''}\mathcal{E}_{j''l''}{}^{J}\mathrm{T}_{l''}(E'')}, \qquad (1)$$

where

$\mathrm{T}_l(E)$: the penetration factor,
E, E' : the initial and the final channel energy, respectively,
j, j' : the initial and the final channel spin, respectively,
l, l' : the initial and the final orbital angular momentum, respectively,
J : the spin of the compound nucleus,

and

$$\varepsilon_{jl}{}^{J} \text{ is equal to } \left\{ \begin{array}{l} 2, \text{ if both } j_1 \text{ and } j_2 \\ 1, \text{ if either } j_1 \text{ or } j_2 \\ 0, \text{ if neither } j_1 \text{ nor } j_2 \end{array} \right\} \text{ satisfy } |J-l| \leqq j_k \leqq J+l\,. \tag{2}$$

Double primed quantities are associated with those channels to which the compound nucleus is feasible to decay.

Fortunately, as the level scheme including the spin and parity had been reported in a recent work of beta decay[14], calculation of the cross sections for Fe^{56}* was feasible to be made. Although contributions of the (n, p) reaction were to be taken into summation in the denominator of the formula (1), they were neglected because the cross section of the (n, p) reaction is small, for example, (0.08 ± 0.12) mb[15] for the neutron energy of 4.4 MeV. The penetration factor $T_l(E)$ was calculated by Beyster et al[16] assuming the Woods-Saxon potential[17]. The calculated results are shown by the dashed curves in Fig. 8. They are in good agreement with the experimental results not only in the absolute values but also in the relative values of the cross sections corresponding to the excitation of the 1st and 2nd excited levels. Therefore, it may be said that the inelastic scattering of the neutrons with the energy of several MeV proceeds mainly through the compound-formation process. The slopes of the calculated curves, however, are less than those of the experimental curves. This deviation may be due not to misapplication of Hauser-Feshbach's formula, but to the fact that undiscovered levels** are not taken into the calculation.

For Ti and Zn, the calculation similar to that for Fe was impossible, because the level schemes were not available in the range higher than 3.4 MeV for Ti and 2 MeV for Zn. Therefore, the formula (1) was modified by using the notion of level density under the following assumption.

> Assumption 3: The residual nucleus has so many excited levels in the range of several MeV that the spins and parities of these levels can be treated as distributed statistically***.

The formula (1) is then modified as follows:

$$\sigma(i/i') = \frac{\pi\lambda\!\!\!^{-2}}{2(2i+1)} \times \frac{\sum_l [T_l(E) \sum_J \{\varepsilon_{jl}{}^J \sum_{j'l'} \varepsilon_{j'l'}{}^J T_{l'}(E')\}]}{\int_0^E \frac{1}{D_0(E-E'')} \sum_{l''} (2l''+1) T_{l''}(E'') dE''} \tag{3}$$

where $(2i''+1)/D_0(U)$ is the level density with spin i'' at the excitation energy U. The derivation of this formula is given in Appendix I. The functional forms of $D_0(U)$ have been given by Newton[19], Cameron[20] and others. Newton's formula is adopted here because of its simplicity. The results of the calculation of the formula (3) are shown by the full curves in Fig. 8. Since the absolute magnitude of level-density formula is not expected to be dependable, these curves are normalized to the experimental values for the excitation of the 1st levels by the neutrons of 3.83 MeV. The normalization factors for the level densities are 0.0538, 0.123 and 0.186 for Ti, Fe and Zn, respectively. In Appendix II, a comparison is made between the calculated values of level density and the experimental

---

* It is apparent from the published level scheme that the energy spectrum of the neutrons shown in Fig. 5 is due to the major isotope of Fe, i.e. Fe^{56} (91.68%).

** In order to check how much the undiscovered highly excited levels contributed to the cross section, it was tried to compare the published total non-elastic cross section[18] $\sigma_{ne}(E_n)$ at the incident-neutron energy E_n with $\Sigma(E_n)$ which was defined as follows,

$$\Sigma(E_n) = 4\pi \int_{E_{exc}} \left(\frac{\partial^2 \sigma_{inel}}{\partial\Omega \partial E} \right)_{obs} dE\,,$$

where $(\partial^2\sigma_{inel}/\partial\Omega\partial E)_{obs}$ is the observed value of the differential cross section per MeV of the excitation energy for the inelastic scattering. The angular distribution was assumed to be isotropic. The integration was taken from the excitation energy of the 1st excited level up to $(E_n - 1.2)$ MeV. In the range of excitation energies higher than $(E_n - 1.2)$ MeV, the cross section could not be observed, because of the decrease of the efficiency of the detector. For Ti, Fe and Zn, $\sigma_{ne} \approx \Sigma$ at 3.6 MeV, but $\sigma_{ne} \approx 2\Sigma$ at $E_n = 4.6$ MeV. This fact suggests that there exist a number of excited levels between the excitation energies of 3.6 and 4.6 MeV.

*** Of course, this assumption holds only approximately. It will not lead, however, to erroneous results as fas as the discussion is limited to the competition between the channels decaying to individual levels of the residual nucleus.

ones is the case of Fe^{56}. The resonance-like structures in these curves are due to the behaviors of the penetration factors.

In the spectra of Ti (in Fig. 4), the peak neighbouring with the elastic peak was due to Ti^{46} and Ti^{48}, so that the calculation was carried out with respect to these isotopes. The peaks corresponding to the excitation of the 2nd and 3rd levels of Ti^{48} were not resolved in this experiment, so that the sum of the cross sections for these levels was calculated. Since the spin and parity of the 3rd excited level of Ti^{48} were not definitely known, two series of calculations were carried out, assuming the spin and parity to be 2^+ and 4^+, respectively. As seen in Fig. 8, better agreement between the observed and calculated results is obtained if one assumes the spin and parity of 4^+, but one cannot conclude the spin and parity of 4^+, because experimental errors are rather large and the contribution from isotopes other than Ti^{48} is neglected in the calculation.

In the case of Fe^{56}, where calculations both by the original Hauser-Feshbach formula (1) and by the modified one (3) were done, the modified Hauser-Feshbach formula shows better fitting at high incident energies. This suggests that Assumption 3 holds, i.e. there exist a number of excited levels, and their spins and parities are distributed statistically.

For Zn^{64}, Zn^{66} and Zn^{68}*, the calculated values of the cross sections corresponding to the excitation of the 2nd and 3rd levels are about twice as large as the observed values. It is not clear why this disagreement** occurs.

In conclusion, it may be possible to say that the compound-formation process is predominant in the inelastic scattering of 3.4 to 4.6-MeV neutrons by Ti, Fe and Zn. In order to get further confirmations, measurements of the angular distributions of scattered neutrons are now in progress.

The authors whould like to express their appreciation to Dr. T. Momota for invaluable help and advice. They are greatly indebted to Mr. C. Kobayashi, Mr. Y. Sato and members of the fast-neutron group for operation and maintenance of the accelerator, and to Dr. A. Sugie, Dr. K. Harada and Dr. T. Terasawa for helpful discussions. The authors also wish to express their thanks to Mr. F. Kurosawa for assistance in these experiments.

Appendix I The Modification of Hauser-Feshbach's Formula

When the energy of the incident particle is high and many levels can be excited in the residual nucleus, Hauser-Feshbach's formula (1) can be modified by taking the following three aspects into consideration.

(A) The numerators of the form must be preserved from the modification to give the dependence of the inelastic-scattering cross section on the spin i' of the residual nucleus, because the most parts of the spin dependence of the formula (1) come from the numerators.

(B) It is assumed that many levels of the residual nucleus are excited, the spins and parities of which are distributed statistically, and the density of the levels with spin i is expressed in the form[19),20)] of

$$\rho(U, i)=\frac{2i+1}{D_0(U)},$$

where $D_0(U)$ is the function of the excitation energy U.

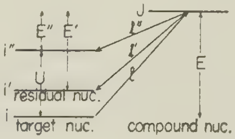

Fig. 9. Schematic energy-level diagram for the inelastic scattering.

(C) To get a good approximation without the detailed knowledge on the levels of the residual nucleus, the denominators of the formula are rewritten in a form of integral, using the expression of level density.

Representing the denominators of the formula (1) by $H(E, J)$,

---

* The predominant isotopes of Zn are Zn^{64} (48.89%), Zn^{66}(27.82%) and Zn^{68}(18.56%), and the level schemes of these isotopes are similar with each other.

The (n, p) reaction cross section for Zn is (56 ± 4.0) mb[20)] at the incident energy of 3.6 MeV. The contribution of this reaction was neglected in the calculation.

** This disagreement may be remedied by revision of the magnitude of imaginary part of the optical potential.

$$\mathrm{H}(E,J)=\sum_{j''l''E''}\varepsilon_{j''l''}{}^{J}\,\mathrm{T}_{l''}(E'')\,, \tag{A.1}$$

where

$$\varepsilon_{j''l''}{}^{J} \text{ is equal to } \left\{\begin{array}{l} 2, \text{ if both } j_1'' \text{ and } j_2'' \\ 1, \text{ if either } j_1'' \text{ or } j_2'' \\ 0, \text{ if neither } j_1'' \text{ nor } j_2'' \end{array}\right\} \text{ satisfy } |J-l''|\leqq j_k''\leqq J+l''\,. \tag{A.2}$$

Taking the aspect (B) into consideration, (A.1) and (A.2) may be replaced by

$$\mathrm{H}(E,J)=\sum_{E''=0}^{E}\sum_{l''=0}^{\infty}\sum_{j''}\mathrm{T}_{l''}(E'') \tag{A.3}$$

and

$$|J-l''|\leqq j''\leqq J+l''\,, \tag{A.4}$$

respectively. The number of the channels with a definite l'' and j'', through which the compound nucleus can decay, is given by

$$\frac{1}{2}\left\{\frac{2(j''+\frac{1}{2})+1}{\mathrm{D}_0(E-E'')}+\frac{2(j''-\frac{1}{2})+1}{\mathrm{D}_0(E-E'')}\right\}dE''=\frac{2j''+1}{\mathrm{D}_0}dE''\,,$$

where dE'' is a small energy interval in the residual nucleus. Here, the factor 1/2 before the parentheses results from the assumption of the equal populations of two parities in the residual nucleus. Then replacing the summation over E'' in (A.3) by an integral,

$$\mathrm{H}(E,J)=\int_0^E\sum_{l''=0}^{\infty}\sum_{j''=|J-l''|}^{J+l''}\mathrm{T}_{l''}(E'')\frac{2j''+1}{\mathrm{D}_0(E-E'')}dE''=(2J+1)\int_0^E\frac{1}{\mathrm{D}_0(E-E'')}\sum_{l''=0}^{\infty}(2l''+1)\mathrm{T}_{l''}(E'')dE''\,.$$

Thus, the formula (3) is obtained.

Appendix II The Level Density of Fe^{56}

The use of the formula (3) requires the knowledge of the level density $(2i+1)/\mathrm{D}_0$. As the expression of the level density, Newton's formula[18] was adopted in this paper, but there is no justification for using Newton's formula in the energy range up to several MeV, because of the following two reasons. One reason is that the pairing energy (~3 MeV) is neglected in the Newton's formula. The other is that this formula is based on the data obtained from the thermal-neutron capture and hence related to levels with excitation energies nearly equal to the binding energy of a neutron. So it will be adequate to remark that, in this paper, it was used only as an approximate formula with an adjustable constant factor (~0.1, See § 4).

This normalized level density was checked by the level scheme of Fe^{56} which had been obtained by the beta-decay experiments[18]. But this level scheme was not sufficient to see the complete level scheme in the energy range related to this paper, because the levels corresponding to the beta-transitions of higher order or small energy difference might have not been found. Tentatively we regarded all transitions in the aforesaid experiments as the allowed transitions and the following process was used for derivation of $1/D_0$ as a function of excitation energy.

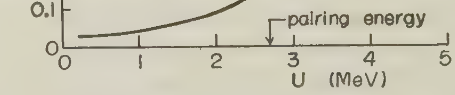

Fig. 10. Level density of Fe^{56}.

$$\left(\frac{1}{\mathrm{D}}\right)_{\mathrm{obs}}=\frac{1}{2}\sum_i\frac{2i+1}{\mathrm{D}_0} \tag{A.5}$$

Here, $(1/\mathrm{D})_{\mathrm{obs}}$ is the level density at an excitation energy obtained from one beta-decay scheme. For Fe^{56}, there are two beta-decay schemes, i.e. $\mathrm{Mn}^{56}\rightarrow\mathrm{Fe}^{56}$ and $\mathrm{Co}^{56}\rightarrow\mathrm{Fe}^{56}$. The range of summation $\sum$ is limited to i's corresponding to the allowed transition. In Fig. 10 these values of $1/D_0$ calculated by the formula (A.5) are compared with Newton's formula normalized by 0.123. The agreement is not bad.

References

1) W. Hauser and H. Feshbach: Phys. Rev. **87** (1952) 366.
2) S. T. Butler: Phys. Rev. **106** (1957) 272. G. E. Owen and L. Madansky: Phys. Rev. **105** (1957) 1766. J. S. Blair: Phys. Rev. **115** (1959) 928.
3) L. Cranberg and J. S. Levin: Phys. Rev. **103** (1956) 343. C. O. Muelhause, S. D. Bloom, H. E. Wegner and G. N. Glasoe: Phys. Rev. **103** (1956) 720. H. H. Landon, A. J. Elwyn, G. N. Glosoe and S. Oleksa: Phys. Rev. **112** (1958) 1192. R. Batchelor and J. H. Towle: Proc. Phys. Soc. London **A73** (1959) 193.
4) P. Stellson and A. Campbell: Phys. Rev. **97** (1955) 1222. G. L. Griffith: Phys. Rev. **98** (1955) 579. I. L. Morgan: Phys. Rev. **103** (1956) 1031. J. B. Guernsey and A. Wattenberg: Phys. Rev. **101** (1956) 1516. J. R. Beyster, M. Walt and E. W. Salmi: Phys. Rev. **104** (1956) 1319.
5) e.g. G. R. Keeping, Jr. and J. H. Roberts: Rev. Sci. Instr. **21** (1950) 163.
6) e.g. Y. Axner and B. Swenson: Arkiv Fysik **3** (1952) 491.
7) e.g. R. Batchelor: Proc. Phys. Soc. London **A65** (1952) 674.
8) e.g. S. J. Bame, Jr., E. Haddad, J. E. Perry, Jr. and R. K. Smith: Rev. Sci. Instr. **28** (1957) 997, **29** (1958) 652.
9) K. G. Malmfors, J. Kjellman and A. Nilson: Nuc. Instr. **1** (1957) 186. A. Elwyn, J. V. Kane, S. Ofer and D. H. Wilkinson: Phys. Rev. **116** (1959) 1490.
10) G. K. O'Neill: Phys. Rev. **95** (1954) 1235. G. C. Neilson and D. B. James: Rev. Sci. Instr. **26** (1955) 1018.
11) W. Weber, C. Johnstone and L. Cranberg: Rev. Sci. Instr. **27** (1956) 166.
12) C. H. Johnson and H. E. Banta: Rev. Sci. Instr. **27** (1956) 132.
13) J. L. Fowler and J. E. Brolley, Jr.: Rev. Mod. Phys. **28** (1956) 103.
14) P. Kienle and R. E. Segel: Phys. Rev. **114** (1959) 1554.
15) J. Terrell and D. M. Holm: Phys. Rev. **109** (1958) 2031.
16) J. R. Beyster, R. G. Schrandt, M. Walt and E. W. Salmi: LA-2099.
17) R. D. Woods and D. S. Saxon: Phys. Rev. **99** (1954) 575; **101** (1956) 506.
18) J. R. Beyster, R. L. Henkel, R. A. Nobles and J. M. Kinster: Phys. Rev. **98** (1955) 1216.
19) T. D. Newton: Can. J. Phys. **34** (1956) 804.
20) A. G. W. Cameron: Can. J. Phys. **36** (1958) 1040.

JOURNAL OF THE PHYSICAL SOCIETY OF JAPAN, Vol. 16, No. 2, FEBRUARY, 1961

The Crystal Structure of $KCuF_3$

By Atsushi OKAZAKI and Yasutaka SUEMUNE

Department of Physics, Faculty of Science, Kyusyu University, Fukuoka, Japan

(Received July 29, 1960)

The crystal structure of potassium trifluorocuprate (II) $KCuF_3$ has been determined by an X-ray analysis. The structure was refined by Fourier method. The crystals are tetragonal, $a=\sqrt{2}a_0=5.855$ and $c=2c_0=7.852$Å; space group $D_{4h}^{18}-I4/mcm$, with four formula units ($KCuF_3$) in the unit cell, where a_0 and c_0 designate the lattice constants of the fundamental pseudo-perovskite structure. This superstructure is due to a displacement of fluorine ions along the copper-fluorine-copper bonds only in the c plane. The atoms are in the following positions: 4 K^+ in (a): $(0, 0, 0; \frac{1}{2}, \frac{1}{2}, \frac{1}{2})+(0, 0, \frac{1}{4}; 0, 0, \frac{3}{4})$: 4 Cu^{2+} in (d): $(0, 0, 0; \frac{1}{2}, \frac{1}{2}, \frac{1}{2})+(0, \frac{1}{2}, 0; \frac{1}{2}, 0, 0)$: 4 F^- in (b): $(0, 0, 0; \frac{1}{2}, \frac{1}{2}, \frac{1}{2})+(0, \frac{1}{2}, \frac{1}{4}; \frac{1}{2}, 0, \frac{1}{4})$: 8 F^- in (h): $(0, 0, 0; \frac{1}{2}, \frac{1}{2}, \frac{1}{2})\pm(x, \frac{1}{2}+x, 0; \frac{1}{2}-x, x, 0)$ with $x=0.228$. In this structure a Cu^{2+} ion is surrounded by a distorted octahedron of F^- ions with copper-fluorine distances of 2.25, 1.96 and 1.89Å.

§1. Introduction

In recent years attention of many researchers has been drawn to the crystal structures and the magnetic properties of ABO_3 compounds with the perovskite structure because the magnetic ions form the simple cubic lattice in this structure. For the same reason antiferromagnetic substances KMF_3 have been investigated on their crystal structures[1] and magnetic properties[2] in our laboratory, where M indicates the $3d$ transition group elements.

At room temperature ($>T_N$) the structures of $KMnF_3$, $KFeF_3$, $KCoF_3$ and $KNiF_3$ are of the ideal perovskite type, but $KCuF_3$ crystallizes as a modification of the perovskite type, which is tetragonal ($a>c$).

In the perovskite structure a $3d$ cation is in an octahedral anion interstice where the crystal field splits the $3d$ levels of the magnetic cation into two groups—a set of three degenerate $d\varepsilon$ orbitals and a set of two $d\gamma$ orbitals of higher energy. The divalent $3d$ ions under consideration have electronic configurations as follows:

	$3d\varepsilon$	$3d\gamma$
Mn^{2+}	↑ ↑ ↑	↑ ↑
Fe^{2+}	↑↓ ↑ ↑	↑ ↑
Co^{2+}*	↑↓ ↑↓ ↑	↑ ↑
Ni^{2+}	↑↓ ↑↓ ↑↓	↑ ↑
Cu^{2+}	↑↓ ↑↓ ↑↓	↑↓ ↑

Since the electronic charge distribution of Cu^{2+} ion has the $d\gamma$ symmetry a distortion of the local octahedron around Cu^{2+} ion to tetragonal symmetry is expected as a result of the Jahn-Teller effect as discussed by Dunitz and Orgel[3]. As to the direction of the distortion, Öpik and Pryce[4] showed theoretically that Cu^{2+} in octahedral coordination always distorts its surroundings so that the central ion has four near and two far neighbours. On the other hand Liehr and Ballhausen[5] predict that the distortion for Cu^{2+} can go either way, that is, with c/a for the distorted octahedron greater than or less than unity.

Besides $KCuF_3$, so far as we know, there are two more examples of distorted octahedron formed by F^- ions around Cu^{2+} ion. These are in CuF_2[6] with distorted rutile structure and in K_2CuF_4[7] with tetragonal K_2NiF_4 structure where the distortions of the local octahedra are both tetragonal, but $c/a>1$ for the former and $c/a<1$ for the latter.**

Recently Kanamori[9] has shown that the sign of the superexchange interaction is closely connected with the cation orbital state, when the cation is subject to the crystalline field arising from octahedrally or tetrahedrally surrounding anions. Therefore it should be interesting to determine the crystal structure of $KCuF_3$ and to compare with the magnetic properties.

---

* The configuration of Co^{2+} can be represented by a single one-electron configuration only in an approximation.

** Kanamori[8] has pointed out that the distortion in K_2CuF_4 can not be attributed to the Jahn-Teller effect, because K_2NiF_4 has the isomorphous structure.

§ 2. Experimental

The compound, prepared by Hirakawa, Hirakawa and Hashimoto[2] of our laboratory, crystallized in the form of pseudo-cubes which were mostly a few mm^3 in volume and pale violet. The specimens on which the X-ray work was performed were formed into nearly cylindrical shape, length 0.4∼0.8 mm and diameter 0.14∼0.12 mm, by cutting with a razor blade and by grinding with sand paper.

The preliminary data were obtained from rotation and oscillation photographs taken with Cu$K\alpha$ radiation. The lattice constants were determined as follows: at first a_0 was determined from high angle $(hk0)$ reflexions about the [001] by graphical extrapolation against $\cos^2\theta$, next using this a_0 value c_0 was determined from high angle $(h0l)$ reflexions about the [010] by the same extrapolation.

Integrated intensities were recorded on multiple film equi-inclination Weissenberg photographs of the $(hk0)$, $(hk1)$, $(hk3)$ and $(h0l)$ layers using Mo$K\alpha$ radiation. The ranges of intensities measured were about 10^4 to 1 for the $(hk0)$, about 10^3 to 1 for the $(h0l)$ and about 10^2 to 1 for the $(hk1)$ and $(hk3)$, the estimate being made visually. Oscillation photographs were used to bring the relative intensities of reflexions in different layers to a common scale.

The integrated intensities were corrected for Lorentz and polarization factors. Since the linear absorption coefficient for Mo$K\alpha$ radiation is 96.9 cm^{-1}, the absorption corrections of Bradley[10] were applied to the intensities, assuming the crystals to be exactly cylindrical. No corrections were made for extinction and dispersion.

§ 3. Structure Analysis

a) *Preliminary analysis*

The oscillation photographs about [100] and [001] as rotation axes were obtained with Cu$K\alpha$ radiation by spending enough time. Very weak reflexions due to a superstructure were found on these films. The cell dimensions of the superstructure are twice as large as those of the fundamental pseudo-perovskite structure, that is:

$$a'=b'=2a_0=8.280\pm0.002\ \text{Å}\ ,$$

$$c'=2c_0=7.852\pm0.004\ \text{Å}\ ,$$

where the prime and the suffix indicate the super- and fundamental structures, respectively. Indexing on the basis of the above superlattice all the reflexions are classified into two groups as follows:

i) h, k, l all even, whose intensities are corresponding to the pseudo-perovskite structure,

ii) h, k, l all odd, which are due to the superstructure.

(hhl) reflexions of the second group are systematically absent. Moreover the relative intensities between the first and the second group reflexions suggest that this superstructure should not be attributed to an ordering of ion vacancies but to an ordered displacement of F^- ions from the original positions of the pseudo-perovskite structure.

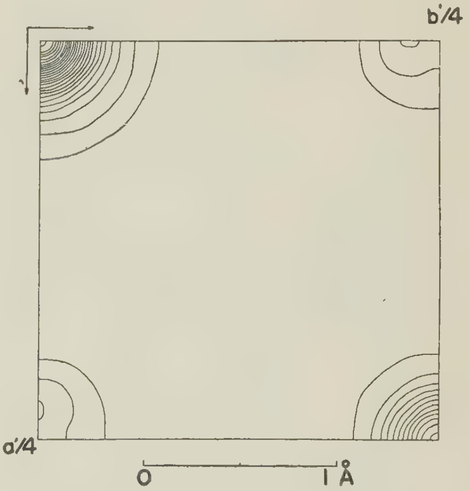

Fig. 1. Electron-density projection along [001], with contours at intervals of 10 e.Å^{-2}. Over the whole region the density is positive.

b) [001] *and* [010] *projections*

Structure factors $F(hk0)$ and $F(h0l)$ of $KCuF_3$ are all positive if the origin is chosen at Cu^{2+} and if the departure from the original pseudo-perovskite structure is not large. Therefore a final F_0 synthesis could be calculated directly using Beevers and Lipson strips. Fig. 1 shows the [001] projection by the F_0 synthesis and the displacement of F^- ions is obvious, although the F^- ions of which displacements are in the opposite direction in successive (001) planes are superposed. A preliminary comparison of calculated and observed $hk0$ structure factors, $F_c(hk0)$ and $F_0(hk0)$, by Wilsons' method[11] for the 34 reflexions out to $(\sin\theta/\lambda)^2=0.99$ provided a provisional temperature factor $B=1.27$ Å^2, and resulted in a reliability factor $R=\sum|F_0-F_c|/\sum|F_0|$ of 0.052 (0.048, if the non-observable reflexions are omitted). The calculated structure factors are based on the atomic scattering factors of Thomas and Umeda[12] for Cu^{2+} and of Berguis et al.[13] for K^+ and F^-.

The refinement of the structure was carried out by the successive use of difference Fourier projection along [001]. The final (F_0-F_c) synthesis is shown in Fig. 2. The final values of the parameters and the temperature factors, given in Table I, were used to calculate a set of structure factors, which is given together with the observed set, in Table II. The reliability factor for the 58 reflexions on the $hk0$ layer is reduced to 0.046 (0.042). The standard deviation of the atomic coordinate of the displaced F^- ion was estimated as 0.008 Å by the methods given by Cruickshank[14].

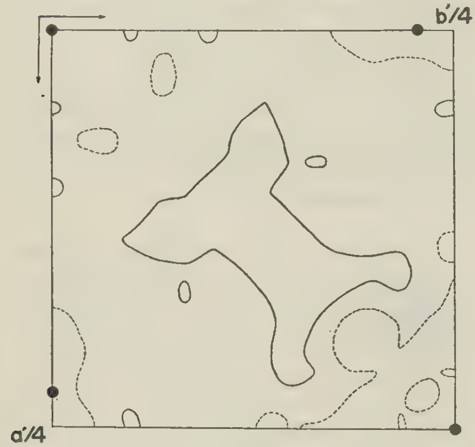

Fig. 2. Final (F_0-F_c) Fourier projection along [001], with contours of ±1 and −3 e.Å^{-2}; negative contours are shown as broken lines. Solid circles represent atomic sites.

Table I. Atomic parameters and temperature factors obtained from [001] projection.

	Parameters		Temperature factors (Å^2)
	x	y	
K^+	$\frac{1}{4}$	$\frac{1}{4}$	1.30
Cu^{2+}	0	0	1.33
F^-	0 0.228 0	0 0 0.228	1.00

A similar procedure was carried out about the $h0l$ data. On the [010] projection by the F_0 synthesis shown in Fig. 3, it is clear that the displacement of F^- ion occurs along the Cu-F-Cu bond only in the c plane. The same parameter value for the shift of F^- ion as the [001] projection was confirmed by the difference

Table II. Observed and calculated structure factors of $(hk0)$ reflexions.

$h\ k\ 0$	$\|F_0\|$	F_c	$h\ k\ 0$	$\|F_0\|$	F_c	$h\ k\ 0$	$\|F_0\|$	F_c	$h\ k\ 0$	$\|F_0\|$	F_c
0 2 0	144.9	138.6	2 10 0	93.7	89.9	4 20 0	15.7	13.0	8 14 0	13.7	15.6
4	347.1	371.7	12	15.6	15.4	22	7.0	6.2	16	22.3	23.0
6	87.5	85.7	14	47.5	47.6				18	10.9	9.4
8	175.2	175.0	16	8.5	4.5	6 6 0	115.3	114.9	20	12.6	9.0
10	44.2	47.0	18	20.7	21.8	8	32.8	34.4			
12	83.3	83.9	20	0	1.0	10	71.8	72.7	10 10 0	47.5	48.9
14	27.1	25.8	22	12.8	8.7	12	14.6	13.8	12	11.6	11.6
16	33.7	37.1				14	41.7	39.4	14	28.0	27.9
18	17.6	14.6	4 4 0	272.1	270.4	16	0	4.7	16	0	4.8
20	15.2	14.6	6	68.6	67.0	18	18.4	18.7	18	15.7	13.9
22	8.5	7.1	8	145.0	146.8	20	0	1.4			
			10	35.0	38.6	22	9.3	7.6	12 12 0	29.8	27.9
2 2 0	240.3	241.3	12	71.3	73.8				14	8.7	8.6
4	102.6	94.6	14	16.7	22.6	8 8 0	90.2	94.2	16	14.8	12.9
6	151.6	153.4	16	31.9	32.9	10	25.5	23.8	18	8.3	5.4
8	47.6	43.4	18	12.0	13.1	12	48.7	50.8			
									14 14 0	17.1	17.0

Fourier projection, while the temperature factors obtained by the third synthesis were somewhat different from those obtained earlier as shown in Table III. In Table IV $F_0(h0l)$ are compared with $F_c(h0l)$. Since the experiments for the $(h0l)$ data were carried out under rather worse condition—shape and size of specimen, exposure time and size of integration—than those for the $(hk0)$ data, the reliability factor for the 92 $(h0l)$ reflexions is 0.087 (0.061).

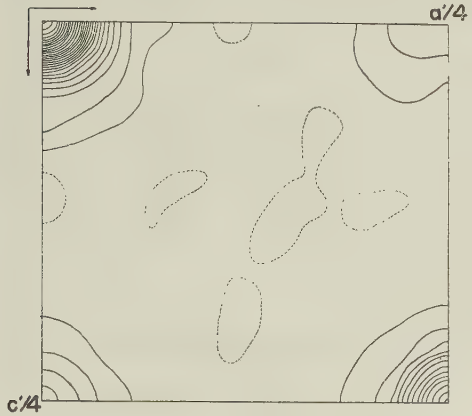

Fig. 3. Electryn-density projection along [010], with contours at intervals of 10 e.Å^{-2}. Broken lines indicate 0 e.Å^{-2}.

Table III. Atomic parameters and temperature factors obtained from [010] projection.

	Parameters x	Parameters y	Temperature factors (Å^2)
K^+	$\frac{1}{4}$	$\frac{1}{4}$	1.23
Cu^{2+}	0	0	1.00
F^-	0 0 0.228	0 $\frac{1}{4}$ 0	1.40

Table IV. Observed and calculated structure factors of $(h0l)$ reflexions.

h 0 l	$\|F_0\|$	F_c	h 0 l	$\|F_0\|$	F_c	h 0 l	$\|F_0\|$	F_c	h 0 l	$\|F_0\|$	F_c
0 0 2	134.6	134.3	2 0 8	57.3	52.0	4 0 20	18.4	15.0	8 0 8	97.5	99.1
4	364.4	363.5	10	82.7	83.3				10	21.2	21.0
6	75.5	75.4	12	27.8	25.8	6 0 4	82.3	71.0	12	53.4	55.4
8	164.4	173.8	14	45.0	42.3	8	147.5	149.8	14	17.7	12.3
10	36.3	38.0	16	27.0	13.4	10	43.1	43.0	16	30.2	26.9
12	90.2	86.9	18	24.6	18.7	12	82.6	79.1	10 0 8	26.6	29.3
14	26.6	18.8				14	28.3	25.1	12	48.0	56.3
16	44.6	40.2	4 0 2	106.6	94.2	16	37.0	38.1	14	0	18.8
18	0	9.7	6	156.7	158.5	18	0	14.0	16	27.9	28.1
20	22.3	16.5	8	58.7	46.8	20	16.3	16.7			
			10	99.6	97.8				10 0 10	43.5	48.5
2 0 0	138.4	138.3	12	0	20.9	6 0 6	120.5	114.6	12	23.0	17.7
4	374.0	377.4	14	52.1	54.2	8	42.4	42.3	14	28.3	26.0
6	98.2	88.0	16	0	10.0	10	72.2	69.4	16	0	9.9
8	175.7	178.2	18	27.9	26.6	12	33.9	22.6			
10	51.3	49.9	20	0	5.4	14	35.6	35.9	12 0 10	20.5	11.8
12	78.0	89.4	22	13.5	11.5	16	0	12.2	14	31.9	29.0
14	21.9	27.7				18	19.4	16.2	16	0	6.7
16	30.8	42.2	4 0 4	270.9	268.7						
18	0	15.3	6	65.4	60.2	8 0 6	30.8	34.3	12 0 12	33.5	33.3
20	19.1	18.4	8	146.6	147.7	10	81.1	76.3	14	18.7	7.7
22	12.4	7.5	10	30.7	32.1	12	28.8	17.1	16	20.8	16.6
			12	78.9	77.1	14	40.7	43.8			
2 0 2	239.4	240.0	14	22.7	16.7	16	0	8.8	14 0 12	21.2	12.3
4	105.3	98.9	16	41.8	36.3	18	20.8	21.8	16	18.3	17.2
6	141.4	145.8	18	0	8.8						
						8 0 8	97.5	99.1	14 0 14	21.7	16.2

c) *Analysis of* (*hk*1) *and* (*hk*3) *data*

Although the [001] and [010] projections of electron density have shown a displacement of F^- ions, a contribution by the displacement to $F(hk0)$ and to $F(h0l)$ is very small in general. Since the superstructure reflexions, on the contrary, are purely due to the displacement, (*hk*1) and (*hk*3) data were examined. The intensities of (*hk*1) and (*hk*3) reflexions were brought into an absolute scale by comparing with those of (*hk*0) reflexions. The parameter and the temperature factor of F^- ion shown in Table V were determined so as to get the best agreement between the observed and calculated structure factors, which are given in Table VI.

Table V. Parameter and temperature factor of the displaced F^- ion.

	From (*hk*1) reflexions	From (*hk*3) reflexions
Parameter	0.232 [1.92]	0.230 [1.90]
Temperature factor (Å²)	2.36	2.36

Values in the brackets show the shortest Cu-F distances (Å) corresponding to these parameters.

Table VI. Observed and calculated structure factors of (*hk*1) and (*hk*3) reflexions.

h k 1	$\|F_o\|$	F_c	*h k* 3	$\|F_o\|$	F_c
1 3 1	20.9	21.4	1 3 3	16.8	17.6
5	14.1	−12.3	5	11.8	−10.9
7	12.9	13.9	7	11.8	12.7
9	8.6	−7.2	9	9.1	−6.6
11	4.7	5.9	11	0	5.5
3 5 1	22.2	−20.7	3 5 3	18.8	−18.6
7	4.0	5.5	7	3.2	−4.9
9	12.3	−11.0	9	12.7	−9.6
5 7 1	12.6	13.6	5 7 3	11.6	12.8
9	0	−2.2	9	0	−1.9
7 9 1	6.8	−7.9	7 9 3	7.1	−7.5

These superstructure reflexions have weak asterism along the c^* axis of the reciprocal lattice†, while the fundamental reflexions have no asterism. Then this parameter may be an upper limit for the displacement and is in good agreement with those obtained from [001] and [010] projections.

Another way to attack this problem is the method of the bounded projection of electron-density[15], that is,

$$\int_{z_1}^{z_2}\rho(x, y, z)dz\ ,$$

which enable to separate the individual atoms if z_1 and z_2 are chosen properly. For the present case it is convenient to choose as $z_1=-1/4$ and $z_2=+1/4$. Then this integral is expressed as follows[16]:

$$\begin{aligned}\int_{-1/4}^{+1/4}\rho(x, y, z)\,dz \\ =\frac{1}{a'^2}\Big[&\frac{1}{2}\Sigma\Sigma\,F(hk0)\cos 2\pi(hx+ky) \\ &+\frac{2}{\pi}\Sigma\Sigma\,F(hk1)\cos 2\pi(hx+ky) \\ &-\frac{2}{3\pi}\Sigma\Sigma\,F(hk3)\cos 2\pi(hx+ky) \\ &+\frac{2}{5\pi}\Sigma\Sigma\,F(hk5)\cos 2\pi(hx+ky)-\cdots\Big]\,.\end{aligned}$$

Although only $F_0(hk0)$, $F_0(hk1)$ and $F_0(hk3)$ are used, the termination error is very small.

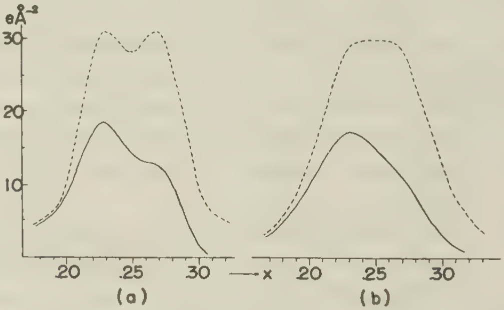

Fig. 4. Cross-section of the bounded projection at $y=0$; in (a) $F(hk0)$, $F(hk1)$ and $F(hk3)$, in (b) $F(h0l)$, $F(hk1)$ and $F(hk3)$ are synthesized, respectively. Broken lines indicate the corresponding cross-sections of [001] and [010] projections.

The cross-section of the projection at $y=0$ is shown in Fig. 4(a). Not only $F_0(hk0)$, but also $F_0(h0l)$ can be used to obtain this cross-section, the result being shown in Fig. 4(b). In these figures the cross-sections of [001] and [010] projections at $y=0$ are also shown by broken lines for comparison. The same results were obtained when $F_c(hk1)$ and $F_c(hk3)$ were used instead of $F_0(hk1)$ and $F_0(hk3)$, respectively.

d) *High and low temperature study*

This superstructure was examined also at high and low temperatures. In the temperature region of 670∼135°K any intensity change was not observed on the super- and fundamental reflexions which were recorded on the oscillation photographs taken using a single crystal high temperature camera having a cylindrical Ni-foil heater (Dent and Taylor[17]) and a low temperature camera by gas cooling method. There was no change of lattice symmetry over the same temperature region.

---

† This asterism will be discussed in § 5.

§ 4. Description of the Structure

Fig. 5 shows the crystal structure of $KCuF_3$ obtained from [001] and [010] projections, where the displacement of F^- ions is exaggerated. For this structure the unit cell should be chosen as indicated by broken lines.

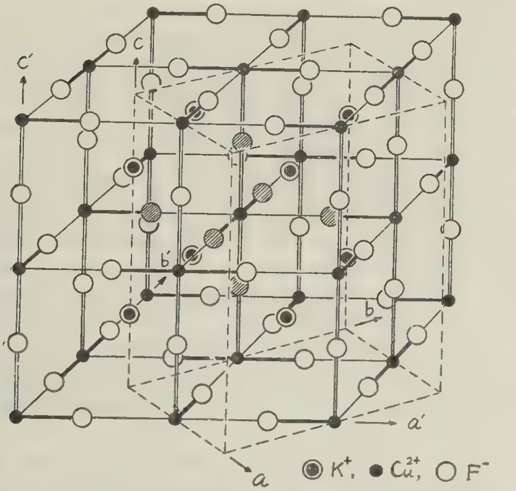

Fig. 5. Structure of $KCuF_3$. Single, double and bold lines are long, medium and short Cu-F distances, respectively, where the displacement of F^- ions is exaggerated. 6 F^- ions which surround a Cu^{2+} ion distorted-octahedrally are shown as shaded circles. Broken lines indicate the unit cell.

Therefore the lattice constants, space group and atomic coordinates are as follows:

$a=\sqrt{2}\,a_0=5.855\pm0.001_5$Å,

$c=2c_0=7.852\pm0.004$Å,

space group: $D_{4h}^{18}-I4/mcm\ (Z=4)$

atomic coordinates: $(0,0,0;\ \frac{1}{2},\frac{1}{2},\frac{1}{2})+$

4 K^+ in (*a*): $(0,0,\frac{1}{4};\ 0,0,\frac{3}{4})$

4 Cu^{2+} in (*d*): $(0,\frac{1}{2},0;\ \frac{1}{2},0,0)$

4 F^- in (*b*): $(0,\frac{1}{2},\frac{1}{4};\ \frac{1}{2},0,\frac{1}{4})$

8 F^- in (*h*): $\pm(x,\frac{1}{2}+x,0;\ \frac{1}{2}-x,x,0)$, $x=0.228$.

In this structure a Cu^{2+} ion is surrounded by a distorted octahedron of F^- ion with copper-fluorine distances as follows:

$$l=2.25\pm0.01\,,\quad m=1.96\pm0.001$$
$$\text{and } s=1.89\pm0.01\text{Å}\,,$$

where l, m and s mean the long, medium and short distances as shown in Fig. 5 by single, double and bold lines, respectively.

Table VII. Cu-F distances (Å) in $KCuF_3$, CuF_2[6] and K_2CuF_4[7].

	$KCuF_3$	CuF_2	K_2CuF_4
	2.25 (2)	2.27 (2)	2.08 (4)
	1.96 (2)	1.93 (4)	1.95 (2)
	1.89 (2)		
mean	2.03_3	2.04_3	2.03_7

Figures in the parentheses show the number of the Cu-F bonds.

In Table VII these Cu-F distances are compared with those in CuF_2 and K_2CuF_4. Although the directions of the distortion are different, the averages of the 6 Cu-F distances are nearly the same. In $CuF_2\cdot2H_2O$[18] the shortest Cu-F distance is 1.89 Å, although the Cu^{2+} surroundings are different from those in the others.

§ 5. Discussion

The electronic configuration of the lowest orbital state of Cu^{2+} ion which is subject to an octahedral cubic field is $(d\varepsilon^6)(d\gamma^2)d\gamma^1$; those in parentheses indicate paired electrons. Therefore a $d\gamma$ orbital oriented to the two far F^- ions (dz^2) should be completely filled.

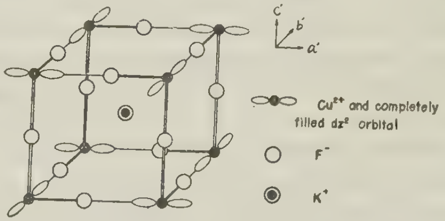

Fig. 6. Ordering of dz^2 orbitals for $KCuF_3$.

The ordering of these dz^2 orbitals is shown in Fig. 6. In the z'-direction, the intervening F^- ion p orbital overlaps on each side a half filled Cu^{2+} ion orbital, while in the x'- or y'-direction, overlapped Cu^{2+} ion orbital is half filled on one side, completely filled on the other. Then superexchange interaction between Cu^{2+} ions on opposite side of F^- ion may be antiferromagnetic for the former and ferromagnetic for the latter as suggested by Goodenough[19] and Kanamori[8]. Below the Néel temperature (243°K), consequently, an A-type antiferromagnetic structure may be expected, that is, all the magnetic moments within any (001) sheet are arranged ferromagnetically but with antiferromagnetic coupling between successive sheets.

The dispositions of the magnetic cations relative to the intervening anions in $KCuF_3$ are very similar to those in MnF_3[20] with distorted ReO_3 structure and in $LaMnO_3$[21] with distorted perovskite ($GdFeO_3$) structure. By neutron diffraction studies the A-type antiferromagnetic structures have been confirmed for both MnF_3[22] and $LaMnO_3$[23]. However the local distortions of these compounds are more complicated than that of $KCuF_3$ and, as pointed out by Gilleo[21], the distortion of $LaMnO_3$ may not be attributed purely to the Jahn-Teller effect, because $LaCrO_3$ and $LaFeO_3$ also have the isomorphous structures, for which the effect cannot be expected.

On the other hand the distortion of $KCuF_3$ seems to be mainly due to the Jahn-Teller effect, because except for $KCuF_3$ there are no such distortions in KMF_3 compounds above their Néel temperatures and the magnitude of the distortion is in good agreement with that found in Mn^{3+}-containing spinels[19]. That is, ratio of long to average of medium and short Cu-F distances is 1.17.

As mentioned in § 3 c), the superstructure reflexions of $KCuF_3$ have weak asterism along the c^* axis of the reciprocal lattice while the fundamental reflexions have no asterism. These features are somewhat similar to those of cobalt[24], and suggest a kind of stacking disorder, say as follows: the displacements of F^- ions in successive (001) planes are in the opposite direction in the regions of perfect crystallization, but in real crystals the displacements in neighbouring (001) planes are in the same direction occasionally. Furthermore one specimen among six examined in detail, showed superstructure reflexions corresponding to the following unit cell: $a'=b'=2a_0$, $c'=c_0$, which means that in this structure the displacements in successive (001) planes are in the same direction. These facts suggest that the difference between the stability of these structures are rather small. This asterism did not disappear down to 135°K. Fortunately the disordered structure assumed here has no influence on $F(hk0)$ and $F(h0l)$.

The authors wish to express their hearty thanks to Prof. T. Okada for his continuous guidance and encouragement, to Dr. K. Hirakawa and Mr. T. Haghimoto for supplying the crystals for this investigation and for discussions, and to Miss K. Hirano for assistance in calculation. This investigation was partly supported by the Scientific Research Expenditure of the Ministry of Education.

References

1) A. Okazaki, Y. Suemune and T. Fuchikami: J. Phys. Soc. Japan **14** (1959) 1823.
2) K. Hirakawa, K. Hirakawa and T. Hashimoto: J. Phys. Soc. Japan **15** (1960) 2063.
3) J. D. Dunitz and L. E. Orgel: J. Phys. Chem. Solids **3** (1957) 20.
4) U. Öpik and M. H. L. Pryce: Proc. Roy. Soc. **A238** (1957) 425.
5) A. D. Liehr and C. J. Ballhausen: Ann. Phys. (N.Y.) **3** (1958) 304.
6) C. Billy and H. M. Haendler: J. Amer. Chem. Soc. **79** (1957) 1049.
7) K. Knox: J. Chem. Phys. **30** (1959) 991.
8) J. Kanamori: J. Appl. Phys. **31** (1960) 14S.
9) J. Kanamori: J. Phys. Chem. Solids **10** (1959) 87.
10) A. J. Bradley: Proc. Phys. Soc. London **47** (1935) 879.
11) A. J. C. Wilson: Nature London **150** (1942) 152.
12) L. H. Thomas and K. Umeda: J. Chem. Phys. **26** (1957) 293.
13) J. Berguis, IJ. M. Haanappel, M. Potters, B. O. Loopstra, C. H. MacGillavry and A. L. Veenendaal: Acta Cryst. **8** (1955) 478.
14) D. W. J. Cruickshank: Acta Cryst. **2** (1949) 65.
15) A. D. Booth: Trans. Faraday Soc. **41** (1945) 434.
16) H. Lipson and W. Cochran: *The Determination of Crystal Structure* (Bell, London, 1953) p. 81.
17) L. S. Dent and H. F. W. Taylor: J. Sci. Instr. **33** (1956) 89.
18) S. Geller and W. L. Bond: J. Chem. Phys. **29** (1958) 925.
19) J. B. Goodenough: J. phys. radium **20** (1959) 155.
20) M. A. Hepworth and K. H. Jack: Acta Cryst. **10** (1957) 345.

21) M. A. Gilleo: Acta Cryst. **10** (1957) 161.
22) E. O. Wollan, H. R. Child, W. C. Koehler and M. K. Wilkinson: Phys. Rev. **112** (1958) 1132.
23) W. C. Koehler and E. O. Wollan: J. Phys. Chem. Solids **2** (1957) 100.
24) O. S. Edwards and H. Lipson: Proc. Roy. Soc. **A180** (1942) 268.

JOURNAL OF THE PHYSICAL SOCIETY OF JAPAN, Vol. 16, No. 2, FEBRUARY, 1961

Hall Effect on Some of the Magnetic Compounds

By Satoshi FUJIME, Miyuki MURAKAMI, and Eiji HIRAHARA
Department of Physics, Faculty of Science, Tōhoku University

(Received September 5, 1960)

A sensitive Hall measuring apparatus has been constructed, and making use of it some of magnetic compounds, nickel oxide, iron telluride, nickel telluride, and iron sulfide have been studied. Especially, iron sulfide was studied because of the interest for its remarkable anisotropies of conductivity and susceptibility. From the results, one may say that the anisotropy of the conduction is responsible to the anisotropy of its mobility but not to the carrier concentration.

§ 1. Introduction

The conduction phenomena of a semiconducting compound containing transition element has some difficult problems not to be explained by the simple current theory, for example, some of these compounds exhibit anomalous resistivity at the temperatures near the Curie or Néel points, and other exhibit a remarkable anisotropy at the temperatures below the Curie or Néel points. Furthermore, the nature of conduction carriers in most cases is unknown whether it is an s-like electron in the energy band or a d-like electron in the discrete levels. In order to elucidate the nature of conduction phenomena, it has been requested to study the Hall Effect for these materials. The Hall voltages of these materials observed in typical conditions, however, are always so feeble to be hardly detected in the ordinary measurements. For the compounds studied in our laboratory, for example, nickel telluride, iron telluride, and iron sulfide, the Hall voltages to be measured for typical conditions seem to be of the order or smaller than 10^{-7} volts. It is, to say, for nickel telluride 8×10^{-7} volts in the case of $H=5000$ oersteds, the sample thickness $d=0.1$ cm, and the sample current $I=200$ mA, so that the ordinary Hall coefficient will be 3.5×10^{-5} cm³/amp.sec.(3.5×10^{-13} volt.cm/amp.gauss).

Therefore, in the construction of the measuring apparatus, the noise level of the detector must be at least of the order of 10^{-9} volts in order to achieve a reasonable signal to noise ratio. The Hall equipment having the sensitivity mentioned above was assembled, and with it the Hall effect has been studied for the compounds above mentioned as well as nickel oxide.

Among these compounds, especially the iron sulfide has been studied in detail, because of the interest for its remarkable anisotropies of conductivity and magnetic susceptibility at the α-transformation.

§ 2. Apparatus and Experimental Procedures

Our apparatus is essentially same as Lavine's apparatus[1] except for some details. The block diagram of our equipments is shown in Fig. 1. The equipment is composed with a 1.025 kc.p.s. power supply, a microvoltor or an attenuater, an amplitude and phase controller, a bucking and adding circuit, a high gain phase sensitive detector, and a pen-recorder or oscilloscope.

The 1.025 kc.p.s. power supply is primarily

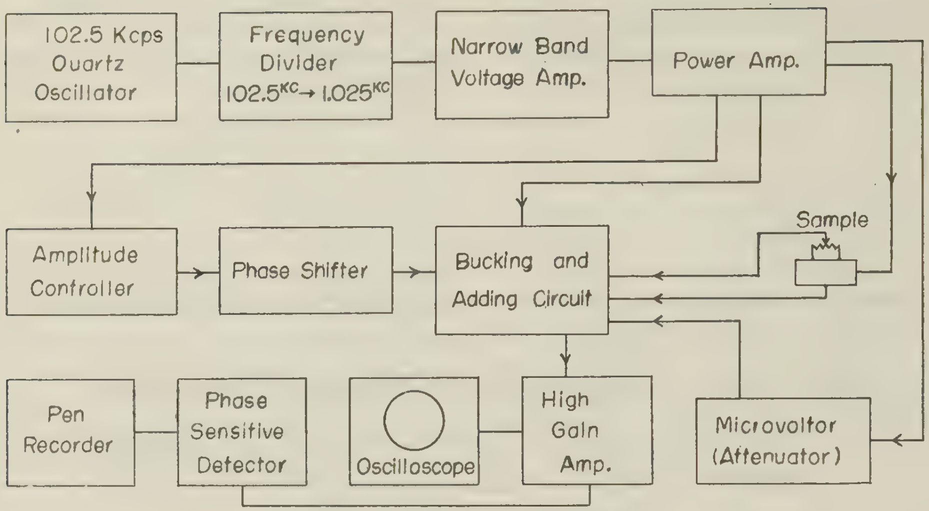

Fig. 1. Block diagram of sensitiue Hall equipment system.

drived by a 102.5 kc.p.s.-quartz oscillator which is stepped down to 1.025 kc.p.s. by a frequency divider or muti-vibrator, and then selected and magnified by a narrow band voltage amplifier and a power amplifier. This power is fed to the sample, the microvoltor, and the amplitude and phase controller, respectively. The voltage signals controled in the bucking and adding circuit are shown by the vector diagram in Fig. 2, in which the picked up voltage independent of magnetic field H is shown as IZ, and the Hall voltage V_H, the magnetoresistance voltage $V_m(H^2)$ and IR drop between the Hall probes are in phase with the current, and are shown collinear in the vector. The resultant vector of these four voltage vectors is shown as the vector $\boldsymbol{A}$. A voltage inverse to $\boldsymbol{A}$ is added by the amplitude and phase controller circuit ajusting the magnitude $|\boldsymbol{A}|$ and the phase as to just vanish the out put signal. The magnetic field is then reversed, the voltage out put of the system becomes $2V_H$ because the Hall voltage changes its sign, and IR and $V_m(H^2)$ does not change sign. The Hall voltage $2V_H$ is recorded by the high sensitive detector and recorder.

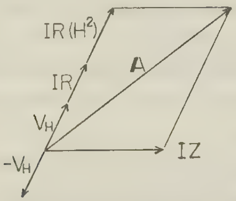

Fig. 2. Vector diagram of voltages controled in the Bucking and Adding Circuit.

A sample holder was constructed in special device to prevent the spurious signals from the sample and the Hall leads. The sample was set in a square hollow in a copper bar of 4 cm in diameter, 25 cm in length, the dimension of square hollow was 3 cm × 3 cm in base area, 2 cm in depth. For a heating furnace, the nichrome wire was wound in a bifilar winding around the mica plate 4 cm × 3.5 cm in area, and this furnace was inserted into the slice-shaped ditch which was cut deeply from the end of the copper bar. The Hall leads and sample current leads were fixed in the narrow channels which were cut along the length of the copper bar, for the sake of preventing a voltage induced in these leads vibrating in the magnetic field.

§ 3. Results

The results of measurement for these compounds are given in Table I. For nickel oxide and nickel telluride*, the Hall measurements could be performed only at the room temperature (at 16°C), because of the high resistivity of the former and of the very feeble Hall response of the latter. For iron telluride and iron sulfide the measurements could be performed in some wider range of temperature. Nevertheless the temperature variations

---

* The authors wish to thank Mr. Y. Nakazumi (Tochigi Chemical Industrial Co.) for supply of this single crystal.

Table I. Results of Hall measurements for Various compounds.

Compounds	Temperature (°C)	V_H (Volt)	R_H (cm³/amp.sec)	n (cm⁻³)	σ (Ω^{-1} cm⁻¹)	μ (cm²/Volt.sec)
NiO	16	4.2×10^{-7}	$+2.6\times 10^{4}$	2.7×10^{14}	1.4×10^{-8}	3.7×10^{-4}
NiTe	16	4×10^{-7}	-3.5×10^{-5}	1.8×10^{23}	1.4×10^{4}	0.49
FeTe	16	1.3×10^{-7}	$+2.1\times 10^{-3}$	2.5×10^{23}	1.5×10^{3}	3.2
FeS						
σ_a	16	0.7×10^{-8}	$+0.70\times 10^{-4}$	8.5×10^{22}	2200	0.16
	115	0.64×10^{-8}	$+0.70\times 10^{-4}$	8.5×10^{22}	2700	0.20
	150	0.64×10^{-8}	$+0.70\times 10^{-4}$	8.5×10^{22}	3000	0.22
σ_c	16	0.7×10^{-8}	$+0.70\times 10^{-4}$	8.5×10^{22}	4	2.8×10^{-4}
	115	0.7×10^{-8}	$+0.70\times 10^{-4}$	8.5×10^{22}	20	14×10^{-4}
	150	0.7×10^{-8}	$+0.70\times 10^{-4}$	8.5×10^{22}	2800	0.21

for only iron sulfide are given in the Table for the purpose of the later discussions. The Hall voltages V_H observed and the Hall constants R_H calculated for these compounds are shown in the third and fourth columns, respectively.

The concentration n, and the mobility μ of the carrier given in the fifth and seventh columns are estimated by the following relations

$$R_H = 1/en \qquad (1)$$

$$R_H \cdot \sigma = \mu\,, \qquad (2)$$

where e is an electronic charge, σ a conductivity. These relations have been originally applicable to a simple band model of a metal and a semiconductor, however they may be, for present, used for the analysis of these compounds. In the present step, the conduction nature of these compounds has been remained obscure and no relations corresponding to Eqs. (1) and (2) have been obtained, it may be inevitable to use the above relations for the analysis of our compounds. Some of results obtained by the use of these relations will be discussed in later part of this paper.

§ 4. Discussions

Nickel oxide: Hall measurements of nickel oxide have not yet been reported, because of its high resistivity and of its very poor Hall response. Morin[2] has determined, by the measurements of Seebeck effect, the nature of conduction was the hole conduction. Our Hall measurement shows a positive Hall constant and so also a hole conduction. The hole mobility is of the order 10^{-4} cm²/volt.sec., and the hole concentration is of the order 10^{14} per unit volume. These values seem to be reasonable for a high resistivity material such as nickel oxide. Yamashita and Kurosawa[3] have investigated theoretically the conduction of this material as a d-hole diffusion with very small mobility. The very small value of mobility obtained as above may be compatible with the concept of the hopping model proposed by them.

Nickel telluride and Iron telluride: These compounds have a considerablly high conductivity with a poor mobility. In general, these compounds, containing a magnetic element and being low resistivity, have a apparent poor mobility estimated by the use of the relation (2), and an extraordinarily large number of carriers estimated by the use of the relation (1), as shown in Table I. These carrier numbers are larger than the lattice concentration, this means the relations (1) and (2) are unreasonable to apply to these compounds and the Hall constants might be under estimated. It may be necessary to consider a two bands model in stead of one simple band model. The extraordinarily small value of Hall constant may be attributed to the cancellation between the contributions from the electrons and the holes. The final conclusion will be reported after the more detailed experiments is made.

Iron sulfide: The iron sulfide has a remarkable anisotropy of conductivity at the temperature range below T_α, the temperature of the α-transformation, as seen in Fig. 3(a)[4]. σ_a and σ_c in the figure are the conductivities in the cases that an external electric field is applied in perpendicular, and in parallel to the c-axis of a single crystal, respectively. The anisotropy at the temperatures below T_α is very large ($\sigma_a/\sigma_c \doteqdot 800$), and becomes to be small ($\sigma_a/\sigma_c=1.5$) above T_α. The Hall measurements were carried out at the temperatures below and above T_α, and the almost same values of Hall constants have been observed both in the cases of σ_a and σ_c, within the limit of experimental error. These Hall constants observed and the mobility estimated by the use of the relation (2), are also shown in Fig. 3 (b). The concentration of carriers in the two cases of σ_a and σ_c, are same order. Nevertheless the mobility exhibits a remarkable anisotropy as seen in the conductivity. It may concluded that the anisotropy of conductivity is owing to the anisotropy of the mobility but not to the carrier number.

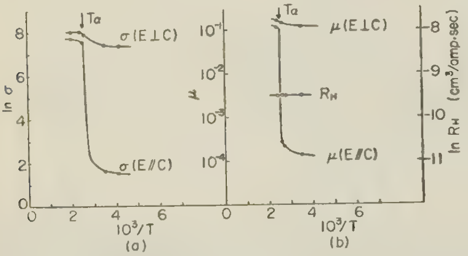

Fig. 3. Conductivity, Hall constants, and mobility for iron sulfide stoichiometric. (a) anisotropy of conduction. σ_a and σ_c are the cases the external electric fields are applied in perpendicular to, and in parallel to c-axis of crystal, respectively[4]. (b) the mobility μ and Hall constant R_H obtained in this work.

In order to interpret the fact that the carrier concentration does not change at the temperatures below and above T_α and that the mobilities very low, it may be natural to assume that there are two kinds of ions of different valences such as Fe^{2+} and Fe^{3+} for the lack of stoichiometry, and the electrons or holes hopping between these ions are responsible for the conduction and the low mobility.

The detailed estimation of this problem will be reported by one of the authors on the paper which will be published in this journal.

This work is supported partly by the fund of the Ministry of Education in Aid of Scientific Research.

References

1) J. M. Lavine: Rev. Sciet. Inst. **29** (1958) 970.
2) E. J. Morin: Phys. Rev. **93** (1954) 1199.
3) J. Yamashita and T. Kurosawa: J. Phys. Chem. Solids **5** (1958) 34.
4) E. Hirahara and M. Murakami: J. Phys. Chem. Solids **7** (1958) 281.

JOURNAL OF THE PHYSICAL SOCIETY OF JAPAN, Vol. 16, No. 2, FEBRUARY, 1961

Anisotropy of Electrical Conduction in Iron Sulfide Single Crystal

By Miyuki MURAKAMI

Department of Physics, Faculty of Science, Tōhoku University

(Received September 5, 1960)

To investigate the anisotropy of the conductivity of iron sulfide single crystal, a simultaneous measurement of the conductivity and the thermal expansion was carried out.

The result is that the conductivity is intimately correlated with the lattice parameter (or exchange energy), but is not necessarily affected by the spin direction. From this result a spin sublattice structure of high temperature type is proposed, and the anisotropy of the conductivity in the range of temperature near the α-transformation temperature is interpreted qualitatively.

§ 1. Introduction

The anisotropies of susceptibility and conductivity in iron sulfide single crystal have been studied in our laboratory[1], the results reproduced are shown in Figs. 1 and 2. In Fig. 1, the solid lines show the susceptibilities in the heating process and dotted lines show those in the cooling process. In these measurement, especially the anisotropic behavior at the α-transformation is characteristic. The qualitative interpretation for the magnetic susceptibility has been given assuming that the exchange energy and anisotropy energy change those values simultaneously at the α-transformation[2),3)]. No report for the interpretation of the conductivity has been published at present.

For the stoichiometric iron sulfide single crystal, the ratio of conductivities, one the current flows along the direction perpendicular to and the other parallel to the c-axis, is of the order of 10^3 at the temperatures below T_α (the temperature of the α-transformation), and is about 1.5 at the temperatures above T_α. One of the purposes of this paper is to interprete the anisotropy qualitatively.

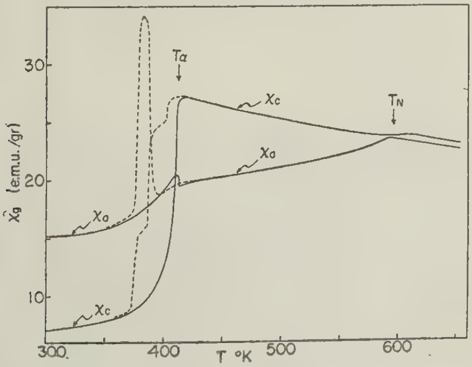

Fig. 1. Susceptibility versus temperature curves. Solid curves are in heating process, and dotted ones are in cooling process[1)].

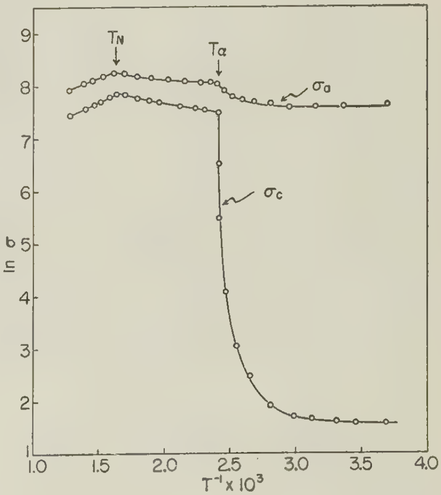

Fig. 2. Conductivity versus temperature curves.

For the interpretation of the anisotropy, it is necessary to perform more detailed investigation of the α-transformation than before (previous cooling experiment[2)]). The previous cooling experiment shows that the exchange energy and the sign of the anisotropy energy change at the different temperatures on the cooling process. On the theoretical consideration, though it is not clear, the exchange energy is considered to change its value with the lattice parameter or c/a of the crystal.

It is well known that a remarkable change of the c/a takes place at the α-transformation[3),4)]. To investigate the correlation between the exchange energy and the conduction, a simultaneous measurement of the conductivity and the thermal expansion of the crystal was carried out in the range of temperature near T_α. From the consideration of the experimental results, an antiferromagnetic sublattice structure of this substance has been proposed which is consistent with the magnetic properties, and explain the anisotropy of the conductivity.

§ 2. Experiments and Results

The apparatus for the simultaneous measurements of conductivity and thermal expansion was built up with a conventional dilatometer and a resistivity measuring potentiometer. The sample was set between the silica pieces, and its thermal expansion was measured by the double mirrors and telescope. Four resistivity probes were attached to the sample as shown in Fig. 3(a). The probes are made of tungsten wire. A plane figure of a probe ring is shown in Fig. 3(b); a small tungsten pin attached on the ring contacts with the sample. Two current leads and two voltage leads are connected with four rings, respectively. The sample crystal used for the measurement was the single crystal with the c-axis parallel to the length of the sample. The conductivity and the thermal dilatation both along the c-axis was measured simultaneously, and the results are shown in Fig. 4.

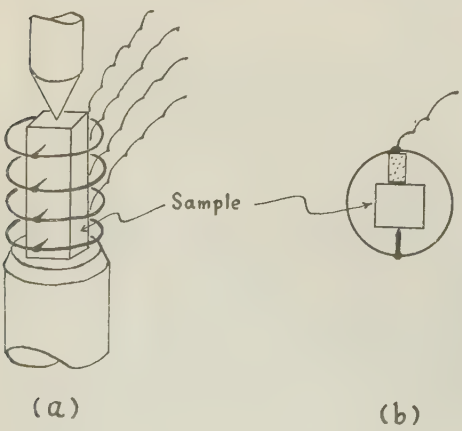

Fig. 3. Detailed figures of sample holder unit in apparatus for the simultaneous measurement of thermal dilatation and conductivity.

The susceptibility χ_a, obtained when the external magnetic field was applied perpendicular to the c-axis of the sample mentioned above, is also shown in Fig. 4. The rate of the temperature change for the susceptibility measurement was taken care to be the same with that of the conductivity and dilatation measurement. The arrows in Fig. 4 show the process of the thermal cycle in each measurement.

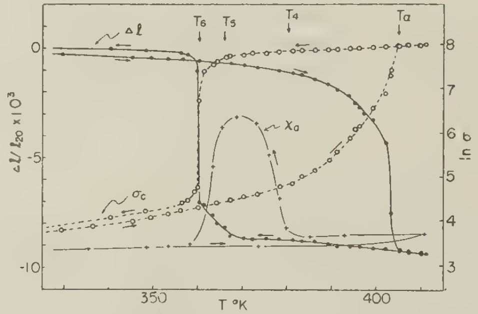

Fig. 4. Results for the simultaneous measurement of thermal dilatation and conductivity, and added to them result for susceptibility of the same sample. Arrows indicate the heating and cooling processes.

It will be significant to call attention to the cooling curves which show a intimate correlation between the conduction and the dilatation, but not between the conduction and the susceptibility or the easy axis direction of magnetization. When the temperature is decreased from T_α, at the temperature T_4 the susceptibility increases abruptly, but the conduction and the dilatation does not change, and at T_5 the susceptibility, conduction and the dilatation bigin to decrease, and then at T_6 the conduction and the dilatation both change abruptly.

§ 3. Discussion

a) *Schematical interpretation of the anomalous cooling curves.*

As mentioned before, the α-transformation on the heating process may be understood by assuming the simultaneous change of the exchange energy and anisotropy energy. The anomalous behavior of the α-transformation on the cooling process may be understood assuming the changes at different temperatures of the two energies.

These situations are schematically given in

Fig. 5. The exchange energy A, which will be intimately correlated with the lattice parameter, decreases abruptly at $T_1 \sim T_3$, and settles on the normal curve on the heating process, but on the cooling process, it jumps up at T_5 toward the normal curve (heating curve) and coinside with it at T_6. The exchange energy is assumed to change like as the lattice parameter. The anisotropy energy constant K, which is assumed uniaxial, will decrease at T_1, and its sign will change from positive to negative at T_2 on the heating process. On the cooling process, its sign will change at T_4 from negative to positive. For the anisotropy energy the change in sign will be important.

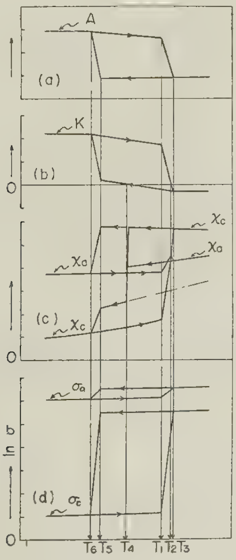

Fig. 5. Schematic interpretation of α-transformation.

a: variation of exchange coupling constant A.
b: variation of anisotropy constant K.
c: variation of susceptibilities of χ_a and χ_c.
d: variation of conductivities of σ_a and σ_c.

Combining the variations of the K and A mentioned above, the temperature variations of the susceptibility and the conductivity near T_α will be represented schematically as in Fig. 5(c) and (d). These figures represent qualitatively the experimental results.

b) *Estimation of the exchange energy at various temperatures*

As mentioned in the preceding paper[5], the Hall measurement for iron sulfide at the temperatures below and above T_α show that the mobility has a remarkable anisotropy and anomaly and the carrier concentration does not change in that temperature range. It may be assumed that the main part of the conduction will be caused by the electron transfer between Fe^{2+} ions and Fe^{3+} ions, and the anisotropy and anomaly will be ascribed to the spin correlation of the conduction electron with the lattice magnetization. There are two distinct cases for the electron transfer in the consideration of spin correlation in an antiferromagnetic material. One is the case in which the electron must transfer along the direction in which the lattice spins align in antiparallel alternately, and in this case the electron transfer will be assumed to need an activation energy for the spin flip, which is equal to the exchange energy J. The other is the case in which the electron will transfer along the direction in which the lattice spins align in parallel, and in this case no activation energy will be needed for the electron transfer. In a rough approximation the ratio of the conductivities in the two distinct directions mentioned above will be $\exp(-J/kT)$. The conductivities in the two cases will be, here after, designated $\sigma_\perp$ and $\sigma_{//}$ respectively.

To estimate the temperature dependence of σ_a/σ_c or $\sigma_\perp/\sigma_{//}$, the temperature variation of J has been estimated by the use of the results of susceptibility measurement. For the temperature range above T_N, it may be put that $J \simeq kT_N$. For $T<T_\alpha$, the estimated T_N' from Eq. (A, 4) in Appendix fitting to the experimental value of $\chi_{//}$ is not the same as T_N because the α-transformation changes the magnetic structure, or the magnitudes of the antiferromagnetic coupling constant A and of the ferromagnetic coupling constant Γ.

A may be estimated from Eq. (A, 1) in Appendix, and S is assumed to be 2, g-value has been estimased by the author[6] to be $g=2.14$ from the analysis for the paramagnetic region. Using these values, T_N' was obtained to be 900°K from Eq. (A, 4) fitting to the experimental values. Therefore, the exchauge energy J may be put as $J=kT_N'=k\times 900°\text{K}$ for $T<T_\alpha$.

For $T_\alpha<T<T_N$, the slightly temperature dependent value of A is estimated from the Eq. (A, 1) which is slightly increasing with temperature as the lattice parameter gradually changes. The value of $\chi_{//}$ in this region has been estimated as $\chi_{//}=2\chi_a-\chi_c$,[1] where χ_a is

the susceptibility when the external magnetic field applied in the direction perpendicular to the c-axis of the crystal. The T_N' in this region is obtained from Eq. (A, 4) using these values mentioned above, which is given in Fig. 6. The values of A and Γ at various temperatures are also given in the same figure.

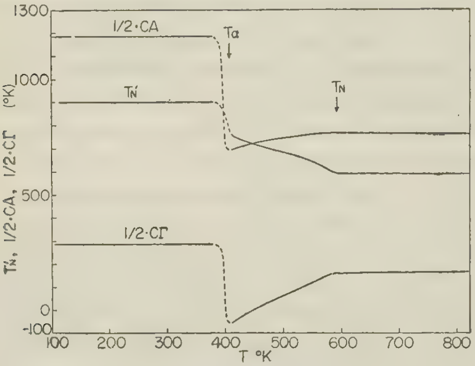

Fig. 6. Estimated values of A, Γ, and $T_N' \equiv \frac{1}{2}C(A-\Gamma)$.

c) *Anisotropy in the conductivity*

For $T<T_\alpha$ the easy magnetization axis is parallel to the c-axis of the crystal, therefore, the ratio $\sigma_a:\sigma_c$ may be approximately $\exp(J/kT):1$. As $J=k\times 900°\mathrm{K}$, this ratio is $\exp(900/100)\simeq 8\times 10^3$ for 100°K, ca. 10^2 for 200°K. Since the actual crystal will have some residual conductivity caused by some sort of lattice defects or by some s-, p- band electrons, these values may be considered to give the observed anisotropy in the conductivity qualitatively.

For the range $T_\alpha<T<T_N$, the spins align in c-plane, or easy magnetization axis lies in perpendicular to the c-axis. As marked in Fig. 5, the conductivity is not affected by the spin direction but intimately correlated with the exchange energy. In fact, it was impossible to evaluate the ratio σ_a/σ_c which agrees with the measured ratio of $\sigma_a/\sigma_c=1.5$, when the sublattices were chosen to be parallel with c-plane. It was considered that the sublattice would change its structure owing to the decrease of A at T_α. Hence it was attempted to find the types of sublattice which could be considered to be consistent with the experimental susceptibility results. Among these sublattices, the one which is able to explain the anisotropy and anomaly of the conductivity is shown in Fig. 7. The sublattice planes in this type incline to the c-axis by about 45° (more exactly 44.5°). In this type, the conductivity along the sublattice plane is $\sigma_{//}$, and $\sigma_\perp$ is the conductivity perpendicualr to the sublattice plane. Considering the experimental results[1)] that the rotationary measurements for the susceptibility around c-axis have shown no anisotropy in this temperature region, the crystal will be assumed to consist of three groups of domains, each domain will have the structure in Fig. 7 and will be disposed keeping angle of 120° with other domains. This domain structure will be designated as "Y-structure" for the sake of brevity.

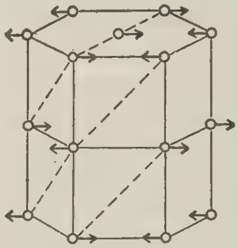

Fig. 7. Magnetic spin sublattice structure proposed in the temperature region between Γ_α and T_N. Circles are iron ions, neglecting sulfur ions for simplicity.

The conductivity along the c-axis may be

$$\sigma_c=\sigma_{//}\cos^2 45°+\sigma_\perp \sin^2 45°=(1/2)(\sigma_{//}+\sigma_\perp)\ .$$

At 420°K, just above T_α, $J=k\cdot 750°\mathrm{K}$ from Fig. 6, so

$$\sigma_c=(1/2)(1/6+1)\sigma_{//}=(7/12)\sigma_{//}\ .$$

At 593°K, the Néel point, $J=593°\mathrm{K}\times k$,

$$\sigma_c=(1/2)(1/2.7+1)\sigma_{//}=(3.7/5.4)\times\sigma_{//}\ .$$

The conductivity along the direction perpendicular to the c-axis may be calculated by Eq. (B, 4) in Appendix. It is

$$\begin{aligned}\sigma_a&=(1/4)(3\sigma_{//}+\sigma_\perp)\\&=(1/4)(3+1/6)\sigma_{//}=(19/24)\sigma_{//} &&\text{at } 420°\mathrm{K}\ ,\\&=(1/4)(3+1/2.7)\sigma_{//}=(91/108)\sigma_{//} &&\text{at } 593°\mathrm{K}\ .\end{aligned}$$

The ratio

$$\begin{aligned}\sigma_a/\sigma_c&\simeq 1.36 \quad \text{at } 420°\mathrm{K}\ ,\\&\simeq 1.23 \quad \text{at } 593°\mathrm{K}\ .\end{aligned}$$

These estimated values agree qualitatively with the experimental value $\sigma_a/\sigma_c=1.5$.

Recently, Hihara et al[7)] have reported the experimental results for the susceptibility and the conductivity of sulfur excess sample FeS_x, $\chi=1.05\sim 1.09$. They found that, in these samples the A and K independently changed at different temperatures. For example, the

K changed its sign at $-20°$C, and the A changed its value at 110°C owing to lattice parameter (c/a) change, for the sample $FeS_{1.05}$. They also have observed that the conductivity changes with A, and does not change at the temperature where K changes its sign.

Their results may be qualitatively explained by our model as follows. For FeS_x ($x=1.05 \sim 1.09$), the sublattice structure will change at T_α from " Y-structure " of the high temperature type to the simple sublattice structure of low temperature one, so that conductivity will be largely affected as expected. At the T_a', the temperature at which K changes its sign, the simple sublattice will be kept unchanged, and only the axis of easy magnetization changes its direction so that the $\chi_{\parallel}$ and $\chi_{\perp}$ interchange mutually their roles, however the conductivity will not be affected approximately by the spin flipping.

Finally the writer wishes to express his thanks to Prof. E. Hirahara for continuous guidance and helpful discussions given during this work.

Appendix

A. Formulas for the susceptibilities

In the simple theory of antiferromagnetism, the susceptibilities[8)] $\chi_{\perp}$ and $\chi_{\parallel}$ are

$$\chi_{\perp}=1/A \qquad (A, 1)$$

$$\chi_{\parallel}=\frac{3SB_s'(y_0)}{S+1}C\Big/\left[T+\frac{1}{2}(A+\Gamma)C\frac{3SB_s'(y_0)}{S+1}\right], \qquad (A, 2)$$

and the Néel temperature T_N is expressed as

$$T_N=(A-\Gamma)\ C/2\ . \qquad (A, 3)$$

The notations used in these formulas are same as in the reference. From the formulas (A, 1), (A, 2) and (A, 3)

$$\frac{1}{\chi_{\parallel}}=\frac{S+1}{3SC}\frac{T}{B_s'(y_0)}+A-\frac{T_N}{C}\ , \qquad (A, 4)$$

is obtained.

B. Calculation of the conductivity

If the $x'\,y'$-plane is chosen in a plane of one sublattice plane of the " Y-structvre ", and then the z'-axis is chosen in perpendicular to the plane, the conductivities along the x'-, y'- and z'-axis, respectively, are $\sigma_{\parallel}$, $\sigma_{\parallel}$ and $\sigma_{\perp}$. An electric field vector $\boldsymbol{E}$, and a current vector $\boldsymbol{I}$ are connected by a tensor $\boldsymbol{\sigma}$ as follows,

$$\boldsymbol{I}=\boldsymbol{\sigma}\cdot\boldsymbol{E}\ , \qquad \boldsymbol{\sigma}=\begin{pmatrix}\sigma_{\parallel} & 0 & 0\\ 0 & \sigma_{\parallel} & 0\\ 0 & 0 & \sigma_{\perp}\end{pmatrix}. \qquad (B, 1)$$

When the $x'\ y'\ z'$-system is rotated around x'-axis in 45°, and z'-axis coincide with the z-axis which is parallel to the c-axis of crystal, the $\boldsymbol{\sigma}$ is represented in the $x\ y\ z$-system as

$$\boldsymbol{\sigma}_{(xyz)}=\begin{pmatrix}1 & 0 & 0\\ 0 & 1/\sqrt{2} & -1/\sqrt{2}\\ 0 & 1/\sqrt{2} & 1/\sqrt{2}\end{pmatrix}\begin{pmatrix}\sigma_{\parallel} & 0 & 0\\ 0 & \sigma_{\parallel} & 0\\ 0 & 0 & 0_{\pm}\end{pmatrix}$$

$$\times\begin{pmatrix}1 & 0 & 0\\ 0 & 1/\sqrt{2} & 1/\sqrt{1}\\ 0 & -1/\sqrt{2} & 1/\sqrt{2}\end{pmatrix}$$

$$=\begin{pmatrix}\sigma_{\parallel} & 0 & 0\\ 0 & \frac{1}{2}(\sigma_{\parallel}+\sigma_{\pm}) & \frac{1}{2}(\sigma_{\parallel}-\sigma_{\perp})\\ 0 & \frac{1}{2}(\sigma_{\parallel}-\sigma_{\pm}) & \frac{1}{2}(\sigma_{\parallel}+\sigma_{\perp})\end{pmatrix}. \qquad (B, 2)$$

The conductivity σ_c along the z-axis is

$$\sigma_c=I_z/E_z=(1/2)(\sigma_{\parallel}+\sigma_{\pm})\ , \qquad (B, 3)$$

To calculate the conductivity perpendicular to the c-axis, it is necessary to take an average over the three sorts of domains distributed in every 120° around the c-axis. The tensor $\boldsymbol{\sigma}_{(xyz)}$ is transformed by rotation of φ around the c-axis to

$$\boldsymbol{\sigma}_{(\varphi}=\begin{pmatrix}\cos\varphi & \sin\varphi & 0\\ -\sin\varphi & \cos\varphi & 0\\ 0 & 0 & 1\end{pmatrix}\cdot\boldsymbol{\sigma}_{(xyz)}\cdot\begin{pmatrix}\cos\varphi & -\sin\varphi & 0\\ \sin\varphi & \cos\varphi & 0\\ 0 & 0 & 1\end{pmatrix}$$

$$=\begin{pmatrix}\sigma_{\parallel}\cos^2\varphi+\frac{1}{2}(\sigma_{\parallel}+\sigma_{\perp})\sin^2\varphi\ , & -\sigma_{\parallel}\sin\varphi\cos\varphi+\frac{1}{2}(\sigma_{\parallel}+\sigma_{\perp})\sin\varphi\cos\varphi\ , & \frac{1}{2}(\sigma_{\parallel}-\sigma_{\perp})\sin\varphi\\ -\sigma_{\parallel}\sin\varphi\cdot\cos\varphi+\frac{1}{2}(\sigma_{\parallel}+\sigma_{\perp}(\sin\varphi\cos\varphi\ , & \sigma_{\parallel}\sin^2\varphi+\frac{1}{2}(\sigma_{\parallel}+\sigma_{\perp})\cos^2\varphi\ , & \frac{1}{2}(\sigma_{\parallel}-\sigma_{\parallel})\cos\varphi\\ \frac{1}{2}(\sigma_{\parallel}-\sigma_{\perp})\sin\varphi\ , & \frac{1}{2}((\sigma_{\parallel}-\sigma_{\perp})\cos\varphi\ , & \frac{1}{2}(\sigma_{\parallel}+\sigma_{\perp})\end{pmatrix}.$$

The conductivity σ_a will be calculated taking average for φ over the three directions $\varphi+0°$, $\varphi+120°$ and $\varphi+240°$, and it will be, independently of φ,

$$\sigma_a=(1/3)\{\sigma_{\parallel}\cos^2\varphi+(1/2)(\sigma_{\parallel}+\sigma_{\perp})\sin^2\varphi+\sigma_{\parallel}\cos^2(\varphi+120°)+(1/2)(\sigma_{\parallel}+\sigma_{\perp})\sin^2(\varphi+120°)$$
$$+\sigma_{\parallel}\cos^2(\varphi+240°)+(1/2)(\sigma_{\parallel}+\sigma_{\perp})\sin^2(\varphi+240°)\}=(1/4)(3\sigma_{\parallel}+\sigma_{\perp})\ . \qquad (B, 4)$$

References

1) E. Hirahara and M. Murakami: J. Phys. Chem. Solids, **7** (1958), 281.
2) M. Murakami and E. Hirahara: J. Phys. Soc. Japan **13** (1958), 1407.
3) M. Murakami: Scie. Rep. Tōhoku Univ. Series 1, **43** (1959), 53.
4) R. Ueda, T. Ichinokawa and T. Mitsui: Busseiron Kenkyu, **33** (1950), 55.
5) S. Fujime, M. Murakami and E. Hirahara: J. Phys. Soc. Japan, **16** (1961), 183.
6) M. Murakami: Sci. Rep. Tohoku Univ. Series 1, **43** (1959), 62. **16** (1961), .
7) T. Hihara, T. Kamigaichi and K. Masumoto: Lecture on the Anual Meeting of Physical Society of Japan, April, 1960.
8) T. Nagamiya, K. Yosida and R. Kubo: Advance in Physics, **4** (1955), 31.

JOURNAL OF THE PHYSICAL SOCIETY OF JAPAN, Vol. 16, No. 2, FEBRUARY, 1961

Heat Treatment Centers in Silicon

By Yasuo MATUKURA*

Electrotechnical Laboratory, Tokyo, Japan

(Received September 7, 1960)

Heat treatment of p-type silicon at temperatures above 900°C frequently results in a decrease of hole concentration. In the present experiments, heat treatment centers have been found to diffuse from the surface during such heat treatments in the case of sufficient concentration to account for the observed changes in the electrical characteristics. The heat treatment center has a deep donor level at 0.4 eV above the valence hand. This level is converted into a donor level 0.51 eV from the conduction band at room temperature. Heat treatment centers may perhaps be introduced into silicon by surface impurity. Diffusion of the surface impurity is classified by its speed into two species. Faster diffusing one is characterized by the diffusion coefficient of 1×10^{-5} cm²/sec at 1017°C and the activation energy for the solution, 1.8 eV. Observed properties on the heat treatment center show that heat treatment in the temperature range 900 to 1265°C results in diffusion of iron from the surface into bulk material.

§1. Introduction

Recently, the growth of silicon single crystals having long lifetime of minority carrier has become possible. However, in subsequent heat treatments to temperatures above 1000°C, the lifetime is frequently degraded.[1-4] The degradation of lifetime is sometimes accompanied by the decrease of hole concentration in p-type silicon, resulting in an increase of resistivity. G. Bemski[1] has reported that these phenomena have been caused by the formation of heat treatment centers at high temperatures, and that these centers are gold. Gold in silicon has an acceptor level at 0.54 eV below the conduction band and a donor level at 0.35 eV above the valece band.[5] By our preliminary experiments, it was seen that heat treated silicons had some donor levels. Neither this discrepancy has yet been made clear, nor the details for the formation of the heat treatment centers.

In the present work, observations are made on the diffusion of heat treatment centers from the surface of specimen and the temperature dependencies of Hall coefficient and resistivity of p-type crystals treated at high temperature. The results show that the heat treatment centers have some donor levels, and that these donors are introduced by diffusion from the surface with the diffusion coefficient of about or over 10^{-5} cm²/sec and precipitate in lattice defect by slow cooling from high temperatures. It seems that these heat treatment centers are originated from some surface impurities, one of which is probably iron atoms.

---

* Present address: Nippon Electric Co. Ltd., Semiconductor division, Kawasaki, Japan.

§ 2. Experimental

The electrical effects in heat treated silicon are studied by standard techniques. The changes in carrier density at room temperature are obtained from resistivity measurements by four point probe method. The energy level of heat treatment centers is obtained from Hall coefficient and resistivity measurements as a function of temperature by using vibrating reed electrometer.

Both pulled and floating zone refined *p*-type crystals are studied, and their resistivities are lying in the range of 10 to 1000 Ω cm at room temperature. For reducing some donors originated from oxygen, pulled crystals are heated for 5 hours at 1050°C and then cooled at the rate of 2°C/min. After cutting, samples are rinsed in a mixture of HNO_3 and HF and then in deionized water by an ultra-sonic machine. Heat treatments of the samples are performed at the temperature range of 900 to 1265°C in quartz tube using argon as a gas ambient.

§ 3. Results

When *p*-type silicon is heated at the temperature above 900°C and quenched, the concentration of hole is reduced to about 10^{14} cm^{-3} and its resistivity becomes high. By a long period treating at high temperature, *p*-type specimens are converted sometimes to the *n*-type of high resistivity indicating that the heat treatment center may act like a donor impurity. While high purity *n*-type silicon is heated at high temperatures and quenched, no change in resistivity or Hall coefficient are not observed. Thus there does not appear more than 10^{13} cm^{-3} of acceptor levels for the heat treatment centers.

Concentrations of the heat treatment center greater or smaller than the initial hole concentration are obtained by treating high purity *p*-type silicon at high temperatures and quenching. On these specimens, Hall coefficient and resistivity are measured as a function of temperature. Fig. 1 shows the typical temperature variations of Hall coefficient. Curve 1 is obtained on an untreated *p*-type specimen. Curve 2 is obtained on a sample treated at 1050°C for 5 hours, whose initial acceptor concentration is 1×10^{14} cm^{-3}, and the slope gives the activation energy of 0.2 eV. Curve 3 is got on another one treated at 1250°C for 5 hours, indicating the activation energy of 0.43 eV. The initial acceptor concentration is equal to the specimen of curve 1. From *p*- to *n*-type conversion is found on a sample which was heated at 1265°C for 2 hours and then kept at room temperature for 4 weeks, shown as curve 4, indicating the activation energy of 0.51 eV. Changes in type were not observed immediately after high temperature treatment but found to occure after 4 weeks. In general, it is seen that the specimen having the higher resistivity after a heat treatment has a tendency to show the larger slope on the Hall coefficient vs the inverse temperature curve. It seems that the decrease of hole concentration may result from the heat treatment center having deep

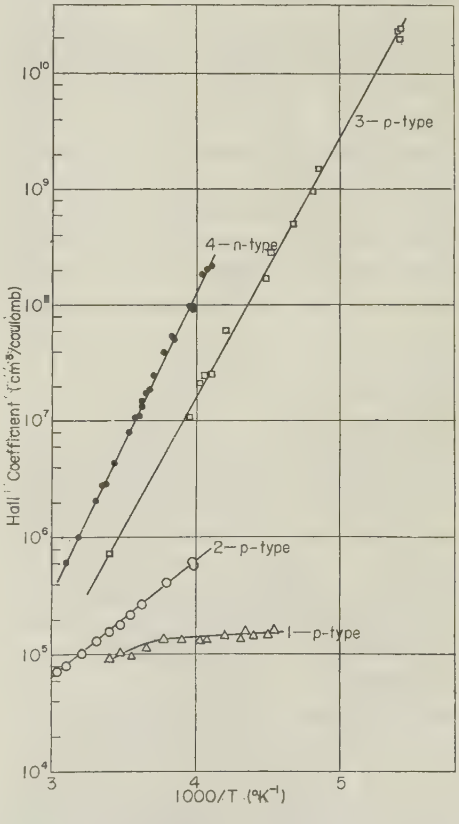

Fig. 1. Hall coefficient *vs* reciprocal temperature for heat treated *p*-type samples.

donor levels above the valence band, and that these centers are nearly ionized at room temperature.

As shown in Fig. 1, the treated *p*-type specimen are converted into *n*-type after about a month at room temperature. However, this conversion does not always take place in heat treated silicon. The specimens in which a large number of heat treatment centers were introduced have a tendency of this conversion.

Since the heat treatment center has deep donor levels lying near the center of forbidden gap, it is henceforth assumed in this work that that the change in hole concentration by heat treatment above 1000°C is a measure of the induced centers.

In order to make clear the mechanism on the formation of the heat treatment center, some experiments were performed. Pulled and floating zone refined *p*-type crystals are cut into rectangular specimens having different surface-to-volume ratios. These specimens are simultaneously heated for 5 hours at 1050°C and then cooled at the rate of 5°C/min. After removing the surface region, the changes of resistivity are measured. Successive lapping of the surface layer shows that the heat treatment centers distribute uniformly in the specimen. The variation of the concentration of formed heat treatment center with the surface-to-volume ratio is shown in Fig. 2. It is seen that the concentration of the heat treatment center increases linearly with the increasing surface-to-volume ratio. Therefore, it seems that the heat treatment centers are not resulted from the bulk properties such as oxygen atoms and quenched-in dislocations but from the surface impurities with high diffusion rate. If the heat treatment centers are resulted from the quenched-in vacancied or some impurities contained in the bulk silicon, it seems that the concentration of heat treatment center does not depend on the surface-to-volume ratio of the treated specimens. This result will predict that the heat treatment centers are formed by diffusion process from the surface into the bulk.

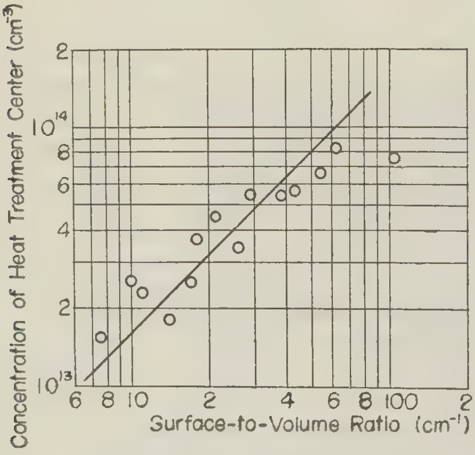

Fig. 2. Concentration of introduced heat treatment center *vs* surface-to-volume ratio of *p*-type sample at 1050°C.

As it is expected for the surface impurities to have a high diffusion rate, *p*-type specimens with the thickness of about 4 mm are used to measure the diffusion constant of these impurities. The specimens are heated for 1 hour at 1017°C and qunenched at the rate of about 800°C/min. Resistivity is measured as a function of the depth from the surface, and the penetration of the surface impurities into the specimen is estimated from the decreased hole density. The distribution of the diffused impurities with the depth from the surface is shown in Fig. 3, where solid line is calculated value obtained by assuming error function for diffusion process and diffusion coefficient $=1\times10^{-5}$ cm²/sec. It is seen that the penetration of the surface impurities nearly agrees with the calculated one. It is noticed that the surface impurities diffuse with large diffusion coefficient such as 1×15^{-5} cm²/sec, and that as shown in Fig. 3 the concentration of heat treatment center near the surface is larger than that in the interior where the diffused centers have a plateau distribution.

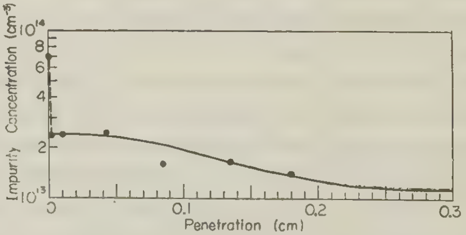

Fig. 3. Penetration curve of surface impurity at 1017°C.

Similar experiments were also performed at 1106°C, and it was seen that the diffusion coefficient at its temperature was greater than 1×10^{-5} cm²/sec. The distribution of the duffused centers shown in Fig. 3 indicates that two species of diffused centers may be present:

a more slowly diffusing species for the shallow penetration with a high surface concentration and a faster diffusing species for the deep penetration.

On the faster diffusing species, the diffusion coefficient is extremely large at the temperatures above 1000°C such as $1\times10^{-5}\,\mathrm{cm^2/sec}$ or more. Therefore, it seems that the diffused impurity in thin specimens distributes uniformly for about 60 min. Then, the plateau in the curve for 1017°C in Fig. 3 measures the surface concentration of a faster diffusing species. Fig. 4 shows the variation of heat treatment center density with the temperature at which the specimens were treated. The specimens of 1 mm thickness with the resistivity of 10 to 200 Ω cm are heated for 2 hours at the temperature range of 1000 to 1265°C and then quenched. The changes of resistivity are measured at 50 μ below the surface, and the diffused center density is obtained. As shown in Fig. 4, the logarithm of the diffused center density varies linearly with the reciprocal of the treating temperature, showing the slope of about 1.8 eV.

It is experienced that the decrease in hole density by heat treatment at high temperatures is larger in the center of pulled crystals than at the edge[3]. Similar results are also obtained in present work. Specimens of 1 mm thickness are prepared by slicing perpendicularly to the pulled axis of crystal. After heating at 1060 and 1200°C, the changes in resistivity are measured along the diameter. Fig. 5 shows the variations of the concentration of heat treatment center along the diameter. It is seen that the concentrations of the diffused center at the edge of the slices are less than those at the center where dislocation density is expected to be small. On the other hand, the concentration of the diffused center depends on the rate at which the specimens are cooled from high temperatures. For example, after the specimens of 200 Ω cm resistivity were heated for 1 hour at 1050°C, the specimens were cooled at the rate of 2°C/min from the treating temperature to 500°C and then rapidly to room temperature. Results obtained from the resistivity measurements show that the diffused centers are nearly zero in the slowly cooled specimens.

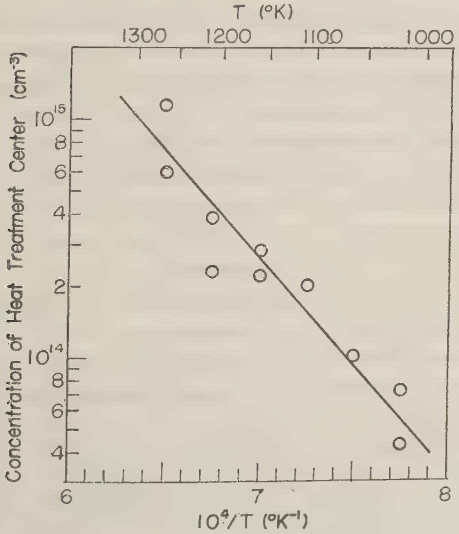

Fig. 4. Solubility of a faster diffusing species *vs* reciprocal temperature.

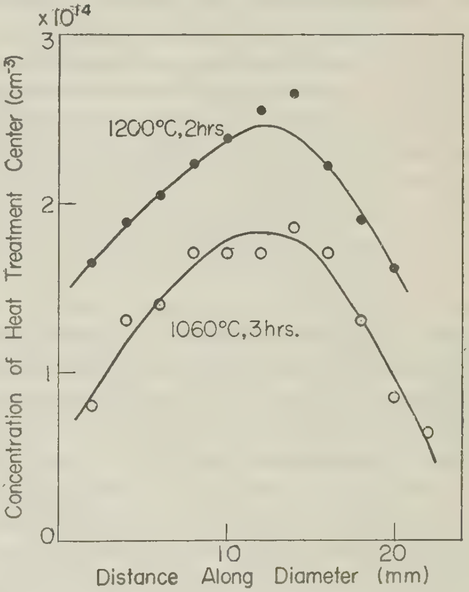

Fig. 5. Concentration of introduced heat treatment center as a function of the distance along the diameter.

§ 4. Discussion

G. Bemski[1] has pointed out that the concentration of carrier in both p- and n-type silicon decreases by heating at high temperatures, and that these decreases result from the introduction of gold as a heat treatment center which has both donor and acceptor levels in silicon. In this work, while the hole density in p-type silicon decreases by the heat treatment at high temperatures, the heat treatment on high resistivity n-type silicon shows no changes in resistivity except the decrease of donor density due to the annihilation of oxygen[6]. Reduction of the hole density in p-type silicon may be explained by an assumption that the heat treatment does not introduce into silicon any deep acceptor levels, but some donor levels. In the elements investigated so far in silicon, the element which has two deep donor levels is only iron, of which the donor levels lie at 0.40 eV above the valence band and at 0.55 eV below the conduction band.[7] If it is permited to assume that one of the impurities of the heat treatment centers is originated from iron, the results obtained in preceeding section may be nearly explained. In Fig. 1, the activation energies 0.43 and 0.51 eV obtained from curve 3 and 4, respectively, are nearly in agreement with the values on iron, but the value obtained from curve 2 is very small compared with 0.40 eV. This discrepancy may be understood as follows: when the amount of the introduced heat treatment centers is small in comparison with the hole density in the initial p-type specimen, the Fermi level will be located below the deep donor level for such centers.

Since the concentration of heat treatment center is proportional to the surface-to-volue ratio, it may be reasonable to assume that the heat treatment centers are originated from the impurities on the surface of specimen. These impurities have a large diffusion constant such as 1×10^{-5} cm²/sec at 1017°C. In the elements investigated so far in silicon, the elements which have such a large diffusion constant are Li, Cu, Au, Zn, Fe,[8] and Ni[9]. Since the heat treatment centers will not have any acceptor levels, it seems that the above mentioned elements are not probable except iron as the impurity of the heat treatment center. The diffusion constant of iron which has been measured by C. B. Collins[7] is 5×10^{-6} cm²/sec at 1000 to 1115°C. It may be noticed that the diffusion constant of iron shows also the good aggreement with the value obtained for the heat treatment centers. As shown in Fig. 4, the activation energy of the surface concentration is about 1.8 eV and much smaller in comparison with the value obtained from the data of C. B. Collins for iron.[7] It seems that this discrepancy may be probably due to the difference in the degree of crystal defect, for the properties of the heat treatment center are very structure sensitive as shown in Fig. 5. The initial surface concentration of the impurity may be roughly estimated from the faster diffusing species as follows; in Fig. 2, the number of diffused center per unit surface-to-volume ratio is about 1.5×10^{12} cm^{-2} at 1050°C. It will be resonable to consider that these amount of the impurities can be supplied on the surface of silicon during the etching process or from argon as a gas ambient.

Heat treatment centers are not observed in the specimens which are cooled slowly from high temperatures. This result is suggestive of the precipitation of the impurity. It seems that the heat treatment centers diffused at high temperature precipitate or aggregate in the site, such as dislocations, having a low potential energy in the course of cooling. This mechanism will agree with the results shown in Fig. 5 that the reduction of hole concentration by heat treatment increases at the center of the slice where the dislocation density is small compared with that at the edge.

It is known that some concentrations of heat treatment center in silicon have a deleterious effect on the lifetime of minority carriers.[1-3] For iron in silicon, the recombination cross section for holes, A, is 3×10^{-16} cm² and for electrons, A_n, is greater than 1.5×10^{-15} cm².[7] In consideration of the diffusion mechanism, energy levels, and recombination properties on the heat treatment centers, it will be reasonable to consider that one of the impurities from which the heat treatment centers in this work originate is probably iron atoms.

The author wishes to thanks Dr. T. Momota for his continual encouragement, and Dr. M. Shibuya for helpfull discussions.

References

1) G. Bemski and J. D. Struthers, J. Electrochemical Soc. **105** (1958) 588.
2) H. C. Theuerer, J. M. Whelan, H. E. Bridgers, and E. Buehler, J. Electrochemical Soc. **104** (1957) 721.
3) Y. Matukura, J. Phys. Soc. Japan, **14** (1959) 918.
4) D. J. Sandiford, J. Appl. Phys. **30** (1959) 1981.
5) C. B. Collins, R. D. Carlson, and C. J. Gallagher, Phys. Rev. **105** (1957) 1168.
6) W. Kaiser, H. L. Frisch, and H. Reiss, Phys.

Rev. **112** (1958) 1546.
7) C. B. Collins and R. D. Carlson, Phys. Rev. **108** (1957) 1409.
8) N. B. Hannay: Semiconductors (Reinhold Publishing Co., New York, 1959) 244p.
9) Y. Matukura and J. Oda, to be published.

JOURNAL OF THE PHYSICAL SOCIETY OF JAPAN, Vol. 16, No. 2, FEBRUARY, 1961

On the Energy of the Interstitial Atom in Graphite

By Tadao IWATA, F.Eiichi FUJITA and Hideji SUZUKI

Japan Atomic Energy Research Institute
Tōkai-mura, Ibaraki-ken

(Received September 16, 1960)

Self- and migration energies associated with interstitial carbon and xenon atoms in graphite are calculated, taking account of the relaxation around the interstitials. Assuming that the graphite lattice consists of thin elastic plates held together by the weak interaction forces and subjected to the transverse force by the interstitial atom, the strain form is obtained by solving the equations for the bending plates. Then, employing a suitably chosen interaction potential between the interstitial and all other atoms, the relaxation and the energies associated with the interstitials are calculated. In case of the carbon atom, the self-energy is 2.5 ev, the migration energy 0.016 ev and the ratio of strain energy to the total self-energy 0.49, and in case of xenon, they are 15.1 ev, 0.03 ev and 0.79 respectively.

§ 1. Introduction

Lattice defects in graphite have been investigated since the development on the first nuclear reactor[1]. Dienes[2] was the first to study the mechanism for self-diffusion in graphite using a simple but pertinent theory: He estimated the energies associated with vacancy, interstitial and direct interchange of atoms, and concluded from these values that either of the vacancy mechanism and the interstitial mechanism may be not always favourable for self-diffusion as compared with the direct interchange. The experiment on the diffusion of carbon stoms in natural graphite was done by Kanter[3], and it was found that the diffusion process can be expressed by $D=40f^2\exp(-163000/RT)$ where f is a constant depending on the crystal shape. He compared this experimental value of activation energy for self-diffusion with the theoretical values obtained by Dienes and revised by him, but didn't find what mechanism actually takes place in self-diffusion in graphite because of the discrepancies between the experimental and theoretical values. It should be noted that the above investigators took no account of the relaxation of atoms around the point defects in their calculations, which would substantially change the above theoretical values.

On the other hand, recent development in the radiation damage experiments seems to emphasize the importance of migration and self-energies of vacancies and interstitials formed by the incident high energy particles[4,5]. Although there are few fundamental irradiation experiments on graphite, it is possible to predict rough values for the energies of the defects; for instance, the self-energies of vacancy and interstitial are probably several electron volts (presumably 3~8 ev), the migration energy of vacancy a few electron volts (3~4 ev), and the migration energy of interstitial very low (of the order 0.1 ev). Actually, Dienes[2] estimated the migration energy of vacancy as 3.1 ev, which seems to be fairly reasonable. However, all other kinds of energies associated with the defects appear to remain not accurately calculated. Therefore, it is quite necessary to do more such calculations using appropriate theoretical methods as well as to do more fundamental experiments.

Another problem concerning the radiation effects on graphite arise from a new development of the nuclear reator; that is the diffusion of fission products such as xenon atoms in graphite. Xenon atoms produced by fission of uranium will migrate in graphite in such a fuel element as the "semi-homogeneous", and their diffusibility sometimes could determine the fundamental design of the reactor. This problem may be treated by a theory similar to that of the migration of the carbon interstitial atoms.

In this paper, we report on the migration and self-energies of the interstitial atoms of carbon and xenon in graphite. It is well known that graphite has a layer structure of hexagonal planes weakly held together by van der Waals forces. The bonds within the planes are very strong covalent bonds, the length of which is 1.42 Å. The inter-layer distance, in which the weak van der Waals interaction is taking place, is 3.35 Å. Accordingly, it may be reasonable to assume the graphite crystal lattice to be a system of thin elastic plates separated at a constant distance by the very weak interaction forces, so far as the lattice can be treated by the elasticity theory.

§ 2. Relaxation of Lattice around an Interstitial Atom

2.1 *Strain form in the layer structure*

There arise two kinds of extra energy increases when an interstitial atom is put into the graphite lattice; namely, (1) the strain energy arising from the change of atomic distances and bond angles as a result of bending of the hexagonal layers around the interstitial, and (2) the interaction energy between the interstitial atom and all other atoms in the crystal lattice. We can treat the former elastically without taking account of the detailed crystal structure. As mentioned before, this treatment is suggested from the layer structure of graphite, and, in fact, had a good success in the interpretation of the specific heat of graphite[6,7]. The latter energy will be obtained if the interaction potential between atoms is suitably chosen and also the strain form of the bent layers is determined, as will be mentioned later.

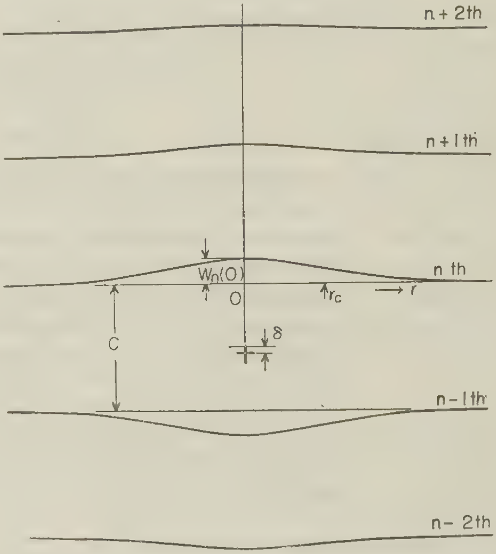

Fig. 1. Relaxation of the graphite lattice around an interstitial.

In this section, we determine the strain form by making the sum of both energy increases minimum. Formally, the latter interaction is introduced as the distribution load on each layer, its strength and distribution form being taken as two parameters in the calculation. The distribution of the load is undoubtedly co-axial as shown in Fig. 1. Therefore, we have the elastic strain energy associated with an interstitial in the form

$$V=\int_0^\infty \sum_{m=-\infty}^{\infty}\left[\frac{1}{2}c\rho\kappa^2\{\nabla^2 w_m(r)\}^2+\frac{1}{2}c\rho\mu^2\{w_{m+1}(r)-w_m(r)\}^2\right]2\pi r dr\,. \tag{1}$$

Here $w_m(r)$ represents the transverse displacement of the m-th layer at a radius r, the displacement parallel to the layer being neglected. c is the distance between the adjacent layers and ρ the volume density. κ^2 and μ^2, each multiplied by $c\rho$, are the bending elastic constant and the Hook's force constant between the neighbouring layers respectively. The first term in the bracket represents the elastic energy in the bent plates, and the second term the interaction energy increase between the neighbouring layers.

We introduce a distribution load $c\rho F_m(r)$ and use the D'Alembert's principle

$$\delta V-\int_0^\infty \sum_{m=-\infty}^{\infty} c\rho F_m(r)\cdot\delta w_m(r)\cdot 2\pi r dr=0 ,$$

in order to find the equations to determine the strain form. Putting the boundary condition that $w_m(r)$ becomes zero as $r\to\infty$, the equation for the strain form of the n-th layer per unit area is obtained[8];

$$-\kappa^2\cdot\nabla^4 w_n(r)+\mu^2\{w_{n+1}(r)+w_{n-1}(r)-2w_n(r)\}=-F_n(r) , \tag{2}$$

where

$$\nabla^2=\frac{d^2}{dr^2}+\frac{1}{r}\frac{d}{dr} .$$

To solve Eq. (2), we assume as following, provided that the interstitial is between the n-th and $(n-1)$-th layer;

$$w_{n-1}(r)=-w_n(r) , \qquad w_{n+1}(r)=\alpha\cdot w_n(r) , \qquad 0\leq\alpha\leq 1 . \tag{3}$$

The former assumption may be quite reasonable as an approximation, unless the crystal structure around the interstitial site is precisely taken into account. The latter assumption is also permissible if $w_m(r)\ll c$ and the region of strain is comparatively small. Thus, the equation to be solved under the above boundary condition is

$$(\nabla^4+h^4)w_n(r)=f_n(r): \quad h=\sqrt[4]{3-\alpha}\cdot\sqrt[2]{\mu/\kappa} , \qquad f_n(r)=F_n(r)/\kappa^2 . \tag{4}$$

To obtain the solution, first we find a Green function $G(r, \xi)$ that is the solution of the equation

$$(\nabla^4+h^4)G(r, \xi)=\frac{\delta(r-\xi)}{2\pi r} \tag{5}$$

and satisfying the boundary condition[9]. The physical meaning of $G(r, \xi)$ is the displacement of the layer at any radius r due to the unit load on the circle of $r=\xi$. By means of the Bessel function representation of δ-function, we have

$$G(r, \xi)=\begin{cases}\dfrac{1}{8h^2}[J_0(\sqrt{i}\,h\xi)\cdot H_0^{(1)}(\sqrt{i}\,hr)-J_0(\sqrt{-i}\,h\xi)\cdot H_0^{(1)}(\sqrt{-i}\,hr)] , & (r>\xi)\\[2ex] \dfrac{1}{8h^2}[J_0(\sqrt{i}\,hr)\cdot H_0^{(1)}(\sqrt{i}\,h\xi)-J_0(\sqrt{-i}\,hr)\cdot H_0^{(1)}(\sqrt{-i}\,h\xi)] , & (r<\xi)\end{cases} \tag{6}$$

where J_0 and $H_0^{(1)}$ are respectively the first and the third kind of Bessel function (Appendix). Thus we can obtain the solution of Eq. (4) by the integration,

$$w_n(r)=\int_0^\infty G(r, \xi)f_n(\xi)2\pi\xi d\xi . \tag{7}$$

By the direct differentiation, it is also possible to verify that Eq. (7) is the solution of Eq. (4). The right hand side of Eq. (7) and therefore Eq. (1) can be obtained analytically, if we assume a step function for $f_n(r)$, that is

$$f_n(r)=\begin{cases}\text{const}: & (0\leq r\leq r_c)\\ 0 \ : & (r_c\leq r) .\end{cases} \tag{8}$$

Then we have

$$\frac{w_n(r)}{w_n(0)}=\begin{cases}\dfrac{1}{C_n}\Big\{1+\dfrac{1}{2}\dfrac{\pi i}{2}\sqrt{i}\,hr_c\cdot H_0'^{(1)}(\sqrt{i}\,hr_c)\cdot J_0(\sqrt{i}\,hr) \\ \qquad +\dfrac{1}{2}\dfrac{\pi i}{2}\sqrt{-i}\,hr_c\cdot H_0'^{(1)}(\sqrt{-i}\,hr_c)\cdot J_0(\sqrt{-i}\,hr)\Big\} & (0\leq r\leq r_c) ,\\[2ex] \dfrac{1}{C_n}\Big\{\dfrac{1}{2}\sqrt{i}\,hr_c\cdot J_0'(\sqrt{i}\,hr_c)\cdot\dfrac{\pi i}{2}H_0^{(1)}(\sqrt{i}\,hr) \\ \qquad +\dfrac{1}{2}\sqrt{-i}\,hr_c\cdot J_0'(\sqrt{-i}\,hr_c)\cdot\dfrac{\pi i}{2}H_0^{(1)}(\sqrt{-i}\,hr)\Big\} & (r_c\leq r) ,\end{cases} \tag{9}$$

$$C_n=\Re\left\{1+\frac{\pi i}{2}\sqrt{i}\,hr_c\cdot H_0'^{(1)}(\sqrt{i}\,hr_c)\right\} ,$$

where $w_n(0)$ is the displacement at $r=0$ of the n-th layer, which is also the maximum value of $w_n(r)$. In spite of the seemingly rough assumption of Eq. (8), the real situation of the lattice strain can be approached by the variation of the parameters, $w_n(0)$ and r_c.

Komatsu and Nagamiya[6] derived the value of μ from data of the force constants between the carbon atoms of benzen molecule and of the compressibility of graphite measured by Bridgeman. Further, they determined κ by fitting their calculated specific heat curve to the observed ones. The results they obtained are; $\mu=1.17\times10^{13}\,\text{sec}^{-1}$ and $\kappa=0.611\times10^{-2}\,\text{cm}^2/\text{sec}$. As will be shown later, α is about 0.30, and h scarcely varies with the change of α. Therefore, we put h as a constant, 0.30 in atomic units.

2.2 *Expression of strain energy in terms of $w_n(r)$*

As mentioned before, the strain energy can be regarded as consisting of the intralayer and the interlayer strain energy, which are represented by the first and the second term in Eq. (1) respectively. Now, extending the assumption of Eq. (3), we assume that the strain form of each layer is similar and has the opposite directions on the upper and lower sides of the interstitial atom. That is,

$$\cdots=\frac{w_{n+2}(r)}{w_{n+2}(0)}=\frac{w_{n+1}(r)}{w_{n+1}(0)}=\frac{w_n(r)}{w_n(0)}=\cdots ,$$

$$w_{n+k}(r)=-w_{n-1-k}(r) . \tag{10}$$

Then, putting

$$\left.\begin{aligned}
&\int_0^\infty\left\{\nabla^2\left(\frac{w_n(r)}{w_n(0)}\right)\right\}^2\cdot 2\pi r dr=2\pi S_1 ,\\
&\int_0^\infty\left(\frac{w_n(r)}{w_n(0)}\right)^2\cdot 2\pi r dr=2\pi S_2 ,
\end{aligned}\right\} \tag{11}$$

we have

$$\begin{aligned}
V=&\frac{1}{2}c\rho\kappa^2\cdot 2\pi S_1\{2w_n^2(0)+2w^2_{n+1}(0)+2w^2_{n+2}(0)+\cdots\}\\
&+\frac{1}{2}c\rho\mu^2\cdot 2\pi S_2\{4w_n^2(0)+2[w_{n+1}(0)-w_n(0)]^2+2[w_{n+2}(0)-w_{n+1}(0)]^2+\cdots\} ,
\end{aligned} \tag{12}$$

where[10]

$$\left.\begin{aligned}
&C_n^2\cdot S_1=\frac{1}{8}h^4r_c^2\cdot s_a-\frac{ih^2}{4}\cdot s_b ,\\
&C_n^2\cdot S_2=\frac{1}{2}r_c^2-\frac{1}{8}r_c^2\cdot s_a+\frac{3i}{4h^2}\cdot s_b ,\\
&s_a=\frac{\pi i}{2}\sqrt{i}\,hr_c\cdot J_0(\sqrt{i}\,hr_c)\cdot H_0'^{(1)}(\sqrt{i}\,hr_c)+\frac{\pi i}{2}\sqrt{i}\,hr_c\cdot J_0'(\sqrt{i}\,hr_c)\cdot H_0^{(1)}(\sqrt{i}\,hr_c)\\
&\qquad+\frac{\pi i}{2}\sqrt{-i}\,hr_c\cdot J_0(\sqrt{-i}\,hr_c)\cdot H_0'^{(1)}(\sqrt{-i}\,hr_c)\\
&\qquad+\frac{\pi i}{2}\sqrt{-i}\,hr_c\cdot J_0'(\sqrt{-i}\,hr_c)\cdot H_0^{(1)}(\sqrt{-i}\,hr_c) ,\\
&s_b=\frac{\pi i}{2}(\sqrt{i}\,hr_c)^2\cdot J_0'(\overline{i}\,hr_c)\cdot H_0'^{(1)}(\sqrt{i}\,hr_c)\\
&\qquad-\frac{\pi i}{2}(\sqrt{-i}\,hr_c)^2\cdot J_0'(\sqrt{-i}\,hr_c)\cdot H_0'^{(1)}(\sqrt{-i}\,hr_c) .
\end{aligned}\right\} \tag{13}$$

2.3 *Interaction energy between the interstitial and all other atoms in the lattice*

First, in case of the carbon interstitial we will determine the interaction potential between the interstitial and all other atoms in the stacking layers. This potential is considered to have two terms, repulsive and van der Waals, and have no possibility of the covalent bond. Therefore, the interaction in question can be regarded as additive of interstitial-lattice site atom pairs.

Brennan[11] calculated the interaction potential between the neighbouring layers of the graphite lattice: He obtained the repulsive term quantum-mechanically, and found the van der Waals term by making the potential minimum at the observed value of c. In order to estimate the elastic constant for shearing c_{44}, Komatsu[7] calculated the interaction potential between two atoms on the neighbouring layers by a method similar to that employed by Brennan, with appropriate modifications and corrections.

We use Komatsu's potential for the interaction between the interstitial and any atom in the layers. This potential seems to be accurate when the distance between two atoms is near to or larger than the c-spacing, but it becomes unreasonably attractive due to the dominant van der Waals term when they approach nearer, as is often the case with the interstitial atom. Therefore, this potential is not applicable in the vicinity of the interstitial. There seems no calculation for the potential in this short-distance region.

Dienes[2] found a solid relation between bond strengths and equilibrium interatomic distances in the C—C bond, the benzen bond and the C=C bond, and, by extrapolating it to the range of interatomic distance between the C—C covalent bond distance and the c-spacing in graphite, he constructed a repulsive potential term of Born-Mayer type. Its physical foundation is recognizable as follows: It is empirically well-known that the nature of the covalent bond can be represented approximately by the Morse potential $U=D\{\exp[-2a(r-r_0)]-2\exp[-a(r-r_0)]\}$. It is likely that, at the equilibrium distance, the bond energy D in this potential is equal to the repulsive energy in magnitude. Therefore, the bond strengths in Dienes' relation can be regarded as the repulsive energies too. On the other hand, the potential we need to construct consists mainly of the repulsive term in the range considered. Consequently, we can employ the repulsive term of the carbon-carbon covalent bond to obtain the necessary potential.

Table I.

	C—C	Benzen	C=C
r_0	1.54	1.39	1.33 Å
D	58.6	86.0	100.0 kcal/mol.

In Table I[12] are shown the bond lengths and the bond stregths, from which the relation $\log D=Ar_0+B$ can be expected as Dienes pointed out, that leads to the potential of Born-Mayer type. We extrapolate the covalent bond data after Dienes' method so as to smoothly connect with Komatsu's potential in the vicinity of c-spacing. Thus, finally, the potentials to be used in our calculation are

$$\varphi_{C-C}(r)=\begin{cases}\exp(1.652-1.386r): & (r\leq 5.56)\\ -\dfrac{309.3}{r^6}+0.5153\exp(-0.2223r-0.07951r^2): & (r\geq 5.56)\end{cases} \tag{14}$$

in atomic units. The minimum interatomic distance to which the former potential will be applied in the present calculation is about 2.2 Å (or 4.1 a.u.). The latter is Komatsu's potential.

In the second, we will determine the interaction potential in case of Xe-interstitial atom in graphite by averaging arithmetically the potential of carbon-carbon and that of xenon-xenon. In spite of lacking in strict verification, this procedure may give a reasonable tendency as in the case of covalent bonds. Komatsu's potential is adopted for this purpose, because, due to the large strain in case of Xe-interstitial, we need not to take account of the potential in the short distance range. After Whalley and Schneider[13], who investigated intermolecular potentials of xenon etc. using the second virial coefficients and the crystal properties at 0°K, we adopt the xenon-xenon potential,

$$\varphi_{\mathrm{Xe-Xe}}(r)=\varepsilon\left\{\left(\frac{r_m}{r}\right)^{12}-2\left(\frac{r_m}{r}\right)^{6}\right\}, \qquad (\varepsilon=7.135\times10^{-4}\,\mathrm{a.u.},\quad r_m=8.630\,\mathrm{a.u.})\,, \tag{15}$$

Thus, the interaction potential between the Xe-interstitial atom and any carbon atom in the graphite lattice is

$$\varphi_{\mathrm{C-Xe}}(r)=\frac{1}{2}\{\varphi_{\mathrm{C-C}}(r)+\varphi_{\mathrm{Xe-Xe}}(r)\}\,. \tag{16}$$

Now, by means of these potentials, we can calculate the interaction energy between an interstitial atom and all other carbon atoms in the strained layers of graphite, the strain form of which is determined by Eq. (9) for given values of parameters, $w_n(0)$ and r_c. This calculation is performed by summing the energies for the atoms of $r\leq 11$ a.u. on the n-th and $(n-1)$-th layers, and then replacing it by the integration for all other atoms. We express the interaction energy ultimately in the form of the quadratic equation of $w_n(0)$ around the equilibrium atate;

$$U=B_1(r_c)\cdot w_n^2(0)+B_2(r_c)\cdot w_n(0)+B_3(r_c) \tag{17}$$

where the coefficients B_1 etc. depend upon the parameter r_c.

2.4 *Determinatian of the strain and the self-energy of interstitial*

The total extra energy increase due to the introduction of an interstitial atom into the lattice from the infinity is given by the sum of Eq. (12) and Eq. (17). We have to find the minimum value of the total extra energy, which is the self-energy of the interstitial atom, varying $w_n(0)$ and r_c. First, in order to vary $w_n(0)$ with r_c fixed, we rewrite the total extra energy W in the form,

$$\begin{aligned}W=&(A_1+B_1)w_n^2(0)+B_2w_n(0)+B_3\\&+A_2\{w_{n+1}^2(0)+w_{n+2}^2(0)+w_{n+3}^2(0)+\cdots\}\\&-A_3\{w_n(0)\cdot w_{n+1}(0)+w_{n+1}(0)\cdot w_{n+2}(0)+w_{n+2}(0)\cdot w_{n+3}(0)+\cdots\}\end{aligned} \tag{18}$$

where

$$A_1=2\pi c\rho\kappa^2S_1+6\pi c\rho\mu^2S_2\,,\qquad A_2=2\pi c\rho\kappa^2S_1+4\pi c\rho\mu^2S_2\,,\qquad A_3=4\pi c\rho\mu^2S_2\,.$$

S_1, S_2, B_1, B_2, B_3, A_1, A_2 and A_3 in the equation are the functions of r_c. In the real crystal the total extra energy increase should have the minimum value with respect to the variation of any one of the parameters $w_{n+1}(0)$, $w_{n+2}(0)$ etc. As it is considered that the real situation is represented by the above calculation in good approximation, we may put the partial derivatives of W with respect to $w_{n+1}(0)$, $w_{n+2}(0)$, etc. equal to zero to eliminate them. Using the above relations and the conditions, $w_{n+m+2}(0)\ll w_{n+m}(0)$ where m is zero or a positive integer, we have

$$w_{n+m}(0)=\alpha^m\cdot w_n(0)\,,\qquad \alpha=\frac{A_3}{2A_2} \tag{19}$$

and

$$W=B_1'\cdot w_n^2(0)+B_2\cdot w_n(0)+B_3=B_1'\left\{w_n(0)+\frac{B_2}{2B_1'}\right\}^2+B_3-\frac{B_2^2}{4B_1'} \tag{20}$$

where

$$B_1'=A_1+B_1-\frac{A_2A_3^2}{4A_2^2-A_3^2}\,.$$

In Eq. (20), W becomes the minimum when $w_n(0)=-B_2/2B_1'$ for a given r_c. Moreover, by varying r_c to minimize W, the self-energy of the interstitial atom can be obtained as is shown in Fig. 2.

§ 3. Migration Energy of Interstitials

Two super-imposed hexagonal networks above and below an interstitial atom are shown in Fig. 3. A and B indicate the interstitial sites, corresponding to the equilibrium point and the saddle point respectively. The migration energy of the interstitial atom is given by the difference between the energies at A and B, that is, $W_B - W_A$. According to the crystal symmetry in regard to the interstitial site, B is located just in the middle of the two layers above and below it. On the other hand, the A site is considered to have a small shift δ in the direction perpendicular to the layers. The total energy increases at B and A configuration are then represented in terms of the interaction energy U and the elastic energy V as follows;

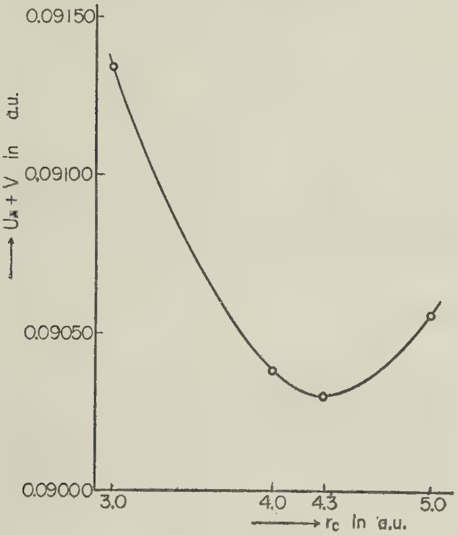

Fig. 2. U_A+V vs. r_c curve for carbon interstitial atom.

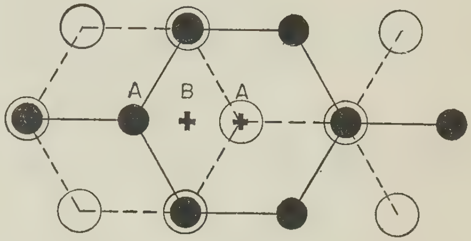

Fig. 3. A and B site for interstitial atom in graphite.

$$\left.\begin{aligned} W_B &= U_B\{w_{nB}(0), r_{cB}, 0\} + V\{w_{nB}(0), r_{cB}\} \\ W_A &= U_A\{w_{nA}(0), r_{cA}, \delta_A\} + V\{w_{nA}(0), r_{cA}\} \end{aligned}\right\} \tag{21}$$

The parameters $w_{nB}(0)$ and r_{cB} in B configuration can be determined after the procedure mentioned in the preceding section, while in A configuration we must determine δ_A to minimize W_A. This is done under the assumption that the strain in A configuration is the same with that in B configuration. δ_A and W_A in this case are denoted as δ_A' and W_A'. Hence,

$$W_A' = U_A\{w_{nB}(0), r_{cB}, \delta_A'\} + V\{w_{nB}(0), r_{cB}\}\ . \tag{22}$$

Now, we expand W_A in the Taylor series around $w_{nB}(0)$, r_{cB} and δ_A'. The result is

$$\begin{aligned} W_A = W_A' &+ \left(\frac{\partial(U_A+V)}{\partial w_n}\right)_{w_{nB}} (w_{nA}-w_{nB}) + \left(\frac{\partial(U_A+V)}{\partial r_c}\right)_{r_{cB}} (r_{cA}-r_{cB}) \\ &+ \frac{1}{2}\left(\frac{\partial^2(U_A+V)}{\partial w_n^2}\right)_{w_{nB}} (w_{nA}-w_{nB})^2 + \frac{1}{2}\left(\frac{\partial^2(U_A+V)}{\partial r_c^2}\right)_{r_{cB}} (r_{cA}-r_{cB})^2 \\ &+ \left(\frac{\partial^2(U_A+V)}{\partial w_n \partial r_c}\right)_{w_{nB}, r_{cB}} (w_{nA}-w_{nB})(r_{cA}-r_{cB}) \\ &+ \frac{1}{2}\left(\frac{\partial^2(U_A+V)}{\partial \delta_A}\right)_{\delta_A'} (\delta_A-\delta_A')^2 + \cdots\ . \end{aligned} \tag{23}$$

Further, if we eliminate $(w_{nA}-w_{nB})$ and $(r_{cA}-r_{cB})$ of the first order terms in the equation by putting $\partial W_A/\partial w_{nA}$ and $\partial W_A/\partial r_{cA}$ equal to zero, the migration energy in the first order approximation can be obtained in the form,

$$W_B - W_A = U_B\{w_{nB}(0), r_{cB}, 0\} - U_A\{w_{nB}(0), r_{cB}, \delta_A'\} + \frac{1}{(ac-b^2)}\{ag^2 - 2bgf + cf^2\} \qquad (24)$$

where

$$a = \left(\frac{\partial^2(U_A+V)}{\partial w_n^2}\right)_{w_{nB}}$$

$$b = \left(\frac{\partial^2(U_A+V)}{\partial w_n \partial r_c}\right)_{w_{nB}, r_{cB}}$$

$$c = \left(\frac{\partial^2(U_A+V)}{\partial r_c^2}\right)_{r_{cB}}$$

$$f = \left(\frac{\partial(U_A+V)}{\partial w_n}\right)_{w_{nB}} = \left(\frac{\partial(U_A-U_B)}{\partial w_n}\right)_{w_{nB}}$$

$$g = \left(\frac{\partial(U_A+V)}{\partial r_c}\right)_{r_{cB}} = \left(\frac{\partial(U_A-U_B)}{\partial r_c}\right)_{r_{cB}} .$$

Table II. Numerical results from the present calculations.

Interstitial atom	$w_{nB}(0)$	r_{cB}	δ_A'	α	Ratio of strain energy to self-energy	Self-energy	Formation energy	Migration energy
C	0.48 Å	2.29 Å	0.04 Å	0.30	0.49	2.5 ev	9.9 ev	0.016 ev
Xe	1.50 Å	2.47 Å	0.003 Å	0.31	0.79	15.1 ev		0.03 ev

§ 4. Discussion

We calculated the self-energies, the migration energies etc. associated with the carbon and xenon interstitial atoms in graphite, taking account of the lattice relaxation. In Table 2 are shown the numerical results obtained.

In case of the carbon interstitial, our calculation might have a slight inaccuracy because of the ambiguity in the interaction potential used in the close-distance region. On the other side, in case of xenon while the potential is rather reliable, the displacement of layers becomes to be not perpendicular to them on account of large strain and will make the strain energy calculation inaccurate. Nevertheless, the calculation of migration energy may be enough reliable, for it is the energy difference which varies with respect to changes of the potential, strain etc. more slowly than the energy itself. The values of migration energy calculated suggest that interstial atoms in graphite are very mobile even at extremely low temperatures. The formation energy is defined as the the sum of the self-energy and the sublimation energy, which is required to move an atom from the crystal surface to the infinity. We adopted the experimental value of the sublimation energy of graphite, 170 kcal/mol.[14] to obtain the formation energy of carbon interstitial in the table. Finally, it should be noted that our result for the self-energy of carbon interstitial is considerably smaller than that obtained by Dienes, 12.9 ev, suggesting the importance of the consideration for the lattice relaxation. In fact, the ratio of the strain energy to the self-energy amounts to 0.49 even in case of the carbon interstitial as cited in Table II.

Acknowledgement

The authors wish to express their hearty thanks to Dr. Y. Takagi for his kind encouragement and interest, and to Prof. T. Inui for his valuable discussions in mathematics.

Appendix

Calculation of Green Function[9]

In order to get Green function which satisfies Eq. (5), we employ the integral representation of the δ-function,

$$\frac{\delta(r-\xi)}{r} = \int_0^\infty kJ_0(kr)\cdot J_0(k\xi)dk . \qquad (25)$$

According to this representation, we assume $G(r, \xi)$ as follows;

$$G(r, \xi)=\int_0^\infty kg(k)\cdot J_0(kr)\cdot J_0(k\xi)dk\,. \qquad (26)$$

Substituting both Eqs. (25) and (26) for Eq. (5), $g(k)$ can be determined. Hence,

$$G(r, \xi)=\frac{1}{2\pi}\int_0^\infty \frac{k}{k^4+h^4}J_0(kr)\cdot J_0(k\xi)dk\,.$$

When $r>\xi$, this is modified in the form,

$$G(r, \xi)=\frac{1}{4\pi}\int_{-\infty}^\infty \frac{k}{k^4+h^4}H_0^{(1)}(kr)\cdot J_0(k\xi)dk\,.$$

Carrying out the complex integration in the upper half of k-plane by virtue of the theorem of residues, finally we have

$$G(r, \xi)=\frac{i}{2}\{\mathrm{Res}\,(\sqrt{i}\,h)+\mathrm{Res}\,(\sqrt{-i}\,h)\}\,,$$

which leads to Eq. (7). When $r<\xi$, the calculation can be performed by either doing in a similar way or using the principle of reciprocity.

References

1) M. Burton and T. J. Neubert: J. Appl. Phys. **27** (1956) 557.
2) G. J. Dienes: J. Appl. Phys. **23** (1952) 1194.
3) M. A. Kanter: Phys. Rev. **107** (1957) 655.
4) F. Seitz and J. S. Koehler: *Solid State Physics* **2** (1956) 305.
5) G. J. Dienes and G. H. Vineyard: *Radiation Effects in Solids, Intersci. Pub., Inc., New York* (1957).
6) K. Komatsu and T. Nagamiya: J. Phys. Soc Japan **6** (1951) 438.
7) K. Komatsu: J. Phys. Soc. Japon **10** (1955) 346.
8) Lord Rayleigh: *Theory of Sound*, Vol. **1**, 2nd Ed. (1894). R. Courant and D. Hilbert: *Methods of Mathematical Physics*, Vol. **1**, Chap. IV (1955) (translation).
9) T. Inui, T. Miyajima and T. Kihara: *Applications of Partial Differential Equation* **I**, Chaps. III and IV (1957) (in Japanese). P. M. Morse and H. Feshbach: *Methods of Theoretical Physics*, Chap. VII (1953).
10) G. N. Watson: *A Treatise on the Theory of Bessel Function*, Chap. V (1952).
11) R. O. Brennan: J. Chem. Phys. **20** (1952) 40.
12) L. Pauling: *The Nature of the Chemical Bond* (1944) 53, 131.
13) E. Whalley and W. G. Schneider: J. Chem. Phys. **23** (1955) 1644.
14) G. Glockler: J. Chem. Phys. **22** (1954) 159.

JOURNAL OF THE PHYSICAL SOCIETY OF JAPAN, Vol. 16, No. 2 FEBRUARY, 1961

Electric Conduction of Ferrites containing Fe^{2+}-ions

By Nahonori MIYATA

Department of Physics, Yokohama National University, Yokohama

(Received October 20, 1960)

The D.C. electric conductivity was measured between 100°K and 300°K for the ferrite solid solution $(MeFe_2O_4)_{1-y}$-$(Fe_3O_4)_y$, where Me=Mn, Ni, Mn-Ni or Zn. Above 120°K the specific conductivity of each specimen depends on temperature as $\sigma=A\cdot\exp(-\varepsilon/kT)/T$. The activation energy ε is $(5\sim8)\times10^{-2}$ eV. A depends on the concentration, y, of Fe_3O_4 as $A=(6.5\pm2.5)\times10^4(y/1-y)$ degree/Ωcm. The analysis of these experimental expressions shows that the dependence of the mobility on temperature for each specimen can be fitted by the expression, $\mu=\mu_0\cdot\exp(-\varepsilon/kT)/T$ and the dependence on the Fe^{2+}-ion concentration, y, by $\mu_0=(3.0\pm1.2)\times10^1(1/1-y)$ degree (cm²/volt sec). μ_0 is independent of the kind and distribution of Me^{2+}-ions.

§ 1. Introduction

The electric resistivity of ferrites at room temperature ranges from about 10^{-2} Ωcm to higher than 10^{11} Ωcm depending on the chemical composition. It has long been known that low resistivities are caused in particular by the simultaneous presence of ferrous and ferric ions on equivalent lattice sites (octahedral sites). Recently, the electric conduction mechanism of ferrites containing Fe^{2+}-ions came to be understood as the hopping motion of electrons between Fe^{2+} and Fe^{3+} on the B-sites (octahedral sites) of the spinel lattice[1]. From the study on the $(MeFe_2O_4)$-(Fe_3O_4) solid solution system, it may be possible to make clear the effect of Me^{2+} or Fe^{2+} on the B-sites on the electric conduction. Previously, the author and his collaborators[2] have reported the conductivity of $MnFe_2O_4$-Fe_3O_4 system. Here the study is extended to the case of Me=Ni, Mn-Ni or Zn, where Ni and Zn are elected on account of the tendency of their preferred occupation of B-site and A-site, respectively. The method of analysis of the experimental results and some conclusions about the ionic distribution mentioned in the previous short note[2] are corrected in this paper.

§ 2. Specimens

Specimens, 3×3×7 mm, were cut from a single crystal or a coarse-grained ingot grown in the Pt-crucible by the Bridgman method in the air atmosphere. The main cations were chemically analysed. The analysis could not determine the excess or deficiency of the oxygen compared with the stoichiometric composition more accurately than ±5% of the oxygen content. The stoichiometry of oxygen will be estimated rather from the electric conductivity. The crystal structure was investigated by the X-ray analysis. All specimens reported here had the spinel type and their lattice constants depended linearly on the concentration of cations. The details of the preparation and structure of specimens will be described in a later other paper[3].

§ 3. Experimental Method

The D.C. specific electric resistance was measured between the temperature range from 100°K to 300°K by the four-probe method with two In-amalgam electrodes on both sides of the specimen for the current flow and two brass electrodes, 4 mm apart, for measuring the potential between them.

§ 4. Results

(a) *Dependence of the electric resistance on the temperature*

Above about 120°K, where a *knick* is observed for almost all specimens, experimental values of the temperature dependence of the specific electric resistance, ρ, are represented by the expression

$$\sigma=1/\rho=A\cdot\exp(-\mathcal{E}/kT)/T^n\,, \tag{1}$$

where A is a constant, $\mathcal{E}$ is the activation energy, T is the absolute temperature and n is a constant which is about unity. An example for a few specimens is shown in Fig. 1, where circle and square represent the observed values and the solid curves show the equation (1) with the suitable choice of the values of A and $\mathcal{E}$.

(b) *Dependence of A and $\mathcal{E}$ on Fe^{2+} concentration*

Two constants in the equation (1), A and $\mathcal{E}$, are determined for each specimen under the assumption $n=1$ and plotted as a function of molar ratio y of $(MeFe_2O_4)_{1-y}$-$(Fe_3O_4)_y$ system in Fig. 2 and 3, respectively. $\mathcal{E}$'s are $(5\sim8)\times10^{-2}$ eV. $A(y)$ is expressed by the relation

$$A=(6.5\pm2.5)\times10^4(y/1-y)\text{degree}/\Omega\text{cm} . \qquad (2)$$

The solid curve and two dotted curves show Eq. (2) together with its dispersion. As the conductivity is very sensitive to the excess or deficiency of oxygen content, the dispersion of the observed value is unavoidable to some extent. It should rather be noticed that, as seen in Fig. 2, equation (2) is common to all ferrite solid solution systems independent of the kind of Me^{2+}-ion.

§ 5. Discussion

Generally, the electric conductivity is given by

$$\sigma=en\mu , \qquad (3)$$

where e is the charge, n the number and μ the mobility, of the charge carrier. The conduction mechanism of ferrites such as those described here is considered as the hopping motion of electrons between Fe^{2+} and Fe^{3+} on the B-site of the spinel lattice[1]. n is now equal to the number of Fe^{2+} and independent of temperature for each specimen.

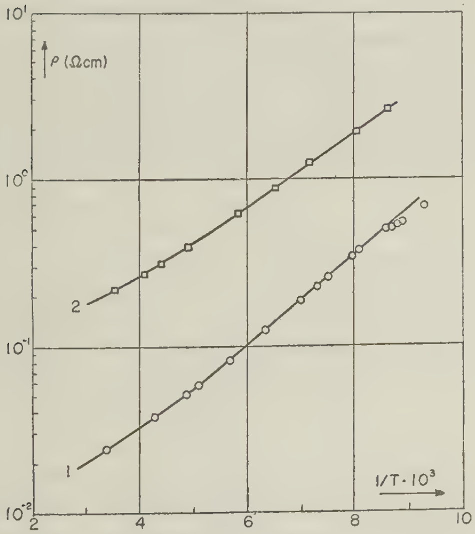

Fig. 1. A few examples of the temperature dependency of the electric resistance (log ρ *vs.* $1/T$).

Composition	Observed values	Solid curves mean $1/\rho=A\cdot\exp(-\varepsilon/kT)/T$ with
$(Zn_{0.3}Fe_{0.7})Fe_2O_4$	○	1; $A^{-1}=6.0\times10^{-6}$ Ωcm/degree $\varepsilon=6.6\times10^{-2}$ eV
$(Mn_{0.85}Fe_{0.15})Fe_2O_4$	□	2; $A^{-1}=7.5\times10^{-5}$ Ωcm/degree $\varepsilon=5.8\times10^{-2}$ eV

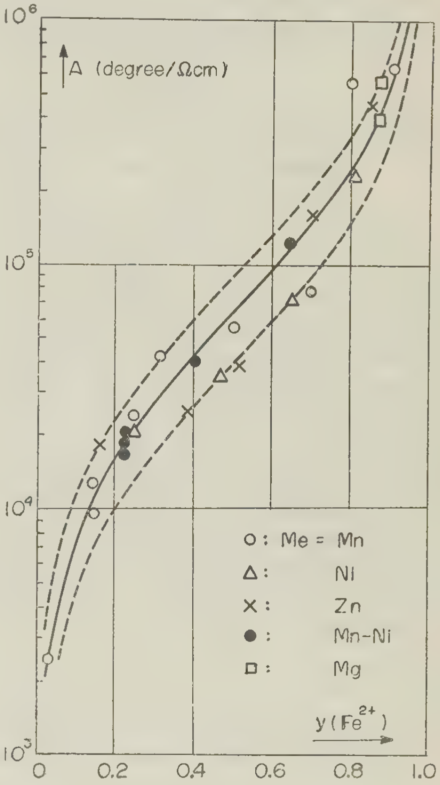

Fig. 2. (A *vs.* y) of $(MeFe_2O_4)_{1-y}$-$(Fe_3O_4)_y$. A solid curve and dotted ones show a center and width of the equation $A=(6.5\pm2.5)\times10^4(y/1-y)$ degree/Ωcm.

As the lattice constant is about 8.4A and there are eight molecules in a unit cell, $n=1.35\times10^{22}\cdot y\,\text{cm}^{-3}$. The cause of the factor proportional to y in equation (2) is understood as the proportionality of n to y. (1) and (3) show that the mobility depends upon temperature as

$$\mu=\mu_0\cdot\exp(-\mathcal{E}/kT)/T , \qquad \mu_0=A/en . \qquad (4)$$

Next, from (2) and (4) with $e=1.60\times10^{-19}$ coulomb and $n=1.35\times10^{22}\cdot y\,\text{cm}^{-3}$,

$$\mu_0=(3.0\pm1.2)\times10^1(1/1-y)\,\text{degree}(\text{cm}^2/\text{volt sec}). \qquad (5)$$

Also, from the usually used equation,

$$\mu=\frac{ea^2}{kT}W \quad \text{and} \quad W=\nu\cdot\exp(-\mathcal{E}/kT)\ ,$$

where a is taken as the distance between nearest B-sites, the jumping frequency, W, is obtained as

$$W=\frac{(2.9\pm1.1)\times10^{12}}{(1-y)}\cdot\exp(-\mathcal{E}/kT)\cdot\mathrm{sec}^{-1}\ . \qquad (6)$$

These relations, (4), (5) or (6), are independent of the kind and distribution of Me^{2+} (Zn^{2+} and Ni^{2+} prefer A-site and B-site, respectively) as seen by the experiment, and show that the mobility, or the transition probability of electrons between Fe^{2+} and Fe^{3+}, becomes large, inversely proportional to $(1-y)$, with the increase of magnetite concentration, y. The theoretical explanation of these relations is not known at present but these facts may provide an important evidence for the hopping mechanism.

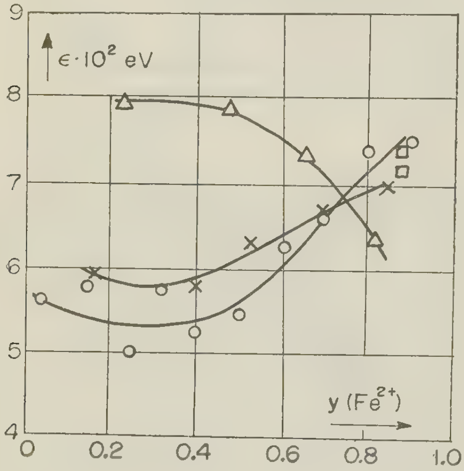

Fig. 3. (ε vs. y) of $(MeFe_2O_4)_{1-y}$-$(Fe_3O_4)_y$. Symbols are the same as in Fig. 2.

Here the experimental results are analysed by the use of (1) with $n=1$. It should be added that for specimens of low magnetite concentration the dependence of σ on temperature is expressed rather by (1) with $n\cong0$, though the reason is not clearly understood.

Acknowledgement

The author wishes to express his hearty thanks to Prof. Z. Funatogawa for his encouragement throughout this work. This work is partly supported by the Scientific Research Expenditure of the Ministry of Education.

References

1) J. Yamashita and T. Kurosawa: J. Phys. Soc. Japan **15** (1960) 802.
2) Z. Funatogawa, N. Miyata and S. Usami: J. Phys. Soc. Japan **14** (1959) 854.
3) N. Miyata: to be published in this journal.

JOURNAL OF THE PHYSICAL SOCIETY OF JAPAN, Vol. 16, No. 2, FEBRUARY, 1961

Dislocations and Fine Lines in Rochelle Salt Crystal

Terutaro NAKAMURA and Kikuo OHI

Department of Physics, Ochanomizu University, Otsuka, Tokyo

(Received November 4, 1960)

Etch pits on c-face of rochelle salt were observed and it was concluded that they correspond to points where dislocations parallel to c-axis emerge on c-face. Some of the dislocations were found to be longer than several millimeters.

Fine lines parallel to c-axis, called *sudaré* among Japanese researchers, were observed to be distributed in quite the same manner as dislocation etch pits are. *Sudarés* are observed at the deepest points of some etch pits.

If surface energy of the interface between rochelle salt and its decomposed products be low, dislocation core may be opened and filled with the decomposed products. It seems likely that this open-cored dislocation may grow into the *sudaré*.

§ 1. Introduction

It has been pointed out that dislocations in ferroelectric crystals have interesting interactions with ferroelectric behaviors[1)-3)]. Screw dislocations in c-direction of rochelle salt crystal were shown to anchor small domains, which will act as nuclei of growing domains.[2)] Shape of the anchored domain was calculated with an electronic computer[3)]. The formation of the anchored domain was shown to stabilize array of parallel screw dislocation lines.[3)] Recently observations of dislocations in ferroelectric GASH[4),5)] and ferroelectric glycine sulfate[6)] have been reported.

The present paper describes observations of etch pits on c-face of rochelle salt crystal, which lead us to the conclusion that these pits correspond to points where dislocations emerge on c-face, and that these dislocations are parallel to c-direction and longer than several millimeters.

It is known that a rochelle salt crystal includes a number of fine lines parallel to c-direction, of $1\mu \sim 10\mu$ in diameter, from tens to several hundreds of microns in length[7)], called *sudaré*.* The *sudarés* are included even in very good crystal which has been grown in the best conditions, while *veils*** are included only in parts which have experienced too rapid crystal growth. These two ideas must be kept separate one from another. Informations heretofore reported about *sudaré* are as follows. They are not visible in the crystal, when the growth has just been completed, but become visible when the days roll on[8)]. Distribution of *sudarés* seems to be related to crystallographic direction[9)]. They increase by irradiation with X- or γ-ray[10),11)].

It was pointed out by Frank[10)] that there exists a state of equilibrium in which a dislocation core is opened if energy of strain at the core is larger than surface energy of created boundary surface. It has been suggested earlier that *sudaré* may be closely related with open-cored dislocation[2)], and this view is supported experimentally by the present work.

§ 2. Dislocation Etch Pits on c-Face

A c-plate crystal of rochelle salt is cut out from a large good crystal by means of a wet

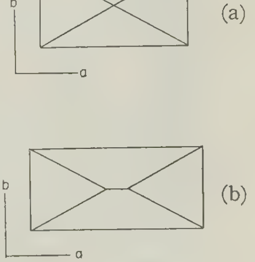

Fig. 1. Etch figures on a c-surface of rochelle salt crystal.

---

* Among Japanese researchers this kind of imperfection is usually called *sudaré*, because these fine lines are distributed forming a wall, which looks like a "*sudaré*", a kind of blind, made of fine bamboo tubes arranged to form a wall.

** Word *veil* is used as a macroscopic imperfection, caused by too rapid crystallization, composed of many small spherical holes.

thread, and carefully polished. This c-cut plate is rubbed lightly with a wet filter paper, and observed under a microscope.

Quadrangular pyramidal etch pits as shown in Photo. 1 are observed. Longer side parallel to a-axis is about 100μ and shorter side parallel to b-axis is about 50μ. Some etch pits have a shape of pointed pyramid as Fig. 1a, while some have shape of hip roof as Fig. 1b*. Experimental results described below lead us to the conclusion that these etch pits correspond to the emergence points of dislocation lines.

(1) There is an imperfect cleavage parallel to c-plane of rochelle salt crystal. Matched cleavage faces parallel to c-plane are etched. Every etch pit on both faces corresponds perfectly to each other as shown in Photo. 1a and b.

(2) By rubbing a crystal with a wet filter paper, water acts not only as an etchant but also as a chemical polisher and dislocations can be followed. Photo. 2 show that etched pattern remains unchanged for about 1 mm, apart from fine details.

(3) The etch pits on the top and the bottom surfaces of one crystal piece even about 5 mm thick are sometimes observed to correspond to each other (Photo. 3). This is the case especially in a sub-grain boundary, most of which are observed to lie parallel to a-, b-, or m-plane.

(4) It is observed that etch pits are nucleated by mechanical stresses which are given by contact with a pin-point or by dropping a steel bar (Photo. 4). Pits caused by the mechanical shock can be followed by chemically polishing for about $50\mu\sim300\mu$, but in the chemical polishing process they become round-bottomed and finally disappear (Photo. 4a and b).

(5) The pit density ranges from 10^3 to $10^4/\text{cm}^2$, but it reaches a value larger than $10^5/\text{cm}^2$ at probably imperfect portions, where some *veils* are found nearby.

§ 3. *Sudaré* and Dislocation Etch Pits

A cube of about $(0.5\,\text{mm})^3$ is cut out from a large rochelle salt crystal by means of a wet thread, so that its faces are nearly perpendicular to a-, b-, and c-axis respectively, and the faces are polished carefully.

Sudaré can be observed through a- or b-faces, under a microscope by dark field illumination, as bright lines shown in Photo. 5.

Observed through c-faces, *sudarés* appear to be fine bright spots under dark field illumination (Photo. 6a), while they appear as fine dark spots under bright field illumination. Immediately after observing *sudarés* through c-face, this c-face is etched by means of the technique shown above in § 2. Some of dislocation etch pits are then ascertained to correspond to *sudarés*. (Photo. 6a and b)

In the process of dissolution of c-surface by water, some spots are observed, which can be identified with emergence points of *sudarés*, at the deepest points of some of the etch pits.

It has been reported by Sakisaka that *sudarés* are always found not to be isolated, but to form walls. Some walls are parallel to a-, b-, or m-face, but some are not plane but form cylindrical surfaces. Photo. 7a shows an arrangement of *sudaré* walls, which was photographed by throwing a parallel ray at a certain angle of incidence (oblique illumination). Photo. 7b shows an arrangement of etch pits, which was obtained by etching the surface of Photo. 7a. Photo. 7a and b clearly indicate that the *sudarés* are distributed quite in the same manner as dislocation etch pits are.

These experimental results seem to be enough to conclude that *sudaré* and dislocation are closely related with each other, and that *sudaré* may be open-cored dislocations proposed by Frank, as discussed below.

§ 4. Discussion

It has been reported that there exist two types of domain structure; i.e. some crystals consist of laminated domains parallel to a–b plane (b-domain crystal), and some consist of laminated domains parallel to a–c plane (c-domain crystal). It was reported that b-domain crystal is obtained only by crystallization in the ferroelectric range, and shows tendency to change into c-domain crystal[2]. In explaining this phenomenon, it was pointed out that screw dislocation parallel to c-axis accompanies strained region having y_z which must anchor small domain at the dislocation[2]. The shape

---

* Similar figures are found in Cady's book[12]. The figures are, however, remarked to be "etch hills" in contradiction with our experimental result which has ascertained them to be "etch pits".

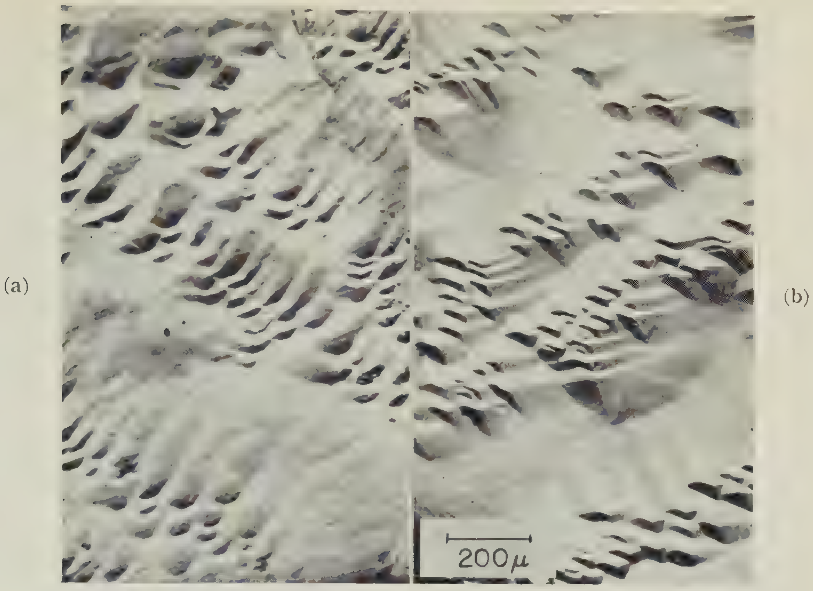

Photo. 1. a), b) Corresponding etch pits on matched cleavage faces.

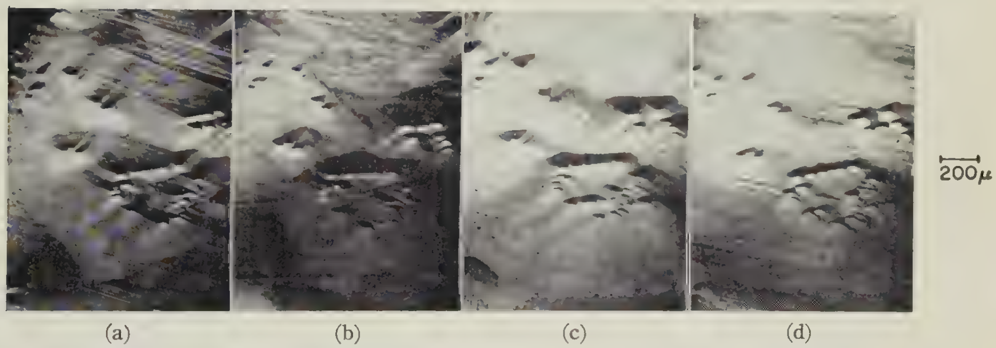

Photo. 2. a)-d) Dislocation etch pits in the process of chemical etching.
distance between a)-b) 190 μ b)-c) 280 μ c)-d) 300 μ

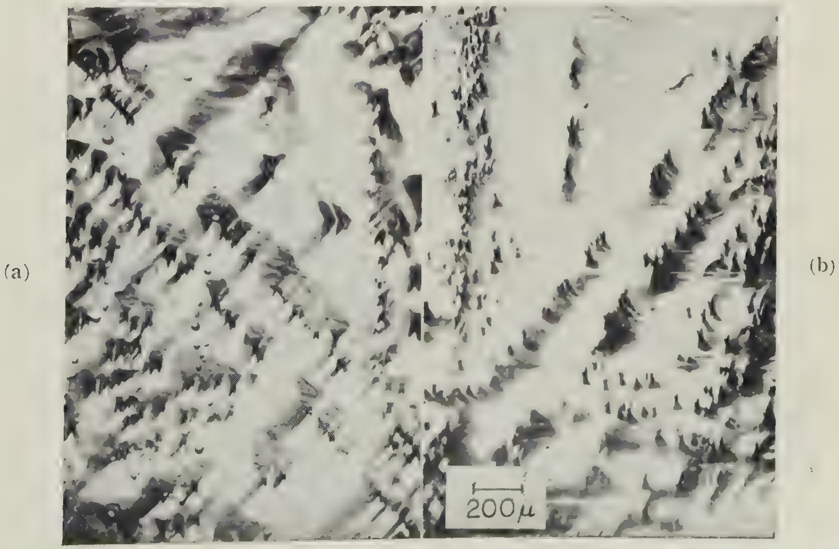

Photo. 3. a), b) Corresponding etch pits on the top and the bottom surfaces of a crystal piece, about 5 mm in thickness.

of the anchored domain was calculated, and it was also pointed out that the array of parallel screw dislocations will be stabilized by formation of anchored domains which relax stresses around dislocation lines, otherwise parallel screw dislocations cannot exist stably[3].

The present experiments revealed that the dislocations in rochelle salt are parallel to *c*-direction and seem to run in parallel straight lines through very long distance by observing both ends of dislocations of about several millimeters (Photo. 3). This fact is rather striking, because dislocations in alkali halides or GASH are reported to form loops when

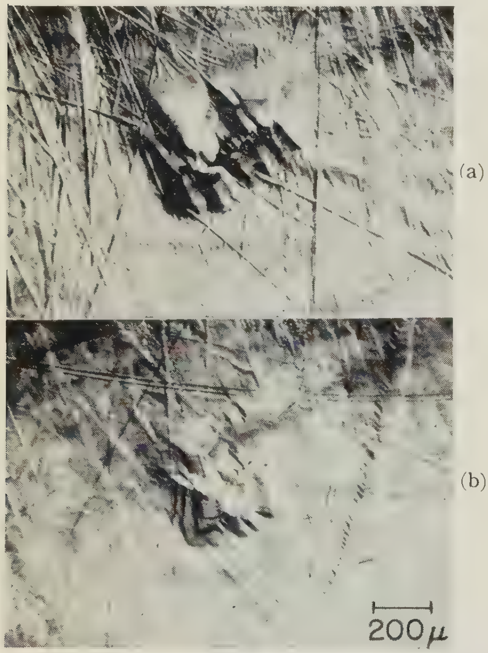

Photo. 4. Etch pits caused by a mechanical shock.
a) pits on the initial surface.
b) pits on the surface 30 μ beneath a).

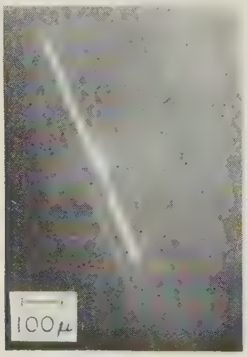

Photo. 5. Photomicrograph of *sudaré* through *a*-face.

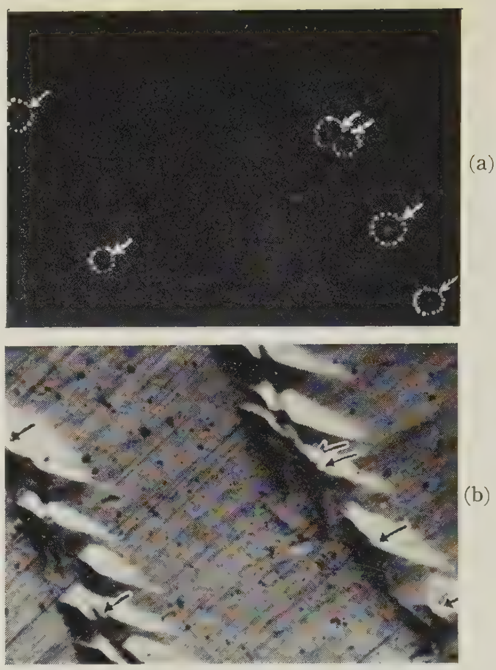

Photo. 6. a) Photomicrograph of *sudarés* through *c*-face, shown by arrows.
b) Etched pattern of the face of a). Pits shown by arrows correspond to *sudarés* in a).

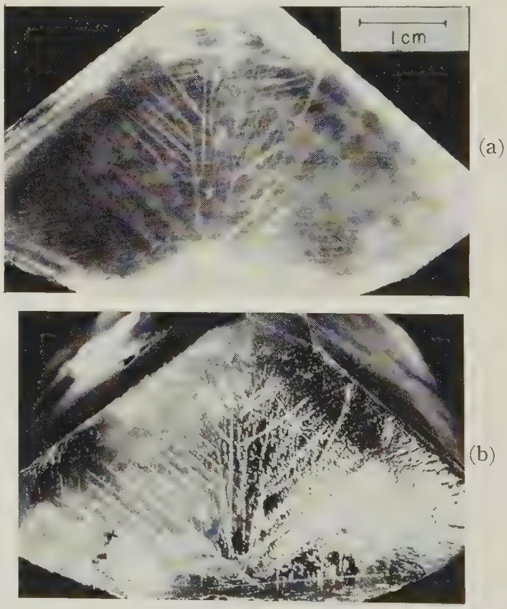

Photo. 7. a) *Sudarés* in a large crystal. Photographed by throwing light at a certain angle of incidence.
b) Etched pattern of the face of a). *Sudarés* are distributed in quite the same manner as dislocation etch pits are.
(Correspondence in left and right end parts looks to be unsatisfactory, owing to lighting condition.)

chemically polished about a few hundred microns. On the present step we cannot distinguish whether the etch pits correspond to edge or screw dislocations, but our experimental results do not show any contradiction with the previously proposed image that a number of screw dislocations run in straight lines parallel to *c*-axis, and anchor nucleus domains.

Our experiment has shown that etch pits are identified with dislocation emergence points and that *sudarés* are distributed in quite the same manner as dislocation etch pits are, and *sudaré* is observed at the deepest point of a pit. These results are leading us to the previously proposed assumption that the *sudaré* may be identified with open-cored dislocation first proposed by Frank. Consider a screw dislocation in a material with isotropic elastic constants. If a strained part near the dislocation core become empty tube of radius r, free energy per unit length increases by

$$\Delta F=\int_0^r 2\pi\gamma\, dr-\int_0^r \frac{\mu b^2}{8\pi^2 r^2}2\pi r\, dr \qquad (1)$$

where γ, μ and b denote specific surface energy, rigidity modulus and Burgers vector respectively. There is an equilibrium when

$$r=\mu b^2/8\pi^2\gamma \qquad (2)$$

for which ΔF takes minimum value. This is Frank's hollow dislocation.. For occurence of open-cored dislocation, large Burgers vector or low specific surface energy is required. Since the lattice constant in *c*-direction of rochelle salt is $c=6.17$Å according to Beevers-Hughes, very large Burgers vector is not expected. However, very low specific surface energy may be expected, since *sudaré* can be conceived not to be empty but to probably contain decomposed products of rochelle salt.* The radius of equilibrium of the tube given by Eq. (2) is conceived to be much smaller than the magnitude which can be observed by an optical microscope. The open-cored tube, however, likely grows up to observable *sudaré* when some additional energy is supplied, for instance thermal energy, irradiation energy of X or γ ray, etc. This supposed process is in agreement with facts reported[8),9),10)].

§ 5. Summary and Conclusion

Etch pits on *c*-face of rochelle salt were observed and concluded to be identified with points where dislocations parallel to *c*-axis emerge on *c*-face. It is rather striking that dislocations are ascertained to be several millimeters long.

Fine lines parallel to *c*-axis, called *sudaré* among Japanese researchers, were observed to be distributed in quite the same manner as dislocation etch pits are. *Sudarés* are observed at the deepest points of some etch pits.

It is proposed that *sudaré* is what is formed by the process that some parts of a dislocation become open-cored, as Frank's hollow dislocation, being filled with decomposed products, and grows gradually when thermal, radiant and other kind of energy are supplied.

This work was financially supported in part by a Grant in Aid for Scientific Research From the Ministry of Education.

References

1) T. Nakamura: J. Phys. Soc. Japan **9** (1954) 425.
2) T. Nakamura: J. Phys. Soc. Japan **11** (1956) 624.
3) H. Takahasi, T. Nakamura and Y. Ishibashi: J. Phys. Soc. Japan **15** (1960) 853.
4) T. Nakamura: J. Phys. Soc. Japan **14** (1959) 1022.
5) T. Nakamura and K. Ohi: J. Phys. Soc. Japan **15** (1960) 1348.
6) H. Toyoda: J. Phys. Soc. Japan **15** (1960) 1539.
7) Y. Sakisaka: unpublished, short remarks appeared in Sci. Rep. of Saitama Univ. **1** (1952) 50; **1** (1953) 63.
8) S. Miyake: Rochelle Salt. Koyama Shoten, Tokyo (1948) p. 9.
9) Y. Sakisaka: unpublished.
10) S. Miyake: Read before the Annual Meeting of Physico-Mathematical Society of Japan. May 1946.
11) Y. Ōta, K. Saheki, T. Nagamura: Read before the Conference on Dielectrics, Sept. 1960, Sapporo.
12) W. G. Cady: Piezoelectricity, McGraw Hill Book Co. Inc., New York (1946) p. 516-517.
13) K. Saheki: Private communication.

---

* A *sudaré* seems not to be empty but to contain decomposed products of rochelle salt, because the atoms which have been existing at the core can hardly come out from crystal. Angle of incidence of light, needed for *sudaré* observation, seems to support this view[13)].

JOURNAL OF THE PHYSICAL SOCIETY OF JAPAN, Vol. 16, No. 2, FEBRUARY, 1961

Observation of Lattice Defects in Graphite by Electron Microscopy, Part I

By F. Eiichi FUJITA and Kazuhiko IZUI

Japan Atomic Energy Research Institute
Tokai-mura, Ibaraki-ken, Japan

(Received September 7, 1960)

In Part I, lattice defects which can *a priori* exist in graphite crystals and be observed by means of electron microscopy, mainly dislocations, are reported. Four kinds of dislocations and their combination predicted from the crystal structure are observed through the diffraction contrast and the disturbances in the moiré pattern such as the extra terminating half lines and the line shift. Their network arrangements and movement are also found. The line grating model reveals the relation between the line shift of the moiré fringes and the Burgers vector of the glissile dislocations. New origins of extra terminating half lines are considered too.

§1. Introduction

In recent years, the study of lattice defects in crystals by means of transmission electron microscopy has been developped mainly in three ways; 1) direct resolution of crystal lattices in such as platinum phthalocyanine[1], and of super lattices in such as antigorite[2] and surpentine[3], 2) direct observation of dislocation lines and stacking faults through the diffraction contrast associated with them in metals including aluminium[4], gold[5] and stainless steel[6], and 3) detection of dislocations by means of moiré patterns from overlapping crystals of copper sulfide[7], gold-paradium[8], etc.

Among these methods, the first one has an advantage that the direct imaging of the crystal lattices is given and dislocations passing through the crystal film and having a component of the Burgers vector perpendicular to the lattice planes manifest in the image as extra terminating half lines. However, its application is limited to the crystals with lattice spacings larger than 6 Å, which is the resolution limit of the present-day electron microscopes. Therefore, many of the substances we want to study lie beyond the reach of this method.

The second method is useful for examining the density, configuration and motion of dislocation lines and is not severely confined by the direction of the lines and the Burgers vectors as in the case of the first method. It would be, however, difficult to determine the Burgers vector by this method even if the selected area electron diffraction method was used in parallel or a careful analysis of the relation between the Burgers vector and the diffraction contrast of the image was performed.

The third method using the moiré pattern is more or less similar to that of the first one, for it reveals dislocations as extra terminating half lines in the moiré pattern. Consequently, the limitation of this method detect the lattice defects is not so different from that of the first method, although in this method indirect resolution of crystal planes of even less than 1 Å in spacing can be obtained and the two dimentional analysis of the Burgers vector is practically possible by using two sets of moiré patterns.

The first attempt to apply both of the second and the third methods in closer relation to the study of lattice defects in graphite has been put into practice by the authors, since various types of disturbances in the moiré pattern from graphite were observed by one of the authors[9]. There have been relatively few number of works of electron microscopy on the lattice defects in graphite such as observation of spiral growth in small particles of graphite by T. Tsuzuku[10], observation of moving dislocations by A. Grenall[11], study of moiré dislocations in synthetic graphite by I. M. Dawson and E. A. C. Follett[12], and observation of sessile dislocation rings in quenched graphite by S. Amelinckx[13]. The present paper reports various kinds of dislocations and stacking faults in graphite crystals predicted and observed through the diffraction contrast as well as by means of the moiré pattern, which enable the determination of the direction of dislocation lines and the Burgers vectors. Various modes of network arrangements of dislocations and the motion of dislocation lines are also observed. The relation between the line shift of moiré fringes across the dislocation lines and their Burgers vectors is discussed, and identification of sessile and glissile, full and half dislocations and their combinations is found to be possible. Origins of extra terminating half lines in the moiré pattern, other than the dislocations passing from the top to the bottom surface of the crystal film, are also discussed.

§ 2. Experimental Procedure

Three kinds of graphite powder were used in the present experiment: Natural graphite powder of SP-1 grade (spectroscopically pure) was supplied by the National Carbon Co., U. S. A. Graphite powder obtained by the reduction from silicon carbide powder by means of high temperature chlorine gas reaction was kindly offered by Dr. Y. Sasaki of the chemistry division of this institute. X-ray and electron diffraction measurements and electron microscopy revealed that the crystallites of this powder of synthetic graphite are as perfect as those of SP-1 natural graphite in respect to the crystal structure. On the other hand, ground powder of artificial graphite supplied by the Showa Denko Co. for the JRR-3 reactor of our institute was found to be rather imperfect, and therefore not used in the present experiment except observation of irradiation effect.

Graphite powder of these kinds was ground between two glass plates with a small amount of distilled water and ether, floated on distilled water, meshed and then dried. This process enables the powder to have a dispersed state suitable for electron diffraction and microscopy, and would also give the crystals appreciable mechanical deformation to produce dislocations, stacking faults, and possibly relative rotations of overlapping crystallite flakes.

In parallel with the observation of unirradiated powder, some irradiation experiments were done which will be mentioned in Part II.

The electron microscopes used in the present observation were of Hitachi HU-10 type with the resolution of 10 Å which has the double condensers in the illumination system and is operated at 75 KV, and of Hitachi HS-5 type with the resolution of 25 Å operated at 50 KV. Electron diffraction study was done by using the same equipments. About 500 pictures were taken at direct magnifications between 10,000 and 30,000, in which many remarkable phenomena were found as illustrated in the following paragraphs.

§ 3. Experimental Results

In general, graphite powder consists of laminar stacking of small crystallite flakes several hundreds angstroms in thickness, a few microns wide in lateral dimensions. This aspect can be seen in Photo. 1. In some areas of the photograph we can see moiré patterns in patches, which indicate the extent of nearly perfect crystal regions or the size of crystallite flakes. Electron diffraction patterns from such areas sometimes show satellites in hexagonal distribution around normal spots as are seen in Photo. 2, indicating that the moiré pattern is arising from interferrence of the direct beam and the doubly diffracted beam from two overlapping crystals with a slight relative rotation around the axis perpendicular to the crystallite planes or *c*-atomic planes of the crystals. In case of the dark field image, the moiré pattern still remains and is considered to be produced by the interference of two primary diffracted beams from two overlapping crystals as pointed out by J. F. Goodman[14]. Some of the moiré patterns observed are formed by three or more overlapping crystals. For example, in Photo. 3 a set of moiré lines with a fine spacing of 50 Å is modulated with a large spacing of 300 Å. A simple geometrical consideration reveals that such a feature of moiré pattern is a result of overlapping of three crystals two of which are rotated by a relatively small angle of the order of 10^{-2} with respect to each other and the rest one by an angle about 6 times larger with respect to the other two. Much more complicated moiré patterns were frequently observed, some of which are apparently highly affected by the Bragg extinction contours or the extinction of equal inclination and some are probably modulated by densely distributed crystal imperfections such as a group of dislocation lines. These features of moiré patterns will be partly discussed in the following paragraph.

Extra terminating half lines in moiré patterns are sometimes observed, as are seen in Photos. 4 (a), (b) and 5. It is generally known that a dislocation having an extra half plane among the crystal planes to form the moiré pattern and passing through the crystal film will give rise to an extra terminating line in the moiré pattern[7,15]. This was further extended to the case of general dislocation by

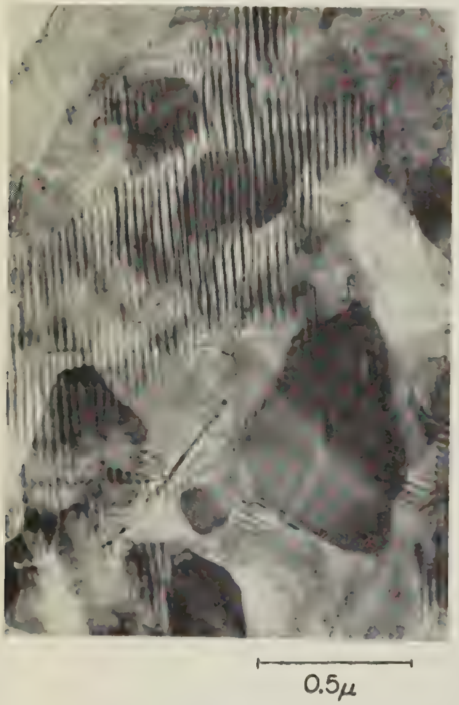

Photo. 1. General aspect of natural graphite powder.

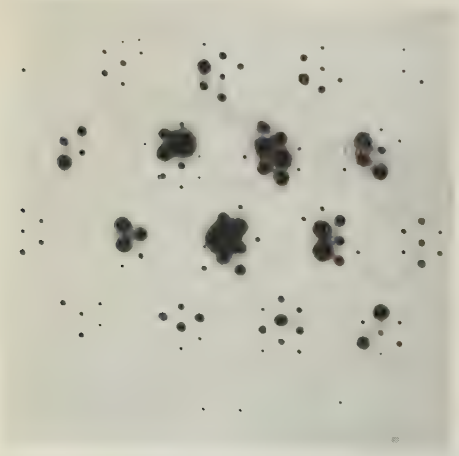

Photo. 2. Electron diffraction pattern from two overlapping crystals.

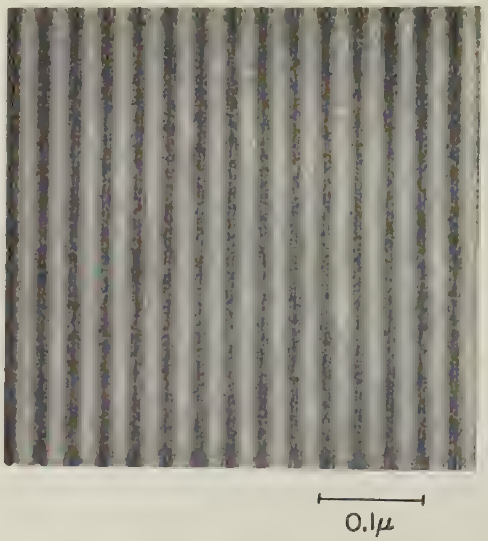

Photo. 3. Moiré pattern from three overlapping crystals.

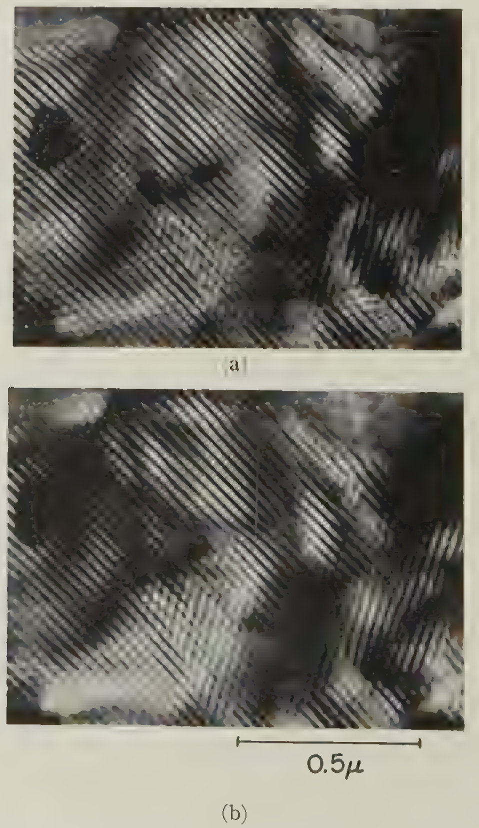

Photo. 4. Extra terminating half lines in moiré pattern and their movement due to the change of illmination condition.

G. A. Bassett, J. W. Menter and D. W. Pashley[8] as discussed later. On the other hand, it was realized that even in absence of a real dislocation such structure in the moiré pattern can be produced by certain kind of contamination of the specimen film[16] and possibly by local distortion of the film. In the present case, when the focus of the objective lens is changed, most of such extra terminating lines are not displaced. While, when changing the angle and the intensity of illumination, many of them are observed to disappear or be displaced as shown in Photos. 4 (a) and (b) which are taken in otherwise the same condition. These facts are apt to lead to a conclusion that most of the observed extra terminating half lines in moiré patterns are not arising from contamination or dislocation lines normal to the *c*-atomic planes. There are, however, a few exceptions in which extra half lints are not displaced and have very clear contrast as shown in Photo. 5, likely indicating the real existence of such dislocations.

Disturbances of moiré patterns along some curved lines are frequently observed as shown in Photos. 6, 7, and 8. As will be mentioned later, these curved lines were verified to be dislocation lines lying in basal or *c*-atomic planes of the crystal. A direct evidence for that seems to be given by Photo. 7, on the left-hand side of which are seen dislocation lines due to the diffraction contrast associated with them like those in metal crystals, while on the right-hand side are the same lines disturbing the moiré pattern in a manner similar to those seen in Photos. 6 and 8. In Photo. 6, two sets of moiré patterns appear in

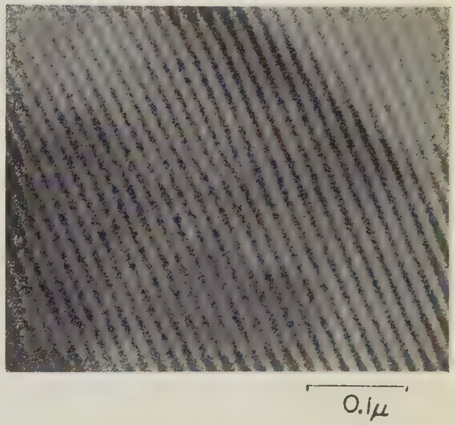

Photo. 5. Extra terminating half line in moiré pattern presumably arising from a dislocation.

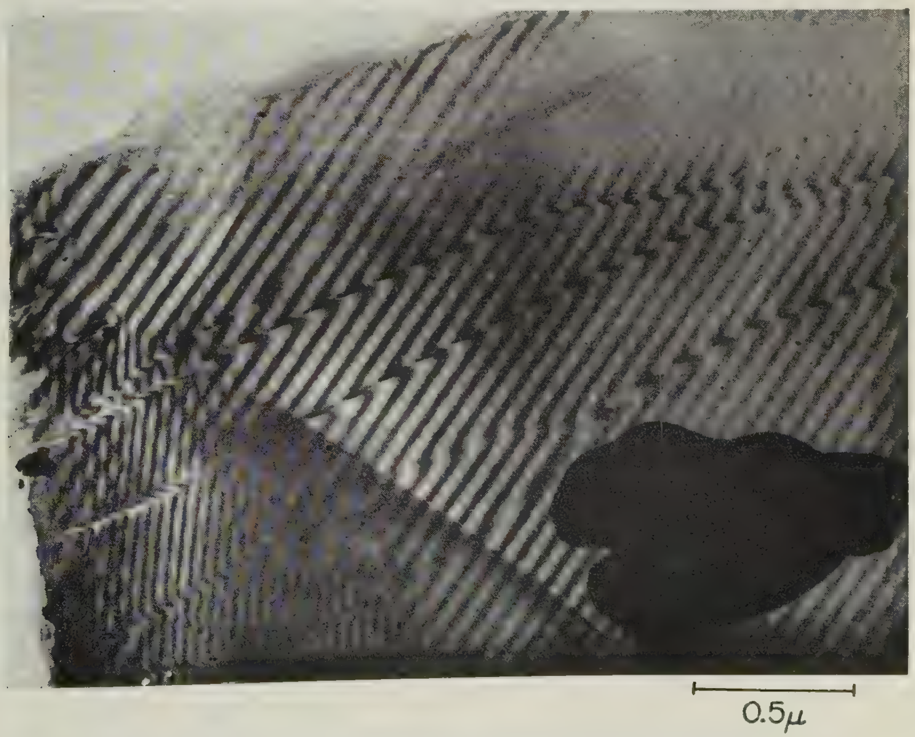

Photo. 6. Disturbance of moiré pattern due to dislocations lying in *c*-plane.

somewhat different ways probably due to the difference in the inclination of crystal; one, parallel to the direction *A*, is predominant in most of the field of the micrograph, and the other, parallel to the direction B, appears only on the lower left-hand side of the picture. We call the former the {100} moiré pattern and the latter the {110} moiré pattern henceforth, since by a closer examination they proved to be arising from double diffraction from the {100} and {110} planes respectively in the hexagonal crystal structure of graphite as shown in Fig. 3. It is noteworthy that, as are seen in this micrograph and Fig. 1 which is a schematical representation of the micrograph, while across the lines such as *ac*, *gh* and *kl* the line shifts of the {100} moire pattern and the {110} pattern take place by just

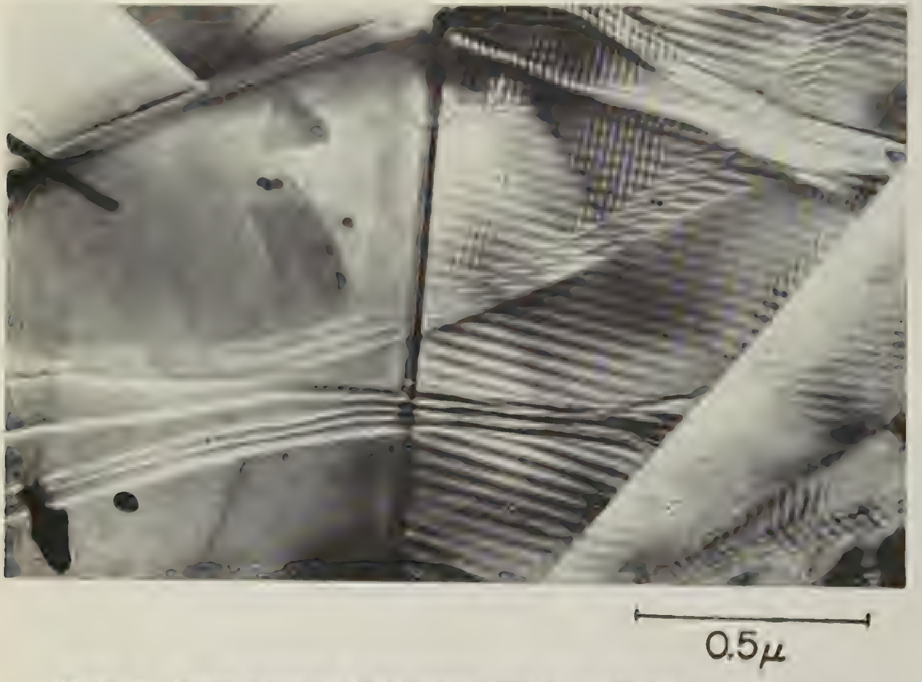

Photo. 7. Image contrast of dislocations and their effect on moiré patterns.

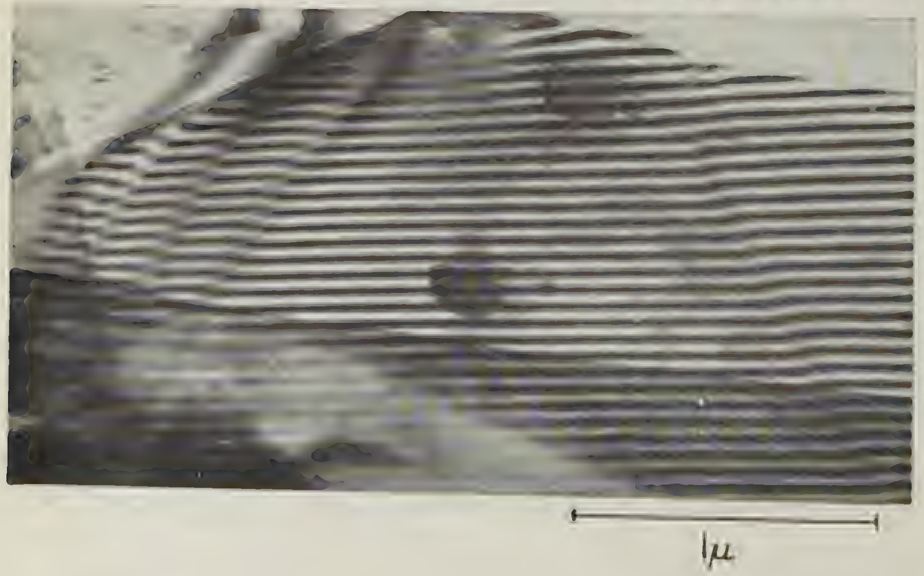

Photo. 8. Line shifts of moiré fringes due to glissile half dislocations.

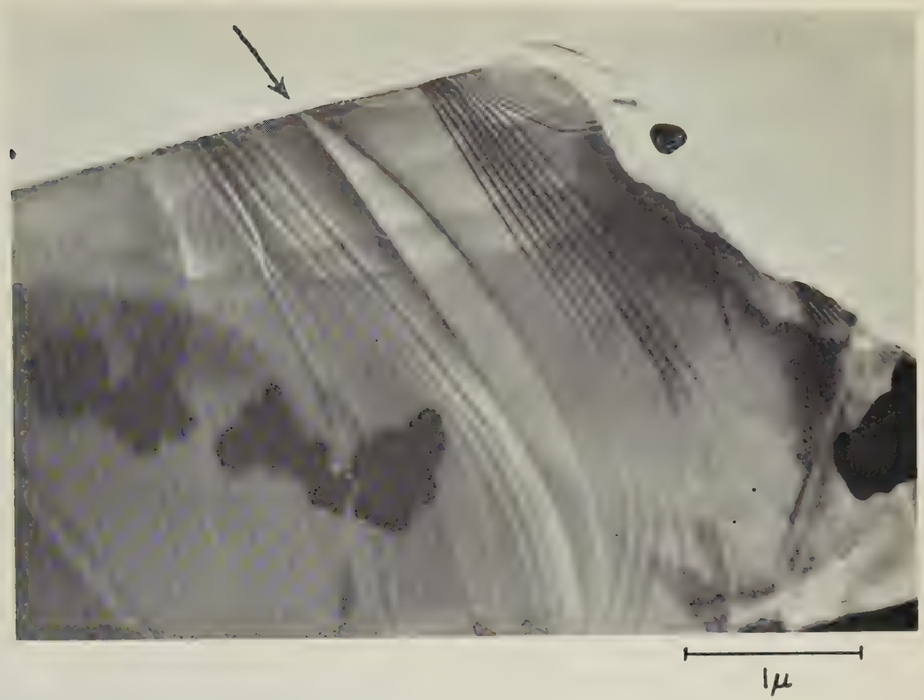

Photo. 9. Sharp image contrast of dislocations.

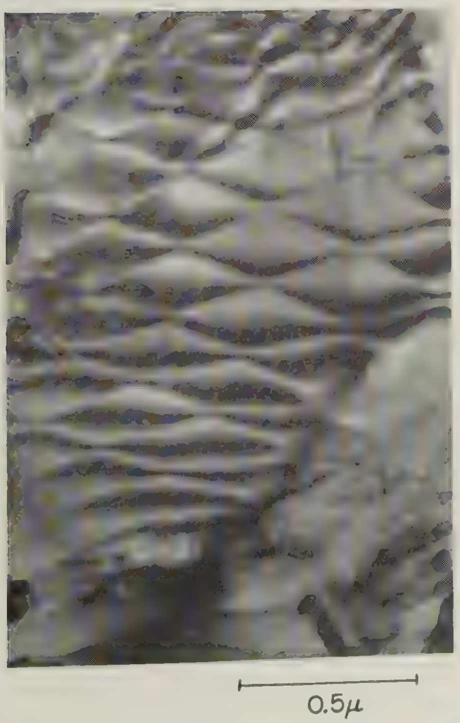

Photo. 10. Triangular network (partly rhombic in appearence) of glissile dislocations.

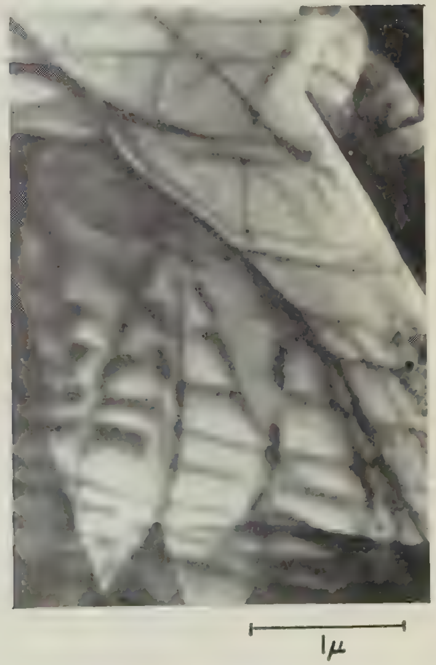

Photo. 11. Random distribution of glissile dislocations.

one and two moiré spacings respectively, across the lines such as *ab*, *jk* and *mk* the shift of the two patterns are about a half and just one moiré spacing respectively. This suggests that the nature, presumably the Burgers vector, of the dislocation lines such as *ac*, *gh* and *kl* is different from that of the lines such as *ab*, *jk* and *mk*. It should also be noted that across five curved lines seen in Photo. 8 the moiré lines shift by the amount of about one third of the moiré spacing, and that generally the line shift takes place gradually across the dislocation line, presumably exhibiting the breadth of the dislocation in the basal plane. By a geometrical analysis based on the kinematical theory a full interpretation of such behaviours of the disturbance of moiré patterns due to dislocation lines as mentioned above can be given, to which we shall refer in the following paragraph.

Apart from the disturbance of moiré pat-

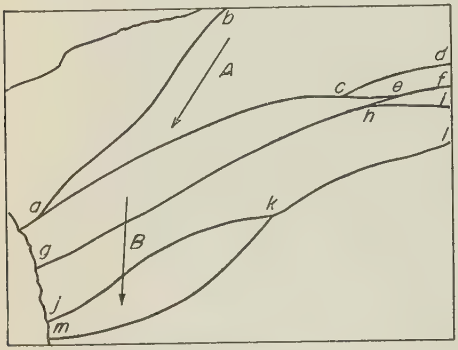

Fig. 1. Schematic representation of Photo. 6.

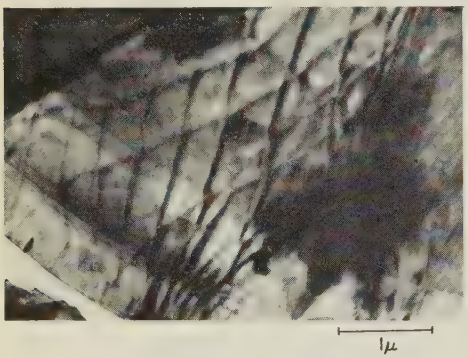

Photo. 12. Square network and double images of dislocations.

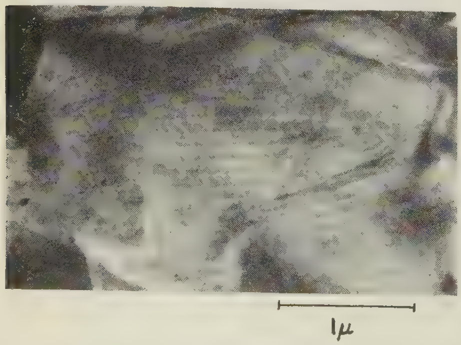

Photo. 13. Parallel array of dislocations with the average distance of 1000 Å.

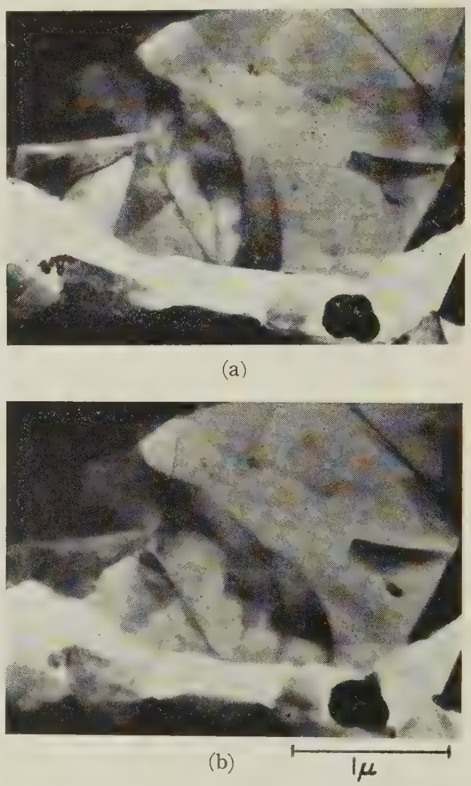

Photo. 14. Motion of dislocation loops.

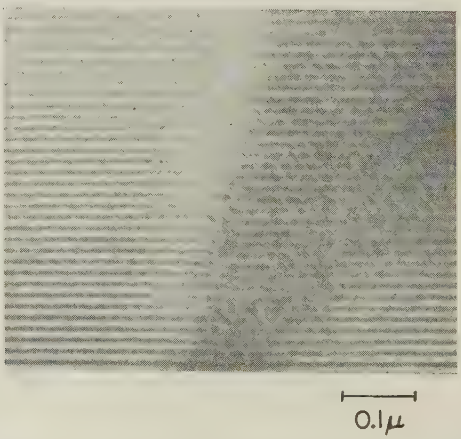

Photo. 15. Moiré dislocation probably caused by a wrinkle of crystal film.

terns, dislocation lines which lie in the basal planes can be directly observed on account of their diffraction contrast. Generally speaking, their appearances and behaviour are similar to those of dislocations observed by many investigators in metal crystals[4,6,17]. In the following are the remarkable features of dislocations in graphite thus observed in the present experiment.

Apparently there are two kinds of dislocations, as are inferable from their difference in the image contrast and mobility, namely one which has sharp, clear contrast and is immobile as shown in Photos. 7 and 9, and the other which has rather obscure, broad contrast and is very mobile as shown in Photos. 10, 11 and 14. As will be discussed later, the Burgers vector of the former is considered to have the main component perpendicular to the basal plane and that of the latter must be in the basal plane. Sometimes paired dislocations which may be the result of split of unit dislocations into their partials are observed. In some cases, such that the thickness of the observed crystal is inadequate or the orientation is not proper for diffraction conditions, it is difficult to identify the kinds of dislocations, unless their motion is observable in the microscope. Moreover, in an extreme case, one cannot distinguish an array of dislocations from a moiré pattern, which will be discussed later on too.

Various types of dislocation networks are observed as well as their random distribution, which are shown in Photos. 9, 10, 11, 12 and 13: Photos. 9 and 13 exhibit parallel arrays of dislocations with the average distance of 1000 Å, a network partly triangular and partly rhombic in appearance is seen in Photo. 10, and a square network in Photo. 12. On the other hand, Photo. 11 shows more or less random distribution of dislocations. Photo. 12 is also remarkable example showing double images of most of the dislocations in the network.

Although many dislocations of various kinds above mentioned are observed in a large number of crystals, there are some crystallites in which no dislocation is observable over several microns in lateral dimensions.

As Grenall[11] first reported, motion of dislocations of the glissile type is easily observed by changing the electron beam current of the microscope. In general, dislocation loops spread from randomly distributed dislocations in certain small area or from a source situated at the periphery of a crystal, move rapidly and more or less discontinuously interacting with other dislocations, and finally form a stable network. Especially the triangular network of about 2000 Å in meshes as shown in Photo. 10 seems to be very stable as a final configuration. Photos. 14 (a) and (b), which were successively taken at the same field in the electron microscope, show the spreading dislocation loops at the initial stage of motion.

§ 4. Discussions

A) *Dislocations in graphite structure*

Dislocations conceivable in the graphite crystal structure are of four kinds as are listed in Table I and schematically shown in Fig. 2 (a), (b), (c) and (d).

Table I. Four kinds of fundamental dislocations in the graphite structure.

Kind	Burgers vector	Line direction	Type
1	// to *c*-plane, a [100]	⊥ to *c*-plane	edge
2	⊥ to *c*-plane, c [001]	⊥ to *c*-plane	screw
3	// to *c*-plane, a [100]	// to *c*-plane	edge and screw
4	⊥ to *c*-plane, c [001]	// to *c*-plane	edge

As is well known[7,15] a dislocation of kind 1 may produce an extra terminating half line or so-called a moiré dislocation such as shown in Photos. 4 (a), (b) and 5, if it actually

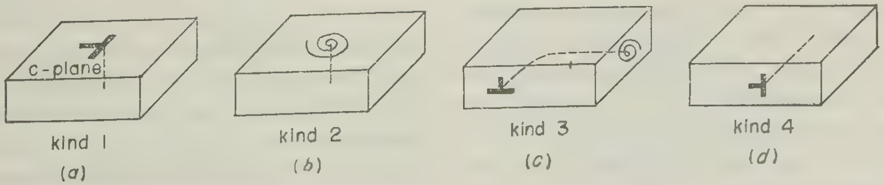

Fig. 2. Schematic representations of four kinds of fundamental dislocations in graphite structure.

exists in graphite crystal. From a theoretical consideration that the interaction force or binding between two succesive c-atomic planes is of van der Waals nature which is very weak as compared with the binding forces in the c-planes, and also from the experimental facts that extraordinarily thin flakes can easily made from a crystal by peeling off c-atomic layers and that the crystal is very glissile along c-planes producing c-plane slip and c-axis rotation, it is rather difficult to conceive that this kind of edge dislocation threading every successive c-atomic plane can stably exist. Dawson and Follett[12)] found many extra terminating half lines in the moiré pattern from synthetic graphite, and refered them to real edge dislocations of kind 1. Although we cannot draw a conclusion on the existence of dislocations of this kind at the present stage of the experiment, so far as the results obtained at least in case of natural graphite most of the extra terminating lines in moiré patterns seem to be not arising from real edge dislocations of this kind, but be the so-called ghosts caused by the local distortion or bending of the crystal, or be due to another kind of dislocations lying in the c-atomic plane such as kind 3. The latter two cases will be explained in detail in the following section.

Kind 2 is of screw type threading c-atomic planes like kind 1. In this case, however, its real existence is more thinkable than the kind 1, if we consider the continuous herical structure of successive c-planes around a screw dislocation of this kind. Actually, Tsuzuku[10)] observed such screw dislocations in small penny shaped graphite crystals grown from carbon black particles, which seem to play very important rôle in the growth of crystals. It may be not unreasonable to expect that this kind of dislocations produces an observable image contrast and a disturbance in the moiré pattern at any rate. However, we have not yet observed them in our graphite crystals.

Kind 3 is the most probable to exist in graphite crystals and is undoubtedly responsible for their very glissile nature along c-layers. Most of the observed dislocations which are mobile and have the obscure, broad contrast such as shown in Photos. 10, 11 and 14 may be of this kind. The very weak van der Waals interaction between c-atomic layers would be again an important factor to determine the breadth of these dislocations, which may in turn govern its electron image contrast. The Burgers vectors of unit dislocations of this kind are shown by $\boldsymbol{a}$, $\boldsymbol{a}'$ and $\boldsymbol{a}''$ in Fig. 3 as well as the Burgers vectors of their partials $\boldsymbol{b}$, $\boldsymbol{c}$ and so on. As a hatched parallelogram in the figure shows, the former form the unit cell of the graphite structure together with the c-axis vector perpendicular to them. It is apparent that a unit dislocation can reduce its energy by splitting into two partials with a stacking fault between them on account of the favourable strain energy relation, $a^2 > b^2 + c^2$ and of very low stacking fault energy. The stacking made of c-layers of the graphite structure can be expressed by $ACACAC\cdots$ or $ABABAB\cdots$ if it is perfect. In Fig. 3, the atomic arrangements in the three configurations, A, B, and C shown by solid circles and solid lines, dotted circles and dotted lines, and open circles and double lines respectively. When we displace the A configuration by the displacement vector or slip vector $\boldsymbol{b}$, we have the B configuration, and by the $\boldsymbol{c}$ vector the C configuration.

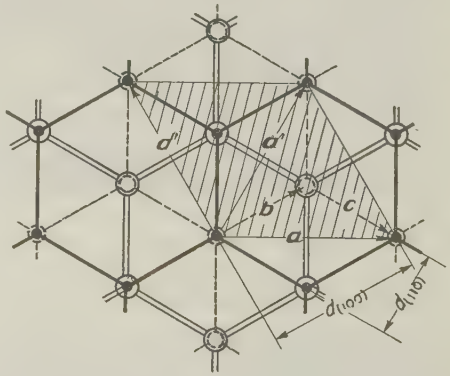

Fig. 3. Three configurations of c-layer stacking and Burgers vectors in c-plane in graphite structure.

It follows that, when a half dislocation of the Burgers vector $\boldsymbol{b}$ moves along a slip plane between a layer of the A configuration and that of the C configuration underneath, a stacking sequence $ACACBABA\cdots$ is obtained behind the dislocation, provided that the lower part of the crystal is fixed for the convenience of understanding. Therefore, if this half dislocation is followed by another half dislocation of the $\boldsymbol{c}$ vector for completion of a unit dislocation, a stacking fault of the *ABCA* type is produced between the two dislocations. This situation is shown in Fig. 4 (a). Similarly, if a half dislocation of the ***c*** vector precedes that of the ***b*** vector, a stacking fault of the *ACCA* type is obtained, which is shown in Fig. 4 (b). The former type of split of a unit dislocation may be more probable than the latter, because the *CC* stacking of the latter type would be associated with a stacking fault energy higher than that of the *ABC* type. Considering, however, that the van der Waals interaction between stacking layers are very weak as compared with the homopolar binding in *c*-atomic layers, well-defined split of a unit dislocation such as in f. c. c. metals seems to be rather difficult to expect in graphite crystals. Actually, among many observed dislocations which can be regarded as kind 3, very few are found clearly splitting in spite of their unmistakably broad contrasts in the direct image or in the moiré pattern. At present we cannot clarify the reason why some dislocations behave themselves like exceptions by clear splitting. Nevertheless, half dislocations of the above types appear to have important rôles in imperfect crystals such as of synthetic graphite or of ground powder of graphite.

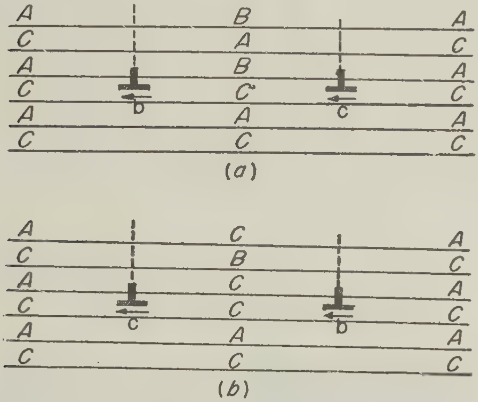

Fig. 4. Partial dislocations of kind 3 and stacking disorders of *c*-layers.

Dislocations of kind 4 are formed at the periphery of *c*-atomic layers inserted in or extracted from the *ACACAC* hexagonal *c*-layer stacking in a crystal as shown in Fig. 5: Unit dislocation, shown by (a), is a result of insertion or missing of two successive layers, and should be associated with a considerabls high strain energy, although it has no stacking fault along the extra or missed planes. Insertion or extraction of a single layer produces a half dislocation with a stacking fault layer of *ABC* type, like (b), or *ACC* type, like (c). A full dislocation (a) would reduce its self energy by splitting into two (c) dislocations if the atomic diffusion can take place in its vicinity, and a (c) dislocation in turn would reduce its stacking fault energy if associated by a glissile half dislocation of kind 3 previously mentioned as shown by Fig. 5 (d). Such behaviours of splitting and association of dislocations seem to be plausible and important, as they can fully account for the disturbances in the moiré pattern by dislocations, which is to be discussed in the next section.

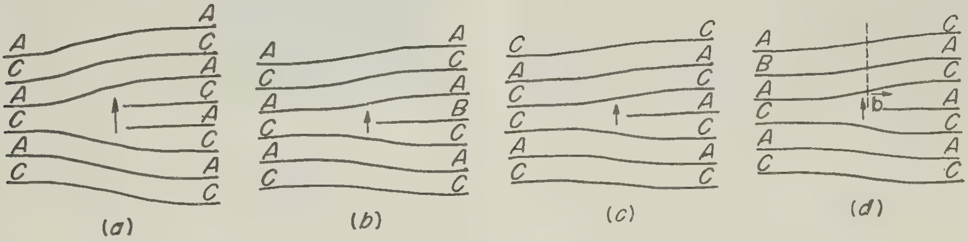

Fig. 5. Dislocations of kind 4.

B) *Disturbances in moiré patterns due to dislocations lying in c-atomic layers*

As is mentioned in the preceding paragraph, origins of extra terminating half lines in the moiré pattern have been discussed by many investigators[7,8,15]. Among these discussions, that by Bassett, Menter and Pashley[8] appears to be worthy of note in regards to another kind of disturbance of moiré pattern due to dislocations lying in *c*-atomic layers: They first pointed out that generally a dislocation line, the Burgers vector of which has a component perpendicular to the lattice planes giving rise to the moiré pattern, can be detected as a number of terminating half lines even if it is not perpendicular to the film examined or it is a screw dislocation. Although they didn't treat the case in which a dislocation passes through the film completely in parallel with it or more specifically the case in question in which the slip plane is parallel to the film, their argument may be extended to such cases to interpret the disturbances in moiré patterns as shown in Photos. 6, 7 and 8.

Apart from the method that Bassett et al[8] have used to illustrate their argument, we first begin with treating a simple line greating model[21] which can be regarded as the lattice projection to form moiré patterns. Consider a portion of a line grating bounded by a curved line is displaced by an amount of fraction of the line spacing, d, in the direction normal to the lines as shown in Fig. 6 (a).

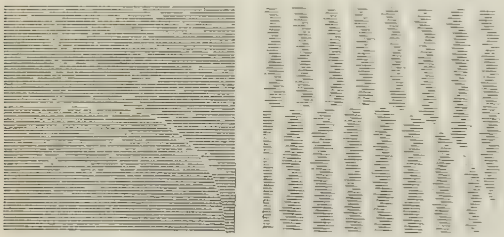
(a) (b)

Fig. 6. Line shift of moiré fringes due to a displacement of a part of a line grating.

By superposing this line grating on a perfect line grating making a small angle α with it, a moiré pattern which has a shift of moiré fringes across the boundary line by a fraction of the fringe spacing, $D=d/\alpha$, is formed. It is easily verified that the amount of displacement of the line grating and that of the moiré fringes have the same fraction in respect to their spacings; as a special case, if the displacement of the line grating is just d, the shift of the fringes is just D too.

Such a displacement as mentioned above will actually take place in a crystal lattice by a dislocation with the Burgers vector and slip plane which are parallel with the film plane. Consider a glissile edge dislocation of possitive sign of kind 3 in a graphite thin crystal as shown in Fig. 7. Due to a component of its Burgers vector perpendicular to the crystal planes to form a moiré pattern, contraction of spacings of the crystal planes will be produced along the dislocation line in the uppermost part of the crystal bounded by the slip plane as shown in Figs. 7 and 8 (a). The latter picture is the same as Fig. 6 (a) in such a sense that there is a displacement corresponding to the displacement vector or the Burgers vector between the upper and lower sides of the lattice, only a difference being that in Fig. 8 (a) the displacement is gradual across the breadth of the dislocation line.

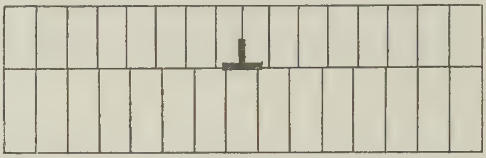

Fig. 7. An edge dislocation of kind 3 and change of lattice spacings in its vicinity.

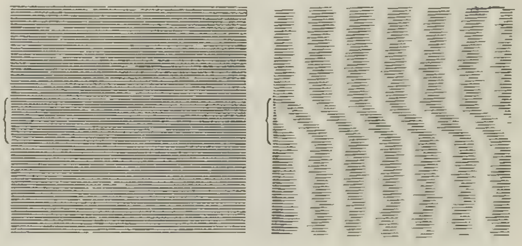
(a) (b)

Fig. 8. Line shift of moiré fringes due to an edge dislocation of kind 3.

Like in the case of Figs. 6 (a) and (b), superposition of Fig. 8 (a) on a perfect line grating produces a curved and shifted moiré pattern as shown in Fig. 8 (b), which can actually be observed very frequently as in Photos. 6, 7 and 8. In the above explanation, we took no account of the lower part of the crystal, which will bear practically the same amount of shift of the moiré fringes in the reverse direction due to the displacement associated with lattice expansion along the dislocation line. In actual observations, therefore, either of the two parts which is thicker or more favourable in the diffraction condition will have a predominant effect on the ultimate image formation.

It is clear from the above model that the breadth of disturbed or curved region of the moiré lines directly gives the width of the dislocation on the slip plane and that the amount of shift of the moiré lines gives the component of Burgers vector perpendicular to the lattice planes concerned. From Photos. 6, 7 and 8, the dislocation width is estimated to be 200 Å or less. This value seems to be much larger than those which are expected for dislocations in metal crystals, but may be not unreasonable if we consider that the difinition of the dislocation width in the present case is different from a usual "half width" difinition, that the very weak interaction between the *c*-atomic layers above and below the slip plane tends to spread the dislocation, and that there is a possibility for a unit dislocation to split into partial dislocations. In fact, a simple calculation following the Peierl's analysis for the isotropic case[18] gives the value of the order of 100 Å which is to be compared with the above observed value. The relation between the Burgers vector and the associated line shift of the moiré pattern in graphite can be predicted by using Fig. 3: Consider a dislocation with the Burgers vector $\boldsymbol{a}$. Since the component of the Burgers vector normal to the (100) lattice planes just corresponds to one lattice spacing, this dislocation will give a relative displacement of this amount to the lattice before and behind it, and therefore will give a full line shift of the (100) moiré fringes. On the other hand, a half dislocation with the Burgers vector $\boldsymbol{b}$ has the normal component of 2/3 of the (100) lattice spacing, and therefore will give the 2/3 line shift of the moiré pattern. Similarly, a half dislocation with the vector $\boldsymbol{c}$ will give 1/3 line shift of the (100) moiré pattern, which is clearly seen in Photo. 8. The same consideration reveals that a dislocation with the Burger $\boldsymbol{a}'$ in Fig. 3 will give the (110) moiré fringes a shift of two line spacings while it gives a full line spacings while it gives a full line shift of the (100) moiré fringes, and that a half dislocation with the vector $\boldsymbol{b}$ will give a full line shift to the (110) moiré fringes. All of these predicted behaviour of dislocations concerning the disturbance on moiré patterns are actually found in Photo. 6 as mentioned in the preceding paragraph. It should also be noted that the Kirchhoff's law in regard to the amounts of line shift is maintained at every junction point of dislocation lines such as *c*, *e*, *h* and *k*, suggesting the preservation of the same low regarding their Burgers vectors.

Two problems seem to remain unsolved: In the first, the line shift of about a half line spacing which is actually observed on dislocation lines such as *ce*, *hi* and *jk* in Photo. 6 cannot be deduced from the above simple line grating model taking account of possible Burgers vectors in the graphite structure. However, careful reexamination of Fig. 7, in which the concerned lattice planes are represented by vertical straight lines even in the vicinity of the dislocation because of the assumption that the crystal film is very thin, will lead to a conclusion that the amount of line shift is determined not only by the Burgers vector of the dislocation but also by some other conditions such as the depth or the distance of crystal part to produce the moiré pattern from the dislocation and possibly the applied stress to the crystal film. For instance, if we assume that the film is very thick, the crystal part far apart from the dislocation underneath or above it has no longer dilatation field and hence no displacement in the lattice planes, so that no line shift will take place in the moiré pattern. Consequently, it is not inconceivable that we could observe a line shift in the moiré pattern the amount of which does not exactly correspond to a Burgers vector possible in the crystal structure. The second problem arises from the fact that two arguments seemingly exclusive to each other are sometimes compatible in one dislocation; one argument is that a sharp, stationry diffraction contrast is due to a sessile dislocation of kind 4 which would not give rise to the line shift of the moiré pattern, and the other that glissile dislocation of kind 3 which produce an obscure contrast can cause the line shift because their Burgers vector have a component normal to the lattice planes to form the moiré pattern. For instance, while several lines on the left-hand side of Photo. 7 have a sharp immobile diffraction contrast peculiar to dislocations of kind 4, the same lines on the right-hand side are associated with the line shift of the moiré pattern which is characteristic of dislocations of kind 3. So far as observed in the present experiment, many dislocations have such an ancipital character. We have, therefore, to draw a conclusion that many dislocations are actually the composite of kind 3 and kind 4. Such association of two kinds of dislocations might arise from two causes, that, as previously mentioned, a dislocation of Fig. 5(c) would reduce its stacking fault energy if associated with a half dislocation of kind 3 as shown in Fig. 5 (d), and that the core energy of either of the two dislocations might be reduced by the association. Recently, Amelinckx[13] observed dislocation rings of kind 4 as a consequence of plane condensation of vacancies in thermally quenched and treated graphite crystals. From their image contrast, he suggested that the dislocation ring is sometimes accompanied by slip on the plane of condensation by a half dislocation to reduce the energy of stacking disorder, which is in good agreement with the above conclusion.

C) *Origins of extra half lines in moiré patterns*

The line grating model in the preceding section for the explanation of the line shift of moiré fringes due to dislocations of kind 3 can easily extended to interpret the occurence of extra terminating half lines in the moiré pattern. Consider a dislocation of kind 3 the Burgers vector of which is such as to produce a full line shift of a moiré pattern. The shift and curvature of the moiré fringes around the edge part of this dislocation is well described by Fig. 8 (b), and is again shown on the left hand side of a schematical representation of Fig. 9. As the dislocation increases its screw component by curving as shown in the latter figure, the curvature of the moiré fringes becomes less sharp although the same amount of line shift still remains as is seen in the middle of the figure. Finally, when the dislocation becomes a pure screw as far as the component of Burgers vector to produce the line shift is concerned, the dislocation line is parallel to the moiré lines and no line shift will be observed. It follows that there must be an extra terminating half line at an end of the pure screw part such as denoted by P in Fig. 9. Such a half line in the moiré pattern, arising from a glissile dislocation of kind 3 lying in the c-plane, may distinctive from that due to a dislocation of kind 1 by its high mobility and anomalous curving of some moiré fringes near the extra terminating half line. Actually, many of the extra half lines observed in the present experiment, for instance those in Figs. 4 (a) and (b), have such characters as above mentioned and therefore seem to arise from this origin.

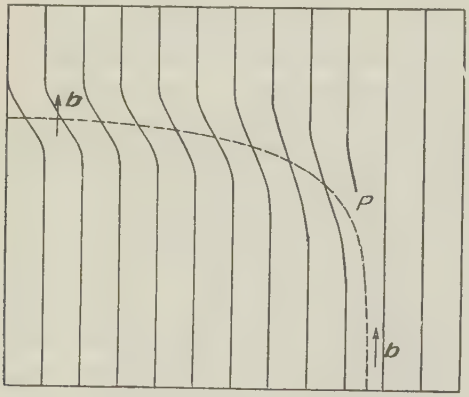

Fig. 9. Extra terminating half line in moiré fringes due to a dislocation of kind 3.

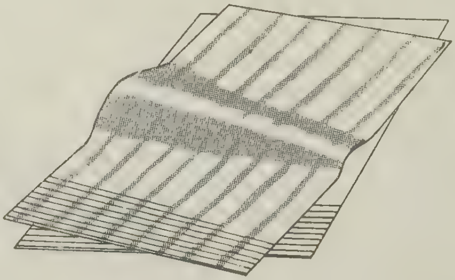

Fig. 10. Small wrinkle on one of two overlapping crystals which can produce an extra half line in the moiré pattern.

Another possible origin for extra half lines in the moiré pattern may be a local distortion of one of the overlapping crystal films otherwise perfect, such as shown in Fig. 10, which would take place especially in case of graphite crystals. An example of this kind of moiré dislocation is given by Photo. 15, in which a distinctive half line is not shown, but instead n half lines are found to meet $n+1$ half lines, n being of the order of 30. As is well known, the spacing of the rotation moiré lines is given by $D=d/\alpha$, where α is the rotation angle and d the spacing of lattice planes to form the moiré lines. α is of the order of 2×10^{-2} rad., when D is about 100 Å. By differenciating the above equation, we have $\delta D/D=-\delta\alpha/\alpha$. Hence, to obtain a value of 1/30 for $\delta D/D$, we may put a value as small as 10^{-3} rad. to $\delta\alpha$, which would easily be produced by a slight wrinkle, as shown in Fig. 10, without extremely disturbing the double diffraction condition there. A wide range disturbance of moiré fringes around the extra half line is characteristic of this kind of moiré dislocation as is seen in Photo. 15.

D) *Diffraction contrast of dislocations in graphite*

P. B. Hirsch, A. Howie and M. J. Whelan[19] treated the electron microscope image contrast of dislocations by a kinematical theory, and clarified that the contrast is essentially phase contrast in the Bragg diffracted beams, the phase difference being due to the displacements of atoms around the dislocations. The theory succeeded in explaining characteristic features of the observed images. Many of such features, for instances, the dependence of the contrast on the Burgers vector of dislocation, the reversal of contrast on bright and dark field images, the invisibility of some dislocations, and the occurrence of double images, are also observed in the present experiment. Especially, as are cited in Table 1, dislocations in graphite have very simple geometrical configurations in spite of the variety in their kinds. Hence, if the dislocation structures, or the atomic displacements around the dislocations, in the graphite lattice were carefully analysed, this would immediately lead to the quantitative verification of the theory and hence to clarifying the problem of the electron image contrast of defects in crystals.

Recently, Y. Kamiya and R. Uyeda[20] found two interesting phenomena concerning the image contrast of dislocations in molybdenite crystals which are also found in our graphite crystals; one is that the diffraction contrast on the crystal film changes abruptly from black to white across a dislocation line as indicated by an arrow in Fig. 9, and the other is that very regular array of dislocations is sometimes indistinguishable from the moiré pattern in their appearences. Kamiya and Uyeda explained the former by taking account of the tilt of the crystal film given by the edge dislocation the Burgers vector of which is parallel to the film. This gives, in our case, an evidence of the association of dislocations of kind 3 and kind 4, because the dislocations in Fig. 9 are regarded as immobile dislocations of kind 4 which would not produce the tilt of the crystal film by themselves. They also explained the latter by replacing the rotation or shear of two overlapping crystals to form the moiré pattern by a twist or shear boundary formed by the cross grating or array of screw dislocations, and concluded the correspondence between the moiré lines and the dislocation lines. This will be again discussed in Part II in regard to the irradiation effect in graphite crystals.

Acknowledgements

The authors wish to express their hearty thanks to Drs. Y. Takagi and K. Motojima for their interest and encouragement in this work, and to Profs. R. Uyeda, T. Suzuki and Dr. H. Suzuki for their valuable discussions. Their thanks are also due to Messrs. H. Ōtsu and Y. Katano for their continued assistance in this work.

References

1) J. W. Menter: Proc. Roy. Soc. **A236** (1956) 119.
2) G. W. Brindley, J. J. Comer, R. Uyeda and J. Zussman: Act. Cryst. **11** (1958) 99.
3) Y. Kamiya, M. Nonoyama and R. Uyeda: J. Phys. Soc. Japan **14** (1959) 1334.
4) P. B. Hirsch, R. W. Horne and M. J. Whelan: Phil. Mag. **1** (1956) 677.
5) J. Silcox and P. B. Hirsch: Phil. Mag. **4** (1959) 72.
6) M. J. Whelan, P. B. Hirsch, R. W. Horne and W. Bollmann: Proc. Roy. Soc. **A240** (1957) 524.
7) H. Hashimoto and R. Uyeda: Act. Cryst. **10** (1957) 143.
8) G. A. Bassett, J. W. Menter and D. W. Pashley: Proc. Roy. Soc. **246** (1958) 345.
9) K. Izui: J. Phys. Soc. Japan **14** (1959) 1829.
10) T. Tsuzuku: J. Phys. Soc. Japan **12** (1957) 778; Proc. *3rd Carbon Conf.*, Pergamon Press, London (1959), 433.
11) A. Grenall: Nature, London **182** (1958) 448.
12) I. M. Dawson and E. A. C. Follett: Proc. Roy. Soc. **A253** (1960) 390.
13) S. Amelinckx: Phys. Rev. Letters **5** (1960) 51.
14) J. F. Goodman: Nature, London **180** (1957) 425.
15) D. W. Pashley, J. W. Menter and G. A. Bassett: Nature, London **179** (1957) 752.
16) H. Hashimoto, T. Naiki and M. Mannami: Electron Microscopy **7** (1959) 174.
17) P. B. Hirsch, R. W. Horne and M. J. Whelan: *Dislocations and Mechanical Properties of Crystals, John Wiley* (1957) 92.
18) A. H. Cottrell: *Dislocations and Plastic Flow in Crystals*, Clarendon Press, Oxford (1953) 58.
19) P. B. Hirsch, A. Howie and M. J. Whelan: Phil. Trans. Roy. Soc. **252** (1960) 499.
20) Y. Kamiya, K. Ando, M. Nonoyama and R. Uyeda: J. Phys. Soc. Japan **15** (1960) 2025.
21) H. Hashimoto: J. Phys. Soc. Japan **13** (1958) 534.

JOURNAL OF THE PHYSICAL SOCIETY OF JAPAN, Vol. 16, No. 2, FEBRUARY, 1961

A Diffraction Pattern caused by Temperature Diffuse Scattering. I. General Theory

By Yoshiro KAINUMA

Physical Institute, Nagoya University, Nagoya

(Received September 24, 1960)

When diffuse X-rays caused by scattering in a thermally vibrating crystal are scattered again in the same crystal, a new diffraction pattern similar to Kossel-pattern is produced. The properties of the new pattern is discussed by the use of the perturbation theory of X-ray scattering in a crystal. This discussion is similar to that given in the author's theory of Kikuchi-pattern (Acta Cryst. 8 (1955) 247).

According to the present theory, the signs of crystal structure factor can be determined by examining the new pattern produced at an appropriate crystal orientation, provided relative values of elastic constants are available.

§1. Introduction

In the present paper, the diffuse scattering of X-rays which is caused by thermal vibration of crystal lattice has been extensively studied. If the diffuse X-rays are reflected by net planes in the same crystal, a new diffraction pattern, geometrically similar to Kossel-pattern, will appear superposed on the diffuse scattering. This was first pointed out by Grenville-Wells[1)*)]. The intensity formulae of this pattern are derived in what follows, and it is pointed out that there is a possibility of a new approach to the phase problem in X-ray crystal analysis by utilizing this pattern.

Calculation of the intensity consists of two steps. In the first step, the intensity is calculated for a crystal in which the vibrating atoms are frozen at a certain instant of time. This calculation is carried out by the use of of a perturbation method in which a generalized theorem of reciprocity in optics plays an important part. In the second step the calculated intensity of the first step is averaged over an interval of time much longer than the periods of lattice vibrations. The time average is estimated by employing the theory of lattice vibration.

It is shown that the new diffraction pattern is superposed on the ordinary temperature diffuse scattering. The new pattern lies on a certain diffraction cone and can be separated into two parts, one with a symmetrical line profile corresponding to Kikuchi-line, the other with an antisymmetical line profile corresponding to Kikuchi-band. The antisymmetrical part gives a pattern similar to the 'Helldunkellinie' of Kossel-pattern.[**)]

In centro-symmetrical crystals the sign of structure factor may be determined by examining the antisymmetrical line profile produced at an appropriate crystal orientation, provided the relative values of the elastic constants are given.

§2. Perturbation Method

Let a beam of parallel X-rays fall upon a crystal. The electric field of the incident X-rays in vacuum is given by

$$\boldsymbol{E}=\boldsymbol{E}_0 \exp(-2\pi i \boldsymbol{K}_0\cdot\boldsymbol{r})\exp(2\pi ict/\lambda)\ , \qquad (1)$$

where λ and $\boldsymbol{K}_0$ are the wavelength and wave vector respectively of the incident X-rays and all other notations have their usual meanings.

The electromagnetic field of X-rays inside and outside the crystal satisfies the following equations:

$$\left.\begin{array}{l}\mathrm{rot}\,\boldsymbol{E}=-(1/c)\partial\boldsymbol{H}/\partial t\\ \mathrm{rot}\,\boldsymbol{H}=(1/c)\partial\boldsymbol{D}/\partial t\end{array}\right\} \qquad (2)$$

and

$$\boldsymbol{E}=\{1+(e^2/mc^2)(\lambda^2/\pi)\rho(\boldsymbol{r})\}\boldsymbol{D} \qquad (3)$$

where $\rho(\boldsymbol{r})$ is the density of electrons. When

---

[*)] N. Norman (Acta Cryst. **11** (1958) 1) observed similar diffraction phenomena due to Compton scattering of X-rays by a diamond crystal.

[**)] The corresponding phenomena in electron diffraction due to thermal diffuse scattering were studied by S. Takagi (J. Phys. Soc. Japan **13** (1958) 278, 287). Takagi's theoretical approach, however, is different from the present author's treatment.

$\rho(r)$ corresponds to the frozen crystal, $\rho(r)$ has no lattice periodicity. However, the same average of the density $\langle\rho(r)\rangle$ is periodic within the crystal. We will hereafter denote $\langle\rho(r)\rangle$ by $\rho_1(r)$. If the incident beam of X-rays falls upon an imaginary crystal with the density $\rho_1(r)$, the field of X-rays $\boldsymbol{E}_1$, $\boldsymbol{H}_1$ and $\boldsymbol{D}_1$ can be easily calculated by the use of Eqs. (2) and (3) in accordance with the ordinary procedure of dynamical theory.

Let us define $\boldsymbol{E}_2$, $\boldsymbol{H}_2$ and $\boldsymbol{D}_2$ by $\boldsymbol{E}_2=\boldsymbol{E}-\boldsymbol{E}_1$, $\boldsymbol{H}_2=\boldsymbol{H}-\boldsymbol{H}_1$ and $\boldsymbol{D}_2=\boldsymbol{D}-\boldsymbol{D}_1$, respectively. Then $\boldsymbol{E}_2$, $\boldsymbol{H}_2$ and $\boldsymbol{D}_2$ describe the diffuse scattering caused by thermal vibration*, including the new pattern besides the ordinary temperature diffuse scattering (§ 3). $\boldsymbol{E}_2$, $\boldsymbol{H}_2$ and $\boldsymbol{D}_2$ satisfy Eq. (2) while Eq. (3) is written

$$\boldsymbol{E}_2=\{1+(e^2/mc^2)(\lambda^2/\pi)\rho_1(r)\}\boldsymbol{D}_2 + (e^2/mc^2)(\lambda^2/\pi)\rho_2(r)\boldsymbol{D}_1\ , \tag{4}$$

where $\rho_2(r)$ is the difference between instantaneous electron density and averaged electron density, i.e. $\rho_2(r)=\rho(r)-\rho_1(r)$. In the derivation of Eq. (3) we neglected a small quantity $(e^2/mc^2)(\lambda^2/\pi)\rho_2(r)\boldsymbol{D}_2$.

We must calculate the electromagnetic wave field with the suffix 2 at a point A which lies far from the crystal. If a radiation of the same wavelength λ, which is emitted from the point A, falls upon the imaginary crystal of an electron density $\rho_1(r)$, the electromagnetic field satisfies the equations

$$\left.\begin{aligned}&\operatorname{rot}(\overline{\boldsymbol{E}}-\overline{\boldsymbol{E}}_e)=-(1/c)\partial\overline{\boldsymbol{H}}/\partial t\\&\operatorname{rot}\overline{\boldsymbol{H}}=(1/c)\partial\overline{\boldsymbol{D}}/\partial t\end{aligned}\right\} \tag{5}$$

and

$$\overline{\boldsymbol{E}}=\{1+(e^2/mc^2)(\lambda^2/\pi)\rho_1(r)\}\overline{\boldsymbol{D}}\ , \tag{6}$$

where $\overline{\boldsymbol{E}}_e$ in Eq. (5) is an external electromotive force present at the singular point A and is given by

$$\overline{\boldsymbol{E}}_e=\overline{\boldsymbol{p}}\exp(2\pi ict/\lambda)\delta(\boldsymbol{r}-\boldsymbol{r}_A)\ , \tag{7}$$

where $\overline{\boldsymbol{p}}$ is a constant dipole moment and $\delta(\boldsymbol{r}-\boldsymbol{r}_A)$ is the delta-function. Hereafter, we call the electromagnetic wave expressed by $\overline{\boldsymbol{E}}$, $\overline{\boldsymbol{H}}$ and $\overline{\boldsymbol{D}}$ the reciprocal wave. By the help of the reciprocal wave we can calculate $\boldsymbol{D}_2$ at the point A by a generalized theorem of reciprocity, which is expressed as follows:

$$\boldsymbol{D}_2(\boldsymbol{r}_A)\cdot\overline{\boldsymbol{p}}\exp(2\pi ict/\lambda) = -(e^2/mc^2)(\lambda^2/\pi)\int\rho_2\boldsymbol{D}_1\cdot\overline{\boldsymbol{D}}\,d\boldsymbol{r}\ . \tag{8}$$

The proof of Eq. (8) is similar to that of the ordinary theorem of reciprocity in optics[2),3)], and is given in Appendix 1.

If the incident radiation does not excite any Bragg reflection, we have the expression for $\boldsymbol{D}_1$ inside the crystal as follows:

$$\boldsymbol{D}_1=\boldsymbol{E}_0\exp(-2\pi i\boldsymbol{k}_0\cdot\boldsymbol{r})\exp(2\pi ict/\lambda)\ , \tag{9}$$

where $\boldsymbol{k}_0$ is the wave vector of the incident wave in the crystal. If the reciprocal wave is reflected by a single net plane $\boldsymbol{G}$, then according to the formula of dynamical theory[4)] we have the following expression for $\overline{\boldsymbol{D}}$ inside the crystal;

$$\overline{\boldsymbol{D}}=\sum_h\sum_s\overline{\boldsymbol{D}}_h{}^s\exp(-2\pi i\overline{\boldsymbol{k}}_h{}^s\cdot\boldsymbol{r})\exp(2\pi ict/\lambda)\ , \tag{10}$$

where $\sum_h$ is a summation over the reciprocal lattice points $\boldsymbol{O}$ (the origin) and $\boldsymbol{G}$, and $\sum_s$ is that over the wave points P' and P'' (Fig. 3).

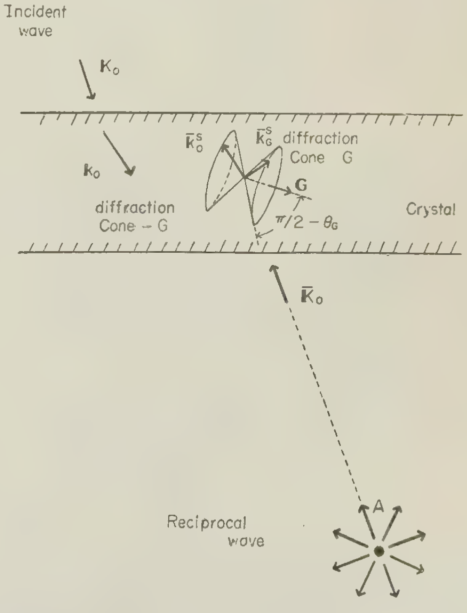

Fig. 1. Incident wave and reciprocal wave in Laue case (transmission pattern).

---

* The total scattering intensity is poportional to the time average $\langle|\boldsymbol{E}|^2\rangle=\langle|\boldsymbol{E}_1|^2\rangle+\langle|\boldsymbol{E}_2|^2\rangle+\langle\boldsymbol{E}_1\cdot\boldsymbol{E}_2{}^*\rangle+\langle\boldsymbol{E}_1{}^*\cdot\boldsymbol{E}_2\rangle$. $\langle|\boldsymbol{E}_1|^2\rangle$ represents the incident wave and Bragg reflections, and thus it vanishes in all directions except the directions of the incident beam and of Bragg reflections. On the other hand, $\langle|\boldsymbol{E}_2|^2\rangle$ vanishes in the exact directions of the incident beam and of Bragg reflections. Therefore, in the above equation the cross terms $\langle\boldsymbol{E}_1\cdot\boldsymbol{E}_2{}^*\rangle$ and $\langle\boldsymbol{E}_1{}^*\cdot\boldsymbol{E}_2\rangle$ vanish in all directions and $\langle|\boldsymbol{E}_2|^2\rangle$ represents diffuse scattering caused by thermal vibration.

$\overline{\boldsymbol{D}}_h{}^s$ is the amplitude of the plane wave with the wave vector $\overline{\boldsymbol{k}}_h{}^s$, where $\overline{\boldsymbol{k}}_G{}^s=\overline{\boldsymbol{k}}_0{}^s+\boldsymbol{G}$. Eq. (10) is derived by the use of the approximation that the reciprocal wave outside the crystal can be regarded as a plane wave at the position of the crystal and given by

$$\overline{\boldsymbol{E}}=\overline{\boldsymbol{E}}_0\exp(-2\pi i\overline{\boldsymbol{K}}_0\cdot\boldsymbol{r})\exp(2\pi ict/\lambda)\,, \tag{11}$$

where

$$\overline{\boldsymbol{E}}_0=-(\pi/R)\{\overline{\boldsymbol{K}}_0\times(\overline{\boldsymbol{K}}_0\times\boldsymbol{p})\}\exp(-2\pi iR/\lambda)\,, \tag{12}$$

where R is the distance between the point A and the crystal, and $\overline{\boldsymbol{K}}_0$ is the wave vector of the plane wave (Fig. 1). $\overline{\boldsymbol{D}}_h{}^s$ in Eq. (10) is given by the fundamental equations and boundary conditions in the dynamical theory of diffraction*.

Introducing unit vectors $\overline{\boldsymbol{e}}_\perp$ and $\overline{\boldsymbol{e}}_{||}$ we have

$$|\boldsymbol{D}_2(\boldsymbol{r}_A)|^2=|\boldsymbol{D}_2(\boldsymbol{r}_A)\cdot\overline{\boldsymbol{e}}_\perp|^2+|\boldsymbol{D}_2(\boldsymbol{r}_A)\cdot\overline{\boldsymbol{e}}_{||}|^2\,, \tag{13}$$

where $\overline{\boldsymbol{e}}_\perp$ and $\overline{\boldsymbol{e}}_{||}$ are perpendicular to each other and both are perpendicular to the wave vector $\overline{\boldsymbol{K}}_0$, and $\overline{\boldsymbol{e}}_\perp$ is, in addition, perpendicular to the reciprocal lattice vector $\boldsymbol{G}$. Therefore $\overline{\boldsymbol{e}}_\perp$ is approximately perpendicular, and $\overline{\boldsymbol{e}}_{||}$ is parallel, to the plane which includes both wave vectors $\overline{\boldsymbol{k}}_0{}^s$ and $\overline{\boldsymbol{k}}_G{}^s$.

§ 3. The time average

The observed intensity at the point A is given by the average

$$J_2(\boldsymbol{r}_A)=(c/8\pi)\langle|\boldsymbol{D}_2(\boldsymbol{r}_A)|^2\rangle. \tag{14}$$

Eq. (14) can be obtained by averaging two terms in Eq. (13) and by multiplying a constant factor $(c/8\pi)$. The averaging is worked out by employing the theory of lattice vibration similar to that in the kinematical treatment of temperature diffuse scattering.

The further treatment differs by the conditions of Laue case and Bragg case. It should be noted that the distinction between Lause case and Bragg case is related to the reciprocal wave but not to the incident wave. In Laue case both vectors $\overline{\boldsymbol{k}}_0{}^s$ and $\overline{\boldsymbol{k}}_G{}^s$ direct inward within the crystal (Figs. 1 and 2a); in Bragg case $\overline{\boldsymbol{k}}_0{}^s$ directs outward while $\overline{\boldsymbol{k}}_G{}^s$ directs inward (Fig. 2b). In Laue case we treat both transmission and reflection patterns; in Bragg case, however, we treat only reflection pattern.

(I) *Laue case*. By substituting $\overline{\boldsymbol{p}}=|\overline{\boldsymbol{p}}|\boldsymbol{e}_{\perp,||}$ into Eqs. (8) and (12) and by the help of Eqs. (9), (10) and (11) we have for non-absorbing crystal the relation

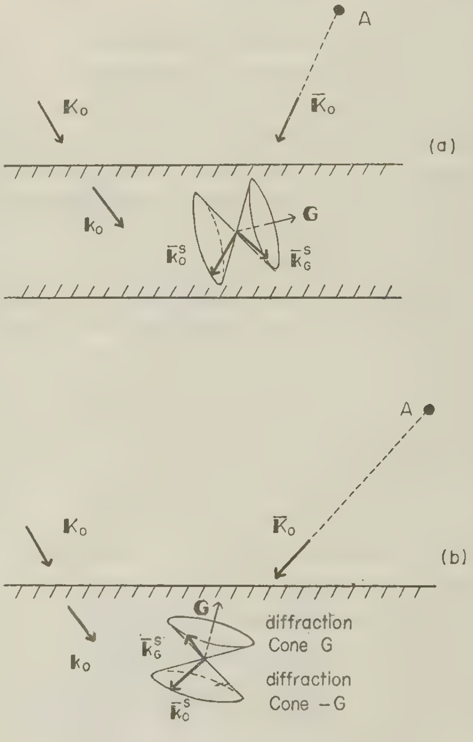

Fig. 2. Incident wave and reciprocal wave.
(a) Laue case (reflection pattern).
(b) Bragg case (reflection pattern).

$$\begin{aligned}\langle|\boldsymbol{D}_2(\boldsymbol{r}_A)\cdot\overline{\boldsymbol{e}}_{\perp,||}|^2\rangle&=NkT(1/R^2)(e^2/mc^2)\\&\times[S_{00}|\boldsymbol{E}_0\cdot\overline{\boldsymbol{e}}_{\perp,||}|^2+\{S_{GG}(\gamma_0/\gamma_G)|\boldsymbol{E}_0\cdot\overline{\boldsymbol{e}}_{\perp,G||}|^2-S_{00}|\boldsymbol{E}_0\cdot\overline{\boldsymbol{e}}_{\perp,||}|^2\}1/2(1+W^2_{\perp,||})\\&+\{S_{0G}F_{-G}+S_{G0}F_G\}(1/|F_G|)\sqrt{\gamma_0/\gamma_G}\,(\boldsymbol{E}_0\cdot\overline{\boldsymbol{e}}_{\perp,||})(\boldsymbol{E}_0{}^*\cdot\overline{\boldsymbol{e}}_{\perp,G||})(C_{\perp,||}/|C_{\perp,||}|)\\&\times W_{\perp,||}/2(1+W^2_{\perp,||})]\,.\end{aligned} \tag{15}$$

In Eq. (15), the derivation of which is given in Appendix 2, F_G is the crystal structure factor,

---

* $\overline{\boldsymbol{D}}_h{}^s$ is given by Eq. (A26), (A27), (A28) and (A29) in appendix 2 and by Eqs. (A38), (A39) and (A40) in Appendix 3.

T is the absolute temperature, k is Boltzmann's constant, N is the total number of unit cells, γ_0 and γ_G are respectively the cosines of the angles Θ_0 and Θ_G (Fig. 3). The parameter $W_{\perp,\parallel}$ determines the direction of $\bar{K}_0$ and is given by

$$W_{\perp,\parallel}=\eta/\{2|F_G|\cdot|C_{\perp,\parallel}|(e^2/mc^2)(\lambda^2/\pi)\sqrt{|\gamma_G/\gamma_0|}\,(1/v_a)\}\,, \tag{16}$$

where

$$\eta=2(\theta-\theta_G)\sin 2\theta_G-(e^2/mc^2)(\lambda^2/\pi)F_0\{1-(\gamma_G/\gamma_0)\}(1/v_a)\,, \tag{17}$$

where θ is the glancing angle of $\bar{K}_0$ on the net plane $\boldsymbol{G}$, and θ_G is the Bragg angle. We have $W_{\perp,\parallel}\gtrless 0$ and $\eta\gtrless 0$ for $\theta\gtrless\theta_G$. The quantity $C_{\perp,\parallel}$ in Eqs. (15) and (16) is given by

$$C_{\perp}=1 \tag{18}$$

and

$$C_{\parallel}=\cos 2\theta_G \tag{19}$$

v_a in Eqs. (16) and (17) is the volume of a unit cell. S_{00}, S_{GG}, S_{0G} and S_{G0} in Eq. (15) are given by

$$S_{hg}\approx\sum_k\sum_l(4\pi^2/\sqrt{m_k m_l})g_k(-\boldsymbol{b}_h)g_l(-\boldsymbol{b}_g)\exp\{-2\pi i(\boldsymbol{b}_h\cdot\boldsymbol{X}^k-\boldsymbol{b}_g\cdot\boldsymbol{X}^l)\}$$
$$\times\{\boldsymbol{b}_h\cdot\boldsymbol{\chi}_{kl}(\boldsymbol{\tau})\cdot\boldsymbol{b}_g\}\,, \tag{20}$$

where

$$\boldsymbol{b}_0=\boldsymbol{k}_0+\bar{\boldsymbol{k}}_0 \tag{21}$$

and

$$\boldsymbol{b}_G=\boldsymbol{b}_0+\boldsymbol{G}\,. \tag{22}$$

The wave vector $\bar{k}_0$ is the weighted mean of $\bar{k}'_{0\perp}$ with the weight $|\bar{D}'_{0\perp}|$ and $\bar{k}_0''$ with the weight $|\bar{D}''_{0\perp}|$. Then $\bar{k}_0$ coincides with the weighted mean of $\bar{k}'_{0\parallel}$ with the weight $|\bar{D}'_{0\parallel}|$ and $\bar{k}''_{0\parallel}$ with the weight $|\bar{D}''_{0\parallel}|$. We have $PO=LO$ for any η (Fig. 3). The effective atomic scattering factor of the kth atom in the unit cell g_k is given by

$$g_k(-\boldsymbol{b}_h)=f_k(-\boldsymbol{b}_h)\exp\{-M_k(-\boldsymbol{b}_h)\}\,, \tag{23}$$

where f_k is the ordinary atomic scattering factor and $\exp\{-M_k(-\boldsymbol{b}_h)\}$ is the temperature factor. m_k is the mass of the kth atom. The vector $\boldsymbol{X}^k$ denotes the position of the kth atom in a unit cell relative to the lattice point. $\boldsymbol{\chi}_{kl}$ is the tensor used by Zachariasen in the kinematical treatment of temperature diffuse scattering and related to the elastic constants of the crystal. The wave vector $\boldsymbol{\tau}$ is given by $\boldsymbol{\tau}=\boldsymbol{b}_0-\boldsymbol{I}$, where $\boldsymbol{I}$ is the reciprocal-lattice-point vector nearest to the vector $\boldsymbol{b}_0$. By the help of Eqs. (13), (14) and (15) we have the intensity of diffraction pattern $J_2(\boldsymbol{r}_A)$ as follows:

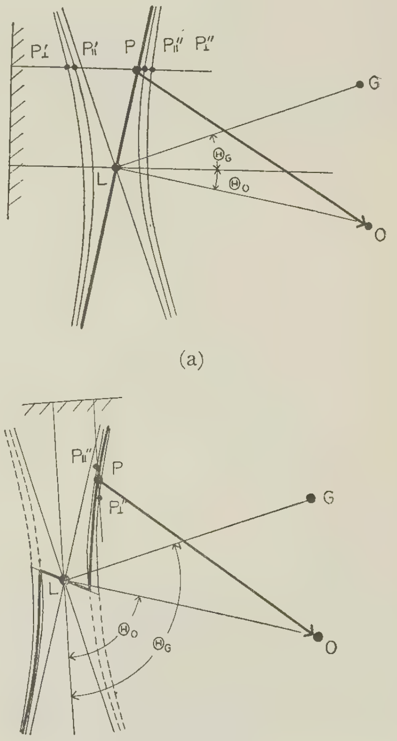

(a)

(b)

Fig. 3. (a) The locus of P in Laue case, where $\overrightarrow{PO}=\bar{K}_0$. (b) The locus of P in Bragg case, where $\overrightarrow{PO}$=mean of the real parts of $\bar{k}^s_{0\perp}$ and $k^s_{0\parallel}$.

$$
\begin{aligned}
J_2(\boldsymbol{r}_A)=NkT[I_eS_{00}+\{&I_e^{\perp}(S_{GG}(\gamma_0/\gamma_G)-S_{00})(1/2(1+W_{\perp}^2))\\
&+I_{eGG}^{||}S_{GG}(\gamma_0/\gamma_G(-I_e^{||}S_{00})(1/2(1+W_{||}^2))\}\\
&+(S_{0G}F_{-G}+S_{G0}F_G)(1/|F_G|)\sqrt{\gamma_0/\gamma_G}\\
&\times(I_e^{\perp}(W_{\perp}/2(1+W_{\perp}^2))+I_{eG}^{||}(W_{||}/2(1+W_{||}^2))\cos 2\theta_G/|\cos 2\theta_G|)]\ ,
\end{aligned}
\tag{24}
$$

For unpolarized incident radiation, we have

$$I_e=I_0(1/R^2)(e^2/mc^2)^2(1+\cos^2\phi_0)/2\ , \tag{25}$$

$$I_e^{\perp}=I_0(1/R^2)(e^2/mc^2)^2(1/2\sin^2 2\theta_G)(\cos^2\phi_0+\cos^2\phi_G-2\cos\phi_0\cos\phi_G\cos 2\theta_G)\ , \tag{26}$$

$$
\begin{aligned}
I_e^{||}=I_0(1/R^2)(e^2/mc^2)^2[&((1+\cos^2\phi_0)/2)\\
&-(1/\sin^2 2\theta_G)(\cos^2\phi_0+\cos^2\phi_G-2\cos\phi_0\cos\phi_G\cos 2\theta_G)]\ ,
\end{aligned}
\tag{27}
$$

$$
\begin{aligned}
I_{eGG}^{||}=I_0(1/R^2)(e^2/mc^2)^2[&((1+\cos^2\phi_G)/2)\\
&-(1/\sin^2 2\theta_G)(\cos^2\phi_0+\cos^2\phi_G-2\cos\phi_0\cos\phi_G\cos 2\theta_G)]\ ,
\end{aligned}
\tag{28}
$$

and

$$
\begin{aligned}
I_{eG}^{||}=I_0(1/R^2)(e^2/mc^2)^2[&(\cos 2\theta_G-\cos\phi_0\cos\phi_G)/2\\
&-(1/\sin^2 2\theta_G)\{\cos 2\theta_G(\cos^2\phi_0+\cos^2\phi_G)-2\cos\phi_0\cos\phi_G\}]\ ,
\end{aligned}
\tag{29}
$$

where I_0 is the intensity of the incident radiation, ϕ_0 is the angle $\angle(\boldsymbol{k}_0, -\bar{\boldsymbol{k}}_0)$ and ϕ_G is $\angle(\boldsymbol{k}_0, -\bar{\boldsymbol{k}}_G)$.

The right-hand side of Eq. (24) can be regarded as the summation of three terms. The first term is the ordinary diffuse scattering around the reciprocal lattice point $-\boldsymbol{I}$. The second term is an even function of η and the third termtan odd function, both amounting to considerable values near the diffraction cone of index G. The second and the third terms correspond to Kikuchi-lines and Kikuchi-band[3] respectively (Fig. 4). In practice, the line

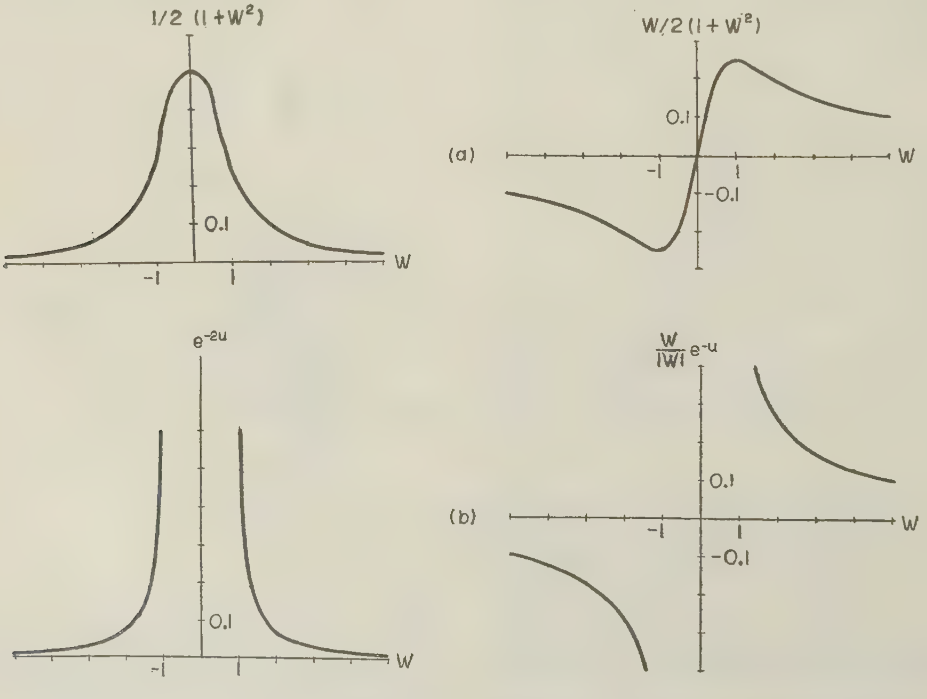

Fig. 4. The line profiles of the symmetric line and the antisymmetric line. (a) Laue case. (b) Bragg case.

corresponding to the superposition of the second and the third terms is observed only when the cone G passes through the diffuse spot $-I$. Hereafter we treat only such cases. Under the influence of the third term, the line on diffraction cone shows a feature similar to ‘Helldunkellinie’ of Kossel-pattern. While in a broad sense, the intensity of Kossel-pattern is independent of the direction of incident electrons or incident X-rays, the intensity of our pattern depends remarkably on the direction of the incident X-rays.

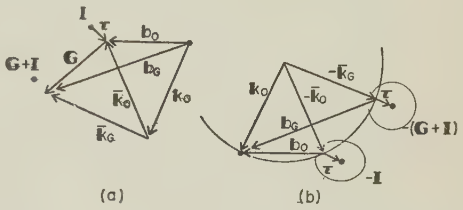

Fig. 5. The geometrical relations between wave vectors.
(a) The definitions in the text.
(b) The same vectors in the Ewald construction.

It is to be noted that in Laue case if $G+I\neq 0$ and the diffraction cone G passes through the diffuse spot $-I$, there appears in the same pattern another diffuse spot $J=-(G+I)$ through which the diffraction cone $-G$ passes. This implies that the direction of the incident beam is near the direction exciting simultaneous reflections $-I$ and J. The above-mentioned geometrical relation occurs because we have $k_0+\bar{k}_G-(G+I)=\tau$ in addition to $k_0+\bar{k}_0-I=\tau$ as shown in Fig. 5.

(II) *Bragg case.* If the crystal is thick enough and not prefectly non-absorbing, the expression for the intensity of our pattern $J_2(r_A)$ becomes very simple. Outside the region of total reflection, $|W_{\perp,||}|>1$, we have

$$\begin{aligned} J_2(r_A)=kT[&(A_\perp I_e{}^\perp+A_{||}I_e{}^{||})S_{00}\\ &+(A_\perp I_e{}^\perp \exp(-2u_\perp)+A_{||}I^{||}_{eGG}\exp(-2u_{||}))S_{GG}|\gamma_0/\gamma_G|\\ &+(A_\perp I_e{}^\perp(C_\perp/|C_\perp|)(W_\perp/|W_\perp|)\exp(-u_\perp)+A_{||}I^{||}_{eG}(C_{||}/|C_{||}|)(W_{||}/|W_{||}|)\exp(-u_{||}))\\ &\times(S_{0G}F_{-G}+S_{G0}F_G)(1/|F_G|)\sqrt{|\gamma_0/\gamma_G|}]\,, \end{aligned} \tag{30}$$

where $|W_{\perp,||}|=\cosh u_{\perp,||}$ and $u_{\perp,||}>0$. Inside the region of total reflection, $|W_{\perp,||}|<1$, we have

$$\begin{aligned} J_2(r_A)=kT\Bigg[&(A_\perp I_e{}^\perp+A_{||}I_e{}^{||})S_{00}\\ &+(A_\perp I_e{}^\perp+A_{||}I^{||}_{eGG})S_{GG}|\gamma_0/\gamma_G|\\ &+\Bigg\{A_\perp I_e{}^\perp(C_\perp/|C_\perp|)\left(S_{0G}F_{-G}\exp i\left(v_\perp+\frac{\pi}{2}\right)+S_{G0}F_G\exp -i\left(v+_\perp\frac{\pi}{2}\right)\right)\\ &+A_{||}I^{||}_{eG}(C_{||}/|C_{||}|)\left(S_{0G}F_{-G}\exp i\left(v_{||}+\frac{\pi}{2}\right)+S_{G0}F_G\exp -i\left(v_{||}+\frac{\pi}{2}\right)\right)\Bigg\}\\ &\times(1/|F_G|)\sqrt{|\gamma_0/\gamma_G|}\Bigg]\,, \end{aligned} \tag{31}$$

where $W_{\perp,||}=\sin v_{\perp,||}$. The derivations of Eqs. (30) and (31) are given in Appendix 3. The factors $A_{\perp,||}$ in Eqs. (30) and (31) represent the effect of primary extinction and of absorption and $A_{\perp,||}$ is a function of η as given by Eq. (A35)*. The factors S_{00}, S_{GG}, S_{0G} and S_{G0} are given by Eq. (20). However it should be noted that in Bragg case b_0 in Eq. (20) is not given by Eq. (21) but is defined as the mean of the real parts of $b^s_{0\perp}$ and $b^s_{0||}$. In Eq. (20) b_G is given by Eq. (22). In Bragg case, PO becomes asymptotically equal to LO as the value $|\eta|$ increases (Fig. 3).

The factors $A_\perp$ and $A_{||}$ become very small in a region of total reflection, especially when $|\eta|$ is near zero. Thus we always have a defect line. Apart from the effect of $A_\perp$ and $A_{||}$ the general feature of the intensity distribution of our pattern in Bragg case resembles that in Laue case (Fig. 4). The intensity of our pattern can be regarded as a summation of three terms similar to those in Laue case. Outside the regions of total reflection, the factors $A_{\perp}$ and $A_{||}$ change slowly if the X-rays are not strongly absorbed.

---

* η is given by Eq. (17) also in Bragg case.

It is noteworthy that in Bragg case even when the diffraction cone G passes through the diffuse spot $-I$ the diffuse spot J does not usually appear in reflection pattern because the cone $-G$ which passes through the diffuse spot J does not cut the reflection pattern (Fig. 2).

§ 4. Possibility of the Determination of the Sign of Struncture Factor

Let us examine the case where the direction of the incident radiation is slightly deviated from the condition of the simultaneous reflections made by two net planes $-I$ and J. Then the diffuse spot $-I$ is cut by both diffraction cones $-I$ and G in both Laue and Bragg cases*. We will examine the line profile of the diffraction cone at the position corresponding to a small value of $|\tau|$. Then the contribution of the acoustic vibrations to the intensity of the pattern predominates over the contribution of the optical vibrations if F_{-I} and F_J are not zero. Thus we have at higher temperatures

$$(1/\sqrt{m_k m_l})\boldsymbol{\chi}_{kl}(\boldsymbol{\tau}) \approx \boldsymbol{\Omega}^{-1}(\boldsymbol{\tau})/(4\pi^2\boldsymbol{\tau}^2 v_a) , \tag{33}$$

where $\boldsymbol{\Omega}^{-1}(\boldsymbol{\tau})$ is a tensor expressed in terms of the elastic constants of the crystal[6)].

Since we have $\boldsymbol{b}_0 \sim \boldsymbol{I}$, $\boldsymbol{b}_G \sim \boldsymbol{I}+\boldsymbol{G}=-\boldsymbol{J}$ and $F_J=\sum_k g_k(\boldsymbol{J}) \exp(2\pi i\boldsymbol{J}\cdot\boldsymbol{X}^k)$, the term $\{S_{0G}F_{-G}+S_{G0}F_G\}$ in Eqs. (24), (30) and (31) reduces to

$$\begin{aligned}\{S_{0G}F_{-G}+S_{G0}F_G\} \approx\ & (\lambda^2/\pi)^2(e^2/mc^2)^2(1/v_a)\{\boldsymbol{I}\cdot\boldsymbol{\Omega}^{-1}(\boldsymbol{\tau})\cdot(\boldsymbol{G}+\boldsymbol{I})\} \\ & \times(1/\boldsymbol{\tau}^2)|F_I|\cdot|F_J|\cdot|F_G|\cdot 2\cos\varphi_I+\varphi_J+\varphi_G) ,\end{aligned} \tag{34}$$

where φ_h is the phase of structure factor

$$F_h=|F_h| \exp(i\varphi_h) . \tag{35}$$

There are three degrees of freedom in the determination of the phase of structure factor corresponding to the three degrees of freedom in selection of the coordinate origin. The value $(\varphi_G+\varphi_I+\varphi_J)$ is invariant for any selection of the origin under the condition that $\boldsymbol{G}+\boldsymbol{I}+\boldsymbol{J}=0$**. In the phase problem we must determine the invariant value of $(\varphi_G+\varphi_I+\varphi_J)$.

Therefore, if the new pattern is observed and if its line profile is measured, then the value of $\cos(\varphi_G+\varphi_I+\varphi_J)$ may be calculated by Eqs. (24), (30) and (34), provided the tensor $\boldsymbol{\Omega}^{-1}(\boldsymbol{\tau})$ is given. Since it would be difficult to measure the line profile, we treat here only a centro-symmetrical crystal where $\cos(\varphi_G+\varphi_I+\varphi_J)$ reduces to ± 1. It would be easy to distinguish whether the antisymmetric line is black-white or white-black. Then by Eqs. (24) and (34) in Laue case or by Eqs. (30) and (34) in Bragg case, we can determine the value of $(\varphi_G+\varphi_I+\varphi_J)$ provided the sign of $\{\boldsymbol{I}\cdot\boldsymbol{\Omega}^{-1}(\boldsymbol{\tau})\cdot(\boldsymbol{G}+\boldsymbol{I})\}$ is given. For the determination of elastic constants, which are necessary to evaluate $\boldsymbol{\Omega}^{-1}(\boldsymbol{\tau})$, the temperature diffuse scattering may be used[7)].

It may be suitable to choose combinations of $\boldsymbol{G}$, $\boldsymbol{I}$ and $\boldsymbol{J}$ where the structure amplitude $|F_G|$ is large, because the width of the line is proportional to $|F_G|$ (Fig. 4 and Eqs. (16) and (17)) and thus the antisymmetrical structure of line would be clearly observed. Generally, Laue case is more suitable for the present purpose. In Bragg case, the antisymmetrical structure of line would be difficult to observe since the effect of extinction, which is expressed by the factor A, is so remarkable that the antisymmetrical structure is likely to be overlooked.

---

* If the cone $-\boldsymbol{I}$ passes through the centre of diffuse spot $-\boldsymbol{I}$, the incident beam excites the Bragg reflection $-\boldsymbol{I}$. In such a case, $\boldsymbol{D}_1$ given by Eq. (9) can not be adopted because Eq. (9) was derived under the assumption that the incident wave is not reflected by any net plane.

** F_h is given by $F_h=\int\rho_1{}^L(X)\exp(2\pi i\boldsymbol{h}\cdot X)\,dX$, where $\rho_1{}^L(X)$ is the averaged electron density and the integration extends over a unit cell. If the lattice point is shifted from O_L to O_L' where $\overrightarrow{O_L O_L'}=\boldsymbol{s}$, $\rho_1{}^{L'}(\boldsymbol{X}')$ is given by $\rho_1{}^{L'}(\boldsymbol{X}')=\rho_1{}^L(\boldsymbol{X}'+\boldsymbol{s})$ and F_h' is given by $F_h'=F_h\exp(-2\pi i\boldsymbol{h}\cdot\boldsymbol{s})$. Thus we have $\varphi_h'=\varphi_h-2\pi i\boldsymbol{h}\cdot\boldsymbol{s}$ If $\boldsymbol{G}+\boldsymbol{I}+\boldsymbol{J}=0$, we have $\varphi_G'+\varphi_I'+\varphi_J'=\varphi_G+\varphi_I+\varphi_J$ for any $\boldsymbol{s}$.

§ 5. Discussions

Booth[8] suggested in 1946 a solution of phase problem according to which the phase of structure factor can be determined in principle by observing whether two diffuse spot ares joined by a diffuse streak or not. His method was criticized by Stokes[9]. Booth paid no attention to the fact that the phase of structure factor has three degrees of freedom (§ 4.). Booth's method takes into consideration the region of large $|\tau|$ where the optical vibrations contribute to the temperature diffuse scattering much more than the acoustic vibrations. On the other hand, the region of small $|\tau|$ is used here. Thus our method is free from the difficulty found in Booth's method.

The calculation in this article was carried out by assuming an ideally perfect crystal although real crystals are not ideally perfect. However, our result of calculation, in the main, are likely to hold for fairly perfect real crystals, if adequate corrections are made for increased intensity and increased breadth due to the mosaic structure of real crystals.

It is assumed that the radiation is almost unabsorbed by the crystal. If the absorption is strong and the effect of absorption is taken into account, remarkable changes will occur in the line profile of the pattern. In Kikuchi-bands it was found that the antisymmetrical line profile is reversed by the effect of absorption[10]. In a phase determination by the present method, the use of a strongly absorbed radiation should be avoided.

The author expresses his deep appreciation to Prof. Ryozi Uyeda for his guidance throughout this work. This research is supported in part by Kagaku Kenkyu Hi, the Science Research Fund established by the Ministry of Education, Japan.

Appendix 1

Here we prove Eq. (8), a generalized theorem of reciprocity. By the use of the well-known formula of vector analysis we have

$$\operatorname{div}(\boldsymbol{E}_2\times\overline{\boldsymbol{H}})=\overline{\boldsymbol{H}}\cdot\operatorname{rot}\boldsymbol{E}_2-\boldsymbol{E}_2\cdot\operatorname{rot}\overline{\boldsymbol{H}}\,.$$

Since $\boldsymbol{E}_2$ and $\boldsymbol{H}_2$ satisfy Eq. (2) and $\overline{\boldsymbol{H}}$ and $\overline{\boldsymbol{D}}$ satisfy Eq. (5) we have

$$\operatorname{div}(\boldsymbol{E}_2\times\overline{\boldsymbol{H}})=\overline{\boldsymbol{H}}\cdot(-1/c)\partial\boldsymbol{H}_2/\partial t-\boldsymbol{E}_2\cdot(1/c)\partial\overline{\boldsymbol{D}}/\partial t\,,$$

which is rewritten

$$\operatorname{div}(\boldsymbol{E}_2\times\overline{\boldsymbol{H}})=(-2\pi i/\lambda)(\overline{\boldsymbol{H}}\cdot\boldsymbol{H}_2+\boldsymbol{E}_2\cdot\overline{\boldsymbol{D}})\,. \tag{A1}$$

By a similar procedure we have

$$\operatorname{div}\{(\overline{\boldsymbol{E}}-\overline{\boldsymbol{E}}_e)\times\boldsymbol{H}_2\}=(-2\pi i/\lambda)(\boldsymbol{H}_2\cdot\overline{\boldsymbol{H}}+\overline{\boldsymbol{E}}\cdot\boldsymbol{D}_2-\overline{\boldsymbol{E}}_e\cdot\boldsymbol{D}_2)\,. \tag{A2}$$

Subtracting Eq. (A2) from Eq. (A1) and integrating with respect to $\boldsymbol{r}$ over the whole space, by the help of Green's theorem, we have

$$\int\{(\boldsymbol{E}_2\times\overline{\boldsymbol{H}})_n-(\overline{\boldsymbol{E}}\times\boldsymbol{H}_2)_n\}dS=(-2\pi i/\lambda)\int(\boldsymbol{E}_2\cdot\overline{\boldsymbol{D}}-\overline{\boldsymbol{E}}\cdot\boldsymbol{D}_2+\overline{\boldsymbol{E}}_e\cdot\boldsymbol{D}_2)d\boldsymbol{r}\,. \tag{A3}$$

In the derivation of the left-hand side of Eq. (A3) we use Eq. (7). Since the left-hand side of Eq. (A3) vanishes, we have

$$\int\overline{\boldsymbol{E}}_e\cdot\boldsymbol{D}_2d\boldsymbol{r}=-\int(\boldsymbol{E}_2\cdot\overline{\boldsymbol{D}}-\overline{\boldsymbol{E}}\cdot\boldsymbol{D}_2)d\boldsymbol{r}\,. \tag{A4}$$

By the use of Eqs. (4), (6), (7) and (A4) we have Eq. (8).

Appendix 2

Here we derive Eq. (15) which holds in Laue case. By the help of Eq. (8) and the definition of $\rho_2(\boldsymbol{r})$, as given in § 2., we have

$$\begin{aligned}\langle|\boldsymbol{D}_2(\boldsymbol{r}_A)\cdot\bar{\boldsymbol{e}}_{\perp,||}|^2\rangle &= (e^2/mc^2)^2(\lambda^2/\pi)^2(1/|\bar{\boldsymbol{p}}|^2)\\ &\times\left\{\iint\langle\rho(\boldsymbol{r})\rho(\boldsymbol{r}')\rangle(\boldsymbol{D}_1(\boldsymbol{r})\cdot\bar{\boldsymbol{D}}(\boldsymbol{r}))(\boldsymbol{D}_1{}^*(\boldsymbol{r}')\cdot\bar{\boldsymbol{D}}^*(\boldsymbol{r}'))\,d\boldsymbol{r}d\boldsymbol{r}'\right.\\ &\left.-\left|\int\langle\rho(\boldsymbol{r})\rangle\boldsymbol{D}_1(\boldsymbol{r})\cdot\bar{\boldsymbol{D}}(\boldsymbol{r})\,d\boldsymbol{r}\right|^2\right\}.\end{aligned}\tag{A5}$$

If the Nordheim's assumption of rigid-atoms[11)] is adopted, i.e. if the electron clouds around atoms are not deformed when nuclei oscillate, the electron density $\rho(\boldsymbol{r})$ is given by

$$\rho(\boldsymbol{r})=\sum_n\sum_k\rho_k(\boldsymbol{r}-\boldsymbol{r}_n{}^k-\boldsymbol{u}_n{}^k)\,,\tag{A6}$$

where $\rho_k(\boldsymbol{\xi})$ is the electron density which is due to the kth atom in the unit cell and is expressed as a function of $\boldsymbol{\xi}$ $(=\boldsymbol{r}-\boldsymbol{r}_n{}^k-\boldsymbol{u}_n{}^k)$ i.e. the coordinate relative to the nucleus of the kth atom. $\boldsymbol{r}_k{}^n$ and $\boldsymbol{u}_k{}^n$ are the equilibrium position and the displacement from equilibrium position, respectively, of the kth atomic nucleus in the nth unit cell.

By the help of Eqs. (9), (10) and (A6), we have

$$\begin{aligned}\int\rho(\boldsymbol{r})\boldsymbol{D}_1(\boldsymbol{r})\cdot\bar{\boldsymbol{D}}(\boldsymbol{r})d\boldsymbol{r} &= \sum_h\sum_s\boldsymbol{E}_0\cdot\bar{\boldsymbol{D}}_h{}^s\sum_n\sum_k\int\rho_k(\boldsymbol{\xi})\exp(-2\pi i\boldsymbol{b}_h{}^s\cdot\boldsymbol{\xi})d\boldsymbol{\xi}\\ &\times\exp\{-2\pi i\boldsymbol{b}_h{}^s\cdot(\boldsymbol{r}_n{}^k+\boldsymbol{u}_n{}^k)\}\exp(4\pi ict/\lambda)\,.\end{aligned}\tag{A7}$$

By the use of well-known relation:

$$f_k(\boldsymbol{b})=\int\rho_k(\boldsymbol{\xi})\exp(2\pi i\boldsymbol{b}\cdot\boldsymbol{\xi})d\boldsymbol{\xi}\,,\tag{A8}$$

Eq. (A7) is rewritten

$$\begin{aligned}&\int\rho(\boldsymbol{r})\boldsymbol{D}_1(\boldsymbol{r})\cdot\bar{\boldsymbol{D}}(\boldsymbol{r})d\boldsymbol{r}\\ &=\sum_h\sum_s(\boldsymbol{E}_0\cdot\bar{\boldsymbol{D}}_h{}^s)\sum_n\sum_k f_k(-\boldsymbol{b}_h{}^s)\exp\{-2\pi i\boldsymbol{b}_h{}^s\cdot(\boldsymbol{r}_n{}^k+\boldsymbol{u}_n{}^k)\}\exp(4\pi ict/\lambda)\,.\end{aligned}\tag{A9}$$

By the use of Eq. (A9) we have

$$\begin{aligned}&\int\langle\rho(\boldsymbol{r})\rangle(\boldsymbol{D}_1(\boldsymbol{r})\cdot\bar{\boldsymbol{D}}(\boldsymbol{r}))d\boldsymbol{r}\\ &=\sum_h\sum_s(\boldsymbol{E}_0\cdot\bar{\boldsymbol{D}}_h{}^s)\sum_n\sum_k g_k(-\boldsymbol{b}_h{}^s)\exp(-2\pi i\boldsymbol{b}_h{}^s\cdot\boldsymbol{r}_n{}^k)\exp(4\pi ict/\lambda)\,,\end{aligned}\tag{A10}$$

where g_k is given by Eq. (23). M_k in Eq. (23) is given by

$$M_k(-\boldsymbol{b}_h{}^s)=2\pi^2\langle(\boldsymbol{b}_h{}^s\cdot\boldsymbol{u}_n{}^k)^2\rangle\,.\tag{A11}$$

By a similar procedure, we have

$$\begin{aligned}&\iint\langle\rho(\boldsymbol{r})\rho(\boldsymbol{r}')\rangle(\boldsymbol{D}_1(\boldsymbol{r})\cdot\bar{\boldsymbol{D}}(\boldsymbol{r}))(\boldsymbol{D}_1{}^*(\boldsymbol{r}')\cdot\bar{\boldsymbol{D}}^*(\boldsymbol{r}')\,d\boldsymbol{r}d\boldsymbol{r}'\\ &=|\sum_h\sum_s(\boldsymbol{E}_0\cdot\bar{\boldsymbol{D}}_h{}^s)\sum_n\sum_k g_k(-\boldsymbol{b}_h{}^s)\exp(-2\pi i\boldsymbol{b}_h{}^s\cdot\boldsymbol{r}_n{}^k)|^2\\ &+\sum_{h,g}\sum_{s,t}(\boldsymbol{E}_0\cdot\bar{\boldsymbol{D}}_h{}^s)(\boldsymbol{E}_0{}^*\cdot\bar{\boldsymbol{D}}^*{}_g{}^t)\sum_{k,l}g_k(-\boldsymbol{b}_h{}^s)g_l(-\boldsymbol{b}_g{}^t)\\ &\times\sum_{n,m}P_{kl}^{nm}(\boldsymbol{b}_h{}^s,\ \boldsymbol{b}_g{}^t)\exp\{-2\pi i(\boldsymbol{b}_h{}^s\cdot\boldsymbol{r}_n{}^k-\boldsymbol{b}_g{}^t\cdot\boldsymbol{r}_m{}^l)\}\,,\end{aligned}\tag{A12}$$

where

$$P_{kl}^{nm}(\boldsymbol{b}_h{}^s,\ \boldsymbol{b}_g{}^t)=4\pi^2\langle(\boldsymbol{b}_h{}^s\cdot\boldsymbol{u}_n{}^k)(\boldsymbol{b}_g{}^t\cdot\boldsymbol{u}_m{}^l)\rangle\ . \tag{A13}$$

By the use of Eqs. (A5), (A9) and (A12), we have

$$\begin{aligned}\langle|\boldsymbol{D}_2(\boldsymbol{r}_A)\cdot\bar{\boldsymbol{e}}_{\perp,\,||}|^2\rangle&=(e^2/mc^2)^2(\lambda^2/\pi)^2(1/|\bar{\boldsymbol{p}}|^2)\sum_{h,g}\sum_{s,t}(\boldsymbol{E}_0\cdot\bar{\boldsymbol{D}}_h{}^s)(\boldsymbol{E}_0{}^*\cdot\bar{\boldsymbol{D}}_g{}^{*t})\\&\quad\times\sum_{k,l}g_k(-\boldsymbol{b}_h)g_l(-\boldsymbol{b}_g)\sum_{n,m}P_{kl}^{nm}(\boldsymbol{b}_h,\ \boldsymbol{b}_g)\exp\{-2\pi i(\boldsymbol{b}_h{}^s\cdot\boldsymbol{r}_n{}^k-\boldsymbol{b}_g{}^t\cdot\boldsymbol{r}_m{}^l)\}\ .\end{aligned} \tag{A14}$$

In the derivation of Eq. (A14) the following approximations are used.

$$g_k(-\boldsymbol{b}_h{}^s)\approx g_k(-\boldsymbol{b}_h) \tag{A15}$$

and

$$P_{kl}^{nm}(\boldsymbol{b}_h{}^s,\ \boldsymbol{b}_g{}^t)\approx P_{kl}^{nm}(\boldsymbol{b}_h,\ \boldsymbol{b}_g)\ , \tag{A16}$$

where $\boldsymbol{b}_h$ is the mean vector given by Eqs. (21) and (22).

By the application of the theory of lattice vibration, we have

$$P_{kl}^{nm}(\boldsymbol{b}_h,\ \boldsymbol{b}_g)=(4\pi^2kT/N\sqrt{m_km_l})(\boldsymbol{b}_h\cdot\boldsymbol{\chi}_{kl}(\boldsymbol{\tau}_p)\cdot\boldsymbol{b}_g)\exp\{2\pi i\boldsymbol{\tau}_p\cdot(\boldsymbol{n}-\boldsymbol{m})\}\ , \tag{A17}$$

where the tensor $\boldsymbol{\chi}_{kl}(\boldsymbol{\tau}_p)$ is given by

$$\boldsymbol{\chi}_{kl}(\boldsymbol{\tau}_p)=(1/kT)\sum_j U_{kj}(p)U_{lj}^*(p)\{Q_j(p)/\omega_j{}^2(p)\}\ . \tag{A18}$$

If the suffix l is replaced by suffix k', Eq. (A18) becomes the same as Eq. (4. 109a) in Zachariasen's textbook[12]. The definitions for $U_{kl}(p)$, $Q_j(p)$ and $\omega_j(p)$ are found in the same textbook. By the help of Eq. (A17), the factor $\sum_{n,m}P\cdots\exp\{\cdots\}$ in Eq. (A14) turns out to be

$$\begin{aligned}&\sum_{n\ m}P_{kl}^{nm}(\boldsymbol{b}_h,\ \boldsymbol{b}_g)\exp\{-2\pi i(\boldsymbol{b}_h{}^s\cdot\boldsymbol{r}_n{}^k-\boldsymbol{b}_g{}^t\cdot\boldsymbol{r}_m{}^l)\}\\&\quad=(4\pi^2kT/N\sqrt{m_km_l})(\boldsymbol{b}_h\cdot\boldsymbol{\chi}_{kl}(\boldsymbol{\tau}_p)\cdot\boldsymbol{b}_g)\exp\{-2\pi i(\boldsymbol{b}_h\cdot\boldsymbol{r}_0{}^k-\boldsymbol{b}_g\cdot\boldsymbol{r}_0{}^l)\}\\&\quad\quad\times\sum_n\exp\{2\pi i(\boldsymbol{\tau}_p-\boldsymbol{b}_h{}^s)\cdot\boldsymbol{n}\}\sum_m\exp\{-2\pi i(\boldsymbol{\tau}_p-\boldsymbol{b}_g{}^t)\cdot\boldsymbol{m}\}\ .\end{aligned} \tag{A19}$$

In the derivation of Eq. (A19) the following approximation is used: $\exp(-2\pi i\boldsymbol{b}_h{}^s\cdot\boldsymbol{r}_0{}^k)\approx\exp(-2\pi i\boldsymbol{b}_h\cdot\boldsymbol{r}_0{}^k)$. If we assume that the crystal is large enough in all directions, Eq. (A19) almost vanishes except when both $\boldsymbol{\tau}_p-\boldsymbol{b}_h{}^s$ and $\boldsymbol{\tau}_p-\boldsymbol{b}_g{}^t$ simultaneously become reciprocal lattice vectors. Since it is not likely that $\boldsymbol{b}_0{}'-\boldsymbol{b}_0{}''$ is equal to any reciprocal lattice vector, the condition for non-vanishing of Eq. (A19) is the simultaneous holding of equations

$$\boldsymbol{\tau}_p-\boldsymbol{b}_h{}^s=-\boldsymbol{h}-\boldsymbol{I} \tag{A20}$$

and

$$\boldsymbol{\tau}_p-\boldsymbol{b}_g{}^t=-\boldsymbol{g}-\boldsymbol{I}\ , \tag{A21}$$

where $\boldsymbol{I}$ is the reciprocal lattice vector nearest both $\boldsymbol{b}_0{}'$ and $\boldsymbol{b}_0{}''$. Eqs. (A20) and (A21) can be satisfied simultaneously only when we have $s=t$. When Eq. (A19) does not vanish, we have

$$\sum_n\exp\{2\pi i(\boldsymbol{\tau}_p-\boldsymbol{b}_h{}^s)\cdot\boldsymbol{n}\}=\sum_m\exp\{-2\pi i(\boldsymbol{\tau}_p-\boldsymbol{b}_g{}^t)\cdot\boldsymbol{m}\}=N\ . \tag{A22}$$

By the help of Eqs. (A19), (A20), (A21) and (A22), we have

$$\begin{aligned}&\sum_{n,m}P_{kl}^{nm}(\boldsymbol{b}_h,\ \boldsymbol{b}_g)\exp\{-2\pi i(\boldsymbol{b}_h{}^s\cdot\boldsymbol{r}_n{}^k-\boldsymbol{b}_g{}^t\cdot\boldsymbol{r}_m{}^l)\}\\&\quad=\delta_{st}NkT(4\pi^2/\sqrt{m_km_l})(\boldsymbol{b}_h\cdot\boldsymbol{\chi}_{kl}(\boldsymbol{\tau})\cdot\boldsymbol{b}_g)\exp\{-2\pi i(\boldsymbol{b}_h\cdot\boldsymbol{X}^k-\boldsymbol{b}_g\cdot\boldsymbol{X}^l)\}\\&\quad\times\exp\{-2\pi i(\boldsymbol{h}-\boldsymbol{g})\cdot\boldsymbol{r}_0\}\ ,\end{aligned} \tag{A23}$$

where $\delta_{st}=1$ if $s=t$, $\delta_{st}=0$ if $s\neq t$, $\boldsymbol{\tau}=\boldsymbol{b}_0-\boldsymbol{I}$, and $\boldsymbol{r}_0{}^k=\boldsymbol{r}_0+\boldsymbol{X}^k$. In the derivation of Eq. (A23) the following approximation is used:

$$\chi_{kl}(\boldsymbol{\tau}^s)\approx\chi_{kl}(\boldsymbol{\tau}) \tag{A24}$$

where $\boldsymbol{\tau}^s=\boldsymbol{b}_0{}^s-\boldsymbol{I}$. The approximation is good except when $|\boldsymbol{\tau}^s|$ becomes very small*.

By the help of Eqs. (A14) and (A23), we have

$$\begin{aligned}\langle|\boldsymbol{D}_2(\boldsymbol{r}_A)\cdot\bar{\boldsymbol{e}}_{\perp,\parallel}|^2\rangle=&(e^2/mc^2)^2(\lambda^2/\pi)^2(1/|\bar{\boldsymbol{p}}|^2)\\ &\times\sum_{hg}\sum_s(\boldsymbol{E}_0\cdot\bar{\boldsymbol{D}}_h{}^s)(\boldsymbol{E}_0{}^*\cdot\bar{\boldsymbol{D}}_g{}^{*s})\exp\{-2\pi i(\boldsymbol{h}-\boldsymbol{g})\cdot\boldsymbol{r}_0\}NkTS_{hg}\,,\end{aligned} \tag{A25}$$

where S_{hg} is given by Eq. (20).

Let us next evaluate the factor $\sum_s(\boldsymbol{E}_0\cdot\bar{\boldsymbol{D}}_h{}^s)(\boldsymbol{E}_0{}^*\cdot\bar{\boldsymbol{D}}_g{}^{*s})$ in Eq. (A25) by the use of the formula of dynamical theory of diffraction[4]. When $\bar{\boldsymbol{p}}=|\bar{\boldsymbol{p}}|\bar{\boldsymbol{e}}_\perp$, we have

$$\bar{\boldsymbol{D}}_h{}^s=\bar{\boldsymbol{e}}_\perp\bar{D}^s_{h\perp}\,. \tag{A26}$$

When $\bar{\boldsymbol{p}}=|\bar{\boldsymbol{p}}|\bar{\boldsymbol{e}}_\parallel$, we have

$$\bar{\boldsymbol{D}}_0{}^s=\bar{\boldsymbol{e}}_\parallel\bar{D}^s_{0\parallel} \tag{A27}$$

and

$$\bar{\boldsymbol{D}}_G{}^s=\bar{\boldsymbol{e}}_{G\parallel}\bar{D}^s_{G\parallel}\,, \tag{A28}$$

where the unit vector $\bar{\boldsymbol{e}}_{G\parallel}$ is perpendicular to wave vector $\bar{\boldsymbol{k}}_G$ and $\bar{\boldsymbol{e}}_{G\parallel}$ is parallel to a plane including both wave vectors $\bar{\boldsymbol{k}}_0$ and $\bar{\boldsymbol{k}}_G$. If the origin of coordinate is assumed to lie on the surface through which the reciprocal wave enters into the crystal, the amplitudes $\bar{D}^s_{h\perp,\parallel}$ in Eqs. (A26), (A27) and (A28) are given by

$$\left.\begin{aligned}&\bar{D}'_{0\perp,\parallel}=(1/2)\{1-(W/\sqrt{1+W^2})\}\bar{E}_0\,,\\ &\bar{D}''_{0\perp,\parallel}=(1/2)\{1+(W/\sqrt{1+W^2})\}\bar{E}_0\,,\\ &\bar{D}'_{G\perp,\parallel}=(-1/2\sqrt{1+W^2})(F_G/|F_G|)\exp(2\pi i\boldsymbol{G}\cdot\boldsymbol{r}_0)\sqrt{\gamma_0/\gamma_G}(C_{\perp,\parallel}/|C_{\perp,\parallel}|)\bar{E}_0\,,\\ &\text{and}\\ &\bar{D}''_{G\perp,\parallel}=(1/2\sqrt{1+W^2})(F_G/|F_G|)\exp(2\pi i\boldsymbol{G}\cdot\boldsymbol{r}_0)\sqrt{\gamma_0/\gamma_G}(C_{\perp,\parallel}/|C_{\perp,\parallel}|)\bar{E}_0\,,\end{aligned}\right\} \tag{A29)**$$

where the quantities found in the right-hand sides of Eq. (A29) are given in the text of this article.

By the help of Eqs. (A26), (A27), (A28), (A29), (11) and (12), we have

---

* If $|\boldsymbol{\tau}^s|$ becomes very small, we have $-\bar{\boldsymbol{k}}_0{}^s-\boldsymbol{k}_0\approx-\boldsymbol{I}$, which is the condition of excitation of the Bragg reflection $-\boldsymbol{I}$. Then the assumtion under which Eq. (9) was derived can not be used.

** The averaged electron density can be expressed as $\rho_1{}^L(\boldsymbol{X})$, a function of the coordinate $\boldsymbol{X}$. The coordinate $\boldsymbol{X}$ denotes the relative position to zero-th lattice point. Thus we have $\boldsymbol{r}-\boldsymbol{r}_0=\boldsymbol{X}$ and $\rho_1{}^L(\boldsymbol{X})=\rho_1(\boldsymbol{r})$. As well-known we have

$$\rho_1{}^L(\boldsymbol{X})=(1/v_a)\sum_h F_h\exp(-2\pi i\boldsymbol{h}\cdot\boldsymbol{X})$$

and

$$F_h=\int_{\text{unit cell}}\rho_1{}^L(\boldsymbol{X})\exp(2\pi i\boldsymbol{h}\cdot\boldsymbol{X})d\boldsymbol{X}\,.$$

Thus we have

$$\rho(\boldsymbol{r})=(1/v_a)\sum_h\{F_h\exp(2\pi i\boldsymbol{h}\cdot\boldsymbol{r}_0)\}\exp(-2\pi i\boldsymbol{h}\cdot\boldsymbol{r})\,.$$

This is the reason that the factor $F_G\exp(2\pi i\boldsymbol{G}\cdot\boldsymbol{r}_0)$ appears in the expressions of $D'_{G\perp,\parallel}$ and $D''_{G\perp,\parallel}$ in Eqs. (A29).

$$\left.\begin{aligned}
&\sum_s (\boldsymbol{E}_0\cdot\bar{\boldsymbol{D}}_0{}^s)(\boldsymbol{E}_0{}^*\cdot\bar{\boldsymbol{D}}_0{}^{*s})=|\boldsymbol{E}_0\cdot\bar{\boldsymbol{e}}_{\perp,\parallel}|^2\{1-(1/2(1+W^2_{\perp,\parallel}))\}(1/R^2)(\pi/\lambda^2)^2|\bar{\boldsymbol{p}}|^2\,,\\
&\sum_s (\boldsymbol{E}_0\cdot\bar{\boldsymbol{D}}_G{}^s)(\boldsymbol{E}_0{}^*\cdot\bar{\boldsymbol{D}}_G{}^{*s})=|\boldsymbol{E}_0\cdot\bar{\boldsymbol{e}}_{\perp,\parallel}|^2(1/2(1+W^2_{\perp,\parallel}))(\gamma_0/\gamma_G)(1/R^2)(\pi/\lambda^2)^2|\bar{\boldsymbol{p}}|^2\,,\\
&\text{and}\\
&\sum_s (\boldsymbol{E}_0\cdot\bar{\boldsymbol{D}}_0{}^s)(\boldsymbol{E}_0{}^*\cdot\bar{\boldsymbol{D}}_G{}^{*s})=(\boldsymbol{E}_0\cdot\bar{\boldsymbol{e}}_{\perp,\parallel})(\boldsymbol{E}_0{}^*\cdot\bar{\boldsymbol{e}}_{\perp,G\parallel})(W_{\perp,\parallel}/2(1+W^2_{\perp,\parallel}))\\
&\qquad\times(F_{-G}/|F_G|)\exp(-2\pi i\boldsymbol{G}\cdot\boldsymbol{r}_0)(C_{\perp,\parallel}/|C_{\perp,\parallel})\sqrt{\gamma_0/\gamma_G}(1/R^2)(\pi/\lambda^2)^2|\bar{\boldsymbol{p}}|^2\,.
\end{aligned}\right\}\qquad \text{(A30)}$$

Substituting Eq. (A30) into Eq. (A25), we have Eq. (15) of the text.

Appendix 3

Here we derive Eqs. (30) and (31), which hold in Bragg case. In Bragg case we can also prove Eqs. (A5), (A6) and (A7) which are derived in Laue case. It must be noted that Eq. (A8) is valid only when $\boldsymbol{b}$ is a real vector. In Bragg case $\boldsymbol{b}_h{}^s$ is a complex vector in the region of total reflection. Since we have assumed that the crystal is not perfectly non-absorbing, $\boldsymbol{b}_h{}^s$ has a small imaginary part even outside the region of total reflection. Thus we have the following equations instead of Eqs. (A10) and (A12) in Laue case.

$$\begin{aligned}
&\int\langle\rho(\boldsymbol{r})\rangle\boldsymbol{D}_1(\boldsymbol{r})\cdot\bar{\boldsymbol{D}}(\boldsymbol{r})d\boldsymbol{r}\\
&\quad\approx\sum_h(\boldsymbol{E}_0\cdot\bar{\boldsymbol{D}}_h{}^s)\sum_n\exp\{2\pi I(\boldsymbol{b}_h{}^s)\cdot\boldsymbol{r}_n\}\sum_k g_k(-R(\boldsymbol{b}_h{}^s))\exp\{-2\pi iR(\boldsymbol{b}_h{}^s)\cdot\boldsymbol{r}_n{}^k\}\exp(4\pi ict/\lambda)\,,
\end{aligned}\qquad\text{(A31)}$$

and

$$\begin{aligned}
&\iint\langle\rho(\boldsymbol{r})\rho(\boldsymbol{r}')\rangle(\boldsymbol{D}_1(\boldsymbol{r})\cdot\bar{\boldsymbol{D}}(\boldsymbol{r}))\,(\boldsymbol{D}_1{}^*(\boldsymbol{r}')\cdot\bar{\boldsymbol{D}}^*(\boldsymbol{r}'))d\boldsymbol{r}d\boldsymbol{r}'\\
&\quad\approx|\sum_h(\boldsymbol{E}_0\cdot\bar{\boldsymbol{D}}_h{}^s)\sum_n\exp\{2\pi J(\boldsymbol{b}_h{}^s)\cdot\boldsymbol{r}_n\}\sum_k g_k(-R(\boldsymbol{b}_h{}^s))\exp\{-2\pi iR(\boldsymbol{b}_h{}^s)\cdot\boldsymbol{r}_n{}^k\}|^2\\
&\quad+\sum_{h,g}(\boldsymbol{E}_0\cdot\bar{\boldsymbol{D}}_h{}^s)(\boldsymbol{E}_0{}^*\cdot\bar{\boldsymbol{D}}_g{}^{*s})\sum_{n,m}\exp2\pi\{I(\boldsymbol{b}_h{}^s)\cdot\boldsymbol{r}_n+I(\boldsymbol{b}_g{}^s)\cdot\boldsymbol{r}_m\}\\
&\quad\times\sum_{k,l}g_k(-R(\boldsymbol{b}_h{}^s))g_l(-R(\boldsymbol{b}_g{}^s))P^{nm}_{kl}(R(\boldsymbol{b}_h{}^s),\ R(\boldsymbol{b}_g{}^s))\\
&\quad\times\exp\{-2\pi i(R(\boldsymbol{b}_h{}^s)\cdot\boldsymbol{r}_n{}^k-R(\boldsymbol{b}_g{}^s)\cdot\boldsymbol{r}_m{}^l)\}\,,
\end{aligned}\qquad\text{(A32)}$$

where $R(\boldsymbol{b})$ and $I(\boldsymbol{b})$ denote the real part and the imaginary part respectively of vector $\boldsymbol{b}=R(\boldsymbol{b})+iI(\boldsymbol{b})$. In Eqs. (A31) and (A32) $\sum_s$ and $\sum_{s,t}$ are removed because either of the pairs $\bar{\boldsymbol{D}}_0{}'$ and $\bar{\boldsymbol{D}}_G{}'$ or $\bar{\boldsymbol{D}}_0{}''$ and $\bar{\boldsymbol{D}}_G{}''$ are negligibly small in Bragg case if the crystal is thick enough and is not perfectly non-absorbing[13]. By the use of Eqs. (A31) and (A32) we have the following equation instead of Eq. (A14).

$$\begin{aligned}
\langle|\boldsymbol{D}_2(\boldsymbol{r}_A)\cdot\bar{\boldsymbol{e}}_{\perp,\parallel}|^2\rangle&=(e^2/mc^2)^2(\lambda^2/\pi)^2(1/|\bar{\boldsymbol{p}}|^2)\sum_{h,g}(\boldsymbol{E}_0\cdot\bar{\boldsymbol{D}}_h{}^s)(\boldsymbol{E}_0{}^*\cdot\bar{\boldsymbol{D}}_g{}^{*s})\\
&\times\sum_{k,l}g_k(-\boldsymbol{b}_h)g_l(-\boldsymbol{b}_g)\sum_{n,m}\exp2\pi\{I(\boldsymbol{b}_h{}^s)\cdot\boldsymbol{r}_n+I(\boldsymbol{b}_g{}^s)\cdot\boldsymbol{r}_m\}P^{nm}_{kl}(\boldsymbol{b}_h,\ \boldsymbol{b}_g)\\
&\times\exp\{-2\pi i(R(\boldsymbol{b}_h{}^s)\cdot\boldsymbol{r}_n{}^k-R(\boldsymbol{b}_g{}^s)\cdot\boldsymbol{r}_m{}^l)\}\,,
\end{aligned}\qquad\text{(A33)}$$

where $\boldsymbol{b}_h$ is a real mean vector defined in the text. By the help of Eq. (A17) the factor $\sum_{n,m}\exp2\pi\{\cdots\}P\cdots\exp\{-2\pi i\cdots\}$ in Eq. (A33) turns out to be

$$\begin{aligned}
&\sum_{n,m}\exp2\pi\{I(\boldsymbol{b}_h{}^s)\cdot\boldsymbol{r}_n+I(\boldsymbol{b}_g{}^s)\cdot\boldsymbol{r}_m\}P^{nm}_{kl}(\boldsymbol{b}_h,\ \boldsymbol{b}_g)\exp\{-2\pi i(R(\boldsymbol{b}_h{}^s)\cdot\boldsymbol{r}_n{}^k-R(\boldsymbol{b}_g{}^s)\cdot\boldsymbol{r}_m{}^l)\}\\
&\quad=(4\pi^2kT/N\sqrt{m_km_l})\sum_p(\boldsymbol{b}_h\cdot\boldsymbol{\chi}_{kl}(\boldsymbol{\tau}_p)\cdot\boldsymbol{b}_g)\sum_{n,m}\exp2\pi\{I(\boldsymbol{b}_h{}^s)\cdot\boldsymbol{r}_n+I(\boldsymbol{b}_g{}^s)\cdot\boldsymbol{r}_m\}\\
&\quad\times\exp\{2\pi i(\boldsymbol{\tau}_p-R(\boldsymbol{b}_h{}^s))\cdot\boldsymbol{n}\}\exp\{-2\pi i(\boldsymbol{\tau}_p-R(\boldsymbol{b}_g{}^s))\cdot\boldsymbol{m}\}\\
&\quad\times\exp\{-2\pi i(\boldsymbol{b}_h\cdot\boldsymbol{X}^k-\boldsymbol{b}_g\cdot\boldsymbol{X}^l)\}\exp\{-2\pi i(\boldsymbol{h}-\boldsymbol{g})\cdot\boldsymbol{r}_0\}
\end{aligned}$$

$$
\begin{aligned}
&= (4\pi^2 kT/\sqrt{m_k m_l})\, v_a \int (\boldsymbol{b}_h\cdot\boldsymbol{\chi}_{kl}(\boldsymbol{\tau}_p)\cdot\boldsymbol{b}_g) \\
&\quad\times |\sum_n \exp\{2\pi i(\boldsymbol{\tau}_p-R(\boldsymbol{b}_0{}^s))\cdot\boldsymbol{n}\}\exp\{2\pi I(\boldsymbol{b}_0{}^s)\cdot\boldsymbol{r}_n\}|^2 d\boldsymbol{\tau}_p \\
&\quad\times \exp\{-2\pi i(\boldsymbol{b}_h\cdot\boldsymbol{X}^k-\boldsymbol{b}_g\cdot\boldsymbol{X}^l)\}\exp\{-2\pi i(\boldsymbol{h}-\boldsymbol{g})\cdot\boldsymbol{r}_0\}\,,
\end{aligned}
\tag{A34}
$$

where the integration is over a unit cell of reciprocal lattice. In Eq. (A34) we use the approximation $\sum_p = Nv_a\int d\boldsymbol{\tau}_p$. Let us put

$$
\begin{aligned}
&\int (\boldsymbol{b}_h\cdot\chi_{kl}(\boldsymbol{\tau}_p)\cdot\boldsymbol{b}_g)|\sum_n \exp\{2\pi i(\boldsymbol{\tau}_p-R(\boldsymbol{b}_0{}^s))\cdot\boldsymbol{n}\}\exp\{2\pi I(\boldsymbol{b}_0{}^s)\cdot\boldsymbol{r}_n\}|^2 d\boldsymbol{\tau}_p \\
&\qquad = (A/N)\int (\boldsymbol{b}_n\cdot\chi_{kl}(\boldsymbol{\tau}_p)\cdot\boldsymbol{b}_g)|\sum_n \exp\{2\pi i(\boldsymbol{\tau}_p-R(\boldsymbol{b}_0{}^s))\cdot\boldsymbol{n}\}|^2 d\boldsymbol{\tau}_p\,.
\end{aligned}
\tag{A35}
$$

Then we have

$$
\int (\boldsymbol{b}_h\cdot\chi_{kl}(\boldsymbol{\tau}_p)\cdot\boldsymbol{b}_g)|\sum_n \exp\{2\pi i(\boldsymbol{\tau}_p-R(\boldsymbol{b}_0{}^s))\cdot\boldsymbol{n}\}\exp\{2\pi I(\boldsymbol{b}_0{}^s(\cdot\boldsymbol{r}_n\}|^2 d\boldsymbol{\tau}_p = (A/v_a)(\boldsymbol{b}_h\cdot\chi_{kl}(\boldsymbol{\tau})\cdot\boldsymbol{b}_g)\,,
\tag{A36}
$$

where $\tau-\boldsymbol{b}_0=-\boldsymbol{I}$. Although we can not give the factor A in any simpler expression than Eq. (A35), it can be seen from Eq. (A35) that the factor A has the properties mentioned near the end of § 3 of the text.

By the help of Eqs. (A33), (A34), (A35) and (19) we have

$$
\begin{aligned}
\langle|\boldsymbol{D}_2(\boldsymbol{r}_A)\cdot\bar{e}_{\perp,\parallel}|^2\rangle &= (e^2/mc^2)^2(\lambda^2/\pi)^2(1/|\boldsymbol{p}|^2) \\
&\quad\times\sum_{h,g}(\boldsymbol{E}_0\cdot\boldsymbol{D}_h{}^s)(\boldsymbol{E}_0{}^*\cdot\boldsymbol{D}_g{}^{*t})\exp\{-2\pi i(\boldsymbol{h}-\boldsymbol{g})\cdot\boldsymbol{r}_0\}AkTS_{hg}\,.
\end{aligned}
\tag{A37}
$$

Let us next evaluate the magnitude of $\bar{\boldsymbol{D}}_h{}^s$ in the factor $(\boldsymbol{E}_0\cdot\bar{\boldsymbol{D}}_h{}^s)(\boldsymbol{E}_0{}^*\cdot\bar{\boldsymbol{D}}_g{}^s)$ in Eq. (A37). Eqs. (A26), (A27) and (A28) are also valid in Bragg case, while Eq. (A29) must be rewritten as follows.

(i) If $W<-1$, we have

$$
\begin{aligned}
&\bar{D}'_{0\perp,\parallel}=\bar{E}_0\,, \\
&\bar{D}'_{G\perp,\parallel}=\sqrt{|\gamma_0/\gamma_G|}\exp(-u)(F_G/|F_G|)\exp(2\pi i\boldsymbol{G}\cdot\boldsymbol{r}_0)(C_{\perp,\parallel}/|C_{\perp,\parallel}|)\bar{E}_0
\end{aligned}
\tag{A38}
$$

and

$$
\bar{D}''_{0\perp,\parallel}=\bar{D}''_{G\perp,\parallel}=0\,,
$$

where $W=-\cosh u$ and $u>0$.

(ii) If $-1<W<1$, we have

$$
\begin{aligned}
&\bar{D}'_{0\perp,\parallel}=\bar{D}'_{G\perp,\parallel}=0\,, \\
&\bar{D}''_{0\perp,\parallel}=\bar{E}_0
\end{aligned}
\tag{A39}
$$

and

$$
\bar{D}''_{G\perp,\parallel}=-i\sqrt{|\gamma_0/\gamma_G|}\exp(-v)(F_G/|F_G|)\exp(2\pi i\boldsymbol{G}\cdot\boldsymbol{r}_0)(C_{\perp,\parallel}/|C_{\perp,\parallel}|)\,\bar{E}_0
$$

where $W=\sin v$.

(iii) If $W>1$, we have

$$
\begin{aligned}
&\bar{D}'_{0\perp,\parallel}=\bar{D}'_{G\perp,\parallel}=0\,, \\
&\bar{D}''_{0\perp,\parallel}=\bar{E}_0
\end{aligned}
\tag{A40}
$$

and

$$
\bar{D}''_{G\perp,\parallel}=-\sqrt{|\gamma_0/\gamma_G|}\exp(-u)(F_G/|F_G|)\exp(2\pi i\boldsymbol{G}\cdot\boldsymbol{r}_0)(C_{\perp,\parallel}/|C_{\perp,\parallel}|)\,\bar{E}_0
$$

where $W=\cosh u$ and $u>0$.

Outside the region of total reflection, by the help of Eqs. (11), (12), (13), (14), (A37), (A38) and (A40), we have Eq. (30) of the text. Within the region of total reflection, by the help of Eqs. (11), (12), (13), (14), (A37) and (A39), we have Eq. (31) of the text.

References

1) H. J. Grenville-Wells: Nature **168** (1951) 291.
2) M. v. Laue: Ann. der Physik **23** (1935) 705.
3) M. v. Laue: Materiewellen und ihre Interferenzen (2nd ed.) (1948) 355. Leipzig, Akademische Verlagsgesellschaft. Y. Kainuma: Acta Cryst. **8** (1955) 247.
4) W. H. Zachariasen: Theory of X-ray Diffraction in Crystals. (1945) 119. New York, John Wiley & Sons.
5) W. H. Zachariasen: ibid. 185.
6) W. H. Zachariasen: ibid. 193.
7) G. N. Ramachandran and W. A. Wooster: Acta Cryst. **4** (1951) 335, 431. J. Hoerni and W. A. Wooster: Acta Cryst. **5** (1952) 386.
8) A. D. Booth: Nature **185** (1946) 380.
9) R. A. Stokes: Nature **161** (1948) 679.
10) H. Pfister: Ann. der Physik **11** (1953) 239. Y. Kainuma: J. Phys. Soc. Japan **8** (1953) 685.
11) L. Nordheim: Ann. der Physik **9** (1931) 607.
12) W. H. Zachariasen: ibid. 185.
13) K. Kohler: Ann. der Physik **18** (1933) 265.

JOURNAL OF THE PHYSICAL SOCIETY OF JAPAN, Vol. 16, No. 2, FEBRUARY 1961

Inelastic Scattering of Thermal Neutrons by Paramagnetic Ions

By Soichiro TOSIMA
Faculty of Science Kyusyu University

(Received July 9, 1960)

For the magnetic scattering of thermal neutrons by paramagnetic ions with discrete energy levels, Trammell's theory is extended to include the inelastic scattering. And the scattering cross section of Eu^{3+}, Sm^{3+}, Co^{2+} in oxide and fluoride and Fe^{2+} in oxide are estimated. In these ions, the cross sections appreciably include the inelastic parts, and depend on the temperature and the energy of the incident neutrons, that is, the cross sections suddenly increase when the energy of the neutron exceeds the level separations.

§ 1. Introduction

The orbital effect on the magnetic scattering of slow neutrons by the rare earth ions, has been discussed by Trammell[1], whose result has proved to explain some features in the magnetic scattering by Nd^{3+} and Er^{3+} [2]. Such an orbital effect is generally small in the iron group compounds, because the orbital angular momentum of the iron group ions is largely quenched by the crystalline field in compounds. On the other hand, in the compounds with the rare earth ion, the electrons in the incomplete 4f shell are deeply buried within the ion and less affected by the crystalline field. However, in some particular compounds, for example CoO and FeO, a large orbital angular momentum surviving under the cubic field brings out a large effect on the neutron diffraction, which Nagamiya and Motizuki[3] have discussed with particular reference to CoO.

These studies are principally concerned with the elastic scattering. But, in some ions, Eu^{3+}, Sm^{3+} on the one hand and Co^{2+}, Fe^{2+} in oxides on the other, the lowest excited level arising from the spin-orbit coupling is rather close to the ground level and the level separation is comparable with kT at room temperature and the energy of the neutrons used in the diffraction experiments. We may therefore expect an appreciable portion of neutrons inelastically scattered, which come from the two processes: the one in which the energy of the incident neutron decreases and the scattering ion goes to the higher energy state, and the other in which the energy of the neutron increases and the ion goes to the lower state. In the present work, we will extend Trammell's theory in order to include such processes of inelastic scattering by the magnetic ion with discrete energy levels.

The cross section of the magnetic scattering is roughly proportional to the square of the effective Bohr magneton number of the magnetic ion. It is, therefore, expected that the cross section has a considerable temperature dependence, because the effective Bohr magneton number of the ion concerned now depends on the temperature. The inelastic scattering process in which the ion goes to the higher energy state can take place only when the energy of the neutron is larger than the level separation, since the total energy of the ion and the neutron must be conserved. Therefore, it is also expected that the cross section increases when the energy of the neutron exceeds the level separation.

As is well-known, L, S and J of the magnetic ion are good quantum numbers in the Russell-Saunders scheme, where L and S are respectively the quantum number of the total oribital angular momentum $\boldsymbol{L}$ and that of the total spin angular momentum $\boldsymbol{S}$ and J the quantum number of $\boldsymbol{J}=\boldsymbol{L}+\boldsymbol{S}$. This scheme remains unaltered for the rare earth ions in compounds, and the situations are similar for Co^{2+} and Fe^{2+} in oxides. For, the orbital angular momentum $\boldsymbol{L}$ for these ions can be replaced by an effective orbital angular momentum $\boldsymbol{L}'$ with $L'=1$ within the lowest orbital manifold under the cubic field, and the spin-orbit coupling leads to the splitting of the energy levels according to the magnitude of effective total angular momentum $\boldsymbol{J}'=\boldsymbol{L}'+\boldsymbol{S}$. Thus, we shall calculate the magnetic scattering cross section of the rare earth ions, and the above-mentioned cases of the iron group ions will also be discussed.

§ 2. The Differential Cross Section of the Magnetic Scattering

Trammell[1) has derived the expression of the differential cross section of the magnetic scattering in the case when both the spin and the orbital angular momentum are operative, and the elastic scattering by the magnetic ions Nd^{3+} and Er^{3+} in the lowest state was calculated in his theory. We will extend his theory to include the transitions between the states with different J value. Now we denote the initial and final wave vectors of the neutron by k_0 and k, and the orbital and the spin angular momentum of the k-th electron in the incomplete shell by $\boldsymbol{l}_k$ and $\boldsymbol{s}_k$. Following his expression, we define the vector $\boldsymbol{P}$ by

$$\boldsymbol{P}=\sum_k\left[\tfrac{1}{2}(\boldsymbol{l}_k f(\boldsymbol{\kappa}\cdot\boldsymbol{r}_k)+f(\boldsymbol{\kappa}\cdot\boldsymbol{r}_k)\boldsymbol{l}_k)+2\boldsymbol{s}_k\exp(i\boldsymbol{\kappa}\cdot\boldsymbol{r}_k)\right], \tag{1}$$

where

$$f(\boldsymbol{\kappa}\cdot\boldsymbol{r})=\frac{1}{(i\boldsymbol{\kappa}\cdot\boldsymbol{r})^2}\int_0^{i\kappa\cdot\boldsymbol{r}}x\,e^x\,dx\ ,$$

$$\boldsymbol{\kappa}=\boldsymbol{k}-\boldsymbol{k}_0$$

For unpolarized incident neutron the differential cross section per magnetic ion, $d\sigma/d\Omega$, is given by

$$\frac{d\sigma}{d\Omega}=\left(\frac{e^2\gamma}{2mc^2}\right)^2\sum_m\sum_n\rho_m\frac{k}{2k_0}\{|(m\,|\,P_+\,|\,n)|^2+|(m\,|\,P_-\,|\,n)|^2\} \tag{2}$$

where γ is the nuclear magneton number of the neutron, ρ_m the statistical weight of the initial state m, $P_\pm=P_x\pm iP_y$, and the z-axis is chosen to be parallel to $\boldsymbol{\kappa}$.

In the Russell-Saunders scheme, the wave function Ψ_{JM} for n electrons in the incomplete shell is the taken to be of the from

$$\Psi_{JM}(\boldsymbol{r}_1,\boldsymbol{r}_2,\cdots,\boldsymbol{r}_n)=\Phi(r_1,r_2,\cdots,r_n)\,\Theta_{l,L,S,J,M},$$

where

$$\Phi(r_1,r_2\cdots,r_n)=\prod_{i=1}^n\varphi_{\alpha l}(r_i)$$

Θ_{lLSJM} is a function of angular and spin variables and $\varphi_{\alpha l}(r_i)$ a radial wave function of the i-th electron.

To calculate the matrix element $(J'\,M'\,|\,P_\pm\,|\,J\,M)$, it is convenient to expand $P_\pm$ in spherical harmonics, thus

$$P_\pm=\sum_{\nu=0}i^\nu(2\nu+1)\sum_k\{f_\nu(\kappa r_k)\tfrac{1}{2}[l_l{}^\pm p_\nu(\theta_k)+p_\nu(\theta_k)l_k{}^\pm]+2g_\nu(\kappa r_k)S_k{}^\pm P_\nu(\theta_k)\}\ , \tag{3}$$

$$g_\nu(x)=(\pi/2)^{1/2}x^{-1/2}\,J_{\nu+1/2}(x)\ ,$$

$$f_\nu(x)=2x^{-2}\int_0^x yg_\nu(y)dy\ ,$$

where θ_k is the angle between the vectors $\boldsymbol{\kappa}$ and $\boldsymbol{r}_k$.

In $(J'\,M'\,|\,P_\pm\,|\,J\,M)$, $g_\nu(\kappa r_k)$ and $f_\nu(\kappa r_k)$ become respectively

$$(\Phi(r_1,r_2,\cdots,r_n)\,|\,g_\nu(\kappa r_k)\,|\,\Phi(r_1,r_2,\cdots,r_n))=(\varphi_{\alpha l}(r_k)\,|\,g_\nu(\kappa r_k)\,|\,\varphi_{\alpha l}(r_k))=G_\nu(\kappa) \tag{4}$$

and

$$(\Phi(r_1, r_2, \cdots, r_n) \mid f_\nu(\kappa r_k) \mid \Phi(r_1, r_2, \cdots, r_n)) \\ =(\varphi_{\alpha l}(r_k) \mid f_\nu(\kappa r_k) \mid \varphi_{\alpha'}(r_k))=F_\nu(\kappa)\ , \qquad (5)$$

which have the same values for all n electrons. In practical calculations, $G_\nu(\kappa)$ and $F_\nu(\kappa)$ are approximated as follows. Expanding $g_\nu(\kappa r)$ in the power series of κr, we have

$$g_\nu(\kappa r)=\frac{2\cdot\nu\,!}{(2\nu+1)!}(\kappa r)^\nu\left(1-\frac{1}{4\nu+6}\kappa^2 r^2+\cdot\right)$$

by which (4) is written as

$$G_\nu(\kappa)=\frac{2\cdot\nu\,!}{2(\nu+1)!}\kappa^\nu\langle r^\nu\rangle\left(1-\frac{1}{4\nu+6}\frac{\langle r^{\nu+2}\rangle}{\langle r^\nu\rangle}\kappa^2+\cdot\right) \\ \doteqdot\frac{2\cdot\nu\,!}{(2\nu+1)!}\kappa^\nu\langle r^\nu\rangle\exp\left[-\frac{1}{4\nu+6}\frac{\langle r^{\nu+2}\rangle}{\langle r^\nu\rangle}\kappa^2\right], \qquad (6)$$

where $\langle r^\nu\rangle$ is defined by

$$\langle r^\nu\rangle=\int_0^\infty \phi_{\alpha l}{}^*\,\phi_{\alpha l}\,r^{\nu+2}dr\ .$$

Similarly

$$F_\nu(\kappa)=\frac{2}{\nu+2}\,\frac{2\cdot\nu\,!}{(2\nu+1)!}\kappa^\nu\langle r^\nu\rangle\exp\left[-\frac{1}{4\nu+6} \times\frac{\nu+2}{\nu+4}\,\frac{\langle r^{\nu+2}\rangle}{\langle r^\nu\rangle}\kappa^2\right]. \qquad (7)$$

The differential cross section has in general a larger value for smaller scattering angle, and those expressions are better approximations for smaller angle.

In order to calculate the angular parts involving the spherical harmonics in $(J'\,M' \mid P_\pm \mid J\,M)$, it is convenient to replace $P_\nu(\theta)$ by the equivalent tensor operator, In the shell with azimuthal quantum number l, the matrix elements of $P_\nu(\theta)$ with odd ν or $\nu>2l$ are zero, and $P_\nu(\theta)$ with even ν are replaced by the tensor operators as follows

$$P_0(\theta)=a_0\times 1=a_0 T_0(l)\ , \qquad (8)$$

$$P_2(\theta)=a_2\left(\frac{3}{2}l_z{}^2-\frac{1}{2}l(l+1)\right)=a_2 T_2{}^0(l)\ , \qquad (9)$$

$$P_4(\theta)=a_4\left(\frac{35}{8}l_z{}^4-\frac{30}{8}l(l+1)_z{}^2\frac{3}{8}l^2(l+1)^2 +\frac{25}{8}l_z{}^2-\frac{6}{8}l(l+1)\right)=a_4 T_4{}^0(l) \qquad (10)$$

and

$$P_6(\theta)=a_6\left(\frac{231}{16}l_z{}^6-\frac{315}{16}l(l+1)l_z{}^4+\frac{735}{16}l_z{}^4 +\frac{105}{16}l^2(l+1)^2 l_z{}^2-\frac{525}{16}l(l+)l_z{}^2+\frac{294}{16}l_z{}^2 -\frac{5}{16}l^3(l+1)^3+\frac{5}{2}l^2(l+1)^2-\frac{15}{4}l(l+1)\right) \\ =a_6 T_6{}^0(l)\ . \qquad (11)$$

The values of a_ν for d- and f-shell are given as follows;

	a_0	a_2	a_4	a_6
d-shell	1	$-2/21$	$-2/63$	
f-shell	1	$-2/45$	$2/495$	$-4/3861$

$P_\nu(\theta)$ with $\nu>4$ in d-shell and $\nu>6$ in f-shell do not appear in our expressions. The product of $T_\nu(l)$ and $l^\pm$ can be expanded in terms of following tensor operators

$$T_1{}^{\pm1}(l)=\frac{1}{\sqrt{2}}l^\pm\ ,$$

$$T_3{}^{\pm1}(l)=\frac{1}{\sqrt{12}}\left\{\frac{15}{4}(l^\pm l_z{}^2+l_z{}^2 l^\pm) -\frac{2}{3}l(l+1)l^\pm-\frac{3}{4}l^\pm\right\}$$

and

$$T_5{}^{\pm1}(l)=\frac{1}{\sqrt{30}}\left\{\frac{315}{16}(l^\pm l_z{}^4+l_z{}^4 l^\pm)-\frac{105}{8}l(l+1) \times(l^\pm l_z{}^2+l_z{}^2 l^\pm)+\frac{15}{8}l^2(l+1)^2 l^\pm -\frac{15}{8}l(l+1)l^\pm+\frac{45}{16}l^\pm\right\}.$$

Using these operators, we have

$$\frac{1}{2}(T_1{}^{\pm1}(l)T_\nu{}^0(l)+T_\nu{}^0(l)T_1{}^{\pm1}(l) \\ =b_\nu T_{\nu-1}{}^{\pm1}(l)+c_\nu T_{\nu+1}{}^{\pm1}(l) \qquad (12)$$

where

$$b_2=\frac{1}{5}\left(\frac{3}{4}-l(l+1)\right), \qquad c_0=1$$

$$b_4=\frac{\sqrt{6}}{9}\left(\frac{15}{4}-l(l+1)\right), \qquad c_2=\frac{\sqrt{6}}{5}$$

$$b_6=\frac{\sqrt{15}}{13}\left(\frac{35}{4}-l(l+1)\right), \qquad c_4=\frac{\sqrt{15}}{9}$$

By use of the relations (8), (9), (10), (11) and (12), $P_\pm$ can be expressed in terms of one-electron tensor operators. In the expression of $P_\pm$, $T_\nu{}^{\pm1}$ with $\nu>2l$ does not appear.

The orbital and spin angular momenta of n electrons are combined to form respectively the resultant total orbital angular momentum $\boldsymbol{L}$ and the total spin angular momentum $\boldsymbol{S}$. It is convenient therefore to rewrite the sum of one-electron tensor operators with respect to $\boldsymbol{L}$ and $\boldsymbol{S}$ as follows

$$\sum_k T_\nu{}^{\pm1}(l_k)=d_\nu T_{\nu\mp}{}^1(L) \qquad (13)$$

and

$$\sum T_1{}^{\pm1}(s_k)T_\nu{}^0(l_k)e_\nu T_1{}^{\pm1}(S)T_\nu{}^0(L)\ . \qquad (14)$$

The values of d_ν and e_ν for Eu^{3+}, Sm^{3+}, Co^{2+} and Fe^{2+}, are given as follows;

	d_1	d_3	d_5	e_0	e_2	e_4	e_6
Eu^{3+}	1	1	1	1	−1/6	−1/6	−1/6
Sm^{3+}	1	0	−1/14	1	−1/15	2/105	1/210
Co^{2+}	1	−1/5		1	−1/5	−1/15	
Fe^{2+}	1	−1		1	1/4	1/4	

By use of (13) and (14) $(J'\,M'\mid P_\pm\mid J\,M)$ is now expressed in terms of tensor operators. Namely

$$\begin{aligned}(J'\,M'\mid P_\pm\mid J\,M)=&\sum_{\mu=0}^{l-1}(-)^\mu\sqrt{2}\,[(4\mu+1)a_{2\mu}\,c_{2\mu}\,d_{2\mu+1}\,F_{2\mu}(\kappa)\\&-(4\mu+5)a_{2\mu+2}\,b_{2\mu+2}\,d_{2\mu+1}\,F_{2\mu+2}(\kappa)](J'\,M'\mid T_{2\mu+1}{}^{\pm1}(L)\mid J\,M)\\&+\sum_{\mu=0}^{l}(-)^\mu 2\sqrt{2}\,(4\mu+1)a_{2\mu}\,e_{2\mu}\,G_{2\mu}(\kappa)(J'\,M'\mid T_1{}^{\pm1}(S)T_{2\mu}{}^0(L)\mid J\,M)\,.\end{aligned}\tag{15}$$

The matrix elements of tensor operators are expressed in terms of the Clebsch-Gorsan coefficients $C(J,\,\nu,\,J';\,M,\,\pm1,\,M')$. From the Wigner-Eckart theorem, the following relations are obtained

$$(J'\,M'\mid T_\nu{}^{\pm1}(L)\mid J\,M)=(J'\,\|\,T_\nu(L)\,\|\,J)C(J,\,\nu,\,J';\,M,\pm1,\,M')\tag{16}$$

and

$$\begin{aligned}(J'\,M'\mid T_1{}^{\pm1}(S)T_\nu{}^0(L)\mid J\,M)&=\sum_{J''}\sum_{M''}(J'\,M'\mid T_1{}^{\pm1}(S)\mid J''\,M'')(J''\,M''\mid T_\nu{}^0(L)\,J\,M)\\&=\sum_{J''}\sum_{\mu}(J'\,\|\,T_1(S)\,\|\,J'')(J''\,\|\,T_\nu(L)\,\|\,J)[(2\mu+1)(2J''+1)]^{1/2}\\&\quad\times W(J\nu J'l;\,J''\,\mu)C(\nu,\,l,\,\mu;\,0,\,\pm1)C(J,\,\mu,\,M,\,\pm1,\,M')\,,\end{aligned}\tag{17}$$

where $W(J\nu J'l;\,J''\mu)$ is the Racah coefficient. The reduced matrix $(J'\,\|\,T_\nu\,\|\,J)$ is not hermitic. For simplicity, we introduce the following coefficient $K_{\mu,\pm}^{\nu}(J',\,J)$

$$\begin{aligned}K_{\mu,\pm}^{\nu}(J',\,J)=&\sum_{J''}(J'\,\|\,T_1(S)\,\|\,J'')(J''\,\|\,T_\nu(L)\,\|\,J)\times[(2\mu+1)(2J''+1)]^{1/2}\\&\times W(J\,\nu\,J'\,l;\,J''\,\mu)C(\nu\,l\,\mu;\,0,\,\pm1).\end{aligned}\tag{18}$$

$K_{\mu,\pm}^{\nu}(J',\,J)$ does not vanish only when two sets of the numbers $\mu,\,l,\,\nu$ and $J',\,\mu,\,J$ respectively from the trigonal relations $\Delta(\mu,\,l,\,\nu)$ and $\Delta(J',\,\mu,\,J)$. And we can easily verify the following relations

$$K_{\nu\pm1,+}^{\nu}(J',\,J)=K_{\nu\pm1,-}^{\nu}(J',\,J)$$

and

$$K_{\nu,+}^{\nu}(J'\,J)=-K_{\nu,-}^{\nu}(J'\,J)$$

Inserting (16) and (17) into (15) and using (18), we obtain

$$\begin{aligned}(J'\,M'\mid P_\pm\mid J\,M)=&\sqrt{2}\sum_{\mu}(-)^\mu F_{2\mu+1}^{\pm}(J'\,J;\,\kappa)C(J,\,2\mu+1,\,J';\,M,\,\pm1,\,M)\\&+\sqrt{2}\sum_{\mu}(-)^\mu F_{2\mu}^{\pm}(J'\,J;\,\kappa)C(J,\,2\mu,\,J';\,M,\,\pm1,\,M')\end{aligned}\tag{19}$$

where

$$\begin{aligned}F_{2\mu+1}{}^{\pm}(J',\,J;\,\kappa)=&\{(4\mu+1)a_{2\mu}\,c_{2\mu}\,d_{2\mu+1}\,F_{2\mu}(\kappa)\\&-(4\mu+5)a_{2\mu+2}\,b_{2\mu+2}\,d_{2\mu+1}\,F_{2\mu+2}(\kappa)\}(J'\,\|\,T_{2\mu+1}(L)\,\|\,J)\\&+2(4\mu+1)a_{2\mu}\,e_{2\mu}\,K_{2\mu+1,\pm}^{2\mu}(J'\,J)G_{2\mu}(\kappa)\\&-2(4\mu+5)a_{2\mu+2}\,e_{2\mu+2}K_{2\mu+1,\pm}^{2\mu+2}(J'\,J)G_{2\mu+2}(\kappa)\end{aligned}\tag{20a}$$

and

$$F_{2\mu}{}^{\pm}(J'\,J;\,\kappa)=2(4\mu+1)a_{2\mu}\,e_{2\mu}K^{2\mu}_{2\mu,\pm}(J'\,J)G_{2\mu}(\kappa)\,. \tag{20b}$$

Among F_ν and G_ν, F_0 and G_0 principally contribute to the scattering amplitude. In the elastic scattering the amplitude is approximately proportional to

$$(J\,||\,T_1(L)\,||\,J)F_0(\kappa)+2K^{0}_{1,\pm}(J',J)G_0(\kappa)=(J\,||\,T_1(L)\,||\,J)F_0(\kappa)+2(J\,||\,T_1(S)\,||\,J)G_0(\kappa)$$

and the ratio x of these two reduced matrices is

$$x=\frac{(J\,||\,T_1(S)\,||\,J)}{(J\,||\,T_1(L)\,||\,J)}=\frac{S(S+1)-L(L+1)+J(J+1)}{L(L+1)-S(S+1)+J(J+1)}\,.$$

For $J=L+S$

$$x=\frac{S}{L}>0$$

and for $J=|L-S|$

$$\begin{aligned} x&=-\frac{S}{L+1}<0 &\qquad &\text{for}\quad L>S\\ &=-\frac{S+1}{L}<0 &\qquad &\text{for}\quad L<S \end{aligned}$$

Therefore, in the ion with more than half-filled shell, the amplitude of the elastic scattering by the ion in the lowest state is approximately proportional to the sum of the orbital and spin contributions, because $J=L+S$ in the lowest state. On the other hand, in the case of the ion with less than half-filled shell, the scattering amplitude is approximately proportional to the difference of the orbital and spin contributions, because $J=|L-S|$ in this case.

Inserting (19) into (2), we have the final expression of the differential cross section

$$\frac{d\sigma}{d\Omega}=\left(\frac{e^2\gamma}{2mC^2}\right)^2\sum_J\sum_{J'}\frac{k}{k_0}(-)^{J'-J}\sqrt{(2J'+1)(2J+1)}\times\sum_\nu\frac{2}{(2\nu+1)}\times F_\nu{}^{+}(J,J';\,\kappa)F_\nu{}^{-}(J'\,J;\,\kappa)\,, \tag{21}$$

with the help of the orthogonal property of the Clebsch-Gordan coefficients

$$\sum_M\sum_{M'}C(J,n,J';\,M,\pm1,M')C(J',n,J;\,M'\mp1,M)=(-)^{J'-J}\frac{1}{2n+1}\sqrt{2(J'+1)(2J+1)}\,\delta_{nn'}\,.$$

In the next section, the magnetic scatterings by various ions with discrete levels are discussed by use of the above expression.

§ 3. The Scattering Cross Sections of Eu^{3+}, Sm^{3+}, Co^{2+} in Oxide and Fluoride and Fe^{2+} in Oxide

The level separations of Eu^{3+}, Sm^{3+}, Co^{2+} in oxide and fluoride and Fe^{2+} in oxide are known to be of the same order of magnitude of kT at room temperature. So we estimate the cross section of the paramagnetic diffuse scattering by these ions.

1) *The rare earth ions* Eu^{3+} *and* Sm^{3+}

In these ions the interactions between the ions and the crystalline fields may be neglected approximately. Then (21) may be applicable in these cases.

The radial wave function $\varphi_{4f}(r)$ is approximated by the hydrogen-like wave function with shielding constant σ of the nuclear charge. Van Vleck[4] has assumed σ to be 34 in order to explain the magnetic susceptibility, and put the numerical value of the spin-orbit coupling parameter λ to be 255 cm^{-1} for Eu^{3+} and 266 cm^{-1} for Sm^{3+}. On the other hand, Gobrecht[5] has found λ to be 355 cm^{-1} and σ to be 32 for Eu^{3+} from the spectroscopic data of $Eu_2(SO_4)_3 8H_2O$.

(a) Eu^{3+} ($L=3$, $S=3$)

The level separations are given bp $E_{J+1}-E_J=(J+1)\lambda$. And the functions $F_\nu^{\pm}(J', J; \kappa)$ for the lowest three states are

$$F_1^{\pm}=(J' \| T_1(L) \| J)(F_0-\frac{1}{2}F_2+A_1^0G_0+A_1^2G_2)\ ,^*$$

$$F_2^{\pm}=(J' \| T_2(L) \|)A_2^2G_2$$

$$F_3^{\pm}=(J' \| T_3(L) \| J)\left(-\frac{2\sqrt{6}}{45}F_2+\frac{\sqrt{6}}{30}F_4+A_3^2G_2+A_3^4G_4\right),$$

where

$$A_1^0=2K_{1,\pm}^{0}/(J' \| T_1 \| J)\ , \qquad A_1^2=-2K_{1,\pm}^{2}/27(J \| T_1 \| J)\ ,$$

$$A_2^2=\mp 2K_{2,\pm}^{2}/(J' \| T_2 \| J)\ , \qquad A_3^2=2K_{3,\pm}^{2}/27(J' \| T_3 \| J)$$

and

$$A_3^4=2K_{3,\pm}^{4}/165(J' \| T_3 \| J)\ .$$

Table I. Coefficients $A_\mu^\nu(J', J)$ for the $J'=0$, 1, 2. $A_\mu^\nu(J', J)$ is symmetric with respect to J and J'. And we define $A_\mu^\nu(J', J)$ to be zero unless the trigonal relations $\Delta(\mu, l, \nu)$ and $\Delta(J', \mu, J)$ be formed.

J'	J	A_1^0	A_1^2	A_2^2	A_3^2	A_3^4
1	0	−2	−0.1667	0	0	0
1	1	2	−0.1333	0	0	0
2	1	−2	−0.5	0.0435	−0.0447	0.0272
2	2	2	−2	0	−0.0163	0.0408

The coefficients $A_\mu^\nu(J', J)$ are tabulated in Table I.

Using these values we can estimate the numerical values of the differential and the total cross sections. The differential cross section, $d\sigma/d\Omega$, monotonously decreases with increasing scattering angle θ as is usual in the paramagnetic scattering. The temperature dependence of $d\sigma/d\Omega$ is shown in Fig. 1, where the wave length of the incident neutron has been taken to be 1.212A. At 300°K, the estimated values of the elastic, inelastic part and the sum of both parts of the total cross section σ are respectively 0.43, 0.74 and 1.17 barns for $\lambda=255\ cm^{-1}$, and 0.36, 0.66 and 1.02 barns for $\lambda=335\ cm^{-1}$. And the elastic, inelastic part and the sum of these parts of the differential cross section $d\sigma/d\Omega(\theta=0)$ are 0.13, 0.27 0.40 barns per steradian for $\lambda=255\ cm^{-1}$, and 0.10, 0.25 and 0.35 barns per steradian for $\lambda=335\ cm^{-1}$. The numerical value of $d\sigma/d\Omega$ in the unit of $2/3(e^2\gamma/2mc^2)^2$ correspond to the square of the effective Bohr magneton number μ_{eff}. For comparison, the curve μ_{eff}^2 vs T is also shown in Fig. 1.

$d\sigma/d\Omega$ and σ depend on the energy ε of the incident neutron, as are shown respectively in Fig. 2 and 3. They suddenly increase when ε exceeds the level separations as were expected previously.

(b) Sm^{3+} ($L=5$, $S=5/2$)

μ_{eff} of Sm^{3+} is about 1/2~1/3 of that of

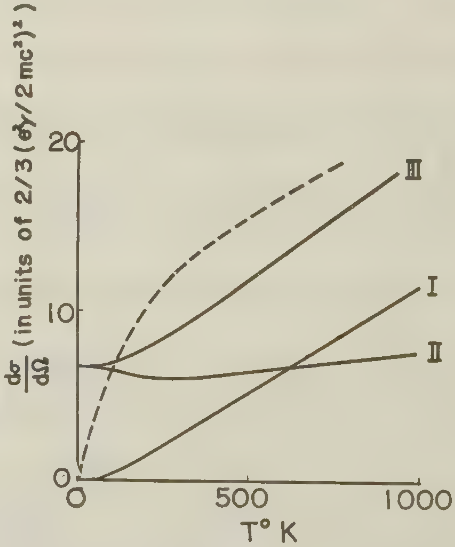

Fig. 1. Temperature dependence of the foreward scattering cross section per ion for $\lambda=255\ cm^{-1}$. Curves I, II and III represent respectively elastic part, inelastic part and the sum of them. The dotted curve represents μ_{eff}^2, where μ_{eff} has been calculated by Van Vleck[4].

---

* The coefficient of F_2 in $F_1^{\pm}$ (J', J) is exactly equal to 1/2 for any ion of the rare earth group. But it is 10.4/20.9 for Er^{3+}, and 8.3/16.3 for Nd^{3+} in Trammell's paper. These are not exact though the numerical values of the cross sections are not affected practically.

Eu^{3+} except at very low temperature, and the cross section is much smaller than that of Eu^{3+}.

2) Co^{2+} *and* Fe^{2+} *in oxide*

Magentic susceptibilities of CoO and FeO have been discussed by Kanamori[6]. According to his theory, L is replaced by $\alpha L'(L'=1; \alpha=-3/2$ for Co^{2+}, and -1 for Fe^{2+}) in the lowest orbital triplet, and the tensor operators are, therefore, replaced by

$$T_1^{\pm1}(L)=-3/2T_1^{\pm1}(L'),$$
$$T_3^{\pm1}(L)=15\sqrt{3}/2\sqrt{2}\,T_1^{\pm1}(L),$$
$$T_2^0(L)=6T_2^0(L)$$

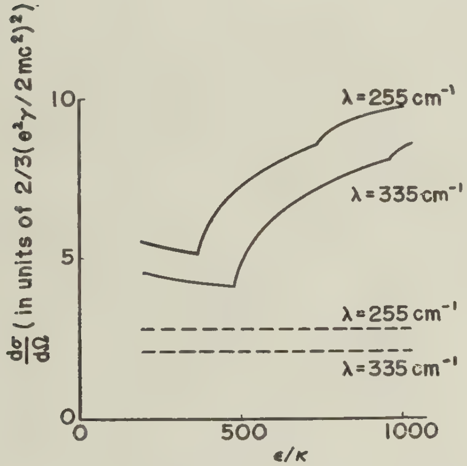

Fig. 2. Dependence of the foreward scattering cross section on the energy ε of the incident neutron. The dotted curve represents the elastic part.

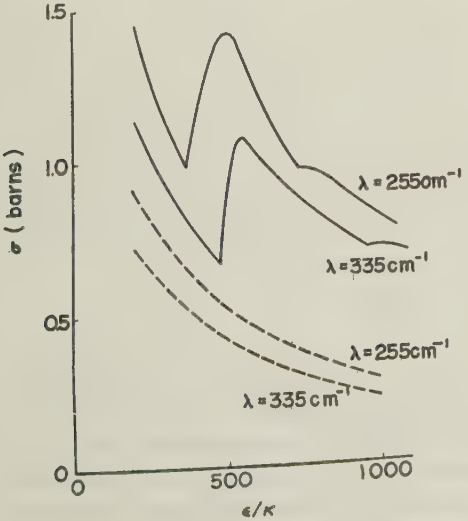

Fig. 3. Variation with ε of the total cross section.

and

$$T_4^0(L)=105/4T_0^0(L')-35/2T_2^0(L')$$

for Co^{2+}. And

$$T_1^{\pm1}(L)=-T_1^{\pm1}(L'),$$
$$T_3^{\pm1}(L)=-3\sqrt{6}/2T_1^{\pm1}(L),$$
$$T_2^0(L)=-3T_2^0(L')$$

and

$$T_4^0(L)=-9/2T_0^0(L')-3T_2^0(L')$$

for Fe^{2+}. The level separations are

$$E_{3/2}-E_{1/2}=405\,\text{cm}^{-1},$$
$$E_{5/2}-E_{3/2}-675\,\text{cm}^{-1}$$

for Co^{2+}, and

$$E_2-E_1=200\,\text{cm}^{-1}$$
$$E_4-E_2=300\,\text{cm}^{-1}$$

In Nagamiya and Motizuki's theory which has discussed the coherent scattering by CoO, the form factor has been calculated by use of the wave functions calculated by Slater[7] and Ariyama et al.[8] On the other hand, the form factor of Co^{2+} in CoF_2 in which the orbital angular momentum is largely quenched has been found experimentally by Erickson[9]. At present, we use the hydrogen-like wave function with shielding constant $\sigma=18.3$, by which we can approximately fit $G_0(\kappa)$ to the form factors by Erickson. The same wave function is approximately used in FeO.

We are not concerned with the short range order effect occuring from the exchange interaction, though the effect is appreciable near room temperature.

(c) Co^{2+} $(L'=1,\ S=3/2)$

The functions $F_\nu^{\pm}(J',\ J)$ for Co^{2+} are

$$F_1^{\pm}=-\frac{3}{2}\left(F_0-\frac{5}{14}F_2-\frac{3}{14}F_4\right)(J'\,||\,T_1(L)\,||\,J)$$
$$+(2G_0-G_4)K_{1,\pm}^{0}(J'\,J)$$
$$-\left(\frac{8}{7}G_2-\frac{2}{3}G_4\right)K_{1,\pm}^{2}(J',J),$$
$$F_2^{\pm}=\left(\frac{8}{7}G_2-\frac{2}{3}G_4\right)K_{2,\pm}^{2}(J'\,J)$$

and

$$F_3^{\pm}=\left(\frac{8}{7}G_2-\frac{2}{3}G_4\right)K_{3,\pm}^{2}(J'\,J)$$

$(J'\,||\,T_4(L')\,||\,J)$ and $K_{\mu,\pm}^{\nu}(J',\ J)$ are tabulated in Table II.

The temperature dependedce of the foreward scattering cross section is shown in Fig. 4. In

Table II. $(J' \| T_1(L') \| J)$ and $K^{\nu}_{\mu,\pm}(J', J)$

J'	J	$(J' \| T_2 \| J)$	$K^{0}_{,1\pm}(J', J)$	$K^{2}_{1,\pm}(J', J)$	$K^{2}_{2\ -}(J', J)$	$K^{2}_{2,\pm}(J', J)$
1/2	1/2	$-1/\sqrt{3}$	$5/2\sqrt{3}$	$-1/4\sqrt{3}$	0	0
3/2	3/2	$2/\sqrt{15}$	$11/2\sqrt{15}$	$17/10\sqrt{15}$	0	$-3\sqrt{14}/5\sqrt{15}$
5/2	5/2	$\sqrt{7}/\sqrt{5}$	$3\sqrt{7}/2\sqrt{5}$	$-3\sqrt{7}/20\sqrt{5}$	0	$9\sqrt{7}/10\sqrt{5}$
3/2	1/2	$\sqrt{5}/\sqrt{6}$	$-\sqrt{5}/\sqrt{6}$	$13\sqrt{5}/40\sqrt{6}$	$-\sqrt{6}/16$	0
1/2	3/2	$-\sqrt{5}/\sqrt{3}$	$\sqrt{5}/\sqrt{3}$	$-13\sqrt{5}/40\sqrt{3}$	$-\sqrt{3}/8$	0
3/2	5/2	$\sqrt{3}/\sqrt{5}$	$-\sqrt{3}/\sqrt{5}$	$-11\sqrt{3}/40\sqrt{5}$	$\sqrt{35}/8$	$4\sqrt{7}/5\sqrt{5}$
5/2	3/2	$-3/\sqrt{10}$	$3/\sqrt{10}$	$33/40\sqrt{10}$	$\sqrt{105}/8\sqrt{2}$	$-2\sqrt{42}/5\sqrt{5}$

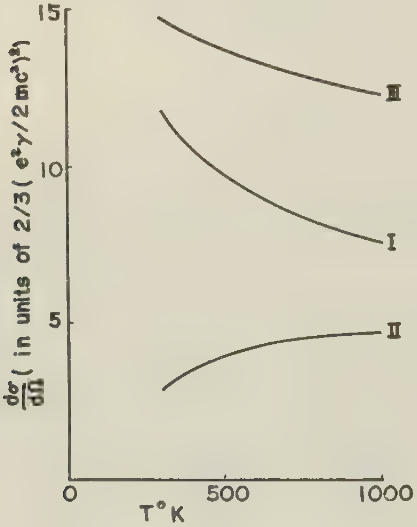

Fig. 4. Temperature pependence of the foreward scattering cross section. Curves I, II and III respectively elastic part, inelastsc part and the sum of them. The wave length of the incident neutron is taken to be 1.212A.

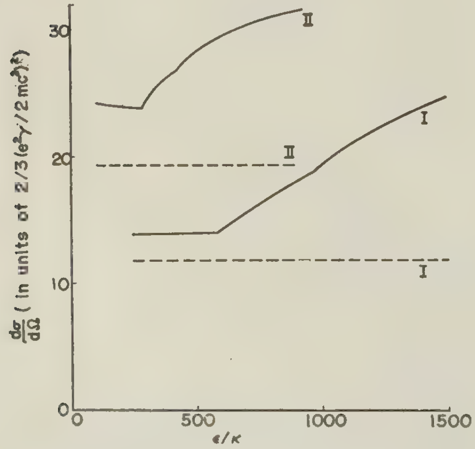

Fig. 5. Variation with ε of the foreward scattering cross sections for Co²⁺ (I) and for Fe²⁺ (II) at T=300°K. The dotted curves represent the elastic parts.

Fig. 5, ε-dependence of $d\sigma/d\Omega$ is shown, and the qualitative behaviour is similar to that of Eu^{3+}.

When the wave length of the neutron is taken to be 1.212A and T=300°K, the elastic and the inelastic parts are estimated respectively 0.56 and 0.14 barns per steradian for the foreward scattering cross section and 0.48 and 0.16 barns for the total cross section.

(d) Fe^{2+} ($L'=1$, $S=2$)

The functions $F_{\nu}^{\pm}(J', J)$ for Fe^{2+} are

$$F_1^{\pm}=-\left(F_0-\frac{19}{14}F_2+\frac{9}{14}F_4\right)(J' \| T_1(L') \| J)$$

$$+\left(2G_0-\frac{9}{14}G_4\right)K^{0}_{1,\pm}(J', J)$$

$$=\left(\frac{5}{7}G_2+\frac{2}{7}G_4\right)K^{2}_{1,\pm}(J'\ J)\ ,$$

$$F_2^{\pm}=\left(\frac{5}{7}G_2+\frac{2}{7}G_4\right)K^{2}_{2,\pm}(J'\ J)$$

and

$$F_3^{\pm}+\left(\frac{5}{7}G_2+\frac{2}{7}G_4\right)K^{2}_{3,\pm}(J'\ J)$$

$(J' \| T_1(L') \| J)$ and $K^{\nu}_{\mu,\pm}(J'\ J)$ are tabulated Table III.

In the same situation as Co^{2+}, the elastic and the inelastic parts are estimated respectively to be 0.92 and 0.50 barns per steradian for the foreward cross section and 0.70 and 0.39 barns for the total cross section. ε-dependence of cross section is similar to the former cases as is shown in Fig. 5.

3) CoF_2

The lowest orbital state of Co^{2+} in the crystalline field with lower symmetry than cubic is nondegenerate. But the orbital angular momentum contributes to the magnetic moment to some extent via spin-orbit coupling, and $\boldsymbol{L}$ is replaced in the perturbation treatment, by

$$\boldsymbol{L}=\boldsymbol{a}\cdot\boldsymbol{S}$$

Table III. $(J' \| T_1(L) \| J)$ and $K_{\mu,\pm}^{\nu}(J', J)$

J'	J	$(J' \| T_1 \| J)$	$K_{1,\pm}^{0}(J', J)$	$K_{1,\pm}^{2}(J', J)$	$K_{2,-}^{2}(J', J)$	$K_{3,\pm}^{2}(J', J)$
1	1	$-1/\sqrt{2}$	$3/\sqrt{2}$	$-3/10\sqrt{2}$	0	0
2	2	$1/\sqrt{6}$	$5/\sqrt{6}$	$13/10\sqrt{6}$	0	$-\sqrt{21}/5$
3	3	$2/\sqrt{3}$	$4/\sqrt{3}$	$-2/5\sqrt{3}$	0	$6/5$
2	1	$3/\sqrt{10}$	$-3/\sqrt{10}$	$6/5\sqrt{10}$	$-\sqrt{3}/2\sqrt{10}$	$-\sqrt{21}/5\sqrt{10}$
1	2	$-3/\sqrt{2}$	$3/\sqrt{2}$	$-2\sqrt{3}/5\sqrt{2}$	$-1/2\sqrt{2}$	$\sqrt{7}/5\sqrt{2}$
3	2	$\sqrt{2}/\sqrt{3}$	$-\sqrt{2}/\sqrt{3}$	$-7\sqrt{2}/20\sqrt{3}$	$\sqrt{3}/2$	$6/5$
2	3	$-\sqrt{14}/\sqrt{15}$	$\sqrt{14}/\sqrt{15}$	$7\sqrt{14}/20\sqrt{15}$	$3\sqrt{7}/2\sqrt{15}$	$-6\sqrt{7}/5\sqrt{5}$

where $\boldsymbol{\alpha}$ is a tensor. CoF_2 belongs to this case. In order to explain the magnetic susceptibility Nakamura and Taketa (hereafter refered to as $N-T$)[10] estimated the components of $\boldsymbol{\alpha}$ to be

$$\alpha_{xx}=0.48$$

$$\alpha_{yy}=0.62$$

$$\alpha_{zz}=0.06$$

choosing the principal axes properly.

The energy levels split into low lying two Kramers doublets and higher ones. The separation between the lowest two doublets has been estimated to be 130 k by $N-T$ or 240 k by Stout and Catalano[11]. We assume that the separation is 240 k though the results are not very dependent on the choice of the value. Using the matrix elements of the spin angular momentum estimated by $N-T$, we can estimate the cross section, we may neglect F_2, G_2, F_4 and G_4 because the contributions of these terms to the cross section are much smaller than that of F_0 and G_0 unless the wave length of the incident neutron is very short.

When the wave length of the neutron is taken to be 1.212A and $T=300°$K. The foreward scattering cross section is estimated to be 0.98 barns per steradian, which is about 25 percent larger than the observed one[9]. Unlike the background due to the nuclear scattering the magnetic scattering is larger for smaller scattering angle. The observed value is obtained from the the extrapolation of the measurements at large angles to $\theta=0$, since the short range order effect is appreciable. Therefore, the observed value may not be accurate. On the other hand, the coherent scattering is in satisfactory agreement with the one calculated from $N-T$'s theory. The elastic and the inelastic parts are respectively 0.65 and 0.33 barns per steradian. The elastic part decreases slightly with increasing temperature, while the inelastic part increases. Then, the sum of them is nearly constant except at low temperatures. But they depend on ε as in the former cases though the increase when ε exceeds 240 k is not so remarkable as in the case of Eu^{3+}.

§ 4. Conclusion

In the case when the level separations of the magnetic ions are comparable with kT at room temperature, we have extended Trammell's theory to include the inelastic scattering, and estimated the scattering cross sections by the ions, Eu^{3+}, Sm^{3+}, Co^{2+} in oxide and fluoride and Fe^{2+} in oxide as the function of the temperature and the energy of the incident neutron. For these ions the inelastic parts of the cross sections are appreciable, and the cross sections depend on the energy of the incident neutron as were expected previously. If the increase of the cross section when ε exceeds the level separations is observed, we may detected the level separations, though they may be more or less affected by the crystalline field for the rare earth ions or the exchange interaction and the effect of the crystal distortion for CoO and FeO. The cross section, more or less, depends on the temperature, but the aspect of this dependence is different for different ions. Unfortunately, we have no experimental data to compare with our results for Eu^{3+}, Co^{2+} in CoO and Fe^{2+} in FeO.

In magnetically ordered state, the spin can change its orientation during the collision if the Curie point is not so high, since the work required to change the spin state is approximately equal to zJ where J is the exchange integral and z the number of the nearest neighbours,and is comparable with energy of the neutron. Therefore, we may expect the inelastic scattering which comes from such a transition. The contribution of the transition to the inelastic scattering is given by $(e^2\gamma F/mc^2)^2\times 2S(1+(\boldsymbol{e}\cdot\boldsymbol{\kappa})^2)$, where F is the form factor and $\boldsymbol{e}$ and $\boldsymbol{\kappa}$ are the unit vectors parallel to the scattering and magnetic vectors, respectively. Magnetic scattering by MnO, FeO, CoO and NiO at low temperature has been observed by Roth[12], and an appreciable diffuse scattering has been observed. Above mentioned transition may contribute to the diffuse scattering, because kT_N of these crystals are smaller than the energy of neutron used in his experiment.

The author wishes to express his sincere thanks to Dr. T. Nakumura for suggesting this problem and for his valuable discussions.

References

1) G. T. Trammell: Phys. Rev. **92** (1953) 1387.
2) W. C. Koehler and E. O. Wollan. Phys. Rev. **92** (1953) 1380.
3) T. Nagamiya and Motizuki: Rev. Mod. Phys. **30** (1958) 89.
4) J. H. Van Vleck: *The Theory of Electric and Magnetic Susceptibilities.* oxford, Clarendon Press, (1932).
5) H. Gobrecht: Ann. Phys. **28** (1937) 673.
6) J. Kanamori: Prog. Theor. Phys. **17** (1957) 177.
7) J. C. Slater: Phys. Rev. **36** (1930) 57.
8) M. Ariyama, K. Kayama and M. Sugimoto: J. Phys. Soc. Japan **12** (1957) 285.
9) R. A. Erickson: Phys. Rev. **90** (1953) 779.
10) T. Nakamura and H. Taketa: Prog. Theor. Phys. **13** (1955) 129.
11) J. W. Stout and E. Catalano: J. Chem. Phys. **23** (1955) 2013.
12) W. L. Roth: Phys. Rev. **110** (1958) 1333.

JOURNAL OF THE PHYSICAL SOCIETY OF JAPAN, Vol 16, No. 2, FEBRUARY, 1961

Time Decrease of Magnetic Permeability in Some Mixed Ferrites

By Keizo OHTA

Kobayashi Institute of Physical Research, Kokubunji, Tokyo

(Received July 30, 1960)

The time decrease of the magnetic permeability after demagnetization, or disaccomodation, was measured for Mn-Zn, Ni-Zn, Cu-Zn and Mg-Zn ceramic ferrites. Considerable disaccomodation was observed with samples containing Fe_2O_3 over the stoichiometric composition. In the case of Mg-Zn ferrites, the disaccomodation is remarkable on both sides of the stoichiometric composition, where it is fairly small. For the specimens sintered in air, the disaccomodation is larger for higher electrical-conductive specimens, while such a correlation to the conductivity disappeared after the specimens were annealed in the nitrogen atmosphere. A single crystal of Ni-Zn ferrite, which is supposed to contain a very small amount of vacancies, also shows a very small disaccomodation. The activation energy determined from the disaccomodation measurements is about 0.5–0.8 eV for Mg-Zn ferrites. It is suggested that the displacement of either vacancies or interstitial ions may possibly be a main origin of the phenomenon.

§1. Introduction

It is normally observed that the magnetic permeability of ferromagnetic materials decreases with time after demagnetization. This phenomenon is termed the *disaccomodation*. The disaccomodation in ferrite was first observed with a Mn-Zn ferrite by Snoek[1] in 1947. He suggested that the electron displacement between divalent and trivalent iron ions in ferrite would be the cause of this phenomenon, just as the diffusion of interstitial carbon or nitrogen atoms was as the cause for the disaccomodation in alpha-iron. Further investigations were made by Enz[2] for a single crystal of Mn-Fe ferrite and by Miyahara and Yamadaya[3] and by Shichijo *et al.*[4] for Mn-Zn ceramic ferrites.

Theory of the *magnetic after-effect*, which is closely related to the disaccomadation, was first proposed by Snoek[5] and then revised by Néel[6],[7],[8], who assumed that the time change in anisotropy energy due to the rearrangement of atom pairs through the diffusion of atoms is the main origin of the magnetic after-effect. The change in anisotropy energy could also be the origin of the disaccomodation. In the case of alpha-iron, the main origin is considered to be the movement of either carbon or nitrogen atoms between different interstitial lattice sites. A similar effect was also proposed for magnetic alloy, where the different sorts of atoms changes their positions substitutionally among the lattice sites. In the case of ferrites, two possibilities can be considered as the origin of the disaccomodation, i.e. the diffusion of electrons between divalent and trivalent iron ions as proposed by Snoek[1], and the diffusion of ions themselves in or among various sites of spinel lattice.

The present author[9] has studied on the disaccomodation of Ni-Zn ferrites, and clarified that the disaccomodation is observed only in the specimens containing excessive iron ions than the content of stoichiometric ferrite, and it becomes remarkable as the content of iron increases. The same result was observed for the time decrease of the permeability after an application of the mechanical compression on the same specimens.

In this paper, the results of the disaccomodation measurements are reported for various mixed ferrite series, such as ceramic Mn-Zn, Ni-Zn, Mg-Zn and Cu-Zn ferrites. The experiment has also been made by using a single crystal of Ni-Zn ferrite.

§ 2. Preparation of Specimens and the Procedure of Measurement

Ceramic ferrites tested were prepared by an ordinary ceramic technique; The mixtures of metal oxides such as Fe_2O_3, CuO, MgO, ZnO, NiO, and or carbonate $MnCO_3$ were baked at 1000°C for two hours, crushed down to fine powders, and then compressed into toroidal forms. They were sintered in the air for two hours at 1250°C for Cu-Zn ferrites, at 1350°C for Ni-Zn and Mn-Zn ferrites, and at 1400°C for Mg-Zn ferrites, and after cooled down to 1000°C, they were rapidly cooled in the air. The specimens prepared were of a ring form, about 25 mm in outer diameter, 20 mm in inner diameter, and 5 mm in thickness. The compositions of the specimens are in the range of $58Ni_{0.4}Zn_{0.6}O$-$42Fe_2O_3$ to $40Ni_{0.4}Zn_{0.6}O$-$60Fe_2O_3$ for Ni-Zn ferrites, and in the range of $58M_{0.6}Zn_{0.4}O$-$42Fe_2O_3$ to $35M_{0.6}Zn_{0.4}O$-$65Fe_2O_3$ for other ferrites, where M represents divalent metal ions such as Mn, Mg or Cu.

A single crystal of Ni-Zn ferrite was grown from the melt by the Bridgeman method. The furnace used for this purpose was similar of Smilten's[10] one. A plutinum crucible containing the raw material was suspended in the furnace, which was held at 1700°C with the temperature gradient of 30°C per cm along its vertical axis, and then lowered down at the rate of 10 mm per hour. A picture frame toroid was cut out from the (110) single crystal plate, by the aid of an ultrasonic vibrating cutter. Each of the four legs of the frame is parallel to one of the ⟨111⟩ directions. The length of each legs is 4.3 mm and its thickness is 2 mm. The composition of this frame specimen was $40Ni_{0.4}Zn_{0.6}O$-$60Fe_2O_3$. All specimens are ascertained to be single phase of spinel structure, except some of the specimens with highest iron content.

Measurements of the permeability were carried out by A.C. bridge method. The specimens were first demagnetized by decreasing

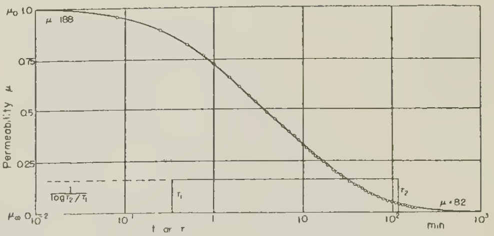

Fig. 1. Typical example of the disaccomodation curves. The specimen is $40Mg_{0.6}Zn_{0.4}O$-$60Fe_2O_3$. The measuring temperature is −10°C. The amplitude of measuring A.C. field, H_m is 10 m Oe.

the amplitude of 50 c.p.s. field from 10 Oe, and then exposed to 1 kc field with the amplitude smaller than 0.05 Oe for the permeability measurements.

A typical example of the time-decrease of permeability is shown as a function of the logarithm of the time *t*, in Fig. 1. The solid curve represents the function proposed by Richter[11]:

$$\psi(t)=\frac{1}{\log \tau_2/\tau_1}\int_{\tau_1}^{\tau_2}\frac{1}{\tau}\exp\left(-\frac{t}{\tau}\right)d\tau\ ,$$

where τ is the relaxation time in a unit process of changing permeability, and τ_1 and τ_2 are, respectively, the lower and upper limits of the assumed flat distribution of τ. The value of τ_1 and τ_2 in Fig. 1 are chosen to get the best fit between theory and experiment. In some cases only a linear portion of the curve of this type was observed, depending upon the measuring temperature. In order to measure the magnitude of the disaccomodation, we adopted the quantity $D=(\mu_{0.1}-\mu_{10})/\mu_{0.1}$, where $\mu_{0.1}$ and μ_{10} are the permeabilities at 0.1 and 10 minutes after demagnetization, respectively.

The electrical conductivity was also measured for the specimens at room temperature by means of the two-point-contact method with D.C. bridge using indium amalgum as a electrode as used by Uitert[12]. The measurements were extended to low temperatures for some specimens in order to determine the activation energies.

§ 3. Experimental Results and Discussions

3.1. *Effect of the Fe_2O_3 content on the disaccomodation*

It has been found that the disaccomodation is very sensitive to the content of Fe_2O_3 for all kinds of ferrites tested. In Fig. 2a) to d), the disaccomodation, *D*, at room temperature are shown as a function of the Fe_2O_3 content. It is seen in these graphs that the disaccomodation is remarkable for specimens containing an excessive Fe_2O_3 (more than 50 mol %), while it is very small for specimens containing a deficient Fe_2O_3 (less than 50 mol %), except for Mg-Zn ferrites which show a fairly large disaccomodation for iron-deficient region.

Electrical resistivities, ρ, of Ni-Zn and Mg-Zn ferrites at room temperature are given as a function of the Fe_2O_3 content in Fig. 3a) and b). The resistivity decreases with an increase of the Fe_2O_3 content, which is in agreement with the measurements by Uitert[12]. This fact looks like to support an idea that

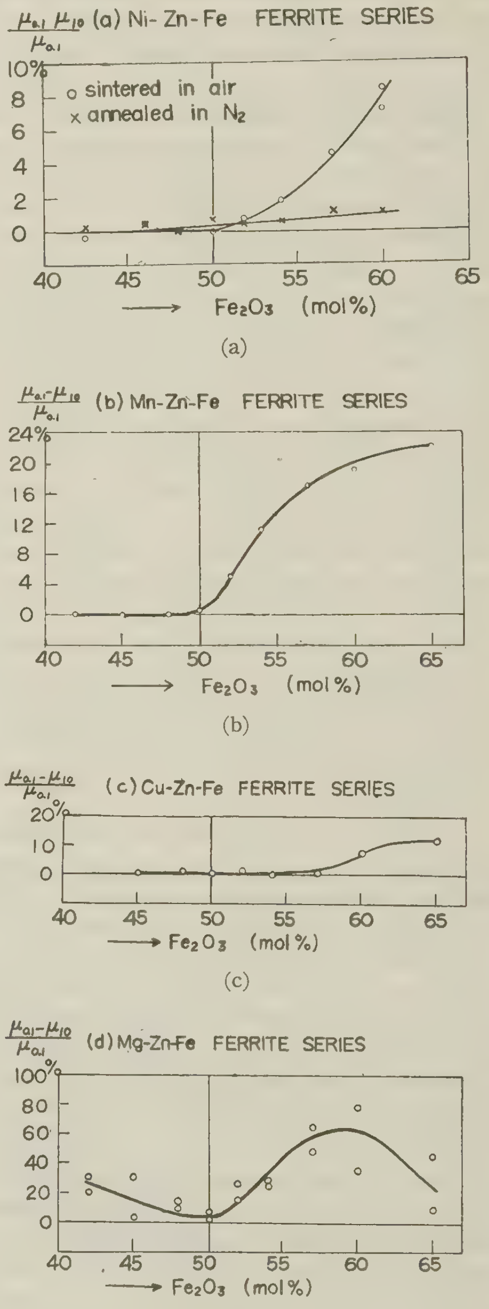

(a)

(b)

(c)

(d)

Fig. 2. Disaccomodation as dependent of the Fe_2O_3 content in several ferrite series;

(a) $Ni_{0.4}Zn_{0.6}O$-Fe_2O_3 sintered at 1350°C; and annealed in nitrogen atmosphere at 1250°C,
(b) $Mn_{0.6}Zn_{0.4}O$-Fe_2O_3 sintered at 1350°C,
(c) $Cu_{0.6}Zn_{0.4}O$-Fe_2O_3 sintered at 1250°C,
(d) $Mg_{0.6}Zn_{0.4}O$-Fe_2O_3 sintered at 1400°C.

the disaccomodation has the same origin as that of the electrical conductivity which is believed to be due to the diffusion of electrons between ferrous and ferric ions in octahedral sites. In the case of Mg-Zn ferrites (Fig. 3b), the resistivity decreases also in the iron-poor region as well as in the iron-rich region. It is interesting to note that the disaccomodation of this ferrite series behaves in the same way as shown in Fig. 2d, which seems to support the idea mentioned above.

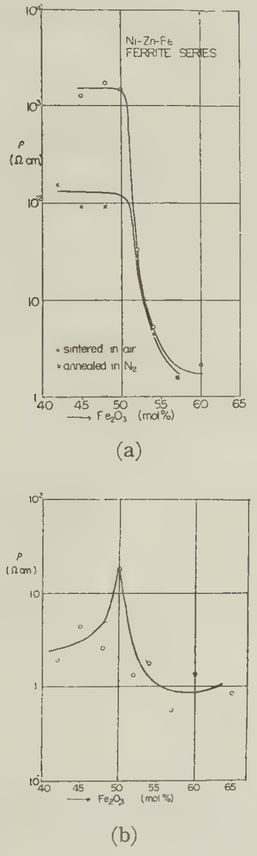

(a)

(b)

Fig. 3. Electrical resistivity as dependent on the Fe_2O_3 content in (a) $Ni_{0.4}Zn_{0.6}O$-Fe_2O_3 and (b) $Mg_{0.6}Zn_{0.4}O$-Fe_2O_3 series.

3.2. *Disaccomodation as a function of the temperature*

Generally speaking, the disaccomodation is strongly dependent upon the measuring temperature. Practically no disaccomodation was detected below the dry ice temperature for all specimens. The μ vs. $\log t$ curves measured at various temperatures are shown in Fig. 4 for Mg-Zn ferrite containing 42 Fe_2O_3, where the permeabilities at $t=0$ and ∞ are taken as 100 and 0, respectively.

The minimum and the maximum relaxation times τ_1 and τ_2 were calculated from the curves in Fig. 4, and plotted as a function of $1/T$ in Fig. 5. The values of the activation energy, E_a, calculated from τ vs $1/T$ lines thus obtained were about 0.7 eV for 42 Fe_2O_3, 0.5–0.8 eV for 54 Fe_2O_3 and 0.5–0.7 eV for 60 Fe_2O_3.

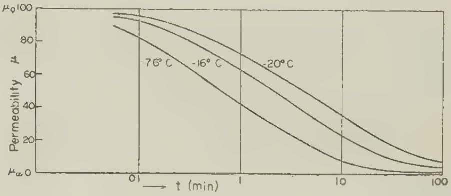

Fig. 4. Thermal change of the disaccomodation in $58Mg_{0.6}Zn_{0.4}O$-42 Fe_2O_3.

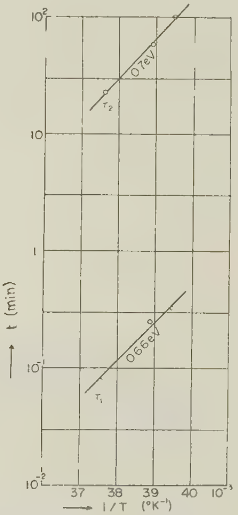

Fig. 5. Maximum and minimum relaxation time τ_1, τ_2 as a function of $1/T$ for $58Mg_{0.6}Zn_{0.4}O$-42 Fe_2O_3.

The temperature dependency of the electrical conductivity in Mg-Zn ferrite with 42 Fe_2O_3 is shown in Fig. 6, from which the activation energy was determined to be 0.18 eV in the vicinity of room temperature. The value for the specimen with 60 Fe_2O_3 is 0.16.

It has been known that many ferrites show large magnetic relaxation losses in the high frequency range, and its activation energy agrees fairly well with that of the electrical conductivity. From this agreement, it has been concluded by Wijn[13] that the origin of the relaxation loss may be the diffusion of electrons between divalent and trivalent iron ions, as is the case for the electrical conductivity.

In the case of the disaccomodartion, however, the activation energies are very large as compared with that of the electrical conductivity, as stated above. Enz[2] also showed that the activation energies of the disaccomodation and of the conductivity were about 0.7 and 1.8 eV, respectively for a single crystal of Mn-Fe ferrite, whose composition is $Mn_{0.84}Fe_{2.14}O_4$. This result was also supported by recent measurement made by Shichijo *et al.*[4] who obtained the values of 0.55 and 0.18 eV, respectively, for the Mn-Zn ferrite ceramics with the composition of $(MnO)_{28}(ZnO)_{19}(Fe_2O_3)_{53}$.

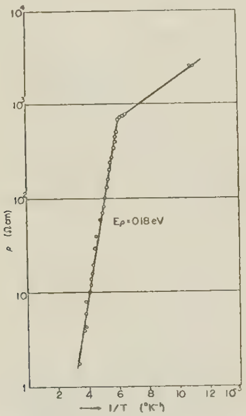

Fig. 6. Thermal change of the electrical resistivity, ρ, in $58Mg_{0.6}Zn_{0.4}O$-$42\ Fe_2O_3$.

Enz[2] explained this discrepancy by assuming that a small amount of Mn^{3+} would be present in both octahedral and tetrahedral sites of spinel lattice, thus giving rise to various types of electron transitions between Mn^{3+}, Mn^{2+}, Fe^{3+} and Fe^{2+} ions which would distribute over octahedral and tetrahedral sites. He assumed that the electron transition with the lowest activation energy will be responsible for the electrical conductivity, while that with a fairly high activation energy will play an important role in giving rise to the disaccomodation.

According to his theory, it must be expected that the relaxation time of the disaccomodation must spread over a fairly wide range which covers the relaxation time of high frequency losses. Actually, however, the relation between τ and $1/T$ for the disaccomodation is confined between the two lines denoted by τ_1 and τ_2 in Fig. 7, and is completely separated from that of high frequency losses. The origin of the disaccomodation, therefore, must be explained by an entirely different mechanism. The fact that Mg-Zn and Cu-Zn ferrites would have very few trivalent metal ions except Fe^{3+} but still show a fairly large disaccomodation conflicts with the idea proposed by Enz.

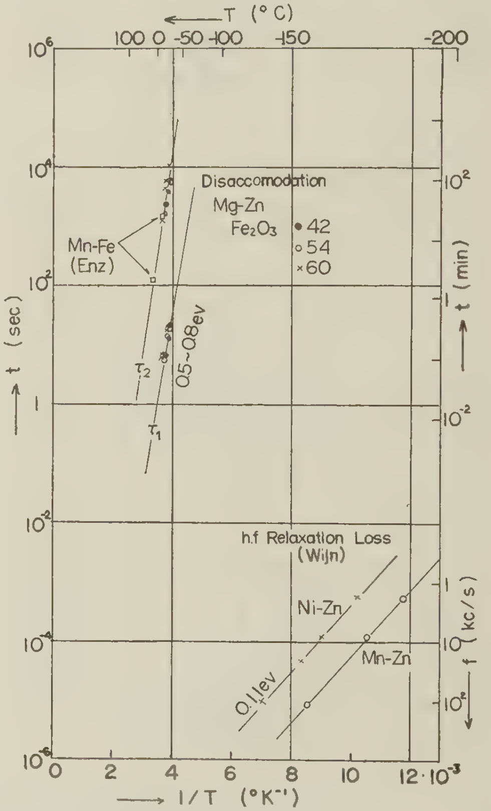

Fig. 7. Relation between τ and $1/T$, for Mg-Zn ferrites as compared to that of high-frequency relaxation losses.

3.3. *Influence of the sintering atmosphere*

The disaccomodation is greatly affected by the sintering atmosphere, which changes the degree of oxidation of the specimens. $40Ni_{0.4}$-$Zn_{0.6}O$-$60Fe_2O_3$ ferrite was used to study these effect, and the results are summerized in Table I.

After sintered at 1350°C for two hours, some specimens were quenched and the remaining specimens were cooled slowly in the furnace. These heat treatments were made in the air. There is a small difference in the

Table I. Effect of the sintering atmosphere on the disaccomodation, D, in $40Ni_{0.4}Zn_{0.6}O$-60 Fe_2O_3.

No.	Heat treatment	D (%)
1	sintered at 1350°C in air and cooled slowly in air	25.3
2	rapidly in air	25.0
3	annealed at 1250°C in air and cooled slowly in N_2	11.5
4	in N_2 and in air	6.8
5	in N_2 and in N_2	1.1

disaccomodation, D, between slowly cooled specimens and rapidly cooled ones. Next, these specimens were annealed again at 1250°C for a half an hour, and then cooled in the furnace. This heat treatment was carried out in nitrogen atmosphere during the whole process, or only during the cooling cycle, or only during the annealing cycle. It may be seen from Table 1 that the disaccomodation decreases with decreasing degree of oxidation. The lowest disaccomodation is observed in the specimen heat-treated in nitrogen atmosphere during the whole process.

The disaccomodation of the Ni-Zn-Fe series which has been annealed at 1250°C in nitrogen atmosphere compared with that of the specimens sintered in air atmosphere in Fig. 2a. It can be seen that D decreases to a considerable extent by nitrogen treatment.

It may be expected that nitrogen treatment deoxidizes the specimens, thus changing some excess ferric ions to ferrous ions. Such an increase in the number of ferrous ion or ferrous-ferric ion pairs, will result in increase in electrical conductivity. This is actually the case, as seen from Fig. 3a. Thus, we might expect that the disaccomodation would be increased by nitrogen treatment, if electron diffusion is really the origin of disaccomodation. The experimental facts, however, are entirely opposite, as mentioned above.

The actual effect of nitrogen treatment can be interpreted as follows: It is commonly recognized that ferrites containing excessive Fe_2O_3 are normally oxidized to some extent, when they are sintered and cooled in the air. It is assumed here that vacancies caused by oxidation is responsible for the disaccomodation. When the specimens are treated in nitrogen atmosphere, however, the number of vacancies will be decreased, thus decreasing the disaccomodation. This model can also explain the effect of iron content on the disaccomodation: That is, when the iron content is increased from the stoichiometric composition, the number of vacancies is expected to increase, because trivalent iron ions are hard to be reduced to divalent ions.

In the case of Mg-Zn ferrites the disaccomodation increases with the deficiency of Fe_2O_3, contrary to the other ferrite series. This can be explained in terms of the effect of excess Mg ions. Since divalent Mg ions can not be oxidized to trivalent, the excess Mg ions added to the stoichiometric composition should enter into the interstitial lattice

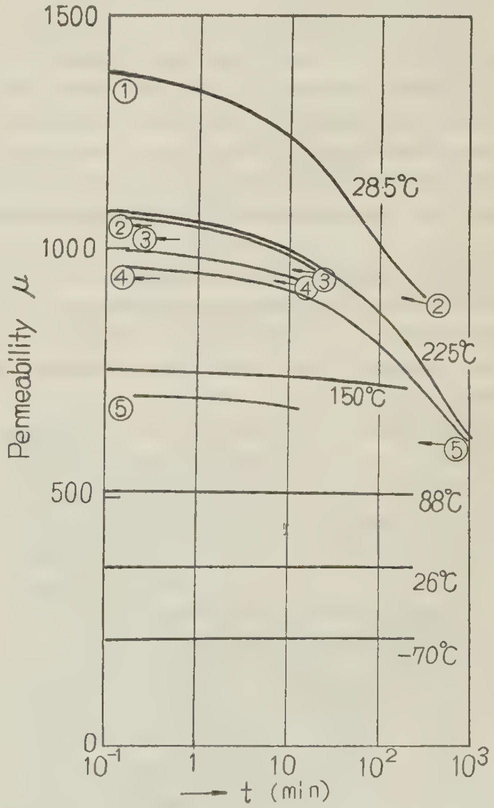

Fig. 8. Time decrease of the permeability in nitrogen-annealed $40Ni_{0.4}Zn_{0.6}O$-60 Fe_2O_3 at various temperatures.

sites. Paladino[14] who recently investigated the phase diagram of Mg-Fe ferrites reached the same conclusion. We can, therefore, explain the experiment by assuming that the interstitial Mg ion is also responsible for the disaccomodation. This effect cannot be expected for Mn-Zn and Ni-Zn ferrites, because in these cases Mn or Ni ions can be changed to trivalent ions, thus maintaing the regular spinel structure.

Furthermore, the time decrease of permeability was measured at higher temperatures for the nitrogen-treated Ni-Zn 60 Fe_2O_3 ferrite, which showed no disaccomodation at room temperature. As shown in Fig. 8, very remarkable changes in permeability were observed above 200°C. The main part of this change, however, was found to be irreversible. In other words, this change is supposed to be acompanied with the change in the structure of the material (*aging effect*). Thus this phenomenon is regarded as independent for the present interest.

In the case of Ni-Zn ferrite single crystal, a negligibly small disaccomodation was observed at and below room temperature ($D\approx 1\%$), although ceramics with the same composition shows a fairly large disaccomodation. It can be considered that this is due to the fact that the single crystal is more perfect and free from vacancies than the air-sintered ceramics. (On the way of the experiment, a large disaccomodation was once observed even at the liquid oxigen temperature. But, it turned out that this was effectuated by heat generation due to the demagnetizing process.)

The value of activation energy obtained from the experiment of disaccomodation, i.e. 0.5–0.8 eV, is also consistent with the model proposed above. Namely, these values are fairly close to 0.9 eV which has been obtained by Bozorth[15] as the activation energy of atomic diffusion from the experiment of magnetic annealing effect of Co ferrites. Lindner[16] has reported about 3 eV as the activation energy of Fe, Ca and Zn ions in Zn and Ca ferrite, basing on the measurements of diffusion by means of the radioactive tracer, but this is expected to include the energy of formation of vacancies or interstitial atoms.

Thus it may be concluded that the main origin of the disaccomdation in various ferrites is the diffusion of either vacancies or interstitial ions generated by oxidation or reduction of the materials.

3.4. *Magnetization process and the field of after-effect*

Here we discuss what kinds of magnetizing processes are responsible for the disaccomodation. The magnetocrystalline anisotropy constant, measured by using the torque magnetometer with the (110) disc of the NiZn ferrite single crystal, is $K_1=-1.7\times10^4$ erg/cc at room temperature. The initial permeability, μ_i, due to the rotational process, as calculated by the formula:

$$\mu_i=\frac{4\pi J_s^2}{3|K_1|}$$

is 60, using the observed value $J_s=490$ gauss. While, the value of measured for the ceramics and the single crystal of Ni-Zn 60 Fe_2O_3 ferrite, are 270 and 750, respectively. This indicates that the displacemet of magnetic domain walls is predominate over the rotational process in these specimens. It can be assumed that this is generally the case for the other kinds of ferrites.

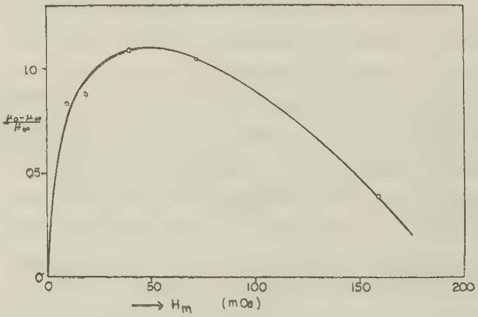

Fig. 9. Relation between the disaccomodation and measuring A.C. field, H_m, for $40Mg_{0.6}Zn_{0.4}O$-60 Fe_2O_3 at 1°C.

Using Mg-Zn 60 Fe_2O_3 ferrite, the disaccomodation at 1°C was measured as a function of the amplitude of the measuring A.C. field, H_m. The ratio $D_\infty=(\mu_0-\mu_\infty)/\mu_\infty$ has the maximum value for $H_m\approx50$ mOe (Fig. 9), where μ_0 and μ_∞ are the values of the permeability at $t=0$ and ∞, respectively. The shape of this curve is similar to the theoretical one proposed by Néel[6] for the after effect due to 180° wall displacements. According to the process adopted by Brissoneau[7] and by others[8],[17], the magnetic induction, B vs H_m curves are constructed for various durations of time from the instant of demagnetization (Fig. 10). From Fig. 10, the *field of magnetic after effect* or *stabilization field*, H_0, which corresponds to the difference of field between two curves of $t=0$ and ∞, was determined as 35 mOe.

According to Néel's[9] theory, the field of after effect for 180° wall displacements is expressed as:

$$2H_0J_s=\frac{cw^2}{3kT}f(U)G(t)\ ,$$

where $f(U)$ the variation of the energy as the function of the position of domain wall U, $G(t)$ a function of time which varies from 0 for $t=0$ to 1 for $t=\infty$, w the change in the atom pair energy due to the displacement of interstitial atom, c the concentration of interstitial atoms, k the Boltzman constant, and T the absolute temperature.

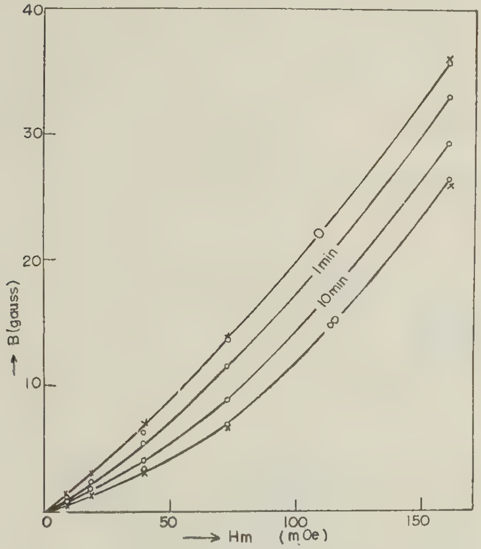

Fig. 10. Relation between magnetic induction, B, and measuring field, H_m, at various times measured from the demagnetization.

Néel has calculated the function $f(U)$ and showed that the maximum value is 2 for 180° wall motion. Here, we consider the case in which $G(t)=1$, $f(U)=2$, $H_0=35\times10^{-3}$ Oe, $J_s=$ $=4.5\times10^2$ gauss, then approximately $w=1.3\times10^{-6}/\sqrt{c}$ is obtained. If we consider the case in which the atomic pairs change their direction, the value of w is changed by the factor 2.9, and thus we have $w=3.8\times10^{-6}/\sqrt{c}$.

There are two possible mechanisms by which vacancy or interstitial ion contributes to the disaccomodation: One is the case that the vacancies accerelate the diffusion of metal ions in the spinel lattice without any direct contribution to the anisotropy. Tne other case is that the vacancies have a direct contribution to the anisotropy through the rearrangement of ion-vacancy pairs. If we assume the second case, and put the vacancy concentration, as $c=2.3\times10^{20}$, which was determined from chemical analysis of ferric and ferrous ions, into the formula of w, we have $w=2.6\times10^{-16}$ erg or 1.5×10^8 erg/mol. This value seems fairly reasonable as compared to the value of the dipole-dipole interaction determined by Néel[18] by using the magnetostriction data of iron-nickel alloys. The same estimation has not been made for the mixed ferrites, but the order of magnitude will be the same, because the magnetostriction constants of ferrites are the same order of magnitude as those of alloys.

§ 4. Summary

1) It was observed for Mn-Zn, Ni-Zn, Cu-Zn and Mg-Zn ceramic ferrites that the disaccomodation increases with an increase of Fe_2O_3 from stoichiometric composition MFe_2O_4.

2) Only in the case of Mg-Zn ferrites, a remarkable disaccomodation was observed also in the region of defficient Fe_2O_3. It takes a minimum value at the stoichometric composition.

3) The tendencies 1) and 2) are also seen for electrical conductivity. But this correlation is found to be superficial, because, when the specimens of Ni-Zn ferrite were annealed in nitrogen atmosphere, the disaccomodation was remarkably decreased, while the electrical conductivity was increased.

4) A negligibly small disaccomodation was observed with the Ni-Zn ferrite single crystal, which is supposed to contain a very small amount of vacancy.

5) The activation energies determined from the disaccomodation measurements with Mg-Zn ferrites are 0.5–0.8 eV, which are fairly large as compaired to that of the electrical conductivity (0.16–0.18 eV).

6) It may be concluded that the disaccomodation is closely related to the vacancy or interstitial ions, the displacement of which may change the local anisotropy, thus changing the permeability.

Acknowledgement

The author should like to express his sincere thanks to Prof. S. Chikazumi for his guidance and kind inspection of the manuscript, and to Prof. S. Miyahara, Dr. T. Yamadaya and Mr. T. Wakiyama for their helpful advices. Thanks are also due to Dr. N. Sakamoto and Dr. N. Miyata for their kind advices for the preparation of single crystal, and to Mr. T. Ikeda for his assistance in this experiment.

References

1) J. L. Snoek: *New Development in Ferromagnetic Materials* (Elsevier Publ., New York 1947) 54.
2) U. Enz: Physica **24** (1958) 609.
3) S. Miyahara and T. Yamadaya: J. Phys. Soc. Japan **14** (1959) 1635.
4) Y. Shichijo, T. Hiraga, O. Ishii and M. Morisawa: Rep. No. 1360, Elect. Comm. Lab. (1959) (in Japanese).
5) J. L. Snoek: Physica **6** (1939) 161.
6) L. Néel: J. de Phys. Rad. **13** (1952) 249.
7) P. Brissoneau: J. Phys. Chem. Solids **7** (1958) 22.
8) G. Biora, A. Ferro and G. Montalenti: A.R. D.C. Contract No. AF 61 (514) 1331, Technical Report 3a (1959).
9) K. Ohta: Bull. Kobayashi Inst. Phys. Res. **8** (1958) 17 (in Japanese).
10) J. Smilten: J. Chem. Phys. **20** (1952) 990.
11) R. Becker and Döring: *Ferromagnetismus* (1939) 247.
12) L. G. Van Uitert: J. Chem. Phys. **23** (1955) 1883.
13) H. P. J. Wijn and H. van der Heide: Rev. Mod. Phys. **25** (1953) 98.
14) A. E. Paradino: J. Amer. Ceramic Soc. **43** (1960) 183.
15) R. M. Bozorth, E. F. Tilden and A. J. Williams: Phys. Rev. **99** (1955) 1788.
16) R. Lindner: J. Chem. Phys. **23** (1955) 410.
17) J. Bindels, J. Bijvoet and G. W. Rathenau: Physica **26** (1960) 163.
18) L. Néel: J. de Phys. Rad. **15** (1954) 225.

JOURNAL OF THE PHYSICAL SOCIETY OF JAPAN, Vol. 16, No. 2, FEBRUARY, 1961

Oxygen Positional Parameters of Tetragonal Mn_3O_4*

By Ken'iti SATOMI**

Tokyo Institute of Technology, Oh-okayama,
Tokyo, Japan

(Received August 6, 1960)

The positions of the oxygen ions of tetragonal Mn_3O_4 are determined through the Debey-Scherrer X-ray analysis, by the extension of the Bertaut's method and with least square method. The assigned correction for the anomalous scattering on Mn to Fe-Kα radiation is somewhat larger than the calculated value. The two oxygen parameters ε and δ for the space-group D_{4h}^{19} are 0.032~0.036 and 0.008~0.010. These values correspond to the case that the tetragonal deformation comes from the octahedral sites but the tetrahedral sites resist to the deformation.

§1. Introduction

Since the investigation by Barth and Posnjak[1] about the existence of the inverse spinels, the cation distribution and the oxygen parameters of the spinels have been investigated by many authors and the main factors which determine the cation distribution are given for the usual ferrites by Verwey et al,[2] being regarded as purely ionic crystals. On the other hand, as they pointed out already, the deviation from the ionic crystal in same spinels, especially in those which do not contain much Fe^{3+} ions, becomes more and more clear. In this respect, Goodenough et al[3] proposed according to the Pauling's theory of the hybridized covalent bond that the Mn^{3+} or Cu^{2+} ions in the spinels prefer the octahedral site and make dsp^2 square covalent bond while the Mn^{2+} and Fe^{3+} ions in the spinels prefer the tetrahedral site and make sp^3 tetrahedral covalent bond. If there are sufficient amount of these ions in the octahedral site to establish the order of the direction of the deformed octahedron, the tetragonal deformation of a crystal as a whole will result[4]. Other authors[5] discussed these problems using the crystalline field splittings of the ionic energy levels.

---

* This paper is presented as partial fulfillment of the requirement for the degree of Doctor of Science in Physics at the Tokyo Institute of Technology.

** Present adress: Nippon Telegraph and Telephone Public Corporation Electrical Communication Laboratory Tokyo, Japan.

Being interested in this deformation, the present author has investigated the oxygen position around the Mn^{3+} ions in the octahedral site of tetragonal Mn_3O_4 by the measurement fo the Debey-Scherrer X-ray diffraction intensities.

§ 2. Experimentals

The powder specimens of Mn_3O_4 were prepared by the decomposition of manganous oxalate precipitated from the mixture of the boiling ammonium oxalate solution and conc. manganous sulphate solution. To prevent the formation of the vacancies of the γ-Mn_2O_3 type, this powder was heated for two hours at 1100°C and then is quenched by putting it between two aluminum plates. The annealing temperature was chosen because it is higher than the decomposition temperature of Mn_2O_3[6] but lower than the transition temperature from the tetragonal to cubic phase[7]. Although the powder was not coase, it was rubbed in an agate-mortar. Then the powder was packed in a frame and the flat surface was used for the measurement of the X-ray diffraction. The diffraction intensities were recorded by the Norelco diffractometer using Fe–Kα radiation with slow scanning speed. All the measured lines of this sample can be indexed according to the space group D_{4h}^{19} with $a=5.76$ Å and $c=9.46$ Å Fig. 1 shows the diffraction lines of Mn_3O_4 and the relations between them and those of a cubic spinel. The observed breadths of the diffraction lines are found to be about 1/5°. This is mainly the instrumental broadening, because the dimension of the powder observed under the microscope were about 10 microns.

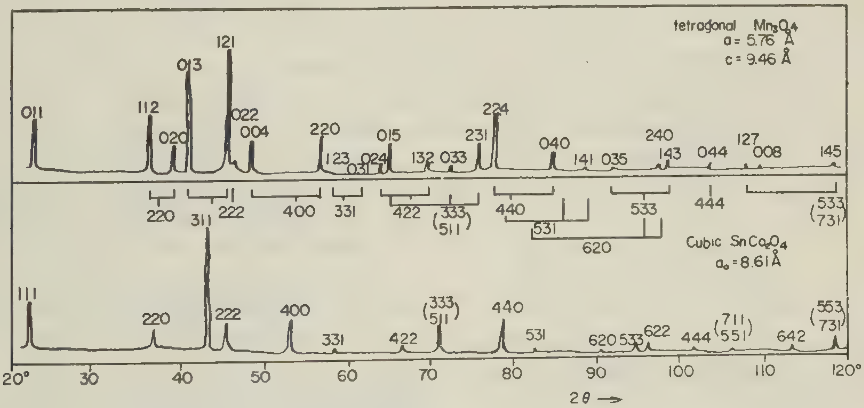

Fig. 1. X-ray diffraction patterns of tetragonal Mn_3O_4 and cubic $SnCo_2O_4$.

§ 3. Method of Analysis

The analysis of the measured integral intensities of the lines (hkl) was performed by a method similar to that used by Bertaut[8] in his investigation of the cation distribution of Cu ferrite. Then the result was refined by the least square method. The author extended the Bertaut's method so as they could be applied to the case of the tetragonally deformed spinel Mn_3O_4. Based upon the description of the International Tables of the D_{4h}^{19}, the positions of the oxygen ion are expressed as 16(h) site and the positions of Mn ions are expressed as 4(a) and 8(d). Their coordinates are respectively $(0, 1/4-\varepsilon, 3/8+\delta)$, $(0, 0, 0)$ and $(0, 1/4, 5/8)$ etc. For $\varepsilon=\delta=0$ the oxygen lattice is only uniformly deformed from the face-centred cubic closepacked to the face-centred tetragonal with the Z-axis streched by $c/\sqrt{2}a$ times. For $\varepsilon=2\delta$ the oxygen position is the same as in the spinel unless the tetragonal deformation is considered. If $\varepsilon>2\delta$ the ratio of the displacements is larger in the XY-plane than parallel to the Z-axis in the sence to compensate the deformation of the tetrahedral site from the regular tetrahedron. To determine the position of the oxygen, first of all we calculate the crystal structure factors for the small values of ε and δ retaining only the contribution of the linear terms of parameters. The result is shown for the relatively low angle lines in the Table I. It is seen that the first order contribution of the oxygen parameters exists for the lines: (011)(013)(121)(123)(031)(015)(033)(231)(035) and (143) etc. Although for the cubic spinels only the intensity of the (111) lines is strongly dependent on the oxygen parameter $u-3/8$, for the tetragonal Mn_3O_4 the intensities of so many diffraction lines are influenced by the oxygen positional parameters that the two parameters ε and δ can be determined fairly well. If we put $\varepsilon/2=\delta=u-3/8$, these structure factors is of course the same as those in the spinels.

Table I. The crystal structure factors $F(hkl)$ and the numbers of the planes $p(hkl)$ of Mn_3O_4.

$h\ k\ l$	p	$\lvert F(h\,k\,l)\rvert$ per formula unit $A(B_2)O_4$
0 1 1	8	$B-\frac{1}{\sqrt{2}}A+(\delta+\varepsilon)\cdot 4\pi O$
1 1 2	8	A
0 2 0	4	A
0 1 3	8	$B+\frac{1}{\sqrt{2}}A-(3\delta-\varepsilon)\cdot 4\pi O$
1 2 1	16	$B+\frac{1}{\sqrt{2}}A+(\delta-\varepsilon)\cdot 4\pi O$
0 2 2	8	$2B \qquad - \qquad 4O$
0 0 4	2	$2B \quad -A \quad + \quad 4O$
2 2 0	4	$2B \quad -A \quad + \quad 4O$
1 2 3	16	$B-\frac{1}{\sqrt{2}}A-(3\delta+\varepsilon)\cdot 4\pi O$
0 3 1	8	$B-\frac{1}{\sqrt{2}}A+(\delta-3\varepsilon)\cdot 4\pi O$
0 2 4	8	A
0 1 5	8	$B+\frac{1}{\sqrt{2}}A+(5\delta+\varepsilon)\cdot 4\pi O$
1 3 2	16	A
0 3 3	8	$B+\frac{1}{\sqrt{2}}A-(3\delta+3\varepsilon)\cdot 4\pi O$
2 3 1	16	$B+\frac{1}{\sqrt{2}}A+(\delta+3\varepsilon)\cdot 4\pi O$
2 2 4	8	$2B \quad +A \quad + \quad 4O$
0 4 0	4	$2B \quad +A \quad + \quad 4O$
0 3 5	8	$B+\frac{1}{\sqrt{2}}A+(5\delta-3\varepsilon)\cdot 4\pi O$
1 4 3	16	$B+\frac{1}{\sqrt{2}}A-(3\delta-\varepsilon)\cdot 4\pi O$
0 4 4	8	$2B \quad -A \quad + \quad 4O$
0 0 8	2	$2B \quad +A \quad + \quad 4O$

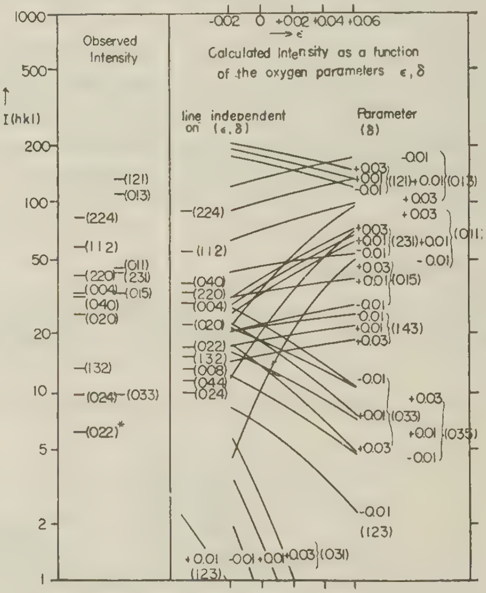

* The correction of f in § 4 can explane the weak observed value but $I(022)$ is not exact for the overlap with (121).

Fig. 2. The observed and the calculated intensities of the diffraction lines of Mn_3O_4.

Upon using the Thomas-Fermi scattering factors for Mn, the Hartree scattering factors for O^{2-} and the Lorentz' and polarization factors of the diffraction intensity for a polycrystalline block i.e. $1+\cos^2 2\theta/\sin^2\theta\cos\theta$, the intensity values were calculated. The results are shown in the Fig. 2, where the ordinate represents the logscale intensity, the abscissa denotes ε and the curves are drawn for various δ's. The lines (123) and (031), which correspond to the spinel line (331), are too weak to be used for the determination of the oxygen parameters.

Looking at the Table I and the Fig. 2 we can see immediately that the intensity ratio of the following lines can be used most effectively, to determine ε and δ separately, and to estimate the deviation from $\varepsilon=2\delta$,

$$\delta: \frac{I(013)}{I(015)}, \quad \varepsilon: \frac{I(013)}{I(033)}, \ \frac{I(121)}{I(231)}; \ \frac{I(011)}{I(015)}, \quad \varepsilon-2\delta: \frac{I(121)}{I(013)}, \ \frac{I(143)}{I(035)}.$$

There are many lines to use for the determination of the average displacement of the oxygen from the tetrahedral site toward the octahedral sites,

$$\varepsilon+2\delta: \frac{I(015)}{I(033)}, \ \frac{I(231)}{I(033)}; \ \frac{I(013)}{I(011)}, \ \frac{I(011)}{I(033)} \qquad \text{etc.}$$

For the ratios coming after the semicolon, the result should deviate if it happens that the structure factors of the Mn ions on the octahedral and the tetrahedral sites are different. What site is more dense in the electronic distribution can be estimated by selecting the lines sensitive for it and by calculating their intensity ratios ξ

$$\xi=\frac{\{I(112),\, I(020)\}}{\{I(004),\, I(220)\}} \cong \frac{\{f_{\text{tet}}\}^2}{\{2f_{\text{oct}}-f_{\text{tet}}+4f_{\text{oxy}}\}^2} \times \frac{\phi(\theta)}{\phi'(\theta')} \times \frac{p}{pp'} \qquad \text{etc.}$$

Where $\phi(\theta)$ is the part of the atomic structure factors and the other geometrical factors which depends upon the scattering angles. The corrections from the ratio $\xi_{\text{calc.}}$ calculated for the distribution $\mathrm{Mn(Mn)_2O_4{}^{2\cdot}}$ are estimated and compared with the experimental data for the most probable distributions

$$\mathrm{Mn^{3+}_{2/3}}V_{1/3}\mathrm{(Mn^{3+})_2O_4{}^{2-}}, \quad \mathrm{Mn^{3+}(Mn^{3+}_{5/3}}V_{1/3})\mathrm{O_4{}^{2-}}, \quad \mathrm{Mn^{2+}(Mn^{3+})_2O_4{}^{2-}}, \quad \text{and} \quad \mathrm{Mn^{3+}(Mn^{2+}Mn^{3+})O_4{}^{2-}},$$

assuming that

$$f_{\mathrm{O^{2-}}}=10\,, \ f_{\mathrm{Mn}}=25\,, \ f_{\mathrm{Mn^{2+}}}=23\,, \ f_{\mathrm{Mn^{3+}}}=22 \text{ and } \phi(\theta)/\phi'(\theta')\cong\text{const. for various distributions,}$$

where the metal ions in the parentheses occupy the octahedral site and the metal ions outside of it occupy the tetrahedral site and v indicates vacancy. The existence of the metal ion vacancies v is considered, because it is believed that the disappearence of the tetragonal deformation by the substitutions of the Mn ions in spinels is dependent on the degree of the oxydation9). In the end, there are no contradiction in assigning the normal 2(33) spinel arrangement for Mn_3O_4,

$$\frac{\xi_{3v(3)}}{\xi_{\text{calc.}}}=0.3^*, \quad \frac{\xi_{3(3v)}}{\xi_{\text{calc.}}}=1.10\,, \quad \frac{\xi_{2(33)}}{\xi_{\text{calc.}}}=0.96\,, \quad \frac{\xi_{3(23)}}{\xi_{\text{calc.}}}=0.82 \quad \text{and} \quad \frac{\xi_{\text{obs.}}}{\xi_{\text{calc.}}}=0.92$$

where the same constant factors for each distribution are eliminated by taking the ratio $\xi/\xi_{\text{calc.}}$.

For the correction of the temperature factor $\exp\{-B(\sin\theta/\lambda)^2\}$ it must be given $B=\dfrac{6h^2}{mk\theta}\left\{\dfrac{\Phi(X)}{X}+\dfrac{1}{4}\right\}$, $X=\dfrac{\theta}{T}$, where θ is the Debey temperature. For NaCl $\theta=281$°K, $m=m_{\mathrm{Cl}}+m_{\mathrm{Na}}/2\cong 30$ and $B=1.43\times 10^{-16}$. Here θ of Mn_3O_4 is estimated using the frequency of the optical mode of the lattice vibrations, as it has been observed by the author10) in the far infrared region. The observed values are 200 $\mathrm{cm^{-1}}$ for NaCl, 600 $\mathrm{cm^{-1}}$ for Mn_3O_4 and then $\theta_{\mathrm{Mn_3O_4}}/\theta_{\mathrm{NaCl}}\cong\nu_{\mathrm{Mn_3O_4}}/\nu_{\mathrm{NaCl}}\cong 3.0$. From this and $m=3m_{\mathrm{Mn}}+4m_{\mathrm{O}}/7\cong 33$, the correction for Mn_3O_4 is given as $B_{\mathrm{Mn_3O_4}}=0.18\times 10^{-16}$. The Mn_3O_4 belongs to relatively hard crystals and the correction for the thermal vibrations is not great for the relatively low angle lines for which $10^{-8}\sin\theta/\lambda$ is smaller than 0.3.

The corrections of the absorption and the extinction can be neglected if the sample is the ideal polycrystalline block. The diffracted intensity is reduced only by a constant factor for the whole lines.

---

* γ-Mn_2O_3 shows this vacancy distribution and a slight existence of the vacancy in the sample have a large effect on the result but the more exact calculation does not show the posibility of the existence of vacancies on this investigation.

Each intensity ratio for the lines dependent upon the oxygen parameters is calculated and the loci which satisfy both the observed and calculated intensity ratios are given on the $\mathcal{E}$-δ plane, as shown in the Fig. 3. If these loci cross at one point, this point gives the result consistent for all the line intensities. This method of determining two parameters has been used by Hastings and Corliss[11] to give the cation distribution x and the oxygen parameter u of the Mn ferrite by the Neutron diffraction method. On the determination of the cross point, one must be careful of the fact that the error in the observed intensity of each line gives rise to a different amount of shifts of the loci on the $\mathcal{E}$-δ plane. Due to the uncertainty of drawing the base lines on the diffraction pattern and the approximations used in the calculations, the result will be given as $\delta=0.008\sim0.012$ and $\mathcal{E}=0.032\sim0.040$.

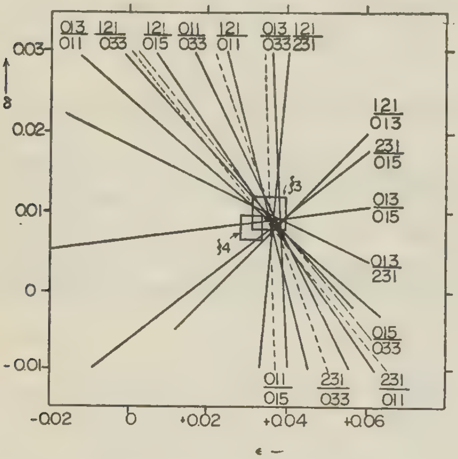

Fig. 3. The graphical determination of the oxygen parameters ε and δ of Mn_3O_4.

§4. Refinements of the Results

In the above calculation, the contribution from the higher order terms of $\mathcal{E}$ and δ, the anomalous scattering of the Mn ion core and the charge difference of Mn ions on the octahedral and tetrahedral sites are neglected. In this section the result obtained graphically is refined by the application of the least square method to the deviations of the calculated line intensities from the observed ones, $\Delta_{hkl}=I_{hkl}(\text{obs.})-I_{hkl}(\text{calc.})$. The exact formula for the dependence on $\mathcal{E}$ and δ and the new $f_{Mn^{2+}}$ and $f_{Mn^{3+}}$ obtained by Thomas and Umeda (TFD) and $f_{O^{2-}}$ in the 2+ wells obtained by Suzuki (HF)[13] are used in the refinement. When many lines can be used for the determination of parameters the least square method is suitable in weighing each line[14),15)].

The calculations are put forward to derive the most probable values of the scaling factor K, oxygen parameters $\mathcal{E}$ and δ, temperature factor B and the real part of the anomalous scattering factor f. The last parameter f is efficient for the correction of f_{Mn} to the Fe-$K\alpha$ radiation, the wave length of which is just in front of the absorption edge of Mn

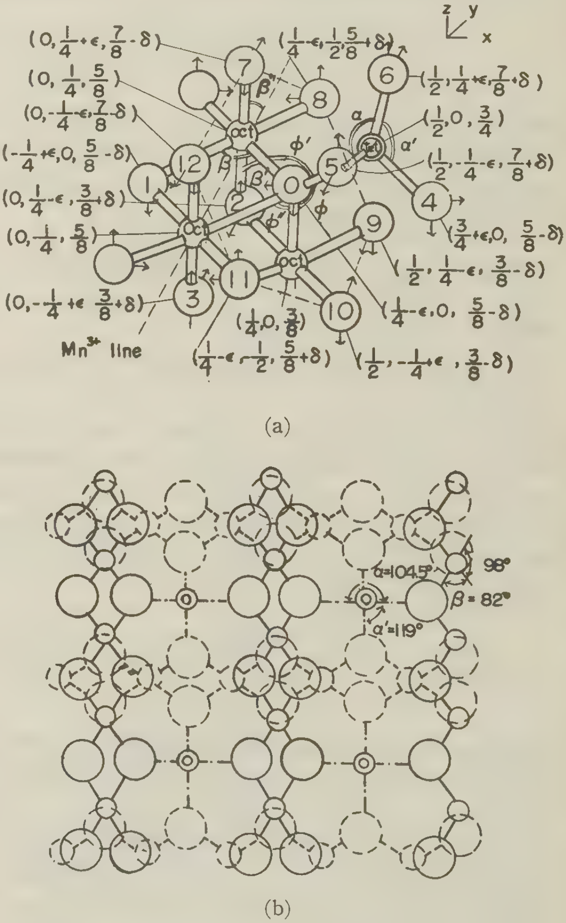
z y x
$(0,\frac{1}{4}+\epsilon,\frac{7}{8}-\delta)$
$(\frac{1}{4}-\epsilon,\frac{1}{2},\frac{5}{8}+\delta)$
$(0,\frac{1}{4},\frac{5}{8})$
$(0,-\frac{1}{4}-\epsilon,\frac{7}{8}-\delta)$
$(-\frac{1}{4}+\epsilon,0,\frac{5}{8}-\delta)$
$(0,\frac{1}{4}-\epsilon,\frac{3}{8}+\delta)$
$(0,\frac{1}{4},\frac{5}{8})$
$(0,-\frac{1}{4}+\epsilon,\frac{3}{8}+\delta)$
$(\frac{1}{2},\frac{1}{4}+\epsilon,\frac{7}{8}+\delta)$
$(\frac{1}{2},0,\frac{3}{4})$
$(\frac{1}{2},-\frac{1}{4}-\epsilon,\frac{7}{8}+\delta)$
$(\frac{3}{4}+\epsilon,0,\frac{5}{8}-\delta)$
$(\frac{1}{2},\frac{1}{4}-\epsilon,\frac{3}{8}-\delta)$
$(\frac{1}{4}-\epsilon,0,\frac{5}{8}-\delta)$
$(\frac{1}{4},0,\frac{3}{8})$
$(\frac{1}{4}-\epsilon,-\frac{1}{2},\frac{5}{8}+\delta)$
$(\frac{1}{2},-\frac{1}{4}+\epsilon,\frac{3}{8}-\delta)$
Mn^{3+} line
1 2 3 4 5 6 7 8 9 10 11 12 0
oct
β β' α α' φ φ'
T α=104.5°
98°
β=82°
α'=119°

(a)

(b)

◯○ : oxygen and octahedral site Mn^{3+} of the upper layer
◌◌ : oxygen and octahedral site Mn^{3+} of the lower layer
◎ : tetrahedral site Mn^{2+}

Fig. 4. Arrangement of the ions and its displacement in tetragonal Mn_3O_4. (a) Coordinates and Interbond angles. (b) Oxygen displacement in the c-plane.

ion[16]. The calculation started with $\varepsilon=0.04$, $\delta=0.01$, $f=-3.5$, $B=0$ and $K=1.9$ and the refined K, ε, δ and f are determined from solving the normal equations:

$$-\sum_{hkl}\Delta\frac{\partial\Delta}{\partial K}=\Delta K\sum_{hkl}\left(\frac{\partial\Delta}{\partial K}\right)\left(\frac{\partial\Delta}{\partial K}\right)+\Delta\delta\sum_{hkl}\left(\frac{\partial\Delta}{\partial K}\right)\left(\frac{\partial\Delta}{\partial\delta}\right)+\Delta\varepsilon\sum_{hkl}\left(\frac{\partial\Delta}{\partial K}\right)\left(\frac{\partial\Delta}{\partial\varepsilon}\right)+\Delta f\sum_{hkl}\left(\frac{\partial\Delta}{\partial K}\right)\left(\frac{\partial\Delta}{\partial f}\right)$$

$$-\sum_{hkl}\Delta\frac{\partial\Delta}{\partial\delta}=\Delta K\sum_{hkl}\left(\frac{\partial\Delta}{\partial\delta}\right)\left(\frac{\partial\Delta}{\partial K}\right)+\Delta\delta\sum_{hkl}\left(\frac{\partial\Delta}{\partial\delta}\right)\left(\frac{\partial\Delta}{\partial\delta}\right)+\Delta\varepsilon\sum_{hkl}\left(\frac{\partial\Delta}{\partial\delta}\right)\left(\frac{\partial\Delta}{\partial\varepsilon}\right)+\Delta f\sum_{hkl}\left(\frac{\partial\Delta}{\partial\delta}\right)\left(\frac{\partial\Delta}{\partial f}\right)$$

$$-\sum_{hkl}\Delta\frac{\partial\Delta}{\partial\varepsilon}=\Delta K\sum_{hkl}\left(\frac{\partial\Delta}{\partial\varepsilon}\right)\left(\frac{\partial\Delta}{\partial K}\right)+\Delta\delta\sum_{hkl}\left(\frac{\partial\Delta}{\partial\varepsilon}\right)\left(\frac{\partial\Delta}{\partial\delta}\right)+\Delta\varepsilon\sum_{hkl}\left(\frac{\partial\Delta}{\partial\varepsilon}\right)\left(\frac{\partial\Delta}{\partial\varepsilon}\right)+\Delta f\sum_{hkl}\left(\frac{\partial\Delta}{\partial\varepsilon}\right)\left(\frac{\partial\Delta}{\partial f}\right)$$

$$-\sum_{hkl}\Delta\frac{\partial\Delta}{\partial f}=\Delta K\sum_{hkl}\left(\frac{\partial\Delta}{\partial f}\right)\left(\frac{\partial\Delta}{\partial K}\right)+\Delta\delta\sum_{hkl}\left(\frac{\partial\Delta}{\partial f}\right)\left(\frac{\partial\Delta}{\partial\delta}\right)+\Delta\varepsilon\sum_{hkl}\left(\frac{\partial\Delta}{\partial f}\right)\left(\frac{\partial\Delta}{\partial\varepsilon}\right)+\Delta f\sum_{hkl}\left(\frac{\partial\Delta}{\partial f}\right)\left(\frac{\partial\Delta}{\partial f}\right).$$

The standard deviations are given by $\sigma_i=\sqrt{\sum_{hkl}\Delta^2_{hkl}/m-s\cdot\Delta_{ii}/D}$, where m is the number of the used lines, s is the number of all the parameters to determine. The result is

$$K=2.28\pm0.21\,,\quad \delta=0.0083\pm0.0015\,,\quad \varepsilon=0.0320\pm0.0027\,,\quad f=-4.4\pm0.7\,.$$

The correction for the anomalous scattering of f_{Mn} turns out to be a little larger than the calculated value -3.5. To take account of B, we selected the lines which depend not so strong on ε and δ and determined K, f and B from these lines. Then based upon these values, ε and δ are obtained from the lines which depend strongly on these parameters. The result is $B=0.4\pm0.3\times10^{-16}$ and the other values are not much altered.

§ 5. Discussion

The coordinate of ions and the angles α, β, ϕ etc. as well as the schematic result are shown in the Fig. 4. Cell dimensions are expressed as $c\cong(1+2\gamma/3)a_0$ and $a\cong(1-\gamma/3)a_0/\sqrt{2}$ using a_0 the edge of the cube and γ the degree of the tetragonal deformation $c/\sqrt{2}a-1$. The volume of the cube is twice as large as the tetragonal unit cell of Mn_3O_4. The observed values $\varepsilon=0.036$, $\delta=0.009$, $\gamma=0.16$ and $a_0=8.54$ Å are used in the calculation.
The oxygen—metal distances are

$$\begin{aligned}
r_{\text{octahedralsite-oxygen in } c\text{-plane}} &\cong(1-2\varepsilon-\gamma/3)a_0/4\cong1.8_8\ \text{Å}\\
r_{\text{octahedralsite-oxygen // } c\text{-axis}} &\cong(1-4\delta+2\gamma/3)a_0/4\cong2.2_8\ \text{Å}\\
r_{\text{tetrahedralsite-oxygen}} &\cong(1+8\varepsilon/3+8\delta/3)\sqrt{3}a_0/8\cong2.0_7\ \text{Å}\,.
\end{aligned}$$

The oxygen—oxygen distances are

$$\begin{array}{lll}
(1\text{–}0) & \cong(1-4\varepsilon-\gamma/3)a_0/2\sqrt{2} & \cong2.4_3\ \text{Å}\\
(2\text{–}0)(3\text{–}0) & \cong(1-4\delta-2\varepsilon+\gamma/6)a_0/2\sqrt{2} & \cong2.7_7\ \text{Å}\\
(4\text{–}0) & \cong(1+4\varepsilon-\gamma/3)a_0/2\sqrt{2} & \cong3.2_9\ \text{Å}\\
(5\text{–}0)(6\text{–}0) & \cong(1+4\delta+2\varepsilon+\gamma/6)a_0/2\sqrt{2} & \cong3.4_2\ \text{Å}\\
(7\text{–}0)(9\text{–}0)(10\text{–}0)(12\text{–}0) & \cong(1+\gamma/6)a_0/2\sqrt{2} & \cong3.1_0\ \text{Å}\\
(8\text{–}0)(11\text{–}0) & \cong(1-\gamma/3)a_0/2\sqrt{2} & \cong2.8_6\ \text{Å}\,,
\end{array}$$

the ion numbers correspond to those in the Fig. 4.
The interbond angles are

$$\begin{array}{llll}
\alpha & \cong2\cos^{-1}\dfrac{1}{\sqrt{3}}+2\dfrac{\sqrt{2}}{3}(4\varepsilon-8\delta-\gamma) & \Delta\alpha & \cong-2\Delta\alpha'\cong-4._8{}^\circ\\
\beta & \cong\pi/2-4\varepsilon & \Delta\beta & \cong-8._2{}^\circ
\end{array}$$

$$\beta' \cong \pi/2-4\delta-2\varepsilon \qquad \Delta\beta' \cong \Delta\beta''/\sqrt{2} \cong -6._2{}^\circ$$

$$\phi \simeq \pi-\cos^{-1}\frac{1}{\sqrt{3}}+2\frac{\sqrt{2}}{3}(4\delta-5\varepsilon+\gamma/2) \qquad \Delta\phi \simeq -3._7{}^\circ$$

$$\phi' \cong \pi-\cos^{-1}\frac{1}{3}-\varepsilon/4-3\delta-\gamma/3\sqrt{2} \qquad \Delta\phi' \cong -4._2{}^\circ$$

$$\phi'' \cong \pi/2+4\delta+2\varepsilon \cong \pi-\beta' \qquad \Delta\phi'' \cong 6._2{}^\circ \,.$$

If the positions of oxygen ions are deformed uniformly by $\gamma=0.16$ from the cubic close-packed arrangement to the tetragonal one, we should have $\Delta\alpha \cong -8._6{}^\circ$. The observed value $\Delta\alpha \cong -4._8{}^\circ$ is nearly half as large. For the regular octahedron, the interbond angles are $\beta=\beta'=\beta''=90^\circ$ but for the observed one they are 82°, 84° and 86° and the longer edge of the rectangle is parallel to the Mn^{3+} line on *c*-plane (c.f. Fig. 4). The similar deformations are known in the octahedron around the ions Cu^{2+}, Pd^{2+}, Pt^{2+} etc. which make the square covalent bond and linear complex in oxides or chlorides[17),18)].

For the sake of comparison let us review the results of spinels $MnFe_2O_4$ and $CuFe_2O_4$. The inter ionic distances in $MnFe_2O_4$, obtained by Hastings' data, are[11)]

$r_{\text{octahedralsite-oxygen}} = 2.0_5$ Å

$r_{\text{tetrahedralsite-oxygen}} = 2.0_0$ Å

(1, 2, 3–0) $\cong 2.7_8$ Å

(4, 5, 6–0) $\cong 3.2_6$ Å

(7, 8, 9, 10, 11, 12–0) $\cong 3.0_1$ Å

and those of $CuFe_2O_4$, calculated by Prince's data, are[19)]

$r_{\text{octahedralsite-oxygen in } c\text{-plane}} \cong 1.9_9$ Å

$r_{\text{octahedralsite-oxygen} \,//\, c\text{-axis}} \cong 2.1_8$ Å

$r_{\text{tetrahedralsite-oxygen}} \cong 1.8_9$ Å

(1–0) $\cong 2.7_2$ Å

(2, 3–0) $\cong 2.9_0$ Å

(4–0) $\cong 3.0_9$ Å

(5, 6–0) $\cong 3.0_9$ Å

(7, 9, 10, 12–0) $\cong 2.9_9$ Å

(8, 11–0) $\cong 2.9_0$ Å .

The summations of the ionic radii give the following lengths:

$Mn^{3+}O_6$ octahedron (Mn-oxygen) $\cong 2.0_2$ Å
(oxygen-oxygen) $\cong 2.8_6$ Å

$Mn^{2+}O_4$ tetrahedron (Mn-oxygen) $\cong 2.2_0$ Å
(oxygen-oxygen) $\cong 3.6_0$ Å

$Fe^{3+}O_6$ octahedron (Fe-oxygen) $\cong 2.0_0$ Å
(oxygen-oxygen) $\cong 2.8_3$ Å

$Fe^{3+}O_4$ tetrahedron (Fe-oxygen) $\cong 2.0_0$ Å
(oxygen-oxygen) $\cong 3.2_9$ Å

In the above results, $r_{\text{oxygen-octahedralsite in } c\text{-plane}}$ are shorter than the sum of the ionic radii, and $r_{\text{tetrahedralsite-oxygen}}$ are also shorter than that but longer than the $r_{\text{tetrahedralsite-oxygen}}$ of the $MnFe_2O_4$ in which it is believed that the tetrahedralsite Mn ion forms covalent bond. The differences in the bond lengths and the interbond angles for the same $Mn^{2+}O_4$ tetrahedron between Mn_3O_4 and $MnFe_2O_4$ might come from the fact that in the $MnFe_2O_4$ the octahedralsite Fe^{3+} is purely ionic while in Mn_3O_4 the octahedralsite Mn^{3+} is covalent and the oxygen *p* orbit cannot be directed to both the tetrahedralsite and the octahedralsite at the same time[3)]. The similar contraction of the bonds of the tetrahedral site by 0.1 Å compared with the sum of the ionic radii exists in $Fe^{3+}O_4$ tetrahedron in the $CuFe_2O_4$ spinel. Although the tetragonal deformation is not so great as Mn_3O_4, Prince et al state that the tetrahedron $Fe^{3+}O_4$ is almost regular in $CuFe_2O_4$.

As is shown in Fig. 5 the above geometrical relations are visualized on the $(\varepsilon-\delta)$ plane by drawing the loci which satisfy the specific conditions for the angle and the length of the tetrahedral bonds. If the tetrahedron does not change its angles for the overall deformation of the unit cell, there must be approximate relations

$$4\varepsilon-8\delta-\gamma \cong 0 \,.$$

Since γ amounts to 0.16 for Mn_3O_4, then ε and δ must be on the line (b). If the deformation is uniform, they must be on the line (a). If the length of the tetrahedral bond does not vary and is put to be equal to the value found on $MnFe_2O_4$ by Hastings the ε and δ must be on the line (c) which satisfies

$$(1+8\varepsilon/3+8\delta/3)\sqrt{3}\,a_0/8 \cong 2.00 \text{ Å} \,.$$

On the other hand, if the sum of the ionic radii is used for this, the line (d) is obtained. By the cross point of the two lines (b) and (c) is represented an extreme case in which the tetrahedron does not deform at all. Another extreme case is given by the cross point of the lines (a) and (d), which means the model of rigid spheres freely slideable. If the octahedron has the six bonds of the same lengths, ε and δ must be on the line (e). If the average length of these bonds is kept constant, the line (f) is obtained for the case in which the average is equal to the summation of the ionic radii and the line (g) is obtained for the case in which the lengths of bonds contract by 0.1 Å from the value of (f).

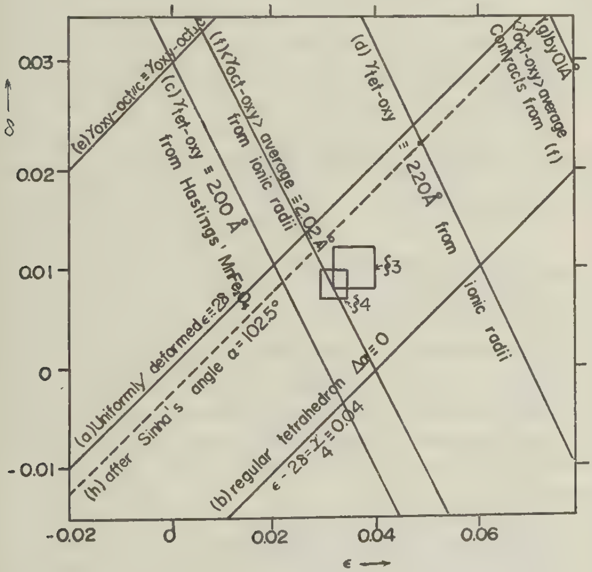

Fig. 5. The specific conditions on the oxygen positions given from the formation of the ideal bond in the each site of the tetragonal Mn_3O_4 and the experimental results given as the squares, the larger from § 3 and the smaller from the § 4. The both are shown on the same ε–δ plane as in Fig. 3.

In the Fig. 5 the probable values of $\mathcal{E}$ and δ measured for Mn_3O_4 are shown by small squares. This square is in the middle of the quadrilateral formed by the lines (a), (b), (c) and (d). This shows that the oxygen position is determined by the balance between the deformation due to the octahedral site becoming tetragonal and the deformations due to the tetrahedron preserving its regular form against the tetragonal deformation of the crystal as a whole. Contrary to the case, if the cause of the tetragonal deformation is not on the octahedral site but on the tetrahedral site, the measured point of the oxygen parameters will be on the other side of the line (a). In the Fig. 5 Sinha's result is also shown by the line (h)[20].

On the contrary to Mn_3O_4, the tetragonal contraction along the *c*-axis exists for the $CuCr_2O_4$ spinel[21] and the tetragonal deformation exists also for the iron-chromite spinels of which the average oxygen parameter u has been given by Derbyshire.[22] When the two oxygen parameters are separated for these spinels, from the reasoning similar to the case of the elongation, it will become clear that whether the tetragonal deformation of these compound comes from the tetrahedral site or the octahedral site. If the contraction of $CuCr_2O_4$ comes from the Cu ions as is stated by Dunitz et al, the displacement of the oxygen should be also $\mathcal{E}>2\delta$ not withstanding the fact that γ is negative. The author hopes that for these oxides a detailed investigation of the electron density around the each site should be performed.

Acknowledgement

The author thanks Mr. K. Kato of Kubo Laboratory of Tokyo Institute of Technology for the measurement of the powder X-ray patterns and he also thanks Professor I. Aoki of Chiba University for helpful suggestions in the analysis. The author is most thankful to Professors Y. Takagi and S. Sawada of Tokyo Institute of Technology for their guidance and encouragement through the investigation.

References

1) F. W. Barth and E. Posnjak: Z. Krist. **82** (1932) 325.
2) E. J. W. Verwey and E. L. Heilman: J. Chem. Phys. **15** (1947) 147.
3) J. B. Goodenough and A. L. Loeb: Phys. Rev. **98** (1955) 391.
4) G. I. Finch, A. P. B. Sinha and K. P. Sinha: Proc. Roy. Soc. A, **242** (1957) 28. P. J. Wojtowig: J. Appl. Phys. **30** (1959) 30.
5) J. D. Dunitz and L. E. Orgel: J. Phys. Chem. Solids **3** (1957) 20, 318.
6) R. T. Meyer and K. Rötgers: Z. anorg. Chem. **57** (1908) 104.

7) F. C. Romeijn: Philips Res. Rep. **8** (1953) 304.
8) F. Bertaut: Compt. rend. **230** (1950) 213.
9) H. J. Van Hook and M. L. Keith: Amer. Mineralogist **43** (1958) 69.
10) to be published.
11) J. M. Hastings and L. M. Corliss: Phys. Rev. **104** (1956) 328.
12) L. H. Thomas and K. Umeda: J. Chem. Phys. **26** (1957) 293.
13) T. Suzuki: Acta Cryst. **13** (1960) 279.
14) W. C. Hamilton: Phys. Rev. **110** (1958) 1050.
15) L. P. Skolnick, S. Kondo and L. R. Lavin: J. Appl. Phys. **29** (1958) 198.
16) A. J. Bradley and J. W. Rodgers: Proc. Roy. Soc. **A**, **144** (1934) 353. C. H. Daufen and P. H. Templeton: Acta Cryst. **8** (1955) 841.
17) W. J. Moore and L. Pauling: J. Amer. Chem. Soc. **63** (1941) 1392.
18) A. F. Wells: Z. Krist. **100** (1938) 189; J. Chem. Soc. (1947) 1670.
19) E. Prince and R. G. Treuting: Acta Cryst. **9** (1956) 1025.
20) K. P. Sinha and A. P. B. Sinha: J. Phys. Chem. **61** (1957) 758; Acta Cryst. **10** (1957) 439.
21) S. Miyahara and H. Ohnishi: J. Phys. Soc. Japan **12** (1956) 1296.
22) W. D. Derbyshire and H. J. Yearian: Phys. Rev. **112** (1958) 1603.

JOURNAL OF THE PHYSICAL SOCIETY OF JAPAN, Vol. 16, No. 2, FEBRUARY, 1961

Nuclear Quadrupole Resonance Under High Pressure, I.

By Tokujiro FUKE

Faculty of Engineering, Tokushima University, Tokushima

(Received September 16, 1960)

The nuclear quadrupole resonance frequencies of I^{127} in stannic tetraiodide (SnI_4), As^{75} in arsenolite (As_4O_6), Br^{81} in paradibromobenzene (p-$C_6H_4Br_2$) and in potassium bromate ($KBrO_3$) were measured as a function of hydrostatic pressure at various temperatures. The pressure range was 1–9000 kg/cm^2 in the temperature range from $-77°$ to 100°C, and 1–1000 kg/cm^2 at liquid oxygen temperature, respectively.

In general, the pressure and the temperature dependence of the resonance frequency is found to agree with Bayer's theory incorporated with Kushida-Benedek-Bloembergen's theory. It is noticed, however, that an anisotropic change of the internal parameters for the positions of atoms in a unit cell would contribute appreciably to the analysis of the data even in the cases of cubic crystals, SnI_4 and As_4O_6 and that a deviation from the Bayer curve is observed in As_4O_6. Doublet lines for SnI_4 are found to behave differently as a function of volume, and it is concluded for the molecular crystal, As_4O_6 that the effective modes of lattice vibration which are responsible for the temperature dependence of the resonance frequency, are intra-molecular modes rather than a tipping mode of the molecule as a whole.

§ 1. Introduction

A theory for the temperature dependence of the nuclear quadrupole resonance frequency was first proposed by Bayer[1], and it was modified by a few investigators[2),3),4)], and the discrepancy between the theories and observed data which exists more or less in almost all cases, was explained by Kushida, Benedek, and Bloembergen[5]*. They observed pressure dependence of the resonance frequency at various temperatures and pointed out that the temperature dependence at constant pressure includes not only an explicit temperature dependenec in the amplitude of particular mode of lattice vibration $\langle\theta^2\rangle$ but also an implicit temperature dependence via the volume dependence of the static field gradient $q(V)$ as well as $\langle\theta^2\rangle$. And KBB obtained the value of q and $\langle\theta^2\rangle$ as a function of volume and concluded that the observed temperature dependence of the resonance frequency is accounted for by Bayer type theory, if the effects of the thermal expansion on q and $\langle\theta^2\rangle$ are properly taken into account. They also obtained many other important informations from the values of $q(V)$ thus derived.

---

* Hereafter their article will be referred as KBB.

Recently Barnes and Engardt[6] explained the anomalous positive temperature dependence of bromine quadrupole resonance frequencies in titanium tetrabromide $TiBr_4$ in terms of the large and negative pressure dependence of these lines on the base of KBB's analysis.

It is the purpose of this article to see how precisely and to what extent the KBB theory is applicable. The resonance frequencies studied under hydrostatic pressure in the present investigation are in the range of 100–250 Mc/sec at various temperatures which include liquid oxygen temperature.

The possibility of deviation from KBB theory was first suggested by Walsh[7] in his pressure experiment of electron spin resonance for ammonium alum $(NH_4)_2SO_4\cdot Al_2(SO_4)_3\cdot 24H_2O$. He pointed out the importance of " out-of scale " displacements of individual atoms in a unit cell under hydrostatic pressure even for a cubic crystal.

The similar idea was also proposed by Bernheim and Gutowsky[8] when they explained the observed deviation from V^{-1} law[5] for the volume dependence of the quadrupole splitting of Na^+ in ionic crystals with the form $NaXO_3$, in which X is either Cl, Br, or N.

Because cubic crystals are appropriate in order to check this kind of mechanism, SnI_4 and As_4O_6 were chosen in the present investigation. And p-$C_6H_4Br_2$ and $KBrO_3$ were also used in order to make comparison with the KBB's results for similar samples p-$C_6H_4Cl_2$ and $KClO_3$ respectivaly.

It was intended also that the volume dependence of the doublet lines in SnI_4 was compared with each other and that their different behavior would be accounted for by the chemical inequivalence of the positions for iodine nuclei. It is suggested that the similar study of the pressure dependence of multiplet lines in many other samples would reveal the detailed origin of such multiplicity.

§ 2. Experimental Method

The apparatus used in the present experiment consists of *a*) a high-pressure pump and a pressure gauge, *b*) a pressure bomb in which an rf coil and the sample are enclosed, and *c*) a spectrometer and a frequency meter.

In Fig. 1 is shown the main part of the apparatus. At the right part of the figure is seen the high-pressure pump* which generates hydrostatic pressure up to 10000 kg/cm². The pressure-generating cylinder is made of Cr-Mo-steel (SCM3) with 120 mm o.d., 16 mm i.d., and 200 mm height. The plunger which is made of high carbon steel (S55C) and has a Bridgman packing[9], is driven by the 30-ton hydraulic rum.

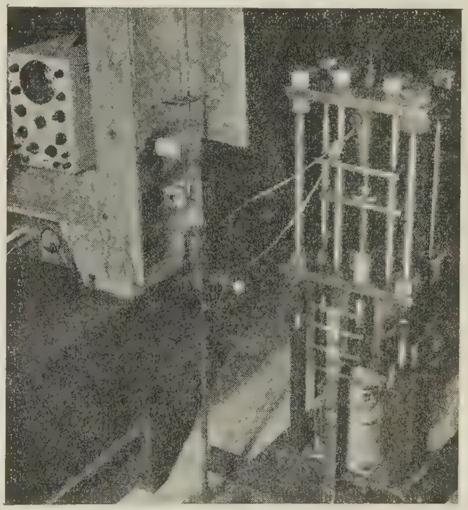

Fig. 1. Photograph of the main part of the experimental apparatus.

It is noted that the active volume of the cylinder is made large enough compared with the sample space of the bomb so that a by-pass pump system[9] can be eliminated.

A pressure gauge which consists of manganin wire[9] is installed in a gauge coil plug at the upper part of the wall of the cylinder. An Amagat cone-seal[9] is used as a high pressure electrode for the gauge coil, and the details of its insulator part will be shown later. The change in the resistance of the coil caused by the pressure is measured with a conventional bridge, and overall accuracy of the pressure measurement with this method is about 5 kg/cm^2. The gauge coil is calibrated against the freezing point of mercury at 0°C[9], using the discontinuity in the resistance of mercury at the freezing point.

---

* The high-pressure pump was designed by Professor Y. Kôi and constructed under his guidance.

In Fig. 2 is shown the high-pressure bomb assembly. It is similar in structure to the one used by Benedek and Kushida[10] when they observed the pressure dependence of NMR line in antiferromagnetic MnF_2. The material of the bomb is, however, the same kind of steel as the pressure-generating cylinder, since it is less expensive than Be-Cu which was used by them, and satisfactory for the present zero-field measurement, if frequency modulation is used. The o.d. and the i.d. of the bomb are 60 mm and 12 mm respectively, and the bomb was tested several times up to 10 000 kg/cm^2 and is used regularly up to 9000 kg/cm^2. The bomb and the pressure-generating cylinder are connected with a piece of flexible stainless-steel tubing (1/8″ o.d. and 0.025″ i.d.)*.

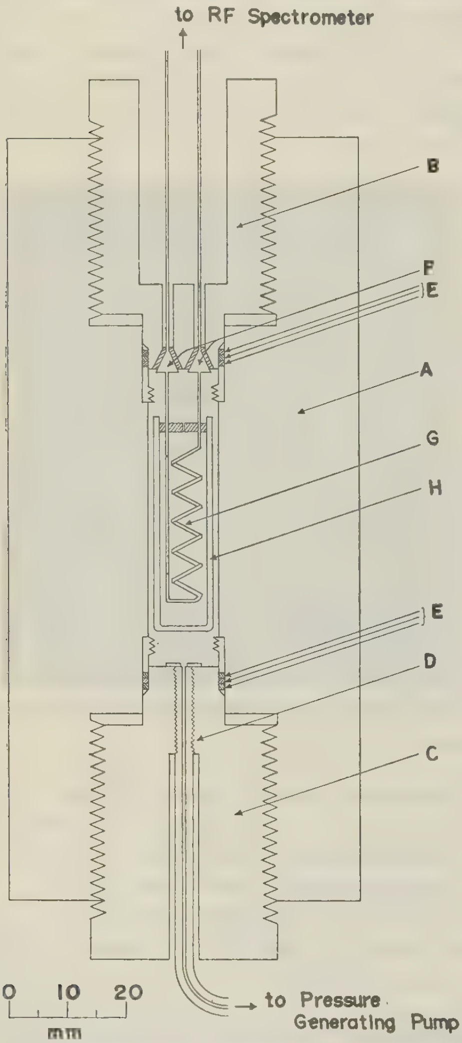

Fig. 2. High-pressure bomb and plug assembly. (*A*) Cr-Mo-steel bomb. (*B*) (*C*) Cr-Mo-steel plug. (*D*) Stainless steel connecting tubing. (*E*) Sealing washers. (*F*) Conical seals for electrical terminals. (*G*) Radio frequency coil. (*H*) Sample holder

A pair of Amagat cones were used as high-pressure electrical leads of the bomb. Since these leads are connected to an rf sample coil in the bomb, the insulator of the high-pressure leads ought to be chosen with a special care. Although the traditional material, pipe stone, was used by KBB[5], this is not appropriate for the present purpose, because of its relatively high dielectric loss in the frequency range of the present experiment. Walsh[7] and Benedek-Kushida[10] reported that artificial mica is satisfactory for this purpose in sub-micro to microwave region.

Therefore, artificial mica, Micalex M-21**, was tried first as the insulating material. Its electrical character was found to be satisfactory, and the initial sealing of the conical shell was achieved with the doping by epoxy resin. Chances of cracking were increased, however, with the increase in thickness of the conical shell, which was necessary at the frequency of 200 Mc/sec or more in order to reduce the capacity between the bomb and the electrodes. More precise machining might improve the situation.

As an easy method epoxy resin shell was tried, which can be made simply by curing the resin between the cone and the bomb without any skillful machining, and was found to give fair result below 150 Mc/sec. This type of electrical lead has been used at the gauge coil plug for a long time without any trouble. Although this method of sealing has a disadvantage of relatively high dielectric loss above 200 Mc/sec, the mixing of either Micalex or MgO_2 powder with this material improved the high frequency character, and the frequency range in the present experiment was safely covered with this method.

---

* This tubing was purchased from Harwood Engineering Co., Inc., U.S.A.

** Product of Toshiba Electric Co.

Petroleum benzine was used as pressure-transmitting medium at and above −77°C. Even at −77°C the pressure in the bomb was believed to be hydrostatic up to 9000 kg/cm², because any abrupt broadening of the line width was unobserved. At liquid oxygen temperature, petroleum ether was used, and the measurement was carried out up to about 1000 kg/cm², using another bomb. Its steel connecting tubing (6 mm o.d. and 2 mm i.d.), comes out through the same plug as the electrical leads in order to minimize the dipping of the tubing in the liquid oxygen. The maximum pressure available at this temperature is limited by the freezing of the transmitting liquid in the tubing instead of by its freezing in the bomb, as is evidenced by the fact that the pressure shift of the resonance frequency stops increasing before the line width increases suddenly when the pressure is increased above this limit. Therefore, it is suggested that the measurement under the higher pressure at this temperature would be possible, if the sample and the gauge coil are installed in the same bomb, the pressure is applied to the bomb first without cooling, and then the whole assembly is cooled down in the liquid oxygen bath.

Kôi's spectrometer[11] is satisfactory for the detection of the resonance line. This spectrometer has Lecher-line tuning circuits and can be used either as a regenerative or a superregenerative spectrometer. Usually superregenerative scheme was used in order to get a better signal to noise ratio. The resonance lines were displayed on a CRO screen, and their frequencies were measured by superposing a signal from a heterodyne wavemeter on the resonance signal, the accuracy of the measurement being better than 5 kc/sec.

§ 3. Experimental Results

A) *Stannic Iodide* SnI_4

The sample is an assembly of fine crystal grains which were prepared by heating the stoichiometric amount of Sn and I in an evacuated ampule.

Doublet quadrupole lines for this sample was first observed by Dehmelt[12] at room temperature, and they were explained in terms of a chemical inequivalence of the positions for iodine nuclei. The temperature dependence of the resonance frequencies for these doublets was measured as well[13),14)].

In the present experiment the resonance frequency was measured as a function of hydrostatic pressure up to 9000 kg/cm² at

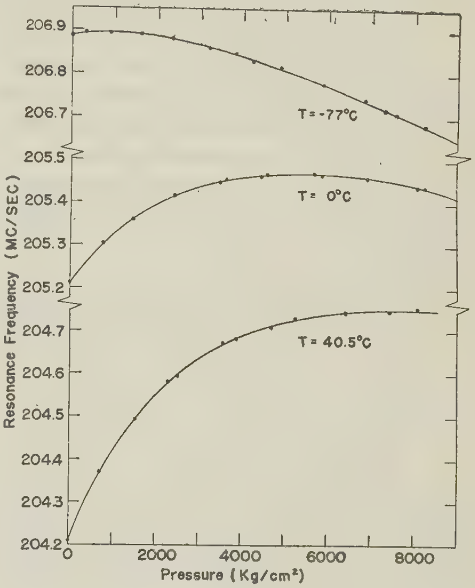

Fig. 3(a). The resonance frequency of the higher frequency line of the I^{127} doublet lines in SnI_4 plotted as a function of pressure at three temperatures.

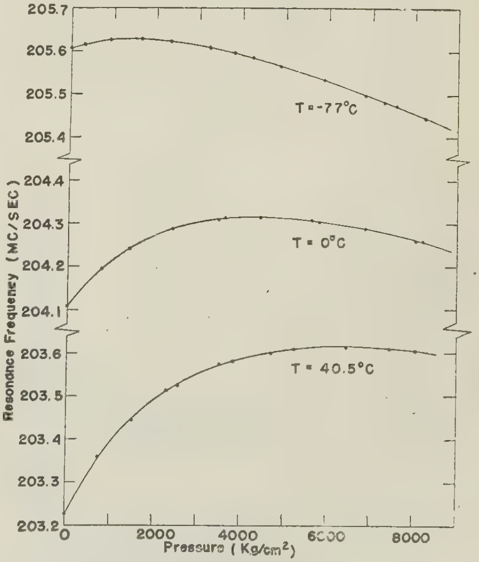

Fig. 3(b). The resonance frequency of the lower frequency line of the I^{127} doublet lines in SnI_4 plotted as a function of pressure at three temperatures.

$-77°$, $0°$, and 40.5°C. At each temperature the measurements were repeated while the pressure was increased and decreased. Right after the pressure was varied, the resonance frequency was not stationary, and it drifted to the direction which can be explained in terms of the recovery from an adiabatic heating or cooling during the change in the pressure. After several minutes the frequency reached the stationary value, which has no hysteresis within the experimental error. Each component of the doublet lines was measured alternatively at each pressure in order to measure the separation between these lines precisely.

The pressure dependence of the resonance frequencies for the higher and the lower frequency lines are shown in Figs. 3(a) and 3(b), respectively. At liquid oxygen temperature the resonance frequency decreased linearly with the increasing pressure up to 1000 kg/cm^2, and the values of $(\partial\nu/\partial P)_{P=0}$ for the higher and the lower frequency lines are 75 and 47 cps/(kg/cm^2), respectively. Their resonance frequencies at atmospheric pressure at this temperature were 208.912 and 207.481 Mc/sec.

B) *Arsenolite* As_4O_6

The sample was of commercial reagent grade with purity of 99.8%. In Fig. 4 the resonance frequency of As^{75} in this sample is plotted as a function of pressure at $-77°$, $0°$, and 97°C, respectively*. The resonance frequency at liquid oxygen temperature is found to be 116.837 Mc/sec*, and the pressure shift at 1000 kg/cm^2 is smaller than the line width, 10 kc/sec, which has been broadened by pressure.

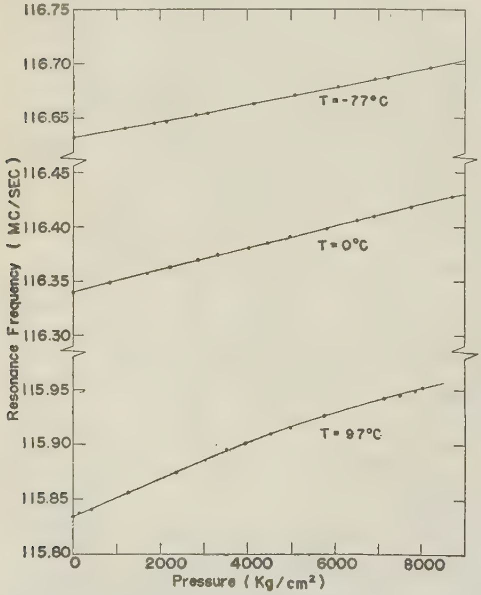

Fig. 4. The resonance frequency of the As^{75} nucleus in As_4O_6 as a function of pressure at three temperatures.

C) *Paradibromobenzene* p-$C_6H_4Br_2$

The sample was recrystallized from an alcoholic solution. In Fig. 5 the pressure dependence of Br^{81} in this sample is shown as a function of pressure at $-77°$, $0°$, and 44.5°C, respectively. It is noted that the resonance frequency decreases almost linearly with increasing pressure at -77°C. This behavior ought to be compared with the similar experiment of KBB[5] for p-$C_6H_4Cl_2$, where *ν-versus-P* curve shows the similar linear decrease only above 4000 kg/cm^2.

The resonance frequency at the liquid oxygen temperature decreased linearly with pressure up to 1000 kg/cm^2, and it was found

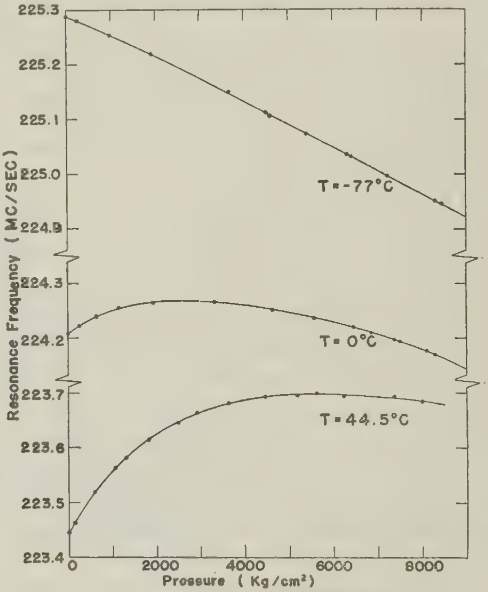

Fig. 5. The resonance frequency of the Br^{81} nucleus in p-$C_6H_4Br_2$ as a function of pressure at three temperatures.

---

* Since the observed temperature dependence of the resonance frequency at atmospheric pressure is slightly different from the value reported by Bray, O'Keefe, and Barnes[15], the measurement of the resonance frequency at -77°C and liquid oxygen temperature was repeated with the regenerative spectrometer.

that $(\partial\nu/\partial P)_{P=0}=85$ cps/(kg/cm^2), and $\nu_{P=0}=$ 226.398 Mc/sec.

D) *Potassium Bromate* $KBrO_3$

The sample is the assembly of fine crystals which were recrystallized from aqueous solution. In Fig. 6, *ν-versus-P* curves are plotted at three temperatures, −77°, 0°, and 97.5°C, respectively. At the liquid oxygen temperature the frequency increases linearly with pressure up to 1000 kg/cm^2, and it was found that $(\partial\nu/\partial P)_{P=0}=86$ cps/(kg/cm^2), and $\nu_{P=0}=$ 149.212 Mc/sec.

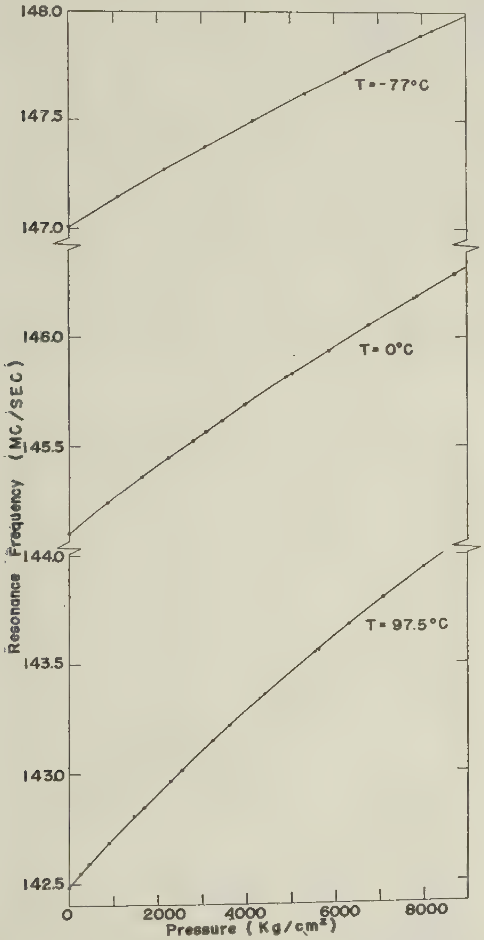

Fig. 6. The resonance frequency of the Br^{81} nucleus in $KBrO_3$ as a function of pressure at three temperatures.

The pressure experiment was also tried for $NaBrO_3$, but this material reacted with the transmitting fluid explosively at about 2000 atmos. The similar explosion was reported by KBB[5] for $NaClO_3$.

§ 4. Analysis of experimental data

Since the experimental results were analyzed on the basis of KBB, theory[5], its essential points will be summarized here.

The pure quadrupole resonance frequency is expressed by

$$\nu=\nu_0(1-3/2\langle\theta^2(t)\rangle_{AV})\ , \qquad (1)$$

where ν_0 is the resonance frequency when the effect of lattice vibration does not exist, $\theta(t)$ is the tipping angle of the maximum principal axis of field gradient tensor caused by the lattice vibration, and $\langle\ \rangle_{AV}$ denotes the average over the time. If $\langle\theta^2(t)\rangle_{AV}$ is expanded with respect to normal modes of vibration, and the energy of each normal mode thus obtained is equated to that of corresponding harmonic oscillator we obtain.

$$\nu=\nu_0\left[1-\frac{3}{2}\sum_{i=1}^{N}\frac{A_i}{\omega_i^2}\hbar\omega_i\times\left(\frac{1}{2}+\frac{1}{\exp(\hbar\omega_i/kT)-1}\right)\right]. \qquad (2)$$

Here the summation ought to be carried out over all the normal modes, but actually the effect of higher-frequency modes can be neglected due to the factor $1/\omega_i$. And Eq. (2) is reduced to the following equations, if the relation $x\equiv\hbar\omega/(kT)\leq 2$ holds,

$$\nu=a(1+bT+c/T)\ , \qquad (3)$$

were

$$a=\nu_0=\frac{eQq_0}{2I(2I-1)}\left(3m_z-\frac{3}{2}\right), \qquad (3a)$$

$$b=-\frac{3}{2}\,k\sum_{1}^{M}\frac{A_i}{\omega_i^2}\ , \qquad (3b)$$

$$c=-\frac{\hbar^2}{8k}\sum_{1}^{M}A_i\ . \qquad (3c)$$

Here a, b, and c, which generally depend of volume, can be obtained as a function of volume, if the $\nu(V, T)$ is measured experimentally. Since the measured value in the present experiment is, however, $\nu(P, T)$, equation of state, either empirical or theoretical, is necessary for this purpose. KBB[5] used the following semi-empirical equation for compressibility χ,

$$\chi(T, V)=-\frac{1}{V}\frac{\partial V}{\partial P}=\frac{V_0}{V}\chi_{00}\Big/\left[1-\zeta\left(\frac{V-V_0}{V_0}\right)\right], \qquad (4)$$

where ζ is a constant, whose value is 3.33 for wide range of solids, if use is made of Birch-Murnagham law[16]. And V_0, χ_{00} denote, respectively, the equilibrium volume and the compressibility at $T=0°K$ and $P=0$ atmos. The integral of Eq. (4) determines P-V isotherms with integration constants determined by thermal expansion coefficient.

Thus a, b, and c can be determined as a function of volume, from ν-*versus*-V isotherms at three different temperatures. Hence, the volume dependence of q_0, ω_i, and A_i can also be deduced respectively, and they can be written as

$$\left.\begin{aligned} q_0(V)&=q_0(V_0)(V/V_0)^{n(V)}\,, && \text{(A)}\\ \omega_i(V)&=\omega_i(V_0)(V/V_0)^{-\gamma_i}\,, && \text{(B)}\\ A_i(V)&=A_i(V_0)(V/V_0)^{+\sigma_i}\,, && \text{(C)}\end{aligned}\right\} \quad (5)$$

If the average over i is taken, one obtains

$$\left.\begin{aligned} d\ln a/d\ln V&=n(V)\,, && \text{(A)}\\ d\ln|b|/d\ln V&=2\gamma+\sigma\,, && \text{(B)}\\ d\ln|c|/d\ln V&=\sigma\,. && \text{(C)}\end{aligned}\right\} \quad (6)$$

When an asymmetry parameter η of the field gradient tensor is small enough, which is the case treated by KBB, the volume change of the resonance frequency can be devided into two parts as follows:

$$\frac{\partial\ln\nu}{\partial\ln V}=\frac{d\ln q_0}{d\ln V}+\frac{\partial\ln\nu}{\partial\ln\langle\theta^2\rangle_{AV}}\frac{\partial\ln\langle\theta^2\rangle_{AV}}{\partial\ln V} \qquad (7)$$

$$=\frac{d\ln a}{d\ln V}+\left[\frac{db}{(d\ln V)}T+\frac{dc}{(d\ln V)}\frac{1}{T}\right]$$
$$/(1+bT+c/T)\,. \qquad (8)$$

These relations can be extended to the case of $\eta\neq0$ by slight modifications in b and c in Eq. (3).

For instance, if tipping motions about x and y axes which are perpendicular to the direction of q, are *assumed* to be sole normal modes of vibration which are responsible to the reduction in resonance frequenny, the following equation is obtained[17),

$$q=q_0\left\{1-\frac{3}{2}\hbar\left[\frac{1+\eta/3}{\Theta_y\omega_y}\left(\frac{1}{2}+\frac{1}{\exp(\hbar\omega_x/kT)-1}\right)\right.\right.$$
$$\left.\left.+\frac{1-\eta/3}{\Theta_y\omega_y}\left(\frac{1}{2}+\frac{1}{\exp(\hbar\omega_y/kT)-1}\right)\right]\right\}, \qquad (9)$$

where Θ_x and Θ_y are moments of inertia of the normal modes along x and y axes, and ω_x and ω_y are their vibration frequencies, respectively.

In this case, therefore, b and c are expressed by

$$b=-\frac{3k}{2}\left(\frac{1}{\Theta_x\omega_x{}^2}+\frac{1}{\Theta_y\omega_y{}^2}\right)$$
$$-\frac{\eta k}{2}\left(\frac{1}{\Theta_x\omega_x{}^2}-\frac{1}{\Theta_y\omega_y{}^2}\right), \qquad (10)$$

$$c=-\frac{\hbar^2}{8k}\left(\frac{1}{\Theta_x}+\frac{1}{\Theta_y}\right)-\frac{\eta}{24}\frac{\hbar^2}{k}\left(\frac{1}{\Theta_x}-\frac{1}{\Theta_y}\right). \qquad (11)$$

The effect of η can usually be neglected, except for the case with a large η, where its temperature and volume dependence ought to be determined experimentally.

A) SnI_4

Thermal expansion coefficient of SnI_4 was measured by Biltz *et al*[18) in the range −195° to 0°C, whereas its compressibility has not been measured yet, so far as the author

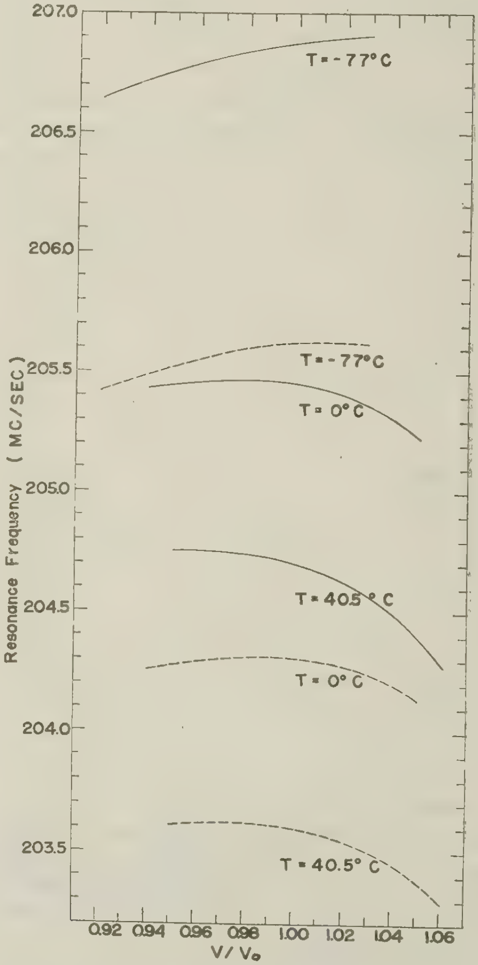

Fig. 7. The ν-*versus-volume* isotherms for SnI_4 derived from the experimental data using an equation of state. The solid curves show the results for the higher-frequency line of the doublet, and the dashed curves show those for the lower-frequency line.

knows. Therefore its compressibility was measured here with a lever piezometer which is the same as was used by Bridgman[9], and the result is $16\times10^{-6}/(\mathrm{kg/cm^2})$ at room temperature (12°C).

By using Eq. (4), the *P-versus-V* isotherms for this sample were determined with these values of thermal expansion coefficient and compressibility, in conjunction with the value 3.33 for ζ. And ν*-versus-P* curves which were obtained experimentally, were transferred into ν*-versus-V* curves as shown in Fig. 7.

First it was tried to determine the value of c at $V/V_0=1$, but the experimental error did not allow this value to be determined definitely. Its value is, however, very small, as is evidenced by the fact that ν*-versus-T* relation at constant volume is almost linear. Therefore, the moment of inertia $\langle\Theta\rangle=1/\langle A\rangle$ has large value. This is compatible with the following estimate of the moment of inertia, namely if one evaluates the moment of inertia of a tetrahedral molecule SnI_4 about an axis which passes through its center of gravity, one obtains $\Theta=3900\times10^{-40}\,\mathrm{g\,cm^2}$, which corresponds to $c=0.005$.

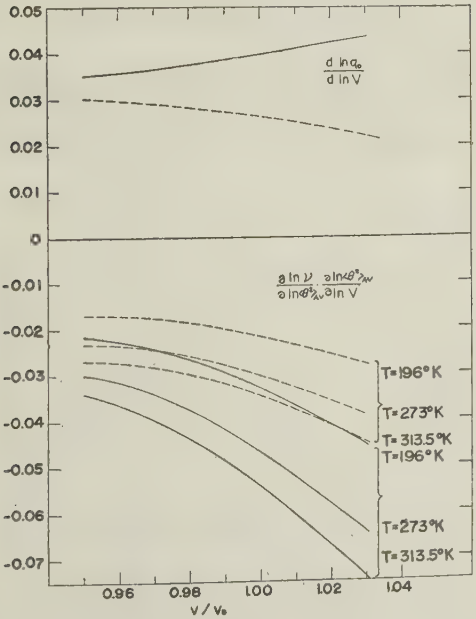

Fig. 8. The contribution from the volume dependence of the static field gradient q_0 and that of the lattice vibration, to the volume dependence of the resonance frequency for SnI_4. The solid and the dashed curves are those for the higher and the lower frequency lines, respectively.

In Fig. 8 are plotted the contributions to $\partial \ln\nu/\partial \ln V$ from q_0 and $\langle\theta^2\rangle_{AV}$, respectively. These two contributions have opposite signs with each other as shown there. This is similar to the results for $p\text{-}C_6H_4Cl_2$ obtained by KBB[5], but here the $\langle\theta^2\rangle_{AV}$ contribution depends more strongly on the volume than the case of $p\text{-}C_6H_4Cl_2$, and this tendency is more striking for the higher-frequency line. The volume dependence of the $\langle\theta^2\rangle_{AV}$ contribution is rather similar to those for $KClO_3$ than to those for $p\text{-}C_6H_4Cl_2$, and its temperature dependence at constant volume is almost linear, indicating $dc/d\ln V$ in Eq. (8) to be negligibly small.

Now let us compare the higher-frequency line (solid curve) with the lower-frequency line (dashed curve). Both the q_0 and the $\langle\theta^2\rangle_{AV}$ contributions for the higher-frequency line are larger in magnitude and stronger in their volume dependence than those for the lower-frequency line, and the differences between the curves for the two lines have the tendency to decrease to zero at a smaller volume. The same tendency is seen for the *b-versus-V* and the $1/2\cdot\partial \ln b/\partial \ln V$*-versus-V* curves in Fig. 9.

It is necessary to estimate the value of σ in order to obtain the value of γ (a modified Grüneisen's constant) from the volume dependence of b. The accuracy of experiment is, however, generally insufficient for the accurate estimate of σ[5]. Although SnI_4 is not an ideal molecular crystal[21], it may be safe to assume that σ is very small as is the case for a typical

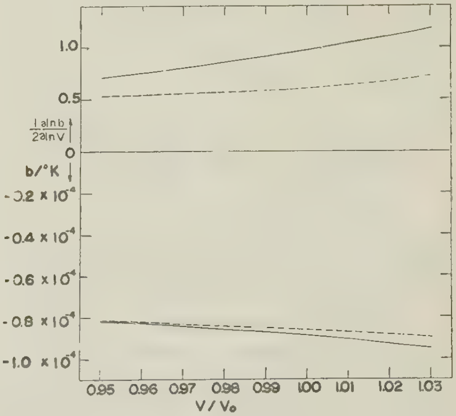

Fig. 9. The volume dependence of $1/2\cdot\partial\ln b/\partial\ln V$ and b for SnI_4. The solid and the dashed curves correspond to the higher and the lower frequency lines for the doublet, respectively.

molecular crystal. And if this assumption is admitted, it is concluded that there is considerable difference between the values of γ for the two resonance lines, and this difference decreases in magnitude with decreasing volume. This deduction is compatible with the following observation in the low-frequency Raman lines in molecular crystals: Ichishima[19] investigated their temperature dependence and found that $1/\omega \cdot d\omega/dT$ is different for different components of multiple lines.

The different behaviors of the doublet lines in SnI_4 stated above may be explained as follows: Stannic iodide crystal[20] consists of SnI_4 tetrahedrons, and each tetrahedron is slightly distorted so that only one I atom (I_I) is at a position with three fold symmetry, and the other three (I_{II}) lie at slightly less symmetric positions, as has been pointed out by Dehmelt[12]. Therefore, the resonance line due to I_{II}'s has non vanishing asymmetry parameter, which amounts to 0.8%. The two SnI_4 tetrahedrons are situated so that the base planes of the tetrahedrons, each of which consists of three I_{II}'s, face each other with the relation of a screw rotation by 60° about an axis of three-fold symmetry, and they have a slight tendency to form a kind of associated molecule Sn_2I_8[21]. The separation of the doublet resonance lines in SnI_4 is caused by an inter-molecular effect as was discussed by Schawlow *et al*[13,14], and the I_{II} atoms which are responsible for the lower-frequency line, must be influenced by neighboring molecules more strongly than the I_I atoms, because inter-molecular hybridization usually decreases the value of q, as is evidenced by the observed positive value of $\partial \ln q/\partial \ln V$ for this specimen. Therefore. it is natural to assume that the relative displacement between the pair of tetrahedrons stated above behave differently from the displacements among the other neighboring tetrahedrons, when the sample is subjected to a hydrostatic pressure. And this assumption enables the explanation of the facts that $\partial \ln q/\partial \ln V$, $\partial \ln \nu/\partial \ln \langle\theta^2\rangle_{AV} \cdot \partial \ln \langle\theta^2\rangle_{AV}/\partial \ln V$, b, and $\partial \ln b/\partial \ln V$ are all larger in magnitude for the higher-frequency line than for the lower one, and the differences between the values for the two lines have a tendency to decrease with decreasing volume.

In another word, it may be concluded that the distance between the pair tetrahedrons is slightly more rigid under the hydrostatic compression than the distances between the other tetrahedrons, therefore, the resonance line originated from I_I atoms is influenced more strongly under the pressure than I_{II} line, and with the increase of the degree of compression, this difference decreases and all the molecular distances would be compressed more homogeneously with the further compression. It should be noted that the effect of asymmetry parameter itself is negligible as stated before.

It is suggested that the study of the pressure dependence of multiplet lines in general would give an important clue for the understandings of the origin of the multiplets and of a detailed behavior of the molecules in a unit cell as well. For instance, the pressure dependence of triplet Cl lines in chloral hydrate $CCl_3CH(OH)_2$ would be interesting, because only two components of the triplets are believed to have hydrogen bonds[17].

B) As_4O_6

Thermal expansion coefficient for As_4O_6 is[22],

$$41.2\times10^{-6}-67.9\times10^{-9}(T-313),$$

and its compressibility at 30°C is[23], 9.29×10^{-6}. P-V isotherms for this specimen were determined with these values in conjunction with the value of 4.8 for ζ.

Since the pressure coefficient of the resonance frequency at liquid oxygen temperature was so small that it was not determined ac-

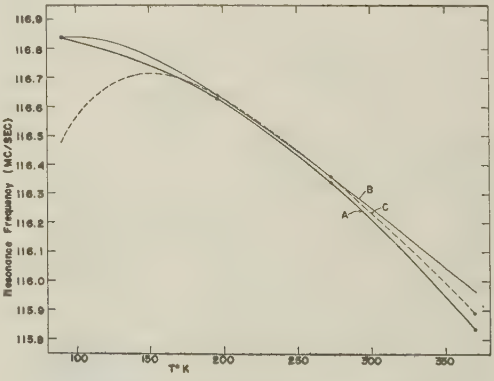

Fig. 10. The ν-*versus-temperature* curves for As_4O_6. Curve (A) is the temperature dependence of ν at atmospheric pressure. Curves (B) and (C) are $a(1+bT+c/T)$ curves calculated from the three lower and the three higher temperatures, respectively, at the constant volume which corresponds to liquid oxygen temperature and atmospheric pressure.

curately enough, $\nu(T)$ curve at constant volume was determined only at the volume which corresponds to the temperature of liquid oxygen and to the atmospheric pressure. This volume was estimated with the thermal expansion coefficient. The resonance frequency at the same volume at −77°, 0°, and 97°C, and the frequency at liquid oxygen temperature under the atmospheric pressure were tried to be fitted to Eq. (3), which is expected from the high temperature approximation of the Bayer type theories. The results are, however, unsatisfactory as are shown in Fig. 10. In this figure curve (B) represents Eq. (3) with the values of a, b, and c determined with the use of the three lower-temperature points, and curve (C) is the similar curve with the same parameter determined at the three higher-temperatures. This discrepancy indicates that the approximate equation (3) at high temperature fails to hold at about 90°K and the relation, $x \equiv \hbar\omega/(kT) < 2$, does not hold at this temperature, because the value of Θ is small and hence ω is large. Therefore, one ought to return to the original equation Eq. (2). Assuming $N=2$, $\omega_1=\omega_2=\omega$, and $A_1=A_2=A=1/\Theta$ on the basis of the crystal structure, one obtains,

$$(\nu_{90}-\nu_{196}):(\nu_{196}-\nu_{273}):(\nu_{273}-\nu_{370})$$

$$=\left(\frac{1}{\exp(\hbar\omega/196k)-1}-\frac{1}{\exp(\hbar\omega/90k)-1}\right)$$

$$:\left(\frac{1}{\exp(\hbar\omega/273k)-1}-\frac{1}{\exp(\hbar\omega/196k)-1}\right)$$

$$:\left(\frac{1}{\exp(\hbar\omega/370k)-1}-\frac{1}{\exp(\hbar\omega/273k)-1}\right).$$

And the best choice for the value of the lattice vibration frequency $\tilde{\nu}$ is in wave number unit, $\tilde{\nu} \equiv \omega/2\pi c = 370\,\mathrm{cm}^{-1}$ at the lower three temperatures, and it is $440\,\mathrm{cm}^{-1}$ at the higher three temperatures. In any case the value of x is greater than 5 at 90°K.

The moment of inertia deduced from the value ω is 17×10^{-40} and $11\times10^{-40}\,\mathrm{g\,cm}^2$ in the two temperature regions respectivly, volume which corresponds to liquid oxygen temperature and atmospheric pressure.

There are two points to be noted. First, the value of the moment of inertia thus obtained is much smaller than that of As_4O_6 molecule about its center of gravity, which amounts to about $1700\times10^{-40}\,\mathrm{g\,cm}^2$. The second point is that the value of ω thus determined appears to depend explicitely on the temperature.

The first point can be explained only by assumming that the dominant mode of lattice vibration which is responsible to the reduction in the resonance frequency, is intramolecular vibration instead of tipping motion of the molecule as a whole as in the case for usuall molecular crystals.

Although a unique explanation for the second point does not seem to be possible from the present experiment, either unharmonicity of the vibration considered above, or some distribution of the intra-molecular vibrations (or both) could account for this point.

The pressure dependence of the resonance frequency in this sample will be considered now. Although negative pressure dependence of ν is usually observed at low temperature in such molecular crystals as p-$C_6H_4Cl_2$ and p-$C_6H_4Br_2$ and even in SnI_4, no such tendency is observed even at liquid oxygen temperature for this specimen.

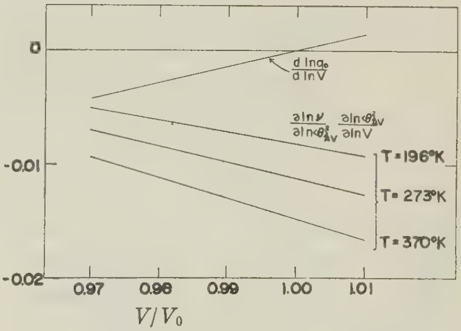

Fig. 11. The contribution of the volume dependence of q_0 and that of the lattice vibration to the volume dependence of the resonance frequency for As_4O_6 at three temperatures.

In spite of the ambiguity mentioned above in applying KBB's analysis to this sample, the volume dependence of the resonance frequency is analyzed along the KBB method. The result thus obtained is shown in Fig. 11, where the contributions to $\partial\ln\nu/\partial\ln V$ from the q_0 and the $\langle\theta^2\rangle_{AV}$ terms are shown. The volume dependence of b is also small, and the value of γ at $V/V_0=1.00$ is only 0.3. This can be explained in terms of the fact that the intramolecular bending motions play the most important role to the temperature dependence of the resonance line.

C) p-$C_6H_4Br_2$ and $KBrO_3$

Mean thermal expansion coefficient of p-$C_6H_4Br_2$ in the temperature ranges 20° to −77°C and 20° to −183°C are 138×10^{-6} and 98×10^{-6} deg^{-1}, respectively. Its compressibility is found to be 15.5×10^{-6}/(kg/cm^2) at room temperature (12°C). From Eq. (4), the equation of state was obtained using these values as well as the value of 3.33 for ζ.

The result of the analysis is shown in Figs. 12 and 13. The contributions of q_0 and $\langle\theta^2\rangle_{Av}$ to $\partial\ln\nu/\partial\ln V$, which are similar to the case of SnI_4, are drawn in the former figure, and the volume dependence of b and γ are shown in the latter one, where the value of γ is found to be roughly equal to that of isomorphic p-$C_6H_4Cl_2$. Using the data of two low-frequency Raman lines[24], the value of b is estimated as $b=-0.55\times10^{-4}$/°K. The agreement between this value and the value shown in Fig. 13 can be regarded as reasonable, if it is taken into account that the compression under the pressure could not be isotropic because of less symmetric crystal structure.

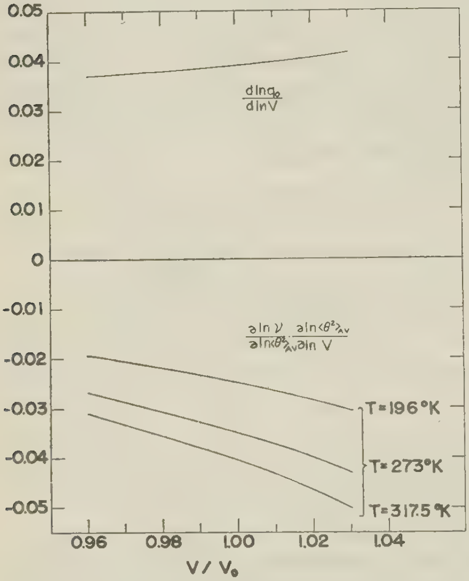

Fig. 12. The contribution of the volume dependence of q_0 and that of the lattice vibration to the volume dependence of the resonance frequency for p-$C_6H_4Br_2$ at three temperatures.

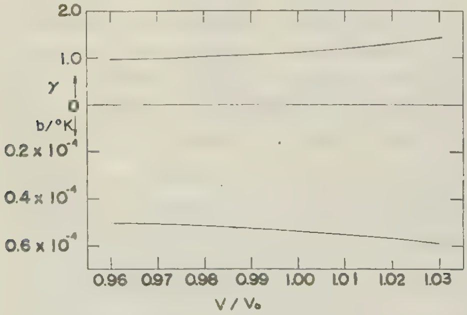

Fig. 13. The volume dependence of b and γ for p-$C_6H_4Br_2$.

The pressure dependence of $KBrO_3$ is found to be quite similar to that of $KClO_3$ which was extensively investigated by KBB already, and therefore, the result will not be shown here.

Acknowledgement

The author wishes to express his sincere thanks to Professor Y. Kôi at Tokushima University for suggestting this investigation and for his guidance throughout this experiment. He also appreciates valuable discussions with Professor T. Kushida at Hiroshima University and Professor J. Itoh at Osaka University. He is grateful to Mr. A. Tsujimura for his cooperation in the earlier stage of this experiment. The present investigation has partly been supported by the fund of the Ministry of Education.

References

1) H. Bayer: Z. Physik **130** (1951) 227.
2) T. Kushida: J. Sci. Hiroshima Univ. **A19** (1955) 327.
3) T. C. Wang: Phys. Rev. **99** (1955) 566.
4) B. Dreyfus: Ann. Physique **3** (1958) 683.
5) T. Kushida, G. B. Benedek and N. Bloembergen: Phys. Rev. **104** (1956) 1364.
6) R. G. Barnes and R. D. Engardt: J. Chem. Phys. **29** (1958) 248.
7) W. M. Walsh, Jr: Phys. Rev. **114** (1959) 1485.
8) R. A. Bernheim and H. S. Gutowsky: J. Chem Phys. **32** (1960) 1072.
9) P. W. Bridgman: The Physics of High Pressures (G. Bell and Sons, Ltd., London, 1949).
10) G. B. Benedek and T. Kushida: Phys. Rev. **118** (1960) 46.
11) Y. Kôi: J. Phys. Soc. Japan **12** (1957) 49.
12) H. G. Dehmelt: Z. Physik **130** (1951) 356.
13) A. L. Schawlow: J. Chem. Phys. **22** (1954) 1211.
14) S. Ogawa: J. Phys. Soc. Japan **13** (1958) 618.
15) P. J. Bray, G. O'Keefe and R. G. Barnes: J. Chem Phys. **25** (1956) 792.
16) F. Birch: J. Geophs. Research **57** (1952) 227.
17) T. P. Das and E. L. Hahn: Nuclear Quadrupole Resonance Spectroscopy in *Solid State*

Physics, Supplement I (Academic Press Inc., New York, 1958).
18) W. Biltz, A. Sapper and E. Wunnenberg: Z. Anorg. Chem. **203** (1932) 285.
19) I. Ichishima: Nihonkagakukaishi **71** (1950) 607 (in Japanese).
20) R. W. G. Wyckoff: Crystal Structures (Interscience Publishers, Inc., New York, 1951).
21) R. Kiriyama: Kozomukikagaku (in Japanese), (Kyoritu Co., Ltd., Tokyo 1952).
22) International Critical Table (McGraw-Hill Book Company, Inc., New York, 1928).
23) P. W. Bridgman: Proc. Am. Acad. Arts. Sci. **67** (1932) 345.
24) A. Rousset: J. Phys. radium **9** (1948) 101.

JOURNAL OF THE PHYSICAL SOCIETY OF JAPAN Vol. 16, No. 2, FEBRUARY, 1961

Magnetic Anisotropy of Chromium Antimonide and its Manganese Substitites

By Ichiro TSUBOKAWA*

The Research Institute for Iron, Steel and Other Metals,
Tohoku University, Sendai, Japan

(Received September 21, 1960)

Magnetic anisotropy of compounds of CrSb, $(Cr_{0.9}Mn_{0.1})Sb$ and $(Cr_{0.8}Mn_{0.2})Sb$ was investigated by using their single crystals. From the measurements of torque curves by means of torsion pendulum magnetometer, the difference between the susceptibilities parallel and perpendicular to the c-axis of the hexagonal crystal lattice was obtained for each specimen. It was confirmed that the magnetic spin axis lies along the c-axis for each compound. (also in the ferrimagnetic region of $(Cr_{0.8}Mn_{0.2})Sb$) The magnetic anisotropy constant K of CrSb was estimated to be about 10^5 erg/gr. at room temperature.

§ 1. Introduction

The magnetic properties of chromium antimonide and its manganese substitutes in powder form were studies by Lotgering and Gorter[1] and Hirone et al.[2] It has been known from these studies that these compounds have either antiferromagnetic spin ordering or both ferromagnetic and antiferromagnetic spin ordering with a temperature transition between them. Snow[3] showed by neutron diffraction experiments that the spin magnetic moment of each cation in chromium antimonide orients along the c-axis of the hexagonal crystal lattice. In order to study the magnetic anisotropy of these compounds and the interesting magnetic behavior, the present author measured the magnetic anisotropy by using single crystals of these compounds.

§ 2. Specimens and the Method of Measurement

Single crystals of chromium antimonide and the manganese substitutes were prepared in the following way. First, the powders of these compounds, CrSb, $(Cr_{0.9}Mn_{0.1})Sb$ and $(Cr_{0.8}Mn_{0.2})Sb$ were made by the ceramic method as described in the pervious paper.[2] The compounds perpared in this way were then pressed into a rectangular rod with a pressure of six tons per square centimeter. These compressed bars were sealed in evacuated silica tubes, heated at temperatures several degrees above the melting points of each specimen, and cooled in a furnace at a rate of a few degrees per minute. The size of single crystals obtained were about 4×4 millimeters square and 10 millimeters in length.

The crystallographic orientation was determined by means of Laue photographs within an accuracy of a few degrees. A magnetic torsion pendulum magnetometer was used to measure the anisotropy of magnetic susceptibility. The difference of principal magnetic susceptibilities can be expressed by the following equation,

---

* Present address is Totsuka Works, Hitachi, Ltd. Yokohama, Japan.

$$\chi_a-\chi_c=\frac{2L}{mH^2\sin 2\theta}\,, \tag{1}$$

where m is the mass of the specimen, L the torque in the specimen due to the magnetic field H and θ the angle between the c-axis and the applied field.

§ 3. Experimental Results

First, an example of the torque curve in the $a-c$ plane for a single crystal of chromium antimonide at various temperatures in a magnetic field with a field strength of 6420 Oe are shown in Fig. 1. Each curve shows that the torque changes nearly as sin 2θ with the angle θ, and its amplitude decreases with a rise of temperature. It was also confirmed that the torque value changes linearly with the square of the applied magnetic field strength, and example at liquid nitrogen temperature being shown in Fig. 2. On the basis of equation, (1) the difference of susceptibilities perpendicular and parallel to the c-axis of the crystal, $(\chi_a-\chi_c)$, are obtained as shown in Fig. 3. On the other hand, the powder susceptibility may be expressed as an average of parallel and perpendicular susceptibilities by the well-known formula

$$\chi_p=\frac{1}{3}\chi_c-\frac{2}{3}\chi_a\,. \tag{2}$$

Using the previous data of powder susceptibility and the difference $(\chi_a-\chi_c)$ obtained by the present experiments, the values of χ_a and χ_c were calculated. The results are shown in Fig. 4. To confirm the results, the author

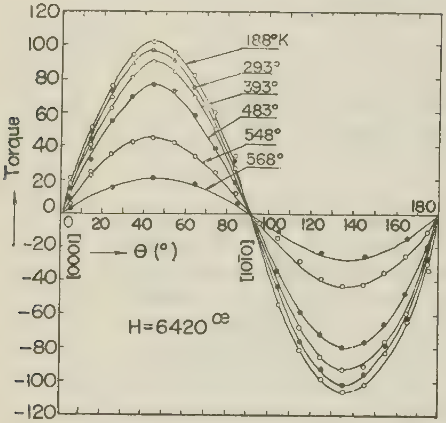

Fig. 1. Torque curves of a single crystal of CrSb in a–c plane.

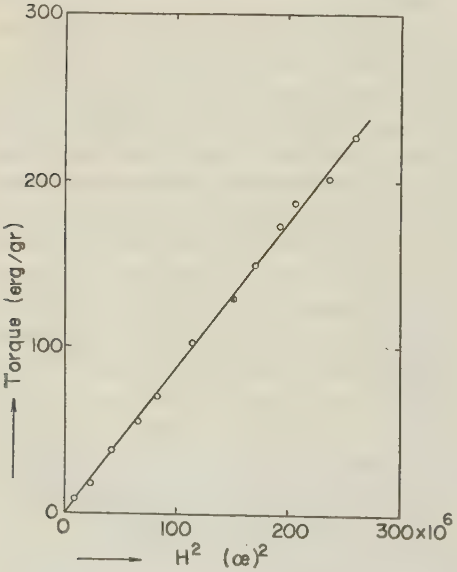

Fig. 2. Torque versus H^2 relation of CrSb.

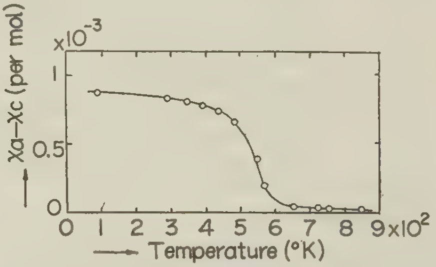

Fig. 3. $(\chi_a-\chi_c)$ of CrSb.

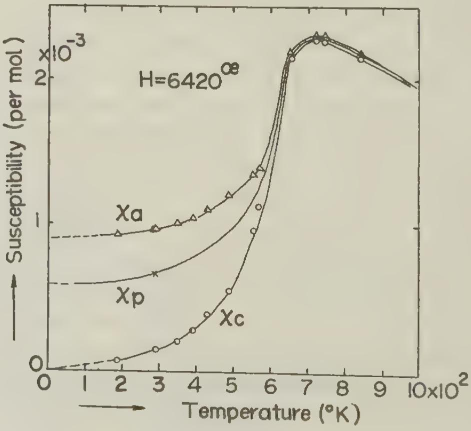

Fig. 4. χ_a, χ_c and χ_p of CrSb. ▲ and × are the values of χ_a and χ_p obtained by using the magnetic balance.

measured χ_a and χ_p of the same crystal at room temperature using a magnetic balance. The powder specimen was prepared from the original single crystal. The results are shown in Fig. 4 by the marks ▲ and ×. Each value agrees very well with the former curves.

The same measurements were also made for the compounds $(Cr_{0.9}Mn_{0.1})Sb$ and $(Cr_{0.8}Mn_{0.2})Sb$. It is known from the measurement of the powder susceptibility that the compounds are antiferromagnetic in a certain range below the Néel temperature, but become ferrimagnetic in the lower temperature range. In the antiferromagnetic region, the torque curves were represented nearly by sin 2θ as shown in Fig. 5 and Fig. 6. However, for the compound $(Cr_{0.8}Mn_{0.2})Sb$ at liquid nitrogen temperature, which is just below the ferrimagnetic transition point, the maximum points of the torque curves are displaced to the side of the c-plane (about 15° at the maximum field strength of 25.2 kOe) (Fig. 7). The relation of the maximum torque value versus the square of the magnetic field at several temperatures are shown in Fig. 8. As shown in Fig. 8, the maximum values of torque at the higher temperatures of the antiferromagnetic region change in proportion to the square of the magnetic field strength, however, at the lower temperature of the

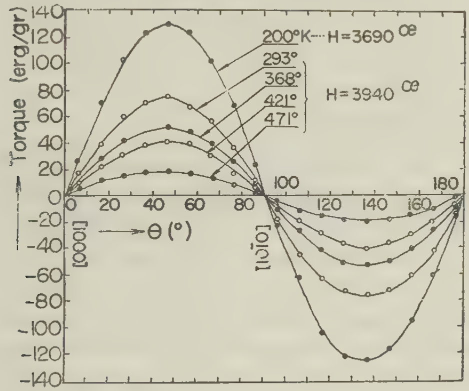

Fig. 5. Torque curves of a single crystal of $(Cr_{0.9}Mn_{0.1})Sb$ in the $a-c$ plane.

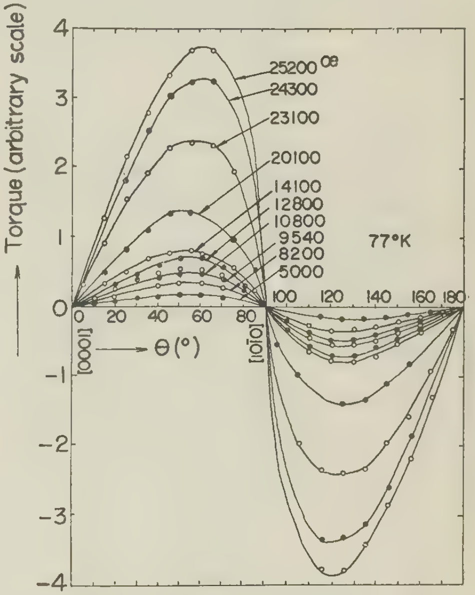

Fig. 7. Torque curves of a single crystal of $(Cr_{0.8}Mn_{0.2})Sb$ in the $a-c$ plane at 77°K.

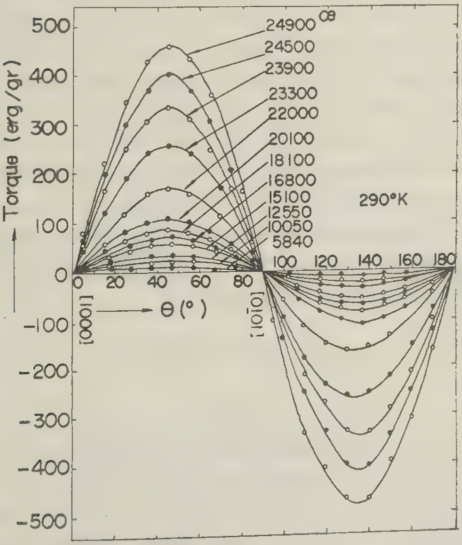

Fig. 6. Torque curves of a single crystal of $(Cr_{0.8}Mn_{0.2})Sb$ in the $a-c$ plane at 290°K.

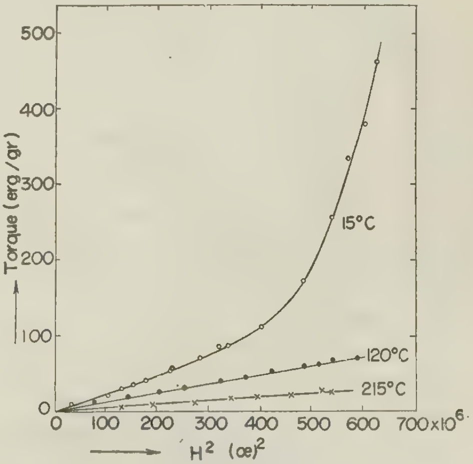

Fig. 8. Torque versus H^2 relation of $(Cr_{0.8}Mn_{0.2})Sb$.

region it increases more rapidly than the linear relation. As in the previous case of chromium antimonide, we obtained $(\chi_a-\chi_c)$ as shown in Fig. 9 and 10. χ_a and χ_c obtained with combining the previous data of powder susceptibilities[2] are shown in Fig. 11 and 12.

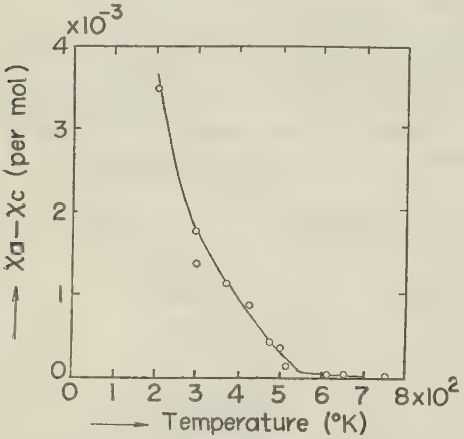

Fig. 9. $(\chi_a-\chi_c)$ of $(Cr_{0.9}Mn_{0.1})Sb$.

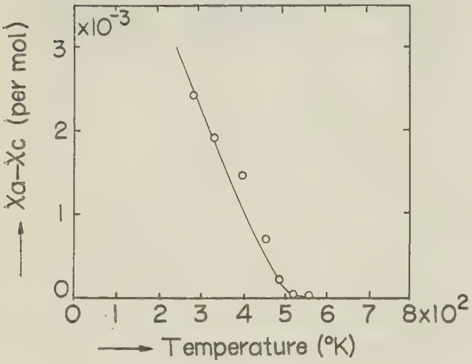

Fig. 10. $(\chi_a-\chi_c)$ of $(Cr_{0.8}Mn_{0.2})Sb$.

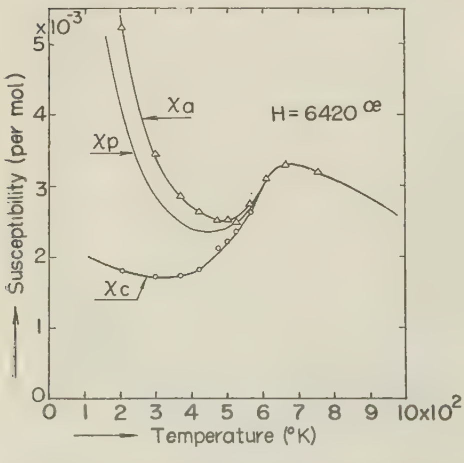

Fig. 11. χ_a, χ_c and χ_p of $(Cr_{0.9}Mn_{0.1})Sb$.

It is considered that the easy axis of the magnetization lies also in the direction parallel to the c-axis of the crystal.

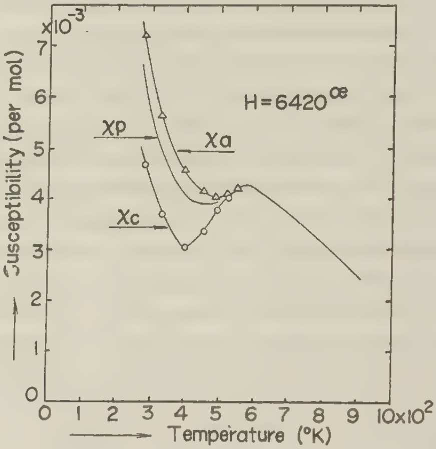

Fig. 12. χ_a, χ_c and χ_p of $(Cr_{0.8}Mn_{0.2})Sb$.

§ 4. Discussions

It is concluded from the torque measurement that the antiferromagnetic easy direction of CrSb is along the c-axis of the crystal. This fact is consistent with the results of neutron diffraction experiments by Snow.[3] In such a case, it is to be expected that the perpendicular susceptibility will be independent of temperature below the Néel point. Contrary to this expectation, present results show that the perpendicular susceptibility of chromium antimonide decreases with falling temperature from the Néel point to 400°K. This fact may be explained by a weakening of the antiferromagnetic interaction which is accompanied by the change of the lattice constant c (according to Snow's X-ray work,[4] the lattice constant c expands several percent during the temperature rise of these ranges). According to a molecular field approximation, the Néel point and the susceptibility of antiferromagnet are expresses as

$$T_N=\frac{2}{3}|J|zk^{-1}S(S+1)\,, \tag{3}$$

$$\chi_N=Ng^2\mu_B^2/4|J|z \tag{4}$$

where J is the exchange integral, z number of the nearest neighbour, K Boltzman's constant, S spin quantum number, χ_N the susceptibility at the Néel point, N Loschmit number, g Landé factor and μ_B Bohr magneton. The same consideration can be applied also to the other two compounds, since the same kind of behaviour appears in χ_a below the Néel point in these and, at the same time the measurement of the dilatation performed by Hirone et al[5] gives the change of lattice constants of the same order of magnitude. It is noticed for $(Cr_{0.8}Mn_{0.2})Sb$, that the torque versus H^2 curve at 15°C displaced from straight line appreciablly at above $H=20000$ Oe. This anomalous behaviour is considered to be based on the induced ferromagnetism of this crystal in the stronger field strengths. (At room temperature, the compound is antiferromagnetic from the previous susceptibility data and present torque measurement.)

Torque curves at liquid nitrogen temperature show that saturation could not be obtained at 13000 Oe. Ferrimagnetic easy direction is in the *c*-axis of the hexagonal crystal and coincide with the antiferromagnetic easy direction at higher temperatures.

Finally, we will show the results of the magnetic anisotropy constant for CrSb. Introducing the anisotropy constant, K, we can express the powder susceptibility by the formula[6]

$$\chi_p=\frac{1}{3}\chi_{||}-\frac{2}{3}\chi_{\perp}-\frac{2}{15K}(\chi_{||}-\chi_{\perp})^2H^2\,. \quad (5)$$

Thus, if we measure the χ_p as a function of H^2, then we can calculate K combining with the observed χ_a and χ_c. The obtained value of K is of the order of magnitude of 10^5 erg/gr at just below room temperature.

Acknowledgements

The author wishes to express his hearty thanks to Professors T. Hirone and H. Watanabe for their kind encouragement throughout the course of the present study. He also wishes to express his sincere thanks to Asistant Professors S. Maeda and N. Tsuya for their useful discussions.

References

1) F. K. Lotgering and E. W. Gorter: J. Phys. Chem. Solids **3** (1957) 238.
2) T. Hirone, S. Maeda, I. Tsubokawa and N. Tsuya: J. Phys. Soc. Japan **11** (1956) 1083.
3) A. I. Snow: Phys. Rev. **85** (1952) 365.
4) A. I. Snow: Rev. Med. Phys. **25** (1953) 127.
5) T. Hirone, S. Maeda and T. Suzuoka: Annual meeting of Japan Physical Society held in Tokyo, March 1958.
6) T. Nagamiya, K. Yosida and R. Kobo: Advances in Physics **4** (1955) 39.

JOURNAL OF THE PHYSICAL SOCIETY OF JAPAN, Vol. 16, No. 2, FEBRUARY, 1961

Extension of High Polymer Molecule and Energy Change by Mixing

By Hiroshi MIZUTANI

Department of Physics, Faculty of Science, Hokkaido University, Sapporo, Japan

(Received September 28, 1960)

The change in intermolecular potential energy produced by mixing some low molecular liquids, which are considered as the substitute for the chain elements of polystyrene molecule, with several non-polar solvents and the extension of polystyrene molecule in these solvents were measured, and the obtained results were compared with the theory⁽¹⁾. Determination of the energy change was made by means of calorimetric method and that of the extension of polystyrene by measuring the intrinsic viscosity of the solution. We found that the variation of the extensions of polystyrene in different non-polar solvents is mainly determined by the difference in the energy change effected by the mixing of benzene, the side group of polystyrene, with the solvents.

§1. Introduction

The fact that the extension of high polymer molecule in solution depends on the kind of solvent may be ascribed to the difference in potential energies between chain elements of the high polymer molecule and solvent molecules. Since many properties of high polymer solution have an intimate relationship with the degree of the extension of high polymer molecule in solution, the investigation on the relation between the molecular extension in solution and the intermolecular potential energies between chain elements and solvent molecules must be of importance not only to the problem of moleculor extension but also to the study of the physical properties of high polymer solution.

According to the theoretical treatment⁽¹⁾, the mean square end-to-end distance $\langle r^2\rangle$ of the high polymer molecule in solution is given by

$$\langle r^2\rangle=\frac{\displaystyle\int \exp\left\{\frac{\sigma N^2}{\nu\tau}\frac{\Delta E}{kT}r^{-3}-\frac{3r^2}{2CN^\gamma}\right\}r^4dr}{\displaystyle\int \exp\left\{\frac{\sigma N^2}{\nu\tau}\frac{\Delta E}{kT}r^{-3}-\frac{3r^2}{2CN^\gamma}\right\}r^2dr}, \cdots\cdots(1)$$

with

$$\Delta E=\frac{E_{pp}+E_{ss}}{2}-E_{ps}, \cdots\cdots\cdots\cdots(2)$$

where $-E_{pp}$, $-E_{ss}$ and $-E_{ps}$ are the mutual potential energies for chain element-chain element, solvent molecule-solvent molecule, and chain element-solvent molecule, respectively, σ the number of the nearest neighbors around a lattice point, N the number of chain elements, ν the number density of lattice points, τ a constant number $[(4\pi/3)\cdot(1/6^{3/2})]$, k Boltzmann constant, and CN^γ the end-to-end distance of high polymer molecule when the volume exclusion effect of chain element is taken into account, C and γ being constants. Eq. (1) is the formula for the end-to-end distance of high polymer molecule in solution obtained with due consideration for the interaction between the chain elements and the solvent molecules as well as for the volume exclusion effect of chain elements. From this equation we see that the end-to-end distance of high polymer molecule in solution is a monotone decreasing function of ΔE, the energy change produced when the chain element and a solvent molecule come in contact with each other (cf. Fig. 5). The problem thus reduces to the experimental investigation into the relation between $\langle r^2\rangle$ and ΔE for different solutions of a high polymer substance.

Since it is practically impossible to measure ΔE directly for high polymer solutions, we had instead recourse to the use of low molecular substance, which might be regarded as the equivalent to the chain element of the polymer. As the chain element we may assume the monomer of high polymer molecule or the units whose size are larger or smaller than monomer.

If we take polystyrene as a high polymer substance:

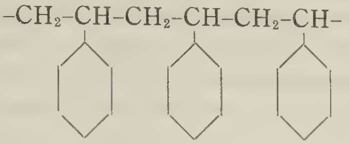

$-CH_2-CH-CH_2-CH-CH_2-CH-$

the conceivable chain elements are:

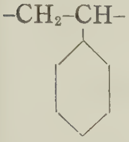

$-CH_2-CH-$

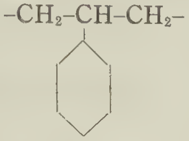

$-CH_2-CH-CH_2-$

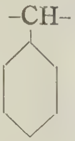

$-CH-$

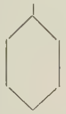

The corresponding stable molecules which might possibly behave in the same manner as these units are:

styrene

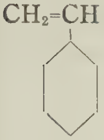

$CH_2=CH$

ethylbenzene

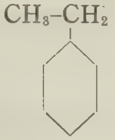

CH_3-CH_2

isopropylbenzen

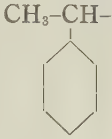

$CH_3-CH-CH_3$

toluene

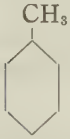

CH_3

benzene

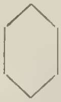

Which molecule of these can be considered as the suitable substitute for the chain element of polystyrene may be judged by determining ΔE-values for that molecule in various solvents and trying to see if the ΔE-values thus determined and the $\langle r^2 \rangle$ -values, which can be obtained from the intrinsic viscosity $[\eta]$ of polystyrene solutions (see later), satisfy Eq. (1). The ΔE-value can be derived, as will be described in § 4, from the energy change ΔU, which in its turn can be determined from the mixing heat ΔH evolved (or absorbed) in the process of mixing the molecules with the solvent by the use of the relation[(2)]

$$\Delta U=\Delta H-T(\alpha/\beta)\Delta V. \cdots\cdots\cdots\cdots(3)$$

Here T is the absolute temperature, α the thermal expansion coefficient, β the isothermal compressibility, and ΔV the volume change brought about by mixing. The methods of measuring ΔH, ΔV and $[\eta]$ will be described in detail in the following sections.

§ 2. Measurement of Mixing Heat ΔH

The easiest and most accurate method of obtaining the mixing heat is perhaps to measure the heat transferred from an electric heater to the mixture of two liquids, which is required for componsation or reproduction of the temperature change according as heat is absorbed or evolved.

I) Apparatus

Employing this method, we constructed an apparatus which is an improved type of that devised by G. H. Cheesman and A. M. Beryl Whitaker[(3)] (Figs. 1 and 2). Main points of improvement are as follows:

i) Up-and-down motion of iron rod for mixing and stirring liquids is drived by an electro-magnet set outside the glass tube. D. C of constant voltage is used for the magnet to prevent the heating of the mixing vessel due to the electric induction. Make and break of circuit of the magnetic coil is performed by a rotary switch connected to a synchronous motor.

ii) As is shown in Fig. 1, a cylindrical piece of copper (indicated by D in the figure) with large heat capacity is used as temperature standard, with reference to which the temperature change in the mixing vessel is to be measured. In this way the measure-

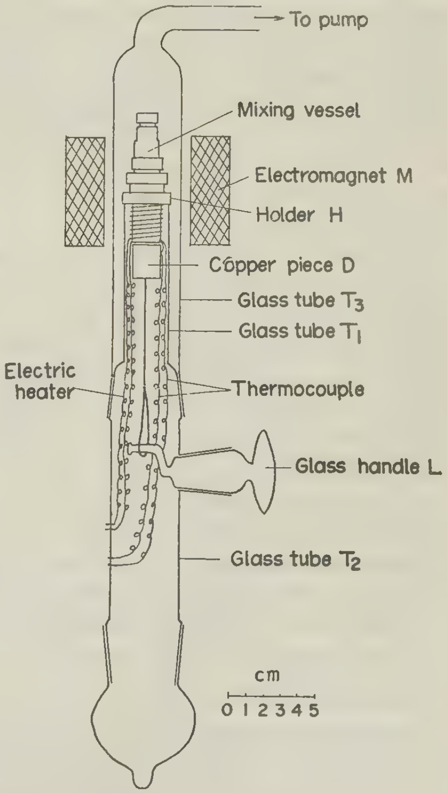

Fig. 1. Scheme of the whole apparatus.

ment is markedly simplified.

As seen in Fig. 1, the mixing vessel supported on a ring holder *H*, which in turn is supported on top of a glass tube T_2, is set in a glass tube T_3. There are several holes in the upper part of the ring holder through which the tube T_2 is evacuated. In order to prevent radiant heat transfer between the mixing vessel and the outer space, inner surface of glass tube T_3 is coated with aluminium by means of vacuum-evaporation technique. Glass handle *L* is used for pulling down the copper piece *D* stated above so that it may be released from contact with the bottom of the mixing vessel.

The heating coil is an enamel-coated constantan wire 0.2 mm in diameter, about 1 meter long, and with resistance of 13 ohms. Voltage applied to the coil ranged from 0.65 volt to 1.3 volt. These values of the current were selected so that the plotting of the "heating curve", as will be illustrated in Fig. 3, may be made easily and quickly.

M is a magnet coil designed so as to let the iron rod move up and down and to break the tinfoil diaphragm (described below). The magnet coil is made of an enamel-coated copper wire 0.4 mm in diameter, total number of turns being 8000. 100 volt D. C. voltage is applied to this magnet coil and the current is closed and cut off at regular intervals of one second by a rotary switch drived by a synchronous moter. The duration of time while the switch is on is 0.01 sec.

Fig. 2 gives the details of the mixing vessel. It is composed of two parts *B* and *C* with respective volumes 2.7 cm³ and 3.4 cm³, into which the liquids to be mixed are introduced. *B* and *C* are separated from each other by a tinfoil diaphragm 0.005 mm in thickness, which is hold tightly by gaskets G_1 made of annular polyethylene sheet 1 mm thick.

In *C* there is an iron rod with a sharp point which is used for breaking the tinfoil diaphragm and mixing the two liquids by its up-and-down motion. Around the vessel *C* are wrapped two sheets of insulating paper *P*, with a heating coil *E* in between.

II) Experimental Procedure

Accurately measured quantities of the two liquids to be mixed are introduced into the vessels *B* and *C*, and the whole apparatus is evacuated down to pressure 10^{-4} mm Hg.

Now, we start the motor which drives the rotary switch. If the readings of galvanometer are found constant we commence mixing and stirring the liquids. The results obtained in endothermic and exothermic cases are shown in Fig. 3a and Fig. 3b, respectively.

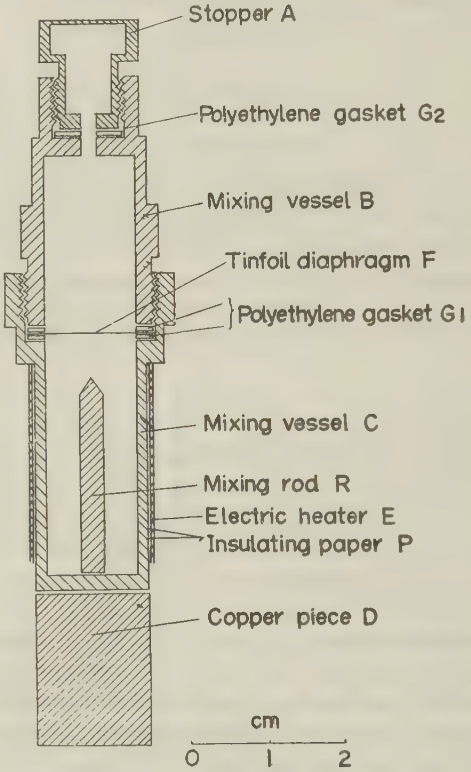

Fig. 2. Mixing vessel.

A in Fig. 3a indicates the point where the mixing is started. The galvanometer reads from *A* to *C* and finally to *D*. The net temperature change due to mixing corresponds to the height *AB* which is obtained by extrapolation of the curve *DC* leftwards down to *B*. In order to obtain the mixing heat ΔH (see section (III)), we close the heater circuit at the moment when the curve arrives at the point *D* (which can be selected arbitrarily*. The "heating curve" *DEF* is then plotted, and the tangent is drawn at *E* which is at the same level as *A*. This tangent means a heating curve which would have been obtained if the heating were solely due to heater current*.

---

* Only, the curve *C D* must be long enough to be extrapolated.

In the case of exothermic mixing (Fig. 3b), the height $A'B'$ corresponding to the net temperature elevation brought about by mixing is obtained by extrapolation of the curve $D'C'$. The plotting of the "heating curve" $E'F'$ is started from the room temperature. The tangent of the curve $E'F'$ at E', is, as before, nothing but the heating curve which would have been obtained, if the heating were only due to the heating coil.

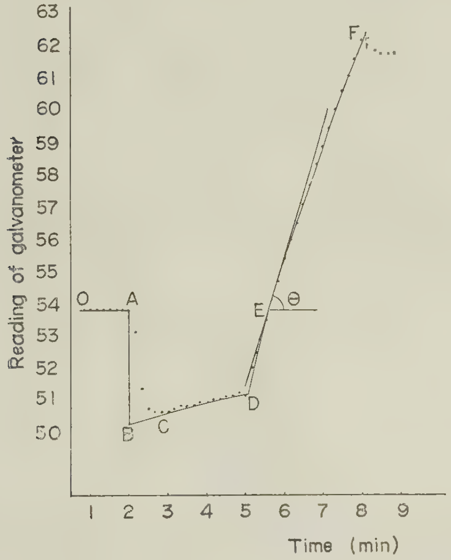

Fig. 3a. Mixing curve of benzene and isopropylbenzene.

III) Calculation of Mixing Heat

i) Endothermic Mixing

In Fig. 3a, AB measures the net temperature depression caused by mixing, and the gradient $\tan\theta$ of the tangent drawn to the curve DEF at E means the temperature elevation of the mixture per unit time when the heat is transferred from none other than the heating coil. Thus the mixing heat ΔH (joule) is given by

$$\Delta H = I^2 R \times \frac{AB}{\tan\theta}\,, \tag{4}$$

where I (ampere) is the heater current, and R (ohm) the resistance of the heating coil.

ii) Exothermic Mixing

From Fig. 3b, and following the same procedure as in the case of endo-thermic mixing, we get the mixing heat

$$\Delta H' = I^2 R \times \frac{A'B'}{\tan\theta'}\,. \tag{5}$$

§ 3. Measurement of the Volume Change Caused by Mixing

A pycnometer with stoppers, as shown in Fig. 4, is used for the measurement of volume change produced by mixing. The stoppers serve for preventing the liquids from evaporation. Measurements of the densities ρ_A and ρ_B of the liquids A and B and of ρ_{AB} of equi-

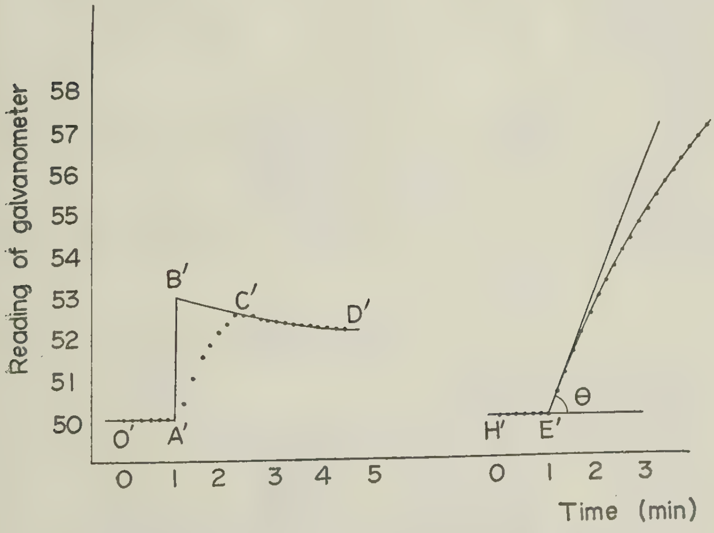

Fig. 3b. Mixing curve of benzene and methylethylketone.

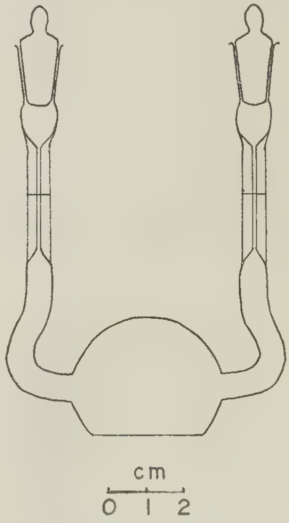

Fig. 4. Pycnometer.

---

* In constructing the heating curve, due corrections must be made by subtracting the heat developed within the mixture (heat of kinetic energy origin), which can be measured by the blank test.

Table I. Volume change by mixing. (cm³/mol. mixt.)

Solvent \ Chain element equivalent	Styrene	Ethylbenzene	Isopropyl-benzene	Toluene	Benzene
Benzene	+0.0504	+0.1193	−0.0583	+0.0715	0
Toluene	−0.2896	−0.0163	+0.1120	0	+0.0715
Xylene	+0.0231	+0.0422	+0.0323	+0.2070	+0.2797
Styrene	0	−0.0136	+0.0478	−0.2896	+0.0504
Ethylbenzene	−0.0136	0	−0.0876	−0.0163	+0.1193
Cyclohexane	+0.5694	+0.4792	+0.4699	+0.6348	+0.6412

molal mixture of A and B are determined by the ordinary manner. The volume change per unit equi-molal mixture is therefore given by

$$\Delta V=\frac{1}{2}\left[\frac{M_A+M_B}{\rho_{AB}}+\left(\frac{M_A}{\rho_A}+\frac{M_B}{\rho_B}\right)\right], \qquad (6)$$

where M_A and M_B are the molecular weights of A and B respectively. Experimental results obtained are shown in Table I.

§ 4. Calculation of Energy Change Due to Mixing

In this section we shall derive the mixing energy of two liquids A and B [$\Delta E=(E_{pp}+E_{ss})/(2)-E_{ps}$] from the change of the intermolecular potential energy ΔU brought about by mixing. We assume for simplicity that the quasicrystalline lattice model for liquid is allowed to use and that the size and shape of molecules of A and B are so similar to each other that the probability for a molecule to occupy a lattice point is the same in both liquids.

Let the numbers of molecules of A and B be N_A and N_B, respectively, the number of the nearest neighbor sites around a lattice point be σ, and the potential energies of molecular pairs $A-A$, $B-B$ and $A-B$ be $-E_{AA}$, $-E_{BB}$ and $-E_{AB}$, respectively. Then the sum of the potential energies of two liquids A and B before mixing is

$$U_A+U_B=-\frac{\sigma N_A}{2}E_{AA}-\frac{\sigma N_B}{2}E_{BB}\,. \qquad (7)$$

Table II.

Solvent	Thermal expansion coefficient α	Isothermal compressibility β cm²/dyne
Benzene	1.229×10^{-3}	0.953×10^{-3}
Toluene	1.051 〃	0.9147 〃
Xylene	0.994 〃	0.798 〃
Styrene	0.738 〃	0.74 〃
Ethylbenzene	1.018 〃	0.833 〃
Cyclohexane	1.20 〃	1.20 〃

Since the numbers of the molecular pairs $A-A$, $B-B$ and $A-B$ are respectively given by

$$\left.\begin{aligned} N_{AA}&=\frac{\sigma N_A^2}{2(N_A+N_B)}\,,\\ N_{BB}&=\frac{\sigma N_B^2}{2(N_A+N_B)}\,,\\ N_{AB}&=\frac{\sigma N_A N_B}{N_A+N_B}\,, \end{aligned}\right\} \qquad (8)$$

we have, for the total intermolecular potential energy of the mixture,

$$\begin{aligned} U_{\text{mix}}&=-N_{AA}E_{AA}-N_{BB}E_{BB}-N_{AB}E_{AB}\\ &=-\frac{\sigma N_A^2}{2(N_A+N_B)}E_{AA}-\frac{\sigma N_B^2}{2(N_A+N_B)}E_{BB}\\ &\quad-\frac{\sigma N_A N_B}{N_A+N_B}E_{AB}\,. \end{aligned} \qquad (9)$$

Thus the change in intermolecular potential energy of the two liquids produced by mixing is, from Eqs. (7) and (9),

$$\Delta U=U_{\text{mix}}-(U_A+U_B)=\frac{\sigma N_A N_B}{N_A+N_B}\Delta E\,, \qquad (10)$$

with

$$\Delta E=\frac{E_{AA}+E_{BB}}{2}-E_{AB}\,, \qquad (11)$$

so that

$$\Delta E=\frac{N_A+N_B}{\sigma N_A N_B}\Delta U\,. \qquad (12)$$

If no change of volume accompanies mixing, ΔU is equal to the mixing heat ΔH, or we have

$$\Delta E=\frac{N_A+N_B}{\sigma N_A N_B}\Delta H\,. \qquad (13)$$

In the case where the volume change $\varDelta V$ is not zero, the system of mixture undergoes a change in energy corresponding to the work done in a form of mechanical work of expansion or contraction. Theory⁽²⁾ requires that

$$\varDelta U=\varDelta H-T(\alpha/\beta)\varDelta V \\ +(\text{higher terms of } \varDelta V)\,, \qquad (3)$$

in which α, thermal expansion coefficient, and β, isothermal compressibility of the mixture, are given in terms of corresponding values of the component liquids, by

$$\left.\begin{aligned}\alpha&=\phi_1\alpha_1+\phi_2\alpha_2\,,\\ \beta&=\phi_1\beta_1+\phi_2\beta_2\,,\end{aligned}\right\} \qquad (14)$$

ϕ_s' being the volume fractions of the components. Eqs. (3) and (12) yield

$$\varDelta E=\frac{N_A+N_B}{\sigma N_A N_B}\{\varDelta H-T(\alpha/\beta)\varDelta V\}\,. \qquad (15)$$

In the special case where unit molal mixture is made of equi-molal liquids A and B, we have

$$N_A=N_B=\frac{N_{AV}}{2}\,,$$

N_{AV} being Avogadro's number. If we put

$$\sigma=12\,,$$

Eq. (15) becomes

$$\varDelta E=\frac{1}{3N_{AV}}\{\varDelta H-T(\alpha/\beta)\varDelta V\}\,. \qquad (16)$$

Table III. Energy change by mixing.

Chain element equivalent	Solvent	Mixing heat $\varDelta H$ cal/mol.	$T(\alpha/\beta)\varDelta V$ cal/mol.	Energy change by mixing	
				$\varDelta U$ cal/mol.	$\varDelta E$ cal/pair
Styrene	Benzene	+ 13.5	+ 4.42	+ 9.1	$+4.99\times10^{-24}$
	Toluene	0.00	−24.46	+ 24.46	$+13.45\times$ 〃
	Xylene	+ 10.4	+ 1.99	+ 8.4	$+2.63\times$ 〃
	Styrene	0	0	0	0
	Ethylbenzene	0.00	− 1.13	+ 1.13	$+0.62\times$ 〃
	Cyclohexane	+205	+37.46	+167	$+92.1\times$ 〃

Table IV. Energy change by mixing.

Chain element equivalent	Solvent	Mixing heat $\varDelta H$ cal/mol.	$T(\alpha/\beta)\varDelta V$ cal/mol.	Energy change by mixing	
				$\varDelta U$ cal/mol.	$\varDelta E$ cal/pair
Ethylbenzene	Benzene	+ 21.1	+10.37	+10.7	$+5.91\times10^{-24}$
	Toluene	− 3.38	− 1.37	− 2.01	$-1.11\times$ 〃
	Xylene	+ 4.68	+ 3.62	+ 1.06	$+0.58\times$ 〃
	Styrene	0.00	− 1.13	+ 1.13	$+0.62\times$ 〃
	Ethylbenzene	0	0	0	0
	Cyclohexane	+102	+30.4	+72	$+39.7\times$ 〃

Table V. Energy change by mixing.

Chain element equivalent	Solvent	Mixing heat $\varDelta H$ cal/mol.	$T(\alpha/\beta)\varDelta V$ cal/mol.	Energy change by mixing	
				$\varDelta U$ cal/mol.	$\varDelta E$ cal/pair
Isopropylbenzene	Benzene	+21.3	− 4.76	+26.1	$+14.34\times10^{-24}$
	Toluene	− 5.53	+ 8.87	−14.40	$-8.92\times$ 〃
	Xylene	− 1.39	+ 2.60	− 3.99	$-2.19\times$ 〃
	Styrene	+ 3.64	+ 3.69	− 0.05	$-0.03\times$ 〃
	Ethylbenzene	0.00	− 6.80	+ 6.80	$+3.74\times$ 〃
	Cyclohexane	+86.0	+29.30	+56.7	$+31.2\times$ 〃

Table VI. Energy change by mixing.

Chain element equivalent	Solvent	Mixing heat ΔH cal/mol.	$T(\alpha/\beta)\Delta V$ cal/mol.	Energy change by mixing	
				ΔU cal/mol.	ΔE cal/pair
Toluene	Benzene	$+12.6$	$+6.36$	$+6.2$	$+3.45\times10^{-24}$
	Toluene	0	0	0	0
	Xylene	$+6.34$	$+18.13$	-11.79	$-6.48\times$ 〃
	Styrene	0.00	-24.46	$+24.46$	$+13.45\times$ 〃
	Ethylbenzene	-3.89	-1.37	-2.52	$-1.38\times$ 〃
	Cyclohexane	$+116$	$+38.00$	$+78$	$+42.7\times$ 〃

Table VII. Energy change by mixing.

Chain element equivalent	Solvent	Mixing heat ΔH cal/mol.	$T(\alpha/\beta)\Delta V$ cal/mol.	Energy change by mixing	
				ΔU cal/mol.	ΔE cal/pair
Benzene	Benzene	0	0	0	0
	Toluene	$+13.9$	$+6.36$	$+7.5$	$+4.13\times10^{-24}$
	Xylene	$+50.6$	$+25.34$	$+25.3$	$+13.86\times$ 〃
	Styrene	$+10.5$	$+4.42$	$+6.1$	$+3.34\times$ 〃
	Ethylbenzene	$+21.6$	$+10.37$	$+11.2$	$+6.15\times$ 〃
	Cyclohexane	$+171$	$+43.90$	$+137$	$+75.5\times$ 〃

Observed values of ΔH for equi-molal mixing and calculated values of ΔE are given in Tables III–VII.

Procedure of deriving the equi-molal mixing heat from the experimental results for non-equi-molal mixing is as follows. Neglecting the effect of volume change ΔV and putting ΔU equal to ΔH, we obtain from Eq. (13) the expression for equi-molal mixing heat per unit molal mixture;

$$\Delta H_{\text{equi-mol. mix.}}/\text{mole} = \frac{N_{AV}}{4}\left(\frac{N_A+N_B}{N_A N_B}\right)\Delta H_{\text{obs.}}\,, \qquad (17)$$

or, introducing the molal fractions of liquids A and B;

$$\left.\begin{aligned} x_A &= \frac{N_A}{N_{AV}}\,, \\ x_B &= \frac{N_B}{N_{AV}}\,, \end{aligned}\right\} \qquad (18)$$

$$\Delta H_{\text{equi-mol. mix.}}/\text{mole} = \frac{x_A+x_B}{4x_A x_B}\Delta H_{\text{obs.}}\,. \qquad (19)$$

§ 5. Measurement of Extension of High Polymer

The end-to-end distance of polystyrene of molecular weight 200,000 in various solutions has been measured. Between the intrinsic viscosity $[\eta]$ of the high polymer solution and the molecular weight M of the high polymer molecule there is an empirical relation

$$[\eta] = KM^{a}\,, \qquad (20)$$

where K and a are constants. For the benzene solution of polystyrene, Eq. (20) becomes(4)

$$[\eta] = 2.7\times10^{-4}\times M^{0.66}\,. \qquad (21)$$

This equation enables one to determine the molecular weight of any fractionated sample of polystyrene. The values of K and a for solvents other than benzene are then obtained from the measurement of $[\eta]$ by using polystyrene of known molecular weight.

With these values of K and a, $[\eta]$ of the solutions of polystyrene with molecular weight 200,000 can be calculated, so that finally the extension of polystyrene in these solutions can be derived from the values of $[\eta]$ and a(5). The measurement of viscosity was carried out by the use of a viscometer of Ostwald type. The concentration of the solution was determined by weighing the high polymer residue after a known quantity of solution was dried by evacuation and

Table VIII. Intrinsic viscosity $[\eta]$ and root mean square end-to-end distance $(\langle r^2\rangle)^{1/2}$ of polystyrene with molecular weight 200,000.

Solvent	$[\eta]$ g/cc	a	$(\langle r^2\rangle)^{1/2}$ Å
Benzene	85.5	0.66	320
Toluene	82.0	0.59	290
Xylene	74.0	0.52	253
Styrene	84.5	0.62	303
Ethylbenzene	77.5	0.50	256

heating. Experimental results are shown in Table VIII.

§ 6. Discussion

As already stated (§ 1), the mean square end-to-end distance $\langle r^2\rangle$ of high polymer molecule in solution must be a monotone decreasing function of ΔE. As can be seen from Tables III–VII, it is only the case where benzene is assumed as the chain element equivalent that $\langle r^2\rangle$ comes out a monotone decreasing function of ΔE (cf. Tables VII and VIII). It may therefore be inferred that, in so far as the solvent molecules are non-polar, the extension of polystyrene is determined mainly by the intermolecular interaction between the benzene group, which is bound on the side of the main chain of polystyrene, and solvent molecules.

That the benzene group acts as a substitute for the chain element of polystyrene may be interpreted as follow; If the structural chain element of polystyrene were free, its nearest neighbor sites (usually 12) should be all equivalent to one another and capable of admitting any other element (chain element or solvent molecule) into them: But the nearest neighbor sites of actual chain element are not all equivalent with respect to the chain element, since some of them are already occupied. The remaining sites which are capable of admitting any other element are perhaps for the most part identical in character with the nearest neighbors of benzene. This may probably be the reason why benzene molecules show a behavior similar to the chain elements of polystyrene.

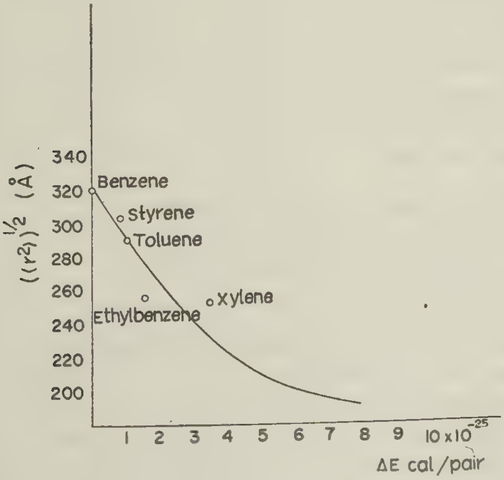

Fig. 5. Relation between root mean square end-to-end distance and energy change by mixing for polystyrene (M.W.: 200,000).
Full line: Theoretical curve ($\sigma=12$, N=1923)
Circle : 1/40 of observed values

The next step to be taken is to compare the relation between ΔE and $\langle r^2\rangle$ with the theory quantitatively. In Fig. 5 the full line gives the theoretical curve and circles give the observed values of ΔE multiplied by 1/40. Theoretical values are those calculated numerically from Eq. (1), where as the lower limit of integration is taken the value of r which is computed from the radius R of a hypothetical sphere considered to consist of close-packed chain elements by the relation based on the random fleight model

$$\langle R^2\rangle=\frac{1}{6}\langle r^2\rangle\,, \tag{22}$$

and as the upper limit is taken the value of the end-to-end distance of the chain with the elements lined up straight. The constants in Eq. (1) are estimated to be: $\sigma=12$, $N=1923$, $\nu=2{,}566\times10^{21}$ and $\tau=0.285$.

The fact that the experimental values of ΔE multiplied by 1/40 come out to fit the theoretical curve fairly well may be interpreted as follows:

(1) For the chain elements constituting a chain some of the configurations of the pairs of "chain element-chain element" and of "chain element-solvent molecule" will be frustrated on account of the steric hindrance by the neighboring chain elements, so that the effective number of the nearest neighbors around a chain element must be less than $\sigma=12$. The diminution in σ-value causes theoretical value of ΔE as calculated by Eq. (1) to increase so that the curve in Fig. 5 should be displaced to the right.

(2) It is generally regarded as true that

the high polymer molecule in solution assumes the form of a thread ball, the density of the chain elements at a point within the ball being the larger, the nearer it approaches the center. Thus, the solvent molecules are more or less prevented from penetrating into the ball; that is to say, it becomes impossible for the chain elements near the center to make free contact with solvent molecules. Consequently, the effective number of chain elements should be considered to be less than $N=1923$. The decrease in N-value also leads to the displacement of the curve in Fig. 5 to the right.

(3) The steric hindrance stated in (1) will cause the destruction of low energy configurations along with the diminution in the number of geometrical nearest neighbors. This implies that the values of ΔE to be observed when the high polymer (polystyrene) is dissolved in various solvents should be smaller than those observed in the present experiment.

Acknowledgments

The author wishes to express his hearty thanks to prof. T. Hori and Prof. J. Furuichi for kind discussion on the present subject. He is also indebted to Mr. I. Asai, Mr. K. Nemoto, Mr. M. Akiyama and Mr. T. Abe for kind assistance and to Mr. T. Noguti and Mr. Y. Kabashima for laborious preparation of the apparatus.

References

1) H. Mizutani: J. Phys. Soc. Japan **15** (1960) 475.
2) G. Scatchard: Trans. Faraday Soc. **33** (1937) 160.
3) G. H. Cheesman and A. M. Beryl Whitaker: Proc. Roy. Soc. London A **212** (1952) 406.
4) P. C. Pepper: J. Polymer Sci. **7** (1951) 347.
5) P. Debye and A. M. Bueche: J. Chem. Phys. **16** (1948) 573.

JOURNAL OF THE PHYSICAL SOCIETY OF JAPAN Vol. 16, No. 2, FEBRUARY, 1961

Proton Magnetic Resonance of Ice Single Crystal

By Kiyoshi KUME
The Institute for Solid State Physics,
University of Tokyo, Tokyo
and Ryosuke HOSHINO
Department of Physics, Faculty of Science,
Hokkaido University, Sapporo

(Received September 10, 1960)

The single crystal of ice was examined by proton magnetic resonance method, and the result was shown to be consistent with Pauling model. The problem of whether the arrangements of protons is ordered or not is, however, still open to the question.

The structure of heavy ice has been investigated by Peterson and Levy[1] by neutron diffraction and the result is found to be consistent with Pauling model[3]. We examined the ice single crystal by proton magnetic resonance method and obtained the result which is again consistent with the model.

The sample was kindly provided by Dr. K. Arakawa. The crystal was examined by the etch-pit method[2]. The etch-pits developed on the surface perpendicular to the c-axis are reproduced in Fig. 1. All of them are regular hexagonal as is expected from the hexagonal crystal lattice of ice. It may safely be concluded that the crystal is quite single and the c-axis is almost parallel throughout the crystal. A cylindrical specimen about 10 mm in diameter and 15 mm in height, the axis of which was perpendicular to the c-axis, was cut from the central part of the original single crystal of

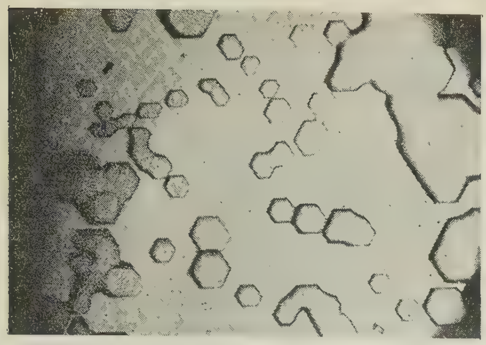

Fig. 1. Ech-pits on the ice single crystal.

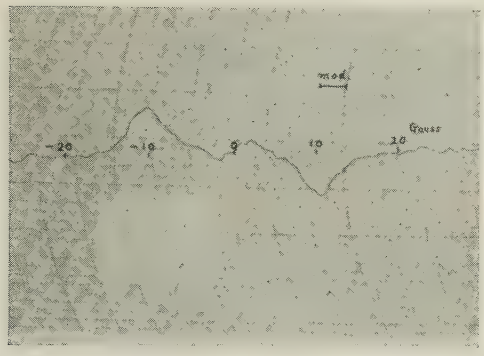

Fig. 2. Derivative of absorption curve of ice single crystal when the magnetic field is applied parallel to the c-axis ($\theta=0°$).
Sample: Ice single crystal, see the text for details
Field: 5630 Gauss
Field sweep: about 3 Gauss/min
Frequency: 24.0 MC
R.f. Field within sample coil: about 50 microgauss
Time constant: about 10 sec
Temperature: 93°K

about 200 mm in diameter and 70 mm in height.

Fig. 2 shows an example of the results. The external magnetic field was applied parallel to the c-axis, within the accuracy of 5 degrees. The temperature was kept as low as $-180°C$, and H_1 was cut down to as low as about 50 microgauss to avoid saturation. A Twin-T bridge-type detector was used throughout this experiment. The upper part of Fig. 3 shows the angular dependence of the absorption, where the external field makes the angle θ from the c-axis in the plane which contains the c-axis and a direction that makes the angle of about 20 degrees with an a-axis in the c-plane.

The calculations of line shapes were based upon Pauling model[3]: first, protons occupy the two among the four possible positions surrounding each oxygen, secondly, the protons lie on the lines connecting two oxygens, and thirdly, only one proton can exist on any oxygen-oxygen line closer to either of the two oxygen atoms at both ends. The assumption of the microscopic random occupation of protons among possible arrangements, however, are immaterial here, because the contribution to the second moment from neighboring protons, which must be used in the calculation of the actual line shape, is practically the same, whether these protons take random or ordered arrangements[4]. Then the number of possible interproton vectors are 18 in all; 6 of them are contained in a c-plane, the remaining 12 being contained in the cone, which is shown in Fig. 4. These interproton vectors were assumed to be equally

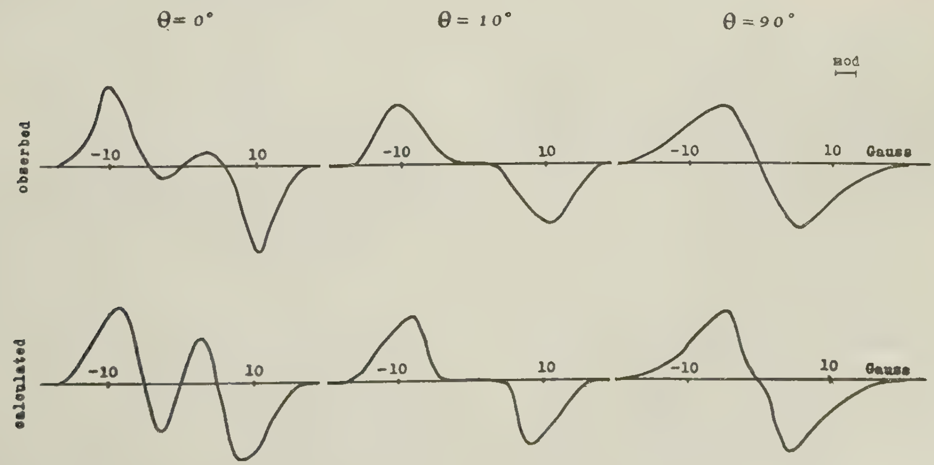

Fig. 3. Derivative of absorption curves of an ice single crystal. For the meaning of θ see text.

occupied throughout the whole specimen. Then the line shapes were able to be calculated by using the data on the interproton distance as well as the intermolecular contribution which were obtained by the powder experiment[4]. The results are shown in the lower part of Fig. 3. In view of the fact that the angular precision was rather poor, the agreement between observed and calculated curves is considered to be satisfactory.

Fig. 5 shows the motional narrowing. Although the experiment is rather qualitative, the general tendency is consistent with the powder experiment[4].

The authors express their hearty thanks to Prof. Y. Kakiuchi, who showed much interest on the experiment, and offered a chance to conduct it. We wish to thank Dr. K. Arakawa who kindly supplied the ice single crystal. We also thank Mr. H. Shimizu for his assistance in taking the etch-pits.

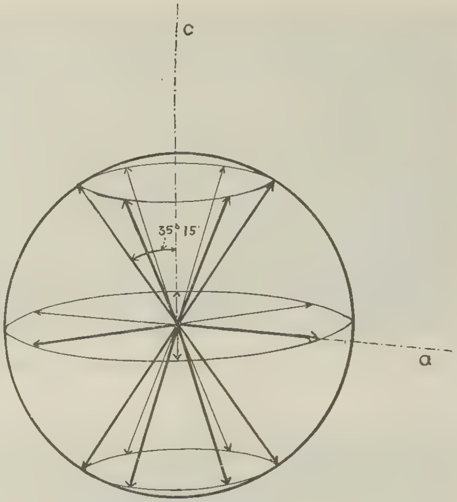

Fig. 4. Possible interproton vectors in ice crystal.

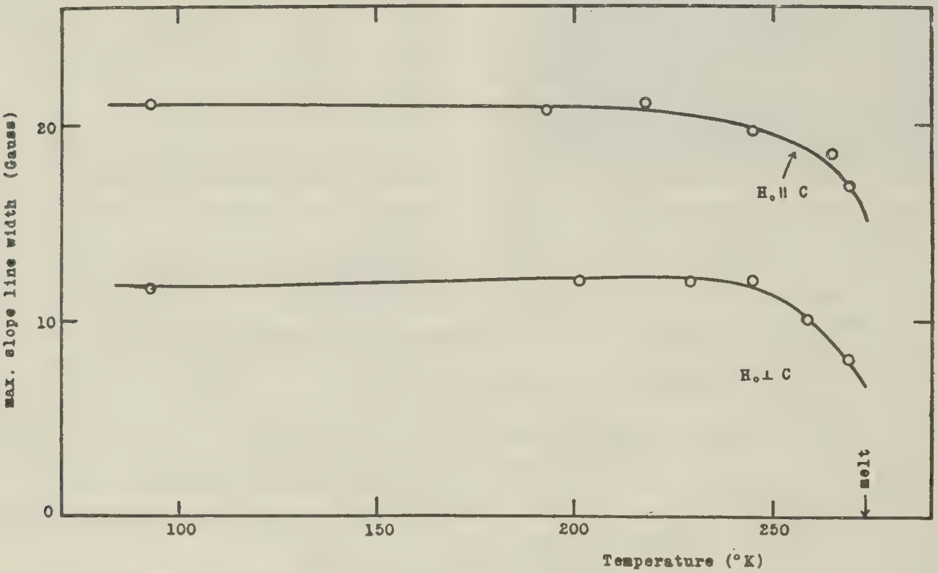

Fig. 5. Narrowing of absorption line of ice single crystal.

References

1) S. W. Peterson and H. Levy: Acta Cryst. **10** (1957) 70.
2) K. Higuchi: Acta Metallurgica **6** (1958) 636.
3) L. Pauling: J. Amer. Chem. Soc. **57** (1935) 2680.
4) K. Kume: J. Phys. Soc. Japan **15** (1960) 1493.

JOURNAL OF THE PHYSICAL SOCIETY OF JAPAN, Vol. 16, No. 2, FEBRUARY, 1961

Microwave Attenuation by Cyclotron Resonance in a Slightly Ionized Gas

By Taro DODO

Hitachi Central Research Laboratory, Kokubunji, Tokyo

(Received Oct. 25, 1960)

The Boltzmann equation is solved for the distribution function of electrons in a static uniform magnetic field $\boldsymbol{B}_0$ and a high frequency electric field. The tensor of dielectric constant and the propagation constant $\boldsymbol{k}$ are obtained from this solution. The calculations are made by neglecting the square of the amplitude of electric field for two cases: (1) $\boldsymbol{k}//\boldsymbol{B}_0$, (2) $\boldsymbol{k}\perp\boldsymbol{B}_0$.

The attenuation spectrum for the case (2) is not a Lorentzian type and its maximum occurs at the microwave frequency

$$\omega\simeq(\omega_c^2+\omega_p^2+\nu_m^2)^{1/2}\ .$$

If the electron density is high, the attenuation spectrum differs from a Lorentzian type even for the case (1).

§ 1. Introduction

For the measurement of plasma temperature (collision frequency), the electron cyclotron resonance method gives more accurate means than the usual microwave diagnostic technique[1], because the half width of the resonance spectrum gives directly the collision frequency. It is then desirable to establish the theory, which would enable us to analyse the results obtained by cyclotron resonance technique. Several works[2][3][4] pertaining to this topic have been published. They are, however, neither rigorous nor convenient for the comparison with the experiment.

Kelly, Margenau and Brown[2] had obtained the cyclotron resonance absorption spectrum by calculating the quantity $\langle \boldsymbol{J}\cdot\boldsymbol{E}\rangle_{time\ average}$. Because the electric field $\boldsymbol{E}$ used in the theory of K. M. B. is the incident external field, which does not include the induced electric field produced by the plasma current $\boldsymbol{J}$, their theory can be applied only to a dilute plasma, i.e. $\omega_p^2\ll\omega^2$. Drummond[3] had carried out more detailed calculations, but his analytical results were complicated and difficult to be interpreted intuitively. Also he had shown many numerical results about the refractive index, but he had aimed at a very dense and hot plasma, so his results were not appropriate to apply to a slightly ionized cold plasma used in ordinary laboratory experiments. Also both authors had introduced phenomenologically the collision frequency, the relation between the collision frequency and the differential collision cross section* had not been clarified. Recently, Kelly[4] has derived conductivity tensors including electron-electron collision, but he has not derived propagation constant. The quantities that should be compared with experiments are propagation constants and these are different for propagation directions in relations to the static magnetic field. K. M. B. and Kelly have assumed without any discussion that the distribution function is uniform in spatial coordinates. When an electromagnetic wave polarized normal to a static magnetic field propagates in normal direction to the static field, a longitudinal current and a longitudinal field are induced. By these longitudinal components the electron density will be made inhomogeneous in the propagation direction.

The "absorption" of the electromagnetic energy can be obtained by calculating the quantity σE^2, where $\boldsymbol{E}$ should include the field induced by the current flowing in the plasma. On the other hand, for the plasma diagnostics, we get the information about the density and the collision frequency of the plasma from the measurement of the "attenuation constant" and the phase shift. The

---

* Desloge, Matthysse and Margenau[5] had made some errors in the treatment of collision term in the Boltzmann equation. They had used the collision frequency instead of the momentum transfer collision frequency, which should be used in such a problem. Recently, Desloge and Matthysse[6] has carried out the correct treatment in this point.

"absorption" and the "attenuation" are not the same. Consider the propagation of microwave of frequency ω through a collision-free plasma without static magnetic field. If $\omega_p>\omega$, as is well known, the amplitude of the wave attenuates, although there is no absorption of the wave energy. Usual plasma diagnostic method is based on the measurement of this attenuation. From this reason, we aimed to derive the "attenuation constant". The attenuation constant is more complicated than the conductivity tensors when the wave propagates perpendicularly to the static field.

§ 2. Distribution Function

The Boltzmann equation is solved for the distribution function f of electrons in a static uniform magnetic field $\boldsymbol{B}_0$ directed in z-axis and a high frequency electromagnetic field, whose electric vector $\boldsymbol{E}$ is in the $x-y$ plane. The Boltzmann transfer equation is

$$\frac{\partial f}{\partial t}+\boldsymbol{v}\frac{\partial f}{\partial \boldsymbol{r}}+\boldsymbol{F}\frac{\partial f}{\partial \boldsymbol{v}}=\left(\frac{\partial f}{\partial t}\right)_{coll}, \tag{1}$$

where $\boldsymbol{F}$ is the Lorentz force and $(\partial f/\partial t)_{coll}$ is the change of distribution function by collisions. Taking the non-relativistic approximation and neglecting the quantities of the order of v/c, $\boldsymbol{F}$ is given by

$$\boldsymbol{F}=-\frac{e}{m}\boldsymbol{E}-\frac{e}{mc}(\boldsymbol{v}\times\boldsymbol{B}_0)\,. \tag{2}$$

In a slightly ionized gas, collisions of the electrons are mainly electron-neutral atom encounters. We neglect the electron-ion and electron-electron collisions and assume that $(\partial f/\partial t)_{coll}$ comes from the electron-neutral elastic collision only and the relative velocity of collision can be replaced by the electron velocity because of (atomic mass)$\gg$(electron mass). By these assumptions $(\partial f/\partial t)_{coll}$ becomes very simple in form. We can assume safely that ions are not influenced by the high frequency microwave field because of their large inertia. Further we neglect the quantities of the order of $\boldsymbol{E}^2$. This is the most essential and severe assumption* in this paper. This means that the increase of mean kinetic energy of electrons by the absorption of microwave energy is not taken into consideration. Actually, for the plasma diagnostics by the measurement of microwave attenuation, we must use the microwave of small amplitude in order that the plasma is not disturbed by the measuring means. Therefore, the neglect of the quantities of the order of $\boldsymbol{E}^2$ is a natural assumption.

With these assumptions we can treat rigorously the problem without ambiguity. To the first order of $\boldsymbol{E}$, we can put the distribution function f into the form

$$f=f_e+f_{odd}=f_e+v_xG_1+v_yG_2\equiv f_e+\boldsymbol{v}\boldsymbol{G}\,, \tag{4}$$

where f_e, G_1, and G_2 are functions of electron speed v. Since

$$\frac{\partial}{\partial \boldsymbol{v}}(f_e+\boldsymbol{v}\boldsymbol{G})=\frac{\boldsymbol{v}}{v}\left(\frac{\partial f_e}{\partial v}+\boldsymbol{v}\frac{\partial \boldsymbol{G}}{\partial v}\right)+\boldsymbol{G}\,, \tag{5}$$

substituting (4) into (1) gives

$$\frac{\partial f_e}{\partial t}+\boldsymbol{v}\frac{\partial \boldsymbol{G}}{\partial t}+\boldsymbol{v}\left(\frac{\partial f_e}{\partial \boldsymbol{r}}+\boldsymbol{v}\frac{\partial \boldsymbol{G}}{\partial \boldsymbol{r}}\right)-\frac{e}{m}\boldsymbol{E}\boldsymbol{G}$$
$$-\frac{e}{m}\boldsymbol{E}\frac{\boldsymbol{v}}{v}\left(\frac{\partial f_e}{\partial v}+\boldsymbol{v}\frac{\partial \boldsymbol{G}}{\partial v}\right)-\frac{e}{mc}(\boldsymbol{v}\times\boldsymbol{B}_0)\boldsymbol{G}=\left(\frac{\partial f}{\partial t}\right)_{coll}. \tag{6}$$

Substracting from (6) the expression obtained by replacing $\boldsymbol{v}$ with $-\boldsymbol{v}$ in (6), we obtain

$$\boldsymbol{v}\left[\frac{\partial \boldsymbol{G}}{\partial t}+\frac{\partial f_e}{\partial \boldsymbol{r}}-\frac{\partial \boldsymbol{E}}{m}\frac{1}{v}\frac{\partial f_e}{\partial v}-\frac{e}{mc}(\boldsymbol{B}_0\times\boldsymbol{G})\right]$$
$$=\left[\left(\frac{\partial f}{\partial t}\right)_{coll}\right]_{odd}, \tag{7}$$

where $[(\partial f/\partial t)_{coll}]_{odd}$ is the odd function part of $(\partial f/\partial t)_{coll}$ with respect to $\boldsymbol{v}$. Neglecting the terms containing (electron mass/neutral atom mass)$^{1/2}$, the right hand side of (7) becomes, as shown in Appendix I,

$$-\nu_m\boldsymbol{v}\boldsymbol{G}\,,$$

where ν_m is the collsion frequency for momentum transfer and is generally a function of v,

$$\nu_m=2\pi\iint(1-\cos\theta)f_n(\boldsymbol{v}_n)g\sigma(g,\theta)\sin\theta d\theta d\boldsymbol{v}_n\,, \tag{8}$$

where $f_n(\boldsymbol{v}_n)$ is the distribution function of neutral atoms, g is the relative velocity given by $g=|\boldsymbol{v}-\boldsymbol{v}_n|\simeq v$, and $\sigma(g,\theta)$ is the differential scattering cross section. Then (7) reduces to a simpler expression

$$\frac{\partial \boldsymbol{G}}{\partial t}-\frac{e}{mc}(\boldsymbol{B}_0\times\boldsymbol{G})+\nu_m\boldsymbol{G}=\frac{e\boldsymbol{E}}{m}\frac{1}{v}\frac{\partial f_e}{\partial v}-\frac{\partial f_e}{\partial \boldsymbol{r}}\,. \tag{9}$$

The solution of (9) is easily obtained by the change of variables

$$E_x+iE_y=E_+,\ E_x-iE_y=E_-,\ G_1+iG_2=G_+,\cdots\,. \tag{10}$$

---

[*] If the collision frequency ν_m is independent of the electron velocity, this assumption is unnecessary for the results derived in § 3(i).

By use of (10), (9) becomes

$$\frac{\partial G_\pm}{\partial t}\mp i\omega_c G_\pm+\nu_m G_\pm =\frac{e}{m}E_\pm\frac{1}{v}\frac{\partial f_e}{\partial v}-\left(\frac{\partial f_e}{\partial x}\pm i\frac{\partial f_e}{\partial y}\right), \tag{11}$$

where ω_c is the cyclotron frequency

$$\omega_c=eB_0/mc\ .$$

If E_+ and E_- vary as
$E_+=e_+\exp(-i\omega t)$, $E_-=e_-\exp(-i\omega t)$, (ω : real), (E_+ : ordinary wave, E_- : extraordinary wave), we obtain the soltuions of (11):

$$G_\pm=\left[\frac{eE_\pm}{m}\frac{1}{v}\frac{\partial f_e}{\partial v}-\left(\frac{\partial f_e}{\partial x}\pm i\frac{\partial f_e}{\partial y}\right)\right]\frac{1}{\nu_m-i(\omega\pm\omega_c)}, \tag{13}$$

and

$$G_1=\left[\frac{e}{m}\frac{1}{v}\frac{\partial f_e}{\partial v}\left\{(\nu_m-i\omega)E_x-\omega_c E_y\right\} -\frac{\partial f_e}{\partial x}(\nu_m-i\omega)+\frac{\partial f_e}{\partial y}\omega_c\right]\frac{1}{(\nu_m-i\omega)^2+\omega_c^2}, \tag{15}$$

$$G_2=\left[\frac{e}{m}\frac{1}{v}\frac{\partial f_e}{\partial v}\left\{\omega_c E_x+(\nu_m-i\omega)E_y\right\} -\frac{\partial f_e}{\partial x}\omega_c-\frac{\partial f_e}{\partial y}(\nu_m-i\omega)\right]\frac{1}{(\nu_m-i\omega)^2+\omega_c^2}. \tag{16}$$

$\partial f_e/\partial v$ of the first term on the right hand side of these expressions can be replaced under our assumption by $\partial f_0/\partial v$, f_0 being the zero-order quantity with respect to the perturbation $\boldsymbol{E}$, i.e. the Maxwell distribution in equilibrium.

§ 3. Propagation Constants (Dispersion Relations)

Calculations are carried out for two different cases, namely (i) when the propagation vector $\boldsymbol{k}$ is parallel to the z-axis, $\boldsymbol{k}//\boldsymbol{B}_0$, and (ii) when $\boldsymbol{k}$ is parallel to the x-axis, $\boldsymbol{k}\perp\boldsymbol{B}_0$. In both cases we treat a plane wave, so that $\partial f_e/\partial y=0$.

(i) $\boldsymbol{k}//\boldsymbol{B}_0$

In this case, $\partial f_e/\partial r\equiv 0$ because the electromagnetic wave propagates as a transverse wave. Using (13), we obtain the current $J_\pm$:

$$J_\pm=-e\int(v_x\pm iv_y)f dv=-(e/3)\int v^2 G_\pm dv =\frac{e^2E_\pm}{3kT}\int\frac{v^2}{\nu_m-i(\omega\pm\omega_c)}f_0 4\pi v^2 dv =\frac{ne^2}{3kT}E_\pm\left\langle\frac{v^2}{\nu_m-i(\omega\pm\omega_c)}\right\rangle. \tag{17}$$

When ν_m is independent* of v, we have, because of $\langle v^2\rangle=3kT/m$, from (17) the relationship

$$J_\pm=\frac{\omega_p^2}{4\pi}E_\pm\frac{1}{\nu_m-i(\omega\pm\omega_c)},\quad \omega_p^2=4\pi ne^2/m\ . \tag*{(17)$'$}$$

When ν_m is proportional to v, i.e. the collision cross section (mean free path) is independent of v, we can obtain an analytical expression and the result is shown in Appendix II. The numerical results is nearly the same as (17)$'$.

By use of (10), the Maxwell equations are rewritten as follows:

$$\left.\begin{aligned} i\frac{\partial H_\pm}{\partial z}&=\frac{1}{c}\frac{\partial E_\pm}{\partial t}+\frac{4\pi}{c}J_\pm\ ,\\ i\frac{\partial E_\pm}{\partial z}&=-\frac{1}{c}\frac{\partial H_\pm}{\partial t}\ .\end{aligned}\right\} \tag{20}$$

Eliminating $H_\pm$ from these equations and substituting (17) into $J_\pm$, we obtain the scalar dielectric constants ε_+ and ε_- for the ordinary and extraordinary waves:

$$\frac{\partial^2 E_\pm}{\partial z^2}=\frac{1}{c^2}\left(\frac{\partial^2 E_\pm}{\partial t^2}+4\pi\frac{\partial J_\pm}{\partial t}\right)\equiv\frac{\varepsilon_\pm}{c^2}\frac{\partial^2 E_\pm}{\partial t^2}\ . \tag{21}$$

As stated at the begining of this subsection, in the case of $\boldsymbol{k}//\boldsymbol{B}_0$ the electron density is independent of the spatial coordinates and so $\partial n/\partial t=0$, $\partial J_\pm/\partial t\propto n(\partial E_\pm/\partial t)$. Then we obtain

$$\varepsilon_\pm=1-\frac{1}{3\lambda_D^2}\frac{1}{\omega}\left\langle\frac{\omega\pm\omega_c-i\nu_m}{(\omega\pm\omega_c)^2+\nu_m^2}v^2\right\rangle, \tag{22}$$

where λ_D is the Debye length and $\lambda_D=(kT/4\pi ne^2)^{1/2}$. When ν_m is independent of v, the above expression comes to

$$\varepsilon_\pm=1-\eta\frac{1\pm\gamma-i\beta}{(1\pm\gamma)^2+\beta^2}, \tag*{(22)$'$}$$

where $\eta=\omega_p^2/\omega^2$, $\gamma=\omega_c/\omega$, $\beta=\nu_m/\omega$.

Substituting

$$\left.\begin{aligned} E_\pm&=E_{\pm 0}\exp i(k_\pm z-\omega t)\ ,\\ k_\pm&=k_{\pm r}+ik_{\pm i}\end{aligned}\right\} \tag{24}$$

into (21), we obtain the real and imaginary parts of propagation constants:

$$\begin{aligned} k_{\pm r}&=k_0(|\varepsilon_\pm|+\varepsilon_{\pm r})^{1/2}/(2)^{1/2}\ ,\\ k_{\pm i}&=k_0(|\varepsilon_\pm|-\varepsilon_{\pm r})^{1/2}/(2)^{1/2}\ ,\quad k_0=\omega/c\ .\end{aligned} \tag{25}$$

---

* If ν_m is independent of v, we get (17)$'$ by the partial integration:

$$\int v\frac{\partial f_e}{\partial v}\frac{1}{\nu_m-i(\omega\pm\omega_c)}4\pi v^2 dv =-\frac{3}{\nu_m-i(\omega\pm\omega_c)}\int f_e 4\pi v^2 dv =-3n/[\nu_m-i(\omega\pm\omega_c)]\ .$$

Therefore, f_e is not necessarily the Maxwell distribution, namely the assumption stated at the last section, the neglect of quantities of the order of $\boldsymbol{E}^2$, is unnecessary.

The attenuation constant $k_{//}$ of wave energy for the linearly polarized wave propagating parallel to the static magnetic field is

$$k_{//}=-\frac{1}{|E_{+}E_{-}|}\frac{\partial}{\partial z}|E_{+}E_{-}|=k_{+i}+k_{-i}\quad \text{nepers/cm.} \tag{26}$$

In the case of a plasma of extremely low density ($\omega_p^2\ll\omega^2$), we expand the square root of (25) into a power series of ω_p^2/ω^2 and take the first term only, then we get the well-known Lorentzian spectrum:

$$k_{//}=\frac{1}{6\lambda_D^2 c}\left[\left\langle\frac{\nu_m}{(\omega+\omega_c)^2+\nu_m^2}v^2\right\rangle+\left\langle\frac{\nu_m}{(\omega-\omega_c)^2+\nu_m^2}v^2\right\rangle\right]\quad \text{for } \omega_p^2\ll\omega^2\,. \tag{27}$$

When ν_m is independent of v, (27) becomes

$$k_{//}=\frac{\omega_p^2}{2c}\left[\frac{\nu_m}{(\omega+\omega_c)^2+\nu_m^2}+\frac{\nu_m}{(\omega-\omega_c)^2+\nu_m^2}\right]\quad \text{for } \omega_p^2\ll\omega^2\,. \tag{27$'$}$$

This expression is already given by K. M. B.[2] from the calculation of conductivity tensor σE^2.

When the value of ν_m is not extremely large, the attenuation spectrum (27)′ has the maximum at $\omega=\omega_c$ and has a symmetrical shape about $\omega=\omega_c$. For a plasma of not extremely low density ($\omega_p^2\gtrsim\omega^2/10$), the attenuation spectrum numerically calculated from (22)′ and (25) has a maximum at $(\omega)_{\max}>\omega_c$ and has an assymmetrical shape about $(\omega)_{\max}$. A numerical example is shown in Fig. 1.

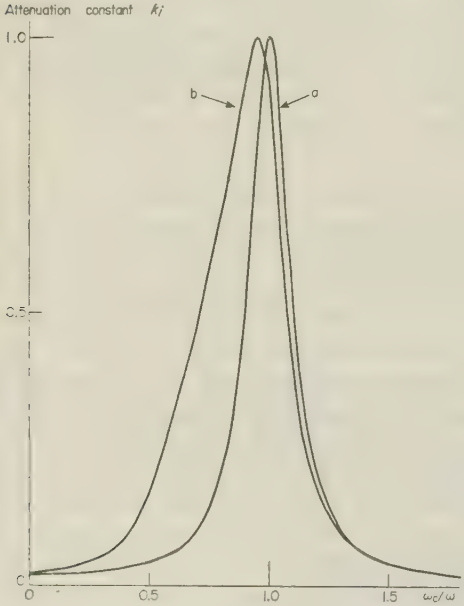

Fig. 1. Attenuation spectra of a Lorentzian type and an exact one as a function of magnetic field strength ω_c/ω.
(a): Calculated by (27)′. $\omega_p^2\ll\omega^2$, $\nu_m/\omega=0.1$.
(b): Calculated by (22)′ and (25). $\omega_p^2=0.5\omega^2$, $\nu_m/\omega=0.1$.
The collision frequency is the same for both cases. The normalization factors are adjusted so as to give the same peak height.

(ii) $\boldsymbol{k}\perp\boldsymbol{B}_0$

In this case, even when the incident microwave has E_y component only, a longitidinal component E_x is produced in the plasma by the current J_x produced by E_y and $\boldsymbol{B}_0$.

The first term of the current obtained by using (15) is a current J_E produced by the electric field and its second term containing $\partial f_e/\partial x$ is a current J_D produced by diffusion. One can prove (as shown in Appendix III*)

$$(J_E/J_D)\propto(\lambda'/\lambda_D)^2\,, \tag{28}$$

where λ' is the wave length of the microwave. Therefore, in case of $(\lambda'/\lambda_D)^2\gg1$, the term containing $\partial f_e/\partial x$ can be neglected. In laboratory experiments, λ_D is usually of the order of 10^{-2} cm and so the condition $(\lambda'/\lambda_D)^2\gg1$ is well established.

On these grounds, calculations are carried out neglecting the term containing $\partial f_e/\partial x$. Currents J_x and J_y are obtained from (15) and (16):

$$\begin{aligned}J_x&=-e\int v_x f dv=-e\int v_x^2 G_1 dv\\&=\frac{ne^2}{3kT}\left[\left\langle\frac{\nu_m-i\omega}{(\nu_m-i\omega)^2+\omega_c^2}v^2\right\rangle E_x-\left\langle\frac{\omega_c}{(\nu_m-i\omega)^2+\omega_c^2}v^2\right\rangle E_y\right],\end{aligned} \tag{29}$$

$$J_y=\frac{ne^2}{3kT}\left[\left\langle\frac{\omega_c}{(\nu_m-i\omega)^2+\omega_c^2}v^2\right\rangle E_x+\left\langle\frac{\nu_m-i\omega}{(\nu_m-i\omega)^2+\omega_c^2}v^2\right\rangle E_y\right]. \tag{30}$$

Substituting these expressions into the Maxwell equation

$$(\Delta^2-\text{grad div})\boldsymbol{E}=\frac{1}{c^2}\left(\frac{\partial^2\boldsymbol{E}}{\partial t^2}+4\pi\frac{\partial\boldsymbol{J}}{\partial t}\right), \tag{31}$$

we obtain the dielectric tensor $\overleftrightarrow{\varepsilon}$. In this calculation, the term $\partial\boldsymbol{J}/\partial t$ is composed of two terms:

$$\frac{\partial\boldsymbol{J}}{\partial t}\propto\frac{\partial n}{\partial t}\boldsymbol{E}+n\frac{\partial\boldsymbol{E}}{\partial t}\,.$$

---

* This discussion was suggested by Professor T. Kihara of Tokyo University.

The first term $(\partial n/\partial t)\boldsymbol{E}$ is the quantity of the order of $\boldsymbol{E}^2$ and can be neglected from our assumption. Then

$$\frac{1}{c^2}\left(\frac{\partial^2 \boldsymbol{E}}{\partial t^2}+4\pi\frac{\partial \boldsymbol{J}}{\partial t}\right)\equiv\frac{\overset{\leftrightarrow}{\varepsilon}}{c^2}\frac{\partial^2 \boldsymbol{E}}{\partial t^2}\,, \tag{32}$$

$$\left.\begin{aligned}
&\varepsilon_{xx}=\varepsilon_{yy}=1-\frac{1}{3\lambda_D^2}\frac{1}{\omega}\left\langle\frac{\omega+i\nu_m}{(\omega+i\nu_m)^2-\omega_c^2}v^2\right\rangle,\\
&\varepsilon_{xy}=-\varepsilon_{yx}=i\frac{1}{3\lambda_D^2}\frac{\omega_c}{\omega}\left\langle\frac{v^2}{(\omega+i\nu_m)^2-\omega_c^2}\right\rangle,\\
&\varepsilon_{xz}=\varepsilon_{yz}=\varepsilon_{zx}=\varepsilon_{zy}=0\,,\\
&\varepsilon_{zz}=1-\frac{1}{3\lambda_D^2}\frac{1}{\omega}\left\langle\frac{v^2}{\omega+i\nu_m}\right\rangle.
\end{aligned}\right\} \tag{33}$$

In the case of plane wave propagating along the x-axis, i.e. $\partial\boldsymbol{E}/\partial y=\partial\boldsymbol{E}/\partial z=0$, (31) and (32) are

$$0=\frac{1}{c^2}\left[\varepsilon_{xx}\frac{\partial^2 E_x}{\partial t^2}+\varepsilon_{xy}\frac{\partial^2 E_y}{\partial t^2}\right],$$

$$\frac{\partial^2 E_y}{\partial x^2}=\frac{1}{c^2}\left[\varepsilon_{yx}\frac{\partial^2 E_x}{\partial t^2}+\varepsilon_{yy}\frac{\partial^2 E_y}{\partial t^2}\right].$$

Eliminating E_x from these equations, we obtain the effective scalar dielectric constant ε for E_y propagating along the x-axis:

$$\frac{\partial^2 E_y}{\partial x^2}=\frac{\varepsilon}{c^2}\frac{\partial^2 E_y}{\partial t^2}\,,$$

$$\begin{aligned}
\varepsilon&=\varepsilon_{yy}-\varepsilon_{yx}\varepsilon_{xy}/\varepsilon_{xx}\\
&=1-\frac{1}{3\lambda_D^2}\frac{1}{\omega^2}\left[\left\langle\frac{1+i\beta}{(1+i\beta)^2-\gamma^2}v^2\right\rangle\right.\\
&\qquad\left.+\frac{\dfrac{1}{3\lambda_D^2}\dfrac{\gamma^2}{\omega^2}\left\langle\dfrac{v^2}{(1+i\beta)^2-\gamma^2}\right\rangle^2}{\left\{1-\dfrac{1}{3\lambda_D^2}\dfrac{1}{\omega^2}\left\langle\dfrac{1+i\beta}{(1+i\beta)^2-\gamma^2}v^2\right\rangle\right\}}\right].
\end{aligned} \tag{34}$$

If ν_m is independent of v, the above expression becomes

$$\varepsilon=1-\eta\frac{1-\eta+i\beta}{(1-\eta-\beta^2-\gamma^2)+i\beta(2-\eta)}\,. \tag{34$'$}$$

Substituting this dielectric constant (34) or (34)′ into (25) instead of $\varepsilon_\pm$, we obtain the propagation constant for E_y. Because this expression is lengthy*, we show the numerical results for the cases of $\eta=0.1$, 0.3, 0.5, 2.0: $\beta=0.1$ in Fig. 2, as an example. The attenuation spectra were calculated numerically by using (34)′ for various combinations of η and β. From these calculations, we found that the half width was given by $2\nu_m$ in good accuracy when $\eta\lesssim 0.3$ and $\beta\lesssim 0.3$. And the maximum of attenuation spectrum occured, as expected from (34)′, at $(\gamma)_{\max}$;

$$(\gamma)_{\max}\simeq(1-\eta-\beta^2)^{1/2}\,. \tag{35}$$

From another point of view, the microwave frequency $(\omega)_{\max}$ at which the attenuation spectrum attains a maximum is given by, instead of ω_c,

$$(\omega)_{\max}\simeq(\omega_c^2+\omega_p^2+\nu_m^2)^{1/2}\,. \tag{36}$$

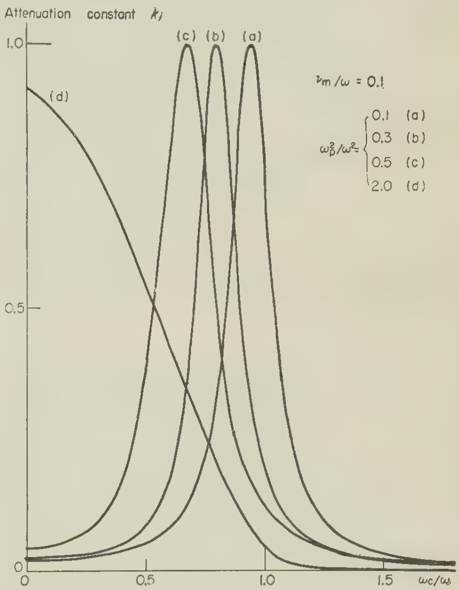

Fig. 2. Attenuation spectra of the microwave propagating normal to the static magnetic field. In this figure the microwave frequency ω is fixed and the cyclotron frequency (field strength) ω_c is varied. The resonance maximum $(\omega_c)_{\max}$ is given by

$$(\omega_c)_{\max}\simeq(\omega^2-\omega_p^2-\nu_m^2)^{1/2}\,.$$

The normalization factors of (a), (b), (c) are adjusted so as to give the same peak height.

The appearance of ω_p^2 in the denominator of the expression (34)′ of the dielectric constant results from the fact that in the case of $\boldsymbol{k}\perp\boldsymbol{B}_0$ the electric field has a longitudinal component leading to fluctuation of the electron density. This density fluctuation is in close connection with the plasma oscillation.

In order to see a characteristic feature for the case of $\boldsymbol{k}\perp\boldsymbol{B}_0$, the relation between the phase velocity V and the frequency ω is shown in Fig. 3 for the particular case of $\nu_m=0$.

---

* Mr. S. Tanaka[7] of Kyoto University has shown an approximate expression for the case of $\omega_p^2\ll\omega^2$ and he has given many numerical examples for this case.

The phase velocity V is given by the relation

$$\left(\frac{V}{c}\right)^2=\varepsilon^{-1}\fallingdotseq\left(1-\frac{\omega_p{}^2}{\omega^2}\frac{\omega^2-\omega_p{}^2}{\omega^2-\omega_p{}^2-\omega_c{}^2}\right)^{-1}. \quad (37)$$

This figure should be compared with the Figures 4.1 and 4.2 in Spitzer's text[8]. In the case of $\omega_p>\omega_c$ (Fig. 3(a)), the phase velocity is similar to that of an ordinary wave. In the case of $\omega_c>\omega_p$ (Fig. 3 (b)), the difference between $\boldsymbol{k}//\boldsymbol{B}_0$ and $\boldsymbol{k}\perp\boldsymbol{B}_0$ is remarkable and the phase velocity has the characteristics of both an ordinary wave and an extraordinary wave. With regard to experiments, if an experiment is carried out by changing the microwave frequency and fixing the static magnetic field strength, a maximum of attenuation occurs at very low frequency $\omega\simeq\omega_p{}^2/\omega_c$ as well as at $\omega\simeq(\omega_c{}^2+\omega_p{}^2)^{1/2}$. On the other hand, the maximum occurs at only one point $\omega_c\simeq(\omega^2-\omega_p{}^2)^{1/2}$ when the magnetic field is varied keeping the frequency constant.

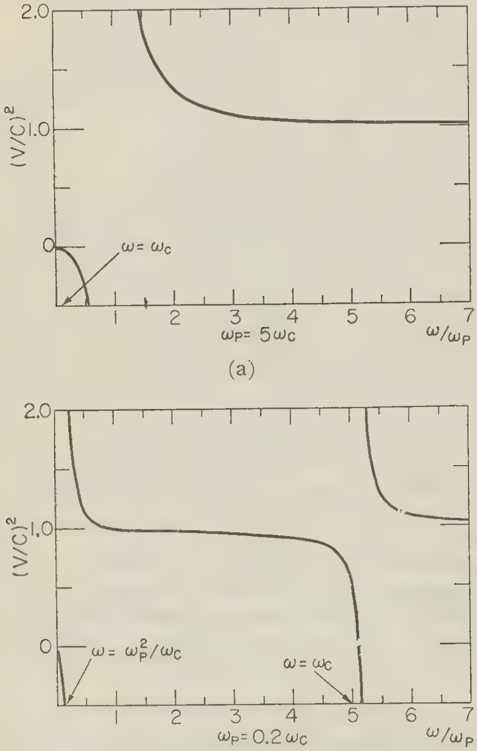

Fig. 3. Dispersion curves for $\nu_m=0$ for the electromagnetic wave propagating normal to the static field. (a): $\omega_p=5\omega_c$, (b): $\omega_p=0.2\omega_c$

§ 4. Conclusion

In this article a theory of cyclotron resonance appropriate to the plasma diagnostics is constructed rigorously with the definite assumption which should be reasonable for the ordinary diagnostic experiments.

The main results are the following two. First, the dielectric tensor is derived from the Boltzmann equation without ambiguity. The collision frequency ν_m, which is treated ambiguously by many authors, is clearly defined and an analytical expression for dielectric tensor is derived when ν_m depends on the electron velocity. It is clarified that the dependence of distribution function on the space coordinates, which is in usual treatment ignored without comment, can be neglected when the wave length of the electromagnetic wave is larger than the Debye length.

Second, the "attenuation spectrum" of microwave is represented as a function of the magnetic field strength. In a rather dense plasma, even for an extraordinary wave, the attenuation spectrum is considerably different from the absorption spectrum calculated by Kelly, Margenau and Brown[2] using the conductivity tensor. (See Fig. 1.) This difference becomes even more pronounced for the wave propagating normal to the magnetic field. This is attributed to the fact that the electromagnetic wave has a longitudinal component. The main feature is the shift of resonance maximum point of attenuation spectrum from $\omega=\omega_c$ as shown in (35) and (36). Nevertheless, for the case of $\boldsymbol{k}\perp\boldsymbol{B}_0$ the collision frequency is found to be given by the half width of attenuation spectrum in good accuracy. The density of plasma can be determined by the peak position using expression (35) as well as by the ordinary method where the peak height is used.

This theory is in good agreement with experiments.[9] [10]

The author is greatly indebted to Mr. S. Tanaka of Kyoto University who suggested this problem and gave valuable discussions. He wishes also to express his sincere thanks to Professor T. Kihara of Tokyo University for his valuable advices and suggestions on the rigorous treatment of the Boltzmann equation. He is deeply obliged to Miss. Y. Nakamura for her performance of numerical calculations and to Mr. K. Matsuoka for his discussions.

Appendix I Change of the Distribution Function by Collisions

As is well known, when the electron-neutral atom collision alone is taken into account, $(\partial f/\partial t)_{coll}$ is

$$\left(\frac{\partial f}{\partial t}\right)_{coll} = \iint [f_n(\boldsymbol{v}_n')f(\boldsymbol{v}')-f_n(\boldsymbol{v}_n)f(\boldsymbol{v})]g\sigma(g,\theta)d\Omega d\boldsymbol{v}_n\,. \tag{A. I. 1}$$

Let $W(\boldsymbol{v},\boldsymbol{v}')d\boldsymbol{v}'$ be the probability that an electron having a velocity $\boldsymbol{v}$ gets a velocity between $\boldsymbol{v}'$ and $\boldsymbol{v}'+d\boldsymbol{v}'$ after a collision. Using W, (A. I. 1) is rewritten as follows:

$$\left(\frac{\partial f}{\partial t}\right)_{coll} = \int [f(\boldsymbol{v}')W(\boldsymbol{v}',\boldsymbol{v})-f(\boldsymbol{v})W(\boldsymbol{v},\boldsymbol{v}')]d\boldsymbol{v}'\,. \tag{A. I. 2}$$

There is no anisotropy of space with respect to collision:

$$W(\boldsymbol{v},\boldsymbol{v}')=W(-\boldsymbol{v},-\boldsymbol{v}') \tag{A. I. 3}$$

The right hand side of (7) is

$$\left[\left(\frac{\partial f}{\partial t}\right)_{coll}\right]_{odd} = \frac{1}{2}\int [f(\boldsymbol{v}')\{W(\boldsymbol{v}',\boldsymbol{v})-W(\boldsymbol{v}',-\boldsymbol{v})\} -f(\boldsymbol{v})W(\boldsymbol{v},\boldsymbol{v}')+f(-\boldsymbol{v})W(-\boldsymbol{v},\boldsymbol{v}')d\boldsymbol{v}]' \tag{A. I. 4}$$

Using the decomposition (4) and (A. I. 3), we get for each term in (A. I. 4)

$$\begin{aligned}\int f_e(v')\{W(\boldsymbol{v}',\boldsymbol{v})-W(\boldsymbol{v}',-\boldsymbol{v})\}d\boldsymbol{v}' &= \int f_e(v')\{W(\boldsymbol{v}',\boldsymbol{v})-W(-\boldsymbol{v}',\boldsymbol{v})\}d\boldsymbol{v}' \\ &= \int f_e(v')\{W(\boldsymbol{v}',\boldsymbol{v})-W(\boldsymbol{v}',\boldsymbol{v})\}d\boldsymbol{v}' \\ &\qquad (\because \text{change of variable}) \\ &= 0\,,\end{aligned}$$

$$\int f_e(v)\{W(\boldsymbol{v},\boldsymbol{v}')-W(-\boldsymbol{v},\boldsymbol{v}')\}d\boldsymbol{v}'=0\,,$$

$$\frac{1}{2}\int \boldsymbol{v}'\boldsymbol{G}(v')\{W(\boldsymbol{v}',\boldsymbol{v})-W(\boldsymbol{v}',-\boldsymbol{v})\}d\boldsymbol{v}' = \int \boldsymbol{v}'\boldsymbol{G}(v')W(\boldsymbol{v}',\boldsymbol{v})d\boldsymbol{v}'\,,$$

$$-\frac{1}{2}\int \boldsymbol{v}\boldsymbol{G}(v)\{W(\boldsymbol{v},\boldsymbol{v}')+W(-\boldsymbol{v},\boldsymbol{v}')\}d\boldsymbol{v}' = -\int \boldsymbol{v}\boldsymbol{G}(v)W(\boldsymbol{v},\boldsymbol{v}')d\boldsymbol{v}'\,.$$

Then, (A. I. 4) becomes

$$\left[\left(\frac{\partial f}{\partial t}\right)_{coll}\right]_{odd} = -\int [\boldsymbol{v}\boldsymbol{G}(v)W(\boldsymbol{v},\boldsymbol{v}')-\boldsymbol{v}'\boldsymbol{G}(v')W(\boldsymbol{v}',\boldsymbol{v})]d\boldsymbol{v}'\,, \tag{A. I. 5}$$

$$= -\int [\boldsymbol{v}\boldsymbol{G}(v)f_n(\boldsymbol{v}_n)-\boldsymbol{v}'\boldsymbol{G}(v')f_n(\boldsymbol{v}'_n)]g\sigma(g,\theta)d\Omega d\boldsymbol{v}_n. \tag{A. I. 6}$$

In a slightly ionized plasma, the temperature of neutral atoms equals to at most the electron temperature, i.e.

$$|\boldsymbol{v}_n| \lesssim (m/M)^{1/2}|\boldsymbol{v}|\,. \tag{A. I. 7}$$

$(m/M)^{1/2}$ is the order of 10^{-2}, we expand $\boldsymbol{v}'$ and $\boldsymbol{v}_n'$ into a power series of $(m/M)^{1/2}$:

$$\boldsymbol{v}_n'=\boldsymbol{v}_n[1+\mathrm{O}(m/M)^{1/2}]\,, \tag{A. I. 8}$$

$$\boldsymbol{v}'=\boldsymbol{v}[\cos\theta+\mathrm{O}(m/M)^{1/2}] +|\boldsymbol{v}|\sin\theta[\boldsymbol{h}\cos\varphi+\boldsymbol{i}\sin\varphi]\,, \tag{A. I. 9}$$

where $\boldsymbol{h}$ and $\boldsymbol{i}$ are the unit vectors normal to $\boldsymbol{v}$. Substituting (A. I. 8) and (A. I. 9) into (A. I. 6) and neglecting the quantities of the order of $(m/M)^{1/2}$, we obtain

$$\left[\left(\frac{\partial f}{\partial t}\right)_{coll}\right]_{odd} = -\boldsymbol{v}\boldsymbol{G}\iint (1-\cos\theta)f_n(\boldsymbol{v}_n)g\sigma(g,\theta)d\Omega d\boldsymbol{v}_n\,, \tag{A. I. 10}$$

$$= -\boldsymbol{v}\boldsymbol{G}\nu_m(v)\,, \tag{A. I. 10$'$}$$

where we have used the fact that the second term of (A. I. 9) after integration by solid angle $d\Omega$ is zero. The quantity ν_m is the momentum transfer collision frequency, and is equal to the collision frequency only when the forward scattering is equal to the backward scattering, i.e. $\sigma(g,\theta)=\sigma(g,\pi-\theta)$.

Appendix II $J_\pm$ When ν_m is Proportional to v

If the cross section $\sigma(g,\theta)$ is independent of the relative velocity g and we neglect the terms containing $(m/M)^{1/2}$, ν_m becomes proportional to the electron velocity:

$$\nu_m = g\iint (1-\cos\theta)f_n(\boldsymbol{v}_n)\sigma(\theta)d\Omega d\boldsymbol{v}_n = N\sigma_m v = v/\lambda_m\,, \tag{A. II. 1}$$

where N is the number of neutral atoms per unit volume and σ_m and λ_m are the total cross section and the mean free path for momentum transfer, respectively. The integral (17) can be carried out analytically:

$$J_\pm = \frac{ne^2E_\pm}{3kT}\int \frac{\nu_m+i(\omega\pm\omega_c)}{\nu_m{}^2+(\omega\pm\omega_c)^2}\left(\frac{\alpha}{\pi}\right)^{3/2} \times \exp(-\alpha v^2)4\pi v^4 dv \tag{A. II. 2}$$

$$= \frac{\omega_p{}^2}{4\pi}E_\pm\frac{2}{3}\tau\left[\frac{2}{\pi^{1/2}}\{1-x^2+x^4\exp(x^2)E_1(x^2)\} +ix\{1-2x^2+4|x^3|\exp(x^2)\,\mathrm{Erfc}(|x|)\}\right], \tag{A. II. 3}$$

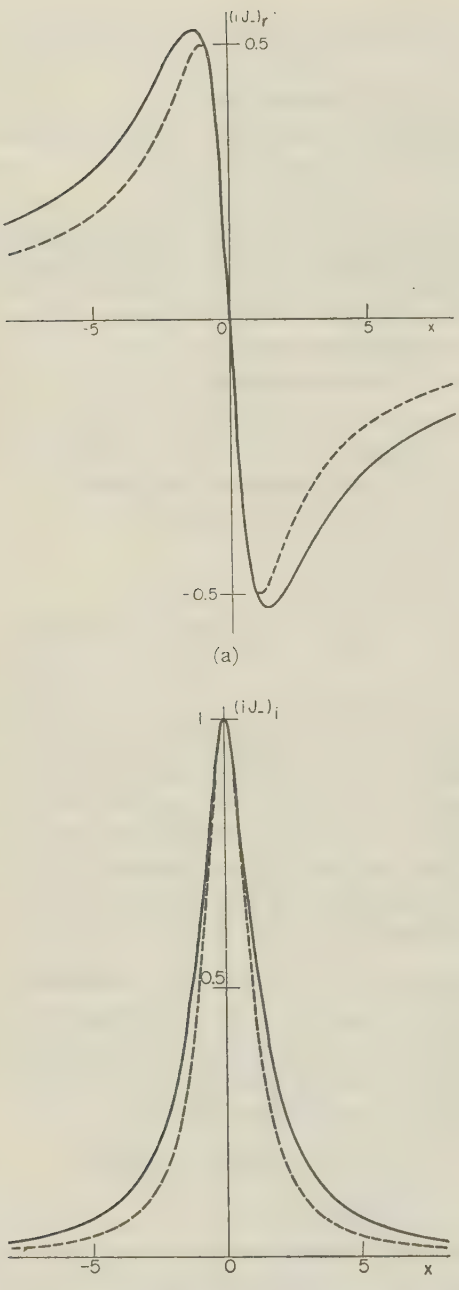

Fig. 4. The current J_- induced by the extraordinary wave is represented as a function of $x=\tau(\omega-\omega_c)$.

(a) Real part of iJ_-
Solid line: constant cross section, $x[1-2x^2+4|x^3|\exp(x^2)\,\mathrm{Erfc}(|x|)]$
Broken line: constant collision frequency, $x/(x^2+1)$

(b) Imaginary part of iJ_-
Solid line: constant cross section, $1-x^2+x^4\exp(x^2)\mathrm{E}_1(x^2)$
Broken line: constant collision frequency, $1/(x^2+1)$

where $\alpha=m/2kT$, mean collision time

$$\tau=\lambda_m/(2kT/m)^{1/2}\ ,$$

$$x=\tau(\omega\pm\omega_c)\ ,\quad \mathrm{E}_1(x)=\int_x^\infty \exp(-t)t^{-1}dt\ ,$$

$$\mathrm{Erfc}\,(x)=\int_x^\infty \exp(-t^2)dt\ .$$

The real and imaginary parts of iJ_- are plotted against $x=\tau(\omega-\omega_c)$ in Fig. 4 (a), (b). The current iJ_-' in the case of constant collision frequency (17)$'$ is also shown by a broken line in the same figure:

$$iJ_-'=-\frac{\omega_p{}^2}{4\pi}E_-\tau\frac{\tau(\omega-\omega_c)-i}{\tau^2(\omega-\omega_c)^2+1}\ ,\quad \tau=1/\nu_m\ .$$

From this figure, we can see that J_- in the case of constant cross section is almost the same as J_-' in the case of constant collision frequency.

Appendix III Current due to grad *f*

Let us compare J_E produced by the longitudinal field E_x with J_D produced by the density gradient $\partial f_e/\partial x$. By use of (15), J_E and J_D are given as follows:

$$J_E=-e\int v_x{}^2\frac{e}{m}\frac{1}{v}\frac{\partial f_0}{\partial v}E_x\frac{\nu_m-i\omega}{(\nu_m-i\omega)^2+\omega_c{}^2}4\pi v^2dv$$

$$=\frac{ne^2}{3kT}\left\langle\frac{\nu_m-i\omega}{(\nu_m-i\omega)^2+\omega_c{}^2}v^2\right\rangle E_x=ne\mu E_x\ , \tag{A. III. 1}$$

$$J_D=\frac{e}{3}\left\langle\frac{\nu_m-i\omega}{(\nu_m-i\omega)^2+\omega_c{}^2}v^2\right\rangle\frac{\partial n}{\partial x}$$

$$=e\frac{kT}{e}\mu\frac{\partial n}{\partial x}=eD\frac{\partial n}{\partial x}\ . \tag{A. III. 2}$$

We can see from the above equations that the Einstein's relation is valid in microwave region. Let the wave length of microwave be λ', we have relations of order estimation:

$$\frac{E_x}{\lambda'}\simeq\mathrm{div}\,\boldsymbol{E}=4\pi e(n-n_0)\ ,$$

$$\frac{\partial n}{\partial x}\simeq\frac{n-n_0}{\lambda'}\ ,$$

where n_0 is the equilibrium value of the density. Finally, we obtain the relation

$$J_E/J_D\simeq n_0e^2\mu4\pi(n-n_0)\lambda'/[kT\mu(n-n_0)/\lambda']$$

$$=4\pi e^2n_0\lambda'^2/kT=\lambda'^2/\lambda_D{}^2\ .$$

References

1) S. C. Brown: Proc. 2nd International Conf. Peaceful Uses of Atomic Energy, Geneva. Paper No. P/387 (1958).

2) D. C. Kelly, H. Margenau and S.C. Brown: Phys. Rev. **108** (1957) 1367.
3) J. E. Drummond: Phys. Rev. **110** (1958) 293, **112** (1958) 1460.
4) D. C. Kelly: Phys. Rev. **119** (1960) 27.
5) E. A. Desloge, S. W. Matthysse and H. Margenau: Phys. Rev. **112** (1958) 1437.
6) E. A. Desloge and S. W. Matthysse: Am. J. Phys. **28** (1960) 1.
7) S. Tanaka: Nuclear Fusion Research **4** (1960) 540, 550. (In Japanese)
8) L. Spitzer: *Physics of Fully Ionized Gases* (Interscience Publ. 1956) pp. 53∼54.
9) S. Tanaka: Nuclear Fusion Research **5** (1960) 283 (In Japanese)
10) T. Dodo: J. Phys. Soc. Japan (to be published)

JOURNAL OF THE PHYSICAL SOCIETY OF JAPAN, Vol. 16, No. 2, FEBRUARY, 1961

Optical Image Formation in Terms of Entropy Transformations*

Edward L. O'NEILL** Toshimitsu ASAKURA

Information Technology Department, ITEK Corporation
Lexington, Massachusetts U. S. A.

(Received October 10, 1960)

Three major developments have been associated with problems in image formation optics in the last decade. They are the application of Communication and Information Theory concepts to optics, the theory of partial coherence and finally the matrix approach to image formation. In this report it is shown that these three developments are intimately related. Starting with E. Wolf's general theory of image formation in terms of the mutual coherence function, it is shown that both the matrix and communication approaches flow naturally from it. In addition, these latter two are themselves closely related. Finally, some new results showing the change in entropy loss as a function of focal position are presented both from a geometrical and physical optics point of view.

The appeal is one of unity. The arguments presented are confined to the special but important case of quasi-monochromatic illumination. For sources of arbitrary spectral width and time varying fields, the generalized theory has not yet been fully developed.

§1. Introduction

The field of opitical image formation has undergone a renaissance in the last decade or so, the impetus for this renewed interest coming from several distinct sources. First, the fact that the equations describing the formation of an optical image could be cast into a form already well known to circuit engineers gave rise to the speculation that optical image formation could be treated from the standpoint of linear filter theory. With certain slight, but important, modifications, the techniques developed in electric filter theory were applied to optical systems with so much success and appeal that today they are an accepted way of treating problems in image formation.

In addition to this stimulating influence, a number of workers began to examine carefully the naive concepts associated with the terms "coherent" and "incoherent" light. By a process of inductive investigation, much of the ambiguity and vagueness of the earlier work was removed from the theory. Culminating in the outstanding work of Emil Wolf in recent years, the theory of partial coherence stands as a self-consistent, conceptually clear, and logical extension of the classical Maxwell description of electromagnetic wave propaga-

---

* This work was supported by the Air Force Office of Scientific Research under Contract No. AF49 (638)-577

** Now at Department of Physics, Boston University, Boston 15, Mass., U. S. A.

tion. A similar treatment has been and is being carried on for vector waves in the theory of partial polarization.

Finally, Gamo[1)] and Gabor,[2)] simultaneously and independently, demonstrated that image formation could be treated by matrix methods in complete analogy to the wave versus matrix formalism of the early days of modern quantum mechanics. Gamo has developed the theory of the point where it now appears that the "illumination matrix" will play a role in statistical optics similar to that played by the density matrix of statistical mechanics.

This paper, in addition to presenting some new results of the application of statistical communication theory concepts to optics, will attempt to demonstrate the the connections among these three approaches. For reasons of logical consistency, a phenomenological treatment of the theory of partial coherence based on Wolf's approach will be given in section 2, while section 3 will develop the two extreme cases of this general approach, emphasizing the notation of linear filtering. The part that entropy plays in image formation will also be presented in section 3, together with illustrations and discussions of the connection between the entropy criterion and the more classical descriptions of image quality. Section 4, will demonstrate the relation between the Gamo matrix description and the partial coherence factors outlined in section 2.

§ 2. Generalized theory of image formation

An excellent historical review of the work in the theory of partial coherence has been given in a recent publication[3)] by Born and Wolf. For our purposes here, we accept the final results of the theory on the basis of the phenomena it is capable of explaining in a logically consistent way. Taking the deductive approach, we start with the most general relation[4)] between observable quantities over the object and image planes and deduce the equation describing the formation of an image in quasi-monochromatic light for the two extreme cases of fully coherent and fully incoherent illumination. It is with these two extreme cases that the remainder of the paper is concerned.

A few definitions, will be needed. Following Wolf† let $\Gamma_{12}(\tau)=\Gamma(\vec{x}_1, \vec{x}_2; \tau)$ represent the mutual coherence of the light vibrations at two points in the wave field at times separated by τ and let $\Gamma(\vec{x}_1, \vec{x}_2; \nu)$ represent its temporal Fourier transform. In terms of the scalar disturbance over the wave field, $\Gamma_{12}(\tau)$ is defined as

$$\Gamma_{12}(\tau)=\langle V(\vec{x}_1, t+\tau)V^*(\vec{x}_2, t)\rangle=\langle V_1(t+\tau)V_2^*(t)\rangle \tag{1}$$

the brackets indicating a time average.

In terms of the sketch below, the relation between the Fourier transforms of $\Gamma_{12}(\tau)$ over the object and image planes is given by

$$ {}_i\hat{\Gamma}(\vec{x}_1, \vec{x}_2; \nu)=\iiiint_{-\infty}^{+\infty} {}_0\hat{\Gamma}(\vec{\xi}_1, \vec{\xi}_2; \nu)K(\vec{\xi}_1-\vec{x}_1; \nu) K^*(\vec{\xi}_2-\vec{x}_2; \nu)d\vec{\xi}_1 d\vec{\xi}_2 \tag{2}$$

where $K(\vec{x}_1, \nu)$ represents the complex amplitude distribution in the image plane due to a monochromatic point source of frequency ν in the object plane. In (2) it is assumed that this distribution does not change appreciably over the region being explored.

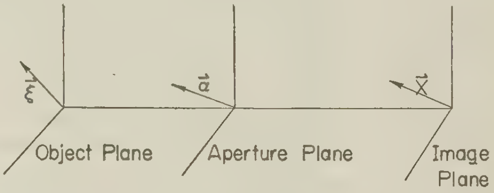

The mutual coherence function itself, it must be recalled, is given by

$$\Gamma_{12}(r)=\int_{-\infty}^{+\infty}\Gamma_{12}(\nu)e^{-2\pi i\nu\tau}d\nu \tag{3}$$

and the actual intensity variations over the object and image planes by

$$ {}_0I(\vec{\xi})={}_0\Gamma_{11}(0)={}_0\Gamma(\vec{\xi}_1, \vec{\xi}_1; 0) \tag{4}$$

$$ {}_iI(\vec{x})={}_i\Gamma_{11}(0)={}_i\Gamma(\vec{x}_1, \vec{x}_2; 0)$$

respectively. Taking the temporal Fourier transform of (2) yields a direct relation between the mutual coherence function over the object and image planes in the form,

$$ {}_i\Gamma(\vec{x}_1, \vec{x}_2; \tau)=\iiiint_{-\infty}^{+\infty} K(\vec{\xi}_1-\vec{x}_1; \nu) \times K^*(\vec{\xi}_2-\vec{x}_2; \nu) {}_0\Gamma(\vec{\xi}_1, \vec{\xi}_2, \nu)e^{-2\pi i\nu\tau}\vec{d}\xi_1\vec{d}\xi_2 d\nu \tag{5}$$

---

† The authors wish to express their gratitude to Dr. G. Parrent for permission to consult a manuscript based on his Doctoral Dissertation at Manchester University.

The time and space Fourier transforms of $\Gamma_{12}(\tau)$ have interesting physical significance[3] in terms of the fringe contrast produced in the Michelson two-beam and stellar interferometers respectively. In the former case, information is obtained about the spectral energy density of the source; while in the latter, information is obtained which describes the brightness of the source as a function of its geometry.

Turning now to the special case of *quasi-monochromatic* illumination over the object plane defined by the set of (5)

a. ${}_0\Gamma_{12}(\tau)={}_0\Gamma_{12}(o)e^{-2\pi i\bar{\nu}\tau}$

b. ${}_0\hat{\Gamma}_{12}(\nu)=-\Gamma_{12}(o)\delta(\nu-\bar{\nu})$

assuming

c. $|\tau|\ll\frac{1}{\Delta\nu}$

equation (5) becomes

$$\Gamma(x_1, x_2; \tau)=\iiiint_{-\infty}^{+\infty}K(\vec{\xi}_1-\vec{x}_1; \bar{\nu})K^*(\vec{\xi}_2-\vec{x}_2; \bar{\nu}) \times {}_0\Gamma(\vec{\xi}_1, \vec{\xi}_2; o)d\vec{\xi}_1 d\vec{\xi}_2 e^{-2\pi i\bar{\nu}\tau} \tag{7}$$

The actual intensity variation over the image plane is then, by (4)

$${}_iI(x)={}_i\Gamma(\vec{x}_1, \vec{x}_1; o)=\iiiint_{-\infty}^{+\infty}K(\vec{\xi}_1-\vec{x}_1, \bar{\nu}) \times K^*(\vec{\xi}_2-\vec{x}_1; \bar{\nu}){}_0\Gamma(\vec{\xi}_1, \vec{\xi}_2; o)d\vec{\xi}_1 d\vec{\xi}_2 \tag{8}$$

We now specialize still further. From *incoherent* illumination over the object plane, for example a self-luminous object, ${}_0\Gamma_{12}(o)$ takes the form

$${}_0\Gamma(\vec{\xi}_1, \vec{\xi}_2; o)={}_0I(\vec{\xi}_1)\delta(\vec{\xi}_1-\vec{\xi}_2) \tag{9}$$

Substituting this into (7) and capitalizing on the sifting property of the δ-function, we arrive at an equation which emphasizes the linear filtering aspect of incoherent image formation:

$${}_iI(x)=\iint_{-\infty}^{+\infty}{}_0I(\vec{\xi})s(\vec{\xi}-\vec{x}, \bar{\nu})d\vec{\xi} \tag{10}$$

where $s(x)=|K(x)|^2$ is the intensity impulse response or spread function for the system. Taking the two dimentional spatial Fourier transform of (10) results in the well known multiplication equation in frequency space for the object and image spatial spectra

$${}_i\hat{I}(\vec{\omega})=\tau(\omega){}_0\hat{I}(\vec{\omega}) \tag{11}$$

where $\tau(\omega)$ is the spatial frequency response or transfer function of the optical system in incoherent light. Because, in practice, most optical instruments are confronted with incoherently illuminated objects, a great deal of attention has been paid to (10) and (11) in the last decase—so much so, in fact, that today a number of industrial instruments are available which yield $\tau(\vec{\omega})$ for lens systems.

At the other extreme, for fully *coherent* illumination over the object plane we must make an appeal to a theorem recently demonstrated by Parrent[5] which states that "in the quasi-monochromatic approximation a coherent field is completely characterized by a complex wave function U which depends on the coordinates of one point only and in terms of it the mutual coherence function is given by

$$\Gamma_{12}(\tau)=U(P_1)U^*(P_2)e^{-2\pi\bar{\nu}\tau}, \ |\tau|\ll\frac{1}{\Delta\nu}.\text{"} \tag{12}$$

Applying this theorem to the mutual coherence function over the object plane in (8), we find for the intensity distribution in the image plane

$${}_iI(x)=\left|\int_{-\infty}^{+\infty}{}_0U(\vec{\xi})K(\vec{\xi}-\vec{x}; \bar{\nu})d\vec{\xi}\right|^2 \tag{13}$$

or in terms of the complex amplitudes over the object and image planes, the system behaves as a linear filter governed by the equation

$${}_iU(\vec{x})=\int_{-\infty}^{+\infty}{}_0U(\vec{\xi})K(\vec{\xi}-\vec{x}; \bar{\nu})d\vec{\xi}. \tag{14}$$

Again, taking the spatial Fourier transform of both sides, we derive the multiplication relation in frequency response

$${}_i\hat{U}(\vec{\omega})=\hat{\tau}(\omega){}_0\hat{U}(\vec{\omega}) \tag{15}$$

where $\hat{\tau}(\omega)$ is here the coherent transfer function.

Before closing this section it is important to emphasize again that this material is being used as both a base and a connecting link for the remainder of the paper. From the standpoint of image formation as linear filtering we are concerned with the extreme cases of fully coherent and incoherent illumination. For the more general case of partially coherent illumination these concepts have been extended considerably in Dr. Parrent's thesis.

§ 3. Entropic Description of Image Formation

Section 2 indicate that, at least in principle, under conditions which are frequently satisfied in practice, it is always possible to predict the variation in intensity over the final image plane in terms of the parameters describing the optical system, the intensity variation over the object plane, and the mode of illumination. In practice, however, most optical systems are required to image incoherently illuminated or self-luminous objects. For this special but important case the equations simplify considerably, leading to the relatively simple relations shown in (10) and (11). In this section, attention will be focused on the problem of image formation in incoherent quasi-monochromatic light with emphasis on the aspect of linear filtering. Many of the results will be directly applicable to systems linear in complex amplitude (coherent).

A study of (10) and (11) shows that $\tau(\vec{\omega})$ and $s(\vec{x})=|K(\vec{x})|^2$ are Fourier transform pairs. A direct application of the Convolution Theorem results in the interesting relation

$$\tau(\vec{\omega})=\frac{\iint_{-\infty}^{+\infty}\hat{K}(\vec{\alpha})\hat{K}^*(\vec{\alpha}+\vec{\omega})d\vec{\alpha}}{\iint_{-\infty}^{+\infty}|\hat{K}(\vec{\alpha})|^2d\vec{\alpha}} \tag{16}$$

But it is well known in scalar diffraction theory that the complex amplitude variations over the aperture plane and Fraunhofer image plane are Fourier transform pairs. Hence, the space frequency response in incoherent light is given by the normalized self-convolution of the complex aperture distribution with its complex conjugate. For a circular aperture with unit amplitude and zero phase (aberrations) over it, $\tau(\omega)$ in (16) is given by the common area of two circles as one slides over the other as a function of the distance between their centers. In this way, the picture of an optical system as a two-dimensional low-pass filter of spatial frequencies is sharpened.

All of this is well known,[6] of course. For periodic objects or for isolated objects on a dark background, (10) and (11) have been used with considerable success to determine the Fourier structure of the image. For random detail in the object plane, the multiplicative relation in frequency space must be written in terms of the Wiener spectra

$${}_i\Phi(\vec{\omega})=|\tau(\vec{\omega})|^2{}_0\Phi(\vec{\omega}) \tag{17}$$

where ${}_0\Phi(\vec{\omega})$ and ${}_i\Phi(\vec{\omega})$ are the spatial Fourier transforms of the auto-correlation of the object and image intensity variations respectively. If, in addition, the object structure is bandlimited to W lines per millimeter then by the Sampling Theorem[7] it is possible to write

$${}_0I(\vec{\xi})=\sum_{n=-\infty}^{+\infty}\sum_{m=-\infty}^{+\infty}{}_0I\left(\frac{m}{2w},\frac{n}{2w}\right)T_{mn}(\vec{\xi}) \tag{18}$$

where $T_{mn}(\xi)$ is the two-dimensional sampling function given by

$$T_{mn}(\vec{\xi})=\frac{\sin(2\pi w\xi-m\pi)}{(2\pi w\xi-m\pi)}\frac{\sin(2\pi w\eta-n\pi)}{(2\pi w\eta-n\pi)} \tag{19}$$

If, in addition, the object is confined to an area L^2, then the Sampling Theorem can be applied directly in frequency space, yielding

$${}_0\hat{I}(\vec{\omega})=\sum_{j=-\infty}^{+\infty}\sum_{k=-\infty}^{+\infty}{}_0\hat{I}\left(\frac{j}{2L},\frac{k}{2L}\right)L_{jk}(\vec{\omega})\,. \tag{20}$$

The relation between the sampled values in the space and frequency planes can be described through the matrix equation

$${}_0\hat{I}_{jk}=\sum_m\sum_n F_{jk,mn}\,{}_0J_{mn} \tag{21}$$

where $F_{jk:mn}$ are the elements of a unitary matrix describing the Fourier transformation between the planes in the form

$$F_{jk:mn}=\exp\left\{i2\pi\left(\frac{jm+kn}{4WL}\right)\right/4WL \tag{22}$$

and where $N=16W^2L^2$ represents the number of degrees of freedom. The complete transformation from the sampled points in object space to those in object frequency space, through the instrument to the image frequency space, and finally to the image sampling points themselves can be described by the matrix equation,

$${}_iI(\vec{x})=F^{-1}\tau F_0I(\vec{\xi}) \tag{23}$$

where τ is a diagonal matrix describing the sine wave response of the instrument and where the elements of the matrix on the left-hand side of (23) can be forced to yield the continuous function ${}_iI(\vec{x})$ by a further application of the Sampling Theorem.

If, further, the probability distribution for the statistically independent intensity values in object space which were sampled is given by $P({}_0I)$, then the entropy of the object set is given by

$$H_0=-\int P({}_0I)\log_2P({}_0I)d_0I \tag{24}$$

and a transformation from the $\vec{\xi}$ to an $\vec{\eta}$

representation results in the entropy

$$\hat{H}_0 = H_0 - \int P({}_0I) \log_2 J({}_0I/{}_0\hat{I}) d_0 I \tag{25}$$

For a linear transformation through the matrix A such that

$${}_0\hat{I} = A_0 I \tag{26}$$

$$J({}_0I/{}_0\hat{I}) = [A]^{-1} \tag{27}$$

where A is the determinant of the matrix A. For the transformation described by (21), $J({}_0I/{}_0\hat{I}) = 1$ so that $\hat{H}_0 = H_0$. In addition the image plane $J({}_iI/{}_i1) = 1$ so that

$$\varDelta H = H_i - H_0 = \hat{H}_i - \hat{H}_0\ . \tag{28}$$

By reasoning similar to that of Shannon[8] and Goldman[7] in two dimensions it is easily shown that

$$\varDelta H = \frac{1}{16\pi^2 w^2} \iint_0^w \log_2 |\tau(\vec{\omega})|^2 d\vec{\omega} \tag{29}$$

Since $0 \leqq |\tau(\omega)|^2 \leqq 1$ over the resolution limit of the system, this entropy change is always a loss. That is, the image is always a smoothed-over version of the object. To illustrate this effect the entropy loss as a function of the defocusing error has been calculated for a one-dimensional slit aperture and a circular aperture from both a physical optics point of view and from the corresponding geometrical approximation. The results are shown in Figures 1 and 2 where only the one-dimensional case is illustrated, while the two-dimensional case can be found in the report[15]. The expressions for the frequency response have been taken from reference 6. One sees that from a geometrical point of view, the image is perfect when properly focused in terms of zero entropy loss, while from the more accurate physical optics description, the entropy undergoes a loss even at best focus due to the finite spread of point image.

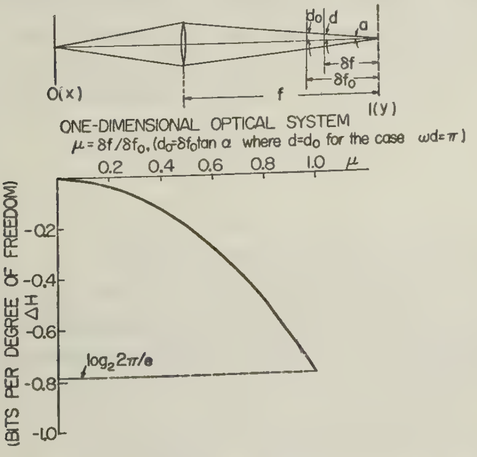

Fig. 1. Entropy loss versus defocusing (one-dimensional geometrical optics case).

It is interesting to point out that, if one substitutes $|\tau(\vec{\omega})|^2$ in (17) into (29), there results a relation between the entropy difference in the object and image planes and the average value of the log $\varPhi(\vec{\omega})$ in the form

$$\varDelta H = \frac{1}{2} \log_{2i}[\varPhi(\bar{\omega})/{}_0\varPhi(\vec{\omega})] \tag{30}$$

indicating that for a number of systems in cascade, the entropy loss is given in terms of the logarithm of the ratio of the final Wiener spectrum to that of the original.

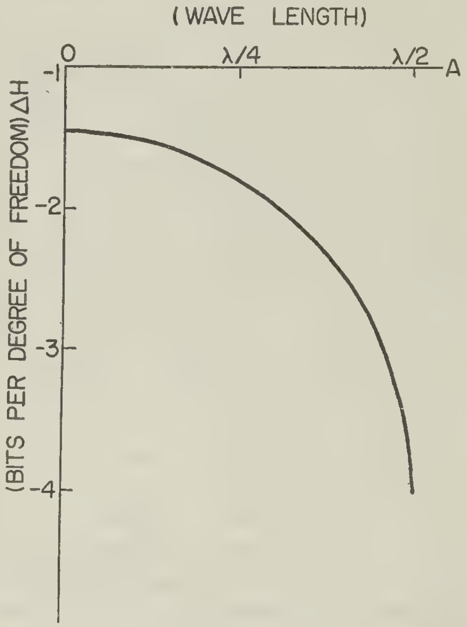

$$\varDelta H = \int_0^1 \log_2 \bigg/ \frac{\sin 4kA\eta(1-\eta)}{4kA\eta} \bigg/ d\eta \quad \{\text{Reference } 6\}$$

Fig. 2. Entropy loss versus defocusing (one-dimensional physical optics case).

Finally, it is important to see if this description of image formation is connected with the more classical and accepted descriptions. Recalling that $0 \leqq \tau(\vec{\omega}) \leqq 1$, a series expansion of (29) in the form

$$\varDelta H = \text{const.} \iint_0^w \Big\{ 1 - \tau(\vec{\omega}) + \frac{1}{2}[1 - \tau(\vec{\omega})]^2 + \frac{1}{3}[1 - \tau(\vec{\omega})]^3 + \cdots \Big\} d\vec{\omega} \tag{31}$$

shows that only the first few terms contribute appreciably to the integral. However, quality factors defined in terms of integrals over $\tau(\vec{\omega})$ and $\tau^2(\vec{\omega})$ have already been suggested and used[9] in optics with some success. It is not surprising, therefore, to find that minimizing the entropy loss between the object and image plane corresponds to maximizing such terms as Schade's equivalent passband N_e[10] or the Strehl Definition[11] of classical optics.

§ 4. Matrix Description of Image Formation

It remains now to relate the treatments in sections 2 and 3 to the recent matrix description which has already reached an advanced state of development at the hands of H. Gamo. For reasons of conceptual ecomony, one-dimensional variations only will be considered in this section. This will preserve the main features of the argument without introducing unwieldy notation. It should be pointed out, however, that the general theory in two dimensions, including the proof of the rotationally symmetric Sampling Theorem, has been given by both Gamo and Gabor. The emphasis here, however, is to demonstrate how this new formulation is related to that already presented. To this end, therefore, the one-dimensional equivalent of (8) can be written as

$$
{}_iI(x)=\iint_{-\infty}^{+\infty}K(\xi_1-x_1;\,\bar{\nu})K^*(\xi_2-x_2;\,\bar{\nu})\times{}_0\Gamma(\xi_1,\xi_2;\,o)\,d\xi_1 d\xi_2 \tag{32}
$$

Since $K(x)$ is the Fourier transform of the complex amplitude over the exit pupil of the optical system, it is certainly band-limited, allowing one to write

$$
\begin{aligned}
K(\xi-x)&=\sum_{m=-\infty}^{\infty}K\left(\xi-\frac{m}{2w}\right)T_m(x)\\
&=\sum_{m=-\infty}^{\infty}K_m(\xi)T_m(x)
\end{aligned} \tag{33}
$$

where $T_m(x)$ is the one-dimensional form of the sampling function defined in (19). Inserting the summations for K and K^* in (32) results in the following matrix expression of the quadratic form,

$$
{}_iI(x)=\tilde{T}AT=\sum_m\sum_n T_m(x)A_{mn}T_n(x) \tag{34}
$$

where A_{mn} are the elements of the "illumination matrix" defined as

$$
A_{mn}=\iint_{-\infty}^{+\infty}K_n(\xi_1)\,{}_0\Gamma(\xi_1,\xi_2;\,o)K_n^*(\xi_2)\,d\xi_1 d\xi_2 \tag{35}
$$

Since $A^*_{nm}=A_{mn}$ and ${}_iI(x)$ is positive, the matrix is of the positive definite Hermitian form. In addition, the total illumination in the image plane is fixed and is given by the integral over ${}_iI(x)$ in (34). Due to the orthogonality of the sampling functions there results the invariance principle for the trace of the matrix

$$
\int I_i(x)\,dx=\frac{1}{2w}\sum_n A_{nn}=\frac{1}{2w}\,\mathrm{trace}\,(A)=\mathrm{const.} \tag{36}
$$

Finally, there exists a transformation S in function space from the T to T' representation such that

$$
I(x)=\tilde{T}'\Lambda' \tag{37}
$$

Where Λ is given by the similarity transformation

$$
\Lambda=\tilde{S}AS\,. \tag{38}
$$

Conventionally now it is convenient to diagonalize Λ so that (37) reduces to a sum of pure square of the form,

$$
{}_iI(x)=\sum_n\lambda_n T_n'^2(x) \tag{39}
$$

where λ_n are the eigenvalues of the illumination matrix A obtained from setting the determinant $|A-\lambda|=0$. These eigenvalues λ_j can then be used to construct the eigenvectors from which the S matrix itself is determined.

From the standpoint of image formation it is an easy matter to show how these matrices reduce for the two extreme cases of fully coherent and incoherent illumination. First, for the coherent case, the insertion of the condition in (12) into A_{mn} results in

$$
A_{mn}=\int_{-\infty}^{+\infty}K_m(\xi_1)\,{}_0U(\xi_1)\,d\xi_1\int_{-\infty}^{+\infty}K_n^*(\xi_2)\,{}_0U^*(\xi_2)\,d\xi_2 \tag{40}
$$

or

$$
A_{mn}={}_iU\left(\frac{m}{2w}\right){}_iU^*\left(\frac{n}{2w}\right) \tag{41}
$$

Now, substituting this back into (34) and making use of the Sampling Theorem, there results an expression for the image intensity distribution

$$
{}_iI(x)=|{}_iU(x)|^2 \tag{42}
$$

which agrees, of course, with (13) and (14).

For the incoherent ${}_0\Gamma_{12}={}_0T(\xi_1)\delta(\xi_2-\xi_1)$ and again the elements of the illumination matrix take the form

$$A_{mn}=\int_{-\infty}^{+\infty}{}_0I(\xi)K_m(\xi)K_n^*(\xi)d\xi \tag{43}$$

and inserting this into (34) a little manipulation results in

$${}_iI(x)=\int_{-\infty}^{+\infty}{}_0I(\xi)\,|\,K(\xi-x)\,|^2d\xi \tag{44}$$

which, again, agrees with (10) and emphasizes the role of the optical system as a linear filter.

It should also be pointed out that for a series of systems in cascade, the multiple convolution integrals of the form in (44) can be replaced by Fourier space by a single equivalent multiplication relation for the equivalent frequency response of the whole chain as a product of the separate frequency responses of each link. Similarly, Gamo has demonstrated that there exists a matrix parallel to this which allows one to determine one equivalent illumination matrix as a product of matrices arising from each system in the chain. Finally, the sinusoidal test chart plays such as important role currently that the image of such an object has been calculated using the matrix method for the cases of coherent, incoherent, and partially coherent illumination. The rather lengthy and tedious manipulations can be found in reference12).

Turning now from the image forming aspect of the matrix description, it is interesting to note that the illumination matrix corresponds formally in many ways with the density matrix of statistical mechanics. Following von Neumann13) we now extend the analogy further and define the entropy of the light beam in terms of the eigenvalues of the diagonalized matrix; thusly

$$H=-\sum_i\left(\frac{\lambda_i}{\sum\limits_j \lambda_j}\right)\log_2\left(\frac{\lambda_i}{\sum\limits_j \lambda_j}\right) \tag{45}$$

which was mentioned by Gamo14). Since the trace is invariant under a unitary transformation, the sum in the denominators represents the total illumination by (36) and is constant. It is proven15), further, that in the coherent limit H goes to zero, while in the incoherent limit H reaches a maximum agreeing with the usual interpretation of the entropy of completely ordered and disordered arrangements respectively.

It is important to mention here that this entropy is not the same as the entropy of the object intensity distribution given in (24). In point of fact, the term "entropy" as used in thermodynamics, statistical mechanics and information theory has caused considerable confusion. Since its introduction by Clausius16), entropy in thermodynamics has been used to describe the irreversibility between equilibrium states. Starting with the pioneering work of Boltzmann17) in the form of his celebrated H theorem and the interpretations given by Gibbs18), entropy in statistical mechanics has came to be understood as a description of the overwhelming tendency for a non-equilibrium state to reach equilibrium. In a strikingly prophetic paper, Szilard19) pointed out in 1929 the similarity between entropy and information in treating the problem of Maxwell's demon. Later, Shannon,8) concerned with practical problems of message transmission, defined an entropy as a measure of the choice of a massage as well as of the average information in long messages. It is clear that these expressions for entropy are certainly not equivalent since they refer to basically different physical quantities. Much confusion can be avoided if it is agreed to define entropy first as a measure of uncertainty in the mathematical theory of probability. In the same way that the various moments, standard deviation, etc. are defined as weighted sums, it is often useful to employ a stronger measure of the unexpectance of an event than the linear measure P_1 itself, where $0\leqq P_i\leqq 1$. The suggested stronger measure is the $\log 1/P_i$ which covers the range $0\leqq\log 1/p_i\leqq\infty$. The average value of this quantity defined in the usual weighted sense is called the "entropy" of the set of probabilities p_i and is given by $H=-\sum_i p_i\log p_i$. One is now free to apply this notion to any fields in the same way that one applies such concepts as variance and standard deviation.

It is in this spirity that the entropy is a perfectly valid measure of the degree of coherence of a light beam. This is not an unexpected result, however. The value that H assumes is determined by the eigenvalues λ_i which in turn arise from elements of the illumination matrix. These elements in turn are derived from Wolf's mutual coherence function which itself, in normalized form, has been defined as the "degree of coherence." It, too, is a statistical description in the form of the complex cross correlation function of the disturbance at two points in space at different times (see (1)). Finally, it is interesting to point out that Planck[20] (1907) mentions Laue's[21] attempt to relate the thermodynamic entropy of the black body radiation field to the tate of partial coherence. The connection between the present work and Laue's has not as yet been demonstrated.

§ 5. Summary and Conclusions

An attempt has been made to relate the three major developments of theoretical optics in the last decade. Starting with the most general theory of scalar wave propagation in the form of Wolf's mutual coherence function, it has been possible to demonstrate how one can incorporate within this framework some of the more important applications of matrix techniques and statistical filter theory. For the most part, progress has been confined to the more restricted case of quasi-monochromatic illumination with special emphasis on the coherent and incoherent limits. It is to be expected that further attempts at unification will be directed toward treatments of polychromatic partially coherent fields. In addition, the similarity between the illumination matrix of statistical optics and the density matrix of statistical mechanics indicates that future research will exploit this analogy still further. Despite the often centrifugal effects of specialized investigation, it is encouraging to note that, in modern optics at least, there is now a tendency for more general formulations to approach a common focus.

References

1) H. Gamo: J. Opt. Soc. Am. **47** (1957) 976; **48** (1958) 136.
2) D. Gabor: "Optical Transmission," Third London Symposium on Information Theory, 1955; "Light and Information," Proc. Symposium on Astr. Optics and Related Subjects, interscience Publishers, 1956.
3) M. Born and E. Wolf: *Principles of Optics*, Pergamon Press, 1959.
4) E. Wolf: Cimento Nuovo **12** (1954) 884.
5) G. B. Parrent: J. Opt. Soc. Am. **49** (1959) 787.
6) E. L. O'Neill: *Selected Topics in Optics and Communication Theory*, Itek Corporation, 1958.
7) S. Goldman: *Information Theory*, Prentice-Hall, 1954.
8) C. E. Shannon: Bell System Tech. J. **27** (1948) 623, 739.
9) E. H. Linfoot and P. B. Fellgett: Phil. Trans. Roy. Soc. A**247** (1955) 369.
10) O. H. Shade: Journal of SMPTE **58** (1959) 181.
11) H. Strehl: Z. F. Instrumkde **22** (1902) 213.
12) T. Asakura: Publ. Theor. Opt. Sec., Itek Corp., (1958) 58-13.
13) J. Neumann: von *Mathematical Foundations of Quantum Mechanics*, Princeton Univ., 1955.
14) H. Gamo: J. Appl. Physics, Japan **25** (1956) 431.
15) E. L. O'Neill and T. Asakura: Itek P-163, April 1960.
16) R. Clausius: Ann. Physik **100** (1857) 358, Phil. Mag. **14** (1857) 108.
17) L. Boltzmann: Wien. Ber. **58** (1868) 517; **66** (1872) 275.
18) J. W. Gibbs: *Elementary Principles in Statistical Mechanics*, Yale Univ. Press, 1902.
19) L. Szilard: Z. Physika **53** (1929) 840.
20) M. Planck: *The Theory of Heat Radiation*, Dover Publ., 1907.
21) M. Laue: von Ann. Phys. **23** (1907) 1; Hand. du exp. Phys. **18** (1928) 272.

JOURNAL OF THE PHYSICAL SOCIETY OF JAPAN, Vol. 16, No. 2, FEBRUARY, 1961

Magnetic Hyperfine Structure in the Rotational Spectrum of H_2CO

By Hiroshi TAKUMA*

Department of Physics, Faculty of Science, University of Tokyo, Tokyo

(Received October 24, 1960)

The theory of magnetic hyperfine interaction of an asymmetric rotor molecule with C_{2v} symmetry in $^1\Sigma$ state was discussed, and the magnetic hyperfine structures in the low frequency rotational spectrum of formaldehyde were studied with a beam maser. The $\Delta F=0$ and the $\Delta F=\pm 1$ components in the $J=4$, $K_{-1}=3$ and the $J=5$, $K_{-1}=3$ Q-branch transitions were observed with good signal-to-noise ratio. The frequency of the $\Delta F=0$ component of the $J=5$, $K_{-1}=3$ line was measured as 18.275 ± 0.004 Mc. The observed hyperfine structures were analysed with the theory, and the hyperfine coupling constants were determined as $\alpha=-13.2\pm 3.4$ kc, $\beta=-3.0\pm 3.4$ kc and $\gamma=30.2\pm 2.7$ kc. The coupling constants were theoretically interpreted, and a proportionality of the hyperfine coupling constans and the rotational g factors for the asymmetric rotor molecule was found. $\langle r^{-3}_{\text{electron}}\rangle_{av}$ arround the proton in H_2CO was obtained as $1.5\times 10^{24}\,\text{cm}^{-3}$ from the comparison of these two quantities.

§1. Introduction

The magnetic hyperfine splittings in the rotational spectrum of a molecule in $^1\Sigma$ state are usually very small, and cannot be observed by a conventional absorption type spectrometer. Recently, the application of beam maser techniques in the field of microwave spectroscopy allowed the observation of the magnetic hyperfine structures of some kinds of molecules with sufficiently good resolutions and sensitivites.

Gordon[1] observed the magnetic hyperfine structures of inversion lines of ammonia, and determined the hyperfine coupling constants. Takuma, Shimizu and Shimoda[2] observed and analysed the magnetic hyperfine structure of the $3_{12}\rightarrow 3_{13}$ transition of H_2CO. Thaddeus, Loubser, Krisher and Lecar[3] observed and analysed the $2_{11}\rightarrow 2_{12}$ transition of H_2CO and HDCO. Shimoda and Kondo[4] observed the magnetic hyperfine structure of the $J=3$, $K=2$ inversion line of ammonia.

The magnetic hyperfine structure of NH_3 was discussed by Gunther-Mohr, Townes and Van Vleck,[4] and by Gordon[1], and experimental results are completely analysed except the anomaly of the hyperfine structure of the (3.2) line found by Shimoda and Kondo.[4]

The theory of magnetic hyperfine structures of asymmetric molecules in $^1\Sigma$ state with C_{2v} symmetry was discussed by Okaya,[7] but his theory and experiment were rather incomplete and did not agree well with the recent studies with masers. The observed patterns of the $3_{12}\rightarrow 3_{13}$ and the $2_{11}\rightarrow 2_{12}$ transitions were explained satisfactorily with the theory in TSS**. However, the hyperfine coupling constants were not obtained from the lack of sufficient number of experimental data.

The physical interpretation of the magnetic hyperfine coupling constants and their relation with rotational g factors were discussed by White[6] for diatomic, linear or symmetric rotor molecules. However, such discussion for asymmetric rotor molecules have not been published.

Thus the problems about the magnetic hyperfine structures are left unaccomplished for asymmetric rotor molecules. The purpose of this paper is to treat such subjects for an asymmetric rotor molecule, H_2CO.

The theory of the hyperfine interaction of H_2CO type molecule was discussed, and the hyperfine coupling constants were theoretically analysed. The hyperfine structures of the low frequency transitions of H_2CO, the $4_{31}\rightarrow 4_{32}$ and the $5_{32}\rightarrow 5_{33}$ transitions, were studied with a low frequency beam maser which was pioneered recently by Shimoda, Takuma and

---

* Present Address, Department of Applied Physics, Faculty of Engineering, University of Tokyo, Tokyo.

** The paper by Takuma, Shimizu and Shimoda[2] on the $3_{12}\rightarrow 3_{13}$ line of H_2CO is reffered as TSS in this paper for convenience.

Shimizu[8]. The magnetic hyperfine satellites in these two transitions were observed with a little improvement of the sensitivity of the spectrometer. From these observations and the experimental result on the $3_{12} \to 3_{13}$ line, the magnetic hyperfine coupling constants were determined.

The results were physically interpreted, and the relation between the magnetic hyperfine coupling constants and the rotational g tensor of the asymmetric rotor molecule was also discussed.

§ 2. Theory of Magnetic Hyperfine Interaction of H₂CO Type Molecules

The Hamiltonian of a formaldehyde type molecule with C_{2v} symmetry in $^1\Sigma$ state can be written as;[1,2,5,9]

$$\boldsymbol{H}=A(J_z-L_z)^2+B(J_y-L_y)^2+C(J_x-L_x)^2 \tag{1.0}$$

$$+(e\mu_N/c)\sum_{K=1,2}\sum_{i} r_{Ki}^{-3}(\boldsymbol{r}_i-\boldsymbol{r}_K)$$

$$\times\left\{\boldsymbol{v}_i-\left(1+\frac{Z_K}{g_H}\right)\boldsymbol{v}_K\right\}g_H\boldsymbol{I}_K \tag{1.1}$$

$$-(e\mu_N/c)\sum_{K=1,2}\sum_{L\neq K} Z_L r_{KL}^{-3}(\boldsymbol{r}_K-\boldsymbol{r}_L)$$

$$\times\left\{\left(1+\frac{Z_K}{g_H}\right)\boldsymbol{v}_K-\boldsymbol{v}_L\right\}g_H\boldsymbol{I}_K \tag{1.2}$$

$$+\mu_N{}^2r^{-3}g_H{}^2\{\boldsymbol{I}_1\cdot\boldsymbol{I}_2-3r^{-2}(\boldsymbol{I}_1\cdot\boldsymbol{r}_{12})(\boldsymbol{I}_2\cdot\boldsymbol{r}_{12})\}\ , \tag{1.3}$$

where J_g is the component of the rotational angular momentum along the molecular fixed $g(g=x, y, z)$ axis, L_g the electronic angular momentum, μ_N the nuclear magneton, r_{Ki} the distance between the K^{th} nucleus and the i^{th} electron, r_{KL} the distance between the K^{th} and the L^{th} nuclei, $\boldsymbol{r}_i$ and $\boldsymbol{v}_i$ the position vector and the velocity vector of the i^{th} electron, $\boldsymbol{r}_K$ and $\boldsymbol{v}_K$ the position vector and the velocity vector of the K^{th} nucleus, g_H the g factor of proton, Z_K or Z_L the effective charge of the K^{th} or the L^{th} nucleus, r the distance between the two protons, and I_K the spin of the K^{th} proton. The nuclei are numbered so that $K=1$ and 2 for the protons. The molecular fixed coordinate axes x, y, and z are chosen as the principal axes of the molecule.

The energy of the hyperfine interaction was given as a function of $\boldsymbol{I}\cdot\boldsymbol{J}$ coupling constants A_{Kg} and spin-spin interaction terms, but the theoretical evaluation of A_{Kg} was not discussed in TSS. In order to obtain a theoretical background about the experimental values and to get informations about the electronic state of the rotating molecule, detailed discussions on A_{Kg} are given below. The electronic state must be excited by molecular rotation, because Eq. (1) contains the coupling terms between the electronic angular momentum and molecular rotation. The Hamiltonian $\boldsymbol{H}$ will be treated by the electronic wave function at first. The Hamiltonian is devided into two parts; $\boldsymbol{H}^{(1)}$ and $\boldsymbol{H}^{(2)}$, the one which is diagonal and the other which is off diagonal in electronic wave function as below;

$$\boldsymbol{H}^{(1)}=\sum_{g\ \ x,y,z} A_gJ_g{}^2 \tag{2.0}$$

$$-(e\mu_Ng_H/c)\sum_{K=1,2}\sum_{L\neq K} Z_L r_{LK}^{-3}(\boldsymbol{r}_K-\boldsymbol{r}_L)$$

$$\times\left[\left(1+\frac{Z_K}{g_H}\right)\boldsymbol{v}_K-\boldsymbol{v}_L\right]\cdot\boldsymbol{I}_K \tag{2.1}$$

$$+\mu_N{}^2r^{-3}g_H{}^2[\boldsymbol{I}_1\cdot\boldsymbol{I}_2-3r^{-2}(\boldsymbol{I}_1\cdot\boldsymbol{r}_{12})(\boldsymbol{I}_2\cdot\boldsymbol{r}_{12})]\ , \tag{2.2}$$

$$\boldsymbol{H}^{(2)}=\sum_{g=x,y,z} A_gL_g{}^2 \tag{2.3}$$

$$-2\sum_{g=x,y,z} A_gJ_gL_g \tag{2.4}$$

$$+(e\mu_Ng_H/c)\sum_{K}\sum_{i} r_{iK}^{-3}(\boldsymbol{r}_i-\boldsymbol{r}_K)\times\boldsymbol{v}_{iK}\cdot\boldsymbol{I}_K\ , \tag{2.5}$$

where $A_x=C$, $A_y=B$, $A_z=A$, and $\boldsymbol{v}_{ik}=\boldsymbol{v}_i-(1+Z_K/g_H)\boldsymbol{v}_K$. The terms (2.0) is neglected because it is independent of rotational energy of the molecule. The second order perturbation calculation by Van Vleck's method can be written as[5]

$$\langle o|\boldsymbol{G}|o\rangle=\langle o|\boldsymbol{H}^{(1)}|o\rangle+\sum_{n\neq0}(E_0-E_n)^{-1}\langle o|\boldsymbol{H}^{(2)}|n\rangle\langle n|\boldsymbol{H}^{(2)}|o\rangle\ , \tag{3.0}$$

where o and n refer to the ground and the n^{th} excited electronic state of the molecule, and $\boldsymbol{G}$ is the effective Hamiltonian.

The first term in Eq. (3.0) is calculated as;

$$\langle o|\,\boldsymbol{H}^{(1)}|o\rangle=\sum_{g=x,y,z}A_gJ_g{}^2-(e\mu_N/c)\sum_{K=1,2}\sum_{L\neq K}Z_Lr_{LK}^{-3}(\boldsymbol{r}_K-\boldsymbol{r}_L)\times\left[\left(1+\frac{Z_K}{g_H}\right)\boldsymbol{v}_K-\boldsymbol{v}_L\right]\cdot g_H\boldsymbol{I}_K$$

$$+\mu_N{}^2g_H{}^2r^{-3}[\boldsymbol{I}_1\cdot\boldsymbol{I}_2-3(\boldsymbol{I}_1\cdot\boldsymbol{r}_{12})(\boldsymbol{I}_2\cdot\boldsymbol{r}_{12})\boldsymbol{r}^{-2}]\ , \tag{3.1}$$

and the second term is obtained as;

$$\sum_{n\neq0}(E_0-E_n)^{-1}\langle o|\boldsymbol{H}^{(2)}|n\rangle\langle n|\boldsymbol{H}^{(2)}|o\rangle$$

$$=\sum_{g}\sum_{g'}\boldsymbol{M}_{gg'}J_gJ_{g'}+\sum_{g}\sum_{g'}\sum_{K}\boldsymbol{N}_{Kgg'}J_g\boldsymbol{I}_{Kg'}+\sum_{g}\sum_{g'}\boldsymbol{S}_{gg'}\boldsymbol{I}_{1g}\cdot\boldsymbol{I}_{2g'}\ , \tag{3.2}$$

where

$$M_{gg'}=\sum_{n\neq 0}(E_0-E_n)^{-1}\cdot 4A_gA_{g'}\langle o|L_g|n\rangle\langle n|L_{g'}|o\rangle\,, \tag{3.3}$$

$$\begin{aligned}N_{Kgg'}=-(e\mu_N/c)\sum_{n\neq 0}(E_0-E_r)^{-1}\{&\langle o|L_g|n\rangle\langle n|\sum_i[(\boldsymbol{r}_i-\boldsymbol{r}_K)\times\boldsymbol{v}_{iK}]_g r_{iK}^{-3}|0\rangle\\&+\langle o|\sum_i[(\boldsymbol{r}_L-\boldsymbol{r}_K)\times\boldsymbol{v}_{iK}]_{g'}r_{iK}^{-3}|n\rangle\langle n|L_g|o\rangle\}g_H\,,\end{aligned} \tag{3.4}$$

$$\begin{aligned}S_{gg'}=-(e\mu_N g_H/c)^2\sum_{n\neq 0}(E_0-E_n)^{-1}\cdot&\langle o|\sum_i[(\boldsymbol{r}_i-\boldsymbol{r}_1)\times\boldsymbol{v}_{iK}]_g r_{i1}^{-3}|n\rangle\\&\times\langle n|\sum_i[(\boldsymbol{r}_i-\boldsymbol{r}_2)\times\boldsymbol{v}_{iK}]_{g'}r_{i2}^{-3}|o\rangle\,.\end{aligned} \tag{3.5}$$

The first term in the right hand side of Eq. (3.2) is the increment of the rotational energy of the molecule due to the excitation of the electronic state, and can be neglected in the present discussion, because it is small compared with the rotational energy and has the same expression as the energy of the molecular rotation.

Because $\boldsymbol{v}_K=\boldsymbol{\omega}\times\boldsymbol{r}_K$, where $\boldsymbol{\omega}$ is the angular velocity of the molecule, and $\boldsymbol{\omega}_g$ is equivalent to $2A_gJ_g/\hbar$, terms such as $(\boldsymbol{r}_K-\boldsymbol{r}_L)\times\boldsymbol{v}_K$ can be substituted by[5]

$$[(\boldsymbol{r}_K-\boldsymbol{r}_L)\times\boldsymbol{v}_K]_g=\sum_{g'=x,y,z}\{\delta_{gg'}(\boldsymbol{r}_K-\boldsymbol{r}_L)\boldsymbol{r}_K-\boldsymbol{r}_{Kg'}(\boldsymbol{r}_K-\boldsymbol{r}_L)_g\}\times\frac{2A_{g'}J_{g'}}{\hbar}\,.$$

On the other hand, the directions of the principal axes of the diadic of $\boldsymbol{I}\cdot\boldsymbol{J}$ coupling constants for each hydrogen nucleus must be parallel to the principal axes of the molecule from symmetry consideration. Therefore, cross products $J_gJ_{g'}$ between different g and g' must vanish in the final form of the effective Hamiltonian. Taking into account of these facts, and by putting $-I_{Kg}=\bar{I}_{Kg}$ in order to discuss with the molecular fixed coordinate axes, we obtain the Hamiltonian for the nuclear magnetic interaction;

$$\begin{aligned}\boldsymbol{G}=&-\sum_{K=1,2}(A_{Kx}\bar{I}_{Kx}J_x+A_{Ky}\bar{I}_{Ky}J_y+A_{Kz}\bar{I}_{Kz}J_z)\\&+\mu_N{}^2g_H{}^2r^{-3}[\sum_g\bar{I}_{1g}\bar{I}_{2g}-3(\sum_g\bar{I}_{1g}r_g)(\sum_g\bar{I}_{2g}r_g)r^{-2}]\,,\end{aligned} \tag{4}$$

which is the same as Eq. (4) in TSS. The hyperfine coupling constants, $A_{Kg}{}^{(1)}$ and $A_{Kg}{}^{(2)}$ are defined below.

$$\begin{aligned}A_{Kg}^{(1)}=-\frac{2e\mu_NA_gg_H}{c\hbar}\sum_{L\neq K}Z_Lr_{LK}^{-3}\Big\{&\Big(1+\frac{Z_K}{g_H}\Big)\\&\times[(\boldsymbol{r}_K-\boldsymbol{r}_L)\boldsymbol{r}_K-\boldsymbol{r}_{Kg}(\boldsymbol{r}_K-\boldsymbol{r}_L)_g]\\&-[(\boldsymbol{r}_K-\boldsymbol{r}_L)\boldsymbol{r}_L-\boldsymbol{r}_{Lg}(\boldsymbol{r}_K-\boldsymbol{r}_L)_g]\Big\}\end{aligned} \tag{5.1}$$

$$\begin{aligned}A_{Kg}^{(2)}=\frac{e\mu_Ng_HA_g}{c}\sum_{n\neq 0}(E_n-E_0)^{-1}&\\\times\{\langle o|L_g|n\rangle\langle n|\sum_i&[(\boldsymbol{r}_i-\boldsymbol{r}_K)\times\boldsymbol{I}_{iK}]_g r_{iK}^{-3}|o\rangle\\+\langle o|\sum&[(\boldsymbol{r}_i-\boldsymbol{r}_K)\times\boldsymbol{v}_{iK}]_g r_{iK}^{-3}|n\rangle\langle n|L_g|o\rangle\}\,.\end{aligned} \tag{5.2}$$

Then A_{Kg} in Eq. (4) is determined as

$$A_{Kg}=A_{Kg}^{(1)}+A_{Kg}^{(2)}\,. \tag{5.3}$$

For the convenience of later discussions, following constants are defined;

$$\left.\begin{aligned}\alpha&=A_{1x}+A_{2x}\\\beta&=A_{1y}+A_{2y}\\\gamma&=A_{1z}+A_{2z}\end{aligned}\right\} \tag{5.4}$$

The indirect spin-spin interaction term, $\sum_g S_{gg}I_{1g}I_{2g}$, is neglected in the above discussion, because it is of the order of $(e\mu_Ng_H/c)\cdot\langle r_{\text{electron}}^{-3}\rangle_{\text{av}}(1/mA_g)A_{Kg}^{(2)}\sim 10^{-12}A_{Kg}^{(2)}$, and $A_{Kg}^{(2)}$ is usually the same order of magnitude as the direct spin-spin interaction term (2.3) in $^1\Sigma$ state molecules.

The physical meanings of $A_{Kg}^{(1)}$ and $A_{Kg}^{(2)}$ are apparently shown in Eq. (5). The former is the part of $\boldsymbol{I}\cdot\boldsymbol{J}$ coupling constant due to the rotation of nuclear charge, and the latter is that due to the excitation of the electrons by rotation. In general, the sign of the value of $A_{Kg}^{(1)}$ is negative, and that of $A_{Kg}^{(2)}$ is positive, as seen from Eqs. (5.1) and (5.2). Therefore, the sign of the value of A_{Kg} is positive if the greater parts of the electrons rotate with the molecular frame, because the electrons get angular momentum and $A_{Kg}^{(2)}$ predominates. On the contrary, the sign of the value of A_{Kg} is negative, when the greater parts of the electrons slip against the molecular frame.

§ 3. Measurement of Hyperfine Structures by a Low Frequency Beam Maser

The rotational spectrum of H_2CO lies in a very wide range. The greater part of the rotational transitions lie in rather short wave length microwave region, and it is difficult to study them by beam masers at the present stage. Only a few $\Delta J=0$ transitions are in centimeter ranges in which a beam maser is operated without difficulties. The $2_{11}\rightarrow 2_{12}$ and the $3_{12}\rightarrow 3_{13}$ transitions, which have already been studied, belong to such transitions. The hyperfine structures in $\Delta J=0$ transitions in microwave ranges consist of three strong $\Delta F=0$ components and weak $\Delta F=\pm 1$ components.[2,3] Therefore, it is difficult to observe a $\Delta F=+1$ or $=-1$ transition, because it overlaps one of $\Delta F=0$ components frequently. Only the value of $\alpha-\beta$ is obtained from the observation of $\Delta F=0$ transitions, as shown in TSS.

On the other hand, some $\Delta J=0$ transitions of H_2CO lie in low frequency ranges, and it has been shown by Shimoda, Takuma and Shimizu[8] that these transitions can be observed by a beam maser. The $\Delta F=0$ components in these transitions are separated by only a few cycles per second, while $\Delta F=\pm 1$ transitions are estimated to be separated from $\Delta F=0$ components by the order of 10 kc, as will be shown later. Therefore, the low frequency beam maser is suited to the study of $\Delta F=\pm 1$ transitions. The measurements in microwave and low frequency ranges give more accurate values of α, β and γ than the measurements in only one of these two ranges.

The low frequency measurements were made on the $4_{31}\rightarrow 4_{32}$ and the $5_{32}\rightarrow 5_{33}$ transitions. The experimental procedure was the same in principle as stated in the previous paper.[8] A high Q resonance circuit was used to improve the sensitivity. The noise figure of the spectrometer was 2 for the $4_{31}\rightarrow 4_{32}$ transition, and 1.5 for the $5_{32}\rightarrow 5_{33}$ transition. A long time constant and slow sweeps were used for the observation of hyperfine structure in the $4_{33}\rightarrow 4_{32}$ transition to improve the sensitivity. The time constant was 10 seconds and the sweep rate was about 3 kc/min. for the $4_{31}\rightarrow 4_{32}$ transition, while the time constant of 2.5 seconds and the sweep rate of about 10 kc/min. was used for the $5_{32}\rightarrow 5_{33}$ transition.

The observed patterns are shown in Fig. 1 and Fig. 2, and the measured values are

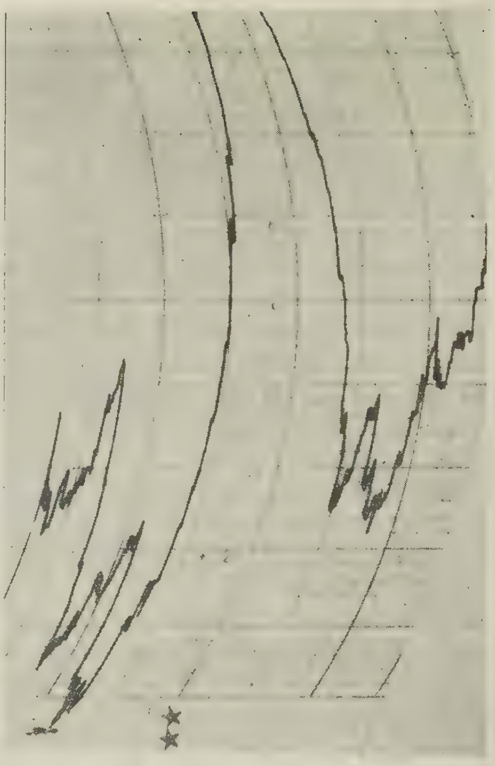

Fig. 1. Trace of the $4_{31}\rightarrow 4_{32}$ transition of H_2CO by beam maser.

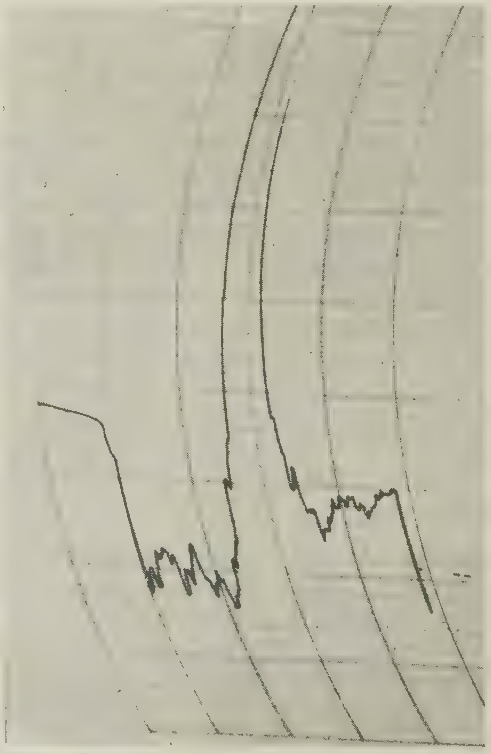

Fig. 2. Trace of the $5_{32}\rightarrow 5_{33}$ transition of H_2CO by beam maser.

Table I. Observed values of hyperfine splittings in the low frequency transitions of H_2CO.

Transitions $J_{K_{-1}K_1} \to J_{K_{-1}K_1}$	$F \to F'$	Splittings (kc)	Frequencies (Mc)
$4_{31} \to 4_{32}$	$\Delta F=0$	0.00	4.5769 ±0.0023*)
	$5 \to 4$ $4 \to 5$	$^{+}_{-}$ 25.7±0.9	
	$4 \to 3$ $3 \to 4$	$^{+}_{-}$ 15.5±1.1	
$5_{32} \to 5_{33}$	$\Delta F=0$	0.00	18.275 ±0.004
	$\left.\begin{matrix}6 \to 5\\ 5 \to 4\end{matrix}\right\}$ + $\left.\begin{matrix}5 \to 6\\ 4 \to 5\end{matrix}\right\}$ −	9.9±0.7	

*) Measured by Shimoda, Takuma and Shimizu.[8)]

listed in Table I.

The frequency shifts due to the magnetic hyperfine interaction for the $F \to F'$ component, $\Delta\nu_{F\to F'}$, are calculated from Eq. (10) of TSS;

$$\left.\begin{aligned}
&\Delta\nu_{F\to F}=0 \qquad (F=J+1,\ J,\ J-1)\,,\\
&\Delta\nu_{J+1\to J}=-\Delta\nu_{J\to J+1}\\
&\quad=\frac{1}{2J}[\alpha\langle J_x^2\rangle+\beta\langle J_y^2\rangle+\gamma\langle J_z^2\rangle]\\
&\quad-\frac{9\mu_N^2 g_H^2 r^{-3}}{2J(2J+3)}\left[\langle J_y^2\rangle-\frac{1}{3}J(J+1)\right],\\
&\Delta\nu_{J\to J-1}=-\Delta\nu_{J-1\to J}\\
&\quad=\frac{1}{2(J+1)}[\alpha\langle J_x^2\rangle+\beta\langle J_y^2\rangle+\gamma\langle J_z^2\rangle]\\
&\quad-\frac{9\mu_N^2 g_H r^{-3}}{2(2J-1)(J+1)}\left[\langle J_y^2\rangle-\frac{1}{3}J(J+1)\right],
\end{aligned}\right\} \qquad (6)$$

because $\Delta\langle J_g^2\rangle \ll 1$ for low frequency transitions.

Eq. (6) shows that the hyperfine spectrum of the low frequency transition of H_2CO consists of a strong center line which corresponds to the $\Delta F=0$ transitions and symmetrically arranged four satellites which correspond to the $\Delta F=\pm 1$ transitions. The $\Delta F=\pm 1$ satellites were completely resolved in the $4_{31}\to 4_{32}$ transition, while only one satellite was observed in the $5_{32}\to 5_{33}$ transition. In the latter case, $\Delta\nu_{6\to 5}$ and $\Delta\nu_{5\to 4}$ or $\Delta\nu_{5\to 6}$ and $\Delta_{4\to 5}$ are nearly equall and two satellites are unresolved.

From the observed values of $\Delta\nu_{5\leftrightarrow 4}$ in the $4_{32}\to 4_{32}$ transition, by putting the values of $\mu_N=5.050\times 10^{-24}$ erg/gauss, $g_H=5.585$ and $r=1.89$Å in Eq. (6), we obtain

$$\alpha\langle J_x^2\rangle+\beta\langle J_y^2\rangle+\gamma\langle {}_z^2\rangle$$
$$=5.500\alpha+5.500\beta+9.000\gamma=188.0\pm 7.2\ \text{kc}. \qquad (7.1)$$

Similary, from the observed value of $\Delta\nu_{3\leftrightarrow 4}$, we obtain

$$5.500\alpha+5.500\beta+9.000\gamma=183.0\pm 1.1\ \text{kc}\,. \qquad (7.2)$$

The right hand sides of Eqs. (7.1) and (7.2) agree will with each other. This is a check for the measurement of $\Delta\nu_{3\leftrightarrow 4}$ and $\Delta\nu_{4\leftrightarrow 5}$. Averaging the values of Eqs. (7.1) and (7.2).

$$5.500\alpha+5.500\beta+9.000\gamma=185.5\pm 9.1\ \text{kc}\,. \qquad (7.3)$$

On the other hand, in the $5_{32}\to 5_{33}$ transition, the average values of $\Delta\nu_{5\leftrightarrow 6}$ and $\Delta\nu_{4\leftrightarrow 5}$ give the frequency shifts of the unresolved satellites in the higher or lower frequency side, which are referred as $\Delta\nu_+$ or $\Delta\nu_-$ respectively. Thus we obtain from Eq. (6),

$$\Delta\nu_+=-\Delta\nu_-$$
$$=\frac{11}{120}(\alpha\langle J_x^2\rangle+\beta\langle J_y^2\rangle+\gamma\langle J_z^2\rangle)-0.07\ \text{kc}.$$

The observed value is put into the above equation, and it becomes;

$$10.50\alpha+10.50\beta+9.000\gamma=107.2\pm 7.6\ \text{kc}. \qquad (8)$$

The value of $\alpha-\beta$ is precisely determined from the observation of the $\Delta F=0$ components in microwave lines. The separation between the $F=4$ and $F=2$ components in the $3_{12}\to 3_{13}$ transition was measured as 23.0±0.6 kc. By putting this value into Eq. (9) in TSS[2)], we obtain*)

$$\alpha-\beta=-10.2\pm 0.9\ \text{kc}. \qquad (9)$$

Thus the values of α, β and γ are determined from Eqs. (7), (8) and (9);

$$\alpha=-13.2\pm 3.4\ \text{kc}$$
$$\beta=-3.0\pm 3.4\ \text{kc}$$
$$\gamma=30.2\pm 2.7\ \text{kc}$$

§ 4. Discussions

The hyperfine structures in the rotational spectrum of H_2CO have been calculated according to the theory and the hyperfine coupling constants determined above. The calculated values are listed in Table II, and compared with the experiments. The agreement between the calculated and the experimental values is very good. Thus the hyperfine structure in the rotational spectrum of H_2CO has been completely analysed, and the theories of hyperfine structure in the rotational spectrum of an asymmetric molecule by Posener[9] or TSS[2] have proved to be useful for a practical analysis.

---

*) The value of $\alpha-\beta$ was determined as −9.1± 0.6 kc in TSS. However, the measurement of the separation between the $F=3$ and the $F=4$ components might have some systematic error, because they were not resolved completely. Therefore, the experimental value of $\Delta\nu_{2\to 2}-\Delta\nu_{4\to 4}$ alone was used to determine the value of $\alpha-\beta$. More precise measurements on the $3_{12}\to 3_{13}$ and the $1_{10}\to 1_{11}$ transitions are now in progress.

Table II. Observed and calculated values of hyperfine structures in the Q-branch transitions of H_2CO.

Transitions $J_{K_{-1}K_1} \to J_{K_{-1}K_1}$	$F \to F'$	Observed (kc)	Calculated (kc)
$2_{11} \to 2_{12}$*)	1→1	−22.1±0.7	−22.8
	1→2	− 8.5±1.0	− 9.0
	3→3	0.0	0.0
	2→2	11.1±1.0	10.6
$3_{12} \to 3_{13}$**)	2→2	−23.0±1.5	−23.8
	3→3	10.4±0.7	9.1
	4→4	0.0	0.0
$4_{31} \to 4_{32}$	4→3 3→4	$\pm$15.5±1.1	$\pm$15.6
	5→4 4→5	$\pm$25.7±0.9	$\pm$25.0
$5_{32} \to 5_{33}$	$\left.\begin{matrix}5\to4\\6\to5\end{matrix}\right\}$ $\left.\begin{matrix}4\to5\\5\to6\end{matrix}\right\}$	+ 9.9±0.7 −	+ 9.3 −

*) Measured by P. Thaddeus, J. Loubser, L. Krisher and H. Lecar.[3]

**) Measured by H. Takuma, T. Shimizu, and K. Shimoda.[2]

The magnetic hyperfine coupling constants are closely related to the electronic state of the rotating molecule. The magnetic hyperfine coupling constant of proton had been determined with H_2, HD and NH_3.[6] It has a negative sign in all these molecules. That is, the magnitude of the magnetic field due to the rotation of nuclei exceeds that due to the excitation of the electronic state. This is because the distribution of the appreciable portion of the valence electrons is spherically symmetric about the center of mass of these molecule.

On the other hand, the hyperfine coupling constant γ in H_2CO has been obtained to have a positive sign. This is the first case in which the coupling constant of proton has been found to have a positive sign. The reason of the positive sign of the $\boldsymbol{I} \cdot \boldsymbol{J}$ coupling constant will be considered in the following.

A portion of the electrons in the CH bonding orbitals in H_2CO may be assumed to be spherically symmetric about each protons, but it is not spherically symmetric about the center of mass of the molecule. Because the electrons in sp^2 hybridized valence orbitals of the carbon atom and the lone pair electrons of the oxygen atom are fixed with respect to the molecular frame, they are easily excited by rotating the molecular frame.

Therefore, a large portion of the valence electrons does not slip about the center of mass of the molecule. The portion of electrons distributed with spherical symmetry around each proton exibits a kind of slippage about the proton and cancells partly the magetic field due to the proton. Moreover, HH distance r in H_2CO is larger than that of H_2 or NH_3, so the absolute value of $A^{(1)}_{Kg}$ is smaller, because it is proportional to r^{-3} as shown in Eq. (5.1).

Both α and β have small negative values. This shows that the magnetic field due to the nuclear charges exceeds that due to the electrons in the rotation along x or y axis, contrary to z direction. This is because the magnetic field due to the carbon and oxygen nuclei is less effective in producing a magnetic field by a revolution of the molecule along z axis compared with a revolution along x or y axis.

Table III. Magnetic hyperfine coupling constants of H_2CO.

Components	Nuclear (Calculated) (kc)	Electronic (kc)	Totals (Experimental) (kc)
α	−37.8	24.6	−13.2±3.4
β	−19.7	16.7	− 3.0±3.4
γ	−18.6	21.6	30.2±2.7

The nuclear parts of the $\boldsymbol{I} \cdot \boldsymbol{J}$ coupling constants α, β and γ, can be calculated from Eq. (5.1), and listed in Table III. Half an electron is assumed to be in the atomic orbital of each hydrogen in the average, slipping about the proton like the chair of Ferris wheel, in the calculation of these constants. The electronic parts are obtained by subtracting the nuclear parts from the experimentally obtained values of α, β and γ. They are also listed in Table III. The nuclear part or the electronic part of γ is much greater than that of the other components of $\boldsymbol{I}\cdot\boldsymbol{J}$ coupling constants, because each diagonal component of the $\boldsymbol{I}\cdot\boldsymbol{J}$ coupling diadic is proportional to the rotational constant along each axis as shown in Eqs. (5.1) and (5.2), and H_2CO has the largest rotational constant along z axis. Physically, this molecule rotates with a much larger angular velocity about z axis than the angular velocity along x or y axis.

In order to derive the relation between the $\boldsymbol{I}\cdot\boldsymbol{J}$ coupling constants and the rotational g factor of the molecule, Eq. (5.2) is somewhat modified.

$$m\sum_i(\boldsymbol{r}_i-\boldsymbol{r}_K)\times\boldsymbol{v}_{iK}=m\sum_i\boldsymbol{r}_i\times\boldsymbol{v}_i+mN\boldsymbol{r}_K\times\boldsymbol{v}_K$$
$$-m\boldsymbol{r}_K\times\sum_i\boldsymbol{v}_i-m\left(1+\frac{Z_K}{g_H}\right)\sum_i\boldsymbol{r}_i\times\boldsymbol{v}_K\ ,$$

where N is the total number of the valence electrons in the molecule, and m the electron mass. The first term of the right hand side of the above equation is the electronic angular momentum of the molecule, and the order of magnitude of the remaining each term is equal to

$$\frac{m}{M}\times(\text{angular momentum of the molecule}),$$

where M is the mass of the molecule. Therefore, the last three terms are smaller than the first term, and $\sum(\boldsymbol{r}_i-\boldsymbol{r}_K)\times\boldsymbol{v}_{iK}$ in Eq. (5.2) can be substituted by $\hbar L_g/m$. Then following relation is derived;

$$A^{(2)}_{Kg}\cong 4\mu_B\mu_N g_H A_g\langle r^{-3}_{\text{electron}}\rangle_{\text{av}}$$
$$\times\sum_{n\neq0}(E_n-E_0)^{-1}|\langle o|L_g|n\rangle|^2\ , \qquad (11)$$

where μ_B is the Bohr magneton. This is the extension of Eq. (19) in the paper by White[6] to an asymmetric top molecule H_2CO. $\sum_{n\neq0}(E_n-E_0)^{-1}|\langle o|L_g|n\rangle|^2$, which we shall abbreviate as $\sum_n(L_n)_g$, is a measure of the excitation of the electrons by a revolution of the molecule along g axis.

It was also shown by White that $\sum_n(L_n)_g$ was closely related to the rotational g factor for diatomic, linear or symmetric top molecules. The simillar relation to be satisfied for asymmetric molecules with C_{2v} symmetry in ${}^1\Sigma$ state is discussed in the appendix of this paper. From Eqs. (11) and (A10), we obtain the following relation;

$$-A^{(2)}_{Kg}/(g_H\mu_N{}^2g^{(2)}_{gg})\cong\langle r^{-3}_{\text{electron}}\rangle_{\text{av}}\ . \qquad (12)$$

Thus the value of $\langle r^{-3}_{\text{electron}}\rangle_{\text{av}}$ can be obtained from the value of $A^{(2)}_{Kg}$ calculated above, if the value of $g^{(2)}_{gg}$ is known.

The Zeeman effect of the microwave spectrum of H_2CO was studied by Kondo et al. with an absorption type spectrometer.[10] Their results are listed in Table IV. From Eq. (A10), nuclear parts of the rotational g tensor of H_2CO are calculated with the same assumptions as have been assumed in calculating $A^{(1)}_{Kg}$. The electronic parts are obtained by subtracting the nuclear parts from the experimental values. The results are listed in Table IV.

Table IV. Molecular g tensor of H_2CO.

Components	Nuclear (Calculated) (kc)	Electronic (kc)	Totals*) (Experimental) (kc)
g_{xx}	0.305	−0.285	0.02±0.10
g_{yy}	0.317	−0.667	−0.35±0.10
g_{zz}	0.503	−3.403	−2.90±0.05

*) Determined by K. Kondo et al.[10]

Putting the values of $A^{(2)}_{Kg}$ and $g^{(2)}_{gg}$ in Eq. (12), we obtain

$$-A^{(2)}_{Kx}/(g_H\mu_N{}^2g^{(2)}_{xx})=2.01\times10^{24}\ \text{cm}^{-3}\ ,$$
$$-A^{(2)}_{Ky}/(g_H\mu_N{}^2g^{(2)}_{yy})=0.58\times10^{24}\ \text{cm}^{-3}\ ,$$
$$-A^{(2)}_{Kz}/(g_H\mu_N{}^2g^{(2)}_{zz})=1.48\times10^{24}\ \text{cm}^{-3}\ .$$

These values should agree to give the value of $\langle r^{-3}_{\text{electron}}\rangle_{\text{av}}$. Though they differ with each other, their differences are not significant because the relative errors for the experimental values of β and g_{xx} exceed 100 percent (See Table III and IV). The most precise value of $\langle r^{-3}_{\text{electron}}\rangle_{\text{av}}$ is obtained from $A^{(2)}_{Kz}/(g_H\mu_N{}^2g^{(2)}_{zz})$, because the relative experimental errors of γ and g_{zz} are much smaller than that of α, β, g_{xx} and g_{yy}.

Then, the value of $\langle r^{-3}_{\text{electron}}\rangle_{\text{av}}$ is determined as;

$$\langle r^{-3}_{\text{electron}}\rangle_{\text{av}}=1.5\times10^{24}\ \text{cm}^{-3}\ .$$

This is very much larger than that of pure $2p$ orbitals in hydrogen, and it shows that assuming the excited state as a p-electron is questionable. This is the same conclusion as

White[6] obtained for H_2, but the circumstances are more complicated in the present case, because the electrons in the bonding orbitals of the sp^2 hybridized carbon atom play a principal role in H_2CO.

Acknowledgements

The auther would like to express his hearty thanks to Professor K. Shimoda, for his encouragements, valuable advice and inspirations throughout this work. He also thanks to Messrs. T. Shimizu and K. Kondo for their assistances in experiment and discussions on this subject.

Appendix

Zeeman effect of the rotational spectrum of H_2CO by an absorption type spectrometer will be discussed here briefly.[*]

The hyperfine splittings are assumed to be negligibly small, and only the first order Zeeman effect is considered. The Hamiltonian for this problem is;

$$\mathscr{H}=C(J_x-L_x)^2+B(J_y-L_y)^2+A(J_z-L_z)^2$$
$$+\frac{e}{2c}\sum_i(\boldsymbol{r}_i\times\boldsymbol{v}_i)\cdot\boldsymbol{H}-\frac{e}{2c}\sum_K Z_K(\boldsymbol{r}_K\times\boldsymbol{v}_K)\cdot\boldsymbol{H}\,. \tag{A1}$$

In order to treat the Hamiltonian in the same way as that of the magnetic hyperfine structure, the external field H will be described by the molecular fixed coordinate system.

$$\left.\begin{aligned}H_x&=\lambda_{xZ}H\\H_y&=\lambda_{yZ}H\\H_z&=\lambda_{zZ}H\end{aligned}\right\}, \tag{A2}$$

where λ_{xZ}, λ_{yZ} and λ_{zZ} are the direction cosines of x, y and z axes with respect to the space fixed Z axis. The direction of the static field is chosen as the Z axis. Zeeman energy is then described as

$$\varDelta W_Z=-\mu_N\sum_g\sum_{g'}g_{gg'}J_gH_{g'}\,, \tag{A3}$$

where $g_{gg'}$ is the rotational g tensor of the molecule.

The Hamiltonian is devided into two parts in the same way as that of the magnetic hyperfine interaction: one which includes only diagonal terms in the electronic wave function and the other which includes off diagonal terms. The diagonal part $\boldsymbol{H}^{(1)}$ is given as

$$H^{(1)}=CJ_x^2+BJ_y^2+AJ_z^2$$
$$-\frac{e}{2c}\sum_K Z_K(\boldsymbol{r}_K\times\boldsymbol{v}_K)\cdot\boldsymbol{H}\,, \tag{A4}$$

After a little manipulation, we find

$$\langle o|\boldsymbol{H}^{(1)}|o\rangle$$
$$=-\mu_N(g_{xx}^{(1)}J_xH_x+g_{yy}^{(1)}J_yH_y+g_{zz}^{(1)}J_zH_z)\,, \tag{A5}$$
$$g_{gg}^{(1)}=\frac{eA_g}{\mu_N c\hbar}\sum_K Z_K(\boldsymbol{r}_K{}^2-r_{Ky}^2)\,,$$

where $g_{gg}^{(1)}$ is the rotational g tensor of the molecule due to the rotation of nuclear charges.

The effective part of the Hamiltonian which includes off diagonal terms is

$$\boldsymbol{H}^{(2)}=-2CJ_xL_x-2BJ_yL_y-2AJ_zL_z$$
$$+\frac{e}{2c}\sum_i(\boldsymbol{r}_i\times\boldsymbol{v}_i)\cdot\boldsymbol{H}\,. \tag{A6}$$

Thus the electronic part in the result of the perturbation calculation is written as

$$\sum_{n\neq0}(E_n-E_0)^{-1}\langle o|H^{(2)}|n\rangle\langle n|H^{(2)}|o\rangle$$
$$=\sum_g\sum_{g'}\mathfrak{M}_{gg'}J_{g'}J_g+\sum_g\sum_{g'}\mathfrak{H}_{gg'}J_gH_{g'}\,, \tag{A7}$$

where the second order terms on H are neglected, and

$$\mathfrak{M}_{gg'}=\sum_{n\neq0}4(E_0-E_n)^{-1}A_gA_{g'}\langle o|L_g|n\rangle\langle n|L_{g'}|o\rangle$$
$$\mathfrak{H}_{gg'}=-\frac{eA_g}{c}\sum_{n\neq0}(E_0-E_n)^{-1}[\langle o|L_g|n\rangle\langle n|\sum_i(\boldsymbol{r}_i\times\boldsymbol{v}_i)_{g'}|o\rangle \tag{48}$$
$$+\langle o|\sum(\boldsymbol{r}_i\times\boldsymbol{v}_i)_{g'}|n\rangle\langle n|L_g|o\rangle]$$

The term $\sum\sum\mathfrak{M}_{gg'}J_gJ_{g'}$, will not be considered here, because it is the same experssion as the rotational energy of the molecule, and included in it.

Therefore, the Zeeman energy due to the excitation of electrons is obtained as

$$\varDelta W_Z^{(2)}=-\mu_N\sum\sum g_{gg'}^{(2)}J_gH_g\,,$$
$$g_{gg'}^{(2)}=-\frac{eA_g}{\mu_N c}\sum_{n\neq0}(E_n-E_0)^{-1} \tag{A9}$$
$$\times[\langle o|L_g[n\rangle\langle n|\sum_i(\boldsymbol{r}_i\times\boldsymbol{v}_i)_{g'}|o\rangle+\langle o|\sum_i(\boldsymbol{r}_i\times\boldsymbol{v}_i)_{g'}|n\rangle\langle n|L_g|o\rangle]\,.$$

---

[*] Recently, after this work was finished, more detailed calculation of the magnetic interaction of $^1\Sigma$ state molecules including the second order Zeeman effect has been developed by K. Kondo.

As $m\sum r_i\times v_i$ is the electronic angular momentum of the molecule, the diagonal terms of the rotational g tensor of the molecule are obtained as below;

$$g_{gg}=g_{gg}^{(1)}+g_{gg}^{(2)}$$

$$g_{gg}^{(1)}=\frac{eA_g}{\mu_N c\hbar}\sum_K Z_K(r_K{}^2-r_{Kg}^2) \tag{A10}$$

$$g_{gg}^{(2)}=-\frac{4A_g\mu_B}{\mu_N}\sum_{n\neq 0}(E_n-E_0)^{-1}|\langle o|L_g|n\rangle|^2 ,$$

where μ_B is the Bohr magneton and m the electron mass. Eq. (A10) is the extension of Eq. (22) by White[6] to an asymmetric top molecule with C_{2v} symmetry.

References

1) J. P. Gordon: Phys. Rev. **99** (1955) 1253.
2) H. Takuma, T. Shimizu and K. Shimoda: J. Phys. Soc. Japan **14** (1959) 1595.
3) P. Thaddeus, J. Loubser, L. Krisher and H. Lecar: J. Chem. Phys. **31** (1959) 1677.
4) K. Shimoda and K. Kondo: J. Phys. Soc. Japan **15** (1960) 1125.
5) G. P. Gunther-Mohr, C. H. Townes and J. H. Van Vleck: Phys. Rev. **94** (1954) 1191.
6) R. L. White: Rev. Mod. Phys. **27** (1955) 276.
7) A. Okaya: J. Phys. Soc. Japan **11** (1956) 249.
8) K. Shimoda, H. Takuma and T. Shimizu: J. Phys. Soc. Japan **15** (1960) 2036.
9) D. W. Posener: Austral. J. Phys. **11** (1958) 1.
10) K. Kondo, H. Hirakawa, A. Miyahara, T. Oka and K. Shimoda: J. Phys. Soc. Japan **15** (1960) 303.

JOURNAL OF THE PHYSICAL SOCIETY OF JAPAN, Vol. 16, No. 2, FEBRUARY, 1961

Some Remarks on Hydrostatic Pressure and Maxwell Model

By Wataru SEGAWA

College of Humanities and Sciences, Nihon University, Tokyo

(Received October 7, 1960)

The difference between hydrostatic pressure and isotropic component of stress tensor was early mentioned by Reiner in his theory of dilatancy. In the recent development of the theory of viscoelasticity, however, it seems that this distinction becomes fade and is slightened. In this paper, this distinction is rigorously discussed in relation to Maxwell model.

It has been shown that as far as we stay at the assumption that actual stress is equivalent to elastic stress and also to viscous stress and the condition that viscous stress vanishes when viscous strain rate becomes zero, derived Maxwell's formulas can not contain hydrostatic pressure.

§ 1. Introduction

The extention of classical Maxwell's formula to three-dimensional case was initially done by T. Alfrey.[1] However, either the classical formula or Alfrey's formula are founded on the assumption that strain and strain rate are sufficiently small and so are not valid to the cases of large strain and strain rate. Recently, new theories have been developed by Yamamoto[2] and Segawa,[3] which are valid for non-linear viscoelasticity, basing on the extended Maxwell model. Now, we must remember that the classical Maxwell model is the series combination of a Hookeian spring and a Newtonian dashpot and the actual stress is equivalent to the elastic stress and also to the viscous stress. On the other hand, the Maxwell model in the theory of non-linear viscoelasticity is the series combination of a non-Hookeian spring and a non-Newtonian dashpot, though the assumption that the elastic stress is the same as the viscous stress is conserved, as far as we stand in the idea of the series combination of a spring and a dashpot.

The viscous stress is such stress as it vanishes when the viscous strain rate becomes zero. Thus, we can expect that either elastic stress or viscous stress becomes zero when the viscous strain rate vanishes, considering the property of the series combination of a spring and a dashpot. Then, hydrostatic pressure must also vanish because it is a kind of the elastic stress.

The difference between the hydrostatic pressure and the isotropic component of stress was early emphasized by Reiner in his mathematical theory of the dilatancy.[4] In the recent development of the theories of viscoelasticity, however, this distinction seems to have been treated carelessly. In this paper, we will discuss how this distinction is important, especially in relation to Maxwell's formula and some remarks will be done, relating to hydrostatic pressure and Maxwell model.

§ 2. Hydrostatic Pressure and Isotropic Component of Stress Tensor

After Reiner,[4] component of the stress, the strain and the strain rate tensor in the liquid are written as follows:

$$T^{*\lambda\mu}=T^*\delta_{\lambda\mu}+T'^{\lambda\mu}\ , \qquad (2.1)$$

$$e_{\lambda\mu}=e\delta_{\lambda\mu}+e'_{\lambda\mu}\ , \qquad (2.2)$$

$$f_{\lambda\mu}=f\delta_{\lambda\mu}+f'_{\lambda\mu}\ , \qquad (2.3)$$

respectively, where $\delta_{\lambda\mu}$ is the Kronecker's delta, and

$$T'^{\lambda\lambda}=e'_{\lambda\lambda}=f'_{\lambda\lambda}=0\ , \qquad (2.4)$$

$$T^{*\lambda\lambda}=3T^*\ ,\quad e_{\lambda\lambda}=3e\ ,\quad f_{\lambda\lambda}=3f\ . \qquad (2.5)$$

In Eq. (2.1), T^* and $T'^{\lambda\mu}$ express the isotropic components and the deviatoric components of the stress tensor, respecticely. Moreover, this equation can be rewritten as follows:

$$T^{*\lambda\mu}=(T-p)\delta_{\lambda\mu}+T'^{\lambda\mu} \qquad (2.6)$$

where p represents the hydrostatic pressure and is regarded as a function of the isotropic components of strain tensor e:

$$p=p(e) \qquad (2.7)$$

and T and $T'^{\lambda\mu}$ are the functions of isotropic components of the strain rate tensor and of components of the strain rate tensor, respectively:

$$T=T(f)\ ,\quad T(0)=0 \qquad (2.8)$$

$$T'^{\lambda\mu}=T'^{\lambda\mu}(f_{\lambda\mu}) \qquad (2.9)$$

Putting

$$T^{*\lambda\mu}+p\delta_{\lambda\mu}=T^{\lambda\mu}\ , \qquad (2.10)$$

Eq. (2.6) becomes

$$T^{\lambda\mu}=T\delta_{\lambda\mu}+T'^{\lambda\mu}\ , \qquad (2.11)$$

which in the case of liquid is a function of only components of strain rate tensor and just corresponds to $T_v^{\lambda\mu}$ in § 3. From Eq. (2.10), we have

$$T^*=T-p=T(f)-p(e)\ . \qquad (2.12)$$

From the above consideration, we can see that hydrostatic pressure p is not equivalent of the isotropic component of the stress tensor T^*, but such part of it as remains when $f_{\lambda\mu}=0$. This fact was initially pointed out by Reiner. We must also take care of the fact that hydrostatic presure vanishes when $e_{\lambda\mu}=0$ because $e=0$ if $e_{\lambda\mu}=0$.

§ 3. Hydrostatic Pressure and Maxwell Model

As it is well-known, characteristic properties of Maxwell model are represented by two assumptions that (1) the actual stress is equivalent to the elastic stress and also to the viscous stress and (2) the actual strain is the sum of the elastic strain and the viscous strain. In the theory of three-dimensional non-linear viscoelasticity,[2,3] the second assumption has been improved so that the actual strain rate is the sum of the elastic strain rate and the viscous strain rate but the first assumption has not been improved substantially.

Let the actual stress, the elastic stress and the viscous stress be denoted by $T^{\lambda\mu}$, $T_e^{\lambda\mu}$ and $T_v^{\lambda\mu}$ respectively, then the first condition is expressed by

$$T^{\lambda\mu}=T_e^{\lambda\mu}=T_v^{\lambda\mu} \qquad (3.1)$$

Moreover, let the actual strain rate, the elastic strain rate and the viscous strain rate be $f_{\lambda\mu}, f_{e\lambda\mu}$ and $f_{v\lambda\mu}$, respectively, then the second conditioned will be represented by

$$f_{\lambda\mu}=f_{e\lambda\mu}+f_{v\lambda\mu}\ . \qquad (3.2)$$

Similarly as above, let the actual strain, elastic strain and viscous strain be denoted by $e_{\lambda\mu}$, $e_{e\lambda\mu}$ and $e_{v\lambda\mu}$, respectively. Then, we can assume that

$$T_e^{\lambda\mu}=T_e^{\lambda\mu}(e_{e\lambda\mu})\ ,\quad T_e^{\lambda\mu}=0 \text{ when } e_{e\lambda\mu}=0 \qquad (3.3)$$

and

$$T_v^{\lambda\mu}=T_v^{\lambda\mu}(f_{v\lambda\mu})\ ,\quad T_v^{\lambda\mu}=0 \text{ when } f_v^{\lambda\mu}=0 \qquad (3.4)$$

It seems that Eq. (3.3) and Eq. (3.4) are surely natural and reasonable assumptions to be employed whenever we want to develop any theory of viscoelasticity. But as soon as we admit these assumptions we will encounter unpleasant results as we shall see just later.

As we have seen in § 2, hydrostatic pressure is such part of the isotropic components of stress tensor as remains when $f_{v\lambda\mu}=0$. But, if $f_{v\lambda\mu}=0$, we have from Eq. (3.4)

$$T_v^{\lambda\mu}=0$$

and from Eq. (3.1) also

$$T_e^{\lambda\mu}=0$$

and at the same time hydrostatic pressure will vanish because it belongs to the elastic stress.

From the above circumstances, we can see that hydrostatic pressure is not contained in Maxwell model and accordingly in Maxwell's formulas and this fact is natural result as far as we admit Eq. (3.1), Eq. (3.4) and the definition of hydrostatic pressure as mentioned above.

If we want to avoid this obstacle, we should adopt any other model different from the Maxwell model as mentioned above. For instance, we could employ such a model as parallel combination of a spring and a Maxwell element, but then we could no longer call that model a Maxwell model in the same sense of this paper and moreover we would face another obstacle.

Finally, we must notice that in Voigt model the circumstances are quite different from the above, there exist no obstacles, because now actual stress is the sum of elastic stress and viscous stress and elastic stress never vanishes even if viscous stress becomes zero.

§ 4. Conclusions

Hydrostatic pressure is such part of the isotropic components of the stress tensor as remains when components of the viscous strain rate tensor vanish. Whereas, as the condition that component of actual stress tensor is equivalent to that of the elastic stress tensor and also to that of the viscous stress tensor is assumed in Maxwell model and as components of the viscous stress tensor vanish when components of the viscous strain rate tensor becomes zero, we can conclude that the hydrostatic pressure can not be contained in the rheological equations of Maxwell model as far as we conserve the above conditions.

References

1) T. Alfrey: *Mechanical Behaviors of High Polymer* (Interscience Publ., New York, 1948) 208.

2) M. Yamamoto: J. Phys. Soc. Japan **14** (1959), 313; Suppl. Prog. Theor. Phys. **10** (1959), 19.

3) W. Segawa: Busseriron Kenkyu **2-4** (1958), 13 (in Japanese); J. Phys. Soc. Japan **14** (1959) 1102; **15** (1960) 339.

4) M. Reiner: Amer. J. Math. **67** (1945) 350.

JOURNAL OF THE PHYSICAL SOCIETY OF JAPAN, Vol. 16, No. 2, FEBRUARY, 1961

Rheological Equations of Generalized Maxwell Model and Voigt Model in Three-Dimensional, Non-Linear Deformation.

By Wataru SEGAWA

College of Humanities and Sciences, Nihon University, Tokyo

(Recieved October 24, 1960)

It is well known that the generalized Maxwell model and Voigt are very useful for description at the mechainical behaviours of the materials having the distribution of relaxation times or retardation times, as far as the deformation of the materials is one-dimensional and the strain and the strain rate are sufficiently small. In this paper, these two models have been extended so as to be applicable to three-dimensional and non-linear deformations of initially isotropic materials and two sets of rheological equations corresponding to each of such extended models have been obtained.

It has been also shown that, the condition of small deformation being introduced, each of the two sets are reduced to three-dimensional extensions of the corresponding classical equations, and moreover, the three-dimensionaly extended formulas, which are applied to simple elongation, are reduced to the corresponding classical (one-dimensional) equations for the case of simple elongation.

§1. Introduction

In the previous papers[1) 2)], we have derived the rheological equations of the Maxwell model and the Voigt model in the case of three-dimensional, non-linear deformation. Similar derivation was also done by Yamamoto[3)], in somewhat different formulation from our's.

In these treatment, one-dimensional, classical models have been extended so as to be applicable to three-dimensional, non-linear deformations. For instance, in the classical Maxwell model actual strain is the sum of elastic strain and viscous strain, whereas in our Maxwell model actual strain rate is the sum of elastic strain rate and viscous strain rate. Moreover, in order to represent nonlinearity, Hookeian spring and Newtonian dashpot have been replaced by non-Hookeian spring and non-Newtonian dashpot, respectively, and to be valid for three-dimensional deformation, various relations have been described by the components of their tensors.

As is well known, in the classical theory of viscoelasticity we considered the generalized Maxwell model and Voigt model having the distribution of relaxation times and retardation times, respectively, in order to represent the mechanical behaviours of materials and the former is the parallel combination of Maxwell elements and the latter is the series combination of Voigt elements.[4)]

In this paper, under the similar considerations of the previous papers, we will derive the rheological equations of the generalized models in the case of three-dimensional and nonlinear deformations of initially isotropic materials and moreover we will make clear how the above equations will be reduced to the corresponding classical formulas or the three-dimensional extensions of them.

§2. Rheological Equation of Generalized Maxwell Model

Let the quantities relating to p-th Maxwell element be denoted by subscript p.

The generalized Maxwell model in three-dimensional case will be specified by the condition

$$T^{\lambda\mu}=\sum_{p=1}^{n}T_p{}^{\lambda\mu} \tag{2.1}$$

where $T^{\lambda\mu}$ is the component of stress tensor (referred to the deformed state), and $T_p{}^{\lambda\mu}$ is the component of stress tensor in p-th Maxwell element.

Let the coordinates of a material particle in underformed state and deformed state (when elastic process alone took place in p-th Maxwell element) be denoted by x^i and $y_p{}^{*\lambda}$, respectively, in a rectangular coordinate system fixed in space. Then, strain rate-stress relation in p-th Maxwell element may be represented by

$$f_{\lambda\mu}=\frac{\partial y_p{}^{*\lambda}}{\partial x^i}\frac{\partial y_p{}^{*\mu}}{\partial x^j}\frac{d}{dt}\left\{\frac{\partial x^i}{\partial y_p{}^{*\alpha}}\frac{\partial x^j}{\partial y_p{}^{*\beta}}(A_p\delta_{\alpha\beta}+B_pT_p{}^{\alpha\beta}+C_pT_p{}^{\alpha\gamma}T_p{}^{\gamma\beta})\right\}+D_p\delta_{\lambda\mu}+E_pT_p{}^{\lambda\mu}+F_pT_p{}^{\lambda\nu}T_p{}^{\nu\mu} \qquad (2.2)^{1)}$$

where $f_{\lambda\mu}$ is the component of strain rate tensor and $A_p, B_p, C_p, D_p, E_p, F_p$ are the functions of stress invariants defined by

$$T_{p1}=T_p{}^{\lambda\lambda}, \qquad T_{p2}=\frac{1}{2}T_p{}^{\lambda\mu}T_p{}^{\lambda\mu},$$

$$T_{p3}=\frac{1}{3}T_p{}^{\lambda\nu}T_p{}^{\nu\mu}T_p{}^{\mu\lambda}. \tag{2.3}$$

In Eq. (2.2), we must notice that $\lambda, \mu, \cdots$, $i, j, \cdots$ etc. are so-called *dummy index*, but p is not so. This convention will be used throughout this article.

A component of strain tensor in p-th Maxwell element will be given by

$$e_{p\lambda\mu}=\frac{1}{2}(y^{*\lambda}_{p,i}y^{*\mu}_{p,i}-\delta_{\lambda\mu}) \tag{2.4}$$

where $y^{*\lambda}_{p,i}$ represents $\partial y_p{}^{*\lambda}/\partial x^i$ and $\delta_{\lambda\mu}$ is the Kronecker's delta. The strain stress relation is written as follows

$$e_{p\lambda\mu}=A_p\delta_{\lambda\mu}+B_pT_p{}^{\lambda\mu}+C_pT_p{}^{\lambda\nu}T_p{}^{\nu\mu} \tag{2.5}$$

which has appeared in Eq. (2.2).

By virtue of Eqs. (2.4) and (2.5), together with other conditions, we can decide $y^{*\lambda}_{p,i}$ (and accordingly $\partial x^i/\partial x_p{}^{*\lambda}$) ($\lambda, i=1, 2, 3$) as the functions of $T_p{}^{\lambda\mu}$($\lambda, \mu=1, 2, 3$), then Eq. (2.2) becomes the relation between $f_{\lambda\mu}$ and $T_p{}^{\lambda\mu}$. Thus, Eqs. (2.1) and (2.2) express the rheological equation of generalized Maxwell model for the material which is isotropic in the natural state.

When deformation is sufficiently small, we can use the relation

$$\frac{\partial y_p{}^{*\lambda}}{\partial x^i}\frac{\partial y_p{}^{*\mu}}{\partial x^j}=\delta_{\lambda i}\delta_{\mu j}\,,$$

$$\frac{\partial x^i}{\partial y_p{}^{*\alpha}}\frac{\partial x^j}{\partial y_p{}^{*\beta}}=\delta_{i\alpha}\delta_{j\beta}, \tag{2.6}$$

and the strain-stress relation and the strain rate-stress relation will become linear. Substituting these conditions into Eq. (2.2), we have

$$f_{\lambda\mu}=\frac{d}{dt}(A_p\delta_{\lambda\mu}+B_pT_p{}^{\lambda\mu})+D_p\delta_{\lambda\mu}+E_pT_p{}^{\lambda\mu} \tag{2.7}$$

where, denoting the shear modulus by μ_p and the coefficient of viscosity by η_p,

$$\left.\begin{aligned}A_p&=-\frac{1}{6\mu_p}T_{p1}, & B_p&=\frac{1}{2\mu_p}\\ D_p&=-\frac{1}{6\eta_p}T_{p1}, & E_p&=\frac{1}{2\eta_p}\end{aligned}\right\}. \tag{2.8}$$

if the material is incompressible and isotropic.

Eqs. (2.1) and (2.7), together with Eq. (2.8), are three-dimensional extension of the classical equation of generalized Maxwell model.

Let us apply Eqs. (2.1) and (2.7) to incompressible, simple elongation which is specified by

$$\left.\begin{aligned}&T^{11}\neq0, \quad \text{all others}=0\\ &T_p{}^{11}\neq0, \quad \text{all others}=0\\ &f_{\lambda\mu}=0 \text{ if } \lambda\neq\mu\\ &f_{22}=f_{33}=-\frac{1}{2}f_{11}\\ &T_{p1}=T_p{}^{11}\end{aligned}\right\} \tag{2.9}$$

Putting $T^{11}=T$, $T_p{}^{11}=T_p$, $f_{11}=f$, we have from Eq. (2.1)

$$T=\sum_{p-1}^{n}T_p \tag{2.10}$$

and from Eq. (2.7)

$$\left.\begin{aligned}&f=\frac{d}{dt}\left(-\frac{1}{6\mu_p}T_p+\frac{1}{2\mu_p}T_p\right)-\frac{1}{6\eta_p}T_p+\frac{1}{2\eta_p}T_p\\ &-\frac{1}{2}f=\frac{d}{dt}\left(-\frac{1}{6\mu_p}T_p\right)-\frac{1}{6\eta_p}T_p\end{aligned}\right\}, \tag{2.11}$$

accordingly,

$$f=\frac{1}{3\mu_p}\frac{dT_p}{dt}+\frac{1}{3\eta_p}T_p \tag{2.11}$$

Eq. (2.10) and (2.11) are equivalent to the classical equation of generalized Maxwell model.4)

§ 3. Rheological Equation of Generalized Voigt Model

Generalized Voigt model for three-dimensional deformations may be characterized by the condition

$$f_{\lambda\mu}=\sum f_{p\lambda\mu} \tag{3.1}$$

where $f_{p\lambda\mu}$ represents the component of strain rate tensor in the p-th Voigt element. (In this paragraph, we will represent the quantities relating to the p-th Voigt element by subscript p)

The rheological equation to the p-th element of Voigtian material which is isotropic in its natural state will be represented by

$$\begin{aligned} T^{\lambda\mu} &= L_p\delta_{\lambda\mu}+M_p e_{p\lambda\mu}+N_p e_{p\lambda\mu}e_{p\nu\mu} \\ &\quad +P_p\delta_{\lambda\mu}+Q_p f_{p\lambda\mu}+R_p f_{p\lambda\nu}f_{p\nu\mu} \qquad (3.2)^{2)\,3)} \end{aligned}$$

where $T^{\lambda\mu}$ is a component of stress tensor, $e_{p\lambda\mu}$ represents a component of strain tensor in p-th Voigt element, and L_p, M_p, N_p, P_p; Q_p, R_p are functions of the strain invariants and the strain rate invariants, respectively, defined by

$$\left.\begin{aligned} & e_{p1}=e_{p\lambda\lambda}, \quad e_{p2}=\frac{1}{2}e_{\lambda p\mu}e_{p\lambda\mu}, \\ & e_{p3}=\frac{1}{3}e_{p\lambda\nu}e_{p\nu\mu}e_{p\mu\lambda} \\ & f_{p1}=f_{p\lambda\lambda}, \quad f_{p2}=\frac{1}{2}f_{p\lambda\mu}f_{p\lambda\mu} \\ & f_{p3}=\frac{1}{3}f_{p\lambda\nu}f_{p\nu\mu}f_{p\mu\lambda} \end{aligned}\right\} \qquad (3.3)$$

If the material is incompressible, L_p will be reduced to an undetermined coefficient φ, and f_{p1} will become zero.

Strain component in the p-th Voigt element may be defined by

$$e_{p\lambda\mu}=\frac{1}{2}(y^{*\lambda}_{p,i}y^{*\mu}_{p,i}-\delta_{\lambda\mu}) \qquad (3.4)$$

where $y^{*\lambda}_{p,i}$ represents $\partial y_p{}^{*\lambda}/\partial x^i$ and x^i and $y_p{}^{*\lambda}$ express the coordinates of a material particle of undeformed and deformed states in the p-th Voigt element, respectively. Moreover, strain components and strain-rate components are related to each other as follows:

$$e_{p\lambda\mu}=y^{*\lambda}_{p,i}y^{*\mu}_{p,j}\int\frac{\partial x^i}{\partial y_p{}^{*\alpha}}\frac{\partial x^j}{\partial y_p{}^{*\beta}}f_{p\alpha\beta}dt \qquad (3.5)$$

or

$$f_{p\lambda\mu}=y^{*\lambda}_{p,i}y^{*\mu}_{p,j}\frac{d}{dt}\left(\frac{\partial x^i}{\partial y_p{}^{*\alpha}}\frac{\partial x^j}{\partial y_p{}^{*\beta}}e_{p\alpha\beta}\right). \qquad (3.5')^{1)}$$

Then, we can express $e_{p\lambda\mu}(\lambda, \mu=1, 2, 3)$ as the function of $f_{p\lambda\mu}(\lambda, \mu=1, 2, 3)$ by virtue of Eqs. (3.4) and (3.5). Thus, Eq. (3.1), Eq. (3.2), together with Eqs. (3.4) and (3.5), constitute the rheological equation of the generalized Voigt model for the material which is isotropic in natural state.

When the deformation is sufficiently small, Eq, (3.2) will become linear, and using the relation

$$y^{*\lambda}_{p,i}y^{*\mu}_{p,j}=\delta_{\lambda i}\delta_{\mu j}, \quad \frac{\partial x^i}{\partial y_p{}^{*\alpha}}\frac{\partial x^j}{\partial y_p{}^{*\beta}}=\delta_{i\alpha}\delta_{j\beta} \qquad (3.6)$$

Eq. (3.5) and Eq. (3.5′) will be reduced to

$$e_{p\lambda\mu}=\int f_{p\lambda\mu}dt \quad \text{and} \quad f_{p\lambda\mu}=\frac{d}{dt}e_{p\lambda\mu} \qquad (3.7)$$

respectively. We must notice that Eq. (3.7) is valid as far as we concern with small deformation, on the other hand in large deformation strain rate is not given mere by the time derivative of strain but by Eq. (3.5′). Thus, Eq. (3.2) will be reduced to

$$T^{\lambda\mu}=L_p\delta_{\lambda\mu}+M_p e_{p\lambda\mu}+P_p\delta_{\lambda\mu}+Q_p f_{p\lambda\mu} \qquad (3.8)$$

where, denoting the shear modulus by μ_p and the coefficient of viscosity by η_p

$$M_p=2\mu_p, \quad Q_p=2\eta_p$$

and L_p and P_p are linear functions of e_{p1} and f_{p1}, respectively. Moreover, if the material is incompressible, Eq. (3.8) will be reduced to

$$T^{\lambda\mu}=\varphi\delta_{\lambda\mu}+2\mu_p e_{p\lambda\mu}+2\eta_p f_{p\lambda\mu} \qquad (3.9)$$

where φ is an undetermined coefficient. Eq. (3.1) and (3.9) express the three-dimensional extension of the classical rheological equation of generalized Voigt model.

In the case of incompressible materials, simple elongation is specified by

$$\left.\begin{aligned} & T^{11}\neq 0, \text{ all others}=0 \\ & f_{\lambda\mu}=0 \text{ if } \lambda\neq\mu, \ f_{22}=f_{33}=-\frac{1}{2}f_{11} \\ & f_{p\lambda\mu}=0 \text{ if } \lambda\neq\mu, \ f_{p22}=f_{p33}=-\frac{1}{2}f_{p11} \\ & e_{p\lambda\mu}=0 \text{ if } \lambda\neq\mu, \ e_{p22}=e_{p33}=-\frac{1}{2}e_{p11} \end{aligned}\right\} \qquad (3.10)$$

Putting $T^{11}=T$, $f_{11}=f$, $f_{p11}=f_p$ and $e_{p11}=e_p$ we have from Eq. (3.1)

$$f=\sum_p f_p \qquad (3.11)$$

and from Eq. (3.9)

$$\left.\begin{aligned} & T=\varphi+2\mu_p e_p+2\eta_p f_p \\ & 0=\varphi+2\mu_p\left(-\frac{1}{2}e_p\right)+2\eta_p\left(-\frac{1}{2}f_p\right) \end{aligned}\right\}$$

or

$$T=3\mu_p l_p+3\eta_p f_p \qquad (3.12)$$

Eqs. (3.11) and (3.12) represent the classical equation of generalized Voigt model in the case of simple elongation.[4]

§ 4. Discussions

In the precedings, we have derived two sets of rheological equations for the generalized Maxwell model and Voigt model in the case of three-dimensional, non-linear deformations, and it has been shown that, the conditions of small deformation being introduced, the derived equations are reduced to three dimensional extensions of the corresponding classical equations, which, in turn, being applied to simple elongation, are reduced to the corresponding classical equations. We can easily show that the three-dimensionally extended formulas are also reduced to the corresponding classical equations in the case of simple shear, the conditions of simple shear being introduced.

As we have seen, any Hookian spring and any Newtonian dashpot have been thoroughly replaced by non-Nookian spring and non-Newtonian dashpot, respectively, and stress-strain-strain rate relations in the most general type have been effectively utilized.

Eq. (2.1) and (2.2), together witn Eq. (2.4), (2.5), can serve for solving actual problems of general deformation of Maxwellian material which is isotropic in natural state, in principle. But, these equations are very complicated and such calculations will be much involved, because of non-linearity of the equations. The same is true in the case of Eq. (3.1), (3.2), (3.4) and (3.5). More detailed discussions relating to these problems and others will be done later.

References

1) W. Segawa: J. Phy. Soc. Japan **15** (1960) 339.
2) W. Segawa: J. Phy. Soc. Japan **14** (1959) 1102.
3) M. Yamamoto: J. Phy. Soc. Japan **14** (1959) 313; Suppl. Prog. Theor. Phy. **10** (1959) 19.
4) T. Alfrey: *Mechanical Behaviors of High Polymer* (Interscience Publ, New York, 1948) 127, 539.
T. Alfrey and E. F. Gurnee: *Dynamics of Viscoelastic Behavior*, Rheology Vol. 1, ed. by F. R. Eirich (Academic Press, New York, 1956) Chap. II.

JOURNAL OF THE PHYSICAL SOCIETY OF JAPAN, Vol. 16, No. 2, FEBRUARY, 1961

The Velocity Distribution at the Interface between Two Liquids

By Setsuo OKUDA

Department of Physics, Okayama University, Okayama

(Received October 31, 1960)

By carrying out detailed experiments in a water flume of dimensions 180 cm×50 cm×15 cm we have observed, by the use of a suitable colouring material, the velocity distribution near the interface between two superposed liquids having different densities, the lighter liquid flowing over the heavier one confined in a hollow. It has thus been found that if there is any difference, however small, between the densities of the two liquids, the velocity of the upper liquid decreases fairly rapidly near the interface, as if it were a solid plane, while the lower liquid is almost at rest in the hollow.

Attempts have then been made to explain the observed flow pattern theoretically. First, a rather simple approximate calculation has been performed by assuming that the two liquids are in direct contact with each other, but no satisfactory explanation of the observed flow pattern has been obtained.

We have next carried out an improved calculation by assuming that there is formed a thin intermediate zone between the two liquids and it has been found that the calculated flow pattern is, in this case, in fairly good agreement with the observed one.

§ 1. Introduction

In natural flows at rivers, lakes and the sea or in artificial flows in chemical engineering process, it is frequently observed that a lighter liquid flows over a heavier one in a concave hollow and that there exists an interface or a thin contacting zone with sharp density gradient between those two liquids. The investigation of such a phenomenon, especially the study of the velocity distribution in the contacting zone, is not only physically interesting for the problem of boundary layer between two liquids, but also practically useful for the technical planning of water supply or the treatment of chemical substance. The purpose of the present study is to observe, by carrying out experiments in a water flume, the velocity distribution in the contacting zone between two liquids having different densities, one of which flows over the other confined in a hollow, and to explain the observed results by theoretical analysis.

§ 2. Experiments

The water flume used in the present experiments is shown in Plate 1.

It consists of two glass side-plates (length being 180 cm and height 50 cm) placed in parallel at a distance of 15 cm and two steel walls and steel bottom. For the scale measurement grid lines with spacing of 10 cm are drawn on the semi-transparent paper pasted on the backside glass plate. For convenience in treatment and application of the obtained results to natural flow, brine was used for heavier liquid and its density was controlled by the concentration of salt, while tap water was used for lighter liquid.

The densities of the liquids were measured by a precise hydrometer (scale interval being 1.000~1.020 gr/cm^3) and it was found that the density difference $\Delta\rho$ between the two liquids did not exceed 0.02 gr/cm^3 which is the maximum value of density difference found in natural water flows under normal conditions.

The thickness of the flowing liquid layer was changed by controlling the positions of the water surface S and the mouths of inlet I and exit E. The lighter liquid was made to circulate by a motor pump M along the course of I→E→C (cock)→M→I and the flow speed was controlled by turning the cock C and regulating the voltage for the motor pump M.

Prior to the present experiments a few physical experiments have been carried out

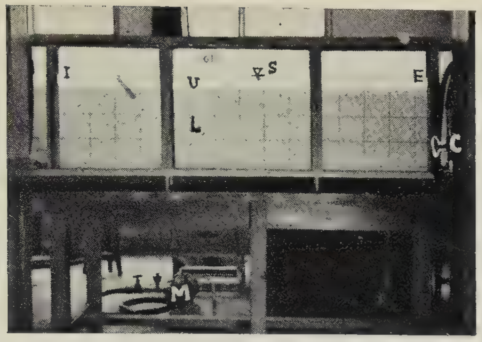

Plate 1. Whole view of water flume and piping system.
I: inlet; E: exit; S: surface; C: cock;
U: upper liquid; L: lower liquid; M: motor

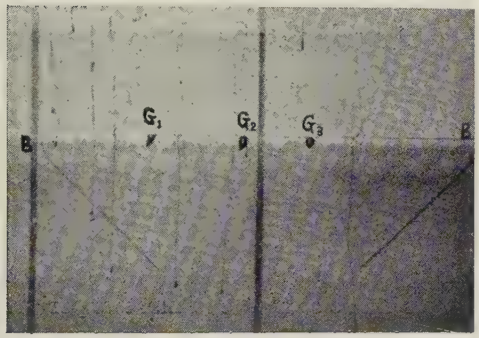

Plate 2. Water-blue lines and small glass spheres G_1, G_2, G_3, whose densities are 1.005, 1.010, 1.015 gr/cm³ respectively. B: bending part of diagonal line at sharp density gradient.

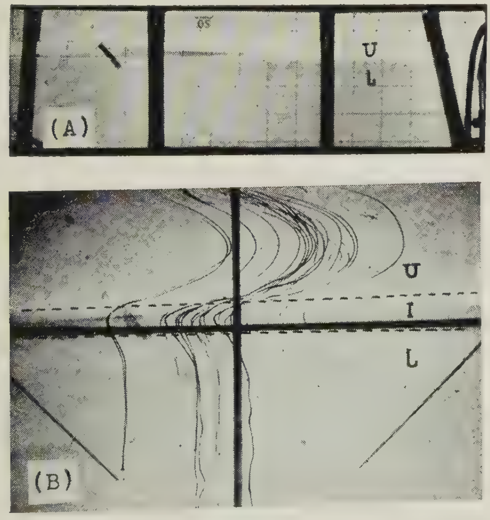

Plate 3. The flow in the upper layer is laminar (Re=250). Re: Reynolds number related to the upper layer.

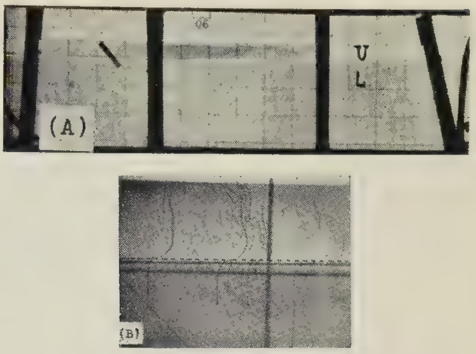

Plate 4. The flow in the upper layer is turbulent (Re=2400).

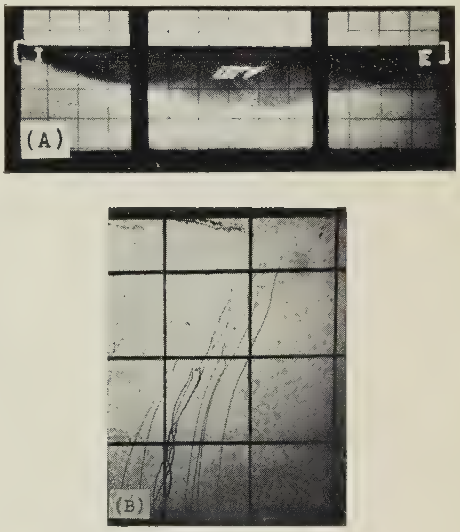

Plate 5. The flow in homogeneous liquid.

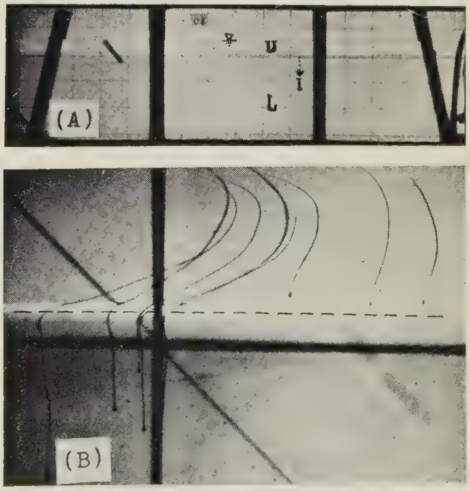

Plate 6. Three-layer flow with intermediate zone.
U: upper liquid: I: intermediate zone;
L: lower liquid

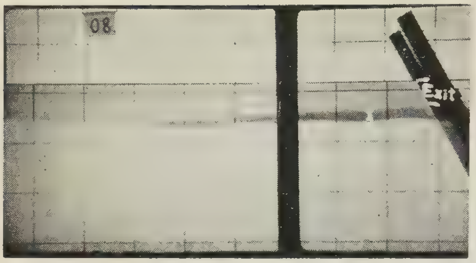

Plate 7. Very thin intermediate zone (I) pressed to the downstream side.

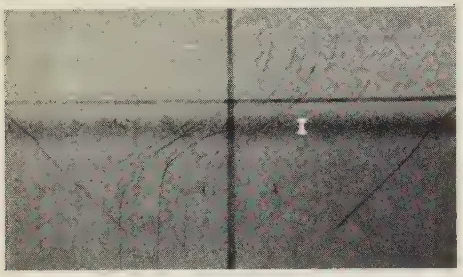

Plate 8. Veloctiy distribution near the intermediate zone (I) which flows out towards the exit.

on stratified water flow.

G. I. Taylor1) observed two-layer flow (tap water flowing over brine in a hollow) in a small water flume (50 cm×6 cm×0.6 cm) in order to explain qualitatively the wind distribution under stabilized condition and G. H. Keulegan2) investigated quantitatively the stability of interface and the mixing of two liquids in various water flumes. In his experiments tap water was made to flow over sugar water.

However, the exact velocity distribution in the contacting zone between two liquids was not determined in their experiments.

In order to determine precisely the velocity distribution in the thin layer, a newly devised "Water-blue Method"3) was applied to the present experiment. When small particles of water-blue (a kind of aniline dye-stuff) of diameters of 0.1∼0.3 mm are plunged into water, they fall down vertically and are dissolved in water and, as shown in Plate 2, there appear blue vertical lines along their paths.

If water flows horizontally, these vertical blue lines shift as time goes on, so that the vertical distribution of the horizontal velocity can be determined by recording the positions of these lines by means of photography or cinematography. It was observed that the flow in the central vertical plane containing flow direction is completely two-dimensional, because the plane is the center of symmetry and the velocity component perpendicular to it vanishes.

In order to determine the density distribution in the contacting zone in motion, small glass spheres4) of various densities, which had been measured precisely beforehand, were put into the zone and their equilibrium positions were observed.

The position at which discontinuous change of density occurs is indicated by a partial bending of the straight line drawn diagonally on the backside wall, as shown in Plate 2, which may be caused by discontinuous change of refractive index5). If ferric chloride is dissolved in brine and potassium ferrocyanide in tap water, prussian blue becomes visible in the mixing zone between two liquids and by observing such a coloured layer it is readily found that the flow in the zone is laminar or turbulent.

For the sake of comparison of the observed results with slow-motion theory, the flow speed was made so slow and the contacting zone was made so stable in most experiments that the coloured layer was very thin and could hardly be recognized in photographs. Lest a small natural convection should occur in the water flume due to the temperature gradient on the side-wall, the temperature of air in the laboratory was kept nearly constant and experiment was not carried out until the temperature of water had become nearly equal to the temperature of air. For convenience in photographing or observation three photo flood lamps (500 W×3) were used to illuminate the wall from behind, but only in short duration lest they should overheat the wall.

Some typical behaviours of the stratified flow as observed by the above-mentioned method are shown in Plates 3, 4, and 5. In each of these plates, the plate with mark (A) shows the general feature of the stratified flow as revealed by pouring the blue ink into the upper liquid at supply mouth, while the plates with mark (B) show the velocity distribution at the central part of the water flume which are visualized by water-blue lines. It is to be noted that the flow in the upper layer is laminar in Plate 3, whereas it is turbulent in Plate 4.

Plate 5 shows the feature of the flow in the case of a homogeneous liquid without density difference.

From these plates it will be seen that when there exists any density difference between two liquids, each liquid flows as if there were a solid plane in the interface, namely, the upper liquid flows with the parabolic velocity distribution in the case of laminar flow or with the flattened one in the case of turbulent flow, while the lower liquid is confined in the hollow and is almost at rest. In the case of a homogeneous liquid without density difference, however, the moving upper layer induces the motion of the lower liquid, and the horizontal velocity decreases continuously.

In the following sections, some analytical calculations are tried in order to explain the remarkable diminution of velocity in the contacting zone between two liquids with density difference.

§ 3. Calculation of the Horizontal Flow in Two Layers, neglecting Vertical Flow

A considerable amount of studies has been carried out so far on two-layer flows stratified vertically. Especially, the velocity distribution in a half jet with infinite layer thickness and infinite horizontal extent has been calculated by G. H. Keulegan[6], R. C. Lock[7] and O. E. Potter[8] for the case of laminar flow, and by S. I. Pai[9] for the case of turbulent flow. But their results that the velocity in the interface is nearly equal to the mean value of the upper and lower velocities are inconsistent with the prompt vanishing of velocity in the contacting zone as observed in the present experiments on a finite flume.

In the branch of estuarine hydrography, on the other hand, many experimental studies[10] have been carried out on the velocity distribution in two-layer flow which consists of upper fresh river water and lower sea water and has finite vertical thickness and infinite horizontal extent. But, their results too cannot be applied to the present experiment for a finite flume.

A. Thom and C. J. Apelt[11] calculated the flow pattern when the horizontally moving liquid with the parabolic velocity distribution flows over the same liquid contained in rectangular hollow whose height is twice as large as its width. The general feature of the calculated flow pattern is very similar to that of the observed one in homogeneous liquid as shown in Plate 5, but as a matter of course their results cannot be applied to the stratified flow with density difference. The stable interface between two liquids with density difference coincides nearly with the ceiling plane of the hollow and the lower liquid is confined and circulates in the hollow.

K. Hidaka[12] calculated the liquid flow in a rectangular hollow subject to the boundary condition that constant tangential stress is acting along the ceiling plane of the hollow. Also, M. Kawaguti[13] calculated a similar flow subject to the boundary condition that there is a constant velocity along the ceiling plane of the hollow. But they did not consider the flow over the ceiling plane. Although both of these authors carried out their rather troublesome calculations by solving the Navier-Stokes equations of motion numerically, yet it will be shown below that a simple calculation can give an approximate flow pattern at the central part of the water flume where the vertical component of velocity is negligibly small.

Hidaka shows that when the liquid circulates in a horizontally long rectangle, the vertical component of velocity is negligible except in the regions near the vertical edgewalls.

This situation does not change even when a horizontal flow contacts with the liquid in the rectangular hollow at its ceiling, and in fact, observation of the motion of the fine materials in the water shows that the vertical flow is negligible in the central region of the long flume.

Thus, a simple calculation for two-layer flow is tried to investigate approximately the flow pattern in the central region of the flume.

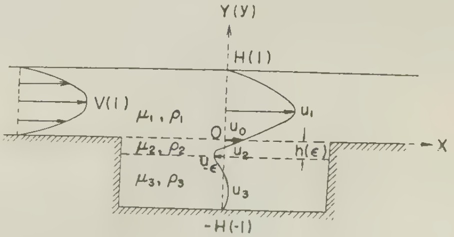

Fig. 1. Two-layer flow.

As shown in Fig. 1, we take the x-axis along the ceiling of the rectangular hollow in the direction of horizontal flow and the y-axis vertically upwards.

Then, if we neglect the vertical component of velocity, the equation of stationary horizontal motion becomes

$$\mu\frac{\partial^2 u}{\partial y^2}=\frac{\partial p}{\partial x}\,, \tag{1}$$

where μ is the coefficient of viscosity, u the horizontal velocity, and p the pressure.

The boundary conditions to be satisfied by the horizontal flow are

$$u_1=0 \qquad \text{at } y=1 \quad \text{(at the fixed surface)},$$

$$\left.\begin{aligned} &u_1=u_2 \\ &\mu_1\frac{\partial u_1}{\partial y}=\mu_2\frac{\partial u_2}{\partial y} \end{aligned}\right\} \qquad \text{at } y=0 \quad \text{(at the interface)},$$

$$u_2=0 \qquad \text{at } y=-1 \quad \text{(at the bottom)},$$

the suffixes 1 and 2 indicating the values in the upper flow and the lower one respectively.

The total flow rate Q_1 through the upper layer is calculated by the use of the initial parabolic velocity distribution $U_{01}=4y(1-y)$ with the maximum value of unity at a section sufficiently upstream of the hollow. Thus we have

$$Q_1=\int_0^1 u_1 dy=\int_0^1 4y(1-y)dy=2/3\,,$$

while the total flow rate Q_2 through the lower layer should vanish, since the lower heavier liquid is confined and circulates in the hollow. Thus,

$$Q_2=\int_0^{-1} u_2 dy=0\,.$$

The solutions of Eq. (1) satisfying the above conditions are given by

$$\left.\begin{aligned} &u_1=\{-(4r+1)y^2+4ry+1\}/(1+r)\,, \\ &u_2=(3y^2+4y+1)/(1+r)\,, \end{aligned}\right\} \tag{2}$$

where $r\equiv\mu_2/\mu_1$ is the ratio of the coefficients of viscosity of the two fluids. From these solutions the pressure gradients in the upper and lower fluids are calculated to be

$$\frac{\partial p_1}{\partial x}=-\frac{8\mu_2+2\mu_1}{1+r}<0\,,$$

$$\frac{\partial p_2}{\partial x}=\frac{6\mu_2}{1+r}>0\,,$$

and the interface inclination γ necessary for balancing with the difference of the pressure gradients in the two layers is given by

$$\gamma=\left(\frac{\partial p_2}{\partial x}-\frac{\partial p_1}{\partial x}\right)\Big/ g\Delta\rho$$

$$=(14\mu_2+2\mu_1)/\{(1+r)g\Delta\rho\}\,, \tag{3}$$

where g is the acceleration of gravity and $\Delta\rho=\rho_2-\rho_1$ is the density difference.

The velocity at the interface, u_0, which indicates the scale of motion in the lower layer, is derived from Eq. (2) as:

$$u_0=(u_1)_{y=0}=1/(1+r)\,. \tag{4}$$

Thus, it will be seen that the larger the viscosity μ_2 of the lower liquid as well as the value of r are, the smaller are the value of u_0 as well as the circulating velocity in the hollow.

The velocity distribution as given by Eq. (2) is very similar to that obtained by Hidaka in the central region of the flume, but it does not coincide with the result observed in the present experiments.

In fact, a slight difference of viscosities between the upper and lower liquids (as measured by the Ostwald viscosimeter) gives the value of $r\fallingdotseq 1$ so that we have from Eq. (4) $u_0\fallingdotseq 0.5$, which conflicts with the prompt vanishing of u_1 near the interface as observed in the experiments.

§ 4. Shear Flow Jumping over the Hollow; Effect of Vertical Walls upon the Flow

In the preceding section the effect of vertical walls upon the flow has been considered only as an indirect condition that the lower liquid is confined in the hollow, which gives rise to $Q_2=0$, and the vertical flow near the vertical walls has not been taken into account in the calculation.

We shall now investigate theoretically the direct effects of the vertical walls upon the

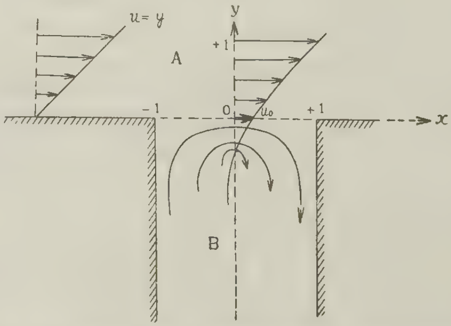

Fig. 2. Shear flow jumping over the hollow.

flow as well as upon the general features of the flow jumping over a narrow and deep hollow.

In order to simplify the calculation and especially to investigate the flow pattern near the interface in detail, we shall study the shear flow jumping over a semi-infinite vertical hollow.

As shown in Fig. 2, the horizontal interface between the two liquids coincides with the ceiling plane of the hollow, and with the origin 0 at the middle point of interface of length 2 we take the x-axis along the direction of the horizontal flow and the y-axis vertically upwards. We call the region of the upper lighter liquid over the interface and the horizontal walls "Region A" and that of the lower heavier liquid in the hollow "Region B", namely:

Region A: $y \geqq 0$,

Region B: $y < 0$, $-1 \leqq x \leqq 1$.

If, in the case of a stationary slow motion of fluid, we neglect inertia terms in the equations of motion, a stream function which satisfies the equation of continuity is a solution of the following biharmonic equation:

$$\Delta\Delta\psi = 0 , \tag{5}$$

where, as usual, Δ stands for the Laplacian operator $\partial^2/\partial x^2 + \partial^2/\partial y^2$.

In Region A, ψ consists of the term $y^2/2$ as originated from the shear flow with velocity distribution $u = y$ and a term ψ_A as originated from the effects of the lower liquid in Region B, while in Region B the flow originates only from the tangential viscous drag exerted by the flowing upper liquid in Region A. Thus,

$$\text{in Region A:} \qquad \psi = (1/2)y^2 + \psi_A , \tag{6}$$

$$\text{in Region B:} \qquad \psi = \psi_B . \tag{7}$$

The boundary conditions to be satisfied by the solution of Eq. (5) are as follows. In Region A the effect of the lower liquid upon the flow is very small at a great distance from the interface, so that

$$\psi_A \to 0 \qquad \text{as } |x|,\ y \to \infty . \tag{8}$$

In Region B, on the other hand, the effect of the upper liquid upon the flow at an infinite distance from the interface vanishes and the liquid sticks to both the vertical walls. Thus,

$$\psi_B \to 0 \qquad \text{as } y \to -\infty , \tag{9}$$

$$\psi_B = \partial\psi_B/\partial x = 0 \qquad \text{at } x = \pm 1 . \tag{10}$$

A particular streamline coincides with the interface line itself, and the horizontal velocities as well as the tangential viscous stresses at both sides of the interface are continuous and the liquid sticks to the horizontal walls. Thus we have

$$\psi_A = \psi_B = 0 \qquad \text{at } y = 0 , \tag{11}$$

$$\frac{\partial\psi_A}{\partial y} = \frac{\partial\psi_B}{\partial y} = \left\{\begin{matrix} 0 & |x| > 1 \\ f(x) & |x| \leqq 1 \end{matrix}\right\} \text{at } y = 0 , \tag{12}$$

$$\mu_A\left(\frac{\partial^2\psi_A}{\partial y^2} + 1\right) = \mu_B\frac{\partial^2\psi_B}{\partial y^2} \qquad \text{at } y = 0 , \tag{13}$$

where μ_A and μ_B are the coefficients of viscosity of the liquids in Region A and Region B respectively, and $f(x)$ is an unknown function which expresses the velocity distribution at the interface.

A solution of Eq. (5) can be obtained by assuming ψ in the form:

$$\psi = e^{ikx}Y(y) ,$$

where $Y(y)$ is a function of y alone. Inserting this into Eq. (5) and solving a resulting ordinary differential equation for $Y(y)$, we get

$$Y(y) = K_1e^{ky} + K_2e^{-ky} + K_3ye^{ky} + K_4ye^{-ky} ,$$

where K_1, K_2, K_3 and K_4 are constants to be determined by the conditions described in the above.

Thus, in Region A the conditions (8) and (11) require that

$$K_1 = K_2 = K_3 = 0 ,$$

so that the function $Y(y)$ becomes

$$Y(y) = Bye^{-ky}$$

and therefore

$$\psi = Bye^{-ky}e^{ikx} ,$$

where B, like K_4, is a constant.

This solution can be generalized by assuming B to be a function of k and then taking all values for k.

Thus, taking into account that the flow pattern is symmetric with respect to x, the appropriate expression for ψ_A in Region A can be put in the form:

$$\psi_A = y\int_0^\infty B(k)e^{\ ky}\cos kx\,dk , \tag{14}$$

and the function $B(k)$ is determined by the boundary condition (12) as:

$$B(k) = \frac{2}{\pi}\int_0^\infty f(\xi)\cos k\xi\,d\xi . \tag{15}$$

In like manner the, appropriate general solution ψ_B of Eq. (5) for Region B can be obtained, which satisfies the conditions (9) and (10), and is symmetric with respect to x. It can be expressed by the sum of two infinite series as:

$$\psi_B=\sum_{m=1}^{\infty} A_m(\psi_m+\psi_m^*)\ , \qquad (16)$$

where A_m's are constant and

$$\psi_m=y\, e^{p_m y}\cos p_m x\ ,$$

$$\psi_m^*=\int_0^\infty c_m(x\sinh kx-\tanh k\cosh kx)\sin ky\, dk\ ,$$

$$p_m=\frac{\pi}{2}(2m-1)\ ,$$

$$c_m=4(-1)^{m+1}kp_m^2/\pi\{(p_m^2+k^2)^2(\sinh k + k\,\mathrm{sech}\, k)\}\ .$$

$m=1, 2, 3, \cdots\cdots$(positive integers) .

From (16) and (12) we get the relation $f(x)$ and A_m's in the form:

$$f(x)=\sum_{m=1}^{\infty} A_m G_m(x)\ , \qquad |x|\leqq 1 \qquad (17)$$

where

$$G_m(x)=\cos p_m x + \int_0^\infty kc_m(x\sinh kx-\tanh k\cosh kx)dk\ ,$$

and this is a completely definite function of x and k.

Also, the relation between the function $B(k)$ and A_m's is obtained by substituting (14) and (16) into (13) as follows:

$$1-2\int_0^\infty kB(k)\cos kxdk = r\pi\sum_{m=1}^{\infty}(2m-1)A_m\cos p_m x\ , \qquad (18)$$

where $r\equiv\mu_B/\mu_A$ is, like r in (2) in § 3, the ratio of the coefficients of viscosity of the liquids in the upper and lower layers.

In order to determine the feature of the flow, it is necessary to get, from the above three relations (15), (17) and (18), definite functional forms of $B(k)$ and $f(x)$ as well as numerical values of A_m's.

First, taking account of the symmetry of flow pattern with respect to x, we expand the horizontal velocity distribution $f(x)$ along the interface into a Fourier cosine series. Thus,

$$\left.\begin{aligned} f(x) &= \sum_{m=1}^{\infty} D_m\cos p_m x\ , && |x|\leqq 1\ ,\\ &=0 && |x|>1\ . \end{aligned}\right\} \qquad (19)$$

Putting this into (15) and carrying out integrations, we get

$$B(k)=\sum_{m=1}^{\infty}\{2D_m p_m(-1)^{m-1}/\pi(p_m^2-k^2)\}\ . \qquad (20)$$

Then the integral on the left-hand side of Eq. (18), which is denoted simply by $F(x)$, can be evaluated as:

$$F(x)\equiv\int_0^\infty kB(k)\cos kxdk=\sum_{m=1}^{\infty} D_m H_m(x)\ , \qquad (21)$$

where

$$H_m(x)= \frac{(-1)^{m-1}}{\pi}p_m\{C_i(p_m^+)\cos(p_m^+)+C_i(p_m^-)\cos(p_m^-) + S_i(p_m^+)\sin(p_m^+)+S_i(p_m^-)\sin(p_m^-)\}\ ,$$

with

$$p_m=\frac{\pi}{2}(2m-1)\ ,\ p_m^+=p_m+p_m x\ ,\ p_m^-=p_m-p_m x\ ,$$

$$C_i(\eta)\equiv-\int_\eta^\infty\frac{\cos u}{u}du\ ,$$

$$S_i(\eta)\equiv\int_0^\eta\frac{\sin u}{u}du\ .$$

$H_m(x)$'s are completely known functions containing the functions $C_i(\eta)$ and $S_i(\eta)$ whose values can be obtained by the use of suitable numerical tables.

Using (21) and (19), Eqs. (18) and (17) become respectively

$$2r\sum_{m=1}^{\infty} p_m A_m\cos p_m x=1-2\sum_{m=1}^{\infty} D_m H_m(x)\ , \qquad (22)$$

$$\sum_{m=1}^{\infty} D_m\cos p_m x=\sum_{m=1}^{\infty} A_m G_m(x)\ . \qquad (23)$$

From these equations approximate values of the first eight constants A_1, A_2, A_3, A_4, D_1, D_2, D_3 and D_4 have been obtained by neglecting terms with suffixes $m\geqq 5$ and using numerical values of $\cos p_m x$, $H_m(x)$ and $G_m(x)$ at four fixed points $x=0$, 0.25, 0.5 and 0.75. Since the ratio r of the coefficients of viscosity of the two liquids is nealy equal to unity in the present experiments, we have put $r=1$ in Eq. (22). Thus, we have

$$\begin{aligned} A_1&=0.2573, & A_2&=-0.0330,\\ A_3&=0.0099, & A_4&=-0.0024,\\ D_1&=0.1875, & D_2&=-0.0160,\\ D_3&=0.0038, & D_4&=-0.0008. \end{aligned}$$

These values show that each series in Eqs. (22) and (23) converges fairly rapidly and that the neglect of the terms with suffixes $m\geqq 5$ does not bring about an error exceeding 1%.

Therefore it may be expected that the general feature of the flow pattern can be obtained with sufficient accuracy by using the above numerical values of the constants.

With the use of the above numerical values of D_1, D_2, D_3 and D_4, the horizontal velocity distribution at the interface $u_{(0)}=f(x)$ has been calculated by Eq. (19). The result is shown in Fig. 3. It will be seen that the interfacial velocity changes rather slowly in the central part whose length is about one third of the total length of the interface and that it decreases rapidly near the vertical walls.

In order to investigate how the interfacial velocity is affected by the value of the ratio $r=\mu_B/\mu_A$, the velocity at the origin has been calculated for various values of r. The result is shown in Fig. 4. It is found that the increase of r, namely the increase of the coefficient of viscosity of the lower liquid brings about the decrease of flow velocity in the lower liquid as in § 3.

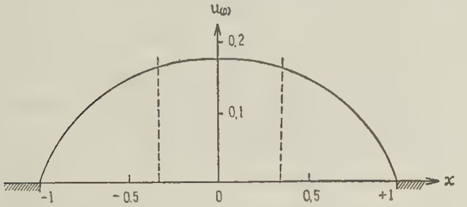

Fig. 3. Velocity distribution along the interface.

Next, the velocity distribution near the interface has been compared with the observed one.

The horizontal velocity u is derived from the stream function as:

$$u=\partial\psi/\partial y\ .$$

Thus, by using (14) we obtain the horizontal velocity in Region A as:

$$u_A=y+\int_0^\infty(1-yk)B(k)e^{-ky}\cos kxdk\ , \qquad (24)$$

while, by (16), the horizontal velocity in Region B becomes

$$u_B=\sum_{m=1}^{\infty}A_m(u_m+u_m^*)\ , \qquad (25)$$

with

$$u_m=(1+yp_m)e^{p_m y}\cos p_m x\ ,$$

$$u_m^*=\frac{4}{\pi}(-1)^{m+1}\int_0^\infty\frac{k^2p_m^2\cos ky(x\sinh kx-\tanh k\cosh kx)}{(p_m^2+k^2)^2(\sinh k+k\operatorname{sech}k)}dk\ .$$

The velocity distribution calculated by these formulae at four fixed points $x=0, 0.5, 1$ and 2 is shown in Fig. 5. The definite integrals involved have been evaluated by the Simpson rule with an accuracy of 0.1%. From this figure it will be seen that even in the central section ($x=0$), where the horizontal velocity is maximum, the flow of the lower layer vanishes at the depths nearly twice as large as the width of the hollow and this result suggests that the flow in a rectangular

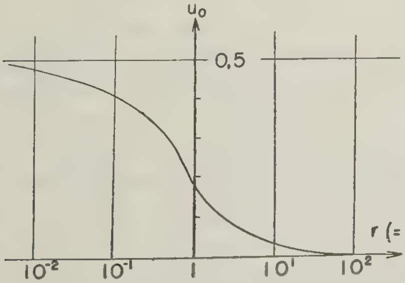

Fig. 4. Relation between the ratio of the coefficients of viscosity of the two liquids and the interfacial velocity.

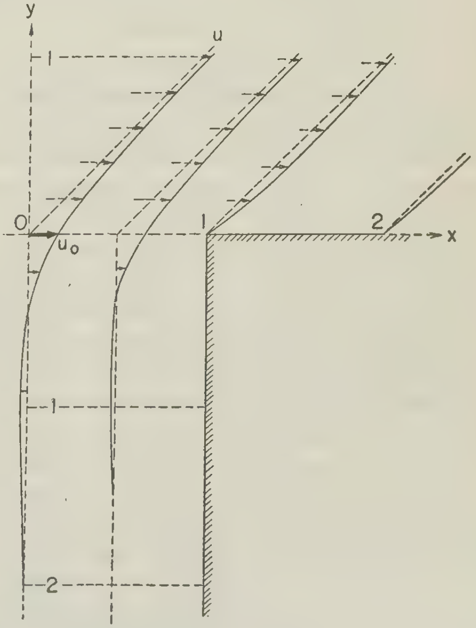

Fig. 5. Distribution of horizontal velocity near the interface.

hollow, whose height is greater than twice of its width, is very similar to the flow in the semi-infinite vertical hollow.

Also, the calculation by M. Kawaguti for the flow in a rectangular hollow with large value of the ratio of height to width gives a similar flow pattern in the central section to that obtained by the present calculation.

According to the present calculation, however, there exists in the central section a horizontally moving layer with considerable thickness in the lower liquid, and this result does not coincide with the observed fact that the horizontal velocity near the interface vanishes rapidly.

§ 5. Horizontal Flow with Intermediate Zone; Three-Layer Flow

In the preceding two sections we have calculated the velocity distribution in two superposed liquids under the assumption that the lower heavier liquid is confined in the hollow and the upper liquid flows over it and that they contact with each other directly at the ceiling of the hollow, but no satisfactory explanation has been obtained for the observed fact that the horizontal velocity vanishes rather rapidly. In the present section, therefore, an attempt will be made to carry out improved calculations, assuming the existence of an intermediate zone between the two liquids.

It is generally observed that when a lighter liquid such as tap water is piled on a heavier liquid such as brine, a thin zone with intermediate density is formed up between these two liquids owing to inevitable mixing even at very slow piling.

In the present experiment, the arrangement of two superposed liquids was obtained practically by pouring tap water very slowly over a filter paper spread on a veneer-sheet which was initially floating on the surface of brine filled the hollow to its ceiling. As the thickness of the upper water layer increased, the veneer-sheet rose up very slowly from its initial position. At the very initial stage of piling, the poured fresh water flowed out of the edge of the filter paper in the form of a very thin film, with a rather considerable speed in spite of very slow pouring of the fresh water. Then, mixing occurred along the interface between brine and fresh water, and a thin intermediate zone was formed up. Not only at the initial stage of arrangement, but also in the course of experiment, such a mixing zone grew up along the initial interface owing to (molecular or turbulent) diffusion and shear flow.

A part of the liquid in the mixing zone, which did not flow into the mouth of exit but impinged upon the vertical wall of the hollow, moved downwards vertically along the wall. Owing to its small density, however, it could not go down to the bottom of the hollow, but rather flowed back horizontally at a small depth from the ceiling, as shown in Fig. 6. Thus, a thin intermediate liquid layer with intermediate density was formed, which circulates between the upper and lower liquids.

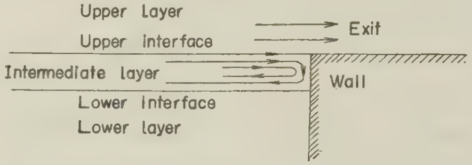

Fig. 6. Growth of intermediate layer.

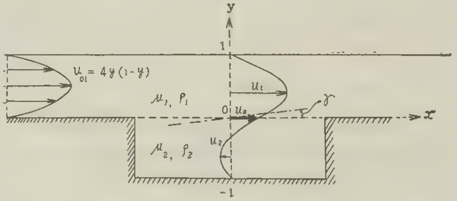

Fig. 7. Three-layer flow.

It has been observed that in a finite time-duration (a few hours) for observation, the thickness of such an intermediate zone is very small in comparison with that of the upper or lower layer. It is likely, however, that the existence of such a thin layer affects the general flow pattern remarkably.

We now calculate the flow pattern approximately, neglecting, for the sake of simplicity as in § 3, the vertical motion in the central major part of the flume which is very long in the horizontal direction as compared with the vertical one. With the coordinate-origin O at the center of the ceiling of the hollow, we take the X-axis along the ceiling in the direction of horizontal flow and the Y-axis vertically upwards, as shown in Fig. 7.

The equation of stationary horizontal motion is then given by Eq. (1), namely:

$$\mu\frac{\partial^2 U}{\partial Y^2}=\frac{\partial p}{\partial X},$$

where μ is the coefficient of viscosity, p the pressure and U the horizontal velocity.

As a simple model for calculation, the three-layer flow is assumed as shown in the figure, which consists of the horizontal flow in the upper layer with thickness H, the circulating flow in the intermediate zone with small thickness h and the circulating flow confined in the hollow with thickness $(H-h)$.

In order to distinguish physical quantities in each layer, suffixes 1, 2 and 3 have been used for the upper, intermediate and lower layers, respectively. For convenience of numerical calculation, the maximum velocity V in the far upstream of the hollow has been taken as the standard scale of the horizontal velocity, while the thickness of the upper liquid layer, H, as the standard scale of the vertical distance.

Then, introducing non-dimensional horizontal velocity u and non-dimensional distance y defined as:

$$u=U/V, \qquad y=Y/H,$$

the equations of motion become

$$\frac{\partial^2 u_i}{\partial y^2}=\frac{H^2}{\mu_i V}\cdot\frac{\partial p_i}{\partial X}, \qquad (i=1,2,3). \tag{26}$$

The non-dimensional thicknesses of the three layers become respectively

$$\begin{array}{ll} 1 & \text{(upper layer)},\\ \varepsilon=h/H(\ll 1) & \text{(intermediate layer)},\\ 1-\varepsilon & \text{(lower layer)}. \end{array}$$

If we assume that the pressure gradients $\partial p_i/\partial X$ $(i=1,2,3)$ are all constant, Eq. (26) can be integrated easily, obtaining

$$u_i=a_i y^2+b_i y+c_i \qquad (i=1,2,3), \tag{27}$$

where

$$a_i=\frac{H^2}{2\mu_i V}\frac{\partial p_i}{\partial x}.$$

The nine constants a_i, b_i, c_i $(i=1,2,3)$ in (27) can be determined by solving simultaneous linear algebraic equations as obtained by substituting (27) into the following six boundary conditions and three flow-rate conditions:

(i) Boundary conditions:

$$\left.\begin{array}{ll} u_1=0 & \text{at } y=1,\\ u_1=u_2,\ \mu_1\partial u_1/\partial y=\mu_2\partial u_2/\partial y & \text{at } y=0,\\ u_2=u_3,\ \mu_2\partial u_2/\partial y=\mu_3\partial u_3/\partial y & \text{at } y=-\varepsilon,\\ u_3=0 & \text{at } y=-1; \end{array}\right\} \tag{28}$$

(ii) Flow-rate conditions:

$$\left.\begin{array}{ll} \int_0^1 u_1 dy=2/3 & \text{(upper layer)},\\ \int_{-\varepsilon}^0 u_2 dy=0 & \text{(intermediate layer)},\\ \int_{-1}^{-\varepsilon} u_3 dy=0 & \text{(lower layer)}. \end{array}\right\} \tag{28}$$

In the first place, we have solved approximately the said simultaneous linear algebraic equations, assuming that the thickness of the intermediate zone is very small so that $\varepsilon\ll 1$. Since, in the present experiment, the coefficients of viscosity of the liquids in the three layers are nearly equal to each other, we have assumed, for simplicity, that $\mu_1=\mu_2=\mu_3$. The results obtained are

$$\left.\begin{array}{l} a_1=-4+4\varepsilon,\\ b_1=b_2=4-5.3\varepsilon,\\ c_1=c_2=1.3\varepsilon,\\ a_2=(2/\varepsilon)-1.3,\\ a_3=-2\varepsilon-2.6\varepsilon^2,\\ b_3=-2.7\varepsilon-4.8\varepsilon^2,\\ c_3=-0.7\varepsilon-2.2\varepsilon^2, \end{array}\right\} \tag{29}$$

Using these values we have calculated approximately the horizontal velocity u_0 at the upper interface $y=0$ as well as the similar quantity $u_{-\varepsilon}$ at the lower interface $y=-\varepsilon$, thus obtaining

$$\left.\begin{array}{l} u_0=1.3\varepsilon,\\ u_{-\varepsilon}=-0.7\varepsilon. \end{array}\right\} \tag{30}$$

From these results it will be seen that the thinner the thickness of the intermediate layer is, the smaller are the velocities in the intermediate and lower layers.

Next, we have also calculated exact values of the nine constants a_i, b_i, c_i $(i=1,2,3)$ by solving, by the use of a digital computer, the above-mentioned simultaneous linear algebraic equations for various values of ε such as 0.1, 0.03 and 0.01, and it has been found that relative errors of the preceding approximate values of a_i, b_i and c_i do not exceed 10%, 3% and 1% for $\varepsilon=0.1$, 0.03 and 0.01 respectively.

The velocity distributions as calculated by using the exact values of a_i, b_i and c_i corresponding to $\varepsilon=0.1$, 0.03 and 0.01 are shown in Fig. 8. In this figure, the observed velocity distribution is also shown for comparison by a dotted curve.

From Fig. 8 it will readily be seen that the calculated velocity distributions are in fairly good agreement with the results of observation and that the existence of a thin intermediate zone between two superposed liquid layers with different densities rather prevents the motion in the lower layer of heavier liquid confined in the hollow.

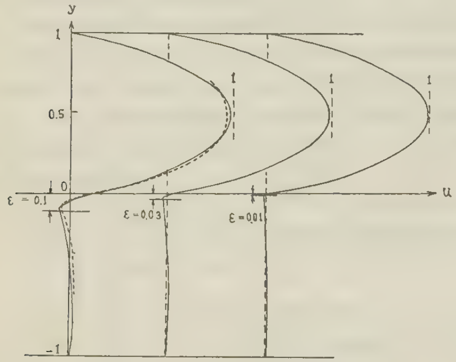

Fig. 8. Calculated velocity distributions in the three-layer flow with various thicknesses of the intermediate layer. The dotted curve shows the observed velocity distribution.

It is worth noticing here that even when the thickness of the intermediate layer is fairly small, the velocity distribution in the three-layer flow is remarkably different from that in the two-layer flow without intermediate layer which has been discussed in §3.

In case when ε is vanishingly small, the value of the constant a_2 as given in (29), namely:

$$a_2 = \frac{H^2}{2\mu_2 V}\frac{\partial p_2}{\partial X} = \frac{2}{\varepsilon} - 1.3$$

becomes large, and therefore the inclinations of the upper and lower interfaces should become very steep in order to balance with the large pressure gradients $\partial p_i/\partial X$. The existence of a thin intermediate layer becomes then difficult and neglect of the vertical velocity component as done in the present calculation becomes inadequate.

Next, in order to investigate the effect of the value of the ratio $r=\mu_3/\mu_1$, of the coefficient of viscosity, μ_3, of the lower liquid to that μ_1, of the upper liquid upon the flow in the lower liquid layer, we have calculated the horizontal velocity u_0 at the upper interface $y=0$ for various values of r, assuming that the coefficient of viscosity, μ_2, of the mixed liquid in the intermediate layer with thickness $\varepsilon=0.1$ is equal to the algebraic mean of μ_1 and μ_3, i.e. $\mu_2=(1/2)(\mu_1+\mu_3)$.

The result of calculation is shown in Fig. 9, in which the interfacial velocity as calculated by Eq. (4) in §3 as well as that derived from Fig. 4 in §4, both for the two-layer flow, are also shown for comparison. Here, the velocity $u_{0.5}$ at $y=0.5$ has been taken as the standard scale of velocity, which is equal to the maximum velocity in the upper layer in the flows treated in §3 and §5.

From this figure it will be seen that the interfacial velocity is much smaller in the case of the three-layer flow than that in the case of the two-layer flow for all values of the ratio $r=\mu_3/\mu_1$.

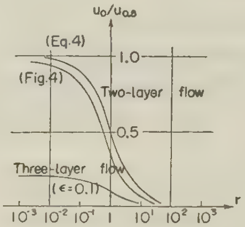

Fig. 9. Effect of the ratio of the coefficients of viscosity of the upper and lower liquids upon interfacial velocity.

§6. Stability of Intermediate Layer

In the preceding section we have given a fairly satisfactory theoretical explanation to the observed velocity distribution near the interface between two superposed liquids having different densities by assuming three-layer flow with a thin intermediate layer.

But we have not yet verified theoretically or experimentally the stable existence of such an intermediate layer. In the present section we shall discuss analytically the stability of the intermediate layer and explain experimentally the effect of the said layer upon the velocity distribution in the superposed liquids.

A few theoretical studies[14] have been made so far on the stability of horizontal flow with vertical density gradient. L. F. Richardson has investigated the atmospheric turbulence by the energy method, and G. I. Taylor and S. Goldstein have studied independently, by the use of the method of small disturbances, the stability of a horizontal shear flow with density stratification. All these authors have shown that the horizontal flow with density stratification is stable when the so-called "Richardson number" Θ defined as:

$$\Theta=-\frac{g}{\rho}\frac{d\rho}{dY}\bigg/\left(\frac{dU}{dY}\right)^2 \tag{31}$$

exceeds a certain critical value, where ρ is the density of the fluid, U the horizontal velocity, g the acceleration of gravity, the Y-axis being taken vertically upwards.

Also, H. Schlichting[15] has studied theoretically the stability of boundary-layer flow near a horizontal solid plane with vertical density gradient by the method of small disturbances, obtaining the result that the flow is stable for all values of Reynolds number if

$$\Theta>1/25\ , \tag{31$'$}$$

and he has shown that this theoretical result is in good agreement with the result of experiment by H. Reichardt who investigated the stability of air flow in a wind tunnel with large temperature gradient.

In our experiment, the lower heavier liquid is almost at rest in the hollow, as mentioned already, and therefore the flow near the upper interface is quite similar to the boundary-layer flow on a solid plane. Thus, we may use the above critical value of $\Theta=1/25$ as the criterion for stability of the flow.

The velocity gradient at $y=0$, where the flow is most liable to be unstable, is given by (29), as:

$$\left(\frac{du_1}{dy}\right)_{y=0}=b_1=b_2=4-5.3\varepsilon\doteqdot4\ ,$$

and therefore we have

$$\frac{dU}{dY}\doteqdot\frac{4V}{H}\ ,$$

for small value of ε.

Also, since the intermediate layer is sufficiently thin, we may put approximately

$$-\frac{d\rho}{dY}=\frac{\Delta\rho}{h}\ ,$$

where $\Delta\rho$ is the difference between the densities of the liquids in the upper and lower layers and h is the thickness of the intermediate layer. In practice, however, there occur sharp density gradients along the upper and lower interfaces, so that the value of $-d\rho/dY$ near the interfaces is much larger than the above mean value and the flow there is more stable than expected by the estimation.

Substituting the above values of dU/dY and $-d\rho/dY$ into Eq. (31), we obtain

$$\Theta\doteqdot\frac{g}{\rho}\frac{\Delta\rho}{h}\bigg/\left(\frac{4V}{H}\right)^2=\frac{g\Delta\rho H^2}{16V^2\rho h}\ . \tag{32}$$

In the present experiment $\rho=1$ gr/cm³, $H=10$ cm, $h=1$ cm and $V=2$ cm/sec approximately. Thus, using these values and adopting the critical value 1/25 for Θ, we obtain, from (32),

$$\Delta\rho\doteqdot2.5\times10^{-5}\quad \text{gr/cm}^3\ .$$

This result shows that only a slight difference in the densities of the upper and lower liquids suffices to stabilize the flow in the intermediate zone.

Although, as can been seen from (32), the flow in the intermediate layer becomes more stable as its thickness becomes thinner, yet the pressure gradient $\partial p_i/\partial X$ becomes then very large and the inclinations of the upper and lower interfaces become very steep. We shall next estimate numerically the slopes of the interfaces.

We write the density differences $\rho_2-\rho_1$ and $\rho_3-\rho_2$ as $\Delta\rho_{12}$ and $\Delta\rho_{23}$ respectively, and we denote the inclination of the upper interface by γ_{12} and that of the lower interface by γ_{23}. Then it is found that if there hold the following relations, the equilibrium of pressure in each layer can be maintained:

$$\Delta\rho_{12}g\gamma_{12}=\frac{\partial p_2}{\partial X}-\frac{\partial p_1}{\partial X}\ ,$$

$$\Delta\rho_{23}g\gamma_{23}=\frac{\partial p_3}{\partial X}-\frac{\partial p_2}{\partial X}\ .$$

If, in these relations, we substitute the expressions for the pressure gradients from (27), namely:

$$\frac{\partial p_i}{\partial X}=\frac{2Va_i\mu_i}{H^2}\ ,$$

we get

$$\left.\begin{aligned}\gamma_{12}&=\frac{2V}{g\Delta\rho_{12}H^2}(a_2\mu_2-a_1\mu_1)\ ,\\ \gamma_{23}&=\frac{2V}{g\Delta\rho_{23}H^2}(a_3\mu_3-a_2\mu_2)\ .\end{aligned}\right\} \tag{33}$$

In case when the three coefficients of viscosity μ_1, μ_2 and μ_3 are nearly equal to each other, as in the present experiment, a_2 is much greater than either of $|a_1|$ and $|a_3|$ for very small values of ε, as can be seen from (29), and therefore

$$\gamma_{12}>0\ ,\qquad \gamma_{23}<0\ .$$

Thus, it will be seen that the thickness of the intermediate layer increases towards downstream.

If we assume that the density of the liquid in the intermediate layer is equal to the algebraic mean of the densities of the upper and lower liquids, so that

$$\varDelta\rho_{12}=\varDelta\rho_{23}=\frac{1}{2}(\rho_3-\rho_1)\equiv\frac{1}{2}\varDelta\rho\ ,$$

and if, for very small ε, we neglect a_1 and a_3 in comparison with a_2, we have approximately

$$\gamma_{12}=-\gamma_{23}=\frac{8V\mu}{g\varDelta\rho H^2\varepsilon}\ . \tag{33'}$$

Under normal conditions in the present experiment, the coefficient of viscosity of water was $\mu=0.01$ poise (c. g. s.), the maximum velocity in the upper layer $V=2$ cm/sec, the density difference between the upper and lower liquids $\varDelta\rho=0.02$ gr/cm^3, the thickness of the upper layer $H=10$ cm, and the thickness of the intermediate layer $h=1$ cm ($\varepsilon=0.1$). Substituting these values into (33′), we get

$$\gamma_{12}=|\gamma_{23}|\doteqdot 8\times10^{-4}\ ,$$

and then the difference in thicknesses, $\varDelta h$, at both ends of the intermediate layer with length of 200 cm is calculated as:

$$\varDelta h=200\times2\times8\times10^{-4}=0.32\text{ cm}\ ,$$

which is considerably large compared with the mean thickness $h=1$ cm, but since the slopes of the interfaces are gentle, the neglect of the vertical velocity component may be allowed.

If, however, the thickness h of the intermediate layer would decrease, for example, to a value of 0.1 cm, then the slopes γ_{12} and γ_{32} would take a large value of 8×10^{-3} and the value of $\varDelta h$ would become 3.2 cm which is much larger than the mean thickness of the layer, and consequently such a very thin intermediate layer cannot exist in the flume.

Lastly, summarizing the above results we may say that as the thickness of the intermediate layer becomes thinner, the flow in the layer becomes more stable, but the slopes of both the upper and lower interfaces become more steep. The limiting thickness of the layer which can exist between the upper and lower liquids depends upon the horizontal velocity V, the density difference $\varDelta\rho$ between the upper and lower liquids and the thickness H of the upper layer. As can be inferred from (33′), even a very thin intermediate layer can exist in case when the horizontal velocity V is small and either or both of the density difference $\varDelta\rho$ and the thickness H of the upper layer are large.

Next, in order to verify experimentally the stable existence of a thin intermediate layer and its effect upon the velocity distribution, some experiments of the three-layer flow have been carried out in the water flume.

Coloured brine of density $\rho_2=1.01$ was poured very slowly, to the thickness of 1 cm, on the heavier brine of density $\rho_3=1.02$ confined in the hollow, and then tap water of density $\rho_1=1.00$ was poured gently on the coloured brine over the ceiling plane of the hollow.

The fresh water in the upper layer was moved horizontally by a motor pump as explained in § 2.

In the first several hours of flowing in the upper layer, the coloured brine remained in the stable state in the intermediate layer, and the inclinations of the upper and lower interfaces were observed to be $|\gamma_{12}|\doteqdot|\gamma_{23}|\doteqdot 10^{-3}$, in fairly good accordance with the theoretically estimated value of 8×10^{-4} given above.

The stable existence of the coloured brine in the intermediate layer and the velocity distribution in the layer are shown in Plate 6 (A) and (B). It will be seen that the velocity distribution as revealed by water-blue lines is very similar to the theoretical curve shown in Fig. 8 for the case of the intermediate layer with thickness of 1 cm ($\varepsilon=0.1$), and this result seems to justify the present analysis on the basis of the three-layer flow.

Further, in order to observe the flow pattern with a very thin intermediate layer, the coloured brine in the layer was sucked up by a small siphon very slowly so as not to disturb the flow. As the volume of the coloured brine decreased, the thickness of the layer became thinner and the slopes of the upper and lower interfaces became steeper, and ultimately the coloured brine became confined in a rather long horizontal triangular region as shown in Plate 7.

In such a state of flow, the upper and lower liquids were in direct contact with each other at the upstream side of the hollow and the two-layer flow occurred there temporarily, which however could not be maintained owing to the turbulent mixing of the upper and lower liquids at irregularly vibrating interface near the vertical wall.

In § 5 we have carried out the theoretical analysis under the condition that the liquid in the intermediate zone is confined and is circulating in the zone. If, however, a part of the liquid in the intermediate layer flows out towards the exit, a remarkable change occurs in the flow pattern. Such a flow could be realized by lowering slightly the horizontal wall surface at the exit side. The velocity distribution in this case is shown in Plate 8. It will be seen that this velocity distribution resembles to that in the case of the two-layer flow treated in § 3 and § 4. It is to be remarked here, however, that in this case too, a new intermediate zone grows up, after a short time-duration, along the interface between the old intermediate layer and the lower liquid and the flow pattern comes soon back to that in the case of the three-layer flow.

§ 7. Summary

The principal results obtained in the present work may be summarized as follows.

(1) Carrying out detailed experiments in a water flume of dimensions 180 cm × 50 cm × 15 cm we have observed, by the use of a suitable colouring material, the velocity distribution near the interface between two superposed liquids having different densities, the lighter liquid (such as tap water) flowing over the heavier one (such as brine) confined in a hollow. It has been found that if there is any difference, however small, between the densities of the two liquids, the velocity of the upper liquid decreases fairly rapidly near the interface, as if it were a solid plane, while the lower liquid is almost at rest in the hollow.

(2) Attempts have been made to explain the observed flow pattern theoretically. In the first place, a rather simple approximate calculation has been carried out by assuming that the two liquids are in direct contact with each other. However, no satisfactory explanation of the observed flow pattern has been obtained, namely, in such a two-layer flow the velocity near the interface is not so small compared with the velocity in the upper layer.

(3) We have next carried out an improved calculation by assuming that there is formed a thin intermediate zone between the two liquids owing to inevitable mixing of the liquids, and it has been found that the calculated flow pattern is, in the present case of the three-layer flow, in fairly good accordance with the observed one.

(4) The effect of the ratio of viscosities of the liquids in the upper and lower layers upon the flow pattern has also been discussed, and it has been found that the larger the viscosity of the lower liquid in the hollow is, the smaller is the velocity near the interface and consequently the weaker is the motion in the hollow.

(5) The stability of thin intermediate layer has been discussed and it has been shown that the thin intermediate layer can exist in stable state, provided that its thickness is not too small.

(6) Further, it has been observed that artificial removal of the intermediate layer makes the two-layer flow appear temporarily, but such a flow cannot be maintained for a long time owing to the growth of a new intermediate zone by inevitable mixing of the liquids at the interface.

In conclusion, it may be remarked that the phenomenon that a lighter liquid flowing over a hollow is prevented by a thin intermediate layer from contacting directly with a heavier liquid which is confined and is nearly at rest in the hollow, is frequently observed in natural circumstances, and such a phenomenon seems to be a cause of the existence of dead water in a deep hollow in storage dam or in estuarine reservoir, where, in the former, cold water originated from snow melting, and, in the latter, sea water flowed in at the time of artificial blocking of estuarine mouth are conserved for a rather surprisingly long period.

Acknowledgements

The author wishes to express his cordial thanks to Professor Keiji Yamashita and Mr. Shigeru Matsubara of Okayama University for their kind guidance in the course of the present work. He is also indebted to Professors S. Tomotika and Kō Tamada of Kyoto

University for their invaluable advices and encouragement.

References

1) G. I. Taylor: Proc. Cambridge Phil. Soc. **23** (1927) 730.
2) G. H. Keulegan: J. Res. Nat. Bur. Stand. **43** (1949) 487.
3) S. Okuda and S. Matsubara: *Preprint* for the Meeting of the Society of Applied Physics of Japan (1957) (in Japanese).
4) M. Masima: *Handbook of Experimental Technique* (Sankaido, 1953) 4 (in Japanese).
5) W. Jost: *Diffusion* (Academic Press, 1952) 449.
6) G. H. Keulegan: J. Res. Nat. Bur. Stand. **32** (1944) 303.
7) R. C. Lock: Quart. J. Mech. & Appl. Math. **4** (1951) 42.
8) O. E. Potter: Quart. J. Mech. & Appl. Math. **10** (1957) 312.
9) S. I. Pai: *Fluid Dynamics of Jets* (Van Nostrand, 1954) 164.
10) D. W. Pritchard: *Advances in Geophysics* Vol. 1 (Academic Press 1952).
11) A. Thom and C. J. Apelt: A. R. C. Reports and Memoranda, No. 3090 (1957).
12) K. Hidaka: Umi to Sora, **17** (1937) 378; **18** (1938) 32, 319. (in Japanese).
13) M. Kawaguti: *Preprint* for the 14th Annual Meeting of the Physical Society of Japan (1959) (in Japanese).
14) Cited in H. Schlichting's "*Grenzschicht-Theorie*" (Verlag G. Braun, 1951) 323.
15) H. Schlichting: Z. A. M. M. **15** (1935) 313.

Short Notes

This section is intended to secure prompt publication of important discoveries in physics. The reports should not exceed 800 words in length. A figure of size 7 cm×7 cm will be counted as 150 words.

J. PHYS. SOC. JAPAN **16** (1961) 339

Annealing of Radiation Damage on Lifetime in Silicon

By Kenji MATSUURA and Yoshio INUISHI
Faculty of Engineering, Osaka University

(Received December 14, 1960)

The annealing of carrier lifetime τ in γ-ray irradiated n type silicon crystals was observed. The lifetime at room temperature was obtained by measuring the decay of photo-injected carrier by microwave absorption method (10 GC) without using any electrode[1].

40 ($\Omega\cdot$cm) Sb-doped, pulled silicon which shows intense infrared absorption (9 μ) and 20 ($\Omega\cdot$cm) floating-zoned n-type silicon containing little oxygen were irradiated with Co^{60} γ-ray at room temperature.

Surfaces were etched with CP4 before measuring lifetime. Since little difference in lifetime was found between etched and non-etched crystals after irradiation, it might be concluded that bulk effects play the important part in the present experiment. Fig. 1 shows the effect of annealing temperature on τ following γ irradiation. According to Shockley-Read theory[2], $1/\tau - 1/\tau_0$ is proportional only to recombination center density provided that the Fermi level does not change appreciably and that the capture cross sections for holes and electrons are kept constant during the annealing cycle. τ_0 and τ are the lifetimes measured at room temperature before irradiation and after each annealing intervals, respectively.

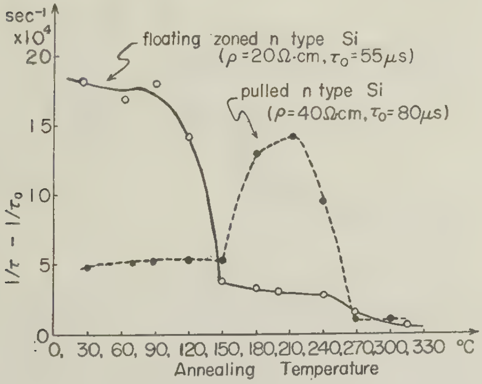

Fig. 1. Isochronal annealing of two different kind n type Si. (Annealing time of these crystals is ten minutes at each temperature.)

An Sb-doped, pulled Si crystal shows different dependence on annealing temperature from floating-zoned crystal, having a peak of $1/\tau - 1/\tau_0$ at about 200°C which is not observed with the latter. Probably, the oxygen in silicon will be mainly related to the mechanism of this behaviour. An isothermal percentage annealing curve for pulled Si at 240°C shown in Fig. 2 also has a peak but those for floating-zoned Si do not show such a peak. From these curves, the activation energy of the annealing process in floating-zoned Si is calculated as 1.2 eV. which is in good agreement with the value reported by Bemski and Augustyniak[3]. These annealing curves, however, represent neither first order process alone describable with an exponential time dependency nor second order process.

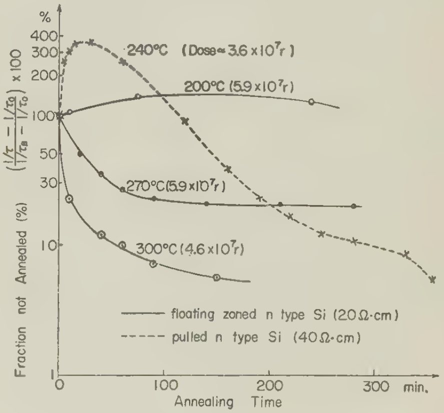

Fig. 2. Isothermal annealing curves of a pulled n type Si and floating zoned n type Si. (τ_B is the lifetime just after γ irradiation.)

Experiments are being prepared to clarify the mechanism of interaction between radiation-induced defect and oxygen or various other imperfections.

References

1) A. P. Ramsa, H. Jacobs and F. A. Brand: J. Appl. Phys. **30** (1959) 1054.
2) W. Shockley and W. T. Read: Phys. Rev. **87** (1952) 835.
3) G. Bemski and W. M. Augustyniak: Phys. Rev. **108** (1957) 645.

J. Phys. Soc. Japan **16** (1961) 340

The Fundamental Absorption of Lithium Fluoride and Sodium Fluoride

Ryumyo Onaka, Atsuo Fukuda and
Arisato Ejiri

Institute for Optical Research, Tokyo University of Education, Shinjuku-ku, Tokyo

(Received December 15, 1960)

The fundamental absorption of alkali halides has been measured by many authors. Eby, Teegarden and Dutton[1] have recently investigated them extensively in the vacuum ultraviolet region both at room temperature and at liquid nitrogen temperatures. Since the alkali halide samples measured by them were of thin films evaporated on lithium fluoride plates, the measurement of the fundamental absorption of lithium fluoride itself was not undertaken.

Thin films of lithium fluoride were prepared by evaporation on thin film substrates in the present study. It was found that celluloid is the best material as the substrate. Substrate films of about 100 A thick were easily prepared by dripping a drop of one percent amylacetate solution of celluloid onto pure water, and by picking up with a frame made of brass wire. The celluloid films gave the transmission of about 30 to 50 percent at 900 A.

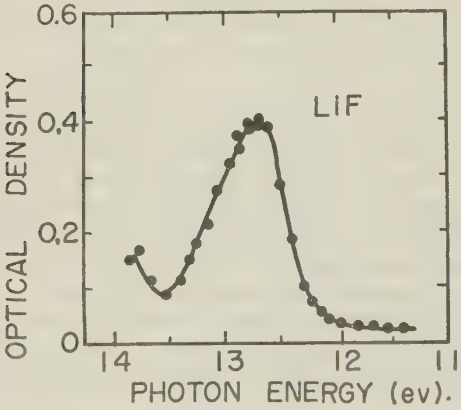

Fig. 1. The fundamental absorption spectrum of lithium fluoride.

The thickness of a lithium fluoride film evaporated on the substrates was so controlled as to give the optical density of about 0.5 to 1.0. No annealing of the sample was tried because the material of the substrate was organic.

A small vacuum spectrophotometer with a 20 cm concave grating was used in measurement of the transmittance. The slit width used corresponded to about 7 A in wavelength. With a hydrogen discharge tube as the light source, the transmittance of lithium fluoride films was measured at wavelengths down to 900 A. The correction for the background intensity was carefully made, since its amount is almost of the same order as the signal below 1000 A.

Transmissions of two portions of the prepared film, on one of which lithium fluoride was evaporated, were measured, and from them the optical density of the lithium fluoride film was deduced, for the absorption of the substrates was almost the same. No correction was applied to the difference of reflection. The measurement was made only at room temperature.

The transmittance of a lithium fluoride film measured is shown in Fig. 1 as a function of the photon energy. A strong absorption band was found with its peak at 12.7 ± 0.1 ev, and a depression at 13.5 ± 0.1 ev on the higher energy side. These values of the peak and the depression agree very well with those in the reflection spectrum recently reported by Kato *et al*[2]. Remarkable asymmetry is observed in the absorption band shape, which seems to imply that the band consists of two or more components. A similar asymmetry of shape of the first fundamental band is seen in the spectrum of sodium fluoride obtained by Eby *et al*[1].

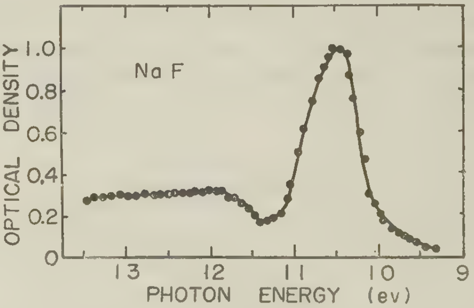

Fig. 2. The fundamental absorption spectrum of sodium fluoride.

The fundamental absorption of sodium fluoride was also measured by the same method described above. (Eby *et al* measured it at wavelengths above 1100 A). The wavelength range of the present measurement was extended down to 900 A, and the second absorption peak was investigated. As shown in Fig. 2, it was found that the second absorption band is broad, similar to that observed in sodium chloride and sodium bromide.

References

1) Eby, Teegarden and Dutton: Phys. Rev., **116** (1959) 1099.
2) Kato, Nakamura, Matsui and Uchida: J. Phys. Soc. Japan, **15** (1960) 2105.

J. PHYS. SOC. JAPAN **16** (1961) 341~342

The Inverse Solution of the TFD Equation*

By Kwai UMEDA, Yasuo TOMISHIMA
and Chikao KAWABATA

Department of Physics, Okayama University

(Received November 8, 1960)

The series expansion of the inverse solution of the TF equation has recently been calculated by Gold[1]. We have carried out in turn the similar calculation for the TFD equation

$$\frac{d^2\psi}{dx^2}=x\left[\beta+\left(\frac{\psi}{x}\right)^{1/2}\right]^3 \qquad (1)$$

with the initial conditions

$$\psi(0)=1 \quad\text{and}\quad -\psi'(0)=B, \qquad (1a)$$

the value of B being dependent on the boundary condition.

For smaller values of x, $\psi(x)$ can be expanded into a semiconvergent power series of the form

$$\psi(x)=1+\sum_{n=2}^{\infty}a_n x^{n/2} \qquad (2)$$

a_n's being listed by several investigators[2] as functions of a_2 only.

As for the inverse solution it is convenient to take not the intrinsic one $x=x(\psi)$ but the alternative one $x=x(\Psi)$ where $\Psi=1-\psi$, since we are concerned in the shaded region ($x\approx0$ and $\psi\approx1$ or $\Psi\approx0$) in Fig. 1. The inverse of (1):

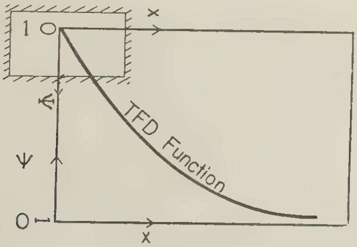

Fig. 1.

$$\frac{d^2x}{d\Psi^2}=x\left(\frac{dx}{d\Psi}\right)^3\left[\beta+\left(\frac{1-\Psi}{x}\right)^{1/2}\right]^3 \qquad (3)$$

allows in the neighborhood of $\Psi=0$ the series expansion of $x(\Psi)$ of the form

$$x(\Psi)=\sum_{n=2}^{\infty}c_n\Psi^{n/2}, \qquad (4)$$

c_n's being given in Table I as functions of c_2 only. The β-free part in c_n reproduces b_{n-1} given by Gold[1] for the TF case exactly, as it must be. The a_n's and the c_n's are connected parametrically by B via the relation

$$c_2=\left(\frac{dx}{d\Psi}\right)_{\Psi=0}=-1\Big/\left(\frac{d\psi}{dx}\right)_{x=0}=-1/a_2=1/B. \qquad (5)$$

Table I. c_n's as functions of c_2 only.

$$c_3=c_2^{1/2}\left[\frac{4}{3}c_2^2\right]$$

$$c_4=\left(\frac{8}{3}c_2^4\right)+\left(\frac{3}{2}c_2^3\right)\beta,$$

$$c_5=c_2^{1/2}\left[\left(\frac{56}{9}c_2^5-\frac{2}{5}c_2^2\right)+\left(7c_2^4\right)\beta+\left(\frac{4}{5}c_2^3\right)\beta^2\right],$$

$$c_6=\left(\frac{1,280}{81}c_2^7-\frac{9}{5}c_2^4\right)+\left(\frac{80}{3}c_2^6-\frac{1}{2}c_2^3\right)\beta \\ +\left(\frac{263}{30}c_2^5\right)\beta^2+\left(\frac{1}{6}c_2^4\right)\beta^3,$$

$$c_7=c_2^{1/2}\left[\left(\frac{1,144}{27}c_2^8-\frac{34}{5}c_2^5+\frac{3}{70}c_2^2\right)\right. \\ +\left(\frac{286}{3}c_2^7-\frac{349}{70}c_2^4\right)\beta+\left(\frac{2,189}{40}c_2^6-\frac{6}{35}c_2^3\right)\beta^2 \\ \left.+\left(\frac{32}{5}c_2^5\right)\beta^3\right],$$

$$c_8=\left(\frac{28,672}{243}c_2^{10}-\frac{656}{27}c_2^7+\frac{58}{105}c_2^4\right) \\ +\left(\frac{8,960}{27}c_2^9-\frac{421}{14}c_2^6\right)\beta+\left(\frac{7,462}{27}c_2^8-\frac{983}{168}c_2^5\right)\beta^2 \\ +\left(\frac{4,991}{72}c_2^7\right)\beta^3+\left(\frac{57}{20}c_2^6\right)\beta^4,$$

$$c_9=c_2^{1/2}\left[\left(\frac{739,024}{2,187}c_2^{11}-\frac{2,288}{27}c_2^8+\frac{16,718}{4,725}c_2^5+\frac{1}{252}c_2^2\right)\right. \\ +\left(\frac{92,378}{81}c_2^{10}-\frac{56,485}{378}c_2^7+\frac{151}{120}c_2^4\right)\beta \\ +\left(\frac{405,977}{324}c_2^9-\frac{1,523,929}{25,200}c_2^6-\frac{1}{42}c_2^3\right)\beta^2 \\ +\left(\frac{1,308,307}{2,592}c_2^8-\frac{1,156}{315}c_2^5\right)\beta^3 \\ \left.+\left(\frac{11,869}{200}c_2^7\right)\beta^4+\left(\frac{11}{15}c_2^6\right)\beta^5\right].$$

Table II. c_n's for free A-atom
($Z=18$, $\beta=0.030835$, $B=1.635403$).

n	c_n	β-free part	β-part	$(\beta)/(\beta\text{-free})$
2	0.611470	0.611470		
3	0.389832	0.389832		
4	0.383369	0.372794	0.010575	0.02837
5	0.322702	0.298970	0.023732	0.07938
6	0.293607	0.253433	0.040174	0.15852
7	0.264282	0.205509	0.058773	0.28599
8	0.241408	0.162868	0.078540	0.48223
9	0.223037	0.124016	0.099021	0.79845

In order to see the effect of exchange on the c_n's, we have evaluated them for free neutral Argon atom[3], as shown in Table II. It is noteworthy that the series (4) converges very slowly and the exchange (β-dependent) part predominates more and more with the increasing sequential order n.

References

1) L. Gold: J. Phys. Soc. Japan **15** (1960) 1132.

---

[*] Financially supported by the Research Grant from the Ministry of Education.

2) R. P. Feynman, N. Metropolis and E. Teller: Phys. Rev. **75** (1949) 1561; N. Metropolis and J. R. Reitz: J. Chem. Phys. **19** (1951) 555; S. Kobayashi: J. Phys. Soc. Japan **10** (1955) 824.
3) Cf. P. Gombás: *Die statistische Theorie des Atoms und ihre Anwendungen*, Wien, 1949, p. 87.

J. Phys. Soc. Japan **16** (1961) 342

Spin Wave Resonance in Cu-Ni Alloy Films

By Hiroshi Nosé
Department of Physics, Faculty of Science, Tokyo Metropolitan University

(Received December 10, 1960)

The studies on the spin wave resonance in Cu-Ni alloy films were carried out at 9300 Mc/sec. These films were prepared by the evaporation of alloyed materials on the glass substrates maintained at room temperature, following the procedure established in the case of pure Ni films[1].

The rate of evaporation in the present work was considerably rapid such as about 500∼1000 Å/sec in order to prevent the films from imperfect alloying. The film thicknesses measured by the multiple beam interferometer were about 2500 Å. The colorimetric analysis on the prepared films showed that the weight contents of Cu had increased by a factor of two. The electron diffraction patterns of these films by the reflection method, however, made clear the facts that the line widths were similar to that of pure Ni films and moreover the lattice constants were nearly consistent with the data of the X-ray diffraction measured on a bulk specimen[2], as shown in Fig. 1. These results were hardly affected by annealing at 300°C for one hour. Therefore, it may be admitted to believe that the present films have a nearly perfect structure.

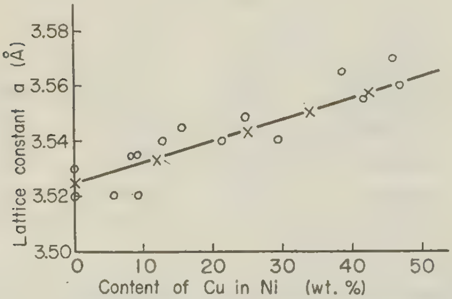

Fig. 1. Concentration dependence of lattice constants of Cu-Ni alloy films; ○: present value by E. D., ×: Coles' value by X-ray as bulk[2].

The exchange coupling constant A can be determined from the term $2A/M_s(p\pi/L)^2$ of spin wave resonance, where M_s is the saturation magnetization, L the film thickness and p the mode number. The values of A in these alloy films are shown in Fig. 2, where the value for pure Ni is somewhat different from that of reference 1 because of the uncertainty of assignments of p. They decreased rapidly in proportion to the concentration of Cu. For reference, the Curie temperature T_c measured for a bulk specimen by Marian[3] are plotted on this figure. It seems that the variation of A with concentration behaves in the similar way to that of T_c.

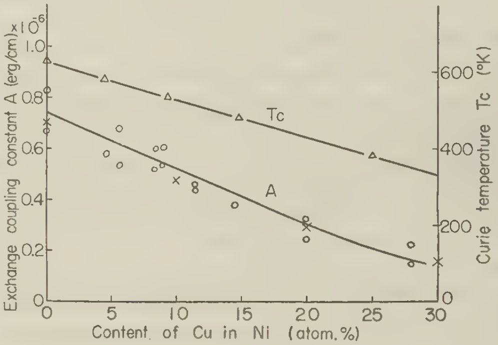

Fig. 2. Concentration dependence of exchange coupling constants of Cu-Ni alloy films; ○: present value, ×: value estimated from measurements by Kondorskij, et al.[4], △: T_c by Marian[3].

We can estimate the values of A in a bulk specimen from the coefficient of $T^{3/2}$ law for the temperature dependence of saturation moment measured by Kondorskij, et al.[4] and compare them with the present values. They are in good agreement. However, it is surprising to note that the observation of spin wave resonance in 28% Cu-Ni alloy at room temperature corresponds to the observation at the temperature as high as about 80% of its Curie temperature.

The author wishes to express his thanks to Prof. R. Kimura for his continued encouragement and to Mr. M. Ichikuni for his colorimetric analysis.

References

1) H. Nosé: J. Phys. Soc. Japan **15** (1960) 1714.
2) B. R. Coles: J. Inst. Met. **84** (1956) 346.
3) V. Marian: Ann. physique [11] **7** (1937) 459.
4) E. I. Kondorskij, V. E. Rode and U. Hoffmann: J. phys. radium **20** (1959) 195.

J. PHYS. SOC. JAPAN **16** (1960) 343~344

Nuclear Magnetic Resonance Study of NaCl Crystal Containing Ca Impurities

By Junkichi ITOH, Mitsuo SATOH*

Department of Physics, Faculty of Science, Osaka University, Osaka

and Akio HIRAKI

Faculty of Engineering, Osaka University, Osaka

(Received December 9, 1960)

Reif[1] first made nuclear magnetic resonance studies of the diffusion of positive-ion-vacancies in AgBr containing Cd impurities. We have made an extensive study on NaCl crystals containing various kinds of divalent impurities. In this note, we shall report only the results of our measurement of the spin lattice relaxation time T_1 of Na nucleus in crystals containing Ca impurity.

Fig. 1 shows the temperature dependence of T_1.

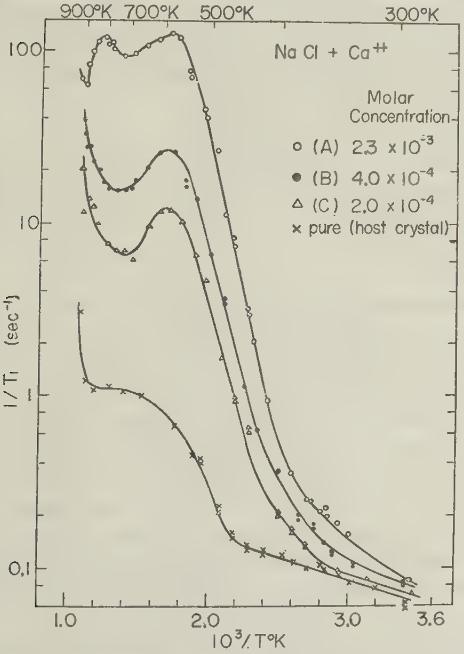

Fig. 1. Spin lattice relaxation rate $1/T_1$ of Na in NaCl+Ca^{++} versus inverse absolute temperature

Samples A, B and C are those containing Ca impurity with concentrations shown in the figure. The contribution of imperfections to $1/T_1$ may be considered as the difference of the curve A, B or C and that of "pure", which will be denoted as $1/T_1°$.

Now these crystals containing Ca impurity will have various types of imperfections; isolated Ca^{++} impurity ions, isolated positive ion vacancies with a concentration equal to that of isolated Ca^{++} ions, the complexes between Ca^{++} and the vacancy, aggregate or precipitate of Ca^{++} (probably accompanying positive ion vacancies), and at high temperatures, thermal vacancies. These various kinds of imperfections may contribute differently to $1/T_1°$.

Above 400°K, $1/T_1°$ first increases exponentially with $1/T$. The line A, B and C in Fig. 1 are all parallel, and the value of $1/T_1°$ is roughly proportional to the concentration of the impurity. This means that $T_1°$ is determined by the motion of isolated positive ion vacancies, and the activation energy for the jump of vacancy is obtained as 0.75 eV[2]. Thus it might be suggested that there is no appreciable number of complexes even at~400°K[3]. At about 580°K, the correlation frequency ν_c of the jump of the vacancy becomes equal to $2\nu_0$ (ν_0: nuclear Zeeman frequency) and a maximum in $1/T_1°$ occurs.

If only the vacancy diffusion contributes to $1/T_1°$ at still higher temperatures, $1/T_1°$ must decrease monotonously above 600°K. Actually, however, there appears a second maximum at about 810°K in A. Also an indication of the tail of the second maximum appears in B and C. This second maximum may be due to the diffusion of Ca^{++} ions. The correlation frequency of the diffusion of Ca^{++} via vacancies which contributes to $T_1°$ is of the order of $Cz\nu_c$, where C is the concentration of Ca^{++} ions and z the number of the nearest neighbor positive ion sites. The maximum of $1/T_1°$ due to this origin will occur at the temperature where $Cz\nu_c \sim 2\nu_0$, and the height of this maximum will be about the same as that due to vacancy diffusion, for the effective charge of the vacancy is $-e$, while that of Ca^{++} is $+e$. In A, this is just the case for the maximum at 810°K, but in B and C the expected maximum lies at a much higher temperature, being masked by the effect to be described next.

Above 900°K, $1/T_1°$ increases sharply with temperature. This may be due to thermal vacancies; the main contribution may come from the negative ion vacancies, which may produce much larger electric quadrupole energy in the surrounding Na nuclei and also moves much more slowly than the positive ion vacancies[4].

References

1) F. Reif: Phys. Rev. **100** (1955) 1957.

2) The values of this activation energy obtained by other methods are 0.77 eV (by diffusion; D. Mapother et al.: J. Chem. Phys. **18** (1950) 1231) 0,85 eV (by ionic conductivity; H. W. Etzel aad R. J. Maurer: J. Chem. Phys. **18** (1950) 1003).

---

* On leave from Okayama University.

3) This conclusion differs from that obtained by Lidiard (A. B. Lidiard: Handbuch der Physik **20** (1956) 246).

4) The activation energy for the jump of Cl^- ion vacancy is obtained as about 1.23 eV from Laurent and Benard's data (J. Phys. Chem. Solids **3** (1957) 7).

J. PHYS. SOC. JAPAN **16** (1961) 344

Temperature Dependence of the Line Width of Ferrimagnetic Resonance in Polycrystalline Nickel Cadmium Ferrite

By Susumu TAKEMOTO

Department of Physics, Faculty of Literature and Science, Shimane University, Matsue

(Received December 16, 1960)

Ferrimagnetic resonance experiments were carried out on polycrystalline nickel cadmium ferrite ($Ni_{0.7}Cd_{0.3}Fe_2O_4$) in the temperature range from −180°C to 100°C at 9500 MC and 24000 MC in order to invesigate the temperature dependence of the line width and the g-value. The writer used a standard electron spin resonance equipment at 9500 MC because of the high fidelity in measurements. But it was modified such that the scanning field was broadened to about 2000 oersted. The sample cavity was of cylindrical H_{111} mode and was kept in a temperature controlled Dewar vessel at low temperature measurements, liquid oxygen being used as low temperature agent. In order to reduce the frequency shift which might be caused by the resonance absorption, it was necessary to make the sample diameter less than 0.30 mm. The samples used in the present experiment were selected, by a microscope, out of scores of spherical samples which were obtained by the Bond sphere grinder. It was found that the resonance condition was greatly affected by a slight deviation of sample shape from sphericity. The absorption curves were almost Lorentzian over the measured region. The derivatives of the absorption curves at various temperatures are shown in Fig. 1, where ΔH_m means the width between the points of maximum slope of the absorption curve. The resonance field was found to strikingly drop as the temperature was lowered. As shown in Fig. 2, the full line width ΔH is affected to a great extent by both the temperature and the frequency. The line width increases at lower temperatures in a similar manner to Healy's result[1] on nickel ferrite and to Tannenwald's result[2] on manganese ferrite. The curves, (a) and (b), were obtained using the conventional resonance apparatus and the curve (c) using the ESR equipment described above. The g-value varies from 2.13 at −180°C to 2.03 at 100°C, gradually increasing with decreasing temperature and the internal field[3] takes values from 300 oersted to 200 oersted in the same temperature range. The writer could not find any subsidiary peaks of the absorption curves in the range of dc magnetic field swept by the scanning field. The line broadening due to the electron migration between ferrous iron and ferric iron seems to be negligiblly small because of the low electrical conductivity[4] of the present ferrite sample. The writer wishes to thank Proffesor I. Takahashi of Kyoto University for many helpful and stimulating discussions and the Central Laboratory of Tôyô Rayon Company for co-operation in part of the present experiments.

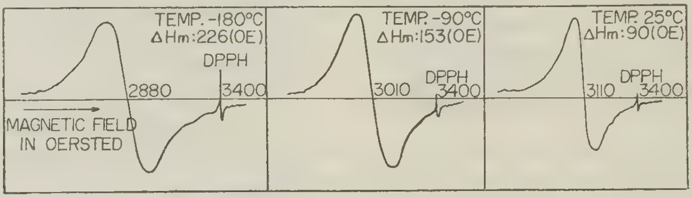

Fig. 1. Temperature variations of the derivatives of the resonance curves of $Ni_{0.7}Cd_{0.3}Fe_2O_4$ at 9500 MC.

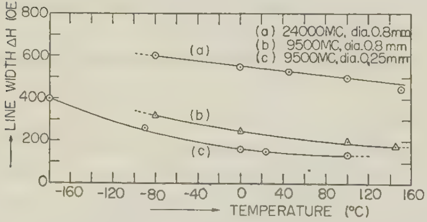

Fig. 2. Temperature dependence of the line width ΔH of $Ni_{0.7}Cd_{0.3}Fe_2O_4$ at 9500 MC and 24000 MC.

References

1) D. Healy: Phys. Rev. **86** (1952) 1003.
2) P. E. Tannenwald: Phys. Rev. **100** (1955) 1713.
3) Y. Kojima: Sci. Repts. Research Insts. Tohoku Univ. **25** (1954) 616.
4) S. Takemoto: Memoirs of the College of Sci. Kyoto Univ. **A-28** (1958) 327.

J. PHYS. SOC. JAPAN **16** (1960) 345~346

Electrical Resistivity of Ferromagnetic Chromium Dioxide

By Buichi KUBOTA and Eiichi HIROTA

Research Department, Wireless Division,
Matsushita Electric Industrial
Co., Ltd. Osaka, Japan

(Received December 9, 1960)

The electrical resistivity of CrO_2 has been studied with the powder specimen, which was prepared in the same way as that described in the previous paper1),2). The measurement of electrical resistivity was carried out by the modified Brentano's method3). Since the electrical resistivity of powder varies with a packing factor, the factor was kept to be about 60% throughout this experiment.

In Table I, the electrical resistivities of CrO_2 prepared under various conditions are tabulated with other properties of CrO_2. It is seen that the resistivity of CrO_2 is in the order of $10^{-1}\Omega$-cm at room temperature and does not seem to be related directly to the ratio, *O/Cr*. The temperature dependence of the electrical resistivity is shown in Fig. 1. It is of interest to note that the resistivity exhibits a peak near the Curie temperature of CrO_2, 116°C, and, except this anomaly, decreases with increasing temperature in the range between −150°C and 350°C. The thermal hysteresis and the absolute value of resistivity are somewhat uncertain due to the powder form of the specimen. Activation energies have also been obtained from this measurement except near the Curie temperature, and the results are about 0.1 to 0.3 ev in the range between 200°C and 350°C, and 0.005 ev between −100°C and the room temperature. To understand the conduction mechanism of CrO_2, the Seebeck effect has been studied. The results are also shown in Table I. It is seen that the thermoelectric power of various oxides is negative.

In view of the above results a probable conclusion to be drawn is that the *N*-type conduction of CrO_2 may be attributed to the interstitial Cr ions of the oxides4), and the peak of resistivity near the Curie temperature may be due to a magnetic interaction between the bulk magnetization and a

Table I. Properties of CrO_2 prepared under various conditions.

Sample number	Preparing condition		O/Cr*1)	Specific gravity	R_0*3) (Ω-cm)	Θ*3) (μV/deg)	T_c (°C)	σ_∞*4) (gauβ/gr)	Lattice contsant*5)	
	Temp. (°C)	Pres. (kg/cm²)							a_o(Å)	c_o(Å)
1	500	317	1.961	4.96	0.20	—	—	92.5	4.421	2.917
2	450	289	1.988	—	0.23	—	—	96.9	—	—
3	480	299	1.997	—	0.17	—	—	96.9	—	|
4	420	128	1.998	—	0.13	−35	—	103.8	—	—
5	355	75	2.005	4.90	0.23	−22	—	—	4.421	2.917
6	560	627	1.985	4.92	0.91	—	116.5	98.0	4.420	2.916
7	520	593	1.997	—	0.31	—	—	100.6	—	—
8	500	578	1.998	—	0.35	−30	—	102.9	—	—
9	400	247	2.000	4.90	0.30	—	—	99.0	4.421	2.916

*1) Ratio, O/Cr, is determined from the ignition loss at 1000°C, 1 hr.
*2) R_0: the resistivity at room temperature.
*3) Θ: the thermo-electric power.
*4) σ_∞: the saturation magnetization at room temperature.
*5) The sample, CrO_2, has a rutile type structure.

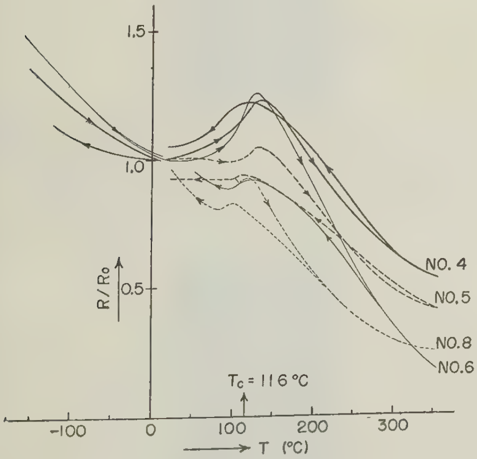

Fig. 1. R/R_0 versus temperature curve for various chromium dioxide; R_0 is the resistivity at room temperature.

spin of charge carrier. Further experiments, however, are necessary to understand and explain the conduction mechanism of CrO_2.

References

1) B. Kubota: J. Phys. Soc. Japan, **15** (1960) 1706.
2) E. Hirota and B. Kubota: J. Phys. Soc. Japan, **15** (1960) 1715.
3) J. C. M. Brentano and C. Goldberg: Phys. Rev., **94** (1954) 56.
4) B. Kubota: to be published at J. Amer. Ceram. Soc.

J. PHYS. SOC. JAPAN **16** (1961) 346

Measurements on Collision Frequencies of Electrons in Neon Gas

By Taro DODO

Hitachi Central Research Laboratory,
Kokubunji, Tokyo

(Received December 12, 1960)

The collision frequency of electrons in an arc discharge in neon gas has been measured by the cyclotron resonance method[1]. The microwave of frequency 9.6 Gc/s was propagated along a square wave guide in TE_{01} mode. The discharge tube was mounted across the wave guide inclined 30 degrees to the H-plane. The values of V.S.W.R. due to the reflection from the discharge tube were found to be less than 1.2 in any case. The attenuation of microwave power transmitted through the discharge tube has been measured as a function of the static magnetic field applied perpendicular to both the axis of the wave guide and the E-vector of the microwave.

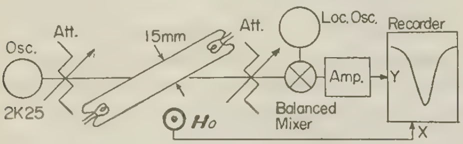

Fig. 1. Abbreviated schematic of experimental apparatus.

The collision frequencies obtained for the various gas pressures from the half-widths of the attenuation spectra are shown in Fig. 2. The electron density in these measurements was $0.3\sim1\times10^{11}/\text{cm}^3$. The collision frequency for momentum transfer of electrons in neon gas obtained from our measurement is

$$\nu_m=7.3\times10^8 p\,, \quad p\text{: gas pressure in mm Hg.} \tag{1}$$

This value is in agreement with the fact that the collision probability P_c[2] (in cm–mm Hg) for the electron of energy 3 eV in neon atoms is 7. The collision frequencies for 0.5 and 1 mm Hg neon gases are larger than the values given by (1). This result could be originated if the electron temperature in these low pressure gaseous discharges is higher than that of high pressure discharge. To confirm this speculation, we have performed a probe measurement[3]. The results indicate that the electron temperatures at 2 mm Hg and 4 mm Hg are 4.1×10^4°K and 3.1×10^4°K, respectively. The collision probability P_c for the 4 eV electron is 8.3[2].

The measurement has been made at higher electron concentration; $n_e\simeq5\times10^{11}/\text{cm}^3$. In this experiment, the discharge tube was mounted across the wave guide parallel to the H-plane and to the static magnetic field. The collision frequencies in this measurement are the same as for the case of low electron density. Therefore, we can conclude that the collisions between charged particles, e–i and e–e, are negligible in these gaseous discharges of low degree of ionization as compared with the electron-neutral atom collision.

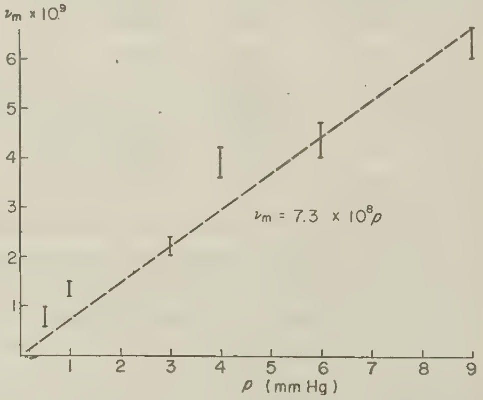

Fig. 2. Electron collision frequencies in neon gas as a function of gas pressure.

The author expresses his thanks to Dr. B. Tadano for his continual encouragements and to Mr. K. Sakai for his assistance in this experiment. He is also obliged to Mr. T. Kuroda of Tohoku University for his assistance and discussions and to Messrs. M. Yamamoto and H. Takano for their preparation of discharge tubes.

References

1) D. C. Kelly, H. Margenau and S. C. Brown: Phys. Rev. **108** (1957) 1367.
2) S. C. Brown: *Basic Data of Plasma Physics* (John Wiley, 1959).
3) L. B. Loeb: *Basic Process of Gaseous Electronics* (Univ. Calif. Press, 1955).

J. Phys. Soc. Japan **16** (1961) 347~348

Observations of Dislocation Network in Neutron-Irradiated LiF Crystal

By Kazuko Kubo and Yoshio Katano

Japan Atomic Energy Research Institute
Tokai-mura, Ibaraki-ken, Japan

(Received November 11, 1960)

Optical-microscopic observations have been made with phase-contrast attachment for LiF crystal which was irradiated with neutrons of about 2×10^{17} nvt in the JRR-1 reactor and annealed at successively higher temperature from 400°C up to 800°C.

Microscopic observations of the same object have been made by several authors[1-4], who have reported that the square cavities, with the faces parallel to (100) and colored by the interference of light, were found densely near cracks and sub-boundaries while often isolatedly in sub-grains. Besides these facts, we have observed the followings:

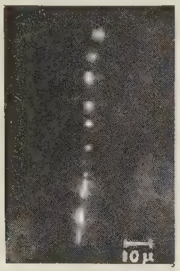

Photo. 1. Square cavities precipitated on a dislocation line.

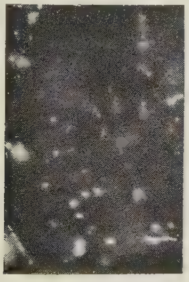

Photo. 2. Isolated dislocation lines, a closed loop and a four-fold node are seen at the lower middle part and a corner respectively.

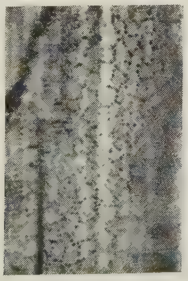

Photo. 3. Polygonal dislocation network.

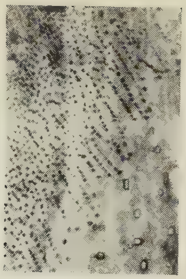

Photo. 4. Parallel dislocation lines found at the terminal part of a network.

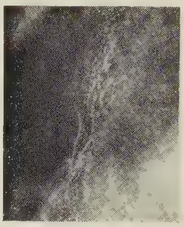

Photo. 5. Dislocation lines on a sub-boundary.

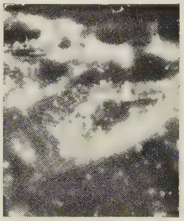

Photo. 6. Cobwebby arrangement of dislocation lines near crack.

(1) Closely formed cavities decorate sub-boundaries and make them visible but few cavities are observed in the region within about 30 μ from the outer surfaces or sub-boundaries of the crystal.

(2) There are isolated dislocation lines, as well as isolated cavities, in sub-grains, which are visually observable by being decorated with light-scatterers. It is almost certain that the most of decorating light-scatterers grow to square cavities with increasing annealing time and temperature (Photo. 1) but there still remains a little uncertainty that some of the quite small light-scatterers might be metallic Li colloids precipitated during thermal annealing but not the nuclei of square cavities which are coagulation of vacancies. It is difficult to find the regularity in distribution of the dislocation lines. The density of the lines is different from one sub-grain to another sub-grain. Those are 30~40 μ in average length and have various shapes, that is, an isolated line, group of lines with nodes, nearly straight line, helical line and closed loop (Photo 2).

(3) Dislocation network exists near the spot with

very dense concentration of the cavities. The decorations of the network appear to be same as described in (2). We show the first picture of the dislocation network in neutron-irradiated LiF crystal. The network consists of either irregular polygons or long parallel lines (Photo 3 and 4).

(4) Dense arrangements of dislocation lines become observable on sub-boundaries and near cracks when the crystal is annealed at about 700°C for a short time (Photo. 5 and 6).

It is certain that tremendous Frenkel pairs are produced by fast neutrons and fission fragments resulted from (n, α) reaction of Li^6 by thermal neutrons during in-reactor irradiation. It is believed that interstitial F-atoms, forming F_2-gas, escape from the crystal and interstitial Li-atoms precipitate to colloids and vacancies coagulate to the square cavities during thermal annealing. The existence of F_2-gas and clloidal Li metal in the crystal lattice, which has been ascertained by nuclear magnetic resonances[5], partly supports this idea. The dislocation lines appear to play an important role which might give F_2-gas some means of escape from the crystal lattice or might offer interstitial Li-atoms and the vacancies the opportunity and the location of coagulation. The microscopic observations in the present note is a part of the studies on the annealing behavior of the neutron-irradiated LiF crystal, which are in progress and the details will be reported soon.

References

1) P. Senio: Science **126** (1957) 208.
2) M. Lambert and A. Guinier: Comptes rend **244** (1957) 2791.
3) R. E. Smallman and T. M. Willis: Phil Mag. **2**(**8**) (1957) 1018.
4) J. J. Gilman and W. G. Johnston: J. Appl. Phys, **30** (1959) 129.
5) P. J. Ring, J. G. O'Keefe and P. J. Bray: Phys. Rev. L. **1** (1958) 453.

J. PHYS. SOC. JAPAN **16** (1961) 348~349

Spectrum of the Electron Cyclotron Resonance in a Plasma

By Taro DODO

Hitachi Central Research Laboratory, Kokubunji, Tokyo

(Received December 15, 1960)

When the electromagnetic wave is propagated through a plasma in the direction perpendicular to the static magnetic field, a cyclotron resonance peak should occur at the angular frequency ω:

$$\omega=(\omega_c{}^2+\omega_p{}^2+\nu_m{}^2)^{1/2}\,, \qquad (1)^{1)}$$

where $\omega_c/2\pi$, $\omega_p/2\pi$, and ν_m are the gyration frequency $eH/2\pi mc$, the plasma frequency $(ne^2/m\pi)^{1/2}$, and the collision frequency for momentum transfer, respectively. We have carried out a measurement on microwave attenuation and verified the relation (1).

The experimental apparatus is the same as the preceeding article.[5] The attenuation spectrum for a constant discharge current is obtained by changing the magnetic field strength and fixing the frequency $\omega/2\pi$ of microwave at 9.6 Gc/s throughout this experiment. The discharge tube is a fluorescent lamp, and it contains 3.5 mm Hg argon and mercury vapour at room temperature. According to the theoretical result (1), the magnetic field strength at which the resonance peak occurs should depend on the electron density $\omega_p{}^2$. In order to confirm this prediction, the attenuation measurements were carried out for various electron densities. The electron density is controlled by the discharge current. Although the magnetic field strength at which the gyration frequency $\omega_c/2\pi$ becomes 9600 Mc/s is 3429 gauss, for a high density plasma the attenuation peak occurs at 2000 gauss or less. The magnetic field strength at which the attenuation peak occurs is shown as a function of the discharge current in Fig. 1.

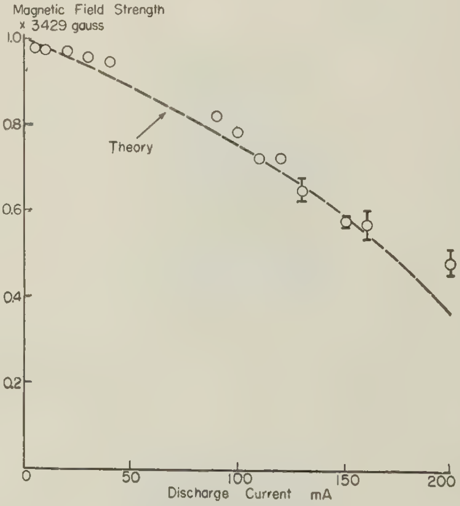

Fig. 1. Field strength at the resonance peak as a function of the discharge current.

From the peak height of the cyclotron resonance spectrum, we can obtain the electron density. From the peak heights of the resonance spectra at the discharge currents of 5, 10, and 20 mA, we find that the electron density is proportional to the discharge current and is $5\times10^{10}/cm^3$ for the discharge current of 10mA*. The plasma frequency $\omega_p/2\pi$ for the electron density $5\times10^{10}/\mathrm{cm}^3$ is 2×10^9 c/s. From this numerical relation and the proportionality of ω_p^2 to the discharge current I, we obtain the relation between $(\omega_p/\omega)^2$ and I for our experiment:

$$(\omega_p/\omega)^2=4.4\times10^{-3}\ I\ (I \text{ in mA}). \qquad (2)$$

When we put the theoretical relation (1) into the form

$$\omega_c/\omega=[1-(\omega_p/\omega)^2-(\nu_m/\omega)^2]^{1/2}\ , \qquad (1)'$$

we can see more easily the relation between the theoretical result and our experimental result. The relation (1)′ tells us that the magnetic field strength, at which the cyclotron resonance peak occurs, decreases as the electron density increases**. The theoretical curve which is obtained by substituting (2) into (1)′ is shown in Fig. 1 by a dotted line***. The theoretical prediction is in good agreement with our experimental result.

Recently, S. Tanaka[3] has carried out the measurement on cyclotron resonance absorption in neon gas and he has also verified the relation (1) in the range of low electron density: $(\omega_p/\omega)^2\sim0.1$ to 0.3. K. Kato[4] has also verified the relation (1) by the measurement on cyclotron radiation from a mercury discharge tube.

Finally, we shall make another remark on the shape of resonance spectrum. Examples of spectra for low and high current discharges are shown in Fig. 2. The half-widths of the spectra for high current discharges (90 mA, 160 mA) are very broad. One may suppose that the width becomes broad because the collisions between charged partcles become frequent. But this is not true and the broadening of spectrum width comes from the inhomogeneity of the electron density in space. By the Lorentz force, the discharge current is pushed to one side of the wall of the tube and the electron density becomes high at this side and low at the other side. As can be seen from (1)′, when the electron density is n_1 in the region 1 in the discharge tube and is n_2 in the region 2, the field strength, at which the resonance peak occurs, is H_1 and H_2 in respective regions. In this way the spectrum is a superpose of many spectra which have peaks at different field strength, and its width becomes broader. When we used an arrangement which insures a uniform distribution of electron density, (for example having the discharge current parallel to the static magnetic field,) the width of spectrum for high current discharge became as narrow as that for low current discharge.

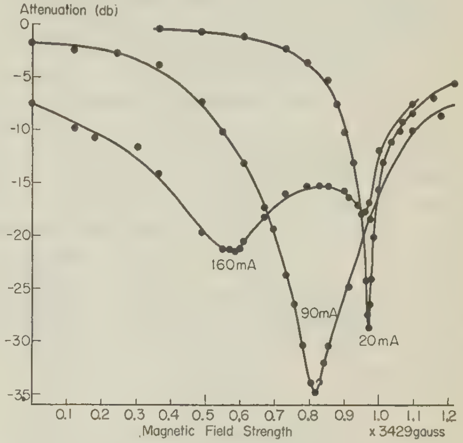

Fig. 2. Attenuation spectra for the discharge currents of 20, 90, and 160 mA. The shape of of spectra for 5, and 10 mA is similar to that of 20 mA.

The author is deeply obliged to Mr. T. Kuroda for his assistance and discussions.

References

1) T. Dodo: J. Phys. Soc. Japan **16** (1961) 293.
2) J. Nakamura: Hitachi Hyoron **36** (1954) 1151 (in Japanese)
3) S. Tanaka: Nuclear Fusion Research **5** (1960) 283 (in Japanese)
4) K. Kato: J. Phys. Soc. Japan **15** (1960) 1093.
5) T. Dodo: J. Phys. Soc. Japan **16** (1961) 346.

---

* J. Nakamura had carried out the measurements on electron density in a discharge tube similar to ours using the double probe method[2]. He found that the electron density was proportional to the discharge current and was $4\times10^{11}/\mathrm{cm}^3$ for the discharge current of 50 mA.

** Note that the microwave frequency $\omega/2\pi$ is fixed throughout this experiment.

*** From the half-width of the resonance spectrum for the discharge current of 20 mA, we obtained the numerical value of 1.8×10^9 c/s for ν_m.

J. PHYS. SOC. JAPAN **16** (1961) 350~351

On the Inelasticity in High-Energy Nuclear Interactions

By Shigeo MATSUMOTO and Shoji MIKAMO
Institute of Polytechnics, Osaka City University

(Received December 5, 1960)

The inelasticity, K, in a nucleon-nucleon collision is defined as the ratio of all the energy of created particles to the available kinetic energy of the nucleons before collision in the center-of-mass system. Let $\langle n_\pm \rangle$ be the average number of charged mesons produced, $\langle E \rangle$ its average total energy in the center-of-mass system. Then the average value of $K, \langle K \rangle$, is expressed by the formula

$$\langle K \rangle = \frac{1.5 \langle n_\pm \rangle \langle E \rangle}{2(\langle \gamma_c \rangle - 1)Mc^2} ,$$

where $\langle \gamma_c \rangle$ is the Lorentz factor of nucleon (in the center-of-mass system) having the average primary energy and M is the nucleon mass. In order to estimate $\langle K \rangle$, we will first try to obtain $\langle n_\pm \rangle$.

A stack of Ilford G5 emulsions (108 sheets of 9″×6″, 600μ thick) was flown at an altitude of 29 km during six hours from Kobe. In this stack, 54 nuclear interactions induced by singly charged particles and 12 by neutral particles* were detected by the tracing-back method. This method consists of tracing star-producing flat tracks back along their passage through successive emulsion strips and finding primary interactions1). The above singly charged particles are mostly the primary cosmic ray protons incident upon the top of atmosphere, but some of them are the protons produced in the atmosphere and the emulsion stack. The effect of the latter protons may be subtracted by the following assumptions: both interactions of these protons and neutral particles are equal in number (12 interactions) and have the same distribution in the number, n_s, of shower particles (particles with blob density less than 1.5 times plateau blob density). Another thing to be considered is a bias against low multiplicity events which is due to the tracing-back method. This bias has been corrected by the probable assumption that the detection probability in this method is proportional to n_s. In this way, the average value of $n_s, \langle n_s \rangle$, was found to be 4.5. We will subtract one track to obtain $\langle n_\pm \rangle$. In the above process, the contamination of π-mesons among singly charged particles which induce nuclear interactions has been neglected. This neglect does not lead to serious error, because the contamination of π-mesons could be estimated to be of the order of 4%. For the primary protons incident upon the stack without undergoing nuclear interactions in the atmosphere, the average kinetic energy can be obtained by the energy spectrum of the primary cosmic ray protons with a sharp geomagnetic cutoff at a kinetic energy of 10 GeV. The value obtained was 26 GeV. Thus, the value of $\langle n_\pm \rangle$ at an average energy of 26 GeV was found to be 3.5. The same method was applied for the interactions with less than 6 heavily ionizing prongs, N_h. In this case, the value of $\langle n_\pm \rangle$ was estimated to be 2.8.

It was found, in this laboratory, that the value of $\langle E \rangle$ in nucleon-nucleon collisions around 40 GeV is 0.44 GeV2). It has to be borne in mind that the events analysed in reference 2 are confined to the relatively large multiplicity showers. We will take the above value of $\langle E \rangle$ to calculate $\langle K \rangle$, because it is known that, for primary energies around several tens GeV, the change of $\langle E \rangle$ with primary energy is small2),3). From the above value of $\langle E \rangle, \langle \gamma_t \rangle = 3.9$, and $\langle n_\pm \rangle = 2.8$, the value of $\langle K \rangle$ was estimated to be 0.34 for the interactions with $N_h \leqslant 5$.

This value is slightly smaller than those of 6.2 GeV4),5) and 8.7 GeV6). If the value of $\langle E \rangle$ for events with low n_s is comparatively large, $\langle K \rangle$ will increase. However, it seems that a considerably large value of $\langle E \rangle$ is less plausible by the following facts. Kalbach et al4). made an analysis of proton-proton collisions using protons of energy 6.2 GeV from the Bevatron. Their observation indicates that the value of $\langle E \rangle$ does not change appreciably as the prong number increases. Analysing the cosmic ray showers, Kaneko and Okazaki3) suggested that the value of $\langle E \rangle$ in each nucleon-nucleon collision does not depend on the inelasticity. This suggestion is also supported by the data observed in reference 2. Thus we reach the conclusion that $\langle K \rangle$ does not change greatly with increasing energy at least up to several tens GeV.

The authors wish to express their sincere thanks to Prof. Y. Watase for his interest and encouragement. Thanks are due to Dr. S. Kaneko for suggesting to obtain the inelasticity. They are also indebted to Mr. O. Kusumoto for his criticisms.

References

1) S. Kaneko, O. Kusumoto, and S. Matsumoto: J. Phys. Soc. Japan **11** (1956) 1129.
2) S. Kaneko, O. Kusumoto, S. Matsumoto, and M. Takahata: *Proceedings of the Moscow Cosmic Ray Conference*, **1** (1960) 107.
3) S. Kaneko and M. Okazaki: Nouvo Cimento **8** (1958) 521.
4) R. M. Kalbach, J. J. Lord, and C. H. Tsao: Phys. Rev. **113** (1959) 330.

---

* It may be reasonable to consider that all of these particles are neutrons.

5) R. R. Daniel, N. Kameswara Rao, P. K. Malhotra, and Y. Tsuzuki: Nouvo Cimento **16** (1960) 1.
6) N. Bogachef, S. Bunyatov, Yu. Merekov, V. Sidorov, and V. Yarba: *Proceedings of the Ninth Conference on High Energy Nuclear Physics, Part* **1** (1959) 199.

J. PHYS. SOC. JAPAN **16** (1961) 351

Enhancement of Photoconductivity upon Cadmium Sulphide Single Crystals

By Saburo KITAMURA, Takao KUBO
and Toshio YAMASHITA

Central Research Laboratory, Matsushita Electric Industrial Co., Osaka

(Received November 30, 1960)

It has been generally accepted that the infrared quenching upon CdS or CdSe crystals was associated with the recombination of electrons and holes made free from traps by irradiation of infrared rays[1,2]. In the case of CdS single crystal, it was reported[1,2] that the photocurrent produced by irradiation with visible rays was reduced by irradiation with infrared rays of 900 mμ or 1400 mμ. But, when a high voltage (of about 2000 volts/cm) was applied to CdS crystal, it was found that the photocurrent was enhanced by irradiation of infrared rays of 900 mμ or 1400 mμ.

Pure CdS crystals used in the present experiment were prepared by the sublimation method[3] in argon gas. The average size of the crystal was 8×6×0.04 mm. A schematic diagram of the experimented arrangement is shown in Fig. 1. Electrodes were formed by indium evaporated on opposite surfaces of a specimen. A specimen to be measured was mounted on a fused quartz plate and was then put in a hard glass tube with quartz windows in which nitrogen gas was flowing.

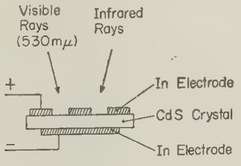

Fig. 1. Schematic diagram of specimen.

Quenching and enhancement of photocurrent by irradiation with infrared rays superposed on visible rays are shown in Fig. 2. When D. C. 750 volts/cm was applied to the crystal, two quenching maxima were observed at 900 mμ and 1400 mμ. On the other hand, when D. C. 1250 volts/cm was applied to the crystal, the quenching value* decreased, most apparent decrease being at 900 mμ and 1400 mμ. When D. C. 2000 volts/cm was applied to the crystal, the enhancement of photocurrent appeared at 900 mμ and 1400 mμ. By irradiation with infrared rays of 900 mμ or 1400 mμ only, there was no photocurrent to be measured. When the electrode on the plane of incidence was negative, the enhancement of photocurrent appeared above 3000 volts/cm of applied voltage.

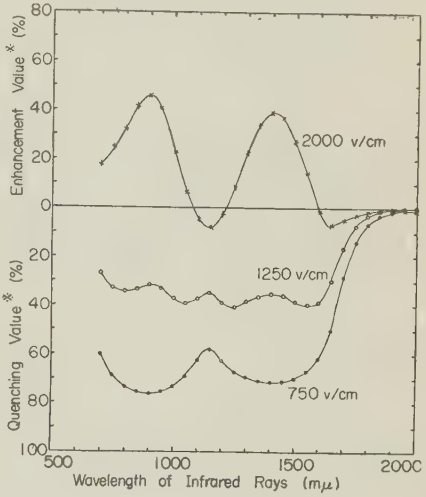

Fig. 2. Quenching and enhancement of photocurrent by irradiation of infrared rays superposed on visible rays.

The above phenomena cannot be understood by the previous interpretation[1,2] that free holes available for recombination are produced by irradiation of infrared rays. Experiments are now being carried on in order to investigate the mechanism of infrared enhancement. The author wishes to thanks Assistant Professor K. Fukuda at Kyoto University for his valuable advice.

References

1) E. A. Taft and M. H. Hebb: J. O. S. A. **42** (1952) 249.
2) R. H. Bube: Phys. Rev. **99** (1955) 1105.
3) S. Ibuki and K. Awazu: J. Phys. Soc. Japan **11** (1956) 1297.

---

* Quenching value is indicated as $\{1-I_{p+s}/(I_p+I_s)\}\times 100(\%)$, where I_{p+s} is the photocurrent produced by the irradiation of infrared rays superpose on visible rays, I_p is the photocurrent produced by irradiation of visible rays and I_s is the photocurrent produced by irradiation of infrared rays. In the present experiments, I_s was nearly zero. When the quenching value is negative, the word infrared enhancement is used.

J. Phys. Soc. Japan **16** (1961) 352~353

A New Phase of an Intermetallic Compound Mn$_{3.4}$Ge and its Magnetism

By Tetuo OHOYAMA,
Department of Physics, Faculty of Science, Tokyo Metropolitan University
Kō YASUKŌCHI and Kazuo KANEMATSU
Department of Physics, College of Science and Engineering, Nihon University, Tokyo

(Received December 10, 1960)

According to Zwicker, et al.[1], an intermetallic compound of manganese with germanium, Mn$_{3.25}$Ge, has a hexagonal close packed structure, in which an ordered, D0$_{19}$ (Ni$_3$Sn) type of structure is induced by annealing the specimen at 750°C for 2 days. The ordered structure, however, was not established in our specimen similarly treated, and a phase transformation into a tetragonal one was found at a lower temperature.

The specimen for this study had a composition of Mn$_{3.4}$Ge (22.7 at. % Ge) and was prepared as follows: Powders of electrolytic manganese (99.9%) and germanium (seven-nine purity) were mixed in the proportion, and the mixture was charged in an alumina crucible, sealed in an evacuated silica tube, and melted by an electric furnace at 1150°C.

Table I. The X-ray diagram of Mn$_{3.4}$Ge, annealed at 430°C (Cu Kα radiation).

obs.			*hkl*	calc.	
2θ (degrees)	*d* (Å)	I/I_0		*d* (Å)	I/I_0
41.8	2.16	100	111	2.16	100
47.8	1.90	30	200	1.90	34
50.4	1.81	15	002	1.81	14
69.8	1.35	17	220	1.35	10
72.0	1.31	20	202	1.31	18
84.9	1.14	25	311	1.14	22
88.7	1.10	8	113	1.10	10
91.0	1.08	8	222	1.08	10
			400	0.951	2
			004	0.904	2
124.5	0.87	10	331	0.870	8
129.8	0.85	20	313	0.852	18
			420	0.850	9

After examined by an X-ray diffractometer to have the same (h.c.p.) structure as Mn$_{3.25}$Ge reported previously[2], the specimen was annealed at 430°C for 9 days and quenched into cold water, with the intention of investigating the effects of heat treatment on the magnetic property and on the atomic arrangement as well. Then, a structure change was brought about, rather than a modification of the original one as has been first expected.

As seen from the X-ray diagram which was obtained by the diffractometer and given in Table I, the specimen thus annealed consisted of a single phase with a face centered tetragonal structure.* No superlattice lines were found and the lattice parameters were determined to be $a=3.80_3$ Å, $c=3.61_8$ Å, and $c/a=0.951$.

As to the magnetic property, the new phase exhibits an anomalous behavior, and has a fairly stronger magnetism than the hexagonal one. Fig. 1 shows the values of the saturation magnetization as a function of temperature, which were determined under a field of 9 kilo-oersteds from the force exerted on the specimen in an inhomogeneous field. The saturation magnetization is nearly constant at low temperatures and extrapolated to be 11 cgs emu/g at 0°K, while, on heating above the room temperature, increases gradually towards its maximum value 17 cgs emu/g at 700°K. Then it falls off quite rapidly and the Debye photograph taken for this specimen after cooled to the room temperature gives only the h.c.p. pattern. Accordingly, the falling off of the thermo-magnetic curve is not due to the magnetic transition of the tetragonal phase, but may be associated with the phase transformation into the hexagonal one, which is paramagnetic at these temperatures. Apart from this point, the magnetic behavior of the tetragonal phase is somewhat similar to that of Néel's P type[3] of ferrimagnetism, but it should be postponed to make that classification until further investigations will be carried out.

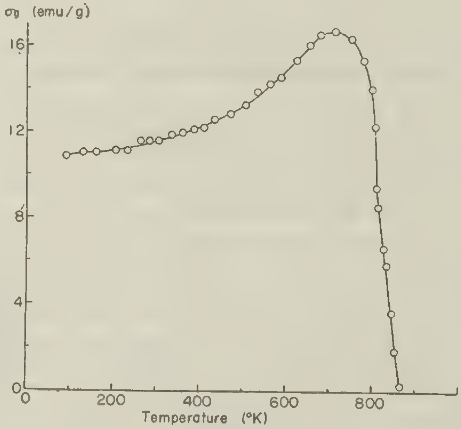

Fig. 1. Temperature dependence of the saturation magnetization of tetragonal Mn$_{3.4}$Ge.

Thus it may be concluded that the hexagonal phase reported by Zwicker, et al. is stable only at higher temperatures, but the transformation from it to the tetragonal one, which is more stable at lower temperatures, takes place so sluggishly that the latter seems to be realized only after a long time annealing.

---

* A f.c.t. structure is equivalent to a b.c.t. structure with $a'=a/\sqrt{2}$. The former is prefered here in relationship to L6$_0$ (Ti$_3$Cu) type of structure, to which D0$_{19}$ type of structure would be transformed.

More detailed examinations of the transformation, as well as as of the anomalous magnetic behavior of the tetragonal phase, are now in progress, and will be reported on later, together with the findings on other compounds of the Mn–Ge system.

References

1) U. Zwicker, E. Jahn and K. Schubert: Z. Metallkde. **40** (1949) 433.
2) K. Yasukōchi, T. Ohoyama and K. Kanematsu: J. Phys. Soc. Japan **14** (1959) 1820.
3) L. Néel: Ann. physique **3** (1948) 137.

Errata

The Magnetic Investigation of Mn^{++}, Co^{++}, Ni^{++}, Cu^{++} Ammine and Anhydrate Salts

By Kiyoshi KIDO and Takashi WATANABE

J. Phys. Soc. Japan **14** (1959) 1217

Page	Column			
1219	right	Table IV		
			C	p
		$Ni(NH_3)_6Cl_2$	1.002	3.08±0.04
1222	right	Table IX		
			g	
		$Ni(NH_3)_6Cl_2$	2.17±0.03	

Errata

On the Superconducting Ground State

By Ziro MIKURA

J. Phys. Soc. Japan **15** (1960) 1783

Page	Column	Line		Should read
1784		Eq. (2.10)	$H_1=\sum_k(\varepsilon_k-\lambda)u_kv_k(\cdots)$	$H_1=2\sum_k(\varepsilon_k-\lambda)u_kv_k(\cdots)$
1784		Eq. (2.11)	$H_2=(ig/2V)\sum_{(\cdots)}\cdots$	$H_2=(ig/\sqrt{2V})\sum_{(\cdots)}\cdots$
1784		Eq. (2.12)	$H_3=(ig/2V)\sum_{(\cdots)}\cdots$	$H_3=(ig/\sqrt{2V})\sum_{(\cdots)}\cdots$
1785	right	The third diagram in Fig. 3	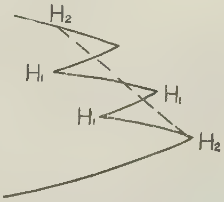	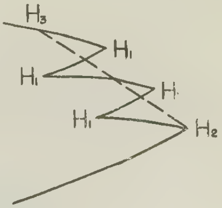
1789	left	Eq. (3.2)	$\kappa=(\pi/3)(H_0{}^3/n^2\gamma_nT_c{}^2)$	$\kappa=(\pi/3)(H_0{}^2/n^2\gamma_nT_c{}^2)$

PROGRESS OF THEORETICAL PHYSICS

CONTENTS

Progress of Theoretical Physics Vol. 24, No. 2, August 1960

On the Problem of Unsaturated Helium Films..A. D. SINGH and R. K. PATHRIA..229
High Energy Scattering of Nucleon from Nuclei—*A Proposed Model and Its Experimental Verification* ....Tatuya SASAKAWA..241
Symmetries of the Interactions among Strongly Interacting Particles and Non-Leptonic Decays of Hyperons ....Kanji FUJII..259
On a Model of Nucleon Structure and Meson-Nucleon Interaction. I ....Hiroshi NAKAMURA..271
Lagrangian Formalism for a Classical Relativistic Particle Endowed with Internal Structure ....Francis Halbwachs..291
Universality of Coupling Constants and Individual Γ_5-Invariance...Kenzo IWATA..308
A New Approach to the Theory of Classical Fluids. II—*Multicomponent System*— ....Kazuo HIRÔIKE..317
On the Collective Motion in Even-Even Spherical Nuclei......Toshio MARUMORI..331
Electron-Electron Interaction in Hot Electron Problems ....Jiro YAMASHITA..357
Photodisintegration of the Deuteron at High Energies ....Tomoya AKIBA..370
Coupling of Dirac Particle and Gravitational Field.............Toshiei KIMURA..386
Information about the Proton-Proton Scattering Matrix from Coulomb Interference ....B. P. NIGAM..407
Electromagnetic Structure of the Nucleon. V—*Numerical Results of Three-Pion-State Contributions* ....K. HIIDA and N. NAKANISHI..414
Collective Excitation of Nuclear Matter ....Shigeaki HATANO..418
Quadrupole Interaction in Crystals ....O. NAGAI and T. NAKAMURA..432

Letters to the Editor:

Influence of Interelectronic Collision on Hall Mobility in Non-Polar Semiconductor ....Y. UCHIYAMA..455
de Haas-van Alphen Effect and Coulomb Interaction ....H. ICHIMURA and S. TANAKA..457
S-Wave Pion-Nucleon Phase Shifts ....K. ISHIDA..459
An Example of a Scattering System in Jauch's Sense........S. KURODA..461
On the Non-Axial Deformation of the Medium and Heavy Even-Even Nuclei ....J. HIURA and S. SUEKANE..462
Contents of Journal of Phys. Soc. of Japan, Vol. 15, No. 7 ....i-ii

Price $ 1.25 per copy
$ 15.00 per year (postage inclusive)
Annual dues for foreign members (individual subscribers)
$ 12.00 (postage inclusive)
〃 for foreign members of the Physical Society of Japan
$ 10.00 (postage inclusive)

Application for membership, subscriptions and orders for back numbers should be sent, directly or through book-dealers, to

The Publication Office
in
Yukawa Hall, Kyoto University, Kyoto, Japan

JOURNAL OF THE PHYSICAL SOCIETY OF JAPAN, Vol. 16, No. 3, MARCH, 1961

Gamma Rays from Inelastic Scattering of Neutrons by Fe, Cu, Zn, Ge and Se

By Kazuaki NISHIMURA

Nuclear Physics Laboratory, Division of Physics, Japan Atomic Energy Research Institute, Tokai-mura, Ibaraki-ken

(Received October 8, 1960)

Gamma rays following inelastic scattering of neutrons by Fe, Cu, Zn, Ge and Se, have been measured with 3.11~4.72 MeV neutrons using a ring geometry arrangement. The excitation functions for the following gamma rays were observed: 0.844, 1.23*, 1.80*, 2.11* and 2.56* MeV in Fe^{56}, 0.665, 0.965 and 1.33 MeV in Cu^{63}, 0.760 and 1.11 MeV in Cu^{65}, 0.810*, 0.995 and 1.81 MeV in $Zn^{64,66,68}$, 0.590 MeV in $Ge^{74,76}$, 0.830 MeV in Ge^{72}, 1.01 MeV in Ge^{76}, 0.560 MeV in Se^{76}, and 0.660 MeV in $Se^{76,78,80}$, respectively. The asterisk indicates the transitions from the higher excited to the 1st excited states. An aspect of de-excitation of higher energy levels was also discussed by analyzing the ratio of probabilities of de-excitation through or not through the 1st excited state as a function of the incident neutron energy.

§1. Introduction

A nucleus, that is raised to an excited state by the inelastic scattering of neutrons, will decay to its ground state with the emission of gamma radiation. It is an important problem to observe the de-excitation gamma rays as well as the inelastically scattered neutrons. These two observations, complementary in nature, present useful informations to clarify the nuclear structure and the mechanism of nuclear reactions.

Measurements of the de-excitation gamma rays following inelastic scattering of fast neutrons have been made by many authors,[1),2),3),4),5)] and yielded valuable data on the structure of nuclear levels, especially in those cases where excitation of the levels is not attainable by beta decay or Coulomb excitation. The excitation functions of gamma rays near the threshold have also been measured by several authors[6),7),8)] for the lowlying levels in various nuclides, and the results have been compared with the theory of Hauser and Feshbach[9)] based on the statistical model.

On the other hand, only a few measurements have been made on the production of gamma rays at neutron energies higher than 3 MeV, well above the threshold for the low-lying levels in medium-weight nuclides. With increase of the incident neutron energy, more levels in the residual nucleus are excited and analysis of data becomes difficult due to the increase of contributions from the higher levels. Some informations about higher levels of the residual nucleus may, however, be obtained by these measurements, since the character of nuclear levels is reflected in the gamma-ray spectra or their excitation functions.

This paper reports the results of measurements on the gamma-ray production in five elements (iron, copper, zinc, germanium and selenium) excited by neutrons of 3.11~4.72 MeV. The gamma-ray spectra observed are illustrated at a neutron energy of 4.04±.10 MeV. Most of these gamma-rays are fitted to known level scheme in relevant nuclide. The absolute production cross sections of gamma rays measured at the neutron energy of 4.04 MeV. are also tabulated.

An analysis on the ratio of transition probabilities from the higher to the 1st and the ground state was also made in iron and zinc, by combining the data of the present work with those obtained with time-of-flight technique[10)].

§2. Experimental Arrangements

The de-excitation gamma rays following neutron inelastic scattering were studied with the ring-geometry arrangements as shown in Fig. 1. Ring scatterers of iron, copper, zinc and carbon had an inner and outer diameter of 9.0 cm and 11.0 cm and a thickness of

5.0 cm. Germanium oxide and selenium were enclosed in aluminum containers, having the same dimensions with a wall thickness of 0.5 mm.

Neutrons were produced by the $D^2(d, n)He^3$ reaction. Deuteron beam of 0.5 μA was focused on a gas target at a distance of 1.7 m from a steering magnet, which was located at 2 m from a 90° beam-analyzing magnet. Measurements were done in a large room, the dimension of which was 25 m by 14 m, and 10 m in height, and which had a pit 2.5 m deep covered with gratings. The target was positioned 1.06 m above the gratings. The neutron background due to the scattering from the wall and floor were found to be negligible.

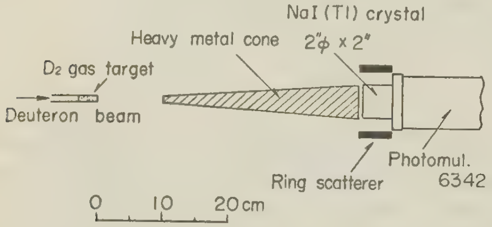

Fig. 1. Experimental arrangement for observing gamma rays from the inelastic scattering of neutrons. The scattering sample has ring geometry.

The gas target was of a cylindrical shape, 3 cm in length and 1 cm in diameter, and had an entrance window covered with a nickel foil of 1.27×10^{-3} mm thickness. The bottom was sealed with a platinum foil of 0.05 mm thickness. The pressure of deuterium gas was 40 cm Hg. The energy loss of the deuterium ions in passing through the nickel foil and the deuterium gas was calculated by use of published data[11].

The scattering ring was placed 45 cm distant from the target with its axis in the direction of the deuteron beam. Owing to its finite dimensions, it received the neutrons emitted in a range of 4.5°~8.5° with respect to the deuteron beam. The average angle between the neutrons incident on the scatterer and the de-excitation gamma rays which entered the detector, was about 100°.

The spread in the energy of the neutrons incident to the sample, which resulted from the spread in the energy of the deuterons in the target and the divergence in the angle of emission of neutrons, was estimated to be less than ±100 keV.

The spread was also checked experimentally by observing the 2.95 MeV resonance in the neutron total cross section of carbon. Both results agreed fairly well with each other.

The gamma rays from the scattering sample were detected with a $2''\phi \times 2''$ NaI(TI) crystal, mounted on a RCA 6342 photomultiplier. Pulses from the scintillation counter was fed into an RCL 256-channel pulse height analyzer through a preamplifier.

A cone of heavy metal, 30 cm in length, was placed between the scintillation counter and the neutron source. The heavy metal cone was made from wolfram, copper and nickel, and had a density of 17 gm/cm^3. It shielded the scintillation crystal against the neutrons and gamma rays from the neutron source effectively.

Neutron flux was monitored using a BF_3 long counter, placed 3.6 m distant from the target in a direction of 60° to the deuteron beam.

§ 3. Experimental Procedures

Day[3] has reported that there are two methods of calculation of inelastic scattering cross sections; one is to neglect completely the effects of all neutron scattering, assuming that the neutron flux is constant throughout the scatterer, and the other is to calculate rigorously taking multiple scattering of neutrons into account. But according to him the root-mean-square difference was only 3.5% between the results mentioned above. We take, therefore, the simple method in which the effects of multiple scattering just cancel out the neutron attenuation.

One can generally determine the gamma-ray intensity by measuring number of counts in a photo-peak. If neutrons enter the scattering ring parallel to its axis, the number of counts C produced in the gamma-ray detector is given approximately by Eq. (1):

$$C = nN\int_V\int_\Omega\left(\frac{d\sigma}{d\Omega}\right)\eta dV\,d\Omega \qquad (1)$$

Here n denotes the number of incident neutrons per cm^2, N the number of nuclei per cm^3 of the scatterer, Ω the solid angle subtended by the scintillator at an elementary colume dV of the scatterer, and V the volume of the scatterer, respectively. $d\sigma/d\Omega$ represents the differential cross section for the gamma-ray production by the neutron inelastic scattering and η the photo-peak efficiency of the NaI detector.

Assuming that the angular distribution of gamma-ray yield does not change greatly in the range of observation, Eq. (1) can be simplified as follows:

$$C=nN\left(\overline{\frac{d\sigma}{d\Omega}}\right)\mathcal{E}V \qquad (2)$$

where $\mathcal{E}\equiv(\overline{\eta\Omega})$ is called the effective photo-peak efficiency, which is determined experimentally by a method to be mentioned later.

The neutron flux n incident to the scatterer was calculated from published data[12)] on the differential cross section of $D^2(d,n)He^3$ reaction.

Then, the differential cross section at $\theta=100°$, $(d\sigma/d\Omega)_{100°}$ can be obtained by measuring the photo-peak yield C and the effective photo-peak efficiency $\mathcal{E}$.

Some of the neutrons, which are scattered at the sample, enter the NaI crystal. These neutrons cause inelastic scattering or neutron capture in the sodium iodide, and result in producing gamma rays which contribute to the background. These scattered neutrons can be closely reproduced by replacing the scattering sample with a carbon scatterer, which does not give an inelastic scattering of neutrons below $E_n=4.43$ MeV, although the energy spectra of scattered neutrons are slightly different in the two cases. The gamma-ray yield C is, therefore, obtained by taking the difference between the measurement with the scattering sample and that with a carbon scatterer.

The pulse-height distribution of the background for neutron energies from 3.11 to 4.72 MeV are shown in Fig. 2 (a) and 2 (b), which are mainly attributed to gamma rays caused by the neutron inelastic scattering in the

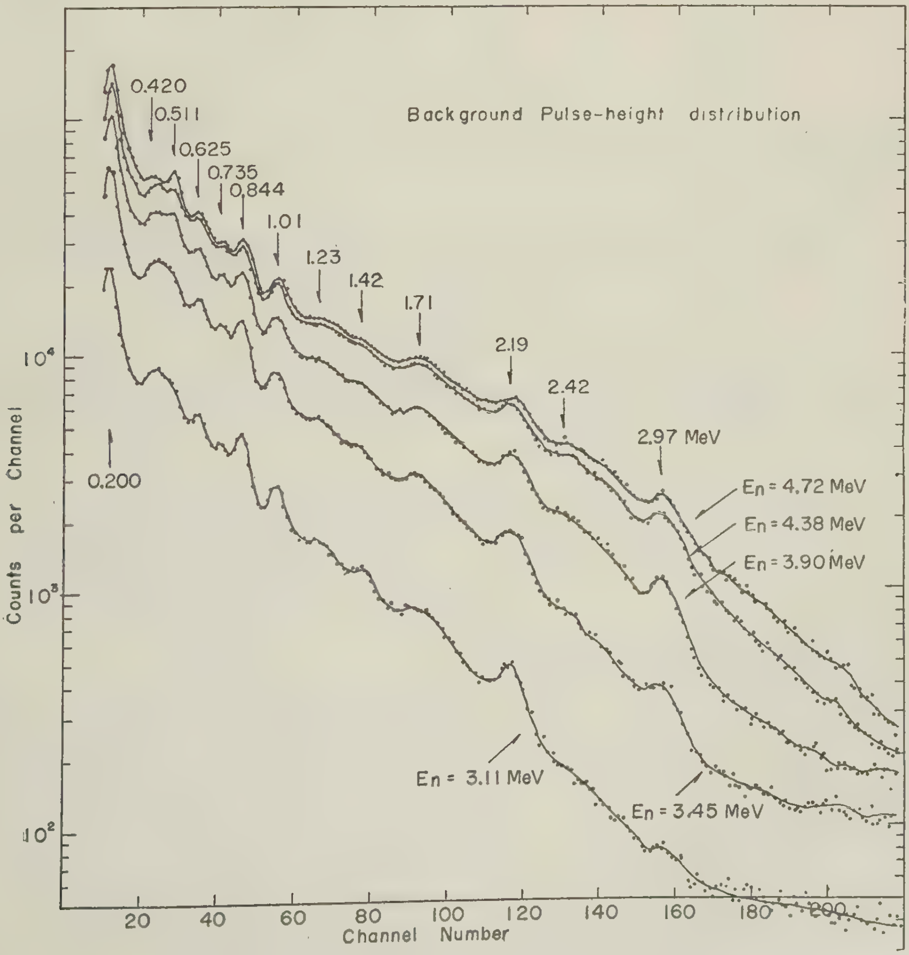

Fig. 2(a).

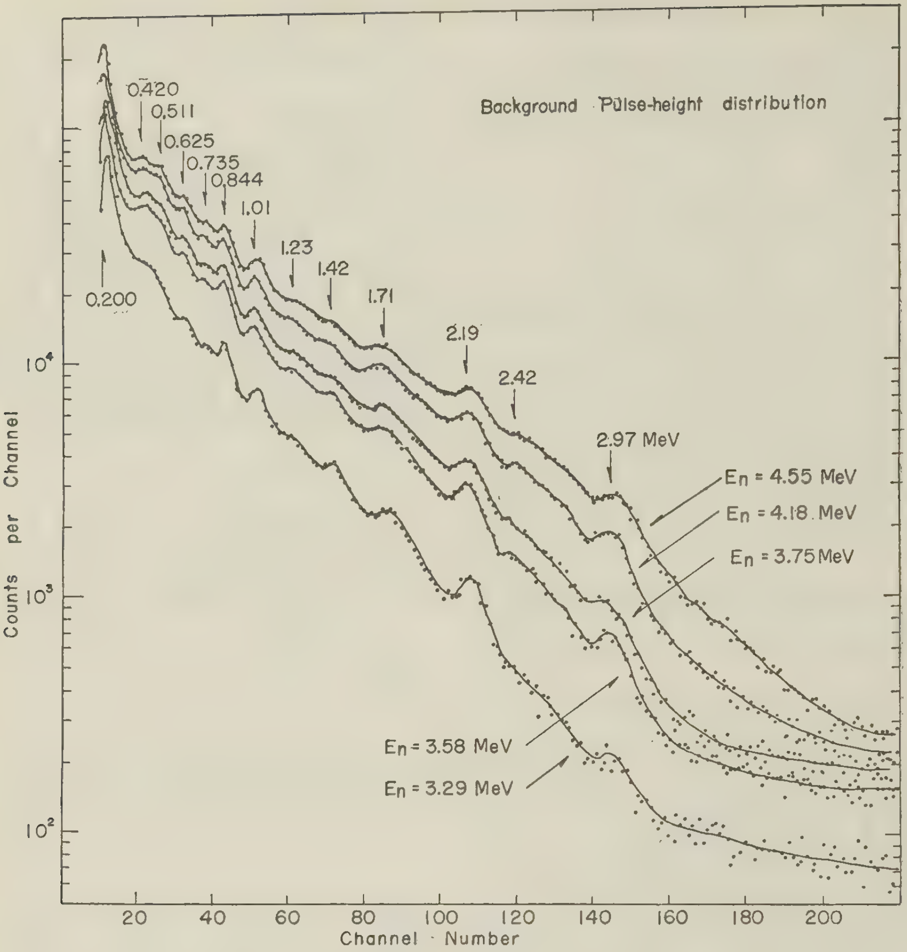

Fig. 2(b).

Fig. 2(a) and 2(b). The pulse-height distribution of the background, which were measured with a carbon ring scatterer. The energies of the incident neutrons are in the range of 3.11∼4.72 MeV. Most of gamma-rays, which are indicated by arrows, arise from inelastic scattering in the NaI(TI) crystal, as listed in Table I.

sodium iodide crystal. Table I gives the energies and de-excitation scheme of these gamma rays at a neutron energy of 4.04±.10 MeV.

The effective photo-peak efficiency $\mathcal{E}$ have to be known as a function of gamma-ray energy E_γ. It depends on the shape of the gamma-ray source and scintillation crystal, and on their relative position. Sodium bicarbonate was irradiated in the JAERI water-boiler reactor (JRR–1) and its absolute activity was measured by a 4π beta counter. Then, this sodium bicarbonate was put in place of the scatterer and the efficiency was determined for the Na^{24} gamma rays of 1.37 and 2.75 MeV, with a result of $(1.04\pm0.04)\times10^{-2}$ and $(4.46\pm0.12)\times10^{-3}$, respectively.

According to Day[3] and Freeman et al.,[8] $\mathcal{E}$ can be expressed by a simple power of E_γ in a range between 0.5 and 2.8 MeV, that is

$$\mathcal{E}=AE_\gamma^{-B} \tag{3}$$

From the efficiency measured for Na^{24} gamma rays, $A=1.55\times10^{-2}$ and $B=1.21$ was obtained.*

The errors in the absolute cross section are originated mainly in the determination of the gamma-ray yield C and the neutron flux n, involved in the published data[12] of $D^2(d, n)He^3$ reaction, is about 7%. The statistical accuracy of gamma-ray counting was 1% or better.

---

* According to Freeman et al.,[8] $A=6.14\times10^{-3}\pm5\%$ and $B=1.09\pm2\%$.

Table I. Background gamma rays which were determined with a carbon ring scatterer in the arrangement shown in Fig. 1. In the second column the de-excitation scheme of the nuclide emitting the gamma ray is given. A comparison with energies given by other authors is listed in the third column.

E_γ (MeV)	De-excitation scheme	Comparisons with other author's E_γ
0.200±.015	$I^{127}(n, n'\gamma)$ 2nd→0	0.204[3] 0.208±.002[7]
0.420±.020	$Na^{23}(n, n'\gamma)$ 1st→0	0.438±.005[8]
	$I^{127}(n, n'\gamma)$ 3rd→0	0.435±.004,[7] 0.441[3]
0.511±.020	annihilation gamma ray	0.50,[4] 0.51[5]
0.625±.015	$I^{127}(n, n'\gamma)$ 4th→0	0.634,[3] 0.632±.006[7]
0.735±.015	$I^{127}(n, n'\gamma)$ 5th→0	0.742,[3] 0.750±.020[7]
0.844±.015	$Fe^{56}(n, n'\gamma)$ 1st→0	0.841[3]
	$Al^{27}(n, n'\gamma)$ 1st→0	0.835±.001,[2] 0.840±.008[3]
1.01±.015	$I^{127}(n, n'\gamma)$	1.012[3]
	$Al^{27}(n, n'\gamma)$ 2nd→0	1.02±.01,[2] 1.017±.010[3]
1.23±.02	$Fe^{56}(n, n'\gamma)$ 2nd→1st	1.24[3]
1.42±.03	$Fe^{54}(n, n'\gamma)$ 1st→0	1.41[3]
1.71±.02	$Al^{27}(n, n'\gamma)$ 4th→2nd	1.72±.02[2]
2.19±.03	$Al^{27}(n, n'\gamma)$ 3rd→0	2.22±.03,[2] 2.21±.02[3]
2.42±.04	$Na^{23}(n, n'\gamma)$ 3rd→0	2.386±.010[8]
2.97±.04	$Na^{23}(n, n'\gamma)$ 6th→0	2.979±.015[8]

The errors due to background subtraction were negligible for large or isolated photo-peaks. But the determination of area under a weak or unresolved photo-peak caused appreciable error; sometimes it amounted to 20%. The correction for absorption of gamma rays in the sample was made by assuming that all gamma rays passed through an average thickness of 5 mm in the sample. The standard error in the effective photo-peak efficiency $\mathcal{E}$, which was within 3.5% as mentioned above, was originated from the statistical accuracy in the absolute beta-counting.

Taking account of these errors, standard errors in the absolute measurement were estimated as follows:

Table II. The energies of gamma rays produced by the inelastic scattering of (4.04±.10)-MeV neutrons, and the differential cross sections for the production of relevant gamma-rays at $\theta=100°$. The cross section values in parentheses have rather large errors (~±30%), since the yields are small compared with other gamma rays. De-excitation schemes are also shown in the fifth column, those in parentheses represent tentative, but most probable assignments. [ ] represents the average energy in the superposition of more than two gamma rays. References are cited in the text.

Element	E_γ(MeV)	$d\sigma/d\Omega$ (mb/ster.)	Nuclide	De-excitation scheme
Iron	.844±.015	81.5	Fe^{56}	1st→0
	1.23±.02	12.0	〃	2nd→1st
	1.42±.02	(10.9)	Fe^{54}	1st→0
	1.80±.03	13.0	Fe^{56}	3rd→1st
	2.11±.04	12.6	〃	4th→1st
	2.56±.04	6.2	〃	7th→1st
	2.97±.04			4th→0
	3.09±.04			
	3.39±.05	(6)	Fe	
	3.51±.05	(3)	〃	

Table II. (cont'd)

Copper	.665±.015	25.3	Cu^{63}	1st →0
	.760±.015	39.0	Cu^{65}	1st →0
	.965±.015	56.2	Cu^{63}	2nd→0
	1.11 ±.02	88.2	Cu^{65}	2nd→0
	1.33 ±.02	31.2	Cu^{63}	3rd→0
	1.46 ±.05	(32)	Cu^{65}	3rd→0
	1.57 ±.04	(12)	Cu^{63}	5th→0
	1.88 ±.04	(8)	Cu^{63}	6th→0
	2.07 ±.04	(5)	Cu	(Cu^{65}: 6th→0)
	2.86 ±.05	(3)	Cu	
	3.11 ±.05			
	3.40 ±.05			
Zinc	[.810±.010]	23.6	Zn	Zn^{64,66,68}: 2nd→1st
	[.995±.015]	83.3	〃	〃 : 1st →0
	1.25 ±.03	(7.2)	Zn^{68}	3rd→1st
	[1.35 ±.03]	(7.3)	Zn^{64,66}	3rd→1st
	1.46 ±.05	(2)	Zn	
	[1.81 ±.04]	21.0	〃	Zn^{64,66,68}: 2nd→0
	[2.36 ±.05]	(6)	〃	(〃 : 3rd→0)
	2.88 ±.05	(5)	〃	
	3.15 ±.05			
	3.48 ±.05			
Germanium	[.590±.010]	84.3	Ge	(Ge^{74,76}: 1st→0)
	.740±.020	(13)	〃	
	.830±.020	65.9	〃	Ge^{72}: 2nd→0
	1.01 ±.020	64.9	〃	Ge^{70}: 1st →0
	1.19 ±.02			Ge^{74}: 2nd→0
	1.49 ±.03			Ge^{72}: 3rd→0
	1.70 ±.02	(22)	〃	Ge^{72}: 4th→0
	1.92 ±.03			
Selenium	.560±.020	28.1	Se	(Se^{76}: 1st→0)
	[.660±.010]	105	〃	Se^{78,80}: 1st→0
				Se^{76,78}: 2nd→1st
	.800±.020	(14)	Se^{80}	2nd→1st
	.900±.020	(4)	Se	(Se^{82}: 1st→0)
	1.19 ±.02	(6)	〃	(Se^{76}: 2nd→0)
	1.30 ±.02	(8)	Se^{78}	2nd→0
	1.42 ±.03	(16)	Se^{80}	2nd→0
	1.57 ±.03			(Se^{82}: 2nd→0)
	1.65 ±.02			
	2.11 ±.03	(12)	Se	
	2.37 ±.03			
	2.90 ±.04	(10)	〃	
	3.25 ±.05			

2.56 MeV (iron): ±20∼25%
1.81 MeV (iron): ±20%
0.56 MeV (selenium): ±20∼35%

Other all gamma rays: ±15%

The standard errors are also represented by vertical bars in the figures.

§ 4. Results

The spectra of gamma rays from iron, copper, zinc, germanium, and selenium excited by the inelastic scattering of (4.04±.10) MeV neutrons are shown in Figs. 3, 5, 7, 9 and 11, respectively. The background spectra as determined with the carbon ring are also shown in these figures with the crossed points.

The differential cross sections for the production of these gamma rays are presented in Table II, together with the scheme of de-excitation. In Table II, the isotropic cross sections of nuclides specified with mass number are calculated taking account of the isotopic abundance. Those described by chemical symbol only, are calculated using the number of nuclei per nuit volume of the natural element.

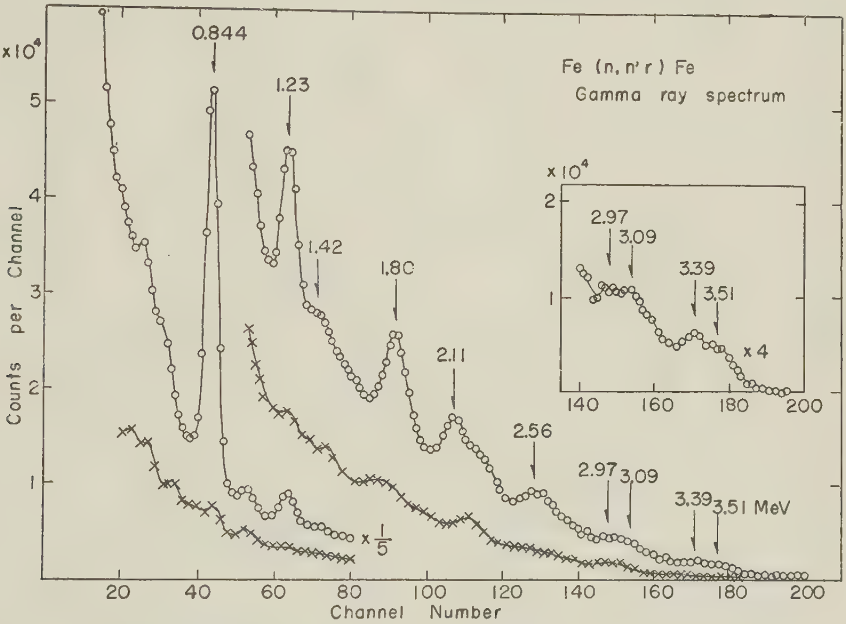

Fig. 3. The spectrum of gamma rays following the inelastic scattering of (4.04±.10)-MeV neutrons in iron. The background spectrum determined with the carbon ring scatterer is illustrated with crossed points. There are subtracted in the inserted figure.

The differential cross sections for gamma-ray production by the neutron inelastic scattering, which were measured in the range of incident neutron energies 3.11∼4.72 MeV, are shown in Figs. 4, 6, 8, 10 and 12. The cross-section values in parentheses in Table II have rather large errors (∼±30%), since the yields are small compared with other gamma rays. Measurements of the excitation functions for these weak gamma rays, therefore, was not performed.

(1) Iron

The gamma rays from low-lying levels in iron are clearly fitted to the known level scheme[13]. The peak around 2.56 MeV in Fig. 3 seems to be composed of three peaks at 2.56, 2.58 and 2.66 MeV; i.e. a peak due to the

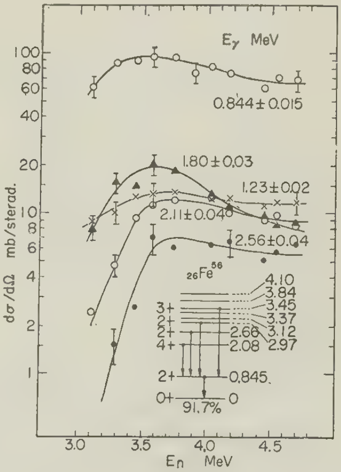

Fig. 4. Excitation curves for gamma-ray production by the neutron inelastic scattering Fe(n, $n'\gamma$) Fe. Those gamma rays which corresponded to the arrows in the inserted level scheme, were investigated.

transition from the 7th (3.45 MeV) to the 1st level (0.844 MeV), one-quantum escape peak of the gamma rays from the 5th (3.12 MeV) to the ground level, and a peak due to the transition from the 3rd (2.66 MeV) to the ground level, respectively.

The excitation curves for iron gamma rays are shown in Fig. 4, together with the known level scheme. The 2.11-MeV gamma ray is considered not to be due to a cross-over transition (2.08 MeV to the ground level) but cascade one (2.97 to 0.844 MeV), since the excitation curve rises steeply above 3.0 MeV.

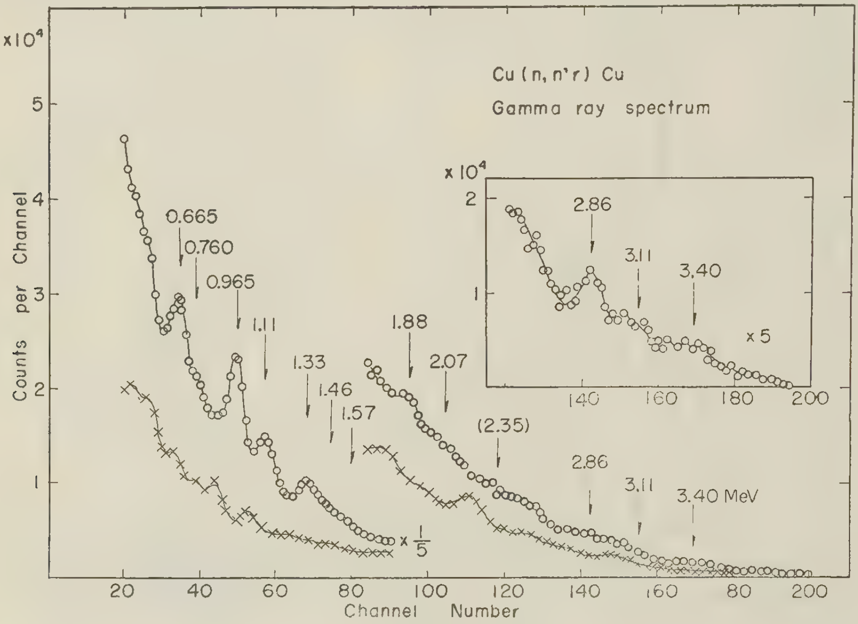

Fig. 5. The spectrum of gamma rays from Cu$(n, n'\gamma)$Cu reaction.

(2) Copper

The gamma-ray spectra of the present measurements are in good agreement with those by Day[3] and Pasechnik et al.[4] as shown in Fig. 5. Furthermore, gamma rays of 2.86, 3.11 and 3.40 MeV were found in our measurement.

The excitation curves of five gamma rays are shown in Fig. 6. Those gamma rays corresponding to the direct transition from the 1st, 2nd and 3rd to the ground state, are predominant. This mode of de-excitation is different from those of even-even nuclei such as iron, zinc, germanium and selenium.

(3) Zinc

The first excited states of zinc isotopes are known to be 0.99 MeV (Zn^{64}), 1.04 MeV (Zn^{66}) and 1.07 MeV (Zn^{68}), respectively[14),15),16)]. The observed photo-peak has an energy of 0.995 ±.015 MeV, which result from the superposition of gamma rays of these energies.

There is almost the same amount of cross-over transition (1.81 MeV) as the cascade one (0.81 MeV). This mode of de-excitation is different from that of iron.

Recently, gamma-ray spectra from the Zn$(n, n'\gamma)$Zn reaction were observed for $E_n=1.0 \sim 3.3$ MeV by Van Patter et al..[17)] The pre-

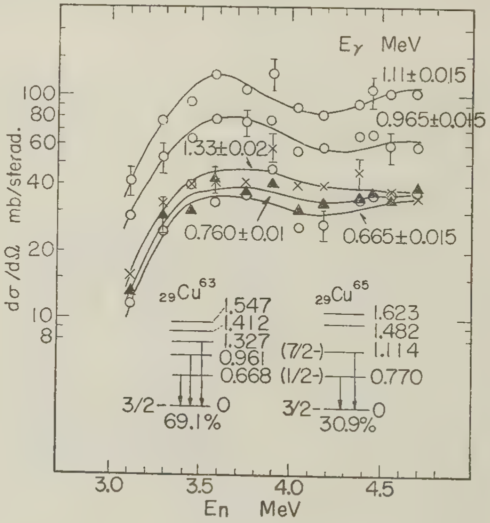

Fig. 6. Excitation curves for Cu$(n, n'\gamma)$Cu reaction.

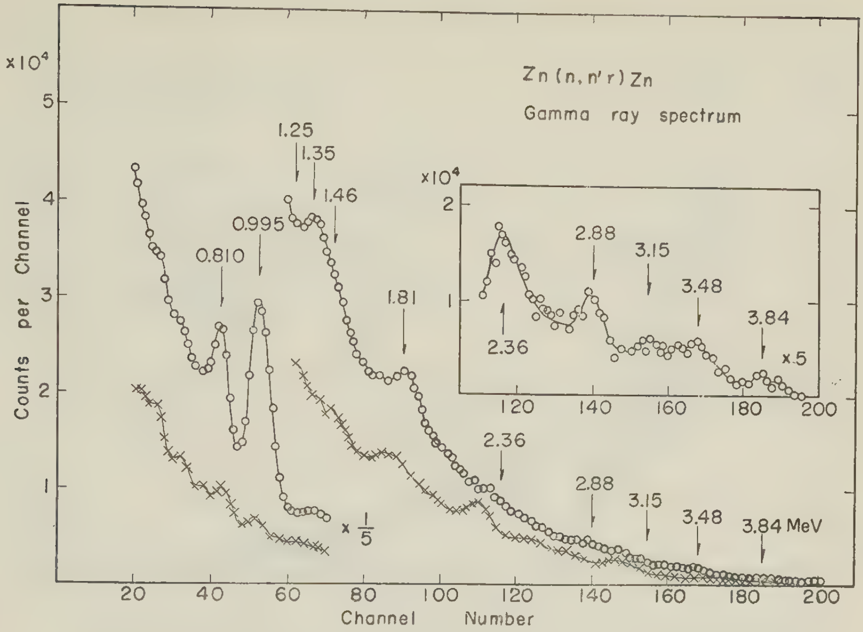

Fig. 7. The spectrum of gamma rays from $Zn(n, n'\gamma)Zn$ reaction.

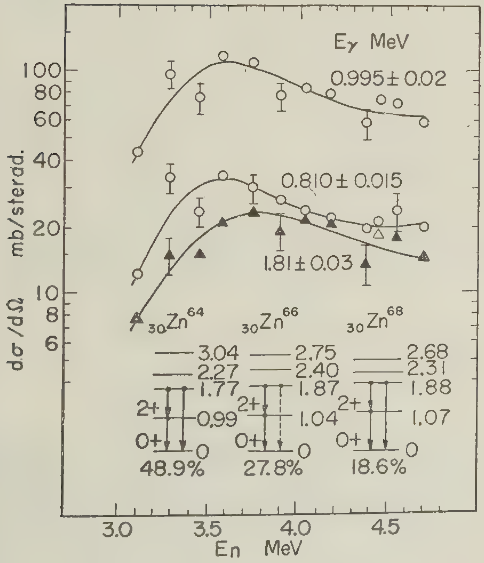

Fig. 8. Excitation curves for $Zn(n, n'\gamma)$ Zn reaction.

sent results will be connected to their excitation function.

(4) Germanium

A detailed pulse-height distribution from 1.0 MeV to 2.0 MeV is shown in the insert of Fig. 9. The transitions from the 1st (1.04 MeV) to the ground state in Ge^{70} and from the 4th (1.73 MeV) to the 1st (0.69 MeV) in Ge^{72} are probably observed as a single peak at 1.01±.02 MeV. Some of gamma rays observed are fitted to known level scheme[15),16)].

The excitation curves for gamma rays of energies 0.59, 0.83 and 1.01 MeV are shown in Fig. 10, and these excitation curves show rather flat variation in the energy range observed.

(5) Selenium

The 0.660 MeV peak is remarkably larger than those of any others. The 0.56-MeV gamma ray is narrowly resolved from the 0.660-MeV gamma ray by the subtraction of background.

The detailed pulse-height spectra are shown in Fig. 11 (a). If one takes the 1st level of Se^{82} as 0.670 MeV[18)] and estimates the energy of its 2nd excited state by the systematics of level scheme for even-even nuclide, the value obtained becomes 1.57 MeV. Then, the gamma ray of 1.57±.03 MeV will be the transition from the 2nd to the ground state of Se^{82}. Furthermore, the 0.900 MeV gamma ray will be the transition from the 2nd (1.57 MeV) to the 1st (0.670 MeV) state of Se^{82}.

Fig. 12 shows the excitation curves for gamma rays of 0.56 and 0.66 MeV. The fact that there is many transitions of rather small intensities in the de-excitation of selenium following the neutron inelastic scattering, agrees with the results of a recent time-of-

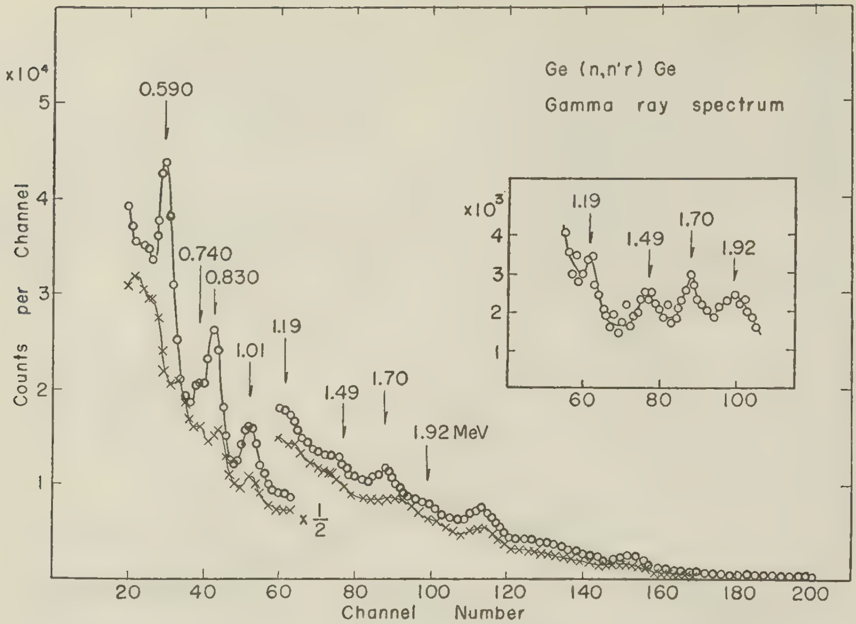

Fig. 9. The spectrum of gamma rays from Ge(n, $n'\gamma$)Ge reaction.

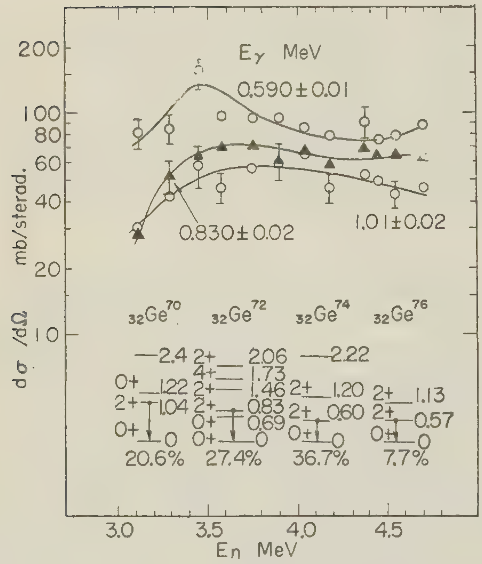

Fig. 10. Excitation curves for Ge(n, $n'\gamma$)Ge reaction.

flight experiment[10].

§ 5. Discussions

In the present measurements of gamma-ray yield from low-lying levels excited by the inelastic scattering of neutrons, we find an amount of cascade transitions from the higher excited states. We can obtain some information about the de-exciting property of higher excited states by combining the present data with the results of time-of-flight measurement of neutron inelastic scattering and the relevant non-elastic scattering cross sections.

For this purpose, we examine the probability that higher states ($E_{i\geq 3}$) excited by the neutron inelastic scattering are de-excited to the ground state by cascading through or not through the 1st excited state. These probabilities are represented by T_1 and T_0, respectively, and expressed by definition as follows:

$$\left.\begin{aligned} T_1 &= \sum_{i=3}^{k} \sigma_i^{n'}(E_n,\, E_i)\, p_1(E_i) \\ T_0 &= \sum_{i=3}^{k} \sigma_i^{n'}(E_n,\, E_i)\, p_0(E_i) \end{aligned}\right\} \qquad (4)$$

where the index i indicates the i-th excited state, k is the index of the highest state excited by the inelastic scattering, $p_1(E_i)$ or $p_0(E_i)$ the probability of transition from the i-th excited state to the ground state by cascading through or not through the 1st excited state, respectively (see Fig. 13) and $\sigma_i^{n'}$ the neutron inelastic scattering cross section leading to the i-th state. In the above equation, the 2nd excited state is excluded from the summation for simplifying the discussion. T_1 and T_0 can be determined experimentally by the following equations as follows:

$$\left.\begin{aligned} T_1 &= \sigma_1^{\gamma} - (\sigma_1^{n'} + \alpha\sigma_2^{n'}),\ \alpha = a/(1+a) \\ T_1 + T_0 &= \sum_{i=3}^{k} \sigma_i^{n'} \simeq \sigma_{\mathrm{non}} - (\sigma_1^{n'} + \sigma_2^{n'}) \end{aligned}\right\} \qquad (5)$$

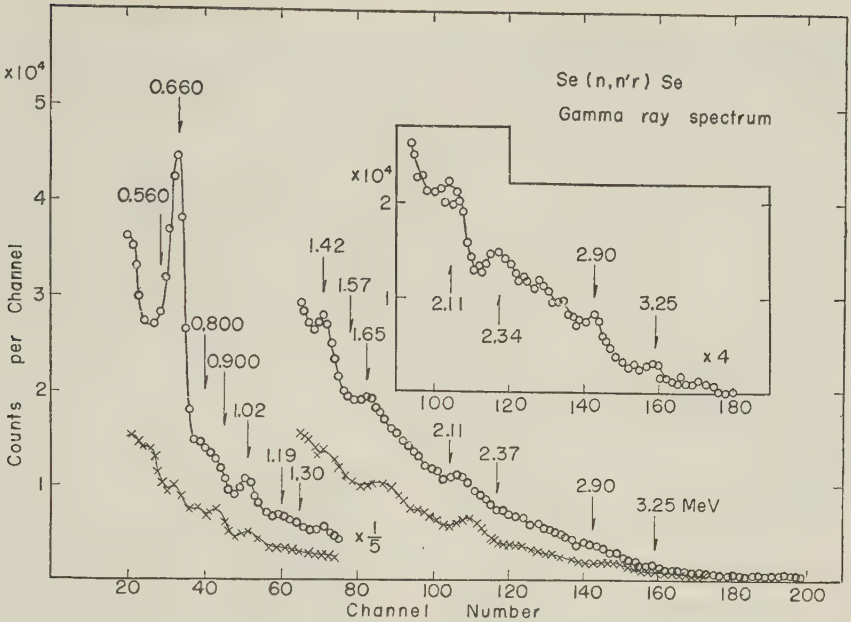

Fig. 11. The spectrum of gamma rays from Se(n, $n'\gamma$)Se reaction.

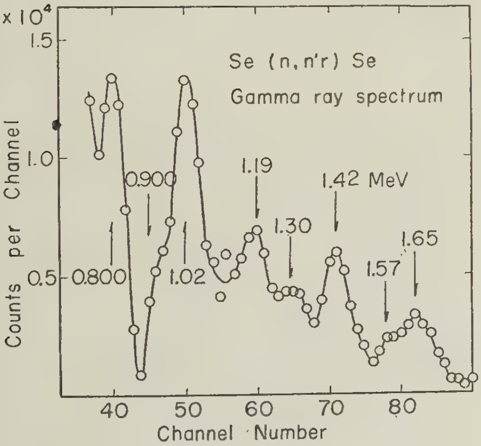

Fig. 11(a). The spectrum of gamma rays from Se(n, $n'\gamma$)Se reaction, especially in the range from 0.80 to 1.65 MeV. The background is subtracted.

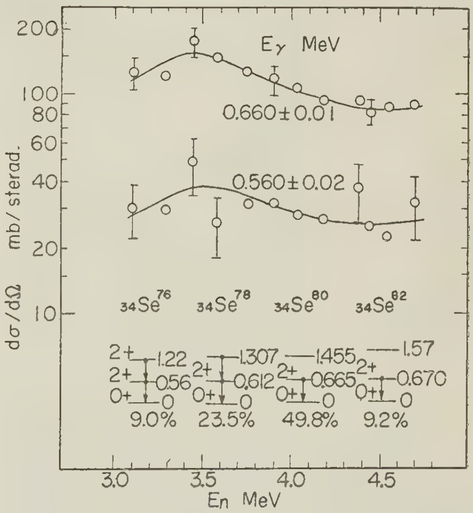

Fig. 12. Excitation curves for Se(n, $n'\gamma$)Se reaction.

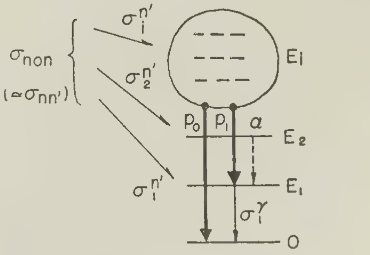

Fig. 13. Notations, which are used in Eq. (6).

Here, σ_1^{γ} is the gamma-ray production cross section which de-excites from the 1st to the ground state, as observed in the present experiment; $\sigma_1^{n'}$ and $\sigma_2^{n'}$ the inelastic neutron cross sections which leave the target nucleus in the 1st and 2nd state, as reported in the time-of-flight experiment[10]. σ_{non} is the non-elastic cross section as given in reference (19). a is the cascade-to-cross-over ratio of the 2nd excited state. $a=(2\text{nd}\rightarrow 1\text{st})/(2\text{nd}\rightarrow \text{ground})$. This quantity is introduced to take account of the cascade transition from the 2nd excited state through the 1st excited state.

Then, the probability ratio R is given as follows:

$$R=\frac{T_1}{T_0}=\frac{\sigma_1{}^{\gamma}-(\sigma_1{}^{n'}+\alpha\sigma_2{}^{n'})}{\sigma_{\text{non}}-\sigma_1{}^{\gamma}-(1-\alpha)\sigma_2{}^{n'}} \qquad (6)$$

The notations used in Eq. (6) are illustrated in Fig. 13.

The results of the calculations of the probability ratio R vs. neutron energy E_n are shown in Fig. 14, where the angular distributions for the emission of gamma rays and neutrons are assumed to be isotropic, the branching ratio for the cascade transition from the 2nd excited state in iron is assumed to be one[13], i.e. $\alpha=1$, and for zinc an isotopic average of reported values[14] is used, i.e. $\alpha=0.55$.

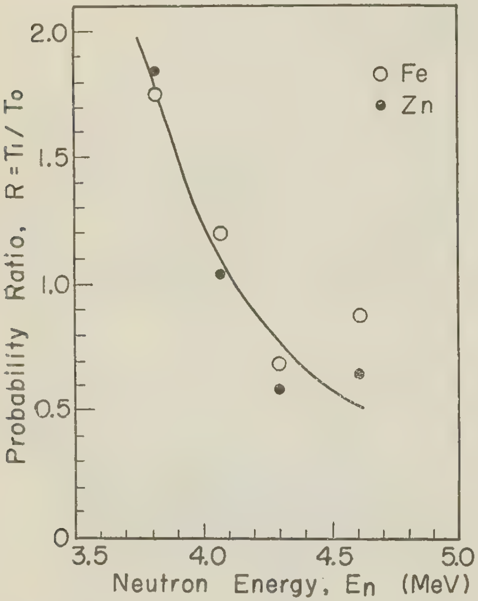

Fig. 14. The results of probability ratio R in Eq. (6).

Fig. 14 shows that the probability ratio R decreases as the incident neutron energy increases. This fact suggests that higher excited states are in general more difficult to be de-excited through the 1st excited state than lower excited states. This property of higher excited states in iron will be explained to some extent by the β-decay data[15] which show that branching ratio to the 1st excited state decreases gradually with increase of the excitation energy.

Acknowledgements

The author would like to express his sincere thanks to Dr. T. Momota for his valuable advice and interest. The author is greatly indebted to Dr. K. Tsukada and Mr. S. Kikuchi for their helpful cooperation throughout this work. Theoretical discussions with Drs. A. Sugie, K. Harada and T. Terasawa are gratefully acknowledged. Thanks are also due to Messrs. T. Kobayashi, Y. Sato and members of the fast-neutron group for operation and maintenance of the Van de Graaf accelerator.

References

1) J. M. Freeman: Phil. Mag. **46** (1955) 12. L. E. Beghian, D. Hicks and B. Milman: Phil. Mag. **46** (1955) 924, 963. R. M. Scinclair: Phys. Rev. **102** (1956) 461; **107** (1957) 1306. I. L. Morgan: Phys. Rev. **103** (1956) 1031. J. B. Weddel: Phys. Rev. **104** (1956) 1069. F. I. Boley, E. H. Thorndike and A. T. Moffet: Phys. Rev. **110** (1958) 915, 1392. M. Hosoe and S. Suzuki: J. Phys. Soc. Japan **14** (1959) 699.

2) M. A. Rothman, H. S. Hans and C. E. Mandeville: Phys. Rev. **100** (1955) 83.

3) R. B. Day: Phys. Rev. **104** (1956) 767.

4) M. V. Pasechnik et al.: International Conference on Peaceful Uses of Atomic Energy, P/2030 (1958) USSR.

5) J. Benveniste: International Conference on Peaceful Uses of Atomic Energy, P/2994 (1958) USA.

6) R. M. Kiehn and C. Goodman: Phys. Rev. **93** (1954) 177. H. C. Martin, B. C. Diven and R. F. Taschek: Phys. Rev. **93** (1954) 199. P. Stelson and A. Campell: Phys. Rev. **97** (1955) 1222. J. M. Freeman, A. M. Lane and B. Rose: Phil. Mag. **46** (1955) 17. J. B. Guernsey and A. Wattenberg: Phys. Rev. **101** (1956) 1516. J. R. Beyster, M. Walt and E. W. Salmi: Phys. Rev. **104** (1956) 1319. M. A. Rothman, D. M. Van Patter, V. S. Dubey, W. C. Porter and C. E. Mandeville: Phys. Rev. **107** (1957) 155. N. Nath, M. A. Rothman, D. M. Van Patter and C. E. Mandeville: Nucl. Phys. **13** (1959) 74, Nucl. Phys. **14** (1960) 78. H. E. Hall and T. W. Bonner: Nucl. Phys. **14** (1959) 295.

7) J. J. Van Loef and D. A. Lind: Phys. Rev. **101** (1956) 103.

8) J. M. Freeman and J. H. Montague: Nucl. Phys. **9** (1958) 181.

9) W. Hauser and H. Feshbach: Phys. Rev. **87** (1952) 366.

10) K. Tsukada, S. Tanaka and M. Maruyama: J. Phys. Soc. Japan **16** (1961) 166.

11) A. B. Chilton, J. N. Cooper and J. C. Harris: Phys. Rev. **93** (1954) 413. D. N. F. Dunbar, H. K. Reynolds, W. A. Wenzel and W. Whailing: Phys. Rev. **91** (1953) 496 (A).
12) J. L. Fowler and J. E. Brolley: Rev. Mod. Phys. **28** (1956) 103.
13) A. N. Diddens, W. J. Huiskanp, J. C. Severien, A. R. Miedema and M. J. Steeland: Nucl. Phys. **5** (1958) 58. L. M. Fagg and S. S. Hanna: Rev. Mod. Phys. **31** (1959) 711. P. Kienle and R. E. Segel: Phys. Rev. **114** (1959) 1554.
14) D. J. Horen: Phys. Rev. 113 (1959) 572.
15) Nuclear data sheet, NRC Series.
16) D. Strominger, J. M. Hollander and G. T. Seaborg: Rev. Mod. Phys. **30** (1958) 585.
17) D. M. Van Patter, N. Nath and M. A. Rothman: Bull. Am. Phys. Soc. Ser. II, **5** (1960) 266.
18) F. K. McGowan and P. H. Stelson: WASH-1013, **48** (1958).
19) D. J. Hughes and R. B. Schwartz: Neutron Cross Sections, BNL 325, Second edition (1958).

JOURNAL OF THE PHYSICAL SOCIETY OF JAPAN, Vol. 16, No. 3, MARCH, 1961

Angular Distributions and Excitation Functions of the Be^9 (d, p) Be^{10} Ground-State Reaction

By Toshiyuki ISHIMATSU, Naoyuki TAKANO, Yûki HACHIYA and Takao NAKASHIMA

Department of Physics, Kyusyu University, Hukuoka, Japan.

(Received November 11, 1960)

Angular distributions and excitation functions of the Be^9 (d, p) Be^{10} ground-state reaction were studied in the energy range of deuteron from 1.7 to 3.0 MeV. Six angular distributions were measured at the deuteron energies of 1.74, 1.97, 2.24, 2.51, 2.73 and 3.03 MeV. Each angular distribution has a forward peak characteristic of the deuteron stripping process for $l_n=1$. The yields in the backward directions, however, are predominant at the lower energies. The excitation curve taken at the laboratory angle of 30°, where the forward peak occurs in the angular distribution, shows a monotone and rather fast rise with deuteron energy. On the other hand, the excitation function of the total cross section of this reaction shows a comparatively slow variation and has a broad peak at about 2.1 MeV of deuteron energy.

§ 1. Introduction

A number of investigations on the Be^9 (d, p) Be^{10} reaction have previously been made in the energy range of deuteron up to about 10 MeV, and there are many informations on the angular distributions of the proton groups from this reaction[1]. At the deuteron energies from 100 keV to 20 MeV, the angular distributions of protons from the Be^9 (d, p) Be^{10} ground-state reaction have been measured at small intervals of deuteron energy and the results show somewhat regular variation of the angular distribution with deuteron energy[2)3)4)]. At the deuteron energies below 800 keV, the differential cross section of this reaction increases smoothly and rapidly with emission angle of protons to the direction of incident deuteron beam. At about 900 keV of deuteron energy, a peak appears at a forward angle and it becomes more and more eminent as deuteron energy increases. At about 2 MeV, however, the proton yield in the backward direction is still predominant. At the deuteron energies of 3.6 and 3.9 MeV, the angular distributions are those of stripping type though they have a relatively high second maximum at about 100°, and the forward peak at the deuteron energy of 3.6 MeV is fitted fairly well by the stripping curve for $l_n=1$ evaluated with Butler's formula using the nuclear radius of 4.5×10^{-13}cm[5)6)]. At the deuteron energies from 8 to 12 MeV, the angular distributions show a more distinct stripping feature having a weaker second peak compared with those at lower deuteron energies, and were well explained by Butler's stripping theory for $l_n=1$ using the nuclear radius of about 5×10^{-13} cm[7)8)9)10)].

The excitation function of the $Be^9(d, p)Be^{10}$ ground-state reaction at the laboratory angle of 90° has been measured by Canavan[2)], using a proportional counter and aluminium absorbers over the energy range of deuteron from 0.55 to 2.95 MeV. The result shows broad maxima in the excitation curve at about 0.9, 1.3 and 2.1 MeV of bombarding deuteron energy, and the last one is thought to be indicative of overlapping resonances due to the compound states at about 17.5-MeV excitation in B^{11} nucleus.

We tried to investigate the variation of the angular distribution of protons from the $Be^9(d, p)Be^{10}$ ground-state reaction with deuteron energy, and investigate the excitation functions of the forward peak in the angular distribution and of the total cross section, over the energy range of deuteron from 1.7 to 3.0 MeV. It was hoped that these informations, together with the previouslv obtained results, would give a clue to understand the mechanism of (d, p) reaction at lower deuteron energies.

§ 2. Experimental Methods

Details of the apparatus used in this experiment are to be reported elsewhere[11)], so here they will be described briefly. The magnetically analyzed deuteron beam emerging from the Van de Graaff accelerator of Kyusyu University passed through a slit of 1 mm in width which served to get error signals for the stabilizer of accelerating voltage and another slit of 4 mm in diameter, and then entered into a scattering chamber and struck a beryllium target mounted at the center of the chamber. These two slits were distant each other about 26 cm and the plane of the target made 45° to the beam direction. The inner diameter of the chamber was 23 cm, and the target was metalic beryllium of 0.27 mg/cm² in thickness evaporated in vacuum on the silver foil of 2.2 mg/cm² in thickness. Charged particles emitted from the target came out of the chamber through the windows made on the side wall of the chamber at intervals of 15°. The windows consisted of openings of 6 mm in diameter covered with aluminium foils of 20 microns in thickness.

A CsI(Tl) crystal of 1 mm in thickness which was mounted on a DuMont 6291 photomultiplier tube was placed close to one of the windows and it stopped all of the charged particles outgoing through this window. Output pulses from the photomultiplier were amplified and then analyzed by a 20-channel differential pulse-height analyzer. A typical pulse-height spectrum obtained by this arrangement is shown in Fig. 1.

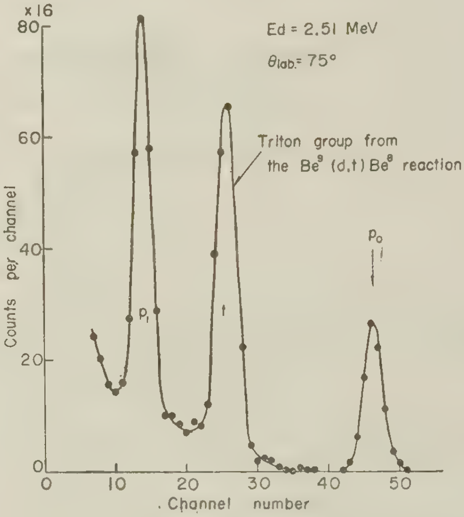

Fig. 1. Pulse-height spectrum of charged particles from the deuteron bombardment of beryllium, obtained at the deuteron energy of 2.51 MeV and at the laboratory angle of 75°.

Another scintillation counter similar to that mentioned above was mounted on the window at 22.5° to the direction of deuteron beam and used as a monitor counter. Output pulses from this counter were discriminated in such a way that only pulses corresponding to the ground-state protons from the $Be^9(d, p)Be^{10}$ reaction were registered.

The deuteron beam was collected in a Faraday cup, 3 cm in diameter and 5 cm in depth, and integrated by a current integrator similar to that designed by Higinbotham and Rankowitz[12)]. To insure accurate measurements of the beam current, the secondary electrons emitted from the cup wall were suppressed by the magnetic field produced by two pieces of Ferite mounted just outside of the cup. The excitation curve was taken at the laboratory angle of 30° where the forward peak occurs in the angular distribution. At that time the Faraday cup was placed as close to the target as possible in order to avoid the effect of deuteron scattering in the backing material of the target, i.e. the distance between the forward edge of the cup and the center of the target was chosen to be 5 cm.

The peaks corresponding to the ground-state protons from the $Be^9(d, p)Be^{10}$ reaction in pulse-height spectra, obtained at different angles and at a certain deuteron energy were integrated to get the areas under them, which give the measures of the intensities of this group at different angles. The angular distribution in the laboratory system at that deuteron energy was obtained by normalizing these areas to a fixed number of monitor counts, and it was transformed to the center-of-mass system.

Experimental points at 0° in the angular distributions were taken, preventing the direct deuteron beam to reach the detector by means of silver absorbers of suitable thickness inserted in front of the window made in 0° direction, and allowing protons of higher energy to enter the scintillation crystal.

To obtain the excitation function, the pulse-height spectra were taken at a fixed counter angle of 30° at different deuteron energies in the same manner as for the angular distribution measurements. Areas under the peaks corresponding to the ground-state proton group in these pulse-height spectra were normalized to a fixed value of integrated beam current, to obtain the excitation function at the laboratory angle of 30°.

Each of the angular distributions at different deuteron energies obtained in this experiment was integrated over the whole solid angles to obtain the total yield of the ground-state protons from the $Be^9(d, p)Be^{10}$ reaction. Six values of the total yield at different deuteron energies derived in this way were normalized with each other using the measured excitation curve at the laboratory angle of 30°. Thus, the excitation function of the total cross section of the reaction concerned was obtained.

§ 3. Results and Discussions

Figs. 2 and 3 show the angular distributions of the ground-state protons from the $Be^9(d, p)$-Be^{10} reaction at different deuteron energies. Deuteron energies indicated in these figures are the mean values in the target material, measured in the laboratory system. The statistical uncertainty of each experimental point is less than 3%. Fig. 4 shows the excitation function of the $Be^9(d, p)Be^{10}$ ground-state reaction at the laboratory angle of 30°. Errors indicated in the figure include uncertanties ascribed to the counting statistics and beam current integration. The relative uncertainty in the beam-current integration was estimated to be less than 1% from the distribution of ratios of integrated beam currents to the corresponding monitor counts in every runs at a certain deuteron energy. Fig. 5 shows the excitation function of total cross section of the $Be^9(d, p)Be^{10}$ ground-state reaction, derived from the angular distributions shown in Figs. 2 and 3, and the 30°-excitation

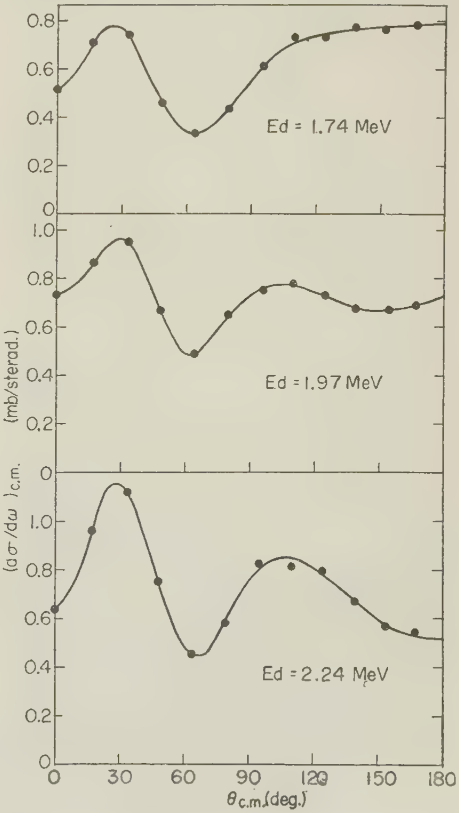

Fig. 2. Angular distributions of the protons from the $Be^9(d, p)Be^{10}$ ground-state reaction at the deuteron energies of 1.74, 1.98 and 2.24 MeV.

function give in Fig. 4.

The scales on the ordinates of these figures were determined with the peak areas and corresponding values of integrated beam current, which were obtained when the 30°-excitation function was measured, and the geometry of the experimental arrangement. They are estimated to have inaccuracy of ±20%, mainly due to the uncertainty in the determination of the target thickness. The target thickness was determined by weighing the backing foil by means of a chemical balance before and after the vacuum evaporation of the beryllium metal.

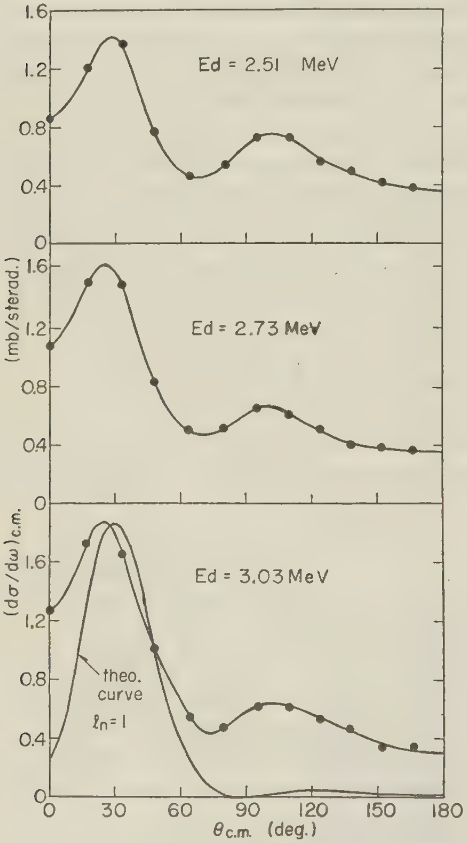

Fig. 3. Angular distributions of the protons from the $Be^9(d, p)Be^{10}$ ground-state reaction at the deuteron energies of 2.51, 2.73 and 3.03 MeV.

Canavan[2)] has measured angular distributions of protons from the same reaction by means of photographic plates at six deuteron energies from 1.0 to 2.2 MeV. He has also studied the excitation function at the laboratory angle of 90° from 0.55 to 2.95 MeV using a proportional counter and aluminum absorbers. His result on the angular distribution at 1.75-MeV agrees well with ours at 1.74 MeV and his result at 2.0 MeV agrees reasonably with ours at 1.98 MeV. In Fig. 5, the points derived from Canavan's results are also shown, where his point at 1.75 MeV is normalized to our 1.74-MeV point.

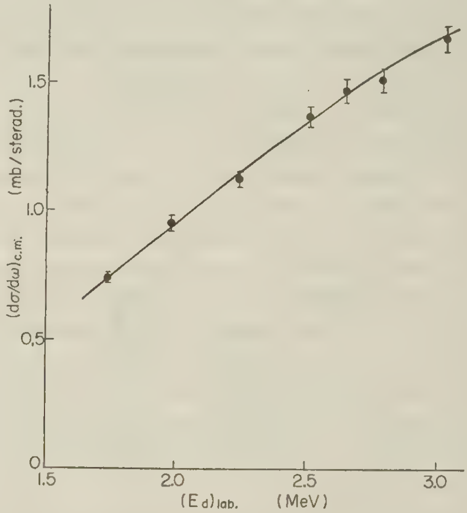

Fig. 4. Excitation function of the $Be^9(d, p)Be^{10}$ ground-state reaction at the laboratory angle of 30°.

It is clearly seen from the results on angular distributions that the forward peak in the angular distribution becomes more and more eminent with increasing deuteron energy and finally the angular distribution approaches to that characteristic of the deuteron-stripping process of Butler type. In Fig. 3, a theoretical angular distribution for $l_n=1$ and $E_d=3.0$ MeV, evaluated by a formula derived by Bhatia *et al.*[13)] on the basis of the deuteron stripping, is also shown. Nuclear radius of 7.0×10^{-13} cm was used in the evaluation. Agreement between the experimental and theoretical angular distributions is not so well and the value of nuclear radius used here is rather large. At such a low deuteron energy, however, in addition to the contribution of the compound-nucleus process to the (d, p) reaction, there may be a considerable amount of contributions of Coulomb and nuclear interaction effects discussed by Tobocman and Kalos[14)], and it is expected that the experimental angular distributions deviate from the theoretical ones derived from a simple theory of the deuteron stripping.

As shown in Fig. 4, the yield of the ground-state protons at the laboratory angle of 30° shows a monotone are rather fast rise with the deuteron energy. Since in the energy range investigated in this experiment the forward peak which is characteristic of the stripping process appears at the laboratory angle of about 30°, the behavior of the excitation function at 30° is thought to give some indication of the gradual growth of the deuteron-stripping process. Tobocman and Kalos[14] have shown that the total cross section of the deuteron-stripping reaction is much reduced by Coulomb interaction, so that the growth of the stripping process with the deuteron energy will be, at least in part, due to the decrease of the Coulomb effect.

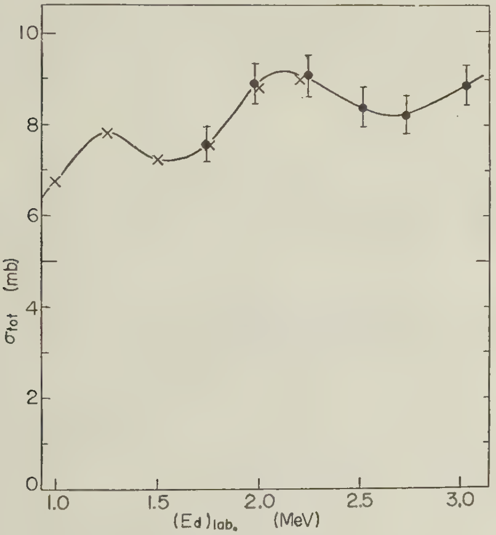

Fig. 5. Excitation function of total cross section of the $Be^9(d, p)Be^{10}$ ground-state reaction. Crosses are points derived from Canavan's results.

On the other hand, it is seen from Fig. 5 that the total cross section of the reaction concerned varies slowly with the deuteron energy, showing a broad maximum at about 2.1 MeV. The general behavior of the total cross section will probably be explained on the basis of the compound-nucleus process. The excitation function at 90° obtained by Canavan also shows a broad peak at about 2.1 MeV of deuteron energy, which was attributed to the overlapping resonances due to the states of about 17.5-MeV excitation in the compound nucleus, B^{11}. Since the stripping process should have little contribution to the excitation function at 90°, the similarity between these two excitation functions suggests that in the $Be^9(d, p)Be^{10}$ ground-state reaction, the contribution of the stripping process to the total cross section is much smaller than that of the compound-nucleus process at deuteron energies below 3 MeV. Neverthless, it must be noticed that even at such a low energy as about 1 MeV, the forward peak in the angular distribution of protons from this reaction is thought to be due to the deuteron-stripping process, because of its growth to a definite stripping peak with increasing deuteron energy.

The authors would like to thank Prof. S. Morita and all other staffs of the nuclear laboratory of Kyusyu University for their supports and discussions throughout this work. Thanks are also due to Mr. T. Maki for the preparation of the beryllium target.

References

1) F. Ajenberg-Selove and T. Lauritsen: Nucl. Phys. **11** (1959) 1.
2) F. L. Canavan: Phys. Rev. **87** (1952) 136.
3) M. K. Jurić: Phys. Rev. **98** (1955) 85.
4) R. K. Smither: Phys. Rev. **107** (1957) 196.
5) H. W. Fulbright, J. A. Bruner, D. A. Bromley and L. M. Goldman: Phys. Rev. **88** (1952) 700.
6) S. A. Cox and R. M. Williamson: Phys. Rev. **105** (1957) 1799.
7) F. A. El-Bedewi: Proc. Phys. Soc. London **A**, **65** (1952) 64.
8) J. R. Holt and T. N. Marsham: Proc. Phys. Soc. London **A**, **66** (1953) 1032.
9) F. S. Eby: Phys. Rev. **96** (1954) 1355.
10) B. Zeidman and J. M. Fowler: Phys. Rev. **112** (1958) 2020.
11) N. Kawai: J. Phys. Soc. Japan **16** (1961) 157.
12) W. A. Higinbotham and S. Rankowitz: Rev. Sci. Instr. **22** (1951) 688.
13) A. B. Bhatia, K. Huang, R. Huby and H. C. Newns: Phil. Mag. **43** (1952) 485.
14) W. Tobocman and M. H. Kalos: Phys. Rev. **97** (1955) 132.

Journal of the Physical Society of Japan, Vol. 16, No. 3, March, 1961

On the Nuclear Interaction of Mu-Mesons*

By Hiroyuki Shibata

Institute of Polytechnics, Osaka City University, Osaka.

(Received November 21, 1960)

The penetrating showers observed with a large multiplate cloud chamber at 50 mwe and 250 mwe underground have been analyzed. The frequencies of the penetrating showers which are experimentally verified to be produced by mu-mesons have been interpreted with the Williams-Weiszäcker method and the constant photonuclear cross section of 1.4×10^{-28} cm^2/nucleon. It has been also shown that the angular distribution of secondary penetrating particles in multiple productions produced by mu-mesons is nearly isotropic in the center-of-mass system of the target nucleon and photon which is virtually associated with the incoming mu-mesons.

§ 1. Introduction

Many investigations on the high energy nuclear interactions produced by mu-mesons were made with cosmic rays underground. It has been pointed out by George and Evans[1] that the frequency of stars underground is understood with the aid of the semiclassical Williams-Weiszäcker method which hereafter will be cited as the W-W method and of the constant photonuclear cross section. Likewise, it has been investigated whether the frequency of the penetrating showers at various depths could be interpreted with the W-W method and a constant or slowly increasing cross section of photonuclear interaction, or not[2-6]. Using a large multiplate cloud chamber, however, we found that about a half of the penetrating showers observed underground had been produced by secondary pi-mesons[7]. Therefore, it can not be realized to investigate the nuclear interactions of mu-mesons, unless they are distinguished from the penetrating showers produced by secondary pi-mesons underground.

The purpose of this paper is to investigate whether or not the frequency of the penetrating showers which are verified to be produced by mu-mesons in the large cloud chamber and its dependence on depth are interpreted in terms of the W-W method with the constant photonuclear cross section and moreover to discuss an angular distribution of the penetrating showers using a kinematics on photo-nucleon interactions.

The observations were performed at 50 mwe and 250 mwe underground from March, 1956 to November, 1957, in the Isohama Tunnel of the National Railway, Yaizu City, Shizuoka, Japan[7].

§ 2. Apparatus and Experimental Results

The experimental arrangement is schematically shown in Fig. 1.

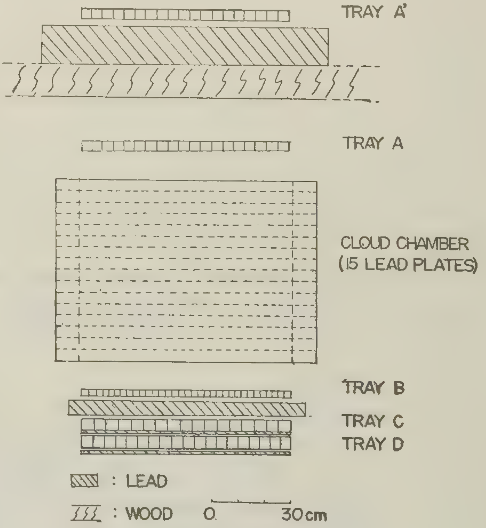

Fig. 1. Experimental arrangement.

The chamber was triggered by coincidences "$(A'\geq1)$ $(A\geq1)$ $(B\geq2)$ $(C\geq2)$ $(D\geq2)$" at 50 mwe, and "$(A'\geq1)$ $(A\geq1)$ $(B\geq2)$ $(C\geq1)$ $(D\geq2)$" or "$(A'\geq1)$ $(A\geq1)$ $(B\geq2)$ $(C\geq2)$ $(D\geq1)$" at 250 mwe, but only the photographs of the cloud chamber which were found to be triggered by the coincidences "$(A'\geq1)$ $(A\geq1)$ $(B\geq2)$

---

* This work has been supported in part by a Grant from the Aid for Fundamental Scientific Research (Institutional Research) from the Ministry of Education.

(C≥2)(D≥2)" were analyzed at both the depths. The penetrating showers are classified into two groups, P-showers and S-showers. P-showers are the penetrating showers produced by the particles assumed as mu-mesons at the lead plates inside the cloud chamber, and S-showers are those produced by secondary particles of the nuclear interactions originated by mu-mesons. For further details on the apparatus and the classification of showers, they will be found in the paper of Higashi et al.[7].

The number of P-showers at the receptive time and the cross section of nuclear interactions of mu-mesons are shown in Table I.

Table I. Receptive time, number of P-showers and the cross section of nuclear interactions.

Depth	Receptive time	Number of P-showers	σ_μ (cm²/nucleon)
50 mwe	667.9^h	7	$(2.4\pm0.6)\times10^{-31}$
250 mwe	3603.1^h	12	$(1.7\pm0.3)\times10^{-30}$

The ratio of the cross sections at both depths ($\sigma_\mu(250)/\sigma_\mu(50)$) is found to be 7.0±2.2[7].

The measurement on the angular distribution of secondary penetrating particles was made by stereo analysis, and the errors of the angle measurements were within 2 degrees. The angular distributions were measured on all of the P-showers observed at 50 mwe and 7 events at 250 mwe. The remaining 5 events at 250 mwe were accompanied with large cascade showers so that their angular distribution can not be measured, and 2 events of them seem to be extra-ordinary high energy ones.

Since it is expected that the angular distributions of incident mu-mesons in their unclear interactions from the original direction are very small, the minimum deflected particle among the secondary particles, without any successive nuclear collision with lead plates, included in each nuclear interaction is assumed to be the surviving mu-meson. The angular distribution of the secondary particles regarded as mu-mesons is shown in Fig. 2 and that of the other secondary particles is shown in Fig. 3, putting together the data obtained at 50 mwe and 250 mwe.

The averaged multiplicity ($\bar{n}_s$) of secondary particles except mu-mesons is found as being 3 per shower. Their interaction m.f.p., λ_π, has been recognized as (22±5) cm in lead which may be concluded to be consistent with the geometrical m.f.p.. The averaged multiplicity of heavily ionizing secondary particles was found to be 0.3 per P-shower and this value shows that the P-showers have 10 times smaller number of heavily ionizing particles than the S-showers have.

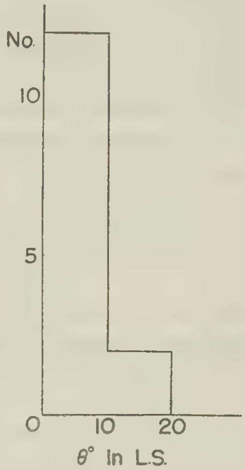

Fig. 2 Angular distribution of the secondary particles regarded as mu-mesons.

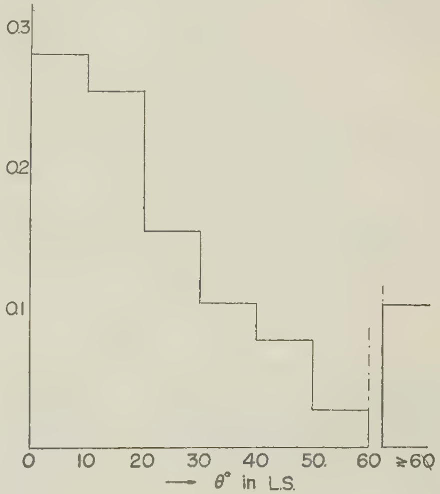

Fig. 3. Angular distribution of the other secondary particles than mu-mesons.

§ 3. Discussion and Conclusions

1) *Cross section of nuclear interactions of mu-mesons and its dependence on depth*

Following the procedure of George and Evans, the nuclear interactions produced by mu-mesons may be accounted for in terms of the interaction of the virtual photon field of mu-mesons with nucleus. If the deflected angle of the incident mu-mesons in nuclear interactions is so small as we may put $\sin\theta \simeq \theta$ and also the transferred energy is small, the virtual photon spectrum may be described by the W-W method[8]. It may be realized from the observed results, as shown in Fig. 2, that the deflection angle of incident mu-mesons is so small that one can now apply the idea of the W-W method for the treatment of the nuclear interactions of mu-mesons.

The number of virtual photons of energy greater than $\mathcal{E}$ associating with a mu-meson of incident energy E is given by[9]

$$\Phi(E,\mathcal{E})=\frac{\alpha}{\pi}\left[\left\{\ln\left(\frac{E}{\mathcal{E}}\right)\right\}^2 2-0.76\ln\left(\frac{E}{\mathcal{E}}\right)\right] \quad \text{for} \quad \mathcal{E} \ll E \qquad (1)$$

where α is the fine structure constant. Here, we assume that $\Phi(E,\mathcal{E})$ is given by the following formula:

$$\left.\begin{aligned}\Phi(E,\mathcal{E})&=\frac{\alpha}{\pi}\left[\left\{\ln\left(\frac{E}{\mathcal{E}}\right)\right\}^2-0.76\ln\left(\frac{E}{\mathcal{E}}\right)\right] && \text{for} \quad \mathcal{E}<\mathcal{E}_0\\ \Phi(E,\mathcal{E})&=0 && \text{for} \quad \mathcal{E}\geq\mathcal{E}_0\end{aligned}\right\} \qquad (2)$$

where $\mathcal{E}_0=\frac{E}{e^{0.76}}\sim\frac{E}{2}$, and equation (1) has a negative value when $\mathcal{E}\geq\mathcal{E}_0$. Hence, the number of photons of energy greater that $\mathcal{E}$ at x mwe underground is given by

$$\Phi(x,\mathcal{E})=\int_{\mathcal{E}}^{\infty}\phi(E,\mathcal{E})\frac{dI_x(E)}{dE}\cdot dE \qquad (3)$$

where $I_x(E)$ is the flux of mu-mesons of energy greater than E at x mwe underground. The photon spectra at 50 mwe and at 250 mwe are obtained by numerical calculations and are shown in Fig. 4. If the photonuclear cross section $\sigma_{h\nu}$ is taken as being independent on the energy of photon at high energy, the cross section $\sigma_\mu(x)$ for shower production by mu-mesons is expressed by:

$$\sigma_\mu(x)=\sigma_{h\nu}\frac{\phi(x,E_{\min})}{I_x} \qquad (4)$$

where I_x is an intensity of the hard component at the depth x mwe, and $E_{\min}$ is threshold energy of the shower observed in the cloud chamber. The expected values of σ_μ(50 mwe) and σ_μ(250 mwe) and the ratio of them, σ_μ(250 mwe)/σ_μ(50 mwe), are given in Table II, as a function of $E_{\min}$*.

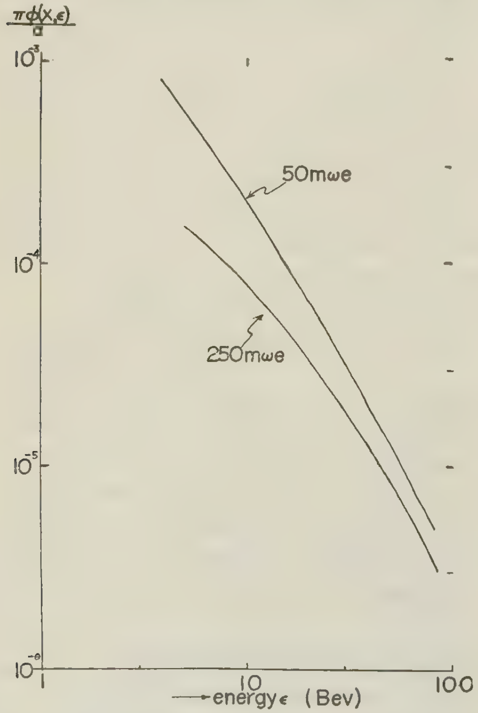

Fig. 4. Integral energy spectra of photons obtained by the W-W method at 50 mwe and at 250 mwe understand.

Table II. The expected values of σ_μ (50 mwe) and σ_μ (250 mwe) and the ratio of them, σ_μ (250 mwe)/σ_μ (50 mwe).

$E_{\min}$ (BeV)	$\sigma_\mu(50)$ (cm²/nucleon)	$\sigma_\mu(250)$ (cm²/nucleon)	$\sigma_\mu(250)/\sigma_\mu(50)$
5	$1.7\times10^{-3}\sigma_{h\nu}$	$10\times10^{-3}\ \sigma_{h\nu}$	5.9
7	1.1 〃	7 〃	6.4
10	0.6 〃	4.5 〃	7.5
20	0.2 〃	2.2 〃	11

Table III. Relation between $E_{\min}$ and $\sigma_{h\nu}$.

$E_{\min}$(BeV)	$\sigma_{h\nu}$ (cm²/nucleon)
5	1.4×10^{-28}
7	2.2 〃
10	4.0 〃

The value of $\sigma_{h\nu}$ was determined by comparing in the observed value of σ_μ(50 mwe) with the above expression, and their results were shown in Table III.

---

* The values of the ratio $\sigma_\mu(250)/\sigma_\mu(50)$, which has been shown in N. C.[7], was obtained from the equation $\Phi(E,\varepsilon)=\alpha/\pi\ [\ln(E/\varepsilon)]^2$ which is given by George and Evans[1].

If the nuclear cross section of virtual photon would be postulated to be identical with that of real photon, and would be taken as a constant at the energy of more than 1 BeV, it may be expected that the value of the photonuclear cross section would be nearly equal to 10^{-28} cm^2/nucleon[10]. The values of cross section of mu-mesons at both the depths and their depth dependence, thus, should be interpreted as a behavior of the showers with the threshold energy of 5 BeV. The threshold energy obtained above is also consistent with the estimated value of $E_{\min}$ from the triggering condition by using the relation between the averaged multiplicity and the shower energy, on the assumption that the nature of the showers of mu-mesons is similar to that of nucleons.

Barrett et al. have obtained the cross section σ_μ(1600 mwe) with a hodoscoped counter arrangement at 1600 mwe underground. They inferred the cross section $\sigma_\mu(1600\ \mathrm{mwe})\geq(4\pm2)\times10^{-29}$ cm^2/nucleon for energies above 5 BeV[12]. The value of σ_μ(1600 mwe) expected from equation (4) is evaluated to be about 6×10^{-30} cm^2/nucleon. But this discrepancy at 1600 mwe is probably not very serious. Because it seems that they did not pay attention to the fact that the tail of a cascade shower is surviving in lead and made them overestimate the number of penetrating showers, and they obtained the maximum cross section of penetrating showers $\sigma_{\max}=3\times10^{-29}/\gamma$ cm^2/nucleon from local absorption[12] at the same depth, where γ is the multiplicity of production resulting from a single interaction of a mu-meson. Therefore, it seems that there is no reason to consider that the value of σ_μ(1600 mwe) is too large.

It should, accordingly, be concluded that the frequencies of penetrating showers produced by mu-measons at the depth down to 1600 mwe are interpreted with the W-W method and the constant photonuclear cross section of 1.4×10^{-28} cm^2/nucleon.

2) *Angular distribution of secondary penetrating particles*

The P-showers, of which secondary penetrating particles are investigated, are occurred in lead plates. It is then doubtful whether or not the angular distribution of the secondary particles of P-showers directly implies that of mu-meson-nucleon interactions. The fact that the heavily ionizing particles are rarely produced in the P-showers, however, suggests that the successive interactions of shower particles in the nucleus may be neglected in the P-showers. It may be therefore considered that the angular distribution of P-showers expresses that of mu-meson-nucleon interactions. As the nuclear interaction of mu-mesons may be understood with the W-W method, the differential energy distribution of the P-showers is given by $\dfrac{d\Phi(x,\mathcal{E})}{d\mathcal{E}}$ where $\Phi(x,\mathcal{E})$ is the number of photons of energy greater than $\mathcal{E}$ at x mwe underground. Then, the angular distribution of secondary penetrating particles of the P-showers at x mwe underground is

$$f(\varphi)d\varphi=\frac{\displaystyle\int_{E_{\min}}^{\infty} n(\mathcal{E})\cdot g(\mathcal{E},\varphi)\frac{d\Phi(x,\mathcal{E})}{d\mathcal{E}}\cdot d\mathcal{E}\cdot d\varphi}{\displaystyle\int_{E_{\min}}^{\infty} n(\mathcal{E})\frac{d\Phi(x,\mathcal{E})}{d\mathcal{E}}\cdot d\mathcal{E}} \qquad (5)$$

where $n(\mathcal{E})$ is the averaged multiplicity and $g(\mathcal{E},\varphi)\,d\varphi$ is the angular distribution of secondary particles of showers produced by photon of energy $\mathcal{E}$. Since the number of photons of energy greater than 40 BeV is less that 10 percents of that of energy greater 5 BeV as shown in Fig. 4 and as a dependence of averaged multiplicity on the incident energy would be expected to be only slight, it does not result so much errors to assume that $n(\mathcal{E})$ is constant. Kessler and Maze[4] have given the anisotropical distribution of the type $(1+\cos\phi)d\Omega$ in the center-of-mass system of photon-nucleon interaction by the use of the F-plot analysis from their observed penetrating showers data. The angle ϕ in the center-of-mass system is transferred to the angle φ in the laboratory system by the relation

$$\tan\varphi=\frac{1}{\gamma_c}\cdot\frac{\sin\phi}{\cos\phi+(\beta_c/\beta_\pi)} \qquad (6)$$

where γ_c and β_c are Lorentz factor and velocity of the center-of-mass system in the laboratory system respectively, and β_π is velocity of the secondary particles in the center-of-mass system. In case that the secondary particles have the angular distribution $(1+\cos\phi)$ $d\Omega$ in the center-of-mass system, the distribution in the laboratory system $f_1(\varphi)\,d\varphi$ was obtained by numerical calculation under such condition as being $\beta_c/\beta_\pi=1$ postulated by Kessler and Maze[4]. The mean value of that expected at both depths is shown in Fig. 5. If we consider the case that there are a few of low energy secondaries in the center-of-mass system, the angular distribution in the laboratory system should tend to increase forward. On the other hand, in case that the angular distribution in the center-of-mass system is isotropic, a different distribution $f_2(\varphi)\,d\varphi$, was evaluated with the same way as above and using the similar momentum distribution of secondary particles in the center-of-mass system as that of pi-meson-nucleon interactions[13] which is shown in Fig. 6. The result is also shown in Fig. 5.

Although the experimental results we obtained till now have still a quite large statistical uncertainties, it seems that the distribution $f_2(\varphi)\,d\varphi$, on the whole, is in better agreement with our results than the distribution $f_1(\varphi)\,d\varphi$ is.

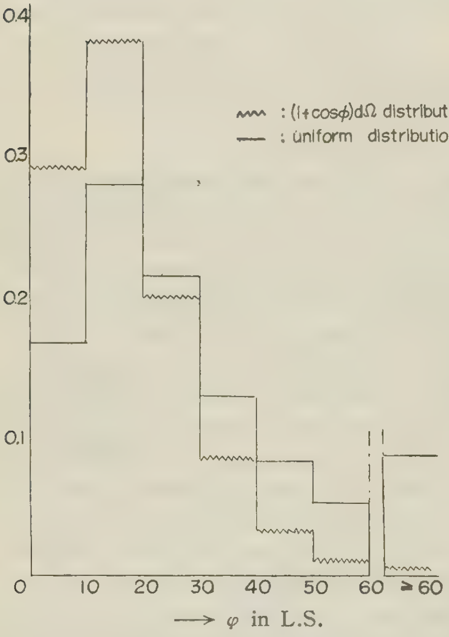

Fig. 5. Expected angular distribution in the lab. system obtained from the distribution $(1+\cos\phi)d\Omega$ in the c.m.s. and from the uniform distribution in the c.m.s.

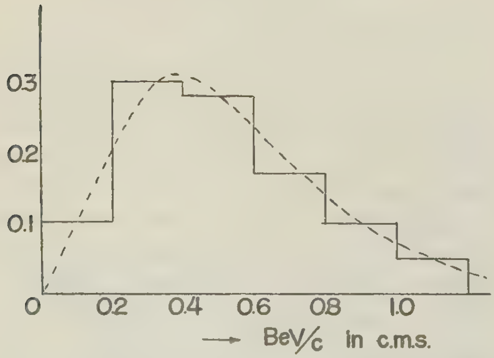

Fig. 6. Assumed momentum distribution of secondary particles in the center-of-mass system.

Namely, the distribution $f_2(\varphi)\,d\varphi$ is similar to the observed one except a few part in 0-10 degrees region. On the other hand, the distribution $f_1(\varphi)d\varphi$ cannot interpret so broad distribution as observed. It may be likely that the anisotropical distribution $(1+\cos\phi)d\Omega$ obtained by Kessler and Maze is due mainly to the narrow arrangement of the observing system. The result that the angular distribution of secondary penetrating particles in multiple productions of photo-nuclear interaction is nearly uniform in the center-of-mass system is of the same behavior as the fact that those of nucleon-nucleon interactions at the energy of 6.2 BeV[15] and of a few tens of BeV[14] and pimeson-nucleon interactions at the energy of 5 BeV[13] seem to be uniform in the center-of-mass system at the first approximation from their observed results. It seems, therefore, that the angular distribution of secondary penetrating particles of multiple production at these energy region is nearly uniform in the center-of-mass system and is not dependent on the character of incident particles.

Acknowledgements

The author wishes to express his great gratitude the Professor Y. Watase of Osaka City University not only for his suggestions, but also for his interest and encouragement. He also wishes to express his thanks to Professors T. Oshio, K. Watanabe, Drs. S. Higashi and S. Mitani for active collaboration, to Professor M. Oda of Tokyo University, Professor S. Ozaki, Drs. T. Kitamura and O. Kusumoto of Osaka City University for suggestions and helpful discussions, and to Mr. H. Nishimura for his aid in measuring.

It is a pleasure to thank the Institute for Food Chemistry for the financial aid.

References

1) E. P. George and J. Evans: Proc. Phys. Soc. London **A 63** (1950) 1248; **A 68** (1955) 829.
2) P. E. Argan, A. Gigli and S. Sciuti: Nuovo Cimento **11** (1954) 530.
3) G. N. Fowler and A. W. Wolfendale: Nucl. Phys. **3** (1957) 299; Progress in elementary particles and cosmic ray physics Vol. IV

(Amsterdam; North-Holland Publ. Co. 1958).
4) D. Kessler and R. Maze: Nuovo Cimento **5** (1957) 1540.
5) S. Higashi, T. Oshio, H. Shibata, K. Watanabe and Y. Watase: Nuovo Cimento **5** (1957) 592.
6) I. B. McLiarmid: Phys. Rev. **109** (1958) 1792.
7) S. Higashi, S. Mitani, T. Oshio, H. Shibata, K. Watanabe and Y. Watase: Nuovo Cimento **13** (1959) 265.
8) T. Murota and A. Ueda: Progr. Theor. Phys. **16** (1956) 497.
9) W. Heitler: Quantum theory of radiation (Oxford Univ. Press. 1954) P. 263.
10) J. M. Sellen, G. Cocconi, V. T. Cocconi and E. L. Hart: Phys. Rev. **110** (1958) 779; **113** (1959) 1323
11) U. Camerini, W. O. Lock and D. H. Perkins: Progress in cosmic ray physics Vol. 1 (Amsterdam; North-Holland Publ. Co. 1952) P. 11.
12) P. H. Barrett, L. M. Bollinger, G. Cocconi, Y. Eisenberg and K. Greisen: Rev. Mod. Phys. **24** (1952) 133.
13) George Maenchen, William B. Fowler, Wilson M. Powell and Robert W. Wright: Phys. Rev. **108** (1957) 850.
14) S. Kaneko, O. Kusumoto, S. Matsumoto and M. Takahata: Proceedings of the Moscow Cosmic Ray Conference, Vol. 1 (1960) P. 107.
15) O. Kusumoto: private communication.
16) R. M. Kalbach, J. J. Lord and C. H. Tsao: Phys. Rev. **113** (1959) 330.

JOURNAL OF THE PHYSICAL SOCIETY OF JAPAN Vol. 16, No. 3, MARCH, 1961

Quantum Statistics of Surface Effect

By Takuji TSUZUKI

Yokohama Municipal University,
Kanazawa-ku, Yokohama, Japan

(Received December 3, 1960)

The quantum mechanical behaviors of a dilute gas in a vessel with finite volume are considered with special reference to the surface effect. It is shown that the thermodynamic function of the system with weak interaction between particles can be expanded in terms of permutation rings with the use of M. Toda's formula, and the result is shown to be in harmony with that derived from the method of grand partition function. An approximate treatment for molecules with hard cores is also given.

§1. Introduction

The theory of gas of interacting particles has been investigated for many years as one of the most typical problems of statistical mechanics. In classical theory, as is well known, J. Mayer has given the expansion formula in terms of interaction of particles. The first term of Mayer's formula (the zero-th approximation) gives the ideal gas law. The deviation from the ideal gas law is generally represented as the 2nd, 3rd, ⋯ virial coefficient. In quantum statistics, however, the symmetricity of wave function must be considered, and Ursell expansion has to be substituted for Mayer's formula. Many authors[1),2),3)] have developed the theories of quantum corrections for systems of interacting particles.

In the present paper, the quantum statistical theories of a dilute gas in a vessel with finite volume are developed. Especially the effect of boundary wall of a vessel on a dilute gas is discussed. When the volume of a container is restricted to be finite, then thermodynamical quantities of a gas are affected by the surface area. In Section 2, the general formula for the surface free energy is developed by the use of M. Toda's[4)] formula. In Section 3, we treat the surface effect assuming that the interaction between molecules is weak. In Section 4, the equation of state of such a gas with surface effect is given. Especially the results derived from the Toda's[4),5)] formula is shown to be in harmony with the result calculated by the method of grand partition function.

In the present work, the potential energy between molecules $u(r)$ and that between a molecule and the boundary wall $u_w(z)$ are nitroduced. The effect of non-comutability of potential energy and kinetic energy is taken into account, and the statistical effect (effect of symmetricity of wave function) is considered. Our results may be applicable to the surface phenomena of substances in which quantum effect is predominant (for example liquid helium[6),7),8)]), or to atomic nuclei[9)] since they consist of only several hundred nucleons even for the heviest atom. In the latter case, however, we must remark that the boundary surface is not plane, but has curvature.

On the other hand, at room temperature, many interesting chemico-physical phenomena between solid and gas have been observed. Adsorption of gas to solid surface is one of them. Some authors[10),11)] have developed the statistical theories of adsorption by the use of grand canonical ensemble. In this case, generally, the quantum treatment need not to be considered, but the potential energy $u_w(z)$ plays an important role. W. A. Steele and G. D. Halsey, JR.[12)] have calculated the excess volume, assuming the inverse cubic attraction between a gas molecule and the boundary wall. Moreover M. P. Freeman and G. D. Halsey, JR.[13)] have introduced the hard sphere repulsion between molecules and have had a good agreement with experimental results. In the previous paper[14)] we have also introduced square-well potentials for the interaction between molecules and between a molecule and the wall. If the interaction between molecules has hard sphere repulsion, the quantum statistical treatment becomes very difficult. In Section 5, we avoid this difficulty by substituting the effective diameter σ for the classical diameter σ_0 of a molecule as we have done in the previous paper[14)].

§ 2. General Formula for the Surface Free Energy

The system we shall consider is a gas composed of N identical molecules in a vessel with volume $V\,(=L_xL_yL_z)$. Molecules are assumed to be nonpolar and spherically symmetric, i.e., the potential energy $u(r)$ between molecules is assumed to be a function only of the distance r between the centers of the molecules. Moreover we introduce the potential energy between a molecule and a wall $u_w(z)$, which is a function of the shortest distance z from the center of the molecule to the surface of the wall. The total energy H is thus

$$H=H_0+\sum_{i=1}^{N}u_w(\boldsymbol{x}_i)+\sum_{i<j}^{N}u(|\boldsymbol{x}_j-\boldsymbol{x}_i|) \qquad (2.1)$$

where H_0 represents the kinetic energy of gas molecules.

The increment of the free energy due to the presence of walls can be written as γA, where A denotes the total surface area of the walls and γ stands for the surface tension. Here we are assuming that the size of the vessel is large compared with the interaction lengths of u_w and u, and further with a certain multiple of the de Broglie wave length of gas molecules. γ is defined by the derivative of free energy F with respect to the surface area A, keeping the volume constant:

$$\gamma=(\partial F/\partial A)_{V,T,N} \qquad (2.2)$$

with

$$F=-kT\log \mathrm{Tr}\,\rho\,, \qquad (2.3)$$

where ρ stands for the density matrix

$$\rho=e^{-\beta H}\,. \qquad (2.4)$$

It is convenient to use Toda's method[4),5)] to make the derivative in Eq. (2.2). In our case there is potential energy due to the wall, which contribute an extra term. Thus we get an extension of Toda's formula[4)]:

$$\gamma=\mathrm{Tr}\left\{2\left[\sum_{i=1}^{N}H_{0z}(i)-\sum_{i=1}^{N}H_{0x}(i)\right]\rho-\sum_{i=1}^{N}z_i\frac{du_w(z_i)}{dz_i}\rho-\sum_{j>i=1}^{N}\frac{z_{ij}^2-x_{ij}^2}{r_{ij}}\frac{du(r_{ij})}{dr_{ij}}\rho\right\}\Big/A\,\mathrm{Tr}\,\rho \qquad (2.5)$$

where the surface perpendicular to the z-axis, with area A is considered, and $H_{0z}(i)$ and $H_{0x}(i)$ are the kinetic energy, for the z-direction and for the x-direction respectively, of the i-th molecule given by

$$H_{0z}(i)=p_{zi}^2/2m\,, \qquad H_{0x}(i)=p_{xi}^2/2m\,. \qquad (2.6)$$

Now, assuming that the potential energy

$$U=\sum_{i=1}^{N} u_w(i)+\sum_{j>i=1}^{N} u(i,j) \tag{2.7}$$

is sufficiently small compared with the kinetic energy

$$H_0=\sum_{i=1}^{N} p_i^2/2m\ , \tag{2.8}$$

we get the expansion of density matrix of the form

$$\rho=\rho_0-\rho_0\int_0^\beta \exp(sH_0)U\exp(-sH_0)\,ds+\cdots\ , \tag{2.9}$$

where

$$\rho_0=\exp(-\beta H_0) \tag{2.10}$$

stands for the density matrix of an ideal gas.

Noting the fact that $H_{0z}(i)$ and $H_{0x}(i)$ commute with H_0 and ρ_0, we have, for the first term of the right-hand side of Eq. (2.5),

$$\begin{aligned}\mathrm{Tr}\,\{(H_{0z}(1)-H_{0x}(1))\rho\}&=\mathrm{Tr}\,\{(H_{0z}(1)-H_{0x}(1))\rho_0\}\\ &-\beta\,\mathrm{Tr}\,\{\sum_i u_w(i)(H_{0z}(1)-H_{0x}(1))\rho_0\}-\beta\,\mathrm{Tr}\,\{\sum_{i>j} u(i,j)(H_{0z}(1)-H_{0x}(1))\rho_0\}\ ; \end{aligned}\tag{2.11}$$

For the second and the third term of Eq. (2.5) we may substitute ρ_0 for ρ if we neglect terms of higher order with respect to interaction potentials. As will be shown later, diagonal element of $(H_{0z}(1)-H_{0x}(1))\rho_0$ vanishes except in a limited region of the order λ (de Brogie wave length) near the wall. So the second and the third terms in the above equation can be neglected in a rough approximation. All these terms can be rewritten using the reduced density matrix of the form[15]

$$\rho_0^{(N)}(\boldsymbol{x}_1,\cdots \boldsymbol{x}_s;\boldsymbol{x}_1',\cdots \boldsymbol{x}_s')=\int\cdots\int \rho_0^{(N)}(\boldsymbol{x}_1,\cdots \boldsymbol{x}_s,\boldsymbol{x}_{s+1},\cdots \boldsymbol{x}_N;\boldsymbol{x}_1',\cdots \boldsymbol{x}_s',\boldsymbol{x}_{s+1},\cdots \boldsymbol{x}_N)\times d\boldsymbol{x}_{s+1}\cdots d\boldsymbol{x}_N \tag{2.12}$$

where the index (N) is attached to clarify the number of molecules.

§ 3. Explicit Formulas for the Surface Tension

As we are interested in the effect of surface perpendicular to the z-axis, we shall impose periodic conditions with respect to the x and y directions. Thus we think of a gas contained in the space between the walls at $z=0$ and $z=L_z$, and between the periodic boundaries at $x=0$, $x=L$, $y=0$ and $y=L$. For brevity's sake we have put $L_x=L_y=L$.

(i) Boltzmann Statistics

For classical statistics we have[15]

$$\rho_0^{(N)}(\boldsymbol{x}_1;\boldsymbol{x}_1')=\frac{1}{N}f^{(N-1)}(\beta)\rho_0(\boldsymbol{x}_1;\boldsymbol{x}_1'|\beta)\ , \tag{3.1}$$

$$\rho_0^{(N)}(\boldsymbol{x}_1,\boldsymbol{x}_2;\boldsymbol{x}_1',\boldsymbol{x}_2')=\frac{1}{N(N-1)}f^{(N-2)}(\beta)\rho_0(\boldsymbol{x}_1;\boldsymbol{x}_1'|\beta)\rho_0(\boldsymbol{x}_2;\boldsymbol{x}_2'|\beta) \tag{3.2}$$

where $f^{(n)}(\beta)$ represents the partition function for an ideal gas with n molecules,

$$\left.\begin{aligned}&f^{(n)}(\beta)=\mathrm{Tr}\,\rho_0^{(n)}=[f^{(1)}(\beta)]^n/n!\ ,\\ &f^{(1)}(\beta)=\mathrm{Tr}\,\rho_0^{(1)}\end{aligned}\right\} \tag{3.3}$$

and $\rho_0(\boldsymbol{x};\boldsymbol{x}'|\beta)$ is the density matrix for a molecule subject to the foresaid boundary conditions[14]:

$$\rho_0(\boldsymbol{x};\boldsymbol{x}'|\beta)=\rho_{0x}\rho_{0y}\rho_{0z} \tag{3.4}$$

where

$$\left.\begin{aligned}\rho_{0x}&=\rho_{0x}(x;x'|\beta)=\lambda^{-1}\exp\{-\pi(x-x')^2/\lambda^2\}\,,\\ \rho_{0y}&=\rho_{0y}(y;y'|\beta)=\lambda^{-1}\exp\{-\pi(y-y')^2/\lambda^2\}\,,\\ \rho_{0z}&=\rho_{0z}(z;z'|\beta)=\frac{2}{L_z}\sum_{n=1}^{\infty}\exp(-\beta\pi^2\hbar^2n^2/L_z^2)\sin\frac{\pi n}{L_z}z\sin\frac{\pi n}{L_z}z'\end{aligned}\right\} \tag{3.5}$$

and

$$\lambda=\sqrt{2\pi\hbar^2\beta/m} \tag{3.6}$$

is the de Broglie wave length. For the lower half $(0\leq z\leq L_z/2)$ of the system we use the integrated form

$$\rho_{0z}(z;z'|\beta)=\lambda^{-1}[\exp\{-\pi(z-z')^2/\lambda^2\}-\exp\{-\pi(z+z')^2/\lambda^2\}]\,, \tag{3.7}$$

as we are assuming that $L_z\gg\lambda$.

We have for the diagonal,

$$[2H_{0z}\rho_{0z}]_{z=z'}=-\frac{\hbar^2}{m}\left[\frac{\partial^2}{\partial z^2}\rho_{0z}\right]_{z=z'}=\frac{kT}{\lambda}\left\{1-\exp(-4\pi z^2/\lambda^2)+\frac{8\pi z^2}{\lambda^2}\exp(-4\pi z^2/\lambda^2)\right\}, \tag{3.8}$$

$$[2H_{0x}\rho_{0x}]_{x=x'}=-\frac{\hbar^2}{m}\left[\frac{\partial^2}{\partial x^2}\rho_{0x}\right]_{x=x'}=\frac{kT}{\lambda}\,. \tag{3.9}$$

Since $L_z\gg\lambda$, we get

$$\int_0^{L_z/2}[2H_{0z}\rho_{0z}]_{z=z'}\,dz=\frac{kT}{\lambda}\frac{L_z}{2}\,, \tag{3.10}$$

$$\int_0^{L_z/2}[\rho_{0z}]_{z=z'}\,dz=\frac{1}{\lambda}\left(\frac{L_z}{2}-\frac{\lambda}{4}\right). \tag{3.11}$$

The same contribution comes from the wall at $z=L_z$. Thus we obtain $(V=L^2L_z,\ A=2L^2)$

$$\mathrm{Tr}\,(2H_{0z}\rho_0)=\frac{kT}{\lambda^3}V\,, \tag{3.12}$$

$$\mathrm{Tr}\,(2H_{0x}\rho_0)=\frac{kT}{\lambda^3}\left(V-\frac{\lambda}{4}A\right), \tag{3.13}$$

$$\mathrm{Tr}\,\rho_0=\frac{1}{\lambda^3}\left(V-\frac{\lambda}{4}A\right). \tag{3.14}$$

Surface tension γ_0 for a gas of free molecules $(u_w=u=0)$ is therefore

$$\begin{aligned}\gamma_0&=N\frac{2\,\mathrm{Tr}\,\{(H_{0z}(1)-H_{0x}(1))\rho_0\}}{A\,\mathrm{Tr}\,\rho_0}\\ &=\frac{N}{V-\lambda A/4}\frac{\lambda}{4}kT\simeq\frac{N}{V}\frac{\lambda}{4}kT\end{aligned} \tag{3.15}$$

which is in agreement with Tada's result[4]. $\lambda/4$ represents the width of the region inaccessible for molecules due to the boundary condition that wave function vanishes at the wall. In fact, it is easy to see in the case of free molecules, that the free energy is

$$F_0^{(N)}=-kT\log\left[\left\{\lambda^{-3}\left(V-\frac{\lambda}{4}A\right)\right\}^N\Big/N!\right] \tag{3.16}$$

and the pressure is given by

$$p_0=-\left(\frac{\partial F_0^{(N)}}{\partial V}\right)_{A,T,V}=NkT\Big/\left(V-\frac{\lambda}{4}A\right). \tag{3.17}$$

Further in this case, we obtain from Eq. (3.15) and Eq. (3.17) the relation

$$(p_0V-\gamma_0A)/kT=N. \tag{3.18}$$

On the other hand, however, from thermodynamical argument, the left-hand side of the last equation is seen to be related to the logarithm of the grand partition function Ξ_0 given by

$$\Xi_0(\zeta)=\sum_{n=0}^{\infty}\zeta^n f^{(n)}=\exp\left\{\zeta\lambda^{-3}\left(V-\frac{\lambda}{4}A\right)\right\}. \tag{3.19}$$

Since the parameter ζ is determined by the condition

$$N=\zeta\,\partial\log\Xi_0(\zeta)/\partial\zeta, \tag{3.20}$$

the thermodynamical relation

$$(p_0V-\gamma_0A)/kT=\log\Xi_0 \tag{3.21}$$

is established.

Since interaction potentials u_w and u are diagonal in the coordinate representation, diagonal elements of ρ_0, $H_{0z}\rho_0$ etc. are sufficient for calculating γ from Eqs. (3.8) and (3.9). We note that for $z<L_z/2$,

$$[2(H_{0z}-H_{0x})\rho_0]_{\boldsymbol{x}=\boldsymbol{x}'}=\frac{kT}{\lambda^3}(-1+8\pi z^2/\lambda^2)\exp(-4\pi z^2/\lambda^2), \tag{3.22}$$

$$[\rho_{0x}]_{x=x'}=[\rho_{0y}]_{y=y'}=\lambda^{-1}, \tag{3.23}$$

$$[\rho_{0z}]_{z=z'}=\lambda^{-1}\{1-\exp(-4\pi z^2/\lambda^2)\}. \tag{3.24}$$

We note the fact that $[2(H_{0z}-H_{0x})\rho_0]_{\boldsymbol{x}=\boldsymbol{x}'}$ is comparable with $kT[\rho_0]_{\boldsymbol{x}=\boldsymbol{x}'}$ only at the distance of the order λ from the wall. We may therefore neglect the terms like

$$\mathrm{Tr}\,\{u_w(i)[H_{0z}(1)-H_{0x}(1)]\rho_0\}$$

and

$$\mathrm{Tr}\,\{u(i,j)[H_{0z}(1)-H_{0x}(1)]\rho_0\}.$$

Thus we get an approximation formula which is valid when the interaction distance of u_w and u are large compared with the de Broglie wave length λ:

$$\begin{aligned}\gamma=N\Bigg[&\frac{kT}{V}\frac{\lambda}{4}-\int z\frac{du_w(z)}{dz}\rho_0(z;z|\beta)dz\Big/\lambda^2f^{(1)}(\beta)\\&-\frac{N-1}{2}\iiiint\frac{z_{12}{}^2-x_{12}{}^2}{r_{12}}\frac{du(r_{12})}{dr_{12}}\rho_0(z_1;z_1|\beta)\rho_0(\boldsymbol{x}_2;\boldsymbol{x}_2|\beta)\\&\times dz_1\,dx_{12}\,dy_{12}\,dz_{12}\Big/\{\lambda^2f^{(1)}(\beta)\}^2\Bigg].\end{aligned} \tag{3.25}$$

(ii) Quantum Statistics

In quantum statistics, we have15),16)

$$\rho_0^{(N)}(\boldsymbol{x}_1;\boldsymbol{x}_1')=\frac{1}{N}\sum_{\nu=1}^{N}(\pm)^{\nu-1}f^{(N-\nu)}(\beta)\rho_0(\boldsymbol{x}_1;\boldsymbol{x}_1'|\nu\beta) \tag{3.26}$$

$$\rho_0^{(N)}(\boldsymbol{x}_1,\boldsymbol{x}_2;\boldsymbol{x}_1',\boldsymbol{x}_2')=\frac{1}{N(N-1)}\sum_{\mu,\nu}^{\mu+\nu\le N}(\pm)^{\mu+\nu}f^{(N-\mu-\nu)}(\beta)\begin{vmatrix}\rho_0(\boldsymbol{x}_1;\boldsymbol{x}_1'|\mu\beta) & \rho_0(\boldsymbol{x}_1;\boldsymbol{x}_2'|\nu\beta)\\ \rho_0(\boldsymbol{x}_2;\boldsymbol{x}_1'|\mu\beta) & \rho_0(\boldsymbol{x}_2;\boldsymbol{x}_2'|\nu\beta)\end{vmatrix}_{\pm} \tag{3.27}$$

where the upper sign corresponds to Bose-Einstein statistics and the lower sign to Fermi-Dirac statistics, and $\rho_0(x;x'|\nu\beta)$ is the density matrix given by Eq. (3.4) and Eq. (3.5) but $\nu\beta$ is substituted for β and is a chain integral of the form

$$\rho_0(\boldsymbol{x}_1;\boldsymbol{x}_1'|\nu\beta)=\int\cdots\int\rho_0(\boldsymbol{x}_1;\boldsymbol{x}_2|\beta)\rho_0(\boldsymbol{x}_2;\boldsymbol{x}_3|\beta)\cdots\rho_0(\boldsymbol{x}_\nu;\boldsymbol{x}_1'|\beta)\,d\boldsymbol{x}_2\cdots d\boldsymbol{x}_\nu\,. \tag{3.28}$$

We see that

$$b_\nu=\mathrm{Tr}\,\rho_0(x;x'|\nu\beta)=\lambda^{-3}\left(\frac{V}{\nu^{3/2}}-\frac{A}{\nu}\frac{\lambda}{4}\right) \tag{3.29}$$

means a permutation ring of ν molecules. The average size of this ring is seen to be $\nu^{1/2}\lambda/4$ because the above equation means that $V-\nu^{1/2}\lambda A/4$ is to be substituted for the geometrical volume V. As is known in the theory of polymers or of Brownian motion, the magnitude $\nu^{1/2}\lambda/4$ can ce interpreted as the length of a chain of ν segments with length λ each. The amount of decrease in effective volume and the effect of surface become more predominant when the permutation ring becomes larger even if we ignore the potential energy between molecules and wall.

The surface tension for an ideal gas in quantum statistics is given by

$$\gamma_0=N\frac{\lambda}{4}kT\frac{\sum_{\nu=1}^{N}(\pm)^{\nu-1}f^{(N-\nu)}/\nu^2}{\sum_{\nu=1}^{N}(\pm)^{\nu-1}f^{(N-\nu)}\left(\frac{V}{\nu^{3/2}}-\frac{A}{\nu}\frac{\lambda}{4}\right)} \tag{3.30}$$

in which the second term in the denominator may be neglected. It can be shown (cf. next section) that the equation of state takes the form

$$p_0=\frac{N}{V}kT\frac{\sum(\pm)^{\nu-1}f^{(N-\nu)}V/\nu^{5/2}}{\sum(\pm)^{\nu-1}f^{(N-\nu)}\left(\frac{V}{\nu^{3/2}}-\frac{A}{\nu}\frac{\lambda}{4}\right)}\,. \tag{3.31}$$

Therefore the equation which corresponds to Eq. (3.18) is

$$\frac{p_0V-\gamma_0A}{NkT}=\frac{\sum(\pm)^{\nu-1}f^{(N-\nu)}b_\nu/\nu}{\sum(\pm)^{\nu-1}f^{(N-\nu)}b_\nu}\,. \tag{3.32}$$

On the other hand, from Eq. (3.26) we see that

$$f^{(n)}=\frac{1}{n}\sum_{\nu=1}^{n}(\pm)^{\nu-1}f^{(n-\nu)}b_\nu\,;\qquad n\ge 1 \tag{3.33}$$

and that the grand partition function $\Xi_0(\zeta)=\sum_{n=0}^{\infty}\zeta^n f^{(n)}$ satisfies the equation

$$\zeta\frac{d}{d\zeta}\Xi_0(\zeta)=\Xi_0\sum_{\nu=1}^{\infty}(\pm)^{\nu-1}\zeta^\nu b_\nu\,. \tag{3.34}$$

Solving this equation with the initial condition that $\Xi_0(0)=f^{(0)}=1$, we get

$$\log\Xi_0(\zeta)=\sum(\pm)^{\nu-1}\zeta^\nu b_\nu/\nu\,. \tag{3.35}$$

ζ is determined by the condition

$$N=\zeta\,\partial\log\Xi_0/\partial\zeta=\sum(\pm)^{\nu-1}\zeta^\nu b_\nu\,. \tag{3.36}$$

The general thermodynamic relation $(pV-\gamma A)/kT=\log \Xi$ can be written as

$$\frac{p_0 V-\gamma_0 A}{NkT}=\frac{\sum(\pm)^{\nu-1}\zeta^\nu b_\nu/\nu}{\sum(\pm)^{\nu-1}\zeta^\nu b_\nu} \tag{3.37}$$

which is to be identified with Eq. (3.32).

To establish this identity we multiply η^N to both the denominator and the numerator of the right-hand side of Eq. (3.32). We note that for an appropriate value of η

$$\eta^N \sum(\pm)^{\nu-1} f^{(N-\nu)} b_\nu=\eta^N f^{(N)} \tag{3.38}$$

has a sharp maximum for a certain value of N, which therefore can be replaced by the average

$$N=\frac{\sum n\eta^n f^{(n)}}{\sum \eta^n f^{(n)}}=\eta\frac{\partial \log \Xi_0(\eta)}{\partial\eta} . \tag{3.39}$$

Comparing Eq. (3.39) with Eq. (3.36), we see that $\eta=\zeta$. For this value of ζ, the right-hand side of Eq. (3.32) can be replaced by the average as follows:

$$\frac{\sum_{\nu=1}^{N}(\pm)^{\nu-1} f^{(N-\nu)} b_\nu/\nu}{\sum_{\nu=1}^{N}(\pm)^{\nu-1} f^{(N-\nu)} b_\nu}=\frac{\sum_{n=1}^{\infty}\zeta^n\sum_{\nu=1}^{n}(\pm)^{\nu-1} f^{(n-\nu)} b_\nu/\nu}{\sum_{n=1}^{\infty}\zeta^n\sum_{\nu=1}^{n}(\pm)^{\nu-1} f^{(n-\nu)} b_\nu}=\frac{\Xi_0(\zeta)\sum_{\nu=1}^{\infty}(\pm)^{\nu-1}\zeta^\nu b_\nu/\nu}{\Xi_0(\zeta)\sum_{\nu=1}^{\infty}(\pm)^{\nu-1}\zeta^\nu b_\nu} . \tag{3.40}$$

Therefore Eq. (3.32) has the same implication to that of Eq. (3.37).

For ideal gas, $\log \Xi_0$ can be written as

$$\log \Xi_0=Q_V V+Q_A A , \tag{3.41}$$

in which both Q_V and Q_A do not depend on the volume V and the surface area A of the system. Thus we get the pressure p as the derivative of $\log \Xi_0$ with respect to the volume V, keeping the surface area A, the chemical potential μ $(\mu=kT\log\zeta)$ and the temperature T constant:

$$p=kT\left(\frac{\partial \log \Xi_0}{\partial V}\right)_{A,\mu,T} . \tag{3.42}$$

We also obtain the surface tension γ as the derivative of $\log \Xi_0/V$ with respect to the volume V, keeping A, μ and T constant:

$$\gamma A=kTV^2\left\{\frac{\partial}{\partial V}\left(\frac{\log \Xi_0}{V}\right)\right\}_{A,\mu,T} . \tag{3.43}$$

Even if there are interactions it can be shown that the above relations (Eqs. (3.42) and (3.43)) hold when Ξ_0 is replaced by Ξ. In this case (non-ideal gas) the explicit expression which corresponds to Eq. (3.25) for surface tension, becomes lengthy which will be published elsewhere. The equation of state becomes complicated, and we shall discuss, in the next section, its relation to the grand partition function.

§4. The Equation of State and the Grand Partition Function

We have seen in the foregoing sections that the formula for surface tension is rather complicated. The reason why the combination $pV-\gamma A$ yields simpler consequence lies in the fact that complicated contributions from the effect of surface on pressure and surface tension cancel out in this combination. To see the circumstances in more detail we have to investigate the pressure equation.

It should be noted that pressure, in general, depends on the surface area of the container.

Even if the wall does not exert any interaction on gas molecules, the volume available for the molecules is diminished if the molecules have hard cores. If the wall repells gas molecules the available volume is decreased and if it attracts molecules the effective number of molecules in gas state is decreased. These affect the pressure which would change proportionally to the surface area. Pressure is given by

$$p=-(\partial F/\partial V)_{A,T,N} \tag{4.1}$$

where the derivative is to be taken keeping the surface area A constant. For the system under consideration Toda's method[5)] gives (Appendix I)

$$pV=\left\{\mathrm{Tr}\,(2\sum_i H_{0z}(i)\rho)-\mathrm{Tr}\left(\sum_i z_i\frac{du_w(i)}{dz_i}\rho\right)-\mathrm{Tr}\left(\sum_{i<j}\frac{z_{ij}^2}{r_{ij}}\frac{du(i,j)}{dr_{ij}}\rho\right)\right\}\Big/\mathrm{Tr}\,\rho\,. \tag{4.2}$$

We make combination $pV-\gamma A$ from Eqs. (4.2) and (2.5), to get

$$pV-\gamma A=\left\{\mathrm{Tr}\,(2\sum_i H_{0x}(i)\rho)-\mathrm{Tr}\left(\sum_{i<j}\frac{x_{ij}^2}{r_{ij}}\frac{du(i,j)}{dr_{ij}}\rho\right)\right\}\Big/\mathrm{Tr}\,\rho\,. \tag{4.3}$$

This is much simpler than Eq. (2.5) or Eq. (4.2), because in the x-direction the system is periodic. In the second term in the right-hand side of Eq. (4.3), we may substitute ρ_0 for ρ just as discussed in Eq. (2.11).

On the other hand, on the assumption that the work done on the system is of the form $dW=-pdV+\gamma dA$ (cf. Eqs. (2.2) and (4.1)), thermodynamic argument leads to the theorem that

$$pV-\gamma A=kT\log\Xi$$

where Ξ denotes the grand partition function. For the case of ideal gas this relation is Eq. (3.21). When the potential energy is present, grand partition function Ξ becomes

$$\Xi=\sum_n^\infty\zeta^n\,\mathrm{Tr}\,\rho^{(n)}=\sum_n^\infty\zeta^n\,\mathrm{Tr}\left\{\left(1-\beta\sum_i^n u_w(i)-\beta\sum_{i<j}^n u(i,j)\right)\rho_0^{(n)}\right\}. \tag{4.4}$$

By the aid of Eqs. (3.26) and (3.27), we get[15)]

$$\begin{aligned}(pV-\gamma A)/kT=\log\Xi=\log\Xi_0&-\beta\sum_n\zeta^n n\,\mathrm{Tr}\,(u_w(1)\rho_0^{(n)})\\&-\beta\sum_n\zeta^n\frac{n(n-1)}{2}\,\mathrm{Tr}\,(u(1,2)\rho_0^{(n)})\,.\end{aligned} \tag{4.5}$$

It should be noted that Eq. (4.5) does not represent the surface tension, but is only a combination of pV and γA. In other words, the derivative of Eq. (4.5) with respect to A (surface area) does not give the surface tension, because the pressure p also depends on the surface area of container.

Eq. (4.3) which is derived from Toda's formula, must be identical with Eq. (4.5) obtained by the use of grand partition function. To verify this identity we shall evaluate Eqs. (4.5) and (4.3) as follows.

(i) Boltzmann Statistics

In Boltzmann statistics, Eq. (4.5) is written

$$\begin{aligned}(pV-\gamma A)/kT=\log\Xi_0&-\beta\zeta\int u_w(\boldsymbol{x})\rho_0(\boldsymbol{x};\boldsymbol{x}|\beta)\,d\boldsymbol{x}\\&-\frac{\beta}{2}\zeta^2\iint u(\boldsymbol{x}_1,\boldsymbol{x}_2)\rho_0(\boldsymbol{x}_1;\boldsymbol{x}_1|\beta)\rho_0(\boldsymbol{x}_2;\boldsymbol{x}_2|\beta)\,d\boldsymbol{x}_1\,d\boldsymbol{x}_2\,.\end{aligned} \tag{4.6}$$

The average number N of particles in the system is

$$N=\zeta\frac{\partial\log\Xi}{\partial\zeta}=\zeta\frac{\partial\log\Xi_0}{\partial\zeta}-\beta\zeta\int u_w(\boldsymbol{x})\rho_0(\boldsymbol{x};\boldsymbol{x}|\beta)\,d\boldsymbol{x}$$
$$-\beta\zeta^2\iint u(\boldsymbol{x}_1,\boldsymbol{x}_2)\rho_0(\boldsymbol{x}_1;\boldsymbol{x}_1|\beta)\rho_0(\boldsymbol{x}_2;\boldsymbol{x}_2|\beta)\,d\boldsymbol{x}_1\,d\boldsymbol{x}_2\,. \tag{4.7}$$

The first term in the right-hand side of Eq. (4.7) is by Eq. (3.19)

$$\zeta\lambda^{-3}(V-A\lambda/4)=\zeta f^{(1)}\,. \tag{4.8}$$

Thus the equation of state derived from the grand partition function becomes

$$\frac{pV-\gamma A}{kT}=N+N^2\frac{\beta}{2}\iint u(\boldsymbol{x}_1,\boldsymbol{x}_2)\rho_0(\boldsymbol{x}_1;\boldsymbol{x}_1|\beta)\,\rho_0(\boldsymbol{x}_2;\boldsymbol{x}_2|\beta)\,d\boldsymbol{x}_1\,d\boldsymbol{x}_2\Big/\{f^{(1)}\}^2 \tag{4.9}$$

higher order terms in u_w and u being neglected.

On the other hand, Eq. (4.3) becomes

$$pV-\gamma A=\frac{\mathrm{Tr}\,\{(1-\beta\sum_i u_w(i)-\beta\sum_{i<j}u(i,j))2NH_{0x}(1)\rho_0{}^{(N)}\}}{\mathrm{Tr}\,\{(1-\beta\sum_i u_w(i)-\beta\sum_{i<j}u(i,j))\rho_0{}^{(N)}\}}$$
$$-\frac{N(N-1)}{2}\frac{\iint\left\{x_1\dfrac{\partial u(1,2)}{\partial x_1}+x_2\dfrac{\partial u(1,2)}{\partial x_2}\right\}\rho_0(\boldsymbol{x}_1;\boldsymbol{x}_1|\beta)\rho_0(\boldsymbol{x}_2;\boldsymbol{x}_2|\beta)\,d\boldsymbol{x}_1\,d\boldsymbol{x}_2}{\{f^{(1)}\}^2}\,. \tag{4.10}$$

The numerator of the first term in the right-hand side of Eq. (4.10) can be evaluated by the aid of Eq. (3.9), and become just NkT times the denominator. The numerator in the second term can be integrated partially and becomes

$$\iint\left\{x_1\frac{\partial u}{\partial x_1}+x_2\frac{\partial u}{\partial x_2}\right\}\rho_0(\boldsymbol{x}_1;\boldsymbol{x}_1|\beta)\rho_0(\boldsymbol{x}_2;\boldsymbol{x}_2|\beta)\,d\boldsymbol{x}_1\,d\boldsymbol{x}_2$$
$$=2\Big\{L\iiint_{x_2<L}[u(\boldsymbol{x}_1,\boldsymbol{x}_2)]_{x_1=L}[\rho_0(\boldsymbol{x}_1;\boldsymbol{x}_1|\beta)]_{x_1=L}\,\rho_0(\boldsymbol{x}_2;\boldsymbol{x}_2|\beta)\,dy_1\,dz_1\,d\boldsymbol{x}_2$$
$$-\iint u(\boldsymbol{x}_1,\boldsymbol{x}_2)\,\rho_0(\boldsymbol{x}_1;\boldsymbol{x}_1|\beta)\,\rho_0(\boldsymbol{x}_2;\boldsymbol{x}_2|\beta)\,d\boldsymbol{x}_1\,d\boldsymbol{x}_2\Big\}\,. \tag{4.11}$$

The factor 2 in the above equation comes from the fact that the coordinate x_1 and x_2 play the same roles. The first term in the right-hand side of Eq. (4.11) gives the half value of the second term, thus we obtain

$$\frac{pV-\gamma A}{kT}=N+\frac{N(N-1)}{2}\beta\iint u(\boldsymbol{x}_1,\boldsymbol{x}_2)\,\rho_0(\boldsymbol{x}_1;\boldsymbol{x}_1|\beta)\,\rho_0(\boldsymbol{x}_2;\boldsymbol{x}_2|\beta)\,d\boldsymbol{x}_1\,d\boldsymbol{x}_2\Big/\{f^{(1)}\}^2\,. \tag{4.12}$$

We may put $N(N-1)\approx N^2$ for large N, thus the selfconsistency of two different methods is satisfied.

(ii) Quantum Statistics

In quantum statistics the verification of identity of two different methods (Eq. (4.3) and Eq. (4.5)) becomes much more cumbersome. For brevity's sake we put

$$\left.\begin{aligned}
b_\nu&=\int\rho_0(\boldsymbol{x};\boldsymbol{x}|\nu\beta)\,d\boldsymbol{x}\,,\\
w_\nu&=\int u_w(\boldsymbol{x})\,\rho_0(\boldsymbol{x};\boldsymbol{x}|\nu\beta)\,d\boldsymbol{x}\,,\\
u(\mu,\nu)&=\iint u(\boldsymbol{x}_1,\boldsymbol{x}_2)\begin{vmatrix}\rho_0(\boldsymbol{x}_1;\boldsymbol{x}_1|\mu\beta) & \rho_0(\boldsymbol{x}_1;\boldsymbol{x}_2|\nu\beta)\\ \rho_0(\boldsymbol{x}_2;\boldsymbol{x}_1|\mu\beta) & \rho_0(\boldsymbol{x}_2;\boldsymbol{x}_2|\nu\beta)\end{vmatrix}_\pm d\boldsymbol{x}_1\,d\boldsymbol{x}_2\,.
\end{aligned}\right\} \tag{4.13}$$

By Eqs. (3.26) and (3.27), Eq. (4.4) becomes

$$\Xi=\Xi_0\left\{1-\beta\sum_{\nu}(\pm)^{\nu-1}\zeta^{\nu}w_{\nu}-\frac{\beta}{2}\sum_{\mu,\nu}(\pm)^{\mu+\nu}\zeta^{\mu+\nu}u(\mu,\nu)\right\}. \tag{4.14}$$

Thus the thermodynamical relation derived from the grand partition function becomes

$$(pV-\gamma A)/kT=\log\Xi=\sum(\pm)^{\nu-1}\zeta^{\nu}b_{\nu}/\nu-\beta\sum(\pm)^{\nu-1}\zeta^{\nu}w_{\nu}-\frac{\beta}{2}\sum_{\mu,\nu}(\pm)^{\mu+\nu}\zeta^{\mu+\nu}u(\mu,\nu). \tag{4.15}$$

A more explicit expression of Eq. (4.15) is given in Appendix II.

On the other hand, Eq. (4.3) becomes

$$pV-\gamma A=\left[N\,\mathrm{Tr}\left\{(1-\beta\sum_{i}u_w(i)-\beta\sum_{i<j}u(i,j))2H_{0x}(1)\rho_0^{(N)}\right\}\right.$$
$$\left.-\frac{N(N-1)}{2}\mathrm{Tr}\left\{\frac{x_{12}^2}{r_{12}}\frac{du(1,2)}{dr_{12}}\rho_0^{(N)}\right\}\right]\Big/\mathrm{Tr}\,\rho^{(N)}. \tag{4.16}$$

The terms in the numerator of the right-hand side of Eq. (4.16) are calculated as the following. First, by Eq. (3.26) and Eqs. (3.4) and (3.5) with β substituted by $\nu\beta$, we get

$$\mathrm{Tr}(2H_{0x}(1)\rho_0^{(N)})=\frac{kT}{N}\sum(\pm)^{\nu-1}f^{(N-\nu)}(\beta)b_{\nu}/\nu. \tag{4.17}$$

Eq. (3.27) gives

$$N(N-1)\beta\int d\boldsymbol{x}_1[2H_{0x}(1)\rho_0^{(N)}(\boldsymbol{x}_1,\boldsymbol{x}_2;\boldsymbol{x}_1',\boldsymbol{x}_2)]_{\boldsymbol{x}_1=\boldsymbol{x}_1'}$$
$$=\sum_{\mu,\nu}(\pm)^{\mu+\nu}f^{(N-\mu-\nu)}(\beta)\left\{\frac{b_{\mu}}{\mu}\rho_0(\boldsymbol{x}_2;\boldsymbol{x}_2|\nu\beta)\pm\frac{1}{\mu+\nu}\rho_0(\boldsymbol{x}_2;\boldsymbol{x}_2|[\mu+\nu]\beta)\right\}$$
$$=\sum_{\mu,\nu}(\pm)^{\mu+\nu}f^{(N-\mu-\nu)}(\beta)\frac{b_{\mu}}{\mu}\rho_0(\boldsymbol{x}_2;\boldsymbol{x}_2|\nu\beta)+\sum_{s}(\pm)^{s-1}f^{(N-s)}(\beta)\left(1-\frac{1}{s}\right)\rho_0(\boldsymbol{x}_2;\boldsymbol{x}_2|s\beta) \tag{4.18}$$

where we have used the identity

$$\int\rho_0(\boldsymbol{x}_2;\boldsymbol{x}_1|\mu\beta)\rho_0(\boldsymbol{x}_1;\boldsymbol{x}_2'|\nu\beta)\,d\boldsymbol{x}_1=\rho_0(\boldsymbol{x}_2;\boldsymbol{x}_2'|[\mu+\nu]\beta).$$

Thus we get

$$N(N-1)\beta\,\mathrm{Tr}\,(u_w(2)2H_{0x}(1)\rho_0^{(N)})=\sum_{\mu,\nu}(\pm)^{\mu+\nu}f^{(N-\mu-\nu)}(\beta)\frac{b_{\mu}}{\mu}w_{\nu}$$
$$+\sum(\pm)^{s-1}f^{(N-s)}(\beta)w_s-\sum(\pm)^{s-1}f^{(N-s)}(\beta)\,w_s/s. \tag{4.19}$$

Similarly

$$N\beta\,\mathrm{Tr}\,(u_w(1)2H_{0x}(1)\rho_0^{(N)})=\sum(\pm)^{\nu-1}f^{(N-\nu)}(\beta)\,w_{\nu}/\nu. \tag{4.20}$$

To calculate terms including $u(i,j)$ we have to use

$$\rho_0^{(N)}(\boldsymbol{x}_1,\boldsymbol{x}_2,\boldsymbol{x}_3;\boldsymbol{x}_1',\boldsymbol{x}_2',\boldsymbol{x}_3')=\frac{1}{N(N-1)(N-2)}\sum_{\mu,\nu,\tau}^{\mu+\nu+\tau\leq N}(\pm)^{\mu+\nu+\tau-1}f^{(N-\mu-\nu-\tau)}(\beta)$$
$$\times\begin{vmatrix}\rho_0(\boldsymbol{x}_1;\boldsymbol{x}_1'|\mu\beta) & \rho_0(\boldsymbol{x}_1;\boldsymbol{x}_2'|\nu\beta) & \rho_0(\boldsymbol{x}_1;\boldsymbol{x}_3'|\tau\beta)\\ \rho_0(\boldsymbol{x}_2;\boldsymbol{x}_1'|\mu\beta) & \rho_0(\boldsymbol{x}_2;\boldsymbol{x}_2'|\nu\beta) & \rho_0(\boldsymbol{x}_2;\boldsymbol{x}_3'|\tau\beta)\\ \rho_0(\boldsymbol{x}_3;\boldsymbol{x}_1'|\mu\beta) & \rho_0(\boldsymbol{x}_3;\boldsymbol{x}_2'|\nu\beta) & \rho_0(\boldsymbol{x}_3;\boldsymbol{x}_3'|\tau\beta)\end{vmatrix}_{\pm}. \tag{4.21}$$

After some calculations we get

$$\frac{N(N-1)(N-2)}{2}\beta\,\mathrm{Tr}\,(u(2,3)2H_{0x}(1)\rho_0{}^{(N)})+N(N-1)\beta\,\mathrm{Tr}\,(u(1,2)2H_{0x}(1)\rho_0{}^{(N)})$$
$$+\frac{N(N-1)}{2}\,\mathrm{Tr}\left\{\frac{x_{12}{}^2}{r_{12}}\frac{du(1,2)}{dr_{12}}\rho_0{}^{(N)}\right\}$$
$$=\frac{1}{2}\sum_{\mu,\nu,\tau}(\pm)^{\mu+\nu+\tau-1}f^{(N-\mu-\nu-\tau)}(\beta)\frac{b_\mu}{\mu}u(\nu,\tau)+\frac{1}{2}\sum_{\nu,\tau}(\pm)^{\nu+\tau}f^{(N-\nu-\tau)}(\beta)u(\nu,\tau)\,. \qquad (4.22)$$

These together give

$$(pV-\gamma A)/kT=\Big\{\sum(\pm)^{\nu-1}f^{(N-\nu)}(\beta)(b_\nu/\nu-\beta w_\nu)$$
$$-\beta\sum(\pm)^{\mu+\nu}f^{(N-\mu-\nu)}(\beta)\frac{b_\mu}{\mu}w_\nu-\frac{\beta}{2}\sum(\pm)^{\mu+\nu+\tau-1}f^{(N-\mu-\nu-\tau)}(\beta)\frac{b_\mu}{\mu}u(\nu,\tau)$$
$$-\frac{\beta}{2}\sum(\pm)^{\nu+\tau}f^{(N-\nu-\tau)}(\beta)u(\nu,\tau)\Big\}\Big/\mathrm{Tr}\,\rho^{(N)}\,. \qquad (4.23)$$

Multiplying ζ^N to both the numerator and the denominator of the right-hand side of the above equation, we sum up over N. Thus the numerator in the right-hand side of Eq. (4.23) becomes

$$\Xi_0\Big\{\sum(\pm)^{\nu-1}\zeta^\nu b_\nu/\nu-\beta\sum(\pm)^{\nu-1}\zeta^\nu w_\nu-\beta\sum(\pm)^{\mu-1}\zeta^\mu b_\mu/\mu\sum(\pm)^{\nu-1}\zeta^\nu w_\nu$$
$$-\frac{\beta}{2}\sum(\pm)^{\nu+\tau}\zeta^{\nu+\tau}u(\nu,\tau)-\frac{\beta}{2}\sum(\pm)^{\nu+\tau}\zeta^{\nu+\tau}u(\nu,\tau)\sum(\pm)^{\mu-1}\zeta^\mu b_\mu/\mu\Big\}$$
$$=\Xi_0\Big\{\sum(\pm)^{\nu-1}\zeta^\nu b_\nu/\nu-\beta\sum(\pm)^{\nu-1}\zeta^\nu w_\nu-\frac{\beta}{2}\sum(\pm)^{\mu+\nu}\zeta^{\mu+\nu}u(\mu,\nu)\Big\}$$
$$\times\Big\{1-\beta\sum(\pm)^{\nu-1}\zeta^\nu w_\nu-\frac{\beta}{2}\sum(\pm)^{\mu+\nu}\zeta^{\mu+\nu}u(\mu,\nu)\Big\}\,, \qquad (4.24)$$

neglecting terms of the second order in u and w. The denominator gives $\Xi(\zeta)$ or

$$\Xi_0(\zeta)\Big\{1-\beta\sum(\pm)^{\nu-1}\zeta^\nu w_\nu-\frac{\beta}{2}\sum(\pm)^{\mu+\nu}\zeta^{\mu+\nu}u(\mu,\nu)\Big\}\,.$$

Then thermodynamical relation derived from Toda's method gives

$$(pV-\gamma A)/kT=\sum(\pm)^{\nu-1}\zeta^\nu b_\nu/\nu-\beta\sum(\pm)^{\nu-1}\zeta^\nu w_\nu-\frac{\beta}{2}\sum(\pm)^{\mu+\nu}\zeta^{\mu+\nu}u(\mu,\nu)\,. \qquad (4.25)$$

This is just the same to Eq. (4.15). The selfconsistency of two different methods, in quantum statistics, is thus satisfied.

§ 5. Formulation when Interaction has Hard Sphere Repulsion

If there exists strong repulsion between molecules at short range, Eq. (2.1) diverges because of the infinite value of potential energy, and we have to take into account the fact that the probability density $|\varphi(x)|^2$ becomes very small in the range $r-\sigma_0\ll\sigma_0$ (r is the relative distance between the centers of two molecules and σ_0 means geometrical diameter of the molecule). To avoid these difficult circumstances, we have introduced in the previous paper[14] effective diameter σ and the effective distance a which are related to the geometrical diameter σ_0 and to the geometrical distance a_0 respectively by

$$\sigma=\sigma_0+\lambda/2\sqrt{2}\,,\qquad a=a_0+\lambda/4 \qquad (5.1)$$

where a_0 means the classical distance of approach to the wall. That is, any molecule can not come closer to the wall than the distance a_0 because of the strong repulsion between a gas molecule and the wall.

In this section we shall assume the potential energies which have strong repulsions and weak attractions given by the following:

$$u_w(z)=\begin{cases} \infty & \text{for } 0\leq z\leq a\,, \\ v_w(z) & \text{for } a<z\,, \end{cases} \tag{5.2}$$

$$u(r)=\begin{cases} \infty & \text{for } 0\leq r\leq \sigma\,, \\ v(r) & \text{for } \sigma<r\,, \end{cases} \tag{5.3}$$

where a and σ are defined by Eq. (5.1). $u_w(z)$ stands for the interaction between a molecule and wall and $u(r)$ the mutual interaction between two molecules.

We shall calculate the effect of surface on the free energy given as[17)]

$$F=-kT\log B^{(1)}-\frac{kT}{2}N^2\frac{B^{(2)}}{(B^{(1)})^2} \tag{5.4}$$

where

$$B^{(1)}=\mathrm{Tr}\,\{\exp\,(-\beta[H_0(1)+u_w(1)])\}\,, \tag{5.5}$$

$$\begin{aligned} B^{(2)}=\mathrm{Tr}\,\{&\exp\,(-\beta[H_0(1)+H_0(2)+u(1,2)+u_w(1)+u_w(2)]) \\ &-\exp\,(-\beta[H_0(1)+u_w(1)])\exp\,(-\beta[H_0(2)+u_w(2)])\} \end{aligned} \tag{5.6}$$

in which $H_0(i)$ means the kinetic energy of the i-th molecule. As we assume that both $v_w(z)$ and $v(r)$ are small, we can use plane waves in the range $a<z$ and $\sigma<r$ as the eigenfunctions of molecules. Thus Eqs. (5.5) and (5.6) become

$$\begin{aligned} \lambda^3 B^{(1)}=A\int_a^{L_z}\exp\{-\beta v_w(z)\}\,dz+\frac{\hbar^2}{2m}A\int_a^{\infty}\Big[&-\frac{\beta^2}{6}\frac{d^2}{dz^2}v_w(z) \\ &+\frac{\beta^3}{12}\Big\{\frac{d}{dz}v_w(z)\Big\}^2\Big]\exp\{-\beta v_w(z)\}\,dz\,, \end{aligned} \tag{5.7}$$

$$\begin{aligned} \lambda^6 B^{(2)}=&\iint_{(V)}[\exp\{-\beta u(r)\}-1][\exp\{-\beta u_w(\boldsymbol{x}_1)-\beta u_w(\boldsymbol{x}_2)\}]\,d\boldsymbol{x}_1\,d\boldsymbol{x}_2 \\ &\pm\iint_{(V)}\exp(-2\pi r^2/\lambda^2)\exp\{-\beta u(r)\}[\exp\{-\beta u_w(\boldsymbol{x}_1)-\beta u_w(\boldsymbol{x}_2)\}]\,d\boldsymbol{x}_1\,d\boldsymbol{x}_2 \\ &\qquad+\frac{\hbar^2}{m}\iint_{(V)}\Big[-\frac{\beta^2}{6}\Big\{\frac{d^2}{dr^2}u(r)\Big\}+\frac{\beta^3}{12}\Big\{\frac{d}{dr}u(r)\Big\}^2\Big] \\ &\qquad\qquad\times\exp\{-\beta u(r)\}[\exp\{-\beta u_w(\boldsymbol{x}_1)-\beta u_w(\boldsymbol{x}_2)\}]\,d\boldsymbol{x}_1\,d\boldsymbol{x}_2 \\ &\equiv\lambda^6(B_0{}^{(2)}\pm B_{\pm}{}^{(2)}+B_{qu}{}^{(2)})\,. \end{aligned} \tag{5.8}$$

in which $r=|\boldsymbol{x}_2-\boldsymbol{x}_1|$.

If we assume the attractive energy between a gas molecule ($\boldsymbol{x}$) and a molecule in the wall ($\boldsymbol{x}_w$) to be of van der Waals type[12)], we get

$$v_w(z)=-\sum_w\frac{\text{const.}}{|\boldsymbol{x}-\boldsymbol{x}_w|^6}=\frac{-\mathcal{E}a^3}{z^3} \tag{5.9}$$

in which $-\mathcal{E}$ means the energy of a gas molecule when it touches the wall. Putting $-\beta\mathcal{E}=w$, we get from Eq. (5.7) the expansion

$$\begin{aligned} \lambda^3 B^{(1)}=V-Aa+Aa\Big(\frac{w}{2}+\frac{w^2}{10}+\frac{w^3}{48}+\cdots\Big) \\ +A\frac{1}{\pi}\frac{\lambda^2}{a}\Big(\frac{w}{8}+\frac{w^2}{112}+\frac{7}{160}w^3+\cdots\Big) \end{aligned} \tag{5.10}$$

and the first term in the right-hand side of Eq. (5.8) becomes

$$\lambda^6 B_0{}^{(2)} = A\int_0^{L_z} dz\Big[\sum_{\mu=0}^{\infty}\frac{(wa^3)^\mu}{z^3}\frac{1}{\mu!}\int_0^{z-a} 2\pi\sum_{\nu=0}^{\infty}\left\{\frac{(wa^3)^\nu}{(z-r)^{3\nu-1}}\frac{r}{\nu!}\frac{1}{3\nu-1}\right\}\{e^{\;\beta u(r)}-1\}\,dr$$
$$+\sum\frac{(wa^3)^\mu}{z^3}\frac{1}{\mu!}\int_{z-a}^{\infty} 2\pi\sum\left\{\frac{(wa^3)^\nu}{a^{3\nu-1}}\frac{r}{\nu!}\frac{1}{3\nu-1}\right\}\{e^{-\beta u(r)}-1\}\,dr$$
$$-\sum\frac{(wa^3)^\mu}{z^3}\frac{1}{\mu!}\int_0^{\infty} 2\pi\sum\left\{\frac{(wa^3)^\nu}{(z+r)^{3\nu-1}}\frac{r}{\nu!}\frac{1}{3\nu-1}\right\}\{e^{-\beta u(r)}-1\}\,dr\Big]. \tag{5.11}$$

Assuming that $v(r)$ is small, above equation is expanded in Appendix III. If we substitute $\exp(-2\pi r^2/\lambda^2)\exp(-\beta u)$ for $\{\exp(-\beta u)-1\}$ in integrand of Eq. (5.11), we can get $B_\pm{}^{(2)}$, and in the same way substituting

$$\frac{\hbar^2}{m}\left[-\frac{\beta^2}{6}\left\{\frac{d^2}{dr^2}u(r)\right\}+\frac{\beta^3}{12}\left\{\frac{d}{dr}u(r)\right\}^2\right]\exp(-\beta u) \qquad \text{for} \quad \{\exp(-\beta u)-1\}\,,$$

$B_{qu}{}^{(2)}$ can be obtained.

§ 6. Conclusion Remarks

In general, quantum statistical theory of gas is treated in the limit of infinite volume, keeping the density constant. Under the restriction of the volume to be finite, the integral region can not be extended to infinity. This circumstance makes the theory more cumbersome. For example, the integral of Gauss's error function $\phi(x)$ appears as is shown in Appendix, which has definite value $\phi(\infty)=1$ when the volume extends to infinity.

When the density of gas increases, our treatments are not suitable. However the circumstance that, in quantum statistics, the surface effect increases with the length of permutation rings will be valid even if the density becomes large.

The surface free energy is affected by the potential energy $u_w(z)$, which does not appear in the treatment of systems with infinite volume. When we make the gas in a vessel very dilute, it is observed that many molecules of the gas adhere to the boundary wall. This tendency may be intensified for large negative value of $u_w(z)$.

Acknowledgement

The author would like to express his sincere thanks to Professor M. Toda of Tokyo University of Education for valuable discussions, suggestions and advices through this work, and to Dr. T. Kotera for useful conversations.

Appendix I

Pressure p is given by

$$p = -\mathrm{Tr}\left\{\left(\frac{\delta H}{\delta V}\right)_A e^{-\beta H}\right\}\Big/\mathrm{Tr}\,(e^{-\beta H})\,. \tag{A.1.1}$$

For the system in the box with volume $V=L^2L_z$ and surface area $A=2L^2$, we write, according to Toda's method[5],

$$x=L\xi\,,\qquad y=L\eta\,,\qquad z=L_z\zeta \qquad (0\leq\xi,\eta,\zeta\leq 1)$$
$$r_{ij}{}^2=L^2(\xi_{ij}{}^2+\eta_{ij}{}^2)+L_z{}^2\zeta_{ij}{}^2\,. \tag{A.1.2}$$

Hamiltonian becomes then

$$H=-\frac{\hbar^2}{2m}\sum_i \nabla_i{}^2+\sum_i u_w(z_i)+\sum_{i<j}u(r_{ij})$$
$$=-\frac{\hbar^2}{2mL^2}\sum_i\left(\frac{\partial^2}{\partial\xi_i{}^2}+\frac{\partial^2}{\partial\eta_i{}^2}\right)-\frac{\hbar^2}{2mL_z{}^2}\sum_i\frac{\partial^2}{\partial\zeta_i{}^2}+\sum_i u_w(L_z\zeta_i)$$
$$+\sum_{i<j}u(\sqrt{L^2(\xi_{ij}{}^2+\eta_{ij}{}^2)+L_z{}^2\zeta_{ij}{}^2}\,)\,. \tag{A.1.3}$$

Keeping A constant we differentiate H:

$$\delta L=0\ ,\qquad \delta V=L^2\delta L_z$$

$$\begin{aligned}\frac{\delta H}{\delta V}&=\frac{1}{L^2}\left\{\frac{1}{L_z}\frac{\hbar^2}{mL_z^2}\sum_i\frac{\partial^2}{\partial\zeta_i^2}+\sum_i\zeta_i\frac{du_w(i)}{dz_i}+\sum_{i<j}\frac{L_z}{r_{ij}}\zeta_{ij}^2\frac{du(i,j)}{dr_{ij}}\right\}\\&=\frac{1}{V}\left\{\frac{\hbar^2}{m}\sum\frac{\partial^2}{\partial z^2}+\sum z_i\frac{du_w(i)}{dz_i}+\sum\frac{z_{ij}^2}{r_{ij}}\frac{du(i,j)}{dr_{ij}}\right\}\ .\end{aligned}\tag{A.1.4}$$

Thus (A.1.1) gives Eq. (4.2).

If we impose the condition that wave functions vanish at $x=0, L$ and $y=0, L$ instead of the periodic condition we have $A=2L^2+4LL_z$. However, as we assume that $L\gg L_z$, the result does not change as is easily verified.

Appendix II

The grand partition function can be written as follows

$$\begin{aligned}\Xi&=\Xi_0\left\{1-\beta\int u_w(\boldsymbol{x}_1)\,\sigma(\boldsymbol{x}_1,\boldsymbol{x}_1)\,d\boldsymbol{x}_1+\frac{1}{2}\beta\iint u(\boldsymbol{x}_1,\boldsymbol{x}_2)\begin{vmatrix}\sigma(\boldsymbol{x}_1,\boldsymbol{x}_1)&\sigma(\boldsymbol{x}_1,\boldsymbol{x}_2)\\\sigma(\boldsymbol{x}_2,\boldsymbol{x}_1)&\sigma(\boldsymbol{x}_2,\boldsymbol{x}_2)\end{vmatrix}_\pm d\boldsymbol{x}_1\,d\boldsymbol{x}_2\right\}\\&=\Xi_0\{1-\beta Q\}\end{aligned}\tag{A.2.1}$$

where

$$Q=\sum_p u_{w\cdot pp}\,g_p+\frac{1}{2}\sum_p\sum_q g_pg_q(u_{pq\cdot pq}+u_{pq\cdot qp})\tag{A.2.2}$$

in which

$$\sigma(\boldsymbol{x},\boldsymbol{x}')=\sum_k g_k\varphi_k^*(\boldsymbol{x}')\varphi_k(\boldsymbol{x})\tag{A.2.3}$$

$$g_k=\{\zeta^{-1}\exp(\beta E_k)\mp1\}^{-1}\tag{A.2.4}$$

and

$$\begin{aligned}u_{w\cdot pq}&=\int\varphi_p^*(\boldsymbol{x})u_w(\boldsymbol{x})\varphi_q(\boldsymbol{x})\,d\boldsymbol{x}\\u_{pq\cdot rs}&=\iint\varphi_p^*(\boldsymbol{x}_1)\varphi_q^*(\boldsymbol{x}_2)u(\boldsymbol{x}_1,\boldsymbol{x}_2)\varphi_r(\boldsymbol{x}_1)\varphi_s(\boldsymbol{x}_2)\,d\boldsymbol{x}_1\,d\boldsymbol{x}_2\ ,\end{aligned}\tag{A.2.5}$$

$\varphi(\boldsymbol{x})$ is eigenfunction of a molecule. Thus the equation of state becomes

$$pV-\gamma A=kT\log\Xi_0-Q\ .\tag{A.2.6}$$

The first term in the right-hand side of Eq. (A.2.2) is

$$\sum_{n_x,n_y,n_z}\frac{1}{\zeta^{-1}\exp\left\{\frac{\pi}{4}\lambda^2\left(\frac{n_x^2}{L_x^2}+\frac{n_y^2}{L_y^2}+\frac{n_z^2}{L_z^2}\right)\right\}\mp1}\frac{A}{\lambda^2}\frac{2}{L_z}\int_0^{L_z}u_w(z)\sin^2\frac{\pi n_z}{L_z}z\,dz\tag{A.2.7}$$

and considering that $u_w(z)$ does not vanish only when z or L_z-z is small, we get

$$\sum_p g_pu_{w\cdot pp}=\frac{1}{\lambda^3}\sum(\pm)^{\nu-1}\frac{\zeta^\nu}{\nu^{3/2}}A\int_0^\infty u_w(z)\{1-\exp(-4\pi z^2/\nu\lambda^2)\}\,dz\ .\tag{A.2.8}$$

In the calculation of the second and the third terms of Eq. (A.2.2), we use the spherical coordinate for $\boldsymbol{x}_2$, and the volume integral of a function takes the form

$$\begin{aligned}\iint_{(V)}F\,d\boldsymbol{x}_1\,d\boldsymbol{x}_2&=\int_0^{L_z}dz_1A\iint F\,2\pi r^2\sin\theta\,dr\,d\theta\\&=A\int_0^{L_z}dz_1\left\{\int_0^{z_1}2\pi r^2\,dr\int_0^\pi F\sin\theta\,d\theta+\int_{z_1}^\infty2\pi r^2\,dr\int_{\cos^{-1}(z/r)}^\pi F\sin\theta\,d\theta\right\}\ .\end{aligned}\tag{A.2.9}$$

Thus we obtain after some calculations

$$\begin{aligned}\frac{1}{2}\sum_{p}\sum_{q} g_p g_q u_{pq\cdot pq} &= \frac{1}{2}\frac{1}{\lambda^6}\sum_{\mu}\sum_{\nu}(\pm)^{\mu+\nu}\frac{\zeta^\mu}{\mu^{3/2}}\frac{\zeta^\nu}{\nu^{3/2}}A\int_0^\infty \{1-\exp(-4\pi z^2/\mu\lambda^2)\}\,dz \\ &\times\Bigg[\int_0^\infty u(r)2\pi r^2\,dr\Bigg\{2-\frac{\lambda\sqrt{\nu}}{4r}\phi\Bigg(\frac{2\sqrt{\pi}}{\lambda\sqrt{\nu}}[z+r]\Bigg)\Bigg\} \\ &+\int_0^z u(r)2\pi r^2\,dr\,\frac{\lambda\sqrt{\nu}}{4r}\phi\Bigg(\frac{2\sqrt{\pi}}{\lambda\sqrt{\nu}}[z-r]\Bigg)+\int_z^\infty u(r)2\pi r^2\,dr\Bigg(\frac{z}{r}-1\Bigg)\Bigg],\end{aligned}\tag{A.2.10}$$

$$\left.\begin{aligned}&\text{where}\qquad \phi(x)=\frac{2}{\sqrt{\pi}}\int_0^\infty \exp(-s^2)\,ds \\ &\text{with}\qquad \phi(\infty)=1 \quad\text{and}\quad \phi(0)=0\,.\end{aligned}\right\}\tag{A.2.11}$$

The third term in the right-hand side of Eq. (A.2.2) is

$$\begin{aligned}\frac{1}{2}\sum_{p}\sum_{q} g_p g_q u_{pq\cdot qp} &= \frac{1}{2}\frac{1}{\lambda^6}\sum_{\mu}\sum_{\nu}(\pm)^{\mu+\nu}\frac{\zeta^\mu}{\mu^{3/2}}\frac{\zeta^\nu}{\nu^{3/2}}A\int_0^\infty dz \\ &\times\Bigg[\int_0^\infty u(r)2\pi r^2\,dr\exp\Bigg(-\frac{\pi}{\lambda^2}\Bigg[\frac{1}{\mu}+\frac{1}{\nu}\Bigg]r^2\Bigg)\Bigg\{2+\frac{\lambda^2\mu}{4\pi zr}\exp\Bigg(-\frac{\pi}{\lambda^2}\frac{4}{\mu}[z^2+zr]\Bigg) \\ &+\frac{\lambda^2\nu}{4\pi zr}\exp\Bigg(-\frac{\pi}{\lambda^2}\frac{4}{\nu}[z^2+zr]\Bigg)-\frac{\lambda^2\mu\nu}{4\pi zr(\mu+\nu)}\exp\Bigg(-\frac{4\pi}{\lambda^2}\Bigg[\frac{1}{\mu}+\frac{1}{\nu}\Bigg][z^2+zr]\Bigg)\Bigg\} \\ &+\int_0^z u(r)2\pi r^2\,dr\exp\Bigg(-\frac{\pi}{\lambda^2}\Bigg[\frac{1}{\mu}+\frac{1}{\nu}\Bigg]r^2\Bigg)\Bigg\{-\frac{\lambda^2\mu}{4\pi zr}\exp\Bigg(-\frac{\pi}{\lambda^2}\frac{4}{\mu}[z^2-zr]\Bigg) \\ &-\frac{\lambda^2\nu}{4\pi zr}\exp\Bigg(-\frac{\pi}{\lambda^2}\frac{4}{\nu}[z^2-zr]\Bigg)+\frac{\lambda^2\mu\nu}{4\pi zr(\mu+\nu)}\exp\Bigg(-\frac{4\pi}{\lambda^2}\Bigg[\frac{1}{\mu}+\frac{1}{\nu}\Bigg][z^2-zr]\Bigg)\Bigg\} \\ &+\int_z^\infty u(r)2\pi r^2\,dr\exp\Bigg(-\frac{\pi}{\lambda^2}\Bigg[\frac{1}{\mu}+\frac{1}{\nu}\Bigg]r^2\Bigg)\Bigg\{\frac{z}{r}-1-\frac{\lambda^2}{4\pi zr}(\mu+\nu)+\frac{\lambda^2\mu\nu}{4\pi zr(\mu+\nu)}\Bigg\}\Bigg].\end{aligned}\tag{A.2.12}$$

Thus the equation of state $pV-\gamma A$ is obtained from Eqs. (A.2.6), (A.2.8), (A.2.10) and (A.2.12).

Appendix III

By the use of Eq. (5.3) and Eq. (5.9) can be written as follows

$$\begin{aligned}\lambda^6 B_0^{(2)} = A\int_{a+\sigma}^{L_z} dz\,2\pi\Bigg\{&\int_\sigma^{z-a} dr\sum_{\mu=0}^\infty\frac{(wa^3)^\mu}{z^{3\mu}}\frac{1}{\mu!}\sum_{\nu=0}^\infty\frac{(wa^3)^\nu}{(z-r)^{3\nu-1}}\frac{r}{\nu!}\frac{1}{3\nu-1}\sum_{\tau=1}^\infty\frac{[v^*(r)]^\tau}{\tau!} \\ &+\int_{z-a}^\infty dr\sum\frac{(wa^3)^\mu}{z^{3\mu}}\frac{1}{\mu!}\sum\frac{(wa^3)^\nu}{a^{3\nu-1}}\frac{r}{\nu!}\frac{1}{3\nu-1}\sum\frac{[v^*(r)]^\tau}{\tau!} \\ &-\int_\sigma^\infty dr\sum\frac{(wa^3)^\mu}{z^{3\mu}}\frac{1}{\mu!}\sum\frac{(wa^3)^\nu}{(z+r)^{3\nu-1}}\frac{r}{\nu!}\frac{1}{3\nu-1}\sum\frac{[v^*(r)]^\tau}{\tau!}\Bigg\} \\ -A\int_{a+\sigma}^{L_z} dz\,2\pi\Bigg\{&\int_0^\sigma dr\sum\frac{(wa^3)^\mu}{z^{3\mu}}\frac{1}{\mu!}\sum\frac{(wa^3)^\nu}{(z-r)^{3\nu-1}}\frac{r}{\nu!}\frac{1}{3\nu-1} \\ &-\int_0^\sigma dr\sum\frac{(wa^3)^\mu}{z^{3\mu}}\frac{1}{\mu!}\sum\frac{(wa^3)^\nu}{(z+r)^{3\nu-1}}\frac{r}{\nu!}\frac{1}{3\nu-1}\Bigg\} \\ +A\int_a^{a+\sigma} dz\,2\pi\Bigg\{&\int_\sigma^\infty dr\sum\frac{(wa^3)^\mu}{z^{3\mu}}\frac{1}{\mu!}\sum\frac{(wa^3)^\nu}{a^{3\nu-1}}\frac{r}{\nu!}\frac{1}{3\nu-1}\sum\frac{[v^*(r)]^\tau}{\tau!} \\ &-\int_\sigma^\infty dr\sum\frac{(wa^3)^\mu}{z^{3\mu}}\frac{1}{\mu!}\sum\frac{(wa^3)^\nu}{(z+r)^{3\nu-1}}\frac{r}{\nu!}\frac{1}{3\nu-1}\sum\frac{[v^*(r)]^\tau}{\tau!}\Bigg\} \\ -A\int_a^{a+\sigma} dz\,2\pi\Bigg\{&\int_0^{z-a} dr\sum\frac{(wa^3)^\mu}{z^{3\mu}}\frac{1}{\mu!}\sum\frac{(wa^3)^\nu}{(z-r)^{3\nu-1}}\frac{r}{\nu!}\frac{1}{3\nu-1}\end{aligned}$$

$$+\int_{z-a}^{\sigma} dr \sum \frac{(wa^3)^\mu}{z^{3\mu}} \frac{1}{\mu!} \sum \frac{(wa^3)^\nu}{a^{3\nu-1}} \frac{r}{\nu!} \frac{1}{3\nu-1}$$

$$\left. -\int_0^{\sigma} dr \sum \frac{(wa^3)^\mu}{z^{3\mu}} \frac{1}{\mu!} \sum \frac{(wa^3)^\nu}{(z+r)^{3\nu-1}} \frac{r}{\nu!} \frac{1}{3\nu-1} \right\}, \tag{A.3.1}$$

where $v^*(r) \equiv -\beta v(r)$ is the function of r. If we put $w=0$ and $v^*=0$ (hard sphere particle), Eq. (A.3.1) becomes

$$\lambda^6 B_0^{(2)} = \frac{4\pi}{3}\sigma^3 V + A\pi\left(\frac{\sigma^4}{4} + \frac{4}{3}\sigma^3 a\right). \tag{A.3.2}$$

This formula is identical with the result of our previous paper[14].

$\lambda^6 B_\pm^{(2)}$ is a small quantity, in which we have only to calculate the hard sphere part and becomes

$$\begin{aligned} \lambda^6 B_\pm^{(2)} = {} & V\sigma\lambda^2 \exp(-2\pi\sigma^2/\lambda^2) + \frac{\lambda^3}{4\sqrt{2}}(V-aA) \\ & - A\sigma a\lambda^2 \exp(-2\pi\sigma^2/\lambda^2) - \frac{\lambda^3}{4\sqrt{2}} A\sigma\phi(\sqrt{2\pi}\,\sigma/\lambda) \\ & - A\sigma^2 \frac{\lambda^2}{4} \exp(-2\pi\sigma^2/\lambda^2) + \frac{\lambda^3 A}{4\sqrt{2}} \int_{\sigma}^{L_z-a} \phi(\sqrt{2\pi}\, s/\lambda)\, ds \end{aligned} \tag{A.3.3}$$

in which ϕ was defined in Eq. (A.2.11). In the high temperature approximation ($\lambda \ll \sigma$), we may put $\phi(\sqrt{2\pi}\,\sigma/\lambda) \approx 1$, and Eq. (A.3.3) becomes

$$\lambda^6 B_\pm^{(2)} \approx A(L_z-a-\sigma)\lambda^3/2\sqrt{2}\ . \tag{A.3.4}$$

This formula is identical with the term in the virial coefficient due to exchange of two free particles in the volume $A(L_z-a-\sigma)$.

$\lambda^6 B_{qu}^{(2)}$ can be obtained substituting

$$\sum_{\tau=0}^{\infty} \frac{\hbar^2}{m} \left\{ -\frac{\beta^2}{6} \frac{1}{(\tau-2)!} v^{*\tau-2}(v^{*\prime})^2 - \frac{\beta^2}{6} \frac{1}{(\tau-1)!} v^{*\tau-1} v^{*\prime\prime} + \frac{\beta^3}{12} \frac{\tau}{(\tau-1)!} (v^{*\tau-1})^2 (v^{*\prime})^2 \right\} \tag{A.3.5}$$

for $\sum_{\tau=1}^{\infty} [v^*(r)]^\tau/\tau!$ in the integrand of Eq. (A.3.5) and omitting the terms which do not include $\sum_{\tau=1}^{\infty} [v^*(r)]^\tau/\tau!$. In Eq. (A.3.5) $v^{*\prime}$ and $v^{*\prime\prime}$ represent the first and the second order derivatives of $-\beta v(r)$ respectively with respect to variable r.

References

1) M. L. Goldberger and E. N. Adams: J. Chem. Phys. **20** (1951) 240.
2) S. Katsura: Progr. Theor. Phys. **16** (1956) 589.
3) K. Ikeda: Progr. Theor. Phys. **19** (1958) 653.
4) M. Toda: J. Phys. Soc. Japan **10** (1955) 512. S. Ono: Handbuch der Physik **X** (1960) 237.
5) M. Toda: *On the Virial Theorem* dated 1943, which was included in *Recent Problems in Physics* (in Japanese), 1948, Iwanami Press, Tokyo, Japan. H. S. Green: *Molecular Theory of Fluids*, 1952.
6) K. R. Atkins: Canad. J. Phys. **31** (1953) 1165.
7) D. R. Lovejoy: Canad. J. Phys. **33** (1955) 49.
8) S. K. Trikha and O. P. Rustgi: Progr. Theor. Phys. **15** (1956) 296; **17** (1957) 303.
9) D. S. Kothari and F. C. Auluck: Nature, Lond. **159** (1947) 204.
10) S. Ono: J. Chem. Phys. **18** (1950) 397; J. Phys. Soc. Japan **6** (1951) 10.
11) F. P. Buff and F. H. Stillinger: J. Chem. Phys. **25** (1956) 312.
12) W. A. Steele and G. D. Halsey, JR.: J. Chem. Phys. **22** (1954) 979; J. Phys. Chem. **59** (1955) 57.
13) M. P. Freeman and G. D. Halsey, JR.: J. Phys. Chem. **59** (1955) 181.
14) T. Tsuzuki: J. Phys. Soc. Japan **15** (1960) 2197.
15) K. Husimi: Proc. Phys. Math. Soc. Japan **22** (1940) 264.
16) H. Ichimura: Progr. Theor. Phys. **11** (1954) 374, 385, 519.
17) T. Yokota: J. Phys. Soc. Japan **15** (1960) 779.

JOURNAL OF THE PHYSICAL SOCIETY OF JAPAN, Vol. 16, No. 3, MARCH, 1961

Effects of the Special Heat-treatment on Permalloys

By Sadami TOMITA

Kinzoku Kogyo Kenkyusho

(Received June 6, 1959, Revised November 29, 1960)

The magnetic property and the electrical resistance of Mumetal and 50-permalloy were measured after low temperature heat-treatment ranging from 200°C to 600°C. It is observed that the maximum permeability of Mumetal is remarkably increased by this heat-treatment. These results can not be explained simply by the existing theories proposed by Néel et al. From the comparison between experimental results obtained in binary permalloy and polynary permalloy and the analysis of the relation between the maximum permeability and the electrical resistance, we introduce the idea of inhomogeneous internal structure to explain the change of μ_0, μ_m of permalloys by this low temperature heat-treatment.

§ 1. Introduction

In the alloy of Fe–Ni–Mo, Fe–Ni–Cu–Mo, it is known that the permeability of these alloys is sensitive to the heat-treatment at a relatively low temperature, and it was reported that the specific resistance of Ultraperm[1] was changed by the low temperature heat-treatment. In these high permeability alloys, the dependence of permeability and electrical resistace on the heat-treatment can not be explained satisfactorily in terms of "superlattice-transformation"[2]. By using two high permeability alloys, namely, Mumetal and 50-permalloy, we measured the magnetic properties and the electrical resistance, and then we try to explain the experimental results.

§ 2. Experimental Method

Specimen: We prepared two kinds of high permeability alloy, namely, (1) 50–Ni–Fe alloy (binary alloy) and (2) Mumetal (Ni; 77% Fe; 16% Cu; 5% Cr; 2%). We used high purity electrolytic nickel, electrolytic iron and other electrolytic elements. They were melted carefully in vacuum. The test samples were punched in the ring-form with 0.6 m/m thickness for Mumetal and 0.35 m/m thickness for 50-permalloy. The mechanical stress due to cold-working was released by an annealing at high temperature. To protect them from oxidation and reduce non-metalic impurities, test samples were annealed at about 1100°C in an atmosphere of pure hydrogen gas. In this way, the scattering of the values of magnetic properties i. e. μ_0, μ_m of each sample was limited within 5%.

Measurement: The magnetic property was measured by the ballistic-galvanometer-method. The specific electrical resistance was measured by the potentiometer, using the knifeedge as a contact with the specimen.

§ 3. Experimental Results

After the annealing at 1100°C, the sample were reheated to 650°C in the non-inductive furnace of small heat capacity, held for 1 hr. at this temperature, and then rapidly cooled in the furnace with the mean cooling rate of about 600°C/hr.. After this treatment, the samples were again heated rapidly in the same furnace to each temperature, ranging from 200°C to 650°C, in order to observe its annealing effect. The samples were annealed for 1 hr. at each temperature.

Fig. 1 shows initial permeability μ_0, maximum permeability μ_m and the fractional change of electrical resistance $\Delta\rho/\rho$ (%) as a function of annealing temperature in the case of Mumetal. The $\Delta\rho/\rho$-value increases in the temperature range from 300°C to 500°C and then decreases from 500°C to 600°C. The decrease of the $\Delta\rho/\rho$ in the range from 500°C to 600°C has not been observed in the case of Ultraperm[3]. The μ_0-curve has a steep maximum at 520°C.

The μ_m-curve is more complicated than the μ_0-curve. The maximum permeability shows a sharp maximum value nearly at the temperature of 400°C which is lower than the Curie-point of Mumetal, 440°C. Another maximum is nearly at 500°C. The minimum point of the μ_m-curve occurs nearly at the Curie-point of this material. The shape of the μ_m-curve is similar to that of $\Delta\rho/\rho$-curve in the whole range of temperature, except the range from 500°C to 600°C where the μ_m-curve has a broad maximum. But, if we plot the magnetic induction value $B_{\mu_m}=\mu_m\cdot H_{\mu_m}$ at the state of maximum permeability instead of μ_m-value, it is noticeable that the temperature-dependence of the B_{μ_m} coincides with that of the $\Delta\rho/\rho$, as shown in Fig. 5.

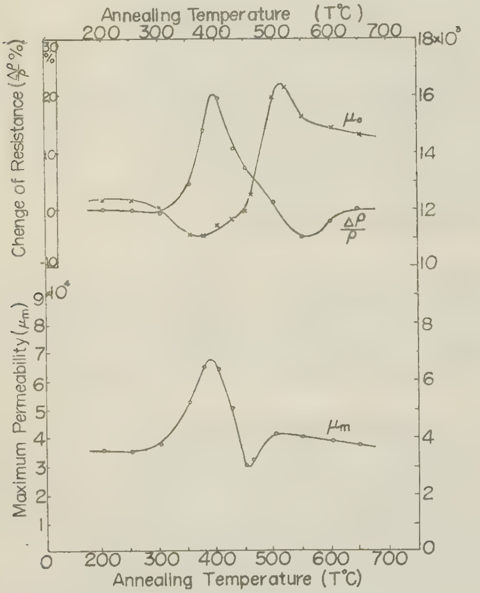

Fig. 1. μ_0, μ_m and $\Delta\rho/\rho$ for Mumetal. The samples were held for 1 hr. at each temperature after rapidly cooled from 650°C.

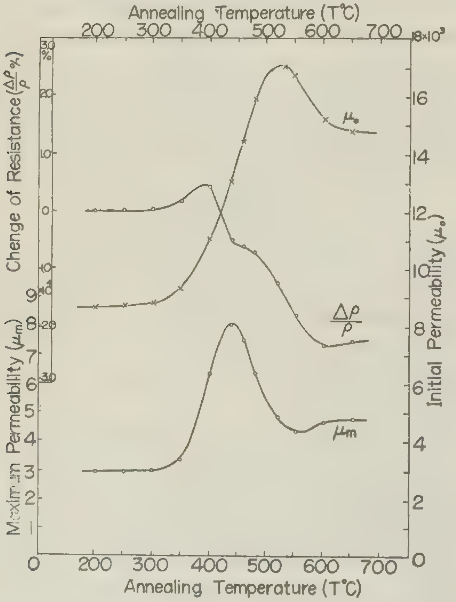

Fig. 2. μ_0, μ_m and $\Delta\rho/\rho$ for Mumetal. The samples were held for 1 hr. at each temperature after cooling in a furnace.

Fig. 2 shows the results which we obtained by the different heat-treatment; i. e. the samples were furnace-cooled before the low temperature heat-treatment. The mean cooling rate of the furnace cooling was about 100°C/hr. between 600°C and 300°C, and the final heat-treatment is the same with the above case.

The curves were not affected by the heat-treatment below 300°C as shown in the figure. The $\Delta\rho/\rho$-curve has a small maximum at about 400°C which coincides with that of Fig. 1. But, the shapes of $\Delta\rho/\rho$-curve in Fig. 1 and Fig. 2, differ from each other. This phenomena at the temperature range from 350°C to 550°C is remarkable. The μ_m-curve has the maximum at 440°C and falls down with slow slope at about 500°C. On the other hand, the μ_0-curve has the maximum at 520°C similarly to the case of Fig. 1. In Fig. 2, the temperature corresponding the peak of $\Delta\rho/\rho$ and μ_m-curve does not coincide, but if we plot the B_{μ_m} instead of μ_m as shown in Fig. 5 (b), the maximum point of this curve coincides with that of $\Delta\rho/\rho$ in Fig. 2 nearly at 400°C, and also the minimum point coin-

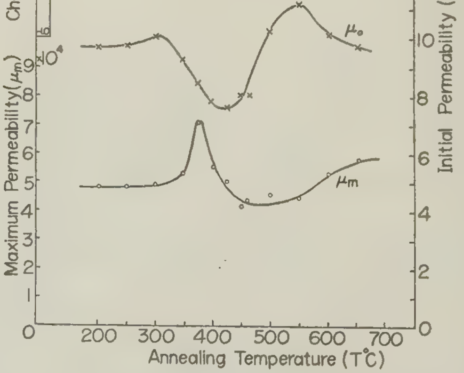

Fig. 3. μ_0, μ_m and $\Delta\rho/\rho$ for Mumetal. The samples were held for 1.5 hr. at 400°C in addition to the heat-treatment for the case of Fig. 1. The $\Delta\rho/\rho$-values are given by adding the change by the heat-treatment at 400°C to that by the initial heat-treatment.

cides at 550°C.

Fig. 3 shows the results of the superposed heat-treatment by the additive annealing for 1.5 hr. at 400°C, giving the largest change of $\varDelta\rho/\rho$ and μ_m. Specimens are initially heat-treated in the same way as in the case of Fig. 1.

The $\varDelta\rho/\rho$-values were obtained by adding the change of resistance by this heat-treatment to those $\varDelta\rho/\rho$-value in Fig. 1. The relation between the increase or decrease of permeability and electrical resistance is complicated by the initial heat-treatment. Namely, in the case of the initial heat-treatment at temperature below 350°C and above 600°C, the change of $\varDelta\rho/\rho$-value by the additive heat-treatment is simple, but in the rest range of temperature, the rate of increasing of $\varDelta\rho/\rho$-value by the additive heat-treatment is not uniform. The μ_0 decreases by the additive heat-treatment at the whole range. But, the μ_m increases by the additive heat-treatment, except for case in which the initial heat-treatment is carried out near 400°C.

Fig. 4 shows the results in the case of 50-permalloy which was annealed for 15 hrs. at each temperature ranging from 350°C to 600°C. The effect of the heat-treatment for few hours on this alloy is not so conspicuous as for Mumetal.

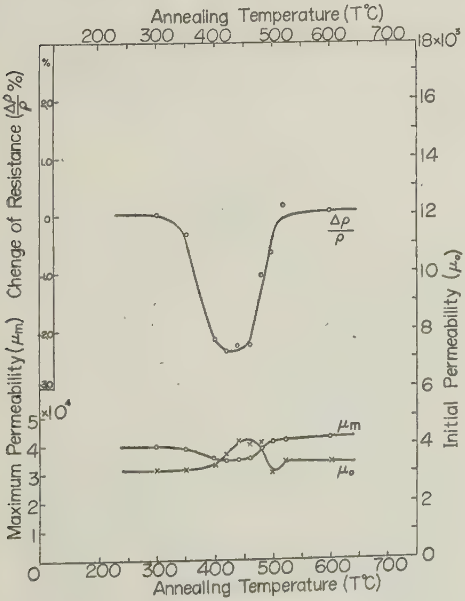

Fig. 4. μ_0, μ_m and $\varDelta\rho/\rho$ for 50-permalloy. The samples were annealed for 15 hrs. at each temperature.

The initial permeability increases ranging from 420°C to 480°C and decreases at 500°C slightly. The maximum permeability decreases ranging from 350°C to 500°C. But these changes are smaller than those in Mumetal. As shown Fig. 4, the fractional change of electrical resistance is similar to the change of the maximum permeability, and the electrical resistance decreases ranging from 350°C to 500°C. These results resemble to 75-permalloy's.

In our experimental results as shown above, we have attached great importance to the fact that the change of maximum permeability caused by the special heat-treatment is analogous to change of electrical resistance. As characteristic quantities for the magnetized state at maximum permeability, we have tried to use the B_{μ_m} and H_{μ_m}-value instead of μ_m-value. We show these values given as a function of annealing temperature in Fig. 5. The B_{μ_m} and H_{μ_m} are obtained by the relation of $\mu_m = B_{\mu_m}/H_{\mu_m}$ from the B-H curve, and

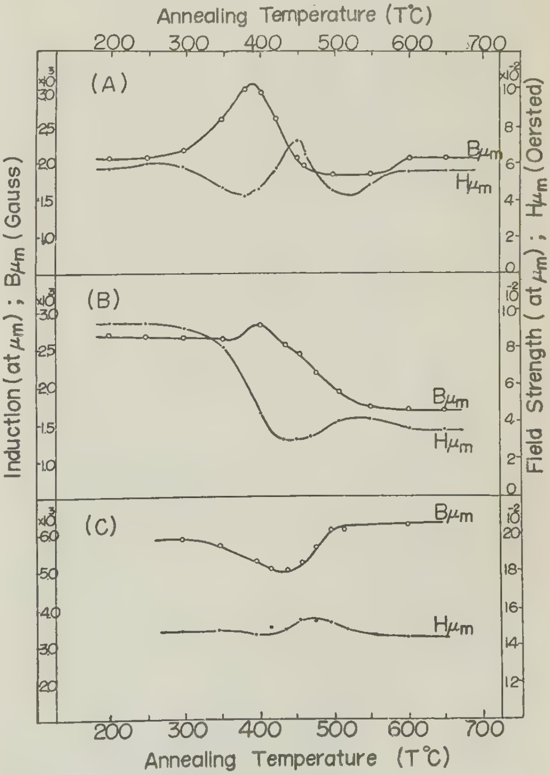

Fig. 5. $H_{\mu m}$ and $B_{\mu m}$-curves: (A) corresponds to μ_m-curve of Fig. 1, (B) corresponds to μ_m-curve of Fig. 2, and (C) corresponds to μ_m-curve of Fig. 4.

each of curves in the figure corresponds to the μ_m-curve of Figs. 1, 2, 4 respectively.

It is noticeable that the variation of the B_{μ_m} in Fig. 5 as a function of the temperature of the heat-treatment is similar to that of $\Delta\rho/\rho$ in Figs. 1, 2, 4. Regarding the variation of maximum permeability, we can find that the peak of the μ_m-curve at 400°C in Fig. 1, corresponds to the highest B_{μ_m} and the small H_{μ_m}, the minimum of μ_m-curve at 450°C to the largest H_{μ_m} and the small peak of μ_m-curve at 520°C to the small H_{μ_m}. The H_{μ_m}-curve for the samples furnace-cooled before the low temperature heat-treatment shows steep slope at the temperature range below the Curie-point, 440°C, and we can find that the peak of μ_m-curve at 440°C is induced by the minimum of H_{μ_m}-value, and the low value of μ_m at 550°C is induced by the increasing H_{μ_m} and the decreasing B_{μ_m}. From the curves illustrated in (C), we can find that the lowering of μ_m between 400°C and 500°C in 50-permalloy, is mainly induced by the lowering of the B_{μ_m}.

§ 4. Discussion

The magnetic properties and the electrical resistance of Mumetal and 50-permalloy are changed remarkably by the low temperature heat-treatment. The correlation between the magnetic property and electrical resistance affected by the special heat-treatment on permalloy have been interpreted by the idea of an atom-ordering[4]. For example, in the case of 79-permalloy[5], the origin of high permeability and high electrical resistance obtained by a rapid cooling from 600°C was explained by the freezing of the disordered phase. However, our experimental results show that such an explanation is not satisfactory for the general kind of permalloy. Namely, in the case of polynary permalloy such as Mumetal, the affected electrical resistance is not always decreased by the heat-treatment in the temperature range of atom-ordering, and is remarkably increased by the annealing near by the Curie-point of Mumetal.

And moreover, the change of magnetic properties of μ_0 and μ_m by the special heat-treatment are not explained by the former theory. The theoretical explanation about the magnetic property on permalloy was proposed by Néel et al.[6),7),8),9)]. But, considering our experimental results, the following facts remain in question.

(1) The magnetic property by the special heat-treatment is very sensitive to the history of heat-treatment.

(2) The variation of μ_0 and μ_m as a function of annealing temperature is very complicated, and the each value can not be explained by the existing atom-ordering theories.

(3) The sign of the change of magnetic property by the special heat-treatment is opposite to each other for the binary permalloy and polynary permalloy.

§ 5. Conclusion

The maximum permeability of Mumetal is remarkably increased by a relatively low temperature heat-treatment. The existing theories for the effects of the heat-treatment are not consistent with our experimental results. In our investigation, however, the assumption of the origination of inhomogeneous structure in the permalloy material such as (1) internal strain caused by the third element added to binary permalloy, (2) lattice defects and (3) short range order of the superlattice seems to be very useful to explain the complex phenomena for the polynary permalloy.

In conclusion, the author wishes to express his hearty thanks to Director Dr. Tamatsu Nishina for his kind guidance and also to those who gave me many advices to my investigation.

References

1) F. Assmus and F. Pfeifer: Entwicklungsberichte **16** (1953) 339.
2) S. Kaya: J. Hokkaido Imp. Univ. **2** (1938) 29.
3) F. Assmus and F. Pfeifer: Entwicklungsberichte **16** (1953) 337.
4) O. L. Boothby and R. M. Bozorth: J. Applied Phys. **18** (1947) 173.
5) H. D. Arnold and G. W. Elmen: J. Franklin Inst. **195** (1923) 621.
6) L. Néel: Compt. Rend. **237** (1953) 1613.
7) L. Néel: J. Phys. et Rad. **15** (1954) 225.
8) S. Taniguchi and M. Yamamoto: Sci. Rep. Res. Inst. Tohoku Univ. **A, 6** (1954) 330.
9) S. Chikazumi: Nippon Buturi Gakkaisi **11** (1956) 92.

JOURNAL OF THE PHYSICAL SOCIETY OF JAPAN Vol. 16, No. 3, MARCH, 1961

Direct Observation of Subgrain-Growth of Cold-Worked Aluminium by means of Electron Microscopy*

Hiroshi FUJITA

Institute of Scientific and Industrial Research, Osaka University, Osaka Japan

(Received April 18, 1960)

Transmission electron micrographs of cold-worked aluminium show that the crystal grain consists of many subgrains the smallest size of which is less than 0.1μ. On subsequent heating, the subgrains grow by two kinds of process, i.e. the formation of subgrain-groups and the usual growth, and finally they grow up to a stable polygonal shape of $3\sim10\mu$ in size. The total area and the structure of sub-boundaries are likely to play a very important role for recrystallization because they act as the sinks of lattice defects in the intermediate course of migration to the recrystallization boundaries, but *the recrystallization in situ* is not found as a special stage of subgrain-growth.

The results obtained in the present work are discussed in relation to a mechanism of the recrystallization which was proposed by the author.

§1. Introduction

It is known that the presence of substructures within a crystal is closely related to the physical phenomena such as deformation, recovery and recrystallization. Formerly the present writer studied the subgrain formation in cold-worked aluminium by electron microscopy using the replica method[1]. Although this method is very convenient for observing the surface details such as slip bands and deformation bands, it is difficult to observe the internal structures of metals. Therefore, some other methods must be used which can directly reveal the internal structure. Heidenreich[2] was the first who observed the structure of metals by transmission electron microscopy. It should be noted that since, in this method, no replica is used, the resolving power of the electron microscope is the only limitation for disclosing fine structure details such as dislocations. Therefore the direct observation method was applied to the study of the subgrains, and some of the results obtained were already reported[3]. The object of the work presented here is to investigate in detail the subgrain-growth of cold-worked aluminium and its relation to the recrystallization.

§2. Specimen Preparation and Experimental Method

Specimens were taken from 99.99% purity aluminium foil which had previously been cold-rolled to 0.01 mm in thickness, well annealed, and hammered at room temperature to 0.5μ or less in thickness. The specimens were annealed at various temperatures and then chemically polished in a two percent aqueous solution or several percent alcohol solution of hydrofluoric acid untill the thickness was reduced to less than 1000Å. Another method of preparation of specimen was also used as follows: The specimens were wet with oil, sandwiched between thin foils of tin and cold-rolled to a thickness less than 1000Å. The final thickness of the specimens prepared by any of these two methods was fairly uniform throughout the specimens. The specimens were finally washed with alcohol and acetone, and were picked up with a mesh for observation.

The transmission electron microscope used had a resolving power of 20Å and was operated at 60 kV. To find the relationships between subgrains and the structure of sub-boundaries, observation was made (A) with different angles of incidence of the electron beam obtained by varying the current of condenser lens, or (B) by tilting the specimen. Method (A) in which the maximum change of angle would be about a few degrees was very useful for changing the image contrast between subgrains. The relative contrast between subgrains and the positions of extinction contours could be varied with the angle of incidence, while the other images, the position of sub-boundaries and the

---

* This is part of the work reported at the annual meeting of the Phys. Soc. of Japan, Oct., 1957.

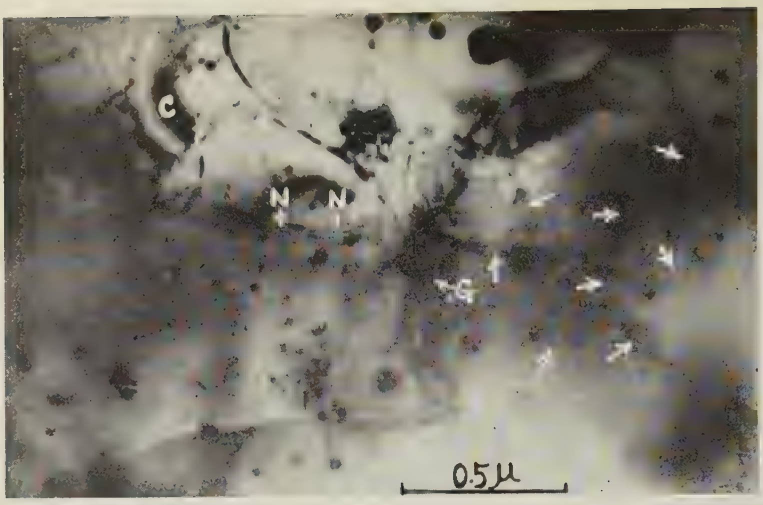

Fig. 1. As beaten. G: dislocation grid. C: extinction contour. N: node of sub-boundary. Arrows show diffused sub-boundaries.

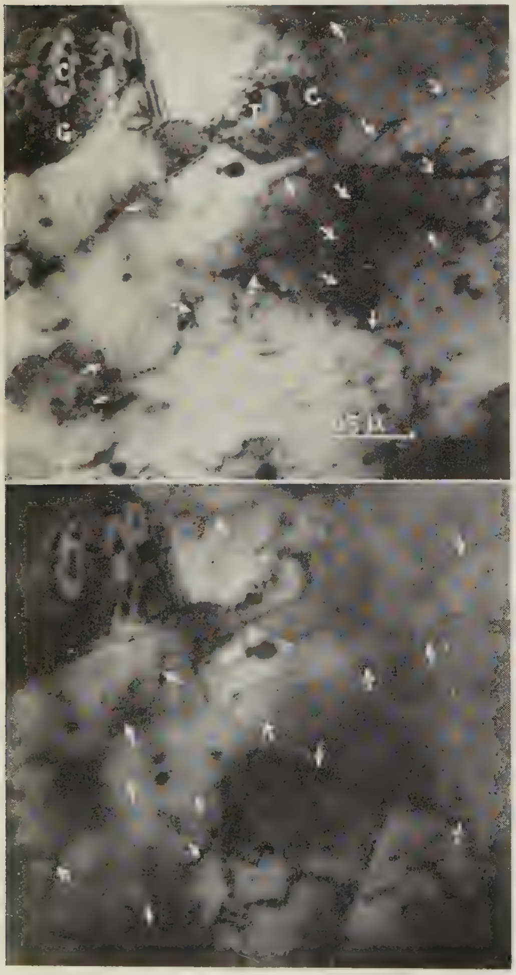

Fig. 2. (a) As beaten, (b) after electron-bombardment for 30 mins. in electron microscope.

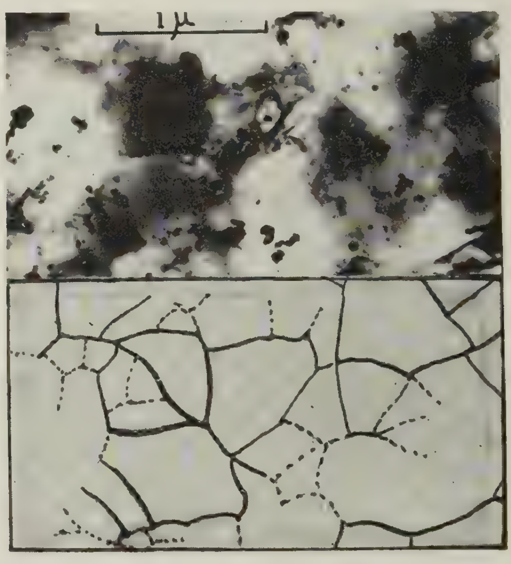

Fig. 3. Annealed for 1 hr. at 200°C. (b) is a sketch of (a).

darkness variation depending on the specimen thickness, were not influenced. It was therefore easy to distinguish each of them from the others.

Method (B) was convenient for examination of the structure of sub-boundaries. The specimen could be rotated up to 45° around an axis perpendicular to the incident beam.

§ 3. Experimental Results

(a) *Cold-worked state*

Figs. 1 and 2(a) are of the specimens as beaten: there are found many relatively dislocation-free regions of $0.1\sim1\mu$ dia., which seem to be bounded by diffused lines (↑) constructing irregular dislocation networks. In some regions where the deformation may be severe, these lines are so more clearly observed that they may be called the sub-boundary. The possibility of formation of such small subgrains was already shown by the replica method[1]. In Figs. 1 and 2, the segmentation of extinction contours (C) and the existense of the nodes of the boundaries (N) are helpful to detect the sub-boundaries.

The misfit angles between the subgrains mentioned above were roughly estimated with method (A) to be less than one degree for the small subgrains and a few degrees for the large ones. Furthermore, it is recognized in Figs. 1 and 2 that the boundaries of larger subgrains are of the dislocation cross-grid structure (G), which means that the sub-boundary is composed of two or more families of dislocations. On the other hand, most sub-bounda-

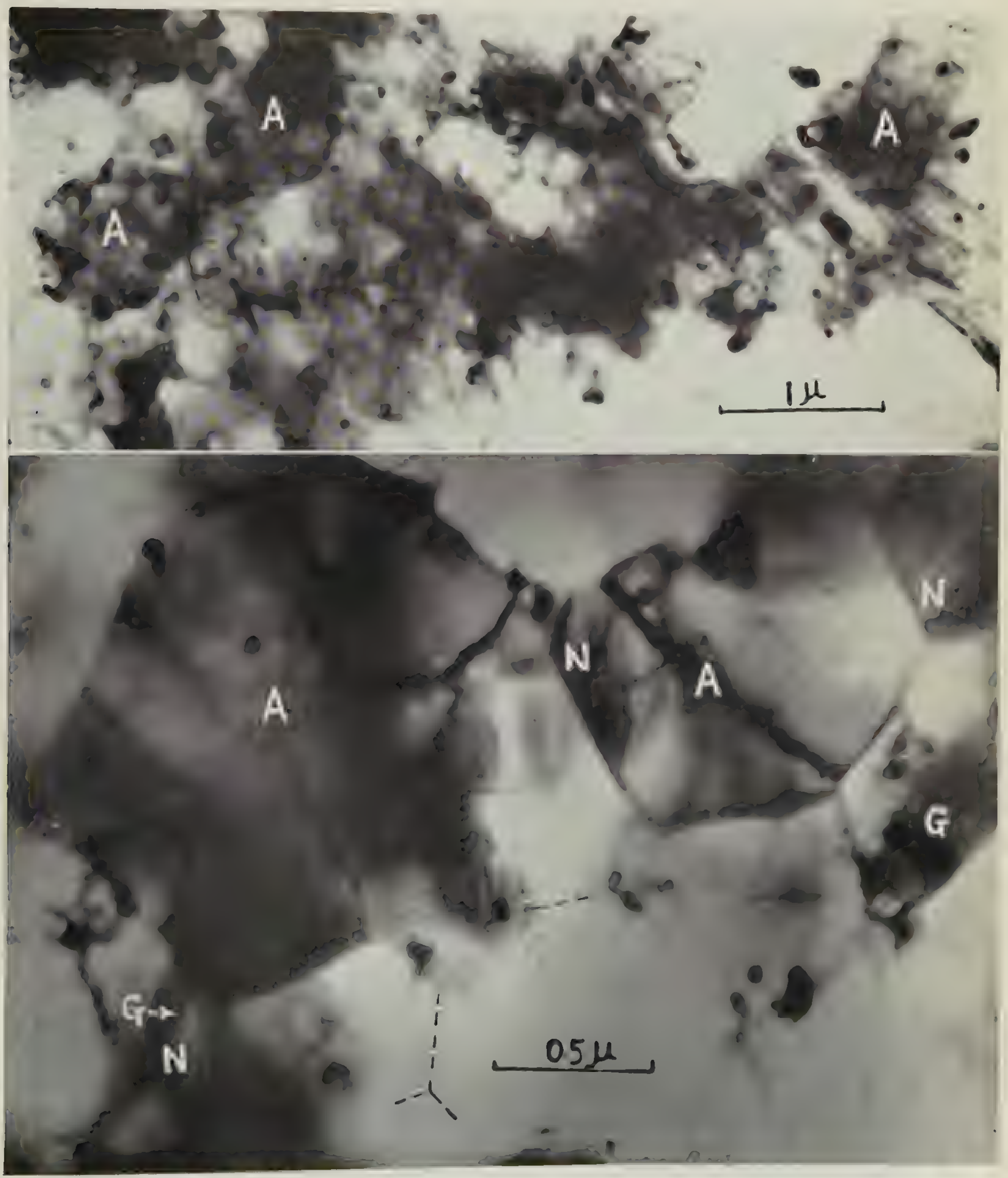

Fig. 4. Subgrain-groups appeared in the course of subgrain-growth. The specimens were annealed for 1 hr. at 260°C. Sign A indicates a subgrain-group consisting of smaller subgrains. (a), (b) were taken from different specimens.

ries of smaller ones seem to have a tendency to take the simple tilt type as slightly seen at the region noted by T in the photographs, which might correspond to K-band[1] reported already.

The temperature rise of the specimen owing to electron-bombardment under observation in the electron microscope was estimated as follows: Fig. 2 (a) and (b) were obtained before and after a strong electron-bombardment in the electron microscope for 30 mins. In these figures it is noticed that there is no visible change in the positions of sub-boundaries. On the contrary, the specimen annealed at 200°C for one hour shows a more marked change, i.e. straightening and sharpening of sub-boundaries as in Fig. 3. It is therefore reasonable to make an estimation that the temperature of the specimen under electron-bombardment was lower than 200°C.

(b) *Subgrain-growth*

On annealing cold-worked specimens, the subgrain-growth occurred in succession to polygonization, as seen in Figs. 3~7 in which the annealing was 200°C×1 hr., 260°C×1 hr., 260°C×2 hrs. and 350°C×1.5 hrs., respectively. These specimens are considered to have still been in the recovery stage, as no recrystallization grain was found by optical microscopy combined with chemical etching. Prolonged annealing caused remarkable subgrain-growth as in Figs. 5 and 7. From these photographs it is recognized that the subgrain-growth proceeds with two kinds of processes; (a) With the sub-boundary migration in the usual sense, (b) with formation of groups of subgrains as region A in Fig. 4(a) which has the size of about 1μ, and it was general that a few groups were formed in the region of 10μ in size. The latter process will be very important not only in the case of subgrain-growth but also in the recrystallization process. In Fig. 4(b) the subgrain-groups are clearly observed.

At the biginning of formation, the subgrain-group has such behaviors as follows: (1) Misfit angles between subgrains composing the group are very small. (2) The sub-boundary of the group is not so smooth but it is only a simple connection of the individual boundaries of composite small subgrains.

Figs. 4 and 5 are examples showing the process of stabilization of the boundary of the group which might be produced due to the absorption of the sub-boundaries within the group.

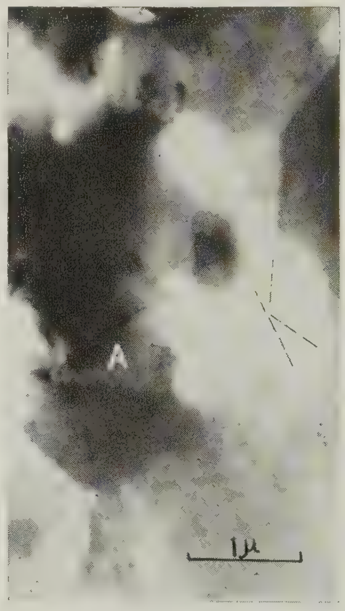

Fig. 5. Annealed for 2 hrs. at 260°C.

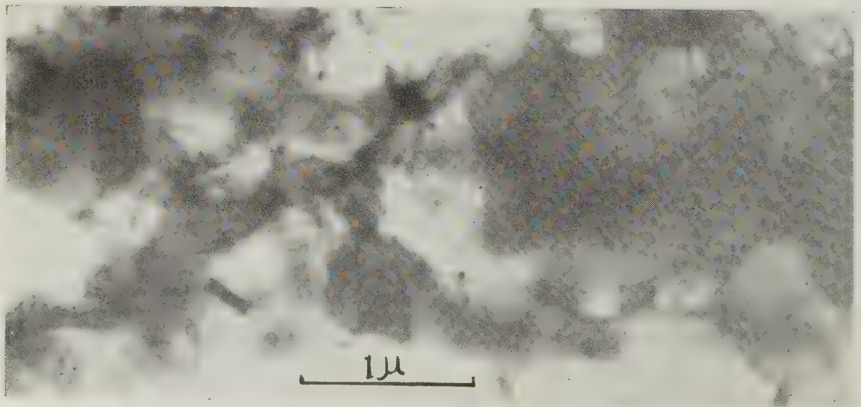

Fig. 6. Annealed for 1.5 hrs. at 350°C, a region outside a recrystallization grain.

On further annealing, the subgrain-growth by the two processes becomes conspicuous as in Fig. 5 (260°C×2 hrs), and finally recrystallization occurs. In the region existing between the groups in Fig. 4(a) (260°C×1 hr) there is no considerable change in size of the subgrains comparing to that of the specimen annealed for one hour at 200°C. After 260°×2 hrs. annealing, however, the subgrains existing between the groups also grew by the usual subgrain growth process. Fig. 6 was obtained with a specimen annealed for 1.5 hrs at 350°C, the photographed region being outside the recrystallization grain where subgrain-growth was delayed.

Fig. 7 is of another region of the specimen (260°C×1 hr.) which is likely to be considered as the beginning of formation of a recrystallization boundary. In order to estimate the misfit angles between subgrains existing inside the boundary noted by *R-R*, Fig. 7(b) was taken at the same region as 7(a) under the different glancing angle of incident beam. Comparing these two photographs it seems

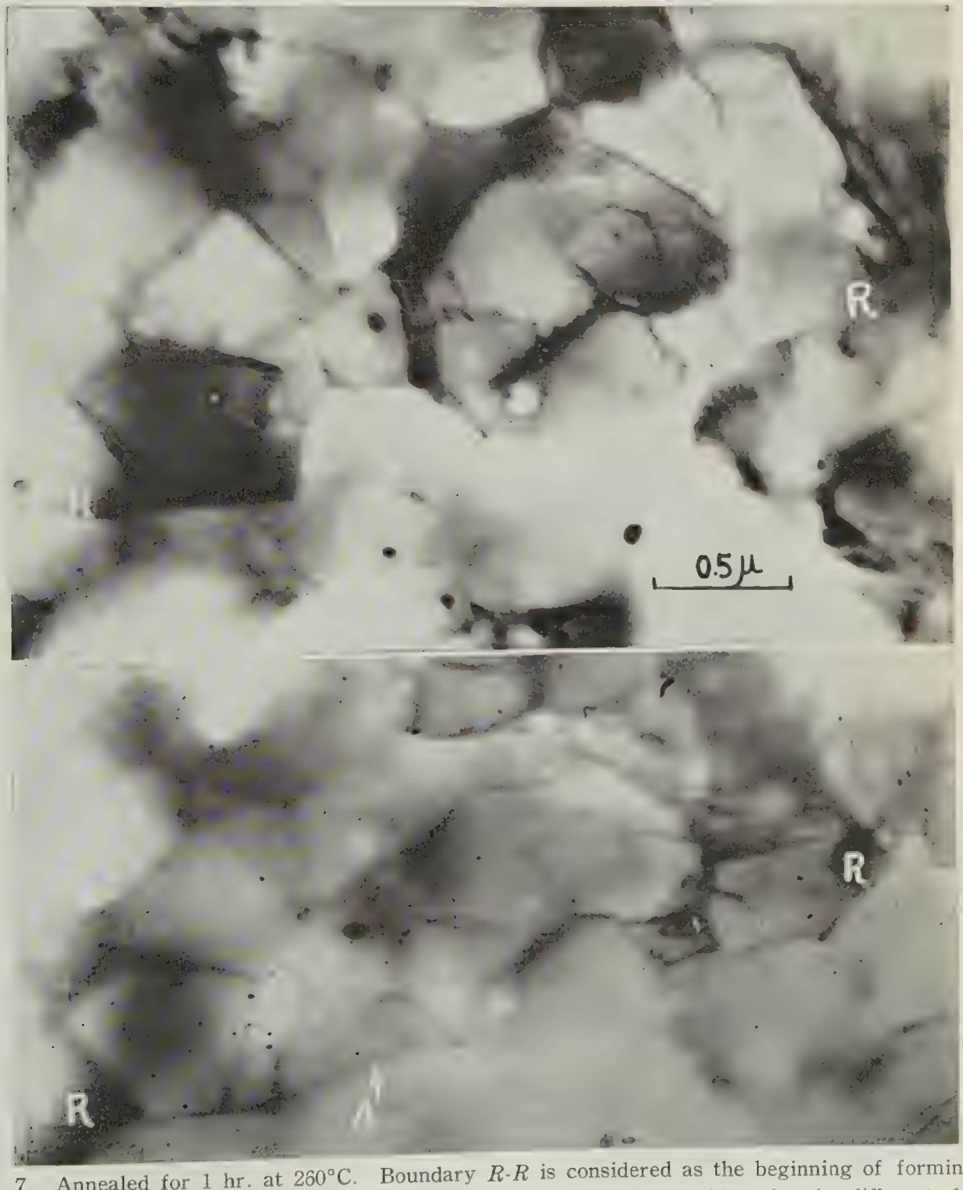

Fig. 7. Annealed for 1 hr. at 260°C. Boundary *R-R* is considered as the beginning of forming a recrystallization boundary. (b) was taken at the same region as (a) under the different glancing angle of incident beam.

that the *R-R* boundary has characters as follows: (1) *R-R* is a boundary of the subgrain-group in a certain sense, because it is a smooth boundary in spite of the presence of many boundaries of small subgrains inside the *R-R* boundary. (2) The grain size of the region surrounded by the *R-R* boundary is much larger than the usual subgrain-group, which is the same order as that of the beginning of recrystallization, 3~10μ in size. (3) The misfit angles between subgrains existing inside the *R-R* boundary are very small as that of the usual subgrain-groups. (4) Outside the *R-R* boundary the recovery process is so delayed that subgrains are not so clearly seen. Furthermore, a part of the boundary, noted by A in Fig. 7 is very faint compared with the other part, and a subgrain exisiting inside the boundary at this part (above the boundary A) has a large misfit angle to any neighbouring subgrains inside the *R-R* boundary. The remainder of this subgrain is observable in the outside region, that is, in the lower part of the photograph. It is, therefore, supposed that the formation of the *R-R* boundary is owing to the deposition of vacancies and dislocations which had existed near the boundary, and this process will be as schematically illustrated in Fig. 8, though more detailed

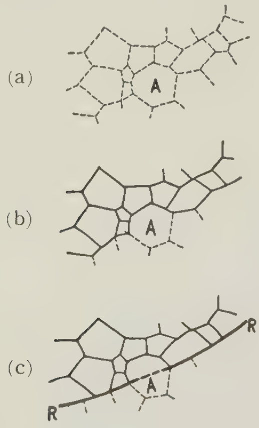

Fig. 8. Schematic illustration of forming a recrystallization boundary.

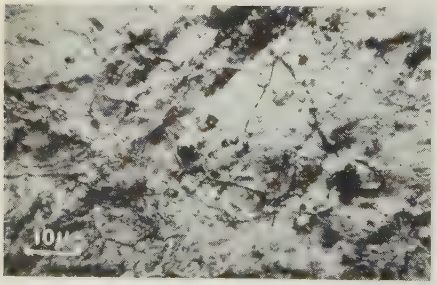

Fig. 9. Optical micrograph of a recrystallized foil specimen annealed for 1.5 hrs. at 350°C.

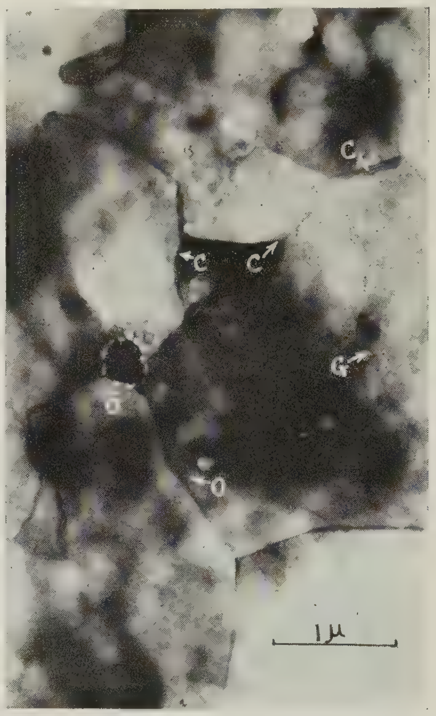

Fig. 10. Annealed for 1.5 hrs. at 350°C. C: boundary fringe. G: dislocation cross-grid. O: oxide film.

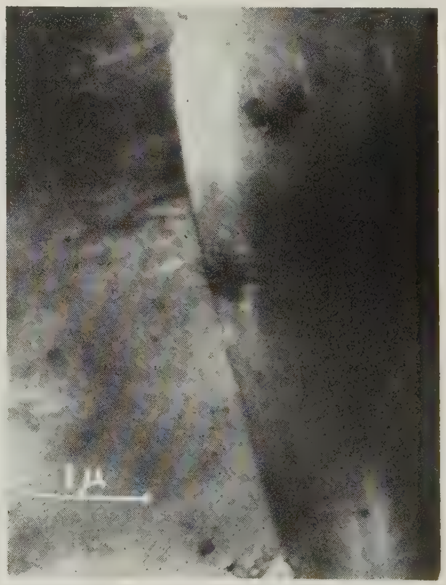

Fig. 11. Recrystallization boundary appeared in a specimen which was subjected to annealing for 3 hrs. at 350°C.

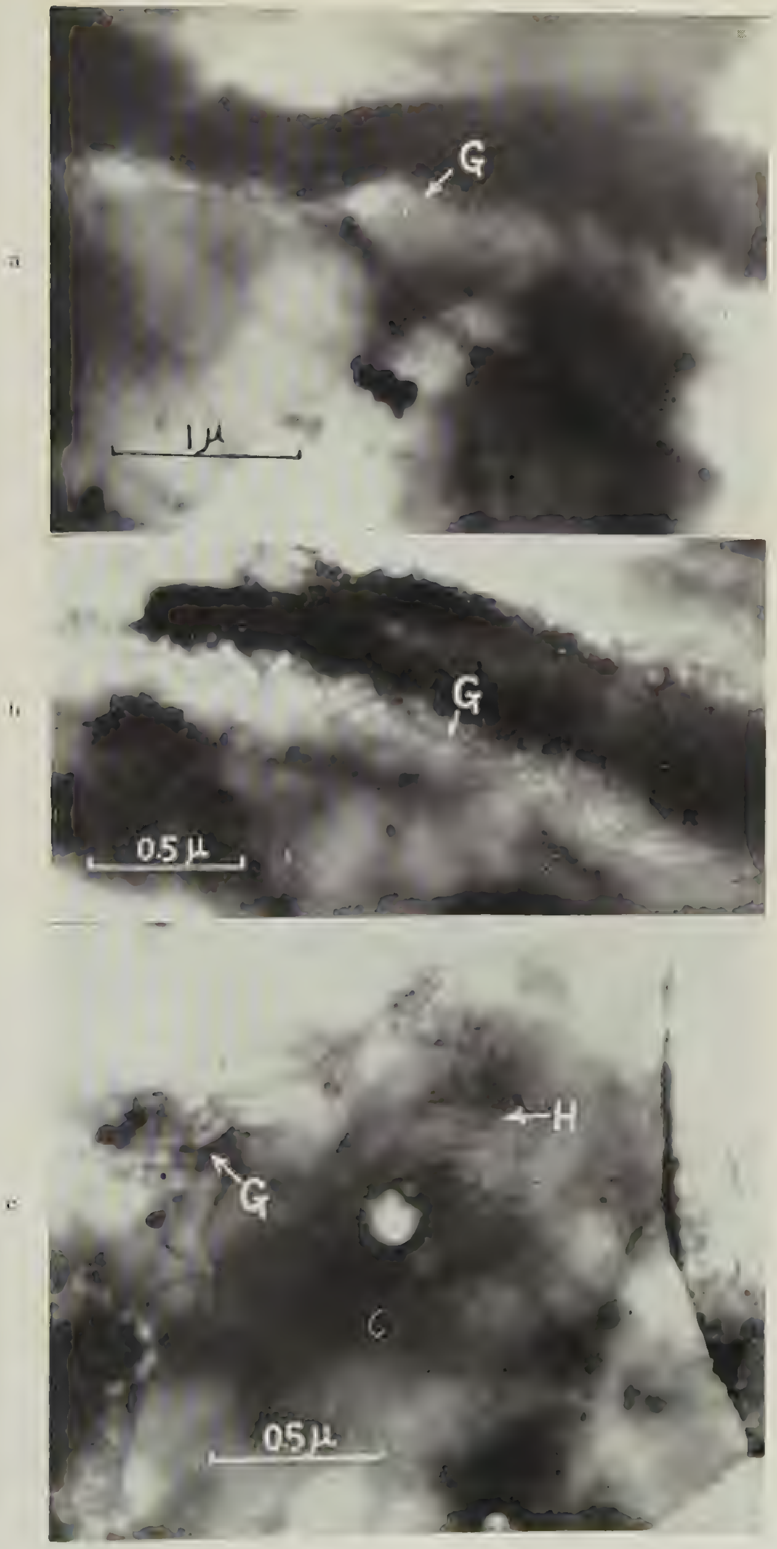

Fig. 12. Dislocation grid appeared in specimens annealed (a) for 1 hr. at 260°C, (b) for 1.5 hrs. at 350°C, (c) for 2.5 hrs at 350°C. H: dislocation hexagonal network.

study is necessary to get the decisive conclusion. Although it is considered that the stage mentioned above corresponds to something like the beginning of the recrystallization, the contrast between the recrystallization grain and the matrix became not yet so strong that it was difficult to observe the recrystallization boundary by optical microscopy. This might be owing to the fact that subgrains inside the boundary *R-R* still play a strong role as the sink for vacancies and dislocations in the intermediate course of migration to the recrystallization boundary so that the formation of the recrystallization boundary was suppressed.

Here, there is some doubt about that in the case of thin foils of metals the recrystallization mentioned above is suppressed by the size effect. To solve this doubt, the specimen used was also observed by optical microscopy and it was verified that the recrystallization occurred even in such thin foils of 0.5μ in thickness as follows. After further annealing (350°C × 1.5 hrs.), the recrystallized grain becomes observable by optical microscopy as in Fig. 9 which was taken of the foil specimen after etching with a reagent (10 g $NaOH$ + 100 cc H_2O) at 40°C. Although there is seen in Fig. 9 a recrystallization boundary which shows only a little growth, it was general that the size of the recrystallization grain at this stage was usually 10～40μ which was one-second to one-third of that before cold-working.

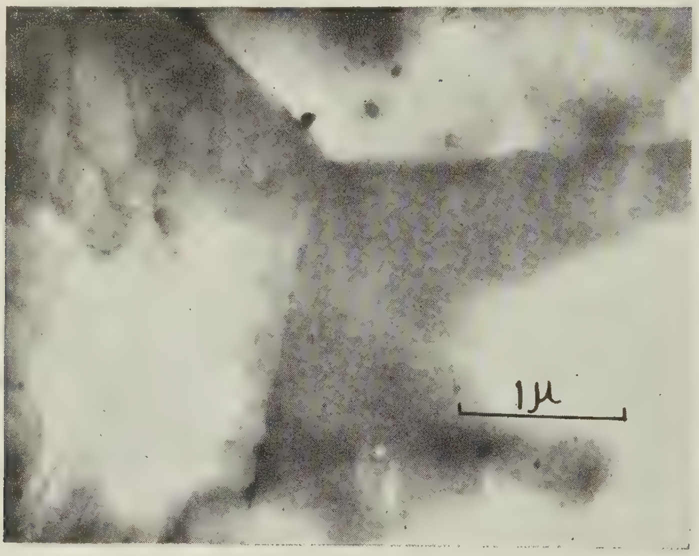

Fig. 13. Annealed for 3 hrs. at 560°C.

By electron microscopy it was found in a specimen annealed for 1.5 hrs. at 350°C that most subgrains grew up to 1～3μ in size as in Fig. 10, and that there were scarcely found both subgrain-groups and small subgrains less than 1μ in size. From the annealing history of this specimen the subgrains in Fig. 10 are considered to have been produced by *the recrystallization in situ* as observed by Crussard[4]. So it is very interesting that they appeared when the recrystallization boundary became observable. However, it is quite clear that they do not belong to a special stage as the subgrain-growth. These subgrains have the size and the shape as similar as those of the stable subgrains that will be mentioned in a later page.

Next, Fig. 11 is an example showing a recrystallization boundary. Comparing Fig. 11 with Fig. 7, it is very interesting that the recrystallization boundary become sharper with the prolonged annealing. This fact is quite reasonably understood if the formation of recrystallization boundary is owing to coagulation of the lattice defects.

Fig. 12 (c) shows a dislocation net-work structure in a sub-boundary formed by *the recrystallization in situ*. In this stage, however, the cross-grid structure of dislocations is apt to take a hexagonal net-work structure under the thermal vibration (compare Fig. 12 (c) with (a) and (b)). It is interesting that in Fig. 12(c) both the cross-grid (G) and the hexagonal net-work structure (H) are observed in a sub-boundary.

After long annealing at high temperatures just below the melting point, the subgrain grows more and more and finally it takes a stable polygonal shape, whose size is 5∼10μ, as in Fig. 13 which were taken of a specimen annealed for 3 hrs. at 560°C. At this stage, it was recognized by optical microscopy that recrystallization grains had grown further.

§ 4. Discussion

About six years ago[5], the author proposed a mechanism* concerning the nucleation of recrystallization. This mechanism is based on the idea that the positions of the recrystallization boundaries are originally decided at the time of cold-working and the nucleus in the usual sense is not needed for the recrystallization. In other words, subgrain-growth plays a very important role for disappearance of the stored energy, but it is not so much important for the formation of recrystallization boundary which needs the coagulation of lattice defects. Since the sub-boundary acts as a sink for lattice defects, it is necessary for formation of the recrystallization boundary that the number of subgrains within the recrystallization boundary decreases to a certain value. Because, for the coagulation of lattice defects to the recrystallization boundary, the defects have to travel for a long distance compared with that in the case of polygonization. In case polygonization has not proceeded so much, most of the lattice defects formed by cold-working may be exhausted for polygonization in the intermediate course of migration to the recrystallization boundary. Furthermore, for the recrystallization boundary the difference of bulk free energy between the recrystallization grain and the matrix around it must be larger than a certain value. So, first of all the subgrains must grow and take the thermally stable structure in order to form the recrystallization boundary.

This idea might be supported by the following experimental results obtained in the present work: (1) remarkable growth of subgrains was observed before the recrystallization, (2) grown subgrains, i.e, so called *the recrystallization in situ*, were observed within the recrystallization grain, (3) outside the recrystallization grain, there remain the subgrains where subgrain-growth was delayed, (4) at the beginning of the recrystallization, boundaries of the recrystallization grain were rather faint and broad.

Fact (1) proceeds by two kinds of process, i.e. (a) formation of subgrain-groups and (b) subgrain-growth in the usual sense. A few subgrain-groups were formed in a region of several micron in size which corresponded to the initial size of a recrystallization grain, and even after the recrystallization, *tne recrystallization in situ* was observed within the recrystallization grain. Thus it is considered that a subgrain-group is not an embryo of recrystallization but it belongs to the category of subgrain.

The fact that some subgrains have a special behavior such as composing the subgrain-group leads us to an imagination that such subgrains were already given a suitable condition for forming the subgrain-group by cold-working so that misfit angles between them are very small. Since the boundary of the group has a larger misfit angle compared with those of subgrains inside the group, it becomes a strong sink for lattice defects such as dislocations and point defects. That is the reason why dislocations composing a sub-boundary within a subgrain-group are absorbed so easily that finally sub-boundaries within a group disappear. This process is one kind of subgrain-growth. Subgrain-growth in the usual sense may also proceed by the same process more or less, in which case formation of subgrain-groups was not observed.

Fact (2) shows that a recrystallization grain is not a resultant formed by the process of subgrain-growth. Because it is hardly possible that there exist some large subgrains within a recrystallization grain, if the recrystallization boundary was formed by means of subgrain-growth.

Fact (3) indicates, however, that the subgrain-growth plays a very important role for recrystallization process. Accordingly, stored energy given by cold-working is released by the process of subgrain-growth so that the recrystallization boundary is thermally stabilized.

---

* Orowan[6] proposed independently the similar idea concerning recrystallization, which was called as *the homogeneous nucleation.*

Fact (4) indicates that a recrystallization boundary is formed by some coagulation of lattice defects, especialy point defects. Such positions playing a role as the sink for lattice defects may be formed during cold-working in the same way as in the case of the subgrain-group. The author reported[7)] already that unpredicted slips occurred in small regions divide a crystal into many domains of a few microns in size. The domain boundary is not so clear that it is recognized only by a difference of slip system or reflected light on both sides of the boundary. Even in the boundary region of the domain, small subgrains less than 1μ in size are formed as well as within the domain with small sink and slip bands[1)]. So, as far as the strained state of the subgrain is concerned, it is rather difficult to find out anything discontinuous at the boundary of the domain.

It should be emphasized, however, that such domains have large misfit angles with each other, so that small subgrains formed within a domain have large relative misfit angles to those within the neighbouring domain, but the subgrains belonging to the same domain have small misfit angles with each other. So, it is reasonable to consider that the boundary region of the domain is a strong sink for coagulation of lattice defects in the case of forming a recrystallization boundary.

From the consideration mentioned above, the following equation* will be deduced, which shows a relationship between the experimental (α) and a theoretical specific surface energy (α_0) of the boundary determined from both misfit angles and boundary structures.

$$\frac{2\alpha}{r_c}=\frac{2\alpha_0}{r_c}-\Delta n\Gamma=\delta F$$

where r_c is a critical size of a recrystallization grain, δF and Δn are the differences of bulk free energies and of the densities of dislocations terminating at the boundary, respectively, between the matrix and the recrystallization grain. Hence

$$r_c=\frac{2\alpha_0}{\delta F+\Delta n\Gamma}\ .$$

α_0 will be very small at the beginning of recrystallization, since the misfit angle is very small because of the diffused structure. If we assume $\Delta n=10^{10}/\text{cm}^2$, $\Gamma=10^{-4}$ ergs/cm, $\alpha_0=$a few ergs/cm$^2\sim 500$ ergs/cm^2, and $\delta F=$the order of 10^6 ergs/cm^3, r_c becomes $1\mu\sim10\mu$ in size, which is in agreement with the experimental results[5)] observed.

Acknowledgement

It is a pleasure to thank Professor Zenji Nishiyama for stimulating discussions.

References

1) H. Fujita and Z. Nishiyama: Memoirs of the Inst. of Sci. and Ind. Research, Osaka Univ. **XIV** (1957) 91; Japan Inst. of Metals, **21** (1957) 607.
2) R. D. Heidenreich: J. Appl. Phys. **20** (1949) 993.
3) Z. Nishiyama and H. Fujita: Metal Phys., Japan, **3** (1957) 108.
4) C. Crussard: Rev. Métall. **41** (1944) 111 and 133.
5) H. Fujita: Submitted to the Report of the Crystal Plastisity Group, Aug., 1954; Read at the Annual Meeting of Japan Inst. of Metals, April, 1955; Light Metals, No. **21** (1956) 39.
6) E. Orowan: *Dislocations in Metals*, **3** (1954) 181.
7) H. Fujita: Light Metals, No. **18** (1956) 15.

---

* See E. Orowan: *Dislocations in metals*, **3** (1954) 186.

Journal of the Physical Society of Japan, Vol. 16, No. 3, March, 1961

Cavity Growth by Vancancy Condensation and Transformation to Dislocation Loop in the Graphite Structure

By Takuro TSUZUKU

College of Science and Engineering, Nihon University,
Kanda-Surugadai, Chiyoda-Ku, Tokyo.

(Received September 22, 1960)

The growth of cavities by vacancy condensation in graphite and the transformation to dislocation loops have been theoretically investigated.

During the heat treatment of carbonaceous substances for graphitization, numerous vacancies and cavities presumably exceeding 10^{-3} atomic per cent are introduced in several ways, *e.g.*, decomposition and evaporation of various impurities. By taking account of the internal surface energy and the configurational entropy of them, it has been concluded that these vacancies and cavities are driven to consolidate to fewer and larger ones lying extensively on the $(00l)$-planes.

In the course of the steady dimensional growth, the cavity is expected to collapse to a prismatic dislocation loop under the compressive thermal stress in c-direction (graphitization stress) caused by the interference between the anisotropically expanding crystallites. The criterion of such transformation has been determined by comparing the self-energy of the dislocation loop with the sum of the surface energy of the original cavity and the compressive strain energy to be released by the collapse; *i.e.*, the critical diameters are ranging from about 100 Å to 1100 Å in accordance with the various conditions concerning the crystal modification and the cavity thickness. These values are in fairly good agreement with the experimental results. It has been remarked that along this course the characteristic intercrystallite voids can be explained.

§ 1. Introduction

In the previous paper[1], the author pointed out that the dislocations in the graphite structure might be produced by the so-called graphitization stress owing to the interference of the anisotropic thermal expansion of each crystallite in some polycrystalline carbons. At the same time, it was remarked that the condensation of point vacancies to fewer flat cavities would be another powerful source of the dislocations in accordance with the suggestion of Seitz[2]. These two origins of the dislocations are both in close connection with the two characteristics of graphite, *i.e.* the heat treatment at elevated temperatures for synthesis and the remarkable anisotropy in the crystal structure.

As generally known, a crystal in thermodynamical equilibrium has to contain a number of lattice vacancies and other imperfections by which the free energy of the system is lowered through the contribution of the configurational entropy. In the case of graphite, since the crystal grows up through the pyrolysis of raw carbonaceous substances, much higher concentration of vacancies are expected to be generated in various ways of impurity dissipation; *e.g.*, (1) volatilization of light organic components at temperature below 1000°C, (2) dehydrogenation arising nearby 1000°C and lasting up to about 1700°C, and (3) evaporation of inorganic impurities* taking place in the final stage of graphitization above 1800°C, *et al.*

Conclusively, the graphite crystal is considerable to be so exceedingly supersaturated with vacancies that the condensation of them to fewer cavities would occur more actively than other crystals. Recently, in the course of the electron microscope study of some graphite flakes, Fujita and Izui[3] have observed circular *moiré* patterns having the diameters of several hundred angstroms. The patterns of this kind can be explained by supposing that such disciform cavities as considered above collapse to the edge dislocation loops, *i.e.*, the peripheral lattice distorsion may give rise to the Bragg reflection of electron waves responsible for the *moiré* patterns.

---

* This is well known to take place sometimes through the intermediate formation and the following decomposition of various metal carbides, *e.g.* silicon carbide, cementite *etc.*

Now, it is worthy to examine a theoretical investigation on the mechanism of vacancy condensation to a small number of cavities in the graphite structure and the following transformation to the same number of dislocation loops.

§ 2. Growth of Cavity by Vacancy Condensation

2.1 *Basic Model*

Owing to the characteristic anisotropy in the crystal structure, an arbitrary cavity lying in graphite may easily take a flat cylindrical form as widely accepted; the diameter and the height in angstroms are denoted by D and h respectively. On the other hand, the area of each unit hexagon containing two C-atoms (Fig. 1) is computed at 5.22 angstrom square. Therefore, the number of atoms emerging on the basal face of such a cylindrial cavity is $m_{\text{basal}}=2.61(\pi D^2/4)=0.30D^2$.

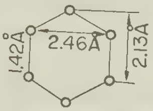

Fig. 1. Unit hexagon of graphite net plane.

Nextly, since the interplanar spacing in c-direction is known to be about 3.36 Å*, the number of point vacancies composing the cavity is $i=3.36m_{\text{basal}}/h=0.089D^2h$.

Finally, supposing that along the periphery of the cavity C-atoms are aligned 2.46 Å apart, one can give the total number of the free bonds (atoms) which are exposed all over the side-face of the cavity,

$$m_{\text{side}}=(\pi D/2.46)(3.36/h)=0.38Dh.$$

2.2 *Surface Energy of Cavity*

According to Pauling[4], the graphite structure is considered to be resulted from the infinite aromatic condensation, so that each carbon-carbon bond achieves one-third double-bond character. Since the energies of pure C–C and C=C valence bonds are known to be 58.6 and 100 kcal/mol respectively, the cohesive energy of graphitic net plane is computed at 58.6×(2/3)+100×(1/3)=72.4 kcal/mol in approximation. On the other hand, the energy of interplanar van der Waals bond of graphite has been calculated by Brennan[5] to be about 4 kcal/mol. At the time of the destruction of these chemical bond, in general, the binding energy may be shared by half with each surface newly exposed. Thus, the total surface energy of such a cylindrical cavity as considered above is given by

$$\begin{aligned}E_s&=2m_{\text{basal}}\times 2+m_{\text{side}}\times 36.2\\&=1.2D^2+13.8Dh \quad \text{(kcal/mol)} \qquad (1)\end{aligned}$$

where the first term in the right-side corresponds to the contribution of the upper and lower basal faces, and the second to that of the side face.

Hereupon, let introduce a quantity "specific surface energy", γ_s, defined by the next equation,

$$\gamma_s=\frac{E_s}{i}=\frac{155}{D}+\frac{13.5}{h} \quad \text{(kcal/mol)} \qquad (2)$$

The physical meaning of γ_s is "the increment (decrement) of the surface energy when a point vacancy pours into (out of) the cavity considered here". For example, if a point vacancy leaves a cavity of $D=20$Å and $h=3.36$Å (one atomic plane missing) and pours into another of $D=80$ Å and $h=6.72$ Å (two plane missing), the internal energy of the crystal is reduced by the difference of the specific surface energies, *i.e.*,

$$\begin{aligned}\Delta\gamma_s&=\left(\frac{155}{20}+\frac{13.5}{3.36}\right)-\left(\frac{155}{80}+\frac{13.5}{6.72}\right)\\&=11.8-3.9=7.9 \quad \text{(kcal/mol).}\end{aligned}$$

Thus, those vacancies and minute cavities generated in the aforesaid ways (§1) are expected to condense successively, through the heat treatment at elevated temperatures for graphitization, to a small number of much larger ones. From Eq. (2), moreover, one can see that the specific surface energies are equalized by degrees with the consolidation of cavities, and, when the vacancies and minute cavities are mostly exhausted the dimensional growth may almost terminate. Such a state can be regarded as a metastable balance, and

---

* The spacing varies in accordance with the degree of graphitization. The lowest value has been reported to be 3.354 Å (at 18°C) on natural graphite of Ceylon, which corresponds to the best graphitization.

γ_s is considerable to give a negative measure of the stability.

2.3 *Configurational Entropy and Free Energy*

In order to describe the mechanism of vacancy condensation (cavity consolidation) more exactly, the contribution of the configurational entropy has to be taken into account. For simplicity, let suppose that n_i cavities consisting of i point vacancies respectively are arranged on N lattice points $(N \gg i)$. This supposition corresponds not only to the aforesaid metastable balance but to the actual state in approximation, if the cavity-size distribution is not so much broad. Thus, the number of possible arrangement, W, is generally given by

$$W = \frac{i^{n_i} \cdot \left(\frac{N}{i}\right)!}{\left(\frac{N}{i} - n_i\right)!\ n_i!} .$$

Putting $n = n_i \times i$ and $c = n/N$, which represent the total number and the concentration of point vacancies (consisting the cavities) respectively, and using Stiring's formula, the configurational entropy, S_{cf}, is expressed in the following form,

$$S_{cf} = k \ln w = \frac{kN}{i}\left[c \ln \frac{i}{c} - (1-c)\ln(1-c)\right]$$
$$= \frac{kN}{0.089D^2h}\left[c \ln \frac{0.089D^2h}{c} - (1-c)\ln(1-c)\right] . \tag{3}$$

Now, in the similar way to that concerning the surface energy, one can define the "specific configurational entropy",

$$\xi = S_{cf}/n = S_{cf}/Nc$$

which may give a measure of entropy change by vacancy migration from a cavity to another.

Hereupon, combining γ_s and ξ, the so-called "specific free energy", φ, is defined by the next equation,

$$\varphi = \gamma_s - T\xi$$
$$= \left(\frac{155}{D} + \frac{13.5}{h}\right) - T\frac{k}{0.089D^2hc}\left[c \ln \frac{0.089D^2h}{c} - (1-c)\ln(1-c)\right]. \tag{4}$$

Now, let make an estimation of the vacancy concentration, c, by using the well-known expression[6)]

$$c = \frac{n}{N} = \left(\frac{\nu}{\nu'}\right)^{3x} \cdot \exp\left(-\frac{E_v}{kT}\right) ,$$

where x is the number of the atoms neighbouring a vacancy, ν' is the Einstein frequency of them, ν is that of the perfect lattice part, and E_v is the formation energy of a vacancy. In approximation, $\nu/\nu' \approx 2$, $x=3$ (taking only the co-planar neighbours around a vacancy) and $T=3000°K$ (temperature of usual industrial graphitization furnace). Moreover, since the three conjugated double-bonds are broken in removing an atom from a lattice point, and, 3/2 bonds are recovered on average in placing it to the periphery of the net plane,

$$E_v = 72.4 \times \{3 - (3/2)\} = 108.6 \text{ kcal/mol}$$

is obtained. Substituting these values to the above equation, vacancy concentration is computed at $10^{-5.2}$. However, as mentioned in § 1, graphite is considerable to be highly supersaturated with the vacancies and cavities in the way of active impurity dissipation, and hence one can put approximately $c \approx 10^{-5}$.

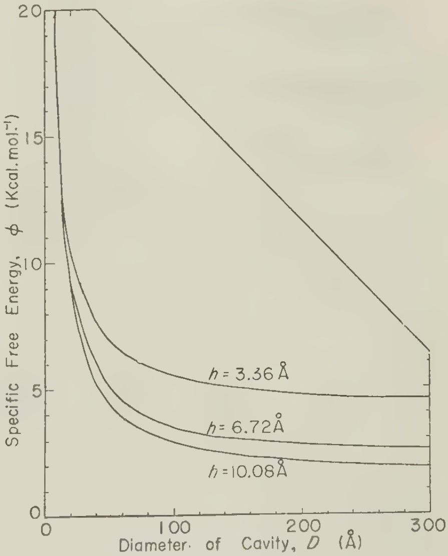

Fig. 2. Dependency of specific free energy on cavity-size.

Thus, the $D-\varphi$ relaction curves at 3000°k are plotted in Fig. 2 for the parameters of $h=3.36$, 6.72 and 10.08 Å (corresponding to that one, two and three planes are deficient respectively). As shown there, the contribution of the configurational entropy is so small that φ decreases monotonically with the growth of cavity-size, indicating no minimum value. Moreover, one can see that when D mounts up to several hundreds angstroms the cavity is hard to make further growth in actual owing to the equalization of φ, similar to the case of the specific surface energy discussed before. In other words, these cavities are possible to be existent only in the so-called metastable balance but impossible in thermodynamical equilibrium, somewhat alike the dislocations.

§ 3. Transformation to Dislocation Loop

3.1 *Geometry of Transformation*

By means of X-ray and electron diffraction it has been established that graphite has two crystal modification[7)8)], the hexagonal (AB-type stacking sequence of $\boldsymbol{c}$-planes) and the rhombohedral (ABC-type sequence), as schematically illustrated in Fig. 3. This gives a cause of the variety of the dislocation loops to be introduced, being in company with the various conditions on the deficient planes, as itemized in the following paragraphs:

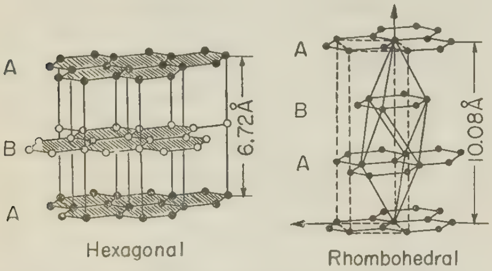

Fig. 3. Two crystal modifications of graphite.

Hexagonal Modification

(h1) One plane missing (h=3.36 Å)

In addition to the prismatic partial dislocation which closes the cavity, another partial dislocation with a Burgers vector connecting the nearest neighbours in (00l)-plane is introduced so as to fit the subtending basal faces. Denoting them by $\boldsymbol{b}_c$ and $\boldsymbol{b}_a$ respectively, the resultant slip is represented by

$$\boldsymbol{b}=\boldsymbol{b}_c+\boldsymbol{b}_a=\tfrac{1}{2}\boldsymbol{c}\cdot[001]+\tfrac{1}{3}\boldsymbol{a}\cdot\langle 210\rangle\ .$$

This causes such a stacking fault as

ABABCBCBC or *ABABACAC*.

(h2) Two planes missing (h=6.72 Å)

$$\boldsymbol{b}=\boldsymbol{b}_c=\boldsymbol{c}\cdot[001]\quad\text{(perfect dislocation).}$$

The dislocation loop can glide along the cylindrical face perpendicular to the basal plane as in Fig. 4 (a), though it might be not so easy.

(h3) Three planes missing (h=10.08 Å)

$$\boldsymbol{b}=\boldsymbol{b}_c+\boldsymbol{b}_a=\tfrac{3}{2}\boldsymbol{c}\cdot[001]+\tfrac{1}{3}\boldsymbol{a}\cdot\langle 210\rangle\ .$$

The possible stacking faults are quite same as those in (h1).

*Rhombohedral Modification**

(r1) One plane missing (h=3.36 Å)

$$\boldsymbol{b}=\boldsymbol{b}_c=\tfrac{1}{3}\boldsymbol{c}\cdot[001].$$

The stacking faults are as follows;

····*ABCBCABC*···· (A-plane missing), or
····*ABCACABC*···· (B-plane missing), or
····*ABCABABC*···· (C-plane missing)

(r2) Two planes missing (h=6.72 Å)

$$\boldsymbol{b}=\boldsymbol{b}_c+\boldsymbol{b}_a=\tfrac{2}{3}\boldsymbol{c}\cdot[001]+\tfrac{1}{3}\boldsymbol{a}\cdot\langle 210\rangle$$

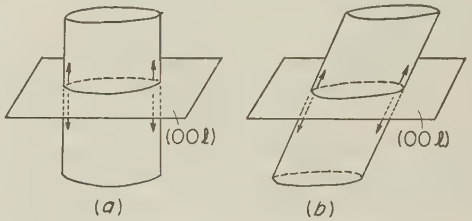

Fig. 4. Clide motion of prismatic dislocation loop.

Table I. Combination of missing planes and basal translation in rhombohedral graphite.

Missing planes	Translation by $\boldsymbol{b}_a$	Stacking disorder
A, B	$C\to\underline{B}$	$\cdots ABC\underline{B}CABC\cdots$
	$C\to A$	None
B, C	$A\to\underline{C}$	$\cdots ABCA\underline{C}ABC\cdots$
	$A\to B$	None
C, A	$B\to\underline{A}$	$\cdots ABC\underline{A}BABC\cdots$
	$B\to C$	None

The under-lined planes in this column correspond just to those in the left-hand column respectively.

In this case, various combinations of the missing planes and the translations by b_a's give rise sometimes to the stacking disorder and sometimes to none. When the stacking order is not altered, the dislocation loop can glide along the surface of such an oblique cylinder as in Fig. 4 (b). All the possible combinations are summarized in Table I.

(r3) Three planes missing (h=10.08 Å)

$$\boldsymbol{b}=\boldsymbol{b}_c=\boldsymbol{c}\cdot[100]\quad\text{(perfect dislocation).}$$

It is easily understood that the same rules as mensioned above can be applied repeatedly and correspondingly to the cases that more than four planes are deficient.

---

* The $\boldsymbol{c}$-dimension of the unit cell is 10.08 Å.

3.2 *Self-Energy of Dislocation Loop*

Several years ago, Foreman showed the expression of the elastic energy per unit length of a dislocation line in an anisotropic crystal as follows[9],

$$E_d=\frac{Kb^2}{4\pi}\ln\left(\frac{R}{r_0}\right), \qquad (5)$$

where b, R and r_0 represent the Burgers vector, radii of the stress field arround it and the effective core respectively. The so-called "energy factor" K in every case of our problem considered before is evaluated in the following way, taking use of his treatise on the hexagonal system. However, the elastic constants c_{ij}'s referred to the dislocation axis in his general expression are rewritten so as to be referred to the normal crystal axis.

(1) Prismatic dislocation (either perfect or partial) with the Burgers vector perpendicular to the basal plane

$$K_{\text{edge}}(\text{prismatic})$$
$$=(\bar{c}_{11}+c_{13})\left\{\frac{c_{44}(\bar{c}_{11}-c_{13})}{c_{11}(\bar{c}_{11}+c_{13}+2c_{44})}\right\}^{1/2} \qquad (6)$$

(2) Partial dislocation connecting the nearest neighbours in the basal plane

$$K_{\text{edge}}(\text{basal})=(\bar{c}_{11}+c_{13})\left\{\frac{c_{44}(\bar{c}_{11}+c_{13})}{c_{33}(\bar{c}_{11}+c_{13}+2c_{44})}\right\}^{1/2} \qquad (7)$$

$$K_{\text{screw}}=\left\{\frac{c_{44}(c_{11}-c_{12})}{2}\right\}^{1/2} \qquad (8)$$

$$K_{\text{mix}}(\text{basal})=K_{\text{edge}}(\text{basal})\sin^2\theta+K_{\text{screw}}\cos^2\theta \qquad (9)$$

where $\bar{c}_{11}=(c_{11}\cdot c_{33})^{1/2}$, and θ is the angle between the slip vector and the dislocation line. In the case of such a dislocation loop as considered here, by averaging Eq. (9) arround it the energy factor is given by

$$\bar{K}(\text{basal})=\frac{1}{2}[(\bar{c}_{11}+c_{13})]\left\{\frac{c_{44}(\bar{c}_{11}-c_{13})}{c_{33}(\bar{c}_{11}+c_{13}+2c_{44})}\right\}^{1/2}+\left\{\frac{c_{44}(c_{11}-c_{12})}{2}\right\}^{1/2} \qquad (10)$$

(3) Combination of prismatic and basal dislocations

Since there is no interaction energy between the orthogonal dislocation components, the separate energy components are additive, and therefore the combined K-factor in this case may be given by the next equation,

$$K\boldsymbol{b}\cdot\boldsymbol{b}=K_{\text{edge}}(\text{prismatic})\boldsymbol{b}_c\cdot\boldsymbol{b}_c+K(\text{basal})\boldsymbol{b}_a\cdot\boldsymbol{b}_a\,. \qquad (11)$$

Table II. Elastic constants of graphite lattice.

c_{11}	c_{12}	c_{13}	c_{33}	c_{44}	(unit)
107	−21.4	−6.3	2.6	1.3	(10^{11} dynes/cm^2)

The elastic constants of graphite lattice, c_{ij}'s, can be determined from the corresponding elastic coefficients, s_{ij}'s, written in the previous paper[1], and are tabulated in Table II. Moreover, substituting them into the above equations from (6) to (10), the energy factors are evaluated as shown in Table III.

Table III. Energy factors of various dislocations.

K_{edge} (prismatic)	K_{edge} (basal)	K_{screw}	$\bar{K}$ (basal)	(unit)
1.53	9.8	9.1	9.5	(10^{11} dynes/cm^2)

Using these K-factors, the elastic energies of the dislocations in various cases itemized in the last sub-section can be calculated from Eq. (5), where R is appropriately assumed to be about $D/2$ (radius of the dislocation loop).

The energy in the dislocation core (residual part of the self-energy) is very difficult to estimate exactly. However, in the case of the prismatic dislocation as considered here, it may be approved to say roughly that the core energy of the dislocation loop is given by the peripheral free bonds exposed at the ends of the extra half-planes. In the other words, the core energy can be said to correspond to the side-face energy of the original cavity represented by the second term in the right side of Eq. (1).

3.3 *Criterion of Transformation*

As previously pointed out, when a polycrystalline carbon is heat-treated for graphitization each crystallite is subjected to the compressive thermal stress and the corresponding elastic strain in $\boldsymbol{c}$-direction. These stress and strain may be partly released by the collapse of the aforesaid flat cavity to the dislocation loop lying on the basal plane. The thermal strain energy owing to this mechanism, E_t, is generally given per unit volume by half of the product of the compressive stress and the constrained expansion in **c**-direction,

$$E_t=\tfrac{1}{2}\times\sigma_r(\varepsilon_r-\alpha_r \mathrm{T})\ ,$$

where the notations are used in the same way as those in the previous paper[1]. For instance, assuming T=3000−1300=1700 (°K)*, and using the expressions for the filamentarily textured polycrystal (typical soft carbon) cited in the previous paper[1], one can obtain such a radial distribution curve of the thermal strain energy as shown in Fig. 5, which indicates the maximum value, 1.87×10^8 ergs/cm^3, at the centre. Therefore, the collapse of a cavity in the neighbourhood of the central axis of the filament is expected to release the energy by

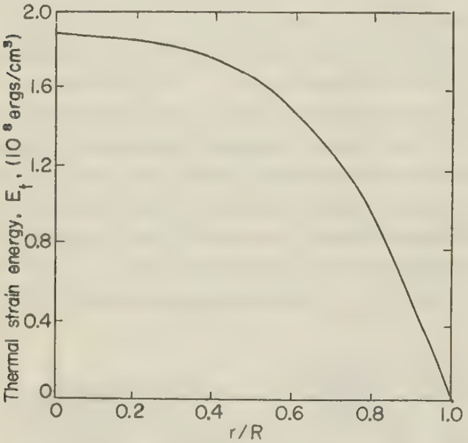

Fig. 5. Distribution curve of thermal strain energy along the radius of the "filamentary polycrystal", owing to the graphitization stress.

$$E_t\times(\text{cavity volume})=\frac{1.87}{4}\pi D^2h\times10^{-16}\quad\text{(ergs).}\tag{12}$$

Thus, the criterion of this transformation is determined by comparing the self-energy of the dislocation loop with the sum of the total surface energy of the original cavity and the thermal strain energy to be released by its collapse. It needs not to compare the free energies, for the contribution of the entropy term is so small that the difference can be neglected in approximation. Besides, as mentioned before, the core energy of the dislocation loop is nearly equal to the side surface energy of the cavity in the present case. Accordingly, one can put

(elastic energy of dislocation loop)
=(basal surface energy of the cavity)
+(thermal strain energy to be released).

Operating in c.g.s. unit, and using Eqs. (2), (5) and (12), this equality is arranged as follows,

$$\frac{Kb^2}{4}\ln\left(\frac{D_c}{2r_0}\right)=D_c(833+0.47\pi h)\times10^{-8}\tag{13}$$

where D_c represents the critical diameter (in angstroms) of the cavity-dislocation transformation. Substituting the K-factors in Table III and the proper Burgers vectors on the assumption that $r_0=3b$, the critical diameters corresponding to the six cases in the subsection 3.1 have been determined as shown in Table IV.

Table IV. Critical diameters of transformation from disciform cavities to dislocation loops, corresponding to various geometrical conditions.

Crystal modification and number of defficient planes	HEXAGONAL			RHOMBOHEDRAL		
	1	2	3	1	2	3
Critical diameter, D_c, in angstrom	225	425	1070	102	535	910

From Table IV, firstly, one can see that the aforesaid round *moiré* patterns having the diameters of several hundreds angstroms, observed by Fujita and Izui[3], correspond to the dislocation loops born of such thin cavities missing one or two atomic plance respectively. On the contrary, those thick cavities missing more than three planes may be hardly transformed to dislocation loops in the crystallite of usual artificial graphite which is seldom over thousands angstroms in diameter. Natural graphite and some special artificial ones carefully prepared may be possible to contain even such large dislocation loops, since the crystallite-size can be up to several micron. However, as mentioned in § 2, when the point vacancies and minute cavities have mostly condensed to fairly large ones, several hundreds angstroms in diameter, the driving force of cavity growth is expected to decline so remarkably that the rate of further consolidation becomes negligible, *i.e.* the state in metastable equilibrium. Accordingly, those large dislocation loops exceeding thousands angstroms in diameter may be scarcely generated except for some special treatment, *e.g.* hard quenching and radiation damage *etc.*.

---

* In this case, T denotes the difference between the graphitization and baking (solidification) temperatures.

Finally, it is worth to point out that the mechanism of cavity consolidation considered here may be applicable to the formation of the characteristic intercrystallite voids extending in nearly parallel to the basal layers. Formerly, by means of the combination of liquid displacement, gas absorption and X-ray diffraction methods, Loch and Austin[10] have evaluated the thickness of those opened voids to be ranging between 3–8 Å, which is in fairly good agreement with our supposition used in the above discussions.

§ 4. Concluding Remarks

The principal results of the preceding theoretical investigation are summerized as follows: (*1*) Through the extremely high temperature treatment for the synthesis of graphite, numerous vacancies and cavities exceeding 10^{-3} atomic per cent are introduced in several ways. (*2*) The so-called "specific free energy" of a cavity has been defined as a measure of the stability, from which it has been concluded that all the cavities and vacancies are driven to consolidate to fewer and larger ones extending on the basal planes. (*3*) In the course of the dimensional growth, the flat cavity is expected to collapse to a prismatic dislocation loop under the compressive graphitization stress in c-direction. The critical size has been determined, by comparing the energies before and after the transformation, to be ranging between, 100∼1100 Å in accordance with the geometrical conditions concerning the crystal modification and the cavity thickness, which is in fairly good agreement with the experimental observation. (*4*) The formation of the characteristic inter-crystallite voids can be explained in the similar way.

References

1) Takuro Tsuzuku: J. Phys. Soc. Japan **15** (1960) 1373.
2) F. Seitz: Phys. Rev. **79** (1950) 890.
3) Eiichi Fujita and Kazuhiko Izui: Orally published in the 14th annual meeting of the Physical Society of Japan, at Hiroshima, Oct. 1959.
4) L. Pauling: *Nature of the Chemical Bond, Cornell Univ. Press*, 1948.
5) R. O. Brennan, J. Chem. Phys. **20** (1952) 40.
6) C. Malmstrom, R. Keen and L. Green, J. App. Phys. **22** (1951) 583
7) H. Lipson and A. R. Stokes: Nature, Lond. **149** (1942) 328.
8) J. Hoerni: Nature, Lond. **164** (1949) 1045.
9) A. J. E. Foreman: Acta Met. **3** (1955) 322.
10) For example, A. J. Decker: *Solid State Physics, Chap. 2, Prentice-Hall Inc.*, 1957.
11) L. D. Loch and A. E. Austin: *Proc. 2nd Carbon Conf.* (1955), 65.

JOURNAL OF THE PHYSICAL SOCIETY OF JAPAN, Vol. 16, No. 3, MARCH 1961

Ferroelectric Properties of X-ray Damaged Rochelle Salt

By Kenkichi OKADA

Department of Natural Science, Nagoya Branch, Aichi-Gakugei University, Nagoya

(Received October 7, 1960)

Radiation damage effects by X-ray in rochelle salt are studied experimentally and theoretically. Double hysteresis loop is explained as a superposition of two biased single loops. Each biased single loop corresponds to each of the two oppositely polarized domains, of which the crystal is composed. Single domain crystals show biased single loops when damaged, and the internal bias thus induced can be compensated by an external dc biasing field. But the Curie point of the damaged crystals compensated by this suitable external field is lower than that of the virgin by ΔT, which depends upon the X-ray dosage. In this respect the effect of damage differs from that of the stress. It is assumed that the irradiation gives rise to polar anisotropy centers which produce effective bias fields in undamaged ferroelectric regions. Irradiation time dependences of the spontaneous polarization, the coercive field and the internal bias are studied. A phenomenological theory is developed to explain the various phenomena. The polarization within the polar anisotropy center is estimated to be the order of 100 esu near the shifted Curie point.

§ 1. Introduction

Since Vigness[1)] found coloring and disintegration in rochelle salt irradiated by X-rays in 1935, there has been no investigation on the radiation damage effects in ferroelectric substances. In 1956 Rogers[2)] observed that dielectric constant of $BaTiO_3$ is decreased and its 120°C peak disappears by pile irradiation. On the same substance several investigators[3-5)] have studied the changes of their properties by radiation damages. Recently, Lefkowitz[6)] found in $BaTiO_3$ with $PbTiO_3$ additive shifts of the Curie point and the other changes of properties due to pile irradiation. On the other hand, Iurin[7)] found double hysteresis loop of γ-irradiated rochelle salt, and Eisner[8)] observed that the dielectric constant of X-ray irradiated rochelle salt is increased by dc biasing field. Chynoweth[9)] studied in detail the same effects and time-dependent phenomena of X-ray damaged triglycine sulfate. Then several investigators gradually became interested in the field of the radiation damage of ferroelectric materials. By Krueger[10)] γ-effects of rochelle salt, by Moulton *et al.*[11)] paramagnetic resonance of X-ray damaged rochelle salt and by Toyoda *et al.*[12)] diffused scattering in X-ray photograph of a heavily γ-damaged rochelle salt have been studied.

Investigations on impure or mixed ferroelectric materials which have similar phenomena to those of damaged crystals have been reported by several authors[13-16)]. But the radiation damage of ferroelectric materials has not been studied theoretically as yet. We developed a phenomenological theory of X-ray damaged rochelle salt and made related observations. Since by the preceding study[17)] it was suggested that there are similar phenomena near the upper and lower Curie points, only the upper Curie point is considered in connection with the ferro-para transition in this report.

§ 2. Specimen and Experimental Apparatus

Specimens were A-cut plates of about $0.1 \times 1.2 \times 1.5\,\mathrm{cm}^3$ cut out from a single crystal of rochelle salt. Electrodes were gold leaves which were attached on the polished surfaces moitsend by breathing without any adhesive. During the X-ray irradiation, the specimen was held in a copper vessel, the temperature of which was kept at about 5°C, unless mentioned otherwise.

The X-ray tube had a tungsten target and a beryllium window, and was running at 40 kV and 15 mA. The electroded specimen was irradiated through two sheets of aluminium foil 0.02 mm thick each (the window of the copper vessel and the electrode of the sample holder) and a bakelite plate 1 mm thick. Hysteresis loops were obtained by means of the well-known Sawyer-Tower circuit at 60 cps on

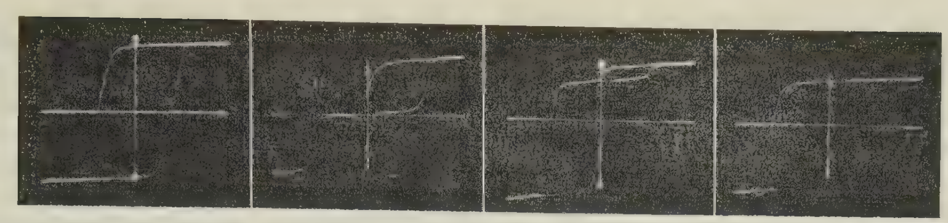
(A) (B) (C) (D)

Fig. 1. Anomalous hysteresis loops of X-ray damaged rochelle salt crystals. (A) normal loop of the virgin. (B) symmetrical double loop. (C) asymmetrical double loop. (D) biased single loop of a damaged single domain crystal.

a cathode-ray oscilloscope. For the measurement of the dielectric constant an ac bridge of frequency 1000 cps and amplitude 5 V/cm was used.

§ 3. Hysteresis Loops of Damaged Crystal and Stressed Crystal

The hysteresis loop of a virgin crystal in in Fig. 1 (A) was changed to a double loop in Fig. 1 (B) after 3 hours irradiation. Sometimes an asymmetrical double loop shown in Fig. 1 (C) was also obtained. By application of a dc field of about 80 V/cm or of a shear stress during irradiation, the loop always became a biased single loop shown in Fig. 1 (D). When the dc field is positive the bias of the loop is negative and *vice versa*. These anomalous hysteresis loops resemble closely those of electrically or mechanically stressed virgin crystals, shown in Fig. 2.

Anomalous hysteresis loops have been found on GASH by Holden *et al.*[18)]. The shape of the loop has been correlated with the location of the specimen in the mother crystal. This anomaly of the loop may be due to an internal stress in the crystal grown in the ferroelectric state. Therefore, at a first glance, the anomalous hysteresis loops of these damaged crystals also may be considered as due to an internal stress produced by lattice imperfections. It will be, however, shown below that they can not be entirely attributed to the internal stresses, and a new mechanism will be proposed.

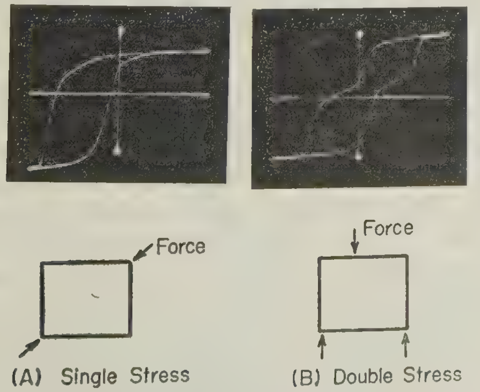

Fig. 2. Hysteresis loops of stressed crystals.

§ 4. Qualitative Explanation of Anomalous Hysteresis Loop of Damaged Crystal

It was shown experimentally that when two ferroelectric condensers showing single loops are biased in the opposite directions, as in Fig. 3 (A) and (B), and are connected in parallel, the resultant hysteresis loop becomes double as illustrated in Fig. 3 (C). This result leads us to a qualitative explanation of anomalous loops of damaged crystals, making use of the method developed by Sawaguchi *et al.*[16)] in the study of aging and double loops of $Pb_{\lambda}Ca_{1-\lambda}TiO_3$.

By the effects of radiation damage, some

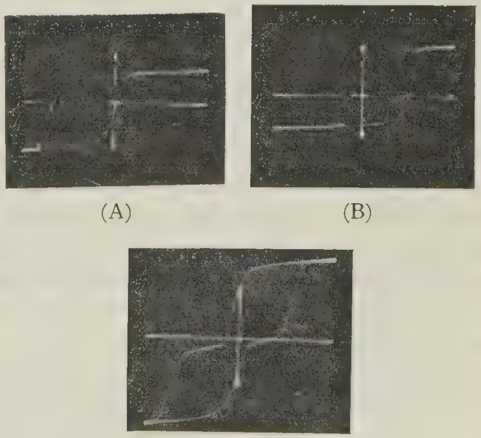
(A) (B)

(C)

Fig. 3. Superposition of two biased loops. (C) is a resultant loop of two ferroelectric condensers of (A) and (B) connected in parallel.

dipoles may be stabilized in the direction of the spontaneous polarization and the crystal may be given a property to be called "polar anisotropy". When a single domain crystal which has positive spontaneous polarization under a mechanical or an electrical bias is brought into a state of positive polar anisotropy, the polarization will become difficult to reverse, and the hysteresis loop will be shifted to the negative E-direction, and *vice versa*. When a multi-domain crystal is damaged, each 180° domain is brought into a state of anti-parallel polar anisotropy. Its hysteresis loop will change into a double loop which is obtained as a superposition of two loops biased in the opposite directions. Therefore, relative height of each partial loop in the double loop will be equal to the volume fraction of each domain.

No change of the domain structure occurs by the damage, but the damage causes the impression of the domain structure in the crystal, that is, the domain walls are stabilized and becomes unable to move until a strong electric field is applied, which is a function of the degree of the polar anisotropy[17]. Recently Abe[19] also proposed a theory to explain the double loop in which the domain wall energy was taken to be a function of the position.

§ 5. Dielectric Susceptibilities *vs.* External DC Biasing Fields* of Damaged Crystal and Stressed Crystal

Fig. 4 is a plot of the dielectric constants of a damaged crystal having a double loop of Fig. 1 (B) and of a virgin crystal at temperatures from −27° to 35°C. Heights of the peaks are reduced and the transitions are blurred in the damaged crystal. Peaks are shifted slightly to get closer to each other. Outside the two peaks, the Curie-Weiss law is no longer satisfied. By applying an external dc biasing field of proper sign and magnitude, the peaks can be sharpened, clear transitions revealed, and the upper peak shifted further to low temperature and the lower peak to high temperature[17].

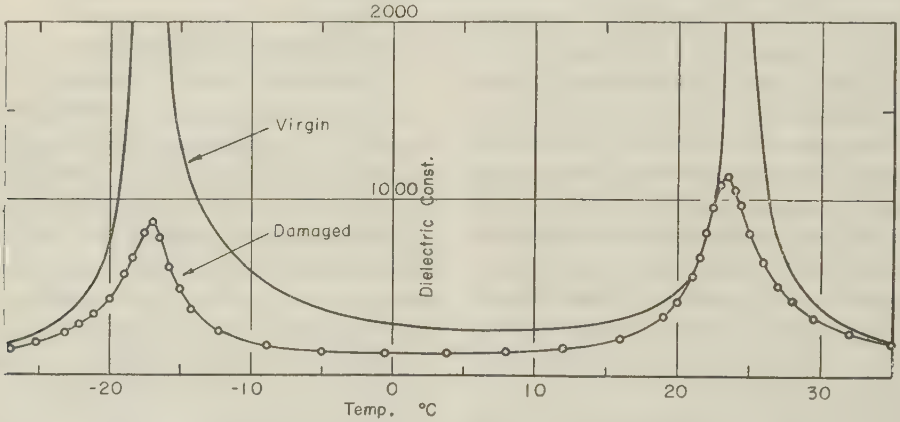

Fig. 4. Temperature dependences of dielectric constant of a double loop crystal damaged by 3 hours irradiation and that of the virgin.

In order to consider theoretically, temperature dependences of susceptibilities of bised single loop crystals and effects of the external dc biasing field on them near the upper Curie point were measured in detail. For comparison those of a stressed crystal were also measured.

(1) *Biased Single Loop Crystal*

On application of a negative external dc biasing field to a crystal having a negatively biased single loop, the clear transition reappears, and re-application of a positive field causes further blurring of the transition. Fig. 5 (A) illustrates this on a specimen having a loop of Fig. 1 (D). Under the external dc biasing field of −220 V/cm, its peak was the sharpest and the position was shifted to the lowest temperature. Negative fields stronger than this blurred the peak and shifted its position to high temperature again as shown by dotted lines in Fig. 5(A). By positive fields, only decreases in the peak height and shifts of the position to the high temperature occurred. Fig. 5(B) is the plot of the reciprocal susceptibility. Under the external biasing field of −220 V/cm, it satisfies the Curie-Weiss law, the constant of which is the same as that of the virgin crystal above the Curie point. The difference of the Curie temperature between the damaged and the virgin is about −1.3°C.

---

* "External dc biasing fiield" means a dc field superposed to the ac field in dielectric constant measurement, distingushing from "internal bias" which means a shift of the hysteresis loop.

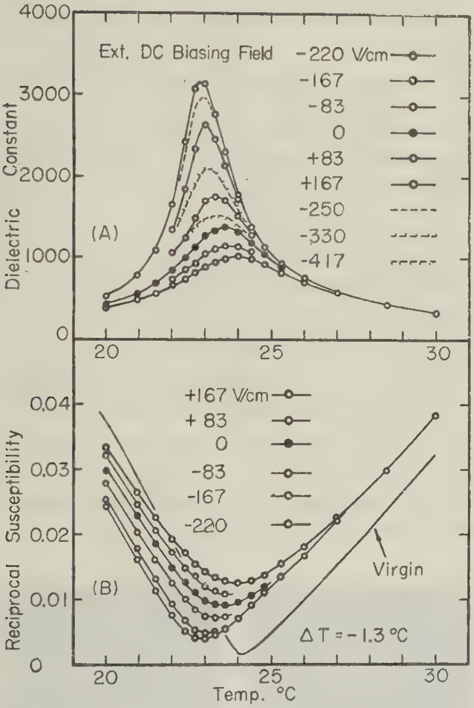

Fig. 5. Effects of external dc biasing fields on dielectric constant and reciprocal susceptibility of a biased single loop crystal damaged by 3 hours irradiation.

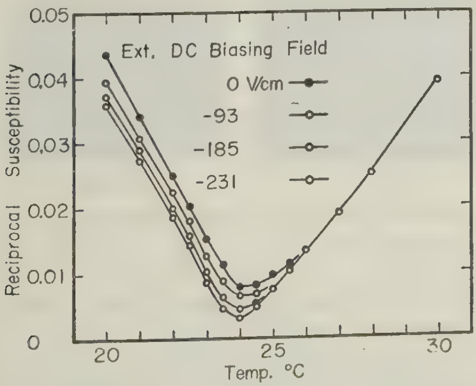

Fig. 6. Effects of external dc biasing fields on reciprocal susceptibility of a stressed crystal of Fig. 2 (A).

(2) *Comparison of Damaged Crystal and Stressed Crystal*

Fig. 6 gives effects of external dc biasing fields on reciprocal susceptibility of a stressed crystal of Fig. 2(A). The same phenomenon is found as in the damaged crystal, but one of the difference is the absence of shift of the Curie point in the case of the stressed crystal. Therefore, it turns out that the effect of radiation is not to introduce some internal stresses into the crystal. Reciprocal susceptibilities of some specimens damaged to different degrees are given as functions of the external dc biasing fields at temperatures near each Curie points in Fig. 7.

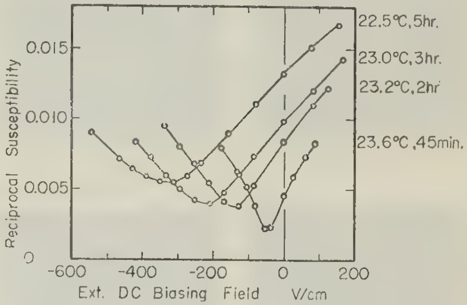

Fig. 7. External dc biasing field *vs.* reciprocal susceptibilities of various damaged crystals of biased single loops at temperatures near each minimum positions in the plot of $1/\eta$ *vs.* T as Fig. 5 (B). Irradiation time of each specimen and the temperature at dielectric constant measurement are written in the figure. Irradiation temperature is 5°C.

§ 6. Temperature Dependence of Internal Bias

Relation between the temperature and the internal bias as defined by Fig. 8 for the oscilloscope data is given in Fig. 9. The internal bias has a weak temperature dependence. Fig. 10 shows hysteresis loops at various temperatures.

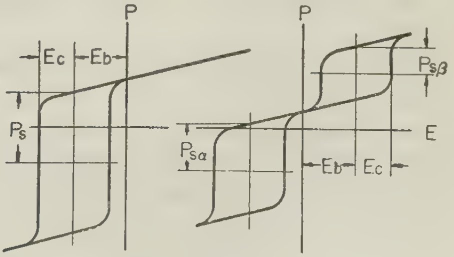

Fig. 8. Definitions of spontaneous polarization P_s, coercive field E_c and internal bias E_b.

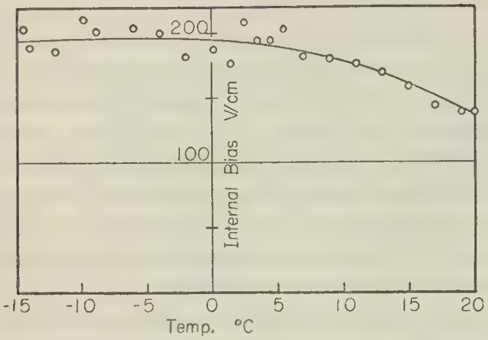

Fig. 9. Temperature dependence of internal bias obtained from oscilloscope data.

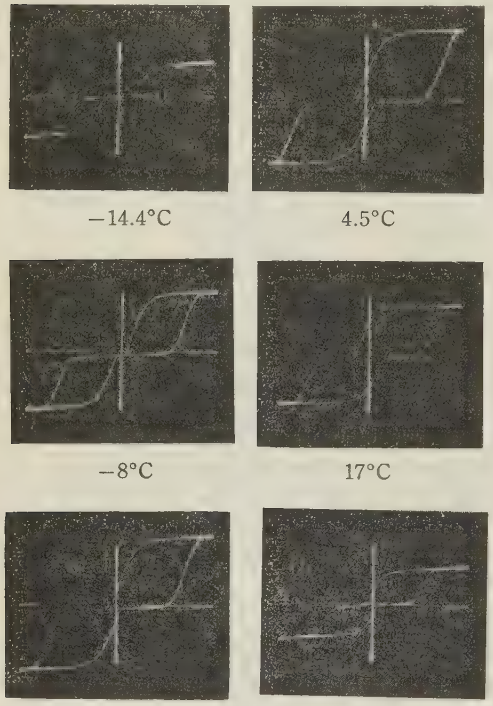
−14.4°C 4.5°C

−8°C 17°C

−2°C 21°C

Fig. 10. Variation of the shape of double loop with temperature.

§ 7. Spontaneous Polarization, Coercive Field and Internal Bias *vs.* X-ray Irradiation Time

Variation of P_s, E_c and E_b with irradiation time are given in Fig. 11 (A). No electric field was applied except an ac field of about 1 minute duration necessary for taking oscillograms. Fig. 12 shows changes of the shape of the hysteresis loop. P_s decreases slightly but steadily, E_c increases and E_b increases almost linearly with irradiation time. These features are somewhat different from those of triglycine sulfate[9]. The sweep amplitude for the loop observation was made sufficiently large in anticipation of increases in E_c and E_b.

Irradiation under influences of an ac field larger than coercive field didn't give any bias effect in the hysteresis loop. As shown in Fig. 11 (B), in comparison to the case of no field in Fig. 11 (A), P_s decreased in the same manner but the increase in E_c was more rapid.

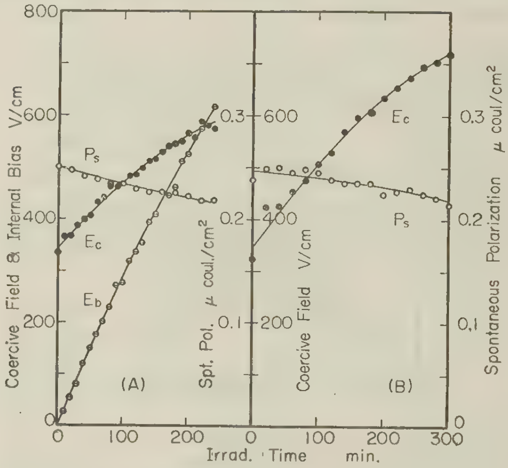

Fig. 11. Spontaneous polarization, coercive field and internal bias *vs.* irradiation time. (A) referes to irradiation without and (B) to with ac field of 2000 V/cm at about 5°C.

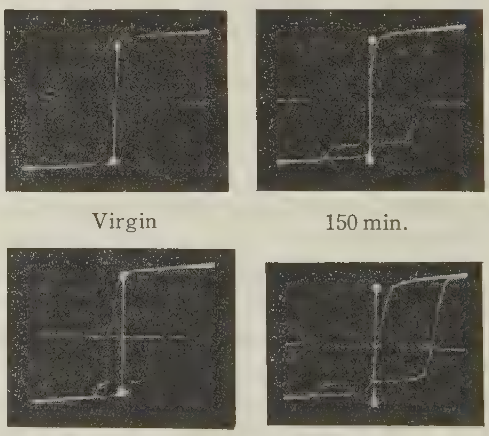
Virgin 150 min.

60 min. 240 min.

Fig. 12. Variation of the hysteresis loop with irradiation time.

This specimen damaged under the influences of the ac field had time-dependent phenomena. At the removal of the ac field there appeared a meta-stable internal bias in the loop which was annealed out gradually either by re-application of the ac field or by heating.

Crystals damaged above the Curie point had the same feature. On the other hand, the internal bias produced by irradiation without an ac field at the ferroelectric temperature region which is treated in this report is stable against electrical and thermal agitations. It seems that the spontaneous polarization which stays constant while the crystal is irradiated is necessary to obtain the permanent internal bias. These phenomena which are important for study of the radiation damage mechanism will be investigated in the near future.

§ 8. Basis for Theoretical Treatment

In order to explain the various phenomena mentioned above theoretically, we assumed, following Sawaguchi *et al.*[16)], a simple model as below.

(1) When a crystal is damaged at the ferroelectric temperature region without an ac field, some dipoles are stabilized in the direction of the spontaneous polarization, that is, polar anisotropy centers are introduced.

(2) The polar anisotropy centers show a paraelectric behavior in response to their external field.

(3) The polar anisotropy centers interact with the other ferroelectric region.

Symbols to be used are;

λ: volume fraction of the ferroelectric part in the crystal,

μ: volume fraction occupied by polar anisotropy centers, where $\lambda+\mu=1$,

P_f: polarization of the λ region,

P_a: polarization of the μ region,

P_0: polarization of the μ region without field,

P: resultant polarization of the crystal observable on the oscilloscope,

E_f: electric field of the λ region,

E_a: electric field of the μ region,

E: external field of the crystal,

k: interaction constant between the λ and μ regions,

σ: dielectric susceptibility of the μ region.

It is assumed that,

$\frac{1}{2}\chi P_f{}^2+\frac{1}{4}\xi P_f{}^4$: free energy of unit volume of the λ region,

$\frac{1}{2}\frac{1}{\sigma}(P_a-P_0)^2$: free energy of unit volume of the μ region, and

$\frac{1}{2}\lambda\mu k(P_f-P_a)^2$: interaction energy between the λ and μ regions.

Then, the free energy of a unit volume of a damaged single domain crystal U is

$$U=\lambda\left(\frac{1}{2}\chi P_f{}^2+\frac{1}{4}\xi P_f{}^4\right)+\frac{1}{2}\frac{\mu}{\sigma}(P_a-P_0)^2+\frac{1}{2}\lambda\mu k(P_f-P_a)^2\,.$$

From $\partial U/\partial P_f=\lambda E_f$ and $\partial U/\partial P_a=\mu E_a$, we obtain

$$E_f=\chi P_f+\xi P_f{}^3+\mu k)(P_f-P_a)\,, \qquad (1)$$

and

$$E_a=\frac{1}{\sigma}(P_a-P_0)-\lambda k(P_f-P_a)\,. \qquad (2)$$

§ 9. Fundamental Formula

Since the distributions and the shapes of the two regions λ and μ in the crystal are unknown, two special cases shown in Fig. 13 are considered.

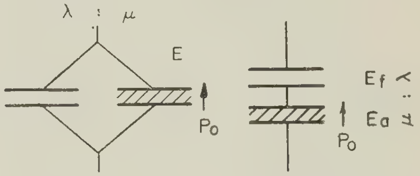

(A) Paraller Type (B) Series Type

Fig. 13. Two types of distribution of polar anisotropy centers.

(1) *Parallel Type*, Fig. 13 (A)

Polarization observed on the oscilloscope is

$$P=\lambda P_f+\mu P_a\,. \qquad (3)$$

External field is $E=E_f=E_a$. Hence, from Eq. (1) and (2)

$$\chi P_f+\xi P_f{}^3+k(P_f-P_a)-\frac{1}{\sigma}(P_a-P_0)=0\,. \quad (4)$$

Reciprocal susceptibility $1/\eta$ as a function of P_f is obtained from Eqs. (1), (3) and (4), that is,

$$\frac{1}{\eta}=\frac{dE}{d(\lambda P_f+\mu P_a)}=\frac{(1+\lambda\sigma k)(\chi+3\xi P_f{}^2)+\mu k}{\mu\sigma(\chi+3\xi P_f{}^2)+\lambda+\sigma k}\,. \qquad (5)$$

From Eqs. (1) and (4) E as a function of P_f is

$$E=\frac{1}{1+\sigma k}\left[-\mu kP_0+(\chi+\lambda\sigma k\chi+\mu k)P_f+(1+\lambda\sigma k)\xi P_f{}^3\right]. \qquad (6)$$

(2) *Series Type*, Fig. 13 (B)

From Eqs. (1) and (2)

$$E=\lambda E_f+\mu E_a=\lambda(\chi P_f+\xi P_f^3)+\frac{\mu}{\sigma}(P_a-P_0)\ . \tag{7}$$

Assuming that the boundary of the two regions has no charge accumulation, electric displacement D is $D=E_f+4\pi P_f=E_a+4\pi P_a$. Therefore,

$$D=\chi P_f+\xi P_f^3+\mu k(P_f-P_a)+4\pi P_f\ , \tag{8}$$

$$D=\frac{1}{\sigma}(P_a-P_0)-\lambda k(P_f-P_a)+4\pi P_a\ . \tag{9}$$

From Eqs. (8) and (9)

$$(\chi P_f+\xi P_f^3)+(4\pi+k)(P_f-P_a)-\frac{1}{\sigma}(P_a-P_0)=0\ . \tag{10}$$

Using Eqs. (7), (8) and (10),

$$\frac{1}{\varepsilon}=\frac{1}{1+4\pi\eta}=\frac{dE}{dD}$$

is calculated, where ε is the dielectric constant. As a result, $1/\eta$ and E are the same functions of P_f as those of the parallel type respectively, but $(4\pi+k)$ substituted for k:

$$\frac{1}{\eta}=\frac{[1+\lambda\sigma(4\pi+k)](\chi+3\xi P_f^2)+\mu(4\pi+k)}{\mu\sigma(\chi+3\xi P_f^2)+\lambda+\sigma(4\pi+k)}\ ,$$

and

$$E=\frac{1}{1+\sigma(4\pi+k)}\{-\mu(4\pi+k)P_0+[\chi+\lambda\sigma(4\pi+k)\chi+\mu(4\pi+k)]P_f+[1+\lambda\sigma(4\pi+k)]\xi P_f^3\}\ .$$

§ 10. Calculation

From the preceding section it is suggested that both the parallel and the series type distribution contribute to changes of ferroelectric properties in a similar way. So we will henceforth calculate on the parallel type only.

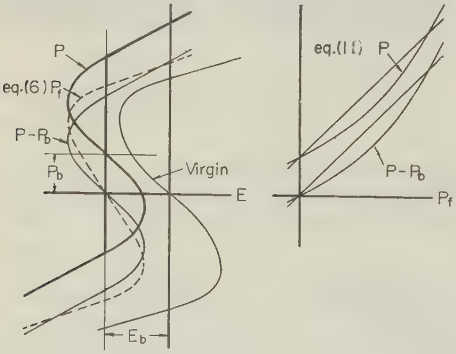

Fig. 14. Theoretical hysteresis loop of damaged single domain crystal. (schematical) E_b is the internal bias. The bias P_b is not observed by the Sawyer-Tower circuit. The coercive field may be reduced largely by the domain wall motion in the experimental result.

(1) *Hysteresis Loop of Single Domain Crystal*

Eq. (6) gives the functional relation between E and P_f. But it is necessary to represent E as a function of P, since observable hysteresis loops are E-P relations. From Eqs. (3) and (4)

$$P=P_f+\frac{\mu}{1+\sigma k}[P_0-(1-\sigma\chi)P_f+\sigma\xi P_f^3]\ . \tag{11}$$

Eqs. (6) and (11) give together the functional relation between E and P, which is illustrated in Fig. 14 schematically. The loop is biased along the E and P axes by E_b and P_b respectively, and its shape is slightly changed, where

$$E_b=-\frac{\mu k}{1+\sigma k}P_0\ , \tag{12}$$

and

$$P_b=\frac{\mu}{1+\sigma k}P_0\ . \tag{13}$$

But the bias P_b is not observed by the Sawyer-Tower circuit[20]. E_b is the internal bias.

(2) *Spontaneous Polarization*

Spontaneous polarization P_s under the external dc field equal to the internal bias of the loop is obtained as below. In Eq. (6) putting $E=E_b$,

$$\xi P_f^2=-\frac{\chi(1+\lambda\sigma k)+\mu k}{1+\lambda\sigma k}\ .$$

Substituting this into Eq. (11),

$$P_s=P-P_b=\lambda\frac{1+\sigma k}{1+\lambda\sigma k}\left[-\frac{\chi}{\xi}-\frac{\mu k}{\xi(1+\lambda\sigma k)}\right]^{1/2}\ . \tag{14}$$

Neglecting the higher order terms of μ, we obtain

$$P_s\simeq\left(-\frac{\chi}{\xi}\right)^{1/2}\left[1-\frac{1-k/(2\chi)}{1+\sigma k}\mu\right]\ . \tag{15}$$

Change of the spontaneous polarization ΔP_s is

$$\Delta P_s\simeq-P_{vs}\frac{1-k/(2\chi)}{1+\sigma k}\mu\ , \tag{16}$$

where $P_{vs}=(-\chi/\xi)^{1/2}$ is the spontaneous polarization of the virgin crystal.

(3) *Reciprocal Susceptibility and Effect of External Dc Biasing Field*

At the Curie point T_c of the virgin crystal where $\chi=0$, from Eq. (5)

$$\frac{1}{\eta}=\frac{3(1+\lambda\sigma k)\xi P_f^2+\mu k}{3\mu\sigma\xi P_f^2+\lambda+\sigma k}>0\ .$$

Therefore, susceptibility stays finite even at T_c.

In order to have infinite dielectric constant it is necessary that $dE/dP=1/\eta=0$ and $d^2E/dP^2=0$. From Eq. (5) the former condition is

$$(1+\lambda\sigma k)(\chi+3\xi P_f{}^2)+\mu k=0\,. \tag{17}$$

Differentiating Eq. (5) with respect to $P=\lambda P_f+\mu P_a$ by the aid of Eq. (11), the latter condition becomes $P_f=0$. Substituting this into Eq. (6),

$$E=-\frac{\mu k}{1+\sigma k}P_0=E_b\,.$$

Therefore, the infinite dielectric constant occurs under the external dc biasing field equal to the internal bias at the temperature satisfying the next equation. Putting $P_f=0$ in Eq. (17)

$$\chi=-\frac{\mu k}{1+\lambda\sigma k}\,. \tag{18}$$

Curie point of the damaged crystal $T=T_c+\varDelta T$ sharpened by the external field is given by means of Eq. (18) and the relation $\chi=(T-T_c)/C$, which is assumed to be satisfied just below the virgin Curie point. T_c and C are the Curie temperature and the Curie-Weiss constant of the virgin crystal respectively. That is,

$$\varDelta T=C\chi=-\frac{\mu k}{1+\lambda\sigma k}C\,. \tag{19}$$

It turns out that the Curie point is lowered by the damage. At this temperature $T_c+\varDelta T$ the spontaneous polarization vanishes from Eqs. (14) and (18). Eliminating μ from Eq. (12) and (19)

$$\frac{\varDelta T}{E_b}=\frac{1+\sigma k}{1+\lambda\sigma k}\frac{C}{P_0}\,. \tag{20}$$

(4) *Curie-Weiss Law*

From the preceding argument $\chi>-\mu k(1+\lambda\sigma k)$ above the Curie point of the damaged crystal. Then, under the external field $E=E_b$, from Eq. (6) $P_f=0$. Eq. (5) becomes

$$\frac{1}{\eta}=\frac{(1+\lambda\sigma k)\chi+\mu k}{\mu\sigma\chi+\lambda+\sigma k}\,.$$

If σ and k are assumed to be temperature independent, temperature dependency of $1/\eta$ is

$$\frac{d}{dT}(1/\eta)=\frac{\lambda}{C}\left(\frac{1+\sigma k}{\mu\sigma\chi+\lambda+\sigma k}\right)^2\,. \tag{21}$$

When $\lambda\simeq 1$, it becomes $d/dT(1/\eta)=1/C$ naturally.

(5) *Hysteresis Loops of Multi-domain Crystals*

As depicted in Fig. 15, volume fractions of anti-parallel 180° domians are put α (for positive P_s) and β (for negative P_s). From Eq. (12), each α and β domains have single loops biased by

$$E_b=\mp\frac{\mu k}{1+\sigma k}P_0\,,$$

respectively. Double loop is considered as a superposition of these biased single loops. Since spontaneous polarizations of both domains per unit area at $E=E_b$ are P_s given by Eq. (14), ratio of the loop heights is equal to α/β.

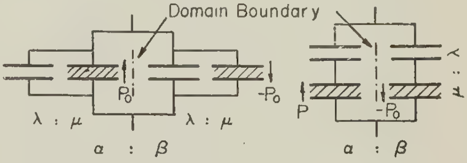

(A) Paraller Type (B) Series Type

Fig. 15. Distributions of polar anisotropy centers in multi-domain crystals.

§ 11. Comparison Between Experimental and Theoretical Results

(1) *Hysteresis Loop and Internal Bias*

The theoretical hysteresis loop Fig. 14 explains qualitatively the experimental result. But the bias P_b can not be observed by the Sawyer-Tower circuit, and owing to the domain wall motion the theoretical hysteresis loop may give a value of the coercive field larger than the experimental value. From Fig. 1, the ratio of heights of the two partial loops of the double loop can be considered to be equal to the ratio of the volumes of the anti-parallel domains. From Eq. (12), if μ is proportional to the X-ray irradiation time, the internal bias E_b must increase linearly with the time. Fig. 11 (A) illustrates this fact. From Eq. (12), assuming that σ and k are temperature independent constants, P_0 may have the same temperature dependency as E_b given in Fig. 9.

(2) *Shift of Curie Point and Estimation of P_0*

Ratio of the shift of Curie point and the internal bias is given by Eq. (20). It depends upon the X-ray dosage through λ. In a slightly damaged crystal $\lambda\simeq 1$, then

$$\frac{\varDelta T}{E_b}=\frac{C}{P_0}$$

at $\lambda\simeq 1$. Fig. 16 shows a relation between the shift of Curie point and the external dc biasing field which gives the sharpest peak in the plot of the dielectric constant *vs.* temperature. Four specimens have been damaged by X-ray dosages of 45 min., 2 hrs., 3 hrs. and 5 hrs. irradiations. E_b in the above equation is the internal bias (shift of the hysteresis loop). This internal bias at the Curie point could be obtained by the exterpolation of the plot of E_b-T, for example Fig. 9. But it is difficult to verify experimentally that the internal bias at the vicinity of the Curie point has the same value as the external dc biasing field which gives the sharpest peak, owing to the fact that the loop becomes slender near the Curie point and E_b is somewhat annealed by the strong ac field. From Fig. 9 the internal bias at about 23°C is suggested to be almost a half of that at 5°C. By the comparison of the external dc biasing field giving the minimum reciprocal susceptibility (shown in Fig. 7) to the internal bias at 5°C plotted in Fig. 11, taking account of the decrease in the internal bias with temperature elevation, these two values may be assumed to be equal.

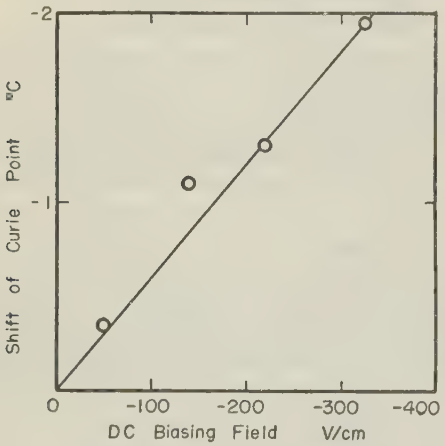

Fig. 16. Relation between the shifts of the Curie point and the external dc biasing fields which give the sharpest transitions in four biased single loop crystals damaged by various X-ray dosages.

$\Delta T/E_b=C/P_0$ is the gradient at the origin of the plot of E_b *vs.* ΔT, and may be approximately 1.8°C/esu from Fig. 16. Putting $C=178$,

$$P_0 \simeq 100 \text{ esu}\ .$$

Dipoles of this magnitude are stabilized by the irradiation, but the value may vary with temperature as mentioned at the end of the preceding subsection.

(3) *Spontaneous Polarization and Coercive Field*

From Eqs. (14), (15) or (16) the spontaneous polarization decreases by increase of μ with irradiation time. Fig. 11 (A) illustrates this fact too. The coercive field increases with the irradiation time. It may be suggested that some lattice imperfections introduced by irradiation prevent the domain wall motion, so that the coercive field is increased.

(4) *On the Quantities μ, σ and k*

In Eq. (21) $\lambda=1-\mu\simeq1$ is necessary for $d/dT(1/\eta)=1/C$ above the Curie point. Curve of $1/\eta$ against temperature under a suitable external dc biasing field is parallel with that of the virgin as shown in Fig. 5. Then, it is suggested that $\lambda\simeq1$ or $\mu\ll1$ in a crystal damaged by such a dosage of irradiation.

From Eqs. (12), (16) and (19) σ and k may be represented by the known quantities and their numerical values may be estimated. Eliminating λ and μ from Eqs. (12) and (19),

$$\frac{1}{\Delta T}=\frac{P_0}{C}\frac{1}{E_b}+\frac{\sigma}{C}\ .$$

From the experiment the linear plot of $1/\Delta T$ *vs.* $1/E_b$ intersects with $1/\Delta T$ axis near the origin, and σ may be considered to be small in comparison with $C=178$. For these estimations a more abundant experimental data are necessary, which are left for the future study.

§ 12. Summary and Discussion

X-ray damage effects in rochelle salt were studied, and a phenomenological theory was developed. Main results are as follows:

(1) X-ray irradiation at the ferroelectric temperature region gives rise to internal bias in the single domain crystal. The hysteresis loop is biased in the E-direction. The ferro-para transition is blurred. These properties resemble those of the externally biased virgin crystal.

(2) This internal bias can be compensated by a suitable external dc biasing field. The dielectric constant is thereby increased and the transition is sharpened again.

(3) There are some effects which are not compensated by the external dc biasing field. The Curie point of the damaged crystal sharpened by the suitable external dc field is lower than that of the virgin crystal. The shift of of the Curie point increases with the irradiation time. The spontaneous polarization is reduced, and the coercive field is increased by the irradiation. Therefore, in comparison with the externally stressed virgin crystal, the ra-

diation damage does not only introduce the internal bias, but also gives rise to a new type of imperfection in the crystal which is treated in the theoretical investigation.

(4) The internal bias increases linearly with irradiation time, and has a weak temperature dependence.

(5) By the irradiation the domain structure is impressed in the initial structure which the crystal possessed before the irradiation. The multi-domain crystal shows double hysteresis loop, which is explained as a superposition of two single loops biased in the opposite directions.

(6) Irradiation under the influences of a strong ac field dose not give rise to any permanent internal bias, but increases in the coercive field occur. Crystals damaged above the Curie point have the same feature.

(7) A phenomenological theory can explain successfully most of the above phenomena. The theory assumes a simple model, that is, some dipoles are stabilized in the direction of the spontaneous polarization by the irradiation, which act as polar anisotropy centers. The region occupied by the centers shows a paraelectric behavior in responce to its external field, and interacts with the other ferroelectric region. The value of this stabilized polarization is estimated to be about 100 esu near the shifted Curie point, and is suggested to have the same weak temperature dependence as that of the internal bias.

The present author wishes to express his sincere thanks to Professor T. Nakamura for the kind guidances and encouragements, to Dr. E. Sawaguchi and Dr. R. Abe for their valuable discussions, and to Mr. K. Toyoda for the helpful informations.

References

1) I. Vigness: Phys. Rev. **48** (1935) 198.
2) F. T. Rogers: J. Appl. Phys. **27** (1956) 1066.
3) M. C. Wittels and F. A. Sherrill: J. Appl. Phys. **28** (1957) 606.
4) R. C. Miller and R. D. Heidenreich: J. Appl. Phys. **29** (1958) 957.
5) I. Lefkowitz and T. Mitsui: J. Appl. Phys. **30** (1959) 269.
6) I. Lefkowitz: J. Phys. Chem. Solids **10** (1959) 169.
7) V. A. Iurin: Izv. Akad. Nauk SSSR Ser. Fiz. **21** (1957) 329.
8) I. Ia. Eisner: Sov. Phys. Crystallography **2** (1957) 293.
9) A. G. Chynoweth: Phys. Rev. **113** (1959) 159.
10) H. H. A. Krueger: Bull. Amer. Phys. Soc. Ser. II **4** (1959) 425.
11) G. C. Mouton, W. G. Moulton and W. B. Ard, Jr.: Bull. Amer. Phys. Soc. Ser. II **5** (1960) 73.
12) K. Toyoda, A. Shimada and T. Tanaka: J. Phys. Soc. Japan **15** (1960) 536.
13) I. Ia. Eisner: Izv. Akad. Nauk SSSR Ser. Fiz. **21** (1957) 334.
14) V. P. Konstantinova and V. A. Iurin: Sov. Phys. Crystallography **2** (1957) 292.
15) L. E. Cross: Nature 4603 (1958) 179.
16) E. Sawaguchi and M. L. Charters: J. Amer. Ceramic Soc. **42** (1959) 157.
17) K. Okada: J. Phys. Soc. Japan **15** (1960) 363.
18) A. N. Holden, W. J. Merz, J. P. Remeika and B. T. Matthias: Phys. Rev. **101** (1956) 962.
19) R. Abe: J. Phys. Soc. Japan **15** (1960) 795.
20) W. G. Cady: *Piezoelectricity* (Mc-Grow Hill 1949) 570 p.

JOURNAL OF THE PHYSICAL SOCIETY OF JAPAN, Vol. 16, No. 3, MARCH, 1961

An Effect of Heat Treatment on WO_3 Single Crystal

I. Various Patterns

By Tadao HORIE and Tsuruji IWAI

Faculty of Science, Osaka University

(Received October 31, 1960)

After having been heated in vacuum with or without metallic vapor at a reduced pressure, WO_3 single crystals show various patterns, that is, a pattern composed of green stripes, a bluish splashed pattern, a pattern of dark lines, and so on. Each of them has its own habits of orientation with respect to the crystal axes as well as of color. Which type of these patterns does come out entirely depends on the condition of heat treatment.

§ 1. Introduction

Much attention has recently been payed by many authors to pretty but tiny pieces of WO_3 single crystals, especially because of an expectation for its being a ferroelectric or antiferroelectric substance.[1)-3)] A good many elaborate works have so far been devoted to measurements of a variety of physical properties, including the X-ray analysis of the crystal structure[4)-11)], the dielectric constant,[12)] the electrical resistivity,[2),10),13)] the optical absorption threshold,[14),15)] the indices of refraction,[16)] the heat capacity,[2)] the thermal expansion coefficient,[9),17)] the domain structures,[10),18)-21)] the Hall constant,[13)] the thermoelectromotivity,[2)] and so on.

However, its high electrical conductivity above room temperature and its volatility at still higher temperatures seem to have prevented its various important characteristics from being disclosed. For instance, its semiconductive behavior blinds the intrinsic dielectric property of the crystal. The temperature dependence of the optical property is also obscured by its sublimation character.

In addition to these circumstances, another strange and complicated phenomenon will be presented here in brief. Roughly speaking, the WO_3 single crystal has a perovskite structure modified from the $BaTiO_3$ one, the W ion being put in place of the Ti, and the site of the Ba ion being left unoccupied. The O_6-octahedra, therefore, are sharing corners with one another throughout the crystal. The crystal has several transition points near −40°, 17°, 330°, 740° and 910°C. After having been heated in vacuum or in metallic vapor at least above its monoclinic-orthorhombic transition temperature (330°C), it shows various patterns in dependence on the condition of heat treatment.

After the crystal has been heated in Zn vapor, it exhibits a pattern composed of a lot of obliquely crossed green stripes. When Na vapor is used instead of Zn, a bluish splashed pattern appears. When the crystal is heated high enough in vacuum without metallic vapor, another type of pattern comes out in the crystal. All of them are obviously different from the well known domain structure patterns of WO_3. Which one of these types of pattern does occur entirely depends on the condition of heat treatment. However, the methods of crystallization have no influence upon this phenomenon, so long as the specimens are grown from the vapor phase.

§ 2. Preparation of Specimens

The specimens used were mostly thin plate-like c-crystals, about $500 \times 500 \times 50\,\mu$ in size. They were grown in crystalline form by condensation of the vapor on a comparatively cold surface. The principle of this method has already been described in detail.[14)]

The powder materials of tungsten trioxide were obtained from both American and Japanese chemicals companies. In order to heat the powder above 1000°C, either kryptol furnaces or siliconite ones were utilized. Fused quartz and platinum crucibles were used with success.

Various combinations of the crucibles, the furnaces, and the powders supplied by different makers were tested. The average size of the crystals produced is more or less dependent on the details of the crystallization procedures. However, the phenomenon which will be described in the present paper is entirely independent of them, as far as the condensation methods are concerned.

§ 3. Green Stripes

Either a fused quartz or a hard glass tube of 1 cm diameter and 20 cm length is set horizontally. One end is fused and the other is connected to a pumping system via a stopcock. The tube contains a number of WO_3 single crystals near the closed end, and a small boat made of hard glass with a piece of zinc metal on it, the latter being a few cm apart from the closed end. When the tube is evacuated, and then heated up to near 400°C by an electric heater wound around it, the vapor pressure of Zn is estimated at about 10^{-1} mmHg.

The crystals prepared by the way mentioned in the last section are transparent and yellowish. After they have been heated up to about 400°C in the atmosphere of Zn vapor, and then cooled down to room temperature, microscopic observation reveals that many of them have green patterns as shown in Photo. 1.

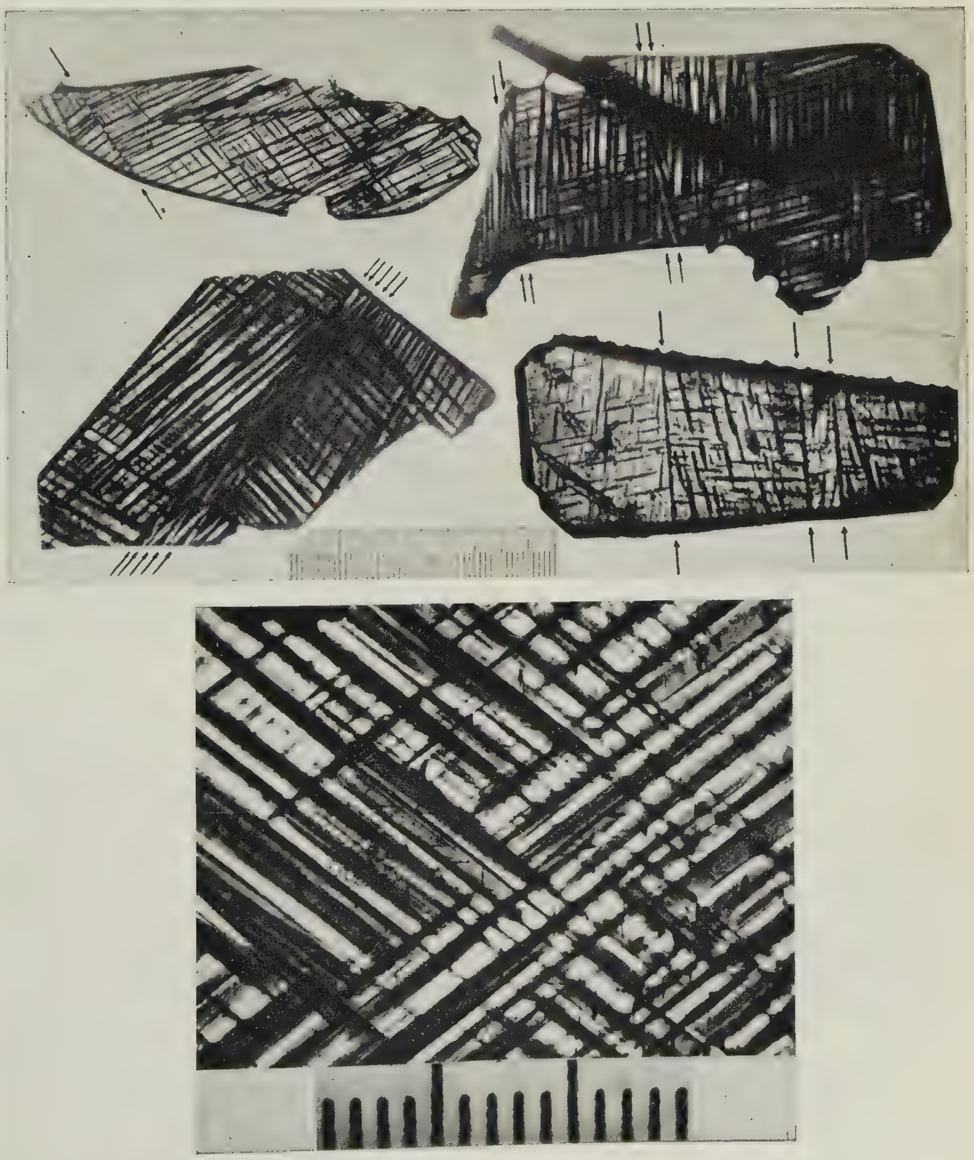

Photo. 1. Patterns of green stripes induced by Zn vapor in thin crystals of WO_3. Arrows indicate *a-b* domain boundaries. (10^{-2} mm/div.)

The pattern is composed of a number of obliquely crossed green stripes against the yellowish background. These stripes appear sometimes thickly and sometimes thinly. The color of the stripes is sometimes dark green and sometimes light green. These variations seem to be due to the experimental conditions, that is to say, the pressure of the metallic vapor, the thickness of the crystal, the duration and the maximum temperature of the heating procedure.

However, several regularities may be pointed out as follows. The pattern is always composed of two groups of green stripes. Each of these groups takes a definite orientation with respect to the crystal axis, or the domain boundary of the monoclinic phase. As depicted in Fig. 1, one encounters the domain boundary at an angle of 8°, and makes an angle of 37.5° with the *a*-axis of the crystal. The other meets the domain boundary at an angle of 83°, and crosses the *a*-axis at an angle of 37.5°. These groups intersect each other at an angle of 75°. So far as these angles are concerned, such patterns in any adjacent domains form mirror images of each other with respect to the boundary wall between them, as shown in Photo. 2.

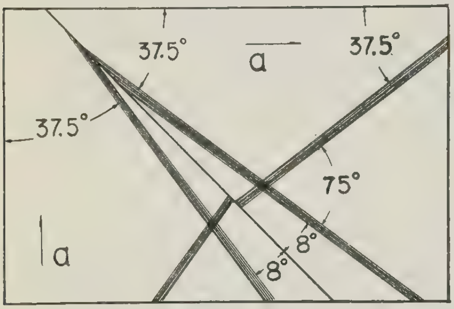

Fig. 1. Schematic drawing of green stripes and a a-b domain boundary in the c-plane.

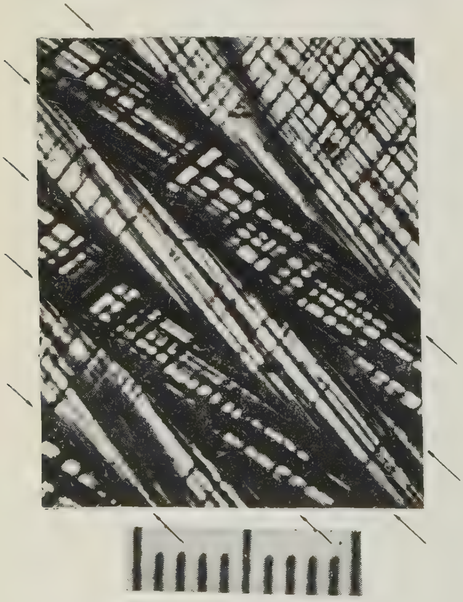

Photo. 2. Green stripes and a-b domain boundaries indicated by arrows in a thin crystal of WO_3. (10^{-2} mm/div.)

Both edges of a stripe are sharply defined, while both ends of the stripe fade out gradually. The stripe seems to be quite a thin band in the interior of the crystal. One of the band edges is located near the top surface of the crystal, while the other near the bottom surface. The inclination of the plane of the band is estimated at about 50° to the crystal surface (c-plane). Furthermore, it has often been recognized that some band has a fine

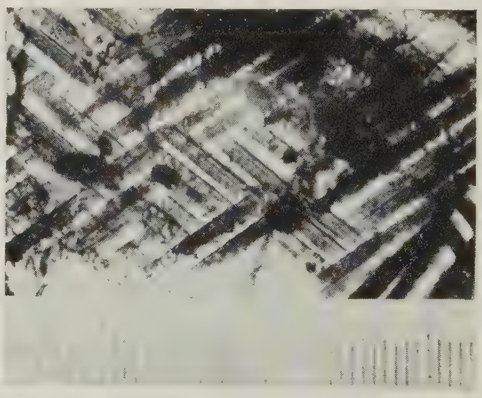

Photo. 3. Fine structure of green stripes in a thin crystal. (10^{-2} mm/div.)

Photo. 4. Green stripes in a thick crystal. (10^{-2} mm/div.)

structure composed of several lines parallel to the band edge, as shown in Photo. 3.

In the previous paper,[14] it has been reported that the same pattern was observed only by heating the crystal in vacuum. At that time, the experiment was done with the aid of a vacuum vessel fitted with a platinum heating coil within it. There was a brass joint connecting the platinum wire with a copper rod in vacuum. Metal vapor which must have had emerged from the joint as a result of current flow was entirely overlooked. According to a series of the later experiments, Zn vapor is essentially necessary for inducing such a pattern of obliquely crossed green stripes in the crystal.

It is, however, too soon to make a plausible decision about the reason why the pattern comes out. Needless to say, any definite conclusion should be preceded by much more detailed studies from all angles on the characteristic property of the pattern. Some informations about its peculiar behavior are being prepared to be published in Part II.

By the way, another type of stripes could occasionally be observed especially when thick crystals were tested. They are quite similar in shape and color to the ordinary ones, as shown in Photo. 4. However, the angle between the stripe of this type and the crystal axis is somewhat different from those mentioned above. Even when there had been no indication directly after the end of heat treatment, some stripes could be detected one or two days later.

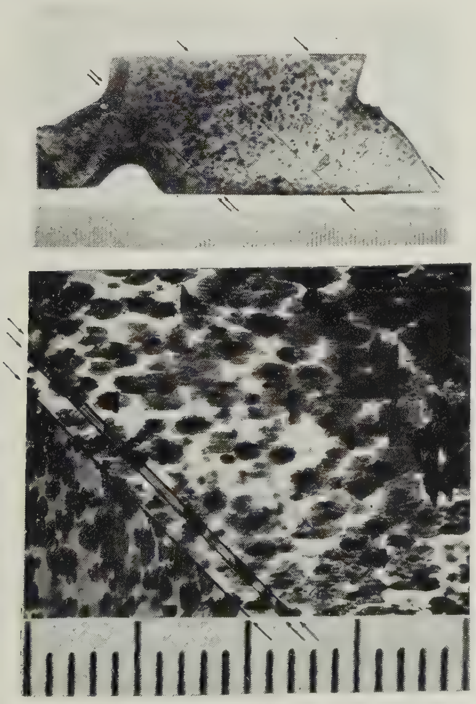

Photo. 5. Splashed patterns induced by Na vapor in WO_3 single crystals. Arrows indicate *a–b* domain boundaries. (10^{-2} mm/div.)

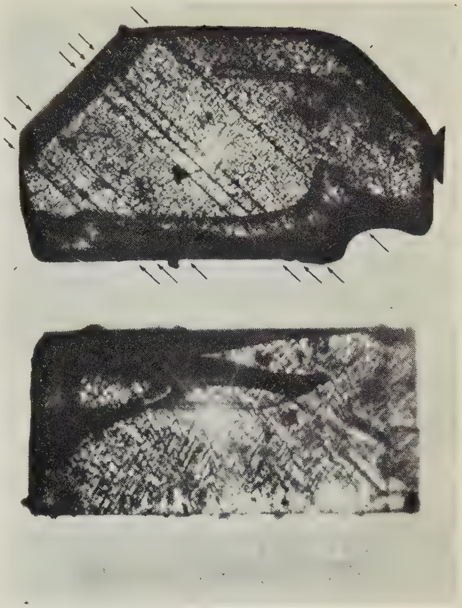

Photo. 6. Dark lines induced in WO_3 single crystals by heating in vacuum at higher temperatures. Arrows indicate *a–b* domain boundaries. (10^{-2} mm/div.)

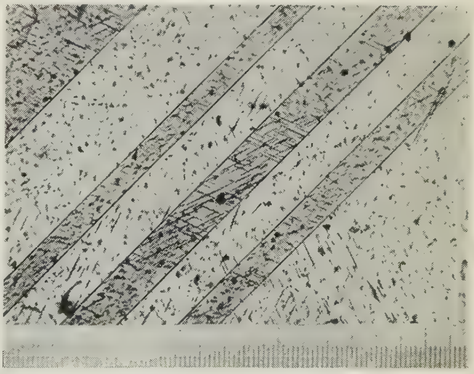

Photo. 7. Dark lines and *a–b* domain boundaries in a specimen placed between Nicols. (10^{-2} mm/div.)

§ 4. Splashed Pattern

If the crystal is treated just in the same way as above in the atmosphere of Na vapor instead of Zn, it shows a complete change in color from yellow to grass green, and besides a quite different kind of pattern is observed in it, as shown in Photo. 5. It resembles a splashed pattern composed of a lot of more or less blurred touches made with a brush in parallel with either the *a*- or *b*-axis of the crystal. These touches are all more or less different in color and in shade both from each other and from the background. Some ones are light greenish blue, and some ones dark blue gray. In addition, the pattern seems to be limited to the crystal surfaces in contrast to the green stripes mentioned in the last section.

Magnéli and others have already performed the X-ray analyses of the structures of the alkali tungsten bronzes Na_xWO_3, where x is larger than 0, and less than 1.[22] The crystal structure is monoclinic for x less than 0.1, tetragonal for $0.1<x<0.3$, and so on. According to many other investigators, WO_3 has also a monoclinic structure at temperatures ranging from 17 to 330°C. On the other hand, according to Straumanis, the color of Na_xWO_3 changes from grass greenish to brighter blue gray, dark blue gray, blue to blue black, violet, red, orange, and yellow, with increasing value of x.[23]

These evidences may lead to an expectation that the splashed pattern might be due to diffusion of a minute amount of Na vapor into the interior of the crystal just near the surfaces. Such an expectation may also be supported by the experiment done by Brown and Banks[24]. They have shown that the alkali tungsten bronzes can be prepared by the powder phase reaction, as a result of heating an evacuated Y-shaped hard glass tube with WO_3 powder in one of the closed ends and with Na metal in the other.

When the crystal with such a pattern in it is heated in the air atmosphere, the crystal turns yellowish, that is, it recovers its original tint, only some traces of the pattern being left visible faintly.

Other metals such as Hg, Cu, and Pb failed to induce any pattern, partly because the equipment used was not suitable for maintaining the vapor of these metals at a desired pressure.

§ 5. Dark Lines

When the crystal is heated as high as about 610°C in a vacuum vessel without any metallic vapor, it turns blue uniformly, and at the same time a number of dark lines crossing obliquely appears in it as shown in Photo. 6. When the crystal is picked out of the vacuum vessel into the air atmosphere, and heated again with a coal gas burner, or a nichrome furnace, it recovers its original tint, while the dark lines remain unchanged against the yellowish background.

These dark lines are rather short compared to the green stripes described above. In addition, these lines seem to be limited to the crystal surface in contrast to the green stripes. As far as a single domain is concerned, they run in the two definite orientations with respect to the crystal axes. They make an angle of either 19° or 71° with the *a*-axis, and intersect each other at an angle of about 52°. Qualitatively speaking, this habit is analogous to that of the green stripes, but they are clearly different from each other as regards the numerical values of their characteristic angles.

In any case, taking a look at Photo. 7, it is readily seen that such a pattern of dark lines in any domain and a similar one in its adjacent domain are symmetric in orientation to each other with respect to the boundary line between the two domains.

When the crystal was heated in vacuum at still higher temperatures than 720°C, dark lines appeared so densely that the crystal turned completely black and no patterns were distinguished.

In conclusion, the authors wish to express their sincere thanks to Professor S. Sawada of Tokyo Institute of Technology for his kind arrangements for the preparation of specimens. The authors are also indebted to the Scientific Research Fund of the Ministry of Education for financial aid.

References

1) B. T. Matthias and E. A. Wood: Phys. Rev. **84** (1951) 1255.
2) S. Sawada: J. Phys. Soc. Japan **11** (1956) 1237.
3) S. Sawada: J. Phys. Soc. Japan **11** (1956) 1246.
4) R. Ueda and T. Ichinokawa: Phys. Rev. **82** (1951) 563.
5) R. Ueda and J. Kobayashi: Phys. Rev. **91** (1953) 1565.
6) W. L. Kehl, R. G. Hay, and D. Wahl: J. Appl. Phys. **23** (1952) 212.

7) G. Anderson: Acta Chem. Scand. **7** (1953) 154.
8) J. A. Perri, E. Banks and B. Post: J. Appl. Phys. **28** (1957) 1272.
9) C. Rosen, E. Banks, and B. Post: Acta Cryst. **9** (1956) 475.
10) S. Tanisaki: J. Phys. Soc. Japan **15** (1960) 566.
11) S. Tanisaki: J. Phys. Soc. Japan **15** (1960) 573.
12) S. Sawada, R. Ando, and S. Nomura: Phys. Rev. **82** (1951) 952.
13) S. Sawada and G. C. Danielson: Phys. Rev. **113** (1959) 803.
14) T. Horie, K. Kawabe and T. Iwai: Ann. Rept. Sci. Works Fac. Sci. Osaka Univ. **4** (1956) 45.
15) T. Iwai: J. Phys. Soc. Japan **15** (1960) 1596.
16) S. Sawada and G. C. Danielson: Phys. Rev. **113** (1959) 1008.
17) M. Foëx: Compt. rend. **220** (1945) 917.
18) K. Hirakawa: J. Phys. Soc. Japan **7** (1952) 331.
19) S. Tanisaki: J. Phys. Soc. Japan **13** (1958) 363.
20) S. Sawada and G. C. Danielson: Phys. Rev. **113** (1959) 1005.
21) R. Ueda and T. Ichinokawa: Phys. Rev. **80** (1950) 1106.
22) A. Magnéli and B. Blomberg: Acta Chem. Scand. **5** (1951) 372; A. Magnéli: Acta Chem. Scand. **5** (1951) 670.
23) M. E. Straumanis: J. Amer. Chem. Soc. **71** (1949) 679.
24) B. W. Brown and E. Banks: J. Amer. Chem. Soc. **76** (1954) 96.

JOURNAL OF THE PHYSICAL SOCIETY OF JAPAN, Vol. 16, No. 3, MARCH, 1961

Magnetic Properties of Intermetallic Compounds in Iron-Germanium System: $Fe_{1.67}Ge$ and $FeGe_2$

By Kō YASUKŌCHI, Kazuo KANEMATSU

Department of Physics, College of Science and Engineering,
Nihon University, Tokyo

and Tetuo OHOYAMA

Department of Physics, Faculty of Science,
Tokyo Metropolitan University

(Received November 5, 1960)

The magnetic properties of the two intermetallic compound β phase ($Fe_{1.67}Ge$) and δ phase ($FeGe_2$), in Fe-Ge system, were investigated. The β phase has $B8_2$ type of crystal structure and is ferromagnetic with the Curie point 485°K, saturation magnetization at 0°K $1.59\,\mu_B$, and paramagnetic moment $3.14\,\mu_B$ per iron atom. The δ phase has C16 type of crystal structure and exhibits a parasitic ferromagnetic behavior in which the Néel point, asymptotic Curie point, saturation magnetization at 0°K, and paramagnetic moment are 190°K, +90°K, $0.11\,\mu_B$, and $2.43\,\mu_B$, per iron atom respectively. Brief discussions on the magnetic structures were given.

§1. Introduction

Recently, we have studied the magnetic properties of intermetallic compounds in the binary systems consisting of iron group transition metals and IVb group elements in the periodic table; Mn-Ge[1], Mn-Sn[2], and Fe-Sn[3]. In the present study, we took up the system of iron-germanium and have carried out some magnetic measurements on the intermetallic compounds of this system. According to the phase diagram adopted by Hansen[4] on the basis of Ruttewit and Masing's work, there are two intermediate phases in the iron-germanium system, i.e. β phase about a composition of 40 at. % Ge and δ phase about a composition of 70 at. % Ge. The crystal structures of these phases have been determined by Laves, Wallbaum[5] and Castelliz[6] to be $B8_2$ (Ni_2In) type for the β phase and C16 ($CuAl_2$) type for the δ phase. No investigations, however, have been made on the magnetic properties of the alloys of this system. According to our investigations[2),3)], the compounds Mn_2Sn and Fe_2Sn, which have the same ($B8_2$) type of structure as the β phase are ferromagnetic, while the compounds $MnSn_2$, $FeSn_2$, and $CoSn_2$, which have the same (C16) type of structure as the δ phase, are not ferromagnetic but antiferromagnetic for the former two and paramagnetic for the last one. Thus, the magnetic properties of the both phases in this system are interesting in relation to those compounds with the same crystal structure. In this paper, will be reported the existence of a ferromagnetism in the β phase and a parasitic ferromagnetism in the δ phase as well as brief discussions on their magnetic structures.

§ 2. Preparation of Specimens and Experimental Method

As seen from the phase diagram, both phases have considerable ranges of homogeneity. To avoid the precipitation of other phases at room temperature, we choose within the homogeneity ranges the compositions Fe_5Ge_3 ($Fe_{1.67}Ge$) and $FeGe_2$ as representatives of β and δ phases respectively. The preparation of the specimens was as follows: Powders of electrolytic iron (99.9%) and pure germanium (seven-nine purity) were mixed at the desired proportions, and the mixtures were charged in alumina crucibles, sealed in evacuated silica tubes, and melted at 1300°C. Finally, after homogenized for several hours at 800°C, they were quenched into water. The specimens thus obtained were examined by an X-ray diffractometer to ascertain their crystal structures. The temperature dependences of the magnetizations of these specimens were measured from the liquid oxygen temperature up to 900°K, under a field of 7.5 kilo-oersteds, by means of a pendulum magnetometer in their ferromagnetic region, and also by means of a magnetic torsion balance in their paramagnetic region. In both apparatus the magnetization was determined by measuring the forces exerted on the specimens placed in an inhomogeneous field.

§ 3. δ phase

For $FeGe_2$ of the δ phase, the temperature dependences of the magnetization σ_g and the reciprocal of the magnetic susceptibility χ_g at higher temperatures are shown in Fig. 1. As seen in the figure, the phase is feebly ferromagnetic at low temperatures. This feeble ferromagnetism appears to be associated with the antiferromagnetism exhibited by the isotypic compounds $FeSn_2$ and $MnSn_2$, and is to be classified under parasitic ferromagnetism. The small value of the saturation magnetization as well as the concavity of the $1/\chi_g - T$ curve of this specimen is in line with this proposal. Further support will be seen below.

The saturation magnetization at absolute zero of temperature is estimated to be 3.15 cgs emu/g, corresponding to $n_f = 0.11$ Bohr magnetons per iron atom. The Néel point was determined to be 190°K by plotting σ_g^2 against T and extrapolating the part with steepest slope to the temperature axis. The asympotic Curie point and the effective Bohr magneton number per ion atom n_p determined from the straight part of $1/\chi_g - T$ curve is 90°K and 2.43, respectively. The X-ray diagram for our specimen could be interpreted by assuming a tetragonal, C16 ($CuAl_2$) type of structure, with the lattice parameters $a = 5.91_1$Å, $c = 4.96_2$Å and $c/a = 0.839$, which is in fair agreement with Wallbaum's results[5)]. The density 7.36 g/cm³ measured by a picnometer gave 3.82 formula weights of $FeGe_2$ per unit cell.

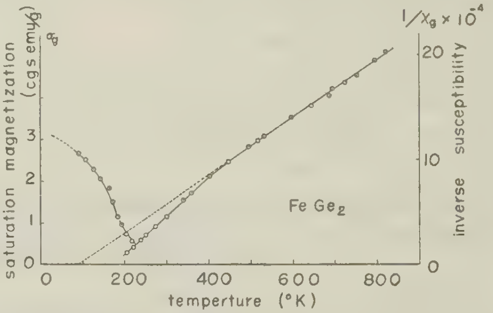

Fig. 1. Magnetic property of $FeGe_2$. Dependences of saturation magnetization and inverse susceptibility on temperature.

Now, we shall give some considerations on the magnetic structure of this compound. As in the case of $MnSn_2$[2)], the whole lattice of the magnetic atom is classified into two crystallographically equivalent sublattices specified by antiparallel spin orientations. Assuming that the spin moments of every iron atom $S = 1$, and Landé factor $g = 2$, n_p is calculated to be 2.82, which may be compared with the experimental value 2.43. Further assumption that the 0.18 vacant sites of iron are distributed only in one of the two sublattices leads to a value $n_f=0.095$, as the uncompensated magnetic moment per iron atom, which is very closed to the experimental value 0.11. Thus the parasitic ferromagnetism of the compound may be considered to come from the destruction of the perfect compensation of spin moments in an otherwise antiferromagnetic substance by vacant sites in the crystal lattice.

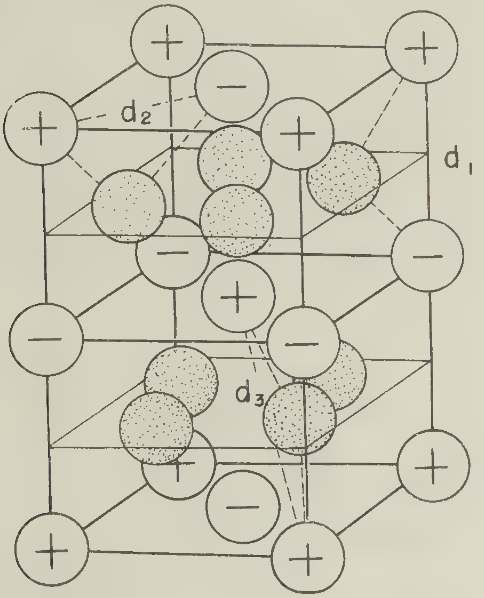

Fig. 2. Crystal structure of δ phase in Fe-Ge system (C16 type) and proposed spin arrangement. Spotted circle: Ge; open circle: Fe. $d_1=2.48$Å, $d_2=4.18$Å, and $d_3=4.86$Å in $FeGe_2$.

Fig. 2 shows the structure of the compound together with the antiferromagnetic spin arrangement which underlies its parasitic ferromagnetism. The nearest neighbor Fe-Fe distances and the angles of Fe-Ge-Fe are 2.48Å and 59° for the pairs of iron atoms along the c axis (first neighbor), 4.18Å and 112° along the face diagonals (second neighbor), and 4.86Å and 148° along the body diagonals (third neighbor).

Now we introduce a positive superexchange interaction between iron atoms through a germanium atom, similar to those proposed by us in manganese-tin alloys[2]. The interaction in the present compound is considered to be stronger than in manganese-tin, because the nature of bonding of germanium is more covalent than that of tin. Then, the magnetic structure may be considered to be as follows: Between the first neighbor iron atoms, the direct interaction may be assumed to be negative and superior to the superexchange interaction through germanium atom, to which the angle of Fe-Ge-Fe may be unfavorable. On the other hand, between the second and the third neighbors, the positive superexchange interaction may be dominant. If the interactions between the first and the third neighbors overshadow that between the second neighbors, the spin arrangement shown in Fig. 2 will be realized in the compound, and, as has been mentioned, the partial failure of this spin arrangement may be localized at the vacant sites in one of the two sublattices, giving rise to the parasitic ferromagnetism of the δ phase.

§ 4. β phase

In the composition of Fe_5Ge_3 ($Fe_{1.67}Ge$) of the β phase, a new ferromagnetic material was found. The saturation magnetization and the reciprocal of the values of the magnetic susceptibility above the Curie point are plotted against temperature in Fig. 3. The σ_g-T curve is similar to that of a typical ferromagnetic substance. It is shown that, near the Curie point, the $1/\chi_g-T$ curve is convex against temperature axis, and that the Curie-Weiss law holds very well at higher temperatures. The saturation magnetization σ_0 at absolute zero of temperature, extrapolated from the σ_g-T curve is 89 cgs emu/g, which corresponds to 1.59 Bohr magnetons per iron atom. The Curie point T_C determined from $\sigma_g{}^2-T$ curve by extrapolation is

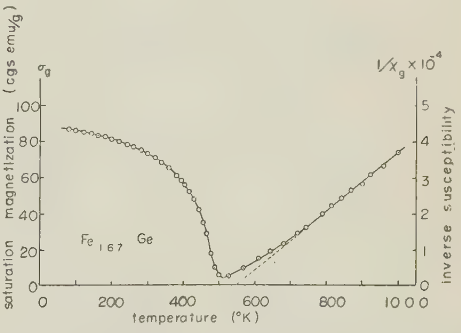

Fig. 3. Magnetic property of $Fe_{1.67}Ge$. Dependences of saturation magnetization and inverse susceptibility on temperature.

485°K. The paramagnetic Curie point θ_p and the effective number of Bohr magnetons per iron atom, which are determined from the linear part of $1/\chi_g - T$ curve, are 540°K and 3.14, respectively.

As examined by an X-ray diffractometer, the specimen of Fe$_{1.67}$Ge used in this study had B8$_2$ type of structure with lattice parameters $a=4.02_1$Å, $c=5.02_7$Å and $c/a=1.25_0$, in accordance with Castelliz, Laves and Wallbaum. And the measured density 7.93 g/cm^3 gives $2.01 \approx 2$ formula weights of Fe$_{1.67}$Ge per unit cell. Then the atomic arrangement in the lattice points is determined by the intensity analysis of the X-ray diagram to have the same feature as that of Mn$_{1.77}$Sn[7], namely,

2 Fe in 2(a) 0, 0, 0; 0, 0, 1/2;
2 Ge in 2(c) 1/3, 2/3, 1/4; 2/3, 1/3, 3/4;
1.33 Fe in 2(d) 1/3, 2/3, 3/4; 2/3, 1/3, 1/4.

It is seen in Table 1 that the intensities of diffraction lines calculated on the basis of this arrangement are consistent with those measured for our specimen. Thus, as shown in Fig. 4, the whole lattice of the compound can be divided into two sublattices; sublattice A consisting of 2(a) (spotted circle), and B consisting of 2(c) and 2(d) (open circle), which are not crystallographically equivalent to each other.

Table I. X-ray diagram of Fe$_{1.67}$Ge

hk. l	observed		calculated	
	$10^3 \sin^2\theta$	I	$10^3 \sin^2\theta$	I
10.0	—		48.92	0.0
10.1	—		72.38	5.7
00.2	93.9	2.5	93.91	3.9
10.2	142.9	34	143.0	63.1
11.0	146.6	26	147.4	71.3
20.0	—		196.4	0.0
20.1	—		219.9	1.1
11.2	—		241.2	0.0
20.2	291.7	7	290.3	21.0
21.0	—		343.7	0.0
21.1	—		367.2	0.5
21.2	439	6	437.6	23.9
30.0			441.9	14.9

Now we assume the magnetic moments of individual iron atom to be those corresponding to the following spin quantum numbers:

$S=1$ for 2 Fe in A sublattice
$S=1/2$ for 1.22 Fe in B sublattice.

Then n_f and n_p^2 may be calculated from these values as the weighted means of gS and $S(S+1)g^2$, giving 1.60 and $(2.45)^2$ respectively, which agree with the experimental values mentioned above.

From a point of view of molecular field theory, the interactions among the magnetic atoms can be described by three coefficients, α, β and γ, which denote the interactions within A sublattice, within B sublattice, and between the two sublattices, respectively. In view of the feature of the $\sigma_g - T$ curve and the convexity of the $1/\chi_g - T$ curve of the β phase, all the interactions α, β and γ may be considered to be positive (ferromagnetic). Assuming the existence of the same kind of indirect interaction as in the case of the δ phase besides the direct one, the three positive coefficients of interaction may be understood as follows: The interaction within A sublatice, α, consists of direct interations between the nearest neighbor iron atoms, which are 2.51Å apart, and of the indirect interactions between second and third neighbors, which are 4.02Å and 4.77Å apart and

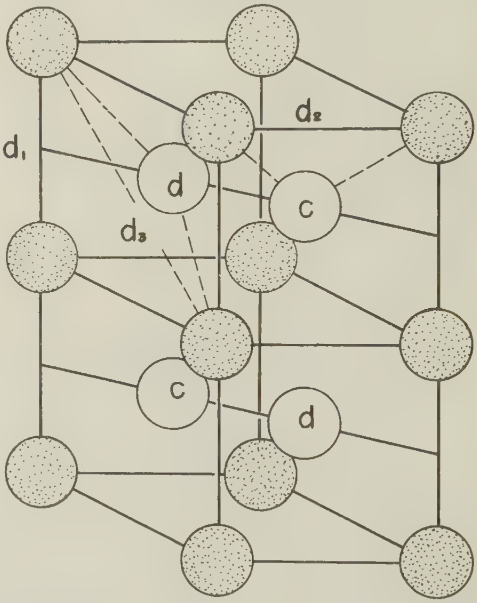

Fig. 4. Crystal structure of β phase in Fe-Ge system (B8$_2$ type). Spotted circle: A sublattice (2(a) site). Open circle: B sublattice (c and d mean 2(c) and 2(d) sites respectively). $d_1=2.51$Å, $d_2=4.02$Å, and $d_3=4.77$Å in Fe$_{1.67}$Ge.

make angles Fe-Ge-Fe of 99° and 128° respectively. Though the Fe-Fe distance which is nearly equal to d_1 in the δ phase (Fig. 2) may lead to a negative direct interaction, it may be probable that, in favor of Fe-Ge-Fe angles, the positive indirect interactions are strong enough to overcome it. Next the interaction within B sublattice, β, is purely due to the superexchange interaction between iron atoms through intervening germanium atom, which is 2.32Å apart from both iron atoms and makes angle of Fe-Ge-Fe 120°. Finally, as to the interaction between the two sublattices, γ, the corresponding Fe-Fe distance is 2.64Å, and it can be considered that the positive superexchange interaction, here again, plays an important role, making the resultant interaction fairly strong positive one.

The authors wish to express their hearty thanks to Prof. S. Iida of Tokyo University and Prof. R. Kimura of Tokyo Metropolitan University who gave them an oppotunity to use the facilites to achieve the work, and are also indebted to Shindengen Electric Manufacturing Co., Ltd. for kindness in supplying germanium metal.

References

1) K. Yasukōchi, T. Ohoyama and K. Kanematsu: J. Phys. Soc. Japan **14** (1959) 1820. K. Yasukōchi, K. Kanematsu and T. Ohoyama: J. Phys. Soc. Japan **15** (1960) 932.
2) K. Yasukōchi, K. Kanematsu and T. Ohoyama: to be published.
3) K. Kanematsu, K. Yasukōchi and T. Ohoyama: J. Phys. Soc. Japan **15** (1960) 2358.
4) M. Hansen: *Constitution of Binary Alloys*, 2nd edi. (McGraw-Hill, New York, 1958) p. 658.
5) F. Laves and H. J. Wallbaum: Z. angew. Min. **4** (1941/42) 17. H. J. Wallbaum: Z. Metallkde. **35** (1943) 218.
6) L. Castelliz: Mh. Chem. **84** (1953) 765.
7) H. Nowotny and K. Schubert: Z. Metallkde. **37** (1946) 17.

JOURNAL OF THE PHYSICAL SOCIETY OF JAPAN Vol. 16, No. 3, MARCH, 1961

Magnetic Properties of Perovskites Containing Strontium, II. Lanthanum-Strontium Manganites.

By Hiroshi WATANABE

The Research Institute for Iron, Steel and Other Metals,
Tohoku University, Sendai.

(Received November 19, 1960)

Magnetic and crystallographic properties have been studied of the system $(La_{1-y}Sr_y)MnO_x$ with varying values of y and x. It is found that the compounds with $y=1$ crystallize in the perovskite-like structures provides that x is lower than a certain limit. Perovskite-like $SrMnO_x$, containing both Mn^{3+} and Mn^{4+} does not show any spontaneous magnetization above the liquid nitrogen temperature, and their paramagnetic Curie temperature is negative, in contrast with the well-known ferromagnetic behavior observed in La-rich manganites. Hence in these compounds no evidence of strong positive $Mn^{3+}-Mn^{4+}$ interaction is obtained. The susceptibility measurements show that $Mn^{3+}-Mn^{3+}$ interaction in Sr-rich cubic perovskite is negative. This fact is consistent with Jonker's results that in cubic perovskite manganites such as $(La, Ca)MnO_3Mn^{3+}-Mn^{3+}$ interaction is positive for large cell dimensions while it is negative for small cell dimensions.

§ 1. Introduction

In the preceding paper[1] we reported magnetic and crystallographic properties of two systems of perovskite-like compounds, $(La, Sr)FeO_x$ and $(La, Sr)CoO_x$. It was found that their crystallographic as well as magnetic properties are greatly influenced by the value of x, or the concentration ratio of tetravalent to trivalent ions. It may be interesting, therefore, to study in a similar way other systems for which properties for "non-correct" samples have not been fully investigated. In this paper we shall report some of the results obtained with respect to the system (La, Sr)-MnO_x.

The properties of La-Sr manganites[2)-4)], as well as analogous manganities[5)-7)] have been the subject of considerable amount of investigation. Strong ferromagnetism has been found in La-rich manganites, and it was ascribed to positive $Mn^{3+}-Mn^{3+}$ and $Mn^{3+}-Mn^{4+}$ interactions. Jonker[4)] points out that these interactions may be of the semicovalent type suggested by Goodenough, and the former interaction is dependent on interatomic distances, being positive for large separations while negative for small separations. But since his conclusion is based on the experimental results on La-rich "correct" perovskites, the range of y is limited, and, moreover, the coexistence of negative $Mn^{4+}-Mn^{4+}$ interaction makes the statement uncertain. We shall show in this paper that evidence for negative $Mn^{3+}-Mn^{3+}$ interaction is fully produced by the experiments on "non-correct" samples.

§ 2. Experimental Procedure

The procedures of preparation of the samples were similar to those in reference 1. Starting materials were pure La_2O_3, $SrCO_3$ and $MnCO_3$. Since higher annealing temperatures, however, were needed for obtaining specimens of low Mn^{4+} ion content, a high-frequency vacuum induction furnace was used; prefired samples, pressed into bricket form, were put in high-alumina crucibles, which were put in graphite crucibles, heated to the scheduled temperatures, maintained about 30 minutes there, and then furnace-cooled.

Each specimen was chemically analyzed for total Mn and Mn^{4+}, following the standard method in the chemical analysis department of our Institute.

X-ray powder patterns were taken of many of the samples in the X-ray research laboratory of our Institute, with 11.46 cm diameter camera and Fe anticathode tube.

Care was taken not to unduly oxidize the pulverized samples before measurement.

Magnetic measurements were made just in the same way as in reference 1.

§ 3. Crystallographic Study

Fig. 1 shows the result of chemical analysis and crystallographic study on a diagram, taking as the abscissa y, Sr concentraction, and as the ordinate Mn^{4+} concentration in total Mn. Samples labeled as A are those heat-treated in the air and have oxygen in excess of correct amount ($x=3$), except for $y=1$, corresponding closely to $SrMnO_3$, which is not perovskite-like. Samples labeled as V are those heat-treated in various temperatures. Roughly estimated phase boundaries are also drawn in the figure.*

One of the striking features of the diagram in Fig. 1 is the appearance of perovskite-like structure at $y=1$; $SrMnO_x$ is cubic when Mn^{4+} concentration is about 25% ($x=2.64$). At higher concentrations of Mn^{4+}, there appears a tetragonal distortion with $c/a>1$, while at lower concentrations (in the presence of Mn^{2+}) there appears a monoclinic distortion with $b/a(=c/a)<1$. The cubic $SrMnO_x$ has the smallest cell volume in the whole system.

Fig. 2 shows the difference in lattice parameter variations with y between A samples and V samples. In the A-preparation, the perovskite-like phase breaks off at $y=0.45$. In the V-preparations, the existence range of the perovskite-like phases is widened, and the cell volume decreases as y increases.

Table I gives the analytical and crystallographical data for several specimens.

The above crystallographical results are consistent with the consideration based on the tolerance factor. Jonker and Van Santen[2)] discussed the stability of the perovskite (ABO_3) compounds in terms of the Goldschmidt tolerance factor

$$t=\frac{r_0+r_A}{\sqrt{2}(r_0+r_B)},$$

where r_A, r_B and r_0 are the radii of the A (large), B (small) and 0 ions, respectively. Using Goldschmidt's values as the radii, they found the maximum possible value of t for the existence of perovskite-type compounds:

$$t_{\max}=0.96_5.$$

If we apply this rule to the system $SrMnO_x$,

---

* The constitution diagram presented here may probably be a very incomplete one, in that the samples are not prepared at the same temperature, nor are they quenched from the preparing temperatures.

Table I. Crystal symmetry and lattice parameters of some of the (La, Sr)MnO_x samples.

Specimen	Mn^{4+}% or Mn^{2+}%*	Crystal symmetry†	Lattice parameters
$LaMnO_xA$	37.1	Rbh	$a=3.88$ A, $\beta=90°38'$
$LaMnO_xV_1$	10.4	Mon	$a=3.95$ A, $b=3.84$ A, $c=a$, $\beta=91°55'$
$LaMnO_xV_5$		Mon	$a=3.97$ A, $b=3.85$ A, $c=a$, $\beta=92°10'$
$La_{0.9}Sr_{0.1}MnO_xA$	36.0	Rbh	$a=3.88$ A, $\beta=90°32'$
$La_{0.9}Sr_{0.1}MnO_xV_1$	20.1	Rbh	
$La_{0.8}Sr_{0.2}MnO_xA$	45.1	Rbh	$a=3.87$ A
$La_{0.8}Sr_{0.2}MnO_xV_5$	9.9	Cub	$a=3.88$ A
$La_{0.7}Sr_{0.3}MnO_xA$	53.0	Rbh	$a=3.87$ A, $\beta=90°13'$
$La_{0.7}Sr_{0.3}MnO_xV_5$	36.4	Cub	$a=3.88$ A
$La_{0.6}Sr_{0.4}MnO_xA$	60.7	Rbh	
$La_{0.6}Sr_{0.4}MnO_xV_1$	39.9	Rbh	$a=3.87$ A
$La_{0.6}Sr_{0.4}MnO_xV_6$	18.8	Cub	$a=3.86$ A
$La_{0.5}Sr_{0.5}MnO_xA$	71.1	Rbh+$SrMnO_3$	
$La_{0.5}Sr_{0.5}MnO_xV_1$	49.7	Rbh	$a=3.86$ A
$La_{0.5}Sr_{0.5}MnO_xV_6$	−8.0*	Cub	$a=3.87$ A
$La_{0.4}Sr_{0.6}MnO_xA$	82.1	Rbh+$SrMnO_3$	
$La_{0.4}Sr_{0.6}MnO_xV_6$	7.6	Cub	$a=3.86$ A
$La_{0.3}Sr_{0.7}MnO_xV_6$	6.3	Cub	$a=3.85$ A
$La_{0.2}Sr_{0.8}MnO_xV_3$	47.3	Cub	$a=3.82$ A
$La_{0.1}Sr_{0.9}MnO_xV_0$	61.0	Cub+$SrMnO_3$	Cub $a=3.84$ A
$La_{0.1}Sr_{0.9}MnO_xV_4$	40.0	Cub	$a=3.80$ A
$SrMnO_xA$	99	$SrMnO_3$	
$SrMnO_xV_2$	65	Tet+$SrMnO_3$	Tet $a''=3.79$ A, $c''=3.84$ A
$SrMnO_xV_5$	23.6	Cub	$a=3.80$ A
$SrMnO_xV_{5.5}$	−5.7*	Cub+Mon	Cub $a=3.80$ A Mon $a'=3.84$ A, $b'=3.79$ A, $c'=a'$, $\beta'=91°36'$

† Cub=cubic, Rbh=rhombohedral, Mon=monoclinic, Tet=tetragonal.

* Negative sign represents Mn^{2+} concentration instead of Mn^{4+}.

we find that the maximum possible value of p, Mn^{4+} concentration, for the existence of perovskite-type structure is

$$p_{\max}=0.67 \quad \text{(Point Q in Fig. 1).}$$

In a similar way we find the corresponding value for the system $LaMnO_x$:

$$p_{\max}=0.88 \quad \text{(Point P in Fig. 1).}$$

The values for the system of (La, Sr)MnO_x should lie on a line connecting P and Q, as indicated by the chain line in Fig. 1.

Although the number of specimens in our study is not sufficiently large for the test of such a criterion, qualitative validity of this expectation is borne out, with somewhat lower critical Mn^{4+} concentrations than expected.

Jonker discusses further distortion from cubic to monoclinic symmetry using Megaw's criterion. If we assume that that the structural change takes place at the value of t

$$t=0.9\,,$$

we find that in the system $LaMnO_x$, the critical value of t corresponds to $p=0.13$ (Point R in Fig. 1). Values found experimentally are: $p=0.125$ after Jonker[4], and $p=0.20$ after Wold and Arnott[8]. Our result is also consistent with these values. In the system ($La_{1-y}Sr_y$)-$MnO_{3-y/2}$, corresponding to $p=0$, *viz.*, with no Mn^{4+} and Mn^{2+} ions, monoclinic distortion would be possible for $y<0.6$ whereas the experimental data (*e.g.* $y=0.2$, V_6 or $y=0.5$, V_6) indicate that the cubic phase is more extended than expectation. In the system $y=1$, *viz.* $SrMnO_x$, the criterion predicts the monoclinic distortion when $p<-0.06$, namely when the compound contains 6% Mn^{2+} ions in total Mn ions. The sample $V_{5.5}$ roughly substantiates this prediction.

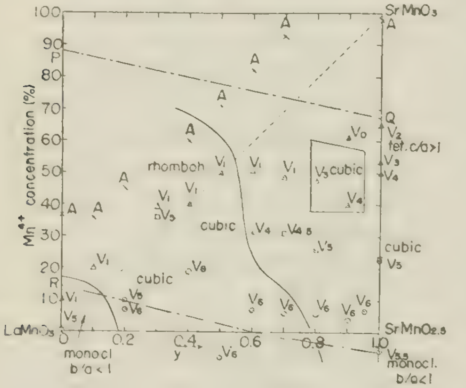

Fig. 1. Mn^{4+} concentration of specimens against y (Sr concentration), as determined by chemical analysis. A: Samples heat-treated in the air at 1300°C. V_i: Samples heat-treated in vacuo at $(1000+i\times100)$°C. The dotted line represents the correct compositions. The upper chain line gives the boundary which separates the perovskite-like phases from others, and the lower chain line gives the boundary between cubic and monoclinic perovskites, as anticipated from the tolerance factor.

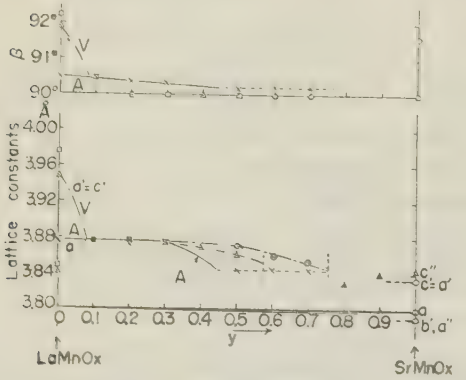

Fig. 2. Lattice parameters against y for A- and V- preparations. a denotes the lattice constant for the cubic structure, a', b', c' $(=a')$ denotes those for the monoclinic structure, and a'', c'' those for the tetragonal structure. ×A samples △V_0 to V_4 samples ⊡V_5 samples ⊙V_6 samples*

§4. Magnetic Study

Measurements of the paramagnetic susceptibility above the Curie temperature have been carried out for all specimens. For samples with compositions $y<0.4$, our results are in qualitative agreement with Jonker's[4]. The significant result in Jonker's measurement that the Curie-Weiss law is obeyed in samples with $0.2<y<0.4$ is also confirmed in our experiment. In the region $y>0.4$ we observed curved $1/\chi-T$ relation. The curvature becomes more and more accentuated as y increases or x decreases (Fig. 3).

$SrMnO_x$ samples with any value of x have no spontaneous magnetization above the liquid nitrogen temperature (Fig. 4), and they have definitely negative Curie temperatures, indicat-

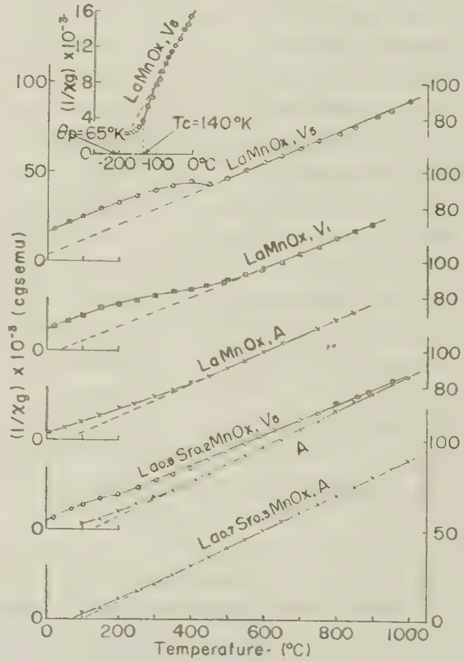

Fig. 3(a)

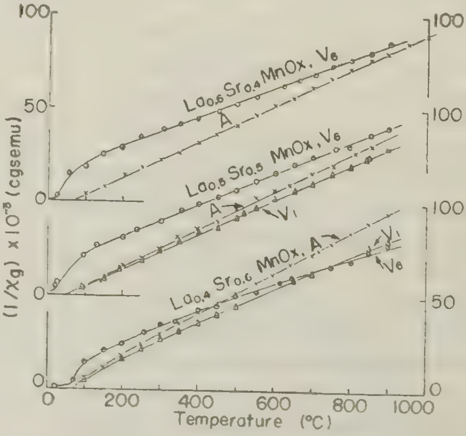

Fig. 3(b)

---

* These lattice constants refer to single perovskite cells, although some of the samples showed fairly apparent doubling of the cell edges.

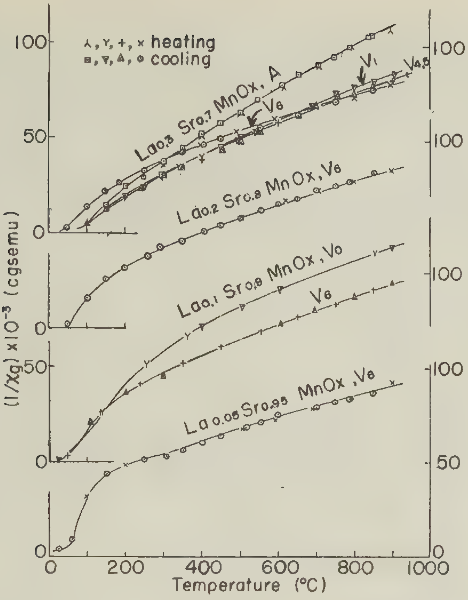

(c)

Fig. 3. $1/\chi-T$ curves of (La, Sr)MnO_x samples.

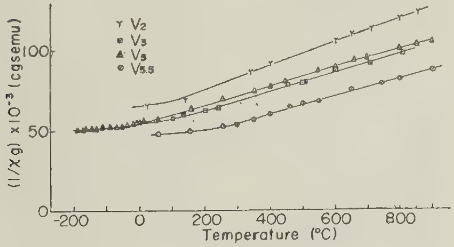

Fig. 4. $1/\chi-T$ curves of (La, Sr)MnO_x samples.

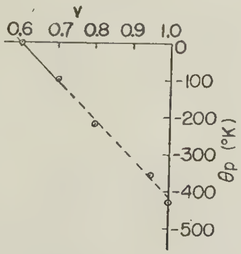

Fig. 5. Paramagnetic Curie temperature (θ_p) vs composition (y) of the V_6-samples ($V_{5.5}$ for $y=1$).

ing predominantly antiferromagnetic interactions between magnetic ions.

$SrMnO_3$, whose crystal structure is different from perovskite[9], is also non-magnetic, and has negative paramagnetic Curie temperature. We may say that in this compond $Mn^{4+}-Mn^{4+}$ interaction is negative.

In Fig. 5 we have plotted the paramagnetic Curie temperature θ_p of Sr-rich specimens with small concentrations of Mn^{4+} ions. θ_p changes its sign near $y\sim0.6$.

Saturation magnetization has been measured of the samples above the liquid nitrogen temperature. Except for details it is similar to Jonker's result (Fig. 6). It is to be noted that the value for $y=0.7$, V_6 is fairly smaller than that for V_1 or $V_{4.5}$.

Temperature dependence of the saturation magnetization of some specimens is given in Fig. 7. It has been found that the reduced saturation magnetization *vs* reduced temperature curves do not agree in general with the usuall Brillouin-type curves.*

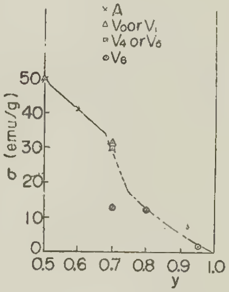

Fig. 6. Saturation magnetization at liquid nitrogen temperature of some (La, Sr)MnO_x samples.

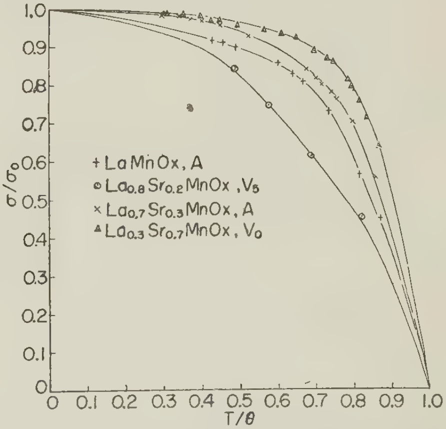

Fig. 7. Reduced magnetization *vs* reduced temperature curves of some of the (La, Sr)MnO_x samples. σ_0 denotes the extrapolated values of magnetization at absolute zero, θ denotes the ferromagnetic Curie temperature obtained by extrapolating the reciprocal susceptibility values to zero.

§ 5. Discussion

Jonker[4] pointed out that $Mn^{3+}-Mn^{3+}$ interaction is positive if the interionic distance is large, while it is negative if this distance is small. This conclusion was drawn from the moment arrangement in $LaMnO_3$, and also from the saturation magnetization in the system $(La, Ca)MnO_3$. Our experiment reveals further evidence of this statement in the system $La_{1-y}Sr_yMnO_x$, since cubic samples with $y>0.6$ have negative $Mn^{3+}-Mn^{3+}$ interaction in increasing amount with decreasing lattice dimension (Fig. 5). Such a dependence on interionic distance may be a result of the combined effect of various types of interaction.

---

* Unusual temperature dependence as was reported in reference 2 for $y=0.6$ has not been found in our experiment.

Goodenough[10)] assumed that $Mn^{3+}-Mn^{3+}$ interaction is antiferromagnetic if cation $d\gamma$ orbitals directed towards the intervening oxygen ion are both occupied or both empty, while it is ferromagnetic if one is occupied and the other is empty. This assumption explains the spin arrangement in $LaMnO_3$. In cubic perovskites the bond ordering as has been suggested by Goodenough is destroyed, both of the degenerate $d\gamma$ orbitals being occupied with equal probability. In such a case the sign of interaction may be determined by the relative magnitude of the various types of interaction. The experimental data suggest that the antiferromagnetic interaction overcomes the ferromagnetic interaction if the interionic distance is small.

In order to estimate the energy of $Mn^{3+}-Mn^{3+}$ interaction as a function of $Mn^{3+}-Mn^{3+}$ interionic distance, the molecular field treatment was applied to the layer-antiferromagnetic spin system as well as to the cubic spin system. In the former system (monoclinic, $b/a<1$), the following equations hold:

$$\theta_{33}(a)+\tfrac{1}{2}\theta_{33}(b)=\tfrac{3}{2}\theta_p$$

and

$$\theta_{33}(a)-\tfrac{1}{2}\theta_{33}(b)=\tfrac{3}{2}T_c,$$

where θ_{33} denotes the energy of $Mn^{3+}-Mn^{3+}$ interaction expressed in degrees Kelvin, θ_p and T_c are the paramagnetic and the Néel temperatures, respectively. As for $LaMnO_3$, V_5 (in the monoclinic range), $\theta_p=65°K$ and $T_c=140°K$ (See the inset in Fig. 3(*a*))*, whence we obtain

$$\theta_{33}(a)=154°K,\quad \theta_{33}(b)=-56°K.$$

On the other hand, the values of θ_{33} for cubic samples with small Mn^{4+} concentrations have been derived by simply equating it to θ_n, neglecting the presence of $Mn^{3+}-Mn^{4+}$ and $Mn^{4+}-Mn^{4+}$ interactions. The result is plotted in Fig. 8. $\theta_{33}(b)$ for $SrMnO_x$, $V_{5.5}$ has been obtained by assuming the value of $\theta_{33}(a)$ for the same specimen to be $-200°K$.

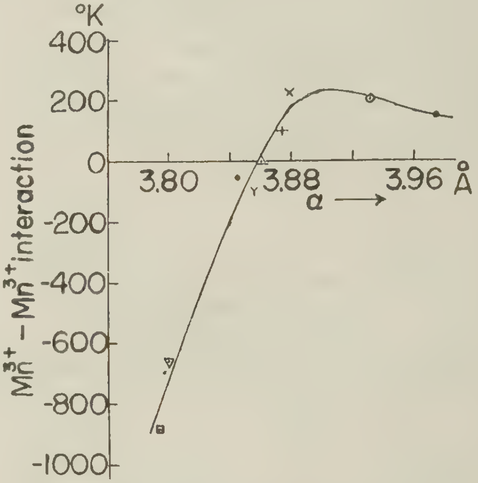

Fig. 8. $Mn^{3+}-Mn^{3+}$ interaction *vs* $Mn^{3+}-Mn^{3+}$ interionic distance, *d*. ● $LaMnO_x$, V_5, low temperature. ∘ $LaMnO_c$, V_5, high temperature. × $La_{0.8}Sr_{0.2}MnO_x$, V_5. + $La_{0.5}Sr_{0.5}MnO_x$, V_6. ⚠ $La_{0.4}Sr_{0.6}MnO_x$, V_6. Y $La_{0.3}Sr_{0.7}MnO_x$, V_6. ⊡ $SrMnO_x$, $V_{5.5}$. ⚠ $SrMnO_x$, V_5.

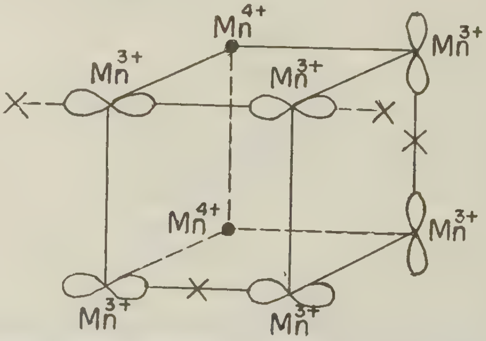

Fig. 9. Effect of oxygen ion vacancies on the half-filled d_{z^2} orbitals of Mn^{3+} in the $SrMnO_x$ compounds. × represents oxygen vacancies.

$Mn^{4+}-Mn^{4+}$ interaction may be considered to be negative, as is seen from the difference in the paramagnetic Curie temperature of $La_{0.1}Sr_{0.9}MnO_x$, V_0 and V_6. As pointed out by Kanamori[11)], this interaction should be antiferromagnetic according to any mechanism which is considered to play an important role in magnetic interaction.

---

* Here it is assumed that incomplete compensation of the magnetizations of the two antiferromagnetically coupled sublattices produces non-zero net magnitization below T_c.

As for $Mn^{3+}-Mn^{4+}$ interaction, we are not certain of its sign for $y=1$, but the fact that the paramagnetic Curie temperature of V_5 ($\sim$23% Mn^{4+}) is strongly negative suggests that it is not strongly positive.

Although $SrMn^{3+}_{0.75}Mn^{4+}_{0.25}O_{2.625}$ (V_5 is close to this composition) has a negative paramagnetic Curie temperature, antiferromagnetic spin ordering does not seem to develop in it (See the low temperature susceptibility in Fig. 4). Goodenough* interprets this as follows. The half-filled d_{z^2} orbitals of a Mn^{3+} ion adjacent to an oxygen vacancy should be directed towards the vacancy (Fig. 8). Since the oxygen vacancies are distributed at random and there is no magnetic interaction across a vacancy, there may be no magnetic ordering.

Acknowledgements

The author wishes to express his hearty thanks to Professor T. Hirone and to Drs. J. B. Goodenough and J. Kanamori for their valuable disscussions. He is also indebted to the members of the chemical analysis department directed by Professor H. Gotô and to those of X-ray research laboratory directed by Professor S. Ogawa of our Institute. Thanks are also due to Mr. K. Ito for aid with the magnetic measurements. A part of the expenditure of this study has been defrayed from the Scientific Research Funds of the Ministry of Education.

References

1) H. Watanabe: J. Phys. Soc. Japan **12** (1957) 515.
2) G. H. Jonker and J. H. Van Santen: Physica **16** (1950) 337.
3) J. H. Van Santen and G. H. Jonker: Physica **16** (1950) 559.
4) G. H. Jonker: Physica **22** (1956) 707.
5) H. L. Yakel: Acta Cryst. **8** (1955) 394.
6) E. O. Wollan and W. C. Koehler: Phys. Rev. **100** (1955) 545.
7) J. B. Goodenough: Phys. Rev. **100** (1955) 564.
8) A. Wold and J. Arnott: J. Phys. Chem. Solids **9** (1959) 176.
9) H. Binder: Z. anorg. allg. Chem. **303** (1960) 105.
10) J. B. Goodenough: J. phys. radium **20** (1959) 155.
11) J. Kanamori: J. Phys. Chem. Solids **10** (1959) 87.

---

* Private communication.

JOURNAL OF THE PHYSICAL SOCIETY OF JAPAN, Vol. 16, No. 3, MARCH, 1961

Regrowth of Germanium Single Crystal from Indium Melt

Masami TOMONO

Central Research Laboratory, Hitachi, Ltd., Kokubunji, Tokyo

(Received November 28, 1960)

A single crystal of *n*-type germanium was heated with a small piece of indium on it, and subsequently cooled rapidly to cause regrowth of the *p*-type germanium on the substract germanium from the indium melt. After removal of the indium, the growth pattern on the surface of the regrown germanium was observed. In some cases relatively large growth pyramids were observed, while in others flat patterns with threefold or sixfold symmetry were observed. After the detailed examination, it was concluded that the former represents the growth due to the screw dislocations and its center is dislocation array resulting from thermal strain. The shape and size of the growth pyramid vary with the number of screw dislocations which exist at center. The latter seems to be caused by surface nucleation.

§ 1. Introduction

Many studies have been made on the growth of single crystal from germanium melt[1)-5)]. However, because of the difficulty in observing the solid and liquid phases of germanium separately, reports dealing with the growing process of single crystal are relatively few[5)].

Many observation have been made on the regrown germanium produced on the substrate crystal as follows: Contact is made between the substrate germanium and the melt of indium, then germanium is dissolved in the melt. After that the system is slowly cooled so as to cause the regrowth of germanium on the substrate[2),6)-10)]. The author made observations on the *p*-type germanium layer which was regrown on the base single crystal with various cooling speeds of the above-mentioned indium melt, and studied the regrowth of the germanium single crystal from the indium melt. As for the regrowth of single crystal, it is necessary to know which of the screw dislocation or the surface nucleation is responsible for it. In the former, peculiar spiral or concentric curved patterns should be found. While, in the latter, those patterns should not be found. Various growth patterns were observed of germanium single crystal which was regrown on the substrate single crystal from the indium melt.

§ 2. Method of Experiment

A small piece of indium was put on the surface of an *n*-type germanium pellet parallel to (111) plane, and this was heated with a high-frequency furnace in hydrogen atmosphere at about 550°C for 10 minutes. Part of germanium in contact with indium melt is then dissolved into the melt until an approximate saturation is reached. At this time, the high-frequency heating is put off and simultaneously the specimen is cooled rapidly by pouring oil. Fig. 1 shows a resulting *p*-type layer regrown from the indium melt.

This method is convenient because the separate observation of *p*-type and *n*-type germanium layers is possible by the chemical etching and other methods. If this specimen is treated with mercury for amalgamation of indium present over *p*-type regrown layer and this amalgam is dissolved away with nitric acid, then the surface of the *p*-type germanium is exposed[9)]. A smooth surface parallel to (111) plane on the bottom of this exposed pan-shaped regrown layer was observed for the crystal growth pattern by the opical or electron microscope. The observations by the electron microscope were made by replica method using the platinum-palladium shadowing from left to right on the photographs. Then, the *p*-type regrown layer was etched with the dilute CP-4 etchant from the surface and etch patterns were observed successively.

§ 3. Results of the Experiment

3.1 *Abnormal growth pattern*

On the flat and smooth bottom surface of pan-shaped *p*-type regrown germanium layer shown in Fig. 1, the growth pattern of the abnormally large truncated hexagonal pyramid is frequently observed as shown in Fig. 2. Such an abnormal growth pyramid is seen, in most cases, to have nearly flat and smooth top surface as shown in Fig. 3 when magnified observation was made. Each side of the hexagon surrounding the top surface is, of course, parallel to [110] axis. Formation of the apparently large steps on the pyramidal surface by bunching together[11),12)] of a great number of fine growth steps is clearly seen.

The photograph shows in the lower left part how several steps are integrated into one step.

Fig. 4 gives an electron microphotograph of another abnormal growth pyramid with the top surface not flat but slightly inclined. The specimen is applied with shadowing from the left, and the step height can be known from the width of white shadow in the left-hand part of the photograph. It is seen that all the steps except those at the periphery of the top surface hexagon are approximately equal in height. Again each side of the hexagon is parallel to [110] axis, of course. For the slope angle obtained in this way, $\tan\theta \doteqdot 0.12$. The slope of the pyramidal surface obtained by this method on the growth pyramid of Fig. 4 is indicated schematically in Fig. 5.

The slope is small at the skirt of the growth pyramid and gradually increases but at the periphery of the top surface indicated by A, the slope decreases suddenly and discontinuously. Thereafter, the slope decreases at the point B near the center of top surface and in the part between B and C, it is nearly zero.

The point C represents the center of the top surface. An $\angle$-shaped rectilinear groove found near the center of top surface in Fig. 4 is a slip line caused in the course of the crystal growth and the detail will be given in the next report[13)]. Fig. 6 shows a photograph of another abnormal growth pyramid having no flat and smooth part on the top surface.

It is seen that in the neighborhood of the top surface the slope of the pyramidal surface becomes somewhat small but is still considerably large.

Fig. 7 shows the specimen with two abnormal growth pyramids developed one on the top of another. Fig. 8 and Fig. 9 are the growth patterns originating from three vicinal centers: in the neighborhood of these centers each of the three independent groups parallel to the special [110] equivalent direction grows in the corresponding [211] equivalent direction, but with increase of distance from the centers they interact and result in such growth patterns as if they were developed from the same center.

3.2 *Center of the abnormal growth and grain boundary*

This paragraph is devoted to the examination of the center of the abnormal growth

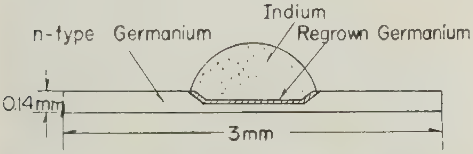

Fig. 1. Cross-section of specimen.

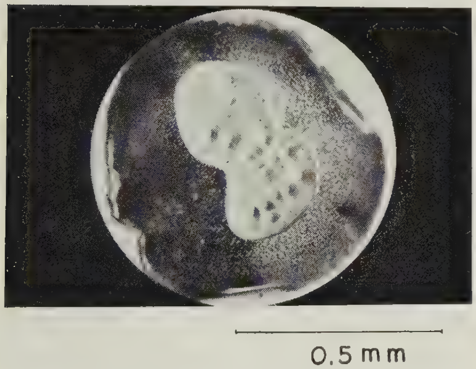

Fig. 2. Growth pattern of the abnormally large truncated hexagonal pyramid observed on the bottom of the *p*-type regrown layer (by optical microscope).

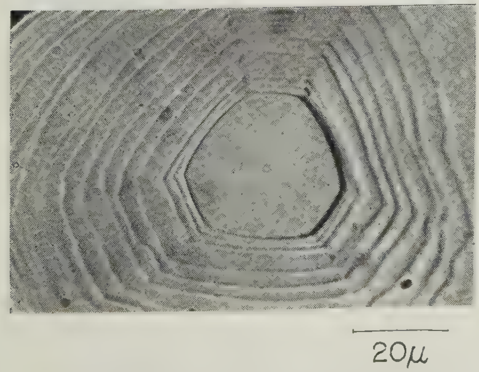

Fig. 3. Abnormal growth pyramid with flat and smooth top surface (by optical microscope).

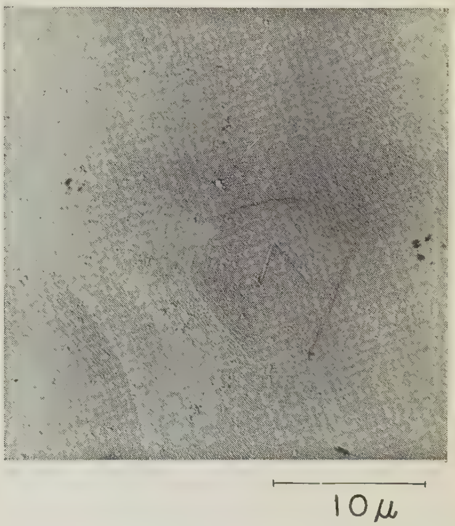

Fig. 4. Abnormal growth pyramid with slightly inclined top surface (by electron microscope).

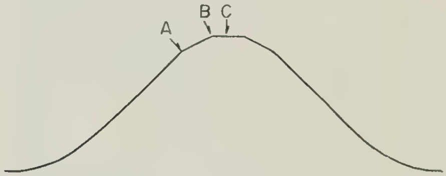

Fig. 5. Schematic indication of the slope of pyramidal surface of growth pyramid of Fig. 4.

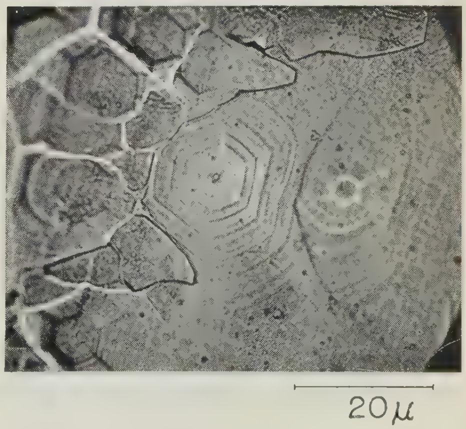

Fig. 6. Abnormal growth pyramid with nearly the same slope of top surface as that of the side (by optical microscope).

described above. In a photograph of Fig. 10, growth pattern is obviously found also on the flat and smooth top face of the growth pyramid. And in the central part, there exists a pattern which seems to be the center of the growth. In some cases, however, the top surface of the abnormal growth pyramid is truly flat and smooth and free from any recognizable growth pattern, as shown in Fig. 3. Fig. 11 gives an enlarged photograph of such a case.

Fig. 12 shows the results which were obtained by etching the area of the abnormal growth pyramid with dilute CP-4 etchant. In (a) the abnormal growth pyramid after 20-second etching.

Near the center of the flat and smooth top surface, etch pit arrays are present in parallel

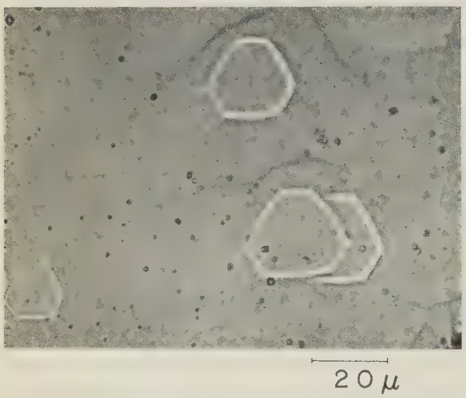

Fig. 7. Abnormal growth pyramids developed one on the top of another (by optical microscope).

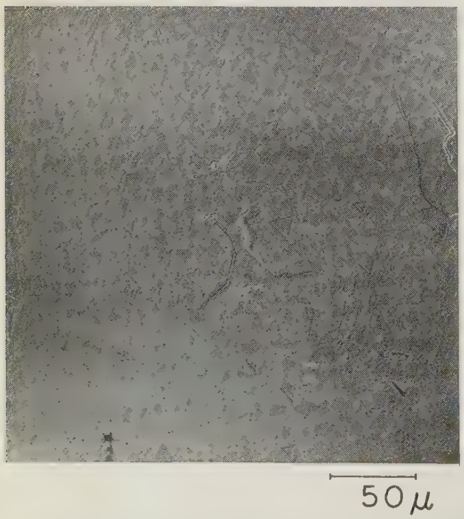

Fig. 8. Composite growth pattern developed from three centers (1) (by electron microscope).

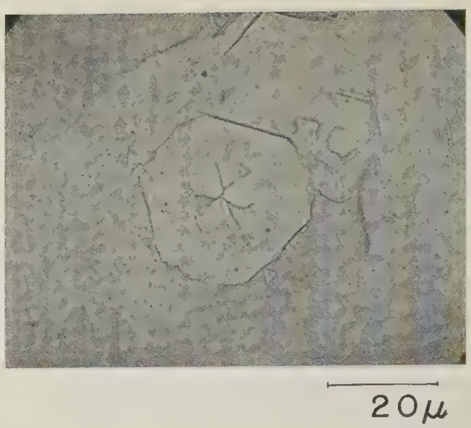

Fig. 9. Composite growth pattern developed from three centers (2) (by optical microscope).

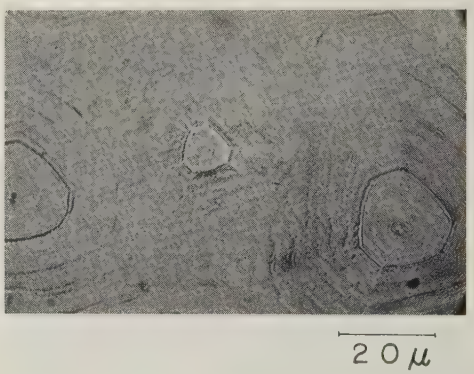

Fig. 10. Growth pattern on the flat and smooth top face of the abnormal growth pyramid (by optical microscope).

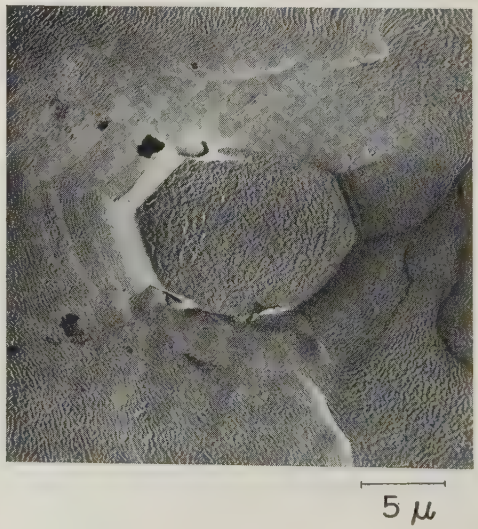

Fig. 11. Enlarged view of the abnormal growth pyramid with no growth pattern on the flat and smooth top surface (by electron microscope).

to the alternate three sides of hexagon (to three [110] axes). Grain boundary surrounding the growth pyramid is distinctive in (a). (b) is the case with 15-minute etching. An equilateral triangle of etch pit arrays in the central part of the top face forms a large hole, and the etch pit arrays appears on the grain boundary and indicate that they are caused by misfitting. Fig. 13 shows the results of the etching of the bottom of the regrown p-type layer, and explains the process of the abnormal growth pyramid being attacked. (a) shows the state after 21-minute etching with dilute CP-4 etchant; the portion of the abnormal growth pyramid has been selectively etched away, and the n-type germanium substrate is exposed. (b) shows the state after complete dissolution of the p-type regrown layer by the etching for about 60 minutes. Etch pits corresponding to edge dislocations of n-type germanium have appeared, and it is shown that there is no correlation between the distribution of dislocations in the substrate single crystal and the growth pattern on the regrown layer.

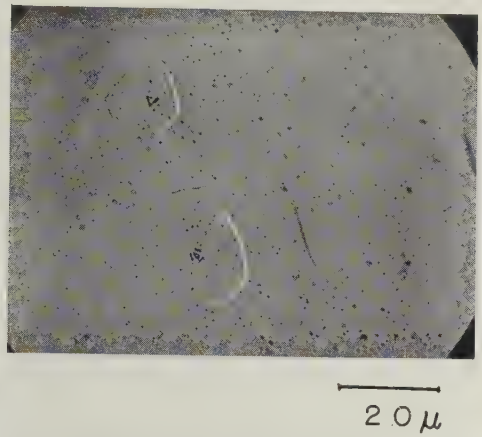

(a) After 20-second etching

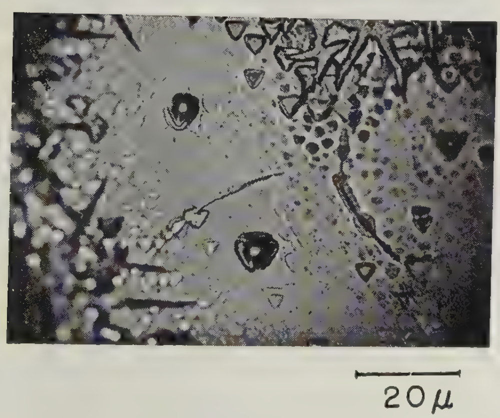

(b) After 15-minute etching

Fig. 12. Etched pattern of abnormal growth pyramids (by optical microscope).

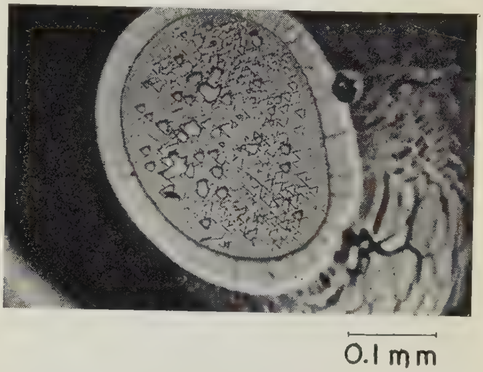

(a) After 21-minute etching

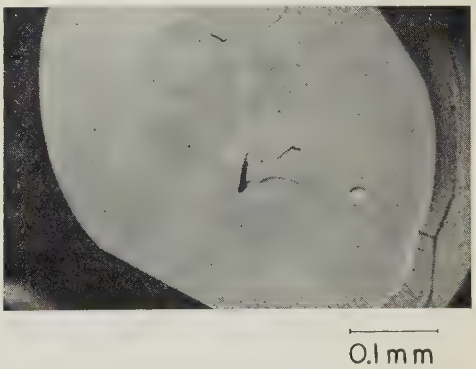

(b) After 60-minute etching

Fig. 13. Etch pattern on the p-type regrown germanium layer (by optical microscope).

As a help to ascertain this fact, photographs are shown in Fig. 14 for an n-type germanium which, while covering the indium alloyed side with wax, has been etched gradually on the reverse side with dilute CP-4 etchant. (a) shows the state of etch pits which appeared after the etching of the reverse side of the n-type germanium. (b) shows the state after further about 1-hour etching; the pointed centers of etch pits appeared on the n-type germanium reached the p-type regrown layer present on the opposite side of the pellet, and the p–n boundary began to appear. Since the etching rate of p-type germanium is smaller than that of n-type, flat and smooth p-type germanium appeared and the etch pits took the truncated cone shape. In the bottom part of each pit, many fine etch pits are recognized. Among them, the etch pit located near the center or the top of the truncated cone is relatively larger than the others. Obviously, it corresponds to the etch pit in the n-type germanium bulk. In other words, it is seen that the dislocations in n-type germanium extend continuously to the p-type regrown layer, and in addition to them, an extraordinarily number of dislocations are present in the p–n junction boundary.

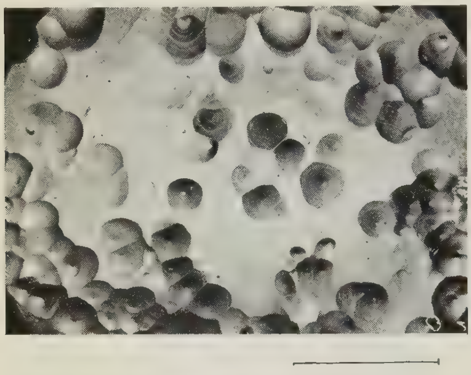

(a) Etch pits on bulk germanium

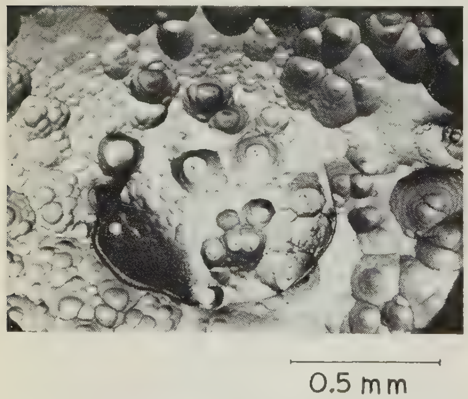

(b) Regrown layer revealed after etching

Fig. 14. Specimen etched on the reverse side of n-type germanium (by optical microscope).

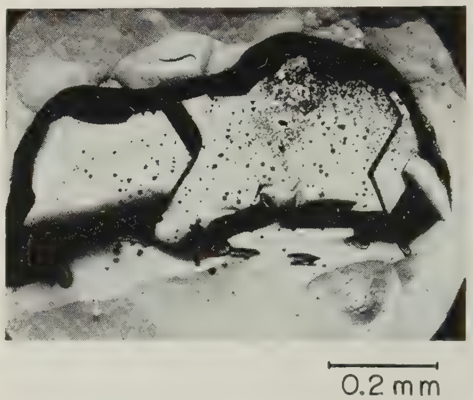

(a) Observation by reflected light

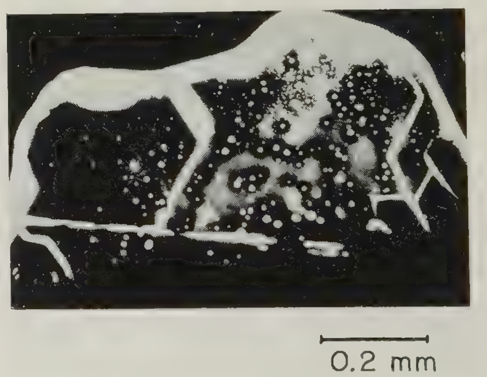

(b) Observation by transmitted light

Fig. 15. Pits which appeared when p-type regrown layer was etched on its reverse side (by optical microscope).

By applying the etching similarly on the reverse side of the n-type germanium neighbouring to the bottom of the pan-shaped p-type regrown layer shown in Fig. 1 was entirely removed away, and the resulting states are shown by the photographs in Fig. 15. The photograph (a) shows the observation of the reverse side of the bottom of such a pan-shaped p-type regrown layer as shown in Fig. 1 by reflected light. This p-type regrown layer was exposed after the n-type germanium layer was removed away by etching. It is seen that the central part of the above mentioned abnormal growth pyramid was easily etched also from the reverse side. In the upper right-hand part of this, ▽-shaped etch pits are seen in a large number, and they indicate that the part corresponding to the center of the abnormal growth pyramid which was visible on the front surface of the regrown layer was easily etched also from the reverse side of the same layer. The star or polygonal shaped pits seen in the other part of the photograph were formed as follows: At first the reverse side of the p-type layer was etched and there appeared ▽-shaped etch pits. With this process wide, curved and dark coloured part seen in the figure was severely attacked by the etchant and penetrated through. Because this part corresponds to the periphery of the regrown layer and here its thickness is remarkably thin as compared to central part. From that part the etchant leaked to the opposite side of the *p*-type layer, thus etch pits appeared also on this side. The triangle of the pits thus formed is rotated by 180° about the first triangle, and these two equilateral triangles overlapped each other to form the star-shaped etch pit. (b) shows the same specimen as (a) but observed by the transmitted light. In this photograph, the part at which the etch pich penetrated through the *p*-type regrown layer looks white. This white etch pit is surrounded by a black area where the transmission of light is not permitted because the abnormally grown layer is thicker than the other part. Another area

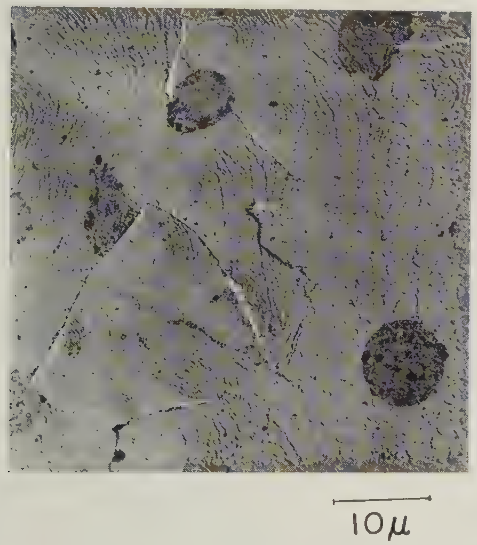

Fig. 16. Small growth pyramid (by electron microscope).

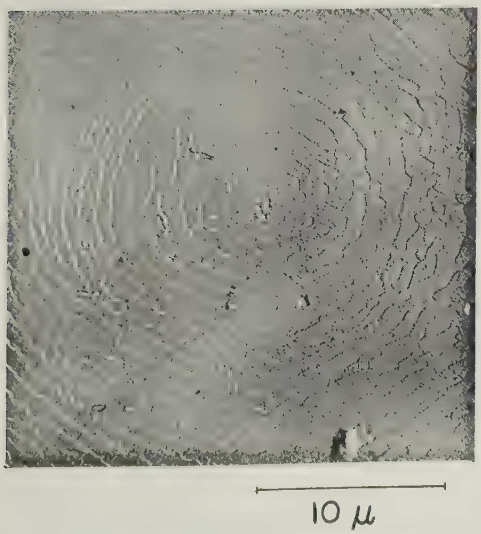

Fig. 17. Pyramidal surface of small growth pyramid (by electron microscope).

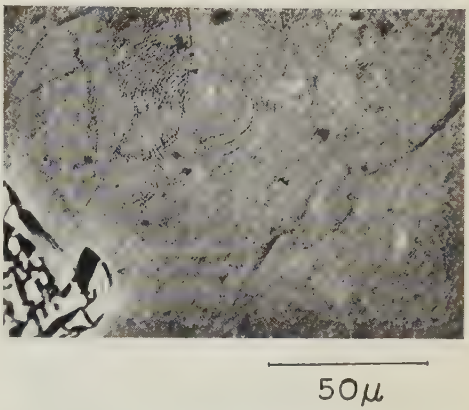

(a) Growth pattern developed by decoration

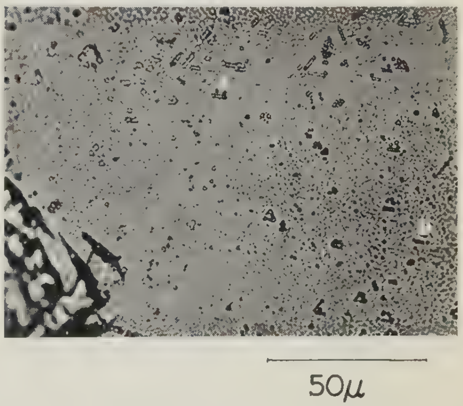

(b) Etch pattern developed by chemical etching

Fig. 18. Small growth pattern developed by decoration (by optical microscope).

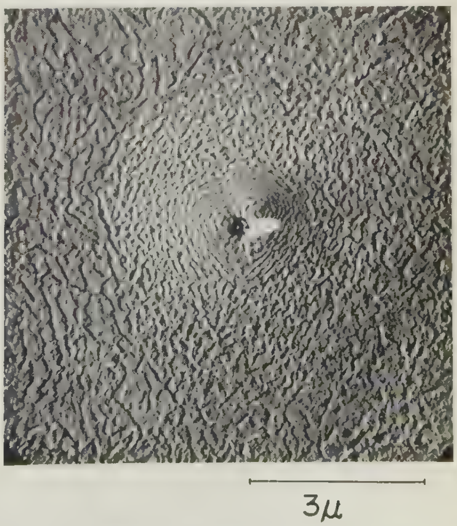

Fig. 19. Three sets of growth patterns developed around the hole (by electron microscope)

free from the abnormal growth looks gray because the light is partially transmitted due to the thin p-type layer of poor growth. This again shows that the triangle of star-shaped etch pit appears in the central part of the abnormal growth. From the results of the experiments so far described, it is clear that the center of the abnormal growth occurs on the p–n junction boundary irrespective of the lattice defect in the n-type germanium substrate.

3.3 *Small growth pyramid*

The growth pattern observed on the bottom surface of the pan-shaped regrown layer shown in Fig. 1 reveals not only the abnormal growth pyramid as described in 3.1 but also very small pyramid as shown in Fig. 16 frequently. The pyramid in this case is characterized in that it has uniform slope all over the pyramidal surface and hence free from any flat and smooth top surface seen in the above-mentioned abnormal growth pyramid.

In the photograph, white or black broken line shows the boundary caused in the course of the growth. An enlarged view of such growth pyramid is shown in Fig. 17. In the lower left-hand part of the step shadow is

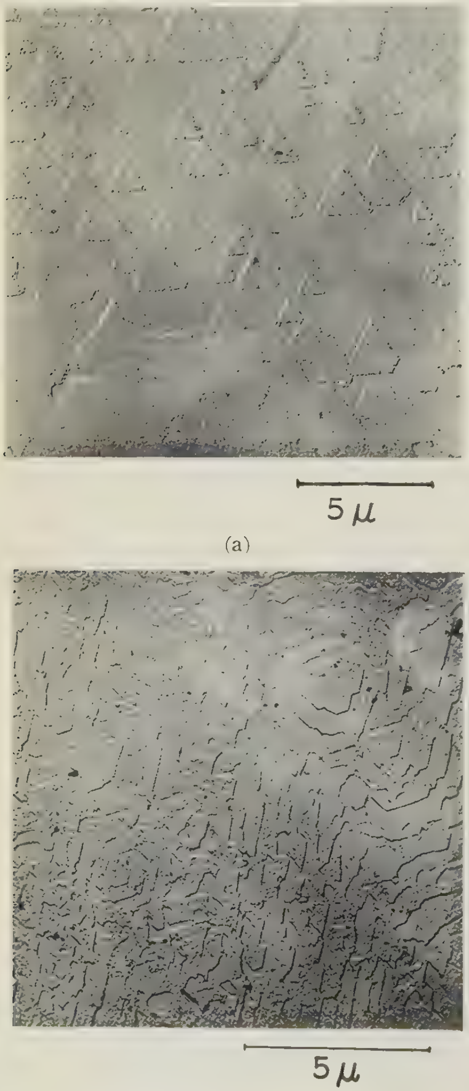

(a)
(b)

Fig. 20. Planar growth pattern composed of a set of polygons having sides parallel to [110] axis (by electron microscope).

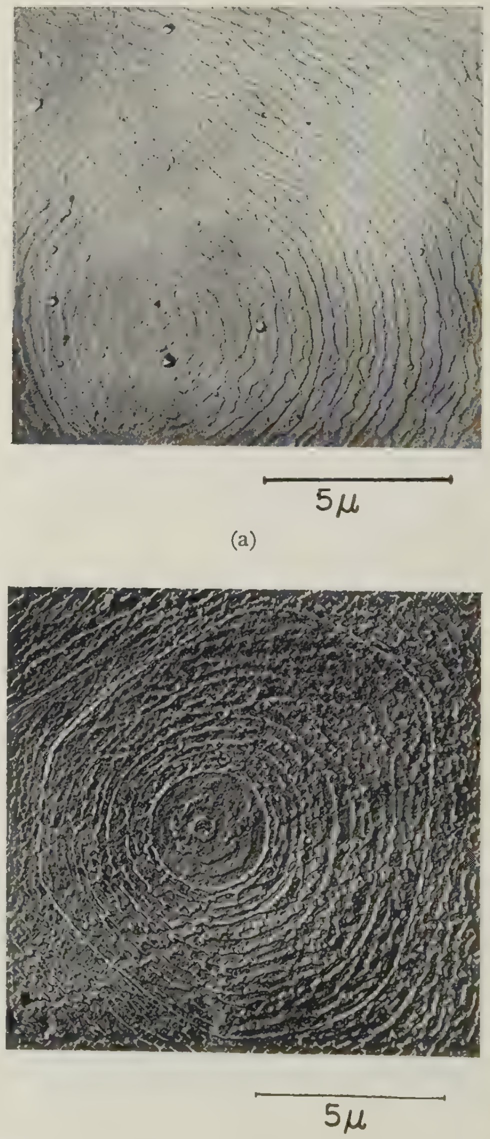

(a)
(b)

Fig. 21. Concentric step pattern compounded with uneven pattern (by electron microscope).

white, while in the upper right-hand part of the step it is black, showing clearly that the pyramidal surface has uniform slope. For the slope angle θ of the pyramidal surface obtained from the width of this shadow, $\tan\theta=0.03$.

In some cases the growth pattern of such a small growth pyramid is not so clearly observed. To obtain the better contrast in such case the author applied the method of decoration. In the first place, a specimen was electrolytically polished anodically in the electrolyte of the composition as shown below. After that, with the polarity inversed, the specimen was applied on its surface with a very thin copper plating, and then it was heat treated in nitrogen atmosphere mixed with a small amount of oxygen at 400°C for 30 minutes. It was known that the growth pattern not so clear at first reveals itself very distinctly by this method.

Composition of the electrolyte:

20% $CuSO_4$ solution	5% (volume)
H_2O_2 (30%)	5% (volume)
HF (48%)	5% (volume)
Deionized water	85% (volume)

The reason for this is probably that copper atoms precipitated at first uniformly on the surface of the specimen moved on the crystal surface by heating and were collected at the growth steps where they were oxidized and fixed. The growth pattern is shown in Fig. 18 (a) which appeared in superior contrast by such decoration on the flat and smooth surface of an abnormal growth pyramid. Before the application of decoration, such pattern was hardly noticeable. It is obvious that this is the growth pattern developed from the central part.

(b) shows the etch pattern developed by 20 minutes etching of this specimen with dilute CP-4 etchant. A large number of etch pit arrays several microns in length parallel to the [110] axis appears, and there is one pit array respectively for each of A and B at the position of major axis of the ellipse which is concentric with the center of the growth pattern as shown in (a). It is remarkable that these pit arrays do not take the complicated triangular shape unlike the case of Fig. 12. Fig. 19 shows the specimen which has three sets of growth centers arround an extremely small hole. At a distance away from the center of the hole, they are integrated into one growth pattern. The depth of the hole is about 0.35 μ as calculated from the shadow.

3.4 *Planar growth pattern*

In the cases described in 3.1 and 3.3, presence of the growth pyramid was recognized, but in some cases, planar pattern is formed by the integration of a number of polygons which have three sides parallel to [110] axis as shown in Fig. 20 (a) and (b).

In Fig. 21 (a) and (b) is shown very slightly sloped concentric step pattern compounded with uneven pattern.

§ 4. Discussion

4.1 *Regrowth of germanium from indium melt*

Consider a system in which (111) plane of a germanium single crystal is, in equilibrium state, in contact with an indium melt. If this system is cooled, germanium precipitates and regrows on the germanium single crystal from the indium melt. As to this regrowth, we may consider it in two cases: in the first case the screw dislocation present on the surface of the substrate single crystal in contact with the melt is responsible for the regrowth, while in the other the surface nucleation is responsible for it. As the supersaturation of germanium in the indium melt becomes remarkable, many critical nuclei are produced on the substrate germanium surface and the regrowth of germanium is caused by them clearly. But in case where the supersaturation is so small, the regrowth is caused, as well known, by the screw dislocation. Now consider the regrowth by the surface nucleation[14)–16)].

Denoting by ρ_c the radius of critical nucleus, we have:

$$\rho_c=\frac{a\phi}{2kT\ln\alpha} \tag{1}$$

where a is the distance between adjacent atoms arround the critical nucleus, ϕ is the bonding energy per bond of the adjacent atoms and α is the saturation ratio of germanium which is related to the supersaturation σ by $(\sigma=\alpha-1)$. Fig. 22 shows the results of calculation of the relationship between σ and ρ_c. The abscissa shows the supercooling temperature ΔT as well as σ.[17)]

Now consider that the step is in the [110] direction on the (111) plane, and one broken bond per atom is present. In this case, the activation energy for nucleation is given by:

$$\varDelta F_c=\frac{\phi^2}{kT\ln\alpha} \tag{2}$$

Further, as to the rate of formation of critical nuclei, I, we have:

$$I=n_0 j\exp(-\varDelta F_c/kT) \tag{3}$$

where n_0 is the number of single atoms which are adsorbed per unit area of the crystal surface, j is the number of atoms which arrive at the surrounding of the critical nucleus per unit time.

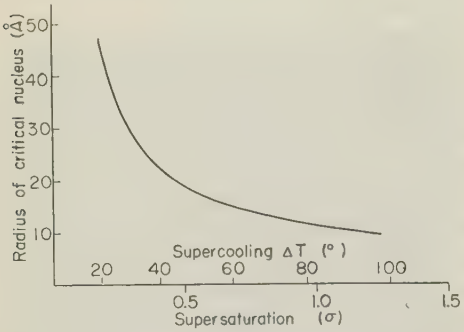

Fig. 22. Relationship between supersaturation and the radius of the critical nucleus ($\varDelta T$ denotes the supercooling assuming that $T_0=773$°K).

The discussion of each constant appearing in Eqs. (2) and (3) is as follows: The heat of melting of germanium into the molten indium, $\varDelta H$, is 11.9 kcal/mol[17], and therefore, $\phi=4.13\times10^{-13}$ erg is obtained as calculated from $\phi=\varDelta H/2N$ (N is Avogadro's constant). As to j, we have:

$$j\approx2\pi\rho_c DN_0 \tag{4}$$

where D is the diffusion coefficient of germanium in the melt, and N_0 is the the concentration of germanium atoms in the indium melt. ρ_c must be calculated with Eq. (1). In Eq. (1), $a=3.97$ Å. According to Y. Sugita $D=5.7\times10^{-5}$ cm²/sec,[18] and by Takabayashi D is estimated to be of the order of 10^{-5} cm²/sec.[19] With reference to the phase diagram of *In—Ge* system at 770K[17),20)], $N_0=3.5\times10^{21}$ cm^{-3}. Thinking from this value of N_0, we may assume $n_0\approx10^{14}$ cm^{-2} in (3) without serious error. Substituting these values into Eq. (4), we have $j\approx10^{11}$ sec^{-1}. With this and the above-shown other values used in Eq. (3), the results as shown in Fig. 23 are derived. As seen from the figure, the error in evaluating n_0 and j does not seriously affect the results, and the order estimation as descrived above is sufficient for the purpose. The abscissa shows the supercooling temperature $\varDelta T$ as well as the supersaturation.

On the assumption that the growth step with sufficiently large radius of curvature exists on the crystal surface and the rate of advance of that step U_∞ is controlled mainly by the diffusion of germanium atom to the step in the melt, the following equation is derived[16),

$$U_\infty=a^2D\pi N_0(\alpha-1)\{\ln(\delta/a)\}^{-1} \tag{5}$$

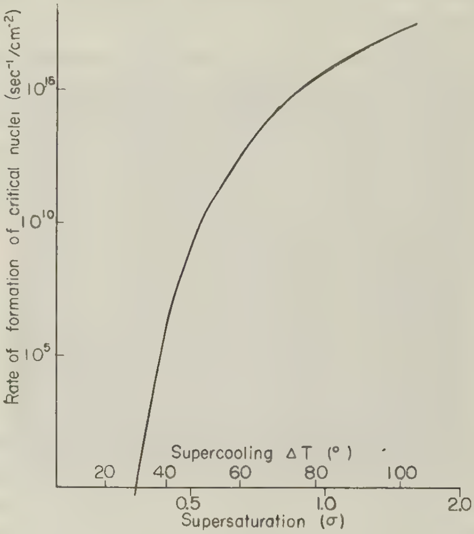

Fig. 23. Rate of formation of critical nuclei.

where δ is the thickness of a molten layer in which the diffusion of solute atom participating in the growth of crystal is carried out, and this layer exists in uniform thickness adjacent to the crystal surface. Now denote the time by t, then δ may be regarded as $\delta\approx\sqrt{Dt}$. If a value $\delta\approx10^{-3}$ cm ($t\approx0.018$ sec) is assumed, Eq. (5) is reduced to:

$$U_\infty\approx97.4\sigma\ \text{cm/sec} \tag{5$'$}$$

Denoting by A the area of the crystal in contact with the indium melt, we have $A\approx1$ mm² for the present case. Thus, the time required for one critical nucleus to grow and cover the entire crystal surface is given roughly by:

$$\frac{\sqrt{A}}{U_\infty}\approx10^{-3}\ \text{sec} \tag{6}$$

Incubation period for the formation of the critical nucleus is expressed as:

$$\tau=\frac{1}{AI} \tag{7}$$

From the value $I \approx 10^5\,\mathrm{cm^{-2}\,sec^{-1}}$ for $\sigma=0.4$ in Fig. 23, $\tau=10^{-3}$ sec follows in this case. Thus, for $\sigma<0.4$ we find $\tau>\sqrt{A}/U_\infty$, and in this case, the growth rate takes the form of:

$$R=\frac{d}{\tau} \tag{8}$$

where d is the spacing of {111} planes, i.e., 3.26 Å which is slightly smaller than the value of earlier-mentioned a. For $\sigma>0.4$, $\tau<\sqrt{A}/U_\infty$ and the surface nucleation becomes remarkable: many steps exist on the crystal surface, and consequently, the growth rate is limited by the diffusion of germanium atom from the indium melt onto the crystal surface. The growth rate R of the crystal in this case is given by[16]

$$R=DN_0\Omega\sigma/\sqrt{Dt} \tag{9}$$

where Ω is the atomic volume of germanium, i.e., $2.25\times10^{-23}\,\mathrm{cm^3}$. For $\sqrt{Dt}=10^{-3}$ cm, the growth rate R was calculated by Eqs. (8) and (9), as a function of the supersaturation σ, and the resnlts are shown by full line in Fig. 24. As σ exceeds 0.4, R increases rapidly according to Eq. (8), but with a little larger value of σ, the growth rate is controlled by the diffusion of germanium atom in the melt, as a result of which R increases linearly with σ according to Eq. (9).

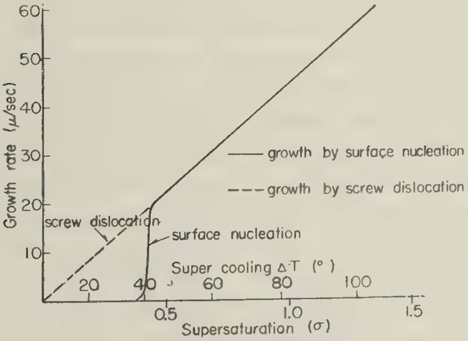

Fig. 24. Relationship between supersaturation and growth rate of the crystal.

For $\sigma<0.4$, the rate of crystal growth due to the surface nucleation is very small, and it can be considered that in this region the screw dislocation is mainly responsible for the crystal growth. After the spiral growth step caused by the screw dislocation is fully developed to cover the entire surface of the crystal and the growth reaches the steady state, the growth rate R is given by Eq. (9). In such case, it varies linearly with the supersaturation σ as shown by the dotted line in Fig. 24. The time required for the growth due to screw dislocation to reach the steady state is roughly of the order of 10^{-3} sec as calculated by Eq. (6). Since this is quite a short time, it may be justified to consider that the rate of growth due to the screw dislocation is represented substantially by the dotted line in Fig. 24. As is commonly known, distance of the growth steps due to a single screw dislocation is $4\pi\rho_c$, but if there exist n screw dislocations of the same sign within the distance of $2\pi\rho_c$, the mean distance of the growth steps is $4\pi\rho_c/n$. In considering that the height d of one step is 3.26 Å, the angle θ between the pyramidal surface of the growth pyramid thus formed and the (111) plane of the crystal surface is expressed by the relation such as:

$$\tan\theta=\frac{nd}{4\pi\rho_c} \tag{10}$$

With the use of Eq. (1), the relationship of the supersaturation σ and $\tan\theta$ was calculated from Eq. (10) for various values of n as a parameter. Fig. 25 gives the results of this calculation.

4.2 *Lattice defects in the regrown layer*

As shown in Fig. 14, the regrown germanium layer has a great number of dislocations independent of the imperfections in the substrate germanium. The mechanism of for-

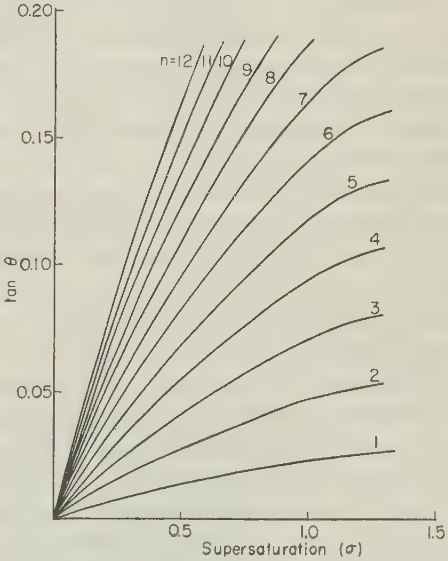

Fig. 25. Relationship between the supersaturation and the slope of the pyramidal surface of the growth pyramid.

mation of these dislocations will be discussed in this paragraph. Consider that an n-type germanium pellet is heated in contact with an indium melt and subsequently cooled rapidly by pouring oil. We consider the state in which indium is in molten state and from this melt, germanium is segregating to form p-type regrown layer. In such condition, the temperature of the upper surface of the regrown layer is raised by the latent heat of solidification of germanium, while the n-type germanium substrate is cooled by pouring of oil. As a consequence, there exists in the p-type regrown layer of Fig. 1 a temperature gradient down from the solid-melt interface towards the substrate germanium. Moreover, the radial temperature gradient exists because of decrease in temperature towards the edge of the regrown layer. Further, in addition to these, local irregularity of temperature is naturally caused when the oil is poured for rapid cooling. Temperature of the thin p-type regrown layer formed in this process is very near to its melting point and so is subject to plastic deformation, but the n-type substrate germanium is difficult to be subject to it at temperatures below 500°C.[21] Thus, at the beginning of the regrowth, many localized slips are caused in the regrown layer, and there is a possibility of generating a great number of dislocations independent of the imperfections in the n-type substrate. For the generation of such many lattice defects, there are other reasons conceivable. That relatively large amount of indium (of the order of 10^{18} cm^{-3})[22] is contained in the p-type layer is, of course, one reason[23]. In some cases, vacancy which is caused in the regrown layer in the solid-melt interface at the beginning of the regrown condenses into a disc form which may collapse and generate dislocation ring.

4.3 *Discussion of the abnormal growth pyramid*

The abnormal growth pyramid mentioned in 3.1 is characterized in that, as seen from Fig. 2, its size is abnormally large compared with the other growth patterns. They can be classified into two cases: first, as shown in Figs. 3, 7 and 11, the top surface of the growth pyramid is flat and smooth, and second, as shown in Figs. 4, 5, 6 and 10, the top surface is inclined a little but its slope is considerably smaller than that of the pyramidal surface. The mechanism of the formation of such abnormal growth pyramid will be discussed in this paragraph. In the centeral part of the top surface of the abnormal growth pyramid of Fig. 12 (a), there exist etch pit arrays parallel to three [110] axes on the (111) surface. Obviously, this is an indication of the existence of the localized slip lines. The reason why such a complicated slip has been created is probably that the area has large localized temperature gradient at the beginning of the regrowth for the reason discussed in 4.2. As to germanium, it has been known that slip is easy to occur in the [110] directions on the {111} planes[21),25),26)]. When the p-type layer is looked down from above in Fig. 1, there are two cases in regard to the orientation of a regular tetrahedron composed of a set of {111} planes. First, the tetrahedron is normal with respect to the (111) plane of the upper surface and the second, it is inverted. For a germanium column with a radial temperature gradient, the slip is possible on either set of {111} planes, but if the column is cooled at its bottom so as to give the axial temperature gradient, the slip is easier to occur on the {111} planes of the inverted regular tetrahedron[27]. If the stress in this case is analyzed into components of the easy-to-slip direction, then both slips, one parallel to [110] axis on the bottom surface (the surface of regrown layer) and the other to [110] axis making an angle of 54°44′ with the bottom surface, should simultaneously occur. The etch pit arrays parallel to [110] axis on the top surface of abnormal growth pyramid in Fig. 12 (a) seem to be the arrays of the edge dislocations caused by the slip of the former direction. The same slip causes also screw dislocations which in the present example do not participate in the growth of crystal. Another screw dislocations from the slip of the latter direction make an angle of 54°44′ with the surface, and coexist with the above-mentioned edge dislocation arrays, and should participate in the subsequent growth of the crystal. The same slip causes also edge dislocation which in the present example is probably invisible because it intersects the surface of the regrown layer at small inclination. It follows from the above that three sets of edge dislocation arrays and screw dislocation arrays, each parallel to [110] axis on the surface of regrown layer but making an angle of 120° with each other, sholud be simultaneously created. In this case, a step whose height inside the three sets of slip lines is larger than that of the outsider is created. In the area with such locally concentrated screw dislocations, regrowth is prominent and hence much heat of solidification is generated, so further formation of screw dislocation is caused enough to form the center of the abnormal regrowth. As to the edge dislocation arrays in the center of the top surface in Fig. 12 (a), the equilateral triangle formed by the arrays is of the same orientation as that of the etch pits present in quantity in the other part of the specimen, and this obviously corresponds to the bottom of the inverted tetrahedron as previously mentioned. Fig. 26 shows a model of the screw dislocation arrays which coexists with the above-mentioned edge dislocation array. Now, considerations are made on the slip line AA' in the figure. Assume that at A n_A screw dislocations of the same sign exist adjacently with one another (or it may be assumed that a single dislocation with a large Burgers vector exists). At A', the existence of the same number n_A of screw dislocations which have the opposite sign is assmed.

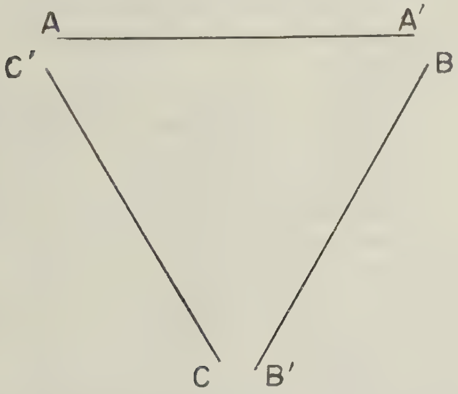

Fig. 26. Model of the dislocation arrays in the central part of the abnormal growth pyramid.

As to B, B' and C, C', existence of concentrated screw dislocations in the respective numbers of n_B and n_C is assumed. With these screw dislocation as centers, growth of crystal takes place. The slip line in Fig. 12 (a) has the length of the order of several microns, so the slip lines $\overline{AA'}$, $\overline{BB'}$ and $\overline{CC'}$ in Fig. 26 may be considered to have nearly the same length. Now assume that $\overline{AC'}$ which indicates the distance between one end of $\overline{AA'}$ and the end of the adjacent slip line is considerably small compared with $\overline{AA'}$, i. e., 0.1 μ or less. Then, for the relatively small supersaturation σ in Fig. 22, the radius of critical nucleus, ρ_c, is relatively large and satisfies the ration $2\rho_c > \overline{AC'}$, and because of the mutually reverse signs, the screw dislocations at A and C' interfere with each other, effecting the growth at the same rate as if there were $|n_A - n_C|$ screw dislocations. While, if σ gradually increases thus resulting in the decrease in ρ_c until the condition $2\rho_c < \overline{AC'}$ is satisfied, the growth will be controlled by the number of screw dislocations, n_A or n_C, namely by larger one of them. For other positions, similar discussion may be applicable. Assume $\overline{AC'} \approx \overline{A'B} \approx \overline{B'C}$, for instance. In the case of $n_A = n_B = n_C$, if σ is small at the beginning of the regrowth, then $2\rho_c > \overline{AC'}$, and the growth due to these screw dislocations does not take place at all. While, if σ gradually increases until $2\rho_c < \overline{AC'}$ is satisfied, then the concentric growth patterns will develop around $\overline{AC'}$, $\overline{A'B}$ and $\overline{B'C}$, from each of the n_A centers and they are integrated in the distance eventually into the concentric growth step around AA', BB' and CC', and the slop increases in proportion to n_A according to Eq. (10). In consideration of $\tan\theta \doteqdot 0.12$ in Fig. 4 as described in 3.1, it follows from Fig. 25 that $n_A \approx 10$ for $\sigma \approx 0.4$. But, towards the end of the regrowth process, the supersaturation σ decreases again resulting in $2\rho_c > \overline{AC'}$, thereby growth by these growth centers is completely stopped. Figs. 3, 7 and 11 seem to represent such case. In general, however, all n_A, n_B and n_C are not necessarily equal. Now, for instance, take up the case of $n_A > n_B > n_C$. For a small σ at the beginning of regrowth, concentric growth patterns are developed from $(n_A - n_C)$ growth centers around $\overline{AA'}$, $\overline{BB'}$ and $\overline{CC'}$, and the pyramid has a small slope. With the gradual increase in σ, concentric growth patterns are developed from n_A centers and the slope of the pyramidal surface is increased in accordance with Eq. (10). Towards the end of the regrowth process concentric growth patterns are developed again from ($n_A - n_C$) growth centers and the slope is made small. This is represented by Figs. 4, 6 and 10 the behavior of the change in the slope is shown by Fig. 5. The possibility of the growth by the screw dislocation arrays as shown in Fig. 26 is clear from Figs. 8 and 9. Either of the figures shows the concentric growth pattern produced around those growth patterns which developed at first from threefold center and subsequently were integrated in the distance away from the center. In Fig. 8, there exist many slip lines of equilateral triangle which are, as previously mentioned, of the same orientation as the etch pits caused by edge dislocation, and in the present example, three centers of growth patterns are also of the same arrangement as above. It is clear that the center of the abnormal growth pyramid has such a complicated structure as mentioned above and a relatively large number of screw dislocations are collected to it.

4.4 *Discussion of small growth pyramid*

In the case of relatively small growth pyramids as shown in Figs. 16 and 17, the slope of the pyramidal surface is nearly unifrom from the skirt to the top. In the central part of the small growth pyramid as seen in Fig. 18 (b), there exists a slip line with a simple structure. This slip line forms one straight line as shown by *A* and *B* in the same figure. As mentioned above, it seems that following this edge dislocation array the screw dislocation array exists. Since the straight lines *A* and *B* are of the order of several microns in length. The distance between the screw dislocations of the different signs may be justifiably considered from Fig. 22 not to become substantially smaller than $2\rho_c$ provided that they exist at a separation of the same order as cited above. It seems from this that the slope of the pyramidal surface of the growth pyramid is constant from the beginning to the end of the regrowth process. Since $\tan\theta \doteqdot 0.03$ from Fig. 17 as discussed in 3.3, the number of the screw dislocations in the present case is about 3 for $\sigma \approx 0.4$ in Fig. 25. It seems that the center of such small growth pyramid has a simple structure compared with that of the abnormal growth pyramid of 4.3, and the number of the screw dislocations existing in that part is relatively small. Fig. 19 shows a specimen which has the growth center of threefold symmetry around a small hole.

4.5 *Discussion of planar growth pattern*

If the rate of growth of the crystal is sufficiently large and exceeds 20 μ/sec in Fig. 24, the growth of the crystal should take place mainly through the surface nucleation. In such case, planar growth pattern should be developed as shown in Fig. 20. Obviously, each of the patterns (a) and (b) has threefold symmetry. Fig. 21 (a) and (b) may be such that the small growth pattern as described in 4.3 appears in good contrast by the oxide decoration.

§ 5. Acknowledgment

The author is indebted to Y. Sugita for his supply of many data and cooperation in experiment, and to T. Mitsuishi and E. Yamada for their discussion about the mechanism of regrowth.

References

1) E. Billig: Proc. Roy. Soc. A, **235** (1955) 37.
2) S. G. Ellis: J. Appl. Phys. **26** (1955) 1140.
3) E. Billig: Brit. J. Appl. Phys. **7** (1956) 375.
4) G. Gressel and J. A. Powell: Progress in Semiconductors **2** (1957) 237.
5) F. D. Rosi: RCA Rev. **19** (1958) 349.
6) J. I. Pankove: RCA Rev. **15** (1954) 75.
7) C. W. Mueller and N. H. Ditrick: RCA Rev. **17** (1956) 46.
8) C. W. Mueller: RCA Rev. **18** (1957) 205.
9) J. I. Pankove: J. Appl. Phys. **28** (1957) 1054.
10) J. W. Peterson, J. Mcglasson and W. C. Hittinger: J. Metals **9** (1957) 823.
11) C. Elbaum and B. Chalmers: Can. J. Phys. **33** (1955) 196.
12) A. R. Lang: J. Appl. Phys. **28** (1957) 497.
13) M. Tomono: To be published.
14) R. Becker and W. Döring: Ann. der Phys. **24** (1935) 719.
15) F. C. Frank: Adv. in Phys. **1** (1951) 91.
16) W. K. Burton, N. Cabrera and F. C. Frank: Phil. Trans. Roy. Soc. **243** (1951) 299.
17) P. H. Keck and J. Broder: Phys. Rev. **90** (1953) 521.
13) Y. Sugita: Unpublished.
19) Takabayashi: J. Appl. Phys. Jap. **25** (1956) 331 (in Japanese).
20) W. Klemm et al.: Z. Anog. Allgem. Chem. **256** (1948) 239.
21) C. J. Gallapher: Phys. Rev. **88** (1952) 721.

22) F. A. Trumbore: B. S. T. J. **39** (1960) 205.
23) J. C. Fisher, R. L. Fullman and G. W. Sears: Act. Metallurgica **2** (1954) 344.
24) B. Chalmers: J. Metals **6** (1954) 519.
25) E. S. Greiner: J. Metals **7** (1955) 203.
26) R. G. Treuting: J. Metals **7** (1955) 1027.

JOURNAL OF THE PHYSICAL SOCIETY OF JAPAN, Vol. 16, No. 3, MARCH, 1961

An Electron Diffraction Study on Cu-Sn Alloys

By Tomokuni MITSUISHI

Hitachi Central Res. Lab. Kokubunji, Tokyo

(Received November 30, 1960)

Intermetallic compounds produced by the interdiffusion of Cu and Sn were examined by electron diffraction. In addition to the known phases, a new phase of structure A4 type is found.

§1. Introduction

Cu-Sn alloys were studied by X ray diffraction, and various intermetallic compounds were reported[1]. (Table I). Related to the investigation on the soldering of copper, the boundary layer of Cu_6Sn_5 at low temperature and the additional layer Cu_3Sn between Cu_6Sn_5 and Cu at high temperatures were found by the microscopic observation of Cu-Sn joint[2]. By the electron diffraction method, Tazaki and Kohra[3] confirmed the formation of Cu_6Sn_5 in heat treated double films of Cu and Sn. Recently Y. Fujiki[4] observed electron diffraction patterns of a Cu-Sn compound of NiAs type structure. However, these data on the interdiffusion of Cu-Sn and on the formation of various compounds are not satisfactory. The author examined Cu-Sn compound layers of various stage of interdiffusion, and identified various intermetallic compounds of Cu-Sn reported literatures in various transient states of interdiffusion. In addition, he found a new compound of structure A-4 type.

Table I. Cu-Sn intermetallic compounds*

Phase	Structure type	Lattice constant a	b	c
β-Cu-Sn (at 25 wt % Sn) (Cu-rich boundary)	A_2	2.975 3.014 (at 672°C)		
γ-Cu-Sn	b.c. cubic ?			
δ-Cu_4Sn	similar to $D8_{1-3}$	17.92		
ζ-$Cu_{20}Sn_6$	trigonal	7.316		7.854
ε-Cu_3Sn (Sn rich boundary)	A_3	2.753		1.569
	orthorhom. superlattice	5.510	38.18	4.319
η-Cu-Sn	superlattice of $B8_1$ type	20.95		25.43

* From "*A Handbook of Lattice Spacings and structures of Metals and Alloys*[1] p 175"

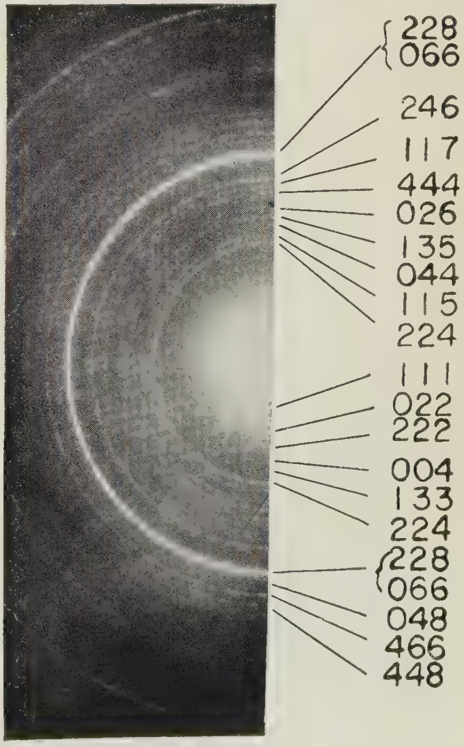

Fig. 1. Diffraction rings of δ′ phase

Table II. Spacings (d's in Å) of δ' (observed) and those of reference (calculated)

δ'		Reference*			
d	*I***	*d*	*h*	*k*	*l*
10.02	m	10.00	1	1	1
6.17	f	6.13	0	2	2
—	—	5.10	1	1	3
5.01	f	5.01	2	2	2
4.29	ff	4.34	0	0	4
3.91	ff	3.98	1	3	3
3.54	m	3.54	2	2	4
3.34	f	3.34	1 3	1 3	5 3
3.06	f	3.06	0	4	4
2.90	f	2.93	1	3	5
		2.89	2	4	4
2.73	f	2.74	0	2	6
—	—	2.64	3	3	5
—	—	2.61	2	2	6
2.50	f	2.50	4	4	4
2.43	f	2.43	1 1	1 5	7 5
2.31	m	2.32	2	4	6
—	—	2.26	1 3	3 5	7 5
—	—	2.17	0	0	8
—	—	2.12	3	3	7
—	—	2.11	4	4	6
2.05	s	2.05	2 0	2 6	8 6
—	—	2.00	1 5	5 5	7 5
—	—	1.99	2	6	6
1.94	ff	1.94	0	4	8
—	—	1.90	1 3	1 5	9 7
—	—	1.89	2	4	8
1.84	f	1.85	4	6	6
—	—	1.82	1	3	9
1.77	f	1.77	4	4	8

* Calculated assuming A4 type $a=17.34$

** Intensities of diffraction rings

§ 2. Experimental Procedures

(a) *Foil specimens*

Foil specimens were prepared by vacuum evaporation. Cu and Sn were deposited one after another on resin films which were spread over glass plates. The resin films were then dissolved away with acetone and the specimens were scooped up by a fine mesh. The thickness of foils was measured by a microscopic interferometer using a sodium lamp as the light source. Thickness of Cu was about 700Å and that of Sn 400Å. The specimens were heated in vacum for 1 or 6 min. at each temperature of 200°C and 470°C.

(b) *Block specimens*

The specimens for electron reflection measurements were prepared by evaporating Sn on Cu blocks, $30^{\mathrm{mm}} \times 4^{\mathrm{mm}} \times 3^{\mathrm{mm}}$. They were heated in vacum for one or five minuites at each temperature of 200°C and 400°C.

§ 3. Results and Discussions

(a) *Foil specimens*

Some of the foil specimens, showed diffraction patterns indicating that Cu_6Sn_5 (η) had been formed before any heat treatment, and others those of Cu only. Upon heating both of these specimes changed to a new phase and then to another. Let us call these phases δ' and X respectively. Phase δ' has the lattice constant close to that of δ phase. However δ' phase shows the diffraction pattern corresponding to A-4 type (Fig. 1, Table II), while δ phase has the D-8_{1-3} structure. The δ' phase is a newly found compound. As for the X phase, we were not able to determine its crystal structure. However, it is doubtless that it is different from η, ε or δ phases. It has some variations both in lattice spacing and in intensities of diffraction lines from one specimen to another. Consequently we concluded that this phase was an intermediate one.

Table III. Summary of observed results

Thickness of Cu (mμ)	70	70	70	Bl.*	Bl.	Bl.	Bl.	Bl.	Bl.	Bl.	Bl.
Thickness of Sn (mμ)	40	40	40	70	40	70	70	40	40	25	35
Temperature of tempering (°C)	—	470	470	—	—	200	200	200	200	470	470
Time of Tempering (min.)	—	6	1	—	—	5	10	1	6	1	5
Diffraction*	T	T	T	R	R	R	R	R	R	R	R
Observed phase	η	δ'	X	Sn	η	η	δ'?	$\eta+\varepsilon$	$\eta+\varepsilon$?	η	ε

* T: Transmision R: Reflection Bl.: Block

(b) *Block specimens*

While specimens deposited with thick layer of Sn (70 mμ) showed the diffraction pattern of Sn before the heat treatment, those deposited with thin layer (40 mη) indicated the diffraction pattern likely to be η phase. With the application of the heat treatment to the latter, η phase became distinct and the continuation of heat treatment resulted in the appearence of the pattern like that of δ' phase or ε phase.

ε phase is not observed in foil specimens. This fact indicates that ε phase layer is too thin for transmission experiments, owing to the condition of material supply restricted by foil thickness. Appearance of X phase in foil specimens is also interpreted as a similar phenomenon. It was rare for any specimen to show the typical diffraction pattern of each phase, and even specimens of the same treament showed more or less different diffraction patterns. This is quite conceivable if the specimens did not attain the thermal equilibrium and were in transient states.

In accordance with Fujiki's results, η phase can be easily formed at relatively low temperatures.

Acknowledgement

The author expresses his sincere gratitude to Dr. Ōhara for many helpful discussions. He is indebted to Mr. T. Takagi for assistance with the experiments.

References

1) W. B. Pearson: *A Handbook of Lattice Spacings and Structures of Metals and Alloys.* Pergamon Press (1958) p. 611.
2) T. B. Crow: J. Inst. Metals **35** (1926) 55; E. J. Daniels: J. Inst. Metals **58** (1936) 199.
3) J. Tazaki and K. Kōhra: J. App. Phps. Japan **21** (1952) 354.
4) Y. Fujiki: J. Phys. Soc. Japan **14** (1959) 913 .

JOURNAL OF THE PHYSICAL SOCIETY OF JAPAN, Vol. 16, No. 3, MARCH, 1961

Diffusion of Cobalt into Silver

By Tokutaro HIRONE and Hisao YAMAMOTO

The Research Institute for Iron, Steel and Other Metals,
Tohoku University, Sendai, Japan

(Received December 3, 1960)

The diffusion coefficient of cobalt into silver has been measured as a function of temperature over the range from 745°C to 943°C by the tracer and lathe-sectioning technique. It has been found that the diffusion coefficient can be expressed as follows;

$$D=(104)\exp\frac{59.9}{RT}10^3\ \text{cm}^2/\text{sec}.$$

The value of activation energy, 59.9K cal/mol, obtained by the present experiment is in good agreement with the result of the screening theory of impurity diffusion, but considerable discrepancy is found between the observed and theoretical frequency factor. The amount of diffused cobalt showes an abnormal decrease near the diffusing surface, which may be caused by the low solubility limit of cobalt in silver.

§1. Introduction

Since Lazarus put forward a screening theory of impurity diffusion in metals, various results of calculations based on the Thomas-Fermi method for the diffusibility of impurity atoms in metallic lattices have been reported[1)-3)]. In order to check these theoretical results experimentally, the diffusion coefficients of various impurity atoms into silver as well as copper have been measured. Although results for both these series are qualitatively consistent with the result of the screening theory, quantitative-agreement is less favorable in the case of copper than in the case of silver: The activation energy of solute diffusion into silver increases regularly from Sb to Ru[4),5)], which belongs to the second transition series, but the activation energies for the diffusion of the first transition elements into copper increase in the order Fe, Co, Ni and decrease from Ni to Zn and increase again at Ga[6)-10)]. However it is uncertain whether the activation energy for the diffusion of the first transition metals into silver is similar to the case of the diffusion into copper or not. For the purpose of finding the difference between the both cases, the diffusion coefficient of cobalt into silver was studied. As silver and cobalt had been reported to be insoluble in each other, special precautions were taken in analyzing the results of the experiment.

§ 2. Experimental Method and Results

The specimens were single crystals of silver 99.99%, 1.5 cm in diameter and 15 cm in length, made by means of the Bridman method. A single crytal rod thus prepared was etched, put into a resin mould and, by means of a cut-off wheel, cut into the shape of a short cylinder, 15 mm in length. To avoid the influence of strains due to the cutting process, the surface layer, about 2 mm in thickness, was removed by electropolishing the cut surface. Then the surfaces were smoothed by polishing with emery paper and electropolished again. Each end surface of the specimen was then plated with cobalt containing Co^{60} isotope.

The amount of plated cobalt was calculated from the product of the time and current-density of electroplating. Then its total radioactivity was measured and the ratio of cobalt quantities to the activity was determined. The estimated thickness of the plated layer ranged from 100 to 500Å. The electroplated specimen was sealed in a quartz tube filled with argon gas and was put in a diffusion annealing furnace. The temperature of the specimen was maintained constant within ±1°C. After the annealing was finished, the specimen was quenched, then mounted in a precision lathe and sectioned.

The total depth of sectioning was measured by a dial-gauge. Each slice thickness was determined from the slice mass as well as from the ratio of total masses to total depth. The sum of each slice mass ranged from 99.6% to 99.9% of the total diminution of the specimen weight due to sectioning.

Fig. 1 shows the logarithms of specific activity of each sliced piece plotted against the square of the penetration depth. As is seen from the figure, each curve shows a steep descent of activity near the surfaces, and then decreases linearly with the square of the penetration depth.

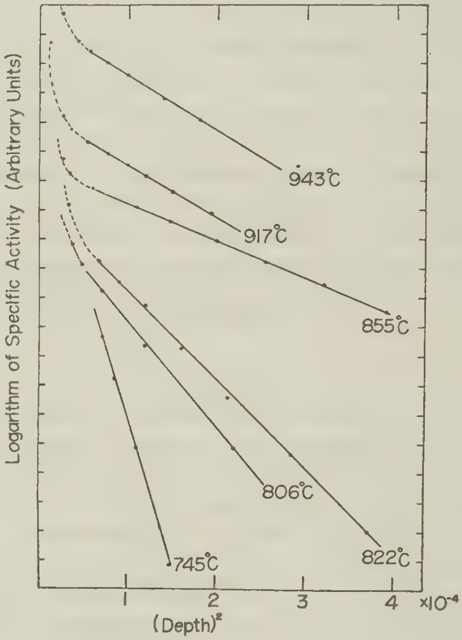

Fig. 1. Penetration curves for the diffusion of Co in Ag.

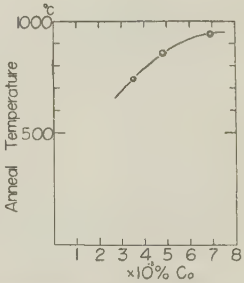

Fig. 2. Co concentrations at the breaking point of the penetration curve versus the annealing temperature.

The analysis of the data was complicated by the existence of the steep descent of the cobalt concentration near the surface. A similar effect has previously been found by Pierce and Lazarus in the case of ruthenium diffusion into silver[5)]. These effects are presumably considered to be caused by the formation of the impermeable intermetallic phase or to the extremely low solubility limit of cobalt or ruthenium in silver. At the present stage it is difficult to give the correct interpretation. However, Tamman proposed previously on the basis of his magnetic measurements that the solubility of cobalt in silver is 0.0007 (at 1000°C) and 0.0004 (at 1200°C) wt. percent respectively.

Fig. 2 shows a temperature dependence of cobalt concentration, which corresponds to the breaking point on the curve of the logarithms of specific activity versus the square of depth where activity ascends sharply. As seen from the curve, these points are roughly in the same order of magnetude as Tamman's result of solubility limit of cobalt in silver.

As in the case of Pierce and Lazarus, the linear part of the x^2-plot of the activity is here assumed to be due to the Fick mechanism of diffusion. Here x means the penetration depth of cobalt into silver. Then the cobalt concentration is expressed by the following equation;

$$c=\frac{c_0}{\sqrt{\pi D t}}\exp\left(-\frac{x^2}{4Dt}\right).$$

In this equation, D represents the diffusion coefficient, t annealing time, c the concentration of diffused atoms and c_0 the concentration of initial solute atom. By comparing the results of the measurements with the above equation, the diffusion coefficient can be obtained as given in the following Table.

Table I. Diffusion of Co in Ag.

Annealing Temperature (deg C)	D (cm²/sec)	Annealing time (sec)
943	2.04×10^{-9}	3.51×10^{4}
917	8.81×10^{-10}	6.57×10^{4}
855	2.78×10^{-10}	26.0×10^{4}
822	1.13×10^{-10}	31.8×10^{4}
806	7.18×10^{-11}	42.5×10^{4}
745	1.50×10^{-11}	59.6×10^{4}

The temperature variation of the diffusion coefficient is shown in Fig. 3.

As can be seen from the curve, the diffusion coefficient can be perfectly expressed by the Arrhenius equation,

$$D=D_0\exp\left(-\frac{Q}{RT}\right).$$

Based on the above results the value of the frequency factor D_0 and the activation energy Q were calculated together with their probable error. The results of the calculations are as follows.

$$Q=(59.9\pm1.2)K\ \text{cal/mol} \qquad (3)$$

$$D_0=(104\pm76)\ \text{cm}^2/\text{sec}. \qquad (4)$$

The present result is shown as one of the points in Fig. 4 together with activation energies obtaineded by other workers versus

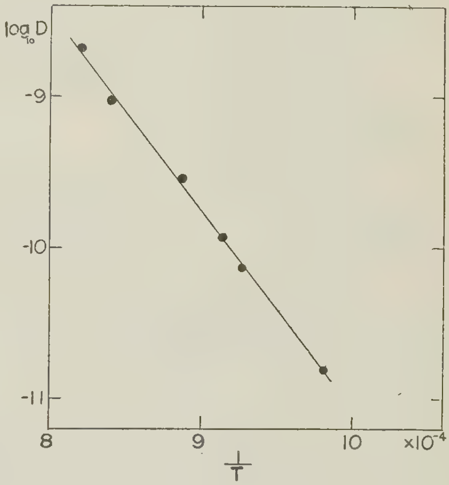

Fig. 3. Diffusion data plotted as log D versus $1/T$.

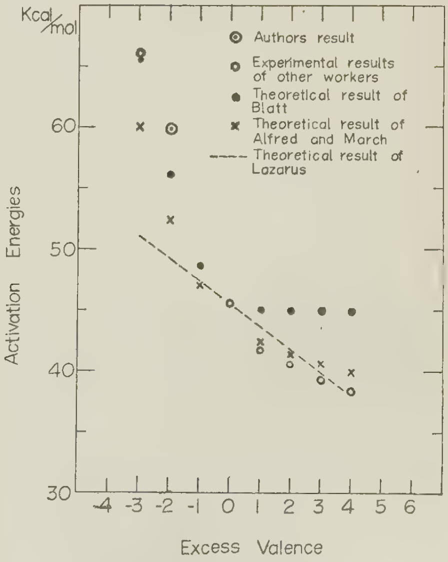

Fig. 4. Calculated and experimental activation energies for the solute diffusion in silver.

the atomic number of diffusing metals. The theoretical results due to Alfred and March, Blatt and Lazarus are also shown in the same figure. As is seen from the figure the present result agrees comparatively well with the result of Blatt[2]. However, the present authors found an unexpected result as for the value of D_0: According to Zener's theory[11], the relation between D_0 and Q is given as follows.

$$D_0=a^2\nu \exp(\lambda\beta Q/RT_m)\,. \tag{5}$$

a: the lattice constant
ν: the Debye frequency
λ: a numerical constant, which should be taken to be 0.55 for diffusion of electronegative impurities in silver[5]
T_m: the melting point.
$\beta=d(\mu/\mu_0)/d(T/T_m)=0.45$[5].
μ: the shear modulus.
μ_0: the shear modulus at absolute zero of temperature.

In very dilute solution all of these quantities except ν and Q are those of the solvent metal. Putting the observed values in Eq. (5), the following result is obtained:

$$D_0=3.5\ \mathrm{cm^2/sec}.$$

Thus the calculated value of D_0 is considerably less than the measured value shown in Eq. (4). The same kind of anomaly in D_0 value was also found by Pierce and Lazarus in the case of ruthenium diffusion into silver. The origin of these large values of D_0 is not known at the present time.

Acknowledgement

The authors wish to express their sincere thanks to Dr. Kunitomi, Prof. H. Watanabe and Mr. T. Suzuoka for their king advice throughout the course of the present investigation. This investigation was supported in part by the Grant-in-Aid of Fundamental Scientific Research of the Ministry of Education.

References

1) D. Lazarus: Phys. Rev. **93** (1954) 973.
2) F. Blatt: Phys. Rev. **99** (1955) 600.
3) L. C. R. Alfred and N. H. March: Phys. Rev. **103** (1956) 877.
4) C. T. Tomizuka and L. Slifkin: Phys. Rev. **96** (1954) 610.
5) C. B. Pierce and D. Lazarus: Phys. Rev. **114** (1959) 686.
6) C. A. Mackliet: Phys. Rev. **109** (1958) 1964.
7) M. Sakamoto: J. Phys. Soc. Japan, **13** (1958) 845.
8) A. Ikushima: J. Phys. Soc. Japan, **13** (1958) 764.
9) A. Kuper, H. Letaw, J. L. Slifkin, E. Sonder and C. T. Tomizuka: Phys. Rev. **96** (1954) 1224.
10) C. T. Tomizuka and D. L. Garett: Bull. Am. Phys. Soc. **4** (1959) 171.
11) C. Zener: J. Appl. Phys. **22** (1951) 372.

JOURNAL OF THE PHYSICAL SOCIETY OF JAPAN Vol. 16, No. 3, MARCH, 1961

Orientation Dependent Mechanical Breakdown of a Model High Polymer Solid*

C. C. HSIAO, J. E. OSBORN, and D. B. ROZENDAL

University of Minnesota, Minneapolis, Minnesota

(Received August 16, 1960)

A theory of mechanical breakdown of a model high polymer solid is given. On the basis of considering a static, a quasistatic, or a dynamic system, the orientation dependent mechanical strength of a linear model polymer solid is analyzed. The maximum breaking strength obtainable is six times that of the unoriented strength and is found to occur in the direction of orientation for a fully oriented static system.

§ 1. Introduction

Recently a number of analyses[1)-4)] have been made of the orientation and strength problem of a model solid. On the basis of considering a quasi-static system of oriented microscopic linear elements the stress tensor in the vicinity of a point in an orthogonal coordinate system has been found to be[1)]:

$$\sigma_{ij}^* = \int El^2 \lambda \rho^* f^* \varepsilon_{mn} s_m^* s_n^* s_i^* s_j^* d\omega^* \tag{1}$$

where

E = the spring modulus,
l = the length of any spring,
λ = the number of springs per unit volume,
ρ^* = the probability density function of the orientation of the springs,
f^* = the fraction of unbroken springs,
$\varepsilon_{mn} s_m^* s_n^*$ = The strain along the instantaneous direction of a spring,
s_i^* = instantaneous direction of a spring,
and $d\omega^*$ = the solid angle.

Depending upon the variations of f^* three different cases may be analyzed. If f^* is constant, i.e. $f^* = f_0$, the system is static[3)]. The system becomes quasi-static when

$$\frac{df^*}{dt} = k_r(\varepsilon_{mn} s_m^* s_n^*)\left(\frac{1}{4\pi} - f^*\right) - k_b(\varepsilon_{mn} s_m^* s_n^*) f = 0 \tag{2}$$

and $f^* \cong (1 - K_1 \varepsilon_{mn} s_m^* s_n^*)$ where k_r and k_b are exponential functions of strain and K_1 is a constant[1)]. The system is dynamic when

$$\frac{df^*}{dt} = k_r\left(\frac{1}{4\pi} - f^*\right) - k_b f^* \neq 0\ ; \tag{3}$$

then

$$f^* = \frac{1}{4\pi} \exp\left[-\int (k_r + k_b) dt\right] \left[\int k_r \exp\int (k_r + k_b) dt\ dt + C\right] \tag{4}$$

where C is an integration constant. To a first approximation for small strains, the foregoing expression reduces to

$$f^* \cong f_0[1 - K_2(\varepsilon_{mn} s_m^* s_n^*)^2]$$

if a linear relation between strain and time is considered where $f_0 = 1/8\pi$ and K_2 is a constant. For both the static[3)] and the quasistatic[1)] case the analyses have already been reported. In order to obtain a better understanding of the subject, the following section gives the analysis for the dynamic case.

§ 2. Behavior of Dynamic Model Solid

With $f^* \cong f_0[1 - K_2(\varepsilon_{mn} s_m^* s_n^*)^2]$, the stress tensor becomes

$$\sigma_{ij}^* = El^2 \lambda f \int_0 [\varepsilon_{mn} s_m^* s_n^* - K_2(\varepsilon_{mn} s_m^* s_n^*)^3] s_i^* s_j^* \rho^* d\omega^*\ . \tag{5}$$

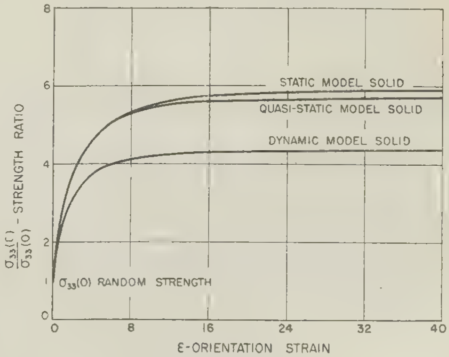

Fig. 1. Fracture strength ratio for three model solids.

---

* Supported in part by the U. S. Atomic Energy commission.

In the case of simple tension in the 33 direction, ε_{mn} has only the principal strain components. Because of symmetry, $\varepsilon_{11}=\varepsilon_{22}=-\nu\varepsilon_{33}$ where ν is the strain ratio. Thus the scalar strain

$$\varepsilon_{mn}s_m{}^*s_n{}^*=\varepsilon_{11}s_1{}^{*2}+\varepsilon_{22}s_2{}^{*2}+\varepsilon_{33}s_3{}^{*2} \tag{6}$$

and

$$s_i{}^*=(\sin\theta^*\cos\varphi^*,\ \sin\theta^*\sin\varphi^*,\ \cos\theta^*)\ .$$

For the uniaxial orientation along the 33 direction, as shown previously[1)], if the orientation strain is ε then the density of the probability distribution function of orientation is

$$\rho^*=\frac{(1+\varepsilon)^3}{[\cos^2\theta^*+(1+\varepsilon)^3\sin^2\theta^*]^{3/2}}\rho \tag{7}$$

where ρ is the density function for the random case. Let $1-(1+\varepsilon)^{-3}=k^2$, then the stress σ_{33}^* may be obtained after integration. The result is

$$\begin{aligned}\sigma_{33}^*=\frac{El^2\lambda\rho\varepsilon_{33}}{8\pi(1+\varepsilon)^{3/2}}\Bigg\{&-\nu\left(\frac{1}{k^2(1-k^2)^{1/2}}-\frac{\sin^{-1}k}{k^3}\right)+(1+\nu)\left(\frac{-1}{2k^2(1-k^2)^{1/2}}+\frac{3}{2k^4(1-k^2)^{1/2}}-\frac{3\sin^{-1}k}{2k^5}\right)\\&-K_2\varepsilon_{33}^2\Bigg[-\nu^3\left(\frac{1}{k^2(1-k^2)^{1/2}}-\frac{\sin^{-1}k}{k^3}\right)+3\nu^2(1+\nu)\left(\frac{-1}{2k^2(1-k^2)^{1/2}}+\frac{3}{2k^4(1-k^2)^{1/2}}-\frac{3\sin^{-1}k}{2k^5}\right)\\&-3\nu(1+\nu)^2\left(\frac{-1}{4k^2(1-k^2)^{1/2}}-\frac{5}{8k^4(1-k^2)^{1/2}}+\frac{15}{8k^6(1-k^2)^{1/2}}-\frac{15\sin^{-1}k}{8k^7}\right)\\&+(1+\nu)^3\left(\frac{-1}{6k^2(1-k^2)^{1/2}}-\frac{7}{24k^4(1-k^2)^{1/2}}-\frac{35}{48k^6(1-k^2)^{1/2}}+\frac{105}{48k^8(1-k^2)^{1/2}}-\frac{105\sin^{-1}k}{48k^9}\right)\Bigg]\Bigg\}\ .\end{aligned} \tag{8}$$

To obtain equilibrium fracture strength, we let $\partial\sigma_{33}^*/\partial\varepsilon_{33}=0$; then

$$\begin{aligned}\varepsilon_{33}^2=\Bigg\{&-\nu\left[\frac{1}{k^2(1-k^2)^{1/2}}-\frac{\sin^{-1}k}{k^3}\right]+(1+\nu)\left[\frac{-1}{2k^2(1-k^2)^{1/2}}+\frac{3}{2k^4(1-k^2)^{1/2}}-\frac{3\sin^{-1}k}{2k^5}\right]\Bigg\}\Bigg/\\3K_2\Bigg\{&-\nu^3\left[\frac{1}{k^2(1-k^2)^{1/2}}-\frac{\sin^{-1}k}{k^3}\right]+3\nu^2(1+\nu)\left[\frac{-1}{2k^2(1-k^2)^{1/2}}+\frac{3}{2k^4(1-k^2)^{1/2}}-\frac{3\sin^{-1}k}{2k^5}\right]\\&-3\nu(1-\nu)^2\left[\frac{-1}{4k^2(1-k^2)^{1/2}}-\frac{5}{8k^4(1-k^2)^{1/2}}+\frac{15}{8k^6(1-k^2)^{1/2}}-\frac{15\sin^{-1}k}{8k^7}\right]\\&+(1+\nu)^3\left[\frac{-1}{6k^2(1-k^2)^{1/2}}-\frac{7}{24k^4(1-k^2)^{1/2}}-\frac{35}{48k^6(1-k^2)^{1/2}}+\frac{105}{48k^8(1-k^2)^{1/2}}-\frac{105\sin^{-1}k}{48k^9}\right]\Bigg\}\ .\end{aligned} \tag{9}$$

Thus the fracture stress as a function of ε is given by

$$\begin{aligned}\sigma_{33}(\varepsilon)=\frac{E\lambda\rho l^2}{(3k_2)^{1/2}12\pi(1+3)^{3/2}}\Bigg\{&-\nu\left[\frac{1}{k^2(1-k^2)^{1/2}}-\frac{\sin^{-1}k}{k^3}\right]+(1+\nu)\left[\frac{-1}{2k^2(1-k^2)^{1/2}}+\frac{3}{2k^4(1-k^2)^{1/2}}\right.\\&\left.-\frac{3\sin^{-1}k}{2k^5}\right]\Bigg\}^{3/2}\Bigg/\Bigg\{-\nu^3\left[\frac{1}{k^2(1-k^2)^{1/2}}-\frac{\sin^{-1}k}{k^3}\right]+3\nu^2(1+\nu)\left[\frac{-1}{2k^2(1-k^2)^{1/2}}+\frac{3}{2k^4(1-k^2)^{1/2}}\right.\\&\left.-\frac{3\sin^{-1}k}{2k^5}\right]-3\nu(1+\nu)^2\left[\frac{-1}{4k^2(1-k^2)^{1/2}}-\frac{5}{8k^4(1-k^2)^{1/2}}+\frac{15}{8k^6(1-k^2)^{1/2}}-\frac{15\sin^{-1}k}{8k^7}\right]\\&+(1+\nu)^3\left[\frac{-1}{6k^2(1-k^2)^{1/2}}-\frac{7}{24k^4(1-k^2)^{1/2}}-\frac{35}{48k^6(1-k^2)^{1/2}}+\frac{195}{48k^8(1-k^2)^{1/2}}-\frac{105\sin^{-1}k}{48k^9}\right]\Bigg\}^{1/2}\ .\end{aligned} \tag{10}$$

§ 3. Generalized Fracture Theory and Stress-Strain Law

An interesting inter-relation common to all the three analyses[1)-3)] has been observed. For clarity the following table is given to bring out the common nature for the three different cases of equilibrium fracture:

In the foregoing table all C's are proportional to $El^2\lambda f_0$;

$$\varphi(\varepsilon)=\left[\frac{3-k^2}{4^4}-\frac{3(1-k^2)^{1/2}}{k^5}\sin^{-1}k\right]-\nu\left[\frac{-3+3k^2}{k^4}+\frac{3-2k^2}{k^5}\sin^{-1}k\right]$$

which varies from 1/3 for $\varepsilon=0$ to 2 for $\varepsilon=\infty$, with

Table II. Comparison of Different Models.

Model	Static	Quasi-Static	Dynamic
f^*	$f_0=\frac{1}{8\pi}$	$f_0[1-K_1(\varepsilon_{mn}s_m s_n)]$	$f_0[1-K_2(\varepsilon_{mn}s_m s_n)^2]$
$\sigma_{33}(\varepsilon)$	$C_0\varphi(\varepsilon)\varepsilon_{33}(\varepsilon)$	$C_1\varphi(\varepsilon)_{33}(\varepsilon)$	$C_2\varphi(\varepsilon)\varepsilon_{33}(\varepsilon)$
$\sigma_{33}(0)$	$\frac{1}{3}C_0\varepsilon_{33}(\varepsilon)$	$\frac{1}{3}C_1\varepsilon_{33}(\varepsilon)$	$\frac{1}{3}C_2\varepsilon_{33}(\varepsilon)$
$\frac{\sigma_{33}(\varepsilon)}{\sigma_{33}(0)}$	$3\varphi(\varepsilon)\frac{\varepsilon_{33}(\varepsilon)}{\varepsilon_{33}(0)}$		

$$k^2=-1(1+\varepsilon)^{-3}$$

and

$$\nu=-\frac{\varepsilon_{11}}{\varepsilon_{33}}=\frac{\left[1-\frac{(1-k^2)^{1/2}}{k}\sin^{-1}k\right]-\frac{1}{2k^2}\left[3-k^2-\frac{3(1-k^2)^{1/2}}{k}\sin^{-1}k\right]}{k^2-2\left[1-\frac{(1-k^2)^{1/2}}{k}\sin^{-1}k\right]+\frac{1}{2k^2}\left[3-k^2-\frac{3(1-k^2)^{1/2}}{k}\sin^{-1}k\right]}$$

which varies from 1/4 for $\varepsilon=0$ to 1 for $\varepsilon=\infty$. The difference between the three analyses is seen to lie wholly in the ratio $\varepsilon_{33}(\varepsilon)/\varepsilon_{33}(0)$. For fracture the numerator is the fracture strain when orientation is present and the denominator is the fracture strain when orientation does not exist. It is reasonable to believe that the fracture process is essentially a brittle one and a linear relation between the stress and the small fracture strain holds while the orientation strain is nearly the total strain and is only associated with the directions of the basic components of the model solid. For any state before fracture the foregoing relations seem to hold. Thus, we have a stress-strain relation which for simple tension is capable of specifying the strength for any particular state of orientation. Mathematically the general linear stress-strain relation is

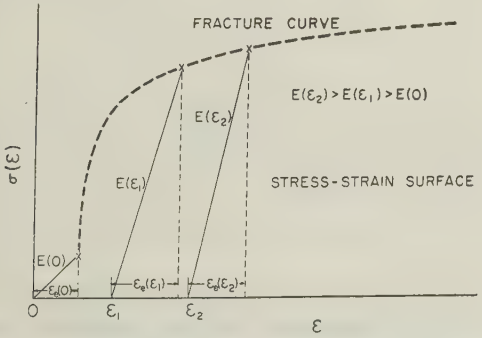

Fig. 2. Schematic stress-strain surface of oriented model solid.

$$\sigma(\varepsilon)=E(\varepsilon)\varepsilon_e(\varepsilon) \tag{13}$$

where ε_e is the elastic strain, and $E(\varepsilon)=C\varphi(\varepsilon)$ is a modulus as a function of orientation strain $\varphi(\varepsilon)$ and C is the material constant depending upon the microscopic model chosen. If we plot this out we obtain an area in the $\sigma(\varepsilon)-\varepsilon$ plane describing the linear and non-linear behavior of the solid as shown in Fig. 2. For oriented solids when the fracture strain is constant it is seen that the modulus increases as the degree of orientation increases. This is quite true in reality. When $\varepsilon=0$ the modulus reduces to the elastic modulus $E(0)$ of the solid.

In spite of the difference in models used if the elastic fracture strain is considered independent of orientation then the strength ratio reduces to the same expression for all the models

$$\frac{\sigma(\varepsilon)}{\sigma(0)}=\frac{E(\varepsilon)\varepsilon_e(\varepsilon)}{E(0)\varepsilon_e(0)}=\frac{E(\varepsilon)}{E(0)}=3\varphi(\varepsilon) \tag{14}$$

which approaches to 6 as ε goes to ∞. By varying the fracture strain ratio we can easily widen the applicability of the general orientation-strength relation.

Furthermore, it seems possible to generalize the stress-strain relations for a model solid with uniaxial orientation strain ε along one of the principal directions in the following form:

$$\sigma_{ij}(\varepsilon)=E_{ij}(\varepsilon)\varepsilon_{ij}(\varepsilon)\ . \tag{15}$$

For biaxial orientation,[4] if ε_x and ε_y are the orientation strains along two mutually perpendicular principal directions then

$$\sigma_{ij}(\varepsilon_x, \varepsilon_y)=E_{ij}(\varepsilon_x, \varepsilon_y)\varepsilon_{ij}(\varepsilon_x, \varepsilon_y)\,. \qquad (16)$$

It is hoped that these relations will be investigated in the future.

References

1) C. C. Hsiao: J. Appl. Phys. **30** (1959) 1924; J. Polymer Science **44** (1960) 71.

2) C. C. Hsiao: AEC AT (11-1)-532, Tech. R No. 1, June; No. 3, July; No. 4, University of Minnesota, July, (1959).

3) J. E. Osborn and C. C. Hsiao: AEC AT (11-1)-532, Tech. R. No. 7, University of Minnesota, Sept., (1959); J. Appl. Phys. Sept., (1960).

4) C. C. Hsiao and J. E. Osborn: AEC AT (11-1)-532, Tech. R. No. 8, University of Minnesota, Oct., (1959).

JOURNAL OF THE PHYSICAL SOCIETY OF JAPAN, Vol. 16, No. 3, MARCH, 1961

X-Ray Line Broadening in Polyethylene Filaments

By Ken-ichi KATAYAMA

Textile Research Laboratory, Asahi Chemical Industry Company, Ltd.
Takatsuki, Japan

(Received August 5, 1960)

The precise methods of obtaining X-ray line profile and broadening in crystalline high polymer using X-ray diffractometer are discussed in detail, and the causes of X-ray line broadening in highly oriented linear polyethylene 'Marlex 50' are investigated. It is found that the main causes are crystallite size effect and lattice-distortion, and the strain distribution function is approximated by Cauchy-form $1/(1+k^2x^2)$. Therefore, the separation of two effects can be made by means of Hall's equation. Using 110 and 220 reflections on the equator, recrystallization of crystallite by annealing, break-up of crystallite with elongation and change in lattice-distortion are observed.

The obtained values of strain (1~2%) are larger by one order of magnitude than those of cold-worked metals, and not changed so greatly by annealing and deformation, whereas crystallite size varies widely (100Å~larger than 700Å).

§ 1. Introduction

It is well known that the X-ray diffraction lines from crystalline high polymers are somewhat broadened as compared with those given by large perfect crystals of inorganic substances.

The X-ray line broadening may be due to several cause; (i) small size effect of crystallite; (ii) distortions in crystal-lattice or other imperfections, and (iii) thermal vibration of high polymer chains. In high polymers, measurements of line profiles of diffracted X-rays contain many difficulties, and the causes of line broadening have not been studied. With recent advances in measuring technique by X-ray diffractometer, it is possible to overcome experimental difficulties and distinguish between probable causes of broadening in some way.

Highly oriented filament of linear polyethylene 'Marlex 50' was chosen as specimen for the following reasons:

(i) Lattice imperfections due to irregularities in chain structure have little effect on broadening, since molecular chains of this type of polyethylene are regular and have few branches.

(ii) The crystal structure was fully analysed by Bunn[1].

(iii) Two orders of reflection, 110 and 220, from the same planes can be observed with intensities enough to measure diffraction profile correctly.

In the present paper, discussions on the causes of broadening and strain distribution function will be given. The thermal and load-induced changes of crystallite size and distortion will also be investigated.

§ 2. Theory of Line Profile and Broadening

The methods of separating lattice-distortion and size effects on broadening in X-ray pattern have been discussed by means of Fourier analysis of powder diffraction line profiles[2,3], and were successfully applied to cold-worked metals by many authors[4]. Some remarkes on using the important results of broadening theory are summarized here.

The profile of the diffraction peak of l-th order from certain set of planes can be represented by a Fourier series:

$$P(h,l)=K\sum_{-\infty}^{\infty}A_n(l)\cos 2\pi nh\,, \tag{1}$$

where $h=(2a\sin\vartheta/\lambda)-l$, a is interplanar spacing, ϑ the Bragg angle, λ the X-ray wave length, and K a proportionality factor involving some slowly varying functions of ϑ. If two types of broadening are present, $A_n(l)$ is represented by the product of small particle size coefficient A_n^P which is independent of l, and distortion coefficient $A_n^D(l)$ which is dependent on l. That is, observed profile is obtained by convolution process on two profiles which would be obtained if two causes were present separately.

If we have a number of orders of reflection from the same planes, it is possible to separate the two effects with complete accuracy. When only one or two orders of reflection are available the following approximation methods[3] can be used.

(1) n small

When n is small,

$$-\frac{\log A_n}{n}=\frac{1}{\bar{N}}+2\pi^2l^2\overline{e^2}n\,, \tag{2}$$

where Na is the thickness of the crystal normal to the reflecting planes, and e is the local strain. $\bar{N}$ value determined from this formula is largely influenced by the tail of the line profile, so the measurements of the tail must be made with great accuracy.

(2) n large

If the displacements of widely separated planes are independent, the line profile due to lattice-distortion will be of the Cauchy-type $1/(1+k^2x^2)$ for small h, and

$$-\frac{\log A_n^D}{n}=f(l)\,. \tag{3}$$

The functional form of $f(l)$ depends on the strain distribution function. For example, $f(l)$ is equal to αl for the Cauchy distribution and αl^2 for the Gaussian distribution, where α is a constant relating to the magnitude of strain. Therefore, we can find the strain distribution function if we know the form of $f(l)$.

Instead of the methods based on the Fourier analysis of line profile, Hall has suggested a simple method[5], which is rather recommended when the intensity measurement of the tail is ambiguous. According to his suggestion, integral line breadth β is expressed by

$$\frac{\beta\cos\vartheta}{\lambda}=\frac{1}{t}+2\xi\frac{\sin\vartheta}{\lambda}\,, \tag{4}$$

where t is 'apparent size' which is equal to $aN^2/\bar{N}$[6], and ξ the integral breadth of the strain distribution function. Eq. (4) is valid if both line profiles are always of the exact Cauchy-form and the breadth due to distortion effect is proportional to the order of reflection, because the convolution of two Cauchy-forms is also of the same form and integral breadths are additive. The line profile due to small size effect is closely approximated by Cauchy-form provided that specimen contains a fairly wide distribution of crystallite size. In fact, exponential distribution of size gives the exact Cauchy-form. Therefore, the applicability of Eq. (4) depends on the nature of the line broadening generated by pure distortion effect.

§ 3. Experimental Procedure and Correction

Difficulties of the measurement of line broadening in high polymer are as follows:

(i) Since scattered X-rays from high polymer contain amorphous scattering besides temperature and incoherent scatterings, the base line of crystalline peak cannot be drawn with certainty.

(ii) For measurement of pure line profile, we must know the instrumental profile[7], but in the present case we cannot consider the line profile of well-annealed sample as instrumental, because the strain in high polymer crystallite does never disappear entirely by annealing.

(iii) Since the intensities of reflections of higher order are weak, we seldom have two or more reflections from the same planes with intensities enough to measure the profiles accurately.

In the present experiment, a highly stabilized X-ray source[8] with Cu target was used, and the monochromatization was achieved by means of balanced filters[9] (Ni and Co foils) which were balanced within 1% at K_β wave length. Highly oriented monofilaments with 0.16 mm diameter were arranged side by side on a flat sample-holder parallel to the line focus of X-ray tube, and the profiles of diffraction peak were obtained by usual spectrometric powder technique.

The general methods of obtaining the true profile and line breadth from observed data have been discussed in detail[10], so only the special aspects in the present experiment are described below.

(1) *Correction of observed intensities*

By transmission technique, the sum of amorphous and incoherent scatterings was measured previously along the meridian of fiber diagram.

On the assumption that this diffuse scattering on the meridian is equal to that on the equator, the background of crystalline peak 110 can be corrected. The error due to this assumption may be small because the peak intensity of amorphous halo is about 0.5% of that of 110 reflection.

Proportionality factor in the formula (1) involves the influence of absorption of X-ray by the sample, geometrical factors (polarization and Lorentz factors*), and the modulation by structure factor which can be calculated from crystal structure data. These corrections are necessary when the lines are fairly broadened.

(2) *Correction of Fourier coefficients*

The Fourier coefficients of true profile are given by Stokes' method[7] using observed profile when instrumental profile is known. Though the profile of well-annealed sample is considered as the instrumental profile in the case of cold-worked metals, we cannot use this simple procedure in the case of high polymers. Therefore the line profile from perfect crystal powder with high absorption coefficient for Cu K_α (for example, KI) is measured near the Bragg angle of high polymer reflection, and the convolution of this profile and the calculated weight function due to finite thickness of high polymer sample is used as the instrumental profile. The measured instrumental profiles were appreciably asymmetrical. Though observed profiles of polyethylene samples were also asymmetrical, this asymmetry could be explained by that of the instrumental profiles.

(3) *Correction of integral breadth*

Simplified correction of observed integral breadth based on Stokes' method has been given by Rudman[11], but it is still troublesome without suitable computer. If we can assume adequate functional forms for the true and instrumental profiles, simpler method[12] may be used. As a matter of fact, the observed profile, which is widely broadened than the instrumental profile, is closely approximated by Cauchy-form, so we can assume that true profile has Cauchy-form. The measured instrumental profiles are asymmetrical, but they can be approximated by Gaussian form so far as they are used for the correction of the integral breadth. Thus, it is written as:

$$\text{true profile:}\quad \frac{1}{\beta}\frac{1}{1+\dfrac{\pi^2}{\beta^2}x^2}\,,$$

$$\text{instrumental profile:}\quad \frac{1}{b}\exp\left(-\frac{\pi}{b^2}x^2\right),$$

and by convolution operation, one finds that the observed integral breadth is

$$B=\frac{b\exp\left(-\dfrac{\beta^2}{\pi b^2}\right)}{1-2\Phi\left(\sqrt{\dfrac{2}{\pi}}\dfrac{\beta}{b}\right)}\,, \tag{5}$$

where

$$\Phi(t)=\frac{1}{\sqrt{2\pi}}\int_0^t \exp\left(-\frac{u^2}{2}\right)du\,.$$

From Fig. 1, we can find β, when B and b are known. The curve in Fig. 1 is somewhat different from Alexander's[12] which was obtained by numerical integration.

§ 4. Strain Distribution

Among many reflections from polyethylene filament, 110 and 220 are only one pair of reflections from the same planes that have appreciable intensities. For this reason, attention was confined to the profiles of 110 and 220 peaks. This would have the generality, for the changes of broadening of reflections on the equator have the same tendency. To obtain a sample which has as large crystallite size as possible, sample filament was annealed for 30 minutes allowing free shrinkage at 110°C and further for an hour at 130°C maintaining constant length. Then, the line profiles of 110 and 220 were measured at 20°C and $-196°C$. Low temperature was attained by cooling the sample-holder by liquid nitrogen. Observed values of A_n and $-\log A_n/n$ are plotted against n in Fig. 2 and Fig. 3 respectively.

---

* Though the theory in § 2 was first obtained for the powder diffraction line profile, it can be applied to highly oriented filaments if we use the Lorenz factor for rotating-crystal method instead of that for powder method.

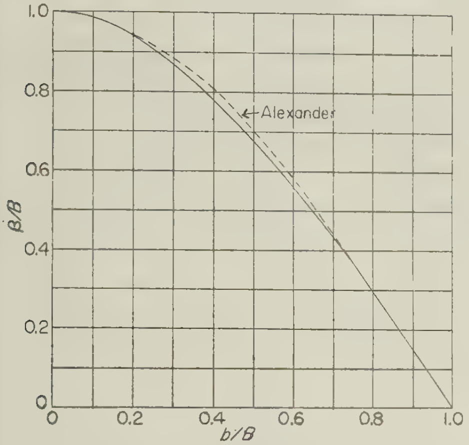

Fig. 1. Curves for correcting X-ray integral line broadening for instrumental broadening. Full-line was obtained from Eq. (5), and dotted-line by Alexander.

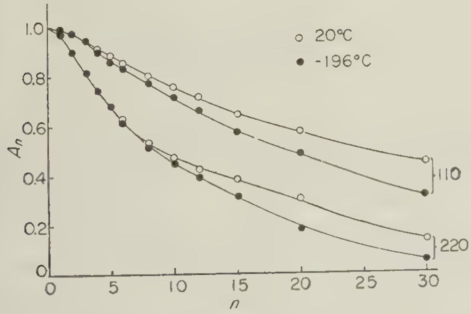

Fig. 2. Fourier coefficients A_n for annealed specimen measured at 20°C and $-196°C$.

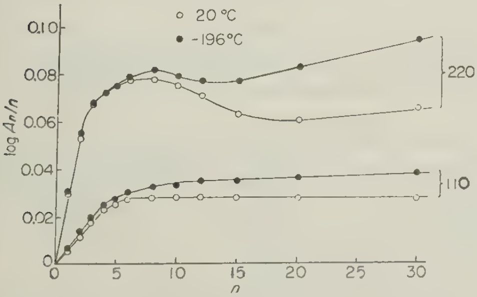

Fig. 3. $-\log A_n/n$ for annealed specimen measured at 20°C and $-196°C$.

In Fig. 3, the curves are straight lines passing through the origin for small n, and therefore, the crystallite size must be very large as seen from Eq. (2), even though measured crystallite size is affected by tail error. Consequently, the line broadening of this sample may be ascribed to pure lattice-distortion. As for the temperature scatterings at 20°C and $-196°C$, it is found that two shapes of tails of line profiles differ little from one another though the background level decreases a little by cooling. Thus it is concluded that the temperature scattering is so diffuse that it has little effect upon the shape of tail. On the other hand, the central part of line profile becomes broader by cooling contrary to the thermal effect in which the line profile becomes usually sharper by cooling. Moreover, this change is reversible, so the increase in line broadening at low temperature can be ascribed to that in elastic strain.

For large n, $-\log A_n/n$ tends to become a constant value. This fact indicates that the displacements of planes far apart become independent. The ratio of saturated value for the second order to that for the first order is about 2, so the strain distribution function for large n is expected to take Cauchy-form[3], but this result is not conclusive unless we have more reflections from the same planes. At any rate, the line profile due to pure distortion effect is nearly described by Cauchy-form, and its integral breadth is proportional to the order of reflection so far as 110 and 220 reflections are concerned. Therefore, Hall's equation (4) may be used hereafter with confidence.

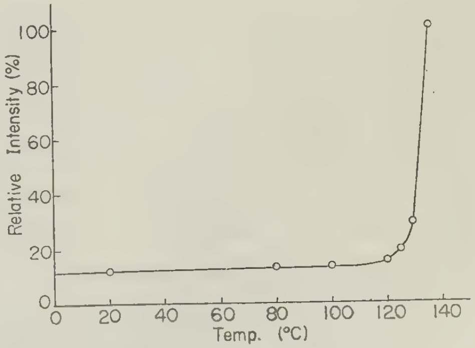

Fig. 4. Change of relative intensity under amorphous peak with temperature.

§ 5. Thermal Changes

The thermal changes of filaments at constant length were followed above room temperature. In highly oriented polyethylene, the crystallinity is not obtained so precisely as in powder specimen by X-ray method[13]. For simplicity, the integrated intensity of amorphous scattering along the meridian obtained by transmission technique was conveniently considered as the measure of the crystallinity*. The ratio of the integrated intensity to that of completely molten sample is plotted against temperature in Fig. 4.

Bragg distance corresponding to amorphous peak is also plotted against temperature in Fig. 5. Beyond 100°C, the coefficient of linear expansion of amorphous region increases and returns to the initial value after melting, but in crystalline region this phenomenon[14] cannot be seen as far as highly oriented filaments are maintained at constant length. From these facts, the thermal motion of chains in amorphous region seems to become more active above 100°C.

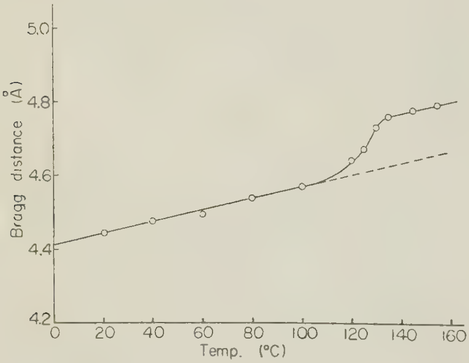

Fig. 5. Change of Bragg distance for amorphous peak with temperature.

To investigate changes in crystallites with annealing temperature, the integral breadths of 110 and 220 reflections were measured by the use of Fig. 1, and β *versus* temperature curve was plotted in Fig. 6. The values of 'apparent size' t and integral breadth of strain distribution function, ξ, were calculated using Hall's equation (4) and are shown in Fig. 7. From the two curves obtained from measurements at annealing temperature, it is seen that the strain decreases rapidly and the crystallite size increases appreciably above 100°C. This implies that the small imperfect crystallites melt and large ones recrystallize, because the crystallinity does not decrease so rapidly with rising temperature as seen from Fig. 4. In cooling process after annealing, as seen from other two curves in Fig. 7, the crystallite size increases further and strain also increases to the value before annealing.

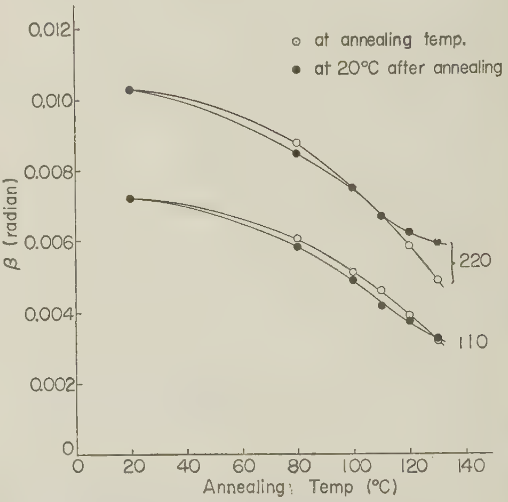

Fig. 6. Change of integral breadth with annealing temperature.

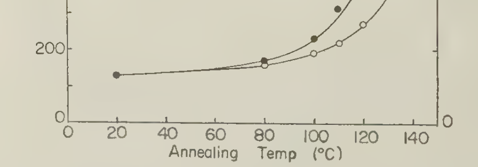

Fig. 7. Change of apparent size, t, and integral breadth of strain distribution function, ξ, with annealing temperature.

These data indicate, therefore, that the distortion or imperfection in crystalline region generates in the course of crystallization by cooling.

§ 6. Load-induced Changes

For the understanding of the mechanical

---

* These values do not express exactly true crystallinity, because the intensity of amorphous halo is not uniform but rather influenced by preferred orientation of chains in amorphous region.

behavior of crystalline high polymer, it is very important to know how microscopic structure changes with microscopic deformation. Therefore, the load-induced changes in crystallites were examined by following changes in line broadening by focusing our attention on crystallite size and distortion. Before loading, the specimens were annealed at 110°C for 30 minutes allowing free shrinkage, and then deformed in tension in a Instron Tensile Testing Instrument at constant rate of deformation of 0.2% per second. The load-elongation curve is shown in Fig. 8 with full-line, the dotted-lines representing 'load-elongation cycles', in which a specimen is elongated to a certain value and contracted till the load drops off to zero. The maximum elongation used in this experiment was almost the elongation at rupture, 40%.

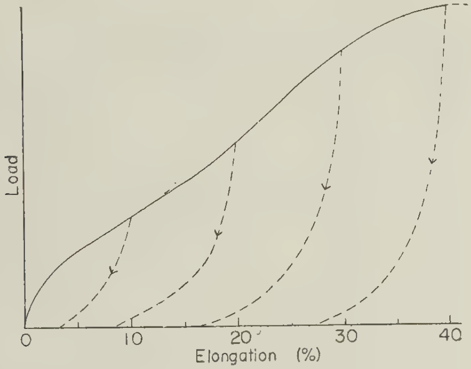

Fig. 8. Load-elongation curve and cycles.

The specimens were clamped on specimen-holders immediately after deformation, and the measurements of line broadening were made after 12 hours. Repeated measurements on the same specimen gave the same results, so the specimen did not change during measurement.

In Fig. 9, t and ξ obtained from integral breadths of 110 and 220 are plotted against elongation*. The changes in t and ξ become large beyond 25% elongation which corresponds to the inflection point on the load-elongation curve in Fig. 8. This results agree with that of Nylon filaments[15].

The difference in apparent size for elongated specimen and contracted one after the same elongation is very little, so break-up of crystallite by elongation is not recovered by contraction after elongation and seems to give rise to the permanent change in microscopic structure. On the other hand the strain decreases a little with contraction, and this is due to the elastic part of strain induced by elongation. Thus, it is worth noticing that the load-induced microscopic structural changes are mainly the break-up of crystallites and the increase in lattice-distortion is unexpectedly small.

The reflections on the first layer line which are expected to be sensitively broadened by the slip occurred among chains were recorded on a photographic film, because the precise method using diffractometer are only applicable for the reflections on the equator. By visual inspection, it is found that the change in broadening of the reflections on the first layer line with elongation has the same tendency as that on the equator.

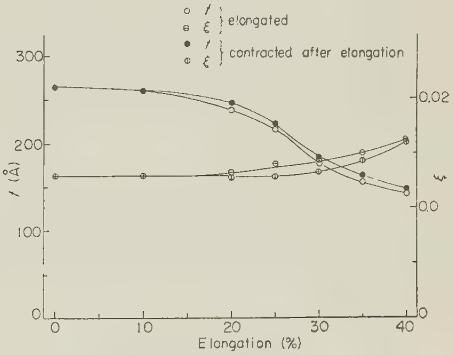

Fig. 9. Changes of apparent size, t, and integral breadth of strain distribution function, ξ, with elongation.

The angular broadening in fiber pattern, which is defined as the width of diffraction arc at half-maximum intensity taken along the arc, is about 7° for 110 reflection and slightly decreases with elongation. So the disorientation of crystallites at large elongation which was found in Nylon filaments[15] are not observed in polyethylene.

New crystalline phase[16] has been reported in polyethylene film extremely deformed by rolling or drawing. In the present work, however, reflections which could not be indexed on the orthorhombic cell were not observed.

---

* In the case of load-elongation cycle, the maximum elongation in the cycle is used as the parameter.

§ 7. Conclusion

There are many difficulties in measuring X-ray line broadening in crystalline high polymers, but careful intensity measurements and appropriate correction methods make it possible to obtain true values of Fourier coefficients or integral breadth of diffraction line with sufficient accuracy.

By analysing line broadening of 110 and 220 reflections from highly oriented linear polyethylene 'Marlex 50', it was found that important causes of broadening are crystallite size effect and lattice-distortion. Fourier analysis of line profiles shows that the strain distribution function is well approximated by Cauchy-form*. Therefore, the simple method suggested by Hall can be used. The crystallite changes widely in its size with annealing (100Å∼larger than 700Å) and breaks up with elongation, whereas the strain does not change so greatly. However, the amount of strain is larger by one order of magnitude even in the case of minimum strain (about 1% in integral breadth) than that in cold-worked metals. Large amount of strain contained in crystallite may be one of the reasons why rather large temperature factors should be used in the crystal structure analysis of polyethylene1) and other high polymers17).

The origin of the distortion is not clear at present, but the Cauchy-type strain distribution suggests that large distortions are localized somewhere in crystallite.

Acknowledgments

The author wishes to express his sincere thanks to Prof. K. Tanaka of Kyoto University for his continued encouragement and Mr. T. Amano for his assistance during the course of this experiment.

References

1) C. W. Bunn: Trans. Faraday Soc. **35** (1939) 482.
2) B. E. Warren and B. L. Averbach: J. Appl. Phys. **21** (1950) 595; B. E. Warren: Acta Cryst. **8** (1955) 483.
3) J. N. Eastabrook and A. J. C. Wilson: Proc. Phys. Soc. London **B, 65** (1952) 67.
4) For example, G. K. Williamson and W. H. Hall: Acta Met. **1** (1953) 22; M. McKeehan and B. E. Warren: J. Appl. Phys. **24** (1953) 52; G. K. Williamson and R. E. Smallman: Acta Cryst. **7** (1954) 574; F. R. L. Schoening and J. N. Van Niekerk: Acta Met. **3** (1955) 10; J. Appl. Phys. **26** (1955) 726; D. Michell and F. D. Haig: Phil. Mag. **2** (1957) 15.
5) W. H. Hall: Proc. Phys. Soc. London **A, 62** (1949) 741.
6) F. Bertaut: Compt. rend. **228** (1949) 187.
7) A. R. Stokes: Proc. Phys. Soc. London **61** (1948) 382.
8) K. Tanaka, K. Katayama and T. Amano: J. Appl. Phys. Japan **29** (1960) 12.
9) P. A. Ross: Phys. Rev. **28** (1926) 425; J. Opt. Soc. Amer. and Rev. Sci. Instr. **16** (1928) 433; K. Tanaka *et al*: Rev. Sci. Instr. **30** (1959) 430.
10) H. P. Klug and L. E. Alexander: *X-Ray Diffraction Procedures* (John Wiley & Sons, New York, 1954).
11) P. S. Rudman: J. Appl. Phys. **30** (1959) 2016.
12) L. Alexander and H. P. Klug: J. Appl. Phys. **21** (1950) 137.
13) J. L. Matthews, H. S. Peiser and R. B. Richards: Acta Cryst. **2** (1949) 85.
14) C. W. Bunn and T. C. Alcock: Trans. Faraday Soc. **41** (1945) 317; C. Sella: Compt. rend. **248** (1959) 2348.
15) J. Kauffman and W. George: J. Appl. Phys. **21** (1950) 431.
16) R. H. Pierce, J. P. Tordella and W. M. D. Bryant: J. Amer. Chem. Soc. **74** (1952) 282; E. R. Walter and F. P. Reding: J. Polymer Sci. **21** (1956) 557; W. P. Slichter: *ibid* **21** (1956) 141; P. W. Teare and D. R. Holmes: *ibid* **24** (1957) 496.
17) C. W. Bunn and E. V. Garmer: Proc. Roy. Soc. **A, 189** (1947) 39.

---

* Presumably, cut-off Cauchy-form is better approximation.

JOURNAL OF THE PHYSICAL SOCIETY OF JAPAN, Vol. 16, No. 3, MARCH, 1961

Study on the Ordered Alloys of Gold-Manganese System by Electron Diffraction, III. Lattice Modulation in the Ordered Au_3Mn.

By Denjiro WATANABE

The Research Institute for Iron, Steel and Other Metals,
Tohoku University, Sendai, Japan

(Received August 5, 1960)

In the present paper, some discussion is given of the nature of the lattice modulation which is believed to cause the satellites to flank main reflections in electron diffraction patterns of the ordered Au_3Mn alloy and also in the case of CuAu (II) as well as of Cu_3Pd. Two types of modulation, i.e. a periodic change of lattice spacing and of scattering factor, are considered. It is pointed out that the valence electron may play an important rôle for the lattice modulation. In order to clarify this problem, a detailed X-ray study will be necessary.

§ 1. Introduction

In Part I of the present study[1], the structure of the ordered Au_3Mn alloy was investigated by electron diffraction, using thin single-crystalline films prepared by evaporation, and it was shown that this alloy possesses a two-dimensional anti-phase domain structure of a new kind, whose fundamental lattice consists of a face-centred orthorhombic cell with the atomic arrangement similar to Cu_3Au. In that case, satellites flanking intense main reflections were observed, as seen in Photo. 1 of Part I, but their intensities could not be derived from the proposed structure model. Such satellites as above have also been observed in other ordered alloys with anti-phase domain structure such as CuAu (II)[2], Cu_3Pd[3], and Cu-Au-Zn ternary ordered alloys[4], and it has been believed that some kind of periodic modulation with the same periods as anti-phase domain size does exist in the ordered lattice. In the case of Au_3Mn, five kinds of satellites were seen in photographic plates, their separations from the relevant main reflections being $m_1=a_1^*/M_1$, $2m_1$, $m_2=a_2^*/M_2$, $2m_2$ and $3m_2$ in reciprocal space respectively. Among these satellites only those with the separations of m_1, m_2 and $3m_2$ were represented in Figs. 2 and 3 of Part I by small open circles.†

For the origin of the satellites, on the other hand, Glossop and Pashley suggested that they are entirely caused by double diffraction of split superlattice-reflections[5]. This explanation is based on the fact that the distances of the satellites from the relevant main reflections are integer times the separations of the splits of the superlattice reflections. Carrying out the same experimental procedure as in cases of CuAu (II)[6] and a Cu-Au-Zn ternary ordered alloy[4], however, the present author confirmed also in the Au_3Mn alloy that the periodic modulation of the lattice plays an important rôle. Photo. 1 shows a pattern obtained from an ordered Au_3Mn film tilted by 45° around the principal axis lying in the film plane. The superlattice reflections seen at normal incidence disappear here, since there is no superlattice reflection in the {110} plane of reciprocal lattice as described in Part I.

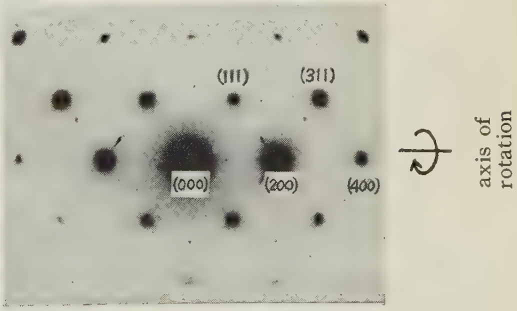

Photo. 1. Electron diffraction pattern of the ordered Au_3Mn film: [110] incidence.

Nevertheless, the satellites remain fairly strong. This fact shows that a greater part of intensity of the satellites is not caused by double diffraction but due to a periodic lattice modulatoin. Recently, we observed, in addition, the satellites flanking the superlattice reflections, {001}, in electron diffraction patterns of the ordered Cu_3Pd (α'') alloy mixed with one-dimensional anti-phase domains[7]. These satellites are also considered to be caused by the periodic lattice modulation.

---

† All the notations, m_1, m_2, a_1^*, a_2^*, M_1 and M_2, have the same significance as in Part I.

In general, either or both of two kinds of modulation in a crystal lattice are conceivable as the cause of the satellites, i.e. a periodic change of lattice spacing, and of scattering factor[8]. For CuAu (II), Ogawa and the present author[2] proposed some explanation about the origin of the satellites, by considering a definite amount of expansion of lattice spacing at each anti-phase domain boundary, but it seems that this explanation is difficult to apply to all cases so far examined, because there are some cases in which contraction takes place along the alignment direction of anti-phase domains.

In the present paper, contribution of a periodic lattice modulation accompanying anti-phase domains to the diffraction pattern will be reconsidered, and some discussion will be given of the origin of the satellites, on the basis of observed intensities.

§ 2. Models of Lattice Modulation and Comparison with the Experimental Facts

First, we shall consider for simplicity the case of one-dimensional anti-phase domains, the fundamental lattice of which is of ordered A_3B type with the first kind of out-of-step having the period of Ma along the x direction, and calculate the structure amplitudes of the satellites for some possible models of lattice modulation.

(1) *Periodic change of lattice spacing*

Let us assume a periodic modulation of the spacing as shown by arrows in Fig. 1 (a), with the period of modulation Ma and with the shifts of lattice planes expressed by a sinusoidal function as shown in Fig. 1 (b). Positions, x_p^1 and x_p^2, of the two kinds of lattice plane, which are parallel to the boundary plane and belong to the p-th fundamental cell, will be given by the following equations, by assuming that the lattice position on the boundary plane as indicated by arrow (↟) is taken as the origin of the crystal lattice:

$$x_p^1 = pa + \delta a \cdot \sin 2\pi \frac{p+(1/4)}{M} \tag{1-1}$$

$$x_p^2 = \left(p+\frac{1}{2}\right)a + \delta a \cdot \sin 2\pi \frac{p+(3/4)}{M} \tag{1-2}$$

The structure amplitude for this crystal is

$$\begin{aligned} S = \sum_{q=0}^{N-1} \exp 2\pi i q(2M)A_1 \times \Biggl[\Psi_1 \sum_{p=0}^{M-1} \exp 2\pi i p A_1 \cdot \exp\left(2\pi i A_1 \delta \cdot \sin 2\pi \frac{p+(1/4)}{M}\right) \\ + \Psi_2 \sum_{p=0}^{M-1} \exp 2\pi i p A_1 \cdot \exp\left(2\pi i A_1 \delta \cdot \sin 2\pi \frac{p+(3/4)}{M}\right) \Biggr], \end{aligned} \tag{2}$$

where N is half the number of anti-phase domain along the x direction, and

$$\Psi_1 = E_B + E_A \exp \pi i(A_2+A_3) + \{E_A + E_B \exp \pi i(A_2+A_3)\} \exp 2\pi i M A_1, \tag{3-1}$$

$$\Psi_2 = E_A\{\exp \pi i(A_1+A_2) + \exp \pi i(A_3+A_1)\} \cdot (1+\exp 2\pi i M A_1), \tag{3-2}$$

in which E_A and E_B are the atomic scattering factor for electron of A-and B-atom respectively, and A_1, A_2 and A_3 are continuous variables in reciprocal space. By expanding $\exp\left(2\pi i A_1 \delta \cdot \sin 2\pi \frac{p+(1/4)}{M}\right)$ and $\exp\left(2\pi i A_1 \delta \cdot \sin 2\pi \frac{p+(3/4)}{M}\right)$ by Bessel functions, we obtain

$$\begin{aligned} S = \sum_{q=0}^{N-1} \exp 2\pi i q(2M)A_1 \times \Psi_1 \times \\ \Biggl[J_0(2\pi A_1 \delta) \cdot \sum_{p=0}^{M-1} \exp 2\pi i p A_1 \\ + J_2(2\pi A_1 \delta) \cdot \left\{ \exp \frac{\pi i}{2M} \cdot \sum_{p=0}^{M-1} \exp 2\pi i p\left(A_1 + \frac{1}{M}\right) - \exp\left(\frac{-\pi i}{2M}\right) \cdot \sum_{p=0}^{M-1} \exp 2\pi i p\left(A_1 - \frac{1}{M}\right) \right\} \\ + J_2(2\pi A_1 \delta) \cdot \left\{ \exp \frac{\pi i}{M} \cdot \sum_{p=0}^{M-1} \exp 2\pi i p\left(A_1 + \frac{2}{M}\right) + \exp\left(\frac{-\pi i}{M}\right) \cdot \sum_{p=0}^{M-1} \exp 2\pi i p\left(A_1 - \frac{2}{M}\right) \right\} \end{aligned}$$

$$+J_3(2\pi A_1\delta)\cdot\left\{\exp\frac{3\pi i}{2M}\cdot\sum_{p=0}^{M-1}\exp 2\pi ip\left(A_1+\frac{3}{M}\right)-\exp\left(\frac{-3\pi i}{2M}\right)\cdot\sum_{p=0}^{M-1}\exp 2\pi ip\left(A_1-\frac{3}{M}\right)\right\}+\cdots\Bigg]$$

$$+\sum_{q=0}^{N-1}\exp 2\pi iq(2M)A_1\times\Psi_2\times$$

$$\Bigg[J_0(2\pi A_1\delta)\cdot\sum_{p=0}^{M-1}\exp 2\pi ipA_1$$

$$+J_1(2\pi A_1\delta)\cdot\left\{\exp\frac{3\pi i}{2M}\cdot\sum_{p=0}^{M-1}\exp 2\pi ip\left(A_1+\frac{1}{M}\right)-\exp\left(\frac{-3\pi i}{2M}\right)\cdot\sum_{p=0}^{M-1}\exp 2\pi ip\left(A_1-\frac{1}{M}\right)\right\}$$

$$+J_2(2\pi A_1\delta)\cdot\left\{\exp\frac{3\pi i}{M}\cdot\sum_{p=0}^{M-1}\exp 2\pi ip\left(A_1+\frac{2}{M}\right)+\exp\left(\frac{-3\pi i}{M}\right)\cdot\sum_{p=0}^{M-1}\exp 2\pi ip\left(A_1-\frac{2}{M}\right)\right\}$$

$$+J_3(2\pi A_1\delta)\cdot\left\{\exp\frac{9\pi i}{2M}\cdot\sum_{p=0}^{M-1}\exp 2\pi ip\left(A_1+\frac{3}{M}\right)-\exp\left(\frac{-9\pi i}{2M}\right)\cdot\sum_{p=0}^{M-1}\exp 2\pi ip\left(A_1-\frac{3}{M}\right)\right\}+\cdots\Bigg] \tag{4}$$

for $A_1>0$. The structure amplitudes of the satellites flanking the main reflections and those flanking the superlattice reflections are given respectively as follows:

(i) Satellites flanking the main reflections ($A_1=h_1\pm(n/M)$, $A_2=h_2$, $A_3=h_3$, where h_1, h_2 and h_3 are unmixed and n=integer.)

$$\begin{aligned}|S_m|&=2N\cdot M\cdot J_n(2\pi\cdot h_1\pm(n/M)\cdot\delta)\cdot|E_B+3E_A|, && \text{for } M>2\\ &=5.656\,N\cdot J_1(2\pi\cdot h_1\pm(1/2)\cdot\delta)\cdot\sqrt{E_B^2+5E_A^2+2E_BE_A}, && \text{for } M=2\end{aligned} \tag{5-1}$$

(ii) Satellites flanking the superlattice reflections undergoing no splitting ($A_1=h_1\pm(n/M)$, $A_2=h_2$, $A_3=h_3$, where h_2+h_3=even and n=integer).

$$\begin{aligned}|S_s|&=2N\cdot M\cdot J_n(2\pi\cdot h_1\pm(n/M)\cdot\delta)\cdot|E_B-E_A| && \text{for } M>2\\ &=|S_m| && \text{for } M=2\end{aligned} \tag{5-2}$$

It is readily known from the above result that the intensities of the satellites increase with the order of reflection and the satellites flanking the main reflections with $h_1=0$ must have the smallest intensity. The circumstances remain the same even when a definite spacing change, i.e. an expansion or a contraction of the lattice, exists periodically only at each domain boundary, as already proposed by Ogawa and the present author for CuAu (II)[2].

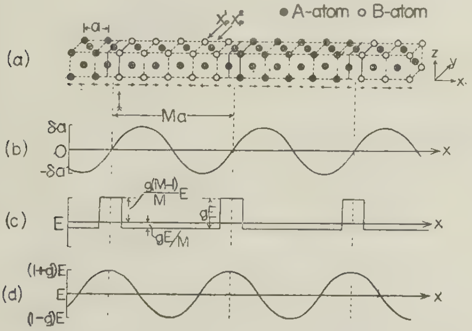

Fig. 1. Some models of periodic lattice modulation.
(a) and (b); Periodic change of lattice spacing. Small arrows in (a) represent the displacements of lattice planes.
(c) and (d); Periodic change of scattering factor.

Experimentally, however, the satellites flanking the direct spot is most pronounced in all cases so far examined, and the higher the order of main reflection, the smaller the intensity of the satellites becomes. Therefore, it becomes clear that the observed satellites are hard to be explained by the periodic change of lattice spacing alone, unless an anomalous value of atomic scattering factor for electron at the lowest scattering angle such as previously proposed[2] is assumed.

2) *Periodic change of scattering factor*

If the scattering factor at each domain boundary is different on the average from that inside each domain, satellites should also arise. Here we shall consider the following two simplified models.

(a) First, let us examine the model as shown in Fig. 1(c), in which the change of scattering factor is gE, that is to say, the scattering factors of atoms on domain boundary and inside domain are given by $\left(1+\frac{g(M-1)}{M}\right)E$ and $\left(1-\frac{g}{M}\right)E$ respectively, where E is the scattering factor for the structure without modulation. The structure amplitude for such a crystal is given by

$$\begin{aligned} S=&\left(1-\frac{g}{M}\right)\cdot\sum_{q=0}^{N-1}\exp 2\pi iq(2M)A_1\cdot\sum_{p=0}^{M-1}\exp 2\pi ipA_1\cdot(\Phi_1+\Phi_2\exp 2\pi iMA_1) \\ &+g\cdot\sum_{q=0}^{N-1}\exp 2\pi iq(2M)A_1\cdot\{\Psi_1+\Psi_2\cdot\exp 2\pi i(M-1)A_1\}\ , \end{aligned} \tag{6}$$

where

$$\Phi_1=E_A\{\exp\pi i(A_1+A_2)+\exp\pi i(A_2+A_3)+\exp\pi i(A_3+A_1)\}+E_B \tag{7-1}$$

and

$$\Phi_2=E_A\{1+\exp\pi i(A_1+A_2)+\exp\pi i(A_3+A_1)\}+E_B\cdot\exp\pi i(A_2+A_3)\ , \tag{7-2}$$

and Ψ_1 and Ψ_2 have the same significance as in Eq. (3). The structure amplitudes of the satellites flanking main reflections and those flanking superlattice reflections become respectively as follows:

$$|S_m|=2g\cdot N\cdot\left|E_B+E_A+2E_A\exp\left(\mp\frac{n\pi i}{M}\right)\right|\ , \tag{8-1}$$

and

$$|S_s|=2g\cdot N\cdot\left|E_B+E_A-2E_A\exp\left(\mp\frac{n\pi i}{M}\right)\right|\ . \tag{8-2}$$

(b) Next, we shall consider a structure in which the scattering factor varies sinusoidally as shown in Fig. 1 (d), where the scattering factors of atoms on the two kinds of lattice plane in the p-th fundamental cell are given by

$$E_p^1=E\left(1+g'\cos 2\pi\frac{p+(1/4)}{M}\right) \tag{9-1}$$

and

$$E_p^2=E\left(1+g'\cos 2\pi\frac{p+(3/4)}{M}\right)\ , \tag{9-2}$$

and g' represents a parameter of the sinusoidal variation. The structure amplitude for such a crystal is given by

$$\begin{aligned} S=\sum_{q=0}^{N-1}\exp 2\pi iq(2M)A_1\Bigg[&\Psi_1\Bigg\{\sum_{p=0}^{M-1}\exp 2\pi ipA_1+\frac{g'}{2}\exp\frac{\pi i}{2M}\cdot\sum_{p=0}^{M-1}\exp 2\pi ip\left(A_1+\frac{1}{M}\right) \\ &+\frac{g'}{2}\exp\left(\frac{-\pi i}{2M}\right)\cdot\sum_{p=0}^{M-1}\exp 2\pi ip\left(A_1-\frac{1}{M}\right)\Bigg\} \\ &+\Psi_2\Bigg\{\sum_{p=0}^{M-1}\exp 2\pi ip\,A_1+\frac{g'}{2}\exp\frac{3\pi i}{2M}\cdot\sum_{p=0}^{M-1}\exp 2\pi ip\left(A_1+\frac{1}{M}\right) \\ &+\frac{g'}{2}\exp\left(\frac{-3\pi i}{2M}\right)\cdot\sum_{p=0}^{M-1}\exp 2\pi ip\left(A_1-\frac{1}{M}\right)\Bigg\}\Bigg]\ , \end{aligned} \tag{10}$$

$$\begin{aligned} |S_m|&=g'NM\cdot|E_B+3E_A| && \text{for}\quad n=1,\quad M>2\ , \\ &=0 && \text{for}\quad n\geq 2,\quad M>2\ , \\ &=2\sqrt{2}\,g'N\cdot|E_B+E_A\mp 2iE_A| && \text{for}\quad M=2, \end{aligned} \tag{11-1}$$

and

$$\begin{aligned} |S_s|&=g'NM\cdot|E_B-E_A| && \text{for}\quad n=1,\quad M>2\ , \\ &=0 && \text{for}\quad n\geq 2,\quad M>2\ , \\ &=2\sqrt{2}\,g'N\cdot|E_B+E_A\pm 2iE_A| && \text{for}\quad M=2. \end{aligned} \tag{11-2}$$

From these calculations it is seen that the ratio of intensity of satellites to that of the relevant main or superlattice reflection is independent of the reflection order, and therefore satellites flanking the direct spot are expected to be most strong if the dependence of scattering factor upon scattering angle is taken into account. Since, however, the result of the model (d) contradicts the experimental fact that the second and the third order satellites ($n=2$, 3) are clearly observed in many cases including Au_3Mn, the observed amplitudes of satellites from the Au_3Mn alloy is now compared with the calculated values based on the more favourable model (c). The calculation for the two-dimensional anti-phase domain structure of Au_3Mn is similar as in the above one-dimensional case, and the structure amplitude of the first order satellites due to the modulation with $M_2=2$ along the y-direction is shown to be

$$|S_m|=2\sqrt{2}\,g\cdot N\cdot|E_{\text{Mn}}+3E_{\text{Au}}|\equiv N\cdot F. \quad (12)$$

In the second column of Table I* the values of the structure amplitude obtained from the square root of the observed intensities of satellites, which have been already given in Table II of Part I, are tabulated again, and these values and the values of $|F|/g$ calculated from Eq. (12) are shown against the change of scattering angle in Fig. 2, where the observed value of (12, 2, 0) reflection is normalized with the calculated one. It is to be noted that the observed values decrease more slowly than the calculated one. If intensities

Table I. The observed and calculated structure amplitudes for the satellites.

H_1	H_2	H_3	$\lvert F_{\text{obs.}}\rvert$	$\lvert F_{\text{cal.}}\rvert$
2	0	0	17	6
6	0	0	11	6
10	0	0	7	5
2	8	0	14	4
6	8	0	8	5
10	8	0	5	5
2	16	0	7	2
6	16	0	5	3
10	16	0	4	4
2	24	0	5	1
0	2	0	17	6
0	6	0	12	7
0	10	0	10	9
0	14	0	7	8
0	18	0	3	8
4	2	0	10	3
4	6	0	8	5
4	10	0	7	7
4	14	0	5	7
4	18	0	3	7
8	2	0	6	2
8	6	0	5	3
8	10	0	5	4
8	14	0	3	5
12	2	0	4	1
12	6	0	3	2

Table II. Some examples of the structure amplitudes of satellites calculated for the model containing both kinds of lattice modulations.

Index	$\lvert S_m\rvert/N$
0, $2-(1/M_2)$, 0	15.2
0, $2+(1/M_2)$, 0	0.3
0, $4-(1/M_2)$, 0	9.8
0, $4+(1/M_2)$, 0	2.2
2, $2-(1/M_2)$, 0	9.8
2, $2+(1/M_2)$, 0	0.2

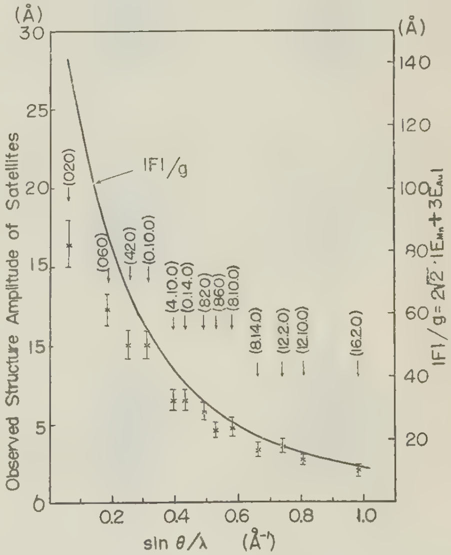

Fig. 2. Comparison of the observed structure amplitude of satellites and $|F|/g$ calculated from Eq. (12).

---

* In this table, the index, $(H_1H_2H_3)$, refers to the large orthorhombic cell $2\times4\times1$ times as large as the fundamental cell. The relation between the indices, $(h_1h_2h_3)$ and $(H_1H_2H_3)$, is given as follows: $h_1=(H_1/2)$, $h_2=(H_2/4)$, $h_3=H_3$.

of the satellites be somewhat strengthened by double diffraction, this tendency should be more pronounced, because such an effect is expected to be conspicuous at small scattering angle. If a fraction of the modulation, g, is assumed to be about 1/8.5, the intensity of the satellites flanking the main reflections of lower order may be explained by the present model (c), but the satellites with large scattering angle seem not to be fully elucidated. These circumstances seem to suggest that the scattering factor variation mainly contributes to the lower angle satellites, while part of the intensity of the higher angle satellites is ascribed to the lattice spacing variation.

Here, the order of magnitude of the spacing variation, if any, can be estimated in the following way: The values of structure amplitudes of satellites are calculated, by assuming various values for the displacements of atoms at the domain boundaries along the x and y directions. In this case, we assumed that along both directions the lattice constant is slightly expanded at domain boundaries. Comparing the observed structure amplitudes with the calculated ones, the most appropriate values of the displacements were so selected that the coincidence between both values might be best for the higher angle satellites. In this way, the displacements of atoms at domain boundaries were estimated to be about 0.01 Å along the x and 0.02 Å along the y direction. It is readily shown that such an order of displacements has little effect on the structure amplitudes of main and superlattice reflections but exerts a large influence upon the structure amplitudes of satellites. In the third column of Table I the structure amplitudes of satellites calculated by taking only the above displacements into account are also tabulated. In this table we see that for the satellites with small H_1 or H_2 value, i.e. $(2H_20)$ and $(6H_20)$,

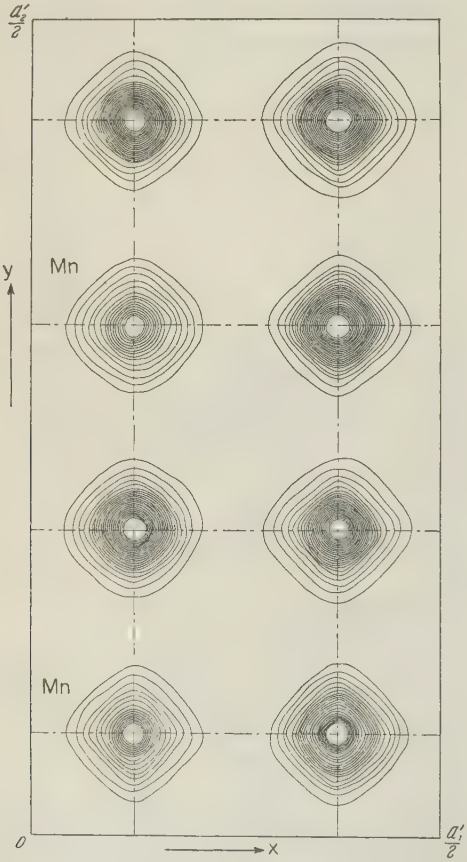

Fig. 3. (a); Two-dimensional Fourier map obtained from reflections except satellites.

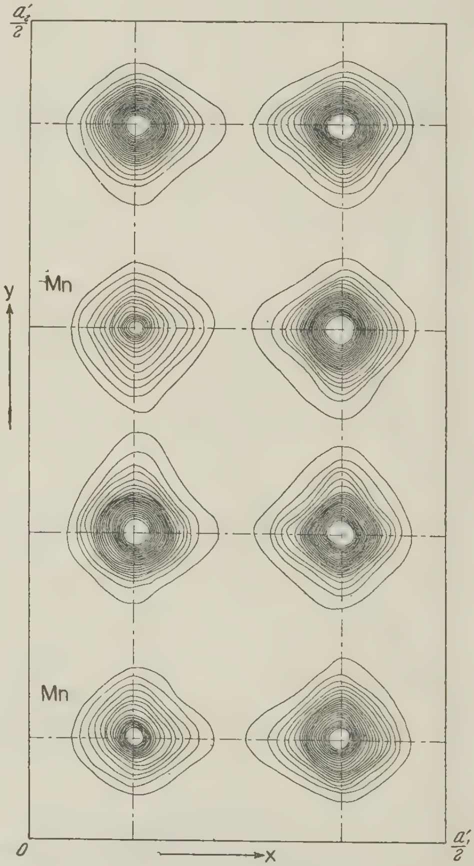

Fig. 3. (b); Two-dimensional Fourier map obtained from all the reflections including satellites.

In (a) and (b), the full lines represent the places where out-of-steps occur, i.e. the domain boundaries.

The contours are drawn at arbitrary unit.

$(H_1 20)$ and $(H_1 60)$, the calculated structure amplitudes are smaller than the observed ones, while for the satellites with relatively large H_1 or H_2 value the agreement is good.

In order to investigate the nature origin of the of the satellites with small H_1 or H_2 value, Fourier synthesis for the potential distribution was tentatively undertaken, using the measured structure amplitudes given in Table II of Part I. The potential distribution estimated from reflections not including the satellites is shown in Fig. 3 (a). In this figure, which is a projection on (001) plane of a quarter of a large orthorhombic unit cell ($a'_1=2a_1$, $a'_2=4a_2$, $a'_3=a_3$), the positions of gold and manganese atoms, showing the potential distribution of nearly spherical symmetry, are clearly distinguished. Fig. 3 (b) is the result obtained by taking account of all the observed reflections including the satellites, with the following assumption regarding the determination of the phase of the structure amplitudes for the satellites:

(i) Along the x direction the lattice constant at every boundary between the domains is assumed to be elongated slightly. The periodic change of the scattering factor is forbidden due to the symmetry operation of the present space group, P_{nnm}-D^{12}_{2h}.

(ii) Along the y direction the modulation of the scattering factor may be present, but in the present case we only assume also for this direction that the lattice constant at every boundary is slightly elongated.

It is remarkable that in Fig. 3 (b) the potential distribution around gold and manganess atoms is fairly distorted in comparison with Fig. 3 (a). The displacements of potential peaks at domain boundaries, however, can not be detected in this figure, because their magnitudes are very small, as mentioned above. Moreover, from the detailed analysis of Fig. 3 (b) we see that the height of potential peaks at the boundaries of domains along the y direction decreases slightly in comparison with Fig. 3 (a).* This fact means that the modulation of the scattering factor also occurs along the y direction, though this has not been assumed beforehand. It was known in the course of Fourier synthesis that the distortion of the potential distribution around each atom is attributable to the satellites with small H_1 or H_2 value. That is to say, this distortion causes the abnormally intense satellites in question, especially those flanking the direct spot.

(3) *Combination of both types of lattice modulation*

In view of the above result that neither the lattice spacing variation alone nor the scattering factor variation alone explains the intensities of the satellites satisfactorily, we shall tentatively consider a two-dimensional antiphase domain structure of Au$_3$Mn type in which both the variations given by Figs. 1 (a) and (c) occur simultaneously along the y direction. In this case we assume that no variation occurs along the x direction. The structure amplitude is given by

$$\begin{aligned}S=\sum_{q=0}^{N-1}\exp 2\pi iq(2M_2)A_2\cdot\Bigg[\,&G_1\Bigg\{\left(1-\frac{g}{M_2}\right)\cdot\sum_{p=0}^{M_2-1}\exp\, 2\pi iA_2\left(p+\delta\cdot\sin 2\pi\frac{p+(1/4)}{M_2}\right)\\&\qquad+g\cdot\exp\left(2\pi iA_2\delta\cdot\sin 2\pi\frac{1}{4M_2}\right)\Bigg\}\\&+G_2\Bigg[\left(1-\frac{g}{M_2}\right)\cdot\sum_{p=0}^{M_2-1}\exp\, 2\pi iA_2\left(p+\delta\cdot\sin 2\pi\frac{p+(3/4)}{M_2}\right)\\&\qquad+g\cdot\exp\left\{2\pi iA_2\left(M-1+\delta\cdot\sin 2\pi\frac{M_2-(1/4)}{M_2}\right)\right\}\Bigg]\Bigg],\end{aligned}\tag{13}$$

where

$$\begin{aligned}G_1=E_{\mathrm{Mn}}+E_{\mathrm{Au}}\exp\pi i(A_3+A_1)+\{E_{\mathrm{Au}}+E_{\mathrm{Mn}}\exp\pi i(A_3+A_1)\}\exp 2\pi iM_2A_2\\+E_{\mathrm{Au}}\{1+\exp\pi i(A_3+A_1)\}\cdot\{1+\exp 2\pi iM_2A_3\}\exp 2\pi iA_1\end{aligned}$$

and

---

* Such a change of peak height, however, can not be detected in Fig. 3.

$$
\begin{aligned}
G_2=E_{\mathrm{Au}}\{&\exp\pi i(A_1+A_2)+\exp\pi i(A_2+A_3)\}\cdot\{1+\exp 2\pi iM_2A_2\}\\
&+\{E_{\mathrm{Au}}\cdot\exp\pi i(A_1+A_2)+E_{\mathrm{Mn}}\exp\pi i(A_2+A_2)\}\cdot\exp 2\pi iA_1\\
&+\{E_{\mathrm{Mn}}\cdot\exp\pi i(A_1+A_2)+E_{\mathrm{Au}}\exp\pi i(A_2+A_3)\}\cdot\exp 2\pi i(A_1+M_2A_2)\ ,
\end{aligned}
$$

and the domain size along the x direction, M_1a_1, is considered to be a_1 ($M_1=1$). Assuming $M_2=2$, we have

$$
\begin{aligned}
|S|\doteqdot N\cdot\Bigg|\,&G_1\Bigg[J_0(2\pi A_2\delta)\cdot\left\{\left(1-\frac{g}{2}\right)(1+\exp 2\pi iA_2)+g\right\}\\
&\qquad+J_1(2\pi A_2\delta)\cdot\left\{\left(1-\frac{g}{2}\right)(1-\exp 2\pi iA_2)+g\right\}\cdot\sqrt{2}\,i\Bigg]\\
&+G_2\cdot\Bigg[J_0(2\pi A_2\delta)\cdot\left\{\left(1-\frac{g}{2}\right)(1+\exp 2\pi iA_2)+g\cdot\exp 2\pi iA_2\right\}\\
&\qquad+J_1(2\pi A_2\delta)\cdot\left\{\left(1-\frac{g}{2}\right)(1-\exp 2\pi iA_2)-g\cdot\exp 2\pi iA_2\right\}\cdot\sqrt{2}\,i\Bigg]\Bigg|\ . \qquad (14)
\end{aligned}
$$

The structure amplitude of satellites located at $A_1=h_1$, $A_2=h_2\pm 1/M_2$), $A_3=h_3$, is given by

$$|S_m|\doteqdot 2\sqrt{2}\,N\cdot|(E_{\mathrm{Mn}}+3E_{\mathrm{Au}})\cdot(gJ_0\mp 2.828J_1)|\ . \qquad (15)$$

It is clear from this equation that for the positive value of g the calculated intensity of the inner satellites ($A_2=h_2-(1/M_2)$) becomes exceedingly larger than that of the outer ones ($A_2=h_2+1/M_2$), provided that g and δ are of the same order of magnitudes as those already estimated. Table II shows some examples of the intensity asymmetry.* If g-value is negative, the asymmetry is reversed.

Furthermore, Eq. (14) predicts that the intensity asymmetry should appear also in a pair of split superlattice reflections, but such an order of magnitude of g and δ as above is so small that the asymmetry does not appear in the superlattice reflections in the present case. The derivation of such an asymmetry of intensity in a pair of satellites is characteristic for the model in which both types of lattice modulation are combined[8]. The circumstances are of course much the same for the one-dimensional domain structure.

Since such an intensity asymmetry in satellites could not actually be observed in all cases so far examined by electron diffraction, the model taking account of both modulations as considered here seems to be not satisfactory in explaining the origin of the satellites. In this connection, it is worth mentioning that in the Au_4Zn alloy which exhibits the two-dimensional anti-phase domain structure of Cu_3Pd type, the intensity asymmetries in both satellites and split superlattice reflections have been observed by X-rays[9).]** In this case, it is reasonable to assume that the scattering factor variation due to a composition change inside each anti-phase domain coexists with the lattice spacing variation.

(4) *On the satellites flanking the superlattice reflections*

As was described in §1, the satellites flank-

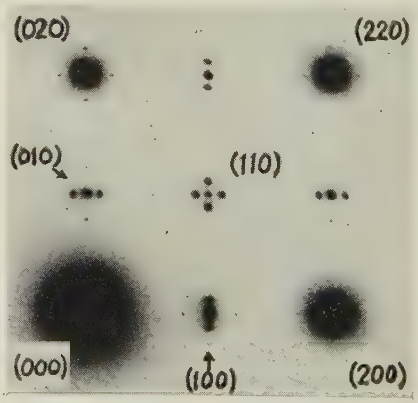

Photo. 2. Electron diffraction pattern of the ordered Cu_3Pd (α'') film mixed with the one-dimensional anti-phase domain structure; normal incidence. Indices refer to the disordered cubic lattice.

---

* Such an asymmetry appears also in the model ($a-b$), in which lattice spacing variation only is considered, as readily known from equation (5).

** However, the satellites flanking the direct spot were hardly detected by X-rays, while they were observed by electron diffraction. This ordered alloy was named $Au_{3+}Zn$ instead of Au_4Zn by Iwasaki *et al*[9). following Wilkens and Schubert[11), ing the {001} superlattice reflections were observed besides those flanking the main reflections in the ordered Cu_3Pd alloy, in which the one-dimensional anti-phase domain structure lined-up along the *z*-direction are mixed with a little amount of the two-dimensional structure[7]. In Photo. 2 is reproduced an electron diffraction pattern taken from this alloy. The intensity distribution in reciprocal space derived from Photo. 2 is shown in Fig. 4, where superlattice reflections and satellites are represented by the small closed and open circles respectively.* As already shown in the preceding calculations and pointed out by Okuzumi, Perio and Tournarie[10], the satellites flanking the superlattice reflections are also expected to appear by the periodic lattice modulation.

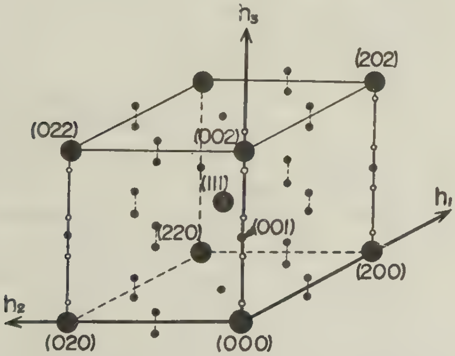

Fig. 4. Fundamental intensity distribution in reciprocal space induced from Photo. 2.

Table III. Structure amplitudes of the satellites flanking (001) and (002) reflections calculated for the Cu_3Pd alloy.

Index	$\|S\|/N$
$0,\ 0,\ 1-(1/M)$,	$24\,g$
$0,\ 0,\ 1+(1/M)$,	$18\,g$
$0,\ 0,\ 2-(1/M)$,	$30\,g$
$0,\ 0,\ 2+(1/M)$,	$24\,g$

In the present Cu_3Pd alloy, the intensity of the satellites in question seems to be explained by the periodic change of scattering factor (model (c)). In Table III, for example, are shown the structure amplitudes of the satellites flanking (001) superlattice reflection and of those flanking (002) main reflection calculated from Eq. (8–2) and (8–1), respectively, for the Cu_3Pd alloy, where *M* was estimated to be about 4. As the observed intensity distribution well coincides with that given in this table, it is supposed that the satellites flanking the superlattice reflections are caused by the same origin as those flanking the main reflections. In the Au_3Mn alloy, however, we could not detect any satellite around superlattice reflection.

§ 3. Further Considerations

Although we can not draw after all a decisive conclusion about the nature of the lattice modulation from the above considerations, it is suggested that the lattice spacing variation is required to be assumed for the satellites with large scattering angle and some kind of the scattering factor variation for those with small H_1 or H_2 values, though the magnitude of these modulations may somewhat be diminished if the effect of double diffraction exists.

If the periodic change of scattering factor, say in the model depicted in Fig. 1 (c), is caused by the difference in degree of ionization between the boundary atoms and inside ones, the appearance of the satellites flanking the direct spot may be explained, and the intensity asymmetry in a pair of satellites may not be expected to occur at $\sin\theta/\lambda$ larger than 0.2 even when the lattice spacing variation co-exists, because the effect of ionization on the atomic scattering factor for electron is negligible except at small values of $\sin\theta/\lambda$ less than 0.2. But, appreciable intensity of the satellites may not be expected for small H_1 and H_2 values, although those for large H_1 and H_2 values may be attributable to the lattice spacing variation. The present difficulty can not be overcome even if we take account of secondary diffraction of the satellites flanking the direct spot[2], because the actual intensity distribution in a pair of the satellites flanking other main reflections, especially of those flanking $\{220\}_{\text{cub.}}$ reflection, remains unexplained. That is to say, the inner satellite flanking $\{220\}_{\text{cub.}}$ reflection has obviously larger intensity than that of the outer, whereas these satellites should have at least the same order of intensity in order to be explained by secondary diffraction. Thus, it seems that the actual nature of the scattering factor variation is more complicated than the above model of ionized atom.

---

* In this figure, the superlattice reflections due to the two-dimensional structure were neglected.

Here, it must be noted that up to the present the satellites flanking the direct spot are hardly observed by X-rays except the only one case. Wilkens and Schubert[11] observed a very weak diffraction line at the satellite position around the direct spot using a polycrystalline specimen of $Cu_5Au_2Zn_8$. In the case of electron diffraction, the distortion of the potential distribution around each atom has a large influence on the satellites with small H_1 or H_2 value including those flanking the direct spot, as already mentioned. From this fact, it is suggested that such a distortion in the distribution of valence electron as ellipsoidal distribution considered in zinc oxide by Johnson[12] exists at each domain boundary and causes the satellites in question to arise. If these satellites are caused by such an effect, they will hardly be observable in an X-ray diffraction pattern, for the abnormality of valence electron distribution seems not so to affect X-ray diffraction as to affect electron diffraction. In this connection, Schubert *et al*[13]. proposed that the valence electron plays an important rôle in the formation of anti-phase domain structure. They found a definite relation between the valence electron density and the domain size in many ordered alloys with stable anti-phase domain structure, and assumed that excess or deficiency of valence electrons to unity is located with the definite period and gives rise to out-of-step of ordering. According to this idea, the distortion of valence electron distribution at domain boundary and also the lattice spacing variation may occur, if the spatial change of valence electron number causes a periodic variation in the cohesive force of the lattice. Accordingly, the idea given by Schubert *et al.* seems to be closely connected with the origin of the satellites. However, a more concrete theoretical foundation might be desired for this idea, and at the same time a more detailed X-ray study about the satellites should be carried out.

The present author wishes to express his sincere thanks to Professor S. Ogawa for the kind guidance and encouragement.

The present investigation has partly been supported by the fund of the Ministry of Education in Aid of Scientific Researches.

References

1) D. Watanabe: J. Phys. Soc. Japan **15** (1960) 1030.
2) S. Ogawa and D. Watanabe: J. Phys. Soc. Japan **9** (1954) 475.
3) D. Watanabe and S. Ogawa: J. Phys. Soc. Japan **11** (1956) 226.
4) S. Ogawa, D. Watanabe, H. Watanabe and T. Komoda: J. Phys. Soc. Japan **14** (1959) 936.
5) A. B. Glossop and D. W. Pashley: Proc. Roy. Soc. **250** (1959) 132.
6) S. Ogawa, D. Watanabe, H. Watanabe and T. Komoda: Acta Cryst. **11** (1958) 872.
7) S. Ogawa and D. Watanabe: to be published.
8) A. J. C. Wilson: *X-Ray Optics* (Methuen and Co. London, 1949) 99.
9) H. Iwasaki, M. Hirabayashi, K. Fujiwara, D. Watanabe, and S. Ogawa: J. Phys. Soc. Japan **15** (1960) 1771.
10) H. Okuzumi, P. Perio and M. Tournarie: Acta Cryst. **12** (1959) 1039.
11) M. Wilkens and K. Schubert: Z. Metallkde., **48** (1957) 550.
12) V. A. Johnson: Phys. Rev. **57** (1940) 613.
13) K. Schubert, B. Kiefer, M. Wilkens and R. Haufler: Z. Metallkde., **46** (1955) 692.

JOURNAL OF THE PHYSICAL SOCIETY OF JAPAN, Vol. 16, No. 3, MARCH, 1961

The Ferroelectric Phase Transition in $(\text{Glycine})_3 \cdot H_2SO_4$ and Critical X-Ray Scattering

By Iwao SHIBUYA* and Toshio MITSUI**

Crystal Research Laboratory, The Pennsylvania State University,
University Park, Pennsylvania, U.S.A.

(Received October 3, 1960)

On the assumption that the ferroelectric phase transition in $(\text{Glycine})_3 \cdot H_2SO_4$ is of the order-disorder type, expressions for Bragg reflections and critical scattering of X-rays are given in terms of a long-range order parameter and pair correlation functions. Temperature dependence of the critical scattering is discussed on the basis of the Bragg-Williams approximation and of a modified Fröhlich theory. Experimental observations agree with theoretical predictions, and prove that the phase transition is of the order-disorder type. The observed critical scattering exhibits a pronounced peak at the Curie point, suggesting that the local field theory is not a good approximation. The shape of the peak appears to be quite different from that in the ferromagnetic case. It has been found that the sulfur atoms do not shift appreciably when the glycine groups rotate. A method for evaluating the pair correlation function is proposed.

§1. Introduction

Critical scattering is one of the effects associated with a condensed material in the vicinity of a phase transition. It may be expected to occur in crystals where there are, under appropriate conditions, atoms of more than one type or atoms existing in more than one state in the lattice. An example of the former case is an order-disorder transition in alloys[1], and the latter a ferromagnetic transition[2]. As has been shown in these cases[1)-3)], investigation of critical scattering provides very valuable information about the mechanism of a phase transition. The purpose of the present paper is to show how critical scattering of X-rays takes place in the ferroelectric transition of $(\text{Glycine})_3 \cdot H_2SO_4$, and to give a foundation for more detailed studies of this phenomenon. (For simplicity, $(\text{Glycine})_3 \cdot H_2SO_4$, triglycine sulfate, will be abbreviated as TGS below). The reasons why we chose TGS as the first sample in our studies of critical scattering by ferroelectrics are as follows: (1) the transition is of second order[4], (2) the transition seems to be of the order-disorder type (see Sec. 2), (3) the crystal structure at room temperature has been analyzed[5], and (4) the unit cell has only two molecular units and the crystal structure is relatively simple.

One can find a general theory on diffuse X-ray scattering by partially ordered crystal in Zachariasen's book[6] and, in more detail, in Matsubara's articles[7]. Our present theory described in Sec. 2 will be based on their formulations. The long-range order parameter and pair correlation function will be defined in an analogous way to the alloy case, and intensities of Bragg reflections and critical scattering will be expressed in terms of them. A method to evaluate the pair correlation function will be proposed in Sec. 2. With the help of statistical mechanics, the pair correlation function will provide information on the interaction between atoms or molecules in the crystal, and thus on the origin of ferroelectricity. Estimation of pair correlation will be made in a later paper. Experimental observations of Bragg spots and critical scatterings will be reported in Sec. 3. Discussions on obtained results will be given in Sec. 4.

§2. Theory

A. *Fundamental assumptions*

Ferroelectricity in TGS was fonnd by Matthias, Remeika, and Miller in 1956[8]. The crystal is ferroelectric along the *b*-axis below 47°C[4], and the transition is of second order[4]. Usually ferroelectric phase transitions are classified into two types[9]; one is the $BaTiO_3$ type sometimes called a displacive type, and the other is the KDP type usually called an order-disorder type. The type of a transition can be decided by examining the order of magnitude of the Curie-Weiss constant or of the transition entropy as has been demonstrated clearly by Anderson[10]. The Curie-Weiss constant of TGS is 3,280°K[4] compared to 3,260°K for KDP[11] and to 170,000°K for $BaTiO_3$[12]. The transition entropy of TGS is 0.48 cal./mol. deg.[4] compared to 0.47[11] or 0.72[13] for KDP and to 0.12 for $BaTiO_3$[12]. These values suggest that the transition of TGS is of the order-disorder type.

---

* Now at the Institute for Solid State Physics, University of Tokyo, Tokyo, Japan.

** Now at Laboratory for Insulation Research, Massachusetts Institute of Technology, Combridge, Massachusetts, U.S.A. On leave from Hokkaido University, Sapporo, Japan.

The crystal structure of TGS has been analyzed recently by Hoshino, Okaya and Pepinsky[5]. The space group is $P2_1/m$ above the Curie point and $P2_1$ in the ferroelectric phase. The *c*-projection of the structure at room temperature is shown in Fig. 1. The figure corresponds to a structure of negative polarity[15]. The structure of positive polarity is a mirror image of Fig. 1, putting the mirror perpendicular to the *b*-axis. A molecular unit is enclosed by the dashed lines. The unit cell has two molecular units, which are related with each other by the twofold screw axis 2_1. Coupling between atoms seems to be strong within this molecular unit and it may be considered a statistical unit. However, for simplicity, the crystallographic unit cell will be assumed to be a statistical unit below. There is some evidence suggesting that this is not a very bad assumption. We get a transition entropy of $R\ln 2 = 1.38$ cal./mol. deg., where R is the gas constant, if we assume that the molecular unit is a statistical unit with two positions of equilibrium, and if we use the Bragg-Williams approximation[16] (for this terminology, see Sec. 4). On the other hand, if we assume that the crystallographic unit cell is a statistical unit, we get a transition entropy of $\frac{1}{2}R\ln 2 = 0.69$ cal./mol. deg., which is close to the observed value of 0.48. Further, existence of the twofold screw axis results in zero Bragg reflection and zero diffuse coherent scattering at (0*k*0), where *k* is odd, due to the extinction

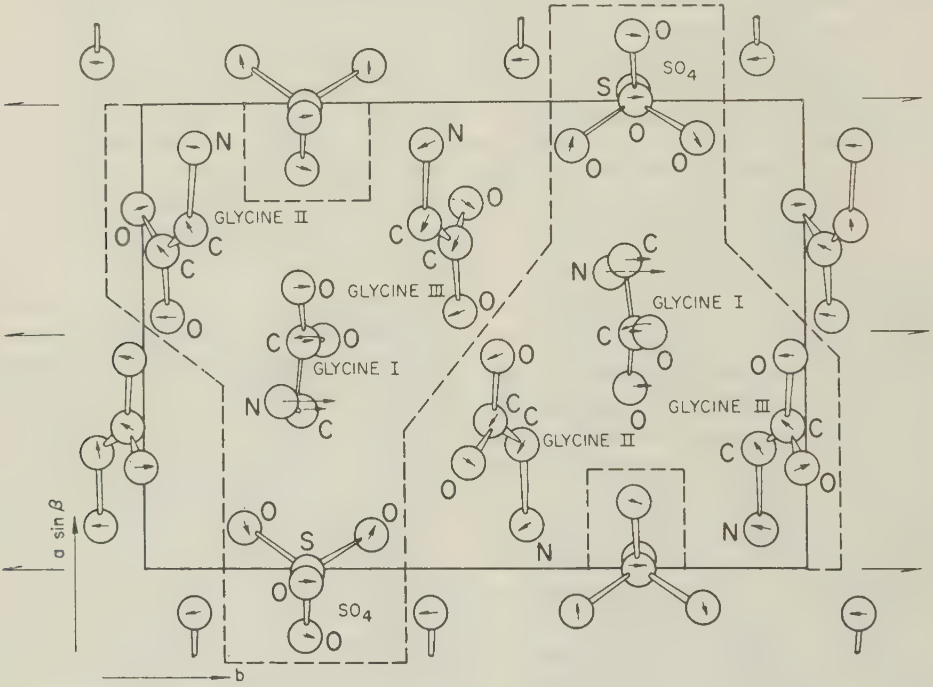

Fig. 1. Projection of the structure of TGS along the *c*-axis (after Hoshino, Okaya and Pepinsky[5]). This structure corresponds to negative polarity. Arrows show displacements of atoms during a reversal of polarity. The molecular unit is enclosed by dashed lines.

law[17)] and to the reasons described below. However, if coupling between the two molecular units in the unit cell is weak, the two molecules could have opposite polarity and destroy 2_1 symmetry frequently due to the thermal agitation at elevated temperatures, and a diffuse peak should be observed also around (0*k*0), where *k* is odd. No well defined peaks, however, have been observed, suggesting that coupling along the *b*-axis is strong.

The phase transition at 47°C will be assumed to be of the order-disorder type, and the actual crystal structure to be a statistical mixture of two basic structures, one of which has positive polarity and the other negative polarity, and which are mirror images of each other. Above the Curie point, the basic structures exist in the same proportion, and the unit cell has a center of symmetry on the time average. Below the Curie point, the ratio of the two structures deviates from $\frac{1}{2}$, and spontaneous polarization appears. The basic structure with negative polarity is assumed to be the same as that determined by Hoshino, Okaya and Pepinsky[5)]. The structure factor which they calculated by placing the sulfur atom at $y=\frac{1}{4}$ will be written as

$$F'=A'+iB' . \qquad (1)$$

For the space group $P2_1$, the origin of the unit cell cannot be determined uniquely along the *b*-axis. If the origin is defined by referring to a special atom which shifts during a reversal of polarity, the origin has to be shifted according to the reversal. This procedure is not convenient for handling the problem, since we cannot superpose origins of two unit cells by the lattice translation when they have different polarities. Suppose that a part of the crystal (or of the domain below the Curie point) has positive polarity, and another part negative polarity simultaneously, and that the two parts were superposed by the lattice translations. The resultant structure should have a center of symmetry. In the present treatment, the origin of the unit cell is put at one of these centers of symmetry which is closest to the origin chosen by Hoshino *et al*. For this new choice of the unit cell, the origin of Hoshino *et al.* is at $(0\delta 0)$; and δ should be added to all *y* coordinates in order to adjust to the new origin. We can now treat the two basic structures in a symmetrical way by this choice of the unit cell. Structure factors F_+ and F_-, which correspond to positive and negative polarity, can be written for the new origin as

$$F_+=A-iB \qquad (2a)$$

and

$$F_-=A+iB . \qquad (2b)$$

By the definition of structure factors[17)], A and B are related to A' and B' by equations

$$A=A'\cos 2\pi k\delta-B'\sin 2\pi k\delta , \qquad (3a)$$

$$B=A'\sin 2\pi k\delta+B'\cos 2\pi k\delta . \qquad (3b)$$

In Sec. 3 it will be found that δ is nearly equal to zero.

Hoshino *et al.* took the effect of the thermal vibration of the atoms into account by isotropic temperature factors when they calculated the structure factor F'. Therefore, in reciprocal space, the weight J for the diffracted coherent X-rays may be written as

$$J=\sum_s \sum_{s'} \langle F^*_{s'}F_s\rangle e^{2\pi i(\boldsymbol{H}\cdot\boldsymbol{r}_{ss'})}+J_T . \qquad (4)$$

Here F_s and $F_{s'}$ are the scattering amplitude of the *s*th and the *s'*th unit cells, $\langle\ \rangle$ is the time average, $\boldsymbol{H}$ a position vector in reciprocal space, $\boldsymbol{r}_{ss'}$ the vector from the *s'*th to the *s*th unit cell, and J_T is the thermal diffuse scattering due to the lattice vibration. The summation should be carried out for all unit cells in the crystal bathed in the incident X-rays. The above expression can be rewritten as

$$J=J_B+J_C+J_T , \qquad (5)$$

where

$$J_B=|\langle F_s\rangle|^2 \sum_s \sum_{s'} e^{2\pi i(\boldsymbol{H}\cdot\boldsymbol{r}_{ss'})} \qquad (6a)$$

and

$$J_C=\sum_s \sum_{s'}\{\langle F^*_{s'}F_s\rangle-|\langle F_s\rangle|^2\}e^{2\pi i(\boldsymbol{H}\cdot\boldsymbol{r}_{ss'})} . \qquad (6b)$$

$\sum_s \sum_{s'} e^{2\pi i(\boldsymbol{H}\cdot\boldsymbol{r}_{ss'})}$ gives the Laue interference function, and J_B represents Bragg spots when the unit cell is defined independent of atomic shift as in our case. J_C gives the critical scattering which is caused by disorder configuration of molecules in the crystal.

B. *Effect of long range order on J_B*

Suppose that the unit volume of TGS has N unit cells, of which N_+ have positive polarity and N_- negative. Then $x_+\equiv N_+/N$ and $x_-\equiv N_-/N$ are the probabilities that a unit cell has positive and negative polarity, respectively. Naturally $x_+ + x_- = 1$.

A long-range order parameter S is defined by

$$S = x_+ - x_- \,. \tag{7}$$

$x_+ = x_- = \frac{1}{2}$ and thus $S=0$ in the paraelectric phase, and $x_+=1$, $x_-=0$, and thus $S=1$ at very low temperatures if a domain of positive polarization is considered. S is related to the spontaneous polarization P_{Ss} by the equation

$$S = \frac{N_+}{N} - \frac{N_-}{N} = \frac{(N_+ - N_-)\mu}{N\mu} = \frac{P_s}{N\mu} \,, \tag{8}$$

where P_s is the spontaneous polarization and μ is the dipole moment of the unit cell. x_+ and x_- are given in terms of S by the equations

$$x_+ = \tfrac{1}{2}(1+S) \quad \text{and} \quad x_- = \tfrac{1}{2}(1-S) \,. \tag{9}$$

Thus we have

$$\langle F_s \rangle = x_+ F_+ + x_- F_- = A - iSB \,, \tag{10}$$

where Eqs. 2 and 9 were used. Therefore, by Eq. 6a, we have

$$J_B \propto |\langle F_s \rangle|^2 = A^2 + S^2 B^2 \,. \tag{11}$$

Here it should be mentioned that B is not the imaginary part of the structure factor of the actual crystal, but that of the basic structure. B has a finite value also above the Curie point, while an imaginary part of the structure factor of the actual crystal disappears above the Curie point as S becomes zero. Measurements of P_s were made from -100°C to the Curie point and values of S have been calculated by Eq. 8 assuming that $S=1$ at -100°C. The result is shown in Fig. 2. $S=0.77$ at about 22°C, and therefore, the room temperature structure is a superposition of 11.5% of one of the basic structure and 88.5% of the other according to Eq. 9.

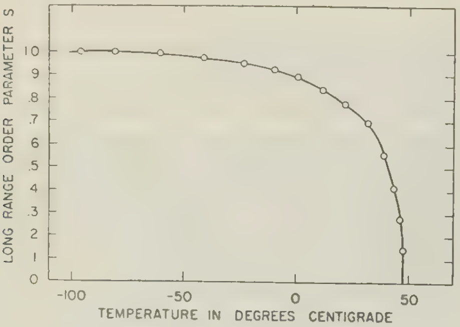

Fig. 2. Long-range order parameter S as a function of temperature. Perfectly ordered structure was assumed and S was put equal to one at -100°C, where $P_S = 3.6$ microcoulombs/cm².

One can easily show that Eq. 11 can be derived also on the assumption that the molecular unit is a statistical unit. In this sense, this equation is free from the assumption made for the derivation described above.

C. *Expression for J_C in terms of pair correlation functions*

A pair correlation function, $g_{ss'}(++)$, is defined as the probability that the sth and the s'th unit cells have positive polarity at the same moment. $g_{ss'}(+-)$, $g_{ss'}(-+)$ and $g_{ss'}(--)$ are defined in analogous ways. Then we have

$$g_{ss'}(++) + g_{ss'}(+-) = x_+ = \tfrac{1}{2}(1+S) \,,$$

$$g_{ss'}(++) + g_{ss'}(-+) = x_+ = \tfrac{1}{2}(1+S) \,,$$

$$g_{ss'}(--) + g_{ss'}(-+) = x_- = \tfrac{1}{2}(1-S) \,,$$

and

$$g_{ss'}(--) + g_{ss'}(+-) = x_- = \tfrac{1}{2}(1-S) \,.$$

For simplicity $g_{ss'}(++)$ will be written as $g_{ss'}$, below. From the above equations we have

$$\left.\begin{aligned} &g_{ss'}(++) \equiv g_{ss'} \,, \\ &g_{ss'}(+-) = \tfrac{1}{2}(1+S) - g_{ss'} \,, \\ &g_{ss'}(-+) = \tfrac{1}{2}(1+S) - g_{ss'} \,, \\ \text{and}\quad & \\ &g_{ss'}(--) = g_{ss'} - S \,. \end{aligned}\right\} \tag{12}$$

$\langle F_{s'}^* F_s \rangle$ and $|\langle F_s \rangle|^2$ are given by

$$\begin{aligned} \langle F_{s'}^* F_s \rangle = {} & g_{ss'}(++)F_+^*F_+ + g_{ss'}(+-)F_+^*F_- \\ & + g_{ss'}(-+)F_-^*F_+ + g_{ss'}(--)F_-^*F_- \end{aligned} \tag{13}$$

and

$$|\langle F_s \rangle|^2 = (x_+ F_+^* + x_- F_-^*)(x_+ F_+ + x_- F_-) \,. \tag{14}$$

Therefore, using Eqs. 2, 9 and 12, we have

$$\langle F_{s'}^* F_s \rangle - |\langle F_s \rangle|^2 = 4\varDelta_{ss'} B^2 \,, \tag{15}$$

where $\varDelta_{ss'}$ is defined by

$$\varDelta_{ss'} \equiv g_{ss'} - \tfrac{1}{4}(1+S)^2 \,. \tag{16}$$

Therefore, J_C given by Eq. 6b becomes

$$J_C = 4B^2 \sum_s \sum_{s'} \varDelta_{ss'} e^{2\pi i (\boldsymbol{H} \cdot \boldsymbol{r}_{ss'})} \,. \tag{17}$$

$g_{ss'}$ has the following tendency:

$$\lim_{r_{ss}\to\infty} g_{ss'} = x_+ x_+ = \tfrac{1}{4}(1+S)^2 \,. \tag{18}$$

Therefore, by Eq. 16, $\lim\limits_{r_{ss'}\to\infty} \varDelta_{ss'} = 0$, and J_C can be written as

$$J_C = 4NvB^2 \sum_s \varDelta_s e^{2\pi i (\boldsymbol{H} \cdot \boldsymbol{r}_s)} \,, \tag{19}$$

where v is the volume of the crystal bathed in the incident X-ray beam, and Δ_s and r_s are $\Delta_{ss'}$ and $r_{ss'}$, respectively, when the origin of the coordinate system is put at the origin of the s'th unit cell. Putting

$$G \equiv J_C/(4NvB^2)\ ,$$

we can rewrite Eq. 19 as

$$G = \sum_s \Delta_s e^{2\pi i(\boldsymbol{H}\cdot\boldsymbol{r}_s)}\ . \qquad (21)$$

$\boldsymbol{H}$ and $\boldsymbol{r}_s$ can be written as

$$\boldsymbol{H} = h\boldsymbol{a}^* + k\boldsymbol{b}^* + l\boldsymbol{c}^* \qquad (22)$$

and

$$\boldsymbol{r}_s = n_1\boldsymbol{a} + n_2\boldsymbol{b} + n_3\boldsymbol{c}\ . \qquad (23)$$

Here $\boldsymbol{a}^*$, $\boldsymbol{b}^*$ and $\boldsymbol{c}^*$ are the reciprocal lattice vectors, $\boldsymbol{a}$, $\boldsymbol{b}$ and $\boldsymbol{c}$ the unit cell vectors, and n_1, n_2 and n_3 are integers. G is a periodic function in the reciprocal space with periods of $h=1$, $k=1$ and $l=1$. By Fourier's theorem, Δ_s is given by

$$\Delta_s = \iiint G e^{-2\pi i(\boldsymbol{H}\cdot\boldsymbol{r}_s)} dh dk dl\ . \qquad (24)$$

Here the integration should be carried out in a unit cell of reciprocal space, say, in the region determined by $m_1 - \frac{1}{2} \leqslant h \leqslant m_1 + \frac{1}{2}$, $m_2 - \frac{1}{2} \leqslant k \leqslant m_2 + \frac{1}{2}$ and $m_3 - \frac{1}{2} \leqslant l \leqslant m_3 + \frac{1}{2}$, where m_1, m_2 and m_3 are integers. It should be noticed that for $\boldsymbol{r}_s = 0$,

$$g_{ss'} = g_{00} = x_+ = \tfrac{1}{2}(1+S)\ , \qquad (25)$$

and

$$\Delta_0 = \tfrac{1}{2}(1+S) - \tfrac{1}{4}(1+S)^2 = \tfrac{1}{4}(1-S^2)\ . \qquad (26)$$

Therefore, Eq. 24 becomes

$$\tfrac{1}{4}(1-S^2) = \iiint G dh dk dl\ . \qquad (27)$$

This relation may be used for the normalization of experimental data, when Δ_s is evaluated experimentally using Eq. 24. The above discussion holds for both the ferroelectric and the paraelectric phases. S should be put equal to zero for the paraelectric phase.

D. *Temperature dependency of J_C*

It is very difficult to predict the temperature dependence of the critical scattering, especially since one does not have any quantitative knowledge about interaction forces between dipoles. If we use the Bragg-Williams approximation (see Sec. 4), however, we have $g_{ss'} = x_+x_+$ except for g_{00} and we may put Δ_s $(s \neq 0)$ equal to zero by Eqs. 9 and 16, and thus Eq. 19 becomes

$$J_C = NvB^2(1-S^2)\ . \qquad (28)$$

Here use was made of Eq. 26. The Curve 1 in Fig. 3 shows values of $J_C/(NvB^2)$ calculated with Eq. 28. The calculation was made using data shown in Fig. 2. A somewhat similar argument has been made for the ferromagnetic case by van Hove[18].

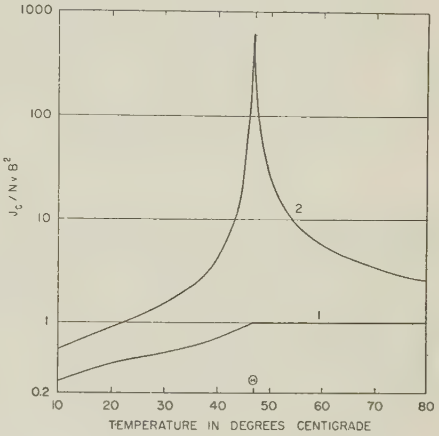

Fig. 3. $J_C/(NvB^2)$ as functions of temperature. The Curve 1 was calculated by Eq. 28, and the Curve 2 by Eq. 33. Experimental observations are expected to be an intermediate of the two curves.

Another approach to this problem may be made by relating the critical scattering to the dielectric constant. Fröhlich[19] developed a general theory of isotropic dielectrics and gave an expression for the dielectric constant in terms of thermal fluctuation of polarization. He considered a macroscopic spherical region of volume V in an infinite homogeneous specimen of which the dielectric constant is ε. The expression he derived is

$$\varepsilon - 1 = \frac{4\pi}{V}\,\frac{\varepsilon}{2\varepsilon+1}\,\frac{\langle M^2\rangle}{kT}\ . \qquad (29)$$

Here k is Boltzmann constant, T temperature in degrees Kelvin, and $\langle M^2\rangle$ the time average of the square of the dipole moment $\boldsymbol{M}$ of the spherical region in the absence of an applied field. The origin of $\boldsymbol{M}$ is in the thermal fluctuation of dipoles. To derive the above equation, however, the specimen was assumed not to have spontaneous polarization, and use was made of the cavity field of isotropic dielectrics. Therefore, the above expression is not directly applicable to TGS. However, the basic idea of Fröhlich's theory can be applied to any dielectric, and below his theory will be applied to our case of TGS with the fictitious assumption that both the ferroelectric and the paraelectric phases are dielectrically isotropic.

To derive an expression for the ferroelectric phase, we consider a single domain crystal of positive polarity, and put the probability that $\boldsymbol{M}$ is in a negative direction equal to zero. Following Fröhlich's procedure and having in mind that $\langle \boldsymbol{M} \rangle$ is not zero in the ferroelectric phase, we obtain the expression,

$$\varepsilon - 1 = \frac{4\pi}{V}\,\frac{3\varepsilon}{2\varepsilon+1}\,\frac{\langle (\boldsymbol{M}-\langle \boldsymbol{M} \rangle)^2 \rangle}{kT}\,. \tag{30}$$

This equation holds for both ferroelectric and paraelectric phases. For the paraelectric phase $\langle \boldsymbol{M} \rangle = 0$, and Eq. 30 is identical with Eq. 29 except for the coefficient 3. This difference comes from the fact that the dipoles can have any direction in Fröhlich's theory while they should be parallel or antiparallel to the b-axis in our model of TGS. If the dipole moment vector of the sth unit cell is denoted as $\boldsymbol{\mu}_s$ and its absolute value as μ_s, naturally μ_s is equal to μ and $\langle \boldsymbol{\mu}_s \rangle$ is a vector parallel to the b-axis with magnitude $S\mu$. Thus, using Eqs. 12 and 16, we have

$$\begin{aligned}
&\langle (\boldsymbol{M}-\langle \boldsymbol{M} \rangle)^2 \rangle \\
&\quad = \Big\langle \sum_s \sum_s (\boldsymbol{\mu}_{s'} - \langle \boldsymbol{\mu}_{s'} \rangle)(\boldsymbol{\mu}_s - \langle \boldsymbol{\mu}_s \rangle) \Big\rangle \\
&\quad = \sum_s \sum_{s'} (\mu_{s'} - S\mu)(\mu_s - S\mu) g_{ss'}(++) \\
&\qquad + (-\mu_{s'} - S\mu)(\mu_s - S\mu) g_{ss'}(+-) \\
&\qquad + (\mu_{s'} - S\mu)(-\mu_s - S\mu) g_{ss'}(-+) \\
&\qquad + (-\mu_{s'} - S\mu)(-\mu_s - S\mu) g_{ss'}(--) \\
&\quad = 4\mu^2 NV \sum_s \Delta_s\,.
\end{aligned}$$

Therefore, for a large value of ε, Eq. 30 becomes

$$\varepsilon \approx \frac{24\pi N\mu^2}{kT} \sum_s \Delta_s\,. \tag{31}$$

If we write G at a lattice point in the reciprocal space as G_0 and put h, k and l equal to integers in Eq. 22, Eq. 21 becomes

$$G_0 = \sum_s \Delta_s\,.$$

Therefore, using Eq. 31, we have

$$G_0 \approx \frac{kT}{24\pi N\mu^2}\,\varepsilon\,. \tag{32}$$

Using Eq. 20, J_C at a lattice point in the reciprocal space is given by

$$J_C \approx \frac{kNvB^2}{6\pi N\mu^2} \cdot \varepsilon T\,. \tag{33}$$

That is, critical scattering at each lattice point in reciprocal space is proportional to εT, and thus should have a distinct peak at the Curie point. The Curve 2 in Fig. 3 shows $J_C/(NvB^2)$ calculated with Eq. 33. The calculation was made by putting ε equal to the dielectric constant measured along the b-axis[4]. N and μ were determined using the known cell dimensions[5], and the spontaneous polarization measured at −100°C (3.6 $\mu Q/\text{cm}^2$); $N = 1/(\text{unit cell volume})$ and $\mu = 3.6/N$ μQ cm. J_C at non-integer values of (kkl) also seem to exhibt a peak at the Curie point, which is an intermediate of the two curves shown in Fig. 3.

§ 3. Experiments

The intensity of diffracted X-rays was measured with a General Electric X-ray unit. CoKα radiation was used with the help of iron filter and a discriminator put in the electronic circuit. An iron filter serves to cut the Kβ radiation and a part of the white radiation with short wavelength. The discriminator sends signals to the scaler only when photons having energy close to that of CoKα radiation come into the counter tube. The applied voltage to excite the CoKα radiation was 45 kv and the current used was 6 ma. A receiving slit with a small pin hole was used for studies of diffuse scattering. Slits wide enough to get proper integrated intensity were used for studies of Bragg reflection. Small cylindrical specimens were used for all experiments.

TGS is a monoclinic crystal and its cell dimensions and monoclinic angle vary with varying temperature due to thermal expansion and to the spontaneous strains. Great care was taken to eliminate the effect of these variations when intensities were measured as function of temperature. The azimuthal and the longitudinal angles of crystal setting were readjusted at each temperature by making the intensity of a Bragg reflection a maximum. The proper angles for the diffuse scattering measurements were determined at each temperature by referring to near-by Bragg points. For example, the diffraction angle for the (0 8.1 0) measurements was determined by referring to the (0 8 0) and (0 10 0) peak positions at each temperature.

In order to check the validity of Eq. 11, several Bragg reflections were measured as functions of temperature. B is zero for $(h0l)$ reflections due to the twofold screw axis existing along the b-axis[17]. Fig. 4 shows temperature dependence of (100), (001) and (004) reflections. These are relatively weak reflections and seem to be free from the extinction effect. Measured intensities were reduced to electron units using calculated F values of Hoshino *et al.*[5] According to Eq. 11, since $B=0$ for these reflections, the curves show the temperature dependence of A^2 of the basic structure. The figure shows that a slight change takes place in A^2, and thus, in the basic structure near the Curie point. However, since (100), (001) and (004) are weak reflections, the curves suggest that the change of the basic structure during the phase transition is very small.

Fig. 5 shows the temperature dependence of Bragg reflections (0 8 0) and (0 6 1). According to Hoshino *et al.*, $A=40.26$ and $B=-19.11$ for (0 8 0), and $A=2.42$ and $B=15.06$ for (0 6 1) in electron units. The dashed curves in the figure show the values calculated using Eq. 11. That calculation was made with the assumption that $\delta=0$ in Eq. 3b, and that A and B are independent of temperature. The first assumption that $\delta=0$ is supported also by the measurement of critical scattering as will be described below. Fig. 4 seems to suggest that the second assumption on the temperature dependence of A and B is not very far from reality.

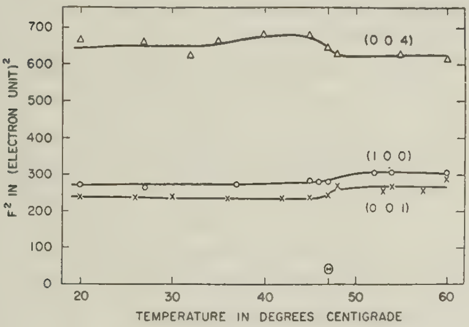

Fig. 4. F^2 of Bragg reflections $(h0l)$ as functions of temperature. Measured integrated intensities were reduced to F^2 by putting their room temperature values equal to F^2 calculated by Hoshino *et al*[5].

The calculated curves agree reasonably well with the observations. The small discrepancy seems to be attributed partly, as has been observed by Lowde in the ferromagnetic case[2], to the fact that the measured intensity of the Bragg reflection includes a contribution from the critical scattering which has a peak at the same place as the Bragg reflection. If the peak height of a proper Bragg reflection is divided by integrated intensity, the quotient is determined only by the divergent angle of the incident X-ray beam and by the mosaic spread of the crystal, and is, therefore, independent of temperature insofar as the mosaic structure remains unchanged*. The peak of diffuse scattering seems to have a flatter shape than that of a Bragg reflection, as seen in other cases.[1),2),20)] Therefore, if the measured Bragg intensity includes a contribution from the diffuse scattering, the above quotient of the measured quantities decreases with increasing contribution from the diffuse scatterings. Fig. 6 shows the peak height of the

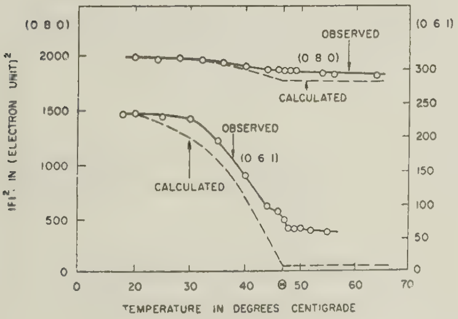

Fig. 5. F^2 of Bragg reflections (080) and (061) as functions of temperature. See the text for the calculated values. Scales of the ordinate were determined so that the room temperature values agree with the square of the structure factor $|F|$ calculated by Hoshino *et al*[5].

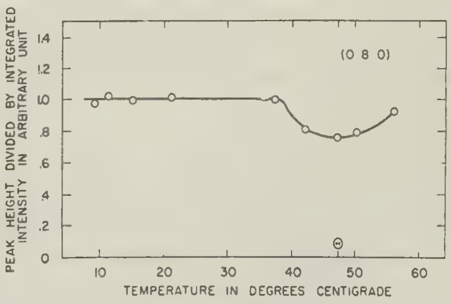

Fig. 6. Temperature dependency of a peak height of (080) Bragg reflection divided by its integrated intensity.

---

* The authors owe this argument to Dr. B. C. Frazer.

(0 8 0) Bragg reflection divided by its integrated intensity as a function of temperature. The curve deviates from a straight line with increasing temperature and reaches its minimum value at the Curie point, suggesting that there is a very definite contribution from the critical scattering to the measured Bragg reflection.

A part of the discrepancy in Fig. 5 could be due to an error in B' of Hoshino *et al.*[5]. They analyzed the crystal structure by putting $S=1$ in Eq. 11, while the actually observed S is 0.77 at room temperature. Therefore, the B' of Hoshino *et al.* could be subject to some errors.

As seen in the curve for (0 6 1) in Fig. 5, the discrepancy between observed and calculated values becomes large at about 30°C. Similar bumps were observed also in some of the other Bragg reflections. At this time no explanation can be presented for these bumps.

The observed total background consists of a critical scattering, thermal diffuse scattering, an incoherent scattering due to the Compton effect, and the natural background counts of the counter tube. We have to subtract the latter three from the observed background, in order to compare the experimental observations with the discussion on the critical scattering given in Sec. 2.

For simple cubic crystals in which lattice points are occupied by identical atoms of scattering factor f_0, the thermal diffuse scattering J_T is given by[21]

$$J_T=|f_0|^2e^{-2M}\sigma ,$$

where M is the Debye-Waller factor and σ is a function of the temperature, of the position vector $\boldsymbol{H}$ in reciprocal space, and of the elastic stiffness c_{ij}. In analogy to this equation, thermal diffuse scattering by TGS is assumed to be expressed by

$$J_T=|F|^2\sigma , \tag{34}$$

where σ is a function of temperature, $\boldsymbol{H}$ and c_{ij} as above, but its functional form must be somewhat different from that in the simple case. The temperature factor e^{-2M} is implicitly included in Eq. 34, since Hoshino *et al.*[5] calculated F by assigning the Debye-Waller factor to each atom.

There are two kinds of elastic stiffnesses, usually written as c_{ij}^E and c_{ij}^D. c_{ij}^E is the elastic stiffness of the electrically shorted crystal and c_{ij}^D is that of the crystal with no electrodes on its surfaces. Some of the c_{ij}^E's could have an anomaly at the Curie point, while there is no reason to expect sharp anomalies in the c_{ij}^D at the Curie point[22]. The crystals used in our measurements had no electrodes on their surfaces. Therefore, the elastic stiffness in our case is c_{ij}^D and we can reasonably assume that σ and thus J_T have no anomaly at the Curie point. This assumption is supported by the experimental observations shown in Figs. 7 and 10, as described below.

$A=B=F=0$ for $(0k0)$ where k is odd, due to the existence of the twofold screw axis[17]. Therefore, $J_B=J_C=J_T=0$ at these points, according to Eqs. 11, 19 and 34, and thus the diffuse background at these points is a sum of an incoherent scattering and the natural background counts. This fact was used to determine the intensity of the incoherent scattering and natural background counts at any (hkl) by assuming that these contributions be the same as for an $(0k0)$ point for which k is odd and which is closest in angle to the relevant (hkl). For instance, J_C+J_T at (0 8±0.1 0) is determined as a total background at (0 8±0.1 0) minus a background at (0 7 0). Here a background at (0 8±0.1 0) means an average value of background at (0 8.1 0) and that at (0 7.9 0). The same notation will be used also for other (hkl)'s below.

Fig. 7 shows diffuse background at $(h0l)$, where B is zero[17] and thus no critical scat-

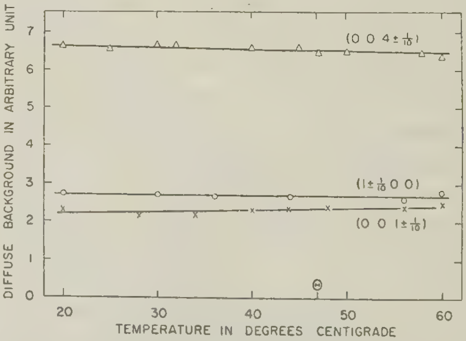

Fig. 7. Temperature dependency of the diffuse background around $(h0l)$. Incoherent scattering and natural background counts have been subtracted and the polarization correction has been made. The plotted values represent the thermal diffuse scattering J_T (see the text).

tering is expected according to Eq. 19. For the data shown in Fig. 7, the incoherent scattering and natural background counts have been already subtracted in the above manner and the polarization correction has been made. Therefore, Fig. 7 shows J_T around (004), (100) and (001). The curves show no anomaly at the Curie point and support our assumption discussed above. Fig. 7 shows also that the J_T around (004), (001) and (100) are almost exactly proportional to F^2 of those Bragg reflections shown in Fig. 4, a fact suggesting that Eq. 34 is not a bad assumption. The agreement of relative intensities at room temperature seems, however, to be too good and probably somewhat accidental, if we consider experimental errors and the H dependence of σ in Eq. 34.

Fig. 8 shows J_C+J_T at (0 8±0.1 0). According to Hoshino *et al.*, $A=40.28$ and $B=-19.11$ for (0 8 0) and the figure shows a peak at the Curie point as discussed in Sec. 2D. In the figure, J_C is separated from J_T by the dashed line, which was drawn using Eqs. 11 and 34 on the assumptions that J_C is negligible at room temperature and that A, B and σ are independent of temperature as suggested by the curves in Figs. 4 and 7.

Fig. 9 shows J_C separated in the above manner for (0 8±0.1 0) and (0 8±0.2 0). The closer to the Bragg reflection (0 8 0), the more pronouced the anomaly.

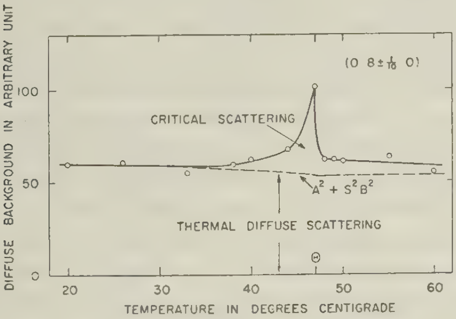

Fig. 8. Temperature dependency of diffuse background at (0 8±0.1 0). Incoherent scattering and natural counts have been subtracted, and the polarization correction has been made. See the text for the separation of the critical scattering from the thermal diffuse scattering.

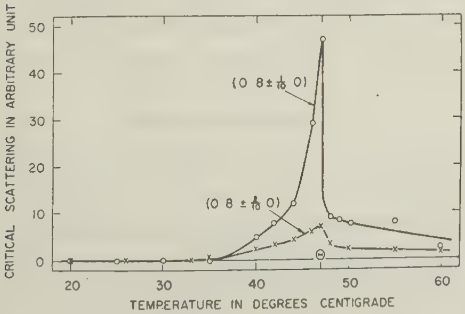

Fig. 9. Critical scatterings at (0 8±0.1 0) and at (0 8±0.2 0) as functions of temperature.

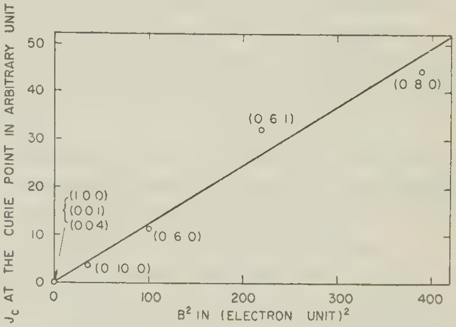

Fig. 10. Relation between the critical scattering J_C at the Curie point and B^2 calculated by Hoshino *et al*[5]. (*hkl*) on the figure shows that the measurements were made at (h k±0.1 l) except for the cases of $B=0$. The data were obtained with the same specimen and measured intensities were corrected by the polarization factor, except for the cases of $B=0$.

Eq. 19 shows that J_C should be proportional to B^2 times a periodic function G in reciprocal space. To examine this relation, J_C was measured at several points corresponding to (h k±0.1 l), where h, k and l are integers, and plotted as a function of B^2 at the (h k l) calculated by Hoshino *et al.*[5] The periodic function G has a period of $h=1$, $k=1$ and $l=1$ and thus should have the same value at the above points. Therefore, the measured values of J_C, for which polarization corrections were made, should be proportional to B^2. Fig. 10 shows that this relation holds at least approximately. Data shown in Fig. 7 for which no anomaly was observed are also added in Fig. 10, though these measurements were not made at (h k±0.1 l). The small disagreements in Fig. 10 seem to be caused by experimental errors which seem to be about 10%, by errors in the background drawn to separate J_C from J_T, by errors in the structure factors of Hoshino *et al.*[5], and by the fact that B^2 at (h k±0.1 l) is slightly different from B at (*hkl*). The proportionality between J_C and B^2 of Hoshino *et al.*[5] shown in Fig. 10 proves that δ is nearly equal to zero in Eqs. 3.

§ 4. Conclusions and Discussions

Our fundamental assumptions for the theoretical treatments given in Sec. 2 were that the phase transition in TGS is of the order-disorder type and that the actual crystal is a statistical mixture of two basic structures. These assumptions led us to the following conclusions: the structure factor F of the actual crystal is given by $\langle F\rangle = A - iSB$ (Eq. 10), the intensity of the critical scattering is expressed by B^2 times a periodic function in reciprocal space (Eq. 19), and that periodic function should have an anomaly at the Curie point as suggested by Eq. 33. Experimental observations described in Sec. 3 agree with these theoretical predictions and prove that the ferroelectric phase transition in TGS is essentially of the order-disorder type.

δ is nearly equal to zero as suggested especially by the relation shown in Fg. 10. From this fact we can decide how much each atom is displaced during a reversal of polarity, referring to the atomic coordinates determined by Hoshino *et al.*[5] For instance, the sulfur atoms do not shift appreciably when the nitrogens of Glycine I (see Fig. 1) move by 0.99 Å along the *b*-axis. Since the sulfur atoms do not move, one can say that the various atoms displace within a framework of sulfur atoms. Existence of such a framework could be a condition for easy domain wall motion, i.e., a condition that a crystal is not simply pyroelectric but also ferroelectric.

Fig. 9 shows that the intensity of critical scattering at (0 8±0.1 0) drops rather abruptly just above the Curie point. This feature appears to be quite different from the ferromagnetic case[2], and to be suggestive of the difference between the interaction forces of ferromagnetic dipoles and those of ferroelectric dipoles. More detailed studies, however, seem to be necessary for definite conclusions.

The curves shown in Fig. 9 are different from Curve 1 of Fig. 3. This fact proves that putting Δ_s $(s\neq 0)$ equal to zero is not a good approximation. This follows, of course, from the Onsager[22], Kirkwood[23], and Fröhlich theories[19]. The approximate theory in which Δ_s $(s\neq 0)$ is put equal to zero is called the Bragg-Williams approximation in the alloy case, the Weiss theory for ferromagnetism, and an internal field theory or a local field theory for ferroelectrics. An internal or local field theory is however, sometimes discussed in connection with the Lorentz-Debye molecular field. The authors used " Bragg-Williams approximation " instead of a " local field theory " in the preceding sections, in order to make it clear that they have no intention to correlate this approximation with the electrostatic molecular field. The electrostatic interaction could make some contribution to the occurrence of ferroelectricity as has been discussed by Pirenne[25] and Devonshire[16]. Probably one can gain more insight into this problem by generalizing Fröhlich's theory[19] to anisotropic dielectrics.

It is interesting to observe that the spontaneous polarization is related to the Bragg reflections by Eqs. 8 and 11, while the dielectric constant is related to the critical scattering at the lattice points of reciprocal space as seen in Eq. 33. These facts imply that studies of weight distribution of critical scattering in reciprocal space can give more detailed information on transition mechanism than the usual dielectric studies. Quantitative information on the anisotropy and nature of the interaction between ferroelectric dipoles are expected to be obtained by evaluation of pair correlation functions, with the help of statistical mechanics. Measurements of diffracted X-rays have to be carried out in wider temperature range than in the present studies for reliable estimation of pair correlation function.

The theory presented in this paper can be applied also to $NaNO_2$. X-ray studies of the phase transition in $NaNO_2$ have been carried out by one of the present authors (I.S.).[27]

Acknowledgements

The authors wish to express their thanks to Professors R. Pepinsky and Y. Okaya for their encouragement during the course of this study. A part of this work was carried out at Brookhaven National Laboratory, Upton, New York, under the auspices of the U.S. Atomic Energy Commission. The authors are much indebted to Dr. B. C. Frazer for his many helpful discussions and his suggestion of the plot in Fig. 6. They are grateful also to Drs. G. J. Dienes and S. Hoshino for their criticism.

References

1) See, for instance, L. Guttman in *Solid State Physics*, edited by F. Seitz and D. Turnbull (Academic Press, Inc., New York, 1956), Vol. 3, p. 146.
2) See, for instance, R. D. Lowde: Rev. Modern Phys. **30** (1958) 69, and A.W. McReynolds and T. Riste: Phys. Rev. **95** (1954) 1161.
3) J. M. Cowley: Phys. Rev. **77** (1949) 669.
4) Hoshino, Mitsui, Jona and Pepinsky: Phys. Rev. **107** (1957) 1255.
5) Hoshino, Okaya and Pepinsky: Phys. Rev. **115** (1959) 323.
6) W. H. Zachariasen: *Theory of X-ray Diffraction in Crystals* (John Wiley and Sons, Inc., London, 1946), Chapter IV, Sec. II.
7) T. Matsubara: X-Rays **5** (1946) 102; **6** (1950) 15.
8) Matthias, Remeika and Miller: Phys. Rev. **104** (1956) 849.
9) For instance, L. Tisza in *Phase Transformation in Solids*, edited by Smoluchowski, Mayer and Weyl (John Wiley and Sons, Inc., New York 1951), p. 1.
10) P. W. Anderson: *Ceramic Age*, Newark, N. J., April, 1951.
11) W. Bantle: Helv. Phys. Acta **15** (1942) 373.
12) W. J. Merz: Phys. Rev. **91** (1953) 513.
13) C. C. Stephenson and J. G. Hooley: J. Amer. Chem. Soc. **66** (1944) 1397.
14) Blattner, Känzig and Merz: Helv. Phys. Acta **22** (1949) 35.
15) Unterleitner, Okaya and Pepinsky (to be published).
16) A. F. Devonshire: Phil. Mag. Suppl. **3** (1954) 85, Section 4.5.
17) *International Tables for the Determination of Crystal Structures* (Cebrüder Bornträger, Berlin 1935).
18) L. Van Hove: Phys. Rev. **93** (1954) 268.
19) H. Fröhlich: *Theory of Dielectrics* (Oxford University Press, London, 1958), Chapter II, §7.
20) See, for instance: R. W. James: *The Optical Principles of the Diffraction of X-Rays* (G. Bell and Sons, Inc., London, 1954), p. 210 for thermal diffuse scattering.
21) See p. 207 of Reference 20.
22) W. P. Mason: *Piezoelectric Crystals and Their Application to Ultrasonics* (D. Van Nostrand Co., Inc., Princeton, N. J., 1950). Especially see p. 129 for rochelle salt, and pp. 152 and 153 for KDP.
23) L. Onsager: J. Amer. Chem. Soc. **58** (1936) 1486.
24) J. G. Kirkwood: J. Chem. Phys. **7** (1939) 911.
25) J. Pirenne: Helv. Phys. Acta **22** (1949) 479.
26) See Section 4.4 of Reference 16.
27) I. Shibuya: J. Phys. Soc. Japan **16** No. 3 490 (1916).

JOURNAL OF THE PHYSICAL SOCIETY OF JAPAN, Vol. 16, No. 3, MARCH, 1961

X-Ray Studies of the Ferroelectric Phase Transition in $NaNo_2$

By Iwao SHIBUYA

The Institute for Solid State Physics, University of Tokyo, Tokyo

(Received October 8, 1960)

Studies of the temperature dependence of Bragg reflections and critical scatterings of X-rays have been carried out for the ferroelectric $NaNO_2$ in a manner analogous to those made by Shibuya and Mitsui for $(glycine)_3 \cdot H_2SO_4$. Experimental observations agree with theoretical predictions which are based on an assumption that the phase transition in $NaNO_2$ is of the order-disorder type. A long-range order parameter and the spontaneous polarization are estimated as functions of temperature by using the temperature variation of Bragg reflections. The observed intensity of the critical scattering drops rather abruptly just above the Curie point in a manner similar to the case of $(glycine)_3 \cdot H_2SO_4$.

§ 1. Introduction

Studies of the temperature dependence of Bragg reflections and critical scatterings of X-rays have been carried out recently by Shibuya and Mitsui[1] for $(glycine)_3H_2SO_4$, TGS, both theoretically and experimentally. The present work on $NaNO_2$ is an extension of their work. As will be described in Sec. 2, the mechanism of the ferroelectric phase transition in $NaNO_2$ seems to have a strong resemblance to that in TGS; therefore, the theory which has been developed for TGS is expected to be applicable also to $NaNO_2$. A brief summary of theoretical assumptions and conclusions will be presented in Sec. 3; experimental results and discussions will be given in Sec. 4.

§ 2. Properties of $NaNO_2$

In 1943, Strijk and MacGillavry[2] found a phase transition in $NaNO_2$ at about 158°C by piezoelectric as well as X-ray studies. The crystal belongs to a pyroelectric class at room temperature[3], while centers of symmetry appear above the transition point[2]. In 1958, Sawada *et al.*[4] found that the pyroelectric phase was also ferroelectric along the *b* axis. (The crystallographic *a*, *b*, and *c* axes adopted by Strijk and MacGillavry[2] will be used throughout the present paper).

Structure analyses have been carried out by several workers for the high[2),5),6] and room-temperature phases[3),7),8),9]. The unit cell has two molecular units, both above and below the Curie point. The space group is *Im2m* at room temperature, and above the Curie point, the crystal gains a mirror plane perpendicular to the *b* axis, centers of symmetry are therefore obtained as in the case of TGS, and the space group becomes *Immm*. Strijk and MacGillavry proposed two models[2] to explain the appearance of mirror symmetry; one is an disordered structure due to large oscillational motions of atoms and the other is a positionally disordered structure. Later, they found that their X-ray data could be explained by the two models almost equally well[5]. The following physical properties of $NaNO_2$, however, suggest that the transition mechanism of this crystal is quite similar to those of TGS and KH_2PO_4, (KDP). The Curie-Weiss constant of $NaNO_2$ is 5000°K[4] compared

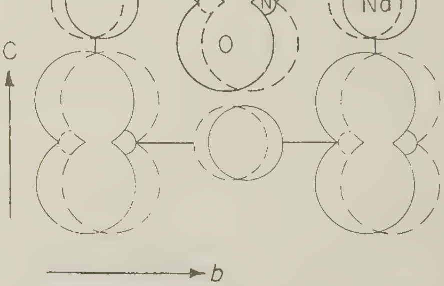

Fig. 1. The unit cell of $NaNO_2$. Atoms depicted by thin lines lie on the $x=0$ plane, and these by thick lines are at $x=1/2$. The solid lines correspond to the positive polarity and the dashed lines to negative polarity, respectively.

to 3280 of TGS[10] and 3260 of KDP[11]; the transition entropy of $NaNO_2$ is 0.7 cal./mol. deg.[4] compared to 0.48 of TGS[10] and 0.47[11] or 0.72[12] of KDP; therefore, the transition in $NaNO_2$ seems to be of the order-disorder type as in the cases of TGS and KDP. (For a detailed discussion, see reference 13).

Fig. 1 shows the unit cell of $NaNO_2$ proposed for the disordered structure by Strijk and MacGillavry[2].

§ 3. Theoretical Assumptions and Conclusions

It is assumed that the Na^+ and NO_2^- ions have two equilibrium positions as shown in Fig. 1. The positions depicted by solid lines will be called a positive position and those by dashed lines a negative position. It will be assumed that at sufficiently low temperature all atoms are in the positive positions in a domain of positive polarity; the corresponding assumption can be made for the case of negative polarity. The probability of finding an atom in the positive position is assumed to be equal to that in the negative position above the Curie point.

This is essentially the same model as is used for TGS, and the conclusions expected from this model are as follows. (See Sec. 2 of reference 1 for the exact definition of quantities and derivation of theoretical conclusions).

If the origin of the unit cell is put at a position where a center of symmetry exists above the Curie point, the structure factor of the unit cell in which all atoms are in the positive positions is given by $A+iB$ and that of the unit cell in which all atoms are in negative positions by $A-iB$. So that the structure factor F of the actual crystal is given, in terms of a long-range order parameter S, by

$$F=A+iSB ,$$

or

$$|F|^2=A^2+S^2B^2 . \qquad (1)$$

The relation holds both above and below the transition temperature.

Another conclusion we can derive from our assumptions (See Sec. 2 D of reference 1.) is that the critical scattering of X-rays should exhibit an anomaly at the Curie point as the dielectric constant does. It can be expected that in $NaNO_2$ the anomaly of critical scattering is observable since the peak height of the dielectric constant of $NaNO_2$ is about 1000, and is comparable to that of about 3000 of TGS.

§ 4. Experimental Results and Discussions

In the case of TGS, we evaluated S as a function of temperature by measuring the spontaneous polarization, and examined the validity of Eq. 1. This procedure can not be used for $NaNO_2$ since the coercive field increases rather rapidly with decreasing temperature. However, it seems certain that S is quite close to unity at room temperature as suggested by the excellent results of the neutron structure analysis of Kay and Frazer[9]; therefore, it is possible to put $F^2=A^2+B^2$ at room temperature according to Eq. 1. By Eq. 1, $F^2=A^2$ above the Curie point where $S=0$. To examine this conclusion, intensities of several Bragg reflections were measured at room temperature and at about 200°C using the usual multiple-film method with CuKα radiation. The crystals used for this experiment were grown from aqueous solution. The intensities were estimated visually by comparison with a standard scale and were corrected for the usual Lorentz and polarization factors. Due to the small liner absorption coefficient and the small radii of the cylindrical specimens (about 0.1 *mm*), no absorption correction was made. Some reflections with strong intensities, *e.g.* (020) and (101), were affected by extinction, and they were corrected for the secondary extinction using the usual formula

$$F_{\text{obs}}^{\text{corrected}}=F_{\text{obs}}\exp(gF_{\text{cal}}^2\,\text{LPF}) ,$$

(All symbols have usual meanings.), with $g=1.32\times10^{-4}$. The results are shown in Table I in comparison with the values of A_c, B_c, and F_c calculated on the basis of Carpenter's results[7]. The values of F_c are those given in Carpenter's paper[7]; A_c and B_c were calculated with his F_c and α_c for the new origin of the unit cell. As has been mentioned in Sec. 3, A and B in Eq. 1 had to be calculated putting the origin of the unit cell at the point where a center of symmetry appears above the Curie point. Carpenter put the origin referring to the position of oxygen atoms[7]. If we use his origin and our unit cell vectors*,

---

* Carpenter's b and c axes must be exchanged to adjust to the notation of the present paper.

Table I.

h	k	l	Room temperature				200°C
			A_c	B_c	$\|F_c\|$	$\|F_0\|$	$\|F_0\|$
0	2	0*	+38.0	+2.8	38.2	37.2	39.3
0	3	1	−4.6	−7.3	8.6	8.9	6.0
0	4	0	+8.5	+2.1	8.8	9.7	8.4
0	5	1	−3.9	−6.7	7.7	8.4	6.0
1	0	1*	+34.5	0.0	34.5	35.2	34.7
1	1	0	+14.5	−7.6	16.2	17.0	13.3
1	2	1	+22.1	+8.7	23.5	19.3	20.7
1	3	0	+1.2	−14.0	14.0	14.2	0.5
1	4	1	−3.6	+1.4	3.9	3.7	4.0
1	5	0	−3.5	−11.0	11.8	11.4	4.9
2	1	1	−2.9	−2.3	3.6	4.4	3.4
2	2	0	+24.3	+2.6	24.5	21.1	20.2
2	3	1	−3.7	−5.4	6.6	7.7	4.2

* Corrections for secondary extinction effect were made for these reflections.

center of symmetry exists at (00.0470) at 200°C according to Strijk and MacGillavry[2]. Therefore, the values of A and B shown in Table I were calculated by putting the origin at the above point. In Table I, A_c, B_c, and F_c are expressed in the electron unit and the scale factors for F_0 were so determined that the following relations hold; $\sum|F_c|=\sum|F_0|$ for the room temperature structure, and $\sum|A_c|=\sum|F_0|$ for the high temperature structure. Table I proves that the relation $|F|^2=A^2$ holds for the high temperature phase at least approximately. The small discrepancy seems to be due partly to the temperature dependence of A. In the Table, one can also see that the large temperature variations of (130) and (150) are explained by their large B values.

Further investigations on the temperature dependence of Bragg reflections were made with another film method. The intensities of the (130), (150), and (200) reflections were recorded at several temperatures on a single film. As seen in Table I, the (130) and (150) reflections have large B values while (200) has zero B value due to the symmetry of the crystal. The obtained photograph again proved the prediction of Eq. 1; drastic intensity changes were observed in the vicinity of the Curie point for (130) and (150), but practically no change for (200).

In order to estimate the long-range order parameter and the temperature dependence of the spontaneous polarization, more accurate measurements of the (130) and (200) reflections were made with a General Electric X-ray unit, XRD-IV. CuKα radiation was used with the help of a nickel filter and a pulse-height discriminator put in the electronic circuit. The applied voltage was 45 KV and the current 15 mA, and a slit wide enough to get proper integrated intensities was used. The crystal was shaped into a small cylinder and rotated around the c axis. A care was taken to eliminate errors in intensity measurements due to the temperature variations of the cell dimensions. Azimuthal and longitudinal angles of the crystal settings were readjusted at each temperature by making the intensity of Bragg reflections maximum. The results obtained are shown in Fig. 2; they prove that the intensity of (130) decreases sharply below the Curie point, while that of (200) is not affected by the phase transition and decreases only slightly and linearly with increasing temperature.

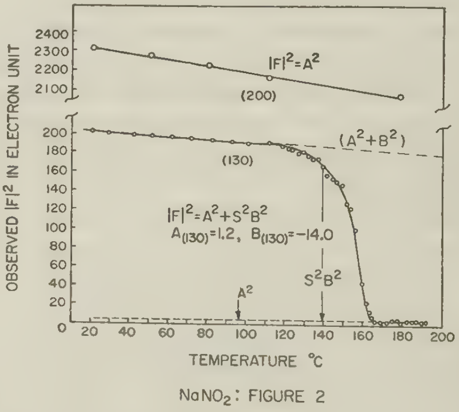

Fig. 2. The temperature dependences of $|F|^2$ of (200) and (130) reflections.

Equation 1 tells us that the long-range order parameter S can be estimated as a function of temperature if the temperature dependence of A and B are known. The $|F_0|^2$ *vs* temperature curve of (130) has a finite tangent at room temperature; this situation could be attributed either to the change of S or changes in A and B; however, an almost strictly linear change of $|F|^2$ from room temperature to about 100°C seems to suggest that the main part of the change is caused by temperature variations of A and B, since S usually has some curvature as a function of temperature when it changes. Therefore, it was assumed that the linear part of the $|F|^2$ *vs* temperature curve and its extrapolation to higher temperature give a temperature dependence of A^2+B^2. $|F|^2$ of (130) is almost constant above 170°C, and it was also assumed that the $|F|^2$*vs* temperature curve in this temperature region and its extrapolation to lower temperature give the temperature dependence of A^2. The extrapolated curves are shown by dashed lines in Fig. 2. The temperature dependence of $|F|^2$ of (200) in Fig. 2 suggests that the above assumptions are not unreasonable. Fig. 3 shows values of S calculated using Eq. 1 and the above assumptions. The transition in $NaNO_2$ is most likely to be of first order[4]; for a first order transition, by its definition, S should change discontinuously as demonstrated by a dashed curve in Fig. 3. (Note that this dashed curve has no quantitative significance.) The discrepancy seems to be attributed to the facts that the measured integrated intensity contained some contributions from the critical scattering as in the case of TGS[1], and also that the temperature was not quite uniform within the crystal during each measurement. The spontaneous polarization P_s is proportional to S as shown by Eq. 8 of reference 1; a scale for P_s is given on the right-hand side of the vertical axis in Fig. 3. This scale was determined using the value of P_s reported by Sawada *et al*[4] (6.4μC/cm² at 143°C). According to Fig. 3, P_s is about 7μC/cm² at room temperature and is consistent with the value obtained by a pyroelectric measurement reported by Nomura[14].

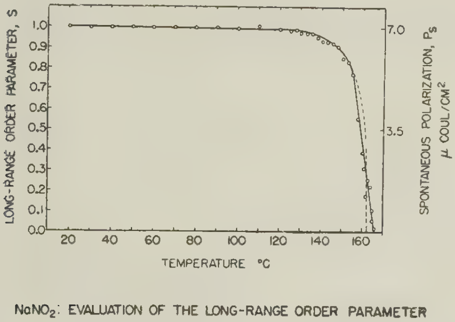

Fig. 3. The long-range order parameter S as a function of temperature (left-hand side of the vertical axis), and the temperature dependence of the spontaneous polarization P_s (right-hand side).

Measurements of the diffuse background were made at $(1-0.02|^{3}+0.05|0)$ and $(1+0.02|3-0.05|0)$ in the same manner as in the case of TGS. Fig. 4 shows the averaged intensities of these two sets of observations.

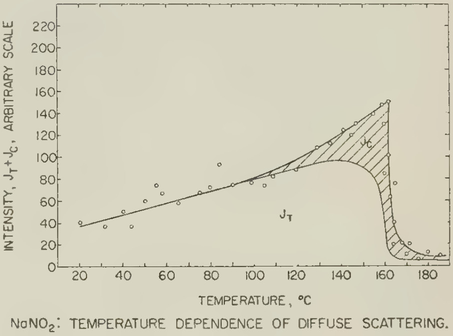

Fig. 4. Temperature dependence of the diffuse background. See the text for the separation of J_C and J_T.

As discussed in Sec. 3, an anomaly was observed at the Curie point. The measured background is a superposition of the critical scattering J_C, the thermal diffuse scattering J_T, incoherent scattering due to the Compton effect, and natural counts of the countertube. To separate J_C from the total diffuse background, the following assumptions were made. (1) The incoherent and natural background is negligible compared to J_C+J_T; the assumption seems reasonable, since the total intensity becomes very weak above the Curie point. (2) The critical scattering J_C is negligible between the room temperature and 100°C. This is consistent with the assumption made in the treatment of Bragg reflections that $S=1$ in the above mentioned temperature range. (3) The expression of J_T, $J_T=|F|^2\sigma$, assumed for TGS (Eq. 34 of reference 1) can be rewritten as

$$J_T=|F|^2(aT+b) .$$

Here $|F|^2$ is given by Eq. 1 and is assumed to depend on the temperature only through S which is shown in Fig. 3. (In other words, for the calculation, the effect of the temperature dependence of A and B were included in $(aT+b)$ and the values of A and B given in Table 1 were put in Eq. 1.) T stands for the temperature, a and b are constants. The values of a and b were estimated by using the curve between 20°C and 100°C, where the backgrounds are equal to J_T according to the assumptions (1) and (2). The separation of J_C and J_T on these assumptions is illustrated in Fig. 4, and thus the separated J_C is shown in Fig. 5 as a function of temperature. These measurements of J_C are only preliminary ones; however, Figs. 4 and 5 show at least that the critical scattering is observable for $NaNO_2$, and it seems also worthwhile to note that J_C dropped abruptly just above the Curie point in Fig. 5 in a manner quite analogous to that of TGS.

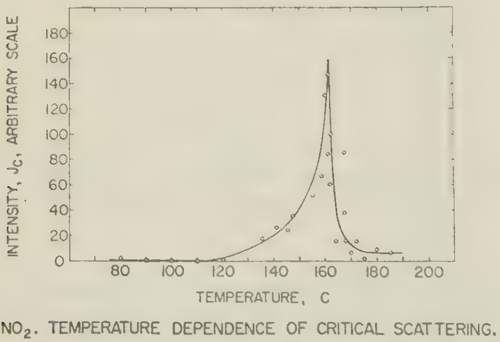

Fig. 5. The critical scattering at (1±0.02|3±0.05|0) as a function of temperature.

In conclusion, it may be stated that the experimental observations agree with the theoretical predictions based on the assumption that the phase transition in $NaNO_2$ is of the order-disorder type. In the case of TGS, it could be said that during a polarization reversal, various atoms displace within a framework of sulfur atoms[1], however, as seen in Fig. 1, there is no such framework in $NaNO_2$, This could be a reason why the coercive field of $NaNO_2$ increases rapidly with decreasing temperature; this feature is quite different from that of TGS.

Fortunately, the structure of $NaNO_2$ is quite simple and there seems to be a good hope of understanding its transition mechanism better than any other ferroelectrics with the order-disorder type phase transition. More detailed studies on the critical scattering is being planned. Estimations of the pair correlation function will be reported in a later paper.

Acknowledgments

A part of the present study was carried out in the Crystal Research Laboratory, Department of Physics, The Pennsylvania State University. The author wishes to thank Professor R. Pepinsky for his generous helps throughout the course of this study. He is particularly indebted to Professor T. Mitsui for his continued guidance in many valuable suggestions and for calling his attention to this problem. He also wishes to express his gratitude to Professor Y. Okaya for his critical reading of the manuscript.

References

1) I. Shibuya and T. Mitsui: J. Phys. Soc. Japan 16, **3** 479 (1961).
2) B. Strijk and C. H. MacGillavry: Rec. trav. chim. **62** 705 (1943).
3) G. E. Ziegler: Phys. Rev. **38** 1040 (1931).
4) S. Sawada, S. Nomura, S. Fujii, and I. Yoshida: Phys. Rev. L. **1** 320 (1958).
5) B. Strijk and C. H. MacGillavry: Rec. trav. chim. **65** 127 (1946).
6) B. C. Frazer, R. Ueda, and M. I. Kay: Paper 15-24 5th International Congress of Crystallography, at Cambridge, England, Aug. 1960.
7) G. B. Carpenter: Acta. Cryst. **5** 132, (1952).
8) M. R. Truter: Acta. Cryst. **7** 73 (1954).
9) M. I. Kay and B. C. Frazer: Acta. Cryst. (1960). (in press)
10) S. Hoshino, T. Mitsui, F. Jona, and R. Pepinsky: Phys. Rev. **107** 1255 (1957).
11) W. Bantle: Helv. Phys. Acta. **15**, 373 (1942).
12) C. C. Stephenson and J. G. Hooley: J. Amer. Chem. Soc. **66**, 1397 (1944).
13) P. W. Anderson: *Ceramic Age*, Newark, N. J., April, 1951.
14) S. Nomura: Butsuri **14** No. 2 (1959).

Journal of the Physical Society of Japan, Vol. 16, No. 3, March, 1961

P_s Function in Electron Diffraction*

By Yoshiro Kainuma
College of General Education, Nagoya University, Nagoya
and William N. Lipscomb**
School of Chemistry, Institute of Technology, University of Minnesota, Minneapolis, Minn.

(Received October 31, 1960)

The property of P_s function in electron diffraction was studied on the basis of the dynamical theory of diffraction. It was proved that P_s function in electron diffraction has the property similar to the P_s function in X-ray diffraction, as expected from pseudo-kinematical theory, i.e. kinematical theory using the complex atomic scattering factor.

§1. Introduction

The aim of the present article is to derive the properties of P_s function in electron diffraction on the firm basis of the dynamical theory of diffraction.

Friedel's law fails to hold in X-ray diffraction by a crystal if the wavelength of the incident X-rays lies in the short wavelength side of the absorption edge of heavy atoms contained in the crystal. Since several years ago many authors applied the failure of the law to the determination of the absolute configuration of atoms in optically active substances. The most direct use of the anomalous dispersion in structure analysis was given by the method of P_s function[1]. The P_s function is a function defined by the substitution of $\sin(2\pi \boldsymbol{h}\cdot\boldsymbol{r})$ for $\exp(2\pi i\boldsymbol{h}\cdot\boldsymbol{r})$ in the ordinary Patterson function. The P_s function gives an antisymmetric configuration of light atoms around heavy atoms. A few years before we tried to study the properties of P_s functions in electron diffraction. In the initial stage of the study it seemed to be promising. The phase shift of the electron wave scattered by heavy atoms was predicted and the complex atomic scattering factor electrons was introduced by Glauber and Schomaker[2] and calculated by Hoerni and Ibers[3]. The phase shift of the scattered electron wave is not an anomalous effect, but occurs generally in the scattering of the wave with any wavelength***. In the application of P_s function in electron diffraction there is no trouble such as selection of an X-ray tube with the target which gives characteristic X-rays with an adequate wavelength. However, we encountered unexpected difficulty that several authors[4,5,6] cast their doubts about the applicabilities of the kinematical theory of diffraction using the complex atomic scattering factors—Hoerni's pseudo-kinematical theory[7]—to crystals. According to them such a theory can be applied only to the diffraction of electrons by gas molecules. Thus only if we construct P_s function using the intensities of reflection calculated on the basis of the dynamical theory of diffraction, the properties of P_s function in electron diffraction can be elucidated.

However, there was another difficulty. According to Miyake, Kohra and Uyeda[8] Friedel's law in electron diffraction fails to hold when the simultaneous reflections by two or more net planes occur in non-centrosymmetric crystals. They had to calculate numerically the solution of the reduced fundamental equations of the dynamical theory taking only three waves into account. At that time there was no well-known method to treat the reflected intensities in many-wave problems in the dynamical theory of electron diffraction.

---

* The main part of this article was read by one of the authors in the seminar on theoretical problems in X-ray and electron diffraction by crystals held at Institute of Solid State Physics, Tokyo University on September 7 to 9, 1959.

** Now at Department of Chemistry, Harvard University, Cambridge, Mass.

*** The phase shift of the scattered electron waves comes from the multiple elastic scattering within a heavy atom. It should be noted that the true counterpart of the anomalous scattering of X-ray in electrons is not the multiple elastic scattering, but the elastic scattering accompanying the virtual transition of electronic state. See (2) of §4 of the present article.

Because the use of P_s function is a positive application of the failure of Friedel's law, we had to face the problem how to obtain the solution of the many-wave problem not numerically, but in an explicit analytical form.

Recently Fujimoto[5] and Niehrs[8] developed Niehrs and Wagner's theory[9] and formulated the dynamical theory by the use of scattering matrix and gave a general method to treat the many-wave problems. At the same time, Fujiwara[10] extended the Artmann's calculation[11] of the wave field within the crystal in the first order Born approximation to higher orders of approximation and derived the results of Cowley-Moodie's formulation[12] of the dynamical theory. The results of the Fujimoto's and Fujiwara's theories are proved to be essentially the same as each other.

These developements of the dynamical theory have enabled us to study the properties of P_s functions of electron diffraction on a firm basis.

§ 2. The Results of Fujimoto's Theory

For the convenience, we refer to the results of Fujimoto's theory. He assumes a thin single crystal, of which surfaces are prependicular to its c-axis. He gave the intensity of reflection, $\boldsymbol{h}=(hko)$, in the power series of the product of thickness of the crystal D and the wavelength of electrons λ as follows:

$$I(\boldsymbol{h})=I_2(\boldsymbol{h})+I_3(\boldsymbol{h})+I_4(\boldsymbol{h})+\cdots\ , \tag{1}$$

where

$$I_2(\boldsymbol{h})=\left(\frac{\lambda D}{4\pi}\right)^2\cdot|v_h|^2\ , \tag{2}$$

$$I_3(\boldsymbol{h})=\left(\frac{\lambda D}{4\pi}\right)^3\cdot\frac{i}{2}\left[v_{-h}\sum_g\sum{}' v_g v_{h-g}-v_h\sum_g\sum{}' v_{-g}v_{g-h}\right]\ , \tag{3}$$

$$\begin{aligned}I_4(\boldsymbol{h})=\left(\frac{\lambda D}{4\pi}\right)^4\cdot\frac{2}{4\,!}\Big[&3\,\Big|\sum_g\sum{}'\,v_g v_{h-g}\Big|^2-4\,|v_h|^2\cdot\mathrm{Re}(v_h{}^2)-8\,|v_h|^2\sum_g\sum{}'\,|v_g|^2\\&-4\,\mathrm{Re}\Big(v_{-h}\sum_g\sum{}'\underset{\neq}{}\sum_l\sum{}' v_g v_{l-g}v_{h-l}\Big)-4\mathrm{Re}\Big(v_{-h}\sum_g\sum{}' p_g v_g v_{h-g}\Big)\Big]\ .\end{aligned} \tag{4}$$

$\boldsymbol{g}=0$ and $\boldsymbol{g}=\boldsymbol{h}$ are excluded from the summation $\sum\limits_g\sum{}'$ in (3) and (4). v_h denotes the Fourier coefficient of the Fourier series:

$$-\frac{8\pi^2 me}{h^2}\cdot V(\boldsymbol{r})=\sum\sum_h\sum v_h\exp(2\pi i\boldsymbol{h}\cdot\boldsymbol{r})\ , \tag{5}$$

where $V(\boldsymbol{r})$ is the electric potential within the crystal. The parameter p_g in the right hand side of (4) has a value depending upon the direction and wavelength of the incident electrons and defined as follows:

$$p_h\equiv p_{(hko)}=-\{(h-\xi)\boldsymbol{a}^*+(k-\eta)\boldsymbol{b}^*\}^2 \tag{6}$$

where $\xi\boldsymbol{a}^*+\eta\boldsymbol{b}^*$ is the component of the wave vector (with the magnitude $1/\lambda$) of the incident electrons parallel to the surface of the crystal.

Fujimoto pointed out that the possibility of the failure of Friedel's law appears first in the term $I_3(\boldsymbol{h})$ of the series (1). We have $I_3(\boldsymbol{h})\neq I_3(-\boldsymbol{h})$ for non-centrosymmetric crystals, while we have always $I_2(\boldsymbol{h})=I_2(-\boldsymbol{h})$ for any kind of crystals.

Integrated intensity of the reflection $\boldsymbol{h}$ can be writtern as

$$J(\boldsymbol{h})=J_2(\boldsymbol{h})+J_3(\boldsymbol{h})+J_4(\boldsymbol{h})+\cdots\ . \tag{9}$$

corresponding to (1). Since there are included no parameters p_h's in the expression of $I_2(\boldsymbol{h})$ and $I_3(\boldsymbol{h})$, we can put

$$J_2(\boldsymbol{h})/I_2(\boldsymbol{h})=J_3(\boldsymbol{h})/I_3(\boldsymbol{h})=K\ , \tag{10}$$

where K is a constant.

§ 3. P_s Function in Electron Diffraction

P_s function in two dimensions can be written as follows:

$$P_s(\boldsymbol{r})=\sum_{h}\sum J(\boldsymbol{h})\sin 2\pi\boldsymbol{h}\cdot\boldsymbol{r} \tag{11}$$

Corresponding to the power series of $J(\boldsymbol{h})$ given in (9), P_s can be expanded as follows:

$$P_s(\boldsymbol{r})=P_{s2}(\boldsymbol{r})+P_{s3}(\boldsymbol{r})+P_{s4}(\boldsymbol{r})+\cdots . \tag{12}$$

From (7) we have always

$$P_{s2}(\boldsymbol{r})=0 . \tag{13}$$

For the calculation of P_{s3} it is convenient to write $I_3(\boldsymbol{h})$ as

$$I_3(\boldsymbol{h})=\left(\frac{\lambda D}{4\pi}\right)\cdot\frac{i}{2}\Big[v_{-h}\sum_{g}\sum v_g v_{h-g}-v_h\sum_{g}\sum v_{-h}v_{g-h}\Big] , \tag{14}$$

where the summation $\sum_{g}\sum$ is over all of g's including $g=o, h$, because we have

$$\left.\begin{aligned} v_{-h}\sum_{g}\sum v_g v_{h-g}&=v_{-h}\sum_{g}\sum{}' v_g v_{h-g}+2v_o\,|\,v_h\,|^2 ,\\ v_h\sum_{g}\sum v_{-g}v_{g-h}&=v_h\sum_{g}\sum{}' v_{-g}v_{g-h}+2v_o\,|\,v_h\,|^2 . \end{aligned}\right\} \tag{15}$$

It is to be noted that even if we use any value of v_o in (15) which is different from v_o defined in (5), we have still (14). In the following it is convenient to select the value of v_o which makes the values of the function

$$U(\boldsymbol{r})=\sum_{h}\sum v_h\exp(2\pi i\boldsymbol{h}\cdot\boldsymbol{r}) \tag{16}$$

vanish at the place far from the projected areas of atoms.

From (16) we have

$$U^2(\boldsymbol{r})=\sum_{h}\sum\Big(\sum_{g}\sum v_g v_{h-g}\Big)\exp(2\pi i\boldsymbol{h}\cdot\boldsymbol{r}) \tag{17}$$

The convolution integral of U and U^2 is given by

$$\begin{aligned}\iint_{S_a} U(\boldsymbol{r})\cdot U^2(\boldsymbol{r}+\boldsymbol{u})d\boldsymbol{r}&=S_a\cdot\sum_{h}\sum v_{-h}\cdot\Big(\sum_{g}\sum v_g v_{h-g}\Big)\exp(2\pi i\boldsymbol{h}\cdot\boldsymbol{u})\\ &=S_a\cdot\sum_{h}\sum v_h\cdot\Big(\sum_{g}\sum v_{-g}v_{g-h}\Big)\exp(-2\pi i\boldsymbol{h}\cdot\boldsymbol{u})\end{aligned} \tag{18}$$

where S_a is the area of the parallelogram with the sides of the unit cell, a_1 and a_2. Similarly the convolution integral of U^2 and U is given by

$$\begin{aligned}\iint_{S_a} U^2(\boldsymbol{r})\cdot U(\boldsymbol{r}+\boldsymbol{u})d\boldsymbol{r}&=S_a\cdot\sum_{h}\sum v_h\Big(\sum_{g}\sum v_{-g}v_{g-h}\Big)\cdot\exp(2\pi i\boldsymbol{h}\cdot\boldsymbol{u})\\ &=S_a\cdot\sum_{h}\sum v_{-h}\Big(\sum_{g}\sum v_g v_{h-g}\Big)\exp(-2\pi i\boldsymbol{h}\cdot\boldsymbol{u})\end{aligned} \tag{19}$$

By the use of (14), (18) and (19) we have

$$\begin{aligned}P_{s3}(\boldsymbol{u})&=\frac{K}{2i}\Big\{\sum_{h}\sum I_3(\boldsymbol{h})\exp(2\pi i\boldsymbol{h}\cdot\boldsymbol{u})-\sum_{h}\sum I_3(\boldsymbol{h})\exp(-2\pi i\boldsymbol{h}\cdot\boldsymbol{u})\Big\}\\ &=K\cdot\left(\frac{\lambda D}{4\pi}\right)^3\cdot\frac{1}{2S_a}\left\{\iint_{S_a} U(\boldsymbol{r})\cdot U^2(\boldsymbol{r}+\boldsymbol{u})d\boldsymbol{r}-\iint_{S_a} U^2(\boldsymbol{r})\cdot U(\boldsymbol{r}+\boldsymbol{u})d\boldsymbol{r}\right\}\end{aligned} \tag{20}$$

If we have a unit cell containing heavy atoms and light atoms, the heavy atoms will appear more emphasized than the light atoms in the function $U^2(\boldsymbol{r})$. Thus the convolution integral

$\iint_{S_a} U(\boldsymbol{r})\cdot U^2(\boldsymbol{r}+\boldsymbol{u})d\boldsymbol{r}$ shows peaks with the positions and weights given in Table I by the help of the same reasoning as given about the weights of the ordinary Patterson peaks[14]. In Table I, w_i^H denotes the weight of the peak of he $U(\boldsymbol{r})$ at the ith heavy atom in the unit cell H_i, i.e. $w_i^H=\iint_{S_a} U_i^H(\boldsymbol{r})d\boldsymbol{r}$, where $U_i^H(\boldsymbol{r})$ is the contribution of the ith heavy atom to the function $U(\boldsymbol{r})$ and the integral is over S_a. $(w^2)_i^H$ denotes the weight of the peak of the function $U^2(\boldsymbol{r})$ at H_i. w_k^L denotes the weight of the function $U(\boldsymbol{r})$ at the kth light atom in the unit cell L_k*. Similarly the convolution integral $\iint_{S_a} U^2(\boldsymbol{r})\cdot U(\boldsymbol{r}+\boldsymbol{u})d\boldsymbol{r}$ shows the peaks given in Table II.

Table I.

Positions	Weights
$\overrightarrow{H_i\ H_j}$	$w_i^H\cdot(w^2)_j^H$
$\overrightarrow{H_j\ H_i}$	$w_j^H\cdot(w^2)_i^H$
$\overrightarrow{L_k\ H_j}$	$w_k^L\cdot(w^2)_j^H$

Table II.

Positions	Weights
$\overrightarrow{H_i\ H_j}$	$(w^2)_i^H\cdot w_j^H$
$\overrightarrow{H_j\ H_i}$	$(w^2)_j^H\cdot w_i^H$
$\overrightarrow{H_j\ L_k}$	$(w^2)_j^H\cdot w_k^L$

Table III.

Positions	Weights
$\overrightarrow{L_k\ H_j}$	$+w_k^L\cdot(w^2)^H$
$\overrightarrow{H_j\ L_k}$	$-w_k^L\cdot(w^2)^H$

Let us assume that there is only one species of heavy atoms in the unit cell. Then, in the difference of the convolution integrals

$$\left\{\iint_{S_a} U(\boldsymbol{r})\cdot U^2(\boldsymbol{r}+\boldsymbol{u})d\boldsymbol{r}-\iint_{S_a} U^2(\boldsymbol{r})\cdot U(\boldsymbol{r}+\boldsymbol{u})d\boldsymbol{r}\right\}$$

the heavy-heavy peaks are cancelled by each other and we have the positive and negative light-heavy peaks given in Table III.

From Table III and (20), it is seen that the function $P_{s3}(\boldsymbol{r})$ gives the relative position of the light atoms to the heavy atoms. Thus the function $P_{s3}(\boldsymbol{r})$ has essentially the same property as P_s function in X-ray diffraction.

Moreover, under the following conditions we have

$$P_s^4(\boldsymbol{r})=0\ . \tag{21}$$

If the incident electrons form a convergent beam with a symmetric distribution of intensity around the normal of the crystal surface, we may aproximate the incident beam by a number of plane waves propagating in various directions. Then we can prove that

$$J_4(\boldsymbol{h})=J_4(-\boldsymbol{h}) \tag{22}$$

by the use (4) and above mentioned symmetrical intensity distribution. Thus we have $P_{s4}(r)=0$.

The same holds also in the case in which the incident beam is a plane wave propagating in a definite direction and the crystal is warped slightly and the average direction of the surface normals is parallel to direction of the incident beam.

Thus we have in these cases

$$P_s(\boldsymbol{r})=P_{s3}(\boldsymbol{r})+P_{s5}(r)+\cdots \tag{23}$$

and we can expect that P_s function has essentially the same property as P_s function in X-ray diffraction if the crystal is thin.

§ 4. Discussions

(1) *Pseudo-kinematical theory and dynamical theory.*

Miyake[4] concluded that the intensity of reflection in the limit $\lambda D\to 0$ does not tend to the pseudo-kinematical theory but to the kinematical theory on the basis of the dynamical theories of Fujimoto and Fujiwara. In the present article we pointed out that P_s function in electron diffraction shows essentially the same property as expected from the pseudo-kinematical theory on the same basis as used by Miyake.

According to Miyake the application of the complex atom scattering amplitude to thin crystal may give nothing but a misleading

---

[*] It should be noted that the value of $U(r)$ is made equal to zero at the places far from the projected areas of atoms by a choice of the adequate value of v_0.

conclusion. However, our present result shows that the use of such a complex atomic scattering factor affords the right clues to the structure of non-centrosymmetric crystals. In our view, Miyake pointed out the negative side of the pseudo-kinematical theory, and we pointed out the opposite positive side of the same theory.

In our view it can be expected that the pseudo-kinematical theory may give a good approximation in the thinnest crystal with a thickness of a unit cell. Our expectation was proved recently by Kainuma and Yoshioka[14], and Hayashi[15].

It should be noted that we tried to find an application of the dynamical theory of Fujimoto and Fujiwara in the initial stage of structure determination and Miyake gave a firm theoretical basis for attaining to higher accuracy in structure determination using the same theory.

(2) *Scattering of electrons accompanying virtual transitions.*

In the present artical we have derived the property of P_s function in electron diffraction by thin crystals taking into account only the existence of many weak reflected-waves on the basis of the dynamical theory of electron diffraction. The result of the calculation in thin crystals has been found essentially the same as expected from the kinematical theory of diffraction using the complex atomic scattering factor due to the multiple elastic scattering within an atom.

However, it should be noted that the true counterpart of the anomalous scattering of X-rays in electrons is not the elastic multiple scattering, but the elastic scattering accompanying the virtual transition of electronic states of the atom, because the anomalous scattering of X-rays accompanies the virtual electronic transitions also.

When atoms compose a crystal, the elastic scattering accompanying the virtual transitions of the electronic states of the crystal and the phonon states of the lattice vibrations can occur. The dynamical theory of diffraction taking into account these virtual transitions have been studied by Yoshioka[16] and Yoshioka and Kainuma[17]. It seems very desirable to study the property of P_s functions taking into account not only the effect of many weak waves but also these virtual transitions. However, it is left still unstudied yet.

(3) *Overlapping of the projections of atoms.*

In § 3 we assumed that the heavy atoms will appear more emphasized than the light atoms in the function $U^2(\boldsymbol{r})$. This assumption was used as the basis of the derivation the property of P_s function.

If the projections of atoms in a unit cell overlap each other, the above assumption cannot be appropriate, because the overlapping light atoms may appear emphasized as well as the heavy atoms in the function $U^2(r)$. Then there will appear the additional positive and negative peaks at the positions from the overlapping light atoms to light atoms and from light atoms to the overlapping light atoms in the two-dimensional P_s function. Thus the overlapping of the projections of atoms will make the two-dimensional P_s function very complicated and diminish the practical merit of the P_s function.

It should be noted that these additional peaks in the P_s function in not expected from the pseudo-kinematical theory. In (1) of this section it was mentioned that in thin crystals pseudo-kinematical theory and dynamical theory of many waves gives essentially the same intensities of reflections. However, the overlapping of the atoms on the projection parallel to the incident beam deteoriates the equivalence of the pseudo-kinematical theory to the dynamical theory even in the thinnest crystal with one molecular thickness. This will be proved also in the forthcoming articles by Kainuma and Yoshioka[14] and Hayashi[15]

(4) *Practical applications of P_s function in electron diffraction.*

We will find several difficulties in the practical use of P_s function in electron diffraction.

The extremely accurate measurement of the reflected intensities is required as it was required for the application of P_s function in X-ray diffraction, because P_s function is estimated from the difference of the reflected intensities, $J(\boldsymbol{h})-J(-\boldsymbol{h})$, as shown in (11)*.

---

* The application of P_s function in electron diffraction will be found only in the analysis of the crystal containing many light atoms for each heavy atom. Cowley[21] concluded that the failure of Friedel's law can be observed in the transmission photograph only by using the specimen of such a crystal. He could not observe the failure of Friedel's law in the transmission through the crystal of basic lead carbonate.

In the present article we have treated P_s function in a two-dimensional projection and the crystal has been assumed to be thin. In many crystals the lattice constant c_0 of the unit is larger than a_0 and b_0, if the crystal has a remarkable crystal habit and it is thin in the direction of c-axis. Then we will have many overlapping peaks in the projection parallel to c-axis.

There is a reason to believe that the property of P_s function does not change essentially even if the crystal is not a thin parallel-sided plate but a small polyhedron. The reason may be found in the implication of Kato's extension[19] of Bethe's dynamical theory[20] to polyhedral crystals. Broadly speaking, the finite areas of the facets of the small crystal cause the diffraction of waves through the apertures with the same shapes and areas as the facets of the crystal. Thus the integrated intensity of reflections by the small crystal connot be very different from that by the thin parallel-sided plate of the same crystal. Although there is still no investigation on the extention of the dynamical theory of many waves to the small polyhedral crystal, the above reasoning will not be far from truth. Thus the property of P_s function will be independent of the external shape of the crystal if the averaged thickness of thin crystal in the direction parallel to the incident beam is the same.

Thus the practical application of P_s function in electron diffraction will be found by the help of the accurate measurement of the reflected intensities by the small polyhedral crystal.

Finally, the authors wish to express their sincere thanks to Professor Ryozi Uyeda for his encouragement during the study.

Our thanks are expressed also to Drs. F. Fujimoto and K. Fujiwara for letting us read their manuscripts of their articles before the publications. The present study was supported partly by the Grant-in-aid for Fundamental Scientific Research from the ministry of education, Japan. The travel grant of Fulbright Commission given to Y. K. and the reasearch fund of the National Science Foundation given to W. N. L. enabled the present study also.

References

1) Y. Okaya, Y. Saito and R. Pepinsky: Phys. Rev., **93** (1955) 1855; R. Pepinsky and Y. Okaya: Proc. Natl. Acad. Sci., **42** (1956) 286.
2) R. Glauber and V. Schomaker: Phys. Rev. **89** (1953) 667.
3) J. A. Hoerni and J. A. Ibers: Phys. Rev. **91** (1953) 1182; J. A. Ibers. and J. A. Hoerni: Acta Cryst. **7** (1954) 405.
4) S. Miyake: J. Phys. Soc. Japan **14** (1959) 1347.
5) F. Fujimoto: J. Phys. Soc. Japan **14** (1959) 1558.
6) J. A. Hoerni: Phys. Rev. **102** (1956) 1534.
7) K. Kohra, R. Uyeda and S. Miyake: Acta Cryst. **3** (1950) 479; K. Kohra: J. Phys. Soc. Japan, **9** (1954) 690.
8) H. Niehrs: Z. Naturforsch. **14a** (1959) 504.
9) H. Niehrs and E. H. Wagner: Z. Phys. **143** (1955) 285.
10) K. Fujiwara: J. Phys. Soc. Japan **14** (1959) 1513.
11) K. Artmann; referred in artical by H. Raether: Handbuch der Physik **32** (1957) 475; Springer-verlag.
12) J. M. Cowley and A. F. Moodie: Acta Cryst. **10** (1957) 609; J. M. Cowley and A. F. Moodie: Proc. Phys. Soc. London **71** (1958) 533.
13) H. Lipson and W. Cochran: The Determination of Crystal Structures (Bell, 1953) 153.
14) Y. Kainuma and H. Yoshioka: To be published.
15) M. Hayashi: J. Phys. Soc. Japan **15**, (1960) 2054.
16) H. Yoshioka: J. Phys. Soc. Japan **12** (1957) 618.
17) H. Yoshioka and Y. Kainuma: To be published.
18) S. Miyake and R. Uyeda: Acta Cryst. **3** (1950) 461.
19) H. Bethe: Ann. Physik **87** (1928) 55.
20) N. Kato: J. Phys. Soc. Japan **7** (1952) 397; **7** (1952) 406.
21) J. M. Cowley: Acta Cryst. **9** (1956) 391.

JOURNAL OF THE PHYSICAL SOCIETY OF JAPAN, Vol. 16, No. 3, MARCH, 1961

Electron Distribution in Cu_2O Crystal

By Tadasu SUZUKI

Institute of Physics, College of General Education, University of Tokyo. Meguro-ku, Komaba, Tokyo

(Received November 5, 1960)

The atomic scattering factor and the electron distribution were studied by X-ray diffractometry in order to know the electronic state of oxygen in crystalline Cu_2O. The intensity measurements were performed within an experimental error of about 1 to 3%. The atomic scattering factor of oxygen was determined referring to the scattering factor of copper, and was compared with theoretical values of O^{2-}, O and O^{2+}. The observed value corresponds best to the scattering factor of O^{2-}. However, a small deviation from the ideally ionic O^{2-} state, for example the state of $O^{1.85-}$, is possible, which may be expected from the positive hole model for Cu_2O crystal. The electron distribution in some special planes of the unit cell of the crystal was determined by three dimensional Fourier synthesis. The electron distributions were found to be almost spherical around each atom except the overlapping of the electron cloud in the region between neighbouring Cu and O atoms.

§1. Introduction

The previous x-ray study of the binding properties of Cu_2O and Ag_2O crystals by the present author[1] has shown that the root-mean-square amplitude of the thermal lattice vibration is 0.26A for Cu_2O and is 0.40A for Ag_2O, the mean lattice strain is 0.15% for Cu_2O and is 1.4% for Ag_2O, and the thermal expansion coefficient of the lattice is $1.9\times10^{-6}/C°$ for Cu_2O. These results suggest that the binding force between the metallic atom and the oxygen atom is much weaker in Ag_2O than in Cu_2O, a result which can not be expected from the purely ionic model for both crystals. Especially, the thermal expansion coefficient of Cu_2O deviates remarkably from Megaw's empirical rule[2] for purely ionic crystals. Furthermore, the nearest Cu-O distance in Cu_2O, 1.85A, is too short to be expected from the ionic radii of O^{2-} and Cu^+, which are known to be 1.36A and 0.96A, respectively.[3]

The purpose of the present work is to study the electron distribution in Cu_2O by x-ray diffractometry in order to know the bonding type of the crystal.

§2. Experimental Conditions

The powder samples used for the intensity measurement were the same as those used in the previous work. The particle size was about one micron as determined microscopically. The purity of the samples was determined to be 98.9% by chemical analysis, and no trace of impurity could be observed in the diffraction patterns. It was shown in the previous work that the lattice constant of the crystal is 4.268±0.001A.

Measurements were performed with a Norelco diffractometer. The x-ray source was a copper target tube operated at 35 kV and 15mA. The scattered intensities were measured by a proportional counter with a nickel filter of 0.013 mm in thickness.

In order to monitor the intensity variation of the incident x-ray beam, an aluminum foil was set up at the another window of the same target tube and the (200) reflection from the foil was observed by a Geiger counter.

§3. Measurements

(1) *Preliminary, Survey*

Preliminarily, integrated intensities were measured on chart with a planimeter. The measurements were repeated twelve times by remounting the samples in each case. The standard deviation of the observed intensities from the mean value of the total measurements was about 2% for the strong reflections and about 9% for the weak ones. It was concluded from this survey that both samples and experimental conditions are satisfactory for precise intensity measurement.

The stepwise- and the continuous-counting methods were compared by measuring the integrated intensities of the two weak reflections, (110) and (331). The fixed count was taken as 10,000 counts and the intensity was measured by scanning stepwise over the diffraction profile with the finest step of 1/100 degree. The continuous counting was performed with the slowest scanning speed, 1/8 degree per minute. The intensities of (110) and (331) obtained by the two methods agree well, as shown in Table I. Therefore, the continuous counting method was adopted for the main measurements in order to survey many specimens.

Table I. A comparison between the fixed counting and the continuous counting. The integrated intensities in counts of (110) and (331) are tabulated.

hkl	fixed counting	continuous counting
(110)	1.657×10^5 counts	1.648×10^5 counts
(331)	1.979×10^5 counts	1.965×10^5 counts

The apparent density of manually packed powder samples, used in the preliminary measurements, was about 2.0 gr/cm³, while the density of the solid Cu_2O is 6.2 gr/cm³. Measurements were performed on specimens having different apparent densities, 3.0~3.4 gr/cm³, which were packed by a hand press machine into a cylindrical specimen holder. The mean value of the observed intensities of these specimens is tabulated in the last column of Table II. No large difference was found among the samples having different densities so far as the relative intensities are concerned.

The effect of extinction was examined by the procedure suggested by Vand.[4] The ratio of the observed intensity, I_0, to the calculated one, I_c, was plotted against the square of the calculated crystal structure factor F_c^2 corrected for the effect of thermal lattice vibration. The structure factor F_c was obtained from the same relation described in § 6 of the previous work. The attenuating factor due to thermal lattice vibration can be expressed by the Debye temperature factor

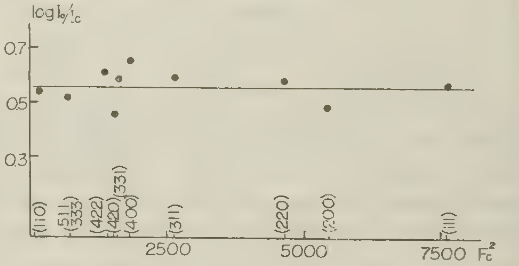

Fig. 1. The logarithmic plot of the ratio I_0 to I_c against to F_c^2. The plots are on a nearly constant line and show that the extinction effects are negligible.

Table II. The main observed intensity with the probable error for the measurements of six times. The third column, *j*, indicates the multiplicity of the reflection by the powder specimen. In the last column, the observed intensity of the pressed specimen is tabulated. The observed intensities were normalized each other to its total sum of all the observed reflections.

hkl	structure factor	*j*	observed intensity (main meas.)	probable error	observed intensity (pressed sample)
110	$2f_0$	12	290	2.3%	287
111	$4f_{Cu}$	8	4820	0.9	4824
200	$4f_{Cu}-2f_0$	6	1664	1.8	1650
211	$2f_0$	24	70	3.0	70
220	$4f_{Cu}+2f_0$	12	1383	1.1	1385
311	$4f_{Cu}$	24	1060	1.1	1066
222	$4f_{Cu}-2f_0$	8	236	3.3	236
400	$4f_{Cu}+2f_0$	6	125	1.1	128
331	$4f_{Cu}$	24	352	1.8	350
420	$4f_{Cu}-2f_0$	24	259	2.3	252
422	$4f_{Cu}+2f_0$	24	343	2.4	338
333 511	$4f_{Cu}$	32	406	2.0	396

M, as $\exp(-2M)$, where M is equal to $B\cdot\sin^2\theta/\lambda^2$, and θ and λ are the Bragg angle and the wave length of the radiation, respectively. B relates to the mean-square amplitude of thermal vibration, $\overline{u^2}$, as $B=8\pi^2\overline{u^2}/3$. An approximate value for B, 1.75A^2, was used, which had been determined in the previous work as an avaraged quantity for copper and oxygen atoms. As is shown in Fig. 1, $\log(I_0/I_c)$ against $F_c{}^2$ is nearly constant within the standard deviation of about 9%, and the extinction effect can be neglected in the present samples.

(2) *Main procedure*

The samples were manually packed into a cylindrical sample holder, which was 20 mm in diameter and 1.5 mm in depth. The sample holder was rotated around its axis one revolution per second in order to avoid the effect of preferred orientation and of surface roughness. The integrated intensity was obtained by subtracting the background counts from the total counts. The half breadths were 0.18 degree for the (110) reflection and 0.5 degree for (333). The background intensity was determined by counting at both tails distant enough from the maximum of the peak, for example 1.5 degrees for (110) and 2.0 degrees for (333). The observed intensities were corrected by monitoring when the variation in intensity of the x-ray out-put exceeded about 1.5% from its mean value. The measurements were repeated six times on remounted samples for each reflection. The standard deviation of the observed values from the mean value was 0.9% for the stronger reflections and about 3% for the weak ones. The obtained integrated intensities were tabulated in Table II with their standard deviations.

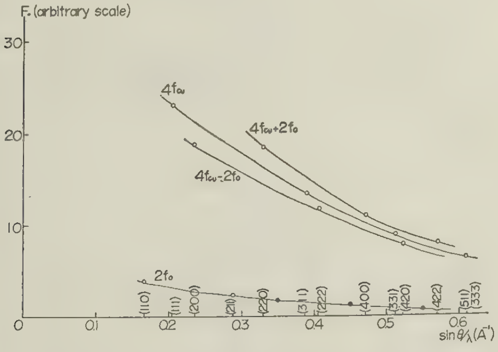

Fig. 2. The crystal structure amplitude F_0 in arbitrary scale, determined from the observed intensity I_0. The open circles are obtained directly from I_0, and the solid circles are deduced from F_0 of the type of $4f_{Cu}\pm2f_0$.

§ 4. Computation Based Upon the Observed Data

(1) *Scattering factors*

The observed structure factor F_0 was determined from I_0 and is shown in Fig. 2. The atomic positions of copper and oxygen in Cu_2O are as follows:

copper: (0, 0, 0,) (0, 1/2, 1/2,) (1/2, 1/2, 0,)
(1/2, 0, 1/2,)
oxygen: (1/4, 1/4, 1/4,) (3/4, 3/4, 3/4,)

and the crystal has cubic symmetry. Therefore, the structure factor for the present crystal consists of the following four combinations of the atomic scattering factors of copper and oxygen: $4f(\text{Cu})$, $2f(\text{O})$ and $4f(\text{Cu})\pm2f(\text{O})$, as is tabulated in the second column of Table II.

The measurements were obtained on a relative scale, and the atomic scattering factor, f, determined from the observed F_0-values must be normalized to the absolute scale. Here, the theoretical value of the atomic scattering factor of oxygen can not be assumed as a standard, since the electron configuration of oxygen atoms in Cu_2O is the present interest and is considered to be quite different according to the models, for example O^{2-} and O^{2+} for the ionic- and the covalent model, respectively. The atomic scattering factor of copper, on the other hand, would be affected not so seriously by its valence electron except in the region of $\sin\theta/\lambda$ smaller than 0.1A^{-1}, because the total electron number of the copper atom is far larger than that of the oxygen atom. The $f_{\text{ob}}(\text{Cu}^+)$ was compared with the theoretical value of the scattering factor $f_{\text{cal}}(\text{Cu}^+)$. The $f_{\text{ob}}(\text{Cu}^+)$ was obtained from F_0-values of (111), (311) and (333)+(511) reflections which were reflected by the atomic plane consisting of copper atoms only.

If the electron distributions around each atom deviate seriously from spherical symmetry, the reflected intensities of (333) and (511) may be different to some extent. The integrated intensities of (333) and (511) were observed to be equal within the experimental error by measurements on single crystals, as will be described in the Appendix. Therefore, the f-values of (333) and (511) were assumed to be equal in the following analysis.

The $f_{\mathrm{cal}}(\mathrm{Cu}^+)$ was taken from the computations of Berghuis et al,[5] and the dispersion effect was corrected by the values of Dauben and Templeton.[6]

The values of $f_{\mathrm{ob}}(\mathrm{Cu}^+)$ and $f_{\mathrm{cal}}(\mathrm{Cu}^+)$ are in the relation

$$f_{\mathrm{ob}}(\mathrm{Cu}^+)=kf_{\mathrm{cal}}(\mathrm{Cu}^+)e^{-M} ,$$

where k is a constant relating to the experimental condition and M is the Debye temperature factor as in §4 (1). Plotting the logarithmic ratio of f_{ob} of f_{cal} against $\sin^2\theta/\lambda^2$ as is shown in Fig. 3, B and k can be determined independently. The scaling constant k was 3.53 and B was 1.40A². The rms amplitude $\sqrt{\overline{u^2}}$ of copper was determined from the value of B to be 0.23 A by the relation described in the last section.

The observed relative f-value of oxygen could now be reduced to the absolute value using the above constant k. The $f_{\mathrm{ob}}(\mathrm{O})$ can be obtained directly from the (110) and (211) reflections and indirectly from structure factors of the type, $4f(\mathrm{Cu})\pm 2f(\mathrm{O})$. The $f_{\mathrm{ob}}(\mathrm{O})$-values are shown in Fig. 4 in absolute scale with the theoretical f-values of O, O^{2-} and O^{2+} computed by Freeman[7] and by the present author.[8] The f-values of the above three electronic states of oxygen differ from one another in the region of $\sin\theta/\lambda$ smaller than about 0.25A⁻¹, since outer electrons contribute mainly to the scattering factor at lower angles. The $f_{\mathrm{ob}}(\mathrm{O})$-value corresponds best to the $f_{\mathrm{cal}}(\mathrm{O}^{2-})$ curve with the appropriate temperature factor for a rms amplitude of 0.29A for oxygen atoms. The $f_{\mathrm{ob}}(\mathrm{O})$ can not be adjusted to the f_{cal}-values of O and O^{2+}, because the normalized f_{ob} is larger than the f_{cal} of O and O^{2+} as seen in Fig. (4).

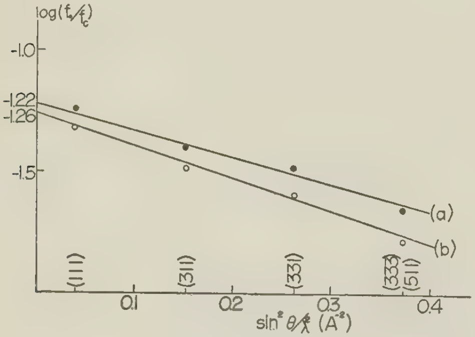

Fig. 3. The plot of $\log(f_0/f_c)$ against to $\sin^2\theta/\lambda^2$. The scaling constant k can be obtained from the section of the $\sin^2\theta/\lambda^2=0$. From the slop of the line, $\overline{u^2}$ can be determined. (a) and (b) refer to the theoretical and experimental f_{Cu}, respectively.

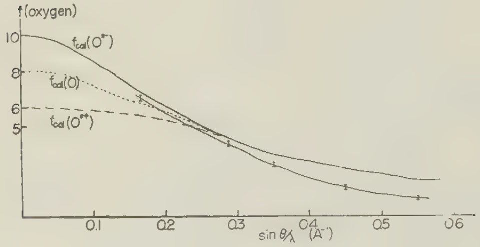

Fig. 4. The calculated scattering factor of oxygen in the O^{2-}, O and O^{2+} state. The observed values are also shown.

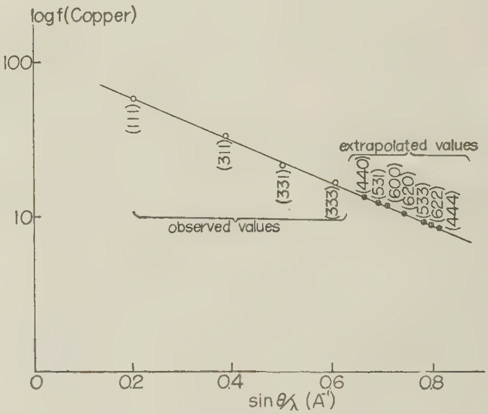

Fig. 5 (a).

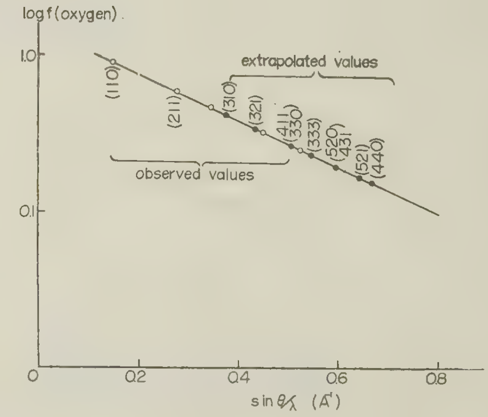

Fig. 5 (b).

Fig. 5. The extrapolation with the exponential approximation of the observed scattering factor to the higher order spectra. (a) for f_{Cu} and (b) for f_{O}.

(2) *Electron distributions*

The electron distributions for the special planes of $(xy0)$, $(xy\frac{1}{4})$ and (xyy) were determined by three dimensional Fourier syntheses. The three dimensional difference Fourier synthesis for the (xyy) plane was also calculated. In order to exclude the termination effect in the synthesis caused by terminating the f_{ob}-values of higher order reflections due to the wave length of the employed radiation, f_{ob}-value was extrapolated after Hartree,[9] to the higher region of $\sin\theta/\lambda$ by an exponential approximation. The logarithmic plot of $f_{\mathrm{ob}}(\mathrm{Cu})$ against $\sin\theta/\lambda$ lies fairly well on a straight line, as shown in Fig. 5(a). The line was extrapolated to about $\sin\theta/\lambda=0.8$, and the f-value of copper was obtained for the reflections from (440) to (444). The f-value of oxygen was also extrapolated by the same method, as is shown in Fig. 5(b). Table III shows the structure factor F_0 of Cu_2O, determined by the observed intensities and the

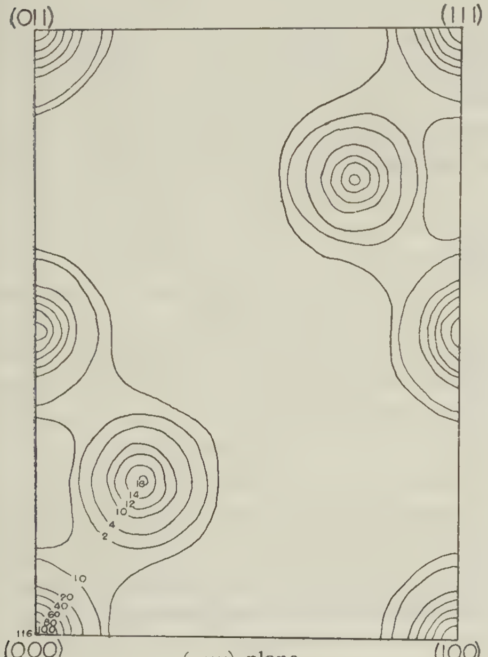

(xyy) plane

Fig. 6(a).

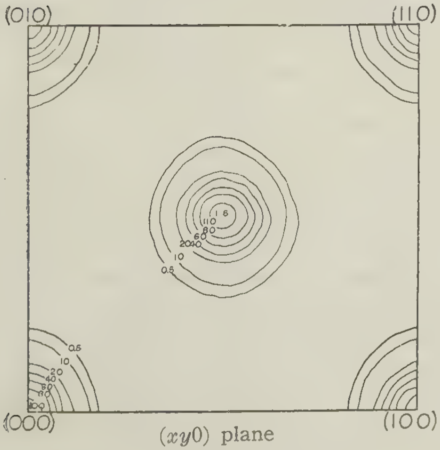

$(xy0)$ plane

Fig. 6(b).

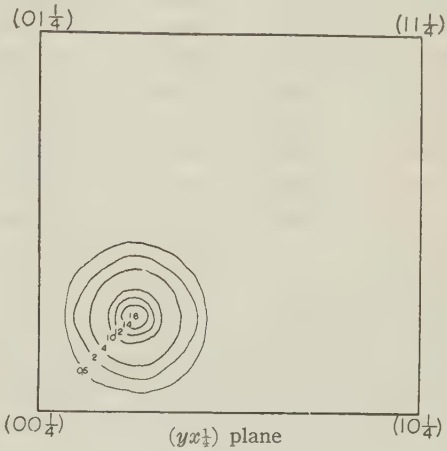

$(yx\frac{1}{4})$ plane

Fig. 6(c).

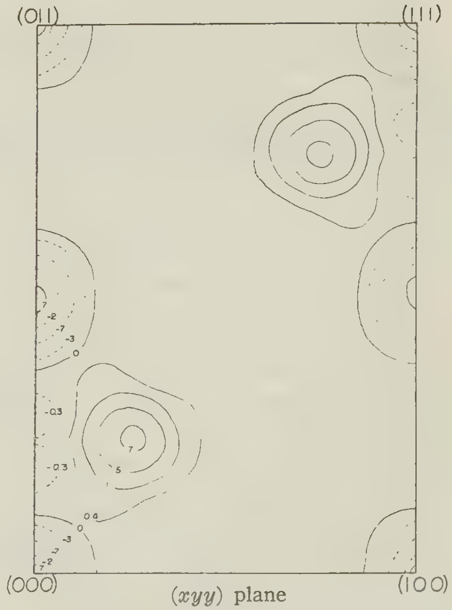

(xyy) plane

Fig. 6(d).

Fig. 6. The electron distributions obtained by the three dimensional Fourier synthesis. (a): (xyy) plane, (b): $(xy0)$ plane, (c): $(xy\frac{1}{4})$ plane. (d): difference Fourier of (xyy) plane.

Table III. The crystal structure amplitude used for the three-dimensional Fourier synthesis. V means the unit cell volum in A^3 unit.

hkl	$8F_0/V$ (A^{-3})	hkl	$8F_0/V$ (A^{-3})
110	−1.34	422	2.85
111	8.35	510	−0.18
200	6.68	431	0.18
211	0.87	511	2.25
220	6.56	333	2.25
310	0.50	521	0.14
311	4.75	440	2.06
222	4.19	531	1.76
321	−0.39	600	1.72
400	3.92	442	1.71
411	−0.28	620	1.50
330	−0.28	533	1.35
331	3.30	622	1.32
420	2.80	444	1.19
332	0.21		

above extrapolations. The values were normalized to the absolute value by comparing the total sum ΣF_{ob} with ΣF_{cal}. The electron distributions obtained are shown in Fig. 6. The calculation was done by the PC–1 computor of the University of Tokyo.

§ 5. Discussion and Conclusion

(1) *The ambiguity of the scattering factor of copper*

The $f_{\mathrm{cal}}(\mathrm{Cu}^+)$ of Berghuis et al, which was taken as a standard for the absolute scale, is based upon the wave function computed with the self-consistent method including the exchange interaction of electrons[10], and is considered to be quite reliable. However, the estimation of the dispersion correction is, in general, not so reliable.

Brindley[11] and Rusterholz[12] determined the absolute $f(\mathrm{Cu}^+)$ experimentally with Cu $K\alpha$ radiation comparing it with the atomic scattering factor of aluminium. The consequence of taking the above experimental $f(\mathrm{Cu}^+)$, instead of the theoretical $f(\mathrm{Cu}^+)$, as an absolute standard must, therefore, be examined. Both $f(\mathrm{Cu}^+)$-values are shown in Fig. 7. The experimental $f(\mathrm{Cu}^+)$-values of Brindley and Rusterholz are smaller than the theoretical value about 1.5 over the whole observed range. However, the scaling constant, k, referred to the different f-values varies not so much, as is shown in Table IV and Fig. 3,

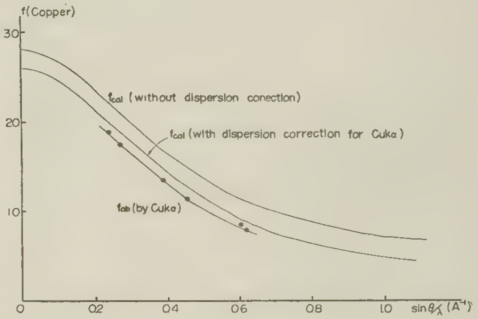

Fig. 7. The scattering factor of copper in absolute scale: without and with the dispersion correction, and the experimental value of Brindley and Rusterholz.

Table IV. (a) The variation of k and $\sqrt{\overline{u^2}}$, and (b) f_{ob}-values for oxygen according to the referred f-value of copper.

	Referred to	
	theoretical vulue	experimental value
k	3.53	3.39
$\sqrt{\overline{u^2}}$	0.23 A	0.21 A

sin θ/λ	hkl	Absolute f_{ob} (0) referred to	
		theoretical value of $f(\mathrm{Cu}^+)$	experimental value of $f(\mathrm{Cu})$
0.16 (A^{-1})	(110)	6.56	6.40
0.28	(211)	4.23	4.07
0.35	interpolated	2.82	2.71
0.45	interpolated	1.59	1.53
0.55	interpolated	1.06	1.02

since there are two adjustable constants k and $\overline{u^2}$. Both the two f_{bo} (oxygen)-values in absolute scale, referred to the different f(Cu), are tabulated in Table IV (b). The difference is appreciable only in the region of smaller $\sin\theta/\lambda$, and is within the experimental error.

(2) *Consideration of the different symmetry for the electron distribution of oxygen*

The f-value of O^{2-}, O and O^{2+}, shown in Fig. 4, were computed with a spherical model for the electron distribution. The electron configuration of O^{2-} is considered to be a neon-like closed shell, and the electron distribution can be safely assumed to be spherically symmetric. However, the electron configuration of O^{2+}, assumed in the co-valent model of Cu_2O, is similar to that of carbon atom in diamond, and the effect of non-sphericity of the electron distribution must be taken into account. McWeeny[13] has computed the scattering factor of a carbon atom in diamond for some particular directions referring to the bonding direction. As can be seen in Fig. 4, the difference between the f-values of the different electron configurations can be recognized only at the (110) reflection in the present case. The scattering direction of the (110) reflection in Cu_2O corresponds to $\hat{S}_3$ of McWeeny's notation. McWeeny's result showed that the f-value of carbon atom in valence- and free-state differs only a little.[*] The difference between the models of spherical and non-spherical electron distribution for O^{2+} may also be assumed to contribute negligibly to the scattering factor. The pure O^{2+} model is, therefore, not adequate for the present case, independently of the difference in symmetry of the electron distribution.

(3) *Electron distribution*

The electron distributions around the copper and oxygen atoms are almost spherically symmetric, as can be seen in the electron density maps of the $(xy0)$ and $(xy\frac{1}{4})$ planes shown in Fig. 6. In the regions between the nearest neighbouring atoms, however, the electron distributions are not zero, but are about 0.5 electrons/A^3, suggesting that the overlapping of the electron distributions of different atoms exists there to some extent.

(4) *Possibility of the deviation from the purely ionic model*

As is discussed in § 5 (2), § 6 (1) and (2), the *purely* co-valent model for the electron configuration of the oxygen atom in Cu_2O is not adequate. Moreover, any model which gives a smaller f-value than f_{ob}(O), can not be adopted. The f_{ob}(O)-value of the (110) reflection lies at about the midpoint between the theoretical f-value of O and O^{2-}. If the electronic state of oxygen atom deviates a little from the purely ionic model, the scattering factor of such an electron configuration might be a little smaller than the f-value of the O^{2-} model and yet larger than f_{ob}(O).

Considering the (100) reflection, the theoretical f(O) value can be brought to fit to the f_{ob}(O)-value with an adequate $\overline{u^2}$. The mean-square amplitude of the thermal lattice vibration of the oxygen atoms was not smaller than that of the copper atoms in the present case, as is described in § 4 (1). So the *possible minimum* f_{cal}(110)-value can be assumed to be 6.65, if the rms amplitude of oxygen atoms is *tentatively* taken as 0.23A, equal to that of copper atoms. The value of 6.65 for f_{cal}(110) corresponds to $O^{1\cdot 85-}$, which is interpolated from the theoretical values of O^{2-} and O.

(5) *Conclusion*

From the above considerations about the atomic scattering factor and the electron distribution, it can be concluded that the oxygen atom in Cu_2O is nearly ionic, but slight deviation from the purely ionic model can not be excluded. The state of $O^{1\cdot 85-}$ is of course an extreme case and the true electronic state of the oxygen atoms in Cu_2O would be between O^{2-} and $O^{1\cdot 85-}$ in its mean value.

The semiconductivity of Cu_2O was investigated by many workers. Dünwald and Wagner[14] studied the electronic conductivity of Cu_2O and concluded that the semiconductivity of Cu_2O should be ascribed to positive holes in the crystal due to excess oxygen atoms. Feldman[15] also supported this result. The comparatively large oxygen ion, however, could not enter interstitially into the crystal. Positive holes of Cu^+ might, therefore, be considered. As a result, one of the O^{2-} ions surrounding the positive hole should be O^{1-} in order to neutralize the electronic charge as a whole. The mean lattice strain of 0.15% in the present sample might be ascribed to the defects of Cu^+, and the possibility of the deviation of oxygen atom from the purely ionic state might correspond to the above consideration.

---

[*] cf. Fig. 4 of McWeeny's paper.[13]

§ 6. Appendix: Measurement on Single Crystals

Measurements on single crystals were performed in order to examine the extinction effect and to obtain the intensity of the (333) and (511) reflection separately, which have the same diffraction angle and can not be separated in the Debye diagram.

Natural single crystals of about 1 mm cube were cracked into small pieces of about 10 ~ 40 microns in diameter. Nearly spherical specimens having about 14, 24 and 48 microns in diameter were selected for the measurement. A small crystal was held by a thin collodion membrane sustained on a small nickel wire ring, and attached on the goniometer head of a Weissenberg camera. A suitable rotation axis, for example, [110] was selected for each specimen, and the sample was oscillated 3 to 4 degrees about the axis through a predetermined scattering angle. The scattered radiation was observed by a scintillation counter instead of photographic films. The collimator for the incident beam was 0.5 mm in diameter and 50 mm in length. The window of the counter was 5mm × 10mm. The counter can be rotated around the sample, having the center of rotation at the sample, so the counter could be always perpendicular to the reflected radiation. The monitoring method was the same as described in § 2 (b). The $K\alpha$ radiations of Mo, Cu, Fe, Co and Cr were used, each with a suitable filter.

An example of the observed integrated intensities was tabulated in Table V(a). Any values which were disturbed by the nickel wire ring were omitted. The variation of the values among the equivalent spectra seems to be due to the absorption effect, since the shape of the samples was not ideally spherical. The observed intensity of the single crystals for various radiations was

Table V (a). An example of the observed intensities of the equivalent reflections from a single crystal. The crystal size was 48 microns in diameter and the radiation of Cu $K\alpha$ was used.

hkl	hkl	$hk\bar{l}$	$\bar{h}\bar{k}l$	$\bar{h}\bar{k}\bar{l}$
111	485	473		
200	328	276		
311	117	121		
222	97	100	109	107
331	158	161	135	132

Table V (b). The observed integrated intensities of single crystals for various radiations. The radius and the diameter of the samples are denoted r and R, respectively.

sample No.	I	II	III				
r in microns	14	24	48				
μR (absorption factor)	0.25	0.50	0.60	0.81	1.24	1.53	2.30
radiation ($K\alpha$)	Cu	Cu	Mo	Cu	Co	Fe	Cr
hkl							
110			37	39	32		
111	1138	835	573	604	479	109	93
200		540	370	382	302	54	53
211				8	8		
220	357	264	226		168	144	57
311		148	164	133	119	104	91
222	100	100	100	100	100	100	100
400			81	96			
331			46	69	147		
422		58	21	82			
511			14	80			
333		60	18	84			

tabulated in Table V(b).

The intensity of (333) is about 5% smaller than that of (511), but the difference is within the range of experimental error, and the intensities of both spectra were assumed to be equal.

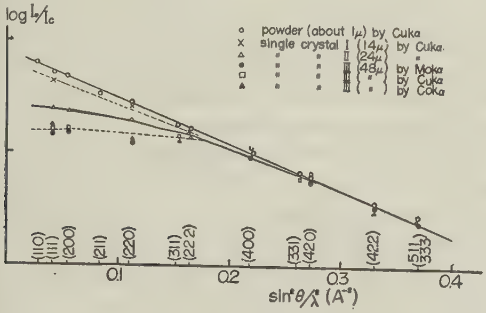

Fig. 8. The plot of log I_0/I_c against to $\sin^2\theta/\lambda^2$. The deviation from the straight line shows the extinction effect.

The logarithms of the ratio of the observed intensity I_0 to the theoretical value I_c were plotted against $\sin^2\theta/\lambda^2$, as shown in Fig. 8. The observed values were corrected with the absorption factor for a spherical crystal according to each μR tabulated in Table V(b). The temperature factor was not included in the theoretical value I_c. The deviation of the plot from a straight line, therefore, implies an extinction effect. It can be concluded that a size of about 15 microns in diameter is not small enough in order to avoid extinction.

Acknowledgement

This work was mainly performed in the Institute for Solid State Physics of the University of Tokyo. The author wishes to express his sincerely thanks to prof. S. Miyake for his kind permission to perform this work in his laboratory. Concerning the use of the PC–1 computor, the author thanks to prof. H. Takahashi, Dr. Marumo and Mr. M. Tokonami.

The author's thanks are due to Mr. T. Sakurai and Mr. S. Togawa for their kind help in the course of the experiment and to profs. S. Miyake, S. Hosoya, Dr. M. Kuriyama and Mr. T. Sakurai for helpful discussions.

This work was partly supported by the Scientific Research Grant of the Ministry of Education.

References

1) T. Suzuki: J. Phys. Soc. Japan (1960).
2) H. D. Megaw: Z. Krist. **100** (1938) 55.
3) L. Pauling: J. Amer. Chem. Soc. **49** (1927) 765.
4) V. Vand: Appl. Phys. **26** (1955) 1191.
5) J. Berghuis et al: Acta Cryst. **8** (1955) 478.
6) C. H. Dauben and D. H. Templeton: Acta Cryst. **8** (1955) 841.
7) A. J- Freeman: Acta Cryst. **12** (1959) 261.
8) T. Suzuki: Acta Cryst. **13** (160) 279.
9) D. R. Hartree and W. Hartree: Proc. Roy. Soc. **A156** 45 (1936).
10) D. R. Hartree and W. Hartree: Proc. Roy. Soc. **A157** (1936) 490.
11) G. W. Brindley and F. W. Ridley: Proc. Phys. Soc. **50** (1938) 96.
12) A. A. Rusterholz: Z. Phys. **82** (1933) 538.
13) McWeeny: Acta Cryst. **7** (1954) 180.
14) H. Dünwald and C. Wagner: Z. Phys. Chem. **322** (1933) 262.
15) W. Feldman: Phys. Rev. **64** (1943) 113.

JOURNAL OF THE PHYSICAL SOCIETY OF JAPAN, Vol. 16, No. 3, MARCH, 1961

A Theory of Electron Impact on Some Polyatomic Molecules

By Tsutomu WATANABE*
Department of Applied Physics, Faculty of Engineering,
University of Tokyo, Tokyo, Japan

(Received January 23, 1960)

A method by which we can get mass spectral pattern of a polyatomic molecule from the data of appearance potentials of various ions and those of optical measurement has been obtained. It is theoretically expected that the total molecular ionization cross section and relative yields of ions do not so much depend on the incident energy, except the low incident energy region, and that the total cross section does not always rise linearly with the increase of incident energy at a threshold.

Applications to CH_4 and CD_4 have been carried out and the results are in plausible agreement with mass-spectroscopic data. In the course of the application, we have taken two ionized states ($^2A_1$, $^2T_2$) into account and have assumed that the potential energy surfaces of ionized states are not so different from that of the ground state of the parent molecule with respect to almost all normal modes except one or two. It is also theoretically expected that we have a larger abundance of parent ion in the CD_4 case than in the CH_4 case by isotope effect. The experimental data shows the tendency predicted by the theory.

§ 1. Introduction

Recently, the experimental researches of electron impact on molecules have drawn much attention not only from the viewpoint of the mass-spectroscopic analysis, but from that of the study of irradiation effects on molecular compounds. It is difficult for us to know immediately the primary processes in which various ions and radicals are produced during irradiation with high energy radiations. It is, however, possible to investigate these processes by means of the electron impact data. These data offer information on what kinds of metastable products are formed under irradiation and how radiation-chemical processes occur. From these data we may gain various informations about, for example, the possibilities of charge transfer, excitation transfer, ion recombination and radical formation. Especially, the relation between appearance potentials of various ion fragments and their relative yields are important for the kinetics of unimolecular decomposition of parent ion into its daughters.

A few theoretical studies on the problem under consideration have been made. Stevenson[1] derived the ratios of H^+/H_2^+ and D^+/D_2^+ theoretically, neglecting the non-orthogonality between the wave functions of H_2 and H_2^+ and applying the Frank-Condon principle. Further, N_2 and CO_2 were treated in the work by Schaeffer[2] who calculated the ratios of N^+/N_2^+ and C^+/CO_2^+, and their isotope effects. In each of these papers, two mechanisms of bond-rupture were considered, that is, (1) the transition to a repulsive electronic level, for instance $^1\Sigma_g^+(H_2)\rightarrow{}^2\Sigma_u^+(H_2^+)$, (2) the transition to an attractive electronic level with nuclear vibrational energy higher than the dissociation energy, for instance $^1\Sigma_g^+(H_2)\rightarrow{}^2\Sigma_g^+(H_2^+)$. The transition probability of (1) was considered to be smaller than that of (2) because of the approximate similarity of the ground state wave function H_2^+ to one electron MO function of the ground state of H_2. The method of treatment adopted by Stevenson as well as by Schaeffer is not ambiguous in principle for the present problem, but unfortunately it is hardly applicable to the problems involving polyatomic molecules. The difficulties in the case of polyatomic molecules are from (1) the lack of sufficient information on their electronic levels as well as on their wave functions, (2) the occurrence of multi-fold integrals in the calculation of relative yields of various ions, and from (3) the ignorance of the potential energy surfaces in ionized states.

---

* Present address: Japan Atomic Energy Research Institute, Tōkai-Mura, Ibaraki, Japan.

However, there are other approaches to the polyatomic cases. Lennard-Jones and Hall[3] estimated the probability of ionization of each bond in *n*-octane by applying the equivalent orbital method. In a strict sence the assumption adopted in their calculation does not generally correspond to the probability of bond rupture by ionization. To obtain it, one must take into account the potential energy surface in ionized state. Rosenstock *et al*[4] studied the spectrum of various ions produced from C_3H_8. They assumed that an electron in each of the levels is ionized with equal probability and the excess electronic energy is imparted to the ion at the time of electron impact and converted into vibration energy through radiationless transitions. These vibrationally excited parent ions decompose adiabatically by competing and successive unimolecular processes. The statistical assumption is essential in the work by Rosenstock *et al*, and is useful for large molecules. There seems, however, to be an ambiguity in the choice of the parameters appearing in the treatment through the work. In almost all the previous works, it was assumed *a priori* that either only one electronic level needed to be taken into account, or, the cross sections of transition to various ionized electronic levels were equal to one another.

In this paper, firstly, the information on the electronic levels and on their wave functions of molecules is obtained by the equivalent orbital method. Secondly, the general formulation of the calculation for each ion abundance is deduced and the dependence of mass spectrum on incident energy is discussed. Finally, applications to CH_4 and CD_4 are carried out as examples.

The following assumptions and treatments have been made in the course of this work:-

(1) The ionization cross section of molecules is assumed to be expressible in terms of its atomic contributions.

(2) The ionization is always considered to occur vertically upward so as to satisfy the Franck-Condon principle.

(3) The various electronic levels of the parent ion are taken into account.

(4) The dissociation of the parent ion occurs along the path on the potential energy surface in the direction in which the entropy due to the motion of nuclear system increases most rapidly.

§ 2. Theoretical Formulation and General Properties of Molecular Ionization Cross Section

When a polyatomic molecule is impacted and is ionized by electron beams with a wave number k_0, the parent ion dissociates into several daughter ions or ion fragments by unimolecular reaction processes. The parent ion is produced in a considerably higher excited state of nuclear vibration by vertical transition. If electronic levels of the molecule under consideration are well separated, the amount of kinetic energy transferred to nuclear vibration is determined both by nuclear configuration of the ground state and by the potential energy surface of the ionized state. The parent ion will remain stable when the amount of the gained kinetic energy is smaller than the dissociation energy of molecular ion in this state. The ion fragment which appears next to the stable parent ion is produced in the case when ionization energy falls into the value between the appearance potential of this ion fragment and the next higher one, as well as in the case when ionization energy is over the next higher appearance potential and the parent ion decomposes into various ions by competing processes which occur in proportion to the change of internal degree of freedom multiplied by the symmetry number of the path of decomposition from the parent ion to its fragments. Other ion fragments are also produced by the same way. As mass spectra are measured about 10^{-5} sec after the time of electron impact, the nuclear motion with period $\sim 10^{-12}$ sec is well considered to be in a thermal equilibrium.

We assume that a cross section of an electron in a molecular orbital (MO) Q is expressed in terms of atomic cross section of rth atomic orbital (AO) Q_r as

$$Q = A \sum_r a_r^2 \cdot Q_r \tag{2.1}$$

where A is a proportional constant of molecular cross section to atomic one, and a_r is the coefficient of rth AO in MO under consideration[5]. The ionization cross section of an AO which has Z_r electrons with ionization potential E is expressed by Bethe[6] as

Table I[6]. Values of c_m for various electronic states.

Shell	$1s$	$2s$	$2p$	$3s$	$3p$	$3d$	$4s$	$4p$	$4d$
c_m	0.28	0.21	0.13	0.17	0.14	0.07	0.15	0.13	0.09

$$\left.\begin{aligned} Q&=\frac{2\pi me^4c_rZ_r}{\hbar^2k_0{}^2E}\log\left(\frac{2\hbar^2k_0{}^2}{\alpha mE}\right) \\ \text{and}\qquad & \\ c_r&=\frac{Z^2_{\text{eff}}}{n^2a_0{}^2}\iint\psi_r x\psi_\kappa d\tau d\kappa\ . \end{aligned}\right\} \qquad (2.1')$$

Here c_r is calculated by Bethe[6] as shown in Table I where α is a parameter of the order of unity, and meaning of the other quantities are as usual. In the incident energy region $E_0 \leq (\hbar^2/2m)k_0{}^2 \leq 200\,\text{eV}$ where E_0 is the appearance potential of the parent ion (*i.e.* between the value of incident energy corresponding to $Q_r=0$ and that neighbourhood of the maximum of Q_r), Q_r shows fairly good agreement with experiment with the choice of $\alpha=4$. Therefore we take 4 as the value of α.

Let us consider a molecule of which q_i is the ith normal coordinate of nuclear motion (an equilibrium point in the ground state is at the origin of every coordinate, *i.e.* at every $q_i=0$), q_{i0} is the coordinate of an equilibrium point in an ionized state, and λ_i is the force constant of nuclear vibration in the ionized state. The ionization potential of the molecule changes as a function of the nuclear configuration with the energy interval between the ground state and the potential surface of ionized state as

$$E=E_0+\sum_{i=1}^{n}(\lambda_i/2)(q_i-q_{i0})^2 \qquad (2.2)$$

where n is the number of degrees of internal freedom.

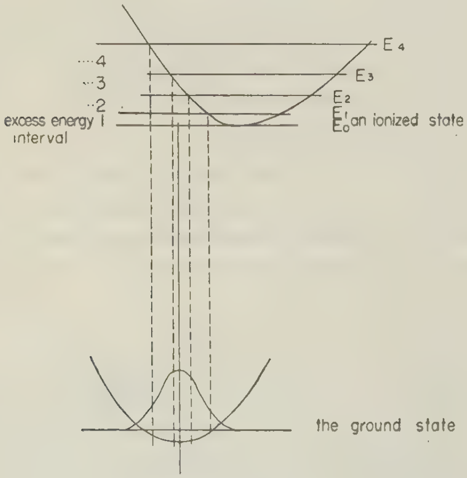

Fig. 1. Schematic figure of the Franck-Condon transion.

The cross sections for the ionizations into the parent ions which have excess energies between E_{l-1} and E_l are determined by the ionization cross section of the molecule not involving the effect of nuclear motion $Q(E)$ and by the ground state probability density $|\Psi_N(q_1, q_2, \cdots, q_{3N})|^2$ of nuclei at any configuration q_i or x_i, y_i, z_i which makes possible the transition into the energy interval $E_0+E_{l-1} \leq E \leq E_0+E_l$ by vertical transition where x_i, y_i, z_i are the Cartesian coordinates and N is the number of nuclei in the molecule. Thus the cross section for the parent ion with excess energy interval between E_{l+1} and E_l $P(E_l, E_{l-1})$ may be given in the form

$$\begin{aligned} P(E_l, E_{l-1})&=\int|\Psi_N|^2Q(E)\prod_{i=1}^{N}dx_idy_idz_i \\ P(E_l, E_{l-1})&=P(E_l, 0)-P(E_{l-1}, 0)\ . \end{aligned} \qquad (2.3)$$

The integration should be made over the whole region of x_i, y_i and z_i of which the nuclear configuration makes possible the transition into the energy interval $E_{l-1}+E_0 \leq E \leq E_l+E_0$, because an ionization energy is a function of x_i, y_i and z_i ($i=1, 2, \cdots, 3N$). We have also the cross section for the total ionization involving the effect of nuclear motion

$$P(\infty, 0)=\int|\Psi_N|^2Q(E)\prod_{i=1}^{N}dx_idy_idz_i \qquad (2.3')$$

where the integration should be made over the whole region of x_i, y_i and z_i. The parent ion with excess internal energy $E-E_0$ ($E_l \leq E-E_0 \leq E_{l+1}$) is considered to decompose into various sets of daughter ions and radical fragments so as to satisfy the condition of energy conservation through the decomposition process. The yield of each set of ion and radical fragments may be in proportion to the number of reaction coordinates along the paths of decomposition from the parent ion into its fragments. The number of reaction coordinates is assumed to be given by $\sigma_\nu(n-n_\nu-\sum_\mu n_\mu)_l$ where n_ν is the degree of internal freedom of an ion fragment ν, n_μ is that of radical fragment μ, and σ_ν is the symmetry number of decomposition. Thus, the sets may be produced in porportion to the ratio of $\sigma_\nu(n-n_\nu-\sum_\mu n_\mu)_l$ to its sum over all sets of ν for lth energy internal. Then the relative aboundance of various ion fragment F_ν's is expressed in the form

$$F_\nu=\sum_l \frac{\sigma_\nu(n-n_\nu-\sum_\mu n_\mu)_l}{\sum_\nu \sigma_\nu(n-n_\nu-\sum_\mu n_\mu)_l}\,\frac{P(E_l, E_{l-1})}{P(\infty, 0)} \tag{2.4}$$

where the sum over the excess energy interval l should be taken for all the cases when the decomposition into the ion fragment ν is considered energetically possible[*].

To carry out the integration in (2.3) we introduce new coordinates, namely $X_i=x_i/(m_i)^{1/2}$, $Y_i=y_i/(m_i)^{1/2}$, $Z_i/=z_i/(m_i)^{1/2}$ where m_i is the mass of ith atom.

We can transform the above coordinates to the normal coordinates by a unitary transformation and can separate the coordinates of translation and rotation of the molecules as a whole from the remaining internal coordinates. The Jacobian of transformation X_i, Y_i, Z_i to q_i is 1 because of its unitarity. Then we have

$$P(E_l, 0)=\prod_{i=1}^{N} \sqrt{m_i}^3 \int\cdots\int |\psi_N(q_{n+1}, \cdots, q_{3N})|^2 \prod_{j=n+1}^{3N} dq_j$$
$$\times\int\cdots\int_{E=0}^{E=E_l} |\psi_N(q_1, q_2, \cdots, q_n)|^2 Q(E) \prod_{i=1}^{n} dq_i \tag{2.5}$$

where $n=3N-6$ for nonlinear molecules, and $n=3N-5$ for linear molecules. We see by (2.5) that the absolute $P(E_l, 0)$ can depend on the states of molecular translation and rotation and therefore on experimental conditions. However the ratio of $P(E_l, 0)/P(\infty, 0)$ does not depend on these conditions. At room temperature we may consider that all the vibrational modes are in the ground states, so that ψ_N is expressed as follows:

$$\psi_N(q_i)=\prod_{i=1}^{n}\frac{1}{N^2}\exp\left(-\sum\frac{\alpha_i}{2}q_i^2\right) \qquad \text{for} \quad 1\leq i\leq n$$
$$\alpha_i=\nu_i/h \qquad N=\sqrt{\frac{\alpha_i}{\sqrt{\pi}}} \tag{2.6}$$

and

$$\psi_N(q_j)=(\text{rotational wave function})\times(\text{translational wave function}) \qquad \text{for} \quad n+1\leq j\leq 3N$$

where ν_i is the frequency of each normal vibrations of nuclei which is obtained from the

---

[*] To illustrate the matter more clearly, we take the case of CH_4^+ as example. According to the experimental data we separate the excess energies into the following intervals $E_0=13.12$ eV, $E_1=1.27$ eV and $E_2=2.28$ eV for ${}^2T_2$ state, and $E_0=19.42$ eV, $E_1=0.68$ eV, $E_2=3.68$ eV and $E_3=7.38$ eV for ${}^2A_1$ state (see Fig. 5a and 5b). Consider the case when $l=2$ for ${}^2T_2$ state, *i.e.* when the parent ion gains its excess internal energy between 1.27 and 2.28 eV, and two ways of decomposition $CH_4 \rightarrow CH_3+H$ and $\rightarrow CH_2+H_2$ are considered to be energetically possible. In the former reaction $n=9$, $n_\nu=6$, $n_\mu=0$ and $\sigma_\nu={}_4C_1$ because σ_ν is the number of ways of choosing one H atom from CH_4^+. In the latter reaction $n_\nu=3$, $n_\mu=1$ and $\sigma_\nu={}_4C_2$,. *ie.* the number of ways of choosing two H atoms from CH_4^+. In this case $\sum_\nu \sigma_\nu(n-n_\nu-\sum_\mu n_\mu)_2=42$ and $\sigma_\nu(n-n_\nu-\sum_\mu n_\mu)_2=12$ for $CH_3^+ + H$, and $=30$ for CH_2+H_2. In order to obtain the relative yield of CH_2^+ from CH_4^+ parent ion with every excess internal energy, one should take account of the two reactions of decomposition $CH_4^+ \rightarrow CH_2^+ + H_2$ and $CH_2^+ \rightarrow 2H^+$. In the former reaction $l=3$ for ${}^2T_2$ state and $l=1, 2, 3, 4$ for ${}^2A_1$ state should be taken into account (see Fig. 5b). For each energy interval between 1 and $l-1$ the quantity

$$\frac{\sigma_\nu(n-n_\nu-\sum_\mu n_\mu)_l}{\sum_\nu \sigma_\nu(n-n_\nu-\sum_\mu n_\mu)_l}\,\frac{P(E_l, E_{l-1})}{P(\infty, 0)}$$

is estimated, one take the sum of it over l and then one can obtain the relative yield of CH_2^+ fragment.

data of Raman and infra-red spectra.

The information about potential surfaces of ionized states has not been obtained experimentally, in most cases, so we do not know the values of λ_i and q_{i0}. But it may properly be said that for the molecule of which the data of Raman and infra-red spectra are well explained by the calculation based on the valence force field picture, the vibrations of nuclei are mainly determined by the valence forces and are almost independent of the contributions of the repulsive interactions between cores which are not directly bonded by chemical valences with each other. The potential energy surface of an ionized state may be obtained by the same procedure as in the case of the ground state, and the change by ionization in the valence force between every couple of atoms is considered to resemble to the case of diatomic molecules.

In some diatomic molecules there are not so large change in the vibrational frequencies and in the internuclear distances by ionization of an electron in a nonbonding orbital, as illustrated in Table II[7]. We assume that the frequencies and the internuclear distances are approximately the same with those of the ground state for almost all the vibrational modes if measured data of vibrational frequencies can be well explained by the calculation based on the valence force field picture. We take the changes of vibrational frequencies and equilibrium points into account only of the modes which may be very different from those of the ground state from the viewpoint of the symmetry of total electronic wave function in the ionized state. The effect of these changes may be important in the case of a molecule in which the stable atomic configuration in the ionized state is quite different from that of the ground state (for example, NH_3 and H_2O).

Table II[7]. Vibration frequencies and internuclear distances of diatomic molecules and molecular ions.

Molecule	Distance (in Å)	Frequency (in cm⁻¹)	Ion	Distance (in Å)	Frequency (in cm⁻¹)
AlH	1.6459	1682.57	AlH^+	1.601	1610
As_2		429.44	As_2^+		318.8
BeH	1.3431	2058.6	BeH^+	1.3121	2221.7
BeD	1.3425		BeD^+	1.3113	
BH	1.2325	2366	BH^+	1.2146	2435
CaH	2.0020	1299	CaH^+	1.733	
CdH	1.761	1430	CdH^+	1.667	1775
CdD	1.748		CdD^+	1.664	
CH	1.1198	2861	CH^+	1.1308	2739
Cl_2^{35}	1.988	564.9	$(Cl_2^{35})^+$	1.891	645.3
CO	1.1281	2170	CO^+	1.1150	2214
CuH	1.463	1940	CuH^+	2.27	1870
H_2	0.7416	4395	H_2^+	1.06	2297
HBr	1.413	2649	HBr^+	1.459	
HCl^{35}	1.2764	2989.7	$(HCl^{35})^+$	1.3153	2675
DCl^{35}	1.2749	2090	$(DCl^{35})^+$	1.3153	1863

We now rewrite (2.5) with the aid of (2.6) as

$$P(E_i, 0)=B\int_{E-E_0}^{E-E_0+E_i} \exp\left(-\sum_{i=1}^{n} \alpha_i q_i^2\right) Q\left(E_0+\sum_{i=1}^{n} \frac{\lambda_i}{2} q_i^2\right) \prod_{i=1}^{n} dq_i$$

$$B=\left(\prod_{i=1}^{n} \sqrt{m_i^3}\right)\left(\prod_{i=1}^{N} \sqrt{\frac{\alpha_i}{\sqrt{\pi}}}\right)\int\cdots\int |\text{rot. wave function}|^2 \qquad (2.7)$$

$$\times\, |\text{trans. wave function}|^2 \times \prod_{j=n+1}^{3N} dq_i\,.$$

Here we have neglected the change in the equilibrium configuration by ionization, *i.e.* we have assumed $q_{i0}=0$ for all i. Let the variable ξ_i be taken in the place of q_i, namely

$$\xi_i=\left(\frac{\lambda_i}{2E_l}\right)q_i^2\,,\quad \beta_i=\beta_0-\frac{2E_l}{\lambda_i}\,,\quad \beta_0=\frac{1}{n}\left(\sum_{i=1}^{n}\frac{2E_l}{\lambda_i}\alpha_i\right),\quad \lambda_i=4\pi^2\nu_i^2\,. \tag{2.8}$$

The function $\exp(\sum_i \beta_i\xi_i)$ is expanded in power series ξ_i and the integration in (2.7) is to be carried out over any value of ξ_i under the condition of $\sum_{i=1}^{n}\beta_i\leq 1$.

The integration in (2.7) can be reduced to a single integral by means of the Dirichlet's integral[8]. In order to make the expression of the result of integration not depend on E_l, we may rewrite the result in terms of y instead of ξ where $y=\beta_0\xi$. Making use of $\sum_{i=1}^{n}\beta_i=0$, we have

$$P(E_l,0)=B\prod_{i=1}^{n}\left(\frac{E_l}{2\lambda_i}\right)^{1/2}\frac{\{\Gamma(\frac{1}{2})\}^n}{\Gamma(\frac{1}{2}n)}\int_0^{\beta_0}\exp(-y)Q\left(\frac{E_l y}{\beta_0}\right)F(y)y^{(n/2)-1}\,dy \tag{2.9}$$

and

$$F(y)=1+\frac{1}{n(n+1)}\sum_{i=1}^{n}\left(\frac{\beta_i}{\beta_0}\right)^2 y^2+\frac{4}{3n(n+2)(n+4)}\sum_{i=1}^{n}\left(\frac{\beta_i}{\beta_0}\right)^3 y^3$$
$$+\frac{1}{n(n+2)(n+4)(n+6)}\left[\frac{1}{2}\left\{\sum_{i=1}^{n}\left(\frac{\beta_i}{\beta_0}\right)^2\right\}^2+\frac{5}{2}\left\{\sum_{i=1}^{n}\left(\frac{\beta_i}{\beta_0}\right)^4\right\}\right]y^4+\cdots \tag{2.10}$$

One finds the integrand in (2.9) does not depend on E_l because y and the argument in Q do not include E_l, but that the integration depends on E_l through the upper limit of the integration β_0. Then, we can obtain any $P(E_l,0)$ from the same integrand $\exp(-y)Q(E_l y/\beta_0)\times F(y)y^{(n/2)-1}$ by taking $\beta_0=(2E_l/n)(\sum_{i=1}^{n}\alpha_i/\lambda_i)$ for the upper limit in integration over y. Thus we may obtain $P(E_l, E_{l-1})$ by taking $(2E_{l-1}/n)(\sum_{i=1}^{n}\alpha_i/\lambda_i)$ for the lower limit and $(2E_l/n)(\sum_{i=1}^{n}\alpha_i/\lambda_i)$ for the upper limit of the integration in (2.9). If $\sum_i(\beta_i/\beta_0)^2<1$ (in ordinary molecules $\langle(\beta_i/\beta_0)^2\rangle\sim 1/10$) the magnitude of higher power terms in (2.10) is negligible as compared with lower power term (see Appendix A).

Next we consider the case where the equilibrium points in normal coordinates change only in one mode or two. In the case of $q_{i0}\neq 0$ in (2.2), we transform variable q_i to ξ_i by the following relations:

$$\frac{\lambda_i}{2E_l}(q_i-q_{i0})^2=\xi$$

and

$$\exp(-\alpha_i q_i^2)=\exp\left(-\alpha_i\frac{2E_l}{\lambda_i}\xi_i\pm 2\alpha_i q_{i0}\frac{2E_l}{\lambda_i}\xi_i-\alpha_i q_{i0}^2\right) \tag{2.11}$$

in (2.7) where $\pm$ is taken as $q_i-q_{i0}\gtrless 0$. If $\alpha_i q_{i0}^2\ll 1$, $\exp(-2\alpha_i q_{i0}(2E_l\xi_i/\lambda_i)^{1/2})$ can be expanded in power series and treated by the same method as before. It is very complicated when $\alpha_i q_{i0}^2>1$ and is necessary to adopt another approximation. We can express the factor $\exp(-\alpha_i q_i^2)$ in terms of y by the method as shown in Appendix B. Thus we can transform $\exp(-\alpha_i q_i^2)$ into $\exp(-y)F(y)$, but in this case $F(y)$ is not always a slowly varying function of y.

As $Q(\xi)$ is a slowly varying function of ξ, for $\hbar^2k_0^2/2m>2E_0$, the dependence of $F_\nu\cdot P(\infty)$ of an ion fragment on k_0^2 are given by

$$E_\nu\cdot p(\infty,0)=\sum\frac{\sigma_\nu(n-n_\nu-\sum_\mu n_\mu)_l}{\sum_\nu\sigma_\nu(n-n_\nu-\sum_\mu n_\mu)_l}P(E_l,E_{l-1})$$
$$\propto Q(K_0^2)\propto A\cdot\log(CK_0^2)/K_0^2 \tag{2.12}$$

where $C=(\hbar^2/2mE)$. The relation between $P(\infty,0)$ or $F_\nu\cdot P(\infty,0)$ and incident energy is similar to that between the cross section of an atom and the incident energy. The general view of k_0^2 dependence of experimental $F_\nu \cdot P(\infty, 0)$ in the case of C_2H_2 is illustrated in Fig. 2[9], showing plausible agreement with tendency predicted by the theory.

The relative ratio of each ion fragment to the total ionization is expressed as

$$F_\nu = \sum_l \frac{\sigma_\nu(n-n_\nu-\sum_\mu n_\mu)_l \int_0^{\beta_0} e^{-y} F(y) y^{(n/2)-1} dy \left(1+\frac{\text{Const.}}{k_0^2-2mE_0/\hbar^2}\right)}{\sum_\nu \sigma_\nu(n-n_\nu-\sum_\mu n_\mu)_l \int_0^{\infty} e^{-y} F(y) y^{(n/2)-1} dy \left(1+\frac{\text{Const.}}{k_0^2-2mE_0/\hbar^2}\right)} \tag{2.13}$$

for high incident energy, namely F_ν is regarded as little dependent on the incident energy $\hbar^2k_0^2/2m$. In the case of CH_4 experimental data of relative abundances to the parent ion as functions of the incident energy are shown in Fig. 3[10] which give plausible agreement with theory.

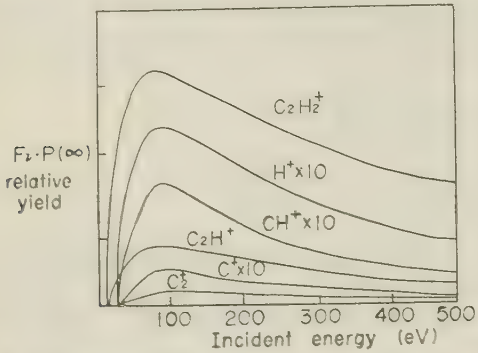

Fig. 2. Dependency of each ion fragment yield on incident energy[9].

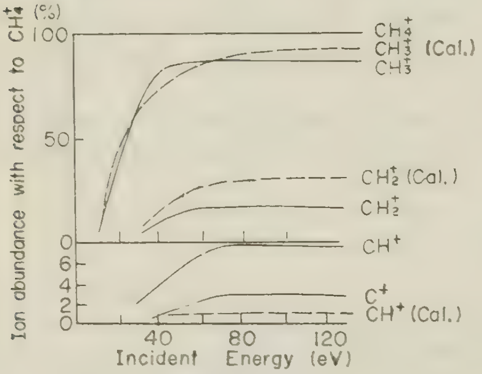

Fig. 3.[10] Energy dependency of each ion abundance with respect to CH_4^+.

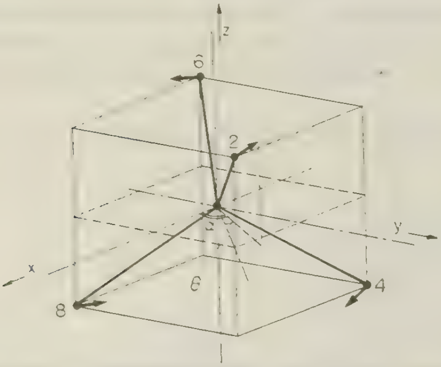

Fig. 4. ν_2 vibration mode and angle α and θ.

In the low incident energy region, the approximation for obtaining the cross section $Q(E, k_0^2)$ in (2.1′) can not be adoptable, and also its additivity of atomic components may not be valid. However, $Q(E, k_0^2)$ may well be given by Const.$\times(2m/\hbar^2k_0^2E)\log(\hbar^2k_0^2/2mE)$ because the general behaviour of the total ionization of molecules is shown experimentally to be resemble the cross section for ionization of atoms. When the incident energy $\hbar^2k_0^2/2m$ lies between E_0+E_{l-1} and E_0+E_l, the parent ion can gain its internal energies only below $\{(\hbar^2k_0^2/2m)-E_0\}$ according to energy conservation.

In the region of $E_0+E_{l-1}<\hbar^2k_0^2/2m<E_0+E_l$ one must take $\{(\hbar^2k_0^2/2m)-E_0\}(\sum_{i=1}^{\mu} \alpha_i/n\lambda_i)$ for the upper limit of integral of (2.9). Therefore, in the low energy region the dependencies of ion currents on incident energy near the threshold of appearance potential are obtained as

$$F_\nu = \frac{P(\gamma, \beta_0(l))}{P(\gamma, 0)} \tag{2.14}$$

where

$$P(\gamma, \beta_0(l)) = \int_{\beta_0(l-1)}^{\gamma} e^{-y} Q\left(\frac{E_l y}{\beta_0(l)}\right) F(y) y^{(n/2)-1} dy$$

$$\gamma = \frac{\Delta E}{n} \sum_{i=1}^{n} \left(\frac{\alpha_i}{\lambda_i}\right), \qquad \Delta E = \frac{\hbar^2k_0^2}{2m} - E_0 \,.$$

Considering that Q for ionization of molecules resembles that for ionization of atoms, $Q(E_l \cdot y/\beta_0(l))$ is given in the form Const. $\times(\log\gamma-\log y)$. When $(\hbar^2k_0^2/2m-E_0)$ is small, the total ion currents $\propto P(\gamma, 0) \propto \Delta E^{(n/2)+2}$, and when $\hbar^2k_0^2/2m$ is a little over E_l, $E_\nu(P(\gamma, \beta_0(l)) \propto (\Delta E-E_l)$ where the suffix ν in F_ν refers to the ion fragment which newly appears at E_l.

Wannier[11] has shown that the ionization yield (cross section) rises at the 1–1.27th power of the energy in excess of the threshold energy for atoms ($Q \propto \Delta E \sim \Delta E^{1.127}$). On the contrary, for molecules, it is expected that the ionization yields do not always rise linearly but can rise at higher power on account of the internal vibration of nucleus. Experimental data are expected to show a tendency that the total ionization rises at the higher power in the more complex molecules, but we have not yet confirmed that the experimental data have a tendency accounted for this effect.

§ 3. Application to CH_4 and CD_4

3.1. *Electronic States of CH_4*

The electronic levels of CH_4^+ have been found by Frost and Mcdowell[12] as shown in Fig. 5a and Table III. We ignore the ionization of electrons in the level of 1st orbital of C atom. $^2A_1$ is the electronic state where an electron in nondegenerate (except spin degeneracy) a_1 orbital is ionized. This state is totally symmetric with respect to all symmetry operations which belong to the point group T_d. $^2T_2$ is the state where an electron in triply degenerate t_2 orbital is ionized. This state has symmetry with respect to three planes of symmetry σ_d and is symmetric with respect to the two planes of symmetry σ_d and antisymmetric with respect to the other plane σ_d. We construct LCAOMO's for a_1 and t_2 from AO's, *i.e.*, the wave function of C2*s* orbital ψ_{2s}, those of C2*px*, C2*py*, C2*pz* orbitals ψ_{2px}, ψ_{2py}, ψ_{2pz}, and those of *i*th H1*s* orbital $\psi_{i(1s)}$ where the orientation *x*, *y*, *z* and the labelled number of H are shown in Fig. 4. The MO wave function of electron in each electronic level are expressed as in the following formula[13]

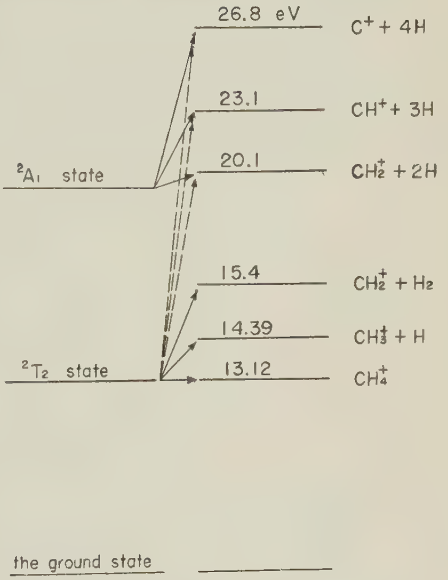

Fig. 5b. Energy diagram of CH_4 and of various ions from CH_4.

Table III[12]. Electronic states of ionized CH_4^+.

Appearance Potential	Total symmetry of state	Ionized orbit
13.16±0.02 V	$^2T_2$	t_2
19.42±0.02 〃	$^2A_1$	a_1

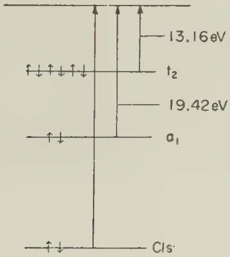

Fig. 5a. Electronic levels of CH_4.

$$\left.\begin{aligned} \psi_s &= \frac{1}{\sqrt{N}}\left\{\lambda\psi_{2s} + \frac{1}{2}(\psi_{2(1s)} + \psi_{4(1s)} + \psi_{6(1s)} + \psi_{8(1s)})\right\} && \text{for } a_1 \text{ state} \\ \psi_x &= \frac{1}{\sqrt{N}}\left\{\lambda\psi_{2px} + \frac{1}{2}(\psi_{2(1s)} - \psi_{4(1s)} - \psi_{6(1s}+)\psi_{8(1s)})\right\} && \\ \psi_y &= \frac{1}{\sqrt{N}}\left\{\lambda\psi_{2py} + \frac{1}{2}(\psi_{2(1s)} - \psi_{4(1s)} + \psi_{6(1s)} - \psi_{8(1s)})\right\} && \text{for } t_2 \text{ state} \\ \psi_z &= \frac{1}{\sqrt{N}}\left\{\lambda\psi_{2pz} + \frac{1}{2}(\psi_{2(1s)} + \psi_{4(1s)} - \psi_{6(1s)} - \psi_{8(1s)})\right\} && \end{aligned}\right\} \qquad (3.1)$$

and λ is obtained from the dipole moment μ of C–H bond by the equation[14]

$$\mu = \frac{(\lambda^2 - 1)eR}{1 + \lambda^2 + 2\lambda S}$$

where R is internuclear distance, the value of λ is 1.15, $N=1+\lambda^2+2\lambda S$, and $S=\frac{1}{2}$. The appearance potentials of various ions from CH_4 are shown in Table IV[15]. A schematic diagram of energy states of ion is illustrated in Fig. 5b, and possible dissociation processes are indicated with arrows.

Table IV[15]. Various ion fragments from CH_4 and their appearance potentials.

Ion	Appearance potential	Procees
CH_4^+	13.12±0.02 V	$CH_4^+ + e$
CH_3^+	14.39±0.02 〃	$CH_3^+ + H + e$
CH_2^+	15.6 〃	$CH_2^+ + H_2 + e$
	20.1 〃	$CH_2^+ + 2H + e$
CH^+	23.0 〃	$CH^+ + 3H + e$
C^+	26.8 〃	$C^+ + 4H + e$

3.2. *Potential Energy Surfaces of Ionized States*

In $^2A_1$ state the symmetry property of the total wave function is the same with that of the neutral ground state (totally symmetric). Moreover, for the CH_4 molecule the vibration spectra of a CH_4 molecule are well explained by the valence force field picture and the contribution of H–H interaction to the potentical surface is considered to be small. Taking into account these features, one may properly consider that the potential energy curve only along the coordinate of ν_1 vibration mode changes by a transition from the ground state to $^2A_1$ state. Further we have assumed that the equilibrium point for $^2A_1$ state is the same with that for the neutral ground state, and also that the force constant for $^2A_1$ state $\lambda_1(^2A_1)$ becomes the value which is obtained by the force constant for the ground state λ_1(ground) multiplied by a ratio of the total binding energy for $^2A_1$ state $V_0(^2A_1)$ to that of the ground state V_0(ground), *i.e.* $\lambda_1(^2A_1)=\{V_0(^2A_1)/V_0(\text{ground})\}\times\lambda_1(\text{ground})$.

In $^2T_2$ state, however, the symmetry property of total wave function is not the same with that of the neutral ground state. One may expect that the atomic configuration in equilibrium is different from that of the ground state to some extent. Now let us consider the case when the electron in one of t_2 orbital that has a same symmetry of φ_{2pz} is ionized. It can easily be expected that the bond angles of H_2–C–H_8 and H_4–C–H_6 become larger (Fig. 4), and of all vibrations the ν_{2a} frequency is considered to render the most remarkable change. To estimate this increased value of the bond angles *i.e.* q_{i0} of the coordinate of ν_{2a} mode in (2.2), we calculate emprically the contribution of ionization of electron in t_2 orbital to the bond angle by the following procedure: (1) The binding energy and vibrational potentials along some normal coordinate of the ground state are expressed in terms of molecular integrals. (2) The binding energies in $^2A_1$ and $^2T_2$ state are also expressed in terms of molecular integrals. (3) The expressions for force constant and for the change of equilibrium point along ν_{2a} vibrational mode in $^2T_2$ are obtained in terms of the same molecular integrals. If V be the potential energy of molecular vibration, it may be expanded along a normal coordinate in a state near $q_i=0$ as

$$V=V_0+\lambda_i' q_i+\frac{\lambda_i}{2}q_i^2\ .$$

Through above procedure we obtain the expressions for V_0, λ_i', λ_i in terms of molecular integrals relating to some normal modes in each state.

To carry out above estimation, the wave functions φ_{2px}, φ_{2py}, φ_{2pz} are transformed by the vector model into their components of the bonds C–H_2, C–H_4, C–H_6 and C–H_8 *i.e.*, $\varphi_{1\sigma}$, $\varphi_{1\pi}$, $\varphi_{1\bar\pi}$: $\varphi_{3\sigma}$, $\varphi_{3\pi}$, $\varphi_{3\bar\pi}$: $\varphi_{5\sigma}$, $\varphi_{5\pi}$, $\varphi_{5\bar\pi}$ and $\varphi_{7\sigma}$, $\varphi_{7\pi}$, $\varphi_{7\bar\pi}$, respectively where we mean by $\varphi_{1\pi}$ one of π component of a C2p orbital with respect to C–H_2 bond and by $\varphi_{1\bar\pi}$ the other π component of a C2p orbital with respect to C–H_2 bond, and so on. Then we have

$$\varphi_{2px}=\frac{\cos\alpha}{\sqrt{1+\sin^2\alpha}}\varphi_{1\sigma}+\frac{2\sin\alpha}{\sqrt{1+\sin^2\alpha}}\varphi_{1\pi}$$

$$\varphi_{2py}=\frac{\sin\alpha}{\sqrt{1+\sin^2\alpha}}\varphi_{1\sigma}+\frac{1}{\sqrt{1+\sin^2\alpha}}\left(\frac{1}{\sqrt{2}}\cos\alpha\cdot\varphi_{1\pi}+\frac{1}{\sqrt{2}}\sqrt{1+\sin^2\alpha}\,\varphi_{1\bar\pi}\right)$$

$$\begin{aligned}
\psi_{2pz}&=\frac{\sin\alpha}{\sqrt{1+\sin^2\alpha}}\psi_{1\sigma}+\frac{1}{\sqrt{1+\sin^2\alpha}}\left(\frac{1}{\sqrt{2}}\cos\alpha\cdot\psi_{1\pi}-\frac{1}{\sqrt{2}}\sqrt{1+\sin^2\alpha}\,\psi_{1\bar{\pi}}\right)\\
\psi_{2px}&=-\frac{\cos\alpha}{\sqrt{1+\sin^2\alpha}}\psi_{3\sigma}-\frac{2\sin\alpha}{\sqrt{1+\sin^2\alpha}}\psi_{3\pi}\\
\psi_{2py}&=-\frac{\sin\alpha}{\sqrt{1+\sin^2\alpha}}\psi_{3\sigma}-\frac{1}{\sqrt{1+\sin^2\alpha}}\left(-\frac{1}{\sqrt{2}}\cos\alpha\cdot\psi_{3\pi}-\frac{1}{\sqrt{2}}\sqrt{1+\sin^2\alpha}\,\psi_{s\bar{\pi}}\right)\\
\psi_{2pz}&=\frac{\sin\alpha}{\sqrt{1+\sin^2\alpha}}\psi_{3\sigma}+\frac{1}{\sqrt{1+\sin^2\alpha}}\left(-\frac{1}{\sqrt{2}}\cos\alpha\cdot\psi_{3\pi}+\frac{1}{\sqrt{2}}\sqrt{1+\sin^2\alpha}\,\psi_{3\bar{\pi}}\right)
\end{aligned}\tag{3.2}$$

and similar expression for $\psi_{2p\text{'s}}$ in terms of $\psi_{5\sigma}$, $\psi_{5\pi}$, $\psi_{5\bar{\pi}}$ and $\psi_{7\sigma}$, $\psi_{7\pi}$, $\psi_{7\bar{\pi}}$ where α is the angle as shown in Fig. 4. The bond eigen-functions of C atom are

$$\begin{aligned}
\psi_{c1}&=\frac{1}{2}(\psi_{2s}+\psi_{2px}+\psi_{2py}+\psi_{2pz})\\
\psi_{c3}&=\frac{1}{2}(\psi_{2s}-\psi_{2px}-\psi_{2py}+\psi_{2pz})\\
\psi_{c5}&=\frac{1}{2}(\psi_{2s}-\psi_{2px}+\psi_{2py}-\psi_{2pz})\\
\psi_{c7}&=\frac{1}{2}(\psi_{2s}+\psi_{2px}-\psi_{2py}-\psi_{2pz})\ .
\end{aligned}\tag{3.3}$$

Then the Coulomb integral Q and the exchange integral J of bond eigen-function between C_1 and H_2 atomic orbitals are given by the following formula:

$$\begin{aligned}
Q(1,2)&=\frac{1}{4}\left[Q_{ss}+Q_{\sigma\sigma}+Q_{\pi\pi}+Q_{\bar{\pi}\bar{\pi}}+\frac{1}{\sqrt{1+\sin^2\alpha}}(2\cos\alpha+4\sin\alpha)Q_{s\sigma}\right]\\
J(1,2)&=\frac{1}{4}\left[J_{ss}+J_{\sigma\sigma}+J_{\pi\pi}+J_{\bar{\pi}\bar{\pi}}+\frac{1}{\sqrt{1+\sin^2\alpha}}(\cos\alpha+2\sin\alpha)(J_{s\sigma}+J_{\sigma s})\right]\ .
\end{aligned}\tag{3.4}$$

In the above expression each integral Q_{ss}, $Q_{\sigma\sigma}$, J_{ss} *etc.*, is defined as

$$\begin{aligned}
Q_{ss}&=\int\psi_s(1)\psi_h(2)\boldsymbol{H}\psi_s(1)\psi_h(2)d\tau_1d\tau_2\\
Q_{\sigma\sigma}&=\int\psi_\sigma(1)\psi_h(2)\boldsymbol{H}\psi_\sigma(1)\psi_h(2)d\tau_1d\tau_2\\
J_{ss}&=\int\psi_s(1)\psi_h(2)\boldsymbol{H}\psi_\sigma(1)\psi_h(2)d\tau_1d\tau_2\\
&\cdots\cdots\cdots\\
\boldsymbol{H}&=\boldsymbol{H}_{\text{total}}-\boldsymbol{H}_{\text{C}}-\sum_{i=1}^{4}\boldsymbol{H}_{\text{Hi}}
\end{aligned}$$

where $\boldsymbol{H}_{\text{total}}$ is the total Hamiltonian of molecule CH_4, $\boldsymbol{H}_{\text{C}}$ is the Hamiltonian of atom C, and $\boldsymbol{H}_{\text{Hi}}$ is that of ith H. The same treatment is carried out in calculating $Q(1,4)$, $Q(1,6)$, $Q(1,8)$, $Q(2,4)$, $\cdots$ and also $J(1,4)$, $\cdots$, that is, $Q(i,j)$ and $J(i,j)$ with all possible combination of i and j.

And we take summations of Q and J according to the following rule

$$V=\sum Q+\sum_a J-\frac{1}{2}\sum_g J+\sum V_{hh}\tag{3.5}$$

where the summation a is taken over the bonding orbitals only, and the summation b is taken over the non-bonding orbitals only. V_{hh} is the interaction potential of H–H, *i.e.*

$$V_{hh}=\frac{1}{4}D_0[\exp\{-2\beta(R-R_e)\}-2\exp\{-\beta(R-R_e)\}]+\frac{3}{4}A_0e^{-2R}R^{-4/3} \tag{3.6}$$

with $D_0=4.747\,\mathrm{eV}$, $\beta=2.0522\,\mathrm{a}_0^{-1}$, $R_e=1.4016\,\mathrm{a}_0$, $A_0=15.159\,\mathrm{eV}$ and $\alpha=0.357\,\mathrm{a}_0^{-1}$ which are derived from the spectroscopic data[7] and from Hirschfelder and Linnett's[16] calculation. We consider the variation for V with the normal coordinate along ν_{2a} vibration mode and put $\alpha=(\pi/4)+\theta$ in Fig. 4 where $\theta\ll 1$. V is expanded in power series of θ, and then one finds that the term of first power vanishes. From the zeroth power term, we obtain V_0, *i.e.* the total binding energy, and from the second power term we obtain also the potential curvature along the normal coordinate of vibration ν_{2a}, $V_{\theta 2}$. Then we have the potential curve along ν_{2a} vibrationed mode in the form

$$\left.\begin{aligned}
&V=V_0+\frac{1}{2}V_{\theta 2}\\
&V_0=\left(4Q_{ss}-\frac{1}{2}J_{ss}\right)+\left(4Q_{\sigma\sigma}-\frac{1}{2}J_{\sigma\sigma}\right)+2\left(4Q_{\pi\pi}-\frac{1}{2}J_{\pi\pi}\right)+\frac{3\sqrt{3}}{8}(J_{s\sigma}+J_{\sigma s})+6V_{hh}\\
&\qquad\qquad\qquad\qquad\qquad\qquad\qquad\qquad\qquad\qquad\qquad\text{for the ground state}\\
&\text{and along } \nu_1 \text{ vibrational mode we also have}\\
&V_{\theta 2}=16\pi^2\nu_2^2c^2m_{\mathrm{H}}R_0^2=-\frac{1}{2\sqrt{3}}(J_{s\sigma}+J_{\sigma s})-\frac{8\sqrt{2}}{3\sqrt{3}}\left(\frac{\partial V_{hh}}{\partial R}\right)R_0+\frac{16}{9}\left(\frac{1}{2}\,\frac{\partial^2 V_{hh}}{\partial R^2}\right)R_0^2\\
&\qquad\qquad(\nu_2\text{ is measured in cm}^{-1})\qquad\qquad\text{for the ground state}
\end{aligned}\right\} \tag{3.7}$$

where m_{H} is the mass of H atom and R_0 is the internuclear distance of C–H in equilibrium.

For ν_1 mode we can easily obtain the following formula by making use of the totally symmetric property, as

$$16\pi^2c^2\nu_1^2m_{\mathrm{H}}R_0^2=\left(\frac{1}{2}\,\frac{\partial^2 V}{\partial R^2}\right)_0R_0^2. \tag{3.8}$$

Since the normal coordinate along ν_3 and ν_4 modes depend both on the mass ratio of C to H, and on its geometrical scheme, each normal coordinate component of bond angle and C–H distance changes can not be obtained easily. However, assuming the valence force field picture, we can acquire relations between the force constants for ν_1, ν_2 and those for ν_3, ν_4, and find them to be in good agreement with the experimental data of Raman and infra-red spectra[17]. So we may expect that the values of molecular integrals which are obtained from the data of ν_1 and ν_2 will be nearly equal to those estimated from ν_3 and ν_4 according to a valence force field picture.

By the same procedure as described above, along ν_2 mode in $^2\mathrm{T}_2$ state is obtained as

$$\begin{aligned}
&V=V_0+V_{\theta 1}\cdot\theta+\frac{1}{2}V_{\theta 2}\theta^2\\
&V_0=\left(4\theta_{ss}-\frac{1}{2}J_{ss}\right)+\frac{5}{6}\left(4\theta_{\sigma\sigma}-\frac{1}{2}J_{\sigma\sigma}\right)+\frac{10}{6}\left(4\theta_{\pi\pi}-\frac{1}{2}J_{\pi\pi}\right)\\
&\qquad+\frac{\sqrt{3}}{2}\left(3-\sqrt{\frac{1}{2}}\right)(J_{s\sigma}+J_{\sigma s})+\frac{21}{4}V_{hh}\\
&V_{\theta 1}=\frac{4}{9}\left(4Q_{\sigma\sigma}-\frac{1}{2}J_{\sigma\sigma}\right)-\frac{4}{9}\left(4Q_{\sigma\sigma}-\frac{1}{2}J_{\sigma\sigma}\right)+\sqrt{\frac{2}{3}}(J_{s\sigma}+J_{\sigma s})\\
&V_{\theta 2}=\frac{4}{27}\left(4Q_{\sigma\sigma}-\frac{1}{2}J_{\sigma\sigma}\right)+\frac{16}{27}\left(4Q_{\pi\pi}-\frac{1}{2}J_{\pi\pi}\right)-\frac{\sqrt{3}}{2}\left(\frac{1}{3}+\frac{1}{\sqrt{2}}\right)(J_{s\sigma}+J_{\sigma s})\\
&\qquad+\frac{7}{4}\sqrt{\frac{2}{3}}\left(\frac{\partial V_{hh}}{\partial R}\right)R_0+\frac{8}{3}\left(\frac{1}{2}\,\frac{\partial^2 V_{hh}}{\partial R^2}\right)R_0^2
\end{aligned} \tag{3.9}$$

In calculation for the above expression, we made an assumption that when an electron is ionized from a given orbital Q, J and V_{hh} become the value of $(N-1)/N$ times the initial values, where N is the total number of electrons in the orbital.

For ${}^2A_1$ state we can calculate V_0 by the same way into the form

$$V_0=\frac{1}{2}\left(4Q_{ss}-\frac{1}{2}J_{ss}\right)+\left(4Q_{\sigma\sigma}-\frac{1}{2}J_{\sigma\sigma}\right)+2\left(4Q_{\pi\pi}-\frac{1}{2}J_{\pi\pi}\right)+\frac{3}{2}\sqrt{\frac{3}{2}}(J_{s\sigma}+J_{\sigma s})+\frac{21}{4}V_{hh} \tag{3.10}$$

The experimental values of various V_0's are given by[18)]

$V_0=-15.50$ eV for the ground state

$V_0=-13.64$ eV for ${}^2T_2$ state

$V_0=-11.04$ eV for ${}^2A_1$ state

where we adopt 11.26 eV as the value of ionization potential of C$2p$ and 3.69 eV as the value of $2s$–$2p$ energy gap. From these values we obtain

$$\begin{aligned}&\sqrt{\frac{3}{2}}(J_{s\sigma}+J_{\sigma s})=-3.13\ \text{eV}\\&\left(4Q_{ss}-\frac{1}{2}J_{ss}\right)=-4.43\ \text{eV}\\&\left(4Q_{\sigma\sigma}-\frac{1}{2}J_{\sigma\sigma}\right)+2\left(4Q_{\pi\pi}-\frac{1}{2}J_{\pi\pi}\right)=-5.94\ \text{eV}\end{aligned} \tag{3.11}$$

Using the experimental data 4.096 eV for V_2 in (3.7) we obtain

$$-\frac{8}{3}\sqrt{\frac{2}{3}}\left(\frac{\partial V_{hh}}{\partial R}\right)R_0+\frac{16}{9}\left(\frac{1}{2}\frac{\partial^2 V_{hh}}{\partial R^2}\right)R_0^2=3.05\ \text{eV} \tag{3.12}$$

To value also obtained from the formula (3.6), being 16.31 eV. The values of the first and the second derivatives of H–H interaction potentials in CH_4 will be smaller than the values theoretically expected (~1/5). The result obtained in (3.12) may provide support for the good agreement by the explanation for vibration spectra in hydrocarbon molecules from the picture of valence force field.

We separate $(4Q_{\sigma\sigma}-(1/2)J_{\sigma\sigma})$ from $(4Q_{\pi\pi}-(1/2)J_{\pi\pi})$ in (3.11) by the method described in appendix C, and obtain $(4Q_{\sigma\sigma}-(1/2)J_{\sigma\sigma})=-8.05$ eV and $(4Q_{\pi\pi}-(1/2)J_{\pi\pi})=+1.05$ eV. Consequently we estimate $V_{\theta1}$ and $V_{\theta2}$ and obtain

$$V_{\theta1}=5.73\ \text{eV}\ ,\qquad V_{\theta2}=6.08\ \text{eV}\ . \tag{3.13}$$

From these results, we can see that the equilibrium point is changed to some extent in ${}^2T_2$ state from that in the neutral ground state, but that the frequency is not so changed from that of the neutral ground state. The equilibrium angle in ${}^2T_2$ state (*i.e.* θ for the minimum V in (3.9) is evaluated to be about 27° from the $V_{\theta1}$ in (3.13). However we can not conclusively determine the shape of nuclear configuration of ${}^2T_2$ state by the value of θ for the minimum V obtained above, because the expression (3.9) is only valid when θ is small, that is, when an ion in ${}^2T_2$ state is suffered small deformation from tetrahedral configuration along ν_2 mode. The result of (3.13) comes mainly from the following features. (1) For the ground state the frequency of ν_2 (1526 cm^{-1}) is smaller than that of ν_1 (2914 cm^{-1}), that is the curvature of potential energy surface along ν_2 vibration is smaller than that for C–H stretching. If the curveture along ν_2 vibrational mode in the ground state takes nearly the same value with that of ${}^2T_2$ state, the equilibrium point easily changes by a small amount of change for each valence force. It is the reason why $V_{\theta1}$ is not so small. (2) The H–H interaction is small and every ν_i is well explained by the valence force field picture in the ground state, and these pictures will be valid in the potential energy surface of $^2T_2$ state because of the smallness of the H–H interaction in ionized state of $^2T_2$ as in the ground state. (3) The little increase in frequency term $V_{\theta 2}$ for $^2T_2$ compared with that for the ground state is due to the effect of H–H interaction. In the above calculation, Q and J may vary to some extent with the adopted values of dissociation energies, but the situations of (1), (2) and (3) do not differ by a small variation of the dissociation energies in every case. As related later, the results of the integration of $P(\infty, 0)$, and of $F_\nu P(\infty, 0)$ are not influenced so much by the change of $V_{\theta 2}$, *i.e.* by the curveture change of surface, but influenced by that of V_1, *i.e.* by the change of internuclear distance in equilibrium.

3.3. *Results of Calculation*

To perform the integration (2.10) the parameters α_l, λ_l, λ_2, E_l, are obtained from experimental data as illustrated in Table V. In Table V we can see $\lambda_2' \neq 0$ for $^2T_2$ state, that is, $q_{20} = \lambda_2'/\lambda_2 \neq 0$ in (2.2), and we take

Table V. Adopted values of parameters α_l, λ_l, λ_2', E_l.

Parameter	Adopted value for the ground state	Adopted value for $^2A_1$ state	Adopted value for $^2T_2$ state
α_1	3.815 $a_0^{-2} m_H^{-1}$		
α_2, α_3	2.016 〃		
α_4, α_5, α_6	3.992 〃		
α_7, α_8, α_9	1.726 〃		
λ_1		0.8759 eV $a_0^{-2} m_H^{-1}$	0.6876 eV $a_0^{-2} m_H^{-1}$
λ_2		0.2401 〃	0.2945 〃
λ_2'			1.269 eV $a_0^{-1} m_H^{-1/2}$
λ_3		0.2401 eV $a_0^{-2} m_H^{-1}$	0.2401 eV $a_0^{-2} m_H^{-1}$
λ_4, λ_5, λ_6		0.9339 〃	0.9339 〃
λ_7, λ_8, λ_9		0.1758 〃	0.1758 〃
E_1		1.27 eV	0.68 eV
E_2		2.78 〃	3.58 〃
E_3			7.35 〃

m_H denotes the hydrogen mass, the symbols with suffix 1 relate to the normal coordinate for ν_1 vibration, those with suffix 2 relate to the normal coordinate for ν_2 vibration, λ_2' is the coefficient of the first power term of q_2 in $^2T_2$ state ($\lambda_2' = \lambda_2 q_{20}$ in (2.11)) and is calculated from V_1 in (3.13), the symbols with suffix 3 relate to the other normal coordinate for ν_2, vibration, those with suffix 4, 5 and 6 relate to the normal coordinates for ν_3 vibration, and those with suffix 7, 8 and 9 relate to the normal coordinate foa ν_4 vibration.

$$\xi_2 = \frac{\lambda_2'}{E} q_2$$

as a new variable in (2.8) because of $\lambda_2' q_2 \gg \lambda_2$ and we take also

$$\exp(-\alpha_2 q_2^2) = \exp(-\beta_2'(\xi_2 - \xi_{20})^2)$$

$$\beta_2' = \sqrt{\frac{E_l}{\lambda_2'}} \cdot \alpha_2, \quad \xi_{20} = \sqrt{\frac{2}{\beta_2}} \tag{3.14}$$

for ξ_2 normal coordinae part of the vibrational wave function of nuclei. Further, the function in (3.14) is calculated by the approximation method which shown in Appendix B.

When we put the relative aboundances of CH_4^+, CH_3^+, CH_2^+, CH^+ and C^+ with respect to the total ionization as F_1, F_2, F_3, F_4 and F_5, respectively, these ion abundances are obtained from Fig. 5 and Table IV according to (2.4) as

$$F_1 P(\infty, 0) = P_1(E_1, 0)$$

$$F_2 P(\infty, 0) = \frac{2}{7} P_1(\infty, 0) + \frac{5}{7} P_1(E_2, 0) - P_1(E_1, 0) + \frac{12}{119} P_2(\infty, 0)$$

$$+\frac{54}{6545}P_2(E_2,\,0)+\frac{96}{2145}P_2(E_1,\,0)$$

$$F_3P(\infty,\,0)=\frac{5}{7}P_1(\infty,\,0)-\frac{5}{7}P_1(E_2,\,0)+\frac{30}{119}P_2(\infty,\,0) \tag{3.15}$$

$$+\frac{27}{1309}P_2(E_2,\,0)+\frac{48}{4290}P_2(E_1,\,0)$$

$$F_4P(\infty,\,0)=\frac{36}{119}P_2(\infty,\,0)+\frac{162}{6545}P_2(E_2,\,0)+\frac{288}{2145}P_2(E_1,\,0)$$

$$F_5P(\infty,\,0)=\frac{9}{119}P_2(\infty,\,0)-\frac{9}{119}P_2(E_2,\,0)$$

where $P_1(E_l,\,0)$ means the symbol for ${}^2T_2$ state, and $P_2(E_l,\,0)$ means that for ${}^2A_1$ state.

The results of calculation are shown in Table VI and Fig. 2.

Table VI. Relative abundances to the parent ion.

Ion	Observed[19]	Calculated
CH_4^+	100	100
CH_3^+	86	93
CH_2^+	16	38
CH^+	8.1	0.6
C^+	2.8	0
CD_4^+	100	100
CD_3^+	83	64
CD_2^+	12.5	24
CD^+	7.23	0
C^+	2.19	0

3.4. *Isotope Effect*

We can find the value of β_0 for CD_4 in (2.8) is $\sqrt{2}$ times that for CH_4 and this increases of β_0 will cause a change of relative yield. We can expect that the parent ion becomes to have larger abundance than that for CH_4, because

$$F_1=\frac{\int_0^{\beta_0} e^{-y}F(y)Q\left(\frac{E_l y}{\beta_0}\right)y^{(n/2)-1}dy}{\int_0^{\beta_0} e^{-y}F(y)Q\left(\frac{E_l y}{\beta_0}\right)y^{(m/2)-1}dy} \tag{3.16}$$

and $Q(y/\beta_0)$ is such a slowly varying function of $(E_l y/\beta_0)$ that it can be regarded as nearly constant. The tendency obtained by the experiments in Table VI shows that the consideration is acceptable. It is considered to be equivalent in view of physical interpretation to the following meaning that the zero point energy of nuclear motion for CD_4 is lower than that for CH_4 and the wave function of nuclear motion concentrates nearer the equilibrium point for CD_4 than for CH_4.

Thus if the equilibrium point in the ionized state is not much different from that in the neutral ground stage, *i.e.* the parent ion can remain stable at considerable rate to the total ionization the nuclear system gains less kinetic energy with the Franck-Condon transition for CD_4 by the isotope effect and then the dissociation take place less easily.

The results of calculation are also shown in Table VI. They tell us that the tendency measured by the experiments from CH_4 to CD_4 is not so striking as is theoretically expected. The reason is not clear, but a part of the discrepancy comes from y depedency of the integrand in (2.14), and the integrand may be supposed to be more slowly varying function of y.

§ 4. **Discussion and Conclusion**

The similarity of the shape of the cross section-incident energy curve of molecules to that of atoms has been deduced in our case by our taking LCAO wave function for MO wave function. However, this similarity does not essentially depend on the structure of the wave function of an orbital to be ionized. Further, there is a possibility that the curve for molecules resembles those for composed atoms even when the additivity rule is not applicable.

The non-linearity behaviour of the curve of the relation between cross section and incident energy near a threshold is due to the effect of strong convergence of the integrand in (2.14) at the origin, that is, the probability of finding nuclei at the equilibrium configuration is rather small and is larger at a distance from it. The effect must appear in the cases of optical transition of an electron in molecules, of an electron capture by molecules or molecular ions, of all the electronic phenomena that are affected by the wave function of nuclear motion. It is, therefore, possible to consider that in optical transition of electronic excitation or ionization the maximum value of observed transition does not always correspond to that from the equilibrium point of nuclear motion in the ground state, even if the atomic configuration in equilibrium in an excited state is the same as that in the ground state. One must not apply the analogous consideration of diatomic molecules to that of polyatomic ones. The curve for the relation between the yield of product and the energy of the incident particle (electron, photon, *etc.*) has not always the maximum that corresponds to the vertical transition from the nuclear configuration of the maximum probability in the ground state (Fig. 6).

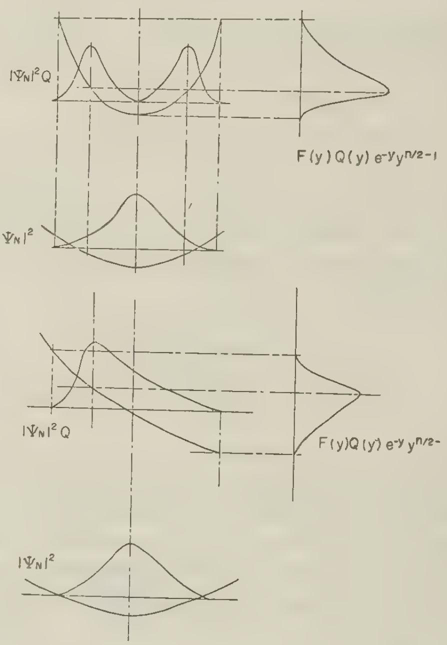

Fig. 6. Schematic figure of transition probabilities when $n>2$.

On account of several approximations adopted in the estimation of $V_{\theta 1}$ and $V_{\theta 2}$, each term of molecular integrals may not be so accurate that we can not discuss other properties of the molecule with these J and Q from the quantitative views. However, one may at least conclude the following remarks. (1) The relative abundance of each ion is much influenced by the change of equilibrium configuration, but not much by the change of force constant. (2) The value of parent ion abundance is considerably large when the equilibrium configuration of ionized state resembles that of the neutral ground state (more than 80% of the total ionization). (3) If the interaction between non-bonding two atoms is not small compared with the valence energy of bonding atoms (for example CCl_4), the feature may be different from that described above and one may consider that the abundance of parent ion is negligibly small in this case.

The poor agreement of the results of calculation with experiments for the abundances of CH^+ and C^+ is due to the assumption that the equilibrium configuration in the potential energy surface is the same with that of the ground state in $^2A_1$ state. We suppose that the integrand in (2.10) should be more slowly varing function and should not decay so rapidly with y in this case. It is also supposed that this correction may have good influence on the descrepancies of isotope effect. There is a possibility of the change of equilibrium configuration in $^2A_1$ state. The discrepancy seems to be due to the fact that the potential surface is not a true basin at the point where every $q_i=0$ in $^2A_1$ and the potential curve of the coordinate along the process such as

$$CH_4^+(^2A_1) \longrightarrow CH_3^+ + H$$

has not a minimum. The slope along these path may be considered to be large and the probability of ionization to $^2A_1$ state may extend over a wide range of the ionization potential E, that is, the integrand in (2.14) may be a more soothing function of y.

The absence of the appearance potential of new CH_3^+ at 19.42 eV, *i.e.* the energy level of $^2A_1$ state, seems to be attributable to the fact that CH_3^+ in the state refered to the surface of CH_4^+ in $^2A_1$ may be unstable, or to the fact that the surface in $^2A_1$ state may be combined with the surface in $^2T_2$ state. Otherwise the amount of this CH_3^+ ion may be too little to be detected by experiment. Generally speaking one must take every ion fragment for each electronic level into account.

In the above consideration, the production of negative ions H_2^-, H^-, *etc.* and positive ions H_2^+, H^+, have been ignored on account of small yields, especially, from the complexity of negative ion production processes. The small amounts of H_2^+ and H^+ ions may be due to the large negativities than those of CH_3^+, CH_2^+, CH^+ and C^+.

Acknowledgements

The author wishes to express his grateful thanks to Professor Ayao Amemiya for his helpful discussions and continuous encouragement for the present work. He is also grateful to Professor Ichirō Kanomata for his suggestions from experimental aspects and to Professor Masao Kotani and the members of his laboratory for their valuable discussions from the theoretical viewpoint. He further appreciates useful comments of Mr. Mitio Inokuti. A part of the calculation in the present work was carried out with the aid of the FACOM-128 Fuji automatic relay computer which is located in the Yurin Denki Seiki Co., and the writer is indebted to Mr. Sugayasu Hirano for use of the machine.

Appendix A

In (2.10) we obtain the formula

$$P(E_2,0)=B\prod_{i=1}^{n}\left(\frac{E_l}{2\lambda_i}\right)^{1/2}\frac{\{\Gamma(1/2)\}^n}{\Gamma\{(1/2)n\}}\left\{f_0+\frac{1}{n}\sum_i\beta_i f_1+\frac{1}{n(n+2)}\left[\sum_{i>j}\beta_i\beta_j+\frac{3}{2}\sum_i\beta_i^2\right]f_2\right.$$
$$\left.+\frac{1}{n(n+2)(n+4)}\left[\sum_{i>j>k}\beta_i\beta_j\beta_k+\frac{3}{2}\sum_{i\neq j}\beta_i^2\beta_j+\frac{5}{2}\sum_i\beta_i^3\right]f_3+\cdots\right. \qquad \text{(A1)}$$

where

$$f_i=\int_0^1\exp(-\beta_0\xi_i)Q(\xi)\xi^{(n/2)+i-1}d\xi$$
$$Q(\xi)=\sum_r\left\{\frac{2\pi Ame^4c_ra_r^2Z_r}{\hbar^2k_0^2E_l[(E_0/E_l)+\xi]}\right\}\log\left\{\frac{2\hbar^2k_0^2}{m\alpha_rE_l[(E_0/E_l)+\xi]}\right\} \qquad \text{(A2)}$$

and $\sum\limits_{i\neq j>k}$ means $\sum\limits_{\substack{i\neq j\\ i\neq k}}\sum\limits_{j>k}$.

Using the fact that $\sum\limits_i\beta_i=0$, (A1) becomes the following formula

$$P(E_l,0)=B\prod_{i=1}^{n}\left(\frac{E_l}{2\lambda_i}\right)^{1/2}\frac{\{\Gamma(1/2)\}^n}{\Gamma\{(1/2)n\}}\left\{f_0+\frac{\sum\beta_i^2}{n(n+2)}f_2+\frac{4\sum\beta_i^3}{3n(n+2)(n+4)}f_3\right.$$
$$+\frac{1}{n(n+2)(n+4)(n+6)}\left[\frac{1}{2}(\sum\beta_i^2)^2+\frac{5}{2}(\sum\beta_i^4)\right]f_4$$
$$+\frac{1}{n(n+2)(n+4)(n+6)(n+8)}\left[\frac{4}{3}(\sum\beta_i^2)(\sum\beta_j^3)+\frac{47}{10}(\sum\beta_i^5)\right]f_5$$
$$+\frac{1}{n(n+2)(n+4)(n+6)(n+8)(n+10)}\left[\frac{1}{6}(\sum\beta_i^2)^3+\frac{49}{8}(\sum\beta_i^2)(\sum\beta_j^4)\right.$$
$$\left.\left.+\frac{241}{72}(\sum\beta_i^6)\right]f_6+\cdots\right. . \qquad \text{(A3)}$$

Since $Q(\xi)$ is a decreasing function of ξ

$$f_i=\int_0^1 \exp(-\beta_0\xi)Q(\xi)\xi^{(n/2)+i-1}d\xi$$
$$\leq\frac{1}{\beta_0{}^{(n/2)+i}}\int_0^{\beta_0}\exp(-y)Q(y)\,y^{(n/2)+i-1}dy$$

where $\beta_0\xi=y$. As we have $f_i<\frac{\{(n/2)+i-1\}}{\beta_0}f_{i-1}$, then

$$f_i<\frac{(n/2)+i-1}{\beta_0{}^{(n/2)+i-1}}\int_0^{\beta_0}\exp(-y)Q(y)\,y^{(n/2)+i-2}dy\ .$$

Then we obtain

$$f_i<\frac{\{(n/2)+i-1\}\{(n/2)+i-2\}\cdots(n/2)}{\beta_0}f_0\ . \tag{A4}$$

We substitute (A4) into (A3), then we have

$$\frac{\sum\beta_i{}^2}{n(n+2)}f_2<\frac{1}{4}\sum\left(\frac{\beta_i}{\beta_0}\right)^2 f_0$$
$$\frac{4\sum\beta_i{}^3}{3n(n+2)(n+4)}f_3<\frac{1}{6}\sum\left(\frac{\beta_i}{\beta_0}\right)^3 f_0$$
$$\text{the term of } f_4<\left\{\frac{1}{32}\left(\sum\left(\frac{\beta_i}{\beta_0}\right)^2\right)^2+\frac{5}{32}\sum_i\left(\frac{\beta_i}{\beta_0}\right)^4\right\}f_0$$
$$\text{the term of } f_5<\left\{\frac{1}{24}\left(\sum\left(\frac{\beta_i}{\beta_0}\right)^2\right)\left(\sum\left(\frac{\beta_i}{\beta_0}\right)^3\right)+\frac{47}{320}\sum\left(\frac{\beta_i}{\beta_0}\right)^5\right\}f_0$$
$$\text{the term of } f_6<\left\{\frac{1}{384}\left(\sum\left(\frac{\beta_i}{\beta_0}\right)^2\right)^3+\frac{39}{512}\left(\sum\left(\frac{\beta_i}{\beta_0}\right)^2\right)\left(\sum\left(\frac{\beta_i}{\beta_0}\right)^4\right)+\frac{241}{4608}\sum\left(\frac{\beta_i}{\beta_0}\right)^6\right\}f_0\ . \tag{A5}$$

β_i/β_0 is the ratio of the difference of inverse frequency to the mean and is given in the form

$$\frac{\beta_i}{\beta_0}=\frac{(1/\nu_0)-(1/\nu_i)}{1/\nu_0}\qquad \frac{1}{\nu_0}=\frac{1}{n}\sum_{i=1}^{n}\frac{1}{\nu_i}\ . \tag{A6}$$

In practice the value of $\beta_i/\beta_0\leq 1/2$ and we may expect for most molecules the mean values of $\langle(\beta_i/\beta_0)^2\rangle\sim 1/10$. We shall consider molecules XY_4 and XY_3 as examples, *i.e.* $n=9$ and $n=6$ respectively. In those cases

$$\sum\left(\frac{\beta_i}{\beta_0}\right)^2\leq 1\ ,\qquad \sum\left(\frac{\beta_i}{\beta_0}\right)^3<1\ ,$$
$$\sum\left(\frac{\beta_i}{\beta_0}\right)^n\ll 1\qquad \text{for}\quad n\geq 4\ . \tag{A7}$$

Thus, we can conclude and that the equation (A3) converges when $n\leqq 9$.

Appendix B

If in (2.11) $q_2\lambda_2<\lambda_2'$ ($\lambda_2'=\lambda_2 q_{20}$), the potential (2.2) will be well expressed as

$$E=E_0+\sum_{i=1}^{n}{}'\frac{\lambda_i}{2}q_i{}^2+\lambda_2' q_2 \tag{B1}$$

where the primed $\sum$ means the summation over i except 2. Then the equation which corresponds to (2.7) becomes

$$P(E_{l1}D)=B\int_{E=E_0}^{E=E_l+E_0}\exp(-\beta_0\sum\xi_i)\exp(\sum_i{}'\beta_i\xi_i)Q(\sum_i\xi_i)\exp(-\beta_2'(\xi_2-\xi_{20})^2+\beta_2\xi_2)$$
$$\times\prod_i{}'\left(\sqrt{\frac{E_l}{2\lambda_i}}\frac{d\xi_i}{\sqrt{\xi_i}}\right)\left(\frac{E_l}{\lambda_2'}\right)d\xi_2 \tag{B2}$$

from the transformation of $\xi_2=(\lambda_2'/E_l)q_2$ and $\xi_i=(2\lambda_i/E_l)q_i^2$ for $i\neq 2$ and

$$\beta_i=\beta_0-\frac{2E_l}{\lambda_i}\alpha_i\,,\qquad \beta_0=\frac{1}{n-1}\Sigma'\left(\frac{2E_l}{\lambda_i}\right)\alpha_i\qquad \text{for}\quad i\neq 2$$

$$\beta_2'=\left(\frac{E_l}{\lambda_2'}\right)^2\qquad\qquad \xi_{20}=\sqrt{\frac{2}{\beta_2'}}\,.$$

The function $\exp(-\beta_2'(\xi_2-\xi_{20})^2+\beta_0\xi_2)$ is expanded in power series of $(\xi_2-\xi_{20})$ at $\xi_2=\xi_{20}$ in the form

$$\exp[-\beta_2'(\beta_2'-\xi_{20})^2+\beta_0\xi_2]=\left\{\sum_{n=0}^{\infty}\frac{(-)^n(\beta_2')^n(\xi_2-\xi_{20})^{2n}}{n!}\right\}\left\{\sum_{n=0}^{\infty}\frac{\beta_0{}^n(\xi_2-\xi_{20})^n}{n!}\right\}\exp(\beta_0\xi_{20})\tag{B3}$$

because the function of ξ_2 must have maximum at ξ_{20}. Then we can obtain $\exp(-\beta_2'(\xi_2-\xi_{20})^2+\beta_2\xi_2)$ in power series of ξ_2.

Appendix C

We consider a virtual vibration in the ground state as shown in Fig. 7 which resembles to ν_4 vibration of XY_4 in the case of $m_X \ll m_Y$. β, β' be the angles which are illustrated in Fig. 7, ψ_{2px}, ψ_{2py}, ψ_{2pz} are expressed in terms of $\psi_{1\sigma}$, $\psi_{1\pi}$, $\psi_{1\bar{\pi}}$, *etc.* by the same method in (3.2), that is

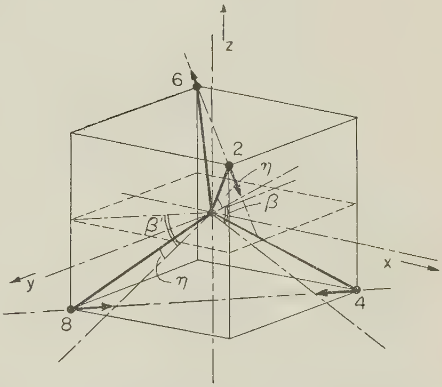

Fig. 7. Virtual vibration mode in Appendix C and angles β, β' and η.

$$\begin{aligned}\psi_{2px}&=-\frac{1}{\sqrt{2}}\cos\beta\psi_{1\sigma}+\sqrt{1-\frac{1}{2}\cos^2\beta}\left(-\frac{1}{\sqrt{2}}\cos\beta\psi_{1\pi}+\sqrt{1-\frac{1}{2}\cos^2\beta}\,\psi_{1\bar{\pi}}\right)\\ \psi_{2py}&=\frac{1}{\sqrt{2}}\cos\beta\psi_{1\sigma}+\sqrt{1-\frac{1}{2}\cos^2\beta}\left(-\frac{1}{\sqrt{2}}\cos\beta\psi_{1\pi}-\sqrt{1-\frac{1}{2}\cos^2\beta}\,\psi_{1\bar{\pi}}\right)\\ \psi_{2pz}&=\frac{1}{\sqrt{2}}\cos\beta\psi_{1\sigma}+\sqrt{1-\frac{1}{2}\cos^2\beta}\,\psi_{1\pi}\end{aligned}\tag{C1}$$

and similar expressions ψ_{2p}'s in terms of $\psi_{3\sigma}$, $\psi_{3\pi}$, $\psi_{3\bar{\pi}}$, $\psi_{5\sigma}$, $\psi_{5\pi}$, $\psi_{5\bar{\pi}}$ and $\psi_{7\sigma}$, $\psi_{7\pi}$, $\psi_{7\bar{\pi}}$.

By the similar procedure adopted in § 3 we make use of the relations

$$\begin{aligned}Q(R_2)+Q(R_4)+Q(R_6)+Q(R_8)&=4\left\{Q(R_0)+\frac{1}{2}\left(\frac{\partial^2 Q}{\partial R^2}\right)_{R=R_0}(\varDelta R)^2\right\}\\ Q(R_2)+J(R_4)+J(R_6)+J(R_8)&=4\left\{J(R_6)+\frac{1}{2}\left(\frac{\partial^2 Q}{\partial R^2}\right)_{R=R_0}(\varDelta R)^2\right\}\end{aligned}\tag{C2}$$

etc., where R_0 is C–H distance in equilibrium, $R_i=R_0+\varDelta R_i$ is C–H_i distance. When $(\varDelta R_i)^2=\eta^2R_0^2$ is taken as the change of C–H_i distance from equilibrium $(\beta=\tan^{-1}(\sqrt{1/2}+\eta))$, we obtain the formula $V=V_0+(1/2)V_{\eta 2}\cdot\eta^2$ where V_0 is the same with that in the case of ν_2 vibration and

$$\begin{aligned}V_{\eta 2}=&\frac{1}{2}\left(\frac{1}{2}\frac{\partial^2 V}{\partial R^2}\right)R_0^2-\frac{1}{4}\left(4Q_{\sigma\sigma}-\frac{1}{2}J_{\sigma\sigma}\right)+\left(4Q_{\pi\pi}-\frac{1}{2}J_{\sigma\sigma}\right)\Bigg|\\ &-\frac{3\sqrt{3}}{8}(J_{s\sigma}+I_{\sigma s})+\left(\frac{1}{2}\frac{\partial V_{hh}}{\partial R^2}\right)R_0^2\end{aligned}\tag{C3}$$

On the other hand, from the point of valence force field picture $V_{\eta 2}$ in (C3) is to be expressed in the form

$$V_{\eta 2}=\frac{1}{2}\left(\frac{1}{2}\,\frac{\partial^2 V}{\partial R^2}\right)R_0{}^2+V_{\theta 2}\ .$$

$$V_{\theta 2}=-\frac{1}{4}\left(4Q_{\sigma\sigma}-\frac{1}{2}\,J_{\sigma\sigma}\right)+\frac{1}{2}\left(4Q_{\pi\pi}-\frac{1}{2}\,J_{\pi\pi}\right)-\frac{3\sqrt{3}}{8}(J_{s\sigma}+J_{\sigma s})+\left(\frac{1}{2}\,\frac{\partial^2 V_{hh}}{\partial R^2}\right)R_0{}^2$$

Using the adjusted value by (3.12) for $\{(1/2)(\partial^2 V_{hh}/\partial R^2)\}R_0{}^2$ (0.187 times theoretical value). We obtain $(4Q_{\sigma\sigma}-(1/2)J_{\sigma\sigma})$ and the $(4Q_{\pi\pi}-(1/2)J_{\pi\pi})$ from (C7) and third equation of (3.11).

References

1) D. P. Stevenson: J. Chem. Phys. **15** (1947) 409.
2) C. A. Schaeffer: J. Chem. Phys. **18** (1950) 1501.
3) J. E. Lennard-Jones and G. G. Hall: Trans. Faraday Soc. **48** (1952) 581.
4) H. M. Rosenstock, M. B. Wallenstein, A. L. Wahrhafting and H. Eyring: Proc. Natl. Acad. Sci. U.S. **35** (1952) 667.
5) T. Watanabe: J. Phys. Soc. Japan **16** (1961) 529.
6) H. Bethe: Ann. der Physk. **5** (1930) 325.
7) G. Herzberg: *Molecular spectra and molecular structure I*, (D. van Nostrand Co., 1950) 658.
8) E. T. Whittaker and G. N. Watson: *A course of modern analysis*, (Cambridge Univ. Press, 1955) 258.
9) J. T. Tate, P. T. Smith and A. L. Vamgjam: Phys. Rev. **48** (1935) 525.
10) Van J. Greeh and H. Neuert: Z. Naturforsh. **5A** (1950) 502.
11) G. H. Wannier: Phys. Rev. **90** (1953) 817.
12) D. C. Frost and C. A. McDowell: Proc. Roy. Soc. **A241** (1957) 194.
13) G. G. Hall and J. E. Lennard-Jones: Proc. Roy. Soc. **A202** (1950) 155.
14) H. O. Pritchard and H. A. Skinner: Chem. Rev. **55** (1955) 745.
15) F. H. Field and J. L. Franklin: *Electron impact phenomena*, (Academic Press, 1957) 243.
16) O. Hirshfelder and J. W. Linnett: J. Chem. Phys. **18** (1950) 130.
17) C. Herzberg: *Molecular spectra and molecular structure II*, (D. van Nostrand Co., 1945) 181.
18) W. Bleakney, E. U. Condon and L. G. Smith: J. Phys. Chem. **41** (1937) 197.
19) American Petroleum Institute of Research Project, No. 44, *Mass spectral data*, (Carnegie Inst. of Tech., Pittsburgh, Pa, USA).

JOURNAL OF THE PHYSICAL SOCIETY OF JAPAN, Vol. 16, No. 3, MARCH, 1961

On the Additivity Rule in the Ionization Cross Section of Molecules

By Tsutomu WATANABE

Japan Atomic Energy Research Institute, Tokai-Mura,
Naka-Gun, Ibaraki-Ken, Japan

(Received April 15, 1960)

Validity of the additivity rule in the ionization cross section of molecules is investigated. So far as the present calculation is concerned, we have concluded that the rule is considered to be approximately valid within the allowance of 20% under the condition where electrons are impacted with incident energies more than 80 eV and the internuclear distance between every couple of atoms in a molecule is more than $2.5a_0$. If the internuclear distance is less than $2.5a_0$, one must take account of the diffraction effects due to the interference of waves scattered by the neighbour atoms. Numerical computation was carried out to the cases of C_nH_{2n+2} and C_nF_{2n+2}. The results for C_nH_{2n+2} were found in plausible agreement with mass spectroscopic data but those for C_nF_{2n+2} were found in small disagreement with data.

§ 1. Deduction

In an inelastic collision of an electron with a molecule, it has often been regarded that the inelastic cross section is given as the sum of the cross sections of atoms. This additivity rule is not necessarily self-evident from the theoretical viewpoint. In order to investigate the validity of the rule in the case of ionization by electron impact, we start with Schrödinger equation of many electron system with may centered field, namely

$$\left[-\frac{\hbar^2}{2m}\sum_{i=1}^{n}\nabla_i^2-E-\sum_{i,\alpha}V_\alpha(r_i)+\sum_{i>j}\frac{e^2}{r_{ij}}\right]\Phi=0 \tag{1.1}$$

where $V_\alpha(r_i)$ denotes the potential of α's core to the ith electron and m and $\hbar$ have their usual meanings. The total wave function Φ is assumed to be written in the form

$$\begin{aligned}\Phi=&F_0(\vec r_1)\Psi_0(\vec r_2,\vec r_3,\cdots,\vec r_n)\\&+\int F_\kappa(\vec r_1)\Psi_\kappa(\vec r_2,\vec r_3,\cdots,\vec r_n)\,d\kappa\\&+\sum_{i\neq1}\int G_\kappa^{i}(\vec r_i)\Psi_\kappa(\vec r_1,\vec r_2,\cdots,\vec r_{i-1},\vec r_{i+1},\cdots,\vec r_n)d\kappa\end{aligned} \tag{1.2}$$

where F_0 denotes the wave function in the field of a neutral molecule, F_κ the wave function of an inelastically scattered electron, G_κ^i that of an exchanged inelastically scattered one, Ψ_0 the total wave function of the neutral molecule, and Ψ_κ the product of the wave function of a molecular ion produced by ionization and that of an ejected electron. In the above description, the symbolic letters with suffix 1 relate to the incident electron, the letters with suffix i except 1 relate to an electron in the molecule, the suffix κ means the magnitude of momentum vector of the ejected electron, i in G_κ^i means the labeled number of which an electron is to be exchanged and scattered for the incident electron.

The wave function Ψ_0 may be written in the form of Slater's determinants which are constructed by one electron wave functions of molecular orbitals, and orthogonality relationship between every two molecular orbital wave functions of different kinds is assumed. When our wave function Ψ_0 in the form of Slater's determinants is expanded in terms of ψ_0 which is to be ionized in the form

$$\Psi_0=\sum_i(-1)^i\psi_0(\vec r_i)\Psi_0'(\vec r_2,\vec r_3,\cdots,\vec r_{i-1},\vec r_{i+1},\cdots,\vec r_n)\,, \tag{1.3}$$

the wave function Ψ_κ is assumed to be expressed by the wave function of the ejected electron ψ_κ and $\Psi_0'(\vec r_2,\vec r_3,\cdots,\vec r_{i-1},\vec r_{i+1},\cdots,\vec r_n)$ in the form

$$\Psi_\kappa=\sum_i(-1)^i\psi_\kappa(\vec r_i)\Psi_0'(\vec r_2,\vec r_3,\cdots,\vec r_{i-1},\vec r_{i+1},\cdots,\vec r_n)\,. \tag{1.4}$$

In short, the above description means that we neglect the change of Ψ_0' by ionization. We have adopted the analogical method of calculation to that for electronic collisions with atoms for use in the calculations of differential cross section for ionization of molecules[1], and then we have taken account of the influence of exchange effect of an incident electron for an electron in the molecule as well as the influence of distortion effect of an incident electron by a neutral molecular field on differential cross sections. Owing to the fact that the interaction potential between an incident electron and a molecule is not spherically symmetrical the calculation of a cross section for ionization needs proper approximation. Our incident electron may be scattered by the electron in the individual atomic orbitals in LCAOMO as independent scattering centers so that the amplitudes for scattering by the electron in the individual AO with proper allowance for phase difference may be determined by the same method as in elastic collision of electron with molecules.

The differential cross section for ionization of a molecule $I_\kappa(\theta,\varphi)$ in terms of the antisymmetrical scattered amplitude by an electron in rth AO $\phi_r^-(\theta,\varphi)$ is given by

$$I_\kappa(\theta,\varphi)=\frac{k_\kappa}{k_0}\left\{\sum_r a_r^2|\phi_r^-(\theta,\varphi)|^2+\sum_{r\neq r'} a_r a_{r'}|\phi_r^-(\theta,\varphi)\cdot\phi_{r'}^-(\theta,\varphi)|\exp\left(-i(\vec{k}_0-\vec{k}_\kappa)\vec{R}_{rr'}\right)\right\} \tag{1.5}$$

where $(k_\kappa/k_0)|\phi^-(\theta,\varphi)|^2$=differential cross section of an atom for ionization of rth AO, a_r is the coefficient of rth AO in LCAOMO, k_0, k_κ, and κ are the magnitudes of wave vectors of incident, scattered and ejected electrons respectively, θ and φ are the angles of scattering and of ejection with respect to the direction of the incident electron, and $R_{rr'}$ is the internuclear distance between r and r'th atom.

Usual experiments are carried out on molecules in the gas phase so that the orientation of molecule with respect to the direction of the incident electron should be considered at random, and one must average $I_\kappa(\theta,\varphi)$ over the molecular orientation, namely

$$\left.\begin{aligned}\frac{1}{4\pi}\int_\sigma I_\kappa(\theta,\varphi)\,d\sigma&=\frac{k_\kappa}{k_0}\left[\sum_r a_r^2|\phi_r^-|^2+\sum_{r\neq r'} a_r a_{r'}|\phi_r^-\cdot\phi_{r'}^-|\,\frac{\sin(K\cdot R_{rr'})}{K\cdot R_{rr'}}\right]\\ Q&=\frac{1}{4\pi}\int_0^{\kappa_{\max}}\int_\Omega\int_\omega\int_\sigma I_\kappa(\theta,\varphi)\,d\Omega\,d\omega\,d\kappa\,d\sigma\end{aligned}\right\} \tag{1.6}$$

where the integration is to be carried out over the solid angle $d\sigma$ of direction of molecule, over the solid angle $d\Omega$ of scattered electron, and over that of ejected electron $d\omega$.

Eqs. (1.5) or (1.6) shows that the total cross section can be expressible only in terms of atomic cross sections and the interactions between all possible couples of antisymmetrical scattered amplitudes caused by different AO's in the molecule which depend on $R_{rr'}$. If cross terms in (1.6) are regarded to be negligible compared with square terms, we can take the total ionization cross section as the sum of its atomic components. To verify this we consider the homonuclear diatomic case. $\phi_r^-(\theta,\varphi)$ does not depend on the coordinate of atom r and $|\phi_r^-\cdot\phi_{r'}^-|=|\phi_r^-|^2$ in the homonuclear case. Then we assume that the θ-, φ- and κ-dependences of each $|\phi_r^-|^2$ and also $|\phi_r^-\cdot\phi_{r'}|$ resemble to the differential cross section of hydrogen atom in its θ-, φ- and κ-dependences. Massey and Mohr[2] obtained analytically the θ-, φ- and κ-dependences of the cross section for hydrogen atom by means of Born's approximation and by taking the Coulomb function for the wave function of an ejected electron and plane wave for that of scattered one. The θ- and φ-dependences for hydrogen atom obtained through Born's approximation are found in plausible agreement with experimental data in the incident energy region above 80 eV[3]. According to the numerical results of θ- and φ-dependences which were obtained by Massey and Mohr[2], we take a following approximate formula for $\int|\phi_r^-|^2 d\omega$

$$\int|\phi_r^-|^2 d\omega=\frac{A}{K^2}\,\kappa\exp\left(-\sqrt{\frac{3\hbar^2}{2mE}}\cdot\kappa\right) \tag{1.7}$$

where A is a constant, K is the magnitude of the momentum change between incident and scattered electrons, i.e.

$$K^2=k_0^2+k^2-2k_0k\cos\theta\ .$$

By numerically integrating $|\phi_r^-|^2$ and

$$|\phi_r^-|^2\sin(K\cdot R_{rr'})/(K\cdot R_{rr'})$$

over K and κ with the aid of IBM–650 computor under the condition of momentum and energy conservation throughout the process of ionization, we have obtained the results as shown in Fig. 1. From this figure we can see that the validity of the additivity depends rather on the magnitude of internuclear distance $R_{rr'}$ than on the magnitude of wave vector of the incident wave k_0. It is found that in the range of the incident energy above 80 eV and in the range $R_{rr'}$ larger than $2.5a_0$ the total ionization cross section is expressible in terms of atomic components rather well within the allowance of 20%.

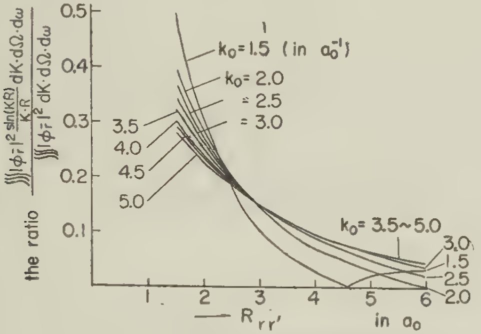

Fig. 1. The $R_{rr'}$ and k_0 dependences of the ratio of cross term to square terms

$$\iiint|\phi_r^-|^2\frac{\sin KR}{K\cdot R}d\kappa\, d\Omega\, d\omega\Big/\iiint|\phi_r^-|^2\, d\kappa\, d\Omega\, d\omega\,.$$

in the H–H case

§ 2. Applications to Hydro- and Fluorocarbons

According to the previous results, we compare the total ionization measurement of saturated hydro- and fluorocarbons with our calculations. Considering the results in Fig. 1 and adopting $2.916a_0$ and $2.083a_0$ as the internuclear distances of C–C and C–H bonds in hydrocarbons, and $2.953a_0$ and $2.499a_0$ as those of C–C and C–F bonds in fluorocarbons[4),5)], we may safely say that it is enough to take account of the cross terms between the nearest neighbour atoms in (1.6) and neglect those between the atoms which are more distant each other. From this we obtain the expression of the total ionization cross sections for hydro- and fluorocarbons in the form

$$\left.\begin{aligned} Q&=\sum_r a_r^2Q_r+\sum_{r\neq r'}a_ra_{r'}Q_{rr'}\\ Q_r&=\iiint|\phi_r^-|^2\, d\kappa\, d\Omega\, d\omega\\ Q_{rr'}&=\iiint|\phi_r^-\phi_{r'}^-|\,\frac{\sin(K\cdot R_{rr'})}{K\cdot R_{rr'}}\,d\kappa\, d\Omega\, d\omega \end{aligned}\right\} \tag{2.1}$$

where the sums $\sum_{r\neq r'}$ are taken only over the couples of nearest neighbour atoms. Assuming that the φ- and κ-dependencies of each ϕ_r^- are not different from each other, we have

$$Q_{rr'}=\int A_0\sqrt{I_r}\sqrt{I_{r'}}\,\frac{\sin(K\cdot R_{rr'})}{K\cdot R_{rr'}}\,d\Omega \tag{2.2}$$

where I_r is a differential cross section for ionization of an atom and A_0 is the ratio of the atomic component of a cross section of a molecule to the cross section of an atom. Each Q_r and I_r were expressed by Bethe in the forms

$$\left.\begin{aligned} Q_r&=A_0\frac{4\pi m^2e^4c_rZ_r}{\hbar^4k_0^2E}\log\left(\frac{2\hbar k_0^2}{mE}\right)\\ I_r&=\frac{4k_\kappa m^2e^4c_rZ_r}{\hbar^4k_0EK^2} \end{aligned}\right\} \tag{2.3}$$

where e is electronic charge, Z_r is the number of electron in an atomic orbital, E is the ionization energy of a molecular level under consideration, and

$$c_r=(Z_{\text{eff}}^2/n^2a_0^2)\int|(r|x|\kappa)|^2\, d\kappa$$

which was calculated and taburated in Bethe's paper[6)]. The expressions (2.3) were obtained by the method of Born's approximation as well as by the treatment in which the plane waves were adopted as the wave functions of scattered and ejected electrons, and only dipole matrix elements were taken into account under calculation. However, we may well take (2.3)'s for the proper calculation, because I_r is not so much different from the experimental data in the point of K dependency over the incident energy above 80 eV[3)].

We ignore the contribution from the ionization of $(1s)$ orbital electrons of C or F atom in the total cross sections for ionization. The bonding orbitals of C atoms are considered to be the tetrahedrally hybridized orbitals of $(2s)(2p)^3$ and the bonding orbitals of F atoms are considered to be $(2p\sigma)$ orbitals. We have the total cross section for ionization in the forms

$$\begin{aligned} Q_{\text{h.c.}}=n[&2a_{\text{H}}^2Q_{\text{H}}+2a_{\text{C}}^2Q_{\text{C}}+2a_{\text{C}}'^2Q_{\text{C}}\\ &+4a_{\text{C}}a_{\text{H}}Q_{\text{CH}}+2a_{\text{H}}^2Q_{\text{HH}}+2a_{\text{C}}^2Q_{\text{CC}}]\\ &-2a_{\text{C}}^2Q_{\text{CC}}+4a_{\text{C}}'a_{\text{H}}Q_{\text{CH}}+4a_{\text{H}}^2Q_{\text{HH}}\\ &+2a_{\text{H}}^2Q_{\text{H}}+2(a_{\text{C}}^2-a_{\text{C}}'^2)Q_{\text{C}} \end{aligned} \tag{2.4}$$

for saturated hydrocarbons

$$Q_{\text{f.c.}}=n[2a_F{}^2Q_F+2a_C{}^2Q_C+2a_C{}'^2Q_C+4a_Ca_FQ_{CF}+2a_F{}^2Q_F+2a_C{}^2Q_{CC}]$$
$$-2a_C{}^2Q_{CC}+4a_C{}'a_FQ_{CF}+4a_F{}^2Q_{FF}+2a_F{}^2Q_F+2(a_C{}^2-a_C{}'^2)Q_C$$

for saturated fluorocarbons, where n is the number of carbon atoms. Here

$$Q_C=\frac{1}{4}Q_{C2s}+\frac{3}{4}Q_{C2p}\ ,$$

$$Q_F=\left[\frac{2}{a_F{}^2}Q_{F2s}+\frac{4}{a_F{}^2}Q_{F2p}+Q_{F2p}\right],$$

$$Q_{CC}=\iiint A_0\left(\frac{1}{4}I_{C2p}+\frac{3}{4}I_{C2p}\right)\frac{\sin(K\cdot R_{CC})}{KR_{CC}}\,d\kappa\,d\Omega\,d\omega\ ,$$

$$Q_{CH}=\iiint A_0\left(\frac{1}{4}I_{C2s}+\frac{3}{4}I_{C2p}\right)^{1/2}I_H{}^{1/2}\frac{\sin(K\cdot R_{CH})}{K\cdot R_{CH}}\,d\kappa\,d\Omega\,d\omega\ ,$$

$$Q_{HH}=\iiint A_0I_H\frac{\sin(K\cdot R_{HH})}{K\cdot R_{HH}}\,d\kappa\,d\Omega\,d\omega\ ,$$

$$Q_{CF}=\iiint A_0\left(\frac{1}{4}I_{C2s}+\frac{3}{4}I_{C2p}\right)^{1/2}I_{F2p}{}^{1/2}\frac{\sin(K\cdot R_{CF})}{K\cdot R_{CF}}\,d\kappa\,d\Omega\,d\omega\ ,$$

and

$$Q_{FF}=\iiint A_0I_{F2p}\frac{\sin(K\cdot R_{FF})}{K\cdot R_{FF}}\,d\kappa\,d\Omega\,d\omega$$

where Q_F denotes the total cross section of F atom for ionization muliplied by A_0, Q_{F2s} that of F2s electron, I_{C2p} the differential cross section of C2p electron and so on. The atomic coefficients a_H, a_C, a_C', and a_F are calculated from the estimated dipole moments of C–H and C–F bonds[7] (a_C is the coefficient of C in C–C bond eigenfunction, a_C' is that in C–H or C–F bond eigenfunction). Here the electronic orbitals are constructed by the bond eigenfunctions of each C–C and C–H in the hydrocarbon case and by those of each C–C, C–F and the wave function of lone pair F2p electron in the fluorocarbon case.

Comparing the calculated values of C_4H_{10} and C_3F_8 with those obtained by experiment, we determine the values of A_0 for hydro- and fluorocarbons respectively. The both results of calculation are shown in Fig. 2 in plausible agreement with experiments[8]. Moreover, from the intercept and the slope of experimental curves (dotted lines), granting that $a_C{}^2=a_C{}'^2$ we can expect

$$\left.\begin{array}{l} -2a_C{}^2Q_{CC}+4a_C{}'a_HQ_{CH} \\ \qquad +4a_H{}^2Q_{HH}+a_H{}^2Q_H>0 \\ \text{for hydrocarbons and} \\ -2a_C{}^2Q_{CC}+4a_C{}'a_FQ_{CF} \\ \qquad +4a_F{}^2Q_{FF}+a_F{}^2Q_F\lesssim 0 \end{array}\right\}\quad(2.5)$$

for fluorocarbons.

The condition in (2.5) is acceptable for hydrocarbons but that for fluorocarbons does not seem to be acceptable. When we considered that Q_{CC}, Q_{CF}, or Q_{FF} are of the order less than one forth of Q_{F2p} or of Q_{F2s} from the condition in (2.5) for fluorocarbons, we may infer that the cross section of F atom is negative. Consequently, the validity of approximation (2.1) is questionable to the data for C_nF_{2n+2} in the strict sence.

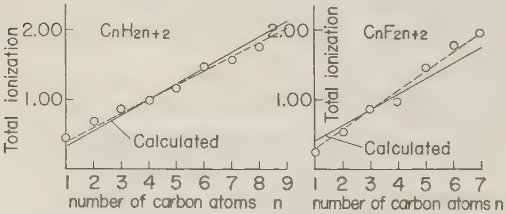

Fig. 2. The relation between total ionization and number of carbon atoms.

References

1) N. F. Mott and H. S. W. Massey: *The theory of atomic collisions*, (Oxford Univ. Press, 2nd ed., 1949), 244, etc.

2) H. S. W. Massey and C. B. O. Mohr: Proc. Roy. Soc. **A**, **140** (1933) 613. T. Yamanouchi

and M. Kotani: Proc. Phys-Math. Soc. Japan **22** (1940) 14.
3) J. T. Tate and R. R. Palmer: Phys. Rev. **40** (1932) 731.
4) C. A. Coulson: *Valence*, (Oxford Univ. Press, 1953), 200.
5) P. W. Allen and L. E. Sutton: Acta. Cryst. **3** (1950) 46.
6) H. Bethe: Ann. der Physik **5** (1930) 325.
7) H. O. Pritchard and H. A. Skinner: Chem. Rev. **55** (1955) 745.
8) F. L. Mohler, et al.: J. Research N. B. S. **45** (1950) 235. F. L. Mohler, et al.: Ibid, **49** (1952) 343.

JOURNAL OF THE PHYSICAL SOCIETY OF JAPAN, Vol. 16, No. 3, MARCH, 1961

The Optical Properties of Cadmium Telluride in the Far Infrared Region

By Akiyoshi MITSUISHI

Department of Applied Physics, Faculty of Engineering, Osaka University, Osaka, Japan

(Received November 9, 1960)

The reflection spectra of CdTe were measured in the spectral region from 20 μ up to about 400 μ at the two different temperatures, 90°K and 300°K. The Reststrahlen band was found at 65 μ with peak reflectivity of 92% at 90°K and 67 μ with the peak reflectivity of 77% at 300°K. The reflection spectra were analysed by Kramers-Kronig dispersion relation to obtain the optical constants n and k. Combining these values, the fundamental lattice dispersion frequencies of the bulk material were determined to be 140 cm^{-1} (71.2 μ) at 300°K and 144 cm^{-1} (69.5 μ) at 90°K. The damping constant was also obtained.

§ 1. Introduction

Cadmium Telluride is one of the $\mathrm{II_B}$–$\mathrm{VI_B}$ semiconductors, and it is also isoelectronic to InSb. The optical properties of this material have not been measured extensively[1]. Garlick *et al*[2] measured the refractive index in the near infrared region and suggested that the binding of the CdTe is almost homopolar, as the difference of the static and optical dielectric constant is small. The measurement of the Reststrahlen band is useful for the estimation of the polar character, and recently such measurements have been made for many diatomic semiconducting materials.

The fundamental lattice dispersion frequency of the powdered $\mathrm{II_B}$–$\mathrm{VI_B}$ compounds suspended in polyethylene have been reported in the recent note[3], but it was found that the value obtained with the powdered material was different from that of the bulk material. As a large crystal of CdTe, which is enough to make reflection measurement by the far infrared spectrometer, was obtained, the investigation was made in the spectral region from 20 μ up to about 400 μ at the two temperatures, 90°K and 300°K. The reflection spectra were analysed by Kramers-Kronig dispersion relation to obtain the optical constants n and k in the wavelength region around the reflection peak. Combining these values with Drude dispersion formula, the fundamental lattice dispersion frequency and the damping constant were obtained.

It is noted that the frequency of CdTe is smaller than that of InSb, but is larger than that of AgI which is also isoelectronic to CdTe.

In the meantime, Moss[4] reported that the effective charge e^*/e of CdTe was 0.83, when the Reststrahlen wavelength of 69 μ calculated from the compressibility data was used.

§ 2. Experimental

The far infrared vacuum grating spectrometer used in this investigation was already reported by Yoshinaga *et al*[5]. For the reflection measurement, the optical attachment shown in Fig. 1 is introduced in the optical path in front of the entrance slit. M_1 and M_3 are the plane mirrors and M_2 is a spherical mirror. These mirrors are mounted on a thick brass base-plate together with the positioning knock located at A to keep the cryostat in the correct position. The optical beam, which is focused on the entrance slit when this attachment is removed, is deflected by M_1 to form the image of source on the specimen mounted in the cryostat and the reflected beam from the specimen is focused on the entrance slit dy M_2 and M_3. The incident angle of the deam to the reflecting surface is 12°.

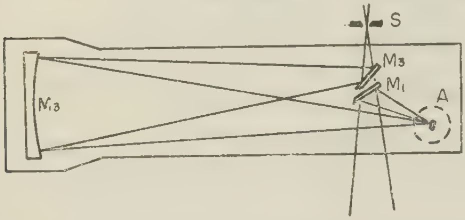

Fig. 1. The optical attachment for use in the reflection measurement at incident angle of 12°. M_1, M_3: plane mirror, M_2: spherical mirror, A: positioning knock, S: entrance slit.

The reference mirror and the sample to be measured were attached to the holder of the cryostat for reflection measurement. The cryostat is made of metal and it is so designed that either the reference mirror or the sample can be brought manually into the optical path by the rack and pinion mechanism without disturbing the vacuum of the spectrometer. The cryostat has the polyethylene window of 1 mm thick inclined to the optical axis of the spectrometer to avoid disturbance by reflection from the window surface and is evacuated separately from the vacuum tank of the spectrometer.

The sample used in this measurement is the zone refined polycrystalline crystal, the surface of which is ground and polished.

The reflectivity was measured by comparing the reflected intensity from the sample with that from the reference mirror. The final measurement was made by the point-by-point procedure to get the higher accuracy. The uncertainty in the percent reflectivity is ±1% in the spectral region shorter than 100 μ and about ±2% in the longer wavelength region.

§ 3. Experimental Result

Fig. 2 shows the reflection curve of CdTe at 300°K from 20 μ up to about 400 μ. General figure of the curve is similar to the other crystals of the zincblende structure and no side band was present. Impurity content of this specimen was not known. And, no free carrier effect was observed in this spectral region.

The change of the Reststrahlen band by lowering the temperature is shown in Fig. 3.

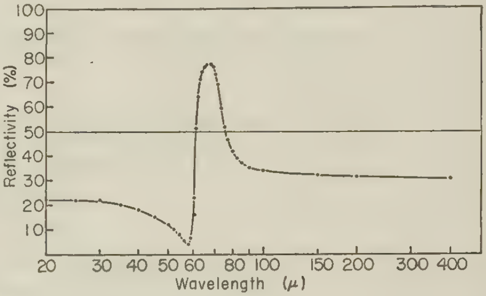

Fig. 2. The reflection spectrum of CdTe in the wavelength region from 20 μ to 400 μ at the temperature of 300°K.

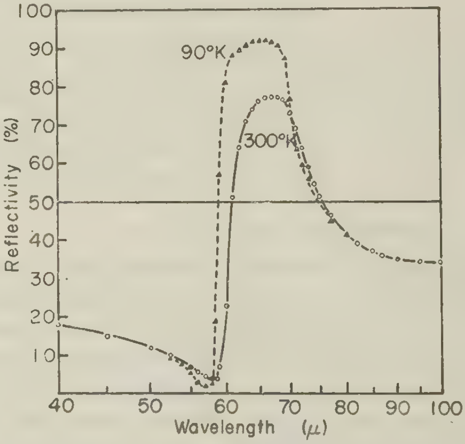

Fig. 3. The Reststrahlen reflection spectra of CdTe at the two temperature 90°K and 300°K

The band became steeper and shifted slightly to the shorter wavelength side with marked increase in the peak reflectivity. The peak reflectivity was 92% at 90°K compared with 77% at 300°K.

The minimum reflectivity was found at 57.5 μ at 90°K and 58.0 μ at 300°K. The Reststrahlen wavelength was 65 μ at 90°K and 67 μ at 300°K (The band center was assumed to correspond to this wavelength).

§ 4. Calculation of the Optical Constants

Kramers-Kronig relation was used to obtain the optical constants from the single reflection spectrum. This method of analysis has recently come into frequent use for various kinds of reflection spectra[6].

For the normal incident light the complex amplitude of reflection is given by

$$\rho=\frac{N-1}{N+1}=\frac{n-ik-1}{n-ik+1}=re^{i\theta}\,, \qquad (1)$$

where N is the complex refractive index and equal to $(n-ik)$, n is the real refractive index, k is the extinction coefficient, r is the square root of the reflectivity R, and θ is the phase shift upon reflection. The reflectivity R is given by

$$R=\left|\frac{N-1}{N+1}\right|^2=\frac{(n-1)^2+k^2}{(n+1)^2+k^2}\,. \qquad (2)$$

Kramers-Kronig dispersion relation interrelates $\ln r$ and θ. In the infrared region the reflectivity is easily measured and θ can be calculated from the following relation[6,7]

$$\theta(\lambda)=\frac{2\lambda}{\pi}\int_0^\infty\frac{\ln\sqrt{R_1}-\ln\sqrt{R}}{\lambda_1^2-\lambda^2}\,d\lambda_1\,. \qquad (3)$$

The integral covers the whole spectral region but, as the contribution from the wavelength remote from λ is small, it is enough if the detailed knowledge of the reflectivity in the spectral region around λ is learned.

With the calculated θ and the observed value of R, n and k can be calculated by the following relations derived from Eq. (1),

$$n=\frac{1-R}{1+R-2\sqrt{R}\cos\theta}\,, \qquad (4)$$

$$k=\frac{-2\sqrt{R}\sin\theta}{1+R-2\sqrt{R}\cos\theta}\,. \qquad (5)$$

The computation of θ was performed by the electronic computer. In this calculation the reflectivity was considered to be constant in the wavelength regions shorter than 20 μ and longer than 400 μ. The phase angle obtained is shown in Fig. 4.

The optical constants which were calculated from these phase angle were given in Fig. 5.

§ 5. Discussion of the Result

The properties of the Restsrahlen band are described by Drude dispersion formula

$$n^2-k^2=\varepsilon_\infty+\frac{(\varepsilon_0-\varepsilon_\infty)\left[1-\left(\frac{\omega}{\omega_0}\right)^2\right]}{\left[1+\left(\frac{\omega}{\omega_0}\right)^2\right]^2+\left(\frac{\omega}{\omega_0}\right)^2\left(\frac{\gamma}{\omega_0}\right)^2}\,, \qquad (6)$$

$$2nk=\frac{(\varepsilon_0-\varepsilon_\infty)\frac{\omega}{\omega_0}\frac{\gamma}{\omega_0}}{\left[1-\left(\frac{\omega}{\omega_0}\right)^2\right]^2+\left(\frac{\omega}{\omega_0}\right)^2\left(\frac{\gamma}{\omega_0}\right)^2}\,, \qquad (7)$$

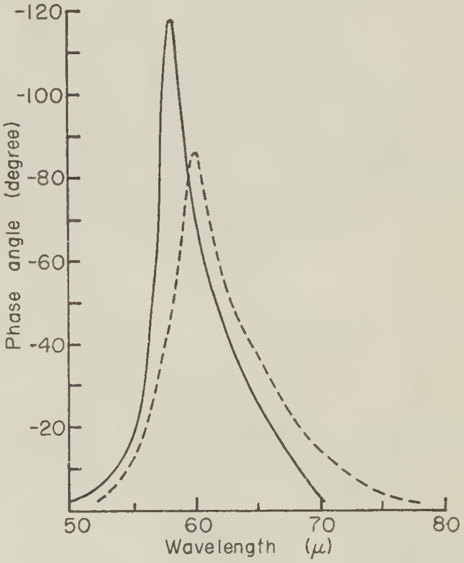

Fig. 4. The phase angle calculated by Eq. (3) for the Reststrahlen spectra of CdTe at 90°K and 300°K

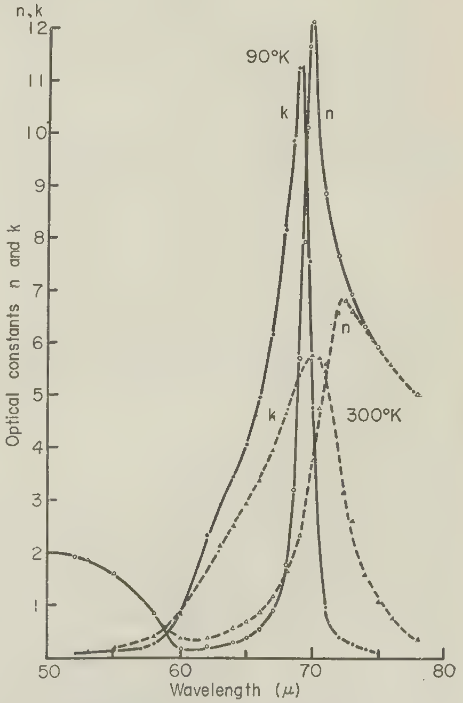

Fig. 5. Optical constant of CdTe around the Reststrahlen peak for the temperatures of 90°K and 300°K.

where ε_0 and ε_∞ are the static and optical dielectric constants, respectively, ω_0 is the fundamental lattice dispersion frequency, and γ is the damping constant. It is clear from Eq. (7) that $2nk\omega$ shows its maximum value at $\omega=\omega_0$. Thus the fundamental lattice dispersion frequency can be obtained from the plot of $nk\omega$ against frequency. Such a plot with wavelength is shown in Fig. 6 using n and k values given in Fig. 5. From the peak of these curve, ω_0 is determined to be 144 cm^{-1} (69.5 μ) at 90°K and 140 cm^{-1} (71.2 μ) at 300°K. From the compressibility data, Moss[4] calculated this wavelength to be 145 cm^{-1} (69 μ), which accords to the data mentioned above. In the previous note[3], the frequency of 150 cm^{-1} was reported as ω_0 with the powdered materials. It is observed for many other compounds[8] that the absorption maximum frequency obtained with the powder suspended in polyethylene is always larger than the infrared dispersion frequency of the bulk or evapolated materials.

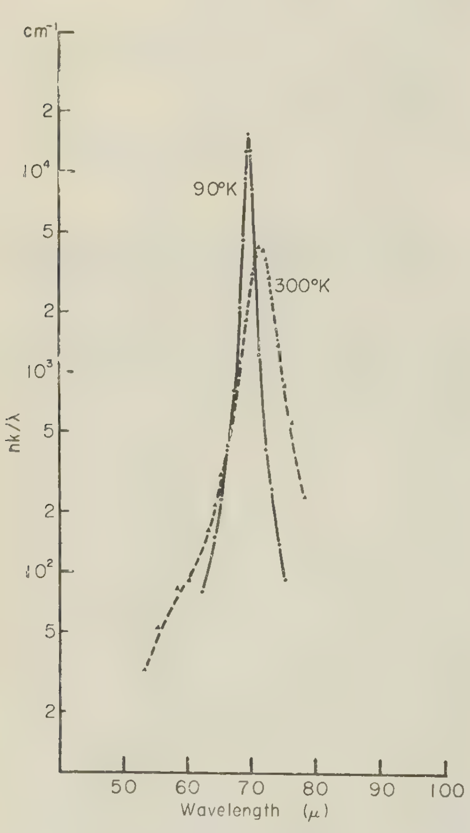

Fig. 6. The plot of $\frac{kn}{\lambda}$ against λ at the temperatures of 90°K and 300°K.

If the damping constant is neglected in Drude dispersion formula, perfect reflection is obtained in the frequency range from ω_0 to $\omega_l=\sqrt{\frac{\varepsilon_0}{\varepsilon_\infty}}\,\omega_0$. When γ increases from zero, the peak reflectivity decreases. Thus, the steep rise of the Reststrahlen band with the marked increase in the peak reflectivity at the low temperature may be understood by the interpretation that the damping constant becomes very small at the low temperature.

The damping constant is given by the following relation which can be derived from Eq. (7),

$$\frac{\gamma}{\omega_0}=\frac{(\varepsilon_0-\varepsilon_\infty)\omega_0}{2(nk\omega)_{\max}}\simeq\frac{\varepsilon_0-\varepsilon_\infty}{2(nk)_{\max}}\,. \tag{8}$$

The damping constant is also available from the following relation

$$\frac{\gamma}{\omega_0}=\left(1-\frac{\lambda_0}{\lambda_{1/2}}\right)\left(1+\frac{\lambda_{1/2}}{\lambda_0}\right), \tag{9}$$

where $\lambda_{1/2}$ is the wavelength by which $\frac{nk}{\lambda}$ becomes the half of its maximum value.

The value of ε_0 is reported to be 11[9]. The value of $\varepsilon_\infty(=n_\infty^2)$ is somewhat uncertain. Moss[4] obtained 2.68 for n_∞ by fitting the two measured values[2] of the refractive index to the simple dispersion formula. If the damping constant is neglected, rough estimate of n_∞ can be made by the relation

$$\frac{\lambda_0}{\lambda_{\min}}=\sqrt{\frac{\varepsilon_0-1}{n_\infty^2-1}}\,, \tag{10}$$

where $\lambda_{\min}$ is the wavelength of the minimum reflectivity. The values obtained are 2.7 for 90°K and 2.8 for 300°K. The reflectivity at 20 μ gives 2.7. Taking 2.68 for n_∞ in Eq. (8), the following values are obtained for $\frac{\gamma}{\omega_0}$.

	90°K	300°K
From Eq. (8)	0.02	0.06
From Eq. (9)	0.02	0.05

At the low temperature the damping constant decreases appreciably.

Recently Merten[10] has derived the following expression from the lattice dynamical theory for the transverse optical lattice frequency ν_t of the zincblende lattice,

$$\nu_t=\frac{1}{\pi}\sqrt{\frac{1}{M}\left(a\,c_{11}-1.30\,\frac{e^{*2}}{v_a}\right)}\,,$$

where M is the reduced mass, a is the lattice constant, c_{11} is the elastic constant, e^* is the effective charge and v_a is the volume of the unit cell. As c_{11} of CdTe, to the author's knowledge, is not known, it is not possible to compare the experimental value with this theory. It may be interesting to note that the fundamental lattice dispersion frequencies of InSb, CdTe, and AgI, which form the isoelectronic series, and the reduced masses and the lattice constants of them are almost the same, differ markedly. The Reststrahlen band of InSb was measured by Yoshinaga and Oetjen[11], and Spitzer and Fan[12]. The former give the Reststrahlen frequency of 183 cm^{-1} (54.6 μ). Analysing this Reststrahlen band, Moss *et al*[13] derived the fundamental lattice dispersion frequency of 177.6 cm^{-1}. The frequency of CdTe is 144 cm^{-1} (71.2 μ). The Reststrahlen band of AgI has not been measured. However, the absorption band at 110 cm^{-1} (91 μ) was observed with the powder suspended in polyethylene. As the higher value is usually obtained with the powdered material the frequency for the bulk material will be smaller than this value.

The effective charge e^*/e is calculated from the dielectric constant and the fundamental lattice dispersion frequency. For CdTe, Moss[4] obtained 0.83 with the wavelength of 69 μ. Present value of 71.2 μ does not change this value after all. The value for InSb is 0.36[12]. That for AgI is not known yet. Thus the lattice frequency increases as the ionicity decreases in this isoelectronic series. This property of the isoelectronic series was pointed out in the other isoelectronic compound[14].

Acknowledgement

The author wishes to express his cordial thanks to Prof. H. Yoshinaga for his valuable suggestion and encouragement throughout this work and is grateful to Dr. N. Munesue of the Electrical Communication Laboratory for providing CdTe crystal and Dr. S. Ibuki of the Mitsubishi Electric Co. for his interest in this work.

References

1) T. S. Moss: "Optical Properties of Semiconductors" (1959) p. 221.
2) G. F. J. Garlick, J. M. Hough and R. A. Fatehally: Proc. Phys. Soc. London **72** (1958) 925.
3) A. Mitsuishi, H. Yoshinaga and S. Fujita: J. Phys. Soc. Japan **13** (1958) 1235.
4) T. S. Moss: Proc. Phys. Soc. London **74** (1959) 491.
5) H. Yoshinaga, S. Fujita, S. Minami, A. Mitsuishi, R. A. Oetjen and Y. Yamada: J. Opt. Soc. Amer, **43** (1958) 315.
6) T. S. Robinson: Proc. Phys. Soc. London **65B** (1952) 910; T. S. Robinson and W. C. Price: *Ibid.* **66B** (1953) 969; F. C. Jahoda: Phys. Rev. **107** (1957) 1261; F. Abeles and J-P. Mathieu: Ann. Physique **3** (1958) 5, H. R. Philipp and E. A. Taft: Phys. Rev. **113** (1959) 1002, M. P. Rimmer and D. L. Dexter: J. Appl. Phys. **31** (1960) 775, M. Gottlieb: J. Opt. Soc. Amer. **50** (1960) 343.
7) See Ref. 1, p. 22.
8) Unpublished result.
9) F. A. Kröger and D. DeNobel: J. Electronics **1** (1955) 190.
10) L. Merten: Z. Naturforsch. **13a** (1958) 662, 1067.
11) H. Yoshinaga: Phys. Rev. **100** (1955) 753; H. Yoshinaga and R. A. Oetjen: *Ibid.* **101** (1956) 526.
12) W. C. Spitzer and H. Y. Fan: Phys. Rev. **99** (1955) 1893.
13) T. S. Moss, S. D. Smith and T. D. F. Hawkins: Proc. Phys. Soc. London **70** (1957) 776.
14) G. Picus, E. Burstein, B. W. Henvis and M. Hass. J. Phys. Chem. Solids **8** (1959) 282.

JOURNAL OF THE PHYSICAL SOCIETY OF JAPAN, Vol. 16, No. 3, MARCH, 1961

Interaction of Exciton with Electron Trapping Centers in Alkali Halide Crystals.

3. Exciton Induced Photoconductivity of U center*

By Masayasu UETA, Masamitsu HIRAI and Mikihiko IKEZAWA
Department of Physics, The Faculty of Science, Tohoku University, Sendai.

(Received November 10, 1960)

Photoconductivity of KCl and KBr crystals containing U centers has been investigated as a function of illuminating photon energy, in both the regions of U absorption and the fundamental absorption bands of host crystals. The maximum conductivity occurs where the fundamental absorption starts. The photoconductivity curve is similar to the spectral distribution of the quantum efficiency of U→F conversion as reported previously. The wavelength of light which enhances the maximum conductivity shifts to the longer wavelength side if the U center concentration is below 5×10^{16}/cc. This fact is in agreement with that of the quantum yield dependence on the concentration. The behaviour of Br-ion band in KCl crystal upon the photoconductivity was also investigated and it was concluded that localized excitons which may be considered to be produced by photons absorbed in Br band, have the same property as the free excitons in the host crystal so far as the effect on U centers is concerned.

§ 1. Introduction

It is believed that excitons are generated in alkali halide crystals when the crystals are irradiated with ultra violet light in the region of their fundamental absorption bands. On the problem of exciton effect upon F center, the investigations of photoelectric emission from the center has been performed by Apker and his co-workers[1]. They showed that excitons can ionize F centers.

Since a few years ago, we have been investgating the similar effect of ultra violet lighit on the color centers from the photochemical point of view and it was found that F, M, R and U centers can be easily destructed by the exciton[2,3]. A U center is considered to be an H^- ion subsititutionaly occupying the site of a halogen ion.

Recently we have reported on the measurements of the quantum efficiency of exciton-induced photochemical conversion of a U center to an F center[4]. It was shown that the ultra violet light absorbed in the host crystal can convert a U center with a quantum yield of nearly unity in both KCl and KBr crystals when the concentration of U center is larger than 1.0×10^{17}/cc, but the yield decreases when the concentration is below 5×10^{16}/cc. From this fact, the diffusion of an exciton has been proposed.

The present report deals with the photoconductivity measurements of U center in both spectral regions of U band and the fundamental absorption bands in KCl and KBr crystals. From the similar investigations in KCl crystals containing Br ion as an impurity, the nature of a localized exciton was discussed.

§ 2. Experimental Procedures

KCl and KBr crystals containing only U centers were prepared by the conventional method as described before. The concentrations were $4.0\times10^{16}\sim6.0\times10^{17}$/cc and $2.3\times10^{16}\sim3.1\times10^{18}$/cc in KCl and KBr crystals, respectively. Some of them were kept at room temperature for as long as five years after the preparation. The other crystals have various histories as tabulated in Table I.

Fig. 1 shows the crystal holder.* Crystals were held between two electrodes made of silver plated copper. One of them has holes of 1 mm in diameter which make light incident on the crystal. The other is the sensitive

---

* A preliminary note has been appeared in this journal vol. **15** (1960), 1356.

* This type of crystal holder was designed by Prof. H. Kanzaki. We are indebted to him for the construction.

Table I. Crystal history and U center concentration.

Sample	Concentration of U centers (per. cc.)		Concentration of Br ions (mole fraction)	Time after coloration	
KCl	1	4.0×10^{16}	7×10^{-5}	10 days	Harshaw
〃	2	1.1×10^{17}	〃	5 years	〃
〃	3	2.7×10^{17}	6×10^{-4}	6 months	Home made
〃	4	3.5×10^{17}	7×10^{-5}	5 years	Harshaw
〃	5	5.9×10^{17}	〃	〃	〃
〃	6	6.0×10^{17}	〃	〃	〃
〃	7	6.0×10^{17}	9×10^{-6}	6 months	Home made
KBr	8	3.5×10^{16}		〃	Harshaw
〃	9	6.4×10^{17}		5 years	〃
〃	10	8.5×10^{17}		6 months	〃
〃	11	3.1×10^{18}		5 years	〃

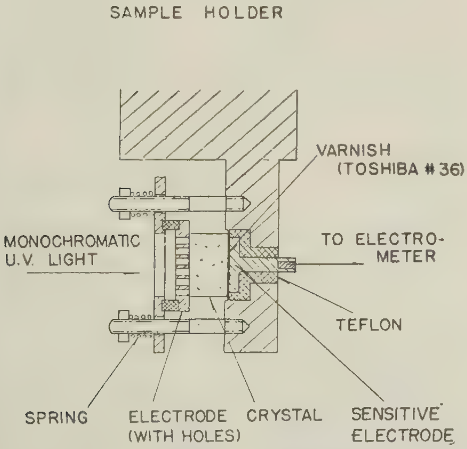

Fig. 1. Crystal holder for the photocurrent measurements.

electrode painted with varnish (Toshiba #36) to prevent the photoelectric emission from the electrode metal. The sensitive electrode was connected to a Cary model 31 vibrating reed electrometer through an input resistance of 10^{12} ohms. An electric field was applied on the crystal along the direction of illuminating light. Such a field direction is denoted here as "+direction". D. C. electric field of about 1000 volt/cm. was supplied with dry cells. Photocurrents were recorded with using a Yokokawa Type ER-22 electronic recorder of which time constant is three seconds. The noise current was 5×10^{-16} Amp. or less through all measurements.

A vacuum grating monochromator constructed in our laboratory was used in the spectral region between $\lambda\lambda$ 240 mμ and 170 mμ. Slit widths of the monochromator were set so that the band pass of each monochromatic light is less than 1 mμ. The intensity of light incident on the crystal was $\sim1\times10^{11}$ and 5×10^{11} photons per cm^2 per sec. in the regions of $\lambda\lambda$170 mμ–200 mμ and 200 mμ–240 mμ, respectively, as described previously.

Spectral distributions of photoconductivity of U center were measured as follows. In the case of KCl crystal, the polarization effect is very small if the intensity of monochromatic light is adjusted to produce the photocurrent of less than 10^{-13} Amp. Therefore, the saturation photocurrents are almost nearly the same but decrease a bit after repeated illuminations. However, it was confirmed that the polarization effect can be avoided by the illumination of the same light for the same period with applying an opposite electric field.

We have measured the saturation values of photocurrents with each monochromatic light. From the saturation values of these photocurrents, the photoconductivity curve of KCl crystal containing U center has been obtained with the correction of both absorption spectrum of the crystal and the relative spectral intensity distribution of illuminating light which was measured as described before³⁾. Corrections of the reflection loss of incident lights by the crystal surface were not made.

In KBr crystals, however, the photocurrents were much smaller, and moreover, the polarization effect was large, so, the measurement of the saturation value could not be carried out. Therefore, we have measured, at first, the response height on the recorder with a standard monochromatic light of λ 200 mμ for the period of three seconds' illumination. Next, the response with any light, for example, λ 205 mμ was measured for the same illumination period. After that, the measurement with the standard light of λ 200 mμ was made again. From these values, the relative photocurrent due to any monochromatic light was obtained with comparison to that of the standard light by the interpolation. The accuracy of measurements in KBr crystals is, therefore, a bit lower than that in KCl crystals.

All measurements in the present report have been done at room temperature, but the extension to the lower temperature has beening undertaken.

§ 3. Experimental Results and Discussions

3–1. *The spectral variation of the potoconductivity in KCl and KBr crystals containing U centers.*

Curve A in Fig. 2 shows an observed spectral variation of photocurrent in KCl crystal containing U center with a concentration of 5.9×10^{17}/cc. The crystal is #5 in Table I. The absorption curve of the crystal and the spectral intensity distribution of ultra violet light shown in curves B and C, respectively, were taken into consideration as corrections to obtain a real spectral variation of the photoconductivity. Curve D shows such a conductivity distribution obtained from curve A. The photocurrent is very small at the absorpsion peak of U band (λ 216 mμ), but it increases rapidly as the photon energy of illuminating light does, and reaches to the maximum value at the spectral region where the exciton absorption band starts.

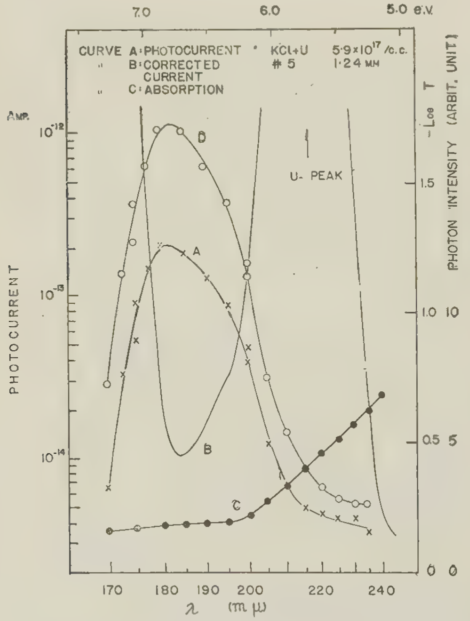

Fig. 2. Photoconductivity curve of KCl crystal containing U centers.

A: Observed photocurrents as a function of illuminating photon energy.

B: Absorption curve of KCl+U crystal.

C: Spectral intensity distribution of illuminating light.

D: Spectral variation of photoconductivity obtained from curve A with corrections of curves B and C.

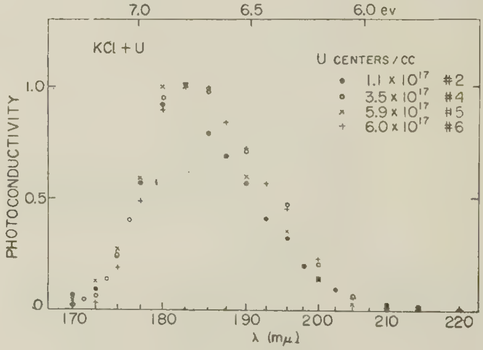

Fig. 3. Photoconductivity curves in KCl+U crystals of different histories.

Fig. 3 shows the similar photoconductivity curves in KCl crystals of different histories, where the maximum values are normalized to unity. The absolute values of photocurrent depend much on their history of preparation and heat treatment; however, all crystals have the maximum conductivity at λ 183 mμ.

On the other hand, U centers can be converted to F centers with ultra violet light. The spectral variation of the quantum yield of this conversion was investigated as reported previously[4)], and it was shown again in Fig. 4 for the comparison. The maximum yield occurs at λ 183 mμ too, and the correspondence between curves of the photoconductivity and quantum yield of U→F is clearly seen.

The similar relation between both curves was also obtained in KBr crystal as shown in Fig. 5. The maxima of the conductivity and the yield η occur at the same photon energy of λ 203 mμ. The photoconductivity curve has a shallow minimum at near the U-absorption peak and it increases toward the longer wavelength side. The shape of conductivity curve measured by Glaser[5)] is somewhat different from ours. He has observed a deep and a shallow minima at U-peak and at λ 210 mμ, respectively. The origin of such a defference is not clear. However, as seen from the Fig. 5 in his paper, U absorption band is much asymmetric and has a large absorption coefficient at the shorter wavelength side. This was considered, by Glaser, to be attributed to the overlapping of a broad band called X center. In our case, such a high concentration of X center was not detected and the U center has the symmetric bell shape.

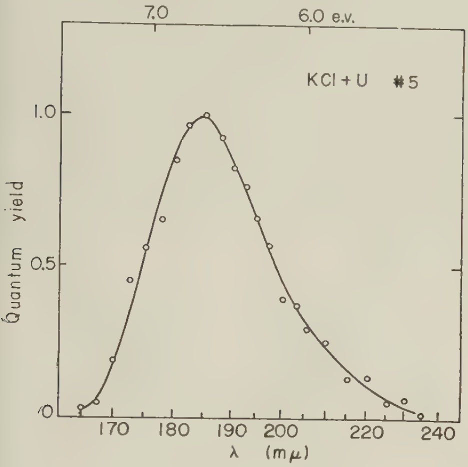

Fig. 4. Spectral variation of quantum yield of U→F in KCl crystal.

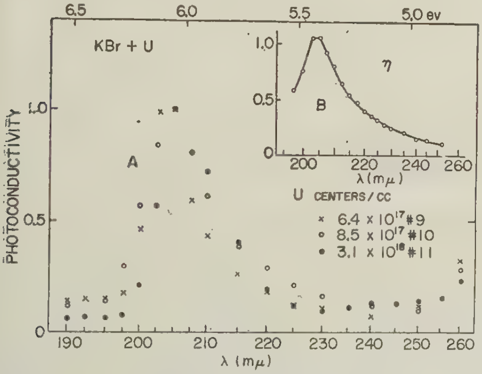

Fig. 5. The correspondence between curves of photoconductivity and quantum yield of U→F in KBr crystal.

A: Photoconductivity curve.

B: Spectral variation of quantum yield.

The OH band was not detected in KBr crystals but existed in KCl crystals. In Harshaw crystals the concentration was 8×10^{15}/cc, and 2×10^{15}/cc in other crystals. These concentrations are negligibly small compared to that of U center. However, it was confirmed that OH band does not show photoconduction.

All measurements of photocurrents were carried out with an electric field of "+direction". When the field was reversed, the photoconductivity curve in KCl was the same as that in "+direction" within an error of 20 per cent as shown in Fig. 6.

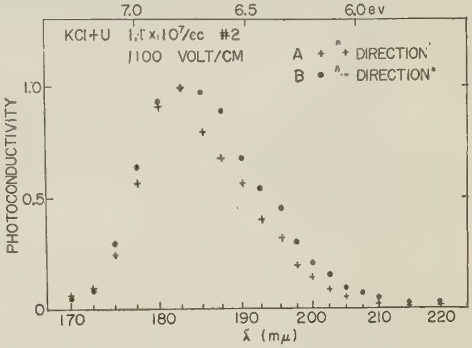

Fig. 6. Photoconductivity curve in KCl crystal with applying electric field of "+direction": curve A and "−direction": curve B.

From the detailed comparison between both curves of photoconductivity in Fig. 2 and quantum efficiency in Fig. 4, which were measured in KCl crystals #5 of the same history, it is seen that the relative value of photoconductivity in the region of U absorption band against the maximum value is very small compared to that in the case of quantum efficiency. For example, at λ 210 mμ, the photoconductivity is a few handredths of the maximum value at λ 183 mμ, but the quantum efficiency is about one fifth. This fact suggests us that the conversion of U→F occures with different mechanisms in both regions of U absorption band-peak and the shorter wavelength side.

The absorption band of U center in KCl crystal shows a shoulder in the shorter wavelength side. This is clearly seen in the absorption band of Fig. 7 measured at low temperatue. Therefore, it is probable to consider that U center has its higher excited or ionized states and absorption bands due to the transitions to these states are overlapping with each other. The similar results showing asymmetry of U band has been observed by Pohl[6] at room temperature.

We have tentatively concluded that in the region of U absorption peak, U center is excited with illumination of light and, in this excited state, the hydrogen atom diffuses to the interstitial position leaving an electron as suggested by Mott and Gurney[7], but in the region of the shorter wavelength side, an electron of U center is ionized directly or after obtaining a small activation energy. The hydrogen atom diffuses away leaving a negative ion vacancy. The ionized electron will come back to the vacancy forming an F center, because of the electrostatic attraction field.

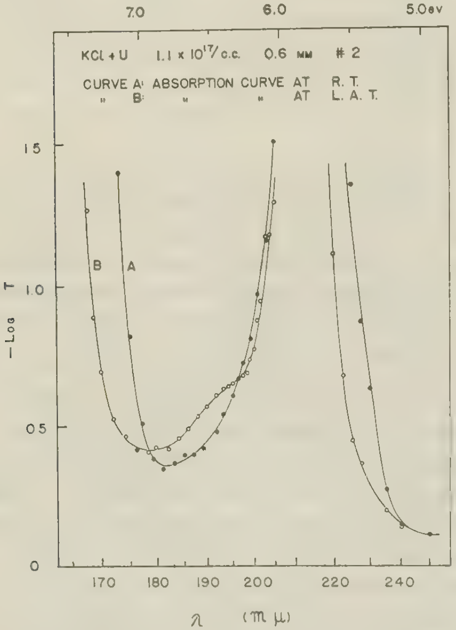

Fig. 7. Absorption curves of KCl+U crystal.
A: Measured at room temperature.
B: Measured at liquid air temperature.

When a crystal is irradiated with light in the tail of the characteristic absorption band, excitons are generated. The large photoconductivity in its absorption region indicates that excitons do ionize U centers. The sharp decrease of photoconductivity toward inside the exciton absorption band, will be attributed to the destruction of an exciton through its diffusion to the crystal surface or being trapped by imperfections probably existing more densely near the surface, because the penetration depth of light becomes small due to the high absorption coefficient.

3-2. *Dependence of Photoconductivity upon U center concentration.*

If the energy of excitons is transferred to U centers by the diffusion of excitons, it is expected that in crystals containing small concentration of U center, the photoconductivity in the exciton absorption band will decrease. As already shown in Fig. 5, in all crystals containing U centers more than 6.4×10^{17}/cc the maximum photoconductivity was observed to occur at λ203 mμ where the exciton absorption band starts. The maximum value was seven times larger than that at λ228 mμ corresponding to U-absorption peak. However in a crystal having a small concentration of 3.5×10^{16}/cc, the wavelength of light which enhance the maximum photoconductivity shifted to λ210 mμ as shown in Fig. 8, and the conductivity at λ203 mμ is only one half of that at λ228 mμ.

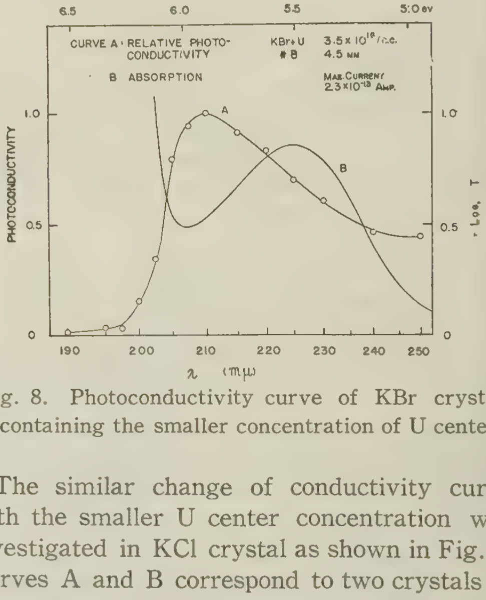

Fig. 8. Photoconductivity curve of KBr crystal containing the smaller concentration of U center.

The similar change of conductivity curve with the smaller U center concentration was investigated in KCl crystal as shown in Fig. 9. Curves A and B correspond to two crystals of #1 and 2, of which U center concentrations are 4.0×10^{16}/cc and 1.1×10^{17}/cc, respectively. The maximum point of conductivity shifted to λ185 mμ from λ183 mμ when the concentration is low, and especially the photoconductivity in the region of the fundamental absorption band decreases remarkably as in the case of KBr crystal. These facts showing the abrupt decrease in efficiency of the energy transfer from an exciton to U center, when the concentration is below 5×10^{16}/cc, will indicate the exciton diffusion through the crystal.

The same conclusion has been also deduced previously from the experiments carried out on the quantum efficiency of U→F conversion with varying the concentration. However, the present results of photoconductivity is more precise.

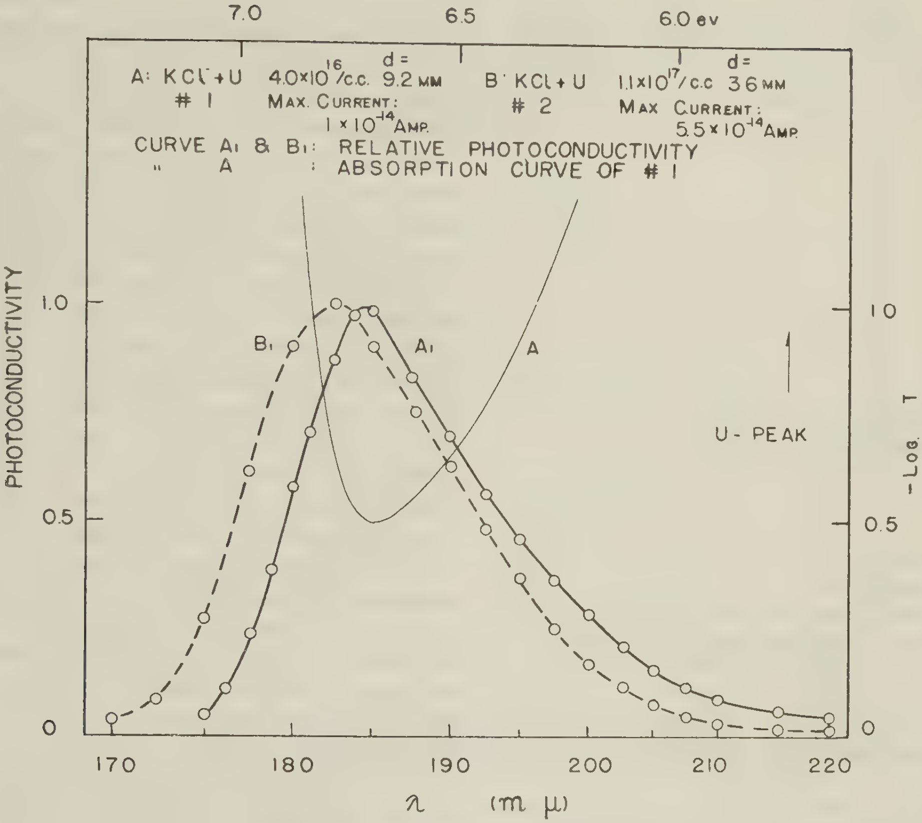

Fig. 9. Photoconductivity curves of KCl crystals containing different amount of U centers. U center concentrations are 4.0×10^{16}/cc, and 1.1×10^{17}/cc in A and B, respectively.

3–3. *Irradiation effect of ultra violet light upon the photocurrent.*

When a KCl crystal was irradiated by ultra violet light from a hydrogen discharge tube, F centers were created from U centers and the photocurrent decreases in the whole spectral region. Fig. 10 shows such an effect. Curve A shows the initial state of photoconductivity curve in a crystal of #6 before the irradiation. Curves B and C show photocurrents after 2 and 8 seconds' irradiation, respectively. The irradiation was performed at a distance of 5 cm in air through the fused quartz window of 2 mm thickness. After the 14 seconds' illumination, photocurrent drops to quite a small value as shown in curve D. At this stage, the concentration of F centers generated from U centers was only 1×10^{15}/cc. That is, inspite of that almost all U centers remain in the crystal, the decrease of photocurrent is quite large.

Next, with illuminating the crystal by white light, all F centers returned to U centers, but photocurrent recovered only a little as shown in curve E. However, it recovered gradually when the crystal was kept in dark at room temperature for 17 and 65 hours as indicated in curves F and G, respectively. Finally the initial height of photoconductivity was recovered after the crystal was annealed at 200°C for 30 hours.

From these results, it is considered that vacancies or imperfections were generated by ultra violet light and they acted as traps for electrons to make their Schubweg short. These traps seem to easily disappear by the annealing.

The similar decrease of photocurrents was observed if the crystals were heated at 520°C for 5 minutes and quenched rapidly to room temperature. Though the concentration of U center decreases to half of the initial value in this heating and quenching treatment, the photocurrent decreased to a very small value as in the case of irradiation of ultra violet light.

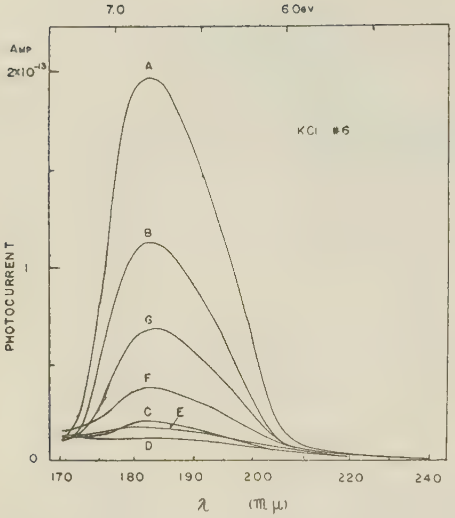

Fig. 10. Effect of ultra violet light upon the photoconductivity.

A: Initial state of photoconductivity curve before irradiation.

B and C: After 2 and 8 seconds' irradiations, respectively.

D: After 14 seconds' irradiation.

E: After white light illumination to bleach F center.

F and G: After keeping in dark at room temperature for 17 and 65 hours, respectively.

3-4. *The effect of Br ion impurity in KCl crystal.*

All KCl crystals investigated so far in the present work were confirmed to contain Br ion as an impurity of which concentration was given in Table I. The Br ion has its own absorption band and its peak locates at λ172 mμ. Due to this band the characteristic absorption tail of KCl crystal shifts to the longer wavelength side. Therefore, the question might exist that the observed phenomena in the region of exciton absorption band, will be attributed to Br ion, and not to the pure exciton in KCl crystal. Kobayashi and Tomiki[8] prepared the purer KCl crystals very carefully from $KHCO_3$ and HCl acid. The crystal is designated by #7. The Br ion concentration is as low as 9×10^{-6} mole fraction.

We have investigated the spectral variation of photoconductivity and efficiency of U→F conversion in the crystals of different amount of Br ion, in order to see the effect of Br absorption band.

Fig. 11 shows two extreme cases of the purest crystal #7 and that of high concentration of Br ion #3. Photoconductivity and absorption curves of crystals are shown by subscripts 1 and 2, respectively. Curves A and B indicate the purest and the other crystals, respectively.

As seen from the figure, the characteristic absorption tail shifts to the shorter wavelength side in the purest crystal and the maximum point of photoconductivity also shifts to λ180 mμ from λ185 mμ. On the other hand, in crystals obtained from Harshaw Chemical Co. in which the concentration of Br ion is 7×10^{-5} mole fraction, the fundamental absorption tail shifts to the longer wavelength side compared to the crystal of #7 and the maximum photoconductivity occurs at λ183 mμ.

The maximum quantum efficiency of U→F conversion occurs at the shorter wavelength side in the purer crystal as the Br ion concentration decreases as shown in Fig. 12 which was measured and will be reported in detail by Ishii. However, in every crystals, the maximum photoconductivity and quantum efficiency occur always near the edge of the host absorption band.

Even in the purest crystal of #7, absorption tail is somewhat modified by the Br ion, because it contains Br ion of 9×10^{-6} mole fraction. From the analysis of the band shape of Br ion, it was concluded that at λ175 mμ, 88 per cent of the total absorption coefficient of the crystal is due to the KCl and the remaining 12 per cent is due to Br ions[8], and at λ177 mμ, 50 per cent of absorption is due to the Br. At<λ173 mμ, almost all absorption is attributed to the pure KCl crystal. Therefore, from the photoconductivity and quantum yield measurements in Fig. 11 and 12, it is concluded that the observed phenomena in the region of absorption band of host crystal is attributed to the pure exciton in KCl crystal.

Inspite of the fact that in the crystal #3, as seen from the Fig. 11, all photon in the region of λλ182 mμ-177 mμ are absorbed in Br band and not in the host crystal, the photoconductivity and quantum yield of U→F have large values. This fact indicates that the photon energy absorbed in Br ion can be transferred to U center with high efficiency as that absorbed in the host crystal. This is very suggestive to the investigations of the nature of Br ion in KCl crystal. Photons absorbed in these ions may be considered to from the localized

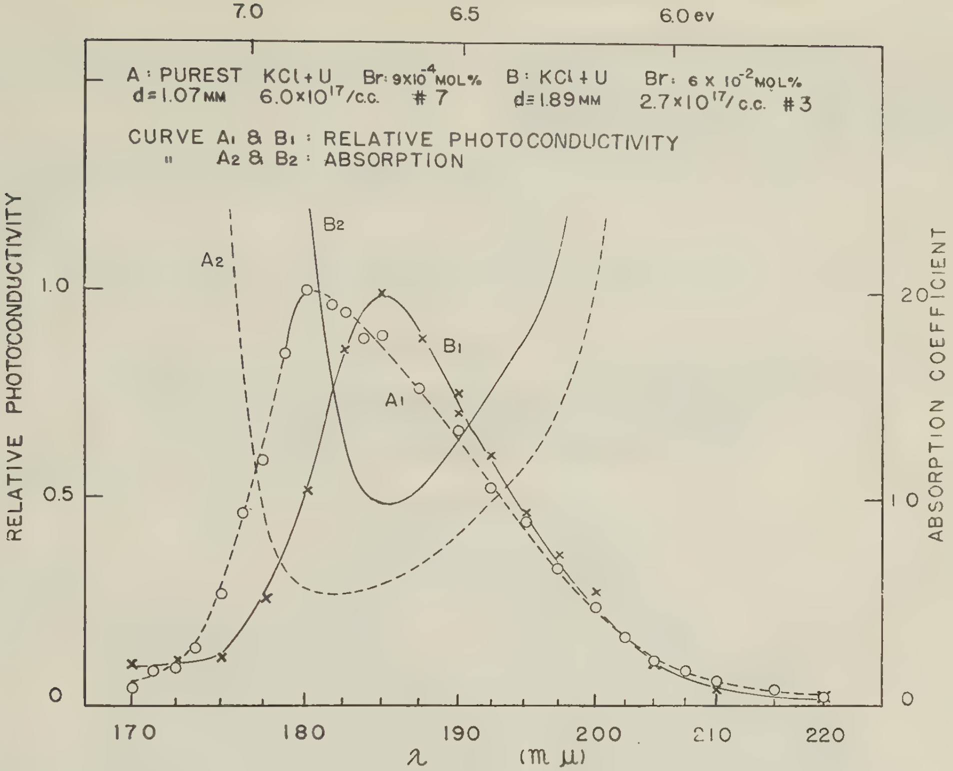

Fig. 11. Photoconductivity curves in KCl crystals containing different amount of Br ion.
A: In case of the purest crystal; Br concentration is 9×10^{-6} mole fraction.
B: Br concentration is 6×10^{-4} mole fraction.

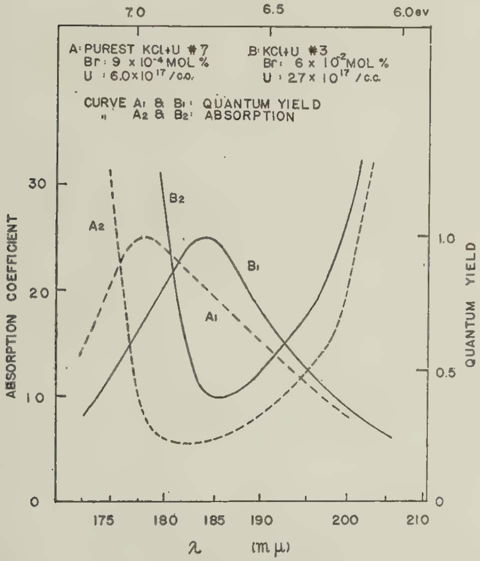

Fig. 12. Spectral variation of quantum yield of U→F conversion in KCl crystals containing different amount of Br ion.
A: The purest crystal, Br concentration is 9×10^{-6} mole fraction.
B: The concentration is 6×10^{-4} mole fraction. Subscripts 1 and 2 indicate quantum yields and absorption curves of the crystals, respectively.

excitons, but so far as the interaction with U center are concerned, there is no difference between these excitons and the free excitons.

Acknowledgements

We would like to thank Professor K. Kobayashi for the discussions on the fundamental absorption tail of KCl crystals containing Br ion as an impurity. One of the authors (M.U.) is indebted to Professor H. Pick for his kindness of discussing and showing the data of Pohl and Glaser. He also wishes to thank Professor Hilsch and Dr. Martienssen for the stimulating discussions. This work was supported by the Scientific Research Fund of the Ministry of Education.

References

1) L. Apker and E. Taft: Phys. Rev. **79** (1950) 914, **81** (1951) 698, **82** (1951) 814.
2) M. Ueta, M. Hirai and H. Watanabe: J. Phys. Soc. Japan **14** (1959) 253.
3) M. Ueta and M. Hirai: J. Phys. Soc. Japan **14** (1959) 546., M. Ueta: Prog. Theor. Phys. Supplt. **12** (1959) 40.
4) M. Ueta, M. Hirai and H. Watanabe: J. Phys. Soc. Japan **15** (1960) 593.

5) G. Glaser: Ann. d. Physik **27** (1936) 219.
6) R. W. Pohl: Acta Physica Polonica (1936) 349.
7) N. F. Mott and R. W. Gurney: *Electronic Processes in Ionic Crystal; Clarendon Press, Oxford* p. 147.
8) K. Kobayashi and T. Tomiki: J. Phys. Soc. Japan **15** (1960) 1982.

JOURNAL OF THE PHYSICAL SOCIETY OF JAPAN, Vol. 16, No. 3, MARCH, (1961)

Theoretical Prediction of the Pressure Distribution on a Non-lifting, Thin Symmetrical Aerofoil at Various Transonic Speeds

By Iwao HOSOKAWA

National Aeronautical Laboratory, Mitaka Shinkawa, Tokyo

(Received October 5, 1960)

Theoretical pressure distributions on a non-lifting, circular-arc aerofoil at various transonic speeds are obtained by application of a new method recently published by the author. The method consists essentially of a refinement of the linearized transonic flow theory in which the nonlinear characteristics of the fundamental equation are taken into account. The results reveal most of principal phenomena observed in experimental studies throughout the whole Mach number range.

§1. Introductory Remarks

Recently, a useful method of analysis on the transonic flows around a thin obstacle was proposed by the author.[1] Its basic idea consists in the correction of the linearized transonic flow theory[2],[3] in which the nonlinearity of the flow field is taken into account. In one of the previous papers,[1] the logical structure of the theory and the main features deduced from it are described together with two examples of calculation for the sonic flow case ($M_\infty=1$).

The other paper[4] treats the transonic flow past a wavy wall as a simple but interesting example of applications of the theory. The result for the lower critical flow is nearly in agreement with Kaplan's more exact one. Furthermore, it illustrates various flows including shock waves plausible for the higher free-stream Mach numbers.

However, there remains another family of the more important cases of the transonic flow, that is, the flow around an isolated aerofoil. In this paper, a symmetrical circular-arc aerofoil is dealt with as a typical example of such problems; first the behaviours of the sonic and shock points on the aerofoil in accordance with the change of the transonic similarity parameter are examined in detail, as a necessary process of the present method, and next, various velocity and pressure distributions on the aerofoil are obtained. Also the pressure drag is plotted against the transonic similarity parameter, and compared with data published by other authors. All the quantities are arranged in the reduced form consistent with the transonic similarity law for the sake of simplicity and convenience of utilization. In the next section, a summarized description of our method is given.

§2. Summary of the Method

The differential equation for the steady, two-dimensional transonic flow is as follows:

$$(1-M_\infty^2)\Phi_{xx}+\Phi_{yy}=(\gamma+1)M_\infty^2\Phi_x\Phi_{xx} \tag{2.1}$$

where $U_\infty\Phi$ is the perturbation velocity potential; γ is the ratio of specific heats; M_∞ and U_∞ are the Mach number and the velocity of the free stream respectively; and the x-axis is taken in the direction of the free stream.

In order to obtain the approximate solution, Oswatitsch[2] and Maeder[3] suggest to deal with the following equation (the linearized transonic flow theory);

$$(1-M_\infty^2)\varphi_{xx}+\varphi_{yy}=K\varphi_x \tag{2.2}$$

in which K is a constant having the meaning of the acceleration at a certain point of the flow field, as is known from comparison of (2.1) and (2.2).

Now it has been derived in the previous paper[1] that a more exact solution of (2.1) based upon reasonable assumptions could be obtained provided the solution of the linearized equation (2.2), $\varphi(x;\ K)$, were found. The procedure of refinement can be written as follows:

$$\Phi_x=(1-M_\infty^2)/[(\gamma+1)M_\infty^2]\pm\sqrt{Y(x)} \tag{2.3}$$

where

$$Y(x)=\left\{\frac{1-M_\infty^2}{(\gamma+1)M_\infty^2}\right\}^2+\varphi_x^2(c^*)-2\frac{1-M_\infty^2}{(\gamma+1)M_\infty^2}\varphi_x(x)+2\frac{K}{(\gamma+1)M_\infty^2}\{\varphi(x)-\varphi(c^*)\} \tag{2.4}$$

and the double sign corresponds to

$$\varphi_x\gtrless(1-M_\infty^2)/[(\gamma+1)M_\infty^2] \tag{2.5}$$

respectively. In the above equation, the unknown constants c^* and K should be determined according to the following prescriptions;

$$1-M_\infty^2=(\gamma+1)M_\infty^2\varphi_x(c^*;\ K) \tag{2.6}$$

$$K=(\gamma+1)M_\infty^2\varphi_{xx}(c^*;\ K) \tag{2.7}$$

The both constitute the simultaneous algebraic equations for c^* and K in case of usual transonic flow. The former represents that $x=c^*$ is the sonic point on the surface of the aerofoil. If (2.6) has more than one root for c^*, $x=c^*$ must be the sonic point in the accelerated region of the flow. The latter equation, on the other hand, serves in determining $K(>0)$ as equal to the acceleration of the flow at the sonic point on the aerofoil. In case of purely sub- or supersonic flow, (2.6) has no root; but also in this case c^* should take the fixed value of the (lower or upper) critical point in order to ensure the continuity of the solution from transonic to sub- or supersonic, and then K is determined by (2.7) for this value of c^*.

Finally, we shall now enumerate some characteristic features of our approach:[1]

1) The constant K is uniquely determined and there is no such ambiguity as is seen in the linearized transonic flow theory.

2) The occurrence of shock is predicted as the discontinuities in the pressure and velocity on the surface.*

3) The procedure of approximation is very simple, because it does not require any assumption or knowledge about the entire flow field and the whole shape of the sonic and shock lines; nevertheless the results obtained by the method are reliable, in so far as our estimation is valid on the order of magnitude of various quantities in the neighbourhood of the obstacle.

§ 3. The Linearized Transonic Flow

According to Maeder's theory, the formal solutions of (2.2) representing the linearized transonic flow past a thin, symmetrical aerofoil are written as follows:

$$\varphi(x,\ y)=-\frac{1}{2\pi}\int_0^1 F'(\xi)\frac{e^{\alpha(x-\xi)}}{\beta}K_0(\alpha\sqrt{(x-\xi)^2+\beta^2y^2})\xi p,\quad M_\infty\leqq1 \tag{3.1}$$

---

* Though it is not affirmed from the standpoint of the exact treatment of the problem (Lin and Rubinov[5]) that a normal shock wave stays on the curved surface, it may be admitted for an approximate treatment.

$$\varphi(x, y)=-\frac{1}{2}\int_0^{x-my} F'(\xi)\frac{e^{\alpha(x-\xi)}}{m} I_0(|\alpha|\sqrt{(x-\xi)^2-m^2y^2})d\xi\ , \quad M_\infty\geqq 1 \tag{3.2}$$

where α, β and m are related to each other as

$$\beta^2=1-M_\infty{}^2=-m^2\ , \quad \alpha=K/2\beta^2; \tag{3.3}$$

$F(x)$ is the cross-sectional area of the aerofoil, whose chord length can be assumed unity without loss of generality, the origin of the co-ordinate being at the leading edge; and K_0 and I_0 are the modified Bessel functions of the zeroth order.

1) *Subsonic case* ($M_\infty\leqq 1$)

On the aerofoil, we can have the limit:

$$\lim_{y\to 0}\varphi(x, y)=-\frac{1}{2\pi}\int_0^1 F'(\xi)\frac{e^{\alpha(x-\xi)}}{\beta}K_0(\alpha|x-\xi|)d\xi \tag{3.4}$$

since the integral is uniformly covergent when y tends to zero. Thus, its derivative is

$$\lim_{y\to 0}\varphi_x=\frac{1}{2\pi\beta}\int_0^1 F'(\xi)\frac{\partial}{\partial\xi}\{e^{\alpha(x-\xi)}K_0(\alpha|x-\xi|)\}d\xi \tag{3.5}$$

$$=\frac{1}{2\pi\beta}\left\{F'(\xi)\, e^{\alpha(x-\xi)}\, K_0(\alpha|x-\xi|)\Big|_{\xi=0}^{\xi=1}-\int_0^1 F''(\xi)e^{\alpha(x-\xi)}K_0(\alpha|x-\xi|)d\xi\right\}. \tag{3.6}$$

If $F(\xi)$ is expressed by a polynomial (which means a sharp-edged aerofoil), we can express $F''(\xi)$ with a power series:

$$F''(\xi)=\sum_{n=0} a_n\xi^n \tag{3.7}$$

and the integral in (3.6) can be reduced to the following forms:

$$J_n=\int\xi^n e^{\alpha(x-\xi)}K_0(\alpha|x-\xi|)d\xi\ , \quad n=0,\ 1,\cdots. \tag{3.8}$$

The integration can conveniently be carried out by taking account of Schläfli's integrals of Poisson's type for the modified Bessel functions[14] and their derivatives:

$$z^{-\nu}K_\nu(z)=z^{-\nu}K_{-\nu}(z)=\frac{\Gamma(1/2)}{2^\nu\Gamma(\nu+1/2)}\int_0^\infty e^{-zt}(t^2-1)^{\nu-1/2}dt \tag{3.9}$$

$$\frac{d}{dz}[z^{-\nu}K_{-\nu}(z)]=-\frac{\Gamma(1/2)}{2^\nu\Gamma(\nu+1/2)}\int_0^\infty te^{-zt}(t^2-1)^{\nu-1/2}dt\ . \tag{3.10}$$

First, we shall deal with J_0:

$$J_0=\int e^{\alpha(x-\xi)}K_0(\alpha|x-\xi|)\,d\xi=\int_0^\infty(t^2-1)^{-1/2}dt\int e^{\alpha(x-\xi)-\alpha|x-\xi|t}d\xi \tag{3.11}$$

$$=\int_0^\infty(t^2-1)^{-1/2}\frac{e^{\alpha(x-\xi)(1\mp t)}}{-\alpha(1\mp t)}dt$$

$$=-\frac{1}{\alpha}e^{\alpha(x-\xi)}\left\{-\int_0^\infty e^{-\alpha|x-\xi|t}(t^2-1)^{-3/2}\,dt\mp\int_0^\infty te^{-\alpha|x-\xi|t}(t^2-1)^{-3/2}dt\right\}$$

$$=-\frac{1}{\alpha}e^{\alpha(x-\xi)}\left\{\alpha|x-\xi|K_1(\alpha|x-\xi|)\mp\frac{d}{d(\alpha|x-\xi|)}\alpha|x-\xi|K_1(\alpha|x-\xi|)\right\} \tag{3.12}$$

in which the double sign corresponds to $x\gtrless\xi$, respectively. Thus we get

$$J_0=-e^{\alpha(x-\xi)}\{|x-\xi|K_1(\alpha|x-\xi|)+(x-\xi)K_0(\alpha|x-\xi|)\} \tag{3.13}$$

by use of the relation $d/dz(zK_1(z))=-zK_0(z)$. In a general case of J_n, a similar procedure leads to the result which includes the modified Bessel functions of the higher order with the aid of (3.9) and (3.10).

For a circular-arc aerofoil which is certainly the simplest case, we can obtain the following integrated expression of (3.1), taking account of $F(\xi)=4t(\xi-\xi^2)$ $(F''(\xi)=-8t)$ and (3.13);

$$\varphi_x=\frac{4t}{\pi\beta}\left[e^{\alpha(x-\xi)}\left\{\left(\frac{1}{2}-x\right)K_0(\alpha|x-\xi|)-|x-\xi|K_1(\alpha|x-\xi|)\right\}\right]_{\xi=0}^{\xi=1} \tag{3.14}$$

or

$$=\frac{4\pi}{\pi\beta}\left[e^{\alpha(x-1)}\left\{\left(\frac{1}{2}-x\right)K_0[\alpha(1-x)]-(1-x)K_1[\alpha(1-x)]\right\}\right.$$
$$\left.-e^{\alpha x}\left\{\left(\frac{1}{2}-x\right)K_0(\alpha x)-xK_1(\alpha x)\right\}\right]. \tag{3.15}$$

In the limit, $\alpha\to\infty$ and $\beta\to 0$ $(M_\infty=1-0)$, (3.15) becomes

$$\varphi_x=-\frac{2t}{\sqrt{\pi K}}(x^{-1/2}-4x^{1/2}) \tag{3.16}$$

as was already proved by another way in the previous work.[1)]

Differentiation of (3.15) gives

$$\varphi_{xx}=\frac{4t}{\pi\beta}\left[e^{\alpha(x-1)}\left\{\left(-\frac{1}{2}\alpha-1\right)K_0[\alpha(1-x)]-\frac{1}{2}\alpha K_1[\alpha(1-x)]\right.\right.$$
$$\left.\left.-e^{\alpha x}\left\{\left(\frac{1}{2}\alpha-1\right)K_0(\alpha x)-\frac{1}{2}\alpha K_1(\alpha x)\right\}\right]. \tag{3.17}$$

In Maeder's theory K should be determined as follows:

$$K=(\gamma+1)M_\infty^2\varphi_{xx}\left(x=\frac{1}{2};\ K\right). \tag{3.18}$$

After rearranging this equation, we get

$$\frac{\pi}{2}(-\xi_\infty)^{3/2}\left(\frac{\alpha}{2}\right)=\left(\sinh\frac{\alpha}{2}-\frac{\alpha}{2}\cosh\frac{\alpha}{2}\right)K_0\left(\frac{\alpha}{2}\right)+\frac{\alpha}{2}\sinh\frac{\alpha}{2}K_1\left(\frac{\alpha}{2}\right). \tag{3.19}$$

We know from this equation that $\alpha/2$ has a non-vanishing solution only when $(\pi/2)(-\xi_\infty)^{3/2}<1$, that is, $-(2/\pi)^{2/3}<\xi_\infty<0$. In addition to that, the equation has a trivial solution $\alpha=0$ for all negative values of ξ_∞. Thus the point $\xi_\infty=-(2/\pi)^{2/3}$ makes a branch point on the diagram of ξ_∞ versus α, or ξ_∞ versus c^*, as is seen in Fig. 1. Within the range between $-(2/\pi)^{2/3}<\xi_\infty<0$, we must of course adopt the finite solution since the significant characteristics of the transonic flow are given only by the non-vanishing solution of $\alpha/2$ or K; in the other range, however, the solution $\alpha=0$ is useful, which provides Prandtl-Glauert's approximation in itself. Maeder's theory is interesting in that it leads to an existence of a symmetric solution $(\alpha=0)$ which results in no pressure drag even at the supercritical state $(\xi_\infty>-(4/\pi)^{2/3}$, which is derived from (3.15)).

2) *Supersonic case* $(M_\infty\geqq 1)$

After the treatment similar to the previous case, we have

$$\lim_{y\to 0}\varphi(x,\ y)=-\frac{1}{2}\int_0^x F'(\xi)\frac{e^{\alpha(x-\xi)}}{m}I_0(|\alpha|(x-\xi)]d\xi \tag{3.20}$$

$$\lim_{y\to 0}\varphi_x=-\frac{1}{2m}F'(x)+\frac{1}{2m}\int_0^x F'(\xi)\frac{\partial}{\partial\xi}e^{-|\alpha|(x-\xi)}I_0[|\alpha|(x-\xi)]d\xi \tag{3.21}$$

$$=-\frac{1}{2m}\left\{F'(0)e^{-|\alpha|x}I_0(|\alpha|x)+\int_0^x F''(\xi)e^{-|\alpha|(x-\xi)}I_0[|\alpha|(x-\xi)]d\xi\right\}. \tag{3.22}$$

In this case I_0 appears in place of K_0 and we are now in a position to calculate

$$J_n' = \int \xi^n e^{-|\alpha|(x-\xi)} I_0[|\alpha|(x-\xi)]d\xi. \tag{3.23}$$

The integral expressions for the I-functions[14] are as follows:

$$z^{-m}I_m(z) = z^{-m}I_{-m}(z) = \frac{1}{2^m\Gamma(m+1/2)\Gamma(1/2)}\int_{-1}^{1} e^{-zt}(1-t^2)^{m-1/2}dt \tag{3.24}$$

$$\frac{d}{dz}[z^{-m}I_{-m}(z)] = -\frac{1}{2^m\Gamma(m+1/2)\Gamma(1/2)}\int_{-1}^{1} te^{-zt}(1-t^2)^{m-1/2}dt \tag{3.25}$$

where m is an integer. (This notation (m) is used only here, so that any confusion with the parameter m implying $\sqrt{M_\infty^2-1}$ does not occur.)

First,

$$J_0' = \int e^{-|\alpha|(x-\xi)} I_0[|\alpha|(x-\xi)]d\xi = \frac{1}{\pi}\int_{-1}^{1}(1-t^2)^{-1/2}dt \int e^{-|\alpha|(x-\xi)-|\alpha|(x-\xi)t}d\xi \tag{3.26}$$

$$= \frac{1}{\pi}\int_{-1}^{1}(1-t^2)^{-1/2}\frac{e^{-|\alpha|(x-\xi)(1+t)}}{|\alpha|(1+t)}dt$$

$$= \frac{1}{\pi|\alpha|}e^{-|\alpha|(x-\xi)}\left\{\int_{-1}^{1} e^{-|\alpha|(x-\xi)t}(1-t^2)^{-3/2}dt - \int_{-1}^{1} te^{-|\alpha|(x-\xi)t}(1-t^2)^{-3/2}dt\right\}$$

$$= -\frac{1}{|\alpha|}e^{-|\alpha|(x-\xi)}\left\{|\alpha|(x-\xi)I_1[|\alpha|(x-\xi)] + \frac{d}{d[|\alpha|(x-\xi)]}|\alpha|(x-\xi)I_1[|\alpha|(x-\xi)]\right\} \tag{3.27}$$

$$= -e^{-|\alpha|(x-\xi)}\{(x-\xi)I_1[|\alpha|(x-\xi)] + (x-\xi)I_0[|\alpha|(x-\xi)]\} \tag{3.28}$$

by use of the relation, $d/dz[zI_1(z)] = zI_0(z)$. Also integration of J_n's will be performed in a similar manner to the previous case.

For a circular-arc aerofoil we get from (3.22) and (3.28)

$$\varphi_x = \frac{4t}{m}e^{-|\alpha|x}\left\{\left(x-\frac{1}{2}\right)I_0(|\alpha|x) + xI_1(|\alpha|x)\right\}. \tag{3.29}$$

In the limit, $|\alpha| \to \infty$ and $m \to 0$ ($M_\infty = 1+0$), the above equation coincides with (3.16)

Differentiation of (3.29) gives

$$\varphi_{xx} = \frac{4t}{m}e^{-|\alpha|x}\left\{\left(\frac{|\alpha|}{2}+1\right)I_0(|\alpha|x) - \frac{|\alpha|}{2}I_1(|\alpha|x)\right\}. \tag{3.30}$$

The corresponding equation to (3.19) for the supersonic case in Maeder's theory is

$$\xi_\infty^{3/2}\frac{|\alpha|}{2} = e^{-|\alpha|/2}\left\{\left(\frac{|\alpha|}{2}+1\right)I_0\left(\frac{|\alpha|}{2}\right) - \frac{|\alpha|}{2}I_1\left(\frac{|\alpha|}{2}\right)\right\}. \tag{3.31}$$

From this we know that $|\alpha|/2$ has only a non-vanishing solution in this case.

§ 4. Sonic and Shock Points on the Aerofoil

The simultaneous equations (2.6) and (2.7) are rewritten in a much simplified form by introducing a new function,

$$f(x;\ \alpha) = \pm(\sqrt{|M_\infty^2-1|}/t)\varphi_x(x;\ K) \tag{4.1}$$

in which the double sign corresponds to $M_\infty \lessgtr 1$, as follows:

$$|\xi_\infty|^{3/2} = f(c^*;\ \alpha), \tag{4.2}$$

$$2\alpha|\xi_\infty|^{3/2}=f_x(c^*;\ \alpha)\ . \tag{4.3}$$

Here c^* and α are unknown, ξ_∞ being a parameter. In the present example, (3.15), (3.17), (3.29) and (3.30) give immediately $f(x;\ \alpha)$ and $f_x(x;\ \alpha)$.

On the other hand, the position of the shock wave on the aerofoil should be determined by the other root c^{**} of the same equation (4.2) for a definite α and ξ_∞, according to the prescription given in the previous work[1].

Actual calculation of the above equations, however, is not easy because they include transcendental functions. In our case of a circular-arc aerofoil, several steps of the successive calculation were necessary with the use of Newton's method.*

In solving (4.2) and (4.3) in the present case, it is useful to know beforehand by investigating analytically the asymptotic behaviours of the equations that for $\alpha=0$, $c^*=1/2$ and $\xi_\infty=-(4/\pi)^{2/3}$; for $\xi_\infty=0$, $\alpha=\pm\infty$ and $c^*=1/4$; and for $c^*=0$, $\alpha=-2$ and $\xi_\infty=2^{2/3}$. At the same time we have a knowledge by dealing with the equation of c^{**} that for $\alpha=0$ and $\xi_\infty=-(4/\pi)^{2/3}$, $c^{**}=1/2$; and for $\xi_\infty=0$ and $\alpha=\infty$, $c^{**}=1$. The calculated results are indicated in Table I as well as in Fig. 1.

In Fig. 1, the present result is compared with the theoretical ones by Maeder (linearized transonic flow theory) and by Spreiter (integral equation method)[6], and many experimental data.[7)-9)] The sonic and shock points appear at first both on the midchord of a circular-arc aerofoil at the critical speed of the free

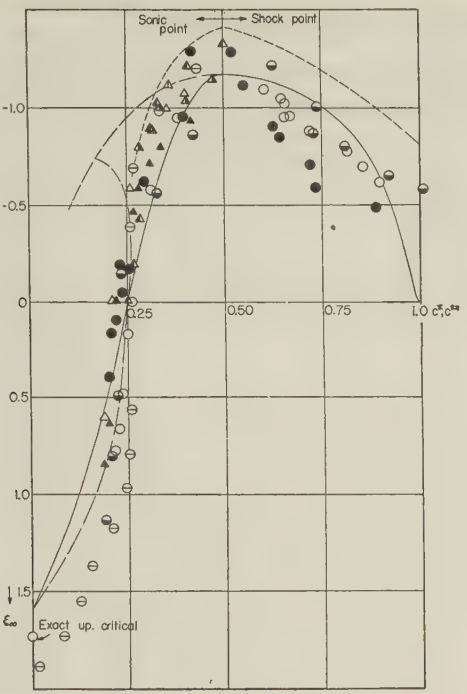

Fig. 1. Behavious of the sonic and shock points on a circular-arc aerofoil.

Theory .... Spreiter[6]

—— —— Maeder

———— Present

Experiment, Kawamura and Karashima[7]

● $t=0.106$ ○ $t=0.0808$

◒ $t=0.0544$

Michel et al[8]

▲ $t=0.06$ ◭ $t=0.10$

△ $t=0.08$ ◮ $t=0.12$

Bryson[9]

⊖ $t=0.088$

Table I. Solutions of (4.2) and (4.3).

c^*	α	$(-\xi_\infty)^{3/2}$	c^{**}	c^*	$\|\alpha\|$	$\xi_\infty^{3/2}$
0.500	0.000	1.2732($=4/\pi$)	0.500	0.250	∞	0.0000
0.475	0.203	1.2468	0.575	0.225	11.300	0.1089
0.450	0.418	1.1838	0.645	0.200	6.480	0.3076
0.425	0.660	1.0908	0.711	0.175	4.807	0.5256
0.400	0.950	0.9697	0.772	0.150	3.900	0.7461
0.375	1.317	0.8227	0.825	0.125	3.325	0.9630
0.350	1.835	0.6500	0.872	0.100	2.912	1.1773
0.325	2.652	0.4594	0.910	0.075	2.605	1.3874
0.300	4.260	0.2648	0.941	0.050	2.360	1.5947
0.275	9.150	0.0970	0.967	0.025	2.165	1.7986
0.2625	19.100	0.0349	0.980			
0.250	∞	0.0000	1.000	0.000	2.000	2.0000

---

* The author had recourse to an electric computer of relay type at Yulin Denki Seiki Co. Ltd..

stream, the former going ahead and the latter receding back monotonously with increasing Mach number. In this respect, Maeder's theory indicates a peculiar behaviour of the sonic point in the neighbourhood of the branch point, $\xi_\infty=-(2/\pi)^{2/3}$. The present result concerning the behaviour of the sonic point is in good accord with experiments throughout the whole transonic range of ξ_∞, though Spreiter's one is better for the smaller range of ξ_∞ near the critical speed. Furthermore the present method predicts the upper critical value of ξ_∞ very close to the exact one ($=1.74$, which can be found from the oblique-shock relation), whereas Spreiter's result by the local linearization method gives the value 2.08.[13]

Now with respect to the position of the shock wave on the aerofoil, it may be pointed out that the present theory predicts it much closer to the experimental data than Spreiter's although the experimental data show certain indefiniteness such that the shock wave changes its position considerably depending on the thickness ratio of the aerofoil and the Reynolds number of the flow*; the shock wave predicted

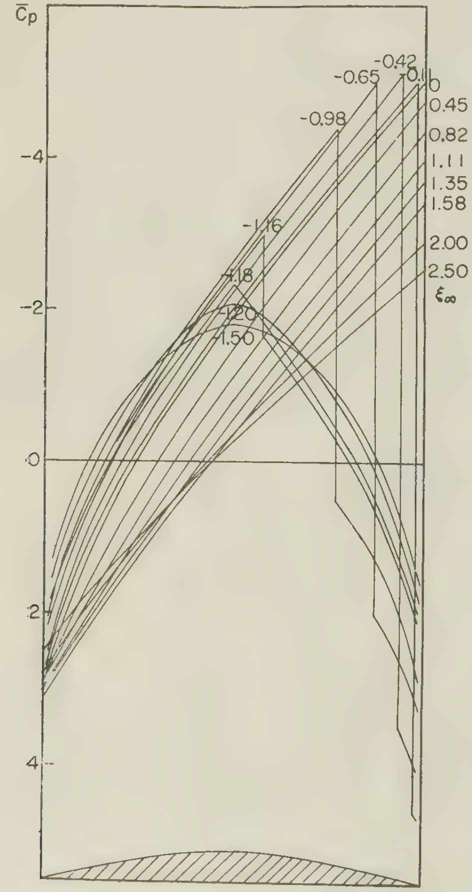

Fig. 2. Theoretical pressure distribution on a circular-arc aerofoil in terms of $\bar{C}_p$, for various ξ_∞.

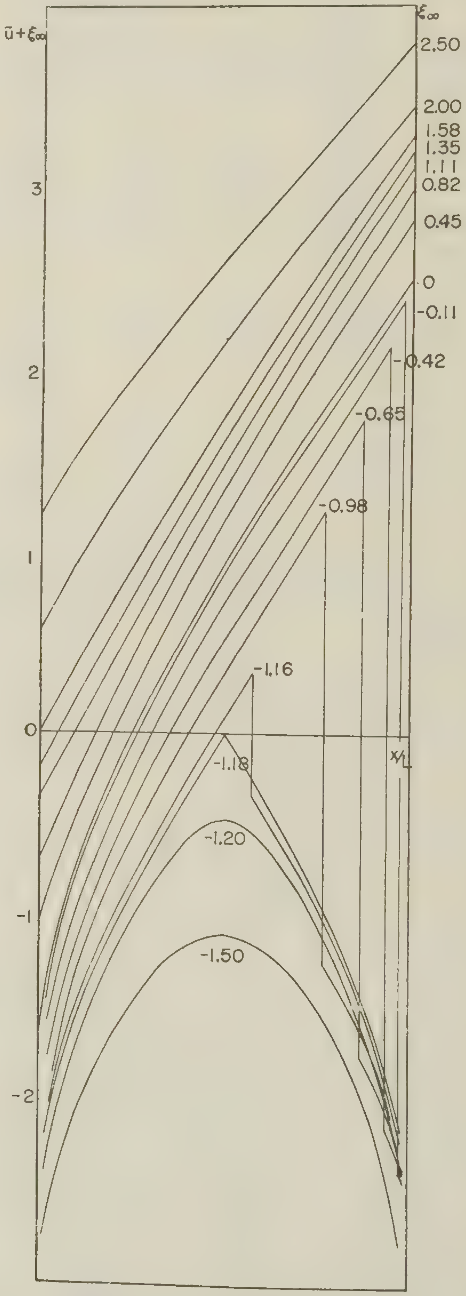

Fig. 3. Theoretical velocity distribution on a circular-are aerofoil in terms of $\bar{u}+\xi_\infty$, for various ξ_∞.

---

* In quoting the experiment of Ref. 7, the unpublished details of experimental data could be utilized thanks to kindness of the authors of Ref. 7.

by Spreiter seem to recede too rapidly with increasing ξ_∞.

It is interesting to note that the nature of our curve which is nearly horizontal and flat at $x=0.5-0.75$ suggests unstableness of the position of the shock wave just after the lower critical value of ξ_∞ is surpassed. Namely if the main flow suffers non-uniformity expressed by ΔM_∞, the shock wave will be unstable and fluctuate from its original position by the amount

$$\Delta c^{**}=\frac{\partial c^{**}}{\partial \xi_\infty}\frac{2M_\infty^2+4}{3M_\infty\{(\gamma+1)M_\infty^2 t\}^{2/3}}\Delta M_\infty\,. \qquad (4.4)$$

The thinner the aerofoil is, the more unstable is the position for the same grade of the assumed non-uniformity of the free stream.

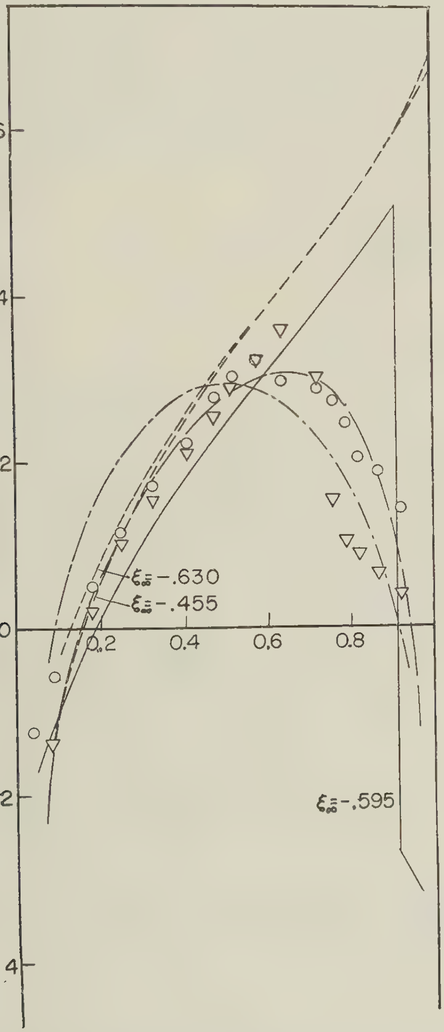

Fig. 4. Pressure distribution on a circular-arc aerofoil in the supercritical flow ($\xi_\infty \cong -0.526$).
Theory ·········· Spreiter[12)]
— — Maeder[11)] ($\xi_\infty=-0.526$)
—— Present
- — Prandtl-Glauert
Experiment, Liepmann[10)]
○ $Re=8.77\times10^5$
▽ $Re=1.75\times10^6$

§ 5. Pressure and Velocity Distributions

By use of the reduced velocity $\bar{u}$ and $f(x, \alpha)$, (2.3), (2.4) and (2.5) are simplified, as follows:

$$\bar{u}=\frac{\{M_\infty^2(\gamma+1)\}^{1/3}}{t^{2/3}}\Phi_x \qquad (5.1)$$

$$=-\xi_\infty\pm\sqrt{\eta(x)} \qquad (5.2)$$

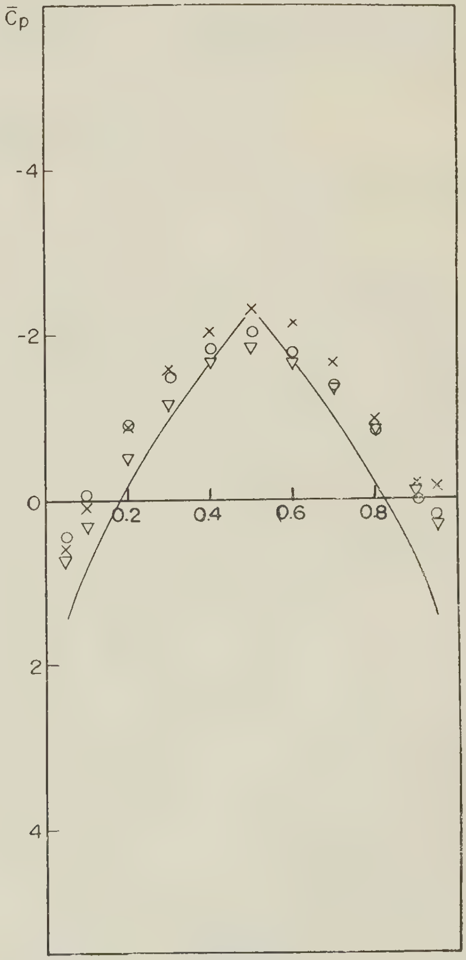

Fig. 5. Pressure distribution on a circular-arc aerofoil in the lower critical flow.
Theory —— Present ($\xi_\infty=-1.1745$)
Experiment, Michel et al[8)]
○ $M_\infty=0.770$, $t=0.12$ ($\xi_\infty=-1.3226$)
× $M_\infty=0.835$, $t=0.08$ ($\xi_\infty=-1.1567$)
▽ $M_\infty=0.870$, $t=0.06$ ($\xi_\infty=-1.0653$)

$$\eta(x)=\xi_\infty^2+(1/|\xi_\infty|)f^2(c^*;\ \alpha)-2\sqrt{|\xi_\infty|}\,f(x;\ \alpha)+4\alpha\sqrt{|\xi_\infty|}\int_{c^*}^{x}f(x;\ \alpha)dx \tag{5.3}$$

the double sign corresponding to

$$\left.\begin{array}{ll}\xi_\infty^2-\sqrt{|\xi_\infty|}\,f(x;\ \alpha)\leqq 0\,, & \text{for } M_\infty<1\\ \text{and} & \\ \xi_\infty^2-\sqrt{|\xi_\infty|}\,f(x;\ \alpha)\geqq 0\,, & \text{for } M_\infty>1\end{array}\right. \tag{5.4}$$

As α is uniquely related to ξ_∞, (5.2) is the expression consistent with the transonic similarity law.

By use of this expression, we obtain the two formulae for reduced physical quantities as follows;
for *pressure coefficient* C_p;

$$\bar{C}_p=\{M_\infty^2(\gamma+1)\}^{1/3}t^{-2/3}C_p=-2\bar{u} \tag{5.5}$$

$$=2\xi_\infty\mp2\sqrt{\eta(x;\xi_\infty)} \tag{5.6}$$

for *local Mach number* M;

$$\begin{aligned}\bar{u}+\xi_\infty&=\{(\gamma+1)tM_\infty^2\}^{-2/3}\{(\gamma+1)M_\infty^2\Phi_x-(1-M_\infty^2)\}\\&=(M^2-1)/\{(\gamma+1)tM_\infty^2\}^{-2/3}\cong2(M-1)/\{(\gamma+1)t\}^{-2/3}\end{aligned} \tag{5.7}$$

and we have only to remark that

$$\bar{u}+\xi_\infty \gtreqqless 0 \text{ corresponds to } M \gtreqqless 1\,. \tag{5.8}$$

The both results calculated for various values of ξ_∞ are shown in Figs. 2 and 3. The variations of them with ξ_∞ seem to be reasonable as a whole. In the sub- and supersonic extremities, they are in accord with the results obtained by the conventional linear theories. At the lower critical value of ξ_∞, the curve of the velocity distribution makes an angular shift at the sonic point and it is interesting to compare with the well-known critical state of the one-dimensional flow. For ξ_∞ above the lower critical value, a normal shock wave appears on the aerofoil, and arrives at the trailing edge at $\xi_\infty=0$.

Fig. 4 is presented for comparison with other theories.[11),12)] They are compared with Liepmann's experiment[10)] which was performed for a circular-arc aerofoil of $t=0.12$ in the supercritical flow of $M_\infty=0.895$ ($\xi_\infty\doteqdot-0.526$). First it is seen that Maeder's result[11)] is better in this régime of transonic flow (*cf.* Fig. 9), probably due to the viscous effect which destroys the formation of a shock wave near the aerofoil. Next, Spreiter's result[12)] overestimates the negative pressure on the aerofoil, particularly in the rear portion. This is in close relation to his prediction of rapid receding of the position of shock wave (described in the previous section). Thus, our prediction could be considered rather successful as a conclusion from the inviscid, nonlinear theory.

Figs. 5, 6 and 7 are provided in addition in order to compare our results with Michel's experiments (ONERA).[8)] They offer three typical examples of flows; that is, the lower critical, supercritical, and supersonic flows.

§ 6. Shock Wave at the Trailing Edge

We have learned that the normal shock arrives at the trailing edge when $\xi_\infty=0$. Then, what happens on the velocity discontinuity when ξ_∞ becomes positive? Certainly the velocity discontinuity will then lose the meaning of a normal shock and take the feature of an oblique shock, which we shall prove mathematically within the present theory as follows.

After the trailing edge, we should have

$$\varphi_x=\frac{1}{2m}\int_0^1F'(\xi)\frac{\partial}{\partial\xi}e^{-|\alpha|(x-\xi)}I_0[|\alpha|(x-\xi)]d\xi \tag{6.1}$$

$$= -\frac{1}{2m}\Big\{F'(0)e^{-|\alpha|x}I_0(|\alpha|x) - F'(1)e^{-|\alpha|(x-1)}I_0[|\alpha|(x-1)]$$

$$+ \int_0^1 F''(\xi)e^{-|\alpha|(x-\xi)}I_0[|\alpha|(x-\xi)]d\xi\Big\} \tag{6.2}$$

$$= \frac{2t}{m}\,[e^{-|\alpha|x}\{(2x-1)I_0(|\alpha|x)+2xI_1(|\alpha|x)\}$$

$$-e^{-|\alpha|(x-1)}\{(2x-1)I_0[|\alpha|(x-1)]+2(x-1)I_1[|\alpha|(x-1)]\}] \tag{6.3}$$

with the aid of (3.28). In the limit when x approaches the trailing edge upstream, this becomes

$$\varphi_x(1+0) = \frac{2t}{m}\,[e^{-|\alpha|}\{I_0(|\alpha|)+2I_1(|\alpha|)\}-1] < 0\ . \tag{6.4}$$

From (3.29), on the other hand, the limit when x approaches there downstream is obtained as

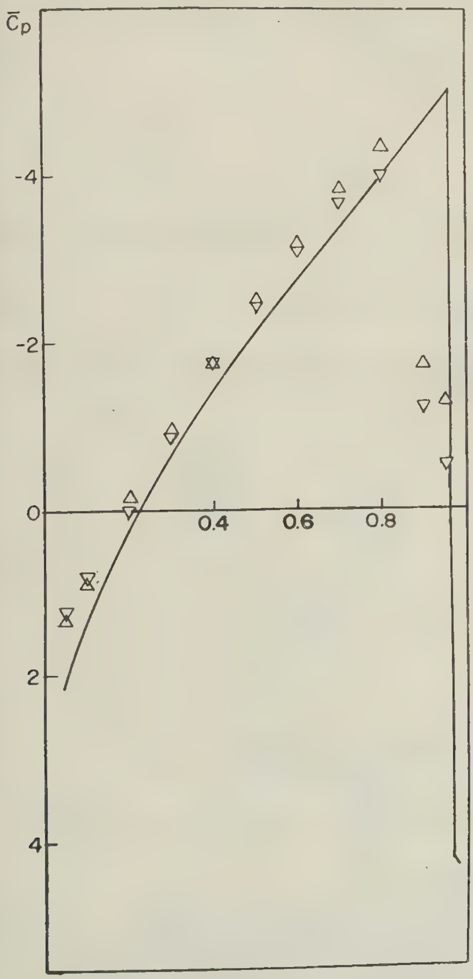

Fig. 6. Pressure distribution on a circular-arc aerofoil in the supercritical flow.
Theory ——— Present ($\xi_\infty=-0.2110$)
Experiment, Michel et al[8)]
△ $M_\infty=0.955,\ t=0.10\ (\xi_\infty=-0.2422)$
▽ $M_\infty=0.970,\ t=0.06\ (\xi_\infty=-0.2240)$

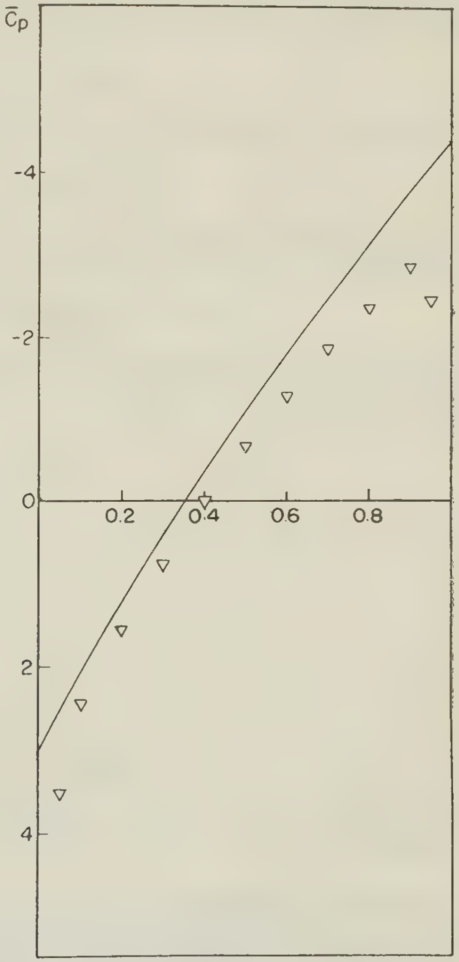

Fig. 7. Pressure distribution on a circular-arc aerofoil in the supersonic, but below upper critical flow.
Theory ——— Present ($\xi_\infty=0.8226$)
Experiment, Michel et al[8)]
▽ $M_\infty=1.125,\ t=0.06\ (\xi_\infty=0.8264)$

$$\varphi_x(1-0)=\frac{2t}{m}\,[e^{-|\alpha|}\{I_0(|\alpha|)+2I_1(|\alpha|)\}>0\,. \tag{6.5}$$

Now from (6.4) and (6.5), the following relation can be derived;

$$Y(1-0)\geqq Y(1+0) \tag{6.6}$$

(Here it is noted that the last term of the right-hand side of (2.4) has the same value in both limits, since $\varphi(1\pm0)-\varphi(c^*)=\int_{c^*}^{1}\varphi_x dx.$)

The equality holds only when $M_\infty=1$ and at the extremity, $M_\infty\to\infty$. These results may be considered to elucidate qualitatively the above-mentioned fact, the resonable behaviour of the supersonic flow at the trailing edge.

Moreover, it can be shown that when ξ_∞ is equal to 0.833 (which is smaller than the upper critical value), the oblique shock changes suddenly to that belonging to the weak family The proof is as follows.

According to the rule (2.5), the sign to be attached to $\sqrt{Y(1+0)}$ should change from minus to plus when

$$\varphi_x(1+0)=(1-M_\infty^2)/[(\gamma+1)M_\infty^2]\,. \tag{6.7}$$

This condition is expressed by use of (6.4) as

$$2[e^{-|\alpha|}\{I_0(|\alpha|)+2I_1(|\alpha|)\}-1]=-\xi_\infty^{3/2}\,. \tag{6.8}$$

Since $|\alpha|$ is already uniquely related to ξ_∞ as described in § 4., we can solve (6.8) and obtain $|\alpha|\doteqdot3.85$ and $\xi_\infty^{3/2}\doteqdot0.76$ ($\xi_\infty\doteqdot0.833$). Then we have

$$Y(1+0)=2K/[(\gamma+1)M_\infty^2]\cdot\{\varphi(1+0)-\varphi(c^*)\}>0\,. \tag{6.9}$$

For example, velocity distributions for two cases are shown in Fig. 8; each corresponds to ξ_∞, a little smaller (a), and larger (b) than this value, respectively.

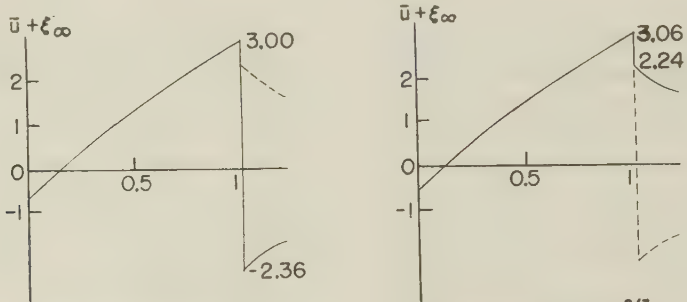

(a) $\xi_\infty=(0.746)^{2/3}=0.823$

(b) $\xi_\infty=(0.963)^{2/3}=0.975$

Fig. 8. Illustration of conversion of the shock-wave family at the trailing edge of a circular-arc aerofoil. ($\xi_\infty=0.833$ is the point of conversion.)

This result is qualitatively correct. Because, first, when the supersonic flow is deflected by a very small angle at the trailing edge, it can either drop to subsonic through a strong shock wave, or remain supersonic through a weak shock wave, as is known from the consideration by the shock polar; next there is a normal shock at the trailing edge in the case of $M_\infty=1$ in the present theory and, on the other hand, naturally we have a weak shock for higher Mach numbers where the flow about there is purely supersonic; and therefore it is quite unavoidable that a sudden, discontinuous change of the family of shock occurs at some value of M_∞ larger than one with increasing Mach number. As is proved already ((6.6)), the weak shock tends to the Mach wave in the supersonic linear theory.

§ 7. Pressure Drag

The reduced drag coefficient $\bar{C}_d$ is evaluated as follows:

$$\bar{C}_d = \frac{\{(\gamma+1)M_\infty^2\}^{1/3}}{t^{5/3}} C_d$$

$$= \frac{\{(\gamma+1)M_\infty^2\}^{1/3}}{t^{5/3}} \int_0^1 F'(x) C_p(x) dx \qquad (7.1)$$

$$= \int_0^1 (1/t) F'(x) \bar{C}_p(x;\ \xi_\infty) dx\ . \qquad (7.2)$$

In case of a circular-arc aerofoil,

$$\bar{C}_d = \int_0^1 4(1-2x) \bar{C}_p(x;\ \xi_\infty) dx\ . \qquad (7.3)$$

For the case of $M_\infty < 1$, the range of integration is conveniently reduced to (0.05—0.95), because the flow has singularities of the same type at the leading and trailing edges, and the maximum error of $\bar{C}_d$ due to this approximation will be within about 0.1.

The calculated results are shown in Fig. 9 with other data. It is noted, however, that in our result a slightly negative drag which amounts to -0.2 at most is obtained within a very small range of ξ_∞ just above the lower critical value. It is probably due to the concentrated effect of the theoretical error in the neighbourhood of the leading and trailing edges;[1] but it may be considered practically insignificant.

Comparing with the experimental data in the figure, Maeder's theory seems to give a

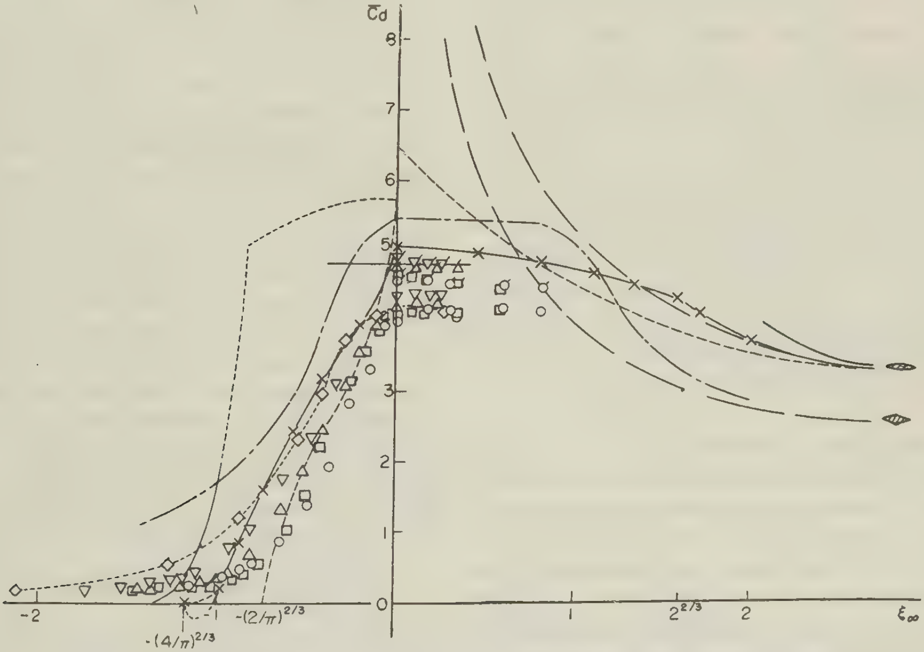

Fig. 9. Reduced pressure drag coefficient $\bar{C}_d$ of a circular-arc aerofoil versus ξ_∞.

Theory —— · · Spreiter (Integral Eq.)[12]
———— Spreiter (Local Linearization)[6),13]
· · · · · · Maeder[11]
× × × Present
— —— Linear Theory
—— — —— Diamond Aerofoil

Experiment, Michel et al[8]

○ $t=0.06$ ○
□ $t=0.08$ □
△ $t=0.10$ △ Extrapolated Drag
▽ $t=0.12$ ▽

(These data have been cited from Spreiter's work[13].)

Maeder[11]

···◇··· $t=0.1$ (slotted wall)

good result at least for ξ_∞ near zero, in the subsonic side but it fails for other ranges of ξ_∞.[11] One of his results that there exists a supercritical, symmetric, shock-free solution for ξ_∞ smaller than $-(2/\pi)^{2/3}$ contradicts the experimental fact. On the other hand, Spreiter's integral equation method[6),12)] results in the unnatural, too rapid increase of drag for ξ_∞ just above the lower critical value, though it predicts that critical value itself rather well. This is considered a reflection of the rapid receding of the shock wave and the overestimation of the velocity distribution in his result as were stated before. The local linearization method gives good results locally for the proper ranges of ξ_∞.[6),13)] But it seems that the phenomenon of sonic freezing is not so remarkable in the subsonic side as expected, in this theory from the experimental point of view. Thus among all these results, the present theory seems to be the most satisfactory as a whole, considering the general trend of experiments.

For reference, the famous drag-curve for a diamond aerofoil is added, which was given theoretically by Trilling, Guderley and Yoshihara, and Vincenty and Wagoner. The both bear a much qualitative resemblance but that the lower critical value of ξ_∞ for a diamond aerofoil vanishes whereas that for the present aerofoil is equal to $-(4/\pi)^{2/3}$.

§ 8. Concluding Remarks

As an example of application of the author's method developed in the previous paper, various transonic flows around a circular-arc aerofoil were calculated with success. This method can be directly applied to any thin aerofoil as far as its profile is expressed by a polynomial. If a high speed computer is available, applicability will further be enlarged.

These results are significant in verifying the following facts: First, transonic flows around a thin aerofoil can be treated by systematical analysis throughout the whole range of Mach number so that a plausible transition of the flows with M_∞ be given in the first-order approximation, and secondly the quadratic nature of the nonlinear equation gives rise to the shock wave in the flow field inevitably in some case. This is also consistent with the general view that it is probably impossible to have a smooth supersonic zone enclosed within a subsonic field.

Finally the author wishes to express his hearty thanks to members of the National Aeronautical Laboratory for their valuable discussions.

References

1) I. Hosokawa: J. Phys. Soc. Japan **15** (1960) 149.
2) K. Oswatitsch and F. Keune: Proc. Conf. on High Speed Aeronautics, Polytech. Inst. Brooklyn (1955) 113.
3) P. F. Maeder and H. U. Thommen: J. Aero. Sci. **23** (1956) 187.
4) I. Hosokawa: J. Phys. Soc. Japan **15** (1960) 2080.
5) C. C. Lin and S. I. Rubinov: J. Math. Phys. **27** (1948) 105.
6) J. R. Spreiter, A. Y. Alksne and B. J. Heytt: NACA Tech. Note 4148 (1958).
7) R. Kawamura and K. Karashima: Aero. Research Inst. Univ. Tokyo Rep. no. 342 (1959).
8) R. Michel, F. Marchaud and J. Le Gallo: ONERA, Publication no. 65 (1953).
9) A. E. Bryson: NACA Tech. Rep. 1094 (1952).
10) H. W. Liepmann: J. Aero. Sci. **13** (1946) 623.
11) P. F. Maeder: Proc. 9th Intern. Congr. Appl. Mech., vol. 2 (1957) 15.
12) J. R. Spreiter and A. Y. Alksne: NACA Tech. Rep. 1217 (1955) 31.
13) J. R. Spreiter and A. Y. Alksne: NACA Tech. Note 3970 (1957) 50.
14) G. N. Watson: *Theory of Bessel Functions* (Cambridge, 1922) 171p.

JOURNAL OF THE PHYSICAL SOCIETY OF JAPAN, Vol. 16, No. 3, MARCH, 1961

Effect of a Magnetic Field upon the Stability of Free Boundary Layers between Two Uniform Streams

By Kanefusa GOTOH

Department of Physics, Faculty of Science,
Kyoto University

(Received December 2, 1960)

The stability of free boundary-layer flows of a viscous, incompressible, electrically conducting fluid is investigated. It is found generally that a uniform magnetic field parallel to the steady flows has an effect of stabilizing the flows. When the magnetic field is weak, i.e. when the Alfvén number A is less than unity, the flows are unstable with zero critical Reynolds number ($R_c=0$). But when the magnetic field is so strong that $A>1$, the flows are absolutely stable ($R_c=\infty$) provided $R_m/R>1$ where R_m is the magnetic Reynolds number. For small values of R_m/R, the flows are unstable even for $A>1$, so long as $(R_m/R)A^2 \ll 1$.

It is also shown that an oblique magnetic field cannot stabilize the flow, however strong it may be.

§1. Introduction

It is generally believed that the magnetic field imposed upon laminar flows of electrically conducting fluid makes the flows less unstable and there are many evidences supporting this conclusion. In the case of two-dimensional parallel flow between parallel planes, Stuart[1] found that if the magnetic Reynolds number R_m is sufficiently small, a uniform magnetic field parallel to the flow causes a steady rise of the critical Reynolds number with increasing magnetic field. For the plane flows of perfect conductor ($R_m=\infty$) between parallel planes, Velikhov[2] showed that the effect of magnetic field is also stabilizing, and if the Alfvén number A exceeds the critical value 0.2 the flow is entirely stabilized by the magnetic field.

In this paper we attempt to discuss the effect of a uniform magnetic field upon the stability of free boundary-layer flows between two parallel streams. The fluid is assumed to be incompressible with the constant density ρ, the kinematic viscosity ν, the electrical conductivity σ, and the magnetic permeability μ.

It was already established in ordinary hydrodynamical case that the free boundary-layer flows are unstable at all Reynolds numbers irrespective of the detailed structure of their velocity profiles (Tatsumi and Gotoh[3]). It may therefore be interesting to investigate whether the magnetic field stabilizes the free flows or not, and, in particular, to study how the critical Reynolds number changes, or does not change, with the intensity of the magnetic field.

It will be found that as in the case of the channel flows the magnetic field has a stabilizing effect in this case too, but the critical Reynolds number R_c rises in somewhat different manner with increasing magnetic field. In contrast with the continuous rise of R_c with increasing A for the bounded flows, R_c in the present case remains to be zero for $A<1$. For values of A greater than unity, R_c changes abruptly to infinity provided $R_m/R>1$. If, on the other hand, $R_m/R \ll 1$, the flow is unstable even for $A>1$ so long as $(R_m/R)A^2$ is small.

§2. Mathematical Formulation

Taking the x-axis of two-dimensional Cartesian coordinates along the direction of a steady plane parallel flow, let $U(y)$ and H be the velocity profile of this flow and the intensity of a uniform magnetic field respectively.

When the undisturbed magnetic field is parallel to the undisturbed velocity, Squire's theorem[4] in the non-magnetic stability theory of plane parallel flows is also valid in magnetic case, and it is sufficient to consider two-dimensional disturbances only (Michael[5]. By making use of the equations of continuity:

$$\operatorname{div} \boldsymbol{u}=0\ , \qquad \operatorname{div} \boldsymbol{H}=0\ , \tag{1}$$

two-dimensional disturbances may be expressed in terms of the stream function ψ and the magnetic stream function χ as follows:

$$\left.\begin{aligned} u_x&=\frac{\partial\psi}{\partial y}\,, & u_y&=-\frac{\partial\psi}{\partial x}\,,\\ h_x&=\frac{\partial\chi}{\partial y}\,, & u_y&=-\frac{\partial\chi}{\partial x}\,,\end{aligned}\right\} \tag{2}$$

If we consider infinitesimal disturbances only, the equations of motion and magnetic induction may be linearized with respect to the intensity of the disturbances, so that by virtue of the principle of superposition it suffices to deal with only one of their harmonic components:

$$\left.\begin{aligned} \psi&=\phi(y)\exp\{i\alpha(x-ct)\}\,,\\ \chi&=\theta(y)\exp\}i\alpha(x-ct)\}\,,\end{aligned}\right\} \tag{3}$$

where $\alpha\,(>0)$ represents the wave number in the x-direction, $\mathscr{R}_e(c)\equiv c_r$ the phase velocity, and $\mathscr{I}_m(\alpha c)\equiv\alpha c_i$ the amplification factor of the disturbance. According as c_i takes positive, zero or negative values, we have amplified, neutral or damped disturbances respectively.

Substituting (2) and (3), together with steady fields, into the equations of motion and magnetic induction, and neglecting quadratic terms of ϕ and θ, we obtain the following equations for the amplitude of disturbances ϕ and θ:

$$(U-c)(\phi''-\alpha^2\phi)-U''\phi-S(\theta''-\alpha^2\theta)=-\frac{i}{\alpha R}(\phi^{\mathrm{iv}}-2\alpha^2\phi''+\alpha^4\phi)\,, \tag{4}$$

$$(U-c)\theta-\phi=-\frac{i}{\alpha R_m}(\theta''-\alpha^2\theta)\,, \tag{5}$$

where primes denote differentiation with respect to y, and all quantities have been made non-dimensional with respect to the representative velocity U_0, magnetic field H_0 and length scale l of the field. Non-dimensional parameters R, R_m and S are defined as

the Reynolds number: $R=lU_0/\nu$,
the magnetic Reynolds number: $R_m=4\pi\sigma\mu lU_0$,
the pressure number: $S=\mu H_0^2/(4\pi\rho U_0^2)$.

In the following, both U_0 and H_0 are chosen such that

$$U(\infty)=-U(-\infty)=1\,,\qquad H=1\,.$$

Eliminating ϕ from Eqs. (4) and (5), we have a sixth-order equation for θ:

$$\begin{aligned}(U-c+A)(U-c-A)(D^2-\alpha^2)\theta+2U'(U-c)\theta'&=-\frac{i}{\alpha R_m}\{(U-c)(D^2-\alpha^2)-U''\}(D^2-\alpha^2)\theta\\ &\quad-\frac{i}{\alpha R}(D^2-\alpha^2)^2(U-c)\theta+\frac{1}{\alpha^2RR_m}(D^2-\alpha^2)^3\theta\,,\end{aligned} \tag{6}$$

where $D=d/dy$ and $A\ (=S^{1/2})$ denotes the Alfvén number. Since all disturbances must vanish at infinity, Eqs. (5) and (6) must be solved subject to the boundary conditions:

$$\left.\begin{aligned}\phi(\infty)&=\phi(-\infty)=0\,,\\ \theta(\infty)&=\theta(-\infty)=0\,.\end{aligned}\right\} \tag{7}$$

§ 3. Solutions for Large R and R_m

When both R and R_m are extremely large, Eq. (6) reduces to

$$\theta''+\frac{2U'(U-c)}{(U-c)^2-A^2}\theta'-\alpha^2\theta=0\,. \tag{8}$$

In order to solve this equation it is convenient to divide the y-space into three separate regions (I), (II) and (III) by two appropriate points y_1 $(>y_c)$, and y_2 $(<y_s)$ as:

$$\text{(I)}\quad y>y_1\,,\qquad \text{(II)}\quad y_1>y>y_2\,,\qquad \text{(III)}\quad y<y_2\,,$$

and to deal with these three regions separately, where y_c and y_s are defined by

$$U(y_c)=c+A\ , \qquad U(y_s)=c-A\ .$$

(i) *Solutions in the outer regions* (I) *and* (III)

Since, in the regions (I) and (III), U' tends to zero as $|y|\to\infty$, the first approximate solution of Eq. (8) may be obtained by neglecting the second term in (8), and the better approximation will be given by iteration process. If we denote the solutions in the regions (I) and (III) by θ_{I} and θ_{III} respectively, the above procedure is equivalent to expanding θ_j ($j=\text{I, III}$) into the following series of functions:

$$\theta_j=C_jF_j=C_j\sum_{n=0}^{\infty}F_j^{(n)}(y;\alpha,c,A)\ , \tag{9}$$

where C_j's are arbitrary constants and $F_j^{(n)}$'s are solutions of the following equations:

$$\left.\begin{aligned}
&F_j^{(0)\prime\prime}-\alpha^2F_j^{(0)}=0\ ,\\
&F_j^{(n)\prime\prime}-\alpha^2F_j^{(n)}=-\frac{2U'(U-c)}{(U-c)^2-A^2}F_j^{(n-1)\prime}\ , \qquad (n\geq 1)\ .
\end{aligned}\right\} \tag{10}$$

Equations (10) are easily solved and, taking the boundary conditions (7) into consideration, we have

$$\left.\begin{aligned}
&F_{\text{I}}^{(0)}=e^{-\alpha y}\ , \qquad F_{\text{III}}^{(0)}=e^{\alpha y}\ ,\\
&F_j^{(n)}(y)=\frac{2}{\alpha}\int_{\pm\infty}^{y}\frac{U'(\xi)\{U(\xi)-c\}}{\{U(\xi)-c\}^2-A^2}\sinh\alpha(\xi-y)F_j^{(n-1)\prime}(\xi)\,d\xi\ ,
\end{aligned}\right\} \tag{11}$$

where $\pm\infty$ in the integrals must be taken as $+\infty$ and $-\infty$ for $j=\text{I}$ and III respectively.

If, in particular, we take

$$U(y)=\tanh y$$

as the basic velocity profile, the integrals in (11) can be evaluated immediately, obtaining

$$\left.\begin{aligned}
F_{\text{I}}(y)=e^{-\alpha y}\Big[\,1&+\frac{2\alpha(1-c)}{(1-c+A)(1-c-A)(1+\alpha)}e^{-2y}\\
&+2\alpha\cdot\frac{(1-c)^2(2+\alpha+c+c\alpha)+(2-c)(1+\alpha)A^2}{(1-c+A)^2(1-c-A)^2(1+\alpha)(2+\alpha)}e^{-4y}+\text{O}(e^{-6y})\Big]\ ,\\
F_{\text{III}}(y)=e^{\alpha y}\Big[\,1&+\frac{2\alpha(1+c)}{(1+c+A)(1+c-A)(1+\alpha)}e^{2y}\\
&+2\alpha\cdot\frac{(1+c)^2(2+\alpha-c-c\alpha)+(2+c)(1+\alpha)A^2}{(1+c+A)^2(1+c-A)^2(1+\alpha)(2+\alpha)}c^{4y}+\text{O}(e^{6y})\Big]\ .
\end{aligned}\right\} \tag{12}$$

(ii) *Solutions in the inner region* (II)

Let f_1 and f_2 denote two particular solutions of Eq. (8) in the region (II).

If we assume f_k ($k=1, 2$) in the form of power series of α^2 as:

$$f_k=\sum_{n=0}^{\infty}\alpha^{2n}f_k^{(n)}(y;c,A)\ , \tag{13}$$

$f_k^{(n)}$'s must satisfy the following equations:

$$\left.\begin{aligned}
&f_k^{(0)\prime\prime}+\frac{2U'(U-c)}{(U-c)^2-A^2}f_k^{(0)\prime}=0\ ,\\
&f_k^{(n)\prime\prime}+\frac{2U'(U-c)}{(U-c)^2-A^2}f_k^{(n)\prime}=f_k^{(n-1)}\ , \qquad (n\geq 1)\ .
\end{aligned}\right\} \tag{14}$$

Formal solutions of (14) are readily obtained as

$$\left.\begin{aligned} &f_1^{(0)}=1\,, \qquad f_2^{(0)}=\int_{y_2}^{y}\frac{d\xi}{\{U(\xi)-c\}^2-A^2}\,,\\ &f_k^{(n)}(y)=\int_{y_2}^{y}\frac{d\xi}{\{U(\xi)-c\}^2-A^2}\int_{y_2}^{\xi}[\{U(\zeta)-c\}^2-A^2]\,f_k^{(n-1)}(\zeta)\,d\zeta\,, \qquad (k=1,2;\ n\geq 1)\,. \end{aligned}\right\} \tag{15}$$

Thus we get the general solution in the region (II) as:

$$\theta_{\mathrm{II}}=C_1 f_1+C_2 f_2\,. \tag{16}$$

The singularities in the integrands of (15) show that f_1 and f_2 are in general many-valued functions, so that we have to choose their correct branches by comparing them with the asymptotic behaviour of the solutions of the full equation (6). In the neighbourhood of $y=y_c$ f_1 and f_2 are expressed as a linear combination of two power series solutions:

$$\left.\begin{aligned} &\mathscr{F}_1(y)=1+\sum_{n=1}^{\infty}B_n^{(1)}(y-y_c)^n\,,\\ &\mathscr{F}_2(y)=\mathscr{F}_1(y)\log(y-y_c)+\sum_{n=1}^{\infty}B_n^{(2)}(y-y_c)^n\,, \end{aligned}\right\} \tag{17}$$

where $B_n^{(1)}$, $B_n^{(2)}$ $(n=1,2,\cdots)$ are numerical constants.

If we put $R_m=\infty$, but retaining R to be finite, Eq. (6) reduces to

$$(U-c+A)(U-c-A)(D^2-\alpha^2)\theta+2U'(U-c)\theta'=-\frac{i}{\alpha R}(D^2-\alpha^2)^2(U-c)\theta\,. \tag{18}$$

Changing the independent variable from y to η, where

$$\varepsilon\eta=y-y_c\,, \qquad \varepsilon=\{2\alpha R U'(y_c)\}^{-1/3}\,,$$

the above equation (18) becomes

$$\frac{d^4\theta}{d\eta^4}-i\left(\eta\frac{d^2\theta}{d\eta^2}+\frac{d\theta}{d\eta}\right)=\mathrm{O}(\varepsilon)\,. \tag{19}$$

Four independent solutions of this equation are expressed as:

$$\left.\begin{aligned} &\theta_1=1+\mathrm{O}(\varepsilon)\,,\\ &\theta_2=\int\left(h_1\int h_2\,d\eta-h_2\int h_1\,d\eta\right)d\eta+\mathrm{O}(\varepsilon)\,,\\ &\theta_3=\int h_2\,d\eta+\mathrm{O}(\varepsilon)\,,\\ &\theta_4=\int h_1\,d\eta+\mathrm{O}(\varepsilon)\,, \end{aligned}\right\} \tag{20}$$

where

$$h_1=\eta^{1/2}H_{1/3}^{(1)}\left[\frac{2}{3}(i\eta)^{3/2}\right], \qquad h_2=\eta^{1/2}H_{1/3}^{(2)}\left[\frac{2}{3}(i\eta)^{3/2}\right],$$

and $H_{1/3}^{(1)}$, $H_{1/3}^{(2)}$ denote the Hankel functions of order 1/3. The asymptotic form of (20) for $R\to\infty$ and for fixed $y-y_c$ is obtained by making $\eta\to\infty$, and for large values of η the solutions (20) become

$$\left.\begin{aligned}&\theta_1\sim 1\,,\\&\theta_2\sim\text{const.}\log\eta\,,\\&\theta_3\sim\text{const.}\,\eta^{-3/4}\exp\left[\frac{2}{3}\eta^{3/2}e^{i\pi/4}\right],\\&\theta_4\sim\text{const.}\,\eta^{-3/4}\exp\left[\frac{2}{3}\eta^{3/2}e^{5\pi i/4}\right],\end{aligned}\right\}\tag{21}$$

under the condition:

$$-\frac{7}{6}\pi\leq\arg\eta\leq\frac{1}{6}\pi\,.\tag{22}$$

It is easily seen that the first two solutions in (21) are identical with the solutions (17) if terms of $O(\varepsilon\log\varepsilon)$ are ignored. The condition (22) shows that the solutions (17) represent the correct solutions of the full equation (6) provided that y lies, if $U'(y_c)>0$, in the region *below* $y=y_c$. Thus, the path of integration in (15) must be taken through this region (see Fig. 1). The same rule is also valid at $y=y_s$.

Although the solutions (13) in power series of α^2 converge for all values of α, they are not conveniently calculated for non-small values of α. For $\alpha\approx 1$ another method of perturbation may be useful.

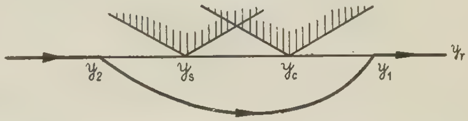

Fig. 1. Path of integration in complex y-plane.

If we take the velocity profile $U(y)=\tanh y$ and take the case in which

$$\alpha=1\,,\qquad A=c=0\,,\tag{23}$$

then Eq. (8) permits two independent solutions:

$$f_1=\operatorname{cosech}\,y,\qquad f_2=y\operatorname{cosech}\,y+\cosh\,y\,.\tag{24}$$

For small but non-zero values of A and c, we can take

$$A,\qquad c\ll U(y)\,,\tag{25}$$

and expand the coefficient of θ' in (8) as follows:

$$\frac{2U'(U-c)}{(U-c)^2-A^2}=\frac{2U'}{U}\left(1+\frac{c}{U}+\frac{c^2+A^2}{U^2}+\cdots\right).\tag{26}$$

Then the solutions of (8) may be expressed in the following series:

$$f_k(y)=\sum_{n=0}^{\infty}f_k^{(n)}(y)\,,\qquad(k=1,2)\,,\tag{27}$$

where $f_k^{(n)}$'s are solutions of equations:

$$\left.\begin{aligned}&f_k^{(0)\prime\prime}+2\frac{U'}{U}f_k^{(0)\prime}-f_k^{(0)}=0\,,\\&f_k^{(1)\prime\prime}+2\frac{U'}{U}f_k^{(1)\prime}-f_k^{(1)}=-2\frac{U'}{U}\left(\frac{c}{U}+\frac{A^2}{U^2}\right)f_k^{(0)\prime}-(1-\alpha^2)f_k^{(0)}\,,\\&\cdots\cdots\cdots\cdots\end{aligned}\right\}\tag{28}$$

§ 4. Eigenvalue Problem for Large Values of R and R_m

The complete solution of Eqs. (8) which satisfies the boundary conditions (7) is obtained by connecting analytically θ_{I} and θ_{II} at y_1, and θ_{II} and θ_{III} at y_2 respectively, that is,

$$\left.\begin{aligned} &\theta_{\mathrm{I}}(y_1)=\theta_{\mathrm{II}}(y_1)\,, && \theta_{\mathrm{I}}'(y_1)=\theta_{\mathrm{II}}'(y_1)\,,\\ &\theta_{\mathrm{II}}(y_2)=\theta_{\mathrm{III}}(y_2)\,, && \theta_{\mathrm{II}}'(y_2)=\theta_{\mathrm{III}}'(y_2)\,. \end{aligned}\right\} \tag{29}$$

In order that Eqs. (29) are satisfied by non-zero C_{I}, C_{III}, C_1 and C_2, the following determinant must vanish:

$$E=\begin{vmatrix} F_{\mathrm{I}}(y_1) & f_1(y_1) & f_2(y_1) & 0 \\ F_{\mathrm{I}}'(y_1) & f_1'(y_1) & f_2'(y_1) & 0 \\ 0 & f_1(y_2) & f_2(y_2) & F_{\mathrm{III}}(y_2) \\ 0 & f_1'(y_2) & f_2'(y_2) & F_{\mathrm{III}}'(y_2) \end{vmatrix}=0\,. \tag{30}$$

equation (30) gives a relationship between eigenvalues of α and c for $R=R_m=\infty$ and for given A.

For small values of α, substitution of (12) and (15) together with $U(y)=\tanh y$ into Eq. (30) gives the eigenvalue equation:

$$\begin{aligned} (1+c^2-A^2)-\alpha[1+(4A)^{-1}(1+c+A)(1-c-A)\{\log(1-c+A)-\log(-1-c+A)\} \\ -(4A)^{-1}(1+c-A)(1-c+A)\{\log(1-c-A)-\log(-1-c-A)\}] \\ +\mathrm{O}(\alpha^2)=0\,. \end{aligned} \tag{31}$$

It may readily be seen that this expression is free from the choice of the matching point. For $\alpha=0$ we have

$$1+c^2-A^2=0\,, \tag{32}$$

so that

$$\left.\begin{aligned} &c_r=0\,,\\ &c_i=\sqrt{1-A^2}\,, \end{aligned}\right\} \tag{33}$$

where the positive root has been taken for c_i, since it must conform with $c_i=1$ for $A=0$. For small values of α an approximate solution of (31) is obtained, by taking the second term into consideration, as:

$$\left.\begin{aligned} &c_r=0\,,\\ &\alpha=\frac{1-c_i^2-A^2}{1+c_i(\pi-\delta)+(4A)^{-1}(1+c_i^2-A^2)\log\dfrac{(1+A)^2+c_i^2}{(1-A)^2+c_i^2}}\,, \end{aligned}\right\} \tag{34}$$

where

$$\tan\delta=2c_i/(1-c_i^2-A^2)\,,\qquad (0<\delta<\pi/2)\,.$$

For $\alpha\approx1$, we substitute (27) and (12) together with $U(y)=\tanh y$ into (30), and obtain the equation:

$$\frac{4}{3}A^2-c\pi i-2(1-\alpha)+\mathrm{O}\{c^2, A^4, (1-\alpha)^2\}=0\,. \tag{35}$$

Thus, we have, for small values of c, A, $1-\alpha$,

$$\left.\begin{aligned} &c_r=0\,,\\ &\alpha=1-\frac{2}{3}A^2-\frac{1}{2}\pi c_i\,. \end{aligned}\right\} \tag{36}$$

The $\alpha-c_i$ curves for constant A are calculated from this result and (34), and are illustrated in Fig. 2.

It is seen in Fig. 2 that for fixed A the neutral disturbance ($c_i=0$) gives the maximum wave-number, α_m, say, and α_m decreases as A increases. For $A \geqq 1$, both α and c_i vanish, and the flow becomes entirely stable under this condition.

§ 5. Eigenvalue Problem for Small R and R_m

Next we proceed to solve the stability problem for small values of R and R_m. The method of approximation which will be employed here is similar to that already used by the author for ordinary hydrodynamical case (Tatsumi and Gotoh[3]).

If we divide the whole y-space into two regions (I) $y \geq y_0$ and (II) $y \leq y_0$, where y_0 is an arbitrary finite point, Eq. (6) may be modified, for these two regions (I) and (II), as:

$$(D^2-\alpha^2)(D^2-\beta_j^2)(D^2-\gamma_j^2)\theta = L_j[\theta]\ , \quad (j=\mathrm{I}, \mathrm{II}) \tag{37}$$

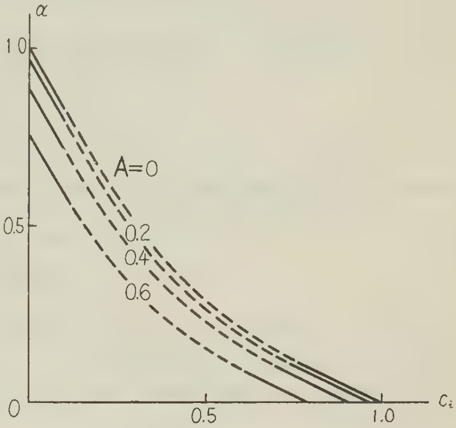

Fig. 2. $\alpha-c_i$ curves for $R=R_m=\infty$.

where

$$\left.\begin{aligned} U_{\mathrm{I}}(y) &= U(y)-U(\infty)=U(y)-1\ , \\ U_{\mathrm{II}}(y) &= U(y)-U(-\infty)=U(y)+1\ , \end{aligned}\right\} \tag{38}$$

$$\left.\begin{aligned} 2\beta_{\mathrm{I}}^2 &= 2\alpha^2+i\alpha(R+R_m)(1-c)+i\{\alpha^2(R-R_m)^2(1-c)^2+4\alpha^2RR_mS\}^{1/2}\ , \\ 2\gamma_{\mathrm{I}}^2 &= 2\alpha^2+i\alpha(R+R_m)(1-c)-i\{\alpha^2(R-R_m)^2(1-c)^2+4\alpha^2RR_mS\}^{1/2}\ , \\ 2\beta_{\mathrm{II}}^2 &= 2\alpha^2-i\alpha(R+R_m)(1+c)+i\{\alpha^2(R-R_m)^2(1+c)^2+4\alpha^2RR_mS\}^{1/2}\ , \\ 2\gamma_{\mathrm{II}}^2 &= 2\alpha^2-i\alpha(R+R_m)(1+c)-i\{\alpha^2(R-R_m)^2(1+c)^2+4\alpha^2RR_mS\}^{1/2}\ , \\ &\mathscr{R}_e(\beta_j, \gamma_j)>0\ , \end{aligned}\right\} \tag{39}$$

and

$$\begin{aligned} L_{\mathrm{I}} = {} & i\alpha R\{U_{\mathrm{I}}(D^2-\alpha^2)-U_{\mathrm{I}}''\}(D^2-\alpha^2)+i\alpha R_m(D^2-\alpha^2)^2U_{\mathrm{I}} \\ & +\alpha^2RR_m[\{U_{\mathrm{I}}(D^2-\alpha^2)-U_{\mathrm{I}}''\}U_{\mathrm{I}}+(1-c)\{U_{\mathrm{I}}(D^2-\alpha^2)+(D^2-\alpha^2)U_{\mathrm{I}}-U_{\mathrm{I}}''\}]\ , \end{aligned} \tag{40}$$

$$\begin{aligned} L_{\mathrm{II}} = {} & i\alpha R\{U_{\mathrm{II}}(D^2-\alpha^2)-U_{\mathrm{II}}''\}(D^2-\alpha^2)+i\alpha R_m(D^2-\alpha^2)^2U_{\mathrm{II}} \\ & +\alpha^2RR_m[\{U_{\mathrm{II}}(D^2-\alpha^2)-U_{\mathrm{II}}''\}U_{\mathrm{II}}-(1+c)\{U_{\mathrm{II}}(D^2-\alpha^2)+(D^2-\alpha^2)U_{\mathrm{II}}-U_{\mathrm{II}}''\}]\ . \end{aligned} \tag{41}$$

It may easily be seen that the right-hand sides of Eq. (37) for $j=\mathrm{I}$ and II tend to zero as $y\to\infty$ and $y\to-\infty$ respectively, so that the first approximate solution is obtained by neglecting the right-hand sides. The second approximate solution will be obtained by substituting the first approximate solution into the right-hand sides of (37), and the approximation may be made arbitrarily better by repeating the iteration. This procedure is equivalent to expanding θ_j into the following series:

$$\theta_j(y)=\sum_{n=0}^{\infty} g_j^{(n)}(y;\, \alpha^2, \alpha R, \alpha R_m, A, c)\ , \tag{42}$$

where $g_j^{(n)}$'s are the solutions of the following equations:

$$\left.\begin{aligned} (D^2-\alpha^2)(D^2-\beta_j^2)(D^2-\gamma_j^2)g_j^{(0)} &= 0\ , \\ (D^2-\alpha^2)(D^2-\beta_j^2)(D^2-\gamma_j^2)g_j^{(n)} &= L_j[g_j^{(n-1)}]\ . \end{aligned}\right\} \tag{43}$$

The series of Eqs. (43) are solved successively, giving the results:

$$\left.\begin{aligned}
&g_{\mathrm{I}1}^{(0)}=e^{-\alpha y}\,, \qquad g_{\mathrm{I}2}^{(0)}=e^{-\beta_{\mathrm{I}}y}\,, \qquad g_{\mathrm{I}3}^{(0)}=e^{-\gamma_{\mathrm{I}}y}\,,\\
&g_{\mathrm{II}1}^{(0)}=e^{\alpha y}\,, \qquad g_{\mathrm{II}2}^{(0)}=e^{\beta_{\mathrm{II}}y}\,, \qquad g_{\mathrm{II}3}^{(0)}=e^{\gamma_{\mathrm{II}}y}\,,\\
&g_{jk}{}^{(n)}(y)=\frac{1}{\alpha(\alpha^2-\beta_j{}^2)(\alpha^2-\gamma_j{}^2)}\int_{\pm\infty}^{y}\sinh\{\alpha(y-\xi)\}L_j[g_{jk}{}^{(n-1)}(\xi)]\,d\xi\\
&\qquad+\frac{1}{\beta_j(\beta_j{}^2-\alpha^2)(\beta_j{}^2-\gamma_j{}^2)}\int_{\pm\infty}^{y}\sinh\{\beta_j(y-\xi)\}L_j[g_{jk}{}^{(n-1)}(\xi)]\,d\xi\\
&\qquad+\frac{1}{\gamma_j(\gamma_j{}^2-\alpha^2)(\gamma_j{}^2-\beta_j{}^2)}\int_{\pm\infty}^{y}\sinh\{\gamma_j(y-\xi)\}L_j[g_{jk}{}^{(n-1)}(\xi)]\,d\xi\,.
\end{aligned}\right\}\tag{44}$$

The general solutions satisfying the boundary conditions (7) are given by

$$\left.\begin{aligned}
&\theta_{\mathrm{I}}=C_{\mathrm{I}1}g_{\mathrm{I}1}+C_{\mathrm{I}2}g_{\mathrm{I}2}+C_{\mathrm{I}3}g_{\mathrm{I}3} \qquad (y\geq y_0)\,,\\
&\theta_{\mathrm{II}}=C_{\mathrm{II}1}g_{\mathrm{II}1}+C_{\mathrm{II}2}g_{\mathrm{II}2}+C_{\mathrm{II}3}g_{\mathrm{II}3} \qquad (y\leq y_0)\,.
\end{aligned}\right\}\tag{45}$$

In order to obtain the complete solution over the whole y-space, we have to connect the two solutions θ_{I} and θ_{II} analytically at $y=y_0$. This is attained by equating the values at $y=y_0$ of θ_{I} and θ_{II} themselves and their first five derivatives respectively. Thus,

$$\left.\begin{aligned}
&(\theta_{\mathrm{I}})_{y_0}=(\theta_{\mathrm{II}})_{y_0}\,,\\
&\left(\frac{d^p\theta_{\mathrm{I}}}{dy^p}\right)_{y_0}=\left(\frac{d^p\theta_{\mathrm{II}}}{dy^p}\right)_{y_0} \qquad (p=1,\cdots,5)\,.
\end{aligned}\right\}\tag{46}$$

In order that these conditions are satisfied by non-zero C's, the following determinant must vanish:

$$E=\begin{vmatrix}
g_{\mathrm{I}1}(y_0) & g_{\mathrm{I}2}(y_0) & g_{\mathrm{I}3}(y_0) & g_{\mathrm{II}1}(y_0) & g_{\mathrm{II}2}(y_0) & g_{\mathrm{II}3}(y_0)\\
g''_{\mathrm{I}1}(y_0) & g'_{\mathrm{I}2}(y_0) & g'_{\mathrm{I}3}(y_0) & g'_{\mathrm{II}1}(y_0) & g'_{\mathrm{II}2}(y_0) & g'_{\mathrm{II}3}(y_0)\\
g''_{\mathrm{I}1}(y_0) & g''_{\mathrm{I}2}(y_0) & g''_{\mathrm{I}3}(y_0) & g''_{\mathrm{II}1}(y_0) & g''_{\mathrm{II}2}(y_0) & g''_{\mathrm{II}3}(y_0)\\
g'''_{\mathrm{I}1}(y_0) & g'''_{\mathrm{I}2}(y_0) & g'''_{\mathrm{I}3}(y_0) & g'''_{\mathrm{II}1}(y_0) & g'''_{\mathrm{II}2}(y_0) & g'''_{\mathrm{II}3}(y_0)\\
g^{\mathrm{iv}}_{\mathrm{I}1}(y_0) & g^{\mathrm{iv}}_{\mathrm{I}2}(y_0) & g^{\mathrm{iv}}_{\mathrm{I}3}(y_0) & g^{\mathrm{iv}}_{\mathrm{II}1}(y_0) & g^{\mathrm{iv}}_{\mathrm{II}2}(y_0) & g^{\mathrm{iv}}_{\mathrm{II}3}(y_0)\\
g^{\mathrm{v}}_{\mathrm{I}1}(y_0) & g^{\mathrm{v}}_{\mathrm{I}2}(y_0) & g^{\mathrm{v}}_{\mathrm{I}3}(y_0) & g^{\mathrm{v}}_{\mathrm{II}1}(y_0) & g^{\mathrm{v}}_{\mathrm{II}2}(y_0) & g^{\mathrm{v}}_{\mathrm{II}3}(y_0)
\end{vmatrix}=0\,.\tag{47}$$

The enormous complexity of Eq. (47) compels us to restrict our consideration to the case of small values of R and R_m.

First we look for the solution of (47) for those values of R and R_m which satisfy $R_m\ll R$, and expand (47) into powers of α^2, αR, αR_m and R_m/R:

$$\begin{aligned}
E=-16(\beta_{\mathrm{I}}-\alpha)(\beta_{\mathrm{II}}-\alpha)(\gamma_{\mathrm{I}}-\alpha)(\gamma_{\mathrm{II}}-\alpha)(\beta_{\mathrm{I}}-\gamma_{\mathrm{I}})(\beta_{\mathrm{II}}-\gamma_{\mathrm{II}})&\\
\times[E_0(\alpha,\beta_j,\gamma_j)+\mathrm{O}(\alpha^{10},\beta_j{}^{10},\gamma_j{}^{10})]=0\,,&
\end{aligned}\tag{48}$$

where

$$\begin{aligned}
&E_0=E_{00}+(R_m/R)E_{01}\,,\\
&E_{00}=\alpha^4(\beta_{\mathrm{I}0}+\alpha)(\beta_{\mathrm{II}0}+\alpha)(\beta_{\mathrm{I}0}+\beta_{\mathrm{II}0})(\beta_{\mathrm{I}0}^2+\beta_{\mathrm{II}0}^2-\beta_{\mathrm{I}0}\beta_{\mathrm{II}0}+\alpha\beta_{\mathrm{I}0}+\alpha\beta_{\mathrm{II}0}+\alpha^2)\,,
\end{aligned}\tag{49}$$

$$\begin{aligned}
E_{01}=\frac{\alpha^4R^2A^2}{4\beta_{\mathrm{I}0}\beta_{\mathrm{II}0}(\beta_{\mathrm{I}0}+\alpha)(\beta_{\mathrm{II}0}+\alpha)}&[\alpha\beta_{\mathrm{I}0}(\beta_{\mathrm{I}0}+\alpha)^4(\beta_{\mathrm{I}0}-\alpha)+\alpha\beta_{\mathrm{II}0}(\beta_{\mathrm{II}0}+\alpha)^4(\beta_{\mathrm{II}0}-\alpha)\\
&+3\alpha(\beta_{\mathrm{I}0}+\alpha)^2(\beta_{\mathrm{II}0}+\alpha)^2(\beta_{\mathrm{I}0}+\beta_{\mathrm{II}0})(2\beta_{\mathrm{I}0}+2\beta_{\mathrm{II}0}+\alpha)\\
&+\beta_{\mathrm{I}0}\beta_{\mathrm{II}0}(\beta_{\mathrm{I}0}+\alpha)^2(\beta_{\mathrm{II}0}+\alpha)^2(3\beta_{\mathrm{I}0}+3\beta_{\mathrm{II}0}-4\alpha)\\
&-\beta_{\mathrm{I}0}\beta_{\mathrm{II}0}(\beta_{\mathrm{I}0}+\alpha)(\beta_{\mathrm{II}0}+\alpha)\{(\beta_{\mathrm{I}0}+\alpha)^3+(\beta_{\mathrm{II}0}+\alpha)^3\}]\,,
\end{aligned}\tag{50}$$

and

$$\beta_{\mathrm{I}0}^2=\alpha^2-i\alpha R(c-1)\,, \qquad \beta_{\mathrm{II}0}^2=\alpha^2-i\alpha R(c+1)\,.\tag{51}$$

The first approximate equation $E_{00}=0$ gives the set of eigenvalues which have already been obtained in ordinary hydrodynamics (Tatsumi and Gotoh[3]), namely,

$$c_r=0\ , \qquad R=\frac{4(\sqrt{3}-c_i)}{(1-\sqrt{3}\,c_i)^2}\alpha\ . \tag{52}$$

Using this result as the first approximation, the second approximate solution is obtained as

$$\left.\begin{aligned} &c_r=0\ ,\\ &R=\frac{4(\sqrt{3}-c_i)}{(1-\sqrt{3}\,c_i)^2}\left[1+\frac{9c_i^2-26\sqrt{3}\,c_i+39}{(1-\sqrt{3}\,c_i)^3(3-\sqrt{3}\,c_i)}\frac{R_m}{R}A^2\right]\alpha+\mathrm{O}(\alpha^2,\,R_m^2/R^2)\ . \end{aligned}\right\} \tag{53}$$

Putting $c_i=0$, we find the following relationship between α, R and R_m for neutral disturbances:

$$R=4\sqrt{3}\left(1+13\frac{R_m}{R}A^2\right)\alpha+\mathrm{O}(\alpha^2,\,R_m^2/R^2)\ . \tag{54}$$

In Fig. 3 the neutral curves as calculated from (54) are plotted in the α-R plane for various values of $(R_m/R)A^2$. All neutral curves pass through the origin, giving the zero critical Reynolds number, and their slope decreases with increasing A, that is, the unstable region becomes narrower for stronger magnetic field.

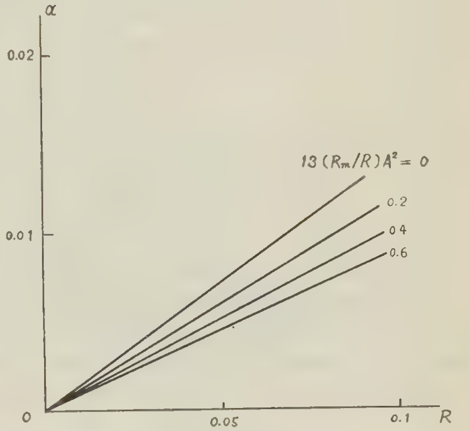

Fig. 3. Effects of magnetic field on neutral curves for $A^2R_m/R\ll 1$.

Next we consider another special case in which $\alpha\ll R\ll R_m$. Then E_0 in (48) is expressed as:

$$-\frac{1}{8}\alpha^5R_m^4[(R/R_m)^{3/2}(\kappa_{\mathrm{I}}+\kappa_{\mathrm{II}})(\kappa_{\mathrm{I}}\kappa_{\mathrm{II}})^{-1}(1+A^2-c^2) \\ \times\{\kappa_{\mathrm{I}}^2(\kappa_{\mathrm{I}}^2+A^2\kappa_{\mathrm{I}}^{-2})^{1/2}+\kappa_{\mathrm{II}}^2(\kappa_{\mathrm{II}}^2+A^2\kappa_{\mathrm{II}}^{-2})^{1/2}\}+\mathrm{O}(\alpha^{1/2},\,R^2/R_m^2)]\ , \tag{55}$$

where

$$\left.\begin{aligned} &\kappa_{\mathrm{I}}^2=-i(c-1)\ , \qquad \kappa_{\mathrm{II}}^2=-i(c+1)\ ,\\ &\mathscr{Re}\{\kappa_{\mathrm{I}},\ \kappa_{\mathrm{II}},\ (\kappa_{\mathrm{I}}^2+A^2\kappa_{\mathrm{I}}^{-2})^{1/2},\ (\kappa_{\mathrm{II}}^2+A^2\kappa_{\mathrm{II}}^{-2})^{1/2}\}>0\ . \end{aligned}\right\} \tag{56}$$

The first approximate equation for $E=0$ is given by

$$\kappa_{\mathrm{I}}^2(\kappa_{\mathrm{I}}^2+A^2\kappa_{\mathrm{I}}^{-2})^{1/2}+\kappa_{\mathrm{II}}^2(\kappa_{\mathrm{II}}^2+A^2\kappa_{\mathrm{II}}^{-2})^{1/2}=0\ , \tag{57}$$

from which it follows that

$$c_r=0\ , \qquad c_i=\sqrt{(1-A^2)/3} \qquad \text{for} \quad A\leq 1\ , \tag{58}$$

where the positive root has been taken for c_i, because it must conform with $c_i=1/\sqrt{3}$ for $A=0$.

Lastly, in case when $\alpha\ll R=R_m$, E_0 takes the form;

$$i\alpha^5R_m^4\Big[(A^2-1-c^2)\Big\{\frac{i}{2}(\beta_{\mathrm{I}}\gamma_{\mathrm{I}}+\beta_{\mathrm{II}}\gamma_{\mathrm{II}})(\beta_{\mathrm{I}}+\gamma_{\mathrm{I}}+\beta_{\mathrm{II}}+\gamma_{\mathrm{II}})^2+4i+2(\beta_{\mathrm{I}}\gamma_{\mathrm{I}}-\beta_{\mathrm{II}}\gamma_{\mathrm{II}})\Big\} \\ +4c(\beta_{\mathrm{I}}+\gamma_{\mathrm{I}})(\beta_{\mathrm{II}}+\gamma_{\mathrm{II}})+4A(\beta_{\mathrm{I}}\beta_{\mathrm{II}}-\gamma_{\mathrm{I}}\gamma_{\mathrm{II}})+\mathrm{O}(\alpha^{1/2})\Big]\ . \tag{59}$$

For small values of A^2 a perturbation of the result $c_r=0$, $c_i=1/\sqrt{3}$ for $A=0$ gives

$$c_r=0\,, \qquad c_i=\frac{1}{\sqrt{3}}\left(1-\frac{9}{8}A^2\right)+\mathrm{O}(A^4)\,, \tag{60}$$

and it may therefore be expected that c_r remains zero for also finite A. Assuming this, β_j and γ_j are expressed as:

$$\left.\begin{array}{ll} \beta_{\mathrm{I}}=(\xi_1+i\eta_1)/\sqrt{2}\,, & \gamma_{\mathrm{I}}=(\xi_2+i\eta_2)/\sqrt{2}\,, \\ \beta_{\mathrm{II}}=\gamma_{\mathrm{I}}^*\,, & \gamma_{\mathrm{II}}=\beta_{\mathrm{I}}^*\,, \end{array}\right\} \tag{61}$$

where the asterisk denotes the complex conjugate, and

$$\left.\begin{array}{l} \xi_1=[\{c_i^2+(1+A)^2\}^{1/2}+c_i]^{1/2}\,, \\ \eta_1=[\{c_i^2+(1+A)^2\}^{1/2}-c_i]^{1/2}\,, \\ \xi_2=[\{c_i^2+(1-A)^2\}^{1/2}+c_i]^{1/2}\,, \\ \eta_2=[\{c_i^2+(1-A)^2\}^{1/2}-c_i]^{1/2}\,. \end{array}\right\} \tag{62}$$

In terms of these (real) variables, approximate equation for $E=0$ is written as:

$$\begin{aligned} &(A^2-1+c_i^2)[(\xi_1\xi_2-\eta_1\eta_2)(\xi_1+\xi_2)^2+4+2(\xi_1\eta_2+\eta_1\xi_2)] \\ &\qquad +2c_i[(\xi_1+\xi_2)^2+(\eta_1+\eta_2)^2]+4A(\eta_1\xi_2-\xi_1\eta_2)=0\,. \end{aligned} \tag{63}$$

The relationship between c_i and A is derived by solving this equation numerically and the result is tabulated in Table I and shown graphically in Fig. 4, together with the result (58). It may be seen that $c_i>0$ for $0\leq A\leq 1$, c_i decreasing monotonously with increasing A, and $c_i=0$ for $A=1$. Consequently it is concluded that the effect of the magnetic field is always stabilizing, however weak it may be, and the flow is completely stabilized at $A\geq 1$ provided $R_m/R>1$. This tendency of the magnetic effect is the same with that obtained in § 4 for $R=R_m=\infty$. There is, however, an exceptional case in which the flow is unstable even for $A>1$, so long as $(R_m/R)A^2\ll 1$ is satisfied.

Table I.

A	c_i
0.3	0.517
0.5	0.405
0.7	0.230
0.8	0.132
0.9	0.048
0.95	0.017
1.00	0.000

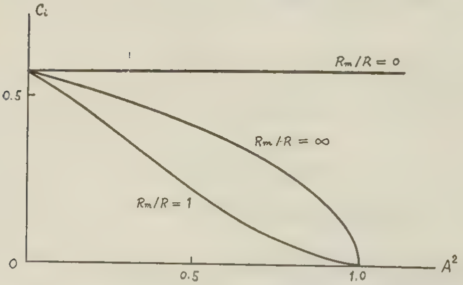

Fig. 4. c_i-A curves for small values of α.

§ 6. Concluding Remarks

The results obtained in the preceding sections all indicate the stabilizing effect of the magnetic field. Although the results of calculation are partial and not sufficient for giving the whole picture of the stability characteristics of the free boundary-layer flow, yet we can draw its outline by interpolating these partial informations. The relationship between eigenvalues α, R, R_m and c_i seems to be as sketched in Figs. 5(a) and 5(b). Different constant values of A determine surfaces in the octant (α, R, c_i)-space. The behaviour of the surfaces is somewhat different for $R_m/R>1$ and $R_m/R\ll 1$. For $R_m/R>1$, the area of the surfaces decreases with increasing A, and for the limit of $A\to 1$ the surface shrinks into the R-axis. For $R_m/R\ll 1$, however, it is seen from Fig. 4 that the circumstance around the c_i-axis does not change appreciably with increasing A, and it is difficult to tell what limiting form will the surface take in this region for $A\to 1$.

It was already verified by Velikhov[2] for the limiting case of $R=R_m=\infty$ that $A>2$ is the sufficient condition for the stability of parallel flows. But the critical value of the Alfvén number A_c, say, which gives the conditions for the marginal stability, is expected to vary with different velocity distributions of steady flows. According to the present result (Figs. 2 and 5a), we have $A_c=1$ for the free boundary-layers between two parallel streams provided $R_m/R>1$, in contrast with the value $A_c=0.2$ for the plane Poiseuille flow (Velikhov[2]). The larger value of A_c in this case agrees with our expectation, because in ordinary hydrodynamical case the free boundary-layer flows were found to be more unstable than bounded flows.

It is seen in Figs. 2 and 3 that the stabilizing effect of the magnetic field appears first in disturbances of short wavelength and then extends gradually to those of longer wavelength as A increases up to unity. This tendency is just opposite to that in the broken-line jet in which the disturbance of the longest wavelength ($\alpha=0$) first become stable (Drazin[6]).

When the ratio R_m/R $(=4\pi\sigma\nu\mu)$ is kept constant, c_i decreases monotonously with increasing A, that is, the stronger magnetic field more stabilizes the disturbances. However, the magnetic field does not change the critical Reynolds number, and R_c remains zero provided $A<1$.

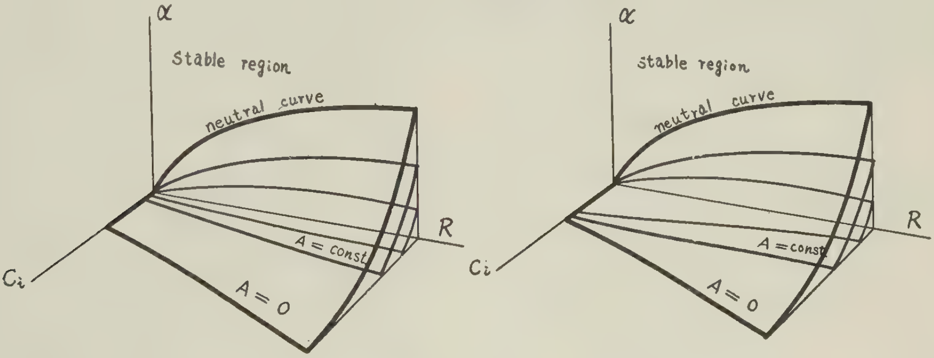

(a) $R_m/R>1$. (b) $R_m/R\ll 1$.

Fig. 5. Relation between α, R and c_i for different constant A and R_m/R.

It is found in Fig. 4 that for fixed values of R and A (<1) the flow of the perfect conductor $(R_m=\infty)$ is more unstable than that with finite conductivity $(R_m<\infty)$ just as was the case for the plane Poiseuille flow (Velikhov[2]).

The conclusions obtained for small values of α apply universally to all velocity profiles of the free boundary-layer type. On the other hand, the results for finite values of α vary with the type of the velocity profile under consideration, and the detailed information obtained here for the profile $U(y)=\tanh y$ may hold only qualitatively for other profiles.

Finally, it should be noted that if the magnetic field is not parallel to the undisturbed velocity, the flow cannot be stabilized by the magnetic field, however strong it may be. This is due to the fact that in this case Squire's theorem referred in §2 is no longer valid and therefore the general three-dimensional disturbances must be considered. Let the magnetic field be $(H_x, 0, H_z)$. One harmonic component of the disturbance may be expressed in vector form as:

$$\boldsymbol{u}=\boldsymbol{v}(y)\exp\{i\alpha(x-ct)+i\gamma z\}\,,$$

$$\boldsymbol{h}=\boldsymbol{f}(y)\exp\{i\alpha(x-ct)+i\gamma z\}\,,$$

where γ denotes the wave-number in the z-direction. The amplitude functions of the y-component of disturbances v_y and f_y are governed by equations:

$$\left.\begin{aligned}&(U-c)(D^2-\beta^2)v_y-U''v_y-S(H_x+\gamma H_z/\alpha)(D^2-\beta^2)f_y=-\frac{i}{\alpha R}(D^2-\beta^2)^2v_y\,,\\&(U-c)f_y-(H_x+\gamma H_z/\alpha)v_y=-\frac{i}{\alpha R_m}(D^2-\beta^2)f_y\,,\\&\qquad\qquad\beta^2=\alpha^2+\gamma^2\,,\end{aligned}\right\}\tag{64}$$

which correspond to Eqs. (4) and (5) in § 2 for the two-dimensional disturbances. If the wave-numbers α and γ satisfy the relation:

$$\alpha H_x + \gamma H_z = 0 , \tag{65}$$

the simultaneous equations (64) become two separate equations for v_y and f_y, and the disturbance velocity has no means of interaction with the magnetic field. The general three-dimensional disturbances always involve the one with those wave-numbers which satisfy the relation (65) and to such disturbances the conclusion of entire instability in ordinary hydrodynamical case applies unchanged. Thus, it is concluded that the oblique magnetic field cannot stabilize the flow, however strong it may be.

Acknowledgements

The writer wishes to express his cordial thanks to Professor S. Tomotika for his interest in this work, and also to Dr. T. Tatsumi for his helpful discussions.

References

1) J. T. Stuart: Proc. Roy. Soc. **A, 221** (1954) 189.
2) E. P. Velikhov: Soviet Phys. JETP **9** (1959) 848.
3) T. Tatsumi and K. Gotoh: J. Fluid Mech. **7** (1960) 433.
4) H. B. Squire: Proc. Roy. Soc. **A, 142** (1933) 621.
5) D. H. Michael: Proc. Camb. Phil. Soc. **49** (1953) 166.
6) P. G. Drazin: J. Math. Phys. **39** (1960) 49.

Short Notes

This section is intended to secure prompt publication of important discoveries in physics. The reports should not exceed 800 words in length. A figure of size 7 cm×7 cm will be counted as 150 words.

J. PHYS. SOC. JAPAN **16** (1961) 571

On the New Magnetic Phase in Manganese-Aluminium-Copper System

By Ichiro TSUBOYA and Makoto SUGIHARA

Electrical Communication Laboratory Nippon Telegraph and Telephone Public Corporation, Musashino-shi, Tokyo, Japan

(Received November 1, 1960)

In Mn-Al-Cu alloys, there is the ferromagnetic phase corresponding to the composition of Cu_2MnAl which is well known as the Heusler alloy[1]. The other ferromagnetic phase, however, in this system has not been discovered. In this note, the present authors would like to report the existence of a new ferromagnetic phase in this alloy system.

The electrolytic Cu (99.9%), electrolytic Mn (99.9%) and pure Al (99.99%) were mixed in the desired proportion and melted in air and cast into rods of 10 mm in diameter. These specimens were annealed for one hour at 900°C in vacuum to remove the segregation, then cooled to room temperature at the rate of 150°C/hr.

The composition range, in which the specimens seem to show ferromagnetism, was determined by the magnetic testing.

According to X-ray powder analysis, the composition range showing ferromagnetism is found to be a single cubic phase. The crystal structures of non-ferromagnetic specimens are the mixture of β-Mn phase and Cu_9Al_4 phase in Cu rich region, the β-Mn in Cu poor and Mn rich region, and orthorhombic Y-phase[2] in Al rich side. These results are shown in Fig. 1.

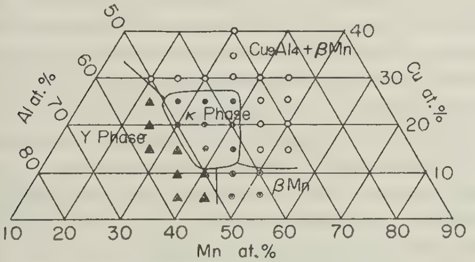

Fig 1. Results of X-ray diffraction
● κ phase (magnetic).
○ $Cu_9Al_4+\beta$-Mn.
▲ Orthorhombic *Y* phase.
⊙ $\beta-$Mn.

The ferromagnetic cubic phase is the same structure as the κ phase of Mn-Al-Fe alloy system[3], but it covers the larger composition range. The structure of this κ phase show the b.c.c. CsCl (B 2) type with the lattice constant 2.984±0.005Å which is not appreciably dependent on the composition. In this structure, it seems that Al atoms occupy body centered sites and Cu and Mn atoms occupy the cube corner sites but the excess of Mn atoms occupy the body centered Al sites.

The magnetic properties of this κ phase such as Curie temperature, $\sigma-T$ curve, and $1/\chi-T$ curve were measured by magnetic balance. The Curie temperatures at 20 at.% Cu specimens increase with an increase of Mn content. Namely it was 370°K at 30 at.% Mn, and 550°K at 40 at.% Mn. The saturation magnetizations at 0°K, however, decrease with an increase of Mn content. Namely it was 270 gauss (per c.c.) at 40 at.% Mn and 160 gauss (per c.c.) at 30 at.% Mn.

Tne temperature dependence of saturation magnetization (I_s-T curve) and inverse susceptibility above Curie temperature ($1/\chi-T$ cnrve) are shown in Fig. 2. $1/\chi-T$ curves of the alloy in this κ phase region show generally non-linear relations. This relations suggest that the magnetic interactions in the κ phase are not ferromagnetic but ferrimagnetic.

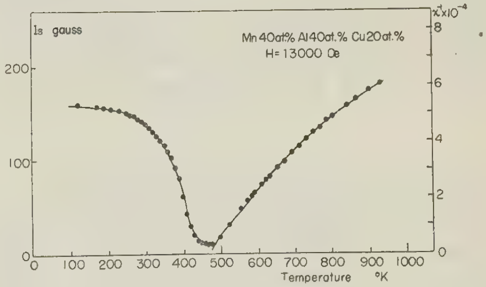

Fig. 2. I_s-T and $1/\chi-T$ curve of 20 at.% Cu, 35 at.% Mn 45 at.% Al specimen at the field strength of 13000 Oe.

As seen in the above results of crystallographic and magnetic observations, the magnetism of this κ-phase seems to be understood by assuming the antiferromagnetic interaction between body centered (Al site) Mn atoms and cube-corner (Cu site) Mn atoms, and ferromagnetic interaction between cube corner Mn atoms.

Further discussion with detailed measurements will be reported later on.

References

1) O. Heusler: Ann. Phys. [5] **19** (1934) 155.
2) W. B. Pearson: *A Handbook of Lattice Spacings and structures of metals and Alloys.* (Pergamon Press, London, 1958) 339P.
3) I. Tsuboya and M. Sugihara: J. Phys. Soc. Japan **15** (1960) 1534.

J. Phys. Soc. Japan **16** (1961) 572~573

Optical Absorption and Electrical Conductivity of Reduced $BaTiO_3$ Single Crystal

Seiji Ikegami, Ichiro Ueda and Yukihiko Ise

Technical Research Department, Wireless Division, Matsushita Electric Industrial Company, Kadoma, Osaka

(Received December 9, 1960)

It has been well known that some properties of $BaTiO_3$ single crystals are changed by reduction treatment. In order to investigate the effects of reduction, preliminary measurements of optical absorption and electrical conductivity were made on untreated and reduced single crystals.

$BaTiO_3$ single crystals were grown from highly purified $BaTiO_3$ powder and KF by H. Sasaki of this department. Crystals were reduced by heating in hydrogen atmosphere, and reduction degree was varied by the temperature and time of heating.

The optical transmissions were measured on a single crystal at room temperature in a range of wavelengths from 0.2 to 33μ. The transmission spectra of weakly reduced specimens are shown together with that for the untreated crystal in Fig. 1. In the case of treatment at 1000°C for 1 hour, no transmission was measurable by our instrument. As shown in Fig. 1, a broad absorption band centered near 2.8μ in the infrared region was observed. The absorption coefficient at 2.8μ for curve 2 is about 70 cm^{-1}. This absorption is similar to that of the slightly reduced rutile[1]. Fig. 1 also shows that the transmission near the absorption edge is decreased by reduction. This change of spectra in the visible region is the cause for the coloration of a reduced crystal.

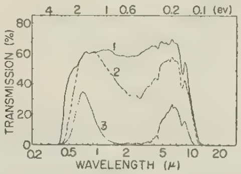

Fig. 1. Transmission spectra of reduced $BaTiO_3$ single crystals at room temperature. (1) untreated; (2) and (3) reduced at 600°C and 700°C, respectively, for 1 hour in hydrogen atmosphere. Thickness of crystal is 0.012 cm.

The measurements of conductivity were made on one untreated crystal and four reduced crystals in a temperature range of −120°C to 400°C. Fig. 2 shows the results of conductivity measurements. The conductivities are plotted against the reciprocal absolute temperatures. The values of thermal activation energy E for each crystal and temperature range are shown in Fig. 2, assuming the conductivity is represented in the form $\sigma=\sigma_0 \exp(-E/2kT)$. Generally E changes at the transition temperatures. As seen in Fig. 2, curve 2 for the slightly reduced crystal is still similar to that for the untreated one, therefore the effect of reduction does not appear on the conductivity. But in the cases of more heavily reduced crystals (curves 3, 4 and 5), the effects clearly appear on their conductivities, and the resistivity and E decrease with increasing reduction. The crystal for curve 3 has the lowest conductivity among these three crystals, therefore the thermal activation energy at room temperature for curve 3 may be compared with the optical one. These two values are 0.44 and 0.39 ev for infrared absorption and conductivity, respectively, and they are in reasonable agreement.

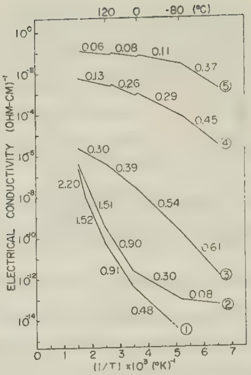

Fig 2. Electrical conductivity *vs.* reciprocal absolute temperature. (1) untreated; (2), (3), (4) and (5) reduced at 600°C, 800°C, 900°C and 1000°C, respectively, for 1 hour in hydrogen atmosphere.

From the results mentioned above, it is probable that: (1) In the reduced $BaTiO_3$ single crystals, the conduction mechanism is similar to that in the reduced rutile involving electrons trapped at the oxygen vacancies. (2) The energy gap between the conduction band and the induced donor level decreases with increasing reduction because of the interaction of individual donor centers. (3) The conduction mechanism of the untreated crystal at room temperature cannot be explained by oxygen vacancy model. (4) The conduction of the untreated crystal at high temperature is intrinsic as suggested by Branwood and Tredgold[2].

In addition, it is expected that the wavelength of maximum absorption increases with increasing reduction, although our instrument could not detect clearly. Further experiments are now in progress.

The authors wish to express their sincere thanks to Mr. S. Kisakà, manager of this department, for his support, and also to Drs. H. Sato and C. Oka-

zaki for their helpful advice.

References

1) D. C. Cronemeyer: Phys. Rev. **111** (1959) 1222.
2) A. Branwood and R. H. Trdegold: Proc. Phys. Soc. **76** (1960) Part 1 93.

J. PHYS. SOC. JAPAN **16** (1961) 573

Impedance Changes Induced by Light in ZnS Phosphors

By Ichizo UCHIDA and Kimihiko SATAKE

Research Laboratory, Nippon Electric Co. Ltd. Tokyo

(Received April 18, 1960)

The impedance changes are induced by light in ZnS phosphor powders which are arranged so as to form the dielectrics of capacitor. This phenomenon is interpreted in terms of the increase in free electron density and the polarization of the phosphor grains caused by electron trapping process1),2),3). The electrical equivalent circuit of the capacitor containning the phosphors as dielectrics is considered to be such as shown in Fig. 12),3). Under illumination, the increase in free electron density causes the decrease of R_P (photoconductive effect) and the polarization of the phosphor grains causes the increase of C_P (photodielectric effect). From the frequency properties of the capacitance, the photodielectric effect is not apreciable in ZnS:Cu:Pb:Cl phosphors used in this experiment3). Therefore, the photoconductivity of the phosphors can be readily estimated from a.c measurement4).

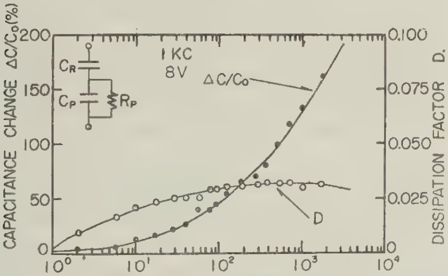

Fig. 1. Equivalent circuit and impedance changes vs incident light intensity (2500°K tungsten lamp). C_R: Capacitance of non sensitive part as resin. C_P, R_P: Capacitance and resistance of sensitive part as phosphors.

ZnS:Cu:Pb Cl phosphors have green emission when excited by 3650Å ultraviolet and show good electroluminescence. The electroluminescent emission is green at lower frequency but becomes blue at higher frequency. The samples were prepared by spraying the phosphor powders mixed with epoxiresin on a quartz plate coated with conductive tin oxide and by evaporating the aluminum film on the phosphor layer as the another electrode.

The capacitance change increases monotonically with the intensity of incident light and dissipation factor has a peak at about 6×10^2 lux as shown in Fig. 1. These properties coinside with the results calculated from the equivalent circuit2),3). Consequently it is adequate to measure the capacitance change in order to estimate the photoconductivity.

In this paper, the spectral sensitivity of the capacitance change induced in ZnS:Cu:Pb:Cl was measured at room temperature. (Fig. 2.) The curve of the spectral sensitivity has high sensitivity in the region of the absorption edge and two peaks at 3580Å and 3860Å. It is supposed that the peak at 3580Å is due to the increase of the free electron density excited from the blue emission centers and the peak at 3860Å is caused by the green emission centers.

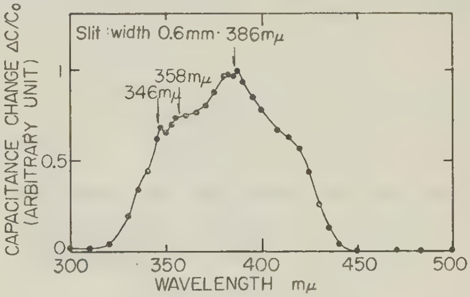

Fig. 2. Spectral sensitivity of the capacitance change.

The authers would like to express their thanks to Dr. Osamu Harashima for his guidance and encouragement.

References

1) Garlick and Gibson: Proc. Roy. Soc. **A188** (1947) 485.
2) Kallmann, Kramer and Perlmutter: Phys. Rev. **89** (1953) 700.
3) Kronenberg and Accardo: Phys. Rev. **101** (1955) 989.
4) Kallmann Kramer and Peter: J. Phys. Chem. Solids **10** (1959) 59.

J. PHYS. SOC. JAPAN **16** (1961) 574

NMR of Co^{59} in Forromagnetic Cobalt Alloys

By Yoshitaka KÔI, Akira TSUJIMURA
Facutly of Engineering, Tokushima University
Tokushima, Japan
Tadamiki HIHARA, and Toshimoto KUSHIDA
Faculty of Science, Hiroshima University
Hiroshima, Japan

(Received January 7, 1961)

Internal magnetic field H_i seen at nuclei in ferromagnets can be measured by observing nuclear magnetic resonance (NMR) of these nuclei.1) Since the intensity of NMR line in ferromagnets is anomalously strong,1) the detailed structures of the resonance line, which are caused by alloying and reflect a distribution of H_i in the alloys most directly, can be observed clearly.

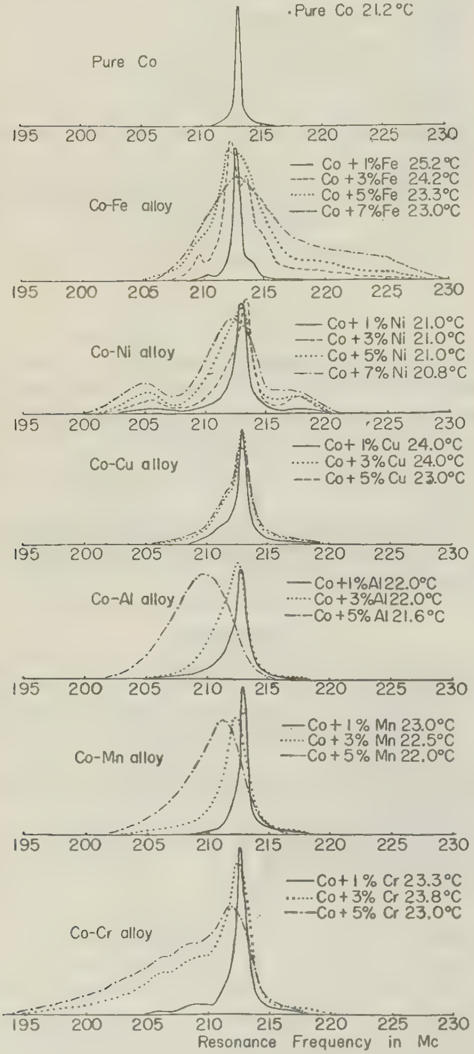

Fig. 1. NMR lines of Co^{59} in cobalt alloys.

Co^{59} resonances in several ferromagnetic cobalt alloys in fcc phase were observed by using a frequency-modulated autodyne spectrometer. The samples were well-annealed powder of the alloys which were prepared from high-purity metals in an induction furnace. The derivatives of the resonance lines of the alloys as well as that for pure cobalt metal thus observed are shown in Fig. 1.

Total integrated intensity of the line is essentially unchanged by alloying, although the vertical scale in the figure is not exactly the same for each specimen.

The alloy lines generally have structures, which are less pronounced in highly-doped specimens. In the case of Co-Fe and Co-Ni, we see resolved satellites at both wings of the main lines, whereas in the other cases investigated here the lower frequency tail (some of them have fine structures) spreads more strongly than the higher-frequency tail by alloying.

One can estimate the quadrupole broadening of the Co lines in the alloys to be of the order of 1Mc, using the value of nuclear quadrupole coupling in copper alloys2−3). Therefore the observed structure is not quadrupole origin, but it describes the distribution of hyperfine field in the alloy.

The present results may well be accounted for in terms of the spacial distribution of hyperfine field around the impurity caused by the spin-dependent scattering of *s*-electrons by the impurity4). Our results, however, do not exclude the possibility of the scattering of *d*-electron waves. The shift in the center-of-gravity of the line is compatible with the observation of average H_i in Co-Fe and Co-Ni alloys by means of low-temperature-specific-heat measurement5).

The details will be published in near future, but it is noted that the similar structure is observed in Fe^{57} resonance in Fe-Ni and Fe-Cr alloys as well.

It is a pleasure to acknowledge the valuable comments made by Professor T. Nagamiya and by Professor N. Bloembergen.

References

1) A. M. Portis and A. C. Gossard: J. Appl. Phys. **31** (1960) 205S.
2) N. Bloembergen and T. J. Rowland: Acta Met. **1** (1953) 731.
3) C. P. Flynn and E. F. Seymour: Proc. Phys. Soc. (London) **76** (1960) 526.
4) Similar idea is used for non-ferromagnetic dilute alloys by many authors. See, for instance, A. Blandin and E. Daniel: J. Chem. Phys. Solids **10** (1959) 126.
5) V. Arp, D. Edmonds and R. Petersen: Phys. Rev. Letters **3** (1959) 212.

J. Phys. Soc. Japan **16** (1961) 575～576

Hot Electron Nonequilibrium Carrier Distribution in a Many-Valley Semiconductor

By Louis Gold

Radiation Laboratory and Department of Nuclear Engineering, University of Michigan, Ann Arbor, Michigan

(Received December 12, 1960)

Recent experiments[1),2)] on hot electron departure from Ohm's law fail to show reasonable agreement with Shibuya's theory[3)] for N-germanium. In particular, the deviation of collinear current and voltage directions was so large as to imply[1)] that a thermal equilibrium distribution of electrons over the several energy minima likely did not prevail as originally supposed[3)]. During the course of preparation of this note the publication by Reik, Risken and Finger[4)] appeared in which an attempt was made to improve Shibuya's theory; but without allowance for intervalley scattering, agreement with experiment was still lacking.

Based on a hot electron formalism already described[5)], a study of the contribution of non-uniform charge density for the ellipsoidal energy surfaces in germanium was carried out. Presumably the imbalance or nonequilibrium distribution of the carriers arises from the anisotropy of the masses which produces differing scattering rates among the valleys. No effort is made to embody details of the various modes of scattering but rather the ad hoc assumption of of different electron densities for the several energy minima is introduced. This approach by-passes the difficult matter of dealing with optical and acoustical modes of scattering and evaluating the role of intra and intervalley effects.

It thus develops that a reasonable departure for collinear current and voltage, (i.e. sensible $\tan \varepsilon$ values) comes about and, moreover, the first clue of temperature dependency is evidenced.

In view of the findings, it appears that such measurements of the angular deviation of the current and voltage coincidence may prove complementary to other techniques for delineating effective masses and carrier density; combined with galvanomagnetic and cyclotron resonance observations, the nonequilibrium redistribution of carriers associated with the hot electron phenomenon may be measured. It may be anticipated that such data ought to shed light on the character of scattering processes responsible for the non-thermal carrier distribution.

The following underlying relation has been deduced for N-germanium:

$$\tan \varepsilon = \frac{1}{N_1}\left(\frac{K-1}{2K+1}\right) \cdot \frac{\sqrt{(\quad)_1^2+(\quad)_2^2+(\quad)_3^2-4[\quad]}}{1-\frac{2}{N_1}\left(\frac{K-1}{2K+1}\right)[\quad]} \qquad (1)$$

where, in terms of the electron densities n_i for the 4 sets of energy surfaces and the directions cosines l_j of the electric vector $\vec{E}$ referred to the cubic axis,

$$\begin{aligned} N_1 &= \sum_i n_i = n_1+n_2+n_3+n_4 \\ N_2 &= (n_1+n_3)-(n_2-n_4) \\ N_3 &= (n_1+n_4)-(n_2+n_3) \\ N_4 &= (n_1+n_2)-(n_3+n_4) \qquad (1a) \\ [\quad] &= N_2 l_1 l_2 + N_3 l_1 l_3 + N_4 l_2 l_3 \\ (\quad)_1 &= N_2 l_2 + N_3 l_3 \\ (\quad)_2 &= N_2 l_1 + N_4 l_3 \\ (\quad)_3 &= N_4 l_2 + N_3 l_1 \,. \end{aligned}$$

If the scattering tensor is of similar symmetry as the mass tensor and the possible variance in the ratio $K'=\nu_l/\nu_t$ for the separate ellipsoids be ignored, then replacement of K by KK' enters[5)]; here ν_l and ν_t are respectively the longitudinal and transverse scattering frequencies, corresponding to the mass ratio $m_l/m_t=K$.

It is instructive to consider formula (1) for the circumstance $l_1 \cong 1$, $l_2=l_3 \cong 0$ (corresponds to E nearly aligned along a cubic axis) which leads to

$$\tan \varepsilon \cong \left(\frac{K-1}{2K+1}\right) \cdot 2\frac{\Delta}{N_1} \qquad (2)$$

where

$$\Delta = n_1 - n_2 = n_3 - n_4 \,. \qquad (2a)$$

As Δ is inclined to be very small, ε itself is seen to be inherently small. Clearly, the existence of an angle between current and voltage is not only a property of the anisotropic mass, but its very manifestation relates to an overall low carrier density. In the extreme case where $\Delta \to 1/2N_1$, the ultimate maximum value of $\tan \varepsilon$ is simply $(K-1)/(2K+1)$ which for N-germanium means $\varepsilon_{\max} \sim 25°$.

The central influence of the total carrier density N_1 emerges and accounts for the experimentally observed fact that larger $\tan \varepsilon$ obtain at reduced temperatures; the exponential behavior $\tan \varepsilon \alpha e^{\varepsilon kT}$ seems indicated, ε being an appropriate activation energy. Furthermore, the maxima for $\tan \varepsilon$ vs electric field may be accounted for on the basis of carrier generation by impact ionization which will cause a fall-off of ε as N_1 rises.

Since K and N_1 can be separately determined, experimental means are now afforded for investigating the manner in which the carrier density redistributes itself in a many-valley semiconductor at increasingly higher electric fields.

References

1) W. Sasaki, M. Shibuya, K. Mizuguchi and G. M. Hatoyama: J. Phys. Chem. Solids **8** (1959) 250.

2) S. H. Koenig: Proc. Phys. Soc. **73** (1959) 959.
3) M. Shibuya: Phys. Rev. **99** (1955) 1189.
4) H. G.. Reik, H. Risken and G. Finger: Phys. Rev. Retter **5** (1960) 423.
5) L. Gold: Phys. Rev. **104** (1956) 1580.

J. PHYS. SOC. JAPAN **16** (1960) 576~577

Nature of the A-Centers in KCl

By Noriko NISHIMAKI, Kazuko KOJIMA
Osaka Women's University
and Tadanobu KOJIMA
Osaka City University

(Received January 6, 1961)

In the previous paper[1], it was reported that the *A*-band in additively colored KCl crystals arises from a sort of impurities involved in the specimens, and that the *A*-center can trap another electron to become an *A′*-center at about −50°C. Further experiments reported here revealed that the *A*-center is probably an *F*-center having a Na^+ ion on one of its six neighboring cation sites.

By quenching an additively colored KCl crystal containing 1 nominal mole % of NaCl, we get only *F*-centers as in the case of pure crystals. Illuminating this sample with *F*-light at −30°C, a much more pronounced *A*-band was found to develop than hitherto obtained (Fig. 1). This band duplicates the characteristic properties of the *A*-band in apparently pure specimens, such as thermal stability, $A \rightarrow A'$ conversion with *F*-light at −50°C, and dichroic properties as explained below.

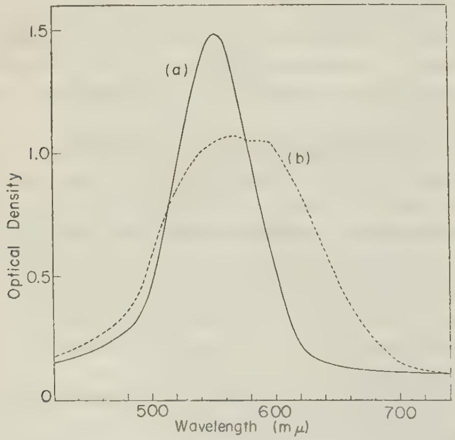

Fig- 1. Absorption curves of an additively colored KCL crystal containing 1 nominal mole % of NaCl, measured at −70°C. (a) initial; (b) after 50 min irradiation with *F*-light at −30°C.

Since the *A*-band is enhanced with the addition of NaCl, the *A′*-band shows similar behavior to the *F′*-band, and the *A*-band has its peak near the *F*-band, we may propose a model for the *A*-center that it consists of an *F*-center adjacent to a substitutional Na^+ ion. A theoretical consideration shows that, as a result of perturbation due to the Na^+ ion, the triply degenerate excited states of the *F*-center split into two levels, the lower (A_1) nondegenerate and the higher (E) doubly degenerate. It can also be shown that among the two the possible absorption bands, the one should lie to the longer wavelength side and the other to the slightly shorter wavelength side of the *F*-band. We call the former the A_1-band and the latter the A_2-band.

Now consider a sample which has been irradiated with A_2-light polarized along the [100] direction. Then our model predicts that the A_1-band will remain unchanged whereas the A_2-band decreases, when measured with light polarized along [100], provided the dichroism is caused only through preferential ionization. When measurement is made with light polarized along [010], we shall find both the bands decreased, and the decrease will be more conspicuous for the A_1-band. Moreover, no difference will be observed between two absorption curves measured with light polarized along [110] and that along [$1\bar{1}0$].

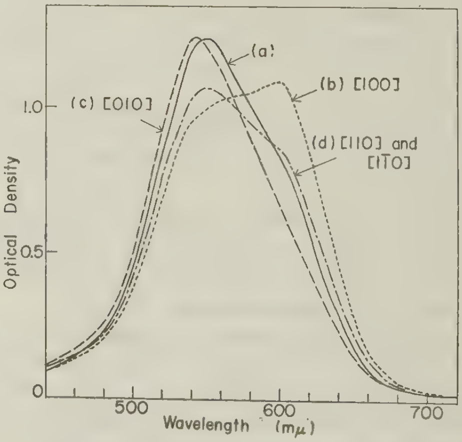

Fig. 2. Dichroic absorption of KCl containing *A*-centers, irradiated with 520 mμ light polarized along [100] at −30°C. (a) before irradiation; (b)-(d) after irradiation, measured with polarized light. All measurements were made at −70°C.

Most of these predictions were confirmed by experiments (Fig. 2). However, the A_1-band in the [100] direction and the A_2-band in the [010] direction were considerably higher than predicted. This indicates that the dichroism was caused primarily by reorientation of the centers rather than through ionization. It should be noted that Ohkura's experiment[2)] on the optical conversion between the *A*- and *B*-bands can also be well accounted for on the basis of our model. The conversion is presumably nothing but a result of reorientation of *A*-centers induced by optical excitation, and the assumptions seem unnecessary such as the existence of *B*-centers or the production of photoelectrons.

A more detailed account of this work will be published elsewhere.

References

1) K. Kojima and N. Nishimaki: J. Phys. Soc. Japan **16** (1961) 121.
2) H. Ohkura and T. Uchida: J. Phys. Soc. Japan **15** (1960) 2114.

J. PHYS. SOC. JAPAN **16** (1961) 577

Impurity Effect upon Mobility in Heavily Doped Silicon

By Yoshitaka FURUKAWA

The Electrical Communication Laboratory, Musashino-shi, Tokyo

(Received December 27, 1960)

Conductivity mobilities of electrons and holes in heavily doped silicon have already been reported by Backenstoss.[1)] In his experiment, measurements were taken with several Group III and Group V impurities up to concentration of 6×10^{19} cm^{-3} and and 6×10^{18} cm^{-3} for n- and p-type silicon, respectively. Resistivity was measured by using a four-point probe method and impurity concentration was obtained with radioactive tracers or from thermal neutron activiation. Resistivity *versus* impurity concentration relations thus obtained were represented with a single curve each for *n*- and *p*-type silicon respectively except for In-doped case.

Recently, however, impurity effect upon mgoility in heavily doped Germanium was observed[2)] and this effect was attributed to the difference in carrier—ionized impurity interaction. The same effect is expected in heavily doped silicon.

In the present experiment, impurity effect upon Hall mobility in heavily doped silicon was measured with the bridge shape samples by using a conventional D.C method and carrier concentrations were obtained from the relation n (or p)$=1/eR$ where R is the Hall coefficient.

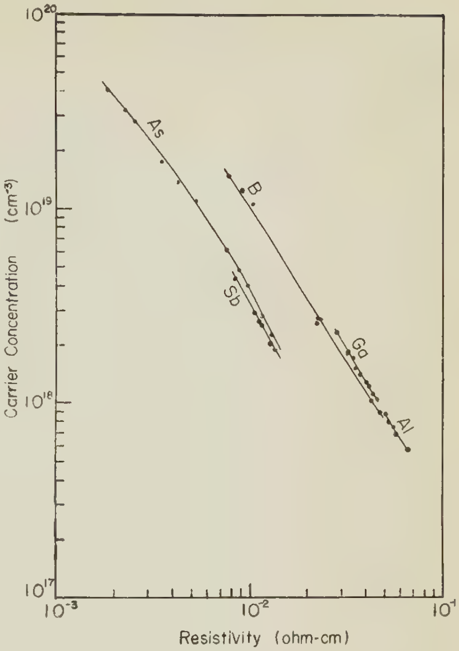

Fig. 1. Resistivity *versus* carrier concentration curves for *n*- and *p*- type silicon at room temperature.

Table I. Mobility at carrier concentration of 2×10^{18} cm^{-3}.

Impurity	donor		acceptor		
	Sb	As	B	Al	Ga
ionization energy (eV)	0.039	0.049	0.045	0.057	00.65
mobility (cm^2 volt^{-1} sec^{-1})	235	220	110		100

The results are shown in Fig. 1. The impurity effect has been observed in heavily doped silicon and there exists some correlation between impurity scattering mobility and ionization energy of impurities. As shown in Table I, the lower the ionization energy of the impurities is, the higher the mobility becomes. This tendency was also observed in heavily doped germanium.

The author thanks Dr. Z. Kiyasu and Dr. T. Niimi heartily for the guidance in this work.

References

1) G. Backenstoss: Phys. Rev. **108** (1957) 1416.
2) Y. Furukawa: J. Phys. Soc. Japan **15** (1960) 730.

J. PHYS. SOC. JAPAN **16** (1961) 578~579

X-ray Small Angle Scattering from Precipitated Platelets in Al-Ag Alloy

By Yasuharu YONEDA and Kouzou NISHIOKA

Department of Applied Physics, Kyushu University, Fukuoka

(Received September 8, 1960)

Geisler et al[1] studied the precipitated platelets of γ' phase iu Al-Ag alloy with diffuse streaks in the Laue pattern. Further, with small angle scattering of X-rays Guinier[2] studied it and measured the mean value of the thickness of the platelets from the length of the streaks.

We have also measured small angle scattering from these platelets and calculated the distribution of their thickness by extending the Fankuchen method to one dimentional case.

In the present experiment Cu $K\alpha$ radiation monochromatized with LiF crystal monochrometer was used. The widths of the 1st and 2nd slit were 0.5 mm and 0.1 mm respectively, the slit distance 320 mm, the distance between the 2nd slit and the sample 10 mm. The path 340 mm long between the sample and the detecter slit was evacuated. 0.07 mm thick sample was prepared from Al-Ag alloy containing 20 weight percent of Ag by etching the surface with Nitric-Acid alcohl.

Fig. 1 (a) shows a scattering photograph of the sample. The two streaks were considered to be the scattering from individual grain. The streaks showed unsymmetrical change with the rotation of the sample. This phenomenon was well explained later by the Eq. (1), which was deduced with the assumption of the platelet structure. In this experiment the double reflection was not observed[3),4)].

For the purpose of evaluating the distribution of thickness of the platelet, we measured the scattering intensity with G.M. counters, diminishing the height of beam so as to measure only one streak from a single grain. The curve is given in Fig. 1 (b).

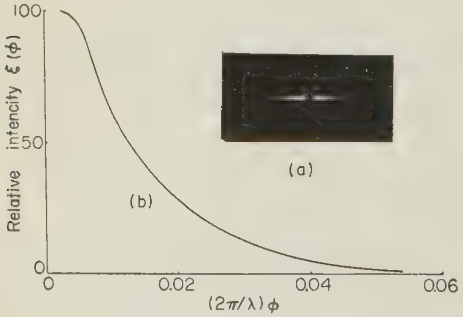

Fig. 1. Photograph (a) and intensity curve (b) of small angle scattering from Al-Ag, water-quenched from 520°C and annealed 240 hours at 140°C.

It is shown by a simple calculation that the coherent scattering intensity except the neighbourhood of zero angle, when the platelets distribute at random both in thickness and relative distance, is given by

$$I(\phi)=I_e\rho^2 4\bar{H}^2 \sum_i \left(\frac{2\sin t_i(2\pi/\lambda)\phi}{(2\pi/\lambda)\phi}\right)^2 \times\left[\frac{2\sin T_i(\pi/\lambda)\{\phi-\psi)^2-\psi^2\}}{(\pi/\lambda)\{(\phi-\psi)^2-\psi^2\}}\right]^2, \qquad (1)$$

where I_e is the scattering intensity of one electron, ρ the differential electron density of the platelets and the matrix, $4\bar{H}^2$ the mean square of platelet's height, $2t_i$ the thickness of platelet, $2T_i$ the length of platelet, ϕ the scattering augle, ψ the angle between incident beam and platelet, and λ the wave length.

When T_i is a constant T, Eq. (1) can be written as follows:

$$\xi(\phi)\equiv I(\phi)\left[\frac{(\pi/\lambda)\{\phi-\psi)^2-\psi^2\}}{2\sin T(\pi/\lambda)\{(\phi-\psi)^2-\psi^2\}}\right]^2 = I_e\rho^2 4\bar{H}^2 \sum_i \left(\frac{2\sin t_i(2\pi/\lambda)\phi}{(2\pi/\lambda)\phi}\right)^2. \qquad (2)$$

This corresponds to the transformation from the scattering intensity on the reflection sphere to that on the perpendicular reciprocal axis of platelets. In the case of practical measurement, $\xi(\phi)$ is obtained directly from measurement by choosing so as to satisfy $(\phi-\psi)^2-\psi^2=0$ as can be seen from Eq. (1). But when T_i is constant as in this case, $\xi(\phi)$ can be obtained from measurement on the reflection sphere by Eq. (2). Eq. (2) agreed well with the result of our experiment by putting $2T$=1000A.

By use of $\xi(\phi)$ we calculated the distribution curve of thickness of the platelet by Fankuchen method[5]: (Fig. 2). The mean value of thickness is about 30A. This is close to the results of Guinier et al.[6] of 30~50A.

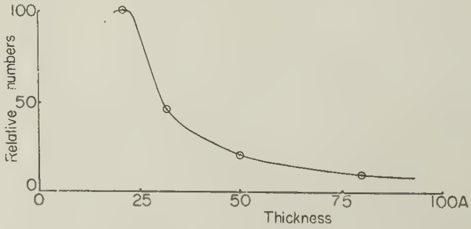

Fig. 2. Distribution curve of thickness of platelet.

We wish to express our sincere thanks to Professor T. Futagami for his continued encouragement during the course of this research.

References

1) A. H. Geisler and J. K. Hill: Acta Cryst. **1** (1948) 238.
2) for example, A. Guinier and G. Fournet: *Small-*

Angle scattering of X-rays, New York, Wiley, (1955) p. 208.
3) H. Fricke and V. Gerold: J. Appl. Phys. **30** (1959) 661.
4) W. T. Ogier, R. L. Wild and J. C. Nickel: J. Appl. Phys. **30** (1959) 408.
5) M. H. Jellinek and I. Fankuchen: Ind. Eng. Chem. **37** (1945) 158; **41** (1949) 2259.
6) Reference 2) p. 210.

J. PHYS. SOC. JAPAN **16** (1961) 579

Microdomain Structure in Paraelectric Phase of NaNO$_2$

By Sigetosi TANISAKI
Faculty of Literature and Science, Yamaguchi University

(Received December 26, 1960)

Sodium Nitrite (NaNO$_2$) was first reported to be a ferroelectric by Sawada et al.[1], Curie point of which is about 160°C. The crystal structure of this material has been studied by several researchers[2),3),4),5),6)]. From these structure analysis, the ferroelectricity in the low temperature phase has been considered to be due to the ordered arrangement of NO$_2$ groups, which becomes disordered above the Curie point. In this note the microdomain structure in the paraelectric phase found by X-ray study will be reported.

Oscillation photographs and Laue photographs were taken with a and b axes vertical just above the Curie point. From these photographs it was found that, besides the normal Bragg- and Laue-reflections and the ordinal thermal diffuse scatterings, two sharp satellites in each side of some of the normal reflections along a axis, and the weak plate like diffuse scatterings around those normal spots whose intensities are distributed vertically to b axis appear. Fig. 1 shows an example of oscillation photograph by 30° with a axis vertical. The satellites correspond to a certain periodical structure along a axis, and the period calculated from the separation between satellite and normal spot is about 8.4 a. These satellites can be interpreted by the following model. Let us consider two kinds of atomic layers parallel to (100) in which the arrangement of NO$_2$ groups is perfectly ordered as shown in Fig. 2(a). It is assumed that the interchanges of the two kinds of layers occur along a axis once in every eight or nine layers of the same kind as shown in Fig. 2(b). This model corresponds to the extreme case in which the width of the (100) domain in ferroelectric phase becomes as short as 4 a or 4.5 a, and so it may be called the "microdomain structure". Suppose that the structure factor F of the basic structure shown in Fig. 2(a) are given by $F=A+iB$, then $|A|^2$ and $|B|^2$ are to be proportional to the intensities of normal Bragg spots and satellites respectively. The result of calculation by the use of the atomic parameters obtained by small modifications of Strijk and MacGillavry's data[5] and on the assumption of the appropriate temperature factors, shows a satisfactory agreement with the observed values.

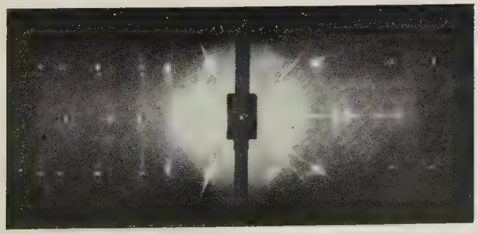

Fig. 1. X-ray oscillation photograph with a axis vertical.

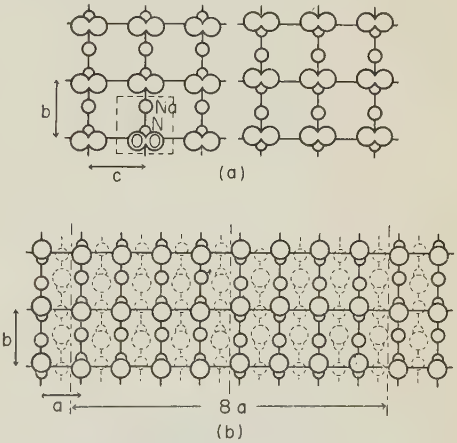

Fig. 2. (a) Two kinds of atomic layers with perfectly ordered arrangement of NO$_2$ groups. The basic structure is shown in the rectangle of broken line. (b) Projection of the microdomain structure along c axis. Circles of broken lines represent atoms whose positions are higher as much as 1/2 c than those of the corresponding atoms represented by circles of full lines.

The detailed investigations about the temperature dependencies of satellites and diffuse scatterings are now in progress.

References

1) S. Sawada, S. Nomura, S. Fujii and I. Yoshida: Phys. Rev. Letters **1** (1958) 320.
2) G. E. Ziegler: Phys. Rev. **38** (1931) 1040.
3) G. B. Carpenter: Acta Cryst. **5** (1952) 132.
4) M. R. Truter: Acta Cryst. **7** (1954) 73.
5) B. Strijk and C. H. MacGillavry: Rec. Trav. Chim. **62** (1943) 705, **65** (1946) 127.
6) B. C. Frazer, R. Ueda and M. Kay: unpublished.

J. PHYS. SOC. JAPAN **16** (1961) 580~581

Measurement of Anomalous Absorption Coefficients of Electrons for MgO Crystals*

By Kazutake KOHRA

Institute of Physics, College of General Education, University of Tokyo, Komaba, Meguro, Tokyo

and Hiroshi WATANABE

Hitachi Central Research Laboratory, Kokubunji, Tokyo

(Received January 9, 1961)

It is well known that anomalous phenomena of absorption take place at the Laue-Bragg reflecting position in a single crystal for X-rays[1]. In electron diffraction, too, similar phenomena take place. Honjo et al[2] found the difference in the absorption coefficients of two wave fields and the present authors[3] observed the anomalous transmission corresponding to the Borrmann effect[4]. On the other hand, it was theoretically explained by Yoshioka[5] that the effect of inelastic scattering in electron diffraction can be represented by the imaginary potential in the same way as in the case of X-ray diffraction. But there has been no quantitative study of the anomalous absorption coefficient for electrons.** We have measured the mean and anomalous absorption coefficients of electrons for MgO crystals by the use of electron micrographs.

Fig. 1 is an example of bright field electron micrographs of MgO crystals, where the equal thickness fringes due to the (200) reflection are seen. Fig. 2 gives the intensity curve along the line indicated by the arrow in Fig. 1. Taking into account the effect of absorption in the dynamical theory, the transmitted intensity is given by the following equation which is analogous to the one in the case of X-ray diffraction[7]:

$$I_t=\frac{1}{2}I_0\left\{\frac{\cos(\sqrt{1+w)}\,|v_h|\lambda t/2\pi)}{\sqrt{1+w^2}}e^{-\mu_0 t}\right.$$
$$+\frac{1}{2}\left(1+\frac{w}{\sqrt{1+w^2}}\right)^2 e^{-(\mu_0-\varDelta\mu)t}$$
$$\left.+\frac{1}{2}\left(1-\frac{w}{\sqrt{1+w^2}}\right)^2 e^{-(\mu_0+\varDelta\mu)t}\right\}, \qquad (1)$$

where

$$\mu_0=\frac{v_{oi}\lambda}{2\pi\sqrt{1+w^2}}, \qquad (1a)$$

$$\varDelta\mu=\frac{|v_{hi}|\lambda}{2\pi\sqrt{1+w_2}}. \qquad (1b)$$

I_0 is the intensity of the incident wave, t the thickness, w a parameter indicating the deviation from the Laue-Bragg condition, v_h the h-th Fourier coefficient, and v_{oi} and v_{hj} the o-th and h-th coefficients of the imaginary potential, respectively. t is known from the magnification of the electron micrograph and w is determined from the period of the fringe. For v_h the calculated value used by Honjo et al[2] is here also used. The first term in (1) corresponds to the fringe pattern indicated by **a** in Fig. 2, and the sum of second and third terms to the background indicated by **b**. From the curve **a** the mean absorption coefficient is determined, and from the curve **b** the anomalous absorption coefficients of the two wave fields.

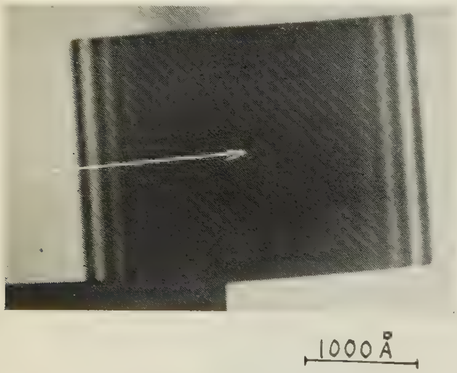

Fig. 1. A bright field electron micrograph of MgO crystal.

Table I.

Accelerating voltage (kV)	$l_0=\mu_0^{-1}$ (A)	$l'=(\mu_0-\varDelta\mu)^{-1}$ (A)	$l''=(\mu_0+\varDelta\mu)^{-1}$ (A)	w	v_{oi} (ev)	$\|v_{hi}\|$ (ev)
40 (theory)	—	—	—	—	1.47	0.068
50	230 260	1840 1460	140 130	0.19 0.14	1.85	1.54
75	670 625	2500 1790	260 490	~0 ~0	0.84	0.62

It is to be noted that the observed intensity involves contributions from not only elastic but also inelastic scatterings, whereas the theory is concerned only with the former. In the present paper, however, neglecting the contribution from inelastic scattering, the values for the (200) reflection at 50 and 75 kV were determined as shown in Table I, where theoretical values at 40 kV[5] are also given for comparison. Measurements are being extended to 100 kV, and similar procedures are applied to the

---

* A part was read at the Ann. Meeting of Phys. Soc. Japan (Tokyo) in April, 1960.

** Studies on the effect of absorption on the interference fringe in thin films of metals have recently reported by Hashimoto et al.[6]

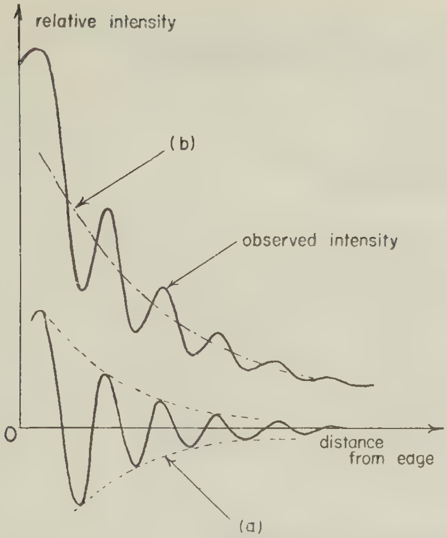

Fig. 2. Intensity curve.

(220) reflection. More accurate values will be obtained by the use of the dark field image. Details will be reported in the near future.

References

1) G. Borrman: Phys. Zs. **42** (1940) 157: Zs. f. Phys. **127** (1950) 297. M. v. Laue: Acta Cryst. **2** (1949) 106. W. H. Zachariasen: Proc. Nat. Acad. Sci. USA. **38** (1952) 378. K. Kohra: *X-sen Kesshogaku* (edited by I. Nitta, in Japanese, *X-ray Crystallography*) II, p. 891, Maruzen, Tokyo, 1961.

2) G. Honjo and K. Mihama: J. Phys. Soc. Japan **9** (1954) 184.

3) K. Kohra and H. Watanabe: J. Phys. Soc. Japan **14** (1959) 1119.

4) G. Borrmann: Phys. Zs. **42** (1940) 157; Zs. f. Phys. **127** (1950) 297.

5) H. Yoshioka: J. Phys. Soc. Japan **12** (1957) 618.

6) H. Hashimoto et al.: Phil. Mag. **5** (1960) 967.

7) for example, W. H. Zachariasen: *Theory of X-ray Diffraction in Crystals*, Wiley, New York, 1945. G. Brogren and Ö. Adell: Ark. f. Phys. **8** (1953) 97. N. Kato: J. Phys. Soc. Japan **10** (1955) 46.

Errata

On the Electron Emission From Oxide Coated Cathode Subject to Strong Electric Field

By Chokichiro SHIBATA

J. Phys. Soc. Japan **16** (1961) 51

Page	Column	Line	Wrong	Corrected
54	left	43	gain in zero	gain is zero
54	right	10	$\sqrt{\frac{2l}{m}V_c}$	$\sqrt{\frac{2e}{m}V_c}$
56	left	26	to Metson's[8]	to Metson's[9]
59	left	28	in Fig. 19.	in Fig. 19.[10]
61	right	2	Bruinings:	Bruining:

Radiation Induced Optical Absorptions in Crystalline Quartz and Fused Silica

By Kazuko KUBO

J. Phys. Soc. Japan **16** (1961) 108

Page			Should be read
111	Fig. 5		(a) Before irradiation
			(b) After γ-irradiation (3×10^8r)
			(c) After 1.5 hrs bleaching
			(d) 〃 4.5 〃
			(e) 〃 12 〃
			(f) 〃 34.5 〃
			(g) 〃 105.5 〃
112	Fig. 8	(a) Before irradiation	(a) Before irradiation
		(b) After 8×10^{16}nvt irradiation (Before optical bleacding)	(b) After irradiation (3×10^8r) (Before bleaching)
		(c) After optical bleaching for 6 days	(c) After optical bleaching for 105.5 hrs
		(d) After 2×10^{16}nvt re-irradiation	(d) After 8.4×10^6r re-irradiation
		(e) After 4×10^{16}nvt re-irradiation	(e) After 8.4×10^6r irradiation to same new specimen
		(f) After 10^{17}nvt re-irradiation	

Addendum

On the Ferrimagnetic Resonance of Europium Iron Garnet

By W. P. WOLF

J. Phys. Soc. Japan **15** (1960) 2104

The following footnote was omitted at the end of the above communication:

(7) Measurements on single crystals have recently been reported by T. Miydai, H. Takata, Y. Shichijo and N. Tsuya, J. Phys. Soc. Japan **15** (1960), 1354. The results are essentially similar to the polycrystalline values, but the agreement with our theory is even closer, especially at low temperatures. It may be noted that the theoretical curve shown by Miydai et al. is identical to our calculated line although it is derived from a basically different assumption: see footnote (6).

JOURNAL OF THE PHYSICAL SOCIETY OF JAPAN, Vol. 16, No. 4, APRIL, 1961

Angular Distributions of Protons from the Alpha Particle Bombardment of B^{10}, N^{14}, O^{16} and Ne^{20}

By Hisashi YAMAGUCHI

Institute for Nuclear Study, University of Tokyo,
Tanashi-Machi, Kitatama-Gun, Tokyo

(Received December 26, 1960)

Angular distributions of protons from the alpha particle bombardment have been obtained for the following transitions, corresponding to discrete states of the residual nuclei: $B^{10}(\alpha, p)C^{13}$ ground at bombarding energies 27.5 and 33.1 MeV; $N^{14}(\alpha, p)O^{17}$ ground, first, second, third at bombarding energies 26.8, 28.1 and 33.3 MeV; $O^{16}(\alpha, p)F^{19}$ ground to second (unresolved), third to fifth (unresolved), sixth at bombarding energies 26.7 and 33.1 MeV; and $Ne^{20}(\alpha, p)Na^{23}$ ground and first (unresolved), second to sixth (unresolved) at bombarding energy 26.9 MeV. These angular distributions show the so-called diffraction patterns and some of them are interpreted with the aid of predictions of the direct interaction theory. However, some deviations from the predictions of the direct interaction theory exist and suggest the effect of other nuclear reaction processes.

§ 1. Introduction

In the past few years a few experimental studies of angular distributions of (α, p) reaction have been reported. Eisberg, Igo and Wegner[1] studied the spectra of protons from heavy elements at 40 MeV alpha particle energy and they suggested noncompound nucleus processes in the region of small excitation energy in the residual nucleus.

On the lighter elements, several angular distributions of protons from B^{10}, C^{12}, F^{19}, Na^{23}, Al^{27} and P^{31} have been measured at low and intermediate alpha particle energies[2)-5)]*. On the reaction mechanism of (α, p) reaction in intermediate energy region, a few theoretical treatments exist so far.[6)-9)] Generally, the treatment analogous to the knock-on process (surface) for the (p, n) or (p, p'), and to the stripping process for the deuteron induced reaction are used. Neglecting the detailed discussion, the differential cross sections for such direct interaction theories are shown to be in proportion to the square of the spherical Bessel function of appropriate order. Some experimental results have been interpreted with the aid of predictions of such direct interaction theories. S. T. Butler[6] compared his formula (surface) to the results for $C^{12}(\alpha, p)N^{15}$ ground at 30.5 MeV alpha particle energy obtained by C. E. Hunting and N. S. Wall. Also C. E. Hunting and N. S. Wall[2] compared their results for $B^{10}(\alpha, p)C^{13}$ ground, $Al^{27}(\alpha, p)Si^{30}$ ground and $P^{31}(\alpha, p)S^{34}$ ground at 30.4 MeV alpha particle energy to the Butler formula. In these comparisons the theoretical curves were fitted well to the experimental ones, but for the case of B^{10} the interaction radius was rather small and for the case of Al^{27} the agreement was not so good. P. von Hermann and G. F. Pieper[3] compared their results for $B^{10}(\alpha, p)C^{13}$ ground at 4.9, 7.0 and 8.1 MeV alpha particle energies and $P^{31}(\alpha, p)S^{34}$ ground at 7.0 and 8.1 MeV alpha particle energies to $|j_l(QR)|^2$ (surface) and got partial fits in these comparisons. G. F. Pieper and N. P. Heydenburg[4] also compared their results for $F^{19}(\alpha, p)Ne^{22}$ ground at 6.25 and 6.40 MeV alpha particle energies to $|j_l(QR)|^2$ (surface) and showed good fits. In the experiment above mentioned[4] Pieper and Heydenburg have measured angular correlations of gamma ray from the first excited state of Ne^{22} with the alpha particle and proton directions at 6.10 and 6.40 MeV alpha particle energies. The results at 6.40 MeV bombarding energy agree with predictions based on simple direct interaction mechanism, but the results at 6.10 MeV do not show the same agreements as that for the 6.40 MeV.

In a previous paper[5] we have showed the angular distributions for the reaction $C^{12}(\alpha,$

---

* In the reference 5), other references of the reaction $C^{12}(\alpha, p)N^{15}$ were listed.

$p)N^{15}$ ground for twelve bombarding energies in the region of 25 to 39 MeV. These angular distributions changed remarkably with the variation of the bombarding energies, particularly in large angles.

To study the mechanism of the (α, p) reaction, such energy dependence of angular distribution is very interesting. In this paper we wish to show the results of the measurements of the angular distributions for the (α, p) reactions of B^{10}, N^{14}, O^{16} and Ne^{20} at 27, 28 and 33 MeV alpha particle energies.

§ 2. Experimental Methods

The external alpha particle beam from the I.N.S. (Tokyo) variable energy cyclotron[10] was brought into a scattering chamber of 100 cm in diameter. The beam focusing system and the scattering chamber used in this experiments are the same as our previous experiment[5] except for the case of gas target bombardment such as nitrogen, oxygen, and neon. In the bombardment of gas target, we used a gas chamber which was made of a brass cylinder of 9 cm in diameter and of 6 cm in height and had two windows extending over the angular range of more than 90° corresponding to "forward counter" and "backward counter," each including the beam entrance (backward) and the beam exit (forward). Each window was covered with a sheet of aluminum foil of 20μ in thickness. The slit front of the scintillation counter which was used in the case of solid target was replaced by a set of slits by which the solid angle and the target thickness were defined.

As the targets we used N_2 of 39 cm Hg, O_2 of 40 cm Hg, Ne of 43 cm Hg at room temperature respectively, and the film of natural boron suspended in polystyrene of about 6.0 mg/cm² thickness. N_2 and O_2 were the commercial gases guranted 99% in purity by the dealer and Ne was a reagent graded gas guranted 98% in purity by the dealer. The boron target was prepared by the method described by N. S. Wall[11].

The beam energy was determined by the measurement of its range in aluminium. For the calculation of alpha particle energy from the measured range in aluminum we used the range-energy curve of protons in aluminum of W. A. Aron et al.[12]. The absolute value of the beam energy is in accuracy of a few %. The incident beam energy spread was estimated to be within about 0.5%.

For identification of the levels[13),14] involved in these reactions, the energies of the detected proton groups were calculated from the kinetics and the incident alpha particle energy, and compared to the energy of the recoil protons produced by the scattering of the alpha particles from the hydrogen atoms contained in the target.

In order to obtain an absolute differential cross section, we used following formula for the gas target

$$\sigma(\Theta)=N\frac{1}{nI}\frac{1}{G}\sin\Theta \qquad (1)$$

where N is the number of protons entering the detector, n is the number of target nuclei in a unit volume, I is the number of alpha particles that traversed the target, and $G=(b\pi r^2)/(hR_0)$ is the geometrical factor of the slit system which is shown in Table I. For the B^{10} case, we could not estimate the absolute differential cross section owing to unknown boron content of the target.

Table I. Slit dimensions (in millimeters).

	Foreward counter	Backward counter
In the case of Boron;		
Diameter of slit, $2r$	8.0	8.0
Distance from the target center to slit, R_0	250	218
In the case of gas target;		
Width of front slit, b	5.0	5.0
Diameter of rear slit, $2r$	8.0	8.0
Distance from the target center to rear slit, R_0	260	223
Distance between slits, h	143	131
Geometrical factor, G	6.76×10^{-3}	8.60×10^{-3}

The errors indicated in the figures of angular distributions include those from two sources, one being the error in the estimation of background subtraction and the other being the statistical errors. These errors were generally small, but in the larger angles increasing background and decreasing energy of detected proton group made these errors serious, particularly in the weak proton groups, such as $N^{14}(\alpha, p)O^{17}$ first and second, estimated errors reached a few tens percent.

§ 3. Results and Discussions

The observed angular distributions for the (α, p) reactions are listed in Table II and shown in Fig. 1. In Fig. 2 the differential

Table II. Observed (α, p) reactions.

(1) Proton group	(2) Energy level[13),14)] in MeV	(3) Spin and parity[13),14)]	(4) E_α(lab) in MeV	(5) Total cross section σ_t in mb
		Reaction $B^{10}(\alpha, p)C^{13}$		
P_0	0	$1/2^-$	27.5	1 (relative)*
			33.1	0.57 (relative)
		Reaction $N^{14}(\alpha, p)O^{17}$		
P_0	0	$5/2^+$	26.8	1.37
			28.1	1.31
			33.3	0.82
P_1	0.871	$1/2^+$	26.8	0.29
			28.1	0.21
			33.3	0.10
P_2	3.058	$(1/2^-)$	26.8	0.29
			28.1	0.27
			33.3	—
P_3	3.846	$(7/2^-)$	26.8	—
			28.1	0.83
			33.3	—
		Reaction $O^{16}(\alpha, p)F^{19}$		
P_{0-2}	0	$1/2^+$	26.7	6.51
(unresolved)	0.110	$1/2^-$	33.1	4.24
	0.198	$5/2^+$		
P_{3-5}	1.35	(3/2)	26.7	4.55
(unresolved)	1.46	1/2, 3/2	33.1	2.41
	1.56	$3/2^+$		
P_6	2.78	(7/2, 9/2)	26.7	7.0
			33.1	3.43
		Reaction $Ne^{20}(\alpha, p)Na^{23}$		
$P_{0,1}$	0	$3/2^+$	26.9	1.33
(unresolved)	0.439	$5/2^+$		
P_{2-6}	2.078	(7/2)	26.9	2.66
(unresolved)	2.39	(1/2)		
	2.64			
	2.71			
	2.98			

* In the case of B^{10} the relative values of the total cross section to the 27.5 MeV's are shown.

cross sections for the case of nitrogen and oxygen at fixed angles are shown as functions of bombarding energies. In Table II and Fig. 3 the total cross sections σ_t are also shown. For the B^{10} case, the relative values of σ_t compared to the value at $E_\alpha=27.5$ MeV are shown in Table II. Tabulated data for all the results are given in Ref. 15).

(1) *Angular distribution*

As mentioned in the Introduction, the angular distributions of the (α, p) reaction are compared to the predictions of the direct interaction theories.

Under the assumption of a knockout process, the differential cross section has the following form

$$\sigma(\theta) \propto |f(\theta) j_l(QR)|^2 \tag{2}$$

where $f(\theta)$ is a form factor, j_l is the spherical Bessel function of order l, Q is the momentum transfer vector defined by the form

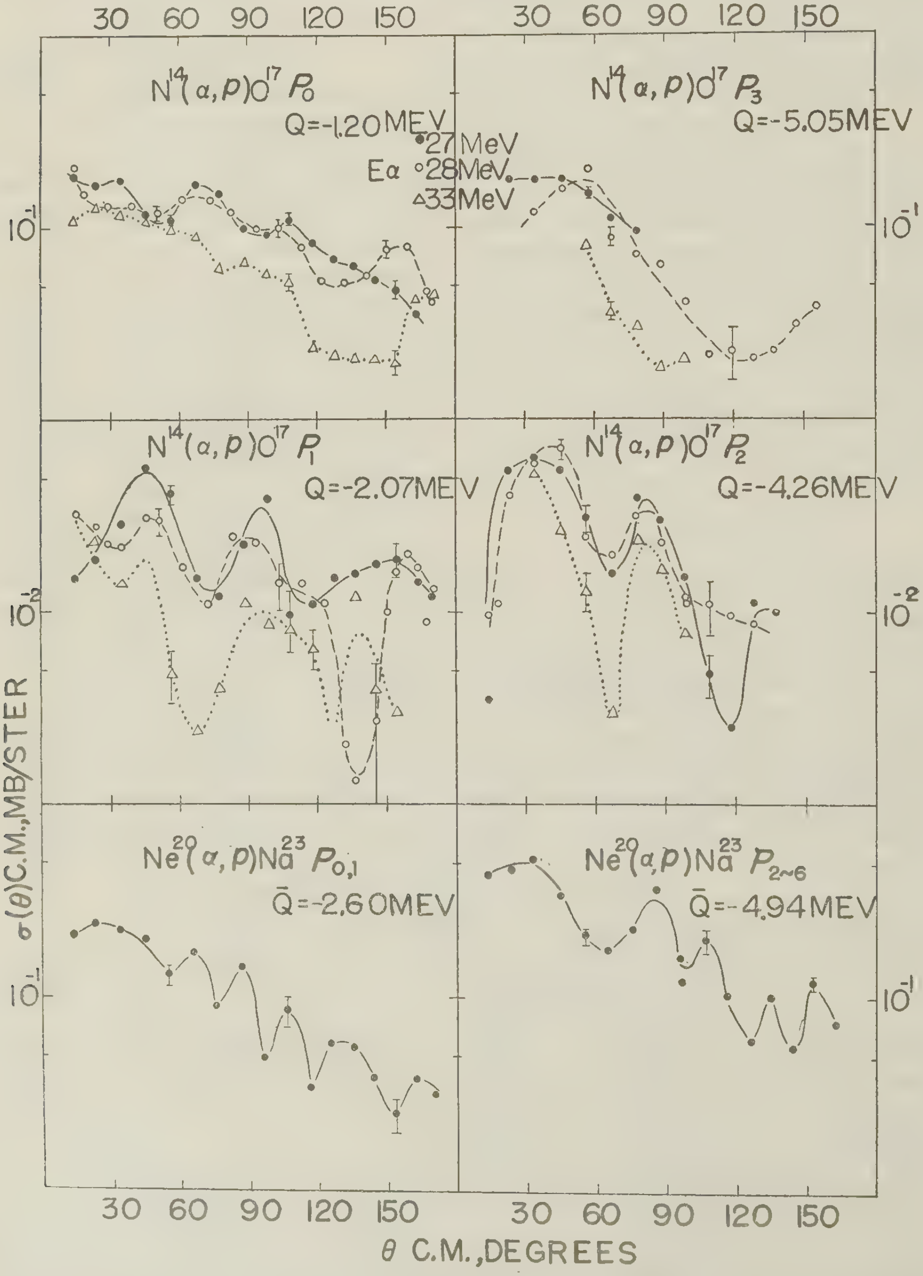

(a)

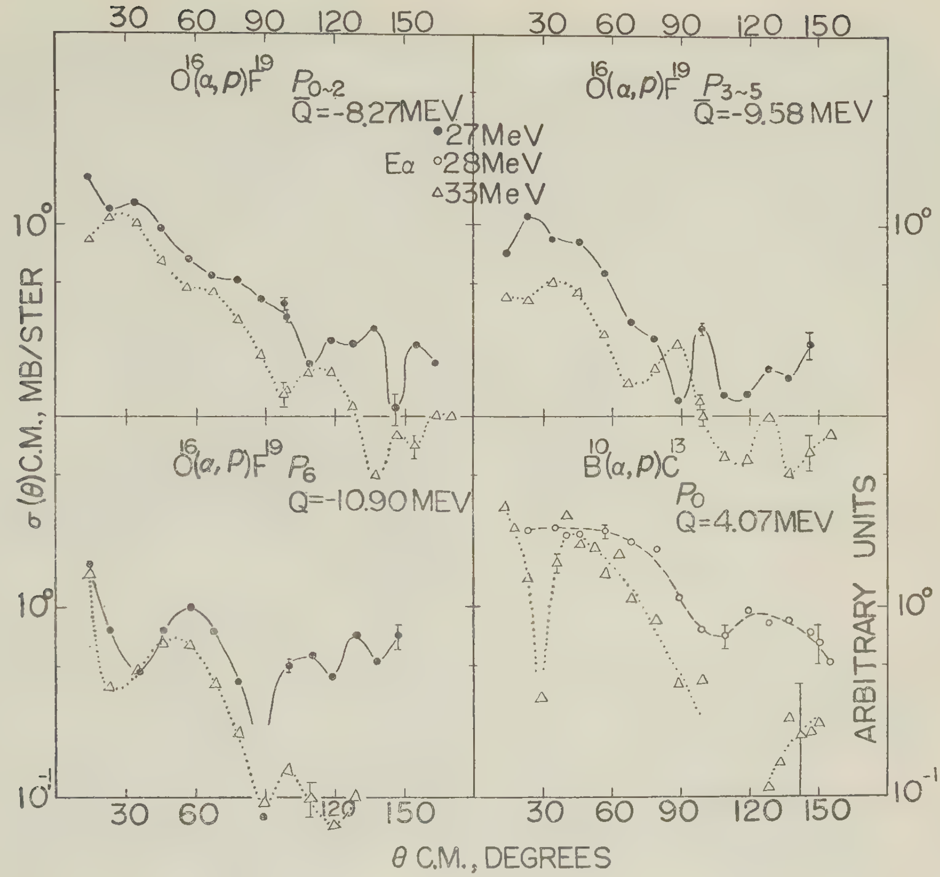

(b)

Fig. 1. Angular distribution of protons from the alpha particle bombardment of B^{10}, N^{14}, O^{16} and Ne^{20} at $E_\alpha=27$(●), 28(○) and 33(△) MeV. Representative errors are shown.

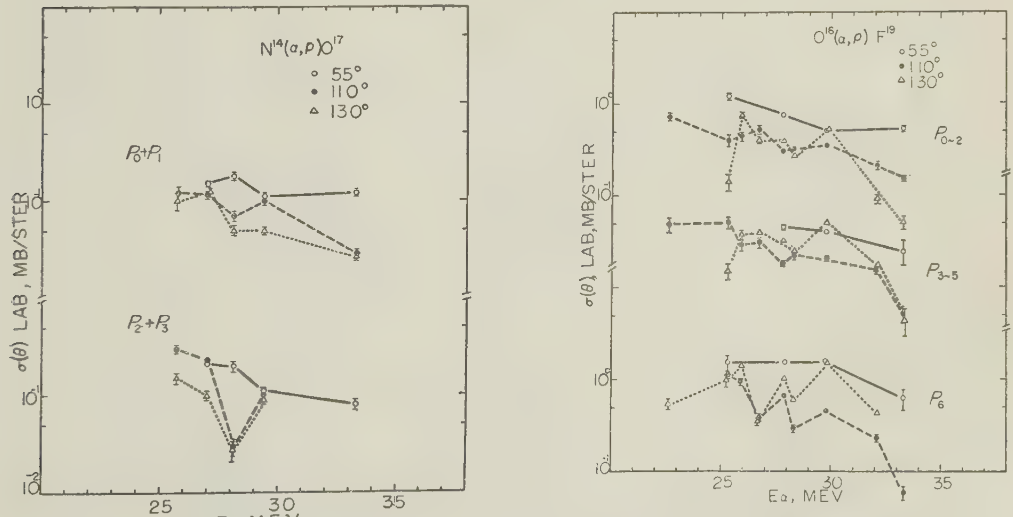

(a)

(b)

Fig. 2. Differential cross sections for the reactions $N^{14}(\alpha, p)O^{17}$ ground and first, second andthird; and $O^{16}(\alpha, p)F^{19}$ ground to second, third to fifth, sixth as functions of alpha particle energies at laboratory angles 55°, 110°, and 130°.

$$Q=\left(\frac{M_x-M_p}{M_x}\right)\left(K_\alpha-\frac{M_x}{M_y}K_p\right) \qquad (3)$$

where M_x, M_y, and M_p is the mass of the target, the residual nucleus and the proton respectively, and the K's are the wave vector of the alpha particle, and proton. R is the interaction radius, and l is the change of angular momentum, which is limited by the selection rule

$$|J_x+J_y+i|_{\min}\leqslant l\leqslant J_x+J_y+i \qquad (4)$$

where J_x is the spin of the target nucleus, J_y is the spin of the residual nucleus, and i is the vector sum of the spins of the entering and emerging particles. l must be odd if the parity of the residual nucleus differs from that of the target nucleus, and must be even if the parities are the same. Under the assumption of a stripping process, the differential cross section, also, has the form of Eq. (2). In this case, Q is defined by the form

$$Q=K_\alpha-\frac{M_x}{M_y}K_p\,. \qquad (5)$$

The differential cross sections of these two processes have similar expressions and we are not able to distinguish these two processes from the results of the angular distribution measurements.

Other mechanisms for the (α, p) reaction are heavy particle stripping and triple or double stripping. In heavy particle stripping, the differential cross section is of the same form of Eq. (2) but Q as defined as $Q=K_\alpha+(M_\alpha/M_y)K_p$ and this process interfers with ordinary stripping. This assumption was originally used by G. E. Owen and L. Madansky[16] for the analysis of the $B^{11}(d, n)C^{12}$ reaction, and in the alpha induced reaction B.

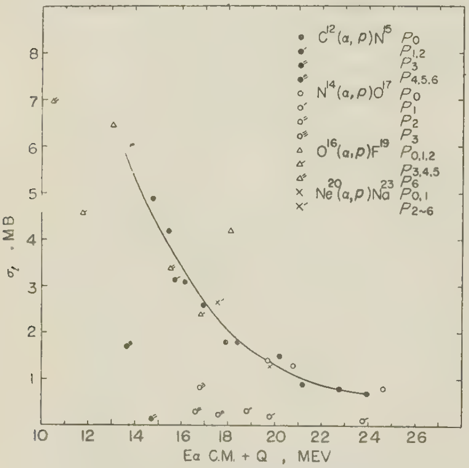

Fig. 3. Total cross sections σ_t as a function of $(E_{\text{c.m.}}+Q)$ in MeV. The data of carbon are replotted from I. Nonaka et al.[5]. A solid curve is of the case of the reaction $C^{12}(\alpha, p)N^{15}$ ground.

Table III. Interaction radii.

(1) Reaction		(2) l-value (experimental)	(3) E_α(lab) in MeV	(4) R in 10^{-13} cm (experimental)	(5) R in 10^{-13} cm from (α, α)*
$B^{10}(\alpha, p)C^{13}$	ground	3 (uniquely)	27.5	3.7	5.1
			33.1	6.3	
$N^{14}(\alpha, p)O^{17}$	ground	2	26.8	6.4	5.4
			28.1	7.9	
			33.3	4.9	
	first	0 (2)	26.8	5.7 (5.4)	
			28.1	5.4 (5.1)	
			33.3	5.2 (4.9)	
	second	1 (uniquely)	26.8	4.7 or 7.3	
			28.1	6.9	
			33.3	6.2	
	third	3	26.8	3.5	
			28.1	5.7	
$O^{16}(\alpha, p)F^{19}$	sixth	3, 4, 5	26.7	7.6, 6.2, 7.0	5.5
			33.1	7.2, 8.1, 9.0	

* Interaction radius expected from the elastic alpha-particle scattering analysis in reference 19): $(1.017A^{1/3}+2.94)$ in 10^{-13} cm.

Zeidman and J. L. Yntema[17)] applied it to the results for the (α, d) reactions on N^{14} and Li^6 at bombarding energy 43 MeV.

S. Hinds and R. Middleton[18)] have compared their results for the (He^3, p) reaction to the double stripping process derived by H. C. Newns. The differential cross section has the form

$$\sigma(\theta) \propto \sum_L |A(L) j_L(QR)|^2 \qquad (6)$$

where j_L is a spherical Bessel function and $A(L)$ is a constant analogous to the capture probability occurring in the Born approximation deuteron stripping theory, and $L = l_n + l_p$. This assumption may be used in the case of the (α, p) reaction in which the nucleons in the incident alpha particle interact with the target nucleus, individually or in a pair.

In order to compare our results to the direct interaction theory, the stripping process is

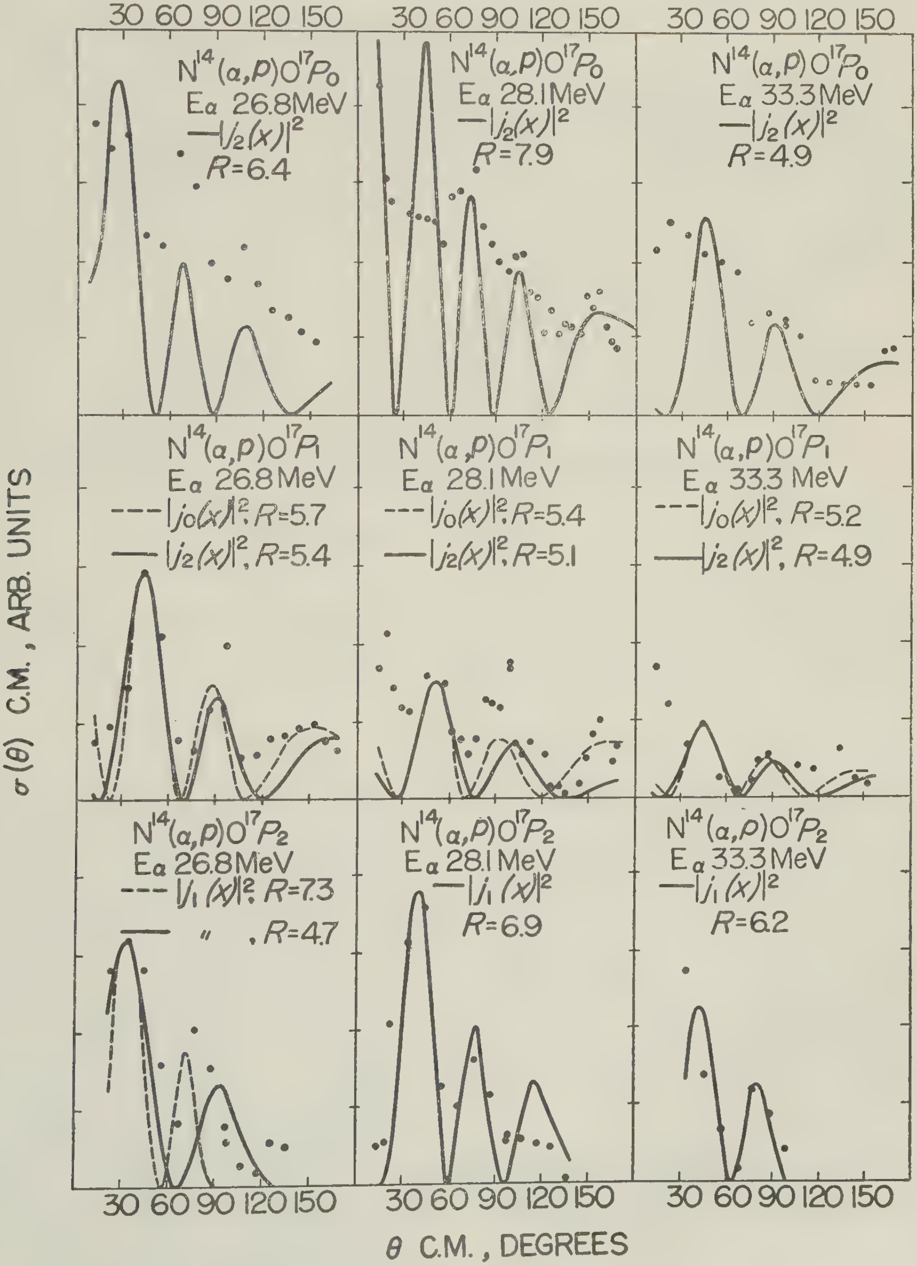

(a)

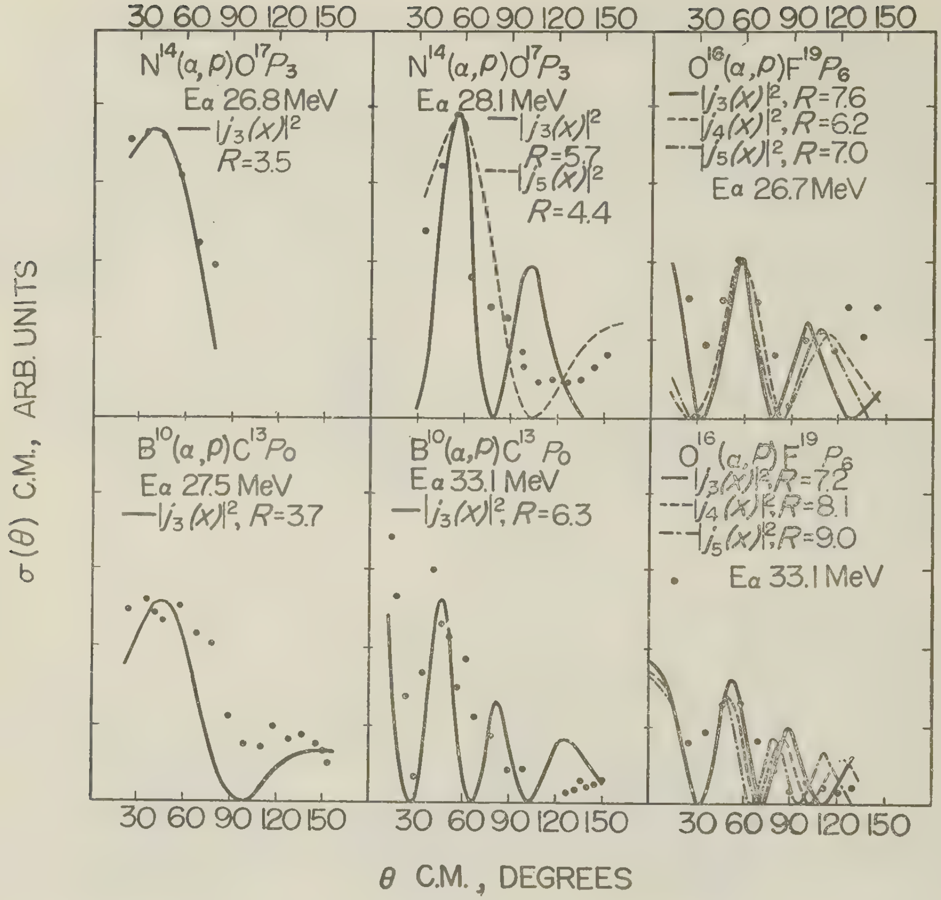

(b)

Fig. 4. Comparisons between the experimental angular distributions and $|j_l(x)|^2$ based on a stripping process. Where $x=QR$, Q is the momentum transfer, and R is the interaction radius in unit of 10^{-13} cm.

assumed, and owing to our capacities of calculation we are limited in these comparison to fit $|j_l(QR)|^2$, where $Q=K_\alpha-(M_x/M_y)K_p$, to each resolved proton group. The results of these fits are shown in Fig. 4 and Table III.

(i) $B^{10}(\alpha, p)C^{13}$ ground $l=3$ (uniquely); For the case of $E_\alpha=27.5$ MeV, we have had to choose a small interaction radius $R=3.7\times 10^{-13}$ cm to explain the broad peaks. This circumstance was seen for the case of $B^{10}(\alpha, p)C^{13}$ ground at $E_\alpha=30.4$ MeV obtained by C. E. Hunting and N. S. Wall[2], choosing the interaction radius $R=3.3\times10^{-13}$ cm in the comparison to the Butler formula. We had to choose, however, the larger interaction radius $R=6.3\times10^{-13}$ cm for the case of $E_\alpha=33.1$ MeV to explain the sharp rise in the small angles.

(ii) $N^{14}(\alpha, p)O^{17}$ ground $l=2$*; For the case of $E_\alpha=26.8$ MeV, we have failed to explain the rise in the small angles by the choice $R=6.4\times10^{-13}$ cm in spite of the success of the reappearance of following maxima and minima. For the case of $E_\alpha=28.1$ MeV, we have failed to explain the first shallow valley by the choice $R=7.9\times10^{-13}$ cm in spite of the success of the reappearance of following maxima and minima too. For the case of $E_\alpha=33.3$ MeV, we have had to choose a smaller radius, $R=4.9\times10^{-13}$ cm than the ones for the case of two lower bombarding energies.

(iii) $N^{14}(\alpha, p)O^{17}$ first, $l=0$ or 2; For the case of $E_\alpha=26.8$ MeV we get the almost same result for $|j_0|^2$ with $R=5.7\times10^{-13}$ cm, or $|j_2|^2$ with $R=5.4\times10^{-13}$ cm to be fitted the experimental results. For the higher two energies, $E_\alpha=28.1$ and 33.3 MeV, where the sharp rises exist in the region smaller than 30 degrees, we have failed to explain these rises. In the larger angle region, $|j_l|^2$ with $l=0$ is preferable to $|j_l|^2$ with $l=2$.

---

* In this case $l=2$ or 4 from the selection rule Eq. 3. We have chosen $l=2$ according to the results of preliminary fit. The situations are the same in the case of other reactions.

(iv) $N^{14}(\alpha, p)O^{17}$ second, $l=1$ (uniquely); For the case of $E_\alpha=26.8$ MeV the first maximum is fitted only, and the first and second maxima are fitted for $E_\alpha=28.1$ MeV.

(v) $N^{14}(\alpha, p)O^{17}$ third, $l=3$; For this proton group, we failed to get the full angular distribution owing to the strong proton group leaving the O^{17} in the fourth excited state. Nevertheless, we are able to see the situation of these proton groups, by comparison with other proton groups.

(vi) $O^{16}(\alpha, p)F^{19}$ sixth, $l=3$ or 4 if the spin of F^{19} sixth is 7/2; $l=4$ or 5 if the spin of F^{19} sixth is 9/2. The spin of the F^{19} sixth is 7/2 or 9/2.[13] In each case, the allowable l-values are 3 or 4 and 4 or 5 depending on whether the parity of F^{19} sixth is odd or even. In our results, the fits of $|j_l|^2$ to the experimental results in the small angles (first maximum) are obtained equally well for $l=3$, 4 and 5 for the case of $E_\alpha=26.7$ and 33.1 MeV. In the calculation of the energy level of F^{19}, by the intermediate $j-j$ coupling shell model[20] or by the collective model[21], this state is assigned to 9/2+. However, we could not affirm this prediction by $|j_l|^2$ fit.

(2) *The cross section*

In Fig. 3, the total cross sections σ_t for all transitions measured are plotted against (E_α in c.m.$+Q$)[*]. The data for $C^{12}(\alpha, p)N^{15}$ ground are plotted from I. Nonaka et al.[5]. The σ_t decrease generally as (E_α in c.m.$+Q$) increase, and they are same order in this energy region. On the other hand, in Fig. 2 we show the strong energy dependence of the differential cross sections at fixed angles for the reaction $N^{14}(\alpha, p)O^{17}$ and $O^{16}(\alpha, p)F^{19}$.

Table IV. $N^{14}(\alpha, p)O^{17}$.

(1) Proton group	(2) Energy level in MeV[13]	(3) l value by shell model	(4) Spin and parity[13]	(5) σ_t relative to P_0		
				$E_\alpha=26.8$ MeV	28.1 MeV	33.3 MeV
P_0	0	2	5/2+	1.0	1.0	1.0
P_1	0.871	0	1/2+	0.21	0.16	0.12
P_2	3.058	(1)	(1/2−)	0.21	0.21	—
P_3	3.846	(3)	(7/2−)	—	0.63	—

For the case of the $N^{14}(\alpha, p)O^{17}$ reaction, we obtained the cross sections for four transitions leaving O^{17} in ground, first, second, and third (only at $E_\alpha=28.1$ MeV) state. In Table IV the result for N^{14} are shown. The transitions to first and second state of O^{17} have relatively small cross sections. It is interesting to compare these results to the ones for the $O^{16}(d, p)O^{17}$ reaction. T. S. Green and R. Middleton[22] measured this (d, p) reaction at $E_d=9$ MeV. In their results, the ground and excited states at 0.87 and 3.85 MeV had large capture probabilities and reduced widths, and the level at 3.06 MeV which exhibited an isotropic angular distribution had small yield. Then, they concluded that the former two were the single particle states formed by the addition of $1d$, $2s$, and $1f$ neutrons to the O^{16} core respectively, and that the latter involved core excitation. Such a situation are not true for our results.

(3) *Reaction mechanism*

The simple calculation based on direct interaction theory are not sufficient to explain the present experimental results. Modifications of the theory are expected to make these comparison better. As we show in Fig. 2, however, the angular distribution have a strong energy dependence. Accordingly we must expect an energy dependence of the reaction mechanism. Such an energy dependence is also seen in the reaction $F^{19}(p,\alpha)O^{16}$ ground[23] in almost the same excitation energy as our reaction $O^{16}(\alpha,p)F^{19}$. As mentioned in the Introduction we showed[5] the backward peaking in the reaction $C^{12}(\alpha,p)N^{15}$ ground at excitation energies of compound nucleus 26.0–30.1 MeV.[*],[**] In this excitation region, a resonance at 26.6 MeV was found by J. P. Schiffer et al.[24] in the reaction $C^{13}(He^{3},p)N^{15}$ ground.

---

[*] (E_α in c.m.$+Q$) means the kinetic energy of the system for the final state of the reaction.

In our experimental results for the elastic and inelastic scattering of alpha particles by carbon[25], nitrogen[26], and oxygen[26] in the region of $E_{\alpha}=25-40$ MeV, we have found a strong energy dependence of the angular distributions for the reactions.

From these experimental results it may be reasonable to think that there are some effects of the compound process for the (α,p) reaction of light nuclei in intermediate energy region.

At any rate more experimental and theoretical work is needed to study the reaction mechanism of the (α,p) reaction.

Acknowledgement

The author wishes to express his thanks to Professor I. Nonaka for his valuable suggestions and encouragement, and Drs. J. Sanada, T. Mikumo, and S. Okai for their valuable suggestions and discussions. He also thanks the cyclotron crew and members of the electronic division for their constant cooperation, and Miss. A. Adati for calculations of theoretical angular distributions. His thanks are also due to Messrs. I. Umeda, T. Tabata and S. Hitaka for their cooperative efforts throughout this work.

References

1) R. M. Eisberg, G. Igo and H. E. Wegner: Phys. Rev. **100** (1955) 1309.
2) C. E. Hunting and N. S. Wall: Phys. Rev. **108** (1957) 901 (L) and ibid **115** (1959) 956.
3) P. von Hermann and G. F. Pieper: Phys. Rev. **105** (1957) 1556.
4) G. F. Pieper and N. P. Heydenburg: Phys. Rev. **111** (1958) 264.
5) I. Nonaka et al.: J. Phys. Soc. Japan **14** (1959) 1260.
6) S. T. Butler: Phys. Rev. **106** (1957) 272.
7) S. T. Butler, N. Austern and C. Pearson: Phys. Rev. **112** (1958) 1227.
8) S. T. Butler and O. Hittmair: *Nuclear Stripping Reactions* (John Wiley and Sons, Inc., New York, 1957).
9) E. M. Henley: Nuclear Phys. **13** (1959) 317.
10) S. Kikuchi et al.: J. Phys. Soc. Japan **15** (1960) 41.
11) N. S. Wall: Rev. Sci. Instr. **24** (1953) 1146.
12) W. A. Aron et al.: USAEC Report AECU 663 (1949) (unpublished).
13) F. Ajzenberg—Selove and T. Lauritsen: Nuclar Phys. **11** (1959) 1.
14) P. M. Endt and C. M. Braams: Rev. Mod. Phys. **29** (1957) 683.
15) H. Yamaguchi et al.: INSJ-35 (1960), Inst. of Nuclear Study, Univ. of Tokyo (unpublished).
16) G. E. Owen and L. Madansky: Phys. Rev. **105** (1957) 1766.
17) B. Zeidman and J. L. Yntema: Nuclear Phys. **12** (1959) 298.
18) S. Hinds and R. Middleton: Proc. Phys. Soc. London **A**, **74** (1959) 196.
19) A. I. Yavin and G. W. Farwell: Nuclear Phys. **12** (1959) 1.
20) J. P. Elliott and B. H. Flowers: Proc. Roy. Soc. London **A**, **229** (1955) 536.
21) E. B. Paul: Phil. Mag. **2** (1957) 311. G. Rakavy: Nuclear Phys. **4** (1957) 375.
22) T. S. Green and R. Middleton: Proc. Phys. Soc. London **A**, **69** (1956) 28.
23) H. Ogata: J. Phys. Soc. Japan **14** (1959) 707.
24) J. P. Schiffer et al.: Phys. Rev. **104** (1956) 1064.
25) T. Mikumo et al.: J. Phys. Soc, Japan **15** (1960) 1158. T. Mikumo: to be published.
26) I. Nonaka et al.: to be published.
27) J. R. Priest et al.: Phys. Rev. **119** (1960) 1301.
28) E. E. Carroll, Jr., and W. E. Stephens: Phys. Rev. **118** (1960) 1256.
29) P. R. Klein et al.: Nuclear Phys, **16** (1960) 374.

---

[*] Recently J. R. Priest et al.[27] measured the angular distributions for $C^{12}(\alpha,p)N^{15}$ at 16.1-19.0 MeV and $F^{19}(\alpha,p)Ne^{22}$ at 18.9 MeV and also showed results similar to ours for the reaction $C^{12}(\alpha,p)N^{15}$. They found a resonance of $C^{12}(\alpha,p)N^{15}$ ground at about $E_{\alpha}=17.5$ MeV in excitation curve at 31.8° (lab), and at this energy (corresponding to 20.3 MeV excitation of O^{16}) there is a peak[28] of the total γ-absorption in O^{16}.

[**] P. R. Klein et al.[29] reported the angular distributions for $Li^{6}(\alpha,p)Be^{9}$ and $Li^{7}(\alpha,p)Be^{10}$ at $E_{\alpha}=30$ MeV and also showed backward peaking there.

JOURNAL OF THE PHYSICAL SOCIETY OF JAPAN, Vol. 16, No. 4, APRIL, 1961

Resonance Levels in the Reactions ^{28}Si(p, γ)^{29}P, ^{29}Si(p, γ)^{30}P and ^{30}Si(p, γ)^{31}P

By Haruko OHMURA[*], Hiroyasu EJIRI, Yutaka NAKAJIMA, Kinuko HORIE[†], Kiichi ETOH[**], Akiji OHUCHI[***] and Yozo NOGAMI

Department of Physics, Faculty of Science, University of Tokyo, Tokyo, Japan

(Received December 27, 1960)

The reactions ^{28}Si(p, γ)^{29}P, ^{29}Si(p, γ)^{30}P and ^{30}Si(p, γ)^{31}P have been studied in the region of proton energy from 300 kev to 1700 kev. We have found in the reaction ^{29}Si(p, γ)^{30}P two new resonances at proton energies 1307.5±3 kev and 1331.5±3 kev, and in the reaction ^{30}Si(p, γ)^{31}P nine new resonances at proton energies 1094, 1179.5, 1209-5, 1290.5, 1300, 1302.5, 1324.5, 1394.5 and 1403 kev with the errors of ±3 kev. No definite resonant level has been observed in the reaction ^{28}Si(p, γ)^{29}P in the range of proton energy between 570 kev and 1400 kev.

§1. Introduction

The reactions ^{28}Si(p, γ)^{29}P, ^{29}Si(p, γ)^{30}P and ^{30}Si(p, γ)^{31}P have been investigated by a number of authors[1-12] using natural and enriched silicon targets measuring gamma rays and positron activities produced in the target.

For the reaction ^{28}Si(p, γ)^{29}P, no resonant level was found by Tsytko et al.[3] from 500 kev to 1000 kev of proton energy. Olness et al.[12] also reported that the capture cross section for ^{28}Si(p, γ)^{29}P had shown no evidence for a level reported on the basis of (d, n) and (p, p) reactions at excitation energy of about 3.7 Mev.[13,14,15] Considering the correspondence between excited states in mirror nuclei, ^{29}P and ^{29}Si, based on the charge symmetry hypothesis of the nuclear force, several resonant levels should be expected for proton capture by ^{28}Si in the region of proton energy below 1650 kev. In Fig. 1 the known level schemes of ^{29}P and ^{29}Si are shown.

Detailed studies on the resonant levels in the reaction ^{30}Si(p, γ)^{31}P have been reported by many authors, especially by Broude et al.[7] and Antuf'ev et al.[10] in the range of proton energy from 500 kev to 1000 kev, while for the proton energy between 1000 kev and 1400 keV, no resonance has been reported.

We have investigated the reactions ^{28}Si(p, γ)^{29}P, ^{29}Si(p, γ)^{30}P and ^{30}Si(p, γ)^{31}P in the region of proton energy between 300 kev and 1700 kev using isotopically enriched thin targets. This paper presents the results of the studies on the excitation functions of those reactions and on the resonant levels in each phosphor isotopes.

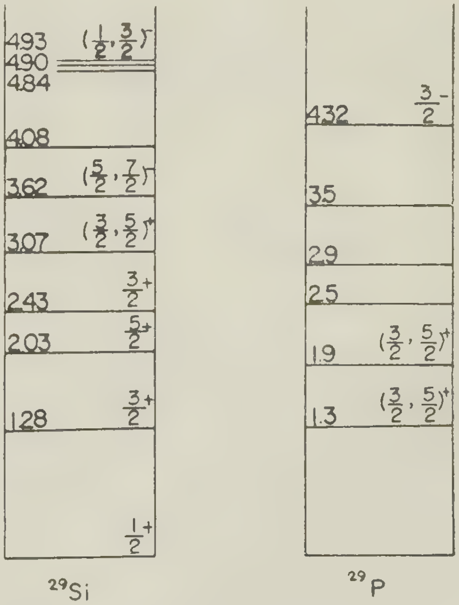
493
$(\frac{1}{2},\frac{3}{2})^-$
490
484
408
362
$(\frac{5}{2},\frac{7}{2})^-$
307
$(\frac{3}{2},\frac{5}{2})^+$
243
$\frac{3}{2}^+$
203
$\frac{5}{2}^+$
128
$\frac{3}{2}^+$
$\frac{1}{2}^+$
^{29}Si
432
$\frac{3}{2}^-$
35
29
25
1.9
$(\frac{3}{2},\frac{5}{2})^+$
1.3
$(\frac{3}{2},\frac{5}{2})^+$
^{29}P

Fig. 1. Level schemes of ^{29}P and ^{29}Si.

§2. Experimental Procedures and Results

The University of Tokyo electrostatic generator provided a proton beam of up to 4 μa in the range of proton energy from 300 kev to 1410 kev. For higher energy protons, J.A.E.R.I. electrostatic generator was used. Above 570 kev in proton energy the H^+ beam was used, while for below energies the H_2^+ beam was also employed. The proton beam energy was analyzed with a magnetic analyzer. Its magnetic field was measured by nuclear magnetic resonance method and was calibrated by referring to the 990.8 keV resonance in the reaction ^{27}Al(p, γ)^{28}Si. The errors in proton energies are estimated to be less than 3 kev.

---

[*] Present Adress: Dept. of Phys., Washington University, St Louis, Mo., U.S.A.

[**] Present Adress: Nippon Atomic Industry Group, Co., Ltd., Yurakucho, Chiyodaku, Tokyo, Japan.

[***] Present Adress: Mitsubishi Atomic Power Industries Incorporated, Otemachi, Chiyodaku, Tokyo, Japan.

[†] Radioisotopes Research Laboratory, University of Tokyo, Tokyo, Japan.

Thin targets enriched in each stable silicon isotope ^{28}Si, ^{29}Si and ^{30}Si, deposited on Ta plates, were obtained by electromagnetic separation at the University of Kyoto. The target chamber is made of 1 mm thick brass wall equipped with two windows of thin mica foils (0.7 mm and 0.14 mm of thickness) for positron detection.

Gamma rays from the target were detected by sodium iodide crystal scintillation counters and analyzed with a twenty-channel pulse height analyzer. To measure positron activities, a Geiger-Müller counter with a mica window of 1.9 mg/cm^2 thick was used.

A. Reaction ^{28}Si(p, γ)^{29}P

The excitation function of the reaction ^{28}Si(p, γ)^{29}P was obtained for the proton energy from 1300 kev to 1700 kev with a proton beam from J.A.E.R.I. electrostatic accelerator. As gamma ray detectors, use was made of 2″ dia.×2″ and 1½″ dia.×1″ sodium iodide crystals, each coupled to 6292 photomultiplier tube. A broad resonance was observed at proton energy 1650 kev, in agreement with the reports by Newton[6] and Olness et al.[12]

The excitation function in the range of proton energy from 570 kev to 1400 kev was observed using a proton beam obtained from the University of Tokyo electrostatic accelerator, and no definite resonant level was found. In this case, a 5″ dia.×4″ sodium iodide crystal attached to a 6099 (B) photomultiplier tube was also used to detect the high energy gamma rays as well as a 2″ dia.×2″ sodium iodide crystal.

There are some evidences for existence of excited levels in ^{29}P in the region of excitation energy 3.4∼3.7 Mev. Calvert et al.[14] and Macefield and Towle[15] reported a level at 3.5 MeV of excitation energy in ^{29}P in the reaction ^{28}Si(d, n)^{29}P. In the elastic scattering of protons by silicon, a resonance may have been observed at proton energy of 1 Mev[13] (3.7 Mev in ^{29}P excitation energy). Corresponding to such excited levels, some resonances might be anticipated in the reaction ^{28}Si(p, γ)^{29}P for the proton energy from 700 kev to 1200 kev. We tried more precise experiment on the excitation function using another type of target chamber. For the detection of gamma rays, we used 4″×4″ and 3″×3″ cylindrical sodium iodide crystals attached to a 6099 (B) photomultiplier tube and a 6363 photomultiplier tube respectively. The target chamber and scintillation counter arrangement is illustrated in Fig. 2. The result of this experiment showed no distinct resonance. Assuming total width Γ_t of the resonant level to be much smaller than the target thickness (about 3 kev for protons of 1 Mev), an upper limit of 5 $\times 10^{-3}$ ev may be set to the value $(2J+1)\Gamma_p\Gamma_\gamma/\Gamma_t$ for the resonant levels in the range of proton energy from 700 kev to 1200 kev.

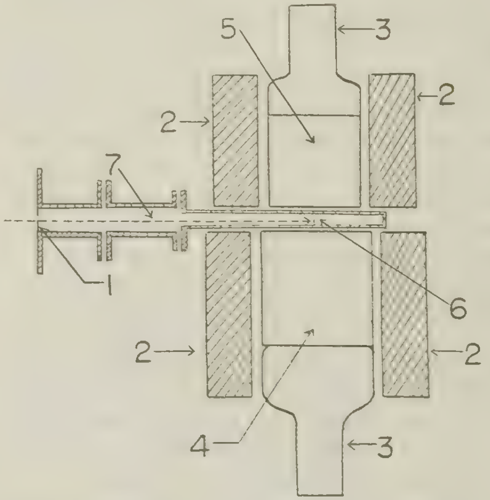

Fig. 2. Schematic view of the target chamber and the detectors.

1. Beam defining slit. 2. Lead shield. 3. Photomultiplier. 4. 4″ dia.×4″ NaI(Tl) crystal. 5. 3″ dia.×3″ NaI(Tl) crystal. 6. Target. 7. Proton beam.

B. Reaction ^{29}Si(p, γ)^{30}P

The excitation function of the reaction ^{29}Si(p, γ)^{30}P was measured for the proton energy from 300 kev to 1410 kev, recording low energy gamma rays with a 2″ dia.×2″ sodium iodide crystal and higher energy gamma rays with a 5″ dia.×4″ sodium iodide crystal. Resonances were observed at proton energies 326, 415, 698, 730, 917.5 and 958.5 kev with the errors of ±3 kev, and they agree well with the results reported by previous investigators.[4,5,8,11] In addition to these, new resonances were found at proton energies 1307.5±3 kev and 1331.5±3 kev. The excitation function of the $^{29}Si(p,\gamma)^{30}P(\beta^+)^{30}Si$ was also observed by an activation method in the region of proton energy from 900 kev to 970 kev with a Geiger-Müller counter detecting 2.5 min. positron activities produced in the target. Yield curves of gamma rays above 1.2 Mev detected in the 2″ dia.×2″ sodium iodide crystal scintillation counter and positrons from the reaction $^{29}Si(p,\gamma)^{30}P$ are shown in Fig. 3 and Fig. 4.

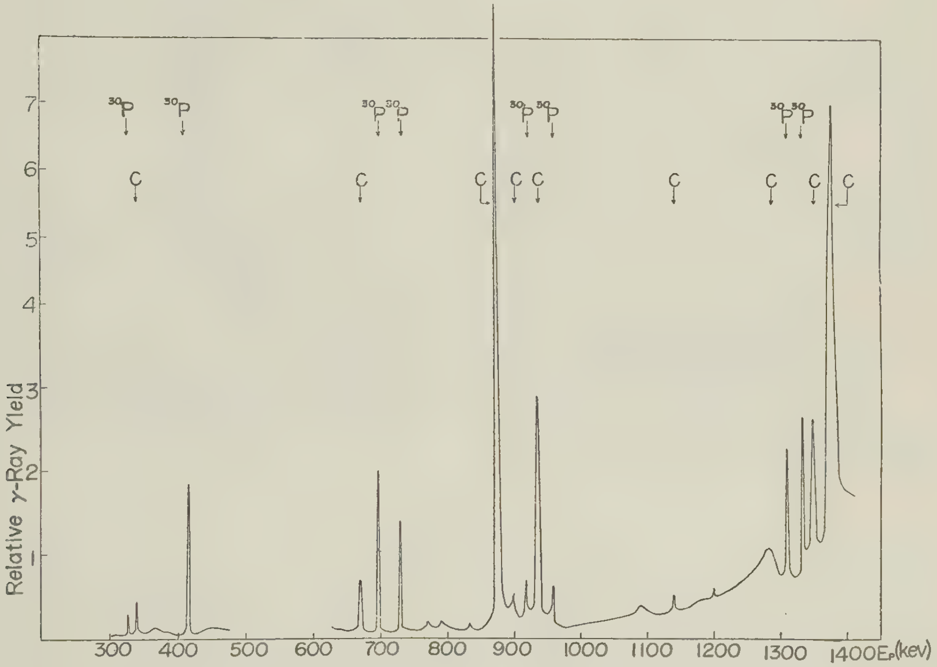

Fig. 3. Excitation function for gamma rays above 1.2 MeV from $^{29}Si(p,\gamma)^{30}P$. Background has been subtracted.
C: γ rays from ^{19}F contamination.

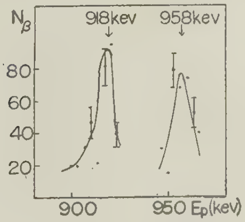

Fig. 4. Yield curve for positrons in the reaction $^{29}Si(p,\gamma)^{30}P$. Background has been subtracted.

At each resonant energy the gamma ray spectrum was measured with a 2″ dia.×2″ sodium iodide scintillation counter and the results, together with the relative yield of the gamma rays in the targets of different isotopic abundances, were used to assign the resonance to proper isotope. We also observed the decays of positron and annihilation gamma activities with a Geiger-Müller counter at several resonant level for the identification of the reaction.

C. Reaction $^{30}Si(p,\gamma)^{31}P$

The reaction $^{30}Si(p,\gamma)^{31}P$ was investigated with the same detector arrangement as in the case of the reaction $^{29}Si(p,\gamma)^{30}P$ for the range of proton energy, 500 kev to 1410 kev. Resonances were observed at 501, 620, 670, 759, 776, 835.5, 945, 961.5, 982 and 986.5 kev in proton energy with the errors of ±3 kev, showing good correspondences with previous reports.[3,7,9,10] Above 1000 kev nine unreported resonances were observed at proton energies 1094, 1179.5, 1209.5, 1290.5, 1300, 1302.5, 1324.5, 1394.5 and 1403 kev with the errors of ±3 kev, which are considered as resonances in the reaction $^{30}Si(p,\gamma)^{31}P$ from the observed

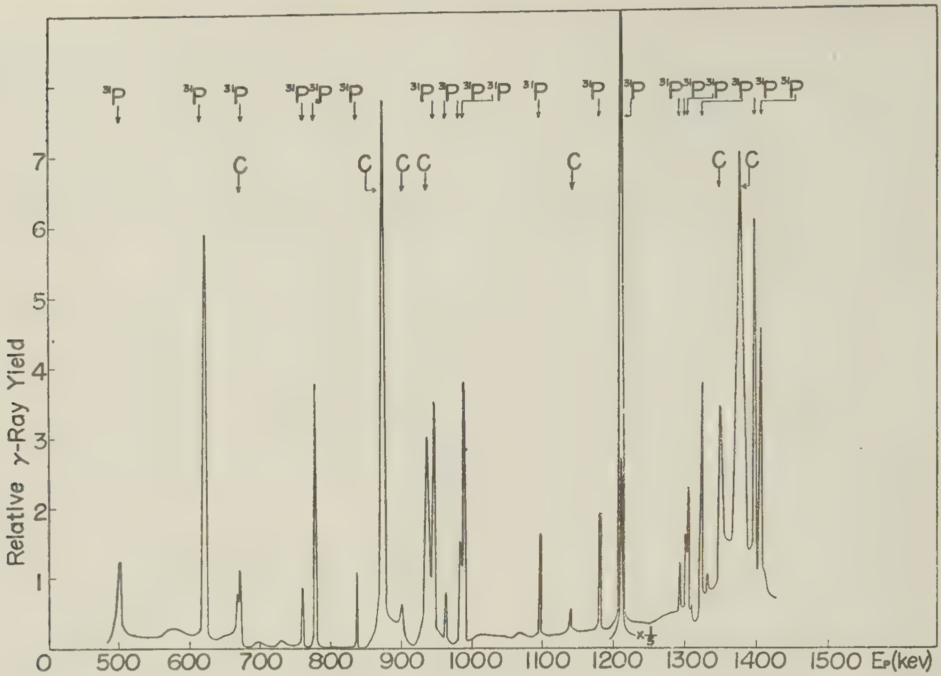

Fig. 5. Excitation function for gamma rays above 1.2 MeV from ^{30}Si(p, γ)^{31}P. Background has been subtracted.
C: γ ray from ^{19}F contamination.

gamma ray spectra and by comparing the relative yield of gamma rays from the targets with different isotopic abundances. In Fig. 5 is shown the excitation function obtained by measuring gamma rays above 1.2 Mev in a 2″ dia. × 2″ sodium iodide scintillation counter.

§ 3. Discussions

The broad resonance observed at the proton energy 1650 kev in the reaction ^{28}Si(p, γ)^{29}P may be considered to be the analog state of 4.93 Mev excited state in the mirror nucleus ^{29}Si. This 1650 kev resonant level was suggested to be a $2p\frac{3}{2}$ single particle-like state from the result of elastic scattering experiments[16]. Studies on the gamma rays emitted from this resonant level would be of interest as to the properties of this level and low lying excited levels in ^{29}P.

Any other resonances corresponding to the excited states in ^{29}Si were not observed in the present experiment on the reaction ^{28}Si(p, γ)^{29}P for the proton energy between 570 kev and 1400 kev, while in this region of proton energy, some excited levels in ^{29}P were observed in the reaction ^{28}Si(d, n)^{29}P.[14,15] Supposing that the excited state at 3.49 Mev observed in the reaction ^{28}Si(d, n)^{29}P[15] is the single particle-like $1f\frac{7}{2}$ level corresponding to the 3.62 Mev excited level in ^{29}Si and that the low lying $\frac{5}{2}^{+}$ excited state has the character of collective excitation, the gamma ray transition probability between these two levels would be highly reduced from that of the electric dipole transition between single particle excited states, and the value $(2J+1)\Gamma_{\gamma}\Gamma_{p}/\Gamma_{t}$ might be very small.

For the levels in ^{29}Si between 3.62 Mev and 4.93 Mev, the characters of the excited levels are not well known, therefore it seems to be difficult to deduce a conclusion on the existence of the corresponding excited levels in ^{29}P from the present (p, γ) experiments. Studies on the reaction ^{32}S(p, α)^{29}P are under progress as well as the experiments on gamma rays from 1650 kev resonant level in order to investigate the structure of the excited states in ^{29}P.

As for the newly observed levels in the reaction ^{29}Si(p, γ)^{30}P, the gamma ray spectra show that from the 1307.5 kev resonant level a strong transition occurs to the first excited state (T=1) of ^{30}P and the 1331.5 kev resonant level decays mainly to the ground state (T=0).

In order to study the characters of the

resonant levels and low lying excited levels in ^{30}P and ^{31}P, we are now undertaking the experiments on the gamma rays emitted from new resonant levels found in the reaction ^{29}Si$(p, \gamma)^{30}$P and ^{30}Si$(p, \gamma)^{31}$P.

Acknowledgements

The authors would like to express their cordial thanks to the staffs of Van de Graff group of the Japan atomic Energy Research Institute for their cooperation. They are also very grateful to the isotope separator group of the University of Kyoto for their kind assistance.

References

1) M. R. Seiler, J. N. Cooper, and J. C. Harris: Phys. Rev. **99** (1955) 340.
2) S. Milani, J. N. Cooper, and J. C. Harris: Phys. Rev. **99** (1955) 645.
3) S. P. Tsytko and Iu. P. Antuf'ev: Sov. Phys. JETP. **3** (1956) 993.
4) C. Broude, L. L. Green, J. C. Willmott, and J. J. Singh: Phys. Rev. **101** (1956) 1052. Physica. **22** (1956) 1139 (A).
5) P. M. Endt, J. C. Kluyver, and C. van der Leun: Phys. Rev. **95** (1954) 580.
6) P. M. Endt and C. M. Braams: Rev. Mod. Phys. **29** (1957) 711.
7) C. Broude, L. L. Green, and J. C. Willmott: Proc. Phys. Soc. London. **72** (1958) 1097; **72** (1958) 1115.
8) C. van der Leun and P. M. Endt: Phys. Rev. **110** (1958) 96.
9) L. Simons: Nuclear Phys. **10** (1959) 215.
10) Iu. P. Antuf'ev, A. K. Val'ter, V. Iu. Gonchar, E. G. Kopanets, A. N. L'vov, P. M. Tutakin, and S. P. Tsytko: *Nuclear Reactions in low and intermediate energies.* (Academy of Science Press, Moscow, 1957) 294p.
11) J. J. Singh: Phys. Rev. **115** (1959) 445.
12) J. W. Olness and J. L. Parker: Bull. Am. Phys. Soc. Ser. **II, 5** (1960) 56.
13) S. Rubin, L. E. Bailey, and T. O. Passell: Phys. Rev. **114** (1959) 1110.
14) J. M. Calvert, A. A. Jaffe, and E. E. Maslin: Proc. Phys. Soc. London. **A70** (1957) 78.
15) B. E. F. Macefield and J. H. Towle: Proc. Phys. Soc. London. **76** (1960) 56.
16) J. Vorona, J. W. Olness, W. Haeberli and H. W. Lewis: Phys. Rev. **116** (1959) 1563.

Journal of the Physical Society of Japan, Vol. 16, No. 4, April, 1961

The Reaction $Mg^{25}(d, p)Mg^{26}$ in the Energy Range of Deuterons from 1.5 MeV to 3.0 MeV

By Naoyuki Takano

Department of Physics, Kyusyu University, Fukuoka, Japan

(Received, January 6, 1961)

Angular distributions and excitation functions of protons from the reaction $Mg^{25}(d, p)Mg^{26}$ leading to the 1.83- and 2.97-MeV state of Mg^{26}, have been investigated in the deuteron energy range from 1.55- to 3.00-MeV. The yield of the protons leading to the ground state were so small that this group was not measured. The results of angular distributions were compared with the deuteron stripping theory, and a qualitative agreement for the second excited state group at the deuteron energies above 2.5 MeV, was obtained in the forward directions, but not for the first excited state group and also in the backward directions for each groups.

The angular distributions of the first excited state group at the deuteron energies above 2.44 MeV, could be fitted to Bhatia's formula with two l_n-values of 0 and 2. Both angular distributions include considerably isotropic part, and show a competition between the deuteron stripping process and the compound nucleus formation. Also, the results of excitation functions for total cross section were compared with the statistical theory and a fairly good agreement was obtained with the interaction radius of $(1.21+1.3\cdot A^{1/3})\times10^{-13}$ cm. Furthermore, a considerably small yield of this reaction seems to show that Coulomb effects play an important role in this lower energy range.

§1. Introduction

An investigation of the reaction $Mg^{25}(d, p)$-Mg^{26} leading to the low-lying state of Mg^{26} had been made by a few authors[1,2,3]. Nevertheless, angular distributions of these proton groups were measured only at the deuteron energy of 8.0 MeV in the forward directions[1]. These results were compared with Butler's theory for the deuteron stripping reaction and a good agreement, in general, was obtained with Bhatia's formula with the interaction radius of $(1.7+1.22\cdot A^{1/3})\times10^{-13}$ cm.

For the first excited state group, a considerably better agreement was obtained with the superposition of two angular distributions corresponding to two l_n-values of 0 and 2. This state also had been investigated using a magnetic analyser and nuclear emulsion[2], and found to be not a doublet but a single state.

Furthermore, theoretical analysis for this group had been made by a few authors[4,5]. They explained this angular distribution with a configuration mixing of $s_{1/2}$ and $d_{3/2}$ level of Mg^{26} in nuclear shell model, and also estimated the mixing ratio of $s_{1/2}$ to $d_{3/2}$ level of Mg^{26}, and deformation parameter using the data at the deuteron energy of 8.0 MeV[1]. In the case where the bombarding energies are higher than the Coulomb potential, angular distributions of the protons from (d, p) reaction in the forward direction, can usually be fitted to the deuteron stripping theory[6] which is based on the Born approximation. But in such a low energy range as in this experiment, the Born approximation may not be applicable. Although it may be difficult to obtain a good agreement between theoretical results and experimental, we carried out the present experiment in order to investigate how the anomalous angular distribution of the 1.83 MeV state proton group would behave in the lower energy range of deuteron, and to obtain some information for the reaction mechanism and the structure of the nucleide Mg^{26}, from angular distributions and excitation functions.

§2. Apparatus and Experimental Procedures

The deuteron beam used in this experiment, was produced by the Van de Graff accelerator of Kyusyu University, whose accelerating voltage was calibrated with resonances of the gamma-ray from the reaction $F^{19}(p, \alpha\gamma)O^{16*}$. The deuteron beam deflected by 45° with a beam analyzing magnet, after passing through a tantalium slit of 1 mm in width located at a distance of 47 cm from the target and another silver slit of 4 mm in diameter located at a distance of 20 cm from the target, entered into the scattering chamber. The enriched $Mg^{25}O$ target was set in such a way that the target plane made 45° with respect to the deuteron beam at the center of the scattering chamber. And then the beam was collected in the Faraday cup located at a distance of 12 cm from the center of the scattering chamber.

The target was prepared by depositing a suspension of MgO powder in alcohol on the silver backing foil of 2.0 mg/cm² and evaporating the alcohol in vacuum. A sample of MgO enriched in Mg^{25} was supplied by the mass separator at the I.N.S. of University of Tokyo. Isotopic content of Mg^{25} was estimated to be about 90%, by comparing the proton yield with that of natural MgO target. A considerably uniform target of about 1.2 mg/cm² in thickness was prepared by this method. This target thickness corresponds to the energy loss of about 150 kev at the deuteron energy of 2.5 MeV⁷⁾.

Scattering chamber, scintillation counter and other electronic circuits used in this experiment, were quite similar to those used in the study of other (d, p) reactions in our laboratory⁸⁾ and are described here briefly. Scattering chamber has an inner diameter of 23 cm and height of 10 cm, having 20 ports in its side wall. The side ports of 6 mm in aperture, bored at intervals of 15°, from 15° to 165° on one half of the side wall of the scattering chamber and from 22.5° to 157.5° on the other half. These ports also play a role as the defining slit to scintillation detector. The solid angle, subtended by these defining slits for the target was estimated to be 2.17 $\times 10^{-3}$ steradian in the average. Angular resolution of these slits was estimated to be ±1.5°.

The beam current, collected by a Faraday cup, was measured by a current integrator of Higinbotham type. But in the case of the measurement of excitation curve, this Farady cup was replaced by another one, which has an inner diameter of 3 cm and length of 5 cm, and located at a distance of 5 cm from the target surface, in order to avoid the effect of scattering of deuteron beam by the target and its backing foil. Furthermore, for the

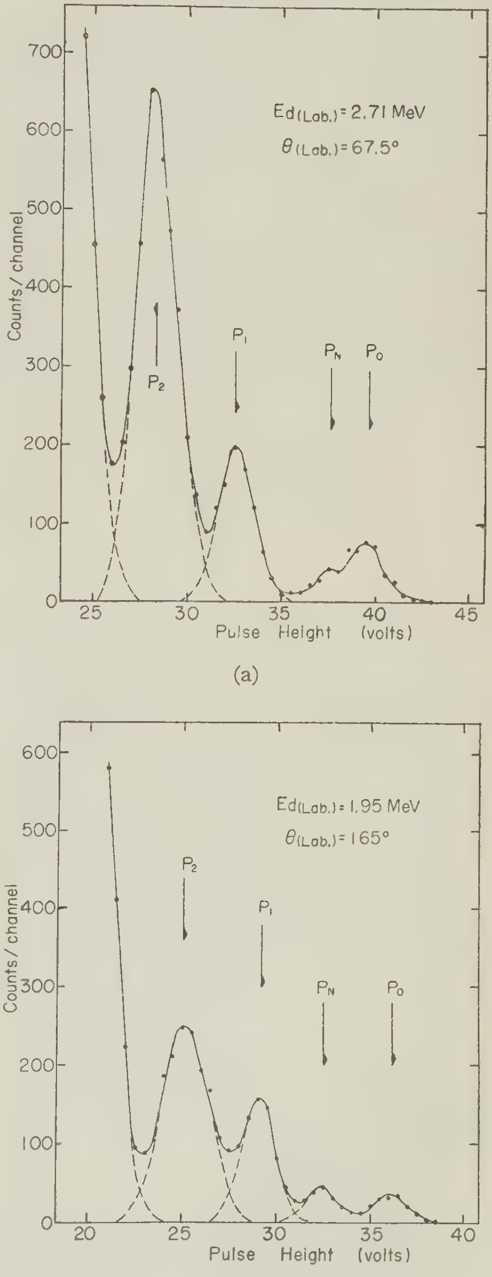

(a)

(b)

Fig. 1. Pulse height spectra from the scintillation counter of the protons emitted by the $Mg^{25}(d, p)Mg^{26}$ reaction, obtained at 67.5° (Lab. system) with $E_d = 2.71$ MeV (a) and at 165° (Lab. system) with $E_d = 1.95$ MeV (b).

measurement of the yield at 0° to the deuteron beam, this Faraday cup was taken away and the same defining slit as that used at another side ports of the scattering chamber was set at the direction of 0°.

The protons emitted by this reaction were measured with a scintillation counter which consisted of CsI(T*l*) of 1 mm in thickness and E.M.I. 6097 photomultiplier. Furthermore, another CsI(T*l*) scintillation counter was fixed to the side port of the scattering chamber making an angle of 82.5° to the deuteron beam in the opposite side to the proton detector, and was used as a monitor counter. The bias of the monitor counter was set to count only the pulse due to the protons of higher energies than those leading to the second excited state of Mg^{26}. The signal pulses, after passing through a cathode follower and an A-1 type linear amplifier, were fed to a 20 channel differential pulse height analyser. The typical pulse height spectra from the scintillation counter obtained in this experiment are shown in Fig. 1.

Assignment of the peaks in these spectra was carried out by reaction kinematics. The first, third and fourth peaks correspond to the protons from the reaction $Mg^{25}(d, p)Mg^{26}$ leading to the ground, the first excited and the second excited state of Mg^{26}, respectively. The second peak corresponds to the protons from the $N^{14}(d, p)N^{15}$ ground state reaction, produced by the nitrogen contamination in the MgO target. Aluminium absorber of $20\,\mu$ in thickness was inserted in front of the scintillation counter in the forward directions, preventing the alpha particles emitted by the reaction $N^{14}(d, \alpha)C^{12}$ from entering the proton detector. And also, in measuring the yields at 0° direction to the deuteron beam, another silver absorber of 40 mg/cm² in thickness was inserted in front of the defining slit at 0° direction, in order to stop the direct deuteron beam.

Background runs were carried out at the several deuteron energies with a silver foil of 2.0 mg/cm² in place of the target. Although the background from the other element was so small that the subtraction of the background was easy, the resolution of each proton groups was not complete, and then the area of each peaks in pulse height spectrum was obtained from the estimated peak, as is shown by dotted curves in Fig. 1.

An uncertainty arising from the group separation was estimated to be 5% at maximum. Excitation curves of the protons from this reaction leading to the 1.83-, and 2.97-MeV state of Mg^{26} were also measured with the CsI(T*l*) scintillation counter, fixed at the 75° side port of the scattering chamber and with the aforementioned Faraday cup and are shown in Fig. 6.

§ 3. Results and Discussions

Angular distributions of the protons from the reaction $Mg^{25}(d, p)Mg^{26}$ leading to the first and second excited state of Mg^{26} at the deuteron energies of 1.65-, 1.95-, 2.20-, 2.44-, 2.71-, and 2.99-MeV are shown in Figs. 2 to 5. Indicated errors at each points include the

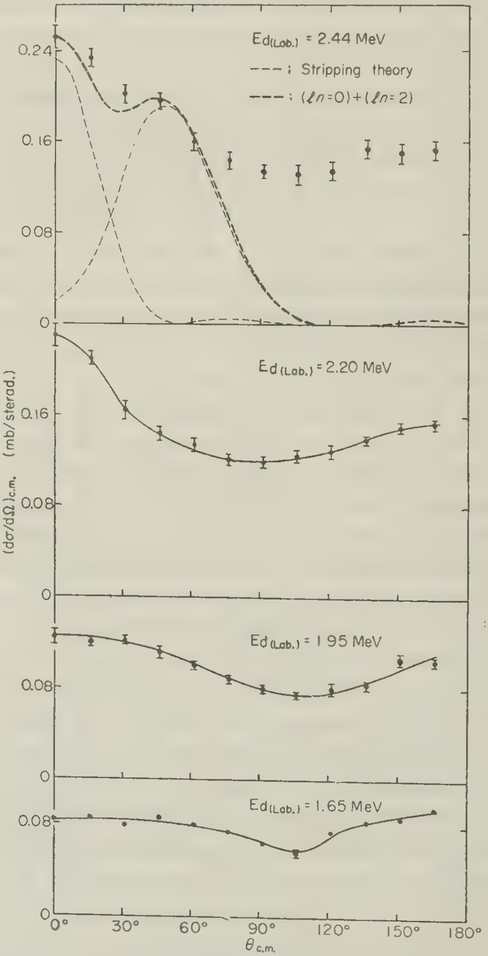

Fig. 2. Angular distribution of the proton from the $Mg^{25}(d, p)Mg^{26}$ first excited state reaction at the deuteron energies of 2.44-, 2.20-, 1.95-, and 1.65-MeV.

over all uncertainty due to the experimental procedures described above. Statistical error amounts to 3% at maximum. Absolute cross section was estimated from the results obtained by measurement of excitation curves at 75° direction. The scale of the ordinate in these figures has an uncertainty of about 40%, which is mainly due to the non-uniformity of the thickness of target.

Although the shape of angular distributions for the first excited state group varies gradually with the deuteron energy, it shows nearly isotropic pattern for the deuteron energies below 2 MeV and shows a characteristic forward peak of the deuteron stripping reaction above this energy, and also two peaks corresponding to the orbital angular momentum $l_n=0$ and $l_n=2$, above the deuteron energies of 2.44 MeV. The second peak at about 50°, in the center-of-mass system, becomes predominant with the increasing deuteron energy.

The dotted curve indicated in Figs. 2 and 3 are theoretical curves calculated from Bhatia's formula[6] with interaction radius of 5.0×10^{-13} cm and $l_n=0$ and 2. Each theoretical curve is normalized to the peak value of experimental curve. The fat dotted curves in these figures indicate the superposition of these two theoretical curves. A qualitative agreement was obtained with Bhatia's formula in the forward direction at the deuteron energy of 2.99 MeV, but not in the backward directions. The shape of the angular distribution for the deuteron energy of 2.99 MeV is similar to that obtained by Holt *et al.*[1] at 8.0 MeV. Furthermore, it must be noted that the ratio of these two peaks is in agreement

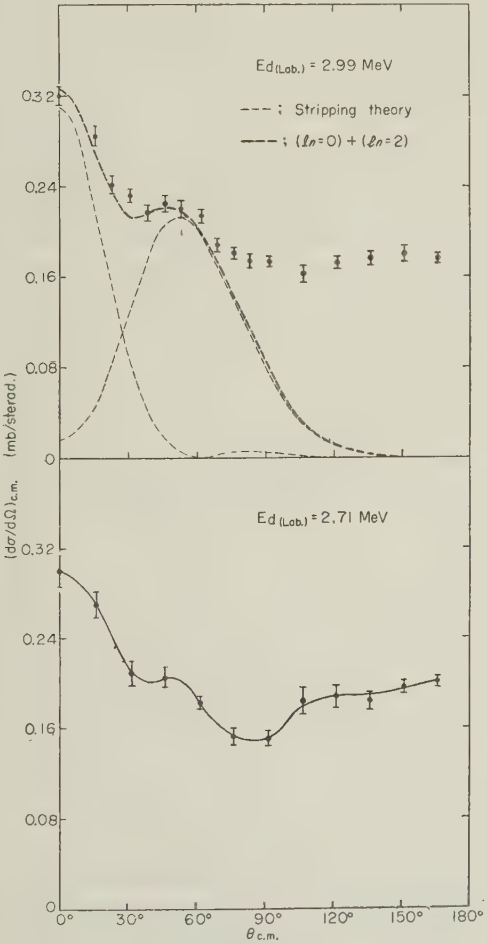

Fig. 3. Angular distribution of the proton from the $Mg^{25}(d, p)Mg^{26}$ first excited state reaction at the deuteron energies of 2.71-, and 2.99- MeV.

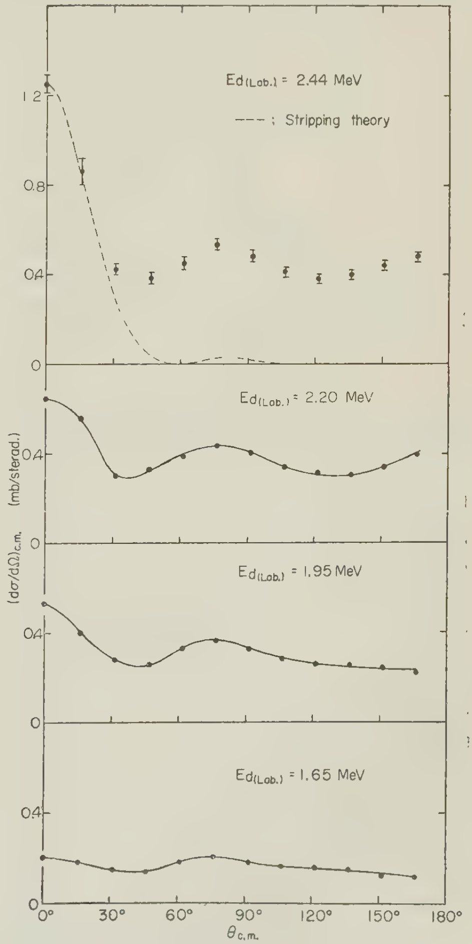

Fig. 4. Angular distribution of the proton from the $Mg^{25}(d, p)Mg^{26}$ second excited state reaction at the deuteron energies of 2.44-, 2.20-, 1.95-, and 1.65- MeV.

with their result within the experimental error. Although these evidences may not be incompatible with those predicted by the nuclear shell model and spheroidal model[4,5] a remarkably small absolute cross section and a feature at the backward directions will not be explained by a direct interaction theory. It seems probable that the compound nucleus formation contributes mainly to this group at these lower deuteron energies.

Angular distributions of the protons from the reaction leading to the second excited state of Mg^{26} are shown in Figs. 4 and 5.

The dotted curve indicated in Figs. 4 and 5 are theoretical curves calculated from Bhatia's formula with interaction radius of 6.0×10^{-13} cm and $l_n=0$. Theoretical curves is normalized to the experimental curves at 0° direction.

A qualitative agreement is obtained with Bhatia's formula in the forward directions, but not in the backward directions and in the energy range of deuteron below 2.2 MeV. The characteristic forward peak of the deuteron stripping reaction, in general, becomes remarkable with the increasing deuteron energy, but angular distributions have rather large isotropic part.

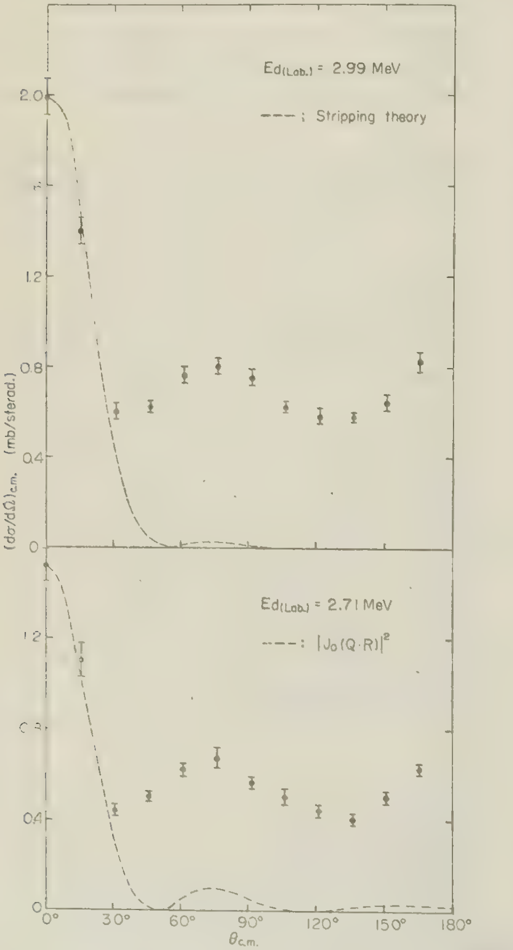

Fig. 5. Angular distribution of the proton from the $Mg^{25}(d, p)Mg^{26}$ second excited state reaction at the deuteron energies of 2.71-, and 2.99- MeV.

The shape of the angular distribution for the second excited state group, in general, shows the oscillatory pattern, as is expressed by

$$|J_0(Q\cdot R)|^2$$

where J_0 is the spherical Bessel function of order 0. R is interaction radius and Q is the magnitude of the momentum transfer, given by

$$Q=\left|K_p-\frac{1}{2}K_d\right|$$

K_p and K_d are the wave vectors for the outgoing proton and the incident deuteron, respectively.

The dotted curve at the deuteron energy of 2.71 MeV is theoretical curve calculated from the above described formula with interaction radius of 7.0×10^{-13} cm. The rise in the backward direction also may be affected by other direct process, such as heavy particle stripping reaction.

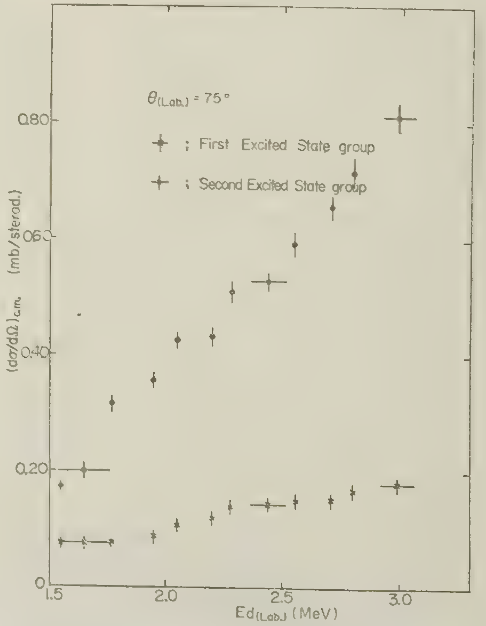

Fig. 6. Excitation curve for the $Mg^{25}(d, p)Mg^{26}$ reaction at $\theta_{(Lab.)}=75°$.

Excitation curves of the protons from the reaction leading to the first and second excited state of Mg^{26} were measured at 75° to the deuteron beam in the energy range of deuteron from 1.55- to 3.00-MeV, and are shown in Fig. 6.

Furthermore, the total cross sections for the first and second excited state groups, obtained from the angular distributions in Figs. 2 to 5 and the excitation curves shown in Fig. 6, were plotted against deuteron energy in the center-of-mass system and are shown in Fig. 7.

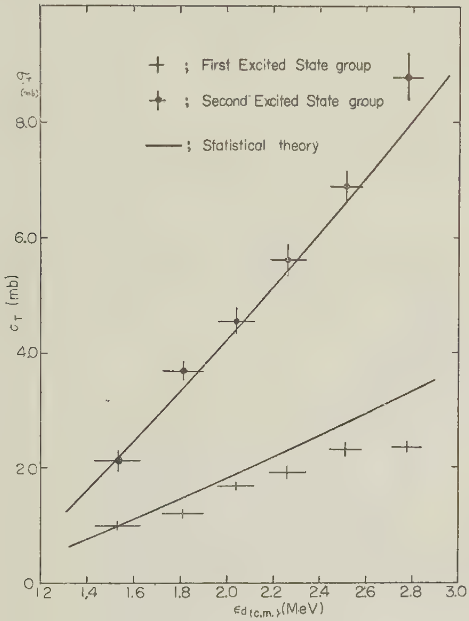

Fig. 7. Excitation function for the $Mg^{25}(d, p)Mg^{26}$ reaction. The full curves show theoretical excitation curve calculated by statistical theory.

From the shape of angular distribution described above, it seems probable that the cross section of the compound nucleus formation considerably contributes to the excitation curve in lower energy range. Therefore, the general this behavior of the total cross section will be shown by the formula of Blatt and Weisskopf for the statistical theory. The full curves are theoretical curves calculated by the formula of Blatt and Weisskopf[9], and are normalized at the deuteron energy of 1.53 MeV (center-of-mass system) to the experimental point of each group. A qualitative agreement for the second excited state group was obtained with the interaction radius of $(1.21+1.3\cdot A^{1/3})$ 10^{-13} cm, but not for the first excited state group. These two excitation functions vary monotonously with the increasing deuteron energy and show no resonance like feature owing to the statistical assumption for the level of compound nucleus.

Furthermore, the ratios of a total cross section for the second excited state group to that for the first excited state group were plotted against the incident energies in the center-of-mass system and are shown in Fig. 8.

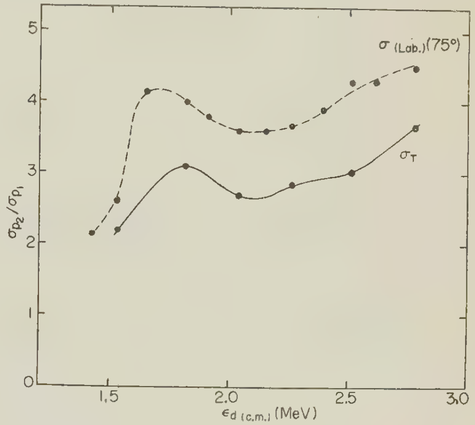

Fig. 8. The ratios of a total cross section for the second excited state group to that for the first excited state group. The dotted curve shown in figure, is the result obtained at 75° direction.

A peak which is unexpected from the statistical theory appears at the deuteron energy of 1.8 MeV in the center-of-mass system. This phenomenon will not be explained by the competition of the branching to these two states of residual nucleus, because the spin and parity of these two states of Mg^{26} both have been found to be $2+$[10]. Taking account of the evidence that the angular distributions of the second excited state group have rather simple form but those of the first excited state group have a complicated form, the first excited state of Mg^{26} seems to have a complex structure, probably of two or more particles excitation. In the case where the incident deuteron are considerably affected by Coulomb potential, direct process may not be a predominant process, but plays only a part of the nuclear reaction.

The author wishes to express his cordial thanks to Prof. S. Morita for his constant encouragement and valuable discussion, and to all other staffs of nuclear laboratory of Kyusyu University for their helpful discussion throughout the present work. He also wishes to express his thanks to the mass separator crew of I.N.S. of University of Tokyo for the preparation of target.

References

1) J. R. Holt, and T. N. Marsham: Proc. Phys. Soc. London **66A** (1953) 258.
2) P. M. Endt, J. W. Haffner, and D. M. Van Patter: Phys. Rev. **86** (1952) 518.
3) J. Ambrosen: Nature **169** (1952) 408.
4) S. Okai, and M. Sano: Progr. Theor. Phys. **15** (1957) 203.
5) J. Sawicky: Nuclear Physics **6** (1958) 575.
6) A. B. Bhatia, K. Huang, R. Huby, and H. O. Newns: Phil. Mag. **43** (1952) 485.
7) S. K. Allison, and S. D. Warshaw: Rev. Mod, Phys, **28** (1953) 779.
8) N. Kawai: (To be published in J. Phys. Soc. Japan.) T. Ishimatsu *et al*: (To be published in J. Phys. Soc. Japan.)
9) J. M. Blatt, and V. F. Weisskopf: *Theoretical Nuclear Physics* (John Wiely and Sons. Inc., New York, 1952) 340p.
10) P. M. Endt, and C. M. Braams: Rev. Mod. Phys. **29** (1957) 683.

JOURNAL OF THE PHYSICAL SOCIETY OF JAPAN, Vol. 16, No. 4, APRIL, 1961

The Structure of Extensive Air Showers Near the Axes

By Shūji FUKUI

Physical Institute, Nagoya University, Nagoya, Japan

(Received August 23, 1960)

The lateral distribution of electrons and also of the mean energy of extensive air showers (EAS) were observed with a detector array composed of 14 scintillation detectors, 15 Čerenkov detectors, an arrival direction detector and a neon hodoscope. In particular the precise structure near the axes could be detected by the neon hodoscope. Each EAS was specified by various parameters, that is, the lateral distributions of electrons and energy flow, μ-mesons, and nuclear active component, and it was found that the structure of the EAS thus observed are different from case to case.

Near the axis the lateral distributions of electrons are rather flat and varied gradually from $r^{-0.4}$ to $r^{-1.0}$ according to the distance from the axis, up to a few meters. The slope of the distribution between 5 m–50 m distance from the shower axis is well fitted by the predicted one from the Nishimura-Kamata theory, adjusting the value of the s-parameter. The observed lateral distribution of mean energy of electrons is expressed by $E=7.5\times10^8\times r^{-0.7\pm0.1}$ ev in the region from the axis to 7 m.

The probable influences on the structure near the axis are discussed.

§1. Introduction

An extensive air shower, abbreviated as EAS, is a phenomenon which is caused by the interaction of a primary cosmic ray particle of ultra-high energy at high altitude in the atmosphere and in which a larger number of particles are accumulated by many successive interactions of the particles in the atmosphere. Numerous experimental studies of EAS carried out up to the present have dealt with the average structure of EAS. The results thus far obtained have been summarlized in several review articles.[1]

It has recently been noticed that the structure of individual EAS fluctuating about the average structure exhibits very important information about the development of EAS. As has been pointed out by several authors,[2] the fluctuation of the depth in the atmosphere of the very early stages of the development may be significant. Besides this, the fluctuation of the development of the nuclear cascade which is caused by the inelasticity of the interaction and the nature of the secondary particles may also play an important role.[3] Therefore, EAS observed at any altitude, even assuming a constant primary energy, show a different structure from case to case owing to the effects of these fluctuations. It is necessary to measure all the characteristics, i.e. the various parameters, of EAS in as much detail and as comprehensively as possible for the purpose of studying ultra-high energy interactions. In this manner the Moscow group has been studying EAS vigorously. Also an air shower project has been founded at the Institute for Nuclear Study, University of Tokyo.

In this report the structures of EAS near their axes are discussed. The lateral distributions of particles were measured by the array of 14 plastic scintillation detectors and the neon hodoscope.* The latter instrument is the same device as the one known as the Conversi counter.[4] The neon hodoscope covers an area of 7 m² and can give precise information about the particle distributions and the position of the shower axis. The energies of the shower particles were measured by Čerenkov detectors. The lateral distributions of electrons and also of mean energies of particles were well determined by means of these detectors and compared with the theoretical ones predicted by the Nishimura-Kamata function.[5] It is noticeable that the observed structure of EAS near the axis is different from case to case and that the variety is not caused by statistical fluctuation but is due to the essential character of EAS. It is emphasized that the individual character of EAS presents information about the development of EAS and the nuclear interactions. The results on the nuclear active and μ-meson components and the interpretations of EAS concerning all of the components will be discussed elsewhere.[6]

§ 2. Experimental

A. General

Observations of EAS were performed with two arrangements. The general features of EAS were examined with Arrangement A and then the fine structure of EAS, especially near the axes, was studied with Arrangement B. As the details of detectors used, with the exception of the neon hodoscope will be reported elsewhere,[7] they are only briefly described here.

a. *Arrangement A*

The experimental arrangement of detectors is schematically illustrated in Fig. 1 a. The n-detector is used to measure the particle density and is a plastic scintillator whose effective area and thickness are 1 m² and 4.5 cm, respectively. 14 detectors are used. The e-detector is used to measure the energy flow carried by particles in an unit area. 9 e-detectors are lead-glass Čerenkov detectors 53 cm in diameter and 30 cm thick (12 radiation length equivalent). 6 e-detectors are $Pb(NO_3)_2$ solution (30%) Čerenkov detectors. The container of the solution is 56 cm in diameter and 80 cm in thickness (6 r.l. equivalent).[8] Each e-detector is surrounded by barytes concrete of 30 cm width in order to compensate the number of particles which scatter out from the detector by those which scatter in from the concrete. Five 0.25 m² plastic scintillation detectors placed at the vertices of a pentahedron are used to determine the arrival direction of the shower by means of fast timing circuit.[9] 4 plastic scintillation detectors each of area 2 m² placed 30 m.w.e. underground and a hodoscope chamber of 1 m² under a concrete block of 20 r.l. are employed to detect μ-mesons of energies of >5 Bev and of >1 Bev, respectively.[10] 2 "transition chambers", which are five layer sandwiches of iron sheets and plastic scintillators give information concerning the nucleon components.[11] The neon hodoscope whose details are presented in the following section is used to observe the lateral distribution of electrons.

The apparatus was triggered by 4-fold coincidences of the n-detectors with the added requirement that more than 7 particles must traverse each detector. This was accomplished by suitable bias to give the proper triggering level. A coincidence between n_6, n_7, n_8, and n_9 was mainly employed, but other coincidences, that is, n_1–n_2–n_3–n_4 and n_8–n_9–n_{10}–n_{12} were used for short periods. The size (the total number of particles) of observed showers were in the range of 10^4 to 10^7.

---

* Prof. J. Nishimura proposed at the symposium held in February of 1956 the utility of this device as a density detector which would display the character of EAS by permitting observation of the precise particle distribution near the shower axis.

b. *Arrangement B*

To obtain the precise structure of EAS near their axes Arrangement B was used and is shown in Fig. 1 b. The locations of the n-detectors are the same as in Arrangement A, except that 4 detectors at the central part of the detector array were rearranged. 10 lead glass e-detectors without concrete compensators are placed in a group under the neon hodoscope. 3 fast timing detectors which detect the arrival direction of the shower are placed at vertices of a triangle. The other detectors, excepting the neon hodoscope, were not operated. 4-fold coincidences between n_6, n_7, n_8, and n_9 triggered the apparatus.

B. Neon Hodoscope

a. *Construction*

The neon hodoscope which covers an area of 7 m^2 is the same device as the hodoscope chamber originally developed by Conversi.[4] These instruments work on the following principles. Glass tubes filled with a mixture of neon and argon are placed between parallel conducting plates, and an intense pulsed

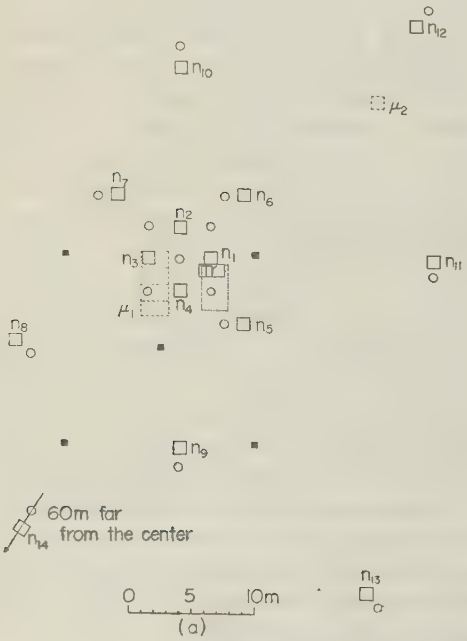

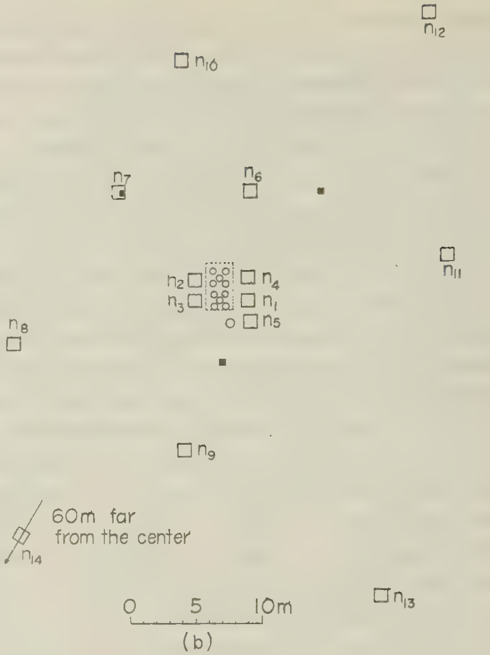

Fig. 1. Experimental arrangement of detectors. a) is employed in Arrangement A and b) in Arrangement B.

□: The plastic scintillators whose effective area and thickness are 1 m^2 and 4.5 cm respectively.

⌣ : The lead-glass or Pb(NO$_3$)$_2$ solution Čerenkov detectors. The size of the lead-glass is 53 cm in diameter and 30 cm in thickness. The container of the solution is 56 cm in diameter and 80 cm in thickness. In Arrangement A each detector is surrounded with barytes concrete of 30 cm width. In Arrangement B, only the lead-glass detectors were used without the concrete compensators.

■: 0.25 m^2 plastic scintillators which were set at the vertices of a pentahedron in Arrangement A and a triangle in Arrangement B. They are used to determine the arrival direction of the shower.

⬚: The neon hodoscope which is placed on the floor 2.5 m above the level of the other detectors. It covers an area of 7 m^2 and contains 5000 tubes. The details are shown in Fig. 2.

μ_1: 4 plastic scintillators each of area of 2 m^2 placed 30 m.w.e. underground.

μ_2: The hodoscope chamber of 1 m^2 placed under the concrete block. μ_1 and μ_2 are used to detect μ-mesons of energies of >5 Bev and >1 Bev respectively.

Tr: 2 transition chambers consisting of five layer sandwiches of iron slabs and plastic scintillators.

electric field is applied across the tube immediately after the passage of ionizing particles. Then the tubes which are traversed by particles become luminous, and the others do not.

Our purpose is to determine the particle density, not the trajectory, so tubes are placed on a horizontal plane. As shown in Fig. 2, tubes are arranged in a lattice, the total number being five thousand. Each tube, 5 cm long and 2 cm in a diameter, is filled with a mixture of (Ne+0.1%A) at a pressure of 30 cm Hg. The pre-treatment of tubes before filling with the gas followed the method described in a previous paper.[12] The operating circuit of the neon hodoscope is shown schematically in Fig. 3. The peak voltage gradient and the time constant of the voltage pulse are fixed at 13.5 kV/2.3 cm and 1 μsec, respectively. The time delay between the passage of the shower particles and the application of the voltage pulse is 1.5 μsec. Under this operating condition the efficiency of detecting particles is estimated to be almost 100%. Light from tubes which are lit is reflected by a mirror and photographed on 35 mm film. Pictures were taken on Fuji SSS film at f/1.8.

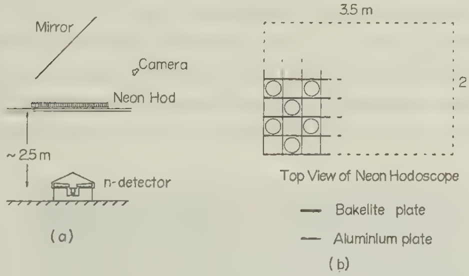

Fig. 2. Arrangement of the neon hodoscope shown schematically. Each tube, 5 cm long and 2 cm in diameter, is filled with a mixture of (Ne+0.1% A) at a pressure of 30 cm Hg. Tubes are set in the lattices and cover an area of 7 m². The instrument including its photographic system is placed in a dark room which serves as well for the electrical shielding. The hodoscope is placed 2.5 m above the level of the other detectors.

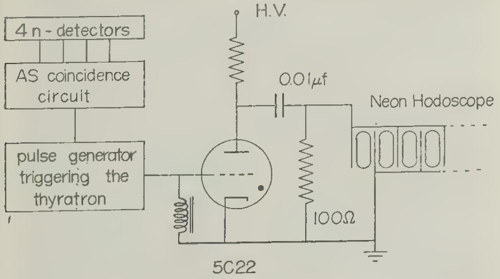

Fig. 3. High voltage pulse generator. The voltage of H. V. is fixed at 13.5 kV. The time constant of the voltage pulse is 1 μ sec. The time delay between the passage of the shower particles and the application of the voltage pulse is 1.5 μ sec.

This instrument can be easily constructed. It is very stable and also has a long operating life. Actually it was confirmed that the detection efficiency does not vary during a few tens of thousands of times of operation.

b. *Estimation of electron density*

The density of electrons is estimated from the number of lighted tubes by the following method. The total area of the neon hodoscope is divided into 28 sections, each of area of 50×50 cm². Assuming that all electrons pass through the tubes parallel to the shower axis and the particle density is uniform throughout the area of each section, the number of lighted tubes, m, is given by

$$m = T(1-\exp(-\Delta s)) + T(1-\exp(-\Delta s'))\exp(-\Delta(s-s')),$$

where T is the total number of tubes in the section, Δ the electron density per unit area in the section, s the effective area of each tube, and s' the effective area for one particle to cross two adjacent tubes. As each tube has a cylindrical shape and stands vertically, the effective area through which particles can pass varies with the inclination of the direction of the particle's path to the axis of the tube. From previous experiment[13] it is confirmed that the detection efficiency of tubes in the present arrangement is not dependent upon the region where a particle crosses. So the effective area, s, is a function only of the inclination of the shower axis and can be easily estimated. When the path of particle is inclined markedly, one particle can cross two adjacent tubes and then two tubes are lighted. The effective area, s', varies with the zenith and the azimuth angles of the shower axis. For the shower for which the axis is inclined at less than 25°, the values of s' are zero or negligibly small. The second term of the above expression has a significant value only when the particle density and the inclination of the axis are large.

From the present arrangement of tubes the details of the local concentration of particles can not be studied. That is, the special resolution is not sufficiently good to analyze the concentration of particles within an area of 10 cm × 10 cm. It is noted from the above expression that the number of lighted tubes is almost saturated when electrons with density of more than 5,000 particles per m^2 strike the neon hodoscope.

§ 3. Results

A. Lateral distribution of electrons

a. *The region from a few m to 80 m from the axis*

From the amplitude of the pulse from each scintillation detector (n-detector), which was recorded on film, the number of particles striking the detector was determined. Pulses from single pentrating cosmic ray particles were used for calibration. It should be noted that the pulse from a scintillation detector depends on the number of ionizing particles falling on it, their energies, and any secondary events produced in it. On the other hand, the neon hodoscope is expected to give a nearly true density of electrons, because the tubes are made of very thin glass and the process of discharges does not depend on the energy of the particles. In the first step of analyzing the data, we used the raw number determined as indicated above, not correcting for the effects of secondary processes and variation in particle energies. The location of the shower axis was determined by using a special-purpose computer whose operation is based on the assumption that the lateral distribution of densities given by the scintillation detectors can be smoothly fitted to some curve representing the function r^{-n}, where r is the distance from the axis. After determining the location of the axis, the distance of each detector from the axis was measured and then the distribution of particle densities was plotted against the distance.

In the region beyond a few m to 80 m from the axis, each lateral distribution of particle density thus obtained is in good agreement with that predicted by the N. K. theory[5], assigning a certain value of the s-parameter, which has an inaccuracy of ±0.2 due to the statistical fluctuation of the electron numbers fell in the detectors and due to the accuracy in determining the location of the shower axis. Each observed lateral distribution can be expressed by one value of s which denotes now only the slope of the distribution rather than its original meaning. Then the size of each EAS can be determined by comparing the observed distribution with that of the N.K. theory, assuming that the lateral distribution of particle density at far distances beyond the observed points can be also given by the N.K. theory with the same value of s and that the N.K. theory keeps its validity in that region.

The two values of observed density given by the scintillation detector and by the neon hodoscope can be compared for various distances from the axis. The ratio of these as a function of the distance from the axis is given in Fig. 4. It is found that the ratios do not depend on the shower sizes or the values of s within the present accuracy. The points in Fig. 4 represent the averaged values.

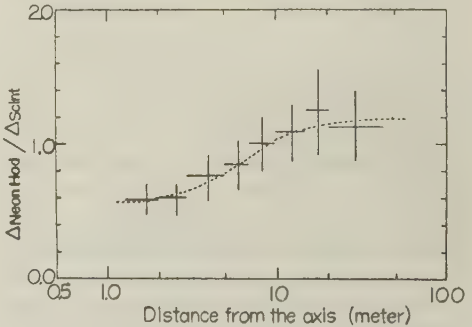

Fig. 4. Comparison between particle densities obtaided by scintillation detectors and by the neon hodoscope as a function of the distance from the shower axis.

Assuming the neon hodoscope data to be correct, Fig. 4 can be used to correct the n-detector data, and thus arrive at corrected lateral distributions. If we use the N.K. function assigning a certain value of the s-parameter to express the lateral distribution of particle density, the corrected value of s for each EAS is about 0.2 greater than the value of s previously obtained. Hereafter in this report, the corrected values of s are used to express the slope of the lateral distribution of particle density.

b. *The region very close to the axis*

When the axis of EAS passed through or very close to the neon hodoscope, the location of the axis and the lateral distribution of electrons could be precisely determined by the spatial distribution of tubes discharged in the neon hodoscope. Two typical examples of photographs are illustrated in Fig. 5. Fig. 6 shows an example of analysis of an EAS derived with the aid of the neon hodoscope. As seen in the figure, the lateral distribution obtained by the neon hodoscope is smoothly connected with the corrected distribution given by the scintillation detectors and changes its slope gradually with the distance from its axis. When the axis of an EAS of size more than a few $\times 10^6$ strikes the neon hodoscope, the number of tubes discharged is almost saturated and it becomes impossible to determined the density of electrons. In most cases the lateral distributions were examined as closed to the axis as 30 cm.

For convenience to discuss the lateral distributions, most of the observed EAS are separated in two groups in terms of the value of s, which is determined as described in the previous section; that is, $s<1.2$ and $s\geq 1.2$. The composite distributions of these two groups, normalized to the shower size of 10^5, are plotted in Fig. 7 a and Fig. 7 b. It is remarkable that only four showers among eighty whose axes passed through the neon hodoscope present very steep distributions, characterized by $s=0.6$, as shown in Fig. 7 c, where the sizes are normalized to $N=10^5$. The averaged distributions of these three groups are illustrated together in Fig. 8.

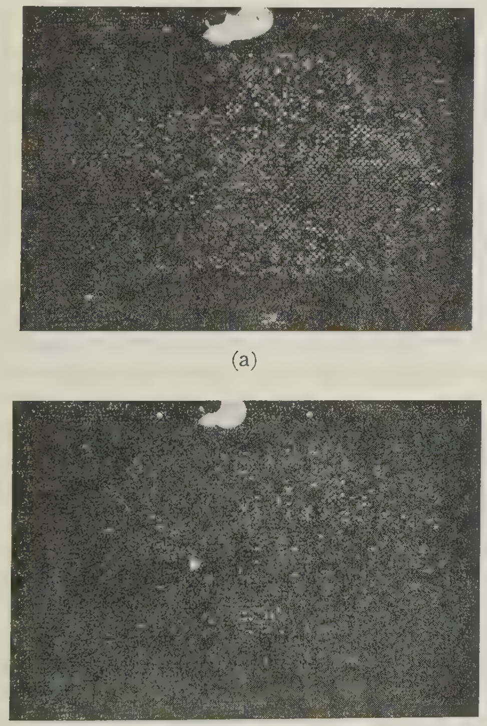
(a)

(b)

Fig. 5 Two typical examples of photographs taken by the neon hydroscope. a) shower size $=1\times 10^5$ and $s=0.8$. b) shower size$=0.8\times 10^5$ and $s=1.2$.

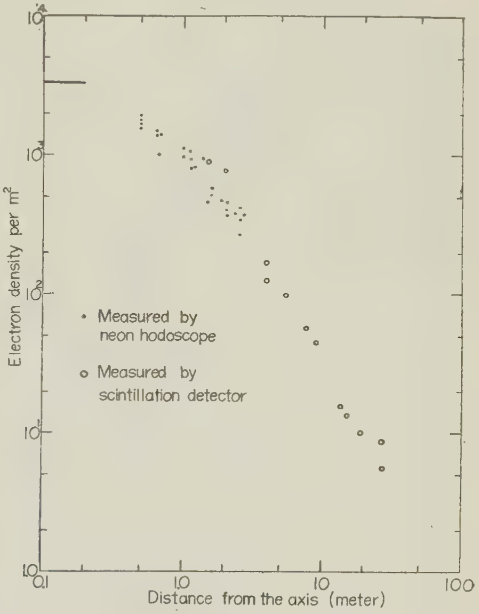

Fig. 6. A typical example of the lateral distribution of electrons, for the shower of Fig. 5. a.

It is noted from the figure that i) the distributions near the axis are rather flat except in the case of the four showers of Fig. 7 c, ii) the character of the distribution for the showers with $s<1.2$ varies gradually from $r^{-0.6}$ to r^{-1} with the distance from the axis and the distribution is represented by $s=1.0\pm 0.2$ in the region beyond a few m from the axis, iii) the character of the distribution for the showers with $1.2\leq s$ varies from $r^{-0.4}$ to $r^{-0.7}$ near the axis and is fitted to $s=1.4\pm 0.2$ in the region beyond a few m from the axis, and iv) the character of distribution of the four showers with steep distributions is nearly equal to r^{-1} near the axis and is well represeted by $s=0.6\pm 0.1$.

B. The lateral distribution of the mean energy of shower particles

The pulses from e-detectors were recorded by photography of the oscilloscopes in the same way as in the case of the n-detectors. The almost of energy dissipated in the detector was calibrated by comparison with pulses from single penetrating μ-mesons. In order to obtain the mean energy of electrons near the shower axis the following procedures were carried out. As the location and the arrival direction of the axis are already determined, the lateral distribution of particles of each EAS given by the neon hodoscope can be traced on the places where the e-detectors are set. The spatial distribution of particles probably does not change from the level of the neon hodoscope to that of the e-detectors, because the only material between the two levels is wood of a few cm thickness. Correcting the effective area of the e-detector by the direction cosine of the shower axis, the dissipated energy divided by the number of particles gives the mean energy of electrons incident on each detector.

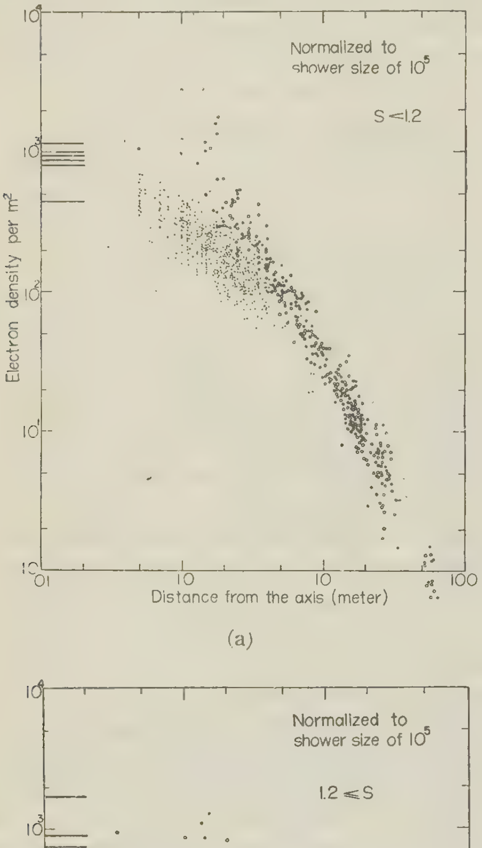

(a)

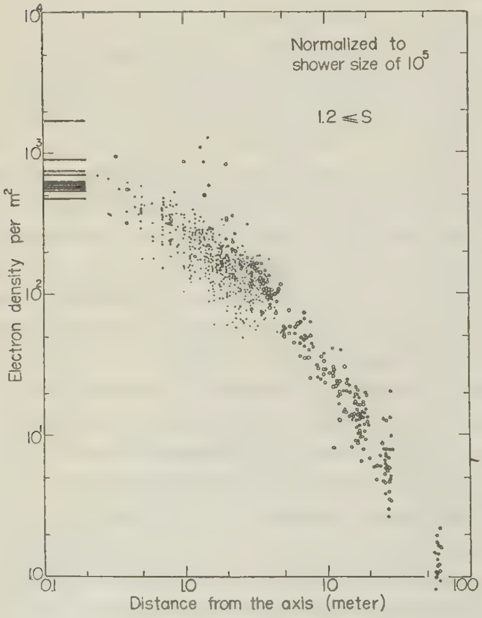

(b)

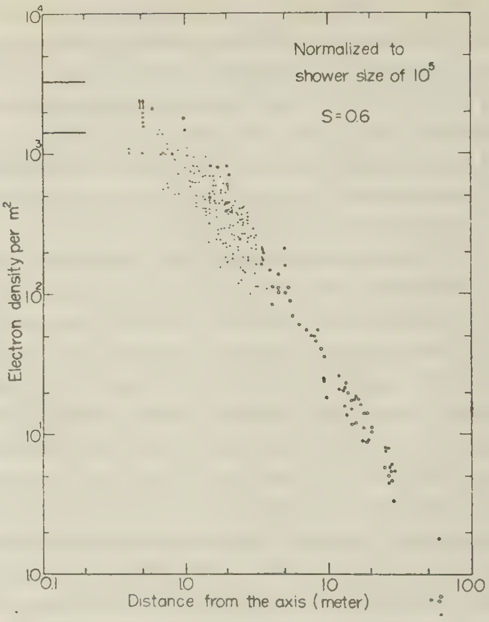

(c)

Fig. 7. The accumulated lateral distributions of electrons, normalized to a shower sizes of 10^5. a) is the case of showers with $s<1.2$, b) showers with $1.2 \leq s$ and c) the showers with $s=0.6$.

The values of the mean energies observed in individual EAS show large fluctuations. However, assuming that the density of particles in each EAS and also the process of the energy loss of particles in the Čerenkov detector show Poissonian fluctuation, the observed fluctuation of the mean energy shows no indication beyond what can be explained by the fluctuation of the Poissonian distributions. No dependence of the lateral distribution of the mean energy on the shower size or on the value of the *s*-parameter was found within the present accuracy. The composite lateral distributions are shown in Fig. 9. The theoretical curve from the N.K. lateral distribution function for mean energy and the experimental results of Dmitriev et al.[14] and Vernov et al.[15] are shown in the same figure. From the observed distributions the lateral distribution of mean energy in the region from the axis to 7 m is expressed by $E=7.5\times10^8\times r^{-0.7\pm0.1}$ ev, where r is measured in meters. The present distribution is in good agreement with the results of Vernov et al.

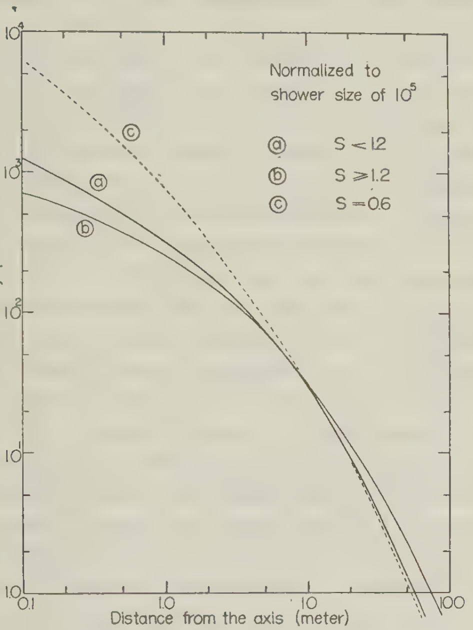

Fig. 8. The averaged lateral distributions of electrons which are shown in Fig. 7. Curve a is the lateral distribution corresponding to Fig. 7a. The r-dependency varies from $r^{-0.6}$ to $r^{-1.0}$ at distances from the axis up to a few meters, and s has the value 1.0 in the region beyond 5 m. Curve b corresponds to Fig. 7b. The r-dependency varies from $r^{-0.4}$ to $r^{-0.7}$ near the axis, and $s=1.4$ in the region beyond 5 m. Curve c is the one corresponding to Fig. 7c. The r-dependency is nearly equal to $r^{-1.0}$ near the axis, and $s=0.6$ in the region beyond 5 m.

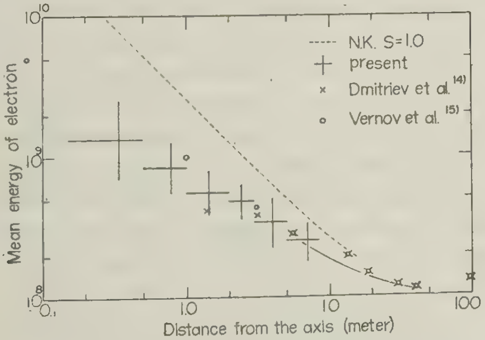

Fig. 9. The lateral distribution of the mean energy of electrons. It is well expressed by $E=7.5\times10^8\times r^{-0.7\pm0.1}$ ev in the region from the axis to 7 m.

§ 4. Discussion

A. Comparison between the density obtained by the scintillation detector and by the neon hodoscope

Concerning the particle density of EAS, the kind of detectors used must be considered. If scintillation detectors are used and the particle density is estimated by the method previously mentioned, the estimated density may not represent the correct electron density, especially near the axis, because of various phenomena caused by electrons of relatively high energy and other particles in scintillation detectors of finite thickness.[16] On the other hand, the neon hodoscope tube has a character similar to that of the G-M counter, and the accuracy of the estimation of the particle density depends only on its geometry and the trajectories of changed particles. At large distances from the axis, the paths of electrons are not strictly parallel to the axis owing to multiple scattering, and therefore the effective area of tubes may be larger than that assumed. In this case the estimated value of the particle density may be a little larger than the true value, but the correction is estimated to be not larger than 20% from the data on the lateral distribution of the mean energy.

The correction for the density observed with the scintillation detector can be made by comparison with the density obtained by the neon hodoscope as a function of the distance from the shower axis.

B. The lateral distribution of electrons

Many workers have observed EAS and discussed the lateral distribution of electrons, comparing the observed distribution with the predicted one from the theory with respect to the averaged features. It is shown from the N.K. theory that the lateral distribution of electrons can be expressed by one value of the *s*-parameter even when the electron components are initiated from many sources distributed in one dimention, namely the longitudinal direction. The lateral structure of electrons of EAS is the superposition of a large number of electron cascade showers which are produced by many sources in successive stages of the development of EAS. It is apt to be considered that the lateral distribution of electrons is expressed by some averaged structure. However, as has been pointed out by various authors[2),3)] the lateral distribution of electrons is influenced by the fluctuations in the development of EAS.

The individual lateral distribution of electrons in the region from a few meter to 80 m from the axis can be well fitted by the N.K. function, the value whose s-parameter is suitably adjusted for each EAS. Here, it must be noticed that the s-parameter is used only to express the slope of the lateral distribution of electrons observed and that the value of s has an error of ± 0.2 due to the statistical fluctuations of the particle numbers in the detectors and due to the accuracy in determining the position of the shower axis. As presented in § **3.A**, about half of the eighty showers whose axes passed through the neon hodoscope have N.K. age parameter in the range $s<1.2$ and about fourty percent of them have values in the range $1.2 \leq s$. Four of the observed showers have a steep slope, that is, $s=0.6$. The observed frequencies of EAS of different values of s may be changed by changing the triggering condition and the arrangement of the detector array.

It is remarkable that, for instance, an EAS of size 2×10^5 and its lateral distribution of electrons with $s<1.2$ can be well represented by the superposition of an EAS of size 1.5×10^5 and lateral distribution of electrons with $1.2\leq s$ and an EAS of size 4×10^4 and the lateral distribution of electrons with $s=0.6$. This example shows the possibility that, if a young shower, though its size is small, is superimposed on an old shower, it can change the apparent lateral distribution of electrons of the composite shower considerably. Taking into account this possibility, the lateral structure of EAS may be affected by the fluctuation of the survival of nuclear-active particles which have relatively high energy.

Direct measurements on the particle distribution very near the axis have been made by some workers. In the work of Hazen,[17)] performed experiments with a cloud chamber at 3000 m altitude, the density gradients within 0.5 m from axes were found to be much smaller than those predicted by the Molière theory. From observations with a large diffusion cloud chamber at sea-level, Relf[18)] concluded that the lateral structure up to 0.6 m from the axis was described by the Molière theory within Gaussian fluctuations, and that each shower, within statistical errors, consists of a single core. He observed only one event which showed a very steep distribution up to 1 m from the axis. Vernov et al.[19)] observed the core structure with a diffusion chamber of 0.6 m^2 together with ionization chamber arrays. As one can see in Fig. 7 a and Fig. 7 b the observed lateral distribution of electrons within a few meter from the axis varies gradually from r^{-1} to $r^{-0.4}$. These features depend slightly on the value of s but do not depend on the shower size. The predicted distribution from the theory can not be adopted in the region very close to the axis because the assumption made in the theory is not correct in that region.

The altitude of first nuclear interaction has a dominant effect on the lateral structure of EAS, but the change of the interaction mean free path of particles with their energy and successive interactions also have some effect. Recently it has been observed that the energy spectrum of γ-rays observed at high altitude shows a steep slope in the region beyond 10^{12} ev compared to its slope in the lower energy region.[20)] If the γ-rays are produced from the decay of π°-mesons, it is considered that the energy spectrum of secondaries at a high energy interaction may be affected by the initial energy and the interaction mean free path may also have some depedency on the particle energy. Indeed, the structure of EAS is the accumulated phenomenon, therefore the lateral distribution of electrons should be discussed considering the nuclear component, μ-meson component, and the electron mean energy which will be discussed in next section.

C. Lateral distribution of the mean energy of particles

Recently Danilova et al.[21)] and Miyake et al.[22)] observed EAS at mountain altitude with a multiplate cloud chamber, and it was observed that the lateral distribution of particles and also the development of showers in the chamber showed a large fluctuation from case to case. Vernov et al.[19),23)] observed the energy flux of the electron-photon component with ion-chamber arrays and found sharp fluctuations therein. Porter et al.[24)] observed the lateral distribution of energy flow at distances of 60–500 m from the axis using a water Čerenkov detector and concluded that the results were consistent with the theoretical distribution predicted by the N.K. function for the mean energy with $s=1.0$. Dmitriev et al.[14)] and Vernov et al.[15)] obtained the lateral distribution of the energy flux using ion-chambers. As seen in Fig. 9, their results are in an excellent agreement with the present results.

In the present experiment the amount of the energy flow estimated by the Čerenkov detector needs a correction which is found to be not very large. The thickness of the detector is not enough to absorb the entire process of the electron cascade shower carried by the high energy electron-photon component. This correction is estimated to be at most 20 to 30% when an electron of energy of more than 1 Bev strikes the detector. The correction for the contribution by the nuclear-active component is estimated using the result obtained with the transition chamber and it does not seem to exceed 20% near the axis. The fluctuation of the particle density and of the process of the energy dissipation in the detector has a large effect on the estimated value of the energy flow. Therefore, it can not be clearly determined whether or not the lateral distribution of the energy flow depends on the shower size and on the value of s-parameter.

The observed lateral distribution of the mean energy of electrons is well expressed by $E \fallingdotseq 7.5\times10^{8}\,r^{-0.7\pm0.1}$ ev within 7 m from the axis, where the distance r is measured in meters. As seen in Fig. 9, the theoretical curve predicted by the N.K. function for the mean energy with $s=1.0$ lies above the experimental points. The initial energy of the electron shower is taken to be infinite in the theory, but that of the actual shower has a finite value. Moreover it should be noted that in the estimation of the mean energy, the energy which is carried by the photons is ignored because the photons are not counted in the particle density.

Even for a composite EAS consisting of the superposition of an old shower and a young one, as discussed in § **4.B**, the energy flow is not clearly distinguished from the average value because of satistical fluctuations. In order to examine the energy flow of EAS precisely, further experimental investigations are needed.

D. Very high electron density observed by scintillation detectors near the axis

Some EAS show the feature that the electron densities estimated by scintillation detectors are three or five times of those obtained by the neon hodoscope in the region 1 m or 2 m from the axis. The discrepancy is too great to be explained by statistical fluctuation and the lateral distribution of particles of these EAS is observed to be very steep in this region. The rate of occurrence of these EAS was observed to be about 40% of the total number of EAS analyzed and to be independent of the s-value. As the amount of material between the neon hodoscope and the scintillation detectors is very small, the materialization of particles in that space should be negligible.

Therefore other possible contribution must be considered. If neutral particles produce secondary events in scintillators, they give a high amplitude of the pulse, but the tubes of the neon hodoscope are not discharged by neutral particles. At first let us assume these particles are photons. As the thickness of a scintillator is about 0.1 r.l., ten photons present an amplitude equivalent to a single electron if the photons produce electron pairs. Therefore, the number of photons required is more than 30 times the number of electrons to increase the pulse amplitude to the observed value. As a second case let us assume neutrons instead of photons. A star produced by a neutron of energy of several hundreds of Mev presents, on the average, a pulse amplitude about 50% of the amplitude produced by an electron of 100 Mev. If the stars thus produced raise the pulse amplitude to the observed value, the number of neutrons needed is several times the number of electrons. Photons and neutrons exist in relatively large number near the axis but from the data already obtained, the amount of increase of the amplitude of the pulse which could be attributed to these components is estimated to be at most several ten percent of electrons. It appears very hard to explain the above mentioned phenomenon in terms of either photons or neutrons.

If local concentrations of charged particles are superposed on the main distribution, the pulse amplitude is raised but the number of lighted tubes in the neon hodoscope can not be changed if the area of the concentration is smaller than 10 cm × 10 cm. These local concentrations, e.g., narrow showers, may be composed of groups of electrons or μ-mesons. If the nuclear interaction occurs at lower atmospheric depth, as discussed above, some of the γ-rays may produce narrow electron showers and such γ-rays will be in the region near the axis. The observed energy flow of EAS which present this phenomenon is not higher than that of other EAS within the present accuracy of estimation, though it shows slight higher value. Therefore, narrow electron showers may be excluded in explaining such phenomena, because the energy flow must be raised considerably by these electron showers.

If this concentration is compose of μ-mesons, the energy flow detected by the Čerenkov detectors is not raised greatly by these μ-mesons. But the mechanism of production of such μ-mesons comes into question. μ-mesons in EAS are considered to be produced in the early stages of development of EAS. These narrow concentrations are not readily explained in terms of μ-mesons because of the high density required unless a narrow shower of μ-mesons can be produced by a process which is unknown.

Recently, Vernov et al.[25)] observed the possible presence of collimated particle beams in the cores by means of a diffusion cloud chamber. The beams were concentrated in a circle of diameter 4 cm and the number of particles within that circle was 5 to 15. The phenomena observed by Vernov et al. may be the same as that observed by us. The lumpy distribution near the axis observed by Heineman[26)] and Davis et al.[27)] was not observed in the present experiment because of the lack of spatial resolution of the neon hodoscope. However, that kind of distribution may be partly attributed to the phenomena described above.

Acknowledgements

The author is greatly indebted to many individuals in connection with this work. In particular he wishes to thank Professor Y. Watase and Professor S. Kikuchi for their encouragement and continuous interest in this experiment and Professor J. Nishimura for his suggestion of the utility of the neon hodoscope and also for his encouragement. The author is especially indebted to Professors I. Miura, M. Oda and K. Suga and Messrs. T. Matano, G. Tanahashi and Y. Tanaka for their help in performing the experiment and for their encouragement and valuable discussions. He would like to thank other staff of the Cosmic-Ray Laboratory of INS for their help in maintenance of the apparatus and for their assistance in analyzing the data. He also wishes to thank Mr. S. Miyamoto and Mr. M. Teranaka for their assistance in preparing the neon hodoscope. Finaly the author wishes to express his thanks to Professor. M. Crouch of Case Institute of Technology, who is a staff member of the Science Office of the American Embassy in Tokyo, and Professor S. Hayakawa for their discussions and help in the preparation of this manuscript.

Addendum

After this observation the subsequent measurements of EAS have been performed with the modified detector array by the members* of INS. By the new arrangement the location of the shower axis can be determined accurately even when the axis does not strike the neon hodoscope and the lateral distribution of particles can be measured at far 200 m from the axis. The preliminary results of these subsequent measurements show that the lateral distribution of particles within 3 m from the axis fluctuates from shower to shower and that if the slope of the lateral distribution is expressed by the s-parameter of N.K. function, s is to be assigned as 0.6∼0.8 for 3 m∼30 m and $s=1.2\sim1.4$

---

* The members of INS are T. Matano, I. Miura, M. Oda, K. Suga, G. Tanahashi and Y. Tanaka.

beyond 30 m from the axis.

It may be pointed that the individuality of the structure of EAS is shown by the lateral distribution close to the axis. The discrepancy in the observed value of s for the region of a few m～several tens m may be understood by considering the accuracy of s dermined in the two different experimental arrangements. The essential parts of discussions in this report will not be changed by this discrepancy. The structure of EAS should be precisely discussed considering the inter-relations between the multi-parameters of EAS.

References

1) K. Greisen: *Progress in Cosmic Ray Physics, Vol. III,* (1956). W. Galbraith: *Extensive Air Showers (Butterworth Scientific Publications, London,* 1958). G. Cocconi: *Extensive Air Showers* (Handbuch der Physik.).
2) Kraushaar: Suppl. Nuovo Cimento **3** (1958) 649. N. L. Grigorov and V. Ia. Shestoperov: Zh. Eks. Teor. Fiz. **34** (1958) 1539. S. Miyake: Prog. Theor. Phys. **20** (1958) 844.
3) H. Messel: *Progress in Cosmic Ray Physics, Vol. II* (1954). M. Oda: Nuovo Cimento **5** (1957) 615. A. E. Cudakov, N. A. Dobrotin, N. L. Grigorov, S. N. Vernov and G. T. Zatsepin: Suppl. Nuovo Cimento **3** (1958) 737. Z. Koba: Prog. Theor. Phys. **17** (1957) 288. A. Ueda and N. Ogita: Prog. Theor. Phys. **18** (1957) 269.
4) M. Conversi and A. Gozzini: Nuovo Cimento **2** (1955) 189. M. Conversi, S. Focardi, C. Franzinetti, A. Gozzini and P. Murtas: Suppl. Nuovo Cimento, **4** (1956) 234.
5) K. Kamata and J. Nishimura: Suppl. Prog. Theor. Phys. No. 6 (1958) 93.
6) S. Fukui, H. Hasegawa, T. Matano, I. Miura, M. Oda, K. Suga, G. Tanahashi and Y. Tanaka: now in press.
7) I. Miura and K. Suga: now in press.
8) T. Matano, I. Miura, M. Oda, K. Suga, G. Tanahashi and Y. Tanaka: INS-J-9, April 10, 1958.
9) G. Tanahashi: INS-J to be published.
10) T. Matano: INS-J to be published.
11) Y. Tanaka: INS-J to be published.
12) S. Fukui and S. Miyamoto: INS-TCA **10** (1957).
13) S. Fukui and S. Miyamoto: INS-TCA **11** (1958).
14) V. A. Dmitriev, G. V. Kulikov, E. I. Massalsky and G. B. Khristiansen: Zh. Eks. Teor. Fiz. **36** (1959) 992.
15) S. N. Vernov, V. A. Dmitriev, V. I. Solobveva and G. B. Khristiansen: Zh. Eks. Teor. Fiz. **37** (1959) 1481.
16) M. H. Brennan, J. A. Lehane, J. Malos, D. D. Millar, C. S. Wallace, and M. M. Winn: Suppl. Nuovo Cimento **3** (1958) 653. C. S. Wallace: Proc. Moscow Conf. **2** (1960) 316.
17) W. E. Hazen: Phys. Rev. **85** (1952) 455.
18) K. E. Relf: Phys. Rev. **97** (1955) 172.
19) S. N. Vernov, N. N. Goryunov, G. T. Zatsepin, G. V. Kulikov, Yu. A. Nechin, Z. S. Strugalsky and G. B. Khristiansen: Zh. Eks. Teor. Fiz. **36** (1959) 669.
20) Proc. Moscow Conf. vol. 1 (1960).
21) T. V. Danilova, O. I. Dovzhenko, S. I. Nikolskii and I. V. Rakoblskaia: Zh. Esk. Teor. Fiz. **34** (1958) 541.
22) S. Miyake, K. Hinotani, I. Katsumata and T. Kaneko: J. Phys. Soc. Japan **14** (1959) 1471, and Proc. Moscow Conf. **2** (1960) 67.
23) S. N. Vernov, Ya. S. Babetsky, N. N. Goryunov, G. V. Kulikov, Yu. A. Nechin, Z. S. Strugalsky and G. B. Khristiansen: Zh. Eks. Teor. Fiz. **36** (1959) 976.
24) N. A. Porter, T. E. Cranshaw, J. F. de Beer, A. G. Parham and A. C. Sherwood: Phil. Mag. **3** (1958) 826.
25) S. N. Vernov, G. V. Kulikov, Z. S. Strugalsky and G. B. Khristiansen: Zh. Eks. Teor. Fiz. **37** (1954) 1193.
26) R. E. Heineman: Phys. Rev. **96** (1954) 161.
27) W. P. Davis, W. E. Hazen and R. E. Heineman: Nuovo Cimento **12** (1954) 233.

JOURNAL OF THE PHYSICAL SOCIETY OF JAPAN, Vol. 16, No. 4, APRIL, 1961

On the Transport Equation in Quantum Mechanics

By Lesser BLUM

Facultad de Ciencias Exactas y Naturales, Buenos Aires Argentina

(Received May 20, 1960)

By means of a time-dependent perturbation procedure similar to that developed by Prigogine, the transport equation for a particle in a Bose-Einstein medium is obtained. This equation shows also a non local character.

§ 1. Introduction

In the theory of quantum transpot processes two ways seem to be most the important in obtaining the evolution equation, namely the time coarsing, which gives the quantum mechanical version of Boltzmnn's equation (classic approximation), and the perturbation theory, which seems more appropriated for the Born approximation. (Prigogine and Ono.[1),2)])

In the present paper we shall make a derivation of the transport equation using a procedure which is very appropriated for the case of the Brownian motion of a particle in an homegoneous medium, that is to say, we take random a priori phases for the states of the medium, but not for the particle. Furthermore, we do not refer to any kind of energy spectrum, as we use the second quantization formalism.

In § 2 we describe the hamiltonian and the basic representation of the system; the Wigner function is used here, and its application to our problem is treated in § 3, the notation is that of Massignon[3)] in which a very good review on this subject is also found. In § 4 the evolution equations for the terms in the Wigner function is obtained. Finally in § 5 we get the transport equation, and some of its features are discussed.

§ 2. Hamiltonian and the Basic Representation

We may write the hamiltonian of our system as

$$H=H_0+\lambda H' \tag{2.1}$$

were we take $\lambda H'$ as the interaction of the particle with the medium λ being the coupling parameter; also we will suppose that only the binary interactions are important.

In the formalism of the second quantization we may then write

$$H'=\frac{1}{2\Omega}\sum_{\alpha\beta kl} v(\alpha kl\beta)a_\alpha{}^+a_k{}^+a_\beta a_l\delta^{Kr}(\alpha+k-l-\beta) \tag{2.2}$$

$$v(\alpha k,\, l\beta)=v(\alpha-\beta)=v^K(k-l)=\int dre^{i(r-r')(\alpha-\beta)}v(r-r'); \tag{2.3}$$

where we take the greek subindices for the states of the particles, the latin for those of the medium, Ω is the total volume of the system of and the a^+, a are usual creation destruction operators. $\delta(x)$ is the tree dimensional kroneker delta $\delta_x{}^{Kr}$, which is 1 if the argument is zero and otherwise 0, and α, β etc. are vector momenta. We shall take $\hbar=1$ for convenience. We shall also assume that the medium obeys the B. E. statistics, i.e.

$$[a_k{}^+a_l]=\delta^{Kr}(k-l) \qquad [a_k{}^+a_l{}^+]=[a_ka_l]=0 \tag{2.4}$$

also we have for our system

$$[a_\alpha{}^+a_k]=[a_k{}^+a_\alpha]=0 \tag{2.4'}$$

in the interaction representation we have

$$H(t)=e^{iH_0t}H'e^{-iH_0t} \tag{2.5}$$

so that from (2.2) and (2.5) we get

$$<n|H(t)|n'>=\frac{1}{2\Omega}\sum_{\alpha\beta ke}\delta^{Kr}(k+\alpha-l-\beta)v(k\alpha l\beta)e^{it(\varepsilon_k+\varepsilon_\alpha-\varepsilon_l-\varepsilon_\beta)}\times\langle n|a_k{}^+a_\alpha{}^+a_la_\beta|n'\rangle \tag{2.6}$$

§ 3. The Wigner Formalism

This formalism is very convenient to show the classical limit of quantum phenomena; let us take the reduced Wigner function for one particle (see for example Massignon (3) p. 213)

$$f_w(x,p)=Tr\left\{\rho,\ \int d\nu\psi^+(x-\pi\nu)\psi(x+\pi\nu)e^{-2\pi i\nu p}\right\} \tag{3.1}$$

with

$$\left.\begin{aligned}\psi^+(x-\pi\nu)&=\sum_\alpha a_\alpha{}^+\varphi_\alpha{}^*(x-\pi\nu)\\ \psi(x+\pi\nu)&=\sum_\beta a_\beta\varphi_\beta(x+\pi\nu)\end{aligned}\right\} \tag{3.2}$$

If we take the φ's as plane waves we get

$$\varphi_\alpha(x)=L^{-3/2}e^{ix\alpha}\quad(\alpha=\text{proportional to }2\pi/L) \tag{3.3}$$

so that in the representation of the occupation numbers n

$$f_w(x,\ p)=\Omega^{-1}\sum_{n,n'}\sum_{\alpha,\beta}\langle n|\rho|n'\rangle\langle n'|a_\alpha{}^+a_\beta|n\rangle e^{ix(\alpha-\beta)}\delta^{Kr}(2p-\alpha-\beta) \tag{3.4}$$

Here as we take an homogeneous medium, the matrix are assumed to be diagonal for the states of the medium, and the only non diagonal states allowed are those for the particle we are studying. We have thus

$$f_w(x,\ p)=\Omega^{-1}\sum_n\sum_{\alpha\beta}\delta^{Kr}(2p-\alpha-\beta)e^{ix(\alpha-\beta)}\langle n1_\alpha|\rho|n1_\beta\rangle \tag{3.5}$$

where 1_α and 1_β are referred to the momentum of the particle under consideration. In the above we should note that the terms in (3–5) have different volume dependence according as they are homogeneous (i.e. diagonal, $\alpha=\beta$) or inhomogeneous (i.e. non-diagonal $\alpha\neq\beta$).

However, only for simplicity, we shall consider only the second case since the first is only a particular case of it.

In the interaction representation, the formule (3–5) can be written as

$$f_w(x,p,t)=\Omega^{-1}\sum_n\sum_{\alpha\beta}\delta^{Kr}(2p-\alpha-\beta)e^{i(\alpha-\beta)[x-t/2m(\alpha+\beta)]}\langle n1_\alpha|\rho|n1_\beta\rangle \tag{3.6}$$

from which we get

$$\partial_t f_w+\frac{(\alpha+\beta)}{2m}\partial_x f_w=\Omega^{-1}\sum_n\sum_{\alpha\beta}\delta^{Kr}(2p-\alpha-\beta)e^{i(\alpha-\beta)[x-t/2m(\alpha+\beta)]}\partial_t\langle n1_\alpha|\rho|n1_\beta\rangle \tag{3.7}$$

in these formulas, m is mass of the particle, and the notation $\partial_t\equiv\partial/\partial t$ is used.

§ 4. The Von Neumann Formalism

Our problem is then to calculate the value of $\partial_t\langle n1_\alpha|\rho|n1_\beta\rangle$ in (3–7); for doing this, let us start with the well known von Neumann equation in the interaction representation

$$i\partial_t\rho(t)=\lambda[H(t),\ \rho(t)];\quad \rho(t)\equiv e^{tH_0t}\rho e^{-tH_0t} \tag{4.1}$$

This equation can be solved by iteration: one can show that the dominant term when $t\to\infty$ and $\lambda\to0$ and $\lambda^2t=$finite (corresponding to the cycle inserted in a line, Prigogine and One (1) and Balescu (4), and in fact, the only terms different from zero under the conditions of our problem) is represented by

$$\partial_t\rho(t)=-\lambda^2\left[H(t),\int_0^t dt_1[H(t_1),\ \rho(t)]\right] \tag{4.2}$$

and in the representation of the occupation numbers

$$\partial_t\langle n1_\alpha|\rho|1_\beta n\rangle=-\lambda^2\int_0^t dt_1\sum_{n''}\sum_{n'''}\Big\{\overbrace{\langle n1_\alpha|H(t)|n''\rangle\langle n''|H(t_1)|n'''\rangle\langle n'''|\rho(t)|n1_\beta\rangle}^{\text{Term I}}$$

$$\overbrace{-\langle n1_\alpha|H(t)|n''))\langle n''|\rho(t)|n'''\rangle\langle n'''|H(t_1)|n1_\beta\rangle}^{\text{Term II}}$$

$$\overbrace{-\langle n1_\alpha|H(t_1)|n''\rangle\langle n''|\rho(t)|n'''\rangle\langle n'''|H(t)|n1_\beta\rangle}^{\text{Term III}}$$

$$\overbrace{+\langle n1_\alpha|\rho(t)|1n''\rangle\langle n''|H(t_1)|n'''\rangle\langle n'''|H(t)|n1_\beta\rangle}^{\text{Term VI}}\Big\}$$

so that because of (2.6) the terms of (4.3) which are non vanishing are

$$\begin{aligned}
\text{T. I}\ &\rightarrow\langle n1_\alpha|a_\alpha{}^+a_k{}^+a_\nu a_l|1_\nu n_k-1,\ n_l+1,\ n\rangle\langle n,\ 1_\nu,\ n_k-1,\ n_l+1|a_\nu{}^+a_l{}^+a_\mu a_k|1_\mu,\ n\rangle\\
&\times\langle n,\ 1_\mu|\rho|n1_\beta\rangle\delta^{Kr}(\alpha+k-l-\nu)\delta^{Kr}(\nu+l-k-\mu)v(\alpha k,\ \nu l)v(\nu l,\ k\mu)\\
&\times\exp\,[it(\mathcal{E}_\alpha+\mathcal{E}_k-\mathcal{E}_\nu-\mathcal{E}_l)]\int_0^t dt_1\exp\,[it_1(\mathcal{E}_\nu+\mathcal{E}_l-\mathcal{E}_k-\mathcal{E}_\mu)]\\
\text{T. II}\ &\rightarrow\langle n1_\alpha|a_\alpha{}^+a_k{}^+a_\nu a_l|1_\nu,\ n_k-1,\ n_l+1,\ n\rangle\langle n1_\nu,\ n_k-1,\ n_l+1,\ |\rho|n_k-1,\ n_l+1,\ 1_\mu,\ n\rangle\\
&\times\langle n_k-1,\ n_l+1,\ 1\mu,\ n|a_\mu{}^+a_l{}^+a_k a_\beta|n1_\beta\rangle\delta^{Kr}(\alpha+k-\nu-l)\delta^{Kr}(\mu+l-k-\beta)v(\alpha k,\ \nu l)\\
&\times v(\mu l,\ k\beta)\exp\,[it(\mathcal{E}_\alpha+\mathcal{E}_k-\mathcal{E}_\nu-\mathcal{E}_l)]\int_0^t dt_1\exp\,[it(\mathcal{E}_\mu+\mathcal{E}_l-\mathcal{E}_k-\mathcal{E}_\beta)|\\
\text{T. III}&\rightarrow\langle n,\ 1_\alpha|a_\alpha{}^+a_k{}^+a_\nu a_l|1_\nu,\ n_k-1,\ n_l+1,\ n\rangle\langle 1_\nu,\ n_k-1,\ n_l+1,\ n|\rho|n_k-1,\ n_l+1,\ n,\ 1_\mu\rangle\\
&\times\langle n,\ n_k-1,\ n_l+1,\ n,\ 1_\mu|a_\mu{}^+a_l{}^+a_\beta a_k|n,\ 1_\beta\rangle\delta^{Kr}(\alpha+k-\nu-l)\delta^{Kr}(\mu+l-k-\beta)\\
&\times v(\alpha k,\ \nu l)v(\mu l,\ k\beta)\exp\,[it(\mathcal{E}_\mu+\mathcal{E}_l-\mathcal{E}_k-\mathcal{E}_\beta)]\int_0^t dt_1\exp\,[it_1(\mathcal{E}_\alpha+\mathcal{E}_k-\mathcal{E}_l-\mathcal{E}_\nu)]\\
\text{T. IV}&\rightarrow\langle n,\ 1_\alpha|\rho|n1_\nu\rangle\langle n1_\nu|a_\nu{}^+a_k{}^+a_l a_\mu|1_\mu,\ n_k-1,\ n_l+1,\ n\rangle\\
&\times\langle n,\ 1_\mu,\ n_k-1,\ n_l+1|a_\mu{}^+a_l{}^+a_k a_\beta|n,\ 1_\beta\rangle\delta^{Kr}(\nu+k-l-\mu)\delta^{Kr}(\mu+l-k-\beta)v(\nu k,\ l\mu)\\
&\times\nu(\mu l,\ k\beta)\exp\,[it(\mathcal{E}_\mu+\mathcal{E}_l-\mathcal{E}_k-\mathcal{E}_\beta)]\int_0^t dt_1\exp\,[it_1(\mathcal{E}_\nu+\mathcal{E}_k-\mathcal{E}_l-\mathcal{E}_\mu)]
\end{aligned}\tag{4.4}$$

Asymptotic time integration of the time dependent terms in the last equation, i.e. considering that significant contributions arise only when the collision time t-t_1 is short in comparison with the time t (this has meaning only if we integrate first over the momenta, but is physically very reasonable) (see for example ref. (4) and (5)) leads to (4–6).

So we make use of the formula

$$e^{\mp i\alpha t}\int_0^t e^{\pm i\alpha t}dt=\pi\delta_\pm(\alpha),\quad\text{if}\quad t\rightarrow\infty\tag{4.5}$$

where δ_+ and δ_- are given by (6)

$$\pi\delta_\pm(\alpha)=\pi\delta(\alpha)\pm iP({}^1/_\alpha)$$

$P({}^1/_\alpha)$ being the principal part; then the time dependent factors in the terms I and IV become simply $\delta_-(\mathcal{E}_k+\mathcal{E}_\alpha-\mathcal{E}_l-\mathcal{E}_\nu)$ and $\delta_+(\mathcal{E}_\beta+\mathcal{E}_k-\mathcal{E}_l-\mathcal{E}_\mu)$, and the terms II and III give no systematic contribution in the limit $t\rightarrow\infty$, $\lambda\rightarrow 0$, $\lambda^2 t$=finite (this can be shown by simple iteration of (4.6)): they must be retained, however, because in certain cases (homogeneous systems, phonon type of spectra), they give: in these cases, there are, of course, not oscillating. We get

$$\partial_t\langle n1_\alpha|\rho|n1_\beta\rangle = -\frac{\lambda^2}{4\Omega^2}\pi\sum n_k(n_l+1)\delta^{Kr}(k+\alpha-l-\nu)\delta^{Kr}(\alpha-\beta+\mu-\nu)|v(k\alpha l\mu)|^2 \tag{4.6}$$
$$\{[\delta_-(\mathcal{E}_k+\mathcal{E}_\alpha-\mathcal{E}_l-\mathcal{E}_\nu)+\delta_+(\mathcal{E}_\beta+\mathcal{E}_k-\mathcal{E}_l-\mathcal{E}_\mu)]\langle n1_\alpha|\rho|n1_\beta\rangle-[\delta_-(\mathcal{E}_\beta-\mathcal{E}_k-\mathcal{E}_l-\mathcal{E}_\mu)$$
$$+\delta_+(\mathcal{E}_\alpha+\mathcal{E}_k-\mathcal{E}_\nu-\mathcal{E}_l)]\ \exp\ [it(\mathcal{E}_\alpha+\mathcal{E}_\mu-\mathcal{E}_\nu-\mathcal{E}_\beta)[\langle n, 1_\nu, n_k-1, n_l+1|\rho|n, n_k-1, n_l+1, 1_\mu\rangle\}$$

to stress the analogy with Prigogine and Ono's result, we may write the (4.6) as

$$\partial_t\langle n,\ 1_{\alpha+(K/2)}|\rho|1_{\alpha-(K/2)},\ n\rangle = -\frac{\pi\lambda^2}{4\Omega^2}\sum_{nkK'}|v(K')|^2 n_k(n_{k-K'}+1)$$
$$\times\exp\ [it(\mathcal{E}_{\alpha+(K/2)}-\mathcal{E}_{\alpha-(K/2)})]\left\{\exp\left[\frac{K'}{2}\left(\frac{\partial}{\partial\alpha}-\frac{\partial}{\partial k}\right)\right]-\exp\left[-\frac{K'}{2}\left(\frac{\partial}{\partial\alpha}-\frac{\partial}{\partial k}\right)\right]\right\}$$
$$\times\{\delta_-(\mathcal{E}_{\alpha+(K'/2)}+\mathcal{E}_{\alpha+(K/2)-(K'/2)}-\mathcal{E}_{k-(K'/2)}-\mathcal{E}_{\alpha+(K/2)+(K'/2)})\ \exp\left[-\frac{K'}{2}\left(\frac{\partial}{\partial\alpha}-\frac{\partial}{\partial k}\right)\right]$$
$$+\left\{\delta_+(\mathcal{E}_{\alpha-(K'/2)}+\mathcal{E}_{\alpha-(K/2)+(K'/2)}-\mathcal{E}_{k+(K'/2)}-\mathcal{E}_{\alpha+(K/2)+(K'/2)})\ \exp\left[\frac{K'}{2}\left(\frac{\partial}{\partial\alpha}-\frac{\partial}{\partial k}\right)\right]\right\}$$
$$\times\exp\left[-it(\mathcal{E}_{\alpha+(K/2)}-\mathcal{E}_{\alpha-(K/2)})\right]\langle n1_{\alpha+(K/2)}|\rho|n1_{\alpha-(K/2)}\rangle$$

where we have put $\alpha-\beta=\nu-\mu=K$; $\alpha-\nu=\beta-\mu=K'$ this last equation may be justified if we carry out the operations of the displacement operators on the functions of the right (this is permitted only in the sens of the Schwartz's distributions, for the δ_+, δ_- are singular functions) we re-obtain then (4-6), by making the suitable change of variables.

§ 5. The Transport Equation

Putting (4-6) in the Wigner function (3-2) we obtain

$$\partial_t f_w+(\alpha/m)\partial_x f_w = -\frac{\lambda^2\pi}{\Omega^3}\sum_n\sum_{klKK'} n_k(n_l+1)\delta^{Kr}(k-l+K')|v(K')|^2 e^{iK(x-(\alpha t/m))}$$
$$\left\{\left[\delta_-\left[\phi\left(\alpha+\frac{K}{2}\right)\right]+\delta_+\left[\phi\left(\alpha-\frac{K}{2}\right)\right]\right]\langle n,\ 1_{\alpha+(K/2)}|\rho|n1_{\alpha-(K/2)}\rangle-\left[\delta_-\left[\phi\left(\alpha-\frac{K}{2}\right)\right]\right.\right.$$
$$\left.+\delta_+\left[\phi\left(\alpha+\frac{K}{2}\right)\right]\right]\langle n,\ n_k-1,\ n_l+1,\ 1_{\alpha+(K/2)+K'}|\rho|n,\ n_k-1,\ n_l+1,\ 1_{\alpha-(k/2)+K'}\rangle$$
$$\left.\times\exp\left[it\left(f\left(\alpha+\frac{K}{2}\right)-f\left(\alpha-\frac{K}{2}\right)\right)\right]\right\} \tag{5.1}$$

in which we have made the following abbreviations

$$\phi\left(\alpha\pm\frac{K}{2}\right)\equiv\mathcal{E}_k-\mathcal{E}_l+\mathcal{E}_{\alpha\pm(K/2)}-\mathcal{E}_{\alpha+K'\pm(K/2)}$$
$$f\left(\alpha\pm\frac{K}{2}\right)=\mathcal{E}_{\alpha\pm(K/2)}-\mathcal{E}_{\alpha+K'\pm(K'/2)}$$

finally this formula can be transformed to give (see Appendix)

$$\partial_t f_w+(\alpha/m)\partial_x f_w = -\frac{\lambda^2\pi}{\Omega^3}\sum_n\sum_{klKK'} n_k(n_l+1)\delta^{Kr}(k-l+K')|v(K')|^2$$
$$\left\{\left[\delta_-\left[\phi\left(\alpha-\frac{i}{2}\frac{\partial}{\partial x}\right)\right]+\delta_+\left[\phi\left(\alpha+\frac{i}{2}\frac{\partial}{\partial x}\right)\right]\right]f_w(x,\ \alpha)-\left[\delta_-\left[\phi\left(\alpha+\frac{i}{2}\frac{\partial}{\partial x}\right)\right]\right.\right.$$
$$\left.\left.+\delta_+\left[\phi\left(\alpha-\frac{i}{2}\frac{\partial}{\partial x}\right)\right]\right]\ \exp\left\{it\left[f\left(\alpha-\frac{i}{2}\frac{\partial}{\partial x}\right)-f\left(\alpha+\frac{i}{2}\frac{\partial}{\partial x}\right)\right]\right\}f_w\left(x+\frac{K't}{m},\ \alpha+K'\right)\right\} \tag{5.2}$$

If the energy spectrum of both components is that of a perfect gas and if we suppose factorized distribution functions, and take continuous spectrum for k and K'

$$\partial_t f_w(x,\alpha,t)+\frac{\alpha}{m}\partial_x f_w(\alpha,x,t)=-\frac{\lambda^2 m}{2}\int dK'\int dk|v(K')|^2\int_0^\infty d\tau$$
$$\cos[\tau K'(\alpha-k+K')]\times\left\{f_w\left(\alpha,x-\frac{K'\tau}{2}\right)\varphi(k)[\varphi(k-K')+1]-f_w\left(\alpha+K',x+\frac{K'\tau}{2}\right)\right.$$
$$\left.\varphi(k-K')\times[\varphi(k)+1]\right\} \tag{5.3}$$

which shows the non-local character observed by Prigogine and Ono.

This effect is noticeable when

$$K^{-1}\le\alpha^{-1}=\lambda_B \quad (de\ \text{Broglie's wave length})$$

Another simple example is a system for which $\mathcal{E}_k=c|k|$ we obtain then

$$\partial_t f_w(x,\alpha,t)+\frac{\alpha}{m}\partial_x f_w(x,\alpha,t)=-\frac{\lambda^2\pi}{2c}\int dkdK'|v(K')|^2$$
$$\times\left\{\varphi(k)[\varphi(k-K')+1]f_w(x,\alpha,t)-\varphi(k-K')[\varphi(k)+1]f_w\left(x+\frac{K't}{m},\alpha+K't\right)\right\}$$

where the uncertainty can be related to the collision process and becomes appreciable when

$$\Delta\mathcal{E}(K')\cdot t<1$$

Aknowledgements

I am very indebted to Prof. Prigogine for many discussions and to the Consejo Nacional de Investigaciones Cientificas of Argentina, who supported this work;

Appendix

The term of (5-1) may generally be written, for this purpose

$$\sum_K e^{ikx}\Psi\left(\alpha-\frac{K}{2}\right)\chi\left(\alpha+\frac{K}{2}\right)\rho(\alpha+K') \tag{A1}$$

which by application of displacement operators becomes succesively

$$=\sum_K\chi\left(\alpha+\frac{K}{2}\right)\rho(\alpha+K')e^{ik(x+(i/2)(\partial/\partial\alpha))}\Psi(\alpha) \tag{A2}$$

$$=\sum_K\chi\left(\alpha+\frac{K}{2}\right)\rho(\alpha+K')e^{(i/2)(\partial/\partial x)(\partial/\partial\alpha)}e^{ixK}\Psi(\alpha) \tag{A3}$$

$$=\sum_K\chi\left(\alpha+\frac{K}{2}\right)\rho(\alpha+K')\Psi\left(\alpha+\frac{i}{2}\frac{\partial}{\partial x}\right)e^{ixK} \tag{A4}$$

$$=\sum_K\rho(\alpha+K')\chi\left(\alpha-\frac{i}{2}\frac{\partial}{\partial x}\right)\Psi\left(\alpha+\frac{i}{2}\frac{\partial}{\partial x}\right)e^{ixK} \tag{A5}$$

one can easily see how this works in the case of (5-1)

References

1) I. Prigogine and S. Ono: Physica **25** (1959) 171.
2) Prigogine I. Superfluidité et équation de transport quantique, Institut interunversitaire de Sciences Nucléaires, Bruxelles, 1960.
3) D. Massignon: Mécanique Statistiqe des Fluides, Dunod, Paris 1957.
4) I. Prigogine and R. Balescu: Physica **25** (1959) 281.
5) I. Prigogine: Non equilibrium Statistical Mechanics Interscience 1960, to be published.
6) W. Heitler: The Quantum Theory of Radiation, Oxford, 1955.

JOURNAL OF THE PHYSICAL SOCIETY OF JAPAN, Vol. 16, No. 4, APRIL, 1961

On the Theory of Adiabatic and Isolated Susceptibilities*

Nobuhiko SAITÔ**

Department of Chemistry, University of Oregon, Eugene, Oregon, U.S.A.

(Received December 8, 1960)

A quantum statistical mechanical proof of the equivalence of adiabatic and isolated susceptibilities in large systems is given by Broer's method using a Gibbs relation. Further a brief mention is made of the susceptibilities in non-equilibrium cases.

§ 1.

According to Broer[1] and Wright[2], a doubt was raised by Polder and Van Vleck that the two susceptibilities χ_s and χ_{iso} which are called adiabatic susceptibility and isolated susceptibility respectively (for the definition see Eqs. (4), (5) and (7)) do not always coincide. A partial solution of this problem was made by Broer. He showed that χ_s is equivalent to χ_{iso} in a large classical system. This is an important contribution to the theories of χ_s and χ_{iso}. However he found a difference between them in the quantum mechanical case. Thus the ratio of these two susceptibilities was calculated quantum mechanically by Wright[2], Broer[1] and Caspers[3]. However it is inconceivable that the difference of χ_s and χ_{iso} is due to a quantum effect. In effect Caspers[4] has shown $\chi_s=\chi_{iso}$ by making use of several assumptions about the structure of the energy levels. Recently Yamamoto[5] discussed more generally the equivalence of χ_s and χ_{iso}. To do this, however, he had to introduce the idea of the *approximate Hamiltonian* with negligible perturbations which give rise to the ergodic property. His argument is correct as far as this approximate Hamiltonian is concerned, but it leaves some doubt about the exact Hamiltonian and the introduction of the approximate Hamiltonian seems rather artificial.

The purpose of this short note is to give a proof of the equivalence of χ_s and χ_{iso} in a large system in the quantum mechanical case.

§ 2.

We consider a Hamiltonian H which is a function of an external parameter F. In the magnetic case, F is a component of the magnetic field. Define an operator A by

$$A=-\partial H/\partial F\,. \tag{1}$$

The density matrix ρ at the temperature T is given by

$$\rho=\exp[(\Omega-H)/kT]\,, \qquad \mathrm{Tr}\,\rho=1\,. \tag{2}$$

where Ω is the free energy of the total system. The average of any dynamical quantity B representing a physical quantity is given by

$$\langle B\rangle=\mathrm{Tr}\,B\rho=\sum_n B_n\exp(\Omega-E_n)/kT\,, \tag{3}$$

where E_n's are the eigenvalues of H and B_n's are the diagonal elements of B in the energy representation which diagonalizes the total Hamiltonian H. Since B is hermitian, B_n's are real quantities.

According to thermodynamics, the isothermal and adiabatic susceptibilities per unit volume are defined by

$$\left.\begin{aligned}\chi_T&=\left(\frac{\partial\bar{B}}{\partial F}\right)_T,\\ \text{and}\qquad&\\ \chi_s&=\left(\frac{\partial\bar{B}}{\partial F}\right)_S\end{aligned}\right\} \tag{4}$$

respectively where $\bar{B}$ is the macroscopic value of B per unit volume, and is given, by statistical mechanics, as

$$\bar{B}=\lim\frac{1}{V}\,\mathrm{Tr}\,B\rho=\lim\frac{1}{V}\langle B\rangle \tag{5}$$

where $\lim(1/V)$ is the abbreviated notation for $\lim\limits_{\substack{V\to\infty,\,N\to\infty\\ N/V=\mathrm{const.}}}(1/V)$. By means of thermodynamical relations and statistical mechanical expressions for thermodynamical quantities, we have[1]

---

* This work was supported in part by a research grant from the National Science Foundation.

** Now returned to the Department of Applied Physics, Waseda University, Tokyo.

$$\chi_T-\chi_s=\lim\frac{1}{V}\frac{1}{kT}\left[\frac{(\langle BH\rangle-\langle B\rangle\langle H\rangle)(\langle AH\rangle-\langle A\rangle\langle H\rangle)}{\langle H^2\rangle-\langle H\rangle^2}\right]. \tag{6}$$

On the other hand statistical mechanics gives another direct expression for the adiabatic susceptibility,

$$\chi_{iso}=\lim\frac{1}{V}\sum_n\frac{\partial B_n}{\partial F}\exp\left[(\Omega-E_n)/kT\right], \tag{7}$$

since the population of the energy levels is to be held constant while taking the derivative of $\bar{B}$ with respect to F. As was mentioned in § 1, this quantity, called isolated susceptibility, has been regarded to be distinguished from χ_s.

Now define an operator $B^{(d)}$ as the operator which is diagonal in the energy representation and has the diagonal elements equal to B_n's. Then we first notice the following property

$$\frac{\partial B_n}{\partial F}=\left(\frac{\partial B^{(d)}}{\partial F}\right)_n \tag{8}$$

where the right hand side means a diagonal element of the operator $\partial B^{(d)}/\partial F$ in the energy representation and is not always equal to a diagonal element of the operator $\partial B/\partial F$. As is defined above, B_n is not always an eigenvalue of B. If B_n happens to be an eigenvalue of B, then we have

$$\frac{\partial B_n}{\partial F}=\left(\frac{\partial B}{\partial F}\right)_n. \tag{9}$$

A proof of the above mentioned property is immediately obtained from the similar discussion by Riddell and Uhlenbeck[6] and is given in the Appendix. As a particular case of Eq. (9), if we take H for B, we have

$$\frac{\partial E_n}{\partial F}=\left(\frac{\partial H}{\partial F}\right)_n=-A_n. \tag{10}$$

From Eqs. (4), (3) and (10), we have

$$\chi_T=\lim\frac{1}{V}\left[\sum_n\frac{\partial B_n}{\partial F}\exp\left(\frac{\Omega-E_n}{kT}\right)+\frac{1}{kT}\sum_n B_nA_n\exp\left(\frac{\Omega-E_n}{kT}\right)-\frac{\langle B\rangle\langle A\rangle}{kT}\right], \tag{11}$$

where

$$\langle A\rangle=\mathrm{Tr}\,A\rho=\sum A_n\exp\left(\frac{\Omega-E_n}{kT}\right)=-\left(\frac{\partial\Omega}{\partial F}\right)_T=kT\frac{\partial}{\partial F}\ln\mathrm{Tr}\exp\left(-\frac{H}{kT}\right). \tag{12}$$

The first term of the right-hand side of Eq. (11) is just equal to χ_{iso} and is rewritten, by virture of Eq. (8), as

$$\begin{aligned}\chi_{iso}&=\lim\frac{1}{V}\sum_n\frac{\partial B_n}{\partial F}\exp\left(\frac{\Omega-E_n}{kT}\right)=\lim\frac{1}{V}\sum_n\left(\frac{\partial B^{(d)}}{\partial F}\right)_n\exp\left(\frac{\Omega-E_n}{kT}\right)\\&=\lim\frac{1}{V}\mathrm{Tr}\frac{\partial B^{(d)}}{\partial F}\rho=\lim\frac{1}{V}\left\langle\frac{\partial B^{(d)}}{\partial F}\right\rangle.\end{aligned} \tag{13}$$

It should be noted that this is not always equal to $\mathrm{Tr}\,((\partial B/\partial F)\rho)=\langle\partial B/\partial F\rangle$. In the same way, the second term of Eq. (11) is equal to

$$\frac{1}{kT}\mathrm{Tr}\,B^{(d)}A^{(d)}\rho=\frac{1}{kT}\langle B^{(d)}A^{(d)}\rangle,$$

where $A^{(d)}$ is defined similarly to $B^{(d)}$. Thus we finally have

$$\chi_T-\chi_{iso}=\lim\frac{1}{V}\frac{1}{kT}[\langle B^{(d)}A^{(d)}\rangle-\langle B\rangle\langle A\rangle]\,. \tag{14}$$

A confusion of Broer's consideration lies here. He wrote Eq. (11) and (14) as (see p. 537 in Broer's paper)

$$\chi_T=\lim\frac{1}{V}\left[\left\langle\frac{\partial B}{\partial F}\right\rangle+\frac{1}{kT}(\langle BA\rangle-\langle B\rangle\langle A\rangle)\right],$$

$$\chi_T-\chi_{iso}=\lim\frac{1}{V}\frac{1}{kT}[\langle BA\rangle-\langle B\rangle\langle A\rangle]\,,$$

which are not always true.

In the notation of Gibbs and of Broer for microcanonical averages, $\mathrm{Tr}\,B^{(d)}A^{(d)}$ is written as

$$\mathrm{Tr}\,(B^{(d)}A^{(d)}\rho)=\sum_n\overline{B_n}|\,\overline{A_n}|\exp(\Omega-E_n)/kT\,. \tag{15}$$

Eq. (15) holds irrespective of whether the energy levels are degenerate or not, because $A_n=-\partial E_n/\partial F$ and $\overline{B_nA_n}|_{E_n}=\overline{B_n}|_{E_n}\overline{A_n}|_{E_n}$. Eq. (14) with Eq. (15) is identical to the result obtained by Yamamoto through the consideration of the approximate Hamiltonian. On the other hand Broer showed that the quantities in $[\cdots]$ in the right-hand sides of Eqs. (14) and (6) are equivalent in the limit of a large system, by making use of the Gibbs expansion which holds for any quantity G in a large system,

$$\langle G\rangle=\overline{G}|_{\langle H\rangle}+\frac{1}{2}(\langle H^2\rangle-\langle H\rangle^2)\frac{\partial^2\langle G\rangle}{\partial\langle H\rangle^2}\,. \tag{16}$$

Therefore it will be redundant to repeat the calculation leading to $\chi_s=\chi_{iso}$ here. Thus we get a proof of the equivalence of the two quantities of χ_s and χ_{iso}.

The condition for $\chi_{iso}=\chi_s$ of Klein[8], and also that of Wright[2], which is a special case of the former, are too severe. They are the condition for χ_{iso} to be *exactly* equal to χ_s irrespective of the size of the system.

§ 3.

In this section another discussion on the papers of Broer[2] and Caspers[3] will be given. We have already pointed out the mistake of Broer's general argument on quantum mechanical case. In a later section of his paper, Broer assumed the energy level of the form,

$$E_n=-FM_n+U_n+D_n/F \tag{17}$$

and under the approximation of high temperature and high magnetic field (large F) he obtained $\chi_{iso}/\chi_s=4/5$. In this calculation, however, there was no complication arising from the difference between, e.g., $A^{(d)}$ and A. Essentially the same calculation was carried out by Caspers[3]. One of their assumptions is that

$$\langle MU\rangle\equiv\frac{1}{p}\sum_n M_nU_n=0\,,$$

where p is the number of levels. However we first assume $\langle MU\rangle\neq0$, then we have, revising the calculations of Broer in case of $A=B$ in the notation of § 2,

$$\chi_s=\chi_TC_M/C_H=\lim\frac{1}{V}\left(\langle U^2\rangle-\frac{\langle MU\rangle^2}{\langle M^2\rangle}-2\langle MD\rangle\right)\Big/kTF^2 \tag{18}$$

and

$$\chi_{iso}=\lim\frac{1}{V}[-2\langle MD\rangle/kTF^2]\,, \tag{18'}$$

where C_M and C_H are specific heats at constant magnetization and at constant magnetic field respectively.

Eqs. (18) and (18′) yield as the condition for $\chi_s=\chi_{iso}$,

$$\langle U^2\rangle\langle M^2\rangle=\langle MU\rangle^2 . \tag{19}$$

This is also derived from Eqs. (6) and (14) by using the energy level (17). The condition (19) is really the case in a large system, as is shown in the following. First if we look at the fact that M_n is a sum of N spins which take either $+1/2$ or $-1/2$, we see that its probability distribution is expressed for large N by a Gaussian function,

$$f(M)=A\exp\left(-\frac{M^2}{2N\alpha}\right), \qquad A=(2\pi N\alpha)^{-1/2} . \tag{20}$$

Thus we have

$$\langle M^2\rangle=A\int_{-\infty}^{\infty}M^2\exp\left(-\frac{M^2}{2N\alpha}\right)dM=N\alpha \tag{21}$$

U_n is regarded as a function of M, and U_n corresponding to $M=0$ is zero. Therefore we obtain

$$\begin{aligned}\langle MU\rangle&=A\int_{-\infty}^{\infty}MU(M)\exp\left(-\frac{M^2}{2N\alpha}\right)dM\\&=A\int\left(U'(0)M^2+\frac{1}{2}U''(0)M^3+\cdots\right)\exp\left(-\frac{M^2}{2N\alpha}\right)dM\\&\simeq AU'(0)\int M^2\exp\left(-\frac{M^2}{2N\alpha}\right)dM ,\end{aligned} \tag{22}$$

where higher order terms of the expansion can be neglected for large N, since $U'''(0)$, for example, is of order N^{-2}. This expression corresponds just to the Gibb's relation (16). Similarly we have

$$\langle U^2\rangle=U'(0)^2A\int M^2\exp\left(-\frac{M^2}{2N\alpha}\right)dM . \tag{23}$$

Eqs. (21), (22) and (23) give Eq. (19) to prove $\chi_s=\chi_{iso}$.

Next we consider the case $\langle MU\rangle=0$. This may be realized in the spin-spin dipolar interaction, because U is regarded as an even function of M. In this case U can be expanded in the form

$$U=\frac{1}{2}U''(0)M^2+\cdots$$

then we have

$$\langle U^2\rangle=\frac{1}{2}[U''(0)]^2\langle M^4\rangle\sim O(N^0) ,$$

since $U''(0)$ is of the order N^{-1} and $\langle M^4\rangle\sim O(N^2)$. On the other hand we have

$$\langle MD\rangle\sim D'(0)\langle M^2\rangle\sim O(N) .$$

Therefore $\langle U^2\rangle$ term can be neglected compared with the term $\langle MD\rangle$ in Eq. (18). Thus we again obtain $\chi_s=\chi_{iso}$. The result $\chi_{iso}/\chi_s=4/5$, obtained by Broer, Wright and Caspers, is valid only for small systems, as was pointed out by Caspers[3),4)].

§ 4.

In this section we take A for B. We have shown that $\chi_s\doteq\chi_{iso}$, so we may write, according to Eq. (14),

$$\chi_T-\chi_s=\lim\frac{1}{V}\frac{1}{kT}[\langle A^{(d)2}\rangle-\langle A\rangle^2]\,. \tag{24}$$

We consider a Hamiltonian given as

$$H=H_0-AF \tag{25}$$

and we limit ourselves to $\langle A\rangle$ linear in F. Then χ is independent of F, and we have from Eq. (10)

$$\left.\begin{aligned}\langle A^{(d)2}\rangle&=\sum_n A_n{}^2\rho_n\simeq\sum_m A^2_{mm}\rho_{0m}\\ \langle A\rangle&=\sum_n A_n\rho_n\simeq\sum_m A_{mm}\rho_{0m}\end{aligned}\right\}\,. \tag{26}$$

where ρ_0 is the equilibrium density matrix of the system with Hamiltonian H_0 and suffix m means the eigenstate of H_0. A quantum statistical derivation of χ_T is given from Eqs. (4) and (12) by making use of the perturbation technique. For example, Nakajima[9] showed the following expansion

$$\begin{aligned}\mathrm{Tr}\,e^{-\beta(H_0-AF)}=&\,\mathrm{Tr}\,e^{-\beta H_0}+F\beta\,\mathrm{Tr}[\exp(-\beta H_0)A]\\ &+\frac{F^2}{2}\beta\int_0^\beta d\lambda\,\mathrm{Tr}[\exp(-\beta H_0)A(\lambda)A]+\cdots\,,\end{aligned} \tag{27}$$

where

$$A(\lambda)=\exp(\lambda H_0)A\exp(-\lambda H_0)\,.$$

Therefore we have

$$\begin{aligned}\chi_T&=\lim\frac{1}{V}\left[\int_0^\beta d\lambda\,\mathrm{Tr}\{\rho_0A(\lambda)A\}-\frac{1}{kT}(\mathrm{Tr}\,\rho_0A)^2\right]\\ &=\lim\frac{1}{V}\left[\sum_{m,m'}\frac{|A_{mm'}|^2(\rho_{0m}-\rho_{0m'})}{E_{0m'}-E_{0m}}-\frac{1}{kT}(\sum A_{mm}\rho_{0m})^2\right].\end{aligned} \tag{28}$$

On the other hand Kubo[10] gave a general method for calculating the dynamic susceptibility of an isolated system under external fields. Because the system does not exchange heat with surroundings, the dynamic susceptibility thus calculated is supposed to be adiabatic. This is in fact the case. In the limit of zero frequency, or in static case, we have[11], in a representation diagonalizing the operator H_0

$$\begin{aligned}\chi(0)&=\lim\frac{1}{V}\sum_{m,m'}\frac{|A_{mm'}|^2(\rho_{0m}-\rho_{0m'})}{\hbar}\,\mathrm{P}\int_{-\infty}^{\infty}\frac{\delta(p+\omega_{mm'})}{-p}dp\\ &=\lim\frac{1}{V}\left[\sum_{m,m'}\frac{|A_{mm'}|^2(\rho_{0m}-\rho_{0m'})}{E_{0m'}-E_{0m}}-\frac{1}{kT}\sum|A_{mm}|^2\rho_{0m}\right]\end{aligned} \tag{29}$$

where use is made of the relation

$$\begin{aligned}\mathrm{P}\int_{-\infty}^{\infty}\frac{\delta(p+\omega)}{p}dp&=-\frac{1}{\omega}\qquad\text{for}\quad\omega\neq0\\ &=0\qquad\text{for}\quad\omega=0\,.\end{aligned}$$

Thus we obtain from Eqs. (28) and (29)

$$\chi_T-\chi(0)=\lim\frac{1}{V}\frac{1}{kT}[\sum_m A^2_{mm}\rho_{0m}-(\sum A_{mm}\rho_{0m})^2]\,. \tag{30}$$

Referring to Eqs. (24) and (26), we see that Eq. (30) is identical to Eq. (24) in the linear approximation. Thus $\chi(0)$ is equal to χ_s.

Another method was developed by Kubo and Tomita[12] to obtain the dynamic susceptibility. However this method gives χ_T in zero frequency. In this method, one assumes that at first the system is in thermal equilibrium under an external field F and has a density matrix $\rho=\exp(\Omega-H_0+AF)/kT$. At the time $t=t_0$, the system is isolated from the heat reservoir and the field F is turned off. Thus the average of A, $\langle A\rangle$, will relax and may be expressed by a function of the type $F\phi(t-t_0)$ which can be obtained by the first order perturbation calculation. The derivative of $\phi(t-t_0)$ with respect to t_0 gives the response due to a single pulse at $t=t_0$. By the superposition of these responses due to pulses at different times, we obtain $\langle A\rangle$ for an arbitrary form of $F(t)$. However as is seen in the above derivation, the system is in thermal equilibrium and in thermal contact with the heat reservoir while the pulse is applied. This is the reason we get χ_T in zero frequency[13]. A more detailed discussion of the interaction of the system with a heat reservoir will be given later.

Acknowledgments

This paper was originated from the paper of Dr. Yamamoto and the discussion with him while he was staying at the University of Oregon. The author wishes to thank Professors T. L. Hill and T. Yamamoto for the pleasant discussion.

Appendix. A Proof of $\dfrac{\partial B_n}{\partial F}=\left(\dfrac{\partial B^{(d)}}{\partial F}\right)_n$

According to the definition of $B^{(d)}$, the Hamiltonian of the system H commutes with $B^{(d)}$. We denote the common normalized eigenfunctions of H and $B^{(d)}$ by ψ_n. B_n is the eigenvalue of $B^{(d)}$. Then we have

$$B^{(d)}\psi_n=B_n\psi_n\,. \tag{A.1}$$

By differentiating (A.1) with respect to F, we have

$$\frac{\partial B^{(d)}}{\partial F}\psi_n+B^{(d)}\frac{\partial\psi_n}{\partial F}=\frac{\partial B_n}{\partial F}\psi_n+B_n\frac{\partial\psi_n}{\partial F}\,. \tag{A.2}$$

Multiplying (A.2) by $\psi_n{}^*$ and integrating it over the whole space we have

$$\left(\frac{\partial B^{(d)}}{\partial F}\right)_n=\frac{\partial B_n}{\partial F}+\int\psi_n{}^*B_n\frac{\partial\psi_n}{\partial F}d\tau-\int\psi_n{}^*B^{(d)}\frac{\partial\psi_n}{\partial F}d\tau\,. \tag{A.3}$$

Since $B^{(d)}$ is hermitian, and B_n is its eigenvalue, the last two terms of the right-hand side of Eq. (A.3) cancel. Hence we have

$$\frac{\partial B_n}{\partial F}=\left(\frac{\partial B^{(d)}}{\partial F}\right)_n\,. \tag{A.4}$$

If B_n is an eigenvalue of B, $B^{(d)}$ in the above equations can be replaced by B, and we have

$$\frac{\partial B_n}{\partial F}=\left(\frac{\partial B}{\partial F}\right)_n\,. \tag{A.5}$$

References

1) L. J. Broer: Physica **17** (1951) 531.
2) A. Wright: Phys. Rev. **76** (1949) 1826.
3) W. J. Caspers: Physica **25** (1959) 43.
4) W. J. Caspers: Physica **25** (1959) 645
5) T. Yamamoto: Phys. Rev. **119** (1960) 701.
6) R. J. Riddell, Jr. and G. E. Uhlenbeck: J. Chem. Phys. **18** (1950) 1066, and also R. W. Zwanzing: J. Chem. Phys. **18** (1950) 1412.
7) See ref. 1 and J. W. Gibbs: *Elementary Principles in Statistical Mechanics* (New Haven, 1902) Chap. IX.
8) M. J. Klein: Phys. Rev. **86** (1952) 807.
9) S. Nakajima: Advances in Physics **4** (1955) 363.
10) R. Kubo: J. Phys. Soc. Japan **12** (1957) 570.
11) N. Saitô: Phys. Rev. **117** (1960) 1163.
12) R. Kubo and K. Tomita: J. Phys. Soc. Japan **9** (1954) 888.
13) See also the discussion of W. Bernard and H. B. Callen: Rev. Mod. Phys. **31** (1959) 1017.

JOURNAL OF THE PHYSICAL SOCIETY OF JAPAN Vol. 16, No. 4, APRIL, 1961

Convex-Core Model of Molecules in Crystalline State. II

By Saburo KOBA

Department of Physics, Faculty of Science, University of Tokyo

(Received December 26, 1960)

The convex-core model of molecules, which has been effective for discussing thermodynamic properties of polyatomic gases, is applied to the crystals of benzene and ethylene as a continuation of a previous article of the same title, in which crystals of methane, carbon dioxide, and nitrogen were treated. By use of model parameters determined from the second virial coefficients, cohesive energies and lattice constants are calculated. When we neglect zero-point energies, potential non-additivities, and electric multipole interactions, then the calculated cohesive energies are close to the observed values for benzene and 16% higher for ethylene. The calculated lattice constants agree well with observed ones in both cases. Stability of the benzene crystal is discussed, but the conclusions are not as definite as in the case of carbon dioxide.

The convex-core model of molecles is applied in this paper to the crystals of benzene and ethylene, as a continuation of a previous article[1] of the same title, which is referred to as Part I.

In Part I, we have explained to some extent the crystal structure of carbon dioxide by taking into account the electric multipole moment. In Part II, we apply similar method to benzene.

In Part II, we neglect the zero point energy and non additivity of the intermolecular potential. The former is positive, and perhaps the latter is also positive (since it is positive for spherical molecules). The electric multipole interaction is negative for benzene and ethylene. Sum of these three effects is presumably less than 20% of the total cohesive energy.

For the purpose of treating polyatomic molecules, Kihara introduced a model which assumes an appropriate convex body called core inside each molecule[2]. The shortest distance between two cores is called intercore distance and denoted by ρ. The potential energy U between two molecules is assumed to be a function of this ρ only, and moreover

$$U(\rho)=U_0\left[\left(\frac{\rho_0}{\rho}\right)^{12}-2\left(\frac{\rho_0}{\rho}\right)^{6}\right]. \qquad (1)$$

Here ρ_0 and U_0 are model constants determined from the second virial conffiicient and, if necessary, from transport coefficients[3].

Benzene C_6H_6

Because of the π electrons, it would be more natural to adopt for a core of a benzene molelcule C_6H_6 a regular hexagon obtained by connecting the centers of six carbon atoms. But calculations show that for this core the cohesive energy is too high and this means that the core is too small. Therefore, giving up consistency with the case of ethylene, we choose, as a core of a benzene molecule a regular hexagon formed by connecting the midpoints of successive CH-bonds. (A more accurate shape would be a hexagon plate with nonvanishing thickness.) Since the length of a CC-bond in a benzene molecule is 1.397A and that of a CH-bond is 1.085A, the length l of one side of the hexagon core is calculated to be 1.940A. The values of ρ_0 and U_0 determined from the second virial coefficient are

$$\rho_0=3.6\text{A}\ , \qquad U_0/k=740°\text{K}\ ,$$

k being the Boltzmann constant. The parallel body of the core at the distance $\rho_0/2$ indicates the shape and size of the molecule as shown in Fig. 3.

At the time of publication of the reference 2 (1953), the value of ρ_0 for benzene was taken from the lattice constant of graphite, since observed values of the second virial coefficient were not sufficient to determine both ρ_0 and U_0. Recently, however, Andon and Cox et al.[4),5)] observed the second virial coefficients of benzene between 67.1°C and 164.6°C. By use of their results together with values of Francis et al.[6)] both ρ_0 and U_0 have been calculated from the second virial coefficient only.

The crystal of benzene is orthorhombic, the corner and the face centers of a unit cell being occupied by centers of molecules. The x-, y-, and z-dimensions of a unit cell are

$a=7.46$, $b=9.67$, $c=7.03$A at −3°C,

$a=7.29$, $b=9.47$, $c=6.74$A at −195°C.

Space group is $Pbca-D_{2h}^{15}$. The cohesive energy measured as sublimation heat at 0°C is −10.67 kcal/mol.

According to Cox[7] details of the molecular orientation are the following. The molecule situated at the corner has, at −3°C, three successive carbon atoms C_1, C_2, and C_3, with coordinates

$x=-0.383$, $y=1.339$, $z=-0.040$A for C_1,

$x=-0.971$, $y=0.465$, $z=0.873$A for C_2,

$x=-0.591$, $y=-0.870$, $z=0.921$A for C_3.

The direction of the normal to the molecular plane is very close to (3, 1, 3). The orientation of the molecule at the center of the c-face is derived from the orientation at the cell corner by reflection with respect to a plane at $x=\frac{1}{4}a$ followed by a translation $\frac{1}{2}b$ in the y-direction; that of the a-face, by reflection with respect to a plane at $y=\frac{1}{4}b$ with a translation $\frac{1}{2}c$; that of the b-face, by reflection with respect to a plane at $z=\frac{1}{4}c$ with a translation $\frac{1}{2}a$.

In order to calculate the cohesive energy and the lattice constants let us somewhat idealize the crystal structure. We namely simplify the orientation of the molecule at the corner to

$x=z=0$ $y=1.397$A for C_1,

$-x=z=0.855$ $y=0.699$A for C_2,

$-x=z=0.855$ $y=-0.699$A for C_3,

the direction of the normal to the molecular plane being (1, 0, 1). The structure is shown in Fig. 1. In Fig. 1, molecules and cores shown by the dotted lines lie at a distance $b/2$ below and above the plane of drawing.

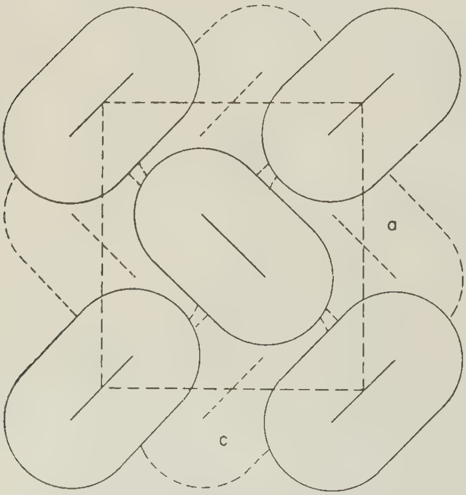

Fig. 1. Benzene crystal.

It should be noted that de Boer[8] has evaluated the sublimation heat of benzene crystal by use of this idealization. He assumed the observed lattice constants and summed up the attractive potential between CH groups which is inversely proportional to the sixth power of the distance. The cohesive energy calculated by him is −11.3 kcal/mol.

Let us denote by n_{ij} the number of (i, j)th neighboring lattice points at the distance r_{ij}. The subscript i is such that $\sum_j n_{ij}$ becomes the number of ith neighbors when the present lattice is reduced to a face-centered cubic lattice. The lattice point distribution is given

Table I

i	j	r_{ij}^2	n_{ij}
1	1	$\frac{1}{4}(a^2+b^2)$	4
1	2	$\frac{1}{4}(b^2+c^2)$	4
1	3	$\frac{1}{4}(c^2+a^2)$	4
2	1	a^2	2
2	2	b^2	2
2	3	c^2	2
3	1	$a^2+\frac{1}{4}(b^2+c^2)$	8
3	2	$b^2+\frac{1}{4}(c^2+a^2)$	8
3	3	$c^2+\frac{1}{4}(a^2+b^2)$	8
4	1	a^2+b^2	4
4	2	b^2+c^2	4
4	3	c^2+a^2	4
5	1	$\frac{1}{4}(9a^2+b^2)$	4
5	2	$\frac{1}{4}(9a^2+c^2)$	4
5	3	$\frac{1}{4}(9b^2+a^2)$	4
5	4	$\frac{1}{4}(9b^2+c^2)$	4
5	5	$\frac{1}{4}(9c^2+a^2)$	4
5	6	$\frac{1}{4}(9c^2+b^2)$	4

in Table I. The intercore distances ρ_{ij} to the cores of (i, j)th neighbors are expressed in the form

$$\rho_{ij}^2 = Aa^2 + Bb^2 + Cc^2 + Dbc + Eca + Fab + Gal + Hbl + Icl + Jl^2 .$$

Here a, b, and c are the lattice constants and l is the side length of the hexagon core of our molecular model. The coefficients A, B, ..under the coditions

$$\sqrt{6}\, l \leq c < a < b ,$$

$$\sqrt{\frac{3}{2}}(a-c) \leq b - \sqrt{\frac{3}{2}}\, a \leq l \leq b - \sqrt{\frac{3}{2}}\, c ,$$

are given in Table II. The core-model interaction energy per molecule

$$\frac{1}{2} U_0 \sum_{ij} n_{ij} \left[\left(\frac{\rho_0}{\rho_{ij}} \right)^{12} - 2 \left(\frac{\rho_0}{\rho_{ij}} \right)^{6} \right] \qquad (2)$$

can be evaluated by use of this table.

The expression (2) takes its minimum -10.2 kcal/mol at

$$a = 7.6\text{A} , \quad b = 11.0\text{A} , \quad c = 6.9\text{A} .$$

These values of the cohesive energy and the lattice constants are satisfactorily close to the corresponding observed values.

The orthorhombic crystal which we have treated is not a structure of closest packing. For the core-model of benzene we consider a structure of closest packing in which the flat hexagonal molecules are piled. This piled structure corresponds to, say, cubic closest packing of spheres.

On the other hand, we approximate electric multipole interactions of benzene molecules by quadrupole interactions. The benzene molecule

Table II $\sqrt{\frac{3}{2}} \equiv \sqrt{}$

i	j	A	B	C	D	E	F	G	H	I	J	n_{ij}
1	1	$\frac{1}{10}$	$\frac{3}{20}$				$\frac{1}{5}\sqrt{}$	$-\frac{4}{5}\sqrt{}$	$-\frac{6}{5}$		$\frac{12}{5}$	4
1	2		$\frac{3}{16}$	$\frac{5}{32}$	$\frac{1}{8}\sqrt{}$				$-\frac{3}{2}$	$-\frac{1}{2}\sqrt{}$	3	4
1	3	$\frac{5}{32}$		$\frac{5}{32}$		$\frac{3}{16}$		$-\frac{5}{8}\sqrt{}$		$-\frac{3}{8}\sqrt{}$	$\frac{15}{16}$	4
2	1	1						$-2\sqrt{}$			3	2
2	2		1						-4		4	2
2	3			1						$-2\sqrt{}$	3	2
3	1	1	$\frac{1}{4}$	$\frac{1}{4}$				$-\sqrt{}$	$-\frac{3}{2}$	$\frac{1}{2}\sqrt{}$	3	8
3	2	$\frac{5}{32}$	$\frac{3}{4}$	$\frac{5}{32}$	$\frac{1}{4}\sqrt{}$	$-\frac{3}{16}$	$\frac{1}{4}\sqrt{}$	$-\frac{1}{2}\sqrt{}$	-3	$-\frac{1}{2}\sqrt{}$	3	8
3	3	$\frac{5}{32}$	$\frac{3}{16}$	$\frac{5}{8}$	$\frac{1}{4}\sqrt{}$	$\frac{3}{8}$	$-\frac{1}{8}\sqrt{}$	$-\frac{1}{8}\sqrt{}$	$-\frac{9}{8}$	$-\frac{7}{4}\sqrt{}$	$\frac{39}{16}$	8
4	1	1	1					$-\sqrt{}$	-3		3	4
4	2		1	1					-4		4	4
4	3	$\frac{1}{2}$		$\frac{1}{2}$		1						4
5	1	$\frac{9}{4}$	$\frac{1}{4}$					$-3\sqrt{}$	-1		$\frac{23}{8}$	4
5	2	$\frac{9}{4}$		$\frac{1}{4}$				$-3\sqrt{}$			$\frac{3}{2}$	4
5	3	$\frac{1}{4}$	$\frac{9}{4}$						-6		4	4
5	4		$\frac{9}{4}$	$\frac{1}{4}$					-6		4	4
5	5	$\frac{1}{4}$		$\frac{9}{4}$						$-3\sqrt{}$	$\frac{3}{2}$	4
5	6		$\frac{1}{4}$	$\frac{9}{4}$					-1	$-3\sqrt{}$	4	4

has an electric quadrupole[9)]

$$Q=6.24\times10^{-26}\text{ e.s.u.}\ ,$$

the axis being perpendicular to the molecular plane.

Contribution of the quadrupole interaction to the cohesive energy is evaluated up to the neighbors corresponding to $i=4$ for both orthorhombic and piled structure. This calculation is elementary but laborious.

If we consider the sums of the core-model interaction (2) and the quadrupole interaction for each of the two strucures, the orthorhombic structure is more stable than the piled one, the difference being of the order of 0.5 kcal/mol.

But if we consider that several approximations and simplifications are introduced in our method, and the difference 0.5 kcal/mol being small, the crystal stability is not explained as definitely as in the case of carbon dioxide.

Moreover, cyclohexane-hexachloride molecule $C_6H_6Cl_6$, which is considered to be oblate, has the crystal structure similar to that of carbon dioxide[10)]. Therefore for a more complete discussion of stability, it is desired to consider the structure in which benzene molecules are arranged as in the crystal of carbon dioxide.

However, we do not go deep into the stability problem because of two reasons. Firstly, a view point which considers the arrangement of benzene molecules as a set of six-toothed bevel gear-wheels is also possible, so the application of the convex-core model itself has some problems. Secondly, as stated before the core used can be improved though calculation will become rather complicated.

Ethylene C_2H_4

As the core of an ethylene molecule C_2H_4 we choose a thin rod connecting two carbon atoms with the length $l=1.33$A. The choice of a rod core may be reasonable because of the π-electrons and because of the fact that each molecule in an ethylene crystal can rotate round the CC-bond. The values of ρ_0 and U_0 determined from the second virial coefficient are

$$\rho_0=4.2\text{A}\ ,\qquad U_0/k=256°\text{K}\ .$$

The parallel body of the core at the distance $\rho_0/2$ indicates the shape and size of the molecule as shown in Fig. 3.

The crystal of ethylene is orthorhombic, the corner and the body center of a unit cell being occupied by centers of molecules. The x-, y-, and z-dimensions of a unit cell are, according to Bunn[11)],

$$a=4.87\text{A}\ ,\qquad b=6.46\text{A}\ ,\qquad c=4.14\text{A}\ ,$$

space group is $Pnnm-D_{2h}{}^{12}$, the CC-bonds being parallel to the ab-plane. Coordinates of carbon atoms of the molecule at the corner are

$$(x,\ y,\ 0)\ \text{ and }\ (-x,\ -y,\ 0)$$

where $x=0.11a$ and $y=0.06b$; and those of

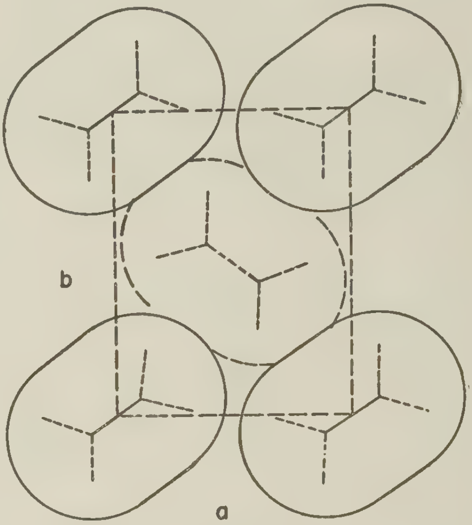

Fig. 2. Ethylene crystal.

Table III

i	j	$\rho_{ij}{}^2$	n_{ij}
1	1	$\frac{a^2}{2}+\frac{c^2}{4}-2au+2u^2$	8
2	1	$a^2-4au+8u^2$	4
2	2	c^2	2
3	1	$2a^2-8au+8u^2$	2
3	2	$2a^2$	2
3	3	$a^2+c^2-4au+8u^2$	8
4	1	$\frac{5}{2}a^2+\frac{c^2}{4}-6au+4u^2$	16
4	2	$\frac{a^2}{2}+\frac{9}{4}c^2-2au+2u^2$	8
5	1	$2a^2+c^2-8au+8u^2$	4
5	2	$2a^2+c^2$	4
6	1	$4a^2-8au+8u^2$	4
6	2	$4c^2$	2
7	1	$\frac{9}{2}a^2+\frac{c^2}{4}-6au+2u^2$	8
7	2	$\frac{5}{2}a^2+\frac{9}{4}c^2-6au+4u^2$	16

the molecule at the body center are

$$\left(\frac{a}{2}-x,\frac{b}{2}+y,\frac{c}{2}\right) \text{ and } \left(\frac{a}{2}+x,\frac{b}{2}-y,\frac{c}{2}\right).$$

The crystal structure is shown in Fig. 2. The angle between the CC-bond and the a-axis is about 35°.

It is impossible to explain the difference between a and b by use of our molecular model. We approximately assume, therefore, that a be equal to b and that the angle between the CC-bond and the a-axis be 45°.

Let us denote by ρ_{ij} the intercore distance to an (i, j)th neighboring molecule, and by n_{ij} the number of (i, j)th neighboring molecules. The subscript i is such that $\sum_j n_{ij}$ becomes the number of ith neighboring lattice points when the present lattice is reduced to a body-centered cubic one:

$$\sum n_{1j}=8\,, \qquad \sum n_{2j}=6\,,\cdots$$

The values of of ρ_{ij} and n_{ij} are given in Table III, which holds for

$$a \geqq 4u \equiv \sqrt{2}\, l\,,$$

l being the length of the rod core.

The cohesive energy and the lattice constants are given by the minimum of the sum (2). The values, which have been calculated by use of the Parametron Computer PC–1, are −3.79 kcal/mol for the cohesive energy and

$$a=b=5.8\text{A}\,, \qquad c=4.3\text{A}\,.$$

The cohesive energy thus obtained is 16% higher than −4.5 kcal/mol, which is the sublimation heat calculated from the specific heat observed by Egan and Kemp[12]. The agreement can be improved by choosing somewhat larger core, although such rectangular core as adopted in the reference 2 is too large.

The ethylene molecule has an electric quadrupole[9]

$$Q=2.30\times10^{-26}\text{ e.s.u.}\,,$$

the axis being the CC-bond. We mention here that, in rod-like molecules, the stability of closest packing structure with parallel arrangement of molecules is much hampered by the electric quadrupole interaction. The discussion of crystal stability is postponed in following papers.

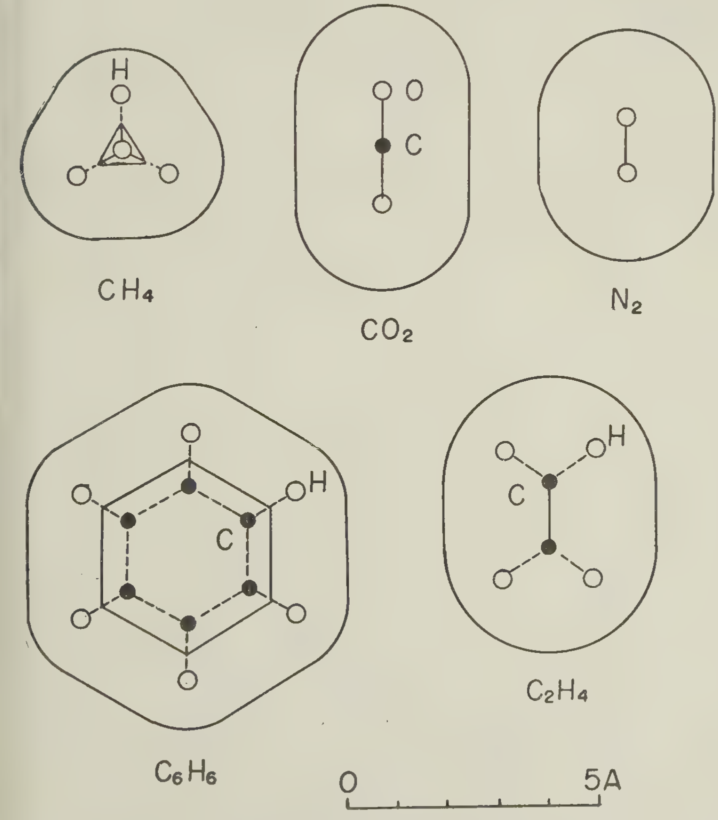

Fig. 3. The used core-models of molecules.

General Conclusion

We have investigated, in Part I and II, methane CH_4, carbon dioxide CO_2, nitrogen N_2, benzene C_6H_6, and ethylene C_2H_4 crystals by use of our convex-core model of molecules. The cores of these molecules are shown in Fig. 3.

When we neglect zero-point energies, potential non-additivities, and electric multipole interactions, then the calculated cohesive energies are 24% lower for methane, 27%, higher for carbon dioxide, 17% lower for nitrogen, little higher for benzene, and 16% higher for ethylene in comparison with observed values. Main cause of the energy discrepancy for methane is the neglect of both the zero-point energy and the potential non-additivity. That for carbon dioxide is the neglect of the quadrupole interaction and the core thickness, because a more appropriate core of the carbon dioxide molecule would be such as shown in Fig. 4. In general, when the core is enlarged, the potential depth U_0 increases and hence calculated value of the cohesive energy becomes lower. The energy discrepancy for ethylene may also be partly due to the choice of the thin core, because a more adequate core would be such as shown in Fig. 4.

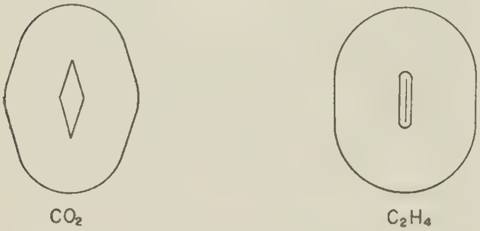

Fig. 4. Cores of carbon dioxide and ethylene which will be closer to the reality, the non-vanishing thickness corresponding to π-electrons.

Thus we reach the following conclusion. For simple non-polar convex molecules the core-model interaction explains the cohesive energies and lattice constants if appropriate cores are chosen, although the stability of their crystal structures depends greatly on the electric multipole interaction as shown recently by Kihara[10].

Acknowledgements

In conclusion the author wishes to express his sincere thanks to Prof. T. Kihara for his continual guidance and valuable suggestions. He also wishes to express his cordial thanks to Dr. Y. Midzuno and Dr. S. Kaneko for their kind guidance in programming and operating the Parametron Computor PC-1.

References

1) T. Kihara and S. Koba: J. Phys. Soc. Japan **14** (1959) 247.
2) T. Kihara: Rev. Mod. Phys. **25** (1953) 831.
3) T. Kihara: J. Phys. Soc. Japan **12** (1957) 564.
T. Kihara and A. Ōuchi: ibid. **12** (1957) 1052.
4) Andon, Cox, Herington, and Martin: Trans. Faraday Soc. **53** (1957) 1074.
5) J. D. Cox and R. J. L. Andon: Trans. Faraday Soc. **54** (1958) 1622.
6) Francis, McGlasham, Hamann, and McManamey: J. Chem. Phys. **20** (1952) 1341.
7) E. G. Cox: Rev. Mod. Phys. **30** (1958) 159.
8) J. H. de Boer: Trans. Faraday Soc. **32** (1936) 10.
9) R. M. Hill and W. V. Smith: Phys. Rev. **82** (1951) 451.
10) T. Kihara: J. Phys. Soc. Japan **15** (1960) 1920.
11) C. W. Bunn: Trans. Faraday Soc. **40** (1944) 23.
12) C. J. Egan and J. D. Kemp: J. Am. Chem. Soc. **59** (1937) 1264.

JOURNAL OF THE PHYSICAL SOCIETY OF JAPAN, Vol. 16, No. 4, APRIL, 1961

Entropy Production and Variation Principle in The Kinetic Theory of Rigid-Sphere Gas Mixture

By Terutosi MURAKAMI

Department of Applied Science, Faculty of Engineering,
Kyushu University, Fukuoka, Japan

(Received January 7, 1961)

The balance equations and the fluxes of thermodynamical variables are obtained on the basis of the modified Boltzmann equation for a multicomponent rigid-sphere gas. The kinetic expression of entropy balance is obtained in terms of the H-theorem, the correction to the entropy due to imperfectness of the gas being added. The correction is calculated from the equation of state, which is derived from the momentum transport equation. The entropy balance is also formulated thermodynamically with the aid of the Gibbs relation. By the use of these two expressions a variational problem concerning the entropy production rate can be set up. The solution of this problem leads to the first approximation equation for singlet distribution function, which is identical with Enskog's one apart from the terms independent of the energy dissipation.

§ 1. Introduction

The variation principles in the kinetic theory of gases[1),2),3)] seem to have a close relation to the extremum properties of the entropy production in thermodynamics of irreversible processes. These principles are established on the basis of the linearized Boltzmann integro-differential equation. Since the kinetic theory of gases based on the linearized Boltzmann equation is limited to the case of low density, it is desirable to inquire to what extent the variation principle is applicable to the transport processes in dense gases.

A great deal of attention has been concentrated to the transport properties of the dense fluid of rigid-sphere molecules.[4)-14)] The modified Boltzmann equation was derived by Enskog[4)] at first on the basis of plausible physical arguments. From the statistical mechanical point of view, Rice and et al.[7),8)] reinvestigated this equation and proposed a new equation of transport different from the Enskog equation, but recently O'Toole and Dahler[9)] and Hollinger and Curtiss[10)] have confirmed independently that the equation for the singlet distribution function has exactly the same form as that originally suggested by Enskog.

In a previous paper[11)] the variation principle in the kinetic theory of gases was extended to the case of a dense gas made of rigid-sphere molecules with finite diameter. It was also shown that the solution of Enskog's first approximation equation for a dense gas can be derived from the variation principle with respect to the entropy production rate, provided that the correction to the entropy due to imperfectness of a gas would be taken into account.

It is the purpose of the present paper to establish a thermodynamical descriptions of linear transport processes in a multicomponent dense gas consisting of rigid-sphere molecules with different diameters and masses on the basis of the kinetic theory.

At first we shall briefly mention of derivation of the modified Boltzmann equation following O'Toole and Dahler's and Enskog's method (§ 2.). The problem of our attention is confined to solving such a fundamental equation with use of suitable approximation methods. For this purpose equations of balance such as equation of continuity, equation of motion and equation of energy balance, will be obtained by means of the general equation of change derived from our modified Boltz- mann equation (§ 3.).

We shall confine ourselves to the study of the system in which the macroscopic state varies so slowly that the system may be well described with use of perturbed singlet distribution function corresponding to small deviation from the Maxwell distribution and of the equilibrium pair correlation function. The the fluxes appearing in the hydrodynamic equations are expressible in terms of these functions (§ 4.).

To determine the perturbation functions, the various approximation methods have been proposed. Enskog's method of direct solution of the basic Boltzmann integro-differential equation is well known. This method will be followed in the present paper for the system of moderately dense gases, and the first approximation equation identical with Thorne's equation[12] for two component system will be derived in § 5. Another purpose of this investigation is to establish the method for obtaining the solution of such a fundamental equation from entirely physical considerations. To complete the description of irreversible processes, we shall consider the equation of entropy balance. In usual kinetic theory of gases the entropy is given as $-k$ time the H-function, which is considered as the average of logarithm of a singlet distribution function assigned to each molecule. Then the balance equation of entropy is derived with help of the general equation of change in terms of statistical expression (§ 6.). In our case of a dense gas the correction to the entropy due to imperfectness of the gas should be taken into account. The first approximation to this correction is achieved by adding the equilibrium value of additional entropy calculated from the virial expansion form of the usual equation of state, which is obtained from the momentum transport equation. The expression of entropy production rate thus obtained is not so simple function of molecular properties, but may be written in quadratic integral form concerning the perturbation function as far as it is confined to linear processes.

On the other hand, the entropy production rate can be expressed as a bilinear form of the fluxes of molecular properties and the conjugate driving forces according to the thermodynamic considerations of irreversible processes based on the Gibbs relation (§ 7.). The equation to be satisfied by the perturbation function is obtained if these two expressions for the entropy productions are equated. Then the variational problem concerning this entropy production rate is established and from this variational problem the first approximation equation for the perturbation function is obtained (§ 8.).

§ 2. The Modified Boltzmann Equation for the Gas Mixtures of Rigid-Sphere Molecules

Let us consider a multicomponent gas consisting of ν kinds of rigid-sphere molecules with different diameters and masses in non-equilibrium state; the mass and diameter of a molecule of the species i will be denoted by m_i and σ_i, respectively. As is well known, a state of the system under consideration is well described by the singlet distribution functions $f_i^{(1)}(\boldsymbol{r}, \boldsymbol{v}_i; t)$ and the pair distribution functions $f_{ij}^{(2)}(\boldsymbol{r}_i, \boldsymbol{v}_i; \boldsymbol{r}_j, \boldsymbol{v}_j; t)$ which are defined in usual manner. The function $f_i^{(1)}$ is normalized to the number density n_i of kind i:

$$\int f_i^{(1)}(\boldsymbol{r}, \boldsymbol{v}_i; t)\, d\boldsymbol{v}_i = n_i(\boldsymbol{r}, t) \ . \tag{2.1}$$

The pair distribution function $f_{ij}^{(2)}$ is assumed to be given in the form

$$f_{ij}^{(2)}(\boldsymbol{r}_i, \boldsymbol{v}_i; \boldsymbol{r}_j, \boldsymbol{v}_j; t) = \chi_{ij}(\boldsymbol{r}_i, \boldsymbol{r}_j)\, f_i^{(1)}(\boldsymbol{r}_i, \boldsymbol{v}_i; t)\, f_j^{(1)}(\boldsymbol{r}_j, \boldsymbol{v}_j; t) \tag{2.2}$$

where the correlation functions $\chi_{ij}(\boldsymbol{r}_i, \boldsymbol{r}_j)$ depend only on the location of the two molecules but not on the momenta, just as in the case of uniform equilibrium state. This is the basic assumption of our kinetic theory of moderately dense gases, besides the assumption of binary collisions. In a uniform equilibrium state the functions χ_{ij} depend only upon the densities and are reduced to the radial distribution functions, while in a non-uniform state the value of χ_{ij} may be expected to involve also the spatial derivatives of the densities. However, if the gradients of temperature, velocities, and concentrations are small, the local equilibrium value χ_{ij}^0 can be used for χ_{ij} in successive points to the second approximation. Then the central problem in the present theory is to determine the singlet distribution function $f_i^{(1)}$ in non-equilibrium state, and to obtain the transport of the molecular properties in terms of this function, regarding χ_{ij}^0 as a parameter of the state.

From statistical mechanics the rate of change in the singlet distribution function $f_i^{(1)}$ is determined by the equation

$$\left\{\frac{\partial}{\partial t}+\boldsymbol{v}_i\cdot\nabla+\frac{\boldsymbol{F}_i}{m_i}\cdot\nabla_{\boldsymbol{v}_i}\right\}f_i^{(1)}(\boldsymbol{r},\boldsymbol{v}_i;t)=\sum_j\iint\{f_{ij}^{(2)}(\boldsymbol{r},\boldsymbol{v}_i';\boldsymbol{r}+\sigma_{ij}\boldsymbol{k},\boldsymbol{v}_j';t)$$
$$-f_{ij}^{(2)}(\boldsymbol{r},\boldsymbol{v}_i;\boldsymbol{r}-\sigma_{ij}\boldsymbol{k},\boldsymbol{v}_j;t)\}\sigma_{ij}^2(\boldsymbol{g}_{ji}\cdot\boldsymbol{k})\,d\boldsymbol{k}\,d\boldsymbol{v}_j\,, \tag{2.3}$$

with

$$\sigma_{ij}\equiv\frac{1}{2}(\sigma_i+\sigma_j)\,, \tag{2.4}$$

where $\boldsymbol{F}_i$ is the external force acting on a molecule of kind i, $\boldsymbol{k}$ the unit vector in the direction of line of centers of the two molecules in contact, $\boldsymbol{g}_{ji}=\boldsymbol{v}_j-\boldsymbol{v}_i$ the relative velocity, and $\boldsymbol{v}_i'$, $\boldsymbol{v}_j'$ the velocities of molecules after the collision characterized by $\boldsymbol{v}_i$, $\boldsymbol{v}_j$ and $\boldsymbol{k}$. The derivation of (2.3) is closely parallel to that given by O'Toole and Dahler[9] for the modified Boltzmann equation in the case of simple dense gases composed of rigid-sphere molecules.

Inserting (2.2) into (2.3), we obtain Enskog's modified Boltzmann equation for multi-component dense gases of rigid-sphere molecules:

$$\left\{\frac{\partial}{\partial t}+\boldsymbol{v}_i\cdot\nabla+\frac{\boldsymbol{F}_i}{m_i}\cdot\nabla_{\boldsymbol{v}_i}\right\}f_i^{(1)}=\left(\frac{\partial f_i^{(1)}}{\partial t}\right)_{\text{coll}}\,,$$

$$\left(\frac{\partial f_i^{(1)}}{\partial t}\right)_{\text{coll}}=\sum_j\iint\left\{\chi_{ij}^0\left(\boldsymbol{r}+\frac{\sigma_{ij}}{2}\boldsymbol{k}\right)f_i^{(1)}(\boldsymbol{r},\boldsymbol{v}_i';t)\,f_j^{(1)}(\boldsymbol{r}+\sigma_{ij}\boldsymbol{k},\boldsymbol{v}_j';t)\right.$$
$$\left.-\chi_{ij}^0\left(\boldsymbol{r}-\frac{\sigma_{ij}}{2}\boldsymbol{k}\right)f_i^{(1)}(\boldsymbol{r},\boldsymbol{v}_i;t)\,f_j^{(1)}(\boldsymbol{r}-\sigma_{ij}\boldsymbol{k},\boldsymbol{v}_j;t)\right\}\sigma_{ij}^2(\boldsymbol{g}_{ji}\cdot\boldsymbol{k})\,d\boldsymbol{k}\,d\boldsymbol{v}_j\,, \tag{2.5}$$

where the local equilibrium value of the function χ_{ij}^0 is evaluated at the center of colliding two molecules.

If the conditions in gases are slowly varying in space, we may expand $f_j^{(1)}(\boldsymbol{r}\pm\sigma_{ij}\boldsymbol{k},\boldsymbol{v}_j;t)$ and $\chi_{ij}\left(\boldsymbol{r}\pm\frac{1}{2}\sigma_{ij}\boldsymbol{k}\right)$ in Taylor's series about the point $\boldsymbol{r}$, and retain the terms only up to the second. Then (2.5) is written in the form:

$$\frac{\partial f_i}{\partial t}+\boldsymbol{v}_i\cdot\nabla f_i+\frac{\boldsymbol{F}_i}{m_i}\cdot\nabla_{\boldsymbol{v}_i}f_i=\sum_{\gamma=1}^{6}\sum_{j=1}^{\nu}J_{ij}^{(\gamma)}\,, \tag{2.6}$$

$$J_{ij}^{(1)}\equiv\chi_{ij}^0\iint(f_i'f_j'-f_if_j)\sigma_{ij}^2(\boldsymbol{g}_{ji}\cdot\boldsymbol{k})\,d\boldsymbol{k}\,d\boldsymbol{v}_j\,, \tag{2.6–1}$$

$$J_{ij}^{(2)}\equiv\chi_{ij}^0\iint\{\boldsymbol{k}\cdot(f_i'\nabla f_j'+f_i\nabla f_j)\}\sigma_{ij}^3(\boldsymbol{g}_{ji}\cdot\boldsymbol{k})\,d\boldsymbol{k}\,d\boldsymbol{v}_j\,, \tag{2.6–2}$$

$$J_{ij}^{(3)}\equiv\frac{1}{2}\iint(\boldsymbol{k}\cdot\nabla\chi_{ij}^0)(f_i'f_j'+f_if_j)\sigma_{ij}^3(\boldsymbol{g}_{ji}\cdot\boldsymbol{k})\,d\boldsymbol{k}\,d\boldsymbol{v}_j\,, \tag{2.6–3}$$

$$J_{ij}^{(4)}\equiv\frac{1}{2}\chi_{ij}^0\iint[\boldsymbol{k}\boldsymbol{k}:(f_i'\nabla\nabla f_j'-f_i\nabla\nabla f_j)]\sigma_{ij}^4(\boldsymbol{g}_{ji}\cdot\boldsymbol{k})\,d\boldsymbol{k}\,d\boldsymbol{v}_j\,, \tag{2.6–4}$$

$$J_{ij}^{(5)}\equiv\frac{1}{2}\iint(\boldsymbol{k}\cdot\nabla\chi_{ij}^0)[\boldsymbol{k}\cdot(f_i'\nabla f_j'-f_i\nabla f_j)]\sigma_{ij}^4(\boldsymbol{g}_{ji}\cdot\boldsymbol{k})\,d\boldsymbol{k}\,d\boldsymbol{v}_j\,, \tag{2.6–5}$$

$$J_{ij}^{(6)}\equiv\frac{1}{8}\iint(\boldsymbol{k}\boldsymbol{k}:\nabla\nabla\chi_{ij}^0)(f_i'f_j'-f_if_j)\sigma_{ij}^4(\boldsymbol{g}_{ji}\cdot\boldsymbol{k})\,d\boldsymbol{k}\,d\boldsymbol{v}_j\,, \tag{2.6–6}$$

where f_i' and f_j' denote $f_i(\boldsymbol{r},\boldsymbol{v}_i';t)$ and $f_j(\boldsymbol{r},\boldsymbol{v}_j';t)$, respectively. This equation (2.6) is our fundamental equation for the singlet distribution function.

§ 3. The General Equation of Change and the Flux Vector

Before solving the equation (2.6), we consider the general hydrodynamic equation of change. The macroscopic conditions in a fluid in non-equilibrium may be well described by a set of thermodynamical quantities and their derivatives in space, together with the equations governing these quantities. These thermodynamical quantities are given as the averages of the molecular properties which are functions of the molecular velocities.

Let us denote one of such properties associated with molecules of kind i by ψ_i. The average of this property $\overline{\psi}_i$ at each point of space is given by

$$n_i\overline{\psi}_i=\int\psi_i f_i\, d\boldsymbol{v}_i\,. \tag{3.1}$$

Thus the stream velocity (mass average velocity) $\boldsymbol{v}_0$ is given by

$$\rho\boldsymbol{v}_0(\boldsymbol{r},t)=\sum_i m_i\int\boldsymbol{v}_i f_i\, d\boldsymbol{v}_i\,, \tag{3.2}$$

in which $\rho(\boldsymbol{r},t)=\sum_i n_i m_i$ is the mass density of the gas at a point $\boldsymbol{r}$.

Multiplying (2.6) by ψ_i and integrating over the velocity space we find the equation of change

$$\frac{\partial(n_i\overline{\psi}_i)}{\partial t}+\nabla\cdot n_i\overline{\psi_i\boldsymbol{v}_i}-n_i\overline{\left\{\frac{\partial}{\partial t}+\boldsymbol{v}_i\cdot\nabla+\frac{\boldsymbol{F}_i}{m_i}\cdot\nabla_{\boldsymbol{v}_i}\right\}}\psi_i=\sum_{\gamma=1}^{6}I_i^{(\gamma)}(\psi)\,, \tag{3.3}$$

where

$$I_i^{(\gamma)}(\psi)\equiv\sum_j\int\psi_i J_{ij}^{(\gamma)}\, d\boldsymbol{v}_i\,. \tag{3.4}$$

If we use (2.6–1) to (2.6–6) and consider the inverse encounters, the collisional changes given by (3.4) are expressed in the form

$$I_i^{(1)}=\sum_j \chi_{ij}^0\sigma_{ij}^2\iiint(\psi_i'-\psi_i)f_if_j(\boldsymbol{g}_{ji}\cdot\boldsymbol{k})\, d\boldsymbol{k}\, d\boldsymbol{v}_i\, d\boldsymbol{v}_j\,, \tag{3.5–1}$$

$$I_i^{(2)}=\sum_j \chi_{ij}^0\sigma_{ij}^3\iiint(\psi_i-\psi_i')(\boldsymbol{k}\cdot f_i\nabla f_j)(\boldsymbol{g}_{ji}\cdot\boldsymbol{k})\, d\boldsymbol{k}\, d\boldsymbol{v}_i\, d\boldsymbol{v}_j\,, \tag{3.5–2}$$

$$I_i^{(3)}=\sum_j \frac{1}{2}\sigma_{ij}^3\iiint(\psi_i-\psi_i')(\boldsymbol{k}\cdot\nabla\chi_{ij}^0)f_if_j(\boldsymbol{g}_{ji}\cdot\boldsymbol{k})\, d\boldsymbol{k}\, d\boldsymbol{v}_i\, d\boldsymbol{v}_j\,, \tag{3.5–3}$$

$$I_i^{(4)}=\sum_j \frac{1}{2}\sigma_{ij}^4\iiint(\psi_i'-\psi_i)[\boldsymbol{k}\boldsymbol{k}:f_i\nabla\nabla f_j](\boldsymbol{g}_{ji}\cdot\boldsymbol{k})\, d\boldsymbol{k}\, d\boldsymbol{v}_i\, d\boldsymbol{v}_j\,, \tag{3.5–4}$$

$$I_i^{(5)}=\sum_j \frac{1}{2}\sigma_{ij}^4\iiint(\psi_i'-\psi_i)(\boldsymbol{k}\cdot\nabla\chi_{ij}^0)(\boldsymbol{k}\cdot f_i\nabla f_j)(\boldsymbol{g}_{ji}\cdot\boldsymbol{k})\, d\boldsymbol{k}\, d\boldsymbol{v}_i\, d\boldsymbol{v}_j\,, \tag{3.5–5}$$

$$I_i^{(6)}=\sum_j \frac{1}{8}\sigma_{ij}^4\iiint(\psi_i'-\psi_i)f_if_j(\boldsymbol{k}\boldsymbol{k}:\nabla\nabla\chi_{ij}^0)(\boldsymbol{g}_{ji}\cdot\boldsymbol{k})\, d\boldsymbol{k}\, d\boldsymbol{v}_i\, d\boldsymbol{v}_j\,. \tag{3.5–6}$$

If ψ_i is one of the summational invariants, we can obtain the contribution of over all kinds to the collisional change, summing over i, and symmetrizing by the same arguments as that in Appendix I in the author's previous paper[11], in the following form

$$\sum_i^{\nu}\sum_{\gamma}^{6}I_i^{(\gamma)}(\psi)=-\nabla\cdot\Big[\sum_{\alpha}^{2}\mathbf{J}_c^{(\alpha)}(\psi)\Big]+\sum_{\alpha}^{2}R^{(\alpha)}(\psi)\,, \tag{3.6}$$

where

$$\mathbf{J}_c^{(1)}(\psi)=\frac{1}{2}\sum_{ij}\sigma_{ij}^3\chi_{ij}^0\iiint(\psi_i'-\psi_i)f_if_j\boldsymbol{k}(\boldsymbol{g}_{ji}\cdot\boldsymbol{k})\, d\boldsymbol{k}\, d\boldsymbol{v}_i\, d\boldsymbol{v}_j\,, \tag{3.7–1}$$

$$\mathbf{J}_c^{(2)}(\psi)=\frac{1}{4}\sum_{ij}\sigma_{ij}^4\chi_{ij}^0\iiint(\psi_i'-\psi_i)f_if_j\left(\boldsymbol{k}\cdot\nabla\ln\frac{f_i}{f_j}\right)\boldsymbol{k}(\boldsymbol{g}_{ji}\cdot\boldsymbol{k})\,d\boldsymbol{k}\,d\boldsymbol{v}_i\,d\boldsymbol{v}_j\,, \tag{3.7–2}$$

$$R^{(1)}(\psi)=\frac{1}{2}\sum_{ij}\sigma_{ij}^4\chi_{ij}^0\iiint f_if_j\{\boldsymbol{k}\cdot\nabla(\psi_i'-\psi_i)\}(\boldsymbol{g}_{ji}\cdot\boldsymbol{k})\,d\boldsymbol{k}\,d\boldsymbol{v}_i\,d\boldsymbol{v}_j\,, \tag{3.8–1}$$

$$R^{(2)}(\psi)=\frac{1}{4}\sum_{ij}\sigma_{ij}^4\chi_{ij}^0\iiint f_if_j\left(\boldsymbol{k}\cdot\nabla\ln\frac{f_i}{f_j}\right)\{\boldsymbol{k}\cdot\nabla(\psi_i'-\psi_i)\}(\boldsymbol{g}_{ji}\cdot\boldsymbol{k})\,d\boldsymbol{k}\,d\boldsymbol{v}_i\,d\boldsymbol{v}_j\,. \tag{3.8–2}$$

As was pointed out for one component gases[13], it is shown that $\mathbf{J}_c(\psi)$'s are the contribution of the collisional transfer of ψ to the flux vector, (see Appendix I). In addition to the abovementioned collisional transfer, there exists a flux due to the flow of molecules across the surface moving with the mass average velocity, given by

$$\mathbf{J}_{k_i}(\psi_i)=\int\psi_i\boldsymbol{V}_if_i\,d\boldsymbol{v}_i\,, \tag{3.9}$$

associated with the ith kind of molecules, where $\boldsymbol{V}_i=\boldsymbol{v}_i-\boldsymbol{v}_0$ is called the peculiar velocity. Then the whole flux in a gas mixture is given by the sum of such fluxes over all components:

$$\mathbf{J}_k(\psi)=\sum_i\mathbf{J}_{k_i}(\psi_i)=\sum_i^{\nu}\int\psi_i\boldsymbol{V}_if_i\,d\boldsymbol{v}_i\,. \tag{3.10}$$

It is now noticed that there remains the terms $R(\psi)$'s given by (3.8), which correspond to energy sources and are necessary for the correct expression of the energy balance.

We shall now consider the summational invariants, m_i, $m_i\boldsymbol{V}_i$ and $m_iV_i/2$ as ψ_i to get the hydrodynamical equations.

(I) *The equation of continuity*: Let ψ_i be m_i. Then using (2.1) and (3.3) we obtain

$$\frac{D\rho_i}{Dt}=-\rho_i\nabla\cdot\boldsymbol{v}_0-\nabla\cdot\boldsymbol{J}_i\,, \tag{3.11}$$

where $\rho_i=n_im_i$ and $\boldsymbol{J}_i=n_i\overline{m_i\boldsymbol{V}_i}$ are the mass density and the diffusion velocity flux of species i, respectively. D/Dt denotes the hydrodynamical operator $(\partial/\partial t-\boldsymbol{v}_0\cdot\nabla)$ and (3.11) is the equation of continuity for the ith species. If the equations of continuity (3.11) are summed over i, since $\sum_i^{\nu}\boldsymbol{J}_i=0$ according to the definition of $\boldsymbol{J}_i$, the overall equation of continuity is obtained:

$$\frac{D\rho}{Dt}=-\rho\nabla\cdot\boldsymbol{v}_0\,. \tag{3.12}$$

(II) *The equation of motion*: If we put $\psi_i=m_i\boldsymbol{V}_i$ in (3.3), and sum over i, then we obtain

$$\rho\frac{D\boldsymbol{v}_0}{Dt}=-\nabla\cdot\mathbf{P}+\sum_i n_i\boldsymbol{F}_i \tag{3.13}$$

where $\mathbf{P}$ is given by

$$\mathbf{P}=\mathbf{P}_k+\mathbf{P}_c\,, \tag{3.14}$$

$$\mathbf{P}_k=\sum_i m_i\int\boldsymbol{V}_i\boldsymbol{V}_if_i\,d\boldsymbol{v}_i=\sum_i\mathbf{P}_{k_i}\,, \tag{3.14–k}$$

$$\mathbf{P}_c=\sum_{\alpha}^{2}\mathbf{J}_c^{(\alpha)}[m_i\boldsymbol{V}_i]\,, \tag{3.14–c}$$

since $R(m_i\boldsymbol{V}_i)$'s all vanish. We can immediately see that (3.13) is the equation of motion and $\mathbf{P}$ is the pressure tensor. The momentum flux arising from the collisional transfer of momentum $\mathbf{J}_c[m_i V_i]$'s are respectively written in the following forms:

$$\mathbf{J}_c^{(1)}[m_i V_i]=\frac{\pi}{15}\sum_{ij}\sigma_{ij}^3\chi_{ij}^0 M_{ji}m_i\iint(2\boldsymbol{gg}+g^2\mathbf{U})f_i f_j\,d\boldsymbol{v}_i\,d\boldsymbol{v}_j \tag{3.15–1}$$

$$\mathbf{J}_c^{(2)}[m_i V_i]=\frac{\pi}{48}\sum_{ij}\sigma_{ij}^4\chi_{ij}^0 M_{ji}m_i\iint f_i f_j\Big[\frac{(\boldsymbol{gg}+g^2\mathbf{U})}{g}\Big(\boldsymbol{g}\cdot\nabla\ln\frac{f_j}{f_i}\Big)$$
$$+g\Big\{\Big(\nabla\ln\frac{f_i}{f_j}\Big)\boldsymbol{g}+\boldsymbol{g}\Big(\nabla\ln\frac{f_i}{f_j}\Big)\Big\}\Big]d\boldsymbol{v}_i\,d\boldsymbol{v}_j\,, \tag{3.15–2}$$

where

$$M_{ij}=2m_i/m_i+m_j\,, \tag{3.16}$$

$\mathbf{U}$ is the unit tensor, and for simplicity the suffices j, i in $\boldsymbol{g}_{ji}$ are droped hereafter. (see Appendix II).

(III) *The equation of energy balance*: If we put $\psi_i=m_i V_i^2/2$ in (3.3) and sum over i, we obtain

$$\rho\frac{D\hat{U}}{Dt}=-\nabla\cdot\boldsymbol{q}-\mathbf{P}:\nabla\boldsymbol{v}_0+\sum_i\frac{\boldsymbol{F}_i}{m_i}\cdot\boldsymbol{J}_i\,, \tag{3.17}$$

where $\hat{U}$ is the kinetic contribution to the internal energy per unit mass given by

$$\rho\hat{U}=\frac{1}{2}\sum_i m_i\int V_i^2 f_i\,d\boldsymbol{v}_i\,, \tag{3.18}$$

and $\boldsymbol{q}$ is the thermal energy flux given by

$$\boldsymbol{q}=\boldsymbol{q}_k+\boldsymbol{q}_c\,, \tag{3.19}$$

$$\boldsymbol{q}_k\equiv\frac{1}{2}\sum_i m_i\int V_i^2\boldsymbol{V}_i f_i\,d\boldsymbol{v}_i=\sum_i\boldsymbol{q}_{k_i}\,, \tag{3.19–k}$$

$$\boldsymbol{q}_c\equiv\sum_{\alpha=1}^{2}\mathbf{J}_c^{(\alpha)}\Big[\frac{1}{2}m_i V_i\Big]. \tag{3.19–c}$$

We use the mark ^ to denote the quantity per unit mass. It should be noted that $R(m_i V_i^2/2)$ does not vanish and is given by (see Appendix II)

$$\sum_{\alpha=1}^{2}R^{(\alpha)}\Big[\frac{1}{2}m_i V_i^2\Big]=-\nabla\boldsymbol{v}_0:\sum_{\alpha=1}^{2}\mathbf{J}_c^{(\alpha)}[m_i V_i]=-\mathbf{P}_c:\nabla\boldsymbol{v}_0\,. \tag{3.20}$$

The energy fluxes arising from the collisional transfer of energy $\mathbf{J}_c[m_i V_i^2/2]$ are respectively given by (see Appendix II)

$$\mathbf{J}_c^{(1)}\Big[\frac{m_i V_i^2}{2}\Big]=\frac{\pi}{15}\sum_{ij}\sigma_{ij}^3\chi_{ij}^0 M_{ji}m_i\iint[2\boldsymbol{g}(\boldsymbol{g}\cdot\boldsymbol{G})+\boldsymbol{g}^2\boldsymbol{G}]f_i f_j\,d\boldsymbol{v}_i\,d\boldsymbol{v}_j\,, \tag{3.21–1}$$

and

$$\mathbf{J}_c^{(2)}\Big[\frac{m_i V_i^2}{2}\Big]=\frac{\pi}{48}\sum_{ij}\sigma_{ij}^4\chi_{ij}^0 M_{ji}m_i\iint\Big[\frac{\boldsymbol{g}}{g}\Big(\boldsymbol{G}\nabla\ln\frac{f_i}{f_j}:\boldsymbol{gg}\Big)+g\Big\{\Big(\boldsymbol{G}\cdot\nabla\ln\frac{f_i}{f_j}\Big)\boldsymbol{g}$$
$$+\Big(\boldsymbol{g}\cdot\nabla\ln\frac{f_i}{f_j}\Big)\boldsymbol{G}+(\boldsymbol{g}\cdot\boldsymbol{G})\nabla\ln\frac{f_i}{f_j}\Big\}\Big]f_i f_j\,d\boldsymbol{v}_i\,d\boldsymbol{v}_j\,, \tag{3.21–2}$$

where $\boldsymbol{G}_{ij}$ is the velocity of mass center of i and j molecules, defined by

$$\boldsymbol{G}_{ij}\equiv\frac{m_i\boldsymbol{V}_i+m_j\boldsymbol{V}_j}{m_i+m_j}\,. \tag{3.22}$$

The local temperature T is defined by

$$\frac{3}{2}nkT=\frac{1}{2}\sum_i m_i\int \boldsymbol{V}_i^2 f_i\,d\boldsymbol{v}_i\ , \tag{3.23}$$

which leads to

$$\rho\hat{U}=\frac{3}{2}nkT\ , \tag{3.24}$$

where n is the number density of the whole gasgiven by the relation

$$n=\sum_i^{\nu} n_i\ . \tag{3.25}$$

§ 4. The First Approximations to Fluxes

If the system is not so far from equilibrium, we may choose as the zeroth approximation to f_i the Maxwell distribution given by

$$f_i{}^0(\boldsymbol{r},\boldsymbol{v}_i;\,t)=n_i(\boldsymbol{r},t)\left(\frac{m_i}{2\pi kT}\right)^{3/2}\exp\left\{-\frac{m_i\boldsymbol{V}_i^2}{2kT(\boldsymbol{r},t)}\right\}, \tag{4.1}$$

where n_i, $\boldsymbol{v}_0$ and T are respectively given by (2.1), (3.2) and (3.23), and are generally functions of the spatial coordinates. Then we may express f_i in terms of a perturbation function ϕ_i:

$$f_i=f_i{}^0(1+\phi_i)\ . \tag{4.2}$$

From (2.1), (3.2), (3.23) and (4.1) we can prove the following relations:

$$\int f_i{}^0\phi_i\,d\boldsymbol{v}_i=0\ , \tag{4.3–1}$$

$$\sum_i m_i\int \boldsymbol{V}_i f_i{}^0\phi_i\,d\boldsymbol{v}_i=0\ , \tag{4.3–2}$$

$$\frac{1}{2}\sum_i m_i\int \boldsymbol{V}_i^2 f_i{}^0\phi_i\,d\boldsymbol{v}_i=0\ . \tag{4.3–3}$$

These auxiliary conditions imposed on f_i imply the physical assumption that the system may be well described by a set of the thermodynamical variables in successive local equilibrium states. Then we can express the fluxes in terms of the perturbation function ϕ_i and the pair correlation function $\chi_{ij}{}^0$.

If we consider the mass flow vector, for which the flux is only kinetic one given by (3.9), then we obtain from (4.3–1)

$$\boldsymbol{J}_i=m_i\int \boldsymbol{V}_i f_i\,d\boldsymbol{v}_i=m_i\int \boldsymbol{V}_i f_i{}^0\phi_i\,d\boldsymbol{v}_i\ . \tag{4.4}$$

The pressure tensor given by (3.16) is reduced to the following form to the first approximation. The kinetic contribution $\mathbf{P}_{k_i}$ is written as

$$\mathbf{P}_{k_i}=n_ikT\,\mathbf{U}+m_i\int \boldsymbol{V}_i\boldsymbol{V}_i f_i{}^0\phi_i\,d\boldsymbol{v}_i\ , \tag{4.5}$$

or we can rewrite, using the hydrostatic pressure $p_{id}{}^0=\sum_i p_{k_i}{}^0=\sum_i n_ikT$ for an ideal gas, as

$$\mathbf{P}_k-p_k{}^0\mathbf{U}=\sum_i\int m_i\boldsymbol{V}_i\boldsymbol{V}_i f_i{}^0\phi_i\,d\boldsymbol{v}_i=\sum_i m_i\int\left(\boldsymbol{V}_i\boldsymbol{V}_i-\frac{1}{3}\boldsymbol{V}_i^2\mathbf{U}\right)f_i\,d\boldsymbol{v}_i\ . \tag{4.6}$$

The collisional transfers of momentum given by (3.15) are respectively reduced after rather tedious but straightforward calculations to

$$\mathbf{J}_c^{(1)}[m_i V_i] = \sum_{ij} n_i n_j b_{ij} \chi_{ij}^0 kT\,\mathbf{U} + \frac{2}{5}\sum_{ij} n_j b_{ij} \chi_{ij}^0 M_{ji} m_i \int V_i V_i f_i^0 \phi_i \, dv_i \,, \tag{4.7-1}$$

$$\mathbf{J}_c^{(2)}[m_i V_i] = -\sum_{ij} \tilde{\omega}_{ij} \left[\frac{6}{5}\frac{\mathbf{S}}{T} + \frac{\nabla \cdot v_0}{T}\mathbf{U} \right], \tag{4.7-2}$$

where $\mathbf{S}$ is the rate of shear tensor defined by (see Appendix III)

$$S_{ij} \equiv \frac{1}{2}\left[\frac{\partial v_{0j}}{\partial x_i} + \frac{\partial v_{0i}}{\partial x_j} \right] - \frac{1}{3}\delta_{ij}(\nabla \cdot v_0) \,, \tag{4.8}$$

$$b_{ij} \equiv \frac{2}{3}\pi \sigma_{ij}^3 \,, \tag{4.9}$$

$$\tilde{\omega}_{ij} \equiv \frac{4}{9} n_i n_j \sigma_{ij}^4 \chi_{ij}^0 (\pi M_{ji} k T^3)^{1/2} \,. \tag{4.10}$$

Consequently the pressure tensor as a whole, is given by

$$\mathbf{P} = \mathbf{P}_k + \mathbf{P}_c = \left[p^0 - \sum_{ij} \tilde{\omega}_{ij} \frac{\nabla \cdot v_0}{T} \right] \mathbf{U} - \frac{6}{5}\sum_{ij} \tilde{\omega}_{ij} \frac{\mathbf{S}}{T}$$
$$+ \sum_i \left(1 + \frac{2}{5}\sum_j M_{ji} b_{ij} \chi_{ij}^0 n_j \right) m_i \int V_i V_i f_i^0 \phi_i \, dv_i \,, \tag{4.11}$$

where

$$p^0 = \sum_i p_i^0 = \sum_i \left\{ p^0{}_{k_i} + \sum_j n_i n_j b_{ij} \chi_{ij}^0 kT \right\} \tag{4.12}$$

is the equilibrium hydrostatic pressure at the local temperature T and densities n_i's. The difference from that of an ideal gas is $\sum_{ij} n_i n_j b_{ij} \chi_{ij}^0 kT$, and means that the gas is imperfect.

On the other hand the equation of state of the equilibrium gases composed of the rigid-spheres can be obtained from the equilibrium statistical mechanics in the virial expansion form:

$$p^0 = kT \left[n + \sum_{ij} n_i n_j B_{ij} + \sum_{ijk} n_i n_j n_k C_{ijk} + \cdots \right], \tag{4.13}$$

where the second virial coefficient B_{ij} is given by

$$B_{ij} = \frac{2}{3}\pi \sigma_{ij}^3 = b_{ij} \,. \tag{4.14}$$

Thus b_{ij} is the second virial coefficient per molecule, and χ_{ij}^0 is expressible in the form

$$\chi_{ij}^0 = 1 + \frac{1}{b_{ij}} \sum_k n_k C_{ijk} + \frac{1}{b_{ij}} \sum_{k,l} n_k n_l D_{ijkl} + \cdots \,, \tag{4.15}$$

which depends only on the concentrations of chemical species.

With use of the perturbation functions the thermal energy fluxes, $\mathbf{q}_k$ and $\mathbf{q}_c$, given by (3.19) are reduced as follows: the kinetic contribution $\mathbf{q}_k$ is written as

$$\mathbf{q}_k = \sum_i \mathbf{q}_{k_i} = \sum_i \frac{1}{2} m_i \int V_i^2 V_i f_i^0 \phi_i \, dv_i \,, \tag{4.16}$$

and the collisional contributions to the energy transfer $\mathbf{J}_c\left[\frac{1}{2} m_i V_i^2\right]$'s are reduced, with use of (3.21) and (4.2), to (see Appendix III)

$$\mathbf{J}_c{}^{(1)}\left[\frac{m_i V_i^2}{2}\right]=\frac{2\pi}{5}\sum_{i,j}\sigma_{ij}{}^3\chi_{ij}{}^0 M_{ij}M_{ji}n_j\boldsymbol{q}_{k_i}+\sum_{i,j}\frac{1}{2}b_{ij}\chi_{ij}{}^0 M_{ij}M_{ji}\frac{m_i-2m_j}{m_i m_j}n_j\boldsymbol{J}_i kT\ , \tag{4.17-1}$$

$$\mathbf{J}_c{}^{(2)}\left[\frac{m_i V_i^2}{2}\right]=\sum_{i,j}\tilde{\omega}_{ij}\left(\frac{3kT}{m_i+m_j}\right)\nabla\frac{1}{T}\ . \tag{4.17-2}$$

Consequently we can write the total energy flux in the form:

$$\boldsymbol{q}=\boldsymbol{q}_k+\boldsymbol{q}_c=\boldsymbol{E}+\sum_i\frac{\bar{H}_i}{m_i}\boldsymbol{J}_i\ , \tag{4.18}$$

where

$$\boldsymbol{E}=\sum_i\left(1+\frac{3}{5}\sum_j M_{ij}M_{ji}b_{ij}\chi_{ij}{}^0 n_j\right)\boldsymbol{E}_{k_i}-\sum_{ij}\tilde{\omega}_{ij}\left(\frac{3kT}{m_i+m_j}\right)\nabla\frac{1}{T}\ , \tag{4.18-1}$$

$$\boldsymbol{E}_{k_i}\equiv\int\left(\frac{m_i V_i^2}{2}-\frac{5}{2}kT\right)\boldsymbol{V}_i f_i\,d\boldsymbol{v}_i\ , \tag{4.18-2}$$

and

$$\bar{H}_i\equiv\left(\frac{5}{2}+\sum_j M_{ij}b_{ij}\chi_{ij}{}^0 n_j\right)kT\ . \tag{4.18-3}$$

The first term in (4.18) is the thermal energy flux and the second is the energy transfer associated with the molecular flows. It is noticed that $\bar{H}_i$ is a partial molar enthalpy in a sense and $\sum_i n_i\bar{H}_i$ is exactly the enthalpy per unit volume of our rigid-sphere gas.

If we find the function f_i which satisfy (2.6), then we have the complete description of the non-equilibrium system by means of the hydrodynamic equations (3.11), (3.13) and (3.17), with the fluxes (4.4), (4.11) and (4.18).

§ 5. Enskog's First Approximation Equation

One of the solution of (2.6) is that analogous to well known Enskog's solution in one component system. We shall derive the first approximation equation following Enskog.

In the left-hand side of (2.6) the terms containing the perturbation function ϕ_i may be neglected to the first approximation, and then the streaming term is written in the form:

$$\begin{aligned}\left\{\frac{\partial}{\partial t}+\boldsymbol{v}_i\cdot\nabla_r+\frac{\boldsymbol{F}_i}{m_i}\cdot\nabla_{v_i}\right\}f_i{}^0=f_i{}^0\Bigg[&\frac{D\ln n_i}{Dt}+\left(\frac{m_i V_i^2}{2kT}-\frac{3}{2}\right)\frac{D\ln T}{Dt}\\&+\frac{m_i}{kT}\boldsymbol{V}_i\boldsymbol{V}_i:\nabla\boldsymbol{v}_0+\boldsymbol{V}_i\cdot\left\{\nabla\ln n_i+\left(\frac{m_i V_i^2}{2kT}-\frac{3}{2}\right)\nabla\ln T+\left(\frac{D\boldsymbol{v}_0}{Dt}-\frac{\boldsymbol{F}_i}{m_i}\right)\frac{m_i}{kT}\right\}\Bigg].\end{aligned} \tag{5.1}$$

The right hand side of (2.6) becomes, if the terms of second order is neglected,

$$\left(\frac{\partial f_i}{\partial t}\right)^0_{\text{coll}}=\sum_\gamma{}^0J_i{}^{(\gamma)}\ , \tag{5.2}$$

$${}^0J_i{}^{(1)}=\sum_j{}^0J_{ij}{}^{(1)}=\sum_j\chi_{ij}{}^0\iint f_i{}^0 f_j{}^0(\phi_i'+\phi_j'-\phi_i-\phi_j)\sigma_{ij}{}^2(\boldsymbol{g}\cdot\boldsymbol{k})\,d\boldsymbol{k}\,d\boldsymbol{v}_j \tag{5.2-1}$$

$$\begin{aligned}{}^0J_i{}^{(2)}=\sum_j{}^0J_{ij}{}^{(2)}=f_i{}^0\sum_j b_{ij}\chi_{ij}{}^0 n_j\Bigg[&\left(M_{ij}M_{ji}-\frac{1}{2}M_{ij}{}^2\right)\boldsymbol{V}_i\cdot\nabla\ln T\\&-2\boldsymbol{V}_i\cdot\nabla\ln n_j-\frac{3}{5}M_{ij}M_{ji}\frac{m_i V_i^2}{2kT}\boldsymbol{V}_i\cdot\nabla\ln T\\&+M_{ij}\left(1-\frac{2}{5}\frac{m_i V_i^2}{2kT}\right)\nabla\cdot\boldsymbol{v}_0-\frac{2}{5}M_{ji}\frac{m_i}{kT}\boldsymbol{V}_i\boldsymbol{V}_i:\nabla\boldsymbol{v}_0\Bigg],\end{aligned} \tag{5.2-2}$$

$${}^0J_i{}^{(3)}=\sum_j{}^0J_{ij}{}^{(3)}=f_i{}^0\left[-\sum_j n_i b_{ij}\boldsymbol{V}_i\cdot\nabla\chi_{ij}{}^0\right], \tag{5.2-3}$$

$$\sum_j {}^0J_{ij}^{(4)}=\sum_j {}^0J_{ij}^{(5)}=\sum_j {}^0J_{ij}^{(6)}=0\ . \tag{5.2–4}$$

Then we have the equation of change in the zero order:

$$\int\psi_i\left(\frac{\partial}{\partial t}+\boldsymbol{v}_i\cdot\nabla+\frac{\boldsymbol{F}_i}{m_i}\nabla\cdot\right)f_i^0\,d\boldsymbol{v}_i=\int\psi_i\left(\frac{\partial f_i}{\partial t}\right)^0_{\text{coll}}d\boldsymbol{v}_i\ . \tag{5.3}$$

If we put $\psi_i=m_i$, $\psi_i=m_iV_i$ and $\psi_i=m_iV_i^2/2$ in the above equation, then we obtain the continuity equation, the equation of motion and the equation of energy balance to the zeroth approximation, respectively,

$$\frac{D\rho_i}{Dt}+\rho_i\cdot\nabla\boldsymbol{v}_0=0\ , \tag{5.4}$$

$$\rho\frac{D\boldsymbol{v}_0}{Dt}=\sum_i\left[\frac{\rho_i}{\rho}\frac{\boldsymbol{F}_i}{m_i}-\frac{1}{\rho}\nabla\left\{n_ikT\left(1+\sum_j n_jb_{ij}\chi_{ij}^0\right)\right\}\right], \tag{5.5}$$

$$n\frac{D\ln T}{Dt}=-\frac{2}{3}(\nabla\cdot\boldsymbol{v}_0)\left\{\sum_i n_i\left(1+\sum_j n_jb_{ij}\chi_{ij}^0\right)\right\}\ . \tag{5.6}$$

Substituting (5.4), (5.5) and (5.6) into (5.1), we obtain the extension of Enskog's first approximation equation to multicomponent gas which determine the perturbation function ϕ_i:

$$\begin{aligned}f_i^0\Bigg[&\left(1+\frac{3}{5}\sum_j M_{ij}M_{ji}b_{ij}n_j\chi_{ij}^0\right)\left(\frac{m_iV_i^2}{2kT}-\frac{5}{2}\right)\boldsymbol{V}_i\cdot\nabla\ln T+\frac{n}{n_i}\boldsymbol{V}_i\cdot\boldsymbol{d}_i\\&+\left(1+\frac{2}{5}\sum_j M_{ji}b_{ij}n_j\chi_{ij}^0\right)\frac{m_i}{kT}\left(\boldsymbol{V}_i\boldsymbol{V}_i-\frac{1}{3}V_i^2\mathbf{U}\right):\nabla\boldsymbol{v}_0\\&+\sum\left(M_{ji}b_{ij}\chi_{ij}^0n_j-\frac{n_j}{n}\sum_k b_{jk}\chi^0{}_{jk}n_k\right)\left(\frac{m_iV_i^2}{3kT}-1\right)\nabla\cdot\boldsymbol{v}_0\\&=\sum_j\chi_{ij}^0\sigma_{ij}^2\iint f_i^0f_j^0(\phi_i'+\phi_j'-\phi_i-\phi_j)(\boldsymbol{g}\cdot\boldsymbol{k})\,d\boldsymbol{k}\,d\boldsymbol{v}_j\ ,\end{aligned} \tag{5.7}$$

where

$$\begin{aligned}\boldsymbol{d}_i\equiv&\frac{\rho_i}{\rho nkT}\left[\sum_j\frac{\rho_j\boldsymbol{F}_j}{m_i}-\rho\frac{\boldsymbol{F}_i}{m_i}\right]+\frac{\rho-\rho_i}{\rho nkT}\nabla p_i^0-\frac{\rho_i}{\rho nkT}\nabla(p^0-p_i^0)\\&+\frac{n_i}{n}\sum_k n_kb_{ik}\chi_{ik}^0\left\{\nabla\ln\frac{n_i}{n}+\frac{1}{2}(M_{ik}-M_{ki})\nabla\ln T\right\}\ ,\end{aligned} \tag{5.8}$$

which agrees with Thorne's equation for a two component system.

§ 6. The Statistical Expressions of the Irreversible Production of Entropy

Thus far in our description of the non-equilibrium system the entropy S, which plays a significant role in the theory of irreversible processes, has been left out of our considerations. We shall now consider the entropy and the balance equation for it, to complete the thermodynamic description of the system.

Let us first consider the equilibrium values of some thermodynamic potentials of an imperfect gas composed of rigid-spheres. The Helmholtz free energy and the entropy of an imperfect gas can be written in the form:

$$F^0=F_{id}^0+\lim_{V_0\to\infty}\int_{V_0}^{V}(p^0-p^0{}_{id})\,dV\ , \tag{6.1}$$

and

$$S^0=S^0{}_{id}+\frac{\partial}{\partial T}\left\{\lim_{V_0\to\infty}\int_{V_0}^{V}(p^0-p_{id}^0)\,dV\right\}\ , \tag{6.2}$$

respectively, where the subscript *id* denote the functions for the corresponding perfect gas with the same temperature and densities. The equation alows us to calculate the equilibrium value of the thermodynamical potentials, if we know the equation of state.

Then we obtain from (6.1) and (4.12) the free energy per unit volume of the rigid-sphere gas mixture:

$$\rho\hat{F}^0=\rho\hat{F}_{id}{}^0+kT\sum_{ij} n_i n_j b_{ij}\left(\frac{1}{n}\int^n \chi_{ij}{}^0\, dn\right), \tag{6.3}$$

where we have used n instead of V as the independent variable. Since $\chi_{ij}{}^0$ is independent of the temperature as seen from (4.13) in a rigid-sphere system, the entropy per unit volume is expressed as

$$\rho\hat{S}^0=\rho\hat{S}_{id}{}^0+\rho\hat{S}^0_{\mathrm{corr}}, \tag{6.4}$$

$$\rho\hat{S}^0_{\mathrm{corr}}=-k\sum_{i,j} n_i n_j b_{ij}\left(\frac{1}{n}\int^n \chi_{ij}{}^0\, dn\right), \tag{6.5}$$

where $\hat{S}_{\mathrm{corr}}$ is the correction to the entropy per unit mass due to imperfectness of the gas. On the other hand, the entropy per unit volume of an ideal gas composed point molecules is known to be

$$\rho\hat{S}_{id}=\sum_i kn_i\left[\frac{3}{2}\ln T-\ln n_i+\ln\left(\frac{2\pi m_i k}{h^2}\right)^{3/2}+\frac{5}{2}\right]-k\sum_i n_i \ln\frac{n_i}{n}. \tag{6.6}$$

According to the H-theorem, the entropy density of the gas of point molecules in non-equilibrium state is given by

$$\rho\hat{S}_{\mathrm{I}}=k\sum_i\int_{-\infty}^{\infty}(1-\ln f_i)f_i\, d\boldsymbol{v}_i, \tag{6.7}$$

which becomes identical with (6.6) for the equilibrium distribution $f_i=f_i{}^0$ apart from an additive constant.

For the present case of a moderately dense gas the correction due to the gas imperfection appears through the pair correlation function χ_{ij}, and furthermore we have assumed that χ_{ij} can be replaced by its equilibrium value $\chi_{ij}{}^0$ without appreciable error. Then we may write the entropy density of an imperfect gas slightly deviated from equilibrium as the sum of (6.7) and (6.5):

$$\begin{aligned}\rho\hat{S}&=\rho\hat{S}_{\mathrm{I}}+\rho\hat{S}_{\mathrm{II}},\\ \rho\hat{S}_{\mathrm{II}}&=\rho\hat{S}^0_{\mathrm{corr}}=-k\sum_{i,j} n_i n_j b_{ij}\left(\frac{1}{n}\int^n \chi_{ij}\, dn\right).\end{aligned} \tag{6.8}$$

Multiplying (2.6) by $k(1-\ln f_i)$, integrating over $\boldsymbol{v}_i$ and summing over i, we obtain the equation of entropy balance

$$\rho\frac{D\hat{S}_{\mathrm{I}}}{Dt}+\nabla\cdot k\sum_i\int(1-\ln f_i)\boldsymbol{V}_i f_i\, d\boldsymbol{v}_i=-k\sum_i\sum_\gamma I_i{}^{(\gamma)}(\ln f_i), \tag{6.9}$$

where $I_i{}^{(\gamma)}$ is given by (3.4). The manner of derivation of (6.9) is similar to that of (3.3). Substituting (4.1) and (4.2) into (6.9), and remembering that $m_i V_i{}^2/2$ is one of the summational invariants, we can write the right-hand side of (6.9), with use of (3.6), (3.7) and (3.8) in the form

$$\begin{aligned}-k\sum_\gamma\sum_i I_i{}^{(\gamma)}(\ln f_i)&=\nabla\cdot\left[\sum_\alpha \boldsymbol{J}_c{}^{(\alpha)}\left[-\frac{m_i V_i{}^2}{2T}\right]\right]-\sum_\alpha R^{(\alpha)}\left(\frac{m_i V_i{}^2}{2T}\right)-k\sum_\gamma^6\sum_i^\nu I_i{}^{(\gamma)}(\phi_i)\\ &=-\frac{1}{T}\nabla\cdot\boldsymbol{q}_0-\frac{1}{T}\mathbf{P}_c:\nabla\boldsymbol{v}_0-k\sum_\gamma^6\sum_i^\nu I_i{}^{(\gamma)}(\phi_i),\end{aligned} \tag{6.10}$$

where we have ignored the terms higher than the square of ϕ_i. $\mathbf{P}_c$ and $\boldsymbol{q}_c$ in (6.10) are given by (4.7) and (4.17), respectively. To the same approximation $\sum_{i=1}^{\nu} I_i(\phi_i)$'s are reduced to

$$k\sum_i^{\nu} {}^0I_i^{(1)}(\phi_i)=k\sum_i^{\nu}\int \phi_i {}^0J_i^{(1)}\,d\boldsymbol{v}_i -\frac{k}{4}\sum_{ij}\chi_{ij}^0\iint f_i^0 f_j^0(\phi_i'+\phi_j'-\phi_i-\phi_j)\phi_i\sigma_{ij}^2(\boldsymbol{g}\cdot\boldsymbol{k})\,d\boldsymbol{k}\,d\boldsymbol{v}_i\,d\boldsymbol{v}_j\,, \tag{6.11–1}$$

$$k\sum_i {}^0I_i^{(2)}(\phi_i)=k\sum_i\int\phi_i {}^0J_i^{(2)}\,d\boldsymbol{v}_i=\sum_i\Big[\mathbf{E}_{k_i}\cdot\nabla\frac{1}{T}\sum_j\frac{3}{5}M_{ij}M_{ji}b_{ij}n_j\chi_{ij}^0 +\boldsymbol{J}_i\cdot\frac{kT}{m_i}\sum_j b_{ij}n_j\chi_{ij}^0\Big(M_{ij}\nabla\frac{1}{T}-2\frac{1}{T}\nabla\ln n_j\Big) +(\mathbf{P}_{k_i}-p_{k_i}{}^0\mathrm{U}):\Big(\frac{\nabla\boldsymbol{v}_0}{T}\Big)\sum_j\frac{2}{5}M_{ji}b_{ij}\chi_{ij}^0 n_j\Big]\,, \tag{6.11–2}$$

$$k\sum_i {}^0I_i^{(3)}(\phi_i)=k\sum_i\int\phi_i {}^0J_i^{(3)}\,d\boldsymbol{v}_i=\sum_i\boldsymbol{J}_i\cdot\Big\{\frac{kT}{m_i}\sum_j b_{ij}n_j\chi_{ij}^0\frac{\nabla\ln\chi_{ij}^0}{T}\Big\}\,, \tag{6.11–3}$$

$$\sum_i {}^0I_i^{(4)}(\phi_i)=\sum_i {}^0I_i^{(5)}(\phi_i)=\sum_i {}^0I_i^{(6)}(\phi_i)=0, \tag{6.11–4}$$

where $(\mathbf{P}_{k_i}-p_{k_i}{}^0\mathrm{U})$ and $\boldsymbol{E}_k$ and $\boldsymbol{J}_i$ are given by (4.6), (4.18–2) and (4.4), respectively. Here ${}^0I_i^{(\gamma)}$ and ${}^0J_i^{(\gamma)}$ indicate the first approximations to the integrals $I_i^{(\gamma)}$ and $J_i^{(\gamma)}$, respectively.

If we use (4.2) and neglect ϕ_i^2 in the second term of the left hand side of (6.9), we immediately obtain from (4.16) and (4.4)

$$k\sum_i\int(1-\ln f_i)V_i f_i\,d\boldsymbol{v}_i=\frac{\boldsymbol{q}_k}{T}-\sum_i\frac{\mu_i^{id}}{T}\frac{\boldsymbol{J}_i}{m_i}\,, \tag{6.12}$$

with

$$\mu_i^{id}\equiv kT\Big[\ln n_i-\frac{3}{2}\ln T+\frac{3}{2}\ln\Big(\frac{m_i}{2\pi k}\Big)\Big]\simeq\frac{\partial}{\partial n_i}(\rho\hat{F}_{id}{}^0) \tag{6.13}$$

which stands for the chemical potential of species i of an ideal gas mixture.

From (6.9), (6.10), (6.11) and (6.12), we finally obtain the expression for the entropy balance equation given by

$$\rho\frac{D\hat{S}_{\mathrm{I}}}{Dt}+\nabla\cdot\boldsymbol{\sigma}_{\mathrm{I}}^{(\mathrm{i})}[s]=\tau_{\mathrm{I}}^{(\mathrm{i})}[s]\,, \tag{6.14}$$

where $\boldsymbol{\sigma}_{\mathrm{I}}$ and τ_{I} are given respectively by

$$\boldsymbol{\sigma}_{\mathrm{I}}^{(\mathrm{i})}[s]\equiv\frac{\boldsymbol{q}}{T}-\sum_i\frac{\mu_i^{id}}{T}\frac{\boldsymbol{J}_i}{m_i}\,, \tag{6.15}$$

$$\tau_{\mathrm{I}}^{(\mathrm{i})}[s]=-k\sum_i {}^0I_i^{(1)}(\phi_i)+\sum_{ij}\tilde{\omega}_{ij}\Big(\frac{3kT}{m_i+m_j}\Big)\Big(\nabla\frac{1}{T}\Big)^2+\frac{6}{5}\sum_{ij}\tilde{\omega}_{ij}\Big[\frac{\mathbf{S}}{T}:\frac{\mathbf{S}}{T}\Big] +\sum_{ij}\tilde{\omega}_{ij}\Big(\frac{\nabla\cdot\boldsymbol{v}_0}{T}\Big)^2+(p^0-p_{id}{}^0)\Big(-\frac{\nabla\cdot\boldsymbol{v}_0}{T}\Big)+kT\sum_{ij}b_{ij}n_j\chi_{ij}^0\Big(2\frac{\nabla\ln n_j}{T}+\frac{\nabla\ln\chi_{ij}^0}{T}\Big)\cdot\frac{\boldsymbol{J}_i}{m_i}\,, \tag{6.16}$$

where we have substituted (4.7) and (4.17) for $\mathbf{P}_c$ and $\boldsymbol{q}_c$ into (6.10).

On the other hand, since the entropy due to the gas imperfection, $\hat{S}_{\mathrm{II}}$, depends on the spatial coordinates only through the number densities n_i's, as seen from (4.15) and (6.8), we can easily obtain

$$\rho\frac{DS_{\mathrm{II}}}{Dt}=(p^0-p_{id}{}^0)\nabla\cdot\boldsymbol{v}_0$$
$$+\sum_i k\left\{\frac{2}{1}\sum_j n_jB_{ij}+\frac{3}{2}\sum_{j,k}n_jn_kC_{ijk}+\frac{4}{3}\sum_{j,kl}n_jn_kn_lD_{ijkl}+\cdots\right\}\nabla\cdot\frac{\boldsymbol{J}_i}{m_i}\,. \tag{6.17}$$

Further the additional chemical of ith species arising from the imperfectness of gas mixtures is given by

$$\mu_i{}^{\mathrm{corr}}\equiv\frac{\partial}{\partial n_i}(\rho\hat{F}_{\mathrm{corr}})=kT\left\{\frac{2}{1}\sum_j n_jB_{ij}+\frac{3}{2}\sum_{jk}n_jn_kC_{ijk}+\frac{4}{3}\sum_{jkl}n_jn_kn_lD_{ijkl}+\cdots\right\}. \tag{6.18}$$

Therefore, the balance equation of the entropy due to imperfectness can be written in the form

$$\rho\frac{D\hat{S}_{\mathrm{II}}}{Dt}+\nabla\cdot\boldsymbol{\sigma}_{\mathrm{II}}{}^{(\mathrm{i})}[s]=\tau_{\mathrm{II}}{}^{(\mathrm{i})}[s]\,, \tag{6.19}$$

where

$$\boldsymbol{\sigma}_{\mathrm{II}}{}^{(\mathrm{i})}[s]=-\sum_i\frac{\mu_i{}^{\mathrm{corr}}}{T}\cdot\frac{\boldsymbol{J}_i}{m_i}\,, \tag{6.20}$$

$$\tau_{\mathrm{II}}{}^{(\mathrm{i})}[s]=-\sum_i\frac{\boldsymbol{J}_i}{m_i}\cdot\nabla\frac{\mu_i{}^{\mathrm{corr}}}{T}+(p^0-p_{id}{}^0)\frac{\nabla\cdot\boldsymbol{v}_0}{T}\,. \tag{6.21}$$

Then the balance equation of total entropy is written as

$$\rho\frac{DS}{Dt}+\nabla\cdot\boldsymbol{\sigma}^{(\mathrm{i})}[s]=\tau^{(\mathrm{i})}[s]\,, \tag{6.22}$$

where

$$\boldsymbol{\sigma}^{(\mathrm{i})}[s]\equiv\boldsymbol{\sigma}_{\mathrm{I}}{}^{(\mathrm{i})}[s]+\boldsymbol{\sigma}_{\mathrm{II}}{}^{(\mathrm{i})}[s]=\frac{\boldsymbol{q}}{T}-\sum_i\frac{\mu_i{}^{id}+\mu_i{}^{\mathrm{corr}}}{T}\cdot\frac{\boldsymbol{J}_i}{m_i}\,, \tag{6.23}$$

$$\tau^{(\mathrm{i})}[s]=\tau_{\mathrm{I}}{}^{(\mathrm{i})}[s]+\tau_{\mathrm{II}}{}^{(\mathrm{i})}[s]=-k\sum_i{}^0I_i{}^{(1)}(\phi_i)+\sum_{ij}\tilde{\omega}_{ij}\left(\frac{3kT}{m_i+m_j}\right)\left(\nabla\frac{1}{T}\right)^2$$
$$+\frac{6}{5}\sum_{ij}\tilde{\omega}_{ij}\left[\frac{\mathbf{S}}{T}:\frac{\mathbf{S}}{T}\right]+\sum_{ij}\tilde{\omega}_{ij}\left[\frac{\nabla\cdot\boldsymbol{v}_0}{T}\right]^2. \tag{6.24}$$

This equation indicates that the change of the entropy $\rho\hat{S}$ of the gas within the local region moving with barycentric velocity $\boldsymbol{v}_0$ is arising from the reversible flow of entropy $\boldsymbol{\sigma}^{(\mathrm{i})}[s]$ and from the irreversible production of entropy $\tau^{(\mathrm{i})}[s]$.

Let us define the bracket expression given by

$$\{\psi,\phi\}\equiv-\sum_{ij}\chi_{ij}{}^0\iiint\psi_i(\phi_i'+\phi_j'-\phi_i-\phi_j)f_i{}^0f_j{}^0\sigma_{ij}{}^2(\boldsymbol{g}\cdot\boldsymbol{k})\,d\boldsymbol{k}\,d\boldsymbol{v}_i\,d\boldsymbol{v}_j\,, \tag{6.25}$$

where ψ_i is an arbitrary function of $\boldsymbol{v}_i$ and ϕ_i is the perturbation function defined by (4.2). This may be symmetrized in the form (see Appendix I of the author's previous paper[11])

$$\{\psi,\phi\}=\frac{1}{4}\sum_{ij}\chi_{ij}{}^0\iiint(\psi_i'+\psi_j'-\psi_i-\psi_j)(\phi_i'+\phi_j'-\phi_i-\phi_j)$$
$$\times f_i{}^0f_j{}^0\sigma_{ij}{}^2(\boldsymbol{g}\cdot\boldsymbol{k})\,d\boldsymbol{k}\,d\boldsymbol{v}_i\,d\boldsymbol{v}_j=\{\phi,\psi\}\,. \tag{6.26}$$

The operator { } is linear, and $\{\phi,\phi\}$ is non negative:

$$\{\psi+\varphi,\phi\}=\{\psi,\phi\}+\{\varphi,\phi\}\,, \tag{6.27}$$

$$\{\phi,\phi\}=\frac{1}{4}\sum_{ij}\chi_{ij}{}^0\iiint(\phi_i'+\phi_j'-\phi_i-\phi_j)^2f_i{}^0f_j{}^0(\boldsymbol{g}\cdot\boldsymbol{k})\,d\boldsymbol{k}\,d\boldsymbol{v}_i\,d\boldsymbol{v}_j\geq0\,. \tag{6.28}$$

Since the integrand can never be negative, the expression $\{\phi, \phi\}$ vanishes if and only if ϕ_i is a linear combination of the summational invariants. With use of this bracket expression, (6.11–1) is reduced as

$$-k\sum_i {}^0I^{(1)}(\phi_i)=k\{\phi, \phi\}\ . \tag{6.29}$$

Then the entropy production rate (6.28) is written in the form:

$$\tau^{(i)}[s]=k\{\phi, \phi\}+\sum_{ij}\tilde{\omega}_{ij}\left(\frac{3kT}{m_i+m_j}\right)\left(\nabla\frac{1}{T}\right)^2+\frac{6}{5}\sum_{ij}\tilde{\omega}_{ij}\left[\frac{\mathbf{S}}{T}:\frac{\mathbf{S}}{T}\right]+\sum_{ij}\tilde{\omega}_{ij}\left(-\frac{\nabla\cdot\boldsymbol{v}_0}{T}\right)^2, \tag{6.30}$$

which can never be negative in accordance with the second law of thermodynamics. The first term is the contribution from the transport due to molecular flows, and the remainings are those from the collisional transfer which become significant in dense gases.

§ 7. Thermodynamic Description of Linear Transport Processes

As in the usual formulation of thermodynamics of irreversible processes, we shall calculate the local entropy production with use of the Gibbs relation:

$$T\,d\hat{S}=d\hat{U}+p^0d\left(\frac{1}{\rho}\right)-\sum_i \mu_i\,d\left(\frac{n_i}{\rho}\right), \tag{7.1}$$

assuming that the transport processes of fluid are completely described by the ordinary thermodynamical variables defined in local equilibrium state. According to (7.1) the change in entropy is given by

$$\rho\frac{D\hat{S}}{Dt}=\frac{1}{T}\left[\frac{1}{\rho}\frac{D\hat{U}}{Dt}-\frac{p^0}{\rho}\frac{D\rho}{Dt}-\sum_i\mu_i\left(\frac{Dn_i}{Dt}-\frac{n_i}{\rho}\frac{D\rho}{Dt}\right)\right]. \tag{7.2}$$

Using the equations of continuity, and the equation of energy balance respectively given by (3.11), (3.12) and (3.17), we obtain the following equation of entropy balance:

$$\rho\frac{D\hat{S}}{Dt}+\nabla\cdot\boldsymbol{\sigma}^{(\text{ii})}[s]=\boldsymbol{\tau}^{(\text{ii})}[s]\,, \tag{7.3}$$

$$\boldsymbol{\sigma}^{(\text{ii})}[s]\equiv\frac{\boldsymbol{q}}{T}-\sum_i\frac{\mu_i}{T}\cdot\frac{\boldsymbol{J}_i}{m_i}=\frac{\boldsymbol{E}}{T}+\sum_i\frac{\bar{H}_i-\mu_i}{T}\cdot\frac{\boldsymbol{J}_i}{m_i}\,, \tag{7.4}$$

$$\begin{aligned}\boldsymbol{\tau}^{(\text{ii})}[s]&\equiv\boldsymbol{q}\cdot\nabla\frac{1}{T}+(\mathbf{P}-p^0\mathbf{U}):\left(-\frac{\nabla\boldsymbol{v}_0}{T}\right)+\sum_i\frac{\boldsymbol{J}_i}{m_i}\cdot\left(\frac{\boldsymbol{F}_i}{T}-\nabla\frac{\mu_i}{T}\right)\\&=\boldsymbol{E}\cdot\nabla\frac{1}{T}+(\mathbf{P}-p^0\mathbf{U}):\left(\frac{\nabla\boldsymbol{v}_0}{T}\right)+\sum_i\boldsymbol{J}_i\cdot\boldsymbol{\Lambda}_i\,,\end{aligned} \tag{7.5}$$

where $\bar{H}_i$ denotes the partial molar enthalpy and $\boldsymbol{\Lambda}_i$ is the affinity for diffusion processes defined by

$$\boldsymbol{\Lambda}_i\equiv\frac{1}{T}\left[\frac{\boldsymbol{F}_i}{m_i}-\frac{T}{m_i}\nabla\frac{\mu_i}{T}+\frac{T\bar{H}_i}{m_i}\nabla\frac{1}{T}\right]. \tag{7.6}$$

Since $\boldsymbol{J}_i=0$ the thermodynamic expression of the entropy production rate is invariant, if $\boldsymbol{\Lambda}_i$ is replaced by

$$\boldsymbol{\Lambda}_i\equiv\boldsymbol{\Lambda}_i-\boldsymbol{C}\,, \tag{7.7}$$

$\boldsymbol{C}$ being an arbitrary constant. If the constant $\boldsymbol{C}$ is chosen such that

$$\boldsymbol{C}=\frac{1}{\rho}\sum_i\rho_i\boldsymbol{\Lambda}_i\qquad(\text{mass average of }\boldsymbol{\Lambda}_i)\,, \tag{7.8}$$

(7.7) is reduced to

$$\boldsymbol{A}_i=\frac{1}{T}\left[\frac{n_i\boldsymbol{F}_i}{\rho_i}-\frac{1}{\rho}\sum_j n_j\boldsymbol{F}_j\right]-\frac{1}{m_i}\nabla\frac{\mu_i}{T}+\frac{\bar{H}_i}{m_i}\nabla\frac{1}{T}+\frac{1}{\rho T}\nabla p^0\,, \tag{7.9}$$

where we have used the relations

$$\sum n_j\bar{v}_j=1\,, \tag{7.10}$$

$$\sum_j n_j\sum_k\left(\frac{\partial\mu_j}{\partial n_k}\right)_{T,p}\nabla n_k=0\,, \tag{7.11}$$

$\bar{v}_j$ being a partial molar volume of the ith component. It follows from the definition of $\boldsymbol{A}_i$ that

$$\sum_i \rho_i\boldsymbol{A}_i=0\,. \tag{7.12}$$

The reason why such an affinity of diffusion $\boldsymbol{A}_i$ is taken is that this choice makes the entropy production due to the diffusion processes to be independent of reference velocity of mass flows. If the diffusion velocity is referred to an arbitrary mean velocity $\boldsymbol{v}^a=\sum_i w_i\bar{\boldsymbol{v}}_i/\sum_i w_i$, where w_i is a weight function, i.e. $\boldsymbol{J}_i{}^a=\rho_i(\bar{\boldsymbol{v}}_i-\boldsymbol{v}^a)$ is employed, we can write the production of entropy with use of the normalized affinities $\boldsymbol{A}_i$:

$$\tau=\sum_i \boldsymbol{J}_i\cdot\boldsymbol{A}_i=\sum_i \rho_i\bar{\boldsymbol{v}}_i\cdot\boldsymbol{A}_i=\sum_i \boldsymbol{J}_i{}^a\cdot\boldsymbol{A}_i\,. \tag{7.13}$$

According to the law of phenomenological linear relation, we can easily obtain the connections between the various diffusion coefficients (i.e. molecular diffusion ($w_i=n_i$), barycentric diffusion ($w_i=\rho_i$) and etc.), by the use of (7.13) and similar arguments as those in mechanical equilibrium case[16] (see p. 109 in References 17)).

If we substitute the kinetic expressions of the fluxes for those in the equation of entropy balance (7.3), we can obtain another microscopic expressions of the entropy flux and the entropy production rate in terms of the distribution functions. These expressions are exact so far as the thermodynamic description is valid. In the present approximation we may employ the kinetic expressions (4.4), (4.11) and (4.18), respectively, for $\boldsymbol{J}_i$, $\mathbf{P}$ and $\boldsymbol{q}$ in (7.4) and (7.5). Then we have the entropy flow

$$\sigma^{(\mathrm{ii})}[s]=\frac{\boldsymbol{q}}{T}-\sum_i\frac{\mu_i}{T}\cdot\frac{\boldsymbol{J}_i}{m_i} \tag{7.14}$$

and the production of entropy

$$\begin{aligned}\tau^{(\mathrm{ii})}[s]=&\sum_{ij}\tilde{\omega}_{ij}\left(\frac{3kT}{m_i+m_j}\right)\left(\nabla\frac{1}{T}\right)^2+\sum_{ij}\tilde{\omega}_{ij}\left(\frac{\nabla\cdot\boldsymbol{v}_0}{T}\right)^2+\frac{6}{5}\sum_{ij}\tilde{\omega}_{ij}\left[\frac{\mathbf{S}}{T}:\frac{\mathbf{S}}{T}\right]\\&+\sum_i\left(1+\frac{3}{5}\sum_j M_{ij}M_{ji}b_{ij}\chi_{ij}{}^0 n_j\right)\boldsymbol{E}_{k_i}\cdot\nabla\frac{1}{T}+\sum_i\boldsymbol{J}_i\cdot\boldsymbol{A}_i\\&+\sum_i\left(1+\frac{2}{5}\sum_j M_{ji}b_{ij}\chi_{ij}{}^0 n_j\right)(\mathbf{P}_{k_i}-p_{k_i}{}^0\mathbf{U}):\left(-\frac{\nabla\boldsymbol{v}_0}{T}\right),\end{aligned} \tag{7.15}$$

where $\mathbf{P}_{k_i}-\boldsymbol{p}_{k_i}\mathbf{U}$, $\boldsymbol{E}_{k_i}$ and $\boldsymbol{A}_i$ are respectively given by (4.6), (4.18–2) and (7.9). Here the chemical potential μ_i only is an unknown quantity. The second law of thermodynamics states that the entropy production rate $\tau^{(\mathrm{ii})}[s]$ never be negative.

If the statistical entropy production $\tau^{(\mathrm{i})}[s]$ given by (6.30) is equated to the thermodynamic entropy production rate $\tau^{(\mathrm{ii})}[s]$ (7.15) obtained from the Gibbs relation, we have the following relation:

$$\begin{aligned}&\sum_i\left(1+\frac{3}{5}\sum_j M_{ij}M_{ji}b_{ij}\chi_{ij}{}^0 n_j\right)\boldsymbol{E}_{k_i}\cdot\nabla\frac{1}{T}+\sum_j \boldsymbol{J}_j\cdot\boldsymbol{A}_j\\&\quad+\sum_i\left(1+\frac{2}{5}\sum_j M_{ji}b_{ij}\chi_{ij}{}^0 n_j\right)(\mathbf{P}_{k_i}-p_{k_i}{}^0\mathbf{U}):\left(-\frac{\nabla\boldsymbol{v}_0}{T}\right)\\&\quad=k\{\phi,\phi\}\geq 0\,.\end{aligned}\tag{7.16}$$

The value of μ_i involved in the affinity $\boldsymbol{A}_i$ is determined by another condition that the entropy flow (7.14) must be equal to that given by (6.23). Thus the chemical potential is given by

$$\begin{aligned}\mu_i&=\mu_i{}^{id}+\mu_i{}^{\mathrm{corr}}\\&=kT\left\{\ln n_i-\frac{3}{2}\ln T+\frac{3}{2}\ln\left(\frac{m_i}{2\pi k}\right)\right\}\\&\quad+kT\left\{\frac{2}{1}\sum_j n_j B_{ij}+\frac{3}{2}\sum_{ij} n_j n_k C_{ijk}+\frac{4}{3}\sum_{jkl} n_j n_k n_l D_{ijkl}+\cdots\right\},\end{aligned}\tag{7.17}$$

and the affinity $\boldsymbol{A}_i$ is also determined.

§ 8. The Variation Principle and Enskog's First Approximation Solution of the Boltzmann Equation Modified for Dense Gases

From (7.16) is seen that the variation principle as shown in the author's previous paper[11] still valid. We shall now reformulate the problem, and establish again the variation principle such that physically reasonable approximation solution f_i of the modified Boltzmann equation for the linear transport processes is given as that to makes the entropy production rate a maximum under the condition compatible with the thermodynamical Gibbs relation.

Let us try to obtain an approximate perturbation function ϕ_i of a singlet distribution function f_i in non-equilibrium state on the basis of the variation principle mentioned above. In the present case this principle is

$$\tau^{(\mathrm{ii})}[s]=\text{Extremum}\tag{8.1}$$

with the restriction

$$\tau^{(\mathrm{ii})}[s]=\tau^{(\mathrm{i})}[s]\,,\tag{8.2}$$

where the variation may be taken with respect to the perturbation function ϕ_i.

With use of the Lagrangian undetermined multiplier λ, we have

$$\delta[(1+\lambda)\tau^{(\mathrm{ii})}[s]-\lambda\tau^{(\mathrm{i})}[s]]=0\,.\tag{8.3}$$

By the same argument as that in derivation of (6.26), the variation of bracket expression is reduced to

$$\begin{aligned}\delta\{\phi,\phi\}&=\frac{1}{4}\sum_{ij}\chi_{ij}{}^0\iiint 2(\phi_i'+\phi_j'-\phi_i-\phi_j)(\delta\phi_i'+\delta\phi_j'-\delta\phi_i-\delta\phi_j)f_i{}^0 f_j{}^0(\boldsymbol{g}\cdot\boldsymbol{k})\\&\quad\times\sigma_{ij}{}^2\,dk\,dv_i\,dv_j=-\sum_i\int\left[2\sum_j\chi_{ij}{}^0\sigma_{ij}{}^2\iint(\phi_i'+\phi_j'-\phi_i-\phi_j)f_i{}^0 f_j{}^0(\boldsymbol{g}\cdot\boldsymbol{k})\,dk\,dv_j\right]\delta\phi_i\,dv_i\,.\end{aligned}\tag{8.4}$$

Then substitution of (6.30) and (7.15) into (8.3) leads to

$$(1+\lambda)\sum_i\int\Xi_i\,\delta\phi_i\,dv_i-\lambda k\delta\{\phi,\phi\}=0\tag{8.5}$$

where

$$\Xi_i \equiv f_i^0\left[\left(1+\frac{3}{5}\sum_j M_{ij}M_{ji}b_{ij}\chi_{ij}^0 n_j\right)\left(\frac{m_i V_i^2}{2}-\frac{5}{2}kT\right)\boldsymbol{V}_i\cdot\nabla\frac{1}{T}+m_i\boldsymbol{V}_i\cdot\boldsymbol{A}_i\right.$$
$$\left.+\left(1+\frac{2}{5}\sum_j M_{ji}b_{ij}\chi_{ij}^0 n_j\right)m_i\left(\boldsymbol{V}_i\boldsymbol{V}_i-\frac{1}{3}V_i^2\mathbf{U}\right):\left(-\frac{\nabla\boldsymbol{v}_0}{T}\right)\right]. \tag{8.6}$$

Then we find

$$(1+\lambda)\Xi_i=-2\lambda k\sum_j \chi_{ij}^0\sigma_{ij}^2\iint f_i^0 f_j^0(\phi_i'+\phi_j'-\phi_i-\phi_j)(\boldsymbol{g}\cdot\boldsymbol{k})\,d\boldsymbol{k}\,d\boldsymbol{v}_j\,. \tag{8.7}$$

In order that this relation is compatible with the condition (8.2), λ must be equal to 1. Thus we obtain from (8.1)

$$\Xi_i=-k\sum_j \chi_{ij}^0\iint f_i^0 f_j^0(\phi_i^{*\prime}+\phi_j^{*\prime}-\phi_i^*-\phi_j^*)\sigma_{ij}^2(\boldsymbol{g}\cdot\boldsymbol{k})\,d\boldsymbol{k}\,d\boldsymbol{v}_j\,, \tag{8.8}$$

where the symbol ϕ_i^* is used to be distinguished from an arbitrary perturbation function ϕ_i. Thus the most probable approximation to the perturbation function ϕ_i is obtained by the solution of (8.8).

Further we can rewrite the variational problem (8.1) and (8.2) as

$$\Gamma(\phi)=2\tau^{(\mathrm{ii})}[s]-\tau^{(\mathrm{i})}[s]=\text{Extremum}\,. \tag{8.9}$$

This form resembles that of Onsager's variation principle[15]. The extremum of (8.9) is shown to be the maximum in the following way. The variational function $\Gamma(\phi)$ is written explicitly as a function of ϕ_i;

$$\Gamma(\phi)=\sum_{ij}\tilde{\omega}_{ij}\left(\frac{3kT}{m_i+m_j}\right)\left(\nabla\frac{1}{T}\right)^2+\sum_{ij}\tilde{\omega}_{ij}\left(-\frac{\nabla\cdot\boldsymbol{v}_0}{T}\right)^2+\frac{6}{5}\sum_{ij}\tilde{\omega}_{ij}\left[\frac{\mathbf{S}}{T}:\frac{\mathbf{S}}{T}\right]$$
$$+2\sum_i\int\Xi_i\phi_i\,d\boldsymbol{v}_i-k\{\phi,\phi\}\,. \tag{8.10}$$

On the other hand, multiplying (8.8) by ϕ_i, integrating $\boldsymbol{v}_i$ and summing over i, we obtain

$$\sum_i\int\Xi_i\phi_i\,d\boldsymbol{v}_i=k\{\phi,\phi^*\}\,,$$

where it must be borne in mind that ϕ_i^* is the solution of variational problem. Then from (6.27) and (6.28) we can obtain the relation

$$\Gamma(\phi^*)-\Gamma(\phi)=k\{\phi^*,\phi^*\}-2k\{\phi,\phi^*\}+k\{\phi,\phi\}=\{\phi^*-\phi,\phi^*-\phi\}\geqq 0\,. \tag{8.11}$$

Hence the extremum of $\Gamma(\phi)$ is the maximum when $\phi_i=\phi_i^*$.

If the expressions (7.17), (4.18–3) and (4.12) are used, we easily obtain the relation between $\boldsymbol{A}_i$ given by (7.9) and $\boldsymbol{d}_i$ given by (5.8)

$$\boldsymbol{d}_i=-\frac{\rho_i}{nk}\boldsymbol{A}_i\,. \tag{8.12}$$

Thus we can rewrite (5.7) as

$$\Xi_i+f_i^0\sum_j\left(M_{ji}b_{ij}\chi_{ij}^0 n_j-\frac{n_j}{n}\sum_k b_{jk}\chi_{jk}^0 n_k\right)kT\left(1-\frac{m_i V_i^2}{3kT}\right)\frac{\nabla\cdot\boldsymbol{v}_0}{T}$$
$$=-k\sum_j\chi_{ij}^0\iint f_i^0 f_j^0(\phi_i'+\phi_j'-\phi_i-\phi_j)\sigma_{ij}^2(\boldsymbol{g}\cdot\boldsymbol{k})\,d\boldsymbol{k}\,d\boldsymbol{v}_j\,, \tag{8.13}$$

which differs by only the second term on the left-hand side from the solution (8.8) of the present variational problem. The extra term appears only in the case of multicomponent dense gas, being small quantity in general. As is easily seen it vanishes both in the case of single-component dense gas and in the case of a dilute gas. As mentioned in previous paragraph the contribution to the entropy production from the transport due to molecular flows is given by $k\{\phi, \phi\}$, then the extra term gives no effect in ϕ_i other than that irrelevant to the dissipation of energy, owing to the relation

$$\int f_i^0 \left[\sum_j \left(M_{ji} b_{ij} \chi_{ij}^0 n_j - \frac{n_j}{n} \sum_k b_{jk} \chi_{jk}^0 n_k \right) kT \left(1 - \frac{m_i V_i^2}{3kT} \right) \frac{\nabla \cdot \boldsymbol{v}_0}{T} \right] \phi_i \, dv_i = 0 \, .$$

Consequently, it seems that the extension of Enskog's first approximation equation to multicomponent system make the entropy production rate a maximum under the constraints that the thermodynamical Gibbs relation is satisfied.

Acknowledgement

The author wishes to express his great gratitude to Professor N. Watanabe for his encouragement. The author is also greatly indebted to Professor S. Ono of University of Tokyo for his invaluable discussions and constant encouragement, and to Professor T. Yamamoto of the Kyoto University for his helpful discussions. This work has been supported in part by a Grant in Aid for Fundamental Scientific Research from the Ministry of Education.

Appendix I

Let us consider the collisional transfer of a molecular property ψ across an element of surface dS at the point $\boldsymbol{r}$. Let the normal to dS, drawn from its negative side to its positive, have a direction specified by unit vector $\boldsymbol{n}$. If a collision is to produce a transfer of ψ across dS, the centers of the colliding molecules must lie on opposite sides of dS, that is, the first molecule i lies on the positive side of dS and the second j on the negative, then the product $(\boldsymbol{k} \cdot \boldsymbol{n})$ is positive. Therefore, the center of molecule i must lie within a cylinder on dS as base with generators parallel to $\boldsymbol{k}$ of length σ_{ij}. The volume of this cylinder is $\sigma_{ij}(\boldsymbol{k} \cdot \boldsymbol{n})\, dS$. The mean position of the two molecules at the instant of the collisions are $\left(\boldsymbol{r} + \frac{1}{2}\sigma_{ij}\boldsymbol{k}\right)$ and $\left(\boldsymbol{r} - \frac{1}{2}\sigma_{ij}\boldsymbol{k}\right)$ and the mean position of the center of two colliding molecules is $\boldsymbol{r}$, at which the correlation function χ_{ij}^0 must be evaluated.

Hence the probable number of collisions in unit time, in which the velocities lie in ranges $d\boldsymbol{v}_i$ and $d\boldsymbol{v}_j$ about $\boldsymbol{v}_i$ and $\boldsymbol{v}_j$ and the collision parameters lie within range $d\boldsymbol{k}$, is

$$\chi_{ij}^0(\boldsymbol{r}) f_i\left(\boldsymbol{r} + \frac{\sigma_{ij}}{2}\boldsymbol{k}\right) f_j\left(\boldsymbol{r} - \frac{\sigma_{ij}}{2}\boldsymbol{k}\right) \sigma_{ij}^2 (\boldsymbol{g} \cdot \boldsymbol{k}) \, d\boldsymbol{k} \, d\boldsymbol{v}_i \, d\boldsymbol{v}_j \, \sigma_{ij} (\boldsymbol{k} \cdot \boldsymbol{n}) \, dS \, . \tag{A-I.1}$$

Since a quantity $(\psi_i' - \psi_i)$ of a property ψ_i is transferred across the surface on each collision of this sort, the total rate of transfer of the property by collisions per unit time and per unit area is

$$\begin{aligned} \{n \cdot \mathbf{J}_c(\psi)\} = n \cdot \frac{1}{2} \sum_{ij} \sigma_{ij}^3 \chi_{ij}(\boldsymbol{r}) \iiint (\psi_i' - \psi_i) \\ \times f_i\left(\boldsymbol{r} + \frac{1}{2}\sigma_{ij}\boldsymbol{k}\right) f_j\left(\boldsymbol{r} - \frac{1}{2}\sigma_{ij}\boldsymbol{k}\right) \boldsymbol{k}(\boldsymbol{g} \cdot \boldsymbol{k}) \, d\boldsymbol{k} \, d\boldsymbol{v}_i \, d\boldsymbol{v}_j \, . \end{aligned} \tag{A-I.2}$$

We thus carried out the integration, obtaining the contribution of the collisional transfer to the flux vector of property ψ_i is

$$\mathbf{J}_c(\psi) = \frac{1}{2} \sum_{ij} \sigma_{ij} \chi_{ij}^0(\boldsymbol{r}) \iiint (\psi_i' - \psi_i) f_i\left(\boldsymbol{r} + \frac{\sigma_{ij}}{2}\boldsymbol{k}\right) f_j\left(\boldsymbol{r} - \frac{\sigma_{ij}}{2}\boldsymbol{k}\right) \boldsymbol{k}(\boldsymbol{g} \cdot \boldsymbol{k}) \, d\boldsymbol{k} \, d\boldsymbol{v}_i \, d\boldsymbol{v}_j \, . \tag{A-I.3}$$

As in the derivation of (2.6), f_i, f_j and χ_{ij}^0 may be expanded in Taylor's series, and derivatives of higher order than the first are neglected. Then we have

$$\begin{aligned}\mathbf{J}_c(\psi)&=\frac{1}{2}\sum_{ij}\sigma_{ij}{}^3\chi_{ij}{}^0\iiint(\psi_i'-\psi_i)\,f_if_j\,\boldsymbol{k}(\boldsymbol{g}\cdot\boldsymbol{k})\,d\boldsymbol{k}\,d\boldsymbol{v}_i\,d\boldsymbol{v}_j\\&\quad+\frac{1}{4}\sum_{ij}\sigma_{ij}{}^4\chi_{ij}{}^0\iiint(\psi_i'-\psi_i)\{(\boldsymbol{k}\cdot\nabla f_i)f_j-(\boldsymbol{k}\cdot\nabla f_j)f_i\}\boldsymbol{k}(\boldsymbol{g}\cdot\boldsymbol{k})\,d\boldsymbol{k}\,d\boldsymbol{v}_i\,d\boldsymbol{v}_j\\&=\mathbf{J}_c{}^{(1)}(\psi)+\mathbf{J}_c{}^{(2)}(\psi)\;. \end{aligned}\tag{A–I.4}$$

We can see from the above equation that $\mathbf{J}_c$'s given by (3.7) are identical with the flux $\mathbf{J}_c$'s arising from the collisional transfer of molecular property.

Appendix II

A. *The derivation of (3.15)*: If we put $m_i\boldsymbol{V}_i$ in (3.7–1), we have

$$\begin{aligned}\mathbf{J}_c{}^{(1)}[m_i\boldsymbol{V}_i]&=\frac{1}{2}\sum_{ij}\sigma_{ij}{}^3\chi_{ij}{}^0\iiint m_i(\boldsymbol{V}_i'-\boldsymbol{V}_i)\,f_if_j\,\boldsymbol{k}(\boldsymbol{g}\cdot\boldsymbol{k})\,d\boldsymbol{k}\,d\boldsymbol{v}_i\,d\boldsymbol{v}_j\\&=\frac{1}{2}\sum_{ij}\sigma_{ij}{}^3\chi_{ij}{}^0m_iM_{ij}\iiint f_if_j\,\boldsymbol{kk}(\boldsymbol{g}\cdot\boldsymbol{k})^2\,d\boldsymbol{k}\,d\boldsymbol{v}_i\,d\boldsymbol{v}_j\\&=\frac{\pi}{15}\sum_{ij}\sigma_{ij}{}^3\chi_{ij}{}^0m_iM_{ij}\iint(2\boldsymbol{gg}+g^2\mathbf{U})\,f_if_j\,d\boldsymbol{v}_i\,d\boldsymbol{v}_j\;,\end{aligned}\tag{A–II.1}$$

where we have used the relation (e.g. see p. 290 in references 13))

$$\int\boldsymbol{kk}(\boldsymbol{g}\cdot\boldsymbol{k})^2\,d\boldsymbol{k}=\frac{2\pi}{15}(2\boldsymbol{gg}+g^2\mathbf{U})\;.\tag{A–II.2}$$

Putting $m_i\boldsymbol{V}_i$ in (3.7–2), we obtain

$$\begin{aligned}\mathbf{J}_c{}^{(2)}[m_i\boldsymbol{V}_i]&=\frac{1}{4}\sum_{ij}\sigma_{ij}{}^4\chi_{ij}{}^0m_iM_{ij}\iiint f_if_j\left(\boldsymbol{k}\cdot\nabla\ln\frac{f_i}{f_j}\right)\boldsymbol{kk}(\boldsymbol{g}\cdot\boldsymbol{k})^2\,d\boldsymbol{k}\,d\boldsymbol{v}_i\,d\boldsymbol{v}_j\\&=\frac{\pi}{48}\sum_{ij}\sigma_{ij}{}^4\chi_{ij}{}^0m_iM_{ij}\iint f_if_j\left[\frac{\boldsymbol{gg}+g^2\mathbf{U}}{g}\left(\boldsymbol{g}\cdot\nabla\ln\frac{f_i}{f_j}\right)\right.\\&\qquad\left.+g\left\{\left(\nabla\ln\frac{f_i}{f_j}\right)\boldsymbol{g}+\boldsymbol{g}\left(\nabla\ln\frac{f_i}{f_j}\right)\right\}\right]d\boldsymbol{v}_i\,d\boldsymbol{v}_j\;,\end{aligned}\tag{A–II.3}$$

using a relation for arbitrary vector $\boldsymbol{\nu}$

$$\int\boldsymbol{kk}(\boldsymbol{\nu}\cdot\boldsymbol{k})(\boldsymbol{g}\cdot\boldsymbol{k})^2\,d\boldsymbol{k}=\frac{\pi}{12}\left\{\frac{\boldsymbol{\nu}\cdot\boldsymbol{g}(\boldsymbol{gg}+g^2\mathbf{U})}{g}+g(\boldsymbol{\nu g}+\boldsymbol{g\nu})\right\}\;.\tag{A–II.4}$$

B. *The derivation of (3.20) and (3.21)*: Putting $\psi_i=\frac{1}{2}m_iV_i{}^2$ in (3.8–1), we can see

$$\begin{aligned}R_c{}^{(1)}\left(\frac{m_iV_i{}^2}{2}\right)&=\frac{1}{2}\sum_{ij}^{\nu}\sigma_{ij}{}^4\chi_{ij}{}^0\iiint f_if_j\left\{\boldsymbol{k}\cdot\nabla\left(\frac{m_i{}^2V_i{}^2}{2}-\frac{m_iV_i{}^2}{2}\right)\right\}(\boldsymbol{g}\cdot\boldsymbol{k})\,d\boldsymbol{k}\,d\boldsymbol{v}_i\,d\boldsymbol{v}_j\\&=-\frac{1}{2}\sum_{ij}^{\nu}\sigma_{ij}{}^4\chi_{ij}{}^0\iiint f_if_j[\boldsymbol{k}m_i(\boldsymbol{V}_i'-\boldsymbol{V}_i):\nabla\boldsymbol{v}_0](\boldsymbol{g}\cdot\boldsymbol{k})\,d\boldsymbol{k}\,d\boldsymbol{v}_i\,d\boldsymbol{v}_j\\&=-\nabla\boldsymbol{v}_0:\mathbf{J}_c{}^{(1)}[m_i\boldsymbol{V}_i]\;.\end{aligned}\tag{A–II.5}$$

In a similar way, we obtain from (3.8–2)

$$R_c{}^{(2)}\left(\frac{m_iV_i{}^2}{2}\right)=-\nabla\boldsymbol{v}_0:\mathbf{J}_c{}^{(2)}[m_i\boldsymbol{V}_i]\;.\tag{A–II.6}$$

If we put $\psi_i=m_iV_i{}^2/2$ in (3.7–1), we have

$$\mathbf{J}_c^{(1)}\left[\frac{m_iV_i^2}{2}\right]=\frac{1}{2}\sum_{ij}\sigma_{ij}^3\chi_{ij}^0\iiint m_iM_{ij}f_if_j(\boldsymbol{G}\cdot\boldsymbol{k})\boldsymbol{k}(\boldsymbol{g}\cdot\boldsymbol{k})^2\,d\boldsymbol{k}\,d\boldsymbol{v}_i\,d\boldsymbol{v}_j$$

$$=\frac{\pi}{15}\sum_{ij}\sigma_{ij}^3\chi_{ij}^0M_{ij}m_j\iint\{2\boldsymbol{g}(\boldsymbol{g}\cdot\boldsymbol{G})+g^2\boldsymbol{G}\}f_if_j\,d\boldsymbol{v}_i\,d\boldsymbol{v}_j\,, \tag{A–II.7}$$

where the following relation has been used

$$\int(\boldsymbol{G}\cdot\boldsymbol{k})\boldsymbol{k}(\boldsymbol{g}\cdot\boldsymbol{k})^2\,d\boldsymbol{k}=\frac{2\pi}{15}\{2\boldsymbol{g}(\boldsymbol{g}\cdot\boldsymbol{G})+g^2\boldsymbol{G}\}\;. \tag{A–II.8}$$

From (3.7–2) we can deduce

$$\mathbf{J}_c^{(2)}\left[\frac{m_iV_i^2}{2}\right]=\frac{1}{4}\sum_{ij}\sigma_{ij}^4\chi_{ij}^0M_{ij}m_i\iint f_if_j(\boldsymbol{G}\cdot\boldsymbol{k})\left(\boldsymbol{k}\cdot\nabla\ln\frac{f_i}{f_j}\right)\boldsymbol{k}(\boldsymbol{g}\cdot\boldsymbol{k})^2\,d\boldsymbol{k}\,d\boldsymbol{v}_i\,d\boldsymbol{v}_j$$

$$=\frac{\pi}{48}\sum_{ij}\sigma_{ij}^4\chi_{ij}^0M_{ij}m_i\iint\left[\frac{\boldsymbol{g}}{g}\left(\boldsymbol{G}\nabla\ln\frac{f_i}{f_j}:\boldsymbol{gg}\right)+g\left\{\left(\boldsymbol{G}\cdot\nabla\ln\frac{f_i}{f_j}\right)\boldsymbol{g}\right.\right.$$

$$\left.\left.+\left(\boldsymbol{g}\cdot\nabla\ln\frac{f_i}{f_j}\right)\boldsymbol{G}+(\boldsymbol{g}\cdot\boldsymbol{G})\nabla\ln\frac{f_i}{f_j}\right\}\right]f_if_i\,d\boldsymbol{v}_i\,d\boldsymbol{v}_j\,, \tag{A–II.9}$$

using the relation

$$\int(\boldsymbol{a}\cdot\boldsymbol{k})(\boldsymbol{b}\cdot\boldsymbol{k})\boldsymbol{k}(\boldsymbol{g}\cdot\boldsymbol{k})^2\,d\boldsymbol{k}=\frac{\pi}{12}\left[\frac{\boldsymbol{g}}{g}(\boldsymbol{ab}:\boldsymbol{gg})+\{(\boldsymbol{a}\cdot\boldsymbol{b})\boldsymbol{g}+(\boldsymbol{b}\cdot\boldsymbol{g})\boldsymbol{a}+(\boldsymbol{g}\cdot\boldsymbol{a})\boldsymbol{b}\}g\right]. \tag{A–II.10}$$

Appendix III

A. *The derivation of (4.7)*: If we use the singlet distribution function given by (4.2), retaining only the first order perturbation, (3.15–1) is reduced to

$$\mathbf{J}_c^{(1)}[m_i\boldsymbol{V}_i]=\frac{\pi}{15}\sum_{ij}\sigma_{ij}^3\chi_{ij}^0M_{ij}m_i\iint(2\boldsymbol{gg}+g^2\mathbf{U})f_i^0f_j^0(1+\phi_i+\phi_j)\,d\boldsymbol{v}_i\,d\boldsymbol{v}_j$$

$$=\frac{\pi}{15}\sum_{ij}\sigma_{ij}^3\chi_{ij}^0M_{ij}m_i\left[\frac{10n_in_jkT}{m_iM_{ij}}\right]\mathbf{U}+\frac{4\pi}{15}\sum_{ij}\sigma_{ij}^3\chi_{ij}^0M_{ij}m_in_j\int\boldsymbol{V}_i\boldsymbol{V}_if_i^0\phi_i\,d\boldsymbol{v}_i$$

$$=\frac{2\pi}{3}\sum_{ij}\sigma_{ij}^3\chi_{ij}^0n_in_jkT\,\mathbf{U}+\frac{4\pi}{15}\sum_{ij}\sigma_{ij}^3\chi_{ij}^0M_{ij}m_in_j\int\boldsymbol{V}_i\boldsymbol{V}_jf_i^0\phi_i\,d\boldsymbol{v}_i\,, \tag{A–III.1}$$

where we have used the relations

$$\iint(2\boldsymbol{gg}+g^2\mathbf{U})f_i^0f_j^0\,d\boldsymbol{v}_i\,d\boldsymbol{v}_j=\frac{10}{m_iM_{ij}}n_in_jkT\,\mathbf{U}\,, \tag{A–III.2}$$

and

$$\iint(2\boldsymbol{gg}+g^2\mathbf{U})f_i^0f_j^0\phi_i\,d\boldsymbol{v}_i\,d\boldsymbol{v}_j=2n_j\int\boldsymbol{V}_i\boldsymbol{V}_jf_i^0\phi_i\,d\boldsymbol{v}_i\,. \tag{A–III.3}$$

Regarding as $b_{ij}=(2/3)\pi\sigma_{ij}^3$, we obtain (4.7–1).

Putting $f_i=f_i^0(1+\phi_i)$ in (3.17–2), and retaining the same order with (A–III.1), we can write $\mathbf{J}_c^{(2)}(m_i\boldsymbol{V}_i)$ as

$$\mathbf{J}_c^{(2)}[m_i\boldsymbol{V}_i]=\frac{\pi}{48}\sum_{ij}\sigma_{ij}^4\chi_{ij}^0m_iM_{ij}[A+B+C]\,,$$

$$A\equiv\iint\left[(\boldsymbol{gg}+g^2\mathbf{U})\left(\frac{\boldsymbol{g}}{g}\cdot\nabla\ln\frac{n_i}{n_j}\right)+g\left\{\left(\nabla\ln\frac{n_i}{n_j}\right)\boldsymbol{g}+\boldsymbol{g}\left(\nabla\ln\frac{n_i}{n_j}\right)\right\}\right]f_i^0f_j^0\,d\boldsymbol{v}_i\,d\boldsymbol{v}_j$$

$$B\equiv\frac{1}{kT}\iint\left[(\boldsymbol{gg}+g^2\mathbf{U})\left\{\frac{\boldsymbol{g}}{g}\cdot(m_i\boldsymbol{V}_i+m_j\boldsymbol{V}_j)\cdot\nabla\boldsymbol{v}_0\right\}+g\{(m_i\boldsymbol{V}_i-m_j\boldsymbol{V}_j)\cdot\nabla\boldsymbol{v}_0\boldsymbol{g}\right.$$

$$\left.+\boldsymbol{g}(m_i\boldsymbol{V}_i-m_j\boldsymbol{V}_j)\cdot\nabla\boldsymbol{v}_0\}\right]f_i^0f_j^0\,d\boldsymbol{v}_i\,d\boldsymbol{v}_j$$

$$C \equiv \frac{1}{2kT}\iint\Big[(\boldsymbol{g}\boldsymbol{g}+g^2\mathbf{U})\Big\{\frac{\boldsymbol{g}}{g}(m_iV_i^2-m_jV_j^2)\cdot\nabla\ln T+g(m_iV_i^2-m_jV_j^2)$$

$$\times\{(\nabla\ln T)\boldsymbol{g}+\boldsymbol{g}(\nabla\ln T)\}\Big\}\Big]f_i^0f_j^0\,d\boldsymbol{v}_i\,d\boldsymbol{v}_j \tag{A–III.4}$$

where the all terms involving ϕ_i are neglected, since (3.17–2) involve the derivatives of the macro-variables. Changing the variables from $\boldsymbol{v}_i$, $\boldsymbol{v}_j$ to the $\boldsymbol{g}_{ji}$, $\boldsymbol{G}_{ji}$, we obtain

$$A=0\,,$$

$$B=-\frac{m_iM_{ji}}{kT}\iint\Big[\frac{1}{g}(\boldsymbol{g}\boldsymbol{g}+g^2\mathbf{U})\boldsymbol{g}\boldsymbol{g}:\nabla\boldsymbol{v}_0+g\{(\boldsymbol{g}\cdot\nabla\boldsymbol{v}_0)\boldsymbol{g}+\boldsymbol{g}(\boldsymbol{g}\cdot\nabla\boldsymbol{v}_0)\}f_i^0f_j^0\,d\boldsymbol{G}\,d\boldsymbol{g}$$

$$=-\frac{32}{3}(2kT)^{1/2}\left(\frac{m_iM_{ji}}{2}\right)^{-1/2}n_in_j\left[\frac{6}{5}\mathbf{S}+\mathbf{U}(\nabla\cdot\boldsymbol{v}_0)\right],$$

and

$$C=0\,.$$

Consequently we have

$$\mathbf{J}_c^{(2)}[m_i\boldsymbol{V}_i]=-\sum_{ij}\tilde{\omega}_{ij}\left[\frac{6}{5}\frac{\mathbf{S}}{T}+\mathbf{U}\frac{\nabla\boldsymbol{v}_0}{T}\right], \tag{A–III.5}$$

where $\tilde{\omega}_{ij}$ is given by (4.10).

B. *The derivation of (4.17)*: In the same manner as in the case of (4.7), we can evaluate the collisional transfer of energy.

Putting $f_i=f_i^0(1+\phi_i)$ in (3.23–1), we have

$$\mathbf{J}_c^{(1)}\left[\frac{m_iV_i^2}{2}\right]=\frac{\pi}{15}\sum_{ij}\sigma_{ij}^4\chi_{ij}^0M_{ji}m_i\iint\{2\boldsymbol{g}(\boldsymbol{g}\cdot\boldsymbol{G})+g^2\boldsymbol{G}\}f_i^0f_j^0(1+\phi_i+\phi_j)\,d\boldsymbol{v}_i\,d\boldsymbol{v}_j$$

$$=\frac{1}{2}\sum_{ij}\sigma_{ij}^3\chi_{ij}^0M_{ji}m_i\iiint f_i^0f_j^0(\phi_i+\phi_j)\{(M_{ij}\boldsymbol{V}_i+M_{ji}\boldsymbol{V}_j)\cdot\boldsymbol{k}\}\boldsymbol{k}(\boldsymbol{g}\cdot\boldsymbol{k})^2\,d\boldsymbol{k}\,d\boldsymbol{v}_i\,d\boldsymbol{v}_j$$

$$=\frac{3}{5}\sum_{ij}b_{ij}\chi_{ij}^0M_{ij}M_{ji}n_j\boldsymbol{q}_{k_i}+\frac{1}{2}\sum_{ij}b_{ij}\chi_{ij}^0M_{ij}M_{ji}\frac{m_i-2m_j}{m_im_j}n_jkT\boldsymbol{J}_i\,, \tag{A–III.6}$$

and from (3.23–2) we have

$$\mathbf{J}_c^{(2)}\left[\frac{m_iV_i^2}{2}\right]=\frac{\pi}{48}\sum_{ij}\sigma_{ij}^4\chi_{ij}^0M_{ji}m_i\iint\Big[\frac{\boldsymbol{g}}{g}\left(\boldsymbol{G}\nabla\ln\frac{f_i^0}{f_j^0}:\boldsymbol{g}\boldsymbol{g}\right)$$

$$+g\left\{\left(\boldsymbol{G}\cdot\nabla\ln\frac{f_i^0}{f_j^0}\right)\boldsymbol{g}+\left(\nabla\ln\frac{f_i^0}{f_j^0}\cdot\boldsymbol{g}\right)\boldsymbol{G}+(\boldsymbol{g}\cdot\boldsymbol{G})\nabla\ln\frac{f_i^0}{f_j^0}\right\}\Big]f_i^0f_j^0\,d\boldsymbol{g}\,d\boldsymbol{G}$$

$$=-\frac{2}{3}\sum_{ij}\sigma_{ij}^4\chi_{ij}^0n_in_j\left(\frac{m_iM_{ji}}{2}\right)^{1/2}\frac{\pi^{1/2}}{m_i+m_j}(2kT)^{3/2}\nabla\ln T$$

$$=\sum_{ij}\tilde{\omega}_{ij}\left(\frac{3kT}{m_i+m_j}\right)\nabla\frac{1}{T}\,. \tag{A–III.7}$$

References

1) E. J. Hellund and E. A. Uehling: Phys. Rev. **56** (1939) 818.
2) C. F. Curtiss and J. O. Hirschfelder: J. Chem. Phys. **17** (1949) 550.
3) S. Ono: Scientific Papers of the College of General Education, University of Tokyo, **5** (1955) 87.
4) D. Enskog: Kungl. Svenska Vetenskaps Akademiens Handle. **63** (1921) No. 4.
5) F. C. Collins and H. Raffel: J. Chem. Phys. **22** (1954) 1728.
6) H. C. Longuet-Higgins and J. A. Pople: J. Chem. Phys. **25** (1956) 884.
7) S. A. Rice, J. G. Kirkwood, J. Ross and W. Zwanzig: J. Chem. Phys. **31** (1959) 575.
8) S. A. Rice: J. Chem. Phys. **31** (1959) 584.
9) J. T. O'Toole and J. S. Dahler: J. Chem.

Phys. **32** (1960) 1097.
10) H. B. Hollinger and C. F. Curtiss: J. Chem. Phys. **33** (1960) 1386.
11) T. Murakami: J. Phys. Soc. Japan **15** (1960) 60.
12) H. H. Thorne: (of the University of Sydney, Australia) see Chapman and Cowling, pp. 292 et seq.
13) S. Chapman and T. G. Cowling: *The Mathematical Theory of non-Uniform Gases*, (Cambridge, 1939, 1953).
14) J. O. Hirschfelder, C. F. Curtiss and R. N. Bird: *The Molecular Theory of Gases and Liquids*, (New York, 1954).
15) L. Onsager: Phys. Rev. **37** (1931) 405.
16) I. Prigogine: *Etude Thermodynamique des Phénomènes Irréversibles* (Dunod, Paris, 1947).
17) S. R. de Groot: *Thermodynamics of Irreversible Processes* (North-Holland, Amsterdam, 1952).

JOURNAL OF THE PHYSICAL SOCIETY OF JAPAN, Vol. 16, No. 4, APRIL, 1961

Temperature Dependence of Magnetic Susceptibilities of $KClO_3$, $KBrO_3$ and KIO_3

By Shōtarō TOBISAWA

Department of Chemistry, Defense Academy, Yokosuka

(Received May 6, 1960)

Magnetic susceptibilities of crushed samples of $KClO_3$, $KBrO_3$ and KIO_3 were measured with a recording magnetic balance which was operated by the Faraday method. The temperature was elevated at a constant rate, 250°C per hour. It was found that, being heated, $KClO_3$ showed irregular paramagnetic susceptibilities in the solid or liquid state, before the evolution of oxygen gas at 500°C. A possible explanation for the irregular paramagnetic behaviors is suggested.

On the contrary, $KBrO_3$ and KIO_3 showed the diamagnetic susceptibilities, which were independent of temperature below the temperatures of the evolution of oxygen gas, 370° and 550°C, respectively.

§1. Introduction

Recently, the paramagnetic resonance spectra of $Ba(ClO_3)_2 \cdot H_2O$, $NaClO_3$ and $Ba(BrO_3)_2 \cdot H_2O$, irradiated by 1 MeV electrons, have been observed by Cowen[1]. From the hyperfine structure of the paramagnetic resonance absorption spectra of a singe crystal of $NaClO_3$, it has been stated by Hastly et al.[2] that the V center produced by X-irradiation is a radical.

It is of particular interest to investigate the changes in physical properties of chlorate, bromate and iodate with elevating temperature. In the present paper, the temperature dependence of magnetic susceptibilities of $KClO_3$, $KBrO_3$ and KIO_3 is studied.

§2. Experimental Procedures

Potassium chlorate of commercial guaranteed reagent was recrystallized from water four times, potassium bromates of Merck (sample A) and of commercial guaranteed reagent (sample B) two and three times, respectively, and potassium iodate of Merck three times. A crushed sample was obtained by carefully squeezing each recrystallized sample in an agate mortar with a pestle.

Measurements were carried out with the recording magnetic balance described in detail in a previous report[3]. The crushed sample of about 15 mg. was charged into a fused quartz bulb made with the same dimension as the previously reported one. This bulb was sealed carefully, after being evacuated for several hours under a vacuum of 10^{-5} mmHg. The measurements were made by elevating the temperature at a constant rate, 250°C per hour, and by applying a constant field, 8650 Oersteds. In every measurement, one millimeter on a recording chart corresponded to 1.6×10^{-9} c.g.s.e.m.u. in magnetic susceptibility. In every experiment, by examining the temperature dependence of magnetic susceptibility of the residue obtained by removing oxygen gas evolved in the bulb as a result of the complete decomposition, it was ascertained that the sample used was not contaminated by paramagnetic or ferromagnetic impurities.

The decomposition temperatures of $KClO_3$, $KBrO_3$ and KIO_3 were determined by measuring losses in weight with a thermal balance without magnetic field. A sample packed in an open bulb, was thermally decomposed under the constant pressure of 50 mmHg. The rate of heating was the same as in the case of the magnetic measurement. When the magnetic balance was used as the thermal balance, one millimeter on the recording chart corresponded to 0.020 mg. In either case, the experiments were carried out under dark condition.

§ 3. Experimental Results

(1) *Paramagnetic susceptibility of $KClO_3$ in the solid or liquid state*

In Fig. 1, the curve (1) indicates that $KClO_3$ decomposes at 500°C. Although the measurements were made for the samples in different weight at constant rate of heating and for the samples in the same weight at different rate of heating, these samples decomposed at 500°C in all the measurements. The decomposition temperature of 500°C is higher than that obtained by Vitoria[4].

The magnetic susceptibility of $KClO_3$, obtained at room temperature, was -0.33×10^{-6} per g., and the value was in good agreement with that obtained by Meslin[5]. The curve (2) shows the first deflection toward paramagnetic side at 158°C, the second change at 352°C, the third change at 446°C, and the fourth change at 500°C. Both the curves (3) and (4) show the first deflections toward paramagnetic sides at 308°C, the second changes at 352°C, then show the third changes at 480° and 474°C, respectively, and the fourth changes at 500°C. In the curves (2), (3) and (4), the deflections toward paramagnetic side above 500°C increase abruptly with increasing temperature. The breaking points at 500°C corresponded to the decomposition temperature shown in the curve (1). The deflection toward paramagnetic side above 500°C can, therefore, be ascribed to paramagnetic contribution due to oxygen gas evolved by the thermal decomposition. It has been reported by Vitoria[4] that the melting point of $KClO_3$, determined by capillary-tube method, is 356°C. The changes in magnetic susceptibilities at

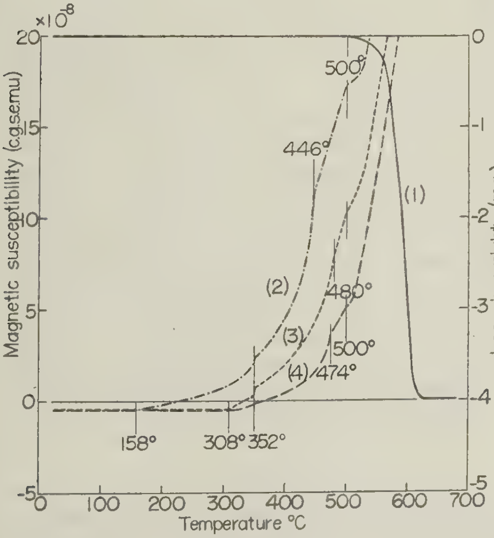

Fig. 1. Magnetic susceptibility and loss in weight versus temperature for $KClO_3$; (1): curve of loss in weight for the sample of 10.1 mg., (2), (3) and (4): curves of susceptibility for the samples of 15.1 mg.

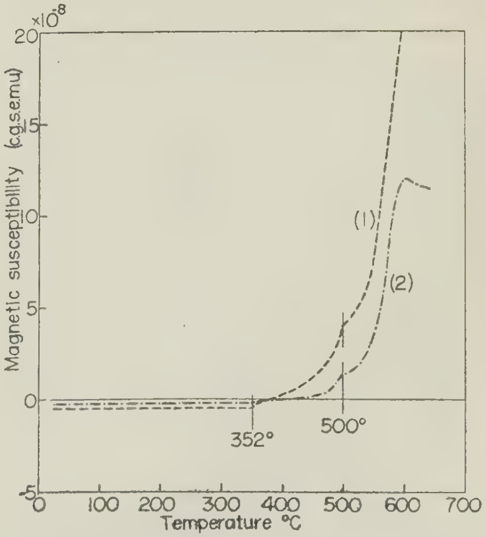

Fig. 2. Magnetic susceptibility versus temperature for $KClO_3$; (1): curve for the sample of 15.0 mg., (2): curve for the sample of 7.0 mg.

352°C in the curves (2), (3) and (4) can, therefore, be owing to the phase transition from solid to liquid. In Fig. 2, both the curves (1) and (2) show the first changes at 352°C, then deflect toward paramagnetic side with increasing temperature. The deflections toward paramagnetic side above 500°C increase abruptly with increasing temperature. In this case, the deflections toward paramagnetic side in the solid state could not be found. Besides, the changes corresponding to the third changes as shown in the curves (2), (3) and (4) in Fig. 1, could not also be recognized.

(2) *Diamagnetic susceptibilities of $KBrO_3$ and KIO_3 before the evolutions of oxygen gas*

The magnetic susceptibility of both the samples A (Merck) and B (commercial G. R.) of $KBrO_3$ was -0.32×10^{-6} per g. and that of KIO_3 was -0.31×10^{-6} per g., at room temperature. In Fig. 3, the curve (1) shows the first loss in weight at 370°C and the breaking point at 396°C. Both the curves (2) and (3) deflect toward paramagnetic side above 370°C and show the breaking points at 395°C. The deflections toward paramagnetic side above 370°C in the curves (2) and (3) can, therefore, be attributed to paramagnetic contribution due to oxygen gas evolved by the thermal decomposition. The breaking point at 395°C is considered to be owing to the phase transition from solid to liquid. This temperature, however, is lower than the melting point of 434°C, reported by Carnelley et al[6].

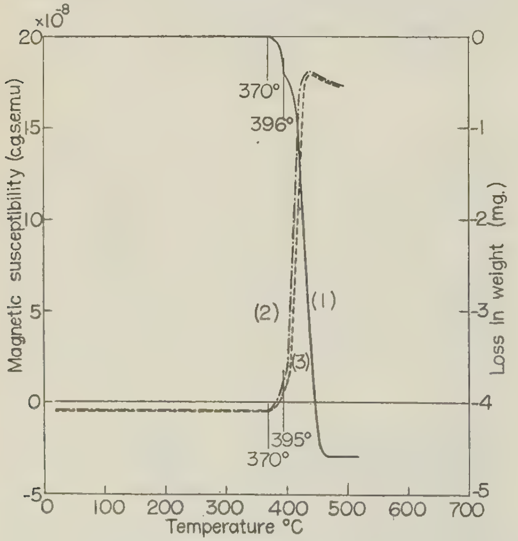

Fig. 3. Magnetic susceptibility and loss in weight versus temperature for $KBrO_3$; (1) curve of loss in weight for the sample of 15.1 mg., (2) and (3): curves of susceptibility for the samples A and B of 15.0 mg.

In Fig. 4, the curve (2) deflects toward paramagnetic side above 550°C and shows the breaking points at 560°C and other temperatures. The temperature of deflection corresponds to the decomposition temperature of 550°C found in the curve (1). The changes in magnetic susceptibility above 550°C can, therefore, be ascribed to paramagnetic contribution due to oxygen gas evolved by the thermal decomposition. The curve (1) also shows the breaking point at 560°C. It has been reported by Day et al.[7] that the melting point of KIO_3 is 560°C. From the above results, the breaking point at 560°C in both the curves (1) and (2) in Fig. 4 is owing to the phase transition from solid to liquid. As indicated in the curve (2), the magnetic behavior of KIO_3 after the evolution of oxygen gas is remarkably different from those of $KClO_3$ and $KBrO_3$.

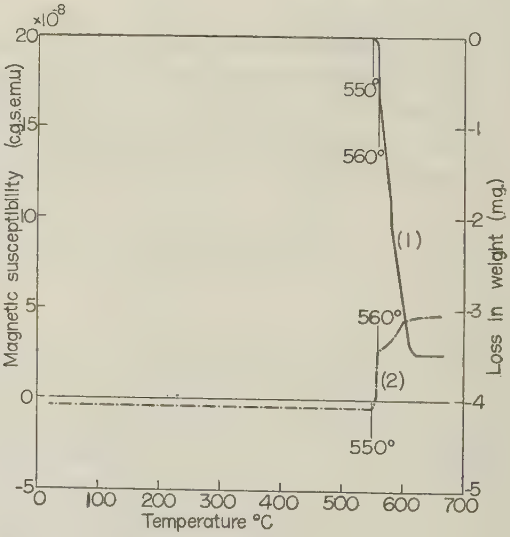

Fig. 4. Magnetic susceptibility and loss in weight versus temperature for KIO_3; (1): curve of loss in weight for the sample of 15.0 mg., (2): curve of susceptibility for the sample of 14.9 mg.

In spite of the fact that the crystal structure of $KBrO_3$ as well as $KClO_3$ contains a discrete XO_3^- ion, the magnetic behavior of $KBrO_3$ before the evolution of oxygen gas is different from those of $KClO_3$. Although KIO_3 is of perovskite structure, KIO_3 showed diamagnetic susceptibilities which were independent of temperature below the temperature of the evolution of oxygen gas similarly to the case of $KBrO_3$.

§ 4. Discussion on Paramagnetic Behavior of $KClO_3$

It has been known that, being heated, $KClO_3$ decomposes without evolution of oxygen gas according to the equation,

$$2KClO_3 \rightarrow KClO_2 + KClO_4 \qquad (1)$$

or

$$4KClO_3 \rightarrow 3KClO_4 + KCl\,. \qquad (2)$$

Osada[8] has found that the reaction (1) takes place at comparatively low temperature, and that the two reaction products release oxygen gas in accordance with the equations, $KClO_2 \rightarrow KCl + O_2$ and $KClO_4 \rightarrow KCl + 2O_2$, respectively. Most of previous investigators[9] have reported that the reaction (2) takes place simultaneously with the reaction $2KClO_3 \rightarrow 2KCl + 3O_2$, while Glasner et al.[10] have stated that the reaction (2) is not a simultaneous reaction with the reaction $2KClO_3 \rightarrow 2KCl + 3O_2$, but a consecutive reaction that $KClO_4$ in the equation (2) is formed according to the equation $KCl + 2O_2 \rightarrow KClO_4$, where KCl and O_2 result from the reaction $2KClO_3 \rightarrow 2KCl + 3O_2$. As it is apparent from these interpretations, the mechanism of decomposition of $KClO_3$ is complicated. Besides, these interpretations seem to suggest that both the reactions (1) and (2) take place indefinitely, and that each amount of the reaction products due to these reactions is not constant. Therefore, the paramagnetic behaviors over the range of temperatures below 500°C, shown in Figs. 1 and 2, lead to suggestion that $KClO_3$ may mainly convert into $KClO_2$ and $KClO_4$ through a certain transition state with unpaired electrons during the course of the reaction (1), in the solid or liquid state when $KClO_3$ is heated. Sometimes $KClO_3$ may partly convert into $KClO_4$ and KCl through an other transition state with unpaired electrons during the course of the reaction (2). This suggestion seems to be supported by appearance of the third changes in the curves of (2), (3) and (4) in Fig. 1. Although the samples of the same weight were decomposed under the same experimental condition, the results obtained showed irregular paramagnetic behaviors, as indicated in Fig. 1. The irregular paramagnetic behaviors may be attributed to the indefinite occurrences of the reactions (1) and (2).

Acknowledgement

The author is particularly indebted to Prof. Y. Nomura for his suggestion and encouragement throughout this work.

References

1) J. A. Cowen: Bull. Amer. Phys. Soc. II, **2** (1957) 317.
2) T. E. Hastly, W. B. Ard and W. G. Moulton: Bull. Amer. Phys. Soc. II, **4** (1959) 260.
3) S. Tobisawa: Bull. Chem. Soc. Japan **32** (1959) 1173.
4) A. P. Vitoria: Anales Soc. Espan. Fis. Quim. **27** (1929) 787.
5) G. Meslin: Ann. chim. phys. **7** (1906) 145.
6) T. Carnelley and L. T. O'Shea: J. Chem. Soc. **45** (1884) 409.
7) R. C. Day and V. Dayal: Trans. Faraday Soc. **32** (1936) 741.
8) H. Osada: Private communication.
9) W. Farmer and J. B. Firth: J. Chem. Soc. **125** (1924) 82. C. E. Otto and H. S. Fry: J. Amer. Chem. Soc. **46** (1924) 272. K. A. Hofmann and P. H. Marin: Sitzber. preuss. Akad. Wiss. Phys.-math. Klasse **1932** 448.
10) A. Glasner and L. Weidenfeld: J. Amer. Chem. Soc. **74** (1952) 2464.

JOURNAL OF THE PHYSICAL SOCIETY OF JAPAN, Vol. 16, No. 4, APRIL, 1961

Luminescence of Doped Silver Chloride Crystals

By Sanemi SONOIKE and Kazuo AKIMOTO

Faculty of Engineering, Chuo University, Bunkyo-ku, Tokyo

(Received July 1, 1960)

Luminescences of silver chloride crystals doped with $CdCl_2$ and $FeCl_3$ are measured spectroscopically at low temperatures. Effects of auxiliary infrared light on them and on photoconductivities are also measured. Cd ions change the normal luminescence of silver chloride of maximum at about 485 mμ to longer wavelength one of 545 mμ at low temperatures. When the latter luminescence is thermally quenched, the usual maximum of 485 mμ recovers and then it is also thermally quenched. The infrared light enhances the luminescence of 545 mμ and quenched that of 485 mμ. This quenching is drastic when Fe ions are added. The photoconductivity is enhanced by the infrared light in Cd doped crystals and almost not quenched in Fe doped crystals. An energy band model is given to explain the experimental results.

§ 1. Introduction

The nature of luminescence centers in solid has complicated character. In spite of a great number of investigations on it, generally acceptable conclusions are few. Especially silver halides are open to question. On the other hand the luminescence of silver halides has a fundamental character of polar crystals', then its investigation is important as the means of research of physical properties of silver halides.

The luminescence of silver halides was observed initially by Randall[1)] and Meidinger[2)], with crystals and emulsions at low temperatures. Farnell and Burton[3)] farther examined it in some detail by means of spectrographical method. They interpreted it as an edge luminescence because they used purest samples and got no after-glow, and explain the thermal quenching of the luminescence by configuration co-ordinates. Makishima and Tomotsu[4)] supported their idea though they noticed the connection with lattice defects, and criticized Seitz's mechanism[5)] which suggested forbidden transitions within silver ions. Moser and Urbach[6)] made some study of the luminescence in which they investigated the buildup of emission under excitation, the effects of infrared radiation of the luminescence, and cation-activated fluorescence. They concluded independently by Dorfner[7)] that the silver halides are clearly in the class of photoconduction phosphors, and proposed a band model with trap levels of electrons and holes. Makishima, Tomotsu and Hayakawa[8)] successively studied the luminescence of silver chloride with anion impurities, and from the buildup and decay types of the luminescence they found many levels of traps besides the centers intrinsic to the matrix.

Aline[8)] measured coincidently the luminescence and photoconductivity in the wide range of excitation spectrum, and obtained good correspondence between them in some peaks, though his interpretation was ambiguous. Wiegand[10)], however, measured the decay times of luminescence and photocurrent, which behaved independently under several treatments. Then he advanced the idea based upon the effects of vacuum and chlorine annealing on the results, that the recombination centers are silver ion vacancies which initially capture free holes radiatively.

Here we encounter a number of interests about the nature of luminescences such that whether the luminescence is only by photoconductive ones, next in that case, which are electrons or holes that radiate the luminescence by being trapped, and farthermore the trappings are whether first trappings or second recombination trappings. Finally we question what are the luminescence centers at which the trappings take place.

Since in silver halides the carrier of photocurrent is known undoubtedly as electrons[11)], Wiegand's measurements are rather affirmative to hole theory. However the experiments of infrared quenching of luminescence by Moser and Urbach suggest the second trapping theory which indirectly contradicts the hole theory. But Moser and Urbach's material was silver bromoiodide, moreover, from the complicated character of the luminescence, unless the comparison of infrared quenching of luminescence and photocurrent be made, the conclusion cannot be drawn. Therefore we try to measure the luminescence of silver chloride and its thermal quenchings, besides infrared quenchings of luminescence and photoconductivity in relation to the cation impurities such as Cd^{++}, Fe^{+++} additives.

§ 2. Apparatus

Silver chloride powder was precipitated from silver nitrate solution and hydrochloric acid using special pure chemical reagent. It was then melted in air in porcelain crucible and the crystal was drawn up from the melt at a point of platinum rod. The crystal then was cut by Ti-saw into discs of 2–3 mm thick and polished on a flat stone with sodium thiosulphate solution and at last rinsed with hydrochloric acid and distilled water. The impurities were added at the molten state in a form of $CdCl_2$ and $FeCl_3$. These processes were done under a safety light.

Such a specimen was settled in a cryostat cooled with liquid oxygen or liquid nitrogen. The temperature of the crystal was measured with a Cu-constantan thermocouple, the junction of which was touched to the crystal covered with a thin mica plate as a protector against chemical reactions.

The stimulating light was thrown through a quartz window from a distance of 40 cm, through a condenser lens and a slit. The light source was 100 W high pressure mercury lamp filtered by Matsuda UV–Dl filter. The infrared light was thrown through another window from a 250 W infrared lamp with Matsuda IR–Dl filter.

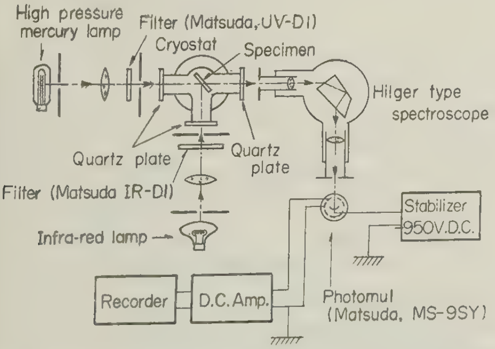

Fig. 1. Arrangement of apparatus to measure the luminescence.

The luminescence was observed from an opposite window and analized by Hilger spectroscope with Matsuda MS–9SY photomultiplier, the output of which was amplified with a sensitive direct current amplifier and automatically recorded. The arrangement of the apparatus is shown in Fig. 1.

The photocurrent was measured separately by a direct current amplifier and a recorder, in similar conditions.

§ 3. Experimental Results

The pure silver chloride powder and crystals showed a proper green luminescence having similar spectroscopic and thermal quenching characters to previous investigators[3),9),10)] the maximum intensity of which is at 485±5 mμ, and the activation energy of the thermal quenching is not far from 0.05 ev. A typical example is shown in Fig. 2. Submaxima were occasionally found at longer wave length side and they often change the form of the main peak at any temperatures to make the activation energy ambiguous.

Origin of these submaxima is attributed to residual impurities or excess silver atoms.

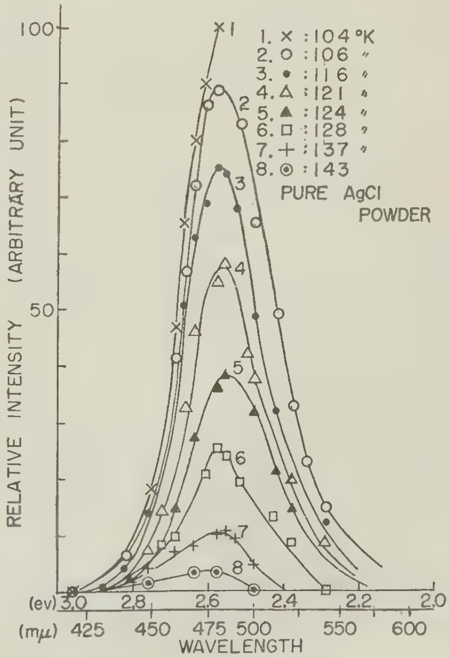

Fig. 2. Luminescence and its thermal quenching of pure AgCl powder.

The silver chloride which was subjected to photolysis and shows violet appearance gives some luminescence at shorter wave length than the maximum, and that of brown appearance shows yellow pink luminescence at longer wave length side. These luminescences were so weak that they can be merely detected as slight deviations from normal back grounds.

Transparent samples also often showed submaximum at about 580 mμ. It is not clear what imperfections are concerned. The room temperature illumination with non-filtered mercury lamp did not change the spectroscopic character essentially, but reduced the intensity over all, even when the darkening was not visible. Strong illumination at room temperature did not reduced the intensity beyond a certain limit —(so for as the shielding effect by photolytic silver dose not cause a remarkable effect)—, but enhanced the intensity slightly by solarization more than that of the specimen let alone after print out.

Silver chloride crystals doped with Cd^{++} ions showed an interesting character in luminescence. At liquid oxygen temperature they gave a luminescence having a single maximum at 545±5 mμ. When the temperature was raised the maximum was weakened, and instead the normal maximum of 485 mμ grew and took its place completely. Then the relief maximum also quenched thermally as usual. This process is shown in Figs. 3, 4 and 5. The greater the amount of Cd ions was, the stronger the intensity of both peaks became. But a small amount of Cd ions was rather suppressive. The amounts of Cd ions added were 2.5×10^{-5}, 5×10^{-5}, 10^{-4} and 5×10^{-4} in mol-ratio.

Auxiliary infrared light enhanced considerably the luminescence of 545 mμ by Cd ions at low temperatures, but it slightly

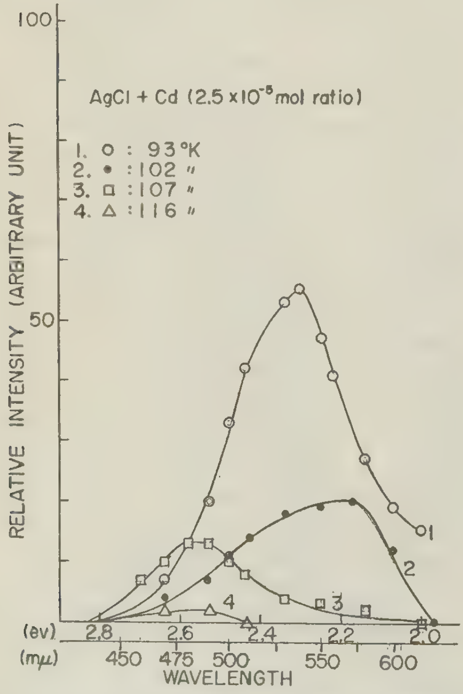

Fig. 3. Luminescence and its thermal quenching of a little Cd doped AgCl Crystal.

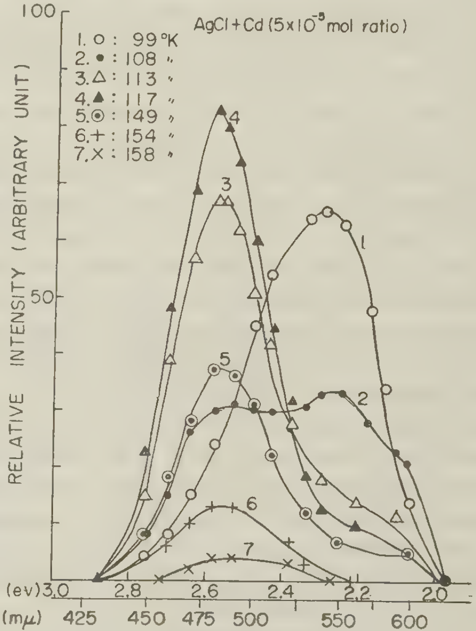

Fig. 4. Luminescence and its thermal quenching of Cd doped AgCl crystal.

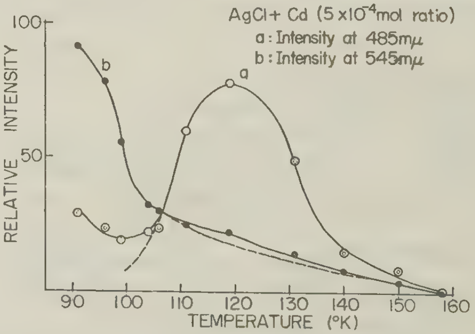

Fig. 5. Transition between two peacks of luminescence intensity with temperature in the Cd doped AgCl crystal. Broken lines avoid the overlapping of peaks one another.

quenched the luminescence of 485 mμ at moderately low temperatures.

Photoconductivity of the sample was also enhanced by the auxiliary infrared light. Those are shown in Figs. 6 and 7.

The buildup of the luminescence was delayed by additions of Cd ions, as well as decay times. The second run of the buildup became faster, but this effect was annihilated by infrared illumination inserted. Effect of the infrared illumination on the decay times was not considerable.

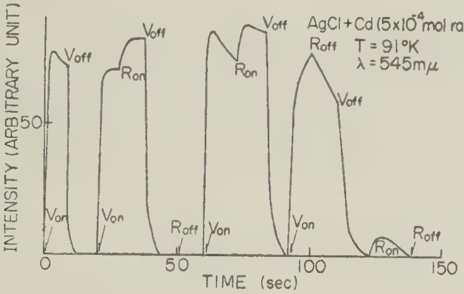

Fig. 6. Effect of auxiliary infrared light on the luminescence of Cd doped AgCl crystal. In diagram, *V* indicates the excitation light and *R* the infrared light.

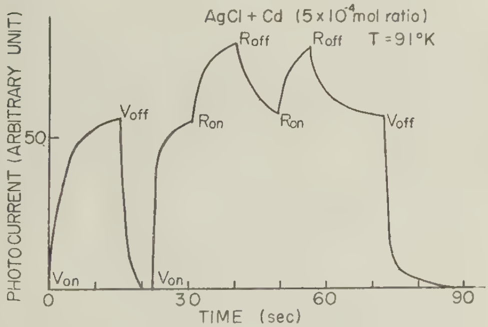

Fig. 7. Effect of auxiliary infrared light on photoconductivity of Cd doped AgCl crystal.

The luminescence of so called pure silver chloride of 485 mμ at low temperatures was also slightly quenched by auxiliary infrared light. In any case spectroscopic forms of individual peaks were not changed by the infrared illumination.

The silver chloride crystals doped with Fe^{+++} ions gave considerably reduced luminescence which besides showed different spectroscopic character. The maximum of 485 mμ was maintained but weak maximum of 550∼560 mμ and a third maximum of longer than 600 mμ were accompanied at low temperatures. These maxima were thermally quenched altogether

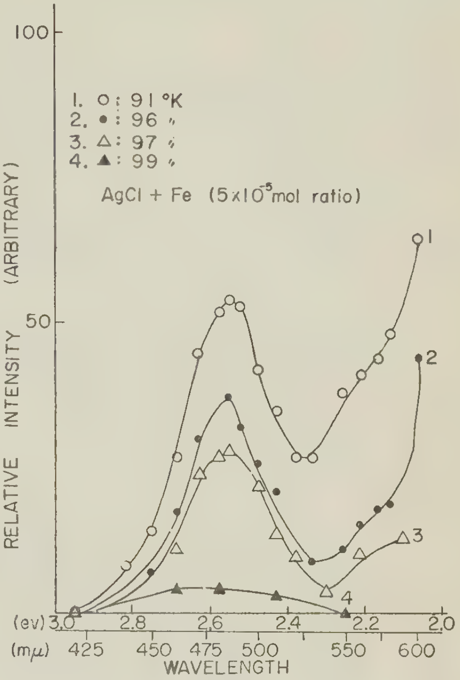

Fig. 8. Luminescence and its thermal quenching of Fe doped AgCl crystal.

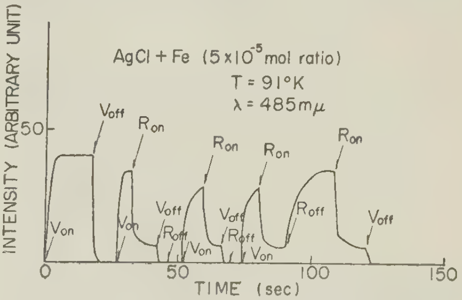

Fig. 9. Effect of auxiliary infrared light on the luminescence of Fe doped AgCl crystal.

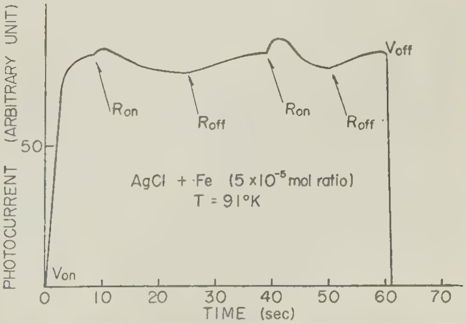

Fig. 10. Effect of auxiliary infrared light on photoconductivity of Fe doped AgCl crystal.

as shown in Fig. 8.

In the Fe doped crystals, the infrared quenching was remarkable at 485 mμ, and less at 555 mμ.

The photoconductivity of the sample showed almost no quenching by the infrared light. At first it enhanced a little and then slowly reduced till slightly under or near the initial current. These are shown in Figs. 9 and 10.

As the solubility of ferric ions in silver chloride is little, the concentration dependence of the luminescence was not determined.

§ 4. Discussion and Summary

The luminescence of maximum intensity at 485 mμ is well known in silver chloride which becomes very strong in purest samples. Then we may attribute it to what is proper to silver chloride. The possible mechanism of luminescence intrinsic to silver chloride is either edge luminescence, or the interstitial silver ions or the silver ion vacancies, both the constituents of Frenkel defects. The fact that this luminescence is replaced by that of at 545 mμ at low temperatures in Cd doped crystals, and quenched by the infrared illumination, suggests that it is not the edge luminescence that is persistent in cooling as suggested by Makishima.

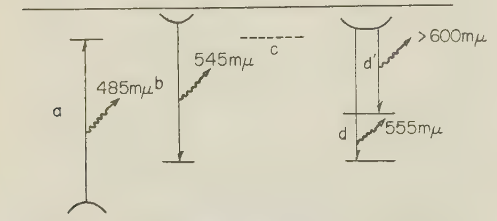

Curved levels represent the excited states

Fig. 11. Energy band model of AgCl phosphor.

Taking account of the influences of the infrared illumination on the luminescence of 485 mμ and 545 mμ, we may assume a band model based on modifying Klick's theory[12] that explained the transition of the blue luminescence of ZnS to the green with temperature. The circumstances are opposit, however, in AgCl(Cd), as the shift of wavelength with temperature is reverse in direction. This is shown in Fig. 11.

In the figure, the notations of the centers are as follows.

a center (485 mμ); this center exists in a purest silver chloride, showing thermal quenching, and being quenched by infrarred illumination. In coexistence of *d* centers, the infrared quenching is drastic, while the photoconductivity is not quenched. In coexistence of *b* centers, it is vanished at low tempratures and appears in warming instead of the thermal quenching of *b* centers, and then also shows thermal quenching as usual. As the concentration of *b* centers is increased from zero, it disappears at once and then increases again as a intensity of relief maximum. After wiegand, the decay constant of the luminescence is very shorter than that of photoconductivity.

b center (545 mμ); this luminescence appears and increases with concentration of added Cd ions. It cancels *a* centers at low temperature completely, but the large amount of it again enhances the *a* center after thermal quenching of itself. Infrared illumination enhances the luminescence as well as photoconductivity.

c ecnter (shallow traps); this increases as the Cd ions are added and delays the decay constant of luminescence of *b* centers.

dd' centers (555 mμ, >600 mμ); this appears as the Fe^{+++} ions are added. It surpresses the efficiency of *a* center, but is thermally quenched together with *a* center. It makes the infrared quenching of *a* center remarkable while is quenched itself somewhat.

This model gives good account of the experimental results.

Thermal quenchings are attributed to the thermal excitation of the electrons or holes in the excited or trapping states of the centers to the conduction or the valence band. We can make any form of the thermal transitions of maxima of luminescence provided the killer centers exist in suitable form. For example we have a equation for stationally state as follows.

$$\frac{dn}{dt}=I-\frac{N_1}{N_c}(1-e^{-E_1/kT})nv\sigma_1\xi_1'-\frac{N_2}{N_c}(1-e^{-E_2/kT})nv\sigma_2\xi_2'$$
$$-\frac{N_3}{N_c}nv\sigma_3\xi_3'-\frac{N_4}{N_c}(1-e^{-E_4/kT})nv\sigma_4\xi_4'=0$$

Where,

n: concentration of conduction electrons
I: excitation rate
N: number of centers
N_c: number of states
E: energy depth of the excited states or the trapping states of centers
V: velocity of electrons
σ: cross section
ξ: recombination probability
1, 2, 3, 4: identification of centers

and prime notation designates that of holes.

Then we get

$$n=\frac{IN_c}{N_1(1-e^{-E_1/kT})v\sigma_1\xi_1'+N_2(1-e^{-E_2/kT})v\sigma_2\xi_2'+N_3v\sigma_3\xi_3'+N_4(1-e^{-E_4/kT})v\sigma_4\xi_4'} .$$

Intensities of luminescence H become

$$H_1=\frac{N_1}{N_c}(1-e^{-E_1/kT})nv\sigma_1\xi_1'$$

$$=\frac{N_1(1-e^{-E_1/kT})\sigma_1\xi_1'I}{N_1(1-e^{-E_1/kT})\sigma_1\xi_1'+N_2(1-e^{-E_2/kT})\sigma_2\xi_2'+N_3\sigma_3\xi_3'+N_4(1-e^{-E_4/kT})\sigma_4\xi_4'} ,$$

$$H_2=\frac{N_2(1-e^{-E_2/kT})\sigma_2\xi_2'I}{N_1(1-e^{-E_1/kT})\sigma_1\xi_1'+N_2(1-e^{-E_2/kT})\sigma_2\xi_2'+N_3\sigma_3\xi_3'+N_4(1-e^{-E_4/kT})\sigma_4\xi_4'} .$$

If $N_4=0$, H_1+H_2 would decrease monotonously.

The transition from H_1 to H_2 with temperature results in $E_1<E_2$ and $N_1\sigma_1\xi_1'\gg N_2\sigma_2\xi_2'$. $N_1\gg N_2$ has been satisfied here, and farther if thermal liberation of holes is important, we take next replacement,

$$\xi'=(1-e^{-E'/kT})n'v'\sigma'$$
$$(1-e^{-E/kT})nv\sigma=\xi ,$$

and we get the similar condition

$$N_1\sigma_1\xi_1'\gg N_2\frac{n'v'}{nv}\sigma_2'\xi_2$$

or

$$N_1\frac{n'v'}{nv}\sigma_1'\xi_1\gg N_2\sigma_2\xi_2' .$$

In either case we may satisfy the conditions represented by the experimental results.

The infrared quenching is also explained from the diagram. In silver chloride, the rate of excitation of holes by the infrared light is less effective than that of electrons, because the photoconductivity does not reduce in this case. Then, *a* centers are quenched liberating free electrons, which have no retiring places without original centers and cannot have remarkable effect in both of luminescence and photoconductivity. The retiring places may be offered by Fe^{+++} ions which protect from holes to recombine because of their charges, and the luminescence is considerably quenched while the photoconductivity is not quenched. On the other hand, *b* centers are electron traps and the infrared light liberates free electrons from other centers and enhances both the luminescence and the photoconductivity.

Now, we shall make some comments about the luminescence centers. We will not enter into the detail constitutions of *b* centers and *d* centers and are only satisfied to say that they are originated from Cd ions and Fe ions. In regard to *a* centers intrinsic to silver chloride, that small amount of Cd ions cancels the intrinsic luminescence may be inconsistent with that the luminescence centers are silver ion vacancies as mentioned by Wiegand. Moreover as the large amount of Cd ions enhances the luminescence though after quenching of Cd owns, the role of interstitial silver ions is excluded. Then we are forced to think of the existence of dislocations which are formed by heavy additions of Cd ions or any impurities accompanying stress fields, or think of more complex reasons as suggested by Rabin[13] in Ca doped sodium chloride.

The detailed discussions of these centers will be given with farther experimental results. We are also studying the effects of anion impurities and the results will be published later.

The authors wish to express their thanks to professor Teturo Inui for helpful criticism to the munuscript, and to Mr. Akira Ito and Mr. Susumu Horie for their untiring assistance throughout the experiments. The present investigation has been partly supported by the Scientific Research Grant from the Ministry of Education and by the Special Research Grant from Chuo University.

References

1) J. T. Randall: Trans. Faraday Soc. **35** (1939) 2.
2) W. Meidinger: Physik. Z. **40** (1939) 517; **41** (1940) 277.
3) G. C. Farnell and P. C. Burton: Fundamental Mechanisms of Photographic Sensitivity, (Butterworths) London, 1951, pp. 61.
4) S. Makishimg and T. Tomotsu: Photographic Sensitivity Vol. 1, (Maruzen) Tokyo, 1956, pp. 69.
5) F. Seitz: Rev. Modern Phys. **23** (1951) 349.
6) F. Moser and F. Urbach: Phys. Rev. **106** (1953) 852.
7) K. R. von Dorfner: Ann. Physik **16** (1955) 331.
8) S. Makishima, T. Tomotsu and S. Hayakawa: Photographic Sensitivity Vol. 2, (Maruzen) Tokyo, 1958, pp. 125.
9) P. G. Aline: Phys. Rev. **105** (1957) 406.
10) D. A. Wiegand: Phys. Rev. **113** (1959) 52.
11) R. S. Van Heyningen and F. C. Brown: Phys. Rev. **111** (1958) 462.
12) C. C. Klick: J. Opt. Soc. Am. **41** (1951) 816.
13) H. Rabin: Phys. Rev. **116** (1959) 1381.

Journal of the Physical Society of Japan, Vol. 16, No. 4, April, 1961

Internal Friction of Synthetic Quartz

By Yosio Hiki

The Government Mechanical Laboratory, Suginami-ku, Tokyo, Japan

(Received October 7, 1960)

Internal friction of twenty six specimens of synthetic quartz was measured at room temperature using the composite oscillator method. Specimens were cylinders, axes of which lay in the crystallographic YZ-plane and made various angles extending from $-35°$ to $+40°$ with the Y-axis. Synthetic quartz had usually smaller values of the internal friction than natural quartz. The internal friction of specimens parallel or nearly parallel to the Y-axis was almost independent of the strain amplitude, while that of specimens inclined to the axis at high angles showed noticeable amplitude-dependence. The orientation-dependence of the values of the internal friction could be well explained by the theory of dislocation damping. The dislocation density in synthetic quartz was estimated to be $10^2-10^3\,\mathrm{cm}^{-2}$, being about one hundredth of the density in natural crystals. Effect of X-irradiation on the internal friction of quartz was also studied for both synthetic and natural ones.

§1. Introduction

It is expected that the state of imperfections in crystals is generally different according as the crystals are grown in different ways. The internal friction measurement is one of the most powerful method to study about the crystal imperfections. There were few works which showed that the internal friction of synthetic quartz had somewhat different nature from that of natural one. King[1] measured the Q^{-1} of the synthetic and natural quartz oscillators at low temperatures and found that the synthetic quartz exhibited an extremely large mechanical absorption at 50°K with frequency of 5 Mc/sec. The absorption peak was almost two or three decades higher than that of the natural quartz. There appeared also a relaxation peak at 20°K both in synthetic and natural crystals. The author mainly studied the 50°K peak and considered that this might be originated from the vibration of the "nonbridging-oxygen defects", and scarcely noticed the 20°K peak which has assumed to arise from the movement of crystal dislocations[2].

In the present investigation, the internal friction of single crystals of synthetic quartz with various crystallographic orientations was measured as a function of the strain amplitude of the vibration at room temperature. The same kind of measurement about the natural crystals has been carried out and the results were already reported in the earlier paper[3] (hereafter called reference I). It was concluded from the results that the internal friction of quartz in the kilocycle range was mainly due to the vibration of dislocations in the crystals. The present study was intended to inspect the above conclusion in the case of synthetic quartz, and also to find the difference of the state of crystal imperfections in the synthetic and natural ones. The variation of the internal friction of both natural and synthetic quartz was also measured when they were annealed isothermally or irradiated with X-rays, because it was expected that they might have different behaviors.

§ 2. Experimental Procedures

The Marx's three-component piezo-electric oscillator was used to measure the internal friction of quartz specimens. The frequency of vibration used was about 64 kc/sec and the strain amplitude ranged from 0.5 to 5.0×10^{-5}. The detailed description of the experimental method is in the earlier papers.[3],[4]

Specimens were prepared from the synthetic quartz, being Y-bar crystals grown hydrothermally by the Sawyer Research Products, Inc. All crystals were free from electrical and optical twinning. The mother crystals were analyzed spectroscopically and it was found that they were purer than natural crystals and that the main metallic impurities were Al and Na. Their contents were considered to be smaller than 10 ppm although accurate determination was impossible. The specimens were of cylindrical form, 2 mm in diameter and about 40–50 mm in length. The length of each specimen l can be determined by the relation $l=(1/2f)\cdot\sqrt{E/\rho}$, where f is the frequency of the measuring oscillator, E the Young's modulus for the lengthwise direction, and ρ the density of the quartz. Using the values of E calculated from the elastic constants of quartz found in usual literatures, it was possible to get the frequency matching between the specimens and the oscillator better than 0.5%. The direction of the specimen axis was chosen to be in the crystallographic YZ-plane and made the angle θ with the Y-axis [cf. Fig. 1 in I]. Twenty six specimens with various orientations were prepared from three mother crystals, 'L', 'M' and 'N', the angle θ being chosen to range from $-35°$ to $+40°$ at an interval of 5°. Specimens inclined to the Y-axis at larger angles could not be prepared owing to the limitation in size and shape of the mother crystals. The specimen will be designated such as "L-$\overline{30}$-1", which refers to that "mother crystal is 'L', angle θ equals to $-30°$, and specimen number is 1".

§ 3. Results and Discussions

3.1 *Amplitude-dependence*

The internal friction, δ, of all specimens

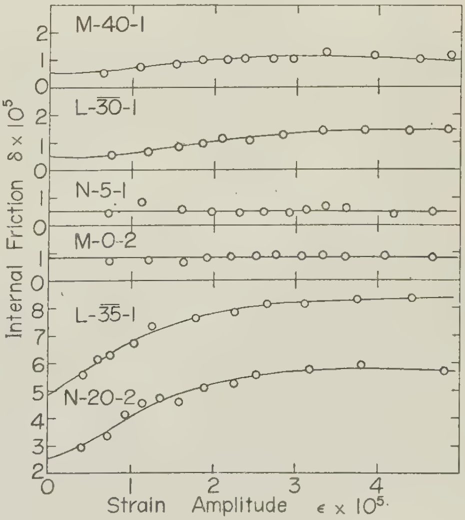

Fig. 1. Internal friction *vs* strain amplitude curves for various specimens.

was measured as a function of the strain amplitude of vibration, ε. Some of the typical results are shown in Fig. 1. In the case of specimens parallel or nearly parallel to the Y-axis, the values of internal friction are small and almost independent of the strain amplitude. Although the internal friction of specimens inclined to the axis at high angles is usually not so large as the case of natural quartz [Fig. 2 in I], the amplitude-dependence is noticeable in these specimens. Some crystals such as L-$\overline{35}$-1 and N-20-2 have larger values and more marked amplitude-dependence of internal friction than usual specimens. These anomalies are sometimes found in specimens with large values of the angle θ. There were four such specimens among seven 'L' specimens, one among seven 'N' specimens, and none among twelve 'M' specimens.

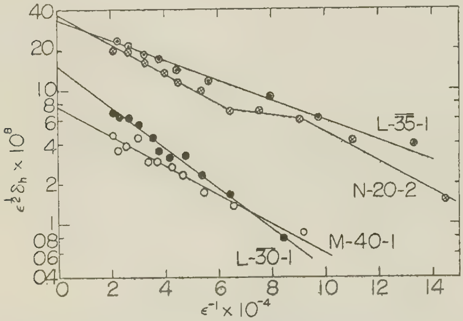

Fig. 2. Analysis of amplitude-dependence of internal friction for various specimens.

In ref. I, experimental results on the internal friction of natural quartz were analyzed using the theory of dislocation damping proposed by Granato and Lücke.[5] The internal friction of crystals due to dislocation damping can be given as[5),6)]

$$\delta=\delta_i+\delta_h=k_1B\omega+c_0\varepsilon^{-1/2}\exp(-c_1/\varepsilon)\,, \quad (1)$$

where ω is the angular frequency of the vibration, B the damping constant for the dislocation movement, and k_1, c_0 and c_1 contain the known quantities such as elastic constants of the crystals and the unknown quantities such as dislocation density in the crystals. The adaptability of this formula will be examined in the case of the synthetic quartz. From the experimental values of internal friction, δ, the amplitude-dependent part, δ_h, is obtained by subtracting the amplitude-independent internal friction which can be got by extrapolating the value of δ to $\varepsilon=0$. In Fig. 2, values of $\log\varepsilon^{1/2}\delta_h$ are plotted against ε^{-1} for four specimens. It is found that linear relationship usually holds between these two variables, which shows an evidence for the dislocation damping occuring in these crystals. Same plotting for the specimen N-20-2 shows anomalous behavior, which may be due to the abundant impurities in this specimen, as suggested in ref. I.

3.2 *Orientation-dependence*

The internal friction of twenty one specimens at strain amplitude equal to 3×10^{-5} are plotted in Fig. 3, where the abscissa is the angle θ. The figure attached to each point represents the specimen number. These values are considerably dependent on the crystallographic orientation of the specimen.

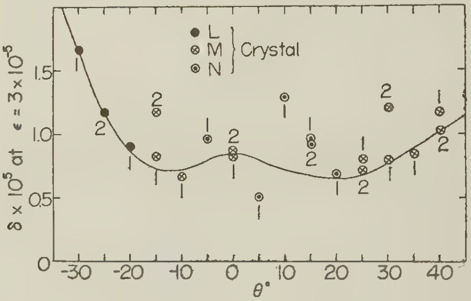

Fig. 3. Orientation-dependence of internal friction.

In the case of natural quartz, the dependence of the amplitude-independent and the amplitude-dependent internal friction on the specimen orientation was found to agree well with the theory of dislocation damping [section 3.4 in I]. In the present case, however, the amplitude-independent internal friction cannot be determined accurately for all specimens. Discussions must therefore be limited to the orientation-dependence of the internal friction at a constant amplitude. The experimental value of the internal friction will be rewritten as[3)]

$$\delta=K_1s^2E+K_2s^{3/2}E^{1/2}\exp(-1/sE)+\delta_0\,, \quad (2)$$

where s is the resolved shear stress factor, E the Young's modulus along specimen axis, δ_0 the internal friction caused from other origin than dislocation damping, K_1 and K_2 are constants independent of specimen orientation. When the dislocations in the crystal have the slip plane parallel to Y- or Z-axis, as assumed in the case of natural quartz, the factor s is proportional to $\sin\theta\cos\theta$. Inserting this into Eq. (2) and assuming that δ_0 has a constant value for all specimens, internal friction at a constant strain amplitude can be obtained as a function of θ. The solid curve in Fig. 3 represents the values calculated by such a method. Three constants δ_0, K_1 and K_2 were chosen so as the curve to pass three experimental points (points for M–40–2, L–$\overline{30}$–1, and midpoint of M–0–1 and M–0–2). The agreement of this curve with other experimental points is considered to be satisfactory. The scatter of some points may be mainly due to the inconstancy of δ_0. The origin of δ_0 may, for example, be the loss in the adhesive between the oscillator and the specimen or incorrectness of the shape of the specimen. Five specimens which have anomalously large internal friction are omitted in this plotting. These may have dislocation density larger than usual specimens, which is verified in the next section.

3.3 *Estimation of dislocation density*

As in the case of natural quartz, the dislocation density, Λ, the mean distance between pinning point, L_c, the maximum binding force between pinning defect and dislocation, F, and the concentration of the pinning points on dislocation, $C=b/L_c$, were calculated with regarding the network length, L_n, as a parameter. The most probable value of L_n was assumed to be $5\times10^{-4}-1\times10^{-3}$ cm [section 3.6 in I]. The results for three specimens, M–40–1, L–$\overline{30}$–1 and L–$\overline{35}$–1, are listed in Table I. The values for a natural crystal, A–45–1, are also shown in the table for the purpose of comparison. The last line represents those for A–45–1 annealed at 500°C for 150 hours, which are reproduced from Table II in ref. I.

Table I.

Specimen	L_n cm	L_c cm	Λ cm^{-2}	F dyne	C
M–40–1	5×10^{-4}	2.0×10^{-4}	1.1×10^{3}	1.2×10^{-4}	2.5×10^{-4}
(Syn.)	1×10^{-3}	3.0×10^{-4}	2.0×10^{2}	1.9×10^{-4}	1.6×10^{-4}
L–$\overline{30}$–1	5×10^{-4}	1.8×10^{-4}	1.4×10^{3}	2.3×10^{-4}	2.8×10^{-4}
(Syn.)	1×10^{-3}	2.6×10^{-4}	2.6×10^{2}	3.4×10^{-4}	1.9×10^{-4}
L–$\overline{35}$–1	5×10^{-4}	2.3×10^{-4}	4.4×10^{3}	1.5×10^{-4}	2.2×10^{-4}
(Syn.)	1×10^{-3}	3.4×10^{-4}	8.3×10^{2}	2.3×10^{-4}	1.4×10^{-4}
A–45–1	5×10^{-4}	1.2×10^{-4}	2.6×10^{5}	0.8×10^{-4}	4.1×10^{-4}
(Nat.)	1×10^{-3}	1.7×10^{-4}	5.0×10^{4}	1.1×10^{-4}	2.9×10^{-4}
A–45–1	5×10^{-4}	2.4×10^{-4}	1.2×10^{4}	1.5×10^{-4}	2.0×10^{-4}
(Ann.)	1×10^{-3}	3.6×10^{-4}	2.3×10^{3}	2.3×10^{-4}	1.4×10^{-4}

The dislocation density in usual synthetic quartz specimens such as M–40–1 and L–$\overline{30}$–1 is of the order of 10^2–10^3 cm^{-2}, which is about one hundredth of that in natural quartz. The density in specimen L–$\overline{35}$–1, which has large values of internal friction as shown in Fig. 1, is several times as large as the density in usual crystals. Synthetic quartz may contain the part with high dislocation density here and there in the crystal. The concentration of the pinning points on the dislocation lines in synthetic quartz seems to be lower than that in natural crystal. This agrees with the fact that synthetic quartz generally contain smaller amount of impurities than natural one. The maximum binding force between pinning defect and dislocation is of the same order of magnitude in synthetic and natural quartz. It may be possible that similar kind of defects, namely, some aggregates of impurities [section 3.7 in I], are pinning the dislocations.

Recently, Nielsen *et al.*[7] observed the etch pits in quartz crystals developed by concentrated hydrofluoric acid, and found that the pit density in synthetic quartz was about three decades lower than that in natural quartz. The authors suggested that the pits might be caused from the etching of impurities precipitated along dislocation line. Accordingly, the dislocation density and impurity concentration in synthetic crystal are conceivable to be lower than those in natural crystal. The results obtained from the internal friction measurements agree with this expectation from etching experiments.

3.4 *Effect of annealing*

The internal friction of a specimen L–$\overline{35}$–1 annealed at 500°C for 5, 10, 20, 50 and 100 hours successively, was measured as a function of the strain amplitude for each state during annealing. The relative values of the concentration of pinning points on the dislocation line, C, were determined through analyzing the ampitude-dependence of the internal friction. The variation of C/C_0 with annealing time is shown in Fig. 4, where C_0 is the initial value of C. The result for the natural quartz specimen, A–45–1, is also drawn in the figure which is reproduced from Fig. 9 in I. In the case of natural quartz, C/C_0 decreases monotonously with annealing time. On the contrary, the value for synthetic quartz increases at first and then decreases.

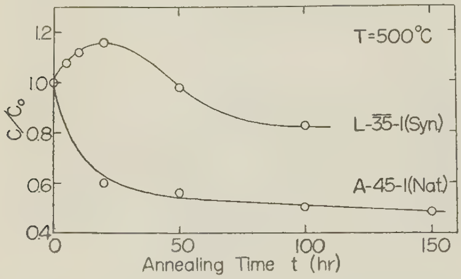

Fig. 4. Variation of C/C_0 for two specimens annealed at 500°C.

The different behaviors of natural and synthetic quartz may be explained as follows. As discussed in section 3.7 in I, the defects pinning down the dislocations in quartz crystals are assumed to be aggregates of impurities near dislocation lines. Natural quartz are considered to have grown very slowly at temperatures 200–350°C and maintained for long time under the ground. The concentration and mean size of impurity aggregates near dislocations may have reached to their equilibrium values at such temperatures. When the crystal is annealed at higher temperatures, some of the aggregates grow larger absorbing small ones on dislocation lines. The number of breakable pinning points may be diminished and C/C_0 be decreased apparently, because external applied stress cannot break dislocations away from the aggregate larger than the possible displacement of the dislocation segment. In the case of synthetic quartz, the concentration of aggregates near dislocations may not reach to the equilibrium value, because the crystals have been growth rapidly. When the specimen is annealed, impurity atoms in crystal are further gathered to the dislocation lines and form new aggregates, and some of the aggregates become large. Accordingly, the apparent number of pinning points may be increased firstly and then decreased.

3.5 *Effect of X-irradiation*

Quartz specimens with different crystallographic orientations were irradiated with X-rays and their internal friction was measured at room temperature. All specimens were annealed at 500°C for 100 hours and then exposed to the X-rays at a definite position separated by 30 cm from the window of the tube with Cu target operated at 40 kV and 20 mA. The results for three natural quartz specimens A–0–3, A–45–2, D–90–1, and a synthetic quartz specimen L–$\overline{30}$–2 are shown in Fig. 5, where the ordinate is the internal friction measured at a constant strain amplitude and the abscissa is the irradiation time. The horizontal line drawn in the left part of

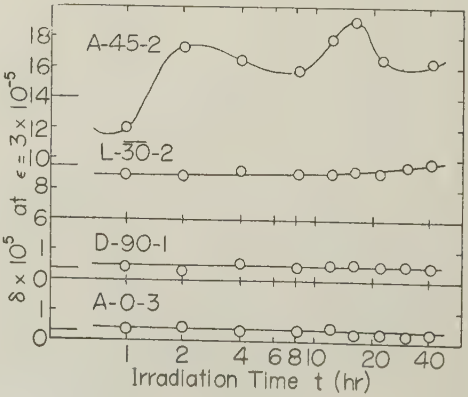

Fig. 5. Variation of internal friction with irradiation time for various specimens.

each curve represents the internal friction for the annealed specimen. The values of internal friction of the specimens A–0–3 and D–90–1 are almost unaffected by the X-irradiation, while that for A–45–2 is changed markedly although its variation with irradiation time is not simple. The internal friction of the synthetic specimen L–$\overline{30}$–2 is increased only slightly by the irradiation.

The above results can be interpreted as follows. When quartz are irradiated with ionizing radiation, the states of lattice defects are somewhat altered. The internal friction originated from the dislocation damping may be varied if the defects are able to act as the pinning points. The internal friction of specimen A–0–3 and D–90–1, which are parallel to Y- and Z-axis, respectively, is not affected by the irradiation because the dislocations in these specimens are inactive for the longitudinal vibration. The value for specimen A–45–2 is changed extremely by irradiation, because the contribution of dislocation damping to the internal friction is most remarkable for specimens with such orientations. The complex feature of the irradiation curve may be originated from the gradual growth of the impurity aggregates which pin down the dislocations. It may be possible that metallic aggregates are grown near dislocation lines promoted by irradiation, as observed in the case of X-irradiated NaCl.[8] Further experiments are desired to understand these phenomena. The synthetic quartz crystals usually contain smaller amount of impurities than natural ones, which is verified by the emission analysis[9] and the experiment of irradiation coloring.[9],[10] Annealed synthetic quartz may contain a few impurity atoms in crystal to grow into the pinning aggregates even when irradiated with X-rays.

§ 4. Reconsideration about Internal Friction of Quartz

It is worthwhile to take into consideration again about the adaptability of the theory of dislocation damping to the internal friction of quartz. The remarkable dependence of the internal friction on the crystallographic orientation was considered to be the most powerful evidence for the dislocation damping in quartz. Some other possible mechanisms which may cause the orientation-dependence of the mechanical damping will be examined:

1) Elastic waves of pure compressional mode can be propagated only in definite directions in an anisotropic medium. Compressional waves excited in other directions are partly converted into transverse waves.[11] Such an effect produces losses dependent on the orientation of the propagation, which must be taken into account in the attenuation measurement using the ultrasonic pulse method. In the case of the resonance method with the composite oscillator, the loss originated from the above effect may be ignored. This may be presumed from the fact that the actual resonant frequencies of all quartz specimens were not so depart from those calculated for the longitudinal vibration.

2) In the interior of the vibrating solid, local thermal flows are generated by the nonuniformity of temperature associated with the stress distribution. These flows originate the thermoelastic damping, the magnitude of which is usually dependent on the crystallographic orientation of the specimen. The thermoelastic damping in quartz is, however, very small, being estimated to be of the order of 10^{-9} in the kc frequency range.[12]

3) Some investigators considered the mechanical damping caused from the vibration of interstitial metallic ions in the " tunnels " of the quartz lattice.[13] The tunnels were considered to be parallel to the Z-axis since the conductivity and dielectric loss were found to be greatest in this direction. The orientation-dependence of the internal friction of natural quartz reported in ref. I cannot be explained by such a mechanism, because the internal friction of the specimens parallel to either the Y- or Z-axis are smaller than those inclined these axes at high angles.

4) It may be possible that the trains of the low temperature peaks[1],[2] contribute to the orientation-dependence of the internal friction at room temperature, although various crystals with different orientations have not been investigated thoroughly at low temperatures. Both peaks are those of relaxation type, which cannot yield the amplitude-dependent internal friction such as observed in the present experiment.

There remains some other questions about the internal friction of quartz crystal. Mason considered the relaxation peak at 20°K (5 Mc) as the Bordoni peak and obtained the result that the Peierls' stress for the dislocation in quartz was rather small.[2] Then dislocations can vibrate easily at room temperature and the theory of Granato-Lücke may be applied to the internal friction of quartz. The same author, however, proposed a new theory about acoustic wave attenuation caused from the viscosity of phonons in crystals, and discussed that the low temperature peak in quartz can be attributed to the phonon relaxation effect.[14] It was also shown that the vibration of dislocations could contribute to the internal friction at higher temperatures, where the damping of the moving dislocations was mainly due to the viscosity of the dragging phonons behind them. The measured value of the damping constant, B, for the dislocation movement was rather coincide with the value calculated by the phonon viscosity theory. The value of B calculated by the phonon scattering theory of Leibfried,[15] which has been used by the present author in the analysis of the experimental results, was about one tenth of the above value.

In conclusion, the large part of the kc-range internal friction of both natural and synthetic quartz crystals may be attributed to the motion of dislocations, because the amplitude-dependence and the orientation-dependence of the internal friction can be well explained through the theory of the dislocation damping. The obtained values of the dislocation density and other quantities concerning these crystals may also be reliable in order of magnitude, although the true origin of the damping force against the motion of dislocations in quartz has not been well understood.

Acknowledgement

The author wishes to express his sincere gratitudes to Dr. T. Kawada for his continued encouragement. He is also greatly indebted to Professor Y. Tomono for his kind instruction and advices. Thanks are also due to Mr. K. Takahashi at the Geological Survey of Japan for his kindness to carry out the spectroscopic analysis of the specimens.

References

1) J. C. King: Phys. Rev. **109** (1958) 1552; Bell Sys. Tech. J. **38** (1959) 573.
2) H. E. Bömmel, W. P. Mason and A. W. Warner: Phys. Rev. **99** (1955) 1894, **102** (1956) 64.
3) Y. Hiki: J. Phys. Soc. Japan **15** (1960) 586.
4) Y. Hiki: J. Phys. Soc. Japan **13** (1958) 1138.
5) A. Granato and K. Lücke: J. Appl. Phys. **27** (1956) 583, 789.
6) Y. Hiki: J. Phys. Soc. Japan **14** (1959) 590.
7) J. W. Nielsen and F. G. Foster: Amer. Mineral. **45** (1960) 299.
8) E. Aerts, S. Amelinckx and W. Dekeyser: Acta Met. **7** (1959) 29.
9) A. J. Cohen and E. S. Hodge: J. Phys. Chem. Solids **7** (1958) 361.
10) R. W. Ditchburn, E. W. J. Mitchell, E. G. S. Paige, J. F. Custers, H. B. Dyer and C. D. Clark: *Defects in Crystalline Solid* (The Phys. Soc., London, 1955) 92.
11) P. C. Waterman: Phys. Rev. **113** (1959) 1240.
12) H. Iwasaki: J. Radio Res. Lab. **5** (1958) 257.
13) M. R. Stuart: J. Appl. Phys. **26** (1955) 1399.
14) W. P. Mason: J. Acoust. Soc. Amer. **32** (1960) 458.
15) G. Leibfried: Z. Phys. **127** (1950) 344.

JOURNAL OF THE PHYSICAL SOCIETY OF JAPAN, Vol. 16, No. 4, APRIL, 1961

The Crystal Structures of $KMnF_3$, $KFeF_3$, $KCoF_3$, $KNiF_3$ and $KCuF_3$ above and below their Néel Temperatures

By Atsushi OKAZAKI and Yasutaka SUEMUNE

Department of Physics, Faculty of Science, Kyusyu University, Fukuoka, Japan

(Received November 7, 1960)

The crystal structures of the antiferromagnets $KMnF_3$, $KFeF_3$ $KCoF_3$, $KNiF_3$ and $KCuF_3$ have been determined above and below their Néel temperatures (T_N) by X-ray diffraction using single crystals. At room temperature (above T_N) the structures of these compounds are of the ideal perovskite type (cubic) except for that of $KCuF_3$ which crystallizes as a tetragonal modification ($a>c$) of the perovskite type. At 78°K (below T_N) the lattice symmetries of $KMnF_3$, $KFeF_3$ and $KCoF_3$ are monoclinic, rhombohedral ($\alpha<90°$) and tetragonal ($a>c$), respectively, while $KNiF_3$ and $KCuF_3$ retain their own symmetries at room temperature. The lattice constants have been determined between these temperatures and their changes near the transition temperature were closely followed. This temperature region was extended up to 670°K for $KCuF_3$.

§ 1. Introduction

The crystal structures of the antiferromagnets KMF_3, where M indicates the $3d$ transition group elements; Mn, Fe, Co and Ni, have been investigated at room temperature by many researchers. The works performed by these researchers were summarized by Martin, Nyholm and Stephenson[1]. All these works have been done with powders and it is perhaps for this reason that the results on the crystal structures of these compounds are rather ambiguous. That is, some have reported as the perovskite structure with cubic symmetry, and others as the pseudo-perovskite structure with lower symmetry for the same compound.

Since the magnetic ions in the perovskite structure form a simple cubic lattice, the magnetic properties of ABO_3 compounds with this structure have been extensively investigated. Therefore it may be interesting to investigate in detail the crystal structures and the magnetic properties of KMF_3 compounds including $KCuF_3$ for which the lattice distortion according to the Jahn-Teller effect may be expected even above the Néel temperature.

The work described herein mainly deals with structural changes of KMF_3 compounds accompanied by their magnetic transitions. The structures at room temperature and at 78°K have been reported shortly[2]. The detailed structure analysis of $KCuF_3$ at room temperature has also been reported[3]. Recently Beckman and Knox[4] have reported a full account of the crystal structure of $KMnF_3$ in the temperature region between 15 and 293°K, and Scatturin et al.[5] have investigated the magnetic structures of KMF_3 compounds including $KCrF_3$ by neutron diffraction.

§ 2. Experiments

These compounds, prepared by Hirakawa, Hirakawa and Hashimoto[6] of our laboratory, crystallized in rectangular forms, their volume being mostly a few mm³. At every step of crystal preparation of each compound—after precipitation, crystallization and additional treatments—the crystal structure was examined by X-ray powder photographs, and almost always the pattern corresponding to the cubic perovskite structure was observed except for $KCuF_3$.

Single crystals were used throughout this work. The specimens on which the X-ray work was performed were formed into nearly cylindrical shape, 0.4∼1.2 mm in length and 0.05∼0.15 mm in diameter, by cutting with a razor blade and grinding with sand paper. Since it was easy to break along the the {100} planes, specimens elongated along the ⟨110⟩ were used without grinding.

At room temperature oscillation and rotation photographs were obtained by using cylindrical cameras, the diameters being 9 cm (Straumanis-Ieviņš arrangement of film mounting) and 10 cm (Bradley-Jay arrangement).

Above and below room temperature, oscilla-

Table I. Constructional details of high-

	Furnace or cooler	Temperature measurement
High-temperature camera	Cylindrical Ni-foil furnace (0.018 mm thick) described by Dent and Taylor[8]. Current was about 20A for 670°K. Controlled manually.	Chromel-Alumel thermocouple was placed 1 mm above specimen. Calibration was made by measuring the melting point of In, Sn, Bi, Pb and InSb. Accuracy: within ±2°C and stability during exposure: within ±0.5°C.
Low-temperature camera	Cooling gas from a liquid nitrogen Dewar was transferred by a double walled glass tube. Temperature was controlled by changing the rate of gas flow, which is regulated by the current through a resistor dipped into liquid nitrogen. The lowest temperature attained was 86°K.	Copper-constantan thermocouple was placed 2 mm above specimen (Fig. 1). Homogeneous temperature destribution was obtained by means of an attachment to the nozzle (Fig. 1). Accuracy within ±0.5°C and stability during exposure within ±1°C.

tion and rotation photographs were obtained by using the high- and low-temperature cameras having a multiple-film carrier which can be moved axially to give a series of 7 to 10 exposures for the equatorial reflexions. Their details are given in Table I. A part of the low-temperature camera (gas cooling type) is shown in Fig. 1. In order to attain 78°K liquid cooling method described by Lonsdale and Smith[7] was used.

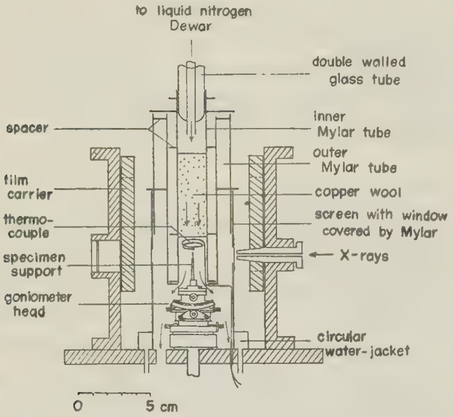

Fig. 1. A part of low-temperature camera using gas cooling method.

§ 3. Structure Determination

a) *at room temperature*

The oscillation photographs about the [100] as rotation axis were obtained for $KMnF_3$, $KFeF_3$, $KCoF_3$ and $KNiF_3$ with Fe$K\alpha$, Co$K\alpha$, Co$K\alpha$ and Cu$K\alpha$ radiations, respectively. In spite of the heavy exposure there was no evidence for superstructure reflexions similar to those observed for $KCuF_3$[3]. Moreover, since these four compounds are cubic and the observed intensities are in good agreement with those calculated by assuming that the structures are of the perovskite type, it seems

Table II. Lattice constants of KMF_3 at room temperature with experimental data.

Compound	Lattice constants (Å) at 298°K	Rotation axis	Radiation	Highest angle reflexion and its Bragg angle
$KMnF_3$	$a=4.190\pm0.001$	[100]	Fe$K\alpha$ Cu$K\alpha$	(330) ~79° (510) ~70°
$KFeF_3$	$a=4.121\pm0.001$	[100]	Co$K\alpha$	(420) ~76°
$KCoF_3$	$a=4.069\pm0.001$	[100]	Co$K\alpha$	(420) ~80°
$KNiF_3$	$a=4.014\pm0.001$	[100]	Cu$K\alpha$ Co$K\alpha$	(510) ~78° (330) ~69°
$KCuF_3$	$a_0=4.140\pm0.001$*	[001]	Co$K\alpha$ Cu$K\alpha$	(420) ~75° (510) ~72°
	$c_0=3.926\pm0.002$ (tetragonal)	[100]	Co$K\alpha$ Cu$K\alpha$	(042) ~78° (034) ~74°

* a_0 and c_0 designate the fundamental structure, because $KCuF_3$ has a superstructure[3].

and low-temperature cameras.

Atmosphere	Film mounting	Windows	Specimen
Vacuum. Both furnace and camera unit were set in the vacuum chamber.	Straumanis-Ievinš type film mounting. Diameter: 9 cm.	Al-foil for inner radiation shield. Mylar sheet for window of outer vacuum chamber.	Cylindrically shaped single crystal was mounted on a quartz fibre by a small amount of potter's clay.
Air. Equipped with a device to prevent frosting of specimen (Fig. 1).	Same as above.	A thin film of Mylar.	Cylindrically shaped single crystal was mounted on a thin quartz rod by adhesive paste.

that these have the ideal perovskite structure.

The lattice constants were determined from high angle equatorial reflexions recorded on rotation photographs. The graphical extrapolation against $\cos^2\theta$ was used for each case. In order to increase the accuracy of the extrapolation, reflexions by two different radiations were recorded on the same film, if necessary. In Table II rotation axis of specimen, radiation used, the highest angle reflexion by the radiation and the approximate value of the Bragg angle θ for each compound are summarized together with the obtained lattice constants, where the errors indicate the maximum deviations at the extrapolations for several runs.

b) *at low temperatures*

The Néel temperature of each compound determined by Hirakawa, Hirakawa and Hashimoto[6] from the magnetic susceptibility measurements is shown in Table III. Below these temperatures $KNiF_3$ and $KCuF_3$ retain their lattice symmetries, but those of $KMnF_3$, $KFeF_3$ and $KCoF_3$ become monoclinic, rhombohedral ($\alpha<90°$) and tetragonal ($a>c$), respectively.

Table III. Néel temperatures (°K) of KMF_3*.

$KMnF_3$	$KFeF_3$	$KCoF_3$	$KNiF_3$	$KCuF_3$
88	113	114	275	243

* A few of these values are somewhat different from those previously reported[2].

Together with these deformations the single crystals are turned into the polycrystalline state which consists of the crystallites having their main crystallographic axis oriented along any of the three former cube axes (for monoclinic and tetragonal cases) or any of the four former body diagonals (for rhombohedral case) with equal probability. Therefore these symmetries can be determined from the splittings of the $\{h00\}$ and $\{hhh\}$ reflextions. The splittings of the $\{400\}$ with Fe$K\alpha$ around the $\langle100\rangle$ and the $\{222\}$ with Cr$K\alpha$ around the $\langle110\rangle$ at 78°K are represented schematically in Fig. 2.

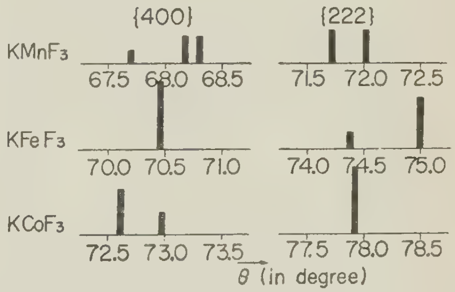

Fig. 2. $\{400\}$ and $\{222\}$ reflexions at 78°K. Abscissa is the Bragg angle. $K\alpha_2$-component of each reflexion is omitted for clarity.

The lattice constants were determined by the same extrapolation as at room temperature. The angles β of $KMnF_3$ and α of $KFeF_3$ were determined from the splittings of the $\{222\}$ with Cr$K\alpha$ and the $\{420\}$ and $\{330\}$ with Fe$K\alpha$, respectively. The results at 78°K are given in Table IV. Fig. 3 shows the temperature dependence of these constants.

Recently Beckman and Knox[4] have investigated $KMnF_3$ in detail down to 15°K. Their lattice constants are in good agreement with ours above 88°K (T_N). But they describe that the monoclinic phase observed by us at 78°K only appears when the crystal warms up from

Table IV. Lattice constants of KMF$_3$ at 78°K.

	Symmetry	Lattice constants (Å)
KMnF$_3$	monoclinic	(a,b,c) $=(4.168, 4.171, 4.185)$* $\beta=89°51'\pm1'$
KFeF$_3$	rhombohedral	$a=4.108\pm0.002$ $\alpha=89.51'\pm1'$
KCoF$_3$	tetragonal	$a=4.057\pm0.002$ $c=4.049\pm0.002$
KNiF$_3$	cubic	$a=4.001\pm0.002$
KCuF$_3$	tetragonal	$a=4.121\pm0.002$ $c=3.911\pm0.002$

* It can not be determined at present which of the three values in the parentheses corresponds to the letters a, b and c.

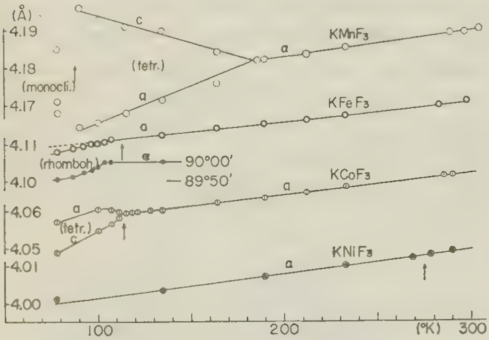

Fig. 3. Lattice constants of KMF$_3$ as a function of temperature. Arrows indicate T_N of each compound.

the antiferromagnetic state to 92°K, and that below T_N the crystal has orthorhombic symmetry with tetragonal pseudo-cell. Therefore reexaminations at 90°K and 78°K by liquid cooling were carried out when a special care was taken for sufficient cooling, and the previous results were confirmed as follows:

i) {222} splits into two components at 78°K but not at 90°K,

ii) {400} splits into three components at 78°K, but the pattern is rather unusual; three components have not the same intensity as shown in Fig. 2.

Therefore it may be true that the crystal becomes at least monoclinic at 78°K. The discrepancy below T_N may be attributed to the experimental method, that is, the temperature was not controlled continuously near T_N in our experiments.

c) lattice constants of KCuF$_3$

Up to 470°K in vacuum the crystal of KCuF$_3$ remains transparent and there is no change in appearance, but at 570°K it becomes opaque and dark. Nevertheless there is no significant change in the diffraction pattern up to 670°K.

The lattice constants of KCuF$_3$ up to 670°K are shown in Fig. 4. c_0/a_0 decreases linearly with increasing temperature and no anomaly can be found at T_N and in the temperature region between T_N and 370°K where an anomaly has been reported⁶⁾ on the magnetic susceptibility.

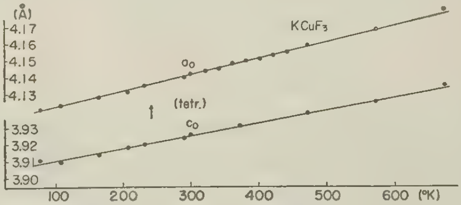

Fig. 4. Lattice constants of KCuF$_3$ as a function of temperature. An arrow indicates T_N.

An irreversible transition of the structure took place between 670 and 720°K, which would not be discussed farther.

§ 4. Discussion

Since the electronic orbital level (the $d\gamma$ level) of the Cu^{2+} ion is degenerate in the undistorted crystal structure, the tetragonal distortion of KCuF$_3$ which is observed even above T_N may be attributed to the Jahn-Teller effect arising from Cu^{2+} ion as discussed previously³⁾. The similar distortion of KCrF$_3$ observed by Scatturin et al.⁵⁾ may be attributed to the same origin.

In Table V the crystal distortions below T_N are compared with those of MO system⁹⁾ with rock-salt structure, which have been investi-

Table V. Crystal distortions of MO and KMF$_3$ compounds below T_N.

MnO	FeO	CoO	NiO
rhombo-hedral $\alpha>90°$	rhombo-hedral $\alpha<90°$	tetragonal $a>c$	rhombo-hedral $\alpha>90°$
KMnF$_3$	KFeF$_3$	KCoF$_3$	KNiF$_3$
monoclinic	rhombo-hedral $\alpha<90°$	tetragonal $a>c$	no distortion

The unit cells of MO compounds for rhombohedrally distorted cases are chosen differently from those in the original paper⁹⁾ for comparison with KMF$_3$ compounds gated theoretically by Kanamori[10]. It has also been pointed out by the same another[11] that the distortion in $KFeF_3$ and $KCoF_3$ seems to correspond to that in FeO and CoO.

Table VI. Tolerance factors of KMF_3 compounds.

$KMnF_3$	$KFeF_3$	$KCoF_3$	$KNiF_3$	$KCuF_3$
0.88	0.91	0.92	0.93	0.92

The ionic radii of Ahrens[12] are used.

In Table VI the Goldschmidt's tolerance factor t of KMF_3 system is given conventionally, which is defined by the following relation:

$$R_K+R_F=t\sqrt{2}(R_M+R_F),$$

where R_K, R_M and R_F are the ionic radii. It is known that while structures of the perovskite family occur for values of t down to about 0.8, the ideal cubic structure is found only if t is much closer to unity. The crystal distortion of $KMnF_3$ that occurs at 184°K (far above T_N) may be attributed to the low value of t.

The authors wish to express their hearty thanks to Prof. T. Okada for his continuous guidance and encouragement, to Dr. K. Hirakawa and Mr. T. Hashimoto for supplying the crystals and for discussions, to Mr. T. Fuchikami for collaboration at the beginning of this research, and to Miss K. Hirano for assistance. This investigation was partly supported by the Scientific Research Expenditure of the Ministry of Education.

References

1) R. L. Martin, R. S. Nyholm and N. C. Stephenson: Chemistry and Industry (1956) 83.
2) A. Okazaki, Y. Suemune and T. Fuchikami: J. Phys. Soc. Japan **14** (1959) 1823.
3) A. Okazaki and Y. Suemune: J. Phys. Soc. Japan **16** (1961) 176.
4) O. Beckman and K. Knox: Phys. Rev. **121** (1961) 376.
5) V. Scatturin, L. Corliss, N. Elliott and J. Hastings: to be published.
6) K. Hirakawa, K. Hirakawa and T. Hashimoto: J. Phys. Soc. Japan **15** (1960) 2063.
7) K. Lonsdale and H. Smith: J. Sci. Instr. **18** (1941) 133.
8) L. S. Dent and H. F. W. Taylor: J. Sci. Instr. **33** (1956) 89.
9) W. L. Roth: Phys. Rev. **110** (1958) 1333.
10) J. Kanamori: Progr. Theor. Phys. **17** (1957) 177, 197.
11) J. Kanamori: J. Appl. Phys. **31** (1960) 14S.
12) L. H. Ahrens: Geochim. et Cosmochim. Acta **2** (1952) 155.

JOURNAL OF THE PHYSICAL SOCIETY OF JAPAN, Vol. 16, No. 4, APRIL, 1961

Anomalous Diffusion at the Interface of Thin Bimetallic Film of Bi and Sb

By Ryōji SUGANUMA, Toshiho YOSHIDA* and Yoshibumi FUJIKI

Institute of Physics, Kyōto Prefectural University of Medicine

(Received November 7, 1960)

The intermetallic diffusion was studied by electron and X-ray diffraction and electrical resistance measurement on vacuum deposited thin bimetallic films of Bi and Sb. The formation of triple-layer, which consisted of two outer layers of Bi and Sb and the intermediate layer of solid solution of the definite composition, was observed in the course of heating in vacuum. Such an anomalous diffusion could not be expected from a usual diffusion couple of bulk specimens. It was found that the degree of such a triple-layer formation depended on the kind and deposition rates of secondary deposits, and the maximum thickness of the intermediate layer attaind by diffusion was confined to a certain limiting value. The defectiveness of films was deduced from electrical resistance measurements, the results of which were related to the triple-layer formation. Tentative explanation and discussions for this were proposed, assuming the existence of some strained intermediate layer of certain thickness where the diffusion rapidly took place.

§ 1. Introduction

At the interface between two metallic films, the interdiffusion and the formation of alloy such as an intermetallic compound or solid solution can be observed in some cases during the successive deposition of two metals[1),2)]. The concentration *versus* distance from the interface for such a bimetallic film immediately after deposition will be such as illustrated by the graph ($t=0$) shown in Fig. 1 (a). In the case where the two metals form a perfect miscible solution, the concentration *versus* distance graph at a time t' ($t'>0$) will follow the form such as shown in Fig. 1 (b) or (b′). The diffraction pattern of the last case will indicate broad bands with sharp edges which correspond to solid solutions of concentrations c_1 and c_2. There seem to be no special compositions other than c_1 and c_2. H. Cramer[3)], however, reported briefly that specimens prepared by the vacuum deposition of very thin layer of Cu on polished Au substrate showed the formation of a solid solution with a definite composition during heating, but no explanation and discussions were given. J. W. Menter[4)] also described that in some circumstances triple layers might be formed consisting of two outer layers of compositions approximating the pure metals and an intermediate layer with a well-defined alloy composition. C. Weaver and R. M. Hill[5)] also proposed the formation of some solid solution for the explanation of his adhesion experiment with thin bimetallic films.

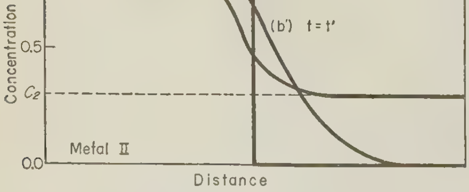

Fig. 1. The concentration *versus* distance curve.

The intermetallic reactions occurring at the interface as mentioned above will intimately be related to the structure and properties of the interface, and the present writers intended to investigate the process of diffusion in thin bimetallic films of Bi and Sb by electron and X-ray diffraction and electrical resistance measurement.

§ 2. Experimental Procedure and Aspects of Diffusion Observed by Electron Diffraction

The specimens were prepared by the successive deposition of Bi and Sb on Formvar

---

* Present Address: Department of Physics, Faculty of Liberal Arts and Science, Shizuoka University, Shizuoka, Japan.

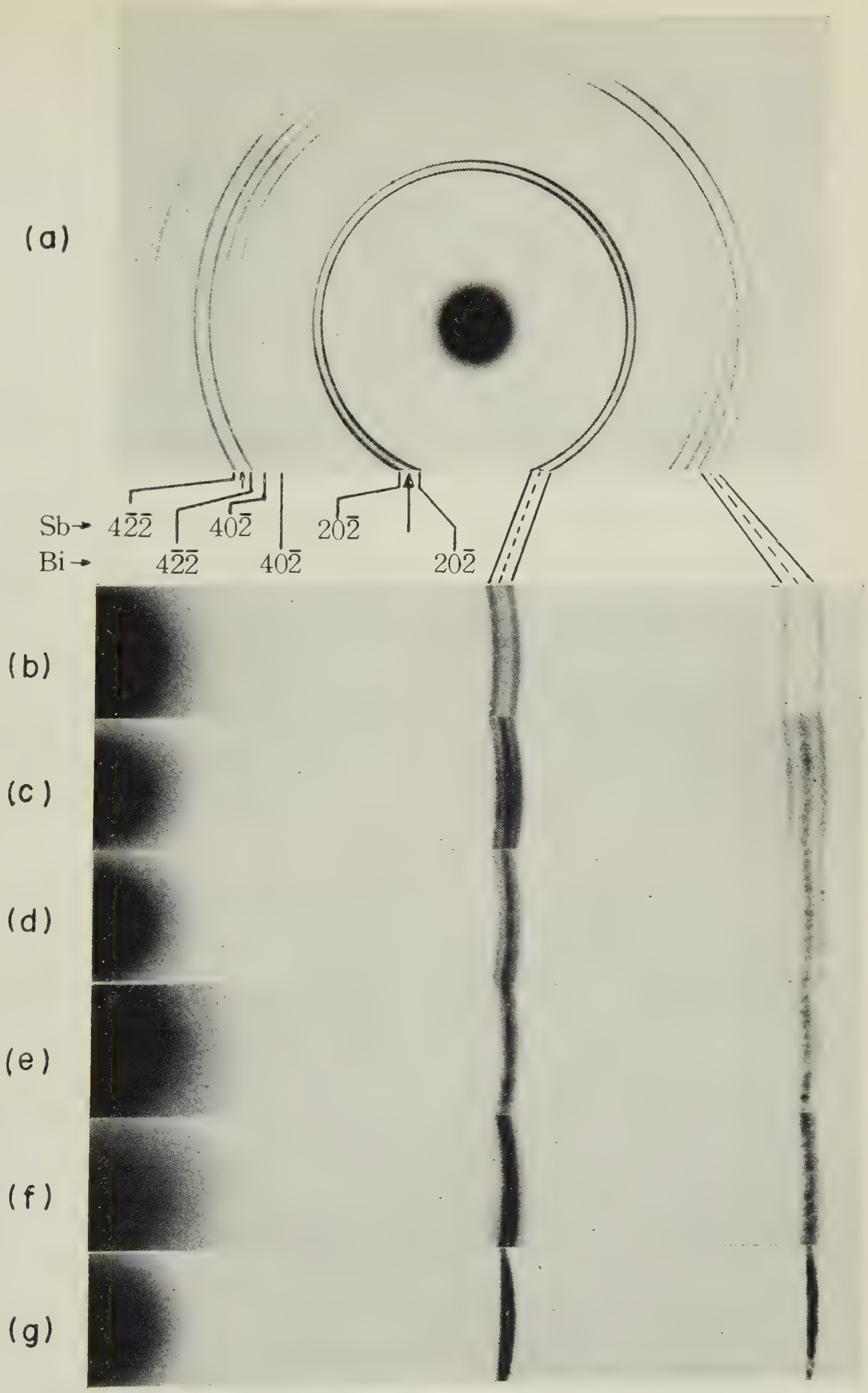
(a)
Sb→ $4\bar{2}\bar{2}$ $40\bar{2}$ $20\bar{2}$
Bi→ $4\bar{2}\bar{2}$ $40\bar{2}$ $20\bar{2}$
(b)
(c)
(d)
(e)
(f)
(g)

Fig. 2. Electron diffraction patterns from the bimetallic film of Sb deposited rapidly on the rapidly deposited Bi under-layer. Heat treatments are as follows:

(a) At room temperature (Normal incidence).
(b) After heating for 5 minutes at about 200°C.
(c) After heating for 10 minutes at about 200°C.
(d) After heating for 15 minutes at about 230°C.
(e) After heating for one hour at about 230°C.
(f) After heating for one hour at about 240°C.
(g) After heating for 6.5 hours at about 240°C.

film in vacuum (about 10^{-5} mmHg). The film thickness was measured by X-ray interference method⁶⁾, using Cu K_α radiation, with a film prepared on a microscopic slide glass at the same time as the specimens for electron diffraction. The thickness of Bi layers was 160∼380 Å and that of Sb 150∼500 Å.

Filaments for evaporation were cylindrical coils of about 15 mm in length and 3 mm in diameter made of W wire of 0.21 mm in diameter. The distance between the substrate and the evaporator was about 6 cm and a shutter of rotating disc-shape made of Al was used during preheating. The condition of vacuum and the geometry of deposition were maintained to be as constant as possible throughout the experiment. The rate of deposition, which had much influence on the results, was about 50∼100 Å/second (rapid deposition) or 0.5∼1 Å/second (slow deposition).

The degree of the formation of intermediate

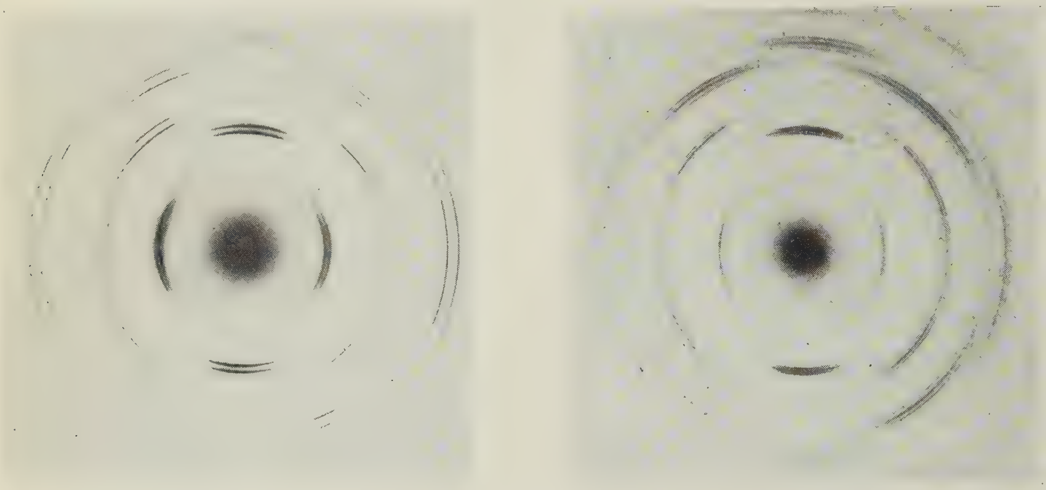
(a) (b)

Fig. 3. Electron diffraction patterns from the specimen of the same type as shown in Fig. 2.
(a) At room temperature (Oblique incidence).
(b) After heating for 10 minutes at about 200°C.

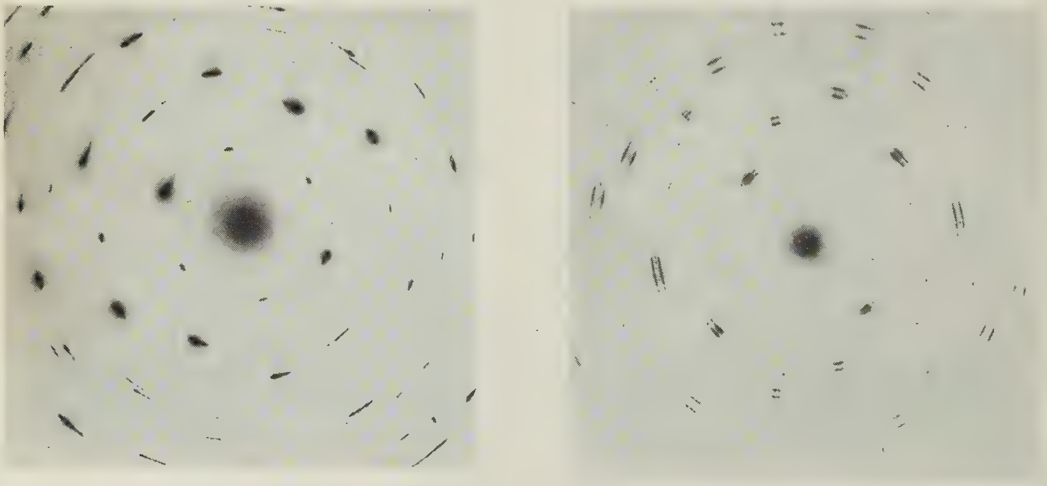
(a) (b)

Fig. 4. Electron diffraction patterns.
(a) The Sb film rapidly deposited on Formvar substrate at room temperature.
(b) The bimetallic film of Bi rapidly deposited on the rapidly deposited Sb under-layer. After heating for 10 minutes at about 220°C.

layer with a definite composition by heat-treatment subsequent to the deposition was influenced by the condition of evaporation, which would be described in detail afterwards. Here, the aspects of diffusion, where the triplelayers were formed by heating, will be described in the first place.

An electron diffraction pattern from a specimen prepared by the rapid deposition of Sb on a rapidly deposited Bi under-layer showed a fibre structure of Bi and Sb, whose {111} planes were parallel to the Formvar substrate, and in addition, very weak $\{20\bar{2}\}$ and $\{4\bar{2}\bar{2}\}$ rings of about 50 at. % Bi solid solution appeared as shown by arrows in Fig. 2 (a) (see also Fig. 3 (a)). This specimen did not show any change of its diffraction pattern even after the aging of about three weeks at room temperature. Then the specimen was heated in the diffraction camera and each stage of diffusion was photographed. The pattern did not show any appreciable change

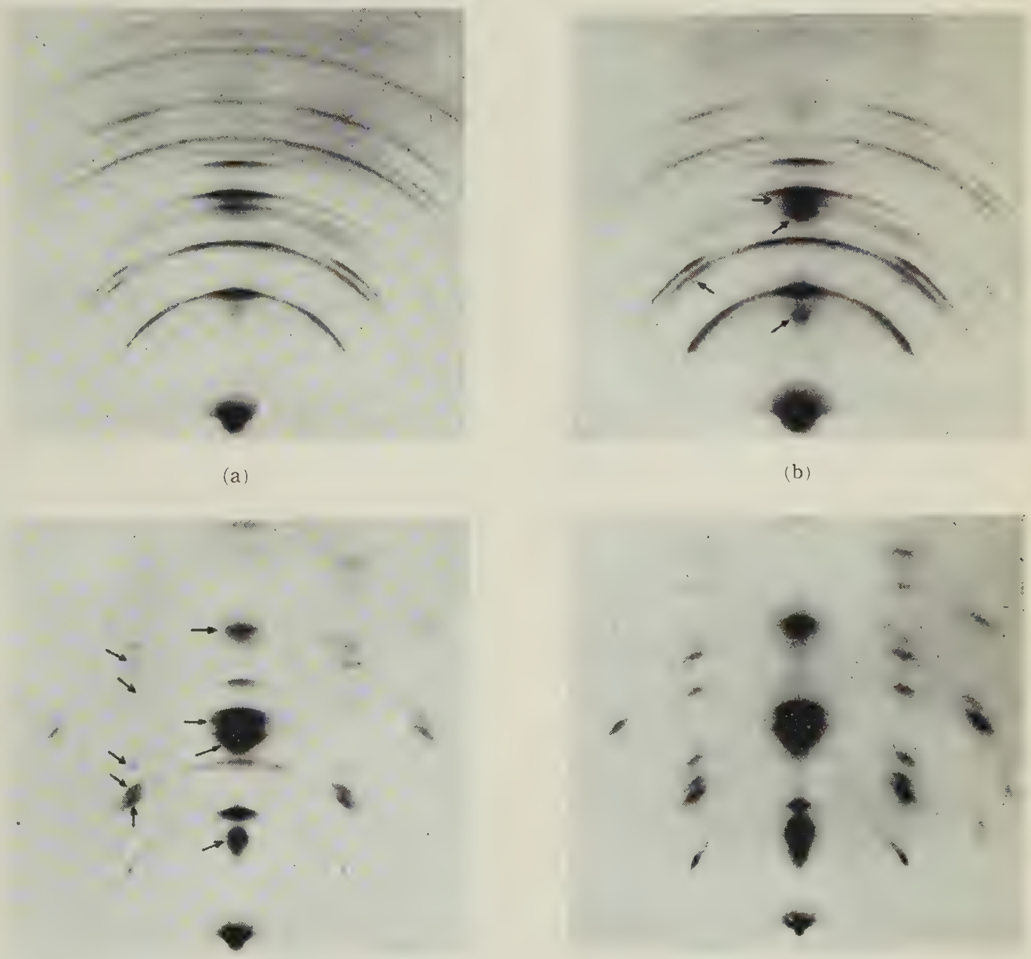
(a) (b)

(c) (d)

Fig. 5. Electron diffraction patterns from the thin Sb film of about 100 Å thick deposited rapidly on the thick Bi layer of about 100 Å thick.

(a) At room temperature. The reflections due to the outer, thin Sb layer alone are observed.

(b) At about 190°C during heating. Weak reflections due to the intermediate layer of solid solution with a definite composition are superposed as indicated by arrows.

(c) After heating for 5 minutes at about 210°C. The reflections due to the intermediate layer are more intense than (b) as indicated by arrows.

(d) After heating for 20 minutes at about 210°C. The reflections due to the Sb layer disappear completely, and those due to the intermediate layer alone are observed.

even after heating for more than 5 hours at about 160°C, but the reflections corresponding to the solid solution of about 50 at. % Bi were sharpened and somewhat strengthened after heating for about 30 minutes at about 180°C.

To maintain the thermal history of all specimens as constant as possible, the heating process was controlled so that it took about 17 minuters for the heating up to about 200°C for all specimens.

After heating for about 5 minutes at about 200～210°C, the reflections due to the intermediate layer became more and more intense without any broadening, while those due to Bi- and Sb-rich solid solutions gradually decreased their intensity but showed no appreciable change of their lattice spacings (Figs. 2 (b), (c) and Fig. 3 (b)). Contrary to the expectation described briefly in § 1, the specimen at this stage is in the state of the triple-layer which is composed of the two outer layers of almost pure Bi and Sb and the intermediate layer of a solid solution with the definite composition.

After heating for about one hour at about 230～235°C, the diffuse scattering was superposed on the ring pattern, and at the same time, the appreciable changes of lattice spacings and intensity of the Bi- and Sb-rich solid solutions could be detected. While, those of the intermediate layer of about 50 at. % Bi solid solution did not show any appreciable change (Figs. 2 (d) and (e)). This indicates that the overall diffusion of usual type became pronounced at this temperature. The change of lattice spacing was greater for the Sb-rich solid solution than for the Bi-rich one, and therefore it was deduced that the diffusion of Bi into the Sb-rich solid solution was greater than that of Sb into Bi-rich one and consequently the net flow of atoms took place from Bi-rich solid solution side to Sb-rich one. Some considerations on this point will be given in § 6.

After the above-mentioned stage, the diffuse rings corresponding to the solid solution with varying lattice constants resulted from further heating (Fig. 2 (f)). Then, after heating for about 6.5 hours at about 235～240°C, the diffusion was almost complete and the diffraction pattern gave the sharp rings corresponding to the definite solid solution (Fig. 2 (g)).

§ 3. Effects of the Order of Successive Deposition and the Rate of Deposition on the Diffusion Process

The aspects of progress of diffusion during heat-treatment were greatly influenced by the

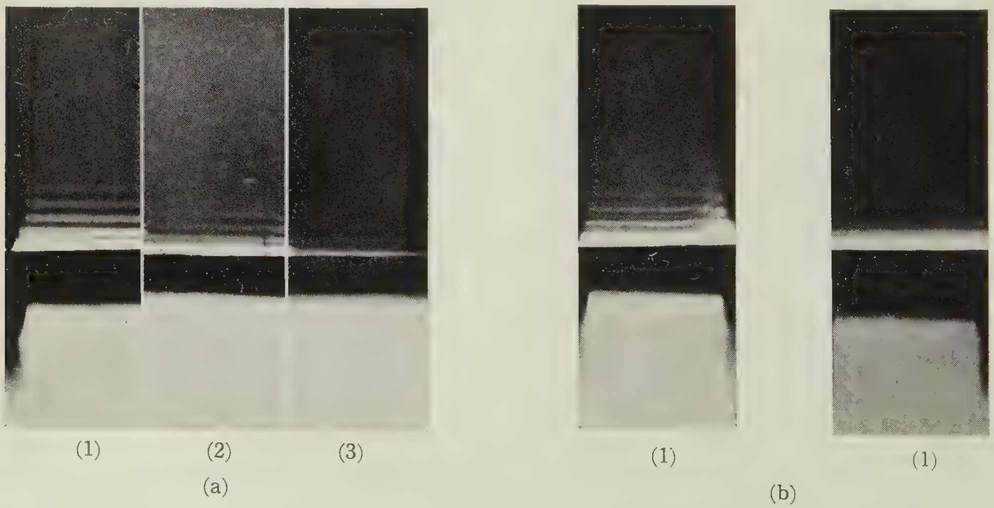

Fig. 6. Photographs obtained by X-ray interference.

(a) (1) Bi film of about 297 Å deposited rapidly.
(2) Sb film of about 302 Å deposited rapidly.
(3) Sb film of about 264 Å deposited slowly.
(b) (1) Double film of Sb (302 Å) deposited rapidly on rapidly deposited Bi under-layer (297 Å).
(2) Double film of Bi (256 Å) deposited rapidly on rapidly deposited Sb under-layer (240 Å)

Table I.

Type of specimen	Primary deposit		Secondary deposit		Temperature at which interdiffusion becomes most pronounced	Degree of triple-layer formation
	Kind	Deposition rate	Kind	Deposition rate		
I	Bi	rapid	Sb	rapid	∼200°C	most pronounced
II	Bi	slow	Sb	slow	∼240°C	
III	Sb	rapid	Bi	rapid	∼220°C	less than above two
IV	Sb	slow	Bi	rapid		
V	Sb	rapid	Bi	slow	∼245°C	not observed
VI	Sb	slow	Bi	slow		

order of successive deposition and the rate of deposition, and specimens are classified in several types. These are summarized in Table I.

(Type I) The results obtained for the specimens of this type were described in the previous paragraph.

(Type II) The specimens prepared by the slow deposition of Sb on the slowly deposited Bi under-layer also exhibited the formation of intermediate layer during heating, but its formation temperature was found to be about 240°C, which was higher than for the case of Type I (200∼210°C), and the considerable overall diffusion took place simultaneously.

(Type III) The Sb layer evaporated rapidly on Formvar film showed a strong perferred orientation as shown in Fig. 4 (a), and this orientation could not be destroyed by the rapid deposition of Bi on it. Examining the spotty arc pattern from the double films and the almost one-to-one correspondence of individual spots, it was supposed that the minute crystallites of Bi and Sb orientate parallel to each other not only in their crystallographic planes but also in their crystallographic directions (see Fig. 4 (b)). Further, many reflections due to double diffraction could be found in this case. The correspondence between individual spots in the reflections due to the intermediate layer of the definite solid solution and those of Bi- and Sb-rich solid solutions is not so perfect as that seen in the case of Bi and Sb. This means that the crystallites of the intermediate layer are not oriented perfectly parallel to those of Bi- and Sb-rich solid solutions. Considering, in addition, that the Debye rings due to the intermediate layer observed with the specimens of Type I are coarser than those due to Bi and Sb (Fig. 2), it will be recognized that the appreciable grain growth can arise in the process of the intermediate layer formation.

The heating at about 220°C for about 10 minutes of these specimens resulted in the formation of triple-layer as shown in Fig. 4 (b). This temperature was slightly higher than that for the films of Type I, and the maximum intensity of reflections due to the intermediate layer attained by heating was somewhat weaker than that for the cases of Types I and II. Further heating for about 20 minuites at about 240°C resulted in the superposition of diffuse lines, and subsequent change was almost the same as that for Type I.

(Type IV) When Sb was deposited slowly on Formvar film, the ring pattern was caused in most cases. After the rapid deposition of Bi on it and subsequent heating at about 220°C, however, the formation of triple layers could be observed just like in the case of Type III.

(Types V, VI) Whenever the secondary Bi deposits were slowly formed, the intermediate layer of the definite composition could never be detected independently of the deposition rate of primary deposits, and the usual overall diffusion as shown in Fig. 1 (b) took place at about 245°C.

The results described above may be summarized as follows:

(1) The specimens of Types I and II seem to indicate the initial alloy formation at the interface during the deposition of secondary

Sb metal, although, in the case of Type II, the reflections due to this initially formed alloy can be detected only occasionally. While, the specimens of any type other than Type I or II never show the existence of such an alloy before heat-treatments. However, it will be likely that there exists a very thin layer of alloy at the interface which cannot be detected by electron diffraction in these cases.

(2) The formation of triple-layer during heating is most pronounced for the specimens of Types I and II and less pronounced for those of Types III and IV, while Types V and VI do not show any triple-layer formation. This is the same sequence as for the initial alloy formation during deposition.

(3) From Table I, it may be deduced that the degree of triple-layer formation depends not on the kinds and deposition rates of primary deposits but on those of secondary deposits.

(4) The temperatures at which the interdiffusion becomes much pronounced can be classified into two groups with the deposition rate of Bi, namely, about 200∼220°C for the specimens of Types I, III and IV where Bi is rapidly deposited, and about 240∼250°C for those of Types II, V and VI where Bi is slowly deposited.

(5) In addition, contaminations of the surfaces of under-layers due to the adsorption of some impurities were found to hardly affect the aspects of diffusion, from the fact that the exposure to air before the second deposition had no effect.

Discussions on these results and some additional informations will be given in §§ 6 and 7.

§ 4. Effects of the Film Thickness on the Diffusion Process

4-1. *Effects of the relative thickness of double film*

To investigate whether the relative thickness of double layers affects the thickness of the intermediate layer formed by heating or not, observations with electron diffraction by the reflection method was carried out, because no appreciable effects could be found within the thickness range where the transmission method was applicable. The thick Bi layer of about 1000 Å in thickness was rapidly deposited on a glass substrate and then the thin Sb layer of about 100 Å was also rapidly deposited on it. The specimen exhibited only the reflections due to the outer, thin Sb layer at room temperature (Fig. 5 (a)), but the weak reflections due to the intermediate layer of about 50 at. % Bi solid solution were superposed on them by subsequent heating in vacuum (Fig. 5 (b)). The reflections due to this layer became more and more intense, while those of Sb-rich solid solution gradually diminished their intensity (Fig. 5 (c)) and finally disappeared after continued heating at about 210°C (Fig. 5 (d)). Again, the formation of the layer of the definite solid solution was seen in this case. This definite solid solution did not show any appreciable change in its lattice constant and intensity during the prolonged heating at about 230°C, and so it was deduced that in this stage the surface of thick Bi layer was covered by the thin layer of the solid solution of the definite composition and further diffusion was almost interrupted.

4-2. *Effects of the total thickness of composite film*

To investigate whether the thickness of the definite solid solution increases or not with the change of total thickness of bimetallic film, some additional experiment by X-rays was performed with the very thick films. The layer of Bi of about 5000 Å in thickness and that of Sb of about 6000 Å were rapidly deposited on a microscopic slide glass successively. The specimens sealed in Pyrex tube in vacuum were heated at various temperatures for various time intervals, and then they were examined by X-rays. The reflections due to Bi and Sb began to change positions after heating for about 10 minutes at about 210°C, showing the change of their lattice spacings, while those due to the layer of the definite composition could never be detected even after prolonged heating.

It is suggested consequently that the thickness of the intermediate layer of the definite composition is not so thick as it can be detected by X-rays but confined to some limiting value where the transmission electron diffraction can be applicable.

The results described in this paragraph will be discussed in § 7.

§ 5. Some Considerations on the Geometrical Structure of the Interface

In § 3, it was described that the formation of triple-layer was appreciably affected by the kinds and deposition rates of secondary deposits. What might be affected by these factors would be, in the first place, the geometrical structure[7),8)] such as grain size, boundaries or porosities etc., in the second place, the stress involved within thin films or defects such as various imperfections[7)]. In the present problem, it seemed very difficult to obtain direct informations about the metal-metal interface, so that we had no other means than to deduce the structure and properties of the interface from those of the individual layer. In this paragraph, some considerations on the first factor will be given.

Some qualitative informations could be obtained from the X-ray interference with thin films which was performed for the determination of film thickness. In the first place, the number of visible interference fringes may be considered to be a measure for the roughness of film surface if it is compared among the films of almost the same thickness. The number of interference fringes observed for the rapidly deposited Sb layer was much less than that for the rapidly deposited Bi layer of almost the same thickness (Figs. 6 (a) (1) and (2)), though the absorption of X-rays was less for the former than for the latter. Consequently, the roughness of the former surface should be greater than the latter. Comparing the slowly deposited Sb film with the rapidly deposited one, the roughness of the former surface seemed to be greater than that of the latter (Figs. 6 (a) (2) and (3)). This is consistent with the results of electron microscopy obtained by E. Cremer and E. Ruedl[8)]. While, the layer of Bi was found to be considerably smooth independently of their deposition rates. It was also found that the surface of outer layer of composite film, irrespective of their kinds and deposition rates, was always smooth even if the surface of under-layer was considerably rough. This was deduced from the facts that many, clear interference fringes could be observed for composite films.

In the second place, the smoothness of interface of composite films can be deduced from an anomalous intensity distribution of interference fringes detected for these composite films, because X-rays reflected partially at the smooth interface will modify the intensity distribution of interference fringes due to the double film as a whole. Considering that such an anomaly could always be detected for the films of Sb deposited on Bi irrespective of their deposition rates, the interface of Sb and Bi under-layer was considered to be smooth. While, the interface of the film of Bi deposited on the slowly deposited Sb under-layer would be considerably rough because the anomaly could never be found. The interface of the film of Bi deposited on the rapidly deposited Sb under-layer would be intermediate in its roughness between the above two cases, because the anomaly could be detected sometimes and the surface of rapidly deposited Sb under-layer was smoother than that of slowly deposited one as described above (Figs. 6 (b) (1) and (2)).

The roughness of interface deduced from these facts depends on the kinds and deposition rates of primary deposits, but not on those of secondary deposits on which the degree of triple-layer formation depends, as shown in § 3. Consequently, no direct relations can be found between the structure and the triple-layer formation.

§ 6. Electrical Resistance Measurement

The electrical resistance measurement was performed in relation to the second factor mentioned in the previous paragraph. The layer of about 400 Å in thickness of Bi or Sb was rapidly or slowly deposited on a microscopic slide glass cut in the dimension of about 30 mm in length and 3.5 mm in width. The leads of Cu foils were soldered on each end where Pt electrodes were prepared by the baking of platinium chrolide solution. The electrical resistance was measured in vacuum by the Wheatstone bridge during aging at room temperature or at subsequent isochronal annealing. The rapid heating and cooling were necessary for the isochronal annealing by pulse heating. The heating, therefore, was performed in vacuum by heat radiation from W coil placed at a distance of about 15 mm from the specimen. The heating coil was wound so carefully that the temperature gradient along the long dimension of specimen became as small as possible and consequently the temperature difference between each end and the mid point of specimen was estimated to be within 1～2°C. The temperature of specimen was measured by Chromel-Alumel thermocouple. The heating to appropriate temperatures could be done within 30 seconds～one minute by manual controlling of heater current. The time interval of about 10 minutes was necessary for the complete cooling to room temperature, but that required for the cooling to about 50°C was within about 2 minutes.

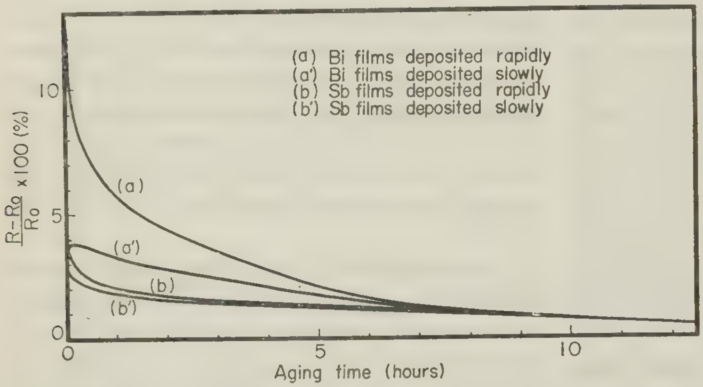

Fig. 7. The percentage decrease in electrical resistance of thin films during the room temperature aging.

The results obtained from the room temperature aging are shown in Fig. 7. The values of $100(R-R_0)/R_0$ are plotted against the aging time, where R is the measured resistance, and R_0 the resistance after the aging of about 24 hours, being nearly constant during subsequent aging. After these measurements, the isochronal annealing was made by the pulse heating for 5 minutes at each temperature. The electrical resistance after each pulse annealing was measured at room temperature and calibrated to the values at 30°C. These results are shown in Fig. 8, taking $100(R-R_0)/R_0$ as the ordinate and the annealing temperature as the abscissa, where R_0 is the same as shown in Fig. 7 and R the calibrated resistance at 30°C.

The percentage decrease in resistance during the room temperature aging shows a marked dependence on the deposition rate. The decay of electrical resistance of vacuum deposited thin films is usually considered to be due to the decay of imperfections[7),9)], and so the less percentage decrease in resistance for the slow deposition rate than for the rapid deposition rate seems to indicate that the decay of mobile imperfections in the slowly deposited films has already begun during deposition[9),10)]. More appreciable decay than the above is seen for the subsequent isochronal annealing as shown in Fig. 8. The decay for the Bi layer is greater for the rapidly deposited one than for the slowly deposited one, while the decay for the Sb layer shows almost the same tendency for both the rapidly and slowly deposited ones. Further, the decay for the Sb layer is much greater than for the Bi layer, which means that the lattice defects are much for the former than for the latter. This is consistent with the results obtained by H. D. Murbach and H. Wilman[11)] by means of stress measurement with thin films. The cause of resistance increase observed for Bi layers as shown in Fig. 8 is not clear in the present stage of investigation.

The results obtained from electrical resistance measurement may be summarized as follows:

(1) The results suggest that the rapidly deposited or slowly deposited Sb layer is most defective, the rapidly deposited Bi layer next defective and finally the slowly deposited Bi layer least defective. This sequence of defectiveness, applying to the secondary deposits of double films, agrees well with the sequence of initial alloy formation during deposition or triple-layer formation during heating as described in § 3.

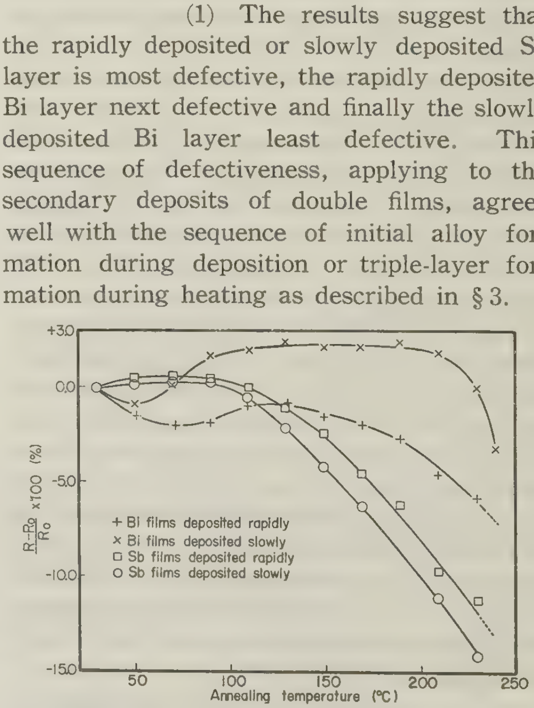

Fig. 8. The percentage decrease in electrical resistance of thin films during the isochronal annealing.

(2) If it is assumed that the interdiffusion in the present bimetallic films is influenced to some extent by vacancies, the net flow of such vacancies will be considered to arise from Sb side to Bi corresponding to the net flow of atoms from Bi side to Sb (§2). It is deduced from Fig. 8 that vacancies are richer in Sb layer than in Bi layer, and therefore, the concentration gradient responsible for such a flow can be expected.

(3) The temperature at which the mobility of imperfections is much increased is about 110∼120°C for the rapidly or slowly deposited Sb layer, about 140°C for the rapidly deposited Bi layer and about 200°C for the slowly deposited Bi layer (Fig. 8). These temperatures should be related to those at which the interdiffusion in double layers becomes much pronounced. The flow of vacancies from one layer to another is necessary for the interdiffusion to take place and the temperature for such a flow to occur may be determined by the temperature at which the vacancies begin to decay in Bi films, because this temperature is higher for Bi films than for Sb ones. Consequently the pronounced interdiffusion is expected to occur at about 140°C for the composite films of Sb and rapidly deposited Bi or about 200°C for those of Sb and slowly deposited Bi, independently of the deposition rate of Sb and the order of successive deposition. While, the temperatures determined by electron diffraction were about 200∼220°C for the former films and about 240∼250°C for the latter ones, as summarized in §3. The general tendency observed by electron diffraction such that the appreciable diffusion takes place at lower temperature for the former (200∼220°C) than for the latter (240∼250°C), coincides with the tendency deduced from the decay of resistance (140°C for the former and 200°C for the latter), but there exists quantitative disagreement between the observed and the deduced temperature in each of the two cases.

Discussions on these results will be given in the next paragraph.

§7. Discussions and Summary

(1) As mentioned in §1, Cramer[3)] observed the same phenomenon for the specimen of thin Au layer deposited on polished Cu as for the composite films of Bi and Sb. Menter[4)] also reported the observation of triple-layer formation in his experiment concerning the Moiré pattern. Although none of them gave any explanation or discussion on thier observations, this phenomenon seems to be a general tendency for thin bimetallic films prepared by vacuum deposition and not particular for the case of Bi and Sb.

(2) Though the clear-cut explanation seems to be difficult in the present stage, the triple-layer formation may be interpreted tentatively by the assumption that the intermediate layer of a certain thickness is separated from two outer layers by some condition, which may be realized by assuming the hightly strained intermediate layer. The very thin layer of solid solution, which was sometimes difficult to be detected, was already formed at the interface of double films during the successive deposition of constituent metals before heating as described in §§2 and 3. This initial alloy formation may be due to the defects in the evaporated metallic films and the latent heat of vaporization of secondary deposit as discussed in the previous papers[2)]. This initially formed layer, whose lattice constant is different from those of upper- or under-layer, may exert the stress on its surroundings and develop the strained layer of a certain thickness. It may be allowed to consider that the relative thickness of the upper and under strained layers is always constant irrespective of the total and the relative thickness of the bimetallic film as a whole, and further the diffusion takes place very rapidly in the intermediate layer including both the initially formed alloy layer and these strained layers, and therefore the state of homogeneous solid solution with the definite composition will be attained very rapidly in this intermediate layer in the early stage of heating. Consequently the triple-layer may be formed.

This assumption may be supported not only by the facts which will be described in (3) and (4), but also by the study of adhesion performed by C. Weaver[5)]. He reported that the values of adhesion obtained for two-layer films of Ag–Pb, Al–Pb and Ag–Cr, which had no miscibility in the solid state at room temperature, were only slightly greater than for the under-layer (Pb or Cr) alone, while the abnormally high adhesion was obtained for the bimetallic films of Cu–Cr and Au–Cr, in which the miscibility of two metals exists in Cu-, Au- or Cr-rich side. Explanation for this high adhesion was given by Weaver on the basis of the formation of a harder, strained intermediate layer at the metal-metal interface, which was due to the formation of a layer of solid solution of somewhat different lattice spacing, causing a resultant strain.

(3) If such a strained intermediate layer exists in the present case, its extent will depend upon the thickness of the alloy formed during deposition, but not upon the thickness of upper-or under-layer itself.

(a) Consequently, in the first place, the thickness of the intermediate layer formed by heating should be confined to such a strained layer of a definite thickness and not increased by the increase of total film thickness. This was actually confirmed by the X-ray diffraction with thick films and by the reflection method of electron diffraction with the specimen of thin Sb layer deposited on thick Bi film, as shown in § 4.

(b) In the second place, the maximum intensity of diffraction rings due to the intermediate layer attained by triple-layer formation should be related to the thickness of the initially formed alloy at the metal-metal interface during successive deposition. As described in § 3, the degree of triple-layer formation is classified into three cases by the kinds and deposition rates of secondary deposits, namely, the most pronounced degree for the films of rapidly or slowly deposited Sb with Bi under-layer (Types I and II), the less pronounced degree for those of rapidly deposited Bi with Sb under-layer (Types III and IV) and the never detected formation for those of slowly deposited Bi with Sb under-layer (Types V and VI). This sequence was found to be just the same as that of the degree of the initial alloy formation (§ 3) and also that of the degree of the defectiveness involved in secondary deposits (see (1) in § 6). These facts will support the assumption considered above.

(4) Finally, some additional support for the assumption stated in (2) may be obtained from the consideration on the discrepancy between the temperature at which appreciable diffusion actually occurs and that deduced from electrical resistance measurement. The former temperature was found to be about 200～210°C for the films of Types I, III and IV or about 240～250°C for those of Types II, V and VI from the results obtained by electron diffraction, while the latter one was estimated to be about 140°C or about 200°C in each case. The discrepancy of about 50°C can be found. If the vacancy mechanism is responsible for the interdiffusion in the present case, the facts that the interdiffusion doe not yet occur at 140° or 200°C though the imperfections such as vacancy in each upper- or under-layer are mobile at these temperatures will probably suggest that vacancies in the intermediate layer may be trapped, for example, at the concentrated dislocations which will be responsible for the structure of the highly strained layer connecting the initially formed layer of solid solution and the upper- or under-layer of pure metal[12]. The activation energy for such trapped vacancies may be greater than for those in upper- or under-layer, and therefore they can hardly decay at 140°C or 200°C. When the temperature is raised to about 200～210°C or about 240～250°C, the vacancies concentrated in the strained region become movable and appreciable diffusion occurs in this strained region, while most of the vacancies in the unstrained upper- and under-layers have already been decayed and the diffusion rate in these layers are much less than that in the intermediate layer. Consequently, the interdiffusion of metals will rapidly take place in the intermediate layer at these temperatures, resulting in the formation of triple-layer. Further, the fact that the appreciable grain growth can be observed in the formation process of the intermediate layer with the definite composition as described in § 3 seems to suggest that the strained intermediate layer mentioned above will play an important role for the triple-layer formation.

For the specimens of Types V and VI, such a triple-layer formation could not be detected. However, these specimens may be considered to be the simple double-layer formed by the superposition of two metals without any intermetallic reactions at the metal-metal interface and to resemble rather the sintering of fine powders of Fe and Cr[13], or the usual diffusion couple of bulk specimens. Accordingly, the strained intermediate layer in these cases, even if it exists, would be confined within the metal-metal interface itself and sufficiently thin for the detection by electron diffraction.

Acknowledgements

The writers wish to express their sincere thanks to Professor K. Tanaka of Kyōto University for his kind and valuable discussions throughout this work. This work was supported in part by the research grant of the Ministry of Education.

References

1) P. Michel: Ann. Physique, Sér. 13 **1** (1956) 719.
2) Y. Fujiki: J. Phys. Soc. Japan **14** (1959) 913, 1308.
3) H. Cramer: Ann. Phys. **34** (1939) 237.
4) J. W. Menter: Adv. in Phys. **7** (1958) 299.
5) C. Weaver and R. M. Hill: Adv. in Phys. **8** (1959) 375; Phil. Mag. **4** (1959) 253, 1107.
6) Y. Fujiki and T. Yoshida: J. Phys. Soc. Japan **14** (1959) 1828.
7) H. Mayer: *Physik dünner Schichten*, II (Wissenschaftliche Verlag., Stuttgart) (1955).
8) M. Auwärter: *Ergebnisse der Hochvakuumtechnik und der Physik dünner Schichten* (Wissenschaftliche Verlag., Stuttgart) (1957).
9) R. A. Aziz and G. D. Scott: Canad. J. Phys. **35** (1957) 785.
10) P. G. Wilkinson and L. S. Birks: J. App. Phys. **20** (1949) 1168.
11) H. P. Murbach and H. Wilman: Proc. Phys. Soc. **B**, **66** (1953) 905.
12) See for example, C. S. Barrett: Acta Met. **1** (1953) 1. D. R. Brame and T. Evans: Phil. Mag. **3** (1958) 971.
13) H. J. Goldschmidt: *The Mechanism of Phase Transformation in Metals* (Inst. of Metals, London) (1956).

JOURNAL OF THE PHYSICAL SOCIETY OF JAPAN, Vol. 16, No. 4, APRIL, 1961

Electrical Properties of Heavily Doped *n*-Type Germanium

By Yoshitaka FURUKAWA
The Electrical Communication Laboratory,
Musashinoshi, Tokyo

(Received November 12, 1960)

Experimental studies were made on electrical resistivity, Hall coefficient and magnetoresistance of *As*- *Sb*- and ($As+Sb$)-doped germanium in the electron concentration range of (10^{18}～$3\times10^{19}\,\mathrm{cm}^{-3}$). The mobility difference between *As*- and *Sb*-doped germanium has been observed at room temperature. This difference seems to be related with the difference in the ionization energy of group V elements. From the present experiment, it has been concluded that in heavily doped germanium, interaction between electron and ionized impurity should be treated as short range force instead of Coulomb force owing to the fairly large screening effect, and as the result the nature of the core of impurity influences directly upon the impurity scattering.

§1. Introduction

Electrical properties of non-degenerate *n*-type germanium containing shallow impurities such as *P*, *As*, *Sb* have been investigated extensively by many authors. One of their result is that the ionization energy of the impurities depends on the impurity concentration as well as the specific element. Therefore the impurity dependence of electrical properties of germanium containing these impurities was observed clearly at low temperatures. However in temperature range where all donors are ionized completely and scattering is mainly due to lattice vibration, the electrical resistivity of germanium is independent substantially on the specific element in group V.

On the other hand, many investigations have been made on heavily doped *n*-type germanium. Lark-Horovitz[1] measured resistivity ρ (ohm-cm) and carrier concentration n (cm^3) at low temperatures and found the approximate validity of the relation $\rho=6270\,n^{-1/3}$ which was deduced from Conwell-Weisskopf formula taking into account Fermi statistics. Bowers[2] measured magnetic susceptivility and Pollack[3] measured piezoresistance. They concluded that four-ellipsoid model is accepted in heavily doped n-type germanium and there is no substantial change in curvature of the conduction band for energies up to 0.08 eV above the band minimum. Goldberg[4] measured magnetoresistance and showed that the symmetry condition $b+c=0$ is satisfied with uncertainty of 30%. These experiments were made on *As*- and *P*-doped germanium.

However, in recent years Esaki-diode was discovered and in its current-voltage characteristics at low temperatures, phonon assisted tunneling[5] was observed in *Sb*- doped junctions of germanium, but not in *As*- and *P*-doped junctions. In addition, the author[6] observed the mobility difference between *As*- and *Sb*- doped germanium at room temperaperature. These results indicate that specification of the kind of impurity is necessary for discussing the electrical properties of heavily doped n-type germanium at room temperature even for the elements in group V.

This paper describes the experimental studies on the impurity dependence of the electrical properties (resistivity, Hall coefficient, and magnetoresistance) of heavily doped n-type germanium.

§ 2. Sample Preparation and Experimental Method

As-, *Sb*- and (*As*+*Sb*)- doped single crystals were grown by pulling from the melt in [100] direction, using the pulling rate of about 7 μ/sec and rotation of about 50 r.p.m. The crystals were sliced perpendicular to the long axis of the single crystals and the bridge shape samples were prepared by using a ultrasonic tool. The samples suitable for making magnetoresistance measurements were prepared by cutting thin plates as shown in Fig. 1. In these samples, the current direction deviates from [100] axis to [010] axis by 22.5°. In cutting the samples, crystal axis was determined optically and confirmed by electron diffraction analysis.

A conventional D.C. method was used for the measurements of resistivity, Hall coefficient and magnetoresistance. The magnetoresistance constant b, c and d are defined in Eq. (1).

$$\frac{\Delta\rho}{\rho H^2}=b+c\frac{(\boldsymbol{I}\cdot\boldsymbol{H})^2}{I^2H^2}+d\frac{\sum_{i=1}^{3}I_i^2H_i^2}{I^2H^2}\,. \qquad (1)$$

In this equation ρ is the resistivity and $\boldsymbol{I}$ and $\boldsymbol{H}$ are the current density and magnetic field respectively. When the angle θ is measured as shown in Fig. 2, Eq. (1) is expressed in the following form.

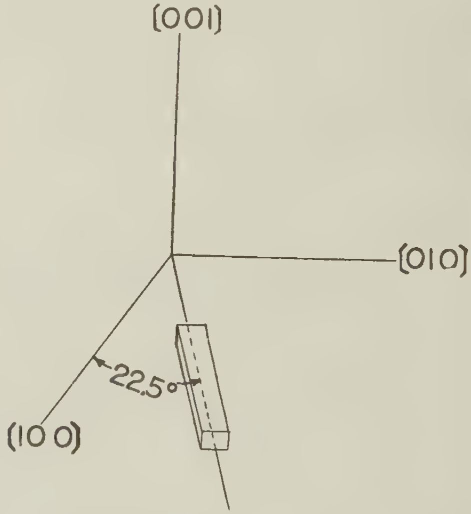

Fig. 1. Cutting direction of samples for measurement of magnetoresistance effect. The crystals were pulled in [001] direction in this figure.

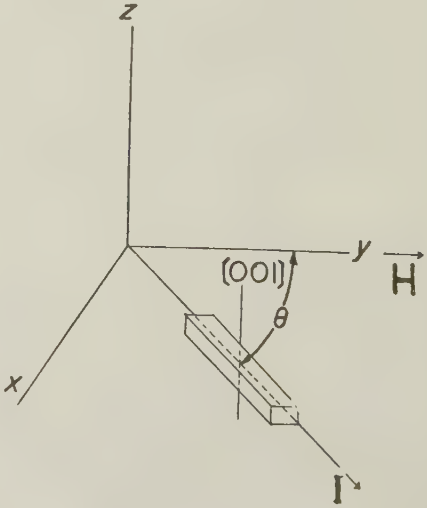

Fig. 2. Position of the samples in magnetic field for the measurement of magnetoresistance.

$$\frac{\Delta\rho}{\rho H^2}=\left(b+\frac{c+d}{2}\right)+\frac{1}{2}\left(c^2+cd+\frac{d^2}{2}\right)^{1/2}\cos(2\theta+\alpha)$$

$$\tan\alpha=\frac{d}{2c+d}\,. \tag{2}$$

Therefore the amplitude, the mean value and the angle $\theta_{\min}$ for the minimum of $\Delta\rho/\rho H^2$ determine b, c and d. This method[7] has the following advantages in the present experiment. (1) All magnetoresistance constants are determined by one rotation of samples in magnetic field. (2) $\theta_{\min}$ is related directly with the ratio c/d so that comparison of magnetoresistance constants of *As*- and *Sb*- doped germanium is made easily.

§ 3. Experimental Results

(a) *Resistivity, Hall Measurements*

Resistivity and Hall measurements were made at 300°K. Magnetic field of 5000 oersteds was used for the Hall measurements. Electron concentration n (cm^{-3}) was calculated by using the relation $n=1/Re$. Where R is the Hall coefficient and the factor[8] arising from the band structure *etc* was neglected in this relation.

Fig. 3 shows *n versus ρ* curves for *As*- and *Sb*- doped germanium. Electron mobility in Sb- dopted germanium is higher than that in *As*- doped germanium. In this figure the experimental points for samples with higher *As* concentration deviate from this straight line to high resistivity side. Such deviation has not been observed in *As*- doped crystals pulled in [111] direction[6] and in *Sb*- doped crystals pulled in [111] or [100] direction. This may be due to anomalous precipitation of *As* or other lattice defects.

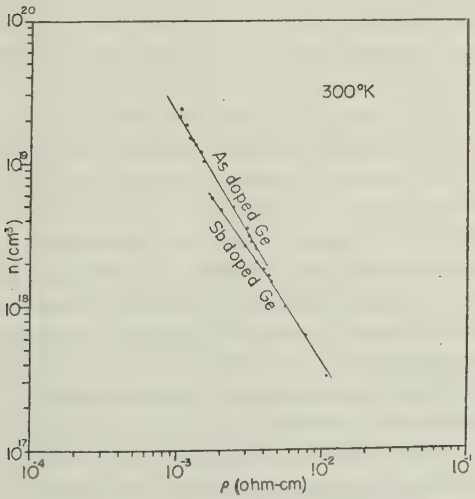

Fig. 3. Resistivity *versus* electron concentration curves for *As*- and *Sb*- doped germanium at 300°K

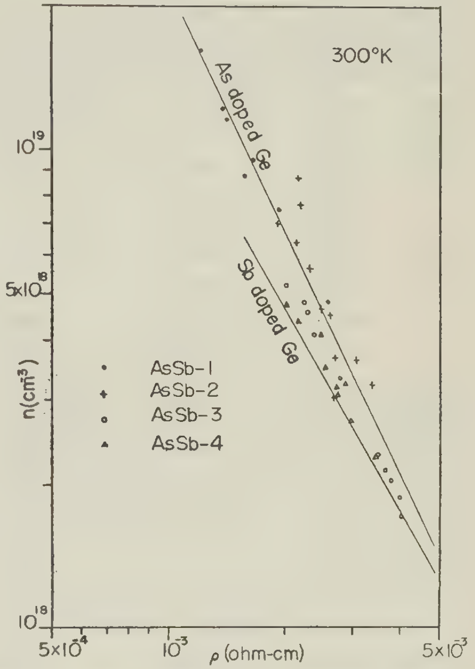

Fig. 4. Resistivity *versus* electron concentration relations for (*As*+*Sb*)- doped germanium at 300°C.

Fig. 4 shows *n versus ρ* relations for the samples containing *As* and *Sb* simultaneously. The straight lines in this figure are the same shown in Fig. 3. Concentration of each impurity in the samples was estimated as follows. In the first place, *As*- doped single crystals were grown and *As* concentration at several points along the pulling direction was determined by measuring the Hall coefficient. Then the crystals were re-melted with *Sb*. Again single crystals of nearly equal size as the original crystals were pulled in [100] direction. Distribution of *As* in the crystals thus obtained was assumed to be same as in original crystals. As concentration estimated at the top of the crystals (seed side) and at the tail where single crystal breaks is shown in Table I.

Table I. *As* concentration estimated from distribution of *As* in the original crystals.

Crystal	*As* Concentration at the top (cm^{-3})	n at the top (cm^{-3})	*As* Concentration at the tail (cm^{-3})	n at the tail (cm^{-3})
AsSb-1	$\sim 2\times 10^{18}$	4.8×10^{18}	$\sim 10^{19}$	1.6×10^{19}
AsSb-2	$\sim 5\times 10^{17}$	3.0×10^{18}	$\sim 3\times 10^{18}$	8.7×10^{18}
AsSb-3	$\sim 10^{17}$	1.7×10^{18}	$\sim 10^{18}$	5.2×10^{18}
AsSb-4	$\sim 2\times 10^{17}$	2.3×10^{18}	$\sim 6\times 10^{17}$	4.7×10^{18}

Table II. Spectroscopic analysis of *As* and *Sb* concentration in $(As+Sb)$-dopted germaninum.

Crystal	Sample	Resistivity (10^{-3} ohm-cm)	Electron Concentration ($10^{18}\,cm^{-3}$)	*As* Concentration ($10^{18}\,cm^{-3}$)	*Sb* Concentration ($10^{18}\,cm^{-3}$)	r	$\frac{\rho-\rho_{Sb}}{\rho_{As}-\rho_{Sb}}$
AsSb-1	No 14	1.67	9.4	13	2.9	0.82	
	No 20	2.62	4.8	5.4	1.6	0.77	1.3
AsSb-2	No 11	2.32	5.7	6.8	4.2	0.62	1.2
	No 15	3.03	3.6	2.7	1.8	0.49	1.3
	No 17	3.34	3.2	2.8	2.3	0.55	1.3
	No 19	2.68	3.0	3.0	2.7	0.53	−0.1
AsSb-3	No 3	2.33	4.6	1.8	4.3	0.3	0.57
	No 5	2.37	4.0	1.2	3.6	0.25	0.24
	No 11	3.78	2.0	0.5	1.6	0.24	0.35
	No 17	3.93	1.7	0.4	0.9	0.31	−0.1
AsSb-4	No 6	3.47	2.3	0.36	2.1	0.15	0.31
	No 12	2.54	3.5	0.62	4.4	0.12	0.16
	No 14	2.50	4.1	0.69	4.4	0.14	0.54
	No 16	2.19	4.4	0.78	3.6	0.18	0.2

Impurity concentration was also determined by spectroscopic analysis. Procedure of this analysis is as follows. Standard samples with different electron concentration were selected from *As*- and *Sb*- doped crystals. Using the standard samples working curves for *As* and *Sb* were drawn by plotting blackness of *As* and *Sb* spectrum lines on the photographic plate against electron concentration determined from the Hall measurements. Concentration of each impurity in $(As+Sb)$-doped samples was determined by measuring the blackness of *As* and *Sb* spectrum lines and comparing it with the working curves. Result is shown in Table II. However this result is not so accurate because the assumption that the impurity concentration is equal to the electron concentration was used in drawing the working curves. The sum of *As* and *Sb* concentration shown in Table II is almost always higher than electron concentration obtained from the Hall measurement. This difference may be due to the precipitation of impurities in the samples.

In Fig. 4 the experimental points for samples with large r, where r is defined by $r=$ *As* concentration/sum of *As* and *Sb* concentrations, lie on *As*- doped line while those for samples with small r lie on *Sb*- doped line. The behavior of transition of experimental points from *Sb*- doped line to *As*- doped one with increasing r will be clearly observed if $(\rho-\rho_{Sb})/(\rho_{As}-\rho_{Sb})$, where ρ_{As}, ρ_{Sb} and ρ (hereafter) are the resistivity of *As*- *Sb*- and $(As+Sb)$- doped germanium, is plotted against r for a fixed electron concentration. However in the present experiment it is difficult to draw such curve because of lack of data for fixed value of n.

In Fig. 5 $(\rho-\rho_{Sb})/(\rho_{As}-\rho_{Sb})$ is plotted against

r for specimens with various electron concentration. Though the dotted curve in this figure will have no physical meaning unless $(\rho-\rho_{Sb})/(\rho_{As}-\rho_{Sb})$ is independent on n, it is shown clearly that the transition of experimental points occurs sharply at $r \approx 0.2 \sim 0.5$ in the concentration range of $n > 10^{18}\,\mathrm{cm}^{-3}$.

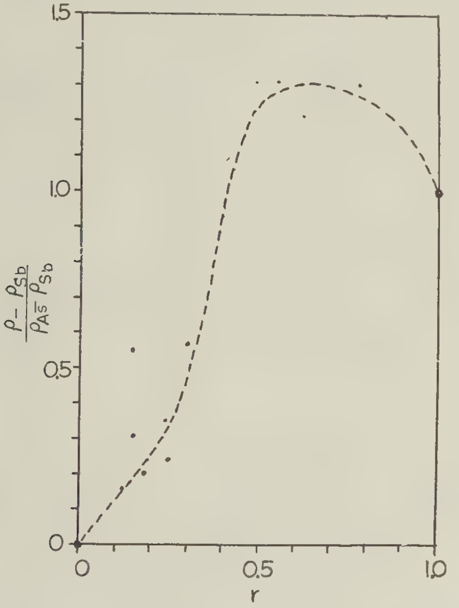

Fig. 5. $(\rho-\rho_{Sb})/(\rho_{As}-\rho_{Sb})$ *versus* r relations.

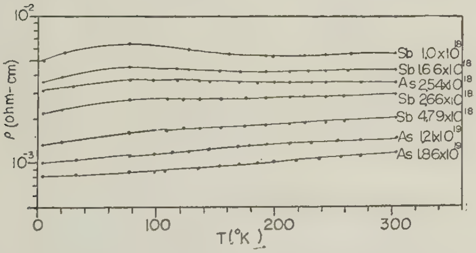

Fig. 6. Temperature dependence of the resistivity for *As*- anp *Sb*- doped germanium.

Fig. 6 shows a typical example of temperature dependence of resistivity of *As*- and *Sb*-doped germanium. The resistivity of the samples with $n > 3\times10^{18}\,\mathrm{cm}^{-3}$ decreases monotomously with decreasing temperatures, while the resistivity of the samples with $n < 3\times10^{18}\,\mathrm{cm}^{-3}$ has a maximum in measured temperature range (4.2°K~300°K).

(b) *Magnetoresistance Measurements*

Magnetoresistance effect of heavily doped germanium was so small that magnetic field of 8500 oersteds was used for this experiment. This magnetic field strength satisfies still the weak field condition. Accuracy of this measurement is lower than that of resistivity and Hall measurements because of appearance of fairly large noise in voltage drop across the resistivity probes.

Fig. 7 shows a typical example of angular dependence of magnetoresistance for *As*- and *Sb*- doped germanium at 300°K Results for $(As+Sb)$- doped germanium are shown in Fig. 8. The minimum of magnetoresistance appears at about 60° for *As*- doped samples

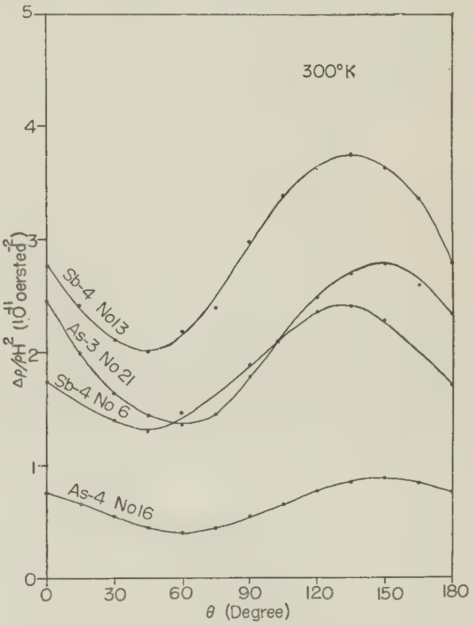

Fig. 7. Angular dependence of magnetoresistance for *As*- and *Sb*- doped germaninum at 300°K. Magnetic field of 8500 oersted was used.

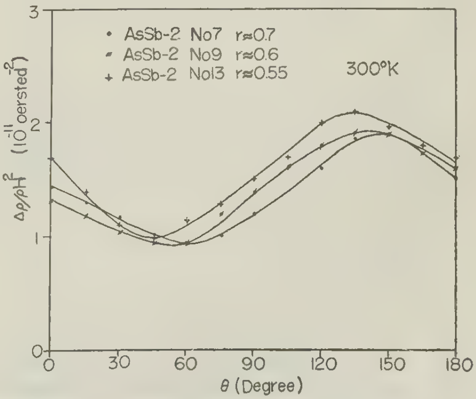

Fig. 8. Angular dependence of magnetoresistance for $(As+Sb)$- doped germanium. $\theta_{\min}$ increases with increasing r from about 45° to about 60°.

Table III. Magnetoresistance of n-type germanium at 300°K.

Crystal	Sample	Resistivity (10^{-3} ohm-cm)	Electron concentration (10^{18} cm^{-3})	Magnetoresistance constant		
				b	c (10^{-11} oersted^{-2})	d
As-3	No 21	3.67	2.4	1.13	−0.51	2.41
As-4	No 16	1.44	12	0.31	−0.18	0.85
	No 22	1.96	7.2	0.48	−0.28	1.32
Sb-4	No 6	1.95	4.5	1.31	−1.11	2.22
	No 13	2.92	2.8	2.0	−1.74	3.48
	No 17	3.48	2.1	1.9	−2.2	4.4
AsSb-1	No 14	1.67	9.4	0.42	−0.26	1.21
	No 20	2.62	4.8	0.96	−0.97	1.94
AsSb-2	No 7	1.92	7.0	0.73	−0.38	1.8
	No 9	2.14	6.5	0.81	−0.71	1.93
	No 13	2.48	4.7	1.0	−1.12	2.24
	No 19	2.68	3.0	1.27	−1.15	2.3

and at about 45° for *Sb*-doped samples. For (*As*+*Sb*)- doped samples $\theta_{\min}$ is equal to about 45° for the samples with small r, increases with increasing r, reaches about 60°. However the transition of $\theta_{\min}$ does not occur simultaneously with the transition of $(\rho-\rho_{Sb})/(\rho_{As}-\rho_{Sb})$ when r is varied. Magnetoresistance constants are listed in Table III.

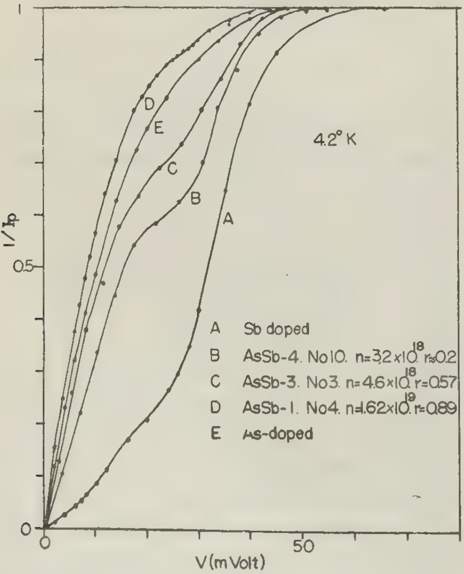

Fig. 9. V–I characteristics for *As*-, *Sb*- and (*As*+*Sb*)- doped junctions at 4.2°K. Phonon assisted tunneling associated with transverse acoustic phonon was quite ambiguous for all (*As*+*Sb*)- doped junctions.

(c) *Observation of Phonon assisted Tunneling*

Fig. 9 shows current-voltage characteristics for *As*-, *Sb*- and (*As*+*Sb*)- doped junctions of germanium at 4.2°K. Phonon assisted tunneling assosisated with longitudal acoustic phonon was observed at about 27 mv, but tunneling associated with transverse acoustic phonon which was observed clearly at about 7 mv for *Sb*- doped junctions was quite ambiguous for all (*As*+*Sb*)- doped junctions.

§ 4. Discussion and Acknowledgement

n versus ρ curve for *P*-doped germanium has been measured only in the electron concentration range of ($1.8\times10^{19}\sim4.5\times10^{19}$ cm^{-3}) and coincided with *As*-doped line shown in Fig. 3 within the experimental error. The observed mobility difference between *Sb*- and *As*- or *P*-doped germanium cannot be expected from Conwell-Weisskopf or Brooks-Herring formula, and seems to be related to the fact that *Sb* has the smallest ionization energy of the group V elements. In havily doped germanium, short range force acts between electron and ionized impurity, and as the result the nature of the core of impurity influences directly upon the impurity scattering.

Another explanation for the mobility difference is as follows. The conduction band structure is modified by heavy doping of impurity in *P*- and *As*-doped germanium, but this is not the case in *Sb*-doped germanium. This assumption[5)] was first proposed for the explanation of the direct tunneling in *P*- and *As*-doped junctions of germanium. However, if the transition of experimental points shown in Fig. 5 is assumed to be due to the band modification, it is difficult to explain the observed phonon assisted tunneling in $(As+Sb)$-doped junctions which were made of the samples with $r>0.5$ (See Fig.9).

The sharp transition shown in Fig. 5 is an unexpected result. As a limiting case of short range force, if the ionized *As* and *Sb* atoms in germanium behave as fixed elastic spheres of radii R_{As} and R_{Sb} respectively, relaxation time τ obtained from classical treatment is as follows.

$$\frac{1}{\tau}=\frac{1}{\tau_{As}}+\frac{1}{\tau_{Sb}} \qquad (3)$$

$$\tau_{As}=\frac{1}{NrR^2_{As}v}$$

$$\tau_{Sb}=\frac{1}{N(1-r)R^2_{Sb}v}\,.$$

Where v is velocity of electrons and N is the sum of *As* and *Sb* concentrations $(N_{As}+N_{Sb})$. Lattice scattering is neglected in above expression.

In this case, the relation $r=(\rho-\rho_{Sb})/(\rho_{As}-\rho_{Sb})$ holds for any value of n. This relation is approximately satisfied for the samples obtained from *AsSb*–3 and *AsSb*–4 crystals. In these samples electron concentration estimated by Hall measurement is nearly equal to the sum of *As* and *Sb* concentrations estimated by spectroscopic analysis. For the samples obtained from *AsSb*–1 and *AsSb*–2 crystals, n differs apprecibly from the sum of the impurity concentrations and the above relation does not hold entirely.

The sharp transition of experimental points shown in Fig. 5 is related with the depature of n from $(N_{As}+N_{Sb})$, therefore it may be due to precipitation of impurities. However, the reason why precipitation of impurity occurs easily in $(As+Sb)$-doped germanium at relatively low impurity concentration and the reason why precipitation occur at $r>0.2$ is not known.

It may be probable that there exists some interaction between *As* and *Sb* atom and as the result a new scattering mechanism is introduced together with ordinary lattice and impurity scattering. Teltow[9)] has suggested that a pairing between two donor ions like P^+ may form in silicon in analogy to hydrogen molecule. Though no evidence of such pairing between donors of the same kind has been reported, pair formation between *As* and *Sb* atom may be expected from the consideration of tetrahedral covalent radii of these impurities. Radius of *Sb* atom is larger than that of germanium, while Radius of *As* atom is smaller than that of germanium. If this is the case in $(As+Sb)$-doped germanium, pairing, hence additional scattering will appear markedly at $r\approx0.5$.

As for the magnetoresistance measurement the symmetry condition $b+c=0$ is satisfied fairly well for *Sb*-doped germanium and also for $(As+Sb)$-doped germanium with small r. The results for *As*-doped germanium show departure from this condition. However more acculate determination of $\theta_{\min}$ is required for discussing the symmetry condition since a slight change in $\theta_{\min}$ affects appreciably on the ratio c/d, therefore on the symmetry condition. However considering the experimental error in the present experiment it may be said that the symmetry condition is sutisfied in *As*- and *Sb*-doped germanium.

On the other hand, $|c/d|$ for *Sb*-doped germanium is obviously larger than that for *As*-doped germanium. This difference in $|c/d|$ may be due to the difference in relaxation time because magnetoresistance constants b, c and d are the functions of relaxation time and the shape of the energy surface, and conduction band structure seems to be the same in both *As*- and *Sb*- doped germanium. Moreover, $|c/d|$ depends only on the specific impurity, but not on the electron concentration (See Table III). So that, the difference in $|c/d|$ may be due to anisotropic character of impurity scattering. In the case of spherical energy surface, $|c/d|$ increases with decreasing anisotropy. If this tendency in $|c/d|$ is true even for germanium, scattering by *Sb* atom will be more isotropic as compaired with *As* atom. This conclusion seems to be related with the fact that electron spin resonance of *As*-doped germanium shows singlet and triplet, while *Sb*-doped germanium shows only singlet.

The author wishes to thank Dr. Z. Kiyasu, Dr. T. Niimi and Prof. Dr. T. Okada for their continual encouragements, Mr. T. Shimozaki for spectroscopic analysis, Mr. K. Ono for electron diffraction analysis and Mr. T. Takahashi for preparation of heavily doped crystals. He is also indebted to Dr. W. Sasaki of the Electrotechnical Laboratory for his helpful discussions.

References

1) K. Lark-Horovitz: Phys. Rev. **71** (1947) 374.
2) R. Bowers: Phys. Rev. **108** (1957) 683.
3) M. Pollak: Phys. Rev. **111** (1958) 798.
4) C. Goldberg, W. E. Howard: Phys. Rev. **110** (1958) 1035.
5) N. Holonyak etal: Phys. Rev. Letter **3** (1959) 167.
6) Y. Furukawa: J. Phys. Soc. of Japan **15** (1960) 730.
7) T. Okada suggested this method to the author.
8) C. Herring: B. S. T. J. **34** (1955) 237.
9) J. Teltow: "*Halbleiter Probleme*" III. W. Schottky, Vieweg, 1956.

JOURNAL OF THE PHYSICAL SOCIETY OF JAPAN, Vol. 16, No. 4, APRIL, 1961

Paramagnetic Resonance of Mn^{++} Associated with Impurities in Alkali Chlorides

By Yasaburo YOKOZAWA

Research Institute of Applied Electricity,
Hokkaido University, Sapporo

and Yukio KAZUMATA

Department of Physics, Faculty of Science,
Hokkaido University, Sapporo

(Received November 18, 1960)

The paramagnetic resonance absorption of Mn^{++} ions associated with the impurities of fluorine or divalent anions has been investigated in the single crystals of NaCl and LiCl. A resolved fine structure was observed in a "not quenched crystal" and it did not fade into a broad single line in contrast with the spectra of Mn^{++} ions which had been usually observed in alkali halides. The ground level splitting parameters have been determined in the spin Hamiltonian $DS_1^2+E(S_2^2-S_3^2)$ as follows: $D=(-420\pm1)\cdot10^{-4}\,\mathrm{cm}^{-1}$, $|E|=(65\pm1)\cdot10^{-4}\,\mathrm{cm}^{-1}$ for $Mn^{++}-F^-$, $D=(-511\pm5)\cdot10^{-4}\,\mathrm{cm}^{-1}$, $|E|=(25\pm5)\cdot10^{-4}\,\mathrm{cm}^{-1}$ for $Mn^{++}-X^{--}$, a manganese divalent anion pair, in NaCl, and $D=(-672\pm5)\cdot10^{-4}\,\mathrm{cm}^{-1}$, $|E|=(12\pm3)\cdot10^{-4}\,\mathrm{cm}^{-1}$ for $Mn^{++}-X^{--}$ in LiCl, the principal axes of the spin Hamiltonian being in nearly agreement with the cubic axes of the crystal. The large value of D suggests the existence of the strong attractive force between Mn^{++} and impurity ion.

§1. Introduction

As the electron spin resonance of paramagnetic ions is affected sensitively by their environment, the state around the paramagnetic ions may be investigated by the structure of the resonace lines. When divalent cations, such as Mn^{++}, are introduced in a monovalent ionic crystal, an equal number of positive ion vacancy may be produced by the principle of charge compensation, or the extra negative charges of divalent anion impurities such as O^{--} or S^{--}, if exist, may be compensated by the extra positive charge of the cations. Then, a Mn^{++} and vacancy may tend to pair with each other experiencing a Coulomb attraction. It may be also possible that a Mn^{++} ion attracts a divalent anion forming a manganese-anion pair, $Mn^{++}-X^{--}$, when the attractive force between them is strong. These circumstances will be investigated by paramagnetic resonance.

The fine structure of Mn^{++} ions in the single crystal of NaCl was observed by Schneider and Caffyn[1], for the first time, quenching the crystal from high temperature, although only a broad single line with a half-width of 400 gauss was observed before quenching[2]. Watkins[3] observed the several types of resonance spectrum with increasing temperature. He classified the spectra according to their appearance and studied the transformations among them. Spectrum I is a broad single line appearing before quenching, arising from Mn^{++} ions in an aggregated state. Spectrum II consists of 6 lines which become conspicuous above 250°C. This arises from isolated Mn^{++} ions which are free from any vacancy. Spectrum III is complex and observable in the temperature around 200°C, or at room temperature after quenching. This spectrum was successfully analyzed by Watkins and Walker[4], and Morigaki, Fujimoto and Itoh[5], assuming Mn^{++} ions associated with a vacancy bound in one of the near cation sites. This can be further divided into two types, one from the Mn^{++} ions with a positive ions vacancy at one of their nearest neighbor cation site, and the other with a vacancy in the next nearest neighbor cation site, designated by spectrum III_1 and III_2, respectively. It was found that spectrum III faded into I in several days after quenching at room temperature. Spectrum III was also observed for Mn^{++} ions in KCl and LiCl single crystals by Watkins[3] and Fukuda, Uchida and Yoshimura.[6],[7] Besides these spectra, Watkins observed spectrum IV, complex one which had lower intensity and larger splitting. He showed that this spectrum arised from Mn^{++} ions associated with a divalent negative impurity ion such as O^{--} for each Mn^{++} ion.

In the present work, different spectra from those described above were observed for Mn^{++} ions in NaCl and LiCl single crystals grown from a melt. All these spectra had fine structure before quenching and were stable at room temperature. The Mn^{++} ions responsible to these spectra are considered to be trapped on some special positions in the crystal, such as a nearest neighbor site with respect to impurities, forming Mn^{++}-impurity pairs. The spectrum from Mn^{++}-F^- pairs is reported in the previous paper[8]. In this report the details of analysis of this spectrum together with others will be given.

§ 2. Experimental Procedure

Mesurements were carried out by a conventional spectrometer, using a rectangular reflection cavity and a barretter for detection. A klystron 2K25 was frequency stabilized to the sample cavity at about 9 kMc/sec working at room temperature. The modulation frequency of the magnetic field was 260 c/s, and the detected signal from the barretter was amplified with a 260 c/s narrow band amplifier and then detected by a lock-in amplifier and recorded as the first derivative of the absorption curve. The magnetic field was produced by an electromagnet with a pole face of 12 cm diameter, 4 cm gap, and a exciting coil of about 10 ohms in D.C. resistance. The exciting current, about 5.5 amperes for 5000 gauss, was supplied through a current-regulator after the rectification of A.C. 100 volts by a semiconductor rectifier. The regulator consisted of power transistors and a chopper amplifier designed similar to that of Garwin[9], where the exciting current was regulated to within 10^{-4}. The magnetic field could be swept from 300 gauss to 6500 gauss continuously, and was measured by proton resonance; g vaule was determined by the comparison of the spectra with the resonance of di-phenyl picryl hydrazil in which $g=2.0036$.

The crystals studied were grown in air by the Kyropulos method from a melt into which about 0.001 mole fraction of $MnCl_2$ or MnF_2 had been added. The starting materials were of reagent grade purity of Kanto Chemical Company. The crystal was attached to the bottom of the cavity and an external magnetic field was rotated in the (001) plane of the crystal. Since LiCl was very hygroscopic, an evacuated cavity was employed.

§ 3. Analysis of the Spectrum

The Mn^{++} spectrum has been discussed in detail in many papers[10]. The spin Hamiltonian of Mn^{++} in a crystalline field can be written, including the hyperfine interaction, as

$$\mathscr{H}=g\beta \boldsymbol{H}\cdot\boldsymbol{S}+\mathscr{H}_{\rm cry}+\boldsymbol{I}\cdot A\cdot\boldsymbol{S}+\sum_j \boldsymbol{I}_j'\cdot A'S\,. \tag{1}$$

Here g is the spectroscopic splitting factor, β the Bohr magneton, $\boldsymbol{H}$ the external magnetic field and $\boldsymbol{S}$ the electronic spin of Mn^{++}. The third and forth terms represent the hyperfine interactions, where $\boldsymbol{I}$ is the nuclear spin of Mn^{++}, $\boldsymbol{I}_j'$ that of the j-th anion, A and A' are h.f. coupling tensors, and the summation is taken over the anions surrounding Mn^{++}. The effect of the crystalline field on Mn^{++} is described by $\mathscr{H}_{\rm cry}$ which can be written as

$$\mathscr{H}_{\rm cry}=DS_1{}^2+E(S_2{}^2-S_3{}^2)\,, \tag{2}$$

neglecting the terms quartic in S.

The crystalline field splitting caused by Eq. (2) can be calculated by a perturbation method and the results up to the second order calculation are given in the literature[10]. In this work, D was so large that a higher order approximation was necessary. The field strengths for resonance up to the third order approximation are given by next expressions.

$$\left.\begin{array}{lll}
\multicolumn{3}{l}{\text{For } \boldsymbol{H}/\!/\text{axis 1}}\\
\quad M=\pm 5/2\rightleftarrows\pm 3/2 & H=H_0\mp 4D+4E^2/H_0\pm 6DE^2/H_0{}^2\,, & \\
\quad M=\pm 3/2\rightleftarrows\pm 1/2 & H=H_0\mp 2D-5E^2/H_0\pm 33DE^2/H_0{}^2\,, & \\
\quad M=+1/2\rightleftarrows -1/2 & H=H_0\qquad -8E^2/H_0\,, & \\
\multicolumn{3}{l}{\text{For } \boldsymbol{H}/\!/\text{axis 2}}\\
\quad D \text{ should be replaced by} & \tfrac{1}{2}(3E-D)\,, & \\
\quad E \qquad\qquad\qquad\quad \text{by} & -\tfrac{1}{2}(D+E)\,, & \\
\multicolumn{3}{l}{\text{For } \boldsymbol{H}/\!/\text{axis 3}}\\
\quad D \qquad\qquad\qquad\quad \text{by} & \tfrac{1}{2}(-D-3E)\,, & \\
\quad E \qquad\qquad\qquad\quad \text{by} & \tfrac{1}{2}(D-E)\,. &
\end{array}\right\} \tag{3}$$

Here M is the component of the electronic spin in the direction of the applied magnetic field, and H_0 is $h\nu/g\beta$, ν being the klystron frequency.

The third term of Eq. (1) adds to these expressions a hyperfine structure. The anisotropy in A is small and A can be treated as a scalar quantity. Then the hyper-fine structure to be added to Eq. (3) is for the $M\rightleftarrows M-1$ transition,

$$-Am-\frac{A}{2H_0}\{I(I+1)-m^2+m(2M-1)\}\,, \tag{4}$$

m being the component of the nuclear spin of Mn^{++}.

The last term in Eq. (1) splits each line in a complex way. For example, 6 chlorine ions surrounding Mn^{++} which form a octahedron split a resonance line into $7^3=343$ components with $I'=3/2$ and these components may not be resolved, contributing only to the line width[11]. But for fluorine ions, as they have nuclear magnetic moments of 3 times larger than those of chlorine ions and $I'=1/2$ for their nuclear spins, the super-hyper-fine structure is so widely splitted and simple as to be observable. Tinkham[12] calculated the shifts and splittings of resonance lines due to this interaction, yielding the result,

$$A_s\sum_j I_{jz}+\mathrm{A}_p\sum_j I_{jz}(3\cos^2\theta_j-1)\,. \tag{5}$$

Here I_{jz} is the component of nuclear spin of F^-, $\pm\frac{1}{2}$ and θ_j the angle between the external magnetic field and the σ-bonding axis of Mn^{++}-F^-. A_s represents the contribution from the admixed fluorine $2s$ orbit and A_p that from $2p$ orbit and also a direct dipole-dipole interaction between Mn^{++} and F^-.

§ 4. Experimental Results

1) *The spectrum of Mn^{++}-F^- pair in NaCl.*

As reported in the previous paper[8], the complex spectrum of Mn^{++} was observed in the single crystal of NaCl which was grown from a melt into which about 0.001 mole fraction of $\mathrm{MnF_2}$ had been added. Each line of the spectrum was a doublet, coming from the super-hyperfine structure of a fluorine ion. This indicates, from Eq. (5) that there exists only one fluorine ion near a Mn^{++} ion, forming a Mn^{++}-F^- pair. The principal axes, 1, 2 3, were found to coincide with the cubic axes of the crystal, one of which was considered to be the direction of Mn^{++}-F^- bond. Although finely resolved doublet structures appeared when an external magnetic field was directed to [100] or [110], no resolved structures could be observed in other directions. This fact is explained by assuming the existence of two types of doublets which correspond to the plus and minus signs of E. $2\times3\times30=180$ doublets appear in the spectrum, 30 being the number of lines for each Mn^{++} ion.

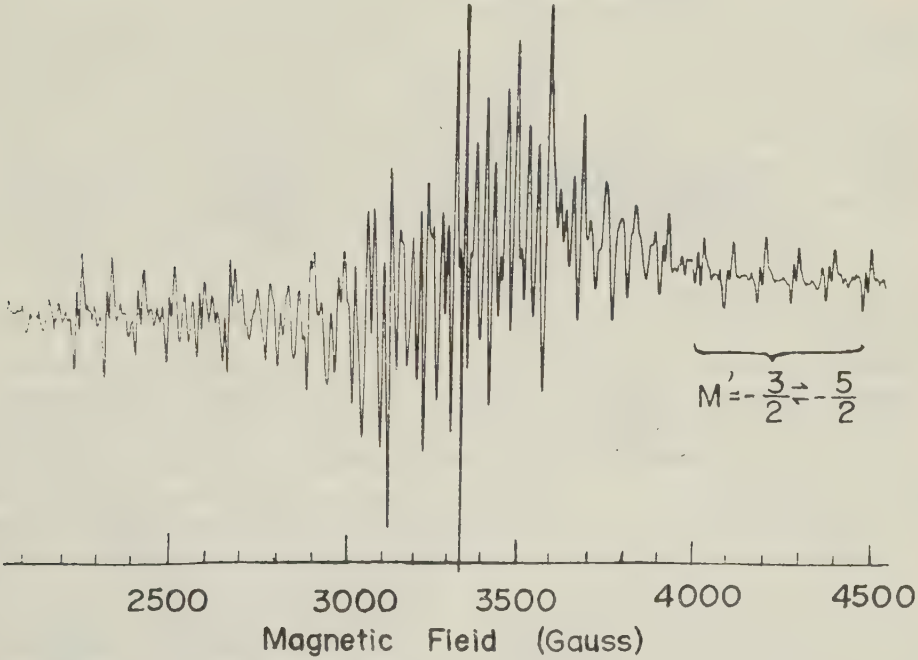

Fig. 1. The spectrum of $Mn^{++}-F^-$ in NaCl, the direction of an external magnetic field being parallel to [110] of the crystal. The transition $M'=-3/2\rightleftarrows-5/2$ for which $Mn^{++}-F^-$ direction is perpendicular to the magnetic field is designated in the figure, where M' is the magnetic quantum number of Mn^{++}. For the spectrum with $\boldsymbol{H}$//[100], see Fig 1 of the previous paper.[8]

The spectrum in [100] direction was already shown in Fig. 1 of the previous report[8]. Fig. 1 of this paper shows the spectrum in [110] direction. In this direction,

$$M'^{*}=(-3/2)\leftrightarrows(-5/2)$$

transition lines of Mn^{++} for which Mn^{++}-F^- bond is perpendicular to the external magnetic field appear separately from other lines as are designated in the figure. The designation of the quantum transitions of the spectrum lines in [100] direction shown in the previous paper was possible with the help of the spectrum in Fig. 1 of this paper. Spin Hamiltonian constants g, D, E and A were determined by the use of Eqs. (3) and (4). Super-hyper-fine coupling constants As and Ap were determined from both spectra of Fig. 1's of two papers.

2) *The Spectrum of Mn^{++}-X^{--} in NaCl.*

Most crystals of NaCl grown from a melt added with $MnCl_2$ had the same resonance spectra as the types I, II and III given in introduction. Among these crystals, there were some in which a different kind of spectrum appeared beside them. The intensity of this spectrum is different from crystal to crystal and in some crystals it is much stronger than those of the other types. Fig. 2 (a) shows the spectrum of this conspicuous one. The condition of the appearance of this spectrum is not yet clear, but it may have some relation with the time of melting before pulling up, the longer the time the stronger the intensity of this spectrum.

Spin Hamiltonian constants of this spectrum are determined as shown in Table I. As

---

[*] M' designates the magnetic quantum number of Mn^{++} for which $Mn^{++}-F^-$ bond is perpendicular to the external magnetic field, using the same notation as in Fig. 1 of the previous paper.[8]

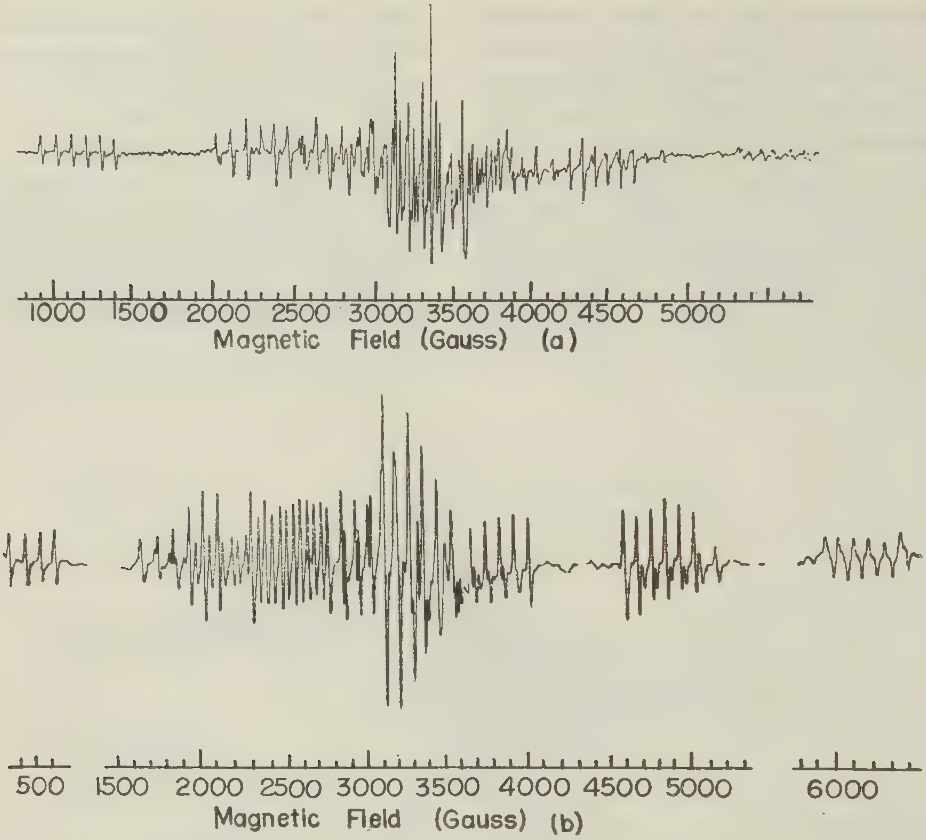

Fig. 2. The spectra of $Mn^{++}-X^{--}$ in the single crystals of (a) NaCl and (b) LiCl. In (a), the magnetic field is slightly misoriented from the principal axis of the spin Hamiltonian, distorting the resonance lines in the group on the highest field side. In (b), the sensitivity is about 3 times larger on the highest field side than on the other side of the spectrum.

these are in good agreement with those of spectrum IV, Mn^{++}-X^- pairs will be responsible to this spectrum.

3) *The spectrum of* Mn^{++}-X^{--} *in LiCl*

Although the spectrum of Mn^{++} ions in LiCl grown from a melt added with $MnCl_2$ was the same as that of type III, that from a melt added with MnF_2 had a different type, as shown in Fig. 2 (b). The principal axes of the spin Hamiltonian are nearly parallel to the cubic axes of the crystal respectively, and splitting parameters are given in Table I. The resonance lines in the group on the highest field side were always weaker than those on the lower field side and disappeared when the magnetic field was rotated from the direction corresponding to Fig. 2 (b) over 1 degree. This is similar to the spectrum discussed in (2), and is explained assuming that the principal axes make a small angle with the cubic axes of the crystal, the angular variation of the positions of resonance lines in the highest field group being larger than that in the lower field. As D is large in this spectrum, the third order perturbation terms of $\mathscr{H}_{\text{cry}}$ make the same order contribution to the second order terms and Eq. (3) is insufficient for the determination of the splitting parameters. However fortunately, as E is small, Eq. (3) is sufficiently accurate for the positions of the resonance lines of Mn^{++} for which the direction of Mn^{++}-F^- bond coincides with the direction of the magnetic field, and D can be calculated. On the other hand, the positions of the lines of other Mn^{++} for which Mn^{++}-F^- is perpendicular to the magnetic field are necessary for the determination of E. However, for this purpose the accurate positions of resonance lines themselves are not necessary but only the difference of positions of two kinds of lines are sufficient, so E can be determined also using

Table I. Spin Hamiltonian constants of Mn^{++} spectra studied in this work.

Crystals	g	A $(10^{-4}\,cm^{-1})$	D $(10^{-4}\,cm^{-1})$	$\lvert E\rvert$ $(10^{-4}\,cm^{-1})$	Axes 1, 2, 3	s.h.f.s. $(10^{-4}\,cm^{-1})$
$Mn^{++}-F^{-}$ in NaCl	1.9988 ± 0.0004	-83.2 ± 1.0	-420 ± 1	65 ± 1	cubic axes of crystals	$\lvert A_s\rvert=14.2\pm0.5$ $\lvert A_p\rvert=2.7\pm0.5$
$Mn^{++}-X^{--}$ in NaCl	2.0023 ± 0.0006	-81.0 ± 2.0	-511 ± 5	25 ± 5	nearly coincide with the cubic axes of crystals*	—
$Mn^{++}-X^{--}$ in LiCl	2.0016 ± 0.0004	-79.7 ± 2.0	-672 ± 5	12 ± 3		—

* Watkins[3)] determined the angle between the principal axes of the spin Hamiltonian and the cubic axes of the crystal to be 1.3° for $Mn^{++}-X^{--}$ in NaCl.

Eq. (3).

As will be discussed in the next paragraph, the small value of E is the evidence of the absence of a vacancy near a Mn^{++} ion. Therefore, the Mn^{++} ion is considered to locate near a divalent anion, forming a Mn^{++}-X^{--} pair.

Watkins considered that the most probable divalent negative ion X^{--} is oxygen negative ion.

The results are summurized in Table I.

§ 5. Discussions of the Results

1) *Mn^{++}-F^{-} pair in NaCl*

As described in § 4, Mn^{++}-F^{-} bond is considered to direct to one of the cubic axes of the crystal. Then a question arises why E is so large, in spite of the equivalence of axes 2 and 3. This can be answered assuming the existence of a vacancy locating in the next nearest neighbor cation site of a Mn^{++} ion perpendicular to the Mn^{++}-F^{-} direction as shown in Fig. 3 (a). The assumption of this model will be supported as follows. The fluorine ion as well as the chlorine ion locating between a Mn^{++} ion and a vacancy may be attracted to the Mn^{++} ion, yielding the quadratic terms in the electrostatic potential at the Mn^{++} ion site which reflect D and E of the spin Hamiltonian. Now, the quadratic part of the potential from a fluorine ion alone and that an from an attracted chroline ion plus a vacancy are represented by φ_1 and φ_2, respectively as follows,

$$\left.\begin{aligned}\varphi_1&=D_1X_1{}^2-(1/3)D_1\cdot r^2\,,\\ \varphi_2&=D_2X_2{}^2-(1/3)D_2\cdot r^2\,,\end{aligned}\right\}\tag{6}$$

where X_1 and X_2 are the components of r with respect to 1 and 2 axes respectively [see Fig. 3 (a)], r being the distance from Mn^{++}. Therefore, the total potential φ is represented as,

$$\varphi=\varphi_1+\varphi_2=D'X_1{}^2+E'(X_2{}^2-X_2{}^2)-(D'/3)r^2\,,\tag{7}$$

where

$$D'=D_1-\tfrac{1}{2}D_2\,,$$
$$E'=D_2/2\,,$$

D' and E' correlate to D and E of the spin Hamiltonian.

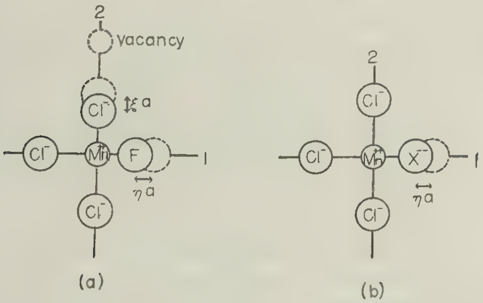

Fig. 3. The arrangement of the anions surrounding a Mn^{++} ion. The displacements of a foreign anion and chlorine ions around a vacancy are shown.

If F^{-} is absent, this model reduce to spectrum III_2. In this case, as $D_1=O$, $D_2=2E'$ corresponding to $\pm2\times65\times10^{-4}\,cm^{-1}=\pm130\times10^{-4}\,cm^{-1}$ and it is in good agreement with the value of spectrum III_2, in which $D=131\times10^{-4}\,cm^{-1}$,[3)] taking only the plus sign of E. In the case of the existence of a vacancy on axes 3, the sign is reversed.

The large value of D suggests the strong interaction between Mn^{++} and F^{-}. This interaction was estimated by Watanabe's theory[14)], following the similar procedure employed by Watkins[3)]. Watanabe calculated the splitting parameter D of Mn^{++}, when an axial crystalline field $V_{\mathrm{axl}}=cr^2Y_2{}^0\ (\theta\varphi)$ existed around a Mn^{++} ion, as follows,

$$D=-9.90\varDelta^2\times10^{-10}+3.62M'\varDelta10^{-5}\,cm^{-1}\,,\tag{10}$$

$$M'=(1/4)(5/\pi)^{1/2}c^2\langle r^2\rangle=-eD'\langle r^2\rangle/3hc\,,\tag{11}$$

Here $\langle r^2\rangle$ is the average value of r^2 for Mn^{++}

ions, that is $\langle r^2\rangle=0.4\times10^{-16}$ as determined from Hartree functions and M' complex expression depending upon the overlap of the wave functions, for which we take the value $0.2\,\mathrm{cm}^{-1}$ as it does not affect the results largely. Now, D' is calculated on the stand-view of a point charge model shown in Fig. 3 (a), ξ and η being the fractional displacements of anions,

$$D_1=-9e\eta/2a^3\cdot\alpha\,, \tag{12}$$

$$D_2=-(3+72\xi)e/16a^3\cdot\beta\,. \tag{13}$$

Here, α and β are corrections to the point charge model and represent the magnitude of the effectiveness of the crystalline field due to the covalency of the ions or the overlapping of the wave functions.

At first, we will consider the case when a F^- ion is absent. In this case, the splitting parameter is expressed by $D=2E=130\cdot10^{-4}$ cm^{-1}, corresponding to $\Delta\sim3500\,\mathrm{cm}^{-1}$ by Eq. (10). On the other hand, Eqs. (11) and (13) give $\Delta\sim280\beta$, taking $\xi=0.048$, the same value as Watkins[3)] employed in his explanation of spectrum III_2, β becomes the order of 12, the same result as Watkins. Now, we will proceed to D. As As and Ap of this spectrum are nearly equal to that of the Mn^{++} in NaF single crystal[13)], the Mn^{++}-F^- distance is considered to be close to the Na^+-F^- distance in NaF, resulting $\eta=0.17$*. Then, from Eqs. (8), (11) and (12), Δ is calculated as $400\alpha-3500/2$, where the result mentioned above is used for D_2. Observed value of D, $-460\times10^{-4}\,\mathrm{cm}^{-1}$ on the other hand, gives $\Delta\sim11000$ by Eq. (10). Thus $\alpha\sim30$, showing the existence of the strong atractive force between Mn^{++} and F^-.

2) *Mn^{++}-X^{--} pair in NaCl and LiCl*

The model of a Mn^{++}-X^{--} pair is shown in Fig. 3 (b), η being the fractional displacement of a X^{--} ion. This model gives

$$\left.\begin{array}{l} D'=-3e/2a^3(1/(1-\eta)^3+3\eta)\cdot\alpha\,, \\ E'=0\,, \end{array}\right\} \tag{14}$$

α having the same meaning as that in the case (1). If the Mn^{++}-X^{--} distance is 2.20 Å, the sum of the radii of both ions where X^{--} is assumed to be oxgen negative ion, then $\eta=0.22$ for NaCl and $\eta=0.14$ for LiCl, a similar calculation as above gives for Mn^{++}-X^{--} in NaCl $\alpha\sim4$, and in LiCl $\alpha\sim7$. On the contrary, if the ion is assumed not to displace at all, $\eta=0$, as assumed by Watkins[3)], the calculation gives $\alpha\sim11$ for NaCl and $\alpha\sim9$ for LiCl. As a Mn^{++}-X^{--} pair is probably considered to make a union which is independent of circumstances, η may not differ largely for both crystals, so the fractional displacement may be small, giving $\eta\sim0$.

§ 6. Concluding Remark

The results of the paramagnetic resonance of Mn^{++}-Impurity in NaCl and LiCl have been described. The splittings of resonance spectra are large, indicating that there exists a strong attractive force between Mn^{++} and impurity ions. Moreover, the resolved fine structure is observed in a " not quenched crystals " and is stable in the room temperature, in contrast to the spectra of Mn^{++} not associated with a impurity as obserbed by other investigators[1)–7)].

The present authors wish to express their sincere thanks to Drs. H. Watanabe and S. Ogawa for their valuable discussions and to Mr. Y. Nakano for the construction of the current regulator for the electromagnet.

References

1) E. E. Schneider and J. E. Caffyn: *Defects in Crystalline Solids* (The Physical Society, London, 1955) 74.
2) K. Oshima, H. Abe, H. Nagano and M. Nagusa: J. Chem. Phys. **23** (1955) 1721.
3) G. D. Watkins: Phys. Rev. **113** (1959) 79.
4) G. D. Watkins and R. M. Walker: Bull. Am. Phys. Soc. Ser. II, **1** (1956) 324.
5) K. Morigaki, M. Fujimoto and J. Itoh: J. Phys. Soc. Japan **13** (1958) 1174.
6) K. Fukuda, Y. Uchida and H. Yoshimura: J. Phys. Soc. Japan **13** (1958) 971.
7) H. Yoshimura: J. Phys. Soc. Japan **15** (1960) 435.
8) Y. Yokozawa: J. Phys. Soc. Japan **15** (1960) 1131.
9) R. L. Garwin: Rev. Sci. Inst. **29** (1958) 223, 900.
10) B. Bleaney and K. W. H. Stevens: Reports on Progress in Physics. **16** (1953) 108.
K. D. Bowers and J. Owen: *ibid.* **18** (1955) 304.
W. Low: *Paramagnetic Resonance in Solids* (Academic Press, New York and London, 1960) p. 113.
11) A. F. Kip, C. Kittel, R. A. Levy and A. M. Phys. Rev. **91** (1953) 1066.
12) M. Tinkham: Proc. Roy. Soc. **A, 236** (1956) 535, 549.
13) W. Hayes and D. A. Jones: Proc. Phys. Soc. London **71** (1958) 503.
14) H. Watanabe: Prog. Theor. Phys. **18** (1957) 405.

---

* This was suggested by R. G. Shulman. We are very grateful to him.

JOURNAL OF THE PHYSICAL SOCIETY OF JAPAN Vol. 16, No. 4, APRIL, 1961

Ferromagnetic Resonance Absorption of Single-Crystal Thin Films of Nickel

By Masao KURIYAMA, Hirokage YAMANOUCHI and Sukeaki HOSOYA

The Institute for Solid State Physics, University of Tokyo,
Shin-Ryudo-cho, Minato-ku, Tokyo, Japan

(Received November 26, 1960)

Single-crystal thin films of nickel having the (100) and the (111) orientations were epitaxially grown by deposition in vaccum onto heated rock salt and zincblende. By electron diffraction, these films were examined to be 100 A to 500 A in size of crystallites without appreciable strain.

By the experiment of ferromagnetic resonance absorption at room temperature, three magnetic quantities were measured at the same time: the saturation magnetization, the crystalline anisotropy and the Landé splitting factor. The first quantity was found to be almost independent of the thickness of films (100 A to 1000 A) and its magnitude was 350 or 400 in gauss, respectively for the (111) or the (100) orientation. This difference may be ascribed to the stress in films. The second one varied in the range between -2×10^4 and -5×10^4 erg/cm^3 and the third was 2.2 in average.

The crystalline anisotropy causes the shift of resonance line as the film is rotated in its plane. Besides, it was found that the more perfect orientation a film has, the narrower is the resonance line.

§ 1. Introduction

There have been a number of experimental works on the magnetic properties of ferromagnetic polycrystalline films. Polycrystalline films, however, give the complicated magnetic properties, which have not yet been completely explained. These properties generally are closely related to both the crystalline anisotropy and the magnetostriction due to the stress in films. Single crystal films, therefore, were used in the present work.

The epitaxial growth of single crystalline films was reported for nickel and iron deposited in vacuum onto the heated cleavage face of rock salt by Shirai[1], and for nickel onto that of zincblende by Miyake and Kubo (Takagi)[2]. Recently Boyd[3] has prepared single-crystal films of Ni, Fe, Ni-Fe and Ni-Co alloys and measured their magnetic crystalline anisotropy with a torque meter. The experiment of ferromagnetic resonance absorption, however, has not so far been carried out for single crystalline films.

In the present work, from the measurement of ferromagnetic resonance absorption three magnetic quantities, such as the saturation magnetization, the cubic crystalline anisotropy constant and the Landé splitting factor, could be obtained at the same time. Single crystal films always give a reproducible and sharp resonance line in spite of the possible contamination and of the unavoidable inhomogeneity such as film granularities, defects and the non-uniformity of thickness.

§ 2. Experimentals

a. *Preparation of specimens*

Nickel films were prepared by deposition in vacuum onto heated single crystal surface of NaCl and ZnS by the method similar to that of previous workers[1),2)]. Rock salt and zincblende crystals were cleaved parallel to the (100) and the (110) planes respectively and placed in a chamber which was evacuated to a pressure of about 3×10^{-6} mm Hg. The substrate was heated to about 550°C for NaCl and to about 400°C for ZnS and held there for about an hour and then cooled slowly to a certain temperature between 430° and 530°C for NaCl and between 230° and 380°C for ZnS. Then nickel was evaporated from a tungsten filament on which nickel was coated by electroplating[4]. In this case, pure nickel (99.99%) supplied from the Sumitomo Mining Co. was used as an electrode. In order to examine whether the impurities appearing in an electroplating process influence the resonance field, other portions of the pure nickel could manage to be evaporated from a tungsten filament in the usual way applicable to metals which are not apt to be alloyed with tungsten. But this way of evaporation gave the same results in resonance absorption as the former way. The former method, therefore, was used throughout the whole experiment.

Evaporation was made in a pressure of 3×10^{-6} mm Hg with the speed of less than 2 A/sec. A polished quartz plate was placed in a chamber as a thickness monitor. The thickness of the evaporated film was measured by an optical multi-beam interference method of Tolansky. Films used for measurements were 20 A to 1300 A in thickness.

b. *Microwave apparatus*

The microwave apparatus of a standard type for X-band was used. With a phase sensitive detector, the differential curve of absorption was automatically recorded at room temperature.

Two types of cavities were used for the two different geometrical settings of a crystal as will be shown in Fig. 3: a. the static field is applied parallel to the surface of a specimen and b. the static field perpendicular to the surface, while the microwave field is in the surface.

The strength of the magnetic field was measured by a flux meter which was calibrated by NMR. The frequency of microwave was determined in each measurement by a sample $MnSO_4\cdot H_2O$, as a standard which has the Landé splitting factor of 2.00[5)]*.

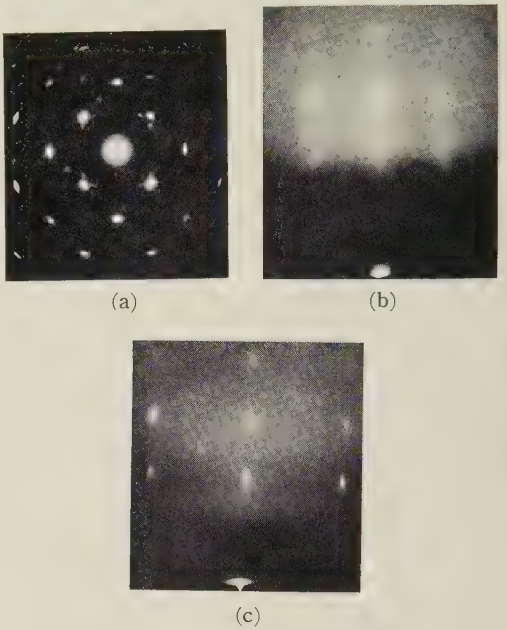
(a) (b)

(c)

Fig. 1. Electron diffraction patterns.

a. Transmission patterns from (100) film stripped off from NaCl.

b. Reflection pattern from (100) film on NaCl with [100] azimuth.

c. Reflection pattern from (111) film on ZnS with [$\bar{1}$10] azimuth.

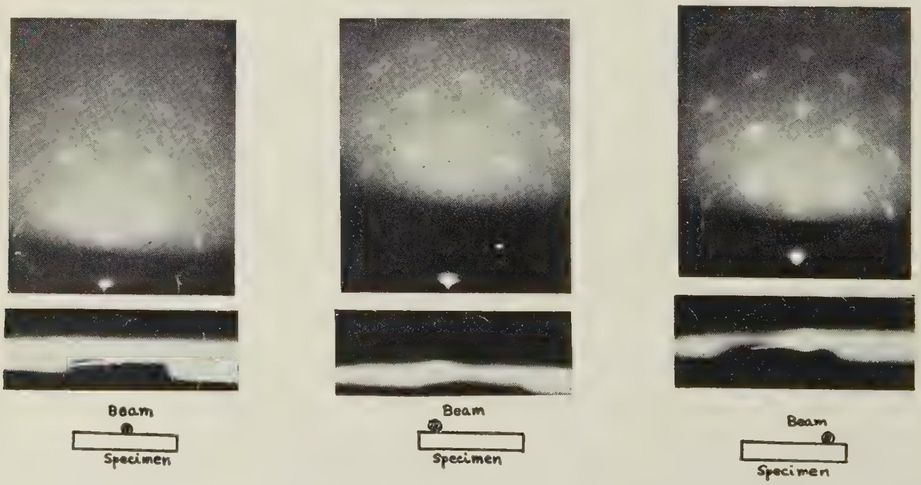

Fig. 2. Electron diffraction patterns from the surface at different positions. Reflection patterns are shown above, and the shadows of specimen with a trace of incident beam are shown in the middle, and the schematic figures of the shadows are shown at the bottom.

---

* In the precise measurement of g value, DPPH should be used as a standard, which has the width of about 3 gauss. As $MnSO_4\cdot H_2O$ has the width of about 300 gauss, Δg can be estimated to be ±0.03 at most. In the present experiment, however, such a magnitude of error is too small to be discussed.

§ 3. Crystal Structure of Thin Films

Films were all examined by electron diffraction: Portions of nickel film on NaCl were removed from a substrate by floating them onto a water surface and were studied by transmission method. Some of them were also studied by reflection method as they were on the substrate. Films on ZnS were all examined by reflection method.

As shown in Fig. 1, films on rock salt have the (100) plane parallel to a substrate surface and either the [100] axis or the [110] axis parallel to the cube edge of the substrate. On the other hand, films on zincblende show the (111) plane parallel to a substrate face with the [110] axis parallel to the [100] axis of the substrate, as also shown in Fig. 1.

In the case of nickel on rock salt the diffraction patterns often show the twin spots due to the microtwins in the (111) planes of the crystal. Magnetic measurements were done for the specimens which were considered to be slightly twinded at worst.

If electron beams deflected by a few minutes impinge the crystal surface at different positions, as shown in Fig. 2, the diffraction patterns show that, exactly speaking, films should consist of many crystallites having slightly different orientations. Applying the line breadth analysis method[6] to the transmission patterns such as Fig. 1, it is found that these crystallites have the crystal size (coherent size) of 100–500 A and no appreciable strain. These results, therefore, implies that a film consists of " mosaic " blocks of a few hundred angstroms having the mis-orientation of at most a few minutes of arc.

A lattice constant agrees well with that of bulk material.

§ 4. Results of Ferromagnetic Resonance

In a ferromagnetic resonance experiment of a single crystal, resonance conditions are given as follows[7),8)]:

a. When the plane of specimen is (100), namely in the case of films on rock salt,

$$\omega_a{}^2=\gamma^2[H_a+4\pi I_s+(K/2I_s)3 \\ +\cos 4\theta)][H_a+(2K/I_s)\cos 4\theta]\ , \qquad (1)$$

$$\omega_b{}^2=\gamma^2[H_b-4\pi I_s+2K/I_s]^2\ , \qquad (2)$$

Here θ is the angle between the [001] axis and the applied dc field.

b. When the plane of specimen is (111), namely in the case of films on zincblende,

$$\omega_a{}^2=\gamma^2[H_a+4\pi I_s-K/I_s]H_a\ , \qquad (3)$$

$$\omega_b{}^2=\gamma^2[H_b-4\pi I_s-4K/3I_s]^2\ . \qquad (4)$$

In the above expressions the subscripts a and b correspond to the two different geometrical positions shown in Fig. 3a and b. ω is the frequency of the microwave and γ is related to the Landé splitting factor g as $\gamma=ge/2mc$. I_s is a saturation magnetization, K, the first order anisotropy constant and H, the resonance field for each case. The second order anisotropic effect and the magnetostriction effect are both neglected here. The latter effect will be discussed later in § 5.

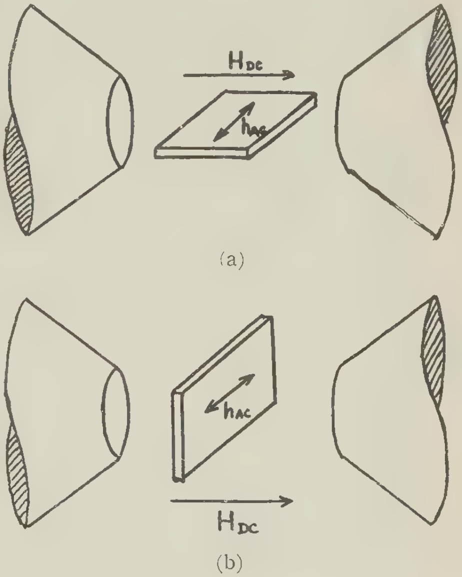

(a)

(b)

Fig. 3. Two different geometrical settings of a crystal.

a. The static field is applied parallel to the surface of film.

b. The static field is applied perpendicular to the surface of film.

In order to obtain three quantities such as the saturation magnetization, the anisotropy constant and the Landé splitting factor at the same time, single crystal films are all measured in two positions as shown in Fig. 3.

Being rotated around the normal of a film in the static magnetic field, the (100) film deposited onto rock salt clearly gives the shift of resonance line, which has the four-fold symmetry as shown in Fig. 4a. Such a symmetry is explained by a term of crystalline anisotropy in equation (1). This phenomenon

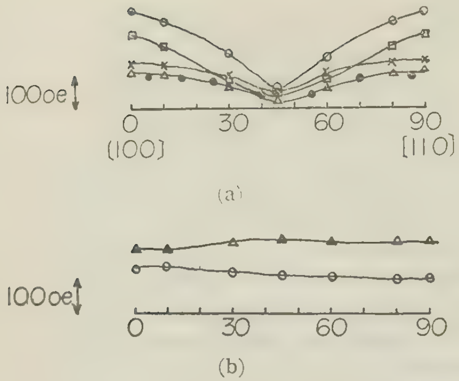

Fig. 4. Shift of the resonance field. Ordinate represents the field direction referred to the crystallographic axis. Frequency of microwave is about 9000 Mc, and the resonance field are about 1000 and 1600 oe. in strength, respectively for (100) and (111) films. Various marks correspond to the specimens with different thickness.

a. (100) Ni on NaCl.
b. (111) Ni on ZnS.

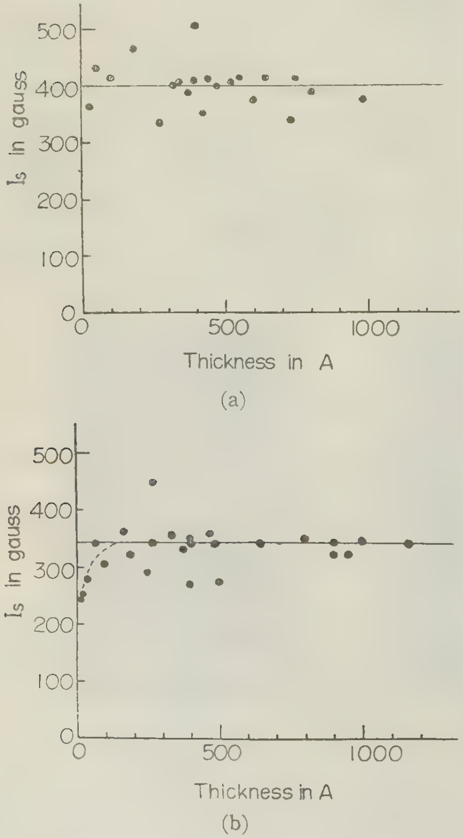

Fig. 5. Variation of the saturation magnetization with the thickness of films.

a. (100) Ni on NaCl.
b. (111) Ni on ZnS.

may be considered to provide the evidence that, even if in some cases the twin crystals exist as a minor part in film, not only the anisotropy constant but also the other magnetic quantities can be regarded as those from a single crystal having, as a whole, the (100) orientation. From the amplitude of the periodic change of field shift, the anisotropy constant is estimated to be -2×10^4 to -5×10^4 erg/cm^3, assuming the magnetization of 400 gauss, and agrees with the values obtained below. On the other hand, the (111) film made on zincblende gives no appreciable shift of the resonance line, as shown in Fig. 4 b.

According to either a pair of (1) and (2) or that of (3) and (4), respectively for the (100) and the (111) films, the magnitudes of the saturation magnetization, the cubic crystalline anisotropy constant and the Landé splitting factor can be obtained from the observed fields in two positions and are plotted against the thickness of films in Figs. 5, 6 and 7. The

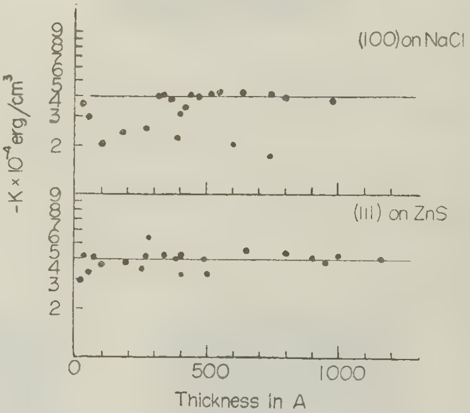

Fig. 6. Variation of the anisotropy constant K with thickness of films.

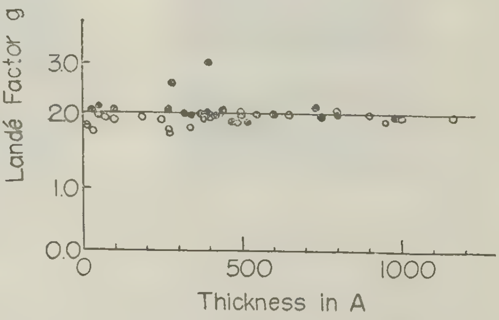

Fig. 7. Variation of the Landé splitting factor g with the thickness of films. Open circles stand for (111) Ni on ZnS, and solid circles for (100) Ni on NaCl.

magnitude of the first is almost constant for various thickness of films, but is found to be 350 and 400 in gauss, respectively for the (111) and the (100) orientations. This difference may be attributed to the stress induced in films as will be discussed in § 5. The anisotropy constant varies in the range between -2×10^4 and -5×10^4 erg/cm³. The value of the Landé splitting factor is obtained to be 2.2 in average.

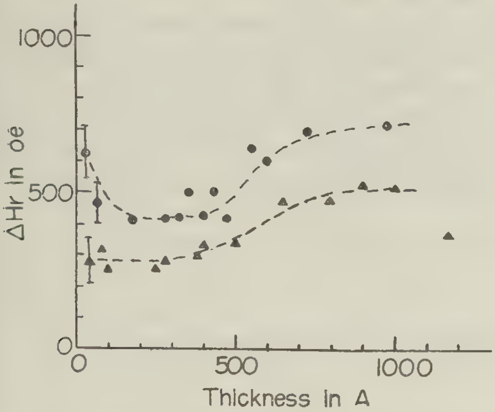

Fig. 8. Half value width of the resonance field against the thickness of films. Circles stand for (100) Ni on NaCl, and triangles for (111) Ni on ZnS.

The half value width of the resonance line is also plotted against the thickness of films in Fig. 8. Usually the polycrystalline film gives broader line (above 700 oe.) than the present specimens do. From the viewpoint of the epitaxial growth, it can be said that crystals grow well if they are not so thick, and moreover, that they give better orientation on zincblende than on rock salt. In fact, the line width of resonance is larger on rock salt than on zincblende and is smaller in the range of thickness of 100 A to 500 A for films on both substrates. It is, therefore, concluded that the broadening of the resonance line depends on the perfectness of orientation in films and hence an observed line consists of many lines shifted by the anisotropy in crystallites with different orientations.

§ 5. Discussions

As described in § 4, the stress in a film may be responsible for the difference of the values of magnetization between films on rock salt and those on zincblende. Since the equations in § 4 contain neither the second order anisotropy effect nor the magnetostriction effect which is more important, the contribution should be discussed of the latter to the resonance field.

If a stress exists in a film, the correction due to magnetostriction must be taken into consideration for the equations in § 4. Since real films may be under stress in a rather complicated way, this correction cannot be estimated exactly. Here we will simply assume that the stress is radially symmetric in the plane of film, and will roughly calculate the order of magnitude of the correction terms, using the general formulae by Macdonald[8].

For the (100) film, the correction term with the order of magnitude of $+\lambda_{[100]}T/I_s$ is inserted in the left side bracket in (1), and $-\lambda_{[100]}T/I_s$ is in (2). For the (111) film, $+(\lambda_{[100]}-\lambda_{[111]})T/I_s$ is inserted in the left side bracket in (3) and $-\lambda_{[111]}T/I_s$ is in (4). Here $\lambda_{[lmn]}$ is the magnetostriction in the $[lmn]$ direction and T, the stress. If T is positive, the stress is tensile.

With these corrections of magnetostriction, the field of resonance becomes larger for the parallel field case and smaller for the perpendicular field case than for those cases without magnetostriction. In other words, if the equations in § 4 without magnetostriction corrections are used for the films with magnetostriction, the magnitude of the saturation magnetization becomes smaller than the true value. Of course, the value of the splitting factor also changes.

If the difference between the value of magnetization obtained from the bulk material and that from the present thin film can be attributed entirely to the magnetostriction effect and besides the magnetostriction constants are assumed to be the same as those for the bulk material, it is derived from the above mentioned calculation that the stress with the order of magnitude of $+10^7$ to $+10^9$ dyne/cm² should be present in films on both kinds of substrates. Such a stress in the film yields the elastic strain of 10^{-5} to 10^{-3}, for Young's modulus of nickel is the order of 10^{12} dyne/cm².

Because the present stress is tensile, the spots in the electron diffraction patterns should be not only broadened but also shifted to one side. Even the elastic strain of 10^{-3}, however, cannot be detected by the electron diffraction camera available at present, because the shift falls within the experimental error.

If the strain in the film could be found by a high resolution electron diffraction camera, the values of the saturation magnetization could have become larger than the values obtained in § 4 and the difference caused by the kinds of substrates would have vanished. The origin of such stress was not investigated in the present work, because we did not try to measure the variation of the resonance field after stripping a film from a substrate and annealing.

The authors wish to express their sincere thanks to Prof. H. Abe and Miss H. Shirai for the use of the microwave equipment.

References

1) S. Shirai: Proc. Phys. Math. Soc. Japan **19** (1937) 937.
2) S. Miyake and M. Kubo (Takagi): J. Phys. Soc. Japan **2** (1947) 15.
3) E. L. Boyd: IBM Journal of research and development **4** No. 2 (1960).
4) L. O. Olsen, C. S. Smith and E. C. Crittenden, Jr.: J. Appl. Phys. **16** (1945) 425.
5) H. Kumagai, K. Ono, I. Hayashi, H. Abe, J. Shimada, H. Shono and H. Ibamoto: Phys. Rev. **83** (1951) 1077.
6) M. Kuriyama, K. Kohra and S. Takagi: J. Phys. Soc. Japan **12** (1957) 151. M. Kuriyama: ibid. **15** (1960) 1426.
7) C. Kittel: Phys. Rev. **73** (1948) 155.
8) J. R. Macdonald: Proc. Phys. Soc. (London) **A 64** (1951) 968.

JOURNAL OF THE PHYSICAL SOCIETY OF JAPAN, Vol. 16, No. 4, APRIL, 1961

Specific Heat of Ti_2O_3

By Shoichiro NOMURA, Tatsuyuki KAWAKUBO
and Taketoshi YANAGI

Physics Department, Tokyo Institute of Technology
Oh-okayama, Meguro, Tokyo

(Received December 5, 1960)

A measurement of the specific heat of Ti_2O_3, prepared by the method of powder metallurgy, was carried out in the temperature range from 50° to 250°C, under the pressure of 10^{-4} mm Hg. A modified method of measurement by the conduction-type calorimeter was adopted, and its reliability of measurement was described in connection with the method of calculation. A broad anomaly of specific heat was observed near 180°C and the amount of anomalous heat was 36 cal/mol, which was smaller than Naylor's result. Some discussions about the anomaly of specific heat were presented.

§ 1. Introduction

Several investigations have been reported about an anomalous behavior of Ti_2O_3 in the temperature range from 160° to 200°C. The lattice parameters of this crystal, which has the corundum-type structure, change markedly in this temperature region,[1),2)] but no symmetry change is observed[3)]. An abrupt change in the magnetic susceptibility,[1),4),5)] accompanied by a marked change in the electrical conductivity, has been observed near the transition temperature[6)].

It has been suggested from the result of measurement of magnetic susceptibility that an antiferromagnetic ordering would be present below the transition temperature. Shirane and coworkers, however, concluded from their neutron-diffraction data that the antiferromagnetic ordering seems to be excluded[7)]. A new model, recently proposed by Goodenough, is favourable to this anomaly in Ti_2O_3[8)].

An anomalous specific heat has been detected by Naylor using the drop method[9)]. This method is not considered to be suitable to give the temperature dependence of heat capacity and so Naylor did not show any explicit curve of the anomalous specific heat near the transition temperature. We have, therefore, examined the temperature dependence of the specific heat of Ti_2O_3 by using a conduction-type calorimeter. In this paper, our measuring method and the results on the specific heat of Ti_2O_3 will be described.

§ 2. Experimentals

a) *Specimen*

The specimen was prepared by the method of powder metallurgy. A mixture of fine powder of highly purified Ti and $3TiO_2$ was pressed into a pellet. This was placed in a graphite crucible, inside of which was covered with a molybdenum sheet, and fired at 1500°C under the pressure of 10^{-4} mm Hg for six hours in a graphite-resistor vacuum furnace. After firing, the pellet was crushed into powder and this was sintered again by the same process. The final product was dark violet in colour. In order to examine the completion of the solid-state reaction, the X-ray powder diffraction photograph was taken by using CuK_α at room temperature. Fig. 1 shows the obtained pattern, where the indices are referred to the hexagonal structure. This pattern coincides with that of the corundum-type structure and the lattice parameters obtained from our data are in good agreement with the former results[1),2)]. In the case that the specimen was fired at 1200°C, the X-ray diffraction pattern showed a few extra-lines in addition to the broad Ti_2O_3 diffraction lines.

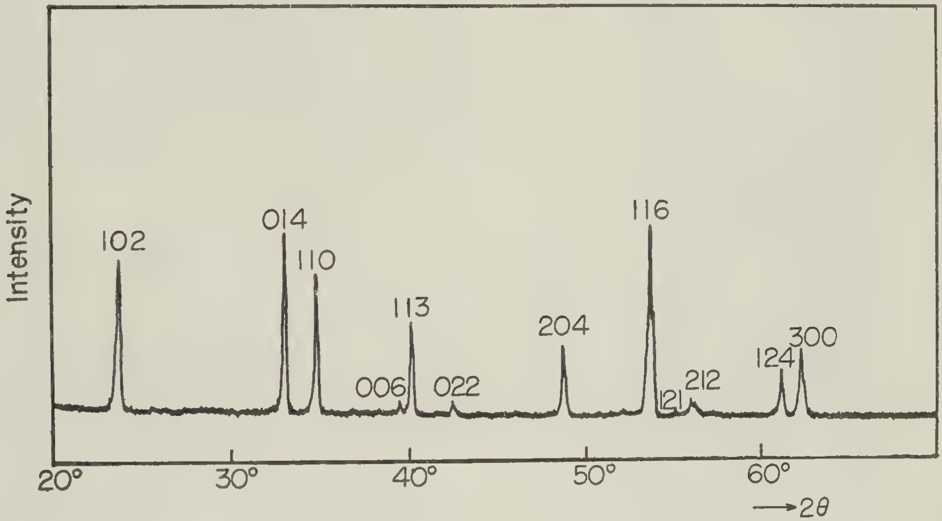

Fig. 1. X-ray diffraction pattern of Ti_2O_3.

b) *Apparatus for the specific heat measurement**

The adopted method was of the conduction type, in which the thermo-electromotive force of the differential thermocouple was recorded when the current of the furnace was varied in a definite manner[10)]. The main part of the calorimeter is shown in Fig. 2. The powder sample is put in a container S, which is made of a thin sheet of nickel. This container is surrounded by a thick outer case C made of a nickel block, and separated from the latter by fine alumina rods R. T_1 is a Pt-Pt 13%Rh thermocouple of 0.2 mmϕ for measuring the temperature of the sample and T_2, T_3 for measuring the temperature difference between the container S and the outer case C. To get a good thermal contact between T_2 and S, T_2 is bound to S at a definite position on its surface with a fine Pt wire. T_3 is inserted into a narrow hole bored in the outer case C. F is a nichrome-resistor furnace to supply heat to the sample and the case C. The heat capacity of the furnace is large owing to its thick alumina tube. In our conduction-type method, however, the temperature difference between S and C is not necessary to be kept constant, and so the large heat capacity is rather favourable for the stable measurement. Surrounding the furnace F, a set of cylindrical sheets of stainless steel D₁, D₂ are used for thermal shields. The pressure in the vessel V is kept under 10^{-4} mm Hg during the measurement in order to prevent the sample from oxidation. The rate of heating of the sample is kept nearly constant, about 1°C/min, by a program control of the furnace input-voltage.

---

* An automatic recording of the measurement was carried out by Y. Murakami and its details will be reported in future.

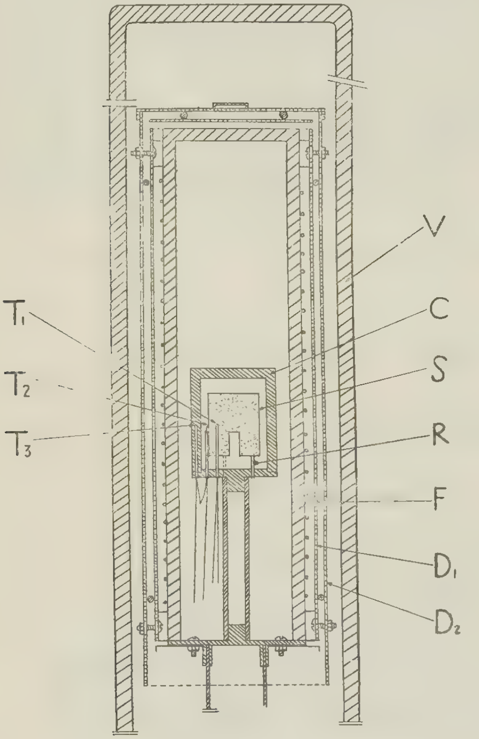

Fig. 2. The main part of the apparatus for the specific heat measurement.

c) *Measuring method*

The masses and the specific heats of the sample and the container S are denoted by m, m_0; $C(\theta)$, $C_0(\theta)$ respectively, where θ represents the absolute temperature. If θ_e is the temperature of the outer case C, the amount of heat which is transfered from C to S during the time interval Δt, can be represented by a function of θ and $\theta_e-\theta$, as $Q(\theta, \theta_e-\theta)\Delta t$. Then a following relation holds between them.

$$\{mC(\theta)+m_0C_0(\theta)+\delta(\theta)\}\frac{\Delta\theta}{\Delta t}=Q(\theta,\theta_e-\theta)\,, \quad (1)$$

where $\Delta\theta$ is the temperature increase during the time interval Δt; $\delta(\theta)$ is a correction term, which is responsible for the heat capacity of the holding rods, the parts of the themocouples inside the outer case C, and the heat conduction through them. The function Q may generally be written as $K(\theta)\{(\theta_e-\theta)-(\theta_e-\theta)_0\}$, where the suffix zero means the value obtained in thermal equilibrium and $K(\theta)$ is a coefficient of thermal transfer between the container and the outer case[10]. Supposing the thermal transfer is mainly due to the radiation, $K(\theta)$ will be proportional to θ^3 [11]. Now Eq. (1) becomes to

$$mC(\theta)+m_0C_0(\theta)+\delta(\theta)$$
$$=K(\theta)\frac{\Delta t}{\Delta\theta}\{(\theta_e-\theta)-(\theta_e-\theta)_0\}\,. \quad (2)$$

Here let us consider the measurement are carried out three times as follows; the first one is for the sample concerned, the second for a standard sample, of which the specific heat is well known in the present temperature range, and the third for the container alone. If the successive experiments are denoted as 1, 2, 3 respectively, the following equations are obtained:

$$m_1C_1(\theta)+m_0C_0(\theta)+\delta(\theta)$$
$$=K(\theta)\left[\frac{\Delta t}{\Delta\theta}\{(\theta_e-\theta)-(\theta_e-\theta)_0\}\right]_1\,, \quad (3)$$

$$m_2C_2(\theta)+m_0C_0(\theta)+\delta(\theta)$$
$$=K(\theta)\left[\frac{\Delta t}{\Delta\theta}\{(\theta_e-\theta)-(\theta_e-\theta)_0\}\right]_2\,, \quad (4)$$

$$m_0C_0(\theta)+\delta(\theta)=K(\theta)\left[\frac{\Delta t}{\Delta\theta}\{\theta_e-\theta)-(\theta_e-\theta)_0\}\right]_3\,. \quad (5)$$

Subtractions (5) from (3) and (4) give

$$m_1C_1(\theta)=K(\theta)A_1\,,$$
$$A_1=\left[\frac{\Delta t}{\Delta\theta}\{(\theta_e-\theta)-(\theta_e-\theta)_0\}\right]_1$$
$$-\left[\frac{\Delta t}{\Delta\theta}\{(\theta_e-\theta)-(\theta_e-\theta)_0\}\right]_3\,, \quad (6)$$

$$m_2C_2(\theta)=K(\theta)A_2\,,$$
$$A_2=\left[\frac{\Delta t}{\Delta\theta}\{(\theta_e-\theta)-(\theta_e-\theta)\}_0\right]_2$$
$$-\left[\frac{\Delta t}{\Delta\theta}\{(\theta_e-\theta)-(\theta_e-\theta)\}\right]_3\,. \quad (7)$$

From these equations, we get $C_1(\theta)$ as follows;

$$C_1(\theta)=\frac{m_2A_1}{m_1A_2}\cdot C_2(\theta)\,. \quad (8)$$

For the relations (3), (4) and (5) to hold simultaneously, the conditions in each measurement

1, 2, 3 should be kept as same as possible; for example, the pressure in the vessel V, the mounting situations of the container and the thermo-couples, the increasing rate of the temperature, etc..

To see how these situations are realized, the measurements for two alumina samples different in mass were carried out, and the relations (6) and (7) were checked. In this case the substances denoted by the suffixes 1 and 2 are both alumina and $m_1=12.75$ g, $m_2=14.02$ g. Fig. 3 shows the values of $A_1/C_1(\theta)$ and $A_2/C_2(\theta)$ in an arbitrary scale and their ratio obtained from the measurements. Provided the conditions stated above are satisfied, this ratio should be constant, m_2/m_1, in the whole range of the temperature. Our result shown in Fig. 3 is just like that. Further, $K(\theta)$ is seemed to vary as θ^{-3} above 90°C. The deviation from θ^{-3} below 90°C seems to be due to the predominance of the heat conduction through the rods and the thermocouples.

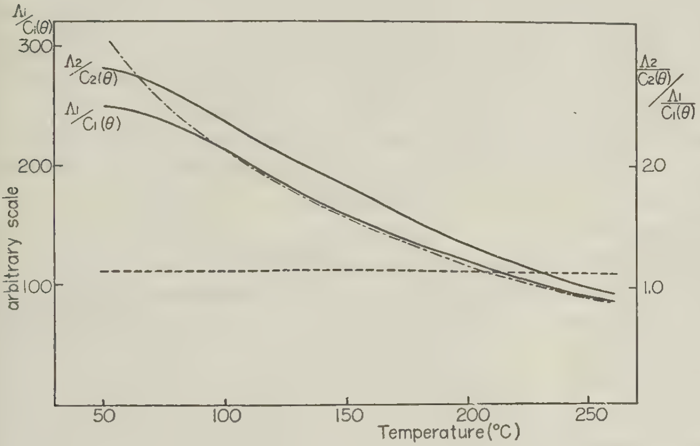

Fig. 3. The calibration characteristics for Al_2O_3 powder. The full lines show the temperature dependences of $A_1/C_1(\theta)$ and $A_2/C_2(\theta)$, the dashed line their ratio, which is nearly constant and equal to $m_2/m_1=1.102$. The hyphenated line represents θ^{-3} curve which is plotted so as to coincide with curve at 100°C.

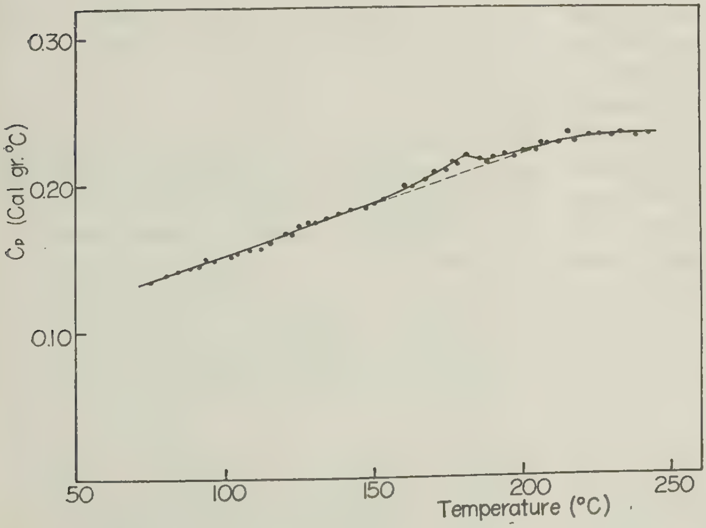

Fig. 4. Specific heat of Ti_2O_3.

§ 3. Results and Discussions

The specific heat of Ti_2O_3 in the temperature range from 50° to 250°C is shown in Fig. 4. A small anomaly is observed near 180°C, the anomalous heat being calculated as *ca* 36 cal/mol. The measurement was carried out under the pressure of 10^{-4} mm Hg. When the pressure was of the order of 10^{-2} mm Hg, a rather large amount of anomaly, over 100 cal/mol, could be observed. The samples, which had extra lines in addition to those of Ti_2O_3 itself in the X-ray analysis, also showed a large specific heat anomaly. These facts suggest that the heat of oxidation might additively be observed in the measurement of the specific heat, if one did not take care of the removal of oxygen in the vessel.

Naylor[9] made the heat-content measurement of Ti_2O_3 by the drop method at temperatures as high as 1750°K. The sample used was prepared by the carbon-reduction of titanium dioxide (the chemical analysis showed 99.4% Ti_2O_3). In his method, the sample was enclosed in a platinum-rhodium alloy capsule during the measurements. The capsule, after being filled with the sample, was evacuated free of air, filled with helium, and sealed-off with platinum. In his paper, he stated that he had found an anomalous heat of about 215 cal/mol near 473°K, but the determination of the transition temperature was difficult and considered to be accurate only to about 20°K.

Comparing our result with Naylor's, following points are noticed;

(1) Naylor's method is considered to be rather superior than ours for determining the mean absolute value of the specific heat, but our method is considered to superior for observing temperature dependence of the specific heat near the anomalous point.

(2) In our case the anomalous heat spreading over the temperature range from 160° to 200°C was observed. This fact corresponds to Naylor's remark that the selection of the transition temperature was difficult in his heat-content measurement. The absolute values of the specific heat in two cases agree well at 200°C, but the amounts of the anomalous heat at the transition show a large discrepancy. This discrepancy may be due to the effect of oxidation of the sample. The small contents of the impurities, further, may play a large role for it, as in the case of the electrical conduction phenomena.

Hitherto, many investigations have been carried out for the properties of Ti_2O_3, and it is supposed that the transition should be caused not by the magnetic ordering but by a change of the bonding character between the cations Ti^{3+} near the transition temperature. In recent papers about oxides[8], Goodenough has pointed out that the electron-pair-bond formation between cations Ti^{3+} plays an important role for the transition of Ti_2O_3 and that only a non-cooperative transition can occur. Any quantitative estimation about the specific heat anomaly of Ti_2O_3 can not be made from Goodenough's model, because of its qualitative nature. But it may be supposed that a large anomoly would not be expected for this substance, because of the lack of the magnetic ordering, the non-cooperative character of the transition and the small lattice deformation by the electron-pair-bond formation. It may be considered that the specific heat anomaly is composed of the electronic term, which is due to the thermal excitation of electrons between fairly splitted levels t_{2g} which would contribute to the semiconducting character below the transition, and the lattice-vibration term which is affected by the electron-pair-bond formation. As Ti_2O_3 is still semiconducting above the transition, a large electronic specific heat anomaly would not be expected near the transition. Noticing that the specific heat anomaly is only about 47 cal/mol even in barium titanate[12], in which the change of the lattice parameters is the same order as that of Ti_2O_3 and the cooperative transition takes place, our results on Ti_2O_3 seems to be reasonable for the electron-pair-bond model.

The authors wish to express their sincere thanks to Prof. S. Sawada for helpful discussions and continual encouragement.

References

1) A. D. Pearson: J. Phys. Chem. Solids **5** (1958) 316.
2) R. E. Newnham: M. I. T. progr. Rep. **XXV** (1959) 39.
3) F. Halla: Z. anorg. allgem. Chem. **184** (1929) 421.
4) M. Foëx and J. Wucher: C. R. Acad. Sci. (Paris) **241** (1955) 184.
5) P. H. Carr and S. Foner: J. Appl. Phys. Suppl. **31** (1960) 344S.
6) F. J. Morin: Phys. Rev. Letters **3** (1959) 34.
7) G. Shirane, S. J. Pickart and R. E. Newnham: J. Phys. Chem. Solids **13** (1960) 167.
8) J. B. Goodenough: Phys. Rev. **117** (1960) 1442.
9) B. F. Naylor: J. Amer. Chem. Soc. **68** (1948) 1077.
10) S. Sawada: Rep. Inst. Sci. Tech. Univ. Tokyo **10** (1956) 107.
11) A. E. De Barr: Rev. Sci. Instr. **19** (1948) 569.
12) S. Sawada and G. Shirane: J. Phys. Soc. Japan **4** (1949) 52.
13) M. Foëx and J. Loriens: Compt. Rend. **226** (1948) 901.

Journal of the Physical Society of Japan, Vol. 16, No. 4, April, 1961

Regrowth of Germanium from Molten Indium or Lead

By Masami Tomono

Central Research Laboratory, Hitachi, Ltd., Kokubunji, Tokyo

(Received December 21, 1960)

A single crystal of n-type germanium was alloyed with indium on its (111) plane and the resulting regrown layer of p-type germanium was observed. When the specimen was cooled at an intermediate speed, dendritic crystal is produced on the flank of the pan-shaped regrown layer. In the case of cooling at very low speed, steps bounded by (111) plane are produced also on the flank. Any of these may be indicative of the growth due to screw dislocation. On the other hand, when the specimen was cooled rapidly, growth due to surface nucleation takes place on the bottom while dendritic growth due to screw dislocation is produced on the flank. As to a specimen made by alloying $Pb-As$ alloy on a p-type germanium pellet and subsequently cooled at low speed, several layers of striations are observed on its cross-section. By this method, it is possible to make observations on the state in which misfit grain boundary is formed in the course of regrowth and also on the anomaly of regrowth produced around a blowhole and other foreign materials.

§ 1. Introduction

Many studies have been made on the shape of regrown germanium crystal produced when the germanium substrate is alloyed with indium, lead or other low-melting-point metal[1),2),3),4)]. As to the cooling process of the temperature cycle during alloying, if the cooling speed is high, uniform regrown layer is produced whether the solid-liquid interface coincides to the (111) plane or not. In the case of intermediate speed, jagged regrowth surface results and inclusion of solvent metal is present in the regrown layer. For a lower speed, it is known that the regrown layer is again uniform[2)]. The author made detailed observations on the regrown germanium layer obtained by alloying indium to an n-type germanium crystal. In an earlier report[5)], the results of the observations were presented on the regrowth pattern on the flat and smooth bottom area of the pan-shaped regrown layer obtained by the rapid cooling of specimen during alloying. Subsequently cooling speed was varied and the corresponding changes in regrowing state of p-type germanium were observed on the sloping flank of the pan-shaped regrown layer. Further, cross section of the regrown layer was made at the bottom of the pan and the layer was made at the bottom of the pan and the layered structure was examined. Finally, $Pb-As$ alloy was alloyed to a p-type germanium single crystal and the resulting distinct layered structure was examined, then the state in which grain boundary is formed by misfitting in the regrown germanium or the growing state of crystal around a blowhole was observed.

§ 2. Experiment

2.1 *Dendritic regrowth*

A single crystal of n-type germanium was heated at about 590°C with a small piece of indium on it, and subsequently cooled at a speed of about 20 deg/sec. The resulting regrowth of the germanium is shown in Fig. 1. In the flat and smooth area on the bottom seen slightly below the center of the figure there exist many spot-shaped patterns, and these correspond to the abnormal regrowth pyramids described in the earlier report[5)]. On the sloping surface of the pan-shaped concave, the dendritic lamellae grow, each of which is bounded by a straight line parallel to [110] axis. In the vicinity of the lamella edge, there exists an upward projection and with this as a center an upward growth takes place. Fig. 2 shows relatively large dendritic lamella appeared on the upper edge of the pan-shaped concave of the specimen which was made by alloying indium at 540°C and subsequently cooling at an intermediate speed—about 60 deg/sec. On the large lamella parallel to the (111) surface of the germanium substrate, there exist in a large number the so-called abnormal regrowth pyramids described in the earlier report[5]. From this, it is known that the regrowth in the direction perpendicular to the lamella has taken place. A specimen obtained under nearly the same condition in the case of Fig. 1 was cleaved with a pincette, and the cleaved surface is shown in Fig. 3. Initially, the dendrites grow along the direction nearly perpendicular to the (111) plane of the substrate surface, but after some progress of the growth, a lateral growth parallel to the same (111) plane takes place dominantly. The hexagonal plates seen layered in Fig. 1 correspond to the latter. Further at the root of the dendrite, it is possible that indium is left pent up in the regrown layer when the adjacent growing dendrites unite together[2]. At the end of the regrown layer located slightly left to the center, upward projections are observed. They may be the same as those on the edges of lamellae of Fig. 1. Fig. 4 shows the cross-sectional view of a specimen which was cooled at a speed as low as 0.3 deg/sec and cleaved again with a pincette. In this case, stepped regrown layers, each bounded by the {111} planes, exist on the sloping flank. At the boundary between the flat area on the bottom and the steps on the flank, there exists a moat which was formed by the delay of the growth as is already known[6]. We see in Fig. 1 that such a moat is also formed by the cooling at a higher speed. When a specimen is kept at 520°C and subsequently cooled rapidly by pouring oil, an extremely thin p-type regrown layer is produced. This specimen was ground at an angle of 18° with its surface and the cross section was etched for about 1 minute with the etchant composed of 40% concentrated nitric acid (48%) and 20% deionized water. The result is shown in Fig. 5. In parallel to the (111) plane of the substrate single crystal surface, regrown layer about 2.7 μ thick is produced. In this case, a striation exists in the regrown layer in parallel to the p-n boundary on the bottom. The regrown lawer on the sloping surface seen in the right-hand part grows in parallel to the p-n boundary at first, but from the part corresponding to the striation on the bottom fine dendritic growth takes place. At the part where the regrown layer on the bottom and that on the sloping surface meet each other, no regrown layer exists at all. The dendritic regrowth pattern on the sloping surface observed under an electron microscope is shown in Fig. 6. The specimen was prepared by rapid cooling by pouring oil as in the case of Fig. 5. In the present example, it is assumed that the temperature was lowered down to below the melting point of the indium within about 0.1 sec. The observations by the electron microscopy were made by replica method using the platinum-palladium shadowing. On the surface of each lamella fine regrowth patterns are seen and they are indicative of the progress of layered growth around some growth centers and in the direction approximately perpendicular to the photograph. From the width of shadow, it was ascertained that the height of these fine growth steps is about 200Å. At the part where the upper and lower adjacent lamellae unite with each other, the growth pattern of the upper lamella overflows and spreads over the lower lamella. Fig. 7 shows the dendritic growth pattern on the less sloped area of the specimen which was prepared by the similar rapid cooling. The photograph shows clearly that the upper and lower steps unite with each other to make the growth pattern continuous. The black irregular pattern is caused by the collapse of replica at the part where intricate structure exists. This area may be a valley caused by the delay of crystal growth due to some obstacles. Blowholes or impurities attached to the crystal surface may be such obstacles. In Fig. 8, the photograph of the part at which the flat and smooth surface on the bottom and the sloping surface of the regrown layer meet together is shown on a specimen prepared similarly by rapid cooling. From the area where the end of the growth step of the lamella in the upper right and the flat and smooth surface on the bottom come in contact with each other, fine concentric growth steps develope locally. In the other part on the bottom it is distinctive that the growth pattern due to the surface nucleation described in the earlier report[5] appears unlike the case of Fig. 1. At the part where the stepped crystal and the bottom surface meet together there is a gap and this gap corresponds to the part which lacks regrown layer on the edge of the flat and smooth surface of Fig. 5.

2.2 *Striation*

In Fig. 5, an example was given to show the striation appeared on the germanium layer regrown from the indium melt. The author prepared a specimen by alloying 97%*Pb*−3%*As* alloy to a *p*-tpye germanium pellet at about 800°C and subsequently cooling the system at a low speed of 0.2 deg/sec. The specimen was then cut and the cross-section was etched with an etchant of 60% concentrated nitric acid and 40% fluoric acid (48%) and observed under a microscope. By this method, it was possible to observe the striation in the regrown germanium layer. An example of this case is

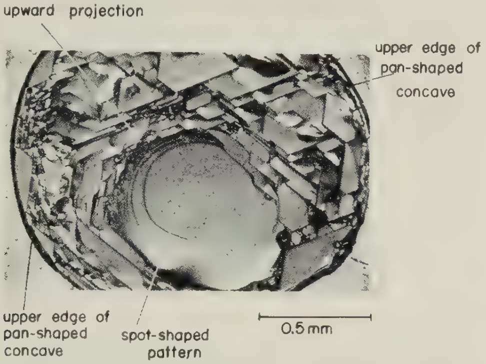
upward projection
upper edge of pan-shaped concave
upper edge of pan-shaped concave
spot-shaped pattern
0.5 mm

Fig. 1. Regrown germanium (intermediate cooling speed)

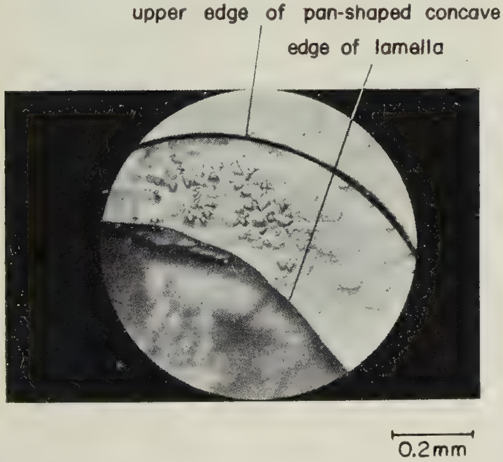

Fig. 2. Relatively large dendritic lamella appeared on the upper edge of the concave (intermediate cooling speed)

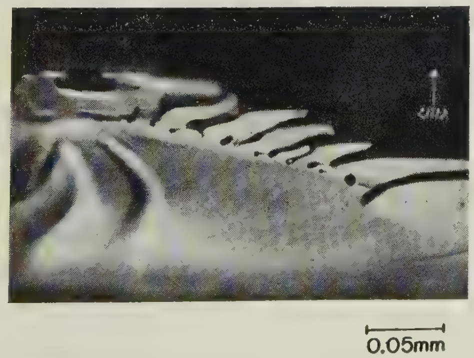

Fig. 3. Cleaved surface of the dendritic regrown layer (intermediate cooling speed)

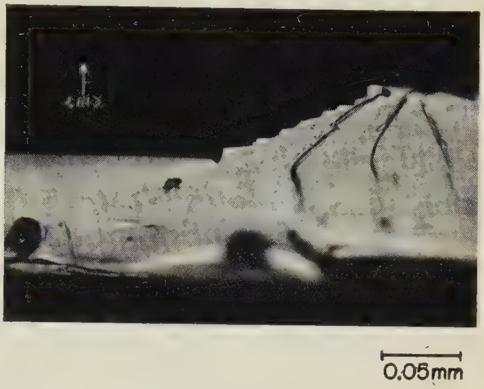

Fig. 4. Cleaved surface of the regrown layer (low cooling speed)

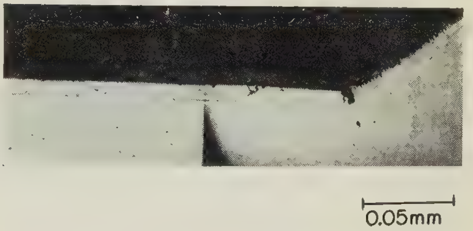

Fig. 5. Cross section of the regrown layer (rapid cooling)

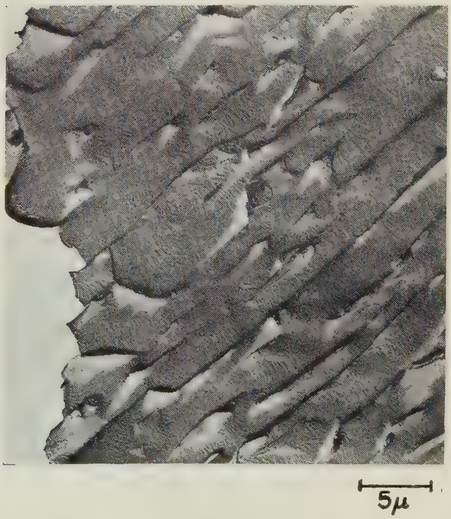

Fig. 6. Dendritic growth pattern developed on the sloping surface of the regrown layer (rapid cooling, electron microscope)

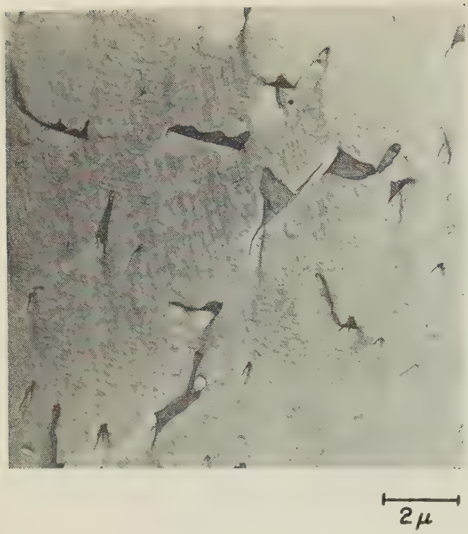

Fig. 7. Growth pattern on the less sloped surface of the regrown layer (rapid cooling, electron microscope)

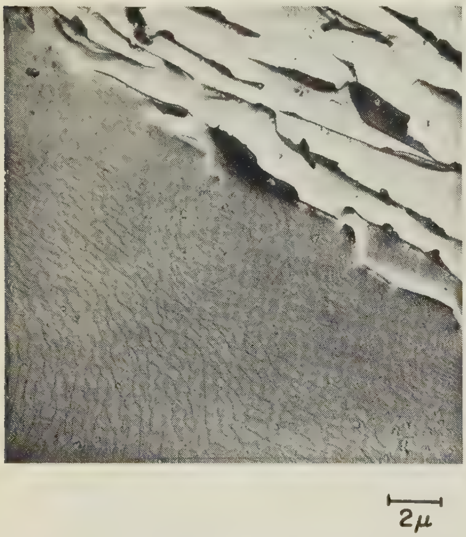

Fig. 8. Growth pattern at the part where the sloping surface and the bottom surface meet together (rapid colling, electron microscope)

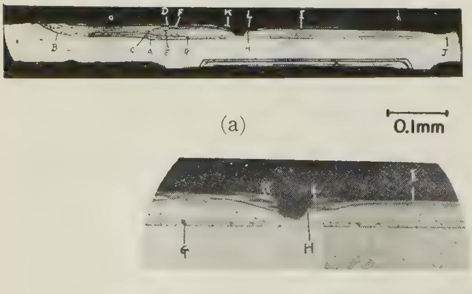

(a)

(b)

Fig. 9. Striations in the *n*-type regrown layer

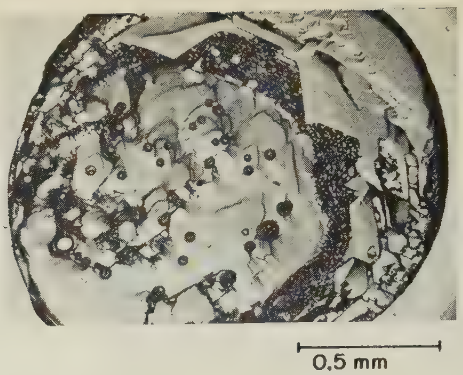

Fig. 10. Growth pattern in the neighborhood of a blowhole in the *p*-type regrown layer (intermediate cooling speed)

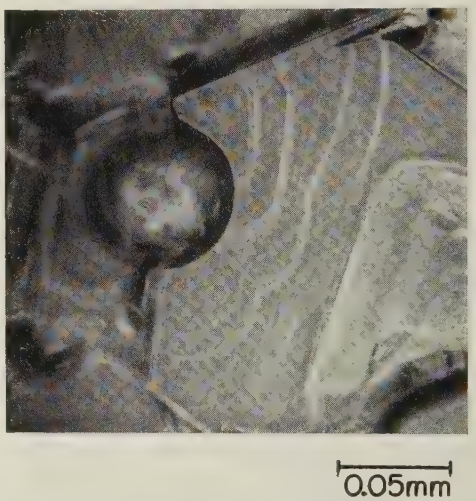

Fig. 11. Composite growth patterns in the neighborhood of the *p*-type regrown layer (intermediate cooling speed)

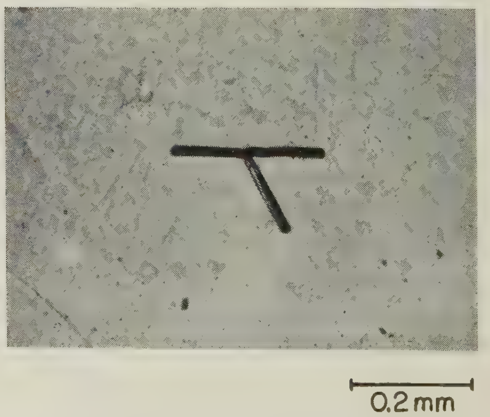

Fig. 12. Special defect in the single crystal grown from germanium melt

given in Fig. 9(a) and (b). (b) is close-up of the central part of (a). A striation in the lower *n*-type regrown layer develops in parallel to *p-n* boundary and the formation of regrown layer is relatively complete. On the contrary, many imperfect structures are seen in the upper regrown layer. In the early stage of the alloying, the molten $Pb-As$ alloy had arrived just at the point A in the figure. At the time when the surface tension decreased due to somewhat elevated temperature, drop of the melt spread to a position B. It is for this reason that the quantity of *p*-type germanium dissolved into the $Pb-As$ melt is smaller in the part between A and B than A and J, and hence stepped structure is caused in the *p-n* boundary at A. The *p-n* boundary between A and J is parallel to the (111) plane. A *p-n* boundary on the flank crossing at J aslant with the above-mentioned boundary will be another {111} plane. On the other hand, the sloping parts of the step at A and B are deviated from such {111} plane macroscopically. At the beginning of the regrowing process, regrowth had taken place nearly in parallel to the *p-n* boundary also in the neighborhood of A, but due to the presence of such a slight non-uniformity as point C (which is probably a fine blowhole or foreign material), difference in growing state had been caused between the right- and left-hand sides and from this part a misfit plane CD had developed. On the right of CD, the slope of the growing surface increases gradually and approaches the {111} plane which makes an angle of 70°32′ with the (111) plane on the bottom.

Further on the right, another misfit plane EF is present against the (111) plane parallel to the bottom. In the part where a fine blowhole G exists, the growth is markedly delayed at first compared with the surrounding part, but once passing over that blowhole the growth makes up the delay resulting in the flat and smooth striation. In the neighborhood of such a large blowhole as H, distinct non-uniformity in growth is seen. At the part neighboring to the bottom of the blowhole, growth of crystal is badly delayed as shown by the striations FHI similarly to the case of G. But, thereafter the growth is made so rapidly that at KL it is rather protruding than in the other part. One end of the *n*-type regrown layer B, in the left-hand part of the figure has grown to have the same height as other parts, but the other end J in the right-hand part is poor in growth and makes a concave.

2.3 *Regrowth in the neighborhood of a blowhole*

We found in Fig. 9 that in the neighborhood of a blowhole the growth is more distinct than in the other areas. To examine this in more detail, Fig. 10 is presented. The specimen was prepared in nearly the same way as in the case of Fig. 1. In the part around a relatively large blowhole, frequently the growth is more advanced than in the other. Some of the growth patterns are developed from a part around the blowhole as a center. Fig. 11 shows an example of the growth patterns developed around a blowhole. The specimen in this case was prepared also in nearly the same way as in the case of Fig. 1.

A terrace seen on the right of the blowhole represents the top surface surrounded by [110] axes of the abnormal growth pyramid described by the author in the earlier report[5]. With at least two centers around the blowhole, two groups of growth patterns are seen. Similar growth patterns are present also in the left-half neighborhood of the blowhole where the growth is delayed compared with the terrace. This suggests that the growth of the terrace and the concentric growth arround the blowhole are independent of each other.

2.4 *Special defect in the single crystal grown from germanium melt*

In Fig. 12, the special defect frequently found in the single crystal which was grown from the germanium melt is shown.

As described in the earlier report, this defect badly affects the electric characteristics of the *p-n* junction[7]. The cause for the formation of this defect will be discussed later.

§ 3. Discussion

3.1 *Regrowth of germanium*

The author pointed out in the earlier report that the regrowth of *p*-tpye germanium from the indium melt is due to the screw dislocation in some cases and the surface nucleation in the others. From the results of that study it follows presumably that for the growth rate exceeding some 20 μ/sec the crystal growth can be caused by the surface nucleation but in the case of lower rate screw dislocation is responsible for the growth[5]. With reference to the experimental results discussed in §2, when the heated specimen of Fig. 5 was cooled rapidly by pouring oil, its temperature might be lowered down to below the melting point of the indium within 0.1 sec. Since the flat and smooth bottom area of the p-type regrown layer is 2.7 μ thick, the growth rate is roughly 30 μ/sec and therefore there is a possibility of growth due to the surface nucleation. In Fig. 5, there is a great difference in the growth patterns between the flat and smooth surface of the bottom and the sloping surface of the flank. Referring to Fig. 8 for the similarly prepared specimen, a planar growth pattern not clear in symmetry exists in the lower left part of the photograph. This is probably indicative of the growth caused by the surface nucleation as described in the earlier report[5]. On the other hand, the growth in the sloping part of Fig. 5 is dendritic clearly. Referring to Fig. 6, each dendritic lamella has some growth centers clearly. In this case, it is assumed that the growth takes place with several very adjacently existing screw dislocations as a center. In the case of Fig. 5, which of the surface nucleation or screw dislocation is responsible for the growth may be dependent on the condition of the substrate crystal surface. In the present case, the flank area is deviated from the (111) plane macroscopically, but it seems microscopically to be formed by bunching together of a great number of fine growth steps surrounded by two {111} planes crossing at an angle of 70°32′ with each other. At the begining, the growth progresses with the concave corner of the step as center and consequently, the regrown layer develops in parallel to the sloping surface of the substrate[2] as seen from Fig. 5, but after a while the new crystal planes thus grown from the adjacent concave corners meet with each other at the convex corner and cause the misfit boundary there. It is quite possible that by the repetition of such process many screw dislocations are produced. It is known that the dendrite is liable to be produced if the temperature gradient from inside the solid towards the solid-liquid interface is larger than that from the interface towards inside the the liquid, especially if the gradient inside the liquid is negative[8],[9],[10]. This condition will be satisfied in case the specimen was cooled rapidly by pouring oil. When the abovementioned two conditions are satisfied simultaneously, the dendritic growth may take place due to the screw dislocations. On the other hand, on the flat and smooth (111) plane of the bottom relatively uniform growth occurs and therefore, the screw dislocations are not produced so much. It is probably for this reason that even when the cooling speed was made extremely high at the end of the cooling period the dendrite due to the screw dislocation is difficult to grow and rather the surface nucleation is responsible for the growth. In comparison with the above, the growing speeds in the cases of Figs. 1, 3, 4, 10 and 11 are extremely small and for these cases it will be doubtless that the growth is effected by the screw dislocation. It has been known that under the special conditions lamellar dendrite is produced[8], and the large lamellar crystal grown on the upper edge of the panshaped concave of Fig. 2 will be a dendritic lamella caused by the presence of twin planes[11],[12]. The growth of this lamella to its thickness direction is effected surely by the screw dislocation because the abnormal growth pyramids described by the author in the earlier report[5] are present in a large number on the surface of the lamella. The mechanism with which dislocation array is produced on such a lamella has already been described[13], and the array conceivably plays the role as the center of the abnormal regrowth. Finally, the discussion on the case of Fig. 9 will be given as follows: For such a markedly slow cooling, it is quite easy to consider that the crystal growth is effected by the screw dislocation[5]. The heat of melting of germanium into the molten indium is 11.9 kcal/mol[14],[15], while that of germanium into lead is 19.2 kcal/mol with reference to the phase diagram G_e-P_b system[16]. Generally, the activation energy for nucleation, ΔF_c, is given by[17].

$$\Delta F_c=\left(\frac{\Delta H}{2N}\right)^2\frac{1}{kT\ln\alpha} \qquad (1)$$

where ΔH is the heat of melting, N is the Avogadro's constant, k is the Boltzmann's constant, T is the absolute temperature and α is the saturation ratio of germanium in the melt. Denoting by I the rate of formation of critical nuclei, we have[17].

$$I=I_0\exp(-\Delta F_c/kT) \qquad (2)$$

I_0 is a constant, and for the growth of germanium from the indium melt, it is expressed as:

$$I_0 \approx 10^{25}\ \mathrm{cm}^{-2}\ \mathrm{sec}^{-1} \qquad (3)$$

As the saturation ratio α exceeds 1.4, the growth due to surface nucleation becomes prominent as described in the earlier report. The growing speed of the crystal in this case is about 20 μ/sec[5]. While, in the case of lead the heat of melting is extremely large compared with indium as described above, and consequently, for the crystal growth to be effected mainly by the surface nucleation, the saturation ratio must be larger than in the case of indium. From this, it follows probably that the possibility of the germanium crystal being grown by the surface nucleation from the melt having lead as its main component is badly poor, especially when the specimen was cooled at considerably low speed as in the case of Fig. 9. On this ground, it is conceived that the regrowth of n-type germanium in the case of Fig. 9 had been effected by the screw dislocation. But, it seems difficult to find the reason why the screw dislocations cause the several layers of striation patterns as seen in Fig. 9 to be presented. In the earlier report[5], the author assumed that the so-called abnormal growth pyramid might be caused, when the pair of the clusters of adjacent screw dislocations with equal sign were present and the clusters had different sign each other. In the course of growth of germanium crystal from the lead melt, because some of the regrown germanium lattice sites are substituted by the larger atom of lead, a great number of lattice defects may be caused at the beginning of growth of n-type germanium on the substrate[10]. As a consequence, there will also be a possibility of producing many pairs of adjacently existing screw dislocation clusters as described above. Denote by ρ_c the radius of critical nucleus and by A the spacing between the adjacent screw dislocation clusters of the same number of dislocations but with different signs each other respectively. Then, if the supersaturation of germanium in the melt is not so high, it is possible that ρ_c is large enough to meet the relation $2\rho_c > A$. In such case, the screw dislocation clusters with different signs interefere with each other and do not participate in the growth. Thus, the crystal growth is effected mainly by the single screw dislocation existing at random on the substrate crystal surface. The growing speed in this case is relatively small, but as the specimen is cooled down gradually, the supercooling becomes large accordingly and hence ρ_c becomes small. And when $2\rho_c < A$ is reached the screw dislocation clusters with different signs begin to act as the centers of of growth independently of one another. This causes the growing speed to be increased and as a result, the supercooling becomes again small. At the same time, heat of solidification is generated so much that the temperature of the solid-liquid interface is raised, thus the the supercooling becomes smaller. Since this is the case, ρ_c becomes again large, thereby the growth due to the above-mentioned screw dislocation clusters being completely stopped and the growing speed considerably reduced. This process is possibly repeated several times before the regrowth of germanium is completed if the specimen was cooled at extremely low speed as in the pressent example. In case the crystal growth is advancing at high speed, effective segregation coefficient of As will be larger and in the regrown layer at that part a larger amount of As is contained. Thus, the growth at high speed and that at low speed will be repeated alternately, probably thereby enabling the several layers of striations to be produced. As to the variation in the effective segregation coefficient with the growing speed of the germanium crystal, it has been well known that in general the donor impurity is liable to be changed[18].

3.2 *Striation*

From the striation patterns of Fig. 9 it is possible to know much about the regrowth. In the lower part of the figure, the n-type regrown layer extends in parallel to the p-n boundary. This is probably because both of bottom and flank areas of the p-n boundary were composed of the single (111) plane respectively, no blowhole was present in the melt during the regrowth, and the cooling was made at a very low speed. In this case the delay of the regrowth at the periphery of the bottom surface as seen in Figs. 4 and 5, at the part J of Fig. 9 and in many other cases cannot be observed. At the part J of Fig. 9, the first striation has grown to nearly the same degree as other parts, but the second, the third, .. etc. have attained very poor growth.

This indicates that in the cooling process the regrowth at the periphery is effected on both the bottom and flank parts simultaneously, and the supply of germanium from the melt is apt to be insufficient. This trend becomes distinct as the regrowing process progresses. Our explanation for such difference between two parts is as follows: In the lower part, molten *Pb—As* maintained nearly the same shape throughout the whole process of alloying, while in the upper part, drops of the molten *Pb—As* collapsed and spread over the region A∼D of the figure in the course of the heating process as described in 3.2. This made the difference in the shape of the drop between the heating and cooling processes, and especially at the periphery reduced the thickness of the molten layer. Next, as to the part A∼B of the photograph, to which the molten *Pb—As* spread at the later time as described above, the solid-liquid interface produced in the course of the heating process was substantially deviated from the single (111) plane though the growth at the beginning was made in parallel to the interface. As the growth progresses, the interface shows a trend to approach the most stable {111} planes, and once encountered with such a disturbance as blowhole C, the left part of C approaches the (111) plane parallel to the bottom and the right part approaches the other {111} plane which makes an angle of 70°32′ with the bottom, and at the same time grain boundary due to misfitting is produced as shown by CD. Further, on the immediately right of CD, as the regrowth progresses the angle between the interface and the bottom plane become large gradually, and then another grain boundary EF is produced. On the other hand in the neighborhood of B, the slope of growth plane with respect to the (111) plane is relatively small and no misfit boundary is produced. At the part neighboring to a small blowhole G, supply of germanium from the melt is less than other parts at first and apparently the growth is delayed. But, once passing over the blowhole, the growth becomes more rapid compared with the other parts, thus resulting in the flat and smooth growth pattern after a while. It is apparent that in the case of such slight uneveness being present on the growth plane a trend to produce flat and smooth growth plane exists. On the other hand, in the case of such a large blowhole as H being present, the growth is badly delayed in that part at first as shown by FHI, but as the specimen is cooled down, the blowhole contracts gradually and fresh melt is pushed and collected in the place from above, thereby possibly starting the growth newly around the blowhole. Then, if any two growth surface which progressed along the blowhole collide with each other anywhere around it, then screw dislocation arrays will be produced with a high possiblility. With this array as a center, rapid abnormal growth takes place resulting in the swollen growth at the area around the blowhole as shown by the parts K and L compared with the other parts. Similarly, in the case of regrowth from the indium melt, swollen growth is produced as shown in Fig. 10 frequently at the area around the blowhole, and many growth centers exist around the blowhole as shown in Fig. 11. Further in Fig. 11, the growth pyramid swollen in a terrace on the right of the blowhole represents the abnormal growth pyramid described in the earlier report[5], and the growth patterns developing from several growth centers around the blowhole are seen to exist also in the delayed growth area on the left of the above-mentioned terrace. This fact will be easily understood on seeing that the growth at K and L of Fig. 9 developed independently of the other areas at the end of the regrowth period.

3.3 *Defect accompanying the dendritic growth*

When the specimen was cooled rapidly, dendritic crystal growth took place in the sloping area deviated from the (111) plane, and each dendritic lamella grows due to screw dislocation as seen in Figs. 6 and 7. In these figures it will be seen how a crystal growth occurs from the upper lamella towards the lower one at the part where the both lamellae unite with each other. As seen from Fig. 3, in this case indium is left at the root of the projection[2]. Such a defect will be possible to occur if the solid-liquid interface is inclined somewht with the (111) plane when the single crystal is grown from the germanium melt containing a trace of impurity. In such case, the impurity in the germanium melt is concentrated there gradually, so that its melting point is lowered down to such value that after the surrounding has been solidified completely and a rapid solidification occurs there. The special defect found frequently in the germanium single crystal as shown in Fig. 12 is considered to be created by such cause. Sometimes, such defect appears as the layered structure independent on the surrounding single crystal at all, and this will be reported by Y. Sugita[19].

Acknowledgement

The author is indebted to Mr. Y. Sugita for his supply of many data and cooperation in experiment.

References

1) J. I. Pankove: R.C.A. Rev. **15** (1954) 75.
2) J. W. Peterson. J. McGlasson, Jr. and W. C. Hittinger: J. Metal **9** (1957) 823.
3) A. S. Rose: R.C.A. Rev. **29** (1958) 423.
4) J. S. Hanson: I.B.M. Journal. **1** (1957) 279.
5) M. Tomono: J. Phss. Soc. Jap. **16** (1961) 439.
6) J. I. Pankove: J. Appl. Phys. **28** (1957) 1054.
7) M. Tomono: J. Phys. Soc. Jap. **15** (1960) 2254.
8) E. Billig: Proc. Roy. Soc. (A) **299** (1955) 346.
9) B. Chalmers: J. Metal **6** (1954) 519.
10) S. G. Ellis: J. Appl. Phys. **26** (1955) 1140.
11) A. I. Bennett and R. L. Longini: Phys. Rev. **116** (1959) 53.
12) R. G. Seidensticker, J. W. Faust, Jr., H. F. John and D. R. Hamilton: Bull. Am. Phy. Soc. **5** (1960) 165. D. R. Hamilton, R. G. Seidensticker, J. W. Faust, Jr., and H. F. John: ibid. D. R. Hamilton: J. Appl. Phys. (1960) 1165.
13) H. F. John. and J. W. Faust, Jr.: Bull. Am. Phys. Soc. **5** (1960) 165. J. W. Fast, Jr., and H. F. John: ibid.
14) P. H. Keck and J. Broder: Phys. Rev. **90** (1953) 521.
15) B. Goldstein: R.C.A. Rev. **18** (1957) 213.
16) C. D. Thurmond and M. Kowalchik: B.S.T.J. **39** (1960) 169.
17) R. Becker and W. Döring: Ann. der Phys. **24** (1935) 719. F. C. Frank: Adv. in Phys. **1** (1951) 91. W. K. Burton, N. Cabrera and F. C. Frank: Phil. Trans. Roy. Soc. **243** (1951) 299.
18) R. N. Hall: Phys. Rev. **88** (1952) 139. R. N. Hall: J. Phys. Chem. **57** (1953) 836. J. A. Burton, E. D. Kolb, W. P. Slichter and J. D. Struthers: J. Chem. Phys. **21** (1953) 1991.
19) Y. Sugita: Unpublished.

JOURNAL OF THE PHYSICAL SOCIETY OF JAPAN, Vol. 16, No. 4, APRIL, 1961

Low-Temperature Electrical Breakdown in Germanium

By Jiro YAMASHITA

Institute for Solid State Physics, University of Tokyo, Tokyo

(Received December 26, 1960)

The low-temperature electrical breakdown effect in n-type germanium which was observed by Sclar and Burstein, and Koenig and Gunther-Mohr, is discussed from viewpoint of the hot electron theory. At first, we assume that the energy loss of conduction electrons comes only from the acoustic scattering, while the mobility is determined by ionized- and neutral impurity scatterings besides the acoustic scattering. We evaluated the electron temperature as a function of applied field and then estimated the rate of ionization of donors and the thermal recombination coefficient. By using these values we estimated the breakdown field of some specimens and compared it with the experiment. The result of the theory seems to be in good agreement with the experiment, when the concentration of donors and acceptors is fairly small. The theoretical result is, however, inconsistent with the experiment, when specimens contain donors above $10^{15}/\text{cm}^3$. It seems to be other mechanisms of the energy loss which work more effectively than the acoustic scattering does, when the concentration of the donors is above $10^{15}/\text{cm}^3$. Further, we proposed a mechanism of the energy loss at compensated germanium which leads to the negative resistance.

§ 1. Introduction

Recently the low-temperature electrical breakdown effect in germanium has been actively investigated.[1] Although some aspects of the phenomenon are qualitatively explained, many experimental facts are still open to further investigations. On the other hand, appreciable progress has been made in both experimental and theoretical studies on warm or hot electron problems at higher temperatures. One of the characteristics of investigation of hot-electron phenomena lies in the fact that it gives a more detailed information about the energy-loss of conduction electrons than the usual ohmic current does.[2] Therefore, it is quite natural to expect that the low-temperature electrical breakdown effect may give a valuable information about a mechanism of the energy-loss of conduction electrons at very low temperature. The purpose of the present paper is to give a result of a preliminary analysis performed by such expectation as mentioned previously. As a result of the analysis we have found that the mechanism of the low-temperature breakdown is rather complicated, because many elementary processes are participated, each in its degree which depends upon a state of each specimen. At present, our knowledge of these elementary precesses is rather poor, so that we are inevitably compeled to introduce somewhat ambiguous assumptions. However, since the low-temperature breakdown effect is a very good source of information of the elementary processes at very low temperature, we hope that the further progress of study on the former will make a good contribution to understanding of the latter.

§ 2. Models and Assumptions

First, we shall give a brief account of models and assumptions with which we shall start the analysis. They are quite conventional ones, but not always free from objections. (1) The shape of energy surfaces is spherical. (2) The conduction electrons are scattered by the acoustic mode of vibrations, ionized-impurity centers and neutral impurity centers. (3) The scattering due to ionized impurities and neutral impurities is elastic. Thus, the energy loss of the conduction electrons comes only from the acoustic lattice scattering. (We shall see later that this assumption is not right, when the density of impurities is above a certain limit.) (4) The rate of the lattice scattering is given by the usual formula, and the acoustic mobility at low temperature is estimated from observed values in the temperature range from 100 to 300°K.[3] Then, it is

$$\mu_L = 2.4\times10^7/T^{3/2} . \tag{1}$$

In germanium mc^2, where m is the average effective mass and c is the sound velocity in the lattice, is much smaller than KT even at liquid helium temperature, so that the so-called high temperature approximation is expected to be valid. (5) The rate of ionized-impurity scattering is given by[4]

$$\mu_i = \frac{8\sqrt{2}\,\kappa^2(kT)^{3/2}}{N_i e^3\sqrt{m'}\,\pi^{3/2}\ln\{1+(\kappa kT/e^2N_i^{1/3})^2\}} , \tag{2}$$

where N_i is the density of charged scatterers. Here $\boldsymbol{m'}$ is regarded as an adjustable parameter to fit the observed datas. However, the accurate value of it is unknown, because the density of the charged centers is not accurately determined. Here we assume tentatively $\boldsymbol{m'}=0.12\boldsymbol{m}_0$ (the averaged effective mass). As is well known, there is another formula of the ionized-impurity scattering, that is, the Brooks-Herring formula. Here we prefer to use the Conwell-Weisskopf formula rather than the *B–H*. The reason will be mentioned in section 7. (6) The rate of the neutral-impurity scattering is given by Erginsoy's formula.[5] The mobility is

$$\mu_n = 8\pi^3 m'' e^4/20\kappa h^3(N_D-N_A) , \tag{3}$$

where N_D is the density of donors and N_A is that of acceptors. Here it is better to interpret $\boldsymbol{m''}$ as an adjustable parameter which has been determined as $0.21\boldsymbol{m}_0$ by Sclar and Burstein.[6] (7) When the energy of the conduction electrons is larger than the ionization energy of the impurity center, they ionize an electron from the impurity center. The rate of energy loss due to the ionization, however, is quite small as compared with that due to the lattice scattering. Thus, the ionization process has little influence on the energy distribution of the conduction electrons.

As to mechanism of the low-temperature breakdown we follow the idea proposed by Koenig.[7] When the intensity of the applied field becomes large, the mean kinetic energy of the conduction electrons becomes large and some of them obtain enough energy to ionize an electron bound to the impurity center. The process which works to reduce the electron density is a capture process of the conduction electrons by empty donors. Since the rate of the ionization increases rapidly with increasing field and the capture cross section decreases with increasing electron energy, there should be a field intensity in which the rate of the ionization becomes as fast as that of the capture process. If the field intensity is above this critical value, no equilibrium state is expected to the conduction electrons. Therefore, this critical field is regarded as the breakdown field. The mathematical formula for this condition is

$$A_t(N_D-N_A-n)+n\{A_i(N_D-N_A-n)-B_t(N_A+n)\}-n^2B_i(N_A+n)=0 . \tag{4}$$

The quantities A_t and A_i represent the rates of carrier production by thermal generation and impact ionization, respectively, and B_t and B_i the respective inverse process, that is, single-electron capture and Auger recombination. The coefficients A_i, B_t and B_i depend both upon the lattice temperature and the electron distribution. In practice we have $n \ll N_A$, N_D-N_A. If in addition the Auger recombination is neglected, the result simplifies to

$$n = A_t(N_D-N_A)/\{B_tN_A-A_i(N_D-N_A)\} . \tag{5}$$

Then, the condition of the breakdown is given by

$$B_tN_A = A_i(N_D-N_A) . \tag{6}$$

§ 3. Distribution Function and Electron Temperature

We start from the Boltzmann equation. Let us denote the distribution function by

$$f(\vec{K}) = f_0(E) + K_x g(E) , \tag{7}$$

where $\vec{K}$ and E are the wave number vector and energy of conduction electrons, respectively, and x is the direction of the applied field. Then, the B.E. is

$$\left[\frac{\partial f}{\partial t}\right]\equiv\left[\frac{\partial f}{\partial t}\right]_F+\left[\frac{\partial f}{\partial t}\right]_{ac}+\left[\frac{\partial f}{\partial t}\right]_i+\left[\frac{\partial f}{\partial t}\right]_n=0\,. \tag{8}$$

The meaning of the sufixes is: F=electric field, ac=acoustic scattering, i=ionized impurity scattering and n=neutral impurity scattering. The explicit expressions of these terms are:

$$\left[\frac{\partial f}{\partial t}\right]_F=\frac{eF}{\hbar}\left[g+\frac{2}{3}E\frac{dg}{dE}+\frac{\hbar^2}{m}K_x\frac{df_0}{dE}\right], \tag{9}$$

$$\left[\frac{\partial f}{\partial t}\right]_{ac}=-\frac{8ec^2}{3\sqrt{\pi}kT}\frac{1}{\mu_a}\frac{1}{\sqrt{E}}\left[E^2\frac{d^2f_0}{dE^2}+\left(\frac{E^2}{kT}+2E\right)\frac{df_0}{dE}+\frac{2E}{kT}f_0-\frac{E}{2mc^2}K_xg\right], \tag{10}$$

$$\left[\frac{\partial f}{\partial t}\right]_i=\frac{4e}{3m\sqrt{\pi kT}}\frac{6(kT)^2}{\mu_iE\sqrt{E}}K_xg \tag{11}$$

and

$$\left[\frac{\partial f}{\partial t}\right]_n=\frac{e}{m\mu_n}K_xg\,. \tag{12}$$

At very low temperature we can neglect the effect of the optical mode of vibrations. Then, it is not hard to find an analytical solution of B.E. In appendix we give the explicit expression of the solutions. If the distribution function is once obtained, the mobility or the rate of ionization of impurity centers will be determined by usual procedures. The distribution functions which were obtained, however, are rather complicated, so that numerical calculations are always required for further applications. An approximate procedure to obtain a more convenient, though less accurate, distribution function was developed by Stratton.[8] (A relation between this approach and the Boltzmann approach was discussed by us.[2]) In that approximation the distribution function $f_0(E)$ is assumed to be

$$f_0(E)=\frac{2}{\sqrt{\pi}(kT_e)^{3/2}}\exp(-E/kT_e)\,. \tag{13}$$

The electron temperature T_e is determined as a function of the applied field by the condition of the energy conservation:

$$e\sigma F^2=\int E\left[\frac{\partial f}{\partial t}\right]_{ac}\sqrt{E}\,dE\,, \tag{14}$$

where σ is the conductivity. Let us examine the condition for following three cases.

(a) Acoustic and neutral impurity scattering. After a simple computation the following condition is derived:

$$p(\mu(F)/\mu_a)=2(T_e/T)^{1/2}(T_e/T-1)\,, \tag{15}$$

where p and $\mu(F)$ are defined by

$$\mu(F)=\mu_a\left(\frac{T_e}{T}\right)^{1/2}\int_0^\infty\frac{x\sqrt{x}\,e^{-x}dx}{\sqrt{x}+\rho(T/T_e)^{1/2}}\,, \tag{16}$$

$$\rho=3\sqrt{\pi}\,\mu_a/4\mu_n \tag{17}$$

and

$$p=3\pi\mu_a{}^2F^2/16c^2\,. \tag{18}$$

When the condition $\mu_n\ll\mu_a$ is fulfilled, $\mu(F)$ is simply expressed as

$$\mu(F)=\mu_n\left\{1-\frac{32}{9\pi}\frac{\mu_n}{\mu_a}\left(\sqrt{\frac{T_e}{T}}-1\right)\right\}. \tag{19}$$

(b) Acoustic and ionized impurity scattering. The electron temperature is determined by

(15) with the definition of $\mu(F)$:

$$\mu(F)=\mu_x\left(\frac{T}{T_e}\right)^{1/2}\left\{1-q^2\int_0^\infty \frac{ue^{-u}du}{u^2+q^2}\right\}. \tag{20}$$

Here q is determined by

$$q=q_0(T/T_e)\{G(T_e)/G(T)\}^{1/2} \tag{21}$$

with the defimition of $G(x)$ and q_0:

$$q_0{}^2=6\mu_a/\mu_i \quad \text{and} \quad G(x)=\ln\{1+(3\kappa kx/e^2N_i{}^{1/3})^2\}. \tag{22}$$

By inserting the electron temperature T_e in $G(x)$ we take into account the energy dependence of q through $G(x)$. Performing a well known integral in (20) we have a final expression of the condition:

$$p\left\{1-q^2\left[\left(\frac{\pi}{2}-S_i(q)\right)\sin q-C_i(q)\cos q\right]\right\}=2\left(\frac{T_e}{T}\right)\left(\frac{T_e}{T}-1\right). \tag{23}$$

(c) When three mechanisms of the scattering are effective, the relation between the field and the electron temperature is again given by (15), but with the definition of $\mu(F)$:

$$\mu(F)=\mu_a\left(\frac{T}{T_e}\right)^{1/2}\int_0^\infty \frac{x^3e^{-x}dx}{x^2+q^2+\rho(T/T_e)^{1/2}x\sqrt{x}}. \tag{24}$$

§4. Rate of Impact Ionization and Rate of Thermal Recombination

Here we consider the impact ionization process in a p-n junction. A conduction electron which has a larger energy than the threshold of the impact ionization can transfer an electron from the valence band to the conduction band. Since this process occurs with a large probability, the distribution function above the threshold is mainly determined by this process and the applied field. In the low-temperature breakdown the situation is completely different. Since the number of impurity ions is much smaller than that of the lattice atoms, the perturbing effect of the impact ionization of the donors on the distribution function is not appreciable. At low temperature the condition $\mu_a \gg \mu_n$, or $\mu_a \gg \mu_i$, is always satisfied, so that the mean free path of the electron is mainly determined by scattering due to the ionized-, or neutral impurities. Then, since the cross section of the elastic scattering for very slow electrons is enormously larger than that of the ionization, the latter process has little influence on the mobility of the conduction electron. As for the energy loss of the conduction electron a more careful consideration is necessary. Let nS be the average number of electrons which enter into the conduction band per unit time by the impact ionization and E_0 be the average energy which is necessary for the ionization, then the energy loss due to the impact ionization is given by

$$n\int E\left[\frac{\partial f}{\partial t}\right]_{ion}\sqrt{E}\,dE=nSE_0. \tag{25}$$

Then, the previous expression of the energy conservation is now extended to:

$$e\mu(F)F^2=\frac{16ec^2}{3\pi\mu_a}\left(\frac{T_e}{T}\right)^{1/2}2\left(\frac{T_e}{T}-1\right)+SE_0, \tag{26}$$

or

$$p\left(\frac{\mu(F)}{\mu_a}\right)=2\left(\frac{T_e}{T}\right)^{1/2}\left(\frac{T_e}{T}-1\right)+\frac{3\pi\mu_a}{16ec^2}SE_0. \tag{27}$$

In the next section we shall make a numerical estimate of each term. The result is that even at the breakdown field the second term in (27) is still smaller than the first and can be safely disregarded, unless the density of impurities is above $10^{16}/\mathrm{cm}^3$. In the following we shall assume that the distribution functions which are derived in the previous section are still approximately valid, even when the applied field is as large as the breakdown field. Then, the time rate of the impact ionization is given by:

$$S=(N_D-N_A)\int_{\Delta E}^{\infty} vQ(E)f_0(E)\sqrt{E}\,dE\,, \tag{28}$$

where $Q(E)$ is the cross section of the impact ionization, v is the velocity of the colliding electron and ΔE is the depth of the donor-level from the bottom of the conduction band. It is a difficult problem to evaluate $Q(E)$ from the first principle. The experiment shows, however, that the cross section of the ionization of a hydrogen atom by a slow electron is nearly equal to its geometrical cross section πa_0^2. Therefore, for the purpose of a rough estimate of $S(T_e)$ it may be allowed to put*

$$Q(E)=\pi(\kappa a_0)^2\,. \tag{29}$$

Then, $S(T_e)$ is evaluated as

$$S(T_e)=2\sqrt{\frac{2\pi kT_e}{m}}(\kappa a_0)^2\left(\frac{\Delta E}{kT_e}+1\right)\exp\left(-\frac{\Delta E}{kT_e}\right)(N_D-N_A)\,. \tag{30}$$

Next, we shall discuss the rate of the thermal recombination. The magnitude of the coefficient for thermal electrons in the temperature range 4–10°K has been determined experimentally by Koenig.[9] However, we have no experimental knowledge about the thermal recombination time of the hot electron, so that we must rely upon theory. In order to estimate temperature dependence of the recombination time we followed the method of Lax.[10] The result is:

$$\tau_c(T_e)\equiv 1/B_tN_A=aT_e/N_A=2\times10^{-8}T_e(5\times10^{12}/N_A)\,. \tag{31}$$

The constant a is determined so as to fit Koenig's data when both lattice and electron temperature are about 4°K.

§ 5. Low Temperature Breakdown and Comparison with Experiments

From Koenig's experiment of the low-temperature breakdown we pick up four specimens in which detailed information of physical properties is available (Table I). At first, by using Eqs. (15) and (24) we evaluate the electron temperature T_e as a function of the apllied field. The results are shown in Fig. 1 and Fig. 2. In Fig. 1 we show also a T_e–F curve of an ideal case in which no impurities exist. We find a tendency that the T_e–F curves come together at the high temperature region, $T_e>10T$, and approach to the ideal curve at high temperature, if the density of donors and acceptors is sufficiently small; $(N_D-N_A)\sim10^{13}$ and $N_A<10^{13}$. Therefore, we except that the electron temperature of these specimens is roughly determined by the applied field irrespective of a

Table I.

No.	T°K	(N_D-N_A)	N_A	$(N_D-N_A)/N_A$	F_b (volt/cm)
1	4.55	1.0×10^{12}	4.0×10^{12}	0.25	14
2	4.55	1.5×10^{13}	5.0×10^{12}	3.0	4.8
3	5.056	2.2×10^{14}	2.8×10^{13}	7.6	9.1
4	4.79	1.9×10^{15}	2.3×10^{13}	83	14.3

---

* This cross section is quite small as compared with that of the elastic scattering, where $Q(E)=20(\kappa a_0)/K$. The ratio $20(\kappa a_0)/K$: $\pi(\kappa a_0)^2$ is equal to 40: 1 when $\Delta E=\hbar^2K^2/2m=0.01$ eV.

impurity content, and the breakdown field depends only upon the ratio $(N_D-N_A)/N_A$. In other specimens, No. 3 and No. 4, the situation is different. The T_e–F curve runs fairly apart from the ideal curve and it does not show a tendency of the convergence to the latter, unless the electron temperature is extremely high. In the following we shall designate the electron temperature which corresponds to the observed breakdown field as

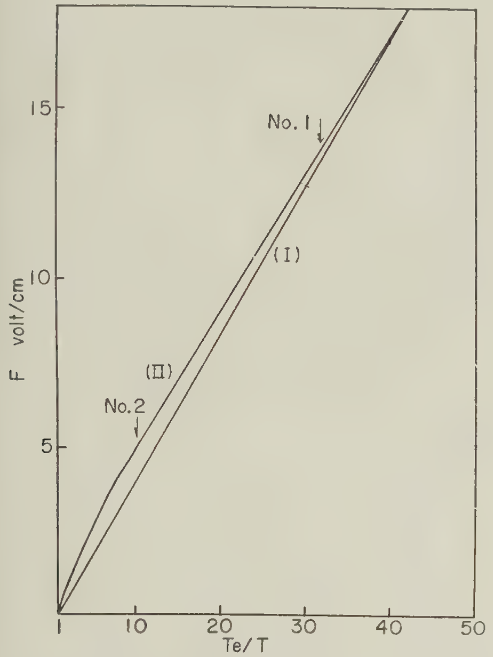

Fig. 1. Electron temperature vs. applied field (I) of ideal case, and (II) of specimens No. 1 and No. 2.

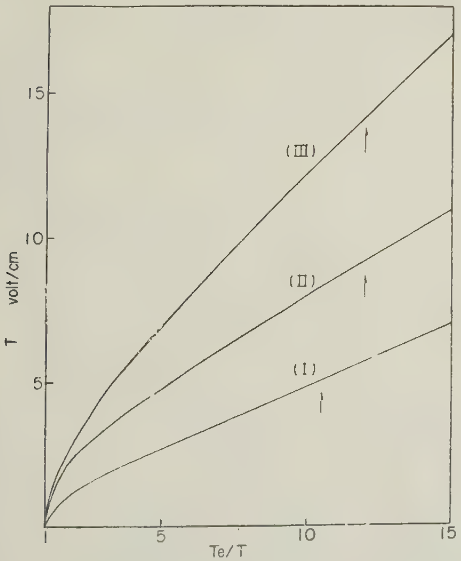

Fig. 2. Electron temperature vs. applied field (I) of specimen No. 2, (II) of specimens No. 3 and (III) of specimen No. 4.

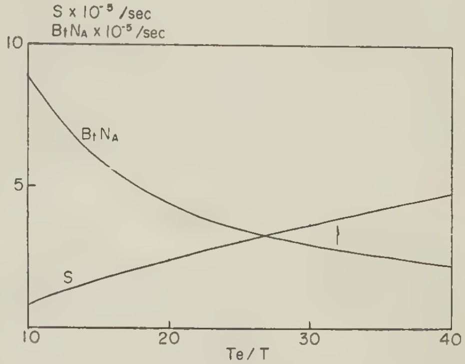

Fig. 3 (a). The rate of the impact ionization S and the rate of the thermal recombination coefficient B_tN_A in specimen No. 1.

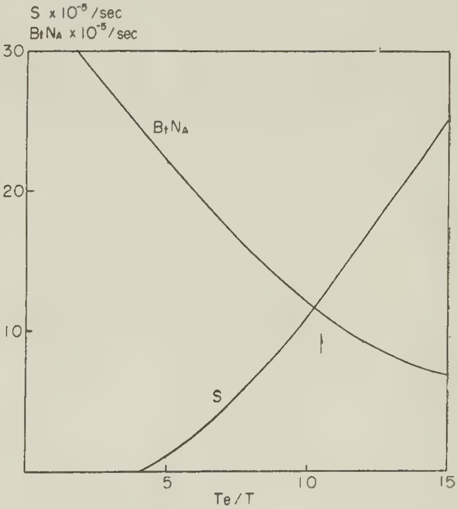

Fig. 3 (b). in specimen No. 2.

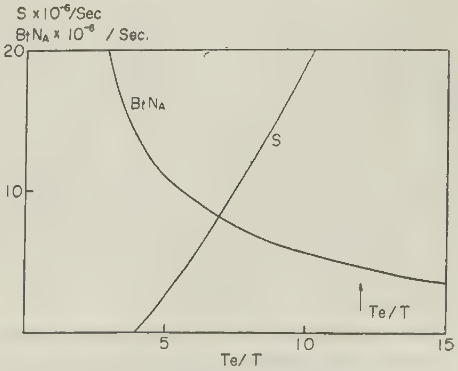

Fig. 3 (c). in specimen No. 3.

the breakdown temperature T_b. We show T_b by an arrow in Fig. 1 and Fig. 2. Next, let us estimate $S(T_e)$ from Eq. (30). The result is shown in Fig. 3. By using Eq. (31) we also estimate the value of $B_t(T_e)N_A$ for these specimens. The result is shown also in Fig. 3. As seen from the figure the condition (5) is roughly satisfied at specimens No. 1 and No. 2. Although the result of the present analysis must be judged very carefully, it seems to be consistent with the model of the low-temperature breakdown proposed first by Koenig.

At specimen No. 3 the agreement between the theory and experiment is not so good as at specimens No. 1 and No. 2, but the accuracy of the present analysis is so poor that we can say nothing definite about this specimen. However, the theoretical result is clearly inconsistent with the experiment at specimen No. 4. (Table II). According to the theory mentioned previously the breakdown temperature must decrease with increasing $(N_D-N_A)/N_A$, but in fact the breakdown temperature has a minimum as a function of $(N_D-N_A)/N_A$.

Table II. $S(T_e)$ and $B_t(T_e)N_A$ of specimen No. 4.

T_e/T	$S(T_e)$	$B_t(T_e)N_A$
3	8.1×10^5	1.6×10^7
5	1.5×10^7	9.6×10^6
8	7.1×10^7	6.0×10^6
10	1.2×10^8	4.8×10^6
12	1.6×10^8	4.0×10^6
15	2.1×10^8	3.2×10^6
17	2.4×10^8	2.8×10^6

Sclar and Burstein[1)] investigated behaviors of the low-temperature breakdown for specimens which contain the donors $10^{14}-2\times10^{16}/\mathrm{cm}^3$. They find that the breakdown field is roughly proportional to (N_D-N_A) when the density of the donors is above $10^{15}/\mathrm{cm}^3$. Although experimental evidence of the proportional relation is not very convincing owing to the limited number of their specimens, it may be regarded as a very important experimental fact.

§ 6. On Specimens Containing High Concentration of Donors

The relation between (N_D-N_A) and F_b observed by Sclar and Burstein seems to be inconsistent with the theory mentioned previouly. In fact, the breakdown field depends upon both the electron temperature and the ratio $N_A/(N_D-N_A)$, but they did not mention about the latter. If we assume, however, that the ratio is nearly the same through their uncompensated specimens and it is of the order of several percent, then it is concluded from the theory that, when the neutral impurity scattering is a main cause of the resistance, the breakdown field is roughly proportional to $(N_D-N_A)^{1/2}$, but not to (N_D-N_A) itself. On the other hand, the observed result maintains that the energy loss of the conduction electrons is proportional to (N_D-N_A), so that there must be other mechanisms of the energy loss which are proportional to (N_D-N_A) and their contribution to the energy loss will surpass that from the acoustic scattering when the density of impurities is above $10^{15}/\mathrm{cm}^3$.

At present, it is not clear what mechanism is really effective to cause such energy loss. In the following we shall examine some of possible mechanisms.

(1) First, we examine the energy loss due to the impact ionization from Eq. (27). This effect, however, does not seems to be hopeful. If we put $T_e/T=10$ and $E_0=0.01\,\mathrm{eV}$, then the ratio of the first and the second term of (27) is:

$$\frac{3\pi\mu_a}{16ec^2}E_0S \Big/ 2\left(\frac{T_e}{T}\right)^{1/2}\left(\frac{T_e}{T}-1\right)\sim10^{-9}S\,.$$

Since the value of S becomes nearly equal to 10^9 when the density of donors reaches $10^{16}/\mathrm{cm}^3$, the energy loss due to the impact ionization alone does not seem to explain the observed facts. The energy loss due to the excitation of the bound electron from the ground state to the lowest excited state of the donor is expected to make nearly the same amount of contribution to the energy loss.

(2) As is well known, the energy levels of an electron bound to a donor split to two sets of singlets and triplets. If the energy of the conduction electron is larger than energy difference of two levels, the conduction electron is able to excite the bound electron from singlets to triplets. If we assume tentatively that the energy difference is 0.001 eV and the cross section of this process is $20\pi(\kappa a_0)^2$, then the energy loss due to

this process at the density of donors of 10^{15}/cm^3 is nearly equal to that due to the acoustic scattering at $T_e=10T$. Therefore, if these assumptions are reasonable, then the energy loss of the conduction electrons is almost proportional to (N_D-N_A) at specimens of high impurity density. (We suppose that this inelastic scattering is caused by an exchange process: a conduction electron falls into an empty triplet level and a bound electron at a singlet level of the same donor jumps into the conduction band with conserving energy.) Since the cross section of the elastic scattering due to a neutral donor is estimated from Erginsoy's formula as about $130\pi(\kappa a_0)^2$ at $E=0.001$ eV, the above assumed value $20\pi(\kappa a_0)^2$ does not seem to be very unreasonable. However, this idea is not quite hopeful because of the following reason. We see easily that this effect is inherent in *n*-type Ge, but not in *p*-type Ge, while Sclar and Burstein observed the proportional relation mentioned previously at both *n*- and *p*-type Ge.

(3) Another possible mechanism of the energy loss is the impurity scattering accompanyed by emission or absorption of a phonon. We, however, have no reliable knowledge of this process. We must wait a new experimental result which suggests an inelastic scattering due to impurities.

Even if we find a mechanism which can reasonably explain the observed relation between (N_D-N_A) and F_b, there remains a question whether or not the thermal recombination coefficient B_t is independent of (N_D-N_A). If B_t is independent of it, we can determine F_b and T_b from the following relations:

$$S(T_b)\equiv A_i(T_b)(N_D-N_A)=B_t(T_b)N_A\ , \qquad (32)$$

$$[p]_{F=F_b}=\frac{\mu_l}{\mu(F_b)}\left[2\left(\frac{T_b}{T}\right)^{1/2}\left(\frac{T_b}{T}-1\right)\right.$$
$$\left.+\alpha(T_b)(N_D-N_A)\right]. \qquad (33)$$

By choosing $\alpha(T_b)$ and F_b so as to fit the observed date at specimen No. 4 we find that $T_b/T\sim5$ and $\alpha(T_b)/2(T_b/T)^{1/2}(T_b/T-1)\sim5$. This value of α is so large that the second term in (33) has an appreciable contribution even at specimen No. 3. If we take into account it, the value of (T_b/T) is newly determined as 7 instead of 12. Then, we see from Fig. 3 that this value of T_b satisfys the condition (32) approximately. In fact, the breakdown field depends upon both the electron temperature and the ratio $(N_D-N_A)/N_A$ through (32). The latter is, however, not important, because $S(T_e)$ increases very rapidly with increasing T_e in the temperature range $T_e<5$, and consequently the breakdown field becomes roughly proportional to the density of the impurities irrespective of the ratio $(N_D-N_A)/N_A$.*

§ 6. Negative Resistance

By studying impact ionization in highly compensated germanium containing both III and V impurities from 5×10^{14} to 10^{16}/cm^3 McWhorter and Rediker[11)] have found a very interesting behavior of the low-temperature breakdown which is not observed in uncompensated specimens. The characteristic feature of the low-temperature breakdown in highly compensated germanium is that a region of negative resistance appears in a voltage-current relation. According to their observation the sustaining field, typically one-third to two-thirds the breakdown field, is approximately proportional to N_D+N_A and agrees with the breakdown field in uncompensated germanium for the same total impurity concentration.

Since this phenomenon is observed only in highly compensated specimens, it compels us to introduce a special mechanism of the energy loss which is inherent in compensated specimens. Although this phenomenon has been observed only in *p*-type germanium, the essential point in the mechanism of the negative resistance may be indifferent to the type of the specimen. In the beginning let us investigate characteristics in these specimens. First, we notice that the prebreakdown conduction is predominantly impurity conduction. The concentration of impurities, however, is still smaller than the critical concentration for possible formation of an impurity band, so that the current is presumably carried by a hopping motion of a bound electron from an impurity center to its adjacent empty center. Secondly, we notice that the specimen contains so many impurities that the potential field in the lattice is by no means regular and consequently the energy levels of donors are not exactly the same, but may be distributed in a certain energy interval. When there is no external field, the bound electrons occupy these energy levels according to the statistical law. When ths external field is applied, the current is expressed as:

---

* However, if B_t increases with increasing density of the impurities, the situation is not so simple as mentioned above. Then, we expect that the breakdown temperature is higher, and $\alpha(T_b)$ is smaller than the respective value estimated before.

$$j=e(n_c\mu_c+n_i\mu_i)F\ , \tag{34}$$

where $en_c\mu_cF$ represents the current carried by conduction electrons and $en_i\mu_iF$ represents the impurity conduction. In the prebreakdown conduction the latter is much larger than the former. Here we consider the energy balance of the conduction electrons which would be given by:

$$en_c\mu_cF^2=(32ec^2/3\pi\mu_a)(T_e/T)^{1/2}(T_e/T-1)n_c+(N_D-N_A)L(T_e)n_c+W(c,\ i)n_cn_i\ . \tag{35}$$

Here the first term in the right side gives the energy loss due to the acoustic scattering, the second term gives that due to other mechanisms which were considered in the previous section and the last term represents the contribution from mutural interaction between the conduction- and impurity electrons. On the other hand, the number of conduction electrons is assumed to be determined by the formula

$$n_c=A_t(N_D-N_A)/\{B_t(T_e)N_A-S(T_e)\}\ , \tag{36}$$

as a function of the electron temperature. From Eq. (35) we see easily that, if $W(c,\ i)$ does not depend upon n_c and n_i, the last term in (35) works only to displace the breakdown field to a higher value. Therefore, we see that a special assumption is necessary for $W(c,\ i)$ in order to have a negative resistance in (34).

Let us introduce an assumption that the mutual interaction between two electron systems is sufficiently strong to keep a thermal equilibrium between them. Then, the impurity electrons distribute among the energy levels according to the Maxwell law with the electron temperature T_e. In this case some amount of energy is transfered from the impurity electron system to the lattice by emission of phonons, because the temperature of the impurity electron eystem is higher than the lattice temperature. Under these circumstances the rate of the energy loss of the conduction electrons due to the mutual interaction of the electron systems is determined by the rate of the energy loss of the impurity electrons due to the interaction between these electrons and the lattice.* This rate is clearly proportional to n_i, but is independent of n_c, if the both electron systems are in equilibrium. Therefore we can write the energy balance condition in the following way:

$$e\mu_cF^2=(32ec^2/3\pi\mu_a)(T_e/T)^{1/2}(T_e/T-1)+L(T_e)(N_D-N_A)+(n_i/n_c)W(i,\ L;\ T_e)\ . \tag{37}$$

Here we note that $W(i,\ L)=0$ at $\Gamma_e=T$. From this condition we can easily derived the negative resistance. Since n_c is much smaller than n_i, the energy loss of the conduction electrons is predominantly determined by the last term of (37). Thus, the electron temperature does not rise to the breakdown temperature, even when the applied field is larger than the field which can lead the breakdown at uncompensated specimens. On the other hand, if the breakdown is supposed to occur, the number of conduction electrons increases much, and then the last term in (37) would be disregarded as compared with other terms. Therefore, the sustaining field should be determined by:

$$e\mu_cF^2=(32ec^2/3\pi\mu_a)(T_s/T)^{1/2}(T_s/T-1)+L(T_s)(N_D-N_A)\ , \tag{38}$$

---

* The distribution of the impurity electrons with T_e may be established through the thermal-and the impact ionization of donor electrons and the thermal recombination of conduction electrons. The equilibrium may be attained within a time interval of 10^{-8} sec. On the other hand, in order to emit a phonon an impurity electron must transfer from a donor site to its adjacent empty site. The life time of this process is expected to be sufficiently long.

and

$$B_t(T_s)N_A=(N_D-N_A)A_i(T_s)\ , \tag{39}$$

where T_s is the electron temperature which corresponds to the sustaining field. According to McWhorter and Reiker's experiment the sustaining field agrees with that in uncompensated specimens containing the same total impurity concentration. They observe also that the sustaining field is roughly proportional to (N_D+N_A). If we assume that the rate of the energy loss due to the inelastic scattering of impurities is nearly the same both for the ionized impurity centers and the neutral impurity centers, their experimental results are easily understood by the discussion mentioned in the previous section. In order to show a theoretical prediction about the negative resistance it is convenient to use the electron temperature as an auxiliary variable. Here we suppose that n_i and μ_i take given values irrespective of the electron temperature, and the functional form of $L(T_e)$ and $W(T_e)$ is also known. We disregard field-dependence of $\mu_c(F)$ for simplicity. By eliminating n_c from (34) and (36) we have a relation between j and T_e, and from (34) and (37) a relation between F and T_e:

$$j=J(T_e) \tag{40}$$

and

$$F=F(T_e)\ . \tag{41}$$

These equations represent a relation between j and F. When T_e is nearly equal to T, the number of the conduction electrons is practically the same as the number of them at thermal equilibrium, and the current is almost carried by the impurity electrons. With increasing T_e, F increases according to (37) and the number of conduction electrons increases according to (36), but the increase is not appreciable, unless the electron temperature is close to the critical temperature. Therefore, the current is still approximately given by $j=en_i\mu_iF$, which is expected to be ohmic. When T_e is close to the critical temperature, the number of conduction electrons increases and its contribution to the current is no more disregarded. Then, the current will be non-ohmic because of increase of n_c with increasing field. Finally when T_e approaches very closely to the critical temperature, n_c increases very rapidly with increasing T_e, and the contribution from the last term in (37) drops off suddenly. Therefore, the field begins to decrease with increasing electron temperature when T_e arrives at a certain limiting value. This value of T_e corresponds to turning point in the j–F curve and it is interpreted as the breakdown field of the compensated specimen. If T_e is equal to the critical temperature given by (39), then the number of conduction electrons becomes sufficiently large to make the last term in (37) negligibly small, and the sustaining field is now determined by (38). In this way we can interpret qualitatively the appearance of the negative resistance in the low-temperature breakdown. According to McWhorter and Rediker the negative resistance disappears rather abruptly in a narrow lattice temperature range, which depends upon the concentration of the impurity. This nature may be interpreted as follows. With increasing lattice temperature the ratio $n_i/n_c(T)$ decreases exponentially, so that the contribution from the last term in (37) becomes unimportant when the lattice temperature rises above a certain limit. Since this limiting temperature is connected with the ratio $n_i/n(T)$, the limiting temperature is expected to be higher, higher the concentration of the impurity. It is observed that the breakdown voltage is considerably reduced by illumination. This effect is also easily interpreted by the model proposed here. The illumination produces conduction electrons, so that it works to reduce the value of n_i/n_c.

§ 7. Number of Conduction Electrons and Mobility

The Hall constant of specimens No. 3 and No. 4 has been measured by Koenig and Gunther-Mohr.[12] A full curve Fig. 4 represents the inverse of the Hall constant of No. 3. The curve is normalized so as to be one

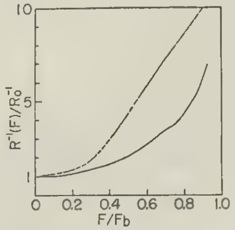

Fig. 4. $R(F)^{-1}/R(0)^{-1}$ vs. applied field in specimen No. 3.

at weak electric field. In fact, when the ionized impurity scattering and the neutral impurity scattering exist, a correction is necessary to derive a number of conduction electrons from the Hall constant.[13] We denote the correction factor as δ, and then we have a relation: $ne=\delta R^{-1}$. In specimen No. 3 the correction factor may amount to 0.7∼0.8 when the field is weak, and it becomes smaller when the electron temperature rises higher. From Eqs. (30) and (31) we see that $S(T_e)$ is quite small as compared with $B(T_e)\cdot N_A$, unless the electron temperature is close to the breakdown temperature. Therefore, in the region of the field $F<0.7F_b$, we expect that increase of the conduction electrons will come from decrease of the thermal recombination coefficient, which was estimated to be inversely proportional to T_e. Then, if we put tentatively δ as one, we can estimate the electron temperature from the observed $R^{-1}-F$ curve. (The correction of δ may increase the electron temperature by a factor 1.2 or 1.3.) In the region of the filled $F>0.8F_b$ the contribution from $S(T_e)$ to the denominator of Eq. (5) is no more negligibly small, so that the $R^{-1}-F$ curve gives only the upper limit of the electron temperature. If we estimate the breakdown temperature from this curve, it may be $7T$ or $8T$, which is in good agreement with the temperature estimated in the previous section. On the other hand, we have calculated the relation between T_e and F by using the assumption that the energy loss comes from only the acoustic scattering.

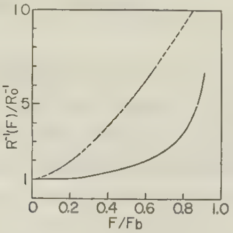

Fig. 5. $R(F)^{-1}/R(0)^{-1}$ vs. applied field in specimen No. 4.

The result is shown in a dotted curve. We find here another evidence for a certain mechanism of energy loss besides the accoustic scattering. The same idea is applicable specimen No. 4. Here the correction factor δ is expected to be close to one, because the contribution from the neutral impurity scattering is dominant in this specimen. In Fig. 5 we show the experimental $R^{-1}-F$ relation by a full curve and the theoretical T_e-F relation by a dotted curve. From the curve the breakdown temperature is estimated as about $5T-6T$, which is again in resonable agreement with the estimation given in the previous section.

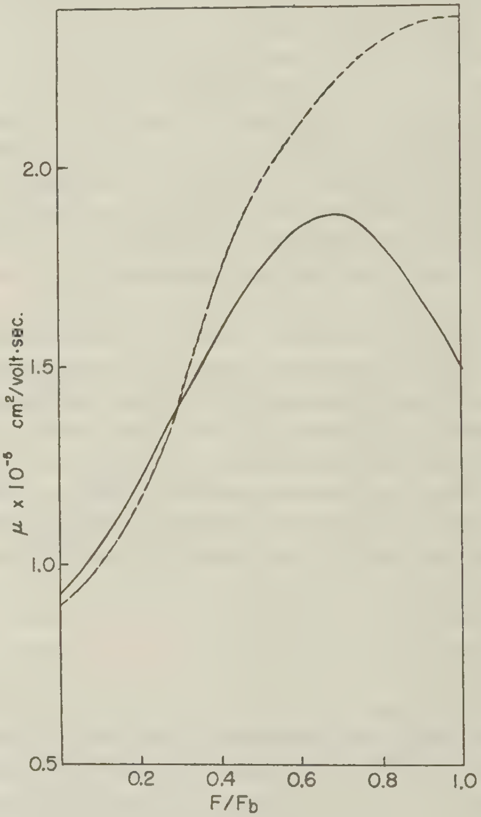

Fig. 6. Observed Hall mobility in a full curve and calculated drift mobility in a dotted curve (specimen No. 3).

The Hall mobility of specimen No. 3 and No. 4 has been observed by Koenig and Gunther-Mohr. In Fig. 6 we show the Hall mobility of No. 3 by a full curve. It may be larger than the drift mobility by a factor 1.2 or 1.3. The drift mobility of No. 3 was calculated in section 4. Accuracy of the theoretical value is not high owing to simplifying assumptions introduced there, but we show it in Fig. 6 by a dotted curve. In Fig. 7 we show the two curves which represent the observed Hall mobility and the calculated drift mobility. An apparent agreement between the theory and the experiment is fairly good.

In the computation of the mobility we have used the Conwell-Weisskopf formula. If we use the Brooks-Herring formula, the ohmic mobility becomes much smaller. For example, the ohmic mobility of No. 3 is 0.1×10^5 cm²/volt sec, and that of No. 4 is 9×10^3 cm²/volt sec, respectively. These values seem to be too small to fit the experimental datas, even when we underestimate the accuracy of the experiment. As is well known, the two formulas give closely the same results, when the conduction electron density is nearly equal to the ionized impurity density. They give quite different result, however, when the conduction electron density is appreciably less than the ionized impurity density. The difference comes from different treatments of the screening for the Coulomb scattering. At very low temperature, the number of conduction electrons is extremely small as compared with the number of changed scattering centers, so that the screening due to the conduction electrons is negligibly small. However, the Coulomb field due to a charged center is still screened by the field of other charged centers of the opposite sign. If the charged centers of both signs are distributed more or less uniformly, the range of the Coulomb field may be nearly equal to the half of the average distance between the nearest neighbour impurity ions. This assumption leads to the Conwell-Weisskopf formula.

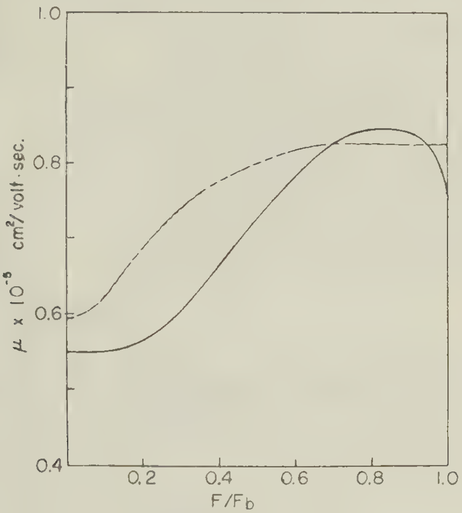

Fig. 7. Observed Hall mobility in a full curve and calculated drift mobility in a dotted curve. (specimen No. 4).

Appendix. Solutions of the Boltzmann equation

(a) There exist the acoustic scattering and the neutral impurity scattering. Since the neutral impurity scattering is nothing to do with energy loss, we derived easily a set of coupled equations:

$$\frac{8ec^2}{3\sqrt{\pi}\,\mu_a}[x^2f_0''+(x^2+2x)f_0'+2xf_0]=\frac{eF}{\hbar}\left(g+\frac{2}{3}x\frac{dg}{dx}\right) \tag{A-1}$$

and

$$g=-[F\hbar/(a\sqrt{x}+b)]\frac{df_0}{dx}\ , \tag{A-2}$$

where $x=E/kT$, $a=4/3\sqrt{\pi}\,\mu_a$ and $b=1/\mu_n$. Then, f_0 is determined as:

$$f_0(x)=Ne^{-x}(x+\rho\sqrt{x}+p)^p\exp\left\{-\frac{p\rho}{\sqrt{p-1/4\cdot\rho^2}}\tan^{-1}\left[\frac{\sqrt{x}+\rho/2}{\sqrt{p-1/4\cdot\rho^2}}\right]\right\}, \tag{A-3}$$

when $p\geqq\rho^2/4$, and

$$f_0(x)=Ne^{-x}(x+\rho\sqrt{x}+p)^p$$
$$\times\left[\sqrt{x}+\frac{\rho}{2}+\sqrt{\frac{1}{4}\rho^2-p}\Big/\sqrt{x}+\frac{\rho}{2}-\sqrt{\frac{1}{4}\rho^2-p}\right]^r, \tag{A-4}$$

when $p\geqq\rho^2/4$. Here p, r and ρ are defined by:

$$p=3\pi\mu_a{}^2F^2/16c^2\ , \tag{A-5}$$

$$r=p\rho/2\sqrt{\frac{1}{4}\rho^2-p} \tag{A-6}$$

and

$$\rho=b/a\,.$$

(b) There exist the acoustic scattering and the ionized impurity scattering. Then the fundamental equations are Eq. (A–1) and

$$g=-[F\hbar x\sqrt{x}/(ax^2+b')]\frac{df_0}{dx}\,, \tag{A-8}$$

where $a=4/3\sqrt{\pi}\,\mu_l$ and $b'=24/3\sqrt{\pi}\,\mu_i$. Then, the equation for $f_0(x)$ is:

$$\left(x^2+\frac{px^3}{x^2+q_0{}^2}\right)f_0{}''+\left\{x^2+2x+\frac{d}{dx}\left(\frac{px^3}{x^2+q_0{}^2}\right)\right\}f_0{}'+2xf_0=0\,, \tag{A-9}$$

where

$$q_0{}^2=6\mu_l/\mu_i \tag{A-10}$$

Then, the solution of (A–9) is

$$f_0(x)=Ne^{-x}(x^2+px+q_0{}^2)^{p/2}\exp\left\{-\frac{p^2}{2}\frac{1}{(q_0{}^2-p^2/4)}\tan^{-1}\left[\frac{x+p/2}{\sqrt{q_0{}^2-p^2/4}}\right]\right\}, \tag{A-11}$$

when $q_0{}^2\geqq p^2/4$, and

$$f_0(x)=Ne^{-x}(x^2+px+q_0{}^2)^{p/2}$$
$$\times\left[x+\frac{p}{2}+\sqrt{\frac{p^2}{4}-q_0{}^2}\Big/x+\frac{p}{2}-\sqrt{\frac{p^2}{4}-q_0{}^2}\right]^{p^2/4\sqrt{p^2/4-q^2_0}} \tag{A-12}$$

when $q_0{}^2\leqq p^2/4$.

(c) In the general case, where three mechanisms of the scattering must be taken into account, the fundamental equations are again (A–1) and

$$g=-[F\hbar x\sqrt{x}/(ax^2+bx\sqrt{x}+b')]\frac{df_0}{dx}\,. \tag{A-13}$$

In this case $f_0(x)$ can not be expressed by a simple analytic function, but it is given by

$$f_0(x)=Ne^{-x}\exp\left\{p\int^x\frac{xdx}{x^2+\rho x\sqrt{x}+px+q_0{}^2}\right\}. \tag{A-14}$$

References

1) N. Sclar and E. Burstein: J. Phys. Chem. Solids, **2**, 1 (1957). S. H. Koenig and G. R. Gunther-Mohr: J. Phys. Chem. Solids, **2**, 268 (1957). S. H. Koenig: J. Phys. Chem. Solids, **8**, 227 (1959).
2) J. Yamashita and K. Inoue: J. Phys. Chem. Solids, **12**, 1 (1959). J. Yamashita: Progr. Theor. Phys. **24**, 357 (1960). L. Adawi: Phys. Rev. **120**, 118 (1960).
3) M. J. Morin: Phys. Rev. **93**, 62 (1954).
4) E. Conwell and W. F. Weisskopf: Phys. Rev. **77**, 388 (1950).
5) C. Erginsoy: Phys. Rev. **79**, 1013 (1950).
6) Sclar and Burstein, loc. cit.
7) S. H. Koenig: Phys. Rev. **110**, 986 (1958).
8) R. Stratton: Proc. Roy. Soc. London A. **242**, 355 (1957).
9) S. H. Koenig: Phys. Rev. **110**, 988 (1958).
10) M. Lax: J. Phys. Chem. Solids, **8**, 66 (1959).
11) A. L. McWhorter and R. H. Rediker: Proc. I. R. E. **47**, 1207 (1959).
12) Koenig and Gunther-Mohr, loc. cit.
13) V. A. Johnston and K. Lark-Horovitz: Phys. Rev. **82**, 977 (1951).

JOURNAL OF THE PHYSICAL SOCIETY OF JAPAN Vol. 16, No. 4, APRIL, 1961

Studies on the Boundary between Etched and Ground Regions of Ge and Si Single Crystal Surfaces by X-Ray Diffraction Topography

By Zensho ISHII*

Electrotechnical Laboratory, Nagatacho, Tokyo

(Received December 3, 1960)

The anomalous boundary effect similar to these found by Fukushima in guartz were studied by x-ray diffraction topography methods in Ge and Si single crystals. Both Laue and Bragg cases are examined using CuKα and AgKα radiations for various net planes. Results are reasonably explained by assuming a strain gradient perpendicular to the boundary as the previous workers. It was shown that the Borrmann effect as well as the ordinary extinction effect are useful in point-by-point examination of lattice distortions in nearly perfect single crystals.

§1. Introduction

It is well known that the integrated intensity of x-rays reflected from a single crystal is generally enhanced by surface treatments such as grinding[1]. Fukushima[2] found that a region produced by the following treatment had higher intensity than a ground region for a quartz crystal: after grinding a Z-cut surface, a part was etched to produce the boundary line parallel to a Y-plane, and then it was found that at the boundary the integrated intensity of x-rays reflected from the Y-plane in transmission was about twice that from the ground region which remained unetched. Afterwards, this effect, which will be called the boundary effect in this paper, was studied in more detail by Kato[3] with the use of a double crystal spectrometer in quartz, $NaClO_3$ and calcite crystals.

Recently, x-ray diffraction topographic methods have been developed to study lattice defects[4]. In the present experiment, the boundary effect for Ge and Si single crystals was studied by x-ray diffraction topography with a parallel beam arrangement[5)-10)]. By this technique, a topographic information from an extended region was easily obtained with higher resolution (about 20 μ) in comparison with the point-by-point measurement with the counter method which had been used by previous workers. For Ge crystals, photographs of transmission as well as reflection by CuKα were taken for several net planes. For Si crystal, a transmission photograph by AgKα was obtained for net plane parallel to the boundary line on the surface.

§2. Experimental Procedures

2.1. *Preparation of specimens*

Specimens of Ge, about 1 mm thick, were cut parallel to the (110) plane from a single crystal grown from the melt by pulling. The surface was polished and etched with CP4 solution. Before the following surface treatment, the dislocation density of the specimens was estimated to be of the order of $10^3/\text{cm}^2$ by counting individual images of dislocation lines in x-ray transmission photographs. Then one side of the specimen was ground with 1,000 mesh carborundum on a glass plate. After grinding, a part of the surface was covered with commercial cellophane tape**, and etched with CP4 solution for about a half minute. The tape was then stripped off from the specimen. Thus a boundary between the etched and the ground region was produced.

Silicon samples were prepared in a similar way by cutting a wafer, about 1 mm thick, parallel to the (111) plane, from a single crystal. In this case, mixture of HF and HNO_3 (volume ratio=1:3) was used for etching instead of CP4.

2.2. *X-ray technique*

For specimens of Ge and Si, CuKα and AgKα were used, respectively. The apparatus was in principle the same one as those in the previous works[7),8)]. The effective size of the source was about $0.01\times5\,\text{mm}^2$. Fuji autoradiographic plates were used; exposures in transmission took about 1 hour both for CuKα (35 kV, 0.3 mA) and AgKα (45 kV, 0.3 mA), and in reflection about 5 minutes. With this, x-ray transmission or reflection photographs from the extended area of the specimen (about 2×5 mm^2 for transmission and 2.5×7 mm^2 for reflection) was obtained.

---

* Present address: Sony Corporation Research Laboratory, 351, Kitashinagawa-6, Tokyo.

** This was neither dissolved nor stripped off during etching processes.

§ 3. Experimental Results and Discussions

For Ge crystals, transmission (Laue case) as well as reflection photographs (Bragg case) were taken for two reflecting planes for each case, to study the direction of strain gradient at the boundary.

3.1. *Transmission photographs*

In one case, the boundary line was produced in a direction of [001] (Fig. 1a), while in another case, in a direction of $[\bar{1}10]$ (Fig. 1b). In both cases, the thickness of the specimens, D, was almost the same, about 1 mm. Since $\mu=379$ cm^{-1}, μD was about 37.9 and very large compared with unity. As transmission photographs, both diffracted beams (denoted by R) and transmitted beams (denoted by R_0) were taken, both of which gave the same results. Therefore, it is concluded that the intensity contrast is caused by the Borrmann effect[11]. X-ray transmission photographs of the $(\bar{2}20)R_0$ with CuKα in the former and latter cases are shown in Fig. 2 and 3.

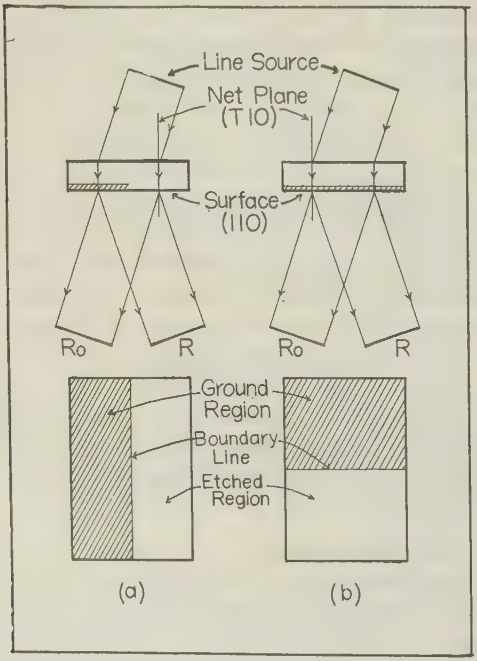

Fig. 1. Schematic diagrams of experimental arrangements.
(a) Boundary Line // [001]
(b) Boundary Line // $[\bar{1}10]$

3.2. *Reflection Photographs*

Photographs of the specimen used in 3.1. was taken by reflection method, that is, the Berg-Barrett method, with the use of CuKα. As reflecting planes the (110) and (100) planes were used. The former is parallel to the surface, whereas the latter intersects the surface at 45 degrees, as shown in Fig. 4, and had not been tried by previous workers. X-ray photographs of the (220) and (400) reflections are given in Fig. 5 and 6, respectively. In the (220) reflection no change of intensity was observed at the boundary, but in the (400) reflection a noticeable change was observed.

3.3. *Discussions on the experiments with Ge*

(a) It has been established that the anomalously transmitted intensity is weakened at distorted regions, such as dislocation lines[5,6,12] and strains[7,8,13], in comparison with the one at perfect regions. It is expected as in the case of extinction effect that the decrease of the anomalous transmission is largest if the direction of the strain gradient is normal to the net plane concerned. For both cases corresponding to Fig. 2 and 3, the mean intensity of the etched region was stronger than that of the ground region, but the intensity change at the boundary was different; for the former case, the intensity decrease compared with that of the ground region was observed, while not for the latter case. From these transmission photographs it is concluded that the distortion is stronger at the boundary than in the ground region, and the strain gradient has a component perpendicular to the boundary. This conclusion is in agreement with that of previous workers.

(b) In the reflection photographs, the boundary effect was not observed for the (220) reflection, whereas it was observed for the (400) reflection. As a cause for the above difference, two possibilities might be considered. Firstly, it might be considered that the strain gradient has no component normal to the surface. As its result, the boundary effect will not be observed for the (220) reflection. However, even if the component of the strain gradient normal to the surface exists, it would be plausible that the boundary effect will not come into observation for the (220) reflection, if the penetrating thickness of x-rays is negligible in comparison with that of the region responsible for the boundary effect.

(c) In transmission as well as in reflection photographs, local fluctuations of the intensity are observed not only on the ground but also on the etched regions. These phenomena

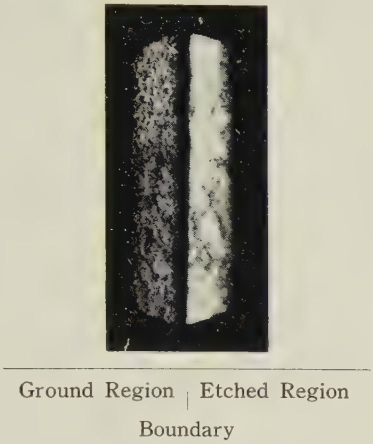

Fig. 2. Transmission photograph of $(\bar{2}20)R_0$ on Ge, the net plane being parallel to the boundary.

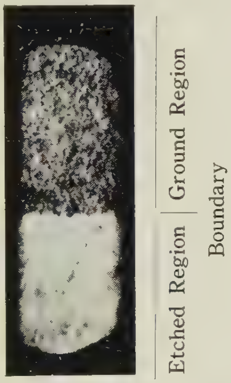

Fig. 3. Transmission photograph of $(\bar{2}20)R_0$ on Ge, the net plane being perpendicular to the boundary.

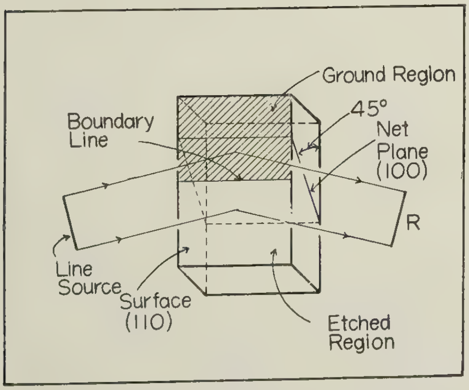

Fig. 4. Schematic diagram of experimental arrangement for reflection photographs.

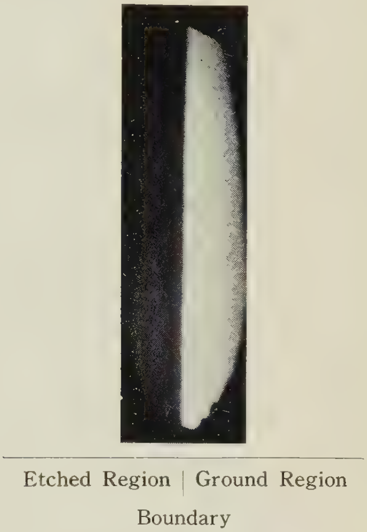

Fig. 5. The (220) reflection photograph of Ge.

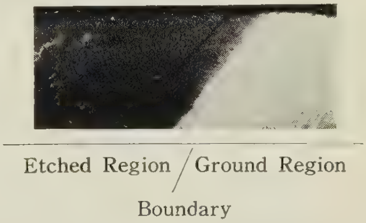

Fig. 6. The (400) reflection photograph of Ge.

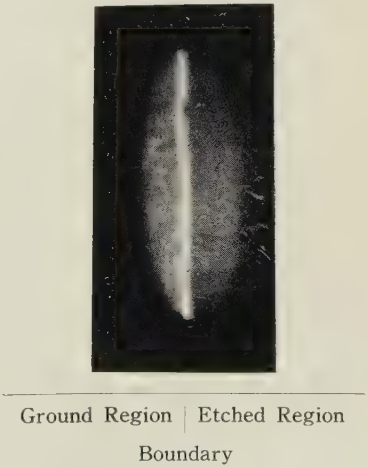

Fig. 7. Transmission photograph of $(\bar{2}20)R$ on Si, the net plane being parallel to the boundary.

mean that some parts remain in a rather perfect state still after grinding, and on the other hand, some parts are still distorted after half-minute etching. It is considered that distortions caused by grinding are localized, and some distortions cannot be removed by the etching.

In Fig. 6, a subsidary intensity decrease on the side of the ground region was also observed near the boundary. This might be probably attributed to the fact that a less distorted region exists close to the boundary.

3.4. *Transmission experiment in Si*

For a specimen of Si, a boundary line perpendicular to $[\bar{1}10]$ on the surface (111) was produced. Diffraction photograph of $(\bar{2}20)$R in transmission with AgKα is shown in Fig. 7. Contrary to the case of Ge, the intensity contrast was caused by the ordinary extinction effect because μD was very small, about 0.8*. The intensity in the ground region was stronger in comparison with the one in the etched region, and at the boundary it was stronger than in the ground region. This result is essentially the same as that of previous workers and also consistent with that of 3.1.

Present informations are insufficient for discussing the fine structures above-mentioned in more detail. But the diffraction topography method proves to be useful for studying the fine structures of the boundary, because the topographic information is easily obtained with high resolution in comparison with the point-by-point intensity measurement.

Acknowledgement

The author should like to express his sincere thanks to Prof. K. Kohra, University of Tokyo, for his guidance throughout this work, to Prof. E. Fukushima, Tokyo Metropolitan University, for his valuable discussion and to Drs. G. M. Hatoyama**, M. Shibuya and N. Sakamoto, Electrotechnical Laboratory, for their encouragements and interests.

References

1) For example, refer to R. W. James: The optical principles of the diffraction of x-rays (G. Bell and Sons LTD, 1954) 340–341p.
2) E. Fukushima: Acta Cryst. **7** (1954) 459.
3) N. Kato: J. Phys. Soc. Japan **11** (1956) 748.
4) For example, as a general survey, K. Kohra: Kinzoku Butsuri (Metal Physics, in Japanese) **5** (1959) 91.
5) H. Barth and R. Hoseman: Z. Naturforsch. **13a** (1958) 792.
6) V. Gerold and F. Meier: Z. Phys. **155** (1959) 387.
7) Z. Ishii and K. Kohra: J. Phys. Soc. Japan **14** (1959) 1250.
8) Z. Ishii, T. Furuoya, Y. Sasaki and K. Kohra: J. Phys. Soc. Japan **15** (1960) 206.
9) M. Yoshimatsu and K. Kohra: J. Phys. Soc. Japan **14** (1959) 1249.
10) M. Yoshimatsu and K. Kohra: J. Phys. Soc. Japan **15** (1960) 1760.
11) For example, refer to the following literatures; G. Borrmann: Z. Phys. **127** (1950) 297. M. von Laue: Acta Cryst. **2** (1949) 106. G. L. Rogosa and G. Schwarz: Phys. Rev. **87** (1952) 995.
12) G. Borrmann, W. Hartwig and H. Irmler: Z. Naturforsch. **13a** (1958) 423.
13) L. P. Hunter: J. Appl. Phys. **30** (1959) 874.

---

* μ of Si is 8.3 cm^{-1} for AgKα and D about 1 mm.

** Now, Sony Corporation Research Laboratory.

JOURNAL OF THE PHYSICAL SOCIETY OF JAPAN, Vol. 16, No. 4, APRIL, 1961

The Switching Circuit Logically or Functionally Equivalent to a System of Biochemical Reactions

By Motoyosi SUGITA

Hitotsubashi University, Kunitachi, Tokyo, Japan

(Received October 26, 1960)

The analogy or the correspondence between the controlled or catalytic reaction and the switching circuit is given, showing that an arbitrary logical circuit can be translated into a system of controlled chemical reactions, which are catalyzed by some of the reaction products of this system. The realizability of such a chemical system is not considered but the logical possibility is discussed using several examples. Nevertheless, we can imagine a way to combine the knowledge of biochemical reactions to various physiological functions and can give useful suggestions to the experimental analysis of the biochemical reactions from the view-point of logical or functional analysis.

§ 1. Introduction

There is an idea of reconstructing a system, which has at least some functions resembling the organism, using the parts of the same organism. For this purpose *logical analysis of the function* of the composed system is necessary. The author has suggested[1] the analogy between switching circuits and enzymatic reactions, where enzyme actions are considered as on-off controls. In this note it is proposed to translate the mutual interaction within a complex chemical system, the reaction rates of which are controlled by the reaction products, to the equivalent logical circuit having the same logical functions.

§ 2. Logical Circuit and Chemical Reaction

Let us consider at first the correspondence of the controlled or catalyzed reaction like $A \xrightarrow{X} B$ to the switching circuit. For simplicity, we consider only the state of the existence or of the non-existence of the catalyzer X. We assign 1 to the former and 0 to the latter. Then $X=1$ corresponds to the *on* state, and $X=0$ to the *off* state of the switching circuit. Only the *on-off control* is considered here.

In the same way only the existence or non-existence of A or B will be considered. The accumulation of the substance B, for instance, will be neglected, considering that the leakage of B due to the consecutive reactions like $A \xrightarrow{X} B \longrightarrow \cdots\cdot$ makes $B=0$ after a short time when the reaction $A \xrightarrow{X} B$ has been repressed. The transient state during the short interval between the cut off of the flux $A \longrightarrow B$ and the terminal state of B, to which 0 is assigned, will be neglected.

If the repression is due to $X=1$, X is called the *repressor*, while, if it is due to $X=0$, X is called the *inducer*. The repression is written as

$$A \xrightarrow{\bar{X}} B \quad \text{or} \quad A \xrightarrow{\overset{X}{\not\downarrow}} B \qquad (1)$$

where $\bar{X}$ is the *negation* of X and $X \not\longrightarrow$ is equivalent to $\bar{X}$. If X is an inducer and $X=1$, the steady level of B will attain a certain value which is not equal to 0. We will consider only the *steady state* of B and assign 1 to the state of B which is not zero. Therefore, we can get the logical relation:

$$\left.\begin{array}{lll} B=X & \text{for inducer} & \text{and} \\ B=\bar{X} & \text{for repressor.} & \end{array}\right\} \qquad (2)$$

Therefore, in the case of a repressor, the existence of $X\,(X=1)$ corresponds to the non-existence of B and the non-existence of X $(X=0)$ to $\bar{X}=1$ and then to the existence of B.

The device for the conversion of X to $\bar{X}$ is called the *Not* element and represented by $\not\longrightarrow$ of (1). The following system of chemical reactions will have function of *Not*.

$$A \xrightarrow{X} B,\ P \xrightarrow{\bar{B}} Q \quad \text{or} \quad \begin{tikzcd} & X \arrow[d, "+"] & & \\ A \arrow[r, no head] & {} \arrow[r] & B \arrow[d, "/" marking] & \\ & P \arrow[r, no head] & {} \arrow[r] & Q, \end{tikzcd} \tag{3}$$

then we have

$$Q=\bar{X} \qquad \text{or} \qquad X \nrightarrow Q=\bar{X}, \tag{4}$$

where the notation $\xrightarrow{+}$ denotes the induction. $+$ is used here to differentiate the transfer of information or of the controlling action from the flux of chemical reaction. It is also true for $\nrightarrow$. The difference between the flux of *information* and that of chemical reaction is very important and should not be confused[2].

Meanwhile, in the following case:

$$\left.\begin{array}{l} \qquad A\xrightarrow{\bar{X}}B,\quad P\xrightarrow{\bar{B}}Q, \\ \text{we can see that} \\ \qquad\qquad Q=X \end{array}\right\} \tag{5}$$

because $Q=\bar{B}$, $B=\bar{X}$,

therefore,

$$Q=\bar{\bar{X}}=X, \tag{6}$$

i.e. the negation of negation of X is X itself. The enzyme induction of the type (5) is indirect. However, we will abstract the difference of the *direct* and the *indirect* types of enzyme induction from the *logical* point of view. According to this view-point the following system of reactions

$$\left.\begin{array}{l} A\xrightarrow{X}B,\ P\xrightarrow{B}Q,\ S\xrightarrow{Q}T,\ U\xrightarrow{T}V, \\ \text{can be expressed simply by} \\ V=X \quad \text{or} \quad U\xrightarrow{X}V. \end{array}\right\} \tag{7}$$

Besides *Not* there are two further logical elements, which are at least necessary for the construction of logical circuit, i.e. *Gate* and *Buffer*.

Gate is rather easy to construct. Let us take the following consecutive reactions

$$A\xrightarrow{X}B\xrightarrow{Y}C. \tag{8}$$

Assuming two valued logic and on-off control of X or Y, we can see that the equation of the *logical product*

$$C=XY, \tag{9}$$

shows the logical structure of that controlled reaction (8). (9) may correspond to the product effect of some medicals.

It is rather painstaking to imagine a chemical system having the character of a *Buffer*, having a series or consecutive structure instead of a parallel one (the parallel one corresponds to the conversion of the bi-path of the metabolic pathway to the main route, for instance). The author has considered the following scheme

$$A\xrightarrow{\bar{X}}B\xrightarrow{\bar{Y}}C,\quad S\xrightarrow{\bar{C}}P. \tag{10}$$

Then we have

$$C=\bar{X}\bar{Y},$$

and

$$P=\bar{C}.$$

From the formula of symbolic logic we have

$$P=\bar{C}=\overline{\bar{X}\bar{Y}}=X+Y. \tag{11}$$

(11) is the equation of the *logical sum*. The correlation of reactions can be written schematically in

$$\begin{tikzcd} & X \arrow[d, "/" marking] & & Y \arrow[d, "/" marking] & & \\ A \arrow[r, no head] & {} \arrow[r] & B \arrow[r, no head] & {} \arrow[r] & C \arrow[d, "/" marking] & \\ & & & S \arrow[r, no head] & {} \arrow[r] & P, \end{tikzcd} \tag{12}$$

§ 3. Chemical Equivalent of Flip-Flop

Concerning the function of *Storage* we can imagine the system of chemical reactions rather easily. For instance, let us translate the logical circuit of flip-flop to a system of controlled chemical reactions. Then we have the scheme given by

$$\left.\begin{array}{l} \quad A_2\xrightarrow{\bar{a}}A_1\xrightarrow{\bar{x}}A, \\ \qquad \sigma_1\xrightarrow{\bar{A}}\sigma,\quad x_2\xrightarrow{\bar{\tau}}x_1\xrightarrow{\sigma}x, \\ \text{and} \\ \quad B_2\xrightarrow{\bar{b}}B_1\xrightarrow{\bar{y}}B, \\ \qquad \tau_1\xrightarrow{\bar{B}}\tau,\quad y_2\xrightarrow{\bar{\sigma}}y_1\xrightarrow{\tau}y. \end{array}\right\} \tag{13}$$

or by Fig. 1

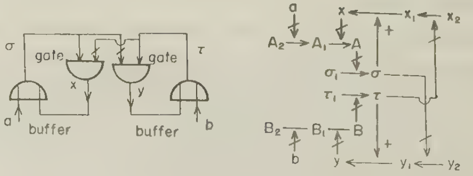

Fig. 1.

The logical equations are common to both systems, electric circuit as well as chemical system, and are given by

$$\sigma=a+x\,,\quad x=\sigma+\bar{\tau}\,;\quad \tau=b+y\,,\quad y=\tau+\bar{\sigma}\,. \tag{14}$$

The analogy of flip-flop and the reaction in vivo may be rather crude. However, many types of the resembling phenomena can be seen, which are the conversion of the course of the reaction systems, like immunological memory, the change of the course of the reaction systems at the start of cell division, the recovery in the resting state of the daughter cells. In such cases this analogy of flip-flop may be suggestive. Rhythmic reaction of iron in HNO_3 solution may also be interpreted from this point of view. The author is not sure whether the change of ionic permeability of cell membrane of nerves can be explained in this manner.

How to realize the system of reactions (13) is neglected here. Only the existence of such a conversion of the mode of reaction systems is considered from the logical point of view.

§4. Translation of a Logical Circuit of Industry into Chemical Systems

Let us try to translate a logical circuit of modern factory responding to the alarm from the control system as is given by Fig. 2,

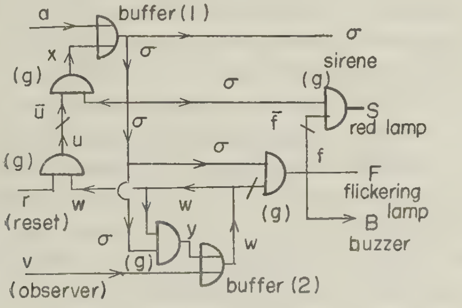

(g): Gate, a: signal from the control system

Fig. 2.

where a is the signal corresponding to an extraordinary state of affairs. σ is the corresponding signal, which will actuate the siren. v is the signal from the button of the watcher. If it is pushed, then $v=1$ and $w=1$, because v and w are connected by the Buffer (2). If $w=1$ and $\sigma=1$ the logical product y is 1, which is put in the Buffer and the signal w is reproduced and is held, though v is cut off. If w and r are not zero, the logical product $u=rw$ is 1, where r is the signal of reset action. Therefore, $\bar{u}=\bar{r}+\bar{w}$ shows that the siren is not stopped during the interval in which $r=0$ or $w=0$, accusing the carelessness of the service men, because the internal instead of external (a) input to the Buffer (1), $x=\sigma+\bar{u}$, reproduces the signal constantly during this interval.

The flickering lamp F will go out, if $w=1$, because there is a *Not* element, i.e. $f=\sigma\bar{w}$. If $f=0$, then $s=\sigma\bar{f}=1$ and the red lamp will go on.

To translate the logical function of this circuit, we have taken the following reaction systems into account

$$\left.\begin{array}{llll}
1) & A\xrightarrow{\bar{a}}B\xrightarrow{\bar{x}}C & 5) & w_1\xrightarrow{\bar{Z}}w \\
2) & \sigma_1\xrightarrow{\bar{C}}\sigma & 6) & Z_2\xrightarrow{\bar{y}}Z_1\xrightarrow{\bar{v}}Z \\
3) & x_2\xrightarrow{\bar{u}}\bar{x}_1\xrightarrow{\sigma}x & 7) & y_2\xrightarrow{\sigma}y_1\xrightarrow{w}y \\
4) & u_2\xrightarrow{w}u_2\xrightarrow{r}u & &
\end{array}\right\} \tag{15}$$

The branched reactions are

$$S_2\xrightarrow{\sigma}S_1\xrightarrow{\bar{f}}S,$$
$$F_2\xrightarrow{\sigma}F_1\xrightarrow{\bar{w}}F.$$

The intuitive representation of (15) is given by Fig. 3. If we assume here that $a=0$, then the reactions (1) and (6) are realized and other reactions are stopped. If a is introduced which corresponds to a substance introduced into our body, 1) is repressed and 2) and 3) will start. Then, if the signal v is put in, the reaction 6) is repressed and 5) and then

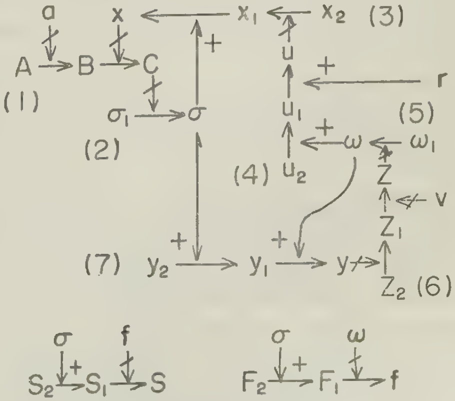

Fig. 3.

7) will start. If the reset key is pushed, the reaction 4) is excited and 3) is stopped. Then x becomes zero and 1) is again set in action. 2) and 7) are then stopped and 6) starts again. Thus 5) and 4) are also stopped and the total system recovers the initial state.

The corresponding logical relations, which are common to Fig. 2 and Fig. 3 are

$$\left.\begin{array}{l} \sigma=a+x\ ,\ x=\sigma\bar{u}\ ,\ u=rw \\ w=v+y\ ,\ y=\sigma w \\ \text{for the main circuit and} \\ f=\sigma\bar{w}\ ,\quad s=\sigma\bar{f} \end{array}\right\} \qquad (16)$$

for the branched reactions.

There may be many other possible block diagrams like Fig. 2 or chemical systems like (15) logically equivalent to (16), while only the logical possibility is considered here. Therefore, the correspondence above considered is not the only one possible but merely tentative. Our aim, however, is to take such logical correspondence into consideration in the analysis of the *physiological* functions of the chemical system in vivo.

§ 5. Concluding Remark

We are not yet well acquainted with the analogy considered above, because our knowledge concerning the biochemical facts is not enough to clarify the correspondence between the chemical reaction systems and the logical circuit in details. So that just an attempt to show the possibility is given in this paper. Some examples of logical circuits are translated into a scheme of chemical system. However, the translation of chemical systems, which are well known, to an equivalent logical circuit is more important and moreover our final aim. While the details of such chemical systems in vivo are not well known to us yet, the above consideration will suggest a way to proceed to the experimental analysis of such systems and to connect biochemistry to physiology.

We have considered here a simplified model of on-off control based on the two-valued logic. There may be many more complex forms of interactions such as, the regulation of the reaction systems, conversion of the mode of the chemical reactions as a whole, adaptive formation of enzymes, the change of the enzyme patterns, immunological memory, and maintenance of the dynamical equilibrium of open systems. In these and other cases, analogue simulation as well as many-valued logic may prove to be more useful, although the analysis may be very difficult.

The interaction or correlation between chemical systems considered above resulted from the catalytic action of some reaction products. In this type of interaction to be called the indirect interaction, one reaction controls the neck factor of the other reaction. The flux J of the latter reaction is determined by

$$J=\text{neck factor}\cdot\text{intensive factor}\ . \qquad (17)$$

Here the intensive factor is a quantity of thermodynamical nature and depends on the chemical potentials, for instance, of the reacting components[3]. The neck factor depends on the rate constants which may be controlled by the catalyzer. There is another type of interaction, to be called the direct interaction, in which the effect of one reaction enters in the intensive factor of the other reaction. In general, we must take both types of interactions, but, for simplicity, we have considered only the indirect one.

In the ordinary theory of irreversible processes, the neck factor has been assumed constant in the phenomenological equations like (17) but the system with indirect correlation cannot be treated by such a formulation. The author has called the theory containing variable neck factors the *flexible neck theory* and the indirect correlation controlled by the flexibility of neck factors the *informational correlation*. Application of this theory to biophysics is given in another paper[2] (in Japanese) and its revised version in English will be published in the near future[4].

References

1) M. Sugita: Vol. 3. Chapter I of Gendai Seibutugaku Koza (Modern Biology), (1957, Kyoritusya).
2) M. Sugita: Bull. Kobayahi Inst. **8** (1958) 159.
3) M. Sugita: The Annals of Hitotsubashi Acad. IV (1954) 163.
4) M. Sugita: J. Theor. Biol. (in preparing).

Addendum

Induction or repression may be replaced by activation and inhibition.

JOURNAL OF THE PHYSICAL SOCIETY OF JAPAN, Vol. 16, No. 4, APRIL, 1961

Mass Spectrometric Study on the Evaporation of Volatile Components in Polyethylene

By Kisaku NAKAGAWA

Electrical Communication Laboratory, Nippon Telegraph and Telephone Public Corporation, Musashino-shi, Tokyo, Japan

(Received December 20, 1960)

Many ions were observed in the spectra of polyethylene heated in the ion source of a mass spectrometer for the temperature range of 150–330°C. With elevation of temperature, the rate of ionic yield displayed a stage of slower increase, Process I, followed by a steeper uprise, Process II. For two commercially available polyethylene, Marlex and Hostalen, it was found that the values of activation energy for the latter stage appeared to be 34 kcal/mol for Marlex and 24.7 kacl/mol for Hostalen. On the contrary, the values for Process I were found to be 6.5 ± 1.2 kal/mol for both samples. According to the mass spectra obtained and the values of activation energy, it was concluded that Process II is corresponding to the stage of thermal degradation, while Process I would be explained by the presence of a stage of evaporation of lighter components included originally in polyethylene.

§ 1. Introduction

A mass spectrometer has been utilized by many investigators to analyze the gaseous components of decomposed polymers[1),2)]. In spite of the various advantages proper to the instrument, the technical difficulties of making the sample into gaseous state and the limited mass range or the finite resolving power have prevented the direct application of this sensitive instrument to the analysis of high polymers. The work carried out by Bradt, et. al.[3)] has been quite unique, but further reports have not been appeared thereafter.

However, the recent advances in the field of high molecular weight mass spectrometry have enabled us to deal with the heavy hydrocarbons with carbon atoms as many as 40 or more[4),5),6)]. Fortunately, moreover, the straight chain hydrocarbons with more than about 15 carbons were shown to exhibit relatively simple spectra[4)]. That is, as the number of carbon atoms increases the mass spectra tend to approach to a particular pattern in which the principal peaks appear within the range of C_3–C_8, followed by the heavier ions diminishing monotonously. This means that the difficulties due to the distribution of molecular weight could be eliminated so long as their structures were concerned. Furthermore, when the short branches or double bonds were present in almost linear chains, the deviation in the spectra from the normal pattern would be expected to appear.

On the other hand, the high polymers may be supposed to have a considerable amounts of low molecular weight components in their wide-spread distribution. Among these lighter components the molecules so small as to be volatile under certain conditions may be expected to exist. Aside from the question whether these smaller molecules are still similar to the longer or not, it may be interesting to make a trial to assure the presence and the possibility of direct analysis of these volatile components. The complete analysis of innumerable members constituting the polymer would be impossible, but a statistical informations about the structure, especially for the branches or terminals, if obtainable, might be much helpful in the future development for the study of the molecular structures of high polymers.

This is a report of a experiment carried out preliminarily for commercially available polyethylene, Marlex 50–15 and Hostalen GD. Emphasis was placed on the confirmation of possibility if the ions could really be detected at the temperature where the thermal degradation has not been taking place.

§ 2. Experimental

A conventional ion source was slightly modified by stringing tungsten heater around the gas inlet glass pipe to serve as a simple furnace. Sample polymer placed in a small glass vessel were pushed into the furnace as seen in Fig. 1. Temperature was estimated by an Alumel-Chromel thermocouple enclosed in a glass tubing.

The mass spectrometer used was the Hitachi RMU-5 type. The ion acceleration was reduced to 1,000 volts to extend the mass range to about C_{18} group. The resolving power at the condition was 170 or slightly less. In this work, sample polymer were sliced to small pieces of about 0.5 mm thick from the raw pellets which had not been undergone any previous treatments.

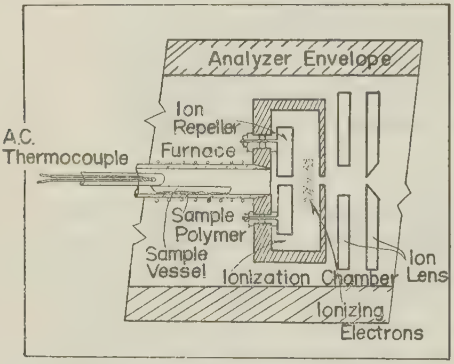

Fig. 1. The ion source with the furnace.

Experiments were carried out at the several points between 150–330°C. The heating to higher temperature could not be performed because the rapid increase of the products from the polymer provoked the electric breakdown between the high voltage electrode and the grounded analyzer envelope. Thus, in our case, the upper limit of temperature was determined by the amounts of sample loaded.

Throughout the experiments the ion source temperature was kept constant at 200°C. The value was determined by a preparatory experiment in which the standard n-$C_{16}H_{34}$ molecules were found to exhibit the smallest fluctuation in the pattern against the ion source temperature variation.

It took about 15 minutes to scan from C_1 to C_{18}, the repeated runs represented no remarkable decrease in ion intensity. The memory effect was examined by ceasing the heating of the furnace before elevating temperature to the next stage. About half an hour was sufficient to reduce the peaks to the amount corresponding to the sample temperature, which was in equilibrium to the ion source temperature. In conclusion, the memories were not essential in this case because the rate of increase of ionic yield was high

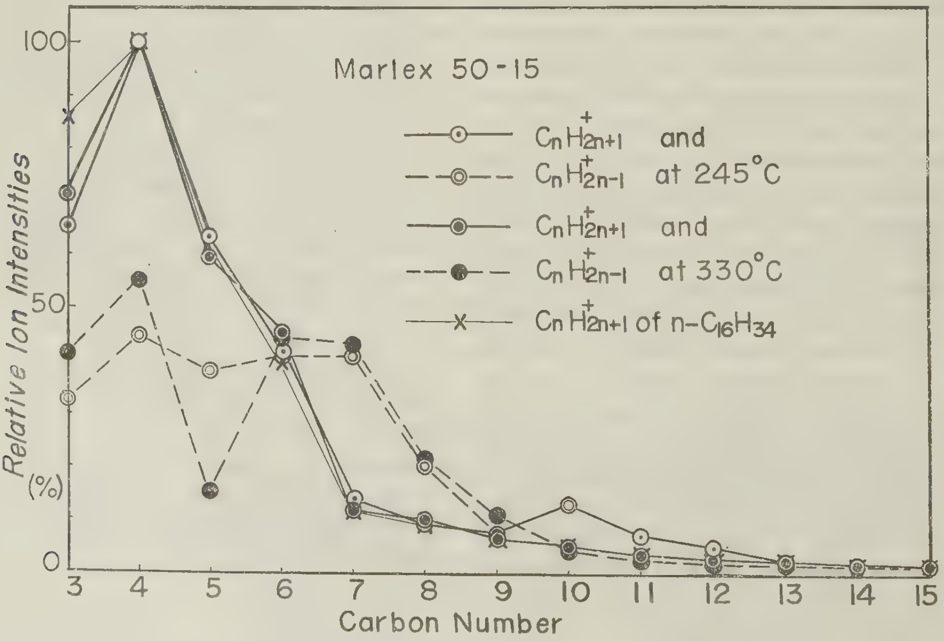

Fig. 2a. The relative intensities of $C_nH^+_{2n+1}$, and $C_nH^+_{2n-1}$ for each C_n-group obtained from Hostalen GD (nominal molecular weight; 70,000). The corresponding values from n-$C_{16}H_{34}$ were shown, too.

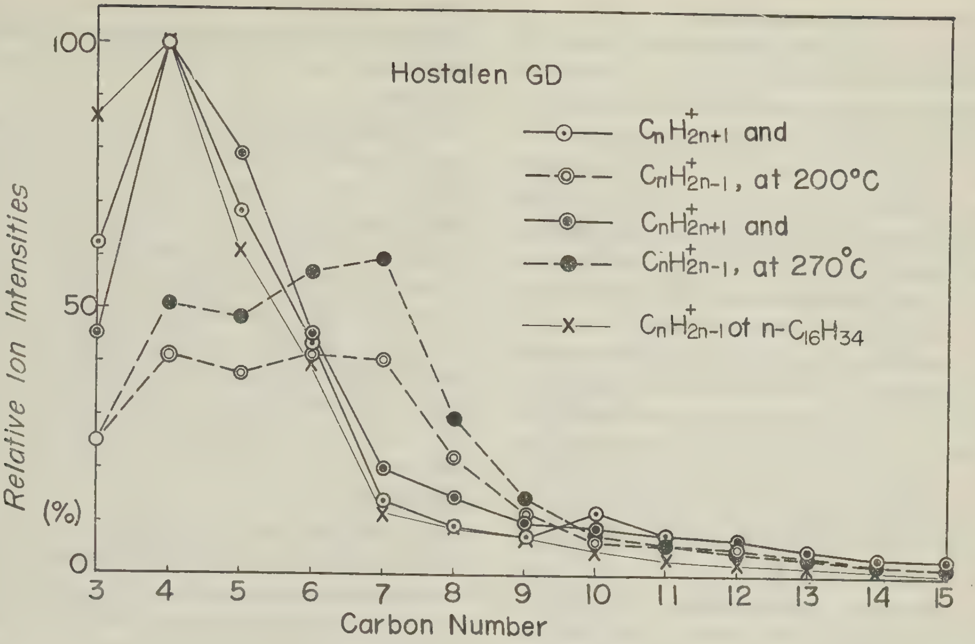

Fig. 2 b. The relative intensities of $C_nH_{2n+1}^+$, and $C_nH_{2n-1}^+$ for each C_n-group obtained from Marlex 50-15. (nominal molecular weight; 70,000) The corresponding values from n-$C_{16}H_{34}$ were shown, too.

enough to neglect the memories of the previous stage.

§ 3. Results and Discussion

F or both polyethylene, lots of peaks were observed in group for every carbon number to the extent of our upper limit of mass range. The succeeding groups, except for the anomalies seen in C_{10}'s and C_{11}'s, displayed a monotonous decrease from group to group with the increase of carbon number. Each group consisted of $C_nH_{2n+1}^+$, $C_nH_{2n-1}^+$, $C_nH_{2n}^+$, $C_nH_{2n-2}^+$, and lower intensity ions. Of all ions and at all temperature stages, $C_4H_9^+$ was the largest (base) peak. The percentage intensities of $C_nH_{2n+1}^+$'s and $C_nH_{2n-1}^+$'s relative to the base peak were illustrated in Fig. 2 a) and b) for two stages of temperature. The corresponding peaks of standard n-$C_{16}H_{34}$ were superimposed thereon. Although the mere resemblance appears to be difficult to bring detailed informations, it is verified that the ions of hydrocarbon molecules having considerable long chains, at least 18 carbon atoms, were obtained from polyethylene under these conditions.

A tentative classification for each sample and for each sequence of $C_nH_{2n+1}^+$ and $C_nH_{2n-1}^+$ was made with respect to their behavior of the relative intensities against the sample temperature. Accoring to the result of this classification, $C_3H_7^+$, $C_{10}H_{21}^+$, $C_{11}H_{23}^+$, and $C_3H_5^+$ were shown to exhibit abnormal behavior to all other ions in their respective

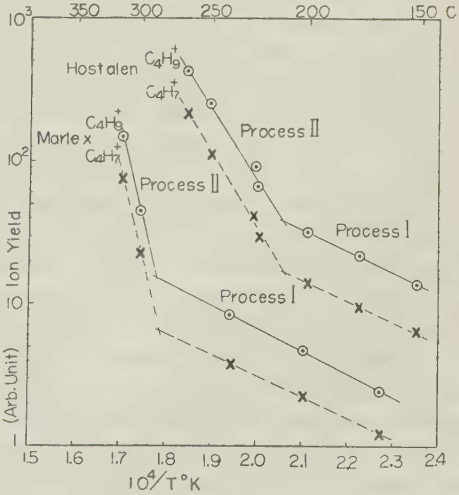

Fig. 3. Ionic yield versus the reciprocal of the temperature heated. Above the top abscissa the temperature in °C was given.

sequence. The disappearance of $C_{10}H_{21}^+$ and $C_{11}H_{23}^+$ at the higher temperature might be correlated to the fact that these ions were quite sensitive to the ion source temperature.

In Fig. 3, the temperature dependence of typical peaks was shown by semi-log plot. As seen clearly from the figure, the processes of ionic production, namely, the production of vapor from the polymer, composed of two stages: gradual increase of the yield in the lower temperature range, Process I, and following steeper uprise at the higher temperature, Process II. Since in our case, the peak-heights could be regarded as to be directly proportional to the rate of yield of vapor products which are to make impacts with electrons in the ionization chamber to form the positive ions, the activation energy could be calculated from the figure directly.

For Process II, the activation energy was calculated to give the values of 24.7 kcal/mol and 34 kcal/mol for Hostalen and Marlex, respectively. Two ionic species for a sample were regarded to behave similarly to each other. These values are much lower than those of thermal degradation presented by Jellinek[7] who offered the values of 46–66 kcal/mol for different molecular weights of polyethylene examined, and Madorsky's value[8] of 71 kcal/mol. Interesting is the fact that one of our values are happened to be very close to the value, 24.5 kcal/mol, which was proposed by Jellinek[7] in his work where polystyrene was degradated in vacuum at the temperature range, 248–340°C. Jellinek assumed that the weak link decomposition and the inhibition take place simultanesusly. In view of the molecular weight of Marlex used (estimated by viscosits measurements to give 47,000), the value, 34, kcal/mol, is too low to correspond to the random C–C scissions. Although it is not obvious at this stage whether the agreement for Hostalen with polystyrene is accidental or it indicates that the proceess of weak link rupture is essentially independent of the kinds of polymer, Hostalen and Marlex might possibly be concluded to begin to degradate at about 200°C and near 300°C, respectively. To determine the reaction mechanism dominating this stage, much more works are required.

The situation was illustrated in Fig. 2 a) and b). The patterns obtained at Process I give almost similar featurs for both polyethylene, whereas the values at Process II exhibited departure from each other as well from the standard.

For the Process I, the calculated values of the activation energy turned to be 6.7 and 5.8 kcal/mol for $C_4H_9^+$ and $C_4H_7^+$ from Hostalen, and 7.6 and 6.5 kcal/mol for the corresponding ions from Marlex. Taking the mean values of all other ions belonging to each sequence, the value for Process I appeared to be 6.5±1.2 kcal/mol. Taking into account the limited accuracy of the measurements, the whole ions which appeared at the temperature range lower than the knick shown in Fig. 3, could be regarded to have been generated through a stage, Process I.

In view of the low values of activation energy obtained for this pre-degradation stage, a process of evaporation were assumed to exist. Employing the spin-echo technique, McCall et. al.[9] estimated the activation energy of the low pressure polyethylene to be 5.3 kcal/mol. The leveling off of this value at about C_{20}–C_{30} was reported by the same authors in correlating to the segmental motion in the molecular flow in polymer. On the other hand, Jensen[10] estimated the vapor pressure of polyethylene (details were not given) by evacuating a oven containing the polymer through an orifice. Jensen reported that the vapor pressure, P, for the temperature range from 30°C up to 180°C, were expressible as $\log P = 7.4 - 4{,}500/T$, which is equivalent to the energy of activation of 8.9 kcal/mol.

Considering the difference in the ratio of the sample area to pump-out speed of outs and Jensen's, our values at Process I would indicate that the evaporation of lighter components aae taking place, and the rate of the process are determined by the diffusion of the components through polymer molecules.

§ 4. Conclusion

The behavior of the production of vapor of polyethylene was examined in a mass spectrometer. The rate of increase of ionic yield was found to be composed of two stages, Process I and II. The values of activation energy were calculated to be 6.5±1.2 kcal/mol for Process I, and 24.7 kcal/mol (for Hostalen) and 34 kcal/mol (for Marlex) for Process II. The latter stage would be correlated (for

Marlex) for Process II. The latter stage would be correlated to the thermal degradation, the mechanism of which was dominated by a reaction having a lower energy of activation, such as, for instances, the weak link rupture or so.

From the view points of the low lying value of activation energy and the mass spectra in which the hydrocarbon ions with a considerable long chains appeared, a stage of evaporation of the ligher components was concluded to exist. In this stage, Process I, the rate of production may perhaps be determined by the stage of diffusion of the lighter components through polymer molecules.

The author wishes to express his grateful thanks to Dr. A. Nishioka in his much instructive suggestions and constant encouragements during this work. He would like also to thank to Mr. Takei for the assistance in the measurements.

References

1) Samuel L. Madorsky, Sidney Straus, Dorothy Thomson, and Laura Williamson: J. Res. Nat. Bur. Stand. **42** (1949) 499.
2) B. G. Achhammer, M. J. Reiney, L. A. Wall, and F. W. Reinhart: J. Polymer Sci. **8** (1952) 555.
3) P. Bradt, V. H. Dibeler, and F. L. Mohler: J. Res. Nat. Bur. Stand. **50** (1953) 201.
4) M. J. O'Neal: *Mass Spectroscopy in Physics Ressarch*, (Nat. Bur. Stand. circular 522, 1953) 217.
5) A. Hood and M. J. O'Neal: *Advances in Mass Spectrometry*, (Pergamon, 1959) 175.
6) Norman Coggeshall: J. Chem. Phys. **33** (1960) 1247.
7) H. H. G. Jellinek: J. Polymer Sci. **3** (1948) 859, **4** (1949) 1, 13.
8) Samuel L. Madorsky: J. Polymer Sci. **9** (1952) 133.
9) David W. McCall, Dean C. Douglass, and Ernest W. Anderson: J. Chem. Phys. **30** (1959) 711.
10) Niels Jensen: J. Appl. Phys. **27** (1956) 1460.

JOURNAL OF THE PHYSICAL SOCIETY OF JAPAN, Vol. 16, No. 4, APRIL, 1961

Interaction between Polyions and Low Molecular Ions

By Nobuhisa IMAI

Faculty of Science, Nagoya University, Chikusa, Nagoya

(Received January 6, 1961)

The characteristic nature of ion-binding of much charged polyions has been investigated mainly on the basis of the Poisson-Boltzmann (P.B.) equation and partly through the conductance experiment. In general, the ion-binding can be classified into two types, the ψ-binding and the P-binding. The former is due to the electrostatic field around polyions, while the latter is due to the short-range interaction between ionized groups of polyions and salt-ions. Through the theoretical analysis of non-linear property of the P.B. equation, we have found, for every shape of polyions, the strong ψ-binding of counterions which greatly depresses the polyion-charge within a thin ion-condensation phase around the polyion. By exactly solving the two-dimensional P.B. equation, we have also obtained the ion-distribution around many rod-like polyions and found the two-step ion-condensation phenomenon; at the first step, counterions are condensed in the neighbourhood of the assembly of polyions, and at the second step, a similar condensation phenomenon occurs around each of the polyions. The alteraction of spatial arrangement of polyions causes a larges change of activity coefficient of small ions.

Through the conductance measurement, we have found the strong P-binding of divalent cations to polyions. Generally, the P-binding is very much strengthened by the effect of ψ-binding.

§ 1. Introduction

Recently, it has been reported that there are many interesting salt-effects upon the aggregation phenomena of polyelectrolytes[1)-4)] or proteins in solutions[5),6)]. For the systematical interpretation of such specific ion-effects, it is one of the important works to study the counterion-binding to a polyion.

In polyelectrolyte solutions, counterions each of which has a charge opposite to polyions are strongly adsorbed to the polyions. Such adsorption of counterions can be classified into two types with respect to the mechanism of interaction. The binding simply due to the strong electrostatic interaction is called ψ-binding and has been investigated theoretically by many authors[7)-13)]. In most cases, there exists the other kind of ion-binding due to the short-range interaction between small ions and ionized groups on polyions. This kind of binding formed by covalent bonds or quasi-covalent bonds is called P-binding. The P-binding is generally strengthened by the ψ-binding, and sometimes bridges of counterions are formed between two groups on polymer chains.

In the study on polyelectrolyte solutions, it is very desirable to simplify or generalize the complicated P-binding phenomenon. Experimentally, the ion-binding problem has been investigated through the measurements of thermodynamical or current carrying properties[14)-16)] of polyelectrolyte solutions, and has been also studied by the transference experiment using isotope ions[17)]. It is, however, not so easy to separate experimentally the effect of P-binding from that of ψ-binding. This separation can be made to a certain degree in the system of polyacids by employing quaternary ammonium ions as counterions, because this cation can be postulated not to be bound to polyanion in the P-binding state on account of its large size and stable electronic structure[14)]. By using this large cation as a standard, the amount of the specific binding of other various cations can be estimated without much difficulty.

Now, in the theoretical studies on the ψ-binding, the ion-distribution around a polyion has usually been calculated mainly on the basis of the Poisson-Boltzmann equation (P.B. equation) to obtain the activity coefficients of counterion and byion. It should be emphasized that in solving the P.B. equation, the linearizing procedure adopted in the Debye-Hückel theory or in the early works on polyelectrolyte[8] is unsuitable for the present system of much charged macro-ions. In fact, no characteristic nature of polyelectrolytes could be deduced from the rough solution by linearization.

Fortunately, the P.B. equation has recently been solved exactly for the system of a single rod-like polyelectrolyte in its neutral free-volume[9] and also has been approximately solved for the system of a much charged coiled polyion in its free-volume[10)-12]. Through these results, one can find the strong adsorption of counterions in the vicinity of polyion and the powerful salt-effect which depress the apparent polymer charges. On the basis of these studies, the abnormal behaviors of activity coefficient of counterion observed in dilute polyion solutions can be explained at least qualitatively. In this paper, we will describe the theoretical analysis of the ion-binding in the cases of rigid and coiled spherical macro-ions, because we have not yet met exact calculations in these cases, and we will discuss the general feature of ψ-binding in the dilute and homogeneous systems of polyions.

Through the theoretical investigation of ψ-binding described in this paper, we found the characteristic phase of condensed counterions around a polyion. That is to say, if the charge ne_0 of a polyion situated in a finite free-volume exceeds a certain constant value n^*e_0, there appears the ion-condensation phase around the polyion in which $(n-n^*)$ counterions are strongly bound, and however larger n may become, the excess of n over n^* is retained in this phase and the total charge inside the condensation phase (n^*) is unaltered. In general, this condensation phase is very narrow and is clearly demarcated from the outer region, but it becomes diffuse with increasing polymer or salt concentration.

Nowadays, however, it is rather important to investigate the interaction of polyions in their concentrated system, such as gel-state or crystal-state. This investigation is of significance also for the physical interpretation of protein interactions. In order to understand such complicated macro-ion systems, we must rather investigate in the first place the general and common characters of counter-ion-distribution on the basis of the P.B. equation than solve the equation concretely for the individual cases. It is also necessary to deal with this problem in the aggregation system of polyions as well as in the homogeneous system. Recently, the P.B. equation for the system of more than two rod-like polyions has been partially solved by us[18], and the characteristic ion-distribution essentially different from that obtained by superposing single polyion systems has been found. We will report in this paper the complete solution for the problem of many rod-like polyions, discussing as generally as possible the ψ-binding in the aggregation state of polyions.

If some polyions (named $1, 2, \cdots, j, \cdots$, and having charges $n_1, n_2, \cdots, n_j, \cdots$) are aggregated in their common free-volume, there appear the following two kinds of ion-condensation. In the first place, if the total charge of these polyions $(\sum n_j)$ exceeds a constant value $n_0{}^*e_0$, condensation phase appears around the whole of these polyions and $(n-n_0{}^*)$ counterions are gathered in this phase. In the second place, when the charge of any polyion n_je_0 becomes larger than n^*e_0 which is the same value with that given in the above single polyion-system, the second condensation phase appears around this j-th polyion. Thus it is the essential fact implied in the P.B. equation that counterions from the condensation phase of the first or the second kind around a polyion or polyions.

In this paper, is also treated the P-binding problem, particularly the problem or divalent cation-binding on the basis of our conductance experiments, in which poly-(acrylic acid) solutions are employed to determine the amount of monovalent and divalent cations bound to carboxyl groups on polyions. A method of analysis to obtain the equivalent conductance of a polyion was adopted. By the use of this equivalent conductance, it was found that every species of salt-cations except quaternary ammonium ions is strongly bound to polyions in the P-binding state. Particularly, in the case of divalent cations, added cations are almost fully bound to polyions so far as dissociated carboxyl groups on the polyions remain unmasked by the cations. It is noteworthy that the counterions in the ψ-binding state, such as quaternary ammonium ions contribute to the ionic conductivity of polyion solutions almost completely. In our experiments, was also confirmed the surprising fact reported by Wall et al.[19] that simple monovalent cations such as sodium ions are pronouncedly bound to polyanions, though these cations are completely dissociated in low molecular acetate solutions. This fact is no doubt due to the ψ-binding effect which strengthens the P-binding. Moreover, our results show that these bound monovalent cations are replaced by newly added divalent cations, and generally P-binding is accompanied by much dehydration.

§ 2. Solution of the Poisson-Boltzmann Equation for the System of Spherical Polyions having Many Charges

It has been proved that the Poisson-Boltzmann equation is available for the determination of electric potential or counterion distribution around fixed polyions in their free-volume neutralized by counterions, but the equation cannot be applied for the calculation of the statistical distribution of polyions around a fixed polyion[10]. Therefore, hereafter we will always adopt the free-volume model for the study of the counterion distribution.

Now, when a rigid spherical polyion with charge ne_0 and radius a is settled in the centre of its neutral free-volume with radius R (Fig. 1), the electric potential ψ around this polyion can be obtained by the following P.B. equation and the boundary conditions;

$$\frac{D}{e_0}\Delta\psi=\frac{(n+j)e^{Y}}{\int_a^R e^{Y}r^2dr}-\frac{j\,e^{-Y}}{\int_a^R e^{-Y}r^2\,dr}\equiv\frac{4\pi\rho}{-e_0}\,, \tag{1}$$

$$(d\psi/dr)_{r=a}=-ne_0/Da^2\,,\qquad (d\psi/dr)_{r=R}=0\,, \tag{2}$$

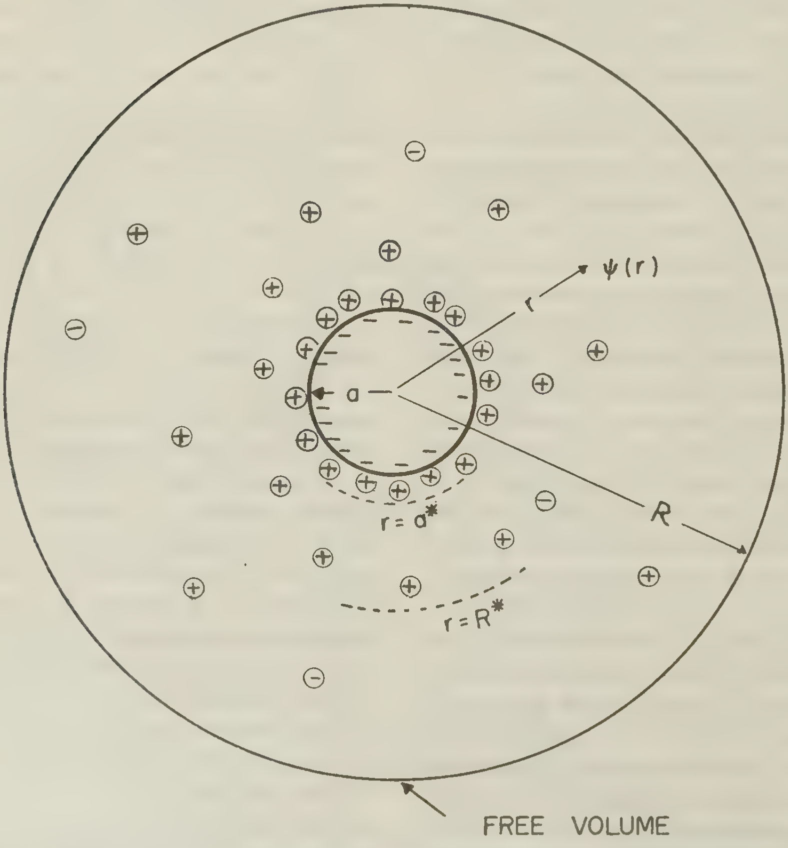

Fig. 1. A rigid spherical polyion having many charges and surrounded by low molecular ions in the neutral free volume.

where

$$Y \equiv e_0\psi/kT\,, \qquad (3)$$

$$\Delta = d^2/dr^2 + (2/r)\,d/dr\,,$$

r is the cubic coordinate whose origin is the centre of the free-volume, the integrals are the normalization factors, kT is the Boltzmann factor, D is the dielectric constant of solvent, and j is the number of byions in this free-volume. The polymer concentration is given by $(a/R)^3$ in our free-volume model.

Putting

$$\kappa^2 \equiv (n+j)\,e_0^2 \Big/ \left[DkT \int_a^R e^Y r^2\,dr\right], \qquad (4)$$

$$\theta^2 \equiv j\int_a^R e^Y r^2 dr \Big/ \left[(n+j)\int_a^R e^{-Y} r^2\,dr\right], \qquad (5)$$

and

$$p \equiv r(dY/dr)\,, \qquad (6)$$

we can rewrite the equation as follows;

$$d(rp)/dr = \kappa^2 r^2 (e^Y - e^{-Y})\,. \qquad (7)$$

Even though the exact solution of this equation cannot be obtained, the physical characters involved in it can be easily deduced through the mathematical analysis of the equation for the following typical cases;

1) The case when $3\log(R/a) \gg 1$ and $(R/a)^2 \gtrsim je_0^2/DkTa \geqq 0$; that is, the case when polyion concentration is extremely dilute but the salt-concentration is practically unrestricted, (d-system)
2) The case when $(je_0^2/DkTa) \gg (R^3-a^3)/a^3$; that is, the case when salt-concentration is high and the polyion is not so dilute. (c-system)

It is then an important character of our method of analysis that no restriction is put for the value of Y, but the polyion or salt concentration is limited as noted above. In this paper, only the results for the above two cases will be described.

[1] *The dilute system of rigid spherical polyions*

Let us define R^*, n^* by the following relations;

$$\frac{n^*e_0^2}{DkTa} = 3\log\frac{R}{a} - \log\left(\frac{je_0^2}{DkTa} + \frac{n^*e_0^2}{DkTa}\right) \qquad (\gg 1)\,, \qquad (9)$$

$$R^*/a = (R/a)^{1/2} \qquad (\gg 1)\,. \qquad (8)$$

Then, in the system satisfying $n \geqq n^*$, the sphere $R = a^*$ which satisfies the following relation can exist in the outside of the polyion;

$$(dY/dr)_{r=a^*} = p(a^*)/a^* = n^*e_0^2/DkTa^*\,, \qquad (10)$$

and the given free-volume can be divided into the following three regions;

(1) the region in which r satisfies $R^* \leqq r \leqq R$ (This region is named D. H. Region.),
(2) the region in which r satisfies $R^* \geqq r \geqq a^*$ (This region is named Intermediate Region.), and
(3) the region in which r satisfies $a^* \geqq r \geqq a$ (This region is named Ion-Condensation Region.).

For the system $n < n^*$, there is no Ion-Condensation Region.

According to our analysis, the following facts can be found without much difficulty.

1) In the D. H. Region, Y is much smaller than unity and accordingly, Y can readily be obtained by linearizing the equation. (The concrete form of Y is not written here.)
2) In the Intermediate region (I-Region), the function $g(r)$ defined by the following relation

is much larger than unity;

$$g(r)=\frac{p}{\kappa^2 r^2(e^Y-\theta^2 e^{-Y})}\,, \tag{11}$$

and by the use of the condition $g\gg 1$, p in this region can be expressed in the form;

$$\left.\begin{array}{ll} p=(a^*/r)\cdot p(a^*) & \text{for}\quad n\geqq n^*\,, \\ p=(a/r)\cdot p(a) & \text{for}\quad n\leqq n^*\,. \end{array}\right\} \tag{12}$$

3) In the present system, g is zero at $r=R$, and increases at the first step with decreasing r, but it becomes small again inside the Condensation-Region (C-Region). The maximum point of g exists in the I-Region.

4) In the Ion-Condensation Region (C-Region), both Y and p are very large compared with unity, and the following important relation can be introduced;

$$1<\frac{a^*}{a}<1+\frac{3\log p(a^*)}{p(a^*)}+O\left(\frac{1}{p(a^*)}\right)\,. \tag{13}$$

5) Near the point $r=a^*$, the conditions $g(a^*)\gg 1$ and $p(a^*)\ll 1$ are both satisfied, and therefore, the approximate solution of Y in the I-Region and that in the C-Region can be analytically connected with each other.

6) Similarly, near the point $r=R^*$, both the conditions $Y(R^*)\ll 1$ and $g(R^*)\gg 1$ are simultaneously satisfied, and then the D. H. Region and the I-Region can be analytically connected with each other. In the domain where r is much smaller than R, the expression of p obtained from the D. H. approximation takes the form of $(1/r)$, which is same with that valid in the I-Region.

7) With increasing value of R/a, the above analytical continuations become incorrect, because two kinds of the approximations can not be simultaneously satisfied at $r=a^*$ or $r=R^*$ unless R/a is sufficiently large.

8) The concrete form of Y in the C-Region can be introduced from the following soluble equation which can be obtained by neglecting the term $\exp(-Y)$ in (7) and using the approximation $p\gg 1$.

$$d(\kappa^2 r^2 e^Y)/dp=(p+2)/(p+\kappa^2 r^2 e^Y)\,.$$

Especially, $Y(a)$ is given in the form;

$$Y(a)=p(a^*)+\log\{p(a)^2-p(a^*)^2+1\}\,. \tag{14}$$

9) The normalization factors κ and θ can be obtained through the above analytical continuation and are given in the form;

$$\kappa^2 a^2=\frac{3(n+j)e_0^2}{DkTa}\frac{a^3}{R^2}\,,\qquad \theta^2=\frac{j}{n+j}:\qquad \text{for}\quad n\leqq n^*\,,$$

$$\kappa^2 a^2=\frac{3(n^*+j)e_0^2}{DkTa}\frac{a^3}{R^2}\,,\qquad \theta^2=\frac{j}{n^*+j}:\qquad \text{for}\quad n\geqq n^*\,.$$

From the above results for the d-system, we can conclude the following facts; when n becomes very large beyond the value of n^*, $(n-n^*)$ counterions are concentrated in the narrow region around a polyion, and the potential-distribution in the outside of this narrow region and the normalization factors are both kept constant for values of n larger than n^*. This means that for the large value of n, the apparent charge of the polyion can be always given by n^*. With decreasing polymer or salt concentration, n^* generally increases, and if n^* becomes larger than n, the ion-condensation region disappears. Inversely, if polymer concentration becomes high, the ion-condensation phase appears even for small

n, but in this case, the boundary of this phase becomes unclear.

[2] *The concentrated system (c-system) of rigid spherical polyions*

In the c-system in which the relation $je_0^2/DkTa \gg (R^3-a^3)/a^3$ is satisfied, the following results can be introduced from the same fundamental P.B. equation.

1) If a' and n' are defined by the relations;

$$p(a')=1\ , \qquad n'e_0^2/DkTa'=1\ ,$$

the free-volume can be divided into the following two regions, the region $a' \leqq r \leqq R$ (named D. H. Region) and the region $a' \geqq r \geqq a$ (named C-Region). In the D. H. Region, Y and p can be obtained by linearizing the equation.

2) The function $g(r)$ defined by (11) is very much smaller than unity everywhere.

3) Under the conditions $g(r) \ll 1$ and $p(r) \geqq 1$, the equation can be approximately solved, and Y in the C-Region is given in the form;

$$e^Y = \left(\frac{q+1}{q-1}\right)^2 ,$$

$$q \equiv 4\sqrt{2}\,\kappa a \cdot \exp\{\sqrt{2}\,(\kappa a - \kappa r)\}\ .$$

4) The solutions of Y thus obtained in the above two regions can be smoothly connected with each other in the neighbourhood $r=a'$, and the normalization factors in this system are determined as follows;

$$\kappa^2 a^2 = \frac{3je_0^2}{DkTa}\,\frac{a^3}{R^3-a^3} \qquad (\gg 1)\ ,$$

$$\theta = 1 - 4\exp\{\sqrt{2}\,(\kappa a - \kappa R)\}\cdot(\sqrt{2}\,\kappa R)^{-1}\ .$$

5) In the C-Region, a' satisfies the following relation;

$$1 < (a'/a) < 1 + O\{(\log \kappa a)/\kappa a\}\ .$$

This shows that the C-Region is very narrow.

Through these results for the c-system, we can find the following ion-condensation phenomena; however larger the polyion charge ne_0 may become, the normalization factor κ is unaltered and $(n-n')$ counterions are condensed in the vicinity of the polyion, and the apparent polyion charge $n'e_0$ is very small, being nearly independent of the polyion charge n.

[3] *Coiled spherical polyion system*

When a coiled polyion which has n ionized groups uniformly distributed in the average volume $v(=(4/3)\pi a^3)$ is situated at the centre of the free-volume (in place of the rigid spherical polyion in the above system) (Fig. 2), the following equation and the boundary conditions are established in the region $r \leqq a$;

$$\frac{D}{4\pi}\Delta\psi = -\rho + \frac{ne_0}{v}\ , \qquad (15)$$

$$\frac{d\psi}{dr}\ ,\ \ \psi \text{ are continuous at } r=a\ , \qquad (16)$$

$$(d\psi/dr)_{r=0} = 0\ , \qquad (17)$$

where n is the total chain-charge of the polyion and ρ denotes the charge density of small ions given in (1). In the region $r>a$, the equation (1) and the boundary condition $(d\psi/dr)_{r=R}=0$ are both valid without any alteration. Although a similar equation to (15) has often been treated by many authors for the same purpose, the general character of the ion-distribution in the internal region of a coiled polyion have not been deeply discussed under the consideration of the strong influence of the outer region of the polyion.

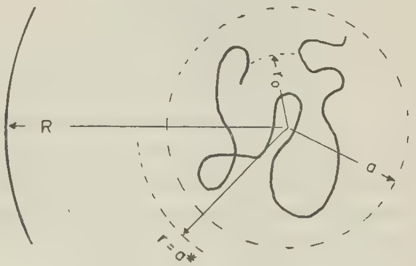

Fig. 2. A much charged coiled polyion with mean radius a in the free-volume.

In this section, we will discuss mainly the important correlation between the ion-condensation phase around a polyion and the characteristic ion-distribution inside the coiled polyion in the dilute system. The main results obtained in this system can be summarized as follows;

(a) In general, there appears the same kind of ion-condensation phase on the surface of the polyion as found in the rigid polyion system, provided that the polyion charge ne_0 exceeds a certain value n_1. This n_1 is expressed for the dilute system by the following relation:

$$\left[\frac{6n_1e_0^2}{DkTa}\cdot\log\left(\frac{3n_1e_0^2}{DkTa}\right)\right]^{1/2} = \frac{n^*e_0^2}{DkTa}\ ,$$

where n^* given in (8) is the critical value for the appearance of the condensation phase in the rigid polyion-system. As seen in this relation, somewhat larger n is necessary for the existence of the C-Region than in the case of rigid polyion-system. In the usual case of the dilute system of much charged polyions, however, the condition $n>n_1$ as well as that $n>n^*$ is satisfied. If n becomes smaller than n_1, the ion-condensation phase disappears and the Intermediate Region (I-Region) is directly continated with the region inside of the coiled polyion (on the surface).

(b) The value of p on the surface of the polyion $p(a)$ increases with increasing n, and is expressed for the case of very large n ($\gg n^*$) as follows;

$$p(a)=\left[2e^{-1}\frac{ne_0^2}{DkTa}\right]^{1/2} .$$

(c) If r_0 is chosen in the internal region of a polyion such that

$$p(r_0)=1 \qquad (r_0<a) ,$$

r_0 satisfies the relation;

$$(a-r_0)/a\approx\left(\frac{12ne_0^2}{DkTa}\right)^{-1/2}\cdot\log\left(\frac{3ne_0^2}{DkTa}\right) .$$

This relation means that p varies sharply near the surface of the coiled polyion.

(d) When we define $\lambda(r)$ as degree of neutralization of chain-charges at r by the following formula;

$$\lambda(r)=\rho v/ne_0 ,$$

it is proved that $\lambda(r)$ is small enough compared with unity except near the edge of the polyion, for instance, at $r=r_0$,

$$\lambda(r_0)=(3ne_0^2/DkTa)^{-1/2} .$$

Therefore, $\lambda(r)$ varies sharply in the surface region $r_0<r<a$, and particularly, at $r=a$, the relation;

$$1-e^{-1}<\lambda(a)<1 .$$

is established. In this relation, the upper limit 1 of $\lambda(a)$ is satisfied in the case $n\leqq n_1$, while the lower limit $1-e^{-1}$ of $\lambda(a)$ is satisfied in the case $n\gg n_1$.

From the above results, the character of the ion-distribution in the system of coiled polyions can be summarized as follows. The polymer charges are nearly completely depressed inside the sphere of the coiled polyion by the counterions. In the outside of the polyion, there appears the same ion-condensation phase as found in the rigid spherical polyion. Thus, the coiled polyion is equivalent, as regards the charge-distribution, to the rigid spherical polyion with a certain surface charge. The whole region inside the sphere $r=a^*$, that is to say, the C-Region plus the inside region of a coiled polyion is the ion-condensation phase in this system.

[4] *The ion-condensation phenomenon in the single polyion system*

A similar **ion-condensation** phenomenon can be easily found also in the single rod-like polyion system, for which the analytical solution of the P.B. equation has been exactly obtained by Lifson, Katchalsky[9]. In this system, potential ψ $(=YkT/e_0)$ around a sufficiently long rod-like polyion with radius a and a linear charge density ne_0 can be expressed in the following form;

$$e^{-Y}=[(1+\delta)(r/R)^{-\delta}-(1-\delta)(r/R)^{\delta}]^2(r/2\delta R)^2 , \tag{18}$$

where r is a cylinder coodinates whose origin is chosen at the axis of the polyion, R is the radius of the cylindrical free-volume, and δ is a constant. Provided that a/R is very small, it is proved that δ takes a real value almost equal to $1-A$ $(A\equiv ne_0^2/DkT)$ when A is smaller than about unity, but with increasing ne_0, δ becomes small, and when A exceeds about unity, it changes to pure imaginary after taking the value of zero. Further, it can be proved that the increase of A beyond unity does not alter the ion-distribution around the polyion except on its surface. Thus, the real—imaginary transformation of the integral constant just corresponds to the ion-condensation phenomenon in the thin rod-like polyion system.

Through the investigations in the above sections, it is found that the ion-condensation phenomenon is a remarkable common character in every system of much charged polyions. This abnormal ion-distribution may be briefly described in another expression; the Donnan equilibrium is approximately established between the ion-condensation phase and its outer region in the free-volume of polyion. In fact, the abnormal behavior of the activity coefficient of low molecular ions can be attributed to the existence of the ion-condensation phase or the Donnan equilibrium state near the polyion. In general, activity coefficient of counterions becomes abnormally small in any case when the counterions are distributed around many fixed charges which are locally and densely gathered with each other, but it takes a normal value when the fixed charges are uniformly dispersed in the system. Thus, even though the analysis of the P.B. equation is not so simple, the final conclusion is essentially concentrated in the concept of the counterion condensation. By using this concept we can find the character of the ion-distribution in more complicated systems without directly solving the P.B. equation. The significancy of Ion-Condensation phenomenon can be more clarified in the system of aggregated polyions as discussed in the next section.

§ 3. Counterion-distribution around Many Rod-like Polyions

It is interesting to study the characteristic nature of ion-distribution around more than two polyions, which results from the co-operative effect of these polyions. The analysis of the P.B. equation upon this problem is further more difficult as compared with that for the single polyion system. This problem, however, can be successfully dealt with for the system of rod-like polyions in salt-free solutions on the basis of the exact solution of the two-dimensional P.B. equation.

For the two-dimensional many-centre problem the following equation can be established;

$$\frac{\partial^2 Y}{\partial r^2}+\frac{1}{r}\frac{\partial Y}{\partial r}+\frac{1}{r^2}\frac{\partial^2 Y}{\partial \theta^2}=\kappa^2 e^Y\,, \qquad (19)$$

$$\kappa^2=4\pi n e_0{}^2\Big/\left(DkT\iint e^Y r\,dr\,d\theta\right), \qquad (20)$$

where r, θ are polar coordinates, n is the total number of counterions out of all polyions and the integral term is the normalization factor. The general solution of this equation has been found and applied by us for the system of two infinitely thin polyions. In this paper we will extend our previous result to the more general system, and describe in detail the procedure of solving this problem.

Now, the general solution of (19) can be expressed by employing two arbitral functions g_1, f_1 as follows;

$$e^{-Y}=\frac{1}{8}\kappa^2[g_1(z)f_1(z^*)-g_2(z)f_2(z^*)]^2\,, \qquad (21)$$

where

$$g_2\equiv g_1\int^z g_1{}^{-2}\,dz\,, \qquad f_2\equiv f_1\int^{z^*} f_1{}^{-2}\,dz^*\,,$$

and z, z^* are defined by $z=re^{i\theta}$, $z^*=re^{-i\theta}$. For the system satisfying $Y(r,\theta)=Y(r,-\theta)$, the solution is written simply in the form[18];

$$e^{-Y}=\frac{1}{8}\kappa^2[g_1g_1{}^*-g_2g_2{}^*]^2\,, \qquad (22)$$

where $g_i{}^*$ is defined by $g_i{}^*=g_i(z^*)$ $(i=1,2)$.

Let $g_1(z)$ be a solution of the following equation including a suitable function $u(z)$;

$$\frac{d^2g_1}{dz^2}+u(z)g_1=0\,, \qquad (23)$$

then, for every kind of $u(z)$, g_2 is the other solution of (23). Thus, ψ can be obtained if the arbitral function $u(z)$ for the given system is determined.

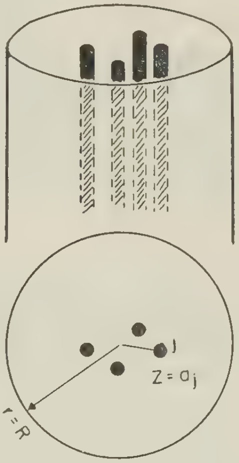

Fig. 3. Rod-like polyions in their common cylindrical free-volume.

The general theory for the dilute system of very thin rod-like polyions

Consider a system in which m rod-like polyions with negative charges $-n_1, -n_2, \cdots, -n_m$ are situated at the points $(r_1,\theta_1), (r_2,\theta_2), \cdots, (r_m,\theta_m)$ in the common cylindrical free-volume (neutrality zone) with radius R (see Fig. 3). In this system, the electric potential resulting from only the fixed polyions (denoted by ψ_p) is written as follows;

$$\frac{e_0\psi_p}{kT}=\sum_{j=1}^{m}A_j\log(z-a_j)(z^*-a_j{}^*)+C\,; \qquad A_j\equiv\frac{n_je_0{}^2}{DkT}\,, \qquad (24)$$

where C is a constant, $a_j=r_je^{i\theta}$, and $a_j^*=r_je^{-i\theta}$. Hereafter, we will deal with only the dilute system in which each of r_k satisfies the condition $r_k \ll R$.

Putting

$$g_{1,2}=q_{1,2}\prod_{j}^{m}(z-a_j)^{-A_j/2}\,, \tag{25}$$

we have the following relation;

$$\exp(-Y+Y_p)=\exp(-Y_g)=\log[g_1g_1^*-g_2g_2^*]^2+C'\,, \tag{26}$$

where Y_g means the electric potential resulting from only the counterions distributed in the free-volume, and C' is a constant. Now, referring to (25), q_1 and q_2 both satisfy the following equation;

$$\frac{d^2q}{dz^2}+\sum_{j=1}^{m}\frac{A_j}{z-a_j}\frac{dq}{dz}+V(z)q=0\,, \tag{27}$$

where $V(z)$ is an arbitral function employed instead of $u(z)$. Our purpose is to determine the form of function $v(z)$ from the following physical conditions established in the present system.

(A) Y should be analytic except at the polyion.

(B) On the surface of the free-volume,

$$(\partial Y/\partial r)_{r=R}\doteqdot 0\,, \qquad \oint(\partial Y/\partial r)_{r=R}\,d\theta=0\,.$$

(C) $dY/d\theta$ becomes very small for large r.

From (27) and the condition (A) neither q_1 nor q_2 becomes infinity except at $z=\infty$ and they must not similtaneously be zero anywhere except at the polyions. On the other hand, from the condition (C), it is evident that q_i $(i=1,2)$ takes a form of z^b at large z. Then, in order to satisfy these conditions, $V(z)$ should be given on the basis of the Liouville's and Frobenius, theorem as follows;

$$V(z)=\sum_{j=1}^{m-2}C_jz^j\Big/\prod_{k=1}^{m}(z-a_k)\,, \tag{28}$$

where C_j $(j=1,2,\cdots,m)$ are constants independent of z. The solution of this equation is composed of many solutions each of which is valid only in its own convergence region. The constants C_j's are determined from the analytical continuation by which these solutions are smoothly connected with each other.

The solution of (27) with $V(z)$ given by (28) can be easily found for large $|z|$, and by applying this solution, Y at large r is deduced as follows;

$$e^{-Y}=\left[D_0\left(\frac{r}{R}\right)^{\delta}-\frac{1}{D_0}\left(\frac{r}{R}\right)^{-\delta}\right]^2\frac{\kappa^2r^2}{8\delta^2}\,, \tag{29}$$

where the constant D_0 is determined by the condition (B) and given in the form $[(1-\delta)/(1+\delta)]^{1/2}$; the constant δ is expressed by C_{m-2} given in (28) and determined by the analytical continuation with the solutions valid in the other region of r. If R/r_j is sufficiently large for every j, δ tends to $1-\sum_j A_j$ and the solution (29) coincides with one centre problem. The expression of Y in (29) is similar to that in (18) established in the single polyion system. Therefore, it is obvious that with increasing $\sum_j A_j$, the constant δ in (29) decreases taking a real value at the first step, and then it changes to pure imaginary. This fact means that the ion-condensation phenomenon appears around the whole assembly of fixed polyions when the total polyion-charge exceeds a critical value $(=1)$. Through the same analysis as done in the single polyion system, it is easily confirmed that however larger the total polyion-charge may become, no appreciable increase of Y takes place at the region apart from the neighborhood of polyions, so far as the constant δ takes an imaginary value. This type of the ion-condensation is called "the first kind of ion-condensation."

On the other hand, the solution of Y available in the neighborhood of j-th polyion (at $z \approx a_j$) may be expressed in the form:

$$e^{-Y} = \left[B_j S_j^{1-A_j} - \frac{1}{B_j} S^{-1+A_j} \right]^2 \frac{\kappa^2 S_j^2}{8(1-A_j)_2}, \tag{30}$$

where S_j is $|z-a_j|$ and B_j is a constant. This expression of Y is the same with (18) valid for the system of an infinitely thin polyion, and therefore, it is obvious that the ion-condensation in the vicinity of a polyion appears similarly to the single polyion system, provided that A_j of each polyion exceeds the value of unity. This type of ion-condensation is called the second kind of ion-condensation.

It is noteworthy that the counterions are condensed in the vicinity of the whole of aggregated polyions before the second kind of condensation appears around each of the polyions, and that with increasing number of polyions coexisting in the system, the first kind of ion-condensation occurs easily.

Now, if m rod-rike polyions having equal charge ne_0 ($\equiv ADkT/e_0$) are arranged axial-symmetrically on a circle with radius a, Y can be concretely expressed by the well-known hyper-geometric functions, and then the analysis in this case is very simple. By putting

$$\left.\begin{aligned} &t = (r/a)^m e^{im\theta}, \qquad t^* = (r/a)^m e^{-im\theta}, \\ &g_j = (1-t)^{(1-\varepsilon)/2} q_j, \qquad (j=1,2), \qquad \varepsilon = 1-A, \end{aligned}\right\} \tag{31}$$

Y_p is written in in the form; $Y_p = A \log(1-t)(1-t^*)$, and the equation (27) is transformed into the following form;

$$\left.\begin{aligned} &t(1-t)\frac{d^2q}{dt^2} + [\gamma - (\alpha+\beta+1)t]\frac{dq}{dt} - \alpha\beta q = 0, \\ &\alpha = \gamma - \varepsilon - \beta, \qquad \gamma \equiv 1 - n^{-1}, \end{aligned}\right\} \tag{32}$$

where β is a constant which should be determined by the analytical continuation. The solution of (32) is composed of several hypergeometric functions each of which has its own convergence region, and then Y is also expressed in various forms corresponding to these convergence regions. For example, in the region $|t-1| \leqq 1$ and $|t-1| \geqq 1$, Y_g is written in the forms;

$$8\exp(-Y_g) = [E_0 H_1 H_1^* - E_0^{-1}\{(1-t)(1-t^*)\}^{\varepsilon} H_2 H_2^*]^2 \kappa^2 \varepsilon^{-2} \qquad \text{for} \quad |t-1| \leqq 1, \tag{33}$$

$$8\exp(-Y_g) = [D_0 (tt^*)^{-\beta} K_2 K_2^* - D_0^{-1}(tt^*)^{-\alpha} K_1 K_1^*]^2 \kappa^2 \delta^{-2} \qquad \text{for} \quad |t-1| \geqq 1, \tag{34}$$

where

$$H_1 = F(\alpha, \beta, \alpha+\beta-\gamma+1; 1-t), \qquad H_2 = F(\gamma-\alpha, \gamma-\beta, \gamma-\alpha-\beta+1; 1-t),$$

$$K_1 = F(\alpha, \gamma-\beta, \alpha-\beta+1; (1-t)^{-1}), \qquad K_2 = F(\beta, \gamma-\alpha, \beta-\alpha+1; (1-t)^{-1}).$$

According to the mathematical relations deduced from the analytical continuation, each of K_1 and K_2 is expressed by the linear combination of H_1 and H_2. Substituting this relation into (34) and comparing this result with (33), we obtain the relation between the constants D_0 and E_0, and at the same time obtain the following transcendental equation to determine the value of β;

$$\frac{1-\delta}{1+\delta}\left(\frac{a}{R}\right)^{2\delta} = \frac{\Gamma^2(\delta)\Gamma(\gamma-\beta)\Gamma(1-\beta)\Gamma(1+\alpha-\gamma)\Gamma(\alpha)}{\Gamma^2(-\delta)\Gamma(\gamma-\alpha)\Gamma(1-\alpha)\Gamma(1+\beta-\gamma)\Gamma(\beta)},$$

where δ is defined by $\delta = n(\beta-\alpha)$. Here, it is proved that this relation is the necessary and sufficient condition for every continuation of various Y's, each having a different available region. From this relation, we can find the following facts;

1) When A is small, β takes a small value of $O(A^2)$.
2) When a/R tends to zero, β becomes zero, and the functions K_1, K_2 become unity, and then, the result coincides with one-centre problem.
3) For the system of infinity thin polyions, ε is given by $1-A$ as noted in (31), but for the system of very thin but finite polyions, ε may generally take other values.
4) When A is smaller than about $(1/m)$, $\varepsilon=1-A$ and $\delta=1-mA$.
5) When A is increased beyond $(1/m)$, δ changes to pure imaginary at the first step. In this case, α and β, C_0 and $(1/C_0)$, $K_1K_1^*$ and $K_2K_2^*$ are conjugated complexes, respectively, but $H_1H_1^*$ and $H_2H_2^*$ are real.
6) At the second step, when A is increased beyond 1, δ and ε both become pure imaginary. In this case, α and $\gamma-\alpha$, β and $\gamma-\beta$, $H_1H_1^*$ and $H_2H_2^*$, $K_1K_1^*$ and $K_2K_2^*$ are conjugated complexes, respectively.

Thus, we can concretely see the two-step ion-condensation phenomenon through the real—imaginary transformation appearing in the transcendental equation. This phenomenon can be found also through the calculation of the force between two rod-like polyions[20]. The argument upon the problem of interaction will be done in the other paper.

§4. The P-binding of Divalent Cations in Poly(-Acrylic Acid) Solutions

The above theoretical treatment was concerned with only the ϕ-binding state of counterions. However, the P-binding also plays a great role in the interaction of counter ions with polyions. Actually, our experiment clearly showed that in general a considerable amount of counterions are tightly bound to

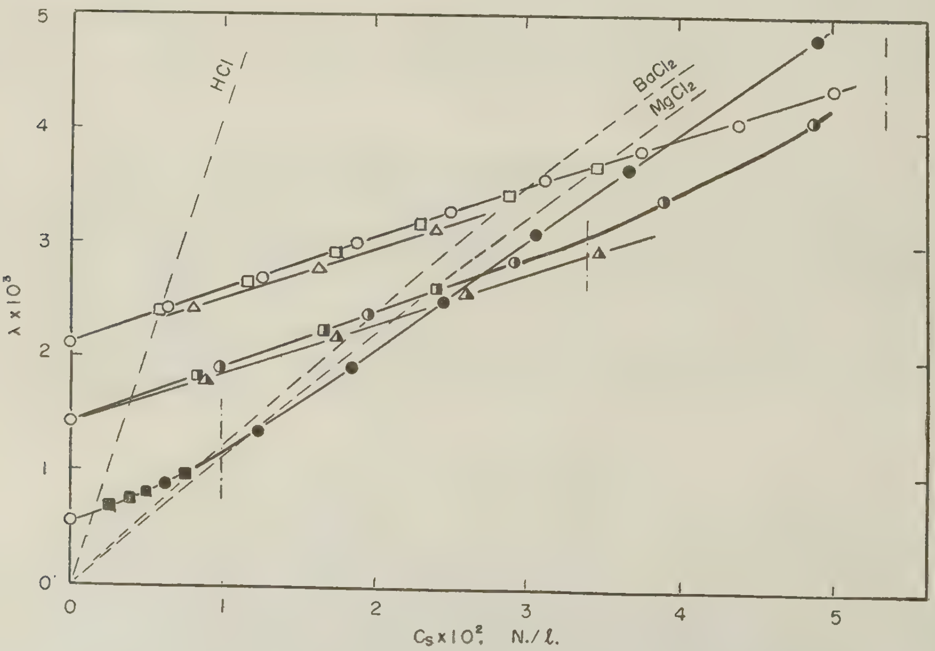

Fig. 4. The relation between specific conductances $\lambda(C_s)$ of polyacid-salt neutralized by tetra-n-butyl ammonium hydroxide and added salt concentration $C_s(N/l)$ at 25°C. The broken lines indicate the corresponding simple salt solutions and the vertical lines indicate the precipitation points with $BaCl_2$. Polymer concentration is always kept constant at 0.06 N/l.

○: $MgCl_2$, $\alpha=1$;	◑: $MgCl_2$, $\alpha=0.7$;	●: $MgCl_2$, $\alpha=0.25$;
□: $BaCl_2$, $\alpha=1$;	◧: $BaCl_2$, $\alpha=0.7$;	■: $BaCl_2$, $\alpha=0.25$;
△: HCl, $\alpha=1$;	◭: HCl, $\alpha=0.7$.	

polyions in the P-binding state. Therefore, we add a brief description on the result of this experiment and point out the importance of the P-binding. We adopted a new method of analysis for the conductance experiments, and determined the amount of bound cations to polyanions having many (5000—20000) carboxyl groups. The solutions employed here are poly-acrylic acid (PAA) solutions neutralized by NaOH or $N(Bu)_4OH$, tetrabutyl ammonium hydroxie, at various degrees of neutralization α, which mean fraction of carboxyl groups not taking a form of COOH but taking a form of COO^- or COO–Me (Me denotes a metal ion).

In Fig. 4, conductances λ of the PAA solutions neutralized by $(NBu)_4OH$ and containing added salt-ions are plotted against the concentration of involved salt-ions C_s (expressed in normal conc.) at a fixed polymer concentration C_p (=0.06 N/l). In this figure, three solid lines correspond to the different α's, and the other two solid lines show similar results in the case of HCl which is added to the polymer solutions at $\alpha=0.7$ and 1.0, respectively. (In the case of HCl, λ's are plotted against the concentration of involved Cl^-.) The conductances of the corresponding simple salt solutions are indicated by the dashed curves. It is seen in this figure, that λ increases linearly with C_s within the value of C_s smaller than αC_p and slope $d\lambda/dC_s$ is much smaller than that of simple salt solution. These facts suggest that added cations are strongly absorbed to polyions so far as COO^- groups remain not to be bound[23].

Now, let λ_c, λ_a, and λ_t denote equivalent conductances of added cation, added anion and tetrabutyl ammonium ion, respectively, then, conductance of polymer solutions can be expressed, on the basis of independent migration of all ions, in the following relation;

$$\lambda=(\alpha C_p-C_m-C_t)\lambda_p+(C_s-C_m)\lambda_c+C_s\lambda_a+(\alpha C_p-C_t)\lambda_t\ , \quad (35)$$

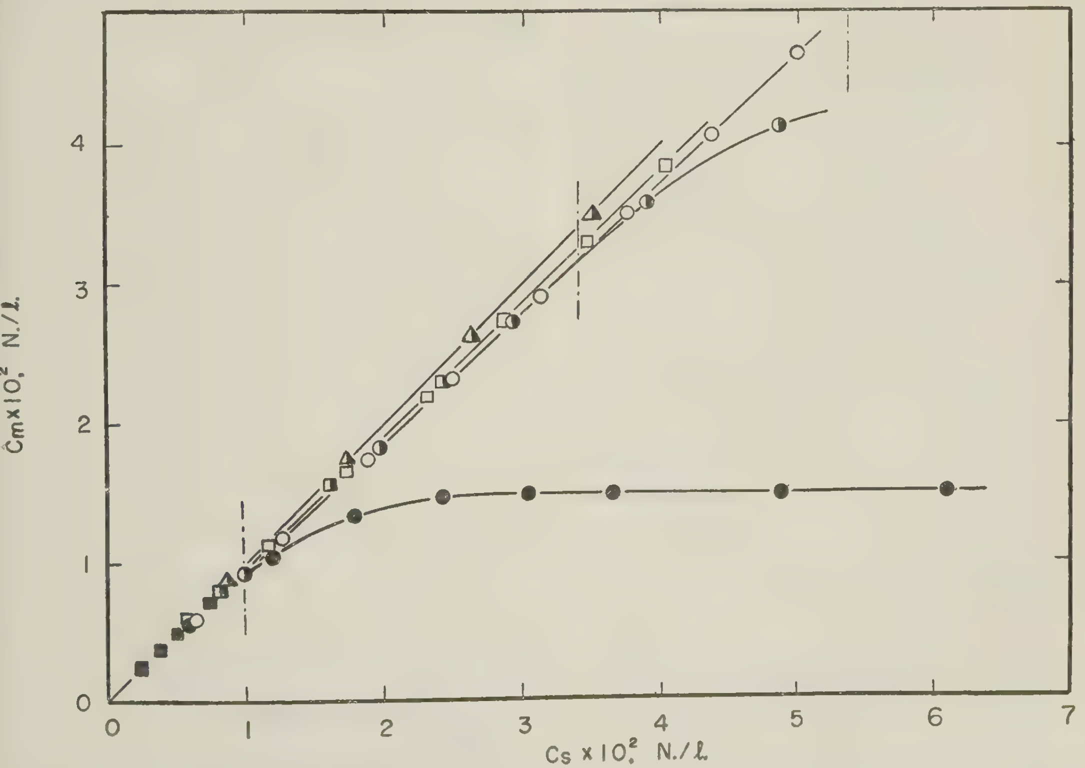

Fig. 5. The relation between the amount of bond cations $C_m(N/l)$ and the concentration of added salts $C_s(N/l)$ at various α's. Polymer concentration is 0.06 N/l.

○: $MgCl_2$, $\alpha=1$; ◑: $MgCl_2$, $\alpha=0.7$; ●: $MgCl_2$, $\alpha=0.25$;
□: $BaCl_2$, $\alpha=1$; ◨: $BaCl_2$, α=0,7; ■: $BaCl_2$, $\alpha=0.25$;
◭: HCl, $\alpha=0.7$.

where C_m and C_t denote the amount of bound salt-cations, and the amount of bound tetrabutyl ammonium ion, respectively.

Differentiating both sides of (35) with respect to C_s, we at once obtain the relation;

$$\frac{\Delta\lambda}{\Delta C_s}=\lambda_a+\lambda_c-\frac{\Delta C_t}{\Delta C_s}(\lambda_p+\lambda_t)$$
$$-\frac{\Delta C_m}{\Delta C_s}(\lambda_c+\lambda_p)\,. \tag{36}$$

Now, according to Fig. 4, it is obvious that for the cases of added Mg^{++}, Ba^{++} and H^+, the value of $\Delta\lambda/\Delta C_s$ at comparatively low C_s is independent of C_s. Therefore, in this case, by putting

$$\Delta C_m/\Delta C_s=h\,, \qquad C_t=b(1-fC_s)\,,$$

the relation (36) can be simply written in the form;

$$\Delta\lambda/\Delta C_s=bf(\lambda_p+\lambda_t)-h(\lambda_c+\lambda_p)+\lambda_x+\lambda_c\,, \tag{37}$$

where h, b, and f are constants independent of C_s, and b and f can be called ion-exchanging parameters which depend on α. Fig. 4 shows that conductances, each of which belongs to different α and the same salt-species, are increased in almost parallel with each other. Therefore, in order to obtain from (37) the expression of λ independent of α, it is necessary to assume that h is nearly independent of α and bf is very small in com-

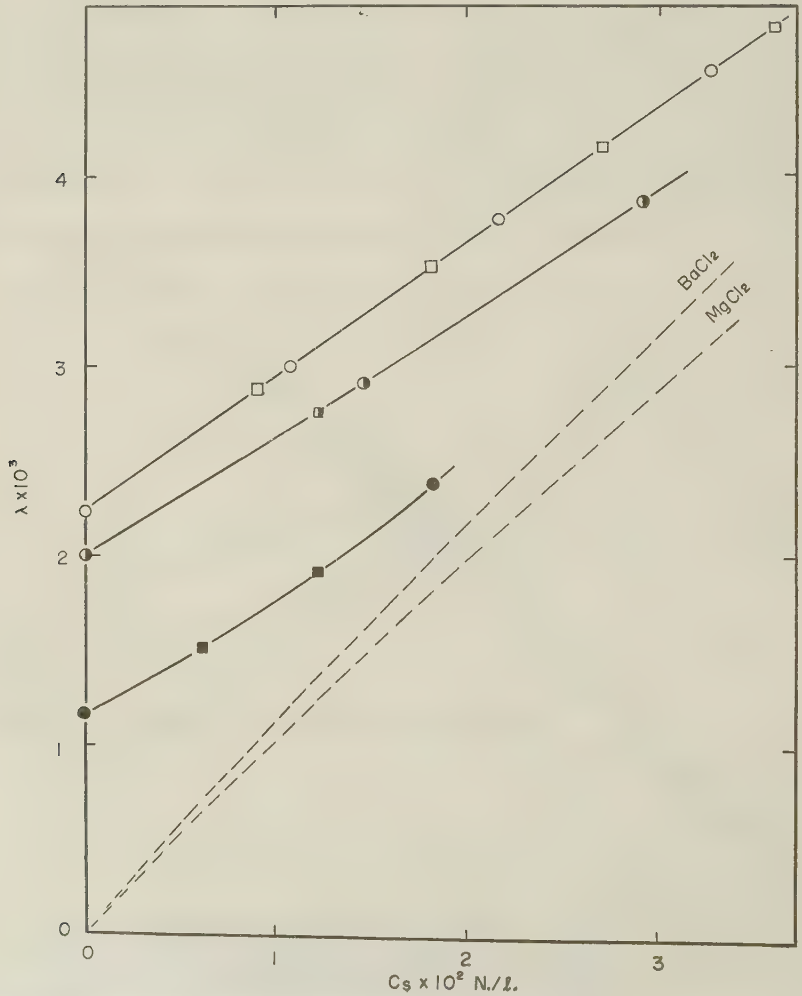

Fig. 6. The relation between specific conductances $\lambda(C_s)$ of polyacid-salt neutralized by NaOH and added salt concentration $C_s(N/l)$ at 20°C. The broken lines indicate the corresponding simple salt solutions. Polymer concentration is always kept constant at 0.089 N/l.

○: $MgCl_2$, $\alpha=1$; ◑: $MgCl_2$, $\alpha=0.7$; ●: $MgCl_2$, $\alpha=0.3$;
□: $BaCl_2$, $\alpha=1$; ◨: $BaCl_2$, $\alpha=0.7$; ■: $MgCl_2$, $\alpha=0.3$.

parison with h. Thus, for the case of these cations, we have the relations;

$$\Delta\lambda/\Delta C_s=\lambda_a+\lambda_c-h(\lambda_c+\lambda_p)\ . \qquad (38)$$

On the other hand, from the pH measurements, it was found that when HCl was added into the polyion solution neutralized by $(NBu)_4OH$ at $\alpha=0.7$ or 1.0, the value of pH changed from 7.2 to 5.2 or from 9.9 to 7.8, provided that the final concentration of added Cl^- is less than αC_p. This pH change corresponds to the increase of H^+-concentration at most about 10^{-5} mol/liter and is negligibly small. Hence, it is reasonable to put $h=1$ in (38) for the case of added H^+.

Thus, we can obtain the value of λ_p without difficulty. By substituting this value of λ_p and the experimental results into (38) or more generally (36) with no ΔC_t term, we obtain the value of C_m in the case of $(NBu)_4OH$—neutralized solutions (Fig. 5). A similar result for the case of added NaCl has been obtained by us, and from the result, it has been concluded that the amount of bound Na^+ is about 60∼70% when Na^+-concentration is nearly αC_p.

Next, by putting $C_s=0$ in (35) and substituting the value of λ_p and the experimental result in the case of no salt into (35), we can calculate the value of C_t/C_p and study the contribution of $(NBu)_4^+$ to the conductance. Although this value cannot be accurately determined because the ionic concentration in our system is too high to assume the independent migration of ions, it can be roughly concluded that about 70–80% of $(NBu)_4^+$ ions can contribute to the ionic conductance of salt-free poly(-acrylic acid) solution.

Turning to the relation (35), it is expected that in the case of the polymer solutions neutralized by NaOH, the value of $\Delta C_m/\Delta C_s$ will depend on α, since bf in this case is is supposed to be a function of α. This fact can be proved by the experimental results shown in Fig. 6. As seen in this figure, the slope of λ increases with increasing α. It is, however, an unsolved problem to determine the concrete values of ion-exchanging parameters.

Thus, through the conductance measurements, we can see very complicated binding phenomena related to both the P-binding and the ψ-binding.

§ 5. Discussion and Conclusions

As discussed in the above sections, there is neither the ideal ψ-binding nor the ideal P-binding in the ion-binding state of polyions. The specific binding of salt-ions to polyions are much strengthened by the *ion-condensation* phase around polyions theoretically expected to appear in the system of much charged macroions. The clear evidence of this effect has been observed in the adsorption phenomenon of various salt-cations to PAA molecules (§ 4).

It must be emphasized here that the ψ-binding effect becomes more conspicuous in the system of locally aggregated polyions than in the system of dispersed polyions. On the basis of the *two-step ion-condensation* which has been deduced in this paper, it is expected that the great change of the activity coefficient of small ions appears when the rearrangement of polyions or the phase change in polymer solutions does occur. This fact may be examined through the experiments of membrane potential.

In general, in order to obtain the information about such complicated ion-binding, it is convenient to adopt the conductance[14)–16)] or dielectric constant measurements[21),22)]. The former method is useful to estimate the amount of salt-ions in specific binding state as described in § 4, while the latter is sometimes convenient to study the ψ-binding effect on the basis of the Maxwell-Wagner effect. The remarkable increase of dielectric constant and its abnormal dispersion in salt-free solutions recently observed by Fuoss and Allgén prove the existence of ionic double phase around a polyion. However, they cannot give the direct support to the ion-condensation phenomenon due to our theory. Nevertheless, it is an interesting problem how the influence of the two-step ion-condensation does appear in the dielectric constant when the aggregation—dispersion transformation is observed in the solution.

It can be briefly concluded through the above investigations that by the concept of the ion-condensation of the first and the second kind deduced from the non-linear character of the P.B. equation, we can make theoretical discussions on the further more complicated polyion system without solving directly the corresponding P.B. equation, and that the strong effect of the ψ-binding appears in reinforcement of the adsorption of cations to polyanions, as observed in the experiment.

There are, however, many unsolved experimental problems upon the ion-binding, such as the influence of added salts, dehydration of bound ions, the relation between the ion-binding and the aggregation phenomena of polyions, etc. These problems are being made clear through the recent work upon the salting-out experiment, the measurements of diffractive index and ultrasonic velocity. Our studies upon this problem will be reported in other papers.

Acknowledgement

It is author's pleasure to acknowledge the useful advice and discussion of Prof. Oosawa. The author is also deeply indebted to the members of author's laboratory for giving him valuable discussions.

References

1) P. J. Flory and J, E. Osterheld: J. Phys. Chem. **58** (1954) 653.
2) R. E. Schachat and H. Morawetz: J. Phys. Chem. **61** (1957) 1171.
3) I. Michaeli, J. Th. G. Overbeek and M. J. Voorn: J. Polymer Sci. **23** (1957) 443.
4) H. Eisenberg and G. R. Mohan: J. Phys. Chem. **63** (1959) 671.
5) See for example, J. D. Ferry: *Advances in Protein Chemistry IV*, (Academic Press, New York, 1948) p. 1.
6) F. Oosawa: J. Polymer Sci. **26** (1957) 29.
7) W. Kuhn, O. Künzle and A. Katchalsky: Helv. Chim. Acta **31** (1948) 1994.
8) J. Hermans and J. Th. G. Overbeek: Rec. trav. chim. **67** (1948) 761.
9) A. Katchalsky and S. Lifson: J. Polymer Sci. **11** (1953) 409.
10) F. Oosawa, N. Imai and I. Kagawa: J. Polymer Sci. **13** (1954) 93.
11) F. T. Wall and J. Berkowitz: J. Chem. Phys. **26** (1957) 114.
12) S. Lifson: J. Chem. Phys. **26** (1957) 700, 727. 1356.
13) S. A. Rice: Rev. Modern Phys. **31** (1959) 69.
14) H. P. Gregor, D. H. Gold and M. Frederick: J. Polymer Sci. **23** (1957) 467.
15) A. Oth and P. Doty: J. Phys. Chem. **56** (1953) 43.
16) H. Eisenberg: J. Polymer Sci. **30** (1958) 47.
17) F. T. Wall and M. J. Eittel: J. Am. Chem. Soc. **79** (1957) 1550, 1556.
18) N. Imai and T. Onishi: J. Chem. Phys. **30** (1959) 1115.
19) J. Huizenga, P. F. Grieger and F. T. Wall: J. Am. Chem. Soc. **72** (1950) 2636.
20) T. Onishi, N. Imai and F. Oosawa: J. Phys. Soc. Japan **15** (1960) 896.
21) H. M. Dintzis, J. L. Oncley and R. M. Fuoss: Proc. Nat. Acad. Sci. **40** (1954) 62.
22) L. G. Allgén and S. Roswall: J. Polymer Sci. **12** (1954) 229.
23) A. Ikegami and N. Imai: J. Polymer Sci. in press. (1961).

JOURNAL OF THE PHYSICAL SOCIETY OF JAPAN, Vol. 16, No. 4, APRIL, 1961

Study of the Hydration-Dehydration in Polyelectrolyte Solutions by the Ultrasonic Technique

By Hiroshi ASAI

Department of Physics, Faculty of Science, Nagoya University, Nagoya Japan

(Received January 9, 1961)

In this study, the ultrasonic velocity and the density of the polycarboxylic acid solutions which are neutralized at various degrees by sodium hydroxide or tetra-n-butyl ammonium hydroxide have been measured. From these results, the amount of hydrated water molecules has been estimated. An abnormal behavior of hydration has been found in polyacid solutions neutralized by NaOH, which is interpreted as being due to the partial dehydration resulting from Na ion-polyion binding at high degree of neutralization. The effects of adding various mono- or di-valent salts upon the hydration state of polyanion were also examined. From these experiments, it has been found that Ba ion-polyion binding gives rise to 40 percent dehydration of the water molecules which were hydrated in no binding state, and Mg ion-polyion binding gives rise to 20 percent dehydration. The whole results in polyacids were always compared with the results in monoacids, and it was concluded that the above dehydration phenomenon was one of the important characteristics of polyacids.

§ 1. Introduction

In the recent studies of polyelectrolyte solutions, it is one of the important subjects to investigate the specific ion-binding and precipitation phenomena in polyelectrolyte solutions. These phenomena are closely related to the hydration of polyions which is much influenced by the various ionic conditions. Although there have been many studies upon the ion-binding[1)-4)] or the salting out of polyions[5-9)], few direct investigations have been made on the hydration problem. It is expected that the information of the hydration in polyelectrolyte solutions can be obtained through the ultrasonic velocity experiment which was employed to estimate the amount of hydration in simple electrolyte solutions[10)-12)]. We have, therefore, undertaken to apply this method for the study of the hydration-dehydration in polyelectrolyte solutions. We measured the ultrasonic velocity and the density of solutions of polyacids (polymethacrylic acid and polyacrylic acid) neutralized by sodium hydroxide and tetra-n-butyl ammonium hydroxide. The comparison of two kinds of counterions gave some new knowledge on the counterion-binding of polyion and the resulting dehydration. We also examined the effects of various mono- and di-valent salts on the neutralized polyacids. As a result, we found the cation binding accompanied by dehydration, the amount of which depends on the species of cations. The same experiments were carried out in monocarboxyl acids and the results were compared with those in polyacids.

§ 2. Experiments

Apparatus

The ultrasonic velocity of the solutions was measured at the frequency of one megacycle by an ultrasonic interferometer which was similar to that used by McMillan and Lagemann[13)] or Gucker and Haag[14)]. The reproducibility of the measured velocities was within 0.3 m/sec. The density of solutions was measured by picnometers. All measurements were made in the water bath at constant temperature 25.0±0.03°C.

Material and preparation

PMA. Crystalline methacrylic acid monomer supplied by the courtesy of Dr. Nagasawa was dissolved in distilled water to a nearly saturated concentration and the degree of neutralization was adjusted to 0.05 with sodium hydroxide. A small amount of the initiator (ammonium persulphate) was added. After incubation for 27 hours at 64°C, monomer solution was polymerized into a jelly-like solution of polymethacrylic acid (PMA). No appreciable amount of unreacted monomer was detected by chemical analysis of the double bond of monomer. The solution was diluted by distilled water. The average degrees of polymerization were found to be 2800 from the intrinsic viscosity[15] in 0.2 M HCl solution.

PAA. The polyacrylic acid (PAA) solution obtained through Towa Gosei Co. as a laboratory sample was dialyzed againt many changes of distilled water for two weeks. The average degrees of polymerization estimated from the intrinsic viscosity[16] in 2 N NaOH solution were found to be 1900.

MMA. The methacrylic acid (MMA) solution obtained by dissolution of the crystalline monomer contained a small amount of the polymerization inhibitor (0.033 percent hydroquinone and 0.05 percent methylene blue), which prevented monomers from photo-polymerization. The presence of small amount of the inhibitor gave no disturbance in our experiments.

Other chemicals were reagent grade. The solute concentration in all original solutions was determined by the titration of carboxylic groups in the presence of sufficient NaCl. The completely neutralized solution in the absence of salt was obtained by addition of the calculated amount of pure hydroxide solution (sodium hydroxide or tetra-n-butyl ammonium hydroxide) into acid solution. Solutions at various degrees of neutralization were prepared by mixing the acid solution and the completely neutralized solution at various ratios.

§ 3. Results

A. *Increase of hydration in acid solution by ionization*

Fig. 1 shows ultrasonic velocity V and density ρ of MMA and PMA solutions at various degrees of neutralization by NaOH. The velocity and the density of MMA solutions increase linearly with the degree of neutralization α. The density of PMA solutions also increases linearly with α. The increment of velocity of PMA solutions by ionization, however, decreases with increasing α. The adiabatic compressibility β of solution is related to the velocity and density by the equation $\beta=1/V^2\rho$; and the apparent partial molar compressibity $\bar{\beta}$ of solute can be calculated by the equation

$$\bar{\beta}=\frac{10^3\beta-v_0\beta_0}{C}\,, \tag{1}$$

where C is the molar concentration of solute in monomer unit, v_0 is the volume of solvent per liter of solution, and β_0 is the compres-

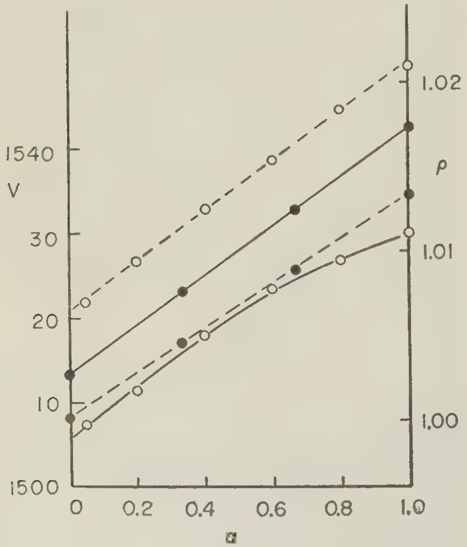

Fig. 1. Ultrasonic velocity V and density ρ of MMA and PMA solutions at various degrees of neutralization α by NaOH. Concentration of MMA, PMA are 0.37 moles/L., 3.34 m/L., respectively. -●-; V of MMA, --●--; ρ of MMA, -○-; V of PMA, --○--; ρ of PMA.

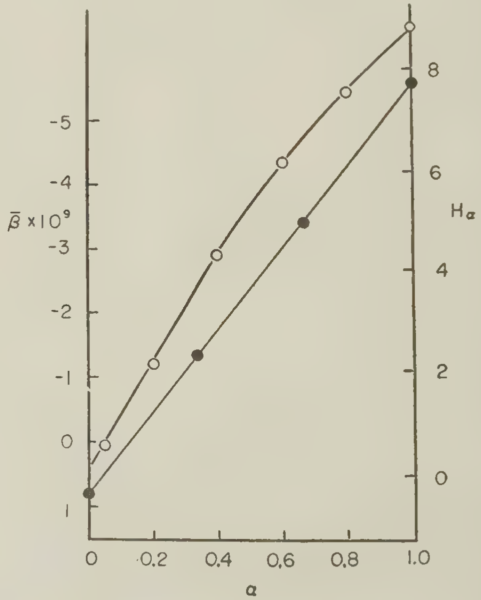

Fig. 2. The apparent partial molar compressibility $\bar{\beta}$ of MMA and PMA at various α. -●-; MMA, -○-; PMA. The right ordinate shows the amount of hydrated water molecules H_α.

sibility of solvent. A non-linear relation between $\bar{\beta}$ of PMA and α can be seen in Fig. 2.

To examine whether or not non-linearity of $\bar{\beta}$ disappears at sufficiently low concentration of polyacid, we made similar experiments at various concentrations of PMA as well as MMA. As shown in Fig. 3, no essential difference was observed in concentration dependence of $\bar{\beta}$ between PMA and MMA. Consequently, $\bar{\beta}$ of PMA at sufficiently low concentration does not vary linearly with α but shows a similar behavior to that at finite concentration.

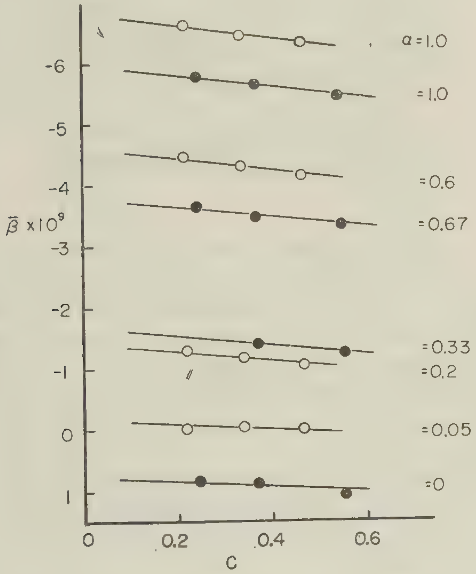

Fig. 3. Relation between $\bar{\beta}$ and acid concentration *C*. -●-; MMA, -○-; PMA.

To evaluate the amount of hydration from the measured value of $\bar{\beta}$ we put the following two assumptions. In the first place, it is assumed that the compressibilities of hydrated water and small ions are negligibly small as compared with that of free water. In simple strong electrolyte solutions, this assumption has been justified[11] by the fact that the amount of hydration estimated under this assumption is in good agreement with that estimated by other experiments. In the second place, it is assumed that the compressibility of the hydrophobic group in acid molecules is not altered by ionization of carboxyl group. Under these assumptions we can estimate the increase of the amount of hydration H_α (moles per mole of solute) by ionization up to α by the following relation, although we can not know the amount of hydration at $\alpha=0$;

$$H_\alpha = -\frac{\beta_\alpha - \beta_{\alpha=0}}{\bar{v}_0 \beta_0} \qquad (2)$$

where $\bar{v}_0$ is the partial molar volume of water. The right ordinate of Fig. 2 shows the value of H_α. Thus, in the term of hydration the results in the figure are described as follows; in MMA the increment of hydration by ionization of each carboxyl group does not depend on α; and in PMA the increment of hydration by ionization of each carboxyl group on polymer chain decreases gradually with increasing α. Such an abnormal behavior of hydration in PMA was also found in PAA. It is then likely that this is a common characteristics of polycarboxyl acids.

Now, in order to examine whether or not this behavior is due to the binding between polyion and Na ion, it is suitable to employ tetra-n-butyl ammonium (TBA) ion as counterion instead of Na ion because this TBA ion can be postulated not to be bound to polyion on account of its large size. Fig. 4 shows the apparent partial molar compressibilities of PAA and acetic acid (Ac) neutralized by TBA-

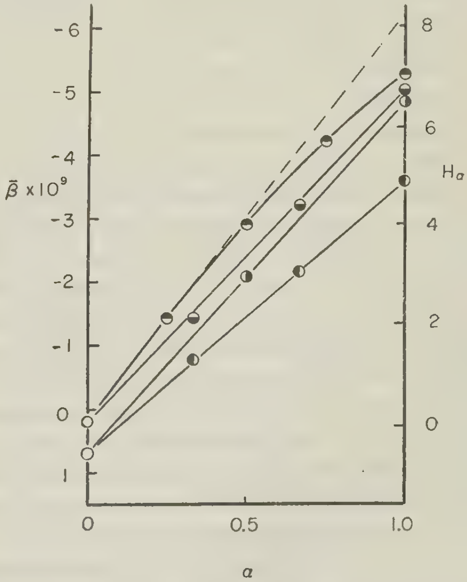

Fig. 4. Plots of $\bar{\beta}$ of acetic acid and PAA neutralized by TBA-OH or by NaOH against α. ◐; TBA-Ac at 0.29 m/L. ◑; Na-Ac at 0.29 m/L, ◒; TBA-PAA at 0.29 m/L, ◓; Na-PAA at 0.30 m/L.

OH and those neutralized by NaOH. The linear relations between $\bar{\beta}$ and α was found in TBA-PAA system as well as in TBA-Ac system, while the non-linear relation was found in Na-RAA system. Therefore, the non-linearity in Na-polyion systems is interpreted as being due to the binding of Na ion to polyion. But for this binding, the difference of $\bar{\beta}$ between Na-PAA and TBA-PAA system should be equal to the difference of $\bar{\beta}$ between Na-Ac and TBA-Ac system. As a matter of fact, the former difference is found to be smaller than the latter. The broken line in the figure gives the value of $\bar{\beta}$ of Na-PAA expected under the supposition of no binding. The actual discrepancy can be attributed to the dehydration accompaning Na ion-PAA ion binding. The estimated amount of dehydration is very small at low α and increases sharply with α. This fact consists at least qualitatively with the experimental results on Na ion binding made by Wall and Eittel[4]. If the fraction of bound Na ion at $\alpha=1$ is about 60 percent as reported by the above authors, the amount of dehydrated water molecules is estimated to be about two molecules per ion binding. This value is fairly small in comparison with the amount of water molecules which were hydrated in no binding state.

B. *Dehydration in polyacid solutions by adding salts*

By using a similar method, we studied the hydration in PMA solutions in the presence of mono- and di-valent salts (NaCl, $MgCl_2$, $BaCl_2$) at various degrees of neutralization by NaOH. The results were compared with those in MMA solutions. The apparent compressibility of the mixed solution of MMA and salts ($10^3\beta-v_0\beta_0$) varies linearly with mixing ratio r. This fact means that hydration of MMA is not affected by the presence of salts. A similar result is obtained in the mixed solution of PMA and mono-valent salt. However, the velocity of the mixed solution of PMA and divalent salts does not vary linearly with r, but has a remarkably low value (except at low α). Typical examples are shown in Fig. 5. The density of the mixed solution of PMA and divalent salt does not appreciably deviate from the straight line. Since the presence of divalent salt gives rise to precipitation of the neutralized polyacid at some critical concentration, the measurements were carried out up to its critical concentration. The experimental results suggest that the added divalent cations are bound to polyions and part or all of the water molecules which were hydrated in no binding state are dehydrated.

The difference $\Delta\Phi$ of the measured value of the apparent compressibility of a mixture from the value expected on the hypothetical

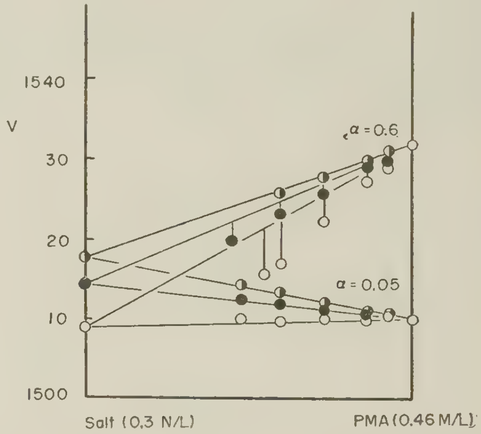

Fig. 5. Plots of V in the mixed solutions of PMA and various salts against mixing ratio r. ◑; NaCl, ●; $MgCl_2$. ○; $BaCl_2$.

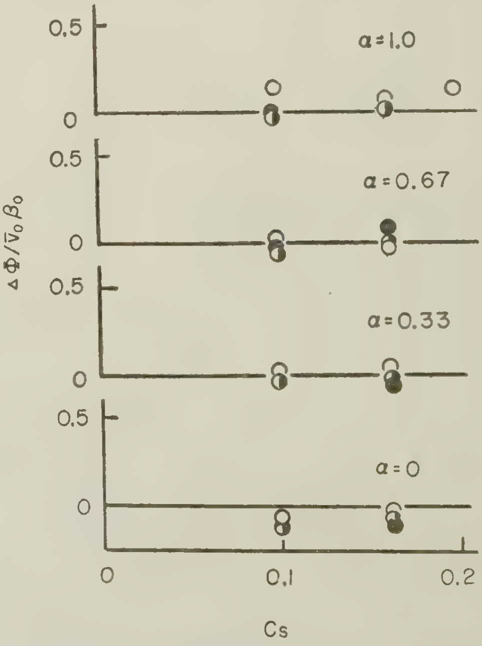

Fig. 6. Plots of $\Delta\Phi/v_0\beta_0$ in the mixed solutions of MMA and various salts against the added salt-concentration C_s (normal/L). ◑; NaCl, ●; $MgCl_2$, ○; $BaCl_2$.

condition of no dehydration can be expressed as follows,

$$\Delta\Phi=(10^2\beta-\beta_0 v_0)-(C_s\bar{\beta}_s+C\bar{\beta})\ , \qquad (3)$$

where C_s is the concentration of salt in a mixed solution and $\bar{\beta}_s$ is the apparent partial molar compressibility of salt. The amount of dehydrated water molecules per liter of solution is given by $\Delta\Phi/\bar{v}_0\beta_0$. Plots of $\Delta\Phi/\bar{v}_0\beta_0$ against salt-concentration are shown in Figs. 6 and 7.

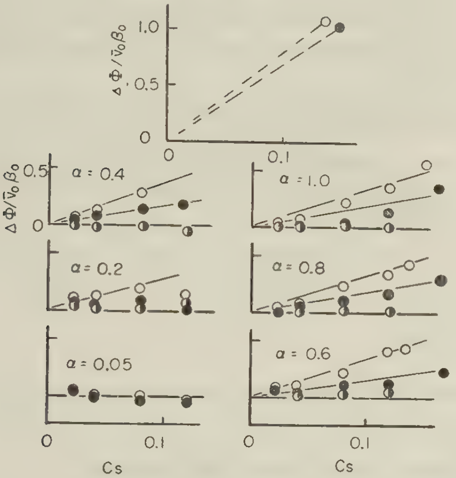

Fig. 7. Plots of $\Delta\Phi/\bar{v}_0\beta_0$ in the mixed solutions of PMA and various salts against C_s. ◑; NaCl, ●; $MgCl_2$, ○; $BaCl_2$. The broken lines show the value of $\Delta\Phi/\bar{v}_0\beta_0$ calculated on the assumption that all of the added divalent cations are bound to polyions and complete dehydration takes places.

It can be seen in Fig. 6 that the addition of various salts does not bring about dehydration of MMA at any α. It can be also seen in Fig. 7 that the addition of monovalent salt to PMA solution does not appreciably bring about dehydration of PMA. On the other hand, the presence of divalent salt brings about a considerable amount of dehydration in PMA solution (except at low α). If it is assumed that the Na ions bound to polyions are not affected by the addition of divalent cations, the amount of dehydrated water molecules estimated from the above equation may be attributed mainly to divalent ion-polyion binding. The fact that the gradient of $\Delta\Phi/\bar{v}_0\beta_0$ against divalent salt-concentration is nearly independent of α suggests that the added cations are almost bound to polyions. This complete divalent cation-polyion binding has been supported by several authors[1),9)]. The broken lines in Fig. 7 show the value $\Delta\Phi/\bar{v}_0\beta_0$ calculated on the assumption that all of the added cations are bound to polyions and the complete dehydration takes place. From the comparison between the broken lines and the measured $\Delta\Phi/\bar{v}_0\beta_0$, it can be said that the Ba ion-polyion binding gaves rise to 40 percent dehydration of the water molecules which were hydrated in no binding state and the Mg ion-polyion binding gives rise to 20 percent dehydration. This difference in the amount of the dehydrated water is originated in the difference in ionic radii between Ba and Mg.

§ 4. Discussion

As seen in Fig. 2 and 4, $\bar{\beta}$ of polyacid is smaller than $\bar{\beta}$ of monoacid at the same α. This fact is due to the low compressibility of polymer skelton formed by the polymerization of monoacids.

In the analysis of dehydration in PMA solutions neutralized by NaOH and containing divalent cations, we assumed that the amount of bound Na-ions is not altered by the absorption of divalent cations to polyanions. It is, however, very possible that when divalent cations are absorbed to polyions, the ion-bridges are formed across the ionized carboxyl groups on polyions. Such bridge-formations might partly release the bound Na ions. This effect will be examined through the studies upon the polyacid solutions neutralized by hydroxides of special cations, such as TBA, having no ability to be bound to polyions.

As described in the above section (Fig. 7), the larger amount of dehydyation is observed in the case of Ba-binding to polyions than in the case of Mg ion-binding. Such difference of the amount of dehydration causes the significant difference of the solubility of polymers between in Ba-ion containing solution and in Mg-ion containing solution.

Through the above experimental results, it is clearly found that the hydration-dehydration change is the very basic and important phenomenon in charged macro-ion system and the ultrasonic measurement is one of the useful method for the study of such hydration phenomenon.

Acknowledgement

I wish to express my thanks to Prof. F...

Oosawa, Dr. T. Ooi, and Dr. N. Imai for their helpful advice and discussion in this investigation. Thanks are also due to Dr. M. Nagasawa for supplying valuable samples.

References

1) F. T. Wall and J. W. Drenan: J. Polymer Sci., **7** (1951) 83.
2) A. Katchalsky and M. Zwick: J. Polymer Sci., **16** (1955) 221.
3) J. Huizenga, P. F. Grieger and F. T. Wall: J. Am. Chem. Soc. **72** (1950) 2636.
4) F. T. Wall and M. J. Eittel: J. Am. Chem. Soc. **79** (1957) 1550, 1556.
5) P. J. Flory and J. E. Osterheld: J. Phys. Chem. **58** (1954) 653.
6) J. Eliassof and A. Sieberberg: J. Polymer Sci. **41** (1959) 33.
7) R. E. Schachat and H. Morawetz: J. Phys. Chem. **61** (1957) 1171.
8) I. Michaeli, J. Th. G. Overbeek and M. J. Voorn: J. Polymer Sci. **23** (1957) 443.
9) A. Ikegami and N, Imai: J. Polymer Sci. (in press).
10) Wada, Shinbo, Oda and Nagumo: Ōyō Butsuri (Japanese) **17** (1948) 257.
11) T. Yasunaga and T. Sasaki: Nihon Kagaku Kaishi (Japanese) **72** (1951) 87.
12) A. Passynski: Acta Phys. Chim. U.S.S.R **8** (1938) 385.
13) D. R. McMillan and R. T. Lagemann: J. Acou. Soc. Am. **19** (1947) 956.
14) F. T. Gucker, Jr. F. W. Lamb, A. Marsh and R. M. Haag: J. Am. Chem. Soc. **72** (1950) 310.
15) A. Katchalsky and H. Eisenberg: J. Polymer Sci. **6** (1951) 145.
16) A. Takahashi, Y. Hayashi and I. Kagawa: Kogyo Kagaku Zasshi (Japanese) **60** (1957) 1059.

JOURNAL OF THE PHYSICAL SOCIETY OF JAPAN Vol. 16, No. 4, APRIL, 1961

On the Theory of Cross Relaxation in Maser Materials

By Motokazu HIRONO

Radio Research Laboratories, Kokubunji, Tokyo

(Received December 15, 1960)

A theoretical study of cross relaxation in Maser materials has been carried out based on the moment method. The energy level splittings due to the crystalline electric field and the applied magnetic field are utilized for the computation of the moments of the cross relaxation. If the lattice points are populated at random by paramagnetic ions in highly diluted salts, the second moment is much greater than the overlap integral of the individual ordinary resonance line shapes and to some extent influenced by the orientation of the applied magnetic field. The shape function of the cross relaxation is roughly Gaussian but takes slightly less values in the wings. The cross relaxation in ruby Maser successfully operated at liquid nitrogen temperatures has been briefly discussed.

§ I. Introduction

In a recent paper the theory of cross relaxation in spin systems was developed by Bloembergen, Shapiro, Pershan and Artman[1] (hereafter referred to as BSPA). This paper shows the mechanism of spin-spin relaxation, i.e. the process by which a common spin temperature is achieved. A number of experiments[2]-[4] have verified this theory at least qualitatively

The most fundamental process of cross relaxation is when two spins make simultaneous opposite flips, the balance in Zeeman energy being taken up by the dipole-dipole interaction. The process was treated in several theoretical papers.[1],[5],[6] The practical computations in BSPA and in reference 2 were based on replacement of the second moment for cross relaxation with the overlap of individual ordinary line shape functions.

Pershan[5] calculated the second moment for the case of nuclear spins of LiF and showed that the above approximation is useful for concentrated salts to which, however, his consideration is confined. The cross relaxation in highly diluted paramagnetic salts was treated by Kiel[6] in terms of moment method and it was shown that the overlap integral method does not suffice for the diluted salts. In his calculations the effect of the crystalline electric field is neglected. This effect is, however, of fundamental importance for the operation of solid state Masers. In the present paper the rate of cross relaxation is calculated in terms of moment method taking into account the effect of the crystalline electric field in the Maser materials and hence the mechanism of relaxation is essentially different from that of Kiel[6].*

In recent years, the ruby Masers were successfuly operated at liquid nitrogen temperatures by Maiman[7] and Ditchfield.[8] Maiman[7] suggested that the cross relaxation is important for the operation. We briefly examined the process in terms of above mentioned results.

§ 2. General Consideration on Cross Relaxation

Consider the spin Hamiltonian,

$$\mathscr{H}=\mathscr{H}_m+\mathscr{H}_{cr}+\mathscr{H}_{\text{int}} \tag{1}$$

$\mathscr{H}_{cr}$ is the sum of the crystalline field couplings of the individual ions. The Zeeman energy in the applied field is given by

$$\mathscr{H}_m=\sum_i \beta \boldsymbol{H}\cdot \boldsymbol{g}_i\cdot \boldsymbol{S}_i\ .$$

The interaction between the spins are assumed to consist of dipolar and exchange terms:

$$\mathscr{H}_{\text{int}}=\sum \tilde{A}_{ij}(\boldsymbol{S}_i\cdot \boldsymbol{S}_j)+\sum_{j>i}\frac{g^2\beta^2}{r_{ij}^3}\left[(\boldsymbol{S}_i\cdot \boldsymbol{S}_j)-\frac{3}{r_{ij}^3}(\boldsymbol{S}_i\cdot \boldsymbol{r}_{ij})(\boldsymbol{S}_j\cdot \boldsymbol{r}_{ij})\right]$$

where one sort of paramagnetic ions is considered and the usual notations are employed. According to BSPA the interaction energy $\mathscr{H}_{\text{int}}$ can be written in the following forms

$$\mathscr{H}_{\text{int}}=A+B+C+D+E+F \tag{2}$$

$$A=\sum_{j>i}[\tilde{A}_{ij}+g^2\beta^2 r_{ij}^{-3}(1-3\cos^2\theta_{ij})]S_{zi}S_{zj}$$

$$B=\sum_{j>i}[(1/2)\tilde{A}_{ij}-(1/4)g^2\beta^2 r_{ij}^{-3}(1-3\cos^2\theta_{ij})](S_{+i}S_{-j}+S_{-i}S_{+j})$$

$$C=\sum_{j>i}(-3/2)g^2\beta^2 r_{ij}^{-3}\sin\theta_{ij}\cos\theta_{ij}\, e^{-i\phi_{ij}}(S_{+i}S_{zj}+S_{zi}S_{+j})$$

$$D=\sum_{j>i}(-3/2)g^2\beta^2 r_{ij}^{-3}\sin\theta_{ij}\cos\theta_{ij}\, e^{+i\phi_{ij}}(S_{-i}S_{zj}+S_{zi}S_{-j})$$

$$E=\sum_{j>i}(3/4)g^2\beta^2 r_{ij}^{-3}\sin^2\theta_{ij}\, e^{-2i\phi_{ij}}\, S_{+i}S_{+j}$$

$$F=\sum_{j>i}(3/4)g^2\beta^2 r_{ij}^{-3}\sin^2\theta_{ij}\, e^{2i\phi_{ij}}\, S_{-i}S_{-j}$$

where θ_{ij} and ϕ_{ij} are the polar angles of the radius vector connecting ions i and j with respect to the z-axis.

Several types of cross relaxations are considered by BSPA and others. In the following we shall examine the most fundamental processes which proceed through the sets of the neighboring two paramagnetic ions. The probability per unit time for the process that ion

---

* Some terms are, however, dropped in the equation (9) of Kiel. An exact calculation shows that the concentration independent term of (9) vanishes for $S=I=1/2$, since the term arises from the fact that $\mathscr{H}_{12}$ does not commute with $\sum' C_{p\xi}S_{zp}I_{z\xi}$ and this condition holds except for $S=I=1/2$.

i increases its energy by an amount $h\nu_\alpha$ and ion j decreases its energy by $h\nu_\beta$, the balance of energy $h(\nu_\beta-\nu_\alpha)$ being taken up by the spin-spin interaction of the whole array of dipoles, is given by

$$w_{ij}=\hbar^{-2}|\langle E_i,\ E_j|\,\mathscr{H}_{ij}|E_i+h\nu_\alpha,\ E_j-h\nu_\beta\rangle|^2 g_{\alpha\beta}(\nu=0)\ . \tag{3}$$

If m_s is a good quantum number the matrix element is obtained from the term B in (2) and its square is given by

$$|\,\mathscr{H}_{ij}|^2=\eta g^4\beta^4(1-3\cos^2\theta_{ij})^2 r_{ij}^{-6}$$

where (4)

$$\eta=(1/16)(S-m_\alpha)(S+m_\alpha+1)(S+m_\beta)(S-m_\beta+1)\ .$$

When m_s is not a good quantum number, the expression of η is more complicated, nevertheless it is estimated to be of the order of unity for the cases considered in the following. The shape function $g_{\alpha\beta}(\nu)$ should be calculated by the moment method. The total second moment is

$$h^2\langle\nu^2_{\alpha\beta}\rangle=-T_r\{[\mathscr{H}(\sum\mathscr{H}_{ij})-(\sum\mathscr{H}_{ij})\mathscr{H}]^2\}/T_r\{[\sum\mathscr{H}_{ij}]^2\}\ . \tag{5}$$

This method was, however, not use by BSPA for practical computation and instead the overlap integral of the line shape function $F(\alpha,\ \beta)$ was used, where

$$F(\alpha,\ \beta)=\iint g_\alpha(\nu')g_\beta(\nu'')\delta(\nu'-\nu'')d\nu' d\nu''\ . \tag{6}$$

If a Gaussian shape is assumed for $g_\alpha(\nu)$ and $g_\beta(\nu)$ with second moments $\langle\varDelta\nu_\alpha{}^2\rangle$ and $\langle\varDelta\nu_\beta{}^2\rangle$ (6) is reduced to

$$F(\alpha,\ \beta)=[2\pi\{\langle\varDelta\nu_\alpha{}^2\rangle+\langle\varDelta\nu_\beta{}^2\rangle\}]^{-1/2}\exp\{-(\nu_\alpha-\nu_\beta)^2/2[\langle\varDelta\nu_\alpha{}^2\rangle+\langle\varDelta\nu_\beta{}^2\rangle]\}\ . \tag{7}$$

By the use of the formulae together with excellent insight into the mechanism of elementary reactions, BSPA obtained several important agreement between the theoretical predictions and the experimental results. However, more rigorous mathematical treatment of the shape functions is very desirable to examine the various phenomena in the solid Masers. In the following section we give the estimation of the shape function using the moment method under consideration of the crystalline electric field.

§ 3. Estimation of the Shape Function by the Moment Method

The estimation of the shape function $g_{\alpha\beta}$ by the moment method was carried out by Pershan[5] and Kiel[6] for nuclear spins of LiF and dilute paramagnetic salts respectively. For their calculations, however, the effect of the crystalline electric field was not taken into account. In the following treatment we used a state of $C_r{}^{+++}$ ion in ruby as a model and hence the influence of the crystalline electric field plays a leading rôle. In the absence of the interaction between paramagnetic ions, the spin Hamiltonian is given by

$$\mathscr{H}_m+\mathscr{H}_{cr}=\beta[g_\parallel H_z S_z+g_\perp(H_x S_x+H_y S_y)]+D[S_z{}^2-S(S+1)]$$

with

$$S=3/2\ .$$

Writing

$$g_\parallel=g_\perp=g \quad \text{and} \quad D=-\delta\ , \tag{8}$$

since $g_\parallel\simeq g_\perp$ and D is negative, we obtain the spin Hamiltonian for the ith ion in the case that the magnetic field is parallel to the crystal c axis, as follows:

$$W_i=-\delta(S^2_{zi}-\xi S_{zi})\ ,\quad \xi=g\beta H/\delta\ . \tag{9}$$

The four energy levels deduced by this expression against magnetic field are shown in Fig. 1.

The total spin Hamiltonian is given by

$$\mathscr{H}=\sum_i W_i+\mathscr{H}_{\text{int}}\,. \tag{10}$$

In order to calculate the moments, we must select the so-called semi-diagonal part of the Hamiltonian, i.e. we take up only that part of the interaction terms that commute with the one-ion energy term $\sum W_i$. This part can be diagonalized simultaneously with the one-ion energy term, so this selection corresponds to the first order perturbation process which was adopted by Ishiguro, Kambe and Usui[9] for the calculation of the moments of the Larmor-lines.

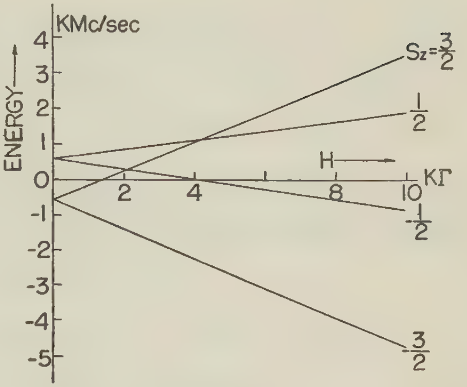

Fig. 1. A model of energy level diagram used for the calculation on the rate of cross relaxation.

The semi-diagonal part of the Hamiltonian may explicitly be written as

$$\overline{\mathscr{H}}=\sum_i W_i+\sum_{j>i}(A_{ij}+B_{ij})S_{zi}S_{zj}+\sum_{j>i}A_{ij}(\overline{S_{xi}S_{xj}}+\overline{S_{yi}S_{yj}}) \tag{11}$$

where

$$\begin{aligned} A_{ij}&=\tilde{A}_{ij}+\frac{g^2\beta^2}{r_{ij}^3}\left(\frac{3}{2}\gamma_{ij}^2-\frac{1}{2}\right), \\ B_{ij}&=-3\frac{g^2\beta^2}{r_{ij}^3}\left(\frac{3}{2}\gamma_{ij}^2-\frac{1}{2}\right) \end{aligned} \tag{12}$$

$$\begin{aligned} \overline{S_{xi}S_{yj}}+\overline{S_{yi}S_{yj}}&=\frac{1}{2}(\overline{S_{+i}S_{-j}}+\overline{S_{-i}S_{+j}}) \\ &=\frac{1}{2}(P_{(3/2)i}P_{(1/2)j}S_{+i}S_{-j}P_{(1/2)i}P_{(3/2)j}+P_{(1/2)i}P_{-(1/2)j}S_{+i}S_{-j}P_{-(1/2)i}P_{(1/2)j} \\ &\quad+P_{-(1/2)i}P_{-(3/2)j}S_{+i}S_{-j}P_{-(3/2)i}P_{-(1/2)j} \\ &\quad+P_{(1/2)i}P_{(3/2)j}S_{-i}S_{+j}P_{(3/2)i}P_{(1/2)j}+P_{-(1/2)i}P_{(1/2)j}S_{-i}S_{+j}P_{(1/2)i}P_{-(1/2)j} \\ &\quad+P_{-(3/2)i}P_{-(1/2)j}S_{-i}S_{+j}P_{-(1/2)i}P_{-(3/2)j}) \end{aligned}$$

where

$$\gamma_{ij}=\cos\theta_{ij} \tag{13}$$

$P_{(3/2)i}$, $P_{(1/2)i}$, $P_{-(1/2)i}$ and $P_{-(3/2)i}$ are the projection operators corresponding to the states $m_i=3/2$, $1/2$, $-1/2$ and $-3/2$ of the i-th ion respectively.

In order to calculate the trace, we select the representation scheme in which each spin is individually space quantized. Thus we have

$$\begin{aligned} P_{(3/2)i}&=(1/6)(S_{zi}+3/2)(S_{zi}^2-1/4)\,, \\ P_{-(3/2)i}&=-(1/6)(S_{zi}-3/2)(S_{zi}^2-1/4)\,, \\ P_{(1/2)i}&=-(1/2)(S_{zi}+1/2)(S_{zi}^2-9/4)\,, \\ P_{-(1/2)i}&=(1/2)(S_{zi}-1/2)(S_{zi}^2-9/4)\,. \end{aligned}$$

Now suppose that one of the two neighboring ions makes $m=1/2\to-1/2$ (α type) transition and the other $m=-3/2\to-1/2$ (β type) transition and the balance of energy $h(\nu_\beta-\nu_\alpha)$ is taken up by the spin-spin interaction.

The operating matrix $\sum\mathscr{H}_{ij}$ in (5) should be replaced by the following expressions

$$\sum_{j>i}\hat{\mathscr{H}}_{ij}=\hat{B}=\sum_{j>i}b_{ij}\Phi_{ij} \tag{14}$$

where

$$b_{ij}=\frac{1}{2}\tilde{A}_{ij}-\frac{1}{4}g^2\beta^2 r_{ij}^{-3}(1-3\gamma_{ij}^2) \tag{15}$$

$$\begin{aligned}\Phi_{ij}=&P_{(1/2)i}P_{-(3/2)j}S_{+i}S_{-j}P_{-(1/2)i}P_{-(1/2)j}+P_{-(1/2)i}P_{-(1/2)j}S_{-i}S_{+j}P_{(1/2)i}P_{-(3/2)j}\\&+P_{-(1/2)i}P_{-(1/2)j}S_{+i}S_{-j}P_{-(3/2)i}P_{(1/2)j}+P_{-(3/2)i}P_{(1/2)j}S_{-i}S_{+j}P_{-(1/2)i}P_{-(1/2)j}\end{aligned} \tag{16}$$

After some elementary calculations we have

$$Tr\{[\sum_{j>i}\hat{\mathscr{H}}_{ij}]^2\}=3(2S+1)^N\sum_{j>i}b_{ij}^2\ , \tag{17}$$

$$\begin{aligned}-Tr\{[\overline{\mathscr{H}}(\sum_{j>i}\hat{\mathscr{H}}_{ij})-(\sum_{j>i}\hat{\mathscr{H}}_{ij})\overline{\mathscr{H}}]^2\}\\=3(2S+1)^N[\sum_{j>i}b_{ij}^2(2\delta+C_{ij})^2\\+\sum_{k\neq(j>i)}\{(5/4)(C_{ik}^2+C_{jk}^2)+(21/8)(A_{ik}^2+A_{jk}^2)\}b_{ij}^2]\end{aligned} \tag{18}$$

where

$$C_{ij}=A_{ij}+B_{ij} \tag{19}$$

and N is the total number of ions in the crystal, and the notation $k\neq(j>i)$ means that k is not equal to j nor i and j is greater than i. In the above expression, terms like

$$\sum_{k\neq(j>i)}C_{ik}C_{jk}b_{ij}^2$$

are neglected compared to the terms like

$$\sum_{j>i}C_{ik}^2 b_{ij}^2\ .$$

Thus we obtain the total second moment using (17), (18) and the equation

$$h^2\langle\nu_{\alpha\beta}^2\rangle=-Tr\{[\overline{\mathscr{H}}(\sum\hat{\mathscr{H}}_{ij})-(\sum\hat{\mathscr{H}}_{ij})\overline{\mathscr{H}}]^2\}/Tr\{[\sum\hat{\mathscr{H}}_{ij}]^2\}\ .$$

For the present case

$$h(\nu_\beta-\nu_\alpha)=2\delta$$

and clearly in the absence of the interaction between ions we have

$$h^2\langle\nu_{\alpha\beta}^2\rangle=(2\delta)^2\ .$$

Thus we get

$$h^2\langle\Delta\nu_{\alpha\beta}^2\rangle=h^2\langle\nu_{\alpha\beta}^2\rangle-(2\delta)^2=M_1+M_2 \tag{20}$$

where

$$\begin{aligned}M_1&=\sum_{j>i}b_{ij}^2C_{ij}^2/\sum_{j>i}b_{ij}^2\\M_2&=\sum_{k\neq(j>i)}\{(5/4)(C_{ik}^2+C_{jk}^2)+(21/8)(A_{ik}^2+A_{jk}^2)\}b_{ij}^2/\sum_{j>i}b_{ij}^2\end{aligned} \tag{21}$$

and the term

$$\sum_{j>i}4\delta C_{ij}b_{ij}^2$$

is neglected compared with the term

$$\sum_{j>i}C_{ij}^2 b_{ij}^2$$

and $C_{ij}=C_{ji}$ and $A_{ij}=A_{ji}$ are assumed.

In the Maser material, usually the paramagnetic ions are highly diluted with diamagnetic ions. Kittel and Abraham[10] suggested that at least two different types of dilution may be contemplated: namely the lattice points are populated at random by the paramagnetic ions or the effect of dilution were to expand the magnetic lattice uniformly. Let us examine the effect of dilution for these cases.

(i) First suppose that the lattice points are populated at random by paramagnetic ions. Let f be the probability that a lattice site is occupied by a magnetic system. For ruby this is the probability that the Al site is replaced by the Cr ion. By a similar method to Kittel and Abraham[10], M_1 and M_2 are reduced to the following expressions:

$$M_1=\sum_j{}' b^2_{ij}C^2_{ij}/\sum_j{}' b^2_{ij}\ , \tag{22}$$

$$M_2=f[\sum_k{}'\{(5/2)C^2_{ik}+(21/4)A^2_{ik}\}-\sum_j{}'\{(5/2)C^2_{ij}+(21/4)A^2_{ij}\}b^2_{ij}/\sum_j{}' b^2_{ij} \tag{23}$$

where $\sum_k{}'$ or $\sum_j{}'$ mean sums over all k or j sites, whether or not occupied. From (12), (19) and (15) we have

$$A_{ij}=\tilde{A}_{ij}-(1/3)B_{ij}\ ,\quad C_{ij}=\tilde{A}_{ij}+(2/3)B_{ij}$$
$$b_{ij}=(1/2)\tilde{A}_{ij}-(1/6)B_{ij}\ . \tag{24}$$

It is seen that M_1 is independent of the dilution and M_2 is proportional to f. When the exchange interaction is absent $\tilde{A}_{ij}=0$ and we get

$$\begin{aligned} M_1&=(4/9)\sum_j{}' B^4_{ij}/\sum_j{}' B^2_{ij}\ ,\\ M_2&=(61/36)f[\sum_j{}' B^2_{ij}-\sum_j{}' B^4_{ij}/\sum_j{}' B^2_{ij}]\ . \end{aligned} \tag{25}$$

According to Van Vleck[11] and Kittel and Abraham[10] the mean square deviation of the frequency from the Larmor value may be written

$$h^2\langle\Delta\nu^2\rangle=[S(S+1)/3]f\sum_j{}' B^2_{ij}=(5/4)f\sum_j{}' B^2_{ij} \qquad \text{for}\quad S=3/2. \tag{26}$$

It is of interest to note that the first term of M_2 resembles this expression.

For the Maser materials, f is of the order of magnitude of 10^{-3} and hence $h^2\langle\Delta\nu^2{}_{\alpha\beta}\rangle$ is expressed by M_1 alone.

(a) If the lattice is simple cubic with the applied magnetic field in the (100) direction, we have

$$\sum_j{}' B^2_{ij}=29.9g^4\beta^4d^{-6} \tag{27}$$

and from (20) and (25) it follows that

$$\langle\Delta\nu^2_{\alpha\beta}\rangle=0.091h^{-2}\sum_j{}' B^2_{ij}=2.7h^{-2}g^4\beta^4d^{-6} \tag{28}$$

where d is the distance between nearest lattice sites. It should be noted that the value is to some extent influenced by the direction of the magnetic field.

(b) If the average of the B^2_{ij} and B^4_{ij} over the sphere, centered at the i-th ion, with the radius r equal to the distance to the (effective) nearest neighbors the number of which is Z, be denoted by $\overline{B^2_{ij}}$ and $\overline{B^4_{ij}}$ respectively, then we have approximately

$$\sum_j{}' B^2_{ij}\simeq Z\overline{B^2_{ij}}\ ,\quad \sum_j{}' B^4_{ij}\simeq Z\overline{B^4_{ij}}\ ,\quad \overline{B^4_{ij}}=2.145(\overline{B^2_{ij}})^2\ ,\quad \overline{B^2_{ij}}=(9/5)g^4\beta^4r^{-6} \tag{29}$$

and hence from (20) and (25) it follows that

$$\langle \Delta\nu_{\alpha\beta}^2\rangle = 1.7h^{-2}g^4\beta^4 r^{-6} \ . \tag{30}$$

If the shape of $g_{\alpha\beta}(\nu)$ is assumed to be Gaussian, we have

$$g_{\alpha\beta}(\nu) = [2\pi\langle \Delta\nu_{\alpha\beta}^2\rangle]^{-1/2} \exp\{-[\nu-(\nu_\beta-\nu_\alpha)]^2/2\langle \Delta\nu_{\alpha\beta}^2\rangle\} \ . \tag{31}$$

In order to compare (31) with (7) we use the following ratio

$$\langle \Delta\nu_{\alpha\beta}^2\rangle/[\langle \Delta\nu_\alpha{}^2\rangle + \langle \Delta\nu_\beta{}^2\rangle] \simeq \langle \Delta\nu_{\alpha\beta}^2\rangle/2\langle \Delta\nu^2\rangle \equiv \lambda^2 \ . \tag{32}$$

For the abovementioned case (a) we have

$$\lambda^2 = (28f)^{-1} \ , \tag{33}$$

and for the case (b)

$$\lambda^2 = 0.38(fZ)^{-1} \ . \tag{34}$$

The former is 36 for $f=10^{-3}$ and the latter 48 for $Z=8$ and $f=10^{-3}$. There is some discrepancy between them. However, in any case the calculated moments are much greater than those deduced by the overlap integral of the individual ordinary resonance line shapes.

(ii) Next suppose that the factor f is unity. From (20) and (25) we have

$$h^2\langle \Delta\nu_{\alpha\beta}^2\rangle = (61/36)\sum_j{}' B_{ij}^2 - (5/4)\sum_j{}' B_{ij}^4 / \sum_j{}' B_{ij}^2 \ .$$

(a) For the cubic lattice with the applied magnetic field in (100) direction we have

$$\langle \Delta\nu_{\alpha\beta}^2\rangle = 1.44h^{-2}\sum_j{}' B_{ij}^2$$

and therefore from (32), (26) and (27),

$$\lambda^2 = 0.58 \ .$$

(b) If the averages over the sphere are taken as in the case (b) of (i), then we have

$$\langle \Delta\nu_{\alpha\beta}^2\rangle = (1.7Z-2.7)\overline{B_{ij}^2}$$

and therefore for $Z=8$, from (32),

$$\lambda^2 = 0.54 \ .$$

Pershan[5] obtained $\lambda^2=(0.8)^2=0.64$, hence our results are nearly equal. If the effect of the dilution changes the location of the magnetic ions as if the magnetic lattice were uniformly expanded, then the ratio λ^2 is constant and $\langle \Delta\nu_{\alpha\beta}^2\rangle$ is proportional to $\langle \Delta\nu^2\rangle$ of Van Vleck.[11] In this case the overlap integral will give a fairly good measure of the cross relaxation.

§ 4. Consideration on the Fourth Moment

In the previous section the shape of $g_{\alpha\beta}(\nu)$ is assumed to be Gaussian. But in principle all higher moments are necessary to determine the exact shape. If we confine our attention to the interval of ν not far from the center, the second and the fourth moment will suffice to outline the shape.

If we write

$$U = \overline{\mathscr{H}}(\Sigma\,\widehat{\mathscr{H}}_{ij}) - (\Sigma\,\widehat{\mathscr{H}}_{ij})\overline{\mathscr{H}} \ ,$$

the total fourth moment is given by

$$h^4\langle \nu_{\alpha\beta}^4\rangle = Tr\{[\overline{\mathscr{H}}U - U\overline{\mathscr{H}}]^2\}/Tr\{[\Sigma\,\widehat{\mathscr{H}}_{ij}]^2\} \ .$$

Here we consider the parts of $\langle\Delta\nu^2_{\alpha\beta}\rangle$ and $\langle\Delta\nu^4_{\alpha\beta}\rangle$ which are independent of the dilution f and much greater than the remaining terms for $f\ll 1$. Then we have after some elementary computations,

$$h^4\langle\Delta\nu^4_{\alpha\beta}\rangle=\sum_j{}' b^2_{ij}C^4_{ij}/\sum_j{}' b^2_{ij}\,. \tag{35}$$

For the diluted magnetic lattice mentioned in (i) (a) of section 3, we have

$$\langle\Delta\nu^4_{\alpha\beta}\rangle=1.35[\langle\Delta\nu^2_{\alpha\beta}\rangle]^2\,,$$

and for the case (i) (b) of section 3

$$\langle\Delta\nu^4_{\alpha\beta}\rangle=1.44[\langle\Delta\nu^2_{\alpha\beta}\rangle]^2\,.$$

If the shape is Gaussian we should have[11)]

$$\langle\Delta\nu^4_{\alpha\beta}\rangle=3[\langle\Delta\nu^2_{\alpha\beta}\rangle]^2\,,$$

hence in the present case the shape will be roughly Gaussian, but will take slightly less value in the wings.

§ 5. Cross Relaxation Time

According to the discussion of the previous section in terms of the moment method the cross relaxation time is obtained as follows:

From (3), (4) and (31) and considering that

$$\sum_j|\mathscr{H}_{ij}|^2=f\sum_i{}'|\mathscr{H}_{ij}|^2$$

we have

$$\sum_j w_{ij}=f\cdot\eta\cdot\hbar^{-2}g^4\beta^4 g_{\alpha\beta}(\nu=0)\sum_j{}'(1-3\gamma^2_{ij})^2 r^{-6}_{ij}\,,$$

and from (12) and (26) this expression is reduced to

$$\sum_j w_{ij}=14\cdot\eta\cdot\langle\Delta\nu^2\rangle\cdot g_{\alpha\beta}(\nu=0)\,,$$

where it should be recalled that $\langle\Delta\nu^2\rangle$ is the second moment of Van Vleck.[11)] To see the relation between the results of the moment method and the overlap integral, we use the notation (32), then it follows that

$$\sum_j w_{ij}=2.8\eta\cdot[2\langle\Delta\nu^2\rangle]^{1/2}\lambda^{-1}\exp\{-(\nu_\alpha-\nu_\beta)^2/4\lambda^2\langle\Delta\nu^2\rangle\}\,. \tag{36}$$

The cross relaxation time T_{21} is obtained by

$$(2T_{21})^{-1}=\sum_j w_{ij}p_j=\frac{1}{4}\sum_j w_{ij}$$

and hence by

$$T_{21}=\left(\frac{1}{2}\sum_j w_{ij}\right)^{-1}. \tag{37}$$

The result of overlap integral is obtained by equating $\lambda=1$ and may agree[2)] with some experimental results of the dilute salts of $K_3(C_0Cr)(CN)_6$. In general, however, the cross relaxation time with $\lambda=1$ gives far longer times than those required by the experimental results, and it is necessary that λ is greater than unity to satisfy the requirement. In this situation BSPA suggested that the relaxation is mainly taking place through the ions with nearest one neighbor in the diluted salts and showed the formulae

$$T_{21}=(Zf)^{-1}\langle\Delta\nu_\alpha^2\rangle_{\mathrm{conc}}^{-1/2}\exp\{Z(\nu_\alpha-\nu_\beta)^2/2[\langle\Delta\nu_\alpha^2\rangle_{\mathrm{conc}}+\langle\Delta\nu_\beta^2\rangle_{\mathrm{conc}}]\}\ . \tag{38}$$

This value is obtained from (36) and (37) with

$$\lambda^2=(fZ)^{-1}\ , \tag{39}$$

namely by equating

$$2(fZ)^{-1}\langle\Delta\nu^2\rangle=2(Z)^{-1}\langle\Delta\nu^2\rangle_{\mathrm{conc}}\simeq Z^{-1}[\langle\Delta\nu_\alpha^2\rangle_{\mathrm{conc}}+\langle\Delta\nu_\beta^2\rangle_{\mathrm{conc}}]$$

and considering that $\eta\sim1$.

Our results (33) and (34) are of the same order of magnitude as the above λ^2, but may be about one third of the latter. The reason that $\lambda\gg1$ seems to be essentially the same as suggested by BSPA. When the value of (34) is adopted we have from (36) and (37)

$$\begin{aligned}T_{21}&=0.21\times(\eta fZ)^{-1}(g^2\beta^2h^{-1}r^{-3})\exp\{(\nu_\beta-\nu_\alpha)^2/3.4(g^4\beta^4h^{-2}r^{-6})\}\\&=(\eta fZ)^{-1}(\rho^3/2.5\times10^{11})\exp\{(\nu_\beta-\nu_\alpha)^2\rho^6/9.25\times10^{21}\}\end{aligned} \tag{40}$$

where ρ denotes the distance of the nearest paramagnetic ions in units of Å. Thus if the lattice points are populated at random by paramagnetic ions the cross relaxation time T_{21} increases very slowly with the decrease of the factor f.

On the other hand if the effect of the dilution changes the location of the magnetic ions as if the magnetic lattice were expanded uniformly, then λ is a constant as shown in the previous section and $\langle\Delta\nu^2\rangle$ is shown to be proportional to the square of the concentration of the paramagnetic ions. Thus we see from (36) and (37) that the cross relaxation time increases very rapidly with the decrease of the concentration of the ions, since $\langle\Delta\nu^2\rangle$ is included in the exponential function.

§ 6. Cross Relaxation in Solid State Masers

We shall evaluate the influence of the cross relaxation on the solid state Masers. First suppose the three level Maser of which the three levels are numbered 1, 2 and 3 from the lowest and n_1, n_2 and n_3 are the spin populations in the three levels as shown in Fig. 2. Let us write $X=2/3\cdot\sum_j w_{ij}$ then the rate equations become, at the steady state,

$$dn_3/dt=W_{13}(n_1-n_3)+S_{32}(n_2-n_3)+w'_{13}(n_1-n_3-\alpha\nu_{31})+w'_{23}(n_2-n_3-\alpha\nu_{32})+X(n_2-n_3)=0\ ,$$

$$dn_2/dt=-W_{31}(n_1-n_3)-w'_{13}(n_1-n_3-\alpha\nu_{31})+w'_{21}(n_2-n_1+\alpha\nu_{12})+X(n_2-n_3)=0\ ,$$

where we introduce such a cross relaxation that $i(1\to2)$ and $j(3\to2)$ transitions simultaneously take place and w'_{ij}, W_{31} and S_{32} denote transition probabilities due to thermal lattice vibrations, strong pumping *rf* power and signal power respectively, and $\alpha=(1/3)Nh/kT_L$, and it is assumed that $h(\nu_{12}-\nu_{23})/kT_{ad}\simeq0$, with T_L the lattice temperature and T_{ad} the final temperature after the spin system has come into internal equilibrium adiabatically. Using the notations

$$w'_{21}\sim w'_{23}\equiv w'=(2T_1)^{-1}\ ,\quad X=(2T_{21})^{-1}$$

we have from the above equations

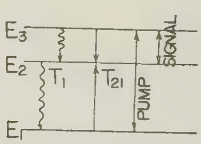

Fig. 2. A three level Maser system used to illustrate the relaxation processes.

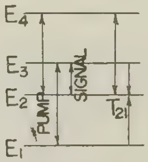

Fig. 3. A push-pull Maser pumping scheme.

$$n_3-n_2=\frac{hN}{6kT}\,\frac{\nu_{12}-\nu_{32}}{(1+2T_1/3T_{21})+T_1\cdot S_{32}} \tag{41}$$

where $T_L=T_{ad}=T$ is assumed. For the push-pull four level Masers as shown in Fig. 3, in the same way we have

$$n_3-n_2=\frac{Nh}{4kT}\,\frac{w'_{12}\nu_{12}+w'_{43}\nu_{43}+w'_{14}\nu_{14}-w'_{23}\nu_{23}}{w'_{12}+w'_{43}+w'_{14}+(w'_{23}+2\sum w_{ij})+S_{32}}$$

again using the notations

$$w'_{43}\sim w'_{21}\sim w'_{32}\sim w'_{12}\equiv w'=(2T_1)^{-1}\,,\quad (3\sum w_{ij})^{-1}=T_{21}\,,\quad \text{and}\quad w'_{41}/w'\equiv\eta\,,\quad \text{with}\quad 0<\eta<1\,,$$

we have

$$n_3-n_2=\frac{hN}{4kT}\,\frac{(\eta\nu_{41}+2\nu_{12})-\nu_{32}}{(\eta+3)+4\cdot T_1/3T_{21}+2T_1S_{32}} \tag{42}$$

where the cross relaxations are due to simultaneous flips $i(1\rightarrow 2)$, $j(3\rightarrow 2)$ and $i(3\rightarrow 4)$, $j(3\rightarrow 2)$.

It is well known that the spin-lattice relaxation time T_1 rapidly decreases with the increase of the temperature, but the cross relaxation time T_{21} is independent of the temperature. We see therefore from (41) and (42) that under certain conditions we would obtain a better Maser action in a relatively high temperatures. This presumption was verified by Maiman[7] using the ruby Maser with (nominal) 0.2 percent Cr ions operated at 77°K and further by Ditchfield.[8] The signals were in the X band and the root-gain-bandwidth products were 14 Mc/s and 22 Mc/s respectively. Maiman suggested that the success of the Maser is due to the effective control of the cross relaxation. For their push-pull scheme, the pump frequency ν_p is roughly related to the signal frequency ν_s as follows:

$$\nu_p=1.9\nu_s+5.8\quad(\text{kMc/s}).$$

Therefore for $\nu_s=9$ we have $\nu_p=22.9$ and hence

$$\nu_\beta(1\rightarrow 2)-\nu_\alpha(3\rightarrow 2)=4.9\quad(\text{kMc/s}).$$

It is surprising that the cross relaxation is effective for such a great difference of transition frequencies, therefore a close examination is needed. Maiman measured T_{21} and obtained the following values: $T_{21}=2\times 10^{-3}$ sec. and $\sim 10^{-6}$ sec for $f=\text{Cr/Al}=$(nominal) 0.2% and 0.6% respectively. In ruby the lattice sites of Al (and hence or Cr) have the near neighbors as shown in the following Table I.

According to Rimai[12] et al, the nearest neighbor is strongly coupled by the exchange interaction and they form rather the molecules and further other antiferromagnetically coupled pairs with smaller exchange constants appear to be present. In addition there is an evidence for the existence of ion pairs coupled by weaker ferromagnetic exchange. These will give rise to different spectrums from the ordinary resonance lines and should probably be omitted from our considerations. Thus we tentatively adopt Z ions at the distance of ρ Å as the effective nearest neighbors and ignor the exchange effect. The real concentrations of Cr are assumed to be one half the nominal.

Fortunately the η and f values do not greatly influence the T_{21} values. We obtain from (40) with $\eta=1$ the values of T_{21} shown in Table II. These values are very rough, however, it may be of interest to note that the values of the first two lines are intermediate of the observed values. It is likely that the cross relaxation would take place in

Table I. Distances and Numbers of the Near Neighbors.

Distance (Å)	2.73	2.81	3.13	3.50	3.78	4.77
Number	1	3	3	6	1	6

Table II. The Cross Relaxation Time T_{21} for the Assumed Nearest Z Neighbors at the Distance ρ.

ρ	Z	$f=10^{-3}$	$f=3\times10^{-3}$
3.50Å	6	3.4×10^{-6} sec	1.1×10^{-6} sec
3.78	1	3.7×10^{-4}	1.24×10^{-4}
4.77	6	$1.4\times10^{+6}$	$4.71\times10^{+5}$

this fashion. Further study is still necessary to confirm the present estimation.

§7. Concluding Remarks

The theory of cross relaxation has been discussed on the paramagnetic salts in general use for solid state Masers. To evaluate the rate of cross relaxation, it is necessary to determine the shape function. Under consideration of the crystalline electric field and the applied magnetic field we estimated the shape function in terms of the moment method. The obtained second and fourth moment for the diluted salt show that the shape function is nearly Gaussian but takes slightly less value in the wings. When the paramagnetic lattice sites are randomly populated the second moment is much greater than that deduced by the overlap integral of observed resonance shape functions. This was already suggested by BSPA on the supposition that the cross relaxation takes place mainly through the ions with one nearest neighbor. However our second moment is about one third of that suggested by BSPA and to some extent influenced by the orientation of the applied magnetic field. In this case the cross relaxation time will slowly decrease in proportion to the concentration of the paramagnetic ions.

On the other hand if the effect of the dilution were to expand the magnetic lattice uniformly the cross relaxation time rapidly decreases with the increase of the concentration of the paramagnetic ions.

The cross relaxation in the ruby Maser which is succesfully operated at the liquid nitrogen temperature is briefly discussed. In spite of various unknown factors it is likely that the process is effective also in this case.

Acknowledgements

The author would like to express his gratitude to Dr. Hiroyuki Uyeda director of the Radio Research Laboratories for his constant interest and to Prof. Kenjiro Kambe of the University of Electro-Communications for his valuable discussions. Many thanks are also due to Professor N. Bloembergen of Harvard University and Dr. P. S. Pershan of National Science foundation who read the manuscript and informed him their opinions.

References

1) N. Bloembergen, S. Shapiro, P. S. Pershan and J. O. Artman: Phys. Rev. **114**, 445 (1959).
2) S. Shapiro and N. Bloembergen: Phys. Rev. **116**, 1453 (1959).
3) C. H· Townes: Quantum Electronics (Columbia Univ. Press, New York, 1960) several papers from pp. 293–369.
4) W. B. Mims and J. D. Mc Gee: Phys. Rev. **119**, 1233 (1960).
5) P. S. Pershan: Phys. Rev. **117**, 109 (1960).
6) A. Kiel: Phys. Rev. **120**, 137 (1960).
7) T. H. Maiman: Quantum Electronics (Ed. C. H. Townes) p. 324, Columbia Univ. Press. (1960).
8) C. R. Ditchfield and P. A. Forrester: Phys. Rev. Letters, **1**, 448 (1958). C. R. Ditchfield: Presented at the Solid State Amplifier Conference at Nottingham (Apr. 1960).
9) E. Ishiguro, K. Kambe and T. Usui: Physica, **17**, 310 (1951).
10) C. Kittel and E. Abraham: Phys. Rev. **90**, 238 (1953).
11) J. H. Van Vleck: Phys. Rev. **74**, 1168 (1948).
12) L. Rimai, H. Statz, M. J. Weber and G. A. de Mars.: Phys. Rev. Letter **4**, 125 (1960).

JOURNAL OF THE PHYSICAL SOCIETY OF JAPAN, Vol. 16, No. 4, APRIL, 1961

"Non-Adiabatic" Behavior in a Low Frequency Beam-Type Maser

By Tadao SHIMIZU and Koichi SHIMODA

Department of Physics, Faculty of Science, University of Tokyo, Tokyo

(Received December 28, 1960)

Characteristics of a low frequency beam-type maser is discussed. A particularly interesting phenomenon is a breakdown of the adiabatic focusing approximation. Theories of electro-static focusing and the line-width of the low frequency transition are obtained by taking into consideration the effect of transition induced by the Stark field which changes with time on a moving molecule.

Saturation of the effective number of focused molecules with the focuser voltage is calculated. The induced radio-frequency transition of a molecule in a mixed state is calculated and the line shape is shown to be the same as for a molecule in a pure state.

§ 1. Introduction

An exploitation of a low frequency spectrometer has been carried out, because some interesting transitions of molecules fall in the megacycle frequency range. The low frequency spectroscopy has become feasible by using maser actions such as a three-level[1] or a beam-type[2] maser. In a conventional spectrometer the intensities of the spectral lines become weaker in the lower frequency range because they are nearly proportional to ν^2. In the maser spectrometer, however, the intensity does not decrease so much at lower frequencies and the noise figure of the amplifier is smaller than that in the microwave range. Thus, many of the low frequency transitions have detectable intensities due to the pumping action in the three-level maser or due to the focusing action in the two-level beam-type maser.

The beam-type maser seems to be more useful, since it can be operated on two levels. Moreover, the focusing efficiency in the beam-type maser is very good when the two levels are close. However, some unexpected phenomena have been found in the operation of a low frequency beam-type maser which have not been observed in the microwave frequency range.

A particularly interesting phenomenon which is found in the low frequency beam-type maser, is a breakdown of the so-called "adiabatic focusing approximation". It may be called a "non-adiabatic" effect. Some years ago a similar problem concerning an atomic orientation in a variable magnetic field was discussed.[3),4),5)]* It was solved, however, for a special case of the magnetic field and their solutions can not be adapted to our problem.

Another phenomenon is an effect of the transition field between the focuser and the resonator. Because of the strong perturbing field on the molecule, the adiabatic approximation that the molecule does not make transition during a flight in this region becomes poor when a low spectral frequency is studied.

Theories of the focusing and the spectral line-width have already been given on the assumption of adiabatic behavior. It is the purpose of this paper to discuss how the focusing and the line shape are affected by the breakdown of the adiabatic approximation. The experimental results on these problems in the case of K-type transitions of formaldehyde molecule will be compared with the present theories in the forthcoming paper.

§ 2. A Breakdown of the Adiabatic Focusing Approximation

A schematic diagram of a low frequency beam-type maser is shown in Fig. 1 of reference (2). Molecules issue from a beam source consisting of a number of fine tubes into the focusing region. High d.c. voltage is supplied on the focuser. The inhomogeneous field inside the focuser is formed so that the molecules in the upper state can be deflected towards the axis and those in the lower state away from the axis.

---

* The authors are grateful to Professors W. A. Nierenberg and W. E. Lamb for notifying these references.

The rf signal valtage $V_0 \cos \omega t = Ed \cos \omega t$ is applied between the electrodes of the parallel-plate condenser which corresponds to a resonant cavity in the microwave maser. Here E is the rf field strength and d is the separation of the electrodes. The molecules make transitions inside the condenser being stimulated by the rf electric field at a proper frequency. The theory of sensitivity of the low frequency beam-type maser spectrometer has already been discussed.[2)]

Now consider the states of molecules in the perturbing field of the focuser and that in the transition field between the focuser and the resonator. Because the gas pressure in the focusing region is low, the molecules do not collide with each other and it is assumed that the state of molecules is not disturbed by molecular collision.

The focuser was constructed from a even number of cylindrical rods. The electric field strength inside a $2n$-pole focuser can be approximated by an expression[7)],

$$E(r) = n \frac{r^{n-1}}{2R^n} V , \qquad (1)$$

where R is the radius of the focuser and V the total voltage applied on the focuser. Therefore, if the Stark effect is such that the energy increases with the electric field, the force acting on the molecule is directed toward the axis and proportional to the gradient of the Stark energy. It is dependent only on r and not on θ of the cylindrical coordinate. The direction of the electric field at any point in a meridional plane is same.

As shown in the following section, a simple analytical expression of the molecular trajectory can be obtained only for the case of a six-pole focuser. The components of the electric field in a six-pole focuser are

$$E_x = a(x^2 - y^2)$$
$$E_y = -a(2xy)$$
$$E_z = 0$$

in a cartesian coordinate, where z is the direction of the axis. Then the ratio of E_x and E_y (the direction of the electric field),

$$\frac{E_x}{E_y} = \frac{1-(y^2/x^2)}{2(y/x)} ,$$

is constant, since y/x is constant for the molecule in a meridional plane.

When the molecules move in the plane, the direction of the electric field seen from the molecules does not change. Therefore, the transition between different M states induced by the focusing field is not considered here.

When a molecule passes through a electrostatic focuser the electric field seen from the moving molecule changes with time during which the molecule takes from the start. A criterion for the adiabatic focusing approximation such that the molecule does not make any transition during the flight through the focuser and that the molecular state itself slowly varies according to the Stark field, can be expressed by

$$\frac{h}{(W_2 - W_1)^2} \left(\frac{\partial H'}{\partial t} \right)_{12} \ll 1 , \qquad (2)$$

where $(\partial H'/\partial t)_{12}$ is the matrix element of the time derivative of the interaction Hamiltonian between the two unperturbed levels. For the six-pole focuser this expression is reduced to a simple form after some manipulations.

$$\frac{\omega_\theta}{\omega_0} \cdot \frac{\Delta W}{\hbar \omega_0} \ll 1 , \qquad (3)$$

where ω_θ is the angular frequency of the perturbing field seen from the molecule and ω_0 the molecular transition frequency between the two unperturbed states. The value of the left-hand side of the formula takes an order of 10^{-7} to 10^{-6} at a microwave frequency near 20 Gc, while it takes a value from 1 to 10 at a radio-frequency of several megacycles. This shows that the adiabatic focusing approximation is not good in the low frequency region.

The perturbing term in the Hamiltonian depends on the trajectory of molecules in the focuser. Since the intensity of the electric field is a function of r, the time dependent perturbing Hamiltonian can be expressed by an explicit function of time from a solution of the molecular motion in a form $r(t)$. Strictly speaking, however, the Schrödinger equation and the equation of motion must be solved simultaneously, but it would be laborious to do so.

As a first approximation, the trajectory of molecules is solved using the potential function which is the Stark energy of the molecule in the "pure" (unmixed) rotational state. Subsequently with the perturbing Hamiltonian which is constructed from the molecular trajectory a time dependent Schrödinger equation of the molecule is worked out.

§ 3. Schrödinger Equation of the Molecule

Approximate solutions of the differential equation of the molecular state in the perturbing field are given in the case of the six-pole focuser.

i) *Schrödinger equation of the perturbed molecule*

In order to describe the molecular state under the time dependent Hamiltonian $H = H_0 - \mu E$, a set of convenient basic functions must be chosen.

Assume that only two levels* take part in the problem, and the wave function of the molecule may be expressed by a linear combination.

$$\psi = a_1(t)u_1(t)\exp\left[-\frac{i}{\hbar}\int_0^t W_1(t')dt'\right] + a_2(t)u_2(t)\exp\left[-\frac{i}{\hbar}\int_0^t W_2(t')dt'\right]. \tag{4}$$

This expression is very convenient in studying "non-adiabatic" behavior of the molecular state in the focuser.

In Eq. (4) $W_1(t)$ and $W_2(t)$ are solutions of the instantaneous stationary problems,

$$H(t)u_n(t) = W_n(t)u_n(t)\,. \tag{5}$$

They are written explicitly as follows:

$$\left.\begin{aligned} W_1(t) &= \frac{1}{2}[W_1^0 + W_2^0 - \sqrt{\delta^2 + 4\mu_{12}^2 E^2(t)}]\,,\\ W_2(t) &= \frac{1}{2}[W_1^0 + W_2^0 + \sqrt{\delta^2 + 4\mu_{12}^2 E^2(t)}]\,, \end{aligned}\right\} \tag{6}$$

where W_1^0 and W_2^0 are the rotational energies of the molecule at zero field and $\delta = W_2^0 - W_1^0$. Here μ_{12} is the dipole matrix element of the molecule and is proportional to the matrix element of the direction cosine, when the direction of the electric field seen from the molecule does not change. In Eqs. (5) and (6), t is not considered as a variable but a parameter which corresponds to the position of the molecule. The basic functions $u_1(t)$ and $u_2(t)$ are the solutions of Eq. (5) and are the instantaneous stationary wave functions of the molecule in the Stark field, including t as a parameter. In Eq. (4) $a_1(t)$ and $a_2(t)$ are the probability amplitudes of $u_1(t)$ and $u_2(t)$, respectively.

The Schrödinger equation of the molecule,

$$i\hbar\frac{\partial\psi}{\partial t} = H(t)\psi\,, \tag{7}$$

is reduced to simultaneous equation between the coefficients $a_1(t)$ and $a_2(t)$, on the assumption of two levels and with an additional condition concerning the phase of the wave functions given by

$$\int u_n^* \frac{\partial u_n}{\partial t} d\tau = 0\,. \tag{8}$$

Substitution of Eq. (4) into Eq. (7) gives after some manipulations

$$\dot{a}_1(t) = -\frac{1}{\hbar\omega}\left(\frac{\partial H}{\partial t}\right)_{12}\exp\left[-i\int_0^t \omega dt\right]\cdot a_2(t) \tag{9}$$

and

---

* For example, the nearest another K-type doublets lies 3×10^5 Mc apart from the $J=4$, $K_{-1}=3$, doublets in the case of formaldehyde molecule. If the perturbing field does not mix the different M states, only two levels are taken into consideration.

$$\dot{a}_2(t)=\frac{1}{\hbar\omega}\left(\frac{\partial H}{\partial t}\right)_{21}\exp\left[\,i\int_0^t \omega dt\,\right]\cdot a_1(t)\;, \tag{10}$$

where

$$\hbar\omega(t)=W_2(t)-W_1(t) \qquad \text{and} \qquad \left(\frac{\partial H}{\partial t}\right)_{12}=\int u_1{}^*\,\frac{\partial H}{\partial t}\,u_2 d\tau\;.$$

Basic functions $u_1(t)$ and $u_2(t)$ can be taken as real functions and written explicitly as functions of the field strength E by

$$u_1\{E(t)\}=a(E)u_1{}^0+b(E)u_2{}^0 \tag{11}$$

$$u_2\{E(t)\}=-b(E)u_1{}^0+a(E)u_2{}^0\;, \tag{12}$$

where $u_1{}^0$ and $u_2{}^0$ are wave functions at zero field and $a(E)$ and $b(E)$ can be written as real functions of E

$$\left.\begin{aligned} a(E)&=\left\{\frac{\sqrt{\delta^2+4\mu_{12}{}^2E^2}+\delta}{2\sqrt{\delta^2+4\mu_{12}{}^2E^2}}\right\}^{1/2}\\ b(E)&=\left\{\frac{\sqrt{\delta^2+4\mu_{12}{}^2E^2}-\delta}{2\sqrt{\delta^2+4\mu_{12}{}^2E^2}}\right\}^{1/2}\\ \{a(E)\}^2&+\{b(E)\}^2=1\;. \end{aligned}\right\} \tag{13}$$

It should be noted that Eq. (8) is satisfied with these basic functions as follows:

$$\begin{aligned}\int u_1{}^*\frac{\partial u_1}{\partial t}d\tau&=\int(au_1{}^0+bu_2{}^0)\left(\frac{\partial a}{\partial t}u_1{}^0+\frac{\partial b}{\partial t}\,u_2{}^0\right)d\tau\\ &=0\end{aligned}$$

Similarly, $\int u_2{}^*\frac{\partial u_2}{\partial t}d\tau=0$ is also satisfied.

By eliminating $a_2(t)$ from Eqs. (9) and (10) a linear differential equation of the second order for $a_1(t)$ is obtained:

$$\ddot{a}_1+\left(i\omega+\frac{\dot{\omega}}{\omega}-\frac{\partial/\partial t(\partial H/\partial t)_{12}}{(\partial H/\partial t)_{12}}\right)\dot{a}_1+\frac{(\partial H/\partial t)_{12}(\partial H/\partial t)_{21}}{\hbar^2\omega^2}a_1=0 \tag{14}$$

In order to obtain explicit expressions of $\left(\frac{\partial H}{\partial t}\right)_{12}$, $\left(\frac{\partial H}{\partial t}\right)_{21}$ and $\frac{\partial}{\partial t}\left(\frac{\partial H}{\partial t}\right)_{12}$, $\int u_1H'u_2d\tau$ is differentiated by t*.

$$\int u_1\frac{\partial H'}{\partial t}u_2d\tau=\frac{\partial}{\partial t}\int u_1H'u_2d\tau-\int\frac{\partial u_1}{\partial t}H'u_2d\tau-\int u_1H'\frac{\partial u_2}{\partial t}d\tau\;. \tag{15}$$

If the direction of the electric field seen from the molecule does not change,

$$\int u_1{}^0H'u_2{}^0d\tau=\int u_1{}^0(-\boldsymbol{\mu}\boldsymbol{E})u_2{}^0d\tau=-E\mu_{12}\;,$$

where μ_{12} is the dipole matrix element on the base of wave functions at zero field and is proportional to the direction cosine matrix element.

By differentiating Eqs. (11) and (12)

$$\frac{\partial u_1}{\partial t}=\dot{a}u_1{}^0+\dot{b}u_2{}^0$$

---

* Because H_0 is time independent, it is apparent that $\partial H/\partial t=\partial H'/\partial t$, where $H=H_0+H'$.

and

$$\frac{\partial u_2}{\partial t}=-\dot{b}u_1{}^0+\dot{a}u_2{}^0$$

are obtained. From these equations

$$\int\frac{\partial u_1}{\partial t}H'u_2d\tau=\int(\dot{a}u_1{}^0+\dot{b}u_2{}^0)(-\mu E)(-bu_1{}^0+au_2{}^0)d\tau$$

$$=(\dot{a}a-\dot{b}b)(-E\mu_{12}) \tag{16}$$

$$\int u_1H'\frac{\partial u_2}{\partial t}d\tau=(a\dot{a}-b\dot{b})(-E\mu_{12}) \tag{17}$$

and

$$\int u_1H'u_2d\tau=\int(au_1{}^0+bu_2{}^0)H'(-bu_1{}^0+au_2{}^0)d\tau$$

$$=(a^2-b^2)(-E\mu_{12}) \tag{18}$$

$$\frac{\partial}{\partial t}\int u_1H'u_2d\tau=(2a\dot{a}-2b\dot{b})(-E\mu_{12})+(a^2-b^2)(-\dot{E}\mu_{12})\ . \tag{19}$$

From Eqs. (16), (17), (18) and (19)

$$\int u_1\frac{\partial H'}{\partial t}u_2d\tau=(a^2-b^2)(-\dot{E}\mu_{12})=\int u_2\frac{\partial H'}{\partial t}u_1d\tau \tag{20}$$

are obtained. Then the explicit forms of functions $\left(\frac{\partial H}{\partial t}\right)_{12}$ and $\frac{\partial}{\partial t}\left(\frac{\partial H}{\partial t}\right)_{12}$ are written by

$$\left(\frac{\partial H}{\partial t}\right)_{12}=\frac{-\delta\mu_{12}\dot{E}}{\sqrt{\delta^2+4\mu_{12}{}^2E^2}} \tag{21}$$

$$\frac{\partial}{\partial t}\left(\frac{\partial H}{\partial t}\right)_{12}=\frac{4\delta\mu_{12}{}^3E\dot{E}^2}{(\delta^2+4\mu_{12}{}^2E^2)^{3/2}}-\frac{\delta\mu_{12}\ddot{E}}{(\delta^2+4\mu_{12}{}^2E^2)^{1/2}}\ , \tag{22}$$

where E is the electric field strength seen from the moving molecule in the focuser and is a function of time. Also, ω and $\dot{\omega}$ are functions of time as follow:

$$\hbar\omega=\sqrt{\delta^2+4\mu_{12}{}^2E^2} \tag{23}$$

$$\hbar\dot{\omega}=\frac{4\mu_{12}{}^2E\dot{E}}{\sqrt{\delta^2+4\mu_{12}{}^2E^2}}\ . \tag{24}$$

The differential equation of $a_1(t)$ is obtained from Eqs. (21), (22), (23) and (24)

$$\ddot{a}_1+\left(\frac{i}{\hbar}\sqrt{\delta^2+4\mu_{12}{}^2E^2}+\frac{8\mu_{12}{}^2E\dot{E}}{\delta^2+4\mu_{12}{}^2E^2}-\frac{\ddot{E}}{\dot{E}}\right)\dot{a}_1+\frac{\delta^2\mu_{12}{}^2\dot{E}^2}{(\delta^2+4\mu_{12}{}^2E^2)^2}a_1=0\ . \tag{25}$$

ii) *The trajectory of molecules in the focuser*

The Lagrangian of the molecular motion in the focuser is written in a cylindrical coordinate as

$$L=\frac{1}{2}m(\dot{r}^2+r^2\dot{\theta}^2+\dot{z}^2)-U(r)\ ,$$

where z is the direction of the axis of the focuser and r is perpendicular to z. The potential $U(r)$ is the Stark energy of the molecule in the focusing field. For a slightly asymmetric top molecule, when $h\nu_0$ is much smaller than the Stark energy*, the potential in the

---

* In more correct words the Stark energy is linearly proportional to the electic field strength.

$2n$-pole focuser is written by*

$$U(r)=\pm\beta_n r^{n-1}\ ,$$

where $\beta_n=\frac{MK}{J(J+1)}\frac{n\mu V}{2R^n}$ and μ the permanent electric dipole moment of the molecule. An upper sign is for the upper state of the molecular energy levels, and *vice versa.*

For the molecule in the upper state Lagrange equations are integrated and become

$$mr^2\dot{\theta}=\text{constant}\equiv j \tag{26}$$

$$m\dot{z}=\text{constant}\equiv mv_z \tag{27}$$

$$\dot{r}^2=v_0{}^2+\frac{2}{m}\left\{\frac{j^2}{m}\left(\frac{1}{r_0}-\frac{1}{r^2}\right)+\beta_n(r_0{}^{n-1}-r^{n-1})\right\}\ , \tag{28}$$

where v_0 is the r-component of the initial velocity of the molecule, and r_0 the initial value of r. Reverse the sign before β_n, and the equation for the lower state molecule is given. Eq. (26) shows a constant angular momentum motion around the z-axis, while Eq. (27) shows a constant velocity motion along the z-direction.

The integral of Eq. (28) can be written in a form,

$$t-t_0=\int\frac{dr}{g(r)}\ . \tag{29}$$

This integration can be expressed by a simple analytical function only for the case of six-pole focuser. In the case of eight- and ten-pole focuser the molecular trajectories are approximately expressed by eliptic functions. For the sake of analytical treatment of the differential equation, the molecular trajectory is discussed for the six-pole focuser as follows.

When $n=3$ (six-pole focuser), from Eq. (28) $g(r)$ is given by

$$g(r)=\frac{1}{r}\sqrt{-ar^4+br^2-c}\ , \tag{30}$$

where

$$\left.\begin{aligned} a&=\frac{2\beta_3}{m}\\ b&=v_0{}^2+\frac{j^2}{m^2r_0{}^2}+\frac{2\beta_3r_0{}^2}{m}\\ c&=\frac{j^2}{m^2}\ . \end{aligned}\right\} \tag{31}$$

Then, the integral of Eq. (29) becomes

$$r^2=\frac{b}{2a}\pm\frac{\sqrt{b^2-4ac}}{2a}\sin^2 2\sqrt{a}\,(t+t_0)\ . \tag{32}$$

The focusing criterion is expressed by

$$r^2_{\max}=\frac{2c}{b-\sqrt{b^2-4ac}}\leqq R^2\ . \tag{33}$$

In a usual experimental condition it may be assumed that the angular momentum of the molecule, j, and the initial value of r-component of the position vector of the molecule, r_0, are very small. When j and r_0 are negligible in the expression of b and c, Eq. (33) is rewritten by

---

* This expression is correct, when the direction of the electric field seen from the moving molecule does not change and the matrix element due to the perturbing interaction is proportional to the direction cosine matrix element.

$$\frac{1}{2}mv_0^2 \leq \frac{MK}{J(J+1)}\mu E_{\max},$$

where $E_{\max}=E(r=R)=\frac{3}{2}\frac{V}{R}$. Similarly, the solution for the lower state molecule is

$$r^2=\frac{\sqrt{b'^2+4ac}}{2a}\cosh 2\sqrt{a}\,(t+t_0)-\frac{b'}{2a}, \tag{34}$$

where

$$b'=v_0^2+\frac{j^2}{m^2r_0^2}-\frac{2}{m}\beta_3 r_0^2 .$$

For the molecule which satisfies the condition, $\frac{1}{2}mv_0^2=\bar{\mu}E_{\max}$, the trajectories are simply expressed by

$$\frac{r}{R}=\sin\sqrt{a}\,t \tag{35}$$

$$\frac{r}{R}=\sinh\sqrt{a}\,t . \tag{36}$$

Then the explicit form of the time dependent perturbation Hamiltonian can be constructed from the trajectory of the molecule.

When $n=3$, electric field strength and its derivatives can be written analytically by

$$\left.\begin{aligned} &E=E_1-E_0\cos\omega_\theta t=E_0(\rho-\cos\omega_\theta t)\\ &\dot{E}=\omega_\theta E_0\sin\omega_\theta t\\ &\ddot{E}=\omega_\theta^2 E_0\cos\omega_\theta t , \end{aligned}\right\} \tag{37}$$

where

$$\omega_\theta=2\sqrt{a}, \qquad E_0=\frac{3V}{2R^3}\frac{\sqrt{b^2-4ac}}{2a}, \qquad E_1=\frac{3V}{2R^3}\frac{b}{2a}\simeq\frac{mv_0^2}{4\bar{\mu}} \quad \text{and} \quad \rho=\frac{E_1}{E_0}\simeq 1 .$$

iii) *Approximate solution of the Schrödinger equation*

Now the differential equation is solved for the case of six-pole focuser. The electric field E is given by Eq. (37) from the trajectory of the molecule, so that the analytical expression of the differential equation can be obtained.

Substitution of Eq. (37) into (25) becomes

$$\frac{d^2a_1}{d\theta^2}+\left(i\frac{\sqrt{F}}{\omega_\theta}-\frac{8x_1^2\sin\theta(\cos\theta-\rho)}{F}-\cot\theta\right)\frac{da_1}{d\theta}+\frac{\omega_0^2x_1^2\sin^2\theta}{F^2}a_1=0 , \tag{38}$$

where

$$\theta=\omega_\theta t , \qquad x_1=E_0\bar{\mu}/\hbar , \qquad \text{and} \qquad F=\omega_0^2+4x_1^2(\cos\theta-\rho)^2 . \tag{39}$$

a) When θ is small so that the coefficient of a_1 in Eq. (38),

$$\omega_0^2x_1^2\sin^2\theta/F^2 ,$$

may be neglected compared with unity, Eq. (38) is reduced to a differential equation of the form

$$\frac{d^2a_1}{d\theta^2}+\left(i\frac{\omega_0}{\omega_\theta}-\cot\theta\right)\frac{da_1}{d\theta}=0 . \tag{40}$$

Here the second order terms of θ in Eq. (38), is neglected and it is taken that $F=\omega_0^2$ because for most of molecules ρ is nearly equal to unity. It should be noted that a_1 is still very small for a small value of θ in this approximation when the initial condition is $a_1=0$, while $da_1/d\theta$ or $d^2a_1/d\theta^2$ may have finite values even for a very small value of θ.

By integrating Eq. (40), one obtains

$$a_1=\frac{-B_1}{1-(\omega_0/\omega_\theta)^2}\left(\cos\theta+i\frac{\omega_0}{\omega_\theta}\sin\theta\right)\exp\left(-i\frac{\omega_0}{\omega_\theta}\theta\right)+B_1' \tag{41}$$

and a similar expression for a_2. With the determined constants from the initial condition, for a very small value of θ, the approximate expressions of a_1 and a_2 are

$$\left.\begin{aligned} a_1&=\frac{\bar{\mu}E_0}{\delta}\theta^2\\ a_2&=1-\frac{1}{2}\left(\frac{\bar{\mu}E_0}{\delta}\right)^2\theta^4\end{aligned}\right\} \tag{42}$$

or

$$\left.\begin{aligned} a_1{}^2&=\left(\frac{x_1}{\omega_0}\right)^2\theta^4\\ a_2{}^2&=1-\left(\frac{x_1}{\omega_0}\right)^2\theta^4+O(\theta^8)\end{aligned}\right\} \tag{43}$$

Since ω_θ is proportional to the square root of the focuser voltage V, $a_1{}^2$ increases in proportion to the square of the voltage V and to the fourth power of t.

$$a_1{}^2=16\left(\frac{x_1}{\omega_0}\right)^2\left(\frac{3MK}{J(J+1)}\frac{\mu}{mR^3}\right)^2V^2t^4 \tag{44}$$

The criterion that the above approximate solutions are applicable is roughly given by

$$\theta\ll\frac{\omega_0}{x_1} \tag{45}$$

A typical value of ω_0/x_1 takes an order of 10^{-3} for the $J=4$, $K_{-1}=3$ transition of formaldehyde molecule.

b) When the transition frequency is so low that $\omega_0\ll x_1$ but θ is not very small, the differential equation, Eq. (38), can be integrated, when

$$\frac{\omega_0{}^2\sin^2\theta}{16x_1{}^2(1-\cos\theta)^2}\ll 1$$

so that the third term in the differential equation can be neglected.

By taking $F=4x_1{}^2(1-\cos\theta)^2$, it becomes

$$a_1=A_1\int_{\theta_0}^{\theta}\frac{\sin\theta}{\sin^4(\theta/2)}\exp\left[-\frac{2ix_1(\theta-\sin\theta)}{\omega_\theta}\right]d\theta\,, \tag{46}$$

where $\theta_0\gg\theta_{00}$ and θ_{00} will be defined later.

Because the typical value of x_1/ω_θ is of the order of 10^6 or more, the second part in the integrand of Eq. (46) is a very rapidly varying function compared with the first part. It may be reasonable that the first part is replaced by its mean value in the interval of the integration and can be factored out from the integration. Then,

$$a_1=-\frac{\omega_\theta}{2ix_1}A_1\overline{f(\theta)}\left\{\exp\left[-\frac{2ix_1}{\omega_\theta}(\theta-\sin\theta)\right]-\exp\left[-\frac{2ix_1}{\omega_\theta}(\theta_0-\sin\theta_0)\right]\right\}, \tag{47}$$

where

$$\overline{f(\theta)}=\frac{\int_{\theta_0}^{\theta}f(\theta)d\theta}{(\theta-\theta_0)}\qquad\text{and}\qquad f(\theta)=\frac{4\sin\theta}{(1-\cos\theta)^3}\,.$$

Multiplied by a_1^* Eq. (47) becomes

$$|a_1|^2=\frac{\omega_\theta^2}{2x_1^2}|A_1|^2\overline{f(\theta)}^2\left\{1-\cos\frac{2x_1}{\omega_\theta}(\theta-\theta_0-\sin\theta+\sin\theta_0)\right\}. \tag{48}$$

Since the second term in the parenthesis is a rapidly varying function, even for a " short time " this term may be averaged out. Then it gives the " non-adiabatic " effect by the following expression.

$$|a_1|^2=\frac{\omega_\theta^2}{2x_1^2}|A_1|^2\overline{f(\theta)}^2. \tag{49}$$

Since ω_θ is proportional to $\sqrt{V}$, it is readily seen from Eq. (49) that $|a_1|^2$ is proportional to the focuser voltage V, when the value of θ is not small and $\omega_0 \ll x_1$.

The approximation is considered to be good when $\theta_0 \ll \theta_{00}$, where θ_{00} is given from

$$\frac{4x_1}{\omega_0}=\frac{\sin\theta_{00}}{(1-\cos\theta_{00})^2}. \tag{50}$$

For a typical condition that $4x_1/\omega_0=1.7\times10^3$ for the $J=4$, $K_{-1}=3$ line, a value of θ_{00} is about 1.0×10^{-1}.

§ 4. Effects of the Transition Field Between the Focuser and the Resonator

The transition field between the focuser and the condenser also disturbs the molecular states appreciably. When the molecular transition frequency is low, this effect is considerably large as shown below. A simple criterion of this effect is given by a comparison between ν_0 and $1/t_0$, where t_0, is a time of flight of the molecule from the end of the focuser to the entrance of the resonator.

i) *Sudden approximation.*

If the time-dependent term in the Hamiltonian of the molecule changes with time very rapidly compared with the molecular frequency, any appreciable change of the molecular wave function does not occur, so that ψ_{final} can be equated to ψ_{initial}, which is the wave function of the molecule at the end of the focuser,

$$\psi_{\text{initial}}=a_1(t_1)u_1(t_1)e^{-i\varphi_1}+a_2(t_1)u_2(t_1)e^{-i\varphi_2}, \tag{51}$$

where t_1 is the time of flight in the focuser. The coefficients a_1 and a_2 are taken as real quantities and their phases are included in φ_1 and φ_2.

When $\frac{\omega_\theta}{\omega_0}\cdot\frac{x_1}{\omega_0}\gg1$ is satisfied, φ_1 and φ_2 are approximatly written by

$$\left.\begin{aligned}\varphi_1&=\int_0^{t_1}\frac{1}{\hbar}W_1dt\\ \varphi_2&=\int_0^{t_1}\frac{1}{\hbar}W_2dt.\end{aligned}\right\} \tag{52}$$

The wave function of the molecule at the reasonator inlet $(t=0)$ is*

$$\psi_{\text{final}}=a_1^0u_1^0+a_2^0u_2^0, \tag{53}$$

where u_1^0 and u_2^0 are the molecular function at zero field.

Then on the assumption of sudden approximation

$$a_1(t_1)u_1(t_1)e^{-i\varphi_1}+a_2(t_1)u_2(t_1)e^{-i\varphi_2}=a_1^0u_1^0+a_2^0u_2^0, \tag{54}$$

---

* This is also the initial state of the molecule for the Schrödinger equation of the molecule in the rf field in the resonator.

where u_1 and u_2 are expressed using zero field functions by

$$\left.\begin{aligned} u_1&=a'u_1{}^0+b'u_2{}^0 \\ u_2&=-b'u_1{}^0+a'u_2{}^0 \end{aligned}\right\} \tag{55}$$

Here a' and b' are given by Eq. (13), when E is replaced by a value at the end of the focuser, E'. Multiplied by $u_1{}^0$ or $u_2{}^0$, Eq. (54) becomes after integration over the space coordinates*

$$\left.\begin{aligned} a_1{}^0&=a_1a'e^{-i\varphi_1}-a_2b'e^{-i\varphi_2}\equiv\mathcal{E}e^{i\theta_1} \\ a_2{}^0&=a_1b'e^{-i\varphi_1}+a_2a'e^{-i\varphi_2}\equiv\lambda e^{i\theta_2} \end{aligned}\right\} \tag{56}$$

or

$$\left.\begin{aligned} |a_1{}^0|^2&=a_1^2a'^2+a_2^2b'^2-a_1a_2a'b'2\cos(\varphi_2-\varphi_1)\equiv\mathcal{E}^2 \\ |a_2{}^0|^2&=a_1^2b'^2+a_2^2a'^2+a_1a_2a'b'2\cos(\varphi_2-\varphi_1)\equiv\lambda^2\,. \end{aligned}\right\} \tag{57}$$

For the case of a six-pole focuser, the field strength seen from the molecule is given approximately by

$$E=\frac{1}{2\bar{\mu}}\,mv_0{}^2\sin^2\frac{\theta}{2}\,.$$

The value at the end of the focuser is approximately

$$E'=\frac{1}{2\bar{\mu}}mv_0{}^2\,,$$

since the value of θ is approximately π near the end of the focuser for the typical values of molecular velocity and the focuser voltage.

The phase difference, $\varphi_2-\varphi_1$, is calculated approximately as follows:

$$\varphi_2-\varphi_1=\frac{1}{\hbar}\int_0^{t_1}(W_2-W_1)dt=\int_0^{t_1}\sqrt{\omega_0{}^2+4x_1{}^2\sin^4\frac{\theta}{2}}\,d\theta\gtrsim\frac{x_1}{\omega_\theta}\pi \tag{58}$$

Since this value is very large compared with π, $\cos(\varphi_2-\varphi_1)$ becomes nearly zero by averaging it over various molecules. Then Eq. (57) becomes

$$|a_2{}^0|^2=\frac{1}{2}\left\{1+\frac{\omega_0}{2x_1}(1-2\gamma^2)\right\}$$

and

$$|a_1{}^0|^2=\frac{1}{2}\left\{1-\frac{\omega_0}{2x_1}(1-2\gamma^2)\right\}$$

where

$$\gamma^2=\{a_1(t_1)\}^2 \qquad \text{and} \qquad 1-\gamma^2=\{a_2(t_1)\}^2\,.$$

It may be noted that as shown in the equation, the effect of the fringing field also occurs even when $\gamma^2=0$ such that the molecule can be focused adiabatically. The line intensity is proportional to

$$|a_2{}^0|^2-|a_1{}^0|^2=\frac{\omega_0}{2x_1}(1-2\gamma^2) \tag{59}$$

The line disappears when $\gamma^2=\frac{1}{2}$, that is, when the molecular state is completely mixed up in the focuser.

ii) *Corrections due to finite time of flight*

Because the time of flight in the transition region is not equal to zero, the wave function of the molecule changes with time during the flight and the wave function at the end of focuser, ψ_{initial}, is not equal to that at the inlet of resonator, ψ_{final}, but somewhat different.

---

* $|a_1{}^0|^2+|a_2{}^0|^2=a_1^2a'^2+a_2^2b'^2+a_1^2b'^2+a_2^2a'^2=(a_1^2+a_2^2)(a'^2+b'^2)=1\,.$

If the perturbing potential $V(t)$ is commutable with the unperturbed Hamiltonian H_0, this difference of the wave functions is expressed by a phase factor of

$$\exp\left[\frac{1}{i\hbar}\int_{t_1}^{t_2}V(t)dt\right].$$

Then Eq. (51) is replaced by

$$\psi_{\text{final}}=\exp\left[-\frac{i}{\hbar}\int_{t_1}^{t_2}V(t)\,dt\right]\cdot\psi_{\text{initial}}$$

and

$$a_1{}^0u_1{}^0+a_2{}^0u_2{}^0=a_1e^{-i(\varphi_1+\beta_1)}u_1+a_2e^{-i(\varphi_2+\beta_2)}u_2\,, \tag{60}$$

where

$$\beta_1=\frac{1}{\hbar}\int_{t_1}^{t_2}W^1(t)dt$$

$$\beta_2=\frac{1}{\hbar}\int_{t_1}^{t_2}W^2(t)dt$$

and $W^1(t)$ and $W^2(t)$ are the eigen values of*

$$\left.\begin{aligned}V(t)u_1&=W^1(t)u_1\\ V(t)u_2&=W^2(t)u_2\end{aligned}\right\} \tag{61}$$

It is readily seen from a comparison of Eqs. (51) and (60) that the expression revised by finite time correction is similar to Eq. (51), where φ_1 should be replaced by $\varphi_1+\beta_1$ and φ_2 replaced by $\varphi_2+\beta_2$.

In order to estimate the validity of sudden approximation, the electric field is assumed to change linearly in the transition region between the focuser and the resonator. Then the argument of cosine function in Eq. (57) becomes

$$(\varphi_2+\beta_2)-(\varphi_1+\beta_1)\simeq x_1\left(\frac{\pi}{\omega_\theta}+t_0\right)$$

The first term in the parenthesis is nearly a time of flight for the length of the focuser under a typical condition stated before, and the second term is that in the transition region. For the $J=4$, $K_{-1}=3$ line of formaldehyde molecule,

$$\frac{\pi}{\omega_\theta}\simeq 1.3\times10^{-3}\,\text{sec}$$

$$t_0\simeq 1.3\times10^{-5}\,\text{sec}\,.$$

This estimation shows that the sudden approximation is good in this case.

§ 5. Number of the Focused Molecules and Saturation Characteristics with the Focuser Voltage

If the upper state is mixed up with the lower state by the perturbation of focusing field, the trajectory of the molecule should deviate from that of the molecule on a pure state and hence the flux of the focused molecules differs somewhat from the expression obtained on the adiabatic approximation[7]. In other words, some molecules in the upper state make transitions to the lower state in the focuser and they are defocused. In addition, the number of molecules which interact with the rf field as the upper state molecules are effectively less than the number of focused molecules because molecular states are not pure at the resonator inlet. This reduced number of molecules is called hereafter an effective number of focused molecules.

---

* Strictly speaking, Eq. (61) can not always be solved as quasi-stationary problems in the similar way as in Eq. (5).

From a kinematical consideration on the adiabatic focusing approximation, the flux of focused molecules by a six-pole focuser can be calculated by using Eqs. (35) and (36)

$$n=\frac{A_i\alpha}{\sqrt{\pi}}N_2\left(1-\exp\left[-\frac{aR^2}{\alpha^2}\right]\right)\left(1-\exp\left[-\frac{4al^2}{\pi^2\alpha^2}\right]\right) \tag{62}$$

where A_i is the inlet area, N_2 the number density of the upper state molecules, and l the length of the focuser. This expression is essentially the same as Eq. (3.9) in reference (7).

In order to take the "non-adiabatic" effect into consideration of the focused molecules the focusing field is treated at first, and secondary the fringing field. Because of the mixing of states induced by the perturbation of Stark field in the focuser, the effective force which acts on the molecule differs from that in a pure state. The expectation value of the potential energy of the molecule in the mixed state can be expressed by

$$U_{\text{eff}}=|a_2(t)|^2U_2+|a_1(t)|^2U_1\ . \tag{63}$$

Since the Stark effect is approximately linear in the low frequency maser[2] the effect of mixing may be calculated by using the effective dipole matrix element which is obtained from Eq. (63) by

$$\mu_{\text{eff}}=\{1-2|a_1(t)|^2\}\mu_{12}\ . \tag{64}$$

This may be interpreted as the decrease of the number of molecules in the upper state and the increase of that in the lower state. It is seen from Eq. (64) that μ_{eff} decreases monotonously with time as the molecule proceeds in the focuser. It is too difficult to obtain $a_1(t)$ from the Schrödinger equation, because the perturbation field must be solved simultaneously with the equation of motion.

Since the argument of the exponential functions in Eq. (62) are small in a ordinary condition, the number of focused molecules is approximately proportional to μ_{eff}^2. Although μ_{eff} is not a constant during the flight of the molecule, a plausible estimate can be obtained by a certain average of μ_{eff}. As shown in Eqs. (44) and (49), $|a_1|^2$ is proportional to V^2 when θ is very small, while $|a_1|^2$ increases linearly with V when θ is not small. Then the rough estimate of the number of focused molecules is expressed by

$$n'=n\left\{1-\left(\frac{V}{V_N'}\right)^{\xi}\right\}^2 \tag{65}$$

where $1<\xi<2$. In a low frequency maser with $V\approx10$ kV, $\nu_0\lesssim10$ Mc and $\mu_{12}\approx1$ Debye, ξ is nearly equal to 1.

Since some of the upper state molecules make transitions to the lower state by the perturbation of the focuser and its fringing field, the effective number of focused molecules should decrease. This effect is supported by the experimental evidence that the saturation of the effective beam flux with the focuser voltage decreases considerably as the distance between the focuser and the resonator increases.

Because the focused molecule is partially in the lower state as given by Eq. (53), the effective number of upper state molecules in a unit time is given after some manipulations by

$$n_{\text{eff}}=n'(1-2\varepsilon^2)\ , \tag{66}$$

where

$$\varepsilon^2=\frac{1}{2}\left\{1-\frac{\omega_0}{2x_1}(1-2\gamma^2)\right\}$$

is the probability amplitude of $u_1{}^0$ in Eq. (53) at the resonator inlet. Since γ^2 is proportional to V near the end of the focuser Eq. (66) can be written by

$$n_{\text{eff}}=n'\frac{\omega_0}{2x_1}(1-2\gamma^2)=n'\frac{\omega_0}{2x_1}\left(1-\frac{V}{V_N}\right). \tag{67}$$

Therefore, from Eq. (65) and Eq. (67) the effective number of focused molecules in a unit time can be written by

$$n_{\text{eff}}=n\left(1-\left(\frac{V}{V_{N'}}\right)^{\xi}\right)\left(1-\frac{V}{V_N}\right), \tag{68}$$

where n is the beam flux on the adiabatic approximation. The expression shows a saturation characteristics with the focuser voltage.

§ 6. Line Shape of the Molecule in a Mixed State

In this section the transition probability of the molecule in the rf field in the resonator is discussed. The induced transition by the rf signal has a different transition probability from that on the adiabatic approximation, when the quantum mechanical state of the molecule is not pure but has been mixed by the perturbation of the focusing field.

As seen in the preceding sections, the molecular state at the resonator inlet is not pure but mixed to some extent. The initial molecular state at $t=0$ is expressed by

$$\psi_0=a_1{}^0u_1{}^0+a_2{}^0u_2{}^0\ .$$

The Hamiltonian of the molecule in the rf field, $E\cos(\omega t+\chi)$, is

$$H=H_0-\mu E\cos(\omega t+\chi)=H_0-\frac{\mu E}{2}\{e^{i(\omega t+\chi)}+e^{-i(\omega t+\chi)}\}\ . \tag{69}$$

Here χ is a phase of the rf field at $t=0$, when the molecule enters the resonator. Express the molecular state in the rf field by*

$$\psi(t)=a_1(t)u_1{}^0e^{i(W_1/\hbar)t}+a_2(t)u_2{}^0e^{i(W_2/\hbar)t}\ ,$$

and the Schrödinger equation is reduced to the differential equations for $a_1(t)$ and $a_2(t)$,

$$\left.\begin{aligned}\dot{a}_2&=\frac{i}{2}xe^{-i(\omega-\omega_0)t-i\chi}\cdot a_1\\ \dot{a}_1&=\frac{i}{2}xe^{i(\omega-\omega_0)t+i\chi}\cdot a_2\ .\end{aligned}\right\} \tag{70}$$

Here $x=E\mu_{12}/\hbar$ and non-resonance terms such as $\exp[\pm i(\omega+\omega_0)t]$ in the differential equations are neglected.

The solutions of the differential equations can be expressed by the following forms,

$$\left.\begin{aligned}a_1&=A_1\exp(i\alpha_+t)+B_1\exp(i\alpha_-t)\\ a_2&=A_2\exp(i\alpha_+'t)+B_2\exp(i\alpha_-'t)\ ,\end{aligned}\right\} \tag{71}$$

where

$$\alpha_\pm=\frac{1}{2}\{(\omega-\omega_0)\pm\sqrt{(\omega-\omega_0)^2+x^2}\}$$

$$\alpha_\pm'=\frac{1}{2}\{-(\omega-\omega_0)\pm\sqrt{(\omega-\omega_0)^2+x^2}\}\ .$$

---

* Though the same notations, a_1 and a_2, are used in the former section for the states in the focuser, they should not be confused.

Substituting Eq. (71) into Eq. (70), the coefficients in Eq. (71) are determined as follows:

$$A_1=\frac{xa_2{}^0\exp(i\chi/2)+2\alpha_-a_1{}^0\exp(-i\chi/2)}{2\sqrt{x^2+\delta\omega^2}}$$

$$B_1=\frac{-xa_2{}^0\exp(i\chi/2)+2\alpha_+a_1{}^0\exp(-i\chi/2)}{2\sqrt{x^2+\delta\omega^2}}$$

where $\delta\omega=\omega-\omega_0$. The expressions of A_2 and B_2 can be obtained similarly. Then, $|a_1|^2$ is given by

$$\begin{aligned}|a_1|^2&=A_1A_1{}^*+B_1B_1{}^*+2Re\,A_1B_1{}^*\exp i(\alpha_+-\alpha_-)t\\&=\frac{1}{2(x^2+\delta\omega^2)}\{x^2+2|a_1{}^0|^2\delta\omega^2-2x\delta\omega|a_1{}^0|\,|a_2{}^0|\cos\delta\\&\quad+[x^2(2|a_1{}^0|^2-1)+2x\delta\omega|a_1{}^0|\,|a_2{}^0|\cos\delta\cos\sqrt{x^2+\delta\omega^2}\,t\\&\quad-2x\sqrt{x^2+\delta\omega^2}\,|a_1{}^0|\,|a_2{}^0|\sin\delta\sin\sqrt{x^2+\delta\omega^2}\,t\}\,,\end{aligned}\tag{72}$$

where δ is the sum of χ and the phase difference between $a_1{}^0$ and $a_2{}^0$.

When $a_1{}^0$ and $a_2{}^0$ are written by Eqs. (56) and (57), $\delta=\chi+\theta_2-\theta_1$. Then

$$\tan(\theta_2-\theta_1)=\frac{a_1(t_1)a_2(t_1)(a'^2+b'^2)\sin\varphi}{a'b'\{a_1(t_1)^2-a_2(t_1)^2\}+a_1(t_1)a_2(t_1)(a'^2-b'^2)\cos\varphi}\,,$$

where $\varphi=\varphi_2-\varphi_1$ is the phase difference between the two states appeared in Eq. (51). Since φ is a very large quantity which depends on the molecular velocity and the field in the focuser, $\sin\varphi$ and $\cos\varphi$ average to zero by the velocity distribution, so that $\theta_2-\theta_1\simeq0$ and $\delta\simeq\chi$.

In ordinary cases when the molecule enters uniformly in the resonator, averages of $\sin\chi$ and $\cos\chi$ for all molecules are zero. Eq. (72) becomes

$$|a_1|^2=\frac{x^2(1-\cos\sqrt{x^2+\delta\omega^2}\,t)}{2(x^2+\delta\omega^2)}+\frac{2\mathcal{E}^2(\delta\omega^2+x^2\cos\sqrt{x^2+\delta\omega^2}\,t)}{2(x^2+\delta\omega^2)}\,,\tag{73}$$

and the emitted power from the molecules is expressed by

$$\Delta P=n'h\nu_0\{|a_1|^2-|a_1{}^0|^2\}=n'h\nu_0\frac{x^2}{x^2+\delta\omega^2}(1-2\mathcal{E}^2)\sin^2\frac{\sqrt{x^2+\delta\omega^2}}{2}t\,.\tag{74}$$

The optimum rf voltage for the maximum output signal is obtained by differentiating $(\Delta P)^2/P_i$, where $P_i\propto x$ is the input power for stimulation.

$$x_{\text{opt}}\frac{L}{2v}=\theta_0=1.1656\tag{75}$$

The saturation broadened line-width can also be calculated from Eq. (74).

$$2\Delta\omega_{\text{sat}}=2\sqrt{x^2+(\Delta\omega_0)^2}\tag{76}$$

Here $\Delta\omega_0/2\pi$ is the half half-width of the line at zero field. These are the same expressions as those derived on the adiabatic approximation, the only difference being that the intensity is $(1-2\mathcal{E}^2)$ times.

It can be concluded that the mixing of states (" non-adiabatic " effect) does not change the resonance width and the optimum voltage when the phase of the molecule is at random with respect to that of the applied rf field. However, when $\langle\sin\delta\rangle$ and $\langle\cos\delta\rangle$ are not zero but take some finite values, the saturation broadened line shape is expressed by

$$\begin{aligned}\frac{\Delta P}{n'h\nu_0}=&\frac{x^2}{x^2+\delta\omega^2}(1-2\mathcal{E}^2)\sin^2\sqrt{x^2+\delta\omega^2}\frac{t}{2}-\frac{2x\delta\omega}{x^2+\delta\omega^2}\mathcal{E}\lambda\langle\cos\delta\rangle\sin^2\sqrt{x^2+\delta\omega^2}\frac{t}{2}\\&-\frac{x}{\sqrt{x^2+\delta\omega^2}}\mathcal{E}\lambda\langle\sin\delta\rangle\sin\sqrt{x^2+\delta\omega^2}\,t\,.\end{aligned}\tag{77}$$

At resonace when $\omega=\omega_0$, the emitted power is

$$\Delta P=n'h\nu_0\left[(1-2\mathcal{E}^2)\sin^2\frac{xt}{2}-\mathcal{E}\lambda\langle\sin\delta\rangle\sin xt\right]. \tag{78}$$

The optimum amplitude for finite values of $\mathcal{E}$ and $\langle\sin\delta\rangle$ is given by

$$x_{\mathrm{opt}}\frac{L}{2v}\simeq\theta_0+\frac{4\theta_0{}^2+1}{4\theta_0{}^2-1}\,\frac{\mathcal{E}\lambda\langle\sin\delta\rangle}{1{-}{-}2\mathcal{E}^2}=1.1656+1.451\,\frac{\mathcal{E}\lambda\langle\sin\delta\rangle}{1-2\mathcal{E}^2}\,, \tag{79}$$

where higher order terms of $\mathcal{E}\lambda\langle\sin\delta\rangle/(1-2\mathcal{E}^2)$ are neglected.

The saturation broadened line-width due to the rf field can be calculated from Eq. (77). The transition probability or the power emitted from the beam is a function of the transit time through the resonator. The distribution of the transit time of molecules in the beam is not exactly but approximately expressed by an exponential function, $\exp(-\Delta\omega_0 t)$. The average of $\overline{\Delta P}$ is obtained from integration of Eq. (77) using this weight factor.

$$\overline{\Delta P}=n'h\nu_0\frac{x}{x^2+\delta\omega^2+\Delta\omega_0{}^2}\left\{\frac{1-2\mathcal{E}^2}{2}x-\mathcal{E}\lambda\langle\cos\delta\rangle\delta\omega-\mathcal{E}\lambda\langle\sin\delta\rangle\Delta\omega_0\right\} \tag{80}$$

Then the total half-width (times 2π) calculated from Eq. (80) is

$$2\Delta\omega_{\mathrm{sat}}=2\sqrt{x^2+(\Delta\omega_0)^2}\left\{1+\frac{\mathcal{E}^2\lambda^2\langle\cos\delta\rangle^2[x^2+(\Delta\omega_0)^2]}{[(1-2\mathcal{E}^2)x/2-\mathcal{E}\lambda\langle\sin\delta\rangle\Delta\omega_0]^2}\right\}^{1/2} \tag{81}$$

This reduces to Eq. (76), when $\mathcal{E}=0$ or when $\langle\cos\delta\rangle=0$.

Acknowledgement

The authors would like to acknowledge helpful discussions with Professor Hidetosi Takahasi, as well as those with Mr. H. Takuma, Mr. K. Kondo, and Dr. T. Oka.

References

1) K. Shimoda: J. Phys. Soc. Japan **14** (1959) 954.
2) K. Shimoda, H. Takuma and T. Shimizu: J. Phys. Soc. Japan **15** (1960) 2036.
3) P. Güttinger: Zeits. f. Physik **73** (1931) 169.
4) E. Majorana: Nuovo Cimento **9** (1932) 43.
5) F. Bloch and I. I. Rabi: Rev. Mod. Phys. **17** (1945) 237.
6) K. Shimoda, T. C. Wang, and C. H. Townes: Phys. Rev. **102** (1956) 1308.
7) K. Shimoda: J. Phys. Soc. Japan **12** (1957) 1006.

JOURNAL OF THE PHYSICAL SOCIETY OF JAPAN, Vol. 16, No. 4, APRIL, 1961

Density vs. Exposure Curves of a Photographic Emulsion for 20~200 kV Electrons

By Mieko TAKAGI, Norihisa KITAMURA and Setsu MORIMOTO*

Physics Department, Tokyo Institute of Technology, Oh-Okayama, Meguro, Tokyo

(Received December 24, 1960)

Density (**D**)-*Exposure* (**E**) curves measured for Fuji Process Orthochromatic plates for electrons with energy 20~200 **kV** were given. Dependence of developing conditions on **D**–**E** curves was also examined. At a suitable developing condition, **D**–**E** curves for electrons with higher energy than 50 **kV** are linear over a wide range of density, and for electrons with lower energy they bend over at lower density.

§ 1. Introduction

For low exposures with fast electrons the photographic density of some emulsions is proportional to the amount of charge per unit area which has reached the emulsion during the exposure. Making use of this property Karle and Karle[1] proposed a method to determine the [*density* (**D**)] vs. [exposure (**E**)] curve, **D**–**E** curve, and their method has been applied by many investigators. For intensity measurement of electrons by the photographic method, the emulsions whose **D**–**E** curves are linear over a wide range of density are most suitable for use.

Some examples of the **D**–**E** curves for electrons in the earlier experiments are shown in Fig. 1. The extent of the linear portion depends on the emulsion. The curves bend over at low density for Agfa Extrarapid[2] and for Agfa Isochrom[3], at **D**=0.8 for Eastman Lantern Slide Medium[4], at **D**=1.3 for Ilford Thin Film Half Tone[5] and at a **D** value larger than 3 for Ilford Nuclear Research B2 plate[5]. The dependence of the extent of the linear portion on the energy of electrons has been studied. Digby et al[5] show that the extent increases as the energy of electrons increases from 25 **kV** to 60 **kV**. Baker et al[4] show that the extent is the same for 40 **kV**~212 **kV** electrons.

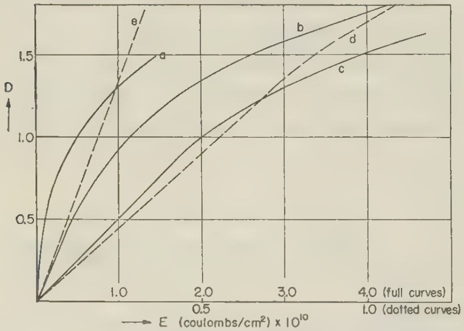

Fig. 1. **D**–**E** curves in the earlier experiments.

- **a**: Agfa Extrarapid, 72.9 **kV** (Backer and Kipphan [2])
- **b**: Agfa Isochrom, 75 **kV** (Borries and Knoll [3])
- **c**: Eastman Lantern Slide Medium, 67 **kV** (Baker, Ramberg and Hillier [4])
- **d**: Ilford Thin Film Half Tone, 66 **kV** (Digby, Firth and Hercock [5])
- **e**: Ilford Nuclear Research B 2,66 **kV** ([5])

Curves **a**, **b** and **c** were given in **D**-log **E** curves in the original papers.

§ 2. Experimental and Results

In this paper the results are given of measurements on **D**–**E** curves of Fuji Process Orthochromatic plate using a high voltage electron diffraction equipment containing two lenses and a rotating sector. The **D**–**E** curves are obtained from the two plates with different exposures applying the method proposed by Karle and Karle[1]. On this method an electron source with any intensity distribution can be used provided that it is stable during the two exposures. However, for precise measurements it is better to use an electron source whose intensity changes continuously with scattering angle. Such a source was obtained by the following method. By adjusting the projector lens current so as to give a large magnification, an almost uniform distribution of electrons is obtained. The electrons are partly masked by a rotating sector above the photographic plate, and the resultant intensity of electrons reaching the plate is nearly, but not exactly, proportional to the distance from the center of the rotating sector.

---

* Now at Ochanomizu University, Tokyo.

Photographic density was read by an optical balancing type microphotometer made by Narumi Mfg. Co. The reading of the density had been calibrated by a standard optical wedge made by Riken Co. The **D–E** curves are obtained from two plates with different exposures applying the method proposed by Karle and Karle[1]. Fig. 2 and Fig. 3 show **D–E** curves for Fuji Process Orthochromatic plates developed for 3 minutes at 20°C in Eastman D–72 developer diluted in ratio 1:1 with water. Fig. 2 is a curve for 80 **kV** electrons which is quite linear up to **D**=1.5. Fig. 3 is the curve for 20~200 **kV** electrons. For electrons with as low an energy as 20 **kV** the curves bend over at low density, and for electrons with higher energy than 50 **kV** the curves are quite linear over a wide range of **D**. This result accords with the earlier experiments[4,5].

Results with different developing conditions for 50 **kV** electrons are shown in Fig. 4. For this emulsion development for 3 minutes in Eastman **D**–72 developer diluted 1:1 with water gives the best result. Digby et al[5] concluded that the extent of the linear portion in **D–E** curves is mainly determined by the nature of the emulsions. The results shown in Fig. 4, however, show that it is also affected to a large extent by the developing conditions.

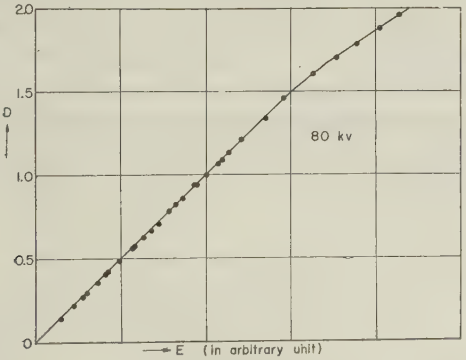

Fig. 2.

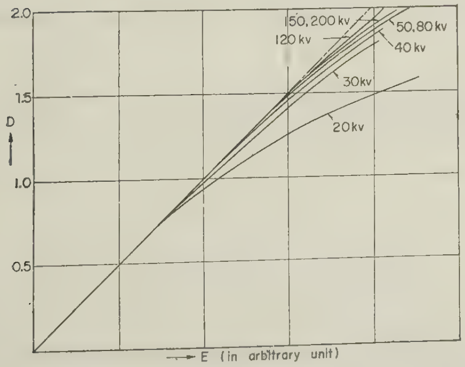

Fig. 3.

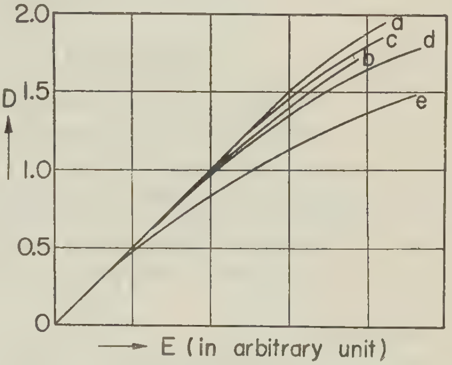

50 kv

a: D-72 dilution 1:1 3 min.
b: D-72 1:1 5 min.
c: D-131 1:0 3 min.
d: D-131 1:1 5 min.
e: D-131 1:1 3 min.

Fig. 4.

On precise intensity measurement of electrons, it is required to control the exposure time so as to make the photographic density to be measured is in a linear range of the **D–E** curve. Hence, it is obvious that the precision will be greatly improved by using plates whose linear range is as wide as suitably developed Fuji Process Orthochromatic plates. Though we have shown only on the results for this emulsion in the above, probably it would be worth while to try various developing conditions for other emulsions to give **D–E** curves linear over a wide range of density.

References

1) J. Karle and I. L. Karle: J. Chem. Phys. **18** (1950) 957.
2) A. Backer and E. Kipphan: Ann. d. Physik [5] **10** (1931) 15.
3) B. v. Borries and M. Knoll: Physik. Zeits. **35** (1934) 279.
4) R. F. Baker, E. G. Ramberg and J. Hillier: J App. Phys. **13** (1942) 450.
5) N. Digby, K. Firth and R. J. Hercock: J.Photographic Science **1** (1953) 194.

JOURNAL OF THE PHYSICAL SOCIETY OF JAPAN, Vol. 16, No. 4, APRIL, 1961

On the Steady Motion of an Indealized Elastico-Viscous Liquid Through Channels with Suction and Injection

By S. K. DATTA

The Calcutta Technical School 110, S. N. Banerjee Road,
Calcutta-13, India

(Received May 12, 1960, Revised December 8, 1960)

In this paper the steady flow of a certain type of elastico-viscous liquid in the annulus between two coaxial circular cylinders and between parallel plane boundaries has been considered. It is assumed that fluid is injected at one boundary and withdrawn at the other, both at the same rate and one of the boundaries is assumed to be moving with a constant velocity parallel to its generator. Numerical values have been given both for the annulus and for the parallel plates.

§1. Introduction

Attention has recently been drawn, due to experimental results on dilute suspensions and emulsions which cannot be explained on classical viscous theory, to the idealized incompressible elastico-viscous liquids. It is generally known that the behaviour of such liquids at small rates of shear is characterized by three constants, a coefficient of viscosity η_0, a relaxation time λ_1 and a retardation time λ_2 e.g., (Oldroyd, 1958)

$$p_{ik}=p'_{ik}-p''\delta_{ik}\ ,$$

$$p'_{ik}+\lambda_1\frac{d}{dt}p'_{ik}=2\eta_0\left(e_{ik}+\lambda_2\frac{d}{dt}e_{ik}\right)\ , \qquad (1)$$

$$e_{ik}=\frac{1}{2}(v_{k,i}+v_{i,k})\ ,$$

where $\delta_{ik}=0,\ i\neq k;\ =1,\ i=k,\ i,\ k=1,2,3$ and e_{ik} is the rate of strain tensor, p_{ik} is the stress tensor, and all these equations are referred to orthogonal cartesian system of axes. It has been shown by Oldroyd (1950, 1951) that among the possible generalizations of equation (1), which are valid for all conditions of motion and stress, and which reduce to (1) for small rates of shear and shear stresses, the simplest are linear in the stresses and include terms of the second degree in stresses and velocity gradients taken together. Thus assuming isotropy and incompressibility, a possible generalization of the second equation of (1) is

$$p'_{ik}+\lambda_1\frac{\mathscr{D}}{\mathscr{D}t}p'_{ik}+\mu_0 p'_{jj}e_{ik}-\mu_1(p'_{ij}e_{jk}+p'_{jk}e_{ij})+\nu_1 p'_{jl}e_{jl}\delta_{ik}$$
$$=2\eta_0\left(e_{ik}+\lambda_2\frac{\mathscr{D}}{\mathscr{D}t}e_{ik}-2\mu_2 e_{ij}e_{jk}+\nu_2 e_{jl}e_{jl}\delta_{ik}\right)\ , \qquad (2)$$

with the equation of incompressibility $e_{ii}=0$, where $\mu_0,\ \mu_1,\ \mu_2,\ \nu_1,\ \nu_2$ are material constants, each of the dimension of time and

$$\frac{\mathscr{D}}{\mathscr{D}t}p'_{ik}\equiv\frac{\partial}{\partial t}p'_{ik}+v_j p'_{ik,j}+\omega_{ij}p'_{jk}+\omega_{kj}p'_{ij}\ ,$$
$$\omega_{ik}\equiv\frac{1}{2}(v_{k,i}-v_{i,k})\ . \qquad (3)$$

Now it was shown by Oldroyd (1950) that for

$$\eta_0>0\ ,\ \lambda_1=\mu_1>\lambda_2=\mu_2\geq 0\ ,\ \mu_0=\nu_1=\nu_2\ ,$$

the liquid will exhibit Weissenberg climbing effect when sheared at a uniform rate between rotating coaxial cylinders. So this may be possible set of values of the constants for a liquid showing Weissenberg climbing effect. In particular, we choose

$$\eta_0>0\ ,\ \lambda_1=\mu_1\ ,\ \lambda_2=\mu_2=\mu_0=\nu_1=\nu_2=0\ .$$

With this choice of constants equation (2) together with (3) gives

$$p'_{ik}+\lambda_1\left(\frac{\partial}{\partial t}p'_{ik}+v_j p'_{ik,j}-v_{i,j}p'_{jk}-v_{k,j}p'_{ij}\right)=2\eta_0 e_{ij}\ . \tag{4}$$

§ 2. Coaxial Circular Cylinders

We choose cylindrical polar coordinates (r, θ, x) with x-axis along the axis of the cylinder. Then from symmetry and when the motion is steady,

$$u_1=u_x=u(r)\ ,\ u_2=u_r=v(r)\ ,\ u_3=u_\theta=0\ ,$$

if we consider the flow at a sufficient distance from the entrance end so that the quantities u_1, u_2, u_3 may be taken as independent of x, and then equation (4) takes the form

$$\begin{gathered}
p'_{rr}+\lambda_1\left[v\frac{\partial p'_{rr}}{\partial r}-2\frac{\partial v}{\partial r}p'_{rr}\right]=2\eta_0\frac{\partial v}{\partial r}\ ,\\
p'_{rx}+\lambda_1\left[v\frac{\partial p'_{rx}}{\partial r}-\frac{\partial u}{\partial r}p'_{rr}-\frac{\partial v}{\partial r}p'_{rx}\right]=\eta_0\frac{\partial u}{\partial r}\ ,\\
p'_{xx}+\lambda_1\left[v\frac{\partial p'_{xx}}{\partial r}-2\frac{\partial u}{\partial r}p'_{rx}\right]=0\ ,\\
p'_{\theta\theta}+\lambda_1\left[v\frac{\partial p'_{\theta\theta}}{\partial r}-2\frac{v}{r}p'_{\theta\theta}\right]=2\eta_0\frac{v}{r}\ ,\\
p'_{r\theta}=p'_x\theta=0\ .
\end{gathered} \tag{5}$$

The equation of continuity is

$$\frac{\partial v}{\partial r}+\frac{v}{r}=0 \tag{6}$$

and the equation of momentum gives

$$\begin{gathered}
\rho v\frac{\partial v}{\partial r}=-\frac{\partial p''}{\partial r}+\frac{\partial p'_{rr}}{\partial r}+\frac{p'_{rr}-p'_{\theta\theta}}{r}\ ,\\
\rho v\frac{\partial u}{\partial r}=\frac{\partial p'_{rx}}{\partial r}+\frac{1}{r}p'_{rx}\ ,
\end{gathered} \tag{7}$$

The boundary conditions are

$$\begin{aligned}
v&=v_a\ , & r&=a\\
&=v_b\ , & r&=b\\
u&=U\ , & r&=b\\
&=0\ , & r&=a
\end{aligned} \tag{8}$$

where a, b are the radii of the outer and inner cylinders respectively.

Integrating (6) and using the first two equations of (8)

$$v=\frac{v_a a}{r}=\frac{v_b b}{r}=\frac{v_a}{\zeta},\quad \zeta==r/a\ . \tag{9}$$

Assuming λ_1 to be small, we eliminate p'_{rr} from the first two equations (5) neglecting squares of λ_1,

$$\lambda_1 v\frac{dp'_{rx}}{dr}+\left(1-3\lambda_1\frac{dv}{dr}\right)p'_{rx}=\eta_0\frac{du}{dr}\ . \tag{10}$$

Substituting v from (9) in the second equation of (7) and integrating

$$rp'_{rx}=\rho v_a a(u+D)\ , \tag{11}$$

where D is a constant of integration. Substituting this in (10) we integrate (10) using the last two equations of (8) and get

$$\frac{u}{U}=\left(\frac{\sigma}{\zeta}\right)^2\frac{\zeta^2(1-KR)^{(R+2)/2}-(\zeta^2-KR)^{(R+2)/2}}{\sigma^2(1-KR)^{(R+2)/2}-(\sigma^2-KR)^{(R+2)/2}}\ ,$$

where

$$K=\frac{\lambda_1 v_a}{a}\ ,\quad R=\frac{v_a a}{\eta_0/\rho}\ ,\quad \sigma=b/a\ .$$

From (12) we may deduce the expression for u for an ordinary viscous liquid by making $\lambda_1=0$,

$$\frac{u}{U}=\frac{1-\zeta^R}{1-\sigma^R}\ . \tag{13}$$

Further, if the walls are rigid having no porosity, $u_a=0$ and then

$$\frac{u}{U}=\frac{\log\zeta}{\log\sigma}\ , \tag{14}$$

which agrees with the expression for laminar flow of a viscous fluid in an annulus when the inner cylinder is moving parallel to its axis.

Table I. (for u/U)
$K=0.05$

R / ζ	1	2	4
.4	1.00	1.00	1.00
.5	0.81	0.91	1.00
.8	0.31	0.45	0.74
1.0	0.00	0.00	0.00

$K=0.00$

R / ζ	1	2	4
.4	1.00	1.00	1.00
.5	0.83	0.89	0.96
.8	0.33	0.43	0.60
1.0	0.00	0.00	0.00

We give in the following table the values of u/U for $K=0.00$, 0.05 when $R=1$, 2, 4 and $\sigma=0.4$. The above table shows that for this particular choice of σ the radius ratio, u/U decreases at a particular position with increase in K if $R<2$ and if $R>2$, u/U increasese with increase in K. It is also noted that as ζ increases u/U decreases and it appears that for a particular choice of radius ratio, if $KR<1$*, then u/U will decrease with increase in K for some values of R and increase for some other values of R. It can also be seen that increase in R increases u/U at any distance.

§ 3. Parallel infinite plates

In this case we choose rectangular cartesian coordinates with x-axis along the upper plate which is fixed and y-axis perpendicular to the plates directed into the fluid. The flow is assumed to be in the x-direction and liquid is injected at the lower plate and withdrawn at the upper one. Then, if we assume the flow to be steady and fully developed,

$$u_x=u(y)\ ,\ u_y=v(y)\ ,\ u_z=0\ .$$

The boundary conditions are

$$\begin{aligned} v&=-V\ ,\quad y=0 \text{ and } h\\ u&=0\ ,\qquad y=0\\ &=U\ ,\qquad y=h\ . \end{aligned} \tag{15}$$

The equation of continuity gives

$$v=-V$$

everywhere. So equation (4) will give

$$\begin{gathered} p_{xx}+\lambda_1\left[v\frac{\partial p'_{xx}}{\partial y}-2\frac{\partial u}{\partial y}p'_{xy}\right]=0\ ,\\ p'_{yy}+\lambda_1 v\frac{\partial p'_{yy}}{\partial y}=0\ ,\\ p'_{xy}+\lambda_1\left[v\frac{\partial p'_{xy}}{\partial y}-\frac{\partial u}{\partial y}p'_{yy}\right]=\eta_0\frac{\partial u}{\partial y}\ ,\\ p'_{zz}=p'_{zx}=p'_{zy}=0\ , \end{gathered} \tag{16}$$

and the equation of momentum gives

---

* By our choice, since λ_1 in small, we may take $KR<1$ ordinary purposes, under the velocity of injection is very large.

$$\rho v\frac{\partial u}{\partial y}=\frac{\partial p'_{xy}}{\partial y}\,,$$
$$0=-\frac{\partial p''}{\partial y}+\frac{\partial p'_{yy}}{\partial y}\,. \tag{17}$$

Eliminating p'_{yy} from the second and third equations of (16) and retaining only first power of λ_1, we have as before

$$p'_{xy}-K_1\frac{dp'_{xy}}{d\eta}=\frac{\eta_0}{h}\frac{du}{d\eta}\,,$$
$$K_1=\frac{\lambda_1 V}{h}\,,\quad \eta=\frac{y}{h}\,. \tag{18}$$

Integrating the first equation of (17) we will obtain

$$p'_{xy}=-\rho V(u+D)\,,\quad \text{where } D \text{ is constant.}$$

Substituting this in (18) and integrating, we have with the help of (15),

$$\frac{u}{U}=\frac{1-e^{-R\eta/(1-K_1R)}}{1-e^{-R/(1-K_1R)}}\,, \tag{19}$$

where

$$R=\frac{vh}{\eta_0/\rho}\,.$$

If $K_1=0$, we obtain the expression for an ordinary viscous fluid as

$$\frac{u}{U}=\frac{1-e^{-R\eta}}{1-e^{-R}}\,. \tag{20}$$

Further if the plates are rigid having no porosity,

$$\frac{u}{U}=\eta \tag{21}$$

which is the known expression for an ordinary viscous fluid without suction or injection.

Table II. (for u/U)

$K_1=0.05$

η \ R	1	2	4
0.0	0.00	0.00	0.00
0.5	0.63	0.75	0.92
1.0	1.00	1.00	1.00

$K_1=0.00$

η \ R	1	2	4
0.0	0.00	0.00	0.00
0.5	0.62	0.73	0.88
1.0	1.00	1.00	1.00

The values of u/U are given in Table II for $K_1=0.00$ and 0.05 when $R=1$, 2, and 4.

So here also we note that when R and K_1 increase, u/U increases, at any particular distance.

The expression (19) can also be deduced from (12) if we make $\sigma\rightarrow 1$.

In conclusion I express my thanks to Prof. B. Sen, D. Sc., for his kind help in the preparation of this paper.

References

1) J. G. Oldroyd: Proc. Roy. Soc., **A 200** (1950) 523.
2) J. G. Oldroyd: Proc. Camb. Phil. Soc. **47** (1951) 410.
3) J. G. Oldroyd: Quart. J. Mech. Appl. Math. **4** (1951) 271.
4) J. G. Oldroyd: Proc. Roy. Soc., **A 245** (1958) 278.

JOURNAL OF THE PHYSICAL SOCIETY OF JAPAN, Vol. 16, No. 4, APRIL, 1961

Flow of Condensing Vapour with Temporary Supersaturated State due to Heat-Removal Effect

By Keishiro NIU

Department of Physics, Faculty of Science,
Tokyo Metropolitan University, Tokyo

(Received November 4, 1960)

This paper deals with the flow of a condensing vapour. The vapour flow in a pipe of constant cross-sectional area with heat-removal effect through the pipe walls has the temporary supersaturated state in the supersonic flow by the effect of surface tension of the droplets which are born in the vapour. In case when the fluid is maintained continually in the supersaturated state, the ratio of the increase in relative humidity to the increase in Mach number or to the decrease in pressure is greater in the flow with heat-removal than in the adiabatic flow. Numerical calculations have been carried out for an example of the flow with definite initial conditions and the region where the condensation shock takes place is predicted theoretically.

§ 1. Introduction

Some studies have been made on the condensation phenomena of the fluid caused by the adiabatic expansion in diverging nozzles[1)-4)], but only few have been done on the same phenomena caused by the heat-removal effect[5)].

In a previous paper[6)], the writer has analysed the flow pattern in the case when the water vapour flows through a pipe of constant cross-sectional area, assuming that there occurs the heat-exchange between the vapour and the pipe wall and that the vapour is kept always in the thermodynamical equilibrium state. The phase change from gas to liquid of the vapour occurs after the fluid reaches the saturated state. In reality, however, a supersaturated state appears in the supersonic flow, since the surface tension of the droplets born in the vapour acts to obstruct the rapid transition of phase. Such a supersaturated state continues for a while, but, owing to the successive heat-removal the temperature of the vapour goes on to decrease and the degree of supersaturation of the fluid reaches ultimately a critical value. Then this unstable state breaks down abruptly and the considerable amount of vapour in the flow changes its phase from gas to liquid. We call the region where this abrupt change occurs the "condensation shock".

In the present paper, we shall investigate the flow pattern in the supersonic flow, by taking account of the appearance of supersaturated state.

§ 2. Flow in Thermodynamical Equilibrium State

For the sake of reference we shall first recapitulate briefly the results obtained in the previous paper[6)]. If we suppose that the fluid is kept always in the thermodynamical equilibrium state, the conservation equations of mass, momentum and energy can be written down for the inviscid vapour flow through a pipe of constant cross-sectional area in case when the heat-exchange occurs between the fluid and the pipe wall. If, then, we take into account the equation of state as well as the proportionality-relation between the enthalpy and the temperature for the ideal gas, the solutions of these conservation equations for the case where the condensation does not occur in the fluid are given by

$$U=\frac{\mu C_P(P_e+m'U_e)\pm\sqrt{\mu^2C_P{}^2(P_e+m'U_e)^2+m'^2R(2\mu C_P-R)(2h'-2H_e-U_e{}^2)}}{m'(2\mu C_P-R)}\,, \tag{1}$$

$$T=(2H_e+U_e{}^2-2h'-U^2)/2C_P\,, \tag{2}$$

$$P=m'RT/\mu U\,. \tag{3}$$

Here, U is the velocity, T the temperature, P the pressure, H the enthalpy, C_P the specific heat at constant pressure, μ the molecular weight of the fluid, R the universal gas constant (R in the previous paper having been replaced here by μR), m' the rate of mass flow through the unit sectional area and h' the removed heat quantity divided by the rate of mass flow. The subscript e refers to the values at the entrance section.

When a part of the vapour condenses so that both the gas and liquid phases coexist in the flow, we can obtain the solutions of the conservation equations by taking into account the following conditions, in addition to the ones for the non-condensing case, that the pressure at the section under consideration is equal to the saturated one, the density of the liquid phase is a known function of the temperature and the enthalpy of the liquid is a linear function of the temperature. Thus we have

$$\begin{aligned}&\frac{\mu\kappa_0 P_S(T)^2}{m'^2RT}+\left\{1+\frac{P_e\rho_L(T)}{m'^2}-\frac{U_e\rho_L(T)}{m'}\right\}\frac{\mu\kappa_0 P_S(T)}{RT\rho_L(T)}+\left\{\frac{1}{2m'^2}-\frac{\mu(C_P-\kappa)}{m'^2R}\right\}P_S(T)^2\\&\qquad-\left[\frac{P_e}{m'^2}+\frac{U_e}{m'}+\left\{1-\frac{P_e\rho_L(T)}{m'^2}-\frac{U_e\rho_L(T)}{m'}\right\}\frac{\mu(C_P-\kappa)}{R\rho_L(T)}\right]P_S(T)+\kappa T\\&\qquad=H_e-\frac{P_e^2}{2m'^2}-\frac{P_eU_e}{m'}-\kappa_0-h'\,,\end{aligned}\tag{4}$$

$$P=P_S(T)\,,\tag{5}$$

$$U=U_e+(P_e-P)/m'\,,\tag{6}$$

where $P_S(T)$ is the saturated vapour pressure, $\rho_L(T)$ the density of liquid phase and κ_0, κ are the coefficients of the zeroth and the first orders of the temperature in the linear relation of the enthalpy of liquid phase, respectively.

Thus, for the equilibrium flow, T, P, U and etc. can be obtained in terms of the parameter h'. When we take into account the appearance of supersaturated state in the flow, however, the variables characterizing the flow depend on the time and cannot be settled by the numerical value of h' only. Consequently, the flow pattern cannot be analysed unless h' is given as a function of the distance measured along the pipe axis from the entrance section.

In this paper, first we assume the pressure distribution in the fluid which is considered to flow down continuously without condensation regardless of the amount of heat-removal, instead of giving h' as a function of the distance defined above. In this case, it is convenient to use, instead of Eqs. (1), (2) and (3), the following equation:

$$h'=\left(\frac{\mu C_P}{R}-\frac{1}{2}\right)\frac{P^2}{m'^2}+\left(\frac{P_e}{m'}+U_e-\frac{\mu C_PU_e}{R}-\frac{\mu C_PP_e}{Rm'}\right)\frac{P}{m'}+H_e-\frac{P_e}{2m'^2}-\frac{P_eU_e}{m'}\,,\tag{7}$$

$$U=U_e+(P_e-P)/m'\,,\tag{8}$$

$$T=\mu PU/m'R\,,\tag{9}$$

then, h' can be obtained from Eq. (7) as a function of the said distance through the known distribution of P.

§ 3. Relation between Relative Humidity and Mach Number or Pressure

If the vapour is in the saturated or supersaturated state and has not sufficient nuclei for condensation, the gaseous molecule must combine with each other so as to form a cluster which develops to a nucleus. Namely, the vapour has to self-nucleate. However, Gibbs' free energy of the cluster is increased by the effect of the surface tension, and the smaller the cluster is, the greater is the rate of increase of the free energy due to the surface tension. Consequently, even if the vapour be in the supersaturated state of rather high degree, the rapid phase transition from gas to liquid would be forbidden by the barrier of high free energy of the clusters which are very small in the early stage of condensation process. Thus we can observe the appearance of supersaturated state in the supersonic flow where all phenomena must be changed during a very short time-duration.

In this section, we shall investigate the relation between the relative humidity and the Mach number or pressure, assuming that the supersaturated state is maintained continuously in the flow as long as we concern.

The Clausius-Clapeyron relation between the temperature T and the saturated vapour pressure P_S is given by

$$\frac{P_S}{P_S{}^*}=\exp\left\{\frac{\mu L}{RT^*}\left(1-\frac{T^*}{T}\right)\right\}, \tag{10}$$

where L is the latent heat of vaporization which is assumed to be constant, and the superscript $*$ refers to the values at the sonic state.

On the other hand, the relation between the Mach number M and the temperature T for the one-dimensional flow in a pipe of constant cross-sectional area in case when there occurs heat-exchange between the fluid and the pipe wall is given by Howarth[7] as follows:

$$\frac{T^*}{T}=\frac{(1+\gamma M^2)^2}{(1+\gamma)^2M^2}, \tag{11}$$

where γ is the adiabatic exponent of the vapour. Accordingly, the relation between the relative humidity and the Mach number for this case is given by

$$\frac{\varphi}{\varphi^*}\equiv\frac{P/P_S}{P^*/P_S{}^*}=\frac{P}{P^*}\exp\left[\frac{\mu L}{RT^*}\left\{\frac{(1+\gamma M^2)^2}{(1+\gamma)^2M^2}-1\right\}\right], \tag{12}$$

The corresponding relation for the one-dimensional flow whose change is caused exclusively by the adiabatic expansion or compression is given by Wegener and Mack[3] as follows:

$$\frac{\varphi}{\varphi^*}=\frac{P}{P^*}\exp\left\{\frac{\mu L(\gamma-1)}{RT^*(\gamma+1)}(M^2-1)\right\}. \tag{13}$$

From these two relations (12) and (13) it will be seen that the ratio of the increase in relative humidy to the increase in Mach number is greater in the flow with heat-exchange than in the adiabatic flow, provided that the change in P is neglected.

As described in § 2, we first employ the pressure distribution along the pipe axis, and enquire after in either case of the above two the change in relative humidity is larger for the same pressure distribution. To this end we shall discuss the relation between M and P, instead of the direct one between φ and P, for the two cases.

According to Howarth[7] we have

$$\frac{P^*}{P}=\frac{1+\gamma M^2}{1+\gamma} \quad \text{namely} \quad M^2=\frac{(1+\gamma)P^*}{\gamma P}-\frac{1}{\gamma} \tag{14}$$

for the one-dimensional flow with heat-exchange, and

$$\frac{P^*}{P}=\left\{\frac{2}{\gamma+1}\left(1+\frac{\gamma-1}{2}M^2\right)\right\}^{\gamma/(\gamma-1)} \quad \text{namely} \quad M^2=\frac{\gamma+1}{\gamma-1}\left(\frac{P^*}{P}\right)^{(\gamma-1)/\gamma}-\frac{2}{\gamma-1} \tag{15}$$

for the corresponding adiabatic flow. From these relations we obtain the values of $dM^2/d(P/P^*)$ as:

$$\frac{1+\gamma}{\gamma} \quad \text{and} \quad \frac{1+\gamma}{\gamma}\frac{1}{(P^*/P)^{1/\gamma}}, \tag{16}$$

respectively. The inequality $P^*/P>1$ holds always in the supersonic flow, so that we can infer from (16) that the ratio of the increase in M^2 to the increase in P^*/P or to the decrease in P itself is larger in the flow with heat-removal than in the flow with adiabatic expansion. Thus this conclusion, together with the result obtained from the relations (12) and (13), implies that in case when the same uniformly decreasing pressure distribution is supposed, the high degree of supersaturation is realized faster in the flow with heat-removal than in the flow with adiabatic expansion.

§ 4. Conservation Equation

In § 3, we have studied the relation between the relative humidity and the Mach number or pressure, assuming that the vapour does not condense after it had been in the supersaturated state. In reality, however, if the degree of supersaturation of the fluid exceeds a certain critical value, this unstable state will be ultimately broken down and consequently the appearance of the considerable amount of liquid phase can be observed by sudden condensation. The mass fraction of the condensed phase of the fluid immediately before and after this abrupt change must be quite different from the one for the equilibrium case. Accordingly, the variables which characterize the flow pattern cannot be obtained from Eqs. (4), (5) and (6) for such a case in our problem.

Here we use the mass fraction of condensed phase q defined as:

$$q=m_L'/m' , \tag{17}$$

where m_L' is the rate of mass flow of condensed phase through the unit sectional area. Then q would increase in company with the increase in h' when the fluid flows downstream. If this q can be known by some considerations of the flow which deviates from the equilibrium one, we can easily obtain the flow variables by solving the conservation equations, instead of using Eqs. (4), (5) and (6). The conservation equations involving q of the mass, momentum and energy in the form of differential equations for the one-dimentional flow which passes through a pipe of constant cross-sectional area with heat-removal effect are written down respectively as

$$\frac{d\rho'}{\rho'}+\frac{dU}{U}=0 , \tag{18}$$

$$-\rho' U dU=dP , \tag{19}$$

$$UdU+C_P dT-d(qL)=-dh' , \tag{20}$$

and the equation of state is also given by

$$\frac{dP}{P}=\frac{d\rho'}{\rho'}+\frac{dT}{T}-\frac{dq}{1-q} . \tag{21}$$

Here, ρ' is the mean fluid density of the gaseous and liquid phases and L the latent heat of vaporization which is given by the difference of the enthalpy of gaseous phase from that of liquid phase as

$$L=(C_P-\kappa)T-\kappa_0 . \tag{22}$$

From the above five equations, we have

$$dU=\frac{1}{\dfrac{U}{\{C_P-(C_P-\kappa)q\}T}+\dfrac{1}{U}-\dfrac{m'}{P}}\left[\frac{\{(C_P-\kappa)T-\kappa_0\}dq-dh'}{\{C_P-(C_P-\kappa)q\}T}-\frac{dq}{1-q}\right] , \tag{23}$$

$$dT=\frac{\{(C_P-\kappa)T-\kappa_0\}dq-UdU-dh'}{C_P-(C_P-\kappa)q} , \tag{24}$$

$$dP=-m'dU , \tag{25}$$

and by successive uses of these equations, we can calculate the values of U, T and P step by step.

§ 5. Mass Fraction of Condensed Phase

In the supersonic flow in which the condensation phenomena are obliged to occur during a very short time-duration, the number of dusts in ordinary vapours is too small to form the nuclei for condensation which play an essential role to break out the supersaturated state. Owing to this result, the nuclei must be supplied by the self-nucleation of vapour. Then the mass fraction of condensed phase q is changed by the following two reasons: first by the self-nucleation and secondly by the growth of the droplets which were born at the preceding sections. In the fluid flow between the interval x and $x+dx$ which are measured from a standard section along the pipe-axis, these changes of mass fraction of condensed phase, described by dq_1 and dq_2 respectively, are given by

$$dq_1=\frac{4}{3m'}\pi\rho_L r_*^3 J dx\ , \tag{26}$$

$$dq_2=\frac{4}{3m'}\pi\rho_L \sum_k \{(r_k+dr_k)^3-r_k^3\}J_k dx_k\ , \tag{27}$$

$$dq=dq_1+dq_2\ , \tag{28}$$

where J is the number of self-nucleation per unit time and unit volume, J_k is the mean rate of self-nucleation in the flow between x_k and x_k+dx_k, r_* is the radius of nucleus of condensation, r_k is the radius of a droplet at x which was born at x_k and grew up during its movement from x_k to x and dr_k is the increase in the radius of the same droplet during its movement along a distance of dx. The radius of nucleus is expressed by[3),8)]

$$r_*=\frac{2\sigma\mu}{\rho_L RT\ln P/P_S}\ , \tag{29}$$

where σ is the surface tension which is given by a semi-empirical expression due to Eötvös and Ramsay-Schield[3),8)] as:

$$\sigma=\frac{\text{const}}{(\mu/\rho_L)^{2/3}}(T_c-T)\ . \tag{30}$$

Here, T_c is the critical temperature of the vapour.

Volmer[9)], Becker and Döring[10)], Frenkel[8)] and others proposed the expressions for the rate of self-nucleation respectively, but these expressions were proved to be practically equivalent to each others.[11,12)] In this paper, we employ Frenkel's one:

$$J=\left(\frac{2}{\pi}\right)^{1/2}\frac{A^{3/2}(\sigma\mu)^{1/2}}{R^2\rho_L}\left(\frac{P}{T}\right)^2\exp\left\{-\frac{16\pi}{3kR^2}\left(\frac{\mu}{\rho_L}\right)^2\left(\frac{\sigma}{T}\right)^3\frac{1}{\ln^2 P/P_S}\right\}\ , \tag{31}$$

where A is the Avogadro number and k is the Boltzmann constant.

So far some investigations have also been made on the growth of the droplet. Oswatitsch ingeniously analysed the adiabatic flow by calculating the growth velocity of the droplet on the basis of the temperature gradient at its surface[13)]. But the density gradient of the vapour due to the absorption of vapour molecules at the droplet surface gives rise directly to the growth of the droplet, though the temperature gradient is buit up conversely by the rate of condensation of the vapour on the droplet. Therefore, with a little modification, we shall follow Wilde's reasoning that the growth velocity of the droplet depends upon the concentration gradient[14)]. Namely, we suppose that the surface of the droplet which exists in the supersaturated vapour is surrounded by the saturated vapour with the pressure $P_S(T)$. Then, Wilde's first approximation is modified to

$$dr_k=\frac{\mu D}{\rho_L RT}\{P-P_S(T)\}\frac{dx}{Ur_k}\ . \tag{32}$$

The coefficient of self-diffusion D is given by[15)]

$$D=\frac{3(RT)^{3/2}}{8(\pi\mu)^{1/2}A\omega^2P}\,, \tag{33}$$

where ω is the effective diameter of molecular collision. Substituting Eq. (33) into Eq. (32), we get the expression for the growth of the droplet as follows:

$$dr_k=\frac{3(\mu R)^{1/2}}{8\pi^{1/2}A\rho_L\omega^2}\left\{1-\frac{P_S(T)}{P}\right\}\frac{T^{1/2}dx}{Ur_k}\,. \tag{34}$$

§ 6. Numerical Discussion

Making use of the results in the preceding two sections, we can analyse the flow in the region where the fluid is not in the equilibrium state. Thus, carrying out numerical calculations, we shall investigate how the flow pattern obtained in the writer's previous paper is altered in the supersonic branch. Water vapour has been chosen as the fluid, and as in the previous paper the following initial values for the flow have been adopted: $P_e=152$ cm Hg $=2.02\times10^6$ dyne cm^{-2}, $T_e=200°\text{C}=473°\text{K}$ and $M_e=1$, from which we have obtained $U_e=5.39\times10^4$ cm sec^{-1}, $\rho_e=9.27\times10^{-4}$ gram cm^{-3}, $m'=5.00\times10$ gram cm^{-2} sec^{-1}. The thermodynamic relations and constants used in this paper are: $P_S(T)=4.98\times10^{11}\exp(-4.89\times10^3/T)$ dyne cm^{-2}, $\kappa=4.19\times10^7$ erg gram^{-1} deg^{-1}, $\kappa_0=-3.13\times10^{10}$ erg gram^{-1}, $\rho_L=\text{const}=1$ gram cm^{-3}, $R=8.31\times10^7$ erg deg^{-1} mol^{-1}, $k=1.37\times10^{-16}$ erg deg^{-1}, $C_P=1.86\times10^7$ erg gram deg^{-1}, $\gamma=1.33$ and $\omega=3.26\times10^{-8}$ cm. Values of the surface tension have been obtained from the existing table[16], instead of calculating them by the use of Eq. (30).

With these values and relations, Eqs. (23)~(25), (27)~(29), (31) and (34) are now reduced respectively to

$$dU=\frac{1}{\dfrac{U}{(1.86\times10^7+2.33\times10^7q)T}+\dfrac{1}{U}-\dfrac{500}{P}}\left\{\frac{(3.13\times10^{10}-2.33\times10^7T)dq-dh'}{(1.86\times10^7+2.33\times10^7q)T}-\frac{dq}{1-q}\right\},$$

$$dT=\frac{(3.13\times10^{10}-2.33\times10^7T)dq-UdU-dh'}{1.86\times10^7+2.33\times10^7q}\,,$$

$$dP=-50.0\times dU\,,$$

$$dq_1=8.38\times10^{-2}r_*^3Jdx\,,$$

$$dq_2=8.38\times10^{-2}\sum_k\{(r_k+dr_k)^3-r_k^3\}J_kdx_k\,,$$

$$r_*=\frac{1.88\times10^{-7}\sigma}{T\log P/P_S}\,,$$

$$\log J=20.36+\frac{1}{2}\log\sigma+2\log P-2\log T-\frac{4.69\times10^2\sigma^3}{T^3\log^2 P/P_S}\,,$$

$$(r_k+dr)^2=r_k^2+2.53\times10^{-5}\left\{1-\frac{P_S(T)}{P}\right\}\frac{\sqrt{T}}{U}dx\,.$$

As described in the preceding sections, we have first given the pressure distribution of the non-condensing vapour and then h' has been determined as a function of x. The pressure distribution used in the present paper is that given by Winnie and Wood's wind tunnel experiment[17]. In Fig. 1 are plotted this pressure P and the corresponding removed heat quantity h' which has been calculated from Eq. (7). The distance x in this figure has been measured from the sonic section. P, T and U for both the equilibrium flow and the non-condensing one are shown in Fig. 2 corresponding to the distribution of h' in Fig. 1. From this figure it will readily be seen that the condensation starts at $x=2.6$ cm in equilibrium flow.

If we take account of the appearance of supersaturated state in the condensing flow, the rate of self-nucleation J, the total number of droplets per unit volume n and the mass fraction of condensed phase q are obtained as shown in Fig. 3. The resulting pressure P, temperature T and velocity U become as shown in Fig. 4, from which it will be seen that, in a very narrow region of 0.2 cm length whose center is at $x=4.8$ cm, the supersaturated state, which has been held from $x=2.6$ cm, is broken down abruptly and a considerable amount of the mass of gaseous phase changes to liquid phase discontinuously. For this region, the term "condensation shock" is used ordinarily. The fluid which behaved as if it were the non-candensing vapour after it was fallen in the supersaturated state is brought back to the nature of equilibrium flow by passing through this condensation shock.

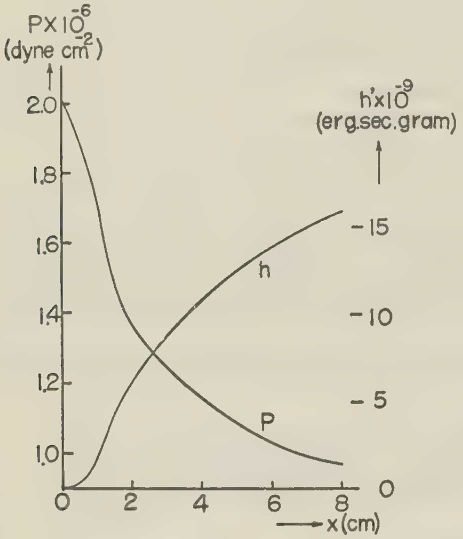

Fig. 1. The pressure distribution given by Winnie and Wood's wind tunnel experiment and the removed heat quantity as calculated from this pressure distribution.

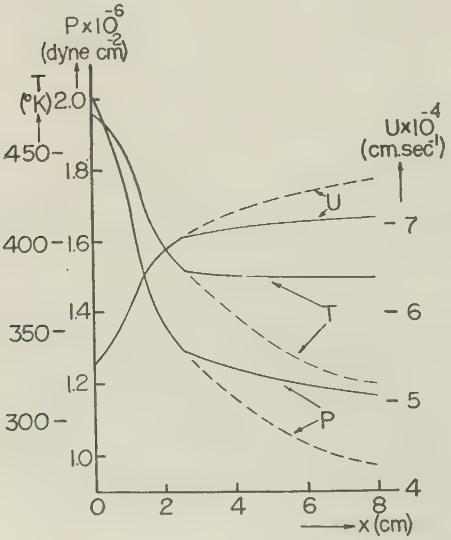

Fig. 2. The pressure, temperature and velocity for the equilibrium flow (continuous line) and for the non-condensing flow (broken line).

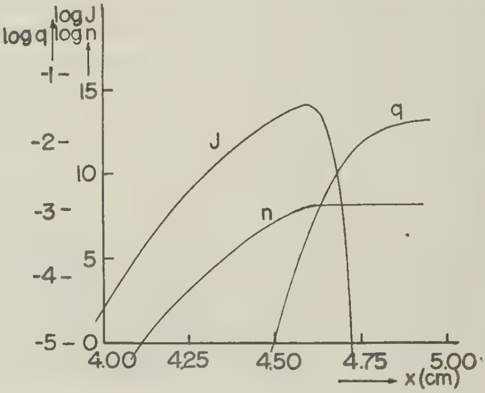

Fig. 3. The rate of self-nucleation, total number of droplets per unit volume and mass fraction of condensed phase.

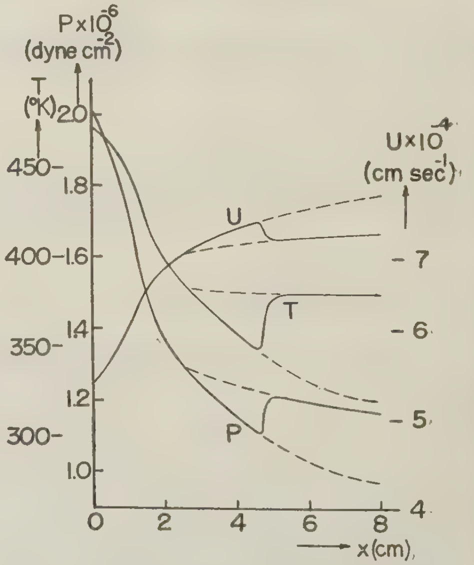

Fig. 4. The resulting pressure, temperature and velocity curves.

Acknowledgements

The writer wishes to express his cordial thanks to Prof. S. Tomotika of Kyoto University not only for his continual encouragement but also for his kind inspection of the manuscript. He is also indebted to Prof. T. Nagakura and Dr. K. Kusukawa of Tokyo Metropolitan University as well as to Prof. T. Simasaki and Dr. K. Hida of the University of Osaka Prefecture where the most part of this work was performed.

References

1) P. P. Wegener: J. Appl. Phys. **25** (1954) 1485.
2) H. Wakeshima: J. Phys. Soc. Japan **10** (1955) 141.
3) P. P. Wegener and L. M. Mack: *Advances in Applied Mechanics*, Vol. V (Academic Press, 1958).
4) H. W. Emmons: *Fundamentals of Gas Dynamics* (Princeton, 1958).
5) P. Chiarulli and R. F. Dressler: J. Appl. Phys. **28** (1957) 990.
6) K. Niu: J. Phys. Soc. Japan **15** (1960) 1108.
7) L. Howarth: *Modern Developments in Fluid Dynamics, High-Speed Flow*, Vol. I (Oxford, 1953).
8) J. Frenkel: *Kinetic Theory of Liquids* (Oxford, 1946).
9) M. Volmer: *Kinetik der Phasenbildung* (Steinkopff, 1939).
10) R. Becker and W. Döring: Ann. Physik (5) **24** (1935) 719.
11) A. Sander and G. Damköhler: Naturwissenschaften **31** (1943) 39.
12) R. T. Probstein: J. Chem. Phys. **19** (1951) 619.
13) K. Oswatitsch: Z. A. M. M. **22** (1942) 1.
14) K. A. Wilde: J. Appl. Phys. **30** (1959) 577.
15) S. Chapman and T. G. Cowling: *The Mathematical Theory of Non-Uniform Gases* (Oxford, 1953).
16) K. Shiba: *Butsuri Josu Hyo* (Iwanami, 1949) (in Japanese).
17) A. M. Winnie and M. W. Wood: Proc. Inst. Mech. Engrs. **138** (1938) 229.

Journal of the Physical Society of Japan, Vol. 16, No. 4, April, 1961

A Simplified Method Calculating The Laminar Boundary Layer

By Shin KAWAMATA

The Aeronautical Research Institute, University of Tokyo

(Received December 1, 1960)

A somewhat simplified method calculating the steady and incompressible laminar boundary layer flow is developed basing on the idea of the "local similarity". The analysis is performed by using the variables proposed by Goertler[1]. The calculated results are utilized to predict the separation points in some decelerated flows and the comparison with other exact solutions shows that the value of the "similar parameter" may be taken as -0.224 at the separation points in this method.

The fundamental equations for the steady incompressible laminar boundary layer flow with an arbitrary pressure gradient in two-dimensions are:

Equation of continuity

$$\frac{\partial u}{\partial x}+\frac{\partial v}{\partial y}=0\,, \tag{1}$$

and Equation of motion

$$u\frac{\partial u}{\partial x}+v\frac{\partial u}{\partial y}=u_1\frac{du_1}{dx}+\nu\frac{\partial^2 u}{\partial y}\,, \tag{2}$$

where x, y are the Cartesian coordinates measured along and normal to the body surface, and u, v the velocity components in x- and y-directions, respectively, u_1 the velocity outside the boundary layer, and ν is the kinematic viscosity which is constant. The boundary conditions are

$$\left.\begin{array}{lll} u=v=0\,, & \text{at} & y=0\,, \\ u\to u_1 & \text{at} & y\to\infty\,. \end{array}\right\} \tag{3}$$

Eq. (1) can be satisfied by the introduction of the stream function $\overline{\Psi}$ which is defined as follows:

$$u=\frac{\partial\overline{\Psi}}{\partial y}\,, \qquad v=-\frac{\partial\overline{\Psi}}{\partial x} \tag{4}$$

Then the following non-dimensional variables are introduced:

$$\left.\begin{aligned} &\xi=\frac{1}{\nu}\int_0^x u_1dx\ , \quad \eta=\frac{u_1y}{\nu}\ , \quad \psi=\frac{1}{\nu}\overline{\Psi}\ , \\ &\zeta=\frac{\eta}{\sqrt{2\xi}}\ , \qquad f(\xi,\eta)=\frac{\psi}{\sqrt{2\xi}} \end{aligned}\right\} \tag{5}$$

With these variables, Eq. (2) and the boundary conditions (3) are transformed into the form

$$f_{\zeta\zeta\zeta}+ff_{\zeta\zeta}+g(\xi)(1-f_\zeta{}^2)=2\xi(f_\zeta f_{\xi\zeta}-f_\xi f_{\zeta\zeta})\ , \tag{6}$$

and

$$\left.\begin{aligned} &f(\xi,0)=f_\zeta(\xi,0)=0\ , \\ &f_\zeta(\xi,\infty)\rightarrow 1\ , \end{aligned}\right\} \tag{7}$$

where $g(\xi)=2\xi d\log u_1/d\xi$.

With the conditions (7), the integration of (6) with respect to ζ from 0 to ∞ gives

$$2\xi\frac{d\Theta}{d\xi}+[1+g(1+H)]\Theta=(f_{\zeta\zeta})_{\zeta=0}\ , \tag{8}$$

where

$$\Theta=\int_0^\infty f_\zeta(1-f_\zeta)d\zeta\ , \text{ and } H\Theta=\int_0^\infty(1-f_\zeta)d\zeta\ .$$

Now, in the case of similar flow, f is the function of ζ only, the right-hand side of Eq. (6) vanishes, and $g(\xi)$ is reduced to a constant independent of ξ, which is called the Falkner-Skan parameter[2], hereafter denoted by β in this paper. For more general flows, the Falkner-Skan parameter does not exist in the strict sense, but it seems reasonable to treat β as a parameter varying slowly with x or ξ.

In this approximation, the Eq. (6) may still be written in the form

$$f_{\zeta\zeta\zeta}+ff_{\zeta\zeta}+\beta(1-f_\zeta{}^2)=0\ , \tag{9}$$

or upon integration

$$[1+\beta(1+H)]\Theta=(f_{\zeta\zeta})_{\zeta=0}\ . \tag{9$'$}$$

Equating Eqs. (8) and (9′), we have

$$2\xi\frac{d\Theta}{d\xi}+(1+H)(g-\beta)\Theta=0\ . \tag{10}$$

Solving for β, we obtain

$$\beta=g+\xi\frac{d\log\Theta^2}{d\xi}\Big/(1+H)\ . \tag{11}$$

Now, the quantity, Θ is a slowly varying function of x, and can be calculated in good approximation by the formula[3]

$$\Theta^2=0.22\,u_1{}^{-4}\int_0^x u_1{}^5dx\Big/\int_0^x u_1dx \tag{12}$$

Then the modified Pohlhausen parameter

$$m=-\frac{\theta^2}{\nu}\frac{du_1}{dx}$$

is calculated in terms of Θ and u_1, where Θ is the momentum thickness, and H is found as a function of m by using the table given by Curle and Skan[4]. Finally we get β from Eq. (11). Once β is determined as a function of x, the velocity profile and skin friction are given numerically by using Howarth's tables[5].

With a view to determining the condition at separation point, the present method of calculation has been applied to some retarded flows, and the value of β are calculated for which the exact or approximate solutions are available. The results are shown in the following table.

u_1/U	separation point x/L	$-\beta$
$1-x/L$	0.120 (H., T.)	0.220
	0.125 (G.)	0.227
$1-(x/L)^2$	0.268 (T.)	0.225
	0.271 (G.)	0.226
$1-(x/L)^4$	0.451 (T.)	0.227
	0.462 (G.)	0.254
$1-(x/L)^8$	0.640 (T.)	0.284
	0.630	0.224
$(1+x/L)^{-1}$	0.159 (G.)	0.222

Here U and L are the reference velocity and length, and the capital letters H, T and G denote the positions of separation point calculated by L. Howarth[5], I. Tani[3] and H. Goertler[1], respectively. It is noticed from these results that the values of β at the separation point are almost the same except the flow of the fourth case of the above table. Omitting this case and taking the arithmetical mean, we have the average value -0.224 for β at the separation point. This result can be utilized for rapidly determining the separation point for a given velocity distribution $u_1(x)$. First, g and Θ are determined as functions of x. Then, they are substituted in Eq. (11), where the value $\beta=-0.224$, and $H=3.55$ which is nearly constant in the vicinity of separation point, are used. The solution of the resulting equation gives the value of x for the separation point. The accuracy of this method determining the separation point seems to be very good. Even when applied to the fourth case of the foregoing table, it gives $(x/L)_{\text{sep}}=0.630$, which is in error of only 1.5 per cent compared with the exact value.

The author is indebted to Dr. Itiro Tani, Professor of Aeronautical Research Institute, University of Tokyo, for his supervision and encouragement during the course of the study.

References

1) H. Goertler: J. Math. and Mech. **6** (1957) 1.
2) V. M. Falkner and S. W. Skan: Phil. Mag. **12** (1931) 865.
3) I. Tani: J. Phys. Soc. Japan **4** (1949) 149.
4) N. Curle and S. W. Skan: The Aeronautical Quarterly **8** (1957) 257.
5) L. Howarth: Proc. Roy. Soc. London **A164** (1938) 547.

JOURNAL OF THE PHYSICAL SOCIETY OF JAPAN, Vol. 16, No. 4. APRIL 1961

Refractive Index and Pore Structure of Acid-Leached Surface Layer of Glass

By Koreo KINOSITA

Department of Physics and Chemistry, Gakushuin University,
Mejiro, Tokyo

(Received December 22, 1960)

It is known that acids leach out metal ions from the outermost layer of glass, leaving a skeleton film. We found that the refractive index of such a film n_f changes with the relative humidity p/p_0, and studied n_f *vs.* p/p_0 relations for some dense flint and dense crown glasses. The following conclusions are derived from the analysis of n_f *vs.* p/p_0 curves: (1) The refractive index of the skeleton n_s ($>n_f$) is always greater than that of fused silica, indicating that metal ions are still contained in the skeleton. (2) The porosity of the film ranges from 0.05 to 0.21, and the mean pore radius from 6Å to 23Å, depending on the composition of glass as well as the leaching conditions.

§ 1. Introduction

According to the widely accepted view[1], the action of acid and alkaline solutions and water on glass can be summarized, in the main, as follows. Acids leach out the alkali and other metal ions from the outermost layer of glass, leaving a porous film of silica skeleton. This surface layer is often recognized by the interference of light, because its index of refraction is lower than that of the bulk of the glass. The reaction of glass with alkaline solution, on the other hand, resembles that with diluted hydrofluoric acid. NaOH, for instance, breaks the existing –Si–O–Si– bond in glass by forming –Si–O–Na, HO–Si– units. Thus the surface layer of glass as a whole is dissolved into the solution. The action of plenty of water is similar to that of acids: it leaches out alkali (and sometimes other metal) ions from the surface layer, only to a lesser extent. If, however, a water droplet is left on the glass surface, the leached out alkali ions remain on the surface and the reaction assumes the characteristics of an alkaline attack.

These phenomena are in close relation with what is known as *yake* (pronounced yah-keh) among the Japanese opticians. *Yake* is a general term for those spontaneously deteriorated areas of a glass surface which differ in reflectivity, scattering power and other properties from the original surface. English word for *yake* would be *stain* (*s*) or *tarnishing*. Frequent outbreak of *yake* on lenses in the manufacturing process, especially in the warm and humid summer season, has been an obstacle to the optical industry of this country.

Yake is classified into two categories: *aoyake* (ah-oh-yah-keh) and *shiroyake* (shee-roh-yah-keh). The former denotes the stains, coloured often amber or purple-blue by the interference of light, which actually are the patches on the glass surface where a surface layer similra to that obtained by acid or water leaching has been formed. The latter represents the white stains which are the patches where light is scattered by small crystallites adhering to the glass surface or by minute irregularities of the surface. It has been found that these crystallites are carbonates, hydroxides and/or other salts of the metals leached out from the glass[2),3),4)].

An extensive study of *yake* by collaboration of a number of physicists and chemists was started around 1955 upon request of the Japan Camera Research Association. As it seemed to me that the most promising approach to the elucidation of the nature of spontaneously developed *yake* was the systematic re-examination by newer techniques of the corrosion of glass by liquid etchants, the work in this laboratory was decided to proceed along this line[5)-8)]. Some workers followed the same line[3),4),9)-14)], some wrestled with the problem of atmospheric attack directly[15)], some looked for sensitive methods for detecting the slightest *aoyake*[16)-18)], and others were engaged in more practical investigations including the search for an effective protecting film to be applied to lens surfaces during the manufacturing process for the prevention of *yake*[19)]. This collaboration was finished in 1959 after making valuable contributions to the optical industry of this country, but still there are many problems left unsolved. Some of these are now being investigated in this laboratory.

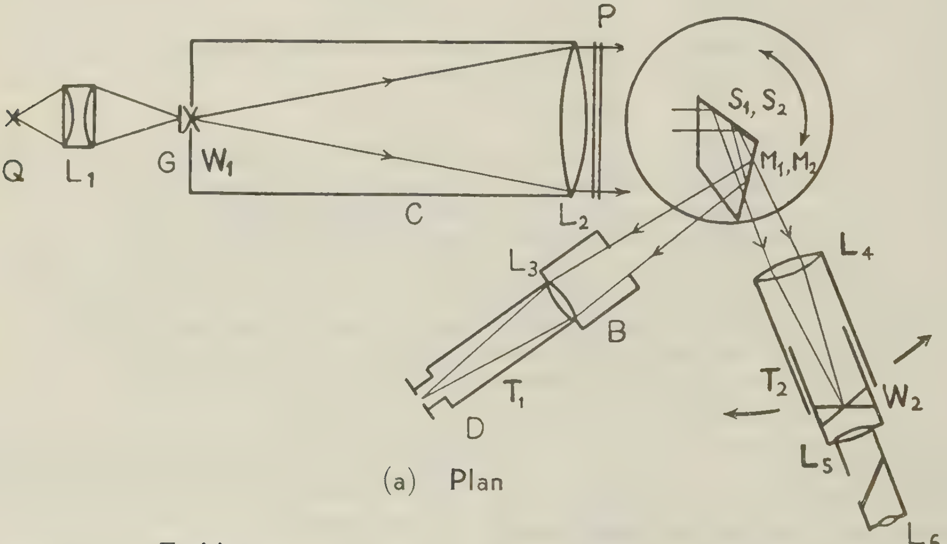

(a) Plan

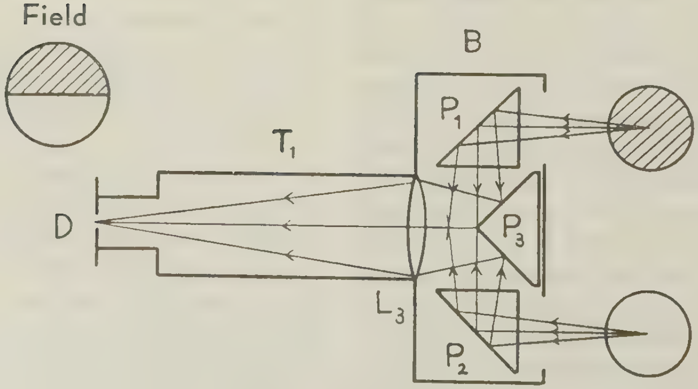

(b) Elevation of B and T_1

Fig. 1. Apparatus for studying relation between n_f and p/p_0. Q: sodium lamp. C: collimator (G: diffuser, W_1: cross wires). P: polarizer. S_1: reference test piece. S_2: test piece with *aoyake* layer. M_1, M_2: plane mirrors. B: prism box (P_1, P_2: rectangular prisms, P_3: aluminized roof prism (field splitter), T_1: tubing with viewing lens L_3). T_2: telescope for reading angle of incidence (W_2: cross wires).

The present paper deals with a recent experiment on the variation with relative humidity of the refractive index of surface layers artificially produced by acid treatment on some dense flint and dense crown glasses. For brevity, such layers shall be called the *aoyake* layers in the following. This variation in refractive index is ascribed to the multilayer adsorption of water vapour on the pore walls of the *aoyake* layer; and the *porosity* (fractional pore volume) as well as the *mean pore radius* are estimated from the refractive index *vs.* relative humidity relations.

§ 2. Experimental Procedures

a) *Measurement of refractive index*

According to the polarimetric study by Tsunekane and Doi[11], the refractive index of the *aoyake* layer is quite uniform throughout its depth. This justifies the application of Abelès's method[20] to the measurement of the refractive index of the *aoyake* layer, n_f. We carried out in 1958 a series of measurements by this method[8], when we found that n_f underwent an observable change if the sample was desiccated or moistened. At once we decided on undertaking a systematic investigation of the humidity dependence of n_f.

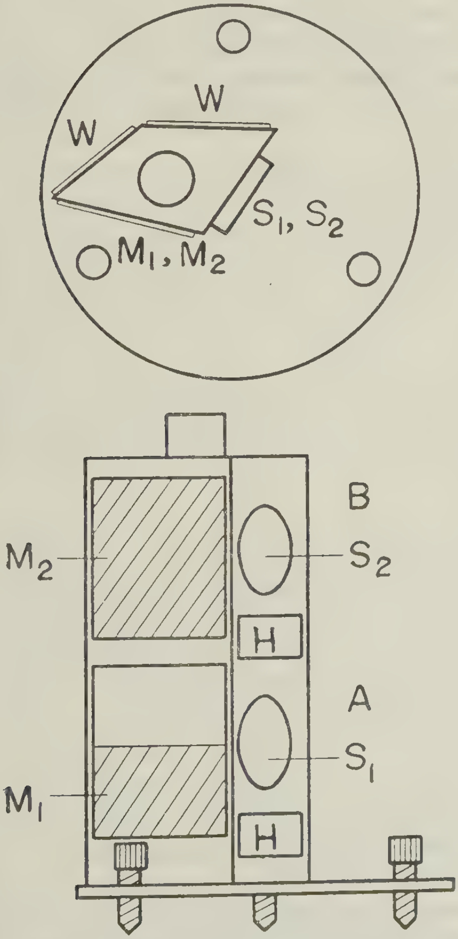

Fig. 2. Sample chamber with air-tight compartments A and B. S_1: reference test piece. S_2: test piece with *aoyake* layer. W: plan-parallel windows. M_1, M_2: plane mirrors. H: gate for inserting humidity controlling agent.

In the experiment cited above our specimen was of the form usually employed in this type of measurement–a glass disk, one half of the surface of which had been subjected to acid attack while the other half was left as freshly polished, with a clear line of demarcation between the two halves. But this was apparently inadequate for the new project, in which it was required to keep the conditions of the reference, or uncoated, surface constant while we change at our will the humidity of the ambient atmosphere of the *aoyake* layer. So we determined on separating the test piece into two, a reference piece S_1 without any surface layer and another piece S_2 of the same kind of glass coated by the *aoyake* layer; and for carrying out the measurement according to Abelès's principle we constructed a new double-head instrument[21]. Later we improved it adopting Traub and Osterberg's idea[22]. A brief description of the improved instrument is given below (see Figs. 1 and 2).

Monochromatic light from a sodium lamp Q, after being collimated and polarized in the *p*-direction*, is allowed to fall on the test pieces S_1 and S_2 which are stored in airtight compartments A and B of the sample chamber (Fig. 2). The sample chamber is mounted on the prism disk of an old spectrometer. Compartment A in which the reference piece S_1 is stored is desiccated throughout the experiment by means of anhydrous phosphoric acid. The test piece on which the *aoyake* layer has been formed, S_2, is enclosed in the other compartment B, and the humidity in this compartment is controlled by keeping appropriate chemicals in it (see § 2 *c*). It is essential to keep the surfaces to be examined of S_1 and S_2 in one and the same plane which is parallel to the revolving axis of the spectrometer. The beams reflected by S_1 and S_2 are again reflected by plane mirrors M_1 and M_2. The last beams take a fixed direction irrespective of the angle of incidence to S_1 and S_2 of the beam from the collimator, and can enter the fixed prism box B. It was found convenient to set M_1 and M_2 at an angle of 110° with S_1 and S_2. The aluminized mirrors M_1 and M_2 are protected by SiO_2 coating. The upper half of M_1 is left transparent, so that a part of the beam from S_1 can go right on and enter a movable telescope T_2. T_2 serves for the precise determination of the angle of incidence. The sample chamber is furnished with plan-parallel windows W, faced at right angles to the beams which fall on and are reflected by S_1 and S_2 at an angle of 56° ($\tan^{-1} 1.483$).

---

* The transmission axis of the polarizer was set within **1′** of the *p*-direction with the aid of Kinosita-Nomura's half-shade device[23].

The beams which enter the prism box B, after being reflected by small rectangular prisms P_1 and P_2, fall on an aluminized *roof prism* P_3 which works as a field splitter. Thus if one observes through a pinhole D at the end of the tubing T_1 the lower and upper halves of the field are seen illuminated by the beams reflected from S_1 and S_2 respectively, with a clear line of demarcation between the two halves. The viewing lens L_3 is focussed on S_1 and S_2.

The method of measurement is quite simple. Observing through D, one adjusts the angle of incidence of the beam from C to S_1 and S_2 by rotating the prism disk until no difference can be recognized in the brightness of the two halves of the field. The angle of incidence φ at this stage can be accurately determined by means of the movable telescope T_2. It is known that[20])

$$\tan\varphi = n_f\,. \tag{1}$$

b) *Preparation of test pieces*

Chemical compositions and refractive indices of the glasses under test are given in Table I. A1 and B1 are commercial optical glasses*, while A2 and A3 are test glasses specially prepared for the study of *yake*.

Table I. Compositions (wt %) and refractive indices (n_D) of glasses under test.

Glass	Composition									n_D
	SiO_2	B_2O_3	Na_2O	K_2O	BaO	PbO	Al_2O_3	Bi_2O_3	As_2O_3	
A1 (analyzed*)	32.4		0.6	1.6		64.6	0.2	0.33		1.760
A2 (calc. from batch)	29.7					70.0			0.3	1.777
A3 (calc. from batch)	29.7			1.0		69.0			0.3	1.771
B1 (analyzed*)	37.1	15.7	0.4		39.5		6.1			1.589

* By the courtesy of Prof. S. Tsuchihashi, University of Kobe.

Test pieces are freshly polished disks, 32 mm in diameter and 3~5 mm in thickness. The top and back surfaces of the test piece make an angle of 2° with each other, in order that the back reflection can be avoided in the measurement of n_f. Techniques for the preservation of the test pieces as well as the cleaning and the leaching treatments have been described previously[5]) (see also Kinosita[24])). The leaching was stopped when the *aoyake* layer showed the sensitive colour of the first order ($n_f d \sim 145\,\text{m}\mu$, where d is the thickness). As was discussed previously[21]), the sensitivity of Abelès's method reaches its maximum at this optical thickness. The test pieces were then rinsed with water, dehydrated with distilled alcohol, and were set in the sample chamber.

c) *Humidity control*

The relative pressure p/p_0 of water vapour in the compartment B, in which the leached test piece S_2 is stored, is controlled by enclosing one of the agents given below in it (see International Critical Tables, Vol. I, p. 67 (1926)):

H_2O $NaCO_3 \cdot 10H_2O$ $NaCl$
NH_4NO_3 $K_2CO_3 \cdot 2H_3O$ $MgCl_2 \cdot 6H_2O$
$ZnCl_2 \cdot 1\frac{1}{2}H_2O$ P_2O_5

It takes some considerable time (of the order of an hour) for the equilibrium value of p/p_0 to be reached in the compartment. For later reference, the variation of p/p_0 with the lapse of time was investigated with the aid of the humidity- and temperature-pick-up of a "Minima" Electric Hygrometer* sealed in the compartment. The time lag of the indication of the hygrometer is believed to be of the order of minutes.

---

* A1 and B1 correspond to Schott SF3 and SK5 respectively.

§ 3. Dependence of n_f on p/p_0

a) Preliminary experiment

The test piece on which an *aoyake* layer had been formed and another test piece of the same glass free from *aoyake* were enclosed in the compartments B and A respectively, one of the humidity controlling agents was inserted in B, and the change with time of n_f was observed. It took some time, say several tens of minutes, for n_f to reach the equilibrium value. A part of this time lag may possibly be attributed to the time required for the completion of adsorption, but the greater part can be ascribed to the time required for the equilibrium in p/p_0 to be established in the compartment B (see the end of § 2 *c*)).

A series of such experiments lead to the conclusion that a wait of one and a half hours was enough for obtaining the equilibrium value of n_f for all agents but H_2O (equil. $p/p_0=1.00$), which needed a longer wait.

On the basis of these preliminary experiments, the equilibrium values of n_f for respective values of p/p_0 between 0.00 and 1.00 were systematically investigated.

b) Experiments with the glasses A1, A2 and A3

The results for the glasses A1, A2 and A3 are illustrated in Fig. 3.

The test pieces were attacked by 0.001 *N* NHO_3, at 60°C. The measurement was started at $p/p_0=0.00$. The relative vapour pressure was then raised step by step up to 1.00 ((1)→), after which it was lowered again step by step down to 0.00 (←(2)). The second (down) run did not follow the path of the first (up) run, but n_f for $p/p_0=0.00$ at the end of the second run was identical with the initial value of n_f for $p/p_0=0.00$. Further up and down runs ((3)→, ←(4)) followed the path of the second run. It took about a week to complete these four runs for one sample.

The observation described above suggests that some structural change had occurred in the first and the second runs which took about four days, after which the layer was stabilized. In this stabilized or *aged* state, the change in the equilibrium value of n_f with the change in p/p_0 was remarkably reversible.

As was reported previously[8)], the absolute values of n_f of the samples prepared in one and the same way are accompanied by some individual fluctuations. But the general trends of the n_f *vs.* p/p_0 relations for the glasses A1, A2 and A3 are well represented by the curves shown in Fig. 3. They are strikingly similar.

c) Experiments with the glass B1

Two experiments were carried out with the glass B1. In the first experiment, the test piece was attacked by 0.001 *N* HNO_3 at 60°C, and in the second by 0.01 *N* HNO_3 at 60°C.

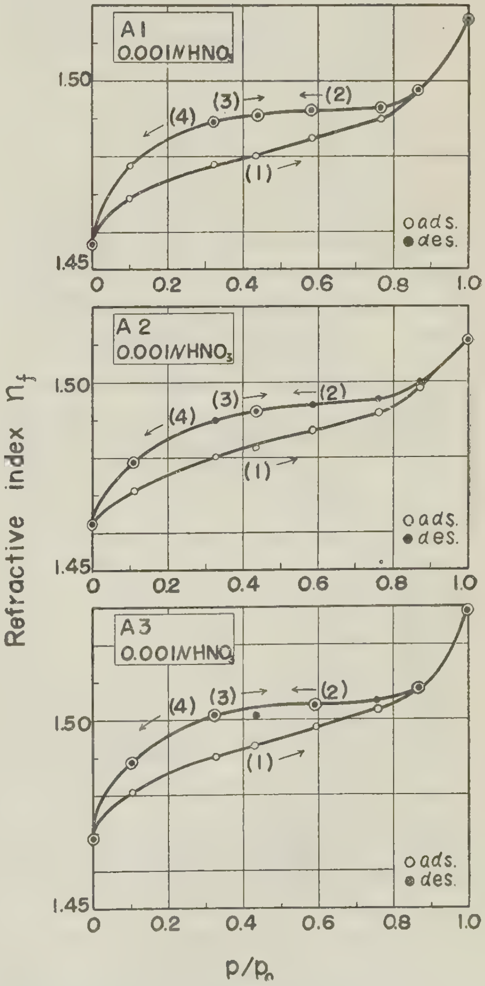

Fig. 3. n_f *vs.* p/p_0 relations for *aoyake* layers on dense flint glasses A1, A2 and A3. Attacked by 0.001 *N* HNO_3, 60°C. $n_f d \sim 145\,m\mu$.

---

* Originally devised by Prof. K. Shiba.

The n_f vs. p/p_0 relations for respective cases are shown in Fig. 4.

Fig. 4 again shows that the path of the second (down) run lies above that of the first (up) run. The third (up) and the fourth (down) runs were found to trace the path of the second run, just as was the case in *b*). One of the differences from the results for the glasses A1, A2 and A3 is that the value of n_f for $p/p_0=0.00$ at the end of the second run is higher than the initial value of n_f for $p/p_0=0.00$. Another difference is found in the form of the n_f vs. p/p_0 curves. The two curves in Fig. 4 are similar in general trends; but they are quite different from those of Fig. 3.

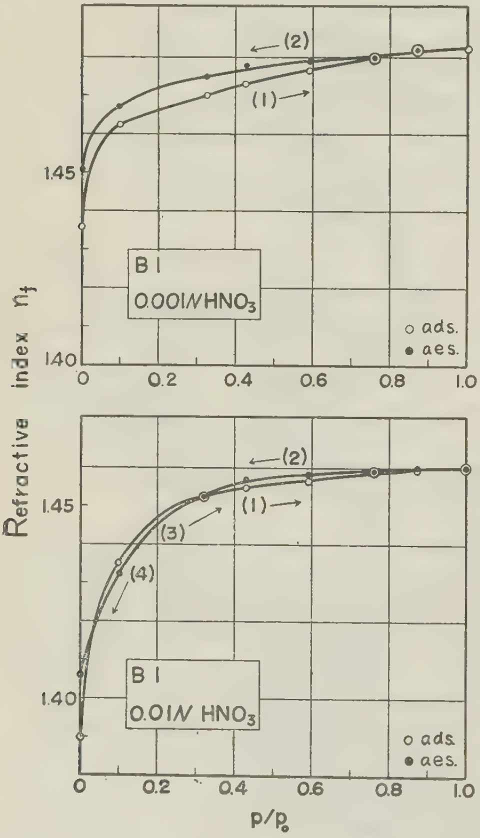

Fig. 4. n_f vs. p/p_0 relations for *aoyake* layers on dense crown glass B1. Attacked by 0.001 *N* HNO_3, 60°C and 0.01 *N* HNO_3, 60°C, resp. $n_f d \sim 145$ mμ.

§4. Estimation of the Parameters of the Pore Structure of the *Aoyake* Layer

It has been discussed[1),7)etc.] that the *aoyake*, from which the alkali and other metal ions have been leached out, is a porous skeleton layer. If this is admitted, the natural consequence will be to suppose that the above described variation in n_f is due to the change in the amount of water adsorbed on the walls of the pores as p/p_0 is varied. The resemblance of the n_f vs. p/p_0 curves in Figs. 3 and 4 to the adsorption isotherms of Type II and Type I (Brunauer, Deming, Deming and Teller's classification[25)]) also supports this view.

According to this idea, the *porosities*, the *refractive indices of the skeletons*, and the *mean pore radii* of the *aoyake* layers we have studied in §3 will be estimated below.

a) *Porosity q and the refractive index of the skeleton* n_s

The skeleton of the *aoyake* layer on a silicate glass has been believed[1)etc.] to be composed almost exclusively of silicic acid which contains some –Si–OH groups besides the original –Si–O–Si– bonds. According to our semi-quantitative spectral analysis[7)], however, it still contains some amount of metal ions which are the constituents of the original glass. Moreover, the skeleton may very probably contain some water, which cannot be desorbed even when p/p_0 is reduced to zero. *The mean refractive index of the skeleton as such* shall be denoted by n_s.

According to the idea mentioned above, the number of water molecules in the pore space will increase as p/p_0 is increased. If v is the volume in the pore space occupied by water at a given value of p/p_0 and v_0 is the total volume of the pores (for convenience' sake, v and v_0 shall be referred to the unit area of the *aoyake* layer), then the mean refractive index of the pore space n_p at that relative pressure will be given by

$$n_p=n_w\frac{v}{v_0}+n_a\left(1-\frac{v}{v_0}\right). \tag{2}$$

Here n_w stands for the refractive index of water, and n_a for that of air.

If V is the volume of the *aoyake* layer per unit area, the following equation will be derived by similar reasoning:

$$n_f=n_s\left(1-\frac{v_0}{v}\right)+n_p\frac{v_0}{v}, \tag{3}$$

or, in terms of the *porosity* of the layer $q=v_0/V$,

$$n_f=n_s(1-q)+n_p q. \tag{4}$$

Now, if we assume that

$$v=0 \quad \text{or} \quad n_p=n_a \quad \text{in case} \quad p/p_0=0.00$$

and

$$v=v_0 \quad \text{or} \quad n_p=n_w \quad \text{in case} \quad p/p_0=1.00\,,$$

we can calculate n_s and q from the observed values of n_f at $p/p_0=0.00$ and 1.00. The results are given in Table II, together with some other data. The numerical values under the headings F and A are those obtained from the lower and upper branches of the curves in Figs. 3 and 4 respectively, and are supposed to represent the properties of the "fresh" and "aged" *aoyake* layers respectively.

In the evaluation of n_s and q described above, it has been tacitly assumed that the *aoyake* layer does not swell nor contract ($V=$ const.) throughout the range of p/p_0. In order to see if it is the case, we examined the change with p/p_0 of the interference colour exhibited by the *aoyake* layer, which is determined by the optical thickness of the layer $n_f d$. It did change as p/p_0 was varied, but quantitative examination proved that this variation can be explained by the change in n_f (Figs. 3 and 4) alone. The interference method is fairly reliable if $n_f d \sim 145\,\mathrm{m}\mu$, which fortunately was the case in our samples. Hence it could be concluded that d, and consequently $V(=d\,\mathrm{cm}^3$ by definition), remains constant throughout the range of p/p_0.

b) *Mean pore radius* $\bar{r}$

As is seen from Eqs. (2) and (4), the relation between n_f and v (the volume of adsorbed water) is linear:

$$n_f=n_a q+n_s(1-q)+(n_w-n_a)\frac{v}{v_0}\,. \tag{5}$$

All parameters included in the right side are known except v_0. The last parameter is at once obtained as*

$$v_0=qV=qd\,. \tag{6}$$

If we plot v as calculated from Eq. (5) against p/p_0, we get the *adsorption isotherms***. (Note that v is the volume as liquid). Figs. 5 and 6 show the adsorption isotherms obtained in this way from Figs. 3 and 4 respectively. The isotherms in Fig. 5 belong to Type II, and those in Fig. 6 to Type I.

Now, let us estimate the total area of the pore walls s by the method of Brunauer, Emmett and Teller[26]. For this, we assume that the adsorption in these cases is multimolecular and obeys the BET equation of multimolecular physical adsorption on a free surface

$$\frac{p}{v(p_0-p)}=\frac{1}{v_m c}+\frac{c-1}{v_m c}\frac{p}{p_0} \tag{7}$$

at low pressures. Eq. (7) includes two parameters, v_m and c: v_m is the so-called monolayer capacity, *i.e.*, the volume of vapour adsorbed when the entire surface of the pores is covered with a complete unimolecular layer; and

$$c=\exp.(E_1-E_L)/RT\,, \tag{8}$$

where E_1 is the heat of adsorption of the first layer, E_L is the latent heat of condensation of vapour, and R and T are the usual constants.

Table II. Properties of acid-leached *aoyake* layers on glasses A1, A2, A3 and B1, as estimated from n_f vs. p/p_0 relations. As for headings F and A, see text.

Glass		Leaching treatment		Index of film n_f at $p/p_0=0.7$	Index of skeleton n_s	Porosity q	Mean pore radius $\bar{r}$ (Å)
Notation	n_D						
A1	1.760	0.001 N HNO_3, 60°C	F A	1.489 1.492	1.558 1.558	0.183 0.183	23 11
A2	1.777	0.001 N HNO_3, 60°C	F A	1.490 1.495	1.541 1.541	0.144 0.144	18 12
A3	1.771	0.001 N HNO_3, 60°C	F A	1.500 1.505	1.572 1.572	0.180 0.180	18 13
B1	1.589	0.001 N HNO_3, 60°C	F A	1.479 1.480	1.503 1.475	0.132 0.051	10 6
B1	1.589	0.01 N HNO_3, 60°C	F A	1.458 1.459	1.494 1.464	0.213 0.123	9 6

---

* The value of d was obtained by dividing the optical thickness $n_f d$, as determined by the interference colour method, by n_f.

** To be exact, it must be admitted that our sample chamber was not thermostatted. But the temperature fluctuation in it seldom exceeded 1°.

If we transform the v *vs.* p/p_0 curves in Figs. 5 and 6 into $p/v(p_0-p)$ *vs.* p/p_0 curves, we find that these can be well approximated by straight lines at low pressures, as demanded by the Brunauer, Emmett and Teller procedure. From these straight lines c and v_m can be found for respective cases*; and from the values of v_m, s can be calculated taking the adsorption cross section of a water molecule as 10.5Å².

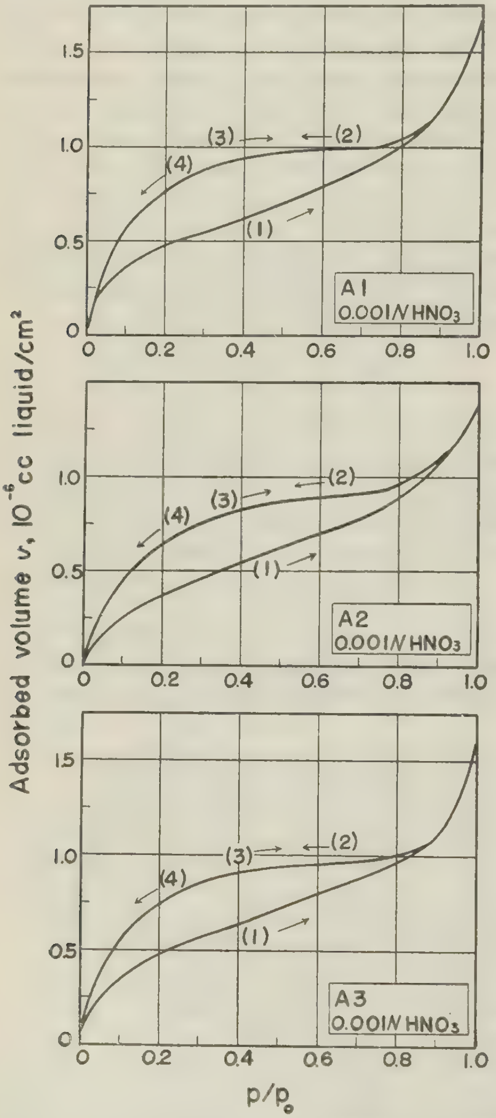

Fig. 5. Adsorption isotherms for *aoyake* layers on glasses A1, A2 and A3. Obtained from Fig. 3.

Now, if we assume for simlicity that the pores are of cylindrical form, s and v_0 are given by

$$s=2\pi\bar{r}l \quad \text{and} \quad v_0=\pi\bar{r}^2l\,, \tag{9}$$

where $\bar{r}$ is the *mean radius*, and l the *total length* of the pores. From the above relations it follows that

$$\bar{r}=2v_0/s\,. \tag{10}$$

The values of the mean pore radius evaluated in this way are given in the last column of Table II.

c) Distribution of pore radius

There is a quite different approach to the evaluation of the pore size, which is based on the capillary condensation theory. The equilibrium vapour pressure p over the meniscus of a liquid filling a capillary of radius r is lower than the normal vapour pressure of the liquid p_0, and is given by the Kelvin equation

$$\log(p/p_0)=-2\sigma V_L/rRT\,, \tag{11}$$

where σ and V_L represent the surface tension and the molar volume of the liquid respectively. Let us assume that at pressure p all capillaries whose radii are smaller than r as

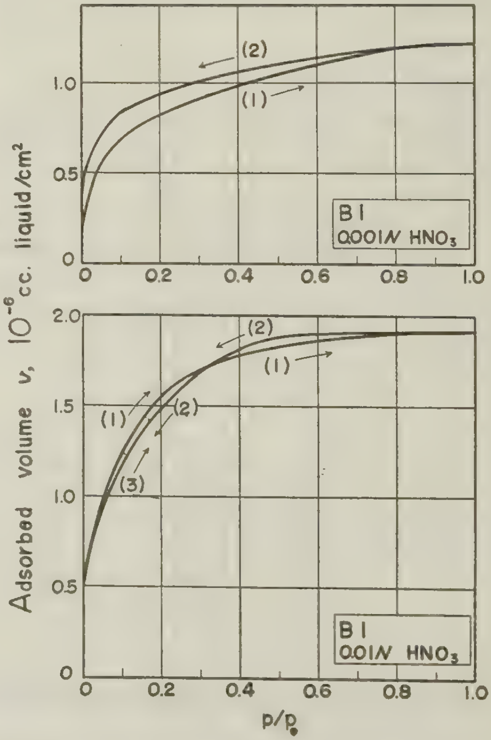

Fig. 6. Adsorption isotherms for *aoyake* layers on glass B1. Obtained from Fig. 4.

---

* The obtained values of v_m (as liquid) range from 0.41 to 1.30×10^{-6} cm³ per unit area of the *aoyake* layer. The values of c range from 11 to 56, which corresponds to $E_1-E_L=1.4\sim2.4$ kcal/mole.

given by Eq. (11) are filled with condensed adsorbate, while larger capillaries are left empty. Then we can transform the adsorption isotherm into a v *vs.* r curve, the ordinate of which represents the volume of liquid condensed in the pores of radii smaller than r. It is more convenient to plot v/v_0 against log r, according to Kubelka[27]. If we differentiate the v/v_0 *vs.* log r curve (the *integral structural curve*) by log r, we get the *differential structural curve*, the ordinate of which is proportional to the frequency of occurrence of the capillaries having radii whose natural logarithms lie between $\log r$ and $\log r + d\log r$.

Our measurements are not so minute as to allow the exact differentiation of the integral structure curves, but if we venture, we get Figs. 7 and 8. The results can be no more than qualitative, but we can get some idea of the pore size distribution from these curves.

The agreement with the estimation of the mean pore radii described in *b*) is not satisfactory, but we would have to be satisfied at this degree of agreement if we consider that the two estimates are based on quite different premises, not to mention the poor reliability of Figs. 7 and 8.

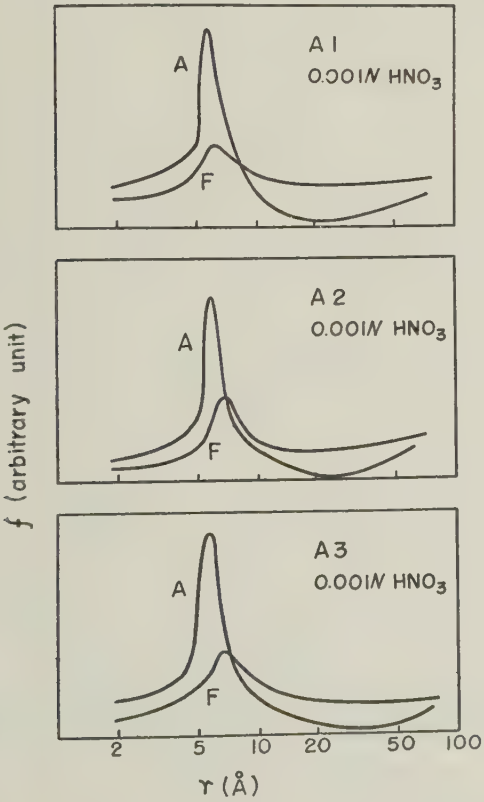

Fig. 7. Differential structural curves for glasses A1, A2 and A3. Obtained from Fig. 5. $f = d(v/v_0)/d(\log r)$.

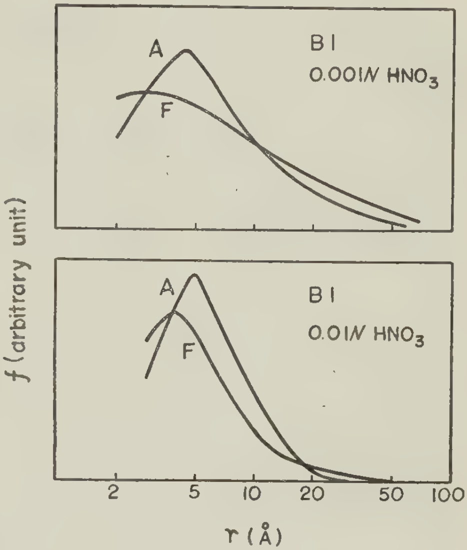

Fig. 8. Differential structural curves for glass B1. Obtained from Fig. 6. $f = d(v/v_0)/d(\log r)$.

§ 5. Discussions

a) n_s and n_f

The present work is believed to be the first attempt to determine n_s, the *refractive index of the skeleton* of an acid-leached surface layer of glass (*aoyake* layer). This has to be distinguished from n_f, the refractive index of the layer as a whole.

The values of n_f of well-developed *aoyake* layers hitherto published[28]–[32]etc.*, as well as the published[11],[13],[17] and unpublished data obtained in our collaboration 1955–59, are scattered between 1.42 and 1.58, most of which being concentrated around 1.47. As the last value is very close to the refractive index of fused silica, 1.46, this has been regarded as evidence in favour of the theory that the well-developed *aoyake* layer is a silica skeleton film, from which the metal ions contained in the original glass has been leached out almost completely. The present work has revealed that this is misinterpretation. The fact is that the refractive index of the material of the *aoyake* layer, or the skeleton, is much higher (see Table II), indicating that a considerable amount of metal ions are still present in the skeleton. The usual method of measurement of the refractive index of the *aoyake* layer gives nothing but the *mean index of the skeleton and the pore space*, which in most cases is close to 1.47. This is demonstrated by the values of n_f at $p/p_0=0.70$ given in Table II.

---

* As regards the interpretation of Bishop's[30] and Hara's[32] results, see Kinosita[33].

This view is consistent with the results of our semi-quantitative spectral analysis of *aoyake* layers[7]. It seems that Anderson and Kimpton's measurement[31] of the infrared spectral reflectivity of the *aoyake* layer also supports this view.

b) *Estimation of the pore structure*

Much has been discussed about the porous nature of the *aoyake* layer. Few, if any, measurements of porosity and pore size have been attempted, in so far as the *aoyake* layer on the polished surface is concerned.

The only data which are to be compared with ours would be those of Russian workers. They seem to have done much in this field, but little is known in this country. In a paper contributed to the Conference on the Structure of Glass, Leningrad, 1953[34], Zhdanov quotes a few estimations of porosities and predominant pore radii of acid-leached surface layers on optical glasses. These are cited in Table III. The estimation is based on "adsorption methods" (volumetric or gravimetric measurements with powdered samples ?). The *predominant radius* is conjectured to have been evaluated from the *differential structural curve*. His values seem to be consistent with ours.

Table III. Porosities and pore radii of acid-leached surface layers on optical glasses estimated by adsorption methods. Zhdanov[34].

Glass	Porosity q	Predominant pore radius (Å)
F3	0.07	<8
BK10	0.12	<8
K1	0.26	<8

Recently Watanabe, Noake and Aiba[35], in their study on microphases in glass, tried an electron microscopic study of the surfaces of some borosilicate glasses which had been subjected to acid attack after heat treatment, and observed small cavities which are believed to have come into existence because of local differences in solubility. The size of the cavities is increased by heat treatment: in air-cooled samples they are of a size of 100Å or less and only a few can be recognized in the electron micrograph*, while in the samples subjected to prolonged heat treatment they are larger and are seen scattered all over the the surface. In our opinion, these "cavities" are the same in their nature as the openings of the "pores" we have been discussing. It is desirable to observe by electron microscopy the openings of the pores in the *aoyake* layers on ordinary polished glass surfaces. For this, however, an essential improvement in the resolving power would be indispensable.

Before concluding this sub-section, an estimate of the area covered by openings of the pores will be given. From either of Eqs. (9) we can calculate l, the total length of the pores. The pores are supposed to form a most complicated labyrinth in the *aoyake* layer, but if we venture to assume that the mean length of a pore is twice the thickness of the layer, we can evaluate the number of pores, and hence the area covered by openings of the pores in the unit area of the surface. This turns out to be 0.03~0.11—not unreasonable.

c) *Further discussions on the pore structure*

It is remarkable that the adsorption isotherms for the dense flint glasses A1, A2 and A3 (Fig. 5) are of the same type, while those for the dense crown glass B1 (Fig. 6) belong to another type. The two isotherms for B1 are much alike notwithstanding the dfference in leaching conditions. These features suggest that the type of the adsorption isotherm is primarily determined by the composition of glass.

This assumpion certainly needs further experimental verifications**, but seems to be highly probable if one admits that the skeletonization of the surface layer of glass is caused by selective dissolution of those microphases in the glass which are easily attacked by acid. The presence of such microphases in the glass, or the microheterogeneous structure of glass, has been keenly discussed by Russian workers[34]; Watanabe's work[35] is also concerned in this problem. According to these workers, the composition and the thermal history of glass determine the chemical nature and the size of soluble (and insoluble) microphases. It will be natural to consider that these in turn will determine the structure characteristics of the *aoyake*. It is known that the adsorption isotherm is highly sensitive to variations in structure characteristics of porous adsorbents.

---

* The resolution of the replicas was of the order of 100Å.

** The adsorption isothem of the *aoyake* on a lantern crown glass, which is now under investigation, seems to belong to Type V isotherm.

The branching of the isoterm (Figs. 5 and 6) is another point to be discussed. The second (down) run goes along a path which differs from that of the first (up) run; further runs follow the path of the second run. This suggests, as was mentioned previously, that some irreversible change—aging—has occurred during the first and the second runs. According to the analysis (Table II), $\bar{r}$ is smaller in the aged layer than in the fresh one. In the glasses A1, A2 and A3 q and n_s are not affected by aging, while in the glass B1 the values of both parameters (especially q) are decreased. Corresponding to these situations, the total length of pores l increases by a factor of 2∼4 in the former glasses, while in the latter the increase of l is not marked.

What kind of irreversible process would have occurred in the *aoyake*, which results in in such structure changes? One of the possible answers would be the following. There are numerous Si–OHg roups in the *aoyake* which have been formed by the hydrolysis of Si–O–X bonds, where X is either an alkali or an alkali earth ion. Whenever two Si–OH groups react with the liberation of water, a strong Si–O–Si bond will be formed which draws two SiO_4 groups closer together. According to Weyl[1], this process can take place at room temperatures*. If it does, the consequent irregular shrinkage of the skeleton may give birth to numerous finer cracks, which will decrease the mean pore radius $\bar{r}$. The total shrinkage of the layer could possibly be so small that the resulting decrease in d cannot be recognized by observation of the interference colour. In some situations it might happen that some water is trapped in the skeleton in the process of deformation, which cannot escape even at $p/p_0=0.00$. Such trapped water will decrease n_s.

Another possible irreversible change which might have occurred in the *aoyake* layers of our samples is the acid attack by NO_3^- ions still left in the layers after rinsing.

There was particular reason why we carried out two experiments on the glass B1, one with the test piece attacked by 0.001 N HNO_3 and another by 0.01 N HNO_3. In our study of the growth rate of the *aoyake* layer[8], we found for this glass that d increases in proportion to $t^{0.4}$ (t is the duration of acid treatment) if the sample is attacked by 0.001 N HNO_3, while d increases in proportion to t if attacked by 0.01 N HNO_3**. This suggested that there would be a substantial difference between the structures of the *aoyake* layers developed by respective treatments. The result, however, was rather contrary to our expectation. The adsorption isotherms were of the same type; and the mean pore radii were almost identical. The only difference was found in that the porosity q and the fractional area covered by pore openings (see the end of § 5 *b*)) were twice as large in the latter case (attack by 0.01 N HNO_3) as in the former case (0.001 N).

It need hardly be said that the study of the growth mechanism of the *aoyake* layer should be based on the knowledge of its pore structure. We have to do much, however, before we can put the study on the right track. At the present status of our knowledge we cannot so much as estimate the resistance experienced by a metallic ion when it goes through a pore of a radius of the order of 10Å.

d) *Application of the method to other fields*

We have developed in this work a method of estimation of the pore structure of a transparent porous film, which is based on the observation of the change in its refractive index due to adsorption of vapour. This method may find applications in other fields, *e.g.*, in the study of the pore structures of evaporated films of transparent materials.

Cordial thanks are due to Mr. Kohzo Natsume, who used to be my assistant, for his collaboration in a series of studies of *yake* on which the present work is founded; and to

---

* It is well known that this aging process can be greatly accelerated by baking the *aoyake*[36].

** If the rate determining process is diffusion of ions through the layer, it is expected that $d \propto t^{0.5}$.

Miss Mizuko Yoshida, Mr. Kiyoshi Ito and Mr. Mitsuo Sasaki who assisted me in the experimental part of this work.

References

1) See, e.g., W. A. Weyl: Glass Ind. **28** (1947) 231; 300; 349; 408. See also S. Tsuchihashi: *Garasu no Hyomen-Kagaku*, Tokyo (1956)*.
2) H. Kamogawa: Nippon Sugaku-Buturigakkaisi **17** (1943) 396*.
3) S. Tsuchihashi, E. Sekido and Y. Nakatani: J. Ceram. Assoc. Japan **66** (1958) 233.
4) S. Tsuchihashi and Y. Nakatani: J. Ceram. Assoc. Japan **67** (1959) 269†.
5) K. Kinosita and K. Natsume: J. Appl. Phys. Japan **28** (1959) 39†.
6) K. Natsume and K. Kinosita: J. Appl. Phys. Japan **28** (1959) 132†.
7) K. Kinosita and K. Natsume: J. Appl. Phys. Japan **28** (1959) 297†.
8) K. Natsume: J. Appl. Phys. Japan **29** (1960) 175†.
9) S. Tsuchihashi: Bull. Chem. Soc. Japan **24** (1951) 161.
10) S. Tsuchihashi and E. Sekido: Bull. Chem. Soc. Japan **32** (1959) 868.
11) S. Tsunekane and Y. Doi: J. Mech. Lab. (Tokyo) **13** (1959) 106†.
12) S. Tsunekane: to be published in J. Appl. Phys. Japan†.
13) T. Kurita and H. Hasunuma: J. Appl. Phys. Japan **28** (1959) 141†; *ibid.* **28** (1959) 539†.
14) M. Kawahara, T. Kurita and H. Hasunuma: J. Appl. Phys. Japan **28** (1959) 547*.
15) Y. Ishida and Y. Doi: J. Mech. Lab. (Tokyo) **12** (1958) 206†.
16) Y. Doi: J. Appl. Phys. Japan **25** (1956) 469*.
17) K. Miyake: Science of Light (Tokyo) **5** (1956) 130; *ibid.* **6** (1957) 85.
18) Y. Doi and Y. Ishida: J. Mech. Lab. (Tokyo) **12** (1958) 201†.
19) Y. Wada and H. Hirose: unpublished.
20) F. Abelès: Compt. rend. **228** (1949) 553.
21) K. Kinosita, T. Matsumoto, K. Natsume and M. Yoshida: J. Appl. Phys. Japan **29** (1960) 205.
22) A. C. Traub and H. Osterberg: J. Opt. Soc. Amer. **47** (1957) 62.
23) K. Kinosita and S. Nomura: J. Phys. Soc. Japan **13** (1958) 1485.
24) K. Kinosita: J. Phys. Soc. Japan **8** (1953) 782.
25) S. Brunauer, L. S. Deming, W. S. Deming and E. Teller: J. Amer. Chem. Soc. **62** (1940) 1723.
26) S. Brunauer, P. H. Emmett and E. Teller: J. Amer. Chem, Soc. **60** (1938) 309.
27) P. Kubelka: Kolloid-Z. **55** (1931) 129.
28) A. Vašíček: Kolloid-Z. **86** (1939) 288; Phys. Rev. **57** (1940) 925; Mitteil. d. Tschech. Akad. d. Wiss. **LI** (1941) Nr. 20.
29) J. Sawai, M. Tashiro, K. Umeya and Y. Kanzaki: J. Ceram. Assoc. Japan **52** (1944) 258†.
30) F. L. Bishop: J. Amer. Ceram. Soc. **27** (1944) 145.
31) S. Anderson and D. D. Kimpton: J. Amer. Ceram. Soc. **33** (1950) 45; **36** (1953) 175.
32) M. Hara: Rep. Res. Lab. Asahi Glass Company **2** (1952) 35†.
33) K. Kinosita: J. Opt. Soc. Amer. **43** (1953) 924.
34) "*The Structure of Glass, Proceedings of a Conference on the Structure of Glass, Leningrad*, 1953", p. 125. English translation from Russian, New York, 1958.
35) M. Watanabe, H. Noake and T. Aiba: J. Amer. Ceram. Soc. **42** (1959) 593.
36) See, *e.g.*, F. L. Jones and H. J. Homer: J. Opt. Soc. Amer. **31** (1941) 34.

---

* Written in Japanese.

† Text in Japanese. Synopsis and figure- and table-captions given in English.

JOURNAL OF THE PHYSICAL SOCIETY OF JAPAN, Vol. 16, No. 4, APRIL, 1961

Diffraction of Plane Sound Wave by Many Equal Circular Holes Arbitrarily Distributed in an Infinitely Large Rigid Plane Plate

By Yûkichi NOMURA
Department of Applied Science, Tôhoku University,
and Tadao OSANAI
Department of Education, Tôhoku University

(Received December 28, 1960)

The solution of the problem, when the holes do not overlap but are distributed arbitrarily in one plane, is obtained by the method of expansion in hypergeometrical polynomials. Formulae of some physical quantities concerned are given. In the case of normal incidence, we also give approximate formulae which are valid when the wave length is large in comparison with the radius.

§ 1. Introduction

The problem of diffracttion of plane wave by a circular plate or circular hole has been solved by Meixner and Andrejewsky[1], Bouwkamp[2], Nimura[3], and other authors by making use of spheroidal coordinates and spheroidal wave functions. One of the present authors[4),5] has succeeded in solving the same problem by using cylindrical coordinates, the discontinuous integral of Weber-Schafheitlin, and the expansion by hypergeometrical polynomials. Following this method, in the familiar coordinate system, and utilizing the addition theorem of Bessel function, we can also solve by perturbation the case of many circular plates or circular holes. In the previous paper[6], we have treated the case of two equal non-overlapping circular holes made in a rigid plane plate. Now we show that the calculation can be easily adapted to the case of any number of non-overlapping equal circular holes arbitrarily distributed in one plane.

By the results, we know that the series of successive approximation, being the functions of wave length and its ratios to the distances between the centres of the holes, has good convergency if the wave length is large.

§ 2. General Solution

Let x, y-axes of rectangular coordinates lie in the rigid plane, origin being arbitrarily taken in this plane. The centres of the circular holes with the same radius a, can be denoted by x_l, y_l ($l=1, 2, 3, \cdots, \mathrm{N}$), or more conveniently by polar coordinates ϖ_l, ψ_l. We denote the distance from the centre x_l, y_l to any other centre $x_{l'}$, $y_{l'}$ by $aq_{l'l}$, its direction from the x-axis being indicated by the angle $\psi_{l'l}$. Cf. Fig. 1.:

$$aq_{l'l}=\sqrt{(x_{l'}-x_l)^2+(y_{l'}-y_l)^2}>2a\ ,$$

$$\cos\psi_{l'l}=\frac{x_{l'}-x_l}{aq_{l'l}}\ ,\qquad \sin\psi_{l'l}=\frac{y_{l'}-y_l}{aq_{l'l}}\ .$$

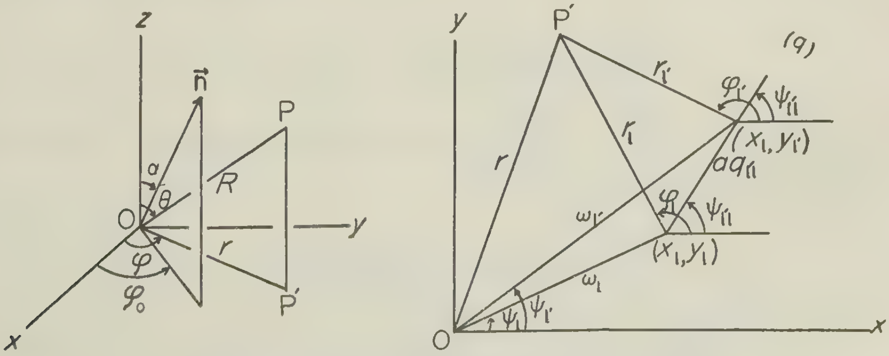

Fig. 1.

Any point P shall be indicated by the polar coordinates R, θ, φ, or more conveniently by the cylindrical ones r, φ, z. The distance from the l-th centre to the point $P'(r, \varphi, 0)$ shall be denoted by r_l. We shall suppose that a plane sound wave comes, whose normal is expressed by unit vector

$$\vec{n}(\sin\alpha\cos\varphi_0, \sin\alpha\sin\varphi_0, \cos\alpha) \ .$$

When the velocity potential for the acoustic field is expressed by $\Phi e^{i\omega t}$, Φ must satisfy the following wave equation:

$$(\nabla^2+k^2)\Phi=0 \ , \tag{1}$$

where $k=(\omega/c)=(2\pi/\lambda)$ in which c is the propagation velocity of sound and λ the wave length.

In the present case, we can put

$$\Phi=\begin{cases} \Phi_0+\overline{\Phi}_0+\sum\limits_{l=1}^{N}\Phi_l \ , & z<0 \\ \sum\limits_{l=1}^{N}\Phi_l \ , & z>0 \end{cases} \tag{2}$$

where Φ_0 and $\overline{\Phi}_0$ are the velocity potential of the incident and the reflected wave respectively,

$$\begin{aligned}\Phi_0&=C\exp\{-ikz\cos\alpha-ikr\sin\alpha\cos(\varphi-\varphi_0)\}\\ &=C\exp\{-ikz\cos\alpha-ik\varpi_l\sin\alpha\cos(\psi_l-\varphi_0)-ikr_l\sin\alpha\cos(\varphi_l-\varphi_0)\}\\ &=C\exp(-ikz\cos\alpha)\sum_{m=0}^{\infty}(2)_m(-i)^m J_m(kr\sin\alpha)\cos m(\varphi-\varphi_0)\\ &=C\exp\{-ikz\cos\alpha-ik\varpi_l\sin\alpha\cos(\psi_l-\varphi_0)\}\sum_{m=0}^{\infty}(2)_m(-i)^m J_m(kr_l\sin\alpha)\cos m(\varphi_l-\varphi_0) \ ,\end{aligned} \tag{3}$$

$$\begin{aligned}\overline{\Phi}_0&=C\exp\{ikz\cos\alpha-ikr\sin\alpha\cos(\varphi-\varphi_0)\}\\ &=C\exp\{ikz\cos\alpha-ik\varpi_l\sin\alpha\cos(\psi_l-\varphi_0)-ikr_l\sin\alpha\cos(\varphi_l-\varphi_0)\} \ ,\end{aligned} \tag{4}$$

and $\sum\limits_{l=1}^{N}\Phi_l$ is that of the scattered wave,

$$\Phi_l=\sum_{s=0}^{\infty}\Phi_l^{(s)} \ , \tag{5}$$

$$\Phi_l^{(s)}=\pm C\sum_{m=0}^{\infty}\sum_{n=0}^{\infty}({}_lA_{mn}^{(s)}\cos m\varphi_l+{}_lB_{mn}^{(s)}\sin m\varphi_l)S_{mn}(r_l, \mp z) \ , \qquad z\gtrless 0 \tag{6}$$

$$S_{mn}(r_l, \mp z)=\int_0^{\infty}\frac{\sqrt{\xi}\,J_m((r_l/a)\xi)\,J_{m+2n+(1/2)}(\xi)}{\sqrt{\xi^2-(ka)^2}}\exp\left\{\mp\sqrt{\xi^2-(ka)^2}\frac{z}{a}\right\}d\xi \tag{7}$$

in which $\Phi_l^{(0)}$ represents the scattered potential due to the l-th hole only, and $\sum\limits_{l=1}^{N}\Phi_l^{(s)}$ the s-th perturbed potential.

§ 3. Boundary Conditions

On the plate where $z=0$ and $r_l>a$ (for all $l=1, 2, 3, \cdots, N$), $\partial\Phi/\partial z$ must vanish. And, in the holes where $z=0$ and $r_l<a$ (for any $l=1, 2, 3, \cdots, N$), $\partial\Phi/\partial z$ and Φ must be continuous.

Since

$$\left[\frac{\partial S_{mn}(r_l, \mp z)}{\partial z}\right]_{z=0}=0 \ , \qquad r_l>a \tag{8}$$

we see that $[\partial\Phi/\partial z]_{z=0}=0$, provided that $r_l>a$. And since $\pm(\partial S_{mn}/\partial z)$ is continuous for $z=0$, we see that $\partial\Phi/\partial z$ is continuous in the holes.

The condition of the continuity of Φ is

$$[\Phi_0+\overline{\Phi}_0]_{z=0}+\left[\sum_{l=0}^{N}\Phi_l\right]_{z=-0}=\left[\sum_{l=1}^{N}\Phi_l\right]_{z=+0} \ ,$$

i.e.

$$[\Phi_0]_{z=0}=\left[\sum_{l=1}^{N}\Phi_l\right]_{z=+0}=\left[\sum_{l=1}^{N}\sum_{s=0}^{\infty}\Phi_l^{(s)}\right]_{z=+0} \ , \tag{9}$$

which shall be satisfied, provided

$$r_l<a: \qquad [\Phi_l{}^{(0)}]_{z=+0}=[\Phi_0]_{z=0}\ , \tag{10}$$

$$[\Phi_l{}^{(s)}]_{z=+0}=-\sum_{l'=1}^{N}{}' \,[\Phi_{l'}^{(s-1)}]_{z=+0}\ , \qquad s=1,2,3,\cdots \tag{11}$$

where Σ' means the summation excluding $l'=l$.

§4. Determination of the Constants

From the condition (10), we have

$$\begin{aligned}&C\sum_{m=0}^{\infty}\sum_{n=0}^{\infty}({}_lA_{mn}^{(0)}\cos m\varphi_l+{}_lB_{mn}^{(0)}\sin m\varphi_l)S_{mn}(r_l,0)\\ &=C\exp\{-ik\varpi_l\sin\alpha\cos(\psi_l-\varphi_0)\}\sum_{m=0}^{\infty}(2)_m(-i)^m J_m(kr_l\sin\alpha)\cos m(\varphi_l-\varphi_0)\ .\end{aligned} \tag{12}$$

If we utilize the hypergeometrical polynomials(7)

$$\left.\begin{aligned}u_n{}^m(x)&=x^{-m/2}\int_0^{\infty}\frac{J_m(\sqrt{x}\,\xi)J_{m+2n+(1/2)}(\xi)}{\sqrt{\xi}}\,d\xi\\ &=\frac{\Gamma(m+n+(1/2))}{n!\sqrt{2}\,\Gamma(m+1)}F(m+n+(1/2),-n,m+1;x)\\ &=\frac{\Gamma(m+n+(1/2))}{n!\sqrt{2}\,\Gamma(m+n+1)}x^{-m}(1-x)^{1/2}\frac{d^n}{dx^n}\{x^{m+n}(1-x)^{n-(1/2)}\}\ ,\end{aligned}\right]\quad 0<x<1 \tag{13}$$

we can expand any function $f_m(x)$ as follows;

$$f_m(x)=x^{m/2}\sum_{n=0}^{\infty}C_n{}^m u_n{}^m(x)\ , \tag{14}$$

where

$$C_n{}^m=\frac{\sqrt{2}\,(m+2n+(1/2))}{\Gamma(n+(1/2))}\int_0^1 x^{-(m/2)}f_m(x)\frac{d^n}{dx^n}\{x^{m+n}(1-x)^{n-(1/2)}\}\,dx\ . \tag{15}$$

Thus, we get

$$(2)_m(-i)^m J_m(kr_l\sin\alpha)=x^{m/2}\sum_{n=0}^{\infty}\beta_n{}^m u_n{}^m(x)\ , \tag{16}$$

$$S_{mn}(r_l,0)=x^{m/2}\sum_{\nu=0}^{\infty}G_{n\nu}^{m}u_\nu{}^m(x)\ , \tag{17}$$

where

$$x=\left(\frac{r_l}{a}\right)^2, \tag{18}$$

$$\beta_n{}^m=(2)_m(-i)^m(2m+4n+1)\frac{J_{m+2n+(1/2)}(ka\sin\alpha)}{\sqrt{ka\sin\alpha}}\ , \tag{19}$$

$$G_{n\nu}^{m}=(2m+4\nu+1)\int_0^{\infty}\frac{J_{m+2\nu+(1/2)}(\xi)J_{m+2n+(1/2)}(\xi)}{\sqrt{\xi^2-(ka)^2}}\,d\xi\ . \tag{20}$$

Therefore, (12) becomes

$$\begin{aligned}&C\sum_{m=0}^{\infty}\sum_{n=0}^{\infty}({}_lA_{mn}^{(0)}\cos m\varphi_l+{}_lB_{mn}^{(0)}\sin m\varphi_l)x^{m/2}\sum_{\nu=0}^{\infty}G_{n\nu}^{m}u_\nu{}^m(x)\\ &=C\exp\{-ik\varpi_l\sin\alpha\cos(\psi_l-\varphi_0)\}\sum_{m=0}^{\infty}x^{m/2}\sum_{n=0}^{\infty}\beta_n{}^m u_n{}^m(x)\{\cos m\varphi_l\cos m\varphi_0+\sin m\varphi_l\sin m\varphi_0\}\ ,\end{aligned}$$

from which we get, by interchanging the letters n and ν in the left hand side,

$$\sum_{\nu=0}^{\infty} G_{\nu n}^{m} \begin{matrix} {}_{l}A_{m\nu}^{(0)} \\ {}_{l}B_{m\nu}^{(0)} \end{matrix} = \beta_n^m \exp\{-ik\varpi_{l}\sin\alpha\cos(\psi_l-\varphi_0)\} \begin{matrix}\cos m\varphi_0 \\ \sin m\varphi_0\end{matrix} \equiv \begin{matrix} {}_{l}a_n^m \\ {}_{l}b_n^m \end{matrix} . \tag{21}$$

Using the solution X_{sn}^{m}, whose numerical tables are already given[4], of the equations

$$\sum_{\nu=0}^{\infty} X_{\nu s}^{m} G_{\nu n}^{m} = \delta_{ns} , \tag{22}$$

we obtain

$$ {}_{l}A_{mn}^{(0)} = \sum_{\nu=0}^{\infty} {}_{l}a_{\nu}^{m} X_{n\nu}^{m} , \qquad {}_{l}B_{mn}^{(0)} = \sum_{\nu=0}^{\infty} {}_{l}b_{\nu}^{m} X_{n\nu}^{m} . \tag{23}$$

By the addition theorem, we have

$$J_m\left(\frac{r_{l'}}{a}\xi\right)\cos m(\varphi_{l'}-\psi_{l'l})$$
$$=(-1)^m \sum_{h=0}^{\infty} \frac{(2)_h}{2} J_h\left(\frac{r_l}{a}\xi\right)\{J_{m+h}(q_{l'l}\xi)+(-1)^h J_{m-h}(q_{l'l}\xi)\}\cos h(\varphi_l-\psi_{l'l}) , \tag{24}$$

$$J_m\left(\frac{r_{l'}}{a}\xi\right)\sin m(\varphi_{l'}-\psi_{l'l})$$
$$=(-1)^{m+1} \sum_{h=0}^{\infty} \frac{(2)_h}{2} J_h\left(\frac{r_l}{a}\xi\right)\{J_{m+h}(q_{l'l}\xi)-(-1)^h J_{m-h}(q_{l'l}\xi)\}\sin h(\varphi_l-\psi_{l'l}) , \tag{25}$$

from which we get

$$J_m\left(\frac{r_{l'}}{a}\xi\right)\cos m\varphi_{l'}$$
$$=(-1)^m \sum_{h=0}^{\infty} \frac{(2)_h}{2} J_h\left(\frac{r_l}{a}\xi\right)\{J_{m+h}(q_{l'l}\xi)\cos(h+m)\psi_{l'l}+(-1)^h J_{m-h}(q_{l'l}\xi)\cos(h-m)\psi_{l'l}\}\cos h\varphi_l$$
$$+(-1)^m \sum_{h=0}^{\infty} \frac{(2)_h}{2} J_h\left(\frac{r_l}{a}\xi\right)\{J_{m+h}(q_{l'l}\xi)\sin(h+m)\psi_{l'l}+(-1)^h J_{m-h}(q_{l'l}\xi)\sin(h-m)\psi_{l'l}\}\sin h\varphi_l , \tag{26}$$

$$J_m\left(\frac{r_{l'}}{a}\xi\right)\sin m\varphi_{l'}$$
$$=(-1)^m \sum_{h=0}^{\infty} \frac{(2)_h}{2} J_h\left(\frac{r_l}{a}\xi\right)\{J_{m+h}(q_{l'l}\xi)\sin(h+m)\psi_{l'l}-(-1)^h J_{m-h}(q_{l'l}\xi)\sin(h-m)\psi_{l'l}\}\cos h\varphi_l$$
$$+(-1)^m \sum_{h=0}^{\infty} \frac{(2)_h}{2} J_h\left(\frac{r_l}{a}\xi\right)\{-J_{m+h}(q_{l'l}\xi)\cos(h+m)\psi_{l'l}+(-1)^h J_{m-h}(q_{l'l}\xi)\cos(h-m)\psi_{l'l}\}\sin h\varphi_l . \tag{27}$$

Putting (26), (27) into (6), (7), we obtain

$$\Phi_{l'}^{(s-1)}=\pm C\sum_{m=0}^{\infty}\sum_{n=0}^{\infty}(-1)^m\sum_{h=0}^{\infty}\frac{(2)_h}{2}\cos h\varphi_l$$
$$\times\int_0^{\infty}J_h\left(\frac{r_l}{a}\xi\right)\Big[\{J_{m+h}(q_{l'l}\xi)\cos(h+m)\psi_{l'l}+(-1)^h J_{m-h}(q_{l'l}\xi)\cos(h-m)\psi_{l'l}\}{}_{l'}A_{mn}^{(s-1)}$$
$$+\{J_{m+h}(q_{l'l}\xi)\sin(h+m)\psi_{l'l}-(-1)^h J_{m-h}(q_{l'l}\xi)\sin(h-m)\psi_{l'l}\}{}_{l'}B_{mn}^{(s-1)}\Big]$$
$$\times\frac{\sqrt{\xi}\,J_{m+2n+(1/2)}(\xi)\exp\{\mp\sqrt{\xi^2-(ka)^2}\,(z/a)\}}{\sqrt{\xi^2-(ka)^2}}d\xi$$
$$\pm C\sum_{m=0}^{\infty}\sum_{n=0}^{\infty}(-1)^m\sum_{h=0}^{\infty}\frac{(2)_h}{2}\sin h\varphi_l$$
$$\times\int_0^{\infty}J_h\left(\frac{r_l}{a}\xi\right)\Big[\{J_{m+h}(q_{l'l}\xi)\sin(h+m)\psi_{l'l}+(-1)^h J_{m-h}(q_{l'l}\xi)\sin(h-m)\psi_{l'l}\}{}_{l'}A_{mn}^{(s-1)}$$

$$
\begin{aligned}
&+\{-J_{m+h}(q_{l'l}\xi)\cos(h+m)\psi_{l'l}+(-1)^h J_{m-h}(q_{l'l}\xi)\cos(h-m)\psi_{l'l}\}\,{}_{l'}B_{mn}^{(s-1)}\Big]\\
&\times\frac{\sqrt{\xi}\,J_{m+2n+(1/2)}(\xi)\exp\{\mp\sqrt{\xi^2-(ka)^2}(z/a)\}}{\sqrt{\xi^2-(ka)^2}}\,d\xi\;,
\end{aligned}
$$

which becomes, by interchanging the letters m and h,

$$
\begin{aligned}
\Phi_{l'}^{(s-1)}=&\pm C\sum_{m=0}^{\infty}\cos m\varphi_l\sum_{h=0}^{\infty}\sum_{n=0}^{\infty}(-1)^h\\
&\times\Big[{}_{l'}A_{hn}^{(s-1)}\{S_{m,n}^{h}(r_l,q_{l'l},\mp z)\cos(m+h)\psi_{l'l}+(-1)^m S_{-m,n}^{h}(r_l,q_{l'l},\mp z)\cos(m-h)\psi_{l'l}\}\\
&+{}_{l'}B_{hn}^{(s-1)}\{S_{m,n}^{h}(r_l,q_{l'l},\mp z)\sin(m+h)\psi_{l'l}-(-1)^m S_{-m,n}^{h}(r_l,q_{l'l},\mp z)\sin(m-h)\psi_{l'l}\}\Big]\\
&\pm C\sum_{m=0}^{\infty}\sin m\varphi_l\sum_{h=0}^{\infty}\sum_{n=0}^{\infty}(-1)^h\\
&\times\Big[{}_{l'}A_{hn}^{(s-1)}\{S_{m,n}^{h}(r_l,q_{l'l},\mp z)\sin(m+h)\psi_{l'l}+(-1)^m S_{-m,n}^{h}(r_l,q_{l'l},\mp z)\sin(m-h)\psi_{l'l}\}\\
&+{}_{l'}B_{hn}^{(s-1)}\{-S_{m,n}^{h}(r_l,q_{l'l},\mp z)\cos(m+h)\psi_{l'l}+(-1)^m S_{-m,n}^{h}(r_l,q_{l'l},\mp z)\cos(m-h)\psi_{l'l}\}\Big]\,,
\end{aligned}
\tag{28}
$$

where

$$
\begin{aligned}
&S_{\pm m,n}^{h}(r_l,q_{l'l},\mp z)\\
&\quad=\frac{(2)_m}{2}\int_0^\infty\frac{\sqrt{\xi}\,J_m((r_l/a)\xi)J_{h\pm m}(q_{l'l}\xi)J_{h+2n+(1/2)}(\xi)}{\sqrt{\xi^2-(ka)^2}}\exp\left\{\mp\sqrt{\xi^2-(ka)^2}\,\frac{z}{a}\right\}d\xi\;.
\end{aligned}
\tag{29}
$$

Utilizing $u_n{}^m(x)$, we get

$$
S_{\pm m.n}^{h}(r_l,q_{l'l},0)=x^{m/2}\sum_{\nu=0}^{\infty}G_{n\nu}^{\pm m,h}(q_{l'l})u_\nu{}^m(x)\;,\qquad x=\left(\frac{r_l}{a}\right)^2
\tag{30}
$$

$$
G_{n\nu}^{\pm m,h}(q_{l'l})=\frac{(2)_m}{2}(2m+4\nu+1)\int_0^\infty\frac{J_{h\pm m}(q_{l'l}\xi)J_{m+2\nu+(1/2)}(\xi)J_{h+2n+(1/2)}(\xi)}{\sqrt{\xi^2-(ka)^2}}\,d\xi\;.
\tag{31}
$$

Thus, from the condition (11) we have

$$
\begin{aligned}
&\sum_{n=0}^{\infty}{}_lA_{mn}^{(s)}\sum_{\nu=0}^{\infty}G_{n\nu}^{m}u_\nu{}^m(x)\\
&=-\sum_{l'=1}^{N}{}'\sum_{\nu=0}^{\infty}u_\nu{}^m(x)\sum_{h=0}^{\infty}\sum_{n=0}^{\infty}\Big[\{G_{n\nu}^{m,h}(q_{l'l})\cos(m+h)\psi_{l'l}+(-1)^m G_{n\nu}^{-m\ h}(q_{l'l})\cos(m-h)\psi_{l'l}\}(-1)^h\,{}_{l'}A_{hn}^{(s-1)}\\
&\qquad+\{G_{n\nu}^{m,n}(q_{l'l})\sin(m+h)\psi_{l'l}-(-1)^m G_{n\nu}^{-m,h}(q_{l'l})\sin(m-h)\psi_{l'l}\}(-1)^h\,{}_{l'}B_{hn}^{(s-1)}\Big]\,,
\end{aligned}
$$

i.e., interchanging the letters n and ν,

$$
\begin{aligned}
&\sum_{\nu=0}^{\infty}G_{\nu n}^{m}\,{}_lA_{m\nu}^{(s)}\\
&\quad=-\sum_{l'=0}^{N}{}'\sum_{h=0}^{\infty}\sum_{\nu=0}^{\infty}\Big[\{G_{\nu n}^{m,h}(q_{l'l})\cos(m+h)\psi_{l'l}+(-1)^m G_{\nu n}^{-m,h}(q_{l'l})\cos(m-h)\psi_{l'l}\}(-1)^h\,{}_{l'}A_{h\nu}^{(s-1)}\\
&\qquad+\{G_{\nu n}^{m,h}(q_{l'l})\sin(m+h)\psi_{l'l}-(-1)^m G_{\nu n}^{-m,h}(q_{l'l})\sin(m-h)\psi_{l'l}\}(-1)^h\,{}_{l'}B_{h\nu}^{(s-1)}\Big]\,,
\end{aligned}
\tag{32}
$$

and similarly,

$$\sum_{\nu=0}^{\infty} G_{\nu n}^{m}\,{}_{l}B_{m\nu}^{(s)}$$

$$=-\sum_{l'=1}^{N}{}' \sum_{h=0}^{\infty} \sum_{\nu=0}^{\infty} \Big[\{G_{\nu n}^{m,h}(q_{l'l}) \sin (m+h)\psi_{l'l}+(-1)^{m} G_{\nu n}^{-m,h}(q_{l'l}) \sin (m-h)\psi_{l'l}\}(-1)^{h}\,{}_{l'}A_{h\nu}^{(s-1)}$$

$$+\{-G_{\nu n}^{m,h}(q_{l'l}) \cos (m+h)\psi_{l'l}+(-1)^{m}G_{\nu n}^{-m,h}(q_{l'l}) \cos (m-h)\psi_{l'l}\}(-1)^{h}\,{}_{l'}B_{h\nu}^{(s-1)}\Big]. \tag{33}$$

Put

$$\begin{matrix} a_{mn}^{(s-1)}(q_{l'l}) \\ \bar{a}_{mn}^{(s-1)}(q_{l'l}) \end{matrix}$$

$$=-\sum_{h=0}^{\infty} \sum_{\nu=0}^{\infty} \left\{G_{\nu n}^{m,h}(q_{l'l}) \begin{matrix}\cos\\ \sin\end{matrix} (m+h)\psi_{l'l}+(-1)^{m} G_{\nu n}^{-m,h}(q_{l'l}) \begin{matrix}\cos\\ \sin\end{matrix} (m-h)\psi_{l'l}\right\}(-1)^{h}\,{}_{l'}A_{h\nu}^{(s-1)}\ , \tag{34}$$

$$\begin{matrix} b_{mn}^{(s-1)}(q_{l'l}) \\ \bar{b}_{mn}^{(s-1)}(q_{l'l}) \end{matrix}$$

$$=\pm\sum_{h=0}^{\infty} \sum_{\nu=0}^{\infty} \left\{G_{\nu n}^{m,h}(q_{l'l}) \begin{matrix}\cos\\ \sin\end{matrix} (m+h)\psi_{l'l}-(-1)^{m} G_{\nu n}^{-m,h}(q_{l'l}) \begin{matrix}\cos\\ \sin\end{matrix} (m-h)\psi_{l'l}\right\}(-1)^{h}\,{}_{l'}B_{h\nu}^{(s-1)}\ , \tag{35}$$

then

$${}_{l}A_{mn}^{(s)}=\sum_{l'=1}^{N}{}' \sum_{\nu=1}^{\infty} \{a_{m\nu}^{(s-1)}(q_{l'l})+\bar{b}_{m\nu}^{(s-1)}(q_{l'l})\}X_{n\nu}^{m}\ , \tag{36}$$

$${}_{l}B_{mn}^{(s)}=\sum_{l'=1}^{N}{}' \sum_{\nu=0}^{\infty} \{\bar{a}_{m\nu}^{(s-1)}(q_{l'l})+b_{m\nu}^{(s-1)}(q_{l'l})\}X_{\nu n}^{m}\ . \tag{37}$$

Thus, we see that ${}_{l}A_{mn}^{(s)}$ and ${}_{l}B_{mn}^{(s)}$ can be calculated if $G_{n\nu}^{\pm m,h}(q_{l'l})$ is evaluated.

§ 5. Evaluation of $G_{n\nu}^{\pm m,h}(q)$

We shall evaluate the integral $G_{n\nu}^{\pm m,h}(q)$. Putting $ka=\gamma$, we have

$$G_{n\nu}^{\pm m,h}(q)=\frac{(2)_m}{2}(2m+4\nu+1)\int_0^{\infty}\frac{J_{h\pm m}(q\xi)J_{m+2\nu+(1/2)}(\xi)J_{h+2n+(1/2)}(\xi)}{\sqrt{\xi^2-\gamma^2}}\,d\xi$$

$$=\frac{(2)_m}{2}(2m+4\nu+1)\{R_{n\nu}^{\pm m,h}-iI_{n\nu}^{\pm m,h}\}\ ,$$

where

$$R_{n\nu}^{\pm m,h}=\int_{\gamma}^{\infty}\frac{J_{h\pm m}(q\xi)J_{m+2\nu+(1/2)}(\xi)J_{h+2n+(1/2)}(\xi)}{\sqrt{\xi^2-\gamma^2}}\,d\xi\ ,$$

$$I_{n\nu}^{\pm m,h}=\int_{0}^{\gamma}\frac{J_{h\pm m}(q\xi)J_{m+2\nu+(1/2)}(\xi)J_{h+2n+(1/2)}(\xi)}{\sqrt{\gamma^2-\xi^2}}\,d\xi\ .$$

These integrals can be calculated as shown in the appendices I, II, III and IV of our previous paper[6]. The results are as follows: When $h\pm m\geqq 0$,

$$R_{n\nu}^{\pm m,h}=\frac{\sqrt{\pi}}{2}\sum_{\mu=0}^{\infty}\frac{(-1)^{\mu}}{\mu!}\frac{(\gamma/2)^{2\mu}}{\Gamma(-\mu+(1/2))}q^{2\mu-h-2\nu-m-2n-1}\sum_{l=0}^{\infty}\frac{(-1)^{l}}{l!}$$

$$\times\frac{q^{-2l}\Gamma\{h+\nu+((1\pm1)/2)m+n-\mu+l+(1/2)\}\Gamma(h+2\nu+m+2n+2+2l)}{\Gamma\{\mu-\nu-((1\mp1)/2)m-n-l+(1/2)\}\Gamma(h+2\nu+m+2n+2+l)\Gamma(m+2\nu+(3/2)+l)\Gamma(h+2n+(3/2)+l)} \tag{I}$$

$$=\left(\frac{\gamma}{2}\right)^{h+m+2\nu+2n+1}\sum_{s=0}^{\infty}\frac{(-1)^{s}\Gamma\{h+((1\pm1)/2)m+\nu+n+s+1\}\Gamma(h+m+2\nu+2n+2+2s)}{s!\,\Gamma(h+m+2\nu+2n+2+s)\Gamma(m+2\nu+(3/2)+s)\Gamma(h+2n+(3/2)+s)}\left(\frac{\gamma}{2}\right)^{2s}$$

$$\times\sum_{\mu=0}^{h+((1\pm1)/2)m+\nu+n+s}\frac{1}{\{h+((1\pm1)/2)m+\nu+n+s-\mu\}!}\frac{(2\mu)!}{(\mu!)^2 2^{\mu}}(q\gamma)^{-\mu}\sqrt{\frac{\pi}{2q\gamma}}\,J_{h\pm m-\mu-(1/2)}(q\gamma)\ , \tag{II}$$

and when $h-m<0$, we can reduce it to the former case by the general relation

$$R_{n\nu}^{-m,h}=(-1)^{h-m}R_{\nu n}^{-h,m}\,.$$

And, we have in general

$$\begin{aligned}
I_{n\nu}^{\pm m,h}&=\frac{\sqrt{\pi}}{2}q^{h\pm m}\left(\frac{\gamma}{2}\right)^{2h+(1\pm1)m+2\nu+2n+1}\\
&\times\sum_{s=0}^{\infty}\frac{(-1)^s}{s!}\frac{\Gamma(h+m+2\nu+2n+2+2s)}{\Gamma(h+m+2\nu+2n+2+s)\Gamma(m+2\nu+(3/2)+s)\Gamma(h+2n+(3/2)+s)}\left(\frac{\gamma}{2}\right)^{2s}\\
&\times\sum_{\mu=0}^{\infty}\frac{(-1)^\mu}{\mu!}\frac{q^{2\mu}}{\Gamma(h\pm m+1+\mu)}\frac{\Gamma\{h+((1\pm1)/2)m+\nu+n+s+1+\mu\}}{\Gamma\{h+((1\pm1)/2)m+\nu+n+s+(3/2)+\mu\}}\left(\frac{\gamma}{2}\right)^{2\mu} \qquad \text{(III)}\\
&=\left(\frac{\gamma}{2}\right)^{h+m+2\nu+2n+1}\\
&\times\sum_{s=0}^{\infty}\frac{(-1)^s\Gamma\{(1\mp1)/2)m+\nu+n+s+1\}\Gamma(h+m+2\nu+2n+2+2s)}{s!\,\Gamma(h+m+2\nu+2n+2+s)\Gamma(m+2\nu+(3/2)+s)\Gamma(h+2n+(3/2)+s)}\left(\frac{\gamma}{2}\right)^{2s}\\
&\times\sum_{\mu=0}^{((1\mp1)/2)m+\nu+n+s}(-1)^\mu\frac{1}{\{(1\mp1)/2)m+\nu+n+s-\mu\}!}\frac{(2\mu)!}{(\mu!)^2 2^\mu}(q\gamma)^{-\mu}\sqrt{\frac{\pi}{2q\gamma}}J_{h\pm m+\mu+(1/2)}(q\gamma)\,. \qquad \text{(IV)}
\end{aligned}$$

In the formulae (II) and (IV), when γ is small and the value of $q\gamma$ is not so small, we see that the term of the order $\gamma/2$ occurs only when $h=m=\nu=n=0$, $s=0$, and that the two terms of the order $(\gamma/2)^2$ occur when $h=1$, $m=\nu=n=s=0$ and $m=1$, $h=\nu=n=s=0$; in this way, we can have expressions of $R_{n\nu}^{\pm m,h}$, $I_{n\nu}^{\pm m,h}$ in power series of $\gamma/2=\beta$. And making use of the expressions[4] of X_{sn}^{m} in power series of β, we can get those of ${}_lA_{mn}^{(s)}$ and ${}_lB_{mn}^{(s)}$ (Cf. § 8.).

§ 6. Diffracted Field at Great Distance

For the scattered wave, we have

$$\Phi=\pm CV=\pm C\sum_{l=1}^{N}V_l\,, \qquad (38)$$

$$V_l=\sum_{m=0}^{\infty}\sum_{n=0}^{\infty}({}_lA_{mn}\cos m\varphi_l+{}_lB_{mn}\sin m\varphi_l)S_{mn}(r_l,\mp z)\,, \qquad (39)$$

where

$${}_lA_{mn}=\sum_{s=0}^{\infty}{}_lA_{mn}^{(s)}\,,\qquad {}_lB_{mn}=\sum_{s=0}^{\infty}{}_lB_{mn}^{(s)}\,. \qquad (40)$$

We use the Kirchhoff solution of the wave equation (1)

$$V=\frac{1}{4\pi}\iint\left\{\frac{\exp(-ikR')}{R'}\frac{\partial V}{\partial n}-V\frac{\partial}{\partial n}\left(\frac{\exp(-ikR')}{R'}\right)\right\}dS_l \qquad (41)$$

to obtain the value of V at a distant point. Here, R' is the distance R_l' between the point Q_l lying in the l-th hole and the distant point P. Cf. Fig. 2.* The integration is to be performed on both sides S_l^+ and S_l^- enclosing the l-th hole:

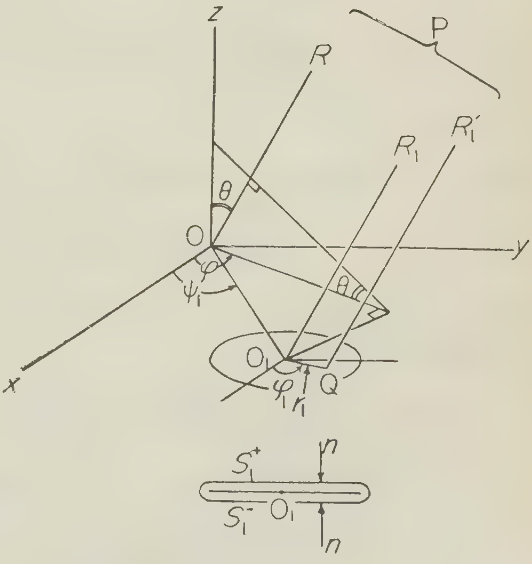

Fig. 2.

---

* Notice that the meanings of the symbols r_l, φ_l in Fig. 2 are just those in the right hand one of Fig. 1, if we identify Q_l and P′.

$$S_l = S_l^+ + S_l^- \,, \qquad l = 1, 2, 3, \cdots, \mathrm{N}\,. \tag{42}$$

Evidently

$$\left(\frac{\partial V_l}{\partial n}\right)_{S_l^+} = -\left(\frac{\partial V_l}{\partial z}\right)_{S_l^+} = \left(\frac{\partial V_l}{\partial z}\right)_{S_l^-} - \left(\frac{\partial V_l}{\partial n}\right)_{S_l^-}\,, \tag{43}$$

$$\left(\frac{\partial V}{\partial z}\right)_{S_l^-} = \left(\frac{\partial V_l}{\partial z}\right)_{S_l^-}\,, \tag{44}$$

$$\left(\frac{\partial}{\partial n}\frac{\exp(-ikR')}{R'}\right)_{S^+} = -\left(\frac{\partial}{\partial n}\frac{\exp(-ikR')}{R'}\right)_{S^-}\,. \tag{45}$$

Therefore

$$V = \frac{1}{2\pi}\sum_{l=1}^{\mathrm{N}}\int \frac{\exp(-ikR_l')}{R_l'}\frac{\partial V_l}{\partial z}\,dS_l^-\,. \tag{46}$$

Now, P being sufficiently distant, we may put

$$R_l = R - \varpi_l \sin\theta\cos(\varphi-\psi_l)\,, \tag{47}$$

$$R_l' = R_l - r_l \sin\theta\cos(\varphi-\varphi_l)\,. \tag{48}$$

And so, we get

$$\begin{aligned} V_l &= \frac{1}{2\pi}\int \frac{\exp(-ikR_l')}{R_l'}\frac{\partial V_l}{\partial z}\,dS_l^- \\ &= \frac{1}{2\pi}\frac{\exp(-ikR_l)}{aR}\sum_{m=0}^{\infty}\sum_{n=0}^{\infty}\int_0^a r_l\,dr_l\int_0^{\infty}\sqrt{\xi}\,J_m\!\left(\frac{r_l}{a}\xi\right)J_{m+2n+(1/2)}(\xi)\,d\xi \\ &\quad\times\int_0^{2\pi}\exp\{ikr_l\sin\theta\cos(\varphi-\varphi_l)\}({}_lA_{mn}\cos m\varphi_l + {}_lB_{mn}\sin m\varphi_l)\,d\varphi_l \qquad (49) \\ &= \sqrt{\frac{2}{\pi}}\,a\,\frac{\exp\{-ikR+ik\varpi_l\sin\theta\cos(\varphi-\psi_l)\}}{R} \\ &\quad\times\sum_{m=0}^{\infty}\sum_{n=0}^{\infty}(i)^m({}_lA_{mn}\cos m\varphi + {}_lB_{mn}\sin m\varphi)\,j_{m+2n}(ka\sin\theta)\,. \qquad (50) \end{aligned}$$

Thus, we obtain

$$\begin{aligned} \varPhi &= \pm\sqrt{\frac{2}{\pi}}\,aC\,\frac{\exp(-ikR)}{R}\sum_{m=0}^{\infty}\sum_{n=0}^{\infty}(i)^m j_{m+2n}(ka\sin\theta) \\ &\quad\times\sum_{l=1}^{\mathrm{N}}\exp\{ik\varpi_l\sin\theta\cos(\varphi-\psi_l)\}({}_lA_{mn}\cos m\varphi + {}_lB_{mn}\sin m\varphi)\,. \end{aligned} \tag{51}$$

At great distance from the holes, the energy flow (mean value about time) per unit solid angle in the direction θ, φ is

$$\begin{aligned} P(\theta,\varphi) &\equiv \frac{1}{2}\mathscr{R}_e\, i\omega\sigma\tilde{\varPhi}\frac{\partial\varPhi}{\partial R}R^2 = \frac{1}{2}\omega\sigma k\tilde{\varPhi}\varPhi R^2 \\ &= \frac{\omega\sigma k a^2|C|^2}{\pi}\sum_{l=1}^{\mathrm{N}}\left|\sum_{m=0}^{\infty}\sum_{n=0}^{\infty}({}_lA_{mn}\cos m\varphi + {}_lB_{mn}\sin m\varphi)\,j_{m+2n}(ka\sin\theta)\right|^2 \\ &\quad+\frac{\omega\sigma k a^2|C|^2}{\pi}\sum_{l=1}^{\mathrm{N}}\sum_{l'=1}^{\mathrm{N}}{}'\exp\{ik\varpi_l\sin\theta\cos(\varphi-\psi_l) - ik\varpi_{l'}\sin\theta\cos(\varphi-\varphi_{l'})\} \\ &\quad\times\sum_{m,n}\sum_{m',n'}(i)^m(-i)^{m'}({}_lA_{mn}\cos m\varphi + {}_lB_{mn}\sin m\varphi)({}_{l'}\tilde{A}_{m'n'}\cos m'\varphi + {}_{l'}\tilde{B}_{m'n'}\sin m'\varphi) \\ &\quad\times j_{m+2n}(ka\sin\theta)\,j_{m'+2n'}(ka\sin\theta)\,, \end{aligned} \tag{52}$$

where $\tilde{\Phi}$ is the conjugate of Φ, and σ the density of the air.

§ 7. Acoustic Impedance and Transmission Coefficient

If we denote by $(p)_l e^{i\omega t}$ the pressure at the l-th hole, we get

$$(p)_l = i\omega\sigma\Big[\sum_{l=1}^{\mathrm{N}} \Phi_l\Big]_{z=+0} = i\omega\sigma[\Phi_0]_{z=0}$$

$$= i\omega\sigma C \exp\{-ik\varpi_l \sin\alpha \cos(\psi_l - \varphi_0)\} \sum_{m=0}^{\infty} (2)_m (-i)^m J_m(kr_l \sin\alpha) \cos m(\varphi_l - \varphi_0)$$

$$= i\omega\sigma C \sum_{m=0}^{\infty} x^{m/2} \sum_{n=0}^{\infty} ({}_l a_n{}^m \cos m\varphi_l + {}_l b_n{}^m \sin m\varphi_l) u_n{}^m(x) \;, \tag{53}$$

conferring (9), (3), (21). Proceeding similarly as in the previous paper[6)], we obtain as to the l-th hole:

mean pressure
$$(p_m)_l = \frac{i\omega\sigma}{2\sqrt{2}} \sqrt{\pi}\, C \sum_{n=0}^{\infty} \frac{\Gamma(n+(1/2))}{n!\,(n+1)!\,\Gamma((3/2)-n)}\, {}_l a_n{}^0 \;, \tag{54}$$

mean velocity
$$(v_m)_l = \frac{2C}{a} \sqrt{\frac{2}{\pi}}\, {}_l A_{00} \;, \tag{55}$$

acoustic impedance
$$(Z_{ac})_l \equiv (R_{ac})_l + i(X_{ac})_l \equiv \frac{(p_m)_l}{(v_m)_l}$$

$$= \frac{i\pi\omega\sigma a}{8\, {}_l A_{00}} \sum_{n=0}^{\infty} \frac{\Gamma(n+(1/2))}{n!\,(n+1)!\,\Gamma((3/2)-n)}\, {}_l a_n{}^0 \;, \tag{57}$$

$$(R_{ac})_l = -\frac{\pi\omega\sigma a}{8} \sum_{n=0}^{\infty} \frac{\Gamma(n+(1/2))}{n!\,(n+1)!\,\Gamma((3/2)-n)}\, \mathscr{Im}\, \frac{{}_l a_n{}^0}{{}_l A_{00}} \;, \tag{58}$$

$$(X_{ac})_l = +\frac{\pi\omega\sigma a}{8} \sum_{n=0}^{\infty} \frac{\Gamma(n+(1/2))}{n!\,(n+1)!\,\Gamma((3/2)-n)}\, \mathscr{Re}\, \frac{{}_l a_n{}^0}{{}_l A_{00}} \;; \tag{59}$$

energy flow (mean value about time)

$$(W)_l = \omega\sigma |C|^2 a \sum_{m=0}^{\infty} \sum_{n=0}^{\infty} \frac{\pi}{(2)_m} \frac{1}{2m+4n+1}\, \mathscr{Im}\, ({}_l A_{mn}\, {}_l \tilde{a}_n{}^m + {}_l B_{mn}\, {}_l \tilde{b}_n{}^m) \;. \tag{60}$$

Energy flow from the whole holes:

$$W = \sum_{l=1}^{\mathrm{N}} (W)_l = \omega o |C|^2 a \sum_{m=0}^{\infty} \sum_{n=0}^{\infty} \frac{\pi}{(2)_m} \frac{1}{2m+4n+1} \sum_{l=1}^{\mathrm{N}} \mathscr{Im}\, ({}_l A_{mn}\, {}_l \tilde{a}_n{}^m + {}_l B_{mn}\, {}_l \tilde{b}_n{}^m) \tag{61}$$

$$= \int_0^{2\pi} d\varphi \int_0^{\pi/2} P(\theta, \varphi) \sin\theta\, d\theta \;. \tag{62}$$

Transmission coefficient of the whole holes:

$$t \equiv \frac{W}{\mathrm{N} W_0} = \frac{2}{\mathrm{N} ka} \sum_{m=0}^{\infty} \sum_{n=0}^{\infty} \frac{1}{(2)_m} \frac{1}{2m+4n+1} \sum_{l=1}^{\mathrm{N}} \mathscr{Im}\, ({}_l A_{mn}\, {}_l \tilde{a}_n{}^m + {}_l B_{mn}\, {}_l \tilde{b}_n{}^m) \;, \tag{63}$$

where

$$W_0 = \frac{1}{2} \pi a^2 \omega\sigma k |C|^2$$

is the normal incident energy flow on each hole.

§ 8. Case of Normal Incidence and Large Wave Length

In the case of normal incidence $\alpha=0$, and for large wave length $\gamma = 2\beta < 1$, we obtain

$$
\begin{aligned}
{}_{\iota}A_{00}&={}_{\iota}A_{00}^{(0)}+{}_{\iota}A_{00}^{(1)}+{}_{\iota}A_{00}^{(2)}+{}_{\iota}A_{00}^{(3)}+O(\beta^4)\\
&=\sqrt{\frac{2}{\pi}}\,X_{00}^{0}\Big\{1-2X_{00}^{0}\sum_{\iota'}{}'G_{00}^{00}(q_{\iota'\iota})+(2X_{00}^{0})^2\sum_{\iota'}{}'G_{00}^{00}(q_{\iota'\iota})\\
&\quad\times\sum_{\iota''}{}'G_{00}^{00}(q_{\iota''\iota'})-(2X_{00}^{0})^3\sum_{\iota'}{}'G_{00}^{00}(q_{\iota'\iota})\sum_{\iota''}{}'G_{00}^{00}(q_{\iota''\iota'})\sum_{\iota'''}{}'G_{00}^{00}(q_{\iota'''\iota''})\Big\}+O(\beta^4)\,,\\
{}_{\iota}A_{01}&={}_{\iota}A_{01}^{(0)}+{}_{\iota}A_{01}^{(1)}+{}_{\iota}A_{01}^{(2)}+O(\beta^4)\\
&=\sqrt{\frac{2}{\pi}}\Big[X_{10}^{0}-2X_{00}^{0}\Big\{X_{10}^{0}\sum_{\iota'}{}'G_{00}^{00}(q_{\iota'\iota})+X_{11}^{0}\sum_{\iota'}{}'G_{01}^{00}(q_{\iota'\iota})\Big\}\Big]+O(\beta^4)\,,\\
\begin{matrix}{}_{\iota}A_{10}\\ {}_{\iota}B_{10}\end{matrix}&=\begin{matrix}{}_{\iota}A_{10}^{(1)}+{}_{\iota}A_{10}^{(2)}\\ {}_{\iota}B_{10}^{(l)}+{}_{\iota}B_{10}^{(2)}\end{matrix}+O(\beta^4)=-\sqrt{\frac{2}{\pi}}\,X_{00}^{0}X_{00}^{1}\sum_{\iota'}{}'\begin{matrix}\cos\psi_{\iota'\iota}\\ \sin\psi_{\iota'\iota}\end{matrix}\\
&\quad\times\Big\{G_{00}^{10}(q_{\iota'\iota})-G_{00}^{-10}(q_{\iota'\iota})\Big\}\Big\{1-2X_{00}^{0}\sum_{\iota''}{}'G_{00}^{00}(q_{\iota''\iota'})\Big\}+O(\beta^4)\,,\\
{}_{\iota}A_{20}&={}_{\iota}A_{20}^{(1)}+O(\beta^4)=-\sqrt{\frac{2}{\pi}}\,X_{00}^{0}X_{00}^{2}\sum_{\iota'}{}'\cos 2\psi_{\iota'\iota}\Big\{G_{00}^{20}(q_{\iota'\iota})+G_{00}^{-20}(q_{\iota'\iota})\Big\}+O(\beta^4)\,,
\end{aligned}
\tag{64}
$$

all the other ${}_{\iota}A_{mn}$, ${}_{\iota}B_{mn}$ being of the order β^4 at most. And, putting

$$\gamma q_{\iota'\iota}=\zeta_{\iota'\iota}\,, \tag{65}$$

we get

$$G_{00}^{00}(q_{\iota'\iota})=\{f(\zeta_{\iota'\iota})-ig(\zeta_{\iota'\iota})\}\beta+\{f_1(\zeta_{\iota'\iota})+ig_1(\zeta_{\iota'\iota})\}\beta^3+O(\beta^5)\,, \tag{66}$$

where

$$
\left.
\begin{aligned}
f(\zeta)&=\sqrt{\frac{2}{\pi}}\frac{1}{\sqrt{\zeta}}J_{-(1/2)}(\zeta)=\frac{2}{\pi}\frac{\cos\zeta}{\zeta}\,,\\
g(\zeta)&=\sqrt{\frac{2}{\pi}}\frac{1}{\sqrt{\zeta}}J_{1/2}(\zeta)=\frac{2}{\pi}\frac{\sin\zeta}{\zeta}\,,
\end{aligned}
\right\}
\tag{67}
$$

$$
\left.
\begin{aligned}
f_1(\zeta)&=-\frac{4}{3}\sqrt{\frac{2}{\pi}}\frac{1}{\sqrt{\zeta}}\Big\{J_{-(1/2)}(\zeta)+\frac{1}{\zeta}J_{-(3/2)}(\zeta)\Big\}=-\frac{4}{3}\frac{2}{\pi}\frac{1}{\zeta}\Big\{\cos\zeta-\frac{1}{\zeta}\Big(\frac{\cos\zeta}{\zeta}+\sin\zeta\Big)\Big\}\,,\\
g_1(\zeta)&=\frac{4}{3}\sqrt{\frac{2}{\pi}}\frac{1}{\sqrt{\zeta}}\Big\{J_{1/2}(\zeta)-\frac{1}{\zeta}J_{3/2}(\zeta)\Big\}=\frac{4}{3}\frac{2}{\pi}\frac{1}{\zeta}\Big\{\sin\zeta-\frac{1}{\zeta}\Big(\frac{\sin\zeta}{\zeta}-\cos\zeta\Big)\Big\}\,.
\end{aligned}
\right\}
\tag{68}
$$

Hence,

$${}_{\iota}A_{00}=\sqrt{\frac{2}{\pi}}\{1+{}_{\iota}\lambda_1\beta+{}_{\iota}\lambda_2\beta^2+{}_{\iota}\lambda_3\beta^3+i({}_{\iota}\mu_1\beta+{}_{\iota}\mu_2\beta^2+{}_{\iota}\mu_3\beta^3)\}+O(\beta^4)\,, \tag{69}$$

where

$${}_{\iota}\lambda_1=-2\sum_{\iota'=1}^{N}{}'f(\zeta_{\iota'\iota})\,, \tag{70}$$

$${}_{\iota}\lambda_2=-\frac{16}{\pi}\sum_{\iota'=1}^{N}{}'g(\zeta_{\iota'\iota})+4\sum_{\iota'=1}^{N}{}'\sum_{\iota''=1}^{N}{}'\{f(\zeta_{\iota'\iota})f(\zeta_{\iota''\iota'})-g(\zeta_{\iota'\iota})g(\zeta_{\iota''\iota'})\}-\Big(\frac{16}{\pi^2}-\frac{4}{3}\Big)\,, \tag{71}$$

$$
\begin{aligned}
{}_{\iota}\lambda_3&=-2\sum_{\iota'=1}^{N}{}'f_1(\zeta_{\iota'\iota})+16\Big(\frac{6}{\pi^2}-\frac{1}{3}\Big)\sum_{\iota'=1}^{N}{}'f(\zeta_{\iota'\iota})+\frac{48}{\pi}\sum_{\iota'=1}^{N}{}'\sum_{\iota''=1}^{N}{}'\{f(\zeta_{\iota'\iota})g(\zeta_{\iota''\iota'})+g(\zeta_{\iota'\iota})f(\zeta_{\iota''\iota'})\}\\
&\quad-8\sum_{\iota'}{}'\sum_{\iota''}{}'\sum_{\iota'''}{}'f(\zeta_{\iota'\iota})f(\zeta_{\iota''\iota'})f(\zeta_{\iota'''\iota''})\\
&\quad+8\sum_{\iota'}{}'\sum_{\iota''}{}'\sum_{\iota'''}{}'\{f(\zeta_{\iota'\iota})g(\zeta_{\iota''\iota'})g(\zeta_{\iota'''\iota''})+g(\zeta_{\iota'\iota})f(\zeta_{\iota''\iota'})g(\zeta_{\iota'''\iota''})+g(\zeta_{\iota'\iota})g(\zeta_{\iota''\iota})f(\zeta_{\iota'''\iota''})\}\,,
\end{aligned}
\tag{72}
$$

$$ {}_{l}\mu_1=\frac{4}{\pi}+2\sum_{l'=1}^{N}{}' g(\zeta_{l'l}) \,, \tag{73}$$

$$ {}_{l}\mu_2=-\frac{16}{\pi}\sum_{l'=1}^{N}{}' f(\zeta_{l'l})-4\sum_{l'=1}^{N}{}'\sum_{l''=1}^{N}\{f(\zeta_{l'l})g(\zeta_{l''l'})+g(\zeta_{l'l})f(\zeta_{l''l'})\} \,, \tag{74}$$

$$\begin{aligned} {}_{l}\mu_3=&-2\sum_{l'=1}^{N}{}' g_1(\zeta_{l'l})-16\left(\frac{6}{\pi^2}-\frac{1}{3}\right)\sum_{l'=1}^{N}{}' g(\zeta_{l'l})+\frac{48}{\pi}\sum_{l'=1}^{N}{}'\sum_{l''=1}^{N}{}'\{f(\zeta_{l'l})f(\zeta_{l''l'})-g(\zeta_{l'l})g(\zeta_{l''l'})\} \\ &+\frac{64}{\pi}\left(\frac{1}{9}-\frac{1}{\pi^2}\right)-8\sum_{l'}{}'\sum_{l''}{}'\sum_{l'''}{}' g(\zeta_{l'l})g(\zeta_{l''l'})g(\zeta_{l'''l''}) \\ &+8\sum_{l'}{}'\sum_{l''}{}'\sum_{l'''}{}'\{f(\zeta_{l'l})f(\zeta_{l''l'})g(\zeta_{l'''l''})+f(\zeta_{l'l})g(_{l''l'})f(_{l'''l''})+g(\zeta_{l'l})f(\zeta_{l''l'})f(\zeta_{l'''l''})\} \,. \end{aligned} \tag{75}$$

The acoustic resistance and reactance becomes respectively,

$$\begin{aligned} (R_{ac})_l&=-\frac{\pi\omega\sigma a}{8}\frac{\Gamma(1/2)}{\Gamma(3/2)}\sqrt{\frac{2}{\pi}}\,\mathscr{Im}\frac{1}{{}_{l}A_{00}} \\ &=\frac{\pi\sigma c}{2}\beta^2\{{}_{l}\mu_1+({}_{l}\mu_2-2{}_{l}\lambda_1\,{}_{l}\mu_1)\beta+({}_{l}\mu_3-2{}_{l}\lambda_1\,{}_{l}\mu_2-2{}_{l}\lambda_2\,{}_{l}\mu_1-{}_{l}\mu_1{}^3+3{}_{l}\lambda_1{}^2{}_{l}\mu_1)\beta^2+O(\beta^3)\} \,, \end{aligned} \tag{76}$$

$$\begin{aligned} (X_{ac})_l&=\frac{\pi\omega\sigma a}{8}\frac{\Gamma(1/2)}{\Gamma(3/2)}\sqrt{\frac{2}{\pi}}\,\mathscr{Re}\frac{1}{{}_{l}A_{00}} \\ &=\frac{\pi\sigma c}{2}\beta\{1-{}_{l}\lambda_1\beta-({}_{l}\lambda_2-{}_{l}\lambda_1{}^2+{}_{l}\mu_1{}^2)\beta^2-({}_{l}\lambda_3-2{}_{l}\lambda_1\,{}_{l}\lambda_2+2{}_{l}\mu_1\,{}_{l}\mu_2+{}_{l}\lambda_1{}^3-3{}_{l}\lambda_1\,{}_{l}\mu_1{}^2)\beta^3+O(\beta^4)\} \,. \end{aligned} \tag{77}$$

And, the total energy flow from the whole holes is

$$\begin{aligned} W&=\omega\sigma a|C|^2\pi\sqrt{\frac{2}{\pi}}\sum_{l=1}^{N}\mathscr{Im}\,{}_{l}A_{00} \\ &=2\omega\sigma a|C|^2\sum_{l=1}^{N}\{{}_{l}\mu_1\beta+{}_{l}\mu_2\beta^2+{}_{l}\mu_3\beta^3+O(\beta^4)\} \\ &=4\sigma c|C|^2\beta^2\sum_{l=1}^{N}\{{}_{l}\mu_1+{}_{l}\mu_2\beta+{}_{l}\mu_3\beta^2+O(\beta^3)\} \,. \end{aligned} \tag{78}$$

Using the formula (55)

$$(v_m)_l=\frac{2C}{a}\sqrt{\frac{2}{\pi}}\,{}_{l}A_{00} \,,$$

we can easily show that

$$\frac{1}{2}\sum_{l=1}^{N}\pi a^2(R_{ac})_l|(v_m)_l|^2=W \,. \tag{79}$$

Transmission coefficient of the whole holes is

$$t=\frac{W}{NW_0}=\frac{1}{N}\frac{2}{\pi}\sum_{l=1}^{N}({}_{l}\mu_1+{}_{l}\mu_2\beta+{}_{l}\mu_3\beta^2)+O(\beta^3) \,. \tag{80}$$

§ 9. Numerical Examples

We notice that the approximation of the previous section gives fairly correct value when $\gamma=2\beta$ is small. For example, we give here the transmission coefficient t for normal incidence computed by the formula (80).

When N=2, the results are as shown in Fig. 3. The abscissa q represents the distance between the centres of the two holes, and the ordinate shows the value of t. Each curve corresponds to $\gamma=0.05$, 0.10, 0.15, 0.20, 0.25.

When $q\to\infty$, t should take the value in the case of single hole

$$t_{\text{single}}=\frac{8}{\pi^2}\left\{1+4\left(\frac{1}{9}-\frac{1}{\pi^2}\right)\gamma^2+O(\gamma^4)\right\}.$$

In fact, continuing the computation for larger q, we see that each curve in Fig. 3 tends to t_{single}, oscillating about the limiting value. The greater the value of γ is, the smaller the oscillation amplitude and the shorter the oscillation peroid is.

As q increases starting from $q=2$, each curve attains to the first maximum point (q_1, t_1), the greatest value t_1 being fairly greater than 1, which fact is worth noticing.

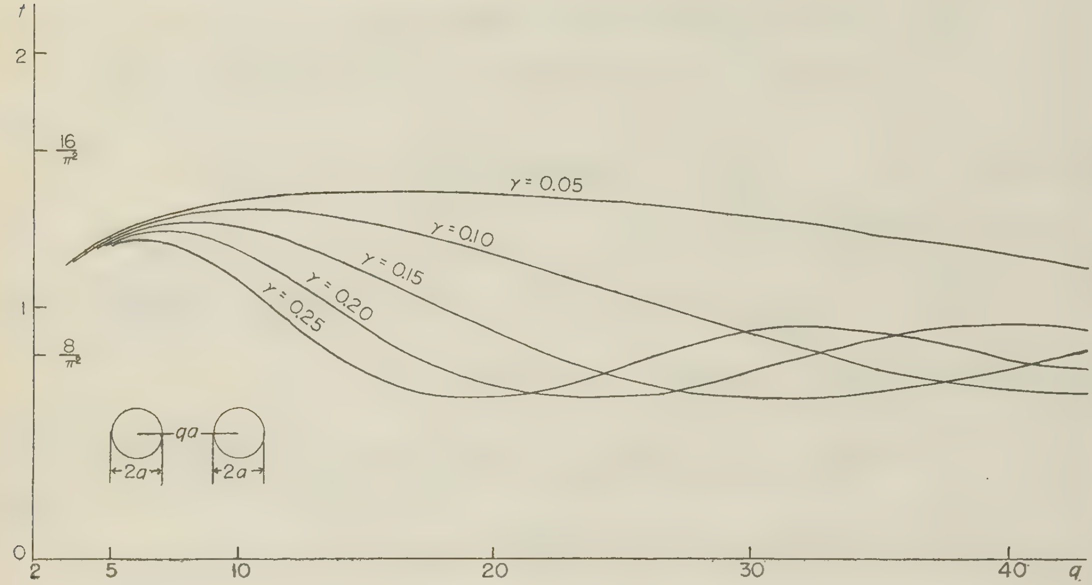

Fig. 3. Transmission coefficient t of two equal circular holes. (γ=circumference of the circle divided by the wave length.)

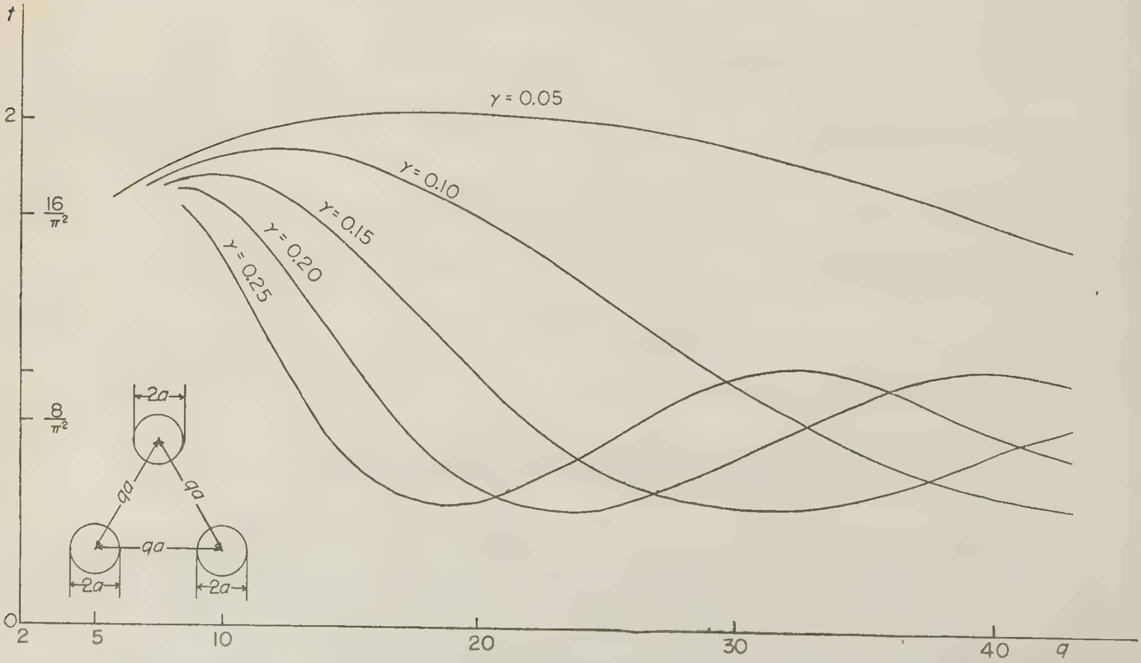

Fig. 4. Transmission coefficient t of three equal circular holes, the centres making a regular triangle. (γ=circumference of the circle divided by the wave length.)

The smaller the value of γ is, the greater the q_1 becomes; $q_1 \to \infty$, $t_1 \to (16/\pi^2) = 1.621$, when $\gamma \to 0$.

When N=3, we calculated two simple cases. Fig. 4 shows the results of the case when the three centres of three equal circular holes make a regular triangle with the lateral sides of length qa. The behaviour of each curve is similar to that in Fig. 3, but the greatest value t_1 becomes greater, and the smallest value smaller.

Fig. 5 shows the results of the case when the three centres of three equal circles are situated on a straight line, the distances from the middle one to the other ones being to qa. The curious curvatures in the descending parts of each curve suggest the appearance of sub-maximums due to the factors $f(2q\gamma)$, $g(2q\gamma)$ and $g_1(2q\gamma)$, when γ is larger.

In both cases, we can show that $t \to t_{\text{single}}$ when $q \to \infty$, and that $q_1 \to \infty$, $t_1 \to (24/\pi^2) = 2.432$, when $\gamma \to 0$.

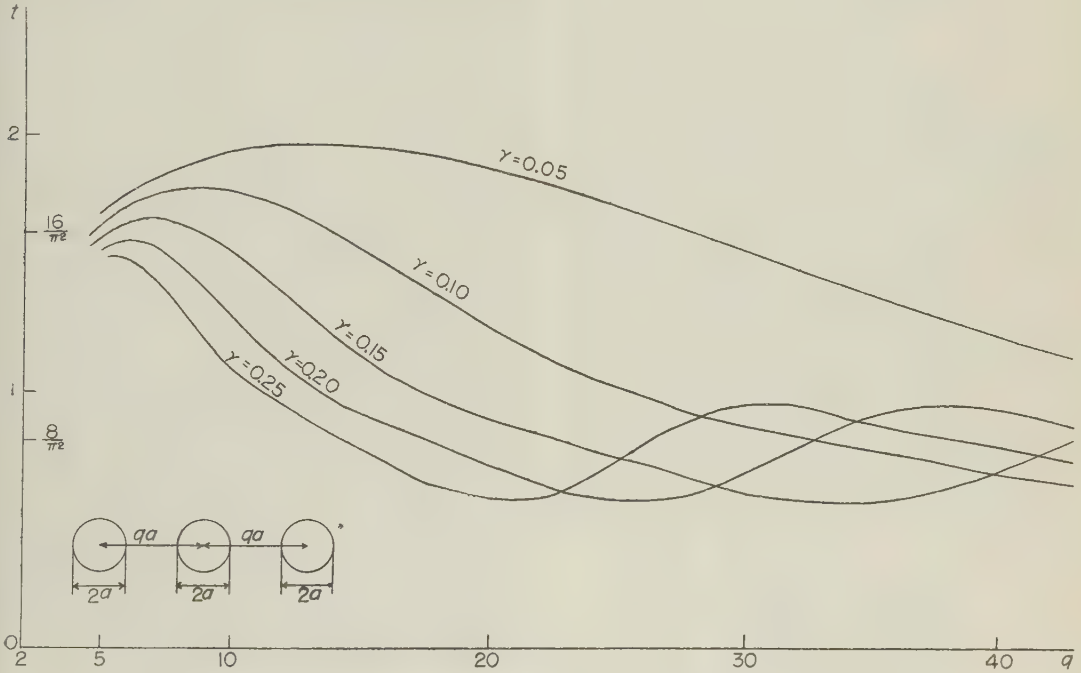

Fig. 5. Transmission coefficient t of three equal circular holes, the centres lying on a straight line. (γ=circumference of the circle divided by the wave length.)

In the above three Figs., the first maximum point (q_1, t_1) and the first minimum point (q_2, t_2) for $\gamma = 0.15$ are read as follows:

	q_1	t_1	q_2	t_2
Fig. 3	8.3	1.33	31.0	0.64
Fig. 4	9.8	1.78	30.6	0.46
Fig. 5	7.1	1.68	34.0	0.57

In the case of $\gamma > 0.25$, we have to compute t by (63). It is necessary to compute ${}_iA_{mn}^{(s)}$, ${}_iB_{mn}^{(s)}$ by (34), (35) and (36), (37) successively taking $s = 1, 2, 3, \cdots$. However, the preparation of the numerical tables of these values for various γ and $q_i\gamma_i$ should be left for electronic computer. If we have such tables, we can compute any physical quantity directly by its formula.

References

1) J. Meixner and W. Andrejewsky: Ann, d. Phys. (6) **7** (1950) 157.
2) C. J. Bouwkamp: Philips Research Reports **5** (1950) 401.
3) T. Nimura: Sci. Rep. Tôhoku Univ. **1**, **2** (1951) 381.
4) Y. Nomura and S. Katsura: Sci. Rep. Tôhoku Univ. **10** (1958) 1.
5) Y. Nomura and N. Kawai: Sci. Rep. Tôhoku Imp. Univ. Series I, **33** (1949) 208.
6) Y. Nomura and T. Osanai: Sci. Rep. Tôhoku Univ. **12** (1960) 97.
7) I. Kobayashi: Sci. Rep. Tôhoku Imp. Univ. Series I, **27** (1939) 365.

Short Notes

This section is intended to secure prompt publication of important discoveries in physics. The reports should not exceed 800 words in length. A figure of size 7 cm×7 cm will be counted as 150 words.

J. Phys. Soc. Japan **16** (1961) 832

Effects of Vacancies on Pulse Photoconductions in CdS Single Crystals

By Junji Shirafuji and Yoshio Inuishi
College of Engineering, Osaka University
Osaka, Japan

(Received January 23, 1961)

The temperature dependence of pulse photocurrent and decay time constant in comparatively pure CdS single crystals have been reported in our previous paper[1]. Here the effect of stoichiometric defect introduction on the pulse photoconduction of the same samples (M-1, M-2) will be mentioned with notations quite similar to the previous report. To introduce the stoichiometric defects, the melt grown CdS crystals were sealed into a silica tube with suitable amount of Cd (denoted "Cd doped") or S ("S doped") in vacuum and heated at 850°C for 1 hour. Thus S or Cd vacancies seem to be introduced, judging from thermally stimulated current data taken by Prof. Tanaka[2]. Fig. 1 shows the temperature dependence of the shortest decay time constant τ_1 of photocurrent excited with 0.5 *μsec* light pulse. τ_1 was found to be shortened very effectively at lower temperatures by S doping having a maximum at about 200°K, while in "Cd doped" crystal τ_1 was rather similar to "pure" crystal. The next shortest decay time constant τ_2 which had been observed in pure crystals did not appear in doped crystals. The peak photocurrent I_1 in this case is shown in Fig. 2, where the introduction of Cd vacancies ("S doped") reduces the current remarkably at lower temperatures and S vacancies ("Cd doped") result in enhancement. As seen in Fig. 3, the longer decay time constant τ_3 when crystals were illuminated with 5 *msec* light pulse is shortened remarkably by Cd vacancy introduction. On the contrary, the crystal with S vacancies shows similar behavior to pure crystals being rather insensitive to temperature. The photocurrent I_3 (dotted lines in Fig. 3) in this case has similar behavior to τ_3, where S vacancies result in the very remarkable enhancement. Transition in photocurrent from the linear to the sublinear relation at high light intensity was seen in "Cd doped" sample. In resume, introduction of Cd vacancies (acceptor) shortens the electron lifetimes, τ_1 and τ_3, very remarkably at lower temperatures. S vacancies (donor) enhance the quantum efficiency enormously, increase the electron lifetime τ_3 and improve the temperature dependency of photoresponse especially at lower temperatures. The experiments on spectral response and surface effects are being continued to clarify the detailed mechanism.

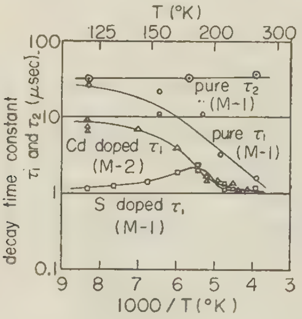

Fig. 1.

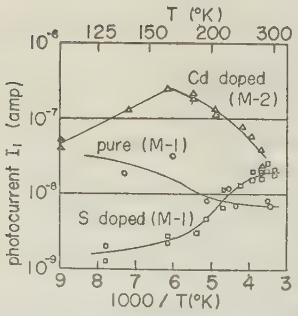

Fig. 2.

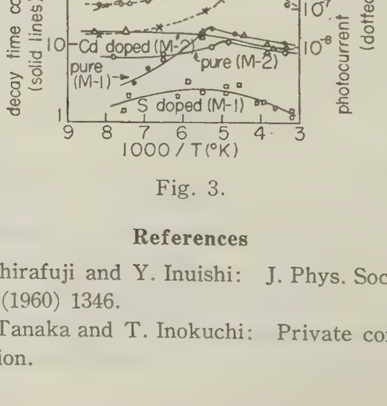

Fig. 3.

References

1) J. Shirafuji and Y. Inuishi: J. Phys. Soc. Japan **15** (1960) 1346.
2) T. Tanaka and T. Inokuchi: Private communication.

J. Phys. Soc. Japan **16** (1961) 833~834

Conductivity of Grain Boundaries in Ge

Yasuo Matukura and Shigezo Tanaka
Semiconductor Division, Nippon Electric Company, Ltd. Kawasaki, Japan

(Received January 12, 1961)

It has been known[1),2)] that grain boundaries in Ge have a p-type character due to the acceptor action of dangling bonds. Conduction in these grain boundaries of Ge was studied by A. G. Tweet[3)] and B. Reed[4)] using measurements of Hall effect and conductance, respectively. As dislocation line has a cylindrical space charge[2)], it is expected that the carrier mobility in small angle grain boundaries may depend upon the direction of the current flow in this sheet.

This work is performed on carefully oriented bicrystals grown by the vertical pulling technique with [100] seeds symmetrically tilted about the [010] axis at angles of 2.5-40°. The intrinsic starting material is doped with Sb and the bulk resistivities are 7 to 20Ω cm. Samples approximately $1.5\times1.5\times10$ mm are cut parallel (A) or perpendicular (B) to the [010] tilt axis, as shown in Fig. 1. In order to minimize the parallel current flow in the bulk material, it is necessary to use contacts which are ohmic on the grain boundary and rectifying on the bulk. Indium alloyed contacts[3)] are used for current electrodes, resistivity and Hall effect probes after electrolytically etching.

Measurements are performed on the resistivity and Hall coefficient at the temperature range of 80 to 300°K. Voltages are checked for linearity as a function of current and magnetic field magnitude and these directions. In the case of the grain boundary space-charge layer conduction, the thickness of the conducting layer can only be estimated and the density of carriers is a function of the perpendicular distance from the grain boundary. Consequently, the reduced Hall coefficient[3)], as $R^*=R/t$, and the reduced resistivity, as $\rho^*=\rho/t$, are measurable.

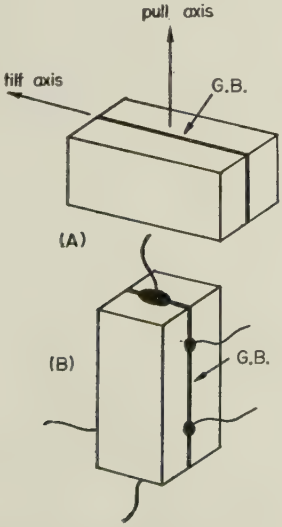

Fig. 1. Schematic drawing of Hall sample containing a grain boundary.

ρ^* on all samples of the various misorientation decreases gradually with the decreasing temperatures, has a minimum value of several kiloohm at about 120°K, and then increases gradually with the decreasing temperatures. However, ρ^* on B samples of the misorientation 2.5° increases with a slope of about 0.1 eV at the temperatures below 120°K. On the other hand, the sign of R^* shows that the current carriers in the grain boundary layer are holes in all samples. R^* on all samples except misorientation 2.5° is nearly constant at the measured temperature range and the values are about 10^6 cm²/coulomb. On the samples of 2.5°, R^* increases with a similar slope to ρ^* of 2.5°B with the decreasing temperatures below 150°K.

If the Hall mobility of holes in the grain boundary is given by $\mu=R^*/\rho^*=R/\rho$, the Hall mobility is not implyed the thickness of the grain boundary layer. Fig. 2 shows Hall mobilities for three samples. There is a high temperature range in which the mobility increases with the decreasing temperatures

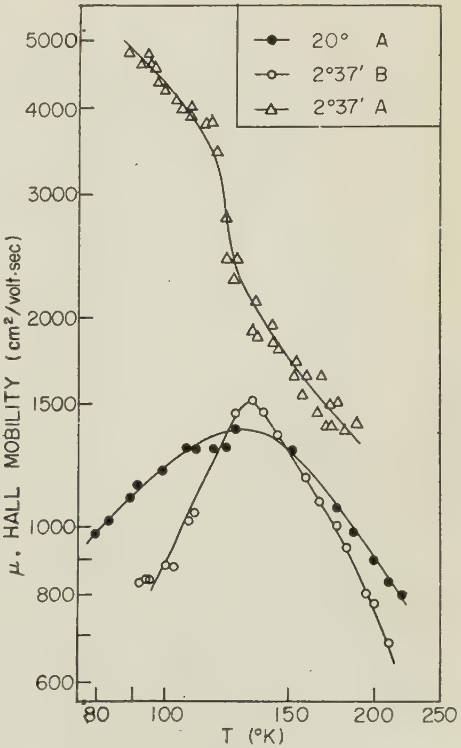

Fig. 2. Temperature variation of Hall mobility.

as does that of the bulk Ge. There is a low temperature range in which the mobility decreases with the decreasing temperatures except the case of 2.5°A.

It seems that the mobility in the high temperature range is determined by a scattering as lattice scattering and in the low temperature range by a scattering as the charged dangling bond scattering. If it is assumed that the hole moving along through the cylindrical space charge is more weakly scattered by the charged dangling bond than the hole moving perpendicular to that, it seems to be reasonable that the mobility of 2.5°A in Fig. 2 is larger than B of the same orientation and does not decrease with the decreasing temperatures. As the misorientation increases, thc feature of the cylindrical space charge in the grain boundary will diminish. In middle-angle grain boundaries, therefore, it seems that the anisotropy of the grain boundary mobility by the direction of current flow will not be observed.

The authors are indebted to Mr. J. Oda in Electrotechnical Laboratory for bicrystal pullings.

References

1) G. L. Pearson: Phys. Rev. **76** (1949) 459.
2) W. T. Read: Phil. Mag. **45** (1954) 775.
3) A. G. Tweet: Phys. Rev, **99** (1955) 1182.
4) B. Reed, O. A. Weinreich, and H. F. Matare: Phys. Rev, **113** (1959) 454.

J. PHYS. SOC. JAPAN **16** (1961) 834

Direct Observation of the Lattice Imperfections in Pearlites by Electron Microscopy

By Zenji NISHIYAMA and Atsuo KORE'EDA
Institute of Scientific and Industrial Research, Osaka University, Japan

Isamu EGUCHI and Koshi KATO
Research Laboratory, Daido Steel Co., Nagoya, Japan

Nishiyama, Kore'eda and Shimizu formerly reported about the morphology of the pearlite observed in specimens of thin foil. The present writers have made further detailed observations by an electron microscope of HU-11 type (100 kV) which is more improved than that formely used.

Specimens were prepared from a sheet of 0.7% carbon steel. It was originally cold-rolled to the thickness of 0.35 mm, and annealed for 1/2 hr at 950°C, followed by slow cooling at the rate of 2°C/min. It was then electropolished with a mixture of phosphoric acid and chromic acid to make thin foils for transmission electron microscopy.

Observations of this specimen have confirmed the results formerly obtained and given finer patterns showing the lattice imperfections. Figs. 1 and 2 are two examples. The bands (θ) appearing in these figures are sections of cementite plates in pearlite. In these bands are seen complex figures probably due to Moiré pattern affected by lattice imperfections which seem to have some relation to the dislocations appearing in the neighbouring ferrite (α). At the boundary between the cementite plate and the ferrited plate a featherlike structure of a certain width is seen although it is diffused in Fig. 1. This boundary structure suggests us that there are parallel arrays of defects due to lattice coherency between cementite and ferrite.

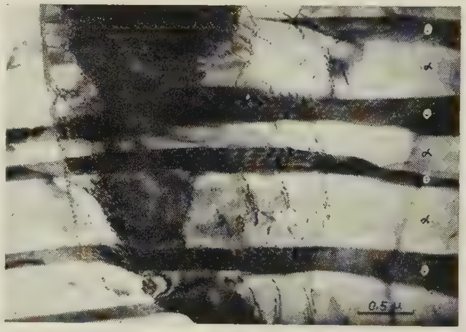

Fig. 1.

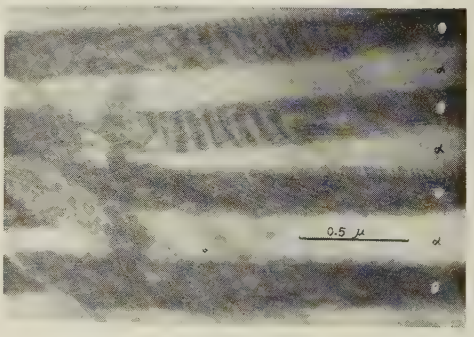

Fig. 2.

Many other photographs showing various aspects of pearlite have been taken, which will be described in "Denki-Seiko" (Electric Furnace Steel).

Reference

1) Z. Nishiyama, A. Kore'eda and K. Shimizu: J. Electron-Microscopy, **7**, 41 (1959).

J. Phys. Soc. Japan **16** (1961) 835~836

Proton Magnetic Resonance in Ferroelectric (CH_3NH_3) $AlSO_4 \cdot 12H_2O$

By Ryosuke Hoshino

Department of Physics, Faculty of Science, Hokkaido University, Sapporo, Japan

(Received February 5, 1961)

Measurements have been made of the proton magnetic resonance absorption in $(CH_3NH_3)AlSO_4 \cdot 12H_2O$, methyl-ammonium aluminum sulfate dodecahydrate (MASD) in the temperature range from 90°K to room temperature.

Fig. 1 (a) shows the observed derivative of the absorption curve for the powdered MASD at room temperature. It showed a rather complicated line shape with a central peak of a width about 4 gauss. On the other hand the absorption of $KAlSO_4 \cdot 12H_2O$, which is an isomorphous compound of MASD, showed only a broad line with flat top as given in Fig. 1 (b). In this case all the nuclei which contribute to the resonance, are the protons in water molecules. And, moreover, the line width 12.8 gauss is of the same order with that of the two-proton system in rigid lattice.[1] Comparing the line shape of $KAlSO_4 \cdot 12H_2O$ with that of MASD, it is resonable to assume that the observed absorption in MASD is the superposition of the two lines: a narrow central line and a broad one indicated by dashed line in Fig. 1 (a). The broad line arises from the effectively fixed protons in water molecules and the narrow line from a rapidly rotating (CH_3NH_3) group.[2] The rotation will bigin at lower temperatures owing to the roughly spherical shape of methyl-ammonium group.[3] The observed absorption derivatives and their second moments as a function of temperature are given in Fig. 2 and Fig. 3, respectively. These results were obtained for rising temperature. Above about 160°K, the sharp line located at the central portion of the line begins to appear and becomes more pronounced as the temperature is raised. The variation of the second moments is rather small owing to the fact that the broad line in water molecules remains constant up to room temperature, but it is evident that the rotation of (CH_3NH_3) group occurs at about 160°K, i.e. about 16° below the Curie temperature, 176°K.[4] The temperature dependence of the ferroelectric behavior, measured by Pepinsky et. al.,[4] shows the same variation as the NMR observation, i.e. the anomaries begin at about 20° below the Curie point. From the above data one may conclude that the rotation of (CH_3NH_3) group is closely related to the disappearance of ferroelectricity in MASD. The measurements in single crystal will be reported later.

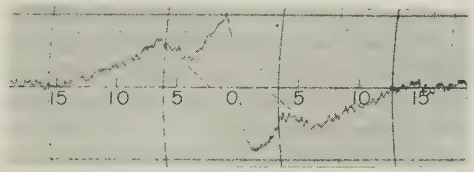

(a) $(CH_3NH_3)AlSO_4 \cdot 12H_2O$

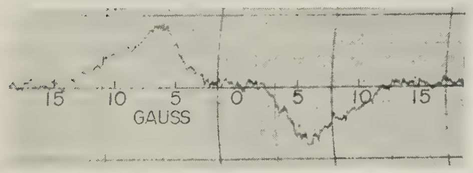

(b) $KAlSO_4 \cdot 12H_2O$

Fig. 1. Absorption curve derivatives for the powdered (a) MASD and (b) $KAlSO_4 \cdot 12H_2O$ at room temperature.

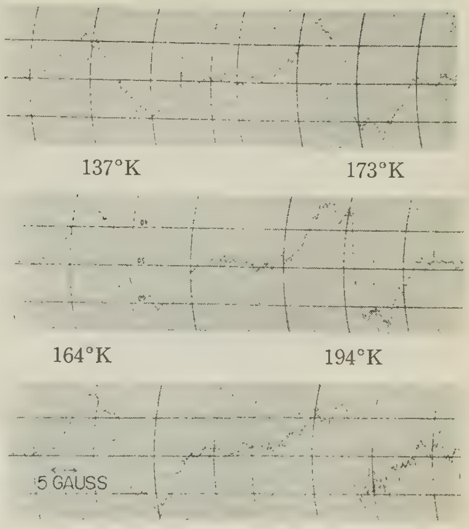

137°K 173°K

164°K 194°K

166°K 253°K

Fig. 2. Absorption curve derivatives for the powdered MASD at several temperatures.

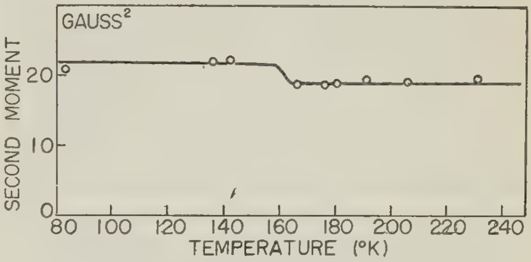

Fig. 3. The variation with temperature of the second moment of the absorption line for powdered MASD.

References

1) G. E. Pake: J. Chem. Phys. **16** (1948) 327.

2) J. G. Powles and H. S. Gutowsky: J. Chem. Phys. **21** (1953) 1695.
3) H. Lipson: Phil. Mag. **19** (1935) 887.
4) R. Pepinsky, F. Jona, and G. Shirane: Phys. Rev. **102** (1956) 1181.

J. Phys. Soc. Japan **16** (1961) 836

Temperature Dependence of ESR Line-Width in $K_2CuCl_4 \cdot 2H_2O$

By Hidetaro Abe

The Institute for Solid State Physics,
University of Tokyo, Azabu, Minato-Ku,
Tokyo, Japan

(Received February 2, 1961)

In the former report,[1] electron spin resonance (ESR) of $K_2CuCl_4 \cdot 2H_2O$ was studied, using seven frequencies, in its single crystals and at room temperature, which gave us some knowledge on the exchange interaction between the copper ions in the crystal. Some preliminary results will be given in the present report about the temperature dependence of the line-width observed at about 24 Gc.

The unit cell of this crystal contains two inequivalent Cu^{++} ions, at (0, 0, 0) and (1/2, 1/2, 1/2). Both ions have the identical g-tensor with rhombic symmetry except that the directions of their principal axes are different, g-tensor of one ion can be obtained from the other by a rotation through 90° about their common principal axis, [0,0,1].

When the static magnetic field H is applied at the [1,1,0] direction, the difference between their Zeeman energies, $\Delta g\beta H$, becomes maximum, whereas it vanishes when H is applied at the [0,0,1] direction, the similar direction.

(a) In case of $H//[1,1,0]$, two separated peaks were observed only at higher frequencies, giving the exchange energy, $2J$, between dissimilar copper ions as

$$2J \gtrsim 0.1\,\mathrm{cm}^{-1} \qquad (1)$$

at room temperature. At 24 Gc, one single lines was observed, the width of which was measured at room temperature to be about 800 oer. This value is mainly ascribed to the difference in the Zeeman energy between the dissimilar ions.[1] At reduced temperature, it becomes narrower as in Fig. 1 (a).

(b) On the other hand, the line-width for $H//$ [0,0,1] observed at the higher most frequency was about 40 oer at room temperature,[1] which can be well described by a relation,[2]

$$\Delta H \simeq (\Delta H_{dip})^2/H_{ex} \qquad (2)$$

where ΔH_{dip} is the dipolar width and H_{ex} the exchange energy between the copper ions expressed in unit of magnetic field. The width observed in our present study, 65 oer., is somewhat larger than that mentioned above, because of the "10/3 effect". Within the experimental errors, it remains constant over the present temperature range as shown in Fig. 1 (b).

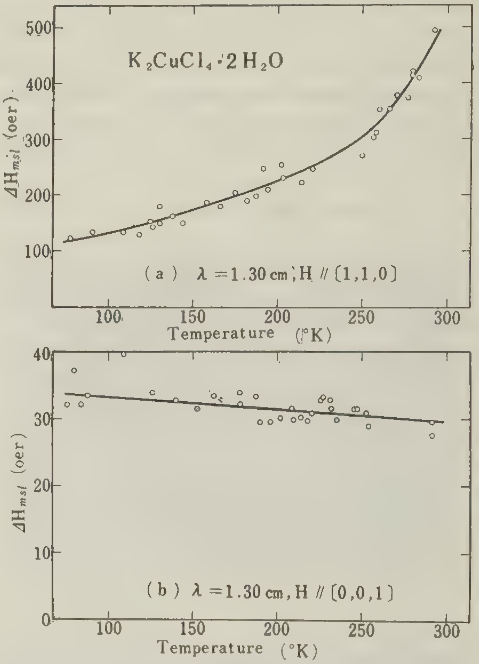

Fig. 1. Temperature dependence of line-width of $K_2CuCl_4 \cdot 2H_2O$.

In both cases of (a) and (b), the line shape fits well the Lorentzian curve at every temperature of measurement from 80°K to 300°K. The origin of this temperature dependence is not yet clear. Some possible models were examined, e.g., the situation that the rhombicity of g tensor of the individual ion decreases in decreasing temperature which can not be expected in the normal case, or that the exchange energy is temperature dependent, such as only that between dissimilar ions increases for decreasing temperature.

In order to make clear the origin, detailed measurements at different frequencies and at lower temperature are now in progress which will be reported in this Journal. A curious behaviour[3] in ESR of this crystal at helium temperature is found at Osaka University.

References

1) H. Abe, K. Ôno, I. Hayashi, J. Shimada and K. Iwanaga: J. Phys. Soc. Japan **9** (1954) 814.
2) P. W. Anderson and P. R. Weiss: Rev. Mod. Phys. **25** (1953) 269.
3) J. Itoh: Private communication.

J. Phys. Soc. Japan **16** (1961) 837~838

E.S.R. of Irradiated DPPH Protected by Polystyrene

By Kohzoh MASUDA
Department of Electronic Engineering
and Tokuo SUITA
Department of Nuclear Engineering College of Engineering, Osaka University, Osaka

(Received February 10, 1961)

The number of the unpaired electrons in DPPH with polystyrene under γ-ray irradiation was studied.

The number of the unpaired electrons in DPPH increased with increasing γ-ray dosage and passing through a maximum point it gradually decreased with increasing of total dosage. Total dose was changed from 10^4 to 10^6 röntgens.

In the experiments the maximum number of unpaired electrons appeared at higher radiation dosage by addition of polystyrene. This phenomena cannot be explained only by the shielding effect of polystyrene but to introduce another mechanism such as the interaction of electrons and polystyrene is necessary.

The number of the unpaired electrons in DPPH was observed by ESR (Electron Spin Resonance) of 10 Gc.[1)]

The number of the electrons produced in DPPH by irradiation of γ-ray is estimated by the equation,

$$n_p/n_{p0}=1-\exp(-k_p t)\,,$$

where n_p is the number of electrons and t is total dose. The number of the electrons remains from annihilation in ESR is estimated at

$$n_a/n_{a0}=\exp(-k_a t)\,.$$

The total number of unpaired electrons is then

$$n/n_0=\exp(-k_a t)+K[1-\exp(-k_p t)]\,,$$

where K is the constant which is determined by the ratio of the number of the unpaired electrons presented in case of non irradiation to the number of atoms which can be ionized by radiation and can produce free radicals.

k_a and k_p are the coefficients of annihilation and production of unpaired electrons. The coefficients k_a and k_p can be introduced by following theoretical assumptions.

1) The chemically stable unpair electrons are annihilated by the recombination of disintegrated molecules.

2) DPPH molecules coagulate in polystyrene and critical concentration for the coagulation R_c can be determined. For concentrations below R_c the hindered rotation of molecules is the dominant term of annihilation mechanisms, while over R_c the recombination of unpaired electrons is suppressed by the polystyrene barriers.

3) Molecules are in some cases ionized by γ-ray and compton electrons termed direct process and in other cases ionized by coagulation of exited states of molecules termed indirect process.

4) In the indirect process there are excited states of electrons which must be transport and are suppresed.

In Fig. 1. and Fig. 2. the heavy lines show the

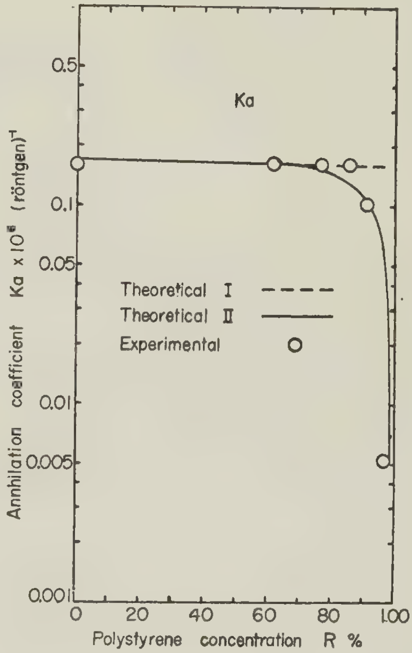

Fig. 1. The annihilation coefficient vs polystyren concentration.

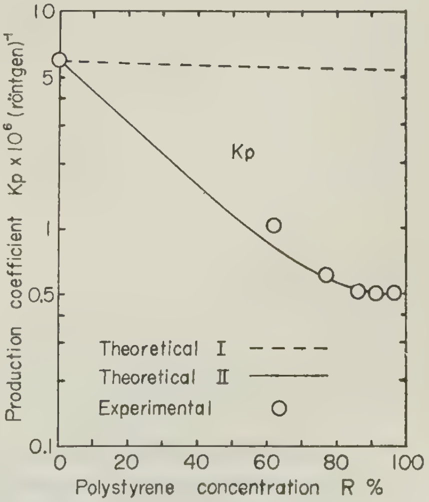

Fig. 2. The production coefficient vs polystyren concentration.

annihilation coefficient k_a and production coefficient k_p versus polystyrene concentration. The dotted lines show the coefficients k_a and k_p including only shielding effect of polystyrene. The points indicate the experimental data.

From the comparison of experimental data and the considerations described above we can conclude that there is not only shielding effect of polystyrene but protection mechanism in DPPH with polystyrene under γ-rays irradiation.

The authors thank to Prof. J. Yamaguchi for his valuable discussions.

Reference

1) K. Masuda and T. Suita: Technol. Repts. Osaka Univ. **8** (1958) 227.

J. PHYS. SOC. JAPAN **16** (1961) 838

Spin Wave Resonance in Pd-Ni Alloy Films

By Hiroshi NOSÉ

Department of Physics, Faculty of Science
Tokyo Metropolitan University

(Received February 7, 1961)

The spin wave resonance in Pd-Ni alloy films was observed in the same manner as in the case of Cu-Ni alloy films[1].

Since the vapour pressures of Ni and Pd resemble each other, it may not be surprising that the concentrations of evaporated films were confirmed to be nearly equal to those of original alloys by means of colorimetric analysis.

On the other hand, since there is a wide difference of lattice constants between Ni and Pd, it is anticipated that the line width of electron diffraction pattern on the evaporated film would be broad, provided that its alloying are imperfect. In practice their lines on the present films, however, were comparably as narrow as those of pure Ni films and furthermore their lattice constants were in good agreement with the results of X-ray diffraction measured on a bulk specimen by Hultgren and Zapffe[2], as shown in Fig. 1. Thus the nearly perfect alloying in present films was confirmed, and this may be perhaps due to the rapid rate of evaporation.

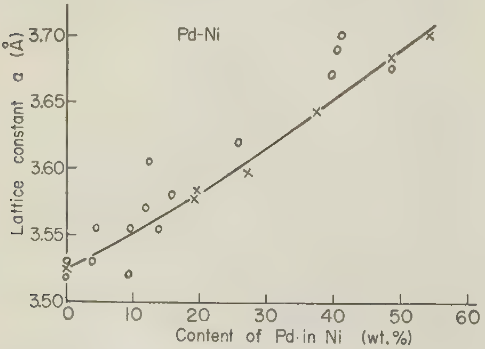

Fig. 1. Concentration dependence of lattice constants of Pd-Ni alloy films; ○: present value by E. D., ×: X-ray value for bulk alloys by Hultgren and Zapffe[2].

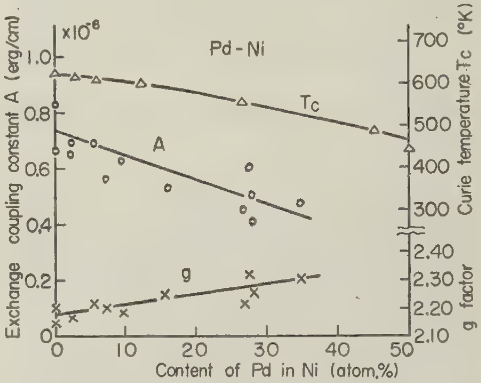

Fig. 2. Concentration dependence of exchange coupling constants and g-factors of Pd-Ni alloy films; ○: present value of A, ×: present value of g, △: T_c by Marian[3].

The exchange coupling constants A of these alloy films were determined from the spin wave resonace at 9300 Mc/sec in a magnetic field being perpendicular to the film plane. These values of A decreased monotonously with increasing concentration of Pd, as shown in Fig. 2. The g-factor was estimated from the main resonances in both perpendicular and parallel field to the plane of each film and plotted also on this figure. For reference, the Curie temperature T_c measured for a bulk specimen by Marian[3] is plotted too. Similarly to the case of Cu-Ni alloy films, it seems that the variation of A in the present case behaves in the similar way to that of T_c and it may be pronounced that the present values of A are the same as those of bulk materials with which there are no data to be compared.

The author wishes to express his thanks to Prof. R. Kimura for his continued encouragement and to Mr. M. Ichikuni for his colorimetric analysis.

References

1) H. Nosé: J. Phys. Soc, Japan **16** (1961) 342.
2) R. Hultgren and C. A. Zapffe: Trans A. I. M. M. E. **133** (1939) 58.
3) V. Marian: Ann. physique [11] **7** (1937) 459.

J. PHYS. SOC. JAPAN **16** (1961) 839

The O-H···O Bond in Orthoboric Acid

James A. IBERS and C. H. HOLM
Sheel Development Company, Emeryville, California, U.S.A.

(Received October 28, 1960)

Recently Kume and Kakiuchi[1)] (hereafter designated KK) concluded that their measured second moment of the proton magnetic resonance absorption spectrum of polycrystalline orthoboric acid (H_3BO_3) was incompatible with the presence of linear or nearly linear O-H···O bonds in the structure. The purpose of this note is to show that their experimental second moment of 10.6±0.9 gauss²* *is* compatible with the presence of linear O-H···O bonds, in support of Zachariasen's[2)] conclusions from his precise X-ray determination of the structure.

The appropriate expression for the second moment $M_2(H_n)$ of a given type of stationary hydrogen nucleus, say H_1, in polycrystalline orthoboric acid is

$$M_2(H_1)=357.97\sum_{H\neq H_1} r_{H_1-H}{}^{-6}+72.12\sum_{B} r_{H_1-B}{}^{-6}$$

The first sum takes into account the interaction of nucleus H_1 with the hydrogen nuclei and the second sum the interaction of nucleus H_1 with the boron nuclei in the structure. The H_1-X distance is r_{H_1-X}. The coefficients are derived from the usual expressions which involve spins, relative isotope abundances, and magnetogyric ratios of the nuclei. The values of $M_2(H_n)$ for each of the six non-equivalent hydrogen nuclei in the unit cell of H_3BO_3 are computed and the results averaged to obtain the total moment M_2. Using the X-ray data of Zachariasen and a Datatron 205 electronic computer we have evaluted the contributions of the nuclei to the total second moment. Contributions from nuclei more distant than 5A were assumed to be the same for each type of hydrogen nucleus and were estimated by integration. (KK also computed directly from the X-ray structure the contributions out to 5A and then applied an integration correction for more distant nuclei.) Table I lists the total second moment, together with the contributions to it of the boron and hydrogen interactions. It is interesting to note that KK obtain for their total second moment a value of 7.7 gauss², just the value we would have obtained had we omitted the boron contributions.

Zachariasen's X-ray data lead to a separation of the maximum oxygen electron density from the maximum hydrogen electron density of 0.88A, and the results in Table I are based on the assumption, known to be erroneous[3)], that the hydrogen electron density coincides with the position of the hydrogen nucleus. However, if we assume the heavy-atom positions of the X-ray study, but take a more reasonable value for the O-H internuclear distance in a linear O-H···O bond, then the hydrogen contributions to the second moment are increased slightly and the boron contributions decreased slightly over those presented in Table I. The overall result is the increase of the calculated second moment by only 0.2 to 0.4 gauss², depending upon the O-H distance assumed. The effect of zero-point motion of the nuclei, particularly the hydrogens, on the second moment is more difficult to calculate, owing to a lack of knowledge of the nuclear motions. However, past experience[4,5)] suggests that the effect will be to increase the calculated second moment by at most 10%. Hence the corrected value of the calculated second moment is about 10 to 11 gauss². It is clear then that the experimental second moment of 10.6±0.9 gauss² is compatible with one calculated from a structure based on the X-ray results. The O-H···O bond in orthoboric acid is thus linear or nearly linear, as suggested by the X-ray results, and the magnetic resonance results do little more than confirm this fact.

Table I Contributions to the Second Moment M_2

Proton No.*	Contributions to M_2 (in gauss²)	
	Hydrogen	Boron
I	7.34	1.69
II	8.29	1.88
III	5.62	1.83
IV	6.95	1.86
V	6.54	1.93
VI	8.13	2.58
Average	7.15	1.96
Integration correction	0.53	0.04
Total contribution	7.68	2.00
Total moment	9.7	

* These correspond to Zachariasen's numbering system.

References

1) K. Kume and Y. Kakiuchi: J. Phys. Soc. Japan **15** (1960) 1277.
2) W. H. Zachariasen: Acta Cryst. **7** (1954) 305.
3) See for example Y. Tomiie: J. Phys. Soc. Japan **13** (1958) 1030.
4) J. A. Ibers and D. P. Stevenson: J. Chem. Phys. **28** (1958) 929.
5) C. H. Holm, C. R. Adams, and J. A. Ibers: J. Phys. Chem. **63** (1958) 992.

---

* We find, from an average of two measurements, an experimental second moment of 9.7±0.8 gauss², in agreement with this value.

J. Phys. Soc. Japan **16** (1961) 840~841

Volume Magnetostriction in Nickel-Iron Alloys

By Yoji Nakamura, Tetsuo Nakajima
and Hideo Takaki
Faculty of Science, Kyoto University

(Received December 27, 1960)

The study on the thermal expansion in iron nickel alloys made by Chevenard1) shows that there are an anomalous contraction in the high nickel content alloys ($>77.2\%$ Ni) and an anomalous dilatation in the low nickel content alloys ($<66.8\%$ Ni) below the Curie temperature.

According to the molecular field theory of ferromagnetism the effects mentioned above correspond to the negative and positive volume magnetostrictions, and also to the positive and negative pressure dependences of the Curie temperature respectively2),3). Theoretical analysis shows that the anomalous expansion and contraction depend on the sign of tangent in Bethe's curve4). Consequently Chevenard's results suggest that the maximum point in the Bethe's curve at which the volume dependence of the spontaneous magnetization vanishes, lies in the region from 66.8% to 77.2% Ni content. The volume magnetostriction, therefore, should change its sign at this region.

The specimens of the Fe-Ni polycrystalline alloys in γ-phase, were prepared by mixing powders of electrolytic iron and those of nickel homogeneously and then melting them at 1600°C. To measure the volume magnetostriction at room temperature, we adopted the D-C Wheatstone bridge with resistance strain gauge whose strain sensitivity was 6.3×10^{-7} per mm scale. The magnetostriction changes linearly with the increasing external magnetic field. When we assume the isotropic forced magnetostriction, we can obtain the volume magnetostriction from the slopes of these curves as shown in Fig. 1.

According to the present author's experimental results the alloy showing no volume magnetostriction is found in the region of higher nickel content side (i.e. from 85.9% Ni to 93.7% Ni) than the region expected from the Chevenard's data.

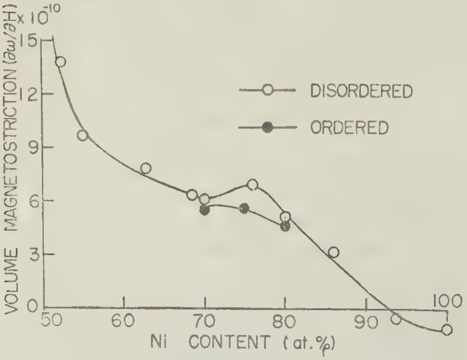

Fig. 1. Volume magnetostriction in nickel iron alloys measured at room temperature.

In recent years, the experimental verification of the following the modynamical relation has been reported for low nickel content alloys by Gugan5)

$$\left(\frac{\partial\omega}{\partial H}\right)_{T.P.}=I\left[-\frac{1}{I}\left(\frac{\partial I}{\partial P}\right)_{T.H.}+\beta\right],$$

where $\frac{\partial w}{\partial H}$ is the volume magnetostriction and β the compressibility. The term $-\frac{1}{I}\frac{\partial I}{\partial P}$ in the above equation can be replaced by $-\frac{1}{2\omega}\frac{\partial\omega}{\partial P}$ when we assume the following relation6)

$$\omega=\omega_0\left(\frac{I}{I_0}\right)^2,$$

where ω and ω_0 are the relative volume change associated with the appearance of the spontaneous magnetizations, I and I_0, at an arbitrary temperature and 0°K respectively. Since the term $-\frac{\partial\omega}{\partial P}$ is always positive, the sign of $-\frac{1}{I}\frac{\partial I}{\partial P}$ depends on the sign of ω which corresponds to the thermal expansion anomaly. In case of low nickel content alloy β is negligibly small as compared to the other terms. However, the measured volume magnetostriction in high nickel content alloys is in the order of 10^{-11} Oe^{-1}. It may, therefore, be impossible to neglect the contribution of the compressibility which is always positive. The shift of the concentration at which the sign of the volume magnetostriction changes, therefore, is due to the effect of compressibility superimposed upon purely magnetic effect, so far as the molecular field approximation is concerned.

In order to investigate the effect of ordering of the alloys upon their volume magnetostriction, we prepared ordered and disordered specimens, the former being annealed at 490°C for 168 hours and the latter quenched from above the critical temperature. As shown in Fig. 1, the volume magnetostriction in the ordered state is smaller than the one in disordered. It is known that the spontaneous magnetization of Ni_3Fe increases by 5.8%7) and the volume of the specimen decreases by 5×10^{-4} when the alloy is brought into the ordered states. Consequently a smaller volume magnetostriction can be expected in the ordered state. Thus the observed result shows a qualitative agreement with the data of the spontaneous magnetization.

References

1) P. Chevenard: Rev. de Met. Mem. **14** (1917) 610.
2) M. Kornetzki: Z. Phys. **98** (1935) 289.

3) R. Bozorth: *Ferromagnetism* (D. Van Nostrand, New York, 1951) 723 p.
4) L. Patrick: Phys. Rev. **93** (1954) 384.
5) D. Gugan: Proc. Phys. Soc. **72** (1958) 1013.
6) L. Néel: *Le Magnetisme* (C.N.R.S., Strasbourg) **2** (1939) 65 p.
7) E. M. Grabbe: Phys. Rev. **57** (1940) 728.

J. PHYS. SOC. JAPAN **16** (1961) 841~842

Decay of Ir^{195} and Ir^{197}

By Saburo HOMMA, Tokihiro KUROYANAGI,*
Department of Physics, Tohoku University, Sendai
and Haruhiko MORINAGA
Department of Physics, University of Tokyo, Tokyo

(Received January 16, 1961)

The systematics of beta-decay energies in iridium predict a total disintegration energy of ≈1 MeV for Ir^{195} and ≈2 MeV for Ir^{197}. Christian et al.[1] reported ≈1 MeV beta ray for Ir^{195}. Butement et al.,[2] however, reported 2.1 MeV and 1.25 MeV beta ray for Ir^{195}, and also reported 1.6 MeV beta ray for Ir^{197}. Since the reported values of the beta-ray energies from Ir^{195} are various and the energy value of the beta ray from Ir^{197} is not consistent with the systematics in iridium, it is interesting to investigate the beta-ray energies of the iridium activities and to compare their values with those from the beta-decay energy systematics.

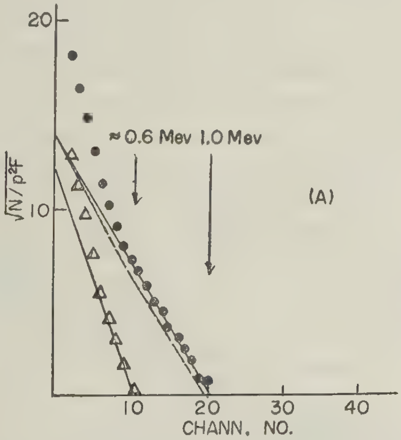

Fig. 1. (A) The Kurie plot of the beta spectrum of Ir^{195}. The contribution for the presence of the beta rays from 19 hr Ir^{194} has been subtracted. The dashed line represents the Kurie plot of Au^{198}, measured under the same conditions.

Ir^{195} was prepared by a (γ, p) reaction in natural platinium using 25 MeV bremsstrahlung from the betatron in the internal target.[3] A chemical separation was performed to get the iridium activities produced in the sample. In order to investigate the beta rays from Ir^{195}, a plastic $(2'' \times 1'')$ scintillation spectrometer, which was calibrated with Au^{198}, P^{32} and In^{114}, was used.

Fig. 1. (A) shows the Kurie plot of the beta-ray spectrum from the decay of 2.3 hr Ir^{195}. The beta rays with the energies of 1 MeV and ≈0.6 MeV were found, and no beta ray above 1 MeV with a half life of 2.3 hr was observed. (The existence of ≈0.6 MeV beta ray was confirmed from comparion with the Kurie plot of Au^{198} shown in Fig. 1. (A)). The intensity ratio of these two beta rays was about 1:0.3. The 1 MeV beta ray agrees with the systematics and the result obtained by Christian et al.

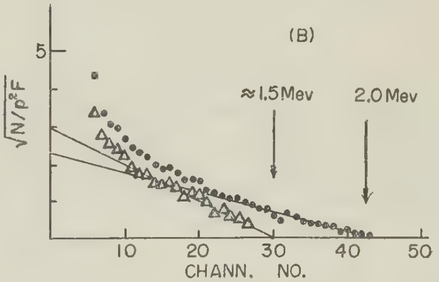

Fig. 1. (B) The Kurie plot of the beta spectrum of Ir^{197}. The contribution for the presence of the beta rays from other iridium and platinium activities has been subtracted.

In the same way the beta rays from Ir^{197} were studied. But in this case no chemistry was performed. 2.0 MeV and ≈1.5 MeV beta rays with the same intensity were found from the Kurie plot of the spectrum (Fig. 1. (B)) and assigned to 7 min. Ir^{197} from their decay curves. The 2 MeV beta ray also agrees very well with the beta-decay energy systematics, so that this beta ray is expected to be the transition to the ground state or the lower excited states in Pt^{197}.

The gamma-ray spectrum was also studied by means of conventional NaI(Tl) $(1\frac{1}{2}'' \times 1\frac{1}{2}'')$ scintillation spectrometer. In addition to the known gamma rays from Ir^{194} and Ir^{195},[2] the strong gamma rays of 100, 130, 330 and 370 KeV decaying with a half life of 2.3 hr were found and very weak gamma rays with the energy between 150 KeV and 250 KeV were also observed. The 880 KeV gamma ray[2] was beyond the limits of detection in the present work. (The gamma rays of 330 KeV and

---

* Present Address: Linac Laboratory, Japan Atomic Energy Reserch Institute, Tokai-mura, Ibaraki-ken.

50 keV were resolved from the corresponding gamma rays of [illegible].

For Ir¹⁸⁶, ≈300 keV gamma ray with the half life of [illegible] min. was found and 1.8 MeV gamma ray was not observed.

The energy and the relative intensity of the gamma rays following the decay of Ir¹⁸⁶ and Ir¹⁸⁸ are listed in Table 1.

Table 1. Gamma rays following the decay of Ir¹⁸⁶ and Ir¹⁸⁸

Energy keV	Relative intensity	Nuclide
130	100	Ir¹⁸⁶
230	50	"
175–250	weak	"
330	30	"
370	40	"
430	30	"
560	20	"
≈300	—	Ir¹⁸⁸

References

1) Christian, Mitchell and Martin: Phys. Rev. 86 (1952) [illegible].
2) [illegible]
3) [illegible]

J. Phys. Soc. Japan 16 (1961) [illegible]

Properties of Grain Boundaries in Silicon

By [illegible]

[illegible]

Japan

(Received January [illegible], 1961)

The non-ohmic character for current flow perpendicular to grain boundaries is frequently experienced in p-type Si. The properties of grain boundaries in Ge were studied by many investigators¹⁻³ and it has been known that this boundary layer has a p-type character due to the acceptor action of dangling bonds⁴. In Si, however, the properties of grain boundaries have not yet been reported. Contrary to Ge, an n-type character has been observed at the grain boundary layer in p-Si.

P-type Si bicrystals are grown by the vertical pulling technique with dual seeds symmetrically tilted about the [110] axis at angles of 10° and 5°. The bulk resistivities are 200 to 400 Ω cm. Photovoltages are measured on the rectangular specimens by scanning a [illegible] perpendicular to the grain boundary. The sign of the photovoltage shows for the grain boundary to be n-type [illegible] crossed the grain boundary.

The resistance of the boundary is non-linear, increasing with increasing voltage, and is [illegible] regardless the current direction. The curve for both directions of current flow resembles the ordinary rectifier characteristics in the blocking direction. In order to measure the voltage drop across the boundary, Au-Sb alloyed contact is used for the boundary and Al-Si contacts for the bulk, as shown in Fig. 1. For the current flow in this figure, the voltage drops V_1 and V_2 are shown with the correction of IR drop. It is seen that V_1 and V_2 resemble the forward and reverse characteristics of p-n junction, respectively. Taking into consideration of the polarities, it may be concluded

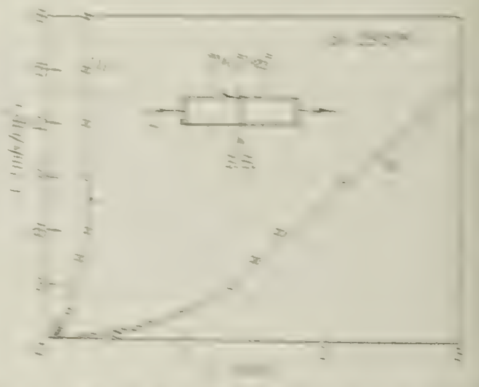

Fig. 1. Voltage drop at both sides of grain boundary as a function of current density.

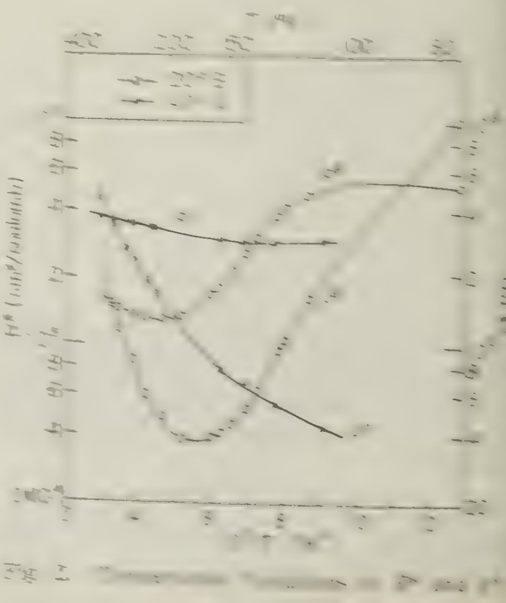

Fig. 2. Temperature dependence [illegible]

[illegible]

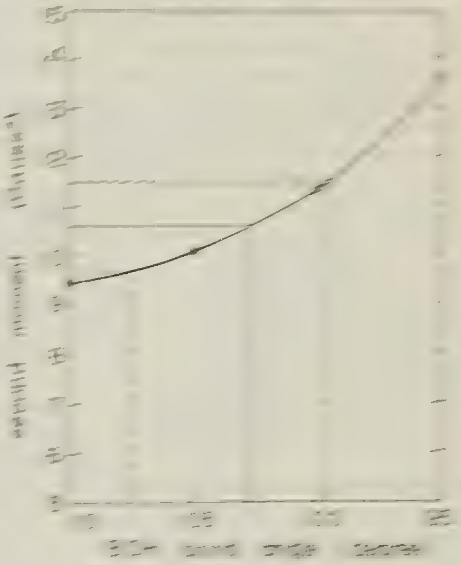

[illegible]

References

1) J. A. Ibers and C. H. Holm: The forgoing paper.
2) K. Kume and Y. Kakiuchi: J. Phys. Soc. Japan, **15** (1960) 1277.

J. PHYS. SOC. JAPAN **16** (1961) 844~845

Linear Potential Barrier Model for Nuclear Surface

By Tutomu INOUE

Nagoya Technical College, Nagoya

(Received February 5, 1961)

Sugiyama[1] developed the theory of surface of Fermi gas on the basis of the charge neutrality condition, and gave the method of correcting a potential barrier which does not satisfy the charge neutrality. He derived expressions for the surface energy σ and the correcting displacement b in terms of a phase shift produced by the barrier. His Eqs. (4.8) and (4.7) can be proved to be equivalent to Swiatecki's formula[2] for surface energy and to the definition of the effective surface, respectively. And they are applicable to the nuclear matter.

Sugiyama applied the expressions to the calculation of the surface energy of linear potential barrier $V(x)=-(\hbar^2k_F{}^2/2M)\cdot(x/x_0)$ for $x\leq 0$. His calculation, however, was limited only to a sharp barrier, i.e., that with smaller slope parameter k_Fx_0, and was not compared with Swiatecki's results[3]. Here, the calculation is made for larger range of k_Fx_0. For a diffused barrier, we can calculate an approximate phase shift by the W-K-B method on one hand; and, on the other hand, the surface energy and the position of the effective surface by the Thomas-Fermi approximation. Thus it is interesting to examine, in the case of this simple barrier, whether his expressions in the W-K-B approximation are reduced to the Thomas-Fermi approximation.

The phase shift $\eta(k_x)$ for this barrier is given by

$$\eta(k_x)=F(\omega)=\tan^{-1}[\{J_{1/3}(\omega)+J_{-1/3}(\omega)\}/\{J_{-2/3}(\omega)-J_{2/3}(\omega)\}]\ ,$$

where J_ν is Bessel function of order ν and $\omega=(2k_Fx_0/3)\cdot(k_x/k_F)^3$. The numerical calculations for $\beta=\sigma/\sigma_s$ and b/b_∞, where σ_s and b are those for the infinite wall, are carried out easily by use of tables of the Bessel function[4] and the results are shown in Table I as a function of k_Fx_0. Taking the same Fermi energy $\hbar^2k_F{}^2/2M=22$ Mev as used by Swiatecki, we obtain the surface coefficient in the mass formula, $a_s=4\pi r_0{}^2\beta\sigma_s$ (r_0 is the radius of the nucleon) as a function of x_0, and it is shown in the curve 1 in Fig. 1. This curve is a quantitative presentation for the qualititative estimation by Swiatecki[3]. The straight line 2 shows the limiting behaviour for $k_Fx_0\ll 1$, given by Sugiyama's Eq. (4.12′).

Table I. The values of β and b/b_∞ as functions of the slope parameter k_Fx_0

k_Fx_0	β	b/b_∞
0.00	1.0000	1.0000
0.15	1.0131	0.3702
0.30	1.0274	0.1976
0.45	1.0426	0.0724
0.60	1.0589	−0.0302
0.90	1.0943	−0.1995
1.2	1.1338	−0.3419
1.5	1.1776	−0.4688
1.8	1.2260	−0.5858
2.1	1.2795	−0.6964
2.4	1.3383	−0.8026
2.7	1.4029	−0.9061
3.0	1.4736	−1.0078
4.5	1.9206	−1.5132
6.0	2.4704	−2.0281
7.5	3.0284	−2.5407
9.0	3.5835	−3.0492
10.5	4.1547	−3.5598
12.0	4.7293	−4.0705
13.5	5.3003	−4.5795
15.0	5.8765	−5.0893

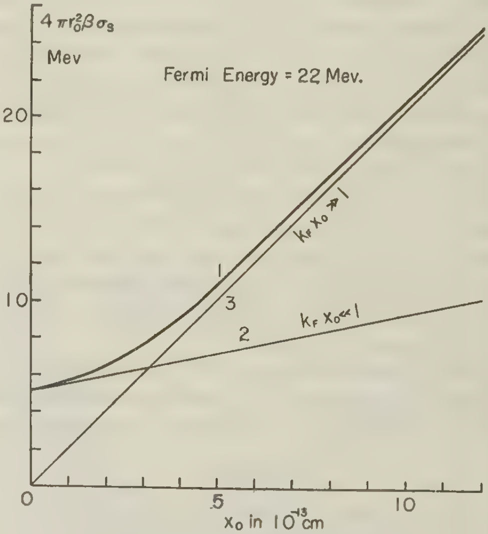

Fig. 1. The surface coefficient in the mass formula as function of the width of surface x_0.

For larger k_Fx_0, the use of the asymptotic expansion of the Bessel functions gives the simple expression

$$F(\omega)\sim\omega+\frac{\pi}{4}\left(+\frac{1}{72\omega}(1+6\cdot\sin 2\omega)\right),$$

which can be obtained also from the W-K-B method. This reduces Sugiyama's Eqs. (4.11) and (4.12) to those of the Thomas-Fermi approximation

$$b/b_\infty=-(15/16\pi)k_Fx_0 \quad \text{and} \quad \beta=(128/105\pi)k_Fx_0,$$

respectively, and the latter is shown as the straight line 3 in Fig. 1.

Fig. 1 shows that the coefficient corresponding to an experimentally reasonable value[5] $x_0\sim2\times10^{-13}$ cm is about 1/3 of the empirical value 17 Mev. This may be due to the defects common to the one-particle treatment and reveal the importance of the contribution of the correlation energy.

The reduction of Sugiyama's expressions to the Thomas-Fermi approximation is practicable not only in the case of the diffused linear barrier but also in that of any diffused barrier, if the phase shift can be calculated by the W-K-B method. The verification will be given in future with that of the equivalency of Sugiyama's expressions to the Swiatecki's.

The author wishes to express his thanks to Dr. Sugiyama for the suggestion of this analysis.

References

1) A. Sugiyama: J. Phys. Soc. Japan **15** (1960) 965.
2) W. J. Swiatecki: Proc. Phys. Soc. London **A**, **64** (1951) 226.
3) W. J. Swiatecki: Phys. Rev. **98** (1955) 203.
4) *Tables of Bessel Functions of Fractional Order*, Colombia Univ. Press, 1948.
5) L. Wilets: Rev. Mod. Phys. **30** (1958) 542.

Errata

Rheological Equations of Generalized Maxwell Model and Voigt Model in Three-Dimensional, Non-Linear Deformation

By Wataru SEGAWA

J. Phys. Soc. Japan **16** (1961) 320

Page	Column	Line		Should be read
320	Synopsis	1	Voigt are	Voigt model are
320	Synopsis	2	at the	of the
321	left	26	$\partial x^i/\partial x_p{}^{*\lambda}$	$\partial x^i/\partial y_p{}^{*\lambda}$
322	left	3	$N_pe_{p\lambda\mu}e_{p\nu\mu}$	$N_pe_{p\lambda\nu}e_{p\nu\mu}$
322	left	7	N_p, P_p;	N_p; P_p,
322	left	11	$\frac{1}{2}e_{\lambda p\mu}$	$\frac{1}{2}e_{p\lambda\mu}$
322	right	34	$3\mu_pl_p$	$3\mu_pe_p$
323	left	16	Nookian	Hookean

The Velocity Distribution at the Interface between Two Liquids

By Setsuo OKUDA

J. Phys. Soc. Japan **16** (1961) 324

Plate 3 (B) and Plate 6 (B) (P. 325) should be interchanged.

Fig. 1 (P. 327) and Fig. 7 (P. 332) should be interchanged, leaving the explanatory titles in the present positions.

Errata

Dislocation Networks and Moiré Patterns of Molybdenite

By Yoshihiro KAMIYA, Keiichi ANDO, Minoru NONOYAMA
and Rhozi UYEDA

J. Phys. Soc. Japan **15** (1960) 2025

Page	Column	Line	wrong	right
2031	right	16	(a)	(c)
			(c)	(a)
2032	left	36	is	in
2034	left	24	(hb)	$(h\cdot b)$
2035	right	9	mikroskope	mikroskopie
		13	mikroskope	mikroskopie
		21	(Oxford, 1953)	(Clarendon Press, Oxford, 1953)
		24	Crysi.	Cryst.
		26	10)	11)
			(1969)	(1959)

10) H. Hashimoto: J. Phys. Soc. Japan **13** (1958) 534.
should be added.

Some Remarks on Hydrostatic Pressure and Maxwell Model

By Wataru SEGAWA

J. Phys. Soc. Japan **16** (1961) 317

Page	Column	Line		Should be read
318	right	8	of the isotropic	to the isotropic
318	right	35	conditioned	condition

JOURNAL OF THE PHYSICAL SOCIETY OF JAPAN Vol. 16, No. 5, MAY, 1961

Lateral Density Distribution of Charged Particles in the Central Region of Extensive Air Shower

Saburo MIYAKE, Kensaku HINOTANI, Itsuo KATSUMATA,
Tatsunosuke KANEKO and Nobuo ITO

Department of Physics, Osaka City University

(Received November 14, 1960)

The lateral density distribution of the ionizing particles around the core of the extensive air shower has been observed with ten plastic scintillation counters at mountain altitude (2775 meters above sea level). The lateral density distribution, which has seemed so far to be expressed by the unique function of the distance from the central axis of extensive air showers, has been clearized as that it could be expressed by $1/r^n$ approximately is a range of 20 meters from the axis and n varies from 0.8 to 2.0 by the character of each shower. The result seems to have a relation to the fluctuation which has been presented in the previous paper or to the fluctuation of nuclear cascade in the development of extensive air showers.

The density spectrum at single counter has been also analysed and the result supports above conclusion.

§ 1. Introduction

It is well known at the present time that the study of an extensive air shower is the only way to get information of nuclear interaction and of primary cosmic radiation at very high energy region (10^{15}–10^{18} ev). The general aspects of the extensive air shower has been also clear at least for the average character of the event. The next steps in the air shower experiment are, then, (1) to analyse the character of individual event, and (2) to study nuclear interactions in very high energy. Only a brief summary of the problems is given here, since a detailed description is available in the previous paper[1].

The lateral density distribution of the charged particles in the extensive air shower has been studied by many authors[2] at various altitude and it has been also estimated by the theoretical calculation of various authors[3]. Most of the results so far obtained were average lateral distribution of all detected showers, or, in some cases, of the shower classified into small groups of fixed range of shower size (total number of shower particles). Their conclusive distribution functions were consistent with estimated distributions of shower particles at age 1.2–1.4, calculated by Nishimura and Kamata[4], at least in altitude lower than mountain altitude and they were not sensitive for any classification. Recent studies on the distribution for individual extensive air shower by the use of large span density detectors array have also shown that the distribution for individual large showers at sea level was approximately consistent with that of age 1.4[5]. Nevertheless, the arrangement of counters in above experiments seems to be too far from the axis of shower to detect the fluctuation because the electromagnetic cascade theory does not show so much sensitivity for the age of showers in such distant region, and statistical error of the observed density, population of μ-meson etc. were not favorable to this item. Then, it can be said that no experiments have yet been made which allow one to evaluate the possibility that each extensive air shower has specific character (individuality) and we have as yet very little information as to what is involved in the fluctuation.

One of the authors has suggested that there may be large fluctuations caused by the fluctuations of the starting altitude of the extensive air showers (level fluctuation) and the characteristic fluctuations of elementary process in the development of nuclear cascade, and their effect should appear especially in the central region of the extensive air shower as the variety of the lateral distribution of density of charged particles. An attempt is made in this paper to determine between the possibilities of above suggestion and further object of the work is to study the characters of primary particles and nuclear interactions in very high energy region. The results obtained here show the existence of large fluctuation and it suggest that we must change the image of the extensive air shower which was considered as the averaged scheme so far.

§ 2. Experimental Method

a) *Experimental arrangement and apparatus*

Fig. 1 shows the arrangement of the apparatus; in this figure, S_1–S_{10} are square plastic scintillation counters of $50\times50\times5\,\mathrm{cm}^3$ large, **C.C.** is a multiplate cloud chamber of $2.0\times1.3\times0.9\,\mathrm{m}^3$ large which containes 21 lead sheets of 1.0 cm thickness[6], and **N.M.** is a neutron monitor of standard type[7]. A thickness of the roof of the laboratory is about 1–3 g/cm² for the scintillation counters.

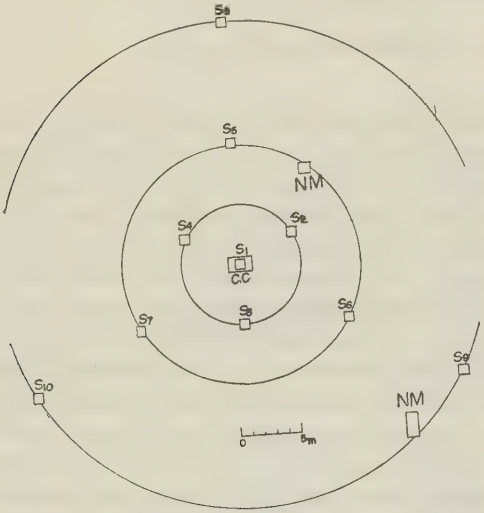

Fig. 1. The arrangement of air shower detectors. $S_1, \cdots S_{10}$ are density detectors which size are $50\times50\,\mathrm{cm}^2$ in area and 5 cm in thickness. **C.C.** is a large multiplate cloud chamber which size is 200 cm wide and 130 cm high and 90 cm deep. **N.M.** is a neutron monitor of standard type which is made for purpose of continual observation of neutron in cosmic ray.

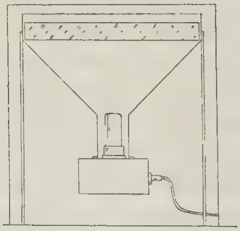

Fig. 2. Crossectional diagram of the plastic scintillator. Photo tube is Du mont 6292 type.

In this report, only the results by the counters are described and the other data concerned to nucleon component will be reported near future.

The detail of the scintillation counter is shown in Fig. 2. The signals from the preamplifier are fed to logarithmic amplifier and amplified. Their logarithmic out put signals are recorded by the method of photographing of the cathode-ray tube. The possible range of pulse height to record is corresponding to the particle density from 4 to 10^6 particles per square meter with the estimated error of about 10%. Starting point of the recorded picture was based on the maximum point of the pulse height distribution curve of the single particle counting by pulse height analyser and the observed pulse height is converted to time interverval as logarithmic scale which is defined as its $6.0\,\mu$sec is twice in this case. The calibration of logarithmic scale has been done by the use of hydrogen discharge tube and romble slit which can vary photo-intensity in the range of six order for the relation of photo-input to recorded output. The frequency of " ghost image " by accidental particles is about one percent of the records, and they can be excluded in the stage of the reading or treatment of observed data. The chance of accidental coincidence between two different extensive air showers can be neglected. These electronic technics employed in this experiment were due to Air Shower Group at Institute for Nuclear Study of Tokyo University[8].

b) *Triggering method*

Three series of observation has been done; These triggering method are as follows;

1. When every pulse from S_1, S_2. S_3, and S_4 exceed 200 particles per square meter.
2. When S_1 exceeds 300 particles/m² and S_2, S_3 and S_4 are more than single particle.
3. When only S_1 exceeds 300 particles/²m.

In these series, average time interval was about 8–13 minutes and the pulse heights from ten scintillation counters and the time when the event occurs are recorded simulteneously.

c) *Treatment of the observed data*

To determine the position of axis and total number of charged particles of the air shower from the recorded particle densities, a simple mechanical analogue computer was used. Nevertheless, since the lateral distribution function is not unique for all showers, the practical method of analysis is as follows; firstly, the position of the axis is searched in the way that the observed data become to show a smooth lateral distribution in axial symmetry, secondly, the exponent of the distribution function, which is expressed approximately the power fuction of the distance from the axis, is given by the comparison of obtained distribution with the already provided curves for the various exponent, and lastly the conventional size is given by the comparison of the density at 10 meters from the axis with the density of standard distribution function which was taken as $r^{-n}\exp-r/r_0$ in this case, where r_0 is taken as 100 meters.

In above treatment, the position of axis is defined with the error of about 1 meter in the central region of experimental arrangement. The exponent n has a error of about 10%, but there is noticeable discrepancy between the showers of low and high value of n and the discrepancy is not artificial.

Since an experiment to determine the relation between the exponent n and r_0 has not yet been made and our counter arrangement is not so wide as to determine r_0 for every shower, the conventional size is not changeable at once to the true size. But it becomes approximated size by multiplying $1/2^{n-1}$, if the lateral distribution function is a standard type mentioned above far from 20 m that is a radius of our counter arrangement.

The pulse height from scintillation counter is not always depend on the particle numbers, and the use of many unshielded G.M. counters are thought to be more available to detect it. Though, the recorded data were calibrated by comparing with track density in the picture of cloud chamber, so as it is mentioned in later section.

The zenith angle of the shower is obtained from the stereoscopic analysis of cloud chamber photographs.

§ 3. Experimental Results

a) *Density distribution in single counter*

The present study was designed to secure the general information about the experimental method and possible significance of the results. Obtained data for S_1 are summarized in Fig. 3 in which low density part is obtained by pulse height analyser and scaling circuits, and the data contributed by air shower are obtained by the coincidence with the signals of other nine counters substituting the probability of accidental coincidence, and high density part is evaluated from all data through the experiment because the frequency is very small and the difference of triggering condition is thought to do not affect to the data in this very high density region.

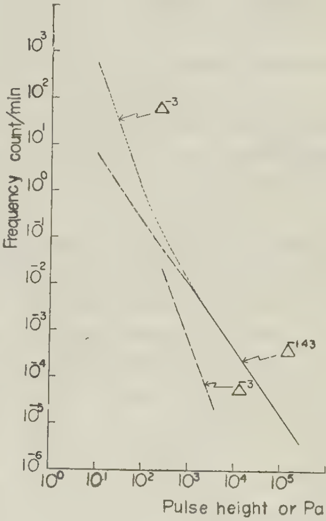

Fig. 3. Density distribution obtained by the density detector S_1. Real line shows that the distribution larger than 10^3 particles per meter square is almost identical to the density distribution obtained by air shower triggering. Dashed line shows density distribution by the event not associated to air shower.

In low density part, the distribution is expressed as the power function of the density with the exponent of -3.0. To analyze what contribute to this density region, the experiment has been done by the cloud chamber under the scintillation counter. The phenomena are divided into following three groups;

1. No significant phenomena are observed.
2. Low energy electron component distributes sparsely.
3. Local high energy electron component are observed only.
4. The others are extensive air showers clearly shown by the signals from other nine counters.

The events belong to group 1) are seemed to be nuclear disintegrations in plastic scintillator and their pulse height distribution is expressed as $\exp(-E/300\,Mev)$ where E is a dissipation energy in the scintillator. Then this events are rapidly decreased according to the output signal is increased and they cannot contribute to high density part.

The events belong to group 2) are seemed to be the core of small size air showers which seemed to be a group of gamma ray distributed mainly in about a few meters.

The events belong to group 3) are young high energy electron cascade and secondaries of high energy nuclear event in the air above the laboratory. The events 2) and 3) are thought to be smaller events, though their age is somewhat different, and their primary energies will be corresponded to larger than 10^{12} ev.

The density distribution by air shower has been seemed so far to be corresponded to the size distribution under the hypothesis that air showers have a unique lateral distribution function for the particle density independent their sizes, and then the exponent of density distribution has to be agreed with the exponent of size distribution, namely, 10 particles/m² and 10^3 particles/m² correspond to sizes of about 10^5 and 10^7 respectively. But in the high density part there exist clear discrepancy. One of the reasons to explain it is the variation of average lateral density distribution function with the size, and the other is variety of the function even in the same size showers, as that described in later section.

In Fig. 4, the rate of contribution from every shower size group has been plotted against the density. It should be noticed that the fixed density is related to very wide range of shower size. The tendency will be more emphasized if the true shower size was used, because the conventional shower size mentioned already have an inclination to strengthen the correspondency of the observed density and shower size.

b) *The distribution and size dependence of the exponent n*

As shown in Fig. 5 the exponent, n, distributes in very wide range, namely, from 0.6 to 2.2. The exponent α of 0.8 and 2.0 is equivalent to the age parameter of about 0.6 and 1.8 in the electromagnetic cascade theory when the culculation by Nishimura and Kamata[4] was applied. Although the relationship between this fluctuation and other character of air shower has never been clear, it seems to us that there are various age of air showers, from young to old, at least in the central region of the showers.

Fig. 6 shows the variation of the mean value of the exponent n for divided shower

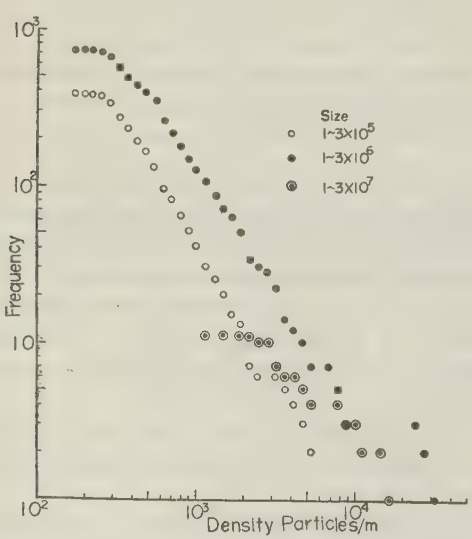

Fig. 4. Three groups of plots show the density distributions of S_1, which are caused by the air showers of size $1-3\times10^5$, $1-10^6$, and $1-10^7$ particles respectively.

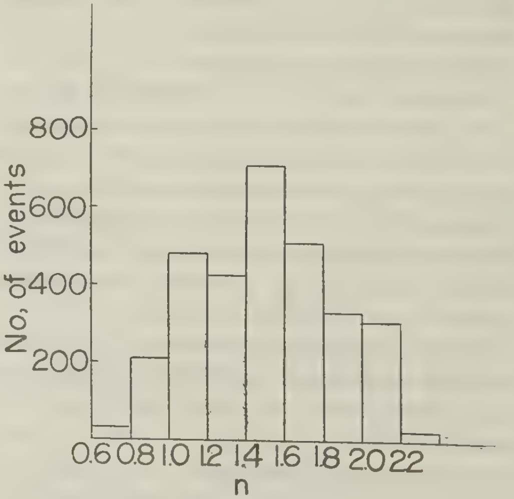

Fig. 5. This histogram shows the distribution of the exponent, n, of lateral density distribution function. We can see from this figure that the exponent fluctuate very wide range.

size groups. In this figure, the value of the exponent at low size must be corrected to smaller one because the showers which have small exponent are missed by the bias of air shower triggering at such small size. Then, it can be said that the mean value of the exponent is increased with the shower size.

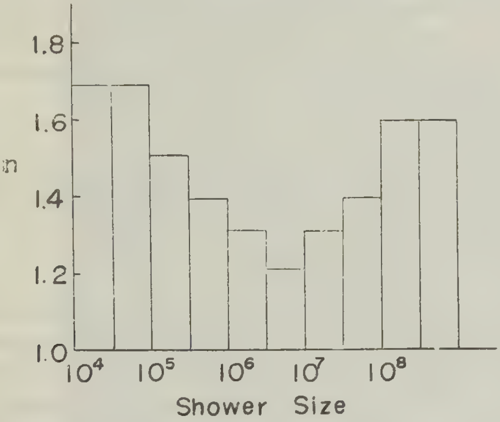

Fig. 6. This histogram shows size dependence of mean value of the exponent, n, of lateral distribution function.

It may be seemed to be natural that the results are, as predicted by electromagnetic cascade theory, understood as larger showers have their maximum at lower atmosphere. But it should be noticed that the exponent is not sensitive to zenith angle of air showers. The difference of the exponent for divided zenith angle group is almost in their error. Then the fluctuation is seen mainly dependent on the character of the showers discussed in later section.

c) *Relation of density distribution to size spectrum*

Fig. 7 shows size spectrum obtained in this experiment. Comparing this size spectrum with density distribution shown in Fig. 3, one can easily find out that the exponent is not identical to each other in larger density and size region. This discrepancy is explained by using the gradual changing of lateral distribution function with the size.

The integral size spectrum $F(N)$ can be represented approximately, in some range of size N, by the following form,

$$F(N) \propto N^{-(\gamma_0 + c \log N')} \tag{1}$$

where N' is the logarithmic mean size of the range. And the size dependent lateral distribution function is assumed as follows,

$$\begin{aligned} \Delta(N, r) &= k(N) N r^{-(a+b \log N)} e^{-r} \\ &= k(N) N^{1-b \log r} r^{-a} e^{-r} \end{aligned} \tag{2}$$

where $k(N)$ is the normalization factor which can be seemed to be constant in some range of size N, in first approximation. The value of γ_0, C, N', a and b will be given in later part of this section. The observed lateral distribution at central region within a few meters from cores shows rather larger fluctuation and there have been few data about the fluctuation. Present data are also not enough to evaluate the fluctuation with some accuracy. Then, the lateral distribution function written in eq. (2) loses its reality in the central region of the air shower. The forms of lateral distribution function at central region plays important role in culculating the density spectrum. By these reasons, it is seemed to be impossible to calculate the accurate density spectrum directly from eq.

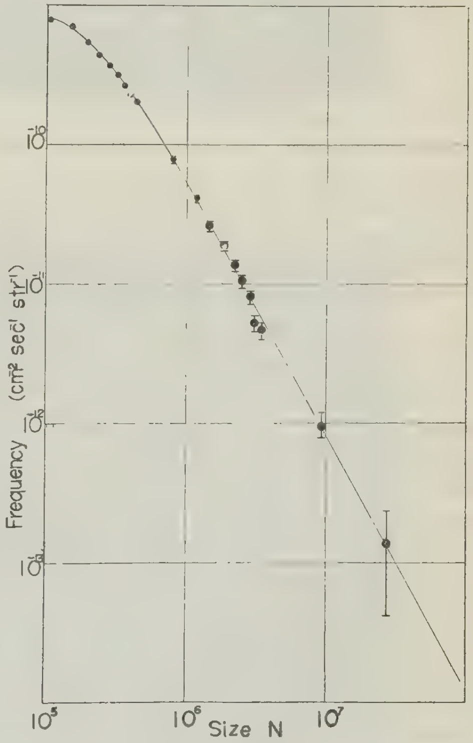

Fig. 7. Size spectrum at Mt. Norikura 2775 m altitude. The size spectrum can be expressed by the following formula;

$$R(>N) = 4.8 \times 10^{-11} \left(\frac{N}{10^6}\right)^{-1.85} \text{cm}^{-2}\,\text{sec}^{-1}\,\text{str}^{-1}$$

for range of size $10^6 - 10^6$.

(1) and (2). Accordingly, it is impossible to show directly that the difference of the exponent between the density distribution and the lateral distribution is due to the size dependency of the lateral distribution. Then, the following method, though it is not directly, is taken.

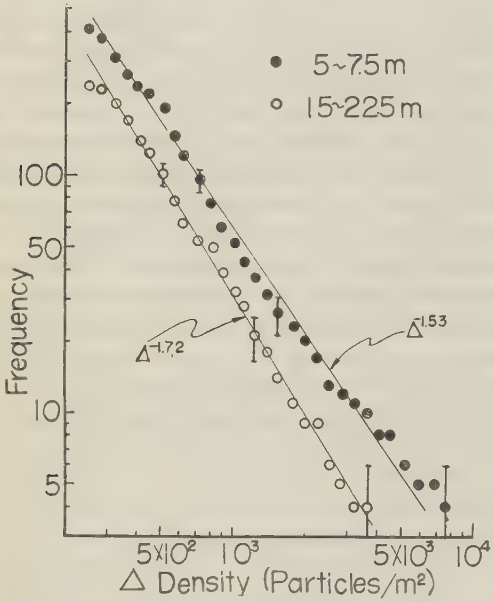

Fig. 8. Two density distributions. One of them (shown by black point) is a density distribution of air showers whose cores strike a ring shaped zone defined by two radii of 5 and 7.5 m from S_1 and the other (shown by circles) is one by two radii of 15 and 22.5 m.

In Fig. 8, two density distribution are shown. One of them (shown by black point in the figure) is a density distribution of air showers whose cores strike a ring shaped zone defined by two radii of 5 and 7.5 *m* from the density detector S_1, and the other distribution curve (shown by circles) is one by two radii of 15 and 22.5 *m*. The exponents of the curves are −1.53 for 5–7.5 *m* and −1.72 for 15–22.5 *m*, respectively, in the range of density $3\times10^2-3\times10^3$ particles per square meter.

On the other hand, the integral density spectrum, $D(\Delta, r)$ by the air shower striking at distance, r, from the density detector S_1 can be written as follows by considering eq. (2),

$$D(\Delta, r)\propto N^{-(\gamma_0+c\log N')}$$
$$=\left\{\frac{1}{k(N)}r^a e^r \Delta\right\}^{-(\gamma_0+c\log N')/(1-b\log\gamma)}$$
$$\propto \Delta^{-(\gamma_0+c\log N')/(1-b\log\gamma)}$$

In this relation, putting, $-\dfrac{\gamma_0+c\log N'}{1-b\log r}=\beta$, we can obtain the follwing relation,

$$b=\frac{\beta-(\gamma_0+c\log N')}{\beta\log r}$$

Mean shower size N' in above relation is 1.4×10^6 and this value corresponds to mean density 10^3 particles per m^2 at distance 5–7.5 *m* from S_1. For distance 15–22.5 *m*, N' is 5×10^6. From these values, we can obtained the following relation,

$$b=0.10$$

This value for b is thought to explain the present experimental results fairly well.

§ 4. Discussion

The present series of experiments shows clearly that there are large fluctuations, although the nature of the fluctuation related to the essential role in individual shower is still a matter of speculation. There appear to be two possible explanations to account for the large fluctuations, namely, (1) the fluctuations of the starting altitude of extensive air showers, as that has been described in the previous paper (level fluctuation) and (2) the characteristic fluctuations of elementary process in the development of nuclear cascade in the core of air shower. These two models, shown in Fig. 9, are different in the inelas-

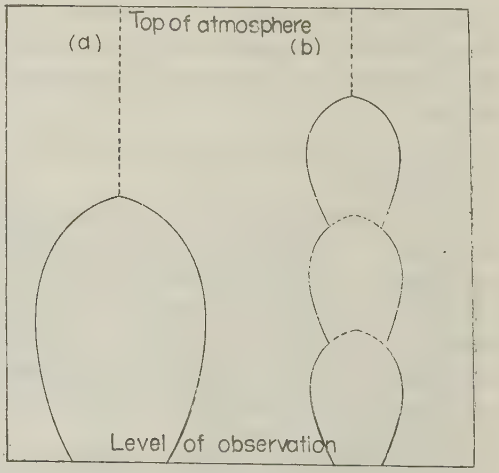

Fig. 9. A schematic figure of the development of air shower in atmosphere. (a) shows the fluctuation of the starting altitude of the air shower. (b) shows the characteristic fluctuations of elementary process in the development of nuclear cascade in the core of air shower.

ticity of high energy nuclear interactions.

Since the experiments in this report give the informations only near the core and the observed particles are small fraction of total, the discrepancy between the above models is not clear. We have not yet sufficient data on the character of individual shower to give an accurate evaluation of these two possibilities.

But if we accept these general specification: By any way the above models essentially equal

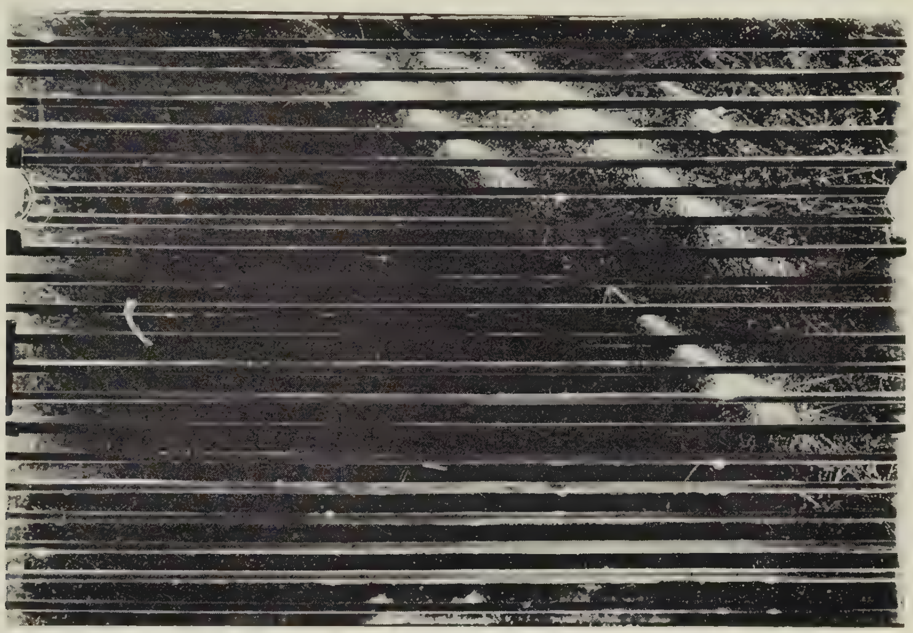

Fig. 10. This picture shows the cloud chamber photograph of the air shower which the core strikes 1.5 m distance from the cloud chamber and the size is 3×10^6 particles. This picture shows very large lateral density fluctuation.

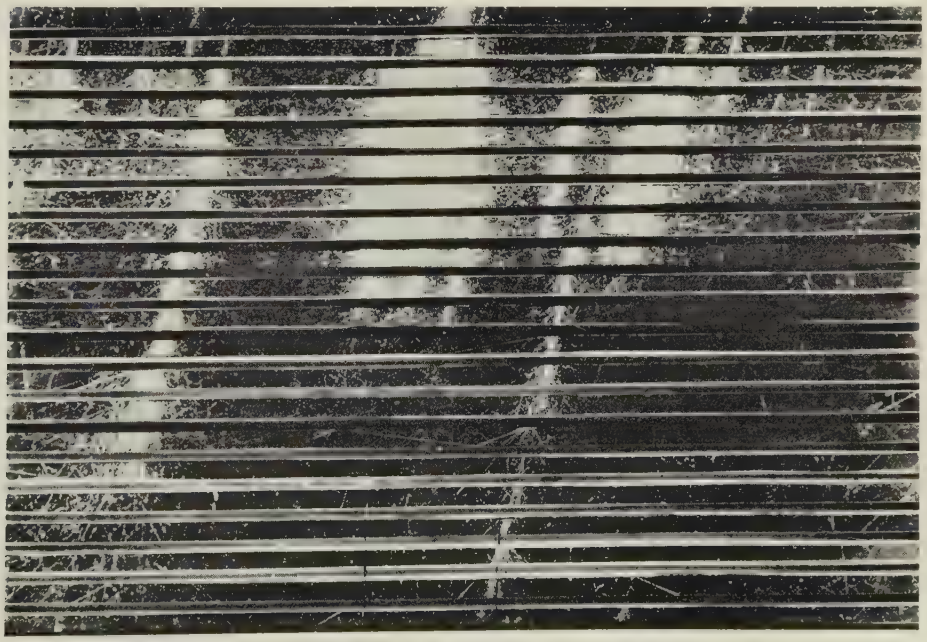

Fig. 11. An example of very young air shower (size$=5\times10^5$, distance from core$=2.5$ m). All particles in this picture are fairly high energy.

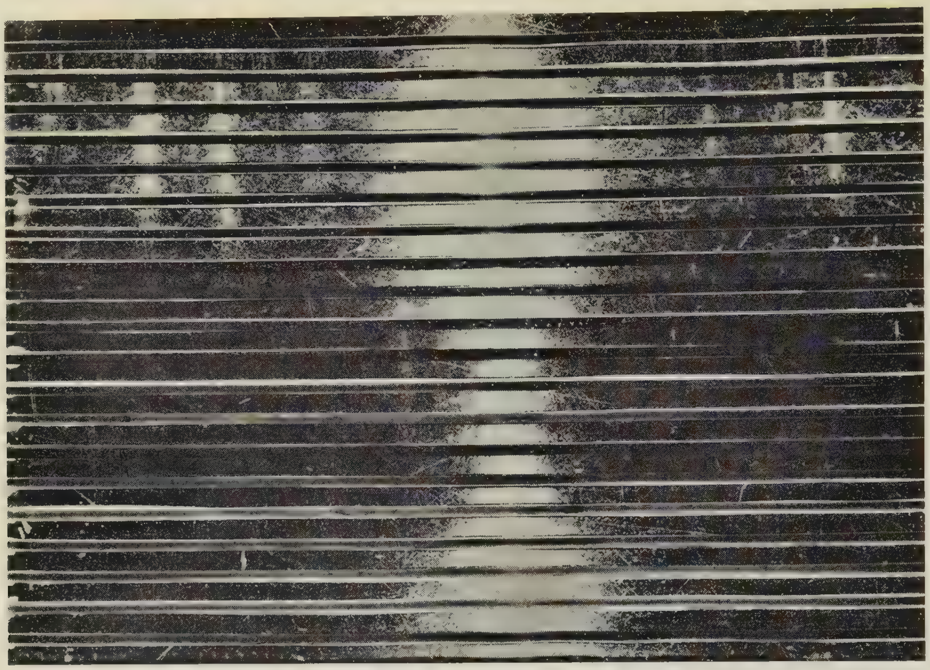

Fig. 12. This picture obtained by triggering of only S_1, so this event is not associated to air shower. It seems that the event is the very early stage of air shower which will develop to the size of about 10^4.

in the fact that core characters are determined by the nearest high energy interaction which occurs with large level fluctuation: It becomes considerable easier to understand some other characters of extensive air shower, for example, high density μ-meson shower in underground, high energy nucleon component in the core and so on which were explained already in the previous paper from the standpoint of model (1).

Several points of interest have come to clear by the use of multiplate cloud chamber, (1) lateral density fluctuation which is understood as azimuthal unisotropy that is shown in Fig. 10. (2) local high energy event as shown in Fig. 11. (3) the very early stage of air shower which will develope to the size of about 10^4. as shown in Fig. 12.

These are seemed to support above explanation. The study for these point will be continued.

Acknowledgement

The authors wish to express their thanks to Professor Y. Watase for his continual encouragements. This study has been supported in part by a Grant in Aid for Fundamental Scientific Research from the Ministry of Education and from Cosmic Ray Laboratory of Tokyo University.

References

1) S. Miyake: Progr. Theor. Phys. **20** (1958) 844.
2) See references of W. Galbraith: Extensive Air shower (Butterworth Scientific Publication co.).
3) M. Oda: Nuovo Cimento **5** (1957) 615. A. Ueda and N. Ogita: Prog. Theor. Phys. **18** (1957) 269. H. Fukuda, N. Ogita and A. Ueda: Prog. Theor. Phys. **21** (1959) 29. S. Olbert: Annals of Physics, **1** (1957) 247.
4) J. Nishimura and K. Kamata: Prog. Theor. Phys. Suppl. No. 6 1958.
5) T. E. Cranshow, W. Galbraith and N. A. Porter: Phil. Mag. **2** (1957) 804, 891 and 900.
6) S. Miyake, K. Hinotani, I. Katsumata and T. Kaneko: J. Phys. Soc. Japan **14** (1959) 1471.
7) M. Kodama, K. Murakami and Y. Sekido: J. Phys. Soc. Japan **12** (1957) 122.
8) T. Matano, I. Miura, M. Oda, K. Suga, G. Tanahashi and Y. Tanaka: The Report of the Institute for Nuclear Study, University of Tokyo.

JOURNAL OF THE PHYSICAL SOCIETY OF JAPAN, Vol. 16, No. 5, MAY, 1961

Mu-Meson Component of Air Shower Below the Ground

By Kenji WATANABE

Osaka City University

(Received January 6, 1961)

Mu-meson component, observed underground, of the extensive air shower is studied, which has come from the nuclear cascade of the shower core in the ground and possibly shows high concentration of mu-mesons below the ground. The total number of them can be estimated independently of energy and multiplicity distributions of secondary particles of the elementary collision each of shower particles undergoes, and also independently of some fluctuations. It is only because they depend upon the whole feature of the nuclear cascade in the shower core.

Experimental data of the multiple penetrating particles (M.P.P.), whose feature is the high concentration of mu-mesons, could not be interpreted in terms of those mu-mesons, i.e., decay products within the nuclear cascades in the ground initiated by impinging nucleons of high energy in the air shower cores, even though the possible contribution of the K-meson and Hyperon production in the high energy collisions within nuclear cascades is taken into consideration.

§ 1. Introduction

It is well known that mu-meson component of the extensive air shower (abbreviated as EAS) penetrates deep into the ground, that has been observed by Cornell group[1], George et al.[2], Osaka group[3] and Sakvarelidze et al.[4] These experiments have revealed that the *mu*-meson component of EAS covers some extension of about 60 m and about 13 m radius at 60 mwe and 1600 mwe respectively, with low particle density of about one particle or less per square meter. These date have been used to construct a model of EAS[5,6,7] together with those obtained at sea level and at mountain altitude.

On the other hand Osaka group has observed the multiple penetrating particles, abbreviated as the M.P.P., by means of a multiplate cloud chamber at 50 mwe and 250 mwe underground[8]. The events occur too frequently with the high concentration of *mu*-mesons to be interpreted by the use of the air shower model so far deduced from previous experiments and calculations of the nuclear cascade[5,6,9]. They shows *mu*-meson concentration from several to a few tens particles per square meter.

About the same time Soviet group has reported experimental results on the nucleon component of EAS at mountain altitute[6,10]. They observed at 3600 m elevation that in the EAS of total 10^5 particles there exists a very high energy nucleon in the shower core of about one hundredth or more of energy of primary cosmic rays, a few nucleons of 10^{12} eV or more energy each being in the EAS of total size more than 10^5 particles. Hence these facts should be taken into account not only for the interpretation of ordinary EAS, but also for the M.P.P., that has firstly suggested by G. Cocconi[6]. The existence of these energetic N-component has afterwards been established extensively by S. Miyake et al.[11], Soviet group[12] and Tokyo group[13].

The *mu*-mesons, observed underground, of EAS, then, are reasonably considered as follows; i) some of them are such *mu*-mesons as to have come from *pi*-meson decays within the nuclear cascades of the shower core in the atmosphere and penetrated into the ground as *mu*-meson, ii) the others are such as to have come within the nuclear cascades below ground, which are initiated by high energy N component impinging on the ground. None has been quantitatively estimated on the latter *mu*-mesons, while about the former several calculations have been performed[5,14,15,16] under various simplifying and sometimes too simplified assumptions. Hence it seems to be worthwhile estimating the contribution of *mu*-mesons generated by the latter mechanism of generation to the air shower *mu*-mesons, observed underground. This problem is studied in this paper and the results of estimate is compared with the experimental results of the M.P.P., discussion being given on its interpretation.

On the other hand it has been also suggested that the M.P.P. comes, because of some fluctuation, from the abruptly developing showers under the mountain altitude[17,18]. This is based upon the new model of air showers presented by S. Miyake[18]. The model may be however not consistent with recent experiments by K. Greisen et al.[18]. In this paper, then, the analysis is performed from the traditional point of view of the air shower.

It needs emphasis that the estimate given in this paper is free from such ambiguities as the adaptation of the energy and multiplicity distributions of secondary particles of elementary collisions in the shower and as their fluctuations. These ambiguities have been of doubtful feature for the calculations, so far attempted, of nuclear cascades in the atomosphere.

§ 2. Inherent Property of Observation of Air Shower *Mu*-Mesons Underground

The EAS so far observed at sea level or mountain altitude gives us an information about the features at some cross sections of the nuclear and electronphoton cascades developing or diminishing in the atmosphere. Then the calculations on the nuclear cascade, to be compared with experimental data, have been required to present the estimates not about the whole cascade but about each cross section along the developing of the nuclear cascade. Hence these estimated results had inherent features directly affected by the assumption adapted for the energy and multiplicity spectra of secondary particles of the elementary collisions in the cascade, and further by their fluctuations. This feature limits the applicability and the confidence of usual EAS theories, since the elementary collision of very high energy has not yet been clarified. It is also because the complexity of EAS calculations requires the various simplifying assumptions, for example the energy equipartition of secondary particles[5,14,15], or the neglection of essential factors, for example the fluctuations. In this way the experimental data of EAS at sea level or at mountain altitudes have to be considered on taking into account various ambiguous factors, but the reason for these complexities is only that the experimental data refer to a cross section of EAS on its developing.

On the contrary, the observation of *mu*-mesons underground of EAS, for example at 250 mwe, gives the information about the whole feature of cascade showers. This is an essential feature of the underground observation, different from those at sea level or mountain altitude: Let us consider a simple example, the EAS initiated from a proton with energy of 10^{15} eV. The inelasticity is assumed to be 0.3 for the nucleon-nucleus collision. On the average exists a high energy proton of 10^{13} eV at sea level (10 mwe), and the proton penetrates into the ground with successively colliding with rock nucleus. In this way at the depth of 30 mwe from the atmosphere the maximum energy particle reaches to have an energy of 1 GeV, where the interaction mean free path is about 1 mwe in the rock. If we observe *mu*-mesons of 1 GeV or more energy by means of a cloud chamber, like the experiment of the M.P.P., the nuclear cascade of EAS of 10^{15} eV may be considered to have disappeared at 30 mwe. Hence the observation of EAS *mu*-mesons at 250 mwe may be contributed from the whole cascade showers, which have disappeared at 30 mwe, through the *mu*-mesons come from the whole developing process of EAS. This fact is the essentially different characteristic from the observation at sea level or at mountain altitudes.

The fact that the probability of *pi*–*mu* decays abruptly changes at the ground surface along the shower developing has to be taken into account, although it has been neglected in the above consideration. If an EAS developed in the atmosphere for 90 % of its age, the underground *mu*-mesons may exist much more than those of another EAS with 50 % of its age in the atmosphere. Thus this fact introduces into consideration such an ambiguous factor that in what partition of the observed *mu*-mesons comes from below the ground. As described above, therefore, only such *mu*-mesons are considered in this paper as to have come from the nuclear cascade initiated by impinging nucleons on the ground. Such *mu*-mesons may be reasonably refered to the experimental data of the

M.P.P. in the first approximation. Then the nuclear cascade under consideration is initiated from the ground surface and developing wholly in the ground, so that it is able to be considered quantitatively with few ambiguity as shown in the following sections.

§ 3. Total Track Length, E_0/E

Considering the nuclear cascades or electron-photon cascades, the physical quantities refering to the whole cascade, but not to each cross section in its developing process, are to be determined by the incident energy and the observing energy, the familiar one being the total track length of the shower particles of more than or equal to E. Let us consider the cascade process initiated from a particle of energy E_0, for convenience. The total track length, $T(E_0, E)$, of the shower particles (of energies more than E) in the whole cascades is expected to be expressed as

$$T(E_0,\ E)=\omega\frac{E_0}{E}\ , \qquad (1)$$

where ω is a constant of about 1/2, as shown in the following, and only a parameter concerning with the energy partition of elementary collisions in the cascade process.

On the basis of the expression (1), the number of *mu*-mesons observed underground is estimated in the next section. In this section it will be shown that, for a few important cases, the expression (1) is valid and independent from the energy and multiplicity distributions of elementary collisions in the cascades. Hence the independency is to be held for the result deduced from the expression (1) on the *mu*-meson numbers observed underground.

i) Electron-Photon Cascade Theory

For the electron-photon cascade theory the expression (1) is described in the radiation unit. As is well known, the total track length is expressed in the so called approximation A, following B. Rossi[20], as

$$T(E_0, E)=0.437\frac{E_0}{E}\ , \qquad (2)$$

if $E_0 \gg E$, being equal to the expression (1). This is the case for the electron-initiating showers, and also the similar expression is valid for the showers initiated by photons, only replacing the numerical factor by the value of 0.572. The elementary processes in the approximation A are the bremsstrahlung by electrons and the pair creation by photons, and the probabilities of energy transfers per radiation length are approximately expressed as

$$\varphi_{\mathrm{brem}}(E_0, E)dE=dE/E$$
$$\varphi_{\mathrm{pair}}(E_0,\ E)dE=\mu_0\frac{dE}{E_0}\ ,$$

respectively, where μ_0 is a constant. In this case, the attention is called that both components, i.e., electrons and photons, contribute to the developing of the cascade showers until each dissipating its energy practically (see the following).

ii) Nuclear Cascade Theory

For the nuclear cascade theory the expression (1) is expressed in the unit of the interaction mean free path. Several nuclear cascade theories[5,14,15,16,21,22] have, so far, been provided, but discussion is given here for the Buddini-Molière theory[22] and the Fukuda-Ogita-Ueda theory[16], the former starting from the Heisenbery theory[23] as the elementary nucleon-nucleon collision and the latter refering to the Landau theory[24]. It is because the Heisenbery theory and the Landau theory are considered as describing comparatively satisfactorily the elementary collisions at high energy though the very high energy collision have not yet been investigated conclusively.

ii-a) Buddini-Molière Nuclear Cascade Theory[22]

In this theory the integral energy spectrum of secondary particles, which contribute to the developing of the nuclear cascade, in the elementary collisions is approximately expressed by

$$F_1(\eta)=\frac{\gamma}{\alpha!}\left(\ln\frac{1}{\eta}\right)^{\alpha}\ , \qquad (3)$$

where $\eta=E/E_0$, E_0 being the energy of the incident particle and E that of the secondary particle. α and γ is constant parameters, and the variation of their values serves to widely reproduce various spectra encountered in high energy collisions. Of course, the approximation cannot be satisfactory in the wide energy range by only a value of the constant α, but the suitable dividing of energy range gives a satisfactory approximation by only one value of α for each energy division. Fig. 1 shows various energy spectra expressed by the expression (3) with corresponding values of α. The Heisenberg theory can be expressed in the satisfactory approximation, following Buddini and Molière, by the one with $\alpha=2.0$ for energy range from $\eta=0.03$ to $\eta=0.3$.

On the other hand the next formula holds,

$$\gamma=\int_0^1 d\eta\cdot\eta\left(-\frac{dF_1(\eta)}{d\eta}\right), \qquad (4)$$

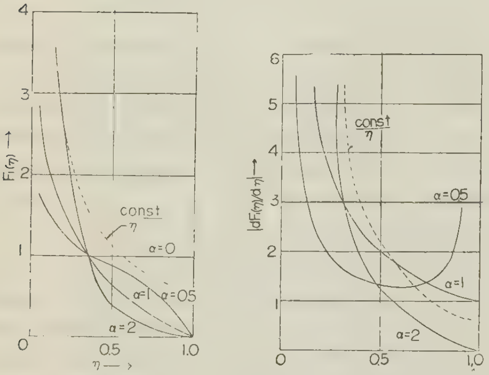

Fig. 1. Integral and differential energy spectra used in the Buddini-Molière nuclear cascade theory (after the authors[22]).

i.e., γE_0 is the energy transfered to the secondaries under consideration. From the view point of the cascade shower, the value of $(1-\gamma)$ is the portion of energies which escape from the cascade in each elementary collision and thereafter does not contribute to the developing of the cascade. When the secondaries of the elementary collision are composed of nucleons, charged *pi*-mesons and neutral *pi*-mesons, regardless of their contribution to the cascade, the energy conservation states that

$$\gamma_n+\gamma_\pi+\gamma_{\pi^0}=1\ ,$$

or more generally,

$$\sum_i \gamma i=1\ .$$

Almost all of the neutral *pi*-mesons decay into two photons, initiating the electron photon cascade showers, and do not contribute to the further developing of the nuclear cascade. In this case, the value of γ in the sense of the expression (4) is to be the value of $(1-\gamma_{\pi^0})$, being a value of about 0.9* at present. The emphasis is that the value of γ is nearly equal to unity, if the portion of the energy escaping from the cascade is small and does not extensively deform the developing of the cascade.

Following Buddini and Molière, the experimental results on the energy spectrum of secondary *pi*-mesons in high energy collisions can be approximated with a set of parameters, $\gamma=0.2$ & $\alpha=2.2$.

The cascade theory based on the expression (3) states that the number, $F(\eta,\ l)$, of particles of energies equal to or more than ηE_0 at the position of l nuclear m.f.p.s. from the initial point is expressed by

$$F(\eta,\ l)=e^{-l}\sum_{n=0}^{\infty}\frac{(\gamma l)^n\left(\ln\frac{1}{\eta}\right)^{n\alpha}}{n!\ (n\alpha)!}\ .$$

Hence the total track length $T(E_0,\ E)$ is obtained as follows,

$$T(E_0,\ E)=\int_0^\infty F(\eta,\ l)dl$$
$$=\sum_{n=0}^{\infty}\frac{\left[\gamma\left(\ln\frac{1}{\eta}\right)^\alpha\right]^n}{(n\alpha)!}\ .$$

The curves representing the expression (5) are shown in Figs. 2a and 2b for various values of α and γ. From these figures it is

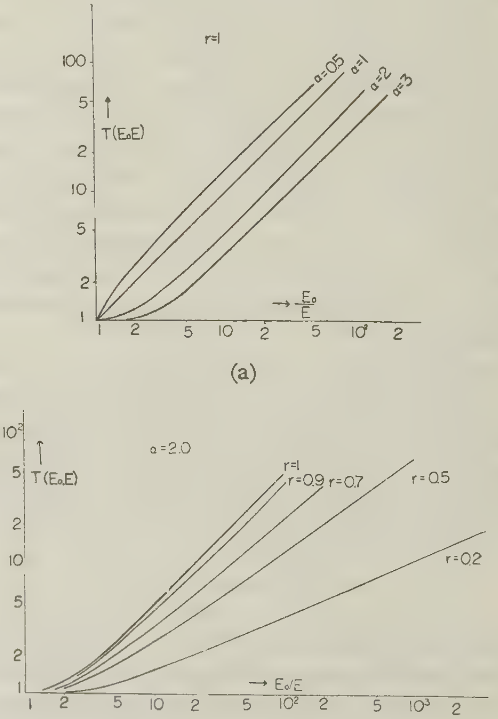

(a)

(b)

Fig. 2. Total track length, $T(E_0,\ E)$, for various pairs of parameters, α and γ.

---

* The value of γ, 0.9, here presented is based on the value of the inelasticity, 0.3, of high energy nuclear collisions in the cascade.

emphasized that the expression (1) can approximately reproduce the expression (5) independently of the values of α, $\alpha=0.5$, 1, 2, 3, i.e., the wide variation of energy and multiplicity spectra if the value of γ is unity. The approximation is satisfactory for the region of E/E_0 smaller than 0.3. The value of ω in the expression is changed from 0.3 to 1.

Even when the spectrum of the elementary collision is changed along the developing of the shower, the expression (1) can be adapted throughout in good approximation. The adaptation of different values of α in different energy regions is also not affect the applicability of the expression (1). These facts may be easily seen from curves of Fig. 2.

In the case of the value of γ smaller than unity, the total track length is reexpressed by the expression (1) in replacing E_0/E by $(E_0/E)^\beta$ with the value of β smaller than unity. For example, the curve with $\gamma=0.5$ and $\alpha=2.0$ is approximated by

$$T(E_0, E)=\text{const.}\,(E_0/E)^{0.71}\,. \qquad (6)$$

Heretofore, the "secondary" particles in this subsection mean those contributing to the further shower developing, regardless of species of particles. But the secondary particles are really considered to be composed of *pi*-mesons and nucleons in the high energy collisions. Both particles contribute concurrently to the developing of the shower. *Pi*-meson induced collisions may be, as usual, considered here to have a same feature as nucleon induced collisions. But energy spectrum of secondary *pi*-mesons may be expected as different from that of secondary nucleons, in which there contains the outgoing of the incident nucleon. Since the secondary particles, both *pi*-mesons and nucleons, undergo further nuclear interactions of the same feature as described above, the secondary energy spectrum may be composed of *pi*-meson spectrum and nucleon spectrum, i.e.,

$$f(\eta)=f_\pi(\eta)+f_n(\eta)\,.$$

In this case, also, the resultant spectrum, $f(\eta)$, may not deviate from the expression (3) with $\alpha=0.5-3$*, and considering that $\gamma=\gamma_\pi+\gamma_n\approx 1$, the expression (1) may be accepted. Also, considering the existence of secondary neutral *pi*-mesons, the curve of $\alpha=2.0$ and $\gamma=0.9$ is approximately proportional to $(E_0/E)^{0.90}$.

ii-b) Fukuda-Ogita-Ueda Theory of Nuclear Cascade[16]

A nuclear cascade theory has been presented, by Fukuda, Ogita and Ueda[16], with reference to the Landau theory of nucleon-nucleon collisions.

The following expression (7) gives the number, dn, of secondary nuclear active particles of energy $(E, E+dE)$, which are produced in the elementary nucleon-nuecleus collision, after Amai et al.[25],

$$dn=\left(\frac{E_0}{E_M}\right)^{1-\delta}\frac{1-\delta}{\delta}\,d\left(\frac{E_0}{E}\right)^{\delta} \qquad (7)$$

where E_0 is the energy of the incident nucleon, δ a constant of about 0.52, and E_M is the energy of the most energetic particle among secondary particles and may be approximately equal to E_0. This expression represents the number of only such secondary particles as to be ejected forward in the center of mass system, but is enough to be used, according to the authors[16], for the calculation of high energy nuclear cascades with the interest in high energy shower particles. The familiar diffusion equations for the nuclear cascade have been formulated on the basis of the expression (7) and have analytically been solved. Suppose that a nucleon of energy E_0 initiates a nuclear cascade at $x=0$, and the number of nuclear particles of energy $(E, E+dE)$ at $x=x$ is expressed[16] by

$$N(E, x)dE=\frac{dE}{E_0}\left(\frac{E_0}{E}\right)^{1+\delta}\left(\frac{Ax}{y}\right)^{1/2}\cdot e^{-x} \cdot I_1(\sqrt{4Axy}\,)\,, \qquad (8)$$

where $y=ln(E_0/E)$, $A=\Delta\left(\frac{E_M}{E_0}\right)^{\delta-1}\cdot(1-\delta)$, and Δ the ratio of the number of charged *pi*-mesons to that of total *pi*-mesons. $I_1(z)$ is the usual imaginary Bessel function of the first order.

The total track length is obtained, using the expression (8), as follows,

$$T(E_0, E)=\int_0^\infty dx\int_E^{E_M} N(E, x)dE$$
$$=\frac{A}{\delta+A}\left[\left(\frac{E_0}{E}\right)^{\delta+A}-\left(\frac{E_0}{E_M}\right)^{\delta+A}\right].$$

When $E_0 \gg E$, it turns out, using $\delta=0.52$ and $\Delta=2/3$,

---

* It is noted that the expression (3) with $\alpha=0.5$ represents such a spectrum as to show the existence of high energy outgoing of the incident particle.

$$T(E_0, E)=0.4\cdot\left(\frac{E_0}{E}\right)^{0.85}.$$

The fact that the power value of 0.85 differs from unity may be attributed to the neglection of the secondary particles ejected backward in the center of mass system. Without the neglection it is expected that the power is unity.

In this way, if the interaction is of the bremsstrahlung type, the expression (1) is valid, for the electromagnetic cascade theory and for the nuclear cascade theory currently accepted, independently of plausible energy and multiplicity spectra of secondary particles.

The problem of fluctuation is essential and can not be neglected for the energy region of $E/E_0>1/10$, but it is apparent that the consideration presented above may be fluctuation-free, because of the statistical averaging, over the energy rigion of $E/E_0<1/50$, which is mainly interest in the cascade theory.

§4. Energy Spectrum of *Mu*-mesons From The Cascade

The energy spectrum of *mu*-mesons come from the nuclear cascades is obtained on the basis of the expression (1). The *pi–mu* decays may affect the nuclear cascades, but is negligible for the case, considered here, in the ground. Each nuclear active particle in the cascade undergoes the next nuclear interaction, upon travelling one mean free path on the average. Hence the total track length, $T(E_0, E)$, can be reinterpreted as intergral energy spectrum, $N(E_0, E)$, contained in the nuclear cascade inititated by a particle of energy E_0, i.e.,

$$N(E_0, E)=T(E_0, E)=\omega\frac{E_0}{E}, \tag{9}$$

since the expression (1) is expressed in the interaction mean free path. Then differential energy spectrum, $n(E_0, E)dE$, of particles contained in the wholly cascades is given by

$$\begin{aligned} n(E_0, E)dE &= \left|\frac{dN}{dE}\right|dE \\ &= \omega\frac{E_0}{E^2}dE\,. \end{aligned} \tag{10}$$

As the nuclear active particles in the nuclear cascades are usually considered to be *pi*-mesons*, the *mu*-meson spectrum from the cascade is the expression (10) multiplied by the decay probability. The decay probability, P, is somewhat different from the usual meaning. In this case, only the interest is in whether the *pi*-meson has ceased its travelling with the interaction or with the decay into the *mu*-meson. On the average, the *pi*-meson is considered to die on travelling one interaction mean free path. Hence the followings are obtained, i.e.,

$$P_{\text{int}}=\frac{dx}{\lambda} \text{ and } P_{\text{decay}}=\frac{dx/\rho}{c\beta}\cdot\frac{1}{\gamma\tau_0},$$

and if $E\simeq pc$,

$$P=\frac{P_{\text{decay}}}{P_{\text{int}}+P_{\text{decay}}}=\frac{B}{E+B}, \tag{11}$$

with

$$B\equiv\frac{mc^2\cdot\lambda}{\rho\cdot c\tau_0}, \tag{12}$$

m being the mass of *pi*-mesons, λ the interaction mean free path, ρ the density of rock in the ground, c the light speed, and τ_0 the mean life time of *pi*-mesons. For the *pi*-mesons in the ground, it turns out, using $\rho=2.6\text{ g/cm}^3$ and $\lambda=100\text{ g/cm}^2$,

$$B_\pi=6.5\text{ MeV}.$$

As the interest at present is in the energy region of more than a few GeV, the developing of nuclear cascades is not affected by the *pi-mu* decays.

Under the assumption of $B\ll E$, the differential energy spectrum of *mu*-mesons is obtained, using (10) and (11), as

$$n_\mu(E_0, E)dE=\omega_\mu\frac{BE_0}{E^3}dE, \tag{13}$$

where

$$\omega_\mu=\frac{\omega}{(m_\pi/m_\mu)^2}=\frac{\omega}{1.72}, \tag{14}$$

this being resulted from the average energy missing in the *pi–mu* transmutation. By the use of the expression (13), the intergral energy spectrum of *mu*-mesons is obtained, under the assumption of $E\ll E_0$, as

$$\begin{aligned} N_\mu(E_0, E) &= \int_E^{E_0} n_\mu(E_0,E)dE \\ &\simeq \frac{\omega_\mu}{2}\cdot\frac{BE_0}{E^2}\,. \end{aligned} \tag{15}$$

---

* For $E>10^{12}$ eV, the K-mesons probably contribute in the cascade, the effect being considered in the next section.

Heretofore the nuclear cascade initiated by a nucleon of energy E_0 has conveniently considered. A glance of the expression (15) gives the estimate for the nuclear cascade initiated by a group of nuclear active particles.

§ 5. Frequency of Observing EAS *Mu*-mensons Underground

In order to compare the estimate, the expression (15), with the experimental results of the M.P.P., we must obtain the frequency of bundles of EAS *mu*-mesons observed below the ground.

As the nuclear active particles in the core of EAS have not yet been investigated thoroughly, the integral frequency of EAS, in which the nuclear active particles carry the energies more than E_s in all, is assumed to be expressed as

$$F(>E_s)=\text{const.}\ E_s^{-\xi}\ . \qquad (16)$$

The nuclear active particles of total energy E_s impinge on the ground, initiate the nuclear cascades in the ground and produce a number of *mu*-mesons of energy more than E, the number of which is given by the expression (15) with E_s replacing E_0. When impinging many particles of total energy more than E_s, *mu*-mesons are to be produced in number of more than N_μ, which is expressed by (15) with E_s replacing E_0. Therefore the frequency, $\mathfrak{F}(\geq n, \geq E)$, of being produced a group of *mu*-mesons (its number is more than n) of energy more than E each in the EAS core in the ground, not from the ground surface, is given, from (15) and (16), by

$$\mathfrak{F}(\geq n, \geq E)=\text{const.}\left(\frac{\omega_\mu}{2}\right)^{\xi}\frac{B^{\xi}}{n^{\xi}E^{2\xi}}$$

$$\propto n^{-\xi}E^{-2\xi}\ .$$

In the above estimate, an assumption is made that each of nuclear active components initiating nuclear cascades in the ground has an energy more than E, the sum ming up of energies of all these nuclear particles being E_s. But it is not the actual case, since the nuclear particles in each EAS are to be in an energy spectrum: Suppose the energy spectrum, $h(E_s, E)dE$, be proportional to dE/E^{φ}, φ is a constant of a value more than two, for the total energy not to diverge. Then it turns out to be

$$\int_{E}^{E_{\max}} E\cdot h(E_s, E)dE=E_s\left(\frac{E_{\min}}{E}\right)^{\varphi-2}\ ,$$

where $E_{\max}$ is assumed to be very large compared to E. The integration with the lower limit of $E_{\min}$ lead to E_s, $E_{\min}$ being determined by the experimental condition. In this case the expression (15) must be changed, on taking into account the energy spectrum of nuclear active particles, as

$$N_\mu(E_0, E)=\frac{\omega_\mu}{2}\cdot\frac{BE_sE_{\min}{}^{\varphi-2}}{E^{\varphi}}\ , \qquad (15')$$

and the frequency, $\mathfrak{F}(\geq n, \geq E)$, leads to be

$$\mathfrak{F}(\geq n, \geq E)=\text{const.}\left(\frac{\omega_\mu}{2}\right)^{\xi}\frac{B^{\xi}E_{\min}{}^{\xi(\varphi-2)}}{n^{\xi}E^{\varphi\xi}}$$

$$\propto n^{-\xi}E^{-\varphi\xi}\ , \qquad (17)$$

where $\varphi>2$.

§ 6. Comparison With the M. P. P. Experiment and Discussion

The energetic nuclear active particles in the core of EAS impinge on the ground, and develop the nuclear cascade in the ground, from which the *mu*-mesons are produced through the *pi*-*mu* decay process. The number of *mu*-mesons produced by this mechanism is estimated almost without ambiguity, as described in the preceding sections. Using the estimate obtained above, the experimental results of the M.P.P. are discussed here from the view point of whether this mechanism being possibly responsible or not.

First of all, the experimental data of M.P.P. so far obtained are summarized in Table I[26]. Underground *mu*-mesons, which are simultaneously falling onto a cloud chamber, with multiple lead plates, of area of about 0.4 m², have been observed in numbers of *mu*-mesons

Table I. Summary of experimental results of the M.P.P.

Depth	Obs. Frequency of M.P.P. of more than 4 P.P.	Integral Number Distribution ($N\geq 4$)	Integral Zenith Angle Distribution	Lateral Spread
50 mwe	$(1.5\pm 0.5)\cdot 10^{-2}$ hr^{-1}	$\sim N^{-1}$	$\sim\cos^{9}\theta$	
250 mwe	$(1.2\pm 0.5)\cdot 10^{-3}$ hr^{-1}	$\sim N^{-1}$	$\sim\cos^{7}\theta$	$\gtrsim$a few meters

in each event up to about thirty. The lateral spread were obtained by means of a few trays of counters aside the chamber, and is likely to be more than a few meters at 250 mwe. Here discussion is given about the absolute frequencies and the number distributions of observed *mu*-mesons of the M.P.P.

In the first place, let us consider, as usual, all of the secondary particles of the elementary collision to be *pi*-meson. Even when the survival of the parent nucleon is taken into account, the results may remain to be unchanged.

Since the nuclear cascades in the EAS is to have vanished in the ground of, at most, 20 mwe from the ground surface, *mu*-mesons observed at 250 mwe could be considered in good approximation to be produced at the ground surface. The energy of a *mu*-meson having the range of 240 mwe is about 60 *GeV*. E in the expression (17) can be replaced by the depth of observation. Further, n in the expression is conveniently replaced by the observing density of particles, Δ. This is because in the cascade the produced *pi*-mesons can reasonably be assumed to have about constant transverse momentum p_t, independently of its energy[27,28], so that the lateral spread of the nuclear cascade remains unchanged along its developing, which implies that the total number, n, is proportional to the particle density, Δ. Therefore the expression (17) may be rewritten as

$$\mathfrak{F}(\geq d,\ \geq\Delta)\propto\Delta^{-\xi}d^{-\varphi\xi}\,. \qquad (\varphi>2) \qquad (18)$$

This relation can directly be compared with the experimental data. The experimental results on the particle density spectrum is $\Delta^{-\xi'}$ with $\xi'\simeq1$ at 50 mwe and at 250 mwe both. Then the expression (18) predicts the depth dependence of the frequencies of the events having the same density to be d^{-2} or more steep with respect to the depths. Contrary to the prediction, the experimental result is expressed as $d^{-1.3}$ or flatter, shown in Fig. 3, where rather large error of 50 mwe point resulted from the producing point of *mu*-mesons along the longitudinal extension of the nuclear cascades. Therefore this mechanism of producing the underground *mu*-mesons in the EAS could not interpret consistently both the data of the M.P.P. at 50 mwe and at 250 mwe.

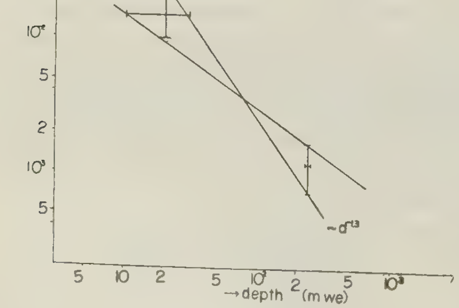

Fig. 3. Depth dependence of the frequency of M.P.P.s. See the text about the comparison with this theory.

Thus the possibility of interpretation by this mechanism leaves only on the data at 50 mwe. The possibility is examined here by the comparison between the spectrum of primary cosmic rays, which refered to the frequency of EAS, and the relation of estimated frequency *vs* E_s, which is obtained from the data of the M.P.P. at 50 mwe. As the lateral spread of the M. P. P. is not well known, let us represent by S the area covered by the events of the M.P.P., S remaining to be a parameter throughout. The absolute frequency, I_v, of the M.P.P. with more than four particles is refered to the observed frequency, I_{obs}, as usual, to be approximately

$$I_{\text{obs}}=\int_0^{\pi/2}I_v\cos^{m-1}\theta d\Omega\cdot T.S=\frac{2\pi}{m}I_v\cdot T.S\,,$$

then it turns out, using the experimental values,

$$I_v\simeq\frac{(6\pm2)\cdot10^{-10}}{S}\,\text{cm}^{-2}\,\text{sec}^{-1}\,\text{sterad}^{-1}\,.$$

On the other hand, if the expression (15) is employed for the estimate of E_s, replacing E_0, then it is obtaind as

$$E_s=(2.7\sim6.8)\cdot10^5\cdot S\ \text{GeV}\,,$$

for which have been used the values, $N_\mu=\dfrac{4}{0.4}\cdot S$, $E=5\sim8$ GeV and $\omega\simeq0.5$. This value of E_s is the lower limit, since the expression (15) is the special case of the expression (15′) with $\varphi=2$, and in general the value of E_s is to be much larger. The pair of values of I_v and E_s is plotted on the energy spectrum of primary cosmic rays, shown in Fig. 4, S being remained as parameter. It is of no doubt experimentally that S is more than some ten m^2, though not yet determined precisely. Hence the plot for E_s

shows unreasonable representation compared with the E_0 spectrum, since the curve, E_s, is necessary to be under the one of E_0 in the Fig. 4. If the expression (15′) is adapted for the estimate of E_s, the impossibility of interpretation by this mechanism increases in much more degree. In conclusion it is confirmed that this mechanism can not interpret even the data of M.P.P. at 50 mwe, too.

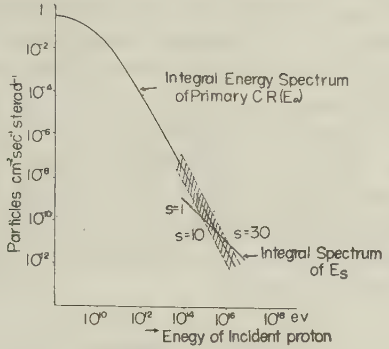

Fig. 4. Intergal energy spectrum, E_0, of primary cosmic rays (after Barrett et al[1)]) and integral energy spectrum, E_s, of the impinging N-component of EAS on the ground, where S is the area covered by the M.P.P.

The contribution of K-mesons and hyperons, though neglected heretofore, must be taken into account in this consideration. It is suggested by the experiment of Bristol group[28)], which shows the existence of X-particles, and also by the experiments of accelerators.

The K_{μ_2}-meson and the $\sum_\mu{}^{\pm}$-particle are mainly found out among so called new particles as to decay into *mu*-mesons[29)], being considered and discussed in the following. It is interesting here that in what partition *pi*-mesons and these heavy particles are produced in the very high energy interactions. So far, only the Bristol group have observed in reference with these problems, showing that X-particles, besides the *pi*-mesons, are produced about 25 % as much as *pi*-mesons in the jet showers produced by about 10^{13} eV particles[27)]. In the more energetic interactions they may be produced more frequently than just described, but have not yet been investigated. In order to investigate the produced *mu*-mesons of energy of a few tens GeV, the production ratio of K-mesons or $\sum$-particles to *pi*-mesons in the interaction of about 100∼1000 GeV must be known, since *mu*-mesons of the lowest energy are to be dominantly observed, as seen from the expression (15). Then the ratio of 25 % is tentatively used here for the K-meson or $\sum$-particle production to *pi*-meson production ratio, as given by Bristol group.

The decay constant B for $K_{\mu 2}$-mesons and $\sum_\mu{}^{\pm}$-particles is given, using $\lambda_k \simeq 3\lambda_\pi$ and $\lambda_\Sigma \simeq \lambda_\pi$[29)], as

$$B_k = 70\,\text{MeV} \text{ and } B_\Sigma = 15\,\text{GeV}\ .$$

Hence the existence of $K_{\mu 2}$-mesons does not deform, as the case of *pi–mu* decays, the nuclear cascade under consideration. The $\sum_\mu{}^{\pm}$-particle is also the case in spite of the large value of B_Σ, since the $\sum_\mu{}^{\pm}$-particle is produced with a branching ration, b, of less than 3 % within the $\sum$-particles.

Then the contribution of $K_{\mu 2}$-mesons and $\sum_\mu{}^{\pm}$-particles is taken into account as follows. The nuclear cascades in the ground are considered unchanged by the existence of the $K_{\mu 2}$-mesons and the $\sum_\mu{}^{\pm}$-particles, as described above, the expression (10) being valid unchanged. Corresponding to the expression (13), the following holds, on taking into account the different decay probability for various components,

$$\begin{aligned} &n_\mu(E_0, E)dE \\ &= \omega \frac{E_0 dE}{E^3} \left\{ \frac{f_\pi B_\pi}{(m_\pi/m_\mu)^2} + \frac{f_k B_k}{(m_k/m_\mu)^2} \right. \\ &\qquad \left. + \frac{f_\Sigma}{m_\Sigma/m_\mu} \cdot \frac{(B_\Sigma/(m_\Sigma/m_\mu)) \cdot E}{(B_\Sigma/(m_\Sigma/m_\mu)) + E} \right\} . \end{aligned}$$

In this expression f_π, f_k and f_Σ is the production ratio of charged *pi*-mesons, $K_{\mu 2}$-mesons and $\sum_\mu{}^{\pm}$-particles in the elementary collisions in the cascades under consideration. It is noticed that the production ratio of *pi*-meson component, K-meson component and $\sum$-particle component is expressed, by notations here used, as $f_\pi/b_\pi : f_k/b_k : f_\Sigma/b_\Sigma$, where b_π is the branching ratio of charged *pi*-mesons in the produced *pi*-meson component, and so on. Charged *pi*-mesons and K-mesons undergo both two body decays into *mu*-mesons, the average energy missing during the transmutation being expressed in the similar expression (see the expression (14)). The $\sum_\mu{}^{\pm}$-prticle undergoes so called the three body decay but in the crude approximation the similar expression being used as the *pi*-mesons, on the average, only considering the mass ratio. Each terms in the curled parenthesis represent the contribution of *pi*-mesons,

$K_{\mu 2}$-mesons and $\Sigma_\mu{}^\pm$-particles, the ratio of which is estimated as follows. It turns out, using $f_\pi \sim (1-0.25)\times\frac{2}{3}$,

$$\frac{f_\pi B_\pi}{(m_\mu/m_\mu)^2}\simeq 1.1\ \mathrm{MeV}\ .$$

It holds experimentally that $\frac{f_k}{b_k}+\frac{f_\Sigma}{b_\Sigma}=0.25$. Assuming that $\frac{f_k}{b_k}\simeq\frac{f_\Sigma}{b_\Sigma}$, it is given, for $K_{\mu 2}$-mesons,

$$\frac{f_k B_k}{(m_k/m_\mu)^2}\simeq 0.23\ \mathrm{MeV}\ .$$

With regard to $\Sigma_\mu{}^\pm$-particles, it holds that

$$\frac{f_\Sigma B_\Sigma}{(m_\Sigma/m_\mu)^2}\simeq 0.45\ \mathrm{MeV}\ .$$

Thus, over the energy range under consideration, the contribution of these particles to the *mu*-meson production is made in the ratio of

$$\pi^\pm : K_{\mu 2} : \Sigma_\mu{}^\pm = 1:0.2:0.5\ .$$

Therefore the contribution of the $K_{\mu 2}$-mesons and the $\Sigma_\mu{}^\pm$-particles could not largely affect the number of *mu*-mesons, $N_\mu(E_0, E)$, obtained when impling only the contribution of *pi*-mesons, and could not accordingly interpret the experimental data of M.P.P. at 50 mwe*. As is also shown in the expression (15), the contribution of the $\Sigma_\mu{}^\pm$-particles could not make flatten the depth dependence of the events under consideration, since the $\Sigma_\mu{}^\pm$-particles of energy more than 100 GeV may mainly contribute because of the energy missing of the $\Sigma_\mu{}^\pm$–*mu* decays.

§ 7. Conclusion

The nuclear active component of EAS impinges onto the ground surface and produces the nuclear cascade showers in the ground, a number of *mu*-mesons being produced in the cascades through the *pi–mu* decay process. The number of the *mu*-mesons underground thus produced has been estimated, given by the expression (15), independently of the energy and multiplicity spectra of secondary particles of the elementary (nucleon-) nucleus collisions in the EAS and further independently of some fluctuations. On the basis of the expression (15) it has been examined whether or not the *mu*-mesons produced by the mechanism just described can interpret the experimental results of so called M.P.P. underground. However no success of interpretation has been obtained, even though the contribution of the $K_{\mu 2}$-meson or the $\Sigma_\mu{}^\pm$-particle production in the very high energy collisions is taken into account.

Acknowledgement

The author wishes to express his sincere thanks to Prof. Y. Watase for his interest and kind encouragement. Thank are due to the underground C. R. group, especially to Prof. S. Ozaki and Dr. S. Miyamoto for helpful discussion and criticism during the course of the work. He is also indebted to Professors J. Nishimura and K. Suga of Tokyo University for valuable advice.

Reference

1) P. H. Barrett, L. M. Bollinger, G. Cocconi, Y. Eisenberg and K. Greisen: Rev. Mod. Phys. **24** (1952) 133.
2) E. P. George, J. W. MacAnuff and J. W. Sturgess: Proc. Phys. Soc. (Lond.) **A**, **66** (1952) 346.
3) S. Higashi, I. Higashino, M. Oda, T. Oshio, H. Shibata, K. Watanabe and |Y. Watase: J. Phys. Soc. Japan **11** (1956) 1021.
4) I. I. Sakvarelidze: Jour. Exp. Theor. Phys. USSR **30** (1956) 458.
5) M. Oda: Nuovo Cimento **5** (1957) 615.
6) G. Cocconi: Handb. d. Phys. Vol. 45 (Springer, Berlin 1957).
7) K. Greisen: Prog. C. R. Phys. IV (North-Holland, Amsterdam 1958).
8) S. Higashi, T. Oshio, H. Shibata, K. Watanabe and Y. Watase: Nuovo Cimento **5** (1957) 597.
9) S. Hayakawa: Nuovo Cimento **5** (1957) 607.
10) S. N. Nikol'skii, Iu. N. Vavilov and V. V. Batov: Doklady. Akad. Sci. USSR **111** (1956) 71.
11) S. Miyake, K. Hinotani, I Katsumata and T.

---

* If the interaction mean free path of *K*-mesons is about three times larger than that of *pi*-mesons, the nuclear cascades might be expected to prolong its range in the ground. Accordingly the nuclear cascades cited for the example in § 2 would penetrate to the deeper depth than 20 mwe, and the observed *mu*-mesons at 50 mwe might have energies less than 5 GeV at their production point, and hence the mechanism just described might be enough to interpret the data of the M.P.P. at 50 mwe. But the estimate in § 2 is based on the experimental data of the inelasticity of 0.3, which must imply the contribution of these heavy particles in high energy collision, if exist.

Kaneko: Proc. Moscow C. R. Conf. Vol. II (Moscow, 1960).

12) S. H. Vernov, N. N. Goryunov, V. A. Dmitriyev, G. V. Kulikov, Yu. A. Nechin and G. B. Kristiansen: Proc. Moscow C. R. Conf. Vol. II (Moscow, 1960).
13) S. Fukui, H. Hasegawa, T. Matano, I. Miura, M. Oda, N. Ogita, K. Suga, G. Tanahashi and Y. Tanaka: Proc. Moscow C. R. Conf. Vol. II (Moscow, 1960).
14) E. Amaldi, L. Mezzetti and G. Stoppini: Nuovo Cimento **10** (1955) 803.
15) A. Ueda and N. Ogita: Prog. Theor. Phys. **18** (1957) 269.
16) H. Fukuda, N. Ogita and A. Ueda: Prog. Theor. Phys. **21** (1959) 29.
17) Y. Sekido: Private communication.
18) S. Miyake: Prog. Theor. Phys. **20** (1958) 844.
19) K. Greisen, J. Delvaille and F. Kendziorski: Proc. Moscow C. R. Conf. Vol. II (Moscow, 1960).
20) B. Rossi: "High Energy Particles", (Prentice Hall, N. Y., 1952).
21) H. Messel: Prog. C. R. Phys. Vol. II (North-Holland, Amsterdam, 1954).
22) P. Buddini and G. Molière: " Kosmische Strahlung " (Springer, Berlin, 1953).
23) W. Heisenberg: Zeits. f. Phys. **126** (1949) 569, **133** (1952) 65, "Kosmische Strahlung" (Springer, Berlin, 1953).
24) L. D. Landau: Izv. Akad. Nauk USSR **17** (1953) 57.
25) S. Amai, H. Fukuda, C. Iso and Sato: Prog. Theor. Phys. **17** (1957) 241.
26) S. Higashi, S. Mitani, T. Oshio, H. Shibata, K. Watanabe and Y. Watase: Proc. Moscow C. R. Conf. Vol. II (Moscow, 1960).
27) O. Minakawa, Y. Nishimura, M. Tsuzuki, H. Yamanouchi, H. Aizu, H. Hasegawa, Y. Ishii, S. Tokunaga, Y. Fujimoto, S. Hasegawa, J. Nishimura, K. Niu, K. Nishikawa, K. Imaeda and M. Kazuno: Nuove Cimento, Suppl. **11** (1959) 112.
28) B. Edwards, J. Losty, D. Perkins, K. Pinkau and J. Reynolds: Phil. Mag. **3** (1958) 237.
29) for example, M. Gell-Mann and A. H. Rosenfeld: Ann. Rev. Nuc. Sci. Vol. 7 (Ann. Rev., California, 1957).

JOURNAL OF THE PHYSICAL SOCIETY OF JAPAN, Vol. 16, No. 5, MAY, 1961

A Study on High-Energy Nuclear-Active Particles in Extensive Air Showers

By Yasuo TANAKA

Institute for Nuclear Study, University of Tokyo

(Received January 21, 1960)

A new type of detector called transition chamber was used to study high-energy nuclear-active particles (N-particles) above 10^{11} ev in extensive air showers (EAS) of size above 10^3. The differential energy spectrum of N-particles is shown to be represented by $E_N^{-2.0\pm0.1}dE_N$ up to 3.10^{13} ev irrespective of shower size. The lateral distribution of nuclear-active particles is obtained within 10 m from the axis. This distribution is tentatively explained by a phenomenological model assuming the Maxwell-Boltzmann distribution for the transverse momentum of N-particles. Total number of N-particles of energy $E_N \geqq 10^{11}$ ev, N_N, in an extensive air shower is expressed as a function of size N_e by $N_N=(50\pm5)(N_e/10^5)^{1.1\pm0.1}$, for N_e ranging from 10^3 to more than 10^6. Then the total energy carried by all N-particles of $E_N \geqq 10^{11}$ ev is estimated to be as much as that of the electron component in an EAS. On the basis of the observed general relationship between the electron component and N-particles for a wide range of sizes, a model of the development of EAS is suggested. The energy spectrum of N-particles is discussed in relation to that of high-energy γ-rays. In particular the existence of very high-energy N-particles implies that the average inelasticity in high energy interactions $\eta=0.4\sim 0.5$, if they are assumed to be survivors of primary particles. Also the possibilities are discussed for the occurrence of N-particles with energies as much as 10% or more of primary particles.

§ 1. Introduction

It is well known that the nuclear cascade in an extensive air shower (EAS) plays a fundamental and basic role in its development in the atmosphere. Therefore, the information on the high-energy nuclear-active particles (N-particles) which are responsible for the development of nuclear cascade is very important for the study of very high-energy nuclear interactions and the development and structure of EAS. However, because of the low frequency of N-particles and the difficulty in detecting them and measuring their energy, the data available on the N-component are much less than those on other components of EAS.

Recently, detectors using ionization chambers which are efficient for detecting high-energy N-particles have been developed mainly by Russian workers. By means of these detectors it has also been possible to estimate the energies of N-particles. These experiments have led to the remarkable result that N-particles in an EAS carry as much total energy as the electron component, and sometimes as much energy could be concentrated in a single N-particle.[1)-4)] Thus the importance of N-particles as the source of energy supply of EAS has been recognized.

In order to arrive at a quantitative description of phenomena from the qualitative understanding we have so far, it is necessary to improve the accuracy of energy measurement of N-particles and also determine the character of associated EAS by fixing the position of shower axis, its incident direction, the total number of particles or the size and other parameters as accurately as possible. The purpose of the present experiment is to study EAS through investigation of the high-energy N-particles as described above. Characteristic features of very high-energy phenomena will be reflected the better in the higher energy N-particles. Therefore, it would be worth while to observe such N-particles for a wide range of sizes of EAS. In fact, this is equivalent to covering a wide range of energy of the primary particles producing EAS, so that one may hope to get possible clues regarding the characteristics of very high-energy phenomena, as well as gain a better understanding of the role of nuclear cascade in EAS.

§ 2. Experimental Arrangement

It has been shown already that the "transition chamber" is quite useful for the detection and energy measurement of high-energy N-particles.[5),6)] The schematic diagram of the transition chamber is shown in Fig. 1. This detector consists of thick material in which five layers of scintillation counters are inserted as illustrated in the figure. The top layer of 5 cm lead absorbs the electron component of EAS efficiently. The total thickness of iron is 320 gcm^{-2} which corresponds to about 3 nuclear mean free paths so that almost all the N-particles which hit the detector will cause nuclear interactions.

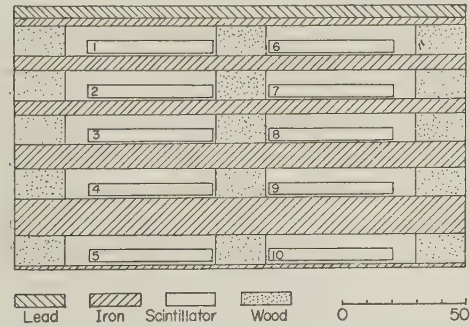

Fig. 1. Schematic diagram of the transition chamber.

In order to measure the energy of N-particles, the so-called "total absorption spectrometer" is perphaps the best detector. It has enough thicknesss of material to absorb the entire nuclear cascade initiated by a N-particle and measures the total energy dissipated by all particles within the detector.

The transition chamber does not have sufficient thickness of material for this purpose, but it can be used to measure the energy of neutral pions produced by nuclear interactions fairly accurately. These neutral pions, each immediately decaying into two γ-rays, initiate electromagnetic cascade showers. As is well known, the number of electrons at shower maximum is almost proportional to the energy of incident γ-rays, and this relation still holds approximately for the superposition of several showers of different energies. In other words the number of electrons at the maximum of the composite shower is proportional to the total energy of the incident γ-rays. On the other hand, the number of electrons varies very slowly, say by less than 20%, within several radiation lengths arround the shower maximum, if the incident γ-ray energy is more than several Bev. Therefore, the particle number at the shower maximum can be obtained with fair accuracy by scintillation counters separated by less than several radiation lengths from each other. Thus, the transition chamber can give the total energy transferred to neutral pions and hence one can estimate the energy of N-particles as explained later.

For the detection of N-particles among the many background electrons of EAS, one should examine the transition curve for a second hump following the rapid absorption, characteristic of pure electromagnetic cascade.

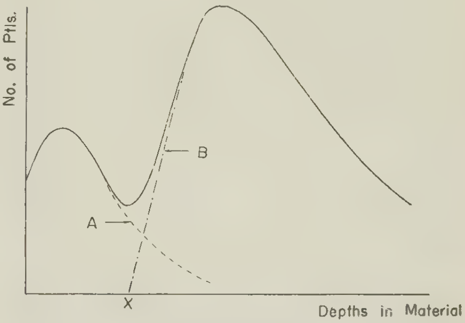

Fig. 2. Shematic figures of transition curves.
A: The transition curve of the electron component.
B: The transition curve of the shower initiated by a high-energy N-particle at X.

This second hump should be obviously due to nuclear interaction which initiates cascade showers through the production of neutral pions. This situation is illustrated schematically in Fig. 2. Since pure electron component is absorbed quite rapidly, almost all N-particles that give rise to neutral pions of more than 10 Bev can be certainly distinguished from the dense background of electrons and photons, unless the nuclear interaction takes place within the lead layer such that the cascade develops too fast to be observed at shower maximum. Thus, the detection efficiency of the transition chamber for high-energy N-particles is considered to be about 70%.

As N-particle detectors, cloud chambers, counter piles, and neutron counters have been used so far. These detectors, however, are not suitable for quantitative measurements on high-energy N-particles. The transition chamber, though it is inferior in accuracy to the method of energy measurement by total absorption, gives the energies of N-particles with a constant degree of accuracy upto very high energies.

Since each layer of transition chamber consists of two scintillation counters each of area 0.25 m^2, it can be used as two independent N-particle detectors. The output signal of each scintillation counter is displayed on the screen of an oscilloscope through a special device by which the pulse height is converted into a signal proportional to the logarithm of the number of particles.[7)]

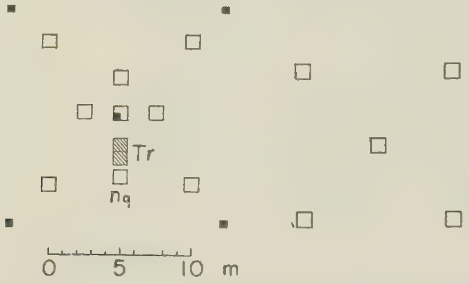

Fig. 3. Arrangement of the detectors. Open squares 1 m^2 each, are n-detectors. Filled squares 0.25 m^2 each, are fast detectors. The detector denoted as Tr is the transition chamber.

An EAS array consisting of 14 scintillation counters was operated in conjunction with the transition chamber. These counters, called n-detectors are each of area 1 m^2. The arrangement of the n-detectors as well as the transition chamber is shown in Fig. 3. One can determine the position of the axis and the size of EAS from the observed density of particles at each n-detector. The output of each n-detector was also represented logarithmically on oscilloscope screen and photographed. Sensitivities of all scintillation counters—counters of the transition chamber as well as the n-detectors—were continuously recorded on a chart of self-recording monitor. They were usually maintained within 10% variation. Besides these counters, a timing network of five 0.25 m^2 scintillation counters was also operated, to obtain information on the incident direction of EAS of more than 10^4 in size. The accuracy was within about 5° near the vertical. These counters are called fast detectors.

The following triggering condition was imposed for efficient selection of N-particles: at least 10 particles in each of any two counters among scintillators No. 1 to No. 5 or No. 6 to No. 10 in the transition chamber, in addition to at least one particle in n-detector n_9 (see Fig. 3). Whenever this condition was satisfied, the recording system was triggered and all the information of the event was recorded. The rate of such events was about 15 per hour. The experiment was carried out at sea level in December 1959. The total working time was about 290 hrs.

§ 3. Identification and Energy Estimation of N-Particles

From the data so obtained, only those events which showed a clear hump of more than 50 particles on the observed transition curve were selected as due to nuclear interactions of N-particles. However, this condition may possibly be satisfied also by the following phenomena: (i) EAS incident at large zenith angle, (ii) nuclear disintegrations occurring within the scintillators, and (iii) radiation burst caused by muons.

When an EAS hits the detector with zenith angle more than 30°, the electron component, without traversal in lead layer, might cause a hump similar to that observed in nuclear interaction. Naturally, such types of events are more likely to occur in inclined EAS. However, the zenith angle distribution obtained for above selected events associated with EAS agrees with that of ordinary EAS well within the limits of experimental errors. Therefore, the contribution of events from (i) should be less than several % if it exists.

Events of type (ii) are caused by relatively low energy N-particles, say more than a few Bev. These N-particles may produce nuclear disintegrations within the scintillation material with some probability, and give rise to a pulse equivalent to that corresponding to more than 50 particles. However, the scintillation efficiency of organic scintillators for heavily ionizing particles is very low. Moreover, the number of such fragments emitted in ordinary nuclear disintegrations is small because the target consists of only light elements. Therefore, a simple estimate shows that this effect is negligible. This type of events can also be picked out and rejected by inspecting the observed transition curves, because only one scintillation counter can show a large pulse height in these cases.

It is possible that the radiation bursts caused by muons satisfy the triggering condition, if muons are coming from directions such that they can penetrate n-detector n_9, or the particles of radiation bursts can hit this n-detector. Since cascade showers of bursts do not develop in the vertical direction for these events, the number of counters which show high density of particles is limited to only one or two from geometrical considerations. Then, the transition curves show an apparent rapid absorption compared to ordinary cascade curves. In fact, a few tens of such events were observed which could be obviously distinguished by inspecting the transition curves.

The rate of radiation bursts of more than 50 particles at shower maximum within the transition chamber caused by muons is about 5 per hour. However, since at least one particle should hit the n-detector n_9 according to the triggering requirement, only those muon-bursts which are associated with EAS could be effectively recorded. Simple estimation shows that such cases could not be more than 10 during the whole period of observation. Moreover, because the energy spectrum of muons is much steeper than that of N-particles, as will be shown later, this effect of muon-bursts on the data of N-particles must be limited to only the low energy regions.

Therefore, the 495 events selected are believed to be due to high-energy N-particles.

As a further confirmation, the distribution in the depths of the points of interactions was checked. The collision mean free path calculated from this distribution turned out to be about 100 gcm^{-2}. Therefore, it is reasonable to suppose that all the selected events are due to N-particles.

The energy of N particles can be estimated as follows. As already mentioned, the total energy of neutral pions is first determined from the number of particles at shower maximum. The number of electrons, $\pi_{\max}$, at shower maximum as a function of primary γ-ray energy $E_0^{(\gamma)}$ is given by Eq. (1) for a single cascade under "Approximation B",

$$\pi_{\max}(E_0^{(\gamma)}) = \frac{0.3}{\sqrt{\ln(E_0^{(\gamma)}/\mathcal{E})}} \frac{E_0^{(\gamma)}}{\mathcal{E}}, \qquad (1)$$

where $\mathcal{E}$ represents the critical energy and is 21 Mev for iron. The cascade shower actually observed is not neccessarily a single cascade but rather a superposition of several showers. However, Eq. (1) can still be applied to the composite cascade showers for obtaining the total energy of neutral pions. The accuracy of the energy determined by the above method can be considered to be of the order of 30%. The event with 50 particles for $\pi_{\max}$ corresponds to about 10 Bev for $E_0^{(\gamma)}$ or the total energy of neutral pions.

In order to estimate the energy of N-particles from the total energy of neutral pions, two quantities should be known. One is the fraction of N-particle energy transferred to secondary particles, or the inelasticity, η, and the other is the ratio of neutral pions to all secondary particles, R. Although either of these might fluctuate from case to case, many experiments on jets by nuclear emulsions allow one to take about 1/3 for the average value of R at high energy. There is much ambiguity in the values of η obtained so far, because they are not of sufficient statistical accuracy and also the accuracy of η in individual events is not good enough. However, one can use a value 0.3 as the average η tentatively for the energy estimation of N-particles. Then the energy of N-particle, E_N, can be estimated as $E_N = 10E_0^{(\gamma)}$. Therefore, the selected events correspond to N-particles of energy $E_N \geqq 10^{11}$ ev. It is difficult to assign the error to the value of E_N thus obtained. However, an uncertainty of factor of 2 may be considered reasonable, because of the above mentioned assumptions.

§ 4. Associated Air Showers

The procedure used to obtain the position of the axis, the lateral distribution and the size of EAS is the same as that described in Ref. 6. That is, the position of the axis is regarded as the point arround which the observed densities at various n-detectors best approach to a certain smoothly decreasing function of radius, r. Then a Nishimura-Kamata (N-K) function[8] which is the best fit to this lateral distribution can be chosen.

The size of EAS, N_e, is assumed to be the area integral of this N-K function.

For the EAS array shown in Fig. 3, the position of the axis can be determined uniquely with the accuracy of usually less than a few metres for EAS which hit the region within 10 m from the centre of the array. Particularly, if EAS of $N_e \geqq 10^4$ hit near the centre, the accuracy in determining the position of the axis can be as good as 1 m (see § 5. (C)). On the other hand, the accuracy becomes worse rather rapidly when the axis is farther than 10 m from the centre. However, these cases do not occur so frequently, because a large majority of N-particles is concentrated within 10 m from the axis as will be shown later.

The accuracy of the size as determined by the above mentioned method is somewhat different from shower to shower, but in general for EAS within 10 m from the centre the statistical accuracy is about 20% for sizes $N_e > 10^4$, and becomes worse for smaller sizes. For a size of 10^3, the error becomes a factor of 2.*

The observed integral size spectrum of EAS for the selected events is shown in Fig. 4. This spectrum can be approximated by $N_e^{-0.4}$ for the region of $N_e <$ several 10^5 whereas it rather fits $N_e^{-0.8}$ for $N_e \geqq 10^6$. These would indicate that the variation of exponent occurs between the sizes 10^5 and 10^6. This fact might be very interesting if it is compared with similar variation of exponent which appears in the same range for the ordinary size spectrum of EAS irrespective of N-particles.[5)]

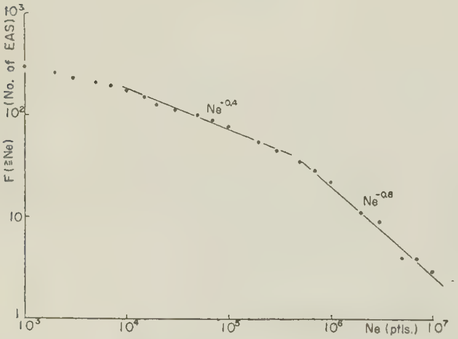

Fig. 4. Observed size spectrum of EAS in which at least one N-particle is detected in transition chamber.

§ 5. Experimental Results

(A) *Energy spectrum of N-particles*

The differential energy spectrum of all observed N-particles is shown in Fig. 5. This spectrum can be fitted very well by a power law $E_N^{-2.0 \pm 0.1} dE_N$ at least for the energy range, 10^{11} ev $\leqq E_N < 10^{12}$ ev. This law can be reasonably extrapolated upto $3 \cdot 10^{13}$ ev though the statistics are poor above 10^{12} ev. Therefore, one could consider that there is no remarkable change in the energy spectrum of N-particles for the energy range 10^{11} ev $\leqq E_N < 3 \cdot 10^{13}$ ev.

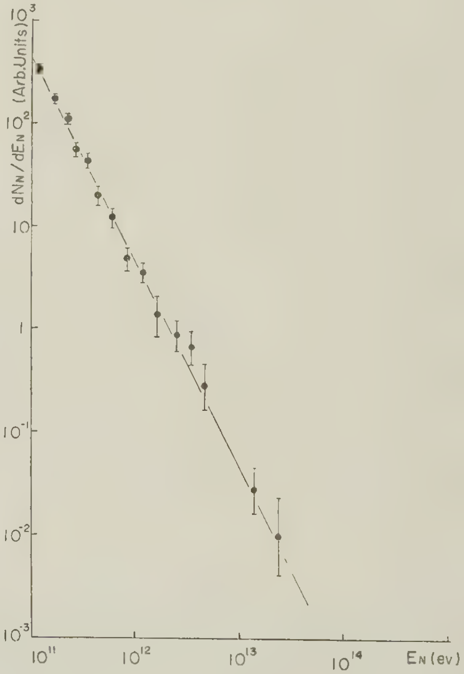

Fig. 5. Differential energy spectrum for all N-particles observed. The straight line represents the spectrum $E_N^{-2.0} dE_N$.

The energy spectra of N-particles have also been obtained for the following intervals of sizes N_e: (i) $10^3 \leqq N_e < 3 \cdot 10^3$, (ii) $3 \cdot 10^3 \leqq N_e < 10^4$, (iii) $10^4 \leqq N_e < 3 \cdot 10^4$, (iv) $3 \cdot 10^4 \leqq N_e < 10^5$ and (v) $N_e \geqq 10^5$. Fig. 6. a) to e) show the integral spectra for different size intervals. It is a remarkable feature that there seems to be no significant dependence of the energy spectrum of N-particles on the size N_e for a wide range of sizes from 10^3 to more than 10^5. It is also to be noted that the energy spectrum is still extending beyond 10^{12} ev even for EAS with $N_e \sim 10^3$. This fact will be discussed later.

---

* Preliminary results of detailed study of lateral distribution of particles from the axis to 200 m show an obvious deviation from the N-K function. Then, the size obtained from the N-K function turns out to be a lower estimation and should be increased by 50%.

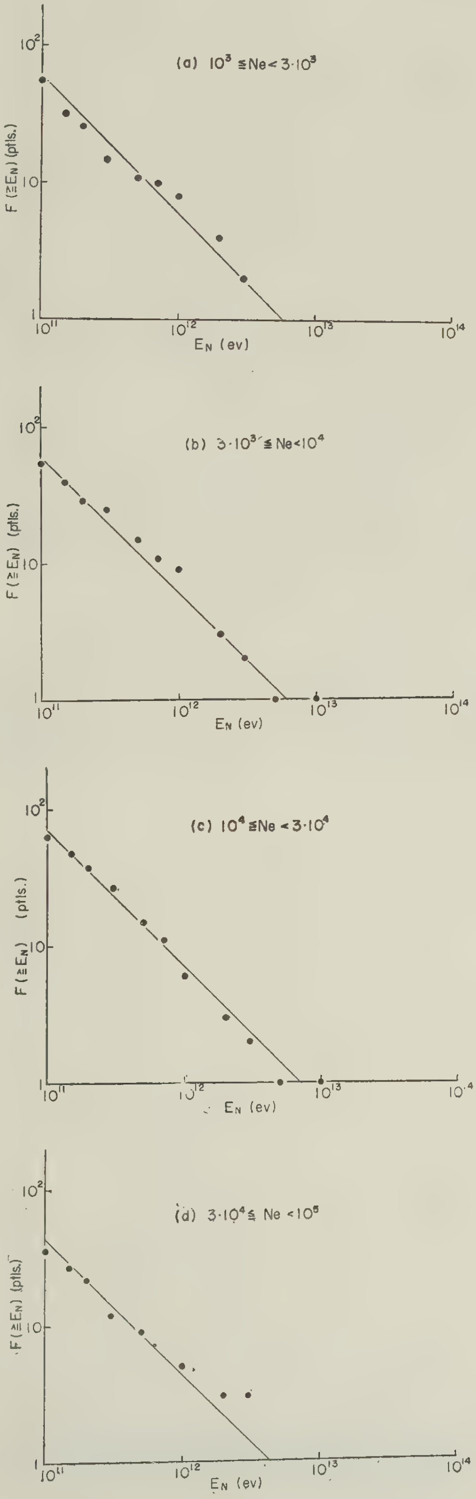

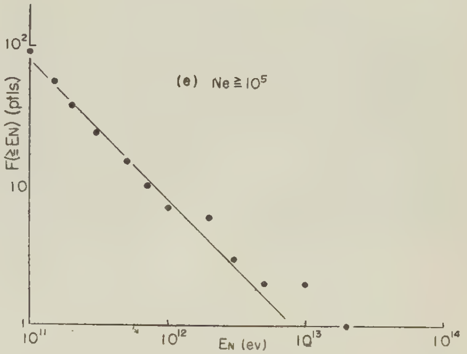

Fig. 6. Integral energy spectra of N-particles for various size ranges.

(B) *Lateral Distribution of N-particles*

As already mentioned, the transition chamber was used as two separate units of N-particle detectors. The frequency of EAS of size (N_e, N_e+dN_e) which hit at a distance $(r, r+dr)$ from either unit detecting an N-particle is given by the following equation.

$$F(N_e, r)dN_edr$$
$$= f(N_e)\Delta_N(N_e, r)2S\,W(N_e, r)dN_e2\pi rdr\,, \quad (2)$$

where $f(N_e)dN_e$ is the size spectrum of EAS, Δ_N is the density of N-particles, S is the area of each unit of transition chamber (0.25 m²) and $W(N_e, r)$ is the detection probability of EAS. (Note that Eq. (2) holds strictly for $S\Delta_N \ll 1$.) Therefore, if $F(N_e, r)$ is known for a fixed size N_e and within the region where $W(N_e, r)$ is almost unity, the lateral distribution of N-particles $\Delta_N(N_e, r)$ can be obtained.

As mentioned in § 4. the accuracy in determining the position of the axis is not very good farther than 10 m, moreover $W(N_e, r)$ is not neccessarily unity for EAS of $N_e < 10^4$ even within 10 m from the transition chamber. Therefore, the lateral distribution of N-particles is studied here only within 10 m from the axis of EAS of $N_e \geqq 10^4$.

The lateral distribution of N-particles of $E_N \geqq 10^{11}$ ev is obtained as shown in Fig. 7. Since the accuracy of r is as good as 1 m, it may be significant that the distribution becomes flatter within 2 m from the axis. If this distribution is approximated by a power low between 2 to 10 m, it can be represented by $r^{-2.5\pm0.5}$. If one assumes tentatively an empirical expression $[1+(r/a)^{2.5}]^{-1}$ for the lateral distribution of N-particles, a value 1.5 m for a can fit this formula to experimental points in the whole range within 10 m. If one supposes that this formula can be applied farther than 10 m upto 30 m as a reasonable cut off point, the fraction of N-particles existing within 10 m corresponds to about 80% and that within 5 m accounts for about 65% of the total.

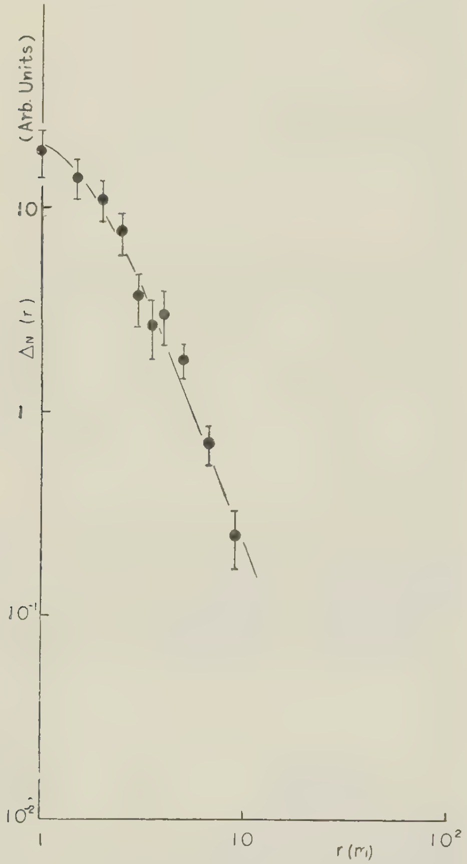

Fig. 7. Lateral distribution of N-particles with $E_N \geqq 10^{11}$ ev in EAS of $N_e \geqq 10^4$. Curve of $1/[1+(r/a)^{2.5}]$ is shown in the figure for $a=1.5$ m.

(C) *An interpretation of the lateral distribution of N-particles*

The lateral distribution of N-particles of certain energy E_N at sea level can be considered as determined by the contributions of N-particles from different altitudes and their angular distribution. Assuming that the number of N-particles of energy E_N produced within the layer $(x, x+dx)$ from the top of the atmosphere is proportional to $\exp(-x/\Lambda_N)dx$, the contribution of these N-particles at sea level, $x=X_0$, without suffering nuclear interaction between x and X_0 is as follows. Since the probability with which a N-particle can arrive at X_0 without nuclear interaction is $\exp[-(X_0-x)/L]$ where L represents the nuclear mean free path, the contribution of N-particles of energy E_N from the layer $(x, x+dx)$ to those at sea level is proportional to $\exp[(1/L-1/\Lambda_N)x]dx$ provided that the effect of decay is negligible.

If the distribution of emitted angles of N-particles is assumed to be proportional to $\exp(-\theta^2/2\theta_0^2)\,2\pi\sin\theta d\theta$ for a certain energy E_N, this corresponds equivalently to the assumption of Maxwell-Boltzmann distribution for the transverse momentum p_T, $\exp(-p_T^2/2p_0^2)\,2\pi p_T dp_T$ where p_0 is the rms average of p_T and is related to θ_0 by the equation $\theta_0 \cong p_0/p$, p being the momentum of N-particle ($cp=E_N$).

For the sake of simplicity, nuclear interaction is supposed to occur once every one mean free path. Then, the lateral distribution at sea level, of N-particles produced n mfps above is expressed by

$$\frac{1}{2\pi(nr_0)^2}\exp\left(-\frac{r^2}{2(nr_0)^2}\right)2\pi r dr\ ,$$

where r_0 is rms radius of those N-particles after traversal of 1 mfp and given by $r_0=(p_0/p)(L/\rho)$, ρ being the average density of air.

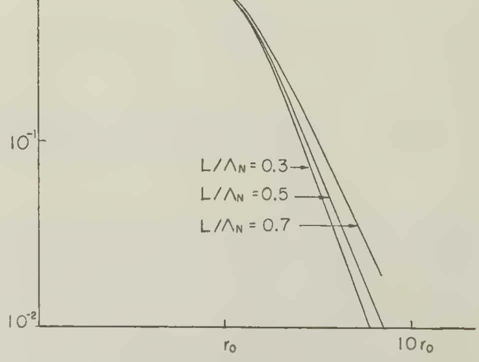

Fig. 8. Lateral distributions of N-particles calculated for different values of L/Λ_N according to Eq. (4), § 5. (C).

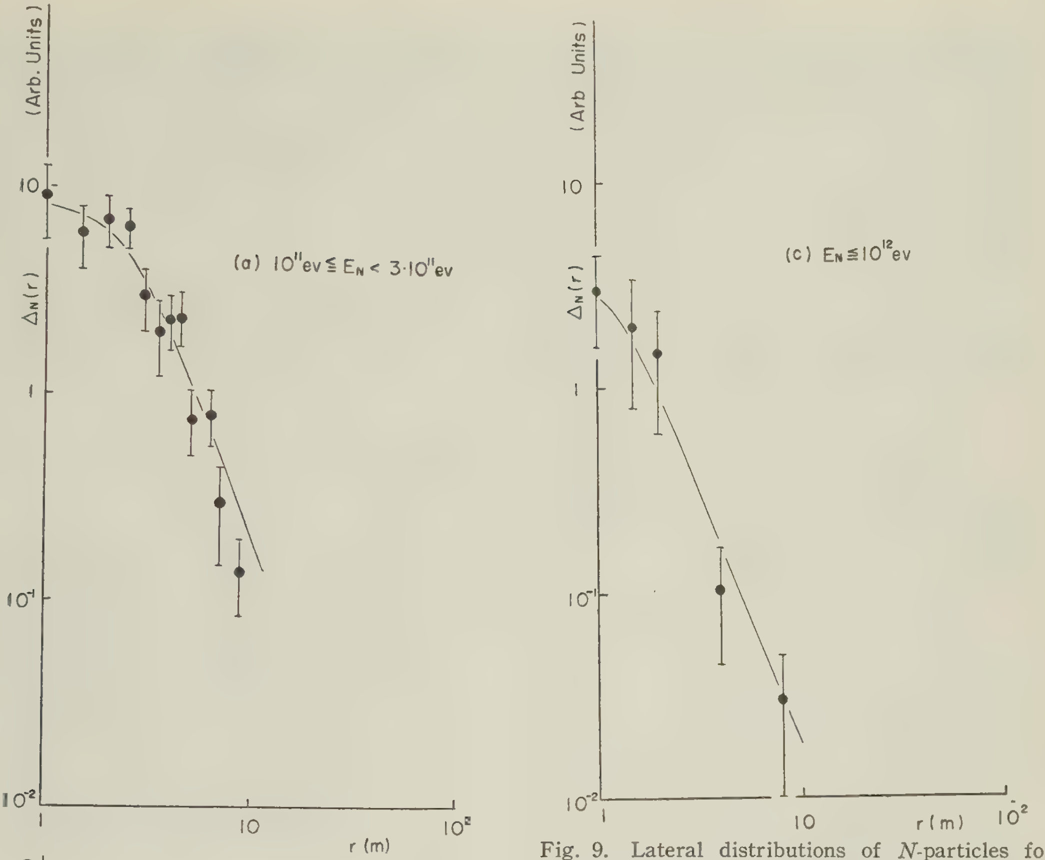

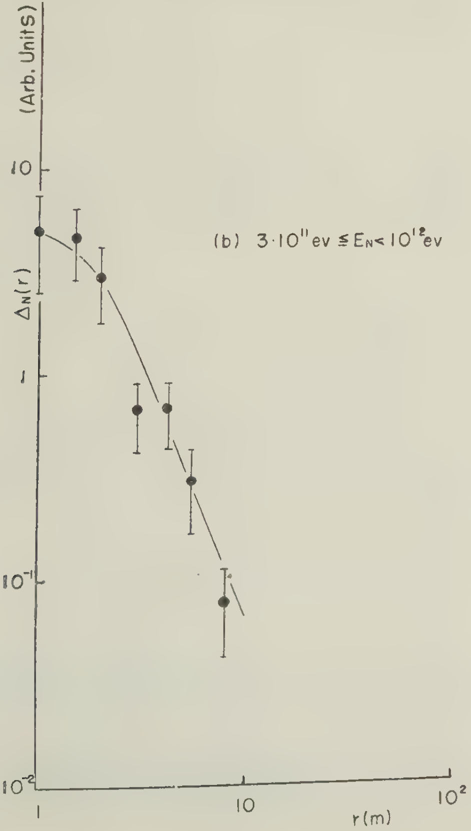

Fig. 9. Lateral distributions of N-particles for different energy ranges. Each of them is compared with calculated curve for $L/\Lambda_N=0.5$ as shown in Fig. 8.

Since the contribution of such N-particles to sea level is proportional to

$$\exp\left[\left(\frac{1}{L}-\frac{1}{\Lambda_N}\right)(X_0-nL)\right]$$

or

$$\exp\left(\frac{L}{\Lambda_N}-1\right)n$$

as given above, the lateral distribution of N-particles of energy E_N can be obtained by the superposition of contributions from various generations using the following expression

$$\Delta_N(r)\propto\sum_{n=1}\frac{1}{2\pi(nr_0)^2}\exp\left[\left(\frac{L}{\Lambda_N}-1\right)n-\frac{1}{2(nr_0)^2}\right]. \tag{4}$$

The results of calculations for three cases, $L/\Lambda_N=0.3$, 0.5 and 0.7 are shown respectively in Fig. 8. These figures illustrate that the above model can account for the part of the distribution expressible by a power function. They are approximated by $r^{-2.8}$, $r^{-2.5}$ and $r^{-2.1}$, respectively.

Fig. 9 (a), (b) and (c) show the experimental lateral distributions of N-particles for different energy intervals: (a) $10^{11}\,\text{ev} \leqq E_N < 3\cdot 10^{11}\,\text{ev}$ ($\langle E_N\rangle_{\text{AV}} = 1.7\cdot 10^{11}\,\text{ev}$), (b) $3\cdot 10^{11}\,\text{ev} \leqq E_N < 10^{12}\,\text{ev}$ ($\langle E_N\rangle_{\text{AV}} = 5\cdot 10^{11}\,\text{ev}$) and (c) $E_N \geqq 10^{12}\,\text{ev}$, respectively, for EAS of $N_e \geqq 10^4$. Curves of Fig. 8, can be fitted to the experimental points in Fig. 9, if we suppose $r_0 = 2.0 \pm 0.2\,\text{m}$ for (a), $r_0 = 1.5 \pm 0.4\,\text{m}$ for (b) and $r_0 = 1.0\,\text{m}$ for (c), respectively. Since the uncertainty in the determination of position of the axis is included in the above values of r_0, the value of r_0 for (c) ($=1\,\text{m}$) would indicate that the accuracy is about 1 m or better. Assuming 1 m for this uncertainty, the spreads of physical significance are (a) $r_0 = 1.8\,\text{m}$ and (b) $r_0 = 1.1\,\text{m}$. These spreads can be attributed to N-particles of the last generation.

Before these are related to the rms values of p_0, one should take into account the angular distribution of primary particles producing N-particles of energy E_N which has been neglected so far. This effect can be estimated by the following simple consideration. Suppose the energy of a secondary particles is $1/k$ of the primary energy on the average. Since the interactions of different generations are independent of each other, it follows that if the angular distribution in each interaction is represented by Gaussian distribution, then the multiplication of effects of successive generations in angular distribution, and hence the spatial distribution again obeys Gaussian distribution. Then the mean square radius $\langle r^2\rangle_{\text{AV}}$ of N-particles with energy $E_N = cp$ is given by

$$\langle r^2\rangle_{\text{AV}} = \left(\frac{p_0}{p}\frac{L}{\rho}\right)^2 + \left(\frac{p_0}{kp}\frac{2L}{\rho}\right)^2 + \left(\frac{p_0}{k^2p}\frac{3L}{\rho}\right)^2 + \cdots$$
$$= r_0^2 \sum_{l=1} \frac{l^2}{k^{2(l-1)}} .$$

Therefore, r_0 seems to be apparently larger by a factor

$$\left[\sum \frac{l^2}{k^{2(l-1)}}\right]^{1/2} .$$

This factor accounts for 1.7, 1.3 and 1.1 for the values of $k=2$, 3 and 5, respectively. Though information on k is still lacking, it can be assumed tentatively as follows: for instance, the ratio of the numbers of mesons to nucleons is $2\sim 5$ to 1, and $k \sim 2$ for nucleons whereas $k \sim 10$ for mesons. Then, the factor would be about 1.2, not very seriously dependent on the above assumptions. Therefore, the apparent values of r_0 have to be reduced by about 20%.

Table I.

	Energy interval (ev)	Average energy (ev)	Apparent r_0 (m)	$\frac{p_0 L}{p\rho}$ (m)	p_0 (Mev/c)
a	$10^{11} \leqq E_N < 3\cdot 10^{11}$	$1.7\cdot 10^{11}$	1.8 ± 0.2	1.5	260 ± 40
b	$3\cdot 10^{11} \leqq E_N < 10^{12}$	$5\cdot 10^{11}$	1.1 ± 0.4	0.9	450 ± 200

The values of p_0 which are shown in Table I, assuming that one nuclear mfp is $100\,\text{gcm}^{-2}$.

These values of p_0, though they are indirect and poor in accuracy, are yet generally in agreement with those obtained for high-energy neutral pions.[9] These results are consistent with the hypothesis that all secondary particles, charged pions and others as well as neutral pions of more than 10^{11} ev still belong to the same class of p_T, and that the distribution of p_T is characterized by a "well-defined" one such as the Maxwell-Boltzmann distribution.

(D) *Total number of N-particles*

Integrating Eq. (2) with respect to radius from 0 to r,

$$dN_e \int_0^r F(N_e, r)dr$$
$$= 2Sf(N_e)dN_e \int_0^r \Delta_N(N_e, r)\, W(N_e, r) 2\pi r dr .$$

Therefore, for the values of r within which $W(N_e, r) = 1$,

$$\int_0^r \Delta_N(N_e, r) 2\pi r\, dr = \frac{dN_e \int_0^r F(N_e, r)dr}{2S\cdot f(N_e)dN_e} , \qquad (3)$$

where the numerator of right hand side is the total number of observed N-particles in association with EAS of size $(N_e, N_e + dN_e)$ that hit within the radius r. Information on this and the size spectrum of EAS give the total number of N-particles within the radius

r from the axis according to Eq. (3). Moreover, if the lateral distribution of N-particles is assumed to be independent of size[6)] and is expressed as already mentioned in (B) of this Section, the total number of N-particles of $E_N \geqq 10^{11}$ ev, N_N, in an EAS can be estimated on the average.

The results of Ref. 6 can be used here for the size spectrum, because the method of determining the position of the axis and the size adopted for this experiment, is the same as that in Ref. 6. Furthermore, the same detectors and almost similar arrangements were used in both the experiments. The spectrum for $N_e < 10^4$ can be inferred by extrapolating that for $N_e \geqq 10^4$ according to $N_e^{-1.4}$.

The results thus obtained are shown in Table II as well as in Fig. 10 where the results of Ref. 6 are also quoted. They seem to be in good agreement within the experimental errors. The errors assigned to the experimental points here include not only statistical error but also inaccuracies of size spectrum.

Table II.

Size interval	Average size	r (m) in Eq. (3)	No. of observed N-ptls. within $r^\dagger$	Flux of EAS ($\mathrm{m^{-2}\,sec^{-1}}$)	Total No. of N-ptls. N_N
$10^3 \leqq N_e < 3\cdot 10^3$	$1.7\cdot 10^3$	3 (5*)	51 (57*)	$5.0\cdot 10^{-4}$	0.4 ± 0.16
$3\cdot 10^3 \leqq N_e < 10^4$	$5.5\cdot 10^3$	5 (10*)	45 (55*)	$1.0\cdot 10^{-4}$	1.3 ± 0.4
$10^4 \leqq N_e < 3\cdot 10^4$	$1.7\cdot 10^4$	10	66	$2.0\cdot 10^{-5}$	8 ± 2
$3\cdot 10^4 \leqq N_e < 10^5$	$5.5\cdot 10^4$	10	31	$4.0\cdot 10^{-6}$	19 ± 5
$10^5 \leqq N_e < 3\cdot 10^5$	$1.7\cdot 10^5$	10	30	$8.0\cdot 10^{-7}$	95 ± 20
$3\cdot 10^5 \leqq N_e < 10^6$	$5.5\cdot 10^5$	10	24	$2.0\cdot 10^{-7}$	290 ± 80
$N_e \geqq 10^6$	$2.4\cdot 10^6$	10	18	$2.0\cdot 10^{-8}$	1700 ± 500

* Not 100% in detection probability.

† Total working time was 290 hrs.

In Fig. 10 the total number of N-particles more than 10^{11} ev, N_N, can be expressed by

$$N_N = (50 \pm 5)(N_e/10^5)^{1.1 \pm 0.1}\,.$$

That is, N_N is almost proportional to the size N_e within the wide range from 10^3 to more than 10^6 without evidence of any change in size dependence.

Since the total number of N-particles as well as their energy spectrum is known, the total energy carried by all N-particles in an EAS can be estimated. The total energy carried by all N-particles between 10^{11} ev and 10^{13} ev in an EAS of size N_e turns out to be about $2\cdot 10^8 N_e$ ev. According to the results of Ref. 6, this value is about the same order of magnitude as that carried by the electron component, i.e. $(1.6\sim 2.2)\cdot 10^8 \cdot N_e$ ev[6)].

§ 6. Discussions

(A) *General relationship between N-particles and electrons*

According to the results obtained so far on N-particles of more than 10^{11} ev in association with EAS, the following characteristics

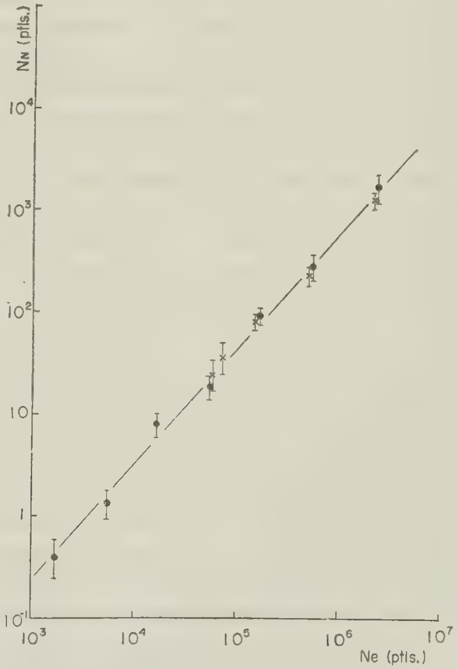

Fig. 10. Total number of N-particles N_N of $E_N \geqq 10^{11}$ ev versus size N_e of EAS. Straight line is represented by $N_N = 50(N_e/10^5)^{1.1}$. Crosses indicate the results of Ref. 6.

are to be noticed. Between a wide range of size N_e, from 10^3 to more than 10^6,

i) the energy spectrum of N-particles is independent of size,

ii) the total number of N-particles N_N is almost proportional to size N_e,

and

iii) the total energy carried by N-particles is nearly equal to that of the electron component in EAS.

Thus the fact that N-particles carry a large proportion of the total energy of EAS and that the general relation between electron component and N-particles seems to be invariant for such wide range of sizes, might suggest that the electron component is in a certain condition of equilibrium with N-particles and the latter are still playing a predominant role even at sea level. In particular, the fact that even EAS as small as 10^3 in size could have almost the same "age" with respect to N-particles as EAS of 10^4 or 10^5 might require such a kind of hypothesis as mentioned above.

In fact the results on the average energy of electrons in EAS[6),10)] as wall as the energy spectrum of high-energy γ-rays studied by emulsion technique[11),12)] would imply that neutral pions more than 10^{12} ev are rarely produced. In this case, the electron component of EAS can be considered as generated for the most part by neutral pions of energies less than 10^{12} ev. Since cascade showers initiated by such relatively low energy neutral pions will be absorbed rather rapidly, the electron component can possibly be in some state of equilibrium with N-particles if N-particles hold enough energy to supply continuously as much electrons as are absorbed[13)]*.

On the other hand, the following features are expected if the above model is supposed to hold. Then the average characters of EAS would not fluctuate very seriously, and further they would not depend on either primary energy or initial altitude of EAS, because the "age" of the EAS would be kept about constant if the electron component is in equilibrium with N-particles. In fact, preliminary results of succeeding study on the lateral structure of particles are consistent with this expectation, namely, the lateral distribution does not seem to fluctuate from case to case except in the region within several metres from the axis. Also, a unique lateral distribution of particles independent of size for almost all EAS of at least $N_e \geqq 10^4$ is not inconsistent with experimental results. Moreover, considering the correlation with the observed number of muons, there has not been found any strong evidence for the dependence of the lateral distribution on the altitude of initiation of EAS.[6)]

Another expectation on the basis of this model would be that the ratio of N_N to N_e is possibly independent of altitude; in other words the attenuation mean free path of the number of electrons is the same as that of N-particles. Although information is still lacking on this problem, the altitude dependence of N-particles could be studied by observations at different altitudes or by taking into account the correlation with the number of muons. This may give a crucial evidence for the model.

Incidentally, the lateral distribution function of N-particles has a close connection with the altitude variation of the production rate of N-particles as has been mentioned in §5 (C). Therefore, detailed study on this distribution would be useful to draw some conclusions regarding the development of EAS.

(B) *Energy spectrum of N-particles*

The energy spectrum obtained for N-particles of $E_N \geqq 10^{11}$ ev can be represented by a single power law $E_N^{-2.0}dE_N$ at least upto $3\cdot 10^{13}$ ev without any evidence of deviation. This gives an integral energy spectrum of $E_N^{-1.0}$. On the other hand, the integral spectrum of N-component not neccessarily associated with EAS has been shown to be $E_N^{-1.5}$ which is considerably different from above spectrum[14),15),16)]. Since the majority of N-particles observed in the present experiment consists of those associated with EAS of $N_e \geqq 10^3$, the difference between the two spectra should be attributed to N-particles associated with EAS of $N_e < 10^3$ as well as the leakage of primary particles to sea level without any interaction in the atmosphere.

By normalizing the spectrum $E_N^{-1.5}$ to the spectrum $E_N^{-1.0}$ of Fig. 5 at $E_N = 10^{13}$ ev, and taking the difference of the two spectra, one obtains a lower limit to the number of N-

---

* In Ref. 13 the authors investigated the transition of EAS under similar assumptions on the energies of neutral pions.

particles that are due to direct leakage of primary particles and those associated with EAS of $N_e<10^3$. If a majority of this difference is due to N-particles accompanying very small showers ($N_e<10^3$), one would expect that the energy spectrum for such N-particles would be much steeper than $E_N^{-1.0}$. However, the present experiment has shown that N-particles in EAS of size as low as 10^3 have the same spectrum $E_N^{-1.0}$ as those in higher size showers (see § 5. (A)) If we assume, therefore, that the same spectrum is likely to persist for showers of $N_e<10^3$, then it follows that the direct leakage of primary particles without any interaction in the atmosphere is appreciable. Even if we consider that 10% of the N-particles which account for the difference of the two spectra are due to such leakage, one obtains a lower limit to the collision mean free path L as 100 gcm^{-2}. It therefore follows that L cannot be much less than 100 gcm^{-2} for high-energy nuclear interactions.

It may be noted here that a comparison of the flux of high-energy N-particles observed at see level and mountain altitude with the primary flux of particles of same energy gives an absorption mean free path of 120~140 gcm^{-2}.15),16) Therefore, the lower and upper limits for L are considered to be fairly well fixed as 100 and 140 gcm^{-2}, respectively.

The energy spectrum of N-particles in Fig. 5 can be compared also with that of high-energy γ-rays, E_γ, observed in nuclear emulsions. Fujimoto et al.11) obtained the integral energy spectrum which is expressed as $E_\gamma^{-1.8\pm0.2}$ for $E_\gamma<10^{12}$ ev and as $E_\gamma^{-2.8\pm0.2}$ for $E_\gamma>10^{12}$ ev. Bristol group12) also had a similar result, that is $E_\gamma^{-3.3\pm0.2}$ for $E_\gamma>10^{12}$ ev. These results may be interpreted as indicating scarcity of production of neutral pions of more than 10^{12} ev. On the other hand, the integral energy spectrum of N-particles can be considered to be still $E_N^{-1.0}$ even in the region of more than 10^{12} ev. Now the question arises what this difference means. Here N-particles would possibly consist of charged pions, nucleons and other strongly interacting particles if they exist. If charge independence hypothesis can still hold at high energy region, charged pions would be expected to be produced as scarcely as neutral pions above 10^{12} ev. Therefore, if the energy spectrum of charged pions above 10^{12} ev is assumed to be the same as that obtained for neutral pions, then it would follow that at least 2/3 of N-particles of more than 10^{12} ev are due to particles different from pions. Of course, possible survivors of primary protons may account for some part of them. However, it is very interesting to investigate whether K-mesons or anti-nucleons exist among observed N-particles, since the composition of high-energy N-particles might give a clue to the development of EAS. The statistical accuracy above 10^{12} ev is not good enough for such analysis in this experiment, and an improved study on this feature is desirable.

(C) *Possible survival of primary particle*

Since it is shown that the integral energy spectrum of N-particles can be represented by E_N^{-1}, in the entire range of shower size and N-particle energy investigated in the present experiment, the total number of N-particles with energy more than E_N may be expressed as $(5\cdot10^{12}\,\text{ev}/E_N)\cdot(N_e/10^5)^{1.1}$. (see § 5. (D)) If the value of E_N is chosen such that the above expression becomes unity for a given size, this would mean that there exists on the average one N-particle of more than that energy in each EAS of that size. The expected values of E_N are $3\cdot10^{10}$ ev, $4\cdot10^{11}$ ev and $5\cdot10^{12}$ ev for EAS of sizes 10^3, 10^4 and 10^5, respectively. Though it is not yet assured that there is always one and only one such high energy N-particle in each EAS, those particles of more than E_N could be tentatively assumed to be surviors of primary particles. Assuming that the average primary energy is approximately given by $10^{10}\,N_e$ ev at sea level, the above values of E_N would indicate that primary particles still hold on the average more than 0.3~0.5% of their initial energies at sea level. If the collision mean free path is equal to 100 gcm^{-2}, it follows that the geometric mean of inelasticity η is approximately 0.4~0.5. This value of η is not very sensitive to the assumptions made above.

Thus, it is found that N-particles carrying about 1% of primary energies normally exist in EAS. Moreover, the existence of N-particles carrying more than several percent to several tens of percent of primary energies may be noticed. Examples of events are listed in Table III in which N-paticles are estimated to carry at least 5% of assumed primary energies, $10^{10}\,N_e$ ev.

The frequency of N-particles carrying more than 10% of primary energies is estimated to be once per 20~30 EASs according to the present energy spectrum. Events listed in Table III show 6 cases for $10^3 \leqq N_e < 3\cdot10^3$ and one case for $3\cdot10^3 \leqq N_e < 10^4$ in which N-particles are estimated to carry more than 10% of primary energies. These frequencies are consistent with those expected above.

Table III.

Size N_e	E_N (ev)	Fraction of primary energy (%)
$1\cdot10^3$	$1.1\cdot10^{12}$	11
$1\cdot10^3$	$1.1\cdot10^{12}$	11
$1.5\cdot10^3$	$1.4\cdot10^{12}$	9
$2\cdot10^3$	$1.4\cdot10^{12}$	7
$4\cdot10^3$	$2.0.10^{12}$	5
1.10^3	$2.1\cdot10^{12}$	21
$2.5\cdot10^3$	$2.1\cdot10^{12}$	8
$1\cdot10^3$	$2.3.10^{12}$	23
$4\cdot10^3$	$2.5\cdot10^{12}$	6
$1.5\cdot10^3$	$3.0\cdot10^{12}$	20
$2\cdot10^3$	$3.9\cdot10^{12}$	20
$3\cdot10^3$	$1.2\cdot10^{13}$	40

Following possibilities can be considered as reasons for such high residual fraction of primary energies; (i) fluctuation in the level of initiation of EAS, (ii) fluctuation in the number of nuclear interactions, and (iii) fluctuation of the inelasticity η.

In the first place, the possibility (i) will be examined. Suppose the EAS is initiated at x gcm^{-2} from the top of the atmosphere. If exponential attenuation is assumed for the total number of particles of EAS, the size $N_e(x)$ at sea level is proportional to $\exp(x/\Lambda_e)$, Λ_e being the attenuation mean free path. Assuming primary energy E_0 is equal to $10^{10}\cdot N_e(0)$ for an EAS started at the top, $x=0$, the relation of N_e vs x is

$$N_e(x)=\left(\frac{E_0}{10^{10}}\right)\exp\left(\frac{x}{\Lambda_e}\right). \qquad (1)$$

Suppose the interaction mean free path of primary particles is L gcm^{-2} and the inelasticity η is constant. Since the average number of interactions from x to sea level, X_0, is $(X_0-x)/L$, the residual energy of primary particle E_N will be

$$\left.\begin{aligned} &E_N=E_0(1-\eta)^{(X_0-x)/L}, \\ \text{or}\quad &E_N=E_0\exp\left[-\frac{K}{L}(X_0-x)\right]. \end{aligned}\right\} \qquad (2)$$

where $K=-\log(1-\eta)$. Therefore, apparent residual fraction of primary energy at sea level, $E_N/10^{10}\cdot N_e$, is

$$\frac{E_N}{10^{10}N_e}=\exp\left[-\frac{K}{L}X_0+\left(\frac{K}{L}-\frac{1}{\Lambda_e}\right)x\right], \qquad (3)$$

Eq. (3) means that an EAS started at lower level gives apparently higher residual fraction if

$$\frac{K}{L}-\frac{1}{\Lambda_e}>0\,.$$

Besides, the fact that $E_N/10^{10}N_e$ is at least 0.3~0.5% for each EAS would imply the following condition, putting $x=0$ in Eq. (3)

$$\exp\left(-\frac{K}{L}X_0\right)=(3\sim5)\cdot10^{-3}\,.$$

Assuming $L=100$ gcm^{-2}, $K=0.53\sim0.58$ or $\eta=0.41\sim0.45$ is obtained. On the other hand, in order to obtain a value $E_N/10^{10}N_e$ of more than 10% by means of variation of x,

$$\exp\left[(K/L-1/\Lambda_e)x\right],$$

should be able to exceed 20~30 for $0<x<X_0$. This requires the condition $\Lambda_e>500$ gcm^{-2}. Therefore, this condition may not be satisfied if the observed EAS are at a stage considerably later than the shower maximum. Rather those events with high residual fractions of primary energies may be interpreted as evidence for EAS near or even before the shower maximum.

The possibility (ii) can be considered as follows. Since the average number of inter-

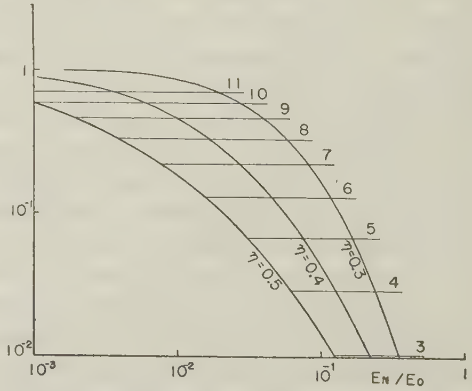

Fig. 11. Integral spectrum of fractional residual energy E_N/E_0 of primary particles for different values of η. Corresponding numbers of nuclear interactions are also shown on the curves.

actions is X_0/L, the probability with which n interactions take place is given by Poissonian distribution $P(X_0/L, \mathrm{n})$. Therefore, the probability of a N-particle having residual energy E_N at sea level greater than or equal to $E_0(1-\eta)^{\mathrm{n}}$, is represented by a partial summation of the Poissonian distribution,

$$\sum_0^{\mathrm{n}} P\left(\frac{X_0}{L}, \mathrm{n}\right).$$

This is nothing but the integral energy spectrum of survived primary particles. The energy spectra calculated for different values of η, 0.3, 0.4 and 0.5 on the assumption $L=100\,\mathrm{gcm}^{-2}$ are shown in Fig. 11. The observed frequency of events in which E_N/E_0 is estimated to be more than 10% is 3~5% of the total. This frequency in Fig. 11 corresponds to an inelasticity $\eta=0.4\sim0.5$ and the number of interactions for such events is something like 3~5. Moreover, the shape of the energy spectrum is not inconsistent with experimental results within the limits of accuracy and can be fitted smoothly with the spectrum E_N^{-1}. However, information is still lacking about EAS corresponding to such few interactions. In these cases, considerable fluctuations in longitudinal development of EAS should be expected. Then the size N_e is not necessarily a good measure of primary energy E_0. Therefore, the observed value of $E_N/10^{10}N_e$ may not be comparable with E_N/E_0 in such cases.

Besides the possibilities (i) and (ii), it can be shown that the fluctuation of inelasticity can also give rise to high residual energies. For the sake of simplicity, it is assumed that the value of inelasticity can be either η_1, or η_2 with probability of occurrence q or $(1-q)$, respectively, among the 10 interactions $(=X_0/L)$. Therefore, the number of interactions with inelasticity η_1 is $10\,q$ whereas that with η_2 is $10(1-q)$ on the average. Suppose a residual energy of 10% occurs in the events in which m interactions with η_1 and (10−m) interactions with η_2 are suffered by primary particles. Then the following equations are satisfied approximately.

$$(1-\eta_1)^{\mathrm{m}}(1-\eta_2)^{10-\mathrm{m}}=10^{-1}\,, \tag{1}$$

$$_{10}\mathrm{C}_{\mathrm{m}}\cdot q^{\mathrm{m}}(1-q)^{10-\mathrm{m}}\cong 4\cdot 10^{-2}\,, \tag{2}$$

$$(1-\eta_1)^{10q}(1-\eta_2)^{10(1-q)}\cong 4\cdot 10^{-3}\,. \tag{3}$$

Eq. (2) means the frequency of such cases as Eq. (1). Eq. (3) represents the fractional residual energy for average cases. Regarding m as a parameter, these equations can be solved. Two possible sets of solutions are shown below.

	m	η_1	q	η_2	$(1-q)$
(a)	0	0.75	0.28	0.20	0.72
(b)	1	0.70	0.40	0.12	0.60

These solutions might suggest a continuous distribution of η such that majority of interactions has η less than 0.5 but some have η values extending beyond 0.5 upto 1 instead of all interactions being necessarily limited to discrete values of η as considered above.

Although this model may only be one of the possible explanations for high residual energies of primary particles, at the same time it can account for the fact that nuclear interactions caused by primary particles studied so far almost always give rather small values of inelasticity.

In order to pursue these possibilities further, it will be inevitably necessary to specify various parameters in addition to the size so as to recognize any differences in individual characters of EAS.

On the other hand, the effect of the existence of N-particles with such high residual energies should be considered. Suppose an N-particle of energy E_N which is about 10% of E_0 interacts. It initiates another " secondary air shower " the size of which is of the order of $E_N/10^9$ at its shower maximum. This is comparable to the size of the original EAS, that is about $E_0/10^{10}$. Therefore, it is likely that such a secondary air shower will modify the structure of original EAS particularly in the vicinity of the core. A variety of effects can also be expected depending on the stage of the development of secondary air shower.

In fact, detailed investigation of cores by means of a large area of neon hodoscope detectors[6),10)] has confirmed that the structure of the core fluctuates remarkably from case to case at least within a few metres from the axis. Particularly, several examples have been found which showed steep cores with steadily increasing densities at least as close as 10 cm to the axis. These could be found in several percent of the total number of events. These events may also be interpreted as due to the superposition of young secondary air shower the energy of which is of the order of 10% of primary energy.

Acknowledgement

The author wishes to express his deepest gratitude to Professors H. Hasegawa, I. Miura, S. Miyake, M. Oda, N. Ogita, K. Suga and Drs. T. Matano, G. Tanahashi for their continuous encouragements and valuable discussions throughout this work. The author is also indebted to Dr. S. Naranan for his discussions of essential importance and many helpful advices on this article. Obligations are due to the efforts of Messrs. S. Shibata, M. Takano, H. Akiyama and K. Uchino for the operation of the apparatus. The author also acknowledges the help of Miss Y. Miura in the treatment of the present data.

References

1) N. I. Dobrotin, G. T. Zacepin, S. I. Nikol'skij and G. B. Hristiansen: Suppl. Nuovo Cim. **3** (1956) 635.

2) N. Dobrotin, O. Dovzhenko, V. Zacepin, E. Murzina, S. I. Nikol'skij, I. Rakobolskaya and E. Tukis: Suppl. Nuovo Cim. **8** (1958) 612

3) V. A. Dmitriev, G. B. Hristiansen and G. V. Kulikov: Suppl. Nuovo Cim. **8** (1958) 587.

4) A. T. Abrosimov, V. A. Dmitriev, G. V. Kulikov, E. I. Massal'skij, K. I. Solov'ev and G. B. Hristiansen: JETF **36** (1959) 751; JETP **9** (1959) 528.

5) T. Matano, I. Miura, M. Oda, K. Suga, G. Tanahashi and Y. Tanaka: INS-TCA-13 (1958)*.

6) S. Fukui, H. Hasegawa, T. Matano, I. Miura, M. Oda, K. Suga, G. Tanahashi and Y. Tanaka: Suppl. Progr. Theor. Phys. (1960).

7) M. F. Crouch, T, Matano, I. Miura, M. Oda, K. Suga, G. Tanahashi and Y. Tanaka: INSJ-8 (1958)*.

8) K. Kamata and J. Nishimura: Suppl. Prog. Theor. Phys. **6** (1958) 93.

9) O. Minakawa, Y. Nishimura, M. Tsuzuki, H. Yamanouchi, H. Aizu, H. Hasegawa, Y. Ishii, S. Tokunaga, Y. Fujimoto, S. Hasegawa, J. Nishimura, K. Niu, K. Nishikawa, K. Imaeda and M. Kazuno: INSJ-7 (1958); Suppl. Nuovo Cim. **11** (1959) 125.

10) S. Fukui: J. Phys. Soc. Japan (in press).

11) Y. Fujimoto, S. Hasegawa, M. Kazuno, J. Nishimura, K. Niu and N. Ogita: INSJ-30 (1960); Proc. Moscow Cosmic Ray Conference **I** (1960) 41.

12) J. Duthie, C. M. Fisher, P. H. Fowler, A. Kaddoura, D. H. Perkins and K. Pinkau: Proc. Moscow Cosmic Ray Conference **I**, (1960) 30.

13) S. Hayakawa and N. Ogita: Proc. Moscow Cosmic Ray Conference **II** (1960) 220.

14) E. A. Murzina, S. I. Nikolskii and V. I. Iakovlev: ZETF. **35** (1958) 1298; JETP **8** (1959) 906.

15) V. A. Dmitriev, G. V. Kulikov and G. B. Khristiansen: ZETF **37** (1959) 893; JETP **10** (1960) 637.

16) O. I. Dovshenko, G. T. Zacepin, E. A. Murzina, S. I. Nikolskij and V. I. Iakovlev: Proc. Moscow Cosmic Ray Conference **II** (1960) 34.

---

* INSJ and INS-TCA are the reports of Institute for Nuclear Study, University of Tokyo.

JOURNAL OF THE PHYSICAL SOCIETY OF JAPAN, Vol. 16, No. 5, MAY, 1961

Experimental Studies on Electronic Trapping Processes Associated with Dislocation Lines in Alkali Halide Crystals

By Hiroshi OHKURA

Department of Applied Physics, Osaka City University, Osaka, Japan

(Received December 3, 1960)

The trapping of conduction electrons by dislocation lines in alkali halide crystals was investigated by measuring the temperature dependence of photoconductances of deformed and undeformed crystals. Furthermore, the effect was verified by observing the thermally stimulated currents. In both cases, measurements of electric currents were carried out under application of ac in order to avoid undesirable effects due to space charge formation. Special care was exerted to obtain crystals having a high degree of purity. From the first mentioned experiment, the effective width of dislocation lines for electron trapping was estimated to be 9.3×10^{-8} cm, by using dislocation densities determined from nuclear magnetic resonance studies. The thermal depth of dislocation lines was estimated to be 0.21 ev for KBr and 0.24 ev for KCl crystals. A current glow peak, which presumably may correspond to trapping by jogs, was also measured. The thermal depth of jogs may be roughly estimated to be 0.48 ev.

§ 1. Introduction

Several intensive and important research efforts to investigate the various effects of dislocation lines on electronic processes in germanium crystals were carried out during the past few years[1),2)]. However, in the case of other crystals, especially such as alkali halides, it seems that little has been done in this respect, although it was well-known that plastic deformations have considerable influence on the electrical and optical properties of alkali halides[3),4)]. Therefore, we started this investigation for the purpose to get some information of trapping effects by dislocation lines with reference to conduction electrons in alkali halides. The work here reported is mainly concerned with measurements and analysis of the decrease of photoconductances in the plastically deformed potassium bromide and potassium chloride crystals at the temperature range below about 150°K.

In order to detect the trapping effect of dislocation lines only, it is quite important to eliminate as much as possible the undesirable effects caused by impurities, vacancy clusters, etc.. Single crystals appropriate for above requirements were obtained by repetitions of Kyropoulos' method. As will be described in § 2 *b*), this method proved to be highly advantageous for potassium bromide crystals. However, as was suggested by Seitz[5)], while a crystal is deformed plastically, a number of vacancy clusters is created in the crystal by moving dislocation lines. Such vacancy clusters may act as effective electron traps and may change the photochemical properties of alkali halides considerably. In fact, as was observed by Ueta and Kaenzing[3)], the *F* band bleaching rate in the plastically deformed colored KCl and NaCl crystals under irradiation with *F*-light at room temperature is much larger than in the case of the undeformed crystals and, moreover, a number of complex color centers is created. In our preliminary tests, the photoconductances of the deformed crystals showed a marked reduction compared with that of the undeformed ones at the whole temperature region from 73°K to 273°K. This fact easily leads us to erroneous interpretations of photoconductive measuremets, if assuming that trapping effects are caused by dislocation lines exclusively. Therefore, as a first step of our experiments, it was necessary to remove such vacancy clusters and also complex color centers, if they were present. We found out that our purposes were fully achieved if the deformed crystals were subjected to a pulse annealing. That is, after the deformed crystal was kept at 400°C for about 30 sec and then it was quenched rapidly on a massive copper block to room temperature. This achievement was confirmed by observing that the optical bleaching properties in deformed crystals subjected to the pulse annealing were exactly the same as for those of undeformed ones. We were worried that the pulse annealing process might decrease a density of dislocation lines which were produced by plastic deformation. The observed increase in the *N.M.R.* signal intensity after the pulse annealing might be attributed to the decrease of dislocation density, but it was confirmed that more than one half of the *N.M.R.* signals due to dislocation lines remained in the case of above mentioned short time annealing. (§ 3 *c*)).

For all insulators, a major problem in photoconductivity measurements is the decrease of apparent conductivity over a few or less seconds after voltage application. This effect can be interpreted as the reduction of an inner field by accumulation of charged carriers near electrodes[6),7),8)]. A number of complicated techniques was tried to remove such space-charge accumulations since Glaser and Lehfeldt's investigation[9)]. In our present work, in order to reduce the space-charge effects, the applied voltage was reversed periodically by applying ac voltage. The effects of elimination of space charges were investigated in some details and the results were summarized and reported in another article[10)].

§ 2. Experimental Details

a) *Apparatus*

Both photoconductive and "current glow" measurements were made between 73°K and 220°K with the sample mounted in a vacuum cryostat of the type shown in Fig. 1. For photoconductive measurements, a sample was fastened to a copper plate connected to the bottom of the liquid oxygen reservoir in the cryostat by a phosphor bronze spring, which is insulated electrically by using a Teflon plate, and the sample was surrounded by a copper radiation shield which was kept at the temperature of the bottom plate. Two electrical leads were brought into the crystal chamber, one of them was connected to the bottom copper plate and the other to the phosphor bronze spring, respectively. Aluminium electrodes were vacuum evaporated on both flat surfaces of cleaved sample plate. Bottom copper plate, crystal, and electrode were optical flat and were in contact with each other. Plates of about 2 mm thickness with 10×10 mm rectangular flat surfaces were used. The light was forcussed on the crystal with an area of about 20 mm². For "current glow" measurements, an electrical and thermal shield was applied on input leads to a preamplifier. The input leads are doubly shielded, the inner shield being driven in phase with an input voltage so as to reduce the stray capacity between grid and cathode of preamplifier. The sample for "current glow" measurements was bar of 2×2×10 mm.

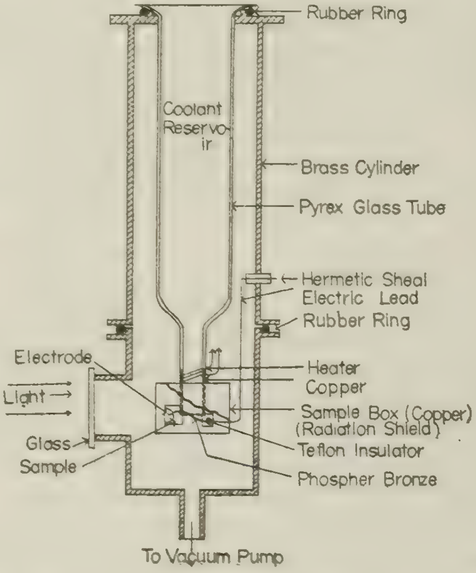

Fig. 1. Schematic block diagram of cryostat. Sample is fastened by spring of phosphor bronze, which is attached to one of electrodes vacuume-evaporated on the sample. Another electrode, the sample, and the bottom plate of the sample box are tightly contacted. Two electrical leads are connected to the phosphor bronze spring and the sample box, respectively.

Silver paint was applied on 2×2 mm faces of the bar. As for an illuminated surface, a cleaved surface was used which is the cleanest obtainable.

The temperatures were measured by a thermocouple of copper constantan attached on the bottom plate.

Block diagram for the photoconductive measurements is shown in Fig. 2. The photoconductive signal was measured by applying ac voltage of 1,000 cps to the sample and an input grid resistance of 100 kilo-ohms, which are connected in series. A rotating-sector disk, driven by a synchronous motor, chopped a light from an incandescent lamp at 30 cps. When the sample was irradiated with the chopped light, a voltage drop at the input resistance consists of 1,000 cps sinusoidal wave modulated with the photoconductive singnal of 30 cps. This modulated wave was sent to a tuned RC-amplifier of 1,000 cps and then was detected to pick up the 30 cps photocurrent signal. The faint 30 cps signal thus obtained was sent to a tuned RC-amplifier of 30 cps and then was lock-in detected. With S–1 in position M, the sensitivity of this apparatus was calibrated with a reference signal of 30 cps picked up by a PbS photo-cell from the same light source.

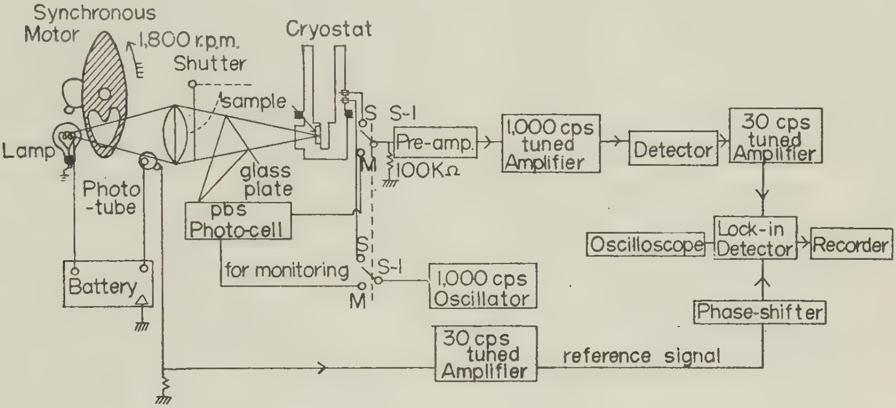

Fig. 2. Block diagram of photocurrent apparatus.

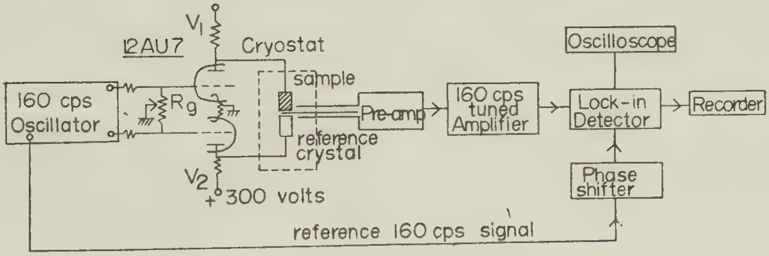

Block diagram of the current glow apparatus

Fig. 3. Block diagram of current glow apparatus. Cryostat is shown in dashed line. Sample, reference crystal, and R_g are arranged to form a balancing bridge. A dark current can be reduced to zero by adjusting R_g.

In Fig. 3, a block diagram of the "current glow" apparatus whose preamplifier consisted of Macdonald's circuit[11] is shown. At the first stage of this apparatus, a null method was used to eliminate a dark current and, furthermore, to increase a signal-noise ratio. An oscillator of 160 cps drives two triodes whose output is applied to both colored sample and control crystal (uncolored) in opposite phase. The variable grid leak resistance of two triodes and these two crystals are arranged to from four arms of a balancing bridge. The output signal due to the dark current can be reduced to zero by adjusting the grid leak resistance R_g. After the dark current has been eliminated, if the impedance of colored sample was changed thermally or by light stimulation, an unbalanced current would flow into a high input impedance in the preamplifier and result in voltage drop. This voltage signal of 160 cps was sent to a 160 cps tuned RC-amplifier and then lock-in detected. This apparatus can be used for photoconductive measurements, too. The sensitivity of this apparatus was calibrated by sending the sinusoidal signal of 160 cps having a known intensity. The input impedance of this Macdonald's preamplifier was about 600 megaohms and the noise level was 1.0×10^{-14} amp.

In a typical run of "current glow" measurements, after the crystal had been irradiated with F-light at 73°K, its temperature was raised at a rate of approximately 0.07°C per second, ac electrical field of about 100 volts per cm being applied to the crystal. The released currents were measured by means of above described apparatus as shown in Fig. 8.

A metal film interference filters were used to obtain a pure F-light irradiation from an 500 watts incandescent lamp of projector.

b) *Sample preparation*

Single crystals of alkali halides were grown from the melt in a platinum crucible by Kyropoulos' method using Yashima's analyzed grade of salt. Pure crystals were obtained by repetitions of Kyropoulos' method and by pulling up the crystal as thinly as possible. F centers were prepared by heating the crystals for about forty hours in either potassium or sodium metal vapor. The temperature of the crystals was maintained at a constant temperature within the range of 450°C and 580°C with an accuracy of ±3°C by using Chino's programmer. The crystals were sealed into an evacuated Pyrex glass tube. The alkali metal was vacuum distilled into the Pyrex tube after several preliminary vacuum distillations. The colored crystals were cleaved into several pieces of about 2 mm thickness, one of which was then plastically deformed by using the oil compressor. The remaining slices were used as reference crystals. The degree of deformation was expressed by a fractional thickness reduction.

Before describing the experimental results, it should be of interest to review the merits of the recrystallization technique which are most impressive in the case of potassium bromide crystals. Some intensitive testings were carried out and the results were summarized as follows. First, recrystallized colored crystals could not be optically bleached by F-light irradiation at room temperature, which is worthy of note. Even plastically deformed crystals, after they had been subjected to the pulse annealing described in §1, resulted in the same optical bleaching phenomena as those of the undeformed ones when they were irradiated with F-light at room temperature. One typical example for both ordinary and recrystallized crystals is illustrated in Fig. 4 a) and b), respectively, in which the soild and the dashed curves show the adsorption curves before and after F-light irradiation, respectively. From these results, we can conclude that the recrystallization technique is advan-

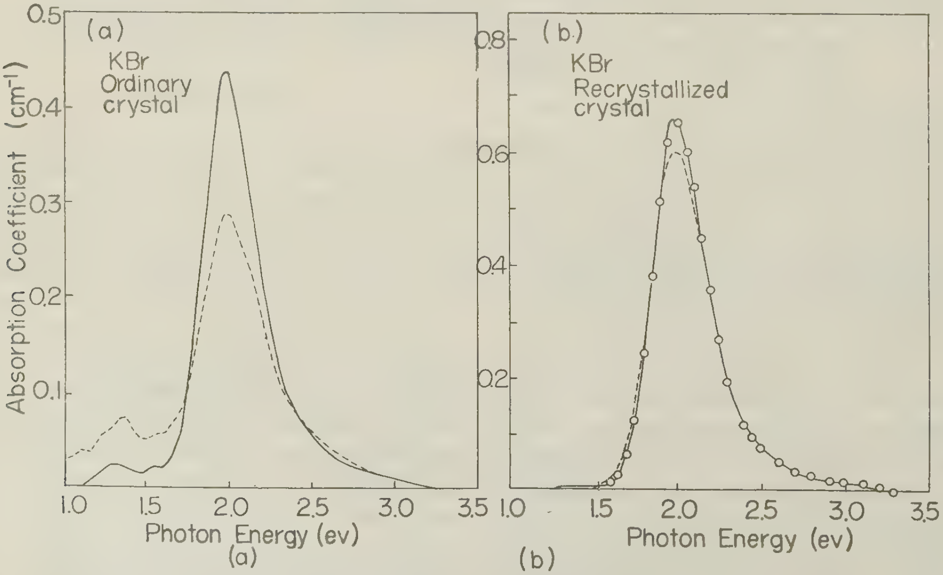

Fig. 4. Absortion coefficient of additively colored KBr crystal against photon energy. a) Ordinary crystal with a 13% plastic deformation; —— before irradiation and --- after ten minutes irradiation with F light. b) Recrystallized specimen a 19% plastic deformation; —— before irradiation and --- thirty minutes irradiation with F light.

tageous to reduce originally present vacancy clusters in the crystal which act to trap photoelectrons to form complex color centers during the F-light irradiation. Furthermore, we proved that the pulse annealing technique is quite effective for deformed crystals to remove vacancy clusters introduced by plastic deformation, as described in § 1. Second, the photoconductances of colored recrystallized crystals tended to increase as the crystal temperature was raised beyond −75°. Subsequent measurements produced the same results when these processes were repeated. On the contrary, the photoconductances of colored ordinary crystals tended to decrease if the crystal temperature raised beyond −75°C and compex color centers were created simultaneously. When these measurements were repeated, we could not obtain reproducible results. For instance, the magnitude of the photoconductance at −50°C in the former case is nearly ten times larger than the maximum value in the latter case. These differences may be attributed to the existence of trapping processes in ordinary crystals due to the vacancy clusters orginally present and the newly created color centers which may act as consecutive traps for photoelectrons[12]. Third, by measuring a secondary current caused by electron bombardment on one surface of KBr crystals, Onuki found that the mean range of conduction electrons in the recrystallized crystals was nearly ten times larger than that in ordinary ones[13]. Fig. 5 shows the saturation behavior of the current responses of both recrystallized and ordinary crystals of about 0.3 mm thickness against an increasingly applied collecting field at room temperature.

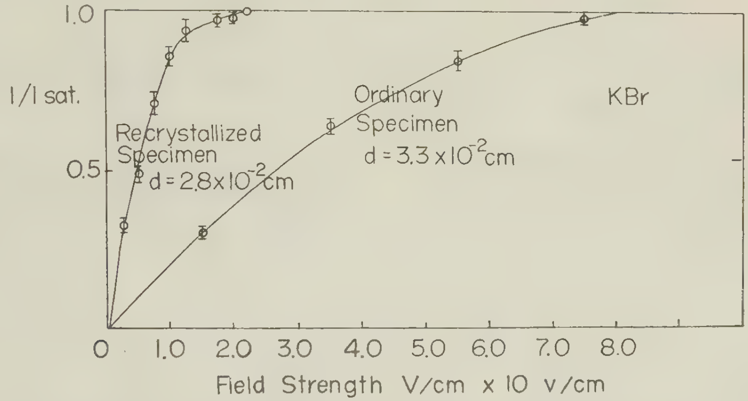

Fig. 5. Normalized secondary current induced by electron bombardment on one side of surfaces of KBr crystal is plotted against the intensity of collecting field strength. The range of conduction electrons in recrystallized crystal is almost ten times larger than that in ordinary crystal.

Comparing these curves with the theoretical curve due to Hecht[14], we can determine the mean ranges of both kinds of crystals. Since the magnitude of the mean range is expressed by a product of electron mobility and mean life time of conduction electrons, if we use the observed value of the electron mobility, $\mu=30\ \mathrm{cm}^2$ per volt-second[15] one can estimate the value of mean life time of conduction electrons in the recrystallized crystal to be in the order of 10^{-8} sec. This value is nearly ten times larger than that in ordinary crystals. If we assume that a cross section of traps responsible for this life time is equal to that of F centers, namely, $1.0\times10^{-14}\ \mathrm{cm}^2$[14], the concentration of corresponding traps can be determined to be in the order of 10^{15} cc, which would be the highest limits.

The potassium bromide crystals were pulled up from the melt as thinly as possible so as to obtain a low concentration of dislocation lines for the recrystallization process. Otsuka et al. have proved by *N.M.R.* studies that the above described procedure is quite suitable for such purpose[16].

§ 3. Experimental Results

a) *Photoconductive measurements*

The photoconductance curve of a colored potassium bromide crystal with 9% plastic strain is shown as the dashed curve in Fig. 6 at the temperature region from 73°K to 223°K.

In the same figure the photoconductance curve of undeformed reference crystal containing the equal amount of F centers is shown with the solid curve. The same photoconductance curve of potassium chloride crystals are shown in Fig. 7 for both undeformed and 18% strained crystals each of which is shown as the solid curve and as the dashed curve in the figure, respectively. The important characteristic of primary interest of these results is that, with

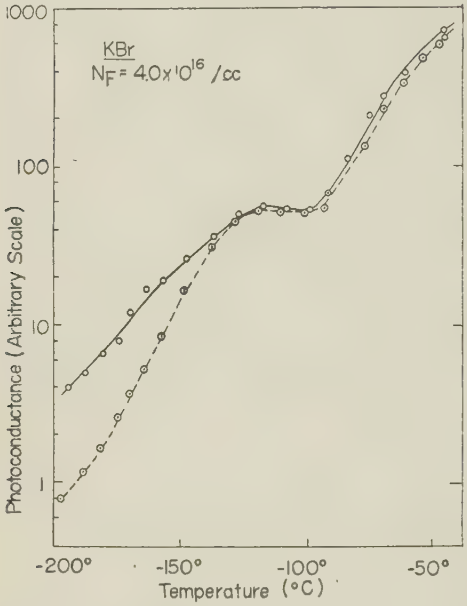

Fig. 6. Ac photoconductance of additively colored KBr crystal against temperature. ——; undeformed crystal and - - -; crystal with a 9% plastic strain.

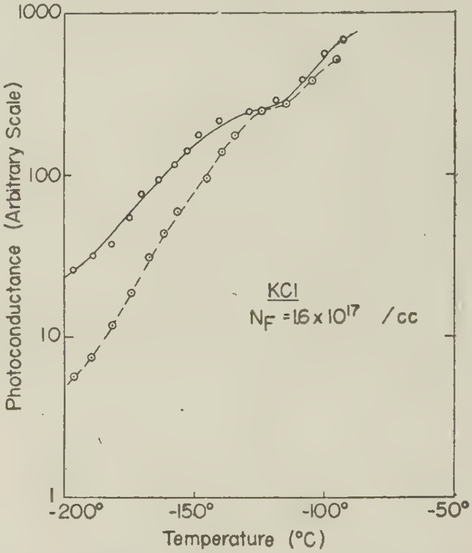

Fig. 7. Ac photoconductance of additively colored KCl crystal against temperature. ——; undeformed crystal and - - -; crystal with a 19% plastic strain.

Table I.

	N_F (cm^{-3})	Degree of deformation (per cent)	T* (°K)	$\frac{N_D w}{N_F \sigma_F}$	$N_D w$ (cm^{-1})	N_D (cm^{-1})	w (cm)
	$\times 10^{16}$				$\times 10^2$	$\times 10^9$	$\times 10^{-8}$
	1.5	16	103	1.4	2.0	7.6	2.6
	1.5	21	106	2.3	3.3	9.6	3.4
	4.3	8	103	0.7	3.2	4.5	7.1
KBr	4.0	9	106	1.0	3.9	4.6	8.5
	3.8	11	106	3.3	12.5	5.8	22
	7.7	9	106	0.9	6.6	4.6	14
	13	18		0.6	7.8	8.4	9.3
	Mean		105				9.3
	$\times 10^{16}$				$\times 10^3$		
	4.0	16	108	3.8	1.5		
KCl	4.0	25	123	7.6	3.0		
	16	19	123	2.2	3.5		
	16	21	120	3.4	5.5		
	Mean		118				

* The first column illustrates the concentration of F centers. The second is the deformation degrees which are expressed by percentage reduction. The sixth is the concentration of dislocation lines determined by *N.M.R.* method (§ 3 (*c*)). The explanations of the other columns will be appeared in § 4.

the exception of the vicinity of the plateau region, the photoconductance of deformed crystals is less than that of undeformed crystals. The plateau of photoconductance is in the range from −125°C to −100°C for KBr from −140°C to −120°C for KCl. The heights of plateaus were found to be inversely proportional to the concentration of *F* centers whithin the range from slightly greater than 10^{15} per cc to 5×10^{17} per cc. This result is excellent evidence that the photoelectrons in the undeformed crystal are trapped only by *F* centers at the temperature below the plateau region[14]. Hence, it appears that the decrease of photoconductance in deformed crystal may be attributed to the shallow traps introduced by plastic deformation. But this interpretation could not be regarded as definite, because other factors which could affect to change the magnitude of photoconductance still remained unexplored. We will revert to discuss these factors in later section.

The result obtained for KBr and KCl containing several concentration are summarized in Table I.

b) *"Current glow" in potassium bromide crystals*

The "current glow", namely, the thermal electric charge release during the warming of a colored KBr crystal containing 3.0×10^{16} *F* centers per cc and with 20% plastic strain is shown in Fig. 8. This crystal had been irradiated at 73°K for one hour with *F*-light. On the contrary, no charge bursts were observed in undeformed KBr crystals during warming from 73°K after *F*-light irradiation.

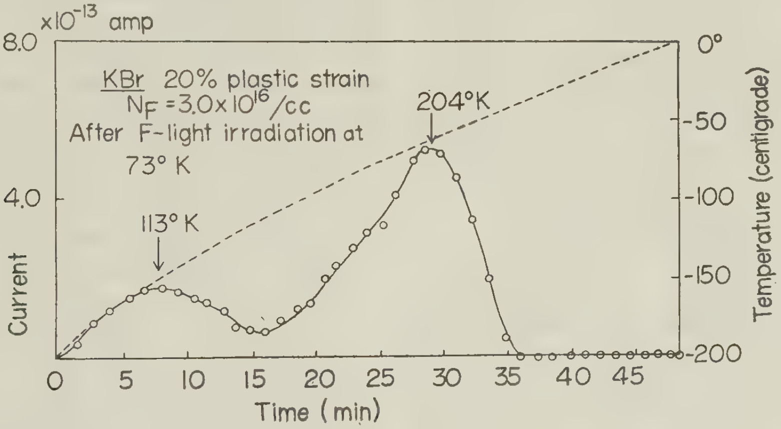

Fig. 8. "Current glow" curve for an additively colored KBr crystal with a 20% plastic strain which has been irradiated for one hour with *F*-light at 73°K. The dashed line shows the variation of temperature of the crystal with time.

Therefore, the current peaks at 113°K and 204°K, in Fig. 8, are characteristic for deformed crystals. These two current peaks may be attributed to the thermal release of electrons from the shallow traps which were created by plastic deformation.

Since the electrons in shallow traps came from *F* centers, being released optically, it is expected that the *F* band in deformed crystals would be bleached during the preliminary irradiation. The *F*-bleachings were measured with the use of Hitachi EPU-2 type spectrophotometer. In the case of undeformed colored crystals, no change was observed in the optical density in the spectral region of both *F* and *F′* bands. This means that an excited electron in an *F* center can hardly be raised thermally into the conduction band at 73°K[14]. Even if a few electrons were raised into it, they may be trapped by the ionized *F* centers causing them to revert into *F* centers unless they reach other *F* centers to form *F′* centers*.

---

* This description is not inconsistent with the Pick's results on the $F\rightarrow F'$ and $F'\rightarrow F$ conversion processes[17),24)]. For instance, in the $F\rightarrow F'$ conversion process, the more the bleaching temperatures increase, the more saturated concentration of bleached *F* centers increase. This may be interpreted in terms of the more predominence of the trapping probability of the negative ion vacancies than that of the *F* centers at low temperatures[25]. The decrease of the quantum efficiency in $F'\rightarrow F$ process due to the increase of temperatures could be interpreted by the same reason as mentioned above.

In the case of *F*-light bleaching of deformed crystals at 73°K, however, there was a slight decrease in the optical density of the *F* band. The saturated values of the decrement of the *F* center density in this case were almost independent of the initial *F* center density and were almost proportional to the deformation degrees; for instance, a saturated decrement of 1.5×10^{15} per cc for a crystal containing 3.0×10^{16} *F* centers per cc and with 27% plastic strain. The *F* band can be recovered by subsequent warming to 100°K.

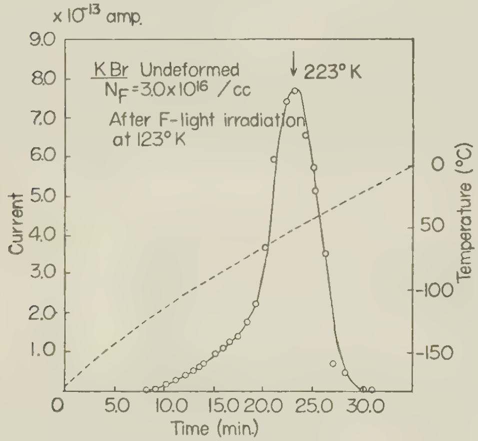

Fig. 9. "Current glow" curve for an additively colored undeformed KBr which has been irradiated for 10 min with *F*-light at 123°K. The dashed line shows the variation of temperature of the crystal with time.

Next, the thermal release curve for undeformed crystals was taken after *F*-light irradiation at 123°K for ten minutes. (Fig. 9) Only a single current peak occurred at 223°K. Exactly the same results were obtained in the case of previous *F*-light irradiation at 173°K. This current glow may be attributed to the thermal destruction of *F′* centers. Optical absorption measurements of the colored and undeformed KBr crystals have shown that *F′*-centers are formed by *F*-light irradiation at both temperatures. More quantitative studies concerning *F*-bleaching are as follows*: When optical measurements were made at liquid oxygen temperature after *F*-light irradiation at 123°K, it was found that the optical density at the peak of the *F* band decreased by approximately 45% of its initial value. After warming this crystal to 173°K subsequently and recooling it rapidly to 100°K, a part of *F′* centers reverted thermally to *F* centers but about 10% of the optical density of the initial *F* centers still remained as *F′* centers. When the crystal was *F*-bleached at 173°K, there was a 15% decrease in the optical density of *F* band. In every case, *F*-bleaching was accompanied with an increase of the *F′* band. Whole *F′* centers can be reverted thermally to *F* centers by a subsequent warming of the crystals to 223°K. These results of optical absorption measurements are consistent with the former description that the current peak at 223°K occurred as a result of the thermal destruction of *F′* centers.

A series of current glow peaks observed in a colored crystal with 18% plastic deformation which had been irradiated with *F*-light both at 123°K and 173°K and then cooled down to 100°K is shown in Fig. 10 *a*) and *b*), respectively. In Fig. 10 *a*), there are three current peaks at 137°K, 204°K, and 290°K, which we denoted as I, II, and III for convenience. In

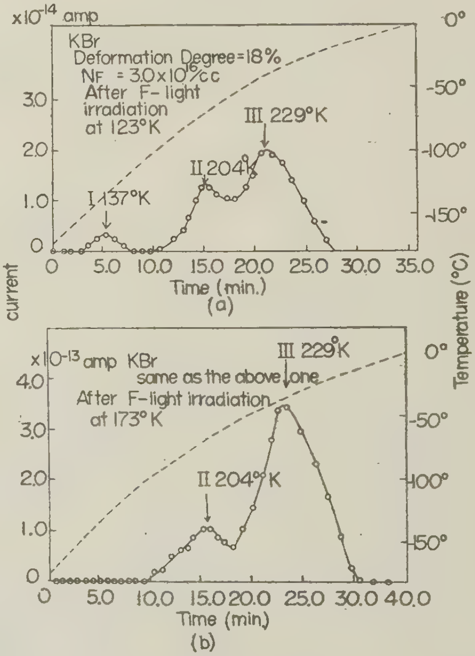

Fig. 10. *a*) "Current glow" curve for an additively colored KBr crystal with a 18% plastic strain which has been irradiated with *F*-light for 10 min at 123°K. *b*) "Current glow" curve for the same sample as that of case *a*) which has been irradiated for 10 min with *F*-light at 173°K. The dashed line shows the variation of temperature of the crystal with time.

---

* These results are somewhat different from Pick's observations[17].

Fig. 10 *b*), peak I disappears and peaks II and III that occur after irradiation at 123°K are also present except that the intensity of peak III becomes larger than that of peak II. Peak I may be considered to be a part of the 113°K peak observed in Fig. 8, if assuming such peaks are caused by the electron release from the traps having an inhomogeneous distribution of energy levels. The idea that the dislocation lines are responsible for this peak I is quite reasonable. Since the dislocation lines in crystals are actually composed of both screw and edge types, it is plausible to assume that trapping levels due to dislocations have an inhomogeneous distribution of energy levels. Peak II is quite consistent with the second peak observed in Fig. 8, which is also caused by a plastic deformation. The interpretation of peak II will be given in § 4. Peak III may be attributed to the destruction of F' band, although there is a slight shift of the peak to higher temperature levels compared with the current glow due to F'-release shown in Fig. 9. Because, as can be confirmed in optical absorption measurements, the creation of F' band at 123°K and 173°K and the subsequent thermal destruction of F' band in deformed crystals are the same as those in undeformed crystals described above.

The most characteristic feature of these results is that the current glow occurred at temperature of 113°K or 137°K signifying that shallow traps were created by the plastic deformation. These shallow traps may be responsible for the decrease of the mean life time of photoelectrons in deformed crystals which was mentioned in § 3 *a*). The temperature at which current peaks were observed are listed in the first column of Table II. The listed temperatures are mean values from several observations and the variation among individual runs was of the order of ±4°C.

The magnitude of the current glow depends on the following two factors; first, the probability that an electron can be removed thermally from a shallow trap to the conduction band and second, the life time of an electron before it is trapped by still deeper traps. If the next two simple assumptions are adopted for these two factors, the method described by Randall and Wilkins[18] in the case of thermoluminescence should be applicable to compute the trap depths for the various glow peaks. First assumption is that the probability of thermal ionization from the original traps p is given by

$$p=s\times\exp(-E/kT) \tag{3.1}$$

where E is the trap depth below the conduction band and s is a frequency factor. Second, a multiple trapping is assumed to be excluded. Then, the trap depth E is related to the temperature T^* of maximum glow by

$$E=kT^*\times\ln s\times\left(1+\frac{\ln(kT^{*2}/\beta E)}{\ln s}\right) \tag{3.2}$$

where β is the warming rate and the frequency factor s is taken to be 10^{10} 1/sec. In the case of a well-separated and appropriately narrow current peak as shown in Fig. 9, another approximate formula derived by Grossweiner[19] can be applicable which permits E and s to be calculated separately from the shape of the observed current temperature curve. According to this analysis, they are given in terms of T^* and T', being the temperature maximum and the temperature at which the increasing current reaches half-maximum, by the following equations:

$$\begin{aligned} &E=1.51\,kT^*T'/(T^*-T') \\ &s=\beta(E/kT^{*2})\exp(E/kT^*) \end{aligned} \tag{3.3}$$

It is still difficult to determine the frequency factor s with high accuracy because of its strong dependence on T^*-T'. In Table II, the trap depths for the various glow peaks calculated by using the equation (3.2) are listed. The trap depth and the frequency factor for F' centers which was calculated by using equation (3.3) is listed in Table II, too.

The charge density of released electrons, N, could be calculated by a time integral of the observed current glow curve, if the life time of the conduction electrons is known at the temperature region where the current bursts are measured. Although the value of life time is not determined yet definitely, we can safely assume it to be 1.0×10^{-8} second as was discussed in connection with Fig. 5. N can be expressed as follows:

$$N=\frac{d}{e\mu\tau VE}\int i\,dt \tag{3.4}$$

where d is the separation of electrodes, e the electronic charge, μ the electron mobility, τ the life time, V a volume of specimen, and E an applied field intensity, respectively. When photoelectrons fill the empty traps entirely under F-light irradiation, the charge density obtained from equation (3.4) would reach a saturation value. A typical example of this saturation curve for the thermal destruction of F' centers is illustrated in Fig. 11. Saturation was reached after about ten minutes irradiation with F-light, which was quite consistent with the results in optical absorption measurements of F-bleaching by irradiation with the light source which was used for current glow measurements. The saturated values for the various traps are listed in the fourth column of Table II. These values may correspond to the density of each trap. It is of interest to note that the density of F' centers is nearly equal to that of optically created F' centers. The tentative assignment of these traps are listed in the last column of Table II, details of which will be discussed in § 4.

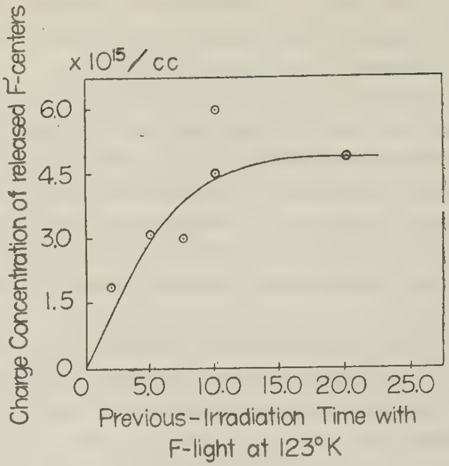

Fig. 11. Concentration of charges released from F' centers in the additively colored KBr crystal containing 3.0×10^{16} F centers per cc against the F-light irradiation time at 123°K.

Table II.

Trap	T^* (°K)	Trap depth (ev)	Frequency factor (1/sec)	Trap density (1/cc)	Assignment
I	113	0.26	Assuming to be 1.0×10^{10}	1.2×10^{14}	Dislocation
II	204	0.48		6.6×10^{14}	Jog
III	229	0.58		3.0×10^{15}	F'
F'	223	0.63	4.0×10^{11}	4.5×10^{15}	

c) *Determination of Dislocation line density through N.M.R.*

N.M.R. method for the determination of dislocation line density in alkali halide crystals had been at first suggested by Watkins[20)] and his findings were largely improved by Otsuka and Kawamura[21)]. They poined out that the observed decrease of a magnitude of nuclear magnetic absorption signal intensity of Br^{79} in deformed KBr crystals is attributed to the second order broadening of the central line of Br^{79}-lines in KBr caused by the introduction of dislocation lines. From this point of view, they have charted the curve showing the relation between dislocation density against deformation degree. The result, however, would not be applicable in our case without taking the special characteristics of our specimens. The following three points were examined with special attention in our present studies;

(1) effects of coloration

(2) effects of pulse annealing after plastic deformation

(3) geometric difference in samples.

We may expect that colored crystals can contain more dislocation lines than uncolored crystals during deformation process due to interaction between dislocation and F centers[22)]. But measurements failed to detect any differences in the dislocation density between uncolored and colored crystals containing 2.0×10^{17} per cc F centers, both of which have been subjected to plastic deformation of 10% strain. Even if such an increase would actually occur, it would be less than 10^8 dislocation line per cm², which is a threshold value detectable by *N.M.R.* technique.

Second, as introduced shortly in § 1, after a deformed crystal was subjected to a pulse annealing process, an increase of the peak intensity together with a simultaneous decrease of a bandwidth in the integrated unclear magnetic resonance absorption signal curve of Br^{79}-line in KBr was observed. This recovering process, obviously, depends on the temperature duration of pulse annealing. For convenience, we defined the recovering rate of *N.M.R.* singnal, R, by the following equation:

$$R = \frac{(I_T - I_R)}{(I_0 - I_R)}, \tag{3.4}$$

where I_T is the peak intensity in the integrated absorption signal curve of a deformed crystal measured after the pulse annealing at the temperature of T, I_R the original peak intensity measured immediately after the plastic deformation, I_0 the peak intensity of the undeformed crystal with the same geometrical construction as the deformed one. Each nuclear magnetic absorption measurement was carried out at room temperature. The numerator of equation (3.4) is inversely proportional to a recovered dislocation density and the denominator is inversely proportional to the dislocation density that has been introduced by plastic deformation. As the proportional constant of both numerator and denominator are equal, R in (3.4) may be called a normalized recovering rate caused by the pulse annealing. Recovering rate R is plotted against the pulse annealing temperature with pulse width of 50 min, 10 min, and 2 min as parameters in Fig. 12. The pulse width is plotted in Fig. 13 against the reciprocal of the characteristic temperature T^* at which temperature the recovering rate reaches its $(1-1/e)$ value in each run. This result shows that the recovering probability per second can be expressed by the following equation:

$$1/\tau = \nu_0 \times \exp(-E/kT^*) \tag{3.5}$$

where E is the activation energy of this process and ν_0 the frequency factor. Although we have no complete knowledge about the activated process which is characterized by above-determined activation energy, it is interesting to note that this energy value ($E = 0.87$ ev) is quite similar to that of the migration of positive ion vacancy. ν_0 is obtained to be 1.0×10^5 per sec.

Hitherto, we treated the recovering process as if dislocation lines were annuled in the crystal by thermal process. But, such a phoenomenon can be interpreted also in terms of the formation of small angle grain boundaries as a result of polygonization or the formation of a cell structure[23]. If these processes occurred predominantly, the dislocation lines would still remain in the crystal and would act as electron traps for conduction electrons. At the present stage, since we have no exact knowledge concerning which of the processes described above is predominant in this thermally recovering process, we did not take into account the result of this observation in analyzing the photoconductive data. Even if the annulment of dislocation lines occurred actually, it is found that, by using equation (3.5), still about one half of them can be expected to remain in the crystal by the pulse annealing at 400°C for 30 sec. Therefor,if we took into account the annulment of dislocation lines, subsequent calculation of the trapping cross section of traps would suffer a difference of factor two.

Third, Otsuka and Kawamura measured the dislocation line density in rod-shaped crystals

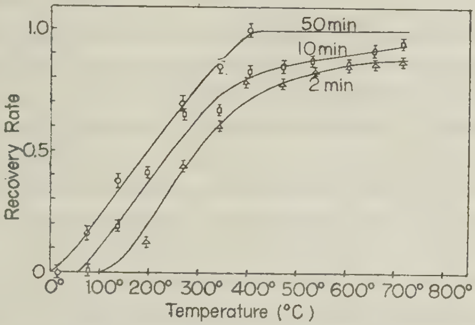

Fig. 12. Recovery rate of Br^{79}-lines in KBr against the pulse-annealed temperature with pulse width of annealing as a parameter.

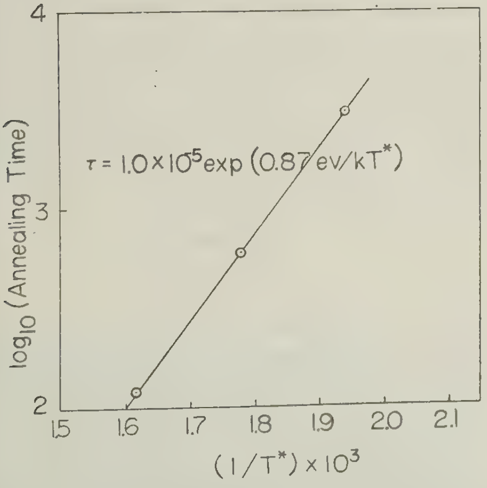

Fig. 13. Pulse-annealed duration against reciprocal of the characteristic temperature T^*.

pressed in the direction of their cylindrical axis. Our deformed crystals used for both photoconductive and current glow measurements were plate-shaped crystals with dimension of about 10×10×2 mm pressed in the direction of their thickness. We may expect that, in the latter case, more dislocation lines may be created than in the former during the deformation process even in the case of the same degree of deformation, because of limited free surfaces through which dislocation lines can escape. In order to verify this expectation, we measured the dislocation density of a plate-shaped specimen deformed in the direction of thickness. From the comparsion with the Otsuka and Kawamura data, we found that the measured density is nearly four times larger than that of theirs, under the same degree of deformation. This evidence quite fits with our expectation. Thus determined dislocation density is listed in the sixth column of Table I for KBr crystals.

§ 4. Discussion

As is well-known, the magnitude of a photoconductance of colored alkali halide crystals depends on the temperature though the opical quantum efficiency, the electron mobility, and the mean life time of conduction electrons[14] Therefore, before discussing the decreasing charactor of photoconductance in deformed crystals described in § 3. *a*), it is necessary to determine in what terms these observations can be interpreted. Fortunately, the experimental fact that the current glow in deformed crystals was observed at the temperature of about 113°K leads us to accept the point of view that new shallow trapping levels are created in deformed crystals during plastic deformation. These shallow traps can enhance a trapping probability for conduction electrons and may contribute primarily to the decrease of mean life time. As we shall show later, the other two factors would not have a marked effect on the temperature dependence of photoconductance. For instance, in order to interpret the decrease of photoconductances in terms of the decrease of the quantum efficiency, one must assume the proximity of dislocation lines and F-centers which results in the considerable variation of the electronic structures of F centers. Then, the following two evidences could be derived. First, the shape and peak location of F band would be changed. Second, under the plastic deformation, the more dislocation lines density would be introduced in the colored crystals than in case of the uncolored crystals. But, these expected evidences are not detected in our observations. (§ 3. *c*)). Therefore, it seems plausible to assume that the invariance of the quantum efficiency together with the uniform distribution of both dislocation lines and F centers*. Furthermore, from the mobility studies[15], the idea that a dislocation line can act to scatter conduction electrons in alkali halide crystals can not be applicable because of its quite short mean free path due to lattice scattering. In n-type germanium, an array of dislocation lines can act as a row of closely spaced acceptor centers which give an appreciable effect on the scattering of electrons[1]. But, in alkali halide, such effect can not be expected because of ionic crystal structure and far lower electronic conductivity compared to germanium.

Trapping effects due to F centers were predominant at the temperature below about 170°K for KBr and 150°K for KCl, respectively. This fact enables us to analyze the characteristic decrease of photoconductances in deformed crystals in these temperature regions. If we assume that shallow traps introduced by plastic deformation act as electron traps, the net mean life time T for plastically deformed crystals can be expressed as follows:

$$1/T=1/T_F+1/T_D\ , \qquad (4.1)$$

where T_F is the mean life time of photoelectrons due to trapping by F centers and T_D the mean life time due to trapping by shallow traps introduced by plastic deformation. Since the magnitude of photoconductance is proportional to the mean lifetime, T_D is calculated from equation (4.1) by using the observed photoconductance as follows:

$$1/T_D=1/T-1/T_F\sim 1/I-1/I_0 \qquad (4.2)$$

and

---

* If the dislocation lines and F centers are uniformly and independently distributed in the crystal, the probability that 10^{16}/cc F centers to be located in the proximity of the dislocation lines must be in the order of 10^{-7}, hence 10^2/cc dislocation lines out of 10^9/cm^2 dislocation lines might combine with the F center, the value of 10^2/cm^2 being too small for the above mentioned evidence to be observed.

$$T_F/T_D = I_0/I - 1 \tag{4.3}$$

where I_0 and I are the photoconductances for the undeformed and deformed crystals, respectively. Thus computed and normalized $1/T_D$ is plotted against temperature by solid line in Fig. 14. The dashed line in this figure shows the temperature derivative of this solid curve. The temperature T^* at which the peak of this derivate curve occurs may be used as the measure of trap depths. T^* are 105°K KBr and 118°K for KCl crystals, respectively.

The order of magnitude of the thermal depths of these shallow traps can be estimated approximately, if assuming that the probability per second for thermal ionization is expressed by the same equation as (3.1), namely, $p = s \times \exp(-E/kT)$, and assuming that the releasing frequency p is one per second at the temperature T^*. Inserting $s = 1.0 \times 10^{10}$ per sec into equation (3.1), the thermal depth E can be computed to be 0.21 ev for KBr and 0.24 ev for KCl crystals, respectively. The latter value would correspond to the thermal depth of trap I listed in Table II obtained from the current glow measurements. As described in §1. and 3, it can be deduced, especially from the optical studies, that these shallow traps are not attributed to point defects such as single vacancies, vacancy clusters, complex color centers etc., but are actually attributed to the characteristic defects caused by plastic deformation. We may speculate that the shallow traps are attributed to either dislocation lines or jogs of the dislocation lines.

A tentative explanation of the shallow traps may be offered by assuming that a dislocation line can trap photoelectrons in this temperature region. In the present experiments, one can estimate the effective trapping width w of dislocation line if the density of dislocation lines N_D (1/cm^2) is known. $N_D w$ and mean life time T_D are related by

$$1/T_D = N_D w u \tag{4.4}$$

where u is a mean thermal velocity. On the other hand, $1/T_F$ is expressed by $N_F \sigma_F u$, where N_F is the density of F centers per cc and σ_F the effective cross section of F center for electron trapping, the value of which can be estimated to be an order of 10^{-14} cm^2 [14]. The ratio of T_F to T_D, which can be obtained with the use of the equation (4.3), maintains at a constant value at low temperature, as shown in Fig. 14, where a release from the traps can be considered negligible. If one inserts equation (4.4) to equation (4.3), one finds

$$\frac{N_D w}{N_F \sigma_F} = \frac{T_F}{T_D} = \frac{I_0}{I} - 1\,, \tag{4.5}$$

from which one can compute $N_D w$. The computed values are summarized in the fourth and fifth column of Table I. Using the values of dislocation densities listed in the sixth column, the trapping widths w are calculated as shown in the last column of Table I. The average value of the effective trapping width of dislocation lines is 9.3×10^{-8} cm, which is a rather reasonable value.

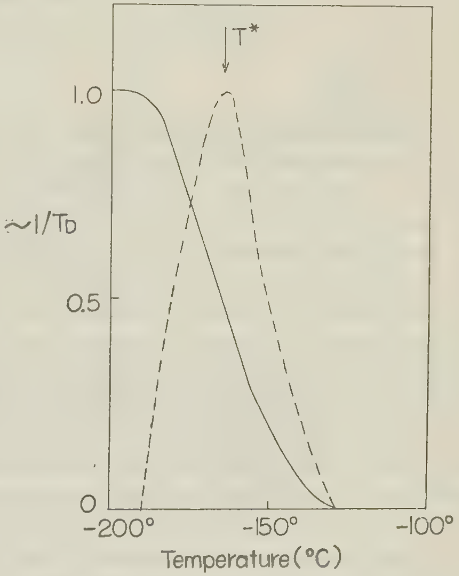

Fig. 14. Reciprocal of the mean life time T_D, which is normalized at the highest value, are plotted against temperature by solid line. Derivative curve of $1/T_D$ is shown by a dashed line.

If this trapping process was attributed only to jogs, $1/T_D$ should be equal to $N_J \sigma_J u$, where N_J is the jog density and σ_J a trapping cross section by jog. If we assume that all electrons which came from bleached F centers would go into jogs, total amount of N_J should be 10^{14} to 10^{15} per cc. By using these values, the order of magnitude of σ_J becomes to be 10^{-13} to 10^{-12} cm^2, which seems to be an unreasonably large. Comparing the observed values of cross sections, we can conclude that the model of dislocation traps is better suited than that of jog traps for explaining the characteristic decrease of photoconductances in deformed crystals.

We would like to advance tentatively the idea that the occurrence of current glow at 204°K, which is also characteristic for plastically deformed crystals, could be attributed to a thermal ionization process from jogs. Adopting this model, we can explain fairly well the occurrence of 204°K peak, though qualitatively. Once electrons trapped along a dislocation line after *F*-light irradiation at 73°K, they move perhaps along the dislocation line until they were trapped by still deeper traps such as jogs, which are located along the dislocation line. These trapped electrons in the jogs would contribute to the 204°K glow peak.

§ 5. Conclusion

By applying ac field on crystals for current measurements and by using single crystal having a high degree of purity, we have confirmed the evidence of trapping processes associated with dislocation lines in plastically deformed colored alkali halide crystals. From the comparison of photoconductances between deformed and undeformed crystals, we can estimate the trap depth of dislocation line to be 0.21 ev for the potassium bromide crystals and 0.24 ev for the potassium chloride crystals, respectively. We obtained also the effective mean trapping width of dislocation line to be 9.3×10^{-8} cm for the potassium bromide crystals, which value is more reasonable than the one obtained by the assumption that the trapping effects are caused by jogs.

Since a dislocation jog could be treated as a point defect having one half of the ionic charge, it could also act as a trap. But, since the net density of jogs is rather small, the trapping due to jogs would not play a role in photoconductive measurements. On the contrary, "current glow" measurement is quite sensitive. "Current glow" measurements gave the thermal depth of jogs to be 0.48 ev.

This evidence of dislocation traps could also throw light on the interpretation of the temperature dependence of photoconductance in undeformed colored crystal at low temperature. Untill now, the decrease of photoconductance in undeformed crystal has been interpreted only in terms of decreasing of the optical quantum efficiency with the decreasing temperature and did not take into account the temperature dependence of mobility[14]. The expected value of photoconductance, which is proportional to the product of the quantum efficiency and the mobilily, is rather flat as the result of the increasing tendency of mobility with the decreasing temperature. Hence, in order to explain the actually observed temperature dependence of photoconductances, it is necessary to either introduce another different mechanism or to add another trapping mechanism besides *F* centers. It seems likely that the trapping role of dislocation lines could contribute to the solution of the problem.

Acknowledgement

The author is indebted to Professor H. Kawamura for his suggestion of this problem and his guidance throughout the course of this study. He also wishes to thank Dr. E. Otsuka and Mr. M. Onuki for many fruitful discussions and suggestions, and Mr. T. Isoi, Mr. Y. Okubo, and Miss S. Miyamoto for technical assistance.

He would express his sincere thanks to Professors T. Nagamiya and J. Itoh, Osaka University, and Professors F. Seitz and R. Maurer, University of Illinois, for their deep interest shown in his work and for their many valuable discussions.

References

1) W. T. Read and G. L. Pearson: Rep. "Defects in Crystalline Solids" Bristol, (1955) 108. R. A. Logan, G. L. Pearson and D. A. Kleinman: J. A.P. **30** (1959) 885.
2) J. Okada: J. Phys. Soc. Japan **10** (1955) 1110.
3) M. Ueta and Kaenzig: Phys. Rev. **97** (1955) 1591.
4) G. Chiarotti: Phys. Rev. **107** (1957) 381. Z. Gyulai and D. Hartly: Z. Physik **51** (1928) 378.
5) F. Seitz: Phys. Rev. **80** (1950) 239.
6) A. von Hippel, E. P. Gross, J. G. Jalias and M. Geller: Phys. Rev. **91** (1954) 568.
7) M. Geller: Phys. Rev. **101** (1956) 1685.
8) J. R. Macdonald: J. Chem. Phys. **23** (1955) 275.
9) G. Glaser and W. Lehfeldt: Gött. Nachr. **2** (1936) 109.
10) M. Onuki and H. Ohkura: J. Phys. Soc. Japan **15** (1960) 1862.

11) J. R. Macdonald: Rev. Sci. Instr. **25** (1954) 144.
12) H. Ohkura, K. Awane, and S. Miyamoto: J. Phys. Soc. Japan **15** (1960) 934.
13) M. Onuki and H. Kawamnra: Reported at the Anual Meeting of the Physical Society of Japan (1957); to be published.
14) N. F. Mott and R. W. Guarnay: "Electronic Processes in Ionic Crystals" (1948) Oxford University Press.
15) M. Onuki and H. Kawamura: J. Phys. Soc. Japan **14** (1959) 967.
16) E. Otsuka, Y. Oshio, T. Kobayashi, and H. Kawamura: J. Phys. Soc. Japan **14** (1959) 1454.
17) H. Pick: Ann. Physik **31** (1938) 365.
18) J. T. Randall and M.H.F. Wilkins: Proc. Roy. Soc. (London) **A**, **184** (1945) 366.
19) L. I. Grossweiner: J. Appl. Phys. **24** (1953) 1306.
20) G. D. Watkins: Thesis, Harvard University, Unpublished.
21) E. Otsuka and H. Kawamura: J. Phys. Soc. Japan **12** (1957) 1071.
22) T. Suzuki and M. Doyama: J. Phys. Chem. Solids **10** (1959) 77.
23) A. H. Cottrel: "Dislocations and Plastic Flow in Crystals" (1953) Oxford University Press.
24) H. Pick: Ann. d. Phys. **37** (1940) 421.
25) M. Lax: Phys. Rev. **119** (1960) 1502.

JOURNAL OF THE PHYSICAL SOCIETY OF JAPAN, Vol. 16, No. 5, MAY, (1961)

Interaction of Electrons and Holes with Acoustic Waves in Intrinsic Semiconductors

By Nobuo MIKOSHIBA

Electrotechnical Laboratory, Nagatacho, Tokyo

(Received December 14, 1960)

A self-consistent semiclassical theory is given for explaining the characteristics of the interaction of electrons and holes with acoustic waves in intrinsic semiconductors. The ultrasonic absorption coefficient can be written as $A=A_R+A_K$, where A_R is due to the change of the deformation potential energies of electrons and holes caused by their recombination, A_K due to the change of the kinetic energy caused by the intraband transition. The formula of A_R is identical with that used by Southgate in the analysis of his experiments, if the frequency at which $\omega\tau=1$ satisfies the inequality $(ql)^2<3(\tau_0/\tau)$, where ω, q are the angular frequency and the wave number of acoustic waves, and l, τ_0, τ are the mean free path, the intraband relaxation time, the lifetime of electrons or holes respectively. Under such condition as the frequency $\omega=1/\tau$ satisfies $(ql)^2>3(\tau_0/\tau)$, no absorption peak can be expected contrary to the simple phenomenological treatment; A_R becomes smaller than the value of Southgate's formula and is obscured by A_K. As a whole, the characteristics of the interaction is very similar with those in many-valley semiconductors. The acousto-electromotive force is too small to be detectable in experiments.

§1. Introduction

Recently Southgate[1),2)] has proposed a mechanism of the utlrasonic absorption due to the electron-hole recombination for the interpretation of his experiments on Ge[3)] and Si[4)] in the intrinsic region. He has analyzed successfully the experiments by the formula[2)] derived from the theory of Weinreich.[5)] There remain some questions, however, about the applicability of the formula, because Weinreich's theory ignores the so-called collision-drag effect[6),7)] and it may be applicable only to the sufficiently low frequency range.

The object of this paper is to give a more detailed theory taking the collision-drag effect into account and to check the applicability condition of the formula used by Southgate. The method used in this paper is the self-consistent semiclassical approach which has been already applied to simple[8] and many-valley[9] semiconductors in the previous papers (hereafter called I and II, respectively). The merits of the method may be that it involves properly the collision-drag effect and can be applied to all frequency ranges.

We shall take a simple model in which the conduction and valence bands have both the single spherical energy surfaces. We consider the interaction of electrons and holes with longitudinal acoustic waves in the intrinsic region. In semiconductors such as Ge and Si with complex energy surfaces, the similar interaction may be expected in the case of transverse waves. In § 2, we shall set up basic equations for the internal electric field E, the internal current densities, J_n and J_p, and the local fluctuations of the number densities, n and p, where n and p refer to electrons and holes, respectively. In § 3, we shall calculate the ultrasonic absorption due to the electron-hole recombination in various frequency ranges. The absorption due to the intraband transition are calculated in § 4. In § 5, the acousto-electric effect is discussed to check whether it is detectable in experiments. In § 6, we shall compare the absorption due the recombination with that due to the intraband transition in various frequency ranges, and discuss the absorption peak expected in intrinsic and many-valley semiconductors.

§ 2. Basic Equations

We make the following approximations throughout this paper.

(a) The effect of the charge of moving impurities on the internal electric field is neglected. The effect of impurities is taken into account implicitly only in the lifetime of electrons or holes.

(b) The velocity dependences of the lifetime τ and the intraband relaxation times, τ_n and τ_p, are neglected. This approximation does not alter all the results except a numerical factor in the high frequency range.

(c) We classify the loss mechanism of the acoustic energy into two parts. One is due to the change of the deformation potential energies of electrons and holes caused by their recombination. When n or p deviates from the local equilibrium fluctuation, n_{eq} or p_{eq}, n or p relaxes to n_{eq} or p_{eq} in the lifetime, being accompanied with the energy transfer from acoustic to lattice systems. The other is due to the change of the kinetic energy caused by the intraband transition. When the distribution fuction f of electrons or holes deviates from the local equilibrium distribution f_0, f relaxes to f_0 in the intraband relaxation time, being accompanied with the kinetic energy transfer. These situations are very similar with those in many-valley semiconductors.[9]

(d) It is assumed that the recombination has no influence on the local space charge. Then, the difference of n_{eq} and p_{eq} can be put equal to $(n-p)$.

It is necessary, for the determinations of E, n, p, J_n and J_p, to solve Maxwell's equation, the equation of continuity and the Boltzmann equation. Maxwell's equation is written as

$$\frac{\partial}{\partial t}\left(\boldsymbol{J}_n+\boldsymbol{J}_p+\frac{\varepsilon}{4\pi}\cdot\frac{\partial \boldsymbol{E}}{\partial t}\right)=-\frac{c^2}{4\pi}\mathrm{curl}\cdot\mathrm{curl}\,\boldsymbol{E}\,, \tag{2.1}$$

where ε is the dielectric constant, c is the light velocity. Since the local velocity of the lattice varies as $u\propto\exp[i(\omega t-qz)]$, we get

$$E=\frac{4\pi i}{\omega\varepsilon}(J_n+J_p) \tag{2.2}$$

for longitudinal waves.

The equations of continuity for electrons and holes are given by

$$\left.\begin{aligned}&\frac{\partial}{\partial t}(ne)+\frac{\partial J_n}{\partial z}+\frac{e}{\tau}(n-n_{eq})=0\,,\\&\frac{\partial}{\partial t}(-pe)+\frac{\partial J_p}{\partial z}+\frac{(-e)}{\tau}(p-p_{eq})=0\,,\end{aligned}\right\} \tag{2.3}$$

respectively, where e is the charge of an electron. The local equilibrium fluctuations associated with the recombination, n_{eq} and p_{eq}, are determined as follows. The well-known relation[10)]

$$N^2=\text{const.}\ T^3\exp(-E_g/kT) \tag{2.4}$$

holds in thermal equilibrium in the absence of acoustic waves, where N is the number density of electrons (holes), E_g the energy gap between the conduction and valence bands. When acoustic waves are being propagated, the energy gap changes into E_g-Cu/V, where V is the sound velocity, $C\equiv C_n+C_p$ is the sum of the deformation potential constants for electrons and holes. Then, from (2.4) we get

$$(N+n_{eq})\cdot(N+p_{eq})=N^2\exp(Cu/VkT)\,. \tag{2.5}$$

Making use of (2.5) and the approximation (d),

$$n_{eq}-p_{eq}=n-p\ , \tag{2.6}$$

we obtain

$$\left.\begin{aligned} n_{eq}&=\frac{1}{2}(n-p)+NCu/2VkT\ ,\\ p_{eq}&=\frac{1}{2}(p-n)+NCu/2VkT \end{aligned}\right\} \tag{2.7}$$

in the case of $Cu/V\ll kT$. Then, we get from (2.3) and (2.7)

$$\left.\begin{aligned} n&=\frac{q}{2\omega e}(J_n+J_p)+\frac{1}{1+i\omega\tau}\left\{\frac{iq\tau}{2e}(J_n-J_p)+\frac{NCu}{2VkT}\right\},\\ p&=\frac{q}{2\omega(-e)}(J_n+J_p)+\frac{1}{1+i\omega\tau}\left\{\frac{iq\tau}{2e}(J_n-J_p)+\frac{NCu}{2VkT}\right\}. \end{aligned}\right\} \tag{2.8}$$

To set up the Boltzmann equation, we should take two facts into account; (1) the collision-drag effect and (2) the force, exerted on electrons or holes, due to the deformation potential, together with the internal electric field E. Thus, the Boltzmann equation for electrons can be written as

$$\frac{\partial f_n}{\partial t}+(\boldsymbol{v}\cdot\boldsymbol{\nabla}_r)f_n+\frac{e}{m_n}(\boldsymbol{E}_n'\cdot\boldsymbol{\nabla}_v)f_n=-\frac{f_n-f_{n0}(|\boldsymbol{v}-\boldsymbol{u}|)}{\tau_n}\ , \tag{2.9}$$

where m_n is the effective mass and

$$E_n'\equiv E-iC_nq^2u/\omega e\ . \tag{2.10}$$

The distribution function can be solved as

$$\left.\begin{aligned} f_n&=f_{n0}(|\boldsymbol{v}-\boldsymbol{u}|)-\Psi_n(\boldsymbol{v})\cdot\partial f_{n0}/\partial v\ ,\\ f_{n0}(\boldsymbol{v})&\equiv\exp\left[\frac{1}{2}m_n(v_{n1}^2-v^2)/kT\right],\\ v_{n1}^2&\equiv\left(\frac{2kT}{m_n}\right)\ln\left\{2^{1/2}\pi^{3/2}\left(\frac{\hbar^2}{m_nkT}\right)^{3/2}(N+n)\right\}, \end{aligned}\right\} \tag{2.11}$$

where

$$\Psi_n(\boldsymbol{v})\equiv\frac{a_nA_n}{ql_n}\cdot\frac{x}{1-ia_nx}+\frac{a_nB_n}{ql_n}\cdot\frac{v_{n0}}{v}\cdot\frac{1}{1-ia_nx}-ux-B_n\frac{v_{n0}}{v} \tag{2.12}$$

for longitudinal waves and we put for brevity as

$$\left.\begin{aligned} &v_{n0}^2 \equiv 3kT/m_n\,, \qquad l_n \equiv \tau_n v\,, \\ &a_n \equiv ql_n/(1+i\omega\tau_n)\,, \qquad x \equiv \cos\theta\,, \end{aligned}\right\} \tag{2.13}$$

and

$$\left.\begin{aligned} &A_n \equiv \frac{eE\tau_n}{m_n} - i\frac{C_n\tau_n q^2 u}{m_n\omega} + u\,, \\ &B_n \equiv nv_{n0}/3N\,. \end{aligned}\right\} \tag{2.14}$$

Then, the local current density,

$$\boldsymbol{J} = \frac{2em^3}{h^3}\int_0^\infty \boldsymbol{v}f(v)d^3\boldsymbol{v}\,,$$

is calculated as

$$J_n = \frac{3NeP_{n0}}{ql_{n0}}\left(\frac{A_n}{a_{n0}} + iB_n\right), \tag{2.15}$$

where

$$l_{n0} \equiv \tau_n v_{n0}\,, \qquad a_{n0} \equiv ql_{n0}/(1+i\omega\tau_n) \tag{2.16}$$

and the modified Pippard's function,[8),9)]

$$\left.\begin{aligned} P_{n0} &\simeq \frac{1}{3}(ql_{n0})^2 - \frac{1}{3}(ql_{n0})^4 \qquad (ql_{n0} \ll 1)\,, \\ &\simeq 1-(3\pi/2)^{1/2}(ql_{n0})^{-1} \qquad (ql_{n0} \gg 1) \end{aligned}\right\} \tag{2.17}$$

is used. The equations, (2.9)-(2.17), are identical in form with those in the paper II. By replacing (n, e) with $(p, -e)$, we can obtain the quantities for holes as

$$J_p = -\frac{3NeP_{p0}}{ql_{p0}}\left(\frac{A_p}{a_{p0}} + iB_p\right). \tag{2.18}$$

The self-consistent solutions for E, n, p, J_n and J_p can be obtained from (2.2), (2.8), (2.15) and (2.18). Here we give the results for J_n and J_p:

$$\left.\begin{aligned} &J_n + J_p = Neu\cdot X/Z\,, \\ &J_n - J_p = Neu\cdot Y/Z\,, \end{aligned}\right\} \tag{2.19}$$

where

$$\begin{aligned} X \equiv {} & \frac{iC}{2kT\omega\tau}(P_{n0}\beta_n - P_{p0}\beta_p) - \frac{3P_{n0}}{ql_{n0}a_{n0}}\left(i\frac{C_n}{3kT}\cdot\frac{(ql_{n0})^2}{\omega\tau_n} - 1\right)(1+P_{p0}\beta_p) \\ & + \frac{3P_{p0}}{ql_{p0}a_{p0}}\left(i\frac{C_p}{3kT}\cdot\frac{(ql_{p0})^2}{\omega\tau_p} - 1\right)(1+P_{n0}\beta_n)\,, \end{aligned} \tag{2.20}$$

$$\begin{aligned} Y \equiv {} & \left\{i\frac{CP_{n0}\beta_n}{2kT\omega\tau} - i\frac{P_{n0}}{a_{n0}}\cdot\frac{C_n}{kT}\cdot\frac{ql_{n0}}{\omega\tau_n} + \frac{3P_{n0}}{ql_{n0}a_{n0}}\right\}\left\{1 - i\frac{6P_{p0}}{ql_{p0}a_{p0}}\cdot\frac{(\omega_p\tau_p)^2}{\omega\tau_p} - i\frac{P_{p0}}{\omega\tau_p}\right\} \\ & + \left\{i\frac{CP_{p0}\beta_p}{2kT\omega\tau} - i\frac{P_{p0}}{a_{p0}}\cdot\frac{C_p}{kT}\cdot\frac{ql_{p0}}{\omega\tau_p} + \frac{3P_{p0}}{ql_{p0}a_{p0}}\right\} \\ & \qquad \times\left\{1 - i\frac{6P_{n0}}{ql_{n0}a_{n0}}\cdot\frac{(\omega_n\tau_n)^2}{\omega\tau_n} - i\frac{P_{n0}}{\omega\tau_n}\right\}, \end{aligned} \tag{2.21}$$

$$\begin{aligned} Z \equiv {} & 1 - i\left(\frac{3P_{n0}}{ql_{n0}a_{n0}}\cdot\frac{(\omega_n\tau_n)^2}{\omega\tau_n} + \frac{P_{n0}}{2\omega\tau_n}\right)(1+P_{p0}\beta_p) \\ & - i\left(\frac{3P_{p0}}{ql_{p0}a_{p0}}\cdot\frac{(\omega_p\tau_p)^2}{\omega\tau_p} + \frac{P_{p0}}{2\omega\tau_p}\right)(1+P_{n0}\beta_n) + \frac{1}{2}(P_{n0}\beta_n + P_{p0}\beta_p)\,, \end{aligned} \tag{2.22}$$

$$\left.\begin{aligned} &\omega_n^2 \equiv 4\pi Ne^2/m_n\mathcal{E}\ , &&\omega_p^2 \equiv 4\pi Ne^2/m_p\mathcal{E}\ ,\\ &\beta_n \equiv (\tau/\tau_n)/(1+i\omega\tau)\ , &&\beta_p \equiv (\tau/\tau_p)/(1+i\omega\tau)\ . \end{aligned}\right\} \tag{2.23}$$

The appropriate approximations of (2.19) to various frequency ranges will be given in the following sections.

§ 3. Ultrasonic Absorption due to Recombination

According to the assumption (c) in § 2, the ultrasonic absorption coefficient $\varLambda$ is written as

$$\varLambda = \varLambda_R + \varLambda_K\ , \tag{3.1}$$

where $\varLambda_R$ is the component due to the recombination and $\varLambda_K$ is due to the intraband transitions. We shall calculate $\varLambda_R$ in this section. When the local fluctuation, n or p, deviates from n_{eq} or p_{eq}, the deformation potential energy, $-Cqu/\omega$, is transferred from acoustic to lattice systems in the lifetime τ owing to one recombination. Thus, the energy W_R absorbed per unit volume and unit time becomes

$$\left.\begin{aligned} &W_R = W_R^n + W_R^p\ ,\\ &W_R^n = \frac{1}{2}\,\mathrm{Re}\left[\left(-\frac{Cqu/\omega}{2\tau}\right)^*(n-n_{eq})\right],\\ &W_R^p = \frac{1}{2}\,\mathrm{Re}\left[\left(-\frac{Cqu/\omega}{2\tau}\right)^*(p-p_{eq})\right]. \end{aligned}\right\} \tag{3.2}$$

Then, from the definition of the absorption coefficient we get

$$\varLambda_R \equiv 2W_R/\rho|u|^2V = \frac{NC}{2\rho V^3\tau}\,\mathrm{Re}\left[\frac{i\omega\tau}{1+i\omega\tau}\left(\frac{C}{kT}-\frac{J_n-J_p}{Neu}\right)\right], \tag{3.3}$$

where ρ is the mass density of materials. In (3.2) we should remark two points; (1) the reason why there is no term involving the energy gap is that it vanishes taking the time or space average and (2) the factor 2 in the denominator in the bracket is due to the fact that one recombination gives rise to a decrease of $(n+p)$ by 2.

First, we shall consider $\varLambda_R$ in the low frequency range where $ql_{n0} \sim ql_{p0} \ll 1$. It is convenient to consider separately three cases;

(A): $$0 \ll (ql_{n0})^2 \ll \frac{3kT}{|C|}\cdot\frac{\tau_n}{\tau}\ ,$$

(B): $$\frac{3kT}{|C|}\cdot\frac{\tau_n}{\tau} \ll (ql_{n0})^2 \ll \frac{3\tau_n}{\tau}\ ,$$

(C): $$\frac{3\tau_n}{\tau} \ll (ql_{n0})^2 \ll 1\ ,$$

where

$$6\omega_n^2/q^2 \gg v_{n0}^2\ , \qquad \omega\tau_n \ll 1$$

are common to all cases. Although we specify three cases by the quantities of electrons, this classification holds approximately for the same quantities of holes. The approximate expressions of (J_n-J_p) and $\varLambda_R$ are calculated as follows.

(A):

$$J_n - J_p \cong 2Neu\ , \tag{3.4}$$

$$\varLambda_R \cong \frac{NC^2}{2\rho V^3kT}\cdot\frac{\omega^2\tau}{1+(\omega\tau)^2}\ . \tag{3.5}$$

(B):

$$J_n - J_p \simeq 2Neu \cdot \frac{Cq}{V} \cdot \frac{\tau_n \tau_p}{m_p \tau_n + m_n \tau_p} \cdot \frac{\omega\tau}{1+i\omega\tau}\,, \tag{3.6}$$

$$\Lambda_R \cong \frac{NC^2}{2\rho V^3 kT} \cdot \frac{\omega^2\tau}{1+(\omega\tau)^2} \left\{ 1 - \frac{4}{(3\tau_n/\tau)/(ql_{n0})^2 + (3\tau_p/\tau)/(ql_{p0})^2} \cdot \frac{1}{1+(\omega\tau)^2} \right\}. \tag{3.7}$$

(C):

$$\begin{aligned} J_n - J_p \cong Neu \cdot \frac{C}{kT} \Bigg\{ 1 &- \frac{1}{2} \left(\frac{3\tau_n/\tau}{(ql_{n0})^2} + \frac{3\tau_p/\tau}{(ql_{p0})^2} \right)(1+i\omega\tau) \\ &+ \frac{1}{4} \left(\frac{3\tau_n/\tau}{(ql_{n0})^2} + \frac{3\tau_p/\tau}{(ql_{p0})^2} \right)^2 (1+i\omega\tau)^2 \Bigg\}\,, \end{aligned} \tag{3.8}$$

$$\Lambda_R \cong \frac{NC^2\omega^2\tau}{2\rho V^3 kT} \cdot \frac{1}{4} \left(\frac{3\tau_n/\tau}{(ql_{n0})^2} + \frac{3\tau_p/\tau}{(ql_{p0})^2} \right)^2 . \tag{3.9}$$

Next, we shall calculate Λ_R in the sufficiently high frequency range such as

(D): $ql_{n0} \gg 1\,, \quad 6\omega_n{}^2/q^2 \ll v_{n0}^2\,, \quad \omega\tau \gtrsim 1\,, \quad \omega\tau_n \lesssim 1\,,$

where electrons and holes may interact independently with acoustic phonon beams. In fact, we get

$$\left. \begin{aligned} J_n &\cong \frac{Neu}{kT} \cdot C_n (1+i\omega\tau_n) \left(1 + \frac{i\omega\tau_n}{P_{n0}} \right)^{-1}, \\ J_p &\cong \frac{N(-e)u}{kT} \cdot C_p (1+i\omega\tau_p) \left(1 + \frac{i\omega\tau_p}{P_{p0}} \right)^{-1} \end{aligned} \right\} \tag{3.10}$$

and

$$\Lambda_R \cong \left(\frac{3\pi}{2} \right)^{1/2} \frac{NC\omega}{2\rho V^2 kT\tau} \left(C_n \frac{\tau_n}{v_{n0}} + C_p \frac{\tau_p}{v_{p0}} \right), \tag{3.11}$$

which is very small compared with Λ_K in (4.8). We shall discuss the obtained results in § 6.

§ 4. Ultrasonic Absorption due to Intraband Transition

As has been shown in the papers I and II, the ultrasonic absorption coefficient Λ_K due to the change of the kinetic energy caused by the intraband transition is given by

$$\Lambda_K = \Lambda_K{}^n + \Lambda_K{}^p\,, \tag{4.1a}$$

$$\Lambda_K{}^n = -\frac{2m_n{}^4}{\rho |u|^2 V \tau_n h^3} \int_0^\infty \frac{\partial f_{n0}}{\partial v} v^3 \, dv \int_{-1}^{1} dx \int_0^{2\pi} d\phi \, |\Psi_n(v)|^2 \tag{4.1b}$$

and the similar formula for $\Lambda_K{}^p$. The approximate expressions for $(J_n + J_p)$ and the calculated formulae for $\Lambda_K{}^n$ and $\Lambda_K{}^p$ are tabulated as follows.

(A):

$$J_n + J_p \cong \frac{\varepsilon q^2 u}{8\pi e} (C_n - C_p) \frac{1-\Delta}{1+\delta/2}\,, \tag{4.2a}$$

where

$$\delta \equiv \frac{m_n}{m_p} \cdot \frac{\tau_p}{\tau_n} - 1\,, \qquad \Delta \equiv \delta \cdot \frac{C/2(1+i\omega\tau) - C_p}{C_p - C_n}\,, \tag{4.2b}$$

$$\Lambda_K{}^n \cong \frac{NC^2\omega^2\tau_n}{4\rho V^3 kT} \cdot \frac{1}{1+(\omega\tau)^2} \left\{ 1 + \frac{1}{3} q^2 v_{n0}^2 \tau^2 \left(2 \cdot \frac{m_n/\tau_n}{m_n/\tau_n + m_p/\tau_p} \right)^2 \right\} \tag{4.3}$$

and the similar formula of $\Lambda_K{}^p$ obtained by replacing the subscript n with p.

(B):

$$J_n+J_p \cong \frac{\mathcal{E}q^2u}{8\pi e}(C_n-C_p)\left\{\frac{1-\Delta}{1+\delta/2}+\frac{(\Delta+\delta/2)(1+\delta)}{(1+\delta/2)^2}\cdot\frac{\tau_n}{m_n}\cdot\frac{q^2kT\tau}{1+i\omega\tau}\right\}, \tag{4.4}$$

$$\Lambda_K{}^n \cong \frac{NC^2\omega^2\tau_n}{4\rho V^3kT}\cdot\frac{1}{1+(\omega\tau)^2}\left[1+\frac{1}{3}q^2v_{n0}^2\tau^2\left(2\cdot\frac{m_n/\tau_n}{m_n/\tau_n+m_p/\tau_p}\right)^2\right.$$
$$\left.\times\left\{1-\frac{4}{(3\tau_n/\tau)/(ql_{n0})^2+(3\tau_p/\tau)/(ql_{p0})^2}\cdot\frac{1}{1+(\omega\tau)^2}\right\}\right] \tag{4.5}$$

and the similar formula of $\Lambda_K{}^p$.

(C):

$$J_n+J_p \cong \frac{\mathcal{E}q^2u}{8\pi e}(C_n-C_p)\left(1-\frac{\Delta+\delta/2}{1+\delta}\cdot\frac{m_n}{\tau_n}\cdot\frac{1+i\omega\tau}{q^2kT\tau}\right), \tag{4.6}$$

$$\Lambda_K{}^n \cong \frac{NC^2\omega^2}{4\rho V^3kT}\cdot\frac{3\tau_n}{(ql_{n0})^2} \tag{4.7}$$

and the similar formula of $\Lambda_K{}^p$.

(D): $$\Lambda_K{}^n \cong \left(\frac{3\pi}{2}\right)^{1/2}\frac{NC_n{}^2\omega}{\rho V^2kTv_{n0}} \tag{4.8}$$

and the similar formula of $\Lambda_K{}^p$.

The comparison of these formulae with those due to the recombination will be discussed in § 6.

§ 5. Acoustoelectric Effect

The acousto-electromotive force F can be defined as the average *dc* force exerted by acoustic waves on an electron or a hole.[11] As in many-valley semiconductors[9] effective forces responsible for the acoustoelectric effect have two components, one associated with the recombination of electrons and holes and the other associated with the intraband transition. Weinreich's relation[12] between the ultrasonic absorption coefficient and the acousto-electromotive force must hold separately for electrons and holes. Thus, we can write as

$$F=F_R{}^n+F_R{}^p+F_K{}^n+F_K{}^p, \tag{5.1}$$

$$\left.\begin{aligned} F_R{}^n&=\Lambda_R{}^n\gamma/NeV, & F_R{}^p&=\Lambda_R{}^p\gamma/N(-e)V,\\ F_K{}^n&=\Lambda_K{}^n\gamma/NeV, & F_K{}^p&=\Lambda_K{}^p\gamma/N(-e)V, \end{aligned}\right\} \tag{5.2}$$

where $\gamma\equiv\rho|u|^2V/2$ is the acoustic energy flow density. From (2.7), (2.8), (3.2) and (3.3) we get $\Lambda_R{}^n=\Lambda_R{}^p$. Then,

$$F_R\equiv F_R{}^n+F_R{}^p=0, \tag{5.3}$$

i.e., the effect due to electrons associated with the recombination is just cancelled by the effect due to holes.

Using the formulae of Λ_K in § 4, we tabulate the formulae of F in various frequency ranges as follows.

(A) and (B):

$$F \cong \frac{C^2\omega^2}{4\rho eV^4kT}\cdot\frac{\gamma}{1+(\omega\tau)^2}\left\{(\tau_n-\tau_p)+\frac{1}{3}\left(2\cdot\frac{m_n/\tau_n}{m_n/\tau_n+m_p/\tau_p}\right)^2q^2\tau^2(v_{p0}^2\tau_n-v_{p0}^2\tau_p)\right\}. \tag{5.4}$$

(C): $$F \cong \frac{C^2\omega^2\gamma}{4\rho eV^4kT}\left[\frac{3\tau_n}{(ql_{n0})^2}-\frac{3\tau_p}{(ql_{p0})^2}\right]. \tag{5.5}$$

(D):
$$F \cong \left(\frac{3\pi}{2}\right)^{1/2} \frac{\omega\gamma}{\rho e V^3 kT}\left(\frac{C_n^2}{v_{n0}} - \frac{C_p^2}{v_{p0}}\right). \tag{5.6}$$

It will be discussed in the next section whether the effect is detectable in experiments.

§ 6. Discussions

(1) *Absorption Coefficient*

From the simple phenomenological treatment of the recombination of electrons and holes given in Appendix I, we can expect in general the absorption peak in the Λ-T diagram at the temperature of $\omega\tau(T)=1$, if $\tau(T)$ is the monotonously decreasing or increasing function of T. As has been shown in § 3, however, this is not the case if the frequency at which $\omega\tau=1$ does not satisfy the inequality

$$(ql_{n0})^2 < 3(\tau_n/\tau)\ , \qquad (\omega\tau=1). \tag{6.1}$$

In the sufficiently low frequency range such as (A), the absorption coefficient Λ_R in (3.5) is identical with the formula used by Southgate[2] and is much larger than Λ_K in (4.3). In this range

$$\frac{\Lambda_R}{\Lambda_K} \cong \frac{\tau}{\frac{1}{2}(\tau_n+\tau_p)} \sim \frac{\tau}{\tau_n} \gg 1\ . \tag{6.2}$$

Even in the higher frequency range such as (B), Λ_K is yet smaller than Λ_R. From (3.7) and (4.5) we get

$$\frac{\Lambda_R}{\Lambda_K} \cong 1 \Bigg/ \left[\frac{1}{2}\left\{\frac{(ql_{n0})^2\tau}{3\tau_n}\left(2\cdot\frac{m_n/\tau_n}{m_n/\tau_n+m_p/\tau_p}\right)^2 + \frac{(ql_{p0})^2\tau}{3\tau_p}\left(2\cdot\frac{m_p/\tau_p}{m_n/\tau_n+m_p/\tau_p}\right)^2\right\}\right]$$
$$\sim 1 \Bigg/ \left[\frac{(ql_{n0})^2\tau}{3\tau_n}\right] \gg 1\ . \tag{6.3}$$

Thus, in good approximation Southgate's formula (3.5) can be used for the analysis of the experimental curve of Λ in the vicinity of the peak, if the frequency $\omega=1/\tau$ is in the range (A) or (B).

If the frequency $\omega=1/\tau$ is in the range (C), the situations are very different from those of (A) and (B). In this range, Λ_R becomes smaller than the value of Southgate's formula and is obscured by Λ_K. From (3.9) and (4.7) we obtain

$$\frac{\Lambda_R}{\Lambda_K} \cong \frac{1}{2}\left\{\frac{3\tau_n}{(ql_{n0})^2\tau} + \frac{3\tau_p}{(ql_{p0})^2\tau}\right\} \ll 1\ . \tag{6.4}$$

In the sufficiently high frequency range such as (D), we get from (3.11) and (4.8)

$$\frac{\Lambda_R}{\Lambda_K} \cong \frac{C}{2}\left(\frac{C_n}{v_{n0}}\cdot\frac{\tau_n}{\tau} + \frac{C_p}{v_{p0}}\cdot\frac{\tau_p}{\tau}\right) \Bigg/ \left(\frac{C_n^2}{v_{n0}} + \frac{C_p^2}{v_{p0}}\right) \sim \frac{\tau_n}{\tau} \ll 1\ . \tag{6.5}$$

Then, if $(ql_{n0})^2 > 3(\tau_n/\tau)$ is satisfied, the absorption due to the recombination can be neglected compared with that due to the intraband transition.

We take up, for example, the sample of Ge of Southgate in which the absorption peak by acoustic waves of 100 Kc/s was observed at $T \cong 690$°K. If we take the values of parameters as $\tau \sim 10^{-6}$ sec, $\tau_n \sim 10^{-12}$ sec, $V \sim 5\times10^5$ cm/sec, $m_n \sim 0.91\times10^{-28}$ g, we get

$$(ql_{n0})^2 \sim 5\times10^{-9} \quad \text{and} \quad 3(\tau_n/\tau) \sim 3\times10^{-6}\ .$$

Thus, the condition (6.1) is satisfied. Since the lifetime of electrons or holes is very much longer than the intraband relaxation time, the condition (6.1) will be satisfied in ordinary situations.

As will be shown in Appendix II, the characteristics of the absorption coefficient Λ_R and

Λ_K in various frequency ranges in intrinsic semiconductors are remarkably similar with that of Λ_p due to the intervalley transition and Λ_K due to the intravelley transition in many-valley semiconductors. The condition (6.1) and the equations (6.2)–(6.5) hold in form in many-valley semiconductors. If we tentatively take the values of parameters in n-Ge as τ (intervalley relaxation time)$\sim 10^{-10}$ sec, $\omega = 10^{10}$ sec^{-1}, τ_0 (intravalley relaxation time)$\sim 10^{-12}$ sec, $T = 100$°K, we get

$$(ql_0)^2 \sim 2\times 10^{-1} \quad \text{and} \quad 3(\tau_0/\tau) \sim 3\times 10^{-2}\,.$$

Then, the condition (6.1) does not hold. Since the intervalley relaxation time is $\sim 10^{-10}$ sec or somewhat longer in n-Ge, it would be difficult to observe the peak[13] of the absorption or the acoustoelectric effect due to the intervalley transition in ordinary situations.

In Figs. 1 and 2 we give the schematic Λ-ω diagrams in intrinsic and many-valley semiconductors respectively, assuming tentatively that the condition (6.1) holds in intrinsic and does not hold in many-valley semiconductors.

(2) *Acoustoelectric Effect*

The acoustoelectric effect due to the intervalley transition by transverse waves in n-Ge has been observed by Weinreich, Sanders and White.[14] They have analyzed the experiment using the formula nearly identical with (A II 5). In intrinsic semiconductors, there is no acoustoelectric effect due to the recombination of electrons and holes. The

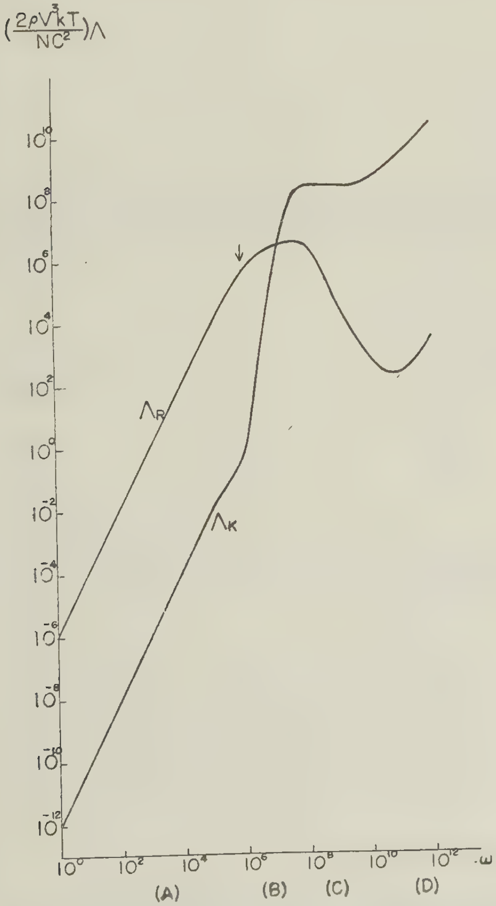

Fig. 1. The schematic Λ-ω diagram in intrinsic semiconductors, where we assume that $\tau_n = 10^{-12}$ sec, $\tau = 10^{-6}$ sec, $T = 690$°K, $m_n = 0.91\times 10^{-28}$ g and $V = 5\times 10^5$ cm/sec. The arrow shows the frequency used by Southgate[1)-4)].

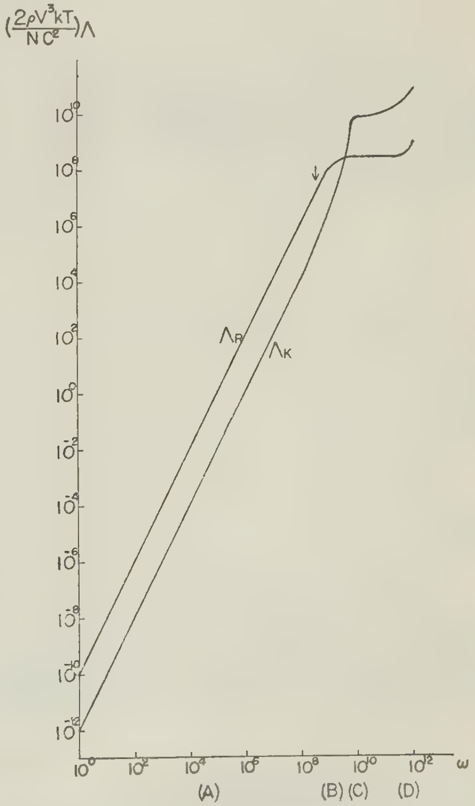

Fig. 2. The schematic Λ-ω diagram in many-valley semiconductors, where we assume that $\tau_0 = 10^{-12}$ sec, $\tau = 10^{-10}$ sec, and $T = 100$°K. The arrow shows the frequency used by Weinreich, Sanders and White[14].

non-vanishing effect is due to the intraband transitions. Comparing (5.4), (5.5), (5.6) with (A II 5) we have the conclusion that the effect in intrinsic semiconductors is too small to be detectable in experiments at present.

The author should express his thanks to S. Gonda for drawing of Figs. 1 and 2.

Appendix I

Simple Phenomenological Treatment

The present author has presented a simple phenomenological theory of the ultrasonic absorption due to electron transfer mechanism in the previous paper.[11] In solids the elastic stiffness constant can be written as

$$c=c_0-c_t\,, \tag{AI 1}$$

where c_0 is the component associated with the stress-induced changes of the electrostatic energy, the exchange energy between ion cores and so forth, c_t is the component associated with electron transfer mechanism. In the problem of acoustic waves we must take into account the relaxation of the energy associated with c_t and we put

$$c=c_0-c_t/(1+i\omega\tau)\,. \tag{AI 2}$$

Solving the equation of acoustic waves, we get

$$\Lambda=\frac{c_t}{\rho V^3}\cdot\frac{\omega^2\tau}{1+(\omega\tau)^2}\,, \tag{AI 3}$$

which shows the peak at $\omega\tau=1$ in the Λ-T diagram.

The calculation of c_t in intrinsic semiconductors are carried out as follows. When there is the strain $\partial R/\partial z$ (R: displacement of the lattice) in the specimen, the bottom of the conduction band and the top of the valence band are raised by $C_n(\partial R/\partial z)$ and lowered by $C_p\cdot(\partial R/\partial z)$, respectively. Then, from (2.4) or (2.5) we obtain

$$\Delta\equiv n_{eq}=p_{eq}=-\frac{NC}{2kT}\cdot\frac{\partial R}{\partial z}\,. \tag{AI 4}$$

If we denote the potential energy of electrons and holes by U, we can write

$$c_t\equiv(U_{\omega\tau\to\infty}-U_{\omega\tau\to 0})/(\partial R/\partial z)^2\,. \tag{AI 5}$$

Since

$$\left.\begin{aligned}U_{\omega\tau\to\infty}&=NC\cdot(\partial R/\partial z)\,,\\ U_{\omega\tau\to 0}&=(N+\Delta)\cdot C\cdot(\partial R/\partial z)\,,\end{aligned}\right\} \tag{AI 6}$$

we get

$$c_t=\frac{NC^2}{2kT}\,. \tag{AI 7}$$

Thus, from (AI 3) and (AI 7) we obtain (3.5). In this phenomenological treatment we ignore the absorption due to the intraband transition.

Appendix II

Many-Valley Semiconductors

In the previous paper II, we have derived the formulae of Λ_p due to the intervalley transition and Λ_K due to the intravalley transition in many-valley semiconductors. In the following, we shall make more careful consideration of the frequency ranges and show the complete correspondence between Λ_p and Λ_R in § 3. Using the basic equations in the paper II, we obtain the following results, which hold for both longitudinal and transverse waves.

(A) and (B):

$$\Lambda_p \cong \frac{NC^2}{2\rho V^3 kT}\cdot\frac{\omega^2\tau}{1+(\omega\tau)^2}\left\{1-\frac{2}{3}(ql_0)^2\frac{\tau}{\tau_0}\cdot\frac{1}{1+(\omega\tau)^2}\right\}, \tag{AII 1}$$

$$\Lambda_K \cong \frac{NC^2}{2\rho V^3 kT}\cdot\frac{\omega^2\tau_0}{1+(\omega\tau)^2}\left\{1+\frac{1}{3}q^2 v_0^2\tau^2\left(1-\frac{2(ql_0)^2\tau}{3\tau_0}\cdot\frac{1}{1+(\omega\tau)^2}\right)\right\}, \tag{AII 2}$$

where $2N$ is the total electron number density, $C\equiv C^{(+)}-C^{(-)}$ is the difference of the deformation potential constants between (+) and (−) valleys; τ_0, l_0, v_0, τ are the intravalley relaxation time, the average mean free path, the average thermal velocity, the intervalley relaxation time, respectively.

(C):

$$\Lambda_p \cong \frac{NC^2\omega^2\tau}{2\rho V^3 kT}\left(\frac{3\tau_0/\tau}{(ql_0)^2}\right)^2, \tag{AII 3}$$

$$\Lambda_K \cong \frac{NC^2\omega^2}{2\rho V^3 kT}\cdot\frac{3\tau_0}{(ql_0)^2}. \tag{AII 4}$$

In all cases including (D) we can see the complete correspondence of Λ between many-valley and intrinsic semiconductors, if we replace as

$C\equiv C_n+C_p\rightarrow C\equiv C^{(+)}-C^{(-)}$,

τ (lifetime)→τ (intervalley relaxation time),

$m_n,\ m_p\rightarrow m,\qquad \tau_n,\ \tau_p\rightarrow\tau_0,\qquad v_{n0},\ v_{p0}\rightarrow v_0,\qquad l_{n0},\ l_{p0}\rightarrow l_0$

in the formulae of intrinsic semiconductors. In many-valley semiconductors, however, there is the acoustoelectric effect due to the intervalley transition. Using Weinreich's relation we obtain

$$F=F_p+F_K\cong\frac{C^2\gamma}{4\rho e V^4 kT}\cdot\frac{\omega^2\tau}{1+(\omega\tau)^2}\left\{1-\frac{1}{3}(ql_0)^2\frac{\tau}{\tau_0}\cdot\frac{1-(\omega\tau)^2}{1+(\omega\tau)^2}\right\} \tag{AII 5}$$

in (A) and (B).

References

1) P. D. Southgate: Bull. Am. Phys. Soc. Ser. II **4** (1959) 462
2) P. D. Southgate: Private communication.
3) P. D. Southgate: Phys. Rev. **110** (1958) 855.
4) P. D. Southgate: Proc. Phys. Soc. **B 70** (1957) 804.
5) G. Weinreich: Phys. Rev. **104** (1956) 321.
6) A. B. Pippard: Phil. Mag. **46** (1955) 1104.
7) T. Holstein: Phys. Rev. **113** (1959) 479.
8) N. Mikoshiba: J. Phys. Soc. Japan **15** (1960) 982.
9) N. Mikoshiba: J. Phys. Soc. Japan **15** (1960) 1189.
10) C. Kittel: *Introduction to Solid State Physics* (John. Wiley & Sons, Inc., New York, 1956) 350P.
11) N. Mikoshiba: J. Phys. Soc. Japan **14** (1959) 1691.
12) G. Weinreich: Phys. Rev. **107** (1957) 317.
13) F. J. Blatt: Phys. Rev. **105** (1957) 1118.
14) G. Weinreich, T. M. Sanders and H. G. White: Phys. Rev. **114** (1959) 33.

JOURNAL OF THE PHYSICAL SOCIETY OF JAPAN Vol. 16, No. 5, MAY, 1961

Growth and Dissolution Prosseses of GASH Crystal

By Terutaro NAKAMURA, Kikuo OHI and Hiroko KUBOTA*

Department of Physics, Ochanomizu University, Otsuka, Tokyo

(Received December 28, 1960)

Growing process of GASH crystal was observed. If a droplet of saturated GASH solution on a slide glass is heated from upper side, platelets obtained afloat on the drop show six-rayed-star-shaped terraces. The mechanism of terrace formation is ascribed to bunching of progressing atomic steps. On the other hand, if heated from lower side, some platelets obtained at the bottom of the droplet are large and thick, which show dislocation etch pits on etching, while some remain small and thin showing no pits on etching. It appears that the growing process is not diffusion-controlled but follows the screw dislocation mechanism.

Dissolution process of GASH crystal was observed. Dissolution takes place by progression of macroscopic steps, which are nucleated book at crystal edges and at dislocation emergence points. The kinetics is controlled by diffusion and macroscopic steps are understood as bunching of atomic steps.

§ 1. Introduction

At a very low supersaturation, crystal growth takes place by the spreading of individual layers of atomic scale across the advancing surface. Solute atoms from a surrounding mother solution are incorporated into the crystal lattice only at the peripheral steps of the uncompleted atomic layers. In completion of the layer, new layers and growth steps are required for continued advance of the surface.

It was recongnized by Gibbs that new layers on a perfect surface are formed by two-dimensional nucleation. It was shown theoretically that two-dimensional nucleation proceeds at substantial supersaturation. Experimental observations, however, indicated that crystals grow at much smaller supersaturation than the theoretical value. In 1949, Frank¹⁾ pointed out that interesection of a screw dislocation on a crystal surface provides a perpetual source of growth steps at very low supersaturations. A detailed analysis of crystal growth from vapor phase was made by Burton, Cabrera and Frank²⁾ on this model. Their analyses were based on the assumption of local equilibrium between the crystal and vapor phase at the growth step. This is equivalent with the assumption that the process of crystal growth is never controlled by the diffusion.

Recently, however, diffusion-controlled growth of crystals draws attention, related with growth of dendrites, growth of crystal whiskers, or anomalous growth of crystals caused by extremely small amount of impurity. In the diffusion-controlled growth, supersaturation is generally high, and advancing faces are not perfect but "non-singular",** in other words, of higher index. Solute atoms can attach to every point of the surface which is everywhere terraced.

The advance of curved surface can be described as progression of individual steps of atomic scale. In progression of many steps of atomic scale on the advancing surface of crystals, the velocity of an individual step is not usually constant, but depends on inclination of the surface in some cases, or on extremely small amount of adsorbed impurity atoms in other cases which hinder the motion of the steps and acts as a poison. The non-uniformity of the velocity of individual step causes overtaking of slower steps by faster ones, which is understood as a shock wave in the flood problem, and was treated by Frank⁵⁾ using the mathematics called kinematic wave theory due to Lighthill and Witham[6]. This shock wave is nominated as " bunching ", and there were some experiments which seemed to observe the bunching[7].

---

* Now at Hitachi Ltd., Musashi Works.

** It was shown by Herring³⁾ that the perfect or low-index surface of the crystal in the equilibrium state corresponds to pointed cusp of polar plot of surface free energy. This surface requires the screw dislocation mechanism for growth at low supersaturation, and Frank⁴⁾ suggested that this surface may be called "singular" face, while continuously curved surface may be called "non-singular".

The dissolution process, in which a crystal is exposed to very high undersaturation, overall kinetics are controlled by diffusion. In the process of etch pit formation, for the study of dislocations in crystals, kinetics are also limitted by diffusion.

The present paper describes the observations of growth and dissolution processes of guanidinium aluminum sulfate hexahydrate (usually abbreviated as GASH), which is known to be ferroelectric. Dislocations in GASH were observed by etching technique[8],[9],[10]. This substance crystallizes in a hexagonal plate, showing a perfect cleavage perpendicular to the (0001) axis, which is identical to the ferroelectric axis. Space group is $P31m$[11]. Etch pits are triangular, and " positively " pointed on the (0001) face, while " negatively " pointed on the $(000\bar{1})$ face.

In the present paper it is shown that the growth of GASH crystal from aqueous solution is, in one case, diffusion-controlled, and in the other case, not controlled by diffusion but dislocations really play parts. It is also shown that in the dissolution process, which is controlled by diffusion, bunching is remarkably observed, and dislocations provide dissolution centers.

§ 2. Growth Process

A droplet of aqueous solution was put on a slide glass and process of growth was observed under a microscope. Appearance of growing crystals depends sharply on the ways of heating, whether the drop is heated with an electric lamp from the upper side, or heated by lighting with a projector from the lower side.

If heated from the upper side, water vaporizes from the free surface of the drop, and the region near the free surface becomes more highly supersaturated, hence nucleation occurs on the surface, and small platelet having edges of about 0.1 mm grows and is afloat on the surface of the droplet. On the other hand, if heated from the lower side, nucleation occurs at the bottom of the droplet and small platelet of the similar size grows in the bottom part. This situation is probably resulted from the facts that, at room temperature solubility is little dependent on temperature and the region between supersolubility curve and solubility curve is rather wide. Energy provided by heating will promote nucleation.

Among crystal platelets obtained by heating from the upper side, a number of crystals exhibit six-rayed star patterns as shown in Photo. 1. This six-rayed star forms a macroscopic terrace, i.e. the part of the star is advanced from the remaining surface area by presumably several tenths of micron in the order of magnitude. Axes of rays form 60° to each other, and the vortex angle of ray α (Fig. 1) is different star by star. Length of the ray is also different star by star. The star is generally situated at the center of the plate. In an individual star, the lengths of the three rays directed in a-axes are almost equal, and those in b-axes are also almost equal, but an inclination is found that the a-axial ray is somewhat longer than the b-axial ray.

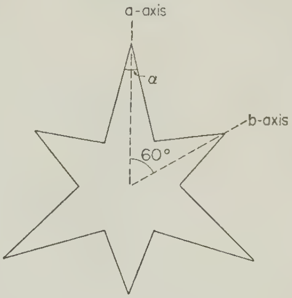

Fig. 1. Shape of six-rayed star, schematic.

Dislocation etch pits were observed on a crystal with the pattern of six-rayed star. No special relations were found between the sites of the dislocation etch pits and the site of six-rayed star.

Mechanism of the formation of six-rayed star will be explained as follows. A crystal floating on the surface of the droplet will be covered by a film of highly supersaturated solution. Transport of solute atoms from the solution into the crystal will be controlled by diffusion. The interface between the solution and the crystal, not singular but of high index, will be considered to be everywhere terraced in atomic scale. Crystal growth will take place by the progression of atomic steps, and bunching will be formed if step velocity is not everywhere constant. This view is supported by the fact that larger crystals which have grown afloat on the solution of the surface have a non-singular face with maroscopic terraces roughly parallel to the star-shaped terrace (Photo. 2). Note here that the remaining faces, which have been immersed in the solution during the growth process, however, are singular.

Crystal platelets obtained by heating from the lower side are clearly divided into two groups. Crystals belonging to the first group (shown as A in Photo. 3) remain thin and small, while those belonging to the second group (shown in the same photograph) show higher growth rate and grow up to thicker crystals. Crystals belonging to the second group which are smaller than A at the earlier stage (a) in the series of photographs become larger than A at the later stage (c). When crystals grow up to a certain size, water is added to the droplet and dislocation etch pits are observed (d). It is very remarkable that no etch pit was observed on the crystals belonging to the first group, while several pits were observed on the crystals of the second group.

It was generally found that the growth rate of crystals increases with increasing dislocation density.

These facts clearly show that in this case the supersaturation is low, the local equilibrium exists between the crystals and the liquid phase at the growth step, and steps accompanied by the screw dislocations are essential for the crystal growth.

§ 3. Dissolution Process

GASH crystal is easily soluble in water. When a drop of distilled water is dripped on the cleaved surface of the crystal under a microscope, it is clearly observed that dissolution takes place by nucleation and remarkable lateral motion of macroscopic steps.

These steps will be understood as the bunching of steps of atomic scale. Over-all kinetics are controlled by the diffusion. Nucleation sites of the macroscopic steps are crystal edges and emergence points of dislocations on a surface.

Steps created at crystal edges

Since the gradient of concentration is highest at the edges of a crystal, dissolution takes place at the edges. In this process, over-all kinetics is controlled by diffusion, the interface between the crystal and the liquid is non-singular, and bunching results in macroscopic steps. It is observed as if macroscopic steps are nucleated at the crystal edges.

The shape of macroscopic steps created at crystal edges are shown in Photo. 4, being almost parallel to the crystal edges. Aspects of the step motion should be divided into two periods, i.e. “adolescence” and “senescence”.

In the adolescence (Photo. 5), steps progress in higher speeds, followed by step nucleation at the crystal edges. In this period, the majority of steps seems to have almost the same height, which was measured to be the order of several tenths of micron from an electron-microscopic study with a low-angle shadowing. The macroscopic steps are not rectangular shouldered (a) but sloping shouldered (b), as shown in Fig. 2. The angle θ in Fig. 2 (b) seems to amount about 10° from the electronmicroscopic study.

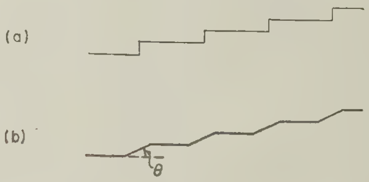

Fig. 2 (a). Steps with rectangular shoulders. (b) Steps with sloping shoulders.

In the senescence, since the crystal edge is no longer sharp, and the gradient of the concentration is no longer high, no steps are created at the crystal edges, but the region where the group of the macroscopic steps swept away remains to be a smoothly curved surface. In this region, it is generally observed that some hillocks are left behind the group of moving steps, as shown in Photo 6. The height of the hillocks is much larger than that of adolescence, exceeding the order of several microns. Formation of the hillocks left behind will be understood, if there is a hindrance of the step motion, such as immobile adsorbed impurity molecules.

In the senescence, in which the creation and motion of steps no longer take place, dissolution is brought about mainly by the lateral shrinkage of periphery of the crystal in the plane of (0001). This aspect can be seen in Photo. 8 (a) and (b).

Steps created at emergence points of Dislocations

Triangular steps as shown in Photo. 7 are created and sent out from the emergence point of a dislocation. The creation of steps at certain definite points supports the conclusion of the previous works that the etch pits correspond to dislocation[8),9)].

Since the undersaturation is very high, the dissolution showing a spiral pattern, which might be seen at screw dislocations, does not take place, but the following process is observed. The initial attack of water to the crystal face gives rise to a small triangular pit at the dislocation emergence point as

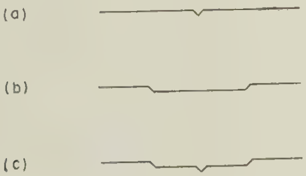

Fig. 3 (a), (b), (c). Process of nucleation and sending out of steps at a dislocation emergence point.

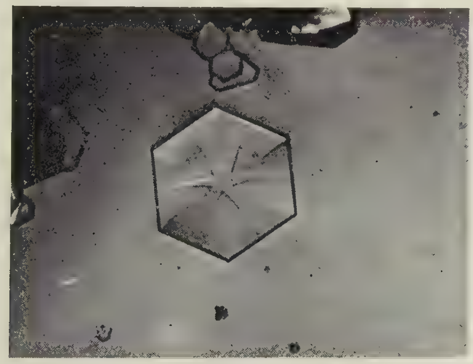

Photo. 1. Photomicrograph of a crystal platelet with a six-rayed star pattern.

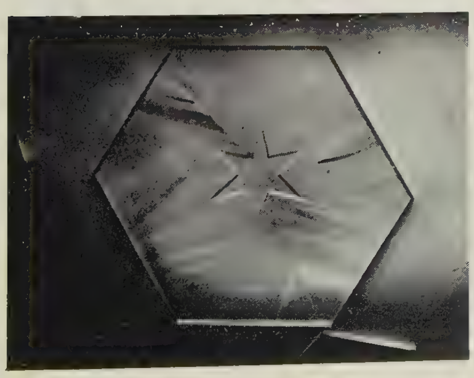

Photo. 2. Photomicrograph of a crystal plate with a star-shaped terrace, together with macroscopic terraces roughly parallel to it.

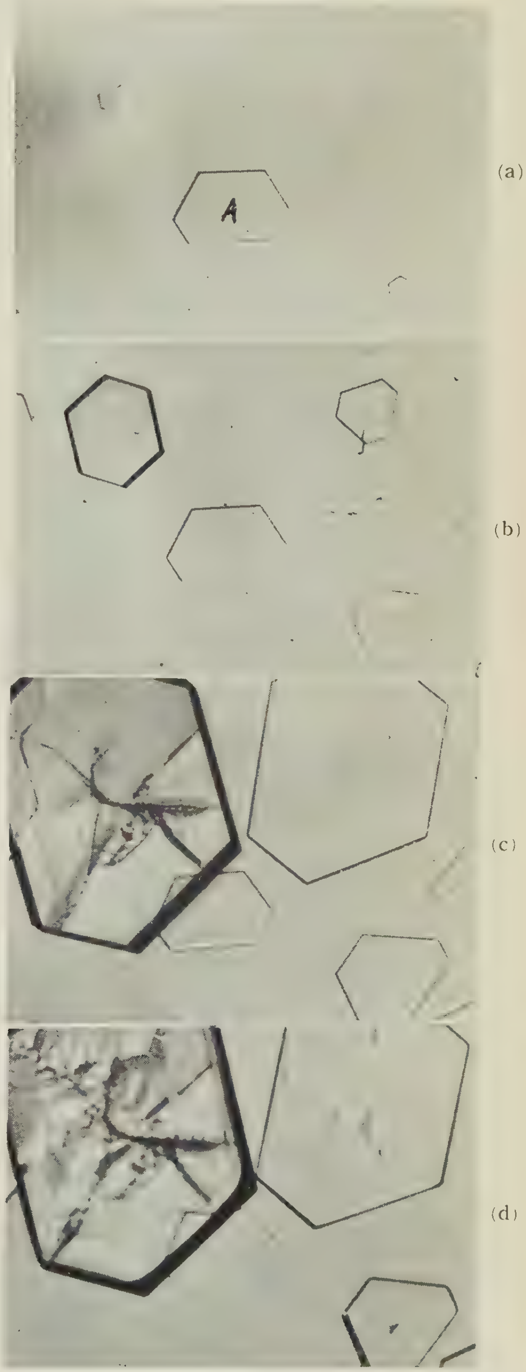

Photo. 3. Photomicrographs of crystals obtained by heating from the lower side. Crystal A remains thin and small during the growth process and shows no dislocation etch pits by an etching treatment.

shown in Fig. 3 (a). When the depth of the pit reaches a certain amount, pit does not grow deeply any more, a triangular step moves so that the pit becomes flat (Fig. 3 b). Strained part in the vicinity of the dislocation is preferentially dissolved again, forming a pit (Fig. 3 (c)). Periodical repetition of this process causes intermittent nucleation and sending out of triangular steps.

Penetrating dissolution

On the top and the bottom faces of a very thin piece of crystal, a couple of etch pits are clearly observed simultaneously, which correspond to the couple of the end points of a dislocation that penetrates the sample, as shown in Photo 8 (a). Note that triangular steps around each dislocation on the both faces are " oppositely sensed ", owing to the trigonal symmetry of GASH crystal.

The observation of " penetrating dissolution " along the dislocation line provides a

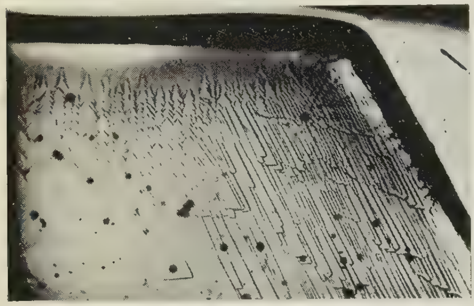

Photo. 4. Photomicrograph of macroscopic steps, which have been created at the crystal edges and have progressed.

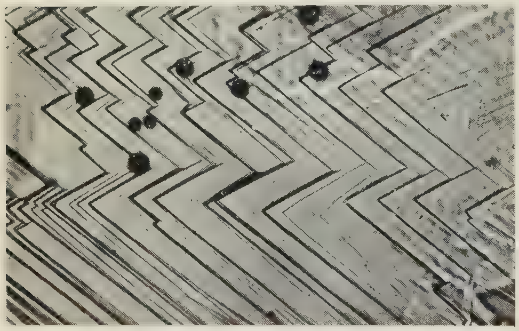

Photo. 5. Photomicrograph of dissolution steps, in adolescence.

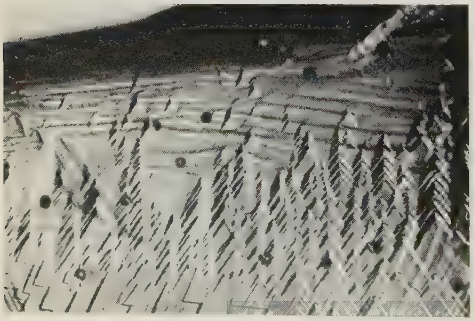

Photo. 6. Photomicrograph of dissolution steps, in senescence.

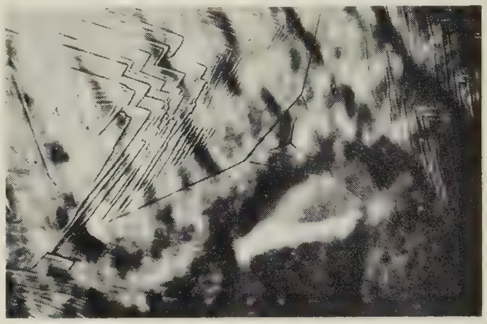

Photo. 7. Photomicrograph of triangular steps, created at and sent out from the emergence point of a dislocation.

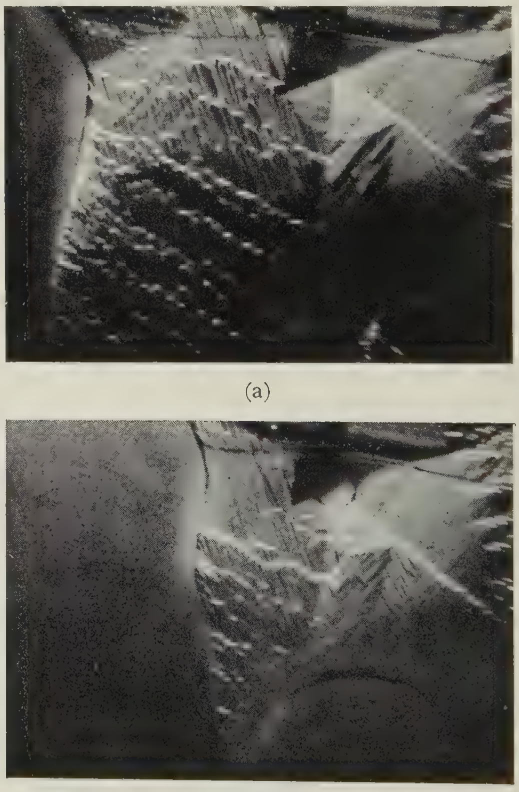

(a)

(b)

Photo. 8. Penetrating dissolution along a dislocation line. (a) before and (b) immediately after penetration.

conclusive evidence for the identification of etch pits with dislocation emergence points.

Interference of two kinds of steps

It is frequently observed that steps created at crystal edges coalesce with each other at the "top of a mountain" which acts as if it were a sink of steps. At the sink, macroscopic steps are triangular, of which sense is "opposite" to that of dislocation etch pits (Fig. 4). This situation will be understood, if we suppose that the rate of lateral progress of macroscopic step is dependent on orientation, i.e. the rate is highest in the *b*-directions, as shown by the arrows in Fig. 4.

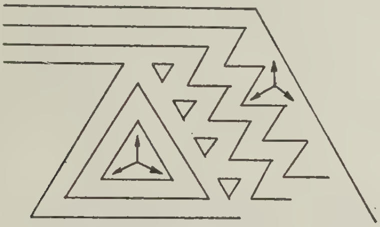

Fig. 4. Shape of steps, directions of the highest rate of lateral progress of steps, and apparent sinks of steps.

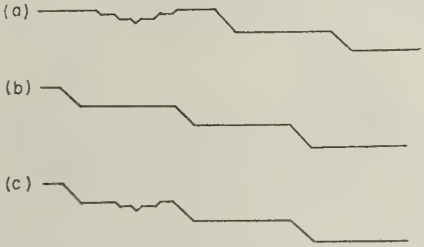

Fig. 5. Interference of steps created at a dislocation emergence point and those created at a crystal edge.

The height of steps, which have been created at a crystal edge, is generally larger than that of steps, which are sent out from a dislocation emergence point (Fig. 5 (a)). Hence the group of triangular steps starting from the dislocation is sometimes "swept" away by the flow of steps from the crystal edge (Fig. 5 (b)). After being swept away, however, close observation can find the continual step creation at the dislocation emergence point on the wider step nucleated at the crystal edges (Fig. 5 (c)).

§ 4. Discussion

GASH shows a characteristic appearance of macroscopic steps and growth pattern of six-rayed star. These phenomena are understood as bunching of progressing steps, so it is conceived that GASH has a characteristic behavior of easy formation of bunching.

Since the phenomena do not seem to be impurity sensitive, it is very likely that the reason for the easy formation of bunching in GASH crystal is not impurity effect but intrinsic one, probably due to the direction dependence of the strength of chemical bond. Crystal structure of this substance[12] suggests that bonding in the {0001} plane is much stronger than that in the ⟨0001⟩ direction, in agreement with the perfect cleavage parallel to the {0001} plane. Surface free energy between aqueous solution and the {0001} face will be, therefore, much smaller than those for other faces. In diffusion-controlled growth or dissolution process, the smoothly curved interface will be then apt to take a stepped form as shown in Fig. 2 (a), in order to make the surface free energy lower. Steps with rectangular shoulders as Fig. 2 (a) are, however, not stable, because diffusion current in the diffusion-controlled process is highest at the rectangular shoulders. Thus the resultant steps must be sloping shouldered as shown in Fig. 2 (b).

Acknowledgement

It is highly acknowledged that an information on observations of remarkable step flow on the surface of GASH crystal in dissolution process was offered by Dr. H. Hirabayashi and Dr. H. Toyoda of Electrical Communication Laboratory, Nippon Telegragh and Telephone Public Corporation, which stimulated the authors to initiate the present work.

This work was financially supported in part by a Grant in Aid for Fundamental Scientific Research from the Ministry of Education.

References

1) F. C. Frank: Disc. Farad. Soc. **5** (1949) 48, 67.
2) W. K. Burton, N. Cabrera and F. C. Frank: Phil. Trans. Royal Soc., London **A243** (1951) 299.
3) C. Herring: Phys. Rev. **82** (1951) 87.
4) F. C. Frank: Growth and Perfection of Crystals (Int. Conf. Reports) John Wiley and Sons Inc. New York, 1958 p 304.

5) F. C. Frank: ibid p 411.
6) M. J. Lighthill and G. B. Witham: Proc. Roy. Soc. London **229** (1955) 281.
7) C. Elbaum and B. Chalmers: Canad. J. Phys. **33** (1955) 196.
8) T. Nakamura: J. Phys. Soc. Japan **14** (1959) 1022.
9) T. Nakamura and K. Ohi: J. Phys. Soc. Japan **15** (1960) 1348.
10) T. Nakamura and K. Ohi: Natural Science Report, Ochinomizu University **11** (1960) 161.
11) E. A. Wood: Acta Cryst. **9** (1956) 618.
12) S. Geller and D. P. Booth: Z. Krist. **111** (1956) 117.

JOURNAL OF THE PHYSICAL SOCIETY OF JAPAN, Vol. 16, No. 5, MAY, 1961

"Angular Distribution of Electrons Suffering Characteristic Energy Loss in Passage through Metal Films"

By Hiroshi WATANABE

Hitachi Central Research Lab. Kokubunji, Tokyo, Japan

(Received January 27, 1961)

The distribution in energy and angle of 20—25 kv electrons scattered by Al, Ag and Au evaporated films was measured with an electron velocity analyser of Möllenstedt type. The energy resolution is about 5×10^{-5}, and the angular resolution better than 5×10^{-4} radian. The angular distribution of the characteristic energy loss was compared with Ferrell's calculation. (Phys. Rev. **101** ('56) 554). The comparison shows that the experimental result is consistent with a simple Bohm-Pines' approach provided that a correction is made for finite resolution of both energy and angle.

§1. Introduction

In the electron energy loss experiment the characteristic energy loss values which we call "eigenloss" values were measured for the large number of elements and compounds.(1) Some people investigated the dependence of the loss value upon the crystal structures,(2) the accelerating voltage,(3,4) the scattering angles(5) and others.(1) A few were reported on the intensity distribution of electrons scattered elastically and inelastically. Marton and his coworkers studied the distribution in energy and angle of 20 kv electrons scattered by thin foils of C, Al, Ni, Cu, Au, Al_2O_3 and formvar. They used an energy analyser of magnetic type having the resolution better than 0.1 % in energy ($\Delta E/E\leq10^{-3}$) and 10^{-3} radians in angle.

Based upon the Bohm-Pines' theory of plasma excitation in metal electrons, Ferrell calculated the angular distribution of the intensities of the eigenloss electrons.(7) He compared the results with the experimental data obtained by Marton and co-workers, and found two significant discrepancies between the theoretical and experimental curves. First, the theoretical intensity at small angles falls short by a considerable amount of accounting for the observed intensity. Second, at large scattering angles the theoretical curve is somewhat stronger than observed. His explanation of the first discrepancy, which is perhaps the more striking one, is that the intense no-loss beam superposes on the eigenloss intensity at small scattering angles because of the insufficient energy resolution of the instrument.

In 1949, Möllenstedt(8) devised a new electron velocity analyser of extremely high resolution. In the analyser the large chromatic aberration of an electrostatic lens is utilized, and the energy resolution better than 5×10^{-5} is easily obtained. In 1960, the present author(9) constructed an analyser of Möllenstedt type with which the angular distribution of electrons scattered inelastically as well as elastically is studied. The resolution of the analyser is about 5×10^{-5} in energy, and better than 5×10^{-4} radians in angle.

Using this instrument the angular distribution of the eigenloss electrons was obtained on evaporated Al, Au and Ag films. The results and the comparison with Ferrell's calculation are described in this paper.

§ 2. Experiment

Figure 1 shows a schematic diagram of the electron optical system of the velocity analyser. A focusing lens and a reducing lens project the reduced diffraction pattern on a plane with a fine slit, and then the part of the projected pattern passing through the fine slit is analysed by the analyser lens. The pattern on the plane of the fine slit and energy loss spectrum obtained in the analysis are shown schematically in (b) and (c) of Fig. 1. Fig 1c gives the relation among energy loss, scattering angle and intensity of scattering electrons.

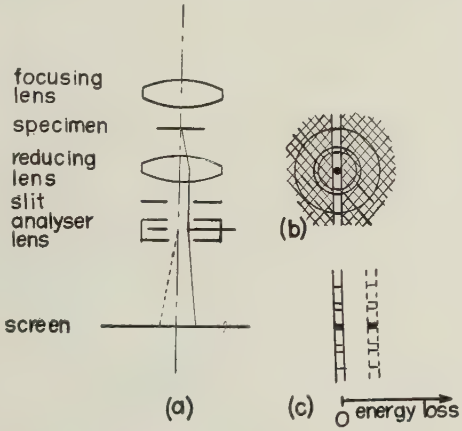

Fig. 1. (a) Schematic diagram of the electron optical system. (b) Diffraction pattern on the fine slit plane. (c) Energy loss spectrum on the final screen.

The intensity measurement was carried out with photometric method. The relative intensity scale was obtained as follows. A shadow image of an aperture diaphragm is shifted discontinuously during the exposure by a magnetic deflector, the electric current through which deflector is varied step-wise in time. An example of the photographic plates thus obtained is shown in Fig. 2a. The microphotometric record of the plate and a curve representing the relative exposure *vs* the distance from the dark line on the photometric record are shown in Figs. 2b and 2c, respectively. A microphotometric record of a photographic plate developed at the same time with the scale plate can be

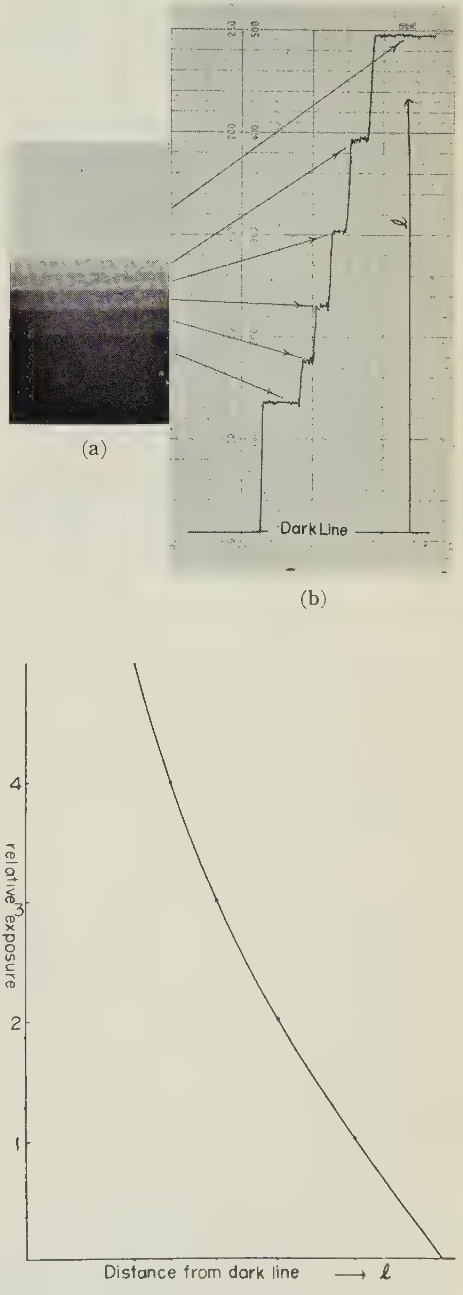

Fig. 2. (a) Exposure steps. (b) Microphotomeritc record of the plate in (a). (c) Relative exposure *vs* distance from dark line.

converted into the relative intensity by means of the intensity scale. The accuracy of this exposure scale is determined by the stability of the electron beam current during the exposure as well as by the accuracy of the exposure time. The stability of the electron beam was tested by recording the characteristic X-ray intensity emitted from the surface of a copper block irradiated by the electron beam. The change of the intensity was less than 1% per minute in the test. The stability of the electron beam current is believed to be better than 1% per minute in the present experiment. The accuracy of the exposure time was tested with a stop-watch. The maximum fluctuation of the exposure time of 5 sec was 0.3 sec, that is, the accuracy is better than 6%. Thus, the accuracy of the exposure scale used in the present experiment is better than 6%.

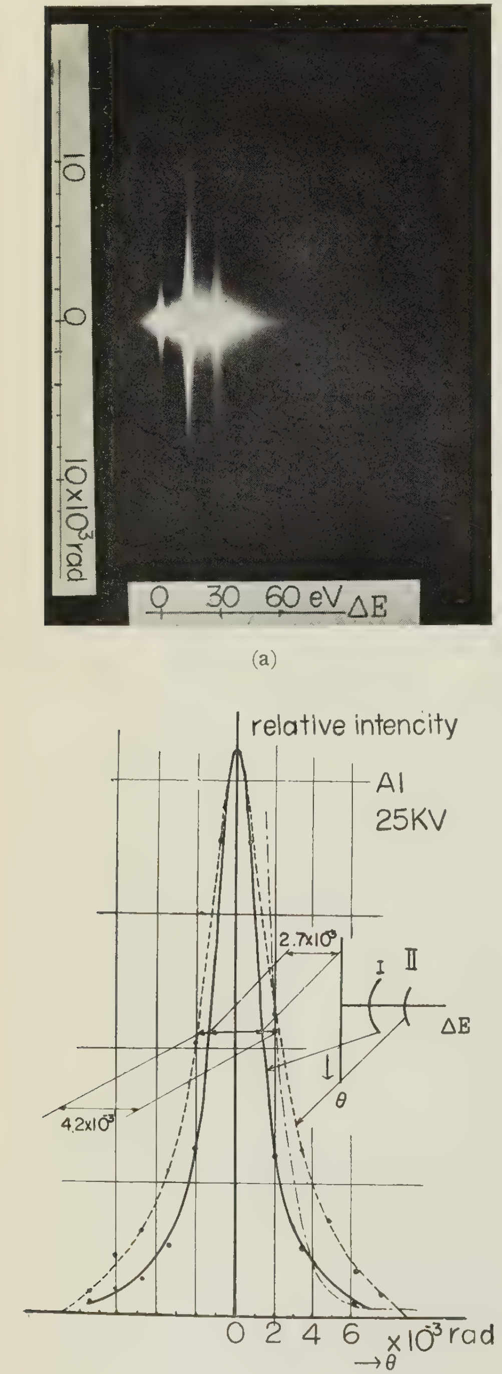

(a)

(b)

Fig. 3. (a) Loss-angle diagram of 25 kv electrons scattered by Al film. (b) Relative intensity *vs* scattering angle for arcs I and II.

§ 3. Experimental Results

Figure 3a shows a loss-angle diagram of 25 kv electrons scattered by an Al evaporated film of about 250 Å thick.

The two arcs I and II in the small angle region indicate that the energy loss value increases with the scattering angle, and they originate from the plasmon excitation in the metal electrons(5). The relative intensity measured along arcs I and II are given in Fig. 3b. The half-value width of bote curves are 2.7×10^{-3} and 4.2×10^{-3} radians, respectively.

Fig. 4a is a cartographic representation of the diagram. The abscissa is the scattering angle, the ordinate energy loss in electron volt unit, and the contours of equal intensity in arbitrary scale. Figure 4b gives the intensity *vs* angle curve at $\Delta E=24$ ev.

Figure 5a shows a cartographic plot of a loss-angle diagram of 25 kv electrons scattered by an Ag evaporated film of about 250 A thick, and Fig. 5b is the intensity *vs* angle

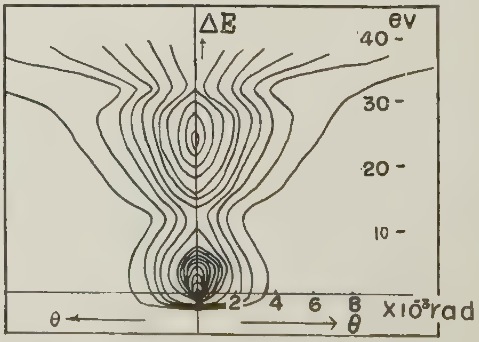

(a)

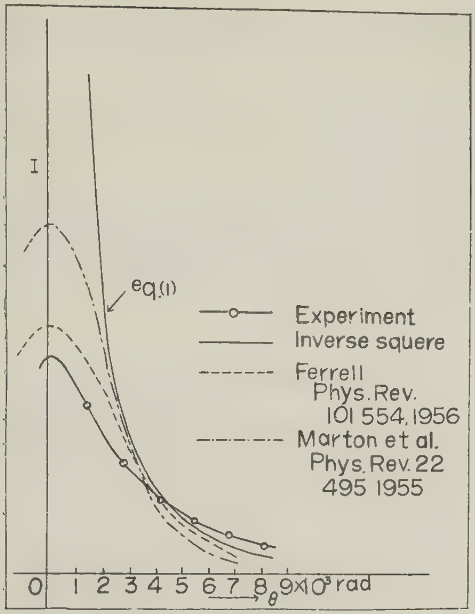

(b)

Fig. 4. (a) Cartographic plot of a loss-angle diagram of 20 kv electrons scattered by Au film. (b) Relative intensity *vs* scattering angle at $\Delta E=24$ ev.

curve at $\Delta E=3.4$ ev.

§ 4. Discussions

The energy loss peaks of Al (15 ev), Au (24 ev) and Ag (3.4 ev) are believed to be originated from the plasmon excitation. Ferrell[7] calculated the differential scattering cross section of electrons exciting one plasmon of energy $\hbar\omega_p$. His result is

$$p(\hbar\omega_p)d\Omega=\frac{d\Omega}{2\pi a_0}\cdot\frac{\theta_E}{\theta^2+\theta_E{}^2}\,, \qquad (1)$$

where $\theta_E=\Delta E/2E$

a_0: Bohr radius

E: accelerating voltage.

Equation (1) is plotted on Figs. 3b, 4b and 5b, being normalized to the experimental values at $\theta=4\times10^{-8}$ radians in Figs. 3b and 4b, and at $\theta=1\times10^{-3}$ radians in Fig. 5b. In cases of Al and Au in Figs. 3b and 4b the calculated values are larger than the experimental ones at angles smaller than 4×10^{-3} rad., and they are smaller than the experimental ones at larger angles. The same tendency in case of Au was observed by Marton and coworkers.

Ferrell treated the problem in more detail, taking the contribution from the multiple scattering into account. The observed eigenloss beam consists of three different parts, (a) electrons scattered first elastically and then exciting a plasmon, (b) electrons exciting a plasmon and then scattered elastically, (c) electrons exciting a plasmon and then lost by inelastic scattering. Summing up these electrons Ferrell obtained the resultant angular distribution in a form of definite integral. The result of the numerical integration for the case of 20 kv electrons exciting a plasmon in Au is presented by the dotted line in Fig. 4b. It agrees with the present experimental result better than the solid line of equation (1) does.

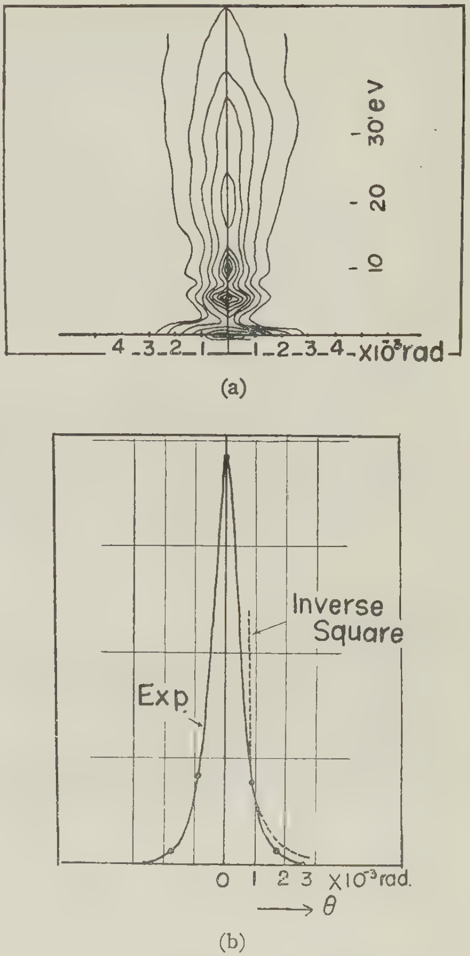

Fig. 5. (a) Cartographic plot of a loss-angle diagram of 25 kv electrons scattered by Ag film. (b) Relative intensity *vs* scattering angle at $\Delta E=3.4$ ev.

Marton and co-workers' experimental result plotted in Fig. 4b agrees with neither the present experiment nor Ferrell's calculations. Since they were forced to sacrifice energy resolution in order to achieve high angular resolution, the superposition of the intense no-loss beam on the eigen-loss beam may cause the large scattering intensity at small angles in their result. In the present experiment both the energy and angular resolutions are high enough to seperate completely the no-loss beam from the eigenloss beam.

§ 5. Conclutions

The relations among scattering intensity, angle and energy loss value were experimentally observed, and represented in cartographic plots. The angular distribution of eigenloss process was compared with Ferrell's calculations.

The following conclusions are drawn from the present experiment.

(a) The plasmon excitation probability given by equation (1) does not agree with the experiment on Al, and Au.

(b) Ferrell's calculation on Au in which the effect of multiple scattering is taken into account agrees with the experimental curve, although his calculation is based upon equation (1).

This agreement means that the eigenloss in Au at 24 ev is caused by the plasmon excitation in Au.

The similar treatment of the plasmon excitation probability in other materials is desired for the further study of plasmon excitation phenomena in solids.

References

1) L. Marton et al: Advances in Electronics and Electron Physics (Academic Press, Inc., New York) **7** (1955) 183.
2) H. Watanabe: J. Phys. Soc. Japan **14** (1959) 1453.
3) G. Ruthemann: Ann. Phisik **2** (1948) 113.
4) G. Haberstroh: Zeits. f. Phys. **145** (1956) 20.
5) H. Watanabe: J. Phys. Soc. Japan **11** (1956) 112.
6) L. Marton et al: Phys. Rev. **99** (1955) 495.
7) R. A. Ferrell: Phys. Rev. **101** (1956) 554.
8) G. Möllenstedt: Optik **5** (1949) 499.
9) H. Watanabe: J. Phys. Soc. Japan **15** (1960) 2368.

JOURNAL OF THE PHYSICAL SOCIETY OF JAPAN, Vol. 16, No. 5, MAY, 1961

Domain Structure of $NaNO_2$

By Shoichiro NOMURA, Yohko ASAO,
and Shozo SAWADA
Department of Physics, Tokyo Institute of Technology

(Received January 31, 1961)

The 180° domains along the *b* direction in $NaNO_2$ single crystals were observed by the etching method at room temperature. The domain boundaries lie parallel to (100). The virgin crystal prepared from the aqueous solution is almost of single-domain, but, after having once been heated above the Curie temperature, it has nearly the same domain structure as the crystal prepared from the melt. These domains were ascertained to be the ferroelectric ones from experiments with *dc* field. By the alkali etchant the positive end of the domain was more rapidly etched than the negative one, and nearly the contrary result was obtained for the acid etchant. The fact that the domain boundaries lie parallel to (100) would be intimately related with the thermal motion of NO_2^- radicals.

§ 1. Introduction

It has been revealed that $NaNO_2$ is ferroelectric below the transition temperature near 160°C.[1] The crystal symmetry of $NaNO_2$ at room temperature is orthorhombic, its space group being $C_{2v}^{20}(Imm)$.[2,3,4] Passing through the transition temperature, it changes to $D_{2h}^{25}(Immm)$, though the crystal structure still remains orthorhombic. The atomic arrangement in the unit cell of $NaNO_2$ at room temperature is schematically shown in Fig. 1. The unit cell contains two $NaNO_2$ molecules and has a polar axis along the *b* direction.

As in the case of other ferroelectrics, a domain structure is expected to appear also in $NaNO_2$ crystal. It is considered, however, that only 180° domain would be realized in $NaNO_2$, owing to its crystal symmetry. So the observation of the domain pattern should be performed, as is well known, not by the method using a polarized-light microscope but the etching method or the colloid method.

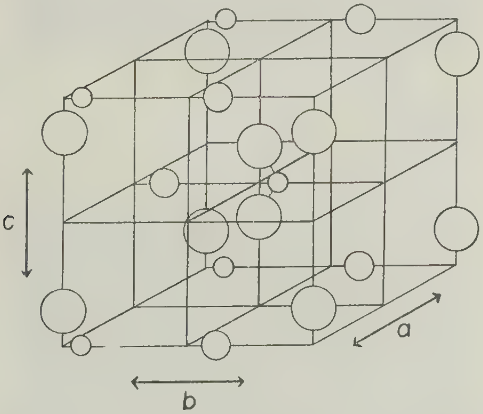

Fig. 1. Parallel perspective drawing of $NaNO_2$ structure at r.t.. Large, medium and small circles represent oxygen, sodium and nitrogen, respectively. The unit cell size is $a=3.55$Å, $b=5.56$Å, $c=5.38$Å.

In this paper, the ferroelectric damain patterns of $NaNO_2$ visualized by the etching method at room temperature are shown and some effects on the domains due to the heat treatment and the application of the electric field one are discribed. It is considered that the feature of the domain boundary is intimately connected with the behavior of NO_2^- radicals in the crystal. Some discussions on it are presented.

§ 2. Preparation of Crystals

Since $NaNO_2$ has a rather low melting point of 277°C and has an adequate curve of solubility into water, single crystals were easily prepared by either the fusion method or the solution method.

In the former case, however, a careful precaution should be taken against humidity because of a considerable deliquescence of $NaNO_2$. $NaNO_2$ powder (special grade in JP) charged in a glazed alumina-crucible of about 400 cc content was first dried at about 100°C during 48 hrs. under the pressure of 10^{-2} mmHg. Next the crucible was set in a vertical electric-furnace, and there the temperature was raised up to *ca* 280°C. Then the crucible was slowly cooled down by lifting it upwards along the axis of the furnace with the aid of a servomotor, while the input power of the furnace was kept constant during the process. A crystal was first nucleated floating on the center of the liquid surface, and then developed towards the wall side of the crucible. In the crystallization process, some stress was applied to the grown-up crystal when it reached the wall of the crucible, and further in the cooling process on account of an anisotropy in the thermal expansion coefficients. Consequently it was cracked into several blocks of which sizes were 1∼3 cm^3 on the average. When we need a crystal of larger size, it was necessary to pick up the grown-up crystal from the melt before it touched the wall side or to flow out the liquid from the crucible in the midst of the cooling process. The crystal prepared was transparent, slightly yellowish and showed the cleavage parallel to $(10\bar{1})$ or (101) planes. The angles between these cleavage surfaces calculated from the X-ray data[2] are shown in Fig. 2, where α and β are 66°52′ and 113°8′, respectively. The angles determined with optical microscope for our crystals agreed well with them.

In the latter case, the method of evaporation was adopted. A saturated aqueous solution of $NaNO_2$ of *ca* 200 cc was gradually dehydrated by conc. sulphuric acid in a desiccator during about ten days. The desiccator was set in a thermostat kept at 35±0.5°C. A little crystal mounted on a glass plate was used as a seed. The obtained tabular crystal was prismatic, elongated along [100], as shown in Fig. 3. As several prismatic crystals generally grew piling on their (001) faces each other, the shape of the grown-up crystal became rather complicated. The dimensions of the obtained crystal were 2 cm×1 cm×0.5 cm at most.

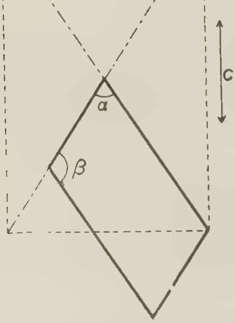

Fig. 2. Angles between the cleavage surfaces (101) and $(10\bar{1})$ denoted by the full lines. The rectangle surrounded by the dashed lines is a projection of $NaNO_2$ unit cell on the b plane and the directions of cleavage are shown by the chain lines.

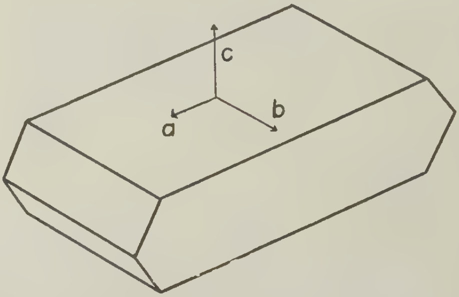

Fig. 3. A prismatic tabular crystal prepared by the solution method.

§ 3. Observation of Ferroelectric Domains

Before etching the crystal, it was necessary to polish its surfaces in order to eliminate a pre-etching effect due to the humidity in air. It was on the *b* surface, perpendicular to the polar axis, that the observations were made. Any patterns were not observed on the other surfaces except the *b* surface, as is expected. As the cleavage does not occur parallel to this face, the crystal was cut perpendicular to the *b* axis with a wet string. The surfaces were polished first with a fine sandpaper and then with a soft filterpaper. Photo. 1 shows the *b* surface before the etching, where any distinguished pattern cannot be seen with the exception of scratches in polishing. 10% NaOH aqueous solution was most used as the etchant and the time required for the etching varied from a few to several tens of seconds, depending upon the desired degree of development of the patterns. Photo. 2 is the etch pattern near the edges of the crystal, where many parallel stripes lie along the *c* direction. Its enlarged picture is exhibited in Photo. 3.

The interval between the stripes, which is the width of the domain, varies considerably according to the place and the specimen. In a virgin crystal prepared by the solution method, any parallel stripes could not be seen. After a heat treatment above the Curie temperature, however, some stripes appeared, though the pattern was somewhat different compared with that shown in Photo. 3. Photos. 4 (a), (b) represent these situations. Supposing that the pattern is resulted from the ferroelectric domains, the crystal shown in Photo. 4 (a) is considered to be composed of a single domain. The effect due to the heat treatment was also recognized on the crystal prepared by the melting method, although the detection was rather difficult because the stripes were fine. It may generally be said that the interval between the stripes

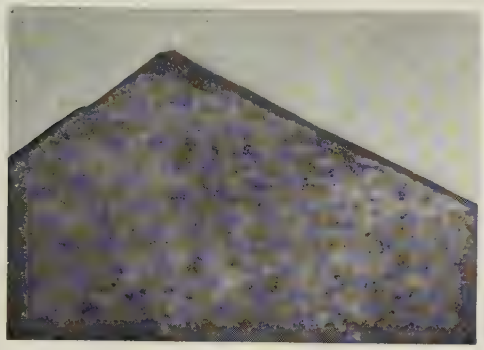

Photo. 1. A (010) surface before etching. The edges are the cleavage faces and the angle between them is β. ($\times 30$)

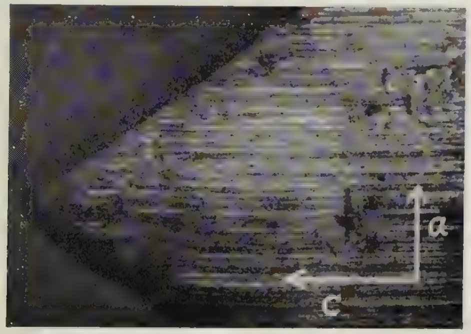

Photo. 2. An etch pattern of the (010) surface near the edges of a crystal. (Etchant: NaOH) The angle between the edges is α. ($\times 70$)

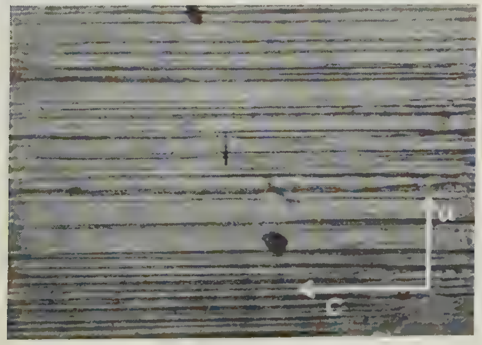

Photo. 3. An enlarged picture of a certain part in Photo. 2. ($\times 140$)

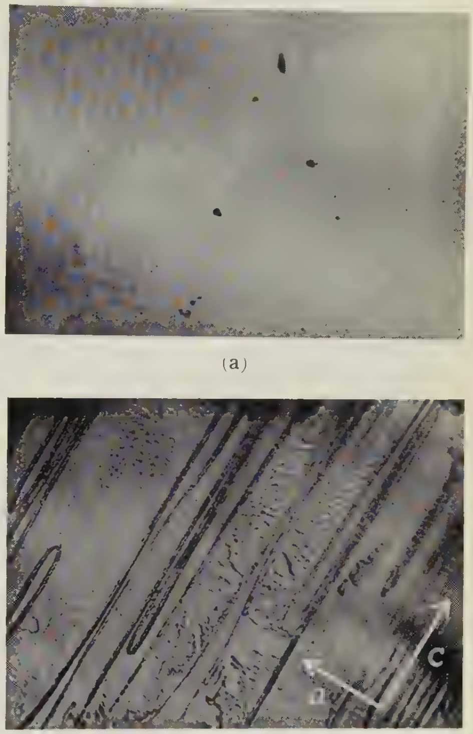

(a)

(b)

Photo. 4. Etch patterns of the (010) surface of a virgin crystal prepared by the solution method. (Etchant: NaOH) ($\times 140$)

(a) before } a heat treatment above the Curie temperature.
(b) after }

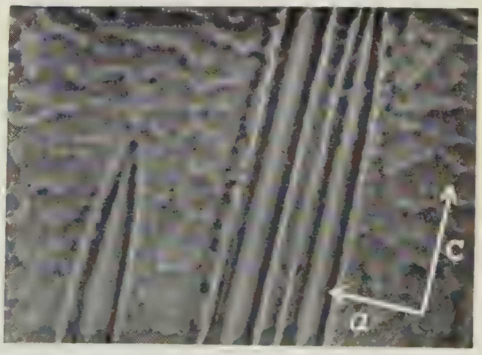

Photo. 5. A wedge-shaped pattern. (Etchant: NaOH) ($\times 790$)

observed on the crystal prepared by the solution method is much larger compared with that by the melting method.

A wedge-shaped pattern can be seen in Photo. 4 (b) and its point is enlarged in Photo. 5.

§ 4. Field Fffect

By observing the etching pattern of the crystal treated by *dc* electric field, it is possible to determine whether it really corresponds to the ferroelectric domain or not, furthermore the sense of the polarization of 180° domain. To ascertain the vanishing of the domain structure in the paraelectric phase by etching the crystal in this temperature-region is also desirable, but such an experiment is not to be easily made.

The $NaNO_2$ crystal shows the *D-E* hysteresis loop for 50 c/sec *ac* field near the transition temperature, and the coercive field observed at 143°C is about 2.3 kv/cm.[1] But the loop does not open out at room temperature even for the field of 25 kv/cm, owing to its high coercive field. While, it was shown by our etching experiments that the sense of the polarization can be pretty easily reversed in the case of the *dc* electric field. The same result about the effect of electric field upon the domain structure was obtained for both of the crystal prepared by the fusion method

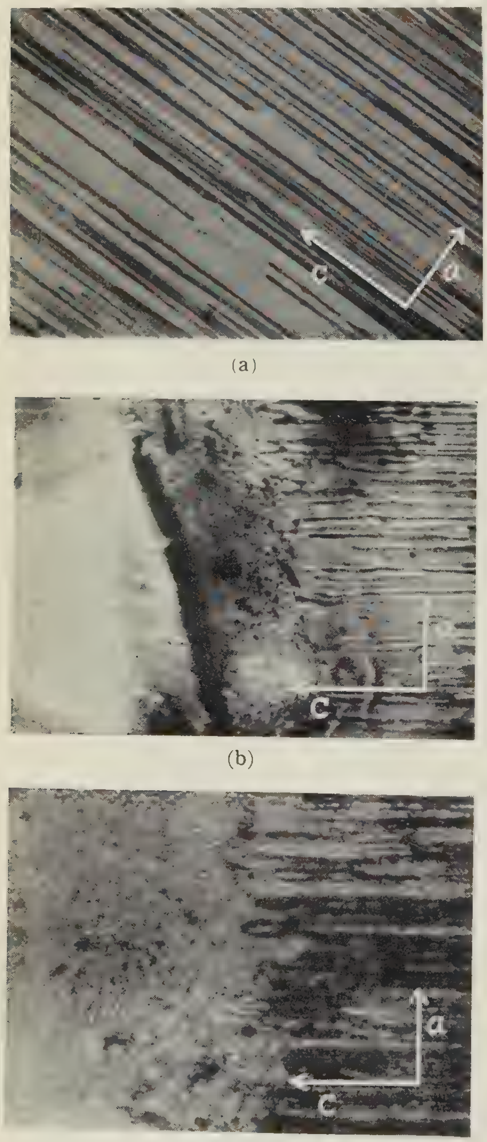

(a)

(b)

(c)

Photo. 6. Etch patterns of the (010) surface near the part where the electrode was attached. (Etchant: NH_4OH)

(a) before (×140)
(b) after (The plus side) } an application of *dc* field (×70)
(c) after (The minus side) (×70)

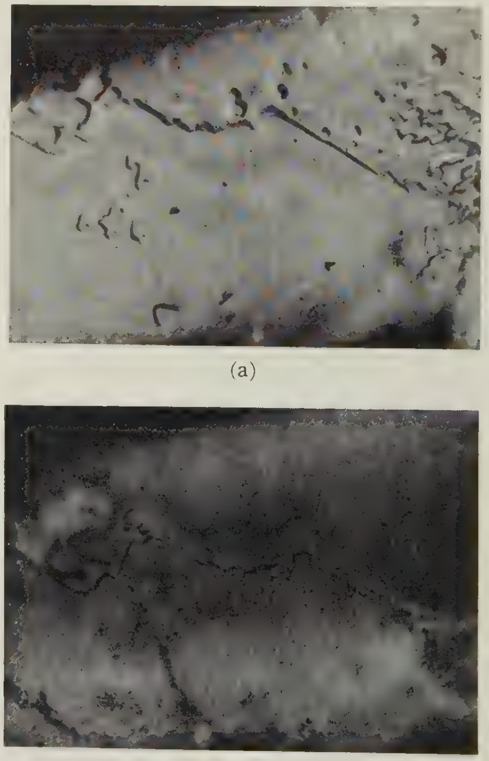

(a)

(b)

Photo. 7. Etch patterns on both (010) surfaces of a crystal plate having irregular domain boundaries created by the effect of *dc* field. (Etchant: CH_3COOH) (×70)

(a) the upper face,
(b) the lower face.

and that by the solution method.

The etch pattern of the crystal before applying the *dc* field was first checked, which is shown in Photo. 6 (a). Then the field treatment was performed as follows. The air-drying silver-paste electrode, of which area was about one tenth of the crystal surface, was attached on the middle of the *b* faces and 2.5 kv/cm *dc* field was applied on it at 120°C during one hour. After removing the electrodes and reetching the crystal, an effect distinctly appeared as is seen in Photos. 6 (b), (c). Any stripe could not be found not only on the part where the electrodes had been attached but also on a larger region beyond it. The same result was obtained even at room temperature by applying the *dc* field of 5 kv/cm during half an hour and if the field was applied more longer, the part without stripes generally became more larger. The stripes reappeared after the poled crystal was once heated above the Curie temperature.

Photos. 6 (b) and (c) are the etch patterns by ammonia obtained on the plus side of the applied field and the minus side,* respectively, where we can see a difference between their etching appearances especially on the part under the electrodes, the plus side being smoother than the minus side. Thus it was easy to discern the sense of the polarization by comparing the roughness of the etched surface. The roughness is considered to depend upon the etching rate and further a step should be formed along a domain boundary owing to the difference of etching rate on plus- and minus-surfaces. Observing the part including the domain boundary, we could easily judge which side was more attacked. It was concluded that the etching rate by the alkali etchant of the positive end was more rapid than that of the negative end and contrary by the acid etchant.

For ascertaining that a domain runs through the crystal along the *b* direction, the location of the domain boundary observed on the upper face of the crystal was compared with that on the lower one by adjusting the focus of the microscope on the both faces without turning over the crystal plate. The similar patterns were observed on the two faces, although the sight of the lower one was a little less clear than the upper one. This situation is shown in Photos. 7 (a) and (b). It may be concluded therefore that a domain runs through the crystal from one face to the opposite one. Further, Photo. 6 and Photo. 7 show that the domain can easily take any shape after an application of the electric field on the crystal.

§ 5. Discussion

It has become clear that the etch patterns observed in our experiments are due to the 180° ferroelectric domain, running through the crystal along the *b* direction. It is considered that the etching rate is determined not only by the chemical activity of the etchant, but also by the electrostatic interaction between the ions in the etchant and the polarization charge appearing on the crystal surfaces. As by the electrostatic interaction the anion drifts towards the positive end of the crystal and the cation towards the negative one, the density of the anions will increase near the positive end and that of the cations near the negative one.**

Considering the case of alkali-etchant, for example, NaOH, we have Na^+ as the positive ion. Supposing that the Na^+ is inactive to $NaNO_2$, it will be natural that the etching rate on the negative end is slower than that on the positive one. A similar interpretation will be possible in the case of other alkali-etchants. In the case of acid, it is presum-

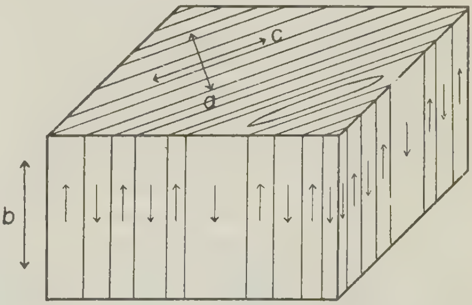

Fig. 4. A schematic model of the domain structure of $NaNO_2$. Side faces are the cleavage ones and the arrows represent the sense of spontaneous polarization.

---

* The plus- and minus-sides are the surfaces connected to the + and − terminals of the battery, respectively.

** The positive- and negative-ends are the surfaces on which the positive- and negative- polarization charge appear, respectively.

ably the cation H^+ that plays an active role for the reaction and leads to the contrary result to alkali-etchant. It is noticeable, however, that the situation is contrary in barium titanate,[7] which is insoluble into water: for example, the etching rate on the positive end was more rapid than that on the negative one when HCl etchant was used.

From our experimental results, we can draw a typical model of the domain structure, including a wedge-shaped domain as shown in Fig. 4, where the sense of the spontaneous polarization is indicated by arrows. The fact that the domain boundary in the natural state only appears parallel to the (100) plane, has to be interpreted in connection with the atomic arrangement in the crystal. Projecting the atomic arrangement of $NaNO_2$ on its (010) plane, we may obtain an illustrative pattern shown in Fig. 5. The cleavage faces, parallel to the (101) or $(10\bar{1})$ planes are indicated there by the chain lines. The strength of the bonding which acts across these faces is considered to be rather weak owing to its large interatomic distance. Supposing that the parts marked A and B represent the antiparallel 180° domains, respectively, their boundaries will probably be located as shown by the full line *pq*. As the O–O distance in NO_2^- radical is 2.09A[2,4], the degree of the overlapping of the oxygen atoms across these planes is not so large. But if the boundary is parallel to the (001) plane, the boundary will be compelled to become a notched face as shown by the dotted line *st*. Comparing these two cases, we may conclude that the latter case occurs less probably than the former. As to why the boundary does not appear parallel to the (101) or $(10\bar{1})$ planes, the situation is not clear, but it might be said that the shape of NO_2^- radical and the character of its thermal motion can not permit the boundary to stand still along these planes. In any cases, however, the difference between their lattice energies would be small, judged from the fact, mentioned in § 4, that the domain can take any shape after an application of the electric field.

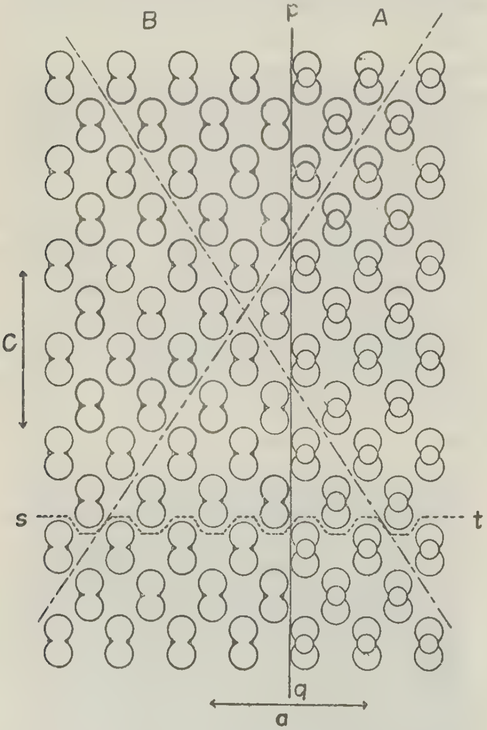

Fig. 5. A projection of the atomic arrangement on the *b* plane in $NaNO_2$ crystal, containing two antiparallel domains. Each unit in the figure represents a superposed projection of Na^+ and NO_2^-. The domain boundary is considered to be located as shown by the full line *pq* and a virtual boundary running along the *a* direction is represented by the notched dashed-line *st*. The directions of cleavage are indicated by the chain lines.

It is probably sure from the X-ray data that the ferroelectricity in $NaNO_2$ is due to the alignment of NO_2^- radicals along the *b* direction, the complete disordering of their sense along the *b*-direction being realized above the Curie temperature.[5,6] From other properties of $NaNO_2$, e.g., the thermal properties,[8] however, it is supposed that the misalignment of NO_2^- would possess some probability to occur also in the ferroelectric phase, so that the domain-wall motion will easily take place with the aid of the thermal vibration of NO_2^- radicals and will presumably show a strong dependence upon the frequency of applied field, because of a short-range interaction between NO_2^- radicals. The reason why the coercive field obtained in the *D–E* hysteresis loop for the *ac* field of 50 c/sec is so different from that of *dc* one seems to be due to this cause.

We may imagine that in a pure and stress-free crystal the sense of the polarization of the whole crystal will be controlled completely by a weak field applied to any point of the crystal, of which strength is of the same order as or a little less than the coercive field.* Qualitative experiments are now in progress. There are many interesting subjects concerning the dynamical properties of the domain-wall motion, but they will be described in a subsequent paper.

The authors wish to express their hearty thanks to Dr. I. Yoshida and Mr. T. Kawakubo for their cooperations in experiments and valuable contributions in discussions.

---

* This means a threshold value of static field in which the domain wall motion begins.

References

1) S. Sawada, S. Nomura, S. Fujii and I. Yoshida: Phys. Rev. Letters. **1** (1958) 320.
2) G. E. Ziegler: Phys. Rev. **38** (1931) 1040.
3) M. R. Truter: Acta Cryst. **7** (1954) 73.
4) G. B. Carpenter: Acta Cryst. **5** (1952) 132.
5) B. Strijk and C. H. MacGillavry: Rec. trav. chim. **62** (1943) 705.
6) B. Strijk and C. H. MacGillavry: Rec. trav. chim. **65** (1946) 127.
7) J. A. Hooton and W. J. Merz: Phys. Rev. **98** (1955) 409.
8) S. Nomura: Unpublished.

Journal of the Physical Society of Japan, Vol. 16, No. 5, May, 1961

Perfectness of Macrodomains of $BaTiO_3$ Crystals

By Kêitsirô Aizu and Osamu Nakada

Hitachi Central Research Laboratory, Kokubunji, Tokyo

(Received January 11, 1961)

Statistico-thermodynamical investigation is made on the size and density of reversely-polarized microdomains contained within a unidomain *c*-plate (or a macrodomain of a multidomain *c*-plate) of $BaTiO_3$ in thermal equilibrium at room temperature, with or without constant electric field applied. Microdomains treated here are confined to ones running through the crystal plate from the surface on the one side to the surface on the other side. It is found that a thinner crystal plate contains more reversely-polarized microdomains, and a plate thicker than about 2×10^{-6} cm contains practically no reversely-polarized microdomains. Reversely-polarized microdomains tend to disperse rather than coalesce, and can hardly be depressed by electric field. Just below the Curie temperature, it is expected that the critical thickness is considerably larger than the above value, since the domain-wall energy per unit area is fairly small.

§1. Introduction

It is generally assumed that a $BaTiO_3$ *c*-plate, in the most stable state, is polarized in the one sense everywhere. But, alternatively, it is conceivable that a unidomain *c*-plate of $BaTiO_3$, in spite of the apparent uniformity of polarization under an opitical microscope, may contain more or less reversely-polarized microdomains. This paper aims to investigate statistico-thermodynamically the size and density of reversely-polarized microdomains which might be contained within a unidomain *c*-plate of $BaTiO_3$ in thermal equilibrium at room temperature with or without constant electric field applied.

Among microdomains, three types are conceivable. The first type of microdomains run through the crystal plate from the surface on the one side to the surface on the other side, the second rise from the surface on either side and end in the interior of the crystal plate, and the third lurk in the interior of the crystal plate. In this paper, only the first type of microdomains are considered. The occurrence of such reversely-polarized microdomains increases on the one hand the internal energy of the crystal plate, but at the same time increases its entropy, too. The former increase is proportional to the thickness of the crystal plate, while the latter increase is independent of the thickness. Therefore, it is expected that the density of reversely-polarized microdomains is larger for a thinner crystal plate.

§ 2. Foundation

Let us consider a unidomain *c*-plate of $BaTiO_3$. A row of unit cells running through the crystal plate perpendicularly to its face is referred to as a *cell-row*. All the unit cells belonging to one cell-row are assumed to be polarized either in the normal sense or in the reverse sense. (Which sense is normal is arbitrary.) A pair of a normal cell-row and a reverse cell-row in planar contact with each other is referred to briefly as a *normal-reverse cell-row pair*. (W. Kinase and H. Takahashi[1] calculated that the thickness of 180° domain walls of $BaTiO_3$ is nearly zero lattice-unit. This is taken into consideration.) When normal-reverse cell-row pairs exist, it is assumed, as an approximation, that a fixed energy increment γ occurs per unit area of their contact planes. Let the crystal plate be L lattice-units thick and contain N cell-rows of which n are reverse and $N-n$ are normal. A cell-row has four other cell-rows in planar contact around it. The central cell-row is referred to as *i-paired* when i of the four are polarized in the opposite sense to it. Let the crystal plate contain n_i i-paired reverse cell-rows and m_i i-paired normal cell-rows ($i=0, 1, 2, 3, 4$). Let the densities of reverse, i-paired reverse, and i-paired normal cell-rows be x, x_i, and w_i, respectively. That is,

$$x=n/N\,, \qquad x_i=n_i/N\,, \qquad w_i=m_i/N\,. \tag{2.1}$$

It follows that

$$\left.\begin{array}{ll}\sum n_i=n\,, & \sum m_i=N-n\,,\\ \sum x_i=x\,, & \sum w_i=1-x\,.\end{array}\right\} \tag{2.2}$$

The probabilities of one cell-row being reverse and being normal are x and $1-x$ respectively, so the probability of one reverse cell-row being i-paired and that of one normal cell-row being i-paired are respectively

$$q_i={}_4C_i\,x^{4-i}(1-x)^i\,, \qquad p_i={}_4C_i\,x^i(1-x)^{4-i}\,. \tag{2.3}$$

The probability of $(n_0, n_1, \cdots, m_3, m_4)$-or shortly (n_i, m_i)-state, wherein n_i reverse cell-rows are i-paired ($i=0, 1, 2, 3, 4$) and m_i normal cell-rows are i-paired ($i=0, 1, 2, 3, 4$), is

$$\frac{n!}{\Pi\, n_i!}\Pi\, q_i^{n_i}\cdot\frac{(N-n)!}{\Pi\, m_i!}\Pi\, p_i^{m_i}\,. \tag{2.4}$$

It is necessary and can be verified easily that the sum of (2.4) over every combination (n_i, m_i) satisfying (2.2) is unity. The number of those configurations wherein n of N cell-rows are reverse is

$$\frac{N!}{n!(N-n)!}\,. \tag{2.5}$$

Ω, the number of configurations of (n_i, m_i) state, is equal to the product of (2.4) and (2.5), so

$$\Omega=\frac{N!}{\Pi\, n_i!\,\Pi\, m_i!}\Pi\, q_i^{n_i}\,\Pi\, p_i^{m_i}\,. \tag{2.6}$$

The entropy (increment) S of the crystal in (n_i, m_i) state is:

$$\begin{aligned}S&=k\log\Omega\\ &=Nk(-\sum x_i\log x_i-\sum w_i\log w_i\\ &\qquad+\sum x_i\log q_i+\sum w_i\log p_i)\,.\end{aligned} \tag{2.7}$$

Here k is the Boltzmann constant.

Let the crystal contain N^* normal-reverse cell-row pairs. Since there occurs energy increment equal to $ac\gamma L$ (a, c: the lattice constants) per one normal-reverse cell-row pair, the internal energy (increment) U of the crystal in (n_i, m_i) state is:

$$U=ac\gamma LN^*\,. \tag{2.8}$$

The number of normal-reverse cell-row pairs is $\sum in_i$ if counted about reverse cell-rows, and is $\sum im_i$ if counted about normal cell-rows. However, in order to maintain the symmetry between the set x, x_i and the set $1-x$, w_i, as required physically, it is improper to set either

$$N^*=\sum in_i \qquad \text{or} \qquad N^*=\sum im_i$$

because either would come to break the symmetry. It will therefore be assumed that $\sum in_i$ and $\sum im_i$ contribute to N^* with certain weights, as

$$N^*=\varphi(1-x)\sum in_i+\varphi(x)\sum im_i\,. \tag{2.9}$$

Here $\varphi(x)$ is a certain function of x satisfying

$$\varphi(x)+\varphi(1-x)=1\,. \tag{2.10}$$

Especially if $\varphi(x)=\text{const.}$, (2.9) becomes a simple arithmetical mean. When n is given, the largest value that $\sum in_i$ takes is $4n$ and the smallest value 0, and the largest value that $\sum im_i$ takes is $4(N-n)$ and the smallest value 0. Therefore when $n_0, \cdots, n_4$ fluctuate within the limits of (2.2), N^* fluctuates at most by $4n\varphi(1-x)$, and when $m_0, \cdots, m_4$ fluctuate within the limits of (2.2), N^* fluctuates at most by $4(N-n)\varphi(x)$. Since one normal-reverse cell-row pair consists of one normal cell-row and one reverse cell-row, the set $n_0, \cdots, n_4$ and the set $m_0, \cdots, m_4$ should have equivalent effects on N^*, so is assumed

$$4n\varphi(1-x)=4(N-n)\varphi(x)\,,$$

i.e.,

$$\frac{\varphi(x)}{x}=\frac{\varphi(1-x)}{1-x}\,. \tag{2.11}$$

Thus from (2.10) and (2.11)

$$\varphi(x)=x\,, \tag{2.12}$$

from (2.9) and (2.12)

$$\begin{aligned} N^*&=(1-x)\sum in_i+x\sum im_i \\ &=N\{(1-x)\sum ix_i+x\sum iw_i\}\,, \end{aligned} \tag{2.13}$$

and from (2.8) and (2.13)

$$U=Nac\gamma L\{(1-x)\sum ix_i+x\sum iw_i\}\,. \tag{2.14}$$

If P is the total polarization of the crystal and P_s is the spontaneous polarization per unit volume of the crystal,

$$P=P_sa^2cL(N-2n)=NP_sa^2cL(1-2x)\,, \tag{2.15}$$

At temperature T and electric field E, the free energy $\varPhi$ of the crystal in (n_i, m_i) state is:

$$\varPhi=U-EP-TS\,. \tag{2.16}$$

The actual state is sought as the one having the lowest free energy. Substituting (2.7), (2.14), and (2.15) into (2.16), solving the variational equation $\delta\varPhi=0$ in allowance for (2.2), and resetting the solution for the sake of convenience, the result is:

$$\frac{x}{1-x}\left\{\frac{x\exp\left(-\frac{ac\gamma L}{kT}x\right)+(1-x)}{x+(1-x)\exp\left(-\frac{ac\gamma L}{kT}(1-x)\right)}\right\}^4 \exp Y\exp\frac{2EP_sa^2cL}{kT}=1\,, \tag{2.17}$$

$$\begin{aligned} Y=4&\left\{1-\frac{ac\gamma L}{kT}x(1-x)\right\} \\ &\times\frac{(2x-1)\exp\left(-\frac{ac\gamma L}{kT}\right)-x\exp\left(-\frac{ac\gamma L}{kT}x\right)+(1-x)\exp\left(-\frac{ac\gamma L}{kT}(1-x)\right)}{\left\{x+(1-x)\exp\left(-\frac{ac\gamma L}{kT}(1-x)\right)\right\}\left\{x\exp\left(-\frac{ac\gamma L}{kT}x\right)+(1-x)\right\}}\,, \end{aligned} \tag{2.18}$$

$$\left.\begin{aligned} x_i&=x\left\{x+(1-x)\exp\left(-\frac{ac\gamma L}{kT}(1-x)\right)\right\}^{-4}q_i\exp\left(-i\frac{ac\gamma L}{kT}(1-x)\right)\,, \\ w_i&=(1-x)\left\{x\exp\left(-\frac{ac\gamma L}{kT}x\right)+(1-x)\right\}^{-4}p_i\exp\left(-i\frac{ac\gamma L}{kT}x\right)\,. \end{aligned}\right\} \tag{2.19}$$

Thus the means has been obtained to calculate those x, x_i, and w_i which make the free energy minimum.

§ 3. Thick Crystal Plates

Applying (2.17), (2.18), and (2.19) to thick crystal plates, it is found that as $L\to\infty$, then $x\to 0$ or $x\to 1$, irrespective of magnitude and sign of electric field. In case $x\to 0$, for sufficiently large L,

$$x\approx\exp\left(-\frac{4ac\gamma L}{kT}\right)\exp\left(-\frac{2EP_sa^2cL}{kT}\right)\,, \tag{3.1}$$

and

$$U\approx\frac{4\gamma x}{a}\,,\qquad S\approx\frac{U}{T}+\frac{2EP_sx}{T}+\frac{kx}{La^2c}\,,\qquad \varPhi+EP_s\approx-\frac{kTx}{La^2c}<0\,. \tag{3.2}$$

Since $\varPhi+EP_s$ is negative, this state is found to be certainly more realizable than the state of perfection ($x=0$). In case $x\to 1$, for sufficiently large L,

$$1-x \approx \exp\left(-\frac{4ac\gamma L}{kT}\right)\exp\frac{2EP_sa^2cL}{kT}\,. \tag{3.3}$$

In general, a crystal plate has two states of minimum free energy, corresponding to (3.1) and (3.3) respectively. The free-energy difference between these states is

$$2EP_s-\frac{2kT}{La^2c}\exp\left(-\frac{4ac\gamma L}{kT}\right)\sinh\frac{2EP_sa^2cL}{kT}\,. \tag{3.4}$$

When $E>0$, the state (3.1) has the lowest free energy and is most stable, while the state (3.3) is metastable, and when $E<0$, situations interchange. When E is present, the depressions of free energy which the metastable state and the most stable state have from the state of perfection nearer to each are different from each other, and the former is deeper than the latter, so (3.4) differs from $2EP_s$. When $E=0$, either the state (3.1) or the state (3.3) has the lowest free energy and is most stable.

In the state (3.1),

$$\begin{aligned}
&x_i \approx {}_4\mathrm{C}_i \exp\left\{-(16-3i)\frac{ac\gamma L}{kT}\right\}\exp\left\{-(5-i)\frac{2EP_sa^2cL}{kT}\right\},\\
&x_4 \approx x\,,\\
&w_i \approx {}_4\mathrm{C}_i \exp\left(-4i\frac{ac\gamma L}{kT}\right)\exp\left(-i\frac{2EP_sa^2cL}{kT}\right),\\
&w_0 \approx 1\,, \qquad w_1 \approx 4x\,.
\end{aligned} \tag{3.5}$$

Since $x_4 \approx x$, almost all the reverse cell-rows present are found to be four-paired, that is, isolated, thus it is reasonable that $w_1 \approx 4x$, what might not have resulted if N^* had been assumed otherwise than (2.13). Incidentally it is found that as $L\to\infty$, then $\sum in_i\to 0$, $\sum im_i\to 0$, and besides $(\sum in_i-\sum im_i)/\sum in_i\to 0$, displaying $\sum in_i \approx \sum im_i$.

Table I.

$L=50$	$E=0$	$E=10^4$	$E=-10^4$
x	1.5×10^{-5}	1.0×10^{-5}	2.3×10^{-5}
x_0			
x_1			
x_2			
x_3	1.5×10^{-8}	6.7×10^{-9}	3.5×10^{-8}
x_4	1.5×10^{-5}	1.0×10^{-5}	2.3×10^{-5}
w_0	1.0	1.0	1.0
w_1	6.0×10^{-5}	4.0×10^{-5}	9.2×10^{-5}
w_2	1.4×10^{-9}	6.3×10^{-10}	3.3×10^{-9}
w_3			
w_4			
U	2.1×10^{3}	1.4×10^{3}	3.2×10^{3}
S	7.8	5.4	1.2
P/P_s			
$\Phi+EP_s$	-190	-130	-290

§ 4. Numerical Calculation

Table I. and Table II. show results of numerical calculation of x, x_i, w_i, U, S, P, and Φ in cases $L=50$ and 20 respectively, where

$$a=4.0\times10^{-8}\,\mathrm{cm}\,,$$

$$c=4.0\times10^{-8}\,\mathrm{cm}\,,$$

Table II.

$L=20$	$E=0$	$E=10^4$	$E=-10^4$
x	1.5×10^{-2}	1.2×10^{-2}	1.8×10^{-2}
x_0	5.3×10^{-8}	1.8×10^{-8}	1.3×10^{-7}
x_1	4.7×10^{-6}	2.0×10^{-6}	9.4×10^{-6}
x_2	1.5×10^{-4}	8.2×10^{-5}	2.6×10^{-4}
x_3	2.3×10^{-3}	1.5×10^{-3}	3.2×10^{-3}
x_4	1.3×10^{-2}	1.0×10^{-2}	1.5×10^{-2}
w_0	9.3×10^{-1}	9.4×10^{-1}	9.1×10^{-1}
w_1	5.6×10^{-2}	4.5×10^{-2}	6.6×10^{-2}
w_2	1.2×10^{-3}	8.1×10^{-4}	1.8×10^{-3}
w_3	1.2×10^{-5}	6.5×10^{-6}	2.1×10^{-5}
w_4	4.6×10^{-8}	1.9×10^{-8}	9.5×10^{-8}
U	2.0×10^{6}	1.6×10^{6}	2.4×10^{6}
S	8.3×10^{3}	6.9×10^{3}	9.6×10^{3}
P/P_s	97.0	97.6	96.4
$\Phi+EP_s$	-4.2×10^{5}	-3.5×10^{5}	-5.0×10^{5}

$$P_s=260\ \text{erg}\cdot\text{volt}^{-1}\cdot\text{cm}^{-2}\ ,$$
$$\gamma=1.4\ \text{erg}\cdot\text{cm}^{-2}\ ,$$

and

$$k=1.38\times10^{-16}\ \text{erg}\cdot\text{deg}^{-1}$$

were used. γ would be like the energy per unit area of macroscopic 180° domain walls. Here γ was assumed to be equal to the value by W. Kinase and H. Takahashi.[1] On the units used in the tables, E, volt·cm^{-1}; U, Φ, erg·cm^{-3}; S, erg·deg^{-1}·cm^{-3}; P/P_s, %. According to Table I., in case $L=50$, reverse cell-rows are very sparse and almost all isolated. According to Table II., in case $L=20$, the density of reverse cell-rows gets to an order of some %, and P is about 97% of P_s. Electric field of 10^4 volt·cm^{-1} can hardly drop the density of reverse cell-rows. Most of reverse cell-rows present are four-paired, but three-paired ones are appreciable, too. When an electric field of 10^4 volt·cm^{-1} is applied, the free-energy depressions of the most stable and metastable states from the state of perfection nearer to each are 3.5×10^5 and 5.0×10^5 erg·cm^{-3} respectively, and the free-energy difference between the most stable and metastable states is 4.9×10^6 erg·cm^{-3}, which is about ten times as large as either of the former two. It is to be noted that the numerical values above calculated are subject to alteration if the estimate of γ is changed.

§ 5. Conclusion

A unidomain c-plate of BaTiO$_3$ thicker than about 2×10^{-6} cm in thermal equilibrium at room temperature can contain in the most stable state practically no reversely-polarized microdomains, whether a positive constant electric field is applied or not. The thinner crystal plate, however, comes to contain reversely-polarized microdomains, which can hardly be depressed by electric fields. Reversely-polarized microdomains tend to disperse rather than coalesce. The critical thickness 2×10^{-6} cm is extremely small, so that usual crystal plates are far thicker. Therefore, if should not be thought that macrodomains of a BaTiO$_3$ c-plate with usual thickness contain any reversely-polarized microdomains, in thermal equilibrium at room temperature. Just below the Curie temperature, however, the critical thickness is expected to be considerably larger, since the domain-wall energy per unit area is fairly small. In this paper, the domain-wall energy per unit area has been assumed 1.4 erg·cm^{-2} at room temperature. If this estimate is changed, the critical thickness suffer alteration. The nearest-neighbor approximation assumed on calculation of the internal energy may be somewhat rough, so that the value 2×10^{-6} cm may not have an exact meaning. In this paper, the second and third types of microdomains, as mentioned in the introduction, have not been considered. They differ from the first type treated here in that the increase of the internal energy caused by the occurrence of each of them is independent of the thickness of the crystal plate and their distribution is three-dimensional. The treatment of them is much more complicated. There seems to be a possibility of their existing in macrodomains in thermal equilibrium.

The authors wish to thank Dr. H. Kitagawa for his encouragement and discussing this work. The authors are also grateful to the colleagues in the laboratory for discussing on this paper.

Reference

1) W. Kinase and H. Takahashi: J. Phys. Soc. Japan **12** (1957) 464.

JOURNAL OF THE PHYSICAL SOCIETY OF JAPAN, Vol. 16, No. 5, MAY, 1961

Study of the Texture of the Boundary of Etched and Ground Regions of Quartz Plate by X-ray Diffraction*

By Einosuke FUKUSHIMA and Hiroshi NIMURA
Department of Physics, Faculty of Science, Tokyo Metropolitan University, Setagaya-ku, Tokyo, Japan

(Received October 26, 1960)

The boundary effect, i.e. the anomalous enhancement of transmitted reflection from the boundary of the etched and ground regions of a quartz plate (E. Fukushima. Acta Cryst. **7** (1954) 459) is studied by an X-ray photographic method. By this method it is found that at the boundary a fairly large strain is produced and the strained layer extends to a deeper layer in the crystal than at the ground region. The influence of annealing on the boundary effect is also studied by a Bragg spectrometer. The anomalous enhancement is reduced by the annealing at the temperature of about 400°C.

From the above results and some supplemental experiments on the ground surface, a model of the zone of strain at the boundary region is proposed and the mechanism of zone formation is considered.

§ 1. Introduction

It is known that the intensity of X-ray reflection from crystals is greatly increased by grinding the surface. It has been reported moreover by one of the present authors (E.F.)[1] that, when a boundary line separating the etched and ground regions on one surface of quartz plate is prepared, the intensity of transmitted reflection from a net plane parallel to the boundary line is found to be anomalously higher at the boundary region even than one at the ground region on the surface. From this "boundary effect", it was inferred that a fairly large strain is produced at the boundary region and the strain gradient is perpendicular to the boundary line and parallel to the surface.

Kato[2,3] investigated the nature of the lattice distortion at the boundary region by means of a double spectrometer. He showed that; (i) for quartz crystals, the half widths of transmitted reflection curves are almost the same at the boundary, ground and etched regions, (ii) the boundary effect is erased by etching the crystal surface in hydrofluoric acid for only a few seconds and (iii) the effect is observed also in $NaClO_3$ crystals, while in calcite the effect is very small. Then he concluded that the boundary effect is due to the reduction of "primary" extinction caused by the elastic strain accumulated there.

Recently, Ishii and Kohra[4] also found the corresponding effect for germanium single crystals with the use of the anomalous transmission.

In the present work, after the boundary effect was confirmed by means of a Bragg spectrometer as in the previous paper[1] (§ 2), the distribution of strain in crystal beneath the boundary region was observed by an X-ray photographic method (§ 3) and the influence of annealing on the boundary effect was studied by means of the spectrometer (§ 4). Some supplemental experiments were also made (§ 5) to interpret more thoroughly the results obtained by the X-ray studies. Finally a strain model of the boundary region was proposed.

§ 2. Boundary Effect

Boundaries were prepared in the same way as in the previous paper[1]: after one surface of quartz plate was ground with 600 mesh carborandum, a part of it was etched. In the present case boundaries as shown in the upper left in Fig. 1 were prepared, where the shadowed regions denoted as *G* are ground regions and the other denoted as *E* is etched region. A beam of MoKα radiation from a source of an appearent size $1\times1\,mm^2$ was collimated by vertical slits about $8\times0.2\,mm^2$ and made to fall upon the range s_1-s_2 in the part $a-b$ on the plate. In this range, boundary line a_0-b_0 is parallel to the plane $(02\bar{2}2)$ which is normal to the surface and was used as the reflecting plane. A quartz plate used was of X-cut and 0.80 mm thick. By moving horizontally the plate the intensities of transmitted reflection were measured at different positions from the etched region to the ground one. In the peak value curve against horizontal positions in the specimen sketched (the p–x curve according to Kato$^{2)}$), the anomalous enhancement of intensity is observed in the range denoted as B on the abscissa. The width of this range amounts to about 0.5 mm. But the true value is estimated as about 0.3 mm after the correction for the width of incident X-ray beam.

---

* Read at Fifth International Congress of IUC in Cambridge. August 1960.

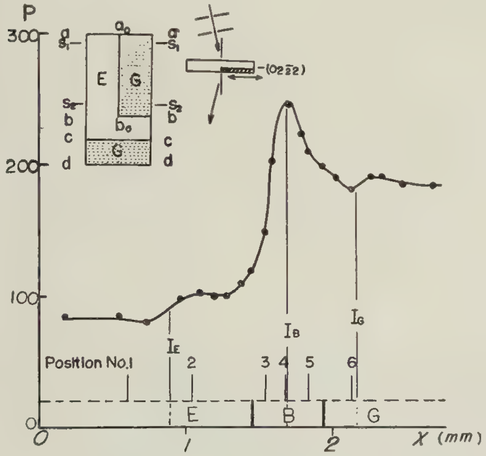

Fig. 1. Peak value curve against horizontal positions in a quartz plate sketched (p–x curve). In this sketch the shadowed regions denoted as G are the ground regions and the other region denoted as E is the etched region. Measurements were carried out only on the upper part s_1-s_2 and the reflection from $(02\bar{2}2)$ plane was used.

§ 3. Observations by the Photographic Method

Diffraction photographs were taken with the same reflecting plane $(02\bar{2}2)$ as in § 2 for the following two cases. The X-ray film was mounted in front of G. M. counter and the width of incident X-rays was reduced to 0.1 mm.

(3.1) *Boundary lines oblique to the reflecting plane* In this case boundary lines oblique to the reflecting plane were prepared. In Fig. 2 (a) the irradiated part is indicated by the

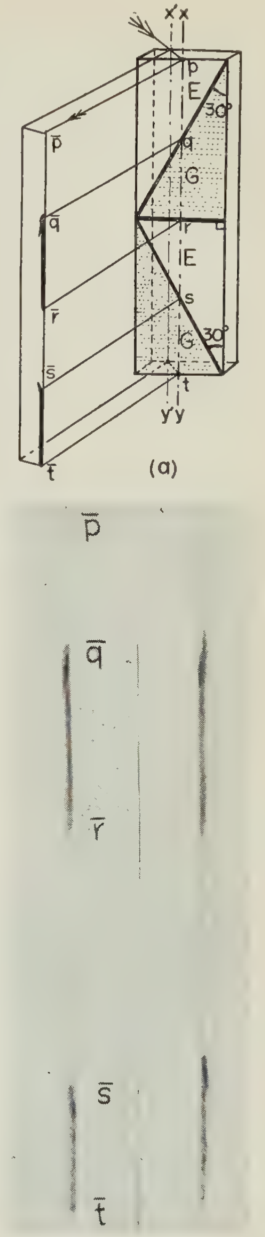

$(0\bar{2}22)$ $(0\bar{2}22)$
(b) (c)

Fig. 2. (a): Schematic illustrations of the specimen and the difiraction pattern. Regions denoted as E or G on the surface are etched or ground regions respectively. The irradiated part is indicated by the line x–y on the transmission side and the line cuts the boundary lines at q, r and s. (b): Diffraction pattern taken in the same arrangement as in (a). Letters denoted correspond to those in (a). (c): Pattern taken by the reflection of opposed sign against (b) and by keeping the incident and transmission sides of the surfaces unchanged.

line connecting x' and y' on the incident side and by the line connecting x and y on the transmission side. The line x–y runs through two E and two G regions and cuts the boundary lines at q, r and s. The boundary lines at q and s make the same angle of 30° to the reflecting plane, but in different directions. The boundary line at r is normal to the reflecting plane. Positions denoted as $\bar{q}$, $\bar{r}$ and $\bar{s}$ at the right margin of a diffraction pattern schematically drawn correspond to q, r and s on the boundaries respectively. The diffraction pattern obtained is shown in Fig. 2 (b). In the ranges $\bar{q}$–$\bar{r}$ and $\bar{s}$–$\bar{t}$, the intensity is, as expected, high, because the reflections came from the ground surface. At $\bar{q}$ and $\bar{s}$ the intensity is more enhanced, while at $\bar{r}$ the enhancement is scarcely seen. This result is consistent with the previous conclusion[1] that the boundary effect is observed for the transmitted reflection from a reflecting plane parallel to the boundary line and can not be observed for the reflection from a reflecting plane perpendicular to the boundary line, because the directions of the boundaries at q and s have parallel components to the reflecting plane, while the direction of the boundary at r has not.

Here will be paid attention to the shapes of reflections at $\bar{q}$, $\bar{r}$ and $\bar{s}$. It is seen that, at $\bar{q}$ and $\bar{s}$, black areas are extended deeply to the interior of the pattern like a tail, the direction of which at $\bar{q}$ is downward and that at $\bar{s}$ upward, while at $\bar{r}$ the extension is hardly seen. These extended black areas are, hereafter, called simply "extensions" with some exceptions.

Fig. 2 (c) shows a pattern taken at nearly the same position as in Fig. 2 (b), but with the reflection of opposed sign, where the incident side of the surface was kept to be unchanged. (Orientations of the quartz plate in Fig. 2 (b) and Fig. 2 (c) in relation to the in cident direction of X-rays are represented schematically by the ones in Fig. 6 (a) and Fig. 6 (b) respectively.) Each of the extensions in the pattern in Fig. 2 (c) extends in the parallel but opposite direction to the corresponding one in Fig. 2 (b).

(3.2) *Boundary lines parallel to the reflecting plane* The specimen, the p–x curve of which is shown in Fig. 1, was used and the lower part from b to d was also used as a reference part in the present case. The boundary line

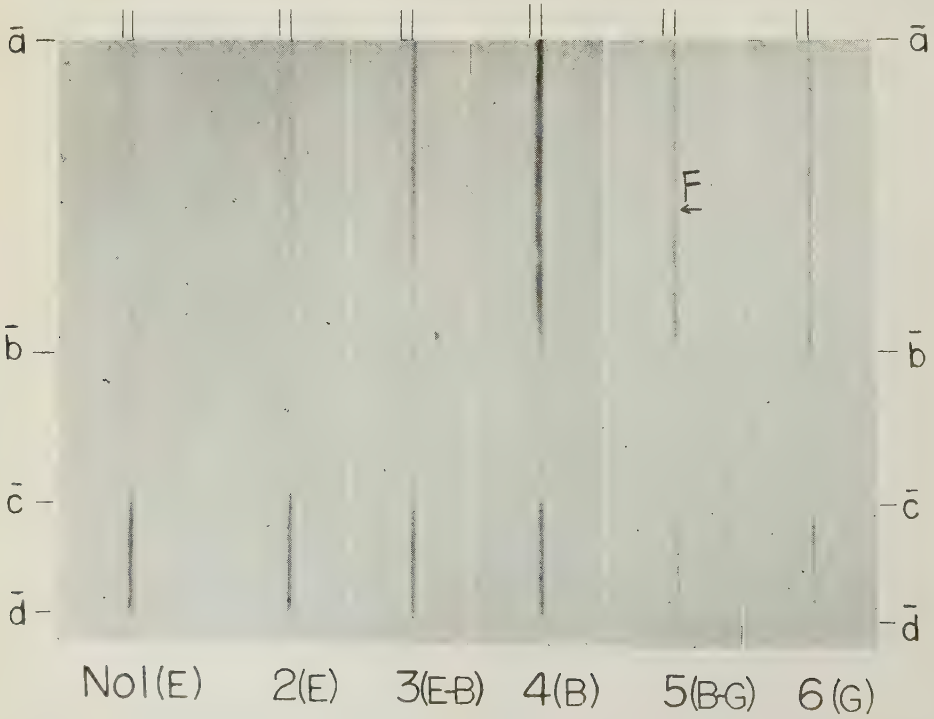

Fig. 3. Diffraction patterns taken at the horizontal positions numbered in Fig. 1. Lower part b–d in the specimen sketched in Fig. 1 is also used in the present case as a reference part.

a_0–b_0 in the upper part from a to b (Fig. 1) is parallel to the reflecting plane and the effect of this boundary was studied by the same photographic method as used in (3.1). Patterns obtained are shown in Fig. 3. These patterns were obtained at the positions numbered on the abscissa of the p–x curve in Fig. 1 and they have the corresponding serial numbers. Features in each pattern will be observed in the part $\bar{a}$–$\bar{b}$ along the pattern. The patterns No. 1 and 2 belong to the etched region. The intensities at the left and right margins of them, corresponding to the incident and transmission sides of the surface, are nearly the same and somewhat higher than at the interior of the pattern. The pattern No. 3 was obtained at the transient region from the etched region to the boundary region. The intensity of the right side margin becomes higher than the left. In the pattern No. 4, which was taken just at the position of the boundary, the margin intensity is the highest and the black area extends deeply to the interior of the pattern. In the transient region from the boundary to the ground region the black area splits into two as shown, for example, by F in the pattern No. 5. The pattern No. 6 was obtained at the ground region and both the margin intensity and the extension of the black area are not so large as in No. 4 and are nearly the same as in the part $\bar{c}$–$\bar{d}$ in that pattern.

Unfortunately the photographing conditions for each pattern were not exactly the same. Accordingly, it is impossible to compare directly the margin intensities or the extensions for all patterns. However, a qualitative comparison can be made by referring to the part $\bar{c}$–$\bar{d}$ of each pattern. Since the homogeneity is expected in the " ground region " in the part c–d on the specimen (Fig. 1), the margin intensity and extension in the corresponding parts $\bar{c}$–$\bar{d}$ of the patterns No. 4 and No. 6 should be the same if the photographing conditions are the same. Then without a serious error the effects of the boundary and ground regions would be compared by the aid of the part $\bar{a}$–$\bar{b}$ and part $\bar{c}$–$\bar{d}$ in the pattern No. 4. In this pattern the width of the extension in the part $\bar{a}$–$\bar{b}$ amounts to about 1/2 of the total width of the pattern and that in the part $\bar{c}$–$\bar{d}$ is about 1/4. The thickness of the specimen is 0.80 mm and accordingly their widths correspond to thicknesses about 0.4 mm and 0.2 mm.

§ 4. The Influence of Annealing on the Boundary Effect

The influence of annealing on the boundary effect was studied, where the $(01\bar{1}0)$ reflection was used and the p–x curves were obtained for three specimens of thickness 0.8 mm. Specimen 1 was annealed successively at 220°C, Specimen 2 at 440° and Specimen 3 at 570°. Measurements were made after the specimens were cooled. After the annealing the reductions of I_B and I_G were observed, while the variation of I_E was not found with the experimental error of 5 %. In Fig. 4, the values of $(I_X-I_E)/(I_{XO}-I_E)$ are plotted against annealing time for three specimens, where I_X means I_B or I_G, and I_{XO} means its initial value. The rates of reductions were large at the beginning of a series of annealings at each temperature, and remarkable for I_B more than for I_G. The data are not yet analysed quantitatively, but the followings can be inferred from the experimental results: No change had occured in the degree of perfection in the interior of the specimens, for the variation of I_B was scarcely detected during the present heat treatments. Thus the reductions of I_B and I_G are attributed to the reduction of strain near the surfaces at the boundary and ground regions. The larger the reduction of I_G is, the more that of I_B is.

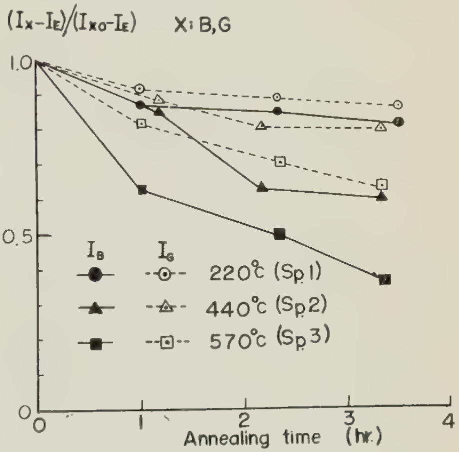

Fig. 4. Plots of $(I_X-I_E)/(I_{XO}-I_E)$ versus annealing time.

Thus it may be said that the magnitude of the strain at the boundary region depends on the one at ground region.

§ 5. Supplemental Studies of Ground Surface

Before proceeding to the nature of the strain beneath the boundary region, a few other results are presented here.

(5.1) *Scratch patterns* By scratching a polished surface of quartz plate with an edge corner of razor under the load of about 1 Kg weight and by etching it in NH_4F solution for about 3 minutes the V-shaped patterns[5] were observed along the scratching direction (Fig. 5). Similar patterns are known for glass[6] and diamond[7] too. The common feature of these patterns is that the shape is always concave to the scratching direction. The patterns are, then, thought to be the tension cracks pulled by a friction between the edge and the surface.

By grinding with carborandum, such cracks would be also produced more finely, densely and in random directions.

(5.2) *Bending of very thin plate by grinding and its easy recovery by etching* It is known that, by grinding one surface of a very thin plate, the surface is bent convexly backward.[8,9] The experiment was made here on a narrow rectangular plate of X-cut, 0.156 mm in thickness and 20 mm in length. By grinding one surface with 600 mesh carborandum, the bending of about 70 cm in radius was observed. This bending was released almost completely by a short etching for about 2 seconds in HF acid (46 %) at 25°C. The reduction of the thickness by this etching was not found and might be less than 1μ if existed.

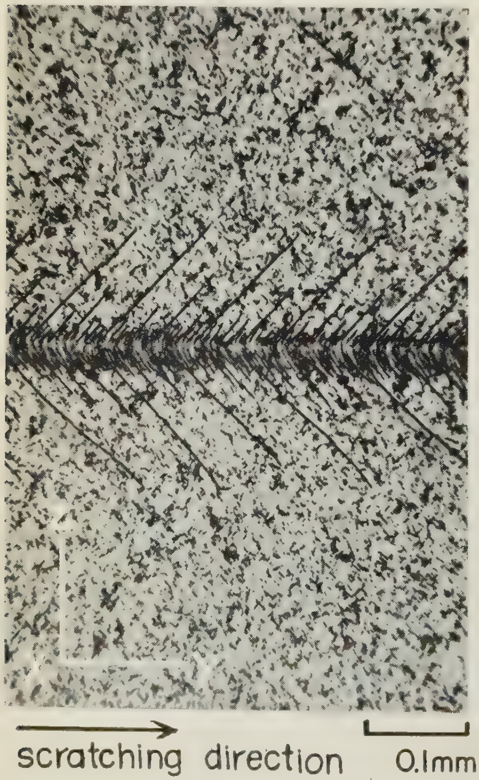

Fig. 5. Scratch patterns on a surface of quartz (Fukushima et al[5]).

§ 6. Discussions and Conclusions

(6.1) *A strain model at the boundary* In

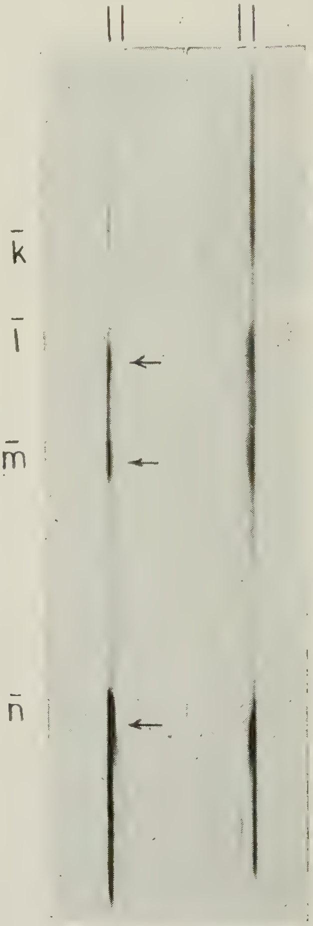

$(0\bar{2}2\bar{2})$ $(02\bar{2}2)$
(a) (b)

Fig. 8. (a): Diffraction pattern taken by the arrangement as shown in Fig. 7 (a). (b): Diffraction pattern taken by the arrangement as shown in Fig. 7 (b).

the diffraction patterns in Figs. 2 (b), (c) and 3, it is observed that the intensity of reflection in the positions corresponding to boundaries which have parallel component to the reflecting plane is greatly enhanced, while in the positions corresponding to boundaries perpendicular to the reflecting plane the intensity enhancement is absent. This result is consistent with previous observations[1,2] by means of a single or double crystal spectrometer.

Moreover, by present photographic method it was found that in the position $\bar{q}$ and $\bar{s}$ in Figs. 2 (b) and (c) the black areas extend to the interior of the patterns deeply like a tail. Such "extension" looks more remarkable in the case of the boundary parallel to the reflecting plane (the part $\bar{a}$–$\bar{b}$ in the pattern No. 4 in Fig. 3). Here, we consider that the intensity distribution in the diffraction pattern represents the topograph of strain distribution in the specimen. Then it will be inferred that the strain exists actually to a deeper layer in the specimen at the boundary region than at the ground region. The strained layers beneath the boundary and ground regions are hereafter, called "the zone of strain". It will be plausible to consider that the width of the extension of the black area is determined from the depth of the zone of strain beneath the surface and the intensity of reflection depends on the strain gradient in the zone of strain.*

Shapes of the extensions at $\bar{q}$ and $\bar{s}$ in Figs. 2 (b) and (c) will be explained by the following illustrations. Figs. 6 (a) and 6 (b) concern with the position q, for instance. Here the width of the zone of strain at the boundary region is neglected and zone of strain is assumed to extend perpendicular to the surface. That is, the zone of strain exists on the plane *abcd* which is normal to the surface and contains the boundary line. The sheet of the incident X-ray beams is expressed by the plane *efgh*. The direction of extension in the pattern is then determined from the projected line of the intersection line of the plane *abcd* and the plane *efgh*. The angle of the direction of the extension to that of the margin is expressed by $\alpha_a=\alpha_b=\tan^{-1}[(2\cos\theta\tan\Omega)/m]$ for both arrangements of Figs. 6 (a) and 6 (b), where Ω is the angle of the boundary line to the reflecting plane, m the vertical magnification and θ is Bragg angle. The equality of α_a and α_b holds actually for the extensions at $\bar{q}$ in Figs. 2 (b) and (c). This supports the above assumption that the zone of strain exists almost perpendicular to the surface. But the value of α's measured is about 10°, which differs greatly from the one, 43.5°, calculated by the above expression. To explain this discrepancy, the widths of both the zone and the incident X-rays will be needed

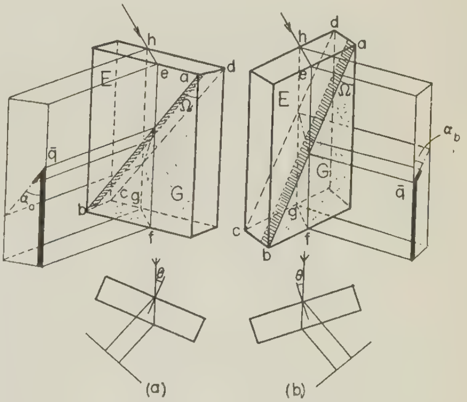

Figs. 6. (a) and (b): Schematic illustrations to explain the difference in the directions of the extensions of black areas at $\bar{q}$ in Figs. 2 (b) and (c).

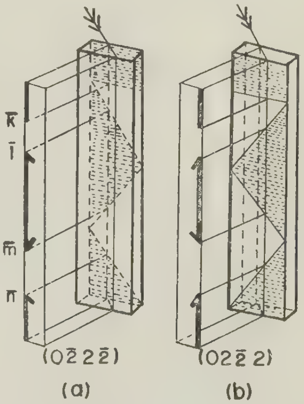

Fig. 7. Schematic illustration of a quartz plate and the diffraction pattern. (a): Boundaries on the incident side of the plate, (b): those on the transmission side.

---

* One of the present authors (E.F.) has measured the intensity of transmitted reflection from different parts of a quartz plate to which a mechanical stress was applied, and came to the conclusoin that the reduction of the extinction effect is proportional to the strain gradient perpendicular to the reflecting plane and not to the strain itself.

to be taken into account.

To study the nature of the lattice distortion in the zone of strain beneath the boundary region, a photographic method as shown schematically in Figs. 7 (a) and (b) was used: in the case (a) boundary lines are set on the incident side of a specimen and a pattern is taken, while in the case (b) the boundary lines are set on the transmission side by turning over the specimen and a pattern is taken again. The corresponding patterns are shown in Figs. 8 (a) and (b) respectively. In the surroundings of the extensions at $\bar{l}$, $\bar{m}$ and especially at $\bar{n}$ in Fig. 8 (a), anomalous reduction of intensity is observed as indicated by arrows, while in Fig. 8 (b) the reduction of intensity is absent. (A boundary line corresponding to $\bar{k}$ is perpendicular to the reflecting plane and neither the extension nor the anomalous reduction of intensity are observed.) This anomalous reduction of intensity in Fig. 8 (a) means that the greater part of the X-rays which satisfies the reflecting condition is reflected from the zone of strain on and near the surface at the boundary region which is set on the incident side of the surface, and thus the intensity of reflection at the interior of the crystal is reduced greatly more than that at the interior beneath the ground or etched region. This means also that the lattice in the zone of strain beneath the boundary region hardly misoriented against the lattice in the perfect region in the crystal. Therefore, it may be said that the boundary effect, i.e. anomalous enhancement of intensity is due to the reduction of so-called " primary " extinction in the zone of strain.[1,2]

The splitting of the extension into two, for instance, at the position indicated by F in the pattern No. 5 in Fig. 3 will be attributed to the fact that the reflection takes place separately in two zones of strain beneath the boundary and ground regions and thus it is concluded that the border of the zone beneath the boundary region is steeper to the surface than the incident angle of X-rays, $\theta=12°15'$, as illustrated in Fig. 9.

From above considerations and the experimental results shown in Figs. 1 and 3, a model of the zone of strain beneath the boundary and ground regions is proposed in Fig. 10. In the zone beneath the boundary region, the gradient of the strain is perpendicular to the boundary line (normal to the plane of figure) and parallel to the surface. The gradient is especially large in the area shaded darkly. In the zone beneath the ground region the strain gradients are present in all directions parallel to surface. Here, the depths of the zones of strain could not be determined quantitatively. According to the experiment by Sakisaka[11] the thickness of the strained layer beneath the ground surface of quartz is about 0.1 mm. On the other hand, if in our present photographs the width of the extension is assumed to express direclty the depth of the zone of strain, the depth of the zone beneath the ground region is calculated as about 0.2 mm as stated in (3.2).

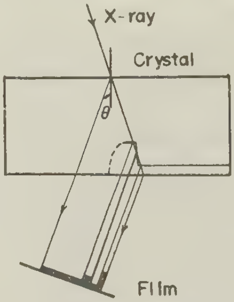

Fig. 9. Schematic illustration to explain the splitting of the extension.

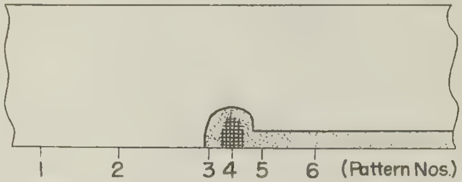

Fig. 10. Side view of the zone of strain derived from the results shown in Figs. 1 and 3.

Here, if the value given by Sakisaka is applied in the present case the depth of the zone of strain beneath the boundary region amount to about 0.2 mm or slightly more, while the depth beneath the ground region is about 0.1 mm.

(6.2) *Texture of the ground surface and the zone formation at the boundary* From the results of the supplemental experiments in § 5, the followings are inferred: Fine cracks produced by grinding the surface are forced to open by debris in them[2] and as a result the surface bending occurs. The crystal is then subjected to the stress by these cracks and the elastic strain would be generated to a considerably deep layer. In this zone of strain, two types of strain will be present: The one strain varies with short period, ideally with the same period as the cracks (Fig. 11) (a) and the other strain is a uniform, positive strain which is superposed.

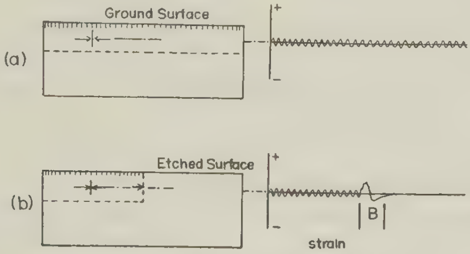

Fig. 11. (a): Schematic illustration of the variation of the strain component parallel to the ground surface. Uniform, positive strain by the bending of the plate is omitted in this figure. (b): Schematic illustration of the magnitude and variation of the strain at the boundary region.

For relatively thick crystals as used in the present X-ray studies, however, the bending by the surface grinding could not be detected. In this case the uniform, positive strain is constrainedly restricted, since the deformation of the plate as a whole is almost absent. The larger stress field is supposed to be conserved in this case than one in the case where the stress is considerably relaxed through the bending of the plate. This stress field is, on the average, compression.

When a part of the surface is etched, the cracks become easily inactive (5.2) probably through the dissolving or removing of the debris in them, and the elastic strains beneath this part disappear. The balance of the compression stress holds no longer at the boundary and new strain would appear in the layer beneath the boundary region, as illustrated in the range B in Fig. 10 (b). In this range the strain will be larger and its period will be long, while at the ground region the period is short. This will be the reason why the zone of strain extends to a deeper layer at the boundary than at the ground region as found in the present X-ray studies. It will be these strain fields that are responsible mostly for the enhancement of reflection intensity at the boundary and ground regions.

The reductions of I_B and I_G by annealing (§ 4) are considered to be attributed to the deformation of the debris in cracks by the creep at high temperature and under high pressure.

Recently, Yoneda¹²⁾ found the anomalous enhancement of the intensity of X-ray reflection from an edge of a ground surface as well as a boundary region of a quartz plate and showed that, at the edge, the strain was generated to a deeper layer than at the portion of the ground surface far from the edge. He considered that nearly the same strain distribution would be formed at the boundary region too. We also think that the similar situation will be realized between the edge and boundary.

E. Aerts, S. Amelinckx and W. Dekeyser¹³⁾ have reported the surface hardenning at the boundary between irradiated and unirradiated regions of NaCl crystal. We consider that a very close relation must exist between the results by them and us.

In conclusion the authors should like to express their sincere thanks to Prof. Ryozi Uyeda of Nagoya University and Prof. Akiya Ookawa of Gakushuin University for their helpful discussions and suggestions. We are greatly indebted also to Mr. Toshio Shinada, the chief of Kinsekisha Laboratory, for his kind discussions and indispensable help. This work was supported by the Scientific Research Fund granted by the Ministry of Education.

References

1) E. Fukushima: Acta Cryst. **7** (1954) 459.
2) N. Kato: J. Phys. Soc. Japan **11** (1956) 748.
3) N. Kato: Bull. Kobayashi. Inst. Phys. Res. **6** (1956) 167 (in Japanese).
4) Z. Ishii and K. Kohra: Presented at the annual meeting of the Physical Society of Japan. October 1958.
5) E. Fukushima, T. Shinada, S. Oinuma and T. Zempo: Presented at the annual meeting of the Physical Society of Japan. April 1960.
6) K. Natsume and K. Kinoshita: J. Appl. Phys. Japan **28** (1959) 132 (in Japanese).
7) R.H. Wentorf: J. Appl. Phys. **30** (1959) 1765.
8) F. Twyman: *Prism and Lens Making*, 2nd ed. 1952 (Hilger and Watts Ltd. Co., London).
9) I. Ida and Y. Arai: Rev. Electr. Commu. Labor. Tech. Journ. N.T.T. **9** (1960) 245 (in Japanese).

10) E. Fukushima: Bull. Inst. Phys. Chem. Res. Japan **14** (1935) 1105. **14** (1935) 1199, **15** (1936) 1 (in Japanese).

11) Y. Sakisaka: Japan J. Phys. **4** (1927) 171.

12) Y. Yoneda: Presented at the annual meeting of the Physical Society of Japan. April 1960.

13) E. Aerts, S. Amelinckx and W. Dekeyser: Acta Met. **7** (1959) 29.

JOURNAL OF THE PHYSICAL SOCIETY OF JAPAN, Vol. 16, No. 5, MAY, 1961

222-Reflection from CuCl in Electron Diffraction

By Fuminori FUJIMOTO

Institute of Physics, College of General Education, University of Tokyo, Komaba, Meguro-ku, Tokyo

(Received January 9, 1961)

The 222-reflection of electron diffraction from CuCl is theoretically and experimentally studied. Ratio of the integrated intensity of the 222-reflection to that of the 111-reflection is calculated by expansion of the scattering matrix and by the solution of Mathieu equation. Calculated results by the both methods agree sufficiently with each other up to the grain size 140 A for 41.3 kV electrons.

The CdS detector and, in addition, the CdS monitor are used in the intensity measurement. The experimental values of the integrated intensity are found to be smaller than the theoretical values at small grain sizes of crystallites. It is, however, confirmed that the ratio of integrated intensity of the 222-reflection to that of the 111-reflection is nearly proportional to the square of grain size and the wave-length, in qualitative accordance with theory.

The 420-reflection is also measured. Dependence of the integrated intensity on wave-length is the same as that of the 222-reflection.

§ 1. Introduction

In electron diffraction, the reflection which is completely or nearly forbidden by kinematical theory has been often observed and studied theoretically by several workers[1)–5)]. Heidenreich[4)] observed abnormally strong 222-reflections from Ge and Si having the diamond structure even in Debye patterns, and attributed the phenomenon to the accidental interactions between the 311- and $\bar{1}$11-reflections. However, Hoerni[5)] pointed out that the intense 222-reflection is also expected from the systematic interactions among *lll*-reflections, and integrated that the intensity of the 222-reflection can attain to a half of the 111-reflection for a thick crystal.

On the other hand, it was reported by Germer[3)] that the intensity ratio of the 222- to the 111-reflection from CuCl decreases rapidly with the decrease of the grain size estimated from the line breadth of Debye rings. A similar phenomenon has been also recently observed in the 222-reflection from Ge[6)].

Applying the dynamical theory developed by the scattering matrix[7)], the author calculated the integrated intensity of the 222-reflection from Ge, and obtained for thin crystals the results that the contribution of the systematic interactions is much larger than the accidental interactions in the 222-reflection and the integrated intensity ratio of the forbidden reflection caused by the systematic interactions to the ordinary reflection is proportional to the square of the crystal thickness and of the wave-length, and that the integrated intensity ratio of the forbidden reflection caused by the accidental interactions such as the 420-reflection, to that due to systematic interactions such as the 222-reflection is independent of the wave-length and is inversely proportional to the crystal thickness[8)].

Table I. Characteristics of CdS detector and monitor.

	Slit width mm	Cryst. width mm	Applied voltage Volt	n	Gain
Detector	0.03	0.67	1.5	0.98	3.5×10^7 (41.3 kV) 2.1×10^7 (23.5 kV)
Monitor	0.08	1.00	1.5	0.93	2.2×10^6 (41.3 kV) 1.3×10^6 (23.5 kV)

In the present paper, we made the similar numerical calculations on the integrated intensities of the 111- and 222-reflections from CuCl by the method proposed by Hoerni making use of the Mathieu function, and checked the range of crystal thickness within which the formula previously deduced by the author is applicable.

The intensity of Debye patterns from CuCl of various grain sizes was measured for various wave-lengths by using the CdS detector developed by us[9], and we performed a quantitative comparison of the 222-reflection between experiment and theory. Further, a qualitative study on the 420-reflection, which is considered to be caused by the accidental interactions exclusively, was also carried out. In the present study, the accuracy of the intensity measurements could be considerably improved by the use of an additional CdS monitor.

§ 2. Experimental

A conventional diffraction camera with a forcussing lens was used. The distance between detector and specimen, and that between plate and specimen were 22.6 and 23.7 cm, respectively. At the front of the specimen, a slit with the diameter 0.08 or 0.25 mm was set. Five specimens having different thicknesses were prepared on collodion films successively by vacuum evaporation in in the camera. The accelerating voltages were 41.3 and 23.5 kV.

The arrangement of the CdS detector was the same as described previously. Another CdS crystal used as monitor was set at about 1 cm apart from the beam stop. The crystals used for the detector and monitor in the present study correspond to the samples No. 8 and 2 described in the previous paper, respectively, and their characteristics are tabulated in Table I, where n is the parameter in the well known formula $i\propto I^n$, i and I being the electron-bombardment-induced-current (EBIC) and the electron intensity, respectively. The parameter n and the gain change to a small extent after the exposure to air. Detailed characteristics are given in the previous paper. Examples of the characteristic curves of the

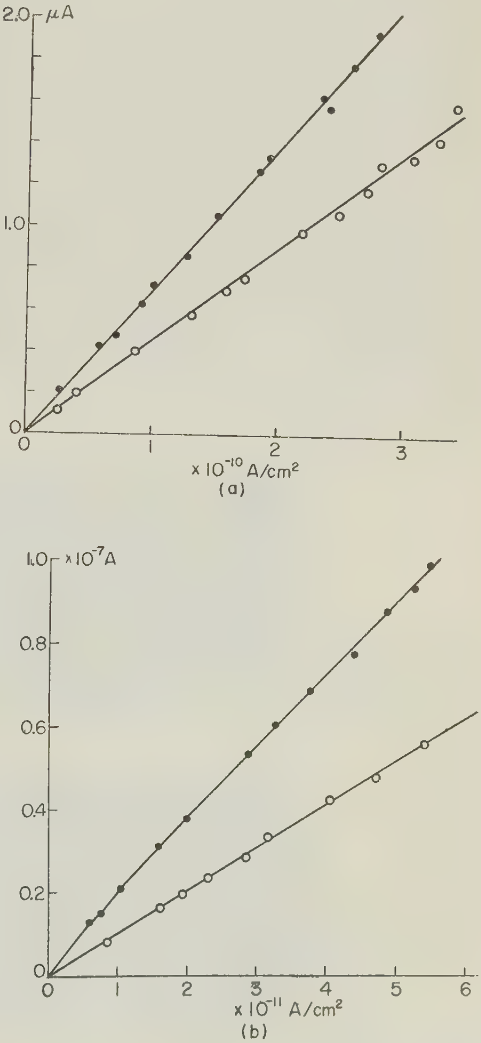

Fig. 1. Characteristic curves for (a) detector and (b) monitor.
●: 41.3 kV; ○: 23.5 kV.

detector and monitor are shown in Fig. 1 (a) and (b), respectively. During the experiment, the characteristic curves were measured at each time after the vacuum was broken.

The incident-beam intensity was controlled so as the EBIC of the detector at the 111-reflection becomes about 1.5 μA, in order to eliminate the error caused by the response time of EBIC. For 41.3 kV, the smaller slit before the specimen was usually used. When the grain size was smaller than 100 A, the diffracted intensity from CuCl gradually decreased by the vaporization of specimen during the measurement and, to avoid this effect, the current density of electrons on the specimen was reduced by using a larger slit and decreasing the total current. For 23.5 kV, the larger slit was used.

The intensity curve for each specimen was measured several times. Long-time fluctuation of the incident intensity was usually within 3%. We corrected the observed diffracted intensities by the EBIC of the monitor assuming the linear relation. When the observed intensity is to be corrected for the change of the monitor current amounting to 10% the error introduced by the linear approximation is 1% with a monitor crystal for which $n=0.9$. The corrected intensity curves coincided with each other within 1%.

The effect of the width of the detector on the line breadth of the observed line profile was as follows. If the sensitive region of detector is assumed to possess a square profile and the intensity profile of ring to be the Cauchy type, the apparent line bread this 5% larger than the true breadth when the slit width is 0.4 of the true breadth. The difference of the apparent breadth from the true one decreases rapidly with the increase of the line breadth. As, in the present experiment, the slit width of the detector was 0.03 mm and the minimum value of the measured line breadth was 0.12 mm, the effect of slit width could be neglected even for the smallest line breadth.

Some examples of the intensity curves of Debye patterns are shown in Fig. 2, in which (a) and (b) are the curves for CuCl with the grain size about 120 A for 41.3 and 23.5 kV, respectively. The intensity scale for the middle and outer parts of the Debye patterns are enlarged respectively twice and 4 times of that for the inner part, by changing the input resistance of a recorder of 2 mV in full scale. The speed of detector was usually 2 mm/min and the running speed of recorder was 8 cm/min.

§ 3. Theory

The crystal structure of CuCl is the ZnS

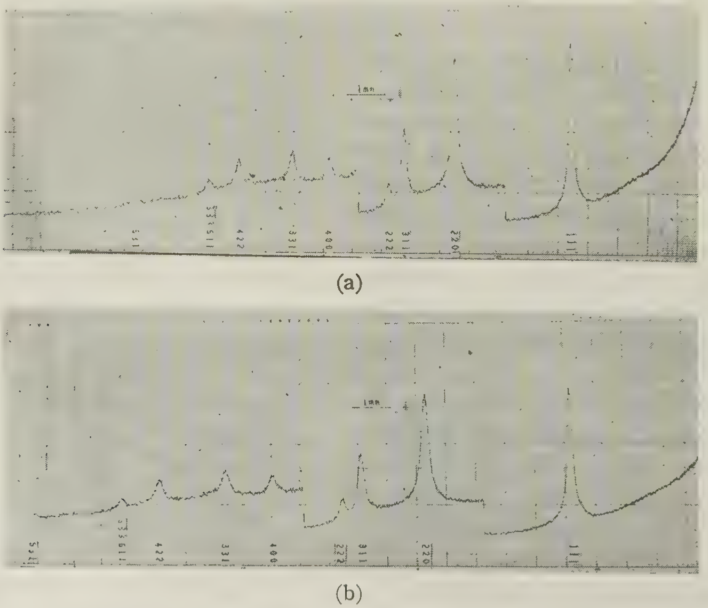

Fig. 2. Intensity curves from CuCl with grain size 120A. The middle and outer parts of the intensity curves are enlarged twice and 4 times of that of the inner part. (a) for 41.3 kV, (b) 23.5 kV.

type with the lattice constant $a_0=5.406$ A and the magnitude of structure factors for the 111- and 222-planes are given by $4(f^2{}_{\text{Cu}}+f^2{}_{\text{Cl}})^{1/2}$ and $4(f_{\text{Cu}}-f_{\text{Cl}})$, respectively, in which f is the atomic scattering factor for electrons. In Table II, the Fourier coefficients calculated from the X-ray scattering factors given by Berghius et al.[10] and James and Brindley[11] are tabulated.

Table II. Fourier potentials of CuCl calculated from X-ray scattering factors given Berghius et al. and James and Brindley.

	Berghius et al.	James & Brindley	
		Hatree	Interpolation
111	6.15 eV	7.3 eV	6.2 eV
222	0.56 eV	0.75 eV	0.29 eV

The author previously deduced the intensity formula for the forbidden 222-reflection from Ge by the use of expansion of the scattering matrix, taking account of the 0-, 111- and 222-waves, assuming the parallel-sided crystal. We can apply the same formula in calculating the intensity of the 222-reflection from CuCl, since the structure factor for the 222-reflection is considerably smaller than that for the 111-reflection as seen from Table II.

The ratio between the total intensities along Debye rings of the 111-reflection and the 222-reflection is given by

$$\frac{J_{222}}{J_{111}}=\frac{\sqrt{2}}{8}v^2{}_{111}\left(\frac{D}{2k}\right)^2\left\{1-\frac{1}{18}\left(\frac{D}{2k}\right)^2 b^4{}_{111}\right\}, \tag{1}$$

where D is the crystal thickness, $k=2\pi/\lambda$, $b_{111}=2\pi/d_{111}$. The Fourier coefficient v_{hkl} is related to the crystal potential $V(\boldsymbol{r})$ given by the following formula:

$$-\frac{8\pi^2m}{h^2}V(\boldsymbol{r})=\sum_h v_h \exp(i\boldsymbol{b}_h\boldsymbol{r})\,. \tag{2}$$

In order to determine the applicable range of (1) with respect to the thickness D, the higher terms should also be calculated. However, such a calculation is very tedious. In order to see the influence of the neglected higher terms, therefore, we compared the calculated result of (1) with the result obtained by the method assuming the harmonic potential as was developed by Hoerni, although this method includes some ambiguities as discussed later.

The solution based on the harmonic potential can be obtained as follows. Assuming v's to be zero except v_{111} and $v_{\bar{1}\bar{1}\bar{1}}$ in (2), we have the following harmonic potential as

$$-\frac{8\pi^2m}{h^2}V(\boldsymbol{r})=2v_{111}\cos b_{111}x\,,$$

where x is the coordinate in the direction of b_{111} and is parallel to the crystal surface. The Schrödinger equation for such a potential reduces to the Mathieu equation, for which the solution of period π and 2π and corresponding eigen values have been tabulated[12]. Through these solutions and eigen values, the normalized eigen vector $\boldsymbol{\psi}^i$ with the components $\psi^i{}_h$ and "Ampassung" ζ^i belonging to i-th wave field can be easily calculated in the case when k_τ/b_{111} is integer or half integer. Here k_τ indicates the tangential component of the incident wave vector. The intensity of the diffracted beam from the crystal is given by

$$I_h=\sum_{ij}\psi_h{}^{i*}\psi_0{}^{i*}\psi_h{}^{j*}\psi_0{}^{j}\exp i(\zeta^i-\zeta^j)D\,.$$

Although the calculation of the intensities at the position where k_τ/b_{111} is neither integer nor half integer is very difficult, we can interpolate between the discrete values reasonably for small values of the crystal thickness. The intensities at larger crystal thickness may be

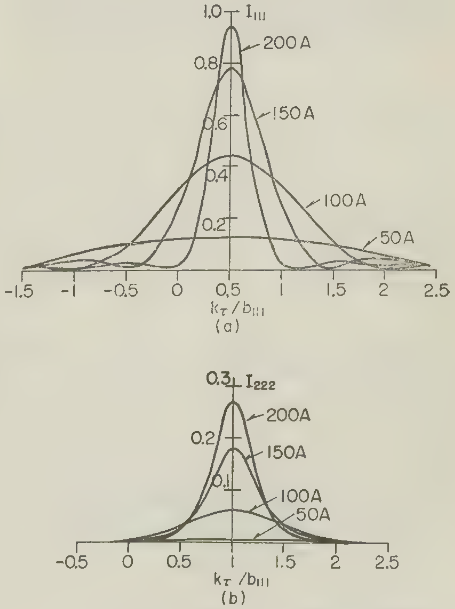

Fig. 3. Rocking curves obtained from the solution of Mathieu equation for various thickness. (a) 111-reflection, (b) 222-reflection.

obtained by considering the successive variation of intensity with thickness.

As shown in Table II, the calculated values of the Fourier coefficients depend on the choice of the atom form factor. In the present numerical calculation of the integrated intensities of the 111- and 222-reflections, the value 6.2 eV for the 111-potential was adopted. Fig. 3 (a) and (b) show the intensity curves of the 111- and 222-reflections calculated for 41.3 kV at various thickness by assuming the harmonic potential. The abscissa indicates the magnitude relating to the tangential component of incident wave vector. The integrated intensity ratio of the 222- to 111-reflection obtained by the numerical integration of Fig. 3 is given by Curve 2 in Fig. 4.

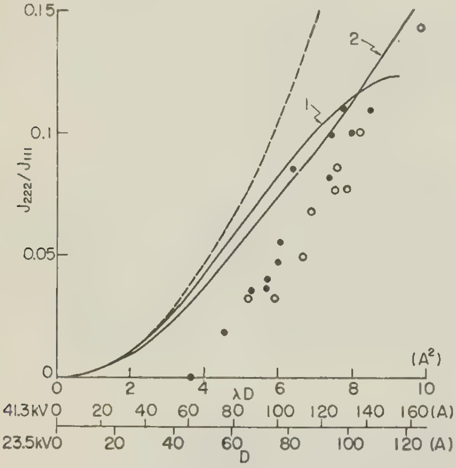

Fig. 4. Integrated intensity ratio J_{222}/J_{111} as the function of λD. Curve 1 shows the calculated values from the expansion of scattering matrix and the dotted line indicates the first term of Eq. (1). Curve 2 shows the calculated values from Mathieu function. Black and white circles are experimental results for 41.3 and 23.5 kV respectively.

The integrated intensity ratio calculated from (1) is given by Curve 1 in Fig. 4, where the dashed line corresponds to the first term of (1).

Curves 1 and 2 are in a satisfactory agreement with each other in the range up to $\lambda D=8$, suggesting that the relation (1) may be applied for $\lambda D<8$ at least.

§ 4. Experimental Results

i) *Grain Size*

In investigating the intensity variation with the grain size, the estimation of the latter quantity is very important. The grain size is usually obtained from the line breadth through the formula[13]

$$\frac{B}{\lambda L}=\frac{1}{D}+\eta\frac{2\sin\theta}{\lambda}\,, \qquad (3)$$

where B is the line breadth, L the camera length, η the mean strain and θ the Bragg angle. In Fig. 5, the values $B/\lambda L$ of each reflection are plotted against $2\sin\theta/\lambda$ on two specimens, where the values of B are corrected by substracting the half breadth of primary beam, 0.028 mm; black circles and triangles represent the values at 41.3 kV and white ones represent those at 23.5 kV.

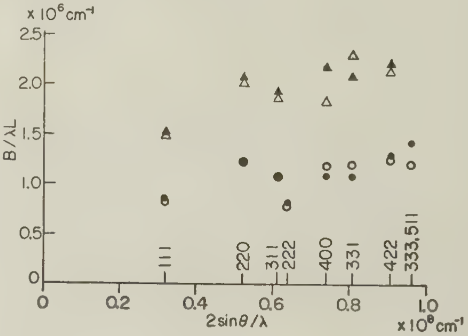

Fig. 5. Line breadth for two specimens.
● and ▲: 41.3 kV, ○ and △: 23.5 kV.

The observed points for the same reflection show fairly good agreements between two voltages, especially for low indeces, and are approximately in accordance with the relation (3). However, for simplicity, we adopt here the values of grain sizes obtained by applying the Scherrer formula, $B/\lambda L=1/D$, to the 111-reflection, as η is not so large and the estimation according to (3) is laborious.

In order to check the values estimated from Scherrer formula, a direct measurement of the grain size were made by electron microphotographs on a specimen for which the grain size estimated from the 111-reflection breadth was 120 A. Although, as seen in Fig. 6, the size of crystallites in the micrographs are widely distributed, the estimated mean size is about 120 A and in a agreement with the diffraction result.

ii) *Intensity of 222-Reflection*

Dependence of the intensity of 222-reflection on the crystal grain size can be observed from the comparison of Fig. 2 (a), and Fig. 7 (a) and

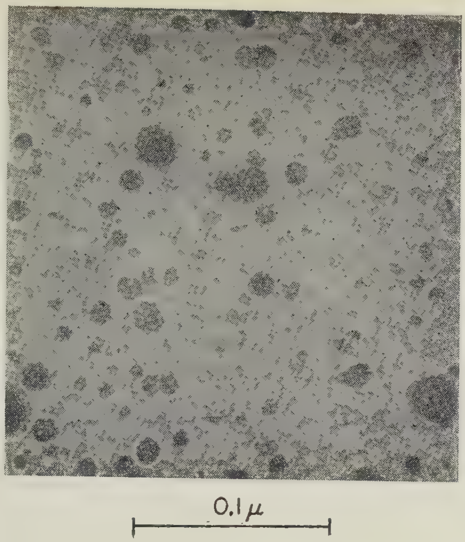

Fig. 6. Electron microphotograph of CuCl.

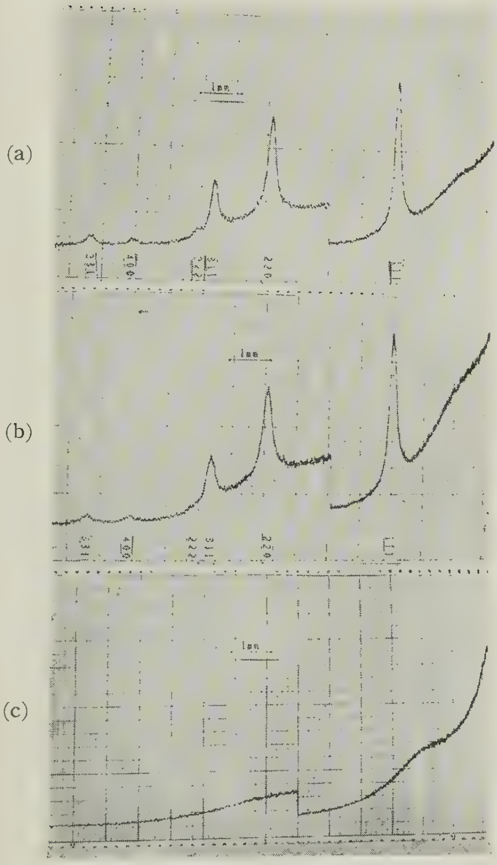

Fig. 7. Intensity curves from CuCl with (a) 100A and (b) 80A. (c) is the intensity curve from collodion. The outer parts are enlarged twice of the inner part.

(b) in the case of 41.3 kV. These curves correspond to the grain sizes of about 120 A, 100 A and 80 A, respectively. Fig. 7 (c) shows the intensity curve for a collodion film as a reference.

Dependence of the intensity from the same specimen on the wave-length is seen in Fig. 2 (a) and Fig. 8 (a) for 41.3 kV and Fig. 2 (b) and Fig. 8 (b) for 23.5 kV. These observations reveal the fact that the change of the 222-reflection with grain size and wave-length is is clearly different from that of the ordinary reflections.

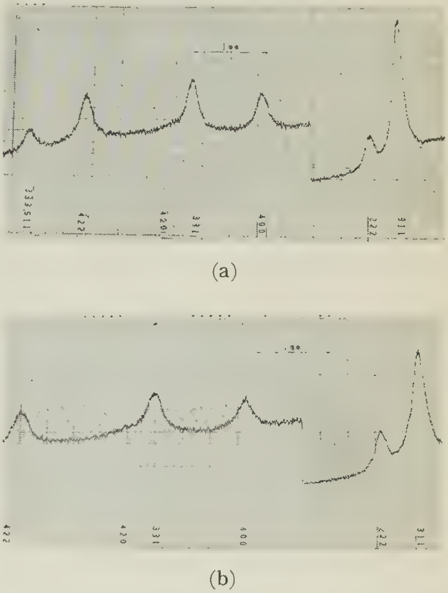

(a)

(b)

Fig. 8. Intensity curves from CuCl with grain size 120A. (a) 41.3 kV and (b) 23.5 kV.

In the comparison of the intensities of the 111- and 222-reflections, the peak areas may be estimated by the product of peak height and half breadth of the reflections. As seen in Fig. 5, the line breadths of 222-reflections agree with those of 111-reflections within the error of measurement. In cases the 222-reflection is weak, however, it is difficult to measure directly the breadth because of the bad separation from the intense 311-reflection. We, therefore, assumed that the breadth of the 222-reflection is always equal to that of the 111-reflection, and the integrated intensity was estimated only from the peak height.

The results are shown in Fig. 4, where the white and black circles correspond to 41.3 kV and 23.5 kV, respectively. The results for both the accelerating voltages agree sufficiently with each other. However, the experimental values are smaller than the theoretical ones, especially at small λD. Discussion about this discrepancy will be given in the next section. If we assume that the experimental results are proportional to $(\lambda D)^n$, the best fit is given by

$$n=2.08 .$$

In thicker specimens, the values of the intensity ratio larger than 0.15 were sometimes observed. However, in such cases, the intensity of background was large and the grain size estimated from the breadth of the 111-reflection was fairly small, probably as the results of plural scattering among crystallites[14]. Thus, these values were omitted from our results.

iii) *Intensity of 420-Reflection*

Fig. 8 (a) and (b) show the intensity curves obtained with strong incident beam from the specimen of the grain size 120 A at 41.3 kV, and 23.5 kV respectively. The driving speed of the detector in these measurements was a half of previous one. In each pattern, the weak 420-reflection appears at outside of the 331-reflection. We may easily notice that the dependence of the 420-reflection intensity on the wave-length is again different from that of ordinary reflections. The relative intensities of ring of the 420-, 222- and 331-reflections are tabulated in Table III, from which we can see that the dependence of the 420-reflection intensity on the wave-length is the same as that of 222, in spite of the difference that the appearance of 420 is caused by only the accidental interactions and that of 222 is mainly due to the systematic interactions. This relation has already been explained in the previous paper. In Ge, the same effect are found[15]. Detailed consideration will be given in the near future.

Table III. Relative intensities of each reflection

	420	222	331
41.3 kV	5	58	56
23.5 kV	5	60	37

§ 5. Discussion

As seen in Fig. 4, the experimental values are smaller than the theoretical values, especially at small λD. We consider now the probable causes for this discrepancy.

In the calculation of the theoretical curves of J_{222}/J_{111}, v's other than v_{111}, in particular v_{222}, are neglected. Although the more precise investigation on the influence of these neglected v's is necessary, it is conceivable that the influence of this approximation will be not appreciable.

As to the accuracy of the intensity measurement, it is probable that the error of the observed intensity of the 222-reflection may be appreciable for the specimen with small grain size for the reason of the bad separation from the intense 311-reflection. However, the same is not the case for the specimen with larger grain sizes, and the deviation of the observed points for larger D from the theorectical curves seems to be outside the experimental error.

The discrepancy may be caused by systematic errors in the estimation of the grain size. In the present experiment, the grain size was estimated from the breadth of the 111-reflection by assuming the Scherrer formula. If the more precise relation (3) is applied, a D-value larger than that deduced from the Scherrer formula is to be obtained, and as the result, the deviation of experimental points from the theoretical curves may become even greater. Therefore, the discrepancy shown in Fig. 4 seem to be not explained by the errors accompanying the measurement of the breadth, though the error of about 20% can not be avoided so long as the grain size is estimated from the line breadth.

In the calculation of the theoretical curves, we assumed that the crystal is perfect and is a parallel-sided plate with a definite thickness. Actually, however, the crystallites are generally granular with widely distributed grain sizes as seen in Fig. 6. Further, the crystallites may not be perfect crystals since the mean strain η estimated from (3) attains 0.5~1.0%. The deviation of the observed points from the linear relation also suggests that the lattice defects are present in crystallites. By taking accout of such circumstances, we can conclude qualitatively as follows:

i) When we assume that the crystal is spherical, the theoretical value of the integrated intensity ratio J_{222}/J_{111} decreases by the factor 3/5, since the integrated intensity of the 222- and 111-reflections are proportional to D^3 and D, respectively*.

ii) If we take account of the distribution of the grain size, the ratio J_{222}/J_{111} should increase for the same reason as mentioned in i)**.

iii) If the crystal is not perfect and contains many faults, the intensity of the 222-reflection will decreases more appreciably than that of 111, since the 222-reflection caused by the dynamical effect is sensitive for the crystal perfectness.

The discrepancy between experiment and theory can be reduced to some extent by the consideration i) and iii), but will be aggravated by the consideration ii).

As considered in the above discussion, there exist a number of complicating factors which may result in the discrepancy between theory and experiment, and it seems to be difficult to reach a satisfactory explanation for the discrepancy at the moment. However, so far as main features are concerned, the observed results in the present experiment may be considered to be in a considerable agreement with the theory.

The author would like to thank Prof. K. Kohra and S. Takagi for their encouragement. This work was partly supported by a research grant of the Minister of Education.

---

* When the crystallite is small and the shape is spherical, the integrated intensity of the 222-reflection J'_{222} is calculated by

$$J'_{222} \propto \int_0^{D/2} 2^3\{(D/2)^2 - x^2\}^{3/2} 2\pi x dx \, .$$

Applying the similar formula for J'_{111}, we get

$$\frac{J'_{222}}{J'_{111}} = \frac{3}{5} \frac{J_{222}}{J_{111}} \, .$$

** Assuming that the size distribution is Gaussian, the integrated intensity of the 222-reflection J''_{222} is calculated by

$$J''_{222} \propto \int_{-\infty}^{+\infty} D^3 \exp(-\alpha(D-D_0)^2) dD \, ,$$

and we get

$$\frac{J''_{222}}{J''_{111}} = \left(1 + \frac{3}{2\alpha D_0^2}\right) \frac{J_{222}}{J_{111}} \, .$$

References

1) H. Raether: Z. Phys. **78** (1932) 527.
2) L. H. Germer: Phys. Rev. **56** (1939) 58.
3) L. H. Germer: Phys. Rev. **61** (1942) 309.
4) R. D. Heidenreich: Phys. Rev. **77** (1950) 271.
5) J. A. Hoerni: Phys. Rev. **102** (1956) 1534.
6) M. Takagi and S. Morimoto: to be published.
7) F. Fujimoto: J. Phys. Soc. Japan **14** (1959) 1558.
8) F. Fujimoto: J. Phys. Soc. Japan **15** (1960) 859.
9) S. Takagi and F. Fujimoto: J. Phys. Soc. Japan **15** (1960) 1607.
10) J. Berghius et al.: Acta Cryst. **8** (1955) 478.
11) R. W. James and G. W. Brindley: Phil. Mag. **12** (1931) 81.
12) Table Relating to Mathieu Functions, U.S. Nat. Bur. Stad. (Columbia Univ. Press, New York, 1951).
13) W. H. Hall: Proc. Phys. Soc. A, **62** (1949) 741.
14) J. S. Halliday: Proc. Roy. Soc. A, **254** (1960) 30.
15) F. Fujimoto and M. Takagi: to be published.

JOURNAL OF THE PHYSICAL SOCIETY OF JAPAN Vol. 16, No. 5, MAY, 1961

The Dipole Moment and End-to-End Length of the Isotactic Vinyl Polymer, III.
Convergence of Neumann Series

By Tsugio MORI

Ôtsu Senior High School, Ôtsu, Shiga-ken, Japan

(Received January 24, 1961)

The theory of dipole moment and end-to-end length of isotactic polymer is described. The problem of convergence of the infinite series in the matrix, which expresses a transformation of the bond vector, is studied in detail, a skeletal chain of linear polymer being regarded as a vector sum of many C–C bond vectors. The method of classifying the chain configurations is given on the basis of the convergence property of the series, which is an extension of the Neumann series. The polymer chain must be Gaussian, if the segments of polymer can rotate independently of each other. The hindrance potential for the internal rotation is assumed to be of the square-well type.

§ 1. Classification of Chain Configurations

We consider the dilute solution of the isotactic vinyl polymer

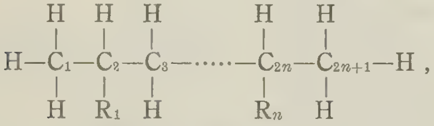

$$\begin{array}{ccccccccccccc} & & \mathrm{H} & & \mathrm{H} & & \mathrm{H} & & \mathrm{H} & & \mathrm{H} & & \\ & & | & & | & & | & & | & & | & & \\ \mathrm{H} & — & \mathrm{C}_1 & — & \mathrm{C}_2 & — & \mathrm{C}_3 & —\cdots\cdots— & \mathrm{C}_{2n} & — & \mathrm{C}_{2n+1} & — & \mathrm{H}\,, \\ & & | & & | & & | & & | & & | & & \\ & & \mathrm{H} & & \mathrm{R}_1 & & \mathrm{H} & & \mathrm{R}_n & & \mathrm{H} & & \end{array}$$

where the skeletal carbon atoms are numbered successively from one end of the skeletal chain, and the notations $\mathrm{R}_1, \cdots, \mathrm{R}_n$ are the numbered dipolar substituents. The mean square dipole moment $\langle\mu^2\rangle$ of this polymer is given by

$$\frac{\langle\mu^2\rangle}{n\mu_0^2}=1+\frac{2}{n}\sum_{i<j}^{n}\sum\langle\cos\omega_{ij}\rangle\,, \qquad (1)$$

where μ_0 is the absolute value of $\boldsymbol{\mu}_i$ which denotes the electric dipole moment vector of the side chain $\mathrm{C}_{2i}—\mathrm{R}_i$, and ω_{ij} is the angle between two vectors $\boldsymbol{\mu}_i$ and $\boldsymbol{\mu}_j$. The mean square end-to-end length $\langle R^2\rangle$ of this polymer is also written in a similar manner. If we put

$$N=2n+1\simeq 2n\,, \qquad (2)$$

we have

$$\frac{\langle R^2\rangle}{Nb_0^2}=1+\frac{1}{n}\sum_{i<j}^{2n}\sum\langle\cos\theta_{ij}\rangle\,, \qquad (3)$$

where b_0 is the absolute value of $\boldsymbol{b}_i$ which denotes the bond vector $\mathrm{C}_i—\mathrm{C}_{i+1}$, and θ_{ij} is the angle between two vectors $\boldsymbol{b}_i$ and $\boldsymbol{b}_j$.

Then the configurations of the polymer skeletal chain are classified as given in Table I which is based upon the order of infinity of the expression

$$\lim_{n\to\infty}\frac{1}{n}\sum_{i<j}^{2n}\sum\langle\cos\theta_{ij}\rangle\,.$$

Therefore, if we wish to calculate $\langle R^2\rangle$, the estimation of $\sum\sum\langle\cos\theta_{ij}\rangle$ is an important problem for us, and it is closely connected with the calculation of $\langle\mu^2\rangle$.

Table I. Classification of chain configurations.

Configuration		$\lim(\sum\sum\langle\cos\theta_{ij}\rangle/n)$
Gaussian chain	Random coil	0
	General Gaussian chain	A const. ($\neq 0$)
Interrupted configuration		The infinity of the order of n^{ν} (where $0<\nu<1$)
Rod configuration (including the crystalline one)		The infinity of the order of n

§ 2. Independent Segment Rotation and Neumann Series

We assume that the polymer skeletal chain in the dilute solution is the connection of many segments as the Markoff process. If the word "segment" signifies the C–C bond itself, and each bond rotates freely only subject to the condition that the bond angle $\pi-\gamma$ and the bond length b_0 are both constant, then (1) and (3) are reduced to

$$\left.\begin{aligned}\frac{\langle\mu^2\rangle}{n\mu_0{}^2}&\longrightarrow 1-\frac{2\alpha^3}{\beta^2}=0.92\\ \text{and}\qquad&\\ \frac{\langle R^2\rangle}{Nb_0{}^2}&\longrightarrow\frac{1+\alpha}{1-\alpha}=2\,,\end{aligned}\right\}\tag{4}$$

respectively. In evaluating this we use the values

$$\alpha=\cos\gamma=\frac{1}{3}\quad\text{and}\quad\beta=\sin\gamma=\frac{\sqrt{8}}{3}\,,\tag{5}$$

where γ is the supplement of the bond angle.

Next, if the segment signifies the monomer $CH_2—CHR$, and the rotations of segments and bonds are hindered by some causes, $\sum\sum\langle\cos\omega_{ij}\rangle$ and $\sum\sum\langle\cos\theta_{ij}\rangle$ are given by

$$\sum_{i<j}^{n}\sum\langle\cos\omega_{ij}\rangle=(001)\,\mathbf{Y}^T\mathbf{X}\left(\sum_{i<j}^{n}\sum\mathbf{X}^{j-i-1}\right)\mathbf{Y}\begin{pmatrix}0\\0\\1\end{pmatrix}\tag{6}$$

and

$$\sum_{i<j}^{2n}\sum\langle\cos\theta_{ij}\rangle=(001)\left\{(\mathbf{Z}+\mathbf{X})\left(\sum_{k<l}^{n}\sum\mathbf{X}^{l-k-1}\right)(\mathbf{1}+\mathbf{Z}')+n\mathbf{Z}'\right\}\begin{pmatrix}0\\0\\1\end{pmatrix},\tag{7}$$

respectively, where $\mathbf{1}$ is the unit matrix, and the notations $\mathbf{X}$, $\mathbf{Y}$, $\mathbf{Y}^T$, $\mathbf{Z}$, $\mathbf{Z}'$ are the matrices given in the preceding papers[1),2)]. The double summation in the right hand sides of these expressions should be read

$$\frac{1}{n}\sum_{i<j}^{n}\sum\mathbf{X}^{j-i-1}=(\mathbf{1}-\mathbf{X})^{-1}\left\{\mathbf{1}+\frac{1}{n}(\mathbf{1}-\mathbf{X})^{-1}(\mathbf{X}^n-\mathbf{1})\right\}\tag{8}$$

when $\mathbf{X}\neq\mathbf{1}$. Here n may be regarded as ∞, for $n=10^2\sim10^5$, and $\mathbf{X}$ is not the number, but the matrix. The infinite geometric series of matrix,

$$\mathbf{1}+\mathbf{X}+\mathbf{X}^2+\cdots\,,$$

is called the Neumann series[3)]. The left hand side of (8) may be regarded as an extension of the Neumann series. Hereupon the following principle can be stated.

Principle 1. The extended Neumann series appears in the calculations of $\langle\mu^2\rangle$ and $\langle R^2\rangle$ so far as we assume that the linear polymer is composed of segments whose rotations are independent of each other.

This principle undergoes no change whatever hindrance the segment rotation suffers. In this way, the convergence of the extended Neumann series becomes our subject.

§ 3. Convergence of Extended Neumann Series, I. General Theory

First we compare two series

$$\mathrm{S}_1=\lim_{n\to\infty}\sum_{i=1}^{n}\mathbf{X}^{i-1}\tag{9}$$

and

$$\mathrm{S}_2=\lim_{n\to\infty}\frac{1}{n}\sum_{i<j}^{n}\sum\mathbf{X}^{j-i-1}\,,\tag{10}$$

where the former is the ordinary Neumann series, and the latter is the extended one. If $\mathbf{X}\neq\mathbf{1}$, we have

$$\mathrm{S}_1=\lim_{n\to\infty}(\mathbf{1}-\mathbf{X})^{-1}(\mathbf{1}-\mathbf{X}^n)\,.$$

Therefore $\lim\mathbf{X}^n$ is a constant matrix if S_1 is convergent. Under this condition, we have

$$\lim_{n\to\infty}\frac{1}{n}\mathbf{X}^n=\mathbf{0}\,,$$

and this formula and (8) yield

$$\mathrm{S}_2=(\mathbf{1}-\mathbf{X})^{-1}\,.$$

In this way, we have the following theorem:

Theorem 1. If the Neumann series S_1 is convergent, then the series S_2 is also convergent.

Next, let us denote the nine elements of $\mathbf{X}$

by X_{kl}:

$$\mathbf{X}=(\mathrm{X}_{kl})=\begin{pmatrix} \mathrm{X}_{11} & \mathrm{X}_{12} & \mathrm{X}_{13} \\ \mathrm{X}_{21} & \mathrm{X}_{22} & \mathrm{X}_{23} \\ \mathrm{X}_{31} & \mathrm{X}_{32} & \mathrm{X}_{33} \end{pmatrix}, \tag{11}$$

and the maximum of the absolute values $|\mathrm{X}_{kl}|$ by X_m, namely,

$$\mathrm{X}_m=\max(|\mathrm{X}_{11}|, |\mathrm{X}_{12}|, \cdots, |\mathrm{X}_{33}|). \tag{12}$$

Then a dominant series of S_1 is

$$(1+\mathrm{X}_m+3\mathrm{X}_m^2+3^2\mathrm{X}_m^3+\cdots)\begin{pmatrix} 1 & 1 & 1 \\ 1 & 1 & 1 \\ 1 & 1 & 1 \end{pmatrix}. \tag{13}$$

This series is convergent when $\mathrm{X}_m<1/3$. Therefore, we conclude that:

Theorem 2. If $\mathrm{X}_m<1/3$, *the Neumann series* S_1 *is convergent.*

Theorem 3. If $\mathrm{X}_m<1/3$, *the series* S_2 *is convergent.*

On the other hand, the following theorem is verified after the diagonalization of S_1 and S_2:

Theorem 4. If all absolute values of eigenvalues of the matrix **X** *are smaller than* 1, *the series* S_1 *and* S_2 *are convergent.*

§ 4. Convergence of Extended Neumann Series, II. Square Well Potential

In the preceding paper[2)], we assumed that the internal rotation of skeletal chain of the polymer was governed by the square well potential,

$$\left.\begin{aligned} V&=0 && (\text{when } 0\leqq|\varphi|\leqq\mathcal{E}) \\ &=\infty && (\text{when } |\varphi|>\mathcal{E}), \end{aligned}\right\} \tag{14}$$

where φ is the rotation angle of the C–C bond, and $2\mathcal{E}$ the parameter which represents the width of the potential well. It was also assumed that the monomer is regarded as the segment, and the linear function

$$\varphi'=\lambda\varphi+\frac{2\pi}{3} \tag{15}$$

was introduced, where the independent variable φ and the dependent variable φ' are the rotation angles of the two adjoining C–C bonds which belong to the same segment. The coefficient λ in (15) is the parameter which signifies a kind of flexibility measure of the segment. In particular, the value $\lambda=0$ corresponds to the rigid segment, and the numerical calculations of $\langle\mu^2\rangle$ and $\langle R^2\rangle$ were carried out in the cases $\lambda=0, 1, -1$. But, in the preceding papers[1),2)], we neglected the discussion whether the extended Neumann series is convergent or not. Then it becomes the main subject of the present paper to verify the convergence of that series with use of the theorems described in § 3.

In the same manner as that of the preceding papers, we can obtain the expressions for nine elements of the matrix **X** under the assumptions (14) and (15), and the results are collected in Table II, where

Table II. X_{kl} expressed as the functions of ε.

	$\lambda=0$	$\lambda=1$	$\lambda=-1$
X_{11}	$-\frac{1}{18}(8+f_1)$	$\frac{1}{18}(1-8f_1-2f_2)$	$-\frac{1}{18}(2+8f_1-f_2)$
X_{12}	$-\frac{\sqrt{3}}{2}f_1$	$-\frac{\sqrt{3}}{6}(1+2f_2)$	$-\frac{\sqrt{3}}{6}(2+f_2)$
X_{13}	$-\frac{\sqrt{2}}{9}(1-f_1)$	$-\frac{\sqrt{2}}{9}(1+f_1-2f_2)$	$\frac{\sqrt{2}}{9}(2-f_1-f_2)$
X_{21}	$\frac{\sqrt{3}}{18}(8+f_1)$	$-\frac{\sqrt{3}}{18}(1-8f_1-2f_2)$	$\frac{\sqrt{3}}{18}(2+8f_1-f_2)$
X_{22}	$-\frac{1}{2}f_1$	$-\frac{1}{6}(1+2f_2)$	$-\frac{1}{6}(2+f_2)$
X_{23}	$\frac{\sqrt{6}}{9}(1-f_1)$	$\frac{\sqrt{6}}{9}(1+f_1-2f_2)$	$-\frac{\sqrt{6}}{9}(2-f_1-f_2)$
X_{31}	$\frac{2\sqrt{2}}{9}(1-f_1)$	$\frac{2\sqrt{2}}{9}(1-f_1)$	$\frac{2\sqrt{2}}{9}(1-f_1)$
X_{32}	0	0	0
X_{33}	$\frac{1}{9}(1+8f_1)$	$\frac{1}{9}(1+8f_1)$	$\frac{1}{9}(1+8f_1)$

$$f_1=\frac{\sin \varepsilon}{\varepsilon} \quad \text{and} \quad f_2=\frac{\sin 2\varepsilon}{2\varepsilon} . \tag{16}$$

According to Table II, we can calculate the values of X_{kl} as the functions of ε within the interval $0\leqq\varepsilon\leqq\pi$, and plot X_{kl} against ε. Corresponding to $\lambda=0, 1, -1$, these plots are illustrated in Figs. 1, 2 and 3, respectively, where the insertion of numerical tables is neglected.

Let us discuss the case $\lambda=1$ as an example in the problem of convergence. It is shown by Fig. 2 that the premise of Theorem 3 is satisfied in the small domain $2.9<\varepsilon\leqq\pi$. However, if we wish to confirm the convergence of the series $\mathbf{S}_2$ in the whole domain $0<\varepsilon\leqq\pi$, we cannot help depending upon Theorem 4, although a further numerical calculation is needed.

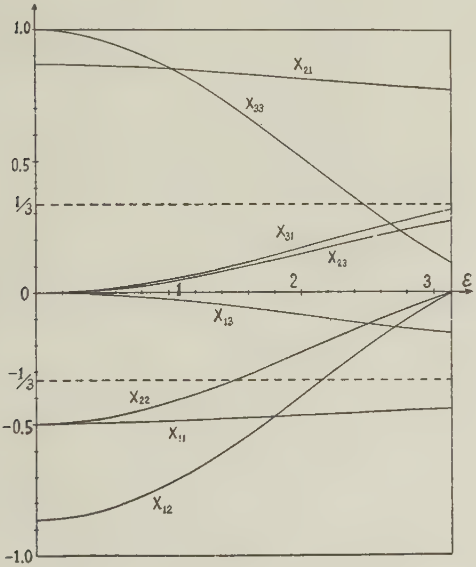

Fig. 1. Plots of X_{kl} against ε in the case $\lambda=0$.

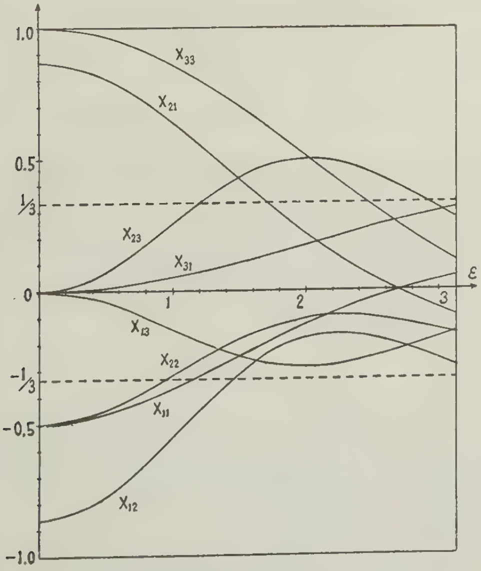

Fig. 2. Plots of X_{kl} against ε in the case $\lambda=1$.

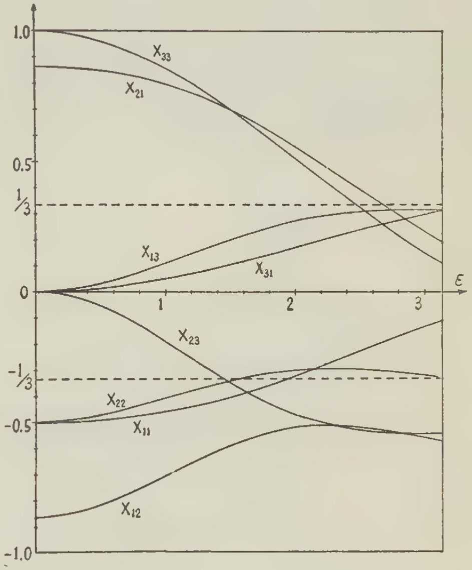

Fig. 3. Plots of X_{kl} against ε in the case $\lambda=-1$.

In this way, we must solve the secular equation of $\mathbf{X}$,

$$|x\mathbf{1}-\mathbf{X}|=\mathbf{0} , \tag{17}$$

and obtain the eigenvalues x_1, x_2 and x_3. If $\lambda=1$ and $\varepsilon=0$, then (17) is reduced to

$$x^3-1=0 ,$$

and the eigenvalues are

$$\left.\begin{matrix} x_1 \\ x_2 \end{matrix}\right\}=\frac{-1\pm\sqrt{3}\,i}{2} \quad \text{and} \quad x_3=1 .$$

If $\lambda=1$ and $\varepsilon=\pi$, then (17) is reduced to

$$x^3+\left(\frac{1}{3}\right)^3=0 ,$$

and the eigenvalues are

$$\left.\begin{matrix} x_1 \\ x_2 \end{matrix}\right\}=\frac{1\pm\sqrt{3}\,i}{6} \quad \text{and} \quad x_3=-\frac{1}{3} .$$

In such a manner, we can obtain various eigenvalues corresponding to values of ε which runs from 0 to π. If these eigenvalues are plotted on the Gaussian plane, then two curves and two straight intervals which are shown in Fig. 4 are generated.

The Gaussian plot thus afforded tells us the solution of our convergence problem. If $\varepsilon=0$, the representative points of the eigenvalues lie on the circumference of the unit circle, and the series S_2 is divergent. However, if $0<\mathcal{E}\leqq\pi$, the representative points of the eigenvalues lie in the unit circle, and the series S_2 is convergent. This result is common to the cases $\lambda=0, 1, -1$. Therefore, if $n\rightarrow\infty$, then $\sum\sum\langle\cos\omega_{ij}\rangle/n$ and $\sum\sum\langle\cos\theta_{ij}\rangle/n$ are convergent in the domain $0<\mathcal{E}\leqq\pi$, but divergent at $\mathcal{E}=0$ which corresponds to the crystalline configuration. Accordingly, we can state the following principle:

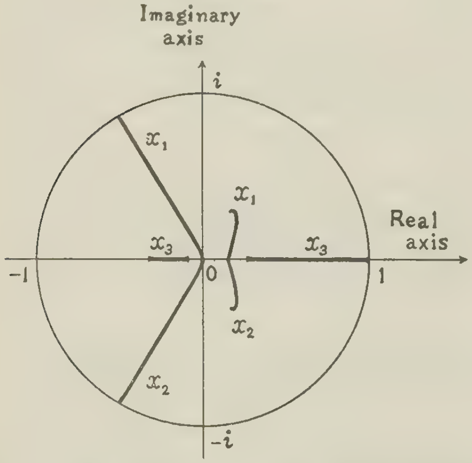

Fig. 4. The Gaussian plot of the eigenvalues of $\mathbf{X}$ in the case $\lambda=1$.

Principle 2. If the linear polymer is composed of segments whose rotations are independent of each other, it must be the Gaussian chain.

This principle has been known in Eyring's case in which the C–C bonds rotate freely and independently of each other[4], and, in this paper, it has been verified that this principle undergoes no change through the replacement of the C–C bonds by the segments which have some flexibility and make the hindered rotation.

§ 5. Discussion

Up to the present, we have used only the square well potential in the treatment of the internal rotation of the polymer chain. Besides it, however, several kinds of potentials may be conceived, e.g., the phonodisk groove potential as given by

$$\left.\begin{aligned} V&=-a\varphi && (\text{when}\quad -\mathcal{E}\leqq\varphi<0) \\ &=a\varphi && (\text{when}\quad 0\leqq\varphi\leqq\mathcal{E}) \\ &=\infty && (\text{when}\quad |\varphi|>\mathcal{E}) \\ &(\text{where}\quad a>0) \end{aligned}\right\}, \quad (18)$$

the harmonic oscillator potential $V=a\varphi^2$, etc. Although these potentials are not studied in this paper, it seems that Principle 2 need not be altered whatever potential we use. On the other hand, so far as we consider $n\rightarrow\infty$, our Principle 2 may undergo no change even if the segment is composed of three or four C–C bonds. Therefore, such a treatment may not be able to afford the interrupted configuration of Table I. However, the Gaussian chain, or the unperturbed configuration, cannot explain the experimental values of $\langle\mu^2\rangle$ and $\langle R^2\rangle$ [2], and hence an actual linear polymer in the solution must take the interrupted configuration. In this way, we are led up to the following imaginations; that is, the segment is composed of many C–C bonds, and sometimes the segment itself contains the crystalline part even in the solution, and the process $n\rightarrow\infty$ is often unadoptable.

If we adopt the above imaginations in the treatments of $\langle\mu^2\rangle$ and $\langle R^2\rangle$, the calculations may be very difficult. Therefore, we keep somewhat the concept of the segment composed of two C–C bonds, and make an attempt to obtain what expressions for $\langle\mu^2\rangle$ and $\langle R^2\rangle$ may represent the interrupted configuration. According to § 3 and § 4, it is evident that

$$\lim_{n\rightarrow\infty}\frac{1}{n}\mathbf{X}^n=\mathbf{0} \qquad (0\leqq\mathcal{E}\leqq\pi) \tag{19}$$

and

$$\lim_{n\rightarrow\infty}\frac{1}{n}(\mathbf{1}-\mathbf{X})^{-1}(\mathbf{X}^n-\mathbf{1})=\mathbf{0} \quad (0<\mathcal{E}\leqq\pi)\,. \tag{20}$$

The formula (20) may be regarded as a mathematical representation of Principle 2, for it reduces S_2 to $(\mathbf{1}-\mathbf{X})^{-1}$ which is independent of n. If we wish to be free from the influence of Principle 2, we must replace the convergent term

$$\frac{1}{n}(\mathbf{1}-\mathbf{X})^{-1}(\mathbf{X}^n-\mathbf{1})$$

by a divergent term $g(n)\mathbf{1}$, where $g(n)$ is a function of n, and is introduced in order to bring the interrupted configuration. Thus we adopt the replacement

$$\frac{1}{n}\sum_{i<j}^{n}\sum\mathbf{X}^{j-i-1}\longrightarrow\{1+g(n)\}(\mathbf{1}-\mathbf{X})^{-1}\,. \tag{21}$$

In the preceding paper¹⁾,

$$g(n)=K(n^{\nu}-1) \tag{22}$$

was attempted as the $g(n)$ term, where the notation ν is the parameter which is also used in Table I. Of course, the three cases $\nu=0$, $0<\nu<1$ and $\nu=1$ correspond to the Gaussian, interrupted and rod configurations, respectively.

In conclusion, some statements which must be corrected are found in the preceding paper¹⁾ after the above discussion, where the correction has already been published as a short note in this Journal⁵⁾.

References

1) T. Mori: J. Phys. Soc. Japan **15** (1960) 1482.
2) T. Mori: J. Phys. Soc. Japan **15** (1960) 1638.
3) R. Courant und D. Hilbert: *Methoden der Mathematischen Physik*, Erster Band, Kap. 1, Berlin Verag von Julius Springer (1931).
4) H. Eyring: Phys. Rev. **39** (1932) 746.
5) T. Mori: J. Phys. Soc. Japan **15** (1960) 2118.

JOURNAL OF THE PHYSICAL SOCIETY OF JAPAN, Vol. 16, No. 5, MAY, 1961

Mathematical Considerations on Chemical Kinetics of Radiation-Induced Polymerization

By Ayao AMEMIYA and Mitio INOKUTI

Department of Applied Physics, Faculty of Engineering,
University of Tokyo, Tokyo, Japan

(Received January 24, 1961)

The chemical kinetics of radiation-induced polymerization is mathematically investigated. The implication of the "stationary state" hypothesis, currently employed in kinetic treatments, is carefully examined. It is shown that the hypothesis is valid only in a certain time interval. Qualitative behaviors of the total number of polymer radicals as well as of polymer molecules as a function of time are derived without resorting to the stationary state hypothesis. In particular, the asymptotic behavior of the total number of radicals proves to be sensitive to the mode of termination reaction. It is also confirmed that the molecular size distribution approaches to the Poisson type asymptotically.

§ 1. Introduction

Recently, experimental researches are carried out on the radiation-induced polymerization of various organic monomers, in which the experimental data are usually analysed in terms of chemical kinetics involving the so-called "stationary state hypothesis". The hypothesis implies, as is well known, that the concentration of radicals or reaction intermediates can be regarded as constant during the over-all process. We have, however, reasons to doubt the validity of the hypothesis in some of radiation-induced polymerization reactions. Firstly, some of the radicals formed during irradiation are quite long-lived, as is shown, for instance, by the decay of radical concentration after irradiation observed by means of electron spin resonance absorption.¹⁾ Secondly, we may sometimes have a very high dose rate, for instance, using charged particle accelerators, and then the substance under irradiation may contain radicals in extremely high concentrations.

In view of the just mentioned situation, we believe that mathematical considerations are necessary concerning the chemical kinetics of radiation-induced polymerizations, and, in particular, the validity of the stationary state hypothesis.

It is well known that the radiation-induced polymerization has many features common to the thermal or catalyst-induced polymerization reaction and that the set of differential equations describing the former is to some extent similar to that appearing in the latter. The only difference consists in the initiation. For, in the case of the radiation-induced polymerization, it is not only a monomer but also a polymer which can be excited, while, only a monomer plays a part in the initiation of the thermal or catalyst-induced polymerization. The difference naturally modifies the set of differential equations we consider, but from mathematical viewpoint, it never introduces an essential difference, but rather brings about a convenience in the formalism.

In our treatment we assume that the rate constant of each of the reactions we consider is independent of time during the over-all process. It may be noted that radical diffusion sometimes modifies rate constants of termination which are known to depend on the spatial distribution of polymer molecules formed (Trommsdorff effect[2]). But our assumption is plausible in the case of the polymerization in a dilute solution.* Anyway, we believe it will never affect essential points of our discussion. Even under the just mentioned assumption, mathematical treatment of the set of differential equations is so difficult on account of the non-linearity that we have not succeeded in obtaining the exact solution.

For this reason, the "stationary state hypothesis", introduced by Bodenstein et al[3], is customarily employed and has proved to be very convenient in many cases. We will examine consequences of this hypothesis in our model reaction scheme and derive some results concerning the behavior of the exact solution without resorting to this hypothesis.**

§ 2. The Model Reaction Scheme

Our reaction scheme is given as follows:

$$\begin{array}{ll} \text{initiation} & \mathrm{M}_s \rightsquigarrow \mathrm{R}_s, \\ \text{propagation} & \mathrm{R}_s+\mathrm{M}_t \rightarrow \mathrm{R}_{s+t}, \\ \text{disproportionation} & \mathrm{R}_s+\mathrm{R}_t \rightarrow \mathrm{M}_s+\mathrm{M}_t, \\ \text{radical transfer} & \mathrm{R}_s+\mathrm{M}_t \rightarrow \mathrm{M}_s+\mathrm{R}_t, \\ \text{recombination} & \mathrm{R}_s+\mathrm{R}_t \rightarrow \mathrm{M}_{s+t}, \end{array} \tag{1}$$

where M_s and R_s stand for the polymer molecule and the polymer radical with degree of polymerization s, respectively. Here we list the symbols we use in the following:

τ: time measured from the beginning of irradiation,
I: dose rate,
k_i: rate constant of initiation per unit dose rate***,
k_p: rate constant of propagation***,
k_d: rate constant of disproportionation***,
k_x: rate constant of radical transfer***,
k_c: rate constant of recombination***,
M_s: ratio of the number of polymer molecules with degree of polymerization s to the total number of monomers at $\tau=0$,
R_s: ratio of the number of polymer radicals with degree of polymerization s to the total number of monomers at $\tau=0$.

Then our set of differential equation reads:

$$\begin{aligned} \frac{dM_s}{d\tau} = & -k_i I M_s - k_p M_s \sum_{t=1}^{\infty} R_t + k_d R_s \sum_{t=1}^{\infty} R_t + \underline{k_d R_s{}^2} + k_x R_s \sum_{t=1}^{\infty} M_t \\ & -k_x M_s \sum_{t=1}^{\infty} R_t + \frac{1}{2} k_c \left[\sum_{h=1}^{s-1} R_h R_{s-h} \right], \end{aligned} \tag{2}$$

---

* In a dilute solution, the possibility of some solvent effect cannot be excluded, but we will not deal with it in the present work.

** Recently, Kyner et al[4] published a work on a subject apparently similar to ours, but it should be noted that non-linear terms, in which the very difficulty consists, do not appear in their scheme and in this respect their problem is quite different from ours.

*** Rigorously speaking, these rate constants may depend on the degree of polymerization, but we regard them as constant here.

$$\begin{aligned}\frac{dR_s}{d\tau} &= k_i I M_s - k_p R_s \sum_{t=1}^{\infty} M_t + k_p \sum_{h=1}^{s-1} M_h R_{s-h} - k_d R_s \sum_{t=1}^{\infty} R_t - \underline{k_d R_s^2} \\ &\quad - k_x R_s \sum_{t=1}^{\infty} M_t + k_x M_s \sum_{t=1}^{\infty} R_t - k_c R_s \sum_{t=1}^{\infty} R_t - \underline{k_c R_s^2}\end{aligned}$$

where

$$\left[\sum_{h=1}^{s-1} R_h R_{s-h}\right] = \begin{cases} \displaystyle\sum_{h=1}^{s-1} R_h R_{s-h} & \text{for odd } s, \\ \displaystyle\sum_{h=1}^{s-1} R_h R_{s-h} + \underline{R_{s/2}^2} & \text{for even } s. \end{cases} \tag{3}$$

It is convenient to regard the degree of polymerization as a continuous rather than discrete variable, and to rewrite $M_s(\tau)$ and $R_s(\tau)$ as $M(s, \tau)ds$ and $R(s, \tau)ds$ respectively, so that we can replace summation by integration.*

Then we have

$$\begin{aligned}\frac{dM(s, \tau)}{d\tau} &= -k_i I M(s, \tau) - \{(k_p + k_x) M(s, \tau) - k_d R(s, \tau)\} \int_1^{\infty} R(t, \tau) dt \\ &\quad + k_x R(s, \tau) \int_1^{\infty} M(t, \tau) dt + \frac{k_c}{2} \int_1^{s} R(h, \tau) R(s-h, \tau) dh\,, \\ \frac{dR(s, \tau)}{d\tau} &= k_i I M(s, \tau) - (k_c + k_d) R(s, \tau) \int_1^{\infty} R(t, \tau) dt \\ &\quad - (k_x + k_p) R(s, \tau) \int_1^{\infty} M(t, \tau) dt + k_p \int_1^{\infty} M(h, \tau) R(s-h, \tau) dh \\ &\quad + k_x M(s, \tau) \int_1^{\infty} R(t, \tau) dt\,.\end{aligned} \tag{4}$$

Further we define the n-th moments of the degree of polymerization with respect to the distributions $M(s, \tau)$ and $R(s, \tau)$ as

$$m_n(\tau) = \int_1^{\infty} s^n M(s, \tau) ds\,, \qquad r_n(\tau) = \int_1^{\infty} s^n R(s, \tau) ds\,. \tag{5}$$

It is easy to derive from (4) the following equation for the moments:

$$\begin{aligned} dr_0/d\tau &= k_i I m_0 - (k_c + k_d) r_0^2 \\ dm_0/d\tau &= -k_i I m_0 - k_p m_0 r_0 + [(k_c/2) + k_d] r_0^2\,. \end{aligned} \tag{6}$$

$$\begin{aligned} dr_1/d\tau &= k_i I m_1 - (k_c + k_d) r_0 r_1 - k_x m_0 r_1 + (k_p + k_x) r_0 m_1\,, \\ dm_1/d\tau &= -k_i I m_1 - (k_p + k_x) r_0 m_1 + k_x m_0 r_1 + (k_c + k_d) r_0 r_1\,. \end{aligned} \tag{7}$$

$$\begin{aligned} dr_2/d\tau &= k_i I m_2 - (k_c + k_d) r_0 r_2 - k_x m_0 r_2 + (k_p + k_x) r_0 m_2 + 2 k_p m_1 r_1\,, \\ dm_2/d\tau &= -k_i I m_2 - (k_p + k_x) r_0 m_2 + (k_c + k_d) r_0 r_2 + k_x m_0 r_2 + k_c r_1^2\,. \end{aligned} \tag{8}$$

We have by (7)

$$d(r_1 + m_1)/d\tau = 0\,, \qquad r_1 + m_1 = 1\,. \tag{9}$$

This assures the conservation of total number of monomers.** Thus (7) can be rewritten as

---

* When we regard s as continuous, the underlined terms in Eqs. (2) and (3) are higher infinitesimals and may be neglected.

** This conservation law also holds even when we regard s as discrete. In other words, it holds exactly.

$$dm_1/d\tau=-[k_iI+(k_p+k_x+k_c+k_a)r_0+k_xm_0]m_1+k_xm_0 \\ +(k_c+k_a)r_0\ , \qquad r_1=1-m_1\ . \tag{7'}$$

We observe by (6), (7′), and (8) that m_1, r_1, r_2, and m_2 can be obtained as a solution of linear differential equation, once the non-linear equations are solved to give $r_0(\tau)$ and $m_0(\tau)$ and this non-linearity is the very subject of our discussion.

In what follows (except in Section 9), we will work with the case where no radical exists at $\tau=0$, or with the initial condition $R(s,\ 0)=0$.

§ 3. The Meaning of the Stationary State

The stationary state hypothesis is generally interpreted in either of the following two ways. The first interpretation implies that we can assume that $dr_0/d\tau=0$ for $\tau_1<\tau<\tau_2$ or that there exist such τ_1 and τ_2 that $r_0=$const. for $\tau_1<\tau<\tau_2$.[5]

The second interpretation is more general, implying that

$$|dr_0/d\tau|\ll|dm_0/d\tau|$$

for $\tau_1<\tau<\tau_2$.[6]

The first interpretation requires that $r_0=r_{00}=$const. Therefore, we have

$$m_0(\tau)=[m_{00}+(k_cr_{00}/2k_p)]\exp[-k_pr_{00}(\tau-\tau_1)]-(k_cr_{00}/2k_p)$$

by (6) under the condition that $m_0=m_{00}$ at $\tau=\tau_1$.

Since $m_0>0$ for any τ, we have

$$\tau_2-\tau_1\leqq(k_pr_{00})^{-1}\log[1+(2m_{00}k_p/k_cr_{00})]\ .$$

This gives the range where the stationary state hypothesis is possible.

On the other hand, using $dr_0/d\tau=0$ and (6), we have

$$k_iI=\frac{(k_c+k_a)r_{00}^2}{[m_{00}+(k_cr_{00}/2k_p)]\exp[-k_pr_{00}(\tau-\tau_1)]-(k_cr_{00}/2k_p)}\ .$$

Thus, if we adopt the first interpretation, we have a definite functional dependence of k_iI in time τ, which is evidently unphysical. Consequently, the first interpretation is unreasonable so that we will adopt the second one.[5]

§ 4. The Expansion with Respect to Time

In order to examine the initial stage, we expand r_0 etc. with respect to τ. For simplicity, we regard k_iI as constant hereafter and put $k_iI\tau=t$, $k_p/k_iI=a$, $(k_c+k_a)/k_iI=b$, $(k_c/2+k_a)/k_iI=c$, $k_x/k_iI=e$. Further, we adopt the initial condition that $r_0=r_1=r_2=0$, $m_0=m_1=m_2=1$ at $t=0$.

$$\begin{aligned} r_0&=t-(t^2/2!)+[t^3(1-a-2b)/3!]+\cdots\cdots\cdots\ , \\ m_0&=1-t+[t^2(1-a)/2!]+[t^3(-1+4a+2c)/3!]+\cdots\cdots\cdots\ , \\ m_1&=1-r_1=1-t+[t^2(1-a)/2!]+[t^3(-1+4a+2b+ae)/3!]+\cdots\cdots\cdots\ , \\ r_2&=t-[t^2(1-3a)/2!]+[t^3(1-2b-10a-3ae+2a^2)/3!]+\cdots\cdots\cdots\ , \\ m_2&=1-t+[t^2(1-a)2/!]+[t^3(-1+4a+6b-4c+3ae)3!]+\cdots\cdots\cdots\ . \end{aligned} \tag{10}$$

Therefore

$$\begin{aligned} m_1/m_0&=1+[t^3(2b-2c+ae)/6]+\cdots\cdots\cdots\ , \\ m_2/m_1&=1+[t^3(2b-2c+ae)/3]+\cdots\cdots\cdots\ , \\ (m_1+r_1)/(m_0+r_0)&=1+(t^2a/2)-[t^3(3a-2b+2c)/6]+\cdots\cdots\cdots\ , \\ (m_2+r_2)/(m_1+r_1)&=1+at^2+[t^3(-3a+2b-2c+a^2)/3]+\cdots\cdots\cdots\ , \end{aligned} \tag{10'}$$

where the last two quantities correspond to the number-average and the weight-average degree of polymerization, respectively.

It should be noted here that the above expansion with respect to t converges for any finite value of t. This fact can be proved by a general theorem concerning the differential equation of the first order.[7]

In each of the above expansion, the constant a begins to appear in the second order term, and the other rate constants in the third order. In particular, e does not appear in $(m_1+r_1)/(m_0+r_0)$ or $(m_2+r_2)/(m_1+r_1)$. This fact means that the effect of radical transfer presents itself only after a considerable time interval. In Fig. 1, the behaviors of $m_0=1-x$, $m_1=u$, $r_0=y$, $m_2=v$, and $r_2=w$ near $t=0$, are schematically shown.

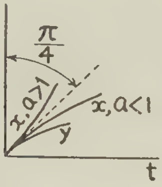

Fig. 1 a.

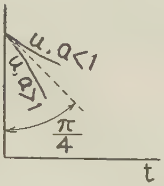

Fig. 1 b.

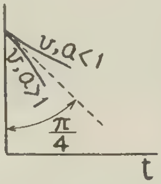

Fig. 1 c.

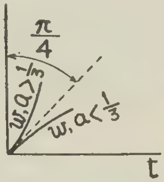

Fig. 1 d.

§ 5. Relation between the Total Number of Radicals and that of Molecules

For convenience, we put $r_0=y$, $m_0=1-x$ and rewrite (6) as*

$$\dot{x}=(1-x)(1+ay)-cy^2\,, \qquad \dot{y}=1-x-by^2\,, \tag{11}$$

where $x(t)$ and $y(t)$ are to satisfy the initial condition $x(0)=y(0)=0$.

If we regard y as a function of x, we obtain by (11) the differential equation.*

$$y'(x)=P(x,\ y)/Q(x,\ y)\,, \qquad P(x,\ y)=1-x-by^2\,, \qquad Q(x,\ y)=(1-x)(1+ay)-cy^2\,, \tag{12}$$

with the initial condition that $y=0$ for $x=0$. According to Painlevé's theorem,[8] the immovable singularities of $y(x)$ are $x=1$, $y=0$ and $x=1-[(b-c)^2/a^2b]$, $y=-(b-c)/ab$, and the movable singularities are algebraic branch points. A little calculation shows that the value of y'' at a point where $y'=0$ is negative in the region where $y>0$, that if $y(x)$ has an extremum, it must be a maximum.

In order to trace the curve for $y=y(x)$, it is convenient to use the curves $P=0$ and $Q=0$. In Fig. 2, we see $P>0$, $Q>0$ in region I. $P<0$, $Q>0$ in region II, and $P<0$, $Q<0$ in region III. Further $dy/dx=\infty$ on the boundary between II and III. Since $y=y(x)$ is a differentiable function, it passes the origin $x=y=0$, increases monotonically to reach a maximum on the boundary between I and II and then decreases monotonically in II to approach the point $x=1$, $y=0$. It never enters the interior of region III. Otherwise, $y(x)$ or $y'(x)$ would be discontinuous on the boundary between II and III.

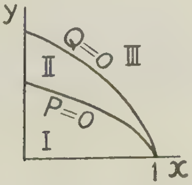

Fig. 2.

In order to determine the behavior of $y=y(x)$, we consider a function $Y_u(x)$ such that

$$Y_u'=(1+aY_u)^{-1}\,, \quad Y_u(0)=0\,,$$

namely,

$$x=Y_u+(aY_u^2/2)\,. \tag{13}$$

Evidently, $Y_u(x)>y(x)$ in the regions I and II. On the other hand, if we define $Y_l(x)$ as

---

* We will hereafter denote differentiation with respect to t and x by dot and prime, respectively. For example, $\dot{x}=dx/dt$, $y'=dy/dx$, $y''=d^2y/dx^2$.

$$Y_l'=(1-x-bY_l^2)/[(1+a/\sqrt{b})(1-x)]\,, \qquad Y_l(0)=0\,, \tag{14}$$

then $y(x)>Y_l(x)$ in the region I. For, since the maximum of $y(x)$ is given by $P=0$, we get $y<1/\sqrt{b}$, and the maximum of $Y_l(x)$ also lies on the curve $P=0$ as is easily seen. If $Y_l(x)$ and $y(x)$ interesects with each other in II, we shall have $y(x)<Y_l(x)$ on the right side of the point of intersection.

To solve Eq. (14), we put

$$X=\sigma(1-x)^{1/2}\,, \qquad \sigma=2b/(a+\sqrt{b})\,,$$

so that the initial condition is written as $Y=0$ for $X=\sigma$. Further the transformation

$$Y_l=-\frac{X}{\sigma\sqrt{b}}\frac{d}{dX}[\log w(X)]$$

yeilds the following equation for $w(X)$:

$$X(d^2w/dX^2)+(dw/dX)-Xw=0\,.$$

Therefore, by making use of the initial condition, we have

$$Y_l=-\frac{X}{\sigma\sqrt{b}}\cdot\frac{I_1(X)K_1(\sigma)-K_1(X)I_1(\sigma)}{I_0(X)K_1(\sigma)+K_0(X)I_1(\sigma)}\,, \tag{15}$$

where $I_n(X)$ and $K_n(X)$ are the modified Bessel functions of the nth order.

For $|X|\ll 1$, Y_l is approximated as

$$Y_l\cong-\frac{1}{\sigma\sqrt{b}}\left\{(\log X)^{-1}+\frac{K_1(\sigma)+CI_1(\sigma)}{I_1(\sigma)}(\log X)^{-2}\right\},$$

where C is the Euler constant. Since $Y_l(\sigma)=0$, there exists an extremum in the interval $0<X<\sigma$ according to Weierstrass' theorem. It is clear that this extremum is a maximum given by $Y_l=X/\sigma\sqrt{b}$ and it is just at the point where $y=Y_l(X)$ and $P=0$ intersect with each other. The value of X corresponding to the maximum is given as the root of the equation.

$$[I_0(X)+I_1(X)]/I_1(\sigma)=[K_1(X)-K_0(X)]/K_1(\sigma)\,,$$

The uniqueness of the root follows from the fact that the left-hand side of the above equation is a monotonically increasing function of X and the right-hand side a monotonically decreasing function.

Next we examine the behaviours of $P=0$. $Q=0$, $Y_l=Y_l(x)$ and the solution $y=y(x)$ of (12) in the neighborhood of $x=1$, or $X=0$. From $P=0$, we have

$$y=X/\sqrt{b}\,\sigma\,,$$

and from $Q=0$,

$$y=(X/\sigma\sqrt{c})+(X^2a/2c\sigma^2)+\cdots\cdots\cdots\,.$$

As seen in Section 7, the solution $y(x)$ of (12) in the neighborhood of $y=1$ satisfies

$$cy^2(1+ay)^{-1}<1-x<by^2\,,$$

so that it can be expanded as

$$1-x=cy^2+L_1y^3+\cdots\cdots\cdots\,,$$

where L_1 is a constant. This equation can be solved with respect to $y(X)$ to give

$$y(X)=\frac{X}{\sigma\sqrt{c}}-\frac{2(b-c)-a}{2\sigma^2 c}X^2+\cdots\cdots\cdots,$$

comparing this result with the behaviors of $P=0$, $Q=0$, $y=Y_u(x)$ and $y=Y_l(x)$ near $x=1$, we have the graph in Fig. 3.

Consequently, we can conclude from the above results that the curve $y=y(x)$ will behave as shown in Fig. 4.

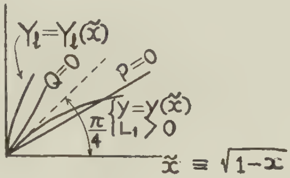

Fig. 3.

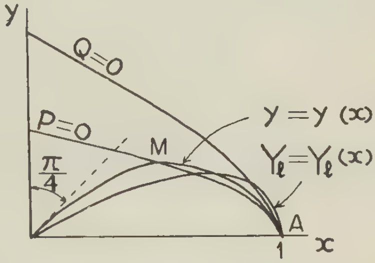

Fig. 4.

§ 6. The Validity of the Stationary State Hypothesis

The second interpretation of the stationary state hypothesis leads to the assumption that $y(x)$ should be approximately given by $P=0$, and therefore it will be possible only between the maximum M and the zero A. (Fig. 4)

Putting

$$bz^2=1-x\,, \qquad y=z(x)+\xi(x)$$

in (12) and neglecting ξ^2 under the assumption $|z(x)|\gg|\xi(x)|$, we have

$$\xi'=(2bz)^{-1}-[2b/z(abz+b-c)]\xi\ .$$

This equation can be solved under the condition

$$\xi=0 \qquad \text{for} \quad x=x_0$$

to give

$$\xi=\frac{\eta_0}{b(a-4b)}\left[\left(\frac{\eta}{\eta_0}\right)^{4b/a}-\frac{\eta}{\eta_0}\right],$$

where $abz+b-c=\eta$, $abz_0+b-c=\eta_0$. The function $\xi(\eta)$ proves to be zero at $\eta=0$ and $\eta=\eta_0$, and to have a maximum

$$\begin{array}{ll} \left(\dfrac{\eta_0}{4b^2}\right)\left(\dfrac{a}{4b}\right)^{a/(4b-a)} & \text{for } b-c=\eta_0[a/4b]^{a/(4b-a)} \\ \dfrac{\eta_0}{b(a-4b)}\left[\left(\dfrac{b-c}{\eta_0}\right)^{4b/a}-\dfrac{b-c}{\eta_0}\right] & \text{for } b-c>\eta_0[a/4b]^{a/(4b-a)} \end{array}$$

This estimation is permissible only if the term proportional to ξ^2 is negligibly small as compared with that proportional to ξ in the equation determining ξ and $|\xi/z|<\varepsilon$ where ε is a sufficiently small positive number, since $z\to 0$ for $x\to 1$. Introducing the notation $\eta/\eta_0=\lambda$, $4b/a=\nu$ and $(b-c)/\eta_0=\theta$, ξ/z is written as

$$\xi/z=(\lambda^\nu-\lambda)(1-\nu)^{-1}(\lambda-\theta)^{-1}\ .$$

Thus ξ/z is a monotonically decreasing function of λ between $\lambda=\theta$ and $\lambda=1$, $\xi/z\to\infty$ for $\lambda\to\theta$ and $\xi/z=0$ for $\lambda=1$ (for any value of ν). If we define λ_ε as the value of λ satisfying

$$(\lambda^\nu-\lambda)(1-\nu)^{-1}(\lambda-\nu)^{-1}=\varepsilon\ ,$$

it is nearly unity for sufficiently small ε and can be expanded as

$$\lambda_\varepsilon=1-(1-\theta)\varepsilon+(1-\theta)[1-\nu(1-\theta)/2]\varepsilon^2+\cdots\cdots\cdots\cdots .$$

The second equation of (11) is written as

$$\dot{\lambda}(t)=-[\eta_0/2b(1-\nu)][(1-\nu)(\lambda-\theta)\lambda+(\lambda-\varphi)(\lambda^\nu-\lambda)] .$$

where $\varphi=(b+c)/\eta_0$. Putting $t=t_1$ for $\lambda=1$ and $t=t_2$ for $\lambda=\lambda_\varepsilon$, we integrate the above equation and obtain

$$t_2-t_1=[2b(1-\nu)/\eta_0]\int_{\lambda_\varepsilon}^{1}[(1-\nu)(\lambda-\theta)\lambda+(\lambda-\varphi)(\lambda^\nu-\lambda)]^{-1}d\lambda .$$

This expression can be simplified for small ε, by making use of the above expansion of λ_ε, in the following form:

$$t_2-t_1=[2b/\eta_0][\varepsilon-\{1+\theta-\varphi-\nu(1-\theta)\}\varepsilon^2/2+\cdots\cdots\cdots\cdots] .$$

The effect of the term proportional to ξ^2 can be estimated as follows. First we note that the equation for $\xi(\lambda)$ is written as

$$\frac{d\xi}{d\lambda}=-\frac{\eta_0}{ab}+\frac{\nu\xi}{\lambda}\left\{1+\frac{ab(2\varphi-\lambda)}{2\eta_0\lambda(\lambda-\theta)}\xi\right\}+O(\xi^3) ,$$

where the second term proportional to ξ in the curly bracket may be written, replacing ξ by the approximate value $\eta_0[(\lambda^\nu-\lambda)/ab(1-\nu)]$, as

$$\frac{1}{2(1-\nu)}\cdot\frac{(\lambda^\nu-\lambda)(2\varphi-\lambda)}{\lambda(\lambda-\theta)}\leqq\frac{1}{2(1-\nu)}\cdot\frac{(\lambda_\varepsilon{}^\nu-\lambda_\varepsilon)(2\varphi-\lambda_\varepsilon)}{\lambda_\varepsilon(\lambda_\varepsilon-\theta)}\cong[(2\varphi-1)\cdot\varepsilon/2] .$$

Consequently, the range of applicability of the stationary state hypothesis is established by calculating t_2-t_1 or λ_ε, where λ_ε is determined in the following way. Given a sufficiently small positive number ε_0. We first determine ε so as to satisfy

$$|(2\varphi-1)\cdot\varepsilon/2|=\varepsilon_0 , \tag{18}$$

and then find λ_ε using this value of ε.

§ 7. The Estimation of the Numbers of Molecules and Radicals

The number of radicals is given by $r_0=y(t)$, the variation of which is described by the following differential equation of the second order deduced by eliminating x in (11)

$$\ddot{y}+(1+2\alpha y)\dot{y}+\beta y^3+\gamma y^2=0 ,$$

where $2\alpha-2b+a$, $\beta=ab$, $\gamma=b-c$. We impose on $y(t)$ the initial conduction that $y=0$, $dy/dt=1$ at $t=0$.

According to investigations of Painlevé and others,8) the equation (11) is known to have movable algebraic singularities, but does not belong to the so-called "canonical type" of their classification, so that it is very difficult to discuss the nature of the solution of (12) in a straightforward manner. Here we will discuss it in a somewhat different way from Painlevé and others'.

In the previous section, we proved that

$$1>y\geqq 0 , \qquad \lim_{x\to 1-0} y(x)=0 .$$

Further it can be shown by (11) that, if $y(t)$ has an extremum, it must be a maximum so that $y(t)$ cannot be a oscillatory function.

We rewrite (11) by making use of the initial condition as

$$y=t-\int_0^t y\,dt-\alpha\int_0^t y^2dt-\int_0^t dt\int_0^t(\beta y^3+\gamma y^2)dt\,.$$

Now we assume that the total number of radicals $y(t)$ reaches a finite saturation value L, or that $y(t)=L>0$ for $t>G$ where G is sufficiently large positive number. Then, for $t>G$,

$$y\cong t-\int_0^G\left[y+\alpha y^2+\int_0^t(\beta y^3+\gamma y^2)dt\right]dt-\int_G^t[L+\alpha L^2-t(\beta L^3+\gamma L^2)]dt$$
$$-\left[t\int_0^t(\beta y^3+\gamma y^2)dt\right]_{t=G}^{t=t}\equiv\Phi_0(G)+\Phi_1(G)t-[(\beta L^3+\gamma L^2)/2]t^2\,.$$

According to this equation, $y(t)$ decreases parabolically for sufficiently large t. This is inconsistent with the assumption $y(t)\cong L>0$. Thus we see that the assumption was false and that no positive saturation value exists. Since on the other hand y cannot be negative as seen in Fig 4, we conclude that

$$\lim_{t\to+\infty} y(t)=+0\,.$$

Further, since the curve $y=y(x)$ lies in the region II in the neighborhood of $x=1$, we have

$$by^2>1-x>cy^2(1+ay)^{-1}\,.$$

Therefore, we may substitute

$$1-x=\sum_{s=0}^{\infty}L_sy^s$$

into (11) and obtain

$$L_0=c\,,\qquad L_1=2c\gamma-ac\,.$$

Using this result, we have, by (2),

$$t=(\gamma y)^{-1}-L_1\gamma^{-2}(\log y)+O(1)\,,$$

where we have assumed that $\gamma>0$. We can solve this equation with respect to y to obtain

$$r_0=y=(\gamma t)^{-1}[1+L_1\gamma^{-2}(\log t)/t]+\cdots\cdots\cdots\,. \tag{20}$$

Thus x is also found as

$$m_0=1-x=c(\gamma t)^{-2}[1+2L_1\gamma^{-2}(\log t)/t]+\cdots\cdots\cdots\,. \tag{21}$$

In particular, if $\gamma=0$ or $b=c$ ($k_c=0$), we have different expressions:

$$\begin{aligned} r_0=y&=(2\beta t)^{-1/2}+(\alpha/\beta t)-(3/4\sqrt{2\bar{\beta}})(\log t)/t^{3/2}+\cdots\cdots\cdots\,,\\ m_0=1-x&=(2at)^{-1}+[(4b+a)/2a(2\beta)^{1/2}]t^{-3/2}-(3/4a)(\log t)/t^2+\cdots\cdots\cdots\,. \end{aligned} \tag{20'}$$

It is easily shown that we have $x\geqq y$ for any finite value of t and x at a point where $x=0$ is positive. Further, $x_l(t)$ and $x_u(t)$ are an upper and lower bounds of $x(t)$, which are defined as follows:

$$\dot{x}_l=1-x_l-cx_l^2\,,\quad x_l(0)=0\,,\qquad \dot{x}_u=(1-x_u)(1+ax_u)\,,\quad x_u(0)=0\,. \tag{22}$$

Again, we can also find such $y_l(t)$ and $y_u(t)$ that

$$y_l(t)<y<y_u(t)\,.$$

The functions $y_l(t)$ and $y_u(t)$ are defined by

$$\dot{y}_l=1-x_u-by_l^2\,,\quad y_l(0)=0\,,\qquad \dot{y}_u=1-by_u^2\,,\quad y_u(0)=0\,. \tag{23}$$

These informations tell us that the behavior of $x=x(t)$ and $y=y(t)$ will be as shown in Fig. 5, and Fig. 6.

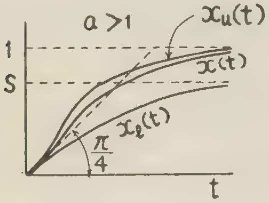

Fig. 5a.

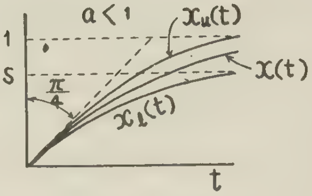

Fig. 5b.

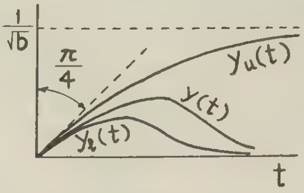

Fig. 6.

§ 8. The Estimation of Higher Moments

The equations (7), (8) for m_1, r_2 and m_2 read:

$$m_1=-(F+G)m_1+G\,, \quad r_2=Fm_2-Gr_2+2am_1(1-m_1)\,, \quad m_2=-Fm_2+Gr_2+2(b-c)(1-m_1)^2\,, \tag{24}$$

where

$$F=1+(a+e)y\,, \quad G=by+e(1-x); \qquad m_1=m_2=1\,, \quad r_2=0 \text{ for } t=0\,. \tag{25}$$

Once the t-dependence of F and G is determined, these equations can be easily integrated. But, since analytic expressions for $x(t)$ and $y(t)$ have not yet been obtained, it is impossible to express m_1, r_2 and m_2 as explicit functions of t. It is also difficult to find these functions by the method used in Section 7. We can only determine an upper and a lower bound of m_1:

$$\begin{aligned} &u_1>m_1>u_2\,, \\ &u_1=(1+a+b+2e)^{-1}\{a+b+2e+\exp[-(1+a+b+ae)t]\}\,, \\ &u_2=\exp[-(a+e+1)t]\,. \end{aligned} \tag{26}$$

The behaviors of the function m_1, r_2 and m_2 for large t are given by putting (20), (21) or (20′), (21′) into (24) and (25). Here we give only the final result:
For $\gamma>0$,

$$\begin{aligned} m_1&=b(\gamma t)^{-1}[1+L_1\gamma^{-2}(\log t)/t]+\cdots\cdots\cdots\,, \\ m_2&=2(b+\gamma)-(2bL_1/c\gamma)(\log t)/t+\cdots\cdots\cdots\,, \\ r_2&=2\gamma t-(2bL_1/c\gamma)\log t+\cdots\cdots\cdots\,. \end{aligned} \tag{27}$$

For $\gamma=0$,

$$\begin{aligned} m_1&=b(2\beta t)^{-1/2}+b(2at)^{-1}-[3b/4(2\beta)^{1/2}](\log t)/t^{3/2}+\cdots\cdots\cdots\,, \\ m_2&=2b+\cdots\cdots\cdots\,, \\ r_2&=2(\beta t)^{1/2}+\cdots\cdots\cdots\,. \end{aligned} \tag{27′}$$

The number-average degree of polymerization $(m_1+r_1)/(m_0+r_0)=1/(1-x+y)$ is a monotonically increasing function of t with the asymptotic form for large t

$$\begin{aligned} 1/(1-x+y)&=\gamma t-L_1\gamma^{-1}\log t+\cdots\cdots\cdots && (\gamma>0)\,, \\ &=(2\beta t)^{1/2}-(a+3b)+\cdots\cdots\cdots && (\gamma=0)\,. \end{aligned} \tag{28}$$

The weight-average degree of polymerization $(m_2+r_2)/(m_1+r_1)=m_2+r_2$ is also a monotonically increasing function of t with the asymptotic form for large t

$$\begin{aligned} m_2+r_2&=2\gamma t-(2bL_1/c\gamma)\log t+\cdots\cdots\cdots && (\gamma>0)\,, \\ &=2(2\beta t)^{1/2}+\cdots\cdots\cdots && (\gamma=0)\,. \end{aligned} \tag{29}$$

The fact that the ratio of the weight-average to the number-average degree of polymerization tends to 2 for large t tells us that the distribution in a sufficiently polymerized system approaches to the Poisson type, as reasonably expected. In Fig. 7, we give schematic curves for the average degrees of polymerization.

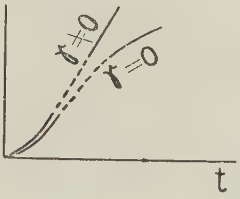

Fig. 7.

It should be noted that the average degrees of polymerization are independent of the recombination rate k_c in the initial stage (see Eqs. (10) and (10′)), but that, for large total dose or after sufficient time interval, they exhibit different dose dependence according as $\gamma>0$ or $\gamma=0$. Namely, the average degrees of polymerization tend to be proportional to D/I for $\gamma>0$ and to $D^{1/2}/k_t I$ for $\gamma=0$, where D means the total dose $D=I\tau$.

§ 9. Solution with a Different Initial Condition

So far we have dealt with the case where only monomer molecules are present at $t=0$. In this section we consider a more general initial condition that that $x=x_i$, $y=y_i$ at $t=0$, which implies that some monomer radicals exist at $t=0$. Analysis similar to that in Section 5 give informations about the behavior of r_0 and m_0. The resulting curves* are shown in Fig. 8 and Fig. 9.

Under the initial condition considered in this section we cannot use the method in Section 6 in order to examine the validity of the stationary state hypothesis. In what follows, we describe a different approach to somewhat rough estimation which gives a sufficient condition for the validity.

Denoting the ordinate for any x of the $P=0$ and the curve $Q=0$ by y_p and y_q, respectively, the quantity

$$l=(y_q-y_p)/y_p$$

can be interpreted as measure of validity, because in the stationary state $y_q=y_p$. By definition l satisfies

$$(c/b)(1+l)^2-ab^{\;1/2}(1-x)^{1/2}(1+l)-1=0\ .$$

When we regard l as a function of $(1-x)^{1/2}$ we have a curve as shown in Fig. 10.

Now we may define the precision ε of the stationary state approximation by

$$|(y-y_p)/y_q|<\varepsilon\ . \tag{30}$$

Thus, provided that $\varepsilon>l_1=(b/c)^{1/2}-1$, the stationary state approximation is reasonable in the sense that by (30) holds in the interval $0<x<x_\varepsilon$, where x_ε is given by

$$(c/b)(1+\varepsilon)^2-ab^{-1/2}(1-x_\varepsilon)^{1/2}(1+\varepsilon)-1=0\ . \tag{31}$$

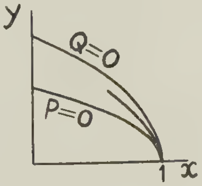

Fig. 8 a.

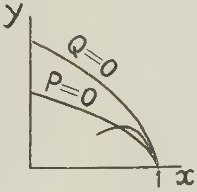

Fig. 8 b.

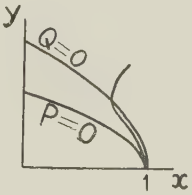

Fig. 8 c.

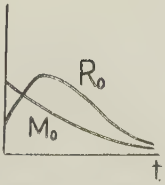

Fig. 9 a.

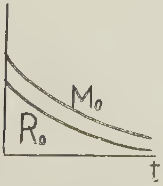

Fig. 9 b.

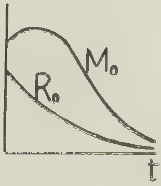

Fig. 9 c.

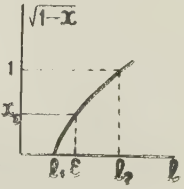

Fig. 10.

---

* When we analyse a very simple model of kinetics treated by Hirschfelder[10] according to our method, the resulting curve are very similar to those shown in Fig. 9. (Unpublished)

This result can be as a criterion for the validity of the stationary state approximation.

§ 10. Concluding Remarks

In conclusion, we will summarize our results.

(I) The stationary state hypothesis leads to mathematical contradiction if it is interpreted to require that the number of radicals should remain constant for a finite time interval.

(II) If we interpret the stationary state hypothesis from a wider standpoint, we find the restricted range of its validity. We have derived an expression by which the range is estimated.

(III) Without resorting to the rather ambigous hypothesis, we can classify various possible behaviors of the number of radicals as well as of molecules as a function of time. In particular, we have given a lower and an upper bound of the number of radicals as well as of molecules at any time.

(IV) It can be shown that the number of radicals generally increases at the beginning, then reaches a maximum and decreases finally, vanishing asymptotically after an infinite lapse of time.

(V) We have discussed the asymptotic behavior of the total number of radicals as well as of molecules to find out that there is a marked distinction in the asymptotic behavior for the case that the recombination between radicals does not occur from that when it does occur. It is also shown that the molecular size distribution approaches the the Poisson type asymptotically. So far our discussions have been formally confined to radiation-induced polymerization described by our model reaction scheme. However, this scheme is also applicable to other cases such as conventional radical polymerization and ionic polymerization, if we adopt properly modified interpretation of the rate constant and regard $R_s(\tau)$ as the fraction of appropriate reaction intermediates having degree of polymerization s. Thus these cases can be also studied by our present method to give similar results although some modifications will be necessary.

Acknowledgement

Finally the authors should like to express thanks to Dr. M. Matsumoto, Kurashiki Rayon Co., for his interests and valuable comments. The authors are also indebted to the Ministry of Education for Scientific Research Fund.

References

1) Cf., e.g., A. M. Bass and H. P. Broida (Ed.): *Formation and Trapping of Free Radicals*, (Academic Press, New York and London, 1960).
2) E. Trommsdorff: Makromol. Chem. **1** (1948) 169.
3) M. Bodenstein u. S. C. Lind: Z. f. phys. Chem. **57** (1906) 168. Ann. Phys. 4. Folge **59** (1919) 633. A. Skrabal: ibid. **82** (1927) 139.
4) W. T. Kyner et al: J. Chem. Phys. **30** (1959) 363.
5) E. A. Moelwyn-Hughes: *Physical Chemistry. An Introduction* (Cambridge, 1940) 544.
6) C. H. Bamford, W. G. Barb, A. D. Jenkins and P. F. Onyon: *The Kinetics of Vinyl Polymerization by Radical Mechanisms* (Butterworth Scientific Publications, 1958) 8.
7) L. Schlesinger: *Einführung in die Theorie der gewöhnlichen Differentialgleichungen auf funktionentheoretischer Grundlage* (Walter de Gruyter and Co., 1922) 31.
8) P. Painlevé: Bull. Soc. Math. France **28** (1900) 201. Acta Math. **25**, (1902). I. B. Gambier: ibid. **33** (1910) 1.
9) E. L. Ince: *Ordinary differential Equations* (Longmans, Green and Co., London, 1927) 304.
10) J. O. Hirschfelder: J. Chem. Phys. **26** (1957) 271.

JOURNAL OF THE PHYSICAL SOCIETY OF JAPAN, Vol. 16, No. 5, MAY, 1961

The Rheological Behavior and Thixotropy of a Fatty Plastic Body

By Toshimaro SONE

Research Laboratory, Snow Brand Milk Products Co., Ltd.,
Shinagawa, Tokyo

(Received January 31, 1961)

The fatty plastic body such as butter or margarine possesses the remarkable non-Newtonian character in its rheological properties. The quantitative study of the viscosity, elasticity and yield value of butter has been performed under various conditions of temperature and shearing stress. The apparatus employed in the measurements involve an oscillating plate viscometer, a cone-plate viscometer and a parallel plate plastometer.

The viscosity, elasticity and yield value decrease remarkably when the specimen is subjected to the kneading on the roll mill, but they recover gradually to their original values after setting the specimen for a long time. The phenomenon can be called as a kind of thixotropy.

The volume dilatometry of the specimen has been also carried out continuously for a setting period of two months. From the comparison of results, the magnitude of viscosity or yield value of butter could be successfully connected to the degree of crystallization of fat in butter which had been evaluated from the specific volume of the specimen. The origin of the thixotropic softening and hardening of butter should be sought for, therefore, in the mechanism of rupture and formation of the three dimensional network of fat crystal in the specimen.

§ 1. Introduction

The fatty plastic body such as butter, margarine and confectioner's fat consists of many small crystals of the order of a few micron or less, enmeshing a considerable proportion of liquid oil within their texture. Consequently its rheological properties are highly dependent upon temperature and pressure. Especially, butter is a typical fatty plastic body which has been widely used as eatables by spreading on bread, and its rheological properties are most important in the practical process as carrying, storage, moulding, and spreading. Many investigations on the rheological properties of butter so far carried out[1)-8)] indicate that the viscosity of butter varies with time during working or setting. Scott Blair et al.[2)-4)] have pointed out that the decrease of viscosity during working and the recovery during setting are a kind of thixotropic phenomena.

In this paper, using butter as an example of plastic bodies, a more quantitative study of the rheological properties of plastic body has been undertaken. In connection with the thixotropic phenomena the variation of crystallinity during working and setting has been also investigated in detail.

§ 2. Experimental Methods

2.1 *Specimen*

The butter employed in our experiment was storaged for about one month before measurements in a constant temperature room at +5°C, so that the tempering of specimen had been completed. Its chemical components are 16% water, 2% salts, 0.8% protein, and 81.0 % fat approximately. The liquid components are being dispersed into the solid fat in the shape of spherical droplets ranging from about one to ten micron in diameter.

2.2 *Procedure and method of kneading*

The duplicate roller used for kneading of butter has the size of 7.5 cm diameter and 17.5 cm length, and the clearance between rollers is varied in four steps of 0.55, 1.65, 3.00 and 4.05 mm respectively. The speed of rotation of roller is 18 r.p.m. and the amount of sample used for kneading at one time is about 500 g. The temperature of working was kept at 25°C or 20°C, but the temperature of sample rose up about 2°C during kneading.

2.3 *Vibrating plate viscometer*

During working at 25°C, about 50 g of worked butter were taken out into a glass beaker at intervals of a few to ten minutes. Immediately, the dynamic viscosity and rigidity modulus were measured using a vibration-plate viscometer.[9),10)] The vibrating porting of this viscometer was a small cylindrical rod of brass which had the size of 3 mm diameter and 30 mm length.

The resonance angular frequency and mechanical loss of this viscometer are connected with the viscosity η and rigidity G of the specimen by the following equations:

$$\eta = K(\tan\delta - \tan\delta_0) \qquad \text{(poise)} \qquad (1)$$

$$G = \frac{K}{\omega_0}(\omega^2 - \omega_0^2) \qquad (\text{dyne/cm}^2), \qquad (2)$$

where K is a constant of apparatus, ω_0, ω the resonance angular frequency in air and in sample respectively and $\tan\delta_0$, $\tan\delta$ the mechanical loss in air and in sample respectively. The constant K was determined by using silicone oils of known coefficients of viscosity.

2.4 *Cone-plate viscometer*

Static viscosity and yield value of butter immediately after working was measured using a cone-plate viscometer which was the same type as developed by Markovitz et al.[11)] A small quantity of viscous butter was taken up from the roller and filled into the wedge-like space between cone and plate. The upper cone was fixed and the lower plate was rotated around its axis at a given torque, and then the rotational velocity of the plate was measured.

The viscosity η is represented by the following equation;

$$\eta = \frac{\tau}{(\Omega/\theta)}, \qquad (3)$$

where τ is the torque of rotation, Ω is the angular velocity and θ is the angle between cone and plate. Thus, Ω/θ represents the rate of shear. In this experiment, the angle θ was 2° and Ω/θ was ranged from 1 to 10^2 sec^{-1}.

Although the worked butter is very fluid, it has still a low yield value and when the rotational torque becomes larger than the yield value, the rotational angular velocity of the plate increases rapidly. The yield value can be determined by extrapolating this flow curve to the zero shear rate.

2.5 *Parallel plate plastometer*

At intervals during working, a batch of viscous butter was taken from the roller and was poured into a metal mould and the cylindrical specimen of 6 cm diameter and 1.4 cm height was made. The viscosity of the specimen was measured by means of a parallel plate plastometer and its change was investigated during setting for a period of 60 days at temperature 16°C, and 20°C and 25°C respectively.

The parallel plate plastometer is the one generally used for measuring the plasticity of rubber. The specimen with cylindrical form is placed between two parallel plates and a constant force F is applied perpendicularly to the plate. The displacement of the upper plate, or the change of the height of specimen, is measured continuously. The viscosity of the specimen can be determined from the time variation of the height of the specimen.

The equation developed by Dienes and Klemm[12)] has been employed in the preliminary experiments. In the present case, the volume of the specimen is constant. Assuming Newtonian flow of the specimen, the reciprocal of the fourth power of the height h is connected with time t by the following equation:

$$\frac{3\mathrm{V}^2}{8\pi}\left(\frac{1}{h^4} - \frac{1}{h_0^4}\right) = \frac{\mathrm{F}}{\eta}t, \qquad (4)$$

where F is the force applied to the specimen, V the constant volume of the specimen, and η the viscosity. The mean shear rate of the specimen can be calculated by the following equation derived by Longworth[13)]:

$$\bar{\dot{\gamma}} = \frac{2}{\pi R^2 h}\int_{r=0}^{r=R}\int_{z=0}^{z=(h/2)} 2\pi r\frac{\partial v}{\partial z}\,dr\,dz$$
$$= \frac{2\pi^{1/2}h_0^{5/2}\mathrm{F}}{3\mathrm{V}^{3/2}\eta}\ (\text{sec}^{-1}), \qquad (5)$$

where R is the radius of the specimen, $\bar{\dot{\gamma}}$ the mean velocity gradient in the direction parallel to the plate, and h_0 the initial height.

When the pressure is removed from the specimen compressed to the height $h_{\min}$, the recovery of the height Δx is observed. The corresponding strain γ is expressed by

$$\gamma = \frac{\Delta x}{h_{\min}}, \qquad (6)$$

Then the Young's modulus E is calculated from the equation

$$E=\frac{F_R}{r}\,,\qquad (\text{dyne/cm}^2) \tag{7}$$

where F_R is the pressure before unloading.

As the above described Dienes' equation has been derived for the Newtonian liquid, the viscosity η calculated from this equation is only apparent for the non-Newtonian material such as butter. Recently, Oka, et al.[14] have developed a new theory which can be applied to the Bingham body with a yield value. According to their theory, when the volume of the specimen is kept constant, the time variation of the distance between parallel plate is expressed by

$$-\dot{h}=\left(F-\frac{fV^{3/2}}{3\pi^{1/2}h^{5/2}}\right)\frac{2\pi h^5}{3\eta V^2}\,, \tag{8}$$

where f is the yield value. Denoting by h_l the limiting height of the specimen for $\dot{h}=0$, one gets from equation (8),

$$h_l=\left(\frac{V^{3/2}f}{3\pi^{1/2}F}\right)^{2/5}. \tag{9}$$

From equation (9) the yield value f is obtained from the height of the specimen when the velocity of decrease of height approaches zero.

From the equation (8) one gets also:

$$\log\left(-\frac{\dot{h}}{h^5}\right)=\log\left(F-\frac{fV^{3/2}}{3\pi^{1/2}h^{5/2}}\right)+\log\frac{2\pi}{3\eta V^2}\,. \tag{10}$$

Thus the plot of $\log(-\dot{h}/h^5)$ against $\log(F-fV^{3/2}/3\pi^{1/2}h^{5/2})$ is linear. From the point where the straight line intersects with the ordinate, the viscosity of the specimen is determined. An example of the experimental data of butter plotted according to equation (10) is represented in Fig. 1, which shows the linear relation over a certain range of $\dot{h}/h^5$.

2.6 *Volume dilatometry of butter, fat and liquid component*

The relation between specific volume and temperature in butter, butter fat, and liquid component were measured by a dilatometric method. The dilatometer consisted of a capillary and a valve, made of Pyrex glass, the volume of the valve being 5.0 c.c. and the diameter of the capillary 1.5 mm. After inserting the specimen, the glass tube was evacuated for one hour, and then purified mercury was filled in the capillary.

The butter fat was obtained by the following procedure. After melting butter of 200 g at 90°C for about one hour, butter fat was separated using a filter paper. The filtered fat was washed three or four times by hot distilled water at 80°C. After confirming no salt reaction by 0.1 N. $AgNO_3$, the filtered warm butter fat was dried in a vacuum oven. In the dilatometry, about 3 g. of molten liquid butter fat was used.

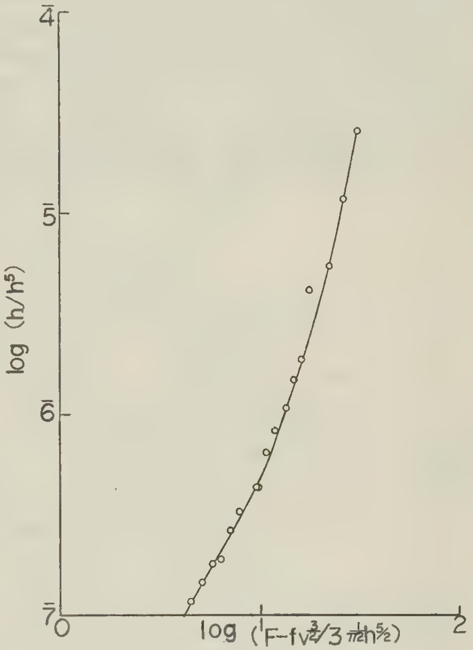

Fig. 1. The plot of experimental data by the equation (10).

The liquid components were separated from butter by mechanical working at +5°C. The most part of the liquid was water, but contained 10.9% salt and 2.9% protein and the very small amount of water soluble inorganic components.

The dilatometer filled with the worked butter was kept at 20°C in a constant temperature room and the height of mercury head was measured every day for about two months. The degree of crystallinity was determined from the specific volume using the correlation curve between specific volume and crystallinity of standard butter. Specific volume—temperature curve corresponding to the solid state was corrected for the deviation by freezing of the liquid components.

§ 3. Experimental results and discussions

3.1 *Temperature dependence of viscosity and elasticity*

A preliminary test was first made for virgin butter at various temperatures, shear rate and pressures. The viscosity and the elasticity of virgin butter was measured at several temperature from 11°C to 25°C, by means of a parallel plate plastometer. The viscosity was calculated by Dienes and Klemm's equation.

Fig. 2 illustrates the relation between the viscosity and the mean shear rate in the logarithmic scales. The change of viscosity with the shear rate or the temperature is not so large in a range from 11°C to 14°C. But when the temperature rose to 20°C, the viscosity of butter decreases rapidly and $\log \eta$ decrease linearly with the increase of $\log \overline{\dot{\gamma}}$. At the temperature over 20°C, the viscosity of butter becomes greatly dependent on the temperature and the shear rate, that is, the rheological behavior is non-Newtonian.

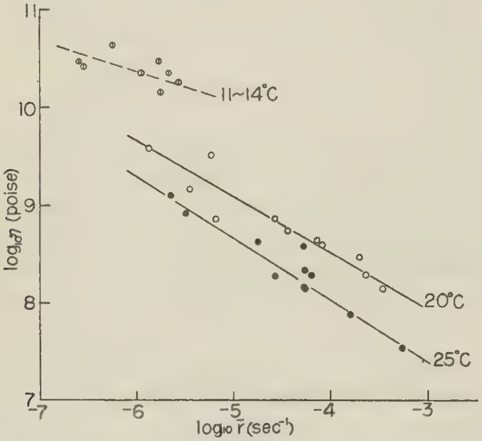

Fig. 2. The variation of the viscosity η with the shear rate $\overline{\dot{\gamma}}$ at the various temperature from 11°C to 25°C.

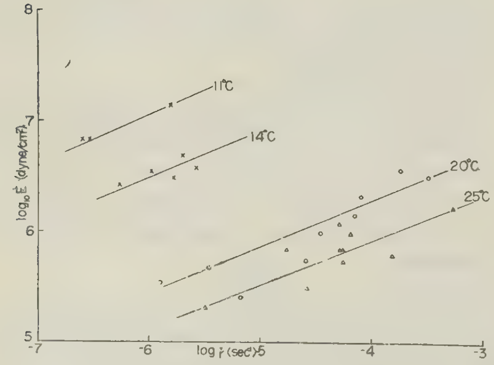

Fig. 3. The variation of the elasticity E with the shear rate $\overline{\dot{\gamma}}$ at the various temperature from 11°C to 25°C.

Fig. 3 depicts the variation of Young's modulus E of virgin butter with the mean shear rate $\overline{\dot{\gamma}}$ for the various temperatures. It is seen that $\log E$ increases linearly with $\log \overline{\dot{\gamma}}$ and that E decreases rapidly with the rise of temperature. The value of Young's modulus obtained is of the same order as the results by Davis[3], 10^5–10^6 dyne/cm^2 at 16°C. The behavior of elastic modulus also indicates the non-Newtonian character in the mechanical property of butter.

3.2 *The variation of viscosity and rigidity during working*

The results described in the previous section has shown that the mechanical properties of butter is largely affected with temperature variation. In order to see the effects of the mechanical processes, it is necessary to investigate the variation of the mechanical properties during kneading. For this purpose, about 500 g. butter was kneaded by a duplicate roller at 25°C and the viscosity and rigidity during kneading were measured by a vibrating plate viscometer with the lapse of time. The temperature rise of butter during rolling was only about 2°C and did not affect the viscosity and the rigidity.

Now denoting by a the clearance of the roller, by v the pheripheral velocity of the two cylinders which have equal velocity, and assuming that the butter does not slip at the surfaces of the rollers, the amount of flow Q through the clearance of the rollers per unit length parallel to roller shaft is roughly calculated by

$$Q = vat_w\,, \tag{11}$$

where t_w is the time of working.

Fig. 4 shows the variation of the viscosity and the rigidity during working with the lapse of time at 25°C. In the abscissa the amount of flow Q is taken instead of time. The decrease in the viscosity and the rigidity of butter is most rapid initially and each values gradually reach to an equilibrium one which varies with the clearance of the rollers.

Intuitively, one sees that the narrowing of the clearance between the two rollers increases the shearing stress and the destruction of the rolled medium continue until the lower viscosity is accomplished.

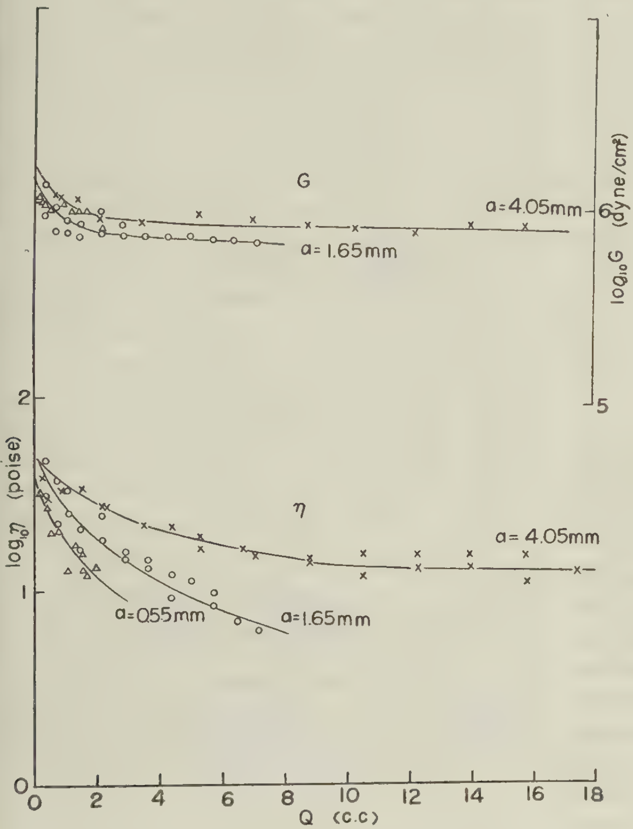

Nig. 4. The variation of the viscosity η and the rigidity G of butter with the amount of working measured at about 500 cps.

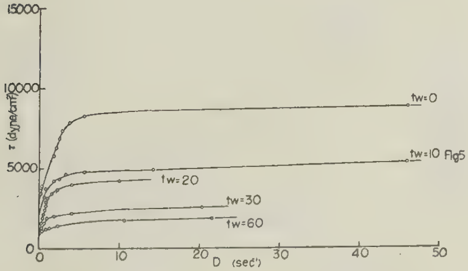

Fig. 5. The flow curve of kneaded butter.

Using a cone-plate viscometer the yield value in addition to the flow curve was measured at 21°C. Through these experiments, the butter was kneaded by the clearance of the rollers which is fixed at 3 mm and the kneading temperature was kept at 20°C. The curves in Fig. 5 show the relation between shear stress τ and shear rate D for different working time in the linear scale. Each flow curve can be separated into two parts, one is over the range 0–10 sec^{-1} being non-linear and the other over the upper range of the rate of shear (10–50 sec^{-1}) being approximately linear. Upper linear parts of each curve have an identical gradient. The lower part is strongly curved, but the yield value is obtained by extrapolation of the lower linear portion. It is remarkable that the butter has a yield value even after working for 60 minutes.

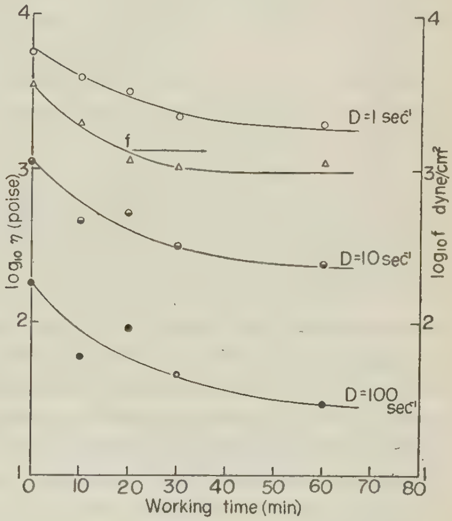

Fig. 6. The variation of viscosity η and the yield value f of butter with working time. Kneading of butter and measurement of viscosity and yield value were carried out at 21°C±1°C.

Fig. 6 shows the variation of yield value and viscosity with the working time. The tendency that the yield value and the viscosity rapidly decrease in the initial period of working, about 30 minutes, and thereafter approaches to the constant value, is similar to the variation of the dynamic rigidity and viscosity during working, which has been already described.

The apparent viscosity η was defined as the ratio of the shear stress to the shear rate τ/D and the relation between the apparent viscosity η and the shear rate D is shown in Fig. 7. The curve of each working time are nearly straight with an almost equal slope.

Recently Tempel[15] has observed the decrease of the viscosity and the rigidity with the increase of shear stress in the fatty gels of 15%-25% glycerol-tristearate suspension in paraffin oil. He assumes that the three dimensional network of tristearate crystals is ruptured by the shearing stress. The reduction of the viscosity, rigidity and the yield value of butter during working seems to involve similar mechanism. Namely, being subjected to the strong shearing stress by compression through the clearance of the roller, the crystal network constituting the body of butter is broken and molten by the mechanical friction between the crystals. These consideration will be further discussed and confirmed in a later section from the dilatometric study.

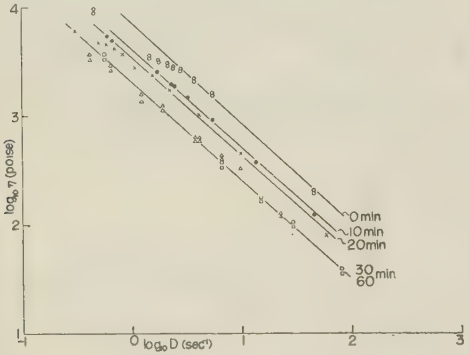

Fig. 7. The variation of the viscosity of butter with the rate of shear at various working time from 0 to 60 minutes.

3.3 *The recovery of viscosity and yield value during setting*

The previous investigators[16),17)] have already reported that the viscosity of butter which had been reduced by working recovered to the original viscosity after a certain time of setting. The variation of viscosity and yield value due to the setting of butter was measured by means of a parallel plate plastometer at 25°C. The butter was kneaded by the roller whose clearance was fixed at 1.65 mm and the temperature of setting after working was kept at 16°C for from one day to ten days. Using the equation of Oka, et al. both the yield value and the viscosity have been determined.

From Fig. 8 and 9, one sees that the relations between the viscosity and the working time and between the yield value and the working time are similar to the results which were obtained by a cone-plate viscometer (Fig. 6), although the present data were obtained at one day after each working time.

However, because the present viscosity measurements were carried out at the different temperature and under much lower shear rate than the case by the cone-plate viscometer, both results can not be quantitatively compared with each other.

The closed points indicate the recovery of

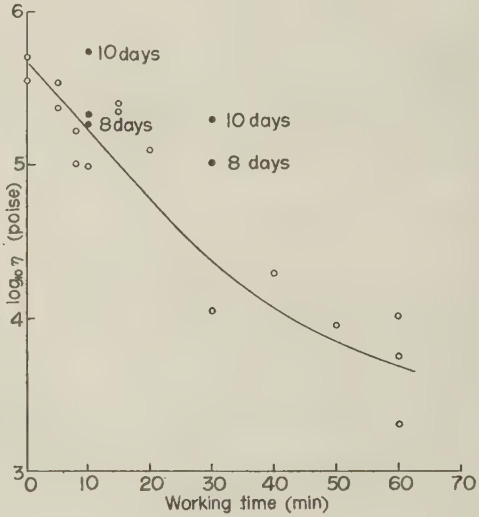

Fig. 8. The variation with working time of the viscosity of butter measured at 25°C after setting for 20 hours at 16°C. Closed points show data after setting 8 days and 10 days at 16°C.

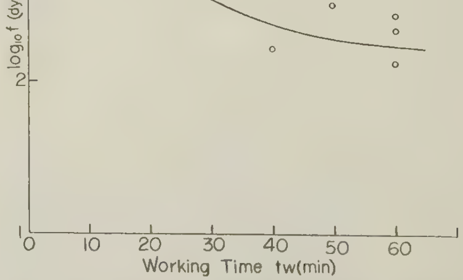

Fig. 9. The variation with working time of the yield value of butter measured at 25°C after setting for 20 hours at 16°C. Closed points show data after 8 days and 10 days at 16°C.

the viscosity and the yield value after eight or ten days setting. It is seen that the thixotropic recovery of the viscosity and the yield value is progressively performed as the lapse of setting days.

Scott Blair[2)], Davis[3)], and Dolby[4)] have previously discussed the recovery of viscosity in connection with the recrystallization of fat which is the mixture of a solid phase and a liquid phase. From the reduction of recovery of the viscosity after the repetition of working, it was concluded that the body or texture of fat could not be completely reproduced to the original state. However, provided that their setting time were long enough as the author's, the recovery of the viscosity might be more perfect.

From the fact that the yield value of butter does not disappear after such long working time and that it gradually recovers by setting as well as the viscosity, the butter can be defined to be a thixotropic plastic substance, as denominated by Burger and Scott Blair[18)].

3.4 *Volume dilatometry of butter, fat and other liquid component*

The relation between temperature and specific volume of butter, butter fat and dispersed dropets were determined by dilatometric measurements (Fig. 10). The temperature range of observation was from −38°C up to 50°C and the rising rate was very slow, about 6°C/hour so that the retardation of phase transition would be perfectly eliminated.

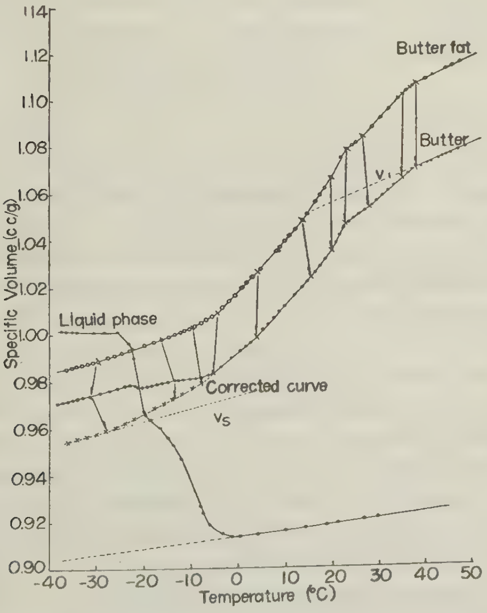

Fig. 10. Specific volume of butter fat, butter and liquid component versus temperature.

Volume-temperature relation of butter fat shows distinctly many breaks at the respective specified temperature. The lower (under −32°C) and upper (over 40°C) linear portion is the specific volume of solid state and liquid state of fat respectively varying with temperature. The breaks between these two parts should correspond to the phase transition temperature of many ingredients (glyceride of fatty acids) involved in the specimen. The specification of each glycerides of fatty acid corresponding to each breaks, however, could not be performed.

The thermal expansion coefficient of butter fat evaluated by Demann, et al.[19)] was 0.58×10^{-3} c.c./g.°C for the solid state and 0.58×10^{-3} c.c./g.°C for the liquid state. From the present experiment the thermal expansion coefficient of butter fat was obtained to be 0.48×10^{-3} c.c./g.°C for the solid state and 1.00×10^{-3} c.c./g.°C for the liquid state. The values obtained in both measurements agree approximately with each other.

In the case of whole butter, a depression of dilation curve occurs around −22°C, which is not observed in the case of butter fat. From the thermal dilation curve of liquid component, however, it is recognized that the above depression is caused by the freezing of liquid droplets contained in the butter. Consequently, in order to obtain the relation between the crystallinity of fat and temperature, the dilation curve of whole butter must be corrected by substituting the extrapolated values which are obtained by extending of the linear portion of the liquid component curve. The corrected curve is shown by the dotted line in Fig. 10. Each transition points of butter are in fairly good agreement with those of butter fat (see Table I).

The degree of crystallization θ is calculated by the following relation,

$$\theta=\frac{v_l-v_t}{v_l-v_s}, \qquad (12)$$

where v_l, v_s is the specific volume of the liquid and solid state of butter respectively. The value v_l and v_s at the measuring temperature t were obtained by the extrapolation of the straight lines at both ends in the dilation curve.

Table I. Thermal transition points of Butter and Butter fat.

Butter fat, $t_{B.F}$ (°C)	Butter, t_B (°C)	Δt ($t_B - t_{B.F}$)
−30.8	−31.0	−0.2
−16.5	−13.8	+2.7
−10.0	− 8.0	+2.0
− 4.8	− 5.5	−0.7
3.8	3.6	−0.2
13.2	16.0	+1.8
19.2	19.5	+0.3
22.6	22.4	−0.2
26.1	27.5	+1.4
35.3	34.5	−0.8
37.6	37.5	−0.1

The degree of crystallization of butter and butter fat obtained from the above calculation is plotted against temperature in Fig. 11. Both curves are very similar with each other. Especially, the fact that the curves fall off in the range from 19°C to 27°C suggests that the large amount of crystallized fat melts at these temperatures, causing the sudden decrease of the viscosity of butter as mentioned previously.

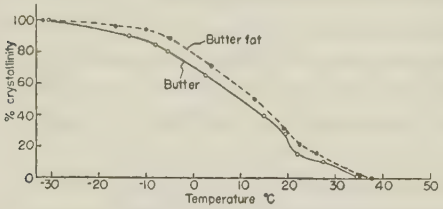

Fig. 11. Crystallinity of butter fat and butter versus temperature.

3.5 *The crystallization of worked butter during setting*

The soft butter which was worked for 30 minutes at 20°C, was filled in a dilatometer and placed in a room regulated to the constant temperature of 20°C. Then the decrease of specific volume was measured for the period of 60 days. The degree of crystallization corresponding to each specific volume can be calculated using the correlation curve which was given in Fig. 10.

Immediately after working of the butter, as is seen in Fig. 12, the degree of crystallization is only about 3%, but it gradually increases through many steps.

Each jumping from step to step probably corresponds to the transformation from the metastable state to crystallized state of each di- or tri-glyceride.

Avrami has theoretically found that the kinetics of phase change is expressed by the following equation[20)]-

$$1-\frac{v_0-v_t}{v_0-v_\infty}=\exp(-kt^n)\,, \qquad (13)$$

where v_t is the specific volume at time t, v_0 and v_∞ the specific volume at the initial and the final state respectively, and k, n are constants. The constant k is proportional to the rate of nucleation and also to the rate of growth, while the constant n is defined by the mechanism of nucleation (see Table II). When the logarithm of $\log(v_\infty-v_t)/(v_\infty-v_0)$ is plotted against the logarithm of time, n is obtained from the slope of line and changes from 1 to 4.

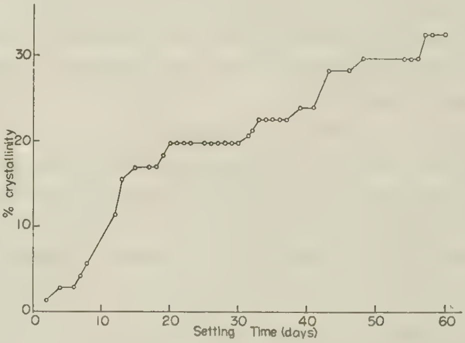

Fig. 12. Crystallization curve of worked butter during setting at 20°C.

Table II.

Value of n.	Shape of crystal	Mechanism of genesis of nuclei
1	needle like	predetermined
2	needle like	sporadic
3	polyhedral like	predetermined
4	polyhedral like	sporadic

According to the equation (13), the results of Fig. 12 were reproduced in Fig. 13. The relation between $\log\log(v_\infty-v_t)/(v_\infty-v_0)$ and $\log t$ is linear and its slope is about 1.1. Thus, it can be said that the crystals in worked butter grow up in the needle-like shape and their nuclei generate predeterminately.

The experimental results obtained at −5°C are also plotted in Fig. 13 in which the slope is about 2.0. Therefore, although the shape of crystals is needle-like, the genesis of nuclei is sporadic.

Few observations have been published on the crystal growth of butter and other fat during isothermal setting. Microscopic observations by Mohr, et al.[17),21)] can only be referred.

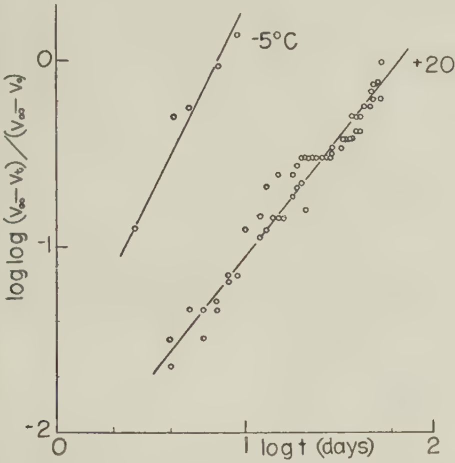

Fig. 13. The analysis of the change of specific volume during setting by Avrami's theory.

Recently, the author and his co-worker[22)] have found with the electron microscope that the shape of the crystal in butter is plate-like at low temperature of −40°C. This fact indicates that the value of constant n should become larger at lower temperatures.

3·6 *The recovery of viscosity, yield value and crystallinity during setting*

As described in the previous section 3.3, the viscosity and the yield value of worked butter recover approximately to their original unworked values after sufficient time of setting. In order to investigate further the relation between the degree of crystallization and the rheological properties of butter, the measurements of the viscosity and the yield value during setting was carried out in parallel with the volume dilatometry.

In Fig. 14, the recoveries of the viscosity and the yield value with the lapse of setting days are represented by the logarithmic scales. The rate of recovery of the viscosity is rapid during the initial ten days and then becomes slower. The recover of the yield value is more rapid than the viscosity and the recovered value after setting of ten days approaches nearly to the yield value of unworked butter.

Assuming that the increase of viscosity during setting is proportional to the decrease of specific volume, the values of viscosity can be replaced for the specific volume in the Avrami's equation as follows,

$$1-\frac{\eta_t-\eta_0}{\eta_\infty-\eta_0}=\exp(-kt^n)\,, \qquad (14)$$

where η_t is the viscosity at time t, η_0 and η_∞ the viscosity at the initial and final state respectively. Using equation (14), the results in Fig. 14, were reproduced in Fig. 15.

It is seen there that the plots are slightly

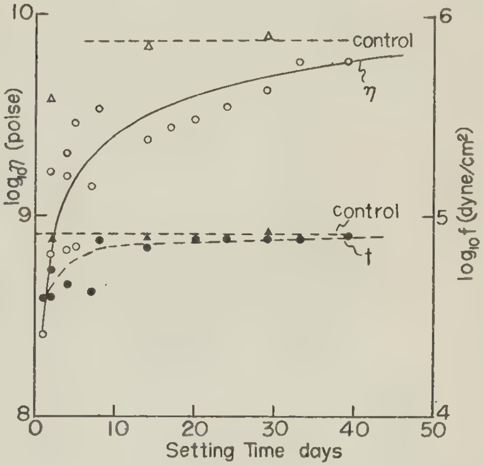

Fig. 14. The recovery of the viscosity η and yield value f of worked butter during setting at 20°C.

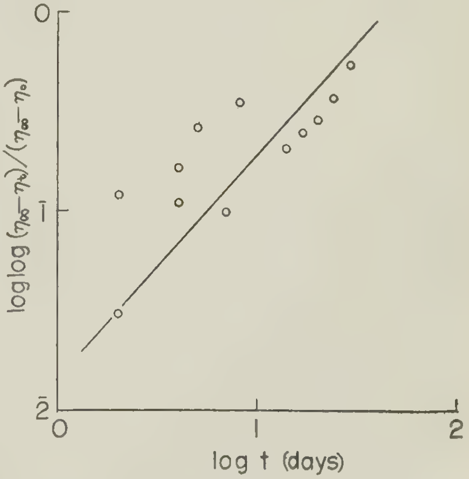

Fig. 15. The analysis of the recovery of viscosity during setting by Avrami's theory. The viscosity was substituted for the specific volume in the Avrami's equation.

disordered but the linear relationship between $\log\log(\eta_\infty-\eta_t)/(\eta_\infty-\eta_0)$ and $\log t$ holds fairly well. The slope of straight line is about 1.2 and agrees with the value of the slope of the straight line in Fig. 13 which expresses the relation between $\log\log(v_\infty-v_t)/(v_\infty-v_0)$ and $\log t$.

From the results mentioned above, it must be admitted that the thixotropic recovery of the viscosity and the yield value is entirely associated with the growth of fat crystals.

§ 4. Conclusion

From all the above described experimental results we may draw some conclusions about the fine structure and the rheological properties of butter which was taken as an example of a soft plastic body. The large temperature dependence, especially around 20°C., is attributed to the melting of fat crystals. The rheological properties are largely dependent on the shear rate and the shear stress and exhibit the non-Newtonian character.

The authors has described in the previous work that the crystals in butter have the dendrical or plate-like shape at low temperatures and their main constituents are the fatty acids of stearin, palmitin and olein. As suggested by Tempel, the fat crystals in butter from a three dimensional network structure, which is deformed under the external force.

Under the low shear stress the breaking of the mechanical interlinks between fat crystals is negligible, but when subjected to higher shear stress as in the case of strong kneading, the junctions between crystals are completely ruptured and causes the softening of the material. Besides, as is seen from dilatometric study, butter includes many kinds of fat which has comparatively low melting temperature. Therefore, the fat crystals are easily melted by the mechanical friction between them during strong kneading.

On the other hand, it is remarkable that the definite yield value is still observed after quite a long working, which suggests the remaining of the crystal network.

It is also noticeable that both the viscosity and the yield value can recover to the original values after setting, which manifests the complete recrystallization of fat crystals.

Phenomenologically butter can be called as a thixotropic substance, or more strictly a plasto-thixotropic substance as defined by Burger, et al.

The isothermal growth of fat crystals during setting can be interpreted by the Avrami's theory. In the fat of kneaded soft butter the needle-like crystals grow during setting and these crystals form a kind of network which occludes liquid oil of low melting temperatures. It has been revealed by the present experiments that the recovery of viscosity during setting is closely related to the crystal growth of butter fat and the formation of crystal network.

A more extended study in the viscoelastic properties of plastic body is now being undertaken. The electron microscope observation would be also helpful in analyzing the microstructure of fat crystals in the texture.

§ 5. Acknowledgements

The author wishes to express his sincere thanks to Dr. Eiichi Fukada, Kobayashi Institute of Physical Research, for his continual guidance and encouragement throughout this work. His particular thanks are due to Prof. Dr. Syoten Oka, Tokyo Metropolitan University, and to Prof. Dr. Jiro Furuichi, Hokkaido University, for their many helpful discussions and advices. He is also indebted to Mr. Masayoshi Fukushima of the Research Laboratory of Snow Brand Milk Products Co. for his contribution in getting the experimental data of this work.

References

1) E. Perkins: J. Ind. Eng. Chem. **6** (1914) 2.
2) G. W. Scott Blair: J. Dairy Res. **9** (1938) 347.
3) J. G. Davis: J. Dairy Res. **8** (1937) 245.
4) R. M. Dolby: J. Dairy Res. **12** (1941) 337.
5) W. Mohr: Fette und Seifen, Anstrichmittel **11** (1955) 925.
6) W. Mohr: Fette und Seifen, Anstrichmittel **59** (1956) 609.
7) W. Mohr: Milchwissenschaft Jahrung **11** (1956) 267.
8) J. Demann and F. Wood: Dairy Ind. **23** (1958) 265.
9) E. Fukada: Kobunshi (in Japanese) **6** (1957) 52.
10) E. Fukada, S. Shimizu and T. Ohno: J. Japan Soc. Testing Material (Special Issue) **8** (1959) 365.
11) H. Markovitz, L. J. Elyash, E. J. Padden and T. W. Dewi: J. Colloid Sci. **10** (1955) 165.

12) G. J. Dienes and H. F. Klemm: J. Appl. Phys. **17** (1946) 458.
13) R. Longworth: J. Polym. Sci. **29** (1958) 307.
14) S. Oka and S. Ogawa: J. Japan Soc. Testing Material (Special Issue) **9** (1960) 321.
15) Van den Tempel: Rheologica Acta **1** (1958) 115.
16) V. R. Hubner and L. L. Thomsen: J. Dairy Sci. **7** (1957) 834; **7** (1957) 839.
17) W. Mohr: Milchwissenshaft Jahrung **11** (1956) 228.
18) J. M. Burger and G. W. Scott Blair: Report on the Principles of Reological Nomenclature. North-Holland Pub. Co. Amsterdam (1949) pp. 51-55.
19) J. M. Demann and F. W. Wood: J. of Dairy Res. **26** (1959) 17.
20) M. Avrami: J. Chem. Phys. **7** (1939) 1103; **8** (1940) 212; **9** (1941) 177.
21) N. King: Dairy Ind. **20** (1955) 311; **20** (1955) 409.
22) M. Okada and T. Sone: J. Appl. Phys. Japan (in Japanese) **29** (1960) 781.

JOURNAL OF THE PHYSICAL SOCIETY OF JAPAN, Vol. 16, No. 5, MAY, 1961

Scattering of Microwaves from a Cylindrical Plasma in the Born Approximation. I

By Yukio MIDZUNO

Department of Physics, Faculty of Science, University of Tokyo

The scattering of a plane microwave incident upon a cylindrically symmetric non-uniform plasma is treated in the Born approximation. When the electric vector is parallel to the axis of the cylinder, the angular distribution function of the cylindrical wave scattered from a cylindrical collisionless plasma is given by

$$f(\theta)=\sqrt{\frac{\pi}{2}}e^{(3/4)\pi j}\int_0^\infty k^2\eta(\rho')J_0\left(2k\rho'\sin\frac{\theta}{2}\right)\rho'd\rho' .$$

Here θ is the scattering angle, $\eta=(\omega_p/\omega)^2$ with the plasma frequency ω_p, and the incident wave is assumed to be proportional to $e^{j(\omega t-kx)}$. The angular distributions for other cases, e.g. waves with the electric vector perpendicular to the axis and/or plasmas with collision loss in a magnetic field, are simply related to $f(\theta)$. For some special density distributions such as that of J_0-type, the integration in $f(\theta)$ can be performed analytically. Finally the same formulas are rederived by summing the radiations from electrons which are forced to oscillate by the incident wave.

§ 1. Introduction

Recently many experiments on the propagation of microwaves in cylindrical discharge tubes have been carried out with the purpose of measuring the density or the density distribution of plasma in the tubes$^{1)}$. Most of them measured the phase shift of the waves effected by the plasma and derived the density using a formula appropriate to the one-dimensional arrangements. In other words, they treated the plasma as if it had the form of an infinite plane slab, upon which a plane microwave is incident normally. But in some of these experiments, the wavelength of the microwaves was comparable with the dimension of the discharge tubes and in such cases the scattering of a plane wave from a cylindrical plasma would be a better approximation to the reality than the arrangements above. Furthermore if we wish to know the density distribution, we must carry out some experiments varying at least one parameter such as the frequency of the microwaves$^{2)}$. In the case of the scattering from a cylindrical plasma, there is a possibility that the angular distribution of the scattered waves can be used for that purpose.

Plasma behaves as a dielectric medium for the propagation of microwaves, and the scattering of microwaves from a cylindrical plasma is nothing but that from a dielectric rod. The effective dielectric constant of a plasma depends on the frequency of the waves and the density of the plasma. It is anisotropic in a magnetic field. Thus we have in general the problem of the scattering from a non-uniform anisotropic dielectric rod[3].

The scatterings of microwaves from a uniform isotropic dielectric rod have been investigated by several authors from both the theoretical and the experimental sides[4),5)]. The same problem from an anisotropic rod was only recently dealt with by Platzman and Ozaki[6], who treated the normal incidence of a plane microwave upon a circular cylinder of a uniform plasma in a uniform magnetic field parallel to the axis of the cylinder. Then the resultant wave equations can be solved in terms of a series of Bessel functions and they got the angular distributions of the scattered waves using an electronic computor. Although their method is rigorous and can be used no matter how dense the plasma is, it would be extremely laborious, were it not prohibitive, to apply this method to a non-uniform cylindrical plasma.

In this paper, we treat the scattering of microwaves from a non-uniform cylindrical plasma in the Born approximation. Although this can be applied only to a plasma of relatively low density, it has such an advantage that the final results are very simple for any cylindrically symmetric density distribution of plasma, especially simple for some realistic distributions. We formulate in section 2 the basic equations of our problem, and in section 3 derive the angular distribution of the wave scattered from a non-uniform cylindrical plasma. Section 4 presents the integrated forms of the angular distributions for some realistic density distributions. Finally in section 5 the same formulas as in section 3 are rederived from another point of view, which will help us to grasp the nature of the scatterings from a plasma.

§ 2. Basic Equations

We start with the Maxwellian equations for the electromagnetic field (in Gaussian units)

$$\mathrm{rot}\, \boldsymbol{E}+\frac{1}{c}\frac{\partial \boldsymbol{B}}{\partial t}=0\,, \tag{2.1}$$

$$\mathrm{rot}\, \boldsymbol{B}-\frac{1}{c}\frac{\partial \boldsymbol{E}}{\partial t}=\frac{4\pi}{c}\boldsymbol{J}\,. \tag{2.2}$$

Let a plasma be at rest. Then the current $\boldsymbol{J}$ in the plasma is determined by the following equation[7]:

$$\frac{m}{ne^2}\frac{\partial \boldsymbol{J}}{\partial t}=\boldsymbol{E}+\frac{1}{ne}\,\mathrm{grad}\, p_e-\frac{1}{nec}\boldsymbol{J}\times\boldsymbol{B}-\frac{m\nu}{ne^2}\boldsymbol{J}\,, \tag{2.3}$$

where m, $-e$, ν are the mass, charge and collision frequency of an electron and n and p_e are the number density and the partial pressure of the electron gas respectively. When the wave-length of the incident wave is much larger than the Debye length, as usually the case, $(ne)^{-1}\,\mathrm{grad}\, p_e$ is much smaller than $\boldsymbol{E}$ induced by the density variations of electrons and can be neglected. Furthermore since we shall treat $\boldsymbol{J}$ as a small quantity induced by the incident waves, $\boldsymbol{B}$ in the right hand side of (2.3) can be replaced by the external uniform static field $\boldsymbol{B}_0$. Then under the assumption that no external electrostatic field exists and that all small oscillating quantities are proportional to $e^{j\omega t}$, where ω is the frequency of the incident wave, (2.3) reduces to

$$(1-j\beta)\boldsymbol{J}-j\gamma\boldsymbol{J}\times\boldsymbol{b}=-j\frac{\omega}{4\pi}\eta\boldsymbol{E}\,. \tag{2.4}$$

Here $\beta=\nu/\omega$, $\gamma=\omega_c/\omega$, $\eta=(\omega_p/\omega)^2$; ω_c and ω_p are the electron cyclotron frequency and the plasma frequency respectively,

$$\omega_c=\frac{e|\boldsymbol{B}_0|}{mc}\,,\qquad \omega_p{}^2=\frac{4\pi e^2 n}{m}\,, \tag{2.5}$$

and $\boldsymbol{b}$ is the unit vector parallel to $\boldsymbol{B}_0$. The solution of (2.4) is expressed as

$$\boldsymbol{J}=\sigma\cdot\boldsymbol{E}\,, \tag{2.6}$$

where σ is the conductivity tensor and given by (with z axis along $\boldsymbol{b}$)

$$\sigma=\frac{\omega\eta}{4\pi j}\begin{pmatrix} L & jM & 0\\ -jM & L & 0\\ 0 & 0 & N\end{pmatrix}, \tag{2.7}$$

$$L=\frac{1-j\beta}{(1-j\beta)^2-\gamma^2}\,,\quad M=\frac{\gamma}{(1-j\beta)^2-\gamma^2}\,,\quad N=\frac{1}{1-j\beta}\,. \tag{2.8}$$

The substitution of (2.6) into (2.2) shows that the plasma is equivalent to a medium whose effective dielectric constant is given by

$$\mathcal{E}=\begin{pmatrix}1-L\eta & -jM\eta & 0\\ jM\eta & 1-L\eta & 0\\ 0 & 0 & 1-N\eta\end{pmatrix}. \tag{2.9}$$

Let us derive the equation for $\boldsymbol{E}$. On eliminating $\boldsymbol{B}$ from (2.1) and (2.2) and using (2.6) we get

$$-\operatorname{rot}\operatorname{rot}\boldsymbol{E}+k^2\boldsymbol{E}=\frac{1}{c}4\pi jk\sigma\cdot\boldsymbol{E}\,, \tag{2.10}$$

where $k=\omega/c$. If we introduce the cylindrical coordinates (ρ, θ, z) with z axis along $\boldsymbol{b}$ and assume all the quantities to be independent of z, (2.10) reduces to

$$\frac{1}{\rho}\frac{\partial}{\partial\rho}\left(\rho\frac{\partial E_z}{\partial\rho}\right)+\frac{1}{\rho^2}\frac{\partial^2 E_z}{\partial\theta^2}+k^2E_z=k^2N\eta E_z \tag{2.11}$$

and other two equations which contain E_ρ and E_θ simultaneously.

The equation for $\boldsymbol{B}$ are derived in a similar manner from (2.1), (2.2) and (2.6) to be

$$\operatorname{rot}\operatorname{rot}\boldsymbol{B}-k^2\boldsymbol{B}=\frac{4\pi}{c}\operatorname{rot}(\sigma\cdot\boldsymbol{E})\,, \tag{2.12}$$

which reduces, under the same assumption as above, to

$$\begin{aligned}&\frac{1}{\rho}\frac{\partial}{\partial\rho}\left(\rho\frac{\partial B_z}{\partial\rho}\right)+\frac{1}{\rho^2}\frac{\partial^2 B_z}{\partial\theta^2}+k^2B_z\\ &\qquad=jk\left\{\frac{1}{\rho}\frac{\partial}{\partial\rho}[\rho(-jM\eta E_\rho+L\eta E_\theta)]-\frac{1}{\rho}\frac{\partial}{\partial\theta}[L\eta E_\rho+jM\eta E_\theta]\right\}\end{aligned} \tag{2.13}$$

and other two equations for B_ρ and B_θ. $\boldsymbol{E}$ is given in terms of $\boldsymbol{B}$ to be

$$\boldsymbol{E}=\frac{1}{jk}\mathcal{E}^{-1}\operatorname{rot}\boldsymbol{B}\,, \tag{2.14}$$

where $\mathcal{E}^{-1}$ means the inverse tensor of $\mathcal{E}$. It is written in components as follows:

$$\left.\begin{aligned}E_\rho&=\frac{1}{jk}\frac{1}{(1-L\eta)^2+(M\eta)^2}\left[(1-L\eta)\frac{1}{\rho}\frac{\partial B_z}{\partial\theta}-jM\eta\frac{\partial B_z}{\partial\rho}\right],\\ E_\theta&=-\frac{1}{jk}\frac{1}{(1-L\eta)^2+(M\eta)^2}\left[jM\eta\frac{1}{\rho}\frac{\partial B_z}{\partial\theta}+(1-L\eta)\frac{\partial B_z}{\partial\rho}\right],\\ E_z&=\frac{1}{jk}\frac{1}{1-N\eta}\left[\frac{1}{\rho}\frac{\partial}{\partial\rho}(\rho B_\theta)-\frac{1}{\rho}\frac{\partial B_\rho}{\partial\theta}\right].\end{aligned}\right\} \tag{2.15}$$

Substitution of (2.15) into (2.13) gives us the desired equation for B_z. In the following throughout this paper we make an assumption that the density distributions of plasmas are independent of θ. Then (2.13) can be reduced to a little more convenient form:

$$\begin{aligned}&\frac{1}{\rho}\frac{\partial}{\partial\rho}\left(\rho\frac{\partial B_z}{\partial\rho}\right)+\frac{1}{\rho^2}\frac{\partial^2 B_z}{\partial\theta^2}+k^2B_z=k^2L\eta B_z\\ &\qquad+jk\left\{-jM\eta\left[\frac{1}{\rho}\frac{\partial}{\partial\rho}(\rho E_\rho)+\frac{1}{\rho}\frac{\partial}{\partial\theta}E_\theta\right]-jE_\rho\frac{\partial}{\partial\rho}(M\eta)+E_\theta\frac{\partial}{\partial\rho}(L\eta)\right\}.\end{aligned} \tag{2.16}$$

From these equations it follows that two modes of waves exist independently each other, one of which has only E_z, H_ρ, H_θ as non-zero components and the other has only H_z, E_ρ and E_θ, and that every normally incident wave can be expressed as a superposition of these waves[3)]. We shall call the former as waves of E-type and the latter as waves of H-type. Then the basic equation for the waves of E-type is (2.11) and that for H-type is given by (2.16) and (2.15).

§ 3. The Scattering Formulas in the Born Approximation

First we discuss the scattering of the waves of E-type. It is shown in Appendix that by means of the two-dimensional Fourier transforms the equation (2.11) is transformed to

$$E_z(\boldsymbol{\rho})=\text{incident wave}+\frac{j}{4}k^2\int H_0^{(2)}(k|\boldsymbol{\rho}-\boldsymbol{\rho}'|)N\eta(\rho')E_z(\boldsymbol{\rho}')d\boldsymbol{\rho}'\,. \tag{3.1}$$

Here $H_0^{(2)}(x)$ is the Hankel function of the second kind; $\boldsymbol{\rho}$ and $\boldsymbol{\rho}'$ are two-dimensional vectors; the integration should be carried out over all the plane, and we have used the boundary condition that at infinity the scattered waves should have only the outgoing components. The expression (3.1) enables us to get $E_z(\boldsymbol{\rho})$ in a power series of η by the successive substitutions. But here we adopt the Born approximation and make the substitution only once. Then $E_z(\boldsymbol{\rho}')$ in the integrand of (3.1) may be replaced by $E_z(\boldsymbol{\rho}')$ of the incident wave itself.

Let the incident wave to be a plane wave*:

$$E_{0z}(\boldsymbol{\rho})=E_0e^{-j\boldsymbol{k}\cdot\boldsymbol{\rho}}\,, \tag{3.2}$$

where $\boldsymbol{k}$ is a wave vector normal to the axis of the cylinder and $|\boldsymbol{k}|=k$. Now we are interested in the field at a remote point, i.e. the case for $\rho\gg\rho_0$ and $k\rho\gg1$, where ρ_0 denotes the radius of the cylindrical plasma. Accordingly we can replace $H_0^{(2)}(k|\boldsymbol{\rho}-\boldsymbol{\rho}'|)$ in the integrand of (3.1) by its asymptotic expression:

$$H_0^{(2)}(k|\boldsymbol{\rho}-\boldsymbol{\rho}'|)=\sqrt{\frac{2}{\pi}}\frac{1}{\sqrt{k\rho}}e^{-jk\rho+jk\rho'\cos\varphi+(\pi/4)j}+O\left(\frac{1}{(k\rho)^{3/2}}\right) \tag{3.3}$$

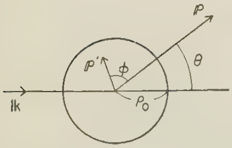

Fig. 1.

where φ is the angle between $\boldsymbol{\rho}$ and $\boldsymbol{\rho}'$ (Fig. 1), and thus we get the following final result:

$$E_z(\boldsymbol{\rho})=E_0e^{-j\boldsymbol{k}\cdot\boldsymbol{\rho}}+E_0f_{\parallel}(\theta)\frac{1}{\sqrt{k\rho}}e^{-jk\rho}+O\left(\frac{1}{(k\rho)^{3/2}}\right) \tag{3.4}$$

with

$$f_{\parallel}(\theta)=\frac{1}{4}\sqrt{\frac{2}{\pi}}e^{(3/4)\pi j}\int k^2N\eta(\rho')e^{jk\rho'(\cos\varphi-\cos(\theta+\varphi))}d\boldsymbol{\rho}'\,, \tag{3.5}$$

or, when the integration with respect to φ is carried out

$$f_{\parallel}(\theta)=\sqrt{\frac{\pi}{2}}e^{(3/4)\pi j}\int_0^\infty k^2N\eta(\rho')J_0\left(2k\rho'\sin\frac{\theta}{2}\right)\rho'd\rho'\,. \tag{3.6}$$

The magnetic field of the scattered wave at a remote place is derived from equation (2.1) to be

$$B_{s\rho}(\boldsymbol{\rho})=O\left(\frac{1}{(k\rho)^{3/2}}\right), \qquad B_{s\theta}(\boldsymbol{\rho})=E_0f_{\parallel}(\theta)\frac{1}{\sqrt{k\rho}}e^{-jk\rho}+O\left(\frac{1}{(k\rho)^{3/2}}\right). \tag{3.7}$$

The waves of H-type can be treated just in the same way as above. We get the following equation corresponding to (3.1):

$$B_z(\boldsymbol{\rho})=\text{incident wave}+\frac{j}{4}k^2\int H_0^{(2)}(k|\boldsymbol{\rho}-\boldsymbol{\rho}'|)[\text{r.h.s. of (2.16) }(\boldsymbol{\rho}')]d\boldsymbol{\rho}'\,. \tag{3.8}$$

In the Born approximation, $\boldsymbol{E}$ and $\boldsymbol{B}$ in the integrand of (3.8) are again replaced by those of the incident wave. Here we note that for the incident wave

$$\frac{1}{\rho}\frac{\partial}{\partial\rho}(\rho E_\rho)+\frac{1}{\rho}\frac{\partial}{\partial\theta}E_\theta$$

vanishes identically because the field must satisfy the Maxwell equations in vacuum. Let the incident wave be a plane wave

$$B_{0z}(\rho)=B_0e^{-j\boldsymbol{k}\cdot\boldsymbol{\rho}} \tag{3.9}$$

$$E_{0\rho}(\boldsymbol{\rho})=B_0\sin\theta e^{-j\boldsymbol{k}\cdot\boldsymbol{\rho}}\,, \qquad E_{0\theta}(\rho)=B_0\cos\theta e^{-j\boldsymbol{k}\cdot\boldsymbol{\rho}}\,. \tag{3.10}$$

---

* In this section we omit the time factor $e^{j\omega t}$.

Then we have

$$B_z(\boldsymbol{\rho})=B_0e^{-j\boldsymbol{k}\cdot\boldsymbol{\rho}}+\frac{j}{4}\int H_0^{(2)}(k|\boldsymbol{\rho}-\boldsymbol{\rho}'|)$$
$$\times\left\{k^2L\eta(\rho')e^{-j\boldsymbol{k}\cdot\boldsymbol{\rho}'}+k\sin\theta' e^{-j\boldsymbol{k}\cdot\boldsymbol{\rho}'}\frac{\partial}{\partial\rho'}(M\eta(\rho'))+jk\cos\theta' e^{-j\boldsymbol{k}\cdot\boldsymbol{\rho}'}\frac{\partial}{\partial\rho'}(L\eta(\rho'))\right\}d\boldsymbol{\rho}'$$

where (ρ', θ') is the components of $\boldsymbol{\rho}'$ in the two-dimensional polar coordinate system. On carrying out the integration with respect to θ', we get the final result

$$B_z(\boldsymbol{\rho})=B_0e^{-j\boldsymbol{k}\cdot\boldsymbol{\rho}}+B_0f_\perp(\theta)\frac{1}{\sqrt{k\rho}}e^{-jk\rho}+\mathrm{O}\left(\frac{1}{(k\rho)^{3/2}}\right), \tag{3.11}$$

$$f_\perp(\theta)=\sqrt{\frac{\pi}{2}}e^{(3/4)\pi j}\left\{\int_0^\infty k^2L\eta(\rho')J_0\left(2k\rho'\sin\frac{\theta}{2}\right)\rho'd\rho'\right.$$
$$+j\cos\frac{\theta}{2}\int_0^\infty k\frac{\partial}{\partial\rho'}(M\eta(\rho'))J_1\left(2k\rho'\sin\frac{\theta}{2}\right)\rho'd\rho'$$
$$\left.+\sin\frac{\theta}{2}\int_0^\infty k\frac{\partial}{\partial\rho'}(L\eta(\rho'))J_1\left(2k\rho'\sin\frac{\theta}{2}\right)\rho'd\rho'\right\}$$
$$=\sqrt{\frac{\pi}{2}}e^{(3/4)\pi j}\int_0^\infty k^2(L\cos\theta-jM\sin\theta)\eta(\rho')J_0\left(2k\rho'\sin\frac{\theta}{2}\right)\rho'd\rho'. \tag{3.12}$$

The electric field of the scattered wave is given by

$$E_{s\rho}(\rho)=\mathrm{O}\left(\frac{1}{(k\rho)^{3/2}}\right),\qquad E_{s\theta}(\rho)=B_0f_\perp(\theta)\frac{1}{\sqrt{k\rho}}e^{-jk\rho}+\mathrm{O}\left(\frac{1}{(k\rho)^{3/2}}\right). \tag{3.13}$$

It should be noted that a resonance phenomenon will occur at $\gamma\ (=\omega_c/\omega)=1$, as easily seen from (2.8). But since one of our basic assumptions is that the scattered wave should be weak compared with the incident wave, (3.12) ought not to be used under the condition $\gamma\approx 1$ and $\beta\ (=\nu/\omega)\ll 1$.

§ 4. Density Distributions of Some Special Types

In fully ionized gases β is proportional to n, but in slightly ionized gases it is independent of n. Accordingly under uniform external magnetic fields, L, M and N can be regarded as constants independent of the density distribution of the plasma in a slightly ionized gas or under the condition $\beta\ll 1$. Then it is convenient to express $f_\parallel(\theta)$ and $f_\perp(\theta)$ in terms of $f_\parallel(\theta)$ for the collisionless plasma, which we denote by $f(\theta)$ in the following.

$$f_\parallel(\theta)=Nf(\theta), \tag{4.1}$$

$$f_\perp(\theta)=(L\cos\theta-jM\sin\theta)f(\theta), \tag{4.2}$$

$$f(\theta)=\sqrt{\frac{\pi}{2}}e^{(3/4)\pi j}\int_0^\infty k^2\eta(\rho')J_0\left(2k\rho'\sin\frac{\theta}{2}\right)\rho'd\rho'. \tag{4.3}$$

For some types of density distributions, the integration in (4.3) can be performed analytically. In this section we shall show some useful examples.

Hereafter we assume $\eta(\rho)=0$ for $\rho>\rho_0$, and give explicitly the dependency of η on ρ only for $\rho<\rho_0$.

1. *The Uniform Distribution*

When

$$\eta=\eta_0\qquad\text{for}\quad\rho<\rho_0, \tag{4.4}$$

$$f(\theta)=\frac{1}{2}\sqrt{\frac{\pi}{2}}e^{(3/4)\pi j}\frac{k\rho_0J_1(2k\rho_0\sin(\theta/2))}{\sin(\theta/2)}\eta_0. \tag{4.5}$$

2. *The Parabolic Distribution*

The distributions of the type ρ^{2n} ($n=0, 1, 2, \cdots$) enable us to perform the integration in $f(\eta)$ analytically by using the formula

$$\int z^{m+1}J_0(z)dz=-m^2\int z^{m-1}J_0(z)dz+z^{m+1}J_1(z)+mz^mJ_0(z)\,. \tag{4.6}$$

The uniform distribution is a special case of them. Another interesting case would be the parabolic distribution:

$$\eta(\rho)=\eta_0[1-(\rho/\rho_0)^2] \qquad \text{for} \quad \rho<\rho_0\,, \tag{4.7}$$

$$f(\theta)=\sqrt{\frac{\pi}{2}}\,e^{(3/4)\pi j}\frac{J_2(2k\rho_0\sin(\theta/2))}{2\sin^2(\theta/2)}\eta_0\,. \tag{4.8}$$

3. *The Distribution of J_0-type*

In a positive column the most plausible density distribution is that of J_0-type[8]:

$$\eta(\rho)=\eta_0J_0(\zeta_1\rho/\rho_0) \qquad \text{for} \quad \rho<\rho_0\,, \tag{4.9}$$

where $\zeta_1=2.4048\cdots$ is the least zero-point of $J_0(x)$. For this distribution also the integration can be performed giving

$$f(\theta)=\sqrt{\frac{\pi}{2}}\,e^{(3/4)\pi j}\zeta_1J_1(\zeta_1)\frac{(k\rho_0)^2J_0(2k\rho_0\sin(\theta/2))}{\zeta_1^2-(2k\rho_0\sin(\theta/2))^2}\eta_0\,. \tag{4.10}$$

§ 5. An Alternative Derivation of the Scattering Formulas

Scattering of microwaves by a plasma is effected by the following mechanism. Electrons in the plasma are forced to oscillate by the field of the incident wave and emit radiations, which in turn perturb the motion of other electrons. In the Born approximation the motion of electrons is assumed to be determined solely by the incident wave and the effect of the scattered waves are neglected. Then it is possible to get the scattering formulas by discussing the motion of each electron directly and summing the radiations from all the electrons in the plasma. Although this procedure gives of course the same formulas as before, it would considerably help us to grasp the very nature of the scattering.

Let us consider the motion of an electron. We neglect the thermal motion of the electron and let the electron oscillate about a point Q($\boldsymbol r'$) under the influence of the incident wave. The equation of motion for the electron is

$$m\frac{d^2}{dt^2}\tilde{\boldsymbol r}=-e\boldsymbol E(\tilde{\boldsymbol r},t)-\frac{e}{c}\frac{d\tilde{\boldsymbol r}}{dt}\times\boldsymbol B(\tilde{\boldsymbol r},t)-m\nu\frac{d\tilde{\boldsymbol r}}{dt}\,. \tag{5.1}$$

Here we can replace $\boldsymbol B(\tilde{\boldsymbol r},t)$ by $\boldsymbol B_0$; and under the assumption that the amplitude of the oscillation is far smaller than the wave length of the incident wave, $\boldsymbol E(\tilde{\boldsymbol r},t)$ can be replaced by $\boldsymbol E_0(\boldsymbol r',t)$. Assuming all the varying quantities are proportional to $e^{j\omega t}$, we can easily solve (5.1) and get the electric dipole moment $\boldsymbol p(t)$ about Q due to this electron.

First we shall consider the case of waves of the E-type. The incident wave is given by

$$E_{0z}(\boldsymbol\rho,t)=E_0e^{j(\omega t-\boldsymbol k\cdot\boldsymbol\rho)}\,, \qquad E_{0x}=E_{0y}=0\,. \tag{5.2}$$

Then from the solution of (5.1) we get

$$\boldsymbol p(t)=-\frac{e^2E_0}{m\omega^2}Ne^{j(\omega t-\boldsymbol k\cdot\boldsymbol\rho')}\boldsymbol e_z\,, \tag{5.3}$$

where $\boldsymbol e_z$ is the unit vector along z axis ($=\boldsymbol b$). Let us take a remote point P($\boldsymbol r$) (Fig. 2). The electromagnetic field at P is[9]

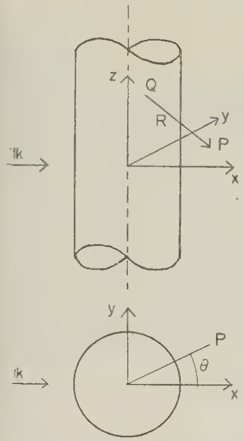

Fig. 2.

$$\boldsymbol{E}(\boldsymbol{r},t)=-\frac{\ddot{\boldsymbol{p}}}{c^2R}+\frac{\boldsymbol{R}(\ddot{\boldsymbol{p}}\cdot\boldsymbol{R})}{c^2R^3}\,, \tag{5.4}$$

$$\boldsymbol{B}(\boldsymbol{r},t)=-\frac{\boldsymbol{R}\times\ddot{\boldsymbol{p}}}{c^2R^2}\,, \tag{5.5}$$

where $\boldsymbol{R}$ is the vector from Q to P, $R=|\boldsymbol{R}|$ and

$$\ddot{\boldsymbol{p}}=\frac{\partial^2}{\partial t^2}\,\boldsymbol{p}\left(t-\frac{R}{c}\right)=-\omega^2\boldsymbol{p}\left(t-\frac{R}{c}\right). \tag{5.6}$$

Thus denoting the cylindrical coordinate of P by $(\rho,\theta,0)$ and that of Q by (ρ',θ',z'), we have the contribution of the electron at Q to the scattered field E_{sz} at P as follows:

$$\begin{aligned}(E_{sz}(\boldsymbol{r},t))_{\mathrm{Q}}&=\frac{\omega^2p_z(t-(R/c))}{c^2R}-\frac{z'(\omega^2\boldsymbol{p}(t-(R/c))\cdot\boldsymbol{R})}{c^2R^3}\\&=-\frac{e^2E_0}{c^2m}N\frac{1}{R}\left(1-\frac{z'^2}{R^2}\right)e^{j(\omega t-kR-k\rho'\cos\theta')}\,.\end{aligned}$$

Then summing the contributions from all the electrons in the plasma, we get

$$E_{sz}(\boldsymbol{r},t)=-\frac{k^2E_0}{4\pi}e^{j\omega t}\int\frac{1}{R}\left(1-\frac{z'^2}{R^2}\right)e^{-j(kR+k\rho'\cos\theta')}N\eta(\rho')d\boldsymbol{r}'\,, \tag{5.7}$$

where the integration should be carried out over the entire space.

In the course of the integration with respect to z', we meet the following type of integral.

$$\begin{aligned}I&\equiv\int_{-\infty}^{\infty}\frac{1}{R^3}e^{-jkR}dz'\\&=\int_{-\infty}^{\infty}\frac{1}{(\xi^2+z'^2)^{3/2}}\exp\{-jk(\xi^2+z'^2)^{1/2}\}dz'\end{aligned} \tag{5.8}$$

where

$$\xi^2=\rho^2+\rho'^2-2\rho\rho'\cos(\theta-\theta')\,. \tag{5.9}$$

Since in our problem $\rho\gg\rho'$ and $k\rho\gg1$, there holds $k\xi\gg1$. Accordingly we need only the asymptotic expression of I for $k\xi\gg1$. When we introduce a new variable $u=k(R-\xi)=k((\xi^2+z'^2)^{1/2}-\xi)$, the integral I reduces to

$$I=2k^2e^{-jk\xi}\int_0^{\infty}\frac{e^{-ju}du}{(u+k\xi)^2\sqrt{u+2k\xi}\sqrt{u}}$$

from which the asymtotic expression can be shown without difficulty to be

$$I=\sqrt{2\pi}k^2\frac{1}{(k\xi)^{5/2}}e^{-jk\xi-(\pi/4)j}\left[1+\mathrm{O}\left(\frac{1}{k\xi}\right)\right]. \tag{5.10}$$

Then the integration over θ' can be carried out as in §3 and we get the final result:

$$E_{sz}(\boldsymbol{r},t)=E_0\sqrt{\frac{\pi}{2}}e^{(3/4)\pi j}\frac{1}{\sqrt{k\rho}}e^{j(\omega t-k\rho)}\int_0^{\infty}k^2N\eta(\rho')J_0\left(2k\rho'\sin\frac{\theta}{2}\right)\rho'd\rho'\,. \tag{5.11}$$

This is just the same expression as (3.6). E_{sx} and E_{sy} are easily shown to vanish in the course of the integration with respect to z'.

When the incident wave is of H-type

$$E_{0y}(\boldsymbol{\rho},t)=B_0e^{j(\omega t-kx)}\,,\qquad E_{0x}=E_{0z}=0\,, \tag{5.12}$$

we have

$$p(t)=-(jMe_x+Le_y)\frac{e^2B_0}{m\omega^2}e^{j(\omega t-kx')}\,, \tag{5.13}$$

where e_x and e_y are unit vectors along x axis and y axis respectively. The contribution to the scattered field B_{sz} at P from an electron at Q is

$$\begin{aligned}(B_{sz}(\boldsymbol{r},t))_Q&=-\frac{1}{c^2R^2}(\boldsymbol{R}\times\ddot{\boldsymbol{p}})_z\\ &\approx\frac{\omega^2\rho}{c^2R^2}\left[\cos\theta p_y\left(t-\frac{R}{c}\right)-\sin\theta p_x\left(t-\frac{R}{c}\right)\right]\\ &=-\frac{e^2B_0}{c^2m}\frac{\rho}{R^2}(L\cos\theta-jM\sin\theta)e^{j(\omega t-kR-kx')}\,,\end{aligned} \tag{5.14}$$

and the scattered field ot P is given by

$$B_{sz}(\mathbf{r},t)=-\frac{k^2B_0}{4\pi}e^{j\omega t}\int\frac{\rho}{R^2}e^{-j(kR+kx')}(L\cos\theta-jM\sin\theta)\eta(\rho')d\mathbf{r}'\,. \tag{5.15}$$

Here the integral,

$$\int_{-\infty}^{\infty}\frac{1}{R^2}e^{-jkR}dz'$$

is evaluated for $k\xi\gg1$ to be

$$\sqrt{2\pi}\,k\frac{1}{(k\xi)^{3/2}}e^{-jk\xi-(\pi/4)j}\left(1+O\left(\frac{1}{k\xi}\right)\right). \tag{5.16}$$

After the integration with respect to θ', we get the final result:

$$\begin{aligned}B_{sz}(\boldsymbol{r},t)=B_0\sqrt{\frac{\pi}{2}}e^{(3/4)\pi j}\frac{1}{\sqrt{k\rho}}e^{j(\omega t-k\rho)}\\ \times\int_0^\infty k^2(L\cos\theta-jM\sin\theta)\eta(\rho')J_0\left(2k\rho'\sin\frac{\theta}{2}\right)\rho'd\rho'\,,\end{aligned} \tag{5.17}$$

which is again equivalent to (3.12). B_{sx} and B_{sy} vanish in the course of the integration with respect to z'.

§ 6. Concluding Remarks

We have derived the formulas for the angular distribution of the microwaves scattered by a cylindrical plasma when a plane wave is incident normally upon the cylinder. Consulting the derivations, we find that our formulas are valid under the following conditions.

1) The scattered wave is very weak compared with the incident wave within the cylindrical plasma.

2) The amplitude of the forced oscillation of electrons in plasma is much smaller than the wavelength of the incident wave.

3) The distance between the electron and the point of observation is much larger than both the wavelength of the incident electromagnetic field and the radius of the cylinder.

The expression for $f(\theta)$ has the form of the Hankel transform[10]:

$$f^*(x)=\sqrt{\frac{\pi}{2}}e^{(3/4)\pi j}(k\rho_0)^2\int_0^\infty\eta^*(y)J_0(xy)ydy\,, \tag{6.1}$$

where we have introduced the dimensionless variables $x=2k\rho_0\sin(\theta/2)$ and $y=\rho/\rho_0$ and the functions $f^*(x)\equiv f(\theta)$ and $\eta^*(y)\equiv\eta(\rho)$. The inversion formula of the Hankel transforms gives

$$\eta^*(y)=\sqrt{\frac{2}{\pi}}e^{-(3/4)\pi j}\frac{1}{(k\rho_0)^2}\int_0^\infty f^*(x)J_0(xy)xdx\,. \tag{6.2}$$

But since x can increase only up to $2k\rho_0$, our knowledge is incomplete to determine $\eta^*(y)$ even if we could measure the angular distribution of the scattered wave completely. And (6.2) shows that the larger $k\rho_0$ is, the more precisely we can determine $\eta^*(y)$, as expected. Although our formula is thus not sufficient to determine the density distribution completely, it would be very useful when we wish to analyse experimental results assuming some reasonable distributions.

The author wishes to express his sincere thanks to Prof. T. Kihara for his continual guidance and his kindness in reading the original manuscript. His thanks are also due to Drs. Y. Sakamoto and S. Miyoshi at the Institute of Physical and Chemical Research, who suggested him this problem and gave kind discussions from the experimental side.

Appendix Derivation of (3.1)

We start with the equation (2.11):

$$\nabla^2 E_z+k^2E_z=k^2N\eta(\boldsymbol{\rho})E_z\,. \tag{A.1}$$

On assuming that E_z is independent of z and introducing the two-dimensional Fourier transform $\tilde{E}_z(\boldsymbol{p})$ of $E_z(\boldsymbol{\rho})$ by

$$\int E_z(\boldsymbol{\rho})e^{j\boldsymbol{p}\cdot\boldsymbol{\rho}}d\boldsymbol{\rho}=\tilde{E}_z(\boldsymbol{p})\,, \tag{A.2}$$

we get from (A.1)

$$\tilde{E}_z(\boldsymbol{p})=G(\boldsymbol{p})+\frac{k^2}{k^2-p^2}\int N\eta(\boldsymbol{\rho})E_z(\boldsymbol{\rho})e^{j\boldsymbol{p}\cdot\boldsymbol{\rho}}d\boldsymbol{\rho} \tag{A.3}$$

where $G(\boldsymbol{p})$ is a function of $\boldsymbol{p}$ corresponding to the incident wave and must satisfy $(k^2-p^2)G(\boldsymbol{p})=0$. On inversing (A.3), we have

$$E_z(\boldsymbol{\rho})=\text{incident wave}+\frac{1}{(2\pi)^2}\iint\frac{k^2}{k^2-p^2}N\eta(\boldsymbol{\rho}')E_z(\boldsymbol{\rho}')e^{j\boldsymbol{p}\cdot(\boldsymbol{\rho}-\boldsymbol{\rho}')}d\boldsymbol{\rho}'d\boldsymbol{p} \tag{A.4}$$

or integrating with respect to the angular component φ of $\boldsymbol{p}$, where $j\boldsymbol{p}\cdot(\boldsymbol{\rho}-\boldsymbol{\rho}')=jp|\boldsymbol{\rho}-\boldsymbol{\rho}'|\cos\varphi$, we get

$$E_z(\rho)=\text{incident wave}+\frac{1}{2\pi}\int k^2N\eta(\boldsymbol{\rho}')E_z(\boldsymbol{\rho}')d\boldsymbol{\rho}'\int_0^\infty\frac{J_0(|\boldsymbol{\rho}-\boldsymbol{\rho}'|p)}{k^2-p^2}pdp\,. \tag{A.5}$$

The integration with respect to p must be carried out in such a manner that the result should express the outgoing cylindrical wave at infinity. For this purpose we consider the following integral[11]:

$$I=\frac{1}{2\pi j}\int_C\frac{zH_0^{(2)}(az)}{r^2-z^2}dz\,, \tag{A.6}$$

where a is a real positive number, r is a complex number with a negative imaginary part and C is the integration path shown in Fig. 3. Then

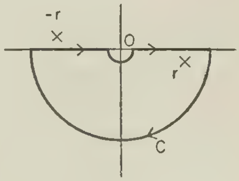

Fig. 3.

$$I=\frac{1}{2\pi j}\int_{-\infty}^{\infty}\frac{zH_0^{(2)}(az)}{r^2-z^2}dz$$
$$=\frac{1}{2\pi j}\left\{\int_0^{\infty}\frac{zH_0^{(2)}(az)}{r^2-z^2}dz-\int_0^{\infty}\frac{zH_0^{(2)}(aze^{-\pi j})}{r^2-z^2}dz\right\}$$
$$=\frac{1}{2\pi j}\int_0^{\infty}\frac{2zJ_0(az)}{r^2-z^2}dz\,. \tag{A.7}$$

On the other hand, the integral I is easily evaluated by means of the residue at the pole. Equating these expressions we get

$$\int_0^{\infty}\frac{zJ_0(az)}{r^2-z^2}dz=\frac{\pi j}{2}H_0^{(2)}(ar)\,. \tag{A.8}$$

Inserting the equation, which is obtained from (A.8) by letting the imaginary part of r tend to zero, into (A.5), we get the desired resut (3.1).

References

1) S. Glasstone and R. H. Lovberg: *Controlled Thermonuclear Reactions* (E. van Nostrand Co. Inc., Princeton, 1960) 170 p.
2) C. B. Wharton and D. M. Slager: J. Appl. Phys. **31** (1960) 428.
3) P. S. Epstein: Revs. Modern Phys. **28** (1956) 3.
4) J. R. Wait: Geophysics **17** (1952) 378. C. Froese and J. Ro Wait: Canad. J. Phys. **32** (1954) 775.
5) M. K. Subbars and A. B. Mclay: Canad. J. Phys. **34** (1956) 546.
6) P. M. Platzman and H. T. Ozaki: J. Appl. Phys. **31** (1960) 1597.
7) L. Spitzer, Jr.: *Physics of Fully Ionized Gases* (Interscience Publ., Inc., New York, 1956).
8) M. J. Druyvesteyn and F. M. Penning: Revs. Modern Phys. **12** (1940) 87.
9) L. D. Landau and E. M. Lifshitz: *The Classical Theory of Fields* (Pergamon Press, London, 1959) § 9-2.
10) I. N. Sneddon: *Fourier Transforms* (McGraw-Hill Book Co., Inc., New York, 1951) Chap. 2.
11) G. N. Watson: *Theory of Bessel Functions* (University Press, Cambridge, 1922) § 13-51.

JOURNAL OF THE PHYSICAL SOCIETY OF JAPAN, Vol. 16, No. 5, MAY, 1961

Photoconductive Hall Effect in Potassium Bromide

By Masami ONUKI

Department of Applied Physics, Osaka City University, Osaka

(Received December 9, 1960)

A.C. method was employed to investigate the mobility of the conduction electron in KBr under space charge free condition at temperatures between 80°K and room temperature. In this experiment white light was used to illuminate the specimen to enhance the conductivity. The mobility which depends on temperature was found to be inversely proportional to the mean density of phonons excited in the crystal. This fact suggests that the mobility is determined mainly by the scattering of the optical mode of lattice vibration. Using the Low and Pines formula, the following values were obtained:

Effective mass of the bare conduction electron, $m^*=0.23\,m$
Effective mass of the polaron, $m_p=0.33\,m$
Strength of interaction between the electron and the polarization, $\alpha=2.56$,

where m is the free electron mass.

§1. Introduction

Experimental studies of electron mobility in polar crystals provide means to check theories of polarons developed by a number of authors.[1-4]

The Hall mobilities of electrons (or holes) in CdS, PbS, PbTe, and ZnO which are polar in nature and have comparatively low specific resistance due to presence of impurities, were measured by several workers.[5-7] The mobilities of carriers in these materials were explained by the combination of the scattering mechanisms of both the optical and acoustic modes of lattice vibration even at room temperature, and therefore it was difficult to separate the mobility due to the optical scattering from the other. The strength of interaction between the electron and the polarization produced by the former was estimated to be less than that in the case of alkali halides. Thus the polaron theories were not necessary to be essential to describe the mobility of above materials.

Recently, Brown and his co-workers made accurate measurements of the drift and Hall mobilities of electrons in silver halide.[8-10] According to their results, the drift mobility (μ_D) was much smaller than the Hall mobility (μ_H) around 80°K and below. This fact is due to the apparent large drift time affected by the trapping of electrons in some shallow traps in the crystals observed in the measurement of the drift time. The Hall mobility measured by them was the mobility which was not affected by the trapping, and thus their results were able to be compared with one predicted by the theory. They concluded that reasonable agreement between the experimental results of the Hall mobility and the polaron theories was observed in the temperature region from about 100°K to 30°K. Further, they estimated that $m^*=0.3\,m$, $m_p=0.4\,m$, and $\alpha=2.2$ for AgCl, where m^* and m_p are the effective masses of the bare conduction electron and the polaron, respectively, and α is the strength of interaction of the electron with the polarization. However, studies of electron mobility in alkali halide, which is the most typical material in ionic crystals, have rather been sluggish in development because of the following difficulties; (1) very high resistivity of the crystal even in the photoconducting state, due to extremely short lifetime of the conduction electron ($10^8\sim10^9\ \Omega$ cm at room temperature), (2) non-uniformity of electic field in the crystal due to the formation of space charge field, resulting difficulty to obtain accurate Hall voltage, (3) slow change of the photoconductivity of the crystal due to bleaching of F centers by the irradiation of light, (4) the flicker noise due to trapping and releasing of electrons by various trapping centers produced by the irradiation.

Redfield has measured the Hall mobilities of electrons in KCl, and NaCl at room and liquid nitrogen temperature by the use of pulsed light.[11] However, the observed results are considerably scattered, and it seems difficult to compare them with theory. Macdonald and Robinson have measured the Hall mobility of electron in KBr only at room temperature by the a. c. method.[12] At present, experimental informations about the mobility of polaron are extremely limited. This fact is due to the difficulties mentioned above and is probably to the uncontrolled impurities in the specimens which might decrease the photoconductivity and increase the noise. Accordingly reliable temperature dependence of polaron mobility has been sought for.

We made experiment with KBr of high purity prepared by recrystallization technique. The conductivity was enhanced by illuminating the additively colored crystal with white light. The Hall voltage was measured by a.c. method at 330 cps in the temperature region between −190°C and room temperature. The crystal impedance between the Hall electrodes was measured at each temperature to correct the apparent Hall voltage into the true Hall voltage, because the crystal impedance was much larger than the input impedance of the amplifier used in this experiment. The Hall mobility of the electron was able to be obtained in the above temperature region under the condition of space charge free and small disturbance noise.

§ 2. Experimental Method and Procedure

Irradiation with strong light results in the decrease of photoconductivity of colored alkali halides due to photo-chemical reaction in them. For this reason, a colored KBr crystal which is the most stable against illumination among alkali halides was adopted. Further, the crystals used were purified by the recrystallization process to avoid the flicker noise inherent to the above reaction and to enhance the photoconductivity in the measurement. KBr crystals were additively colored and the concentration of the F center was estimated to be $1\sim2\times10^{16}/\mathrm{cm}^3$. The dimension of specimens was about $4\times1.5\times1.2\,\mathrm{mm}^3$. The electrodes were made of silver paint.

The photoconductivity of colored KBr decays with time if d. c. electric field is applied, because of the formation of space charge.[13–14] This undesirable effect, however, can be eliminated by the use of a. c. field and steady illumination.[15] A. c. 330 cps was adopted for the measurement of the Hall voltage, in consideration of the results of frequency-dependence of a. c. photoconductivity, and to avoid the 60 cps hum noise and flicker noise, the latter of which is inversely proportional to frequency.

The measuring apparatus is shown in Fig. 1. A 330 cps oscillator (A), whose push-pulled outputs are 100 volts maximum with respect to the ground, is connected to the current electrodes (***a*** and ***b***). This oscillator is

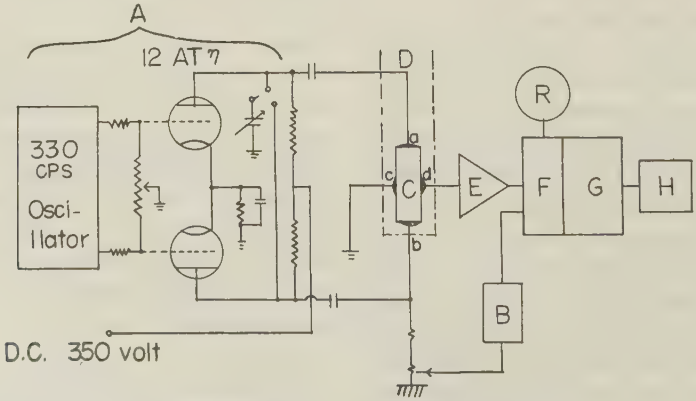

Fig. 1. Apparatus to measure the Hall voltage and the crystal impedance.
(A): 330 cps oscillator; (E): pre-amplifier; (F): differential amplifier; (G): tuned amplifier for 330 cps; (H): d.c. detector; (B): phase-shifter; (C): specimen; (D): cryostat.
For the measurement of crystal impedance, one of the Hall electrodes (c) is connected to the output of the oscillator and the other (d) to the input of the amplifier.

stabilized so that the voltages of the push-pulled outputs are constant and the output wave form has very little distortion. This push-pull driver was devised so that both the voltage and the phase of either output can be changed independently. The background input voltage of the pre-amplifier (***E***) due to the non-uniform illumination over the surface of the specimen and the unbalance-setting of the Hall electrodes could be eliminated to nearly zero by adjusting the voltage and phase of each output of the oscillator.

The input system of the pre-amplifier consists of a cascode circuit after Macdonald, where the input impedance was as large as 80 $M\Omega$ at 330 cps, the input capacitance formed between shielding being eliminated by the feed back device.[16] This pre-amplifier contains also an *RC* tuned amplifier whose pass band is made comparatively wide so as to ensure good phase characteristics vs. frequency. The main amplifier (***F***, ***G***) consists of a differential (***F***) and an *RC* tuned (***G***) amplifier for 330 cps. The d. c. detector (***H***) is set next to the above device. One of the input of the differential amplifier is connected to the output of the oscillator through an attenuator and phase-shifter (***B***). The differential amplifier serves to avoid the effect of induced current through the capacity between the Hall electrodes in the measurement of the crystal impedance and also to adjust the unbalanced voltage between the two Hall electrodes in the measurement of the Hall voltage. A cathode ray oscilloscope (***R***) is attached to the output of the differential amplifier to observe the balancing of the input and to detect the phase of the Hall voltage. The total maximum sensitivity of the device was 3×10^{-3} volt/mA.

A 500 watt projection lamp was used as the light source. The light was filtered with water to eliminate the flicker noise caused by long wave irradiation. Using a focusing lens and mirror, the light was projected uniformly upon the specimen (***C***) in the cryostat (***D***). The gap width of the magnet was 43 mm and the maximum field was 4500 oersteds.

Since the impedance between the Hall electrodes (***c*** and ***d***) which is about $1\sim3\times10^{9}\ \Omega$ at room temperature under illumination, is much higher than the input impedance ($\simeq 80\ M\Omega$), the true Hall voltage V_H is calculated from the apparent Hall voltage V_H' by the use of the following formula,

$$V_H'/V_H = Z_{in}/(Z_{in}+Z_{cry}) \simeq Z_{in}/Z_{cry}\ , \qquad (1)$$

where Z_{in} and Z_{cry} are and the input and the crystal impedance, respectively. Hence, in this work it is necessary to measure Z_{cry} as well as V_H' in order to get V_H.

The Hall mobility μ_H is expressed as follows:

$$\theta = \mu_H H\times10^{-8} = (V_H/t)/(KV_l/l)\ , \qquad (2)$$

(in practical units),

where θ is the Hall angle, H the magnetic field, V_l the applied electric field, t the width, l the length of the specimen, and K the numerical factor due to the non-uniformity of the electric field near the Hall electrodes.

The temperature-dependence of μ_H can be obtained by measuring Z_{cry} and V_H' at each temperature, if we use formula (1), (2), and the measured sensitivity of the detector, where Z_{in}, V_l, t, l, and H are constant and independent of temperature for a given specimen.

The value of K was determined to be 0.83 by the following method. A conducting carbon sheet similar to the specimen in shape, upon which silver-paint electrodes were attached on the same position as that of the specimen, was prepared.[17] A pattern of equipotential lines of the sheet was obtained by a simple experimental procedure. The ratio of the effective electric field estimated from the equipotential line between the Hall electrodes to the average applied field between the two current electrodes was calculated to be 0.83 in the present case.

§ 3. Results and Discussion

(1) *A. c. method of measurement of photoconductivity*

The space charge effect in the measurement of photocurrent is eliminated by adopting the a. c. field and steady illumination. Electrons that approach the anode surface in a half cycle of the a. c. field may fill the ionized F centers (negative ion vacancies) which were formed near the surface in the previous half cycle, thereby the surface regions of the specimen tend to be neutralized.[13]

It has been known that there are non-photoconducting layers between the electrodes and the specimen. These layers behave as constant capacities in series with the true crystal impedance. Fig. 2 shows the equivalent circuit of the specimen in the photoconducting state. If the frequency of the applied a. c. field is comparatively low, almost all of the applied a. c. voltage is fed in these charge-free layers, resulting in small photoconductivity. This effect should cause small Hall voltage, because the longitudinal voltage V_l is not applied uniformly through the specimen. Further, inaccuracy in estimating Z_{cry} should result from this effect.

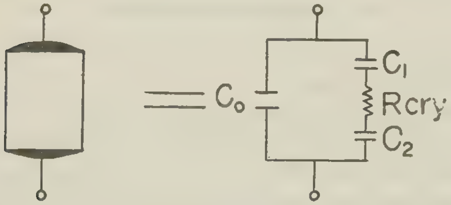

Fig. 2. The equivalent circuit of the specimen in the photoconducting state.
In the circuit diagram, C_0 represents the capacity between the electrodes, R_{cry} the resistance of the photoconducting region in the specimen, and C_1 and C_2 the capacities of the charge-free regions near the electrodes.

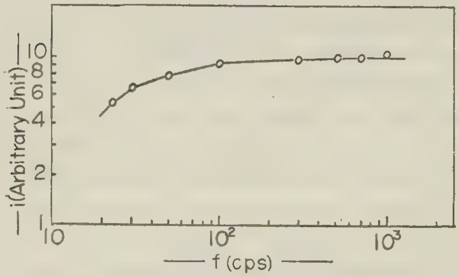

Fig. 3. The frequency-dependence of photocurrent at room temperature.

Frequency-dependence of photocurrent was measured in order to have informations about this surface effect. In this measurement the RC tuned systems contained in the detector were omitted. The frequency of the applied voltage was varied from 20 cps to 1000 cps, the applied voltage being kept at 5 volts throughout this frequency range. The results are shown in Fig. 3. As is seen in the figure, the photocurrent under illumination increases with frequency up to 200 cps and then saturates thereafter. The frequency at which saturation starts shifted to the lower frequency side as the intensity of illumination was decreased. Using this characteristics and the saturated value of the crystal impedance, the capacity of the charge-free layer per unit area may be estimated to be $1.5\times10^2\ \mu\mu F/\text{cm}^2$. If equal charge-free regions about on each electrode, that is, $C_1=C_2$ in Fig. 2, the thickness of the regions may be calculated to be 1.4×10^{-3} cm. At present the cause of the formation of these charge-free layers is not clear.[15] In the measurement of the Hall voltage, the impedance between the two Hall electrodes and that between the two current electrodes under illumination of white light were $1\sim3\times10^9\ \Omega$, and $8\sim25\times10^9\ \Omega$, respectively, which were much larger than the capacitive impedance of the charge-free layers of $2\times10^8\ \Omega$ at 330 cps. For this reason it should be concluded that the undesirable effect of the charge-free layers becomes negligible by adopting 330 cps as the measuring frequency.

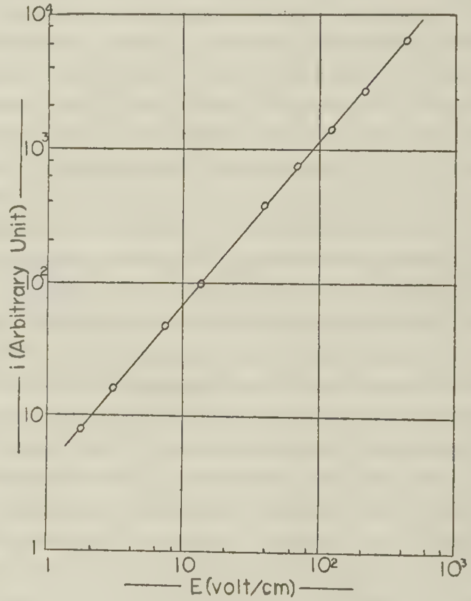

Fig. 4. The field-dependence of photocurrent at 330 cps.

As for the dependence of photocurrent on the applied electric field, results shown in Fig. 4 were obtained. The measuring frequency was 330 cps. The photocurrent was linearly dependent on the field strength from 1.8 volts/cm up to 4×10^2 volts/cm in this measurement. The saturation effect of the photocurrent could not be observed for low fields used in the present work. This fact suggests that the space charge free condition is realized in this experiment.

F centers in KBr are known to behave as trapping centers for conduction electrons at low temperatures below −100°C. In other words, the electrons released from *F* centers are capable of being trapped by other *F* centers which are not ionized, and consequently, *F′* centers may be formed at low temperatures. The *F′* center bleaches thermally to two *F* centers in several seconds at about −100°C. The decay current due to this thermally releasing effect after the turn-off of illumination was observed by the authors.[13] For the reason mentioned above, the temperature-dependence of photocurrent under illumination with white light differed from that under illumination with *F*-band light, as seen in Fig. 5. In the figure the solid line corresponds to the case of the steady white light illumination and the dotted line to the case of the steady *F*-band illumination, the measuring frequency being 330 cps in both cases. In the former case the photocurrent was more enhanced than in the latter case at low temperatures, because of the optical excitation of *F′* electrons by the *F′*-band light contained in white light. As the thermal excitation of *F′* electrons becomes effective at higher temperatures, the curves in Fig. 5 corresponding to the above two cases show identical inclination. To avoid the complicated trapping effect and to enhance the photoconductivity of the specimen, it is desirable to adopt white illumination for the measurement of the Hall voltage.

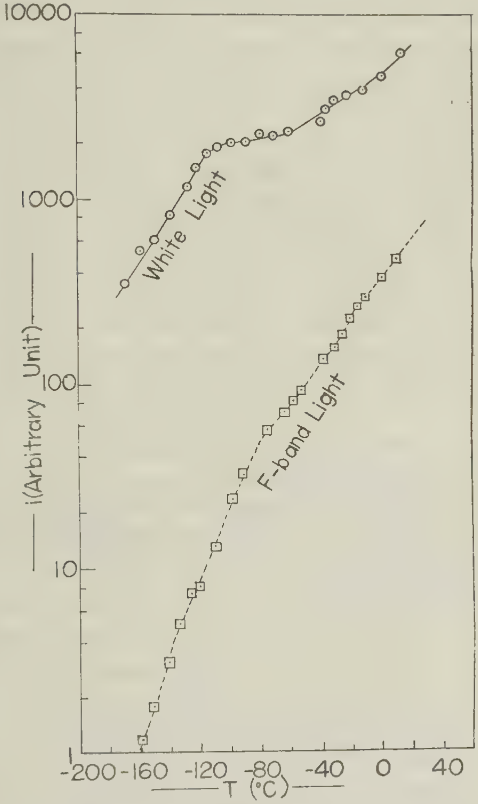

Fig. 5. The temperature-dependence of photocurrents due to white light and F-band light.
———: In the case of white light.
…………: In the case of F-band light.

(2) *The Hall mobility*

The apparent Hall voltage V_H' was found to depend linearly on the applied magnetic field. Fig. 6 shows these results. At low magnetic fields it was difficult to detect V_H' on account of disturbance noise. Noise became smaller as the temperature was decreased. As is seen in Fig. 6, V_H' is linearly dependent on H, $\mu_H H/c$ being much smaller than unity in this case. Further, the signal of V_H' was ascertained to change by 180° in its phase relative to the applied electric field by mean of varying the polarity of the magnetic field H.

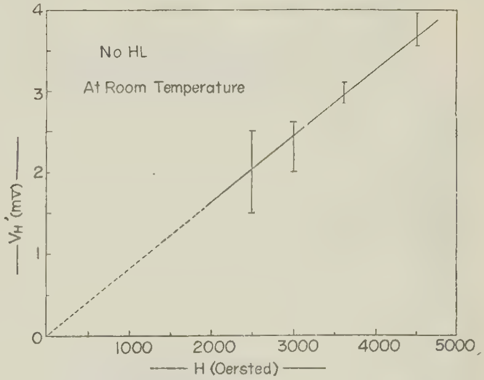

Fig. 6. V_H' as a function of the applied magnetic field.

Fig. 7 and 8 show the photoconductivity σ which is the reciprocal of Z_{cry}, V_H', and V_H in arbitrary scale as functions of temperature for *NO. R1* and *NO. S1* specimens, respectively. The values of μ_H at room temperature were calculated to be 31±6 cm²/volt-sec and 27±5 cm²/volt-sec, respectively, from the analysis mentioned in § 2. These values may be compared with ~30 cm²/volt-sec, the mobility estimated indirectly from the photocapacitive effect by Kahn.[18] Macdonald has given the value as 7.5~12.5 cm²/volt-sec, and it seems to be far smaller. The small value of Macdonald might be due to the neglect of the correction for Z_{cry}.

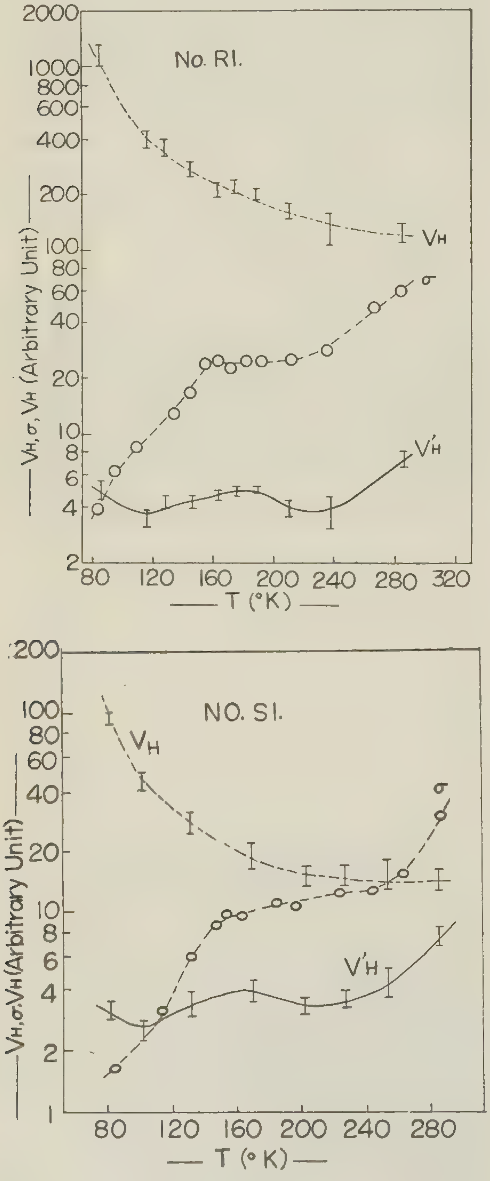

Figs. 7 and 8. V_H', σ and V_H vs. temperature, the ordinate being in arbitrary scale.

Average values of μ_H for more than ten specimens are plotted as a function of temperature in Fig. 9. These points fit better to $\mu_H=A(exp\,\Theta/T-1)$ rather than to $\mu_H=BT^{-n}$. If we fit the data to $\mu_H=BT^{-n}$, the value of n varies from 1 to 2.2 and is not constant over the experimental temperature range. In conclusion, the temperature-dependence of μ_H obtained in this experiment shows clearly exponential type behavior of conduction electrons in ionic crystals. Further, μ_H should be equal to the microscopic mobility μ, because the relaxation time of collision by the optical mode of lattice vibration is independent of mean velocity of electrons.[16),19)] The best fit for the low temperature region was obtained with $A=16.4$ cm²/volt-sec and $\Theta=255$°K.

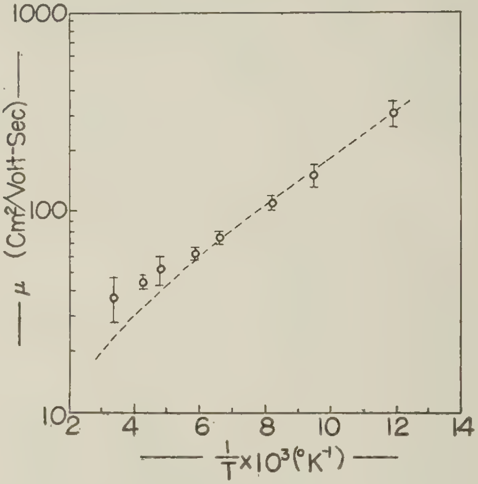

Fig. 9. Mobility of conduction electrons in KBr as a function of temperature.

The dotted line shows the theoretical curve calculated from the Low and Pines formula, $\mu_H=A(\exp\Theta/T-1)$, with $A=16.4$ cm²/volt-sec and $\Theta=255$°K.

According to the polaron theory of Low and Pines, the mobility of the polaron is given as follows in the temperature region $T<\Theta$:

$$\mu=\frac{1}{2\alpha\omega}\cdot\frac{e}{m^*}\left(\frac{m^*}{m_p}\right)^3\cdot f(\alpha)\cdot(exp\,\Theta/T-1), \quad (3)$$

$$m_p=m^*\left(1+\frac{\alpha}{6}\right), \quad (4)$$

$$\alpha=\frac{e^2}{\hbar}\left(\frac{m}{2\hbar\omega}\right)^{1/2}\frac{\mathcal{E}_s-\mathcal{E}_0}{\mathcal{E}_s\mathcal{E}_0}\left(\frac{m^*}{m}\right)^{1/2}, \quad (5)$$

where m^* and m_p are the effective masses of the bare conduction electron and the polaron respectively, $f(\alpha)$ the slowly varying function nearly equal to 1.2 for $\alpha=2\sim5$. ω and Θ are the logitudinal frequency and its associated Debye temperature which are related to the reststrahl frequency ω_t in the following formulas:

$$\omega=\sqrt{\frac{\varepsilon_s}{\varepsilon_0}}\,\omega_t,\ \hbar\omega=k_0\Theta \tag{6}$$

For KBr, values, $\varepsilon_s=4.78$, $\varepsilon_0=2.33$, and $\hbar\omega_t=0.015$ ev lead to $\Theta=246$°K.20) This is to be compared with the experimental value which is 255°K. From the measured value of A, $m_p=0.33\,m$, $m^*=0.23\,m$, and $\alpha=2.65$ are obtained by numerical calculation, where m is the free electron mass. Considering the value of α which is larger than unity, the polaron theories should be adopted for the conduction electron in KBr. In the analysis after the Low and Pines theory, the discrepancy between the observed data and the theory was found at temperatures higher than Θ. This fact, however, is not surprising, because Low and Pines treated the behavior of polarons at temperatures below Θ.21)* So far as the discussion is limited in low temperature range, there is no contradiction between the theory and the experimental data.

We shall consider the co-existence of other scattering mechanisms with that of the optical scattering. The apparent mobility μ obtained in the experiment is expressed as follows by using the combination of μ_i which are supposed to be due to various scattering mechanisms:

$$1/\mu\simeq\sum_i(1/\mu_i)\,, \tag{9}$$

In the present case μ_{opt}, which corresponds to optical scattering, is the smallest and is the most effective in defining the resultant mobility. Now, we shall consider μ_{ac} corresponding to acoustic scattering and μ_n corresponding to neutral impurity scattering by F centers.

μ_{ac}, which is due to acoustic scattering, is given as follows by using the deformation potential E_1:19)

$$\mu_{ac}=\frac{e\hbar^4C_{ll}}{E_1{}^2m^{*3}}(k_0T)^{-3/2}\,, \tag{10}$$

where k_0 is the Boltzmann constant, C_{ll} the elastic constant for longitudinal acoustic wave. Assuming that $E_1=5.4$ ev, which Kawamura calculated for KCl,22) is applicable for KBr, and using that $m^*=0.23\,m$, μ_{ac} is obtained to be equal to about 9000 cm²/volt-sec at room temperature. The temperature-dependence of μ_{ac} follows the $T^{-3/2}$ law, and the mobility μ_{ac} has little effect on the resultant mobility μ in the present temperature range. The temperature at which μ_{ac} is the same order as μ_{opt} should be around 25°K.

Next, we shall consider the mobilities due to impurity scattering by ionized or neutral centers in the crystal. In the present case, the most effective impurity for scattering seems to be neutral F centers in the crystal, the density of which is about 2×10^{16}/cm³ in this case. The most part of F centers are hardly ionized under illumination. From the experiment of the photoconductivity and Hall mobility, we note that the density of the vacant F centers, which is nearly equal to the density of the conduction electron ($\simeq10^9$/cm³), should be much smaller than the density of F centers which are not ionized ($\simeq2\times10^{16}$/cm³) even at room temperature. On the other hand crystals used in this work were checked up to contain unknown impurities whose density was about 4×10^{15}/cm³.13) The densities of these impurtities are so small that their effects to the resultant mobility may be negligible. For the mobility corresponding to the neutral impurity scattering μ_n (due to non-ionized F centers in this case),23) we have

$$\mu_n=\frac{m^*e^3}{20\varepsilon_sN_n\hbar^3}\,, \tag{11}$$

where N_n is the density of the neutral center. Substituting $N_n=2\times10^{16}$/cm³ and $m^*=0.23\,m$, μ_n is estimated to be about 3000 cm²/volt-sec, the value being independent of temperature.

Considering the temperature-dependence of the μ_{ac}, μ_n, and μ_{opt}, the maximum value of the mobility μ is expected to be about 1500 cm²/volt-sec around 40°K. However, μ_{ac} and

---

* For the explanation of the temperature-dependence of the mobility at temperatures higher the Debye temperature, the expression of m_p given by Yokota, $m_p=m^*\left[\frac{\alpha}{6(2\bar{n}+1)^{3/2}}\right]$, where $\bar{n}=1/(exp\,\Theta/T-1)$, might offer some interesting suggestion.3) The better fit of the data to the Yokota mobility formula, which contains the above expression of m_p, was obtained even in the temperature range, $T\geq\Theta$. However, it seems premature to adopt the Yokota expression of the mobility in the high temperature region, because the theory lacks ample theoretical foundation for using it at high temperatures.

μ_n in this experiment should have little effect upon the resultant mobility, μ, because the measuring temperature was not so low. In conclusion, the resultant mobility μ should be equal to μ_{opt}, the mobility due to the optical scattering.

§ 4. Summary

In this work the behavior of the conduction electron in KBr has been investigated between 80°K and room temperature. The decrease of photocurrent due to space chage polarization was prevented by the use of the a. c. 330 cps field and steady illumination of white light. Exact Hall mobility was measured, by assuring that uniform electric field was applied through the specimen.

The mobility was found to be determined by the scattering of the optical mode of lattice vibration, the other scattering mechanisms being estimated to be effective below about 40°K.

Using the Low and Pines formula for the mobility, we obtained that $m^*=0.23\,m$, $m_p=0.33\,m$, and $\alpha=2.65$.

Acknowledgement

The author wishes to express his sincere thanks to Prof. H. Kawamura for his guidance and encouragement throughout the course of this work. The author has received a great deal of valuable critisism and important comments from Professors T. Nagamiya, J. Itoh, M. Ishiguro, and T. Nakamura. The author is also greatly indebted to Prof. F. C. Brown and Dr. D. Kahn for their helpful discussions and suggestions, and to Mr. H. Okura for furnishing good specimens. In addition, the author wishes to thank Mr. T. Tatsumi for his laborious assistance.

This work was supported by the Scientific Research Fund of the Ministry of Education.

References

1) H. Froehlich: Advances in Physics **3** (1954) 325.
2) F. E. Low and D. Pines: Phys. Rev. **98** (1955) 414.
3) T. Yokota: Busseiron Kenkyu **69** (1953) 137.
4) T. D. Shultz: Phys. Rev. **116** (1959) 526.
5) R. S. Allgaier and W. W. Scanlon: Phys. Rev. **111** (1958) 1029.
6) R. L. Petritz and W. W. Scanlon: Phys. Rev. **97** (1955) 1620.
7) A. H. Hutson: Phys. Rev. **108** (1957) 222.
8) F. C. Brown and F. E. Dart: Phys. Rev. **108** (1957) 281.
9) F. C. Brown: Phys. Rev. **97** (1955) 355.
10) K. Kobayashi and F. C. Brown: Phys. Rev. **113** (1959) 507.
11) A. G. Redfield: Phys. Rev. **94** (1954) 537.
12) J. R. Macdonald and J. E. Robinson: Phys. Rev. **95** (1954) 44.
13) M. Onuki and H. Okura: J. Phys. Soc. Japan **15** (1960) 1862.
14) D. Kittel: *Introduction to Solid State Physics* (John Wiley & Sons, Inc.) p. 521.
15) J. R. Macdonald: J. Chem. Phys. **23** (1955) 275.
16) J. R. Macdonald: R. S. I. **25** (1954) 144.
17) K. Yazawa: Toshiba Review **10** (1955) 58.
18) D. Kahn and A. J. Glass: Private communication and to be pulished.
19) W. Shockley: *Electrons and Holes in Semiconductor* (D. Van Nostrand Company, Inc.) Chapter 11.
20) H. B. Callen: Phys. Rev. **76** (1949) 1394.
21) T. D. Lee, F. E. Low and D. Pines: Phys. Rev. **90** (1953) 297.
22) H. Kawamura: J. Phys. Chem. Solids **5** (1958) 256.
23) C. Erginsoy: Phys. Rev. **79** (1950) 1013.

JOURNAL OF THE PHYSICAL SOCIETY OF JAPAN, Vol. 16, No. 5, MAY, 1961

Structures of Photoconductivity Spectra near the Fundamental Absorption Edge of Cadmium Sulfide

By Hiroji MITSUHASHI

Technical Research Laboratories, Japan Broadcasting Corporation, Setagayaku, Tokyo

(Received February 2, 1961)

The photoconductivity structures of CdS single crystals near the adsorption edge were investigated using polarized light at about 81°K. Field dependence of wavelengths of peaks and spectral dependence of decay time of the response were measured as well. From these experimental results, the structures are classified into two groups, one is attributed to the photoconductivity due to excitons which occurs in the shorter wavelength range ($\lambda<4870$Å) and the other to that from some imperfections involved in the crystal, which appears on the longer wavelength side.

§ 1. Introduction

The optical property of CdS crystal has been studied by plenty of investigators[1),2)], partly due to amenability of growing single crystal, in view of clarifying the phenomena which it shows. This crystal is noted as a typical photoconductor and an efficient luminescent material as well. Some of the experimental investigations[2),3)] report that the crystal of high response has quite a sharp single photoconductivity peak near the fundamental absorption edge at room temperature, from which one may estimate the energy gap between conduction and valence band to be 2.4 ev. At lower temperature the specimen shows fairly distinct structures.

The main purpose of the present investigation is to study the origin of photoconductivity structure and the related phenomena.

The photoconductivity at 77°K has been investigated by Böer and Gutjahr[4)], who found a number of fine structures near the adsorption edge. However, no attempt was made for the interpretation of the origin of the structures, irrespective of well-defined result of the structures. Bube[2)] investigated the correlation between the height of the peak at the absorption edge and the magnitude of response of the specimen at room temperature. Gross and co-workers[5)] described the complex structures of photoconductivity on the exciton model, which did not seem to make a consistent explanation on correlation with the investigations by other workers.

In the photo-electric measurements of absorption and reflection spectra of CdS with polarized light, Dutton[1)] determined accurately the temperature and frequency dependence of the absorption coefficient in the intrinsic absorption edge. According to his experiment for polarized light with E vector parallel to the crystalline c axis ($E||c$), there occurs one absorption peak at 4844Å near 80°K which is called B band; for polarized light with E vector perpendicular to the c axis ($E\perp c$), another line appears at 4874Å called A band. Appearance of the reflectance spectrum at lower temperature, as Dutton reported in his paper, gives some indication of the relationship of the exciton-like absorption structure. Recently Thomas and Hopfield[6)] found well-defined reflection peaks at lower temperatures, which lead to the assignment of three exciton series, two of which are associated with the above mentioned A and B bands and the other with C band situated at shorter wavelength than the two bands. Namely the new band C occurred near 4735Å as a considerably broader hump at 77°K. Using the Kramers-Kronig relation they determined oscillator strengths and oscillator frequencies of the reflection lines, which must correspond to the direct allowed excitons. The strength and reproducibility of the lines also made clear that the reflection spectra were not due to some impurities. The existence of three types of excitons was described in terms of the splitting of the valence band. Further quantitative estimation was made for the three valence bands at 4°K. The analysis[7)] of the absorption coefficient in the wavelength range of the absorption edge confirmed a process involving simultaneous creation of an exciton and absorption of a phonon.

The present paper describes that some of the structures of the photoconductivity near 5000Å can be explained in terms of the existing exciton model suggested by Gross and supported by reflectance and fluorescent study of Thomas and Hopfield[6].

§ 2. Experimental Procedures and Results

While a very thin sample is required for transmission measurement, conditions for the thickness of the sample will be relaxed for photoconductivity measurement. It must be taken into first consideration for the experiment that the specimen should retain the intrinsic properties of the crystal. Such treatment as polishing, etching, thermal soldering, intense heating or cooling or so must be avoided[8]. According to our experience, best results were obtained on the fresh crystals, which were grown from vapor phase and showed small traces of striants over the surfaces.

The photoconductivity data were obtained by measuring photo-induced current in the crystals with constant applied voltage. Most of the exact experiments have been made on two crystals (Nos. 7 and 8). One of the experimental difficulties was to make an adequate contact of metallic electrode with the crystal. Ohmic contact with indium is to be unexceptionally recommended for usual photoconductivity measurement of CdS[9]. During In-soldering to the specimen, however, the crystal undergoes thermal or mechanical stress with undesirable result of destroying the photoconductivity structures. Hence precaution was taken for setting the specimen in the cryostat. In-Hg paste was selected as electrode material for that purpose[10]. At first, thin small indium blocks were pasted with polystyrol binder on the Maylar polyester film, sticked to a cooling copper rod. Wiring to the specimen was made by soldering lead wires to the In blocks. On the surface of each indium block a small pellet of In-Hg paste was dropped. After the crystal was bridged across the two In electrodes, thin flakes of indium were placed over the ends of the specimen, which was left for two or three days to be enough amalgamated that stable rest of the crystal was brought about. Ohmic contact is the main consideration in the photoconductivity measurement. However,

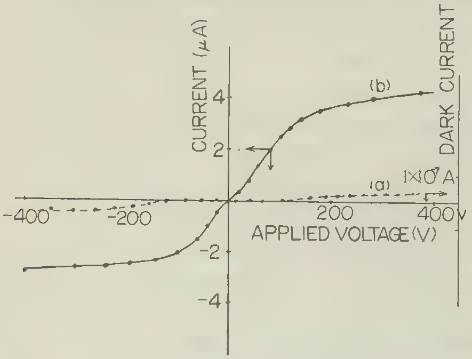

Fig. 1. Ohmic characteristic of the sample soldered with In-Hg paste (specimen No. 7, measured at room temperature), (a) in the dark (b) under ambient illumination.

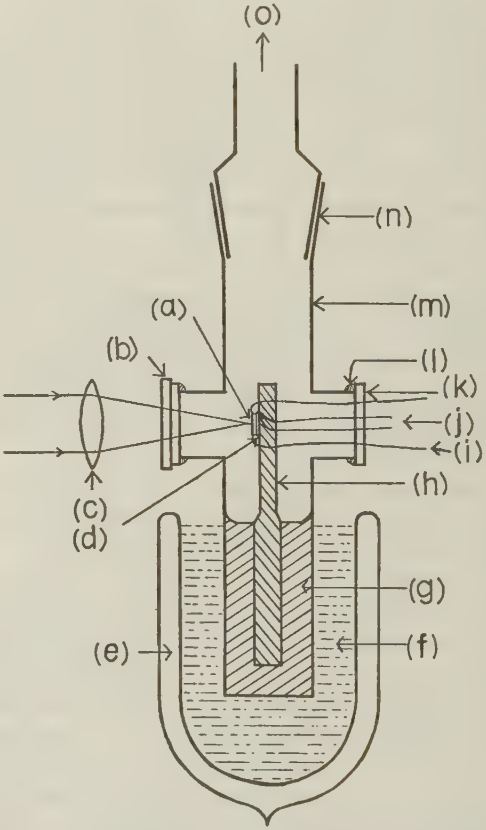

Fig. 2. Cryostat for the low temperature measurement. (a) CdS crystal under study, (b) Polaroid film polarizer, (c) achromatic glass lens, (d) Maylar film of 10 micron thick, (e) Dewar vessel, (f) liquid nitrogen, (g) copper block, (h) cooling copper block, (i) wirings to electrodes, (j) thermocouple, (k) transparent fused quartz window, (l) wax, (m) glass envelope, (n) grounded glass connection, (o) connection to vacuum pump.

the current vs. voltage curve reveals that somewhat non-ohmic nature was unavoidable as shown in Fig. 1. Electric field was applied parallel to the c axis for all measurements.

For the low temperature experiment, a copper rod on which the crystal rested served as a conductor for cooling the specimen, as illustrated in Fig. 2. The temperature of the crystal was measured by means of a thermocouple placed in the In electrode in the visinity of the sample. Variations of the temperature were noticed from one sample to another, possibly depending on conduct of the cooling copper rod to the copper block, which was immersed in the liquid nitrogen in a Dewar. The equilibrium temperature of the crystals was estimated to be 81°±3°K.

The monochromators employed were an instrument with double flint glass prisms made by Tokyo Optical Company and modified Cary Spectrophotometer Model 14, using a tungsten lamp as a light source. The resolution of the instruments was adjusted to be about 2Å, the wavelength accuracy being within 2Å. The direction of incident light was always normal to the c axis of the crystals. Monochromatic light from the instrument was too weak to carry out wavelength scanning at tolerable speed, due to the fact that time delay of photoconductivity becomes exaggerated for feeble intensity of irradiation. Hence the scanning rate was chosen at 0.15Å/sec or less, where almost coincident data of spectral distribution were obtained for both scanning directions, i.e. from longer to shorter wavelength side and *vice versa*. Photocurrent was introduced into a vibrating reed electrometer, the output of which was lead to a recorder. Reproducibility of the data was so conspicuous as to facilitate analysis of the photoconductivity structures. The spectral intensity of the incident radiation was measured beforehand with a sensitive thermocouple connected with an amplifier at wider slit of the spectrometer. Thus correction was made for both spectral distribution of the energy of the tungsten lamp used as the light source and dispersion of the prism of the instrument. However, further corrections for the reflection loss at the crystal surface and the transmitted light were disregarded. Any traces of luminescence were not observed for the wavelength region of the incident radiation.

The photoconductivity data on two specimen are shown in Fig. 3 for different polarizations of the incident light, i.e. with E vector paralleled

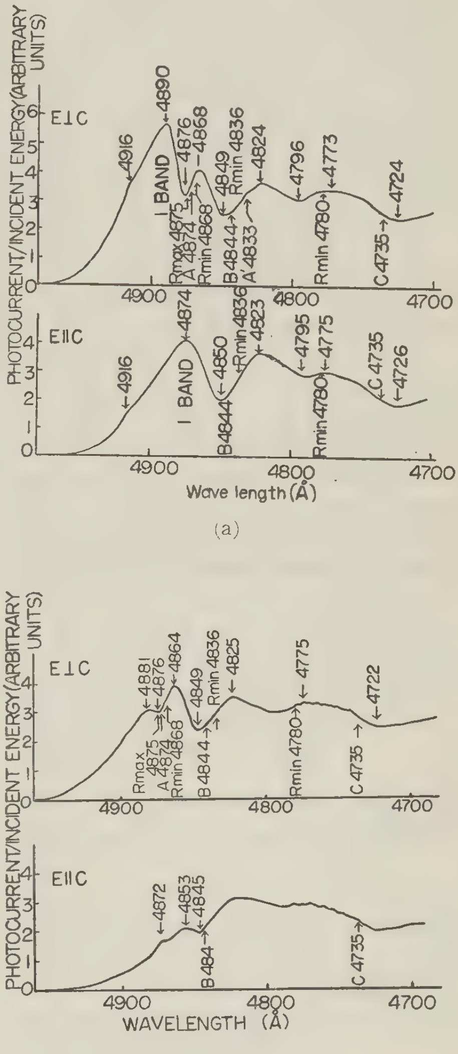

(a)

(b)

Fig. 3. Photoconductivity spectra of CdS for light polarized with $E\perp c$ and A, B and C refer to the exciton bands of $n=1$ and A' to that of $n=2$, identified by Thomas and Hopfield.[6] $R_{\max}$ and $R_{\min}$ correspond to the reflection maximum and minimum observed by Dutton.[1] Electrode distance was 2.5 mm. The temperature of the specimens was 81°K

(a) For the sample No. 7 [3.5 mm $(\|c)\times 1.5$ mm $\times 0.2$ mm], at the field strength of 560 V/cm. Besides the structures due to exciton bands of $n=1$, there is a trace of a structure, presumably due to A' band.

(b) For the sample No. 8 [4 mm $(\|c)\times 1.3$ mm 0.3 mm], at the field strength of 600 V/cm.

to and perpendicular to the *c* axis. Several distinct peaks stand out in the background of the photoconductivity in the fundamental absorption region. From the appearance of the photoconductivity data presented here as compared with the reflectance structure previously reported[1], there seems to be some definite similarities between them, indicating correlation of optical and photoelectric phenomena.

A prominant photoconductivity band presents its maximum at the longer wavelength side of the absorption edge which is denoted as *I* band in Fig. 3. Its peak is generally higher for the more photoconductive material. One of the notable properties of this band is that the peak is field dependent. The wavelength at which the maximum occurs shifts to longer wavelength as the applied field strength is increased as shown in Fig. 4. A sample of poor response has, in general not well-defined shapes as seen on the specimen No. 8 (Fig. 3b). In addition such a sample does not show its band at a fixed wavelength. Other bands except *I* peak near the adsorption edge do not show a field dependent shift within the experimental errors.

The rate of decay in photocurrent vs. wavelength of the incident radiation is illustrated in Fig. 5 as determined by the time intervals required for the current to decrease to 10 percents of the initial value, due to a sudden removal of the illumination.

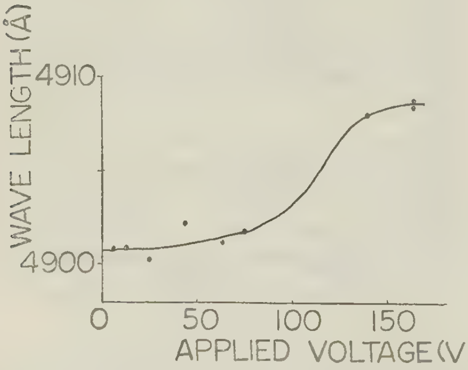

Fig. 4. Dependence of wavelength of the peak for *I* band on the electric field at 109°K (specimen No. 7, $E \perp c$).

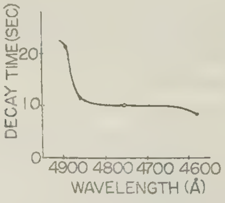

Fig. 5. Photoconductivity decay time vs. wavelength of exciting radiation, for the sample No. 8 at 81 K. ($E \perp c$)

§ 3. Assignment of the Photoconductivity Spectra

Light has been thrown on the energy band structure of the CdS by a lot of experimental investigations, such as optical studies involving adsorption, reflection and luminescence[11], and measurement of cyclotron resonance at liquid helium temperature[12]. On the other hand no attempt seems to have succeeded to make a consistent interpretation of the photoconductivity spectra near the fundamental absorption edge from the standpoint of the energy band structure.

Analysis of the photoconductivity spectra must be carried out, taking into consideration of electrical properties of carriers as well as optical behaviors of the crystal. In general some experimental difficulties are encountered in the course of the investigation, because the photoconductivity occurs by drift of free carriers generated by absorption of photons. Further the electric field seems to be not uniformly applied, especially for the sample which is "soft" soldered with In paste as mentioned in the section 2. Thus the field strength may vary from the surface to the interior of the crystal. Now owing to the fact that lifetime of the carrier depends on the wavelength of the incident light, another complication will be involed in the phenomena of the photoconductivity. An accurate information could be obtained under the favorable conditions. After making correction to various repeated experiments on several samples, we will try to describe the origin of the photoconductivity spectra. In spite of the complexity a fairly accurate nature of the photoconductivity is disclosed on some crystals which have well-defined spectral peaks.

It applies to the reflection spectra that the wavelength midway between a reflectance maximum and minimum should correspond closely with the position of an absorption peak. The analogy will hold for the photoconductivity spectra also. Careful examination of the data reveals an interesting fact that in the absorption edge some wavelengths at which the photoconductivity response shows steep slope agree with the absorption lines associated with above cited A, B and C bands reported by other investigators[1),6)]. Spectral response distribution in the ranges from 4880Å to 4868Å for $E\perp c$ and those from 4848Å to 4825Å for both $E\perp c$ and $E\|c$ are coincident quite well with the reflection spectra measured by Dutton at nearly same temperature (80°K), each dip of the photoconductivity corresponding to the reflection peak and *vice versa*. Near the wavelength range of 4750Å, another broad hump appears which occurs at the separate dip of the reflection spectrum corresponding to the C band. Spectra due to I band of some samples show complex form of one peak or more which sometimes emerge in the range of A band, causing confusion in assignment of the spectra. In addition, a difference in the lifetime of the carrier is noticed between excitations by the I band and by other bands. Thus the I band is different in nature from those due to A, B and C bands.

It will be reasonably admitted that the photoconductivity structures in the wavelength range of A, B and C bands occur from exciton absorption, owing to the close correspondence between the structures and exciton lines with regard to the positions and the number of peaks which can be just inferred from the selection rule according to the direction of polarization of incident light. On the other hand the band denoted as I emerges outside the exciton band where the absorption coefficient is considerably lower[7)] (about $10^2\ \text{cm}^{-1}$ or less). Therefore the free carriers are primarily generated in the bulk while the exciton creation is restricted near the surface of the crystal.

There is some trace of fine structures which appear as several extraordinarily sharp lines overlapped with the main peak of the I band. Origin of such fine structures cannot be understood at present.

Physical interpretation of the I band is difficult according to the experimental data of the present work. It may be supposed, however, that some defect or impurity involved in the crystal is accounted for. This band is supposed to be located near the conduction band. Therefore we tentatively make an assignment for the center corresponding to the I band after the Lambe-Klick model[13)], in which the trapping level responsible for luminescence and photoconductivity is located near the conduction band in the forbidden band. Thus the electron in the I band will be in the similar state to that of the trapping center of the above model, whose wave function has the same symmetry of conduction band (Γ_7) or is close to it. Birman[14)] made the same assumption for describing the polarization of 6200Å luminescence of CdS.

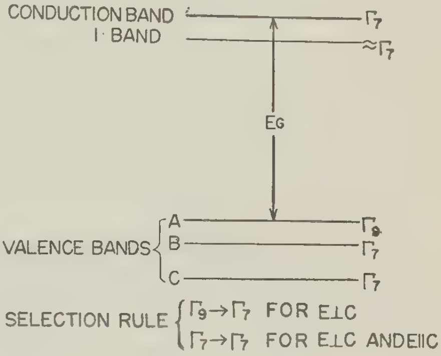

Fig. 6. Energy band structure of CdS. The levels A, B and C correspond to the valence bands to which the excitons series A, B and C belong. The symmetry is expressed by the Bethe's notations for hexagonal symmetry.

In Fig. 6 is shown the schematic diagram indicating the energy band structure of the crystal.

It may be summarized for the assignment of the structures that photoconductivity near the absorption edge peaks can be described along the line consistent with the existing exciton scheme and the impurity center model.

§ 4. Discussion

The mechanism of exciton photoconductivity is not clearly explained for the present situation of the investigations. However, it may be inferred that (i) exciton generated by the optical absorption will migrate through the crystal and happens to dissociate by absorption of a phonon into a free electron and a free hole, drift of the electron inducing the current; (ii) when the migrating exciton comes to the neighbourhood of some imperfection where an electron is trapped and this electron will be ionzed into the conduction band by the interaction of the exciton; (iii) an alternative but related explanation is the indirect optical absorption, simultaneously participated by an exciton and a phonon, which may produce a free electron. Some of the above-mentioned processes will be in action to exciton photoconductivity. On the other hand, the photoconductivity due to the imperfections is different from that due to exciton in feature.

As the stated in the section 2 the peak of *I* band undergoes field-dependent shift, although such a shift is hardly observed for the exciton spectra of photoconductivity within the experimental errors. These phenomena are possibly due to the difference of field strength in the region where generation of the free carriers occurs. The spectral characteristics due to the impurity photoconduction varies from one sample to another. Exact identification of the centers responsible for this band will provide some clue to growing the crystals of high sensitivity which are to be used as photoelectric detectors. Furthermore the non-ohmic character of the crystal shows similarity to the field dependence of the wavelength of the peak due to *I* band, as readily seen in comparison of the plots of Fig. 1 with Fig. 4, suggesting existence of the regions of strong local field strength, presumably near the imperfections involved in the crystal. Other investigators[15),16),17)] report that the optical absorption edge tends to shift to longer wavelength with an increase of applied electric field on account of space charge effect or tunnel effect of optically excited electrons. It must be pointed out here that the decay time of photoconductivity is longer for the *I* band than for the exciton band. The trend of the decay time is in principal accord with the interpretation of the lifetime of the free carrier by Bube[2)], i.e. for a photosensitive material, the volume lifetime is much longer than the surface lifetime. The latter should be associated with exciton absorption and the former with impurity absorption for our case. Thomas and Hopfield[6)] discussed the fluorescence phenomenon of CdS, suggesting that the radiative decay of excitons occurs from "impurity" exciton states and "impurity" states provide a favorable mechanism for the radiative decay of excitons. There seems to exist a close correlation between the imperfection that gives rise to the *I* band photoconductivity and the "impurity" states which take part in the fluorescence.

Several interesting problems remain to be investigated. At lower temperature (e.g. 4°K) the photoconductivity structures will become more sharp. Hence it is expected that identification of the spectra will be made feasible. The structure due to excited state of exciton ($n=2$) would be expected. It would be quite interesting to study temperature dependence of the response at the *I* band in the wider range of temperature. This study would also provide a fairly accurate information on the nature of the imperfections of the crystal. In spite of the experimental troubles involved in the measurement owing to obscurity of the behaviors of the free carriers, a qualitative explanation of the structures on the basis of the reproducible data should lead to clarification of the precise nature of photoconductivity.

§ 5. Conclusion

The photoconductivity structures near the absorption edge in pure CdS can be divided into two classes from the above argument:

(i) One is closely associated with the excited absorption. Photoconductivity structures belonging to this class are intrinsic to the crystal. The carrier lifetime of the carriers due to this band is rather short.

(ii) The other is presumably due to the imperfection of the crystal. The structures occur on the longer wavelength side of the exciton band, though the peaks and the shape vary from sample to sample. The physical nature of the center responsible to the structures cannot be clarified enough by the present work.

The author wishes to express his appreca-tion to Prof. S. Makishima, Dr. G. Kuwabara and Dr. S. Shionoya of Tokyo University for illuminating discussions and to the members of the Research Group on Solid State for helpful advice and to Director S. Shima, Vice Director T. Nomura and Dr. H. Kuroda of the Laboratories for their continued encouragement. The author is indebted to Dr. S. Ibuki of Mitsubishi Electric Company for the crystals used in this study.

References

1) D. Dutton: Phys. Rev. **112** (1958) 785.
2) R. H. Bube: Phys. Rev. **101** (1965) 1668.
3) J. J. Lambe: Phys. Rev. **93** (1955) 985

4) K. W. Böer, H. Gutjahr: ZS. f. Phys. **152** (1958) 203.
5) E. F. Gross, *et al*: Nauk SSSR **110** (1956) 761, quoted from R. H. Bube: Photoconductivity of Solid, J. Wiley, (1960) p. 228.
6) D. G. Thomas, J. J. Hopfield: Phys. Rev. **116** (1959) 573.
7) D. G. Thomas, J. J. Hopfield, M. Power: Phys. Rev. **119** (1960) 570.
8) E. F. Gross, B. V. Novikov: Soviet Physics-Technical Physics, p. 2071, Vol. **1** [p. 1723 in English Ed. (1960)].
9) R. W. Smith: Phys. Rev. **97** (1955) 1525.
10) G. Diemer: Philips Res. Repts. **13** (1958) 458.
11) R. J. Collins: J. App. Phys. **30** (1959) 1135.
12) R. N. Dexter: J. Phys. Chem. Solids, **8** (1959) 494.
13) J. Lambe, C. C. Klick: Phys. Rev. **98** (1955) 909.
14) J. L. Birman: Phys. Rev. Letters, **2** (1959) 157.
15) K. W. Böer, H. J. Hänsch, U. Kümmel: ZS. f. Phys. **155** (1959) 170.
16) K. W. Böer: ZS. f. Phys. **155** (1959) 194.
17) R. Williams: Phys. Rev. **117** (1960) 1487.

JOURNAL OF THE PHYSICAL SOCIETY OF JAPAN, Vol. 16, No. 5, MAY, 1961

Smoke Observation on Boundary Layer Transition Caused by a Spherical Roughness Element

By Masako MOCHIZUKI

Department of Physics, Ochanomizu University,
Otsuka, Tokyo, Japan

(Received December 2, 1960)

Observations were made in the boundary layer along a flat plate in a wind tunnel. A sphere of various diameters was placed on the plate as an isolated roughness element and the resulting flow patterns were examined by the smoke emitted from various heights and positions relative to the sphere. The patterns were stereographically photographed from upper and lateral sides, in order to make clear the mechanism of the change of patterns with varying velocities, namely Reynolds numbers. At low velocities, peculiar vortex filaments are formed. With increasing velocity, they begin to be deformed periodically and a characteristic row of arch-shaped vortices is formed. As the velocity is further increased, the wedge-shaped turbulent region appears downstream and gradually approaches the sphere, encroaching upon the laminer part. Vortex filaments parallel to the direction of the main stream appear with a constant spacing with their heads along the sides of the wedge. These observations were compared with measurements by hot-wire and with the results of visualization reported by other investigators.

§1. Introduction

In the early stage of development, the prime object of researches in turbulence was isotropic turbulence, but recently anisotropic turbulence, and furthermore, as a fundamental problem, the production mechanism of turbulence itself, have come to attract more and more attention. Schubauer and Klebanoff[1] have examined natural transition and the transition caused by spark or three-dimensional roughness by hot-wire technique, and interpreted the transition with the conception of turbulent spot. Gregory and Walker[2] and Weske[3] have investigated, by visualization techniques the transition mechanism and the process caused by three-dimensional roughness in boundary layers. However, the final conclusion on the production mechanism of turbulence seems to have been not yet obtained.

In the present stage, it seems to be the first necessity to examine the mechanism visually. With a view to clarifying the production mechanism, we examined in detail the process in which flow patterns around a sphere changed with Reynolds numbers, by photographing the flow structure in each process.

For the visualization of the flow patterns in the air, the smoke or china clay method has usually been used. The latter only shows results in which the intensities of disturbances of air flow over a solid surface are averaged over a long time. On the other hand, the smoke method is able to show not only the fluid motion at any position by changing the positions of the smoke source, but also the patterns of flow over a wide region and in detail at every moment; moreover, the method can show mean behavior of fluid motion by taking long-exposure photographs. For these reasons, we adopted the smoke method for the present study.

§ 2. Experimental Arrangement and Method

The experiments were made in a 50×50×200 cm closed Göttingen-type wind tunnel in our University, having windows on both lateral and upper sides. A laminar boundary layer was formed on a flat plate which was placed holizontally at a distance of 15 cm above the bottom of the tunnel. The plate was made of black-enameled aluminum and black acryl resin to get good photographic effect, and it was divided into 2 or 3 parts in order to emit the smoke from the gaps. The arrangement is shown in Fig. 1. In order to regulate the flow for zero pressure gradient, wire gauzes were stretched across above the plate at the downstream end of the measuring section.

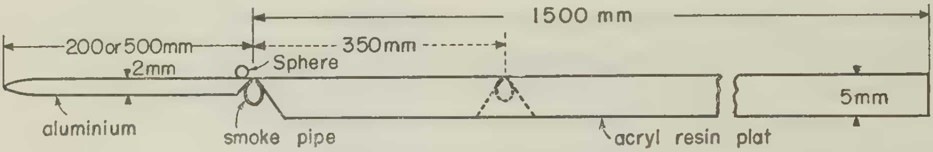

Fig. 1. Arrangement.

As the roughness element, a bearing ball was used, whose diameter (k) was 0.71, 0.55, 0.33 and 0.23 cm, respectively. The roughness element was set at various distances from the leading edge of the plate.

Flattend pipes, which were made from brass pipes of 0.3 mm in diameter and 35 cm in length, were attached to the lower side of the gaps (about 1 mm wide) between the parts of the plate, with their sharpened sides up and down. These pipes have holes at an interval of 2 mm along their upper side. In order that the smoke blown in from both ends of the pipe might be emitted uniformly, the hole size was increased gradually from the ends towards the center (0.4~0.7 mm). In the early stage of experiments the smoke of tobacco was used, but it turned out inconvenient for continuous emission for a long time. Therefore, the smoke of evaporated liquid paraffine was used for the subsequent observation. Without the roughness element, the smoke crept in clear lines along the plate. In order to examine in detail the pattern in the neighborhood of the roughness element, the smoke was emitted at various streamwise positions and heights by the following methods. In the early stage the smoke was emitted from a flattend pipe which was made from a brass pipe of 1 mm in diameter and pierced with holes at an interval of 1 mm. But at a later stage, in order to diminish disturbances to the flow, a smoke sheet was formed by electrically heating a nichrome ribbon (0.1 mm thickness, 0.8 mm width) with liquid paraffine rubbed on.

The flow patterns revealed by the smoke were photographed stereographically both from the upper and lateral sides.

§ 3. Outline of Changing Process of Flow Pattern

Placing the sphere in front of the gap in the plate surface and emitting smoke from it, the changes in the flow pattern produced by the sphere were observed by increasing the wind velocity. Some of the results are

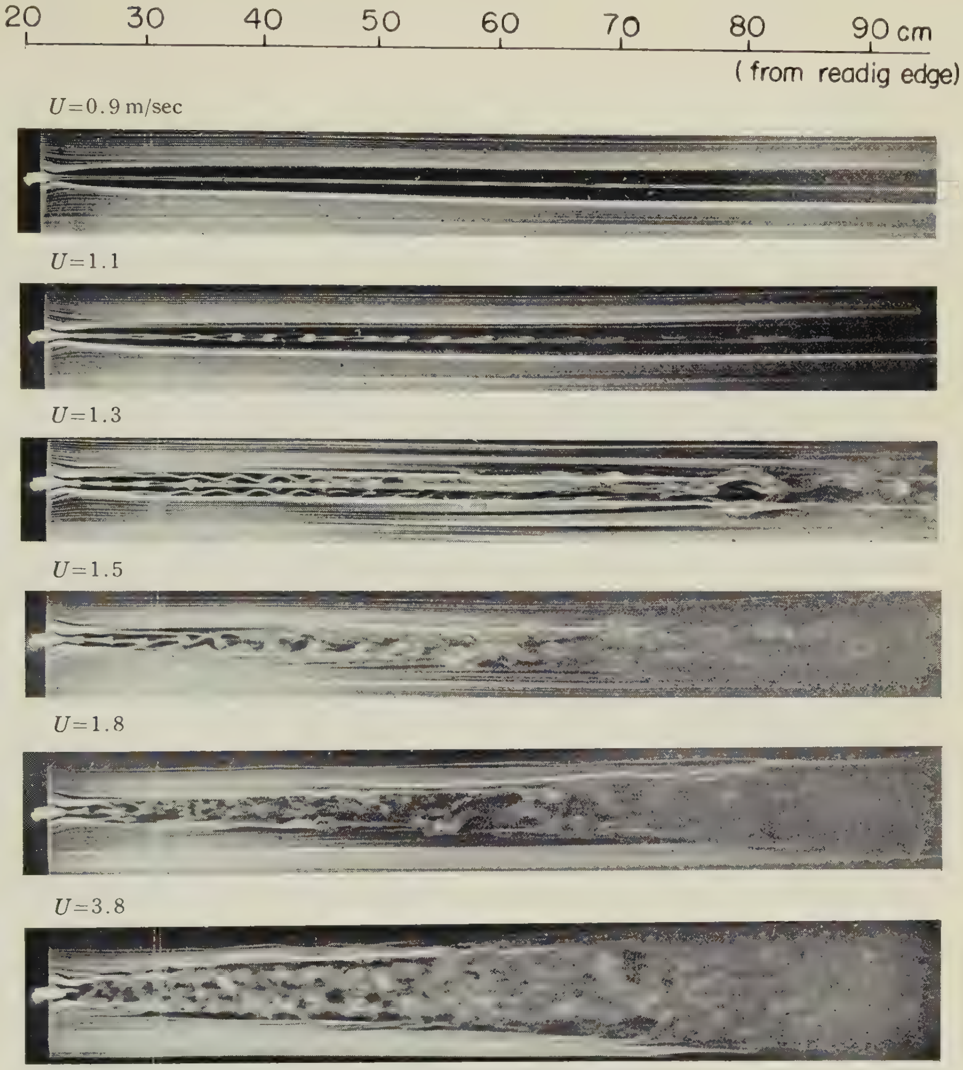
20
30
40
50
60
70
80
90 cm
(from readig edge)
U=0.9 m/sec
U=1.1
U=1.3
U=1.5
U=1.8
U=3.8

(A-a)

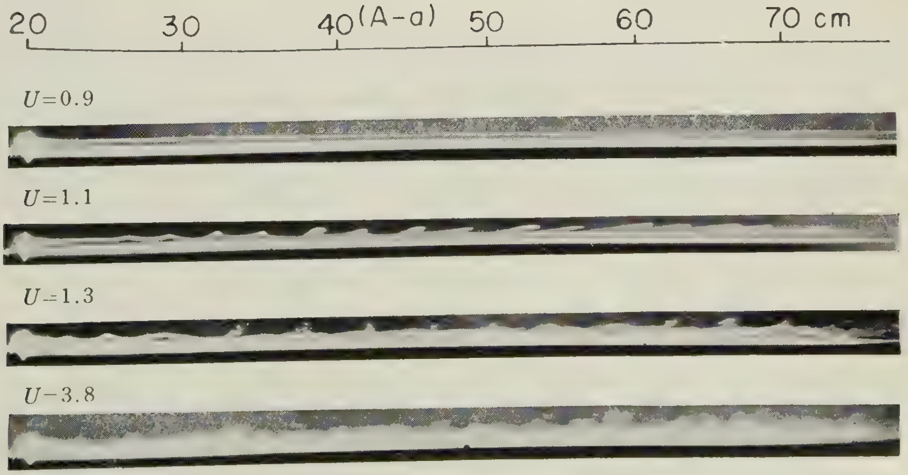
20
30
40(A-a)
50
60
70 cm
U=0.9
U=1.1
U=1.3
U=3.8

(A-b)

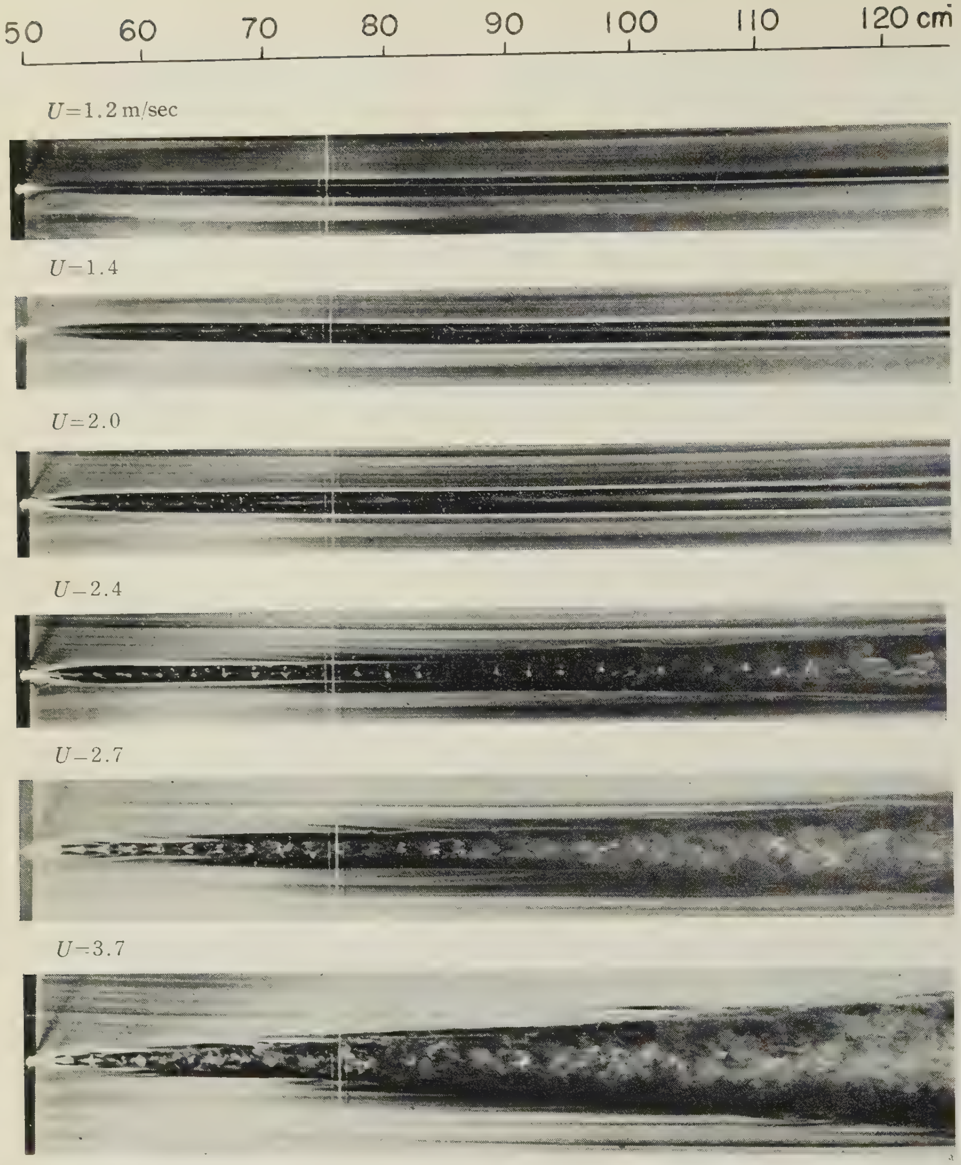
50
60
70
80
90
100
110
120 cm
$U=1.2$ m/sec
$U-1.4$
$U=2.0$
$U-2.4$
$U-2.7$
$U-3.7$

(B-a)

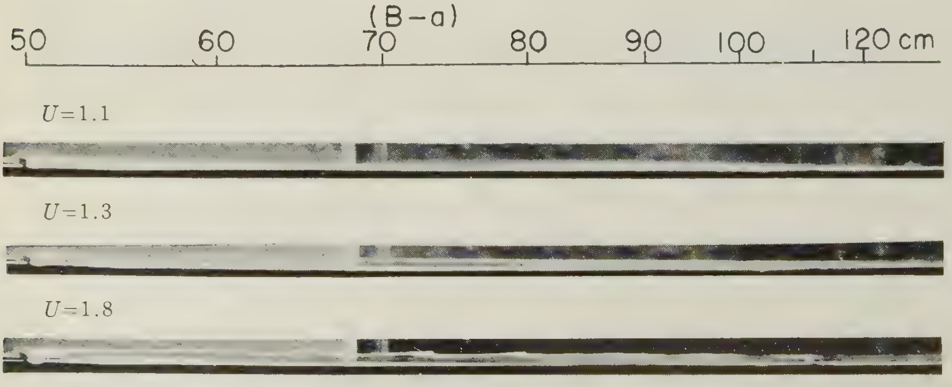
(B-a)
50
60
70
80
90
100
120 cm
$U=1.1$
$U=1.3$
$U=1.8$

(B-b)

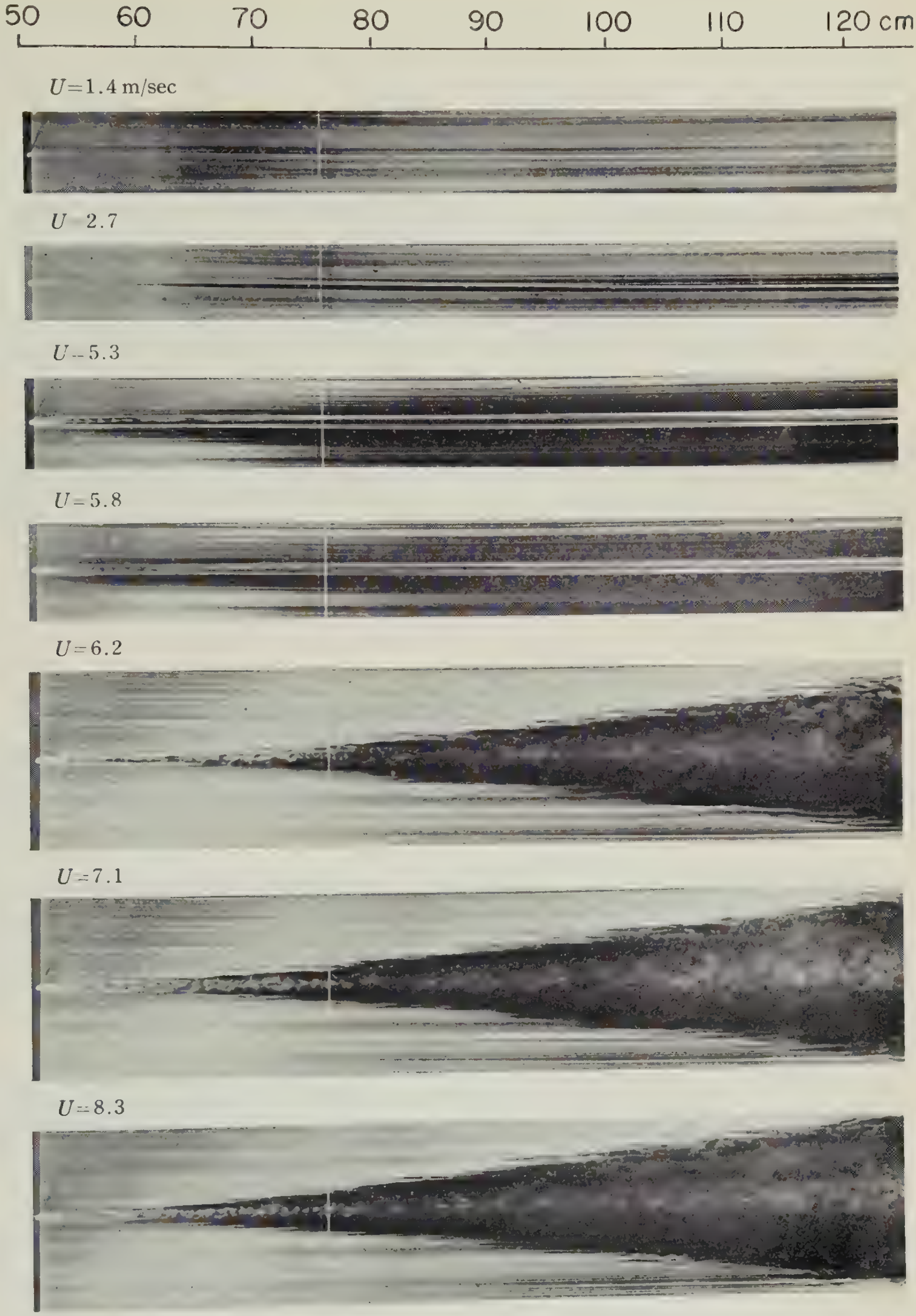

(C)

Fig. 2. Smoke flows produced by spherical roughness element. Smoke is emitted on the plate downstream of the sphere. (A) $x_k \fallingdotseq 20$ cm, $k=0.71$ cm. (B) $x_k \fallingdotseq 50$ cm, $k=0.55$ cm. (C) $x_k \fallingdotseq 50$ cm, $k=0.23$. (a) Plane view. (b) Side view.

shown in Fig. 2. When the wind velocity was very small, there were observed only a reversed flow of smoke close behind the sphere and a single smoke streak trailing downstream from it. As the velocity was increased a little, a pair of smoke spirals (we may call them fixed vortices) appeared close behind the sphere and two parallel smoke filaments (we may call them trailing vortices) trailed downstream parallel to the plate from the top of the spiral vortices. At the same time a horseshoe-shaped smoke filament (we may call it horseshoe vortex) appeared, which circled round the front of the sphere (Fig. 3). These filaments changed their shapes successively as the velocity is in-

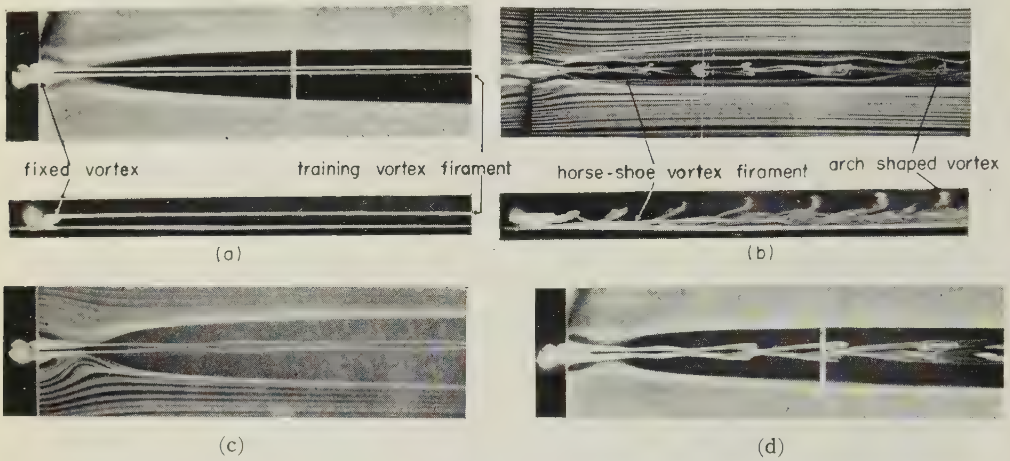

Fig. 3. (a) Stationary state. (b) State of shedding periodic vortices. (c) Waving state. (d) Saw-shaped state.

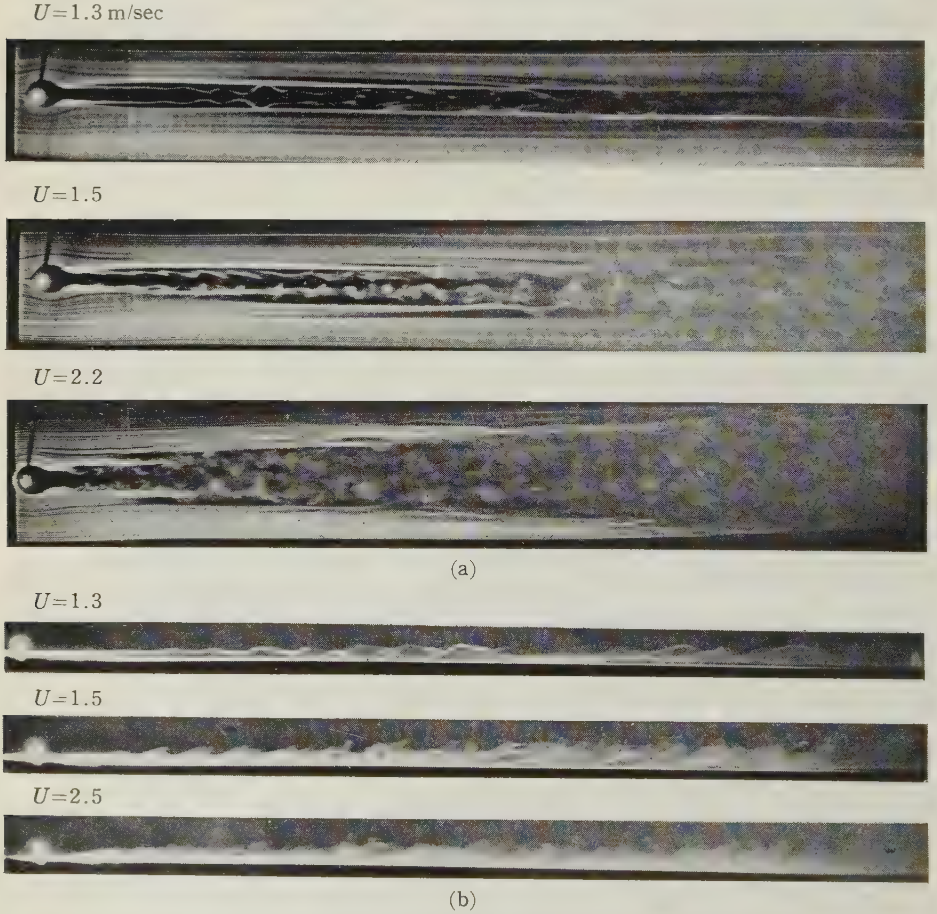

Fig. 4. The case of smoke emitted on the plate upstream of the sphere. $x_k \doteqdot 20$ cm, $k=0.71$ cm.

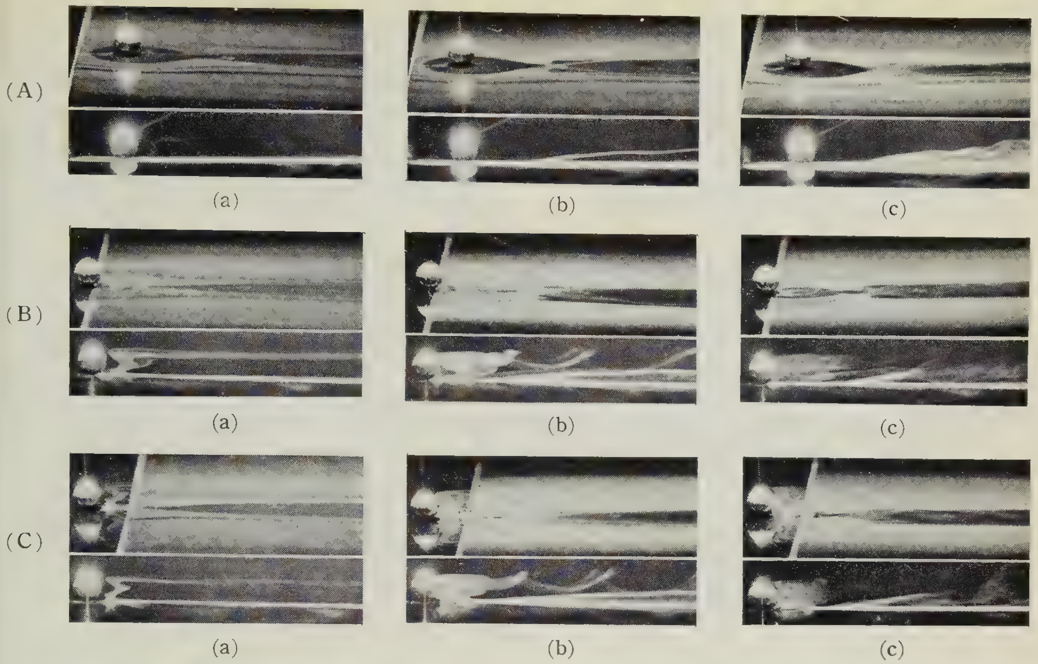

Fig. 5. Structure of fixed vortices. (A) Smoke is emitted on the plate upstream of the sphere, (B) immediate downstream and (C) more downstream. (a) Stationary state. (b) State of shedding of arch-shaped vortices. (c) Turbulent state. $k=0.71$.

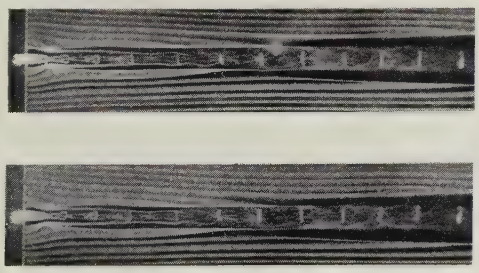

Fig. 6. Stereograph of arch shaped vortices.

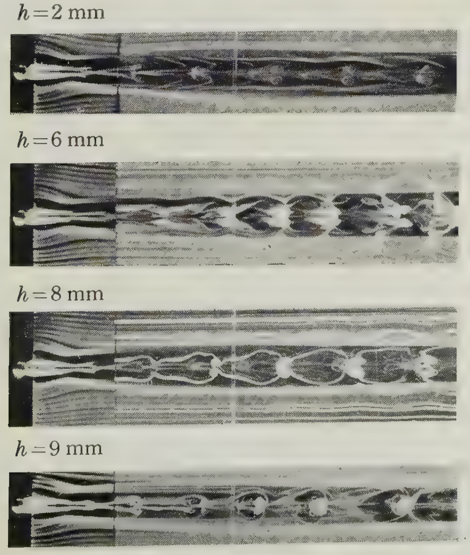

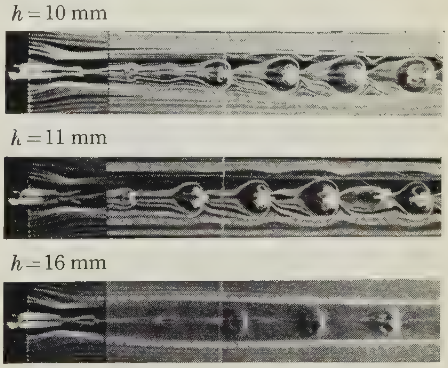

Fig. 7. Structure of arch-shaped vortices. Smoke is emitted both from the plate and upper height (h).

creased.

The trailing vortex filaments begin to wave and then the raised parts begin to show an evident twist (Fig. 3-c and d). These transformations are small near the sphere and develops over some distance, and beyond there, they ceases to grow; the raised parts are stretched by shearing stress in the boundary layer. The horseshoe vortex filament detaches itself upward from the plate as the velocity is increased. Then, the twist of trailing vortex filaments develops into rol-

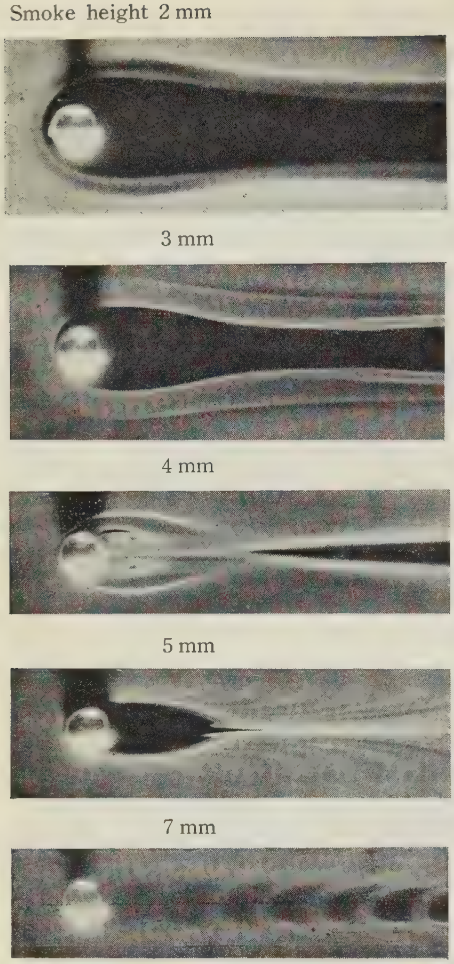

(a)

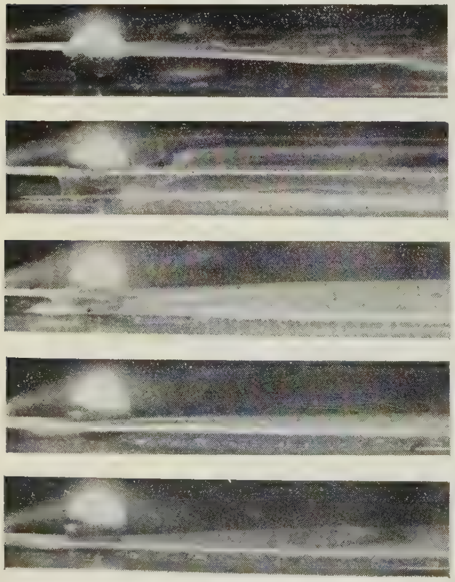

(b)

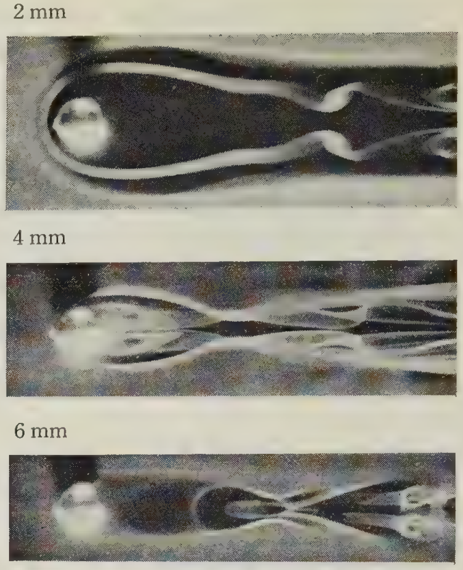

(c)

Fig. 8. Structure of horseshoe vortex. Smoke height is varied. (a) Stationary state. (b) Side view of stationary state. (c) State of shedding of arch shaped vortices. $k=0.71$ cm.

ling-up and the rolled up parts of the two filaments stand in pairs at equal intervals. These vortex-shaped patterns have their axes rising gradually upright until they become nearly vertical at some distances from the sphere. Beyond that, the rotating energy of the vortex-shaped patterns is weakened, and they were stretched downstream owing to the shearing stress. Finally, the vortex-shaped patterns take an arch-shaped configuration. In this stage, the horseshoe vortex filament also show three-dimensional deformations with the period which is the same as that of the arch-shaped vortices.

As the velocity is further increased, the definite periodic shapes of these patterns disappear to be replaced by a turbulent state starting from the downstream location. At the same time the turbulent part gradually encroaches the laminar part of parallel smoke lines. This turbulent part may be regarded as the so-called turbulent wedge, whose apex proceeds upstream and finally reaches the sphere.

These transition processes hold good for different sizes and positions of spheres. In the following sections, each process may be considered in detail.

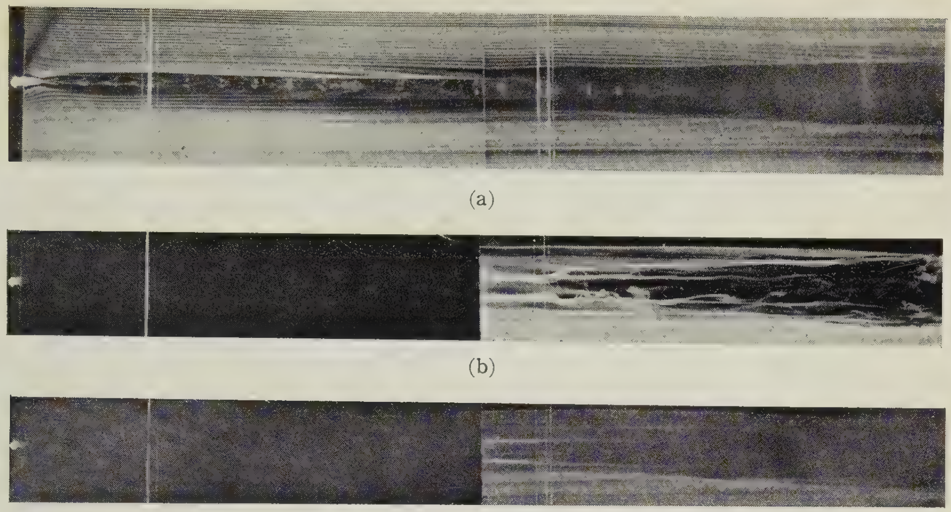

(a)

(b)

(c)

Fig. 11. (a) Smoke is emitted on the plate close downstream of the sphere; photographed instantaneously. (b) Emitted 35 cm downstream from the sphere and photographed instantaneously. (c) Emitted from 35 cm downstream; long exposure (0.5 sec).

§ 4. Structure of Vortex

When we compare Fig. 2, in which smoke is emitted from downstream of the sphere, with Fig. 4, in which smoke is emitted from upstream, it may be considered that the horseshoe vortex filament is formed from upstream of the sphere and the trailing vortex filaments are formed in its downstream. In order to make clear the structure of these vortex filaments, the smoke is emitted from various positions relative to the sphere and the plate, and the photograph was taken of the flow pattern in the neighborhood of the sphere in magnified scale.

The following processes are observed from Fig. 5 in which the smoke is emitted from downstream of the sphere. There appear a pair of spiral smoke filaments vertical to the plate at about one diameter downstream from the sphere (the distance seems to increase with the flow velocity). On rising level with the top of the sphere, the smoke filaments trail downstream parallel to each other and to the plate. It is observed from Figs. 5–B and 5–C in which the smoke is emitted from up- and downstream positions of the center of the spiral, respectively, that these spiral filaments are cylindrical vortices. It is seen from the photographs that the smoke deposited over a certain region on the plate is sucked up and raised spirally. At low velocity, the rotation of the fixed vortices is weak and the trailing vortex filaments are straight lines; with increasing velocity, the trailing vortex filaments show waviness as stated above (Fig. 3-c). At still larger velocity, the fixed vortices become a large turbulent lump (Fig. 5-C-c) so that the spiral motion disappears and the trailing vortex filaments show turbulence at slightly downstream of the sphere.

At a certain velocity, a row of vortices is formed very clearly by the following process. A pair of waving trailing vortex filaments are distored into saw-teeth shapes at regular intervals (Fig. 3-d). Their oblique sides of the saw-teeth are twisted in such a way that, looking from downstream, the right filament rotates clockwise, while the left filament anticlockwise. With increasing velocity, the tips of the saw-teeth are raised and the bottoms lowered. Further, the twisted sides are strengthened until finally rolled up two or three times to form seemingly a series of vortex pairs (Fig. 3-b). These vortex-shaped structures are clearly noticed in the stereographs. As the vortex-shaped patterns grow still further, the individual vortex pair joins together at the heads and takes arch-type shape (Fig. 6). The height of the vortices increases rapidly near the sphere and their tops are raised out of the boundary layer. In further downstream region, the vortices cease to grow and then diffuse gradually.

When the largest sphere is used and the smoke is emitted from the plate surface, these arch-type vortices are not easy to observe. In this case, it can be surmised that the smoke emitted from the surface is not always able to wind around the arch-shaped vortices up to their tops. In order to make sure this explanation the smoke source (nichrom wire) was set at various heights downstream of the sphere, and the resulting patterns of flow were photographed stereographically. Some of them are shown in Fig. 7. The smoke emitted from rather low height is rolled up higher than that emitted from the plate surface. The smoke emitted from a certain height indicates a pattern rotating just around the horizontal part of the arch.

The frequency of shedding vortices is measured from the photograph of row of vortices, with a view to examining the relation between the Strouhal number based on sphere diameter and the Reynolds number, based on velocity at sphere top. The Strouhal number is smaller than that of a sphere but larger than that of a cylinder, both placed in a free stream, and it increases from about 0.1 to 0.23 as the Reynolds number is increased.

In the next place the horseshoe vortex is considered. There is a region around the sphere in which the smoke does not enter as shown in Fig. 4 and 5-A, in which the smoke is emitted from upstream of the sphere. This fact shows that there is a horseshoe-shaped vortex which wraps round the front of the sphere and trails downstream, as has been observed by other researchers. The flow patterns upstream of the sphere are further examined with the smoke source at various heights upstream of the sphere (Fig. 8). The results show that the smoke emitted from lower than sphere center descends and turns back in front of the sphere, and that there exists a vortex having its center close to the sphere and the plate. In the downstream of the sphere and at low velocity, the vortex trail two filaments which are parallel to each other and approach the plate. As the velocity is increased, the filaments raise from the plate and show periodic transformations induced by the arch-shaped vortices. In the case of the smoke emitted from the plate, the smoke filaments stand up rapidly at about three diameters downstream of the sphere and combine with the horseshoe vortex filament.

We shall compare the above-mentioned phenomena with that in the flow around a sphere in a free stream. The photographs of the flow around a sphere were taken in water by Möller[4] and Taneda[5]. In these cases, the fixed vortex takes a rising shape close behind the sphere; but in the present case of boundary layer flow two vortices are formed rising vertically from the surface, and two vortex filaments trail downstream from the respective head of the fixed vortices; these filaments correspond to that from the center of the ring-shaped vortex in the case of the free stream. In the free stream case the vortices shed from the sphere can orientate freely, but in the boundary layer case the vortices can be shed only in such a way that they take the arch shape. Thus the vortices formed at the back of the sphere are considered to originate in quite the same process both in the free flow and the boundary layer. However, the horseshoe vortex is occasioned only by the existence of the solid surface. The parallel flow diverges in every direction at the stagnation point of the sphere in the free flow, while in the boundary layer, the flow which would be directed to the surface turns back against the sphere resulting the formation of the horseshoe vortex.

§ 5. Turbulence Wedge

As the velocity is increased, the turbulent region or the so-called turbulence wedge is formed downstream. With further increase in velocity, the vertex of the wedge advances upstream until finally attaches to the sphere. Gregory and Walker[2] have observed by means of the china clay technique that the wedge formed by a cylindrical or conical roughness on a flat plate has the vertex angle of 7°～16°. Schubauer and Klebanoff[1] have examined the turbulence wedge of a sphere by using a hot-wire anemometer. They found a half vertex angle of 6.4° for a fully turbulent region and that of 10.6° including an intermittent region. Tani, Komoda and Iuchi[6] have also made the measurements on the transition effect of a cylinder on a flat plate with zero pressure gradient by using a hot-wire anemometer. In this case the transition was defined by the point where the fluctuation had the intermittency factor of about 50%. Under the condition that $x_t=x_k$, the relation between critical roughness Reynolds number $R_k=ku_k/\nu$ and transition Reynolds number $R_k=Ux_k/\nu$ was obtained, where k is the height of the roughness element, u_k the mean velocity at the top of the element, ν the kinematic viscosity of fluid, x_k the distance along the surface to the roughness location, x_t the distance along the surface to the transition location and U the velocity outside the boundary layer.

In the present experiment, the position of the vertex of the wedge and wedge angle are determined on the photographs, by drawing border lines between the turbulent region and the outer laminar region and the position of the vertex is considered as the transition point. By placing a sphere (of diameter k) at a certain distance x_k, the transition location x_t for various velocities are measured from the respective photographs. From the curve of x_t against the velocity, the velocity corresponding to $x_t=x_k$ is determined. R_k and R_t are evaluated from these values for various k and x_k. The result is shown in Fig. 9, in which the above-mentioned result obtained by Tani, Komoda and Iuchi is shown by a solid line, and the extrapolated curve which corresponds to the present measurement is shown by a broken line. It is interesting to note that the transition point determined by the smoke observation coincides with those determined by the hot-wire observation. The side of the wedge is not a single straight line but is composed of two straight lines linked together at lower velocities, inclusive of critical velocity when the vertex attaches to the sphere. At higher velocity or when the wedge developed into a fully turbulent one, the side becomes a straight line and a definite wedge angle can be determined. Consequently, at the critical velocity two wedge angles are obtained, namely near the sphere and downstream, respectively, while at large velocities, a single angle is measured. These angles are plotted against the velocity in Fig. 10. It can be seen from this figure that all the measured points for various sizes and positions of the sphere are on the lines for respective cases. Above mentioned result of Schubauer and Klebanoff may be regarded to be on the extrapolated line of the present results of the fully developed turbulence wedge. It is interesting to see that the results obtained from the smoke pattern and those from the hot-wire measurements are in

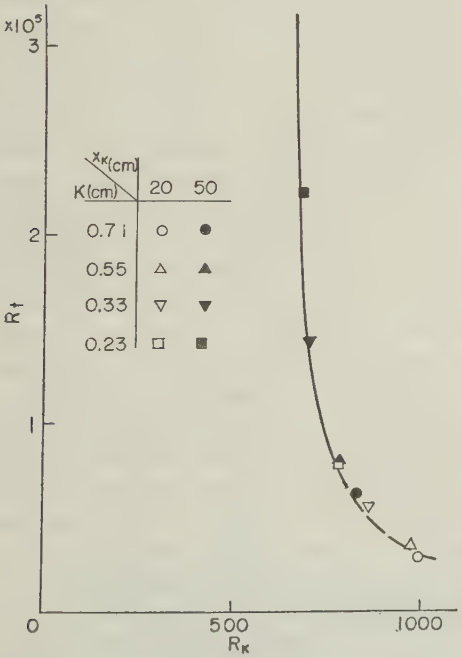

Fig. 9. Variation of transition Reynolds number with critical roughness Reynolds number.

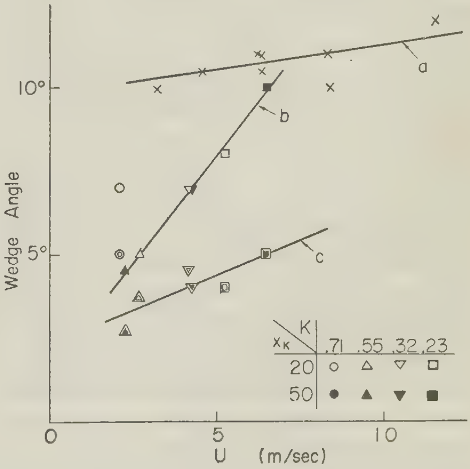

Fig. 10. Relation between angle of turbulence wedge and mean velocity. (a) State of developed turbulence wedge; (b) Near the sphere; (c) Downstream, critical state at which vertex attach to sphere.

good agreement. As the sides of the wedge are seen clearly in the smoke observation, the conception of the wedge is more easily to be understood.

Gregory and Walker have observed that the china clay record of the wedge revealed the fine structure. We examined what corresponds to the fine structure in the present case. The china clay method shows the time averaged results occurred on the plate surface. Smoke particles can depart from the plate surface following the local motion of fluid, even though they are emitted initially on the surface. In order to make the results of the smoke method equivalent to those of the china clay method, another smoke is emitted on the plate further downstream, and the pattern is photographed exposed for a long time. The results show some strong filaments (cf. Fig. 11) which may be regarded as those corresponding to the fine structure of the china clay record. The Reynolds numbers at which the fine structure appears in the experiment of Gregory and Walker are lower than the Reynolds number at which the wedge just attaches to the sphere in the present experiment. Before the wedge developes fully, some dense filaments are observed, which are considered to correspond to the fine structure of china clay. As the wedge develops, however, the smoke filaments disappear just after they are formed. Before the turbulence wedge is formed, the dense smoke filaments parallel to the direction of the main stream appear behind the sphere, but after the turbulent wedge is formed, the smoke filaments which converge and then twist appear along the side of the wedge. It may be thought that these filaments suggest the existence of a vortex in their neighborhood, though it can not be asserted that the position of the filament shows immediately that of the vortex. Such converging and twisting of smoke seem to occur at a constant spacing along the sides of the wedge. The interval measured perpendicularly to the direction of the main stream is about 7 mm, though it becomes larger with decreasing velocity. If it is considered that the filaments are Görtler vortices on the concave wall, the wave length corresponds to those within the unstable region. Therefore, this consideration does not contradict with the present result. But the details will be left for future consideration.

§ 6. Discussion and Conclusion

The transition process of flow patterns caused by a spherical roughness element on the flat plate may be summarized here. The process begins with the formation of distinct vortex filaments, namely two trailing vortex filaments which trail from the head of the fixed vortices behind the sphere and horseshoe vortex filament which circles round the front of the sphere and trails downstream. Weak waviness occurs on the trailing vortex filaments and it grows as the velocity increases. Then at a certain velocity arch-shaped vortices are formed by the rolling up of the trailing vortex filaments. In each stage, the degree of transformation reaches its maximum at a certain distance downstream from the sphere, and the distance varies with the velocity; further downstream these transformed parts cease to grow and are stretched obliquely by shearing stress of the stream. The arch-shaped vortices raise their heads out of the boundary layer, so they are no longer stretched and are diffused as twisting force weakens. The horseshoe vortex filament is also waved owing to the influence of the arch-shaped vortices. At still larger velocities the characteristic forms are lost and a wedge-shaped turbulent state is formed from downstream. The turbulent wedge encroaches the laminar region, and its vertex advances toward the sphere as the velocity is increased. There appear vortex filaments parallel to the main stream, having a constant spacing along the sides of the wedge. The region in which an isolated roughness element can make the flow turbulent is restricted within the wedge. The vertex angle of the wedge becomes larger in proportion to the velocity, as is shown in Fig. 10. It is thought from the above observation that in the transition process the flow pattern passes through the vortical state or state of rotating motion until finally developing into turbulence. The rotations are due to the shearing flow caused by the boundary layer of the plate and the wake of the sphere.

In order to examine the process of the change of the flow pattern a little more quantitatively, the velocities at which the trailing vortex filaments begin to show waviness and those at which the arch-shaped vortices take the maximum height are determined for each size and position of the sphere from the photographs such as Fig. 2. The roughness Reynolds numbers $R_k = ku_k/\nu$ and k/δ_k were calculated for these states, where δ_k is boundary layer thickness at the position of the sphere. The results are shown in Fig. 12 together with the roughness Reynolds number at which the vertex of the wedge reachs to the sphere. The marks in the figure scatter considerably, because of the ambiguity of determining from the photographs the states such as the initiation of waviness and the most developed state of vortices. However, a tendency may be noticed: namely, as R_k is increased, in the case of large k/δ_k, first the trailing vortex filaments begin to wave, the periodic vortices appear and reach to their maximum height, and then the turbulence wedge is formed; but in the case of small k/δ_k the wedge is formed before the most developing state is attained. This means that the vortices grow still in the wedge, and therefore that the arch-shaped vortices have necessarily to raise their heads out of the boundary layer. This state can be clearly recognized in Fig. 6 in which the bottom part begins to be turbulent, in spite of the tops of arch-shaped vortices being still very clear. From above mentioned results the heads of the arch-shaped vortices seem to be independent of the transition. Accordingly, the transition to turbulence should be influenced by the vortices existing in the boundary layer, namely the horseshoe vortex, the trailing vortices and leg of arch-shaped vortices. In the periodic vortices including those of very slight waviness of the trailing vortices, the resulting deformation reach to a maximum at a certain distance from the sphere. This may be regarded as the same phenomenon as the existence of the unstable state of the Tollmien-Schlichting wave. However, the waviness of the trailing vortex filament does not seem to fit with the same stability curve. If the state of initiation of waviness is compared with the condition of the neutral stability by Shen[7], R_δ shows nearly the critical value 420, but $\beta_r\nu/U^2$ shows too large a value, where β_r is circular frequency of the partial oscillation.

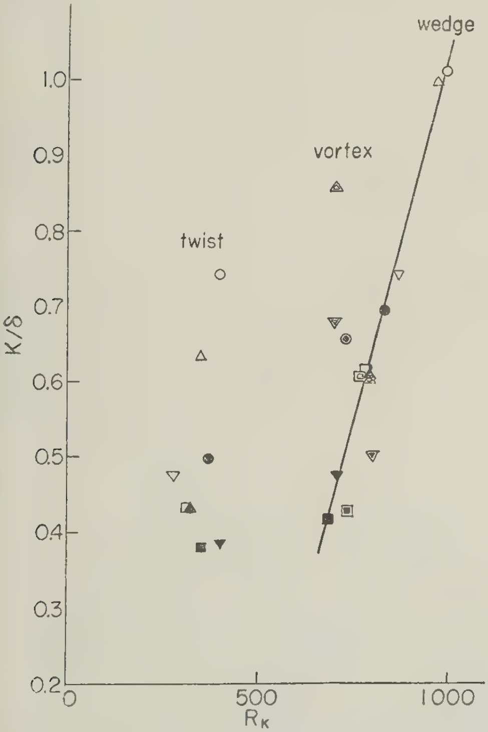

Fig. 12. Relation between roughness Reynolds numbers at which waviness of trailing vortex filament begins, arch-shaped vortices develope mostly and vertex of turbulence wedge attachs to sphere.

The visulization techniques by smoke can grasp well the appearance in the flow field, but on the other hand, a full understanding of the meaning of each pattern is difficult to obtain. Therefore, in order to understand the indication of smoke patterns more clearly, experiments are now being carried on by using the smoke and the hot-wire techniques simultaneously.

The author wishes to express her cordinal thanks to Prof. Jiro Sakagami for his kind guidance and constant encouragement throughout the course of this investigation. She is also grateful to the members of the Boundary Layer Research Group directed by Prof. Itiro Tani for their helpful discussions.

References

1) G. B. Schubauer and P. S. Klebanoff: NACA Rep. 1289 (1956).
2) N. Gregory, and W. S. Walker: A.R.C. Tech. Rep. 13436 (1950).
3) J. R. Weske: Tech. Note BN-91, Inst. Fluid Dyn. and Appl. Math., Univ. Maryland, (1957).

4) W. Möller: Phys. Zeitschr. **39** (1938) 57.
5) S. Taneda: J. Phys. Soc. Japan **11** (1956) 1104.
6) I. Tani: To be published in the Rep. Aero. Res. Inst., Univ. Tokyo.
7) S. F. Shen: J. Aero. Sci. **21** (1954) 62.

Journal of the Physical Society of Japan, Vol. 16, No. 5, May, 1961

Vibration of a Plate and Sound Radiation Generated by an Impulsive Force

By Yasuo Tokita

Kobayasi Institute of Physical Research, Kokubunji, Tokyo

(Received January 25, 1961)

Measurements were made on the vibrational acceleration of a point on a plate and the sound pressure near the plate surface. Attention was given to the initial values of the above quantities, together with coincidence frequency and the waveform of impulsive force, and the following results were obtained.

1) There is a close relation between the hammer momentum (mv) and the initial value (A_0) of the acceleration or the sound pressure, as expressed by the empirical formula; $A_0=K_2(mv)^{K_1}$. The physical meaning of these coefficients is considered.

2) The correspondence between vibrational acceleration and sound pressure is fairly complex and depends upon the mechanical properties and thickness of the plate. The coincidence effect was observed.

3) The waveform of the impulsive force was observed with different stiffnesses and with various velocities of the hammer. The frequency spectrum of the vibration depends on this waveform.

§ 1. Introduction

The modes and responses of vibrational systems have been investigated fairly well in the steady state case, and the steady state sound radiation from vibrating bodies have also been studied and reported as the radiation and scattering problems[1]. However, the transient phenomena for the complicated systems have not yet been solved.

An important class of sound is that the sounds produced when an elastic body is set into vibration by some sort of impulses. The sound from musical instruments and bells; the noises from machines and vehicles; tapping noises in corridors, all these are transient phenomena excited by impulses.

The purposes of this work are, first, to find techniques for investigating complicated transient phenomena, through observation of the transient vibration excited by an impulse on a specific vibrating system, and the sound emitted thereby, second, to obtain, for practical purposes, fundamental knowledges that might be useful for the reduction of noise and of the excess vibration, and third, to study the mechanisms of transmission of impulsive waves through elastic materials. The transient response of simple bodies such as a stretched string or a drum head and three dimensional bodies such as a sphere[1], as well as their sound radiation have been throughly studied[1)-4)]. It has also been reported that a pistol noise which contains many frequency components over a wide band of frequency may be used for the study of architectural acoustics[5),6)]. The present work was started with the hope that the study of vibrations, excited by an impulsive force might likewise be useful in the study of acoustical and vibrational properties of materials.

In this paper, the relationship between the vibration and the sound generated when an impulsive force is applied to a two-dimensional homogeneous plate is studied.

§ 2. Experimental Procedure

2.1 *Experimental method*

When a homogeneous plate suspended by a fine string is subjected to an impulsive force almost at the center, a great many modes of flexural vibration are excited. These modes of vibration decay gradually on account of the radiation of sound and the internal friction of the plate.

The amplitude of the vibration and the sound pressure for each mode can be described in an exponential form;

$$A = A_0 \exp(-\alpha t) \qquad (1)$$

here A is the amplitude of either the vibration or the sound pressure, A_0 is its initial value and α is a reduction constant. If we observe the amplitudes of the vibration and the sound pressure of a single point as a whole at the same time, these quantities would not be described by Eq. (1), because the values of A_0 and α for each mode excited by the impulsive force are different from each other. In the observation within a narrow band of frequency, however, the amplitude of these may be almost represented by Eq. (1).

A schematic diagram of the experimental equipments is shown in Fig. 1. The vibration is detected by an acceleration pick-up fixed near the center of the plate. The sound pressure is received by a microphone at about 10 cm apart from the plate.

The wave patterns of these two quantities, acceleration amplitude and sound pressure, can be observed by a double beam oscilloscope, and at the same time they are recorded on a two channel magnetic taperecorder, and afterwards they are analyzed by a frequency analyzer.

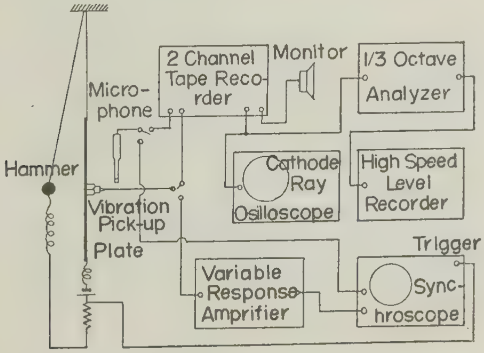

Fig. 1. Schematic diagram of the experimental equipment.

In order to observe how the impact force behaves during the contact, a piezo-electric elements was fixed on the plate and was struck directly by a hammer.

2.2 *Experimental apparatus*

Three different materials were chosen as the sample of plate; iron, glass, and plywood. The dimensions of these plates (length × width × thickness in cm) were (50×50×0.5), (50×50×0.3), (50×50×0.1), (100×100×0.3), (125×125×0.1) and (150×150×0.3) for iron plates, (50×50×1.1) for glass plate and (50×50×2), (60×90×0.6) for plywood plates.

The measurements were carried out under various conditions of the impact; that is different materials of hammer (impact instrument), say steel and rubber; different weights of hammer; various impact velocities and different shapes of the contact surface of the hammer.

A tiny condenser-type microphone was used for receiving the sound. The vibration pick-up used[7] was acceleration type and was made of $Pb(Zr\text{–}Ti)O_3$ ceramics. The weight and the acceleration sensitivity were 25 grams and 40 mv/g (where g is acceleration of gravity) respectively. The pick-up was cemented by "Eastman 910" almost at the center of the plate. The reason why the pick-up was cemented is to prevent some unexpected resonances for fixing the pick-up[8].

At each observation of the frequency responses for each impact, the output voltages of the microphone and the pick-up were recorded simultaneously on a two-channel magnetic tape recorder (a modified "Sony" type 552), in order to enable observation of the correspondence. The reproduced voltage of the tape recording was analyzed by a one-third octave analyzer ("Rion" type SA 2704). The frequency spectra thus obtained were recorded on high-speed level recorder ("Brüel and Kjaer" type 2204). Fig. 2 shows the characteristics of the magnetic recording systems, which record the out-put voltage of the microphone under a constant sound pressure, and also the induced voltage of pick-up under a constant acceleration amplitude. As is clear from this figure, it is not necessary to make correction in the range of frequency used.

A synchroscope (" Iwasaki " type 5101) was used for the observation of wave forms of the vibration and the sound, and the time duration of contact and the wave pattern of impulsive force. The sweep was triggered by the galvanic contact of the hammer with the plate so that it operates just at the instant of contact. A conductive silver paint (" Du pont ") was used for the non-conductive materials like rubber, plywood and glass.

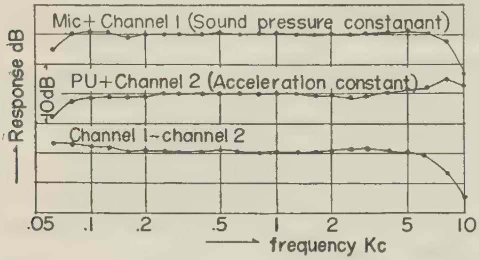

Fig. 2. The frequency characteristics of the two channel tape recorder.

The out put voltage of the pick-up which is proportional to the acceleration of the vibration were transformed to velocity and displacement through an amplifier which has an integrating circuit in itself. The cut-off frequency of the amplifier is 30 c.p.s.

§ 3. Experimental Results

3.1 *Decay curve*

Both the sound pressure and the acceleration of vibration behave almost in the way described by Eq. (1) within a range of one-third octave frequency band, and the slope of these patterns becomes straight in a logarithmic scale. The value of A_0 has been determined by extrapolating these straight lines into the time of zero. An example of the decay curve is shown in Fig. 3, in which each number indicates a center value of one-third octave band.

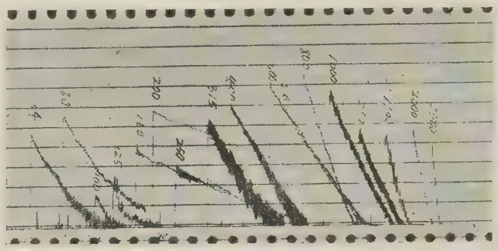

Fig. 3. Example of decay curve.

3.2 *One-third octave band spectrum*

By arranging the values of A_0 for each frequency band, as shown in Fig. 3, in respect to the frequency values concerned, a one-third octave band spectrum for the vibration and the sound is obtained. An example of the results is shown in Fig. 4. The dimensions of plates examined were (50×50×0.5), (50×50×1.1) and (50×50×2.0) for iron, glass and plywood respectively. The hammers used were a steel ball (3.0 cm in diameter), and three rubber hammers which had 80–85° hardness which was given different stiffness, by changing the radius of curvature of the balls (refer Table I). The sound pressure and the acceleration of the vibration are shown in decibel scale (dB) in Fig. 4. The characteristic pattern of each spectrum in this figure doubtlessly resulted from the distri-

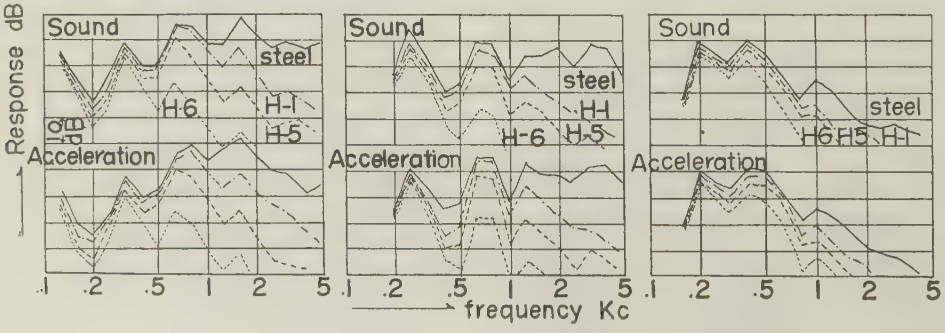

(a) (b) (c)

Fig. 4. Example of one-third octave band spectrum.
(a) iron plate, (b) glass plate, (c) plywood plate.

Table I.

Hammer	Hardness (Shore)	Radius of contact face (mm)	Stiffness ($\times 19^9$ dyne/cm)	Compliance ratio (reference to H-1)
H-1	80-85	25	2.94	1
H-5	80-85	5	1.06	2.76
H-6	80-85	0.5	0.38	7.65
M-1	60-65	25	0.80	3.67
M-5	60-65	5	0.36	8.25
M-6	60-65	0.5	0.17	17
S-1	30-35	25	0.24	12.3

bution of the characteristic frequencies of each plate itself.

3.3 *Variation of spectrum with the stiffness of hammer*

It has been well known that the tone of the sound emitted by a body struck by a hammer differs according to the difference in stiffness of hammers. In Fig. 5 it is shown how the spectra of vibration are affected by the stiffness of hammers. In these experiments, the steel and rubber hammers had almost same weight, and they struck the plates with the same impact velocity. In Fig. 5, all the spectra are shown relative to that for the steel ball. Pertinent data for the rubber hammers are shown in Table I. In this table, stiffness have been determined from the observation of the weight-to-deflection curves, and weight of these hammers are almost 75 grams.

It can be concluded from these experimental results that; with decreasing stiffness of the hammer, the levels of the spectrum in the high frequency range decrease considerably, while no substantial differences can be found in the low frequency range. This will be discussed in detail paragraph 4.

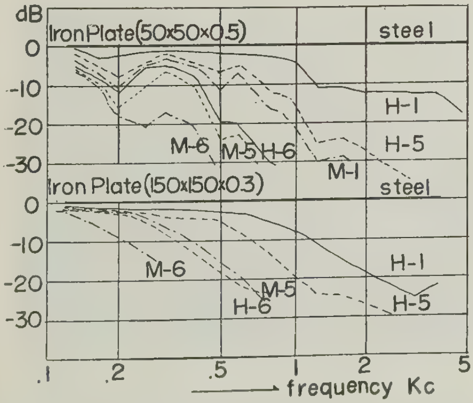

Fig. 5. Spectrum variation due to the hammer stiffness.

3.4 *Relation between A_0 and the momentum of the hammer*

The quantity A_0, the initial value of the sound pressure or of the acceleration of vibration, may be assumed to be a certain function of the impact condition of the hammer. It was therefore examined which quantity was just responsible for the determination of this initial value, among velocity, momentum and the kinetic energy of the hammer. Fig. 6 shows an experimental result for the

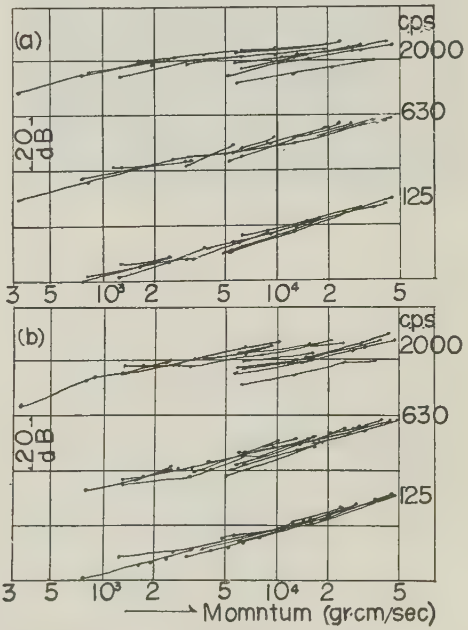

Fig. 6. Relation between A_0 and the momentum of the hammer.
(a) acceleration, (b) sound pressure.

relationship between A_0 and the momentum of the steel ball, both axes being shown in logarithmic scale.

In the case of the rubber hammer which has smaller stiffness than steel ball, the relation between A_0 and the momentum is not as uniform as in the case of the steel ball. When the observed values of A_0 are arranged in respect of velocity and kinetic energy, the relation between A_0 and the velocity or that between A_0 and kinetic energy looks like more fluctuating compared with the case of A_0 and momentum. There exists almost a linear relation in logarithmic scale between the momentum and the relative value of A_0. In the range of low frequency, the increase of twice of the momentum just corresponds to the change of +6 dB of A_0. However, the slope of this line gradually decreases and the linearity becomes diffuse in the range of high frequencies.

3.5 *The correspondence between the vibration and the sound pressure*

It is important to know the correspondence between the vibration of the body and the sound emitted from the vibrating body. In Fig. 7, the experimental data of the ratio of sound pressure to the acceleration of the vibration are plotted in dB scale against the frequency. Fig. 7(a) shows results for an iron plate (50×50×0.5), a glass plate (50×50×1.1) and a plywood plate (50×50×2.0), and (b) shows those for an iron plate of size (150×150×0.3), (100×100×0.3) and (50×50×0.3) respectively. The fluctuations of response curves seem to be caused by the resonance of the plates.

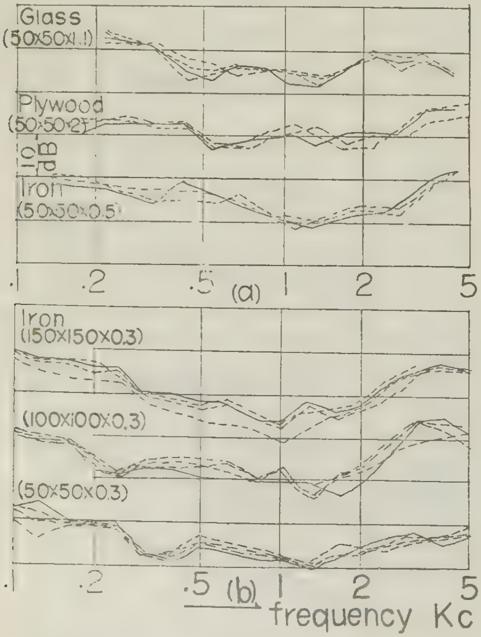

Fig. 7. Relation between the acceleration level and the sound pressure level.
(a) various samples with same size,
(b) various size of iron plate.

It can be concluded from the experiment that the behavior of the correspondence between the sound pressure and the vibration follows different characteristic patterns for each plate according to the physical properties of the plates, but that the correspondence is independent of the properties of the hammer for each same plate.

If the correspondence line is parallel to the abscissa, this behavior means that the sound pressure corresponds to the acceleration of the vibration. According as the slopes of these correspondence curves decline at a rate of −6 dB/octave or of −12 dB/octave, the sound pressure would correspond to the velocity or the displacement of the vibration respectively. If it goes upwards at a rate of +6 dB/octave, it would means that the sound pressure corresponds to the derivative of the acceleration.

From the experimental results shown in Fig. 7, it is hard to decide which correspondence is the most favorable among the velocity, the acceleration, the derivative of acceleration and the displacement. These behaviors seem to be dependent on the geometrical and physical properties of the plates themselves. This problem will be discussed later.

3.6 *Photographic observation*

Next, the experimental results on the waveform of the sound and the vibration and on the force pattern observed by a synchroscope will be described. The waveform are affected by the properties of both plate and hammer. Fig. 8 shows the waveforms for various kinds of plates, which are struck approximately at the center of plate. The hammer is a rubber H-1. The results for the sound pressure and the acceleration are shown in the upper and the lower traces of Fig. 8 respectively. Fig. 8(a) shows the result for an iron plate (100×100×0.1), in which case the sweeping speed of the synchroscope is 5 msec/unit scale. Fig. 8(b) is for an iron plate (100×100×0.3) and

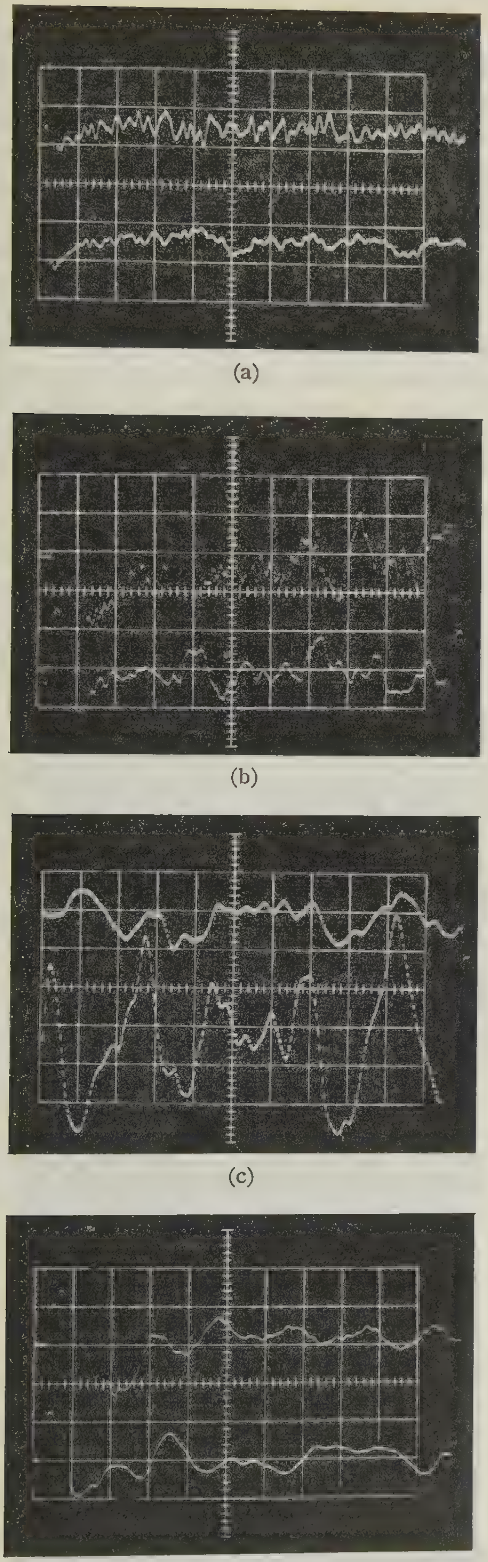

(a)

(b)

(c)

(d)

Fig. 8. Examples of sound and acceleration wave form for various kinds of plate.

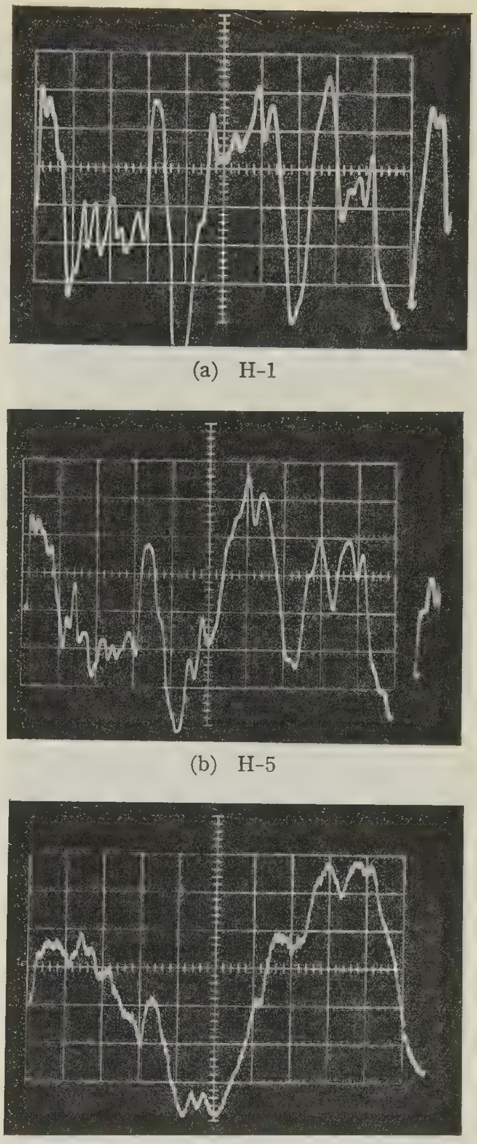

(a) H-1

(b) H-5

(c) M-5

Fig. 9. C.R.O. traces for acceleration of the glass plate which is struck by rubber hammers of various stiffnesses.

the sweeping speed is 500 μsec/unit scale. Fig. 8 (c) is also for an iron plate (50×50×0.5) under the same sweeping speed as Fig. 8 (b). Fig. 8 (d) is the case of plywood (60×90×0.6), in which the sweeping speed is 1 msec/unit scale. It is observed clearly that the waveform for thin plates, for example Fig. 8 (a) and Fig. 8 (d), contain less amounts of high frequency components. When they are struck by a steel ball, which has a greater stiffness than a rubber hammer, these waveformes contain more amounts of high frequency components and also have more complicated and fine appearance.

The effect of the stiffness of the hammer on the vibrational behavior of the plate will be seen not only in the spectrum, but also in the waveform. Fig. 9 shows the waveform of the acceleration of a glass plate, which has been struck by rubber hammers of various stiffnesses. As is shown in Fig. 9 the fine maxima and minima in the waveform tend to disappear with decrease of the stiffness of the hammer, or, in other words, a remarkable change occurs in the high frequency range, but no significant difference can be observed in the low frequency range.

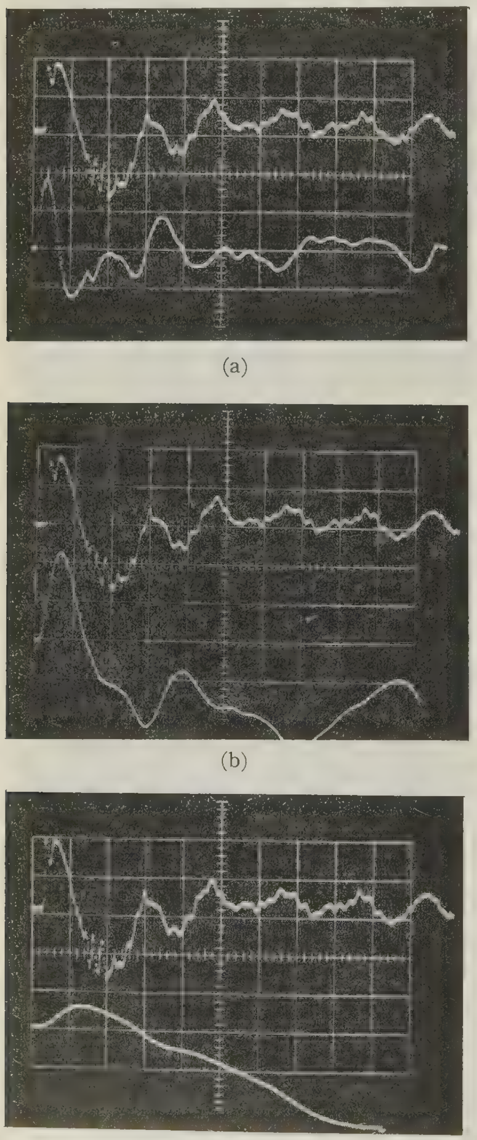
(a)

(b)

(c)

Fig. 10. Waveforms of sound pressure and vibration.

(a) sound pressure and acceleration.

(b) sound pressure and velocity.

(c) sound pressure and displacement.

Next, it was examined what correspondence existed between the waveform of the sound and that of the velocity or the displacement of the vibration, both of which was obtained from the acceleration by an amplifier of suitable characteristics. The results are shown in Fig. 10. The material of plates is plywood (60×90×0.6). Fig. 10 (a) indicates the correspondence between the waveform of the sound pressure and that of acceleration of the vibration, (b) gives sound pressure and velocity of vibration, and (c) gives sound pressure and displacement. Fig. 10 (a) indicates that there exists a fairly good correspondence between sound wave and the acceleration except for a maximum observed at the initial period.

An example of the observation of the contact time is shown in Fig. 11. These photographs are the results for an iron plate (50×

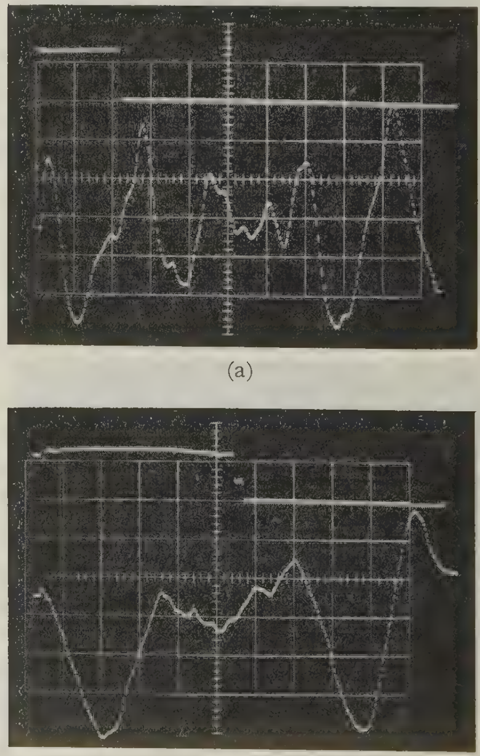
(a)

(b)

Fig. 11. Contact time and the acceleration.

50×0.5) which was struck by a rubber hammer H-1, (a), and H-6, (b). The upper trace shows the current through the contact point. The irregularity of the contact current as in Fig. 11 (b) has been observed very often, and would have been caused by the rebound of the hammer on the plate.

An example of the observation of the impact force is shown in Fig. 12. These figures have been obtained for the iron plate (150×150×0.3) and using various hammers. The upper curves indicate the voltages induced in a piezoelectric ceramic caused by the impact force, the lower curves in Fig. 12 (a), (b), (c) show the acceleration, and those in (d), (e), (f) show the velocity. The sweeping speed is 500 μsec/unit scale, and the hammer velocity is about 55 cm/sec.

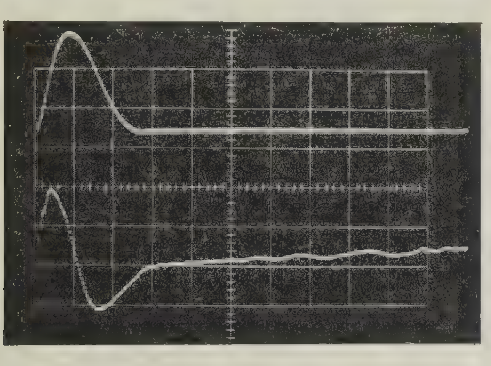
(a)

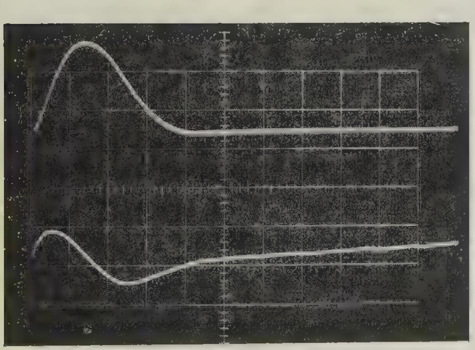
(b)

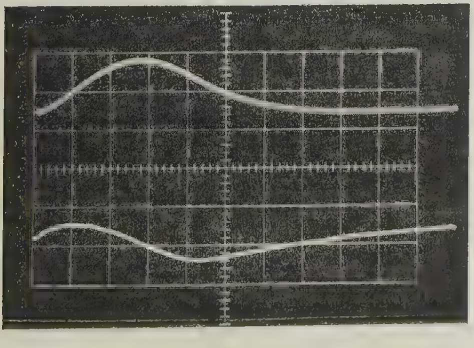
(c)

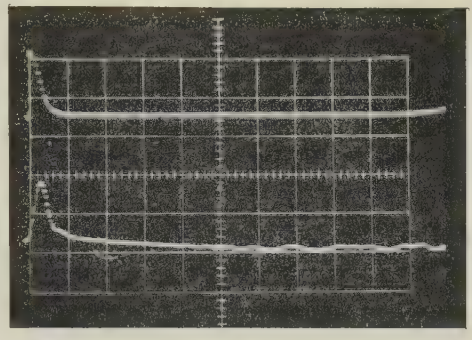
(d)

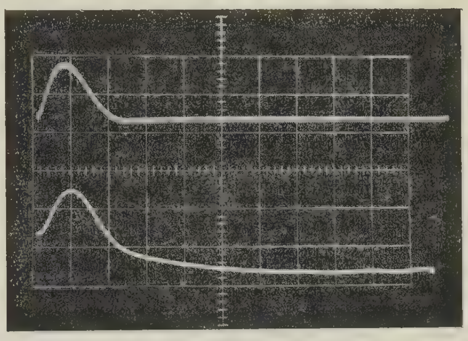
(e)

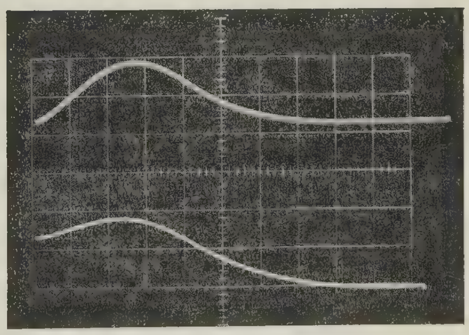
(f)

Fig. 12. The impact force and the vibration. (a) struck by H-1, (b) H-5, (c) H-6, (d) Steel ball, (e) H-1, (f) H-6.

§ 4. Discussion

4.1 *Relation between the spectrum and the stiffness of the hammer*

Let us observe the experimental results when an iron plate was struck by rubber hammers with different stiffnesses. Fig. 13 indicates haw the waveform of the force is affected by the stiffness of the hammers in the impact of constant velocity (about 55 cm/sec). In this case the slope of the force at the initial instant: $(dF/dt)_{t=0}$, becomes less steep with the decrease of stiffness of the hammer, and also the duration of the force becomes longer.

Fig. 14 shows the results when the impact velocity of the hammer is changed. The stiffness of this hammer H–5′ is equal to that of H–5 but the weight is 175 grams. From these data it can be observed that the force figure becomes steeper with increase of hammer stiffness, and also, the time duration becomes longer with increase of the impact velocity.

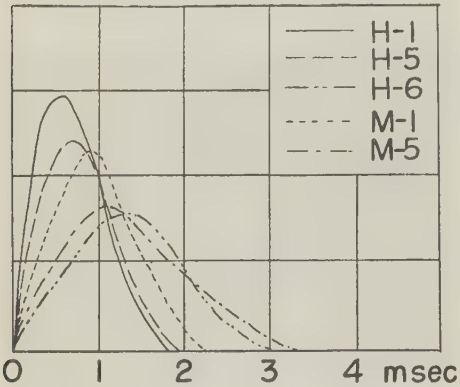

Fig. 13. Waveforms of the impact force for hammers of various stiffnesses.

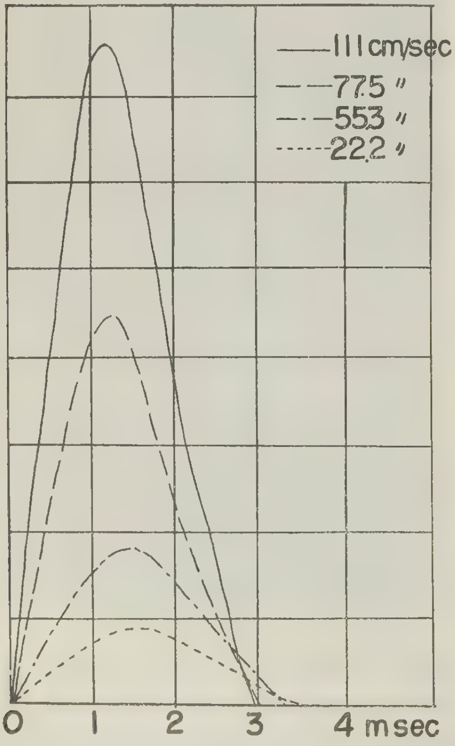

Fig. 14. Waveforms of the impact force for various velocities of the hammer (H–5′).

Let us consider the frequency components involved in the force figure. The sharp pattern in the force figure means that the wave contains more amount of high frequency component and the short time duration means that the impulsive force have a higher cut off frequency. As is seen from Figs. 13 and 14, the case with a harder hammer shows a sharper pattern in the force figure. This evidence just coincides with the fact that the higher components appear in the one-third octave spectrum with increase of the stiffness of hammer. The C.R.O. observation of the acceleration also indicates the same behavior (refer Fig. 9). Similar patterns were obtained even if the rubber hammer of different hardness was used.

The contact time can be determined from Fig. 11. But no definite relationship between the contact time and the duration of the impact could be found. This indefinite relationship seems to be caused by the movements of the plate and the hammer in the same direction, or the plastic deformation of both materials.

However it can be seen from Fig. 11 that the contact time is shorter with the larger hammers, and also with increasing velocity of the hammers. Also, the contact time becomes longer, as we may suppose, in the cases of low stiffness hammer, or in the case of a plywood plate which is struck by a hard steel ball, because of the plastic deformation during impact.

4.2 *Relationship between A_0 and hammer momentum*

The results in Fig. 6 are reproduced by

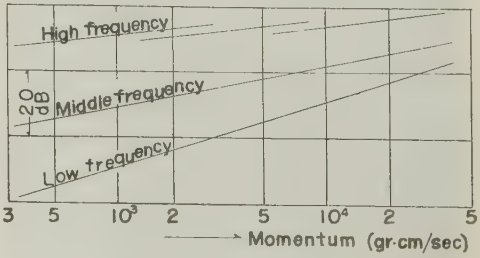

Fig. 15. Reproduction of Fig. 6 to show general trend.

single lines in Fig. 15, in which each line shows fairly well the characteristic relationship between A_0 and momentum at the low frequency region. The fact that the line goes up linearly means that there exists a parallelism between A_0 and momentum. In the medium frequency region, however, the slope of the line tends to go downwards, and at a high frequency region, there is some scattering in the plots.

The behavior of A_0 and momentum can be related by the following empirical formula;

$$A_0 = K_2(mv)^{K_1} \qquad (2)$$

where A_0 is an initial value of sound pressure or of vibration described by Eq. (1), (mv) is the momentum of hammer, and K_1 and K_2 are the coefficients which will be explained now.

K_1 is a coefficient which represents the slope of the straight line in Fig. 15. In the low frequency region, the value of K_1 is unity, in which case A_0 is proportional to (mv). K_1 becomes less than unity in the high frequency region. This means that, in the high frequency region, the increase of momentum of the hammer is not used effectively for the excitement of vibration. When the plate is struck vigorously, the component of high frequency is relatively weakly excited, and the low frequency component predominates.

It is supposed that an excess amount of impact energy above a certain level only contributes to extend the impact duration because of the elastic deformation of material, and is not used effectively to increase the initial amplitude of vibration. The same situation is observed in the waveform just after the impact.

K_2 is another coefficient which may be called the reduction factor. This factor shows how much amount of momentum can be transferred effectively to the vibration, and may be a complicated function of frequency, physical property and shape of contact surface of the hammer etc.. If a certain amount of momentum is applied at an impact, the vibration, corresponding to the momentum multiplied by K_2, is excited. Accordingly, if we try to shift the waveform parallel to the time axis by an amount that depends on K_2, the pattern becomes a simple line, the slope of which is determined by K_1.

The scattering of the data from the straight line in Fig. 6 seems to be caused by the fact that a part of impact energy is spent in some other forms of energy, for instance plastic deformation. Such a behavior is conspicuous in soft materials like plywood. The coefficient K_2 is too complex to be analyzed quantitatively.

When a rigid object like a steel ball is used as a hammer, the impact momentum can be transferred without hardly any rebound on the surface. However, in the case of elastic ball like rubber, a part of the momentum of the hammer is spent for the deformation of the ball. Accordingly, the experimental data in such a cases scatter considerably.

4.3 *Correspondence between the vibration and the sound pressure*

It has been well known in the problems of sound radiation due to the flexural vibration of a plate that there exist abnormal phenomena which have been called by L. Cremer[9] as coincidence effect. Afterwards, it was made clear by M. J. Brillouin[10], K. Gösele[11], W. Westphal[12], and M. Heckel[13] that the coincidence effect can be observed above a certain value of frequency, at which the wave length of the flexural vibration of the plate just coincides with that of sound in air.

The radiation factor, which means the efficiency of the sound radiation, becomes substantially different above and below this critical frequency, f_c. Taking the efficiency above f_c as a standard, there is an abnormal maximum of efficiency in the vicinity of f_c, and it falls off considerably in the lower frequency region.

The propagating velocity of flexural vibra-

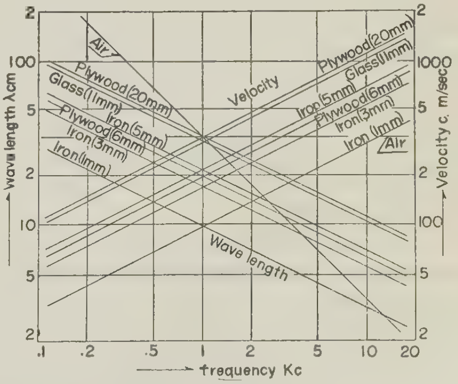

Fig. 16. Propagation velocity and wave length of flexural vibration.

tion of the plate is described as follows[9];

$$c^2=\omega\bar{r}\sqrt{\frac{E}{\rho(1-\mu^2)}}\ , \qquad (3)$$

here c is the propagating velocity, ω is the angular frequency, E is Young's modulus, ρ is the density, μ is the Poisson ratio and $\bar{r}$ is the radius of gyration which is $t/\sqrt{12}$ for a plate with a thickness t.

In Fig. 16, the wave lengths of the plates calculated by Eq. (3) are shown, together with that of sound in air. The values of f_c for the plates used are shown in Table II.

Table II.

Sample	Thickness (cm)	f_c (c.p.s.)
Iron	0.5	2,500
〃	0.3	4,000
〃	0.1	12,500
Glass	1.1	1,150
Plywood	2.0	1,000
〃	0.6	3,000

No anomaly as remarkable as would be expected from the theory was observed above and below the frequency, f_c, as shown in Fig. 7. It is remarked that Westphal also did not find any large anomaly but just a trend of being lower in the lower frequency range.

From our observation, it is found that the sound pressure is almost proportional to the velocity of the plate at lower frequencies, tends to be proportional to the acceleration with increase of frequency, and becomes proportional to the derivative of acceleration in the vicinity of f_c. In the case of high damping materials like a plywood, the amount of reduction of efficiency is so small in a lower frequency range than f_c, that sound pressure can be regarded as proportional to acceleration. As the radiation factor is a certain function of the internal friction of the plate[12),13)], it would be possible to treat this case theoretically.

It is necessary and important to examine what type of vibration pick-up attached to the plate can best reproduce the sound emitted by the plate. It is concluded that neither velocity nor acceleration type is satisfactory, but that the acceleration type looks like better below a few thousands cycles. However, in case f_c is too low or too high, the sound pressure would rather correspond to the velocity.

In Fig. 10, the waveforms of acceleration, velocity and displacement are shown together with that of sound pressure, and as will be seen from this figure, the best fit is found between sound pressure and acceleration. However, for the initial segment of the waveform, a better fit is obtained between sound pressure and velocity (Figs. 10 and 11). This correspondence can be understood from the consideration that in the vibration of a piston, the sound pressure is described by a function of vibrational velocity of the surface of the piston. It seems reasonable that the waveform of the sound pressure is just proportional to that of acceleration, because A_0 is the extraporated initial value of the sound pressure associated with the vibration of the plate, after its own characteristic vibrations have been excited.

§ 5. Conclusions

From the observation of the initial values of the sound and the vibration, A_0, of a plate subjected to an impact, it is concluded that;

1) With reducing stiffness of the hammer, the components of high frequency of sound and vibration tend to disappear, but no much difference is observed in the lower frequency region.

2) The initial value A_0 is closely related to the momentum of the hammer, and this relationship can be represented by Eq. (2). The coefficients K_1, K_2 in Eq. (2) is interpreted qualitatively.

3) The correspondence between the vibration and the sound is fairly complex and depends upon the properties of materials. The coincidence effect was observed in the radiation of sound from a plate, but it is not so marked as expected from the theory.

4) A good coincidence was observed in waveforms of A_0 between impulsive force, velocity and sound pressure just at the initial stage of impact. However, after the characteristic frequencies of the plate were excited, acceleration had a better correspondence with sound for common materials.

5) The relation between the contact time and the duration of the impact force has not yet been clarified.

Acknowledgement

In conclusion I wish to express my sincere thanks to Dr. H. Kawai and Dr. U. Kohasi whose help in discussion has been invaluable. I am also indebted to Mr. M. Koyasu, Mr. K. Negishi and Mr. S. Nakamura for their helpful suggestions, and to Mr. T. Shimizu and Mrs. K. Takeda for their willing aid for the experiment.

References

1) e.g. Lord Rayleigh: *Theory of Sound.* I and II. Cambridge. P. M. Morse: *Vibration and Sound.* McGraw-Hill. I. B. Crandall: *Theory of Vibration System and Sound.* D. Van Nostrand Co.
2) C. E. Crede: *Vibration and Shock Isolation.* John Willy and Sons. Inc.
3) E. Skudrzyk: J. Acoust. Soc. Amer. **30** (1958) 1140, 1152.
4) S. Morita: Lecture on Acoustical Society Meeting (in Japan) (1954, Oct.).
5) J. Igarashi: J. Acoust. Soc. Japan. **10** (1954) 230.
6) J. Igarashi and M. Koyasu: J. Acoust. Soc. Japan. **10** (1954) 261.
7) Y. Tokita: Bull. Kobayasi Inst. Phys. Res. **10** (1960) 47.
8) Y. Tokita: Bull. Kobayasi Inst. Phys. Res. **8** (1958) 234.
9) L. Cremer: *Die Wissenschaftlichen Grundlagen der Raumakustik.* Band III. 178p.
10) M. J. Brillouin: Acustica. **2** (1952) 65.
11) K. Gösele: Acustica. **3** (1953) 143, **6** (1956) 94.
12) W. Westphal: Acustica. **4** (1954) 603.
13) M. Heckel: Acustica. **9** (1959) 371.

JOURNAL OF THE PHYSICAL SOCIETY OF JAPAN, Vol. 16, No. 5, MAY, 1961

On the Relation between the Change in Modulus of Rigidity of Brass Wires by Cold-Rolling and Rolling Textures

By Jun KUROYANAGI

Department of Physics, Faculty of Liberal Arts and Science, Yamagata University

(Received December 28, 1960)

Pole figures for the brass specimens which had been used for the measurement of the change in modulus of rigidity in the previous investigation[1] and had received 90 per cent reduction in cross-sectional area by cold-rolling were obtained. In the pole figure of copper, the most intense rolling texture was {112}<111>. In the pole figure of brass containing 10.14 per cent zinc, the most intense texture was {110}<112> and the {110}<001> texture also appeared in the figure in considerable degree. The intensity of the {110}<001> texture increases with the increase of zinc content. The existense of the β-phase in the brass wire containing 40.24 per cent zinc was ascertained, which had been predicted in the previous paper[1]. On the basis of these results the variation in the modulus of rigidity of the specimens, 57.5 per cent cold-rolled, with various zinc contents was investigated.

§1. Introduction

Previously[1] the present author studied on the change of rigidities of brass wires containing 10.14, 30.15 and 40.24 per cent zinc caused by cold-rolling. The results showed that (1) in well annealed state, the modulus of rigidity of the specimens decreased quasi linearly with the increase of zinc content, (2) the modulus of rigidity of all specimens decreased with the increase of the degree of cold-rolling (3) the relative decrease of the modulus of rigidity of brass wires compared with the decrease of the equally cold-rolled pure copper wire was different according to the zinc content, for instance, in the specimens cold-rolled by 10.5 per cent in cross-sectional area, the modulus of rigidity of the brass wire containing 10.14 per cent zinc was larger than that of pure copper wire and the modulus of rigidity in the brass wires containing 10~40 per cent zinc content decreased slower than that for the well annealed specimens with increasing zinc content, (4) in the specimens cold-rolled by 57.5 per cent, the modulus of rigidity of the brass wire containing 10.14 per cent zinc was greater considerably than that of pure copper wire and it increased gradually with the increase of zinc content up to 30.15 per cent zinc, but the modulus of of rigidity of the brass wire containing 40.24 per cent zinc was grater considerably than that of the brass wire containing 30.15 per cent zinc.

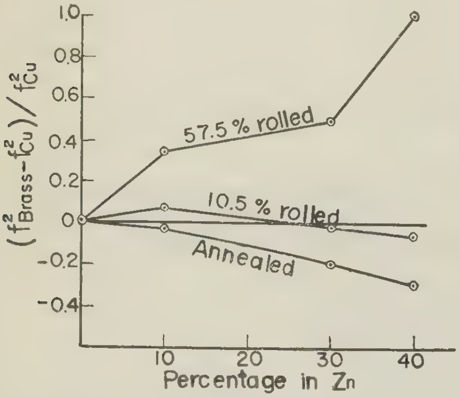

Fig. 1. Modulus of rigidity *vs* percentage of zinc content for annealed and cold-rolled brass wires.

The above relations are represented again in Fig. 1. The cause of the change in modulus of rigidity of the well annealed specimens and of the specimens cold-rolled by 10.5 per cent have discussed in detail in the previous paper[1)], but the discussion of the cause of the change in modulus of rigidity of the specimens cold-rolled by 57.5 per cent was unsatisfactory. Consequently, the present author investigated this problem again.

Cook and Richards[2)] found the following facts from X-ray studies; (1) when polycrystalline copper and brass strips are cold-rolled, the deformation proceeds by a slip mechanism up to about 33 per cent in thickness for copper and slightly more for brass, and beyond this stage it proceeds by a breakdown of the crystals into minute blocks (2) marked preferred orientation increases progressively with the increase of cold-rolling. The large variation in modulus of rigidity of brass wires with cold-rolling must arise from the formation of the preferred orientation, because the modulus of rigidity of copper single crystal decreases from 7,700 kg/mm^2 in the direction [100] to 3,100 kg/mm^2 in the direction [111][3)] and the modulus of rigidity G of *f.c.c.* metal depends on the orientation according to the formula[4)],

$$\frac{1}{G}=\frac{1}{G_{\max}}+3\left(\frac{1}{G_{\min}}-\frac{1}{G_{\max}}\right)\cdot F$$

$$F=\frac{h^2k^2+k^2l^2+l^2h^2}{(h^2+k^2+k^2)^2}$$

where h, k, l are the Miller indices. As $F_{\min}=0$ for [100] and $F_{\max}=1/3$ for [111], it follows that the modulus of rigidity is largest in the direction [100] and smallest in the direction [111]. On account of the above mentioned reasons it is expected that the variation in modulus of rigidity of the specimens, 57.5 per cent cold-rolled, with the change in zinc content to be affected in great degree by the preferred orientations developed during cold-rolling. Thus the preferred orientations in the cold-rolled specimens developed during cold-rolling were studied using the same materials which were used for the measurement of the change in modulus of rigidity. And also the existence of the β-phase in the brass wire containing 40.24 per cent zinc was ascertained, which was predicted in the previous investigation[1)].

§ 2. Experimental Procedure

(1) *Measurement of preferred orientation*

Specimens for pole figure determination were prepared from the wires which had been used for the change in modulus of rigidity and had received 90 per cent reduction in cross-sectional area by cold-rolling in order to obtained diffraction patterns showing the preferred orientation. Cu K_α radiation obtained with 15 mA at 30 KV was used for all diffraction patterns. The X-ray beam was collimated through a pinhole system. The specimen was mounted in a goniometer which permitted accurate measurement of the angle of rotation about the vertical axis of the specimen without removing the specimen from its mounting during the entire series of exposure. The starting position was selected such that the X-ray beam was perpendicular to the rolling plane and the rolling direction of the sheet specimen was vertical. A series of transmission patterns was obtained from 0° to 60° at intervals of 10°, by rotating the specimen clockwise about the vertical axis. The distance from the specimen to the X-ray, film was 40 mm.

(2) *Confirmation of the existence of β-phase*

In the previous investigation the existence of β-phase which should coexist with α-phase in the brass wire containing 40.24 per cent zinc could not be confirmed. Nevertheless, the coexistence of β-phase with α-phase in annealed brass containing 40.24 per cent zinc was successfully confirmed using FeK($\alpha+\beta$) radiation obtained with 20 mA at 15 KV and with the exposure of 10 hours in the present case.

§ 3. Results

(1) *Preferred orientation*

The {111} pole figures obtained from the diffraction patterns for the cold-rolled copper and brass sheets are shown in Figs. 2∼5. The {200} pole figures for these specimens were also obtained to ascertain the results obtained from the {111} pole figures. The intensity of Debye rings for the {111} and {200} planes were estimated by eye and graded into seven classes. These grades are indicated in these figures with cross lines, lines at regular intervals, lines and dots, crosses, and dots respectively in order of intensity.

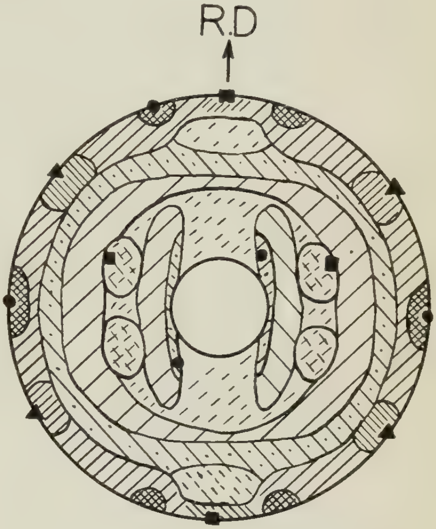

Fig. 3. {111} pole figure for 90 pct cold-rolled brass sheet containing 10 pct zinc. Ideal orientations indicated as follows: Solid circle, {110} <112>. Solid square, {112}<111>. Solid triangle, {110}<001>.

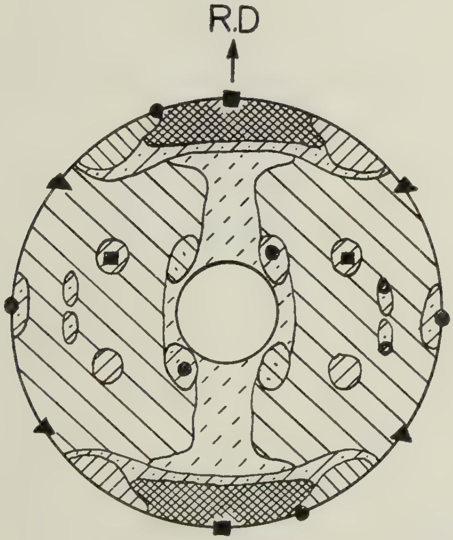

Fig. 2. {111} pole figure for 90 pct cold-rolled copper sheet. Ideal orientations indicated as follows: Solid circle, {110}<112>. Solid square, {112}<111>. Solid triangle, {110}<001>. Open circle, {210}<001>.

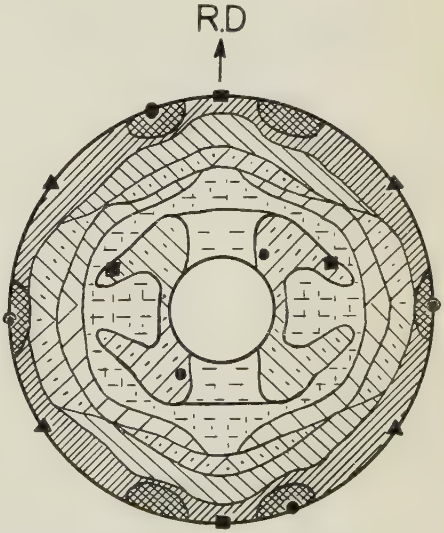

Fig. 4. {111} pole figure for 90 pct cold-rolled brass sheet containing 30 pct zinc. Ideal orientations indicated as follows: Solid circle, {110} <112>. Solid square, {112}<111>. Solid triangle, {110}<001>.

Comparison of these pole figures with one another indicates a number of gradual changes taking place with increasing zinc content. In the pole figures of copper, Fig. 2, the most intense orientation spread is the one centered around the {112}⟨111⟩ orientation. Moreover, a {110}⟨112⟩ texture and a twin {210}⟨001⟩ texture can be found in Fig. 2. Nevertheless, these textures are present to a less degree than the {112}⟨111⟩ texture. In the pole figure of brass containing 10.14 per cent zinc, Fig. 3, the most intense texture is the {110}⟨112⟩ orientation and the intensity of the {112}⟨111⟩ texture becomes weaker as compared with that of copper. Moreover, a {110}⟨001⟩ texture appears in this figure in considerable degree.

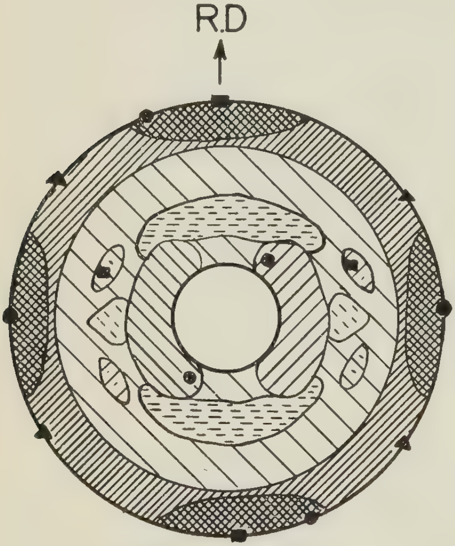

Fig. 5. {111} pole figure for 90 pct cold-rolled brass sheet containing 40 pct zinc. Ideal orientations indicated as follows: Solid circle, {110} <112>. Solid square, {112}<111>. Solid triangle, {110}<001>.

As seen in the pole figures, Figs. 3∼5, the texture represented by {011}⟨112⟩ is present in large amount for any zinc content in the range from 10 to 40 per cent and the intensities of which increase with zinc content; relative intensity of {112}⟨111⟩ texture is almost independent on the zinc content but is weak as compared with that of copper; the intensity of the {110}⟨001⟩ texture increases with increasing zinc content.

(2) *Existence of β-phase*

Fig. 6 shows the powder X-ray photograph of the annealed brass containing 40.24 per cent zinc obtained by the above mentioned method. From this figure the coexistence of of β-phase (*b.c.c.*) with α-phase (*f.c.c.*) in this brass is clear.

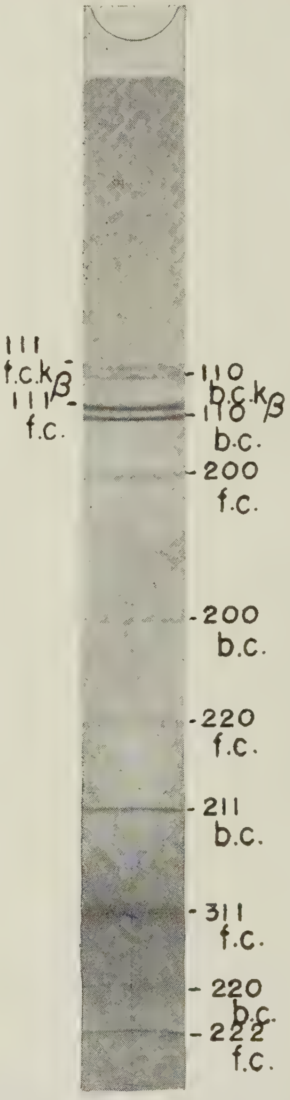

Fig. 6. Power photogram of annealed brass contatining 40 pct zinc. FeK($\alpha+\beta$) radiation, 15 KV, 20 mA 10 hrs.

§ 4. Discussion

The above mentioned rolling textures obtained for the copper and brasses are not completely consistent with the results obtained by Merlini and Beck[5]. These discrepancies may be due to the difference of compositions or history of the specimens and method of measurement. Especially, the specimens used for the measurement of rolling textures in this experiment were prepared from the wires about 1 mm in diameter. Nevertheless, the change in modulus of rigidity of the brass wires cold-rolled 57.5 per cent associated with the change of zinc content, reported in the previous paper[1], can be explained with the above mentioned experimental results as follows. (1) The variation in the modulus of rigidity of the heavily cold-rolled specimens such as in this case should be greatly affected by the preferred orientations developed by cold-rolling. (2) The decrease of the modulus of rigidity should chiefly be due to the development of the preferred orientation represented {112}⟨111⟩, for which the value of the modulus of rigidity is smallest, among the textures of various orientations. (3) The fact that the modulus of the brass wire containing 10.14 per cent zinc surpasses that of pure copper wire in amount at this stage of cold-rolling should be attributed to the change of the strongest preferred orientation from {112}⟨111⟩ to {110}⟨112⟩ by the addition of 10 per cent zinc. (4) The gradual increase of the relative amount of the modulus of rigidity of the 57.5 per cent cold-rolled brass wires against that of copper wire with the incrase of zinc content from 10 per cent to 30 per cent, as shown in Fig. 1, should be due to the gradual increase of the intensity of the preferred orientation represented by {110}⟨001⟩, for which the value of modulus of rigidity is largest, with the increase of zinc content. (5) For the rapid increase of the relative amount of the modulus of rigidity of the 57.5 per cent cold-rolled brass wire containing 40 per cent zinc against that of copper wire, as shown in Fig. 1, two factors may be considerable, namely, (a) the increase of the intensity of preferred orientation {110}⟨001⟩, (b) influence of the β-phase coexisting with α-phase. The difficulties of the confirmation of the existence of β-phase by x-ray photograph, the rapid increase of Vickers hardness at the neighbourhood of 40 per cent zinc content as shown in the previous investigation, and furthermore the fact that the tensile strength shows a maximum value at about 40 per cent zinc content may indicate the existence of the precipited β-phase in the form of very minute particles in the brass containing 40.24 per cent zinc. The decrease of the grain size would increase the modulus of rigidity. This problem is now under investigation.

The author wishes to express his sincere thanks to Mr. Toyojirō Isano for his assistance.

References

1) J. Kuroyanagi: J. Phys. Soc. Japan **15** (1960) 1386.
2) M. Cook and T. L. Richards: J. Inst. Metals **66** (1940) 1.
3) C. S. Barrett: *Structure of Metals*, McGRAW-HILL, (1952) 533.
4) W. Boas: *An Introduction to the Physics of Metals and Alloys*, Mellborn (1947) 49.
5) A. Merlini and P. A. Beck: J. Metals **7** (1955) 385.

Short Notes

This section is intended to secure prompt publication of important discoveries in physics. The reports should not exceed 800 words in length. A figure of size 7 cm×7 cm will be counted as 150 words.

J. PHYS. SOC. JAPAN **16** (1961) 1024

Dielectric α- and β-dispersions in Polyvinyl Butyral (PVB)

By Yūzō TAKAHASHI

Laboratory, Hokkai Can Mfg. Co., Ltd., Otaru, Hokkaido

(Received March 9 1961)

Since there is relatively few reports concerning both dielectric α- and β-dispersions measured for the same sample of polymers, this paper deals with these two dielectric dispersions in PVB. The sample of PVB, which is heat-treated at 200°C for 30 min., was measured for the frequency dependence of dielectric loss ε'' in the temperature region from -70 to 120°C and over the frequency range of 0.3 to 10^6 c/s. The apparatus was the same as the previous one[1].

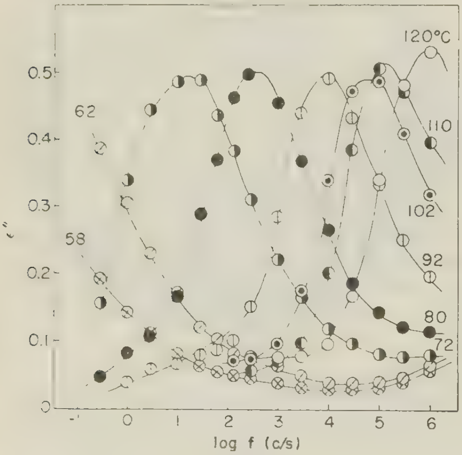

Fig. 1. Frequency dependence of ε'' at various temperatures for PVB (in high temperature region)

The results obtained are shown in Fig. 1 and 2. Two dielectric dispersions, i.e., the higher and lower temperature dispersions which are labled as α and β respectively, can be observed, while these two dispersions are also detected by the mechanical measurement[2]. If $\log f_m$ is plotted against $1/T$, where f_m is the frequency at which ε'' is maximum, we obtain a curve for the α-dispersion, but a straight line for the β-disperion as shown in Fig. 3. Therefore, the apparent dielectric activation energy ΔH^* for the former are 93, 66, 53, 42 and 34 kcal/mol at 80°, 92°, 102°, 110° and 120°C respectively, calculated using the equation of WLF[3]. On the other hand, ΔH^* for the latter is about 12 kcal/mol and independent of the temperature. This difference between the α- and β-dispersions in PVB seems to be based on the difference whether the dielectric relaxation is related to the segmental movements of the main chain or to the movements of the local parts such as the side groups.

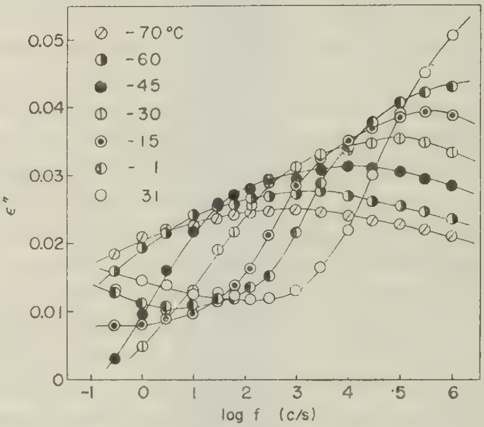

Fig. 2. Frequency dependence of ε'' at various temperatures for PVB (in low temperature region).

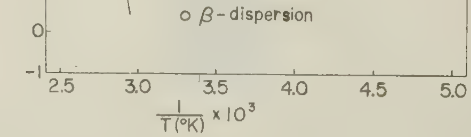

Fig. 3. Plot of logarithmic dispersion frequency against reciprocal of absolute temperature.

The author wishes to thank Professors J. Furuichi and M. Kaneko, Faculty of Science, Hokkaido University, for their continual interest and discussion.

References

1) Y. Takahashi: to be published in J. Phys. Soc. Japan, **16** (1961) 1028.
2) Y. Takahashi: J. Appl. Polymer Sci., in Press.
3) M. L. Williams, R. F. Landel, and J. D. Ferry: J. Am. Chem. Soc., **77** (1955) 3701.

J. PHYS. SOC. JAPAN **16** (1961) 1025

The Double-Grid Ionization Chamber

By Iwao OGAWA and Tadayoshi DOKE

Department of Physics,
Rikkyo (St. Paul's) University, Tokyo

(Received February 15, 1961)

Pulses extracted from the grid of a gridded ionization chamber may be conveniently used as a signal containing the information on the orientation of tracks of alpha particles emitted from the cathode of the chamber[1]. As was shown by Botchagov *et al.*, the negative pulse-height V_g of a grid pulse is approximately given by

$$V_g=(Q_0/C_g)\cdot\{1-(R^*/d_1)\cos\theta\}\ , \qquad (1)$$

where Q_0 denotes the total charge of the ions produced by an alpha particle, C_g the capacity of the grid system, d_1 the distance between the cathode and the grid, and θ the angle between the particle track and the normal to the cathode K, while R^* is a quantity representing a length very close to the particle range R independent of $\cos\theta$.

From (1) it is seen that the pulse-height distribution of those grid pulses which are counted in coincidence with the collector pulses belonging to a particular peak in the energy spectrum would represent the angular distribution in terms of $\cos\theta$ for the particles of the particular energy.

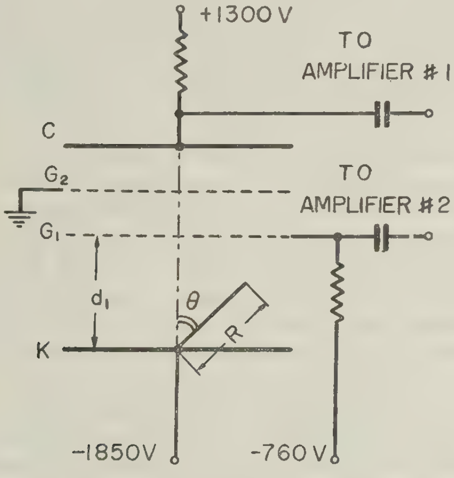

Fig. 1. Schematic view of the double-grid chamber.

In an ordinary *single*-grid ionization chamber, however, simultaneous extraction of both the collector and grid pulses generally impairs the shielding efficiency of the grid and results in a serious loss in the energy resolution.

In order to overcome this difficulty, we have constructed a *double*-grid ionization chamber shown schematically in Fig. 1. Signals are taken out from the first grid G_1 as well as from the collector C. An additional grid G_2 is directly grounded and serves as a screen grid.

The energy spectrum of the alpha particles from a natural uranium source ($\sim 50\,\mu$g/cm^2 thick) obtained with this chamber is given in Fig. 2A. The resolution is fairly good despite the simultaneous extraction of the grid pulses. Fig. 2B shows the grid pulse-height distributions due to U^{234} (curve (a)) and U^{238} (curve (b)) obtained by the collector-grid coincidence method described above, by which we can select a praticular peak of the energy spectrum. The corresponding ranges in the collector pulse-height are indicated by the arrows in the energy spectrum. Thus we can see that the separation of the grid pulses is satisfactory in spite of the rather small difference in energy of the both alpha particles.

Grid pulses due to the particles emitted from G_1, G_2 or C are essentially *positive* at least in the first approximation. Making use of this fact, we have succeeded in a background reduction by a factor of about three in the energy spectrum merely by counting those collector pulses which are accompanied by a *negative* grid pulse. The full account will shortly be published elsewhere.

Reference

1) B. A. Botchagov, A. A. Vorob'ev and A. P. Komar: Izv. Akad. Nauk SSSR, Ser. Fiz. **20** (1956) 1455; Zh. Tekhn. Fiz., **27** (1957) 1575.

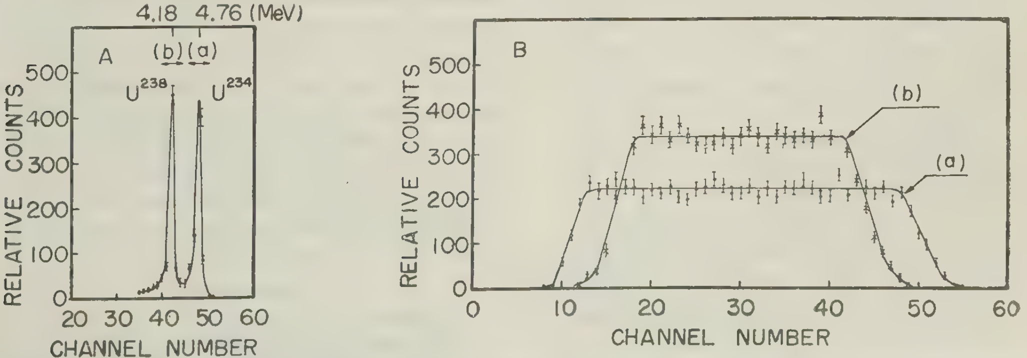

Fig. 2. Pulse-height distributions of natural uranium. A: Energy spectrum. B: Grid-pulse spectra. (a): U^{234}; (b): U^{238}, $R/d_1=0.87$ for U^{234}.

J. PHYS. SOC. JAPAN **16** (1961) 1026

Thermoelectric Behaviours of Rutile

By Kimiko SAKATA

National Research Institute for Metals,
Meguro-ku, Tokyo, Japan

(Received February 20, 1961)

The present note describes the results of experiment in which the temperature dependence of conductivity and that of thermo e.m.f. were simultaneously measured for rutile samples sintered in different oxygen atmosphere. The experimental procedures are the same as previously described[1].

Curves in Figs. 1 and 2 represent, respectively, σ vs. $1/T$ and Q vs. $1/T$ for various oxygen partial pressures P_{O_2} (σ: conductivity in $\text{ohm}^{-1}\,\text{cm}^{-1}$, Q: e.m.f. per degree in mV/degree, T: absolute temperature in °K). Each curve was obtained by successive measuremeuts carried out with decreasing temperature. Each measurement at a certain temperature was carried out after assuring that an equillibrium state had been established in the sample, although below 700°C it could not be attained within a defined time, when a certain final state has been settled. An exception is the case of curve 6, i.e., it was obtained by successive measurements with increasing temperature for the sample which had been rapidly quenched from the equilibrium at 1200°C in the prescribed atmosphere.

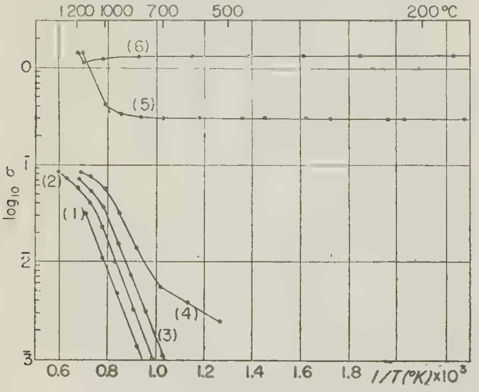

Fig. 1. Conductivity vs. reciprocal absolute temperature for various oxygen partial pressures.
(1) 1 at. O_2 (2) 1 at. air
(3) 100 mm Hg air (4) 10 mm Hg air
(5) 1 at. deoxidized Ar (6) 1 at. deoxidized Ar

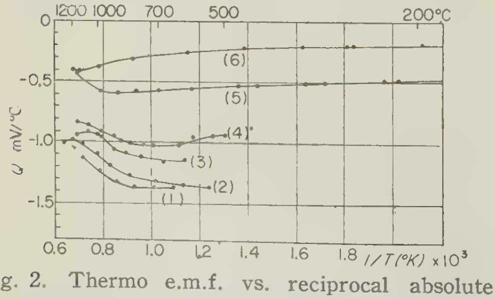

Fig. 2. Thermo e.m.f. vs. reciprocal absolute temperature for various oxygen partial pressures.
(1) 1 at. O_2 (2) 1 at. air
(3) 100 mm Hg air (4) 10 mm Hg air
(5) 1 at. deoxidized Ar (6) 1 at. deoxidized Ar

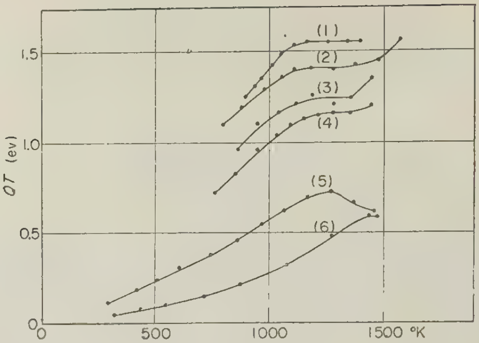

Fig. 3. QT product vs. absolute temperature various oxygen partial pressures.
(1) 1 at. O_2 (2) 1 at. air
(3) 100 mm Hg air (4) 10 mm Hg air
(5) 1 at. deoxidized Ar (6) 1 at. deoxidized Ar

The activation energy of conduction determined by each curve in Fig. 1, in the temperature range of 700°~1000°C, tends to increase with increasing P_{O_2} up to 3.0 ev (curve 1), which may correspond to the value of forbidden energy gap reported by Cronemeyer[2]. The asymptotic value of corresponding QT-curve (Fig. 3, curve 1) tends to 1.55 ev, indicating that the Fermi level approaches to half way of the forbidden gap in the intrinsic region. The conductivy behaviour as well as the corresponding thermo e.m.f. (curve 6 in each figure) suggest that in highly reduced rutile its metallic conduction takes place in the narrow d-band, as pointed out by Morin[3], and the intrinsic conduction begins to predominate at about 1150°C.

Curves 2, 3, 4 and 5 in each figure show intermediate behaviours between those of curve 1 (nearly intrinsic) and curve 6 (highly reduced). It should be pointed out that a contribution to these observed behaviours from a temperature dependent change in oxide composition cannot be ignored. This fact is obvious when one compares curve 5 with curve 6; in the latter case, the above contribution may be neglected. In the former case, on the other hand, the composition change is proceeding in the direction of approaching to stoichiometry with decreasing temperature in the range from 1200°C to about 700°C, where a certain state with a certain composition is frozen in.

References

1) T. Sakata and K. Sakata: J. Phys. Soc. Japan **13** (1958) 675.
2) D. C. Cronemeyer: Phys. Rev. **87** (1952) 876.
3) F. J. Morin: Bell System Tech. J. **37** (1958) 1047.

J. Phys. Soc. Japan **16** (1961) 1027

Magnetic Anisotropy of Heusler Single Crystal

By Keizô Aoyagi and Makoto Sugihara

Electrical Communication Laboratory, Nippon Telegraph and Telephone Public Corporation 1551, Kichijoji, Musashino-shi, Tokyo, Japan

(Received February 25, 1961)

The Heusler alloy of which the typical composition is Cu_2MnX, where X=Al, In, Sn, is the well known ferromagnetic alloy composed of non ferromagnetic elements. It was found by many investigators[1)] that ferromagnetism of the Heusler alloys is associated with body-centred cubic β phase with a face-centred cubic superlattice in the highly ordered state and especially both the saturation magnetization and the curie temperature of Cu_2Mn Al alloy change with the condition of heat treatments, namely both show minimum values in the state quenched from high temperatures and increase with aging at low temperatures. It may be interesting to investigate the effect of heat treatment on the ferromagnetic crystal anisotropy of Cu_2MnAl, in connection with the experimental facts mentioned above. Furthermore, so far any quantitative measuring datum on the ferromagnetic crystal anisotropy of Cu_2MnAl was not publicated except the qualitative datum of small single crystal specimens by Potter[2)]. The authors have tried to grow a large single crystal of Cu_2MnAl and to measure ferromagnetic crystal anisotropy using the crystal and they have got satisfactory results.

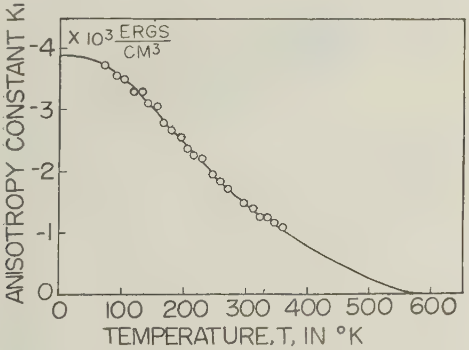

Fig. 1. The temperature dependence of anisotropy constants, K_1, of a Cu_2MnAl alloy in the state quenched from 750°C.

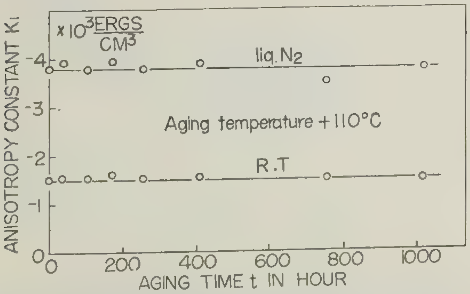

Fig. 2. The change with aging at 110°C of anisotropy constants, K_1, of a Cu_2MnAl alloy.

A single crystal employed was grown in argon furnace from the melt of the ingot of Cu_2MnAl alloy which was preliminary cast and grinded to remove the scale. To prevent the precipitation of non ferromagnetic phase, after the melt was solidified it was immediately cooled rapidly, and then circular disk, 11.834 mm in diameter and 1.001 mm in thickness, with plate surface coinciding with the (100) plane, was cut out from the single crystal ingot. The results of chemical and X-ray analysis on the remainder of a single crystal ingot showed that its accurate composition was $Cu_{1.990}Mn_{1.007}Al_{1.003}$. The crystal structure was exactly the same Heusler type as observed by Bradley et al[3)], and any other line was not observed in X-ray analysis. Anisotropy measurements by the automatic recording torque magneto meter[4)] were performed at the temperature between liq.N_2 and +80°C in the state cooled rapidly by the cold jet of argon gas after annealing for one hour at 750°C, and were performed also at liq.N_2 and room temperature in the state aged at 110°C after heat treated as mentioned above. Measuring magnetic field applied parallel with the (100) plate surface was about 8200 oe, and cubic anisotropy constants, K_1, were determined accurately by Fourier analysis of the measured torque curves.

The results obtained are summarized as follows:

(1) The values of K_1 were -3.7×10^3 ergs/cm³ and -1.5×10^3 ergs/cm³ at liq.N_2 and room temperature, respectively, in the state cooled rapidly from 750°C. Change of K_1 with the measuring temperature was shown in Fig. 1. This temperature dependence was well described by $[I_T/I_0]^5$ curve, where I_T and I_0 were the intensity of Magnetization observed by Heusler[5)] on Cu_2MnAl at the temperatures of T and 0°K, respectively.

(2) Measurements of change of K_1 with aging at 110°C were made from 0 to 1000 hours, but any change of K_1 was not observed. (Fig. 2)

References

1) O. Heusler: Ann. Physik **19** (1934) 155.
L. A. Carapella and R. Hultgren: Trans. Am. Inst. Mining Met. Eng. **147** (1942) 232.
S. Valentiner: Z. Metallkd. **44** (1953) 59.
B. R. Coles, W. Hume-Rothery, F. R. S. and H. P. Myers: Proc. Roy. Soc. **196A** (1949) 125.
A. J. Bradley and J. W. Rodgers: Proc. Poy. Soc. **A 144** (1934) 340.
2) H. H. Potter: Proc. Phys. Soc. London **41** (1929) 135.
3) A. J. Bradley and J. W. Rodgers: loc. cit.
4) C. Kuroda: J. Phys. Soc. Japan **15** (1960) 2355.
5) O. Heusler: loc. cit.

J. PHYS. SOC. JAPAN **16** (1961) 1028~1029

Dielectric α-, β- and γ-Dispersions in the Thermosetting Phenolic Resins

By Yūzō TAKAHASHI

Laboratory, Hokkai Can Mfg. Co., Ltd., Otaru, Hokkaido

(Received February 4, 1961)

A number of works on the dielectric behavior of the thermosetting phenolic resins have been reported. However, systematic classification of the characteristic dielectric dispersions of this resin based on measurements over a wide range of frequency and temperature is lacking. It is of interest to classify the dielectric dispersions since it generally gives us informations about the state of motions of the molecules or its local groups. In the present work, the frequency dependence of the dielectric constant ε' and the loss ε'' was measured for the ammoniac resol type of phenolic resin, cured at 200°C for 30 min. over the frequency range of 0.3 to 10^6 c/s and the temperature range of -60 to 170°C. Three characteristic dispersions were either obtained or suggested and are labeled as α, β and γ in the order from higher temperature or from lower frequency side.

The resin was synthesized from phenol, o-cresol and formaldehyde under a catalyser NH_4OH aq. (weight ratio of phenol to o-cresol is 60:40). The sample film had been dried almost completely. The measurements were made by means of a mutual inductance bridge¹⁾ and a modified resistive-ratio-arm bridge¹⁾. Values of ε'' at high temperatures have been corrected for the steady d-c conductance. Results are shown in Fig. 1 and Fig. 2. In Fig. 1, the values of ε'' show rapid increase at high temperature and low frequency side, although no maximum of ε'' can be observed within the range investigated. There will possibly be a maximum outside this region due to the motions of macromolecules of phenolic resin, i.e., the α-dispersion. On the other hand, Hartshorn et al.²⁾ have reported the dielectric α-dispersions of novolac type of phenol- or cresol-formaldehyde resin at 1 kc/s. in the temperature range of 37 to 75°C. The difference between the behaviors of the α-dispersion for these two types may be due to the complexity of their molecular structures after curing. In Fig. 2 a maximum of ε'', i.e., the β-dispersion, is observed for each curve in the frequency range of about 0.3 to 10^3 c/s. They may be caused by the motions of local parts such as unreacted methylol and amino groups in the phenolic resin molecule³⁾. Finally the remarkable upswing of ε'' values on the high-frequency side suggests the existence of another maximum, i.e., the γ-dispersion. This may corre-

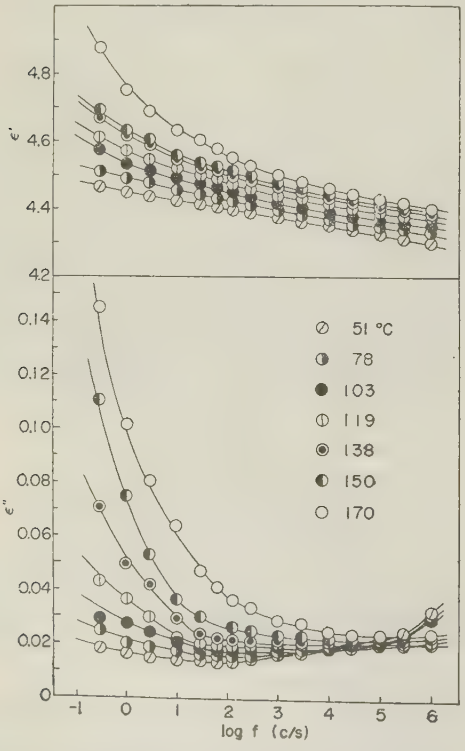

Fig. 1. Frequency dependences of dielectric constant and loss for the ammoniac resol type of phenolic resin in high temperature region.

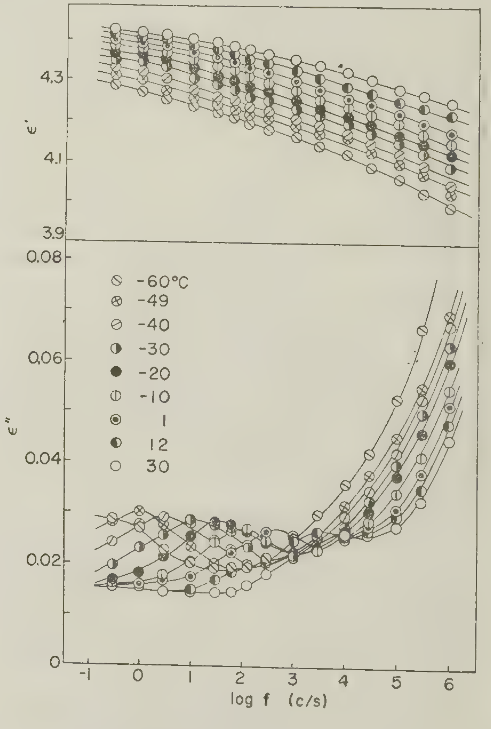

Fig. 2. Frequency dependences of dielectric constant and loss for the ammoniac resol type of phenolic resion in low temperature region.

spond to the dielectric dispersion found by Yager[4] and Kawai et al.[5] at about 10^7 c/s at room temperature for the dried paper-laminated phenolic resin, although Yager interpreted this dispersion as due to an intrinsic properties of cellulose contained in the specimen. In order to confirm the γ-dispersion, it would be necessary to extend the measurement to higher frequencies or to lower temperatures.

The author wishes to thank Professors J. Furuichi and M. Kaneko, Faculty of Science, Hokkaido University, for their invaluable discussions.

References

1) T. Nakajima and S. Saito: J. Polymer Sci., **31** (1958) 423.
2) L. Hartshorn, N. Megson and E. Rushton: Proc. Phys. Soc. (London) **52**, (1940) 796.
3) Y. Takahashi: J. Japan Soc. Test Materials, **10** (1961) No. 92, in Press.
4) W. A. Yager: Trans. Electrochem. Soc., **74** (1938) 113.
5) R. Kawai, G. Sato and Y. Harada: J. I. E. E. Japan, **74** (1954) 120.

J. PHYS. SOC. JAPAN **16** (1961) 1029～1030

Forward Characteristics of Si *pπn*-Junctions

By Masakatsu TOKUNAGA and Katsufusa SHONO

Research Institutes, Yuasa Battery Company, Takatsuki, Osaka

(Received February 10, 1961)

A series of Si *pπn*-junctions were manufactured from *p*-type Si with resistivity ranging between 2 and 5 ohm cm as the starting materials. The junction was formed by diffusing boron from the one side and phosphorous from the other side. This process was done on (111) faces of the crystal at about 1250°C and the width of π-region of junction was adjusted by changing the duration time of diffusion.

Sah, Noyce and Shockley[1] predicts an apparent $\exp(qV/kT)$ dependence of the forward current in a *pn*-junction, where $1 \leqq n \leqq 2$. It is pointed out that the forward current consists of two parts, the diffusion current and the recombination-generation current; and in usual devices the effect of the body resistance of the π-region is added. The diffusion current outside the space charge layer at large forward bias is expressed as

$$J_d = \frac{2qn_pL_0}{\tau_0} \exp\left(\frac{qV}{kT}\right) \qquad (1)$$

where n_p is the density of holes, L_0 and τ_0 are the diffusion length and the lifetime of minority carries, respectively. The recombination-generation current in the space charge layer at small forward bias is given by

$$J_{rg} = \frac{kTn_i}{\tau_0 E} \exp\left(\frac{qV}{2kT}\right) \qquad (2)$$

where n_i is the density of carriers in an intrinsic specimen and E is the electric field at the junction, provided the recombination centers are not very close to the band edge.

We have measured the forward voltage-current characteristics at the temperature range between 200°K and 500°K of *pπn*-junctions which had various width of π-region. The solid lines in Fig. 1 shows the forward characteristics at 300°K. As shown in the figure, in case of $W=0$ (W: width of π-region), the forward current in proportional to $\exp(qV/1.74kT)$ at small forward voltages and to $\exp(qV/1.00kT)$ at larger voltages. With the increasing of W, the forward characteristics deviates from the straight line corresponding to the case of $W=0$. This is due to the body resistance of π-region.

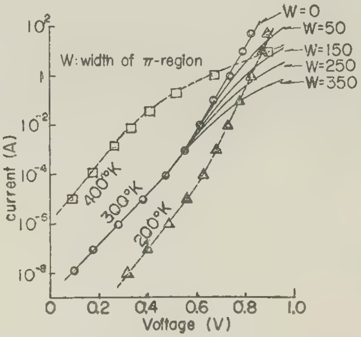

Fig. 1. Forward current voltage characteristics for Si *pπn*-junctions of various width of π-region.

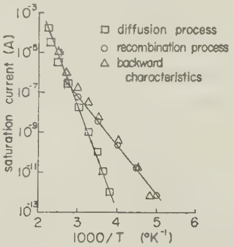

Fig. 2. Saturation current vs 1000/T for Si *pπn*-junctions.

The dashed lines in Fig. 1 show the current-voltage characteristics at 200°K and 400°K of the sample with $W=0$. The dependence of the characteristics on the width of π-region was similar to that observed at 300°K. At 200°K the forward current is proportional to $\exp(qV/2.00kT)$ at small forward voltages and to $\exp(qV/1.00kT)$ at larger voltages. It is found that the experimental results at 200°K are consistent with the theoretical considerations, expressed by Eq. (1) and (2). At 400°K, we can only observe the straight line which is expressed by $\exp(qV/1.00kT)$ in the small forward bias region and the curved line resulting from the body resistance of Si material.

Since the experimental curve for the sample with $W=0$ at each temperature in Fig. 1 can be approximated by two straight lines, we can get the two kinds of forward saturation current I_s in the temperature range between 200°K and 500°K, extrapolating these straight lines to $V=0$, and obtain the results illustrated in Fig. 2. From Fig. 2 we obtain an activation energy of about 0.6 eV for recombination-generation current and the activation energy of 1.2 eV for the diffusion current. This temperature dependence is to be expected from equations (1) and (2), and hence would verify the assumptions made in the calculations, that is, that the recombination centers lie near the center of the energy gap. The reverse saturation current has also been measured and we have obtained the activation energy which is in good agreement with the value from the forward saturation current as shown in Fig. 2.

The author is deeply indebted to Professor J. Yamaguchi and Mr. Y. Hamakawa of Osaka University for their encouragement and interest in this work.

Reference

1) C. T. Sah, R. N. Noyce and W. Shockley: Proc. I.R.E. Sept. (1957) 1228.

J. Phys. Soc. Japan **16** (1961) 1030~1031

Viscous Forces and Brownian Motion

By Naokata Takeyama

Institute of Biophysics,
Kyushu University, Fukuoka

(Received February 24, 1961)

This note describes an attempt to investigate the interrelation between the molecular dynamical theory[1)] of irreversible processes and the thermodynamical ensemble theory[2)].

The common starting point of any theory can be found in the Liouville's equation

$$i\,\partial f/\partial t=Lf\,, \tag{1}$$

where L is the Liouville's operator which is defined by

$$Lf=\begin{cases} i[H,f] & \text{(for the phase space distribution function } f\text{)}\,, \\ \hbar^{-1}[H,f] & \text{(for the density matrix } f\text{)}\,, \end{cases}$$

and H is the Hamiltonian function or operator of the total system.

Our interest is focused on the temporal behavior of a Brownian particle, whose Hamiltonian is $H_0=\vec{\boldsymbol{p}}^2/2M+U(\vec{q})$, interacting with and immersed in the eqilibrium liquid system of its Hamiltonian H_l and statistical temperature $kT\equiv\beta^{-1}$. The interaction between the systems is called V. The Hamiltonian of the total system is given by

$$H=H_0+H_l+V\,, \tag{2·a}$$

and the corresponding Liouville's operator becomes

$$L=L_0+L_l+L'\,. \tag{2·b}$$

The initial f is adopted in the form of

$$\bar{f}=Z^{-1}\exp\{-\beta(H-\vec{\boldsymbol{p}}\langle\vec{\boldsymbol{v}}\rangle+M\langle\vec{\boldsymbol{v}}\rangle^2/2)\} \tag{3}$$

with

$$Z=\mathrm{Trace}\,[\exp\{-\beta(H-\vec{\boldsymbol{p}}\langle\vec{\boldsymbol{v}}\rangle+M\langle\vec{\boldsymbol{v}}\rangle^2/2)\}]\,,$$

where $\langle\vec{\boldsymbol{v}}\rangle$ is a macroscopic and averaged velocity of a Brownian particle obtained by

$$\langle\vec{\boldsymbol{v}}\rangle=\langle\vec{\boldsymbol{p}}\rangle/M=\mathrm{Trace}\,(\vec{\boldsymbol{p}}/Mf)\,.$$

It can be easily seen that $\bar{f}$ is a solution of the equation

$$M\langle\vec{\boldsymbol{v}}\rangle f=\vec{\boldsymbol{p}}\,f+M\beta^{-1}\,\partial f/\partial\vec{\boldsymbol{p}} \tag{4·a}$$

for the classical case; quite similarly

$$M\langle\vec{\boldsymbol{v}}\rangle f=f\int_0^\beta d\lambda/\beta\,\vec{\boldsymbol{p}}(-i\hbar\lambda)+M\beta^{-1}\,\partial f/\partial\vec{\boldsymbol{p}} \tag{4·b}$$

for the quantum case, where $\vec{\boldsymbol{p}}(s)$ stands for

$$\vec{\boldsymbol{p}}(s)=\exp(isL)\vec{\boldsymbol{p}}\,,$$

and the quantum mechanical differential operator with respect to $\vec{\boldsymbol{p}}$ is defined by

$$\partial f/\partial\vec{\boldsymbol{p}}=(i\hbar)^{-1}[\vec{q},f]\,.$$

After performing formally differentiation of Eqs. (4·a) and (4·b) with respect to $\vec{\boldsymbol{p}}$, we obtain

$$M\langle\vec{\boldsymbol{v}}\rangle\,\partial f/\partial\vec{\boldsymbol{p}}=\frac{\partial}{\partial\vec{\boldsymbol{p}}}(\vec{\boldsymbol{p}}f+M\beta^{-1}\,\partial f/\partial\vec{\boldsymbol{p}})\,, \tag{5·a}$$

and

$$M\langle\vec{\boldsymbol{v}}\rangle\,\partial f/\partial\vec{\boldsymbol{p}}=\frac{\partial}{\partial\vec{\boldsymbol{p}}}\left\{f\int_0^\beta d\lambda/\beta\,\vec{\boldsymbol{p}}(-i\hbar\lambda)+M\beta^{-1}\,\partial f/\partial\vec{\boldsymbol{p}}\right\}. \tag{5·b}$$

By dividing $f(t)$ into $f(t)=\bar{f}+f'(t)$, Eq. (1) reduces to

$$\partial f'/\partial t-i^{-1}Lf'=i^{-1}L\bar{f}\,. \tag{6}$$

The steady solution of Eq. (6) for f', to the first order of $\langle\vec{\boldsymbol{v}}\rangle$, can be written as

$$\begin{aligned} f_{st}'=+\lim_{t\to\infty}f_e\int_0^t dt'\int_0^\beta d\lambda \\ \times\exp\{-i(t-t')L\}\dot{\vec{\boldsymbol{p}}}(-i\hbar\lambda)\langle\vec{\boldsymbol{v}}\rangle\,, \end{aligned} \tag{7·a}$$

or in another equivalent from

$$\begin{aligned} f_{st}'=-\lim_{\sigma\to 0}f_e\int_0^\infty dt\int_0^\beta d\lambda \\ \times\exp(-\sigma t)\exp(-itL)\dot{\vec{\boldsymbol{p}}}(-i\hbar\lambda)\langle\vec{\boldsymbol{v}}\rangle\,, \end{aligned} \tag{7·b}$$

where $\dot{\vec{\boldsymbol{p}}}(s)=-i^{-1}L\vec{\boldsymbol{p}}(s)$, and $f_e=Z_e{}^{-1}\exp(-\beta H)$.

The viscous force in the steady state is obtained by

$$\begin{aligned}\langle\dot{\vec{p}}\rangle_{st}&=\mathrm{Trace}\,(\dot{\vec{p}}\,f_{st}{}')\\&=-\int_0^\infty dt\int_0^\beta d\lambda\langle\dot{\vec{p}}(-i\hbar\lambda)\dot{\vec{p}}(t)\rangle_e\langle\vec{v}\rangle\\&\equiv-\zeta\langle\vec{v}\rangle\,.\end{aligned}\tag{8}$$

Here the friction coefficient ζ has been defined by

$$\zeta=\int_0^\infty dt\int_0^\beta d\lambda\langle\dot{\vec{p}}(-i\hbar\lambda)\dot{\vec{p}}(t)\rangle_e$$

for the quantum system, and it becomes

$$\zeta=\beta\int_0^\infty dt\langle\{\dot{\vec{p}},\dot{\vec{p}}(t)\}\rangle_e$$

for the classical system, where $\langle A\rangle_e$ means to take an average of A referring to f_e.

Eq. (1) for $f_0\equiv\mathrm{Trace}_{(l)}f$, where $\mathrm{Trace}_{(l)}$ denotes to take the trace with respect to the equilibrium liquid system only, is written as

$$\begin{aligned}&\partial f_0/\partial t+i^{-1}L_0f_0\\&\quad=+i^{-1}\,\mathrm{Trace}_{(l)}L'f=-(\partial f_0/\partial t)_{\mathrm{drift}}\,,\end{aligned}\tag{9}$$

where the right hand side term of the above expresses a drift term for f_0 owing to the effect of the interaction with the liquid system, which can be written as $(\partial f_0/\partial t)_{\mathrm{drift}}=-\mathrm{Trace}_{(l)}(i\hbar)^{-1}[V,f]$.

Writing formally $(\partial f_0/\partial t)_{\mathrm{drift}}$ as $(\partial f_0/\partial\vec{p})\langle\dot{\vec{p}}\rangle_{\mathrm{drift}}$, the drift force $\langle\dot{\vec{p}}\rangle_{\mathrm{drift}}$ can be approximately replaced by the steady viscous force $\langle\dot{\vec{p}}\rangle_{st}$, Eq. (8). Thus, we obtain

$$\partial f_0/\partial t-i^{-1}L_0f_0\cong-\partial f_0/\partial\vec{p}\,\langle\dot{\vec{p}}\rangle_{st}=\langle\vec{v}\rangle\,\partial f_0/\partial\vec{p}\,\zeta\,.\tag{10}$$

The wanted Kramers-Chandrasekhar's equation[3], which governs the Brownian motion, can be derived from Eqs. (5) and (10) as the following:

$$\begin{aligned}&\partial f_0/\partial t-i^{-1}L_0f_0\\&\quad=\frac{\partial}{\partial\vec{p}}\,[\zeta(M^{-1}\vec{p}\,f_0+\beta^{-1}\,\partial f_0/\partial\vec{p})]\end{aligned}\tag{11·a}$$

for the classical system, and

$$\begin{aligned}&\partial f_0/\partial t-i^{-1}L_0f_0\\&=\frac{\partial}{\partial\vec{p}}\left[\zeta\left\{f_0M^{-1}\int_0^\beta d\lambda/\beta\,\vec{p}(-i\hbar\lambda)+\beta^{-1}\,\partial f_0/\partial\vec{p}\right\}\right]\end{aligned}\tag{11·b}$$

for the quantum system.

It has been clarified that the essential feature in the above treatment is concentrated in the replacement $(\partial f_0/\partial t)_{\mathrm{drift}}\rightarrow(\partial f_0/\partial\vec{p})\langle\dot{\vec{p}}\rangle_{st}$, and in the application of the steady viscous force derived from the thermodynamical ensemble theory, and that the correlative effect of the interaction with the "external" system on the system under consideration is brought in the friction coefficient.

References

1) M. Toda: J. Phys. Soc. Japan **13** (1958) 1475. T. Kotera and M. Toda: ibid., **14** (1959) 1266.
2) H. Mori: J. Phys. Soc. Japan **11** (1956) 1029. R. Kubo: ibid., **12** (1957) 570. R. Kubo, M. Yokota and S. Nakajima: ibid., **12** (1957) 1203.
3) H. A. Kramers: Physica **7** (1940) 284. S. Chandrasekhar: Rev. Mod. Phys. **15** (1943) 1.

J. PHYS. SOC. JAPAN **16** (1961) 1031~1032

Fine Structures of Photoprotons from Si^{28}

By Katsufusa SHODA, Keisuke KOBAYASHI,
Shoichi SIINA, Ken ABE and
Motoharu KIMURA
Department of Physics, Tohoku University, Sendai, Japan

(Received February 20, 1961)

We investigated photoprotons from Si^{28} using 24 MeV bremsstrahlung. The target was the powder of natural Si (9.38 mg/cm²) depositted on a Au foil (0.19 mg/cm²). The energy loss of protons by the half target thickness is about 30% for 3 MeV and about 10% for 6 MeV protons.

The Ilford G-special 600 μ emulsions were scanned by a Tiyoda binocular microscope. The number of detected proton tracks was 4366 in the

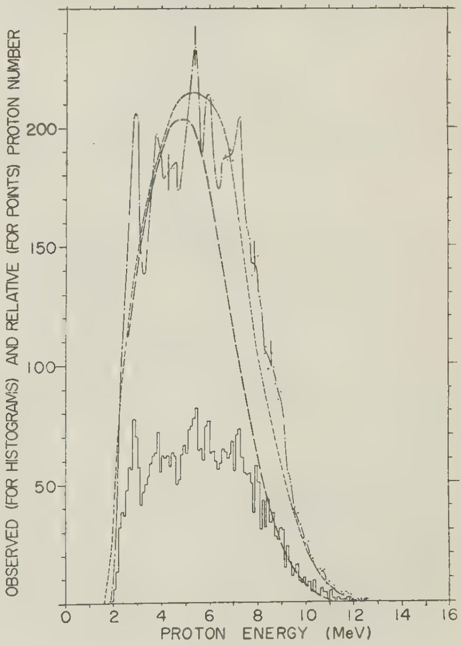

Fig. 1. The energy spectrum of photoprotons from Si. The solid line is a smoothed curve. The broken line and the dotted one are calculated curves of the statistical model with the level densities $\omega=C\exp[2\sqrt{0.45E}\,]\ \mathrm{MeV}^{-1}$ and $\omega=C\exp[E/2.8]\ \mathrm{MeV}^{-1}$, respectively.

scanned area of 1.6 cm^2.

The observed histogram is shown in Fig. 1 along with the smoothed curve using the Valoshek method$^{1)}$. Fig. 1 also includes the calculated energy spectra deduced by the statistical model with two types of level density$^{2)-4)}$. Apart from the fine structures, the calculated curve with the level density ω given by

$$\omega = C \exp[E/2.8] \text{ MeV}^{-1}$$

is in good agreement with the data.

Many fine structures were observed. They may be explained by a resonating group model$^{5)}$, which yields similar fine structures.

It may be interesting to compare the energy distribution with the cross section calculated from inverse reaction $Al^{27}(p, \gamma)$ by detailed balance. This comparison is shown in Fig. 2. For $Al^{27}(p, \gamma)^{6)-8)}$, the energy of γ_1, leading to the first excited state of Si^{28}, was used. γ_0, leading to the ground state of Si^{28} were weak by about a factor of ten, and were not separated from $\gamma_1$$^{8)}$.

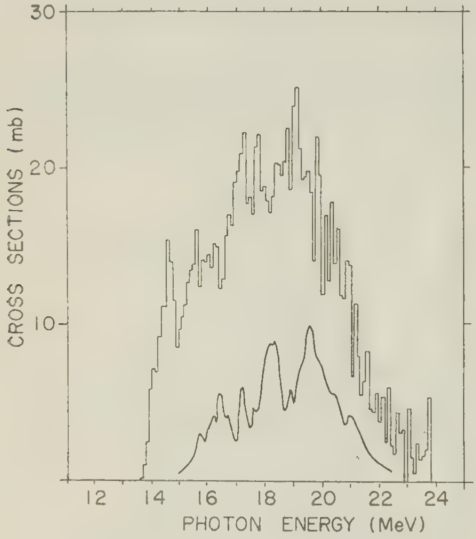

Fig. 2. The comparison of cross section of $Si^{28}(\gamma, p)Al^{27}$ (histogram) and that from $Al^{27}(p, \gamma)Si^{28}$ (solid line).

If we assume that all protons in $Si^{28}(\gamma, p)$ are emitted leaving Al^{27} in the ground state, we get the cross section of $Si^{28}(\gamma, p)$ as shown in Fig. 2 which is obtained by correcting Fig. 1 for bremsstrahlung spectrum.

The shapes of cross sections coincide fairly well, though their energy scales are not the same. This may be reasonable, because they are not exact inverse reactions.

We gratefully acknowledge helpful discussion with Dr. K. Okamoto. Authors are also indebted to Mr. Ishizuka for useful help in calculating the data.

References

1) E. P. Ferreira and P. Y. Valoshek: *Proceedings of the International Conference in Geneva* (August, 1955) **2** (1958) 147.
2) J. M. Blatt and V. F. Weiskopf: *Theoretical Nuclear Physics* (John Wiley and Sons, 1954) p. 311.
3) P. M. Endt and J. C. Kluyver: Rev. Mod. Phys. **26** (1954) 95.
4) P. C. Gugelot: Phys. Rev. **93** (1954) 425.
5) S. Igarashi, K. Izumo and T. Udagawa: Prog. Theor. Phys. **21** (1959) 468.
6) H. E. Gove, A. E. Litherland and R. Batchelor: Phys. Rev. Letter **3** (1959) 177.
7) D. S. Gemmel, A. H. Morton and W. I. B. Smith: Nuc. Phys. **10** (1959) 45.
8) M. Kimura, K. Shoda, N. Mutsuro, T. Tohei, K. Sato, K. Kuroda, K. Kuriyama and T. Akiba: J. Phys. Soc. Japan **15** (1960) 1128.

J. PHYS. SOC. JAPAN **16** (1961) 1032~1033

Observation of Lattice Defects in Fission Fragment-irradiated Graphite*

By Kazuhiko IZUI and F. Eiichi FUJITA**

Japan Atomic Energy Research Institute
Tokai-mura, Ibaragi-ken, Japan

(Received February 27, 1961)

It is generally known that solid materials irradiated with high energy particles undergo structural damages consisting of not only single defects, but also of considerably large size defects, which were first predicted by the theory of temperature spikes$^{1),2)}$ and supported by a few experiments$^{3)}$. Evidences in electron microscopy for such damage effect are relatively few except the observations of fission fragment tracks in mica$^{4)}$ and uranium oxide etc.$^{5)}$ and of small dots and loops formed in neutron irradiated copper$^{6)}$ and graphite$^{7)}$. The present note reports some electron microscopic observations of large defects in graphite induced by fission fragment irradiation.

Refined powder of natural graphite, mixed with uranium oxide powder in the ratio of 10/1, was exposed to thermal neutrons in the reactor to the total doses of the order of 10^{16} n/cm^2, and observed with Hitachi electron microscopes, HU-10 and HS-5. As shown in Photo. 1, tracks of fission fragments from U^{235} were sometimes observed as straight lines about 100 Å wide accompanied by some small dots. By tilting the specimen, their contrasts turn from black to white as that of the matrix changes from white to black. This indicates that they are essentially the diffraction contrasts caused by variations in the Bragg conditions in the crystal and that these narrow linear regions have a crystallographic nature or orientation slightly different from the matrix, possibly exhibiting the thermal spike effect of fission fragments passing through the crystal. A concentric fringe pattern seen on the left hand side of the picture seems to be a large damaged region, where the lattice is buckled, presumably in such a manner as schematically shown in Fig. 1, due to the spike effect producing a number of atomic displacements. Photo. 2 shows a highly damaged region representing many concentric fringe patterns and their complex couplings. In view of the fact that these concentric fringe patterns have a close connection with moiré fringes, their image contrasts seem to be essentially the phase contrast. The dynamical calculation for their image contrast formation based on a model like one in Fig. 1, which was done by H. Hashimoto[8] will give a detailed analysis of the structure of the damaged regions. Dislocation lines became to be rugged and changed their contrasts after the irradiation, as shown in Photo. 3, probably partly due to the spike effect and partly due to absorbing many interstitial atoms produced by the irradiation.

---

* First reported at the Fifth General Assembly, International Congress and Symposia, International Union of Crystallography, August, 1960, Cambridge, England.

** Present address; Brookhaven National Laboratory, Upton, L. I., N. Y., U. S. A.

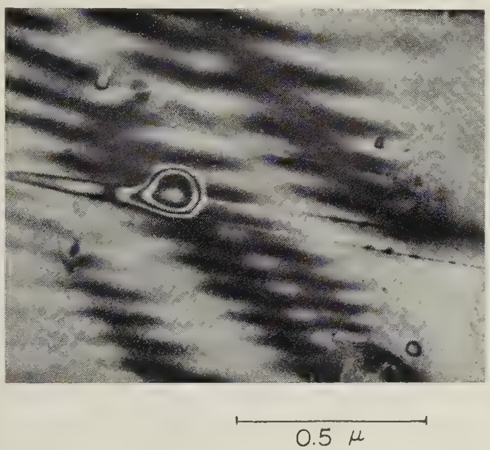

Photo. 1.

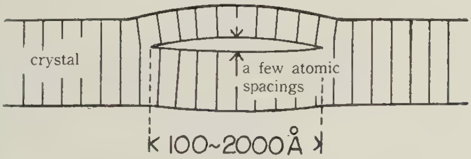

Fig. 1.

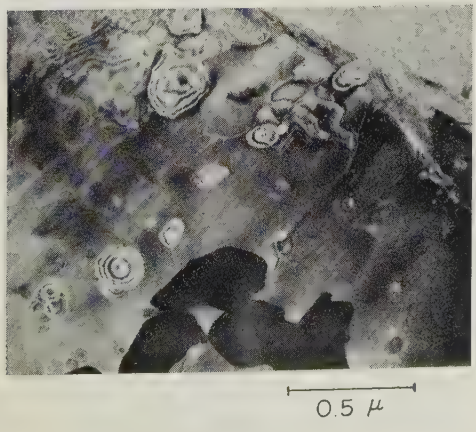

Photo. 2.

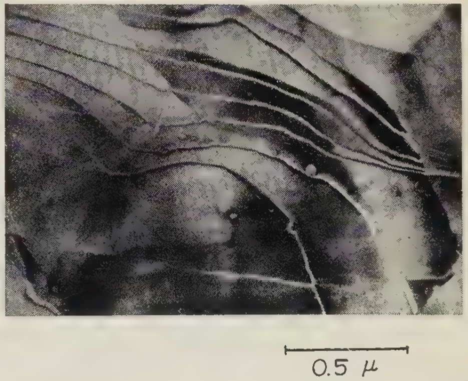

Photo. 3.

A full discussion will be given elsewhere in the near future.

References

1) F. Seitz and J. S. Koehler: *Solid State Physics,* **2** (1956) 305.
2) J. A. Brinkman: J. Appl. Phys. **25** (1954) 961.
3) F. E. Fujita and U. Gonser: J. Phys. Soc. Japan, **13** (1958) 1068.
4) E. C. H. Silk and R. S. Barnes: Phil. Mag., **4** (1959) 970.
5) T. S. Noggle and J. O. Stiegler: J. Appl. Physics, **31** (1960) 2199, also J. J. Kelsch and O. F. Kammerer: private communication.
6) J. Silcox and P. B. Hirsch: Phil. Mag. **4** (1959) 1356.
7) W. Bollmann: Phil. Mag., **5** (1960) 621, and private communication.
8) H. Hashimoto: private communication.

J. Phys. Soc. Japan **16** (1961) 1034~1035

A Note on The Electron Diffusion and The Wall Relaxation in Ferrites

By Hisashi SEKIZAWA

Department of Physics, Faculty of Science, University of Tokyo, Tokyo

(Received February 24, 1961)

A Richter type peak of magnetic loss is known to occur in ferrites[1] and in ferromagnetic garnet[2]. Snoek[3] attributed such phenomena to the diffusion of the electrons between ferrous and ferric ions in 16d sites in the ferrite. In discussions of that loss, it is mentioned[4],[5] that there is a close similarity between it and the loss due to the diffusion of carbon atoms in iron, but the remarkable difference in their situations seems to be unnoticed. And there is a confusion with regard to the interpretation of the relaxation times obtained from the loss peaks in ferrites[6]. This note wishes to clarify the relation between the motion of the electrons and the wall relaxation, and to establish the distinction between the relaxation times of them.

As is well known, the motion of a 180° domain wall can well be expressed by the following simple equation[7],

$$m\ddot{x}+\beta\dot{x}+k_w x=2\mathrm{M_s H}\ ,$$

where x is the displacement of the wall, m the effective mass which can be neglected because of its smallness, k_w the coefficient of force restoring the wall to its equilibrium position, and β the coefficient giving viscous damping. On putting $\mathrm{H}=\mathrm{H_0}\exp(j\omega t)$ and $x=x_0\exp(j\omega t)$, we get for the μ due to the wall[4]

$$\mu_w=\mu_w'-j\mu_w''\propto[1/(1+j\omega\beta/k)]\ .$$

Including the part of μ due to domain rotation μ_r, $\tan\delta$ of $\mu=\mu_r+\mu_w$ has a maximum when

$$\omega_w=1/\tau_w=\sqrt{(\mu_{r0}+\mu_{w0})/\mu_{r0}}\cdot k_w/\beta\ .$$

Clogston[8] made a calculation on the velocity of steadily moving wall based on a semi-microscopic model of the electron diffusion similar to the one proposed by Néel[9]. He assumed that there are N electrons which are migrating among ferric ions in 16d sites through jumps with a relaxation time τ_e and that each one of them accompanies a uniaxial anisotropy energy $w\cos^2\theta$ along certain crystallographical direction specified to each site. His result can be expressed in the present notation

$$\beta\approx\tau_e\sqrt{-K/12A}\,(N/kT)w^2\ .$$

Néel[9] made a theory on diffusion after-effect and calculated the pressure on the wall. His results can be expressed in the present notation

$$k_w\propto\frac{(\omega\tau_e)^2}{1+(\omega\tau_e)^2}\ ,\qquad \mu_w''\propto\frac{\omega\tau_e}{1+(w\tau_e)^2}\ ,$$

The calculation has been made on a wall moving as $x=x_0\sin\omega t$, considering the influence of the potential trough dug by the wall as a small perturbation. But it is the change with ω of x_0 that we are interested in, when discussing the wall relaxation in ferrites. Only in the cases in which the restoring force due to the other mechanisms than that due to the trough dug by the wall is dominant, and also $\tan\delta\ll 1$ even at $\omega=\omega_e=1/\tau_e$, then the calculation can be applied and the activation type loss peak will be observed at ω_e. In the region $\omega\gg\omega_e$, the trough is quenched and does not follow the wall any more. This is the case of iron containing small amount of carbon, discussed by Néel[9] and observed by Tomono[10]. On the other hand, in ferrous ferrites the trough follows the wall though lagging a little. But as β is so large that the condition $\beta\dot{x}\geq kx$ is realized on increasing ω, and the wall motion damps out[4]. This occurs at $\omega=\omega_w$ far below ω_e on the lower side slope of the peak of $\omega\tau_e/\{1+(\omega\tau_e)^2\}$. Note that as

$$\tau_w=\sqrt{\frac{\mu_{r0}}{\mu_{r0}+\mu_{w0}}}\cdot\frac{\beta}{k_w}$$

$$\approx\sqrt{\frac{\mu_{r0}}{\mu_{r0}+\mu_{w0}}}\cdot\frac{1}{k_w}\sqrt{\frac{-K}{12A}}\left(\frac{N}{kT}\right)\tau_e=C\tau_e\ ,$$

the activation energy E obtained by fitting it to $\tau_w=\tau_{w\infty}\exp(E/kT)$ coincides approximately with that of τ_e. But $\tau_{w\infty}=C\tau_{e\infty}$ has a factor C which can not be deduced merely from the elementary process of diffusion but is related with the other quantities such as k_w. So, τ_w and τ_e are two entirely different quantities only having the same activation energy, and must be strictly distinguished to each other.

The disaccommodation of the permeability observed in various ferrites would be closely related with the diffusion of electrons or ions[11]. But the relaxation time of disaccommodation is τ_e and not τ_w. Since $\tau_w\gg\tau_e$ if they belong to the same origin, the disaccommodation observed at room temperature and the loss peak at lower temperatures can not have the same origin. Only the peaks appearing at higher temperatures such as observed by Krupička[12] can have a connection with the disaccommodation at room temperature. Because $\tau_{e\infty}$ should be related with the lattice vibration and is not so sensitive to the process occurring, it seems to be of the order of 10^{-12}—10^{-14} sec. Then, such processes mentioned above must have an activation energy of the order of 1 eV no matter what are the causes of them, electrons or ions.

References

1) H. P. J. Wijn and M. van der Heide: Rev. Mod. Phys. **25** (1953) 98.

2) H. Sekizawa, S. Iida and T. Miyadai: J. Phys. Soc. Japan **13** (1958) 658. D. J. Epstein and

B. Frackiewicz: J. Appl. Phys. **30** (1959) 295S.
3) J. L. Snoek: New Developments in Ferromagnetic Materials (1947).
4) P. A. Miles, W. B. Westphal and A. von Hippel: Rev. Mod. Phys. **29** (1957) 279.
5) L. Néel: J. Appl. Phys. **30** (1959) 3S.
6) A. v. Kienlin: Z. angew. Phys. **9** (1957) 245.
7) W. Döring: Z. Naturforsch. **3A** (1948) 373. R. Becker: J. phys. rad. **12** (1951) 332.
8) A. M. Clogston: Bell System Tech. J. **34** (1955) 739.
9) L. Néel: J. phys. rad. **13** (1952) 249.
10) Y. Tomono: J. Phys. Soc. Japan **7** (1952) 174, 180.
11) U. Enz: Physica **24** (1958) 609. W. A. Crapo: J. Appl. Phys. **31** (1960) 267S.
12) S. Krupička and F. Vilim: Czech. J. Phys. **7** (1957) 723.

J. PHYS. SOC. JAPAN **16** (1961) 1035~1036

Weak Field Behaviour of the $\varDelta E$ Effect in Ferromagnetic Cubic Solid Solution Alloys

By Mikio YAMAMOTO and Satoshi TANIGUCHI

The Research Institute for Iron, Steel and Other Metals, Tôhoku University, Sendai

(Received March 2, 1961)

The experimentally known $\varDelta E$ effect of polycrystalline ferromagnets may be classified into three types[1]. The third-type $\varDelta E$ effect, in which Young's modulus, E, shows a maximum and then a minimum, is observed with cobalt and h c.p. Ni-Co alloys[2] and it may be interpreted as associated with the process of reversible rotation of magnetization vectors from the [0001] direction of easy magnetization towards the direction of an applied magnetic field. The first type, in which E increases monotonously with magnetization, and the second-type, in which E decreases at first and then increases to a value larger than that in unmagnetized state, are observed with cubic metals and alloys[1],[2]. Particularly, the second-type $\varDelta E$ effect is especially conspicuous in f.c.c. Ni-Co alloys. The minimum (negative) value for 50% Co-Ni alloy attains to 5% which is of the same order of magnitude as the saturation value[2].

It has already been confirmed experimentally[1] that the decrease of E at weak magnetic fields in the second-type $\varDelta E$ effect is associated with the displacements of non-180° domain walls. The second-type $\varDelta E$ effect may be resulted from the fact that the occurrence of non-180° wall displacements is difficult in unmagnetized state, and, as the specimen is magnetized, it once becomes easier but again becomes difficult. Thus, in the case where the non-180° wall displacements are extremely easy to occur, the negative minimum of the $\varDelta E$ effect may appear in very weak fields so that it may not be observed. This may be regarded as the first-type $\varDelta E$ effect.

Let us consider, for simplicity, the $\varDelta E$ effect due to the displacements of (100) 90° walls, which is expressed as

$$(\varDelta E)_{SH}/E_S \fallingdotseq (E_S-E_H)/E_S \fallingdotseq E_S(\partial\varepsilon_m/\partial\sigma)_H$$
$$=(3/2)A\lambda_e E_S/W''(U)\,, \qquad (1)$$

where E_H and E_S are the values of E under magnetic field, H, and in magnetically saturated state, respectively, ε_m is the magnetostrictive strain, σ is the stress, A is a numerical factor, λ_e is the saturation magnetostriction along the direction of easy magnetization, and $W(U)$ is the wall energy at the position displaced by U. $W''(U)=d^2W/dU^2$, and it is assumed that $E_S-E_H \ll E_S$. It can be shown, from Eq. (1), the second-type $\varDelta E$ effect occurs when internal stresses or inclusions distribute at random in the specimen, but the second-type $\varDelta E$ effect arising from such origins may change according to specimens or their states even for the same material, so that it can not explain remarkable extreme values of the $\varDelta E$ effect and their systematic composition dependence in f.c.c. Ni-Co alloys[2].

Now, when domain walls are stabilized by the induced uniaxial ferromagnetic anisotropy energy and this energy of stabilization, W_S, predominates over energies of other origins, we can put

$$W''(U)=W_S''(U/d_0)\,, \qquad (2)$$

where d_0 is the thickness of the domain wall concerned. Since the form of $W_S(U)$ curve does not strongly depend on the type of crystal lattice and on the kind of domain walls, we consider, for simplicity, (100) 90° wall in an *ideal simple cubic* alloy with the <100> direction of easy magnetization. Then, its stabilization energy is given by[3]

$$W_S=-K_u U \coth(U/d_0)\,, \qquad (3)$$

and the $\varDelta E$ effect due to the displacement of this domain wall is expressed by

$$(\varDelta E)_{SH}/E_S=(3/2)(d_0/2K_u)A\lambda_e^2 E_S/\mathrm{cosech}^2(U/d_0)$$
$$\times\{1-(U/d_0)\coth(U/d_0)\}\,, \qquad (4)$$

where K_u is the uniaxial magnetic anisotropy constant, which depends on the alloy composition, n, approximately as

$$K_u=16K_0 n^2(1-n^2)\,, \qquad K_0=\text{constant}\,. \qquad (5)$$

The behaviour of the $\varDelta E$ effect in weak magnetic fields as calculated from Eq. (4) shows a good agreement with the measured results on 50% Co-Ni alloy[2]. Also, the alloy composition dependence of the extreme value of the $\varDelta E$ effect as usually defined experimentally is expressed as

$$[(\varDelta E)_{H0}/E_0]_{\mathrm{ext}}=(\varDelta E)_{S0}/E_0-[(\varDelta E)_{SH}/E_S]_{\mathrm{ext}}$$
$$=[(\varDelta E)_{S0}/E_S]_{n=0.5}\{a-1/16n^2(1-n^2)\}\,, \quad (6)$$

where a is a numerical factor, and the composition dependence of the field where the extreme value of the $\varDelta E$ effect locates, H_{ext}, is given by

$$H_{\mathrm{ext}}=(K_0/I_S)/16n^2(1-n^2)\,, \quad (7)$$

where I_S is the saturation magnetization. Eqs. (6) and (7) are found to be in accordance with the measured results on f.c.c. Ni-Co alloys[2].

Thus, it can be concluded that the main cause of the second-type $\varDelta E$ effect is the stabilization of domain walls by the induced uniaxial ferromagnetic anisotropy. The $\varDelta E$ effect due to this origin may appear in all cubic solid solution alloys, but the occurrence of remarkable second-type $\varDelta E$ effect must satisfy several conditions. According to those conditions, the second-type $\varDelta E$ effect must be remarkable only in the composition range of 55~75% Co of b.c.c. Fe-Co alloys, it must be small in b.c.c. Fe-Al alloys, and remarkable second-type $\varDelta E$ effect can not be expected for f.c.c. Ni-Fe and Ni-Cu alloys. These expectations have already been ascertained by the observational results[1].

References

1) M. Yamamoto: Sci. Rep. RITU, **A 12** (1960) 291 (Fe-Co), and literature cited in it.
2) M. Yamamoto and S. Taniguchi: Sci. Rep. RITU, **A 7** (1955) 35 (Ni-Co).
3) S. Taniguchi: Sci. Rep. RITU, **A 8** (1956), 173.

J. PHYS. SOC. JAPAN **16** (1961) 1036~1037

Remarks on the Electrical Properties of Alkali Antimonides

By Shunji IMAMURA

Technical Research Laboratories, Japan Broadcasting Corporation, Kinuta-machi, Setagaya-ku, Tokyo, Japan

(Received March 3, 1961)

This note presents the remarks on the complexity of the characteristics of rubidium antimonide and on the assignment of the acceptors in cesium antimonide.

When an evaporated antimony film is exposed to the alkali vapor, the resistivity varies in complicated ways. In the present work the high reaction temperature (about 250°C, the upper limit restricted by sublimation and dissociation of the specimen) and the thin film of antimony (about 200 Å) were employed, in order to diffuse the alkali atoms quickly. It was also necessary to increase the alkali vapor pressure at slow rate so as to overcome that of the specimen during formation process. The variation of the resistivity was continuously recorded. The other experimental details have been described in the previous paper[1]. The results are shown in Fig. 1. In the Cs-Sb system the compound corresponding to the fourth maximum was determined as Cs_3Sb by X-ray experiment.

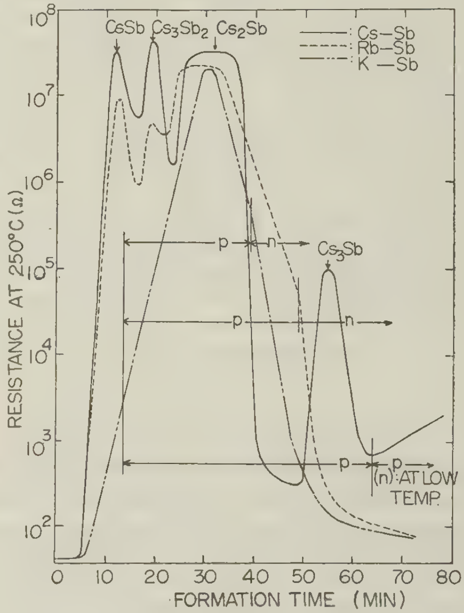

Fig. 1. Variation of the resistance of alkali antimonides. The sign of the predominant carriers at 250°C is denoted by n or by p. According to the X-ray work[5] the compounds Rb_3Sb and K_3Sb are formed just before the transition from p to n-type.

The compositions associated with the other maxima are identified as shown, by comparing with the data of Miyazawa *et al*[2] and Miyake[3]. The K-Sb system behaves in a different way from the Cs-Sb one, i.e., only one maximum exists, differing from the data of Suhrmann and Kangro[4], in which two maxima are shown. The behavior of the Na-Sb was entirely the same as that of the K-Sb. The above data suggest that the Cs-Sb system and the K-Sb (and Na-Sb) one are crystallized in different ways at each other through the formation process. The result for the Rb-Sb is interesting. It seems to indicate that the crystallization of the Rb-Sb proceeds in a similar manner to the Cs-Sb initially and to the K-Sb finally. This is not also inconsistent with the fact, recently found by our X-ray work[5], that Rb_3Sb is crystallized initially in a cubic lattice, which is the same as that of Cs_3Sb, and is transformed into a hexagonal one, which is the same as that of K_3Sb and Na_3Sb, by introducing a plenty of excess Rb atoms. From the present results it may be said that if the formation treatment of the Rb-Sb system is stopped before the transformation into a hexagonal lattice, the electrical and optical properties of the specimen are similar to those of the Cs-Sb system, and after the transformation they are simillar to those of the K-Sb (and Na-Sb). This is thought as a cause of the complexity reported in the work of several investigators[1),6),7)].

Jack and Whachtel[8)] have explained that the structure of Cs_3Sb is a disordered pseudo body-centered cubic lattice*, in which some of Cs and Sb atoms are randomly distributed. This structure makes possible to replace the Sb sites by excess Cs atoms to a certain extent. Moreover, this is describable as consisting of two interpenetrating diamond-type lattices, suggesting some of homopolar nature. Chemical analysis showed also the stoichiometric excess of cesium. In view of these facts, they have suggested that the Cs atom, which is less valent than Sb atom, positioned at Sb site is an acceptor. On the other hand, Sommer[6)] and Spicer[9)] have proposed that the vacancies of Cs atoms caused by evaporation of cesium are responsible for the acceptors. In the present experiment, the resistivity in the last stage increases gradually under an extremely high vapor pressure of cesium, which is estimated to be about 10^{-2} mm Hg, probably due to a compensation of acceptors by donors. Even in this stage, the thermo-electromotive force measurement shows p-type conduction at 250°C. This indicates that the Cs_3Sb containing excess Cs atoms is essentially a p-type semiconductor. Although the n-type conduction is observed when the cesium supply is ceased and the temperature is lowered to below about 120°C, it seems to be an apparent one due to a surface conduction caused by adsorbed Cs atoms. Consequently the author believes at present a propriety of Jack and Wachtel's model, although the other kind of acceptors may exist together with it.

References

1) S. Imamura: J. Phy. Soc. Japan **14** (1959) 1491. **14** (1959) 1497.
2) H. Miyazawa, K. Noga, S. Chikazumi and A. Kobayashi: J. Phys. Soc. Japan **7** (1952) 647.
3) K. Miyake: J. Appl. Phys. **31** (1960) 76.
4) R. Suhrmann and Cl. Kangro: Naturwiss. **40** (1953) 137.
5) J. Chikawa, S. Imamura, K. Tanaka and M. Shiojiri: To be published in J. Phys. Soc. Japan.
6) A. H. Sommer: J. Appl. Phys. **29** (1958) 1568.
7) W. E. Spicer: Phys. Rev. **112** (1958) 114.
8) K. H. Jack and M. M. Wachtel: Proc. Roy. Soc. **A**, **239** (1957) 46.
9) W. E. Spicer: J. Appl. Phys. **31** (1960) 2077.

---

* We have found that the desirable structure of the cubic Rb_3Sb is the same as that of the disordered one of Cs_3Sb[5)]. Hence, in an analogy the author supports the disordered one of Cs_3Sb, though Scheer and Zalm (Philips Res. Rep. **14** (1959) 143.) have proposed an ordered structure.

J. PHYS. SOC. JAPAN **16** (1961) 1037~1038

The Characteristics of the Discharges in the Crossed Electric and Magnetic Field

By Shigeru HAYAKAWA

Technical Research Department, Wireless Division, Matsushita Electrical Ind. Co., Ltd., Osaka, Japan

and Tokuo SUITA

Faculty of Engineering, Osaka University, Osaka, Japan

(Received March 6, 1961)

Various peculiar and interesting phenomena are observed in the case of gas discharge in crossed electric and magnetic field, however this report is mainly based on some of the experimental results having obtained along our projects on the prior stage of gas discharge in such fields.

The apparatus is shown in Fig. 1, which is similar to the Homopolar at Berkeley except for the difference that the inner electrode consists of the upper and the lower separate parts.

A uniform axial magnetic field is initially applied and an electric field introduced between cylindrical co-axial electrodes sets up the discharge to lead the formation of the so called rotating plasma round the symmetric axis. In case that voltage is introduced rapidly between electrodes, a rather long pre-

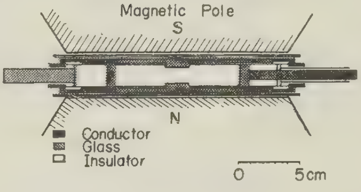

Fig. 1.

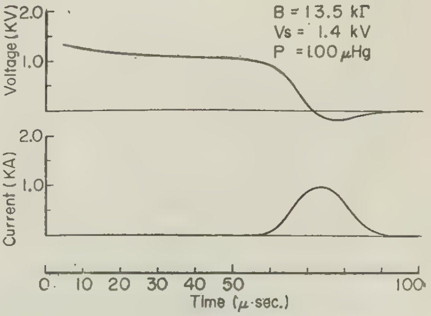

Fig. 2.

discharging period is detected before the discharge is set up. This delay time is closely related to the applied voltage, the magnetic field strength and the vacuum pressure of the system. The current-voltage characteristic for a particular discharge is shown in Fig. 2, with which the delay time of 55 μ. s. is associated.

How the applied voltage is related to the delay time under the constant magnetic field strength and the vacuum pressure is plotted as in Fig. 3.

In order to detect the space potential distribution in this pre-discharging period, double floating probes are inserted radially into the apparatus.

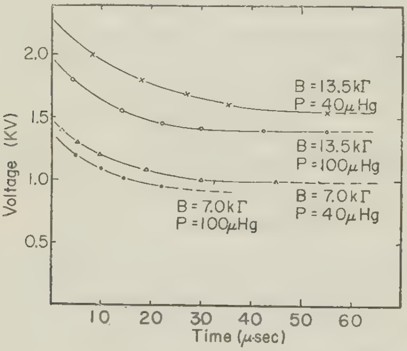

Fig. 3.

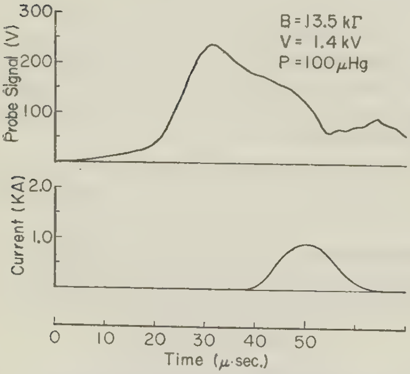

Fig. 4. Double probe signal and discharge current (probe position: 1-probe 3 mm and 2-probe 8 mm from cathode).

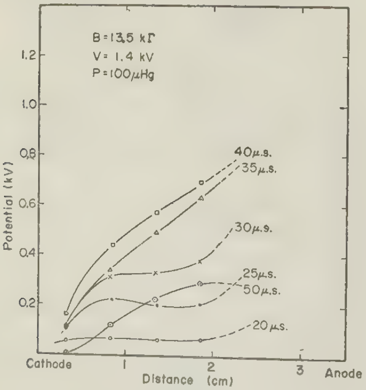

Fig. 5. Time Variation of the Potential Distribution (Discharge starts at 40 μs).

Figure 4 is an example of the detected out-put, in which the corresponding current characteristic is shown in order to make clear the discharge starting time.

By moving the double floating probes radially, the time-variation of the space potential difference between any two points is detected. Figure 5 shows the time variation of the space potential between electrodes after voltage is introduced.

It is to be assumed according to the experimental results that the space charge is accumulated between electrodes during the pre-discharging period, due to which the discharge is initiated. Therefore, if the other factors are kept constant, the delay time is dominantly related to the ion density due to the collision between molecules and electrons under the sudden application of the electric field, and Fig. 3 indicates that the delay time decreases considerably with respect to the increase in the ionization efficiency of electrons as the applied voltage is raised up.

Although we have mentioned only the effects of the applied voltage, the magnetic field strength and the vacuum pressure to the experimental results as stated above, dV/dt in the application of the voltage is so related to the delay time as is effective to the motion of electrons and therefore to the generation of the stable rotating plasma, and our projects are concentrated in this point. The experimental results on this subject matter will be reported soon in future.

The authors are grateful to S. Kisaka for his encouragement, to T. Sekiya and H. Hishida for their discussion, and to K. Wasa for his measurments.

J. Phys. Soc. Japan **16** (1961) 1038~1039

The Electrical Properties of Zinc Telluride

By Hirosi TUBOTA, Hiromichi SUZUKI
and Kazuyoshi HIRAKAWA

General Education Department, Kyushu University, Fukuoka

(Received March 14, 1961)

Some reports have been published on the electrical properties of ZnTe in the form of evaporated thin films[1] or of polycrystalline specimens[2]. However, this compound in single crystals has been studied optically, especially on its photoconduction[3], transmission and reflection[4], but not on any purely electrical properties. We here report the information obtained about the single crystals prepared from the melt of stoichiometric composition and about those doped with indium and selenium[5].

Fig. 1 shows the electrical resistivities and the Hall coefficients. (The Hall coefficient of samples doped with In was not measurable.) The Hall coefficients of both stoichiometric and Se-doped specimens have positive signs. No reversal of the Hall coefficient is observed. We consider that the positive carriers contributing to the electrical conduction come presumably from the Zn vacancies, because the vapor pressure of Zn is much higher than that of Te, and then Zn may escape in the process of crystallization1),6). The energy gap ΔE of ZnTe, 2.12 eV, was determined for the specimen doped with In from the equation $\rho=\rho_0 \exp(\Delta E/2kT)$. This value is in good agreement with that determined from the optical data3),4).

Fig. 2 shows the Hall mobilities μ_H obtained from the Hall coefficients R_H and the electrical resistivities ρ by the use of the equation $\mu_H=(8/3\pi)\cdot(R_H/\rho)$. The temperature dependence of the Hall mobilities of ZnTe is given by $\mu_H \propto T^{-1.50}$ in the region in which the lattice scattering is predominant. This figure, 1.50, suggests that at higher temperatures the electrons are scattered mainly by the acoustical mode. Therefore, the bond in ZnTe crystal seems to be rather covalent, presumably in agreement with the fact that the difference in electronegativity between Zn- and Te-atoms is relatively small, as seen from Table I.

The authors wish to express their sincere thanks to Prof. T. Okada for his kind advice.

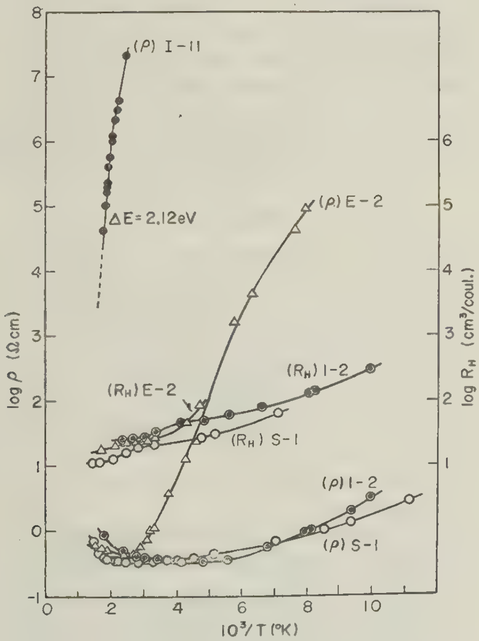

Fig. 1. Resistivity and Hall coefficient versus reciprocal temperature for p-type ZnTe.

1-2: stoichiometric (prepared by slow cooling),

S-1: stoichiometric (prepared by Bridgman's method)

E-2: doped with Se,

I-11: doped with In.

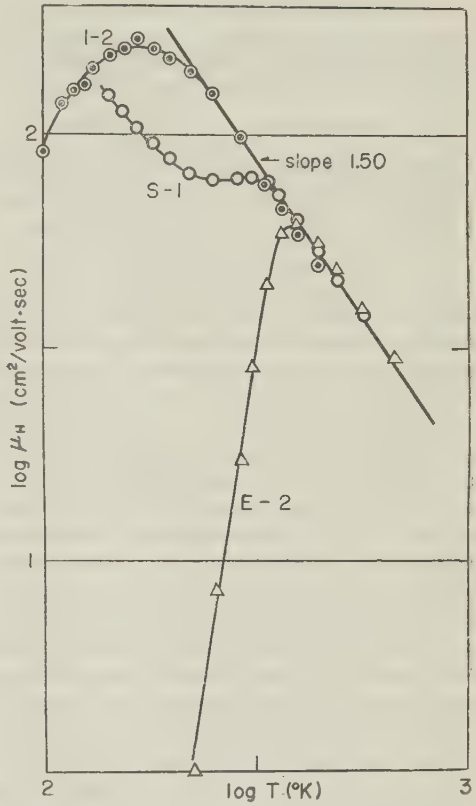

Fig. 2. Hall mobility versus temperature for p-type ZnTe.

Table I. Electronegativity of certain elements evaluated by L. Pauling.

II	III	V	VI
Mg 1.2	Al 1.5	P 2.1	S 2.5
Zn 1.7	Ga 1.7	As 2.0	Se 2.4
Cd 1.7	In 1.7	Sb 1.8	Te 2.1

References

1) J. Horák, M. Machovec and F. Kosek: C. A. **52** (1957) 16043c.

2) B. I. Boltaks, O. A. Matveev and V. P. Savinov: C. A. **50** 3065d (1956).

3) R. H. Bube and E. L. Lind: Phys. Rev. **105** (1957) 1711; ibid **110** (1958) 1040. Y. Simon and J. Bok: Comt. Rend. **248** (1959) 2176.

4) S. Larach, R. E. Schrader and C. F. Stocker: Phys. Rev. **108** (1957) 587.

5) The results on ZnTe single crystals with other various doping elements will be reported.

6) H. Tubota, H. Suzuki and K. Hirakawa: J. Phys. Soc. Japan **15** (1960) 1701.

J. PHYS. SOC. JAPAN **16** (1961) 1040

Internal Magnetic Field in Iron and Iron Alloys Measured by NMR

By Yoshitaka KÔI and Akira TSUJIMURA
Faculty of Engineering, Tokushima University
Tadamiki HIHARA and Toshimoto KUSHIDA
Faculty of Science, Hiroshima University

(Received March 5, 1961)

Nuclear magnetic resonance (NMR) experiments have been made in pure natural iron and iron alloys in order to measure the internal magnetic field, H_i.

The resonance frequency of Co^{59} in (Fe+1%Co) alloy is shown in Fig. 1 as a function of temperature along with newly extended measurement of Fe^{57} NMR frequency in pure iron. The values of the internal field corresponding to the resonance frequencies are shown as well. The resonance frequency extrapolated to 0°K by assuming $T^{3/2}$ law is 289.2 Mc/sec, corresponding to an internal field of 289.7 koe. This value is smaller by about 30 koe than the value deduced from specific-heat measurements at low temperatures[1)]. Here it is to be emphasized that the NMR measurement is by orders of magnitude more accurate. The H_i at Co nuclei in the alloy is larger in magnitude than that in pure cobalt metal by about 60∼70 koe[2),3)]. The possibility that Co atoms lose some of their 3d electrons when dissolved in iron[4)] would be responsible for this increase of H_i.

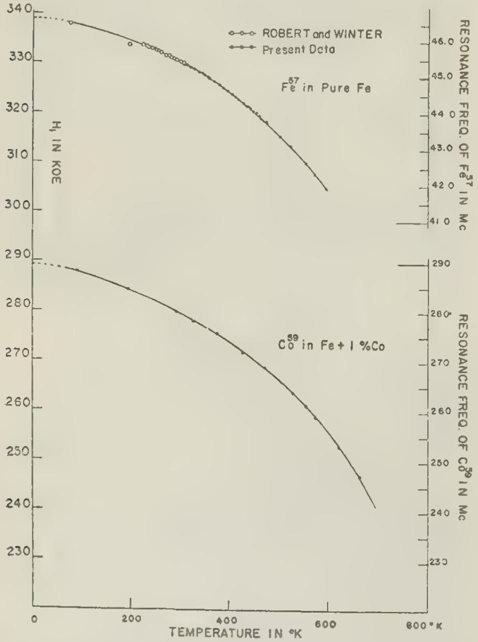

Fig. 1. Fe^{57} NMR frequency in pure iron and Co^{59} NMR frequency in (Fe+1%Co) alloy as a function of temperature.

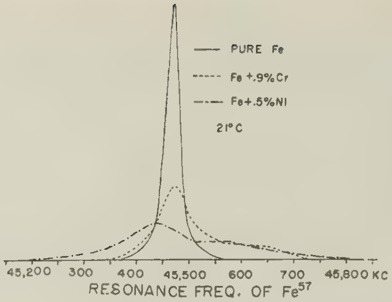

Fig. 2. The line shape of Fe^{57} NMR line (shown as the derivative of the resonance line) in iron alloy.

Since it is interesting to compare the temperature dependence of the resonance frequency of Co^{59} embedded in iron with that of Fe^{57} in pure iron[5),6)], the latter has been measured up to 320°C. Above this temperature the intensity of the line decreased below the noise level. It is to be noted that the resonance frequency of Co^{59} drops off with increasing temperature more rapidly than that of Fe^{57} in spite of the fact that the alloy has a higher Curie point than pure iron[7)].

The line shape of Fe^{57} resonance is strongly affected by alloying; preliminary results for alloying are presented in Fig. 2. Flat satellite lines are observed at higher-frequency wing of the main line for (Fe+0.9%Cr) and (Fe+0.5%Ni) alloys. These structures reflect the distribution of H_i caused by alloying more directly than the observed structures in Co^{59} resonance lines in cobalt alloys[8)], because Fe^{57} nucleus has no quadrupole moment.

References

1) V. Arp, D. Edmonds, and R. Petersen: Phys. Rev. Letters **3** (1959) 212.
2) A. C. Gossard and A. M. Portis: Phys. Rev. Letters **3** (1959) 164.
3) Y. Kôi, A. Tsujimura and T. Kushida: J. Phys. Soc. Japan **15** (1960) 2100.
4) W. M. Lomer and W. Marshall: Phil. Mag. **3** (1957) 185.
5) C. Robert and J.-M. Winter: Compt. rend. **250** (1960) 3831.
6) A. C. Gossard, A. M. Portis and W. J. Sandle: quoted in reference 5. J. I. Budnick, L. J. Bruner, E. L. Boyd, and R. J. Blume: Bull. Am. Phys. Soc. Ser. II **5** (1960) 491. D. E. Nagle, H. Frauenfelder, R. D. Taylor, D. R. F. Cochran, and B. T. Matthias: Phys. Rev. Letters **5** (1960) 364. S. S. Hanna: private communication.
7) P. Weiss and R. Forrer: Ann. Physik **12** (1929) 279.
8) Y. Kôi, A. Tsujimura, T. Hihara and T. Kushida: J. Phys. Soc. Japan **16** (1961) 574.

J. PHYS. SOC. JAPAN **16** (1961) 1041~1042

Slow Decay of Reverse Current and Noise in Field Effect on Ge P^+-N Junction

By Hiroshi EDAGAWA, Yoshinori MORITA,
Syun-ichi MAEKAWA
Kobe Kogyo Corp. Kobe
and Yoshio INUISHI
College of Engineering, Osaka University

(Received March 6, 1961)

Slow decay measurement of the reverse current increment ΔI_r and the mean square short circuit noise current increment $<\Delta i^2>$ due to D.C. surface field effect[1,2] were made simulteneously on Ge p^+-n junctions. Nickel plates were attached to the p^+-n junction specimen surfaces through thin mica spacer as field effect electrode as stated in the previous paper[2]. The glass tubes containing the specimen were evacuated at about 10^{-6} mm Hg for one day and sealed[2]. Fig. 1 (a), (b) are the decay characteristics of the reverse current increment ΔI_r add the noise current increment $<\Delta i^2>$ after the D.C. surface field application at $t=0$ for various temperature. The reverse bias voltage V_c on junction and applied surface field voltage V_F were 50 volt and ±360 volt respectively. By A. U. MacRae and H. Levinstein[1], the field effect decay of the $1/f$ noise in Ge single crystal was already reported. The authors have found that the decay characteristics of ΔI_r and $<\Delta i^2>$ are different depending on the type of surface layer, namely inversion or accumulation layer on high resistivity n-side. As well known, inversion or accumulation is formed on high resistivity n-side surface by negative or positive voltage respectively on the field effect electrode, while field effect on heavily-doped p-side was small[2]. In Fig. 1 (a), (b) the increment ΔI_r and $<\Delta i^2>$ at $t=0.5$ minute after the application of the field voltage were taken to be 100%. The $<\Delta i^2>$ decay associated with inversion layer on n-side follows a log t decay curve at various temperature. On the other hand, $<\Delta i^2>$ decay associated with accumulation on n-side and small inversion layer on p-side deviates from log t decay at larger t. The ΔI_r decay seems to be described by log t curve approximately. The decay time constants for ΔI_r and $<\Delta i^2>$ increase re-

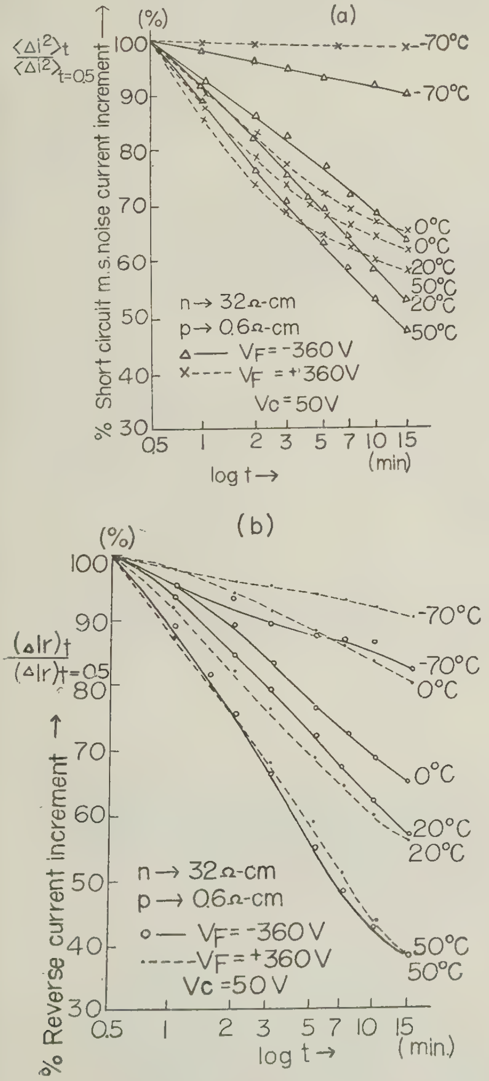

Fig. 1.

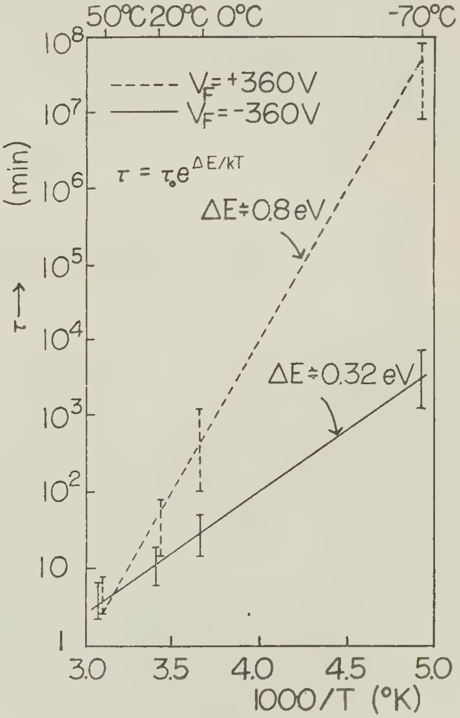

Fig. 2.

markably at lower temperature as seen in Fig. 1 (a), (b) which may be closely related to the relaxation time of carrier exchange with slow states. The time τ at which the increment ΔI_r reduces to a half of the initial value $t=0.5$ minute were plotted as a function of $1/T$ in Fig. 2. The decay time constants associated with accumulation layer on n-side and small inversion layer on p-side was larger than that with inversion layer on n-side.

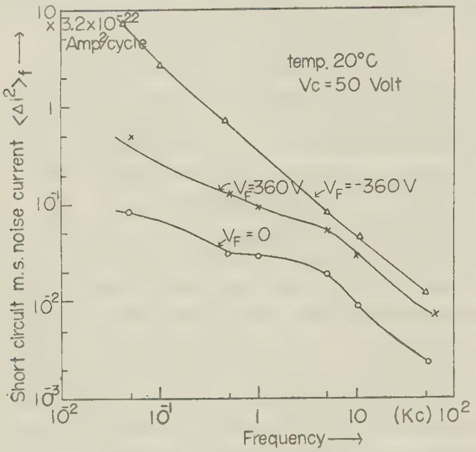

Fig. 3.

The frequency spectrum of the noise contains $1/f$ noise component, especially in case the of inversion layer on n-side surface as shown in Fig. 3.

The ratio $<\Delta i^2>/\Delta I_r$ increases with decreasing temperature below room temperature as was reported by MacRae et al.[1].

References

1) A. U. MacRae and H. Levinstein: Phys. Rev. **119** 62 (1960).
2) K. Komatsubara, Y. Inuishi, H. Edagawa and T. Shibaike: J. Phys. Soc. Japan **15** 1713 (1960).

Errata

Cavity Growth by Vacancy Condensation and Transformation to Dislocation Loop in the Graphite Structure

By Takuro TSUZUKU

J. Phys. Soc. Japan **16** (1961) 407

Page	Column	Line	Wrong	Corrected
408	left	25	$m_{\text{basal}}=2.61(\pi D^2/4)$ $=0.30D^2$	$m_{\text{basal}}=(\pi D^2/4)/2.61$ $=0.30D^2$
		29	$i=3.36m_{\text{basal}}/h$ $=0.089D^2h$	$i=m_{\text{basal}}h/3.36$ $=0.089D^2h$
		35	$m_{\text{side}}=(\pi D/2.46)(3.36/h)$	$m_{\text{side}}=(\pi D/2.46)(h/3.36)$
410	left	Fig. 3	The notation A of the third layer of the Rhombohedral crystal in the right-hand figure should be read C.	

Anomalous Diffusion at the Interface of Thin Bimetallic Film of Bi and Sb

By Ryōji SUGANUMA, Toshiho YOSHIDA and Yoshibumi FUJIKI

J. Phys. Soc. Japan **16** (1961) 676

Page	Column	Line	wrong	right
679	Fig. 5	caption	100° Å	1000 Å
680	left	10	minuters	minutes

JOURNAL OF THE PHYSICAL SOCIETY OF JAPAN, Vol. 16, No. 6, JUNE, 1961

Elementary Processes Related to the Catalytic Action of μ^- for the p-d Fusion Reaction

By Yukio MIZUNO

Department of Physics, University of Tokyo

(Received February 4, 1961)

In this paper the following four problems are studied theoretically.
a) The solution of the three-body problems associated with one meson and two hydrogen nuclei.
b) The number and type of bound states belonging to the mesonic hydrogen molecular ions.
c) The determination of the dominant mechanism of molecular ion formation.
d) The relation of the process, $(p\mu d)_s \longrightarrow \mathrm{He}^3+\gamma$, to the so-called mirror reaction, $n+d \longrightarrow \mathrm{H}^3+\gamma$.
At the end of the paper, it is shown that the theory is in a good quantitative agreement with the experiment for the nuclear as well as the molecular processes.

§ 1. Introduction

Alvarez et al.[1], in observing high energy negative mesons in a normal-hydrogen bubble chamber, discovered that some of these mesons, after having once come to rest, began to move again with the high energy of 5.3 MeV. Their discovery was followed by active investigations in this and related phenomena; theoretically by Hayashi et al.[2], Zel'dovitch et al.[3], Jackson[4], Skyrme[5], and others, and experimentally by Ashmore et al.[6] and Alvarez et al.[1]. This explanation for the present phenomenon is illustrated in a slightly simplified form in Fig. 1, where the control processes are shown by dotted arrows.

In this paper, we present a theoretical study of each of those elementary processes appearing in Fig. 1. The main problems, in which we have been interested, are as follows.

(a) The solution of the three-body problems associated with one meson and two hydrogen nuclei.

(b) The number and type of bound states belonging to the mesonic hydrogen molecular ions.

(c) The determination of the dominant mecha-

$$\begin{tikzcd}
 & \text{decay} & \text{decay} & \text{decay} & \\
\mu\,(\text{stopped}) \arrow[r] & (p\mu)_{1s} \arrow[u, dashed, "\lambda_0"] \arrow[r, "c\lambda_{\mathrm{ex}}"'] \arrow[d, dashed, "\lambda_{m1}"] & (d\mu)_{1s} \arrow[u, dashed, "\lambda_0"] \arrow[r, "\lambda_{m2}"'] & (p\mu d) \arrow[u, dashed, "\lambda_0"] \arrow[r, "\lambda_\mu"'] \arrow[d, dashed, "\lambda\gamma"] & \mathrm{He}^3+\mu\,(5.3\,\mathrm{MeV}) \\
 & (p\mu p) & & \mathrm{He}^3+\gamma &
\end{tikzcd}$$

Fig. 1. Main mechanism of the reaction, $\mu\,(\text{stopped}) \longrightarrow \mu\,(5.3\,\mathrm{MeV})$, in a liquid hydrogen with deuteron impurities of very low concentration c. First, the μ^- in question is trapped by a proton in liquid hydrogen, and then forms a very small neutral atom in the ground state, $(p\mu)_{1s}$, whose radius is about 10^{-11} cm. This atom wanders in the liquid hydrogen with thermal velocity (20°K), like a neutron. Next, when this atom collides with a deuteron impurity, the μ meson transfers from the proton to the deuteron to form a neutral μ mesonic deuteron atom, $(d\mu)_{1s}$, stabler than $(p\mu)_{1s}$ by 135 eV. This newly formed $(d\mu)_{1s}$ is ejected with the energy of 45 eV, but rapidly comes down to the thermal velocity by repeating elastic collisions with the nuclei in liquid hydrogen. Then, this atom captures a proton and forms a very small molecular ion, $(p\mu d)$. In some these molecules, finally, the nuclear fusion reaction between the proton and the deuteron, $p+d \longrightarrow \mathrm{He}^3+5.5\,\mathrm{MeV}$, occurs of which 5.3 MeV is given to the μ^- and 0.2 MeV to the created He³ nucleus. This process can be repeated. The dotted lines in the above figure show the main hindrance processes against the reaction in question. "Decay" means the natural decay of the μ meson, $\mu \longrightarrow e+2\nu$, whose decay constant λ_0 is $4.5\times10^5\ \mathrm{sec}^{-1}$.

nism of molecular ion formation.

(d) The relation of the process, $(p\mu d) \longrightarrow \mathrm{He}^3+\gamma$, to the so-called mirror reaction, $n+d \longrightarrow \mathrm{H}^3+\gamma$.

The first problem is discussed in § 2, by adopting the charge transfer process as an example. The second and third problems are treated in § 3 and § 4, respectively*. The last problem is studied in § 5, where the reader will find a good quantitative agreement between theory and experiment for not only the molecular but also the nuclear process. To avoid duplication of the calculation by Cohen et al.⁸⁾, of which the details have recently been published, we do not treat the problems (b) and (c) quantitatively on the basis of an approximation similar to that in § 2. A numerical value found by Cohen et al. is used in § 5 to make quantitative comparison between theory and experiment. Except for the last problem (d) and a few problems related to the $(d\mu d)$ molecule, there is no marked disagreement between Cohen et al.'s conclusion and ours.

§ 2. The Charge Transfer: $d+(p\mu)_{1s} \longrightarrow p+(d\mu)_{1s}$.

We here attempt a theoretical evaluation of the cross-section for the above process. The incident energy may be thought of as less than the zero-point energy of the proton bound in the ordinary hydrogen molecule, ($\sim\frac{1}{4}$ eV). The simplest treatment will be to apply the first order Born approximation. However, its validity for the present slow collision is somewhat doubtful, because the interaction between d and $(p\mu)$ or p and $(d\mu)$ is strong enough for the $(p\mu d)$ system to have a few bound states, though not many. This interaction causes not only the deviation of the interatomic motion from the plane wave but also the distortion of $(p\mu)_{1s}$ and $(d\mu)_{1s}$ themselves. In our calculation, we intend to take into account both effects at the same time. A feature of the present system is that the mass ratios of the nuclei to the meson are somewhat larger than unity. We then adopt the adiabatic approximation. However, the ratios are never so large as they are for electronic molecular systems, to which the naive adiabatic approximation has been applied with great success. Accordingly, a certain refinement of this approximation will be made.

In the usual approximation, the Hamiltonian of the present system is given by

$$\mathscr{H}_{\text{total}} = -\frac{\hbar^2}{2M_p}\Delta_p - \frac{\hbar^2}{2M_d}\Delta_d - \frac{\hbar^2}{2\mu_0}\Delta_\mu - \frac{e^2}{r_p} - \frac{e^2}{r_d} + \frac{e^2}{R}. \quad (2.1)$$

The meaning of these symbols will be obvious to the reader, the meson mass μ_0 being taken to be 207 times the electron mass throughout the paper. The part of (2.1) associated with the internal motion can be expressed as

$$\mathscr{H} = -\frac{\hbar^2}{2M}\Delta_R - \frac{\hbar^2}{2\mu}\Delta_r - \frac{e^2}{r_p} - \frac{e^2}{r_d} + \frac{e^2}{R}. \quad (2.2)$$

The first term is the kinetic energy operator for the relative motion between the proton and the deuteron. The second is that between the meson and the centre of gravity G of the two nuclei. The reduced masses M and μ are, of course, given by

$$\frac{1}{M} = \frac{1}{M_p} + \frac{1}{M_d}, \quad (2.3a)$$

$$\frac{1}{\mu} = \frac{1}{\mu_0} + \frac{1}{M_p+M_d}. \quad (2.3b)$$

The symbols $\boldsymbol{R}$ and $\boldsymbol{r}$ stand for the distance vectors from d to p and G to μ, respectively. Now, in the ordinary adiabatic approximation, every low-energy eigenfunction of (2.2) can be written in the form:

$$\Phi(\boldsymbol{r}, \boldsymbol{R}) = \varphi_1(\boldsymbol{r}; \boldsymbol{R})G(\boldsymbol{R}) + \varphi_2(\boldsymbol{r}; \boldsymbol{R})U(\boldsymbol{R}). \quad (2.4)$$

Here, φ_1 and φ_2 denote respectively the normalized lowest σ_g and σ_u molecular orbitals. They are exactly the same as the corresponding orbitals for the electronic hydrogen molecular ion, except for the scale factor. The G and U are eigenfunctions describing the relative nuclear motions under the respective adiabatic potentials. As is well-known, with increasing R, the φ_1 and φ_2 approach the forms:

$$\varphi_1 \sim \frac{1}{\sqrt{2}}\{\varphi(r_p)+\varphi(r_d)\},$$

$$\varphi_2 \sim \frac{1}{\sqrt{2}}\{\varphi(r_p)-\varphi(r_d)\},$$

where $\varphi(r)$ means the $1s$ orbital of the mesonic hydrogen atom. Therefore, (2.4) takes the form, for large R,

---

[*] §§ 2, 3, 4 form a detailed report of our study which has been published in form of short note.⁷⁾

$$\Phi \sim \frac{1}{\sqrt{2}}(G+U)\varphi(r_p) + \frac{1}{\sqrt{2}}(G-U)\varphi(r_d) . \tag{2.5}$$

Hence, if G and U are the eigenfunctions having the asymptotic forms:

$$G+U \sim e^{i\boldsymbol{K}_+\cdot\boldsymbol{R}} + F_+(\Omega)\frac{e^{iK_+R}}{R} , \tag{2.6a}$$

$$G-U \sim F_-(\Omega)\frac{e^{iK_-R}}{R} , \tag{2.6b}$$

then Φ corresponds to the collision of interest. The total cross-section for charge transfer is related to the scattering amplitude $F_-(\Omega)$ through

$$\sigma_{\text{ex}} = \frac{K_-}{K_+}\int |F_-(\Omega)|^2\, d\Omega . \tag{2.7}$$

However, the above treatment based on the naive adiabatic approximation has a serious defect. Namely, that it cannot explain the energy release of 137 eV at all. In other words, it results in the relation, $K_- = K_+$. Hence, the σ_{ex} is greatly underestimated, so long as the formula (2.7) is adopted, and some improvement must be made. If an arbitrary, but physically acceptable, function $\Psi(\boldsymbol{r}, \boldsymbol{R})$ is orthogonal to (2.4) in the extended sense that $\int \Psi^*\Phi\, d\boldsymbol{r} = 0$, its energy expectation value must be much higher than the energy of interest. Added to this, in (2.2), the mass ratio M/μ is somewhat larger than unity. Accordingly, the deviation of the exact eigenfunction from the form of (2.4) is expected to be inconsiderable. We, therefore, here attempt to refine the above naive treatment without extending the functional form (2.4).

To determine the functions G and U, we use the variation method based on the Schrödinger variation principle:

$$\delta\iint \Phi^*(\mathscr{H} - E)\Phi\, d\boldsymbol{r}\, d\boldsymbol{R} = 0 .$$

Substituting (2.4) in the above, we obtain the simultaneous equations:

$$\Delta_R G + \frac{2M}{\hbar^2}(E - \mathcal{E}_1)G + \Delta_{11}G = -\left(\Delta_{12} + \nabla_{12}\frac{\partial}{\partial R}\right)U , \tag{2.8a}$$

$$\Delta_R U + \frac{2M}{\hbar^2}(E - \mathcal{E}_2)U + \Delta_{22}U = -\left(\Delta_{21} + \nabla_{21}\frac{\partial}{\partial R}\right)G , \tag{2.8b}$$

where

$$\mathcal{E}_i(\boldsymbol{R}) = \int \varphi_i\left(-\frac{\hbar^2}{2\mu}\Delta_r - \frac{e^2}{r_p} - \frac{e^2}{r_d} + \frac{e^2}{R}\right)\varphi_i\, d\boldsymbol{r} , \tag{2.9a}$$

$$\nabla_{ij}(\boldsymbol{R}) = \int \varphi_i \frac{\partial}{\partial R}\varphi_j\, d\boldsymbol{r} = -\nabla_{ji}(\boldsymbol{R}) , \tag{2.9b}$$

$$\Delta_{ij}(\boldsymbol{R}) = \int \varphi_i \Delta_{\boldsymbol{R}}\varphi_j\, d\boldsymbol{r} . \tag{2.9c}$$

The first interals $\mathcal{E}_i$ are the so-called adiabatic potentials, for which we here adopt the highly accurate values calculated by Teller[9]. The ∇_{ij} and Δ_{ij} are both the integrals which are neglected in the naive adiabatic approximation. In this paper, they are evaluated by using the simple LCAO approximation for φ_1 and φ_2:

$$\varphi_1 = \frac{\varphi(r_p) + \varphi(r_d)}{\sqrt{2(1+S)}} , \tag{2.10a}$$

$$\varphi_2 = \frac{\varphi(r_p) - \varphi(r_d)}{\sqrt{2(1-S)}} , \tag{2.10b}$$

S being the overlap integral: $S = \int \varphi(r_p)\varphi(r_d)\, d\boldsymbol{r}$.

The results for $R=0$ and $R=\infty$ are as follows, the full expressions being given in Appendix 1.

$$\lim_{R\to\infty}\nabla_{12} = \lim_{R\to\infty}\nabla_{21} = 0 , \tag{2.11a}$$

$$\lim_{R\to\infty}\Delta_{11} = \lim_{R\to\infty}\Delta_{22} = -\frac{1}{2}\left\{\frac{M_p{}^2 + M_d{}^2}{(M_p + M_d)^2}\right\}\frac{1}{a^2} , \tag{2.11b}$$

$$\lim_{R\to\infty}\Delta_{12} = \lim_{R\to\infty}\Delta_{21} = -\frac{1}{2}\left(\frac{M_d - M_p}{M_d + M_p}\right)\frac{1}{a^2} , \tag{2.11c}$$

$$\lim_{R\to 0}\nabla_{12} = -\lim_{R\to 0}\nabla_{21} = -\frac{1}{2\sqrt{3}}\left(\frac{M_d - M_p}{M_d + M_p}\right)\frac{1}{a} , \tag{2.12a}$$

$$\lim_{R\to 0}\Delta_{11} = -\frac{1}{2}\left\{\frac{M_p{}^2 + M_d{}^2}{(M_p + M_d)^2} - \frac{1}{2}\right\}\frac{1}{a^2} , \tag{2.12b}$$

$$\lim_{R\to 0}\left(\Delta_{22} + \frac{2}{R^2}\right) = \text{finite} , \tag{2.12c}$$

$$\lim_{R\to 0}\left(\Delta_{12} - \frac{4}{R}\nabla_{12}\right) = \text{finite} , \tag{2.12d}$$

$$\lim_{R\to 0}\Delta_{21} = -\frac{1}{2\sqrt{2}}\left(\frac{M_d - M_p}{M_d + M_p}\right)\frac{1}{a^2} , \tag{2.12e}$$

where a represents the mesonic Bohr radius: $a = \hbar^2/\mu e^2$. The first three of these results are exact, and fortunately the following five are also exact so far as their divergent terms are concerned, because the nature of the singularity at the origin is uniquely determined simply from the values of angular momentum associated with the atomic orbitals to which φ_1 and φ_2 tend as $R \to 0$. The non-divergent parts, however, are fairly sensitive to the detail of the approximation, although this is considered to be not serious for our purpose. Approximate curves of our $\mathcal{E}_i$, Δ_{ij}, ∇_{ij} are illustrated in Figs. 2, 3, 4, 5. Clearly, the Δ_{ii} gives a direct correction to the $\mathcal{E}_i$; Δ_{11} makes the valley of $\mathcal{E}_1$ deeper, while Δ_{22} does the slope of $\mathcal{E}_2$ steeper. We here note the inequality:

$$\Delta_{ii}(R) \leqq 0 \ . \tag{2.13}$$

It is easily proved that (2.13) is always valid if the φ_i is a real function having a definite norm independent of R. The physical meaning will be clear for the reader. The negative sign of Δ_{12} and Δ_{21} (cf. Fig. 3) means that the energy of the total system can be lowered by transferring the meson from the proton to the deuteron. This tendency is, however, sometimes intensified and sometimes deminished by the velocity-dependent terms, $\nabla_{ij}(\partial/\partial R)$. If $M_p = M_d$, of course, all these non-diagonal integrals vanish identically.

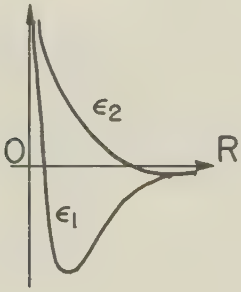

Fig. 2.

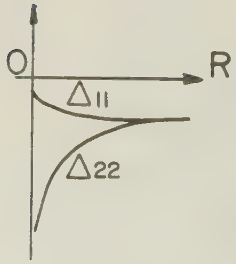

Fig. 3.

The above $\mathcal{E}_i$, ∇_{ij}, Δ_{ij} are all spherically symmetric. Hence, the coupled equations (2.8a, b) are invariant with respect to the rotation of the $\boldsymbol{R}$ space, and we can conveniently use the partial wave method to find the collision solution. Each partial wave (harmonic wave) has the form:

$$G = g_K(R) Y_{KM}(\Omega) \quad \text{and} \quad U = u_K(R) Y_{KM}(\Omega) \ , \tag{2.14}$$

where Y_{KM} denotes the spherical harmonic of angular momentum K and magnetic quantum number M. It is easy to see that the related full wave functions $\varphi_1 g_K Y_{KM}$ and $\varphi_2 u_K Y_{KM}$ have a definite total orbital angular momentum and a definite component of it, which are just equal to K and M, respectively. They are, howeve., not eigenfunctions of L^2, the squared angular momentum operator associated with the relative rotation of the two nuclei. Instead, the component of the total angular momentum along the molecular axis is quantized to zero. If $K=0$, this is strictly a constant of the motion, together with K and M. If $K \neq 0$, however, this is not the case but, in the region of short nuclear distance, the function $\varphi_2 u_K Y_{KM}$ couples strongly with the wave function associated with the $2p\pi$ molecular orbital. This results in the phenomenon called the L uncoupling in the field of molecular physics.[10),11)]

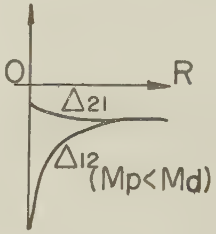

Fig. 4.

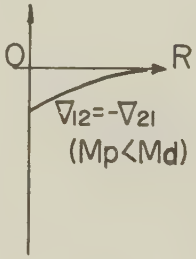

Fig. 5.

Now, substituting (2.14) in (2.8a, b), we obtain for g_K and u_K the coupled equations:

$$\left[\frac{1}{R^2}\frac{d}{dR}\left(R^2\frac{d}{dR}\right)+\frac{2M}{\hbar^2}\left\{E-\mathcal{E}_1-\frac{\hbar^2}{2M}\left(\frac{K(K+1)}{R^2}-\varDelta_{11}\right)\right\}\right]g_K=-\left(\varDelta_{12}+\nabla_{12}\frac{\partial}{\partial R}\right)u_K\,, \tag{2.15a}$$

$$\left[\frac{1}{R^2}\frac{d}{dR}\left(R^2\frac{d}{dR}\right)+\frac{2M}{\hbar^2}\left\{E-\mathcal{E}_2-\frac{\hbar^2}{2M}\left(\frac{K(K+1)}{R^2}-\varDelta_{22}\right)\right\}\right]u_K=-\left(\varDelta_{21}+\nabla_{21}\frac{\partial}{\partial R}\right)g_K\,. \tag{2.15b}$$

On the other hand, the boundary conditions for large R can be found by multiplication of (2.6a, b) by Y_{KM}^* and integration over angles. The result is

$$g_K+u_K\sim\int Y_{KM}^*(\Omega)e^{i\boldsymbol{K}_+\cdot\boldsymbol{R}}\,d\Omega+f_{KM}^+\frac{e^{iK_+R}}{R}\,, \tag{2.16a}$$

$$g_K-u_K\sim f_{KM}^-\frac{e^{iK_-R}}{R}\,. \tag{2.16b}$$

The $f_{KM}^\pm$ are expansion coefficients of the scattering amplitudes $F_\pm(\Omega)$ in terms of the spherical harmonics:

$$F_\pm(\Omega)=\sum_{KM}f_{KM}^\pm Y_{KM}(\Omega)\,. \tag{2.17}$$

The boundary conditions at the origin are clearly that

$$\lim_{R\to0}Rg_K=\lim_{R\to0}Ru_K=0\,, \tag{2.16c}$$

in so far as we neglect the phase shifts due to the nuclear force between p and d, cf. § 5. As one would naturally expect, Eqs. (2.15a, b) have two and just two sets of linearly independent solutions, which obey the condition (2.16c) at the origin:

$$g_K{}^{(i)}\sim a^{(i)}R^K\,, \tag{2.18a}$$

$$u_K{}^{(i)}\sim b^{(i)}R^{(\sqrt{4K(K+1)+9}-1)/2}\,. \tag{2.18b}$$

Therefore, the general solution subject to (2.16c) is given by

$$g_K=\lambda_1g_K{}^{(1)}+\lambda_2g_K{}^{(2)}\,, \tag{2.19a}$$

$$u_K=\lambda_1u_K{}^{(1)}+\lambda_2u_K{}^{(2)}\,, \tag{2.19b}$$

where λ_i are arbitrary constants. The value of the exponent in (2.18b) is not an integer, except for $K=0$. This is due to the fact that the $\varphi_2u_KY_{KM}$ is not an eigenfunction of L^2 even at the origin, unless $K=0$. To remove the defect, it is necessary to take into account the L uncoupling effect stated above.

With increasing R, the differences $\mathcal{E}_2-\mathcal{E}_1$, $\varDelta_{22}-\varDelta_{11}$, $\varDelta_{21}-\varDelta_{12}$, $\nabla_{21}-\nabla_{12}$ go to zero as rapidly as $\exp(-R/a)$. Hence, for large R, (2.15a, b) may be transformed into the two independent equations:

$$\left[\frac{1}{R^2}\frac{d}{dR}\left(R^2\frac{d}{dR}\right)-\frac{K(K+1)}{R^2}+K_\pm{}^2(R)\right](g_K\pm u_K)=0\,, \tag{2.20}$$

where

$$K_\pm{}^2(R)=\frac{2M}{\hbar^2}\left\{E-\frac{\mathcal{E}_1+\mathcal{E}_2}{2}+\frac{\hbar^2}{2M}\left(\frac{\varDelta_{11}+\varDelta_{22}}{2}\pm\frac{\varDelta_{12}+\varDelta_{21}}{2}\right)\right\}. \tag{2.21}$$

Further, in these regions, the above $K_\pm{}^2$ may be approximated as

$$K_\pm{}^2(R)\simeq K_\pm{}^2(\infty)+\frac{2M}{\hbar^2}\frac{\alpha_\pm e^2}{2R^4}\,. \tag{2.22a}$$

The last term means the contribution from the polarization force, α_+ and α_- being respectively the electro-static polarizabilities of the $(p\mu)$ and $(d\mu)$ atoms:

$$\alpha_\pm \cong \frac{9}{2}a^3 . \tag{2.22b}$$

The relation between $K_+(\infty)$ and $K_-(\infty)$ can be found from (2.21) and (2.11c);

$$\frac{\hbar^2}{2M}\{K_-^2(\infty)-K_+^2(\infty)\} = -\frac{\hbar^2}{M}\Delta_{12}(\infty)=\frac{1}{2}\left(\frac{\mu}{M_p}-\frac{\mu}{M_d}\right)\frac{\hbar^2}{\mu a^2}\cong 157\text{ eV} . \tag{2.23}$$

This may be compared with a value of 137 eV, the exact internal energy difference between $(p\mu)_{1s}$ and $(d\mu)_{1s}$. This good agreement is, of course, one of the reasons why we have chosen the trial form (2.4). Now, the above polarization force is certainly not strong, but it has a comparatively long range. Accordingly, it might have a serious effect on the low-energy collision, $K_+(\infty)\sim 0$. This is the case for electronic molecular systems, as is well-known. We must now discuss whether this effect is important in the present μ mesonic system. It will be sufficient to examine the solution of (2.20) for the special case where $K=0$ and $K_+(\infty)=0$.* To the first order of the polarization force, the solution of interest can be expressed as

$$g_0+u_0 \cong A\left\{1+\frac{9}{4}\frac{M}{\mu}\frac{a^2}{R^2}\right\}+\frac{B}{R}\left\{1+\frac{M}{\mu}\frac{a^2}{R^2}\right\} , \tag{2.24}$$

where A and B are arbitrary constants. Consequently, for the distortion to be negligibly small, the following condition must be satisfied:

$$\frac{9}{4}\frac{M}{\mu}\frac{a^2}{R^2} \ll 1 . \tag{2.25}$$

In other words, the value of R must be much larger than the critical value:

$$R_c \equiv \frac{3}{2}\sqrt{\frac{M}{\mu}}\,a \cong 3.6a . \tag{2.26a}$$

For the corresponding electronic problem, the μ and a must be replaced by the electron mass m_e and the electron Bohr radius a_e. Hence, we obtain the value:

$$R_c \cong 3.6\sqrt{207}\,a_e \cong 50a_e . \tag{2.26b}$$

These two values suggest that the Born approximation will be not so drastic for mesonic molecular systems as it is for electronic systems. This is due to the following quantum effect. The value of M measured in mesonic atomic units is much smaller than that measured in electronic atomic units, while all the other quantities are exactly same for the both systems, if they are also expressed in terms of the respective atomic units. Hence, the zero-point motions of nuclei related to the uncertainty principle must be far more active in mesonic molecular systems. As a result, the effect of the potential force on the nuclear motion must be largely averaged out. Considering these favourable circumstances, we adopt the equation for a free particle, in the region $R>6a$,

$$\left[\frac{1}{R^2}\frac{d}{dR}\left(R^2\frac{d}{dR}\right)-\frac{K(K+1)}{R^2}+K_\pm^2(\infty)\right] \times(g_K \pm u_K)=0 . \tag{2.27}$$

The resulting error in the cross-section is expected to be less than a factor of 2. The solutions of (2.27) having the asymptotic forms (2.16a, b) can, of course, be written down analytically, the amplitudes $f^\pm_{KM}$ being involved in them as unknown parameters. However, the solutions (2.19a, b) for $R<6a$ need to be culculated numerically. It will be clear that the parameters λ_i and $f^\pm_{KM}$ can be determined uniquely from the requirement that these two kinds of solutions must be connected smoothly at $R=6a$. Further, it will be needless to note that the amplitudes $f^\pm_{KM}$ for $K\neq 0$ go to zero rapidly with decreasing incident energy.

In Table I, our value of

$$\lambda_{\text{ex}} \equiv N\lim_{K_+\to 0}\left(\frac{\hbar K_+}{M}\sigma_{\text{ex}}\right)=\frac{N\hbar}{M}\lim_{K_+\to 0}(K_-|f^-_{00}|^2)$$

is shown, together with those found by the other authors. Here, N represents the number density of proton in pure liquid hydrogen at 20°K, $N=3.5\times 10^{22}\text{ cm}^3$. The quantity $c\lambda_{\text{ex}}$ may be interpreted as the rate for charge transfer in liquid hydrogen of deuteron concentration c.

Now, in Table I, the value due to Skyrme[5]

---

* For this special case, (2.20) can be solved exactly.

Table I. Calculated values of λ_{ex} (in $10^{10}\,\mathrm{sec}^{-1}$).

	Skyrme	Ours	Cohen et al.	Burke et al.
λ_{ex}	60	1.50	1.14	0.18

was estimated by using the first order Born approximation. The calculation by Cohen et al.[8] is in principle similar to ours, though much more elaborate. Their value may be thought of, in practice, as the true answer which can be derived from the basic assumption (2.4) without further simplification. They found that their λ_{ex} can explain the observed value of $\lambda_{\mathrm{ex}}/\lambda_0+\lambda_{m1}$ quite satisfactorily, together with their theoretical value of λ_{m1}. The main origin of the discrepancy between their value and ours is probably the difference in the range of numerical integration: they integrated Eqs. (2.15a, b) up to $R=20a$. In Burke et al.'s calculation[12], the φ_1 and φ_2 in (2.4) was replaced by those of the naive LCAO approximation from the start. They integrated their equations up to $R=16a$.

§ 3. The Bound States: ($p\mu p$) and ($p\mu d$)

As was noted in § 2, if $M_p=M_d$, all the non-diagonal dynamic correction integrals vanish identically. For ($p\mu p$), therefore, the two equations (2.15a) and (2.15b) are exactly uncoupled with one another. For ($p\mu d$), on the other hand, the coupling terms do not vanish. Their effect is, however, expected to be only of secondary importance, except for shallow bound states and continuous states. We then put, in Eqs. (2.15a, b)

$$\Delta_{ij}(\boldsymbol{R})=\nabla_{ij}(\boldsymbol{R})=0 \qquad \text{for} \quad i\neq j\,, \tag{3.1}$$

independently of whether we are interested in ($p\mu p$) or ($p\mu d$). The effective potential in (2.15b) is certainly attractive outside the region of overlap force, if $K=0$. However, it is so weak that no bound state can exist. Hence, we have only to examine the former equation. To simplify the calculation furthermore, we replace the associated effective potentials:

$$U_K(R)=\varepsilon_1+\frac{\hbar^2}{2M}\left\{\frac{K(K+1)}{R^2}-\Delta_{11}(R)\right\} \tag{3.2a}$$

by Morse potentials:

$$V_K(R)=D_K\left\{\exp\left(-2\frac{R-R_K}{A_K}\right)\right.$$
$$\left.-2\exp\left(-\frac{R-R_K}{A_K}\right)\right\}+C_K\,. \tag{3.2b}$$

The parameters A_K, C_K, D_K, R_K are here fixed by the four requirements that $V_K(\infty)=U_K(\infty)$, $V_K(4a)=U_K(4a)$, $V_K(R_K)=U_K(R_K)$, and the position of the minimum point of V_K, $R=R_K$, should coincide with that of $U_K(R)$.

The above approximate treatment results in three bound states in all, for each of ($p\mu p$) and ($p\mu d$). Two of them are S states ($K=0$), while one is a P state ($K=1$). In the following we wish to discuss whether or not the Hamiltonian (2.2) really has three bound states of these symmetries. The present calculation of energy levels is based on the ordinary variation method. The trial function is clearly given by $\varphi_1 g_K Y_{KM}$. Therefore, the resulting energy values of S, P, D, $\cdots$ states must be respectively upper bounds for the eigenvalues of the lowest S, P, D, $\cdots$ eigenfunctions of the total Hamiltonian (2.2), although this is, of course, not strictly true on account of the Morse potential approximation. On the other hand, the energies obtained for the lower S state and the P state are both somewhat lower than the exact energy of the related dissociation products: $p+(p\mu)_{1s}$ for ($p\mu p$), and $p+(d\mu)_{1s}$ for ($p\mu d$), not $d+(p\mu)_{1s}$. We can, therefore, conclude that the existence of the above two bound states is quite certain. Concerning the upper S state, which is an extremely loosely bound state for each system, our present calculation is certainly rough. For ($p\mu p$), however, that would not be so drastic as the result is wholly wrong. Accordingly, there is every possibility that the ($p\mu p$) system actually has a real or virtual S level near the dissociation limit. For ($p\mu d$), however, this is not the case. The approximation (3.1) is obviously drastic for large R. Accordingly, if we take into account the coupling between g_K and u_K, the present result would be greatly changed. On the other hand, the coupling results in localization of the meson on the deuteron in the region of large nuclear separation. This inevitably weakens the molecular binding between the proton and the deuteron. As a result, we are led to the expectation that the real ($p\mu d$) system would have no excited S state.*

---

* This expectation is opposite to those expressed by Skyrme[5] and Zel'dovitch[3]. The former author suggested that the existence of this level might be essential for the reaction, $p+(d\mu)_{1s}\longrightarrow(p\mu d)$, to take place.

Table II. Calculated dissociation energies (in ev.)

	$(p\mu p)$	$(p\mu d)$	$(d\mu d)$
$S(K=0)$	284 (284)	239 (235)	359 (343)
$P(K=0)$	113 (136)	88 (111)	228 (244)
$D(K=2)$	——	——	80 (103)
$S'(K=0)$	14	−79	30 (202)*

* The figures in brackets are those found by Cohen et al. based on an approximation similar to that of § 2. Their value for the excited S state of $(d\mu d)$ would be wrong.

Table II shows the dissociation energy of each bound state found by the above approximate calculation, together with that of $(d\mu d)$. Here, the energy of the related dissociation products is chosen to be

$$E_{\text{dis.}}=U(\infty)-\frac{\hbar^2}{2M}|\Delta_{12}(\infty)|^2 . \tag{3.3}$$

This expression is exact to the approximation of (2.8a, b). For $(p\mu p)$ and $(d\mu d)$, the last term vanishes, and so (3.3) reduces to the usual one.

§ 4. The Molecular Formation

We first mention the formation of the ground state $(p\mu d)$ molecule by the slow collision of a mesonic deuteron atom with a proton bound in an ordinary hydrogen molecule. As has been shown in the previous section, the $(p\mu d)$ system has one excited state, P, besides the ground state, S. Therefore, the ground state molecule can be formed in the following two ways. One is the direct transition from the incident state, I. The other is the indirect transition through the excited state, P. Clearly, these transitions must be accompanied by emission of some other particle than p, d, μ under consideration. Conforming to the usual convention[13)], we here examine only the two possibilities: the emission of a photon and the emission of an electron bound around the proton. Now, the incident energy of interest is so low that we consider the transitions simply from the S wave component of the incident state eigenfunction. Then, the direct transition is just the so-called 0–0 transition, in which the radiative process is forbidden. Consequently, the transition $I\rightarrow S$ takes place exclusively by electron emission. In the indirect transition, on the other hand, both are possible, and each step of the transition is induced by an electric dipole. Table III shows our calculated values of the associated reaction rates in the pure liquid hydrogen. They have been found by making a number of simplifying assumptions given below.

(a) We used a plane wave approximation for the incident state eigenfunction:

$$\Phi_{\rm I}(\boldsymbol{r},\boldsymbol{R})=\varphi(r_d)\cdot\exp(i\boldsymbol{K}_-\cdot\boldsymbol{R})\,, \tag{4.1}$$

$\varphi(r_d)$ being the $1s$ orbital of the mesonic hydrogen atom.

(b) The bound state eigenfunctions were simplified as

$$\Phi_{KM}(\boldsymbol{r},\boldsymbol{R})=\frac{\varphi(r_p)+\varphi(r_d)}{\sqrt{2(1+S)}}\cdot\frac{1}{R}\cdot\exp[-\alpha_K(R-R_K)^2]\cdot Y_{KM}(\Omega)\,. \tag{4.2}$$

The R_K is the same as that in (3.2b), the α_K being chosen so that it shall give the correct zero-point energy. This harmonic oscillator approximation results in an under-estimation of the reaction rates for $I\rightarrow P$ and $I\rightarrow S$.

(c) The wave function for the bound electron was replaced by the $1s$ orbital of the hydrogen atom.

(d) The plane wave approximation was adopted for the ejected electron.

(e) The perturbation for electron emission was chosen as

$$\mathscr{H}_e=e^2\left(\frac{1}{r_{e\mu}}-\frac{1}{r_{ep}}-\frac{1}{r_{ed}}+\frac{1}{r_{eg}}\right), \tag{4.3}$$

r_{eg} being the distance between the electron and the centre of gravity of the $(p\mu d)$ system. From Table III, we see that the ground state $(p\mu d)$ molecule will be formed predominantly by making the two successive electron-emission transitions, $I\rightarrow P$ and $P\rightarrow S$.* In addition, the rate for $P\rightarrow S$ is so large that neither the meson decay nor the p-d fusion process cannot compete with the transition $P \rightarrow S$ at all.

---

* Jackson[4)] also estimated the rate for 0–0 transition, and obtained a very large value ($\sim10^7\ \text{sec}^{-1}$). His result is, however, not acceptable. The plane wave (4.1) orthogonalized to the bound states (4.2) will be a better approximation of the incident state eigenfunction than (4.1) itself. If this improved one is used in his calculation, the result is in good agreement with ours. His calculation is based on the formula, $\lambda\propto|\langle\Psi^-{}_f|\mathscr{H}_f|\Psi\rangle|^2$, which is famous in the formal theory of scattering[14)]. This expression results in the exact reaction rate, when Ψ is the exact eigenfunction corresponding to the present collision, $(pe)+(d\mu)\longrightarrow(p\mu d)+e$.

We next discuss the formation of $(p\mu p)$. In this case there are two independent incident state, I_+ and I_-. The former is symmetric with respect to interchange of the space coordinates of two protons, and the related wave function is given by $\varphi_1 G$ in the approximation of § 2. The latter is anti-symmetric and the wave function is given by $\varphi_2 U$. Their statistical weights are 1 and 3, respectively. On the other hand, the bound state S is symmetric, and P is anti-symmetric with respect to the same symmetry operation.

Table III. Calculated rates for formation of $(p\mu d)$ in pure liquid hydrogen (in sec^{-1}).

	$I \rightarrow S$	$I \rightarrow P$	$P \rightarrow S$
Electron emission	10^{-1}	10^5	10^{10}
Photon emission	0	10^{-1}	10^6

Therefore, the allowed transitions are two in all, $I_+ \rightarrow S$ and $I_- \rightarrow P$, $P \rightarrow S$ being forbidden in the usual approximation. The latter transition, $I_- \rightarrow P$, can occur by $E1$, just as before. The electric dipole operator for $(p\mu d)$ may be expressed as

$$\mathscr{D} = \frac{e}{2} \frac{M_d - M_p}{M_d + M_p + \mu} \boldsymbol{R} - e \frac{M_d + M_p + 2\mu}{M_d + M_p + \mu} \boldsymbol{r}' , \tag{4.4}$$

where $\boldsymbol{r}'$ stands for the distance vector from the geometrical centre of p and d to μ^-. When $M_p = M_d$, the first term vanishes identically, so that the second term alone exists for $(p\mu p)$. However, the analysis of our calculation for $(p\mu d)$ tells that the contribution of the first term to the transition matrix element is negligibly small. Hence, the reaction rate for $I_- \rightarrow P$ will be of the same order of magnitude as the corresponding value for $(p\mu d)$. This will be roughly true of $I_+ \rightarrow S$ as well. However, if $(p\mu p)$ has an extremely loosely bound S state, whether real or virtual, the situation changes. For, in this case, the collision between p and $(p\mu)$ exhibits resonance. As a results, the amplitude of the I_+ incident state wave function becomes quite large in a region of small R. Consequently, the reaction rate for $I_+ \rightarrow S$ increases considerably. We can, however, hardly expect $I_+ \rightarrow S$ to predominate over $I_- \rightarrow P$.

Lastly, we touch on the formation of $(d\mu d)$. As is shown in Table II, $(d\mu d)$ has four bound states in all, although the existence of the excited S state might be slightly uncertain. Therefore, the following four transitions can take place by collision of d and $(d\mu)$: $I_+ \rightarrow S'$, $I_+ \rightarrow D$, $I_+ \rightarrow S$, and $I_- \rightarrow P$. The last two will be essentially the same as those for $(p\mu p)$. We can, however, expect a somewhat remarkable decrease in the reaction rate, especially for $I_- \rightarrow P$.* The first reason is that the amplitude of the incident state wave function U_{I} will be smaller for $(d\mu d)$ than for $(p\mu p)$. This is because it becomes harder for a particle to penetrate into a potential barrier as the mass increases, the potential to determine U_{I} being repulsive for $R < 10a$. The second reason is that the $(d\mu d)$ molecule is smaller than $(p\mu p)$ in size. The $E1$ transition probability is roughly proportional to $R_0{}^5$, R_0 being the size of the molecule formed by collision. The third reason is the decrease in the statistical weight of the I_- state from $\frac{3}{4}$ to $\frac{1}{3}$. The fourth is the increase in the energy of ejected electron. We must now consider $I_+ \rightarrow S'$. If the energy released is not enough to ionize a bound electron, this transition is forbidden. On the other hand, if the energy is only just enough, then $I_+ \rightarrow S'$ might be able to compete with $I_- \rightarrow P$. This is because the rate for the 0–0 transition increases rapidly with increasing R_0, in proportion to $R_0{}^7$. Of course, R_0 increases as the dissociation energy decreases. According to Zel'dovitch's estimation,[3] the reaction rate amounts to $\sim 10^5\,\mathrm{sec}^{-1}$ in the limiting case that the released energy is just equal to the ionization potential. Thirdly, we must consider $I_+ \rightarrow D$. This can occur by $E2$. Usually, the $E1$ transition is more important than the $E2$. In the present case, however, the $E1$ transition $I_- \rightarrow P$ has a number of handicaps as was mentioned above. Accordingly, $I_+ \rightarrow D$ might also compete with $I_- \rightarrow P$. However that may be, the formation of the $(d\mu d)$ molecule is almost certainly more difficult than that of $(p\mu p)$ or $(p\mu d)$.*

---

* Cohen et al.'s value is $5.9 \times 10^4\,\mathrm{sec}^{-1}$ for $(d\mu d)$, while $6.5 \times 10^6\,\mathrm{sec}^{-1}$ for $(p\mu p)$[8]. Their explanation for this decrease is not acceptable. It seems possible that they may have used G_{I}, by mistake, instead of U_{I} to evaluate the former value.

§ 5. The Radiative p–d Fusion: $(p\mu d)_s \longrightarrow \mathrm{He}^3+\gamma$

1) *The initial state*: $(p\mu d)_s$

We here briefly mention the hyperfine structure associated with the $(p\mu d)_s$ state. The spins of the particles μ, p, d are respectively $\frac{1}{2}$, $\frac{1}{2}$, 1. Hence, the ground state can split into one quintet, two triplets, and one singlet. In the quintet state, the two nuclear spins are parallel; in the singlet they are antiparallel. In the triplet states, both spin states are mixed. Their mixing ratios cannot be determined, until the hyperfine interaction is specified. The ground state has zero total orbital angular momentum: $K=0$. Therefore, the most important hyperfine interaction is considered as the Fermi contact interaction of p and d with μ. The splitting caused by this interaction is estimated to be of the order of magnitude of 0.1 eV, The nuclear force between p and d, which may be expressed in the form of contact interaction in the first order approximation, is also spin-dependent. However, its contribution to the splitting is negligibly small ($<10^{-3}$ eV), cf. (5.14). The rate for p–d fusion depends, clearly, on the relative spin orientation of p and d in the initial state. Hence, each of the spin multiplets has its own reaction rate. In this paper we treat only their statistical average, which is in practice independent of the hyperfine splitting.

2) *The final state*: He^3

In the notation of Russell-Saunders coupling, the He^3 ground state is $^2S_{1/2}$ and "even" in parity. As is well-known, there are just two linearly independent doublet spin functions for three-nucleon systems. Hence, in the approximation of neglecting the non-central nuclear force the He^3 ground state wave function can be expressed in the form:

$$\Psi_f=\Lambda_f{}^+\Theta_+ + \Lambda_f{}^-\Theta_- \,. \tag{5.1}$$

Here, $\Lambda_f{}^\pm$ mean the orbital parts and $\Theta_\pm$ the spin parts. For convenience, Θ_+ and Θ_- are here chosen to be anti-symmetric and symmetric with respect to the exchange of the two protons, respectively. From well-known energy arguments, we can easily see that if the nuclear force is wholly spin-independent, the above $\Lambda_f{}^-$ must be zero.

3) *The photon emission process*: $p+d \longrightarrow {}^3\mathrm{He}+\gamma$.

In the region of short p–d distance of the order of n–d interaction range ($\sim 4\times 10^{-13}$ cm), the two nuclei in the $(p\mu d)_s$ molecule would be to such an extent in an S state, $L=0$, that their fusion reaction occurs exclusively in the S state. Accordingly, we here again examine only the transition from the S wave component. The deuteron ground state is $^3S_1$. Therefore, if the proton spin is parallel to the deuteron spin, the initial state has the symmetry $^4S_{3/2}$ as a whole, and if antiparallel, $^2S_{1/2}$. On the other hand, the final state —the He^3 ground state—is $^2S_{1/2}$. Hence, the radiative transitions can occur by a magnetic dipole. The related transition matrix elements are given, in the usual approximation, by

$$\begin{aligned} M_{if} &= \langle \Psi_i | \mu_p(s_{p_1}+s_{p_2})+\mu_n s_n | \Psi_f\rangle \\ &= (\mu_n-\mu_p)\langle \Psi_i | s_n | \Psi_f\rangle \,. \end{aligned} \tag{5.2}$$

Here, the obvious relation, $\langle \Psi_i | S | \Psi_f\rangle=0$, was used, S being the total intrinsic nuclear spin operator. From the last expression of (5.2), it will be clear that the so-called mirror reaction, $n+d \longrightarrow T+\gamma$, can be a true mirror to a fairly good approximation, notwithstanding that proton and neutron are somewhat different in their magnetic moments.** This is the case for electric dipole transitions as well, though not for higher multipole transitions. Now, suppose that the nuclear force is spin-independent, then the last term of (5.1) must vanish as was noted there. Hence, the two proton spins must be exactly antiparallel in the final state. While, in the ^4S initial state, they are always parallel. Accordingly, the $M1$ transition is forbidden for ${}^4S\rightarrow{}^2S$. We now consider the transition ${}^2S\rightarrow{}^2S$. Clearly, the initial ${}^2S$ wave function has the general form:

---

* For the $(d\mu d)$ molecule, the rate for nuclear fusion might be appreciable even in the excited states, S, P, and D. To the approximation in § 2, the D state wave function falls off much more rapidly than the P state wave function, with decreasing nuclear separation R. However, this is not true of the exact D eigenfunction, but there must be some amount of admixture of S component ($L=0$) which is finite at $R=0$. This is not applicable to the P state, whose wave function must vanish at the origin by symmetry.

** This is one of the reasons why Cohen et al.'s criticism[8] on Jackson's semi-emiempirical treatment[4] is not acceptable. The other reason would be seen from the expression (5.20c).

$$\Psi_i=\Lambda_i^+\Theta_++\Lambda_i^-\Theta_-\ , \tag{5.3}$$

so that the two proton spins can be partly antiparallel. However, (5.3) is required to be orthogonal to the one-term final state wave function, $\Lambda_f^+\Theta_+$. On the other hand, $\langle\Lambda_i^-|\Lambda_f^+\rangle=0$ by symmetry. Therefore, $\langle\Lambda_i^+|\Lambda_f^+\rangle=0$. As a result, ${}^2S\rightarrow{}^2S$ is also forbidden.* To summarize, if the nuclear force is spin-independent, the thermal radiative fusion can hardly take place. In fact, however, the nuclear force is spin-dependent, so that the above arguments cannot be applied. Actually, we can show that if the spin-dependency is taken into account, the above $M1$ transition becomes possible for both ${}^4S\rightarrow{}^2S$ and ${}^2S\rightarrow{}^2S$.** However, it does not seem easy to predict which is faster. In the well-studied case of thermal radiative p–n capture, on the contrary, one of the two possible transitions, ${}^3S\rightarrow{}^3S$, is still forbidden.[13]

4) *Semi-empirical calculation of the reaction rate for* $(p\mu d)_s\longrightarrow\mathrm{He}^3+\gamma$

We first discuss the distortion of $(p\mu d)_s$ wave function due to the nuclear force. Let R_0 be a distance of the order of the range of the nuclear force between p and d, $\sim5\times10^{-13}$ cm. Our main interest is in the region of $R>R_0$. We make the conventional assumption that, for $R>R_0$, Eqs. (2.15a, b) remain valid and the effect of the nuclear force can be taken into account simply by adjusting the boundary conditions (2.16c). For simplicity, we hereafter consider just the g component by omitting the coupling with the u. The new boundary condition may be expressed as

$$\left[\frac{d}{dR}\log(Rg)\right]_{R=R_J}=\frac{1}{R_0+F}\ . \tag{5.4}$$

The constant F is here replaced simply by the scattering length for thermal n–d elastic collision. Let E_1 be the energy shift resulting from the change of the boundary condition. The magnitude will be negligibly small as compared with the original energy E_0. We therefore consider the distortion of g just to the first order of E_1:

$$g\cong g_0+E_1g_1\ . \tag{5.5}$$

The equation for g_1 can be found by differentiation of (2.15a) with respect to the energy E:

$$\left[\frac{1}{R^2}\frac{d}{dR}\left(R^2\frac{d}{dR}\right)+\frac{2M}{\hbar^2}\left(E_0-\mathcal{E}_1+\frac{\hbar^2}{2M}\Delta_{11}\right)\right]g_1$$
$$=-\frac{2M}{\hbar^2}g_0\ . \tag{5.6}$$

As is easily seen, the solution g_1 which is bound at infinity is given by

$$g_1=-\frac{2M}{\hbar^2}\left[g_\infty+g_0\int_0^R g_\infty g_0R^2\,dR\right.$$
$$\left.-g_\infty\int_0^R g_0g_0R^2\,dR\right]\ , \tag{5.7}$$

where g_∞ denotes the improper solution of the original homogeneous equation. In the close proximity of the origin, the above g_0 and g_∞ have the forms:

$$g_0\cong g_0(0)\cdot\left(1+\frac{R}{A}\right)\ , \tag{5.8a}$$

$$g_\infty\cong\frac{1}{g_0(0)}\left(\frac{1}{R}+2\frac{1}{A}\log\frac{R}{B}\right)\ . \tag{5.8a}$$

Here, A is the distance characteristic for the Coulomb scattering:

$$A=\frac{\hbar^2}{Me^2}\cong4.32\times10^{-12}\ \mathrm{cm}\ . \tag{5.9}$$

On the other hand, B is the distance which is determined from the condition:

$$\int_0^\infty g_1g_0R^2\,dR=0\ , \tag{5.10}$$

which results from the normalization condition: $\int g^2R^2\,dR=\int g_0^2R^2\,dR=1$. However, the value of B is considered to be quite insensitive to the potential shape in the region of large R where the Coulomb repulsion is not dominant. For, the Coulomb force is so strong for small R that even a negligibly small change in B can induce an appreciable variation in g_1 for large R. Hence, B may be chosen so that the resulting g_1 of (5.7) shall coincide with the Hankel function which vanishes at infinity. After a short calculation, we find the following connection formula:

---

* Cohen et al.[8] thought ${}^2S\rightarrow{}^2S$ is allowed although ${}^4S\rightarrow{}^2S$ is forbidden. On this basis they reanalysed Ashmore et al.'s experiment[6] and found a new internal conversion coefficient which is nearly twice as large as the old one due to Ashmore et al.

** Accordingly, it is not clear whether or not Cohen et al.'s value of internal conversion coefficient is more reliable than Ashmore et al.'s value. The latter authors implicitly assumed that both transitions have the same reaction rate.

$$-\frac{\hbar^2}{2M}g_0(0)\,g_1(R)\cong\frac{1}{R}+2\frac{1}{A}\log\frac{R}{B}$$

$$\cong-\pi\sqrt{\frac{2A}{R}}H_1^{(1)}(i\sqrt{8R/A})\,. \qquad (5.11)$$

From this we obtain

$$B\cong0.42_9A\,. \qquad (5.12)$$

Substituting (5.11) and (5.8a) in (5.5) we have

$$g(R)\cong g_0(0)\Big[\Big(1+\frac{R}{A}\Big)$$

$$+\frac{\lambda}{R}\Big(1+2\frac{R}{A}\log\frac{R}{B}\Big)\Big]\,. \qquad (5.13)$$

This approximate form will be valid for R up to about $B/4$. The relation between the energy shift E_1 and the above scattering length λ is given by

$$E_1=-\frac{\hbar^2}{2M}\lambda\cdot|g_0(0)|^2\,. \qquad (5.14)$$

Substitution of (5.13) in (5.4) results in

$$\lambda=\frac{R_0^2+(A+2R_0)F}{(A-2R_0)-2(1+\log R_0/B)F}\,. \qquad (5.15)$$

Thus we obtain, for the value of g at $R=R_0$,

$$g(R_0)=C\cdot g_0(0)\cdot\Big(1+\frac{F}{R_0}\Big)\,, \qquad (5.16a)$$

where

$$C(F,R_0)=\frac{1-2\Big(\dfrac{R_0}{A}\Big)^2\cdot\Big(1-\log\dfrac{R_0}{B}\Big)}{\Big(1-2\dfrac{R_0}{A}\Big)-2\Big(1+\log\dfrac{R_0}{B}\Big)\dfrac{F}{A}}\,. \qquad (5.16b)$$

As would have been expected physically, the factor C tends to 1 with decreasing R_0/A and F/A. Hence, C may be taken as the nuclear size correction factor. Now, putting $R_0=A/10$, which would be appropriate for the present case, we obtain

$$C\cong\frac{1.19}{1+1.14F/A}\,. \qquad (5.17)$$

(5.17) diverges to infinity at $F=-0.9A$. Hence, if the n–d system has an "actual" bound state of quite low binding energy, the $(p\mu d)_s$ wave function will be distorted considerably by the nuclear force. However, this does not seem to take place, at least, in the present case. Judging from a calculation by Buckingham and Massey[15], we may expect the magnitude of F for n–d collision to be of the order of $A/10$. The sign is positive for the quartet state collision, and negative for the doublet. Accordingly, the deviation of C from 1 will not be appreciable:

$$C^2\cong1 \quad \text{for the quartet}\,, \qquad (5.18a)$$

$$C^2\cong2 \quad \text{for the doublet}\,. \qquad (5.18b)$$

In the following, for simplicity, we put $C^2=1$, independently of the relative nuclear spin orientation.

We next evaluate the reaction rate for $(p\mu d)_s\longrightarrow He^3+\gamma$. Following Jackson[4] and others, we make use of the reaction constant for $n+d\longrightarrow T+\gamma$, let σv. As was mentioned at the beginning of this section, the ground state of $(p\mu d)$ is split into four sets of spin multiplets by hyperfine interaction, and each multiplet has its own reaction rate. However, the only available experimental result for σv is the statistical average of the two possible values, $(\sigma v)_+$ and $(\sigma v)_-$:

$$\sigma v=\frac{2}{3}(\sigma v)_+ +\frac{1}{3}(\sigma v)_-$$

$$=1.25\times10^{-22}\ \text{sec}^{-1}\cdot\text{cm}^3\,. \qquad (5.19)$$

Hence, it is impossible to determine each of the four reaction rates separately. Consequently, we here estimate only their statistical average, λ_γ. Now, σv can be interpreted as the transition probability from the incident state normalized so that $\Phi_I=1+(F/R)$. We then relate λ_γ to σv through the expression:

$$\lambda_\gamma=\frac{3}{4\pi}\Big[\frac{2}{3}(\sigma v)_+\cdot\Big|\frac{g_+(R_0)}{1+(F_+/R_0)}\Big|^2$$

$$+\frac{1}{3}(\sigma v)_-\cdot\Big|\frac{g_-(R_0)}{1+(F_-/R_0)}\Big|^2\Big] \qquad (5.20a)$$

$$=\frac{3}{4\pi}\Big[\frac{2}{3}(\sigma v)_+\cdot C_+^2+\frac{1}{3}(\sigma v)_-\cdot C_-^2\Big]\cdot|g_0(0)|^2 \qquad (5.20b)$$

$$\cong\frac{3}{4\pi}(\sigma v)\cdot|g_0(0)|^2\,.^* \qquad (5.20c)$$

The value of $g_0(0)$ will be insensitive to the details of the approximation adopted in the calculation, as long as the Coulomb repulsion between p and d is correctly taken into account in the region of small R. However, one of our objects in this section is to see the true result of the basic approximation

---

* This is just the expression which can be derived from the most naive consideration. Jackson[4] adopted (5.20c) with $g_0(0)$ replaced by $g_0(R_0)$. This seems, however, difficult to justify.

(2.4) as quantitatively as possible. We therefore use the value calculated by Cohen et al.:

$$|g_0(0)|^2=1.11\times10^{28}\ \mathrm{cm}^{-3}\,. \qquad (5.21)$$

Then, we have, from (5.20c) and (5.19),

$$\lambda_\gamma=0.33\times10^6\ \mathrm{sec}^{-1}\,. \qquad (5.22)$$

If the *n–d* fusion reaction takes place predominantly from the doublet incident state, this might be an underestimate because of (5.18b).

5) *Comparison with experiment*

Ashmore et al.[6] detected the γ rays from the above *p–d* fusion process. They analyzed the related time distribution to obtain the values of λ_γ and λ_{m2}, cf. Fig. 1. As a result, they found that the following set of values can reproduce their observations satisfactorily within the error of their results:[*]

$$\lambda_{m2}\cong2.5\times10^6\ \mathrm{sec}^{-1}\,, \qquad (5.23a)$$

$$\lambda_\gamma\cong0.3\times10^6\ \mathrm{sec}^{-1}\,. \qquad (5.23b)$$

The theoretical value of λ_{m2} calculated by Cohen et al.[8] is just equal to the above λ_{m2}. In addition, a good agreement with respect to λ_γ can be seen from a comparison of (5.23b) with (5.22).

Ashmore et al.'s analysis is based on the single decay constant approximation. They implicitly assumed that all the multiplets of $(p\mu d)_s$ have the same reaction rate, which would be a defect of their analysis. However, as far as the statistical average is concerned, their simplification does not seem serious. In fact, the experimental value of λ_γ proposed by Cohen et al., who analysed the same experiment on the assumption that ${}^4S\rightarrow{}^2S$ is forbidden, is essentially equal to (5.23b), i.e. $\lambda_\gamma=3.1\times10^5\ \mathrm{sec}^{-1}$.[**] Accordingly, the error of (5.23b) would be minor. If the ${}^2S\rightarrow{}^2S$ transition takes place much faster than ${}^4S\rightarrow{}^2S$ as was supposed by Cohen et al., the theoretical value of λ_γ must be chosen to be nearly twice as large as (5.22) on account of (5.18b). This makes the above agreement slightly poor. It would, however, dangerous to arrive at a definite conclusion from this that ${}^2S\rightarrow{}^2S$ is not dominant. However that may be, the agreement between theory and experiment seems quite satisfactory.

Acknowledgment

The author wishes to express his cordial thanks to Prof. Kotani for his hearty guidance and encouragement. His thanks are also due to Dr. M. Shimizu and Dr. T. Izuyama for their assistance in the numerical calculation and their discussion.

Appendix 1.

The full expressions of $\varDelta_{ij}(R)$ and $\nabla_{ij}(R)$ associated with the orbital functions (2.10a) and (2.10b) are given below, in μ mesonic atomic units.

$$\varDelta_{\substack{11\\22}}=-\frac{1}{2}\frac{M_d{}^2+M_p{}^2}{(M_d+M_p)^2}$$

$$\pm\frac{e^{-R}}{1\pm S}\left[\frac{1}{2}(1+R)+\frac{1}{3}\left\{\frac{M_d{}^2+M_p{}^2}{(M_d+M_p)^2}-\frac{1}{2}\right\}R^2\right.$$

$$\left.\pm\frac{1}{36}\frac{R^2(1+R)^2e^{-R}}{1\pm S}\right],$$

$$\varDelta_{\substack{21\\12}}=-\frac{M_d-M_p}{M_d+M_p}\left\{\frac{1}{2}\sqrt{\frac{1\mp S}{1\pm S}}\right.$$

$$\left.\pm\frac{1}{3}\frac{R^2e^{-R}}{\sqrt{1-S^2}}-\frac{1}{18}\frac{R^2(1+R)^2e^{-2R}}{(1\pm S)\sqrt{1-S^2}}\right\},$$

$$\nabla_{\substack{21\\12}}=\pm\frac{M_d-M_p}{M_d+M_p}\frac{R(1+R)e^{-R}}{6\sqrt{1-S^2}}\,,$$

where

$$S=\left(1+R+\frac{R^2}{3}\right)e^{-R}\,.$$

The upper/lower signs on the right hand side belong to the upper/lower suffices on the left-hand side.

References

1) L. W. Alvarez et al.: Phys. Rev. **105** (1957) 1127. Alvarez et al.: Nuovo Cim. **5** (1957) 1026.
2) C. Hayashi et al.: Prog. Theor. Phys. **17** (1957) 615.
3) Y. W. Zel'dovitch: Doklady Akad. Nauk. **95** (1954) 493. Y. W. Zel'dovitch and A. D. Sakharov: J.E.T.P. **8** (1959) 451.
4) J. D. Jackson: Phys. Rev. **106** (1957) 330.
5) T. H. R. Skyrme: Phil. Mag. **2** (1957) 910.
6) A. Ashmore et al.: Proc. Phys. Soc. **71** (1958) 161.
7) M. Shimizu et al.: Prog. Theor. Phys. **20** (1958) 777. Y. Mizuno et al.: Prog. Theor. Phys. **21** (1959) 479.
8) S. Cohen et al.: Phys. Rev. **119** (1960) 384, 397.
9) E. Teller: Zeit. für Physik **61** (1930) 458.

---

[*] Fit *b* in Figs. 7 and 8 on their paper.

[**] Their value of R_n is overestimated by the factor of 4/3, because of a trivial mistake in their expressions for $P_t{}^{(s)}$.

10) G. Herzberg: *Spectra of Diatomic Molecules* (Van Nostrand, New York, 1950).
11) Y. Mizuno and H. Yoshizumi: Busseiron-Kenkyū (in Japanese), No. **82** (1955) 21.
12) P. G. Burke et al.: Proc. Phys. Soc. **73** (1959) 912.
13) J. M. Blatt and V. E. Weisskopf: *Theoretical Nuclear Physics* (Wiley, New York, 1952).
14) M. Gellman and M. L. Goldberger: Phys. Rev. **91** (1953) 398.
15) R. Buckingham and H. S. W. Massey: Proc. Roy. Soc. (London) **A**, **179** (1941) 123.

JOURNAL OF THE PHYSICAL SOCIETY OF JAPAN, Vol. 16, No. 6, JUNE, 1961

Inelastic Scattering of Deuterons from C^{12}, Mg^{24} and Ni^{60}

By Yoshihide ISHIZAKI

Institute for Nuclear Study, University of Tokyo
Tanashi-machi, Tokyo

(Received February 4, 1961)

The absolute differential cross sections for the inelastic scattering of deuterons leading to the first excited state of C^{12} has been measured at the bombarding deuteron energies of 14.7, 15.9 and 18.1 MeV. Similar measurements were made on Mg^{24} at deuteron energies of 15.9 and 17.5 MeV and also on Ni^{60} at 18.1 MeV.

Deuterons are detected with thin CsI crystals, so that protons from (d, p) reactions do not contribute to the cross section. The energy resolution of the detectors is less than 4 percent.

The obtained angular distributions show a prominent peak at small angles in all the cases and the cross sections decrease at the extremely forward angles. Therefore it is not necessary to take into account the electric interaction to explain these reactions. These angular distributions are compared with the results at different deuteron energies given by other authors, and are observed to have an unusual energy dependence.

The data are analysed with the nuclear interaction theory of Huby and Newns. When the theoretical curve is normalized to fit to the measurement at the forward peak, disagreement between the theoretical curve and the experimental one occurs at the other places, which shows the need of modifing the theoretical calculations with the distorted wave approximation taking a proper optical potential to explain the reaction.

§ 1. Introduction

Measurements of inelastic scattering of deuterons are fewer than the cases for protons and alpha particles.

Haffner[1)] obtained the angular distributions of inelastically scattered deuterons from Li^6, Li^7, Be^9, C^{12}, Mg^{24} and Al^{27} at the bombarding energy of 15 MeV. He analysed his data according to the nuclear interaction theory of Huby and Newns[2)], the electric interaction theory of Mullin and Guth[3)], and from the stand point of compound-nucleus formation. According to his conclusion, for small angles the electric interaction theory seems to fit to the data better and for large angles the nuclear direct interaction theory gives better agreement, and the compound-nucleus formation does not seem to play a major role in the inelastic scattering of deuterons.

Yntema and Zeidman[4)] measured the inelastic scattering of 21.6 MeV deuteron by Ni, Cu, Zn, Ry, Ag, Sn, Gd, Ta, Pt and Au at the four angles of 30°, 60°, 90° and 140°. The angular distribution in each case shows a pronounced peaking in the forward direction, and no increases in the cross sections at backward angles are observed with increasing excitation of the residual nucleus. These facts suggest that the direct process plays a major role in the nuclear interaction of a deuteron and the evaporation process of deuterons from compound-nucleus does not contribute to the cross section.

The above mentioned conclusion about the formation of the compound nucleus, for the experiments at the deuteron energy near to 20 MeV, is reasonable since a deuteron is a loosely bound system and easily breaks under a slight influence of nuclear force, consequently it can not enter into the nucleus as a whole. Near 10 MeV, some experiments of inelastically scattered deuterons from relatively light nuclei were carried out by several authors[5)–14)]. These angular distributions also show a forward peak or peaking in the forward directions.

Recently the angular distributions of elastically and inelastically scattered protons and alpha particles have been found to depend strongly on the incident energy in some energy regions.[15)] This fact seems to show that, in order to discuss the reaction mechanism, measurements have to be made at various incident energies.

We also examined whether the diffrential cross section would decrease or not at extremely forward angles in order to analyse the contribution of the electric interaction process to the cross section. In our measurements at forward angles, the elastically scattered deuterons from hydrogen, which contaminates the targets, were eliminated very carefully. According to the theory of the electric interaction given by Mullin and Guth, the cross section should have a maximum in the forward direction. Most measurements of the inelastic scattering of deuterons carried out so far show a maximum in the forward direction, but these for protons do not. The influence of the electric interaction is considered to be similar for deuterons as well as for protons. Therefore, it is necessary to measure the cross sections at extremely forward angles.

§ 2. Experimental Procedure

The deuteron beam was obtained from INS (Tokyo) variable energy cyclotron.[16)] The beam entered through a focusing system into a scattering chamber. The arrangement of them and the beam collector were quite similar to those described in reference.[17)] The scattering chamber has seventeen windows with 10° interval from 10° to 170° on the wall on the right side of the incident beam direction and sixteen from 15° to 165° on the left side. Each window was covered with a sheet of aluminized mylar of 1 mil. in thickness.

Fourteen scintillation counters attached to the side windows were used at the same time.

The solid angle subtended by the detector was determined by the defining slit attached to the side window. The solid angles were made to increase from forward to backward angles. The diameters of the defining apertures, placed 505 mm apart from the center of the chamber, were 3 mm at 10° and 15°, 5 mm at angles from 20° to 60°, 8 mm from 65° to 85°, and 10 mm from 90° to 165° Such change of the solid angles made the measurements easier without large change of the beam intensity.

The scattered deuterons were detected by CsI crystals. In our targets, (d, p) reactions leading to the excited states produce protons with approximately the same energy as the inelastically scattered deuterons, and therefore it is necessary to exclude the protons having the energy near to that of the desired deuteron. We made use of the fact that the range of a deuteron in the energy region of this experiment is considerably less than that of a proton with the same energy.

Table I shows the thickness of CsI crystals used in the present experiment and energies of a deuteron and a proton corresponding to the range equal to the thickness.

Between a window of the scattering chamber and a detector, an aluminium absorber

Table I. Deuteron energy and proton energy corresponding to the range equal to the thickness of CsI crystals used in this experiment.

thickness of CsI crystal (mm)	1.1	0.77	0.70	0.51	0.36	0.22	0.16
deuteron energy (MeV)	20.0	16.0	15.0	12.5	10.0	7.2	6.0
proton energy (MeV)	15.5	12.5	11.5	9.5	7.5	5.5	4.6

was inserted, which reduced the energies of alpha particles produced by (*d*, *α*) reactions to much lower energy than that of a measured deuteron, when necessary.

We made about ten pieces of uniform crystal for each one shown in Table I.

Energies of all protons which stopped in the crystal were always made at least 1 MeV smaller than the energy of a measured deuteron. Thus, even at the widely different incident deuteron energies, we could use the fourteen scintillation counters at the same time to measure the angular distribution of the inelastically scattered deuterons from C^{12} ($Q=-4.43$ MeV), Mg^{24} ($Q=-1.37$ MeV), and Ni^{60} ($Q=-1.33$ MeV) by adjusting the thicknesses of absorbers and crystals.

The detectors were similar to those described elsewhere[16)], except for the crystals. RCA 6342 and 5819 photomultipliers were used.

The foil targets were set at the center of the scattering chamber making an angle of 45° on the right or left side of the incident beam direction. In almost all cases, detection was made at angles with 5° intervals from 10° or 15°, but in some cases at 10° intervals.

In order to minimize the fluctuation of the gains of photomultipliers, high voltage was always being fed to each counter, and the pulses from it were sent through a cathode follower and a coaxial cable to the measuring room, where electronic circuits were located. We used ten linear amplifiers and four multichannel pulse height analysers, so that we could measure the energy spectra at four angles simultaneously. For the investigation of the angular distribution, we measured the beam current by a current integrator and the yield of the monitor counter in each run of measurement. We repeated the measurement at the same angle several times on different days, and results were in satisfactory agreement with each other.

The target of self-supporting film of natural carbon was prepared from colloidal solution of graphite, and the thickness was 2.38 mg/cm²*. This did not contain any detectable impurity except hydrogen. The targets of self-supporting film of natural magnesium were measured to be 2.22 mg/cm² and 2.37 mg/cm² in thickness. Both of them were used. The foil target of Ni^{60} was manufactured by A.E.R.E. and its thickness was 2.42 mg/cm². After the measurements at fourteen angles, the scintillation counters were removed to the other angles, and exchanges of absorbers and crystals to those with proper thickness were carried out, when necessary.

The error involved in the measurement of beam energy is estimated to be 100 KeV, and energy spread may be within 1 percent.

The corrections for the slit edge effect and the multiple scattering were neglected in the analysis of the present data.

The pulse height spectra obtained for the charged particles resulting from the deuteron bombardment of the targets are shown in

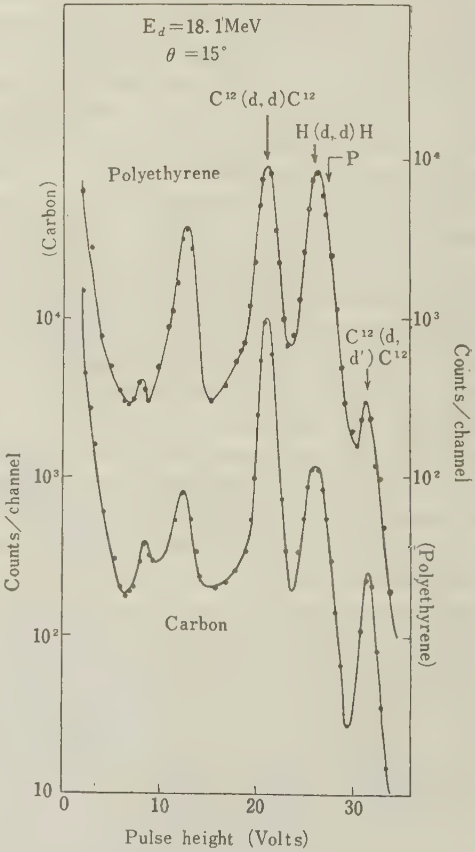

Fig. 1. The pulse height spectra of the charged particles resulting from deuteron bombardment on carbon target and polyethylene with $E_d=18.1$ MeV at 15°. Elastically scattered deuterons pass through the scintillator. Arrow *P* indicates the maximum pulse height of protons obtained in the scintillator.

---

* We are indebted to Dr. Mikumo of Institute for Nuclear Study for the preparation of the target.

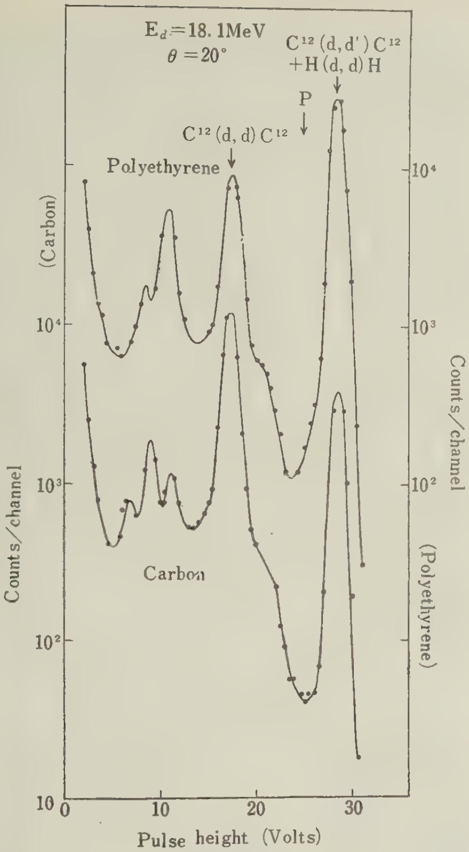

Fig. 2. The pulse height spectra of the charged particles resulting from the deuteron bombardment on carbon target and polyethlene with E_d=18.1 MeV at 20°. Elastically scattered deuterons pass through the scintillator.

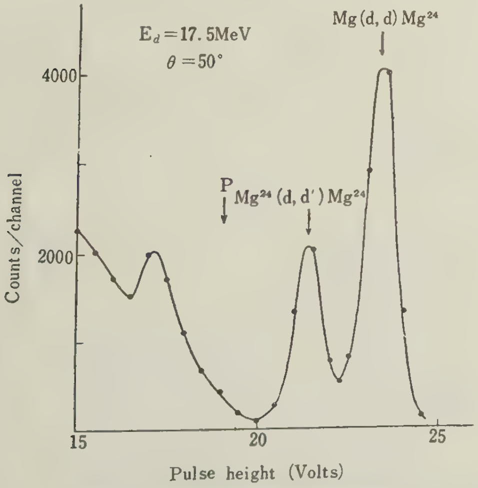

Fig. 3. The pulse height spectra of the charged particles resulting from the deuteron bombardment on Mg^{24} with E_d=17.5 MeV at 50°.

Figs. 1 to 5. Arrows *P* in Figs. 1 to 5 indicate the maximum pulse heights of protons obtained in the CsI scintillators used in the detection of deuterons. In the case of C^{12} the elastically scattered deuterons passed through the CsI crystal. As shown in Figs. 1 and 2, in which we compared the energy spectra resulting from carbon target with those from polyethylene, our carbon target is thought to contain a little amount of hydrogen, and at 20° the energy of an inelastically scatter-

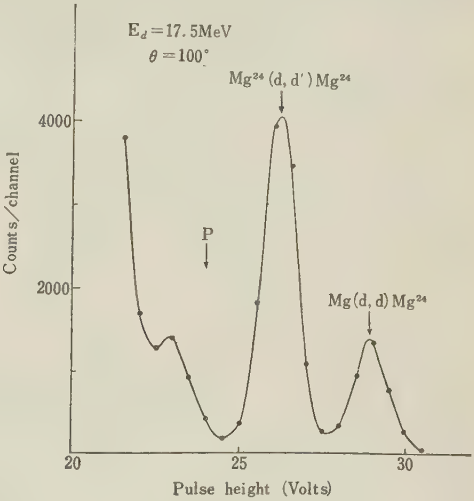

Fig. 4. The pulse height spectra of the charged particles resulting from the deuteron bombardment on Mg^{24} with E_d=17.5 MeV at 100°.

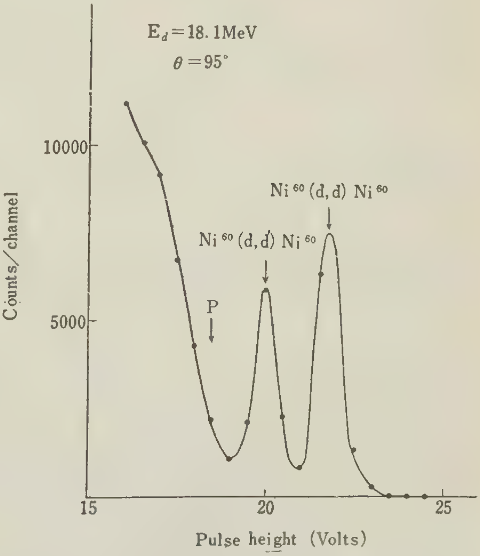

Fig. 5. The pulse height spectra of the charged particles resulting from the deutron bombardment on Ni^{60} with E_d=18.1 MeV at 95°.

ed deuteron from C^{12} leading to the first excited state nearly agrees to that of an elastically scattered deuteron from hydrogen at our bombarding energies. We can not resolve these two deutrons. Therefore, we deduced the angular distribution of deuterons elastically scattered by hydrogen from our data measured at angles of 10°, 15° and 25°, with reference to other experiments.[18)–19)] Then, we could obtain the cross section of inelastically scattered deuterons from C^{12} at 20° by subtraction.

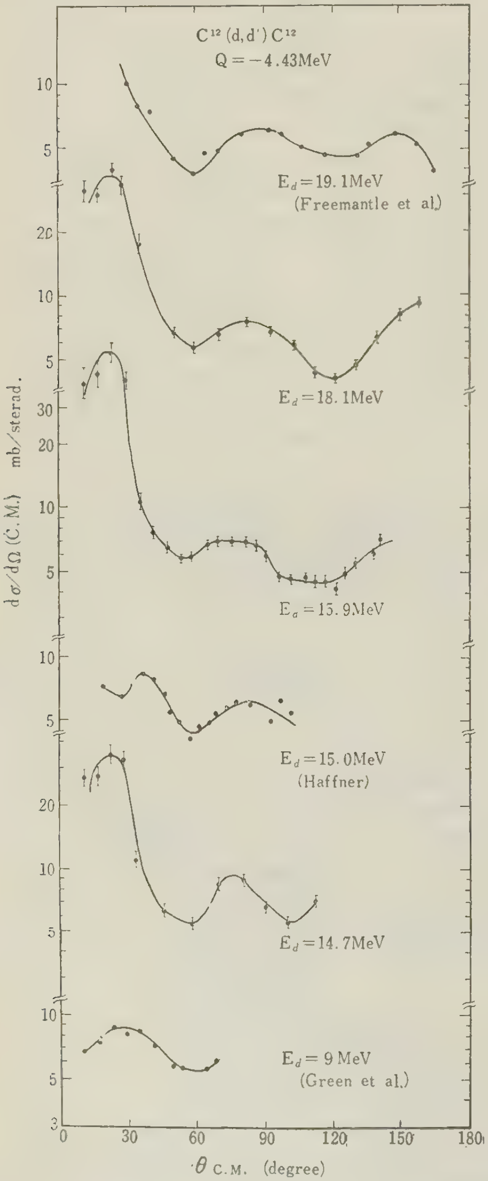

Fig. 6. Angular distributions of the inelastically scattered deuterons from C^{12} leading to the 4.43 MeV state at various bombarding energies.

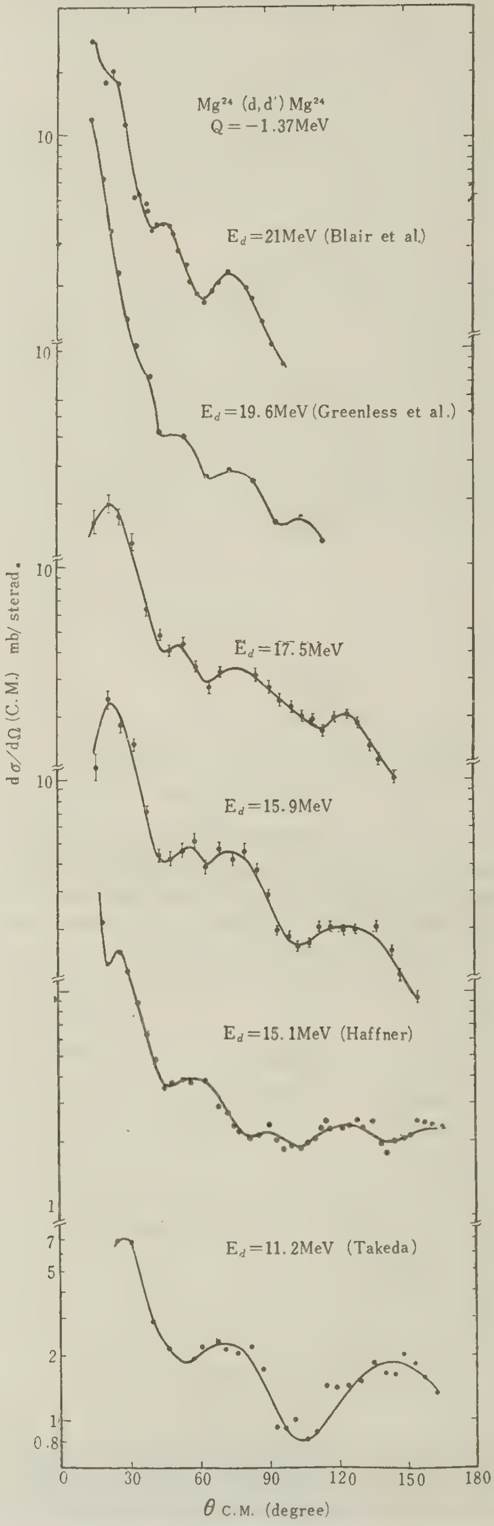

Fig. 7. Angular distributions of the inelastically scattered deuterons from Mg^{24} leading to the 1.37 MeV state at various bombarding energies.

§ 3. Results and Discussions

Angular distributions of the inelastic scattering leading to the 4.43 MeV state of C^{12} were obtained at the incident deuteron energies E_d=14.7, 15.9 and 18.1 MeV. In Fig. 6, we show the results together with those obtained by other authors at different energies. The curves obtained by us are very similar with one another, however not so similar to the quoted data, and have a forward peak at the angle near to 25°.

The angular distributions of inelastically scattered deuterons from Mg^{24} leading to the 1.37 MeV state are shown in Fig. 7. The curves at E_d=15.9 and 17.5 MeV were obtained in this experiment. The curves have a forward peak near to 22°.

The electric interaction theory, given by Mullin and Guth, assumes the interaction potential

$$V=\sum_{n=1}^{Z}\frac{ze^2}{|\mathbf{r}-\mathbf{R}_n|}, \quad \text{for } r\geq r_0 ,$$

$$=0 , \quad \text{for } r\leq r_0$$

where $\mathbf{r}$=the distance of the incident deuteron from the center of the target nucleus, Z, z are the atomic number of the scattering nucleus and the projectile, the sum of their radii is taken as r_0 and $\mathbf{R}_n$ is the coordinate of the n-th particle in the nucleus.

The important factor determining the angular distribution for electric quadrupole transition is

$$\frac{d\sigma}{d\Omega}\propto\left[\frac{j_1(Kr_0)}{Kr_0}\right]^2,$$

where $K=|\mathbf{K}_1-\mathbf{K}_2|$ is the difference between the wave numbers of the initial and the final deuteron, and $j_1(Kr_0)$=spherical Bessel function. This theory predicts a maximum in the forward direction for our cases concerned here.

According to the present experimental results obtained for C^{12} and Mg^{24}, the cross section decreases in the extremely forward direction. Therefore, we can conclude that in the inelastic scattering of a deuteron, the electric interaction process between a deuteron and a nucleus has scarcely any contribution to the cross section.

Fig. 8 shows the angular distribution of inelastically scattered deuterons from Ni^{60} to the 1.33 MeV state. The curve shows a typical diffraction pattern.

One of the characteristic features of the present angular distributions is the increase of the number of diffraction oscillations with atomic mass. The ratio of the cross sections at the forward to backward angles increases with increasing energy and atomic mass.

From all the curves shown in Fig. 6, we see that all the first minima (in the case of Haffner, second minimum) appear at the same angle of 60°, and the second peak shifts a little to larger angles, and broadens out when the energy of bombardment increases from 14 to 20 MeV.

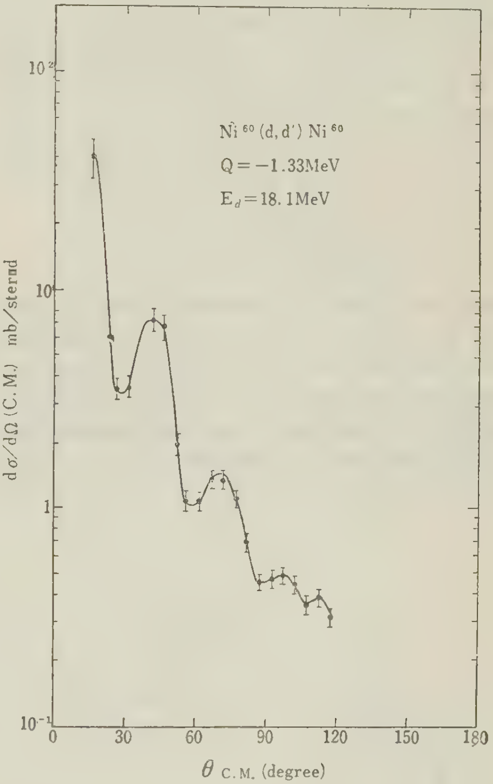

Fig. 8. Angular distribution of the inelastically scattered deuterons from Ni^{60} leading to the 1.33 MeV state.

Fig. 7 shows that the first maximum and the first minimum shift by small amounts to the forward direction with a large increase of the incident energy. The second peak of the curve obtained at E_d=11.2 MeV splits into two peaks, which we call peaks A and B, as the bombarding energy increases. Peak A is much larger than Peak B at E_d= 15.1 MeV. Then, A moves to the forward angle and its amount decrases gradually with increasing energy, and B grows up suddenly at $E_d=15.9$ MeV largely shifting to smaller angles. B decreases gradually with increasing energy from $E_d=15.9$ MeV. These characters do not appear in the case of elastic scattering of deuterons at the same range of the energy in our other experiments.[20]

As mentioned in § 1, compound-nucleus process does not contribute to the cross section. Huby and Newns have developed the direct interaction theory for the inelastic scattering of deuterons in somewhat analogous way to the (d, p) theories of Butler and others.[21] The angular distribution was derived in the plane-wave Born approximation.

We compared our results with the theory of Huby and Newns, in which the differential cross section is of the form

$$\frac{d\sigma(\theta)}{d\Omega}=\sum|A_l|^2\left\{\left[\frac{4\alpha}{K}\cdot\tan^{-1}\left(\frac{K}{4\alpha}\right)\right]\cdot\left(\frac{\pi}{2K\alpha}\right)^{1/2}J_{l+1/2}(Ka)\right\}^2$$

where $\alpha=(1/\hbar)\times(M_p\times\text{deuteron binding energy})^{1/2}=0.23\times10^{13}\ \mathrm{cm}^{-1}$, K is the difference of wave numbers of the deuteron before and after the collision; $K=|\mathbf{K}_i-\mathbf{K}_f|$, $a=$the interaction radius, and $J_{l+1/2}(Ka)=$Bessel functions of the half-integral order. The A_ls are constants suitably chosen. The most important factor determining the angular distribution is $[J_{l+1/2}(Ka)]^2/Ka$. This theory predicts the drop in the forward direction except for the case where $l=0$.

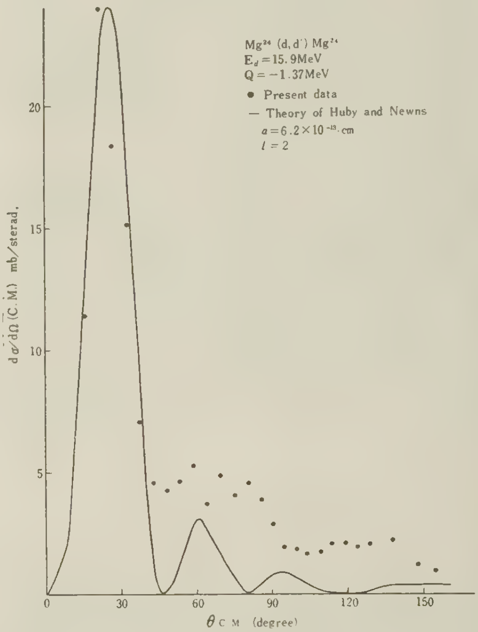

Fig. 10. Comparison of the $Mg^{24}(d, d')Mg^{24}$ angular distribution at $E_d=15.9$ MeV with the nuclear interaction theory of Huby and Newns.

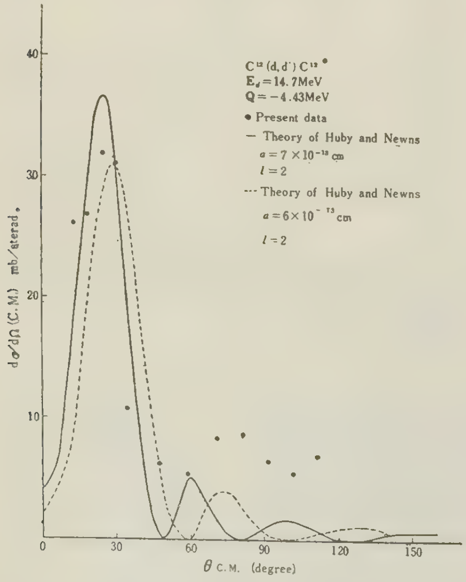

Fig. 9. Comparison of the $C^{12}(d, d')C^{12}$ angular distribution at $E_d=14.7$ MeV with the nuclear interaction theory of Huby and Newns.

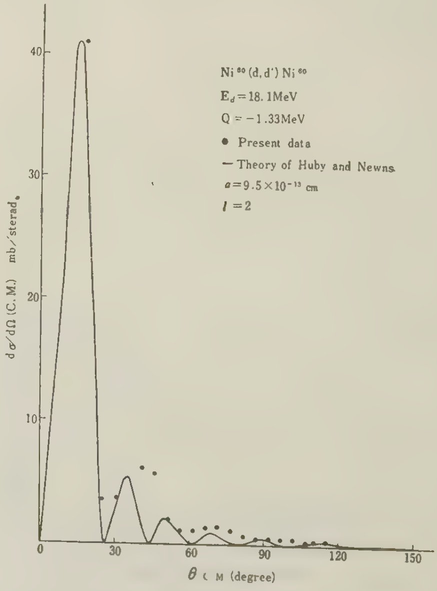

Fig. 11. Comparison of the $Ni^{60}(d, d')Ni^{60}$ angular distribution at $E_d=18.1$ MeV with the nuclear interaction theory of Huby and Newns.

In Figs. 9 to 11 results are shown in the cases of C^{12}, Mg^{24} and Ni^{60} at $E_d=14.7$, 15.9 and 18.1 MeV, respectively. The characteristic features are rather well reproduced by the theory except that the interaction radius of C^{12} for deuteron is too large.

If theoretical values are normalized to fit the experiment at the forward peak, however, theoretical cross sections are so much small at rather large angles. The data at forward angles were also analysed in terms of the diffraction scattering formula of Blair,[22] in which the cross section of inelastic scattering by quadrupole surface excitation of an even-even nucleus is expressed as

$$\frac{d\sigma(\theta)}{d\Omega}(0\rightarrow 2)=(ka^2)^2\left(\frac{5}{4\pi}\right)\cdot\left(\frac{\hbar\omega_2}{2C_2}\right)\cdot\left\{\frac{1}{4}\,[J_0(ka\theta)]^2+\frac{3}{4}[J_2(ka\theta)]^2\right\},$$

where $\hbar\omega_2$ is the excitation energy of the final nucleus and C_2 is the surface tension parameter.

Some results are given in Figs. 12 and 13. The values of a in the Figs. 12 and 13 are those that fit the data of the elastic scattering obtained in our other experiment.[20]

In order to explain the present experiments by direct nuclear interaction process at all angles, it seems to be necessary to calculate with a distorted wave approximation, using a proper optical potential. However, it is uncertain if the strong dependence on energy in the angular distributions for Mg^{24} can be explained with the optical potential having a large imaginary part. Further measurements of the angular distributions seem to be

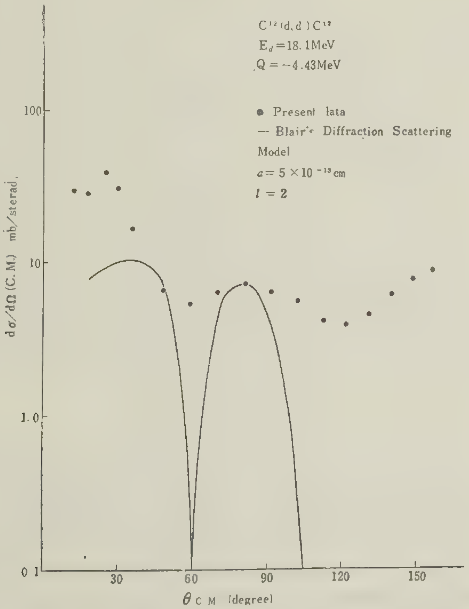

Fig. 12. Comparison of the $C^{12}(d, d')C^{12}$ angular distribution at $E_d=18.1$ MeV with Blair's diffraction scattering model.

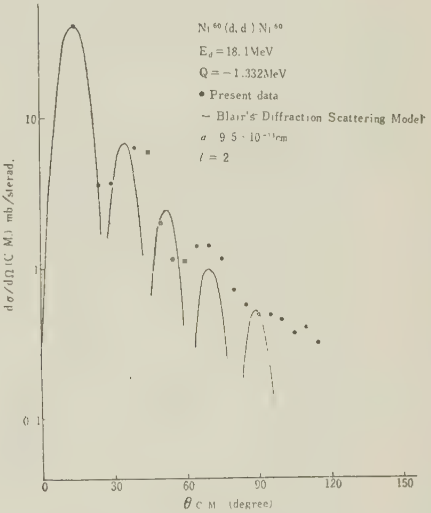

Fig. 13. Comparison of the $Ni^{60}(d, d')Ni^{60}$ angular distribution at $E_d=18.1$ MeV with Blair's diffraction scattering model.

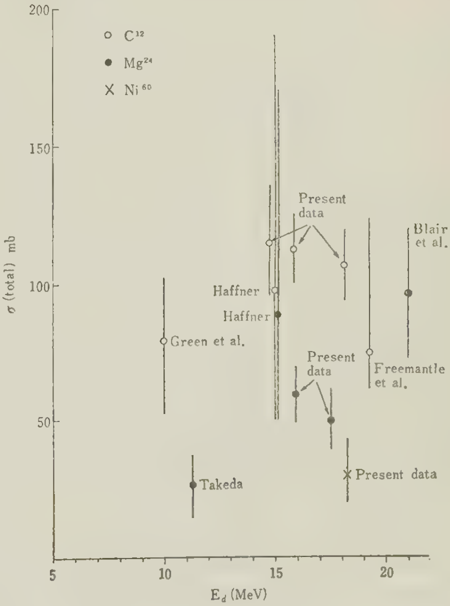

Fig. 14. The total cross sections for inelastic scattering leading to the 1st excited states of C^{12}, Mg^{24} and Ni^{60}.

desirable with smaller changes of the incident energy in order to clarify what is responsible for such a strong dependence.

Fig. 14 gives the total cross sections for the inelastic scattering leading to the first excited states of C^{12}, Mg^{24} and Ni^{60} at the various deuteron energies. All the values are calculated from the absolute differential cross sections reported here, except for the value given by Haffner. The error shown in Fig. 14 comes from an uncertainty in estimating the total cross section from the given differential cross section.

The total cross sections for C^{12} and Mg^{24} seem to increase up to about 14 MeV incident energy, and then decrease gradually with increasing energy. The values for the deuterons are about 2/3 times those for the protons in the case of C^{12}, about 1/2 in Mg^{24} and nearly 2/3 in Ni^{60}, in the measurements at nearly equal deuteron and proton energies.[23)]

In the general form, the differential cross section for the direct process is given by

$$\frac{d\sigma(\theta)}{d\Omega}=\frac{K_f}{K_i}\cdot\left(\frac{M_i}{2\pi\hbar^2}\right)^2\cdot\frac{1}{2I_i+1}\cdot\sum_{i,f}|\langle f\,|V|i\rangle|^2\,,$$

where K=the wave number, i and f indicate the initial and final state respectively, M_i= the mass of the incident particle, I_i=the total spin of the target nucleus in the initial state and V=the interaction potential. If we measure the cross sections of inelastic scattering of a deuteron and a proton of the same wave number, the geometrical factor of the cross section shows that the cross section for a deuteron is four times the cross section for a proton. When the energy of the incident beam is much larger than the absolute Q value, K_f/K_i is nearly equal to 1. Therefore, the ratio of the total cross section for a deuteron to that for a proton may be estimated as about 4 for the same target and Q value, provided that transition matrix elements are also same. However, these ratios in our measurements for C^{12} ($Q=-4.43$ MeV), Mg^{24} ($Q=-1.37$ MeV) and Ni^{60} ($Q=-1.33$ MeV) are nearly equal to 1/2. This suggests that the matrix element for deuteron is about one-third to that for protons. The reduction of the transition probability for a deuteron is infered to be due to large imaginary part of optical potential for a deuteron than that for a proton.[24)]

In the collective model of a nucleus, the interaction between a incident particle and a nucleus is approximated to occur mainly on the nuclear surface. The target nuclei used in this experiment have some evidence of the collective nature.

The transition probability from the first excited state with 2^+ spin to the ground state with 0^+ spin gives a useful information on the structure of the nucleus. The Table II shows the measured mean lives and the ratios of theoretical and experimental values of the nuclear transitions concerned here.

Table II. Measured mean lives of $2^+ \to 0^+$ transitions and the ratios of theoretical and experimental values.

Nucleus	Mean life τ	ratio $\tau_{exp.}/\tau_{theo.}$
C^{12}	2.6×10^{-14} sec	22
Mg^{24}	2.5×10^{-11}	0.32
Ni^{60}	1×10^{-12}	5.1

Data are taken from references 27)~29).

Here the theoretical values of the mean lives are calculated on the basis of the single particle model. As can be seen from the table, the ratios are remarkably large in C^{12} and Ni^{60}. These large values are probably due to the contribution from the collective excitations in these nuclei. In case of nucleus with closed shell, the effect of the collective excitation may be smaller, but can not be neglected, as shown in the analysis by Kisslinger and Sorensen on Sn^{120}, for which the ratio is 4.4.[25),26)] The small value of the ratio in Mg^{24} is hard to be understood and might be due to mistake of the measurement or some selection rule which makes the collective excitation improbable. We think that the study of nuclear reaction gives frequently useful informations on the structure of nuclei.

Acknowledgement

The author wishes to thank Professor I. Nonaka for continuous encouragement. His thanks are also expressed to Drs. T. Ishimatsu, T. Nakamura, Y. Nakano, Y. Saji and S. Yasumi for their helps through this experiment. He thanks Drs. M. Sano, S. Okai and R. Eisberg for discussion and comments to the manuscript. His thanks are due to Mr. T. Karasawa and other operating crew of the cyclotron, and Mr. Y. Yoshimura for the preparation of the electronic circuits.

References

1) J. W. Haffner: Phys. Rev. **103** (1956) 1398.
2) R. Huby and H. C. Newns: Phil. Mag. **42** (1951) 1442.
3) C. J. Mullin and E. Guth: Phys. Rev. **82** (1951) 141.
4) J. L. Yntema and B. Zeidman: Phys. Rev. **114** (1959) 815.
5) T. S. Green and R. Middleton: Proc. Phys. Soc. London **69A** (1956) 28.
6) R. Middleton and C. T. Tai: Proc. Phys. Soc. London **65A** (1952) 752.
7) R. G. Freemantle, W. M. Gibson and J. Rotblat: Phil. Mag. **45** (1954) 1200.
8) F. A. El-Bedewi: Proc. Phys. Soc. London **69A** (1956) 221.
9) S. Hinds, R. Middleton and G. Parry: Proc. Phys. Soc. London **70A** (1957) 900.
10) I. J. Van Heerden: Nuclear Phys. **6** (1958) 55.
11) F. Nemets and G. A. Prokopets: J.E.T.P. **11** (1960) 499.
12) W. F. Vogesang and J. N. Mcgruer: Phys. Rev. **109** (1958) 1663.
13) M. Takeda: J. Phys. Soc. Japan **15** (1960) 557.
14) G. W. Greeless and J. Lowe: Proc. Phys. Soc. London **76** (1960) 143.
15) K. Matsuda et al and T. Mikumo et al.: Private commu. and The Report from Proceeding of the International Conference on Nuclear Structure at Kingston Canada.
16) S. Kikuchi et al. J. Phys. Soc. Japan **14** (1959) 861.
17) S. Kobayashi et al.: J. Phys. Soc. Japan **15** (1960) 1151.
18) S. Kikuchi et al.: J. Phys. Soc. Japan **15** (1960) 9.
19) J. C. Allred et al.: Phys. Rev. **88** (1952) 433.
20) T. Ishimatsu, Y. Ishizaki, T. Nakamura, Y. Nakano, Y. Saji and S. Yasumi: to be published.
21) S. T. Butler: Proc. Roy. Soc. London **A208** (1951) 599.
22) J. S. Blair: Phys. Rev. **115** (1959) 928.
23) K. Matsuda et al.: Private comm. and J. Phys. Soc. Japan **16** (1960) 1151.
24) Levinson and Banerjee: Annals of Physics **3** (1958) 67.
25) P. H. Stelson and F. K. McGowan: Bull. Am. Phys. Soc. **2** (1957) 69. H. Ikegami: Phys. Rev. **120** (1960) 2185. T. Udagawa and H. Ikegami: to be published in Prog. Theor. Phys.
26) L. S. Kisslinger and R. A. Sorensen: Private Communication (to be published).
27) C. P. Swan, F. R. Metzger and V. K. Rasmussen: Phys. Rev. **110** (1958) 154.
28) C. Coleman: Phil. Mag. **46** (1955) 1135.
29) F. R. Metzger: Phys. Rev. **103** (1956) 983.

Journal of the Physical Society of Japan Vol. 16, No. 6, June, 1961

Anomalies in the Scattering of Alpha Particles by Carbon

By Takashi Mikumo

Institute for Nuclear Study, University of Tokyo,
Tanashi-machi, Kitatama-gun, Tokyo, Japan

(Received February 4, 1961)

Angular distributions of elastic and inelastic scattering ($Q=-4.43$ MeV) of alpha particles by the carbon nucleus have been measured at eight different alpha particle energies between 27.0 and 35.5 MeV. These data are discussed together with those reported previously in this journal and with those of other authors.

Angular distributions for both elastic and inelastic alphas show remarkable variation with bombarding energy and cannot be explained with simple direct interaction theories. There appear anomalies in the angular distributions for E_α in the neighbourhood of 30 MeV. Also in the excitation energy near 30 MeV in the compound system, some resonances were found in the elastic excitation function and in the integrated cross section for the inelastic scattering ($Q=-4.43$ MeV). Even at such high excitation energies the effect of the compound system seems to be important.

§ 1. Introduction

In the course of our experiments, previously done in this Institute[1], angular distributions of alpha particles scattered elastically and inelastically ($Q=-4.43$ MeV) by the carbon nucleus were measured at incident alpha particle energies 33.4, 30.7 ahd 28.2 MeV.* (At the last energy, angular distributions of inelastic alpha groups corresponding to $Q=-7.66$, -9.63 and $\simeq -12.7$ MeV were also measured.) In that paper it was reported that some features for the elastic and the inelastic scattering ($Q=-4.43$ MeV) at forward angles seemed to reflect an important contribution of diffraction scattering mechanism such as that discussed by Blair[2]: for example, sharp diffraction patterns in both elastic and inelastic angular distributions; the general out-of-phase relation between both angular distributions; and the large absolute cross sections for the inelastic scattering. On the other hand, the following characteristics were not likely to be explained by Blair theory: the remarkable changes of cross sections and angular distributions with energy in both scattering; the rise of the cross sections at backward angles, especially for the inelastic scattering; the change of the value of the interaction radius R_0 wifh incident alpha energy E_α for the elastic scattering, as calculated after Blair theory, especially the sudden change of R_0 for E_α around 30 MeV.

In addition, Watters[3] had found an anomaly in the elastic angular distribution at 31.5 MeV, which appeared as a plateau at $\theta_{\text{c.m.}} \simeq 60°$. Such an anomaly cannot be understood with the current theories. Nobody else,[4)–12)] however, found such an anomaly at this angular region. Many circumstances for $E_\alpha < 30$ MeV seemed different from those for $E_\alpha > 30$ MeV, for example, the number of the peaks in the angular distributions appeared smaller at $E_\alpha < 30$ MeV than at higher energies. In the energy region, $E_\alpha \simeq 30$ MeV, however, there were very few data published.

Even if the separate data of $\alpha' - \gamma$ angular correlation[13] and some of the angular distributions[14] seemed compatible with the predictions of direct interaction theories, the ensemble of the data reflected the complicated character of the scattering mechanism. In order to elucidate the mechanism it was considered to be necessary to obtain more data, especially to know behaviours around 30 MeV. So, in the present experiment, angular distributions of elastic and inelastic scattering were measured at eight more incident alpha energies ranging from 27.0 to 35.5 MeV. For the study of such an energy-sensitive behaviour the variable-energy cyclotron of this Institute is particularly suitable.

---

* Energy values quoted here are slightly smaller than those reported in ref. 1. This is due to the different references from which range-energy relation are taken. See discussions in § 2B.

The data obtained here show several anomalies for $E_\alpha \simeq 30$ MeV: reproduction of Watters' plateau at somewhat different energy; disappearance of a peak in the angular distributions for both scattering found at higher energies; large value of R_0 compared with that obtained at other energies; some resonance phenomena in the elastic excitation function and in the integrated cross section σ_t for the inelastic scattering.

These facts, together with similar phenomena recently found in this Institute with oxygen and nitrogen, may throw some light on the study of the reaction mechanism and the structure of light nuclei.

§ 2. Experimental Produce

A. *Experimental apparatus*

Details of the 160 cm INS (Tokyo) variable-energy cyclotron[15], the beam focussing system[15] and the scattering apparatus[1],[16] were reported previously. Several modifications were made which are described in the following:

i) In order to see the change of angular distributions of scattered alpha particles with a slight change of beam energy, the target was made as thin as possible. A self-supporting carbon target 1.37 mg/cm² thick was made by the method described in refs. 1 and 16. This corresponds to energy loss of 200 to 300 keV at the relevant alpha particle energies. With this target much better resolution in the histogram was obtained even at backward angles:

ii) Three detectors were placed on the turntable in the 100 cm scattering chamber, instead of two. They were called "extreme-forward," "forward" and "backward" detectors; the last two were 180° apart and the first was on the same side as the third with regards to the beam direction and made an angle of 45° with each other. Fig. 1 shows the arrangement in the scattering chamber. The defining slits for the three detectors were of 2 mm, 3 mm and 6 mm diameter, respectively. Thus we could obtain data at small angles without unduly diminishing the beam intensity. In doing so, however, the minimum laboratory angle attainable was as large as

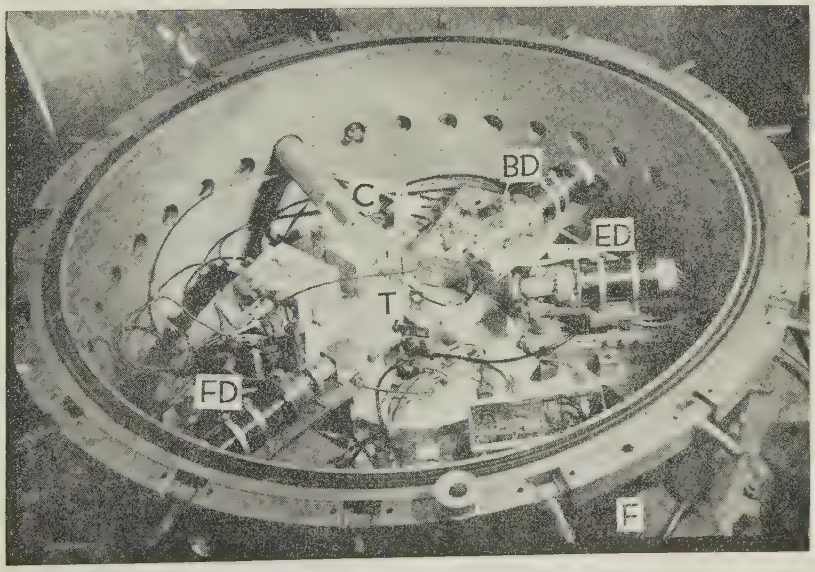

Fig. 1. Arrangement of detectors in the scattering chamber.

C : Beam collimator.
F : Faraday cup.
T : Target holder.
FD: Forward detector (Proportional counter not used is seen between defining slit and scintillation counter).
BD: Backward detector.
ED: Extreme-forward detector.

20°; the lack of data at extremely small angles was somewhat of a handicap in making the analysis.

The angular resolutions for three detectors were about, 0.5°, 0.8° and 1.7° (full angles).

The extreme-forward detector took data between 20° and 35°, the forward detector between 30° and 100°, the backward detector between 85° and 150°, the last two took data simultaneously.

iii) A proportional counter-scintillation counter telescope was used only as the backward detector; each of the other two detectors consisted of only a scintillation counter. During the course of earlier experiments[1)], we had confirmed that it is not necessary to employ proportional counters for α_0 (elastic alphas) and α_1 (inelastic alphas, $Q=-4.43$ MeV) for the small angles, (In Fig. 1 a proportional counter not used is shown in front of the forward scintillation counter.) The proportional counter for the backward detector contained about 30 cm Hg of Argon-CO_2 mixture (5% CO_2). Pulses from the proportional counter, amplified and biased adequately so as not to miss elastic alphas but to discriminate out singly charged particles, opened the gate for pulses from the scintillation counter into multi-channel pulse height analysers.

iv) The CsI(Tl) crystals used for scintillation counters were made as thin as possible. The thicknesses of crystals for three detectors were 0.45 mm, 0.45 mm and 0.3 mm, respectively. At the highest energies an aluminium absorber was inserted in front of the extreme-forward detector in order to stop elastic alphas in the crystal.

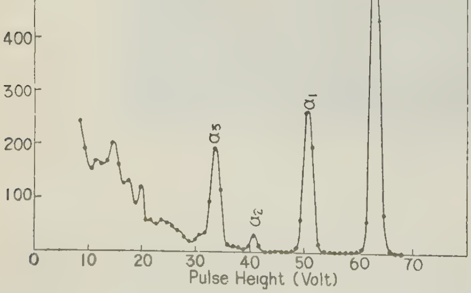

Fig. 2. Typical histogram obtained with extreme-forward detector at $\Theta_{lab}=35°$ and $E_\alpha=35.5$ MeV.

A typical histogram obtained with the forward detector is shown in Fig. 2.

B. *Beam energy measurement*

The energy of the alpha particle beam was determined with the same apparatus as was used in refs. 1 and 16, i.e., a device consisting of aluminium absorbers and an ionisation chamber placed just behind the rear flange of the Faraday cup of the scattering chamber, at the centre of which was a small window of an aluminium foil. Changing the thickness of absorbers one could obtain a Bragg curve and the mean energy of incident alpha beam was determined. At the beginning and/or at the end of each energy run the energy was measured. In refs. 1 and 16 we used range-energy relations of protons in aluminium, carbon and air after Aron et al.[17)] and converted them to alpha particles. This time range-energy relations of protons in aluminium after Bichsel et al.[18)] were used. For carbon and air we were obliged to make use of those of Aron et al. With the aid of these relations, effective energies were estimated to be 35.5, 34.5, 30.7, 30.2, 30.0, 29.8, 29.6 and 27.0 MeV. In order to get the last energy, an aluminium absorber was inserted in front of the beam collimator at the entrance of the scattering chamber.

The beam energies reported in refs. 1 and 16 are higher than would be calculated with Bichsel's relation, according to which the mean alpha particle energies used in 1 were 33.4, 30.7 and 28.7 MeV. In the following discussions these corrected energy values will be used.

C. *Errors*

The width of beam energy was estimated, using a beam analysing magnet (whose momentum resolution being less than 0.1%), to be around 0.5%[19)]. The drift of beam energy in the course of an energy run is due to drifts of the magnetic field of the cyclotron and the focusing magnet, of oscillation frequency, and of dee voltage. The drift of mean energy due to these causes was estimated to be less than 0.5%. This slight drift of energy introduced, however, as will be mentioned below, a considerable change in the differential cross sections of elastic scattering in some angular region at $E_\alpha \simeq 29.8$ MeV.

Uncertainty in the absolute value of each energy was within 300 keV or so, but that in the relative value was much less.

At higher energies ($E_\alpha = 35.5$, 3.45 and 31.4 MeV), because of an improper path, the focused beam did not hit the target at the centre. This caused a disagreement in reading of about 1° between the extreme-forward and forward detectors at a corresponding angle, as these two detectors viewed the beam from oposite sides. Corrections to the angles were therefore made. At lower energies the beam passed through the centre of the target and the readings of angles with three detectors were very consistent. (Uncertainty in the scattering angles: ±0.2°)

The errors in the solid angles of three detectors were estimated to be less than a few per cent. Absolute cross sections obtained with the forward and backward detectors showed, however, disagreements as high as 20% at some corresponding angles, particularly when the overlapping angles corresponded to steep sides of angular distributions. The backward cross sections were normalized to the corresponding forward ones.

The uncertainty in target thickness, mainly due to its inhomogeneity, was estimated to be less than 10%.

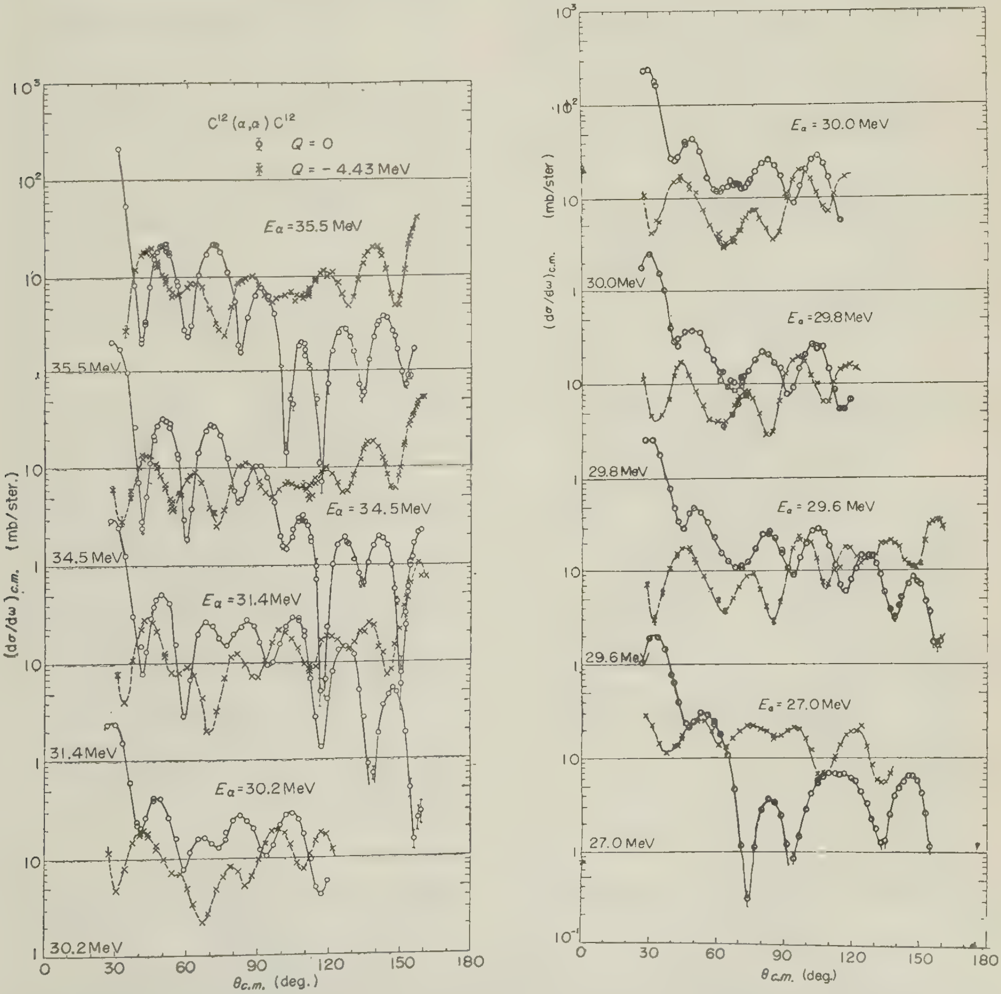

Fig. 3. Angular distributions for both elastic and inelastic (α_0) scattering (α_1) obtained at eight alpha particle energies.

Statistical errors ranged from less than 1% to about 20% depending on the angular position.

Errors due to background subtraction were small, except for α_1 at backward angles at the lowest energy (27.0 MeV), where these errors were sometimes as large as 20%.

The absolute values of cross sections were estimated to be correct to within 20 to 30%.

§ 3. Experimental Results

Differential cross sections for both elastic and inelastic scattering ($Q=-4.43$ MeV) obtained at eight alpha-particle energies are shown in Fig. 3.

Angular distributions for α_0 expressed as ratios to Rutherford cross sections are in Fig. 4, where data of our previous experiments at 33.4, 30.7 and 28.2 MeV* and those

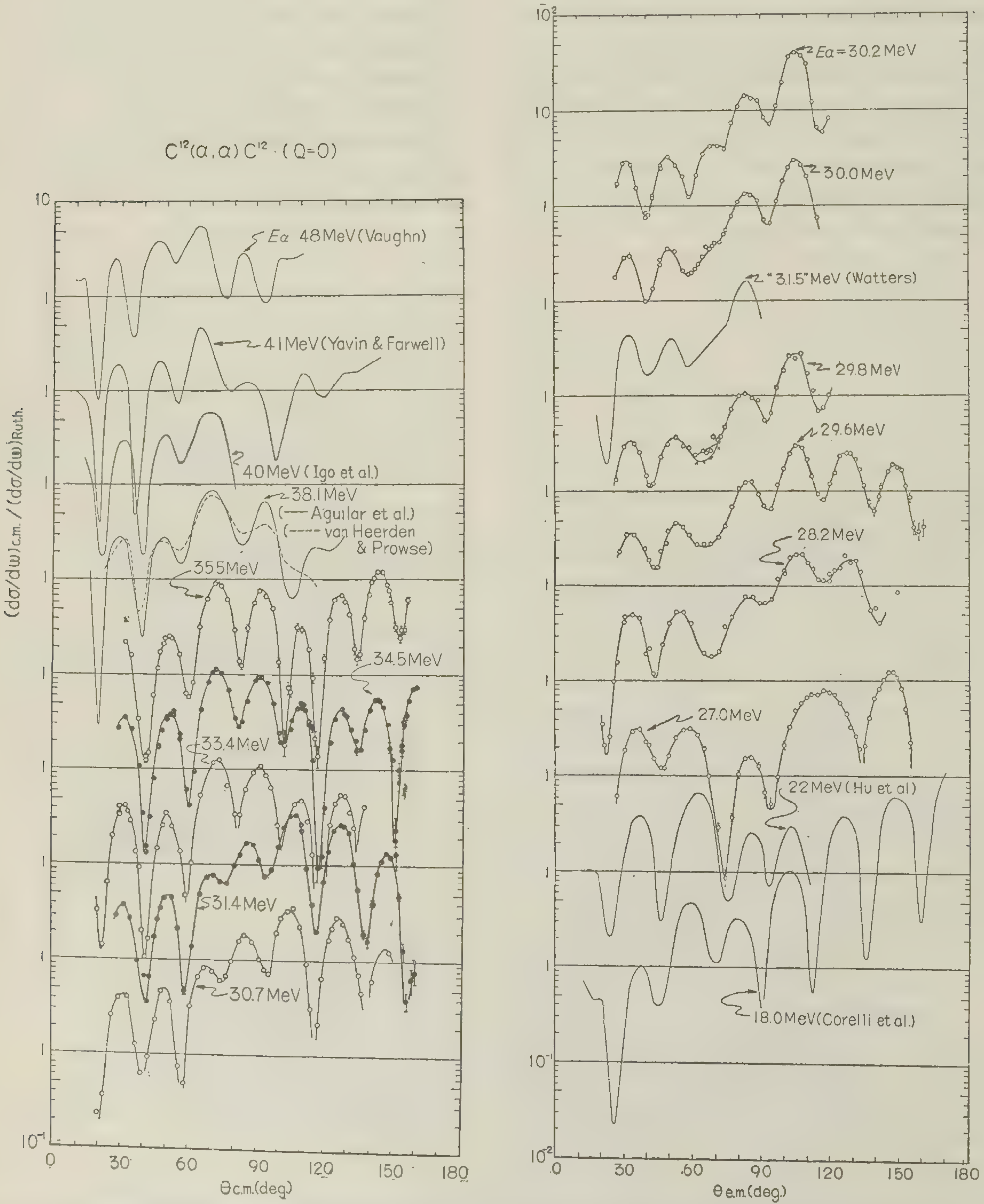

Fig. 4. Angular distributions for α_0 expressed as ratios to Rutherford cross sections. Points × show the change of angular distribution at $E_\alpha \simeq 29.8$ MeV with non-measurable variation of cyclotron energy.

---

* See caption of p. 2 and Sec. 2B.

published by many authors are also presented.

Angular distributions for α_1 are shown in Fig. 5, together with our previous data and those of other authors.

At first sight, angular distributions for both α_0 and α_1 show striking diffraction patterns. It is very difficult to find any systematic variation of the angular distributions with energy. In general the out-of-phase relation between the α_0 and α_1 angular distributions are roughly satisfied, except at several singular points. Elastic scattering and inelastic scattering are therefore closely correlated, but the peak cross sections do not decrease monotonically with increasing angles as Blair's diffraction theory[2] predicts.

The energy variation of the α_0 and α_1 angular distributions is very complicated, nevertheless we may point out some of its characteristics.

i) *Elastic scattering* (α_0)

There are some very deep minima in the angular distributions, especially at $\theta_{c.m.} \simeq 115°$ for $35.5\text{ MeV} \geq E_{\alpha(\text{lab.})} \geq 30.7\text{ MeV}$, and at some other angles. There is also a deep first minimum at extremely forward angles, where our new data are lacking. The ratio $(d\sigma/d\omega)_{c.m.}/(d\sigma/d\omega)_{\text{Ruth.}}$ oscillates and becomes higher at larger angles, especially for the lowest energies. This ratio is extremely high around the fourth and fifth maxima in the energy region of 29 to 32 MeV. This feature

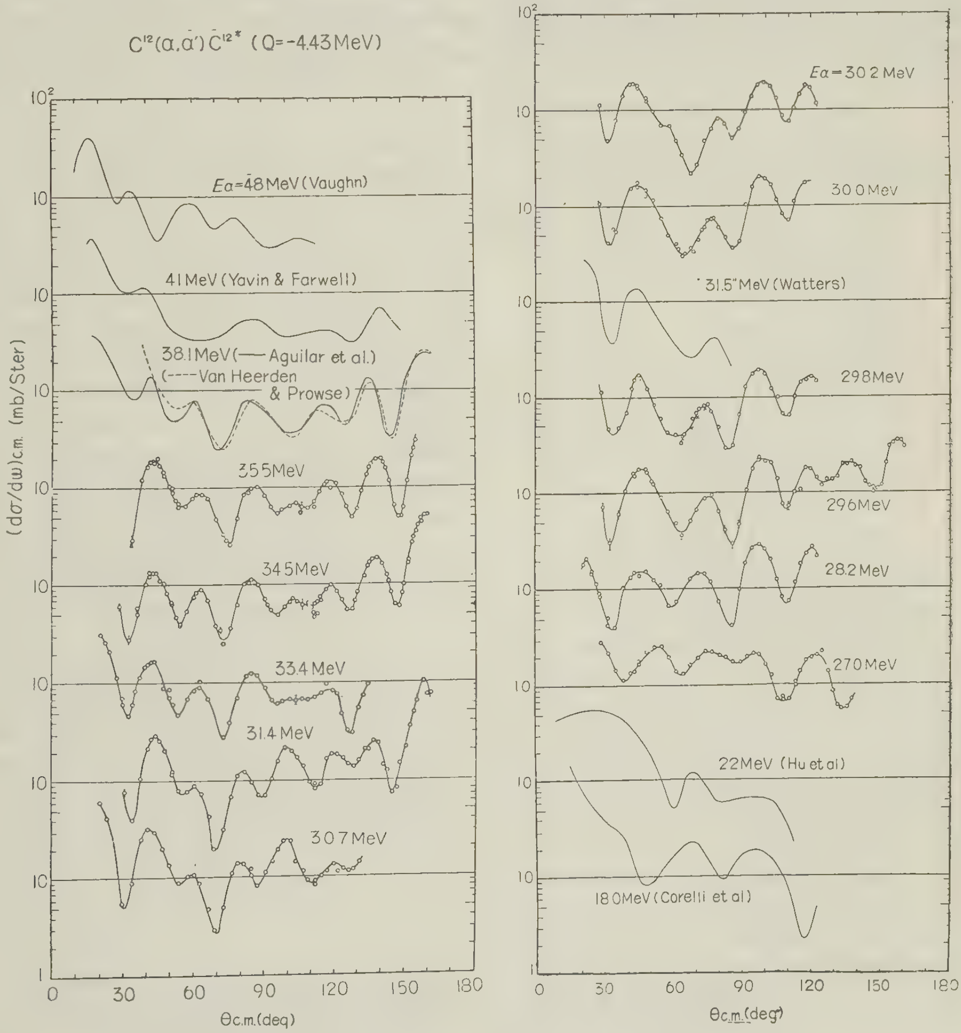

Fig. 5. Angular distribution for α_1.
Points × show the change of angular distribution at $E_\alpha \simeq 29.8$ MeV with non-measurable variation of cyclotron energy.

will be discussed in more detail.

The most dramatic phenomenon is the behaviour around 60° to 70°. There is a strong peak for $E_{\alpha} \geq 33.4$ MeV (the third maximum). This peak decreases with energy and it disappears at $E_{\alpha} \simeq 30.0$ MeV. For lower energies, it becomes hidden in a valley (the third minimum) which becomes deeper as E_{α} becomes lower.

In order to investigate this behaviour we made measurement of cross sections at every 200 keV between 29.6 and 30.2 MeV in the forward angular region. As the cyclotron beam has an energy spread of about 0.5% (See Sec. 2 C), this change corresponds to about the width of the beam. The cross sections and angular distributions changed, however, remarkably with slight variations of the mean energy of cyclotron. At $E_{\alpha}=29.8$ MeV, a non-measurable variation of cyclotron energy changed the shape of angular distribution in the angular region in question. This behaviour is shown in Fig. 4 with the points χ. The energy spread of the beam being taken into account, the change of the angular distributions must be considered as more energy-sensitive than is shown in Fig. 4. This strange behaviour appearing as a plateau in the angular distribution had been found by Watters at E_{α}="31.5" MeV. His angular distribution agrees very well with ours at $E_{\alpha}=30.0$ MeV. The effective energy at the centre of his target is not precisely known because of the lack of information concerning the target thickness. (He used carbon targets between 0.2 and 1 mil thick. The last target would have reduced $E_{\alpha\text{eff}}$ to about 30.6 MeV,

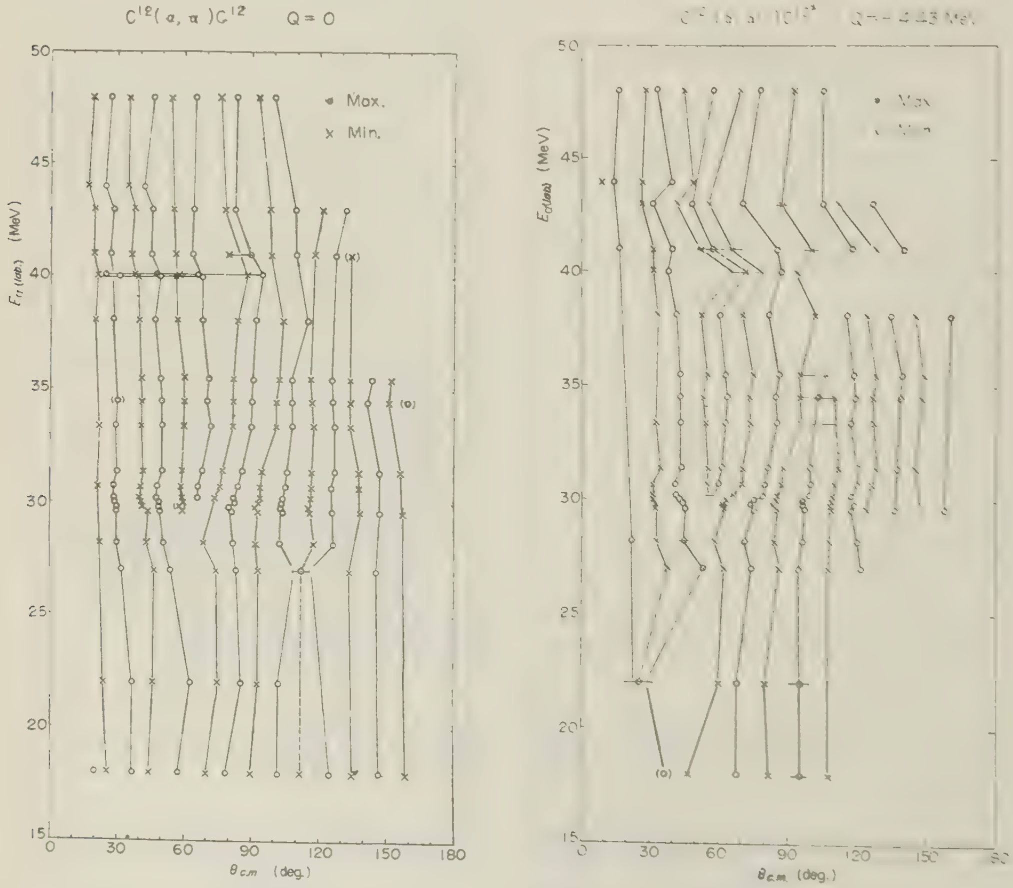

(a) (b)

Fig. 6 (a). Angular positions of maxima and minima in α_0 angular distributions plotted against E_{α} (lab).
(b). Angular positions of maxima and minima in α_1 angular distributions plotted against E_{α} (lab).

which is still higher than our energy.* His rather thick target would have caused him to observe some average behaviour in this energy region.) The energy-sensitive behaviour just mentioned may not be explained by simple diffraction theories, nor by direct reaction theories. Whether this anomaly can be attributed to a resonance in a compound system will be discussed later.

In Fig. 6 (a) the angular positions of maxima and minima are plotted against E_α, where the anomalous behaviour in the region around 30 to 31 MeV is clearly shown.

Another singular phenomenon is observed around 110° at $E_\alpha=27.0$ MeV. A very broad peak is observed in this region, which is split into two peaks for both higher and lower energies. Unfortunately we have not made measurement at either slightly higher or lower energies, nevertheless the singularity is clearly shown also in Fig. 6 (a).

ii) *Inelastic scattering* (α_1, $Q=-4.43$ MeV)

From Figs. 3 and 5, we can point out some of the characteristics in the angular distributions.

At $E_\alpha \simeq 30$ MeV, there appears a similar phenomenon to that found in the elastic scattering case. Here a valley and a peak, observed around 50° to 60° at higher energies, disappear. This valley and peak corresponds to the peak and valley in the α_0 angular distributions discussed in Sec. 3 i). This fact reflects a close correlation between α_0 and α_1, although the out-of-phase relation is violated in the angular region in question.

There are some plateaus around 100° for $33.4\text{ MeV} \leq E_\alpha \leq 35.5\text{ MeV}$ and for $E_\alpha=41$ MeV.

Another remarkable feature is the rise of the cross sections at backward angles ($\theta \gtrsim 150°$). This rise, especially remarkable at $E_\alpha=31.4$ MeV, reminds us of the rise of the backward cross sections observed in the reaction $C^{12}(\alpha, p_0)N^{15}$ ($Q=-4.96$ MeV)[16] for $E_\alpha \lesssim 31$ MeV. This point will be discussed later more fully.

§4. Discussion

i) *Elastic scattering*

As is seen in Fig. 6 (a), angular positions of minima and maxima do not shift systematically towards the smaller angles with an increase of energy as diffraction theories predict. According to these theories, in order that the interaction radius R_0 between a carbon nucleus and an alpha particle be constant, $\theta_{\text{c.m.}}$ for corresponding maxima and minima must decrease as $1/k$, where k is the c.m. wave number of the incident alpha particles. The angular positions of the first minimum and maximum being almost constant, the interaction radius R_0 calculated by diffraction theories (e.g. Blair theory) would decrease as $1/k$, as shown in the previous paper[1]. The reason for this fact is not yet clear. The larger value of R_0 around 30 MeV, shown in ref. 1, seems also established with the aid of the present data. The relation between R_0 and E_α based upon the diffraction model is shown in Fig. 7. (R_0 was obtained from angular positions of second maximum and minimum, because the data of the first ones are lacking in the present results.)

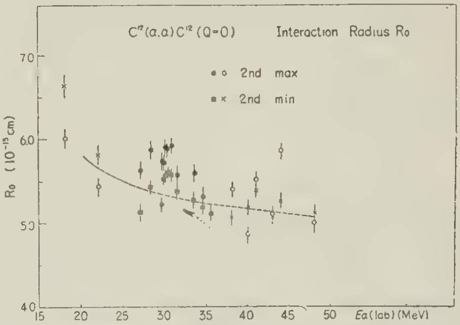

Fig. 7. Interaction radius R_0 obtained from simple diffraction theory plotted against $E_{\alpha(\text{lab})}$.

Aside from the forward angular region where Coulomb scattering must be important, the excitation function for elastic scattering is shown in Fig. 8 at every ten degrees from 70° to 150° (c.m.). This function was obtained from the data of angular distributions. At all these angles, there appears a broad peak (or two narrow peaks) for $E_{\alpha(\text{lab.})}$ around 30 MeV. At other energies less well established peaks are also observed. Unfortunately the behaviour around $E_\alpha \lesssim 27$ MeV is obscured because of the lack of data.

The resonance at $E_\alpha \simeq 30$ MeV corresponds to an excitation energy E_{ex} in the O^{16} nucleus of around 30 MeV. It is surprising that such a resonance exists, and it is not likely that this resonance be attributed to a "compound nucleus" resonance, in the ordinary sense. It seems, however, that in addition to the shape elastic and the diffraction scattering, some particular states in the compound system $C^{12}+\alpha$, which have a large alpha-particle width, contribute to the elastic scattering, even at such a high excitation energy. Interferences among these modes would make the phenomena very complicated.

---

* According to N. S. Wall (private communication), Watters' energy measurements were off by about 1 MeV, and at the centre of his target the effective energy would be about 30.2 MeV which agrees with ours.

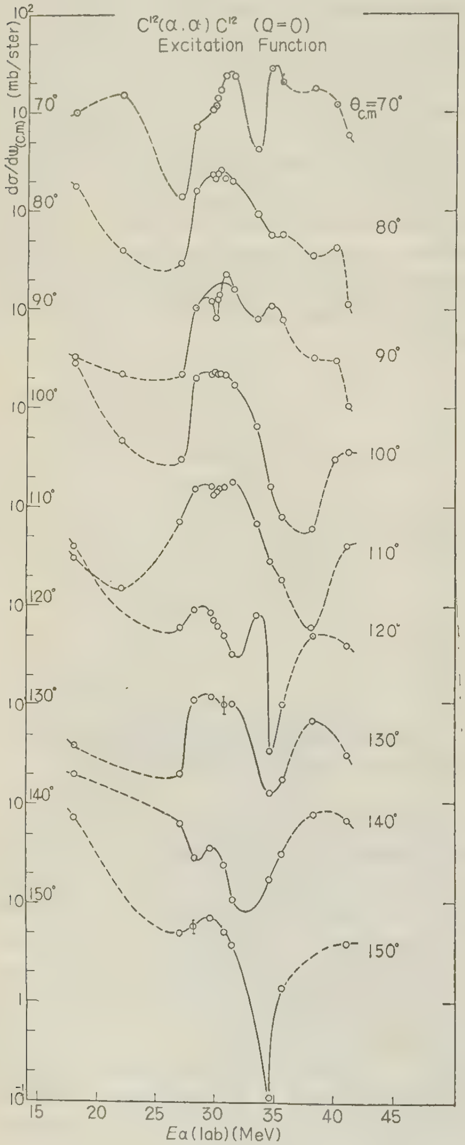

Fig. 8. Excitation function for elastic scattering at every ten degrees from 70° to 150° (c.m.), obtained from angular distribution data.

It is not yet clear whether the Watters' plateau, found in this energy region, is attributed to this resonance or it is nothing else than a transient phenomenon, in which contributions of certain waves of high l-values increase gradually with energy. Optical model calculations would be a powerful tool to solve this problem.

ii) *Inelastic scattering*

Angular positions of the maxima and minima of the angular distributions are shown in Fig. 6 (b). Still less systematic shifts of angular positions with energy were obtained than in the case of elastic scattering, nevertheless singularities at $E_\alpha \simeq 30$ MeV and $E_\alpha \simeq 27$ MeV are observed.

In Fig. 9 is shown the integrated cross section σ_t for α_1 as a function of $E_{\alpha(\text{lab.})}$ and $E_{\text{ex}}(O^{16*})$. σ_t was obtained by integrating the observed differential cross sections by extraporation to 0° and th 180°. (Absolute value of σ_t is not shown, but the values in the coordinate may roughly be read as mb.) σ_t decreases, in general, as the increase of E_α, which is not expected from Blair theory. Although the errors in σ_t are large, especially at energies where data at small or large angles are absent, two peaks at $E_\alpha \simeq 31.5$ MeV and at $E_\alpha \simeq 27$ MeV are observed. For comparison, σ_t for the reaction $C^{12}(\alpha, p_0)N^{15}$ ($Q=-4.96$ MeV)[16),20),21)] is also shown in Fig. 9. (The energy scale is corrected in our present scale.) While it was concluded in ref. 16 that σ_t decreased monotonically as the increase of energy, there appear a peak at $E_\alpha \simeq 25$ MeV and a bump at $E_\alpha \simeq 31$ MeV.

The resonance for α_1 at $E_\alpha \simeq 31.5$ MeV corresponding to $E_{\text{ex}}(O^{16*}) \simeq 31$ MeV has a width of less than 2 MeV. It is surprising that such a resonance (the actual width seems to be narrower, the width of beam energy being taken into account) does exist in such a high excitation of nucleus. It is difficult to consider it to be a "compound nucleus" resonance, since the evaporation mechanism can hardly explain why $\sigma_t(\alpha_1)$ exceeds 10 to 20% of geometrical cross section. ($\pi R_0^2 \simeq 80 \sim 100$ mb)

It is interesting that the energy position where the peak around 60° disappears in the α_0 and α_1 angular distributions turns out to be just at the valley between two peaks in σ_t vs. E_α curve.

In Fig. 9 the energy levels of O^{16} known from the reactions $N^{14}(d, n)$, $C^{13}(He^3, p)$ and $O^{16}(\gamma, 4\alpha)$ are also shown for comparison[22]. Whether the resonances found here correspond to some of these levels is left for future investigation.

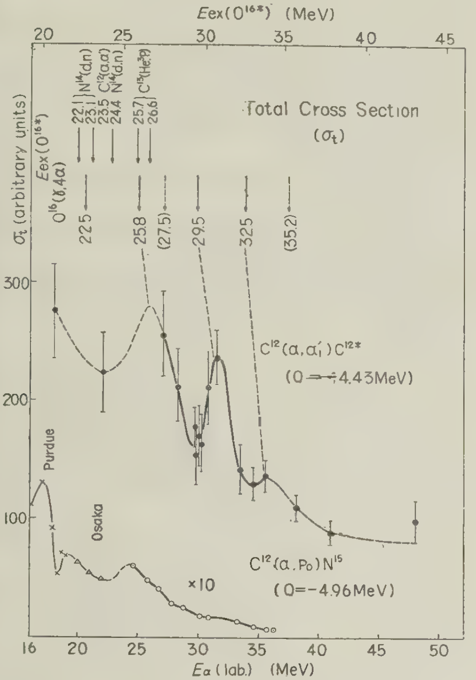

Fig. 9. Integrated cross section σ_t for α_1 plotted against $E_{\alpha(\text{lab})}$ and $E_{\text{ex}}(O^{16*})$.
Energy levels in O^{16*} are taken from the paper of Ajzenberg-Selove and Lauritsen: Nucl. Phys. **11** (1959) 1.

A comparison among the reactions $C^{12}(\alpha, \alpha')C^{12*}$, $C^{12}(\alpha, p)N^{15}$, $C^{12}(\alpha, d)N^{14}$, etc. would elucidate the behaviour of the entrance channel, while a comparison among the reactions initiated by $N^{15}+p$, $N^{14}+d$ and $C^{12}+\alpha$ would be helpful to determine whether the resonant or singular phenomena are open to different entrance channels. The angular distributions of $N^{14}(d, \alpha_0)C^{12}$ and $N^{14}(d, \alpha_1)C^{12*}$ [23] show sharp diffraction patterns and strong energy dependence. At some energies there is a pronounced rise in the cross sections at backward angles and $(d\sigma/d\omega)_{\alpha_1}$ is larger than $(d\sigma/d\omega)_{\alpha_0}$. These features are similar to those in the case of $C^{12}(\alpha, \alpha_0)$ and $C^{12}(\alpha, \alpha_1)$. (At backward angles inelastic cross sections are larger than elastic cross sections. See Fig. 3.) Angular distributions of $N^{14}(d, p_0)N^{15}$ obtained in this Institute by Kyushu University group[24] at $E_d=14\sim16$ MeV resemble those of $C^{12}(\alpha, p_0)N^{15}$ data[16] near the same O^{16} energy. These similarities might be a reflection of the fact that the compound system plays an important role in these scattering and reactions.

In the study of $Mg^{24}(\alpha, \alpha_0)Mg^{24}$ and $Mg^{24}(\alpha, \alpha_1)Mg^{24*}$ ($Q=-1.37$ MeV), Blair et al.[25] found a systematic variation of angular distributions (experiments were done only in the forward angular region), both in size and in shape and in the angular positions of maxima and minima, and they could obtain a " universal " curve in the relation $1/k^2\, d\sigma/d\omega$ *vs.* $2kR_0 \sin\theta/2$. It was impossible to obtain such a curve even in the extremely forward angular region with carbon. We have recently studied $O^{16}(\alpha, \alpha_0)O^{16}$, $O^{16}(\alpha, \alpha')O^{16*}$, $N^{14}(\alpha, \alpha_0)N^{14}$ and $N^{14}(\alpha, \alpha')N^{14*}$ and and found energy variation of angular distributions similar to those found in the case of carbon[26]. The resonance energies in the elastic excitation function for oxygen and the energies where the third peak in the elastic angular distributions disappear for both oxygen and nitrogen are found to be in the region of E_{ex} between 25 and 30 MeV. It is not clear whether these anomalies occur with every light nucleus or are accentuated with nuclei of $n\alpha$-type on the one hand, and for what mass numbers and excitation energies it is possible to obtain " universal " curves on the other hand.

It is also to be investigated whether the same resonances are observed with different incident particles and to compare with the case of alpha scattering. In elastic and inelastic scattering of protons many resonances were observed, by Matsuda et al., with many nuclei, including carbon, corresponding to $E_{\text{ex}}=10\sim30$ MeV[27], on the contrary Ishizaki et al.[28] found no significant anomalies in their study of $C^{12}(d, d_0)C^{12}$ and $C^{12}(d, d_1)C^{12*}$ at $E_d=15$, 16 and 18 MeV ($E_{\text{ex}}(N^{14*})=22\sim25$ MeV). It is also of interest to compare these resonances with those found by Bromley et al. in carbon-carbon elastic scattering[29] and carbon-carbon reactions[30].

Acknowledgement

The author wishes to express his appreciation of the valuable counsel of Professor I. Nonaka during the course of this investigation. He is also very grateful to Dr. H. Yamaguchi for his continual collaboration and discussions, and to the research staff of I.N.S. (Tokyo). Sincere appreciation is extented to Messrs. S. Hitaka, T. Maki, M. Mukae and T. Nakashima for their collaboration during this investigation. Sincere thanks are due to the cyclotron crew of I.N.S. especially to Messrs. A. Suzuki and T. Yamada.

References

1) T. Mikumo, H. Yamaguchi, I. Nonaka, M. Odera, Y. Hashimoto, M. Kondo and T. Maki: J. Phys. Soc. Japan **15** (1960) 1158.
2) J. S. Blair: Phys. Rev. **115** (1959) 928.
3) H. J. Watters: Phys. Rev. **103** (1956) 1763.
4) F. J. Vaughn: UCRL 3174 (1955)
5) R. Beurty, P. Catillon, R. Chaminade, H. Faraggi, A. Papineau and J. Thirion: C.R. Acad. Sc. **249** (1959) 2189.
6) G. W. Farwell, G. B. Shook and A. I. Yavin: Univ. Washington Annual Progress Report 1957.
7) A. I. Yavin and G. W. Farwell: Nucl. Phys. **12** (1959) 1.
8) G. Igo, H. E. Wegner and R. M. Eisberg: Phys. Rev. **101** (1956) 1508.
9) J. Aguilar, W. E. Burcham, J. Català, J. B. A. England, J. S. C. McKee and J. Rotblat: Proc. Roy. Soc. A, **254** (1960) 395. See also J. Català, L. Miralles, J. Aguilar and M. de la Cuadra: Proc. of 2nd. U.N. Internat. Conf. on the Peacefull Use of Atomic Energy **14** (1958) p. 143. and J. B. A. England and J. S. C. McKee: C.R. du Congrès International de Phys. Nucléaire, Paris (1958) p. 402.
10) I. J. Van Heerden and D. J. Prowse: Nucl. Phys. **15** (1960) 356.
11) C. Hu, S. Kato, Y. Oda and M. Takeda: J. Phys. Soc. Japan **14** (1959) 1184.
12) J. C. Corelli, E. Bleuler and D. J. Tendam: Phys. Rev. **116** (1959) 1184.
13) G. B. Shook: Phys. Rev. **114** (1959) 310.
14) E. Rost and N. Austern: to be published.
15) S. Kikuchi et al.: J. Phys. Soc. Japan **15** (1960) 41. K. Matsuda, T. Mikumo, K. Nisimura, S. Kobayashi, H. Ogawa and H. Adachi: INSJ-14, (Jan. 15, 1959)
16) I. Nonaka, H. Yamaguchi, T. Mikumo, I. Umeda, T. Tabata and S. Hitaka: J. Phys. Soc. Japan **14** (1959) 1260.
17) W. A. Aron, B. G. Hoffman and F. C. Williams: AECU 663 (1949)
18) H. Bichsel, R. F. Mozley and W. A. Aron: Phys. Rev. **105** (1957) 1788.
19) T. Karasawa, A. Suzuki, H. Ogawa, N. Yoshimura, H. Adachi, Y. Miyazawa and T. Yamada: to be published.
20) S. Yamabe, M. Kondo and T. Yamazaki: to be published.
21) J. R. Priest, D. J. Tendam and E. Bleuler: Phys. Rev. **119** (1960) 1301.
22) Data are taken from the paper of F. Ajzenberg-Selove and T. Lauritsen: Nucl. Phys. **11** (1959) 1.
23) G. E. Fischer and V. K. Fischer: Phys. Rev. **114** (1959) 533. D. Bodansky, S. F. Eccles, G. W. Farwell, M. E. Rickey and P. C. Robisson: Phys. Rev. Letters **2** (1959) 101. C. Hu: J. Phys. Soc. Japan **15** (1960) 1741. T. Yanabu et al.: to be published.
24) S. Morita et al.: J. Phys. Soc. Japan **15** (1960) 361, and private communication.
25) J. S. Blair, G. W. Farwell and D. K. McDaniels: Nucl. Phys. **17** (1960) 641.
26) S. Hitaka, T. Maki, T. Mikumo, M. Mukae, T. Nakashima, I. Nonaka and H. Yamaguchi: to be published.
27) See for example, S. Kobayashi, K. Matsuda, Y. Nagahara, Y. Oda and N. Yamamuro: J. Phys. Soc. Japan **15** (1960) 1151. S. Kobayashi: J. Phys. Soc. Japan **15** (1960) 1164. Y. Nagahara: J. Phys. Soc. Japan **16** (1961) 133. K. Matsuda et al: to be published.
28) Y. Ishizaki et al.: to be published.
29) D. A. Bromley, J. A. Kuehner and E. Almqvist: Phys. Rev. Letters **4** (1960) 365.
30) E. Almqvist, D. A. Bromley and J. A. Kuehner: Phys. Rev. Letters **4** (1960) 515.

JOURNAL OF THE PHYSICAL SOCIETY OF JAPAN Vol. 16, No. 6, JUNE, 1961

He^3-Alpha Scattering

Ren CHIBA*, Homer E. CONZETT**, Haruhiko MORINAGA***,
Naoshi MUTSURO, Katsufusa SHODA and Motoharu KIMURA
Department of Physics, Tohoku University, Sendai, Japan

(Received February 9, 1961)

Differential cross sections for scattering of He^4 by He^3 have been measured at E_α=27.7, 28.5, 29.4, 30.0, 32.0, 33.4, 34.7, 36.5, 38.4, 41.0 MeV using a scintillation counter spectrometer, at the center of mass angles from ~30° to ~150°. Three distinct minima were found at about 45°, 100°, and 140°. The absolute cross-section and the pattern of the angular distribution showed no appreciable change in the energy range investigated: thus, there was found no sharp resonance in the He^3+He^4 system corresponding to an excited state of Be^7 between 13.4 and 19.2 MeV.

Differential cross-sections of the protons from $He^3(\alpha, p)Li^6\ Li^{6*}$ were observed. Differential cross-sections of alpha-alpha scattering were also measured at E_α=33.5 and 35.5 MeV.

§1. Introduction

Elastic scattering of He^4 by He^3 has not been extensively studied, but is an interesting problem. The scattering mechanism should be quite similar to that of alpha-alpha scattering of which a considerable amount of work has been accumulated making a very fine analysis possible[1]. There are, however, many fundamental differences between those two cases since for alpha-alpha scattering both incident and target particles are identical and have spin zero but in the latter case they are different and have different spins. Moreover, in the energy range of our experiment, reaction other than the elastic scattering can take place. These possibilities will make a phase-shift analysis similar to the case of alpha-alpha scattering difficult but still many interesting features should reveal themselves in the scattering cross-sections.

One of the most interesting things and the major motive of the present experiment is the investigation of the excited states of Be^7. The lower states of Be^7 or Li^7 are known from various experiments[2], and the four low lying odd-parity states have been successfully explained by the intermediate coupling shell model[3),4)]. However, a striking thing is that these states are also explained quantitatively applying the wave functions given by Nilsson[5]. Namely, the moment of inertia and the decoupling factor derived from the experimental energy of the ground, 1st, and the 3rd excited states, assuming that these are the rotational band of $K=\frac{1}{2}^-$ intrinsic states are, in good agreement with the values expected from Nilsson's theory and the 2nd excited state of $7/2^-$ comes very close to the calculated energy. Such a fit may be theoretically expected under certain condition as proved by Elliott[6]. It is extremely interesting to see if this is of the nature discussed by the latter author or if Nilsson's simple theory actually applies.

If Nilsson's theory is applicable, one can expect $9/2^-$ and $11/2^-$ states at around 13 to 15 MeV excitation as a continuation of the low-lying rotational states. The Elliott's theory does not assure this, since such a rotational character is of a pseudo nature.

One support for the rotational nature of these lower states may be attributed to the experimental results of the 3 to 5 MeV He^3-alpha scattering involving the $7/2^-$ state of Be^7[7]. The scattering cross-section is very close to that of Wigner's sum rule limit indicating that this state is made of He^4 and He^3. This may also imply that this state is of the "rotating cigar" type.

The situation is quite similar to that of Be^8. Here, the ground state is probably of the dumbbell type and this is expected from Nilsson's theory, too. Experimentally, the 0–2–4 series seems[1] to represent the rotational spectrum of such a dumbbell. However, such a 0–2–4 series can also be obtained from the intermediate coupling shell model. A dumbbell model predicts a 6^+ state in the energy range investigated, but so far no indication of such a state has been seen[8],[9]. The intermediate coupling shell model will not uniquely predict such a state.

---

* Present Address: Research Division, Nippon Atomic Industry Group Co., Ltd, Hibiya Mitsui Bldg., 12, Yurakucho 1-chome, Chiyoda-ku, Tokyo.

** Fulbright Exchange Schlar at University of Tokyo. Present Address: Lawrence Radiation Laboratory, University of California, Berkely, California Berkely, California, U.S.A.

*** Present Address: Department of Physics, University of Tokyo, Motofuji-cho, Bunkyo-ku, Tokyo.

From the cyclotron at the Institute for Nuclear Study of the University of Tokyo, alpha-particles with energies from 28 to 42 MeV are obtained. These alphas incident on He^3 correspond to Be^7 excitations of 13.4 and 19.2 MeV, which are about the region where a $9/2^-$ or $11/2^-$ state with a width close to the Wigner limit should be observed if Nilsson's simple theory applies. Such states would show up as resonances with $l=5$. However our experimental results seems to have disproved the existance of such a simple Nilsson state in Be^7. This is agreement with the present theoretical interpretation of the rotational spectra in light nuclei[4].

In our energy range a reaction,

$$He^4+He^3 \longrightarrow Li^{6(*)}+p$$

can take place[10]. This reaction is well worth studying since many states involved are of a well-known nature. Therefore, it could be used to test various simple theories about these states and the reaction mechanism involved.

§ 2. Experimental Arrangement

The alpha-particle beam, furnished by the variable energy cyclotron was successively passed through a deflectihg magnet, Q magnets and led into a scattering chamber.

The beam entered through a collimeter of 5 mm diameter and passed through a gas target chamber and was collected in a Faraday cup. A detailed description of the apparatus may be found elsewhere[11].

The target chamber, 8.5 cm in diameter, was mounted at the center of the scattering chamber and was filled with 98% He^3 to a pressure of 10–15 cm Hg. Both incoming and outgoing windows of the target chamber were sealed by 25-micron aluminum foils. A small mercury manometer mounted on the target chamber made it possible to monitor the He^3 gas pressure during the experiment.

In order to get the pulse height distributions at various angles, a counter and a slit system were mounted on a movable disc which could be rotated about the center of the scattering chamber in vacuum. The detecter consisted of a thin CsI(TI) crystal mounted on a multiplier phototube. A proportional counter was mounted in some cases in front of the scintillation counter to separate proton groups from double charged particles by determing the dE/dX of the particles.

A multiple slit system of 1 mm aperture was used for the scintilllation counter and a system of 2 mm was employed for the proportional and scintillation counter assembly. The angular resolution of these slits was about 2 degrees and 4 degrees respectively in the center of mass coordinate.

Another scintillation counter and slit system, mounted at a fixed position (20 or 30 degrees) on the wall of the scattering chamber was used as a monitor.

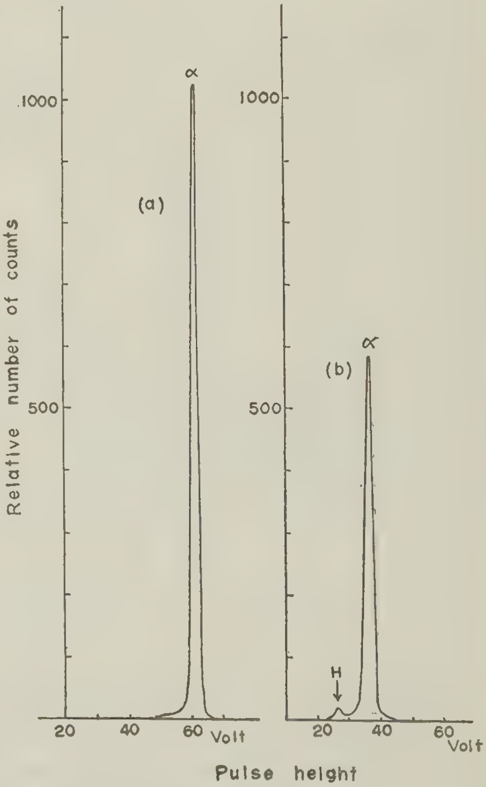

Fig. 1. Scintillation counter spectrum of alpha-alpha scattering in multichannel pulsle height analyzer. $E_\alpha=32.5$ MeV
(a): at 21°, (b): at 41° lab. angle. H indicate recoil proton from hydrogen impurity.

§ 3. Alpha-Alpha Scattering

In order to check the apparatus and experimental arrangement, the scattering of Alpha-particles by helium was investigated at two different energies; 32.5 MeV and 35.5 MeV.

The apparatus used was the same as that for the He^3-alpha scattering, except that the gas filling system and manometer were mounted outside the scattering chamber. The spectrum of the scintillation counter showed a clear alpha-particle peak with an energy resolution of about 4%. A small peak of protons due to hydrogen impurity was observed at some angles. (Fig. 1)

The differential cross-sections as a function of scattering angle are shown in Fig. 2. The angular resolution due to the finite size of the slit system was about 4 degrees in the center of mass system. The angular distribution of alpha-alpha scattering changes appreciably with energy in this energy range. The present result is in good agreement with that of Birmingham group$^{8)}$.

§ 4. He^3-Alpha-Scattering

Experimental procedure

In the present He^3-alpha scattering experiment the bombarding energies of the alpha-particles were 27.5±0.5, 28.5±0.5, 29.4±0.4, 30.0±0.5, 32.0±0.5, 33.4±0.5, 34.7±0.5, 36.5±0.5, 38.4±0.5, 41.0±1.0 MeV at the scattering portion of the gas target.

Since the incident particle is heavier than the target particle, the transformation from tne center of mass to the laboratory system reveals a somewhat unusual behavior in the scattered particle. The scattered particle loses its energy more rapidly than He^3 as the scattering angle increases and appears only up to a critical angle, 48°35′. Actually, from 0° to this critical angle, the energy of alpha-particle is double valued. (Fig. 3) The lower energy corresponds to back scattering in the center of mass system. This low energy particle usually did not pass through the aluminum foil of the scattering chamber or did not give a large enough pulse to be distin-

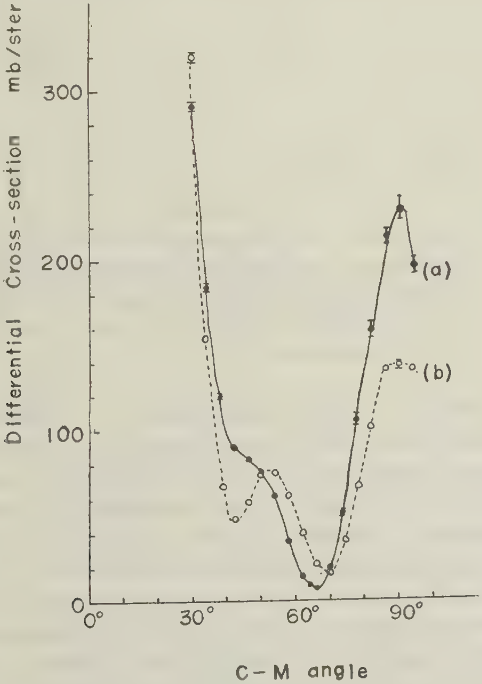

Fig. 2. Differential cross-section of alpha-alpha elastic scattering.
(a) $E_\alpha=35.5\pm0.5$ MeV
(b) $E_\alpha=32.5\pm0.5$ MeV

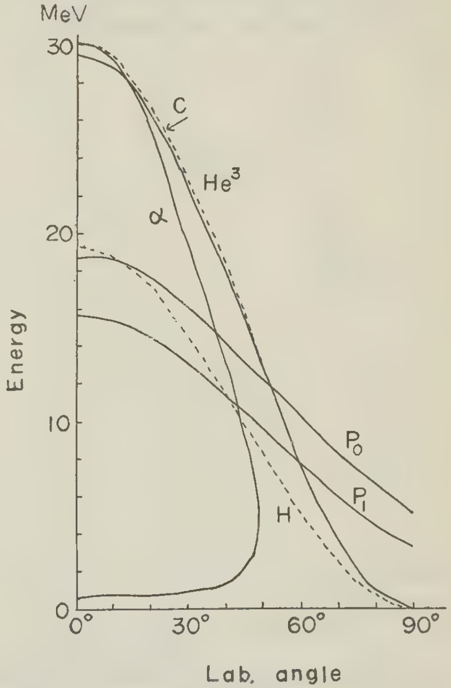

Fig. 3. Kinematics of He^3-alpha scattering at $E_\alpha=30$ MeV.

α : alpha-particles scattered by He^3
He^3 : recoil He^3-particles
H : recoil protons
C : alpha-particles if He^4 exist as a impurity in He^3 target gas.
P$_0$: protons from the reaction He$^3(\alpha, p)$Li^6 gnd.
P$_1$: protons from the reaction He$^3(\alpha, p)$Li^6 1st excited

guished from the gamma and neutron background from the cyclotron in the scintillation-counter spectrum. In the pulse height spectrum, several peaks were observed as shown in Fig. 4. The identification of these peaks was rather complicated since the scintillation-counter does not distinguish alpha, He^3 and proton (at small angles, Li^6 is also expected).

In order to identify these peaks, the pulse heights of these peaks were plotted at every 2 degrees (Fig. 5) The energy-pulse height curves of alpha-particles, He^3 and protons were obtained at those angles where the spectra were comparatively simple, and identification of the peaks was made by comparing the diagram (Fig. 5) with the calculated energy curve.

The pulse height of He^3 is higher than that of alpha-particle of the same energy. At small angles, the He^3 energy is lower than that of the alpha, but the pulse height was higher over the measured angular range. Also, alpha-particles doubly scattered from the entrance and exit foils of the target chamber, and alpha-particles scattered by impurity gases (O_2, N_2) have higher energies, and these are intense at small angles. The intensity of doubly-scattered alpha-particles is proportional to $1/(\sin\theta/4)^3$ if coulomb scattering is assumed.

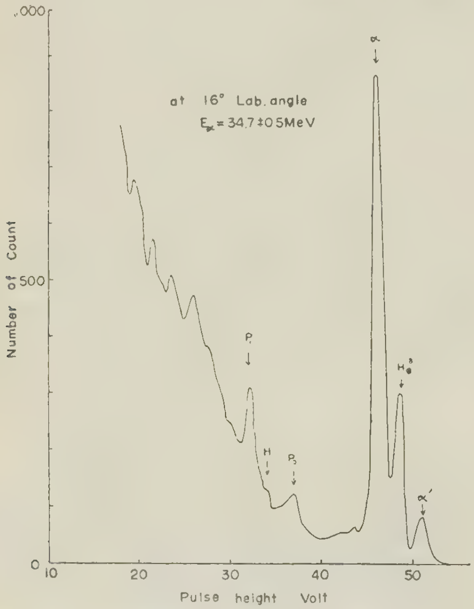

Fig. 4. Pulse height spectrum observed at a lab. angle of 16° in the He^3-alpha scattering in the CsI scintillation counter.

α' : alpha-particles scattered by impurity heavy gas (O_2, N_2) and that of doubly scattered by aluminum windows.
He^3: recoil He^3-particles
α : alpha-particles scattered by He^3
P_0 : protons from $He^3(\alpha, p)Li^6$ gnd.
P_1 : protons from $He^3(\alpha, p)Li^{6*}$ 1st excited state
H : recoil protons from hydrogen impurity

Since the energies of these three groups of alpha's and He^3 are close together at small angles, there is some ambiguity in the cross-section due to imperfect separtion of these groups in the spectra.

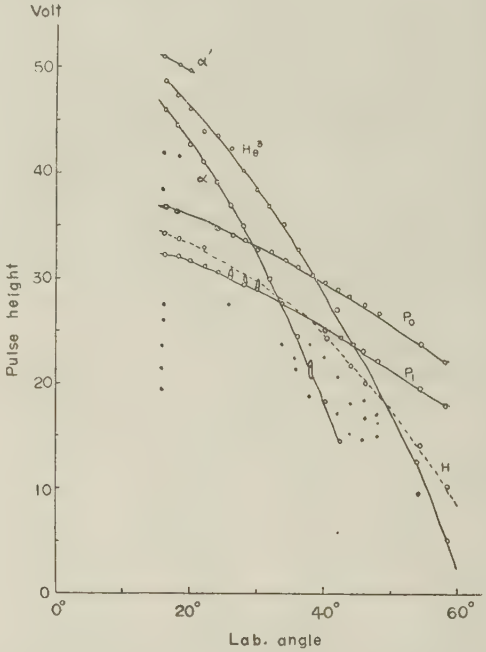

Fig. 5. Pulse height of peaks of various charged particles with scintillation counter spectra were plotted as a function of lab. angle. (E_α=34.4 MeV). Same notations as Fig. 4 were used for identified particles.

Besides alpha-particles and He^3, protons from $He^3(\alpha, p)Li^6$ (to the ground and 1st excited states) and from the impurity hydrogen recoil were observed and separated at larger angles. However, quite frequently these peaks were not completely resolved. For example, around 30 degrees, a proton peak overlapped the alpha's. In order to separate these particles, a proportional counter was used in coincidence with the scintillation counter in the measurements at 33.4 MeV and 41 MeV. The different energy losses of protons and alphas in the proportional counter made it possible to separate these particles with the same pulse height in the scintillation counter spectrum. Because of the poorer resolution of the proportional counter, however, both groups were not very well separated (Fig. 7). Thus the errors between 70–100 degrees (center of mass system) due to overlap of protons and alphas were reduced but not completely eliminated. Near 40 degrees (laboratory angle), the intensities of alpha-particles and He^3 were very low, and overlapping protons were not negligible. Also the rapid decrease of the alpha and He^3 energy with increasing angle made it more difficult to separate the peaks from background as the angle increased. The background subtraction and the finite resolution of the measuring instrument always led to some ambiguity in determing the number of counts in the spectrum. The determination was made from symmetry considerations of the peaks. The errors include both the uncertainty due to separation of the peaks and statistics.

The discriminater level of monitor counter was set at a minimum of the spectrum, to count known groups of particles; the statistical uncertainty was 2–3%. However, in the measurements at 27.5 MeV, 29.4 MeV and 32.0 MeV, the fluctuation of the monitor counts was larger than the statistics. This was caused by a leak of the beam current integrator. It was difficult to correct for the effect of this leak, since it depended strongly on the fluctuation of the beam intensity. In these cases, a plot of the monitor counts v.s. run time was extrapolated to zero run time and the value at zero was accepted as a normalization factor corresponding to a correct integrated charge.

The uncertainty in the absolute scale of the whole angular distribution for each energy was estimated to be 5%. This arises from the uncertainties in the measurement of solid angle, normalization by monitor counts or integrated beam current, alignment of beam

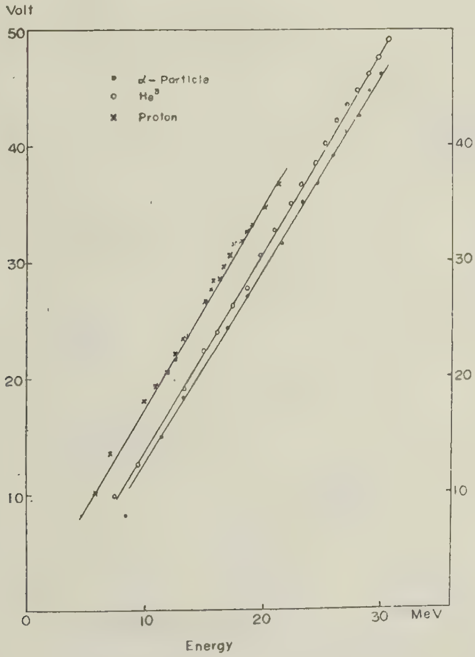

Fig. 6. Experimentally measured pulse-height response of He^3, alpha-particle, and proton in the CsI scintillation counter as a function of energy.

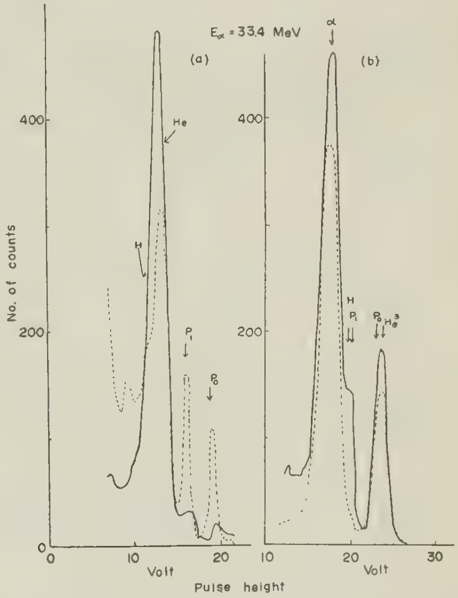

Fig. 7. Pulse height spectrum in scintillation counter. Charge 1 particles and charge 2 particles were separated by coincidence with proportional counter,

(a) $\theta_{Lab}=46°$, beam integrator: 20 micro coulomb
  solid line: charge 2 particles (coincidence)
  broken line: charge 1 particle (anticoincidence)

(b) $\theta_{Lab}=34°$, beam integrator: 5 micro coulomb
  solid lind: total spectrum (without coincidence)
  broken line: charge 2 particles (coincidence)

and slit system, and measurement of target gas pressure.

To obtain the full angular distribution curves, the cross-sections for the forward angle in the center of mass system was obtained from the forward scattered alpha-particles and that for the backward was deduced from the forward scattered He^3.

§ 5. Results and Discussion

The differential cross-sections of elastic scattering of He^3-alpha are shown in Figs. 8 and 9. No significant change in the angular distribution was observed between E=32 MeV

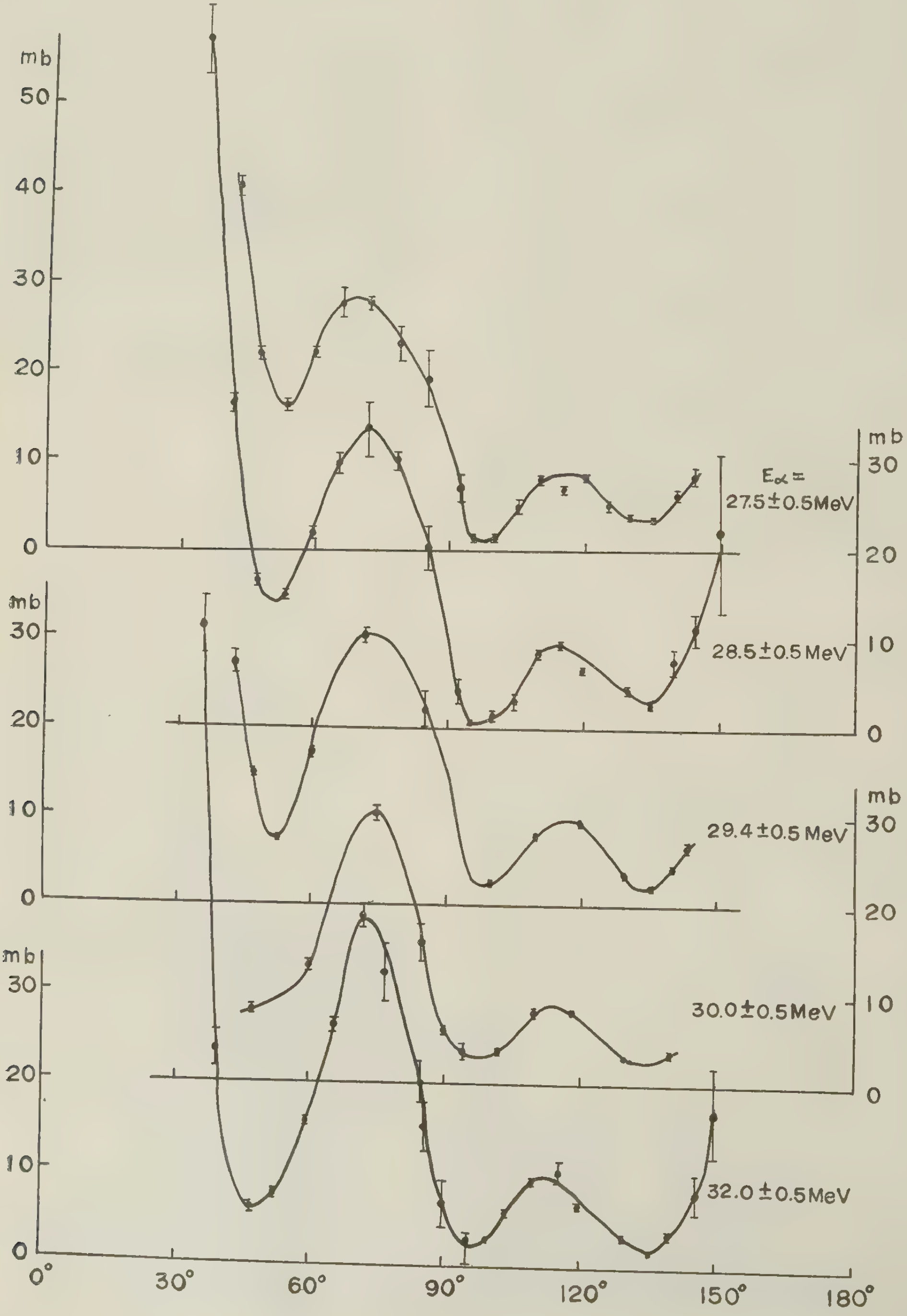

Fig. 8.

and 41 MeV, within the experimental accuracy. The results are consistent with the angular distribution measured by the Birmingham group at 16.6 MeV (center of mass energy[10]).

The whole range of the angular distribution may be fitted approximately by a broad 1=3 resonance. The phase shift analysis of experimental results is difficult since at these energy high 1 values contribute to the scat-

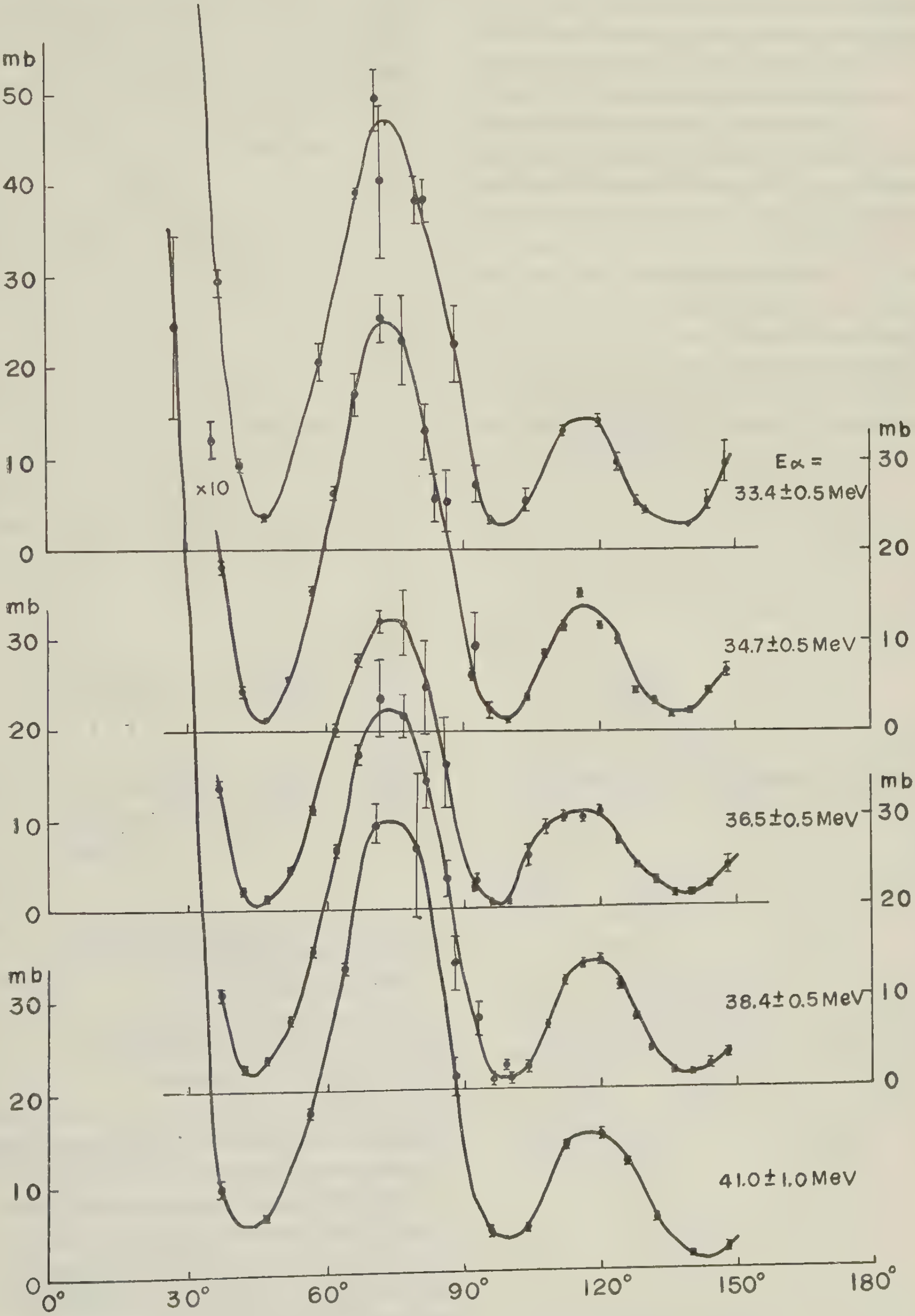

Fig. 9.

Fig. 8 and 9. Angular distributions of He^3-alpha elastic scattering in the center of mass co-ordinate. Energy of alpha-particles indicated are of lab. system. Ordinate are differential cross-section in mb/sterad.

tering. Moreover, it was not possible to estimate the total inelastic cross-section from present experiment which determines the imaginary part of the phase shift. However, it seems to us that the elastic scattering is governed by some mechanism which is slowly energy dependent in these energy range.

The 1=5 resonance which would have been observed was not detected in present experiment. In our experimental region, it is rather difficult to suppose that we have skipped such resonance. It may be that such resonances lie in the energy region different from that was scanned in our experiment because of some other perturbation effect, or may be that they do not exist. It seems to be very interesting to see the result of experiment in broader energy region.

The proton groups from $He^3(\alpha, p)Li^6$ reaction and the large number of unresolved particles below alpha-particles in the spectrum suggest that the reaction cross-sction is not negligible compared with the elastic scattering cross-section (Fig. 4).

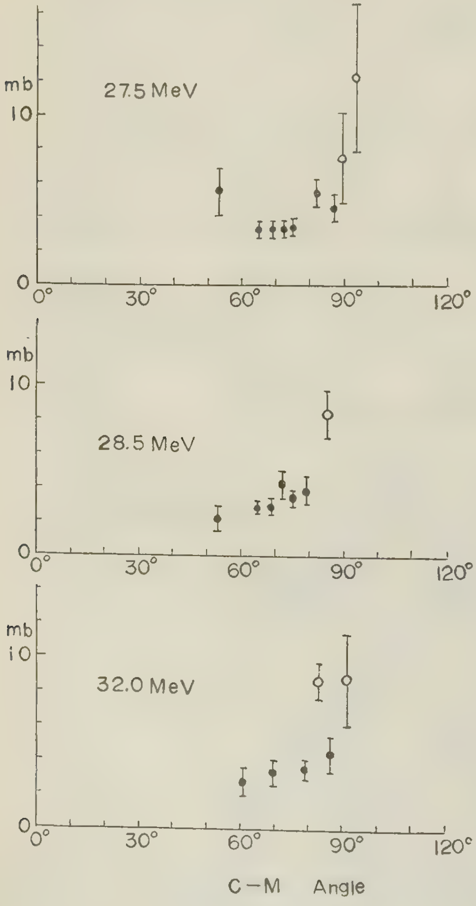

(a)

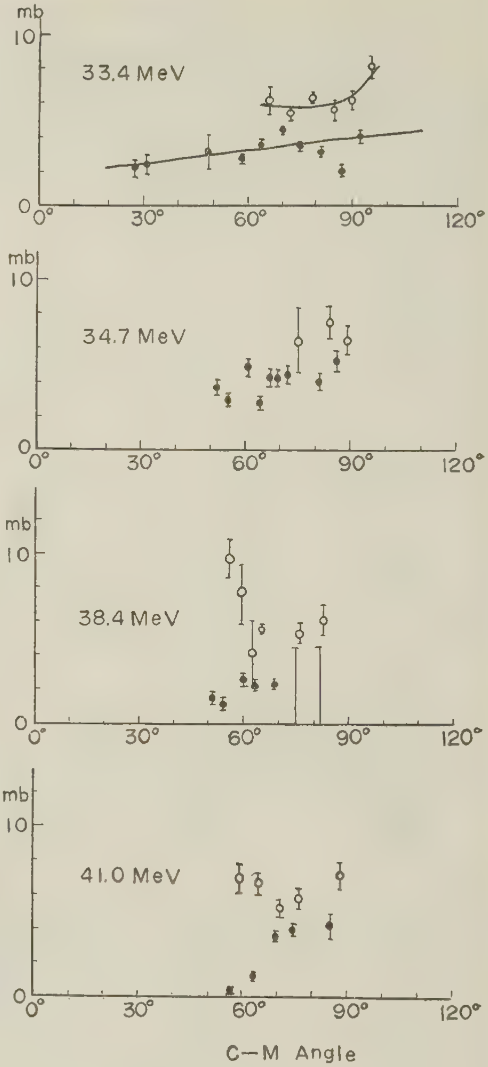

(b)

Fig. 10 a and b. Differential cross-sections of protons from $He^3(\alpha, p)Li^6$ and $Li^{6(*)}$.

●: gnd. state of Li^6

○: 2.18 MeV state of Li^6

Ordinate are in mb/sterad.

The differential cross-sections of the protons from above reaction leading to Li^6 gnd. state ($J=1$, $T=0$) and first excited state ($J=3$, $T=0$, 2.18 MeV) which were resolved at large angles (Fig. 11) were transformed to center of mass system and shown in Fig. 10 a and b. The angular distributions of these two groups of protons were measured by Birmingham group and the cross-sections at about 90° are in agreement with our results$^{10)}$. The intensity of protons to the 2nd excited state ($J=0$, $T=1$, 3.56 MeV) was less than 1/5 of to the gnd. state, or may be less than 1/10 at about 90° of center of mass system if the smooth background was subtracted. It is interesting, however, to point out that not any angular momentum, Parity, nor isotopic spin selection rules imposed on the $He^3+He^4 \longrightarrow Li^{6*}+p$ reaction can suppress the formation of the $Li^{6*}(0^+, T=1)$ state.

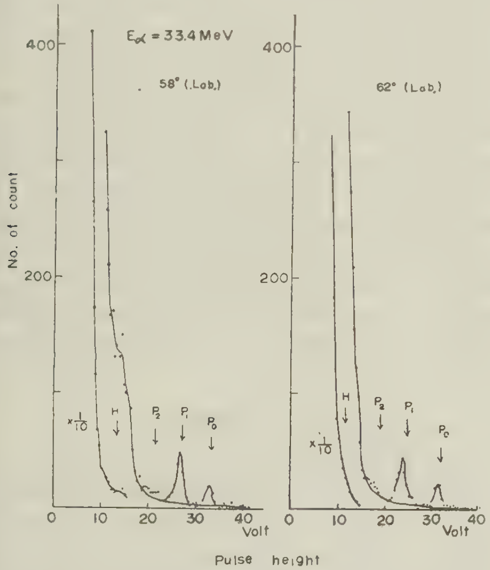

Fig. 11. Pulse height spectrum at large angles. P_0, P_1 and P_2 indicate expected positions of ground, 1st and 2nd excited state protons respectively.

Acknowledgement

This experiment was performed as one of the co-operating project of Institute for Nuclear Study of University of Tokyo. We are grateful to the staff members of the Institute who made it possible for us to use the facilities in this work.

We wish to express our appreciation to the crew of the cyclotron for their assistance during the cyclotron runs.

One of the author (H.E.C.) is grateful to Fulbright grant which made his stay at Institute for Nuclear Study of University of Tokyo possible.

One of the author (H.M.) is grateful to Prof. A Bohr. for the discussions concerning the possibility of applying unified model to Be^7-Li^7 pair and want to take this chance for expressing his sincere gratitude.

Colaborations of graduate students of Tohoku University during the experiments are highly appreciated.

References

1) R. Nilson, R. O. Kerman, G. R. Briggs and W. K. Jentschke: Phys. Rev. **104** (1956) 1673. R. Nilson, W. K. Jetschke, G. R. Briggs, R. O. Kerman and J. N. Snyder: Phys. Rev. **109** (1958) 850.
2) F. Ajzenberg-Selove and T. Lauristen: Nuclear Physics **11** (1959) 1.
3) D. Kurath, Phys. Rev. **101** (1956) 216.
4) D. R. Inglis: Rev. Mod. Phys. **25** (1953). 390.
5) Sven Gösta Nilsson, Dann. Mat: Phys. Medd. **29** No. 16 (1955).
6) J. P. Elliott: Proc. Roy. Soc. **A245** (1958) 128.
7) P. D. Miller and G. C. Phillips: Phys. Rev. **112** (1958) 2048.
8) W. E. Burcham, W. M. Gibson, D. J. Prowse, and J. Rotblat: Nuclear Physics **3** (1957) 217. D. J. Bredin, W. E. Burcham, E. Evans, W. M. Gibson, J. S. C. McKee, D. J. Prowse, J. Rotblat and J. N. Snyder: Proc. Roy, Soc. **A251** (1959) 143.
9) Homer E. Conzett, George Igo, Harlan C. Shaw, and Rodolfo J. Slobodrian, Phys. Rev. **117** (1960) 1075.
10) D. J. Bredian: private communication: D. J. Bredin, J. B. A. England, D. Evans, J. S. C. McKee, P. D. March, E. M. Mosinger and W. T. Toner: preprint on the scattering on He^3-particles by ^{1}H, ^{2}H, ^{3}He and ^{4}He nuclei.
11) Seishi Kikuchi et al: J. Phys. Soc. Japan **15** (1960) 41. J. Sanada: J. Phys. Soc. Japan **14** (1959) 1463.

JOURNAL OF THE PHYSICAL SOCIETY OF JAPAN, Vol. 16, No. 6, JUNE, 1961

Angular Correlation of the Mo^{95} Gamma-Gamma Cascades

By Atsushi AOKI

Department of Physics, Kyoto Prefectural University, Kyoto

(Received February 10, 1961)

The directional correlation and the polarization-direction correlation of the 838 Kev–204 Kev and 584 Kev–204 Kev gamma-gamma cascades in Mo^{95} have been measured. It is found that the spin of 788 Kev level is 1/2, and that of the 1042 Kev level is either 1/2 or 3/2. The branching ratio of the positron decay is also obtained as 0.4%.

§ 1. Introduction

The 60 days isomer of Tc^{95} decays to Mo^{95} by orbital electron capture competing with weak positron emission. The spin of the ground state of Mo^{95} is established to be 5/2 from the investigation of the paramagnetic resonance by Owen and Ward[1]. In addition, from the angular distribution and the polarization-direction correlation of the 204 Kev gamma ray in Coulomb excitation experiments, McGowan and Stelson have shown that the spin of the first excited state must be 3/2, and the multipolarity of the 204 Kev transition is a mixture of $E2$ and $M1$ with the mixing parameter $\delta=-0.6\pm0.2$[2]. Furthermore, many spectroscopic investigations of the decay of Tc^{95} have been made in the last decade[3–7]. Recently, Unik and Rasmussen reported on the decay of Tc^{95m}[8]. Their work was based principally on the results of high-resolution conversionelectron spectroscopic studies, supplemented by gamma ray scintillation spectroscopy and coincidence experiment. The decay scheme proposed by them are shown in Fig 1. As will be seen in this figure, the spins of the 1042 Kev and the 788 Kev levels are both assigned to be either 1/2 or 3/2. They concluded that the 584 Kev transition is more likely to be $M1$ and the 838 Kev transition $M1$ or $E2$. However, since the conversion coefficients for $E2$ and $M1$ are very similar at this particular atomic number for the energies of 838 Kev and 584 Kev[9], the multipolarity assignment for these gamma rays from the conversion coefficients is very difficult. Therefore it seems worthwhile to remove these ambiguities by measuring the angular correlation of the relevant gamma rays.

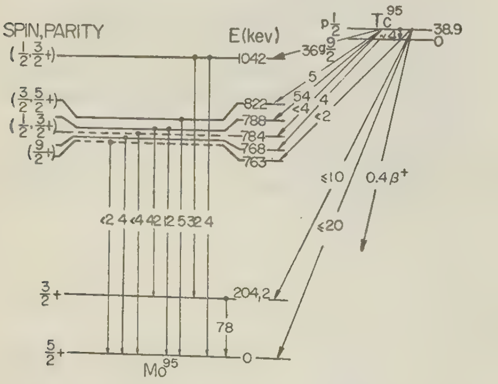

Fig. 1. Decay scheme of Tc^{95m}. Transition intensities are given as percent of total decay. (from Unik and Rasmussen[8]).

§ 2. Experimental Procedure

2.1 *Source preparation*

The Tc^{95m} source was prepared by bombarding the separated Mo^{95} (abundance in enriched element: 94%) as well as the molybdenum metal with 1200 microampere hours of 10 Mev proton particles in the 160 cm cyclotron at the Institute for Nuclear Study of the University of Tokyo, leading to the reaction $Mo^{95}(p, n)Tc^{95,95m}$. The enriched isotope, supplied from Oak Ridge National Laboratory in the chemical form of very volatile MoO_3, was reduced by hydrogen to metallic powder by heating in an electric furnace. The gamma ray from enriched source was measured one month after the bombardment by use of a scintillation spectrometer consisting of a cylindrical NaI (Tl) crystal, 5 in. in diameter and 4 in. high, coupled with a EMI type 6099B photomultiplier tube and a Sunvic 100-channel pulse height analyzer, and the spectrum is presented in Fig. 2. It can be regarded as the gamma ray spectrum following the decay of Tc^{95m} because of the far shorter half-life (20 hr[10]) of Tc^{95}.

Measurements using the sources prepared by natural molybdenum target were started several months after the bombardment to allow the short-lived activities to decay sufficiently. The gamma ray spectra of these sources were in good agreement with the result shown in Fig. 2, except for the contribution from the long-lived (90 days) isomer of Tc^{97}, which has no gamma-gamma cascade[11], and has no significant influence upon the present angular correlation experiments.

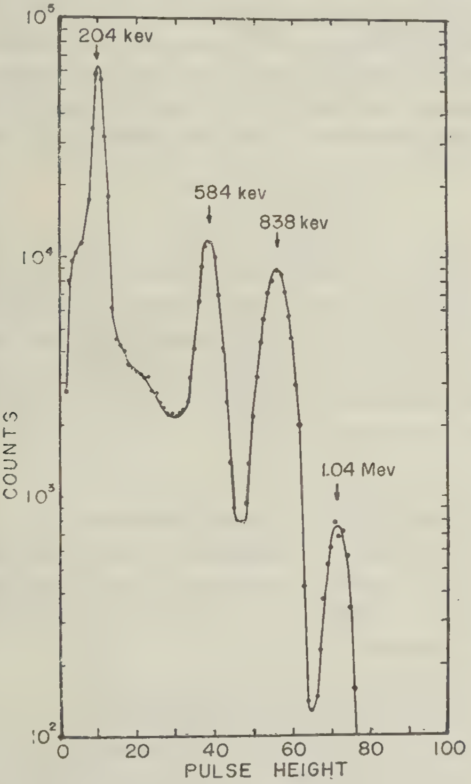

Fig. 2. Gamma ray spectrum of Tc^{95m}.

Thus the sources produced from natural molybdenum were used in the present experiment because of their strong intensity. The part with high activity of the bombarded target of natural molybdenum was peeled off and crushed up to fine powder. Then, the powder, packed in a cylindrical glass container with the inner diameter of 2 mm and depth of 4 mm, was used as the source for the directional correlation experiments. The remaining part of the target was chemically processed[12], and the activities of technetium were then electrodeposited on a thin copper foil[13], which was used for the measurement of the polarization-direction correlation.

2.2 *Directional Correlation Experiments*

The coincidence spectrometer used was the same as reported previously by Hayashi[14], whose detectors consisted of NaI (Tl) crystals of $1\frac{1}{2}$ in. in diameter by 1 in. thick, coupled to RCA-5819 photomultiplier tubes. The measurements of directional correlation were carried out for the 838 Kev–204 Kev gamma-gamma cascade as well as the 584 Kev–204 Kev one. The distance between the source and the front face of each crystal was 7 cm in both cases. If the gamma rays having the energies of 800 Kev or so are scattered backwards by Compton effect in the crystal which is to detect the radiations with energy of 838 Kev or 584 Kev, they give the energy of about 600 Kev to the crystal[15] and some portions of them are counted in the present experimental arrangement. Furthermore, since the back-scattered gamma rays degrade their energy to about 200 Kev, they may be counted in the detector for the 204 Kev radiation. Thus, in order to avoid these undesirable coincidences the front face of the crystal detecting the 838 Kev or 584 Kev gamma rays was covered with a lead disk of 5 mm thick. Besides, the lateral surface of each crystal was surrounded with cylindrical lead shields of 2.5 mm in thickness. The windows of the pulse height analyzers were set so as to pick up the full energy peaks of relevant gamma rays. The results of the directional correlation experiments measured with the metallic source are shown in Figs. 3 and 4. The solid curves drawn in these figures represent the least-squares fit of the experimental data[16], in which the terms up to $P_2(\cos\theta)$ are taken into consideration, owing to the spin value of 3/2 for the 204 Kev level[2]. A deviation of the experimental points at 165° and 180° from the curve appearing in the case of 584 Kev–

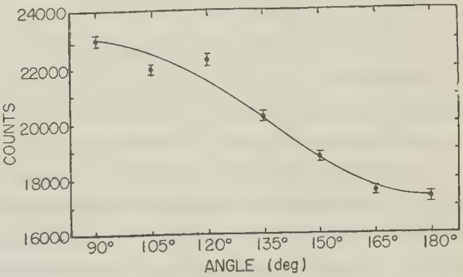

Fig. 3. Directional correlation of the 838 Kev–204 Kev cascade in Mo^{95}. The solid curve represents the least-squares fit of the experimental data.

204 Kev cascade (Fig. 4) can be attributed to the effect of the annihilation gamma rays created at the source position, and these points are omitted in drawing the curve. From these most fitted curves, the measured correlation functions for each case are

$$W'(\theta)=1-(0.178\pm0.005)P_2(\cos\theta)\ ,$$

for the 838 Kev–204 Kev cascade, (1)

and

$$W'(\theta)=1-(0.223\pm0.006)P_2(\cos\theta)\ ,$$

for the 584 Kev–204 Kev cascade. (2)

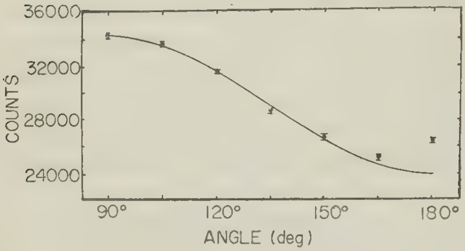

Fig. 4. Directional correlation of the 584 Kev–204 Kev cascade in Mo^{95}. The solid curve represents the least-squares fit of the experimental data obtained by omitting the experimental points at 165° and 180°.

In the case of the 584 Kev–204 Kev cascade, the contribution of the 838 Kev-204 Kev cascade was estimated to be 58% in the present experimental condition. Subtracting this contribution, Eq. (2) becomes

$$W''(\theta)=1-(0.285\pm0.016)P_2(\cos\theta)\ . \quad (3)$$

Then, corrected for finite angular resolution of the detectors[16], Eqs. (1) and (3) give the following equations as the experimentally determined correlation functions.

$$W(\theta)=1-(0.195\pm0.006)P_2(\cos\theta)\ ,$$

for the 838 Kev–204 Kev cascade. (4)

$$W(\theta)=1-(0.321\pm0.017)P_2(\cos\theta)\ ,$$

for the 584 Kev–204 Kev cascade. (5)

2.3 *Polarization-direction correlation*

As will be described in the next section, two possible mixing ratios are obtained for both of the 838 Kev and the 584 Kev gamma rays from the data of the directional correlation experiments. In order to accept alternative, the measurement of the polarization-direction correlation of the gamma-gamma cascades under consideration was carried out. The polarimeter employed was the same as used in the previous experiments[17], and the details of the apparatus were described in the previous paper[18]. The asymmetry ratio R was estimated to be 2.8 and 2.3 for the 548 Kev and the 838 Kev gamma rays, respectively. The mean scattering angle of the polarimeter was adjusted to 80 degree so as to obtain the maximum asymmetry ratio concerning the relevant gamma rays. Since it is difficult to discriminate the 838 Kev and the 584 Kev gamma rays from each other in the polarimeter, there is no other alternative besides measuring the composed polarization-direction correlation for these cascades.

The asymmetry thus obtained in the case of $\theta=90°$ is

$$\frac{N_{\parallel}(\theta)}{N_{\perp}(\theta)}=1.03\pm0.03\ , \quad (6)$$

where $N_{\parallel}(\theta)$ and $N_{\perp}(\theta)$ represent the counting ratios for the cases in which the plane of scattering of the incident gamma ray into the phosphor is parallel, and perpendicular to the plane containing both of the cascade gamma rays, respectively.

§ 3. Analysis and Discussion

In order to analyze the results of the directional correlation experiment, the coefficient of the Legendre polynomial $P_2(\cos\theta)$ in the correlation function, A_2, is calculated for the spin sequence of

$$j_1(Q, D;\ \delta_1)3/2(Q, D;\ \delta_2=-0.6)5/2\ ,$$

where the spin of the initial state, j_1, is 1/2 and 3/2. The results are shown in Fig. 5 as a function of the quadrupole content, which is defined as $\delta_1^2/(1+\delta_1^2)$ by Arns and Wiedenweck[19]. It is readily concluded from Fig. 5 that the spin of 788 Kev level must be

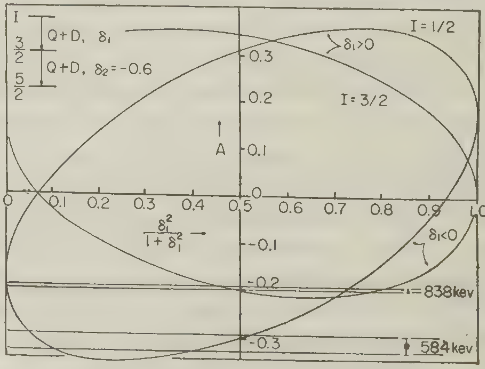

Fig. 5. Analysis of the dipole-quadrupole mixing of 838 Kev and 584 Kev transitions according to Arns and Wiedenweck[19].

1/2, while two possibilities for the spin of the 1042 Kev level are left undecided. The quadrupole contents determined from Fig. 5 for the 838 Kev and the 584 Kev transitions are presented in Table I.

Table I. The quadrupole contents determined from directional correlation experiments. ($\delta_1<0$, $\delta_2<0$)

Level (Kev)	Spin	Gamma ray (Kev)	Quadrupole content (%)
788	1/2	584	8±3 or 48±5
1042	1/2	838	0 or 73±1
1042	3/2	838	44±2 or 78±2

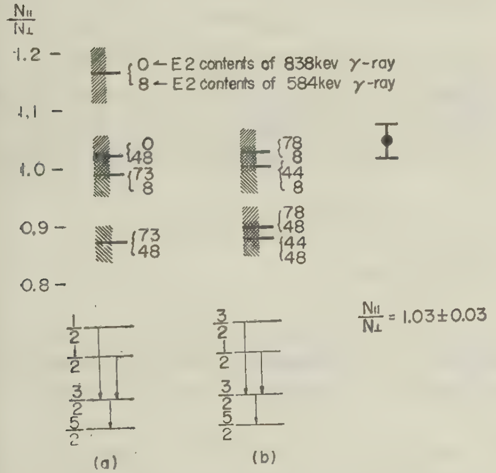

Fig. 6. Expected asymmetry in the polarization-direction correlation experiment for possible combinations of spins and $E2$-$M1$ admixture of the 838 Kev and 584 Kev gamma rays. The shades attached to each line correspond roughly to the error caused by the uncertainty of the experimentally determined A_2.

Under the present experimental condition, the asymmetry expected in the polarization-direction correlation measurements is estimated for these combinations of spins and quadrupole-dipole mixings by using Eq. (2A) in the Appendix, and is shown in Fig. 6 schematically, where (a) and (b) represent the case of $j_1=1/2$ and 3/2, respectively. The shades attached to each line in the figure correspond roughly to the error caused by the uncertainty of the experimentally determined A_2.

Table II below summarizes the results consistent with the angular correlation experiments. The experimental ratios of the K-conversion coefficients for the 584 Kev transition to that of the 838 Kev one, estimated by Unik and Rasmussen[8] and Takazawa *et al.*[20], suggest the small electric quadrupole content for the 548 Kev gamma ray more plausibly. In the above analysis, the quadrupole-dipole mixing parameter of the 204 Kev gamma ray is regarded as −0.6. In paractice, however, since this value includes the error of ±0.2, the quadrupole contents listed in Table II vary about 10% correspondingly.

Table II. The $E2$ contents which are consistent with the angular correlation experiments.

Spin of 788 Kev level	Spin of 1042 Kev level	$E2$ content (%)	
		838 Kev	584 Kev
1/2	1/2	0($M1$ pure)	48±5
1/2	1/2	73±1	8±3
1/2	3/2	78±2	8±3
1/2	3/2	44±2	8±3

In addition to the experiments mentioned above, similar directional correlation experiments with liquid source (TcO_4^- in water) were also put into practice. The measured directional correlation coefficients are 0.166±0.004 and 0.212±0.005 for the case of the 838 Kev–204 Kev and the 584 Kev–204 Kev gamma-gamma cascades, respectively. These coefficients are more attenuated than in the case of the metallic source. The fact suggests the existence of the influence caused by the extranuclear field in the intermediate state. Since the metallic molybdenum has the crystalline structure of the body-centered cubic lattice[21], no attenuation in angular correlation coefficients is expected as far as radio-active technetium atoms sit in the regular lattice sites[22]. Accordingly, the corresponding attenuation factors for the liquid source are evaluated as 0.93±0.03 and 0.95 ±0.03, which are in good agreement whithin their experimental error. Averaging them, we obtain $\bar{G}=0.94\pm0.02$. Recently, Bodenstedt *et al.*[23] observed strong attenuation in measuring the directional correlation of gamma-gamma cascades in W^{184}, following the electron capture of Re^{184}. The half-life of 1.28×10^{-9} sec of the intermediate state in these cascade[23] is comparable with that of 0.76×10^{-9} sec in the case of Mo^{95}.[2] Since they used liquid source containing the activity as ReO_4^-, the situation is considered to be quite similar to the present work. They estimated the attenuation factors as $G_2=0.54$ and $G_4=0.673\pm0.020$. The result of the present work is consistent with these ones if we assume the time-dependent quadrupole interaction[24] as the influence of extranuclear field in both cases and attend to the large quadrupole moment of the intermediate state of W^{184}.

Finally, from the coincidence counts obtained at $\theta=180°$ in the 584 Kev–204 Kev directional correlation measurements, the branching ratio of positron emission is estimated to be 0.4% of the total disintegration. This value is consistent with the results reported in the previous works[6,8,20].

Acknowledgments

The author wishes to express his heartly gratitude to Prof. K. Kimura at Kyoto University for his sustained interest and encouragement throughout the present research. He also expresses his sincere thanks to Prof. T. Hayashi and Dr. M. Kawamura for their many helpful discussions. The helps given by Prof. M. Ishibashi and Mr. M. Koyama at Kyoto University on the chemical separation of the radio-active isotopes are deeply appreciated. His thanks are also due to the cyclotron crew at the Institute for Nuclear Study of the University of Tokyo for their kindly cooperations. This work was partly supported by a grant-in-aid for scientific research of the Ministry of Education.

Appendix

According to Biedenharn and Rose[25], the general formula of the gamma-gamma double correlation concerning the cascade of $j_1(L_1, L_1')j(L_2, L_2')j_2$ is represented as follows:

$$W(\alpha\beta\gamma)\sim\sum(-)^{L_1+L_2}c_{\nu\tau_1}(L_1L_1')c^*_{\nu\tau_2}(L_2L_2')(j_1\|L_1\|j)(j_1\|L_1'\|j)(j_2\|L_2\|j)(j_2\|L_2'\|j)$$
$$\times W(jjL_1L_1';\nu j_1)W(jjL_2L_2';\nu j_2)D(\nu,\tau_2\tau_1;\alpha\beta\gamma),$$

where the notations are the same as those used by Biedenharn and Rose. Now we consider the case that both radiations are mixture of 2^L and $2^{L'}$ pole radiation, and the polarization of the second radiation is to be observed. Then, further calculation of Eq. (1A) yields

$$\begin{aligned}W(\beta,\varphi)\sim&\sum_{\nu\geq0}P_\nu(\cos\theta)\{F_\nu(L_1j_1j)+\delta_1^2F_\nu(L_1'j_1j)+2\delta_1(-)^{j_1-j-1}[(2j+1)(2L_1+1)(2L_1'+1)]^{1/2}G_\nu(L_1L_1'j_1j)\}\\&\times\{F_\nu(L_2j_2j)+\delta_2^2F_\nu(L_2'j_2j)+2\delta_2(-)^{j_2-j-1}[(2j+1)(2L_2+1)(2L_2'+1)]^{1/2}G_\nu(L_2L_2'j_2j)\}\\&+(-)^{\sigma(L_2')}\sum_{\nu\geq2}\{F_\nu(L_1j_1j)+\delta_1^2F_\nu(L_1'j_1j)+2\delta_1(-)^{j_1-j-1}[(2j+1)(2L_1+1)(2L_1'+1)]^{1/2}G_\nu(L_1L_1'j_1j)\}\\&\times\left\{\frac{-2\nu(\nu+1)L_2(L_2+1)}{\nu(\nu+1)-2L_2(L_2+1)}F_\nu(L_2j_2j)+\delta_2^2\frac{2\nu(\nu+1)L_2'(L_2'+1)}{\nu(\nu+1)-2L_2'(L_2'+1)}F_\nu(L_2'j_2j)\right.\\&\left.+2\delta_2(L_2'-L_2)(L_2'+L_2+1)(-)^{j-j_2-1}[(2j+1)(2L_2+1)(2L_2'+1)]^{1/2}G_\nu(L_2L_2'j_2j)\right\}\\&\times\left[\frac{(\nu-2)!}{(\nu+2)!}\right]\cos2\varphi P_\nu^2(\cos\beta),\end{aligned}\tag{2A}$$

provided $L_2+L_2'+\nu$ is an odd integer. Also the parity index $\sigma(L_2')$ is determined by the character of $2^{L_2'}$ pole radiation, that is, $\sigma(L_2')=1$ for magnetic and 0 for electric radiation. In Eq. (2A), φ is the angle between the polarization vector and the normal to the plane determined by the cascade radiations, and P_ν^2 is the associated Legendre polynomial; the first term of Eq. (2A) describes the directional correlation function for the unpolarized radiations.

References

1) J. Owen and I. M. Ward: Phys. Rev. **102** (1956) 591.
2) F. K. McGowan and P. H. Stelson: Phys. Rev. **109** (1958) 901.
3) O. Huber, P. Marmier, H. Medicus, P. Preiswerk and R. Steffen: Phys. Rev. **73** (1948) 1208.
4) O. Huber, H. Medicus, P. Preiswerk and R. Steffen: Phys. Rev. **73** (1448) 1211.
5) E. E. Motta and G. E. Boyd: Phys. Rev. **73**

(1948) 1470, Phys. Rev. **74** (1948) 220, Phys. Rev. **74** (1948) 344.

6) H. Medicus, P. Preiswerk and P. Scherrer: Helv. Phys. Acta **23** (1950) 299.
7) C. Levi, L. Papineau and N. Saunier: Compt. rend. **245** (1957) 1918.
8) J. P. Unik and J. O. Rasmussen: Phys. Rev. **115** (1959) 1687.
9) M. E. Rose: *Internal Conversion Coefficients* (North-Holland Publishing Co., 1958).
10) D. T. Eggen and M. L. Pool: Phys. Rev. **74** (1948) 57.
11) J. M. Cork, M. K. Brice, L. C. Schmid and R. G. Helmer: Phys. Rev. **100** (1955) 188.
12) M. Ishibashi, T. Fujinaga and M. Koyama: Nippon Kagaku Zasshi **81** (1960) 1260.
13) N. Matsuura and H. Yumoto: Radioisotopes **8** (1959) 28.
14) T. Hayashi: J. Phys. Soc. Japan **13** (1958) 117.
15) W. Heitler: *The Quantum Theory of Radiation*, 3rd ed. (Oxford Univ. Press, 1954) p. 211.
16) M. E. Rose: Phys. Rev. **91** (1953) 610.
17) M. Kawamura: J. Phys. Soc. Japan **15** (1960) 3.
18) M. Kawamura, A. Aoki and T. Hayashi: Sci. Rep. Kyoto Pref. Univ. **3** (1959) A 5.
19) R. G. Arns and M. L. Wiedenweck: Phys. Rev. **111** (1958) 1631.
20) K. Takazawa, K. Ohira, H. Matsui and M. Higuchi: Genshikaku Kenkyu, Mimeographed Circular in Japanese **4** (1960) 51.
21) J. M. Mellor: *A Comprehensive Treatise on Inorganic and Theoretical Chemistry* (Longmans, Green and Co., 1931) **XI** p. 499.
22) H. Frauenfelder: *Beta- and Gamma-Ray Spectroscopy* edited by Kai Siegbahn (North-Holland Publishing Co., 1955) Chap. **XIX** p. 531.
23) E. Bodenstedt, E. Matthias, H. J. Körner, E. Gerdau, F. Frisius and D. Hovestadt: Nuclear Physics **15** (1960) 239.
24) A. Abragam and R. V. Pound: Phys. Rev. **92** (1953) 943.
25) L. C. Biedenharn and M. E. Rose: Revs. Mod. Phys. **25** (1953) 729.

JOURNAL OF THE PHYSICAL SOCIETY OF JAPAN, Vol. 16, No. 6, JUNE, 1961

Angular Distribution of (α, p) Reactions in Some Light Nuclei

By Michiya KONDO, Takashi YAMAZAKI and Shotaro YAMABE

Department of Physics, Faculty of Science, Osaka University, Osaka

(Received February 17, 1961)

The angular distributions of the proton groups corresponding to the lower states of the residual nuclei from the reactions $C^{12}(\alpha, p)N^{15}{}_{\rm gnd}$; $F^{19}(\alpha, p)Ne^{22}{}_{\rm gnd,\ 1.28\ MeV}$; $Al^{27}(\alpha, p)Si^{30}{}_{\rm gnd,\ 2.24\ MeV}$; and $Si^{28}(\alpha, p)P^{31}{}_{\rm gnd,\ 1.27,\ 2.23,\ 3.13\sim3.51\ MeV}$ have been measured using 22.5±0.2 MeV alpha particles. The angular distributions of the $C^{12}(\alpha, p)N^{15}{}_{\rm gnd}$ reaction are energy dependent. At 20.6 MeV steep rise in the forward angles is observed, but at 22.2 MeV the steep rise in the backward angles appears instead of the forward rise. The angular distributions of the $F^{19}(\alpha, p)Ne^{22}$ reaction are both peaked in the backward angles. The angular distributions of the $Al^{27}(\alpha, p)Si^{30}$ and the $Si^{28}(\alpha, p)P^{31}$ reactions show the diffraction-like patterns and they are interpreted with Butler's direct interaction theory.

§1. Introduction

The angular distributions of the (α, p) reactions for light nuclei have been measured at various energies[1-6], and the results for the proton groups corresponding to discrete levels in the residual nucleus have been usually compared with the surface direct interaction theory[7].

The angular distributions of the ground state proton group of the reaction $C^{12}(\alpha, p)N^{15}$ have been measured for alpha particle energies between 16 and 19 MeV[3], and between 25 and 40 MeV[4-6]. The angular distributions at the energies higher than 34 MeV show the diffraction-like patterns expected by the direct interaction mechanism. But the angular distributions at the energies below 30 MeV become energy dependent and show steep backward peaking which is unable to be explained by the simple direct interaction theory[7]. We have measured the angular distributions at the alpha particle energies of 22.2, 21.4 and 20.6 MeV.

The angular distributions of the $F^{19}(\alpha, p)Ne^{22}$ reaction have been measured at alpha particle energies of 18.9 MeV[1], and between 6.0 and 6.55 MeV[5]. At 18.9 MeV the angular distributions of the p_0, p_1 and p_2 proton groups (p_i is the group leaving residual nucleus in its i'th excited state.) are all peaked in the backward angles. We have measured the angular distributions of the p_0 and p_1 groups at the energy of 22.2 MeV.

In the case of the reaction $Al^{27}(\alpha, p)Si^{30}$, the angular distributions of the p_0 and p_1 groups at 30 MeV[6] give qualitative agreement with the calculation of the direct interaction theory. But there are some points of disagreement such as (*a*) the marked filling in the regions between the maxima and (*b*) a much higher degree of forward peaking. This higher degree of forward peaking not expected by the theory is also found in the reaction $C^{12}(\alpha, p)N^{15}$.[2] We have measured the angular distributions of the p_0 and p_1 groups of the reactions $Al^{27}(\alpha, p)Si^{28}$ at the energy of 21.8 MeV, and especially for the p_0 group we have also measured the angular distribution at 22.2 MeV to study the energy dependence of this reaction.

We have also measured the angular distributions of the $Si^{28}(\alpha, p)P^{31}$ reaction corresponding to the lower levels of the residual nucleus at the energy of 22.2 MeV, and compared the results with the direct interaction theory.

2. Experimental Procedures

The general experimental arrangement and procedure are similar to that described in the previous experiment[8].

The beam of 22.5±0.2 MeV alpha particles accelerated by the 44 inch Osaka University Cyclotron was lead to a scattering chamber (Fig. 1). Protons emerged from the target were detected by Ilford C-2 nuclear emulsion, 200 microns thick, and the angular distributions were measured every 7.5° from 7.5° to 165° at the laboratory angles. The angular setting of the plate camera was accurate within 1/2°. The angular resolution was determined by the scanned regions of the plate and was about ±1°. Aluminum and gold foils of suitable thickness were inserted between the target and emulsion to stop the scattered alpha particles and to get suitable lengths of tracks of the emitted protons in the emulsion. The beam current was collected by a Faraday cup connected to a polystyrene condenser and the charge was measured by an electrometer. The beam energy was degraded by aluminum foils placed in front of the collimator system.

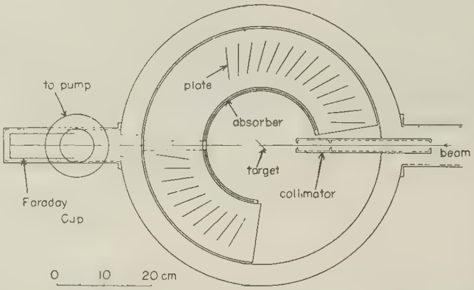

Fig. 1. Schematic diagram of scattering chamber and plate camera.

A thin polyethylene foil of 1.74 mg/cm² thick was used for the carbon target. For the study of fluorine a foil of teflon, 2.1 mg/cm² thick, was prepared. The aluminum target was 1.82 mg/cm² thick. A foil of fused silica, 2.0 mg/cm² thick, was used for silicon experiment. They were all self-supporting and set at 45° with respect to the beam direction.

§ 3. Results

A typical example of the range distribution for the emitted protons is shown in Fig. 2. This is the distribution for $Si^{28}(\alpha, p)P^{31}$ at the laboratory angle of 52.5° induced by 22.5 MeV alpha particles.

The results of the angular distributions for the (α, p) reactions are shown in Fig. 3 to Fig. 6. The energy values shown in the figures are those at the center of target. The errors indicated in these figures are only the statistical ones. The plots in which the errors are not indicated in the figures are due to their smallness. The estimated errors in the absolute differential cross sections are less than 30%, but for teflon target the absolute error is somewhat larger owing to the nonuniformity of the target thickness.

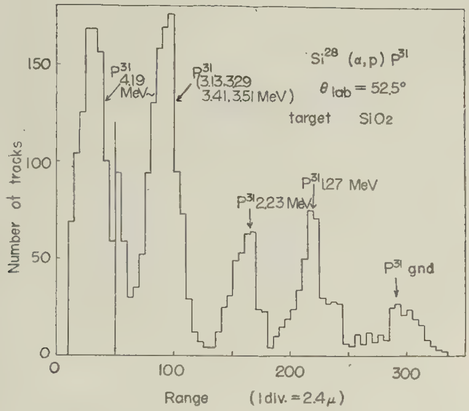

Fig. 2. Range distribution of the protons from the $Si^{28}(\alpha, p)P^{31}$ reaction observed at the laboratory angle of 52.5°. An aluminum foil of 1080 microns was inserted between the target and emulsion.

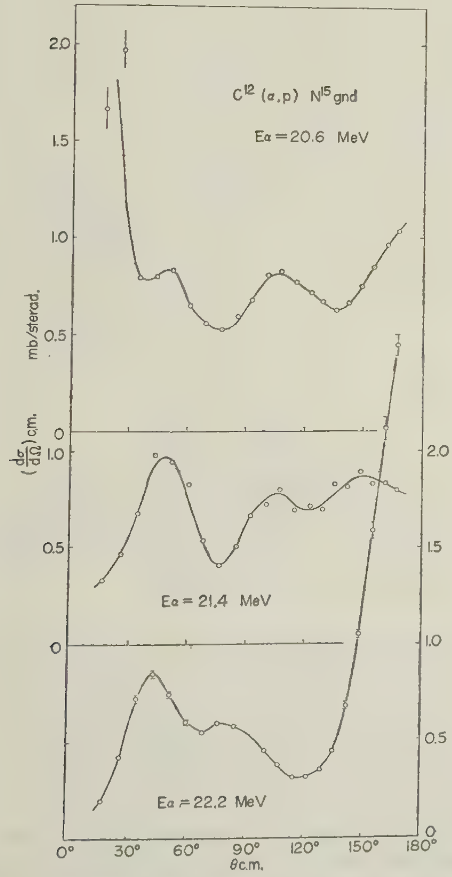

Fig. 3. Angular distributions of protons from the $C^{12}(\alpha, p)N^{15}_{gnd.}$ reaction.

4. Discussion

(i) $C^{12}(\alpha, p)N^{15}$

The angular distributions of the ground state protons from the reaction $C^{12}(\alpha, p)N^{15}$ show remarkable energy dependence. At 22.2 MeV steep rise in the backward angle is observed, at 21.4 MeV the angular distribution shows oscillation without steep rise in both

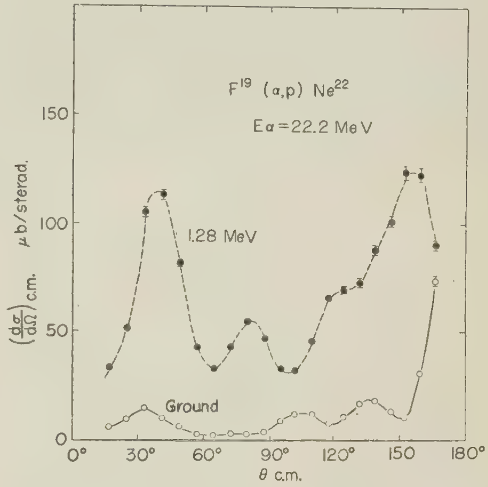

Fig. 4. Angular distributions of protons from the $F^{19}(\alpha, p)Ne^{22}_{gnd, 1.28 MeV}$ reactions.

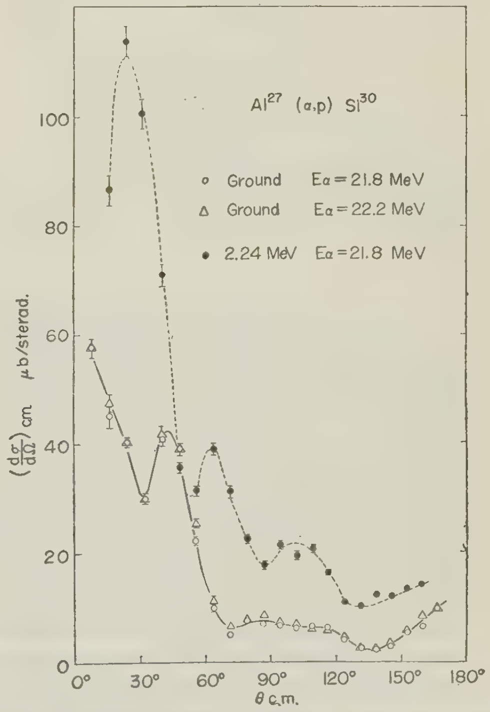

Fig. 5. Angular distributions of protons from the $Al^{27}(\alpha, p)Si^{30}_{gnd, 2.24 MeV}$ reactions.

the forward and backward angles, and at 20.6 MeV the rise in the forward angle appears. The peak near 45° is observed in all of these angular distributions.

The steep backward peak appeared at the alpha particle energy of 22.2 MeV has been observed also at other energies[1),2)]. The excitation curve of this reaction at $\theta_{cm}=165°$ obtained by the interpolation of the angular distributions is shown in Fig. 7. It seems that the backward rise in the angular distributions shows the maximum at about 25 MeV excitation energy of compound nucleus O^{16}, though just at this energy the experimental data are not yet obtained. The steep rise in the backward angle is also observed at 19.2 MeV of the excitation energy of $O^{16}(E_\alpha=16.1\text{ MeV})$[1)]. The backward peak has remarkable energy dependence at the alpha particle energy near 20 MeV, and this behavior may not be explained by the heavy particle stripping[13)] or by the reflection of the outgoing proton waves at the nuclear surface[14)].

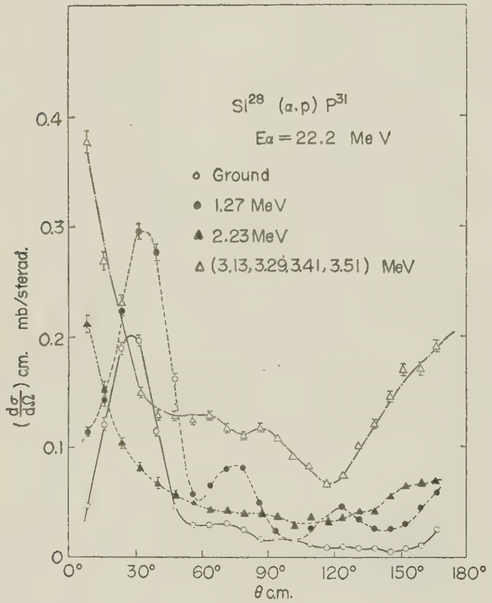

Fig. 6. Angular distributions of protons from the $Si^{28}(\alpha, p)P^{31}_{gnd}$, 1.27 MeV, 2.23 MeV, (3.13, 3.29, 3.41, 3.51 MeV) reactions.

The excitation energy of the compound nucleus O^{16} produced by 21 MeV alpha particle is about 23 MeV, and it is expected that the level density is not so high in this region because O^{16} is a double magic nucleus. In the region higher than 21 MeV in the excitation energy of O^{16} resonances are found in the excitation curves of the reaction $N^{14}(d, n)O^{15}{}_{gnd}$ and the angular distribution of this reaction is energy dependent (Fig. 7)[9)]. Some levels are found in the yield curve of $O^{16}(\gamma, n)O^{15}$.[10)] At the excitation energies of O^{16} between 21 and 26 MeV the excitation curve of $N^{15}(p, \gamma)O^{16}$ is obtained at 90° and shows large resonances at 21.8 and 24.8 MeV (Fig. 7)[11)].

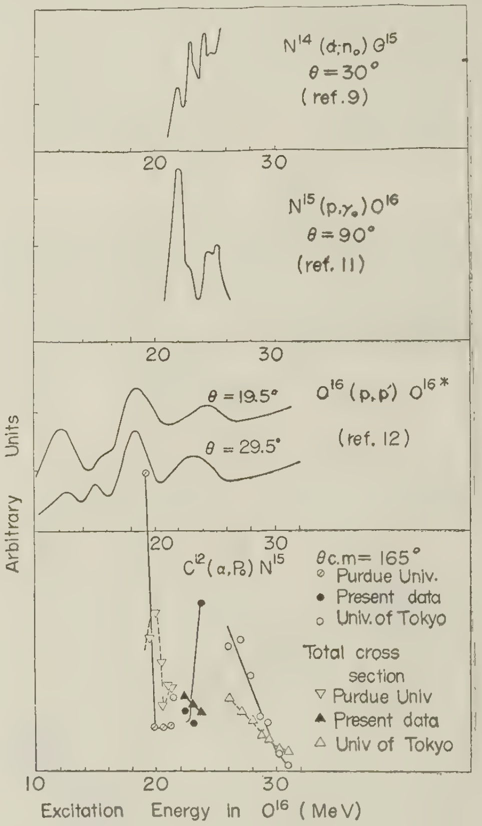

Fig. 7. The integrated cross section and the differential cross section at $\theta_{cm}=165°$ of $C^{12}(\alpha, p)N^{15}$ vs. the excitation energy of the compound nucleus O^{16}. Some other data relating this excitation energy of O^{16} are also shown.

The energy spectra for the inelastic scattering of 185 MeV protons on oxygen[12)] show peaks at 18.5 and 24 MeV of the excitation energy of O^{16} and these peaks roughly coincide in energy with the backward peak of the reaction $C^{12}(\alpha, p)N^{15}{}_{gnd}$ (Fig. 7). The effects of the levels of compound nucleus O^{16} are seen in these reactions and it is probable that similar circumstance exists on the reaction $C^{12}(\alpha, p)N^{15}{}_{gnd}$.

The integrated cross sections of the reaction $C^{12}(\alpha, p)N^{15}{}_{gnd}$ obtained from the angular distributions are shown in Table I. The energy dependence of the integrated cross sections is shown in Fig. 7 together with other results[1),2)]. This shows that the integrated cross section decreases generally as the energy increases though small bumps are observed. The integrated cross section does not show the strong energy dependence though the angular distributions change remarkably as shown in Fig. 3. This is perhaps due to the fact that the amplitude of the compound nucleus formation adds to the amplitude of the direct interaction.

Table I. The integrated cross sections of the reaction $C^{12}(\alpha, p)N^{15}{}_{gnd}$

E_α (MeV)	20.6	21.4	22.2
σ (mb)	6.30	5.50	4.94

(ii) $F^{19}(\alpha, p)Ne^{22}$

The angular distributions of the p_0 and p_1 proton groups from the reaction $F^{19}(\alpha, p)Ne^{22}$ at the alpha particle energy of 22.2 MeV are both peaked in the backward angles. The intensity of the p_1 proton group is greater by a factor of about ten than that of the p_0 proton group. The steep backward peaks of the p_0 and p_1 proton groups observed at 22.2 MeV have been also found at 18.9 MeV[2)]. The angular distribution of p_1 group at 22.2 MeV is very similar to that at 18.9 MeV at the angle larger than 90°, and the difference of these angular distributions is that the forward rise observed at 18.9 MeV is not seen at 22.2 MeV.

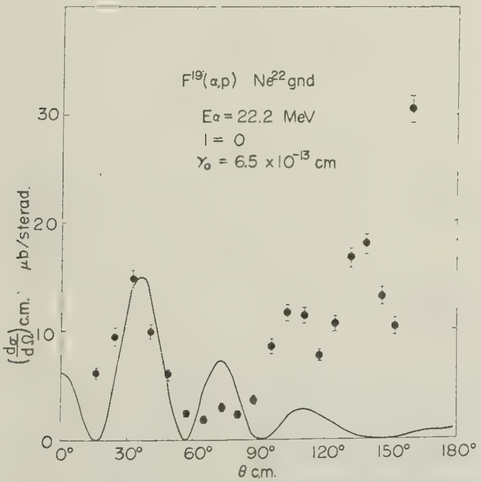

Fig. 8. Theoretical fit to the angular distribution of the $F^{19}(\alpha, p)Ne^{22}{}_{gnd}$ reaction using Butler's formula (Knock on; Eq. 57 of ref. 1) with $l=0$ (uniquely) and $r_0=6.5\times10^{-13}$ cm.

The theoretical fit to the angular distributions of the p_0 and p_1 groups using Butler's formula[1)] are shown in Figs. 8 and 9. For the p_0 and p_1 groups the unique l value of 0 and 2 are allowed, respectively. The interaction radius of 6.0×10^{-13} cm for the p_1 group is larger than that at the other energies[2)]. The fitting of the p_0 group using Butler's formula is rather poor. The steep backward peak of p_0 group and the peak of p_1 group at 155° can not be explained by Butler's theory[7)].

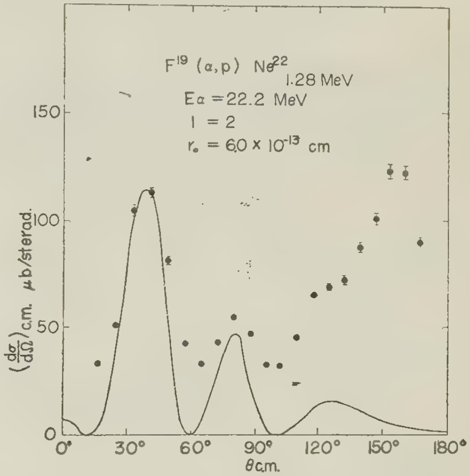

Fig. 9. Theoretical fit to the angular distribution of the $F^{19}(\alpha, p)Ne^{22}{}_{1.28\,MeV}$ reaction using Butler's formula with $l=2$ (uniquely) and $r_0=6.0\times10^{-13}$ cm.

(iii) $Al^{27}(\alpha, p)Si^{30}$

The angular distributions of the p_0 and p_1 proton groups from the reaction $Al^{27}(\alpha, p)Si^{30}$ at the alpha particle energy of 21.8 MeV show the oscillation with forward peaking and no remarkable backward peaking as observed in the reactions $C^{12}(\alpha, p)N^{15}$ and $F^{19}(\alpha, p)Ne^{22}$. The result of the p_0 proton group at 22.2 MeV is similar to that at 21.8 MeV, and therefore it seems that any strong energy dependence does not exist in this energy region. These facts suggest that the direct interaction mechanism plays an important role. The results of fitting Butler's formula[7)] to these data are shown in Figs. 10 and 11.

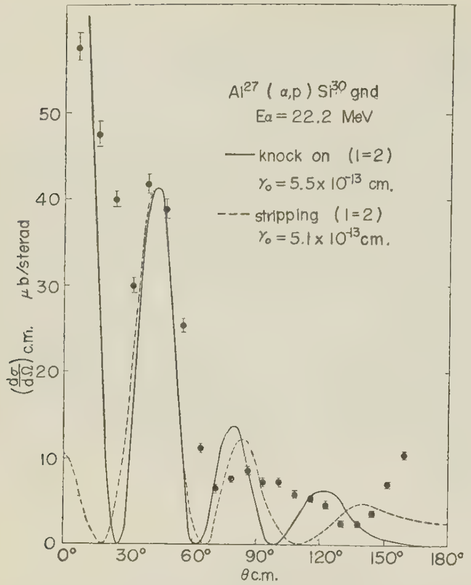

Fig. 10. Theoretical fit to the angular distribution of the $Al^{27}(\alpha, p)Si^{30}_{gnd}$ reaction using the formula of knock-on theory with $l=2$ (uniquely) and $r_0=5.5\times10^{-13}$ cm and the formula of stripping theory with $l=2$ (uniquely) and $r_0=5.1\times10^{-13}$ cm.

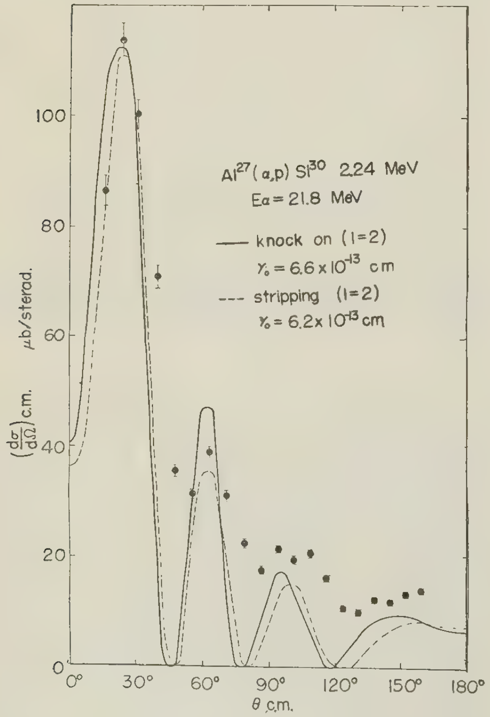

Fig. 11. Theoretical fit to the angular distribution of the $Al^{27}(\alpha, p)Si^{30}_{2.24\,\mathrm{MeV}}$ reaction using the formula of knock-on theory with $l=2$ and $r_0=6.6\times10^{-13}$ cm and the formula of stripping theory with $l=2$ and $r_0=6.2\times10^{-13}$ cm.

At the alpha particle energy of 30.4 MeV[6] the angular distributions of the p_0 and p_1 groups show marked filling in the regions between the maxima. This tendency is also observed in our results, but the filling is not so marked as that of 30.4 MeV[6]. Butler, Austern and Pearson[12] have shown in semi-classical calculation that the filling of minima in the angular distribution is produced by the absorption of either the incident or the emergent particles. This calculation suggests that the difference of the filling of minima at 21.8 MeV and 30.4 MeV is due to the difference of the absorption coefficient of either the incident or the emergent particles.

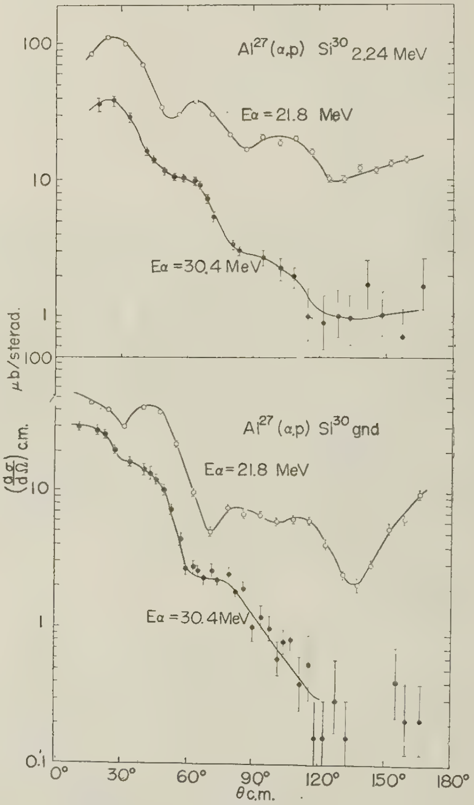

Fig. 12. Differential cross section of $Al^{27}(\alpha, p)Si^{30}_{gnd,\ 2.24\,\mathrm{MeV}}$ at $E_\alpha=21.8$ and 30.4 MeV[7] vs. c.m. scattering angle.

If we assume the interaction radius r_0 is constant in Butler's prediction[7] on direct interaction, the shapes of the differential cross sections plotted against momentum transfer q should be same at different energies. However, as shown in Fig. 12, the positions of maxima and minima in the angular distributions of the $Al^{27}(\alpha, p)Si^{30}_{gnd,\ 2.24\,\mathrm{MeV}}$ reactions at 21.8 MeV are almost same as those at 30.4 MeV, so the positions of maxima and minima will shift at different energies if the differential cross sections are plotted against the momentum transfer q (Fig. 13). Butler's prediction is based on the plane wave assumption, and if we use the distorted waves on the incident and the emergent particles this behavior of the differential cross section may be explained. This independence of the angles of maxima and minima on bombarding energies is also observed in the reaction $C^{12}(\alpha, p)N^{15}{}_{\mathrm{gnd}}$ at the alpha particle energies between 28 and 38 MeV[2] and in some (d, p) reactions at the deuteron energies higher than 10 MeV[15].

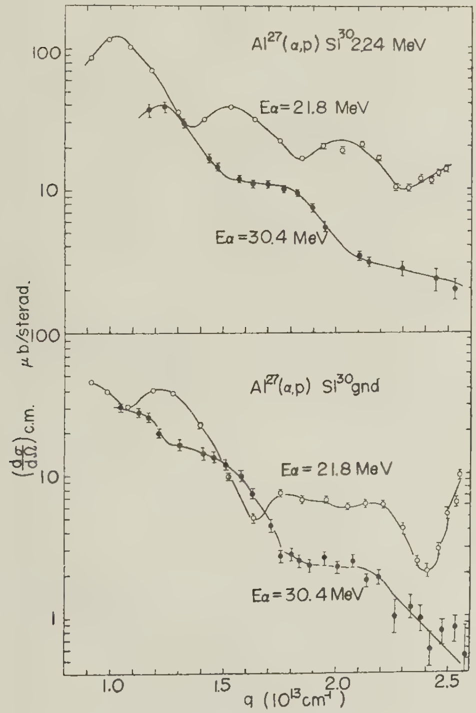

Fig. 13. Differential cross sections of $Al^{27}(\alpha, p)$ $Si^{30}{}_{\mathrm{gnd,\ 2.24\ MeV}}$ at $E_\alpha=21.8$ and 30.4 MeV[7] vs. momentum transfer q.

In the deuteron stripping reaction Satchler[16] has investigated the intrinsic probability of capture of nucleons by nuclei which exhibit collective rotations in addition to an underlying shell structure of independent nuclear orbits. In the case of (α, p) reaction, though we cannot distinguish from the angular distributions only whether the reaction proceeds through knock on or stripping process, we assume stripping for the reaction. Then the probability of triton capture by deformed nuclei is given by

$$\Lambda = \mathrm{const.} \sum_j |C_j|^2 (J_i j K_i \Omega | J_f K_f)^2 ,$$

where (J_i, K_i) and (J_f, K_f) are the angular momenta and their projections along the axis of symmetry of the nucleus for the initial and final states, and (j, Ω) are the corresponding quantities for the added triton. C_j is the probability that the triton has total angular momentum j in the spheroidal potential. In the case of $Al^{27}(\alpha, p)Si^{30}{}_{\mathrm{gnd,\ 2.24\ MeV}}$, if we assume $K_i=5/2$ and $K_f=0$, the addition of s-wave triton $(\Omega=1/2)$ is forbidden. Then only the $d_{5/2}$ triton capture is allowed for both p_0 and p_1 groups, and the ratio of the p_0 and p_1 groups $\Lambda(2^+)/\Lambda(0^+)$ becomes C_j independent,

$$\Lambda(2^+)/\Lambda(0^+) = 1.8 .$$

This explains the experimental result,

$$\Lambda(2.24\ \mathrm{MeV})/\Lambda(\mathrm{gnd}) \cong 3.5 ,$$

qualitatively.

(iv) $\mathbf{Si^{28}(\alpha, p)P^{31}}$

In the $F^{19}(\alpha, p)Ne^{22}$ reaction at 22.2 MeV and the $Al^{27}(\alpha, p)Si^{30}$ reaction at 21.8 MeV, the intensity of the p_1 group is greater than that of the p_0 group, but in the $Si^{28}(\alpha, p)P^{31}$ reaction at 22.2 MeV the intensities of the p_0, p_1 and p_2 groups are almost same. The

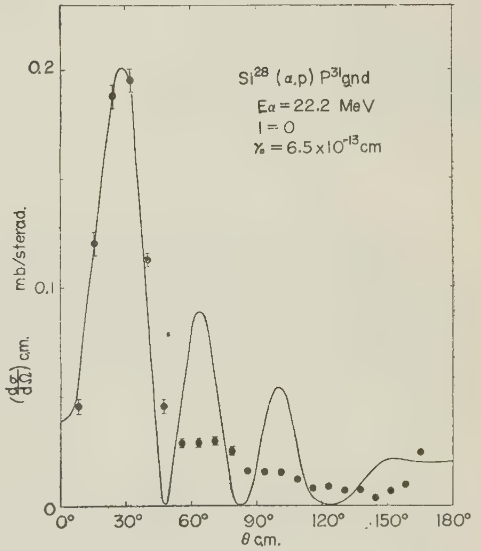

Fig. 14. Theoretical fit to the angular distribution of the $Si^{28}(\alpha, p)P^{31}{}_{\mathrm{gnd}}$ reaction using Butler's formula with $l=0$ (uniquely) and $r_0=6.5\times10^{-13}$ cm.

angular distributions of the p_0 and p_1 proton groups show oscillation, but that of the p_2 proton group does not show such a pattern and has monotonic forward peaking.

For the p_0, p_1 and p_2 groups the unique l values of 0, 2 and 2 are allowed, respectively. Therefore the angular distributions of the p_1 and p_2 groups are expected to be almost same each other in contradiction to our experimental results. The structure of P^{31} is well explained by the Nilsson model by assuming that a proton couples to the deformed Si^{30} core of 0^+.[17] In this model the first and second excited states belong to the different bands, and this circumstance may influence the angular distributions.

The results of fitting Butler's formula[7] to the data are shown in Figs. 14 and 15. The theoretical fittings of these angular distributions are satisfactory. The angular distribution of the protons consisting of unresolved p_3, p_4, p_5 and p_6 groups shows the backward peaking which is not noticeable in the p_0, p_1 and p_2 groups.

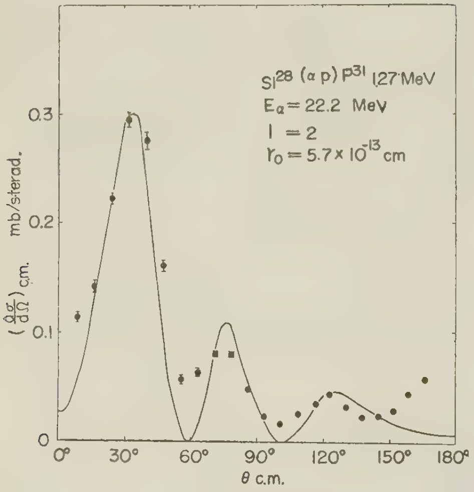

Fig. 15. Theoretical fit to the angular distribution of the $Si^{28}(\alpha, p)P^{31}{}_{1.27\,\mathrm{MeV}}$ reaction using Butler's formula with $l=2$ (uniquely) and $r_0=5.7\times10^{-13}$ cm.

Acknowledgments

The authors are indebted to Professor T. Wakatsuki for his guidance and Miss M. Kitatani for her helps in scanning the nuclear plates. The authors are also grateful to the Nishina Memorial Fundation for its financial support.

References

1) J. R. Priest, D. J. Tendam, and E. Bleuler: Phys. Rev. **119** (1960) 1301.
2) I. Nonaka, H. Yamaguchi, T. Mikumo, I. Umeda, T. Tabata and S. Hitaka: J. Phys. Soc. Japan **14** (1959) 1260.
3) C. E. Hunting and N. S. Wall: Bull. Am. Phys. Soc. Ser. II, **2** (1957) 181.
4) R. Sherr and M. Rickey: Bull. Am. Phys. Soc. Ser. II, **2** (1957) 29.
5) G. F. Pieper and N. P. Heydenburg: Phys. Rev. **111** (1958) 264.
6) C. E. Hunting and N. S. Wall: Phys. Rev. **108** (1957) 901; **115** (1959) 956.
7) S. T. Butler: Phys. Rev. **106** (1957) 272.
8) M. Takeda, M. Kondo, S. Kato, C. Hu, R. Nakasima and S. Yamabe: J. Phys. Soc. Japan **12** (1957) 561.
9) S. Morita, N. Kawai, Y. Goto, T. Maki and M. Mukae: J. Phys. Soc. Japan **15** (1960) 2170; J. Retz-Schmidt and J. L. Weil: Phys. Rev. **119** (1960) 1079.
10) B. M. Penfold and A. S. Spicer: Rev. **100** (1955) 1377.
11) S. G. Cohen, P. S. Fisher and E. K. Warburton: Phys. Rev. Letter **3** (1959) 433.
12) H. Tyrén and Th. A. J. Maris: Nuclear Physics **4** (1957) 637.
13) L. Madansky and G. E. Owen: Phys. Rev. **99** (1955) 1608; G. E. Owen and L. Madansky: Phys. Rev. **105** (1957) 1766.
14) S. T. Butler, N. Austern and C. Pearson: Phys. Rev. **112** (1958) 1227.
15) E. W. Hamburger: preliminary report. S. Morita: private communication.
16) G. R. Satchler: Ann. Phys. **3** (1958) 275.
17) C. Broude, L. L. Green and J. C. Willmott: Proc. Phys. Soc. **A**, **72** (1958) 1122.

JOURNAL OF THE PHYSICAL SOCIETY OF JAPAN, Vol. 16, No. 6, JUNE, 1961

A Cloud Chamber Study of High Energy Nuclear Interactions of Cosmic Ray Particles (I)—A Possible Evidence of Successive Collisions in Carbon Nuclei

By Isao KITA

Department of Physics, Kobe University, Kobe, Japan

(Received February 10, 1961)

In an attempt to study the high energy nuclear interactions of cosmic ray particles, a momentum cloud chamber was operated at Mt. Norikura, 2740 meter high above the sea level, and about ten thousand pairs of stereoscopic pictures of the events were taken. Selected showers were transformed to the C.M.S. of the collisions to obtain the intrinsic features of the nuclear interactions. In the energy range around 100 Gev of incident nucleons, the successive collision model in carbon nuclei, rather than the complete collision model, seems to be consistent with the experimental evidences.

§ 1. Introduction

This and the succeeding papers* report the results of the experimental study of the nuclear interactions of cosmic ray particles with energies around 100 GeV. The interactions which occurred in carbon blocks were observed by a momentum cloud chamber. The chamber was operated at the Cosmic Ray Laboratory on Mt. Norikura, 2740 meter high above the sea level.

In the experiments using cloud chambers, to the contrary in the nuclear emulsion technique, the target material can be chosen as is liked and hydrogen[1], berillum[2], carbon[3),4], or other light materials[5),6] have been used to reduce the probability of successive collisions within the same nucleus. Carbon was used as the target material in this experiment because it does not have a too complex nucleus to obtain the informations on the nucleon-nucleon collisions and also is very easy to get in hand. It is expected that the nucleon-nucleon collisions can take place in a pretty large probability by the peripherical collisions of the incoming particles with the nuclei or due to the transparency of the target nuclei. Although the successive collisions can also occur in the carbon nuclei, there is a prospect that these could be treated in some way or other in such a simple nucleus as carbon.

The momentum of the individual charged particles in this chamber can be measured in a magnetic field up to 25 GeV/c. The ionization density of a track can also be estimated. Hence from the knowledge of the momenta, velocities, and the space angles of all charged particles of a shower, the Lorenz transformation to the centre of mass system of the collision can be calculated. Then the momenta and the angles of emission in the C.M.S. of the collision can be deduced, giving the intrinsic informations on the nuclear interactions of cosmic ray particles.

In this experiment it was hoped that the successive collisions within carbon nuclei could be possibly separated from nucleon-nucleon collisions in a more or less unquestionable way. The results on the successive collisions thus obtained are described in this paper and the results on the single collisions of nucleons will be reported in the succeeding paper.

§ 2. The Experimental Procedures

a) *The cloud chamber and the magnet*

The experimental apparatus used in this experiment is shown in Fig. 1. The cloud chamber situated in a magnetic field has the illuminated volume of 64 cm×64 cm×14 cm and is filled with 35 cm of argon, together with a mixture of ethyl alcohol and water. It was surrounded by a thick copper thermal jacket with flattened copper tubings soldered on its outside surface. Water of which the temperature was controlled within ±0.02°C was circulated through these tubings, and the temperature of the chamber, as measured by thermistors at different four places, was proved within±0.1°C. The dead time was 15 minutes after each expansion for repeating slow expansions and achieving the thermal equibrium of the gas in the chamber.

---

* These papers are referred to in the following as Paper I and Paper II respectively.

The illumination was achieved through the storm windows of the jacket by two Xe-filled flash tubes, each with 200 μF at 3500 volts. The stereoscopic camera which was designed in this laboratory was set at f:16 and unperforated 70 mm Fuji X ray film was used to take the pictures of the events in the chamber. The film is very sensitive and the grains of the film were found to be fine enough to be used for the droplet counting technique.

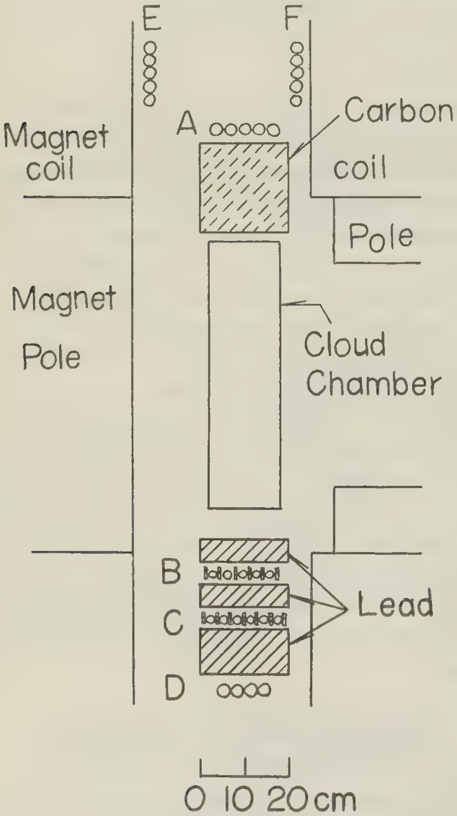

Fig. 1. The experimental arrangements.

The weight of the magnet is about 30 tons in total and the magnetic field of 7350 gausses in the average was yielded by the consumption of 55 kilowatts of power. The gap of the poles is 40 cm wide and there is a hole of 50 cm diameter in a pole for photographing.

b) *Selection of the events*

The simultaneous discharges of at least one counter of the tray A, two of the tray B, two of the tray C, and one of the tray D in Fig. 1 were required to trigger the chamber. In a part of the period of the experiment the E and F were used as anti-coincidence trays to eliminate the dense electron showers or the showers originating in the magnet coils from triggering the cloud chamber.

The photographs were taken at the average rate of 2.3 per hour and about ten thousand stereoscopic pairs of the pictures were taken during the experiment.

The film was scanned by a stereoscopic viewer and the events which were seemed to be nuclear in character were selected. The events which were clearly decided as electron showers were rejected by the visual scanning, and the showers with three or less lightly ionizing tracks were also discarded because it was thought that they were not suitable for finding the velocities of the C.M.S. of the individual events. Thus 277 events which were thought to be prospective for the analysis were picked up from the pictures taken as the first step of the selection procedure. It was realized, however, that all of these events were not fit for the full analysis, and hence more rigorous criteria which will be described later were imposed for the final selection. The analysis was made for each of these events and the results in this and the succeeding paper are mainly based on the analysis of these events.

c) *Measurements of the events*

To obtain the momentum of a charged particle, comparator measurements of the track in both views of the stereoscopic camera were made and a least-square fit was made to each track to calculate the curvature of the track on film. In case that the radius of curvature was smaller than 200 cm, it was measured by fitting the track to the circle of known radius in the full scale projection. The momentum of the particle, p_i, was then determined by applying the magnification factor and the correction of the effect due to the orientation of the track in the magnetic field.

Number of no-field tracks were photographed and the spurious curvatures in the cloud chamber were measured by the same procedures as described above. The maximum detectable momentum, thus obtained, was 25 GeV/c for 40 cm tracks in this chamber. The error in determining the momentum of a particle was assigned using this maximum value of the momentum.

The individual views of the stereoscopic pairs were projected one after the other on a sheet of drawing paper marked with the fiducial lines in full size and the differences of the horizontal coordinates of the track in the both views were measured. Then the side view of the orthogonal projection of the track was constructed, using the numerical table previously prepared. 8% of the linear dilatation was included in this table to account for the expansion of the cloud chamber. Thus the angle of the particle to the vertical line in the side orthogonal projection could be measured. The position of the origin of a shower in the carbon block was then determined from the side orthogonal view. The emission angle of the particle in the front view of the orthogonal projection was obtained, after the effect of the deflection of the particle in the magnetic field was taken into consideration. The space angle of the track was then calculated from the knowledge of the angles in the front and the side views of the orthogonal projections.

As all of the nuclear interactions selected took place in the carbon blocks placed above the chamber and the track of the incoming particle could not be seen in this experiment, the direction of the resultant momentum of the visible particles was assumed to be the axis of the shower. Then θ_i, the angle between a shower particle and the shower axis was calculated. The error in finding the space angle was estimated by repeating the measurements of the angle of a track and was found to be 1.5°.

The ionization of a particle in the cloud chamber was measured by counting the number of the droplet images along the track. Clusters of droplets which had more than 40 drops were rejected in order that the measurement was referred to the primary ionization only. As a fast particle rarely appears actually at the minimum ionization, the minimum level of the ionization was estimated by comparing the measured values with the theoretical ionization curve and the droplet density of the minimum ionization obtained was 18.0±0.6 droplets per cm in the cloud chamber. Once the minimum ionization density was obtained, $I/I_{\text{min.}}$, the ratio of the ionization of a track to the minimum ionization was used to find the velocity of the particle. The image size of a droplet on film was 15 μm.

In some cases of the events observed, however, the droplet counting technique was not available due to the unfavorable condition of the cloud chamber and hence the visual inspection of the ionization was made. In these cases it was estimated that a track could be distinguished from the minimum ionization track if the ratio of its ionization density to the miuimum value, $I/I_{\text{min.}}$ was greater than 2. As $I/I_{\text{min.}}$ exceeds 2 for a charged pion with the momentum less than 105 MeV/c and for a proton with the momentum less than 695 MeV/c, it was considered that pions and protons with the momenta less than the corresponding values given above could be identified by the visual inspection of the ionization. Hence the lightly ionizing particle with the momentum higher than 100 MeV/c was assumed to be a pion, though fast protons might be included in a minor fraction of the presumed pions. All particles below 100 MeV/c with the nearly minimum ionization were considered to be electrons.

d) *Determination of the velocity of the C.M.S.*

The velocity of the C.M.S. of the nuclear collision was determined by finding the frame of reference in which the momenta of the charged particles emitted were balanced in the forward and backward directions. Therefore the events in which the momenta of all charged particles could be measured were picked up for this analysis.

For each particle the value of the momentum p_i and its angle of emission θ_i were measured and the energy E_i was calculated by assigning the mass of the particle in the L.S. According to the Lorenz transformation, the longitudinal component $p_ic\cos\theta_i$ in the C.M.S. is given by

$$p_ic\cos\theta_i^*=\gamma_c(p_ic\cos\theta_i-\beta_cE_i)\ . \qquad (1)$$

In the C.M.S. the sum of the longitudinal components of the momenta is zero if the summation is made over all particles, charged and neutral. It was assumed, however, that the balance of the momenta should hold independently for charged and neutral particles. Hence for the charged particles measured,

$$\sum\gamma_c(p_ic\cos\theta_i-\beta_bE)=\sum p_i^*c\cos\theta_i^*=0\ . \qquad (2)$$

Thus

$$\beta_c = \frac{\sum p_i c \cos\theta_i}{\sum E_i}, \qquad (3)$$

and

$$\gamma_c = \frac{1}{\sqrt{1-\beta_c^2}}.$$

The equation (2) or (3) is rigorously true for any kind of colliding particles when the collision is considered as a single process, and is not restricted to the necleon-nucleon collisions. In fact the incoming particle can be a pion in calculating the γ_c from the equation (3). However, when the interactions are more complex, such as nucleon-nucleus collisions, the significance of γ_c, if any, depends upon the phenomenological model that is used to describe the interactions. If two or more nucleons were hit inside the target nucleus, the value of γ_c calculated in the same way as above can hardly have a definite physical meaning.

The γ_c which was obtained in the present analysis is liable to be smaller than the true value for the very high energy events. The reason for this and also the reason for the fact that the measured highest momentum is much less than the assigned energy of the incident particles is that the maximum detectable momentum of this chamber is 25 GeV/c in the present experiment. Thus one of the particles which should retain the considerable fraction of the incident energy due to the elasticity of the collision will not give the measured momentum of higher than 25 GeV/c. If a neutral particle of very high energy was emitted in the collision, it can only give the same consequence as above. On the other hand if a neutral particle whose value of $pc \cos\theta/E$ is smaller than β_c of the equation (3) is produced in the collision, this will give the larger apparent value of γ_c than the true transformation factor. There is also an error due to the statistical fluctuation by an unfavorable sharing of the momenta among the charged and neutral particles in the collision, which is inevitably introduced in calculating the velocity of the C.M.S. of the individual event.

In spite of these situations, it is presumably believed that the velocity of the C.M.S. thus calculated will give the most reliable value which can be obtained from the experimental measurements. The over-all errors in evaluating γ_c are estimated to be less than 50%.

§ 3. Nature of the Nuclear Collisions Observed

In Fig. 2 the distribution of the multiplicties of 277 events selected was plotted. This multiplicity, n_s, was defined as the number of the particles which appeared to be lightly ionizing and had the momentum of higher than 100 MeV/c. The lightly ionizing particles with the momenta of less than 100 MeV/c were considered to be electrons, as described before. The mean multiplicity calculated from the spectrum in Fig. 2 is 5.1.

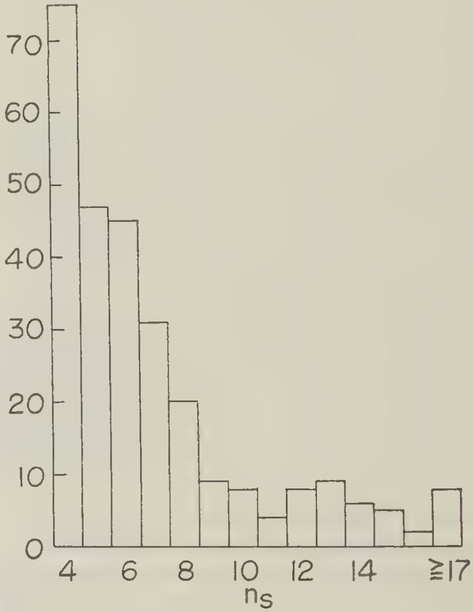

Fig. 2. The histgram of multiplicities of 277 penetrating showers selected.

It was found, however, that more rigorous criteria had to be assigned in order that the full analysis for the individual shower could be made successfully. The criteria used here are the following.

(i) The number of the nearly minimum ionizing nuclear particles with the momenta of >100 MeV/c, n_s, must be four or more, and the momenta of all of them can be measured within the admittable experimental errors.

(ii) The resultant momentum of the charged secondary particles must be 10 GeV/c or more, or three or more particles must have the momenta of >1 GeV/c.

(iii) Each of n_s tracks must be longer than 30 cm, so that a precise measurement of the momentum of the track can be made. This criterion does also confirm that all the particles are located in the well-illuminated region of the chamber.

(iv) When the front and the side views were constructed, all of the tracks must concentrate into a common origin of the shower in the carbon block within the experimental error.

Among 277 events selected above, 32 events were finally found to satisfy these criteria.

With respect to the angular distribution of the secondary particles in the C.M.S. of the collision, as will be reported in Paper II, there was a slight anisotropy with concentrations of particles in the forward and backward directions, but it was thought that the distribution could not be distinctly distinguished from an isotropy when the error in evaluating the transformation factor was taken into account. In fact the angular distribution was not appreciably different from an isotropy for each of the showers in many cases of the events analysed. These showers were designated as the *n-n* group. In the same energy range of cosmic ray interactions, an isotropic distribution in the C.M.S. of emitted particles has been reported by several authors[3),7),8)].

In some cases of showers named the *n-N* group, however, a considerably remarked anisotropy of the angular distribution with quite sharp peaks in the forward and the backward directions was observed. In these showers 80% of the secondary particles of the individual shower were included in the range of $|\cos\theta^*|>0.8$ in the C.M.S., whereas 30% of the emitted particles was included in the same range in the showers of the *n-n* group. There were nine showers of the *n-N* group.

The showers of the *n-N* group can not be regarded as the evidence of the anisotropic distribution of the secondary particles observed in the extremely high energy jet events, because the average γ_c of these showers, if calculated conventionally, is as small as 4.38, whereas the corresponding value of the showers of the *n-n* group is 9.61 as will be reported in Paper II. A possible interpretation of this small value of γ_c in the *n-N* group is that these events were produced by successive collisions of the incoming or emitted particles inside the target nucleus. In fact, if two collisions took place inside a carbon nucleus and if the emitted particles in these collisions were superposed, an apparent anisotropic angular distribution could be resulted by a Lorenz transformation of the collision in which all emitted particles of the two collisions were supposedly included. This is what is expected to occur in case that a simple nucleus like carbon was used as the target of the nuclear collisions. If the successive collisions occurred in a heavier nucleus like bromine or silver in nuclear emulsion, the interaction would be too complex to give such a simple interpretation as above.

On the other hand, the showers of the *n-n* group which showed nearly isotropic angular distributions of the emitted particles were regarded to have been produced by the nucleon-nucleon collisions of the cosmic ray particles. The events of the *n-N* group which were attributed to the successive collisions inside carbon nuclei will be discussed in the following in some detail.

§ 4. Successive Collision in Carbon Nuclei

In considering the shower events using the equation (2), the fundamental assumption was that the secondary particles were emitted in a single process of the collision of two elementary particles. It is very likely, however, that nucleon-nucleus collisions do exist among the events observed[9)], and in such an interaction two or more nucleons can be hit by the incident nucleon or by the emitted particles in the first collision. Attempts have been made to establish the interpretation of such an event in two different ways: the successive collisions[10)] and the composite collision[11)].

A picture of the successive collisions is to assume that an incoming nucleon has an interaction with a nucleon inside a nucleus and then the emitted pions or the nucleons which were concerned in the collision collide with the other nucleons in the same nucleus. Hence in this kind of collisions, the time needed to emit the pions must be shorter than the time interval between the first collision and the second. Thus

$$\frac{\hbar}{E^*} > \frac{\varLambda}{\gamma_c c}, \tag{4}$$

where E^* is the average energy of the pions produced in the C.M.S. of the first collision and Λ is the mean distance between two nucleons in a nucleus in the L.S. Λ is assumed to be of the order of the Compton wave length of a pion and E^* is taken to be 350 MeV from the result of Paper II. Then the equation (4) stands for the value of γ_c which is smaller than 15.

In a model of the composite collision, the pions are not emitted from the excited state of nucleons in the first collision before the succeeding collision takes place inside the target nucleus, or a more reasonable picture is to assume that the incident nucleon interacts with a lump of n nucleons in the nucleus as a whole. In order that this model is accepted, $\Lambda/\gamma_c c$ must be smaller than $\hbar/E^*$ instead of the equation (4): that is $\gamma_c>15$.

As the equation (4) and the corresponding equation for the composite model stand just in the order of magnitude, neither of these two models can be excluded in the energy range of this experiment from the consideration of the time sequence of the collision.

In the nine examples of the showers presented here, it was assumed that an incoming nucleon collided with a nucleon in a carbon nucleus and some ten particles were emitted isotropically in the C.M.S. of the interaction. One or more of these particles collided successively with another nucleon in the target nucleus and several particles were created with an isotropic angular distribution in the C.M.S. of the second interaction.

As the transformation factor γ_1 of the first collision is, as a matter of course, larger than that of the second collisirn γ_2, the apparent γ_{1+2} calculated by taking all the particles involved should be just between γ_1 and γ_2. Hence, if all the particles of this events were transformed by the factor γ_{1+2}, the particles produced in the first collision should show the forward peak and the particles of the second collision should be peaked in the backward direction in this supposed frame of reference. The apparent angular distribution obtained by Lorenz transformations using the wrong values of γ_c will be discussed in Paper II in detail. Therefore the particles in the forward peak were assumed to have been emitted in the first collision and the transformation factor γ_1 was calculated just in the same way as before by taking these particles into account. The vectorial resultant of the momenta of the particles in the backward peak was included in the calculation of γ_1 as one of the constituent of the collision. In the similar way γ_2 was calculated as the transformation factor of the particles in the backward peak and γ_{1+2} taking all the particles was also calculated, though it hardly has a definite physical meaning. Their average values are given below respectively.

$$\gamma_1 = 12.03 \pm 3.5\ ,$$
$$\gamma_2 = 2.22 \pm 0.5\ ,$$
$$\gamma_{1+2} = 4.38 \pm 1.6\ .$$

The second terms assigned are the root mean deviations of γ's of the events adopted. It is quite plain that the γ_{1+2} presented above is too low to be regarded as the transformation factor of the very high energy jet with a peaked anisotropic angular distribution in the C.M.S. of the collision. The average value of γ_1 is a little higher than but is pretty close to the average value of the γ_c's, 9.61, of the events of the n-n group which were attributed to the nucleon-nucleon collisions. This should be naturally accepted, because the γ_1 refers to the energy of the incoming nucleon, just as the γ_c of the nucleon-nucleon collision does so.

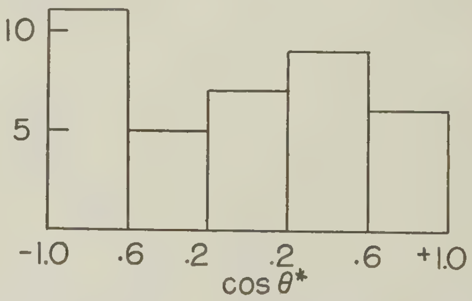

Fig. 3. The angular distribution in the C.M.S. of the emitted particles in the first interactions of the successive collisions.

In Fig. 3 the angular distribution in the C.M.S. of the emitted particles in the first collisions was plotted, which is essentially isotropic within rather poor statistics. This probably means that the first interactions of the successive collisions can be interpretated as the pure nucleon-nucleon collisions of the incoming particles in nature.

The relation between the multiplicities of the all emitted particles in the successive collisions and their corresponding values of γ_1 of the first collisions for the n-N group were plotted in Fig. 4. For comparison the multiplicities of the events of the *n-n* group which were considered as of nucleon-nucleon collision were also presented. As seen in the figure, the multiplicity of each event suffers from a large fluctuation from event to event, but if considered in the average, the multiplicities of the events of successive collisions are appreciably larger than those in nucleon-nucleon collisions. The average values are

$n_s = 7.4 \pm 2.7$ for nucleon-nucleon collisions,

$n_s = 10.6 \pm 2.3$ for successive collisions,

respectively. The difference should be interpretated as the average number of emitted particles of the second interactions in the target nuclei.

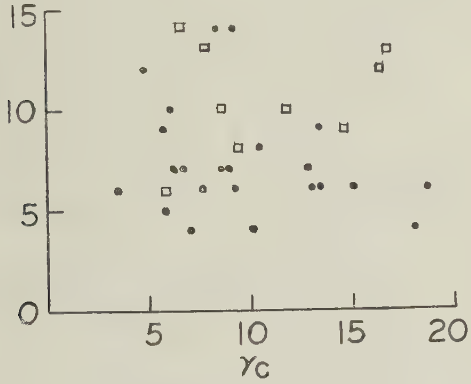

Fig. 4. Multiplicities versus transformation factors. Successive collisions are shown by squares and single collisions by solid circles.

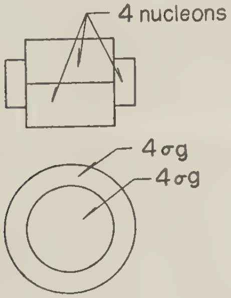

Fig. 5. A static model of carbon 12 nucleus.

In order to treat the successive collisions in more detail, a static model of a carbon nucleus was considered. As the mean free path length through a carbon 12 nucleus is 1.50 times the nucleon diameter, which was just geomertrically calculated, it was assumed that a carbon nucleus was consisted of three layers, each of which included four nucleons. This is shown in Fig. 5, which gives the nucleus a more or less spherical shape and also implys that the incoming fast nucleon can not collide with more than two nucleons in succession. If each nucleon in the target nucleus has the geometrical nuclear cross section, σ_g, and hence, if each layer is opaque for the incoming nucleon, the rate of the occurrence of nucleon-nucleon collisions should be the same as that of successive collisions. If, however, these layers have the transparency of η, the ratio of the rate of the successive collision to that of single collisions is calculated to be

$$R_n = \frac{4\sigma_g(1-\eta)(1-\eta^n)}{4\sigma_g(1-\eta)(1+\eta+\eta^n)} = \frac{1-\eta^n}{1+\eta+\eta^n}, \qquad (5)$$

where n is the number of the particles which were produced in the first collision and could give rise three or more pions in the succeeding collision, so that the backward peak could be noticed. n was assumed to be one third of the multiplicity of the first interaction. As there is no definite information on η of the incident nucleon or of the produced pions in such high energy nucler interactions, the transparencies were assumed to be the same for the successive two interactions in the target nucleus.

In Fig. 6 the calculated curves of R_n are shown for the values of n of 2, 3, 4, and 5. As seen in the figure the curves of R_n are not too sensitive to the variation of n. As the average multiplicity of nucleon-nucleon

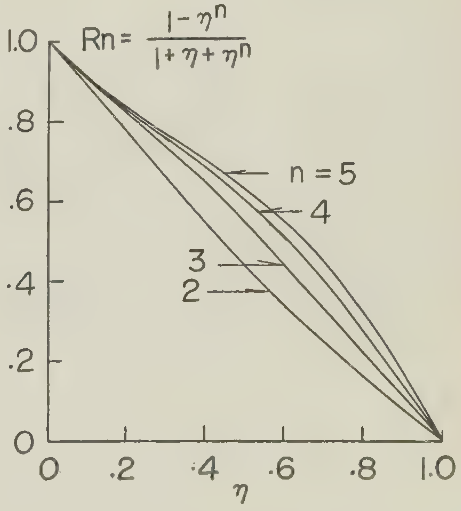

Fig. 6. Calculated curves for the ratios of the cross section for the successive collisions to that of the single collisions.

interactions in this experiment was 11.1, taking the contribution of the neutral pions into account, the value of n adopted was 3.7. There probably is an error due to the uncertainty in identifying the events of the n-N group, which was estimated to be ±3. Then the observed ratio of R_n is $9 \pm 4/23 \pm 6 = 0.39 \pm 0.19$. Thus from the curves in Fig. 6, the transparency η was estimated to be 0.68 ± 0.16. Therefore, if the geometrical nuclear cross section of a nucleon was taken to be 60 mb, the nuclear interaction cross section of a nuclear particle in a carbon nucleus is evaluated to be 19±9 mb. This is in a pretty good agreement with the results obtained in the experiments using the protons or pions of accelerators[12),13)].

When it is accepted that $n = 3.7$ and $\eta = 0.68$, the number of the secondary particles which collide with another nucleon in the carbon nucleus in succession is quite close to one. As this particle is most probably a pion which was emitted in the forward direction in the first interaction, the energy of the particle in the L.S. is calculated to be $E = 8.1$ GeV, using the Lorenz factor of the first collision $\gamma_1 = 12.03$ and the average energy of the pion $E^* = 350$ MeV in the C.M.S. The Lorentz transformation factor between the L.S. and the C.M.S. of the succeeding collision of this particle is calculated from the equation

$$E_\pi = M_N\{\gamma_2\sqrt{\gamma_2^2 - 1 + (M_\pi/M_N)^2} + \gamma_2^2 - 1\}\,, \tag{6}$$

resulting $\gamma_2 = 2.30$, which is in a fairy good agreement with the average value of $\gamma_2 = 2.22$ observed. This is probably another possible evidence of the succession collision model.

In conclusion, from the results of analysis presented above, it might be difficult to treat the successive collisions inside the target nucleus too quantitatively, but it is very plausible that the successive collision model is valid in the nucleon-nucleus collisions in the energy range of this experiment around 100 GeV/c.

Finally the author wishes to express his gratitudes to Professor O. Minakawa for his interest and discussions on this experiment. Thanks go also to Mr. C. Yokoyama, without whose help this work would not have been possible. Dr. Y. Toyoda and Mr. T. Maeda helped the mountain observation. He is indebted to the authorities of Cosmic Lay Laboratory for offering him the facilities for making the experiment on Mt. Norikura. This work was done in collaboration with Professor G. Fujioka.

References

1) A. B. Weaver, Phys. Rev. **90**, (1953) 86.
2) N. G. Birger, N. L. Grigorov, V. V. Guseva, G. B. Zhdanov, S. A. Slavatinskii and G. M. Stashkov, Sov. Phys. JETP **4**, (1957) 872; N. G. Birger, V. V. Guseva, K. A. Kotelinikov, V. M. Maksimenko, S. V. Riabikov, S. A. Slavatinskii and G. M. Stashkov, Sov. Phys. JETP **4**, (1957) 836.
3) N. M. Duller and W. D. Walker, Phys. Rev. **93** (1954) 215.
4) L. F. Hansen and W. B. Fretter, Phys. Rev. **118**, (1960) 812.
5) E. R. T. Awunor-Reener, L. Plaskovitch, B. R. French, C. Ghesquiere, I. B. De Minvielle-Devaux, W. W. Neale, C. Pelletier, P. Rivet, A. B. Sahiar and I. O. Skillicorn, Nuov. Cim. **17**, (1960) 134.
6) L. Montanet, J. A. Newth, G. Petrucci, R. A. Salmeron and A. Zichichi, Nouv. Cim. **17**, (1960) 166.
7) E. Lohrmann, Nuov. Cim. **6** (1957) 1074.
8) S. Kaneko, O. Kusumoto, S. Matsumoto, and M. Takahata, Proceedings of the Moscow Cosmic Ray Conference I (1960) 107.
9) T. Gozani and K. Sitte, Nuov. Cim. **11** (1959) 26.
10) U. Harber-Shaim, Phys. Rev. **84** (1951) 1199.
11) G. Cocconi, Phys. Rev. **93** (1954) 413.
12) V. S. Parashenkov, V. A. Belyakov, E. G. Bubelev, Wang Shou Feng, W. M. Maltsev, Ten Gyn and K. D. Tolstov, Nucl. Phys. **9** (1958) 74.
13) R. M. Kalbach, J. J. Lord and C. H. Tsao, Phys. Rev. **113** (1959) 330.

JOURNAL OF THE PHYSICAL SOCIETY OF JAPAN Vol. 16, No. 6, JUNE, 1961

A Cloud Chamber Study of High Energy Nuclear Interactions of Cosmic Ray Particles. (II)—Results of Single Nucleon-Nucleon Interactions

By Goro FUJIOKA

Department of Physics, Kobe University, Kobe, Japan

(Received February 10, 1961)

30 possible nucleon-nucleon interactions of primary energies around 100 GeV observed in a magnet cloud chamber were analyzed in their center of mass systems. The angular distribution of secondary particles was nearly isotropic. The average values of E^* and p_T were 350 MeV and 220 MeV/c, respectively, the R.M.S. deviations about mean values being 225 MeV and 160 MeV/c. The energy spectrum can be represented as $E^{*-2}dE^*$. The inelasticity of interactions had a tendency to decrease with increasing primary energies. The average inelasticity in the center of mass system was 0.27 ± 0.05. All interactions had almost equal number of shower particles in the foreward and backward directions in the center of mass system.

§ 1. Introduction

The production of secondary π-mesons in a single nucleon-nucleon collision at the range of primary energies above those obtained by accelerators is a very important problem and has been investigated by various authors with cloud chambers[1)-5)] and nuclear emulsion[6)] utilizing cosmic ray particles.

From nuclear interactions in a carbon block caused by cosmic ray particles with energies around 100 GeV observed at Mt. Norikura (alt. 2740 m) in a magnet cloud chamber, 30 events which can be attributed to a single collision have been treated in this article. The apparatus and the procedure of measurements were reported in the preceding paper (hereafter referred to as Paper I).

The primary energy of the collision was calculated from momenta and angles of emission of shower particles in the laboratory system, assuming that the collision was nucleon-nucleon, and the analysis of the interaction in its center of mass system was presented. It is considered that about a quarter of events observed was caused by charged π-mesons, but results obtained can be regarded as those of nucleon-nucleon collisions without giving any appreciable error.

The analysed events were confined to those in which momenta of all particles could be measured, that is, no momentum of shower particles should exceed our M.D.M., 25 GeV/c, and in which four or more shower particles should be included. These criteria were necessary because the calculation of the primary energy needed momenta of all particles, and because fluctuation of calculated values might be fairly large, if number of particles considered was too small. Other conditions of selection of events were that the total visible momentum should exceed 10 GeV/c or three or more particles should have momenta greater than 1 GeV/c, and that the convergence of shower particles on the origin should be good enough.

§ 2. The Nature of the Collision and the Primary Energy

As described in Paper I, the shower axis, i.e. the direction of the primary particle, was determined from the balance of the transverse momenta of shower particles, and then the Lorentz transformation factor γ_c of the C.M.S. was obtained from the balance of the longitudinal momenta in that system assigning appropriate masses for secondaries.

As carbon was chosen as the target material in this experiment, there were some cases in which the target was not a single nucleon. The method to estimate the number of target nucleons participated to the interaction was also given in Paper I. If the angular distribution of secondaries in the C.M.S. transformed by the above-obtained γ_c showed too much concentration in the forward and backward directions, it seemed reasonable to interprete that more than two nucleons took part in this collision. Those events in which more than 80% of particles were included in the region of angle, where $|\cos\theta^*|>0.8$, were classified as n-N group. The other events were assumed to be with the only one nucleon of the target carbon nucleus in this analysis, and were classified as n-n group.

In n-N group, particles in the forward hemisphere in the frame transformed by the above-obtained γ_c were considered to be emitted from the first collision with a single nucleon, and the same procedure was applied to calculate γ_c for this first collision. It was found that the features of collisions in the C.M.S. thus obtained were similar to those of collisions in n-n group, and therefore those two types of 30 collisions (23 events of n-n group and 7 first collisions of n-N group) were included in the next analysis. In two cases of n-N group, the number of particles of first collisions was three, and such events were discarded.

The primary particles responsible to the interactions are protons and π-mesons. At this altitude and in this energy-region the ratio of the number of charged π-mesons to the number of protons is less than 40%.7) Assuming that these two types of particles have the same cross sections and that interactions were caused by charged particles as expected from our triggering counter system, about 30% of our interactions might be caused by charged π-mesons. There is some possibility that interactions caused by neutrons were included, as accompanying charged particles could hit the upper counter tray. Therefore the fraction of intractions caused by charged π-mesons may be slightly lower. The rough estimate from the positive excess (1.0 per interaction) assuming the same number for primary positive and negative π-mesons gave the value of 25% for the fraction of π-meson induced interactions.

Though this fraction is not negligibly small, we have considered that our results were those of nucleon-nucleon interactions, because we did not find any peculiar features in individual cases, and because jet showers in nuclear emulsion showed not much difference, whether they were produced by the singly charged primary cosmic-ray particles (which were mainly nucleons at the balloon altitude) or by the singly charged secondary particles from the jets (mainly π-mesons).8) If the interactions caused by nucleons and charged π-mesons are slightly different in character, this postulation will not give important errors in interpreting the results.

Thus 30 nucleon-nucleon collisions were analysed in the C.M.S.. γ_c's range from 3.5 to 18.9, and the mean value is 10.2.

When the target is a single nucleon, the energy of the primary particle in the L.S. is approximately

$$2\gamma_c^2 M_N \qquad \text{for } \gamma_c^2 \gg 1,$$

where M_N is the rest energy of the nucleon, and is nearly independent of the mass of the primary particle. The distribution of primary energies is given in Fig. 1.

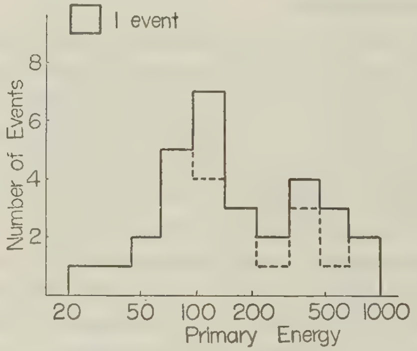

Fig. 1. The distribution of primary energies of nucleon-nucleon interactions. Events above broken lines are of n-N group.

§ 3. The Angular Distribution of Shower Particles in the C.M.S.

The angle of emission of the shower particle in the C.M.S. was calculated by the usual transformation formula,

$$\tan\theta_i^* = \frac{\sin\theta_i}{\gamma_c(\cos\theta_i - \beta_c/\beta_i)}\,. \tag{1}$$

The angular distribution of secondary pions in the C.M.S. thus obtained is shown in Fig. 2. It shows a little peak in the forward direction and a fairly sharp peak in the backward direction.

The average of $|\cos\theta_i^*|$ for each shower was also calculated, and the histogram of this quantity is shown in Fig. 3. The mean value for all events is 0.58 ± 0.03. If the distribution is isotropic, this average should be

0.5, and if the distribution is $|\cos\theta^*|d(\cos\theta^*)$, this should be 0.61, for $\beta_c/\beta^*=1$.

To determine whether the distribution is anisotropic or not, the systematic error caused by the wrongly assigned value of γ_c can not be overlooked. If we use a wrong value γ_c' for the transformation, the solid angle element in the true C.M.S. is transformed in this assigned C.M.S. by the formula,

$$\sin\theta^* d\theta^* = \frac{4\alpha^2}{[(1+\cos\theta^{*\prime})+\alpha^2(1-\cos\theta^{*\prime}]^2}\sin\theta^{*\prime}d\theta^{*\prime}\,, \qquad (2)$$

where $\alpha=\gamma_c/\gamma_c'$, and the assumption that $\beta_c/\beta^*=\beta_c'/\beta^{*\prime}$ is made. The curves of $\sin\theta^* d\theta^*/\sin\theta^{*\prime}d\theta^{*\prime}$ are shown in Fig. 4 for various α values. They are the angular distributions, which we shall obtain due to the erroneous estimate of the primary energy, when the distribution in the true C.M.S. is isotropic. Thus the error in γ_c gives the obtained distribution an apparent an isotropy; it also makes the average of $\langle|\cos\theta^*|\rangle$ larger than 0.5 as shown in Fig. 5, even if the true distribution is isotropic.

There are two sources of error in estimating γ_c that should be considered. The first is the fluctuation on account of the neglection of unseen particles, and perhaps this gives the average error of about 30%. The second is the plural interaction in the nucleus. As shown in Paper I some events

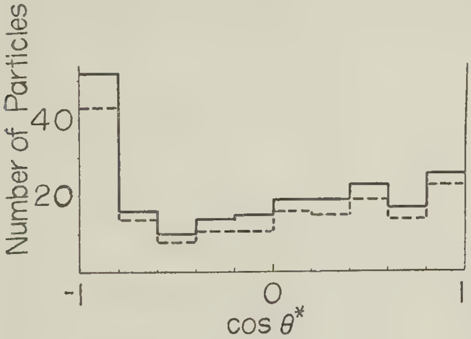

Fig. 2. The angular distribution of shower particles in the C.M.S.. Particles above broken line are of n-N group.

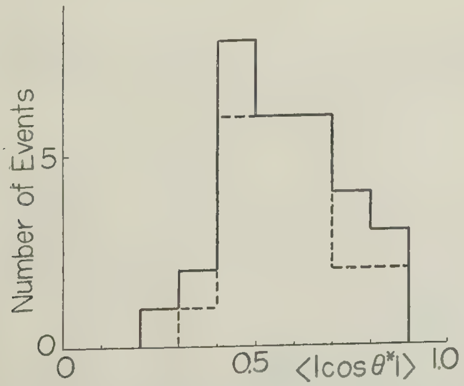

Fig. 3. The distribution of $\langle|\cos\theta_i^*|\rangle$. Events above broken lines are of n-N group.

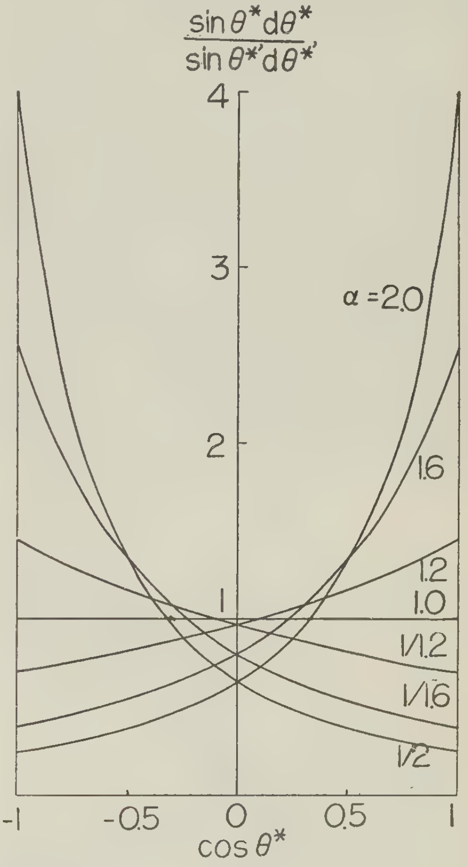

Fig. 4. $\sin\theta^* d\theta^*/\sin\theta^{*\prime}d\theta^{*\prime}$ for various α values, assuming $\beta_c/\beta^*=\beta_c'/\beta^{*\prime}$.

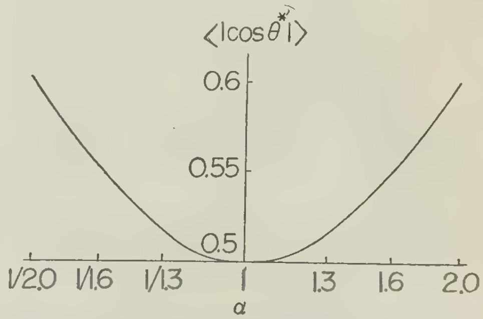

Fig. 5. $\langle|\cos\theta^{*\prime}|\rangle$ *vs.* α, when the distribution in the C.M.S. is isotropic, for $\beta_c'/\beta^{*\prime}=1$.

were interpreted as such and they were discarded from this analysis as stated in § 2. But if the multiplicity of the interaction in the same nucleus caused by the secondary particle emitted from the first interaction was small, or if the energy of the shower particle responsible to this second interaction was not far smaller than that of the primary which had caused the first interaction, such events would not show remarkable separate peaks and might be included in the *n-n* group in this analysis. As $\gamma_1/\gamma_{1+2}\sim 2$ for *n-N* group as shown in Paper I, this source of error will not give the error over 50%.

Considering the effect of the error in γ_c, Figs. 2 and 3 can not be considered as the definite evidence for the anisotropic distribution. But we may go too far if we attribute this anisotropy only to the apparent effect due to the error in γ_c. Our conclusion is that the angular distribution of secondaries in the C.M.S. is not far from isotropy in this range of primary energy.

As the another approach to this problem the indirect but widely used so-called *F*-plot[9] was also considered. To treat all events as a whole, each value of $\tan\theta_i$ was multiplied by γ_c. This means that $\log(F/1-F)$ versus $\log(\gamma_c\tan\theta)$ should be the straight line with the gradient 2 crossing the abscissa at $\gamma_c\tan\cdot\theta=1$ when the distribution is isotropic and β_c/β^* is 1, because

$$\log(F/1-F)=\log(\gamma_c\tan\theta)^2$$

in this case. The *F*-plot constructed from 208 particles is shown in Fig. 6, together with the expected curves for isotropic distribution with $\beta_c/\beta^*=1.0$ and 1.09 (which is the average value in our case). The experimental points can be approximated by these curves if all γ_c values are multiplied by 1.35. This horizontal displacement of *F*-plot is hard to explain but may reflect the fact that the energy estimate from the angular distribution gives high values systematically.[10] Thus the *F*-plot also shows that the angular distribution in the C.M.S. is nearly isotropic.

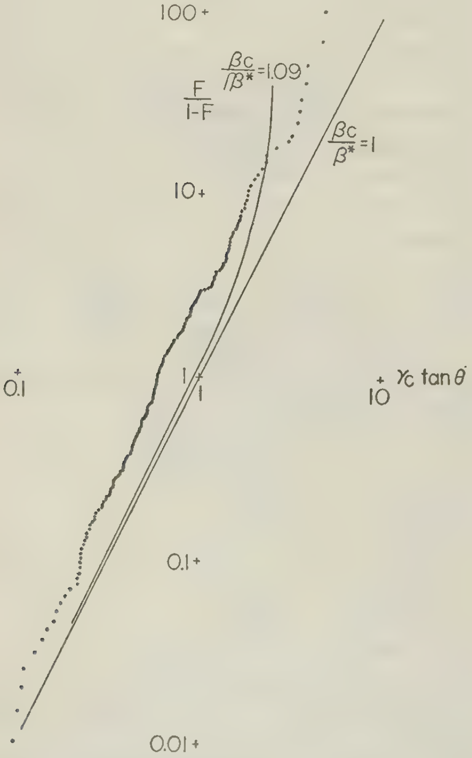

Fig. 6. The normalized *F*-plot constructed from 208 particles of 30 showers.

§ 4. The Energy of Secondaries in the C.M.S.

The energy of secondary pions was calculated according to the usual formula,

$$E_i^*=\gamma_cE_i-\sqrt{\gamma_c^2-1}\,p_ic\cos\theta_i\,. \tag{3}$$

At first, we consider the effect of the error in γ_c. Differentiating (3) by γ_c,

$$\frac{\partial E_i^*}{\partial\gamma_c}=E_i-\frac{\gamma_c}{\sqrt{\gamma_c^2-1}}\,p_ic\cos\theta_i\,. \tag{4}$$

Therefore, if $\Delta\gamma_c$ is not large,

$$\begin{aligned}\frac{\Delta E_i^*}{E_i^*}&=\frac{\Delta\gamma_c}{\gamma_c}\Big[E_i-\frac{\gamma_c}{\sqrt{\gamma_c^2-1}}\,p_ic\cos\theta_i\\&\qquad\Big/E_i-\frac{\sqrt{\gamma_c^2-1}}{\gamma_c}\,p_ic\cos\theta_i\Big]\\&=\frac{\Delta\gamma_c}{\gamma_c}[\beta_cE_i-p_ic\cos\theta_i\\&\qquad/\beta_cE_i-\beta_c^2p_ic\cos\theta_i]\,.\end{aligned} \tag{5}$$

The absolute value of the term in the bracket of (5) is smaller than 1, if

$$\cos\theta_i<\frac{E_i}{p_ic}\;\frac{2\gamma_c\sqrt{\gamma_c^2-1}}{2\gamma_c^2-1}\,, \tag{6}$$

which in many cases holds. Therefore the error in E_i^* introduced by the error in γ_c is in many cases smaller than that of γ_c in percentage and its sign is the same with the sign of the error of γ_c, if the particle is in the backward hemisphere, and the opposite if in the forward hemisphere.

Thus the error in γ_c does not give the systematic error to the energy distribution in the C.M.S., not as in the case of the angular distribution.

The energy distribution is given in Fig. 7. The mean energy was 350 MeV, and the R.M.S. deviation about the mean was 225 MeV. This distribution is expressed fairly well by the formula $1/E^{*2}$ as shown in the figure.

To see if there is any correlation between the energy and the emitted angle, the average energies of particles emitted in given ranges of angles are plotted against the angle of emission in the C.M.S. in Fig. 8. It can be considered as constant, though there are some fluctuations; this shows that there is little dependence of the energy upon the emitted angle in the C.M.S.

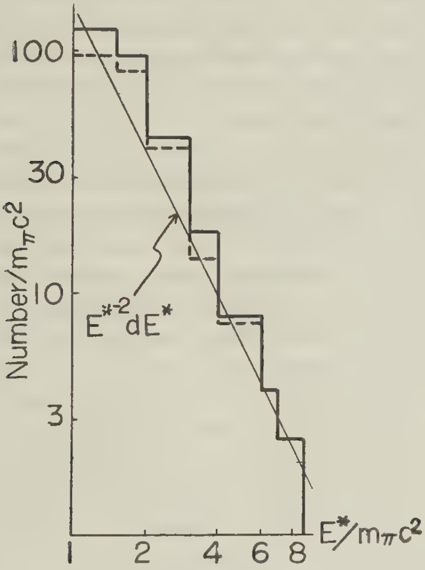

Fig. 7. The energy distribution of secondary π-mesons in the C.M.S.. Particles above broken lines are of n-N group.

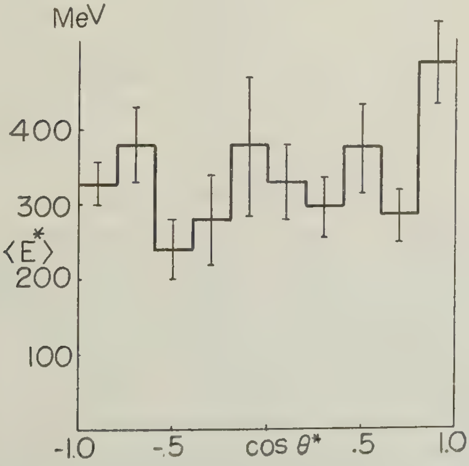

Fig. 8. The average π-meson energy vs. the emitted angle in the C.M.S..

§ 5. The Transverse Momentum of Secondary Particles

The transverse momentum is, of course, Lorentz invariant and independent of γ_c. The distribution of transverse momentum obtained in this experiment is shown in Fig. 9. The average value was 220 MeV/c, and the R.M.S. deviation about the mean was 160 MeV/c.

As the direction of primary particles was determined from the balance of transverse momenta, the transverse momenta were slightly underestimated as pointed out by Minakawa et al.[11] They presented a statistical treatment to obtain the $2n$-th moment of the true distribution of transverse momenta from the observed one. By this method the second moment of the true distribution was calculated. This was $(9.3\pm1.6)\times10^4(\mathrm{MeV/c})^2$, whereas the observed second moment was the

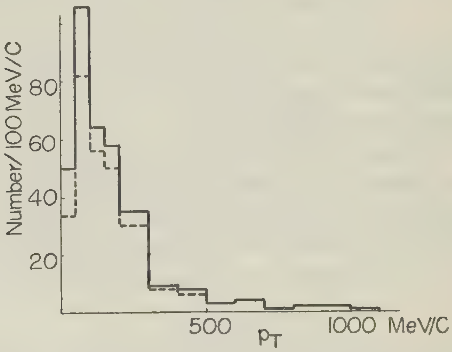

Fig. 9. The distribution of transverse momentum. Particles above broken lines are of n-N group.

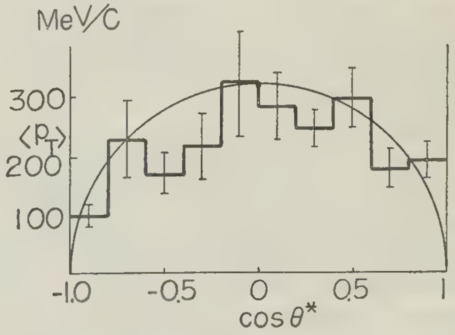

Fig. 10. The average transverse momentum vs. the emitted angle in the C.M.S..

$(7.5\pm1.4)\times10^4(\mathrm{MeV/c})^2$. This shows that the obtained distribution does not differ appreciably from the true one and that the error of determining the primary direction in this analysis is not important.

As it is interesting to see the angular dependence of p_T, the average transverse momentum of pions emitted in given ranges of angles in the C.M.S. is also shown in Fig. 10, though this is not independent of the similar graph for the C.M.S. energy. If there is little correlation between E^* and θ^*, as shown in § 4, p_T should be represented as $\langle p^*\rangle \sin\theta^*$. This curve is drawn in Fig. 10, where $\langle p^*\rangle$ corresponds to $\langle E^*\rangle=350$ MeV. The obtained histogram is rather better approximated by this curve than constant p_T, suggesting again that E^* has little correlation with θ^*.

§ 6. Inelasticity of Collisons

The inelasticity K, that is, the fraction of energy carried out by created particles, was considered in the C.M.S.. This is defined by

$$K=\frac{\sum E_i^*}{2(\gamma_c-1)M_N}, \qquad (7)$$

for the nucleon-nucleon collision, where the summation should be taken over all particles, charged and neutral.

If the primary particle is a π-meson, the velocities of the primary and the target are not the same in the C.M.S.. Putting the suffix π for quantities of the primary π-meson in this system, by the definition of the C.M.S.,

$$\beta_\pi\gamma_\pi M_\pi=\beta_c\gamma_c M_N\,. \qquad (8)$$

The available energy in the C.M.S. including the primary rest mass is

$$\gamma_\pi M_\pi+(\gamma_c-1)M_N\approx(2\gamma_c-1)M_N\,,$$

because $\beta_c\approx\beta_\pi\approx1$. Therefore, in this case K is overestimated if we calculate it from (7), but the error seldom exceeds 10% in our range of γ_c.

If the most energetic positive particle had an energy two times greater than that of any other particle in the L.S., this particle was assumed to be a proton and was not summed up in the numerator of (7). If this particle were a π-meson, K would be underestimated by about 0.2. This was estimated assuming a pion mass for this particle.

To take account the unseen π^0-mesons, the sum for all charged secondaries assuming pion masses was multiplied by 1.5 and was used as $\sum E_i^*$ in (7).

The assumption of all secondaries with momenta greater than 110 MeV/c as π-mesons gives an underestimate of the inelasticity, if K-mesons are produced in that event. The error introduced by this assumption was estimated in each case, assuming that the charged particle, which had the momentum in the L.S. higher than and nearest to 410 MeV/c, was a K-meson and that the neutral K had the same energy with it. This assumption is the very extreme one which gives the highest inelasticity, but was adopted to see the limit of the error. This error seldom exceeded 0.2 under this extreme assumption in our cases.

Thus our value of K assuming that all secondaries are π-mesons and the neutral π-mesons carry half of the energy of all charged π-mesons is correct within the error or 0.2 in the average. K's are plotted against γ_c in Fig. 11. The mean value of K was 0.27 ± 0.05, where the error cited was the standard deviation.

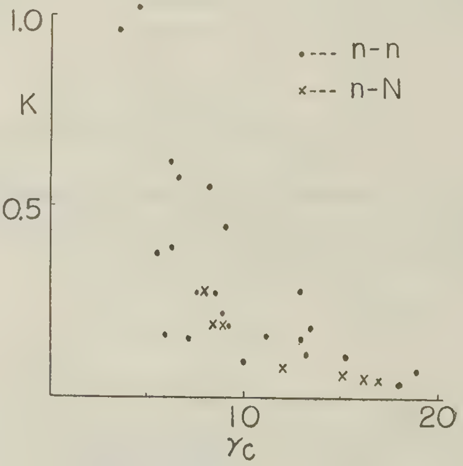

Fig. 11. The inelasticity K *vs.* γ_c.

There is a tendency that K decreases with increasing γ_c. This is not to be taken literally, because many of the high K events with high γ_c might contain too many particles to be analysed or might contain π-mesons with the momentum higher than 25 GeV/c, and those were excluded from this analysis. But the lower limit of K shows the same tendency with increasing γ_c, and, therefore, this is perhaps the true effect.

§ 7. Comparison with Other Results and Discussions

The angular distribution of secondary pions in the C.M.S. is similar to those obtained by Hansen and Fretter,[1] and by Montanet et al.,[2] and shows a slight anisotropy. Kaneko et al.[6] obtained a nearly isotropic distribution in the region of a little lower primary energies. This difference may be due to the difference of altitudes, because at mountain altitudes about one fourth of interactions are caused by charged π-mesons as described in § 2. But considering the systematic error introduced by the fluctuation of γ_c and by the secondary interactions in the nucleus, the discrepancies seem not serious. Though the possibility that there are some events with a weak anisotropy can not be excluded, the angular distribution is not very far from isotropy in the average at this range of primary energies.

The distributions of energy in the C.M.S. and of the transverse momentum are similar between those experiments and ours. Our mean values of E^* and p_T are somewhat lower than those of other authors, but the differences are not significant. $E^{*-2}dE^*$ spectrum seems to hold rather well. This spectrum is just the same with that assigned by Heisenberg[12] in his theory. But this only one point should not be trusted too much as the evidence to support his theory. The independence of the energy and the angle of emission of secondary pions in the C.M.S. shown in § 4 and 5 may favour the statistical model.[13] Perhaps at $\gamma_c \sim 10$ any theory at present can hardly explain satisfactorily all features of interactions.

The tendency that the inelasticity decreases with increasing primary energy was also pointed out by Hansen and Fretter. The average values of K obtained by several authors lie around 0.3 and agree well with ours.

In this analysis we found no example of assymmetric emission of secondaries found by Dobrotin et al.[5] Such assymmetric events, if they exist, contain a high energy particle in many cases, and we might exclude such events as we analysed events in which the momentum of no particle exceeded 25 GeV/c. But assymmetric events with a high energy backward proton in the C.M.S. should be included in this analysis. Even in such cases longitudinal momenta of charged particles should nearly balance in the C.M.S., as it is very implausible that one neutral particle carries an extraordinary momentum in these cases of the presence of one high energy backward proton in the C.M.S.. Our method of estimating γ_c did not depend on the symmetricity of the emission of secondary particles in the forward and backward directions in the C.M.S., but utilized the balance of longitudinal momenta. Therefore it is very unlikely that our calculated γ_c is mistaken by a factor of more than 2, even if we assumed these protons as π-mesons in such cases. Thus we can not find any reason, except the fluctuation of the occurence, why we found no such cases.

We can not say much about the fraction of assymmetric interactions, if any, but our results hold for the symmetric emission of secondaries.

The author wishes to thank Prof. O. Minakawa for his valuable suggestions and discussions. The collaboration with Prof. I. Kita and Mr. C. Yokoyama throughout this work and with Mr. S. Hozumi at the earlier stage of this work was extremely pleasant. Dr. Y. Toyoda and Mr. T. Maeda helped the mountain observation. We are indebted to the Director of Norikura Cosmic Ray Laboratory and his staff, who made this experiment possible. The work was partly supported by the Scientific Research Expenditure of the Ministry of Education.

References

1) L. F. Hansen and W. B. Fretter: Phys. Rev., **118** (1960) 812.

2) L. Montanet, J. A. Newth, G. Petrucci, R. A. Salmeron, and A. Zichichi: Nuovo Cimento, **17** (1960) 166.

3) E. R. T. Awunor-Renner, L. Blaskovitch, B.R. French, C. Ghesquiere, I. B. de Minvielle-Devaux, W. W. Neale, C. Pelletier, P. Rivet, A. B. Sahiar, and I. O. Skillicorn: Nuovo Cimento, **17** (1960) 134.

4) N. G. Birger, N. L. Grigorov, V. V. Guseva, G. B. Zhdanov, S. A. Slavatinskii, and G. M. Stashkov: Sov. Phys. JETP, **4** (1957) 872; N. G. Birger, V. V. Guseva, K. A. Kotelinikov, V. M. Maksimenko, S. V. Riabikov, S. A. Slavatinskii, and G. M. Stashkov: Sov. Phys. JETP, **4** (1957) 836.

5) N. L. Grigorov, V. V. Guseva, N. A. Dobrotin,

K. A. Kotelnikov, V. S. Murzin, S. V. Ryabikov, and S. A. Slavatinsky: Proceedings of the Moskow Cosmic Ray Conference (1960) 143; N. A. Dobrotin and S. A. Slavatinsky: Preprint A-24 of P. N. Lebedev Physical Institute of Academy of Sciences USSR (1960).

6) S. Kaneko, O. Kusumoto, S. Matsumoto and M. Takahata: Proceedings of the Moscow Cosmic Ray Conference (1960) 107.

7) K. Greisen: Progr. Cosmic Ray Phys., **3** (1956) 108.

8) P. K. Malhorta, and Y. Tsuzuki: Nuovo Cimento, **5** (1960) 982.

9) N. M. Duller and W. D. Walker: Phys. Rev., **93** (1954) 215.

10) E. M. Friedlander: Nuovo Cimento, **12** (1959) 483.

11) O. Minakawa, Y. Nishimura, Y. Tsuzuki, H. Yamanouchi, H. Aizu, H. Hasegawa, Y. Ishii, S. Tokunaga, Y. Fujimoto, S. Hasegawa, J. Nishimura, K. Niu, K. Nishikawa, K. Imaeda and M. Kazuno: Suppl. Nuovo Cimento, **11** (1959) 125.

12) W. Heisenberg: Z. Phys., **133** (1952) 65.

13) E. Fermi: Progr. Theor. Phys., **5** (1950) 570.

JOURNAL OF THE PHYSICAL SOCIETY OF JAPAN, Vol. 16, No. 6, JUNE, 1961

Effects of *s–d* Exchange Interaction and Temperature-Independent Paramagnetism on Susceptibilities of Nickel, Palladium and Platium

By Masao SHIMIZU

Department of Physics, Faculty of Science, Tokyo Metropolitan University, Tokyo

(Received September 9, 1960)

The well-known discrepancy between the number of the Bohr magneton obtained from the saturation magnetization at 0°K and that obtained from paramagnetic susceptibilities for Ni is explained by taking into account the s–d exchange interaction, instead of the s–d electron transfer, and the temperature-independent paramagnetism due to the orbital moments of d electrons. The similar discrepancy between the number of magnetic carriers obtained from the paramagnetic susceptibility measurement at lower temperatures and that at higher temperatures for Pd is explained in the same way. The same discussion is applicable to Pt. It is concluded that the temperature-independent paramagnetism is important to understand the temperature variations of susceptibilities of transition metals. The paramagnetic susceptibilities for Ni, Pd, and Pt at higher temperatures are expressed in the form, $C/(T-\theta_p)+\chi_0$. The temperature-independent susceptibility, χ_0, is the sum of the paramagnetic susceptibility of the conduction electron (or s electron) spins and that due to the orbital moment of d electrons.

§1. Introduction

It is well-known that the numbers of the Bohr magneton obtained from the saturation magnetization at 0°K for ferromagnetic iron-group metals are different from those numbers estimated from the paramagnetic susceptibility above the Curie temperature¹⁾.

There are two ways at present to obtain the number of the Bohr magneton from the experimental measurements of the paramagnetic susceptibility above the Curie temperature. One is to use the Curie-Weiss law and the other is to use the $1/\chi-T^2$ law where the variation of $1/\chi$ with T^2 is linear.

Using a modified electron gas model, we have attempted to explain the temperature variations of paramagnetic susceptibilities of the iron-group metals above the Curie temperature, but a satisfactory quantitative agreement between the experimental results and our theoretical results for the susceptibilities has not been obtained.[2]

Especially, the variation with temperature of $1/\chi$ for Ni follows neither the Curie-Weiss law nor the $1/\chi - T^2$ law. At higher temperatures the curve $1/\chi$ vs. T follows the Curie-Weiss law apparently. Also, for Pd the curve $1/\chi$ vs. T follows the Curie-Weiss law apparently at higher temperatures. However, the numbers of the Bohr magnetons obtained from these Curie constants for Ni and Pd at higher temperature regions are also larger than the numbers which are obtained from the experimental results at lower temperatures.

Then, it seems that a new mechanism is necessary to explain the temperature variation of the susceptibilities above the Curie temperature for the ferromagnetic iron-group metals, especially for Ni, and that of Pd.

On the other hand these discrepancies have so far been studied by Watanabe[3], Wohlfarth[4], and Krinchik[5], introducing the mechanism of electron transfer between s and d bands, and by Vonsovskii and Vlasov[6] introducing the s–d exchange interaction. Especially Wohlfarth has examined the effect of the s–d transfer on the paramagnetic susceptibilities for pure Ni and Ni–Cu alloys in detail. He has concluded that an increase, with temperature, of the number of holes in the $3d$ band accounts for the major part of the down-ward curvature of the $1/\chi - T$ curves at higher temperatures, but it does not suffice to explain the whole of it.

Moreover, Wohlfarth has found that the electronic specific heat of the $3d$ band increases at higher temperatures because of the increase of the number of holes in the $3d$ band. It seems, however, that experimental results for the specific heat of Ni at higher temperatures do not show the same increase as the one that Wohlfarth has obtained theoretically, although the experimental results at higher temperatures are not absolutely certain. The specific heats at higher temperatures for Ni, Pd, and Pt are discussed in § 4.

Then, consistently to explain the temperature variation of the susceptibilities and the specific heats at higher temperatures for the ferromagnetic iron-group metals, especially for Ni, and Pd, it seems that a new mechanism besides the electron transfer between s and d bands is necessary.

In this paper we take into account the exchange interaction between s and d electrons and examine the effect on the paramagnetic susceptibilities for Ni, Pd, and Pt (§ 2). We assume that the s–d exchange interactions for these metals are ferromagnetic but we do not think that the ferromagnetism of Ni is caused entirely by this s–d exchange interaction. The exchange interaction between d electrons is assumed to be larger than the s–d interaction. By the modified electron gas model we can ascertain this fact (§ 3).

If we take into account the temperature-independent paramagnetic susceptibility which is expected to derive from the contribution of the orbital moment of d electrons to the total magnetic moment, we can satisfactorily explain the temperature variations of the paramagnetic susceptibility for Ni and Pd.

§ 2. Effect of Exchange Interaction between s and d Electrons on Paramagnetic Susceptibility of Transition Metals

In order to consider the s–d exchange interaction in transition metals, we use the approximation of tight-binding for d and s electrons. Let the spin operators for d and s electrons be $\boldsymbol{s}_k$ and $\boldsymbol{\sigma}_{k'}$ respectively. The s–d exchange energy is $-2\sum_{k,k'} J_{kk'}\boldsymbol{s}_k\cdot\boldsymbol{\sigma}_{k'}$. $J_{kk'}$ is an exchange integral between d electron with wave vector k and s electron with wave vector k', and is nearly equal to J/N, where J is an atomic s–d exchange integral and N is the total number of lattice points.

The mean value of the s–d exchange energy becomes

$$-2\sum_{k,k'} J_{kk'}\langle \boldsymbol{s}_k\cdot\boldsymbol{\sigma}_{k'}\rangle_{\mathrm{AV}} = -2JN^{-1}\boldsymbol{M}_s\cdot\boldsymbol{M}_d/(g_s g_d \mu_B{}^2)\,, \tag{2.1}$$

where

$$\left.\begin{aligned} \boldsymbol{M}_d &= N_d g_d \mu_B \langle \boldsymbol{s}_k\rangle_{\mathrm{AV}}\,,\\ \boldsymbol{M}_s &= N_s g_s \mu_B \langle \boldsymbol{\sigma}_{k'}\rangle_{\mathrm{AV}}\,, \end{aligned}\right\} \tag{2.2}$$

and N_d and N_s are the numbers of d holes and s electrons respectively.

From (2.1), the effective fields for d holes and s electrons become respectively, as shown by Owen et al.[7],

$$\left.\begin{aligned} \boldsymbol{H}_d &= \lambda \boldsymbol{M}_s\,,\\ \boldsymbol{H}_s &= \lambda \boldsymbol{M}_d\,, \end{aligned}\right\} \tag{2.3}$$

where

$$\lambda=2J/(Ng_s g_d \mu_B^2)\ . \tag{2.4}$$

Let the paramagnetic susceptibility of the d holes above the Curie temperature and that of the s electrons be χ_d and χ_s respectively. The magnetizations of d holes and s electrons are given by

$$\left.\begin{aligned} M_d&=\chi_d(H_0+\lambda M_s)\ ,\\ M_s&=\chi_s(H_0+\lambda M_d)\ , \end{aligned}\right\} \tag{2.5}$$

where H_0 is an external magnetic field.

Then, the total magnetic susceptibility χ is given by

$$\chi=(M_d+M_s)/H_0=\chi_d\frac{(1+\lambda\chi_s)^2}{1-\lambda^2\chi_s\chi_d}+\chi_s\ . \tag{2.6}$$

If there is a contribution from the orbital moment of d electrons to the total magnetic moment, we must take into account the temperature independent paramagnetic susceptibility[8], $\chi_{d,\mathrm{orbit}}$, and this should be added to the susceptibility given by (2.6). Kubo and Obata have pointed out that this is important in paramagnetic metals with partly filled non-s bands[8]. Then in this case we have for the paramagnetic susceptibility of transition metals,

$$\chi=\chi_d\frac{(1+\lambda\chi_s)^2}{1-\lambda^2\chi_s\chi_d}+\chi_s+\chi_{d,\mathrm{orbit}}\ , \tag{2.7}$$

where we neglect the diamagnetic susceptibility of atomic core. $\chi_{d,\mathrm{orbit}}$ and g_d are estimated roughly as follows: $\chi_{d,\mathrm{orbit}}\simeq N_d\mu_B^2/\Delta\mathcal{E}$, and $\Delta g_d=g_d-2\simeq\xi/\Delta\mathcal{E}$, where ξ is the coefficient of spin-orbit interaction and $\Delta\mathcal{E}$ is the mean of the separations of energy levels in the d band.

For Ni, Pd, and Pt, the numbers of d holes are few and the widths of d bands are narrow, so that the degeneracy temperatures of these metals are relatively low. If the temperature is so high that the d holes, as a gas, are not degenerate, the paramagnetic susceptibility due to the d hole spins follows the Curie-Weiss law[2),9)], and is given by

$$\left.\begin{aligned} \chi_d&=C_d/(T-\theta)\ ,\\ C_d&=N_d g_d^2\mu_B^2/(4k)\ . \end{aligned}\right\} \tag{2.8}$$

In this case, from (2.7) and (2.8), we have

$$\chi=\frac{C}{T-\theta_p}+\chi_c\ , \tag{2.9}$$

where

$$\left.\begin{aligned} \theta_p&=\theta+C_d\chi_s\lambda^2\ ,\\ C&=C_d(1+\lambda\chi_s)^2\\ &=N_d(g_d/2)^2\mu_B^2(1+\lambda\chi_s)^2/k\ ,\\ \chi_c&=\chi_s+\chi_{d,\mathrm{orbit}}\ . \end{aligned}\right\} \tag{2.10}$$

The formula of this type, (2.9), was already proposed by Néel[10] for Ni alloys.

In the ferromagnetic state and at 0°K, the spontaneous magnetization is given by

$$\begin{aligned} M&=M_d+M_s=(1+\lambda\chi_s)M_d\\ &=N_d(g_d/2)(1+\lambda\chi_s)\mu_B\ . \end{aligned} \tag{2.11}$$

Usually, χ_s is written, by making use of the free electron model, as $\chi_s=3N_s g_s^2\mu_B^2/8\zeta_0$, where ζ_0 is the energy of the Fermi level for the s electrons. As we have calculated the paramagnetic susceptibility of conduction electrons using the Bohm-Pines collective description of electron interactions[11], and the values of χ_s can be obtained if the effective mass and the electron density are given, we shall make use of these values for χ_s in this paper.

§ 3. Comparison with Experimental Results

At very high temperature the paramagnetic susceptibility for transition metals is expected to follow the formula (2.9). For Ni, Pd, and Pt the degeneracy temperatures of d holes will be relatively low since the numbers of d holes per atom are small. Then it will be supposed that Ni, Pd, and Pt are the best examples to interpret their susceptibilities by (2.9) at the highest temperature where the susceptibilities have so far been measured (~1800°K).

The experimental values of susceptibility for Ni, Pd, and Pt are plotted against $(T-\theta_p)^{-1}$

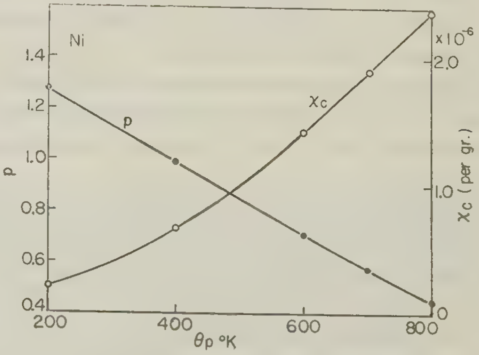

Fig. 1. Values of p and χ_c as functions of θ_p when susceptibility of Ni at high temperatures is expressed as $C/(T-\theta_p)+\chi_c$, where $p=kC_{\mathrm{mole}}/(N_0\mu_B^2)$.

where the value of θ_p is given as a parameter and at higher temperatures these curves χ vs. $(T-\theta_p)^{-1}$ become linear. By extrapolating these lines to the value $(T-\theta_p)^{-1}=0$ we can find the values of C, or $p=kC_{\text{mole}}/(N_0\mu_B^2)$ where N_0 is Avogadro's number, and χ_c as functions of θ_p. These analyses are shown in Figs. 1, and 2 by making use of Terry's data for Ni[12] and Wucher's data for Pd[13]. The values of p for Pt, which are obtained from Honda's data[14] in this way, become smaller than the value which has been estimated before from the susceptibility at lower temperatures[2]. The values of susceptibility for Pt measured by Honda may be inaccurate, because these values are not smoothly connected with the values at lower temperatures obtained by Hoare and Matthews[15].

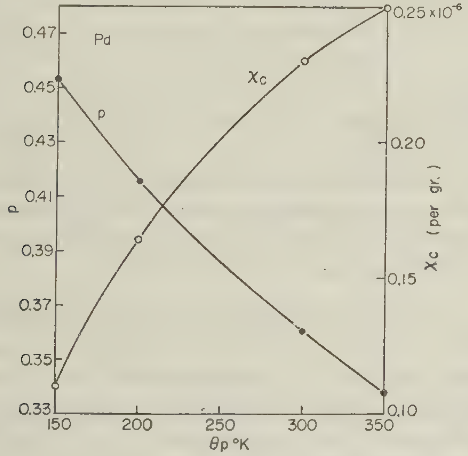

Fig. 2. Values of p and χ_c as functions of θ_p when susceptibility of Pd at high temperatures is expressed as $C/(T-\theta_p)+\chi_c$, where $p=kC_{\text{mole}}/(N_0\mu_B^2)$.

Table I. The values of exchange integral between s and d electrons for Ni, Pd, and Pt.

Element	Ni	Pd	Pt
$2J=h\Delta\nu$ cm^{-1}	2678.5	4054.7	11211.3

The values of λ in (2.4) for Ni, Pd, and Pt are determined by using their atomic spectra. We make use of the energy differences between the atomic states, $^1D(nd^9, (n+1)s)$ and $^3D(nd^9, (n+1)s)$, where $n=3$, 4, 5 for Ni, Pd, and Pt respectively, that is, $h\Delta\nu=2J=E(^1D)-E(^3D)$, where $E(^3D)$ is the weighted mean of the energies of the multiplet for ^3D.[16] The values of $2J$ are shown in Table I.

The paramagnetic susceptibility for the s electrons has been calculated before and is given by[11]

$$\chi_s\,(\text{per gr.})=3.178\times10^{-6}/(\rho r_s^3\gamma)\,, \qquad (3.1)$$

where ρ is density, γ is the coefficient of the increase of energy when conduction electrons have magnetic moment (e. g. $E=E_0+\gamma(n/N)^2$, where (n/N) is the degree of magnetization), and r_s is the inter-electronic spacing of s electrons measured in units of the Bohr radius, a_0,. We have $r_s=(3/16\pi)^{1/3}(a/a_0)p_s^{-1/3}$, where a is a lattice constant and p_s is the number of s electrons per atom.

Let the number of holes in the d band per atom be p_d, then $p_d=p_s=(3/16\pi)(a/a_0r_s)^3$ for Ni, Pd, and Pt.

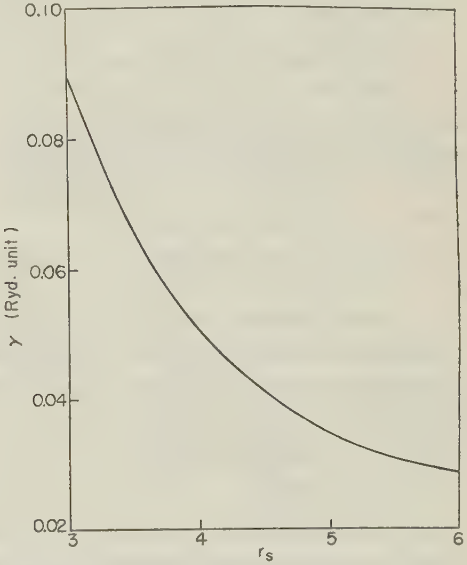

Fig. 3. Values of γ as a function of r_s when $m^*/m=1$.[11]

The values of γ, which have been obtained by the present author making use of the Bohm-Pines collective electron model[11], are shown in Fig. 3 as a function of r_s when $m^*/m=1$, where m^* is an effective mass of s electrons.

First we discuss the case of Ni. The g-factor of Ni at ferromagnetic state, g_{df}, is about 2.2[17] and that at paramagnetic state, g_{dp}, becomes about 2[18]. Then the values of λ at ferromagnetic state and at paramagnetic state which are obtained from (2.4) and J in Table I are different, and they are denoted by λ_f and λ_p respectively. Using $g_{df}=2.2$ and $g_s=2$, we have from (2.4), (3.1) and the value of J for Ni in Table I,

$$\lambda_f \chi_s = 0.0489 r_s^{-3} \gamma^{-1} . \qquad (3.2)$$

From the number of the Bohr magneton at 0°K[19] and (2.11) we have

$$p_d(g_{df}/2)(1+\lambda_f \chi_s) = 0.604 . \qquad (3.3)$$

p_d is calculated from the lattice constant and we have for Ni

$$p_d = p_s = 17.783 r_s^{-3} . \qquad (3.4)$$

From (3.2), (3.3), (3.4), and γ in Fig. 3 where $m^*/m=1$ is assumed, we can obtain the values of r_s, γ, $p_d=p_s$, $\lambda_f \chi_s$, and $\lambda_p \chi_s$ for Ni as follows:

$$\left.\begin{array}{l} r_s = 3.21 , \\ \gamma = 0.0788 , \\ p_d = p_s = 0.539 , \\ \lambda_f \chi_s = 0.188 , \\ \lambda_p \chi_s = (g_{df}/g_{dp}) \lambda_f \chi_s = 0.0207 , \\ \lambda_p^2 \chi_s C_d = 10.7\text{°K} . \end{array}\right\} \qquad (3.5)$$

From these numerical values and (2.10) and (3.1), the values of p, where p is defined by $C_{\text{mole}} = N_0 p \mu_B^2/k$ (N_0=Avogadro's number), and χ_s (per gr.) become

$$p = (1+\lambda_p \chi_s)^2 p_d = 0.562 , \qquad (3.6)$$

and

$$\chi_s = 1.37 \times 10^{-7} \text{ (per gr.)} . \qquad (3.7)$$

When the value of p is given by (3.6) the corresponding values of C, θ_p, and χ_c are obtained from Fig. 1 as follows:

$$\left.\begin{array}{l} C = 0.00358 \text{ (per gr.)} , \\ \theta_p = 708\text{°K} , \\ \chi_c = 1.92 \times 10^{-6} \text{ (per gr.)} . \end{array}\right\} \qquad (3.8)$$

Using the values of C, θ_p, and χ_c given by (3.8) and from (2.9) we calculate χ as a function of T and the result and the experimental results by Terry[12] are shown in Fig. 4.

The value of χ_c is fairly larger than that of χ_s in (3.7). The difference between these two values may be attributable to the temperature independent paramagnetic susceptibility, $\chi_{d,\text{orbit}}$. From the resonance experiments it has been found that $1.95 \leq g_{dp} \leq 2.05$[18]. Assuming $\Delta g_{dp} = g_{dp} - 2 \simeq |\xi|/\Delta\mathcal{E} = 0.05$ and using $|\xi| = 282.5 \text{ cm}^{-1}$ we have $\Delta\mathcal{E} \simeq 5650 \text{ cm}^{-1}$ and $\chi_{d,\text{orbit}} \simeq N_d \mu_B^2/\Delta\mathcal{E} \simeq 8 \times 10^{-7}$ (per gr.).

As the above estimation for $\chi_{d,\text{orbit}}$ is rough, it may be changed by the factor 2 or 3. At present we must inevitably satisfy this rough estimation for $\chi_{d,\text{orbit}}$.

On the other hand, as we have assumed for the sake of simplicity that the d holes are completely non-degenerate and the number of holes is constant with temperature, a part of the difference between χ_c and χ_s may be attributable to the effect of the electron transfer between s and d bands and the different temperature dependence of susceptibility when d holes are partly degenerate.

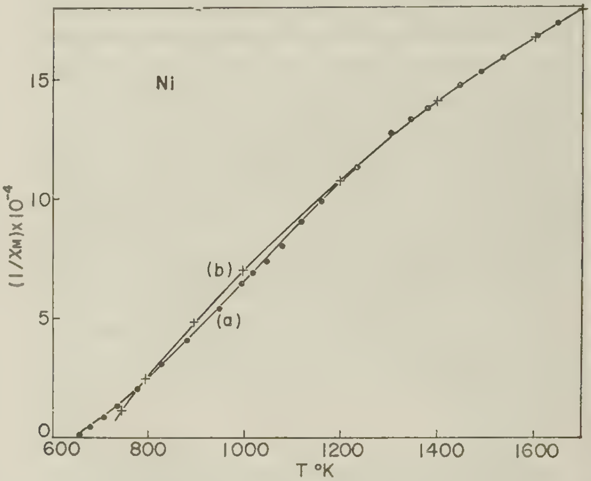

Fig. 4. Paramagnetic susceptibility of Ni. Curve (a) is Terry's experimental result[12]. Curve (b) is calculated by $C/(T-\theta_p)+\chi_c$ with $C=0.00358$ (per gr.), $\theta_p=708$°K and $\chi_c = 1.92 \times 10^{-6}$ per gr.

If the effective mass of s electrons is larger, that is, $m^*/m > 1$, we can explain the temperature dependence of susceptibility for Ni satisfactorily without introducing the temperature independent paramagnetism. For example, if we determine p and $\lambda\chi_s$ to satisfy $p = 0.604(1+\lambda\chi_s)(g_{dp}^2/2g_{df})$ and the relation between p and χ_s given in Fig. 1, we have $p=0.675$, $\chi_s = 1.54 \times 10^{-6}$ (per gr.), and $\theta_p = 624$°K. From these values we obtain $\lambda\chi_s = 0.232$, $p_d = 0.446$, $r_s = 3.42$, and $\gamma = 5.805 \times 10^3$, and from the previous calculation of the susceptibility of an electron gas[11] the effective mass for the s electron is obtained as $m^*/m = 2.51$. This value of m^*/m is large and the former interpretation where $m^*/m=1$ is assumed is more natural.

In the former interpretation, the effective field of the d holes from the s electrons is given by $\lambda M_s = \lambda^2 \chi_s M_d$ and the value of the coefficient of this effective field for Ni is obtained from (2.4) and (3.5) and Table I as

$$\lambda^2 \chi_s N_d \mu_B^2 = 6.79 \times 10^{-5} \text{ Ryd. unit.} \qquad (3.9)$$

This is fairly smaller than the value of the coefficient of the molecular field between the *d* holes, as a gas, which has been obtained (from Fig. 5 in the reference 2) as $\alpha N_d\mu_B^2=3.95\times10^{-2}$ Ryd. unit at $r_s=3.21$, although this value of α is larger by the factor 2.6 than the value which explains the temperature variation of magnetization at low temperatures. From this result it seems that the *s–d* exchange interaction is not a main origin of the ferromagnetism of Ni, although this has already been assumed in our consideration. This conclusion can also be obtained from the fact that the value of $\lambda^2\chi_sC_d$ is fairly smaller than the value of θ_p for Ni.

Now we consider the temperature dependence of susceptibility for Pd at higher temperatures. Wohlfarth[20] has analysed the magnetic properties of Pd and Pt at relatively low temperatures on the basis of the Stoner theory. The similar treatment for Pd with that for Ni will be done although Pd is not ferromagnetic. In the reference 2, we have determined the number of *d* holes for Pd as $p_d=0.32$, $r_s=4.18$ from the temperature dependence of the susceptibility at lower temperatures. We use these values, $p_d=0.32$, $r_s=4.18$, for Pd, in this paper.

From (2.4), (3.4) with $m^*/m=1$, and Table I, we have

$$\chi_s=7.75\times10^{-8}\text{ (per gr.)}\,, \tag{3.10}$$

$$\lambda\chi_s=3.21\times10^{-2}\,, \tag{3.11}$$

for Pd where we assume that $g_d=g_s=2$. Then we have

$$\left.\begin{aligned} p&=(1+\lambda\chi_s)^2p_d=0.341\,,\\ C_d\lambda^2\chi_s&=15.0^\circ\text{K}\,.\end{aligned}\right\} \tag{3.12}$$

From Fig. 2 we find the values of C, θ_p, and χ_c, which are proper to explain the temperature variation of susceptibility by the formula (2.9) with the above value of p, as follows:

$$\left.\begin{aligned} C&=0.00120\text{ (per gr.)}\,,\\ \theta_p&=343^\circ\text{K}\,,\\ \chi_c&=2.48\times10^{-7}\text{ (per gr.)}\,.\end{aligned}\right\} \tag{3.13}$$

This value of χ_c is larger than the value of χ_s in (3.10). The difference will be attributable also to the temperature independent paramagnetism. If we assume that $m^*/m=1.75$ for *s* electrons, we can explain the temperature variation of susceptibility for Pd by (2.9) without introducing the temperature independent paramagnetism as well as in the case of Ni.

Using the values of C, θ_p, and χ_c given by (3.13) we can calculate χ from (2.9), and the result and the experimental results by Wucher[13] are shown in Fig. 5.

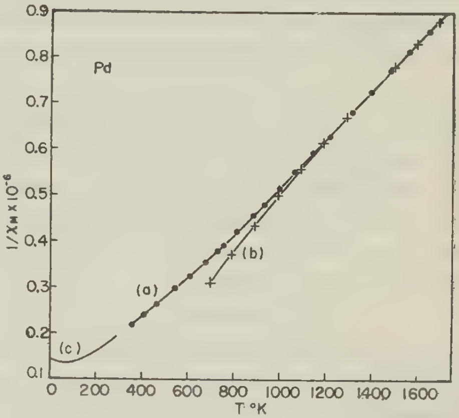

Fig. 5. Paramagnetic susceptibility of Pd. Curve (a) is Wucher's experimental result[13]. Curve (b) is calculated by $C/(T-\theta_p)+\chi_c$ with $C=0.00120$ (per gr.), $\theta_p=343^\circ$K and $\chi_c=2.48\times10^{-7}$ (per gr.). Curve (c) is Hoare and Matthews' experimental result[15]

It will be expected that there is the effect of the *s–d* exchange interaction on the temperature variation of paramagnetic susceptibility for Pd at lower temperatures too. But, as in Ni, the molecular field between *d* holes is fairly greater than the *s–d* exchange field, e. g. for Pd $\lambda^2\chi_sN_d\mu_B^2=9.51\times10^{-5}$ Ryd. unit and $\alpha N\mu_B^2=7.2\times10^{-3}$ Ryd. unit at $r_s=4.18$, and χ_c is a small part of the total susceptibility at lower temperatures, so that we can neglect the effect of the *s–d* exchange interaction at lower temperatures.

The same analysis will be applied to the temperature dependence of susceptibility for Pt. Unfortunately, there is no satisfactory experimental result for the paramagnetic susceptibility of Pt at higher temperatures.

However, we have determined the number of *d* holes for Pt as $p_d=0.30$, $r_s=4.31$ from the temperature dependence of the susceptibility at lower temperatures[2]. Then, from (2.4), (3.1) with $m^*/m=1$, and Table I, we have for Pt

$$\left.\begin{aligned} \chi_s&=4.17\times10^{-8}\text{ (per gr.)}\,,\\ \lambda\chi_s&=8.74\times10^{-2}\,,\\ p&=p_d(1+\lambda\chi_s)^2=0.355\,,\\ C&=5.41\times10^{-4}\text{ (per gr.)}\,.\end{aligned}\right\} \tag{3.4}$$

§ 4. Specific Heats of Ni, Pd, and Pt at Higher Temperatures

In this section we determine the part of the specific heats, which is considered to be the contribution from the d holes, for Ni, Pd, and Pt at higher temperatures. The dilatation terms are evaluated in the following way.

$$C_P-C_V=9TV\alpha_l^2/\beta\ , \tag{4.1}$$

where V, α_l and β are an atomic volume, linear expansion coefficient, and compressibility, respectively. As there is no measurement of the compressibilities of Ni, Pd, and Pt except at room temperature, we make use of the empirical formula[21],

$$C_P-C_V=\zeta TC_P^2\ , \tag{4.2}$$

where ζ is a proportional constant, and the value of ζ is determined by using (4.1) and the experimental values of V[22], α_l[23], and β[24] at room temperature. The results for Ni, Pd, and Pt are shown in Table II.*

Table II. Values of ζ and the Debye temperatures, Θ_D, for Ni, Pd, and Pt.

Metal	Ni	Pd	Pt
ζ cal^{-1} mol	1.001×10^{-5}	1.262×10^{-5}	1.186×10^{-5}
Θ_D°K	450	275	233

In the second place, we consider the contribution of the anharmonic terms of lattice vibrations, C_A, to the specific heat. The electronic specific heat of Cu is definitely determined by the extrapolation of the specific heat at lower temperatures, γT, also at higher temperatures because the degeneracy temperature of conduction electrons is very high. Then, by subtracting the Debye specific heat of lattice vibrations, the contribution of the dilatation term, and the electronic specific heat γT, from C_P, we can estimate the specific heat due to the anharmonic terms for Cu. It should be noted that this part of the anharmonic terms may contain the increase of the specific heat due to the s–d transfer in Cu if the energy difference between the Fermi level of s band and the top of d band is small. But we assume that this energy difference is large and the s–d transfer does not occur in Cu up to the melting point. Also for Ni we use the same values of specific heat of the anharmonic term with those of Cu.

The Debye specific heats, C_D, are calculated from the numerical tables[25] and the Debye temperatures given in Table II.

The electronic specific heats of s electrons for Ni, Pd, and Pt, $C_s=\gamma_sT$, are calculated from the values of p_s and r_s given above, by making use of the collective correction given by Fletcher and Larson[26]. The results are shown in Table III, where we assume $m^*/m=1$ for s electrons.

Table III. Electronic specific heats of s electrons, γ_sT, and classical limits of specific heats of d holes, $(3/2)Rp_d$, for Ni, Pd, and Pt.

Metal	Ni	Pd	Pt
$p_s=p_d$	0.539	0.32	0.30
r_s	3.21	4.18	4.31
$\gamma_s\times10^4$ cal/(deg.^{2} mole)	1.10	1.18	1.19
$(3/2)Rp_d$ cal/(deg. mole)	1.60	0.953	0.894

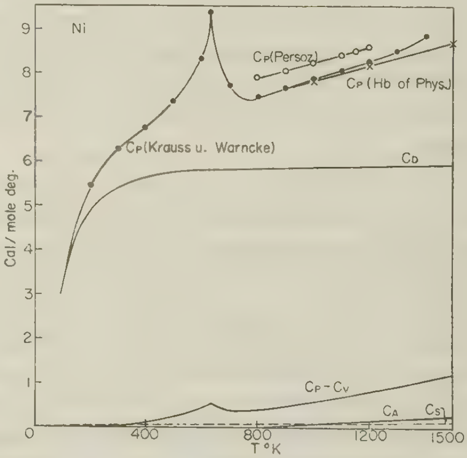

Fig. 6. Specific heats of Ni, e.g. C_P, C_P-C_V, the Debye specific heat C_D, anharmonic term C_A, and electronic specific heat of s electrons C_s, are shown. Curves (1), (2), and (3) are, respectively, Persoz's data[27], Krauss and Warncke's data[28], and data given in reference 29.

The respective parts of specific heat of Ni and the observed results of C_P[27),28),29] for Ni are shown in Fig. 6. In Fig. 7 the residual specific heats, $C_R=C_V-C_D-C_A-C_s$, which are considered to be the d holes, calculated from the various results of C_P, and the extrapolation of the specific heat at lower temperatures, $\gamma T=1.74\times10^{-3}T$ cal/mole deg., are shown.

---

* The analysis of specific heat of Ni has been worked out by E. Sawado and the detail will be published elsewhere.

From the result shown in Fig. 7 it is found that the d holes are almost non-degenerate at $T>1200$°K, the equipartition of energy holds, and the specific heat of d holes is nearly equal to $(3/2)Rp_d=1.6$ cal/mole deg. Thus the effect of the s–d transfer of electrons and accordingly the increase of the specific heat for Ni cannot be expected to be large, although it is, perhaps, certain that the mechanism of the s–d transfer exists practically. The same will be said of the cases of Pd and Pt.

The assumptions, made use of in § 3, that the number of d holes is constant and the d holes are nondegenerate at higher temperatures where we discuss the paramagnetic susceptibility are thus justified.

The same analyses of specific heats of Pd and Pt at higher temperatures are shown in Figs. 8, 9, 10 and 1129), where the anharmonic terms are neglected because the melting points

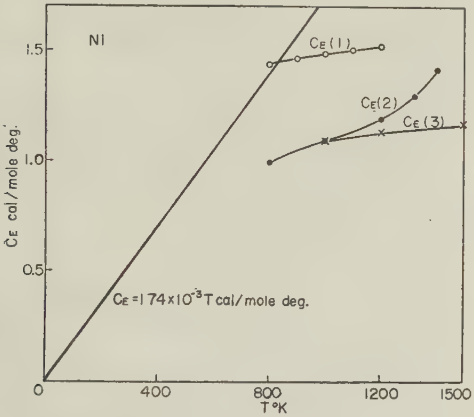

Fig. 7. Residual specific heat of Ni, $C_E=C_V-C_D-C_A-C_S$, and the extrapolation of the specific heat of Ni at lower temperatures, $\gamma T=1.74\times10^{-3}T$ cal/mole deg., are shown. Curves (1), (2), and (3) are, respectively, the residual specific heats obtained from Persoz's data27), Krauss and Warncke's data28), and data given in reference 29.

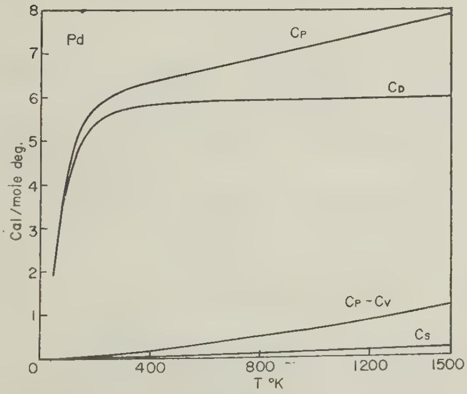

Fig. 8. Specific heats of Pd, e.g. C_P29), C_P-C_V, the Debye specific heat C_D, and electronic specific heat of s electrons C_S, are shown.

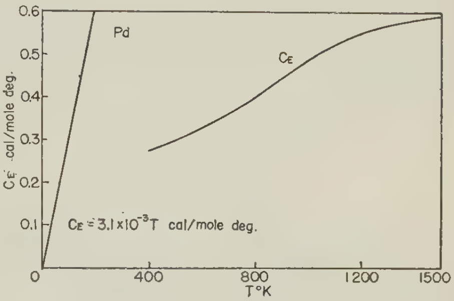

Fig. 9. Residual specific heat of Pd, $C_E=C_V-C_D-C_S$, and the extrapolation of the specific heat of Pd at lower temperatures, $\gamma T=3.1\times10^{-3}T$ cal/mole deg., are shown.

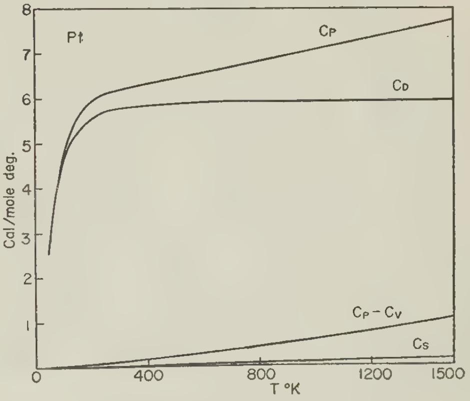

Fig. 10. Specific heats of Pt, e.g. C_P29), C_P-C_V, the Debye specific heat C_D, and electronic specific heat of s electrons C_S, are shown.

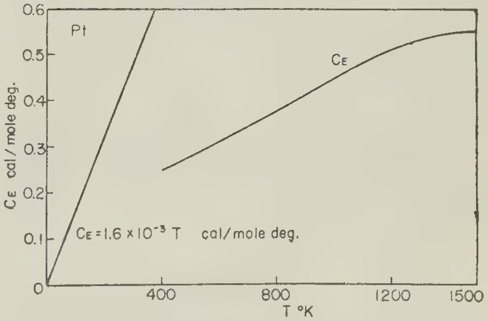

Fig. 11. Residual specific heat of Pt, $C_E=C_V-C_D-C_S$, and the extrapolation of the specific heat of Pt at lower temperatures, $\gamma T=1.6\times10^{-3}T$ cal/mole deg., are shown.

of Pd and Pt are high and they are expected to be small at temperatures under investigation.

§ 5. Conclusion

The temperature variations of the paramagnetic susceptibility for Ni, Pd, and Pt are explained by the itinerant model of d electrons with taking into account the s–d exchange interaction and the temperature-independent paramagnetism. The susceptibility at higher temperatures is approximately expressed by

$$\chi=\frac{C}{T-\theta_p}+\chi_c\ .$$

The values of χ_c obtained for Ni and Pd are fairly larger than the values which are expected to be due to the susceptibility of s electrons. The main parts of χ_c are attributable to the temperature-independent orbital paramagnetism of d electrons.

From the values of specific heats of Ni, Pd, and Pt at higher temperatures, it seems that the increases of electronic specific heat due to s–d transfer do no exist or are very small even if they exist.

From the above analyses and the results of the previous calculations²⁾, it is found that the s–d exchange interactions in Ni, Pd, and Pt are not stronger than the interactions between d holes when they are treated as an electron gas. Thus, contrary to the Zener theory³⁰⁾, we conclude that the s–d exchange interaction is not a main origin of the ferromagnetism of Ni, but gives only a slight modification to it.

It is supposed that the effect of the s–d exchange interaction on the paramagnetic susceptibility may exist also in the cases of Co and Fe. As the degeneracy temperatures of d holes for Co and Fe are fairly higher than Ni, the formula (2.9), just as it is, does not hold in Co and Fe, but the formula (2.7) with χ_d given by (7.9) in the reference 2 will be applicable and the experimental results of susceptibility for Co and Fe will be satisfactorily explained.

References

1) E. C. Stoner: *Magnetism and Matter* (Methuen and Co. Ltd., London, 1934), 381.
2) M. Shimizu: J. Phys. Soc. Japan **15** (1960) 376.
3) H. Watanabe: J. Phys. Soc. Japan **3** (1948) 317.
4) E. P. Wohlfarth: Proc. Roy. Soc. **A, 195** (1949) 434.
5) G. S. Krinchik: Izv. Akad. Nauk S. S. S. R., Ser. Fiz. **21** (1957) 869; Fiz. Metal. Metalloved. **4** (1957) 36.
6) S. V. Vonsovskii and K. B. Vlasov: Zh. Eks. Teor. Fiz., **25** (1953) 327.
7) J. Owen, M. Browne, W. D. Knight, and C. Kittel: Phys. Rev. **102** (1956) 1501.
8) J. H. Van Vleck: *The Theory of Electric and Magnetic Susceptibilities* (Oxford at the Clarendon Press, 1932) 194; R. Kubo and Y. Obata: J. Phys. Soc. Japan **11** (1956) 547.
9) E. C. Stoner: Proc. Roy. Soc. **A, 165** (1938) 372.
10) L. Néel: Ann. Physique **5** (1936) 232.
11) M. Shimizu: J. Phys. Soc. Japan **15** (1960) 2220.
12) E. M. Terry: Phys. Rev. **9** (1917) 394; W. Sucksmith and R. R. Pearce: Proc. Roy. Soc. **A, 167** (1938) 189; M. Fallot: J. phys. radium **5** (1944) 153; Y. Nakagawa: J. Phys. Soc. Japan **11** (1956) 855.
13) M. J. Wucher: Ann. physique **7** (1952) 317; Compt. rend. **242** (1956) 1143.
14) K. Honda: Ann. Physik **32** (1910) 1027.
15) F. E. Hoare and J. C. Matthews: Proc. Roy. Soc. **A, 212** (1952) 137.
16) *Atomic Energy Levels* Vols. 2 and 3 (National Bureau of Standards, 1952).
17) e.g. C. Kittel: *Introduction to Solid State Physics*, 2nd ed. (John Wiley and Sons. Inc., New York, 1956) 413.
18) D. M. S. Bagguley and N. J. Harrik: Proc. Phys. Soc. London **A, 67** (1954) 648.
19) R. M. Bozorth: *Ferromagnetism* (D. Van Nostrand Co., New York, 1951) 270.
20) E. P. Wohlfarth: Proc. Leeds Phil. Soc. **5** (1949) 89.
21) W. Nernst und F. A. Lindemann: Z. Elektrochem. **17** (1911) 817.
22) R. W. G. Wyckoff: *Crystal Structures* (Intersci. Publ., Inc., New York, 1948).
23) *American Institute of Physics Handbook* (Mc Grow-Hill Book Comp., Inc., New York, 1957) **4**-52.
24) P. W. Bridgman: *The Physics of High Pressure* (G. Bell and Sons, Ltd., London, 1958) 160.
25) See reference 23, p. **4**-44.
26) J. G. Fletcher and D. C. Larson: Phys. Rev. **111** (1958) 455.
27) B. Persoz: Ann. physique **14** (1940) 237.
28) F. Krauss und H. Warncke: Z. Metallkunde **46** (1955) 61.
29) See reference 23, p. **4**-40.
30) C. Zener: Phys. Rev. **18** (1951) 440.

JOURNAL OF THE PHYSICAL SOCIETY OF JAPAN, Vol. 16, No. 6, JUNE, 1961

Magnetic Properties of Intermetallic Compounds in Manganese-Tin System: $Mn_{3.67}Sn$, $Mn_{1.77}Sn$, and $MnSn_2$

By Kō YASUKŌCHI, Kazuo KANEMATSU
Department of Physics, College of Science and Engineering, Nihon University, Tokyo
and Tetuo OHOYAMA
Department of Physics, Faculty of Science, Tokyo Metropolitan University

(Received September 29, 1960)

The magnetic properties of $Mn_{3.67}Sn$, $Mn_{1.77}Sn$, and $MnSn_2$ were investigated. In $Mn_{3.67}Sn$, an anomalous magnetic phenomenon was found, which may be due to its antiferromagnetism. The Néel temperature T_N, the effective number of Bohr magnetons per Mn n_p, and the asymptotic Curie point θ_a are 365°K, 3.58, and −275°K, respectively. $Mn_{1.77}Sn$ is ferrimagnetic. The estimated saturation magnetization per Mn at 0°K, $n_f\mu_B$, as well as n_p and the Curie temperature T_C, were determined after various heat treatments. With lowering the annealing temperature, T_C was increased from 226° to 263°K, and n_f was increased from 0.92 to 1.23, while n_p stayed nearly constant at about 3.4. These behaviors are interpreted in terms of the effect of atomic ordering. It was also found that $MnSn_2$ exhibited an antiferromagnetic behavior. T_N, θ_a, and n_p are 324°K, +190°K, and 3.48, respectively.

§ 1. Introduction

The phase diagram of the whole range of manganese-tin system was first studied by Williams[1], and the existence of three intermetallic compounds was confirmed by the thermal analysis and also by the microscopical observation. His assignments on the compositions of these compounds, Mn_4Sn, Mn_2Sn, and probably MnSn, were corrected later by Nial[2] and by Nowotny and Schubert[3], who carried out the detailed X-ray analysis and also determined the crystal structures of these compounds. The results obtained by both X-ray works were substantially in agreement. Nowotny and Schubert concluded as follows: The most manganese-rich compound is $Mn_{3.67}Sn$ ($Mn_{11}Sn_3$) with a hexagonal, $D0_{19}$ (Ni_3Sn) type of structure. The second compound has a homogeneity range of $Mn_{2.05}Sn$ to $Mn_{1.77}Sn$, and has a hexagonal, $B8_2$(Ni_2In) type of structure. And the third compound is not MnSn as regarded earlier, but $MnSn_2$ which has a body centered tetragonal, C16 ($CuAl_2$) type of structure.

The magnetic properties of the alloys of this system have been studied by several authors, but the results are not in agreement with one another. Based upon the simple observations using a magnetic compass, Williams[1] reported that the transitions from ferromagnetism to paramagnetism took place in Mn_4Sn and Mn_2Sn at 117°C and 263°C, respectively. First quantitative measurements of the magnetization over the whole range of composition in this system were carried out by Honda[4], and a sharp maximum of the thermo-magnetic remanence was found at the composition of Mn_4Sn. Potter[5] measured the magnetization of the alloys at the liquid air temperature as well as at the room temperature, and roughly estimated the Curie points of the compounds at 0°C for Mn_4Sn and 150°C for Mn_2Sn. Guillaud[6] reported that ferromagnetism was exhibited throughout the composition range from 13 to 78 at% Mn with the Curie point ca. −11°C, while all alloys containing more manganese, including Mn_4Sn, were non-magnetic after annealed at 500°C. Recently, Ochsenfeld[7] found an anomalous antiferromagnetic behavior in the range of composition less than 15.5 at% Mn. He also concluded, standing upon the older phase diagram, that Mn_4Sn and Mn_2Sn were ferromagnetic with Curie points of 178°C and −11.5°C, respectively. The ferromagnetism of the alloys in this system was noticed by some authors to be very sensitive to the heat treatment[5),6)].

The present paper reports the results of some magnetic measurements which have been carried out on all the three compounds $Mn_{3.67}Sn$, $Mn_{1.77}Sn$, and $MnSn_2$, as well as the effects of heat treatments on the magnetic behaviors of $Mn_{1.77}Sn$.

§ 2. Preparation of Specimens and Experimental Procedures

The compositions of the intermetallic compounds used for this study were $Mn_{3.67}Sn$, $Mn_{1.77}Sn$, and $MnSn_2$. These specimens were prepared as follows: Powders of electrolytic manganese (99.9%) and tin (five-nine purity) were mixed at the desired proportions, and the mixtures were sealed in evacuated glass tubes, and heated by an electric furnace at 500°C for two days to promote the reactions. The starting materials thus obtained were next subject to the following heat treatments: For $MnSn_2$, the starting material was first crushed into powder, heated to promote the peritectic reaction, and the same procedures were repeated for several times, until the X-ray diagram confirmed a fairly complete formation of the compound. For $Mn_{1.77}Sn$ and $Mn_{3.67}Sn$, the starting materials were charged in alumina crucibles, sealed in evacuated silica tubes, and melted at 1100°C. Finally, after homogenized at 840°C for 40 hours, they were quenched into water. After this treatment, the specimens of $Mn_{1.77}Sn$ were held at every 50°C from 750°C to 400°C for several days, and then quenched into water. On the other hand, the specimens of $Mn_{3.67}Sn$ were annealed at 750°C and 550°C for several days, and quenched into water.

The specimens were examined by means of an X-ray diffractometer to ascertain their crystal structures. The temperature dependences of the magnetizations of these specimens were measured from the liquid oxygen temperature up to 900°K, under the field of 7.5 kilo-oersteds, by means of a pendulum magnetometer in their ferromagnetic region, and also by means of a magnetic torsion balance in their paramagnetic region. In both apparatus the magnetization was determined by measuring the forces exerted on the specimens placed in an inhomogeneous field.

§ 3. Experimental Results and Discussions

$Mn_{3.67}Sn$

The X-ray diagram for our specimen of $Mn_{3.67}Sn$ had a similar feature to that reported by Nowotny and Schubert[3], and then could be interpreted as corresponding to a hexagonal, $D0_{19}$ (Ni_3Sn) type of structure. But the lattice parameters are $a=5.67_5$Å, $c=4.52_9$Å, and $c/a=0.798$, and somewhat different from theirs. This forms a superstructure based on the close packed hexagonal one. According to the detailed examination of intensities of diffraction by Nowotny and Schubert, tin atoms in the structure for the stoichiometric (3:1) composition are randomly substituted by the excess atoms of manganese.

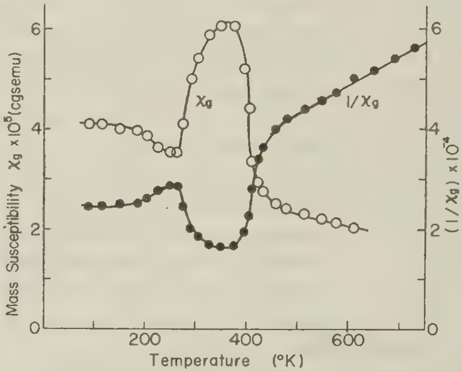

Fig. 1. Magnetic property of $Mn_{3.67}Sn$. Dependences of magnetic susceptibility and its reciprocal on temperature.

Recently we reported that $Mn_{3.25}Ge$[8], which has the same structure as $Mn_{3.67}Sn$, was antiferromagnetic in its disordered state. In Fig. 1, are plotted the values of magnetic susceptibility for $Mn_{3.67}Sn$ and its reciprocals against temperature. As seen in the figure, the susceptibility begins to increase strikingly at 270°K with increasing temperature and falls off rather abruptly at 400°K, and then decreases gradually. The reciprocal susceptibility *vs.* temperature curve has a minimum and the Curie-Weiss law holds very well at higher temperatures. These features were not affected by the heat treatments mentioned above. Thus an antiferromagnetic behavior was also found in this phase of manganese-tin system, and the point of minimum of the $1/\chi_g - T$ curve, 365°K, might be the Néel temperature. The asymptotic Curie point and the effective number of Bohr magnetons, calculated from the straight part of the $1/\chi_g - T$ curve, are -275°K and 3.58 respectively.

Williams and Honda have made some remarks on the existence of a thermo-magnetic remanence. We also observed the thermomagnetic effect below the Néel point besides the antiferromagnetic behavior described above. This phenomenon is quite simillar to the magnetic behavior of Mn_2Pd_3[9], which is antiferromagnetic and exhibits thermo-magnetic remanence too. The complex situation of the magnetic properties of the compound is presumably understood by introducing a coexistence of ferromagnetic and antiferromagnetic regions coupled by exchange interaction. But, taking into accout the non-stoichiometry of the compound, an alternative explanation for this phenomenon may be possible if we assume that an unbalance of spin arrangement is caused by the excess of manganese atoms. To clarify the mechanism of the phenomenon, more detailed investigations will be necessary.

$Mn_{1.77}Sn$

The saturation magnetizations σ_g of $Mn_{1.77}Sn$ after the heat treatments are plotted against temperature in Fig. 2. As seen from the figure, it is ferromagnetic below the room temperature. The reciprocals of the values of the magnetic susceptibilities above Curie points are shown in the same figure. It is seen that, by the effect of heat treatments, the saturation magnetization σ_0 at absolute zero of temperature, extrapolated from the $\sigma_g - T$ curves, varies from 44 to 59 cgs emu/g and the Curie point T_C, determined from $\sigma_g^2 - T$ curves, also varies from 226° to 263°K. The $1/\chi_g - T$ curves are concave against abscissa, and all asymptotic Curie points may be regarded to be positive.

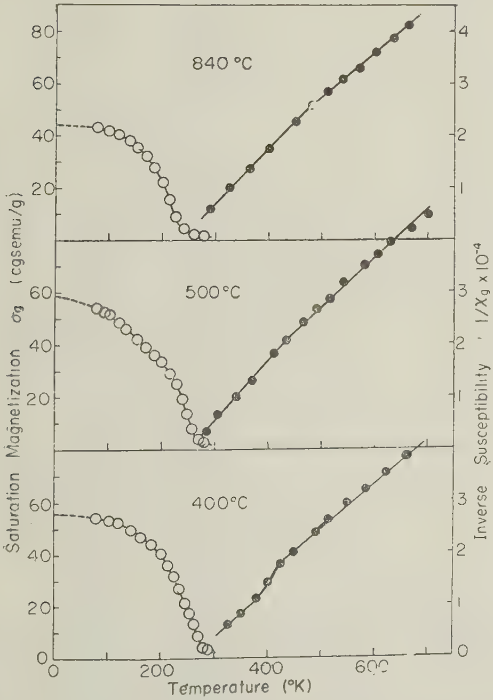

Fig. 2. Magnetic property of $Mn_{1.77}Sn$. Temperature dependences of saturation magnetization and inverse susceptibility after annealed at 840°C, 500°C and 400°C.

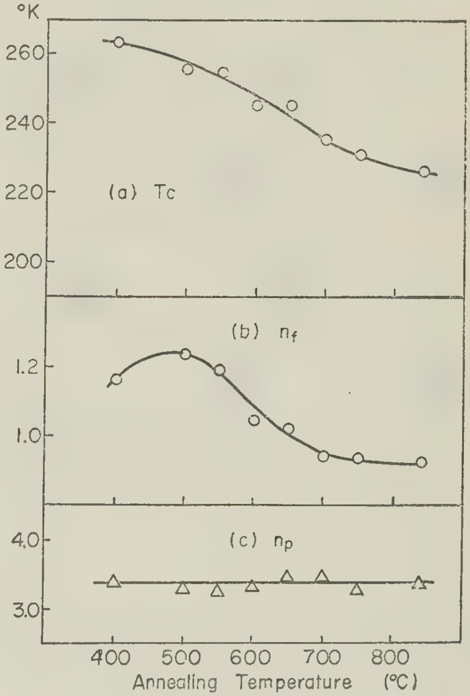

Fig. 3. Dependences of Curie temperature, saturation magnetization, and paramagnetic moments of $Mn_{1.77}Sn$ on annealing temperature. The latter two are expressed in terms of the number of Bohr magnetons per manganese atom.

The dependences of various magnetic constants on the annealing temperature are shown in Fig. 3, where T_C is the Curie temperature, n_f is the saturation magnetization at 0°K expressed in terms of the Bohr magneton, and n_p is the effective number of Bohr magnetons calculated from the slope of $1/\chi_g - T$ curves. As the annealing temperature is lowered from 840°C, (a) T_C increases monotonically from 226° to 263°K; (b) n_f remains nearly constant, 0.92, until the annealing temperature is lowered to 650°C, then increases gradually toward its maximum value 1.23

at 500°C and finally decreases slightly at 400°C; (c) n_p does not change appreciablly, about 3.4.

As to the crystal structure of $Mn_{1.77}Sn$, fortunately the result of detailed examination by Nowotny and Schubert[3] was available.

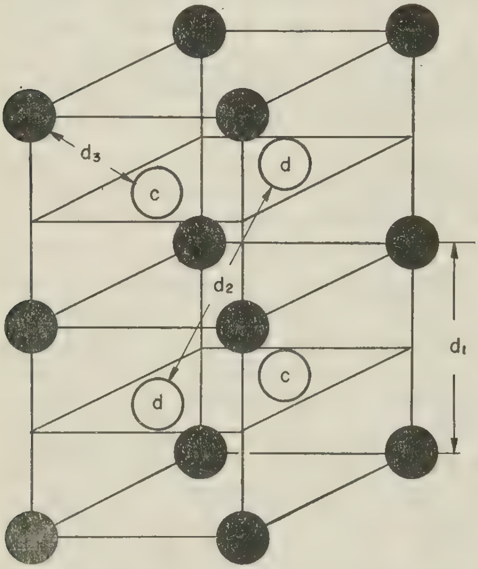

Fig. 4. Crystal structure of $Mn_{1.77}Sn$ ($B8_2$ type). Closed circles: A sublattice (2 (a) site). Open circles: B sublattice (c and d mean 2 (c) and 2 (d) sites, respectively). $d_1=2.76$Å, $d_2=3.75$Å, $d_3=2.89$Å.

According to their result, the Mn_2Sn phase has a hexagonal, $B8_2$ type of structure, which is illustrated in Fig. 4, and has the atomic positions as follows:

2 (a) 0, 0, 0; 0, 0, 1/2;
2 (c) 1/3, 2/3, 1/4; 2/3, 1/3, 3/4;
2 (d) 1/3, 2/3, 3/4; 2/3, 1/3, 1/4.

They reported that the lattice parameters were $a=4.37_0$Å, $c=5.47_5$Å, $c/a=1.25_0$, and the picnometric density was 7.40 g/cm³. These values gave 1.87 formula weights of $Mn_{1.77}Sn$ per unit cell, and the atomic arrangement was determined as follows:

2 Mn in 2 (a)
1.87 Sn+0.13 Mn randomly distributed in 2 (c)
1.18* Mn distributed in 2 (d).

Now the X-ray diagrams for our specimens annealed at temperatures above 650°C had quite similar feature to that of theirs, but the lattice parameters and the picnometric density had somewhat different values: $a=4.39_8$Å, $c=5.51_6$Å, $c/a=1.25_4$, and 6.9 g/cm³, respectively, giving 1.74 formula weights of $Mn_{1.77}Sn$ per unit cell. Therefore, the atomic arrangement in these specimens may be as follows:

2 Mn in 2 (a)
1.74 Sn+0.26 Mn in 2 (c)
0.82 Mn+1.18 atomic holes in 2 (d).

However, it was clearly shown by the X-ray diagrams for our specimens that the hexagonal structure was modified in three stages in the course of heat treatments. The three stages correspond to the following ranges of annealing temperature: (1) above 650°C, (2) between 600°C and 450°C, and (3) below 400°C. In the first stage, neither the diffraction angles

Table I. X-ray Diagrams of $Mn_{1.77}Sn$ (Cu Kα radiation).

Index	Annealing Temperature						Index*
	840°C		500°C		400°C		
hk.l	2θ	*I*	2θ	*I*	2θ	*I*	*hk.l*
10.0	23.4	3	23.4	5	23.4	4	30.0
					25.7	4	21.1
					26.7	5.5	22.0
10.1	28.8	23	28.5	34	28.8	30	30.1
					31.4	2	22.1
00.2	32.4	13.5	32.4	11	32.4	12	00.2
					33.4	9	10.2
					34.3	6	32.0
					35.2	4	11.2
					35.5	7	40.0
					36.2	8	20.2
					39.7	9	41.1
10.2	40.4	31	40.4	43	40.5	50	30.2
11.0	41.0	57.5	41.2	32	41.4	53	33.0
			41.7	11	41.8	31	42.0
					42.8	8	22.2, 50.1
					47.2	3	51.1
20.1	50.7	6	50.8	5	51.0	6	60.1
					51.6	6	11.3
11.2	53.3	10	53.3	13	53.6	9	33.2
					54.1	5	21.3
10.3	55.5	19	55.5	5	55.7	6	30.3
20.2	58.9	9.5	59.0	7	59.0	5	60.2
					59.7	7.5	40.3, 43.2
21.0					64.8	4	63.0
			65.7	3	65.8	6	44.2, 54.1
00.4	68.0	5	67.9	4	68.0	7	00.4
20.3	71.3	5.5	71.3	3	71.3	2	60.3
					73.6	4	73.0
21.2	74.2	11	74.4	11	74.7	6	63.2, 61.3
30.0	74.7	8	75.0	6	75.0	6	90.0
					76.1	5	73.1
			79.6	3	79.7	6	82.1
11.4	82.6	6.5	82.6	8	82.8	8.5	33.4, 71.3 73.2

* Indices in the last column are those with respect to the larger unit cell, $a'=3a$.

---

* This number of Mn in 2 (d) was 1.30 in Nowotny and Schubert's paper, but here the corrected number is shown.

nor the intensities of the individual lines were varied appreciably, showing that the structure was essentially unchanged from that described above. In the second stage, a few superstructure lines which could be indexed with lattice constants $a'=3a$ and $c'=c$, the (42.0) line being the strongest among these, appeared and became stronger and stronger with lowering the annealing temperature. Finally, in the third stage, a great number of additional diffraction lines, which also could be indexed with $a'=3a$ and $c'=c$, appeared.

The picnometric density of our specimen was nearly constant at 6.9 g/cm³, irrespective of preceding heat treatment. This value is considerably smaller than that of Nowotny and Schubert, and our X-ray diagram gives the lattice parameters larger than theirs. These disagreements may be ascribed to the different procedures in the preparation of the specimens; ours were melted and solidified in vacuum, while theirs were made in the atmosphere under salt flux.

Now, the atomic sites 2 (a) are different from 2 (c) and 2 (d) with respect to their surroundings. Thus, as shown in Fig. 4, the whole lattice can be divided into two sublattices; sublattice A consisting of 2 (a) (closed circle) and sublattice B consisting of 2 (c) and 2 (d) (open circle).

From the X-ray examinations, it appears that, in this compound, the crystal structure is not drastically changed and the population of manganese atoms among the two sublattices is not largely affected by the heat treatment. Moreover, n_p stays nearly constant. Thus it seems that the magnetic moments of individual manganese atoms also are not changed by these heat treatments. We further assume that the magnetic moments of individual manganese atom on the two sublattices have the following spin quantum numbers:

$S_A=3/2$ for 2 Mn in A sites
$S_B=\ 1$ for 1.08 Mn in B sites

n_p^2 may be calculated from these values as the weighted mean of $S(S+1)g^2$ and, if we assume the Landé factor to be $g=2$, this gives $n_p=3.54$, which may be compared to the experimental values 3.48 to 3.25. In addition, when the two partial magnetizations are absolutely saturated in the oposite directions, the above S values give $n_f=1.25$ as the ferrimagnetic moment, which is in good agreement with the experimental value for the specimen annealed at 500°C. Thus we are led to assume a negative (antiferromagnetic) interaction between the two sublattices, A and B*. It should be noted here that, in $Fe_{1.67}Ge$[10], which has the same crystal structure and also the same type of distribution of atoms among the atomic sites as in the present compound, the experimental values of both the saturation magnetization at 0°K and the paramagnetic moment above T_C are in good agreement with those calcutated from the assignments $S=1$ for Fe in the A sites, and $S=1/2$ for Fe in the B sites**. Since the manganese atom has one less electrons than iron atom, this may be regarded as another support to the above assumption of spin moments for manganese atoms in $Mn_{1.77}Sn$.

It may be interesting that the heat treatments do not affect the paramagnetic moment (n_p) of the compound above the Curie temperature, but give rise to changes in the saturation magnetization at 0°K (n_f) and the Curie temperature (T_C). The constancy of n_p, together with the result of X-ray analysis, has led us to assume the magnetic moments for individual manganese atoms to be constant. We shall discuss the variations in n_f and T_C below, in relation to changes in the interactions between manganese atoms owing to the change in the atomic distribution among the lattice sites, which is brought about by the effect of annealing.

In addition to the above assumption that the interaction between the two sublattices (A–B interaction) is negative, we further assume that the interactions within the A lattice (A–A interaction) is negative and that within the B lattice (B–B interaction) is positive. These assumptions are equivalent to the assumptions that the exchange interactions for Mn_A–Mn_A, Mn_B–Mn_B, and Mn_A–Mn_B are negative, positive, and negative respectively, and do not conflict with the interaction *vs.* Mn–Mn distance curve (*J-r* curve) proposed experimentally by Guillaud[6] and by Willis and Rooksby[11], since the corresponding nearest neighbor Mn–Mn distances in the present compound are 2.76Å, and 3.75Å and 2.89Å, respectively. The positive asymptotic Curie point, however, suggests the existence of fairly strong positive interaction, while the *J-r* curve leads to a weak one. Thus we propose a relatively strong positive one between the manganese atoms within the B sublattice, by the effect of superexchange interactions through the tin atoms, which lie in the same sublattice, the angle of Mn–Sn–Mn being 120°. This proposal of a superexchange interaction between manganese atoms through IVb elements is also supported by the fact that the magnetic behaviors of $MnSn_2$, $FeGe_2$ and $Fe_{1.67}Ge$[10] can be also well understood by magnetic structures based on the superexchange interactions of this kind.

---

* The ferrimagnetic structure of this compound is supported also by the dependence of the saturation magnetization upon the manganese concentration within the region of the same phase, measured for the specimens annealed at the same temperature, 500°C. The details will be reported later.

** According to our measurements, $n_f=1.59$ and $n_p=3.14$ for $Fe_{1.67}Ge$, and the calculated values are 1.60 and 2.45, respectively.

Now we shall consider the behaviors of the magnetic constants n_f and T_C of the compound in relation to the variation of interactions caused by the structural variations in three stages. First we make the following assumptions: (1) In the initial state realized in the specimens annealed at 840°C, the (negative) A–B interaction is not so strong that the triangular configuration of the partial magnetizations such as discussed by Yafet and Kittel[12] is brought about by the negative A–A interaction, lowering the partial magnetization M_A slightly (still $M_A > M_B$), and (2) the A–B interaction is not affected by the short range order, but is increased by the formation of the long range order in the B lattice, i.e. 2(c) and 2(d) sites of the $B8_2$-type structure. Then the observed behaviors of the magnetic constants may be phenomenologically interpreted as in the following paragraphs.

In the first stage, with the annealing temperatures above 650°C, it can be considered that a short range ordering takes place within the B lattice, giving no essential changes in the X-ray diagram. This ordering in the B lattice may bring about an increase in the positive B-B interaction which originates from the superexchange interaction proposed above. Then T_C may be increased by this increase in the positive interaction, while by the above assumptions, the partial magnetizations M_A and M_B, and also n_f, are not changed appreciably, as long as the ordering is a short range one.

It may be probable that the second stage corresponds to the growth of a long range order in the arrangement of the atoms and holes within the B sublattice, as a few superstructure lines appear and increase their intensities with lowering the annealing temperature. Then, by the above assumptions, the A–B interaction increases and makes the alignment of the individual moments within the A lattice more perfect, leading to an increase in the ferrimagnetic resultant magnetization $M_A - M_B$ and therefore in n_f. The increases in the positive B–B interaction and also in the negative A–B interaction must bring about an increase in T_C. It can be considered that, with the development of the ordered structure at the end of this stage, 500°C, the partial magnetization of the A sublattice, M_A, reaches the value corresponding to the perfect alignment of the individual moments, and the resultant magnetic moment of the compound takes the value which may be approximated by the calculation based on the assignments $S_A = 3/2$ and $S_B = 1$, as mentioned above.

In the third stage, with the annealing temperatures below 400°C, in addition to the superstructure lines which appear in the second stage, a large number of additional lines appear. It may be allowable to ascribe the increase in the number of the diffraction lines and the complication of the X-ray diagram to some displacements of constituent atoms from the normal positions in $B8_2$-type structure, which may presumably be induced by the perfect ordering of the atomic holes in a lower symmetry. Such a deformation of the whole lattice makes the situation so complex that it is difficult to ascribe the observed behaviors of n_f and T_C to some changes in the interactions in a simple way. But it may be considered that the behaviors in this stage does not conflict with the above interpretations.

$MnSn_2$

The X-ray diagram for the specimen with the composition of $MnSn_2$ was quite similar to that reported by Nowotny and Schubert[3], except the diffractions from white tin phase.

Thus the main phase in the specimen was identified with $MnSn_2$, which was determined by them to have C16 type of structure.

Fig. 5 (a) shows the temperature dependence of the magnetic susceptibility of the specimen. As seen in the figure, the $\chi_g - T$ curve has an anomalous feature; a small peak at 324°K followed by a sharp rise toward lower temperature. The reciprocals of the susceptibilities are plotted against temperature in Fig. 5 (b). The $1/\chi_g - T$ curve indicates the validity of the Curie-Weiss law at higher temperatures, and the straight part of the curve is extrapolated to the asymptotic Curie point of +190°K, and the slope of it corresponds to a paramagnetic moment of 3.48 Bohr magnetons per manganese atom.

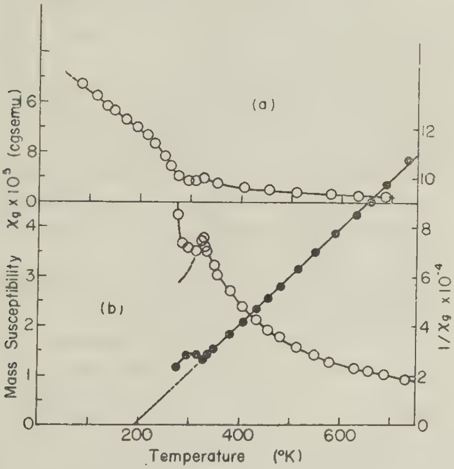

Fig. 5. (a) Temperature dependence of magnetic susceptibility of the specimen with a composition $MnSn_2$. (b) Temperature dependence of inverse susceptibility of the same specimen, with a part of (a) enlarged and estimated susceptibility of the compound $MnSn_2$ (dotted line).

The rapid rise in the magnetization at lower temperatures may be ascribed to the ferrimagnetism of Mn_2Sn phase, because the rise begins at a temperature corresponding to the Curie point of this phase. Moreover, though the X-ray diagram could not detect the presence of this phase, it is rather natural to consider that the specimen of this composition contains this phase, because of the peritectic nature of the reaction in the formation of $MnSn_2$ phase. It is seen in Fig. 5 (b) that the susceptibility of $MnSn_2$ corrected by subtracting the estimated contribution of Mn_2Sn phase (dotted line) behaves like an antiferromagnetism. Thus the temperature of the peak, 324°K, may be considered as the antiferromagnetic Néel point of the compound $MnSn_2$.

Recently, it was reported by Ochsenfeld[7] that the inverse susceptibility *vs.* temperature curves of the tin alloys containing less manganese than 15.5 at% exhibited anomalous antiferromagnetic behaviors. But these behaviors can be interpreted as a superposition of the antiferromagnetism of $MnSn_2$, mentioned above, and the paramagnetism of dilute manganese alloy with tin, observed by Busch and Mooser[13].

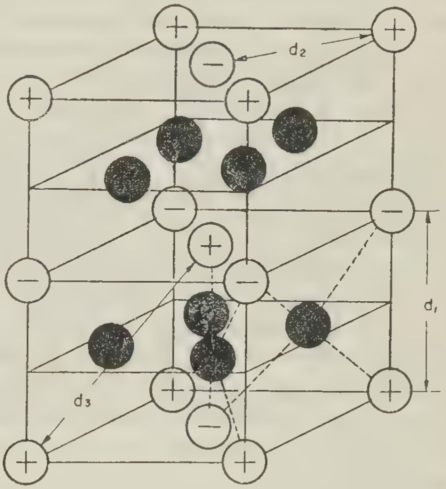

Fig. 6. Crystal structure of $MnSn_2$ (C16 type) and proposed magnetic structure. Closed circle: Sn; open circle: Mn. $d_1 = 2.72$Å, $d_2 = 4.70$Å, $d_3 = 5.43$Å.

Now we shall discuss the magnetic structure of this compound. The structure of the compound is shown in Fig. 6. The nearest neighbor Mn–Mn distances are 2.72Å along the *c* axis, 4.70Å along the face diagonal in the basal plane, and 5.43Å along the body diagonal. The angles of Mn–Sn–Mn for the pairs of manganese atoms along the face diagonal (second neighbor) and along the body diagonal (third neighbor) are 111° and 146°, respectively. According to the *J-r* curve for the manganese atom, mentioned in the discussion of $Mn_{1.77}Sn$, the direct interactions between manganese atoms may be negative for the pair of the first neighbors and positive for the pairs of the second and the third neighbors, corresponding to the interatomic distances above mentioned. The experimental fact that the asymptotic Curie point of this antiferromagnetism is positive suggests the existence of fairly strong positive interaction. Thus, in addition to the direct interactions, it is likely that the positive superexchange interaction between manganese atoms through tin atoms, proposed in the compound $Mn_{1.77}Sn$, plays an important role in this compound, too. In this structure, the superexchange interaction can exist between second and third neighbor manganese atoms. The interaction between the third neighbors would be stronger than that of the second neighbors for the sake of the proper angle of Mn–Sn–Mn. If the negative (direct) interaction between the first neighbors and the positive (indirect) interaction between the third neighbors overshadow the interaction between the second neighbors, the arrangement shown in Fig. 6 will be realized, since it makes all first neighbors antiparallel and all third neighbors parallel. The whole lattice is divided into two, crystallographically identical, sublattices. Therefore, all manganese atoms may have the same value of spin moment, to which we propose the value $S=3/2$. The effective Bohr magneton number per manganese atom in the compound is given by $g\sqrt{S(S+1)}$ and calculated to be 3.87, if we assume the Landé factor to be $g=2$, which is fairly in good agreement with the experimental value, 3.48.

The authors wish to express their hearty thanks to Prof. S. Kaya, the President of Tokyo University, for his constant encouragement and are also very grateful to Prof. R. Kimura of Tokyo Metropolitan University and Profs. Y. Tomono and S. Iida of Tokyo University who gave them opportunities to use the facilities to achieve the work.

References

1) R. S. Williams: Z. anorg. Chem. **55** (1907) 1. M. Hansen: *Constitution of Binary Alloys*, 2nd edit. (McGraw-Hill, New York, 1958) p. 955.
2) O. Nial: Svensk. Kemi. Tidskr. **59** (1947) 165.
3) H. Nowotny and K. Schubert: Z. Metallkde. **37** (1946) 17.
4) K. Honda: Ann. Physik **32** (1910) 1003.
5) H. Potter: Phil. Mag. [7] **12** (1931) 255.
6) C. Guillaud: Thesis Strasbourg, 1943. R. M. Bozorth: *Ferromagnetism*, (Van Nostrand, New York, 1951) p. 340.
7) R. Ochsenfeld: Z. Metallkde. **46** (1958) 472.
8) K. Yasukōchi, T. Ohoyama and K. Kanematsu: J. Phys. Soc. Japan **14** (1959) 1820.
9) J. P. Burger, R. Wendling and J. Wucher: J. phys. radium **20** (1959) 427. N. Perakis, J. Wucher, G. Parravano and R. Wendling: Compt. rend. **246** (1958) 3037.
10) K. Yasukōchi, K. Kanematsu and T. Ohoyama: J. Phys. Soc. Japan **16** (1961) 429.
11) B. T. M. Willis and H. P. Rooksby: Proc. Phys. Soc. London B **67** (1954) 290.
12) Y. Yafet and C. Kittel: Phys. Rev. **87** (1952) 290.
13) G. Busch and E. Mooser: Helv. Phys. Acta **26** (1953) 611.

JOURNAL OF THE PHYSICAL SOCIETY OF JAPAN, Vol. 16, No. 6, JUNE, 1961

The Magnetic Investigation of Mn^{++}, Co^{++}, Ni^{++} and Cu^{++} Ammine and Anhydrate Salts at Low Temperatures

By Takashi WATANABE

Department of Physics, Faculty of Science, Tokyo Metoropolitan University, Tokyo, Japan

(Received October 1, 1960)

The magnetic susceptibility measurements of ammine salts and anhydrate salts of Mn^{++}, Co^{++}, Ni^{++} and Cu^{++} ions at the temperature above 90°K have been carried out previously by Kido and the present author. The magnetic susceptibilities of these salts obtained by them show no deviation from the Curie-Weiss law down to 90°K. The results for magnetic susceptibility measurements of these salts at liquid helium and liquid hydrogen temperatures are given in the present report. The susceptibility measurements were carried out by the Hartshon bridge method. The salts which were studied are $Mn(NH_3)_6Cl_2$, $Mn(NH_3)_2Cl_2$, $Mn(NH_3)Cl_2$, $MnCl_2$, $Co(NH_3)_6Cl_2$, $Co(NH_3)_2Cl_2$, $Co(NH_3)Cl_2$, $CoCl_2$, $Ni(NH_3)_6\cdot Cl_2$, $Ni(NH_3)_6(ClO_4)_2$, $Ni(NH_3)_2Cl_2$, $Ni(NH_3)Cl_2$, $NiCl_2$, $Cu(NH_3)_4SO_4\cdot H_2O$, $Cu(NH_3)_2SO_4$ and $CuSO_4$. The antiferromagnetic or metamagnetic behavior in all other salts except $Mn(NH_3)_6Cl_2$, $Mn(NH_3)_2Cl_2$, $Co(NH_3)_2Cl_2$, $Ni(NH_3)_6Cl_2$, $Ni(NH_3)_6(ClO_4)_2$ and $Cu(NH_3)_2SO_4$ was found in the temperature range from 1.5°K to 20.4°K. The magnitude of the Weiss temperatures θ is largest for Ni^{++} and smallest for Mn^{++} in each coordinated salts of $M(NH_3)_6Cl_2$, $M(NH_3)_2Cl_2$, $M(NH_3)Cl_2$ and MCl_2 (M is one of Mn^{++}, Co^{++} and Ni^{++} ions). The unexpected results are found in the case of $Ni(NH_3)_6Cl_2$ and $Ni(NH_3)_6(ClO_4)_2$, as compared with the results of N.M.R. by Kim and Sugawara.

§1. Introduction

The reports of the magnetic susceptibility measurements of ammine complex salts are very few up to this time, especially, at low temperatures. Most of measurement in the present report was carried out from 20.4°K down to 1.5°K. The magnitude of the Weiss constant θ obtained from the susceptibility for Mn^{++}, Co^{++}, and Ni^{++} salts except the hexammine salts is largest for Ni^{++} and smallest for Mn^{++} in the temperature above 90°K[1]. This order of magnitude is not changed also in the hexammine salts below liquid hydrogen temperatures. The Weiss temperatures θ's defined in Eq. (1) of the salts of $M(NH_3)_2Cl_2$ and $M(NH_3)Cl_2$ type (M is Co^{++} and Ni^{++} ions) are negative and these salts show the nature of metamagnetics like in $CoCl_2$ and $NiCl_2$. The unexpected results of $Ni(NH_3)_6Cl_2$ and $Ni(NH_3)_6(ClO_4)_2$ will be seen in the later chapter.

The magnetic measurement for $CuSO_4$ was carried out by de-Haas and Gorter[3], Borovik-Romanov, Kalasik and Kleines[4], and Borovik-Romanov and Kleines[5]. But these results for a powder sample show the complicated behaviors, as seen in the later chapter.

The method of the preparation of each sample was given in the previous report[1]. The measurements are made with an A. C. Hartshon bridge[2] and the frequency for measurement is 120 c/s, where as a static method was used in the previous study[1]. The thermocouple of copper-constantan is inserted into measuring vessel for the measurement of temperatures in the intermediate temperature range (from 20.4°K to 60°K), as shown in Fig. 1. The diameter of thermocouple wire is selected as small as 0.06 mm, in order to reduce the heat leakage from the thermocouple lead and to minimize the experimental error by eddy current loss. The caliblation of e.m.f. of thermocouple has been carried out by the measurement of magnetic susceptibility for $Fe(NH_4)$-alum. By darkening the inside of Déwar vessel, the time for the ascent of temperature in a sample is reduced to about one hour and seven hours in the temperature ranges from 4.2°K to 20.4°K and from 20.4°K to 70°K, respectively. The susceptibilities of $Ni(NH_3)_2Cl_2$, $Ni(NH_3)Cl_2$, $NiCl_2$ and $CuSO_4$ in intermediate temperatures are measured by the above mentioned method. The sensibility of the thermocouple is not enough when the measurement is started from 4.2°K and the error of temperature measurement is ±1.5~3°K.

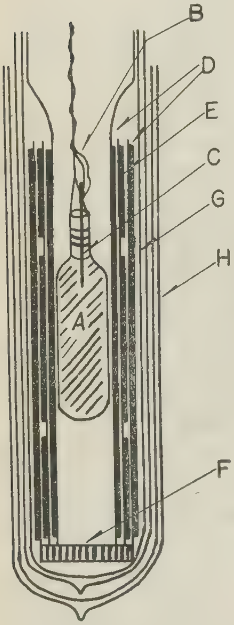

A. Sample.
B. Cu-constanten thermocouple.
C. Copper wire.
D. Primary coil.
E. Secondary coil
F. Heater of constantan wrire (0.5 mm ϕ).
G. Déwar vessel for liquid helium.
H. Déwar vessel for liquid air.

Fig. 1. Schematic picture of the coil system and sample.

§ 2. The Experimental Results

The values of molar susceptibility χ_m, the magnetic moment p_{exp} (the Bohr magneton unit) and g-value in paramagnetic region are written as

$$\chi_m=\frac{C}{T+\theta}, \tag{1}$$

$$p_{\text{exp}}=\frac{1}{\mu_B}\sqrt{\frac{3kC}{N}}=2.839\sqrt{C} \tag{2}$$

and

$$g=p_{\text{exp}}\{S(S+1)\}^{-1/2}, \tag{3}$$

where C, θ, k, μ_B, N and S are respectively the Curie constant, the Weiss constant, the Boltzmann factor, the Bohr magneton, the Avogadro number and spin quantum number.

The values of p_{exp}, g, θ and T_{tr} (the magnetic transition temperature) determined in the low temperature range are given in the following tables and figures.

(1) $Mn(NH_3)_6Cl_2$, $Mn(NH_3)_2Cl_2$, $Mn(NH_3)Cl_2$ and $MnCl_2$ (Table I, Figs. 2 and 3)

(2) $Co(NH_3)_6Cl_2$, $Co(NH_3)_2Cl_2$, $Co(NH_3)Cl_2$ and $CoCl_2$ (Table II, Figs. 4 and 5)

(3) $Ni(NH_3)_6Cl_2$, $Ni(NH_3)_6(ClO_4)_2$, $Ni(NH_3)_2Cl_2$, $Ni(NH_3)Cl_2$ and $NiCl_2$ (Table III, Figs. 6 and 7)

(4) $Cu(NH_3)_4SO_4\cdot(H_2O)$, $Cu(NH_3)_2SO_4$ and $CuSO_4$ (Table IV, Figs. 8 and 11)

§ 3. Discussion of the Results

The crystal structures of these hexammine

Table I.

	p_{exp}	g	θ	T_{tr}
$Mn(NH_3)_6Cl_2$	5.92±0.04	2.00±0.02	0.2±0.2°C	——
$Mn(NH_3)_2Cl_2$	5.84 〃	1.98 〃	1 〃	——
$Mn(NH_3)Cl_2$	5.82 〃	1.97 〃	3 〃	2.6°K
$MnCl_2$	5.79 〃	1.96 〃	3 〃	2.0

Table II.

	p_{exp}	g	θ	T_{tr}
$Co(NH_3)_6Cl_2$	3.70±0.04 4.88±0.06	4.27±0.02 (S=1/2) 2.53±0.03 (S=3/2)	2.6±0.2°C* 17 ±3°C**	——
$Co(NH_3)_2Cl_2$	5.00 〃	2.58 〃	−10 〃 **	16°K
$Co(NH_3)Cl_2$	5.10 〃	2.63 〃	−14 〃 **	20
$CoCl_2$	5.16 〃	2.67 〃	−28 〃 **	24

Table III.

	p_{exp}	g	θ	T_{tr}
$Ni(NH_3)_6Cl_2$	3.08±0.04	2.20±0.02	8 ±0.2°C*	——
$Ni(NH_3)_6(ClO_4)_2$	3.07 〃	2.16 〃	0.5 〃	——
$Ni(NH_3)_2Cl_2$	3.20±0.06	2.26±0.03	−38 ±3°C**	30°K
$Ni(NH_3)Cl_2$	3.24 〃	2.28 〃	−46 〃 **	——
$NiCl_2$	3.28 〃	2.32 〃	−67 〃 **	50°K

* The results in the range below liquid hydrogen temperatures.

** The results in the range above liquid nitrogen temperatures.

Table IV.

	p_{exp}	g	θ	T_{tr}
$Cu(NH_3)_4\cdot(H_2O)\cdot SO_4$	1.78±0.04	2.09±0.02	1.20±0.1°C	3.4°K
$Cu(NH_3)_2SO_4$	1.92±0.06 1.47±0.04	2.22±0.03	22 ±3 ** 0 ±0.2*	
$CuSO_4$	2.10±0.06	2.43 〃	67 ±3 **	33°K and 50°K ?

* The results in the range below 4.2°K.

** The results in the range above liquid nitrogen temperatures.

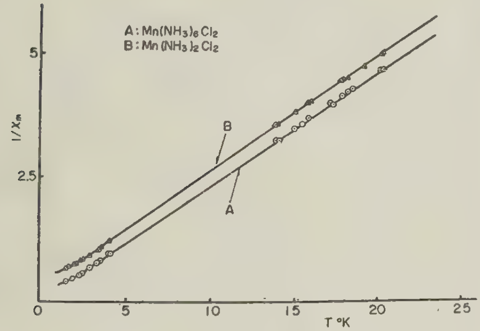

Fig. 2. Reciprocal molar susceptibility versus temperature (°K) for $Mn(NH_3)_6Cl_2$ and $(Mn(NH_3)_2Cl_2$.

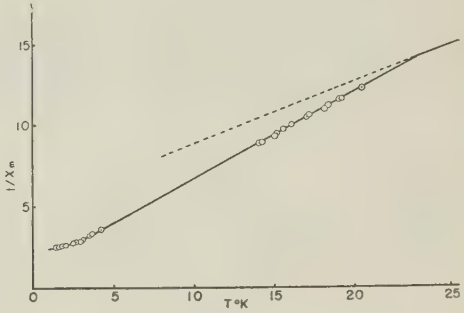

Fig. 4. Reciprocal molar susceptibility versus temperature (°K) for $Co(NH_3)_6Cl_2$.

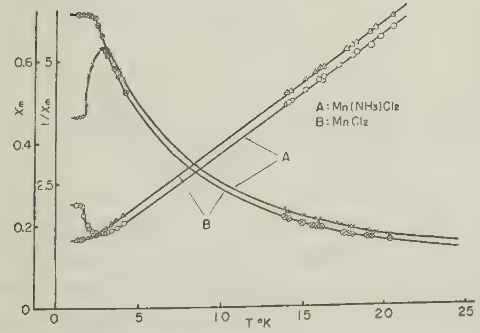

Fig 3. Molar susceptibility and receprocal molar susceptibility versus temperature (°K) for $Mn(NH_3)Cl_2$ and $MnCl_2$.

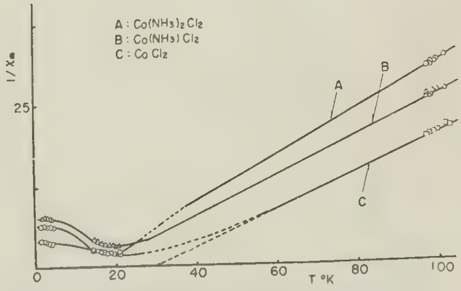

Fig. 5. Reciprocal molar susceptibility versus temperature (°K) for $Co(NH_3)_2Cl_2$, $Co(NH_3)Cl_2$ and $CoCl_2$.

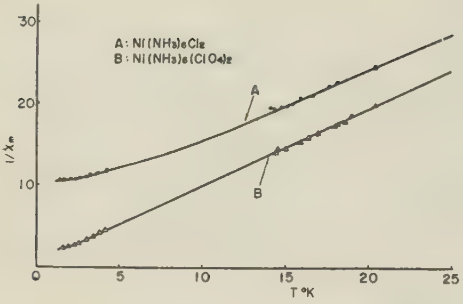

Fig. 6. Reciprocal molar susceptibility versus temperature (°K) for $Ni(NH_3)_6Cl_2$ and $Ni(NH_3)(ClO_4)_2$.

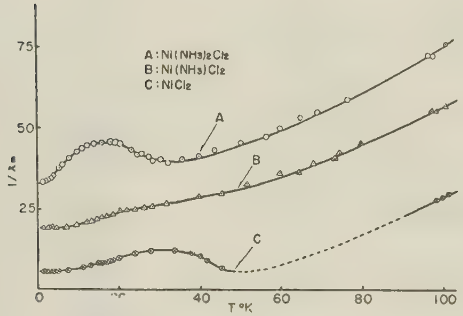

Fig. 7. Reciprocal molar susceptibility versus temperature (°K) for $Ni(NH_3)_2Cl_2$, $Ni(NH_3)Cl_2$, $NiCl_2$.

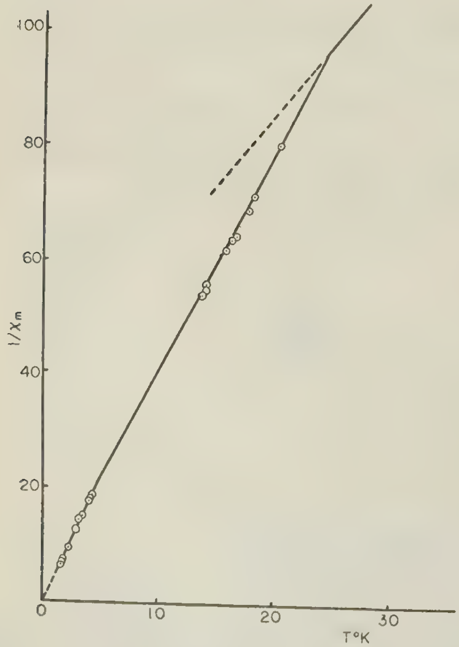

Fig. 8. Reciprocal molar susceptibility versus temperature (°K) for $Cu(NH_3)_2SO_4$.

complex salts belong to anti CaF_2 type[6], and it seems that the symmetry charactor of crystalline field is almost cubic. The crystal structures of diammine and monoammine salts are not yet known, and the crystal structure of anhydrous salt $MnCl_2$ belongs to CdI_2 type[7] and these of $CoCl_2$ and $NiCl_2$ belong to $CdCl_2$ type.[8] Hammel[9] has suggested that the symmetry of $CuSO_4$ belongs to the hexagonal symmetry and that three copper ions are contained in the unit cell.

1) Mn^{++} ($3d^5$, $^6S_{1/2}$)

Since the orbital level of this ion is singlet, the energy level of Mn^{++} ion is not splitted by crystalline field and an anisotropy caused by the crystalline field does not remain. Thus, the most of the Weiss constant originate from the isotropic exchange interaction.

$Mn(NH_3)_6Cl_2$ and $Mn(NH_3)_2Cl_2$: $\theta \simeq 0.2°C$, $g = 2.00 \pm 0.02$ and the susceptibility obeys the Curie-Weiss law down to 1.5°K in the case of manganous hexammine chloride $Mn(NH_3)_6Cl_2$, as seen in Table I and Fig. 2. The temperature at which magnetic anormally of this salt appears, is perhaps below 1°K. $\theta = 1°C$ and $g = 1.98 \pm 0.02$ in the case of manganous diammine chloride $Mn(NH_3)_2Cl_2$. The values of susceptibility of this salt decrease somewhat below the values expected from the Curie-Weiss law in the range below 1.8°K, as seen in Table I and Fig. 2.

$Mn(NH_3)Cl_2$ and $MnCl_2$: Manganous monoammine chloride $Mn(NH_3)Cl_2$ shows the antiferromagnetic behavior, as seen in Fig. 3. The value for susceptibility of this salt represents a maximum at the temperature about 2.6°K and this value decreases in the range below 2.6°K. The value of susceptibility of manganous chloride anhydrate $MnCl_2$ deviates from the Curie-Weiss law below about 2.0°K, but it is constant in the temperature range from 1.4°K to 2.0°K. The anomaly that Murray and Robert[10] have pointed out, did not appear down to 1.4°K.

2) Co^{++} ($3d^7$, $^4F_{5/2}$)

$Co(NH_3)_6Cl_2$: The value of the Weiss constant θ of cobaltous hexammine chloride $Co\cdot(NH_3)_6Cl_2$ is larger than that of nickel hexammine chloride $Ni(NH_3)_6Cl_2$ above 90°K ($\theta = 17°C$). Values of g-factor and θ of $Co(NH_3)_6\cdot Cl_2$ below 20.4°K are different from these at high temperatures, as follows.

	high temperature region (above 90°K)	low temperature region (below 20.4°K)
p_{exp}	4.88 ± 0.06	3.70 ± 0.04
g	2.53 ± 0.03 ($S=3/2$)	4.27 ± 0.02 ($S=1/2$)
θ	17°C	2.7°C
	(from Table II and Fig. 4)	

These phenomena arise from the level splitting of ground state due to spin orbit coupling $\lambda(L \cdot S)$ ($\lambda = -200\,\text{cm}^{-1}$). The susceptibility becomes nearly constant below 1.5°K. But the possibility that the value of susceptibility of this salt becomes constant in the very low temperatures, may be doubtfull, because each orbital level of Co^{++} ion has the Kramers' doublet. The antiferromagnetic charactor of $Co(H_2O)_6Cl_2$ at very low temperatures has been found by T. Haseda.[11)]

$Co(NH_3)_2Cl_2$, $Co(NH_3)Cl_2$ and $CoCl_2$: The values of g-factor and θ for $Co(NH_3)_6Cl_2$ decrease at low temperatures. Such behaviors would be expected also in the cases of $Co \cdot (NH_3)_2Cl_2$, $Co(NH_3)Cl_2$ and $CoCl_2$, but could not be observed in the case of powdered samples. $Co(NH_3)_2Cl_2$ and $Co(NH_3)Cl_2$ have respectively the magnetic transition points of 16°K and 20°K, and the Weiss temperatures θ for both salts have negative signe ($\theta < 0$), as seen in Figs. 4 and 5. The magnetic characters of these salts are similar to that of $CoCl_2$ and it seems that these salts are metamagnetic. The present result of $CoCl_2$ agrees well with the result given by Bizette et al.[12)]

3) Ni^{++} ($3d^8$, $^3F_4$)

$Ni(NH_3)_6Cl_2$: The susceptibility of nickel hexammine chloride $Ni(NH_3)_6Cl_2$ becomes nearly constant in the temperature range below 1.6°K, as shown in Fig. 6. The possible explanations of this behavior are such as the following two.

i) The value of susceptibility seems to decrease below 1.42°K to which the present measurement was performed and the Neél point may be somewhere about 1.5°K.

ii) The ground level of Ni^{++} ion which is splitted by the combined action of cubic field and spin-orbit coupling, is orbital singlet. And so the value of susceptibility becomes constant in the temperature range corresponding to λ^2/Δ_i, where Δ_i is the level separation.

The present experiment could not make clear the above two possibilities, because the measurement could not be carried out down to 1.0°K and the single crystal was not used. But if it is allowed to assume the latter situation (ii) for the explanation of the present result, we may conveniently use the spin Hamiltonian method[12)–14)] in the analysis of the result for $Ni(NH_4)$-Tutton salt. The Hamiltonian is, in this case,

$$\mathscr{H} = -DS_z^2 - E(S_x^2 - S_y^2) + g\mu_B H(\alpha S_x + \beta S_y + \gamma S_z)\,. \qquad (4)$$

From the above Hamiltonian (4), the relation between the susceptibility and the temperature is derived (in the case of Ni^{++} ion, $S=1$) as follows,

$$\chi_{m(\text{powder})}(T) = \chi_{m(\text{powder})}(0) \times \frac{1 - \dfrac{(D+E)(D-3E)}{(D-E)(D+3E)} e^{-2E/kT} - \dfrac{4DE}{(D-E)(D+3E)} e^{-(D+E)/kT}}{1 + e^{-2E/kT} + e^{-(D+E)/kT}} \qquad (5)$$

and at absolute zero degree,

$$\chi_{m(\text{powder})}(0) = \frac{2Ng^2\mu_B^2}{3} \cdot \frac{D+3E}{2E(D+E)}\,. \qquad (6)$$

Some couples of the trial values of D and E are estimated from the relation (6) using extrapolated value to $T=0$. Substituting such values of D and E into the relation (5), final couple of the values are determined by comparison with the experimental result. These values thus obtained at low temperatures are respectively

$$D = 43\,\text{cm}^{-1} \quad \text{and} \quad E = 5\,\text{cm}^{-1}\,.$$

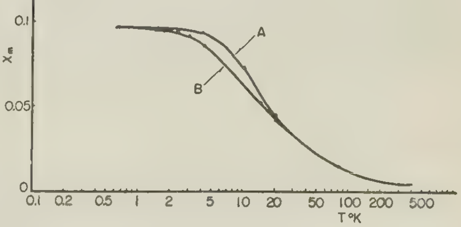

Fig. 9. Calculated and measured molar susceptibility versus temperature (°K) for $Ni(NH_3)_6Cl_2$. A-calculated curve and B-measured curve.

Table V.

Temperature	χ_{exp}*	χ_{calc}**	Temperature	χ_{exp}*	χ_{calc}**
0°K	0.0926***	0.0926***	10.0°K		0.0725
1.42	0.09505		14.3	0.0520	
1.75	0.09433		14.75	0.0516	
2.00		0.0957	15.4	0.0508	
2.33	0.09416		15.9	0.0488	
2.97	0.09099		17.6	0.0457	
3.60	0.08851		20.0		0.0446
4.00		0.0937	20.4	0.0415	
4.20	0.08547		79.0	0.0143	0.0146
			293	0.00395	0.00394

* χ_{exp}:—the experimental values of susceptibility.

** χ_{cal}:—the calculated values of susceptibility.

*** This is the inserting value in Fig. 9.

The estimated values of susceptibility using above numerical values of D and E, and the measured values of susceptibility in any temperature are given in Fig. 9 and Table V.

The values of $D-E$ and $2E$ are about twenty times larger than those of Ni(NH$_4$)-Tutton salt which are determined from the results of E.S.R. or magnetic susceptibility. These values in nickel hexammine chloride salt may be hardly accepted as reasonable values, but they may explain the fact that the reasonance line of $Ni(NH_3)_6Cl_2$ could not be observed in the range below 74°K, although the wave length of 0.8 cm was used.[16]. While E.S.R. of this salt can be observed from room temperature down to 74°K. The color of this salt is blush purple in the region from room temperature down to liquid oxygen and pinky purple below liquid nitrogen temperatures. If above behaviors for $Ni(NH_3)_6Cl_2$ have been considered, the crystal structure of this salt may happen to deform in the range from 70°K to 80°K. It may be said that g-value of $Ni(NH_3)_6Cl_2$ in the range below liquid hydrogen temperatures is 2.20±0.02 which is somewhat larger than 2.17±0.03 in the range above 90°K.

$Ni(NH_3)_6(ClO_4)_2$: The magnetic character of $Ni(NH_3)_6(ClO_4)_2$ is different from that of $Ni(NH_3)_6Cl_2$ below 4.2°K, as seen Fig. 6. The values of susceptibility of $Ni(NH_3)_6(ClO_4)_2$ increase even at 1.5°K, and the result for this salt obeys the Curie-Weiss law down to about 2°K. The color of this salt changes from bluish purple to pinky purple below 80°K similarly to $Ni(NH_3)_6Cl_2$.

If the exchange interaction energy is neglected, from the relation (5) and (6) the values of D and E are estimated respectively, as follows:

$$D=6.0\ \mathrm{cm}^{-1} \quad \text{and} \quad E=1.0\ \mathrm{cm}^{-1}.$$

If the exchange interaction $A\cdot S_iS_j$ is considered, the spin-Hamiltonian becomes[17]

$$\mathscr{H}=-DS_z^2-E(S_x^2-S_y^2)+\mu_B g(H_xS_x+H_yS_y+H_zS_z)+AS\cdot\langle S\rangle\,. \tag{7}$$

$AS\cdot\langle S\rangle$ in the above Hamiltonian represents the thermal equiliblium approximation of $A\cdot S_iS_j$. When the magnitude of exchange interaction is smaller than that of crystalline field splitting, the relation of χ_m and T in any temperature derived from the Hamiltonian (7) is given by (in the case of Ni^{++} ion, $S=1$),

$$\begin{aligned}\chi_{m(\text{powder})}(T)&=\frac{1}{3}(\chi_x+\chi_y+\chi_z)\\&=\frac{2}{3}Ng^2\mu_B^2[\{1-e^{-(D+E)/kT}\}/[(D+E)\cdot\{1+e^{-2E/kT}+e^{-(D+E)/kT}\}+2A\{1-e^{-(D+E)/kT}\}]\\&\quad+\{e^{-2E/kT}-e^{-(D+E)/kT}\}/[(D-E)\cdot\{1+e^{-2E/kT}+e^{-(D+E)/kT}\}+2A\{e^{-2E/kT}-e^{-(D+E)/kT}\}]\\&\quad+(1-e^{-2E/kT})/[2E\cdot\{1+e^{-2E/kT}+e^{-(D+E)/kT}\}+2A(1-e^{-2E/kT})]]\end{aligned} \tag{8}$$

and in the absolute zero degree the relation of χ_m is

$$\chi_{m(\text{powder})}(0) = \frac{2Ng^2\mu_B{}^2}{3}\left(\frac{1}{D+E+2A} - \frac{1}{2E+2A}\right). \qquad (9)$$

The relation of the Curie-Weiss law in the high temperature range is

$$\chi_{m(\text{powdcr})}(T) = \frac{2Ng^2\mu_B{}^2/3}{3kT+2A}. \qquad (10)$$

Above relations for the susceptibility have been kindly derived for the present author by Dr. T. Moriya. Each values of A, D and E whicn are determined by the similar process to the case of $Ni(NH_3)_6Cl_2$ are

$$A = 0.7 \pm 0.1\ \text{cm}^{-1},$$
$$D = 4.0\ \text{cm}^{-1}$$

and

$$E = 0.38\ \text{cm}^{-1}.$$

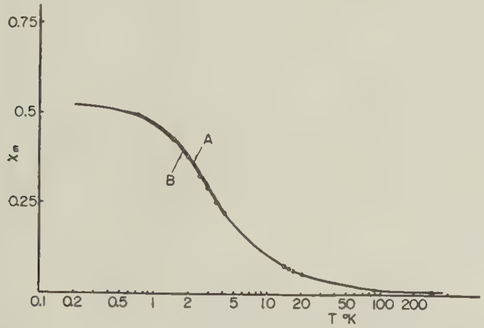

Fig. 10. Calculated and measured molor susceptibility versus temperature (°K) for $Ni(NH_3)_6(ClO_4)_2$.
A-calculated curve and B-measured curve.

The calculated values of susceptibility using above values of A, D and E, and the experimental values of susceptibility in any temperatures are shown in Fig. 10 and Table VI. According to the observation by Kim and Sugawara[18),19)] the proton resonance lines of $Ni(NH_3)_6Cl_2$ (in powder and single crystals) and $Ni(NH_3)_6(ClO_4)_2$ (in powder) disappear respectively at 1.6°K and 7°K. But the values of θ estimated from magnetic susceptibility and the temperatures for disappearance of N.M.R. lines in $Ni(NH_3)_6Cl_2$ and $Ni(NH_3)_6 \cdot (ClO_4)_2$ do not agree with each other as shown in Table VII. The proton line of $Ni(NH_3)_6Cl_2$ disappears at 1.6°K where the value of susceptibility becomes nearly constant, but the proton line of $Ni(NH_3)_6(ClO_4)_2$ disappears at about 7°K while the susceptibility obeys the Curie-Weiss law down to 2°K. On

Table VI.

Temperature	χ_{exp}*	χ_{calc}**	Temperature	χ_{exp}*	χ_{calc}**
0°K	0.525***	0.525***	10.0°K		0.110
1.50		0.420	13.9	0.0748	
1.57	0.4251		15.4	0.0709	
1.86	0.3963		16.1	0.0686	
2.50	0.3294	0.331	17.2	0.0655	
2.95	0.2930		20.0		0.0510
3.37	0.2692		20.4	0.0522	
4.00		0.235	81.0	0.0149	0.0147
4.20	0.2261		293	0.00408	0.00408

* χ_{exp}:—the experimental value of susceptibility.
** χ_{cal}:—the calculated value of susceptibility.
*** This is the inserting value in Fig. 10.

Table VII.

	θ	The temperature of disappearance of N.M.R. line
$Ni(NH_3)_6Cl_2$	8°K	1.6°K (by Kim and Sugawara)
$Ni(NH_3)_6(ClO_4)_2$	0.7	7 (〃)

the other hand, the proton line of $Ni(H_2O)_6 \cdot Cl_2$ disappears at about 7°K. This salt is antiferromagnetic below 6.2°K[20] and the specific heat of this salt exhibits a lambda-shaped anamalous peak at 5.34°K.[21] It seems that the disappearance of proton line in this case can be explained by the antiferromagnetic transformation[22]*. But when the results of Table VII are considered we can not infer that the disappearance of the proton lines of $Ni(NH_3)_6Cl_2$ and $Ni(NH_3)_6(ClO_4)_2$ are due to the antiferromagnetic transition. On the other hands, if the disapperance are due to the spin-quenching below the temperature comparable to an interval of the splitting of ground levels, the temperature of disappearance of N.M.R. line should coincide with that of spin-quenching. But it is not the case.

$Ni(NH_3)_2Cl_2$, $Ni(NH_3)Cl_2$ and $NiCl_2$: The observed relations of $\chi - T$ of $Ni(NH_3)_2Cl_2$ and $Ni(NH_3)Cl_2$ are similar to each other, except the detail in the low temperature range as shown in Fig. 7. The sign of the Weiss constant θ are negative ($\theta<0$) and the order of magnitude of θ is

$$|\theta_{Ni(NH_3)_2Cl_2}| < |\theta_{Ni(NH_3)Cl_2}| < |\theta_{NiCl_2}| \; .$$

(as seen in Table III)

So, it may be probable that the magnetic characters of these salts are metamagnetic like in $NiCl_2$. The order of magnitude of θ indicates that Ni^{++} ions are diluted magnetically by NH_3 ligand. The present result of $NiCl_2$ agrees well with the results of Bitter, Starr and Kaufmann[23], and Bizette, Tisaï and Terrier[12].

4) Cu^{++} ($3d^9$, $^2D_{5/2}$)

$Cu(NH_3)_4SO_4 \cdot (H_2O)$: The result of this salt in the temperature range between 1.02°K and 20.4°K was already published by the present author and T. Haseda[24]. We have proposed the possibility that the magnetic interaction is probably linear chain like in this salt, in order to explain the magnetic susceptibility of single crystals in that report.

$Cu(NH_3)_2SO_4$: The magnetic susceptibility of $Cu(NH_3)_2SO_4$ in the temperature below 20.4°K deviates from the Curie-Weiss law in the temperature above 90°K. And the Weiss constant θ of this salt is almost zero degree in the temperature range from 1.5°K to 4.2°K, as seen in Fig. 8 and Table IV. The following data of the magnetic moment p_{exp} and the Weiss temperature θ are the quotation from Table IV.

	high temperature region (above 90°K)	low temperature region (below 4.2°K)
p_{exp}	$1.92 \pm 0.03\,\mu_B$	$1.47 \pm 0.02\,\mu_B$
θ	22 ±3°C	0 ±0.2°C

The magnetic moment p_{exp} of this salt is 1.47 μ_B in the temperature range from 1.5°K to 4.2°K as shown in the above results. If 1.47 μ_B at the low temperature range is compared with 1.92 μ_B at the high temperature range, these results mean that 73% of the magnetic moment at high temperatures is free and that 27% of this is quenched by some reason in liquid helium temperatures. 27% of magnetic moment corresponds to 15% of electron spin for $S=1/2$. The partial quenching of magnetic moment can be found

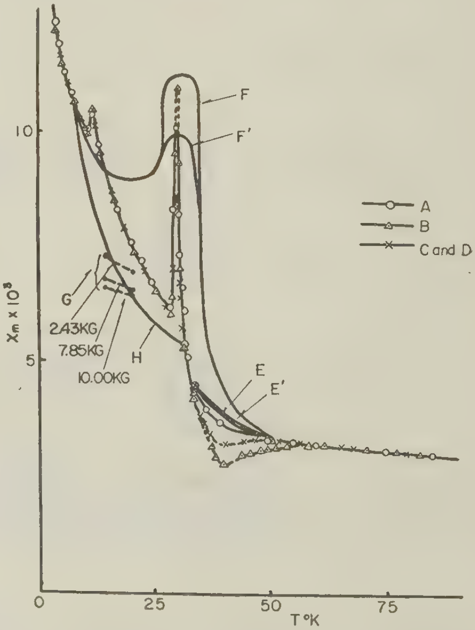

Fig. 11. Molar susceptibility versus temperature (0°K) for $CuSO_4$ anhydrate. E' and F' are the susceptibility curve under the external applied field of 1000 and they correspond to E and F respectively.

---

* Recently, Prof. T. Sugawara of Tokyo University have found the symmetric pattern on proton line with 180° period in $Ni(H_2O)_6Cl_2$ due to the antiferromagnetic ordering at liquid helium temperatures.—private communication.

Table VIII.

$CuSO_4$	The temperature of dehydration	time	condition
A	300°C	1 hr	in air
B	270	2 hrs	〃
C	300	1 hr	in vacuum
D	300	——	+conc. H_2SO_4
E	270	——	〃
F	300	——	$+(NH_4)_2SO_4$

also in the case of $Cr_3(CH_3COO)_6(OH)_2Cl_2 \cdot 8H_2O$[25], but it seems that such a result can not probably be expected in the case of spin state of $S=1/2$ only.

$CuSO_4$: The magnetic measurement of $CuSO_4$ anhydrate was carried out previously by de-Hass and Gorter[3] (1931), recently by Romanov-Borovik, Kalasik, Kleines[4] and Romanov-Borovik, Kleines[5]. The about twenty kinds of samples are prepared for the present experiment according to the several conditions of dehydrating process from the separate sources. The results of magnetic susceptibility of $CuSO_4$ anhydrate are different from sample to sample at about 35°K. The curves of A, B, C, D, E and F in Fig. 11 are respectively for the samples that were prepared by the conditions in Table VIII.

The curve G in Fig. 11 is the results by de-Haas and Gorter. The curve H corresponds to the case in which the external magnetic field of about 1000 Oe is applied to the specimens A, B, C, D and E in the range between 10°K and 35°K, and E′ is for the case in which the external field of about 1000 Oe is applied to the specimen E at the range between 38°K and 45°K. The curve F′ is also the result of application of magnetic field of about 1000 Oe in the case of F.

All the samples in the present results show the magnetic transition at about 35°K as shown in Fig. 11. The transition point of specific heat of lambda-type at 35°K was found by Stout[26] and following to his report this peak of the specific heat corresponds to 1/3 spin quenching (at $S=1/2$ state). The value of susceptibility in the transition point at 35°K is different for the each run, as mentioned above. The magnetic field dependency of susceptibility can be found respectively in the ranges from 10°K to 36°K and from 38°K to 45°K. The values of susceptibility decrease with increasing magnetic field in the former range and increase somewhat with increasing magnetic field in the latter range. It seems that the magnetic property in the former temperature range is parasitic ferromagnetism. The magnetic field dependency of susceptibility could not be found below 10°K, but the results in this temperature range do not obey the Curie-Weiss law and these resulting curves (for the relation of $\chi \sim T$) have the asymptotic line to $T=0$. On the other hand, the sample of $CuSO_4$ which is produced from the mixed fusion state of $CuSO_4+(NH_4)_2SO_4$ was measured in the present experiment and the results are given by the curves F and F′ in Fig. 11. These results is different from the former results of the present experiment at about 35°K, as seen in Fig. 11. The antiferromagnetic character in this case does not appear in the range between 38°K and 45°K, but this result is in agreement with the former results in the temperature below 10°K. The narrow peaked values at 35°K in the former results may be enhanced by the crystal defect. It seems that such ambigous results are attributed to the crystal imperfection existing in the powder sample. Above all, the parasitic ferromagnetic character of this salt in the temperature range from 10°K to 35°K may be also attributed to the existence of crystal imperfections probably.

§ 4. Conclusion

The following conclusions are derived from the results and the discussion of former chapter.

i) The values of the Weiss constant θ decrease with the increasing number of coordinated ligand in Mn^{++}, Co^{++}, Ni^{++} and Cu^{++}

salts.

ii) The values of the Weiss constant θ in each ammine and anhydrated salts are minimum in the case of Mn^{++} ion salt.

iii) It seems that $Co(NH_3)_6Cl_2$ in the temperature below 1.5°K shows antiferromagnetic character, because as pointed out in the preceding chapter the ground orbital level of Co^{++} ion is triplet state and each orbital level has the Kramers' doublet. The expectation that the susceptibility of $Co(NH_3)_6Cl_2$ has constant value in low temperatures may be hardly probable.

iv) The Weiss temperatures θ of $Co(NH_3)_2 \cdot Cl_2$, $Co(NH_3)Cl_2$, $Ni(NH_3)_2Cl_2$ and $Ni(NH_3)Cl_2$ are negative and it seems that these salts show the nature of metamagnetism like in $CoCl_2$ and $NiCl_2$.

v) The crystalline fields of $Ni(NH_3)_6Cl_2$ and $Ni(NH_3)_6(ClO_4)_2$ are predominantly cubic. But the magnetic properties of these salts below 10°K are inconsistent with each other salts as mentioned in preceding chapter. The reliability of values of D and E in $Ni(NH_3)_6 \cdot Cl_2$ (in section 3) is not enough. On the other, if the consideration in section 3 is allowed, the values of level splitting of $(D-E)$, $2E$ and the value of the exchange interaction A of $Ni(NH_3)_6(ClO_4)_2$ are very smaller than the values of $Ni(NH_3)_6Cl_2$, and these values of the former salt are the same order with the values of Ni-Tutton salt. Kim and Sugawara[18),19)] reported the result that proton resonance lines of $Ni(NH_3)_6(ClO_4)_2$ and $Ni(NH_3)_6 \cdot Cl_2$ disappeared respectively at 7°K and 1.6°K. So we can not produce any conclusion from the said dissimilarity between the result of N.M.R. by Kim and Sugawara and the present result of the magnetic susceptibility below 10°K. The proton resonance lines of $Ni(NH_3)_6Cl_2$ and $Ni(NH_3)_6(ClO_4)_2$ disappear in low temperatures, and these behaviors can not be interpreted by the magnetic transformation and can be hardly interpreted by the energy level splitting.

vi) The magnetic transformation of $CuSO_4$ anhydrate is probably at about 35°K. But the reproducible result of magnetic susceptibility of this salt can be hardly obtained from the measurement of sample used in the present experiment. Such a nonreproducibility of magnetic measurement at about 35°K might be caused by the crystal imperfections which would be created in the dehydrated process. And it seems probable that the parasitic ferromagnetic character of this salt in the temperature range 10°K to 35°K is also attributed to the existence of crystal imperfections.

Acknowledgement

The present author wish to express his sincere thanks to Prof. K. Kido who has encouraged him for the present study, and Prof. E. Kanda and Dr. T. Haseda of Tohoku Univ. who have given him many facilities throughout this investigation. He says his thanks also to Mr. Takashi Sato of the Research Institute for Iron, Steel and Other Metals of Tohoku Univ. for his helpful assistance. This work was indebted to the Scientific Research Expenditure of the Section of Low Temperature of the Ministry of Education.

References

1) K. Kido and T. Watanabe: J. Phys. Soc. Japan **14** (1959) 1217.
2) C. J. Gorter: Paramagnetic Relaxation (Leiden 1947).
3) W. J. de-Haas and C. J. Gorter: Leiden communication (1931) 215a.
4) A. S. Borovik-Romanov, V. R. Karasik and N. M. Kleines: J. Exptl. Theor. Phys. (U.S.S.R.) **31** (1956) 18.
5) A. S. Borovik-Romanov and N. M. Kleines: J. Exptl. Theor. Phys. (U.S.S.R.) **33** (1959) 1119.
6) R. W. G. Wyckoff: Crystal Structures. Vol. 2 Interscience Pub. New York (1951) 34.
7) R. W. G. Wyckoff: ibid Vol. 1 (1948) IV 19.
8) R. W. G. Wyckoff: ibid IV 21.
9) F. Hammel: Ann. Chem. **11** (1939) 247.
10) R. M. Murray and L. D. Roberts: Phys. Rev. **100** (1955) 1067.
11) T. Haseda: J. Phys. Soc. Japan **12** (1959) 1051.
12) H. Bizette, B. Tsaï and C. Terrier: Compt. rend **243** (1956) 1295.
13) A. Abragam and M. H. L. Pryce: Proc. Roy Soc. **A205** (1951) 135.
14) J. H. E. Griffice and J. Owen: Proc. Phys. Soc. A (1952) 459.
15) T. Haseda and M. Date: J. Phys. Soc. Japan **13** (1958) 175.
16) M. Date: J. Phys. Soc. Japan **16** (1961).
17) T. Moriya: Private communication.
18) P. H. Kim and T. Sugawara: J. Phys. Soc. Japan **13** (1958) 968.

19) P. H. Kim: J. Phys. Soc. Japan **15** (1960) 445.
20) T. Haseda, H. Kobayashi and M. Date: J. Phys. Soc. Japan **14** (1959) 1724.
21) W. K. Robinson and S. A. Friedberg: Phys. Rev. **117** (1960) 402.
22) T. Sugawara: Private communication.
23) C. Starr, F. Bitter and A. R. Kaufmann. Phys. Rev. **58** (1940) 977.
24) T. Watanabe and T. Haseda: J. Chem. Phys. **29** (1958) 1429.
25) J. Wücher and H. M. Gijsman: Physica **20** (1954) 361.
26) J. W. Stout: J. Chem. Phys. **9** (1941) 285.

JOURNAL OF THE PHYSICAL SOCIETY OF JAPAN, Vol. 16, No. 6, JUNE, 1961

Ultrasonic Attenuation in Tin Single Crystals at Low Temperatures*

By Kazuo KAMIGAKI
The Research Institute for Iron, Steel and Other Metals,
Tohoku University, Sendai

(Received November 14, 1960)

The ultrasonic attenuation coefficient and velocity in the superconducting and the normal states of tin single crystals were measured at temperatures between 1.5° and 4.2°K. It was found that (1) the anisotropy of ultrasonic attenuation in different crystallographic directions exists in the case of comparatively long wavelengths (the product of the mean free path of conduction electrons and wave number of sound waves is less than unity). (2) Also the ratio of longitudinal to shear wave attenuation was found to be larger than that predicted from the free electron model.

§1. Introduction

The recent theory of superconductivity prosed by Bardeen and others (BCS)[1] makes clear the nature of phonon-electron interaction in the superconducting state. This theory is founded on the spherical or isotropic energy distribution of conduction electrons in momentum or wave vector space. In real metals, however, the Fermi surface is not spherical. Recently, Morse[2] and Bezuglji[3] found in tin single crystals the anisotropic deviation of the ultrasonic attenuation from the BCS theory in the frequency range of $ql>1$, where q is the wave vector of ultrasonic waves and l the mean free path of the conduction electrons. In connection with these experiments, the present author planned to measure the ultrasonic attenuation and velocity of the longitudinal and the shear waves along different crystallographic directions of tin single crystals for the frequency range $ql<1$.

§2. Test Piece and the Method of Measurements

The tin single crystals (99.98 per cent) were prepared by the Bridgman method. Each specimen was machined into a rod about 1.2 cm in diameter and 1.2 cm in length. The crystallographic directions of the specimens were determined within ±1° by the light figure method[4]. The specimen was placed in a liquid helium cryostat of the usual type.

The ultrasonic attenuation coefficient was measured by the pulsed wave technique. The electronic apparatus and the measuring procedure were the same as those used in the previous measurements[5]. The frequencies of the ultrasonic waves used in the present experiment were 9, 15 and 25 Mc/s respectively. Quartz crystals were used as transducers: an X-cut disk 0.7 cm in diameter was prepared

---

* The expense of this work was partly defrayed by the Grant-in-Aid for Fundamental Scientific Research of the Ministry of Education.

for the longitudinal waves and a rectangular Y-cut plate 1×1.02 cm in size for the shear waves. The crystals were cemented to the specimens with Bond CA 100. The accuracy of the attenuation measurement was ±3 per cent. Sound velocity was determined by measuring the time difference of successive pulses by means of an electronic delay circuit, and the accuracy of measurement in this case was about 2 per cent. A maximum magnetic field of 600 Oe was applied to destroy the superconducting state of the specimen.

§ 3. Results of Measurements and Discussions

First, the variation of longitudinal attenuation at 15 Mc/s with the magnetic field was measured and the results are shown in Fig. 1.

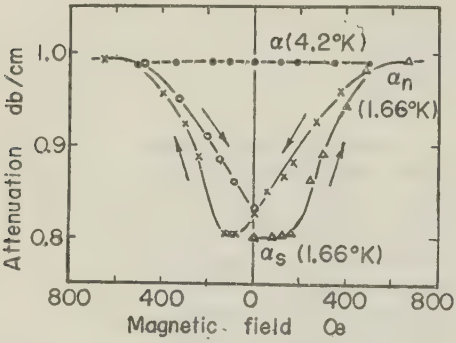

Fig. 1. Dependence of longitudinal ultrasonic attenuation on the magnetic field. The broken line shows the attenuation at 4.2°K and the solid line at 1.66°K.

The broken line shows the attenuation at 4.2°K, which is a temperature above the superconducting transition point T_c; only a slight effect due to the magnetic field could be observed. While the measurement at 1.66°K, which is below T_c, shows that the attenuation increases with the field strength gradually from about 200 Oe and becomes saturated at about 500 Oe as is shown by a solid curve in Fig. 1. By reversing the field direction the attenuation follows the hysteresis curve, this would be due to the heterogeneous transformation between the normal and the superconducting states. The same feature was observed in the shear wave attenuation.

Longitudinal and shear wave attenuation coefficients at 15 Mc/s were measured at temperatures between 1.5°K and 4.2°K. The results are plotted in Fig. 2, the direction of transmission being shown on the pole figures. As was shown by the previous measurements[6,7,8] the attenuation coefficient in the superconducting state decreased rapidly just below T_c and then slowly with further lowering of temperature. On the contrary, attenuation in the normal state was found to remain almost unchanged with temperatures. The same attenuation behavior was also observed at 9 and 25 Mc/s.

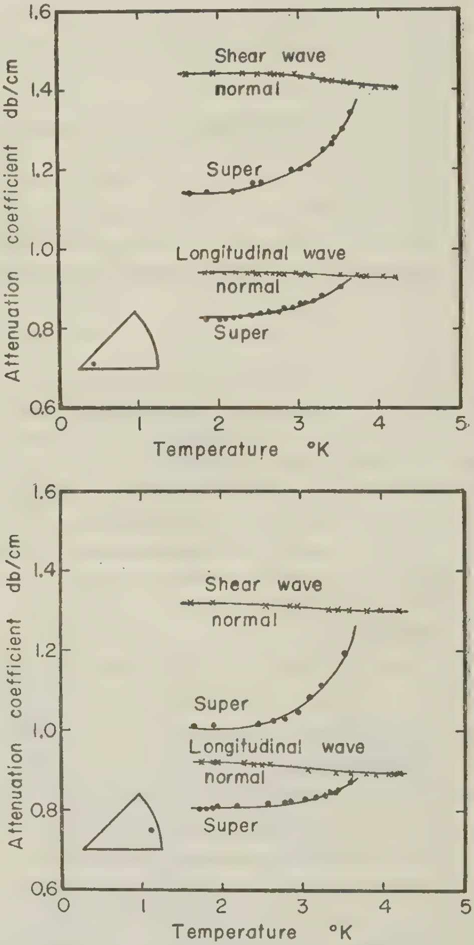

Fig. 2. Longitudinal and shear wave attenuation coefficients at 15 Mc/s.

Longitudinal and shear wave velocities v_L and v_T were measured for the same specimen and the results obtained are shown in Fig. 3. In the present case, both v_L and v_T were almost unchanged with temperature and with the transformation between normal and superconducting states within the accuracy of the measurement[8,9].

It is to be noted here that there is, of course, a background attenuation which is non-electronic in origin. The electronic attenuation was determined by extracting the extrapolated superconducting attenuation to 0°K. Both superconducting and normal state attenuations, which are electronic, are taken from this extrapolated value and written as $\alpha_s(T)$ and $\alpha_n(T)$ at T°K. Now in Fig. 4 the values of $\alpha_n(0)$ along the same crystallographic direction at different frequencies are plotted against the square of the frequency. As this figure shows, the value of attenuation is proportional to the square of the freqency. The dependence of attenuation on frequency f was discussed by several authors in a classical[10,11] and in a quantum mechanical way[12], which showed that α_n is proportional to f or f^2 according as $ql>1$ or <1; hence it is concluded for the present case that $ql<1$. In such a case the attenuation of the longitudinal waves is written in the following form

$$\alpha_n = \frac{8}{15}\frac{\pi^2 f^2}{\rho v_L^3}\frac{\hbar^2(3\pi^2 N)^{2/3}}{e^2}\sigma\,, \qquad (3)$$

where ρ is the density, σ the electrical conductivity, N the number of electrons in the unit volume, and e the electron charge. From the slope of the curve in Fig. 3, the value of product $N^{2/3}\sigma$ is found to be 0.63×10^{34}.*

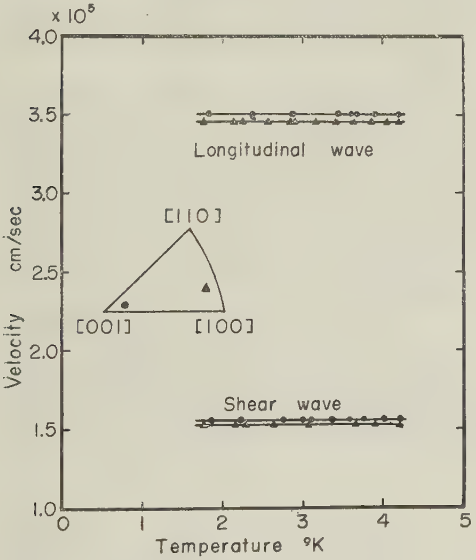

Fig. 3. Velocity of the longitudinal and the shear waves.

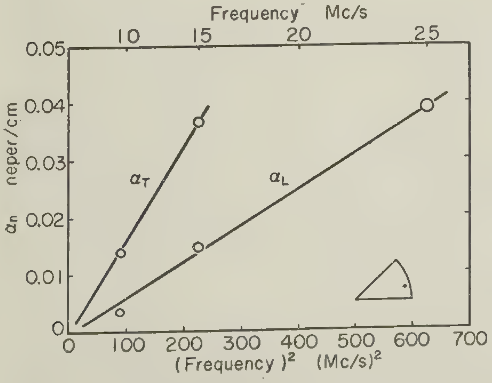

Fig. 4. Relations between α_n and the square of the frequency for longitudinal and shear waves.

According to the BCS theory of superconductivity which was based on the spherical Fermi surface assumption, the variation of ultrasonic attenuation with temperature is given for the case of $ql>1$. However, this assumption is not exactly applicable to the real metals. Some deviation from the theoretical curve was found out in the measured values for different directions of a crystal in the case of $ql>1$[2,3]. Now, in Fig. 5 the ratio α_s/α_n is plotted against reduced temperature for different crystallographic directions, which shows that also in the case $q<1$ the observed values for different orientations deviated from each other. α_s/α_n is slacker in the directions near [100] than the other. This tendency

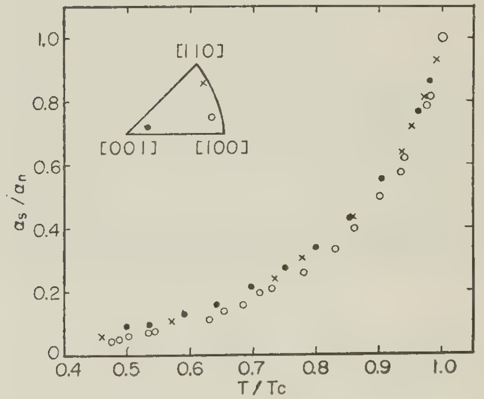

Fig. 5. Ratios between superconducting and normal state attenuation of longitudinal waves at 15 Mc/s for various orientations of tin single crystals.

---

* The residual electrical resistance of the present specimen is estimated at $2\times10^{-8}\,\Omega$-cm, making use of equation (1) and measured values of resistance $1\times10^{-10}\,\Omega$-cm and attenuation 0.82 neper/cm (10.3 Mc/s) in 99.999% tin single crystal[8].

agrees closely with the results obtained in the case of $ql > 1$. The origin of such anisotropy will be the deviation of the electronic energy contour from the spherical symmetry in the tetragonal tin crystal.

Moreover, according to the classical calculations[10,11], the ratio of the electronic attenuation of longitudinal waves α_L to that of shear waves α_T at the same frequency is given

$$\frac{\alpha_L}{\alpha_T}=\frac{4}{3}\frac{v_T^3}{v_L^3}, \qquad (2)$$

assuming the isotropic velocity distribution for conduction electrons. Making use of the observed values in Figs. 3 and 4, the applicability of the above equation is examined. As shown in the following Table, $4v_T^3/3v_L^3$ is obtained as 0.18; while from the slope of both curves in Fig. 4, α_L/α_T is found to be 0.35 in the direction shown in the pole figure, so that the ratio of both sides of equation (2) is calculated as 0.51. This value is less than the value 0.92 due to Mason and Bömmel[8] in the direction near [100]. The deviation of both values from unity would result from the assumption of isotropy used in the theory.

Table I.

	$\frac{4}{3}\frac{v_T^3}{v_L^3}$	$\frac{\alpha_L}{f^2}$	$\frac{\alpha_T}{f^2}$	$\frac{\alpha_L}{\alpha_T}$	Ratio
		$10^4\frac{(\text{neper/cm})}{(\text{Mc/s})^2}$			
Author's result	0.18	0.60	1.7	0.35	0.51
Mason, Bömmel	0.22	0.29	1.2	0.24	0.92

The author wishes to express his sincere thanks to Prof. T. Hirone and Prof. Z. Mikura for their kind guidance throughout the present work.

References

1) J. Bardeen, L. N. Cooper and J. R. Schrieffer: Phys. Rev. **108** (1957) 1175.
2) R. W. Morse, T. Olsen and J. D. Gavenda: Phys. Rev. Letters **3** (1959) 15, 193.
3) P. A. Bezuglji, A. A. Galkin and A. D. Korolyuk: Sov. Phys. JETP **9** (1959) 1388.
4) M. Yamamoto and J. Watanabe: Sci. Rep. Res. Inst. Tohoku Univ. **A 7** (1955) 161.
5) T. Hirone, K. Kamigaki: Sci. Rep. Res. Inst. Tohoku Univ. **A 7** (1955) 456.
6) H. E. Bömmel: Phys. Rev. **96** (1954) 220.
L. Mackinnon: Phys. Rev. **98** (1955) 1181, 1210.
7) R. W. Morse and H. V. Bohm: Phys. Rev. **108** (1957) 1094.
8) W. P. Mason and H. E. Bömmel: J. Acoust. Soc. Amer. **28** (1956) 930.
9) C. F. Squire: Phys. Rev. **93** (1954) 1126.
J. K. Landauer: Phys. Rev. **96** (1954) 296.
B. Welber and S. L. Quimby: Acta Met. **6** (1958) 351.
10) W. P. Mason: Phys. Rev. **97** (1955) 557.
C. Kittel: Acta Met. **3** (1955) 295.
R. W. Morse: Phys. Rev. **97** (1955) 1716.
11) A. B. Pippard: Phil. Mag. **46** (1955) 1104.
12) K. Yoshida: to be published.

Journal of the Physical Society of Japan, Vol. 16, No. 6, June, 1961

The Thermoelectric Power of Magnesium-Cadmium Alloys

By Seiichiro Noguchi

Department of Physics, Tokyo Metropolitan University Tokyo

(Received December 2, 1960)

The thermoelectric power of magnesium-cadmium alloys was measured relative to pure copper at temperatures between room temperature and 300°C. The measurements were made in the entire ranges of the composition and the data were analyzed by a band-model approximation to obtain some information about the band structure of the alloys in the magnesium-cadmium system.

The thermoelectric power at 300°C as a function of composition shows a smooth trend as well as that of an earlier investigation of the Hall measurements[1], although the result of the thermoelectric power at room temperature shows that there are three maxima and two minima, while the result of the Hall coefficient gives two maxima and one minimum. In the alloys of the composition corresponding to the ordered phase, anomalies in the thermoelectric power are observed at the transition point. The results of the thermoelectric power indicate that there is no evidence of any extinction or initiation of a band by the alloying. The situation of the Fermi level in A-overlap is discussed.

§ 1. Introduction

The relation between an axial ratio and an electronic band structure of some hexagonal alloys has been studied by a number of investigators[2-6]. The measurement of axial ratio, however, gives only indirect evidence of a variation of the band structure with alloying.

The experiments on transport properties, such as the Hall effect and the thermoelectric power which are sensitive to the condition of the conduction electrons, are desirable to obtain the direct information on the band structure. It is of great interest to study magnesium-cadmium system because there is a solid solution range in the entire compositions at higher temperatures, and the variation of the axial ratio is appreciably large, namely, the ratios are 1.887 for cadmium and 1.623 for magnesium[2]. The Hall measurements have indicated that the variation of the assumed bands is partly agreement with what is supposed by the results of the axial ratio measurements. The both measurements can not, however, show the detailed features, such as the initiation and the extinction of a band.

The present work will give a further information to this question. The variation of the thermoelectric power on the order-disorder transition is also investigated, and is discussed at the comparison with the results of the Hall effect which have been reported recently by Yonemitsu and Sato[7].

§ 2. Experimental Procedure

Eleven alloys were prepared for this investigation in the same way as for the Hall measurement[1]. The purity of the constituent metals is 99.9% for both magnesium and cadmium.

In the present measurement, a differential methods was used in place of a usual one, and the thermoelectric power of the specimens was obtained relative to pure copper and then the absolute thermoelectric power of the sample was determined by adding the known absolute thermoelectric power of pure copper observed by Cusack and Kendall[19]. The thermoelectric power of the specimens in the temperature range of the order-disorder transformation can not be observed by means of a usual method of measuring the thermoelectric force. The reason is as follows: In this method, one end of the sample is held at some constant temperature, for instance, at 0°C, and the other end is heated slowly up to scheduled temperature, then the thermoelectric voltages with increasing temperature are obtained and are differentiated with respect to temperature in order to obtain the thermoelectric power at every temperature. Therefore, when we try to measure the thermoelectric power during the order-disorder transition with this method, the lower end of the specimen is in an ordered state while the higher end is in a disordered state. Thus, observed thermoelectric voltage between these two ends may have no physical meaning.

We have employed the differential method for above reason, but this method has the same sort of disadvantage as the former one, although the extent of the disadvantage is far smaller. In an ordered alloy the order parameter is given as a function of temperature. When the two ends of such an alloy are kept at some different temperatures each other, these two ends have different states of order in their equilibrium. Unfortunately, without keeping two points of a specimen at the different temperatures, we essentially can not measure the thermoelectric power. This is the reason why the thermoelectric measurement can not be used in the investigation of the kinetics of the orderdisorder transition in spite of its sensitivity to the transition. This flaw, however, may be able to be diminished appreciably with the reduction of the temperature difference between the two ends. In the differential method used here, the difference of temperature was four to six degrees near the transition points.

When we measure the thermoelectric power of a specimen at the temperature at which the order-disorder transition occurs, we shall meet the other difficulty, that is the anomalous heat absorption during the transition. The variation of temperature difference between two ends of the specimen is so rapid that we could hardly observe the thermoelectric power at these temperatures. In the present measurements, heating of the specimens was made at the rate as slow as possible in order to avoid the above effect. The rate was about 0.5°C/min. or less. In spite of various experimental cares, the thermoelectric power in equilibrium state during the order-disorder transition can not essentially be measured by the above reasons. For the present discussion, however, the accurate data for perfect ordered and disordered states are necessary rather than the data for intermediate states. In the present work, all the specimens were measured in argon atmosphere.

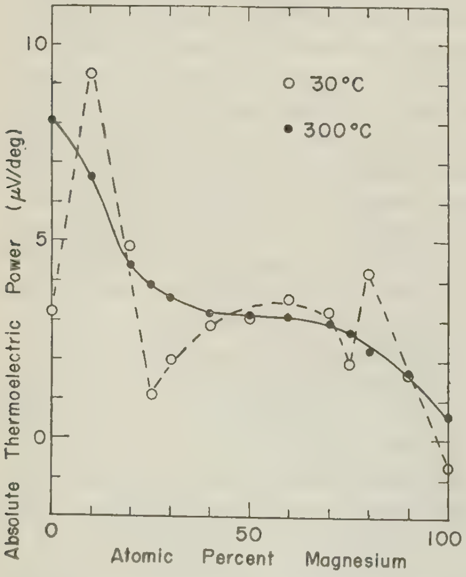

Fig. 1. The concentration dependence of the absolute thermoelectric power in Mg-Cd alloys.

§ 3. Results

Concentration dependence

The absolute thermoelectric power of cadmium at 300°C is obtained to be 8.03 microvolt per degree, and decreases monotonically with the increasing contents of magnesium, then, for the pure magnesium, reaches the value of 0.77 microvolt per degree. The magnesium-cadmium system has a single phase over the entire compositions at higher temperatures than 253°C. At these temperatures, all the alloys have a hexagonal close-packed structure but the axial-ratios are appreciably different for different compositions. On the other hand, at the lower temperatures, e. g. at room temperature, it has been reported that three ordered phases are present. Because of the existence of these phases, there is a notable difference between the composition dependence of the thermoelectric power at 300°C and that at room temperature. The concentration dependence of the both cases are given in Fig. 1. The thermoelectric power as a function of composition has two minima for the compositions corresponding to $MgCd_3$ and Mg_3Cd and it has a maximum for the approximate composition corresponding to MgCd. This behavior is in contrast to that for the Hall coefficient which shows two maxima for $MgCd_3$ and Mg_3Cd and a minimum for MgCd. In both cases, however, the compositions of ordered phases correspond to the extreme value. Extra two maxima are observed in the result of the thermoelectric power.

Temperature dependence

The temperature dependences of thirteen alloys are shown in Fig. 2–6. At higher temperature region, i. e. in the disordered state, all the specimens except cadmium have the tendency that the thermoelectric power de-

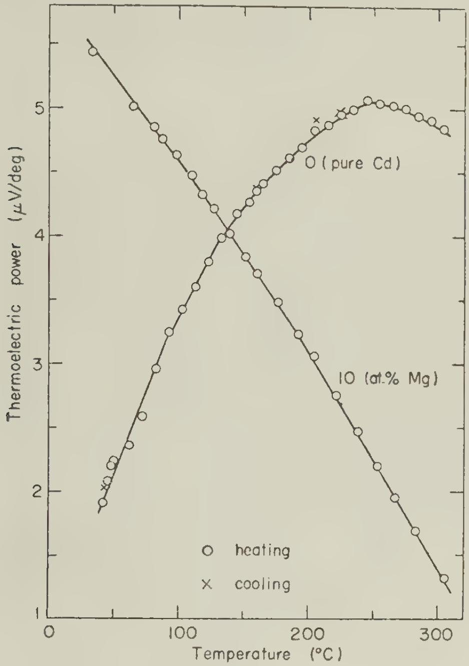

Fig. 2.

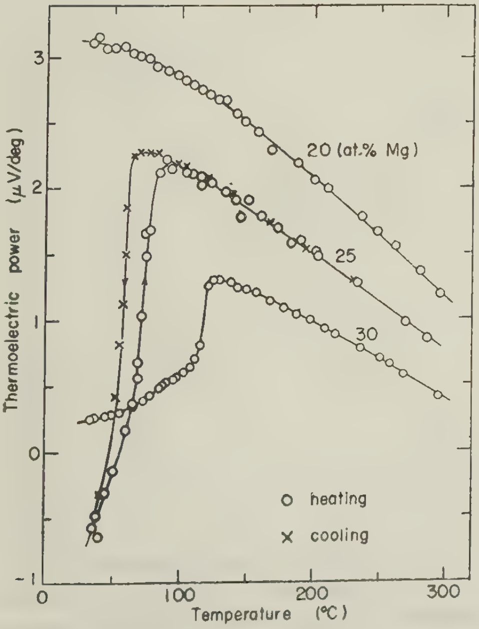

Fig. 3.

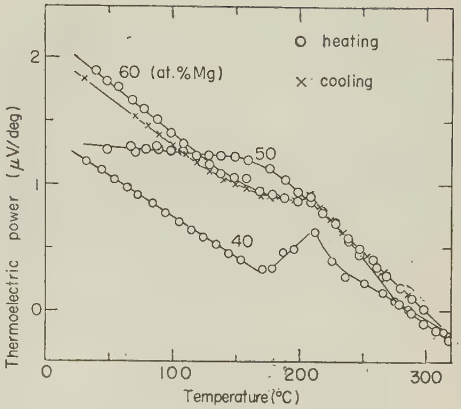

Fig. 4.

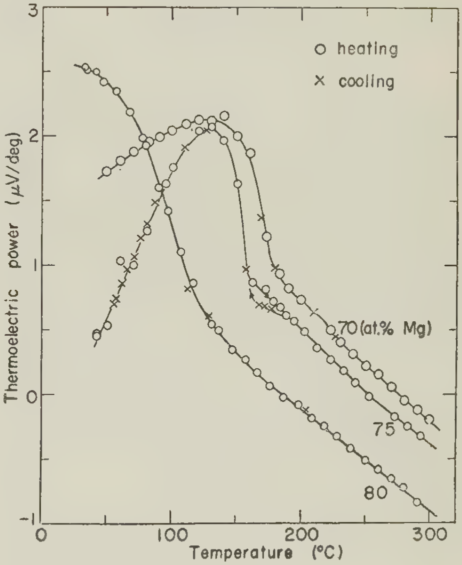

Fig. 5.

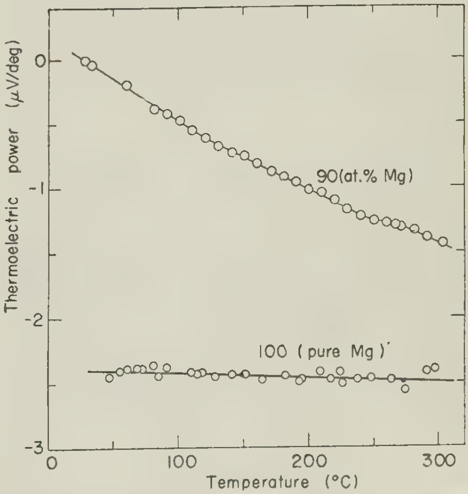

Fig. 2–6. The thermoelectric power relative to copper as a function of temperature.

creases with increasing temperature. For cadmium the thermoelectric power shows an anomalous behavior which has a maximum at about 250°C.

For the ordered phases, the temperature dependence is more complicated than that for the disordered phase. The thermoelectric power increases with increasing temperatures for both ordered phases, $MgCd_3$ and Mg_3Cd, while for MaCd its thermoelectric power appears to decrease with elevating temperature.

§ 4. Discussion and Conclusions

The magnesium forms the substitutional solid solution with the cadmium in any compositions at high temperatures. Although magnesium and cadmium are both divalent metals, each axial ratios are 1.6235 and 1.885 at 310°C, respectively. It has been found by Hume-Rothery and Raynor that the axial-ratio of the alloys of both metals shows a monotonic and continuous change with composition. The lattice-spacing relation has been interpreted in terms of the electronic structure and the sizes of their constituent atoms. As for the variation of the electronic structure is concerned, however, the measurements of the electrical properties are more suitable than the lattice parameter is. In the earlier work[1], we observed the concentration dependence of the Hall coefficient in order to study the electronic structure of magnesium-cadmium alloys. The Hall effect measurements show that most of the results agree with those given by the lattice-spacing measurements. There are some disagreements, however, between them if we study in detail. The present work is done in order to obtain further informations about the overlaps and the holes.

The first Brillouin zone of a hexagonal close-packed structure can contain just two electrons per atom, and the alloys in this system have two conduction electrons per atom. Therefore, we may consider that the number of electrons in the overlaps and of holes are relatively small and they will behave as free electrons. So we can write the thermoelectric power of this system as follows[8]

$$S=\sum_i \sigma_i S_i / \sum_i \sigma_i \,, \tag{1}$$

where σ_i is conductivity, S_i is the thermoelectric power when only the band i is presented in the system and i refers the species of band. In order to interpret the results of Hall measurements obtained by us we have assumed that there are two overlaps and two holes. These overlaps and holes may contain less carriers than a quarter per atom, therefore the relaxation times of them have such a dependence as $\tau=\tau_0 E^{-1/2}$, τ_0 is independent of the energy. If such a dependence and the standard form of bands are assumed, it can be expressed as

$$\begin{aligned}\sigma_i S_i &= \alpha_i (n_i e^2 \tau_i / m_i^*)(\pi^2 k^2 T / 3e\zeta_i) \\ &= \alpha_i e \pi^2 k^2 T C_i \tau_{i0} / 3m_i^* \,, \end{aligned} \tag{2}$$

where n is the number of carriers and n_i is given as $C_i^{3/2}\,\zeta_i$, ζ is the Fermi energy, and α is the dimensionless constant being -1 for a normal band and $+1$ for an inverted one. C_i is an energy-independent parameter. The other symbols have their ordinary meanings. The equation (2) indicates that $\sigma_i S_i$ is independent of the Fermi energy of the band i. In other word, the term $\sigma_i S_i$ becomes to be independent of the number of carriers, the number being changed by alloying[8].

As a fact, the resultant thermoelectric power would be proportional to the total resistivity[10]. This provisional composition-dependence, however, is quite different from the

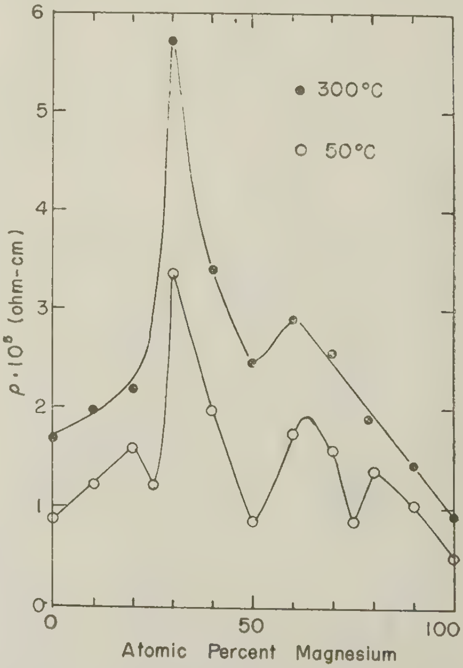

Fig. 7. The concentration dependence of electrical resistance in Mg-Cd alloys. (After Grube and Schiedt.)

observed one as compared with Fig. 7. This difference may indicate that either of our assumptions is wrong. Since the assumption that all the carriers behave as nearly free electrons is allowed for a band possesing small number of carriers, the another assumption that there exist only four bands, α, β, γ and δ, should be corrected. Then, let us try to find any other band in the alloys by which we can explain the present results. The first Brillouin zone of the close-packed hexagonal structure is shown in Fig. 8. For electron moving in all directions, there is an energy discontinuity across the A-faces in the figure, except the edges of the faces, such as PQ and QR. The Brillouin zone shown in the figure is the smallest volume in k-space surrounded everywhere by an energy discontinuity for electrons moving in all directions. It is called the complete zone. With the subtraction of the small truncated prisms from the complete zone, we can get the so-called incomplete zone. One of the truncated prisms is shown in the figure by dotted lines. There may exist an overlap from the incomplete zone across the A-faces into the truncated prisms.

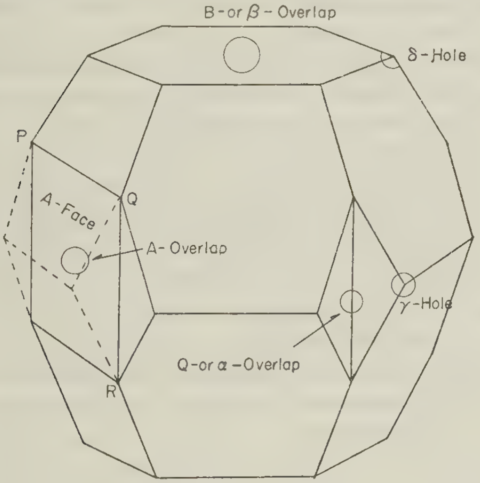

Fig. 8. The first Brillouin zone of h.c.p. structure.

The overlap will be termed the A-overlap. By taking into account this overlap, we will qualitatively explain the present experimental results.

The relation between the state density and energy in A-overlap is shown in Fig. 9. If the Fermi level in this overlap passes from L to M with increase of magnesium contents, we will expect the actual concentration dependence[18]. If we concern with only the variation of axial ratio, the movement of Fermi level should occur in the opposite direction as suggested by Hume-Rothery and Raynor. However, we can interpret this situation by the fact that the energy gap at A-face will be changed with alloying.

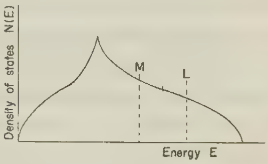

Fig. 9. The assumed energy density of A-overlap.

Let us consider the initiation and extinction of bands in this system. Mott and Jones expected that there exist A- and B-overlaps in cadmium and A- and Q-overlaps in magnesium by their calculation[11]. If this conclusion is true, the Q-overlap will extinct and the B overlap will initiate at some compositions when the concentration of cadimum increase from pure magnesium. If it is assumed that the initiating or extincting bands are normal form, the initiation or extinction gives rise to a discontinuous change in the thermoelectric power of the system[8,9]. From our results such a discontinuity can not be detected. Therefore, there are no evidence of the initiation or extinction of bands in the whole ranges of concentration.

The influence of ordering formation on the thermoelectric power also will be discussed. The Hall measurement shows the following results: In all the super-lattice alloys in this system their Hall coefficients are increased by the formation of order[7]. As given in the preceding section, however, the variation of thermoelectric power in the order-disorder transition is not so simple. When ordered states are destroyed near transition temperature, a decrease of the thermoelectric power is observed in the cases of Mg_3Cd and MgCd, but an increase for $MgCd_3$.

The variation of the Hall coefficient has been interpreted in terms of newly formed Brillouin zones being established by the formation of ordered state. Such a disagrement between the Hall coefficient and the thermoelectric power in the tendency of the variation by the transition may be interpreted by considering the following factor: The *A*-overlap will make an important role for the thermoelectric power than for the Hall coefficient, because all the bands in these alloys except *A*-overlap may be supposed that they posses the standard form and considerably small numbers of carriers. The both ordered structures, Mg_3Cd and $MgCd_3$, are hexagonal close packed but their lattice parameters and axial ratios are of course different from those of the disordered structures. In MgCd, the structure makes a slight deformation into a orthorohombic structure by the formation of order[12]. These variations of the structure may give inevitably rise to the variations of Brillouin zone boundaries and of the energy gaps across the zone boundaries[13-15].

The first Brillouin zone of the disordered structure is closely related to the Fermi surface since the magnesium-cadmium alloys are divalent. On the contrary, the Fermi surface of Cu_3Au may be fairly apart from the Brillouin zone boundaries of the disordered structure, but it may be closely related to the boundaries of the ordered structure[16,17]. For such a system, we may conclude that the variation of the transport properties in order-disorder transition is responsible for the interaction between the Fermi surface and the Brillouin zone of the ordered state.

In the case at hand, the Brillouin zone of the disordered structure is in strong interaction with the Fermi surface. When the ordered state is formed, the Brillouin zone which has been formed in the disordered structure is deformed and the energy gap across its zone boundary may be influenced appreciably. These changes will make an important role to the conduction phenomena of these alloys, though the interaction between the newly established Brillouin zone on the formation of ordered state and the Fermi surface will produce an effect. Then it is difficult to say how the Brillouin zone formed by ordering contributes to the physical properties of the alloys in this system.

Acknowledgements

The author is grateful to Professor T. Sato for his support and many valuable discussions.

References

1) S. Noguchi and T. Sato: J. Phys. Soc., Japan **15** (1960) 1944.
2) W. Hume-Rothery and G. V. Raynor: Proc. Roy. Soc., **A174** (1940) 471.
3) T. B. Massalski and B. Cockayne: Acta Met. **7** (1959) 762.
4) H. Jones: Proc. Roy. Soc. **A147** (1934) 396, Phil. Mag. **41** (1950) 663.
5) J. Goodenough: Phys. Rev. **89** (1953) 282.
6) J. W. McClure: Phys. Rev. **98** (1955) 449.
7) K. Yonemitsu and T. Sato: Phys. Soc. Japan. **13** (1958) 15.
8) S. Noguchi: To be published.
9) W. J. Tomasch and J. R. Reitz: Phys. Rev. **111** (1958) 757.
10) G. Grube and E. Schiedt: Z. anorg. Chem. **194** (1930) 190.
11) N. F. Mott and H. Jones: The Theory of the Properties of Metals and Alloys. Oxford, 1936.
12) H. Steeple: Acta Cryst. **5** (1952) 247.
13) T. Muto: Sci. Pap. Inst. Phys. Chem. Res. Tokyo **34** (1938) 377.
14) J. F. Nicholas: Proc. Phys. Soc. **21** (1950) 23.
15) J. C. Slater: Phys. Rev. **84** (1951) 179.
16) K. Komar and S. Sidrov: J. Phys. USSR **4** (1941) 552.
17) K. Yonemitsu and T. Sato: J. Phys. Soc. Japan **13** (1958) 998.
18) H. Jones: Proc. Phys. Soc. **A68** (1955) 1191.
19) N. Cusack and P. Kendall: Proc. Phys. Soc. **72** (1958) 898.

JOURNAL OF THE PHYSICAL SOCIETY OF JAPAN, Vol. 16, No. 6, JUNE, 1961

Resonance Transfer of Ionization Energy in Semiconductors*

By Shigeharu KOSHINO

Radiation Center of Osaka Prefecture, Shinke-Cho, Sakai, Osaka

and Toshihiko ANDO

Department of Physics, Kyoto University, Kyoto

(Received January 11, 1961)

The thermal conductivity of semiconductor due to the resonance transfer of ionization energy of impurity state caused by the interelectronic interaction is calculated in each of three temperature ranges, the extrinsic, the exhaustion and the intrinsic ranges. The obtained conductivity increases exponentially with the temperature in the extrinsic range, but decreases in the exhaustion range. In the intrinsic range it increases again exponentially with the temperature when the temperature is lower than a critical point, but decreases as the temperature increases beyond the critical point. The experimental detection of our conductivity is possible under an appropriate condition in the intrinsic range, while impossible for almost all other cases.

§1. Introduction

It is well known that the thermal energy is transported by electrons as well as by phonons in semiconductors. The former transport is in general essentially analogous to the metalic one, which means that the thermal and the electrical conductivities satisfy the Wiedemann-Franz law. Recently, however, an anomalous thermal conduction which does not satisfy the Wiedemann-Franz law has been observed in several kinds of semiconductor.[1),2)] Because of the inapplicability of the Wiedemann-Franz law the mechanism giving rise to the anomalous conduction will not contribute to the electrical conduction. The exciton conduction and the ambipolar diffusion have been proposed by Joffe[2)] and Prise[3)], respectively. In the present paper we propose the third mechanism, the resonance transfer of ionization energy of impurity state.

Let us first consider two localized donor (or acceptor) states, one of which is occupied by an electron and the other is open. The interelectronic interaction between the trapped electron and a conduction electron can cause the resonance transition in which the trapped electron is excited into the conduction band and the conduction electron is trapped simultaneously by the open donor. This transition transfers the ionization energy of donor state from the latter donor to the former. If there is the temperature difference between the two donor states, the net current of ionization energy is produced. This process will be formulated in the next section.

When the temperature gradient is present in the sample, the resonance transfer of ionization energy between every two donors produces the net current of the thermal energy throughout the sample. We shall discuss how to formulate the thermal conductivity in §3. The calculation of matrix elements will be performed with the neglect of their dependence on the wave number of electron and the thermal conductivity will be obtained in §4. The explicit formula of thermal conductivity will be obtained in the extrinsic range in §5, in the exhaustion range in §6 and in the intrinsic range in §7. In these sections numerical values for n-Ge and n-InSb will be obtained and it will be shown that our conductivity is hard to be observed in the extrinsic and the exhaustion ranges. In the intrinsic range, however, it can be observed experimentally under an appropriate condition. It is necessary for the observation that the impurity concentration is sufficiently large. When the concentration is so large that the impurity band model is useful, on the other hand, the resonance transfer will be inefficient since it is based on the localization of impurity state.

---

* A short note on this work has been published in J. Phys. Soc. Japan **15** (1960) 1538.

§ 2. Elementally Process

Our discussions will be restricted in n-type semiconductors. Let us first formulate the probability of the resonance transfer of ionization energy between two donors. The resonance transfer is caused by the interelectronic interaction. According to the one-electron approximation method, electronic states are obtained by taking up only an average of the interelectronic Coulomb interaction. The rest part which remains by the substraction of the average field from the true interaction is the perturbation which induce the resonance transition.

Now we assume that the interelectronic interaction is the screened Coulomb type and that the donor state is hydrogen-like. Furthermore, for the simplification, we assume that electronic wave functions in the conduction band are plane waves and the electronic mass is isotropic. The matrix element V of the resonance transition in which an electron in $\boldsymbol{k}$-state is trapped by the donor 1 and the electron which has been trapped by the donor 2 is excited to $\boldsymbol{k}'$-state is given by

$$V=\frac{e^2\alpha^3}{\pi\mathcal{E}}\int\frac{d\tau_1\,d\tau_2}{|\boldsymbol{r}_1-\boldsymbol{r}_2|}\exp\{i\boldsymbol{k}\cdot\boldsymbol{r}_1-i\boldsymbol{k}'\cdot\boldsymbol{r}_2-\beta|\boldsymbol{r}_1-\boldsymbol{r}_2|-\alpha|\boldsymbol{r}_1-\boldsymbol{R}_1|-\alpha|\boldsymbol{r}_2-\boldsymbol{R}_2|\}\,, \tag{1}$$

where $\mathcal{E}$ is the dielectric constant, e the electronic charge, α the modified reciprocal Bohr radius defined by

$$\alpha=m^*e^2/\hbar^2\mathcal{E} \tag{2}$$

and β the screening constant defined by

$$\beta=(4\pi e^2n/kT\mathcal{E})^{1/2}\,. \tag{3}$$

Here m^* is the effective mass of electron, $\hbar$ the Plank constant devided by 2π, k the Boltzmann constant, T the temperature and n the electron concentration in the conduction band.

We assume next that the temperature of the donor state 1 is T_1 and that of the donor 2 is given by

$$Q_1=\frac{1}{(2\pi)^5\hbar}\int(E_0+E)|V|^2f(T_1)\{1-f'(T_2)\}\,g(T_2)\{1-g(T_1)\}\delta(E'-E)\,dk\,dk'\,, \tag{4}$$

where f and g are the distribution function of electrons in the conduction band and in the donor state, respectively, and E_0 is the energy difference between the donor state and the bottom of the conduction band. The inverse thermal current Q_2 is given by (4) in which T_1 and T_2 are replaced by each other. The net thermal current from the donor 1 to the donor 2 is given by Q_1-Q_2. Expanding f and g in power series with respect to $\Delta T=T_1-T_2$ and retaining to the first order terms, we obtain the net thermal current

$$\begin{aligned}Q&=\Delta T\cdot Q'\\&=\Delta T\cdot\frac{1}{(2\pi)^5\hbar}\int(E_0+E)|V|^2\delta(E'-E)\left\{g(1-g)\frac{\partial f}{\partial T}-f(1-f)\frac{\partial g}{\partial T}\right\}dk\,dk'\,.\end{aligned} \tag{5}$$

§ 3. Thermal Conductivity

An electron trapped by a donor interacts with phonons as well as with other electrons. The thermal energy is transported to and from the donor by the electron-phonon interaction from and to the phonon system as well as by the resonance transfer from and to other donors. Let us devide the discussion into three cases: a) the electron-phonon interaction is weaker than the interelectronic interaction, b) the electron-phonon interaction is stronger than the interelectronic interaction while the thermal current due to the phonon conduction is smaller than due to resonance transfer and c) the electron-phonon interaction is stronger than the interelectronic interaction while the thermal current due to the phonon conduction is larger than due to the resonance transfer.

In the first case the temperature of the donor electron is in large part governed by the thermal current due to the resonance transfer and the thermal conductivity may be calculated independently within the electron system neglecting the electron-phonon interaction. In the second case it is expected that the donor electron is in thermal equilibrium with the local phonon system as far as phonons are in the internal local equilibrium. The temperature is governed by the thermal current due to the resonance transfer, which is similar to the first case. The difference of this case from the first one is in the heat capacity of the donor electron. In the last case the temperature of the donor electron is in large part governed by the phonon current. If the temperature at every donor position is known from the phonon current, the thermal current due to the resonance transfer can be calculated in principle. In every case we encounter the difficulty which results from the random distribution of donor. In the first and the second cases we encounter furthermore another difficulty that the temperature of donor is not independent of the thermal current. In order to avoid these difficulties, we assume that the position probability of every donor is uniform and that the temperature gradient is uniform and every donor electron is in the local equilibrium.

Let us now imagine a plane which is perpendicular to the temperature gradient in the sample. The thermal conductivity may be given by the total net thermal current through the plane devided by the area of the plane and by the temperature gradient. By the perpendicular plane the sample is devided into two parts, the higher and the lower temperature parts. We choose then a donor in the higher temperature part. The distance of the donor from the plane is denoted by a. We specify the position of every donor in the lower temperature part by using the spherical coordinate system, the origin of which is the donor chosen in the higher temperature part and the basic axis is vertical to the plane. The temperature difference between the origin donor and a lower temperature donor, the position of which is (R, θ, φ), is given by

$$\Delta T = R\cos\theta (dT/da)\,. \tag{6}$$

Inserting the relation (6) into Eq. (5), multiplying by the donor density N and integrating over the position of the lower temperature donor within the whole volume of the lower temperature part, we obtain the total net thermal current from the donor chosen in the higher temperature part to the lower temperature part beyond the perpendicular plane

$$2\pi N(dT/na)\int_a^\infty\int^{\cos^{-1}(a/R)} Q'\cos\theta\sin\theta\, d\theta\, R^3\, dR\,. \tag{7}$$

Integrating (7) over the position of the higher temperature donor within the whole volume of a cylinder, the axis of which is parallel to the temperature gradient and the cross section is so large that the surface effect is negligible, multiplying by the density of donor, deviding by the area of the cross section of the cylinder and by the temperature gradient, we obtain the thermal conductivity due to the resonance transfer

$$\kappa = 2\pi N^2\int_0^\infty\int_a^\infty\int_0^{\cos^{-1}(a/R)} Q'\cos\theta\sin\theta\, d\theta\, R^3\, dR\, da\,. \tag{8}$$

§ 4. Matrix Element

In the proceeding section we have obtained the formal expression (8) for the thermal conductivity. In order to calculate the integral (8) we must obtain the explicit formula of the matrix element (1). The integral (1) cannot be calculated analytically. Let us neglect $\boldsymbol{k}$ and $\boldsymbol{k}'$ in the integrand of (1) in order proceed the analytical calculation. The neglect of $\boldsymbol{k}$ and $\boldsymbol{k}'$ corresponds to the replacement of every matrix element by that of the process in which one electron is transferred to and the other electron is transferred from the bottom of the conduction band. In this approximation we obtain the matrix element

$$V=-(4\pi e^2/\mathcal{E})F(R)\,, \tag{9}$$

where

$$F(R)=\{\alpha/(\alpha^2-\beta^2)R\}\{C_1(e^{-\alpha R}-e^{-\beta R})+e^{-\alpha R}(C_2R+C_3R^2+(\alpha/3)R^3\}\,. \tag{10}$$

Here R is the distance between the two donors, and

$$C_1=(2\alpha)^4/(\alpha^2-\beta^2)^3\,, \qquad C_2=(11\alpha^4-4\alpha^2\beta^2+\beta^4)/\alpha(\alpha^2-\beta^2)^2$$

and

$$C_3=(3\alpha^2-\beta^2)/(\alpha^2-\beta^2)\,.$$

Inserting the matrix element (9) into Eq. (5), we obtain

$$Q'=(16m^{*3}e^4k/\pi\hbar^7\mathcal{E}^2)\,g(1-g)IF(R)^2\,, \tag{11}$$

where

$$I=\int_0^\infty(E_0+kTx)^2f(1-f)x\,dx\,. \tag{12}$$

The thermal conductivity (8) is then reduced to

$$\kappa=(16m^{*3}e^4k/\pi\hbar^7\mathcal{E}^2)N^2g(1-g)IJ\,, \tag{13}$$

where

$$J=\pi\int_0^\infty\int_a^\infty F(R)^2(1-a^2/R^2)R^3\,dR\,da\,.$$

Inserting Eq. (10) into the integrand of the above equation, we obtain

$$\begin{aligned}J=\{\pi\alpha^2/(\alpha^2-\beta^2)^2\}[&(C_1{}^2/8)\{\alpha^{-3}+\beta^{-3}-16(\alpha+\beta)^{-3}\}\\&+(C_1C_2/2)\{\alpha^{-4}-16(\alpha+\beta)^{-4}\}+(1/2\alpha^5)\{C_2{}^2+2C_1C_3\}\\&-32C_1C_3/(\alpha+\beta)^5+(5/2\alpha^6)\{(\alpha/3)C_1+C_2C_3\}\\&-\{160\alpha/3(\alpha+\beta)^6\}C_1+(15/4\alpha^7)\{C_3{}^2+(2\alpha/3)C_2\}\\&+35C_3/4\alpha^7+35/6\alpha^7]\,,\end{aligned} \tag{14}$$

where $\int_a^\infty\exp(-2\beta R)\,dR/R$ has been replaced by $(1/2\beta a)\exp(-2\beta a)$. Eq. (14) is asymptotically reduced to

$$J=\begin{cases}2^5\pi/\alpha^6\beta^3 & (\alpha\gg\beta)\,,\\ 143\pi/6\alpha^5\beta^4 & (\alpha\ll\beta)\,.\end{cases}$$

Asymptotic expressions for the thermal conductivity are then given by

$$\kappa=\begin{cases}(2^9m^{*3}e^4k/\hbar^7\mathcal{E}^2\alpha^6\beta^3)N^2g(1-g)I & (\alpha\gg\beta)\,, & (15)\\ (1144m^{*3}e^4k/3\hbar^7\mathcal{E}^2\alpha^5\beta^4)N^2g(1-g)I & (\alpha\ll\beta)\,. & (16)\end{cases}$$

From Eqs. (2) and (3) the condition $\alpha\gg\beta$ is reduced to

$$n/T\ll1.7\times10^{18}(m^*/m)^2/\mathcal{E}\,. \tag{17}$$

§ 5. Extrinsic Range

It is convenient to divide the discussion into three cases corresponding to the three temperature ranges, the extrinsic, the exhaustion and the intrinsic ranges. At sufficiently low temperature conduction electrons are supplied by donors and the electron distribution in the conduction band may be given by

$$f=(N/2A)^{1/2}\exp\{-(2E+E_0)/2kT\}\,,$$

where

$$A=2(m^*kT/2\pi\hbar^2)^{3/2}\ .$$

The probability of the exsistence of electron in the donor state and the concentration of conduction electron may be given by

$$g=1-(A/2N)^{1/2}\exp\{-E_0/2kT\}$$

and

$$n=(AN/2)^{1/2}\exp\{-E_0/2kT\}\ ,$$

respectively. It is obvious that the Bohr radius is much smaller than the screening radius at low temperature. In fact the condition (17) is reduced to

$$T^{-1/4}e^{-E_0/2kT}\ll 3.3\times 10^{10}(m^*/m)^{5/4}/\mathcal{E}N^{1/2}$$

at low temperature. It is noted that our discussion is restricted to the case of the low donor concentration since the donor electron has been assumed to be well localized. Then the thermal conductivity may be expressed by the asymptotic equation (15). We obtain

$$\kappa=9.5\times 10^{-2}(m/m^*)^{33/8}\mathcal{E}^{11/2}N^{5/4}T^{3/8}(E_0^2+4E_0kT+6k^2T^2)\exp\{-E_0/kT\}$$
$$\text{erg/cm-sec-degree}\ . \qquad (18)$$

It is noted that the temperature dependence of the thermal conductivity is influenced strongly by the temperature dependence of the screening constant. The thermal conductivity (18) is much smaller than the conductivity due to the phonon current.

§ 6. Exhaustion Range

The exhaustion of the donor electron occurs in general at sufficiently high temperature which is even lower than the intrinsic temperature. If the electron concentration in the conduction band is not so large, the distribution of conduction electron may be given by the Boltzmann distribution

$$f=(N/A)\exp\{-E/kT\}\ .$$

The occupation probability of donor state is then given by

$$g=(2N/A)\exp\{E_0/kT\}\ ,$$

and also it may be assumed that the electron concentration in the conduction band is equal to the donor concentration.

If $\alpha\gg\beta$, we obtain the thermal conductivity

$$\kappa=7.7\times 10^{-25}(E_0^2+4E_0kT+6k^2T^2)\mathcal{E}^{11/2}(m/m^*)^6N^{5/2}T^{-3/2}\exp\{E_0/kT\}$$
$$\text{erg/cm-sec-degree}\ . \qquad (19)$$

It is noted that the thermal conductivity (19) decreases as the temperature increases. The condition $\alpha\gg\beta$ is reduced to

$$T\gg 6\times 10^{-19}\mathcal{E}(m/m^*)^2N\ ,$$

which is usually satisfied. The thermal conductivity (19) is reduced to

$$\kappa=2.8\times 10^{-49}(1+3.5\times 10^{-2}T+4.5\times 10^{-4}T^2)N^{5/2}T^{-3/2}e^{116/T}\qquad \text{cal/cm-sec-degree} \qquad (20)$$

for n-Ge, where we have assumed $m/m^*=5$, $\mathcal{E}=16$ and $E_0=0.01$ ev., and

$$\kappa=4.5\times 10^{-44}(1+0.35T+0.046T^2)N^{5/2}T^{-3/2}e^{11.6/T}\qquad \text{cal/cm-sec-degree} \qquad (21)$$

for n-InSb, where we have assumed $m/m^*=50$, $\varepsilon=16.8$ and $E_0=0.001$ ev. The thermal conductivity (20) is always smaller than the conductivity due to the phonon current in Ge. The thermal conductivity (21) is also generally smaller for InSb, but it may be detectable experimentally when the concentration of donor is of the order of 10^{16}.

§ 6. Intrinsic Range

Conduction electrons excited from the valence band are important at sufficiently high temperature. When the electron concentration in the conduction band is governed by the interband excitation, the distribution function may be given by

$$f=(m'/m^*)^{3/4}\exp\{-(2E+E_1)/2kT\}\ ,$$

where m' is the effective mass of hole in the valence band and E_1 is the energy width of the forbidden band. The occupation probability of donor state is also given by

$$g=2(m'/m^*)^{3/4}\exp\{-(E_1-2E_0)/2kT\}\ .$$

The concentration of donor electron may be given by

$$n=(m'/m^*)^{3/4}A\exp\{-E_1/2kT\}$$

We obtain the thermal conductivity

$$\kappa=7.4\times10^{-45}(m'/m^*)^{3/8}(m/m^*)^{21/4}\varepsilon^{11/2}T^{5/4}N^2\exp\{-(E_1-4E_0)/4kT\}\quad \text{erg/cm-sec-degree}\ , \tag{22}$$

provided $\alpha\gg\beta$, and also

$$\kappa=1.3\times10^{-42}(m/m^*)^5\varepsilon^5N^2T\exp\{E_0/kT\}\qquad \text{erg/cm-sec-degree}\ , \tag{23}$$

provided $\alpha\ll\beta$. It is concluded that the thermal conductivity due to the resonance transfer increases exponentially with the temperature when the temperature is much lower than the critical point T_c. The temperature T_c is defined by the relation $\alpha=\beta$, which is

$$T_c^{1/2}\exp(-E_1/2kT_c)=3.5\times10^2(m^*/m')^{3/4}(m^*/m)^{1/2}/\varepsilon\ .$$

For n-Ge we obtain

$$\kappa=5.1\times10^{-42}\,T^{5/4}N^2e^{-2200/T}\qquad \text{cal/cm-sec-degree}\ , \tag{24}$$

when $T<T_1$, and

$$\kappa=1.0\times10^{-49}\,TN^2e^{116/T}\qquad \text{cal/cm-sec-degree}\ , \tag{25}$$

when $T>T_1$, where T_1 is nearly equal to 2000°K. For n-InSb we obtain

$$\kappa=1.1\times10^{-36}\,T^{5/4}N^2e^{-780/T}\qquad \text{cal/cm-sec-degree}\ , \tag{26}$$

when $T<T_2$, and

$$\kappa=1.5\times10^{-35}\,TN^2e^{12/T}\qquad \text{cal/cm-sec-degree}\ , \tag{27}$$

when $T>T_2$, where T_2 is nearly equal to 500°K. From (24) it is expected that the thermal conductivity due to the resonance transfer can be observed in n-Ge samples in which the donor concentration is of the order of 10^{17} or 10^{18}, when the temperature is near 10^3 °K. The thermal conductivity (26) for n-InSb is almost consistent with Busch's experimental data provided the magnitude of N is of the order of 10^{15}.

As shown above, the thermal conduction due to the resonance transfer of ionization energy is a delicate phenomenon because of the dependence on the impurity concentration. It cannot be observed unless the impurity concentration is large. When the concentration is too large, on the other hand, it also cannot be observed because of the violation of the localization of impurity state.

§ 8. Discussions

We have obtained the thermal conductivity due to the resonance transfer of ionization energy in the extrinsic, the exhaustion and the intrinsic ranges. The obtained conductivity increases exponentially with the temperature in the extrinsic range, but it decreases in the exhaustion range. In the intrinsic range it increases again exponentially with the temperature when the temperature is lower than the critical point. As the temperature increases beyond the critical point, the obtained conductivity decreases.

The magnitude of our conductivity is much smaller than the phonon conductivity in the extrinsic range. In the intrinsic range, on the other hand, our conductivity can be observed experimentally under an appropriate condition which is, for example, the donor concentration of the order of 10^{15} for InSb and 10^{17} or 10^{18} for Ge. In the exhaustion range the observation will be possible for InSb which contains donor of the order of 10^{16}, but impossible for Ge.

The temperature dependence of the obtained conductivity is strongly dependent on the temperature dependence of the screening constant as is obvious from Eqs. (15) and (16). The β-dependence of Eqs. (15) or (16) results from our approximation, the neglect of the dependence of the matrix element (1) on the wave number of electron. If we calculated the matrix element (1) rigorously, we should obtain a somewhat different type of the β-dependence and then a somewhat different dependence of the thermal conductivity. Our calculation is only useful in the lowest approximation.

In the calculation of the thermal conductivity in § 3, we have assumed that donors are distributed quite at random and that the temperature gradient is uniform and every donor electron is in the local equilibrium. These assumptions are inevitable for us since we have no information on the donor distribution.

References

1) G. Busch and M. Schneider: Physica **20** (1954) 1084.
2) A. F. Joffe: Nouvo Cimento Supplement **3** (1956) 702; Rep. Prog. Phys. **22** (1959).
3) P. J. Price: Phil. Mag. **46** (1955) 1252.

JOURNAL OF THE PHYSICAL SOCIETY OF JAPAN, Vol. 16, No. 6, JUNE, 1961

Ferroelectricity in (K, NH_4), (K, Rb) and (K, Tl) Ferrocyanide Mixed Crystals

By Shigeru WAKU, Kunio Masuno and Toshisuke TANAKA

Electrical Communication Laboratory, Nippon Telegraph and Telephon Public Corporation, Kichijoji, Musashino-shi, Tokyo

(Received January 21, 1961)

Substitutions of potassium ion in potassium ferrocyanide by the other mono-valent positive ions were examined. Substituents to give isomorphous ferroelectric substances through replacing some part of the K ion were found to be NH_4, Rb and Tl ions respectively. The peak of the dielectric constant versus temperature curves shifts to the low temperature side by increasing the amount of these substituents. Substituted compounds containing relatively small amount of these substituents show ferroelectric behavior similar to that of potassium ferrocyanide trihydrate.

§ 1. Introduction

In the previous papers[1),2),3)], we reported the ferroelectric behavior in potassium ferrocyanide trihydrate, $K_4Fe(CN)_6 \cdot 3H_2O$, and its isomorphous substances obtained through replacing the Fe ion by Ru, Os and Mn ions, and H_2O by D_2O. These substances crystallize with monoclinic symmetry, of which crystal class is $C_{2}h$ and space group is C_2/c at room temperature. The ferroelectric axis lies in $[1\bar{0}1]$ direction.

Subsequently, we have attempted to substitute some part of the K ion of potassium ferrocyanide trihydrate by the other monovalent ions to obtain new isomorphous ferroelectric substances.

§ 2. Preparation of the Samples

Mixed crystals were grown by the slow cooling of mother solutions, which had been Prepared beforehand by dissolving monovalent ion ferrocyanide and potassium ferrocyanide in various proportions. The preparation of monovalent ion ferrocyanide was done by mixing hydroxide of the corresponding ion and hydrogen ferrocyanide in the molecular ratio of 4:1. Mono-valent substituents to be examined were NH_4, Li, Na, Rb, Cs, Tl, CH_3NH_3, $C_2H_5NH_3$, NH_2NH_3, and NH_3OH. Among these substituents, NH_4, Rb, and Tl ions gave the isomorphous ferroelectric mixed crystals.

The mixed crystals were cut perpendicular to the cleavage plane (010) and silver-painted to measure the electric properties. The dielectric constant was measured by the tuning method in 1 MC. The hysteresis loop in 50 cps was measured by the ordinary Sawyer-Tower's circuit.

§ 3. Experimental Results

(1) *Relation between the composition of mother solution and that of the mixed crystal obtained*

The ammonium content in the mixed crystals is determined by the colorimetric analysis using Nesslar's reagent. The thallium content is determined by the gravimetric analysis in the form of TlCl. In the case of the Rb ion, however, we have failed to obtain the Rb content, because the flame photometric analysis was confused by the spectrum of K ion.

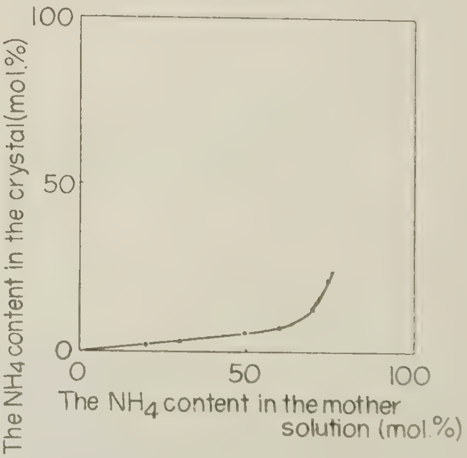

Fig. 1. Relation between the compositions of the mother solution and the obtained crystal in the case of the $(K, NH_4)_4Fe(CN)_6 \cdot 3H_2O$ type mixed crystals.

Figs. 1 and 2 show the relations between the compositions of mother solution and the obtained crystal. The composition of the grown crystal shows a considerably large deviation from that of the mother solution.

(2) *Dielectric behavior*

Figs. 3, 4 and 5 show the small signal dielectric constant versus temperature curves of these mixed crystals, having various molar percentages of the substitution ions. In the case of (Rb, K) mixed crystal, the amount of Rb ion in the mother solution is indicated, as the analysis of the crystals was not performed. The peak height and sharpness of these curves at the dielectric anomaly decrease with the increasing content of replacing ions. Figs. 6, 7 and 8 show the relation between the Curie temperature and the amount of substituting

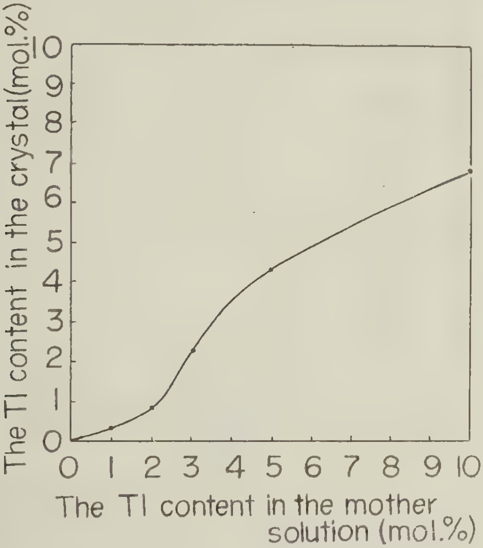

Fig. 2. Relation between the compositions of the mother solution and the obtained crystal in the case of the $(K, Tl)_4Fe(CN)_6 \cdot 3H_2O$ type mixed crystals.

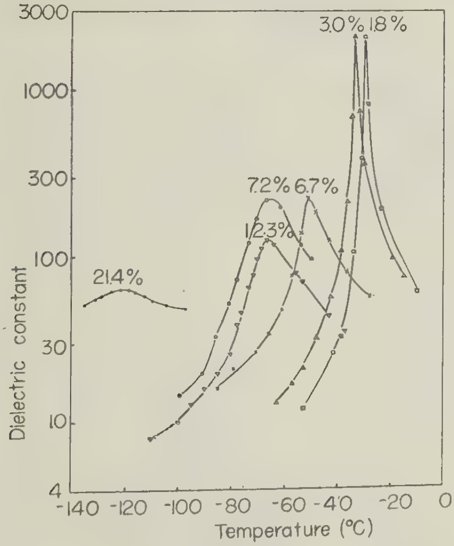

Fig. 3. Dielectric constant versus temperature curves of the $(K, NH_4)_4Fe(CN)_6 \cdot 3H_2O$ type mixed crystals in the [10$\bar{1}$] direction.

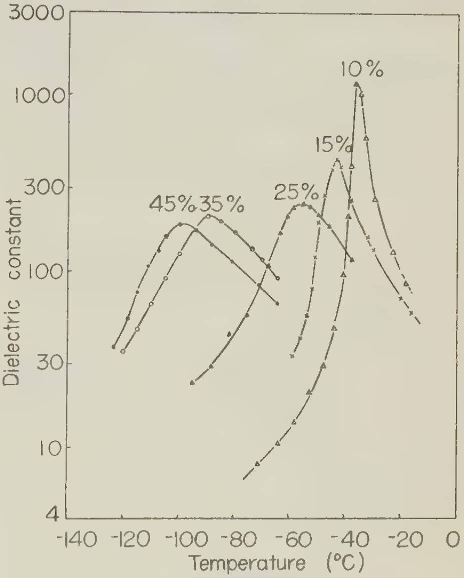

Fig. 4. Dielectric constant versus temperature curves of the $(K, Rb)_4Fe(CN)_6 \cdot 3H_2O$ type mixed crystals in the [10$\bar{1}$] direction.

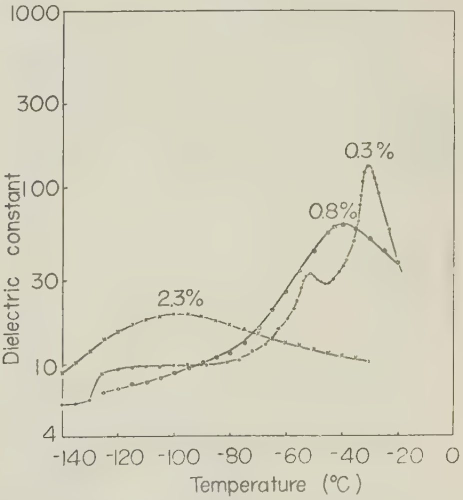

Fig. 5. Dielectric constant versus temperature curves of the $(K, Tl)_4Fe(CN)_6 \cdot 3H_2O$ type mixed crystals in the [10$\bar{1}$] direction.

ions in these three cases, respectively. A linear relation holds approximately in each case.

(3) *Ferroelectric behavior*

Ferroelectric properties of these mixed crystals disappear for relatively small content of the substituting ions. Figs. 9 and 10 show the temperature dependencies of the spontaneous polarization Ps and coercive field Ec of (Rb, K) and (NH_4, K) ferrocyanide, respectively. The ferroelectric hysteresis loop disappears or can be observed only slightly for the replacing ion contents higher than 5% for NH_4 ion, 15% for Rb ion. In the case of the Tl ion, however, hysteresis loop disappears even for very small content of replacing ion. The ferroelectric axis is [$10\bar{1}$] direction similarly to the ordinary potassium salt.

§ 4. Discussion

The ionic radii of K^+, NH_4^+, Rb^+ and Tl^+

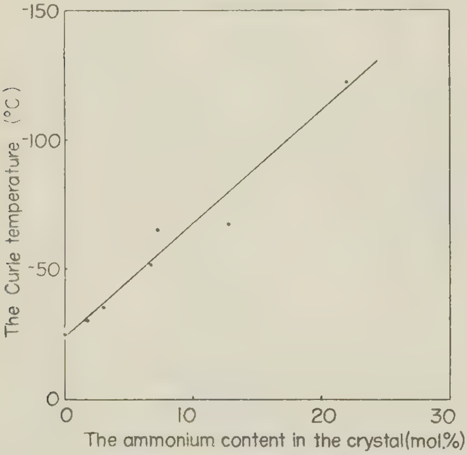

Fig. 6. Relation between the Curie temperature and the content of the replacing NH_4 ion in the case of the $(K, NH_4)_4 \cdot Fe(CN)_6 \cdot 3H_2O$ type mixed crystals.

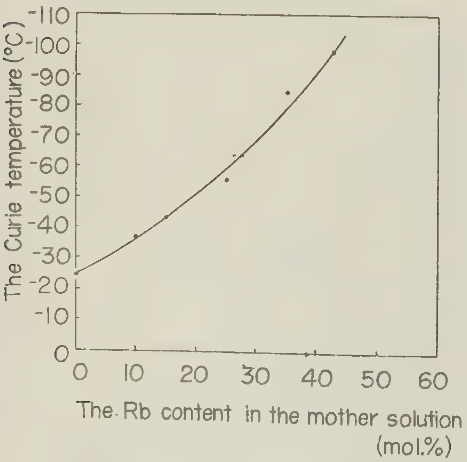

Fig. 7. Relation between the Curie temperature and the content of the replacing Rb ion in the case of the $(K, Rb)_4Fe(CN)_6 \cdot 3H_2O$ type mixed crystals.

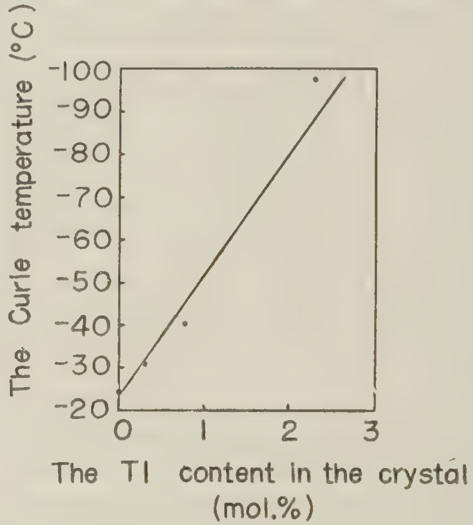

Fig. 8. Relation between the Curie temperature and the content of the replacing Tl ion in the case of the $(K, Tl)_4Fe(CN)_6 \cdot 3H_2O$ type mixed crystals.

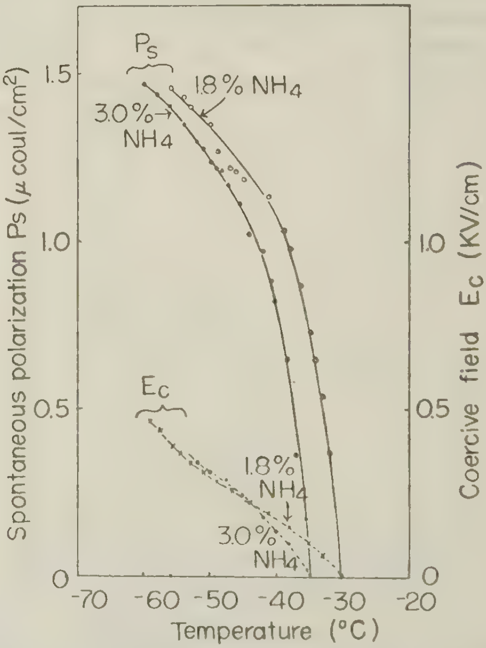

Fig. 9. Spontaneous polarization and coercive field versus temperature curves of the $(K, NH_4)_4Fe(CN)_6 \cdot 3H_2O$ type mixed crystals.

ions are 1.33, 1.59, 1.49 and 1.44Å, respectively. This means that, by substituting some part of the potassium ion in potassium ferrocyanide by the ion having larger ionic radius, the transition point shifts toward the low temperature side. Contrary to this, the ferroelectric transition temperature increases by substituting Fe^{++} ion of potassium ferrocyanide by the divalent ion having larger covalent radius of octahedral coordination[2].

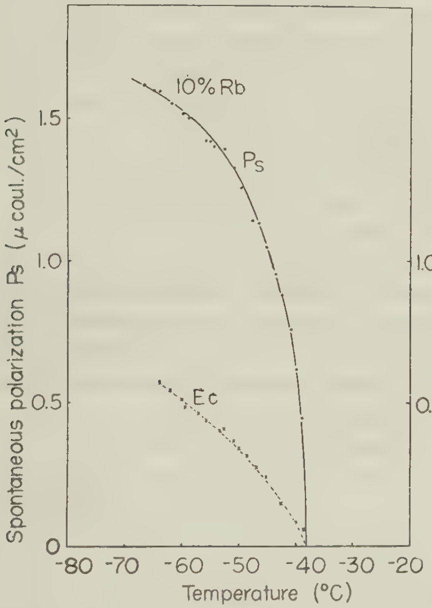

Fig. 10. Spontaneous polarization and coercive field versus temperature curves of the $(K, Rb)_4Fe(CN)_63H_2O$ type mixed crystals.

The peak height and sharpness of dielectric constant versus temperature curve decrease with the increasing content of the substituting ions. As stated before, the ion content in the mother solution and in the grown crystal shows relatively large deviation with each other. For this reason, the grown crystal shows a lamellar structure having gradually segregated concentration of the replacing ion. From the relations such as shown in Figs. 1 and 2, the segregation degree of the substituting ion in the crystal is supposed to increase with increasing concentration of the ion in the mother solution.

Considering the fact that the Curie point of the mixed crystal varies linearly with the concentration of the replacing ion in the crystal, this local change of the concentration can be taken as the reason why the peak height and sharpness of dielectric constant decrease with the increasing content of replacing ion. The ferroelectric hysteresis disappears or can be observed only slightly in these mixed crystals with the relatively small amount of replacing ion. This phenomenon may be explained as follows. The coercive field strength of potassium ferrocyanide group ferroelectrics increases rapidly with decreasing temperature. Consequently, for the mixed crystals with the Curie point varying locally, the domain switching may occur only in the limited region in the crystal having relatively small coercive field strength.

Acknowledgement

The authors are very grateful to Dr. H. Hirabayashi for his helpful discussion.

References

1) S. Waku, H. Hirabayashi, H. Toyoda, H. Iwasaki and R. Kiriyama: J. Phys. Soc. Japan. **14** (1959) 973.
2) S. Waku, K. Masuno and T. Tanaka: J. Phys. Soc. Japan: **15** (1960) 1185.
3) S. Waku, K. Masuno and T. Tanaka: J. Phys. Soc. Japan. **15** (1960) 1698.

JOURNAL OF THE PHYSICAL SOCIETY OF JAPAN, Vol. 16, No. 6, JUNE, 1961

The Superstructures of Iron Selenide Fe_7Se_8

By Atsushi OKAZAKI

Department of Physics, Faculty of Science,
Kyusyu University, Fukuoka, Japan

(Received February 4, 1961)

Iron vacancies in Fe_7Se_8 are confined to the alternate iron layers parallel to the c plane of the fundamental lattice with the NiAs structure. The origin of the ferrimagnetism of Fe_7Se_8 (T_c=187°C) may be attributed to this ordered arrangement similarly to the case of Fe_7S_8. There are two types of the superstructure: low- and high-temperature ones. The unit cell dimensions and the lattice symmetries of these structures are as follows:

low-temperature type: $A=\sqrt{3}B$, $B=2a$, $C=4c$, triclinic,
high-temperature type: $A=2a$, $C=3c$, hexagonal,

where the capital and small letters designate the super- and fundamental lattices, respectively. The transition from the triclinic structure to the hexagonal one, which means a rearrangement of the iron vacancies, begins at 240°C, proceeds gradually and finishes at 298°C.

§1. Introduction

The crystal structures and ferrimagnetic properties of iron selenide $FeSe_x$ were investigated by Hägg and Kindström[1] and Hirone, Maeda and Tsuya[2], respectively, with powder specimens. The more detailed investigation on single crystal of $FeSe_x$ system was undertaken by Hirakawa of our laboratory and it was expected that such an investigation would give us some information about the complex structural changes and ferrimagnetic properties of pyrrhotite Fe_7S_8, which had been studied by many researchers. But it was almost impossible to synthesize the single crystal of pyrrhotite.

At the beginning of the present work Fe_7Se_8 and Fe_3Se_4 were found to have superstructures[3] which stimulated our interests. In Fe_7Se_8 the iron vacancies are confined to the alternate c planes of the fundamental lattice with the NiAs structure similarly to those in Fe_7S_8 [4], but the stacking sequences of these planes along the c axis are different for the selenide and the sulphide. That is, if the capital and small letters designate the unit cell dimensions of the super- and fundamental lattices, respectively, $C=3c$ for Fe_7Se_8 and $C=4c$ for Fe_7S_8. Moreover Fe_7Se_8 (strictly speaking, Fe_7Se_8 with $C=3c$) has hexagonal symmetry, although Fe_7S_8 is monoclinic.

The work on the magnetic properties of Fe_7Se_8 by Hirakawa[5] using a torque magnetometer pointed out that the torque curves in the c plane showed a six-fold symmetry as well as small amount of component with a two-fold symmetry. The origin of this component was attributed to a lattice deformation of an undetectable order.

On the other hand, the crystal structure at high temperature was examined by the present author to resolve the following problems:
(1) Whether the superstructure disappears or not at high temperature.
(2) Whether the temperature of the disappearance coincides with Curie temperature T_c(187°C) or not, if the disappearance of the superstructure would be observed. Many specimens obtained from different ingots were examined and the results were reported shortly[6] as follows: the crystals cooled down slowly to room temperature have a superstructure with $C=4c$ (triclinic symmetry) and is very similar to that of Fe_7S_8 [4] except for the lattice symmetry. With increasing temperature from 240 to 298°C the superstructure transfers gradually to that with $C=3c$.

In the present paper the experimental and analytical details of the X-ray work on these superstructures of Fe_7Se_8 will be described together with some additional experiments to confirm the above results.

§2. Experimental

The preparation of single crystals of Fe_7Se_8 was described in the previous papers[3],[5]. Most of specimens used in the present investigation, however, were prepared by an improved method. That is, iron rods (Johnson-Matthey) were used instead of electrolytic iron powder and the reaction with selenium was performed in an evacuated silica tube by induction heating. An additional heat treatment to obtain single crystals was similar to that of the original method.

At room temperature oscillation and rotation photographs with Co*Kα* radiation were obtained by using a cylindrical camera, the diameter being 10 cm. Above room temperature these photographs were obtained by using a high-temperature camera designed and built for the present investigation. Requirements for this camera were as follows: (1) Temperature is to be measurable precisely. (2) Not only an equatorial line but also higher layer lines are to be recorded, if necessary. (3) Successive exposures are to be carried out without disturbing specimen to follow a crystal transformation. (4) To be convenient in operation.

This camera is shown in Figs. 1, 2 and 3, the details being as follows:

Furnace: It is necessary to record the higher layer lines without disturbing the homogeneity of temperature distribution around the specimen. Therefore a cylindrical Ni-foil furnace (0.018 mm thick) described by Dent and Taylor[7] is used. Current of about 20 A (20 W) is sufficient for 400°C. This furnace is durable for more than 40 hours, which is sufficient for one series of experiment. Vertical, lateral and rotational adjustment and exchange of the heater are made easily.

Temperature measurement: A junction of Chromel-Alumel thermocouple (0.3 mm dia.) is placed 1 mm above specimen, not to intercept the X-ray path. The wire of the couple is placed in such a way as shown in Fig. 1 to reduce the effect of thermal conduction through itself. Calibration by melting specimens of In, Sn, Bi, Pb and InSb having similar shape and size to those of Fe_7Se_8 specimen was carried out before and after each run. The difference between true melting point and temperature recorded by the

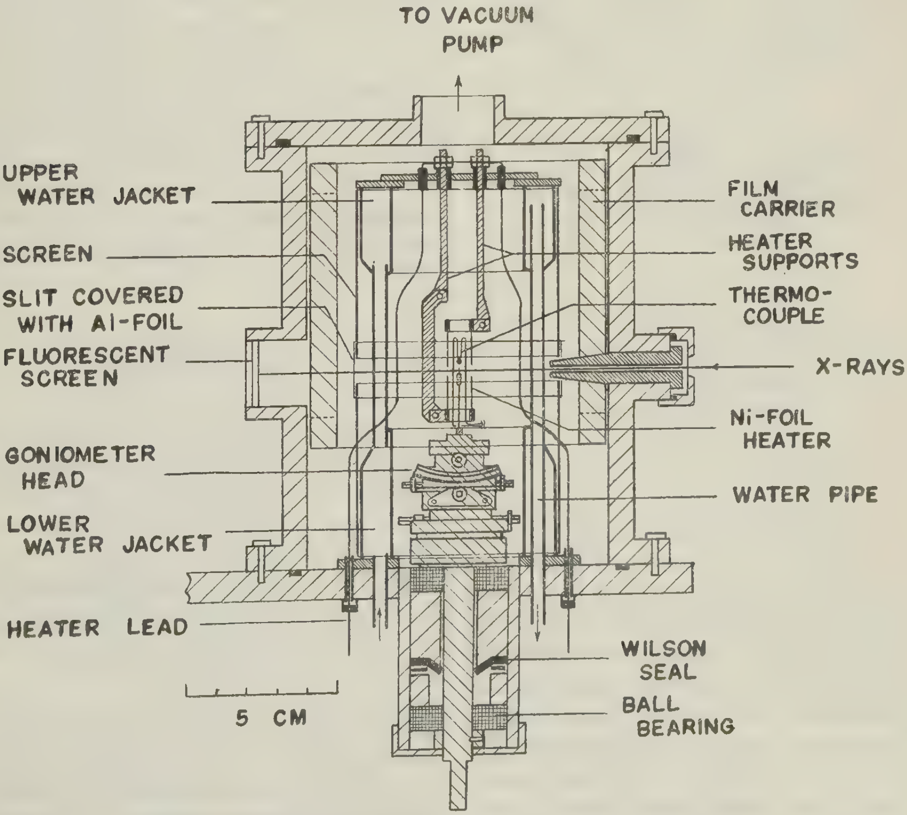

Fig. 1. Main part of the high-temperature camera.

thermocouple was less than 4°C in every specimen and a good linearity between these two temperatures was found in every case. Therefore the accuracy of temperature measurement of specimen after this calibration would be within ±2°C, and the stability of temperature during exposure (less than half an hour) was within ±0.5°C. Another thermocouple (not shown in Fig. 1) could be attached simultaneously, and its junction was placed close to shielding paper of cassette. This thermocouple indicated 10°C higher than room temperature when that of specimen was 400°C.
Atmosphere: Both furnace and camera unit are inside vacuum chamber.

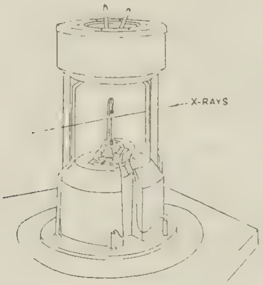

Fig. 2. A sketch of the inside of the camera. Screen and heating element are removed.

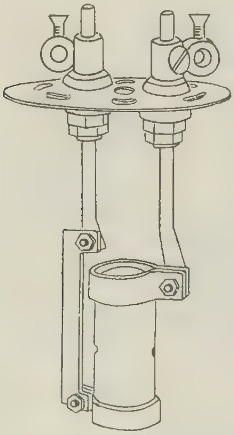

Fig. 3. A sketch of the heating element.

Film mounting: The film carrier with Straumanis-Ieviņš type film mounting, 9 cm in diameter, can be moved axially to give a series of 10 exposures of the equatorial reflexions.
Windows: Inner radiation shield is Al-foil which covers a slit of a cylindrical brass screen wound on upper and lower water jackets. Higher layer reflexions can be recorded by using another screen with a wide slit. A window for X-ray of outer vacuum chamber is Mylar sheet. Shadow of specimen during exposure is observable on a fluorescent screen. Brass pipes connecting the two water jackets, two heater leads juxtaposed to these pipes and one of supporting arms of the heater are placed in the low- and high-angle position, and reflexions with θ between 7.5 and 82.5 degrees are observable.
Specimen: The specimens on which the X-ray work was performed were formed into nearly cylindrical shape, about 1.3 mm in length and about 0.4 mm in diameter, by cutting with a small sawteeth and grinding with sand paper. These were mounted on a quartz fibre support, 15 mm in length and 0.2 mm in diameter by a small amount of potter's clay. Since a movement of arcs of goniometer head was limited to ±6 degrees by the contact of the support with the furnace and with the thermocouple wire, the axis of the specimen was made parallel to the crystallographic axis within ±2 degrees.

So far as a determination of positions of vacancies is concerned, a precise data of intensities are not necessary, if the fundamental structure is well-known. These data must be obtained to determine the displacement of the individual atoms, neighbouring to the vacancies, from the original positions caused by the existence of these vacancies. But this problem will not be mentioned in the present paper. Therefore Weissenberg photographs were taken only subsidiarily at room temperature.

§ 3. Structure Determination

(a) '*4c structure*'

Rotation, oscillation and Weissenberg photographs about each crystallographic axis indicated that Fe_7Se_8 crystallized by slow cooling has a superstructure superposed on the fundamental structure of the NiAs type. If the capital and small letters designate the unit cell dimensions of the super- and fundamental lattices, respectively, this superstructure has the following dimensions:

$$A=\sqrt{3}\,B\,,\quad B=2a\quad \text{and}\quad C=4c\,.$$

This structure will be named as the '4c structure'. Since the pycnometric density is in very good agreement with the calculated value assuming that one eighth of iron sites in the fundamental lattice are vacant, this superstructure may be attributed to an ordered arrangement of iron vacancies. Moreover the (0001) and (0003) reflexions prohibited for the ideal NiAs structure are observed. These suggest that the vacancies are confined to the alternate c planes, where the arrangement as shown in Fig. 4 is reasonable, because the periodicity of this superstructure in the c plane is twice as great as that of the fundamental lattice and one fourth of iron sites must be vacant.

For all the observed reflexions h, k and l are all even or all odd, where the indices are on the basis of the superstructure. Furthermore the ($hk0$) reflexions are observed if $(h+k)/2$ is even, indicating that, if this structure is projected on the C plane, these iron vacancies are at every iron site with equal probability. Therefore the structure as shown in Fig. 5 is the most probable one. 8 vacancies in the unit cell are at the following positions:

$$(0, 0, 0;\ 0, 1/2, 1/2;\ 1/2, 0, 1/2;\ 1/2, 1/2, 0)\ +0, 0, 0;\ 1/4, 1/4, 1/4\ .$$

From another point of view this arrangement resembles the diamond structure and the (hkl) reflexions should be systematically absent unless the following condition besides that for the face-centred lattice is also fulfilled: $h+k+l=2n+1$ or $4n$ (n: integer). This rule is satisfied for all the observed reflexions.

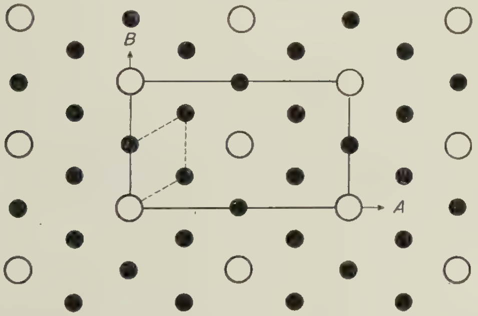

Fig. 4. Ordered arrangement of Fe atoms and vacancies in the alternate metal layer parallel to the c plane. Solid and open circles represent Fe atoms and vacancies, respectively. Unit cells of super- and fundamental lattices are indicated by full and broken lines, respectively.

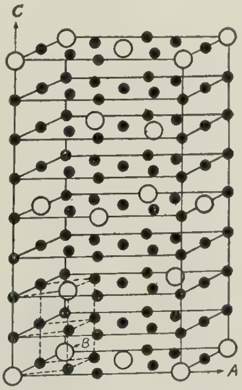

Fig. 5. Unit cell of the '4c structure' of Fe_7Se_8. Open and solid circles represent vacancies and Fe atoms, respectively. Se atoms are omitted for clarity. Broken lines indicate the fundamental unit cell. These notations will be used also in Figs. 6 and 7.

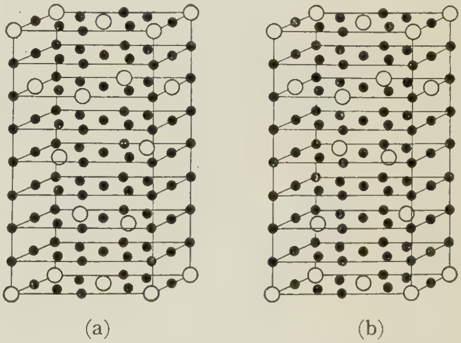
(a) (b)

Fig. 6. Superstructures obtained from that shown in Fig. 5 by turning both the A and B axes around the C axis; (a): through +60 and (b): −60 degrees. (b) is turned upside down for the sake of contrast with (a).

Now, if both the A and B axes are turned around the C axis through +60 and −60 degrees, the superstructures as shown in Figs. 6(a) and 6(b) are obtained, respectively, where (b) is turned upside down for the sake of contrast with (a). The diffraction records of these structures should contain different systematic extinctions which are different also from those of the first structure.

This was proved by turning a specimen around the C axis through 30 degrees successively, by taking oscillation photographs about the A or B axis at every step and by comparing the observed systematic extinctions with those obtained by calculation on the above models, where the maximum numbers of h, k and l are 13, 7 and 25, respectively.

The lattice constants at room temperature are as follows:

$$A=\sqrt{3}\,B=12.53\,,\quad B=2a=7.23_6\ \text{and}\ C=4c=23.5_4\,\text{Å}\,,$$
$$\alpha=89.8^\circ\,,\quad \beta=89.4^\circ\ \text{and}\ \gamma=90.0^\circ\,.$$

Except for the lattice symmetry, the superstructure of Fe_7Se_8 at room temperature is identical to that of natural pyrrhotite Fe_7S_8 described by Bertaut[4]. It was rather difficult to find a specimen of complete single crystal and there are twin structures in general. That is, reflexions corresponding to the three structures as shown in Figs. 5 and 6 are observed frequently on an oscillation photograph.

(b) *'3c structure'*

On the specimen quenched from 320°C another hexagonal superstructure, having the following unit cell dimension, was observed:

$$A=2a\ \text{and}\ C=3c\,.$$

This structure will be named as the '3*c* structure'. For convenience of comparison with the '4*c* structure', the following orthohexagonal cell was chosen throughout the analysis:

$$A=\sqrt{3}\,B\,,\quad B=2a\ \text{and}\ C=3c\,.$$

Similarly to the case of the '4*c* structure', it is found that the iron vacancies are in the alternate *c* planes with the arrangement as shown in Fig. 4.

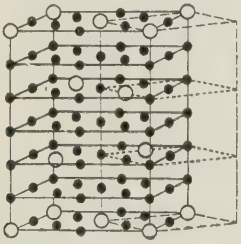

Fig. 7. An orthohexagonal unit cell of the '3*c* structure' of Fe_7Se_8. A hexagonal cell is shown by broken lines.

For all the observed reflexions $h+k$ is even, where the indices are based on the superstructure. One of the possible models is shown in Fig. 7 and this is the most probable*. 6 vacancies in the unit cell are at the following positions:

$$(0,0,0;\ 1/2,1/2,0)$$
$$+0,0,0;\ 1/4,1/4,1/3;\ 1/4,3/4,2/3^{**}\,.$$

This structure is stable even at liquid air temperature. The crystal with this structure is also ferrimagnetic and the Curie temperature is nearly the same as that of the crystal with the '4*c* structure', i.e., 189°C for the former and 187°C for the latter[8].

(c) *Transition from '4c structure' to '3c structure'*

The structural changes at high temperature were examined systematically with eleven specimens cut out from several ingots and the structure of them was examined at room temperature. To obtain information most effectively the axes of these specimens were made parallel to the *B* axis and oscillation photographs with an angular range of 20 degrees about this axis were taken at intervals of 2~10°C.

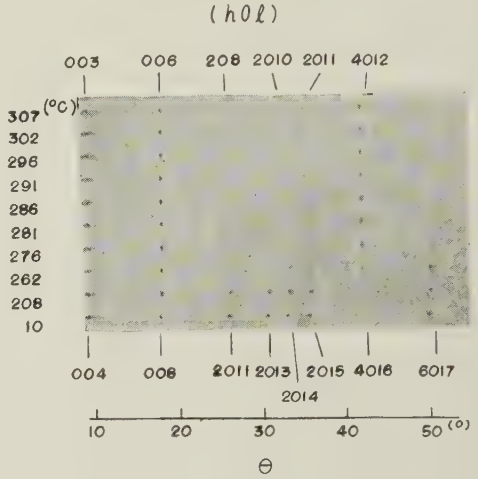

Photo. 1. Oscillation photograph indicating transition from '4*c* structure' to '3*c* structure.' Indices referred to each structure are given at the bottom or top.

At first the transition from the '4*c* structure' to the '3*c* structure' was investigated. An example is shown in Photo. 1. Indices based on the '4*c*' and '3*c*' structures are given at the bottom and the top, respectively. On the pattern of the '4*c* structure', the twin structure described in § 3 (a) is presumable. The intensity of the (008) reflexion which is one of the weakest reflexions from the fundamental lattice is reduced to 1/10 by a filter of metal foil to compare with that of the superstructure pattern, where the indices are given on the basis of the '4*c* structure'. As shown obviously in this photograph this tran-

---

* Details of this analysis have been reported previously[3].

** These positions are described incorrectly in the previous paper[3].

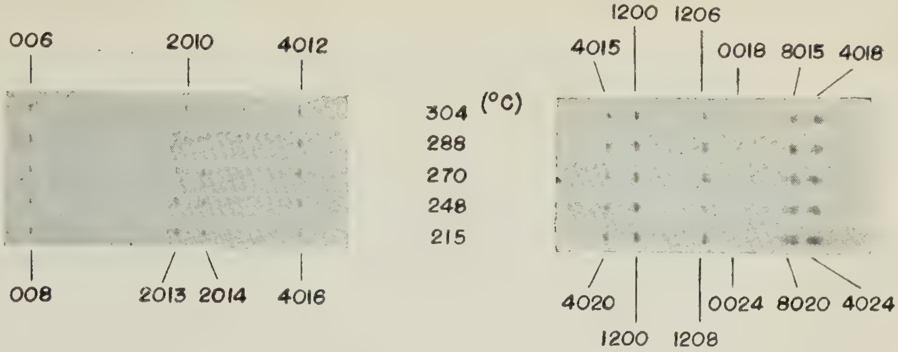

Photo. 2. A part of oscillation (left) and rotation (right) photographs in the temperature range of the '4*c* to 3*c*' transition.

sition proceeds gradually through the temperature range of about 60°C. At the intermediate state the patterns corresponding to both of these structures are observed. As shown in Photo. 2, on rotation photographs taken in this temperature range the splittings of high angle reflexions due to the triclinic deformation of the hexagonal lattice are decreasing gradually and disappear at the temperature where the pattern of the '4*c* structure' disappear on oscillation photograph. The Photo. 2 was obtained by the following procedure: a pair of an oscillation and a rotation photographs with the same specimen were taken successively at each temperature.

This transition which is independent of the magnetic transition from the ferrimagnetic state to the paramagnetic one, begins at 240°C* and finishes at 298°C**. These values are reproducible within ±2°C for specimens prepared from the same raw materials.

The reverse transition from the '3*c* structure' to the '4*c* structure' was difficult to observe in a complete form by the above method. This might be due to oxidation of specimens during exposure at high temperature and was consistent with the fact that crystals prepared from electrolytic iron powder often had the '3*c* structure' at room temperature, even if they were cooled down slowly, because it might be rather difficult to reduce iron powder completely. The reversibility and reproducibility of this transition, however, were proved by another method described in § 4.

Intensity of certain reflexion from the fundamental lattice, for example the (4012) in Photo. 1, changed remarkably with temperature. This suggested that atoms near the iron vacancies changed their positions with temperature. But this problem will not be discussed further.

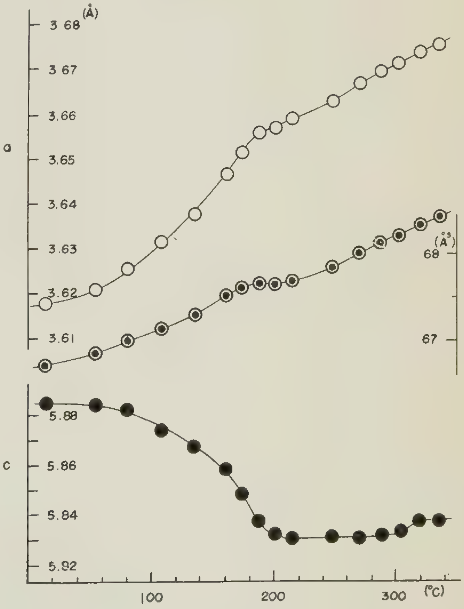

Fig. 8. Lattice constants and volume of the fundamental unit cell of Fe_7Se_8 as a function of temperature.

The lattice constants of the fundamental lattice up to 350°C are shown in Fig. 8. This is in good agreement with the results obtained with a dilatometer[5]. The anomalous behaviour below 190°C is corresponding to the magnetic transition and is observed clearly on the rotation photographs as shown in Photo.

---

*, ** These values for the specimens prepared from electrolytic iron powder were about 302 and 317°C, respectively.

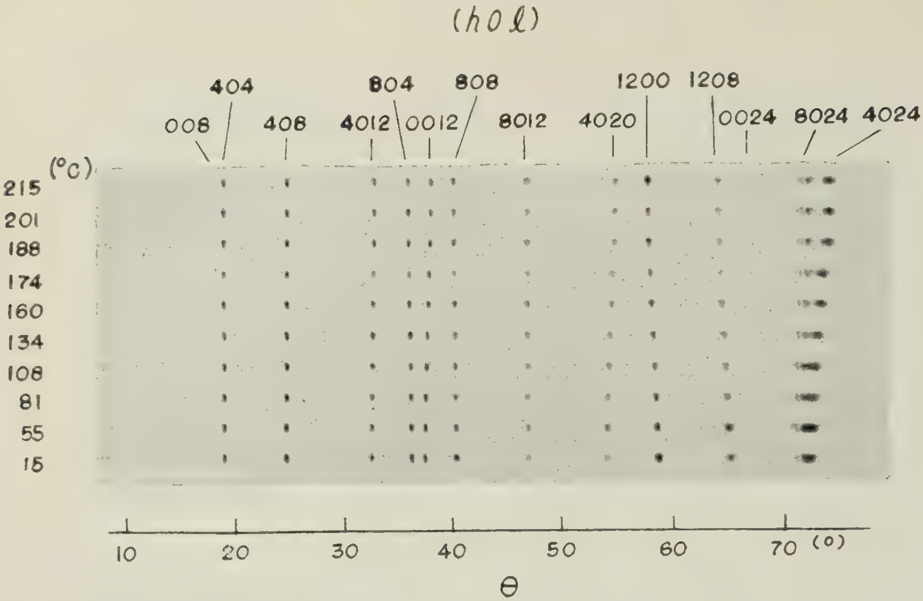

Photo. 3. Rotation photographs displaying an anisotropic thermal expansion below T_c. Indices are given on the basis of the ‘4c structure’.

3[*]. A similar behaviour has been reported by Willis[9] and Snow[10] on CrSb which is antiferromagnetic compound with the NiAs structure. Below the transition the axis of easy magnetization in Fe$_7$Se$_8$[5] and CrSb[10] is parallel and perpendicular to the c plane, respectively. This may be the cause of an opposite behaviour with respect to the a and c axes for these compounds.

(d) *At higher temperature*

The following two types of structural change were observed on the ‘3c structure’ when specimens were heated to higher temperature:

i) ‘$3c \rightarrow 1c$ type’. The transition from the ‘3c structure’ to ‘1c structure’ was observed in the temperature range from 360 to 375°C, which proceeded gradually like that from ‘4c’ to ‘3c’. The term ‘1c structure’ means a partial ordered state in which the iron vacancies remain within the alternate c planes but are distributed at random in these planes. This is concluded from the disappearance of the superstructure reflexions except for the (0003) and (0009) etc. referred to the ‘3c structure’. Such a situation has been reported by Jellinek on Cr$_7$S$_8$[11]. This transition was reversible and reproducible. At about 400°C the distribution of the vacancies became completely disorder.

ii) ‘$3c \rightarrow 2c \rightarrow 1c$ type’. For some specimens an intermediate phase was found between the ‘3c’ and ‘1c’ structures. The diffraction pattern of this intermediate phase could be indexed on the basis of a hexagonal unit cell with $A=2a$ and $C=2c$. Oscillation photographs were taken at 400°C, but the observed extinction rule could not be explained from any arrangement of iron vacancies. The intensities of this ‘2c structure’ were of the order of 1/5 compared with those of the ‘4c’ and ‘3c’ structures. Therefore this structure may be somewhat disorder. The gradual transition from ‘3c’ to ‘2c’ begins at 320°C and finishes at 385°C and the ‘2c structure’ disappears at about 450°C.

To make clear the essential behaviour, the experiments described below were carried out. Specimens with the ‘4c structure’ at room temperature were sealed into evacuated silica tubes, heated up to 450°C and quenched, but the diffraction pattern showed the ‘3c structure’ only. Consequently the reason for these different behaviours at high temperature has been unknown. The ‘2c’ and ‘1c’ structures seemed to accompany oxidation or any other chemical change.

---

[*] The relative intensities of the superlattice reflexions to those of the fundamental ones may be estimated if the (008) reflexion is compared with that in Photo. 1.

§ 4. Additional Experiments

It was found by the experiments described in § 3 (c) that the crystals with the '4*c*' and '3*c*' structures were obtained when they were cooled down slowly and quenched from 320°C, respectively. The experiments with a torque magnetometer by Hirakawa[8)], using crystals to which the heat treatments described above were applied, suggested that the torque curves in the *c* plane for specimens with the '3*c* structure' had no detectable anisotropy, but those for specimens with the '4*c* structure' showed a component of two-fold symmetry superposed on a six-fold one. This fact was confirmed directly by examining the crystal structure of the specimen on which the torque curve was measured. This was carried out as follows: Several disks with the axis parallel to the *c* axis were cut out from crystals quenched from 320°C. The planes of the disks were made flat with sand paper and polished with powder of Cr_2O_3. The torque curves in these planes showed no anisotropy. Oscillation photographs indicated that these had the '3*c* structure.' Then these disks were sealed into an evacuated silica tube and annealed at 290°C and cooled down slowly. Oscillation photographs indicated the '4*c* structure.' The torque curves contained a component of two-fold symmetry superposed on a six-fold one. On the planes of these disks three sets of parallel folds crossing each other at an angle of 60 degrees were observed. These folds might be due to twins and were parallel to the *A* axes. These processes were reversible, and moreover, when these disks were quenched from 275°C, the oscillation photographs showed the patterns of both the '4*c*' and '3*c*' structures coexisting with nearly equal proportion. When these heat treatments were repeated more and more, however, it became difficult to obtain crystals in state of the pure '4*c* structure'. These results are consistent with those described in § 3 (c).

§ 5. Discussion

On some chalcogenides of the 3*d* transition group elements, of which structures are related to the NiAs type and of which compositions are non-stoichiometric, superstructures have been reported by several researchers. Above all on pyrrhotite Fe_7S_8, synthesized crystals were examined systematically with powder specimens[12),13)] and some natural crystals were also examined[13),14)]. The origin of these superstructures, however, had not been revealed for a long while. In 1952 Néel suggested that the ferrimagnetism of pyrrhotite should be due to the ordered arrangement of iron vacancies and the superstructure might be explained also by this ordering.

The first to find such an ordered arrangement was Bertaut who investigated single crystals of natural pyrrhotite[4)]. A similar ordered structure has been found on natural smythite Fe_3S_4 by Erd et al.[15)] in which the iron vacancies are confined to every fourth metal layer and $C=6c$. Another example of such an ordering has been reported on CrS_x system by Jellinek[11)]. He found superstructures on Cr_7S_8, Cr_5S_6, Cr_3S_4 and Cr_2S_3. In each compound chromium vacancies are confined to every second metal layer. Cr_3S_4 has the same structure as that of Fe_3Se_4[3)] with $C=2c$. Cr_2S_3 has two types of superstructure: with $C=2c$ (trigonal) and with $C=3c$ (rhombohedral). These are similar to the case of Fe_7Se_8, but are attributed to the slight difference of compositions: $Cr_{0.69}S$ for the former and $Cr_{0.67}S$ for the latter, respectively. Most of these compounds are ferrimagnetic or antiferromagnetic and at their Curie or Néel temperature these ordered structures still remain as expected. It seems that similar ordered structures may be observed in many other compounds if they are examined in detail.

The author wishes to express his hearty thanks to Prof. T. Okada for his continuous guidance and encouragement and to Dr. K. Hirakawa for suggestion of the present problem, for discussions and for supplying the crystals. He is also indebted to Mr. Y. Suemune for drawing the figures. The present investigation was partly supported by the Scientific Research Expenditure of the Ministry of Education.

Note added in proof. A partial ordered arrangement has been reported also on titanium vacanies in the non-stoichiometric phase $Ti_{2+x}S_4 (0.2<x<1)$. [A. D. Wadsley: Acta Cryst. **10** (1957) 715.]

References

1) G. Hägg and A. L. Kindström: Z. phys. Chem. **22** (1933) 453.
2) T. Hirone, S. Maeda and N. Tsuya: J. Phys. Soc. Japan **9** (1954) 496.
3) A. Okazaki and K. Hirakawa: J. Phys. Soc. Japan **11** (1956) 930.
4) E. F. Bertaut: Acta Cryst. **6** (1953) 557.
5) K. Hirakawa: J. Phys. Soc. Japan **12** (1957) 929.
6) A. Okazaki: J. Phys. Soc. Japan **14** (1959) 112.
7) L. S. Dent and H. F. W. Taylor: J. Sci. Instr. **33** (1956) 89.
8) K. Hirakawa: private communication.
9) B. T. M. Willis: Acta Cryst. **6** (1953) 425.
10) A. I. Snow: Rev. Mod. Phys. **25** (1953) 127.
11) F. Jellinek: Acta Cryst. **10** (1957) 620.
12) H. Haraldsen: Z. anorg. allg. Chem. **246** (1941) 169, 195.
13) F. Grønvold and H. Haraldsen: Acta Chem. Scand. **6** (1952) 1452.
14) M. J. Buerger: Amer. Miner. **32** (1947) 411.
15) R. C. Erd, H. T. Evans, Jr. and D. H. Richter: Amer. Miner. **42** (1957) 309.

JOURNAL OF THE PHYSICAL SOCIETY OF JAPAN, Vol. 16, No. 6, JUNE, 1961

Ultrasonic Attenuation in Magnetite at Low Temperatures

By Kazuo KAMIGAKI

The Research Institute for Iron, Steel and Other Metals,
Tohoku University, Sendai

(Received February 20, 1961)

The ultrasonic attenuation coefficients in magnetite crystals were measured over the temperature range of 4.2°K–300°K and two kinds of attenuation peaks were observed below the transformation temperature of of ionic ordering. The attenuation is attributable to the relaxed electron diffusion between Fe^{2+} and Fe^{3+} ions on the octahedral sites in the ordered lattice of magnetite. The electron diffusion processes are classified into the single electron process and the coupled transition. The activation energy of the former process is determined to be 0.055 ev and the latter 0.36 ev.

§ 1. Introduction

Recently, low temperature internal friction was investigated on single crystals of magnetite and several kinds of ferrite in the frequency range 10^4–10^5 c/s by Fine and Kenney[1)] and Gibbons[2)]. They found the relaxation peaks in magnetite at about 40°K and 95°K. The origin of these peaks were considered as the relaxed motion of electrons between Fe^{2+} and Fe^{3+} ions induced by a lattice deformation due to the alternating stress. This consideration is based on a model that the ions of different size redistribute under the action of the external stress to reduce the elastic strain energy by the electron diffusion process. But the previous measurements mentioned above were limited to the lower frequency range and the exact evaluation of the activation energies for the relaxed electron diffusion processes have not yet been achieved. The present author planned to measure the ultrasonic attenuation at 10^6–10^7 c/s and to determine the activation energies for both peaks. Some discussions on the mechanism of both relaxation processes are also given.

§ 2. Experimental Method

The specimens were natural single crystals* obtained at Hidaka, Hokkaido, Japan and their volumes were about 1 to 2 cubic centimeters. The ultrasonic waves were transmitted through (111) or (100) plane. The former was a natural surface lapped carefully to be flat and parallel to the opposite surface. The (100) plane was cut, lapped and oriented by the X-ray diffraction method within 1°. Their low temperature transformation point at about 120°K was confirmed by the magnetic method.

---

* Kindly furnished by the Miyahara Laboratory, Hokkaido University.

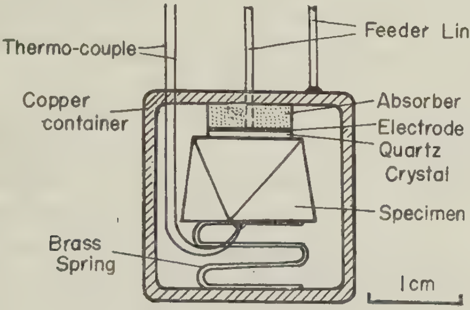

Fig. 1. Specimen holder.

The specimen was mounted in a liquid helium cryostat of the usual type together with the quartz crystal transducer. Details of the specimen holder are shown in Fig. 1. The copper container was made light in weight and the specimen occupied a greater part of the heat capacity. The temperature of the specimen was measured by an Au(2%Co)-Ag(0.2%Cu) thermo-couple. After the evaporation of liquid helium, the specimen was kept under natural heating and the rise in temperature was about fifty degrees per hour.

The apparatus and the method of the attenuation measurements were the same as those used by the author for the previous measurements[3]. The error in the present measurements was within ±3 per cent.

In the course of the measurements a maximum magnetic field of 5000 Oe was applied to the specimen to reduce the secondary effect due to the magnetic domain wall motion. Since the magnetic anisotropy of magnetite vanishes at about 130°K[4], the resistance for the domain wall motion becomes small. The attenuation took a very large value in zero field and was reduced radically in the high field as shown by **X** in Fig. 2b.

Owing to the technical difficulty in supplying liquid helium, the specimen was cooled down through the transformation point without application of the magnetic field. So the specimen must have been composed of twins of the ordered structure.

§ 3. Results of Measurements

Attenuation of the longitudinal waves transmitted along the ⟨111⟩ direction is shown in Figs. 2a and 2b at 5 Mc/s and 15 Mc/s respectively. On both curves, sharp peaks of attenuation are observed at about 60°K (first peak) and 110°K (second peak). At temperatures near the peaks, attenuation varied remarkably with temperature, so the determination of the peak point was made by observing the temperature where the attenuation was inflected from increasing to decreasing. In the

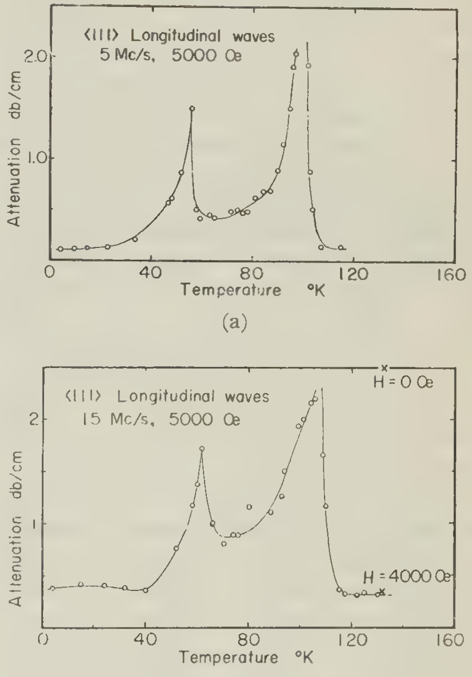

(a)

(b)

Fig. 2. (a) Ultrasonic attenuation of the longitudinal waves in magnetite along ⟨111⟩ at 5 Mc/s and (b) at 15 Mc/s.

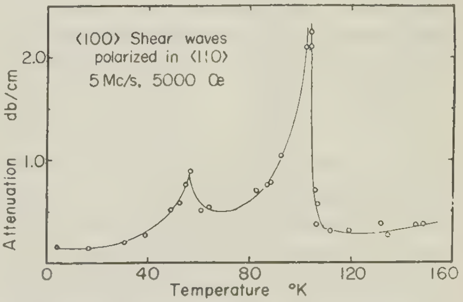

Fig. 3. Ultrasonic attenuation of the ⟨110⟩ polarized shear waves in magnetite along [010] at 5 Mc/s.

case of the first peak, both peak value of attenuation and the corresponding temperature were determined, but in the second peak attenuation increased hugely and only the temperature of inflection was determined.

Attenuation of the shear waves polarized in the ⟨110⟩ direction transmitted from the (100) plane is shown in Fig. 3. In this case similar results to those in Fig. 2 are obtained and two peaks are observed.

§ 4. Discussions

Since the half width of attenuation peaks is narrow, the attenuation is attributable to single relaxation phenomena. In Fig. 4, the ultrasonic frequency of the attenuation measurement is plotted against the inverse of the absolute temperature T at which the first or the second peak was observed. The relaxation peaks obtained by Fine and Kenney[1] and Gibbons[2] are also plotted on the same figure. As this figure shows, the relaxation frequency falls linearly with the increase of the $1/T$ value covering the points obtained at lower frequencies. Making use of the simple Arrhenius type equation activation energies and frequency factors for each sequence of the relaxation peaks are calculated and listed in Table I.

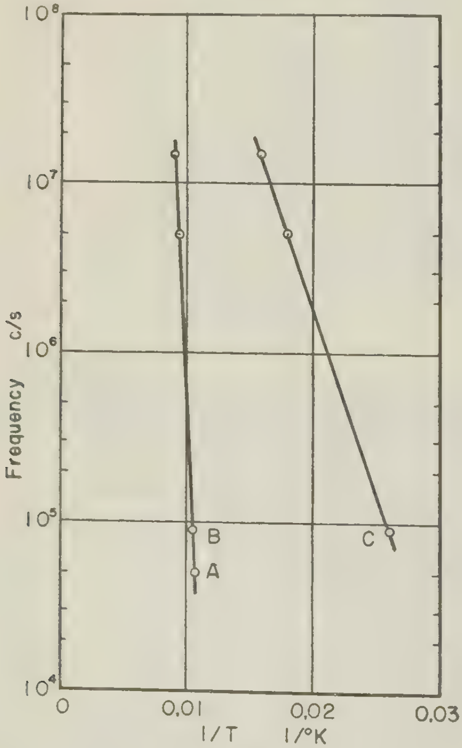

Fig. 4. Relaxation frequency against $1/T$ for the two relaxations in magnetite. Point A was determined by Fine and Kenney[1] and B and C by Gibbons.[2]

Table I.

	Activation energy ev	Frequency factor sec^{-1}
first peck	0.055	4.3×10^{11}
second peck	0.36	6.5×10^{23}

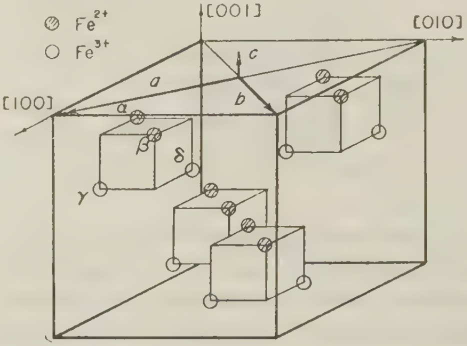

Fig. 5. The ordered arrangement of Fe^{2+} and Fe^{3+} ions in the octahedral sites of magnetite. The principal axis of disordered magnetite are shown conventionally.

The origin of the attenuation peaks is considered to be the stress-induced relaxation in the distribution of Fe^{2+} and Fe^{3+} ions occurring as a result of the transmission of the ultrasonic waves. At first, various types of deformation of the ordered magnetite crystal and the resultant distribution of Fe^{2+} and Fe^{3+} ions to reduce the strain energy should be considered. The ion arrangement in octahedral sites of the ordered magnetite crystal is shown in Fig. 5, where hatched or unhatched circles correspond to Fe^{2+} and Fe^{3+} respectively. b is in the direction of preferred distribution of Fe^{2+} and about 0.55% shorter than a, which is in the direction preferred for Fe^{3+}.[5] For simplicity, the cubic crystal axis of the spinel lattice is used and the four types of the octahedral sites are designated by α, β, γ and δ as shown in Fig. 5.

First, consider the ⟨100⟩ transmission of the longitudinal ultrasonic waves. For the compression along [100] it is preferred for Fe^{2+} to sit on α and β, and for Fe^{3+} on γ and δ, each arrangement of ions is described as $\mathrm{Fe}^{2+}(\alpha\beta)$ or $\mathrm{Fe}^{3+}(\gamma\delta)$ respectively. For the extension $\mathrm{Fe}^{2+}(\gamma\beta)\,\mathrm{Fe}^{3+}(\alpha\delta)$ or $\mathrm{Fe}^{2+}(\alpha\delta)\,\mathrm{Fe}^{3+}(\gamma\beta)$ are preferred. To complete these rearrangements, Fe^{2+} on α or β must exchange the sites with Fe^{3+} on γ or δ, respectively. These rearrangements of ions are effectively caused by the transition of an electron between Fe^{2+} and Fe^{3+} and this is expressed by the single electron process of the following type:

$$\mathrm{Fe}^{2+} \rightleftharpoons \mathrm{Fe}^{3+} + e^- \tag{1}$$

For simplicity, only the Fe^{2+} arragements are discussed hereafter. For the compression along [010] $(\alpha\beta)$ is preferred and for the extension $(\alpha\gamma)$ or $(\delta\beta)$. For the compression along [001] $(\alpha\gamma)$ or $(\delta\beta)$ and for the extension $(\alpha\beta)$. These ion rearrangements are expressed by the same process of single electron migration as in (1).

Next is the case of the ⟨110⟩ longitudinal wave transmission. For the compression along [110], preferential arrangement of Fe^{2+} is $(\alpha\beta)$ and for the extension $(\gamma\delta)$. To complete this rearrangement two Fe^{2+} on α and β migrate simultaneously into γ and δ. Such migration is completed not by the process (1) but by a simultaneous migration of two electrons, or the coupled electron migration process. By this rearrangement the axis a and b are interchanged. For the [011] compression $(\gamma\beta)$ is preferred and for the extension $(\alpha\delta)$, and for the [101] compression $(\delta\beta)$ and for the extension $(\alpha\gamma)$. In both processes of rearrangement there is an intermediate state $(\alpha\beta)$, and the process is divided into two parts, in each of which only one electron moves. Hence these processes are principally the single electron process of (1).

Also in the case of the ⟨111⟩ longitudinal wave transmission, for the [111] compression $(\alpha\beta)$ is preferred and for the extension $(\alpha\gamma)$, $(\alpha\delta)$ and $(\gamma\delta)$ are preferred. In these rearrangements the former two are the single electron process but the last is the coupled electron process.

In the case of the shear wave or the torsional wave transmission, the processes of deformation are similar to those of the longitudinal waves. Hence all the types of ion rearrangement are contained in the above considerations and listed in Table II; the unit processes are classified into the single electron process and the coupled one. Owing to the limitation in the experimental procedure, the specimens are composed of multiple twins at the ordered state. Hence the relaxation process observed in a certain direction is the superposition of the unit processes in the equivalent directions.

Table II. The preferred arrangements of Fe^{2+} in the octahedral sites of magnetite for the transmission of ultrasonic waves along various directions.

Direction of transmission		One electron process		Coupled electron process	
		Compression	Extension	Compression	Extension
⟨100⟩	[100]	$\alpha\beta$	$\begin{cases}\gamma\beta\\ \alpha\delta\end{cases}$		
	[010]	$\alpha\beta$	$\begin{cases}\alpha\gamma\\ \delta\beta\end{cases}$		
	[001]	$\begin{cases}\alpha\gamma\\ \delta\beta\end{cases}$	$\alpha\beta$		
⟨110⟩	[110]			$\alpha\beta$	$\gamma\delta$
	[011]	$\gamma\beta$	$\alpha\delta$		
	[101]	$\delta\beta$	$\alpha\gamma$		
⟨111⟩	[111]	$\alpha\beta$	$\begin{cases}\alpha\gamma\\ \alpha\delta\end{cases}$	$\alpha\beta$	$\gamma\delta$

Now, the first peak of attenuation is explained as a stress-induced relaxation of one electron diffusion expressed by the equation (1). The first reason for such conclusion is that in the case of electric conduction in magnetite, current is carried by electrons hopping between neighbouring pairs of a ferrous and a ferric ion as represented by the equation (1). In pure magnetite, the activation energy for the electric conduction was determined by Calhoun[6] to be 0.06 ev (40°–52°K), 0.09 ev (56°–77°K) and 0.11 ev (78°–90°K). The value 0.06 ev fairly coincides with the activation energy of ultrasonic relaxation 0.055 ev obtained for the first peak, lying near 50°K. Next, the first peak was observed in all the cases of longitudinal wave transmission along ⟨100⟩, ⟨111⟩ and shear waves along ⟨100⟩. The single electron process, expressed by the equation (1) can occur in all the above cases as will be seen from Table II. The low temperature peak was also observed by the previous investigators[1,2] in some ferrites without low temperature transformation of ionic ordering, and peak height varied with the content of Fe^{2+}. This fact also supports the above explanation for the origin of the first peak.

The activation energy for the second peak observed directly below the transformation point is 0.36 ev and considerably higher. This peak is regarded as a stress-induced relaxation corresponding to the simultaneous exchange of paired Fe^{2+} ions with paired Fe^{3+} or the coupled electron process in Table II. According to the previous measurements,[1),2)] the second peak was not observed in magnetite for the ⟨100⟩ longitudinal waves nor in various ferrites without low temperature ionic ordering in octahedral sites. From Table II, it can be seen that in these cases the coupled exchange of ions does not occur. In the conductivity measurements, the activation energy was obtained as 0.11 ev at temperatures near the second peak. This value is considerably lower than the activation energy of ultrasonic relaxation, so the latter can not be considered as the single electron process expressed by (1). As a consequence, it is concluded that the second peak of attenuation is a stress-induced relaxation, the elementary process of which is the coupled exchange of ions through the coupled diffusion of electrons in the ordered octahedral sites of magnetite.

The author wishes to expresss his hearty thanks to Professor T. Hirone of this Institute for his kind guidance throughout the present work and to Professor S. Miyahara of the Hokkaido University for his kind furnishing with specimens and helpful discussions. He is also indebted to the members of Hirone Laboratory and those of Miyahara Laboratory for their kind advices on the present study.

Addendum Shear wave attenuation was measured at 35 Mc/s in the same way as in the case of Fig. 3. The first peak was observed at 68°K and the second at 112°K, both are to be plotted in Fig. 4.

References

1) M. E. Fine and N. T. Kenney: Phys. Rev. **94** (1954) 1573; **96** (1954) 1487.
2) D. F. Gibbons: J. Appl. Phys. **28** (1957) 810.
3) T. Hirone and K. Kamigaki: Sci. Rep. Res. Inst. Tohoku Univ. **A7** (1955) 456.
4) L. R. Bickford, J. M. Brownlow and R. F. Penoyer: Proc. Inst. Electr. Eng. **B104** (1947) 238.
5) W. C. Hamilton: Phys. Rev. **110** (1958) 1050.
6) B. A. Calhoun: Phys. Rev. **94** (1954) 1577.

JOURNAL OF THE PHYSICAL SOCIETY OF JAPAN, Vol. 16, No. 6, JUNE, 1961

Crystal Structures and Electrical Properties of Alkali Antimonides

By Jun-ichi CHIKAWA, Shuji IMAMURA
Technical Research Laboratories, Japan Broadcasting Corporation, Setagaya-ku, Tokyo, Japan
Kenzo TANAKA and Makoto SHIOJIRI
Department of Physics, Faculty of Science, Kyoto University

(Received March 2, 1961)

Both X-ray study and electrical measurement were simultaneously carried out keeping the specimen in vacuum. In K–Sb and Na–Sb, the crystallization into the hexagonal structure from amorphous state and the transition from *p*-type semiconductor to *n*-type one occur simultaneously with successive activation by alkali metal. But Cs–Sb keeps constantly *p*-type in spite of the crystallization into the cubic structure from amorphous state. In Rb–Sb, the transition of the structure occurs, i.e., amorphous→cubic→hexagonal, and *n*-type conduction appears in the hexagonal structure. In order to explain these facts, the relation between the excess alkali atoms and the crystal structure was considered.

The cubic phase of Rb_3Sb was found to be the same as the structure of Cs_3Sb. The unit cell ($a=8.84\pm0.02$Å) is described by the space group $Fd3m$-O_h^7 with eight rubidium atoms at $(0,0,0;\ 0,\frac{1}{2},\frac{1}{2};\ \frac{1}{2},0,\frac{1}{2};\ \frac{1}{2},\frac{1}{2},0)+0,0,0$ and $\frac{1}{4},\frac{1}{4},\frac{1}{4}$ and four antimony and four rubidium atoms occupying at random the other positions $(0,0,0;\ 0,\frac{1}{2},\frac{1}{2};\ \frac{1}{2},0,\frac{1}{2};\ \frac{1}{2},\frac{1}{2},0)+\frac{1}{2},\frac{1}{2},\frac{1}{2}$ and $\frac{3}{4},\frac{3}{4},\frac{3}{4}$.

§ 1. Introduction

Alkali antimonides are intermetallic compounds composed of alkali metal and antimony as represented by M_3Sb, the film of which is photosensitive to visible light. Among them, cesium antimonide has been investigated by many investigators in relation to its electrical and photoelectrical properties because of its excellent photo-emissivity.

Brauer and Zintl[1] showed that the crystal structures of K_3Sb and Na_3Sb are hexagonal (Na_3As type) and that Li_3Sb has a hexagonal structure (the high-temperature modification) and a cubic structure (the low-temperature modification, probably Cu_3Al type). For Cs_3Sb, two different cubic types has been reported; Gnutzmann[2] found that the unit cell of Cs_3Sb is a perfectly ordered cubic lattice of Cs and Sb (Cu_3Al type); on the other hand, Jack and Wachtel[3] found that it is randomly distributed by Cs and Sb atoms over equivalent positions to a certain extent. Recently we became aware that the structure of Rb_3Sb were reported independently by Gnutzmann[2] and by Zhuravlev, Smirnov and Mingazin[4], who found that Rb_3Sb has a hexagonal structure (Na_3As type). However, these X-ray studies have been made on powder specimen only and therefore the structure of practical photosensitive film has been unknown at all.

Imamura[5], one of the authors, studied the behaviors of the electrical properties of the alkali antimonide films in the process of preparation of the specimens, and suggested that Rb_3Sb might exist in both the hexagonal and the cubic forms. In order to study such relation between the physical properties and the structure as in the case of Rb_3Sb, X-ray work must be done by use of the same specimen film for which the physical properties are measured. However, it is difficult to accomplish this purpose, because an extremely thin air-tight window is needed to reduce the absorption of X-ray. In all the X-ray work made in the past, powder specimens were used, and there was no definite evidence that the photosensitive film has the structure as in the case of powder specimens. Hence, employing the test tubes with which both X-ray study and observation of the electrical properties of alkali antimonide films could be carried out, the relation between the electrical properties and the crystal structure of alkali antimodes were investigated. We also found a new cubic phase of Rb_3Sb in this experiment.

§ 2. Experiment

Rubidium-antimony film was prepared in an evacuated glass tube as shown in Fig. 1. In order to obtain X-ray photographs, the entrance and the exist window were mounted on both sides of the tube and covered with mica plates (10 μ in thickness) to admit X-rays.

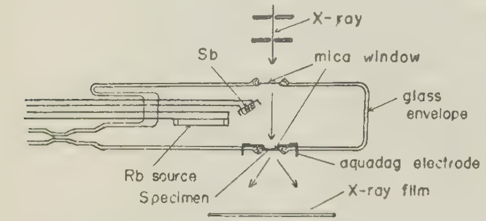

Fig. 1. Preparation of alkali antimonide film and arrangement in X-ray diffraction.

A tungsten filament with antimony and a rubidium source were mounted in the tube. The tube was evacuated and baked at 350°C for three hours. After antimony was evaporated on the exist mica window, metallic rubidium vapour was made by reducing rubidium chromate with silicon powder in an ordinary way to react with the antimony film at 150°~250°C. During the reaction, the sign of the thermoelectromotive force and the electrical resistance of the film were measured with two aquadag electrodes mounted near the exit window. After the measurements, the tube was tipped off from the evacuation system in a vacuum of 3×10^{-6} mmHg and then X-ray diffraction was carried out with placing an X-ray film at a distance of 26 mm from the exit window of the tube, as shown in Fig. 1.

In the above method, however, diffraction lines at high angles disappeared owing to the increase in absorption of the exit mica window. So we also prepared the powder specimen by using tiny flakes of antimony films which were made by tearing off evaporated films from glass substrate, as shown in Fig. 2. After reacting with rubidium under the same condition, the powder specimen was manipulated into the X-ray capillary and sealed off under vacuum to mount on a Debye-Scherrer camera. In this case, we could not measure the electrical properties of powder specimens, but a composition of specimen, Rb/Sb, was measured as follows: weighed tiny flakes of antimony films (about 2 mg) were put into the glass envelope in Fig. 2. After the X-ray photographs were taken with the capillary containing the powder specimen prepared as mentioned above, which was weighed, and the capillary was broken and washed with Aqua regia, so that the capillary without the specimen was weighed. The amount of the specimen was calculated as the difference of two weighing values of the capillary with the specimen and without the specimen, and the amount of rubidium as the difference between the amount of the specimen and the amount of the used tiny flakes of antimony films. Thus, a composition of specimens was calculated.

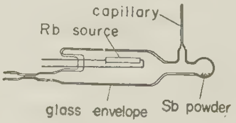

Fig. 2. Preparation of powder specimens of alkali antimonides.

All the X-ray photographs of specimens in this experiment were taken at room temperature with copper radiation.

§ 3. Results

Structure of Rb_3Sb

The electrical resistance of the specimen increases rapidly with successive activation by rubidium, and then it reaches a maximum value at which the specimen has stoichiometric composition Rb_3Sb. With supplying rubidium furthermore, the resistance remarkably decreases[5].

When the resistance of the specimen approached the maximum value in the process of reaction, the X-ray photograph of the specimen showed a halo diffraction pattern at low Bragg angle, as shown in Fig. 3 (A). Consequently, the specimen was considered to be amorphous. After the specimen was annealed at 150~200°C for 5 hours, many diffraction lines appeared which, however, have not yet been interpreted.

Just after the peak resistance was attained by supplying rubidium, the specimen had the cubic structure which was a new phase of

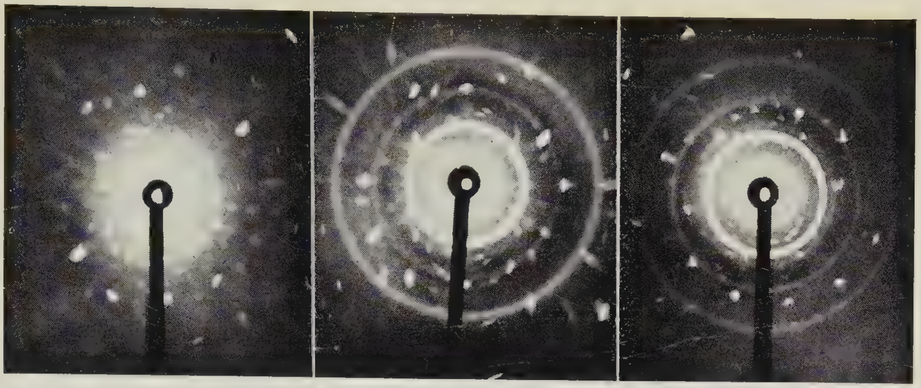

Fig. 3. Diffraction patterns of rubidium-antimony film. (A): At the initial stage in activation process. (B): Cubic phase of Rb_3Sb. (C): Hexagonal phase of Rb_3Sb.

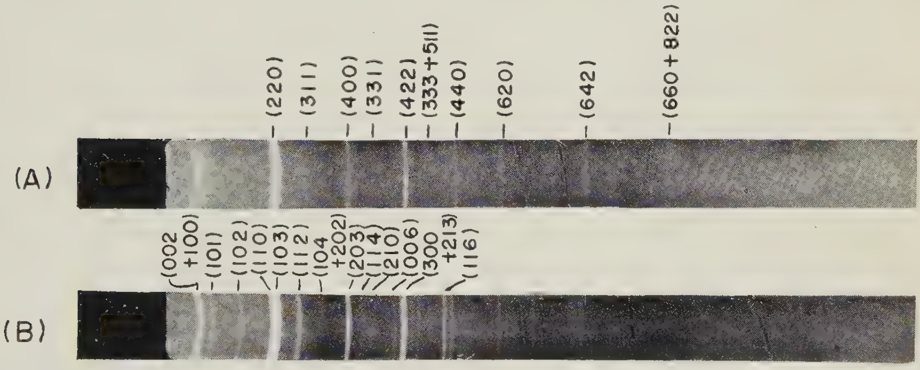

Fig. 4. Diffraction patterns of powder specimens of Rb_3Sb. (A): Cubic phase. (B): Hexagonal phase.

Rb_3Sb. By supplying rubidium a little more the cubic phase was transformed into the hexagonal phase. The X-ray photographs of the cubic and the hexagonal phases which were taken after the reaction at 180°C are shown in Figs. 3(B) and (C), respectively. X-ray photographs were also taken with the powder specimens, as shown in Figs. 4(A) and (B). The diffraction patters in Figs. 4(A) and (B) were respectively identified with those in Figs. 3(B) and (C). In Figs. 3(B) and 4(A), however, very weak diffraction lines of the hexagonal structure appear among the strong diffraction lines of the cubic structure. This shows that these specimens have not a homogeneous composition.

The diffraction pattern in Fig. 4(A) indicates a cubic cell with the constant:

$$a = 8.84 \pm 0.02\ \text{Å}\ ,$$

and can be interpreted by the same structure of Cs_3Sb as that found by Jack and Wachtel[3] (see Fig. 5(A)). That is, the structure is represented by space group $Fd3m\text{-}O_h^7$ and eight rubidium atoms occupy the positions at $(0,0,0;\ 0,\frac{1}{2},\frac{1}{2};\ \frac{1}{2},0,\frac{1}{2};\ \frac{1}{2},\frac{1}{2},0)+0,0,0$ and $\frac{1}{4},\frac{1}{4},\frac{1}{4}$, and four antimony and four rubidium atoms occupy at random other positions at $(0,0,0;\ 0,\frac{1}{2},\frac{1}{2};\ \frac{1}{2},0,\frac{1}{2};\ \frac{1}{2},\frac{1}{2},0)+\frac{1}{2},\frac{1}{2},\frac{1}{2}$ and $\frac{3}{4},\frac{3}{4},\frac{3}{4}$. The crystal structure factors are

$$F = 4(f_{Sb} + 3f_{Rb})$$

$$\text{for } h, k, l \text{ all even and } h+k+l = 4n\ ,$$

$$F = 0$$

$$\text{for } h, k, l \text{ all even and } h+k+l = 4n+2\ ,$$

and

$$F = \sqrt{8}\,(f_{Sb} - f_{Rb})$$

$$\text{for } h, k, l \text{ all odd}\ .$$

The calculated spacings and intensities of the reflections for this structure are in good agreement with the observed values (see Table I).

Gnutzmann[2] reported that Cs_3Sb has the structure of Cu_3Al type. Scheer and Zalm[2]

Table I. Calculated and observed X-ray data with CuKα radiation for the cubic phase of Rb_3Sb. ($a=8.84\pm0.02$ Å)

d obs.	*d* calc.	*h.k.l.*	Int.*) calc.	Int. obs.
—	5.11	111	0.9	—
—	4.42	200	0	—
3.08	3.13	220	100	v.s.
2.63	2.67	311	0.7	w.
—	2.55	222	0	—
2.19	2.21	400	18.4	m.s.
2.01	2.05	331	0.3	w.
—	1.98	420	0	—
1.79	1.80	422	37.9	s.
1.69	1.70	333+511	0.2	w.
1.55	1.56	440	11.5	m.
1.48	1.49	531	0.2	v.w.
—	1.47	442+600	0	—
1.39	1.40	620	15.4	m.
1.36	1.35	533	0.07	v.w.
—	1.33	622	0	—
1.27	1.28	444	3.7	v.w.
1.24	1.24	551+711	0.11	v.w.
—	1.23	640	0	—
1.17	1.18	642	18.0	m.
1.14	1.15	553+731	0.14	v.w.
1.10	1.11	800	2.0	v.w.
1.08	1.08	733	0.05	v.w.
—	1.07	644+820	0	—
1.04	1.04	660+822	10.2	w.m.
1.02	1.02	555+751	0.09	v.w.
—	1.014	662	0	—
0.986	0.989	840	6.4	v.w.
0.968	0.971	753+911	0.11	v.w.
—	0.964	842	0	—
0.940	0.942	664	6.4	w.
0.927	0.927	931	0.09	v.w.
0.902	0.903	844	6.6	w.
0.889	0.889	755+771+933	0.12	v.w.
0.865	0.870	862+10,20	21.9	w.
0.853	0.855	773+951	0.13	v.w.

*) The intensities were corrected for Lorentz-polarization factors, and not for absorption and temperature factor.

expected the ordered Cu_3Al-type structure to be the stable modification of Cs_3Sb and the disordered structure of proposed by Jack and Wachtel to be an unstable modification and suggested that this might account for the observations that a prolonged heating of photocathodes resulted in an irreversible decrease in photosensitivity. It is important to determine whether the photosensitive film has an ordered or a disordered structure. In Cu_3Al type, four antimony atoms are situated at $(0, 0, 0;\ 0, \frac{1}{2}, \frac{1}{2};\ \frac{1}{2}, 0, \frac{1}{2};\ \frac{1}{2}, \frac{1}{2}, 0)$ and twelve rubidium atoms at $(0, 0, 0;\ 0, \frac{1}{2}, \frac{1}{2};\ \frac{1}{2}, 0, \frac{1}{2};\ \frac{1}{2}, \frac{1}{2}, 0)$ $+\frac{1}{2}, \frac{1}{2}, \frac{1}{2};\ \frac{1}{4}, \frac{1}{4}, \frac{1}{4};$ and $\frac{3}{4}, \frac{3}{4}, \frac{3}{4}$, and the crystal structure factors are

$$F=4(f_{\mathrm{Sb}}+3f_{\mathrm{Rb}})$$

for h, k, l all even and $h+k+l=4n$,

$$F=4(f_{\mathrm{Sb}}-f_{\mathrm{Rb}})$$

for h, k, l all even and $h+k+l=4n+2$,

and

$$F=4(f_{\mathrm{Sb}}-f_{\mathrm{Rb}})$$

for h, k, l all add .

It was impossible to observe the reflection lines for which $h+k+l=4n+2$ with h, k, l all even, notwithstanding that the intensities of the reflections with h, k, l all odd were observed (see Table I). Consequently, it does not seem to be proper to consider the structure of the cubic phase of Rb_3Sb as Cu_3Al-type.

Recently, Zhuravlev, Smirnov and Mingazin[4] reported that Rb_3Sb has the structure of Na_3As type (Fig. 5 (C)). This agrees with our result for the hexagonal phase of Rb_3Sb. (The photograph of Fig. 4 (B) give the lattice constants: $a=6.32\pm0.02$ Å, $c=11.19\pm0.02$ Å).

Electrical properties

Imamura[5] found several facts from observation of the sign of the thermo-electromotive force during the preparation: In Cs–Sb, the sign is always negative, indicating that positive charge carriers are predominant, but in K–Sb and Na–Sb the transition from *p*-type to *n*-type takes place just after, or in some case even before, the peak resistance has been attained. In Rb–Sb, this transition occurs rather later than the former two. He also suggested that the transition from *n*-type to *p*-type is associated with the structure change from the amorphous to the hexagonal or from the cubic to the hexagonal, and that rubidium antimonide has either the cubic or the hexagonal phase.

In order to examine whether the structures are responsible for the electrical properties, the X-ray photographs of Cs–Sb, K–Sb and Na–Sb were taken by the method as described in § 2. The sign of thermo-electromotive force was also observed. In Cs–Sb, the transition from the amorphous to the cubic phase took place by supplying cesium and the transition to hexagonal phase did not appear by supplying cesium furthermore, and the sign was always negative. In K–Sb and Na–Sb, the transition from amorphous to hexagonal phase (Na_3As type) took place after attaiment to the peak resistance and the transition from *p*-type to *n*-type. In this case, the cubic phase was not observed. In Rb–Sb, the transition from *p*-type to *n*-type took place in the cubic phase containing the hexagonal phase. These results are almost in agrement with the Imamura's suggestions. It may be concluded that an alkali antimonide of the amorphous or cubic phase is a *p*-type semiconductor and of the hexagonal phase is an *n*-type one.

The space among the atoms in the hexagonal lattice is larger than that in the cubic lattice, as seen from Table II. The excess alkali atoms can be easily accommodated at the interstitial positions in the hexagonal lattice and act as donors. On the other hand, the cubic lattice cannot accommodate so many excess alkali atoms at the interstitial position that the cubic phase indicate an *n*-type conduction. This can be seen from the fact that the cubic lattice of Rb_3Sb is transformed into the hexagonal one by diffusing rubidium in a large quantity. The excess alkali atoms in the cubic lattice may occupy the Sb sites to indicate *p*-type conduction, because such substitution is possible to a certain extent in the disordered lattice as shown in Fig. 5 (A). The transition from the cubic phase to the hexagonal one is prohibited for Cs_3Sb. This may be assigned to the large ionic radius of Cs atom. In fact, although we also prepared a specimen of Cs–Sb by evaporating antimony at 180°C in a glass tube which was filled with Cs vapour, the hexagonal phase was not observed. In this case, excess Cs atoms may initially occupy Sb sites substitutionally. The more excessive cesium may deposit on the wall of the glass envelope or on the surface of the specimen.

Table II. Comparison of the hexagonal and the cubic phase in Rb_3Sb.

Crystal type	Lattice constants (Å)		Density g/cm³	Small distance (Å)		
	a	*c*		Sb–Sb	Sb–Rb	Rb–Rb
Hexagonal	6.32	11.19	3.25	6.32	3.65	3.73
Cubic	8.84		3.64	3.83	3.83	3.83

The diameter of the halo in Fig. 3 (A) agrees with that of the strongest diffraction line of Rb_3Sb. Probably, owing to deficiency in the quantity of rubidium, grains could not grow so large in size that they gave the sharp diffraction lines. The origin of the *p*-type conduction in the amorphous state in all kinds alkali antimonides may be assigned to vacancies of alkali atoms in such tiny grains.

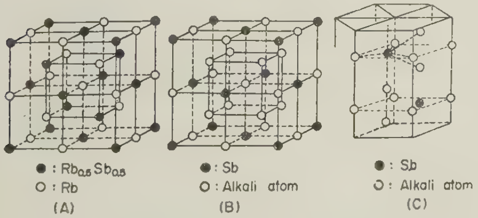

Fig. 5. Unit cells of alkali antimonides. (A): Unit cell of the cubic phase of Rb_3Sb (the same as the unit cell of Cs_3Sb according to Jack and Wachtel). (B): Unit cell of Cu_3Al type (unit cell of Cs_3Sb according to Guntzmann). (C): Unit cell of Na_3As type (unit cell of Na_3Sb, K_3Sb and the hexagonal phase of Rb_3Sb).

§ 4. Discussion

Although many specimens of Rb_3Sb were prepared, we could not make a specimen of the cubic phase which contained no hexagonal phase, so that we could not show experimentally with the pure specimen of the cubic phase that the cubic phase is a *p*-type semiconductor. However, the transition from *p*-type to *n*-type in Rb–Sb occurs rather later than that in K–Sb and Na–Sb in the process of activation with alkali and Cs_3Sb has the cubic structure and is a *p*-type semiconductor. These facts seem to support the conclusion that the cubic phase of Rb_3Sb is a *p*-type semiconductor.

A thick film of the specimen was necessary to obtain X-ray photographs with sharp diffraction patterns. But, in a thick specimen (few microns), the transition of the structure in the process of preparation occurred considerably later than the transition from *n*-type to *p*-type and attainment to the peak resistance. This might be due to the fact that the reaction between alkali metal and antimony proceeded rapidly at the surface of the film and the surface layer of the film had a considerable effect on the electrical properties of the specimens. Therefore, it was desirable to make the specimens as thin as possible. In fact, even with the semi-transparent specimens clear diffraction patterns were obtained, using a thin mica window. It is probable that the specimen containing both the cubic and the hexagonal phase has layer of the hexagonal phase near the surface.

Jack and Wachtel[3)] made X-ray specimens of Cs_3Sb by reaction at 200°∼210°C between antimony powder and cesium vapour, and reported that many specimens gave X-ray photographs with a high background intensity and only one or two broad and diffuse reflexions at low Bragg angle. But we obtained a clearer cubic diffraction pattern with the specimens of Cs_3Sb that were prepared by reaction at 180°C between evaporated thin antimony films and cesium vapour and were not annealed after reaction. This shows that cesium may not easily diffuse into antimony and a highly crystalline specimen of Cs_3Sb can be prepared by diffusing sufficiently cesium into antimony. Therefore, it may be noted that such a thin film of Cs–Sb as a practical photocathode with the maximum photosensitivity just after the establishment of a maximum resistance has the cubic structure, though the relation between the photoemissive properties and the crystal structure is not the main subject in the present work.

Acknowledgements

The authors wish to express their sincere thanks to Dr. H. Kuroda and Dr. H. Mitsuhashi for their continued guidances and encouragements throughout this work, and to Mr. H. Horie for his valuable and kind assistance.

References

1) G. Brauer and E. Zintl: Z. Phys. Chem. **B**, **37** (1937) 323.
2) G. Gnutzmann: Diss., München (1953). Gnutzmann's results have been referred by J. J. Scheer and P. Zalm in Philips Res. Reports **14** (1959) 143.
3) K. H. Jack and M. M. Wachtel: Proc. Roy. Soc. **A**, **349** (1957) 46.
4) N. N. Zhuravlev, V. A. Smirnov and T. A. Mingazin: Sov. Phys. Cryst. **5** (1960) 124.
5) S. Imamura: J. Phys. Soc. Japan **14** (1959) 1491.

JOURNAL OF THE PHYSICAL SOCIETY OF JAPAN, Vol. 16, No. 6, JUNE, 1961

Weak Ferromagnetism in β-NaFeO$_2$

By Hiroshi WATANABE
The Research Institute for Iron, Steel and Other Metals, Tohoku University, Sendai
and Masahiro FUKASE
Konishiroku Photo Industries Company, Limited, Hino-machi, Tokyo

(Received March 3, 1961)

The high temperature modification of sodium ferrite, β-NaFeO$_2$, has weak ferromagnetism, whose Curie temperature is about 450°C. The magnetic property resembles that of LaFeO$_3$. The origin of weak ferromagnetism of β-NaFeO$_2$ can be attributed to the presence of the Dzyaloshinsky type interaction in this compound.

§ 1. Introduction

It is known from the works of French researchers[1)–5)] that sodium ferrite, NaFeO$_2$, crystallizes in two modifications: (1) the low-temperature- or α-modification which is rhombohedral with the space group D_{3d}^5-$R\bar{3}m$[1)], and (2) the high-temperature- or β-modification which is orthorhombic with the space group C_{2v}^9-Pna[2)]. In the present work, thermomagnetic study was made with β-NaFeO$_2$, and it was found that this substance shows weak ferromagnetism when cooled in a magnetic field from temperatures above 500°C. The magnetic property is like that found in LaFeO$_3$ which was studied previously[6)]. The origin of this weak ferromagnetism can be interpreted on the basis of symmetry consideration as due to the presence of the Dzyaloshinsky type interaction[7)] in the compound.

§ 2. Experimental

2.1. *Experimental Procedure*

Powders of Na$_2$CO$_3$ and α-Fe$_2$O$_3$ of average particle size of 0.5 μ in diameter were mixed in the desired proportions, ground in an agate mortar, and sintered at 900°C for 20 hrs in air. The sintered products thus obtained were more stable at room temperature than those with shorter sintering periods. Unstable products were subject to hydration in moist air. Sintering above 1000°C caused sticking of the molten samples to the crucibles.

X-ray powder diffraction patterns were taken of the samples with varying ratios of Na to Fe. Samples ware vacuum-sealed in thin glass tubes.

Samples for thermomagnetic measurements were made in a form of a rectangular prism, 4 mm × 4 mm × 8 mm in size, and were supported by platinum wires, whose one end was buried tight in the sample. Sample mounting as well as the magnetic measurements were made as fast as possible after sintering since even the well-reacted samples were apt to be attacked by moisture.

2.2. *Crystallographic Study*

Fig. 1 shows schematically the positions and intensities of the observed lines on powder photographs. It is seen that samples with $0.9 \leqslant x \leqslant 1.1$ (x denotes Na content: Na$_x$Fe$_{2-x}$O$_{3-x}$) have essentially the same crystal structure, which should correspond to the β-NaFeO$_2$ structure. The pattern was compatible with the structure given by Bertaut and Blum[2)],

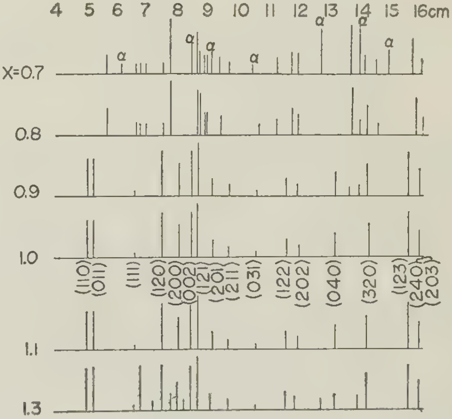

Fig. 1. Schematical representation of the powder diffraction parterns of sintered products of mixtures of Na$_2$CO$_3$ and α-Fe$_2$O$_3$. The abscissa represent the distance between lines of given indices. x stands for the value in the formula Na$_x$Fe$_{2-x}$O$_{3-x}$. Lines with the label α are pertinent to α-Fe$_2$O$_3$. Camera diameter: 114.6 mm. Radiation: FeKα. $x=0.8$ corresponds to 2Na$_2$O$_3$-3Fe$_2$O$_3$, and $x=1.0$ to β-NaFeO$_2$.

except for a small difference in lattice constants from theirs (the present data: $a=5.65$ Å, $b=7.13$ Å, $c=5.37$ Å). Observed and calculated line intensities of β-NaFeO$_2$ are listed in Table I.

Table I. Interplanar distance, d, and observed and calculated line intensities of β-NaFeO$_2$.

No.	(hkl)	d_{obs}	d_{cal}	I_{obs}	I_{cal}
1	110	4.43	4.43	s	54
2	011	4.27	4.29	s	47
3	020	—	3.57	—	0
4	111	3.40	3.42	w	13
5	120	3.02	3.02	vs	77
6	200	2.83	2.83	s	30
7	002	2.68	2.68	vs	55
8	121	2.63	2.63	vs	99
9	210	—	2.63	—	1
10	201	2.48	2.50	m	38
11	211	2.36	2.36	m	7
12	112	—	2.29	—	3
13	220	—	2.22	—	0
14	130	—	2.20	—	3
15	031	2.17	2.18	w	6
16	022	—	2.14	—	1
17	221	—	2.05	—	1
18	131	—	2.03	—	2
19	122	2.00	2.00	m	23
20	202	1.93	1.94	m	7
	040	1.78	1.78	m	22
	320	1.66	1.66	s	32
	123	1.54	1.54	s	39
	203 240	1.50	1.51	m	11

For $x=0.8$, there appears a new structure. The composition corresponds approximately to 2Na$_2$O3Fe$_2$O$_3$. According to Collongues and Thery[3], the compound of this composition has a tetragonal structure, and our data are in rough accord with theirs. Samples with $x \leq 0.7$ are mixtures of 2Na$_2$O3Fe$_2$O$_3$ and α-Fe$_2$O$_3$.

For $x \geq 1.3$, additional lines are superposed on the pattern of β-NaFeO$_2$. It is not yet clear whether these lines are due to admixing of a different phase or they are some superlattice lines of the original β-NaFeO$_2$ structure.

2.3. *Magnetic Study*

Thermomagnetic measurements were made of three samples, with $x=1.0$, 1.1 and 0.7. Figs. 2 (a) and (b) show specific magnetization *vs* temperature curves of the samples with $x=1.0$ and 1.1, respectively. The Curie temperature of these samples are 450°C and 550°C, respectively. The dotted curve in (b) seems to indicate that for this sample treating field of 6800 Oe is not sufficiently strong to produce full remanence.

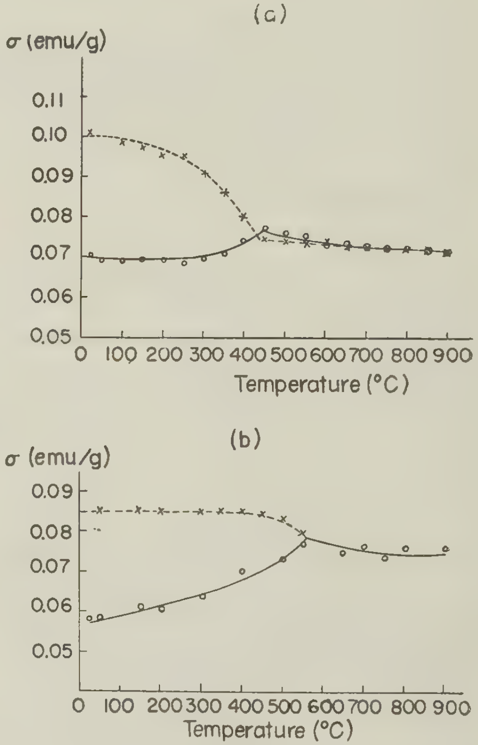

Fig. 2. Specific magnetization σ against temperature of (a) NaFeO$_2$ and (b) Na$_{1.1}$Fe$_{0.9}$O$_{1.9}$. Solid curve: not field-cooled. Dotted curve: cooled from temperatures above 550°C in a field of 6800 Oe. Measuring field: 6800 Oe.

As in LaFeO$_3$, the field-cooled sample has a magnetization *vs* field curve displaced along the magnetization axis. This is shown in Fig. 3. The displacement, however, is very small as compared with the case of LaFeO$_3$. The relation between the remanent magnetization (σ_r) and the field applied during cooling (H_t) is shown in Fig. 4. As is seen from the figure, σ_r is roughly proportional to the square root of H_t. According to Néel's theory of thermoremanent magnetization[8], this behavior corresponds to the case of fine grains with very high coercive force.

Fig. 5 shows the result of the thermomagnetic measurement on a sample with $x=0.7$. As was stated in 2.2, this sample is a mixture of $2Na_2O3Fe_2O_3$ and α-Fe_2O_3. The anomaly in the curve near 650°C may probably corresponds to the Curie temperature of α-Fe_2O_3.* Then the peak at 100°C may be identified with the critical temperature of antiferromagnetic $2Na_2O3Fe_2O_3$.

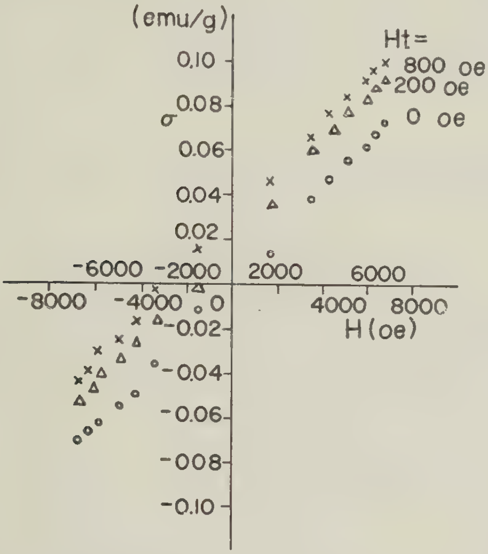

Fig. 3. Specific magnetization (σ) *vs* field (H) curves of field-cooled and not-field-cooled specimens of β-$NaFeO_2$ (at room temperature). H_t: the field during cooling.

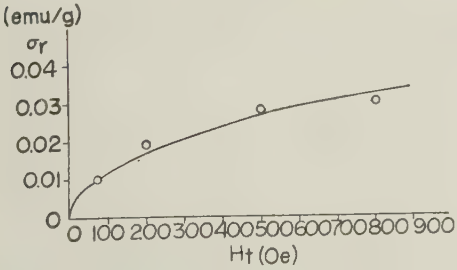

Fig. 4. Thermoremanent magnetization (σ_r) against field applied during cooling (H_t) of β-$NaFeO_2$.

§ 3. Discussion

As was shown in § 2, β-$NaFeO_2$ shows weak ferromagnetism, and it resembles $LaFeO_3$ in that the σ *vs* H curve is shifted along the magnetization axis if it is cooled from temperatures above the Curie temperature of weak ferromagnetism. It has become more and more confirmative that $LaFeO_3$, together with other earth orthoferrites[9], is an intrinsically non-compensating antiferromagnetic because of an angular coupling between almost antiferromagnetically arranged spins. We shall now discuss the possibility of a similar interpretation of weak ferromagnetism in β-$NaFeO_2$.

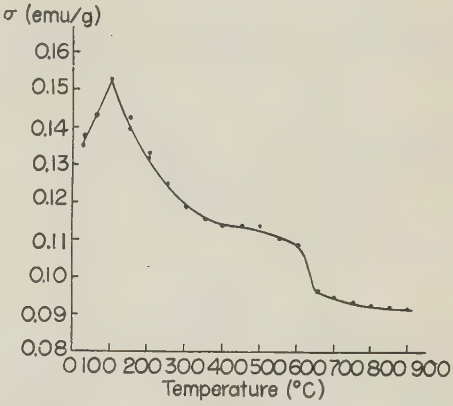

Fig. 5. Specific magnetization (σ) against temperature of $Na_{0.7}Fe_{1.3}O_{2.3}$.

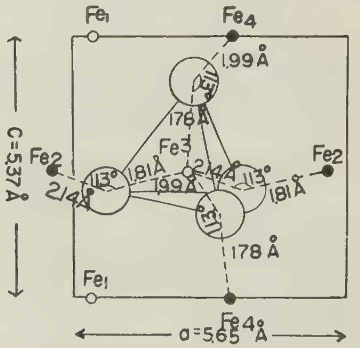

Fig. 6. Environment of an Fe^{3+} ion in β-$NaFeO_2$ structure projected on the *ac*-plane. Large (white) circle: O^{2-} ion. Small white circle: Fe^{3+} ion with + spin. Small black circle: Fe^{3+} ion with − spin.

First of all, Fe^{3+} ions in β-$NaFeO_2$ from a distorted simple monoclinic lattice, so that an antiferromagnetic spin lattice can be formed with antiparallel spin arrangement between near-neighboring Fe^{3+} ions. Each Fe^{3+} ion has four Fe^{3+} neighbors (see Fig. 6). All of them are separated from the central Fe^{3+} ion by intervening O^{2-} ions. Interionic distances and angles Fe–O–Fe are given in the figure. As can be seen, from the figure neighbors of Fe_1 (or Fe_3) are Fe_2 and Fe_4, and those of Fe_2 (or Fe_4) are Fe_1 and Fe_3.

The structure has four screw axes parallel to the c-axis, two planes of gliding reflection n, and two other planes of gliding reflection a. Consideration of these symmetry elements leads to the following relation between the components of $\boldsymbol{S}_i$ (for numbering of spins, see Fig. 6):

---

* Supplementary measurements revealed that this anomaly was absent in a sample with $x=0.8$.

$$\left.\begin{array}{lll} S_{2x}=-\varepsilon S_{1x}\,, & S_{2y}=-\varepsilon S_{1y}\,, & S_{2z}=\varepsilon S_{1z}\,, \\ S_{3x}=-\varepsilon' S_{1x}\,, & S_{3y}=\varepsilon' S_{1y}\,, & S_{3z}=\varepsilon' S_{1z}\,, \\ S_{4x}=\varepsilon\varepsilon' S_{1x}\,, & S_{4y}=-\varepsilon\varepsilon' S_{1y}\,, & S_{4z}=\varepsilon\varepsilon' S_{1z}\,, \end{array}\right\} \tag{1}$$

where ε and ε' take the values ±1. The components of the net moment vector

$$\boldsymbol{m}=\boldsymbol{S}_1+\boldsymbol{S}_2+\boldsymbol{S}_3+\boldsymbol{S}_4$$

can be written as:

$$\left.\begin{array}{l} m_x=(1-\varepsilon)(1-\varepsilon')S_{1x}\,, \\ m_y=(1-\varepsilon)(1+\varepsilon')S_{1y}\,, \\ m_z=(1+\varepsilon)(1+\varepsilon')S_{1z}\,. \end{array}\right\} \tag{2}$$

As mentioned above, $\boldsymbol{S}_1$ and $\boldsymbol{S}_2$ (or $\boldsymbol{S}_3$ and $\boldsymbol{S}_4$) should be nearly antiparallel to each other, while $\boldsymbol{S}_1$ and $\boldsymbol{S}_3$ (or $\boldsymbol{S}_2$ and $\boldsymbol{S}_4$) are parallel, so that the vector

$$\boldsymbol{l}=\boldsymbol{S}_1-\boldsymbol{S}_2+\boldsymbol{S}_3-\boldsymbol{S}_4$$

should have a non-zero absolute value. From (1) it follows that:

$$\left.\begin{array}{l} l_x=(1+\varepsilon)(1-\varepsilon')S_{1x}\,, \\ l_y=(1+\varepsilon)(1+\varepsilon')S_{1y}\,, \\ l_z=(1-\varepsilon)(1+\varepsilon')S_{1z}\,. \end{array}\right\} \tag{3}$$

The case $\varepsilon=\varepsilon'=-1$ is inhibited, because, then, all of the components of $\boldsymbol{l}$ in (3) vanish. Hence we have three cases:

1. $\varepsilon=1$, $\varepsilon'=-1$.

From (3) we have $l_x=4S_{1x}$ and $l_y=l_z=0$ so that the approximate spin direction lies along the a-axis. From (2) $m_x=m_y=m_z=0$ and no net moment appears.

2. $\varepsilon=1$, $\varepsilon'=1$.

$l_x=l_z=0$ and $l_y=4S_{1y}$, so that the approximate spin direction lies along the b-axis. From (2) $m_x=m_y=0$, $m_z=4S_{1z}$ and a small moment appears in the c-direction.

3. $\varepsilon=-1$, $\varepsilon'=1$.

$l_x=l_y=0$ and $l_z=4S_{1z}$, so that the approximate spin direction lies along the c-axis. $m_x=m_z=0$, $m_y=4S_{1y}$ and a small moment appears in the b-direction.

The origin of these non-vanishing net moments may by the Dzyaloshinsky type interaction $\boldsymbol{D}_{ij}[\boldsymbol{S}_i \times \boldsymbol{S}_j]$[7]. The following relation holds between the components of $\boldsymbol{D}_{ij}$'s:

$$\begin{array}{lll} D_{12}(u_x, u_y, 0) & D_{13}(0, v_y, v_z) & D_{14}(-w_x, 0, w_z) \\ & D_{23}(w_x, 0, w_z) & D_{24}(0, -v_y, v_z) \\ & & D_{34}(u_x, -u_y, 0)\,. \end{array}$$

Of these only u_x and w_x are responsible for producing net moments.

Acknowledgements

The authors are indebted to Professor T. Nagamiya and Dr. K. Motizuki of Osaka University for stimulating discussions. One of the authors (M. F.) expresses his thanks to Professor T. Hirone of Tohoku University for providing the facilities to carry out this study in Hirone's laboratory and to Konishiroku Photo Industuries Company for fellowship aid. A part of the expenditure of this study has been defrayed from the Scientific Research Funds of the Ministry of Education.

References

1) S. Goldsztaub: Compt. rend. **196** (1933) 280.
2) F. Bertaut and P. Blum: Compt. rend. **239** (1954) 429.
3) R. Collongues and J. Thery: Bull. soc. chim. **7-8** (1959) 1141.
4) J. Thery and R. Collongues: Bull. soc. chim. **7-8** (1959) 1144.
5) J. Thery and R. Collongues: Compt. rend. **250** (1960) 1070.
6) H. Watanabe: Sci. Rept. RITU **A8** (1956) 14. G. H. Jonker: Physica **22** (1956) 707. H. Watanabe: J. Phys. Soc. Japan **14** (1959) 511.
7) I. E. Dzyaloshinsky: Sovj. Phys. JETP **5** (1957) 1259. T. Moriya: Phys. Rev. **120** (1960) 91.
8) L. Néel: Advances in Physics **4** (1955) 191.
9) R. M. Bozorth: Phys. Rev. Letters **1** (1958) 362.

JOURNAL OF THE PHYSICAL SOCIETY OF JAPAN Vol. 16, No. 6, JUNE, 1961

The Crystal Structure of Chloranil and Bromanil

By Ikuhiko UEDA

General Education Department, Kyushu University, Japan

(Received January 6, 1961)

The Crystal structure of chloranil and bromanil has been determined by X-ray diffraction technique based on the two-dimensional Fourier analysis. Chloranil and bromanil are isomorphous. The cell constants are: $a_0=8.86_2$, $b_0=5.83_7$, $c_0=8.76_3$Å, $\beta=72.6°$ for chloranil and $a_0=8.62_4$, $b_0=6.17_3$, $c_0=9.02_7$Å, $\beta=74.2°$ for bromanil. There are two molecules in the unit cell and the space group is $P\ 2_1/a\ (C_{2h}^5)$. The crystal consists of two layers of substituted halogen atoms which are parallel to the (001) plane, and the skeletons consisting of oxygen and carbon atoms lie between these two layers. The juxtaposition of molecules is such that the dipole interactions between C=O bonds stabilize the structure. There is definite localization of the double bonds in the benzene ring. In the molecule the adjacent halogen and oxygen atoms protrude respectively up and down from the plane of the benzene ring making a puckered form. The thermal motions of the molecules in this crystal have been analysed from the anisotropic thermal parameters of chlorine and oxygen atoms. A theoretical analysis shows that the puckered form is more stable, as a molecule, than the planar form. A clear correspondence is found between this fact and the anisotropic thermal motions of Cl and O atoms.

§ 1. Introduction

Although the molecular shapes of *p*-benzoquinone and its derivatives are symmetrical, they have small but definite values of atomic polarization. Hammick and Coop[1] suggested that this fact was due to the bending effect of the molecule. If it be so, molecules in the crystals may be bended much more by the crystalline field. These effects may become clear by a accurate determination of their crystal structures.

The crystal structure of *p*-benzoquinone was determined by Robertson and Trotter[2]. If this structure is compared to that of chloranil and bromanil, the influence of substitution by halogen atoms to the C=O bond may be estimated. Due to the large size of the halogen atoms the distortion of C=O bonds is expected to be discernible.

Harding and Wallwork[3] determined the crystal structure of the chloranil-hexamethylbenzene complex. According to their results, the oxygen atom and its adjacent two chlorine atoms in the chloranil molecule protruded in the same direction from the plane of the carbon skeleton.

In this paper the detailed crystal structure of chloranil and bromanil will be reported. The structure of chloranil was determined in details which enabled us to discuss the structure of the molecule.

§ 2. Experimental

Both chloranil and bromanil were purified by recrystallizing from saturated benzene solution. Single crystals suitable for X-ray diffraction work were obtained by crystallizing from benzene solution at about 30°C.

The X-ray absorption coefficients of bromanil are $\mu_{\mathrm{Cu}K\alpha}=217\ \mathrm{cm}^{-1}$, $\mu_{\mathrm{Mo}K\alpha}=188\ \mathrm{cm}^{-1}$ and those of chloranil are $\mu_{\mathrm{Cu}K\alpha}=121\ \mathrm{cm}^{-1}$, $\mu_{\mathrm{Mo}K\alpha}=14\ \mathrm{cm}^{-1}$. To minimize the effect of absorption, in the case of bromanil, single crystals were cut and polished to form cylindrical rods 0.2 mm in diameter. The softness and cleavage of these crystals made it very difficult to obtain good samples. Therefore, some systematic error in the intensity data was unavoidable. In the case of chloranil the absorption correction was neglisibly small for Mo*Kα* since we used crystals having a diameter about 0.2 mm.

For the structure determination a complete set of relative intensity for (0*kl*), (*h*0*l*) and (*hk*0) was obtained by integrating Weissenberg goniometer. For chloranil Mo*Kα* radiation and for bromanil Cu$K\alpha$ radiation were used. The relative intensities of reflexions on Weissenberg photographs obtained by the multiple-film technique were measured by visual comparison with an intensity scale.

The crystals were often found twinned in the (001) plane. The temperature factor was fairly large and the reflexions over $\sin\theta/\lambda = 0.8$ Å^{-1} could not be observed. The diffuse scattering was often observed in the cut and polished crystals.

The crystals are monoclinic and the unit cell dimensions determined from high angle reflexions on Weissenberg photographs are:

$$a_0 = 8.86_2 \pm 0.02_5, \quad b_0 = 5.83_7 \pm 0.01_6,$$
$$c_0 = 8.76_3 \pm 0.02_5 \text{ Å}, \quad \beta = 72.6° \pm 0.4°$$
for chloranil

$$a_0 = 8.62_4 \pm 0.01_2, \quad b_0 = 6.17_3 \pm 0.00_9,$$
$$c_0 = 9.02_7 \pm 0.01_3 \text{ Å}, \quad \beta = 74.2° \pm 0.4°$$
for bromanil.

The space group is $P2_1/a$ (C_{2h}^5). The density determined by the floatation method is 1.67 g/c.c. for chloranil and is 3.02 g/c.c. for bromanil. Since the general position in $P2_1/a$ is fourfold and the unit cell contains only two molecules, the centres of gravity of the molecules should occupy a set of twofold special positions. Thus each molecule displays a centre of symmetry in the crystal. Therefore it is clear that their atomic polarization is not due to the asymmetry of the molecules. Since the diffracted intensities of chloranil and bromanil show the same behaviour, both crystals are isomorphous.

§ 3. Structure Determination

From the Patterson maps of the b-projection and a-projection the positions of the heavy atoms were determined. Then the structure factors were calculated with a few models in which the carbon and oxygen skeleton was placed in addition to these heavy atoms. It was possible to arrive at a model which gave fairly good agreement between $F_{cal.}$ and $F_{obs.}$. This was done first with bromanil. In the case of chloranil the model obtained for bromanil was adopted as a starting point.

§ 4. Refinement

In the earlier stage the refinement was repeated by Fourier syntheses. Then, it was followed by subsequent (F_0–F_c) syntheses. In the later stage the thermal anisotropy of heavy atoms and oxygen atom was taken into account. In the structure factor calculation the atomic scattering factors were taken from McWeeny[4] for the light atoms, those from Tomiie and Stam[5] for chlorine, and those from James and Brindly[6] for bromine.

From the ($\rho_0 - \rho_c$) maps the corrections for atomic co-ordinates Δr were estimated by the equation:

$$\Delta r = [d(\rho_0 - \rho_c)/dr]_{r=0} / 2p\rho(0) ,$$

where $\rho(0)$ is the electron density at an atomic centre and p is a constant whose value is deduced from the Fourier map by the equation:

$$\rho(r) = \rho(0) \exp(-pr^2) .$$

The values of $2p\rho(0)$ given by Burbank[7] were used in this refinement but the results of corrections with his values showed some tendency of overestimation.

At this stage of refinement, the temperature factors for each atom were introduced according to the method suggested by Atoji[8] and modified by Sasada[9]. In the final stage

Table I. Final atomic parameters and temperature factors of chloranil.

	x/a	y/b	z/c	a-projection			b-projection			c-projection		
				ψ_c	B	Δ	ψ_a	B	Δ	ψ_a	B	Δ
Cl_1	0.4759	0.7267	0.1778	$-120^\circ.5$	5.19	2.06	$+6^\circ.1$	6.06	1.81	$+100^\circ.3$	5.57	0.06
Cl_2	0.6917	0.2812	0.1707	-59.9	5.03	1.76	$+53.2$	5.75	1.19	-95.3	5.05	0.75
O	0.3307	0.8940	0.5075	$+4.7$	6.54	3.75	-73.0	7.88	3.61	$+65.0$	3.53	1.23
C_1	0.0938	0.2100	0.4972	—	4.50	—	—	6.25	—	—	2.17	—
C_2	0.4973	0.5952	0.3493	—	2.90	—	—	4.81	—	—	1.71	—
C_3	0.0810	0.0933	0.3490	—	3.20	—	—	4.90	—	—	2.55	—

the thermal anisotropy of chlorine and oxygen atoms was taken into account by the method suggested by Schomaker[10] which was modified for the two-dimensional case. By this correction the disagreement factor for each projection was reduced by 2~3% and the positions of light atoms were adjusted slightly. Since in this paper the author wants to discuss small distortion of the C=O bond, even this slight influence should be taken seriously.

Table II. Final atomic parameters and temperature factors of bromanil.

	x/a	y/b	z/c
Br_1	0.4685	0.7203	0.1812
Br_2	0.6970	0.2822	0.1702
O	0.3199	0.8081	0.5087
C_1	0.0983	0.1638	0.4953
C_2	0.4913	0.5634	0.3571
C_3	0.0840	0.0620	0.3505

a-projection $\boldsymbol{B}=6.2$
b-projection $\boldsymbol{B}=6.5$
c-projection $\boldsymbol{B}=5.5$.

The final atomic parameters and temperature factors are shown in Tables I and II. In Table I each atom is assumed to have its stationary scattering factor multiplied by a temperature factor,

$$\exp-[B-\varDelta\sin^2(\phi-\psi)](s/2)^2\ ,$$

where $\boldsymbol{B}$ and $\varDelta$ are constants, ψ is the angle between the direction of maximum vibration and the c^* or a^* axis and $(2s,\ \phi)$ are the polar co-ordinates of a point in each projection plane of the reciprocal lattice. The final structure factors F_{0kl}, F_{h0l} and F_{hk0} are shown in Tables III and IV. The F_0 values have been put on the same scale as the F_c values by making the value of $\sum||F_0|-|F_c||$ minimum. Fig. 1 (a) shows the final *b*-projection of electron density and Fig. 1 (b) shows the *b*-projection of $(\rho_0-\rho_c)$ at the step $R_{h0l}=0.15$.

The disagreement factors $R=\sum||F_0|-|F_c||/\sum|F_0|$ for the refined projections, excluding all reflexions too weak to be observed, are shown below:

$$R_{0kl}=0.09,\ R_{h0l}=0.13,\ R_{hk0}=0.10$$
for chloranil,

$$R_{0kl}=0.13,\ R_{h0l}=0.15,\ R_{hk0}=0.22$$
for bromanil.

Table III. Observed and calculated structure factors for chloranil. In the columns of $F_0/2$ the signs "<" indicate none observed structure factors.

$h\ k$	l	$F_0/2$	$F_c/2$
0 0	1	9.28	10.05−
	2	19.23	16.02−
	3	48.12	47.37−
	4	10.68	7.68−
	5	13.35	10.62
	6	30.64	30.10
	7	5.88	4.49−
	8	7.33	7.09−
	9	8.50	8.54−
	10	<1.80	0.48
	11	2.72	4.66
	12	2.23	3.64
0 1	1	<0.68	0.28
	2	<0.78	0.22−
	3	4.37	3.71−
	4	<1.07	0.00
	5	<1.17	0.73
	6	3.69	3.19
	7	<1.41	0.07
	8	<1.55	1.24−
	9	<1.70	1.83−
	10	<1.89	0.03
	11	<1.94	0.76
	12	<2.04	0.86
0 2	0	38.41	40.50−
	1	17.82	18.12−
	2	17.29	16.81
	3	36.52	37.65
	4	<1.17	4.14
	5	13.84	12.96−
	6	14.67	15.65−
	7	<1.51	2.88−
	8	7.72	7.86
	9	7.77	8.28
	10	<1.85	1.06−
	11	<1.99	3.05−
	12	<2.09	2.45−
0 3	1	1.55	1.28−
	2	<1.22	0.06−
	3	<1.17	0.01
	4	<1.26	1.57
	5	<1.36	0.58−
	6	<1.46	0.26−
	7	<1.55	0.85−
	8	<1.70	0.29−
	9	<1.80	0.51
	10	<1.89	0.33
	11	<2.04	0.27−
	12	<2.14	0.18−
0 4	0	7.67	8.38
	1	11.85	12.62
	2	10.63	9.55−
	3	12.95	14.31−
	4	<1.41	2.78−
	5	8.98	8.28
	6	4.90	5.67
	7	<1.70	3.27
	8	5.00	5.04−
	9	3.35	4.69−
	10	2.81	0.89
	11	<2.09	0.32
0 5	1	<1.46	0.82
	2	<1.46	1.33
	3	<1.51	0.36
	4	<1.55	0.64−
	5	<1.65	1.13−
	6	<1.70	0.48−
	7	<1.80	0.41
0 5	8	<1.89	0.88
	9	<1.99	0.26
	10	<2.07	0.25−
0 6	0	7.43	8.47−
	1	<1.60	1.14
	2	2.91	2.01
	3	<1.70	2.74
	4	<1.75	1.87
	5	2.53	1.54−
	6	<1.85	4.42−
	7	<1.94	1.35
	8	<2.04	0.99
	9	<2.09	0.86
0 7	1	<1.80	0.66−
	2	<1.85	0.82−
	3	<1.85	0.51−
	4	<1.89	0.29
	5	<1.94	1.12
	6	<1.99	0.57
	7	<2.07	0.30−
	8	<2.14	0.68−
0 8	0	<1.99	1.67
	1	<1.99	0.14−
	2	<1.99	0.01
	3	<2.04	0.75−
	4	<2.09	0.06
	5	<2.14	0.16
	6	<2.19	0.54
0 0	1	8.80	10.00−
	2	18.48	15.86−
	3	41.05	46.10−
	4	8.89	7.28−
	5	11.82	10.10
	6	27.97	25.88
	7	5.31	3.04−
	8	7.91	6.14−
	9	7.68	6.60−
	10	<1.82	0.64−
	11	2.33	3.06
	12	1.86	2.04
	13	<2.28	0.54−
2 0	−12	<2.23	0.20
	−11	<2.14	0.26
	−10	<2.00	0.52−
	− 9	<1.86	0.80
	− 8	<1.72	0.74−
	− 7	<1.58	0.40−
	− 6	2.37	3.04
	− 5	3.86	1.30−
	− 4	7.91	7.64−
	− 3	9.35	8.54
	− 2	7.35	8.16−
	− 1	11.22	11.32
	0	16.43	15.86
	1	18.15	18.72−
	2	13.12	12.38−
	3	3.35	4.80
	4	3.07	3.10−
	5	11.40	11.08
	6	5.82	4.86
	7	8.33	6.78−
	8	2.56	2.68−
	9	<1.68	1.24−
	10	<1.82	0.92
	11	<1.95	2.34
	12	<2 09	0.46
	13	<2.23	0.88−

Table III. Continued.

h k	l	$F_0/2$	$F_c/2$
4 0	−11	<2.23	1.30
	−10	2.14	1.68
	− 9	<2.00	0.18
	− 8	6.10	5.34−
	− 7	4.61	5.04−
	− 6	<1.63	2.44
	− 5	12.38	11.84
	− 4	8.75	8.52
	− 3	<1.30	2.12−
	− 2	31.69	29.72−
	− 1	7.26	7.50−
	0	8.10	10.02
	1	31.93	33.64
	2	6.89	7.24
	3	7.59	8.22−
	4	29.79	30.70−
	5	4.05	1.94
	6	7.45	7.98
	7	9.96	11.38
	8	<1.58	0.22
	9	3.54	5.04−
	10	4.70	4.54−
	11	<1.95	1.30
	12	<2.09	1.66
	13	<2.23	0.86
6 0	− 9	<2.19	0.80−
	− 8	<2.05	0.82−
	− 7	<1.95	0.74
	− 6	2.37	2.84
	− 5	<1.72	1.86
	− 4	2.84	2.14−
	− 3	8.14	7.06−
	− 2	2.51	2.34−
	− 1	4.33	3.50
	0	11.64	12.46
	1	4.19	1.84
	2	5.86	4.74−
	3	12.61	13.60−
	4	3.49	1.62−
	5	5.31	5.22
	6	9.45	9.20
	7	2.05	1.24
	8	3.21	4.02−
	9	3.82	4.42−
	10	<1.91	0.70−
	11	<2.00	2.00
	12	<2.14	1.60
	13	<2.23	0.16
8 0	− 8	<2.28	0.10
	− 7	<2.19	1.40−
	− 6	<2.05	1.84−
	− 5	<1.95	1.00
	− 4	4.79	2.36
	− 3	4.24	3.60
	− 2	<1.72	1.46−
	− 1	6.19	5.48−
	0	5.07	4.06−
	1	4.89	4.62
	2	4.93	3.60
	3	4.33	4.88
	4	3.77	4.12−
	5	4.47	4.82−
	6	<1.68	0.34−
	7	2.84	3.10
	8	4.89	1.40
	9	<1.91	0.26
	10	<2.00	1.68−
	11	<2.09	0.70−
	12	<2.23	0.60
10 0	− 5	<2.19	1.36
	− 4	<2.14	0.46
	− 3	<2.05	0.90−
10 0	− 2	<2.00	2.30−
	− 1	2.70	2.20−
	0	4.00	3.34
	1	2.37	3.94
	2	<1.82	0.38
	3	2.79	1.66−
	4	3.49	4.40−
	5	2.98	1.40−
	6	2.89	3.36
	7	<1.91	2.56
	8	<2.00	0.04−
	9	<2.05	1.06−
	10	<2.14	1.80−
	11	<2.23	0.04−
12 0	− 2	<2.23	0.68
	− 1	<2.19	0.52−
	0	<2.14	0.46
	1	<2.09	1.26−
	2	<2.09	0.20
	3	<2.09	0.46
	4	<2.09	0.50
	5	<2.09	0.80−
	6	<2.09	0.78
	7	<2.14	0.88−
	8	<2.19	0.50
	9	<2.23	0.06
2 0	0	18.64	16.47
4		10.04	10.27
6		14.45	13.62
8		5.48	4.76−
10		5.82	5.43
12		4.37	3.76
1 1	0	18.64	18.10
2		37.46	42.23−
3		13.93	13.08
4		5.22	5.64
5		<0.89	0.52
6		14.56	13.49−
7		2.26	2.27−
8		1.82	1.39−
9		3.11	3.14
10		<1.37	1.45
11		<1.44	1.75
12		2.78	2.76−
13		<1.67	0.92
0 2	0	38.87	39.81−
1		5.41	4.56−
2		4.59	3.34−
3		7.26	7.11−
4		8.97	8.05−
5		8.45	7.41−
6		6.30	5.31−
7		1.07	0.87
8		4.48	3.34
9		2.74	1.98
10		2.33	2.70−
11		<1.48	1.30−
12		<1.59	0.81
1 3	0	13.26	11.89−
2		6.34	4.56
3		3.04	1.37−
4		1.07	0.79−
5		4.19	3.77−
6		8.45	6.98
7		1.70	1.53
8		<1.26	0.67
9		<1.37	1.43−
10		<1.44	1.63
11		<1.52	1.26−
12		<1.63	1.42
0 4	0	8.48	6.94

Table III. Continued.

h k l	$F_0/2$	$F_c/2$
1 4 0	9.11	9.27
2	2.07	1.18
3	<1.04	0.43−
4	5.22	3.62
5	<1.15	0.93−
6	<1.19	0.72
7	2.67	3.41
8	<1.33	1.22−
9	<1.44	0.35−
10	<1.52	0.56
11	<1.59	0.77
1 5 0	4.96	4.29
2	4.30	4.01−
3	6.45	6.46−
4	<1.19	0.33−
5	4.15	3.44
6	2.30	2.54−
7	<1.37	1.71−
8	<1.44	0.21−
9	<1.52	1.51−
10	<1.59	0.13−
0 6 0	8.82	8.31−
1	5.93	5.52−
2 6 0	3.15	2.89−
3	<1.30	0.45−
4	<1.33	1.74−
5	<1.37	0.31
6	<1.41	2.09−
7	<3.33	1.83−
8	<1.52	0.27−
9	<1.59	1.09
1 7 0	4.08	4.69−
2	1.96	2.07
3	<1.41	0.11−
4	<1.44	0.11−
5	<1.48	1.24−
6	<1.52	0.82
7	<1.59	0.69
8	<1.63	0.46
0 8 0	<1.52	1.10
1	<1.52	1.63
2	<1.52	0.01−
3	<1.56	1.53
4	<1.56	0.45
5	<1.59	1.14
6	<1.63	0.77

Table IV. Observed and calculated structure factors for bromanil. In the columns of $F_0/4$ the signs " < " indicate none observed structure factors.

h k	l	$F_0/4$	$F_c/4$
0 0	1	7.29	10.44
	2	24.82	25.38−
	3	49.15	48.15−
	4	10.79	8.45−
	5	19.71	15.84
	6	25.87	21.97
	7	<	1.28−
	8	7.34	5.97−
	9	7.47	5.55−
	10	<	0.19
	11	2.27	1.95
0 1	1	<	0.52
	2	<	1.34−
	3	3.85	5.02−
	4	1.18	0.64−
	5	3.08	2.40
	6	3.99	2.89−
	7	<	0.12−
	8	1.09	1.65−
	9	1.50	1.76−
	10	<	0.18
0 2	0	45.03	45.55−
	1	15.55	16.80−
	2	18.67	17.95
	3	33.21	37.49
	4	3.58	3.29
	5	13.99	12.87−
	6	16.13	13.90−
	7	0.99	1.21−
	8	6.70	5.43
	9	5.35	4.41
	10	0.45	0.57−
0 3	1	0.45	0.74−
	2	<	0.56
	3	1.77	2.51
	4	1.58	0.66
	5	0.99	1.39−
	6	1.36	2.03−
0 3	7	<	0.34−
	8	1.18	1.09
	9	0.64	1.00
	10	<	0.08−
0 4	0	12.64	15.43
	1	8.33	7.22
	2	8.33	8.78−
	3	11.78	11.79−
	4	1.18	3.18−
	5	7.29	5.99
	6	4.48	5.45
	7	<	0.65
	8	4.21	2.58−
	9	1.58	1.64−
0 5	1	<	0.51
	2	<	0.02−
	3	<	0.55−
	4	<	0.63−
	5	<	0.44
	6	<	0.63
	7	<	0.20
	8	<	0.34−
0 6	0	3.80	2.95−
	1	0.91	1.69−
	2	2.81	2.46
	3	1.50	1.44
	4	<	1.38
	5	2.22	1.63−
	6	1.50	1.08−
	7	0.77	0.11−
0 7	1	<	0.24−
	2	<	0.09−
	3	<	0.07
	4	<	0.20
0 0	0	—	—
	1	8.2	9.3
	2	17.5	25.1−

Table IV. Continued.

h k	*l*	$F_0/4$	$F_c/4$	*h k*	*l*	$F_0/4$	$F_c/4$
0 0	3	33.7	46.3−	8 0	− 3	2.7	2.6
	4	9.2	8.3−		− 2	0.8	1.7−
	5	15.3	15.4		− 1	6.1	5.6−
	6	21.4	20.7		0	4.4	3.5−
	7	<	1.1−		1	4.6	4.6
	8	6.7	5.5−		2	6.1	6.0
	9	7.0	5.0−		3	4.7	3.4
	10	<	0.2−		4	4.0	4.7−
	11	2.0	1.6		5	5.4	5.2−
2 0	−10	<	0.1		6	<	0.8−
	− 9	0.9	1.0		7	2.3	2.8
	− 8	<	0.4−		8	1.4	2.0
	− 7	<	1.0−		9	<	0.3
	− 6	<	0.5−	10 0	− 1	0.9	1.0−
	− 5	<	0.8		0	1.4	0.9
	− 4	3.5	2.5−		1	1.9	2.1
	− 3	5.0	4.2		2	<	0.6
	− 2	2.7	4.1−		3	0.7	1.0−
	− 1	6.4	6.7		4	2.0	2.4−
	0	9.6	6.6		5	0.9	0.7−
	1	11.9	8.6−		6	1.4	1.6
	2	10.6	11.0−		7	0.8	1.5
	3	<	0.5				
	4	1.0	2.4	2 0 0		9.34	6.97
	5	8.4	9.5	4		15.57	15.92
	6	2.5	1.8	6		10.45	9.20
	7	5.4	5.1−	8		6.56	5.07−
	8	2.7	2.6−	10		2.84	2.07
	9	<	0.2−	1 1 0		12.06	16.33
	10	0.9	1.5	2		26.40	34.96−
	11	1.5	1.2	3		5.56	3.05
4 0	− 9	<	0.1	4		5.23	4.36
	− 8	4.8	3.2−	5		3.22	2.79
	− 7	5.3	4.1−	6		19.40	18.25−
	− 6	4.0	1.2	7		<	0.87−
	− 5	12.2	10.6	8		2.33	2.41−
	− 4	10.3	11.1	9		1.11	0.53
	− 3	4.5	5.1−	10		0.95	1.33−
	− 2	28.6	26.3−	0 2 0		28.85	46.83−
	− 1	14.8	14.3−	1		8.17	10.22−
	0	14.0	14.3	2		1.78	1.27
	1	38.3	33.6	3		3.67	3.68−
	2	12.0	11.9	4		12.73	11.49−
	3	16.1	15.7−	5		7.45	4.51−
	4	27.3	26.8−	6		7.62	6.87−
	5	2.2	2.5−	7		2.22	2.81−
	6	9.4	9.8	8		5.67	4.22
	7	10.4	10.4	9		1.11	0.22
	8	<	0.5	10		1.22	0.96−
	9	4.3	4.0−	1 3 0		12.29	11.39−
	10	3.7	3.1−	2		13.40	12.65
4 0	11	<	0.5	3		2.17	0.66−
6 0	− 7	0.5	0.0	4		3.78	4.25−
	− 6	1.0	0.6	5		5.89	5.93−
	− 5	<	1.0	6		12.17	10.72
	− 4	1.2	0.5−	7		3.00	1.79
	− 3	3.7	3.1−	8		1.67	1.97
	− 2	1.5	1.9−	9		1.33	0.24−
	− 1	3.2	1.6	0 4 0		16.34	18.09
	0	8.0	7.0	1		10.11	8.08
	1	3.7	3.4	2		2.22	1.07
	2	5.1	4.7−	3		<	0.10−
	3	9.9	8.9−	4		7.45	5.91
	4	3.3	2.0−	5		3.78	3.42
	5	5.2	4.7	6		2.89	3.19
	6	6.4	6.3	7		3.17	3.77
	7	1.1	0.6	8		2.67	1.80−
	8	2.2	0.3−	9		<	0.06
	9	2.5	2.7−	1 5 0		7.39	7.79
	10	<	0.1	2		4.94	3.99−
8 0	− 5	0.6	0.7	3		2.56	0.24
	− 4	2.5	2.4	4		<	0.08

Table IV. Continued.

h k l	$F_0/4$	$F_c/4$	*h k l*	$F_0/4$	$F_c/4$
5 5 0	4.89	5.18	5 6 0	1.95	2.30−
6	4.73	3.95−	6	1.45	0.77−
7	1.95	1.29−	7	1.45	2.48−
8	<	0.70−	1 7 0	4.67	4.09−
0 6 0	7.11	3.87−	2	1.56	0.03−
1	6.39	5.04−	3	<	0.38−
2	2.67	1.19−	4	<	0.10
3	<	0.41−	5	1.95	2.67−
4	2.33	1.88−			

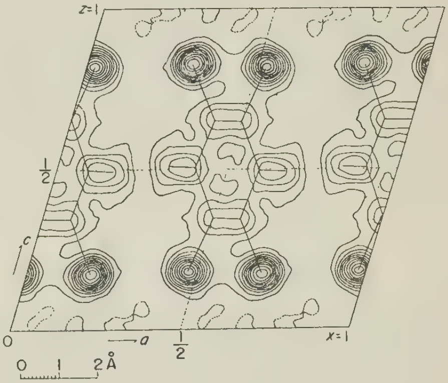

Fig. 1 (a). The final projection of the electron density along the *b*-axis. Contours at intervals of 2 eÅ^{-2}. Contour at 0 eÅ^{-2} is broken.

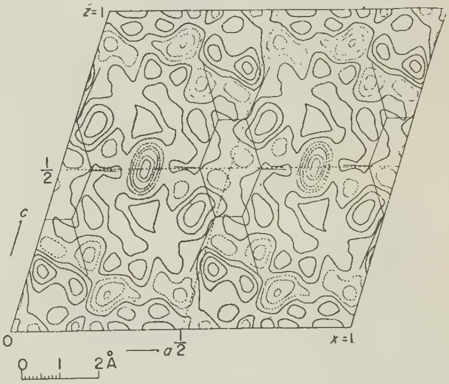

Fig. 1 (b). The $(\rho_0-\rho_c)$ map, (*b*-projection), at the step that the disagreement factors $R=0.15$. Contours at intervals of 0.4 eÅ^{-2}. The negative contours are broken.

§ 5. Accuracy of the Structure Determination

In the case of bromanil the systematic error in the observed structure factors was inevitable because of its large absorption coefficient. Moreover, because of the large atomic number of bromine, the accuracy of the position of light atom was not satisfactory enough to discuss its detailed structure. The standard deviations for atomic positions were calculated by Cruicksnank's[11] method. Those values $\sigma(r)$ were about 0.01 Å for bromine atoms and about 0.1 Å for the light atoms.

In the case of chloranil there is no systematic error except the extinction effect. The standard deviations of atomic positions are: $\sigma(r)=0.003$ Å for chlorine, $\sigma(r)=0.009$ Å for oxygen and $\sigma(r)=0.012$ Å for carbon. Therefore the standard deviations of the bond lengths are: $\sigma=0.017$ Å for the C–C, C=C bonds, $\sigma=0.015$ Å for the C=O bond and $\sigma=0.012$ Å for the Cl–C bond. The average standard deviation of the bond angles is about 1.2°.

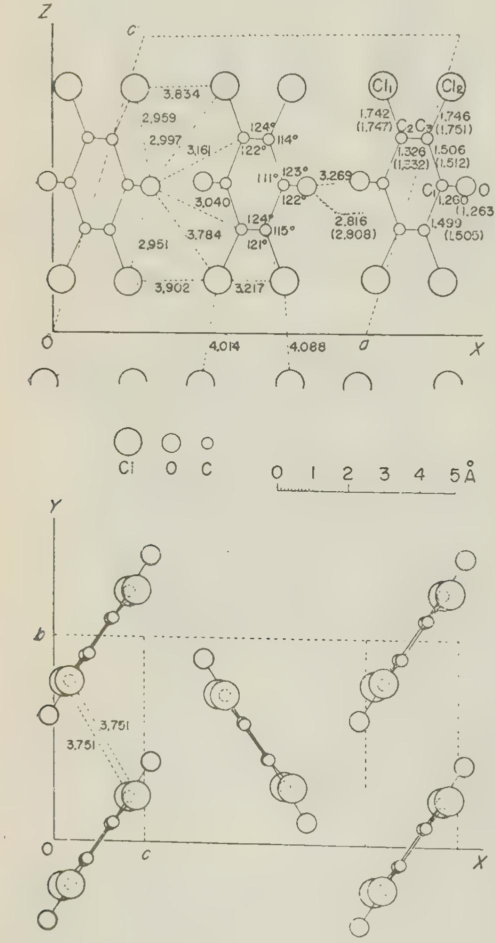

Fig. 2. The arrangement of molecules of chloranil with interatomic distances in Å and bond angles in degrees. The values in the parentheses are the corrected distances by Cruickshank's method.

§ 6. Discussion

(1) Molecular Structure:

The crystal axes were transformed to the orthogonal axes such that a, b axes were parallel to X, Y axes with the common origin. In this orthogonal co-ordinate system the structural calculations of the molecule and the crystal were performed. The results are shown in Fig. 2. The plane through which all carbon atoms in one molecule and its centre of symmetry lie is calculated to be

$$1.0000X+0.6731Y-0.0316Z-7.5584=0\ ,$$

for the molecule at (1/2, 1/2, 1/2). The perpendicular displacements of atoms in this molecule from the above plane are shown in Fig. 3. It is certain that the adjacent chlorine and oxygen atoms protrude respectively up and down from this plane. Moreover the distances between these adjacent oxygen and chlorine atoms are fairly shorter than that expected from the sum of their van der Waals radii. Thus these atoms around the carbon skeleton construct a puckered form.

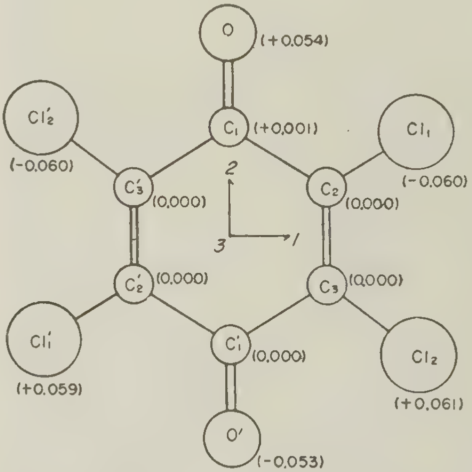

Fig. 3. Molecule of chloranil. The value in the parenthesis for each atom is the perpendicular displacement in Å from the carbon skeleton plane. The axes *1*, *2* and *3* are those concerning U_{ij}.

The bond lengths are found to have fairly typical values, from which it follows that $C_2=C_3$ is the double bond and C_1–C_2, C_2–Cl_1, C_3–Cl_2 are the single bonds. The distance between C_1 and O atoms is somewhat longer than that expected from the C=O bond. Therefore, this bond may have a single bond

(C–O⁻) character to some extent, although it is mainly of double bond character. Thus the $C_1=O$ bond may have a dipole moment. (cf. Figs. 2 and 3.)

(2) Molecular Arrangement:

In the crystal the chlorine atoms form layers parallel to the *XY* plane. The distance between these chlorine layers is slightly larger than that calculated from their van der Waals radii. The cleavage of the (001) plane is well explained by this structure. In these layers the distances between chlorine atoms in adjacent molecules are also slightly larger than that expected from their van der Waals radii. These may indicate that the van der Waals potentials arising from interaction between chlorine atoms are much less than exerting in crystals of usual poly halogenated molecules.

A layer consisting of light atom skeleton lies between these two chlorine layers. In this layer an oxygen atom is found nearest to a carbon atom forming a C=O bond in the adjacent molecule. The distance between these atoms is much shorter than that expected from their van der Waals radii. The two oxygen atoms belonging to these two C=O bonds are even disposed as if they repulse each other. It is suggested that the cohesive factors between molecules arise mainly from the dipole interaction of the C=O bonds. This fact supports Hammick and Coop's[1] theory about the atomic polarization of *p*-benzoquinone and its derivatives. But it cannot be decided whether the bending of the C=O bonds in this crystal is caused by the packing of oxygen to the adjacent carbon and chlorine atoms, or it is due to the interaction between the dipoles of C=O bonds and the crystalline field.

When the structure of molecule as found here is compared with that of Harding and Wallwork[3] from the crystal structure of the chloranil-hexamethylbenzene complex, there is found a remarkable difference in the orientation of the C=O bond relative to the two adjacent chlorine atoms. The chloranil crystal is yellow and that of complex is purple red. In the complex some interaction between the two kinds of molecules should take place resulting the change of electronic state of the molecule of chloranil, which may cause the bending of the C=O bonds.

(3) Anisotropic Thermal Motion:

Using Cruickshank's[12] method the thermal motions of chloranil molecule were analysed from the observed thermal anisotropic parameters of the oxygen and chlorine atoms. The thermal vibration tensors U_{ij}^{obs}'s for Cl_1, Cl_2 and O atoms were calculated from the data of $\boldsymbol{B}$, Δ and ψ in the three projections, such that

$$\overline{u^2}=\sum_{i=1}^{3}\sum_{j=1}^{3}U_{ij}^{obs}l_il_j\ ,$$

where the mean square amplitude of vibrations of these atoms in the direction specified by a unit vector $\boldsymbol{l}=(l_1, l_2, l_3)$. In these calculations the adopted axes are indicated in Fig. 3 and the results are listed in Table V.

The problems to be solved here are the rigid body vibrations of this molecule. The tensors T_{ij}'s of molecular translational vibrations and the tensors ω_{ij}'s of molecular librations about the centre of molecule then can be calculated by the equations:

$$\sum_{i=1}^{3}\sum_{j=1}^{3}U_{ij}^{obs}l_il_j$$
$$=\sum_{i=1}^{3}\sum_{j=0}^{3}[T_{ij}l_il_j+\omega_{ij}(\boldsymbol{l}\wedge\boldsymbol{r})_i(\boldsymbol{l}\wedge\boldsymbol{r})_j]\ ,$$

where $\boldsymbol{r}$'s were the positions of atoms referred to the molecular co-ordinates shown in Fig. 3. These equations were solved under the condition that the molecule was approximately planar, namely $r_3^2=0$. For the small values of r_3's, the value of ω_{12} was rather

Table V. Observed and Calculated U_{ij}.
(Values in 10^{-2} Å^2)

Atom	U_{11}		U_{22}		U_{33}		U_{12}		U_{13}		U_{23}	
	Obs.	Cal.	Obs.	Cal.	Obs.	Cal.	Obs.	Cal.	Obs.	Cal.	Obs.	Cal.
Cl_1	7.33	6.21	6.99	7.76	7.49	7.51	−3.50	−4.87	3.08	3.06	−0.72	−0.86
Cl_2	7.19	6.09	6.08	7.79	6.43	6.46	−0.91	−0.04	3.23	3.11	−0.09	0.10
O	22.06	8.85	3.68	3.68	5.22	5.15	−2.84	−2.38	3.83	3.62	−0.30	−0.29

indefinite. Moreover this affected the values of T_{33}, ω_{11} and ω_{22} very much. Therefore the value of ω_{12} was determined as to give resonable value for T_{33} compared to those of T_{11} and T_{22}. The results are shown in Table VI. From these results the calculated values of U_{ij}^{cal} are compared to those of U_{ij}^{obs} which are shown in Table V.

Table VI. Values of T_{ij} and ω_{ij}.
(Values of T_{ij} in 10^{-2} Å^2 and ω_{ij} in deg^2.)

$$T=\begin{bmatrix} 4.73 & -2.41 & 2.80 \\ & 3.68 & -0.30 \\ & & 4.86 \end{bmatrix} \qquad \omega=\begin{bmatrix} 1.3 & -2.0 & -3.6 \\ & 8.8 & -0.3 \\ & & 18.1 \end{bmatrix}.$$

From these results, it seems certain that the value of ω_{11} is fairly smaller than those ω_{22} and ω_{33}. This means that the libration about the axis *1* is small but those about the axes *2* and *3* are not so much restricted. These facts are consistent with the orientations of the inter-molecular bonds in this crystal, and with the short distance between an oxygen atom in one molecule and its nearest carbon atom in neighbouring molecule. (cf. Figs. 2 and 3.)

The small corrections for atomic positions due to these librations were calculated by Cruickshank's[12)] method. The corrected bond lengths are shown in Fig. 2.

(4) Puckered Molecular Form:

From the results of X-ray analysis it becomes clear that the oxygen and chlorine atoms connected to the benzene ring construct a puckered form. This steric effect is in harmony with the results calculated by the method of Gafner and Herbstein[13)].

a) The angular distortion energy E_1 for each atom is calculated from:

$$E_1=1/2\cdot k(\Delta x)^2\ ,$$

where Δx is the displacement of an atom from the plane of the carbon skeleton and k is the force constant of its displacement. The force constant for out of plane displacement is generally smaller than that for in plane. Accordingly the value of force constant for each atom is assumed to be: $k=0.05\times10^5$ dyne/cm equally.

b) The van der Waals interaction between a pair of adjacent and non-bonded atoms was treated by Hill[14)]. The van der Waals energy E_2 is given by,

$$E_2=\mathcal{E}_a(r_a{}^*/r)^{12}-2\mathcal{E}_a(r_a{}^*/r)^6\ ,$$

where r is the distance between these atoms and $\mathcal{E}_a$, $r_a{}^*$ are energy parameters for this pair of atoms. The distance r depends upon Δx when the adjacent atoms displace antiparallel whereas it is constant when these atoms displace parallel. The values $\mathcal{E}_a$ and $r_a{}^*$ of a single Cl atom have been determined by Hill[14)] and the values of a single O atom are calculated by the method of Hill[14)] from the data of O_2 gas given by Johnston and McCloskey[15)]. The values $\mathcal{E}_a$ and $r_a{}^*$ of a pair of A and B atom are calculated by the formulas: (cf. Hirschfelder, Curtiss and Bird[16)].)

$$\mathcal{E}_a=\{\mathcal{E}_a(A)\cdot\mathcal{E}_a(B)\}^{1/2}\ ,$$
$$r_a{}^*=1/2\{r_a{}^*(A)+r_a{}^*(B)\}\ ,$$

where the value of $r_a{}^*(A)$ or $r_a{}^*(B)$ means the van der Waals diameter of the atom. Since the van der Waals radii have not been determined very accurately and the energy E_2 depends on $r_a{}^*$ strongly, the energy differences E_2's between planar and puckered molecules are calculated for a few different values of $r_a{}^*$, such that:

if Δx's of adjacent atoms are in the opposite direction,

$$E=E_1+1/2\{(E_2-E_0)_{\mathrm{Cl-O}}+(E_2-E_0)_{\mathrm{Cl-Cl}}\}\quad \text{for Cl atom,}$$
$$E=E_1+(E_2-E_0)_{\mathrm{Cl-O}}\quad \text{for O atom,}$$

and if Δx's are in the same direction,

$$E=E_1\ ,\quad \text{for both atoms,}$$

where E_0 is the van der Waals energy at $\Delta x=0$.

The constants used in the calculations are shown in Table VII and VIII. The results are shown in Figs. 4 (a) and (b).

From these results, for the probable values of k, $\mathcal{E}_a$ and $r_a{}^*$, the energy differences E's of Cl and O atoms show the flat valleys in

Table VII. The constants used in the calculations of potential energy differences of Cl and O atoms.

Atoms and pairs		Cl	O	Cl-Cl	Cl-O
$\varepsilon_a \times 10^{15}$ ergs		21.8	7.56	21.8	12.8
r_a^* Å	Case I	3.825	3.425	3.825	3.600
	Case II	3.814	3.364	3.814	3.589
	Case III	3.805	3.355	3.805	3.580
	Pauling[17]	3.6	2.8	3.6	3.2
	Author	3.88	—	3.88	—
$k \times 10^{-5}$ dyne/cm		0.05	0.05	—	—

fairly wide ranges of anti-parallel Δx. The condition which gives the minimum of this potential difference is:

$$(r_a^*)^6 = \frac{1}{2} r^6 \left(1 + \sqrt{1 + \frac{kr^2}{12\varepsilon_a}}\right).$$

In these calculations the value of k may have been estimated somewhat less. When the value of r which gives the minimum of the potential difference is kept constant (the observed atomic distance) and let the value of k increase, r_a^* does not increase very much. (cf. Table VIII.) Moreover, the mean value of van der Waals diameter of Cl atom which has been obtained in this X-ray analysis is 3.88 Å. (cf. Table VII.) Now, the exact values of r_a^*'s are not known, the direct correlation between the theoretical calculations and the results of X-ray analysis of chloranil can not be given with high reliabili-

Table VIII. The combinations of k's and r_a^*'s for which the energy differences show minima at the observed atomic distances $r(\text{Cl-Cl}) = 3.217$ and $r(\text{Cl-O}) = 2.955$ Å.

$k \times 10^{-5}$ dyne/cm		0.05	0.10	0.15
r_a^* Å	Cl-Cl	3.814	3.998	4.116
	Cl-O	3.589	3.768	3.882

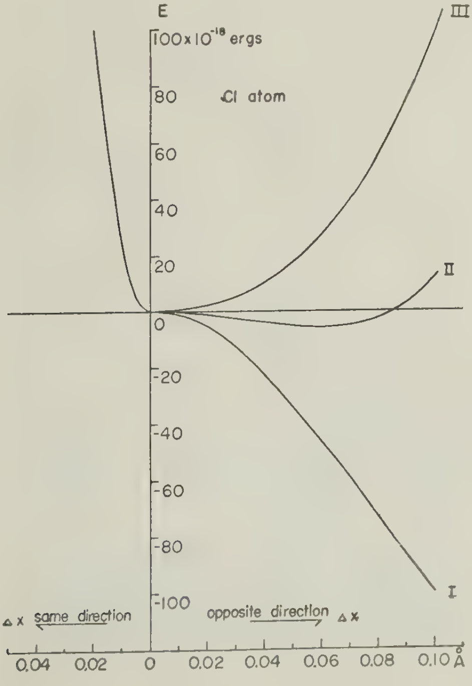

Fig. 4 (a).

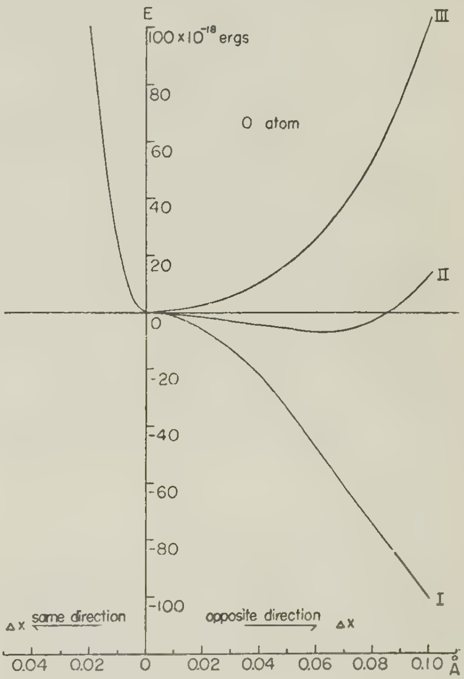

Fig. 4 (b).

Fig. 4. The energy differences between the puckered and planar form of chloranil for various cases of r_a^*'s. (a) for Cl atom and (b) for O atom.

ty. However, from the calculations given above it can be concluded that the puckered form is stable and that the thermal vibrations are pronounced perpendicular to the molecular plane and anti-parallel to each other.

In the above calculations only the adjacent atoms in the same molecule are taken into account. The oxygen atom has another neighbouring carbon atom which belongs to a neighbouring molecule. (cf. Fig. 2.) The influence of the carbon atom to this oxygen atom should be very large and should give the decisive effect in making the puckered form of the molecule. Moreover, the influence may act also co-operatively to make the puckered form of chlorine atoms. Since there is no such influence in the gaseous state, the O and Cl atoms have even chances protruding to the two sides of the carbon skeleton plane so that the positions of these atoms would be diffused by the thermal vibrations in the shallow potential barriers. Therefore chloranil molecules in the gaseous state may look like planar. The influence of the carbon atom may also hinder the thermal vibration of O atom as we see from the fact that the observed values of U_{22} and U_{33} of O atom are smaller than their corresponding values of Cl atoms. (cf. Table V.)

§ 7. Conclusion

Chloranil and bromanil are isomorphous. These crystals form a sandwich type structure which is composed of two layers of halogen atoms parallel to the (001) plane containing light atom skeletons sandwiched between them. The interactions between the molecules are mainly due to the dipole interaction of C=O bonds, which is also supported by the mode of the thermal librations of chloranil molecules in the crystal. The molecule has a centre of symmetry and the oxygen and chlorine atoms around the plane of carbon skeleton are arranged in a puckered form. By a theoretical calculation of potential difference between the planar and puckered molecules, it is shown that the puckered form is more stable. Moreover there are some found correlation between these potential difference valleys and the anisotropic thermal motions of the oxygen and chlorine atoms. Although the bending of C=O bonds as found by the present analysis which is also supported by a theoretical calculation of the molecular structure, there is still a possibility that this bending is caused by the interaction between molecules. The bond lengths found here have normal values except the C=O bond suggesting there is a small contribution of the single bond.

The author wishes to express his sincere thanks to Professor I. Nitta and Professor T. Watanabé for their guidance and encouragement throughout this work. He also thanks Dr. Y. Sasada for his kind advice and Mrs. K. Sugahara for her help in calculations.

References

1) D. L. Hammick, G. C. Hampson and G. I. Jenkins: J. Chem. Phys. **6** (1938) 1263. I. E. Coop and L. E. Sutton: J. Chem. Phys. **6** (1938) 1269.
2) J. M. Robertson: Proc. Roy. Soc. **A150** (1935) 106. J. Trotter: Acta Cryst. **13** (1960) 86.
3) T. T. Harding and S. C. Wallwork: Acta Cryst. **8** (1955) 787.
4) R. McWeeny: Acta Cryst. **4** (1951) 513.
5) Y. Tomiie and C. H. Stam: Acta Cryst. **11** (1958) 126.
6) R. W. James and G. W. Brindley: Phil. Mag. **12** (1931) 81.
7) R. D. Burbank: Acta Cryst. **6** (1953) 55.
8) M. Atoji: Acta. Cryst. **10** (1957) 291.
9) Y. Sasada: To be published.
10) Y. C. Leung, R. E. Marsh and V. Schomaker: Acta Cryst. **10** (1957) 650.
11) D. W. J. Cruickshank: Acta Cryst. **2** (1949) 65. F. R. Ahmed and D. W. J. Cruickshank: Acta Cryst. **6** (1953) 385. D. W. J. Cruickshank: Acta Cryst. **7** (1954) 519.
12) D. W. J. Cruickshank: Acta Cryst. **9** (1956) 747. D. W. J. Cruickshank: Acta Crst. **9** (1956) 754. D. W. J. Cruickshank: Acta Cryst. **9** (1956) 757.
13) G. Gafner and F. H. Herbstein: Acta Cryst. **13** (1960) 706.
14) T. L. Hill: J. Chem. Phys. **16** (1948) 399.
15) H. L. Johnston and K. E. McCloskey: J. Phys. Chem. **44** (1940) 1038.
16) J. O. Hirschfelder, C. F. Curtiss and R. B. Bird: *Molecular Theory of Gases and Liquids* (Willey, New York, 1954) 168p.
17) L. Pauling: *The Nature of the Chemical Bond* (Cornell Univ. Press, Ithaca, 1945) 189p.

JOURNAL OF THE PHYSICAL SOCIETY OF JAPAN Vol. 16, No. 6, JUNE, 1961

Study on Precipitation Phenomena in Thin Films of Supersaturated Gold-Nickel Alloy

By Yasushige FUKANO*

The Research Institute for Iron, Steel and Other Metals, Tohoku University, Sendai

(Received January 7, 1961)

Structure changes of supersaturated gold-nickel alloy after successive agings were studied by means of electron diffraction and electron microscopy. Specimens were prepared by vacuum evaporation and subsequent quenching (Y. Fukano and S. Ogawa, J. Phys. Soc. Japan 14 (1959) 1671). After aging at temperatures lower than 165°C, side maxima appear beside the main spots from the matrix. The side maxima disappear after aging at 250 - 300°C, indicating that they correspond to pre-precipitations. The side maxima were interpreted by assuming a modulated structure similar to that found in Au-Pt alloy by Tiedema et al. (T.J. Tiedema, J. Bouman and W.G. Burgers, Acta Metallurgica 5 (1957) 310). This implies that gold-nickel alloy at the pre-precipitation stage contains a modulated structure similar to that in Au-Pt alloy. After aging at temperatures higher than 300°C, two stable phases with parallel lattices appear. In this state, Widmanstätten structure was found in electron micrographs.

§ 1. Introduction

Since quenching of thin films was difficult so far,[1] aging of alloys has not been studied with thin films prepared by vacuum evaporation. Recently, the present author and Ogawa[2] developed a new technique to quench thin films and studied the aging of Al-Ag alloy. In the present experiment, single crystalline films of Au-Ni alloy were quenched by this technique and structure changes of the films after aging were studied by electron diffraction and electron microscopy.

After aging at temperatures lower than 165°C, side maxima appear at low angle side of main spots from the matrix. The side maxima disappear after aging at 250–300°C. This implies that pre-precipitates formed by low temperature aging are dissolved. The side maxima were explained as a kind of the so-called "side bands" investigated by Daniel and Lipson.[3] After aging at temperatures higher than 300°C, two stable phases with parallel lattices appear. In this state, Widmanstätten structure was found in electron micrographs.

§ 2. Experimental

The present study was carried out using single crystalline films of Au-20 atomic % Ni alloy (Fig. 1) prepared by vacuum evaporation.

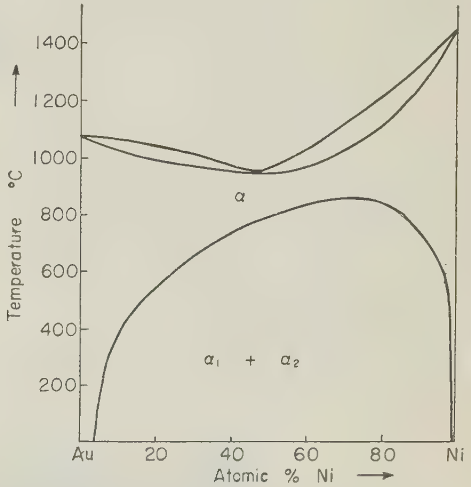

Fig. 1. Equilibrium phase diagram of Au–Ni system.

a) Specimen preparation

The two component metals of this alloy were simultaneously evaporated in vacuum onto fresh cleavage surfaces of rocksalt which were maintained at about 430°C after preheating up to 500°C. The mean thickness of films was about 700 A estimated from the total amount of evaporated metals. Films prepared in this way were well orientated, their surfaces being parallel to (001) plane. It was observed by means of electron microscopy that the thickness of the films were not uniform in most cases. In the present work, however, four most uniform films were selected as specimens. Non uniform films were destroyed during the quenching.

---

* Now at Department of General Education, Nagoya University.

b) Quenching and aging

The specimens were first homogenized by heating in vacua at about 700°C for 2 hr and then quenched to room temperatures by the method described in the previous section. Thus the films of homogeneous supersaturated solid solution were obtained. They were aged in vacua at various temperatures for various periods of time. For temperatures below 165°C, the aging was carried out in the chamber immersed in boiling water or oil bath, and for temperatures above 200°C, in a transparant quartz tube tightly wound by nickrome-wire.

c) Electron diffraction and electron microscopy

The diffraction camera used was a conventional type with a single lens and had camera length about 30 cm. The electron microscope used was Hitachi HU-7. The operating voltage of electron diffraction camera and electron microscope was 50 kV. Electron micrographs were taken at magnification 4,000 X. For the measurement of lattice constants, evaporated gold films aged at about 500°C for 2 hr in vacua were used as standard, adopting lattice constant a=4.070 kX (Wyckoff[4]).

§3. Experimental Results

The four specimens were examined through all the subsequent agings after quenching. The diffraction patterns were taken at various stages of aging. The results are summarized in Table I.

a) Aging at room temperatures

Photo. 1 shows a diffraction pattern of the specimen aged for 2 hr at room temperatures. The pattern shows that the specimen consists of a single phase of the face centered cubic lattice. The lattice constants obtained from all the specimens are listed in Table II. They are independent of the period of aging. The mean value 3.98±0.01 kX agrees with the X-ray value of the homogeneous solid solution of Au-20 atomic % Ni alloy.[5]

Table I. The results obtained from electron diffration patterns at various of aging.

Heat treatment		Results	
Temperature (°C)	Period (hr)	Lattice	Lattice constant (kX)
10– 30	2—72	f.c.c.	3.98±0.01
100	2—13	f.c.c.*	3.98±0.01
165	2	f.c.c.*	3.98±0.01
250–300	0.5– 1	f.c.c.*	3.98±0.01
250–300	4	f.c.c.	3.98±0.01
400–500	1	f.c.c. (α_1) f.c.c. (α_2)	4.05±0.01 3.52±0.01
700	2	f.c.c. (α_1) f.c.c. (α_2)	4.05±0.01 3.52±0.01

* Main spots are accompanied with side maxima on low angle side.

Table II. Lattice constants obtained from specimens aged at room temperature for various periods of time.

No. Sp.	Duration of aging (hr)	Lattice constant (kX)
1	2	3.98±0.01
2	10	3.99±0.01
3	24	3.98±0.01
4	72	3.97±0.01
	mean	3.98±0.01

b) Aging at temperatures 100–200°C

The diffraction patterns were taken at the stages of aging for 2 hr, 7 hr and 13 hr at 100°C and for 2 hr at 165°C. Some of the main spots are accompanied by weak side maxima or are pear-shaped. The main spots correspond to the face centered cubic lattice. The lattice constant is 3.98±0.01 kX which is the same as that of the quenched specimen.

Photo. 2 shows a diffraction pattern taken from the specimen aged at 100°C for 2 hr. In Photo. 2 the incident beam is in [001] direction. The (200)-spots are pear-shaped, elongated towards the low angle side. On the original plate of Photo. 2 it can be observed that the (220)-spots and other higher order spots are also elongated towards the low angle side, parallel to the elongation of (200)-spots. When, however, the specimen is

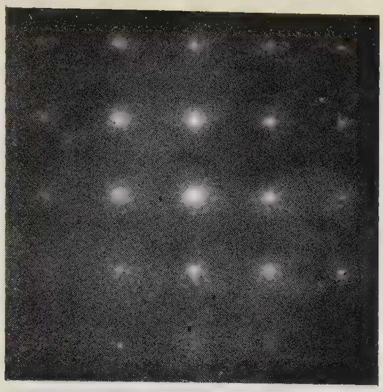

Photo. 1. Electron diffraction pattern of the specimen aged for 2 hr at room temperatures after quenching.

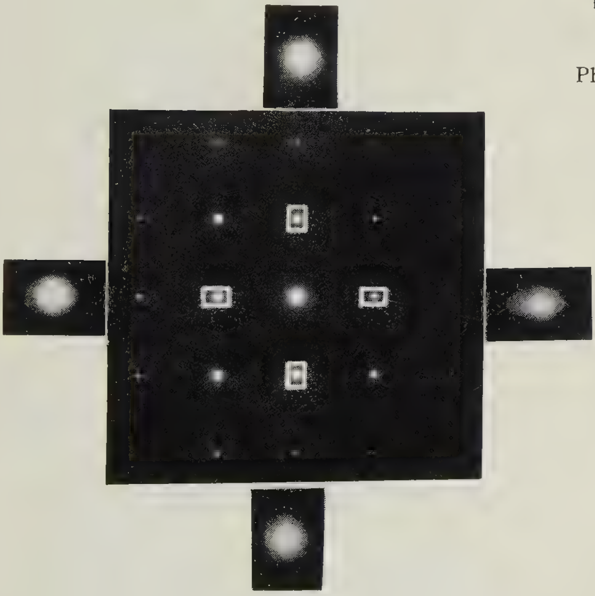

Photo. 2.

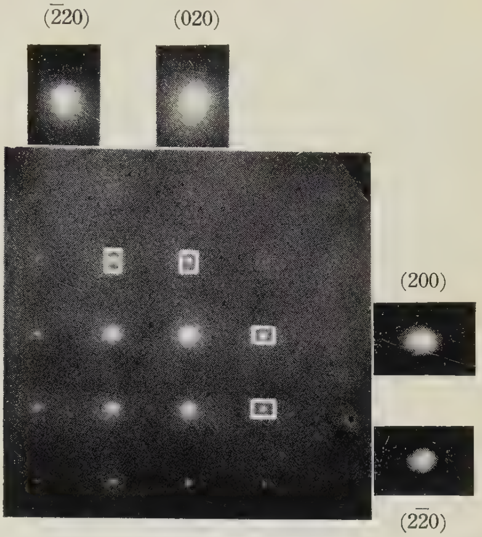

Photo. 3.

Photos. 2—3. Electron diffraction pattern of the specimen aged for 2 hr at 100°C. Enlargements correspond to marked parts.

slightly tilted, pear-shaped spots are observed to split into weak side maxima and main spots, although it is difficult to reproduce the details of this splitting on the print. Photo. 3 was taken by rotating the specimen about 45′ around $[1\bar{1}0]$ axis from the position in which Photo. 2 was taken. The spots (200), (020), $(2\bar{2}0)$ and $(\bar{2}20)$ which lie near the boundary of 0-th Laue zone are accompanied by weak side maxima. Photo. 3 is reproduced schematically in Fig. 2, where dots and crosses represent the side maxima. Side maxima corresponding to the dots in

Photo. 4. (200)-spot and the associated side maximum from the tilted specimen. θ is the angle between the normal of the specimen surface and the incident beam. Arrows in (b) and (c) indicate the side maxima.

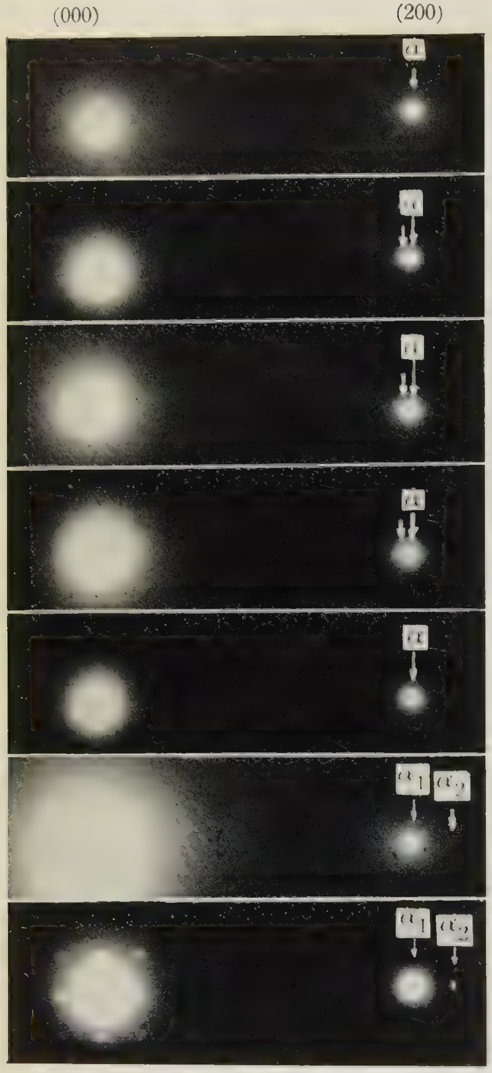

Temperature of aging (°C)	Duration of aging (hr)
room temp.	2
100	2
165	2
250—300	1
250—300	4
400—500	1
700	2

Photo. 5. The variation of (200)-spot and the associated side maximum during aging at various temperatures. α, α_1 and α_2 indicate the main spot from α, α_1 and α_2-phases, respectively. Arrows in (b), (c) and (d) indicate the side maxima.

Fig. 2 are reproduced in the enlargements given in Photo. 3. Those corresponding to the crosses are extremely weak and can be observed only on the original plates. The spots $(\bar{2}00)$, $(0\bar{2}0)$ and $(\bar{2}\bar{2}0)$ lie on the Kikuchi bands with the same indices in Photo. 3. The side maxima accompanying these spots are hardly observed. When Bragg condition is exactly satisfied each main spot is so strong that it masks the weak side maxima associated to it. The effect of masking may become serious by the strong diffuse inelastic scattering which accompanies each Bragg spot.

Since it was impossible to observe all the side maxima at the same time, the side maxima around each main spot were investigated by tilting the specimen films. The distance Δr between a main spot and the associated side maximum was measured in many diffraction patterns (Table III). It is found in Table III that the value of Δr is constant independent of the angle of inclination θ. θ is the angle between the normal of the specimen surface and the incident beam. Photo. 4 shows this fact: Distance Δr remains constant, although Photo. 4 (b) and 4 (c) are taken at $\theta=45'$ and $2°10'$, respectively. Based upon the fact that Δr is constant, it is concluded that the intensity regions of the main maximum and the associated side maximum in the reciprocal space are juxtaposed in (010) plane, as illustrated in Fig. 3. The elongation of the region normal to (001) reciprocal plane in Fig. 3 may be caused by bending of the specimen films. For higher order spots the side maxima are not observed although each spot is slightly elongated towards the low angle side. Summarizing the observations, the intensity distribution on the (001) reciprocal plane as shown in Fig. 4 is concluded.

c) *Aging at 250–300°C*

Photo. 5 shows the variation of (200)-spot from the specimen at the various stages of aging. At 250–300°C the side maximum still remains after aging for 1 hr. When, however, the specimen is further aged for 3 hr the side maximum disappears. Thus the diffraction pattern looks similar to that taken just after quenching (Photo. 5 (a)). The lattice constant is also the same as that of the quenched specimen. However, the background of Photo. 5 (e) is much lower than that of Photo. 5 (a), although the change is

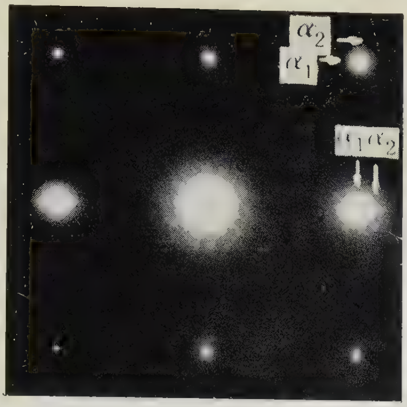

Photo. 6. Electron diffraction pattern of the specimen aged for 1 hr at 400—500°C and then slowly cooled to room temperatures.

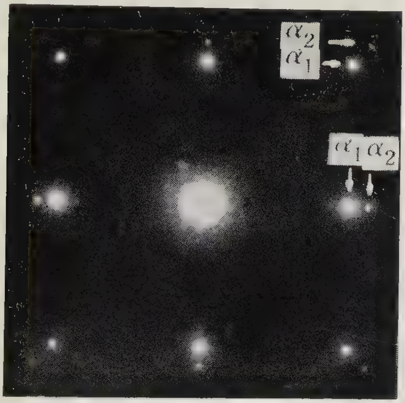

Photo. 7. Electron diffraction pattern of the specimen aged for 2 hr at 700°C and then slowly cooled to room temperatures.

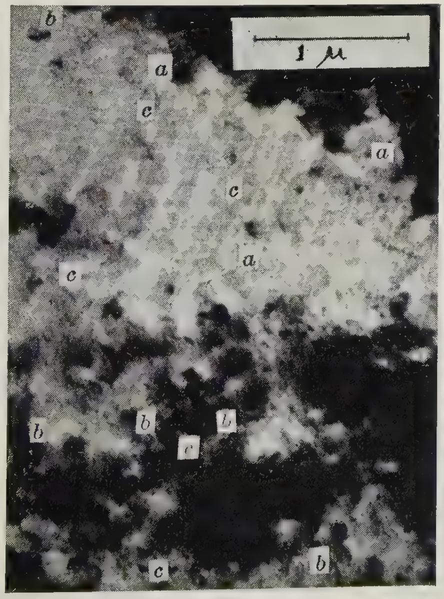

Photo. 8. Electron micrograph of the specimen aged for 2 hr at 165°C.

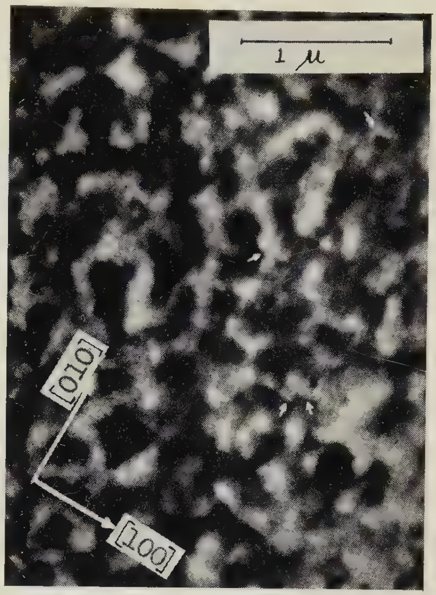

Photo. 9. Electron micrograph corresponding to Photo. 7. Arrows indicate L-shaped precipitates.

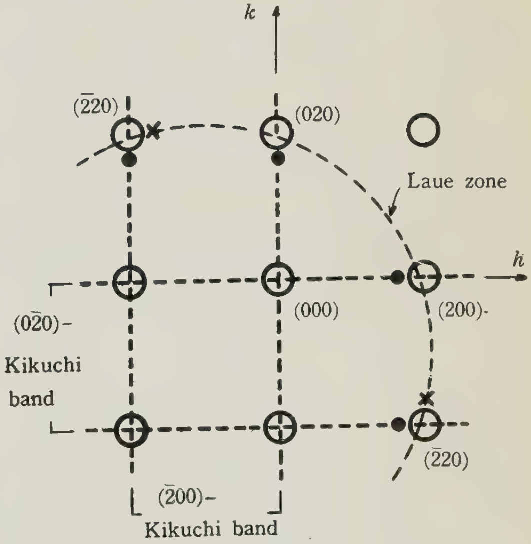

Fig. 2. The scheme of the original plate of Photo. 3. The main spots are represented by circles and the side maxima by dots and crosses.

hardly recognized in the reproduction. This change indicates that imperfections in the specimen have been decreased. The specimen which has once been aged at 300°C for more than 4 hr and has lost its side maxima shows none of them even when it is again aged at temperatures 100–200°C.

d) *Aging at 400–500°C*

The specimens were successively aged at

Table III. The observed valve of Δr.

Pl. No.	θ	°C	Δr (mm)							Δr	$2_{\Lambda}L$ (mm kX)	$Q\ a_0$ (kX)
			(200)	(021)	$(\bar{2}00)$	$(0\bar{2}0)$	(220)	$(2\bar{2}0)$	(220)			
10	45′	100	0.23	0.23			0.23	0.23		0.23	32.1	70
11	45′	100			0.23	0 23	0.24	0.23		0.23	32.1	70
19	2°10′	100	0.25	0.25		0.25	0.25			0.25	32.8	66
40	2°10′	165		0.25	0.25					0.25	32.6	65
43	45′	165			0.25	0.25	0.25			0.25	32.9	66
44	45′	165	0.25		0.25		0.25			0.25	33.1	66
49	32′	165	0.23	0.23		0.23	0.23		0.23	0.23	32.4	71
53	45′	250			0.25	0.23	0.24	0.24		0.24	32.2	67
											mean	68

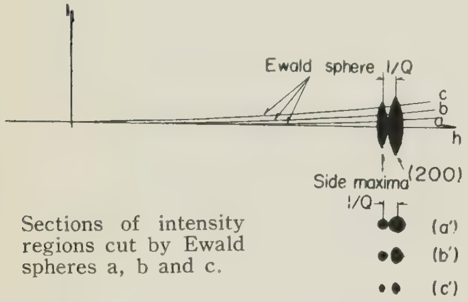

Sections of intensity regions cut by Ewald spheres a, b and c.

Fig. 3. The illustration of the intensity region of (200)-spot and the associated side maximum. Sections of intensity regions (a′), (b′) and (c′) correspond to Photos. 4 (a), 4 (b) and 4 (c), respectively.

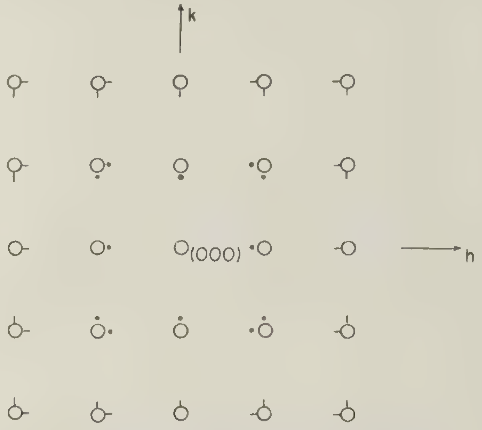

Fig. 4. The illustration of the intensity distribution on (001) reciprocal plane. Open circles and dots indicate main spots and the side maxima, respectively.

high temperatures after the side maxima disappeared. Photo. 6 shows a diffraction pattern taken from the specimen aged at 400–500°C for 1 hr and then cooled slowly to room temperatures. The main spots (α_1 in Photo. 6) correspond to a face centered cubic lattice of lattice constant 4.05±0.01 kX. They are accompanied by weak spots (α_2 in Photo. 6) corresponding to another face centered cubic lattice of lattice constant 3.52±0.01 kX. The two lattices are parallel to each other.

Photo. 7 shows a diffraction pattern of the specimen further aged at 700°C for 2 hr and then cooled slowly to room temperatures. The weak spots in Photo. 6 have become a little stronger in Photo. 7 and spots are multiplied by double reflections. The lattice constant of each lattice remains the same as that given above.

The lattice constants 4.05 kX and 3.52 kX agree respectively with X-ray value of Au-6 atomic % Ni (α_1-phase) and that of Ni-1 atomic % Au (α_2-phase) given by Köster et al.[5] Since the α_2-phase has grown parallel to the matrix phase, it can be expected that there is Widmanstätten structure.

e) *Electron microscopy*

Photo. 8 shows an electron micrograph taken from the specimen aged for 2 hr at 165°C. In this micrograph the images of the modulated structure, details of which will be described later, corresponding to the side maxima are not observed. Small black dots, loops and short lines are visible on the original plate at the locations denoted by a, b and c. They may be images of dislocations.6) 7) Loops have irregular elliptic shapes and the smallest diameter was estimated to be 200 Å. The distribution of loops is not uniform.

Photo. 9 is the electron micrograph corresponding to Photo. 7. White short lines nearly parallel to ⟨100⟩ are visible in Photo. 9. The average dimension of short lines is estimated to be 200 Å in width and 500 Å in length. Some of short lines appear to have L-shape. Since they are not observed in Photo. 8, the appearance of them may be related to the precipitation of α_2-phase. The distribution of white short lines is not uniform. We consider that this pattern corresponds to Widmanstätten structure which is expected from the diffraction pattern (Photo. 7).

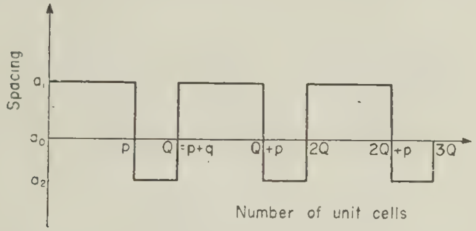

Fig. 5. A model of modulated structure given by Tiedema et al.8)

§ 4. Interpretation of Side Maxima

In interpreting Fig. 4, it might be possible to assume that a new phase with a tetragonal lattice, which is parallel to the lattice of the matrix, had precipitated in the matrix, c-axis taking three orientations parallel to the cubic axes of the matrix. If so, the lattice constant a of the new phase is $a=3.98\pm0.01$ kX, the same as the lattice constant a_0 of the matrix, and the lattice constant c is $c=4.11\pm0.01$ kX calculated from the distance between the incident spot and the side maximum of (200). This tetragonal phase must be either the matrix phase deformed from the face centered cubic lattice or a newly precipitated phase. According to Vegard's law, however, spacing larger than that of gold, $a=4.070$ kX, is impossible in any substitutional solid solution of gold and nickel. Thus the assumption that the new tetragonal phase exists is impossible and the side maxima must be interpreted from a different standpoint.

According to X-ray study of Au-Pt alloy by Tiedema et al.,8) two side bands besides main reflections appear in the early stages of aging and disappear at the later stages. These side bands are attributed to the following modulated structure: The modulation occurs along a cubic axis and its wave-length is Qa_0, where a_0 is the lattice constant of the matrix (Fig. 5). Out of Q layers, p layers are Au rich and q layers are Pt rich, where $q=Q-p$. The spacing of p layers and that of q layers are assumed respectively to be $a_1=a_0(1+q\delta)$ and $a_2=a_0(1-p\delta)$, where δ is a parameter. Ratio p/q is assumed to be the same as that of the amount of the two stable phases which would be obtained at room temperatures.

Au-Ni alloy system studied in the present experiment has the equilibrium phase diagram similar to that of Au-Pt alloy system (Fig. 1). The behavior observed for Au-Ni that the side maxima appear at the early stage and disappear at the later stage of aging is also similar to the behavior for Au-Pt. From these similarities, it is reasonable to attribute the side maxima to the modulated structure as that of Au-Pt alloy. The wave-length of modulation Qa_0 is given by the distance between a main spot and the associated side maxima (Δr of Table III) using the relation

$$\Delta r\cdot Qa_0=\Lambda L, \qquad (1)$$

where Λ is the wave-length of electron wave and L, the camera length. Value of Q turned out to be 17. The ratio p/q is determined from the phase diagram (Fig. 1) and thus $p=14$ and $q=3$ are obtained. It may be reasonable to determine parameter δ by assuming that ratio $(1+q\delta)/(1-p\delta)$ is equal to ratio $a_1/a_2=4.05/3.52$, where a_1 and a_2 are lattice constants of stable α_1 and α_2-phases, respectively. Then δ turns out to be 0.008.

The amplitude of electron wave diffracted by the modulated structure is given by

$$A=\sum_{m=0}^{M-1}\{\sum_{s=0}^{p-1}F_A\exp 2\pi ihs(1+q\delta)+\sum_{t=0}^{q=1}F_B\exp 2\pi iht(1-p\delta)$$
$$\times\exp 2\pi ih\,p(1+q\delta)\}\exp 2\pi ihmQ, \qquad (2)$$

where F_A and F_B are the structure amplitudes of each layer of Au-rich phase and Ni-rich phase, respectively; h, the index of reflection and M, the number of wave-lengths Qa_0. The intensity is, therefore, given by

$$I=\Bigg[\,|F_A|^2\frac{\sin^2\pi hp\,(1+q\delta)}{\sin^2\pi h\,(1+q\delta)}+|F_B|^2\frac{\sin^2\pi hq\,(1-p\delta)}{\sin^2\pi h\,(1-p\delta)}$$
$$+2|F_A|\,|F_B|\,\frac{\sin\pi hp\,(1+q\delta)}{\sin\pi h\,(1+q\delta)}\cdot\frac{\sin\pi hq\,(1-p\delta)}{\sin\pi h\,(1-p\delta)}$$
$$\times\cos\pi hQ\,(1+\delta)\Bigg]\frac{\sin^2\pi MQh}{\sin^2\pi Qh}. \tag{3}$$

The intensity given by the formula (3) has the subsidiary maxima at $h=h_0+\frac{n}{Q}$, where h_0 is the index of main maxima and n, an integer.

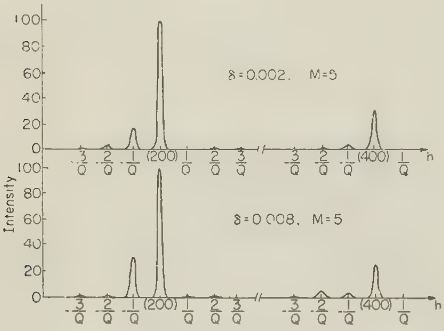

Fig. 6. The calculated intensity curves of (200) and (400)-spots in the reciprocal space.

Fig. 6 shows the intensity curves in the reciprocal space calculated for $\delta=0.002$ and 0.008. Value of M is assumed to be 5. Independent of the value of δ, subsidiary maxima appear only on the low angle side of (200) and (400) main maxima. Subsidiary maxima around (220) are expected to appear on [100] axis similarly to those of (200). The modulated structure in specimen films may be formed along three main axes of the matrix. Thus a diffraction pattern corresponds to the superposition of the intensity regions of three orientations.

The agreement between the observation and the theory is good in the fact that no side maxima is observed in high angle side. It may be reasonable that the second order side maximum at low angle side was not observed, because the expected intensity is too weak. The elongation of (400) spots towards low angle side (Fig. 4) is also in accordance with the theory.

§ 5. Discussions and Conclusions

a) *Side maxima*

The side maxima observed in the present experiment are a kind of the so-called "side bands" investigated by Daniel and Lipson.[3] The side bands observed by them were symmetric across a main reflection and interpreted by assuming sinussoidal modulation of spacing (Fig. 7 (a)). In the case of Al-Cu,

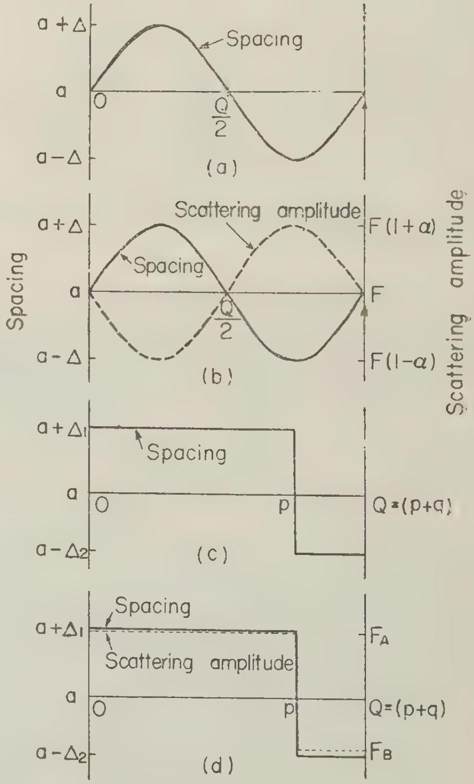

Fig. 7. Modulations given by Daniel-Lipson (a), Wilson (b), Tiedema et al. (c) and the present author (d). Δ and α are amplitudes of the modulation in spacing and scattering amplitude, respectively. Q, p and q are the number of unit cells.

Guinier[9] and Preston[10] observed asymmetric streaks extending towards high angle side. Wilson[11] explained the streaks as follows: Asymmetric side maxima are expected if modulations are assumed both for the spacing and for the scattering amplitude (Fig. 7 (b)). Moreover, the side maximum on low angle side vanishes provided $h_0 Q \Delta = \alpha$, where h_0 is the index of the main reflection and Δ and α are amplitudes of the modulation in spacing and scattering amplitude, respectively. If parameter Q is not a constant, the side maximum extends into a streak. In the case of Au-Pt, Tiedema et al.[8] observed asymmetric side bands. The intensity of the side band on low angle side was stronger than that on high angle side. Tiedema et al. assumed a periodic modulation as illustrated in Fig. 7 (c) to interpret the difference of intensity of both side bands. In the present case of Au-Ni, the side maxima are observed on the low angle side alone. We assumed modulations as illustration in Fig. 7 (d) to interpret the side maximum on low angle side. Each type of the modulations (Fig. 7) depends on the size of atoms and the scattering factor (Table IV).

Table IV. Size and scattering factor of component atoms.

Author	Alloy	Scattering amp.	Size of atoms
Daniel-Lipson	Cu–(Fe–Ni)	$f_{Cu} \sim (f_{Fe}$ or $f_{Ni})$	$r_{Cu} > (r_{Fe}$ or $r_{Ni})$
Wilson	Al–Cu	$f_{Al} < f_{Cu}$	$r_{Al} > r_{Cu}$
Tiedema et al.	Au-Pt	$f_{Au} \sim f_{Pt}$	$r_{Au} > r_{Pt}$
Present author	Au-Ni	$f_{Au} > f_{Ni}$	$r_{Au} > r_{Ni}$

b) *Formation of modulated structure*

For aluminium alloys, the formation of pre-precipitates at low temperatures has been explained as due to quenched-in vacancies which increase the diffusion rate of solute atoms.[12] In the present case of Au- Ni, the formation of modulated structure at low temperatures may also be explained as due to quenched-in vacancies. This explanation is supported by the result that the modulated structure is not produced by re-aging at low temperatures after reversion. Because the excess vacancies have been annealed out in the reversion process, the diffusion rate of Ni-atoms becomes too small to produce pre-precipitates again. The decrease of vacancies in the matrix has been proved also by the decrease of background intensity in diffraction pattern (§ 3(c)).

In the present case, the aging is carried out in the region of temperatures where the second derivative of free energy to composition is negative.[13] The segregates formed in the matrix, therefore, will grow further by mechanism of up-hill diffusion. The surrounding matrix becomes Au-rich. Thus, the modulated structure will be formed by the periodic repetition of the segregation and growth.

Flinn et al.[14] supposed that the homogeneous solid solution of Au-Ni alloy must have a locally ordered structure to reduce the large strain energy in the supersaturated solid solution. In the present experiment, such an ordered structure is not found. The large strain energy may be reduced by the formation of the modulated structure.

Based upon the measurements of electrical resistivity and other physical properties, Sivertsen et al.[15] suggested that metastable precipitates are formed in Au-30 atomic % Ni alloy during aging below 225°C. They supposed that the metastable precipitates are solute rich clusters, solvent-rich clusters or highly ordered regions in the matrix. In the present experiment, it has been made clear that the pre-precipitates have the modulated structure. The pre-precipitates in the present experiment are formed below 300°C while in Sivertsen's experiment, below 225°C. The difference may be due to the difference of compositions of alloys used in both experiments.

c) *True precipitation*

Köster et al.[5] found that the supersaturated solid solution of Au-Ni alloys decomposed by a discontinuous reaction into two phases of an Au-rich solid solution (α_1-phase) and a Ni-rich solid solution (α_2-phase) for aging at temperatures higher than 400°C. According to them, the process of the precipitation proceeds by inhomogeneous precipitation.

In the present work, the homogeneous solid solution of Au-20 atomic % Ni alloy decomposed into two phases of α_1 and α_2 in the whole specimen film after aging at 400–500°C for 1 hr. Since the rate of precipitation in thin evaporated films is larger than that in bulk crystals, we consider that the inhomogeneous precipitation could not be observed in the present experiment.

Tiedema et al.[8] found Widmanstätten structure in Au-Pt alloy. Although Köster et al.[5] did not find Widmanstätten structure in bulk crystals of Au-Ni alloys, the structure is observed in the present experiment (Photo. 9). However, the structure is of dimension several hundred Ångstroms. This may be attributed to the large difference between lattice parameters of two phases, because well-developed Widmanstätten structures are observed for nearly equal lattice parameters.[16] α_2-phase precipitates as the plate parallel to the cubic plane in the matrix. Such a precipitation was also found in Cu-Ag alloys.[17]

Ellwood et al.[18] found from the density measurement that there are very many vacancies in the homogeneous solid solution of Au-Ni alloys, particularly in Au-20 atomic % Ni and Ni-10 atomic % Au. We, therefore, consider that small loops shown in Photo. 8 are dislocation rings which are formed by the collapse of aggregates of vacancies.[7]

§ 6. Acknowledgement

In conclusion the author should like to thank to Prof. S. Ogawa for suggesting this investigation and for guidance throughout the work. Thanks go to Prof. R. Uyeda and Prof. K. Kimoto for helpful discussions.

References

1) A. Winkelmann: Z. Metallkunde **47** (1956) 621.
2) Y. Fukano and S. Ogawa: J. Phys. Soc. Japan **14** (1959) 1671.
3) V. Daniel and H. Lipson: Proc. Roy. Soc. A **181** (1943) 368, Proc. Roy. Soc. A **182** (1944) 378.
4) R. W. C. Wyckoff: The Structure of Crystals, 3rd Edition Supplement.
5) W. Köster and W. Dannöhl: Z. Metallkunde **28** (1936) 248; W. Köster and A. Schneider: Z. Metallkunde **29** (1937) 103.
6) D. W. Pashley: Phil. Mag. **4** (1959) 324.
7) P. B. Hirsch, J. Silcox, R. E. Smallman and K. H. Westmacott: Phil. Mag. **3** (1958) 897.
8) T. J. Tiedema, J. Bouman and W. G. Burgers: Acta Met. **5** (1957) 310.
9) A. Guinier: Compt. Rend. **206** (1938) 1641.
10) G. D. Preston: Nature **142** (1938) 570; Proc. Roy. Soc. A **167** (1938) 526.
11) A. J. C. Wilson: *X*-Ray Optics (London, 1949).
12) T. Federighi: Acta Met. **6** (1958) 379.
13) G. Borelius: J. Metals **3** (1951) 477.
14) P. Flinn, B. L. Averbach and M. Cohen: Acta Met. **1** (1951) 673.
15) J. Sivertsen and C. Wert: Acta Met. **7** (1959) 275.
16) A. H. Geisler and J. B. Newkirk: Trans. Am. Inst. Mining. Met. Engrs. **180** (1949) 101.
17) G. S. Barrett, H. F. Kaiser and R. F. Mehl: Trans. Am. Inst. Mining. Met. Engrs. **117** (1935) 39.
18) E. C. Ellwood and K. Q. Bagley: J. Inst. Metals **80** (1951–52) 617.

JOURNAL OF THE PHYSICAL SOCIETY OF JAPAN Vol. 16, No. 6, JUNE, 1961

A Direct Determination of the Crystal Structure of Ethylenediammonium Sulphate

By Kiichi SAKURAI

Department of Physics, Faculty of Science, Osaka University,
Nakanoshima, Osaka, Japan

(Received February 28, 1961)

The Harker-Kasper inequality method was applied successfully to determine most of the signs of structure factors of ethylene diammonium sulphate. Starting from these signs the final Fourier projections on (001) and (100) were obtained. The dimensions of the unit cell containing eight formula units are $a=8.47\pm0.02$ A, $c=18.03\pm0.04$ A, and the space group is $D_4^4-C4_122_1$ or $D_4^8-C4_322_1$. The ethylenediammonium group is of gauche type with an azimuthal angle of 75.7°. The hydrogen bond distances found in this crystal are 2.80 A, 2.81 A, and 2.82 A. The existence of only one kind of two mirror-image configurations of the ethylenediammonium ion in one of the enantiomorphous forms of this crystal may be an important cause of the strong optical rotatory power of the crystal.

§1. Introduction

Crystals of ethylenediammonium sulphate, $(NH_3CH_2CH_2NH_3)SO_4$, are tetragonal and are known for the strong optical rotatory power, 15.5°mm^{-1} for the *D*-line of sodium.[1] In order to obtain a structural basis for the interpretation of the optical activity as well as information on the role of hydrogen bond in this crystal, its structure has been analyzed by X-ray methods. The accurate determination, if possible, of the sulphate and the ethlyenediammonium groups in this crystal is another purpose of this investigation.

From the structure-analytical point of view, this crystal proved to be a suitable example for the application of the inequality method,[2] which permits many of the signs of structure factors to be determined from intensity data. The present author devised a convenient graphical method for applying some important inequalities and used it for the determination of the signs of structure factors $F(hk0)$'s and $F(0kl)$'s of this crystal.[3] The intensity data were also used by Okaya and Nitta as the first example of the application of their linear inequalities.[4]

§2. Experimental

(1) *Unit cell and space group*

The crystallographic description of this substance is given by Groth.[1] Single crystals used in this investigation were obtained by slow evaporation of an aqueous solution at room temperature in a desiccator. Laue photographs showed the tetragonal holohedral symmetry. Oscillation photographs about the *a* and *c* axes, and equatorial Weissenberg photographs about the *c* axis were taken with filtered Cu $K\alpha$ radiation. The diameters of the rod specimens along the *a* and *c* axes used for the oscillation and Weissenberg photograghs were 0.13 mm and 0.22 mm respectively. The dimensions of the tetragonal unit cell obtained from oscillation photographs are $a=8.47\pm0.02$ Å, $c=18.03\pm0.04$ Å. The density given by Burgers[5] is 1.625 g.cm^{-3}, and the value calculated for eight formula units per cell is 1.62 g.cm^{-3}. Systematic absences of reflections are observed in (hkl) when $h+k\neq 2n$, in $(hh0)$ when $h\neq 2n$, and in $(00l)$ when $l\neq 4n$. Hence the space group is $D_4^4-C4_122_1$ or $D_4^8-C4_322_1$. By axial transformation the lattice parameters become $a=5.99$Å, $c=18.03$Å, and the notation of the space group $P4_12_1$ or $P4_32_1$. These crystallographic data are in good agreement with those given by Burgers.[5] In the present investigation the former set of axes was chosen, because it was easier to obtain rod specimens along the *a* axis based on the former axial system.

(2) *Intensity data*

The $(hk0)$ and $(0kl)$ intensities of oscillation photographs were measured with a microphotometer using a standard intensity scale, and the ($hk0$) intensities recorded on multiple-film integrated Weissenberg photographs were estimated visually by comparison with a standard intensity scale. Corrections for polarization and Lorentz factors were applied in the usual way. As the dimensions of the specimens were small, no correction for absorption was considered neccessary. Approximate values for a scale factor and a temperature-factor parameter were obtained by Wilson's method,[6] due allowance being made for overlapping of atoms in the (001) projection as anticipated from the cell dimensions. The value of the temperature-factor parameter was found to be 2.0 Å². The final values of the scale factor and the temperature-factor parameter were determined by comparison of observed structure factors with calculated values.

§ 3. Structure determination

For the space group $D_4^4-C4_122_1$, there exist two sets of positions, special eight-fold and general sixteen-fold position:

$(000:\ \frac{1}{2}\,\frac{1}{2}\,0)+$

8: (a) $x, 0, 0:\ \bar{x}, 0, \frac{1}{2}:\ \frac{1}{2}, x, \frac{1}{4}:\ \frac{1}{2}, \bar{x}, \frac{3}{4}.$

16: (b) $x, y, z:\ \bar{x}, \bar{y}, \frac{1}{2}+z:\ \frac{1}{2}-y, x, \frac{3}{4}+z:$
$\frac{1}{2}+y, \bar{x}, \frac{3}{4}+z:$
$x, \bar{y}, \bar{z}:\ \bar{x}, y, \frac{1}{2}-z:\ \frac{1}{2}+y, x, \frac{3}{4}-z:$
$\frac{1}{2}-y, \bar{x}, \frac{3}{4}-z.$

As the number of formula units in the unit cell is eight, sulfur atoms occupy the special eight-fold positions, and nitrogen, carbon, and oxygen atoms the general positions. The Harker-Kasper inequality method was applied, for it was expected that this structure could be solved by this method. Although the structure does not possess a center of symmetry, its projection on (001) and (100) are both centrosymmetric, and it is sufficient to determine the sings of $F(hk0)$'s and $F(0kl)$'s to obtain the Fourier projections onto these two planes. One of the fundamental set of inequalities[7)]

$$(U_H \pm U_{H'})^2 \leq (1 \pm U_{H+H'})(1 \pm U_{H-H'}),$$

where U_H is the unitary structure factor for the reflection $H=hkl$, was used. The magnitudes of structure factors, $U(hk0)$'s and $U(0kl)$'s, were derived from the structure factors converted into an absolute scale by Wilson's method. The application of the above inequality was carried out using a chart devised by the present author. A detailed description of the use of the chart and the procedure of sign determination has already been published.[3)]

(1) (001) *projection*

The values of the unitary structure factors and the signs determined by the inequality method are given in Table I. An arbitrary parameter ξ is connected with $U(hk0)$'s with h and k both odd, and this corresponds to the arbitrariness of the choice between the two sets of origins (00), ($\frac{1}{2}\frac{1}{2}$) and ($\frac{1}{2}$0), (0$\frac{1}{2}$). Putting $\xi=-1$, a Fourier projection on (001) was synthesized. It is shown in Fig. 1. After the completion of analysis, it was found that the signs of (400), (390), and (570) were wrong. A Fourier projection including all $F(hk0)$'s with their correct signs is shown in Fig. 2. A comparison of these two Fourier maps shows that the inequality method leads to an essentially correct map except minor details. As anticipated from the unit-cell dimensions, there is a considerable overlapping of atoms in the (001) projection, and the parameters of

Table I. $U(hk0)$'s and the signs determined by the inequality method

$h \backslash k$	0	1	2	3	4	5	6	7	8	9	10
0	1.00	—	|0.08|	—	+0.17	—	0.00	—	+0.69	—	0.00
1	—	—	—	+0.10ξ	—	0.00	—	−0.37ξ	—	+0.32ξ	—
2	|0.08|	—	−0.30	—	|0.09|	—	−0.45	—	0.00	—	−0.40
3	—	−0.10ξ	—	—	—	+0.24ξ	—	0.00	—	−0.39ξ	—
4	+0.17	—	|0.09|	—	+0.84	—	|0.09|	—	0.00	—	0.00
5	—	0.00	—	−0.24ξ	—	—	—	+0.32ξ	—	0.00	
6	0.00	—	−0.45	—	|0.09|	—	−0.60	—	|0.13|		
7	—	+0.37ξ	—	0.00	—	−0.32ξ	—	—			
8	+0.69	—	0.00	—	0.00	—	|0.13|				
9	—	−0.32ξ	—	+0.39ξ	—	0.00					
10	0.00	—	−0.40								

the atoms other than the sulfur atom cannot be obtained from this projection. However, the symmetry of the structure allows the x and y parameter of the light atoms to be determined simultaneouly from the (100) projection.

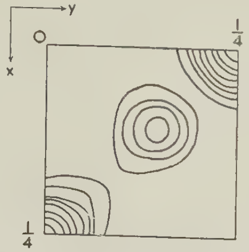

Fig. 1. Fourier projection on (001) based on the signs determined by the inequality method alone. Contours are drawn at equal arbitrary intervals.

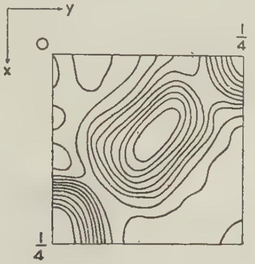

Fig. 2. Final Fourier projection on (001). Contours are drawn at intervals of 2 e.A^{-2}, except around sulfur atom where contours are at intervals of 4 e.A^{-2} starting at 14 e.A^{-2}.

(2) (100) *projection*

The values of the unitary structure factors and the signs determined by the inequality method are given in Table II. In this case two arbitrary parameters, η and ζ, are connected with reflections with $k=2\times$odd, $l=$even and those with $k=2\times$even, $l=$odd respectively. This corresponds to the arbitrariness of the choice of origin out of four points (00), (0$\frac{1}{2}$), ($\frac{1}{4}$0), and ($\frac{1}{4}\frac{1}{2}$). Putting $\eta=+1$ and $\zeta=-1$, a Fourior projection on (100) was synthesized. It is shown in Fig. 3. In this projection all atoms are fairly well resolved, and it was possible to obtain approximate parameter values. From the Fourier projections on (001) and (100) using the signs obtained by the inequality method, it can already be seen that the configuration of the ethylenediammonium ion is gauche. By successive Fourier approximation, the final projection on (100) was synthesized using all the observed F's. It is shown in Fig. 4. In order to refine the struc-

Table II. $U(0kl)$'s and the signs determined by the inequality method

l \ k	0	2	4	6	8	10
0	1.00	$\|0.08\|$	$+0.17$	0.00	$+0.69$	0.00
1	—	$+0.20\eta\xi$	$\|0.08\|$	$\|0.03\|$	-0.41ξ	$+0.67\eta\xi$
2	—	$+0.29\eta$	$\|0.08\|$	$+0.34\eta$	0.00	$+0.37\eta$
3	—	0.00	$\|0.10\|$	$\|0.27\|$	$\|0.24\|$	$+0.23\eta\zeta$
4	$+0.22$	0.00	$+0.24$	$\|0.12\|$	$+0.49$	0.00
5	—	$+0.26\eta\xi$	-0.27ξ	$\|0.13\|$	$\|0.17\|$	$+0.35\eta\xi$
6	—	$+0.16\eta$	$\|0.13\|$	$+0.53\eta$	$\|0.15\|$	$\|0.26\|$
7	—	$\|0.10\|$	$+0.24\xi$	$-0.39\eta\xi$	0.00	
8	$+0.33$	$\|0.11\|$	$+0.47$	$\|0.22\|$	$+0.33$	
9	—	$+0.26\eta\xi$	-0.28	$+0.28\eta\xi$	0.00	
10	—	$+0.07\eta$	0.00	$+0.39\eta$	0.00	
11	—	$\|0.15\|$	$+0.30\xi$	0.00	0.00	
12	0.00	0.00	$+0.40$	0.00	0.00	
13	—	0.00	0.00	0.00	0.00	
14	—	$+0.13\eta$	0.00	0.00	$\|0.31\|$	
15	—	0.00	0.00	$\|0.14\|$	$\|0.22\|$	
16	$+0.52$	0.00	$+0.37$	0.00		
17	—	0.00	0.00	0.00		
18	—	$+0.57\eta$	0.00	$+0.29\eta$		
19	—	0.00	0.00	$-0.34\eta\xi$		
20	$+0.37$	0.00	$+0.58$			
21	—	0.00	-0.23ξ			
22	—	-0.52η				

ture, (F_o-F_c) syntheses were calculated, and, after eight successive calaulations, the final atomic parameters and the temperature-factor parameter were determined by the same procedure as mentioned by Cochran.[8] The final difference map is shown in Fig. 5. It shows peaks in the positions expected for the hydrogen atoms from a model of the ethylenediammonium ion, and reasonable parameter values can be assigned to them. Using the formula of Cruickshank[9] for the standard deviation of electron density, $\sigma(\rho_o)$,

$$\sigma(\rho_o)=\frac{1}{A}[\sum(F_o-F_c)^2]^{1/2}$$

where A is the area of the cell in projection, $\sigma(\rho_o)$ for the (100) projection was found to be 0.69 e.Å^{-2}

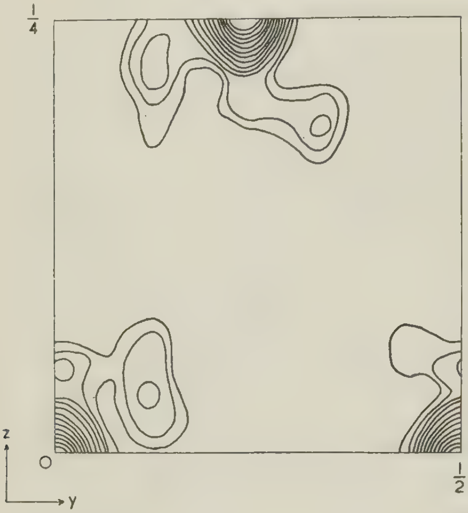

Fig. 3. Fourier projection on (100) based on the signs determined by the inequality method alone. Contours are drawn at equal arbitrary intervals.

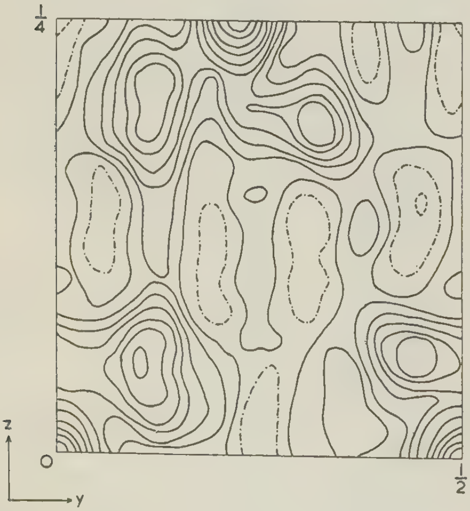

Fig. 4. Final Fourier projection on (100). Contours are drawn at intervals of 2 e.A^{-2}, except around sulfur atom where contours are at intervals of 4 e.A^{-2} starting at 10 e.A^{-2}. Chain lines represent zero contour and broken lines negative contours.

The final atomic parameters are listed in Table III. The observed and calculated structure factors, F_o and F_c, are given in Table IV. The calculated values include the contribution from hydrogen atoms. The average temperature-factor parameter is 1.72 Å^2. The atomic scattering factors used in the calculation are those given in the 'Internationale Tabellen'.[10] The values of R indices for ($hk0$) and ($0kl$) zones are 12% and 16% res-

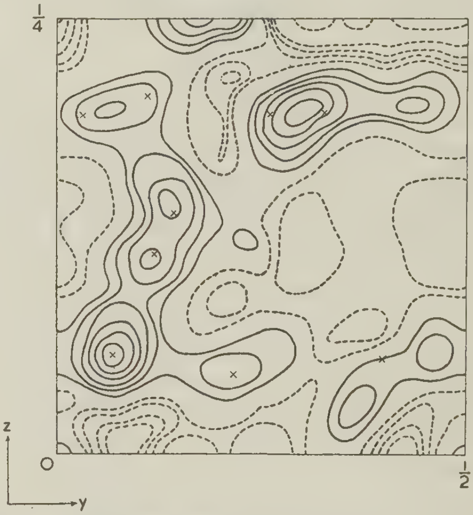

Fig. 5. Difference synthesis projection on (100). Contours are drawn at intervals of 0.2 e.A^{-2}. Negative contours are drawn in broken lines and zero contour is omitted. Crosses mark the positions of hydrogen atoms.

Table III. Atomic parameters

	x	y	z
S	0.2291	0	0
O_I	0.123	0.125	0.0296
O_{II}	0.329	0.063	0.0608
N	0.611	0.111	0.0643
C	0.744	0.005	0.0430
H_I	0.64	0.12	0.114
H_{II}	0.61	0.21	0.044
H_{III}	0.53	0.07	0.055
H_{IV}	0.83	0.07	0.055
H_V	0.76	0.10	0.055

Table IV. Observed and calculated structure factors.

h	k	l	F_o	F_c	h	k	l	F_o	F_c	h	k	l	F_o	F_c
0	2	0	13	14	0	2	10	< 5	3	0	6	6	32	31
0	4	0	16	18	0	2	11	11	11	0	6	7	23	20
0	6	0	< 3	4	0	2	12	< 6	0.8	0	6	8	13	9
0	8	0	24	33	0	2	13	< 6	2	0	6	9	15	10
0	10	0	5	8	0	2	14	23	21	0	6	10	20	18
1	3	0	11	12	0	2	15	7	8	0	6	11	< 6	8
1	5	0	< 3	4	0	2	16	< 6	4	0	6	12	< 6	2
1	7	0	16	16	0	2	17	< 5	3	0	6	13	7	7
1	9	0	8	7	0	2	18	25	24	0	6	14	< 5	2
2	2	0	82	86	0	2	19	< 5	3	0	6	15	6	5
2	4	0	9	13	0	2	20	< 5	0.1	0	6	16	< 5	0.7
2	6	0	22	22	0	2	21	< 5	2	0	6	17	< 5	3
2	8	0	< 3	3	0	2	22	17	15	0	6	18	9	7
21	0	0	9	13	0	4	1	8	8	0	6	19	11	10
3	5	0	13	13	0	4	2	8	6	0	8	1	19	19
3	7	0	< 3	2	0	4	3	9	10	0	8	2	< 5	3
3	9	0	14	13	0	4	4	21	21	0	8	3	11	10
4	4	0	81	76	0	4	5	23	23	0	8	4	24	26
4	6	0	8	11	0	4	6	< 5	0.2	0	8	5	8	7
4	8	0	6	4	0	4	7	19	18	0	8	6	7	5
4	10	0	< 2	0.4	0	4	8	35	40	0	8	7	< 6	0.2
5	7	0	15	13	0	4	9	20	18	0	8	8	14	11
5	9	0	< 2	3	0	4	10	< 6	3	0	8	9	< 5	2
6	6	0	28	26	0	4	11	16	15	0	8	10	< 5	4
6	8	0	5	7	0	4	12	22	21	0	8	11	< 5	5
0	0	4	100	109	0	4	13	< 6	3	0	8	12	< 5	5
0	0	8	42	43	0	4	14	< 6	1	0	8	13	< 5	5
0	0	12	< 6	4	0	4	15	< 5	0.3	0	8	14	< 5	2
0	0	16	32	31	0	4	16	17	13	0	8	15	8	8
0	0	20	15	12	0	4	17	< 5	1	0	10	1	21	21
0	2	1	40	46	0	4	18	< 5	2	0	10	2	14	13
0	2	2	100	100	0	4	19	< 5	1	0	10	3	6	5
0	2	3	< 4	8	0	4	20	22	24	0	10	4	< 5	4
0	2	4	< 4	0.5	0	4	21	7	8	0	10	5	13	15
0	2	5	36	36	0	6	1	17	16	0	10	6	9	9
0	2	6	19	18	0	6	2	23	21	0	10	7	< 5	5
0	2	7	10	6	0	6	3	14	15	0	10	8	< 4	2
0	2	8	10	8	0	6	4	< 6	3	0	10	9	< 4	1
0	2	9	21	19	0	6	5	9	10					

pectively, non-observed reflections being included.

§ 4. Discussion of the structure

Interatomic distances and bond angles are given in Table V. Owing to the overlapping of atoms, the standard deviations of the interatomic distances cannot simply be estimated by the usual formula,[9] so that any significance cannot be attached to the differences between the values found in the present work and those reported. Therefore a mere comparison of the former with the latter will be made. In the following discussion the sulphate group and the ethylenediammonium group are first dealt with, and then the linkage of ions in the

Table V. Interatomic distances and bond angles.

SO_4 group		N—H··O hydrogen bonds	
S—O_I	1.49 Å	N··O_I	2.82 Å
S—O_{II}	1.48	N··O'_I	2.80
O_I··O_I	2.37	N··O_{II}	2.81
O_{II}··O_{II}	2.44	<C—N··O_I	103.6°
O_I··O_{II}	2.42	<C—N··O'_I	106.5
O_I··O_{II}	2.44	<C—N··O_{II}	108.7
NH_3^+·CH_2·CH_2 NH_3^+ group		<O_I··N··O'_I	125.0
		<O_I··N··O_{II}	94.5
C—C	1.55 Å	<O'_I··N··O_{II}	114.8
C—N	1.49	Non-bonded N··O distances	
N··N	2.99	N··O_{II}	3.26 Å
N—H_I	0.93	N··O'_{II}	3.31
N—H_{II}	0.93	N··O''_{II}	3.32
N—H_{III}	0.80		
C—H_{IV}	0.92		
C—H_V	0.93		
<C—C—N	106.2°		
azimuthal angle 75.7°			

structure is described.

(1) *Sulphate group*

The S–O distance in the sulphate group has been discussed be Wells[11] and Pauling.[12] Pauling has given a value of 1.51 Å as a predicted S–O distance after taking into account the ionic character of σ bond and the amount of π bond character and has stated that this value is in good agreement with an average of observed distances, 1.50Å. The average S–O distance of 1.49 A found in the present investigation is close to this predicted value.

(2) *Ethylenediammonium group*

A striking feature of this crystal structure is that the configuration of the ethylenediammonium group is not trans but gauche with the symmetry C_2. (see Fig. 6.) The azimuthal angle of one half of the group with respect to the other is 75.7°, which is much larger than 60°. This large azimuthal angle may be due to the intramolecular repulsion between two NH_3^+ groups. The C–N^+ distance of 1.49Å is in good agreement with those found in amino hydrohalides, amino acids, and peptides.* The reported values range from 1.46Å to 1.52Å. Cox and Jeffrey[13] have reviewed reported values of the C–N single bond distance and have concluded that they lie within a small range about the average value 1.47Å. Hall and Llewellyn[14] have examined C–N^+ bond distances reported until 1953 and have concluded that the best value is 1.47–1.48 Å. They have also compared C–N^+ distances with C–N distances and have pointed out that there is no evidence of bond shortening of the former, relative to the latter, due to the formal charge effect which is estimated to be about 0.03Å by Pauling. In a review concerning the structural data of amino acids and carboxylic acids published by Hahn,[15] it has been remarked that the C–NH_3^+ distance is 1.50 Å, which is 0.03 Å longer than the normal C–N single bond length.

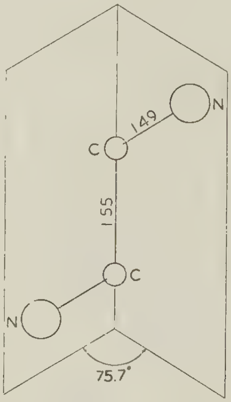

Fig. 6. Structure of the ethylenediammonium group. Bond lengths are given in Angström units.

As the ethylenediammonium ion has the gauche configuration, two mirror-image configurations are possible, and only one kind of the two forms exists in one of the enantiomorphous forms of this crystal. This may be considered to be an important cause of the strong optical rotatory power of this crystal.

(3) *Linkage of sulphate and ethylenediammonium groups*

The structures projected on (001) and (100) are shown in Fig. 7 and Fig. 8 respectively. As can be seen from Fig. 8, the structure can conveniently be described as built up of layers, parallel to (001), containing ethylenediammonium and sulphate groups. Each nitrogen atom is surrounded by six oxygen atoms at distances 2.80, 2.81, 2.82, 3.26, 3.31, and 3.32Å The N-···O distances, 2.80, 2.81, and 2.82Å can be interpreted as hydrogen bonds. These values lie within the range of values reported by Donohue[16] in his list of N–H···O hydrogen bond distances and of those reported later for amino acids and peptides. The arrangement of these three oxygen atoms around the nitrogen atom is shown in Fig. 9, where their positions are projected upon the plane perpendicular to the C–N bond. In this figure the positions of the hydrogen atoms derived from the difference synthesis are also shown. The C–N···O angles are found to be 108.7°, 106.5°, and 103.5°, all being near-tetrahedral value, and the hydrogen atoms lie nearly on the lines connecting the nitrogen and the oxygen atoms. This situation favors the formation of strong hydrogen bonding.16) In each layer ethylenediammonium and sulphate groups are linked by two sets of hydrogen bonds of lengths 2.80, 2.81Å and N···O contacts with distances 3.31, 3.32Å, while these layers are held together by hydrogen bonds of length 2.82A and N···O contacts with a distance 3.26Å. As the number of linkages between layers formed by each nitrogen atom is smaller than that within a layer, a nearly perfect cleavage parallel to (001) can be accounted for by this structure.

---

* The C—N bond considered here refers to the C—NH_3^+ bond of a terminal nitrogen atom.

§ 5. A remark on the use of the inequality method

In this structure the ethylenediammonium ion has the gauche configuration, and this unexpected result has been established unambiguously by the use of the inequality method. This work has thus demonstrated the usefulness of the inequality method in determining a crystal structure in which molecules or molecular ions have an unknown or unexpected strucrure. It will be useful also in determining the average structure of a disordered crystal without any trial-and-error process.

In order that the first Fourier synthesis may

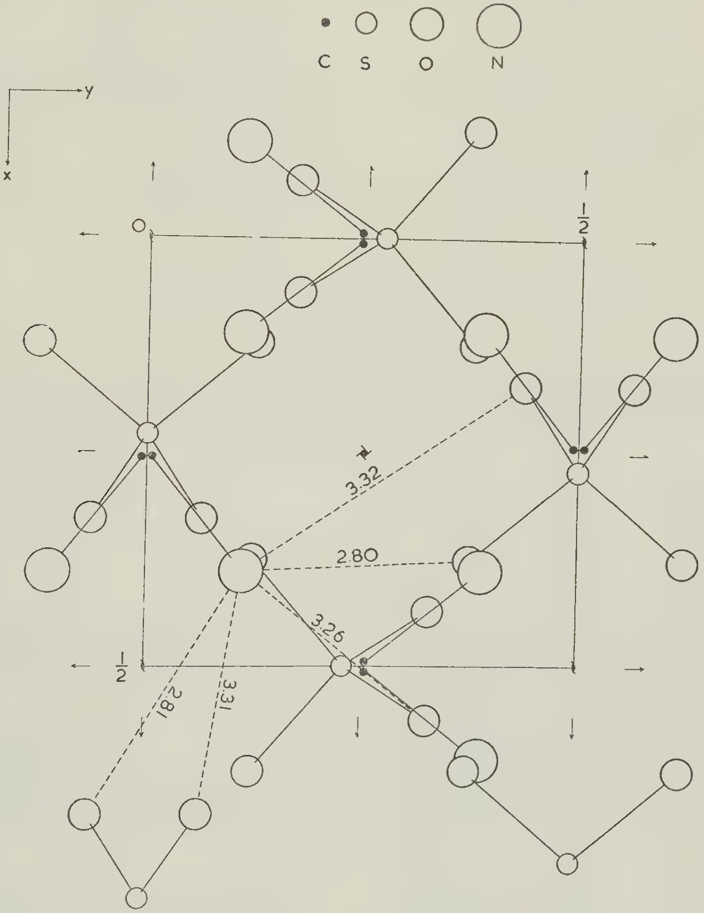

Fig. 7. Projection of the structure on (001). Broken lines represent N-H···O hydrogen bonds and N···O contacts. Interatomic distances are given in Angström units. The N-H···O hydrogen bond of length 2.82 A is not shown owing to the overlapping of participating atoms.

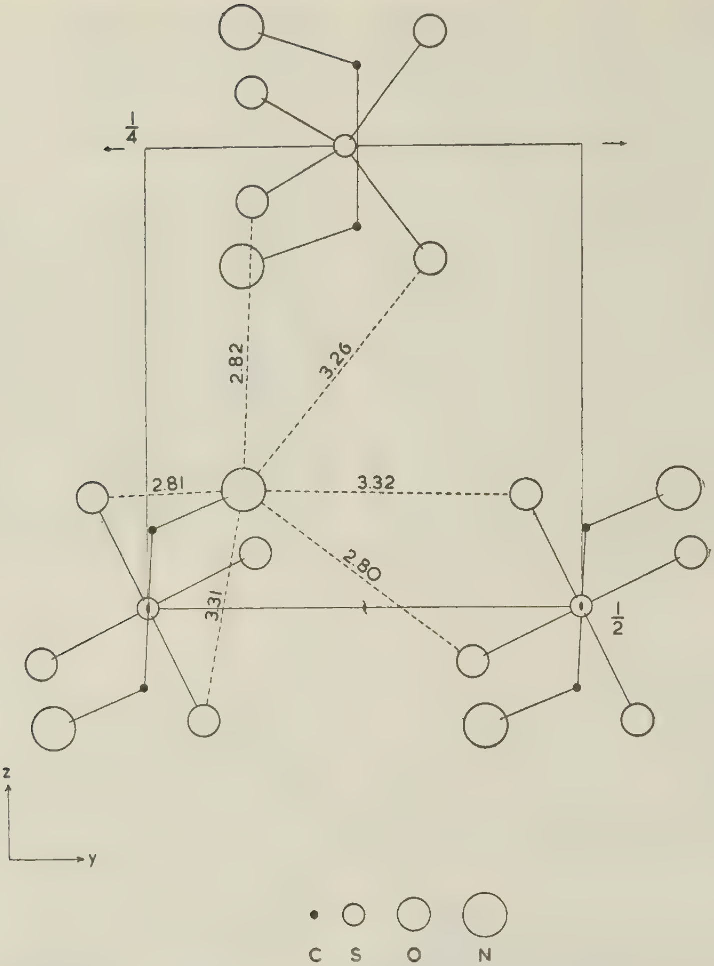

Fig. 8. Projection of the structure on (100). Broken lines represent N–H···O hydrogen bonds and N···O contacts. Interatomic distances are given in Angström units.

give a correct approximate structure, about 20% of larger structure factors must be given their correct signs. In this work the signs of about 70% of the observed structure factors could be determined for the $(hk0)$ and $(0kl)$ reflections, and the minimum magnitudes of $U(hk0)$ and $U(0kl)$ of which the signs could be determined were 0.10 and 0.07 respectively. Obviously the magnitudes of unitary structure factors are important for the successful application of the inequality method. The presence of the comparatively heavy sulfur atom in this structure makes σ, the standard deviation for the Gaussian distribution of unitary structure factors greater, than that expected when the atoms in the unit cell are all equal, and this causes unitary structure factors with large magnitude to be observed. This situation has favored the application of the inequa-

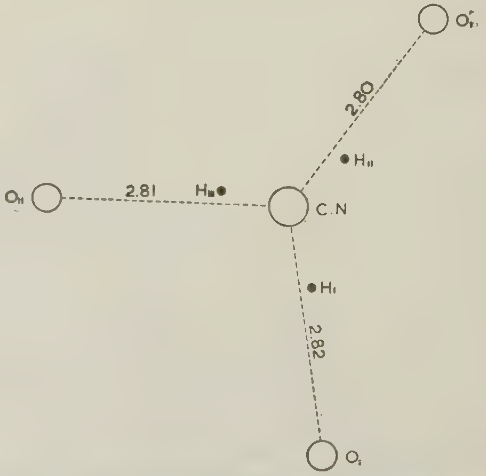

Fig. 9. Arrangement of three hydrogen-bonded oxygen atoms around a nitrogen atom viewed along the C—N bond. The positions of hydrogen atoms are shown by filled circles.

lity method.

The author wishes to express his thanks to Prof. Emeritus I. Nitta and Prof. T. Watanabé for their interest and helpful advice during the course of this investigation. He is also indebted to Dr. Y. Tomiie for his help in experimental work and many tedious calculations.

References

1) P. Groth: *Chemische Krystallographie* Teil 3 (Engelman, Leipzig, 1910) 54.
2) D. Harker and J. S. Kasper: Acta Cryst. **1** (1948) 70.
3) K. Sakurai: Acta Cryst. **5** (1952) 546.
4) Y. Okaya and I. Nitta: Acta Cryst. **5** (1952) 564.
5) W. G. Burgers: Proc. Roy. Soc. London **A 116** (1927) 553.
6) A. J. C. Wilson: Nature **150** (1942) 151.
7) P. M. DeWolff and J. Bouman: Acta Cryst. **7** (1954) 328.
8) W. Cochran: Acta Cryst. **4** (1951) 81.
9) D. W. J. Cruickshank: Acta Cryst. **2** (1949) 65.
10) *Internationale Tabellen zur Bestimmung von Kristallstrukturen* (Borntraeger, Berlin, 1935).
11) A. F. Wells: J. Chem. Soc. **1949**, 55.
12) L. Pauling: *The Nature of the Chemical Bond* (Cornell University Press, Ithaca, 1940) 240. J. Phys. Chem **56** (1952) 361.
13) E. G. Cox and G. A. Jeffrey: Proc. Roy. Soc. London **A 207** (1951) 110.
14) D. Hall and F. J. Llewllyn: Acta Cryst. **9** (1956) 108.
15) T. Hahn: Z. Kristallogr. **109** (1957) 438.
16) J. Donohue: J. Phys. Chem. **56** (1952) 502.

JOURNAL OF THE PHYSICAL SOCIETY OF JAPAN, Vol. 16, No. 6, JUNE, 1961

Study of Metallic Carbides by Electron Diffraction
Part IV. Cobalt Carbides

By Sigemaro NAGAKURA

Tokyo Institute of Technology, Oh-okayama, Meguro-ku, Tokyo

(Received March 3, 1961)

Thin cobalt films formed by evaporation were carburized in town gas at temperatures below 550°C for several hours. Electron diffraction studies of these films confirmed the existence of two kinds of carbide, Co_2C and Co_3C. Co_2C is an orthorhombic crystal with lattice constants $a=2.910$, $b=4.469$ and $c=4.426$ Å, and has a distorted c.p.h. structure. The lattice relation between Co_2C and Co is $(001)_{Co_2C}//(00.1)_{\alpha\text{-}Co}//(111)_{\beta\text{-}Co}$ and $[100]_{Co_2C}//[10.0]_{\alpha\text{-}Co}//[10\bar{1}]_{\beta\text{-}Co}$. Co_2C is formed at temperatures in a range 450°~500°C, and decomposes gradually to α-Co containing stacking faults and graphitic carbon at temperatures in a range 450°~470°C. Co_3C is an orthorhombic crystal with lattice constants $a=4.483$, $b=5.033$ and $c=6.731$ Å and is isomorphous with cementite (Fe_3C). The lattice relation is $(1\bar{2}1)_{Co_3C}//(10.1)_{\alpha\text{-}Co}//(100)_{\beta\text{-}Co}$, and $[111]_{Co_3C}//[0\bar{1}.0]_{\alpha\text{-}Co}//[001]_{\beta\text{-}Co}$. Co_3C is formed at temperatures in a range 450°~500°C and decomposes gradually to α-Co containing stacking faults and to graphitic carbon at temperatures in a range 480°~490°C. The mechanisms of Co_2C and Co_3C formation and decomposition are discussed.

§ 1. Introduction

In the previous papers[1),2),3)] the electron diffraction studies on the nickel and iron carbides were published and it was shown that the method is useful for the study of metallic carbides. The method is applied to the study of cobalt carbides in the present paper.

The cobalt carbide Co_2C was found by Bahr and Jessen,[4)] and Hofer and Peebles[5)] after the CO-gas cementation of cobalt powder at temperatures below 300°C. X-ray studies by Drain,[6)] and Juza and Puff[7)] showed that the

Co_2C is orthorhombic. Juza and Puff carried out the structure analysis, but Clark and Jack[8] reported that their structure was not correct and proposed another structure. Although the above mentioned authors found only the carbide Co_2C, Meyer[9] produced another carbide by the cementation of cobalt bars. His carbide gave the X-ray powder pattern similar to that of cementite, Fe_3C, so that it was considered to be Co_3C. In the present study both kinds of carbide were produced by the cementation of the evaporated cobalt films, and their structures, lattice relation between the carbides and cobalt, processes of carbide formation and decomposition were studied.

§ 2. Experimental

Cobalt films of about 400Å in thickness were prepared on the cleavage faces of rock-salt crystals by the evaporation of electrolytic cobalt. The films were polycrystalline when they were deposited on the faces of rock-salt kept at room temperature, while they were single crystalline on the faces kept at about 500°C. The cementation was carried out according to the method described in the previous paper.[1] The town gas through the converter furnace at about 1000°C was used to carburize the evaporated films. Carburizing temperature was changed in a range from 250 to 550°C. Carburizing period was about 5 hrs., and rate of gas flow was 100~150 cc per min. Composition of the gas was as follows: C: 25, CH_4:5, H_2:40, N_2:30 (in vol %). The electron diffraction patterns were taken by the camera operated at 65kV. The 200kV electron diffraction camera* was used for the measurement of intensities.

§ 3. Results

1. *Evaporated films*

Photo. 1 (a) is an electron diffraction pattern of a cobalt film formed on a surface of rock-salt kept at room temperature. The pattern is due to α-Co crystallites (c.p.h. structure) of random orientation. In the pattern it can be seen that the (hkl) Debye ring having the relation $h-k\neq 3n$ (n: integer) is broad. The breadth increases as the index l becomes higher. The (hkl) ring having the relation $h-k=3n$ is sharp. This shows that many stacking faults are produced on the close packed planes[10] during the deposition. The mean particle size calculated from the half -breadth of the sharp rings was 30Å. When α-Co film was heated in vacuum it transformed to the β-Co film (f.c.c.) gradually, accompanying the crystal growth. Photo. 1 (b) reproduces a diffraction pattern of cobalt film heated at 650°C for 30 min. The mean particle size was 60Å. When the α-Co films were heated in the electron diffraction camera, the transformation from α to β did not occur at the transformation temperature of builk cobalt, 420°C, but occured in a wide temperature range above about 500°C. The amount of transformation depended on the period of heating and on the temperature, and the rate of transformation was very slow at 500°C. The β to α transformation did not take place on cooling.

Photo. 2 reproduces an electron diffraction pattern of a cobalt film with single crystalline orientation prepared on a surface of rock-salt kept at 500°C. The lattice relation was found to be $(00.1)_{\alpha\text{-Co}}//(111)_{\beta\text{-Co}}$ and $[10.0]_{\alpha\text{-Co}}//[10\bar{1}]_{\beta\text{-Co}}$, i.e. the closest packed atomic planes and atomic rows are parallel to each other. The streaks in the pattern can be ascribed to the effect of stacking faults.

2. *Co_2C films*

Photo. 3 reproduces an electron diffraction pattern of a polycrystalline film carburized for 6 hrs. at 500°C. The pattern can be indexed by an orthorhombic unit cell of dimensions

$$a=2.910\,\text{Å},\ b=4.469\,\text{Å}\ \text{and}\ c=4.426\,\text{Å},$$

which agree well with the X-ray data of Co_2C, $a=2.897$ Å, $b=4.447$ Å and $c=4.371$ Å.[8] The mean particle size calculated from the half-breadth of the ring was 40 Å. The patterns of single crystalline film carburized partly and completely are reproduced in Photo. 4 (a) and (b), respectively. The lattice relation is

$$(001)_{Co_2C}//(00.1)_{\alpha\text{-Co}}//(111)_{\beta\text{-Co}}\,,$$
$$[100]_{Co_2C}//[10.0]_{\alpha\text{-Co}}//[10\bar{1}]_{\beta\text{-Co}}\,.$$

The Juza and Puff's structure of Co_2C[7] does not take the positions of carbon atoms into consideration and cannot interpret the reflection (011). According to Clark and Jack,[8] the structure of Co_2C belongs to the space group P_{mnn} and the positions of cobalt atoms are 0, y, z; 0, y, z; 1/2, $1/2+y$, $1/2-z$; 1/2, $1/2-y$,

---

* The author wishes to express his thank to Prof. G. Honjo and Dr. N. Kitamura for giving permission to use the 200 KV camera.

$1/2+z$ with $y=0.347 \pm 0.001$, $z=0.258 \pm 0.002$, and the positions of carbon atoms 0, 0, 0; 1/2, 1/2, 1/2. The structure is illustrated in Fig. 1. Intensities calculated from the model are tabulated in Table I and compared with the observed intensities. The intensity measurement was carried out according to the Karle and Karle's method,[11] and the peak area of Debye ring was measured. Honjo and Kitamura's method[12] was applied to correct the effect of primary extinction using the 200 keV electron diffraction apparatus. The extinction effect was observed in the (002), (111) and (021) rings. The observed intensities agree with the

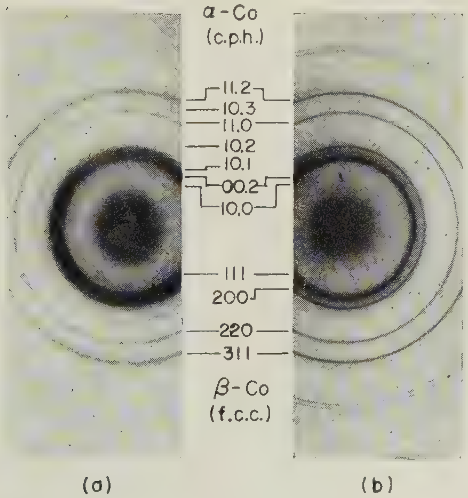

Photo. 1. Electron diffraction patterns of evaporated Co films.
(a) α-Co film deposited on the rock-salt kept at room temperature.
(b) After heating the above film at 650°C for 30 min in vacuum. The pattern is composed of rings due to β-Co and a small amount of α-Co.

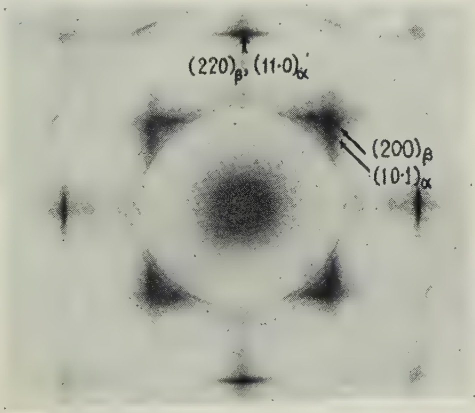

Photo. 2. Electron diffraction pattern of evaporated Co film having single crystalline orientation. Co-existence of α- and β-Co with definite orientation is observed.

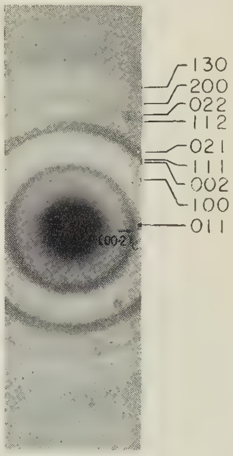

Photo. 3. Electron diffraction pattern of polycrystalline Co_2C film formed by the cementation at 480°C for 8 hrs.

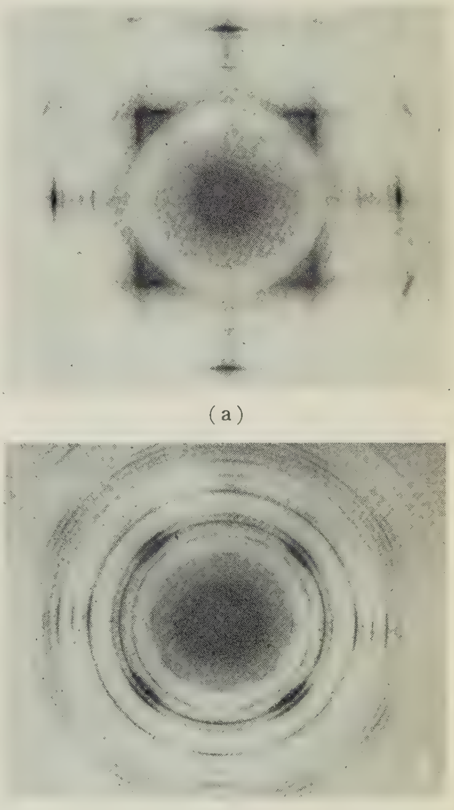
(a)

(b)

Photo. 4. Electron diffraction patterns of Co_2C formed from the single crystalline Co films.
(a) Partly carburized at 450°C for 4 hrs.
(b) Completely carburized at 450°C for 4 hrs.

calculated in the experimental error.

After carburizing for 5 hrs. the carbide was not produced below 400°C, while the film was carburized to Co_2C at 450°C, leaving small amount of α-Co. The completely carburized films were obtained at 500°C. In this case the deposition of free carbon on the films were observed in many cases. Above 550°C the pattern was composed of Debye rings due to α- and β-Co and graphitic carbon.

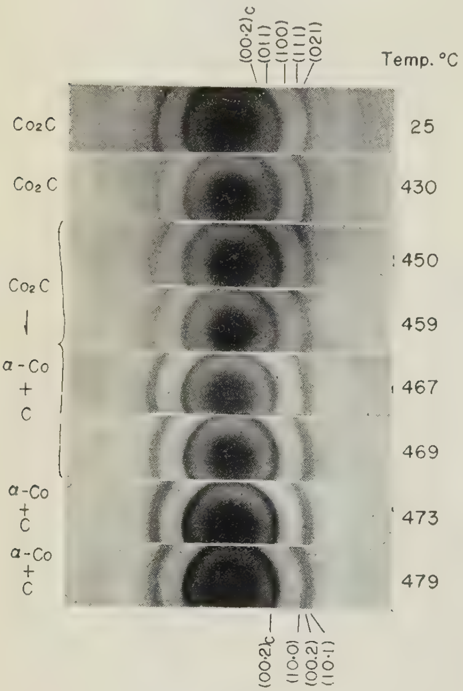

Photo. 5. A series of diffraction patterns showing the decomposition of Co_2C into α-Co and graphitic carbon.

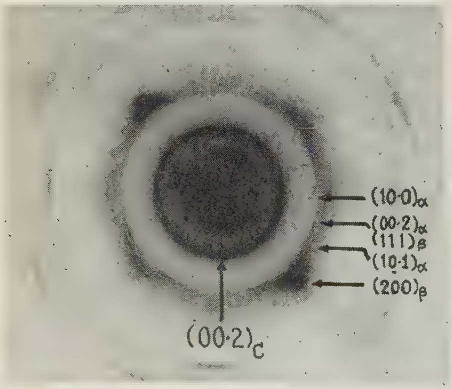

Photo. 6. Electron diffraction pattern after heating the film of Photo. 4 (b) at 500°C for 10 min in vacuum, showing the decomposition of Co_2C to α- and β-Co and graphitic carbon.

When the carburized films were heated in vacuum, Co_2C was found to decompose into α-Co and graphitic carbon. The process of decomposition was continuously observed in the electron diffraction camera. Heating rate was 2°~4°C per min. and the accuracy of temperature was within a few degrees.[1] Photo. 5 reproduces a series of the changes of diffraction patterns. The decomposition began at 450°C and finished at 469°C, leaving the rings due to α-Co and graphitic carbon. α-Co crystallites produced by the decomposition contained the stacking faults as in the evaporated films. Photo. 6 reproduces the diffraction pattern after heating the carburized single cry-

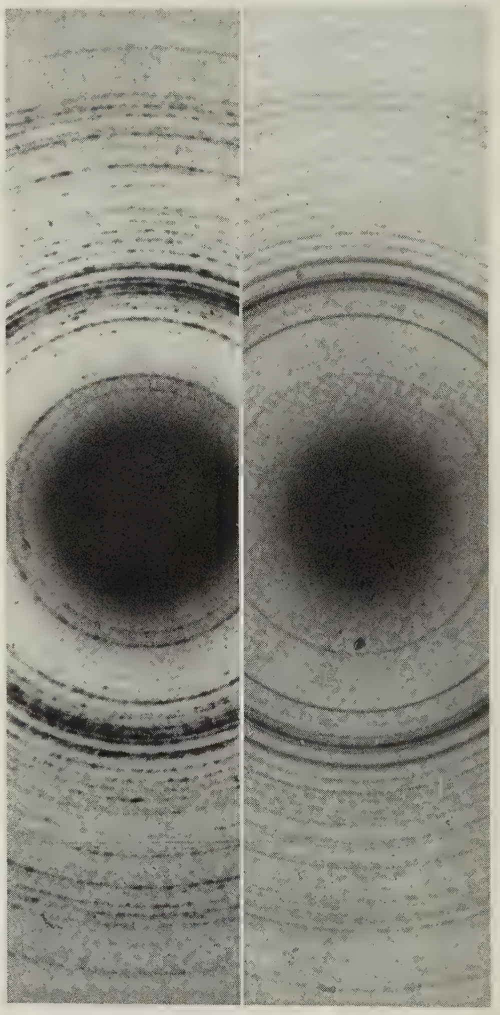
(a) (b)

Photo. 7. Electron diffraction pattern of (a) polycrystalline Co_3C film formed by the cementation at 450°C for 4 hrs., and of (b) Fe_3C film (cementite, see reference 3).

Table I. Spacings and Intensities of Co_2C

No.	*hkl*	Spacing (Å) d_{obs}	Spacing (Å) d_{cal}	Intensity (arbit. unit) I_{obs}	Intensity (arbit. unit) I_{cal}
1	011	3.120	3.014	45	41
2	101	2.421	2.432	68	7
3	110		2.432		70
4	020	—	2.224	400*	5
5	002	2.179	2.213		109
6	111	2.125	2.136		376
7	021	1.989	1.994	200*	194
8	012	—	1.983		1
9	121	1.640	1.645	106	6
10	112		1.639		100
11	022	1.574	1.572	15	19
12	200	1.455	1.455	21	38
13	031	—	1.410	—	0.6
14	013	—	1.402	—	0.3
15	122	—	1.384	—	0.8
16	130	1.326	1.325	50	45
17	211		1.321		2
18	103		1.316		3
19	113	1.261	1.262	46	37
20	131		1.261		4
21	032		1.235	45	0.0
22	023	1.221	1.231		22
23	220		1.219		1
24	202		1.216		17
25	221	1.182	1.176	36	36
26	212		1.175		0.2
27	132	1.135	1.137	30	23
28	123		1.134		0.3

* Obtained by the Honjo-Kitamura's extrapolation method.

stalline film at 500°C for 10 min. It can be seen that the film is composed of the spots due to α-Co, small amount of β-Co and graphitic carbon without orientation. It is noteworthy that the pattern of cobalt is still single crystalline.

3. Co_3C films

Photo. 7 (a) is an electron diffraction pattern of polycrystalline film carburized at 450°C for 4 hrs. and Photo. 7 (b) is the pattern of cementite, Fe_3C. Their spacings and visual intensities are tabulated in Table II. It is evident from the photographs that the carbide is isomorphous with the cementite and can be identified with Co_3C. The orthorhombic lattice constants are

$$a=4.483\ \text{Å},\ b=5.033\ \text{Å}\ \text{and}\ c=6.731\ \text{Å},$$

which are nearly equal to the lattice constants of cementite, $a=4.516$ Å, $b=5.077$ Å, and $c=6.727$ Å.[13] Photo. 8 reproduces an electron diffraction pattern of Co_3C formed by the cementation of a single crystalline cobalt film. The lattice relation may be

$$(\bar{1}11)_{Co_3C}//(10.1)_{\alpha-Co}//(100)_{\beta-Co}\ ,$$

$$[0\bar{1}1]_{Co_3C}//[01.0]_{\alpha-Co}//[001]_{\beta-Co}\ .$$

This relation is gradually destroyed in the growth stage of carbide crystal.

The temperature range of Co_3C formation was 450~500°C. The diffraction rings of Co_3C are always spotty, showing that the particle size of Co_3C is of the order of several hundred Å. This is much larger than that of α-Co. When Co_3C film was headed in vacuum, it was found that Co_3C decomposes to α-Co and graphitic carbon as in the case of Co_2C. Photo. 9 illustrates the process of the decomposition of Co_3C: the decomposition began at 477°C and finished 491°C. α-Co crystallites produced

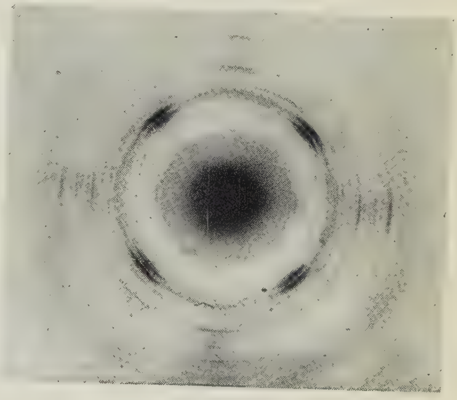

Photo. 8. Electron diffraction pattern of Co_3C film formed from the single crystalline Co film.

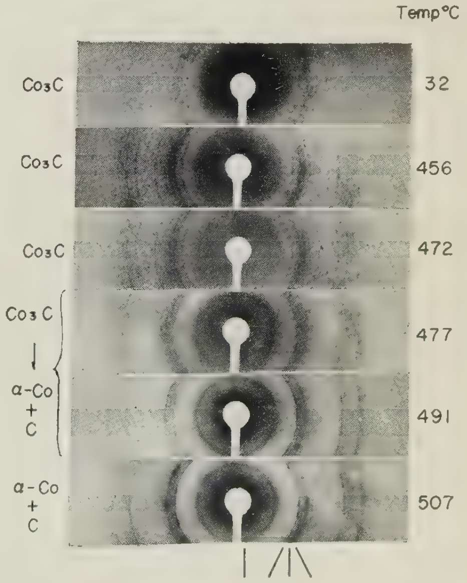

Photo. 9. A series of diffraction patterns showing the decompossition of Co_3C into α-Co and graphitic carbon.

Table II. Diffraction data of Co_3C and Fe_3C

No.	Co_3C		hkl*	Fe_3C (cementite)	
	Int.	d (Å)		Int.	d (Å)
1	s	6.807	(001)	s	6.925
2	m	5.058	(010)	w	5.077
3	vw	4.502	(100)	vw	4.518
4	vw	4.040	(011)	vw	4.052
5	w	3.738	101	w	3.750
6	m	3.376	110	m	3.374
7			002		3.364
8	w	3.005	111	w	3.017
9	vw	2.808	(012)	w	2.803
10	vw	2.703	(102)	w	2.697
11	m	2.520	020	w	2.538
12	s	2.371	112	vs	2.382
13			021		2.375
14	m	2.244	200	s	2.258
15	—	—	(003)	vw	2.242
16	m	2.195	120	m	2.213
17	—	—	(201)	vw	2.140
18	w	2.129	121	m	2.105
19	s	2.089	210	s	2.063
20	—	—	(013)	—	2.051
21	m	2.050	022	m	2.026
22	vs	2.013	103	vs	2.008
23	s	1.961	211	s	1.972
24	s	1.868	202	vs	1.873
25			113		1.867
26	m	1.838	122	s	1.849
27	vw	1.751	212	m	1.758
28	vvw	1.690	(030)	—	1.693
29	m	1.679	220	m	1.687
30			004		1.682
31			023		1.680
32	—	—	(031)	vw	1.641
33	m	1.622	221	m	1.636
34	—	—	(014)	vw	1.596
35	—	—	(203)		1.591
36	m	1.570	130	w	1.585
37	—	—	(104)	vvw	1.576
38	—	—	123		1.575
39	vw	1.529	131	w	1.542
40	vw	1.510	213	vw	1.518
41			(032)		1.512
42	m	1.502	222	m	1.508
43			(300)		1.505
44			114		1.505
45	vw	1.462	301	vvw	1.469
46	—	—	310	vvw	1.443
47	vvw	1.430	132	vvw	1.433
48	—	—	311	w	1.412
49	w	1.402	024	w	1.402
50	—	—	(302)	—	1.375
51	vvw	1.352	230	vvw	1.354
52	—	—	(033)	vvw	1.351
53	vvw	1.341	204	w	1.349
54			223		1.348
55			(005)		1.345
56	vw	1.332	124	w	1.339
57	m	1.318	231	m	1.327
58			312		1.326
59	—	—	214	w	1.303
60	—	—	320		1.301
61	—	—	(015)	—	1.300
62	vvw	1.292	133	w	1.294
63			105	vvw	1.289
64	—	—	321	vvw	1.271
65			040		1.269
66	vw	1.254	232	vw	1.256
67	—	—	303	w	1.250
68			115		1.250
69			041		1.247
70	—	—	140	w	1.222
71	w	1.211	313	m	1.213
72	m	1.210	322		1.208
73	—	—	141	vvw	1.203
74	w	1.191	(034)	m	1.193
75			224		1.191
76			025		1.189
77			042		1.188
78	—	—	215	vw	1.164
79	—	—	233	m	1.159
80	—	—	(205)	—	1.156
81	m	1.152	134	m	1.153
82			125		1.150
83			142		1.149
84	s	1.125	400	s	1.129
85			330		1.125
86	m	1.116	(304)	m	1.121
87			323		1.121
88			006		1.121
89	—	—	(401)	—	1.113
90	w	1.108	331	w	1.109
91			240		1.106
92	vw	1.101	043	vw	1.105
93			410		1.102

* Indices in the brackets correspond to the forbidden reflections.

by the decomposition contained the stacking faults.

§ 4. Discussion

The c-projection of the structure of α-Co and Co_2C are illustrated in Fig. 1 (a) and (b), respectively. Here, large circles A, B (Fig. 1 (a)) and A′, A″, B′, B″ (Fig. 1 (b)) represent cobalt atoms and small circles (C_1), (C_2) carbon atoms. In the structure of α-Co each close packed atomic plane formed by A and B is parallel to the c-plane, but in the structure of Co_2C atomic planes A′—A″ and B′—B″ make an angle of 17°37′ to the c-plane, since height of each atom is different. In both of the

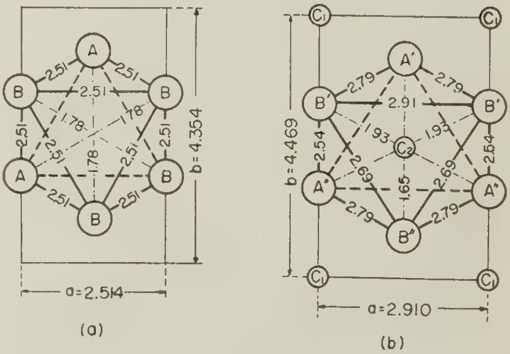

Fig. 1. Structures of α-Co (a) and Co_2C (b) (c-projection). Height of atoms: A: 1/4; B: 3/4; A′: 0.242; A″: 0.258; B′: 0.742; B″: 0.758; C : 0; C_2: 1/2. Heavy lines indicate octahedrons formed by cobalt atoms. Atomic distance is shown in A unit.

structure, however, there are octahedrons formed by cobalt atoms, and in the Co_2C the octahedral interstices are occupied by carbon atoms. Both structures are different only in the orientation of the octahedrons in the lattice. This fact and the lattice relation between α-Co and Co_2C suggest that the Co_2C is formed by the diffusion of carbon atoms into the octahedral interstices of α-Co. By the carbon atom moving in the octahedron, it expanded and distorted in such a way that the distance $A''-A''$ becomes longest and $A''-B'$ shortest. The mean particle size of Co_2C crystallites is nearly equal to that of α-Co and this fact suggests that each crystal of α-Co changes to Co_2C crystal without crystal growth. In the carbide lattice carbon atoms are distributed regularly so as to minimize the lattice distortion. Unlike the case of Ni_3C[2] and ε-Fe_3C, the distribution of carbon atoms in the crystal does not form any sublattice structure. The degree of orientation of α-Co crystallites produced by the decomposition of the single crystalline Co_2C film was not different from the degree of orientation of the original α-Co crystallites. This shows that the decomposition of Co_2C is caused by the carbon atoms moving out of the octahedral interstices of Co_2C. When α-Co films are carburized, the Co_2C may be produced mainly from α-Co even when the carburizing temperature is above the transformation temperature, since the rate of transformation from α- to β-Co is slow. However, Co_2C can be produced also from β-Co and in this case the mechanism can be considered to be similar to the case of Ni_3C formation from nickel.[1]

The arrangement of cobalt atoms in Co_3C crystal has no simple relation to the atomic arrangement in α- or β- crystal and the particle size of Co_3C is much larger than that of α- or β-Co. These situations are similar to the case of Fe_3C (cementite) formation from α-Fe. In contrast to the case of Co_2C, therefore, Co_3C may be formed in such a way that nuclei of Co_3C are produced on the cobalt surface and grow up gradually at the expense of cobalt crystal.

The temperature range of Co_2C and Co_3C formation were nearly same. Therefore, it could not be predicted which carbide would be produced by the cementation. It is worthwhile to mention that the decomposition product of both carbides was mainly α-Co but not β-Co, in spite of the fact that the decomposition temperature is higher than the transformation temperature of bulk cobalt. This may be due to the fact that the atomic arrangement of cobalt atoms in the carbides is more closely related to that of α-Co than that of β-Co.

The author should like to express his thanks to Professors S. Oketani and G. Honjo for their valuable discussions. This work was partly supported by a Grant in Aid for Fundamental Scientific Research from the Ministry of Education.

References

1) S. Nagakura: J. Phys. Soc. Japan, **12** (1957) 482.
2) S. Nagakura: J. Phys. Soc. Japan, **13** (1958) 1005.
3) S. Nagakura: J. Phys. Soc. Japan, **14** (1959) 186.
4) H. A. Bahr and V. Jessen: Ber. deut. chem. Ges., **63** (1930) 2226.
5) L. J. E. Hofer and W. C. Peebles: J. Am. Chem. Soc , **69** (1947) 893.
6) J. Drain: Ann. de chemie, **8** (1953) 900.
7) R. Juza and H. Puff: Naturwiss., **38** (1951) 331.
8) J. Clark and K. H. Jack: Chem. and Ind., **46** (1951) 1004.
9) W. F. Meyer: ZS. f. Krist., **97** (1938) 145.
10) A. J. C. Wilson: *X-ray Optics*, Methuen & Co., Ltd. (London) 1946.
11) J. Karle and I. L. Karle: J. Chem. Phys., **17** (1949) 1025; *ibid*. **18** (1950) 963.
12) G. Honjo and N. Kitamura: Acta Cryst., **10** (1957) 533.
13) W. Hume-Rothery, G. N. Raynor and A. T. Little: J. Iron & Steel Inst., **145** (1942) 143.

JOURNAL OF THE PHYSICAL SOCIETY OF JAPAN, Vol. 16, No. 6, JUNE, 1961

Study on the Internal Motions of Some Acryl- and Methacryl-group High Polymers by Pulsed NMR Method

By Takao KAWAI

Yoshida College, Kyoto University

(Received February 1, 1961)

The internal motions of some high polymers were investigated by measuring the spin-lattice relaxation time (T_1) together with its minima ($T_{1\,\mathrm{min}}$) in proton resonance in the temperature range from liquid air up to about 300°C by pulsed NMR method at 25 Mc/sec. For acryl-group high polymers (PMA, PEA, PBA), two minima of T_1 were observed, one at higher temperature corresponding to the segmental motion and the other at lower temperature to the internal motion of side chain ester alkyl group. For methacryl-group high polymers (PMMA, PEMA, PBMA), three minima of T_1 were observed, of which one at the highest temperature corresponds to the segmental motion, the next at the middle temperature to the internal motion of both main chain methyl group and side chain ester alkyl group and the last at the lowest temperature to the internal motion of the latter group alone.

Thus, we could definitely separate the internal motion of amorphous high polymers. The rigorous analysis of the behavior is considered to be a rather difficult problem, because of the complexity of the circumstances and the lack of both existing suitable formulas and precise experimental data.

§1. Introduction

Nuclear magnetic resonance (NMR) methods have been widely applied to investigate the internal motion of high polymers. Some researches are summarized in a recent review by Sauer and Woodward.[1] However, the methods which have been widely used are steady state methods to measure the line width, the second moment, or the line shape. Relatively few works have been performed on the spin-lattice relaxation time (T_1) of high polymers.[2,3,4,5] We have undertaken a systematic investigation about the internal motion of some high polymers, by measuring T_1 in proton resonance in the temperature range as wide as possible. Some preliminary results were already published.[6] In the present study, we have succeeded in separating clearly the internal motion of high polymer into the segmental motion and the component motions of side chain. The samples used, the experimental methods and results, and discussions will be given in detail below.

§2. Samples

We have investigated the internal motion of the amorphous high polymers but not of the the partially crystalline ones, because the formers are fit to simple analyses. As to the partially crystalline high polymers, the investigations

Table I. Samples used.

	Acryl-group	Methacryl-group
Methyl ester	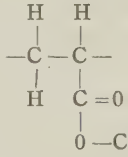 $\begin{array}{cc} H & H \\ \vert & \vert \\ -C- & C- \\ \vert & \vert \\ H & C=0 \\ & \vert \\ & 0-CH_3 \end{array}$ Poly methyl acrylate (PMA)	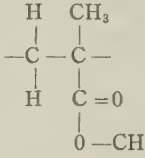 $\begin{array}{cc} H & CH_3 \\ \vert & \vert \\ -C- & C- \\ \vert & \vert \\ H & C=0 \\ & \vert \\ & 0-CH_3 \end{array}$ Poly methyl methacrylate (PMMA)
Ethyl ester	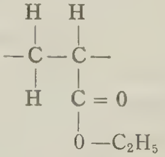 $\begin{array}{cc} H & H \\ \vert & \vert \\ -C- & C- \\ \vert & \vert \\ H & C=0 \\ & \vert \\ & 0-C_2H_5 \end{array}$ Poly ethyl acrylate (PEA)	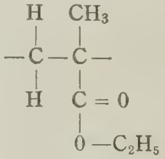 $\begin{array}{cc} H & CH_3 \\ \vert & \vert \\ -C- & C- \\ \vert & \vert \\ H & C=0 \\ & \vert \\ & 0-C_2H_5 \end{array}$ Poly ethyl methacrylate (PEMA)
Buthyl ester	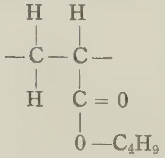 $\begin{array}{cc} H & H \\ \vert & \vert \\ -C- & C- \\ \vert & \vert \\ H & C=0 \\ & \vert \\ & 0-C_4H_9 \end{array}$ Poly buthyl acrylate (PBA)	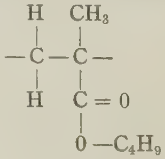 $\begin{array}{cc} H & CH_3 \\ \vert & \vert \\ -C- & C- \\ \vert & \vert \\ H & C=0 \\ & \vert \\ & 0-C_4H_9 \end{array}$ Poly buthyl methacrylate (PBMA)

will be done in a near future.

Six samples were used, as tabulated in Table I.

All samples were kindly supplied by Asahi Kasei Mfg. Co. and some were polymerized by Prof. Kozasa at Kyoto University who measured the average polymerization factors for PMA and PEA by Ostwald's viscometer and found them to be about 4600 and 5560 respectively. The samples are otherwise thought to be of commercial grade.

§ 3. Experimental Method and Results

To measure T_1, a standard 90°~90° pulse method was used.[7,8] The experiments were performed at 25 Mc/sec, using the apparatus already reported.[9] Some improvements were made, however, in order to increase the stability, to obtain stronger *r.* f. pulse, to measure T_1 at lower temperatures and to observe spin echo decay time. All the modifications will be reported in detail elsewhere. The obtained data on the temperature dependence of T_1 for six amorphous high polymers are given in Figs. 1~6.

The estimated error in the measured T_1 is about ±10% above−50°C, but for lower temperature range, it grows worse up to about ±30%. This inaccuracy may be due partly to weak signal and short free induction decay time (T_2*) at lower temperatures and partly to the transition between the modes of internal motion which mainly determine T_1. The error in measuring the temperature T is about ±1°C through nearly the whole range but about ±3°C for lower temperature range, due to the performance of the modified Gutowsky type cryostat[10] which was used.

Some remark must be made about the amplitude of the nuclear signal just after the first pulse (y_1). In principle, y_1 is proportional to the number of resonant nuclei. As already pointed out,[9] however, our apparatus cannot detect the nuclear resonance signal due to protons in the rigid state. So y_1 may be considered to be a rough measure of the number of moving protons. The results of measurement of the temperature dependence of y_1 for PMA and PMMA are shown in Figs, 7 and 8 respectively. The interpretion of y_1 as being proportional to the number of moving protons may contain some errors, because y_1 will be very sensitive to the adjustment of 90°~90° pulse condition, to the change of the "Q" of

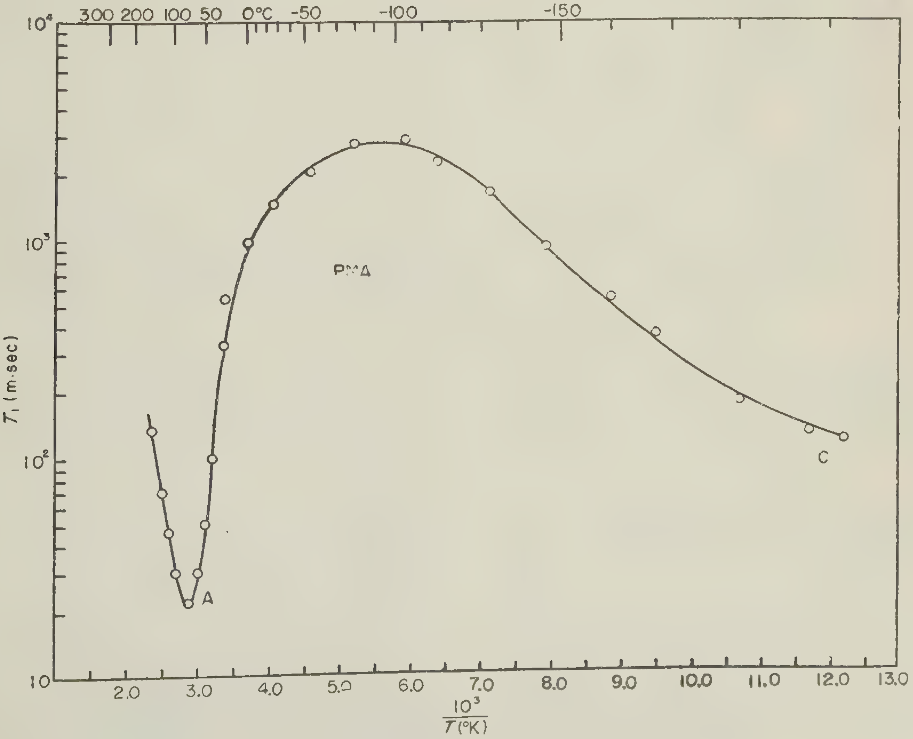

Fig. 1. Temperature dependence of T_1 of proton in PMA.

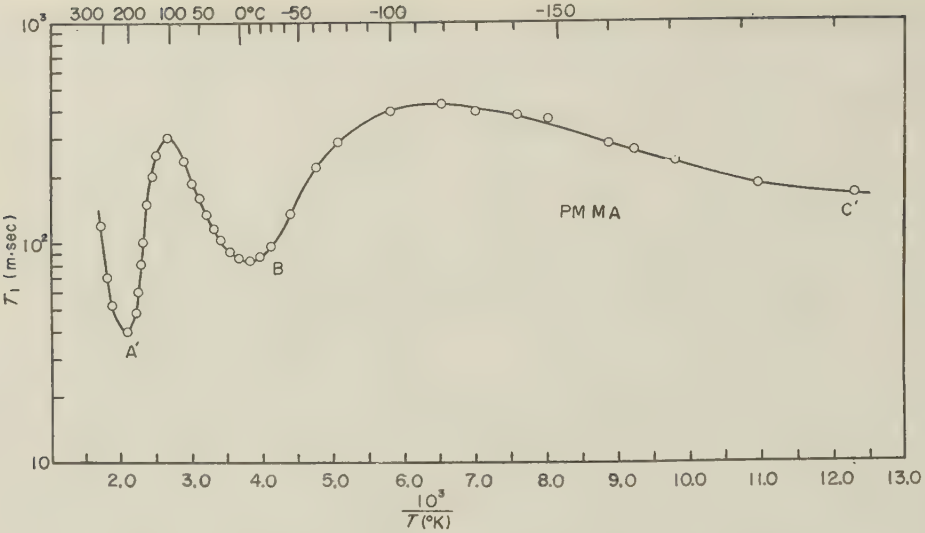

Fig. 2. Temperature dependence of T_1 of proton in PMMA.

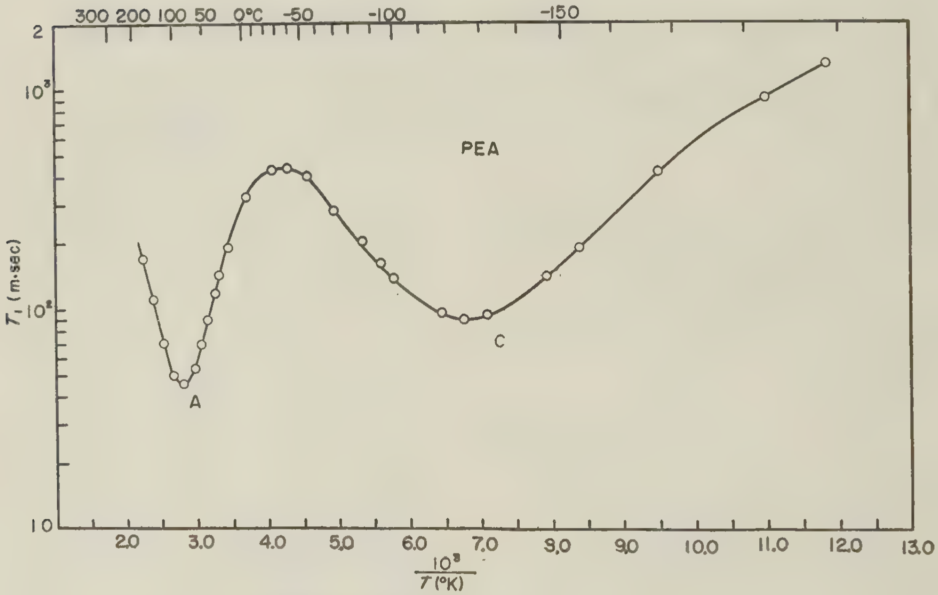

Fig. 3. Temperature dependence of T_1 of proton in PEA.

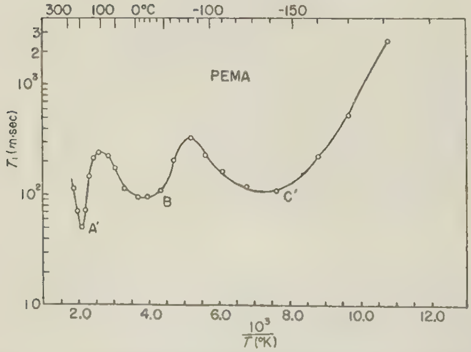

Fig. 4. Temperature dependence of T_1 of proton in PEMA.

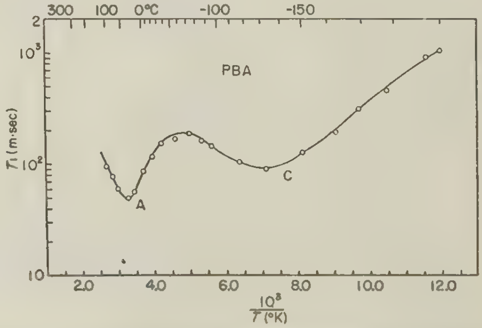

Fig. 5. Temperature dependence of T_1 of proton in PBA.

the sample coil with temperature and to the change of the filling factor of the sample at high temperature, where the sample is in viscous liquid state. However, Figs. 7 and 8 are considered to be useful supports for the interpretation of the data on T_1, as will be shown in the next section.

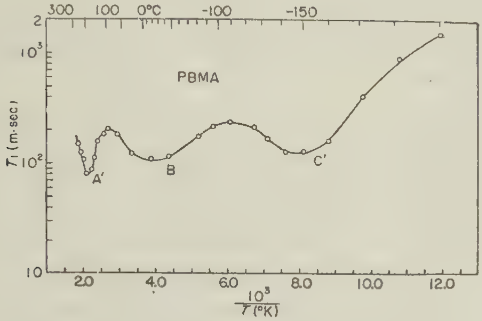

Fig. 6. Temperature dependence of T_1 of proton in PBMA.

§ 4. Interpretation of Data

To interpret the data on T_1, we follow the BPP theory[11] and consider that one mode of the internal motion corresponds to one V-shaped part of the curve T_1 versus $1/T$. But we do not directly apply their formula, which is based on the assumption of a single correlation time.

Thus, first, the V-shaped curves at highest temperatures, maked with *A* and *A'* in Figs. 1~6, obviously correspond to the segmental motions. The data in this temperature range for PMA and PMMA were already published,[6] having been analysed tentatively by using the BPP formula. Recently, A. Miyake used these published data to obtain a distribution spectrum of the correlation time and succeeded in interpretation.[12]

Second, the V-shaped curves marked with *B*, in which a minimum of T_1 occurs at about -10°C for three methacryl-group samples as seen in Figs. 2, 4 and 6, are due to the existence of main chain methyl groups. This conclusion can be derived by comparing the data for each methacryl-group high polymer with those for corresponding acryl-group. In this temperature range, we can consider that in methacryl-group high polymers, both the side chain ester alkyl group and the main chain methyl group are moving and that the magnetic interaction between these two groups are rather strong, for otherwise we would be able to observe two T_1's separately as in the study of the sorbed water.[13]

Third, the V-shaped curves at lowest temperatures marked with *C* and *C'* in Figs. 1~6, can be considered, of course, to correspond to the motions of side chain ester alkyl groups. At the present stage, however, we cannot decide by NMR whether only alkyl groups or the whole C–O–O–R groups are moving. As to the solution of this problem, the study of β transition by dielectric relaxation experiments may be useful. For PMA and PMMA, the V-shaped curves are not completed, which show that the side chain methyl groups are moving even at the liquid air temperature. It is reasonable to consider that it is not so easy for the ethyl buthyl and perhaps propyl radicals to move as for the methyl radicals.

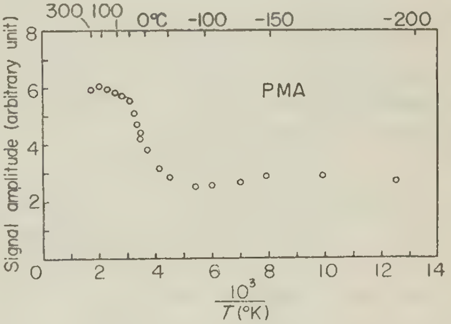

Fig. 7. Signal amplitude (arbitrary unit) *versus* $1/T$ for PMA.

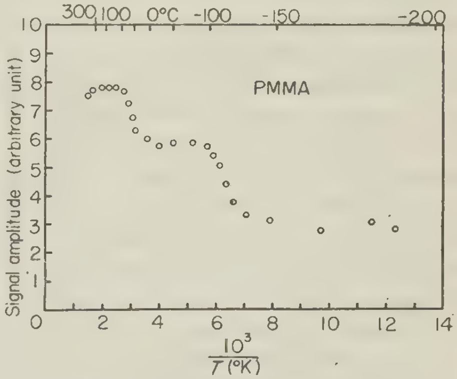

Fig. 8. Signal amplitude (arbitrary unit) *versus* $1/T$ for PMMA.

Finally, we consider the data shown in Figs. 7 and 8. As already pointed out in the preceding section, y_1 is a measure of the number of moving protons. According to the above interpretation of the data on T_1, the respective y_1's should be in the ratio of 6:3 in the temperature ranges corresponding to A and C for PMA, and 8:6:3 in the temperature ranges corresponding to A′ B and C′ for PMMA, considering the molecular structure of each polymer (Table 1). As seen in Figs. 7 and 8, these expectations are fairly satisfied, showing the correctness of the above interpretation.

§ 5. Discussions

Here we consider the use of the BPP formula[11,14] based on the "single correlation time (τ_c)." According to it, the relation between T_1 and τ_c can be represented as follows:

$$\frac{1}{T_1}=\frac{3}{10}\frac{\gamma^4\hbar^2}{b^6}\left(\frac{\tau_c}{1+\omega^2\tau_c^2}+\frac{4\tau_c}{1+4\omega^2\tau_c^2}\right),$$

where b is the "effective" interproton distance, that is an appropriate average of the distances between propons which are effective for the relaxation. Further, if we consider the internal motion of high polymers as an activation process, we have

$$\tau_c=\tau_0\exp(\Delta E/RT).$$

If we use the above formula, we can analyse the data on the temperature dependence of T_1, taking b, τ_0 and ΔE as three adjustable parameters. Then the minimum of T_1 gives b and the temperature dependence gives τ_0 and ΔE. These processes were, indeed, carried out for the segmental motions of PMA and PMMA previously.[6] For other modes of the internal motion, we have tried these analyses for the two representative cases, that is, for the V-shaped curve marked with B for PMMA, and for that marked with C for PEA. It would be desirable to treat the V-shaped curve marked with C for PMA, since it corresponds to the motion of methyl group, which has been widely studied. Unfortunately, however, we could not attain the temperature where the minimum of T_1 for that mode occurs.

The results of the analyses are as follows: $b=2.1$Å, $\tau_0=3.5\times10^{-12}$ sec and $\Delta E=3.6$ Kcal/mol for curve B of PMMA, $b=2.2$Å, $\tau_0=4.5\times10^{-12}$ sec and $\Delta E=1.9$ Kcal/mol for curve C of PEA. The plots of τ_c *versus* $1/T$ are shown on semilogarithmic scale in Fig. 9 (a) and (b) for these two cases respectively, where open circles (for PMMA) and filled circles (for PEA) are derived from the data on T_1, using the BPP formula, and the straignt lines connecting these give $\tau_c=\tau_0\exp(\Delta E/RT)$.

For the curve B of PMMA in Fig. 2, where not only main chain methyl groups but also side chain ester methyl groups are moving and further there are strong coupling between both, the circumstances are very complicated.

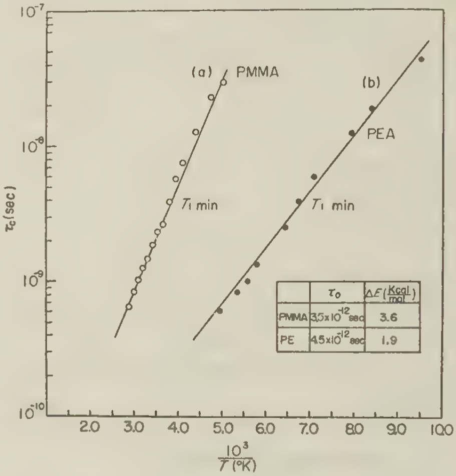

Fig. 9. Plot of τ_c against $1/T$ for PMMA (a) and PEA (b).

But we notice that the value of 2.1Å is somewhat larger than that estimated from the molecular structure (about 1.8Å for H—H distance in methyl group). The same can be said about b for the curve C of PEA in Fig. 3. As for the activation energy ΔE, the values derived above seem to be a little smaller than that derived from T_1 for methyl groups in smaller molecules.[5] It may perhaps be unnecessary to confirm the existence of the distribution of correlation times, though in general, both the increase in the value of $T_{1\,min}$ (which is equivalent to the increase in the apparent value of b) and the flatness of the V-shaped curve (which is equivalent to the decrease in the apparent activation energy) are the results which are expected when we take the distribution of correlation times into account.

§ 6. Conclusions

We could definitely separate the various modes of the internal motion of amorphous high polymers, by measuring T_1 in proton resonance by pulsed NMR method. Recently, the similar investigations were performed by Odajima, Woodward, and Sauer, by measuring the second moment by steady state method.

Our results are excellently consistent with theirs, and we think our results are more direct. We could not discuss our data quantitatively, because of the complexity of the affairs, the lack of both the suitable formula for analysis and the precise experimental data. For further discussions, the progress in the theory of T_1 of high polymers and the measurements of T_1 at various frequencies would be necessary.

Acknowledgements

The author would like to express his sincere gratitude to Professor I. Takahashi for his continual interest and discussions. The author is also indebted to Professor H. Kozasa for his kindness of making and testing the samples. The author's thanks are also due to Dr. A. Hirai for his helpful assistance throughout this investigation and to Dr. S. Ishida of Asahi Kasei Co. for his kindness of providing the samples.

References

1) J. A. Sauer and A. E. Woodward, Rev. Mod Phys. **28** (1960) 88.
2) C. W. Wilson and G. E. Pake, J. Chem. Phys. **27** (1957) 115.
3) H. S. Gutowsky, A. Saika, M. Takeda, and D. E. Woessner, J. Chem. Phys. **27** (1957) 534.
4) A. W. Nolle and J. J. Billings, J. Chem. Phys. **30** (1959) 84.
5) E. O. Stejskal, D. E. Woessner, J. C. Farrar, and H. S Gutowsky, J. Chem. Phys. **31** (1959) 55.
6) T. Kawai, M. Sasaki, A. Hirai, T. Hashi and A. Odajima, J. Phys. Soc. Japan **15** (1960) 1700.
7) E. L. Hahn, Phys. Rev. **80** (1950) 580.
8) E. L. Hahn, Phys. Today **6** No. 11 (1953) 4.
9) T. Hashi, A. Hirai, M. Sasaki and T. Kawai, Memoirs of the College of Science, University of Kyoto, Series A **29** (1959) 205.
10) H. S. Gutowsky, L. H. Meyer and R. E. Mcclure, Rev. Sci. Instr. **24** (1953) 644.
11) N. Bloembergen, E. M. Purcell and R. V. Pound, Phys. Rev. **73** (1948) 679.
12) A. Miyake, High Polymers, **9** (1960) 383 (in Japanese).
13) M. Sasaki, T. Kawai, A. Hirai, T. Hashi and A. Odajima, J. Phys. Soc. Japan **15** (1960) 1652.
14) R. Kubo and K. Tomita, J. Phys. Soc. Japan **9** (1954) 888.
15) A. Odajima, A. E. Woodward and J. A. Sauer, Private communication.

Journal of the Physical Society of Japan, Vol. 16, No. 6, June, 1961

Mechanical Dispersions and Transition Phenomena in Semicrystalline Polymers

By Yasaku Wada

Department of Applied Physics, Faculty of Engineering, University of Tokyo, Bunkyo-ku, Tokyo, Japan

(Received March 3, 1961)

The existing data of mechanical dispersions in seven semicrystalline polymers (polyethylene, polypropylene, polyethylene terephthalate, polytrifluoromonochloro ethylene, polyamide, polyurethane and polytetrafluoroethylene) are compiled and the frequency dependence of loss peak temperature ("transition map") is illustrated. The primary and secondary dispersions occuring in the amorphous regions are identified on the basis of these results. The correspondence of the mechanical dispersions to dielectric ones, transition temperatures found in dilatometric measurements and change in NMR line width with temperature is discussed for these polymers.

§ 1. Introduction

A mechanical dispersion phenomenon in amorphous polymer is observed above glass transition temperature T_g: the mechanical loss exhibits a maximum at a temperature T_r higher than T_g, the temperature gradient of storage modulus has a discontinuity at T_g[1] and the modulus largely decreases in the vicinity of T_r from the order of 10^{10} to 10^6 or 10^7dyn/cm^2.

Recent investigations about the glass transition of amorphous polymers have revealed that the transition occurs in a rather broad temperature range.[2] In many amorphous polymers the upper limit of this range, $T_g{}^+$, is about twenty or thirty degrees higher than the lower limit, $T_g{}^-$.[1]

The temperature dependence of volume, elastic modulus and loss factor in the vicinity of the transition region, is schematically illustrated in Fig. 1. As is apparent in the figure, the glass transition temperature T_g in existing literatures which was determined as an intersection of two straight line portions in the volume-temperature curve lies between $T_g{}^+$ and $T_g{}^-$, being rather nearer to $T_g{}^+$.

It should be particularly mentioned here that the transition region and the dispersion region are not identical, though closely related to each other.[2] The former is determined by the interrelation between frequency of external excitation and temperature dependence of relaxation time, while the latter is determined by the relation between cooling or heating rate of the sample and the temperature dependence of the relaxation time. The glass transition temperature depends indeed on the cooling rate, but it can be taken practically as a material constant, since the cooling rate cannot be varied in the order of magnitude in usual experiments.

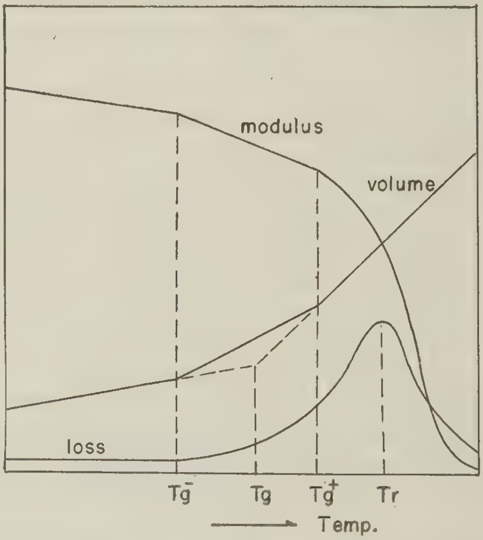

Fig. 1. Schematical representation of the temperature dependence of the volume, the mechanical loss factor and the storage modulus near the glass transition temperature.

In the case of semicrystalline polymers also, the glass transition has been believed to take place in the amorphous part and the associated mechanical dispersion has been observed. This dispersion is usually termed "primary disper-

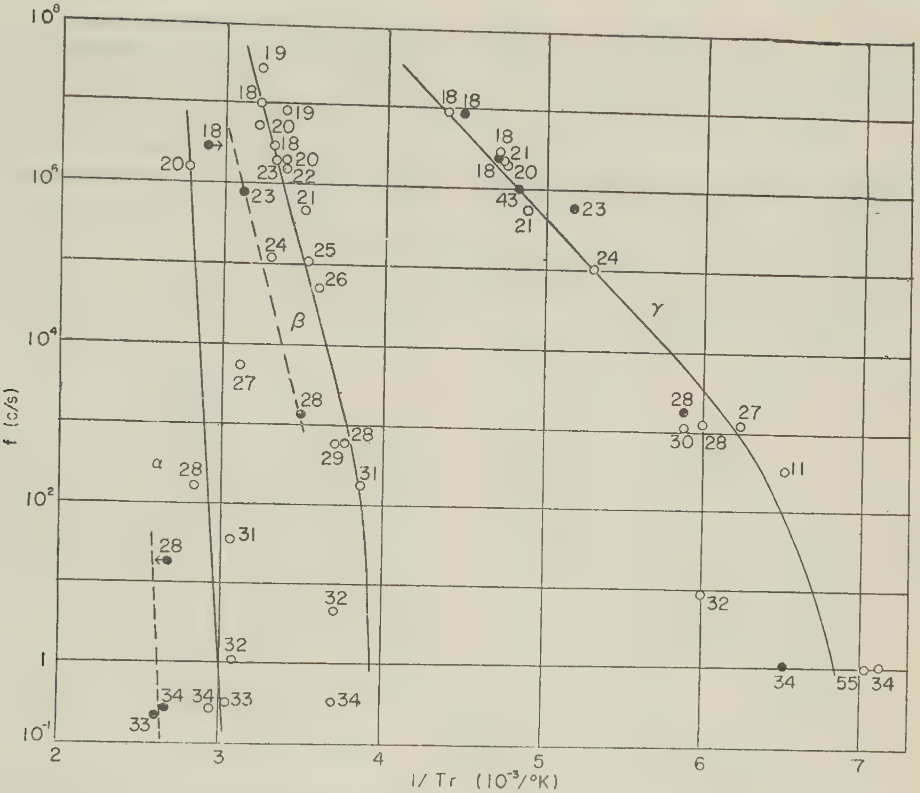

Fig. 2. Transition map of polyethylene. (Circle and dot represent values for branched and linear polyethylene respectively.)

sion." Besides this there has been found in lower temperatures another dispersion associated with the local motion of chain molecules in the amorphous part, named "secondary dispersion." Furthermore, a third dispersion originating from the crystalline part has been also exhibited in some polymers.

Owing to the complicated behavior abovementioned, there is even at present a large scatter of the opinion among authors about the problem which dispersion should correspond to the primary or the secondary dispersion. It is our purpose here to compile the existing data on the mechanical dispersion of semicrystalline polymers and to identify the primary and the secondary dispersions. The data of the thermal expansion, dielectric dispersion and nuclear magnetic resonance will be also referred to.

Seven kinds of semicrystalline polymer are dealt with in this paper:

(1) Polyethylene (PE)
(2) Polypropylene (PP)
(3) Polyethylene terephthalate (PET)
(4) Polytrifluoromonochloroethylene (PTFMCE)
(5) Polyamide (PA)
(6) Polyurethane (PU)
(7) Polytetrafluoroethylene (PTFE)

Nylon 6 and nylon 66 among many modifications of PA have been most extensively studied and are the subjects of the present study. In the case of PU the data are available only for polytetramethylene-hexamethy-

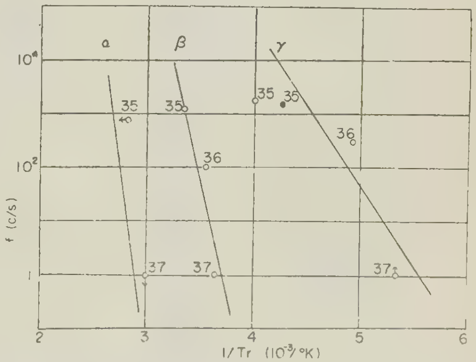

Fig. 3. Transition map of polypropylene. (Circle and dot represent isotactic and atactic polymers respectively.)

lene-urethane. Polymers other than these seven are not treated here because the available data have been too scanty up to the present.

§ 2. Transition Maps of Semicrystalline Polymers

The frequency dependence of the temperature of loss factor maximum T_r is illustrated in Figs. 2 to 8 for seven kinds of polymers. Numbers in the figures indicate the reference numbers. The names of dispersion follow mostly the nomenclature in the review article by Woodward and Sauer,[3] in which the upswing, not the peak, of damping near the

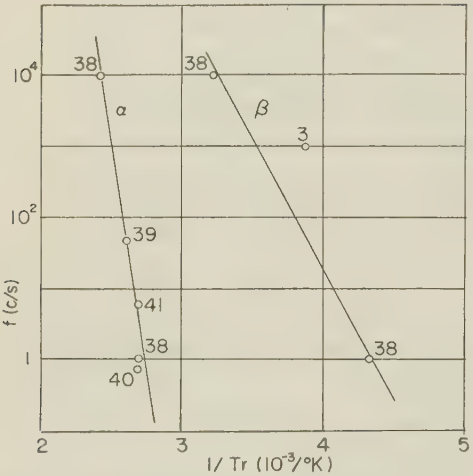

Fig. 4. Transition map of polyethylene terephthalate.

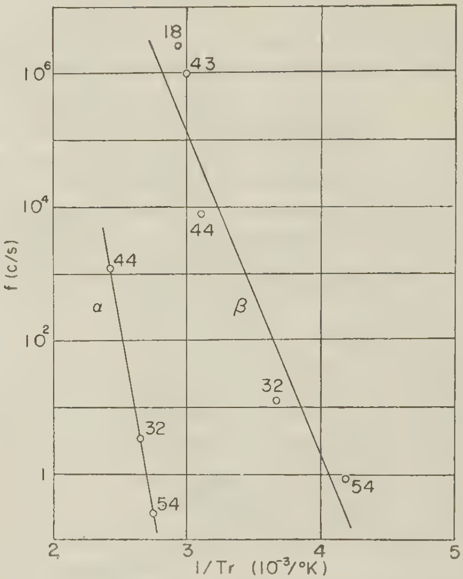

Fig. 5. Transition map of polytrifluoromonochloroethylene.

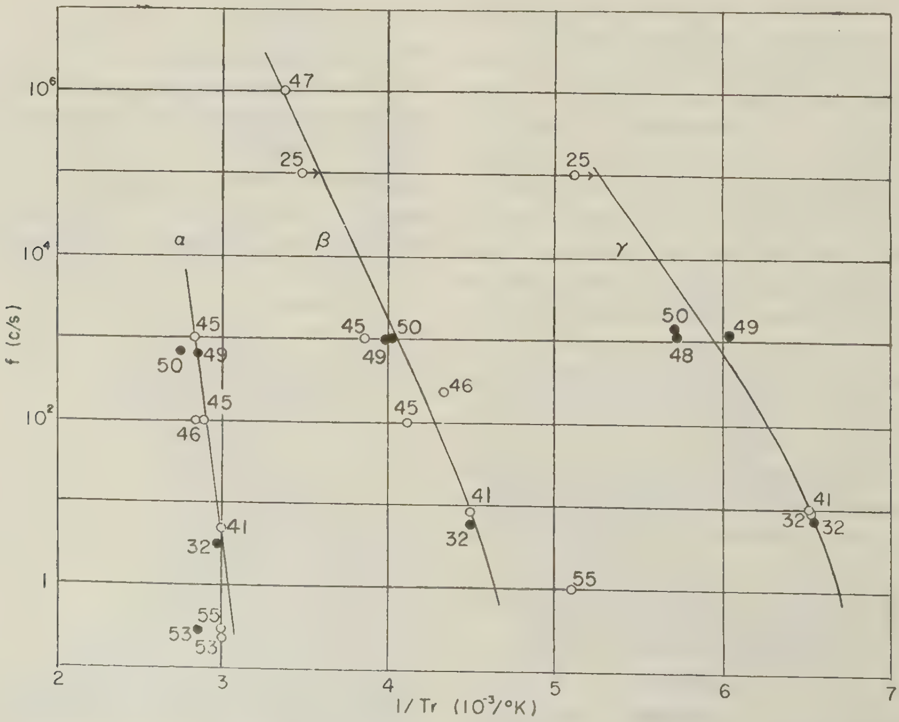

Fig. 6. Transition map of polyamide. (Circle and dot represent nylon 6 and nylon 66 respectively.)

melting point was often called "α peak" and the peak just below was called "α′ peak." This α′ peak is named "α peak" in this paper and the name "α′" is not used.

It is apparently seen from these transition maps that the relation between log *f* and $1/T_r$ is linear in most of the dispersions, though in some cases the linear relation does not hold in low frequencies. The apparent activation energy *E* is calculated from the straight line portion by

$$E=-2.30R\frac{\partial \log f}{\partial(1/T_r)}, \tag{1}$$

where *R* is the gas constant. The values of *E* are listed in Table I, together with T_r values at 1 cps frequency. The values of PE in this table are related to the branched polymer.

The relationship between transition phenomena and dielectric dispersion in polar polymers has been the subject of many papers. The data of dielectric dispersion are shown in Table I for comparison, reproduced from the very extensive study by Nakajima and Saito.[4] The values of PE was obtained with an oxidized sample. T_r in Table I is not to be directly compared with ε'' maximum temperature, since the loss factor corresponds to $\varepsilon''/\varepsilon'$, rather than ε'' in dielectric property. The ε'' maximum temperature should be higher than T_r, if the mechanical and dielectric dispersions are associated with the same mole-

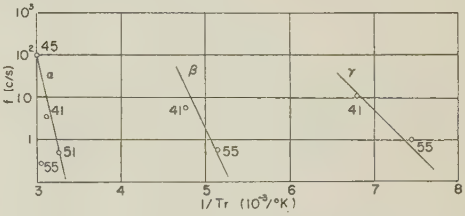

Fig. 7. Transition map of polyurethane.

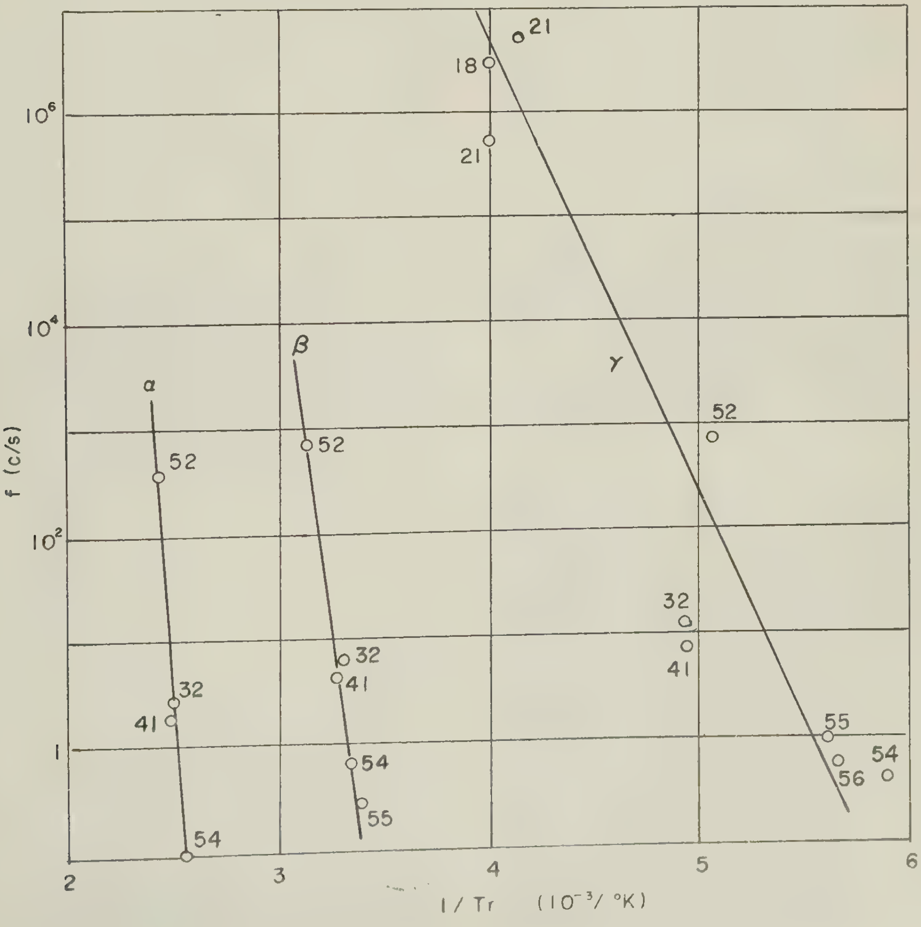

Fig. 8. Transition map of polytetrafluoroethylene.

Table I.

Polymer	T_m (°K)	Dispersion	Mechanical		Dielectric		T_k (°K)
			E (kcal/mole)	T_r at 1 cps (°K)	E (kcal/mole)	ε'' max. temp. at 1 cps (°K)	
PE	370	α	130	333			
		β	34	250	26	265	253[5]
		γ	9.5	145	13		140[5]
PP	440	α		345			
		β	40	275			250[6,7]
		γ	13	178			
PET	537	α	65	365	100	420	340,[8,13] 360[9]
		β	17	230	18	200	
PTFMCE	483	α	50	370	60	380	320[9,10,11]
		β	21	248	18	240	
PA	496, 538	α	62	330	48	310	330[9]
		β	21	214	17	220	
		γ	16	148	9		
PU	450	α	43	310			
		β	20	200			
		γ	10	140			
PTFE	600	α	170	400			400[9]
		β	70	300			
		γ	20	180			160[12]

cular mechanism. Taking this into consideration, one sees in Table I that the values of mechanical dispersion are in a satisfactory agreement with those of the dielectric one.

The last column of Table I shows the temperature T_k where the volume-temperature curve was found to exhibit a discontinuity in slope

§ 3. Criteria for Primary and Secondary Dispersions

The primary dispersion, being caused by movements of large sections of chain molecules in the amorphous phase, may be expected to follow the criteria below:

(1) The loss peak height should increase with increase in the fraction of the amophous phase.

(2) The activation energy should be relatively large, say several tens kcal/mole as estimated from that of perfectly amorphous polymers, owing to the large unit of motion.

(3) The thermal expansion curve should have a point of discontinuity in slope (T_g) in the vicinity of the loss peak temperature at a very low frequency.

(4) T_g should be roughly two-thirds of crystalline melting temperature T_m, when measured in absolute temperature scale.[14,15] This relationship is only an empirical one, but has been confirmed for many substances exhibiting the glass transition. Fig. 9 represents the relation of break temperatures in thermal

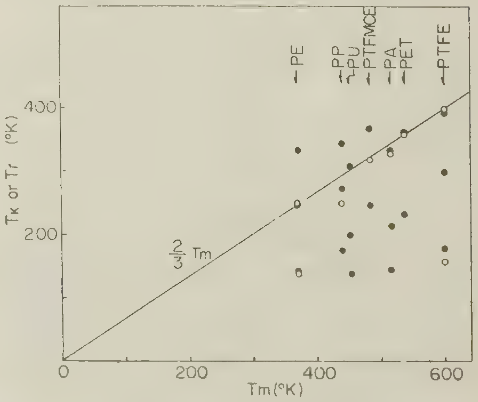

Fig. 9. Break points in thermal expansion curves (circle) and loss peak temperatures at 1 cps (dot) plotted against melting points.

expansion curves (T_k) and loss peak temperatures at 1 cps (T_r) against T_m for seven polymers.

Recently some theoretical studies have been made on the mechanism of the secondary dispersion,[16,17] the conclusion being not yet arrived. Okano[17] attributed this dispersion to the vibration of chain segments and achieved a qualitative agreement with experiment. It may be inadequate at the present stage to ascribe the secondary dispersion of a specific polymer to the rotation of a specific group of atoms in a chain molecule.

In any case, since it is at least valid that the secondary dispersion comes from the local motion of segments in the amorphous phase, the dispersion may be expected to obey the following criteria:

(5) The loss peak height should increase with increase of the relative amount of the amorphous phase.

(6) The dispersion should be observed at lower temperatures than the primary one.

(7) The activation energy should be smaller than that of primary disperson, roughly estimated as ten kcal/mole or so.

Identification of the primary and secondary dispersions for specific polymers will be made in the next section on the basis of the above criteria.

§ 4. Discussions on Specific Polymer

Polyethylene

The peak height of β dispersion is very small, often undetectable in linear PE which has a small fraction of the amorphous regions. Further, the increase in the amorphous regions by irradiation brings about the increase in height of the β peak of PE.[29] It is apparent from Table I and the above facts that the β dispersion fulfils all the criteria for the primary dispersion.

It is seen from Table I that the γ dispersion fulfils the criteria for the secondary dispersion except (5). The loss peak height of this dispersion is almost the same in branched PE as in linear PE.[18,28] This discrepancy may be explained under the assumption that some of the so-called crystalline regions in linear PE may be in an intermediate state between the crystalline and the amorphous states and the local motion of molecules which contributes to the secondary dispersion can take place also in this intermediate region.

The change in shape of the proton magnetic resonance absorption line of PE with temperature seems to support the view of regarding the β and γ dispersions as primary and secondary ones respectively. The narrow line component, caused by moving protons in the amorphous regions, at first appears at 200°K or below, then begins to become rapidly narrower at about 250°K.[29]

Many investigators have agreed in attributing the α dispersion of PE to the presence of the crystalline regions.[28,29]

Polypropylene

The behavior of the mechanical dispersions in PP is closely similar to PE so far as the data available at present concern.[57] A similar assignment of mechanisms to the dispersions as given to PE applies seemingly to PP.

Two extra loss peaks (δ and ε peaks) have been found in this polymer at very low temperatures and have been attributed to the rotation of methyl groups in the crystalline and amorphous regions respectively.[37] This explanation seems, however, not easy to understand. The rotation of such an axially symmetrical group as methyl group can result in no strain in the polymer and hence may not bring about any mechanical relaxation. In any cases, it may be important to explore the mechanical response over an extremely low temperature range for other polymers also.

Polyethylene terephthalate

The α dispersion of this polymer, the loss peak height of which was found to increase with increase of the amorphous regions,[39] satisfies well the criteria (1) to (4). According to the study of dielectric properties,[4] the relaxation strength of this dispersion begins to fall at about 100°C with decreasing temperature. This is indicative of the fact that the segmental motions of molecules begin to be "frozen-in" from this temperature. This temperature therefore can be regarded as the upper limit of glass transition region.

Polytrifluoromonochloroethylene

As is apparent from Table I, the criteria (2) to (4) hold true well for the α dispersion. Nakajima and Saito[58] have investigated the dielectric dispersion of this polymer in detail. According to them the relaxation strength of both α and β dispersions increases almost linearly with increasing fraction of the amorphous regions. Further, the relaxation strength of α dispersion falls rapidly from 50°C with lowering temperature. This indicates definitely that this temperature is the upper limit of glass transition region. They also found that the narrowing in the distribution of relaxation times for the β dispersion starts at 20°C with increasing temperature. This behavior can be accounted for by considering that the local motion of segments is modified above this temperature by the rotationary motion of segments.[59] This temperature therefore can be regarded as the starting point of glass transition, i.e. the lower limit of the transition region.

The γ dispersion satisfies the criteria (5) to (7) and can be safely concluded to be the secondary dispersion.

The temperature dependence of maximum slope width of magnetic resonance absorption line of fluorine nuclei in PTFMCE supports our conclusions. According to Nishioka,[65] narrowing occurs slightly first at around 240°K, then falls rapidly from 340°K.

Polyamide

The mechanical dispersion of polyamides has been most fully investigated by Woodward, Crissman and Sauer.[50] According to them, three loss peaks, α, β and γ, are all affected in height and/or peak temperature by absorbed water, hence all of them are considered as contribution of the amorphous regions. It was further verified that the β dispersion disappears for polymers perfectly free from water. It may be quite natural to say, on the basis of these facts and the data in Table I, that the α and γ dispersions correspond to the primary and secondary dispersions respectively.

One possible explanation for the appearance of the β dispersion may be that the amorphous regions are microscopically separated into two phases, one including water molecules, the other not. The local motions in the former phase contribute to the β dispersion, those in the latter to the γ dispersion. As is widely known,[60] absorbed water in polymers at low temperatures hinders the molecular motion, hence the β dispersion is located at a higher temperature. The primary dispersion results from the motions in regions including both phases and may not be separated into two peaks.

Investigation of the dielectric dispersien of nylon 6[4] shows that the relaxation strength of α dispersion falls from 75°C with decreasing temperature. This indicates that this temperature is the upper limit of glass transition region.

The line width of nuclear magnetic resonance absorption in dry nylon 6 first decreases slightly from ca. 150°K with increasing temperature, then rapidly from 310°K;[61] this is favorable to our conclusions.

Polyurethane

Behavior of the mechanical dispersions of PU very much resembles to PA, reflecting the similarity in chemical structures. With less uncertainty a similar assignment of mechanisms as given for PA appears to apply to PU.

Polytetrafluoroethylene

Many authors have confirmed[62,63,64] that the β dispersion of PTFE comes from the crystalline phase transition.

The α dispersion, though very well fits the criterion (4) as seen in Fig. 9, cannot be regarded as the primary dispersion on account of the following reasons. First, the apparent activation energy is too large as seen in Table I. Secondly, change in the X-ray pattern has been observed at elevated temperatures, being correlated with this dispersion.[64] Though some discrepancies exist among the data of nuclear magnetic resonance study in PTFE, it may be at least valid that the line width of the narrow component caused by moving fluorine nuclei in the amorphous regions exhibits narrowing far below room temperature,[52] indicating the glass transition located at low temperatures.

Taking the above facts into consideration, it may be reasonable to regard the γ dispersion as the primary one. Indeed, McCrum[56] has found that the loss peak height of γ dispersion decreases with increasing crystallinity and the storage shear modulus falls in this dispersion range from 2×10^{10} to 4.5×10^{9} dyn/cm^2 for the sample of 45% crystallinity. The γ dispersion thus satisfies well the criteria for the primary dispersion except (4). The definite explanation about the misfit of the criterion (4) to PTFE cannot be given here, but some remarks must be added. Nonpolar polymers such as PE and PP have generally lower glass transition temperatures than polar ones as PA, PTFMCE and PET, owing to the larger chain flexibility. Then the low transition temperature of PTFE may be reasonable. The misfit therefore seems to be due to the *too* high melting point, presumably resulting from the crystal structure of PTFE. If we take the crystalline phase transition temperature (285°K) as a hypothetical melting point, the criterion (4) applies very well also to this polymer.

It is not unreasonable to compare the α dispersion of PTFE to those of PE and PP.

§ 5. Conclusion

In this paper we have correlated the dynamic mechanical behavior of seven semicrystalline polymers with other types of behavior such as the dielectric, thermal and magnetic ones and classified the transition or dispersion regions without considering the specific chemical structures of polymers.

The conclusions are shown in Table II, the upper and lower limits of glass transition region being also listed. Of course values are only approximate ones. The glass transition temperature is affected by degree of crystallinity, degree of orientation, cooling rate and other numerous factors and varies from sample to sample by ten degrees or so.

Table II. Classification of dispersions

Polymer	Disperision due to crystalline region	Dispersion due to amrphous region		Glass transition region (°K)
		Primary	Secondary	
PE	α	β	γ	220—250
PP	α	β	γ	230—260
PET		α	β	340—360
PTFMCE		α	β	290—320
PA		α	β^*, γ	310—340
PU		α	β^*. γ	ca. 310
PTFE	α, β	γ		150—180

* Observed only for polymers including water.

References

1) Y. Wada, H. Hirose, T. Asano & S. Fukutomi: J. Phys. Soc. Japan, **14** (1959) 1064.
2) T. Hideshima: Progr. Theor. Phys. Suppl., No. 10 (1959) 174.
3) A. E. Woodward & J. A. Sauer: Fortschr. Hochpolym.-Forsch., **1** (1958) 114.
4) T. Nakajima & S. Saito: J. Appl. Phys. Japan, **27** (1958) 294.
5) P. R. Swan: J. Polym. Sci., **42** (1960) 525.
6) M. L. Dannis: J. Appl. Polym. Sci., **1** (1959) 121.
7) B. Baccareda & E. Butta: Chem. e Ind. (Milano), **40** (1958) 6.
8) I. Uematsu & Y. Uematsu: Chem. High Polym. (Japan), **17** (1960) 222.
9) Y. Yano: J. Appl. Phys. Japan, **27** (1958) 274.
10) J. D. Hoffman & J. J. Weeks: J. Polym. Sci., **28** (1958) 472.
11) D. Mandelkern, G. M. Martin & E. A. Quinn: J. Res. Nat. Bur. Stand., **58** (1957) 137.
12) R. F. Boyer: J. Appl. Phys., **25** (1954) 825.
13) H. J. Kolbs & E. F. Izard: ibid, **20** (1949) 564.
14) W. Kauzmann: Chem. Rev., **43** (1948) 219.
15) E. Jenkel: Kolloid-Z., **130** (1953) 472.
16) K. Yamafuji: J. Phy. Soc. Japan, **15** (1960) 2295.
17) K. Okano: Paper presented before the Annual Meeting of Phys. Soc. Japan, Hiroshima (1959).
18) Y. Maeda: Chem. High Polym. (Japan), **14** (1957) 442.
19) W. P. Mason & H. J. McSkimin: Bell Sys. Tech. J., **21** (1952) 112.
20) H. Thurn: Z. angew. Phys., **7** (1955) 44.
21) S. P. Kabin: Zh. Tech. Fiz. USSR, **26** (1956) 2628.
22) Y. Wada: J. Appl. Phys. Japan, **24** (1955) 287.
23) V. A. Solov'ew: Mem. Lenningrad Univ. (Phys. & Chem.), **1** (1958) 30.
24) I. G. Mikhailov & V. A. Solov'ew: Akust. Zh. (USSR), **3** (1957) 65.
25) K. Yamamoto & Y. Wada: J. Phys. Soc. Japan, **12** (1957) 374.
26) Y. Wada & H. Hirose: J. Appl. Phys. Japan, **27** (1958) 652.
27) E. Butta: J. Polym. Sci., **25** (1957) 237.
28) D. E. Kline, J. A. Sauer & A. E. Woodward: J. Polym. Sci., **22** (1956) 455.
29) N. Fuschillo & J. A. Sauer: J. Appl. Phys., **28** (1957) 1073.
30) J. A. Sauer & D. E. Kline: J. Polym. Sci., **18** (1955) 491.
31) W. G. Oakes & D. W. Robinson: ibid., **14** (1954) 505.
32) K. Schmieder & K. Wolf: Kolloid-Z., **134** (1953) 149.
33) L. F. Nielsen: J. Appl. Phys., **25** (1954) 1209.
34) K. H. Hellwege, R. Kaiser & K. Kuphal: Kolloid-Z., **147** (1956) 155.
35) J. A. Sauer, R. A. Wall, N. Fuschillo & A. E. Woodward: J. Appl. Phys., **29** (1958) 1385.

36) A. H. Willbourn: Trans. Far. Soc., **54** (1958) 717.
37) L. T. Muus, N. G. McCrum & F. C. McGrew: Soc. Plastic Engrs. J., **15** (1959) 368.
38) A. B. Thompson & D. W. Woods: Trans. Far. Soc., **52** (1956) 1383.
39) Y. Uematsu & T. Matsudaira: Chem. High Polym. (Japan), **17** (1960) 305.
40) D. W. Woods: Nature (London), **174** (1954) 753.
41) K. Wolf & K. Schmieder: Suppl. Ric. Sci., Vol. 25 (1955).
42) Y. Wada: J. Phys. Soc. Japan, **13** (1958) 1408.
43 Y. Wada, H. Hirose, H. Umebayashi & T. Otomo: ibid., **15** (1960) 2324.
44) M. Baccaredda & E. Butta: J. Polym. Sci., **44** (1960) 421.
45) G. W. Becker & H. Oberst: Kolloid-Z., **152** (1957) 1.
46) T. Kawaguchi: Chem. High Polym. (Japan), **13** (1956) 283.
47) Y. Wada & K. Yamamoto: J. Phys. Soc. Japan, **11** (1956) 887.
48) C. W. Deeley, A. E. Woodward & J. A. Sauer: J. Appl. Phys., **28** (1957) 1124.
49) A. E. Woodward, C. W. Deeley, D. E. Kline & J. A. Sauer: J. Polym. Sci., **26** (1957) 383.
50) A. E. Woodward, J. M. Crissman & J. A. Sauer: ibid., **44** (1960) 23.
51) E. Jenkel: Kolloid-Z., **136** (1954) 142.
52) J. A. Sauer & D. E. Kline: Int. Congress Appl. Mech., Brussels, Vol. 5 (1956) 368.
53) A. M. Thomas: Nature (London), **179** (1957) 862.
54) A. K. Schulz: J. chim. Phys., **53** (1956) 933.
55) K. H. Hellwege, R. Kaiser & K. Kuphal: Kolloid-Z., **157** (1958) 27.
56) N. G. McCrum: J. Polym. Sci., **27** (1958) 555.
57) K. Nagamatsu: High Polymers (Japan), **9** (1960) 899.
58) T. Nakajima & S. Saito: J. Polym. Sci., **20** (1958) 423.
59) T. Hideshima: Rep. Inst. Phys. Chem. Res. (Japan), **35** (1959) 1.
60) Y. Maeda: J. Appl. Phys. Japan, **26** (1957) 22.
61) R. E. Glick, R. P. Gupta, J. A. Sauer & A. E. Woodward: J. Polym. Sci., **42** (1960) 271.
62) D. Hyndman & G. F. Origlio: J. Appl. Phys., **31** (1960) 1849.
63) T. Kuroda & H. Sakami: Rep. Gov. Ind. Res. Inst., Nagoya (Japan), **7** (1958) 315.
64) R. H. H. Pierce, Jr., E. S. Clark, J. F. Whitney & W. M. D. Bryant: Paper presented before the Division of Polymer Chemistry at the 130–th Meeting of Am. Chem. Soc., Atlantic city (1956).
65) A. Nishioka: J. Appl. Phys. Japan, **27** (1958) 269.

JOURNAL OF THE PHYSICAL SOCIETY OF JAPAN, Vol. 16, No. 6, JUNE, 1961

Microwave Spectrum of Formaldehyde
III. Vibration-Rotation Interaction

By Takeshi OKA and Yonezo MORINO

Department of Chemistry, Faculty of Science,
The University of Tokyo, Tokyo, Japan

(Received, November 15, 1960)

The centrifugal distortion constants and the inertia defects necessary for the analysis of the microwave spectrum of formaldehyde molecule were calculated by the vibration-rotation theory.

Nielsen's formulation was used throughout together with the useful relations found by the present authors. The calculated centrifugal distortion constants, inertia defects and Coriolis coupling constants fit well to the experimental values.

§ 1. Quantum Mechanical Hamiltonian

The quantum mechanical Hamiltonian for a vibrating rotator was derived by Wilson and Howard as follows,[1)]

$$H=\frac{1}{2}\sum_{\alpha,\beta}\mu^{1/4}(P_\alpha-p_\alpha)\mu_{\alpha\beta}\mu^{-1/2}(P_\beta-p_\beta)\mu^{1/4}+\frac{1}{2}\mu^{1/4}\sum_s p_s\mu^{-1/2}p_s\mu^{1/4}+V \tag{1}$$

where P_α's are the components of the rotational angular momentum along the molecule-fixed axes and p_s's are momenta of vibration. p_α's are components of the angular momentum due to the vibration and can be written in terms of p_s as

$$p_\alpha=-\sum_s\sum_{s'}{}'\,\zeta_{ss'}{}^{(\alpha)}Q_sp_{s'}$$

where Q_s are normal coordinates of vibration and $\zeta_{ss'}{}^{(\alpha)}$ are Coriolis coupling constants. μ is the inverse of the inertia tensor and when the moments of inertia are expanded in terms of the normal coordinates, its determinant μ and components $\mu_{\alpha\beta}$ are vibrational operators.

$$\mu_{\alpha\beta}=\mu_{\alpha\beta}{}^{(e)}-\mu_{\alpha\alpha}{}^{(e)}\mu_{\beta\beta}{}^{(e)}\Big[\sum_s a_s{}^{(\alpha\beta)}Q_s+\sum_s\sum_{s'}\Big\{\Big(A_{ss'}{}^{(\alpha\beta)}-\sum_{s''}\zeta_{ss''}{}^{(\alpha)}\zeta_{s's''}{}^{(\beta)}\Big)-\sum_\xi\mu_{\xi\xi}{}^{(e)}a_s{}^{(\alpha\xi)}a_s{}^{(\beta\xi)}\Big\}Q_sQ_{s'}\Big]$$

$$\mu=\mu^{(e)}\Big[1-\sum_s\sum_\alpha\mu_{\alpha\alpha}{}^{(e)}a_s{}^{(\alpha\alpha)}Q_s+\sum_s\sum_{s'}\sum_\alpha\Big\{\mu_{\beta\beta}{}^{(e)}\mu_{\gamma\gamma}{}^{(e)}a_s{}^{(\beta\gamma)}a_{s'}{}^{(\beta\gamma)}-\mu_{\alpha\alpha}{}^{(e)}\Big(A_{ss'}{}^{(\alpha\alpha)}-\sum_{s''}\zeta^{(\alpha)}{}_{ss''}\zeta^{(\alpha)}{}_{s's''}\Big)\Big\}Q_sQ_{s'}\Big]$$

where $a_s{}^{(\alpha\beta)}$ and $A_{ss'}{}^{(\alpha\beta)}$ are expansion coefficients of the moments of inertia and are defined as follows;

$$I_{\alpha\beta}=I_{\alpha\beta}{}^{(e)}+\sum_s a_s{}^{(\alpha\beta)}Q_s+\sum_s\sum_{s'}\Big\{A_{ss'}{}^{(\alpha\beta)}-\sum_{s''}\zeta^{(\alpha)}{}_{ss''}\,\zeta^{(\beta)}{}_{s's''}\Big\}Q_sQ_{s'}\,.$$

V is the potential energy of vibration composed of harmonic quadratic terms and anharmonicity terms;

$$V=\sum_s\frac{\lambda_s}{2}Q_s{}^2+hc\sum_s\sum_{s'}\sum_{s''}k_{ss's''}q_sq_{s'}q_{s''}+hc\sum_s\sum_{s'}\sum_{s''}\sum_{s'''}k_{ss's''s'''}q_sq_{s'}q_{s''}q_{s'''} \tag{4}$$

When these expressions are substituted into Eq. (1) and appropriate Van Vleck's transformation which eliminates the first order off-diagonal terms is carried out[2)], the rotational Hamiltonian for an asymmetric rotor can be written as

$$H=\frac{1}{2}\sum_{\alpha,\beta}\sigma_{\alpha\beta}P_\alpha P_\alpha+\frac{1}{4}\sum_{\alpha,\beta,\gamma,\delta}\tau_{\alpha\beta\gamma\delta}\,P_\alpha P_\beta P_\gamma P_\delta \tag{5}$$

with

$$\frac{h}{\hbar^2}\frac{1}{2}\sigma_{\alpha\beta}=\frac{1}{2}[I^{-1}]_{\alpha\beta}+\sum_s\left[\frac{1}{4\pi}\sqrt{\frac{h}{c}}\left\{\frac{3k_{sss}}{\omega_s^{3/2}}a_s^{(\alpha\beta)}+\sum_{s'}{}'\frac{k_{sss'}}{\omega_{s'}^{3/2}}a_{s'}^{(\alpha\beta)}\right\}\right.$$
$$\left.+\frac{h}{8\pi^2c}\left\{4\sum_{s'}{}'\frac{\omega^2_{s'}}{\omega_s(\omega_s^2-\omega_{s'}^2)}\zeta_{ss'}^{(\alpha)}\zeta_{ss'}^{(\beta)}+3\frac{A_{ss}}{\omega_s}\right\}\right]\frac{(v_s+\frac{1}{2})}{I_{\alpha\alpha}^{(e)}I_{\beta\beta}^{(e)}}$$

and

$$\frac{h}{\hbar^4}\tau_{\alpha\beta\gamma\delta}=-\sum_s\frac{a_s^{(\alpha\beta)}a_s^{(\gamma\delta)}}{8\pi^2c^2\omega_s^2}\cdot\frac{1}{I_{\alpha\alpha}^{(e)}I_{\beta\beta}^{(e)}I_{\gamma\gamma}^{(e)}I_{\delta\delta}^{(e)}}$$

For a planar molecule $I_{cc}^{(e)}-I_{aa}^{(e)}-I_{bb}^{(e)}=0$ but $\Delta=I_{cc}-I_{aa}-I_{bb}$ is not equal to zero due to the additional terms in the expression of $\sigma_{\alpha\beta}$ in Eq. (5). The formula for this quantity, inertia defect, was derived by the present authors from Eq. (5) by using properties of vibration-rotation quantities as[3)]

$$\Delta=\frac{h}{\pi^2c}\left[\sum_s\left(v_s+\frac{1}{2}\right)\sum_{s'}{}'\frac{\omega_{s'}^2}{\omega_s(\omega_s^2-\omega_{s'}^2)}\{(\zeta_{ss'}^{(a)})^2+(\zeta_{ss'}^{(b)})^2-(\zeta_{ss'}^{(c)})^2\}\right.$$
$$\left.+\frac{3}{2}\sum_t\frac{1}{\omega_t}\left(v_t+\frac{1}{2}\right)\right]-\tau_{abab}\left(\frac{3}{4}\frac{I_{cc}}{C}+\frac{I_{bb}}{2B}+\frac{I_{aa}}{2A}\right)$$
$$-\frac{m}{M}[I_{cc}g_{cc}-I_{bb}g_{bb}-I_{aa}g_{aa}] \tag{6}$$

where t expresses the out-of-plane vibration and $g_{\alpha\alpha}$ are the components of the g-tensor for the rotational magnetic moment of the molecule. The purpose of this report is to evaluate the centrifugal distortion constants $\tau_{\alpha\beta\gamma\delta}$ and the inertia defects $\varDelta$ for the formaldehyde molecules.

§2. *l* Matrix

In order to calculate the vibration-rotation interaction, the transformation which relates the Cartesian displacements of atoms with the normal coordinates of vibration is necessary. This is the $\boldsymbol{l}$ matrix used by Nielsen and his coworkers, the elements of which are defined by

$$\sqrt{m_i}\,\delta\alpha_i=\sum_s l_{is}^{(\alpha)}Q_s \tag{7}$$

where $\delta\alpha_i$ represents the Cartesian displacement of the i-th atom. Eq. (7) can be written in matrix form as

$$\boldsymbol{x}=\boldsymbol{M}^{-2/1}\,\boldsymbol{l}\boldsymbol{Q} \tag{8}$$

where $\boldsymbol{M}$ is a 3N×3N diagonal matrix and $\boldsymbol{x}$ and $\boldsymbol{Q}$ are vectors with 3N and 3N−6 elements, respectively.

The $\boldsymbol{l}$ matrix can be calculated if the normal vibration treatment is completed. Thus, if we define the internal coordinates and the symmetry coordinates by $\boldsymbol{R}$ and $\boldsymbol{S}$, respectively, and the transformation matrices between them as

$$\boldsymbol{x}=\boldsymbol{AR},\quad \boldsymbol{R}=\boldsymbol{U'S}\ \text{and}\ \boldsymbol{S}=\boldsymbol{LQ}\ , \tag{9}$$

the $\boldsymbol{l}$ matrix is expressed as

$$\boldsymbol{l}=\boldsymbol{M}^{\frac{1}{2}}\boldsymbol{AU'L}. \tag{10}$$

$\boldsymbol{L}$ matrix can be obtained from the normal vibration calculation $(\boldsymbol{GF}-\lambda_k\boldsymbol{E})\boldsymbol{L}_k=0$. $\boldsymbol{A}$ matrix for such molecules as formaldehyde can be derived analytically by inverting the $\boldsymbol{B}$ matrix ($\boldsymbol{R}=\boldsymbol{Bx}$) with the Eckart's condition. For HDCO, where the symmetry is low, it can be obtained from the relation

$$\boldsymbol{A}=\boldsymbol{M}^{-1}\boldsymbol{B'G}^{-1} \tag{11}$$

where G^{-1} denotes the inverse of the G matrix calculated with respect to the internal coordinates. From the properties of these matrices and the $\boldsymbol{e}$ matrix which represents the normalized Eckart's condition, following relations are obtained[3].

$$\begin{aligned} \boldsymbol{l}'\boldsymbol{l} &= \boldsymbol{E}_{3N-6} \\ \boldsymbol{l}'\boldsymbol{e} &= \boldsymbol{e}'\boldsymbol{l} = 0 \\ \boldsymbol{l}\boldsymbol{l}' &= \boldsymbol{E}_{3N} - \boldsymbol{e}\boldsymbol{e}' \end{aligned} \tag{12}$$

They are expressed in scalar form as

$$\begin{aligned} &\sum_i \sum_\alpha l_{is}{}^{(\alpha)}\, l_{is'}{}^{(\alpha)} = \delta_{ss'} \\ &\sum_i \sqrt{m_i}\, l_{is}{}^{(\alpha)} = 0 \\ &\sum_i \sqrt{m_i}\, (\gamma_i\, l_{is}{}^{(\beta)} - \beta_i\, l_{is}{}^{(\gamma)}) = 0 \\ &\sum_s l_{is}{}^{(\alpha)}\, l_{js}{}^{(\alpha)} = \delta_{ij} - \sqrt{m_i m_j} \left(\frac{1}{M} + \frac{\gamma_i \gamma_j}{I_{\beta\beta}} + \frac{\beta_i \beta_j}{I_{\gamma\gamma}} \right) \\ &\sum_s l_{is}{}^{(\alpha)}\, l_{js}{}^{(\beta)} = \frac{\sqrt{m_i m_j}}{I_{\gamma\gamma}}\, \alpha_j \beta_i \quad (\alpha \neq \beta) \end{aligned} \tag{13}$$

They can be used for checking the calculated $\boldsymbol{l}$ matrix as well as for obtaining useful relations between the vibration-rotation quantities. Attention must be paid in calculating the $\boldsymbol{l}$ matrix to the fact that the Cartesian coordinate is fixed to the molecule along of the principal axes of inertia. Thus for the case of HDCO where the a-axis of the inertia tensor does not coincide with the C=O axis, a slight modification is necessary, because the $\boldsymbol{B}$ matrix, independent of the masses of the atoms, is common to all isotopic species and was calculated with respect to the coordinate along the C=O axis. The matrix Θ which expresses the rotation of the molecule-fixed coordinate must be multiplied. It is easily seen that the Θ matrix and the $\boldsymbol{M}^{2/1}$ matrix commute each other, and the $\boldsymbol{l}'$ matrix related to the principal axes of inertia can be expressed by

$$\boldsymbol{l}' = \Theta \boldsymbol{l} \tag{14}$$

The quantities $a_s{}^{(\alpha\beta)}$, $A_{ss}{}^{(\alpha\beta)}$ and $\zeta_{ss'}{}^{(\alpha)}$ are expressed by the components of $\boldsymbol{l}$ matrix as follows.[2]

$$\begin{aligned} &a_s{}^{(\alpha\alpha)} = 2 \sum_i \sqrt{m_i}\, (\beta_i\, l_{is}{}^{(\beta)} + \gamma_i\, l_{is}{}^{(\gamma)}) \\ &a_s{}^{(\alpha\beta)} = -2 \sum_i \sqrt{m_i}\, \alpha_i\, l_{is}{}^{(\beta)} = -2 \sum_i \sqrt{m_i}\, \beta_i\, l_{is}{}^{(\alpha)} \qquad (\alpha \neq \beta) \\ &A_{ss'}{}^{(\alpha\alpha)} = \sum_i (l_{is}{}^{(\beta)}\, l_{is'}{}^{(\beta)} + l_{is}{}^{(\gamma)}\, l_{is'}{}^{(\gamma)}) = \delta_{ss'} - \sum_i l_{is}{}^{(\alpha)}\, l_{is'}{}^{(\alpha)} \\ &A_{ss'}{}^{(\alpha\beta)} = -\sum_i l_{is}{}^{(\alpha)}\, l_{is'}{}^{(\beta)} \qquad (\alpha \neq \beta) \\ &\zeta_{ss'}{}^{(\alpha)} = \sum_i (l_{is}{}^{(\beta)}\, l_{is'}{}^{(\gamma)} - l_{is'}{}^{(\beta)}\, l_{is}{}^{(\gamma)}) \end{aligned} \tag{15}$$

It is obvious from the third formula of Eq. (15) and the first formula of Eq. (13) that the following relations exist for a planar molecule.

$$\left.\begin{aligned} &A_{ss}{}^{(aa)} + A_{ss}{}^{(bb)} = A_{ss}{}^{(cc)} = 1, \\ &a_s{}^{(aa)} + a_s{}^{(bb)} = a_s{}^{(cc)}, \end{aligned}\right\} \quad s\text{: in-plane vibration}$$

and

$$\left.\begin{aligned} &A_{ss}{}^{(aa)} = A_{ss}{}^{(bb)} = 1, \ A_{ss}{}^{(cc)} = 0, \\ &a_s{}^{(aa)} = a_s{}^{(bb)} = a_s{}^{(cc)} = 0. \end{aligned}\right\} \quad s\text{: out-of-plane vibration} \tag{15'}$$

It can be seen from Eq. (15) using Eq. (13) that the following relations exist:[3]

$$
\begin{aligned}
&\sum_{s} \zeta_{ss'}{}^{(\alpha)} \zeta_{ss'}{}^{(\beta)} = A_{ss'}{}^{(\alpha\beta)} - \frac{1}{4} \sum_{\xi} \frac{a_s{}^{(\alpha\xi)}\, a_{s'}{}^{(\beta\xi)}}{I_{\xi\xi}} \\
&\sum_{s} (a_s{}^{(\alpha\alpha)})^2 = 4I_{\alpha\alpha} \\
&\sum_{s} (a_s{}^{(\alpha\beta)})^2 = \frac{I^2{}_{\gamma\gamma} - (I_{\alpha\alpha} - I_{\beta\beta})^2}{I_{\gamma\gamma}} \\
&\sum_{s} (a_s{}^{(\alpha\alpha)}\, a_s{}^{(\beta\beta)}) = 2(I_{\alpha\alpha} + I_{\beta\beta} - I_{\gamma\gamma})
\end{aligned}
\qquad (16)
$$

These relations can be used to check the calculation.

§ 3. Symmetry Considerations

In applying the formulation given above to actual molecules many terms are shown to vanish from the symmetry considerations. Among many quantities appearing in Eq. (5), only those terms which are totally symmetric with all symmetry operations remain. For example, k_{sss} is non-vanishing only when s belongs to the totally symmetric species, because otherwise $k_{sss}\, q_s{}^3$ is antisymmetric with some symmerty operations. In the same way, whether $a_s{}^{(\alpha\beta)}$ $A_{ss}{}^{(\alpha\beta)}$, and $\zeta_{ss'}{}^{(\alpha)}$ vanish or not are determined from the symmetry properties of $q_s P_\alpha P_\beta$, $q_s{}^2 P_\alpha P_\beta$, and $q_s q_{s'} P_\alpha$, respectively.

Table I

Character Table for C_s symmetry

C_s	I	$\sigma\ (ab)$	
A'	$+1$	$+1$	R_c
A''	$+1$	-1	R_a, R_b

Table II

Non-vanishing elements for C_s symmetry

k_{sss}	$s \subset A'$	
$k_{sss'}$	$s' \subset A'$	s arbitrary
$A_{ss}{}^{(\alpha\alpha)}$ and $A_{ss'}{}^{(ab)}$	s arbitrary $\alpha = a, b, c,$	
$\zeta_{ss'}{}^{(c)}$	$s \subset A'$ and $s' \subset A'$ or $s \subset A''$ and $s' \subset A''$	
$\zeta_{ss'}{}^{(a)}$ and $\zeta_{ss'}{}^{(b)}$	$s \subset A'$ and $s' \subset A''$ or $s \subset A''$ and $s' \subset A''$	
$a_s{}^{(\alpha\alpha)}$ and $a_s{}^{(ab)}$	$s \subset A'$ $\alpha = a, b, c$	
$(a_s{}^{(bc)}$, $a_s{}^{(ac)})$	$s \subset A''$	

i) C_s symmetry, HDCO

The character for C_s symmetry is shown in Table I, in which the c-axis is taken as the out-of-plane axis. Non-vanishing elements are listed in Table II. $a_s{}^{(bc)}$ and $a_s{}^{(ac)}$ are shown to be zero from Eq. (15) for a planar molecule.

ii) C_{2v} symmetry, H_2CO

The character for C_{2v} symmetry is shown

Table III

Character Table for C_{2v} symmetry

C_{2v}	I	$C_2(a)$	$\sigma(ab)$	$\sigma(ac)$	
A_1	$+1$	$+1$	$+1$	$+1$	
A_2	$+1$	$+1$	-1	-1	R_a
B_1	$+1$	-1	$+1$	-1	R_c
B_2	$+1$	-1	-1	$+1$	R_b

Table IV

Non-vanishing elements for C_{2v} symmetry

k_{sss}	$s \subset A_1$	
$k_{sss'}$	$s' \subset A_1$	s arbitrary
$A_{ss}{}^{(\alpha\alpha)}$	s arbitrary, $\alpha = a, b, c$	
$\zeta_{ss'}{}^{(c)}$	$s \subset A_1$ and $s' \subset B_1$, ($s \subset A_2$ and $s' \subset B_2$)	
$\zeta_{ss'}{}^{(b)}$	$s \subset A_1$ and $s' \subset B_2$, ($s \subset A_2$ and $s' \subset B_1$)	
$\zeta_{ss'}{}^{(a)}$	$s \subset B_1$ and $s' \subset B_2$, ($s \subset A_1$ and $s' \subset A_2$)	
$a_s{}^{(\alpha\alpha)}$	$s \subset A_1$ $\alpha = a, b, c$	
$a_s{}^{(ab)}$	$s \subset B_1$	
$(a_s{}^{(bc)})$	$s \subset A_2$	
$(a_s{}^{(ac)})$	$s \subset B_2$	

in Table III. Non-vanishing elements are listed in Table IV. The rotational Hamiltonian described in the previous report was derived from these considerations.[5]

§ 4. Centrifugal Distortion Constants

The centrifugal distortion constants defined in Eq. (5) are calculated if the $\boldsymbol{l}$ matrix is obtained. Since they are expressed by $a_s^{(\alpha\beta)}$'s the non-vanishing constants are shown to be $\tau_{\alpha\alpha\alpha\alpha}$, $\tau_{\alpha\alpha\beta\beta}$ and τ_{abab} for C_{2v} planar molecules and $\tau_{\alpha\alpha\alpha\alpha}$, $\tau_{\alpha\alpha\beta\beta}$, τ_{abab} and $\tau_{\alpha\alpha ab}$ for C_s planar molecules.

The centrifugal distortion constants are calculated directly from Eq. (5), which can be transformed into a more convenient form. When Eq. (15) is substituted for example to the expression of $\tau_{\alpha\alpha\alpha\alpha}$ in Eq. (5), it is seen that

$$\begin{aligned}\tau_{\alpha\alpha\alpha\alpha} &= -\frac{1}{2(I_{\alpha\alpha}^{(e)})^4}\sum_s \frac{(a_s^{(\alpha\alpha)})^2}{\lambda_s} \\ &= -\frac{2}{(I_{\alpha\alpha}^{(e)})^4}\sum_i\sum_j \sqrt{m_i m_j}\left[\beta_i\beta_j\sum_s \frac{l_{is}^{(\beta)}\,l_{js}^{(\beta)}}{\lambda_s} + \beta_i\gamma_j\sum_s \frac{l_{is}^{(\beta)}\,l_{js}^{(\gamma)}}{\lambda_s}\right. \\ &\qquad\left. + \gamma_i\beta_j\sum_s \frac{l_{is}^{(\gamma)}\,l_{js}^{(\beta)}}{\lambda_s} + \gamma_i\gamma_j\sum \frac{l_{is}^{(\gamma)}\,l_{js}^{(\gamma)}}{\lambda_s}\right]\end{aligned}$$

The terms appearing in the bracket can be written in a matrix form. If we define a matrix X which is a square diagonal matrix with the equilibrium coordinates of particles as the diagonal elements, the following relation exists

$$\sqrt{m_i m_j}\,\alpha_i\beta_j\sum_s \frac{l_{is}^{(\alpha)}\,l_{js}^{(\beta)}}{\lambda_s} = |\boldsymbol{X'M^{1/2}\,l\lambda^{-1}\,l'M^{1/2}X}|_{\alpha_i\beta_j} \tag{17}$$

where the suffix represents the $\alpha_i\beta_j$-th component of the matrix. When the Eqs. (10) and (11) and the familiar relation $\boldsymbol{F}^{-1} = \boldsymbol{U'L\lambda^{-1}L'U}$ are substituted, the matrix appearing in the right hand side of Eq. (17) becomes $\boldsymbol{X'MAF^{-1}A'MX} = \boldsymbol{K}$. The matrices $\boldsymbol{X}$, $\boldsymbol{M}$, and $\boldsymbol{A}$ can be calculated from the masses of the atoms and the geometry of the molecule without solving the normal coordinate problem. Thus the centrifugal distortion constants can be used to determine the potential constants when there is not sufficient vibrational frequencies. The centrifugal distortion constants can be represented by the K matrix as

$$\begin{aligned}\tau_{\alpha\alpha\alpha\alpha} &= -\frac{2}{(I_{\alpha\alpha}^{(e)})^4}\sum_i\sum_j (K_{\beta i\beta j}+K_{\beta i\gamma j}+K_{\gamma i\beta j}+K_{\gamma i\gamma j}) \\ \tau_{\alpha\alpha\beta\beta} &= -\frac{2}{(I_{\alpha\alpha}^{(e)})^2\,(I_{\beta\beta}^{(e)})^2}\sum_i\sum_j (K_{\beta i\gamma j}+K_{\beta i\alpha j}+K_{\gamma i\gamma j}+K_{\gamma i\alpha j})\end{aligned} \tag{18}$$

This equation is essentially the same as the one derived by Kivelson and Wilson but is more straightforward.[6]

For a planar molecule such as formaldehyde, c elements of the X matrix vanish and $K_{\alpha icj} = 0$. Thus the following relations which was pointed out by Kivelson and Wilson are valid for all planar molecules.

$$\begin{aligned}\tau_{cccc} &= \tau_{aaaa}\frac{C^4}{A^4} + 2\,\tau_{aabb}\frac{C^4}{A^2B^2} + \tau_{bbbb}\frac{C^4}{B^4} \\ \tau_{bbcc} &= \tau_{bbbb}\frac{C^2}{B^2} + \tau_{aabb}\frac{C^2}{A^2} \\ \tau_{aacc} &= \tau_{aaaa}\frac{C^2}{A^2} + \tau_{aabb}\frac{C^2}{B^2}\end{aligned} \tag{19}$$

This relation can also be derived from the definition of the centrifugal distortion constants and the relation between $a_s^{(\alpha\beta)}$ in Eq. (15′).

Table V

Observed and calculated vibrational frequencies in cm^{-1} and the potential constants

s	H_2CO* (obs.)	H_2CO* (calc.)	$\delta\%$	D_2CO** (obs.)	D_2CO** (calc.)	$\delta\%$	HDCO*** (obs.)	HDCO*** (calc.)	$\delta\%$
1	2766.4	2782.2	−0.6	2055.8	2045.1	0.5	2844.1	2831.2	0.5
2	1746.1	1755.7	−0.6	1700	1684.5	0.9	2120.7	2087.8	1.6
3	1500.6	1502.6	−0.1	1105.7	1101.3	0.4	1723.4	1714.6	0.5
4	2843.4	2875.4	−1.1	2159.7	2129.3	1.4	1400.0	1396.4	0.3
5	1247.4	1247.9	0.0	990	989.3	0.1	1041	1030.2	1.0
6	1163.5	1175.3	−1.0	938	938.0	0.0	1074	1063.3	1.0

$f_{RR}=12.374\times10^5$ dyne/cm
$f_{rr}=4.407$ 〃
$f_{Rr}=-0.038$ 〃

$f_{\alpha\alpha}=0.3406\times10^{-11}$ dyne cm
$f_{\theta\theta}-f_{\theta\theta'}=0.7930$ 〃
$f_{\theta\theta}-f_{\theta\varphi}=0.8671$ 〃

$f_{R\theta}-f_{R\varphi}=0.4046\times10^{-3}$ dyne
$f_{r\theta}-f_{r\varphi}=0.3766$ 〃
$f_{r\theta'}-f_{r\varphi}=0$

* Blau and Nielsen (8)
** E. S. Ebers and H. H. Nielsen, J. Chem. Phys. **6** (1938) 311.
*** D. W. Davidson, B. I. Stoicheff and H. J. Bernstein, J. Chem. Phys. **22** (1954) 289.

§ 5. Calculation

i) Normal vibration

The formaldehyde molecule has six modes of vibration. In the cases of H_2CO and D_2CO, three of them belong to A_1, two to B_1 and one to B_2 species and in the case of HDCO five of them belong to A' and one to A'' species. An elaborate normal vibration treatment for the formaldehyde molecule was given by Miyazawa[7] using Urey-Bradley potential field. His potential constants were slightly modified in order to fit the calculated values to the values recently observed by Blau and Nielsen.[8] Internal coordinates were taken as shown in Fig. 1. The following equilibrium structure was assumed:

$$C=O=1.21\ A,\ C-H=1.08\ A,\ <HCO=120°.$$

The observed and calculated vibrational frequencies are listed in Table V, together with the potential constants. The agreement is satisfactory. $\boldsymbol{l}$ matrix was calculated from the $\boldsymbol{L}$ matrix obtained in the course of normal vibration treatment. The calculated $\boldsymbol{l}$ matrix was checked by Eq. (13).

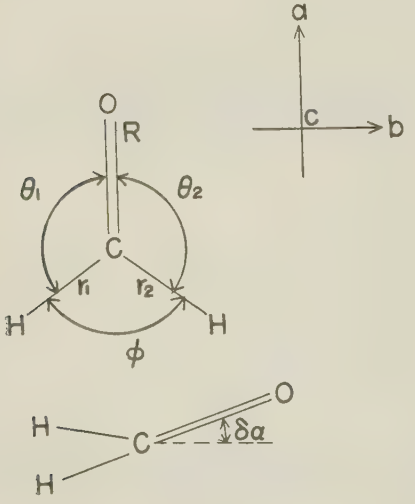

Fig. 1

ii) $a_s^{(\alpha\beta)}$, $A_{ss}^{(\alpha\beta)}$, and $\zeta_{ss'}^{(\alpha)}$

$a_s^{(\alpha\beta)}$, $A_{ss}^{(\alpha\beta)}$, and $\zeta_{ss'}^{(\alpha)}$ were calculated from Eq. (15). It was seen that the calculated values of these constants satisfied the relations in Eq. (16). Some of them are written here.

$$H_2CO: \quad (\zeta_{16}^{(b)})^2+(\zeta_{26}^{(b)})^2+(\zeta_{36}^{(b)})^2=1$$

$$(\zeta_{46}^{(a)})^2+(\zeta_{56}^{(a)})^2=1$$

$$(\zeta_{1s}^{(c)})^2+(\zeta_{2s}^{(c)})^2+(\zeta_{3s}^{(c)})^2=1 \quad (s=4,\ 5)$$

$$HDCO \quad (\zeta_{16}^{(\alpha)})^2+(\zeta_{26}^{(\alpha)})^2+(\zeta_{36}^{(\alpha)})^2+(\zeta_{46}^{(\alpha)})^2+(\zeta_{56}^{(\alpha)})^2=1 \quad (\alpha=a,\ b,\ c)$$

$$\sum_s\sum_{s'}(\zeta_{ss'}^{(\alpha)})^2=4 \quad (s,\ s'=1,\ 2,\ 3,\ 4,\ 5)$$

iii) Centrifugal distortion constants

The centrifugal distortion constants are calculated either by Eq. (5) or by Eq. (15). The explicit formula by Eq. (5) was given by Silver.[9] The calculated values are listed in

Table VI

Calculated centrifugal distortion constants in Mc/sec

	H_2CO	$H_2C^{13}O$	H_2CO^{18}	D_2CO	HDCO
τ_{bbbb}	−0.40331	−0.38084	−0.36350	−0.31250	−0.36106
τ_{cccc}	−0.23114	−0.22222	−0.21356	−0.12503	−0.16993
τ_{aaaa}	−101.831	−101.833	−101.823	−25.494	−57.187
τ_{ccaa}	−0.38358	−0.38286	−0.31746	−0.27237	−0.23698
τ_{aabb}	1.41014	1.31228	1.31432	0.92728	1.45748
τ_{bbcc}	−0.29166	−0.27852	−0.26730	−0.17460	−0.22790
τ_{abab}	−3.29200	−3.16220	−3.01747	−1.78082	−2.30378
τ_{abbb}					−0.19466
τ_{aaab}					2.71209
τ_{abcc}					−0.07943

Table VII

Calculated inertia defect in amu A^2

$$\Delta = \Delta_{vib} + \Delta_{cent} + \Delta_{elec}$$

$$\Delta_{vib} = \sum_s \Delta_s (v_s + \tfrac{1}{2})$$

	H_2CO	$H_2C^{13}O$	H_2CO^{18}	D_2CO	HDCO
Δ_1	0.0086	0.0071	0.0085	0.0752	−0.0127
Δ_2	0.0546	0.0591	0.0693	0.0241	−0.0065
Δ_3	0.0955	0.0891	0.0758	0.1625	0.0355
Δ_4	−0.0271	−0.0261	−0.0272	−0.0907	0.1373
Δ_5	0.4341	0.3913	0.4062	0.6002	−0.3473
Δ_6	−0.4464	−0.4013	−0.4132	−0.6093	0.3358
Δ_{cent}	0.0016	0.0016	0.0016	0.0014	0.0014
Δ_{elec}	−0.0052	−0.0052	−0.0052	−0.0051	−0.0052
$\Delta_{vib,\,0}$	0.0561	0.0561	0.0561	0.0772	0.0674

Table VI.

iv) Inertia defect

The inertia defect was calculated as shown in Table VII. It depends on the vibrational states of the molecule. The additional terms which come from the centrifugal effect and electronic interaction are given separately. The effect of elentrons is not very small. This is due to the out-of-plane π electrons of the C=O bond. In calculating the electronic interaction the g-values listed in Table I of II were used.

§ 6. Discussions

The calculated constants of vibration-rotation interaction are compared with the observed ones in Table VIII. There is only one experimental value for the Coriolis coupling constant.[8] This value has been obtained from infra-red spectrum. Since ν_5 and ν_6 vibrations have nearly equal frequencies, the two levels $v_5=1$ and $v_6=1$ mix through $\zeta_{56}^{(a)}$.

Table VIII
Comparison with the experimental values

		calc.	obs.
$\zeta_{56}^{(a)}$	H_2CO	0.563	0.54*
τ_{bbbb}	H_2CO	-0.40331	-0.39220
τ_{bbbb}	$H_2C^{13}O$	-0.38084	-0.37283
τ_{bbbb}	D_2CO	-0.31250	-0.31942
τ_{bbbb}	HDCO	-0.36106	-0.37016
$\varDelta_0$	H_2CO	0.0561±0.0016§	0.0574±0.0002
$\varDelta_0$	HDCO	0.0674±0.0018§	0.0679±0.0004

* Blau and Nielsen (8).

§ The quoted error came from the experimental error of g-factor (5).

The calculated value is found to be in good agreement with the experimental value.

The calculated centrifugal distortion constants were used in the analysis of the K-type doubling spectra in the first part of this series of reports. As was shown there, the observed frequencies were fit with the calculated ones by a small adjustment on τ_{bbbb}. The calculated values and observed ones are listed in Table VIII.

Since the frequencies for the R-type transition were available only for H_2CO and HDCO, the observed inertia defects are listed only for these two species. They agree with the calculated values within the probable error. The rotational constants for other isotopic species were computed using the calculated inertia defects. The measurement of $1_{01} \leftarrow 0_{00}$ lines for these isotopic species would be of interest to test the accuracy of the present result.

§ 7. Acknowledgement

The authors are indebted to Prof. Koichi Shimoda of the Department of Physics for his valuable advice and encouragement during the course of this investigation.

References

1) E. B. Wilson, Jr., and J. B. Howard: J. Chem. Phys. **4** (1936) 260.
2) H. H. Nielsen: Revs. Mod. Phys. **23** (1951) 90.
3) T. Oka and Y. Morino: J. Mol. Spectroscopy to be published.
4) E. B. Wilson, Jr., J. C. Decius and P. C. Cross: "Molecular Vibrations" McGraw-Hill Book Co., Inc. (1955).
5) I. T. Oka, H. Hirakawa and K. Shimoda: J. Phys. Soc. Japan, **15** (1960) 2265.
II. T. Oka: J. Phys. Soc. Japan, **15** (1960) 2274.
6) D. Kivelson and E. B. Wilson, Jr.: J. Chem. Phys. **20** (1952) 1575.
7) T. Miyazawa: J. Chem. Soc. Japan **76** (1955) 1132.
8) H. H. Blau and H. H. Nielsen: J. Mol. Spectroscopy **1** (1957) 124.
9) S. Silver: J. Chem. Phys. **9** (1941) 565.

JOURNAL OF THE PHYSICAL SOCIETY OF JAPAN, Vol. 16, No. 6, JUNE, 1961

Double Quantum Transition in Electron Spin Resonance of Diphenyl-Picryl Hydrazyl at Low Magnetic Fields

By Tsuneo HASHI

Department of Physics, Faculty of Science, Kyoto University

(Received February 3, 1961)

Two radiation fields (ν_1 of about 150 Mc and ν_2 of 30, 20, and 15 Mc) are applied at static fields of about 50 gauss. The line shape, the peak position, and the intensity of the signal are well interpreted on the basis of the Bloch phenomenological equation choosing $T=4.8\times10^{-8}$ sec, except for slight discrepancies near $H_0=\omega_1/|\gamma|$. Some experimental results at $\nu_2=4.5$ Mc are also given.

§ 1. Introduction

When a two-level system of energy separation $h\nu_0$ is simultaneously irradiated by two radiation fields of different frequencies ν_1 and ν_2 ($\nu_1>\nu_2$), the double quantum transition can take place[1,2,3] under the condition of conservation of energy ($\nu_0=\nu_1-\nu_2$ or $\nu_0=\nu_1+\nu_2$) and that of angular momentum. In the case of $\nu_0=\nu_1-\nu_2$, a quantum with frequency ν_1 is absorbed and a quantum with frequency ν_2 simultaneously emitted, while in the case of $\nu_0=\nu_1+\nu_2$, two quanta with frequencies ν_1 and ν_2 are simultaneously absorbed. Though each process is accompanied by the inverse process, the weight of the inverse process is smaller by the population ratio of the two energy levels. The net emission at the frequency ν_2 in the case of $\nu_0=\nu_1-\nu_2$ is of particular interest, since this mechanism can be used to realize a maser on a system with the positive temperature,[3] and recently much attention has been paid to the role of the double quantum transition in the masers.[3,4,5]

The present paper is concerned with this type of double quantum transition associated with the electron spin resonance of diphenyl-picryl hydrazyl (DPPH) at low magnetic fields. In the field of the magnetic reasonance, the experimental work reported by Winter[2] seems to be the only one as the experimental work on such a double quantum transition.[*] He observed a double quantum transition in DPPH at high magnetic fields, but gave no detailed descriptions of characters of the transition such as the line shape, the peak position and the intensity of the signal. The aim of the present work consists in the detailed study on the double quantum transition relating to the relaxation in the non-isolated system.

We used two radiation fields of the frequency ν_1 of about 150 Mc and of the frequency ν_2 in the range of 4.5 Mc to 30 Mc, and the static magnetic field of about 50 gauss. The signals were observed at the frequency ν_2. The low field magnetic resonance is particularly suitable for the study of the line shape, since the sufficient field strength of rf magnetic field is readily obtainable and the inhomogeneity of the static magnetic field is easily reduced to such an amount that the line shape is not seriously affected by it.

The description of the apparatus, the experimental results and the comparison with the calculations based on the Bloch phenomenological equation[6] are given in the following.

§ 2. Apparatus and Experimental Procedure

The block diagram of the apparatus is shown in Fig. 1. The directions of three magnetic fields (H_0, $2H_1\cos\omega_1t$ and $H_2\cos\omega_2t$) are so arranged that the conservation of the angular monentum is preserved for the double quantum transition, as shown in Fig. 2.

The static magnetic field H_0 of about 50 gauss is produced by a Helmholtz coil which

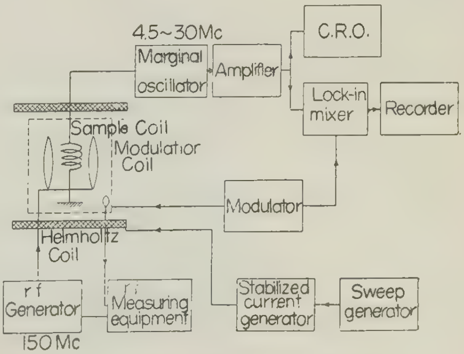

Fig. 1 Block diagram of apparatus

is supplied by a low voltage stabilized current generator using power transistors. At the same time, this generator gives a gradual change in the magnetic field drived by sweep generator of the Miller integrator type. The value of H_0 is measured by an ordinary absorption signal of DPPH using a low field electron spin resonance spectrometer operating in the range of 10 Mc to 200 Mc, which is not shown in Fig. 1.

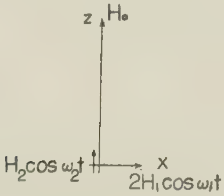

Fig. 2. Arrangement of magnetic fields.

The rf magnetic field $2H_1\cos\omega_1t$ ($\nu_1\simeq150$Mc) perpendicular to the static magnetic field H_0 is produced by a Helmholtz coil with diameter of 3 cm supplied by an rf generator constructed by the stage of master oscillator and that of power amplifier. The maximum available value of H_1 is about 4 gauss. The value of H_1 is measured by a pickup coil-VTVM system. It is also chequed by use of the pulsed pure quadrupole resonance of Br^{81} in $NaBrO_3$,[7] as follows. A single crystal of $NaBrO_3$ is inserted in the coil and the frequency of the rf generator is set at the pure quadrupole reasonance frequency of Br^{81}, i.e. about 150Mc which is also the frequency of the radiation field used throughout the present experiment. The rf generator is then operated in pulsed fashion and the signal from Br^{81} is detected in a usual way as in the standard pulsed pure quadrupole reasonace experiment (the details of the calibrating apparatures are not given in Fig. 1.). From the observed 90° pulse-width t_w and the relation $\sqrt{3}\gamma_{Br}H_1t_w=\pi/2$, the value of H_1 is obtained.

The rf magnetic field $H_2\cos\omega_2t$ ($\nu_2=4.5\sim30$ Mc) parallel to the static magnetic field H_0 is produced by a marginal oscillator of Pound-Knight type.[8] The marginal oscillator serves also as a detector for the double quantum transition, whose output is amplified and coherently detected in the same manner as in the usual magnetic resonance experiment.[9]

The 32c modulation field is produced by an auxiliary coil parallel to the static magnetic field H_0 and the peak-to-peak amplitude used for all of the measurements is 0.1 gauss or less. The frequency modulation and frequency sweep scheme is more desirable than the present magnetic field modulation and magnetic field sweep scheme, but it is not practical because a relatively wide frequency range must be swept. Since our main purpose is the detailed study of the line shape, particular attention was paid to the setting of modulation amplitude, the linearity of the sweep, the balancing of lock-in mixer, and the homogeneity of magnetic fields H_0 and H_1.

The sample consisted of approximately 0.3 g of polycrystalline diphenyl-picryl hydrazyl. All measurements were made at room temperatures.

§ 3. Experimental Results and Discussion

The measurements were made at the frequencies ν_1 of about 150 Mc and ν_2 of 30, 20,

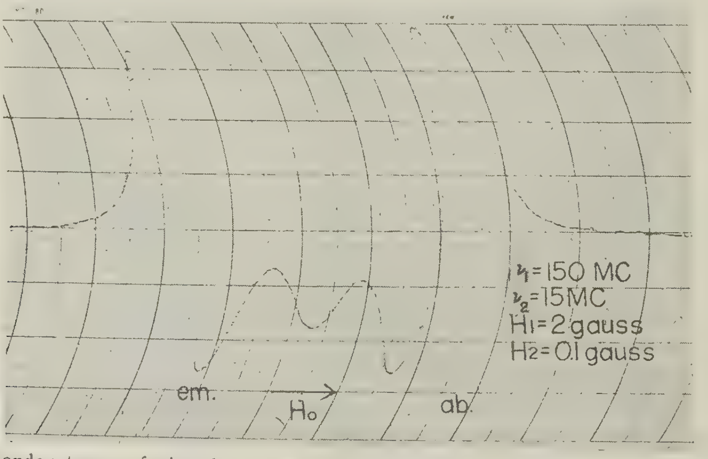

Fig. 3. A typical recorder trace of signal at $\nu_1=150$Mc, $\nu_2=15$Mc $H_1=2$ gauss and $H_2=0.1$ gauss.

15 and 4.5 Mc for various values of H_1 from 1 to 3 gauss. The value of H_2 was fixed at 0.1 gauss.

First we shall show the experimental results at $\nu_2=30$, 20 and 15 Mc. A typical recorder trace and its integrated curve at $\nu_2=15$ Mc and $H_1=2$ gauss are represented in Figs. 3 and 4. All of the integrated curves of the signals obtained at $\nu_2=30$, 20 and 15 Mc have the similar profile. The characteristic features of the curve are as follows. The curve shows opposite polarities on both sides of the magnetic field $H_0=\omega_1/|\gamma|$. By comparing it with the polarity of the ordinary absorption signal obtained by the same apparatus at the frequency ν_2, it was decided that the emission takes place below that field value (i.e. $\omega_0<\omega_1$) and the absorption above it (i.e. $\omega_0>\omega_1$). The fact that the emission takes place in the present case was also confirmed by detecting it with the aid of a high gain regenerative amplifier, in which the oscillation occurred when coupled with it in the case of 2 g of DPPH.

The emission and the absorption parts of the integrated curve are similar in form except for the polarities. More precisely, however, the height of the absorption curve is slightly larger than that of the emission curve. The ratio of the two peak heights is equal to that of the values of H_0 at which the peaks appear. If the curves are transformed by dividing the ordinate by the corresponding abscissa, the emission and the absorption curves become coincident in form. So, in the following, we deal with only the half of the whole curve obtained by the above procedures.

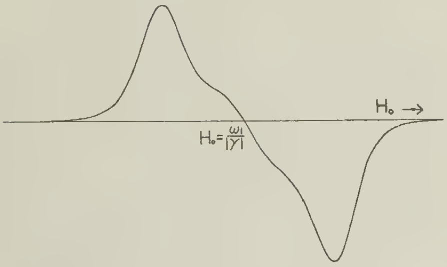

Fig. 4. Integrated curve of the signal given in Fig. 3, the left-hand half showing the emission and the right-hand one absorption.

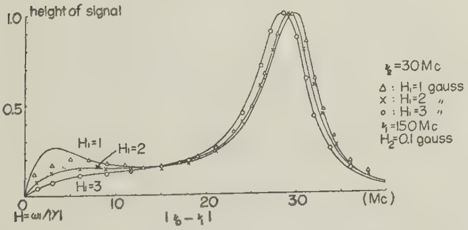

Fig. 5. Calculated half line shapes and experimental points at $\nu_1=150$Mc, $\nu_2=30$Mc, $H_1=1$, 2, 3 gauss and $H_2=0.1$ gauss. The formers are obtained by using (8) and normalizing the peak to unity, and the latters obtained by the procedures stated in the text.

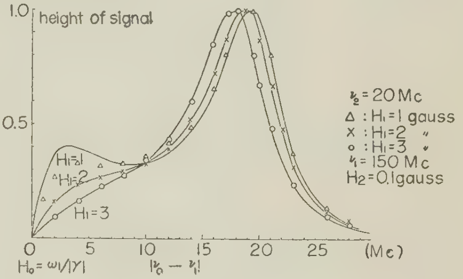

Fig. 6. Calculated half line shapes and experimental points at $\nu_1=150$Mc, $\nu_2=20$Mc, $H_1=1$, 2, 3 gauss and $H_2=0.1$ gauss. These are obtained in the same way as in Fig. 5.

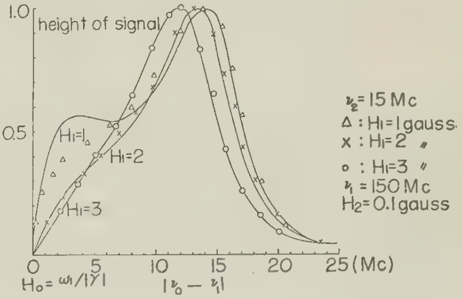

Fig. 7. Calculated half line shapes and experimental points at $\nu_1=150$Mc, $\nu_2=15$Mc, $H_1=1$, 2, 3 gauss and $H_2=0.1$ gauss. These are obtained in the same way as in Fig. 5.

The transformed emission (or absorption) curve is not symmetrical with respect to its peak axis, but some bulges or bumps appear on the higher (or lower) field side. The detailed line shapes are given by experimental points in Figs. 5∼7 for various values of ν_2 and of H_1.

The positions of the peaks do not coincide exactly with the field values $H_0=(\omega_1\pm\omega_2)/|\gamma|$, shifting to the higher field side in the case of emission (lower field side in the case of absorption). The amount of the shift is approximately proportional to H_1^2.

The variation of the peak height (signal intensity) with H_1 is shown in Fig. 8 (where the heights are not divided by the corresponding values of H_0). It is proportional to H_1^2 at $\nu_2=30$ Mc, but at $\nu_2=15$ Mc, the increase of it becomes more gradual than H_1^2 for larger values of H_1. Since it is difficult to maintain the equal sensitivity of the spectrometer at different frequencies, the precise comparison between peak heights at different frequencies was not made. But it was observed that the peak height is approximately proportional to $1/\nu_2^2$ at the fixed values of H_1.

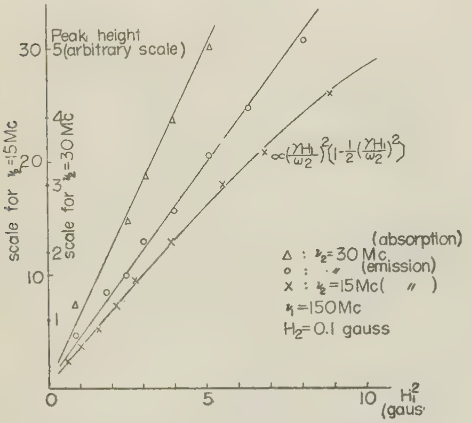

Fig. 8. Variation of peak height with H_1 at $\nu_2=$ 30Mc, 15Mc, $\nu_1=150$Mc and $H_2=0.1$ gauss. ∘, Δ, × are experimental points corresponding respectively to emission and to absorption at $\nu_2=30$Mc and to emission at $\nu_2=15$Mc. Curves are obtained by using (10) and multiplying by appropriate factors for best fits. Different multiplication factors are used for $\nu_2=30$Mc and $\nu_2=15$Mc.

The signal intensity decreases as $\cos^2\theta$, if the direction of the field $H_2\cos\omega_2 t$ is rotated by the angle θ in the zx plane (Fig. 2). No signals could be obtained when the direction of $H_2\cos\omega_2 t$ became perpendicular to both H_0 and H_1. We tried to observe, in this case, the signals due to the higher order transitions at the field $H_0=(2\omega_1\pm\omega_2)/|\gamma|$, but without success.

Now, we shall compare the above results with the calculations based upon the Bloch phenomenological equation.

In non-diluted DPPH, the strong exchange coupling markedly narrows the resonance lines,[10] so the application of the Bloch equation was justified[11] from the microscopic point of view. It holds in the present case of the double quantum transition. Further we assume $T_1=T_2$ after Lloyd and Pake,[10] though recently it was pointed out[12] that in some cases the relation $T_1=T_2$ does not hold exactly for non-diluted DPPH.

The Bloch equation is

$$\frac{d\boldsymbol{M}}{dt}=\gamma(\boldsymbol{M}\times\boldsymbol{H})-\frac{1}{T}(\boldsymbol{M}-\boldsymbol{M}_0)\,. \qquad (1)$$

In the present case, $\boldsymbol{H}$ consists of three components H_0, $2H_1\cos\omega_1 t$ and $H_2\cos\omega_2 t$, namely

$$\boldsymbol{H}=(H_0+H_2\cos\omega_2 t)\boldsymbol{k}+(2H_1\cos\omega_1 t)\boldsymbol{i}\,. \qquad (2)$$

Using a coordinate system rotating about H_0 with angular frequency ω_1, the phenomena described by Eqs. (1) and (2) can regarded as a kind of magnetic resonance in the rotating coordinate system, "nutation resonance." The time dependent magnetization M_z of frequency ν_2 obtained from the equation is

$$M_z=(\chi' H_2\cos\omega_2 t+\chi'' H_2\sin\omega_2 t)\,, \qquad (3)$$

with

$$\chi''=\frac{1}{2}|\gamma|M_0 T\frac{(\omega_0-\omega_1)(\gamma H_1)^2}{\omega_e^3}\cdot\frac{4\omega_e\omega_2}{(\omega_e+\omega_2)^2+1/T^2}\cdot\frac{1}{1+(\omega_e-\omega_2)^2T^2}\,, \qquad (4)$$

where

$$\omega_e=|\gamma|H_e=\sqrt{(\omega_0-\omega_1)^2+(\gamma H_1)^2}\,,$$

and further, following assumptions have been made:

$$|\gamma|H_2\ll\left|\frac{\omega_e^2}{(\omega_0-\omega_1)}\right|,\quad \gamma^2H_2^2\ll\frac{1}{T^2}\,. \qquad (5)$$

Using the values of T already reported,[10,12,13,14] it can be shown that the inequalities (5) hold under the present experimental conditions. In addition, $\omega_2 T\gg1$ at $\nu_2=30$, 20 and 15 Mc, so that Eq. (4) becomes

$$\chi''=\frac{1}{2}|\gamma|M_0T\frac{(\omega_0-\omega_1)(\gamma H_1)^2}{\omega_e^3}\frac{4\omega_e\omega_2}{(\omega_e+\omega_2)^2}\frac{1}{1+(\omega_e-\omega_2)^2T^2}\,. \qquad (6)$$

The power absorbed by the sample is

$$P=\frac{1}{2}\omega_2 H_2^2\chi''\,. \qquad (7)$$

According to the formulas (4) and (7), P becomes negative for $\omega_0<\omega_1$ and positive for $\omega_0>\omega_1$, corresponding to the experimentally observed facts.

Since the line shapes in Figs. 5~7 are obtained from the experimental curves devided by the corresponding value of H_0 and normalized as the peak height becomes unity, they should be compared with a factor

$$\frac{|\omega_0-\omega_1|(\gamma H_1)^2}{\omega_e^3}\cdot\frac{4\omega_e\omega_2}{(\omega_e+\omega_2)^2}\frac{1}{1+(\omega_e-\omega_2)^2T^2} \quad (8)$$

appeared in (6).

Best fits are obtained by choosing the value of T as 4.8×10^{-8}sec. The solid curves in Figs. 5~7 are the polts of the factor for various values of H_1 using the above value of T. The same value of T was also obtained by use of ordinary absorption signal of the same sample at the frequency of about 150 Mc. The signal was obtained in the course of measuring H_0.

The asymmetry in the line shape is mainly due to the factor $\frac{|\omega_0-\omega_1|(\gamma H_1)^2}{\omega_e^3}$ which can be written as $\cos\Theta\ \sin\Theta$ and has the peaks at $H_0=\frac{\omega_1}{|\gamma|}\pm\frac{H_1}{\sqrt{2}}$, where Θ is the angle between H_0 and H_e in the coordinate system rotating about H_0 with the angular frequency ω_1. If the resonance lines were traced using the frequency modulation and frequency sweep technique, the asymmetry in the line shape would not appear.

The factor $\frac{4\omega_e\omega_2}{(\omega_e+\omega_2)^2}$ represents the fact that the magnetic field causing the transition is linearly polarized rather than circularly.

As will be seen in Figs. 5~7, the agreement between the experimental points and the calculated curves is nearly satisfactory. In the region near $H_0=\omega_1/|\gamma|$, however, some disagreements appear, especially for the case of $H_1=1$ gauss. They may be attributed to the experimental error due to the poor signal-to-noise ratio, frequently encountered in the case of lower H_1 and to the rather crude assumption that $T_1=T_2$. The rf field $2H_1\cos\omega_1 t$ is "on resonance" in the region near $H_0=\omega_1/|\gamma|$, so that the direct transition (not the double quantum transition) is strongly saturated. At first sight, the saturation might be considered to be an origin of the disagreements. However, the effects of the saturation caused by the rf field $2H_1\cos\omega_1 t$ on the line shape of the double quantum transition are already taken into account when the Bloch equation is used. So, the anomalous saturation effect which cannot be described by the Bloch equation, if any, might be another origin of the disagreements in the region near $H_0=\omega_1/|\gamma|$. The study of the double quantum transition under the saturation condition which is closely related to the "rotary saturation"[15] is now under way on diluted DPPH, where $T_1\fallingdotseq T_2$ and the applicability of the Bloch equation is doubtful.

It is difficult to calculate the exact values of H_0 at which the factor (8) is maximum. But considering the fact that the first two factors of (6) are rather slowly varying functions of H_0 near the peak, the approximate peak position is obtained as

$$H_0=\frac{\omega_1}{|\gamma|}\pm\frac{1}{|\gamma|}\left(\omega_2-\frac{1}{2}\frac{(\gamma H_1)^2}{\omega_2}-\frac{1}{8}\frac{1}{\omega_2T^2}\right). \quad (9)$$

The term $\frac{1}{8|\gamma|}\frac{1}{\omega_2T^2}$ is about 0.1 gauss or less in magnitude under the present experimental conditions and it cannot be detected by the used experimental apparatus. The term $\frac{1}{2|\gamma|}\frac{(\gamma H_1)^2}{\omega_2}$ becomes of the order of one gauss and gives a main contribution to the shift of the peak position from $H_0=(\omega_1\pm\omega_2)/|\gamma|$, which agrees with the experimental results.

The approximate peak value of χ'' is calculated from (6) by putting $\omega_e=\omega_2$, as:

$$\frac{1}{2}|\gamma|M_0T\left(\frac{\gamma H_1}{\omega_2}\right)^2\left[1-\frac{1}{2}\left(\frac{\gamma H_1}{\omega_2}\right)^2\right], \quad (10)$$

which explains the experimental variation of the peak height with H_1 at the fixed ν_2 as shown in Fig. 8, and that with ν_2 at the fixed H_1. The difference between the gradients of two curves for $\nu_2=30$ Mc in Fig. 8 can be interpreted by the difference between the values of $M_0=\chi_0H_0$ at which the peaks appear.

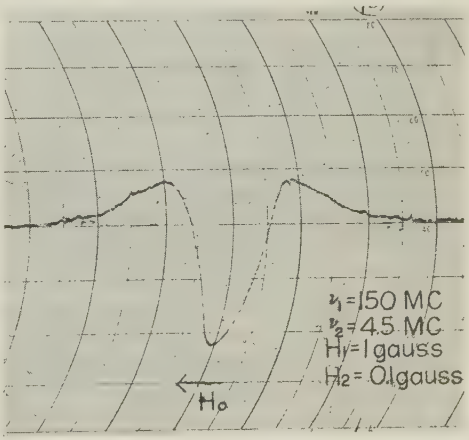

Fig. 9. A recorder trace of signal at $\nu_1=150$Mc, $\nu_2=4.5$Mc $H_1=1$ gauss and $H_2=0.1$ gauss.

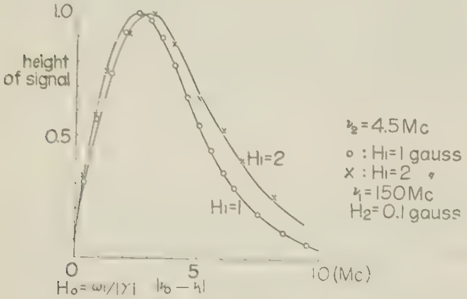

Fig. 10. Calculated half line shapes and experimental points at $\nu_1=150$Mc, $\nu_2=4.5$Mc, $H_1=1$, 2 gauss and $H_2=0.1$ gauss. These are obtained in the same way as in Fig. 5.

Next we shall mention about the signal at the frequency ν_2 of 4.5 Mc. One of the recorder trace of the signals is shown in Fig. 9. The integrated curve is similar in form to the ordinary dispersion signal. Though it seems to have different profile from the results observed at $\nu_2=30$, 20 and 15 Mc, it consists of two parts, emission and the absorption part. After the treatment described above, the line shape becomes the same as those at the higher ν_2 frequencies. The half of the whole line shape is shown by experimental points in Fig. 10. The rf field $2H_1 \cos \omega_1 t$ is always "on resonance" over the whole curve, but as mentioned above, Eq. (4) can be used for analysis. Two calculated line shapes at $H_1=1$ and $H_1=2$ gauss are shown in Fig. 10, where $T=4.8\times10^{-8}$sec is used. So far as the curves in Fig. 10 are concerned, the agreement between the experimental and the calculated line shapes is satisfactory. The observed variations in the position and in the height of the peak are different from those at $\nu_2=30$, 20 and 15Mc, and are rather complicated functions of H_1. The peak height is proportional to H_1^2 up to the field $H_1=0.5$ gauss, but for heigher values of H_1 the increase in the peak height becomes more gradual. For the values of $H_1>1$ gauss, the peak position lies on the lower (or higher) field side for higher values of H_1 in the case of the emission (or absorption). Though these features can be interpreted qualitatively by the expression (4), no precise comparison has been made as yet. The detailed study of the case of $\nu_2=4.5$ Mc will be published in a near future.

Acknowledgement

The author would like to express his sincere thanks to Prof. I. Takahashi and Prof. K. Tomita for their continued interest and discussion. The author's thanks are also due to the members of our laboratory for their assistance. The samples were kindly supplied by Mr. Y. Deguchi of the Department of Chemistry of this University.

References

1) M. G. Mayer: Ann. Physik **9** (1931) 273.
2) J. M. Winter: J. Phys. Radium **19** (1958) 802.
3) A. Javan: J. Phys. Radium **19** (1958) 806.
4) A. Javan: Phys. Rev. **107** (1957) 1579.
5) S. Yatsiv: Phys. Rev. **113** (1959) 15.
6) F. Bloch: Phys. Rev. **70** (1946) 460.
7) T. Hashi: J. Phys. Soc. Japan **13** (1959) 911.
8) R. V. Pound and W. D. Knight: Rev. Sci. Instr. **21** (1950) 219.
9) See e.g. E.R. Andrew: *Nuclear Magnetic Resonance* (Cambridge University Press, New York, 1955).
10) J. P. Lloyd and G. E. Pake: Phys. Rev. **92** (1953) 1976.
11) R. K. Wangsness and F. Bloch: Phys. Rev. **89** (1953) 728.
12) J. P. Goldsborough, M. Mandel and G. E. Pake: Phys. Rev. Letters **4** (1960) 13.
13) N. Bloembergen and S. Wang: Phys. Rev. **93** (1954) 72.
14) M. A. Garstens, L. S. Singer and A. H. Ryan: Phys. Rev. **96** (1954) 53.
15) A. G. Redfield: Phys. Rev. **98** (1955) 1787.
*) Whlie the manuscript was in the press, we became aware of
J. Burget, M. Odehnal, V Petricek and J. Sacha: Czech. Z. Phys. **10** (1960) 547.

JOURNAL OF THE PHYSICAL SOCIETY OF JAPAN, Vol. 16, No. 6, JUNE, 1961

On the Pendent Drop, I

By Ko TAMADA
Department of Aeronautical Engineering, Faculty of Engineering, Kyoto University
and Yoshio SHIBAOKA
Department of Physics, Faculty of Science, Osaka City University

(Received February 27, 1961)

In the present paper is discussed the equilibrium of a pendent drop which appears on the film of water covering a horizontal surface. It is found that the volume of the drop takes a maximum value at a special configuration of $D/H \cong 3$, where D is the diameter and H the depth, of the drop. The solutions for the equilibrium beyond this maximum cannot be realized in the actual drop, since there is slight but steady current of water into the drop from the surrounding film. The drop, in reality, will become unstable for external disturbance and collapse just before the said limit is reached.

An analytical solution is obtainable for the case of a two-dimensional drop, the cross sectional area of which is also seen to attain a maximum at $D/H \cong 1.9$.

§ 1. Introduction

When a glass or metal plate is wetted fully by water and set horizontally, there will soon appear pendent drops on the lower surface of the plate. As far as the present writers are aware, the theoretical consideration concerning the pendent drop of this kind was first made by S. Moriguchi.[1] He linearized the fundamental equation of equilibrium for small thickness of the drop at its initial stage of formation, and determined the diameter of the drop as a characteristic value of the equation. In the present paper is considered the more developed and thick drop on the basis of the equilibrium equation in its full nonlinear form. The process of growth and breakdown of the drop will be of special interest.

As the result of calculation, it turns out that the volume of the drop attains a maximum at a special geometry $D/H \cong 3$, where D is the diameter and H the depth, of the drop. This may be regarded as the final stage of equilibrium for an actual drop, since its volume must increase monotonously owing to the inflow of water induced by the negative pressure at the base of the drop.

The drop, in reality, will collapse just before the said limiting stage is reached. The discussion of the dynamical instability of the drop will however be given in a subsequent paper.

§ 2. Fundamental Equation

The shape of the pendent drop in question is symmetric about a vertical axis and we take it as the z-axis (positive direction downward) of the cylindrical coordinates (r, z) (Fig. 1).

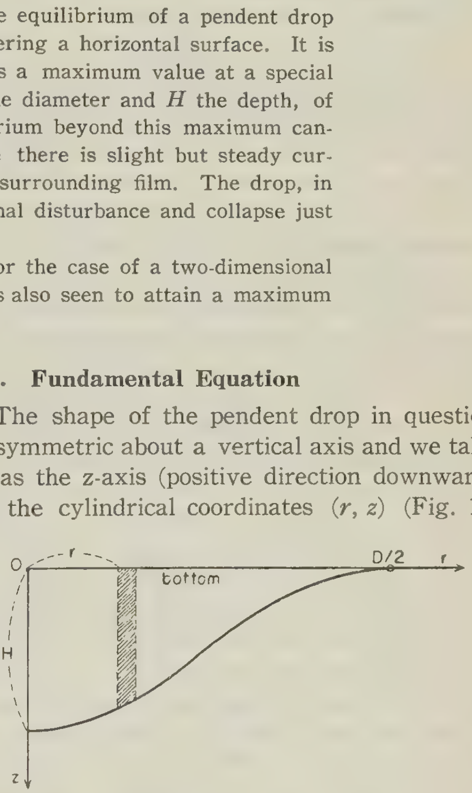

Fig. 1

Let $z(r)$ be the surface of the drop, T the surface tension, ρ the density of water, g the accelaration of gravity and p the excess pressure of the surrounding air over the pressure of water at the bottom $(z=0)$ of the drop. Then, by considering equilibrium of the mass of water contained between the two coaxial cylinders r and $r+dr$, we may write down the equation of equilibrium in the following form:

$$T\frac{d}{dr}\left\{\frac{r\,dz/dr}{\sqrt{1+(dz/dr)^2}}\right\}+r(\rho gz-p)=0 . \qquad (1)$$

Putting here

$$\sqrt{\frac{T}{\rho g}}=l , \quad r=l\xi , \quad z-\frac{p}{\rho g}=l\eta , \qquad (2)$$

we reduce Eq. (1) to a nondimensional form

$$\frac{1}{\xi}\frac{d}{d\xi}\left\{\frac{\xi d\eta/d\xi}{\sqrt{1+(d\eta/d\xi)^2}}\right\}+\eta=0\,. \tag{3}$$

The parameter l is the representative length of the present problem, whose value is determined by the physical constants T, ρ and g. Assuming, for example, $\rho=1\,\mathrm{gr/cm^3}$, $T=73\,\mathrm{dyne/cm}$ and $g=980\,\mathrm{cm/sec^2}$ for water, we obtain the result $l=0.27\,\mathrm{cm}$.

Appropriate boundary conditions for the present problem may be such that

$$\text{at } \xi=0 \text{ and } \xi=\alpha \quad d\eta/d\xi=0\,. \tag{4}$$

Here α is the nondimensional radius of the rim of the drop, which may be taken as the characteristic value of Eq. (3). As is shown below, it may take finite values. This might be seen somewhat unnatural, since any observed drop continues smoothly to the surrounding film of water and hence has no difinite radius. The discrepancy may however be explained as follows: Since the surface tension acts horizontally at the rim $\xi=\alpha$, the weight of the drop as a whole must be sustained by the sum of the pressure difference p. Therefore the pressure of water at the bottom $z=0$ of the drop must be lower than the air pressure, while the pressure in the thin film of water surrounding the drop is obviously equal to the air pressure. The result will be slight but steady inflow of water into the drop from the surrounding. Thus, the actual drop is never in equilibrium in the strict sence, and precise argument about the shape of the drop near the rim will call for the consideration of the inflow of water (viscosity will be important) mentioned above. However, for the case of very slow growth, the shape of the drop may be expected to agree practically with the profile of equilibrium to be determined by (3) and (4).

Since the drop is relatively flat at its initial stage of formation, we may safely neglect the term $(d\eta/d\xi)$ in Eq. (3). Then, it reduces to the Bessel equation of the zero order. This is the case treated by S. Moriguchi. The radius α is determined as the first characteristic value of the equation for the boundary condition (4).* Now, for the consideration of the drop at its intermediate and final stages, it seems to be impossible to make any neglect in Eq. (3). Further, owing to its nonlinearity, it is difficult to obtain analytical solution of the full equation (3), and so we shall appeal to a method of numerical integration in the following section.

§ 3. Integration of the Equation

Let $\Delta\xi$ be a small increment of ξ and $\xi_j=j\Delta\xi$ $(j=0, 1, 2, \ldots)$. Then, Eq. (3) may be approximated by the difference equation

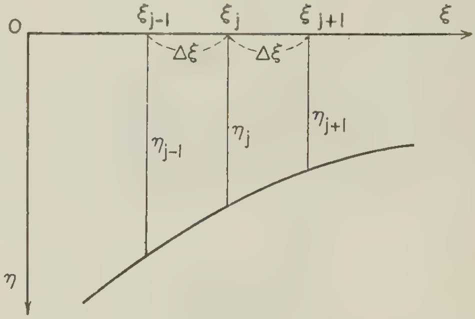

Fig. 2

$$(\xi_j\Delta\xi)^{-1}(\zeta_{j+1/2}-\zeta_{j-1/2})+\eta_j=0\,, \tag{5}$$

where

$$\left.\begin{aligned}\zeta_{j+1/2}&=\frac{1}{2}(\xi_{j+1}+\xi_j)\,\frac{\eta_{j+1}-\eta_j}{\Delta\xi}\times\\&\qquad\left\{1+\left(\frac{\eta_{j+1}-\eta_j}{\Delta\xi}\right)^2\right\}^{-1/2}\\\zeta_{j-1/2}&=\zeta_{(j-1)+1/2}\,,\quad \eta_j=\eta(\xi_j)\end{aligned}\right\} \tag{5a}$$

Solving for η_{j+1} we get

$$\left.\begin{aligned}\eta_{j+1}&=\eta_j+k(1+k^2)^{-1/2}\Delta\xi\,,\\k&=\frac{2j-1}{2j+1}\frac{\eta_j-\eta_{j-1}}{\sqrt{(\Delta\xi)^2+(\eta_j-\eta_{j-1})^2}}+O(\Delta\xi)\end{aligned}\right\} \tag{6}$$

This formula enables us to calculate η_{j+1} with the known data η_j and η_{j-1}. For the starting value η_0 and η_1 we use the power series solution

$$\eta=\eta_0\left\{1-\frac{1}{4}\xi^2+\frac{1}{64}(1-\eta_0^2)\xi^4-\frac{1}{4608}(2-20\eta_0^2+9\eta_0^4)\xi^6+\cdots\right\} \tag{7}$$

which satisfies the initial condition $\eta=\eta_0$ and $d\eta/d\xi=0$ at $\xi=0$. By means of (6) and (7) we may calculate the successive values of η_j until $d\eta/d\xi=0$ at $\xi=\alpha$. This α may be taken as the radius of the drop. Further, the numerical result thus obtained may be refined in the following way. We first integrate once the equation (3) formally and obtain

---

* $\alpha\cong3.83$ and the diameter of the drop $2l\alpha\cong2\,\mathrm{cm}$ for water.

$$d\eta/d\xi = -\left\{\xi^2 - \left(\int_0^\xi \xi\eta\, d\xi\right)^2\right\}^{-1/2} \int_0^\xi \xi\eta\, d\xi\,. \quad (8)$$

Then, inserting the values of $\eta(\xi)$ previously obtained into the right hand side, and carrying out numerical integration,* we can obtain the second approximation for $\eta(\xi)$. We repeat the process till the result converges.

§ 4. Result and Discussion

Fig. 3 shows the calculated profiles of the pendent drop for several values of the parameter η_0. The diameter-depth ratio D/H for each case is tabulated in Table I.

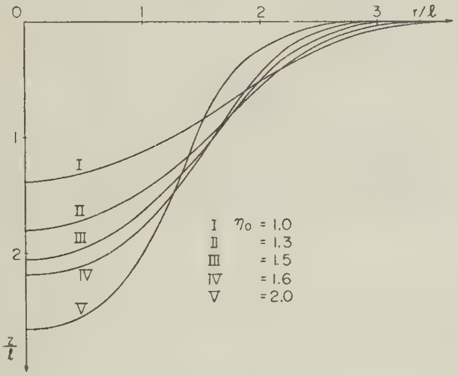

Fig. 3

Table I.

η_0	1	1.3	1.5	1.6	2
D/H	5.173	3.786	3.175	2.924	2.092

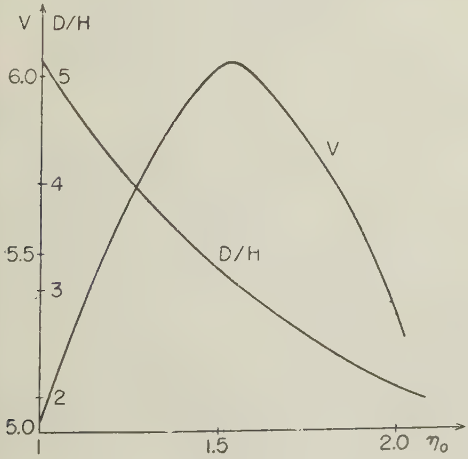

Fig. 4

Now, the volume V of water contained in the drop is obviously given by the equation

$$V = 2\pi \int_0^{D/2} r z(r) dr \qquad (9)$$

Evaluating the integral numerically for each values of η_0, we obtain the relation between V and D/H as shown in Fig. 4. As is seen in the figure, the volume of the drop becomes maximum at about $D/H \simeq 3$. This stage of the maximum volume may be taken as the static limit of the actual drop, since as mentioned before the volume of the drop must increase steadily.** As a matter of fact, the drop will break down just before the said stage is attained owing to its instability for external disturbances.

§ 5. Two-dimensional Case

The corresponding problem for the two-dimensional case seems to be rather artificial, yet it may be of some interest since exact analytical treatment is possible. The result turns out to be qualitatively similar to that of the preceding case.

Taking the rectangular coordinates (x, y) in place of (r, z) and applying the corresponding transformation (2), the fundamental equation becomes

$$\frac{d}{d\xi}\left\{\frac{d\eta/d\xi}{\sqrt{1+(d\eta/d\xi)^2}}\right\} + \eta = 0\,. \qquad (10)$$

Solving this equation under the conditions (4), we get

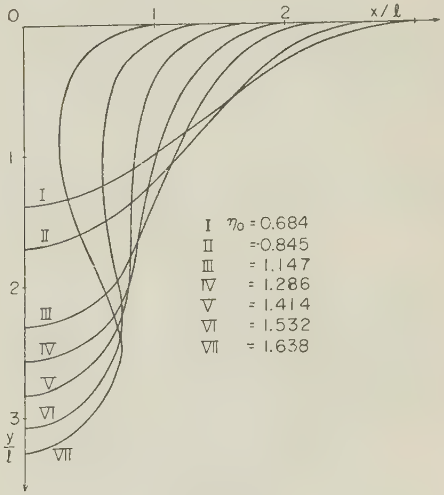

Fig. 5

---

* We have used the formula $\int_{xj-1}^{xj} y dx = \frac{1}{12}(5y_{j-1} + 8y_j - y_{j+1}) \Delta x$

** Part of the profile for $D/H < 3$ can be realized in a pendent drop from the lower tip of a vertical capillary (Reference 2).

$$\left.\begin{aligned} \eta &= \eta_0 \cos\theta\,, \\ \xi &= 2E(\eta_0/2, \theta) - F(\eta_0/2, \theta) \end{aligned}\right\} \quad (11)$$

where $F(\lambda, \theta)$ and $E(\lambda, \theta)$ are respectively the elliptic integral of the first and the second kinds. Since $\eta(\xi) = -\eta(\alpha - \xi)$ in this case, the reduced radius α of the drop is given by the expression

$$\begin{aligned} \alpha &= [\xi]_{\theta=\pi/2} = 4E(\eta_0/2) - 2K(\eta_0/2) \\ &= \pi\left\{1 - \frac{3}{16}\eta_0^2 - \frac{15}{1024}\eta_0^4\right. \\ &\qquad \left. - \frac{35}{16384}\eta_0^6 - \frac{1575}{4194304}\eta_0^8 - \cdots\right\} \quad (12) \end{aligned}$$

where K and E are the complete elliptic integrals. Further, the volume (or cross sectional area, to be exact) S of the drop is $S = 2\alpha\eta_0$, and it can be shown that S becomes maximum for $\eta_0 \simeq 1.187$. Corresponding value of $D/H = \alpha/\eta_0$ is found to be about 1.85. In Fig. 5 are shown some of the calculated shapes of the two-dimensional drop. The value of D/H for each case is given in Table II.

Table II.

η_0	0.684	0.845	1.147	1.286	1.414	1.532	1.638
D/H	4.174	3.187	1.976	1.554	1.198	0.882	0.589

After completing the present work, the writers became aware of the paper due to S. Fordham,[2)] in which are given detailed results of calculation for the shapes of pendant drops. Fordham's work however concerns the determination of surface tension from measurements of pendant drops and hence the calculation of the shape of drop was carried out only up to the point of inflexion on the profile of the drop.

References

1) S. Moriguchi: J. Japan Soc. for Appl. Mech. **3** (1949) 27.
2) S. Fordham: Proc. Roy. Soc. **A 194** (1948) 1.

Short Notes

This section is intended to secure prompt publication of important discoveries in physics. The reports should not exceed 800 words in length. A figure of size 7 cm×7 cm will be counted as 150 words.

J. PHYS. SOC. JAPAN **16** (1961) 1253

Observation of Dislocations in Germanium Single Crystal

By Masakazu SHOJI, Shoji TAUCHI,
Tomokuni MITSUISHI and Masami TOMONO
Hitachi Central Research Laboratory
Kokubunji, Tokyo

(Received February 28, 1961)

It is well known that the density of small etch pits of germanium revealed by slow etching is several orders of magnitude larger than that of CP–4 etch pits[1),2)]. These small etch pits were believed to be screw dislocations[1),2)], but their high density has not been explained. Correspondence between the dislocation line and etch pits was reported[3),4)], although above-mentioned point is not decided.

In this experiment, dislocation lines in germanium were observed by the method of Borrmann[4)] and the density of etch pits was compared with that of X-ray images. From the crystal ingots two groups of specimen A and B were taken very near to each other as shown in Fig. 1(a).

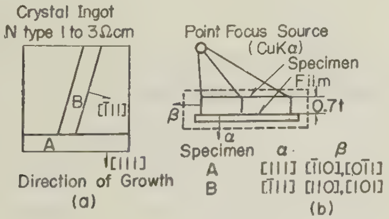

Fig. 1. Orientation of the specimen and the method for X-ray observation.

Nearly isotropic distribution of the direction of Burgers vector was assured by the comparison of X-ray photographs taken for the specimen A and B as shown in Fig. 1(b). After the X-ray observation, CP–4 etch pits and small spiral etch pits reported by Rhodes et al.[2)] were revealed successively. The density of the latter was considerably larger than that reported. The density of etch pits was compared with that of X-ray images obtained for one of the (110) planes. The result is shown in Fig. 2. This might be a extension of the data of Kurtz et al.[5)]

Agreement between the density of X-ray images and that of CP–4 etch pits becomes good because both of them are underestimated. Factor of underestimation in X-ray observation must be smaller than six because one of the six <110> is perpendicular to the diffracting plane. This is shown by *L* in the figure. For the etch pit, this factor must be smaller than four[5)] in the worst case[6)]. This is given by *H*. Overlapping of images prevents precise determination of the density.

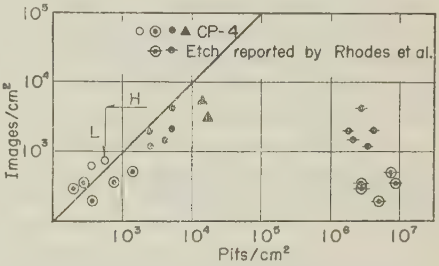

Fig. 2. Comparison of the density of images and that of etch pits.

Density of small etch pits was nearly uniform all over the ingots from which specimen A and B were taken. If these pits correspond to the dislocation lines, some of the photographs taken for different (110) planes must show their images. But the densities of images determined from several photographs agreed within the factor six and the density of small pits was about 10^3 times larger than these. So these small etch pits never correspond to the usual dislocation lines.

They may be clusters of vacancies, some kind of defects related to the impurity[2)], or loops of dislocation which are too small to be resolved. Relation to the rocking curve data[1)] is not clear at present.

The authors wish to express their thanks to Dr. H. Hagihara and Professor K. Kohra for their kind advice and encouragement.

References

1) S. G. Ellis: J. Appl. Phys. **26** (1955) 1140.
2) R. G. Rhodes, K. O. Batsford and D. J. Dane-Thomas: J. Elec. and Cont. **3** (1957) 403.
3) W. C. Dash: J. Appl. Phys. **27** (1956) 1193.
4) G. Borrmann, W. Hartwig und H. Irmler: Z. Naturforsch. **13**(a) (1958) 423.
5) A. D. Kurtz, S. A. Kulin and B. L. Averbach: Phys. Rev. **101** (1956) 1285.
6) W. G. Pfann and F. L. Vogel: Acta Met. **5** (1957) 377.

J. PHYS. SOC. JAPAN **16** (1961) 1254~1255

Anomalous Temperature Dependence of Lattice Constants of Ferroelectric Sodium Nitrite

By Sadao HOSHINO and Iwao SHIBUYA

Institute for Solid State Physics
The University of Tokyo, Tokyo

(Received March 18, 1961)

In order to study the mechanism of the ferroelectric phase transition in $NaNO_2$, the temperature dependence of lattice constants was measured precisely by x-ray diffraction methods. $NaNO_2$ is ferroelectric below 160°C[1] with the space group I*m*2*m*[2]. The spontaneous polarization along the orthorhombic *b* axis disappears above the Curie point as the space group becomes I*mmm*[3].

Single crystals grown from aqueous solution were used throughout the experiment. In the preliminary stage of the experiment, back reflection photographs were taken at various temperatures with a high temperature x-ray camera. The result suggested the existence of a weak anomaly just above the Curie point in addition to the expected one at the Curie point. Because the accuracy of the film method was not sufficient for the present study, additional precise measurements were made using an x-ray diffractometer with an electric furnace. The distance from the specimen to the receiving slit in front of the G–M counter was 200 mm, considerably longer than the radius of the camera previously used (50 mm). The resolving power for measuring the change of diffraction angles was quite high, so that even a small change of the unit cell dimensions (about 0.0001Å) could be detected. Special care was taken for temperature control of specimens; the maximum error of temperature measurements did not exceed ±0.2°C. A very slow heating rate of at least ten minutes per degree was chosen to attain thermal equilibrium of the specimen. Results obtained are shown in Fig. 1.

As is shown, the *c* axis decreases its length moderately with increasing temperature, while the *a* and *b* axes increase their magnitudes. In the figure, one can observe two anomalies at 163°C and 178°C, respectively. The one at 163°C apparently corresponds to the known transition point where the spontaneous polarization disappears, while the other at 178°C has not been reported previously. If the second anomaly observed in this thermal expansion experiment corresponds to a new phase transition, it should indicate the existence of an unknown phase between the well-known ferro- and para-electric phases, although no indication of such an anomaly was shown in the dielectric[1] and specific heat[4] measurements. Recently, Tanisaki[5] discovered the presence of a microdomain structure just above 163°C. Referring to his result, one might call $NaNO_2$ in the new phase region as antiferroelectric. However, no perfectly ordered state would be attained in this phase range, therefore, further structural investigations together with the evaluation of the pair-correlation function illustrated recently[6,7] appear to be necessary for the detailed discussion on the phase transition mechanism of this crystal.

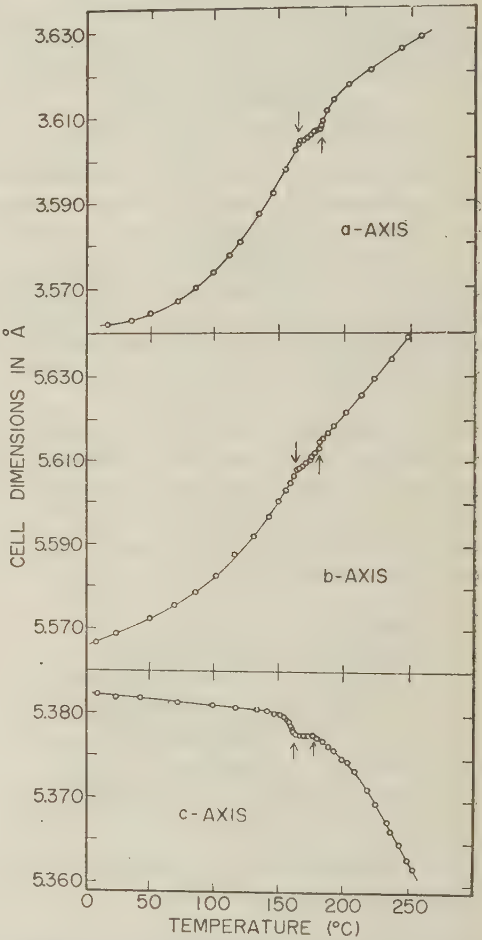

Fig. 1. Temperature dependence of the *a*, *b*, and *c* axes obtained by measuring temperature variations of diffraction angles of (*400*), (*060*), and (*006*) Bragg reflections, respectively.

The phase transition at 163°C was deduced to be of the first order[1], however, the results of the present investigation seem to contradict the above statements, since no appreciable jump in the temperature variation of the cell constants was observed at the transition point (Fig. 1).

A part of this work (film method) was made at the Tokyo Institute of Technology getting assistances of Messers Y. Takeuchi and T. Kato to whom the authors' thanks are due.

References

1) S. Sawada, S. Nomura, S. Fujii and I. Yoshida: Phys. Rev. Letters **1** (1958) 320.
2) G. E. Ziegler: Phys. Rev. **38** (1931) 1040.
3) B. Strijk and C. H. MacGillavry: Rec. trav. chim. **62** (1943) 705.
4) S. Sawada: Private Communication.
5) S. Tanisaki: J. Phys. Soc. Japan **16** (1961) 579.
6) I. Shibuya and T. Mitsui: J. Phys. Soc. Japan **16** (1961) 479.
7) I. Shibuya: J. Phys. Soc. Japan **16** (1961) 490.

J. PHYS. SOC. JAPAN **16** (1961) 1255

Moving Striation in Microwave Discharge Plasma

By Mikio TAKEYAMA,
Yoshida College, Kyoto University
Tanehiro NAKAU, Sōzaburo YAMASAKI
Osaka University of Liberal Arts and Education
and Takeshi ISA
Himeji Technical College

(Received February 23, 1961)

Recently many investigations[1,2] have been carried out on the moving striation in glow discharge plasma. The present note reports that a similar sonic wave can also be observed in stationary microwave discharge plasma under certain conditions.

The experimental apparatus and procedures are as follows: A JRC-2M10 magnetron (maximum output power is 200 W C.W. at 2450 Mc/s) was mounted in a rectangular waveguide (72×34 mm). The discharge tube 20 mm in diameter was placed 2 cm apart from one end of the guide, in the first case, perpendicular and in the second case, parallel to the microwave electric field, as shown respectively in Figs. 1 and 2. Commercial pure argon gas of 8 mmHg pressure was sufficiently cleaned off active gases and used.

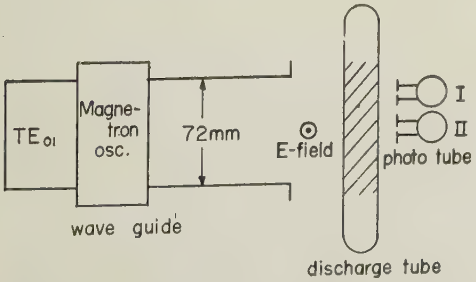

Fig. 1. Microwave electric field perpendicular to plasma column.

The power and the heater supplies for the magnetron oscillator were well regulated to make stable the plasma excited by microwave. In the first case (Fig. 1), we could observe a sonic wave in a plasma under certain condition, when the discharge tube was placed unsymmetrical to the waveguide. The plasma light intensity when the sonic wave was excited was detected by the photomultiplier tubes I and II placed apart from each other in Fig. 1. The output signals from the photo tubes were observed on an oscilloscope. In Photo. I, we can recognize a phase difference between the waves detected by the photo tubes I and II, that is, the existence of progressing wave. We also observed that the amplitude of oscillation built up with wave progression. The frequency shifted from ~500 c/s to ~900 c/s with the change in microwave power, the wave velocity was about 20 m/s, and the wave length about 4 cm. This wave might be so-called "moving striation".

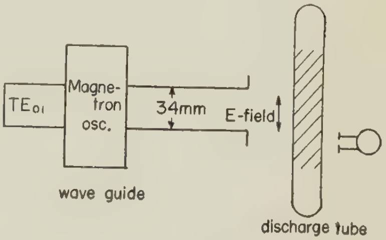

Fig. 2. Microwave electric field parallel to plasma column.

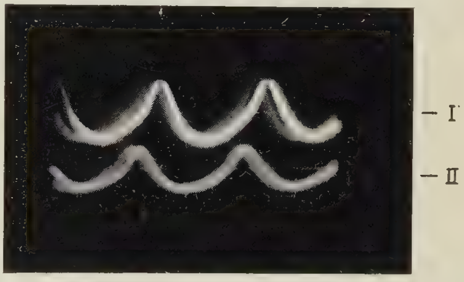

Photo. I. Moving striation pattern in microwave discharge.

In the second case (Fig. 2), on the contrary, any sonic wave was not observed.

The authors wish to thank Prof. I. Takahashi and Prof. K. Mitani at Kyoto University, and Prof. H. Takeyama at Hiroshima University for their kind advices and discussions.

References

1) T. Donahue and G. H. Dieke: Phys. Rev. **81** (1951) 248.
2) Von H. Rother: Ann. Physik **5** (1960) 252.

J. PHYS. SOC. JAPAN **16** (1961) 1256

Electron Spin Resonance of Manganese in $MgCl_2$

By Kuniya FUKUDA, Hiroaki MATSUMOTO,
Toru TAKAGI and Yoichi UCHIDA

*Department of Physics, Faculty of Science,
Kyoto University*

(Received January 23, 1961)

Electron spin resonance of manganese ion in $MgCl_2$ single crystal has been measured at room temperature by using 1.2 cm wavelength microwave.

The material of $MgCl_2$ containing one mole percent of $MnCl_2$, after having been thoroughly baked and sealed in a quartz tube under vacuum of about 10^{-3} mmHg, was heated up to 800°C and then slowly cooled down to room temperature at a rate of 20°C per hour. $MgCl_2$-Mn crystal obtained in this way has a layer structure. From its Laue pattern in Fig. 1, it is seen that the crystal is single and has a three-fold symmetry axis (c-axis) perpendicular to the cloven plane. $MgCl_2$ single crystals as well as $MnCl_2$ belong to $CdCl_2$ crystal type and have a trigonal symmetry about the c-axis[1].

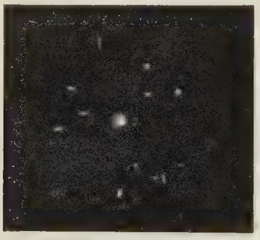

Fig. 1. Laue pattern of $MgCl_2$-Mn. Incident X-ray is perpendicular to the cloven plane of a sample (parallel to the c-axis).

Electron spin resonance was measured by rotating the static magnetic field around the c-axis in the plane perpendicular to it. Resonance spectra are independent of the direction of static magnetic field in this plane within experimental error and they consist of a broad line of about 450 oe. peak to peak width and many sharp lines of about 40 oe. peak to peak width, as shown in Fig. 2.

The sharp lines can be analyzed with the spin Hamiltonian:

$$\mathscr{H} = g\beta \boldsymbol{HS} + \boldsymbol{D}S_z^2 + \boldsymbol{E}(S_x^2 - S_y^2) + \boldsymbol{ASI}\,,$$

where $A = (-82 \pm 4) \times 10^{-4}\,\mathrm{cm}^{-1}$, $|D| = (140 \pm 10) \times 10^{-4}\,\mathrm{cm}^{-1}$, $E = 0$ within experimental error, and $g = 2.002 \pm 0.003$. Therefore, these sharp lines must be attributed to the hyperfine structure of Mn^{++} ion, the local field around which has axial symmetry about c-axis of the host crystal. The values of A and g show considerably good agreement with those of $MgBr_2$-Mn[2].

From the above results, it would be plausible to consider that Mn^{++} ions occupy the regular sites in host crystal.

The broad line, which overlaps hyperfine lines, seems to have nearly Gaussian shape rather than Lorentzian and the g value of 1.996 ± 0.007, as shown in Fig. 2. The intensity of this broad line did not change when a sample was heated at 450°C for one hour and quenched to room temperature. The ratio of the intensities of a hyperfine line and the broad line changed sample to sample when they were cloven from different parts of an original crystal. Further experiments are necessary to see the relations between the hyperfine lines and the broad line.

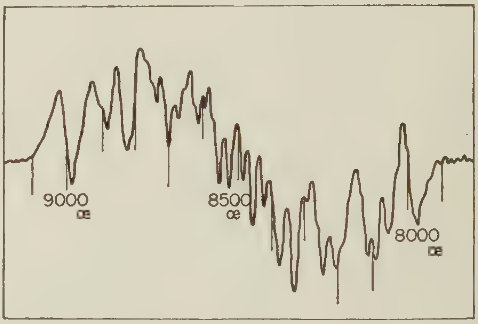

Fig. 2. Electron spin resonance pattern of $MgCl_2$-Mn. Static magnetic field is perpendicular to the c-axis of a sample.

During X-ray irradiation, $MgCl_2$-Mn crystals showed red luminescence (broad band at about 650 mμ) and $MgCl_2$ crystals without manganese weak green luminescence. Electron spin resonance spectra of Mn^{++} ion changed and a few sharp lines (about 10~20 oe.) appeared in the neighbourhood of $g=2$ after X-ray irradiation.

The more detailed investigations of the broad line and the analysis of the new spectra which appeared after X-ray irradiation are now in progress.

The authors wish to express their thanks for the facilities of X-ray diffraction measurements offered by Mr. Tsuneo Seto.

References

1) R. W. Wyckoff: *Crystal Structure* (Interscience Publishers, New York, 1948).
2) H. Koga, K. Horai and O. Matsumura: J. Phys. Soc. Japan, **15** (1960) 1340.

J. PHYS. SOC. JAPAN **16** (1961) 1257

The New Magnetic Phase in Manganese-Aluminium-Nickel System

By Ichiro TSUBOYA and Makoto SUGIHARA

Electrical Communication Laboratory
Nippon Telegraph and Telephone
Public Corporation
Musashino-shi, Tokyo, Japan

(Received March 16, 1961)

The new magnetic phase is observed in Mn-Al-Ni ternary alloy system. The nature of this ferromagnetic phase seems to be the same as κ phase in Mn-Al-Cu¹⁾ and Mn-Al-Fe²⁾ alloy systems reported by the present authors. The composition range of this phase, however, extends more widely than Mn-Al-Cu or Mn-Al-Fe alloys.

For preparation of the specimens, electrolytic Mn (99.9%), electrolytic Ni (99.9%) and pure Al (99.99%) were melted in suitable proportion in air and cast into rods of 10 mm in diameter. The cast specimens were annealed for 1 hour at 900°C in vacuum to remove the segragation, then cooled to room temperature at the rate of 150°C per hour.

The composition range showing ferromagnetism was determined by magnetic examination. The results are shown in Fig. 1 with the results of X-ray analysis.

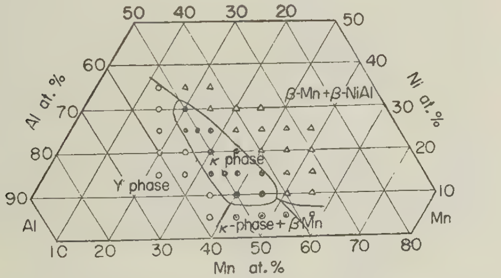

Fig. 1. Results of magnetic examination and X-ray analysis.

- ●: κ phase; magnetic
- ⦿: κ phase and β-Mn phase; weakly magnetic
- ○: orthorhombic Y phase; non magnetic
- △: β-Mn phase and β-NiAl phase; non magnetic
- □: β-Mn phase; non magnetic

According to X-ray analysis, there is a single cubic phase in the composition range of 25 to 50 at.% Mn, 10 to 30 at.% Ni and 40 to 52.5 at.% Al. This composition range nearly coincides with the one which is determined by magnetic examination. It is observed that this cubic phase has the same ordered structure of CsCl type as the κ phase in Mn-Al-Cu and Mn-Al-Fe alloy systems. The lattice parameter of κ phase in this system changes with an increase of Ni content from 2.970 to 2.920Å. The other phases which exist in the composition adjoining to the κ phase are the mixture of β-Mn and β-NiAl phases in the Ni rich region, the orthorhombic Y phase in the Al rich region and the β-Mn phase in the Mn rich and Ni poor region. These phases do not show ferromagnetism.

The magnetic properties such as Curie temperature, $\sigma-T$ curve and temperature dependence of inverse susceptibility are also measured. The Curie temperature and the saturation magnetization show an appreciable composition dependence. The Curie temperature becomes the highest, 550°K, at the Mn rich side and the lowest, 360°K, at the Ni rich side. The saturation magnetization reaches the maximum value 4000 gauss (per mol) near the phase boundary of the Mn and Ni poor side, decreases with an increase of Mn or Ni content, and reaches 1500 gauss at the phase boundary of Ni rich side. The temperature dependence of the saturation magnetization ($\sigma-T$) and of the inverse susceptibility ($1/\chi-T$) are shown Fig. 2 for typical specimens. The $1/\chi-T$ curves almost shows the non-linear relation except for specimens containing nearly 50 at.% Al.

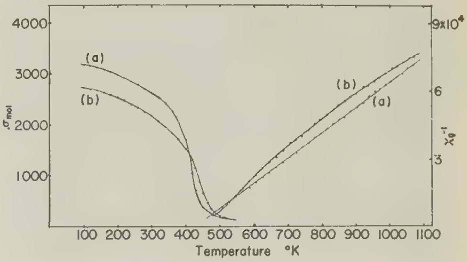

Fig. 2. Temperature dependence of saturation magnetization and inverse susceptibility of a) Mn 35 Ni 15 Al 50 and b) Mn 40 Ni 15 Al 45.

These magnetic properties of the κ phase in Mn-Al-Ni alloy are similar to the κ phase in Mn-Al-Cu alloy¹,³⁾, and can be qualitatively explained by the ferrimagnetism which originates from the antiferromagnetic interactions between Mn atoms occupying two different sublattices of CsCl type structure.

Futher discussion and detailed measurements will be reported later.

References

1) I. Tsuboya and M. Sugihara: J. Phys. Soc. Japan **16** (1961) 571.
2) I. Tsuboya and M. Sugihara: J. Phys. Soc. Japan **15** (1960) 1534.
3) I. Tsuboya: to be published

J. PHYS. SOC. JAPAN **16** (1961) 1258~1259

Effect of Current Injection on Properties of Cadmium Sulfide Crystals

By Hiroji MITSUHASHI

Technical Research Laboratories, Japan Broadcasting Corporation, Setagayaku, Tokyo

(Received March 30, 1961)

In order to study the effects due to the excitation by Tesla's coil, the specimen was rested in a simple cryostat[1] evacuated at a pressure of about 10^{-2} mm Hg. Green gleams came out from the surface of the crystal when the excitation by the coil was attempted from outside the glass envelope of the cryostat, i.e. a discharging tip of the coil approached the crystal or the wiring connected to the specimen which was kept at the temperature of liquid nitrogen. Immediately after the excitation the conductivity of all the crystals was increased by several orders of magnitude and the photoconductivity became largely overwhelmed by the increased dark conductivity. The higher temperature peaks in the thermally stimulated current curve of the most original crystals disappeared as seen in Figs. 1 and 2, although those of lower temperature kept their shapes. With subsequent gradual heating the increased conductivity began to decrease and approached to the value at its initial state. The stimulated current peaks which once disappeared resumed their shapes. One of the most prominent effects on a few samples was inversion of the quenching spectra (Fig. 3), that is, the crystal got photoconductive at 0.9 and 1.4 microns where the original crystals showed salient quenching[2]. This photoconductivity is quite stable in nature except for the further bombardment and/or heating of the specimen and appears as more exaggerated situation of the enhancement observed by Kitamura[3].

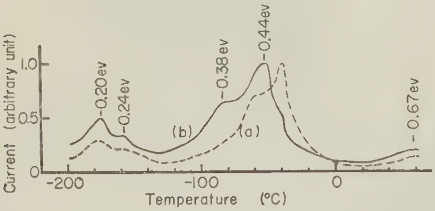

Fig. 1. Thermal stimulation of the unbombarded crystals of (a) No. 3 [0.6 mm×0.15 mm×0.9 mm (|| *c*)] and (b) No. 5 [1.1 mm×0.20 mm×1.5 mm (|| *c*)]. The heating rate was 10 degrees C. per min. The trap depths indicated were calculated on the assumption that attempt to escape frequency was 10^{10} per sec. *c* axis of every specimen was always made parallel to the electric field.

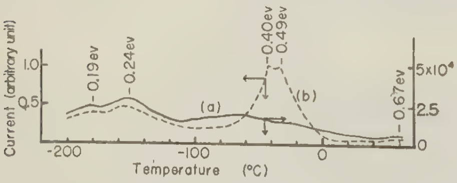

Fig. 2. Variation of thermal stimulation for the crystal No. 3, (a) just after the bombardment and (b) when the crystal came to equilibrium after annealing.

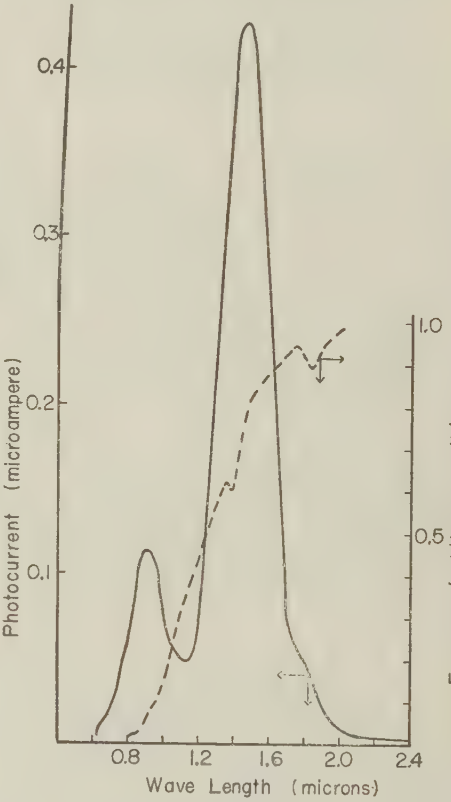

Fig. 3. Inverted photoconductivity for the crystal No. 3 measured at −12°C. with 51 volts applied. The dotted curve shows the incident energy to the sample.

All of these phenomena seem to be closely associated with the change of the lattice imperfections which act as donors and acceptors. The function of the Tesla's coil is understood as providing bombarding ions and electrons of high energy by ionization of the residual gas. The inverted photoconductivity is thought of as occurring from the considerable increase in the imperfections corresponding to the hole trapping centers advanced by Taft[2] and Rose[4].

References

1) H. Mitsuhashi: J. Phys. Soc. Japan **16** (1961) 989.
2) E. A. Taft and M. H. Hebb: J. Opt. Soc. Am. **42** (1952) 249.
3) S. Kitamura *et al*: J. Phys. Soc. Japan **16** (1961) 351.
4) A. Rose: Phys. Rev. **97** (1955) 322.

J. PHYS. SOC. JAPAN **16** (1961) 1259

Absorption and Reflection Spectra of Afterglow Plasma

By Shigetoshi TANAKA

Department of Physics, Faculty of Science
Kyoto University, Kyoto

(Received March 24, 1961)

The plasma resonance, which occurs at $\omega=\omega_p/\sqrt{2}$ (ω_p: plasma frequency) for a circular cylindrical plasma column, has been studied by many workers[1),2)]. It has further been reported that a series of small peaks occur, in addition to the main peak, at lower electron densities, but it was not explained so far, though various mechanisms can be considered[3),4)].

In the present work, both absorption and reflection powers from an afterglow plasma generated by pulsed discharge (pulse width: 15μ sec., peak voltage: 2500 volt, peak current: 2 amp.) were measured at a fixed microwave frequency ($\omega/2\pi=8{,}705$ mc/s), with the plasma column placed across waveguides as shown in Fig. 1. The absorption spectra are shown in Figs. 2 and 3, but the reflection spectra are omitted since they were similar to the former. The plasma resonance did not appear, as seen from Fig. 2 in the case I, where the microwave electric vector E_{rf} was parallel to the tube axis, but did appear in the case II, as shown in Fig. 3, where E_{rf} was perpendicular to the tube axis. Figs. 2 and 3 were photographed in succession by switching over between microwave channels leading to I and II.

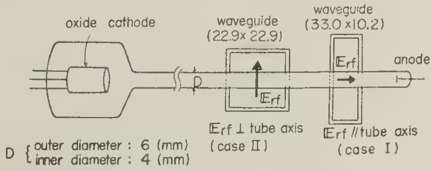
oxide cathode
waveguide (22.9× 22.9)
waveguide (33.0 ×10.2)
Erf
Erf
anode
D
Erf ⊥ tube axis (case II)
Erf // tube axis (case I)
D { outer diameter : 6 (mm) / inner diameter : 4 (mm)

Fig. 1. Waveguides and discharge tube (with neon gas filled at 7.55 mm Hg).

The followings are to be noted: The multiple peaks did not appear at electron densities lower than that of $\omega_p/\sqrt{2}=\omega$ in our experiment on afterglow, as seen from Fig. 3, in contrast to the experiment on the active plasma[3),4)], in which a discharge field was kept impressed. The multiple peaks rather appeared at electron densities higher than that of $\omega_p/\sqrt{2}=\omega$ in the case II, as shown in Fig. 3, but they also appeared in the case I, though both are not alike in detail.

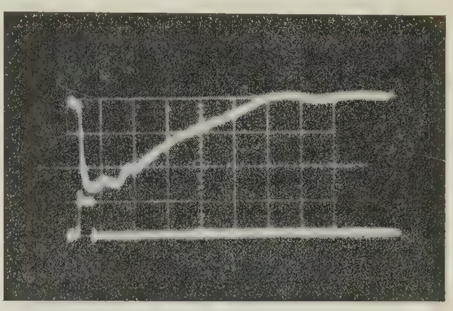

Fig. 2. Absorption spectrum (upper) and tube current (lower, 2 amp/div.) in the case I (swept at 20μ sec/div.).

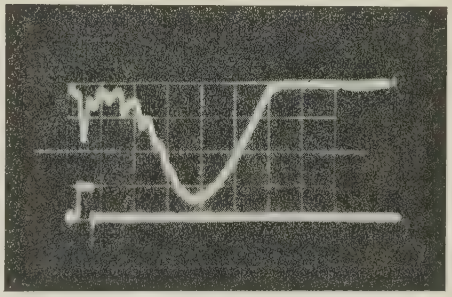

Fig. 3. Absorption spectrum (upper) and tube current (lower, 2 amp/div.) in the case II (swept at $20\,\mu$ sec/div.).

The author wishes to express his thanks to Prof. I. Takahashi for his guidance.

References

1) F. H. Clauser: *Symposium of Plasma Dynamics* (Addison-Wesley Publ. Co., 1960) p. 111.
2) S. Tanaka: Memoirs of the College of Science, University of Kyoto (to be published).
3) A. Dattner: Ericsson Technics, Stockholm, No. **2** (1957) 310.
4) W. D. Hershberger: J. Appl. Phys. **31** (1960) 417.

J. PHYS. SOC. JAPAN **16** (1961) 1260~1261

The Base Resistance of the Transistor in the Saturated Region

By Osamu NAKAHARA

Semiconductor Plant, Sanyo Electric Company, Daito City, Osaka Prefecture, Japan

(Received February 6, 1961)

Base resistance of the transistor is heavily modulated by the collector voltage in the saturation region by the conductivity modulation induced by the minority carrier injection from the collector junction. The space charge layer width variation of the junction also take part for it, but it is found that the effect is much smaller than the former effect.

For simplicity of calculation, we consider the external base resistance due to the part shown by the hatched annular part of the *pnp* transistor in Fig. 1. In this case, the external base resistance is given by the well-known formula[1]

$$R_{bN}=\rho_N \ln(r_c/r_e)/2\pi W_N \qquad (1)$$

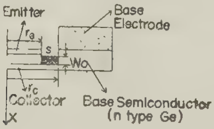

Fig. 1. Transistor geometry for the calculation.

where ρ_N and W_N represent the specific resistivity and the effective width of the hatched part respectively, both functions of the collector voltage. In the operating situation, injected minority carriers from the emitter would affect them, but we neglect the effect here. r_e, r_c denote the emitter and collector radius. We get the approximate expression for ρ_N as a function of V_{bc} (voltage applied between the base and the collector electrodes) as

$$\begin{aligned}\rho_N&=1/q\mu_n\langle n\rangle\\&=1/q\mu_n[p_n\{\exp(qV_{bc}/\lambda kT)-1\}(1+s/2D_P\cdot W_N)\\&\quad/(1+s/D_P\cdot W_N)+n_n]\end{aligned} \qquad (2)$$

where $\langle n\rangle$ means the one dimensional (x-direction) average of the number of the conduction electrons from the emitter side surface to the collector junction in the annular region; q, μ_n, p_n, n_n, k, T and D_P their usual meaning; s, surface recombination velocity for the minority carrier at the emitter side surface. Index λ in the exponential term means the correction factor for the injection relation. We take $\lambda=2$ for $V_{bc}>0$ and $\lambda=1$ for $V_{bc}<0$. In deriving (2), we assume the one dimensional hole distribution from collector junction to emitter side surface in the annular region which induces the same number of free electrons in the conduction band there and take the average for them. It is also assumed $W_N/L_P \ll 1$ where L_P denotes the diffusion length for the hole. In ordinary transistors, $n_n \gg p_n$ is assured to reduce R_{bN} and the effect of V_{bc} on it can not be observed except the case of deep bias. The expression for W_N can be found in the text book.[2]

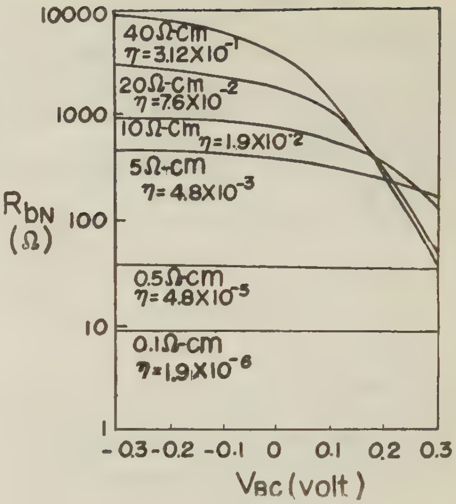

Fig. 2. Variation of R_{bN} with V_{bc} for six different η's. We assume the values W_0 (geometrical width of the annular region)$=10^{-3}$ cm, $s=300$ cm/sec, $T=300$°K, $r_c/r_e=1.5$.

In Fig. 2, the dependence of R_{bN} on V_{bc} is shown graphically with a parameter $\eta=p_n/n_n$ for germanium base. In this example, we take the case for V_{bc} varying from 0.3 to -0.3 volts. This covers the saturation and part of the active region of the grounded-base operation for the transistor with V_{be} (forward bias voltage applied between the emitter and the base electrodes)$=0.3$ volts. It is to be noted that as η approaches unity, R_{bN} varies in a wide range in the saturation region.

Such a rapid charge in R_{bN} results in an interesting phenomenon of negative collector resistance within the saturation region of the transistor of certain types.[3,4] That is, if R_{bN} increases drastically so that the decrease of the minority carriers at the emitter is accompanied by the increase in the d.c. voltage drop (the product of the base current and R_{bN}) in the base circuit with V_{bc}, the collector current in turn decreases, thus the dynatron type negative resistance can be observed in the collector circuit. In the saturation region, the decrease of the minority carriers at the collector junction with V_{bc} is the dominant agent for the internal feedback effect and it is necessary for the negative resistance that the above mentioned external base resistance negative feedback does overcome such internal feedback in the transistor.

The author thanks Dr. S. Iwase, the chief of the plant, for the encouragements given during the work.

References

1) J. M. Early: Transistor Technology (Van Nostrand 1959) **2**, 321.
2) For instance, J. N. Shive: Semiconductor Devices. (Van Nostrand 1959) 359.
3) O. Nakahara: J. Phys. Soc. Japan **15** (1960) 1537.
4) I. A. Lesk et al.: Proc. Inst. Radio Eng. **48** (1960) 1835.

J. Phys. Soc. Japan **16** (1961) 1261

On the Secondary Tunnelling Phenomena in a *p-n* Junction of Gallium Arsenide

By Akikazu Shibata
SONY Corporation, Shinagawa, Tokyo, Japan

(Received March 10, 1961)

Several workers have reported the fine structures of the I–V characteristics of a tunnel diode indicating the phonon interaction at low temperature[1),2)] or the presence of intermediate states in the energy gap[3)]. Very recently, an evidence of the possible existence of impurity bands in the energy gap and the tunnelling between the conduction and/or valence bands and impurity band(s) was observed in a *p-n* junction of GaAs. A similar phenomenon was also reported by Holonyak[4)] who observed tunnelling between these impurity bands at 78°K.

The observed I–V characteristics of a typical GaAs *p-n* junction at room and at liquid nitrogen temperatures are shown in Fig. 1. This junction was formed by alloying a Sn-Pb-Te dot to very heavily doped GaAs with Zn ($>10^{19}\,\mathrm{cm}^{-3}$). This junction exhibits very small current peaks of about 50μa at about 0.1 and 0.43 volts at room temperature. (The significance is the appearance of a secondary tunnelling peak even at room temperature.)

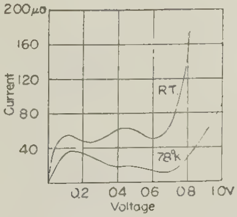

Fig. 1. I–V characteristics of a Zn-doped GaAs *p-n* junction (IP∼50μa at R.T.).

Similar secondary tunnelling current peak was reported in an epitaxially formed P-doped Ge *p-n* junctions at about 0.4 volts at 4.2°K[5)] and a Si tunnel diode in a form of a hump at about 0.8 volts[2)]. Esaki proposed possible existence of a deep impuriy level.

In comparison to the GaAs *p-n* junctions, several P-doped Ge *p-n* junctions were formed and the existence of a hump at about 0.4 volts at 78°K was confirmed. Several As-doped Ge backward diodes having comparable peak currrent were also investigated at 78°K. In this case, however, no evidence of such a hump was observed. In contrast with Zn-doped GaAs *p-n* junctions, a Cd diffused GaAs *p-n* junction showed a clear structure in the current peak at about 0.05 volts at 78°K and did not show a secondary tunnelling hump as illustrated in Fig. 2. This structure may be attributed to the distortion of the energy band edge due to the high impuirty concentration which has been recently investigated by Pankove[6),7)]. A simple calculation of tunnelling current also indicated that such a distorted band edge could produce a structure in the tunnelling current peak.

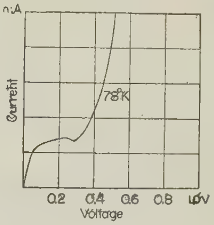

Fig. 2. characteristics of a Cd-diffused GaAs *p-n* junctian at 78°K (IP=0.70 ma).

It could be concluded that these experimental facts, together with those by Holonyak and others, strongly indicate the existence of impurity bands in the energy gap and also the distortion of the energy band edges. However, no such a deep lying impurity band is reported yet. In any case, these secondary tunnelling current peaks are revealed only when specific combinations of impurities and semiconductors are used. It should be a most urget project to elucidate these possible deep lying impurity bands. These phenomena should be observed in all the semiconductors and we are continuing the investigation using other III–V compound semiconductors.

References

1) N. Holonyak, Jr., et al: Phys. Rev. Letters, **3** (1959) 167.
2) L. Esaki and Y. Miyahara: J. Solid-State Electronics, **1** (1960) 13.
3) T. A. Longo: Bull. Am. Phys. Soc., Ser. II, **5** (1960) 160.
4) N. Holonyak: Jr., J. A. P., **32** (1961) 130.
5) J. C. Marinace: IBM Journ., **4** (1960) 280.
6) J. I. Pankov: Phys. Rev. Letters, **4** (1960) 20.
7) J. I. Pankove: Phys. Rev. Letters, **4** (1960) 454.

J. Phys. Soc. Japan **16** (1961) 1262

The Optical Absorption of Localized Exciton in KCl-KI Crystal

By Kaizo NAKAMURA, Kuniya FUKUDA, Riso KATO, Atsuo MATSUI and Yoichi UCHIDA

Department of Physics, Faculty of Science, Kyoto University

(Received April 3, 1961)

It has been shown in earlier works[1] that a definite peak is observed at room temperature on longer wavelength side of the fundamental absorption edge of KCl or NaCl crystal containing I^- impurity, and that this peak is ascribed to the localized exciton at I^- ion occupying Cl^- lattice site. Recently, Kobayashi and Tomiki have reported[2] that commercial KCl or NaCl powder contains a considerable amount of Br^- impurity, and that this impurity causes a remarkable shift of the absorption edge to longer wavelength side.

In the present work, the starting material of KCl powder was prepared by the chemical reaction of filtered aqueous solution of potassium bicarbonate and distilled hydrochloric acid. The single crystals of pure KCl and those containing 0.05 mole % of KI in melt were grown by the Kyropoulos method in air with a platinum crucible. The optical absorption spectra of both crystals were measured at low temperature by the vacuum ultraviolet spectrometer[3].

Fig. 1 shows the absorption spectra of KCl single crystals both at room and liquid nitrogen temperatures. The shift of absorption edge due to the presence of Br^- or of other impurities is more than 0.2 ev at room temperature and about 0.4 ev at liquid nitrogen temperature, respectively. The slope from 7 ev to absorption edge which appears in synthetic KCl at liquid nitrogen temperature might be ascribed to the defects such as dislocations.

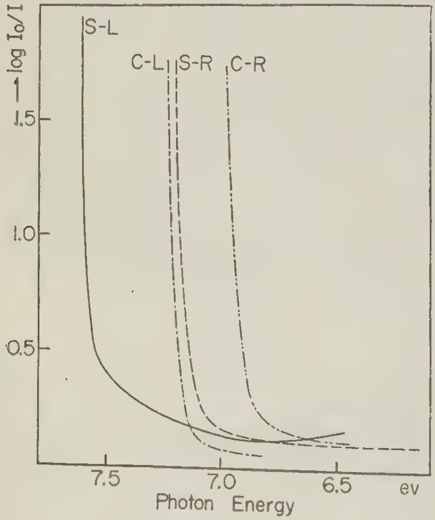

Fig. 1. Absorption spectra of KCl crystals. *C*: crystal from commercial powder, *S*: from synthetic powder, *−R*: measured at room temperature, *−L*: at liquid nitrogen temperature. *C* and *S* are almost the same in thickness.

Fig. 2 (a) shows the absorption spectra of KCl-KI crystals at room temperature. A peak is at 6.58 ev (A) and a hump appears at about 7.1 ev (B) on absorption edge. This hump is masked by the shift of absorption edge in commercial KCl.

Fig. 2 (b) shows the absorption spectra of KCl-KI crystals at liquid nitrogen temperature. The A-band shifts to 6.71 ev and the B-hump appears as a narrow band at 7.2 ev which is observed as a shoulder in commercial KCl. Further, near the absorption edge a shoulder (C) is observed at about 7.5 ev. The half widths of these bands are 0.22 ev for A-band and about 0.1 ev for B-band.

The above three bands may correspond to the "iodine doublet" and the perturbed exciton near I^- ion. Further experiments will be necessary to decide the correspondence. Similar experiments on synthetic NaCl-NaI crystals are now in progress.

References

1) R. Hilsch and R. W. Pohl: Z. Phys. **57** (1929) 145. K. Fukuda, R. Kato, K. Nakamura and Y. Uchida: J. Phys. Soc. Japan **15** (1960) 1344.
2) K. Kobayashi and T. Tomiki: J. Phys. Soc. Japan **15** (1960) 1982.
3) Y. Uchida *et al.*: J. Appl. Phys. Japan **29** (1960) 492.

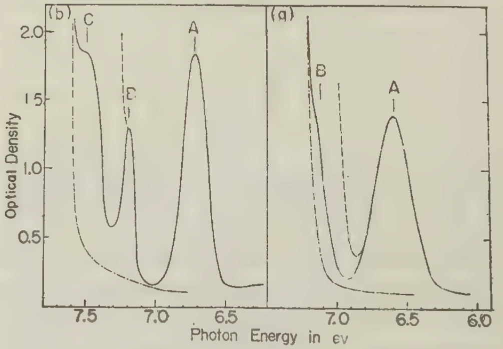

Fig. 2. (a) Absorption spectra of KCl-KI crystals at room temperature and (b) those at liquid nitrogen temperature. Solid curve is for the crystal from synthetic powder, and dashed curve for the crystal from commercial one in each figure, where reference curve of pure KCl crystal is given.

J. PHYS. SOC. JAPAN **16** (1961) 1263

Refractive Index Difference of Dilute Aqueous Solution of Polyvinylpyrolidon

By Yasuhiro MIYAKE and Jiro FURUICHI

Department of Physics, Faculty of Science, Hokkaido University, Sapporo, Japan

(Received March 6, 1961)

Recently, the anomalous behavior of the concentration dependence of the reduced viscosity in the very dilute solution of high polymer has been reported and interpreted as either due to (1) the peculiarities of the viscosity, such as the effects of Non-Newtonian or of the adsoption of polymer molecules on the capillary wall of the viscometer or due to (2) the disentanglement and the expansion of polymer molecules occurring below a critical concentration or the nonuniformity of the solution[1]. In order to decide the above interpretations it is desirable to adopt the methods using other than the viscometer and giving a sufficient accuracy in the region of the very dilute concentration. The differential refractometer seems to be the useful one for this purpose. The concentration dependence of the refractive index difference in the dilute aqueous solution of polyvinylalcohol(PVA) has already been investigated by M. Matsumoto and Y. Ohyanagi[2], who have found out the anomaly. On the other hand, the measurement based on the determination of the concentration using the more accurate interferometer for polyvinylacetate in toluene solution by C. A. F. Tuijnman and J. J. Hermans[3], who studied the precision viscometry of this system, suggests that such an anomaly cannot be found out. From these results, one may expect that the anomaly in PVA solution is due to the destruction of the structure of water caused by the strong interaction of the hydroxyl group of every structural unit with water just as the interpretation of M. Matsumoto et al. Therefore the sample which has no such group strongly interacting with a solvent as the hydroxyl group should not show the anomaly. Then, in the present work, the refractive index difference Δn of the dilute aqueous solution of polyvinylpyrolidon(PVP), which is soluble in water like PVA but has not the hydroxyl group, has been precisely measured. Molecular weights of the sample used are 700,000, 40,000 and 20,000 respectively, whicn are obtained from Kyorin medicine manufacture Co. The measurements have been done at 25°C with the cell of the inner angle 125° for the wave length of 436 mμ using Debye-type differential refractometer*. The result is shown in the figure.

It is evident from this that the index difference Δn between the solution and water plotted against the concentration does not show the anomalous behavior. This is likely to confirm the above inference, that is, the disagreement is attributed to the hydroxyl group so that the destruction of the structure of water may be the origin of the anomalous behavior in the static measurement like this as well as in the specific volume one[4] which is not the kinetic method such as the viscometric[5]. It corresponds to the interpretation (2) as the origin of the anomaly. However, the results of the anomalous behavior of polystyrene in various solvents obtained by the authors' viscometric investigation[6] have also to be interpreted as due to the other origin than the interpretation (2). Hence, it is necessary to consider the structure of the polymer and the solvent and also the method of the measurement in the investigation of the polymer solution.

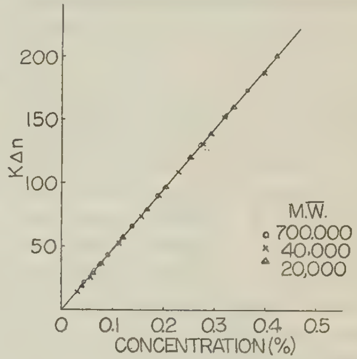

Fig. 1. Refractive index difference between solution and water, Δn, plotted against concentration for aqueous solution of PVP at 25°C. K is constant.

References

1) D. Streeter and R. Boyer: J. Polymer Sci. **14** (1954) 5. O. Ohrn: Arkiv for Kemi **12** (1958) 397. H. Batzer: Makro. Chem. **12** (1954) 145.
2) M. Matsumoto and Y. Ohyanagi: J. Polymer Sci. **31** (1958) 225.
3) C. A. F. Tuijnman and J. J. Hermans: J. Polymer Sci. **25** (1957)385.
4) K. Nakanishi and M. Kurata: Busseiron Kenkyu **101** (1956) 105 (in Japanese).
5) "*Polyvinylalcohol*" edited by Ichiro Sakurada (High Polymer Society of Japan, Tokyo 1955) p. 333.
5) to be published.

---

* This apparatus is made by Narumi CO. For example.

J. PHYS. SOC. JAPAN **16** (1960) 1264~1265

The Electron-Coupled Nuclear Spin Interactions in Ionic Crystals by the Overlap Model

By Tatsuo SHIMIZU

Department of Physics, University of Tokyo

(Received February 16, 1961)

Various properties of the ionic crystal have been investigated by two different approaches. The first is based on the model in which partially covalent bonds are assumed to work, and the second is based on the model in which the overlap between atomic orbitals is explicitly taken into account. The first and the second will be referred to as the covalent and the overlap model, respectively. Yoshida and Moriya[1] calculated nuclear quadrupole relaxations and chemical shifts by the covalent model, and Kondo and Yamashita[2] calculated the same quantities by the overlap model. The results based on the overlap model seem to be more reasonable than those based on the covalent model. Besides these quantities Yoshida-Moriya[1] have calculated the electron-coupled nuclear spin interactions by the covalent model, and Bloembergen and Sorokin[3] have extended them later. The calculation of them on the basis of the overlap model, however, has not yet been carried out. In this note we shall mention the result of such calculation.

The electron-coupled nuclear spin interaction energy is obtained as the second order perturbations of the following interaction operator:

$$\begin{aligned}\mathscr{H}'=\sum_{k,N}&[(16\pi/3)\beta\hbar\gamma_N(\boldsymbol{I}_N\cdot\boldsymbol{S}_k)\delta(\boldsymbol{r}_{kN})\\&+2\beta\hbar\gamma_N\{3(\boldsymbol{I}_N\cdot\boldsymbol{r}_{kN})(\boldsymbol{S}_k\cdot\boldsymbol{r}_{kN})r_{kN}{}^{-5}\\&-(\boldsymbol{I}_N\cdot\boldsymbol{S}_k)r_{kN}{}^{-3}\}]\,.\end{aligned}$$

The notations are those usually used. In calculating the second order perturbations, we approximate the excitation energies by an appropriate average value $\varDelta E$ as is usually done. As the ground state wave function, we take the Slater determinant constructed from the atomic orbitals of the free ions, and we rewrite it with the Löwdin orthogonalized atomic orbitals. We take into account the overlaps S between the orbitals belonging to the nearest neighbor ions only, and retain them up to the order of S^2 in the results. For that sake, we need retain S only in the first order in the Löwdin orbitals. Moreover we retain

$$\int\phi_\mu{}^*(1/r^3)\phi_\nu d\tau$$

only in the case where both atomic orbitals μ and ν belong to the same ion, and neglect the electron densities of the atomic orbitals at the nuclei other than those which they belong to. The results are as follows:

$$\begin{aligned}&(8\beta h/3)^2\gamma_m\gamma_h(1/\varDelta E)[S_{mshs}^2|\phi_{ms}(0)|^2\,|\phi_{hs}(0)|^2\boldsymbol{I}_m\cdot\boldsymbol{I}_h\\&-(3/20\pi)\{S_{hsmp}^2|\phi_{hs}(0)|^2\langle1/r^3\rangle_{mp}\\&+S_{mshp}^2|\phi_{ms}(0)|^2\langle1/r^3\rangle_{hp}\}\\&\times\{\boldsymbol{I}_m\cdot\boldsymbol{I}_h-3(\alpha I_{mx}+\beta I_{my}+\gamma I_{mz})(\alpha I_{hx}+\beta I_{hy}+\gamma I_{hz})\}\\&+(9/400\pi^2)S_{mphp}^2\langle1/r^3\rangle_{mp}\langle1/r^3\rangle_{hp}\\&\times\{\boldsymbol{I}_m\cdot\boldsymbol{I}_h+3(\alpha I_{mx}+\beta I_{my}+\gamma I_{mz})(\alpha I_{hx}+\beta I_{hy}+\gamma I_{hz})\}].\end{aligned}$$

Here m and h designate the metal ions and the halogen ions respectively, and s and p respectively designate the outermost s orbitals and the outermost p orbitals directed to the nearest neighbor ions. α, β, γ are direction cosines of the nearest neighbors. In the above expression, $\varDelta E$ was assumed for simplicity to be common for various terms in braces. The results can also be expressed in the exchange and pseudo-dipolar type coupling, that is:

$$A\boldsymbol{I}_m\cdot\boldsymbol{I}_h+B\{\boldsymbol{I}_m\cdot\boldsymbol{I}_h-3R_{mh}^{-2}(\boldsymbol{I}_m\cdot\boldsymbol{R}_{mh})(\boldsymbol{I}_h\cdot\boldsymbol{R}_{mh})\}\ ;$$

where

$$\begin{aligned}A=&(8\beta h/3)^2\gamma_m\gamma_h(1/\varDelta E)(S_{mshs}^2|\phi_{ms}(0)|^2|\phi_{hs}(0)|^2\\&+(9/200\pi^2)S_{mphp}^2\langle1/r^3\rangle_{mp}\langle1/r^3\rangle_{hp})\,,\\B=&-(8\beta h/3)^2\gamma_m\gamma_h(1/\varDelta E)\{(3/20\pi)\\&\times(S_{hsmp}^2|\phi_{hs}(0)|^2\langle1/r^3\rangle_{mp}+S_{mshp}^2|\phi_{ms}(0)|^2\langle1/r^3\rangle_{hp})\\&+(9/400\pi^2)S_{mphp}^2\langle1/r^3\rangle_{mp}\langle1/r^3\rangle_{hp}\}\,.\end{aligned}$$

Here $\boldsymbol{R}_{mh}$ is a vector connecting the metal ion and the nearest neighbor halogen ion. The above expressions for A, B have the same form as those obtained using covalent model, if we replace $2S_{mshp}^2$ etc. by $\lambda|a_{ms}|^2|a_{hp}|^2$ etc. respectively. This correspondence is similar to that in the case of the chemical shift[2].

Only experimental results on A and B in ionic crystals, which have been published, are those of CsBr, and the results are $Ah^{-1}=55$ cps, $Bh^{-1}=+15$ cps or -89 cps[3]. The theoretical prediction shows that B is always negative, so that we must take -89 cps as the experimental value of Bh^{-1}. Since there are many unknown parameters in the theoretical expressions, we can not obtain convincing theoretical values of A and B. However, we may make a rough estimate of them in order to see whether our model gives a reasonable result. We assume the following values: $\varDelta E=10$ eV, $S_{mphp}=0.080$, which has been obtained by Kondo-Yamashita from the experimental value of the chemical shift[2], $\langle1/r^3\rangle_{mp}=29$ A.U. and $\langle1/r^3\rangle_{hp}=13.6$ A.U. which have been obtained by Barnes and Smith semiempirically[4], and $|\phi_{ms}(0)|^2=65$ A.U. which is calculated by the Hartree-Fock wave function[5]. Furthermore if we assume $1/9S_{mphp}=1/3S_{hsmp}=1/3S_{mshp}=S_{mshs}$, we obtain the experimental value of A for $|\phi_{hs}(0)|^2\sim40$ A.U. which seems reasonable. From these parameter values, we find $Bh^{-1}\sim-20$ cps. If we assume $1/4\ S_{mphp}=1/2\ S_{hsmp}=1/2\ S_{mshp}=S_{mshs}$, we obtain the experimental value of A for $|\phi_{ks}(0)| \sim 8$ A.U., and Bh^{-1} again becomes ~ -20 cps. The discrepancy between -20 cps and -89 cps does not seem to be serious in view of the rough nature of our estimation.

Finally, we note that if we take into account the overlaps between the next nearest neighbor ions, the interactions between metal ions or halogen ions will be obtained in the form exactly the same as the expressions obtained above. Therefore the unpublished experimental results on the coupling between Tl ions cited in Yoshida-Moriya's paper[1] may be explained by our model, although it is apparently very difficult to explain it by the covalent model.

References

1) K. Yoshida and T. Moriya: J. Phys. Soc. Japan **11** (1956) 33.
2) J. Kondo and J. Yamashita: J. Phys. Chem. Solids **10** (1959) 245.
3) N. Bloembergen and P. P. Sorokin: Phys. Rev. **110** (1958) 865.
4) R. G. Barnes and W. V. Smith: Phys. Rev. **93** (1954) 95.
5) D. R. Hartree: Proc. Roy. Soc. **A 143** (1934) 506.

J. PHYS. SOC. JAPAN **16** (1961) 1265~1266

Magnetic Properties of B8 Type Compounds in Manganese-Tin System

By Mitsuru ASANUMA

Department of Physics, Faculty of Science, Hokkaido University

(Received January 21, 1961)

In previous report[1], it has been pointed out that $Fe_{1.3}Sn$ has a B8 type structure and shows ferromagnetism with the Curie temperature at 676°K. In this system, the composition range of B8 phase is so narrow that it was not possible to observe the variation of the magnetic moments of the compounds as a function of the composition.

However, in manganese-tin system, as the homogeneous range of B8 structure is considerablly wide, being estimated to be 35~40 atomic per cent tin by Nial[2], it has been possible to observe the variation of the magnetic moments of the system in this range of composition. This fact is important, since, from this result, it is possible to estimate the magnetic moments of manganese atoms in each lattice site theoretically.

The specimens were prepared as follows; after melting the mixture of each component in argon atmosphere, it was crushed, baked at 600°C for a week in evacuated silica tube, and quenched in water.

The obtained specimens were examined by X-ray Debye-Scherrer method with Fe-Kα, and it was recognized that $Mn_{1.5}Sn$, $Mn_{1.6}Sn$, $Mn_{1.7}Sn$ and $Mn_{1.8}Sn$ have all B8 type structure.

The dependence of saturation magnetization at absolute zero temperature on manganese content is shown in Fig. 1 and Table I, together with the lattice parameters and the Curie temperature in the latter. The value of saturation magnetization at 0°K decreases as manganese content increases.

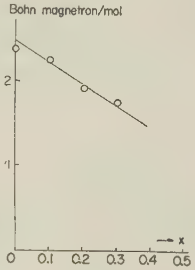

Fig. 1. The dependence of saturation magnetization at 0°K on manganese contents in $Mn_{1+x}Sn$.

Table I.

	$\sigma(\mu_B)$/mol	Curie Temp. (°K)	a (Å)	c (Å)	c/a
$Mn_{1.5}Sn$	2.38	269	4.37_2	5.50_8	1.26_0
$Mn_{1.6}Sn$	2.27	263	4.37_7	5.51_7	1.26_0
$Mn_{1.7}Sn$	1.92	258	4.39_1	5.52_4	1.25_8
$Mn_{1.8}Sn$	1.76	256	4.39_4	5.51_8	1.25_6

The fact that the magnetic moment per mol decreases as the manganese content increases suggests that the phase is probably ferrimagnetic.

When one assumes the variation in population of the manganese atoms takes place mainly on the B sites in Fig. 2, the magnetic moment of manganese atom on B sites is calculated to be $2.2\,\mu_B$.

The same assumption leads to the value of $3.5\,\mu_B$ as the magnetic moment on A sites.

B8 type structure extends from $B8_1$ type to $B8_2$ type for certain kinds of metalloid element. Here, $B8_1$ type structure corresponds to a filling of octahedral interspaces with transition metal atoms, in a hexagonal close packed structure of metalloid elements, and $B8_2$ type structure corresponds to a filling of both octahedral and trigonal interspaces with transition metal atoms, in a hexagonal close packed lattice. Since the volume of octahedral interspace is larger than that of trigonal interspace, it is reasonable to assume that the octahedral interspaces, i.e. A sites are always filled up and the variation in population takes place only on the trigonal interspace, i.e. B site.

Guillaud[3] has suggested that the critical distance of ferromagntic and antiferromagnetic interaction between manganese atom may be 2.81 Å as deduced from the analysis of the variation of the Curie temperature in MnAs, MnSb and MnBi. In a specimen $Mn_{1.8}Sn$, Mn–Mn distance in A site is 2.75_9 Å and the distance between A and B sites is 2.88_7 Å.

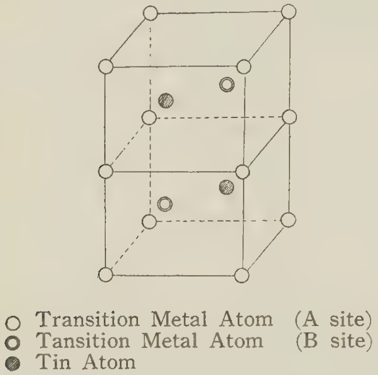
○ Transition Metal Atom (A site)
○ Tansition Metal Atom (B site)
● Tin Atom

Fig. 2. The crystal structure of $B8_2$ type structure.

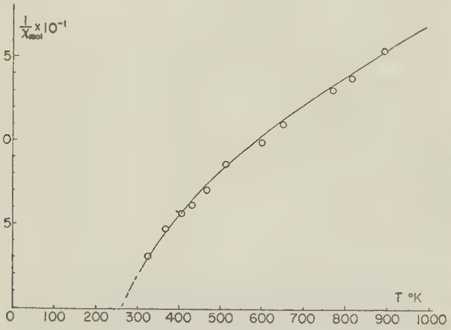

Fig. 3. The curve of the inverse of magnetic susceptibility *vs* temperature.

Therefore, according to Guilland, it is expected that J_{AA} is negative, while J_{AB}, J_{BB} are positive, and present result is inconsistent with Guillaud's criterion. The behavior is also same in $Mn_{1.5}Sn$.

The dependence of the inverse of magnetic susceptibility above the Curie temperature in $Mn_{1.7}Sn$ is slightly concave against temperature axis as shown in Fig. 3. This result also suggest the B8 phase in manganese-tin system is ferrimagnetic. The details will be published in this Journal.

References

1) M. Asanuma: J. Phys. Soc. Japan **15** (1960) 1343.
2) O. Nial: Arkiv. Kemi, Mineral. Geol. **17 B** (1944) No. 11.
3) C. Guillaud: Rev. Mod. Phys. **25** (1953) 119.

J. Phys. Soc. Japan **16** (1961) 1266~1267

On the Decomposition of the Ferromagnetic Phase of the Heusler Alloy, Cu_2MnAl

By Ren'iti Kimura, Tetuo Ohoyama
and Keizo Endo
Department of Physics, Faculty of Science,
Tokyo Metropolitan University

(Received March 6, 1961)

Through our recent study of isothermal change in the electrical resistance, the decomposition of the metastable β-phase of a Cu-Mn-Al alloy has been found to be complicated by the cooperation of two mechanisms of different kinds. These processes consist of the precipitation of more stable phases, but the different values of the activation energy seem to suggest that different processes predominate in higher and lower temperature regions.

The specimen for this study had the composition of Cu_2MnAl and was prepared as follows: Mother alloys with composition of Cu_3Mn and Al_3Mn were first prepared from electrolytic copper (99.9%), electrolytic manganese (99.9%), and pure aluminum (99.99%). The metals of desired proportion were charged in an alumina crucible, melted in an induction furnace, and cast into an iron mold. Then the mixture of the mother alloys in an optimum proportion to obtain the composition of Cu_2MnAl was melted in an atmosphere of argon, and a rod of ca. 1.5 mm in diameter was drawn up into a quarz pipe. The specimen thus obtained was attached with appropriate electrical lead wires and placed in an electrical furnace. On heating and cooling as well as at definite temperatures, the potential drop in the specimen on passing a stationary current was recorded, as a function of time, on an electromagnetic oscillograph paper by means of a feed back device[1].

In Fig. 1, the electrical resistance of the specimen which was quenched into water from 800°C and was ascertained to be of the β-phase by the X-ray diffraction is shown as a function of temperature. The resistance observed on heating at a rate of ca. 250°C per hour is shown by the full curve. It increases first as though it is the disordering process, and at 350°C, with the beginning of the precipitation, becomes to increase more slowly, and after a sudden fall at about 500°C, increases again toward the knick point at 700°C, after which it remains constant or rather decreases slightly*.

---

* Further investigations will be necessary to ascertain whether the temperature coefficient is realy negative at these temperatures, and to discuss the origin of it, if it is the case.

Then the change in the resistance when the temperature was held constant after having been raised up to that point at the same rate as before were also recorded and plotted in the same figure. The points corresponding to the equal time duration held at each temperature are connected by dotted curves. It is clearly seen in the figure that the rate of change in the resistance becomes much greater at the temperatures above 410°C. The logarithm of the time necessary for 50% of the total isothermal change to take place is plotted against the reciprocal of absolute temperature in Fig. 2. It forms a knick point at about 410°C and the activation energies can be calculated from the slope of the straight lines to be 0.42 and 1.5 eV for the lower and the higher temperature ranges, respectively.

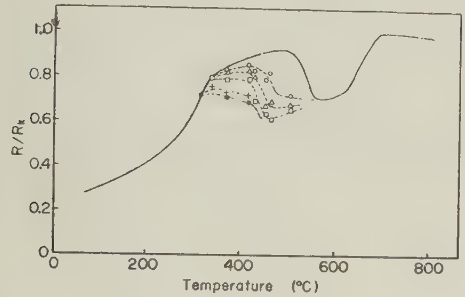

Fig. 1. Full curve: The change in electrical resistance of β-Cu_2MnAl when heated at a rate of 250°C per hour. R_k is the value at the knick point 700°C. Dotted curves: The resistance after held at constant temperatures for 9 min. (○), 18 min. (△), 36 min. (□), 90 min. (+), and 135 min. (●).

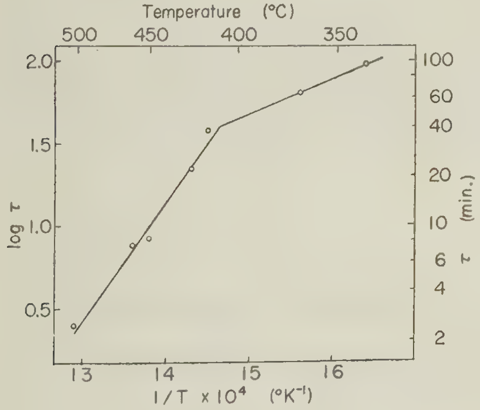

Fig. 2.

To obtain more informations about the difference of the two processes, microscopical observations and Debye-Scherrer X-ray analysis have been undertaken. More dispersed fine precipitations were observed under a microscope in the specimen held at lower temperature range, but unfortunately, the Debye photographs taken at room temperature for the powdered specimen quenched at each stage of the resistance change could not offer any clue to this problem, presumably owing to the instability of the phases in the quenched specimen. Thus the high-temperature X-ray technique seems to be essential to proceed further. As it is in preparation, we hope the result will be reported in future.

The authors wish to express their hearty thanks to Profs. E. Fukushima and T. Sato for their kindness to afford them facilities to achieve the work, and are also grateful to Mr. T. Kuwajima for the design of the feed-back device for the automatic recording.

References

1) T. Kuwajima: To be published on J. Appl. Phys. Japan.

J. PHYS. SOC. JAPAN **16** (1961) 1267~1268

Microwave Measurement of Fast Time varying plasmas

By Susumu Takeda

Nagoya University, Nagoya, Japan

(Received April 21, 1961)

The electron density ($5\times11^{11}\sim2\times10^{13}\,\mathrm{cm}^{-3}$) and the collision frequency in a decaying plasma are deduced from the simultaneous recording of two X-band microwave detector siginals displayed on the dual trace oscilloscope. The electron temperature, except in its very early period, decreases more slowly than expected on the basis of the simple assumption of energy equipartition between electrons and ions. The collision frequency measured here is compared with other results.

The principle of the measurement is a modification of the method previously described[1]. This method can yield the instantaneous value of both the electron density and the collision frequency of a time varying plasma.

In order to confirm the applicability and the validity of this measurement, it was tested to a typical recurrent decaying plasma. Since the two detector signals are photographically recorded, this tecenique can be especially adapted to plasmas produced by non repeated discharges.

The electron density n and the collision frequency ν are related to the plasma impedance $r+jx$, as follows[2]

$$n=\frac{A}{x-B}\,,\qquad \frac{\nu}{n}=\frac{\omega r}{A}\,.$$

where A and B depend on the dimension of the wave guide and the glass tube which contains the plasma and penetrates through the wide side of that waveguide.

Figure 1. shows ν_{ei}/n (here electron-ion collision frequency ν_{ei} predominates and is almost equal to total ν) and the electron temperature T_e calculated from $\nu_{ei}/n \sim (T_e/300)^{-3/2}$ versus time. The characteristic time for equipartition of the temperature between electrons and ions, τ_{ei}, is difined $\tau_{ei}=1/\nu_{ei}\,M_i/2m$ where M_i is the ion mass. And the theoitical value[3] of τ_{ei} in this experimental condition is of the order of a few μ sec; that is much shorter than the measured one. One reason which can possibly explain the measured long decay time of the electron temperature would be the presence of metastable atoms, heating the electron gas by the intermediary of the ion gas.

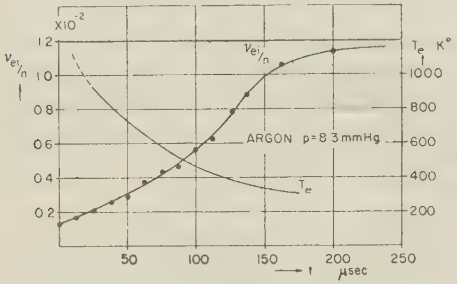

Fig. 1. Ratio of the electron-ion collision frequency ν_{ei} to the electron density n, and the electron temperature T_e versus time.

It was usually assumed that the maximum light intensity originating from the afterglow close to the beginning of a pulsed discharge occured at the time when the electron temperature reached 300°K. The photomultiplier datas of these experiments, especialy in Neon afterglow, contradict this assumption, since the light intensity maximum appears in less than 20 μ sec, whereas the electron temperature reaches 300°K after more than 100 μ sec.

The value of ν_{ei}/n in the late time in Fig. 1 approaches the value 1.2×10^{-2} cm^3/sec, which is compared to the theoretical and experimental values derived by other authors and listed in Table 1.

Table I. Theoretical and experimental values of ν_{ei}/n (cm^{-3}/sec) at room temperature.

	Theory			Experiment			
Electron Density	Spitzer[4]	Ginsburg[5]	Dougal[3]	Anderson[6]	Dougal[3]		This work
					(I)	(II)	
1×10^{11}	3.2×10^{-3}	3.8×10^{-3}	9.6×10^{-3}	3.0×10^{-3}	9.8×10^{-3}	1.2×10^{-2}	1.2×10^{-2} at $n=5\times10^{11}$
1×10^{12}	2.4×10^{-3}	2.9×10^{-3}	5.5×10^{-3}				

(I) Phototube datas of luminous intensity.
(II) Microwave interaction.
(3), (4) ν_{ei} deduced from τ_{ei}.

References

1) S. Takeda and M. Roux: Phys. Soc. Japan **16** (1961) 95.
2) To be published in detail.
3) A. A. Dougal and L. Goldstein: Phys. Rev. **109** (1958) 615.
4) L. Spitzer: "Physics of Fully Ionized Gases" p 50 Eq. (4-4).
5) V. L. Ginsburg: J. Physics (USSR) **8** (1944) 253.
6) J. M. Anderson and L. Goldstein: Phys. Rev. **100** (1955) 1037.

J. PHYS. SOC. JAPAN **16** (1960) 1269

Hot Electron Behavior at High Pressures

By Louis GOLD

Radiation Laboratory and Department of Nuclear Engineering, University of Michigan, Ann Arbor, Michigan

(Received March 17, 1961)

Changes produced in the hot electron behavior of many-valley semiconductors by high (hydrostatic) pressures afford a means for securing information on the energy gap pressure coefficient. This brief communication discloses how a newly developed phenomenological theory[1] for the nonequilibrium carrier distribution in such multivalued band minima structures characterizes hot electron departure from Ohm's law, to the extent where the role of high pressure may be appraised.

It has been demonstrated that the angular deviation ε from collinear current and voltage directions relates to the all important total carrier density via

$$\tan\varepsilon \propto e^{\varepsilon/kT}\,, \tag{1}$$

where ε was identified as an appropriate activation energy[1]. Now interpreting ε as essentially an energy gap E_g for the intrinsic range, the relation (1) may be reexpressed as

$$\tan\varepsilon \propto e^{E_g/2kT} \cdot e^{\pm\alpha P/2kT}\,, \tag{2}$$

where α is the pressure coefficient for the increase or decrease ($\pm$) of E_g with hydrostatic pressure P. Hence, provided the mounting pressure does not expend itself in merely redistributing carriers over the various band minima, a state should exist where the dominant effect contributing to $\tan\varepsilon$ is the gap change per se.

Now the high pressure-hot electron researches by Koenig et al.[2] do indeed manifest findings along the lines of indicated expectations. Thus in the neighborhood of electric fields near 3000 v/cm small increases of ε in N-germanium were detected at 77°K when pressures up to $\sim 10^9$ dynes/cm^2 were impressed; according to Eq. (2), perceptible pressure effect becomes favorable for $\alpha P \gtrsim kT$. Numerically then, with $\alpha = +5\times10^{-12}$ ev/dyne/cm^2 and $P_{\max} = 5.2\times10^9$ dynes/cm^2, $\alpha P \sim 0.025$ ev which exceeds $kT \sim 0\text{-}0066$ ev ($T = 77°$K). Hence the theory appears in sensible agreement with these experimental observations.

Future studies of high pressure-hot electron interaction may be judiciously guided by the foregoing considerations. For example, in view of the negative coefficient for N-silicon $\alpha = -1.3\times10^{-2}$ ev, higher pressures and lower temperatures are called for to detect the anticipated decrease of ε. More generally, with recognition of the crucial role played by the free carrier density, it becomes of interest to explore the influence of impurity concentration, optical excitation, etc. It is conceivable that the presently advocated scheme for determining energy gap changes with hydrostatic pressure may lend itself to band structure exploration in less familiar semiconductors.

Refereuces

1) L. Gold: J. Phys. Soc. Japan **16** (1961) 575.
2) Koenig, Nathan, Paul and Smith: Phys. Rev. **118** (1960) 1217.

Errata

On the Viscosity of Irradiated Polymers. III. Effect of Branching

By Kanji KATSUURA

J. Phys. Soc. Japan **15** (1960) 2310

Page	Column	Line		Should read
2311	left	23		$n(p, q, R)/N=m(p, q, R)$
2311		2nd of Eq.'s (4)	$-G'(z_0, x)$	$+G'(z_0, x)$
2311		Eq. (7)	$R_e(p. 0)^2$	$R_e(p, 1)^2$
2315		Eq. (34)		$1-\frac{4}{\lambda}+\frac{4}{\lambda}\frac{1}{urR_g}\left\{1-\left(\frac{b}{b+urR_g}\right)^b\right\}=0 .$
2315		Eq. (36)		$a_1=A_1R_g .$
2315	right	9		We plot a_1's against b for $\alpha=1$.
2315	right	21	0.74	0.70
2317		Reference 7)	J. Chem. Phys.	J. Phys. Chem.
2315		Fig. 5		Values of a_1 plotted against b.

Fig. 5.

Values of a_1 plotted against b.

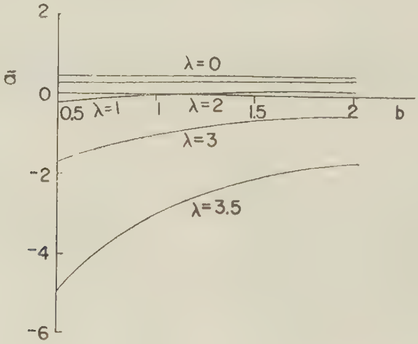

Contents

(Vol. 16)

No. 1

Page

Study on Spark Counters of the Rosenblum Type for Counting α Particles and Neutrons .... Suekichi KAWATA 1

On the Theory of the Fracture of Liquids .... Hiromu WAKESHIMA 6

On the Irreversible Behavior of Coupled Oscillators with Application to Time of Flight .... Youzou KOGURE 14

A New Picture of the Vibration of Linear Lattices .... Jun-ichi HORI 23

Crystal Distortion in Copper Ferrite-Chromite Series .... Haruyuki OHNISHI and Teruo TERANISHI 35

Distribution of Interstitials and Vacancies Produced by an Incident Fast Neutron .... Masayuki YOSHIDA 44

On the Electron Emission from Oxide Coated Cathode Subject to Strong Electric Field .... Chokichiro SHIBATA 51

Resistivity Striations in Germanium Single Crystals .... Hiroshi UEDA 61

X-ray Studies on Precipitation of Metastable Centers in Mixed Crystals NaCl-CdCl$_2$ .... Kazuo SUZUKI 67

Theory of Ferro- and Antiferromagnetic Resonance Absorption .... Takehiko OGUCHI and Akio HONMA 79

A Method for Measuring High Electron Densities in Plasmas .... Susumu TAKEDA and Michel ROUX 95

Energy Spectrum of Mn^{++} Ion in Calcium Fluorophosphate I .... Koziro NARITA 99

The Wavelength Dependence of Quantum Efficiency and Absorption Coefficient of ZnSiO$_3$/Mn Powder Phosphor .... Isoo MASUDA 105

Radiation Induced Optical Absorptions in Crystalline Quartz and Fused Silica .... Kazuko KUBO 108

Propagation of Ultrasonics in Triethylamine-water Mixture .... Seiken SHIMAKAWA 113

SHORT NOTES

Paramagnetic Resonance Study in Some Copper Salts .... Hidetaro ABE and Hiroko SHIRAI 118

Magnetic and Crystallographical Properties of Hexagonal Barium Mono-Ferrite, BaO·Fe$_2$O$_3$ .... Chisato OKAZAKI, Saburo MORI and Fumikazu KANAMARU 119

Electron Linear Accelerator as a Source of Intense Secondary Particle Beams .... Kazuto OKAMOTO 120

A-Centers in Potassium Chloride Crystals .... Kazuko KOJIMA and Noriko NISHIMAKI 121

Vibrational Effect on the Nuclear Quadrupole Coupling in ND$_3$ .... Yoshifumi KATO 122

Proton Resonance and Spin Quenching Effect in NiSO$_4$·7H$_2$O .... Hiroshi NAGASAWA and Yuzo TOMONO 123

Electrical Properties of Sb-Doped n-Type SnSe .... Jun-ichi UMEDA 124

Change of Surface State of Ge by Electron Bomberdment .... Kiichi KOMATSUBARA 125

Antiferromagnetic Magnetostriction in CoO and NiO Single Crystals .... Takuro NAKAMICHI and Mikio YAMAMOTO 126

The Purification of KCl by the Zone Refining Method .... Morio INOUE and Hiroyuki MIZUNO 128

Heat Capacities of Two Manganese Salts .... H. FORSTAT and G. O. TAYLOR 128

Excitation Function for the Reaction O^{16}(α, pn)F^{18} .... Michiaki FURUKAWA and Shigeo TANAKA 129

Mass Spectra of Baryons .... Seitaro NAKAMURA and Ken KAWARABAYASHI 130

Preferential Plastic Deformation in the Surface Region of Al and α-Fe Single Crystals .... Kôji SUMINO and Mikio YAMAMOTO 131

Errata

Study on the Ordered Phases with Long Period in the Gold-Zinc Alloy System .... Hiroshi IWASAKI, Makoto HIRABAYASHI, Kunio FUJIWARA, Denjiro WATANABE and Shiro OGAWA 132

Anisotropic Hall Coefficients in n-Type Germanium .... Hisao MIYAZAWA and Hajime MAEDA 132

No. 2

Elastic and Inelastic Scattering of Protons from Carbon Nucleus from 6.5 to 16 Mev .... Yukio NAGAHARA 133

Short-lived Activity of Ag^{106} .... Mitsuo SAKAI, Hidetsugu IKEGAMI and Toshimitsu YAMAZAKI 148

Counting Efficiency of Gamma Rays in Counter Tubes .... Tatsusaburo SUZUKI and Jiro YUHARA 152

On the Protons from the N$^{14}(d, p)$N^{15} Reaction .... Nawoyuki KAWAI 157

Inelastic Scattering of Neutrons by the Time-of-Flight Method .... Kineo TSUKADA, Shigeya TANAKA and Michio MARUYAMA 166

The Crystal Structure of KCuF$_3$ .... Atsushi OKAZAKI and Yasutaka SUEMUNE 176

Hall Effect on Some of the Magnetic Compounds .... Satoshi FUJIME, Miyuki MURAKAMI and Eiji HIRAHARA 183

Anisotropy of Electrical Conduction in Iron Sulfide Single Crystal .. Miyuki MURAKAMI 187

Heat Treatment Centers in Silicon .... Yasuo MATUKURA 192

On the Energy of the Interstitial Atom in Graphite .... Tadao IWATA, Eiichi FUJITA and Hideji SUZUKI 197

Electric Conduction of Ferrites Containing Fe^{2+}-ions .... Nahonori MIYATA 206

Dislocations and Fines Line in Rochelle Salt Crystal .... Terutaro NAKAMURA and Kikuo OHI 209

Observations of Lattice Defects in Graphite by Electron Microscopy, Part I .... F. Eiichi FUJITA and Kazuhiko IZUI 214

A Diffraction Pattern caused by Temperature Diffuse Scattering. I. General Theory .... Yoshiro KAINUMA 228

Inelastic Scattering of Thermal Neutrons by Paramagnetic Ions ...... Soitiro TOSIMA 241

Time Decrease of Magnetic Permeability in Some Mixed Ferrites .... Keizo OHTA 250

Oxygen Positional Parameters of Tetragonal Mn$_3$O$_4$ .... Ken'iti SATOMI 258

Nuclear Quadrupole Resonance Under High Pressure, I. .... Tokujiro FUKE 266

Magnetic Anisotropy of Chromium Antimonide and its Manganese Substitutes .... Ichiro TSUBOKAWA 277

Extension of High Polymer Molecule and Energy Change by Mixing .... Hiroshi MIZUTANI 282

Proton Magnetic Resonance of Ice Single Crystal .... Kiyoshi KUME and Ryosuke HOSHINO 290

Microwave Attenuation by Cyclotron Resonance in a Slightly Ionized Gas .... Taro DODO 293

Optical Image Formation in Terms of Entropy Transformations .... Edward L. O'NEILL and Toshimitsu ASAKURA 301

Magnetic Hyperfine Structure in the Rotational Spectrum of H$_2$CO ... Hiroshi TAKUMA 309

Some Remarks on Hydrostatic Pressure and Maxwell Model .... Wataru SEGAWA 317

Rheological Equations of Generalized Maxwell Model and Voigt Model in Three-Dimensional, Non-Linear Deformation .... Wataru SEGAWA 320

The Velocity Distribution at the Interface between Two Liquids ...... Setsuo OKUDA 324

SHORT NOTES

Annealing of Radiation Damage on Lifetime in Silicon .... Kenji MATSUURA and Yoshio INUISHI 339

The Fundamental Absorption of Lithium Fluoride and Sodium Fluoride .... Ryumyo ONAKA, Atsuo FUKUDA and Arisato EJIRI 340

The Inverse Solution of the TFD Equation .... Kwai UMEDA, Yasuo TOMISHIMA and Chikao KAWABATA 341

Spin Wave Resonance in Cu-Ni Alloy Films .... Hiroshi NOSÉ 342

Nuclear Magnetic Resonance Study of NaCl Crystal containing Ca Impurities .... Junkichi ITOH, Mitsuo SATOH and Akio HIRAKI 343

Temperature Dependence of the Line Width of Ferrimagnetic Resonance in Polycrystalline Nickel Cadmium Ferrite .... Susumu TAKEMOTO 344
Electrical Resistivity of Ferromagnetic Chromium Dioxide .... Buichi KUBOTA and Eiichi HIROTA 345
Measurements on Collision Frequencies of Electrons in Neon Gas......... Taro DODO 346
Observations of Dislocation Network in Neutron-Irradiated LiF Crystal .... Kazuko KUBO and Yoshio KATANO 347
Spectrum of the Electron Cyclotron Resonance in a Plasma .... Taro DODO 348
On the Inelasticity in High-Energy Nuclear Interactions .... Shigeo MATSUMOTO and Shoji MIKAMO 350
Enhancement of Photoconductivity upon Cadmium Sulphide Single Crystals ...... Saburo KITAMURA, Takao KUBO and Toshio YAMASHITA 351
A New Phase of an Intermetallic Compound Mn$_{3.4}$Ge and its Magnetism .... Tetuo OHOYAMA, Kō YASUKŌCHI and Kazuo KANEMATSU 352

Errata

The Magnetic Investigation of Mn^{++}, Co^{++}, Ni^{++}, Cu^{++} Ammine and Anhydrate Salts.................................. Kiyoshi KIDO and Takashi WATANABE 353
On the Superconducting Ground State .... Ziro MIKURA 353

No. 3

Gamma Rays from Inelastic Scattering of Neutrons by Fe, Cu, Zn, Ge and Se .... Kazuaki NISHIMURA 355
Angular Distributions and Excitation Functions of the Be^9(d, p)Be^{10} Ground-State Reaction .... Toshiyuki ISHIMATSU, Naoyuki TAKANO, Yûki HACHIYA and Takao NAKASHIMA 367
On the Nuclear Interaction of Mu-Mesons.......................... Hiroyuki SHIBATA 372
Quantum Statistics of Surface Effect .... Takuji TSUZUKI 377
Effects of the Special Heat-treatment on Permalloys .... Sadami TOMITA 393
Direct Observation of Subgrain-Growth of Cold-Worked Aluminium by means of Electron Microscopy.. Hiroshi FUJITA 397
Cavity Growth by Vacancy Condensation and Transformation to Dislocation Loop in the Graphite Structure .... Takuro TSUZUKU 407
Ferroelectric Properties of X-ray Damaged Rochelle Salt .... Kenkichi OKADA 414
An Effect of Heat Treatment on WO$_3$ Single Crystal, I. Various Patterns........ Tadao HORIE and Tsuruji IWAI 424
Magnetic Properties of Intermetallic Compounds in Iron-Germanium System: Fe$_{1.67}$Ge and FeGe$_2$... Kō YASUKŌCHI, Kazuo KANEMATSU and Tetuo OHOYAMA 429
Magnetic Properties of Perovskites Containing Strontium, II. Lanthanum-Strontium Manganites .... Hiroshi WATANABE 433
Regrowth of Germanium Single Crystal from Indium Melt .... Masami TOMONO 439
An Electron Diffraction Study on Cu-Sn Alloys................. Tomokuni MITSUISHI 453
Diffusion of Cobalt into Silver .... Tokutaro HIRONE and Hisao YAMAMOTO 455
Orientation Dependent Mechanical Breakdown of a Model High Polymer Solid .... C. C. HSIAO, J. E. OSBORN and D. B. ROZENDAL 459
X-Ray Line Broadening in Polyethylene Filaments............... Ken-ichi KATAYAMA 462
Study on the Ordered Alloys of Gold-Manganese System by Electron Diffraction, III. Lattice Modulation in the Ordered Au$_3$Mn .... Denjiro WATANABE 469
The Ferroelectric Phase Transition in (Glycine)$_3$·H$_2$SO$_4$ and Critical X-Ray Scattering .... Iwao SHIBUYA and Toshio MITSUI 479
X-Ray Studies of the Ferroelectric Phase Transition in NaNO$_2$......... Iwao SHIBUYA 490
Ps Function in Electron Diffraction...... Yoshiro KAINUMA and William N. LIPSCOMB 495
Electron Distribution in Cu$_2$O Crystal .... Tadasu SUZUKI 501
A Theory of Electron Impact on Some Polyatomic Molecules.... Tsutomu WATANABE 510
On the Additivity Rule in the Ionization Cross Section of Molecules .... Tsutomu WATANABE 529
The Optical Properties of Cadmium Telluride in the Far Infrared Region .... Akiyoshi MITSUISHI 533

Interaction of Exciton with Electron Trapping Centers in Alkali Halide Crystals
3. Exciton Induced Photoconductivity of U center .... Masayasu UETA, Masamitsu HIRAI and Mikihiko IKEZAWA 538
Theoretical Prediction of the Pressure Distribution on a Non-lifting, Thin Symmetrical Aerofoil at Various Transonic Speeds .... Iwao HOSOKAWA 546
Effect of a Magnetic Field upon the Stability of Free Boundary Layers between Two Uniform Streams .... Kanefusa GOTOH 559

SHORT NOTES

On the New Magnetic Phase in Manganese-Aluminium-Copper System .... Ichiro TSUBOYA and Makoto SUGIHARA 571
Optical Absorption and Electrical Conductivity of Reduced BaTiO$_3$ Single Crystal .... Seiji IKEGAMI, Ichiro UEDA and Yukihiko ISE 572
Impedance Changes Induced by Light in ZnS Phosphors .... Ichizo UCHIDA and Kimihiko SATAKE 573
NMR of Co^{59} in Ferromagnetic Cobalt Alloys .... Yoshitaka KŌI, Akira TSUJIMURA, Tadamiki HIHARA and Toshimoto KUSHIDA 574
Hot Electron Nonequilibrium Carrier Distribution in a Many-Valley Semiconductor .... Louis GOLD 575
Nature of the A-Centers in KCl .... Noriko NISHIMAKI, Kazuko KOJIMA and Tadanobu KOJIMA 576
Impurity Effect upon Mobility in Heavily Doped Silicon .... Yoshitaka FURUKAWA 577
X-ray Small Angle Scattering from Precipitated Platelets in Al-Ag Alloy .... Yasuharu YONEDA and Kouzou NISHIOKA 578
Microdomain Structure in Paraelectric Phase of NaNO$_2$ .... Sigetosi TANISAKI 579
Measurement of Anomalous Absorption Coefficients of Electrons for MgO Crystals .... Kazutake KOHRA and Hiroshi WATANABE 580

Errata

On the Electron Emission from Oxide Coated Cathode Subject to Strong Electric Field .... Chokichiro SHIBATA 582
Radiation Induced Optical Absorptions in Crystalline Quartz and Fused Silica .... Kazuko KUBO 582

Addendum

On the Ferrimagnetic Resonance of Europium Iron Garnet .... W. P. WOLF 582

No. 4

Angular Distributions of Protons from the Alpha Particle Bombardment of B^{10}, N^{14}, O^{16} and Ne^{20} .... Hisashi YAMAGUCHI 583
Resonance Levels in the Reactions ^{28}Si$(p, \gamma)^{29}$P, ^{29}Si$(p, \gamma)^{30}$P and ^{30}Si$(p, \gamma)^{31}$P .... Haruko OHMURA, Hiroyasu EJIRI, Yutaka NAKAJIMA, Kinuko HORIE, Kiichi ETOH, Akiji OHUCHI and Yozo NOGAMI 593
The Reaction Mg$^{25}(d, p)$Mg^{26} in the Energy Range of Deuterons from 1.5 MeV to 3.0 MeV .... Naoyuki TAKANO 598
The Structure of Extensive Air Showers Near the Axes.................. Shūji FUKUI 604
On the Transport Equation in Quantum Mechanics..................... Lesser BLUM 616
On the Theory of Adiabatic and Isolated Susceptibilities............. Nobuhiko SAITÔ 621
Convex-Core Model of Molecules in Crystalline State. II................ Saburo KOBA 627
Entropy Production and Variation Principle in the Kinetic Theory of Rigid-Sphere Gas Mixture.. Terutoshi MURAKAMI 633
Temperature Dependence of Magnetic Susceptibilities of KClO$_3$, KBrO$_3$ and KIO$_3$.. .... Shōtarō TOBISAWA 654
Luminescence of Doped Silver Chloride Crystals.... Sanemi SONOIKE and Kazuo AKIMOTO 658
Internal Friction of Synthetic Quartz .... Yosio HIKI 664
The Crystal Structures of KMnF$_3$, KFeF$_3$, KCoF$_3$, KNiF$_3$ and KCuF$_3$ above and below their Néel Temperature ...... Atsushi OKAZAKI and Yasutaka SUEMUNE 671
Anomalous Diffusion at the Interface of Thin Bimetallic Film of Bi and Sb........ .... Ryōji SUGANUMA, Toshio YOSHIDA and Yoshibumi FUJIKI 676

Electrical Properties of Heavily Doped *n*-Type Germanium......Yoshitaka FURUKAWA 687
Paramagnetic Resonance of Mn^{++} Associated with Impurities in Alkali Chlorides.. ....Yasaburo YOKOZAWA and Yukio KAZUMATA 694
Ferromagnetic Resonance Absorption of Single-Crystal Thin Films of Nickel .... Masao KURIYAMA, Hirokage YAMANOUCHI and Sukeaki HOSOYA 701
Specific Heat of Ti_2O_3 .... Shoichiro NOMURA, Tatsuyuki KAWAKUBO and Taketoshi YANAGI 706
Regrowth of Germanium from Molten Indium or Lead .... Masami TOMONO 711
Low-Temperature Electrical Breakdown in Germanium................Jiro YAMASHITA 720
Studies on the Boundary between Etched and Ground Regions of Ge and Si Single Crystal Surface by X-Ray Diffraction Topography................Zensho ISHII 733
The Switching Circuit Logically or Functionally Equivalent to a System of Biochemical Reactions...Motoyosi SUGITA 737
Mass Spectrometric Study on the Evaporation of Volatile Components in Polyethylene .... Kisaku NAKAGAWA 741
Interaction between Polyions and Low Molecular Ions ....Nobuhisa IMAI 746
Study of the Hydration-Dehydration in Polyelectrolyte Solutions by the Ultrasonic Technique...Hiroshi ASAI 761
On the Theory of Cross Relaxation in Maser Materials .... Motokazu HIRONO 766
"Non-Adiabatic" Behavior in a Low Frequency Beam-Type Maser ....Tadao SHIMIZU and Koichi SHIMODA 777
Density vs. Exposure Curves of a Photographic Emulsion for 20∼200 kV Electrons .... Mieko TAKAGI, Norihisa KITAMURA and Setsu MORIMOTO 792
On the Steady Motion of an Idealized Elastico-Viscous Liquid Through Channels with Suction and Injection ....S. K. DATTA 794
Flow of Condensing Vapour with Temporary Supersaturated State due to Heat-Removal Effect .... Keishiro NIU 798
A Simplified Method Calculating The Laminar Boundary Layer ......Shin KAWAMATA 805
Refractive Index and Pore Structure of Acid-Leached Surface Layer of Glass...... .... Koreo KINOSITA 807
Diffraction of Plane Sound Wave by Many Equal Circular Holes Arbitrarily Distributed in an Infinitely Large Rigid Plane Plate .... Yûkichi NOMURA 819

SHORT NOTES

Effects of Vacancies on Pulse Photoconductions in CdS Single Crystals .... Junji SHIRAFUJI and Yoshio INUISHI 832
Conductivity of Grain Boundaries in Ge.......Yasuo MATUKURA and Shigezo TANAKA 833
Direct Observation of the Lattice Imperfections in Pearlites by Electron Microscopy .... Zenji NISHIYAMA, Atsuo KORE'EDA, Isamu EGUCHI and Koshi KATO 834
Proton Magnetic Resonance in Ferroelectric $(CH_3NH_3)\ AlSO_4\cdot 12H_2O$....Ryosuke HOSHINO 835
Temperature Dependence of ESR Line-Width in $K_2CuCl_4\cdot 2H_2O$.......... Hidetaro ABE 836
E.S.R. of Irradiated DPPH Protected by Polystyrene...Kohzoh MASUDA and Tokuo SUITA 837
Spin Wave Resonance in Pd-Ni Alloy Films .... Hiroshi NOSÉ 838
The O-H···O Bond in Orthoboric Acid ....James A. IBERS and C. H. HOLM 839
Volume Magnetostriction in Nickel-Iron Alloys................................... ....Yoji NAKAMURA, Tetsuo NAKAJIMA and Hideo TAKAMI 840
Decay of Ir^{195} and Ir^{197} ....Saburo HOMMA, Tokihiro KUROYANAGI and Haruhiko MORINAGA 841
Properties of Grain Boundaries in Silicon.. .... Yasuo MATSUKURA 842
The O-H···O Bond in Orthoboric Acid ......Kiyoshi KUME and Yoshinobu KAKIUCHI 843
Linear Potential Barrier Model for Nuclear Surface.....................Tutomu INOUE 844

Errata

Rheological Equations of Generalized Maxwell Model and Voigt Model in Three-Dimensional, Non-Linear Deformation ....Wataru SEGAWA 845
The Velocity Distribution at the Interface between Two Liquids........Setsuo OKUDA 845
Dislocation Networks and Moiré Patterns of Molybdenite......................... ......Yoshihiro KAMIYA, Keiichi ANDO, Minoru NONOYAMA and Ryozi UYEDA 846

Some Remarks on Hydrostatic Pressure and Maxwell Model..........Wataru SEGAWA 846

No. 5

Lateral Density Distribution of Charged Particles in the Central Region of Extensive Air Shower ....Saburo MIYAKE, Kensaku HINOTANI, Itsuo KATSUMATA, Tatsunosuke KANEKO and Nobuo ITO 847

Mu-Meson Component of Air Shower Below the Ground ....Kenji WATANABE 855

A Study on High-Energy Nuclear-Active Particles in Extensive Air Showers ....Yasuo TANAKA 866

Experimental Studies on Electronic Trapping Processes Associated with Dislocation Lines in Alkali Halide Crystals ....Hiroshi OHKURA 881

Interaction of Electrons and Holes with Acoustic Waves in Intrinsic Semiconductors ....Nobuo MIKOSHIBA 895

Growth and Dissolution Processes of GASH Crystal ....Terutaro NAKAMURA, Kikuo OHI and Hiroko KUBOTA 906

Angular Distribution of Electrons Suffering Characteristic Energy Loss in Passage through Metal Films ....Hiroshi WATANABE 912

Domain Structure of $NaNO_2$ .....Shoichiro NOMURA, Yohko ASAO and Shozo SAWADA 917

Perfectness of Macrodomains of $BaTiO_3$ Crystals ...Kêitirô AIZU and Osamu NAKADA 923

Study of the Texture of the Boundary of Etched and Ground Regions of Quartz Plate by X-ray Diffraction ....Einosuke FUKUSHIMA and Hiroshi NIMURA 928

222-Reflection from CuCl in Electron Diffraction ....Fuminori FUJIMOTO 936

The Dipole Moment and End-to-End Length of the Isotactic Vinyl Polymer, III. Convergence of Neumann Series ....Tsugio MORI 944

Mathematical Considerations on Chemical Kinetics of Radiation-Induced Polymerization..........Ayao AMEMIYA and Mitio INOKUTI 949

The Rheological Behavior and Thixotropy of a Fatty Plastic Body ...Toshimaro SONE 961

Scattering of Microwaves from a Cylindrical Plasma in the Born Approximation. I. ....Yukio MIDZUNO 971

Photoconductive Hall Effect in Potassium Bromide ....Masami ONUKI 981

Structures of Photoconductivity Spectra near the Fundamental Absorption Edge of Cadmium Sulfide..........Hiroji MITSUHASHI 989

Smoke Observation on Boundary Layer Transition Caused by a Spherical Roughness Element..........Masako MOCHIZUKI 995

Vibration of a Plate and Sound Radiation Generated by an Impulsive Force .... Yasuo TOKITA 1008

On the Relation between the Change in Modulus of Rigidity in Brass Wires by Cold-Rolling and Rolling Textures ....Jun KUROYANAGI 1019

SHORT NOTES

Dielectric α- and β-dispersions in Polyvinyl Butyral (PVB) ....Yūzō TAKAHASHI 1024

The Double-Grid Ionization Chamber ....Iwao OGAWA and Tadayoshi DOKE 1025

Thermoelectric Behaviours of Rutile ....Kimiko SAKATA 1026

Magnetic Anisotropy of Heusler Single Crystal ..Keizô AOYAGI and Makoto SUGIHARA 1027

Dielectric α-, β- and γ-Dispersions in the Thermosetting Phenolic Resins ....Yūzō TAKAHASHI 1028

Forward Characteristics of Si $p\pi n$-Junctions ....Masakatsu TOKUNAGA and Katsufusa SHONO 1029

Viscous Forces and Brownian Motion ....Naokata TAKEYAMA 1030

Fine Structures of Photoprotons from Si^{28} ....Katsufusa SHODA, Keisuke KOBAYASHI, Shoichi SIINA, Ken ABE and Motoharu KIMURA 1031

Observation of Lattice Defects in Fission Fragment-irradiated Graphite..........Kazuhiko IZUI and F. Eiichi FUJITA 1032

A Note on the Electron Diffusion and the Wall Relaxation in Ferrites ....Hisashi SEKIZAWA 1034

Weak Field Behaviour of the ΔE Effect in Ferromagnetic Cubic Solid Solution Alloys ....Mikio YAMAMOTO and Satoshi TANIGUCHI 1035

Remarks on the Electrical Properties of Alkali Antimonides..........Shunji IMAMURA 1036

The Characteristics of the Discharges in the Crossed Electric and Magnetic Field
....................................Shigeru HAYAKAWA and Tokuo SUITA 1037
The Electrical Properties of Zinc Telluride ....
.................Hirosi TUBOTA, Hiromichi SUZUKI and Kazuyoshi HIRAKAWA 1038
Internal Magnetic Field in Iron and Iron Alloys Measured by NMR ....
Yoshitaka KÔI, Akira TSUJIMURA, Tadamiki HIHARA and Toshimoto KUSHIDA 1040
Slow Decay of Reverse Current and Noise in Field Effect on Ge P^+-N Junction ..
Hiroshi EDAGAWA, Yoshinori MORITA, Syun-ichi MAEKAWA and Yoshio INUISHI 1041

Errata

Cavity Growth by Vacancy Condensation and Transformation to Dislocation Loop
in the Graphite Structure ....Takuro TSUZUKU 1042
Anomalous Diffusion at the Interface of Thin Bimetallic Film of Bi and Sb ......
...................Ryōji SUGANUMA, Toshiho YOSHIDA and Yoshibumi FUJIKI 1042

No. 6

Elementary Processes Related to the Catalytic Action of μ^- for the p-d Fusion
Reaction ....Yukio MIZUNO 1043
Inelastic Scattering of Deuterons from C^{12}, Mg^{24} and Ni^{60}..........Yoshihide ISHIZAKI 1056
Anomalies in the Scattering of Alpha Particles by Carbon ....Takashi MIKUMO 1066
He^3-Alpha Scattering.............................Ren CHIBA, Homer E. CONZETT,
Haruhiko MORINAGA, Naoshi MUTSURO, Katsufusa SHODA and Motoharu KIMURA 1077
Angular Correlation of the Mo^{95} Gamma-Gamma Cascades ....Atsushi AOKI 1086
Angular Distribution of (α, p) Reactions in Some Light Nuclei ....
.... Michiya KONDO, Takashi YAMAZAKI and Shotaro YAMABE 1091
A Cloud Chamber Study of High Energy Nuclear Interactions of Cosmic Ray
Particles (I)—A Possible Evidence of Successive Collisions in Carbon Nuclei
....Isao KITA 1099
A Cloud Chamber Study of High Energy Nuclear Interactions of Cosmic Ray
Particles. (II)—Results of Single Nucleon-Nucleon Interactions..Goro FUJIOKA 1107
Effects of s-d Exchange Interaction and Temperature-Independent Paramagnetism
on Susceptibilities of Nickel, Palladium, and Platinum ....Masao SHIMIZU 1114
Magnetic Properties of Intermetallic Compounds in Manganese-Tin System: $Mn_{3.67}Sn$,
$Mn_{1.77}Sn$, and $MnSn_2$ ....
.....................Kō YASUKŌCHI, Kazuo KANEMATSU and Tetuo OHOYAMA 1123
The Magnetic Investigation of Mn^{++}, Co^{++}, Ni^{++} and Cu^{++} Ammine and Anhydrate
Salts at Low Temperature ....Takashi WATANABE 1131
Ultrasonic Attenuation in Tin Single Crystals at Low Temperatures..Kazuo KAMIGAKI 1141
The Thermoelectric Power of Magnesium-Cadmium Alloys ....Seiichiro NOGUCHI 1145
Resonance Transfer of Ionization Energy in Semiconductors ....
.... Shigeharu KOSHINO and Toshihiko ANDO 1151
Ferroelectricity in (K, NH_4), (K, Rb) and (K, Tl) Ferrocyanide Mixed Crystals ....
......................Shigeru WAKU, Kunio MASUNO and Toshisuke TANAKA 1158
The Superstructures of Iron Selenide Fe_7Se_8 ....Atsushi OKAZAKI 1162
Ultrasonic Attenuation in Magnetite at Low Temperatures ....Kazuo KAMIGAKI 1170
Crystal Structures and Electrical Properties of Alkali Antimonides...............
....Jun-ichi CHIKAWA, Shunji IMAMURA, Kenzo TANAKA and Makoto SHIOJIRI 1175
Weak Ferromagnetism in β-$NaFeO_2$ ....Hiroshi WATANABE and Masahiro FUKASE 1181
The Crystal Structuae of Chloranil and Bromanil ....Ikuhiko UEDA 1185
Study on Precipitation Phenomena in Thin Films of Supersaturated Gold-Nickel
Alloy ....Yasushige FUKANO 1195
A Direct Determination of the Crystal Structure of Ethylenediammonium Sulphate
.... Kiichi SAKURAI 1205
Study of Metallic Carbides by Electron Diffraction Part IV. Cobalt Carbides ....
.... Sigemaro NAGAKURA 1213
Study on the Internal Motions of Some Acryl- and Methacryl-group High Polymers
by Pulsed NMR Method ....Takao KAWAI 1220

Mechanical Dispersions and Transition Phenomena in Semicrystalline Polymers.... .... Yasaku WADA 1226
Microwave Spectrum of Formaldehyde III. Vibration-Rotation Interaction .... Takeshi OKA and Yonezo MORINO 1235
Double Puautum Transition in Electron Spin Resonance of Diphenyl-Picryl Hydrazyl at Low Magnetic Fields .... Tsuneo HASHI 1243
On the Pendent Drop, I .... Ko TAMADA and Yoshio SHIBAOKA 1249

SHORT NOTES

Observation of Dislocations in Germanium Single Crystal........ ..Masakazu SHOJI, Shoji TAUCHI, Tomokuni MITSUISHI and Masami TOMONO 1253
Anomalous Temperature Dependence of Lattice Constants of Ferroelectric Sodium Nitrite .... Sadao HOSHINO and Iwao SHIBUYA 1254
Moving Striation in Microwave Discharge Plasma ....Mikio TAKEYAMA, Tanehiro NAKAU, Shōzaburo YAMASAKI and Takeshi ISA 1255
Electron Spin Resonance of Manganese in $MgCl_2$........ .....Kuniya FUKUDA, Hiroaki MATSUMOTO, Toru TAKAGI and Yoichi UCHIDA 1256
The New Magnetic Phase in Manganese-Aluminium-Nickel System .... Ichiro TSUBOYA and Makoto SUGIHARA 1257
Effect of Current Injection on Properties of Cadmium Sulfide Crystals .... Hiroji MITSUHASHI 1258
Absorption and Reflection Spectra of Afterglow Plasma........ Shigetoshi TANAKA 1259
The Base Resistance of the Transistor in the Saturated Region ....Osamu NAKAHARA 1260
On the Secondary Tunnelling Phenomena in a *p-n* Junction of Gallium Arsenide .. .. Akikazu SHIBATA 1261
The Optical Absorption of Localized Exciton in KCl-KI Crystal........ Kaizo NAKAMURA, Kuniya FUKUDA, Riso KATO, Atsuo MATSUI and Yoichi UCHIDA 1262
Refractive Index Difference of Dilute Aqueous Solution of Polyvinylpyrolidon .... Yasuhiro MIYAKE and Jiro FURUICHI 1263
The Electron-Coupled Nuclear Spin Interactions in Ionic Crystals by the Overlap Model .... Tatsuo SHIMIZU 1264
Magnetic Properties of B8 Type Compounds in Manganese-Tin System........ .... Mitsuru ASANUMA 1265
On the Decomposition of the Ferromagnetic Phase of the Hausler Alloy, Cu_2MnAl .... Ren'iti KIMURA, Tetuo OHOYAMA and Keizo ENDO 1266
Microwave Measurement of Fast Time Varying Plasmas .... Susumu TAKEDA 1267
Hot Electron Behavior at High Pressures .... Louis GOLD 1269

Errata

On the Viscosity of Irradiated Polymers. III. Effect of Branching ..Kanji KATSUURA 1270

AUTHOR INDEX TO VOL. 16 NOS. 1~6.

ABE Hidetaro;

—— and H. SHIRAI: Paramagnetic Resonance Study in Some Copper Salts.. 118

——: Temperature Dependence of ESR Line-Width in $K_2CuCl_4\cdot 2H_2O$ (S.N.).. 836

ABE Ken: [cf. SHODA Katsufusa (1031) S.N.]

AIZU Kêitirô;

—— and O. NAKADA: Perfectness of Macrodomains of $BaTiO_3$ Crystals.... 923

AKIMOTO Kazuo: [cf. SONOIKE Sanemi (658)]

AMEMIYA Ayao;

—— and M. INOKUTI: Mathematical Considerations on Chemical Kinetics of Radiation-Induced Polymerization 949

ANDO Kei-ichi: [cf. KAMIYA Yoshihiro (846) Errata]

ANDO Toshihiko: [cf. KOSHINO Shigeharu (1151)]

AOKI Atsushi: Angular Correlation of the Mo^{95} Gamma-Gamma Cascades 1086

AOYAGI Keizô;

—— and M. SUGIHARA: Magnetic Anisotropy of Heusler Single Crystal (S.N.)..1027

ASAI Hiroshi: Study of the Hydration-Dehydration in Polyelectrolyte Solutions by the Ultrasonic Technique 761

ASAKURA Toshimitsu: [cf. O'NEILL Edward L. (301)]

ASANUMA Mitsuru: The Magnetic Properties of B8 Type Structure Compounds in Manganese-Tin System (S.N.) 1265

ASAO Yohko: [cf. NOMURA Shoichiro (917)]

BLUM Lesser: On the Transport Equation in Quantum Mechanics.................... 616

CHIBA Ren;

——, H. E. CONZETT, H. MORINAGA, N. MUTSURO, K. SHODA and M. KIMURA: He^3-Alpha Scattering 1077

CHIKAWA Jun-ichi;

——, S. IMAMURA, K. TANAKA and M. SHIOJIRI: Crystal Structures and Electrical Properties of Alkali Antimonides 1175

CONZETT H. E.: [cf. CHIBA Ren (1077)]

DATTA S. K.: On the Steady Motion of an Idealized Elastico-Viscous Liquid Through Channels with Suction and Injection.. 794

DODO Taro: Microwave Attenuation by Cyclotron Resonance in a Slightly Ionized Gas.. 293

——: Measurements on Collision Frequencies of Electrons in Neon Gas (S.N.).. 346

——: Spectrum of the Electron Cyclotron Resonance in a Plasma (S.N.).... 348

DOKE Tadayoshi: [cf. OGAWA Iwao (1025) S.N.]

EDAGAWA Hiroshi;

——, Y. MORITA, S. MAEKAWA and Y. INUISHI: Slow Decay of Reverse Current and Noise in Field Effect on Ge P^+-N Junction (S.N.) 1041

EGUCHI Isamu: [cf. NISHIYAMA Zenji (834) S.N.]

EJIRI Arisato: [cf. ONAKA Ryumyo (340) S.N.]

EJIRI Hiroyasu: [cf. OHMURA Haruko (5931)]

ENDO Keizo: [cf. KIMURA Ren'iti (1266) S.N.]

ETOH Kiichi: [OHMURA Haruko (593)]

FORSTAT H.;

—— and G. O. TAYLOR: Heat Capacities of Two Manganese Salts (S.N.)... 128

FUJIKI Yoshibumi: [cf. SUGANUMA Ryôji (676)]

FUJIME Satoshi;

——, M. MURAKAMI and E. HIRAHARA: Hall Effect on Some of the Magnetic Compounds 183

FUJIMOTO Fuminori: 222-Reflection from CuCl in Electron Diffraction............... 936

FUJIOKA Goro: A Cloud Chamber Study of High Energy Nuclear Interactions of Cosmic Ray Particles (II) Results of Single Nucleon-Nucleon Interactions 1107

FUJITA Eiichi;

—— and K. IZUI: Observations of Lattice Defects in Graphite by Electron Microscopy, Part I 214

——— [cf. IWATA Tadao (197)]
FUJITA Hiroshi: Direct Observation of Subgrain-Growth of Cold-Worked Aluminium by means of Electron Microscopy 397
FUJIWARA Kunio: [cf. IWASAKI Hiroshi (132) Errata]
FUKANO Yasushige: Study on Precipitation Phenomena in Thin Films of Supersaturated Gold-Nikel Alloy 1195
FUKASE Masahiro: [cf. WATANABE Hiroshi (1181)]
FUKE Tokujiro: Nuclear Quadrupole Resonance Under High Pressure, I. 266
FUKUDA Atsuo: [cf. ONAKA Ryumyo (340) S.N.]
FUKUDA Kuniya: [cf. NAKAMURA Kaizo S.N. (1262)]
———, H. MATSUMOTO, T. TAKAGI and Y. UCHIDA: Electron Spin Resonance of Manganese in $MgCl_2$ (S.N.)........1256
FUKUI Shūji: The Structure of Extensive Air Showers Near the Axes 604
FUKUSHIMA Einosuke;
—— and H. NIMURA: Study of the Texture of the Boundary of Etched and Ground Regions of Quartz Plate by X-ray Diffraction 928
FURUICHI Jiro: [cf. MIYAKE Yasuhiro (1263) S.N.]
FURUKAWA Michiaki;
and S. TANAKA: Excitation Function for the Reaction $O^{16}(\alpha, pn)F^{18}$ (S.N.)........ 129
FURUKAWA Yoshitaka: Impurity Effect upon Mobility in Heavily Doped Silicon (S.N.).. 577
———: Electrical Properties of Heavily Doped n-Type Germanium 687
GOLD Louis: Hot Electron Nonequilibrium Carrier Distribution in a Many-Valley Semiconductor (S.N.) 575
———: Hot Electron Behavior at High Pressures (S.N)........1269
GOTOH Kanefusa: Effect of a Magnetic Field upon the Stability of Free Boundary Layers between Two Uniform Streams 559
HACHIYA Yûki: [cf. ISHIMATSU Toshiyuki (367)]
HASHI Tsuneo: Double Quantum Transition in Electron Spin Resonance of Diphenyl-Picryl Hydrazyl at Low Magnetic Fields........1243
HAYAKAWA Shigeru;
—— and T. SUITA: The Characteristics of the Discharges in the Crossed Electric and Magnetic Field (S.N.)........1037
HIHARA Tadamiki: [cf. KŌI Yoshitaka (574, 1042) S.N.]
HIKI Yosio: Internal Friction of Synthetic Quartz........ 664
HINOTANI Kensaku: [cf. MIYAKE Saburo (847)]
HIRABYASHI Makoto: [cf. IWASAKI Hiroshi (132)]
HIRAHARA Eiji: [cf. FUJIME Satoshi (183) Errata]
HIRAI Masamitsu: [cf. UETA Masayasu (538)]
HIRAKAWA Kazuyoshi: [cf. TUBOTA Hiroshi (1038) S.N.]
HIRAKI Akio: [cf. ITOH Junkichi (343) S.N.]
HIRONE Tokutaro;
—— and H. YAMAMOTO: Diffusion of Cobalt into Silver 455
HIRONO Motokazu: On the Theory of Cross Relaxation in Maser Materials 766
HIROTA Eiichi: [cf. KUBOTA Buichi (345) S.N.]
HOLM. C.H.: [cf. IBERS. James A. (839) S.N.]
HOMMA Saburo;
———, T. KUROYANAGI and H. MORINAGA: Decay of Ir^{195} and Ir^{197} (S.N.).... 841
HONMA Akio: [cf. OGUCHI Takehiko (79)]
HORI Jun-ichi: A New Picture of the Vibration of Linear Lattices 23
HORIE Kinuko: [cf. OHMURA Haruko (593)]
HORIE Tadao;
—— and T. IWAI: An Effect of Heat Treatment on WO_3 Single Crystal, I. Various Patterns 424
HOSHINO Ryosuke: [cf. KUME Kiyoshi (290)]
———: Proton Magnetic Resonance in Ferroelectric $(CH_3NH_3)AlSO_4\cdot12H_2O$ (S.N.)........ 835

Hoshino Sadao;
—— and I. Shibuya: Anomalous Temperature Dependence of Lattice Constants of Ferroelectric Sodium Nitrite (S.N.)....1254
Hosokawa Iwao: Theoretical Prediction of the Pressure Distribution on a Non-lifting, Thin Symmetrical Aerofoil at Various Transonic Speeds.... 546
Hosoya Sukeaki: [cf. Kuriyama Masao (701)]
Hsiao C. C.;
——, J. E. Osborn and D. B. Rozendal: Orientation Dependent Mechanical Breakdown of a Model High Polymer Solid 459
Ibers James A.;
—— and C. H. Holm: The O-H....O Bone in Orthoboric Acid (S.N.)...... 839
Ikegami Hidetsugu: [cf. Sakai Mitsuo (148)]
Ikegami Seiji;
—— I. Ueda and Y. Ise: Optical Absorption and Electrical Conductivity of Reduced BaTiO$_3$ Single Crystal (S.N.) 572
Ikezawa Mikihiko: [cf. Ueta Masayasu (538)]
Imai Nobuhisa: Interaction between Polyions and Low Molecular Ions.... 746
Imamura Shunji: [cf. Chikawa Jun-ichi (1175)]
——: Remarks on the Electrical Properties of Alkali Antimonides (S.N.) ..1036
Inokuti Mitio: [cf. Amemiya Ayao (949)]
Inoue Morio;
— and H. Mizuno: The Purification of KCl by the Zone Refining Method (S.N.).... 128
Inoue Tutomu: Linear Potential Barrier Model for Nuclear Surface (S.N.) 844
Inuishi Yoshio: [cf. Matsuura Kenji (339); Edagawa Hiroshi (1041) S.N.]
Ise Yukihiko: [cf. Ikegami Seiji (592) S.N.]
Ishii Zensho: Studies on the Boundary between Etched and Ground Regions of Ge and Si Single Crystal Surface by X-Ray Diffraction Topography 733
Ishimatsu Toshiyuki;
——, N. Takano, Y. Hachiya and T. Nakashima: Angular Distributions and Excitation Functions of the $Be^9 (d, p) Be^{10}$ Ground-State Reaction 367
Ishizaki Yoshihide: Inelastic Scattering of Deuterons from C^{12}, Mg^{24} and Ni^{60}. ......
Ito Nobuo: [cf. Miyake Saburo (847)]
Itoh Junkichi;
——, M. Satoh and A. Hiraki: Nuclear Magnetic Resonance Study of NaCl Crystal containing Ca Impurities (S.N.) 343
Iwai Tsuruji: [cf. Horie Tadao (424)]
Iwasaki Hiroshi;
——, M. Hirabayashi, K. Fujiwara, D. Watanabe and S. Ogawa: Study on the Ordered Phases with Long Period in the Gold-Zinc Alloy System (Errata).... 132
Iwata Tadao;
——, E. Fujita and H. Suzuki: On the Energy of the Interstitial Atom in Graphite 197
Izui Kazuhiko: [cf. Fujita F. Eiichi (214)]
—— and F. E. Fujita: Observation of Lattice Defects in Fission Fragment-irradiated Graphite (S.N.) 1032
Kainuma Yoshiro: A Diffraction Pattern caused by Temperature Diffuse Scattering. I. General Theory.... 228
—— and William N. Lipscomb: P_s Function in Electron Diffraction 495
Kakiuchi Yoshinobu: [cf. Kume Kiyoshi (843) S.N.]
Kamigaki Kazuo: Ultrasonic Attenuation in Tin Single Crystals at Low Temperatures 1141
——: Ultrasonic Attenuation in Magnetite at Low Temperatures 1170
Kamiya Yoshihiro;
——, K. Ando, M. Nonoyama and R. Uyeda: Dislocation Networks and Moiré Patterns of Molybdenite (Errata) 846
Kanamaru Fumikazu: [cf. Okazaki Chisato (119) S.N.]

KANEKO Tatsunosuke: [cf. MIYAKE Saburo (847)]
KANEMATSU Kazuo: [cf. OHYAMA Tetuo (352) S.N.; YASUKOCHI KŌ (429), (1123)]
KATANO Yoshio: [cf. KUBO Kazuko (347)]
KATO Koshi: [NISHIYAMA Zenji (834) S.N.]
KATO Riso: [cf. NAKAMURA Kaizo (1262) S.N.]
KATO Yoshifumi: Vibrational Effect on the Nuclear Quadrupole Coupling in ND$_3$ (S.N.) 122
KATSUMATA Itsuo: [cf. MIYAKE Saburo (847)]
KATSUURA Kanji: On the Viscosity of Irradiated Polymers. III Effect of Branching (Errata) 1270
KAWABATA Chikao: [cf. UMEDA Kwai (341) S.N.]
KAWAI Nawoyuki: On the Protons from the N$^{14}(d, p)$N^{15} Reaction 157
KAWAI Takao: Study on the Internal Motions of Some Acryl- and Methacryl- group High Polymers by Pulsed NMR Method 1220
KAWAKUBO Tatsuyuki: [cf. NOMURA Shoichiro (706)]
KAWAMATA Shin: A Simplified Method Calculating the Laminar Boundary Layer.... 805
KAWARABAYASHI Ken: [cf. NAKAMURA Seitaro (130) S.N.]
KAWATA Suekichi: Study on Spark Counters of the Rosenblum Type for Counting α Particles and Neutrons 1
KAZUMATA Yukio: [cf. YOKOZAWA Yasaburo (694)]
KIDO Kiyoshi;
—— and T. WATANABE: The Magnetic Investigation of Mn^{++}, Co^{++}, Ni^{++}, Cu^{++} Ammine and Anhydrate Salts. (Errata) 353
KIMURA Motoharu: [SHODA Katsufusa (1031) S.N.; CHIBA Ren (1077)]
KIMURA Norihisa: [cf. TAKAGI Mieko (792)]
KIMURA Ren'iti;
——, T. OHOYAMA and K. ENDO: On the Decomposition of the Ferromagnetic Phase of the Heusler Alloy, Cu$_2$MnAl (S.N.) 1266
KINOSITA Koreo: Refractive Index and Pore Structure of Acid-Leached Surface Layer of Glass 807
KITA Isao: A Cloud Chamber Study of High Energy Nuclear Interactions of Cosmic Ray Particles (I) A Possible Evidence of Successive Collisions in Carbon Nuclei..1099
KITAMURA Saburo;
——, T. KUBO and T. YAMASHITA: Enhancement of Photoconductivity upon Cadmium Sulphide Single Crystals (S.N.) 351
KOBA Saburo: Convex-Core Model of Molecules in Crystalline State, II 627
KOBAYASHI Keisuke: [cf. SHODA Katsufusa (1031) S.N.]
KOGURE Youzou: On the Irreversible Behavior of Coupled Oscillators with Application to Time of Flight 14
KOHRA Kazutake;
—— and H. WATANABE: Measurement of Anomalous Absorption Coefficients of Electrons for MgO Crystals (S.N.) 580
KŌI Yoshitaka;
——, A. TSUJIMURA, T. HIHARA and T. KUSHIDA: NMR of Co^{59} in Ferromagnetic Cobalt Alloys (S.N.) 574
——, A. TSUJIMURA, T. HIHARA and T. KUSHIDA: Internal Magnetic Field in Iron and Iron Alloys Measured by NMR (S.N.) 1040
KOJIMA Kazuko: [cf. NISHIMAKI Noriko (576) S.N.]
—— and N. NISHIMAKI: A-Centers in Potassium Chloride Crystals (S.N.) .. 121
KOJIMA Tadanobu: [cf. NISHIMAKI Noriko (576) S.N.]
KOMATSUBARA Kiichi: Change of Surface State of Ge by Electron Bomberdment (S.N.) 125
KONDO Michiya;
——, T. YAMAZAKI and S. YAMABE: Angular Distribution of (α, p) Reactions in Some Light Nuclei 1091
KORE'EDA Atsuo: [cf. NISHIYAMA Zenji (834) S.N.]
KOSHINO Shigeharu;
—— and T. ANDO: Resonance Transfer of Ionization Energy in Semiconductors 1151

KUBO Kazuko: Radiation Induced Optical Absorptions in Crystalline Quartz and Fused Silica 108
——— and Y. KATANO: Observations of Dislocation Network in Neutron-Irradiated LiF Crystal (S.N.) 347
———: Radiation Induced Optical Absorptions in Crystalline Quartz and Fused Silica (Errata) 582
KUBO Takao: [cf. KITAMURA Saburo (351) S.N.]
KUBOTA Buichi;
——— and E. HIROTA: Electrical Resistivity of Ferromagnetic Chromium Dioxide (S.N.) 345
KUBOTA Hiroko: [cf. NAKAMURA Terutaro (209)]
KUME Kiyoshi;
——— and R. HOSHINO: Proton Magnetic Resonance of Ice Single Crystal.... 290
——— and Y. KAKIUCHI: The O-H....O Bond in Orthoboric Acid (S.N.) 843
KURIYAMA Masao;
———, H. YAMANOUCHI and S. HOSOYA: Ferromagnetic Resonance Absorption of Single-Crystal Thin Films of Nickel 701
KUROYANAGI Jun: On the Relation between the Change in Modulus of Rigidity in Brass Wires by Cold-Rolling and Rolling Textures 1019
KUROYANAGI Tokihiro: [cf. HOMMA Saburo (841) S.N.]
KUSHIDA Toshimoto: [cf. KŌI Yoshitaka (574), (1040) S.N.]
LIPSCOMB William N: [cf. KAINUMA Yoshiro (495)]
MAEDA Hajime: [cf. MIYAZAWA Hisao (132) Errata]
MAEKAWA Syun-ichi: [cf. EDAGAWA Hiroshi (1041) S.N.]
MARUYAMA Michio: [cf. TSUKADA Kineo (166)]
MASUDA Isoo: The Wavelength Dependence of Quantum Efficiency and Absorption Coefficient of $ZnSiO_3$/Mn Powder Phosphor 105
MASUDA Kohzoh;
——— and T. SUITA: E.S.R. of Irradiated DPPH Protected by Polystyrene (S.N.) 837
MASUNO Kunio: [cf. WAKU Shigeru (1158)]
MATSUI Atsuo: [cf. NAKAMURA Kaizo S.N. (1262)]
MATSUKURA Yasuo: Properties of Grain Boundaries in Silicon 842
———: Heat Treatment Centers in Silicon 192
MATSUMOTO Hiroaki: [cf. FUKUDA Kuniya (1256) S.N.]
MATSUMOTO Shigeo;
——— and S. MIKAMO: On the Inelasticity in High-Energy Nuclear Interactions (S.N.) 350
MATSUURA Kenji;
——— and Y. INUISHI: Annealing of Radiation Damage on Lifetime in Silicon (S.N.) 339
MIKAMO Shoji: [cf. MATSUMOTO Shigeo (350) S.N.]
MIKOSHIBA Nobuo: Interaction of Electrons and Holes with Acoustic Waves in Intrinsic Semiconductors 895
MIKUMO Takashi: Anomalies in the Scattering of Alpha Particles by Carbon 1066
MIKURA Ziro: On the Superconducting Ground State (Errata) 353
MIDZUNO Yukio: Scattering of Microwaves from a Cylindrical Plasma in the Born Approximation. I. 971
MIZUNO Hiroyuki: [cf. INOUE Morio (128) S.N.]
MIZUNO Yukio: Elementary Processes Related to the Catalytic Action μ-for the p-d Fusion Reaction 1043
MITSUHASHI Hiroji: Structures of Photoconductivity Spectra near the Fundamental Absorption Edge of Cadmium Sulfide 989
———: Effect of Current Injection on Properties of Cadmium Sulfide Crystals (S.N.) 1258
MITSUI Toshio: [cf. SHIBUYA Iwao (479)]
MITSUISHI Akiyoshi: The Optical Properties of Cadmium Telluride in the Far Infrared Region 533

MITSUISHI Tomokuni: [cf. SHOJI Masakazu (1253) S.N.]

———: An Electron Diffraction Study on Cu-Sn Alloys 453

MIYAKE Saburo;

———, K. HINOTANI, I. KATSUMATA, T. KANEKO and N. ITO; Lateral Density Distribution of Charged Particles in the Central Region of Extensive Air Shower 847

MIYAKE Yasuhiro;

- and J. FURUICHI: Refractive Index Difference of Dilute Aqueous Solution of Polyvinylpyrolidon (S.N.) 1263

MIYATA Nahonori: Electric Conduction of Ferrites Containing Fe^{2+}-ions 206

MIYAZAWA Hisao;

——— and H. MAEDA: Anisotropic Hall Coefficients in n-Type Germanium (Errata) 132

MIZUTANI Hiroshi: Extension of High Polymer Molecule and Energy Change by Mixing 282

MOCHIZUKI Masako: Smoke Observation on Boundary Layer Transition Caused by a Spherical Roughness Element 995

MORI Saburo: [cf. OKAZAKI Chisato (119) S.N.]

MORI Tsugio: The Dipole Moment and End-to-End Length of the Isotactic Vinyl Polymer, III. Convergence of Neumann Series 944

MORIMOTO Setsu: [cf. TAKAGI Mieko (972)]

MORINAGA Haruhiko: [cf. HOMMA Saburo (841) S.N.; CHIBA Ren (1077)]

MORINO Yonezo: [cf. OKA Takeshi (1235)]

MORINO Yoshinori: [cf. EDAGAWA Hiroshi (1041) S.N.]

MURAKAMI Miyuki: [cf. FUJIME Satoshi (183)]

———: Anisotropy of Electrical Conduction in Iron Sulfide Single Crystal...... 187

MURAKAMI Terutoshi: Entropy Production and Variation Principle in the Kinetic Theory of Rigid-Sphere Gas Mixture 633

MUTSURO Naoshi: [cf. CHIBA Ren (1077)]

NAGAHARA Yukio: Elastic and Inelastic Scattering of Protons from Carbon Nucleus from 6.5 to 16 Mev 133

NAGAKURA Sigemaro: Study of Metallic Carbides by Electron Diffraction Part IV. Cobalt Carbides 1213

NAGASAWA Hiroshi: [cf. TOMONO Yuzo (123) S.N.]

NAKADA Osamu: [cf. AIZU Kêitirô (923)]

NAKAGAWA Kisaku: Mass Spectrometric Study on the Evaporation of Volatile Components in Polyethylene 741

NAKAHARA Osamu: The Base Resistance of the Transistor in the Saturated Region (S.N.) 1260

NAKAJIMA Tetsuo: [cf. NAKAMURA Yoji (840) S.N.]

NAKAJIMA Yutaka: [cf. OHMURA Haruko (593)]

NAKAMICHI Takuro;

——— and M. YAMAMOTO: Antiferromagnetic Magnetostriction in CoO and NiO Single Crystals (S.N.) 126

NAKAMURA Kaizo;

———, T. FUKUDA, R. KATO, A. MATSUI and Y. UCHIDA: The Optical Absorption of Localized Exciton in KCl-Kl Crystal (S.N.) ....

NAKAMURA Seitaro;

——— and K. KAWARABAYASHI: Mass Spectra of Baryons (S.N.) 130

NAKAMURA Terutaro;

——— and K. OHI: Dislocations and Fines Line in Rochelle Salt Crystal 209

———, K. OHI and H. KUBOTA: Growth and Dissolution Processes of GASH Crystal 906

NAKAMURA Yoji;

———, T. NAKAJIMA and H. TAKAMI: Volume Magnetostriction in Nickel-Iron Alloys (S.N.) 840

NAKASHIMA Takao: [cf. ISHIMATSU Toshiyuki (367)]

NAKAU Tanehiro: [cf. TAKEYAMA Mikio (1255) S.N.]

NARITA Koziro: Energy Spectrum of Mn^{++} Ion in Calcium Fluorophosphate I........ 99
NIMURA Hiroshi: [cf. FUKUSHIMA Einosuke (928)]
NISHIMAKI Noriko: [cf. KOJIMA Kazuko (121) S.N.]
———, K. KOJIMA and T. KOJIMA: Nature of the *A*-Centers in KCl (S.N.) .. 576
NISHIMURA Kazuaki: Gamma Rays from Inelastic Scattering of Neutrons by Fe, Cu, Zn, Ge and Se 355
NISHIOKA Kouzou: [cf. YONEDA Yasuharu (578)]
NISHIYAMA Zenji;
———, A. KORE'EDA, I. EGUCHI and K. KATO: Direct Observation of the Lattice Imperfections in Pearlites by Electron Microscopy (S.N.) 834
NIU Keishiro: Flow of Condensing Vapour with Temporary Supersaturated State due to Heat-Removal Effect 798
NOGAMI Yozo: [cf. OHMURA Haruko (593)]
NOGUCHI Seiichiro: The Thermoelectric Power of Magnesium-Cadmium Alloys 1145
NOMURA Shoichiro;
———, T. KAWAKUBO and T. YANAGI: Specific Heat of Ti_2O_3 706
———, Y. ASAO and S. SAWADA: Domain Structure of $NaNO_2$........ 917
NOMURA Yûkichi: Diffraction of Plane Sound Wave by Many Equal Circular Holes Arbitrarily Distributed in an Infinitely Large Rigid Plane Plate 819
NONOYAMA Minoru: [cf. KAMIYA Yoshihiro (846) Errata]
NOSÉ Hiroshi: Spin Wave Resonance in Cu-Ni Alloy Films (S.N.) 342
———: Spin Wave Resonance in Pd-Ni Alloy Films (S.N.) 838
OGAWA Iwao;
——— and T. DOKE: The Double-Grid Ionization Chamber (S.N.)........1025
OGAWA Shiro: [cf. IWASAKI Hiroshi (132) Errata]
OGUCHI Takehiko;
——— and A. HONMA: Theory of Ferro- and Antiferromagnetic Resonance Absorption 79
OHI Kikuo: [cf. NAKAMURA Terutaro (209, 906)]
OHKURA Hiroshi: Experimental Studies on Electronic Trapping Processes Associated with Dislocation Lines in Alkali Halide Crystals........ 881
OHMURA Haruko;
———, H. EJIRI, Y. NAKAJIMA, K. HORIE, K. ETOH, A. OHUCHI and Y. NOGAMI: Resonance Levels in the Reactions $^{28}Si(p,\gamma)^{29}P$, $^{29}Si(p,\gamma)^{30}P$ and $^{30}Si(p,\gamma)^{31}P$.. 593
OHNISHI Haruyuki;
——— and T. TERANISHI: Crystal Distortion in Copper Ferrite-Chromite Series 35
OHOYAMA Tetsuo;
———, K. YASUKŌCHI and K. KANEMATSU: A New Phase of an Intermetallic Compound $Mn_{3.4}Ge$ and its Magnetism (S.N.) 352
OHOYAMA Tetuo: [cf. KIMURA Ren'iti (1266) S.N.; YASUKŌCHI Kō (429, 1123)]
OHTA Keizo: Time Decrease of Magnetic Permeability in Some Mixed Ferrites 250
OHUCHI Akiji: [cf. OHMURA Haruko (593)]
OKA Takeshi;
———, Y. MORINO: Microwave Spectrum of Formaldehyde III. Vibration-Rotation Interaction........1235
OKADA Kenkichi: Ferroelectric Properties of X-ray Damaged Rochelle Salt 414
OKAMOTO Kazuto: Electron Linear Accelerator as a Source of Intense Secondary Particle Beams (S.N.) 120
OKAZAKI Atsushi;
——— and Y. SUEMUNE: The Crystal Structure of $KCuF_3$ 176
——— and Y. SUEMUNE: The Crystal Structures of $KMnF_3$, $KFeF_3$, $KCoF_3$, $KNiF_3$ and $KCuF_3$ above and below their Néel Temperature 671
———: The Superstructure of Iron Selenide Fe_7Se_8........1162
OKAZAKI Chisato;
———, S. MORI and F. KANAMARU: Magnetic and Crystallographical Properties of Hexagonal Barium Mono-Ferrite, $BaO\cdot Fe_2O_3$ (S.N.)........ 119
OKUDA Setsuo: The Velocity Distribution at the Interface between Two Liquids 324

———: The Velocity Distribution at the Interface between Two Liquids 845

ONAKA Ryumyo;

———, A. FUKUDA and A. EJIRI: The Fundamental Absorption of Lithium Fluoride and Sodium Fluoride (S.N.) 340

O'NEILL Edward L.;

——— and T. ASAKURA: Optical Image Formation in Terms of Entropy Transformations 301

ONUKI Masami: Photoconductive Hall Effect in Potassium Bromide 981

OSBORN J. E.: [cf. HSIAO C. C. (459)]

ROUX Michel: [cf. TAKEDA Susumu (95)]

ROZENDAL D. B. [cf. HSIAD C. C. (459)]

SAITÔ Nobuhiko: On the Theory of Adiabatic and Isolated Susceptibilities 621

SAKAI Mitsuo;

———, H. IKEGAMI and T. YAMAZAKI: Short-lived Activity of Ag^{106} 148

SAKATA Kimiko: Thermoelectric Behaviours of Rutile (S.N.) 1026

SAKURAI Kiichi: A Direct Determination of the Crystal Structure of Ethylenediammonium Sulphate 1205

SATAKE Kimihiko: [cf. UCHIDA Ichizo (573) S.N.]

SATOH Mitsuo: [ITOH Junkichi (343) S.N.]

SATOMI Ken'iti: Oxygen Positional Parameters of Tetragonal Mn_3O_4.......... 258

SAWADA Shozo: [cf. NOMURA Shoichiro (917)]

SEGAWA Wataru: Some Remarks on Hydrostatic Pressure and Maxwell Model.......... 317

———: Rheological Equations of Generalized Maxwell Model and Voigt Model in Three-Dimensional, Non-Linear Deformation.......... 320

———: Rheological Equations of Generalized Maxwell Model and Voigt Model in Three-Dimensional, Non-Linear Deformation (Errata) 845

———: Some Remarks on Hydrostatic Pressure and Maxwell Model (Errata).. 846

SEKIZAWA Hisashi: A Note on the Electron Diffusion and the Wall Relaxation in Ferrites (S.N.) 1034

SHIBAOKA Yoshio: [cf. TAMADA Ko (1249)]

SHIBATA Chokichiro: On the Electron Emission from Oxide Coated Cathode Subject to Strong Electric Field.......... 51

———: On the Electron Emission from Oxide Coated Cathode Subject to Strong Electric Field (Errata) 582

SHIBATA Hiroyuki: On the Nuclear Interaction of Mu-Mesons.......... 372

SHIBUYA Iwao: X-Ray Studies of the Ferroelectric Phase Transition in $NaNO_2$.......... 490

SHIBUYA Iwao;

——— and T. MITSUI: The Ferroelectric Phase Transition in $(Glycine)_3 \cdot H_2SO_4$ and Critical X-Ray Scattering 479

———: [cf. HOSHINO Sadao (1254) S.N.]

SHIMAKAWA Seiken: Propagation of Tltrasonics in Triethylamine-water Mixture...... 113

SHIMIZU Masao: Exchange Interactions between s- and d-Electrons and Paramagnetic Susceptibilities in Nickel, Palladium, and Platinum 1114

SHIMIZU Tadao;

——— and K. SHIMODA: "Non-Adiabatic" Behavior in a Low Frequency Beam-Type Maser 777

SHIMIZU Tatsuo: The Electron-Coupled Nuclear Spin Interactions in Ionic Crystals by the Overlap Model (S.N.) 1264

SHIRAFUJI Junji;

——— and Y. INUISHI: Effects of Vacancies on Pulse Photoconductions in CdS Single Crystals (S.N.) 832

SHIRAI Hiroko: [cf. ABE Hidetaro (118)]

SHODA Katsufusa: [cf. CHIBA Ren (1077)]

———, K. KOBAYASHI, S. SIINA, K. ABE and M. KIMURA: Fine Structures of Photoprotons from Si^{28} (S.N.) 1031

SHOJI Masakazu;

———, S. TAUCHI, T. MITSUISHI and M. TOMONO: Observation of Dislocation in Germanium Single Crystal (S.N.) 1253

SHONO Katsufusa: [cf. TOKUNAGA Masakatsu (1029) S.N.]
SIINA Shoichi: [cf. SHODA Katsufusa (1031) S.N.]
SONE Toshimaro: The Rheological Behavior and Thixotropy of a Fatty Plastic Body.. 961
SONOIKE Sanemi;
——— and K. AKIMOTO: Luminescence of Doped Silver Chloride Crystals.... 658
SUEMUNE Yasutaka [cf. OKAZAKI Atsushi (176, 671)]
SUGANUMA Ryōji;
——— T. YOSHIDA and Y. FUJIKI: Anomalous Diffusion at the Interface of Thin Bimetallic Film of Bi and Sb 676
——— T. YOSHIDA and Y. FUJIKI: Anomalous Diffusion at the Interface of Thin Bimetallic Film of Bi and Sb (Errata) 1042
SUGITA Motoyosi: The Switching Circuit Logically or Functionally Equivalent to a System of Biochemical Reactions 737
SUITA Tokuo: [cf. MASUDA Kohzoh (837) S.N.]
———: [cf. HAYAKAWA Shigeru (1037) S.N.]
SUGIHARA Makoto: [cf. TSUBOYA Ichiro (571, 1255) S.N.]
———: [cf. AOYAGI Keizô (1027) S.N.]
SUMINO Kôji;
———, and M. YAMAMOTO: Preferential Plastic Deformation in the Surface Region of Al and α-Fe Single Crystal (S.N.).......... 131
SUZUKI Hideji: [cf. IWATA Tadao (197)]
SUZUKI Hiromichi: [cf. TUBOTA Hirosi (1038) S.N.]
SUZUKI Kazuo: X-ray Studies on Precipitation of Metastable Centers in Mixed Crystals NaCl-CdCl$_2$.......... 67
SUZUKI Tadasu: Electron Distribution in Cu$_2$O Crystal 501
SUZUKI Tatsusaburo;
——— and I. YUHARA: Counting Efficiency of Gamma Rays in Counter Tubes.. 152
TAKAGI Mieko;
———, N. KITAMURA and S. MORIMOTO: Density vs. Exposure Curves of a Photographic Emulsion for 20～200 kV Electrons 792
TAKAGI Toru: [cf. FUKUDA Kuniya (1256) S.N.]
TAKAHASHI Yûzō: Dielectric α- and β-dispersions in Polyvinyl Butyral (PVB) (S.N.) ..1024
———: Dielectric α-, β- and γ-Dispersions in the Thermosetting Phenolic Resins 1028
TAKAMI Hideo: [cf. NAKAMURA Yoji (840) S.N.]
TAKANO Naoyuki: [cf. ISHIMATSU Toshiyuki (367)]
———: The Reaction Mg$^{25}(d, p)$Mg^{26} in the Energy Range of Deuterons from 1.5 MeV to 3.0 MeV 598
TAKEDA Susumu;
M. ROUX: A Method for Measuring High Electron Densities in Plasmas........ 95
———: Microwave Measurement of Fast Time-varying Plasmas (S.N.) 1267
TAKEMOTO Susumu: Temperature Dependence of the Line Width of Ferrimagnetic Resonance in Polycrystalline Nickel Cadmium Ferrite (S.N.) 344
TAKEYAMA Mikio;
———, T. NAKAU and S. YAMAZAKI: Moving Striation in Microwave Discharge Plasma (S.N.) 1255
TAKEYAMA Naokata: Viscous Forces and Brownian Motion (S.N.)..........1030
TAKUMA Hiroshi: Magnetic Hyperfine Structure in the Rotational Spectrum of H$_2$CO.. 309
TAMADA Ko;
———, and Y. SHIBAOKA: On the Pendent drop, I 1249
TANAKA Shigeo: [cf. FURUKAWA Michiaki (129) S.N.]
TANAKA Shigetoshi: Absorption and Reflection Spectra of Afterglow Plasma (S.N.) ..1259
TANAKA Shigeya: [cf. TSUKADA Kineo (166)]
TANAKA Shigezo [cf. MATUKURA Yasuo (833) S.N.]
TANAKA Toshisuke: [cf. WAKU Shigeru (1158)]
TANAKA Yasuo: A Study on High-Energy Nuclear-Active Particles in Extensive Air Showers 866
TANIGUCHI Satoshi: [YAMAMOTO Mikio (1035) S.N.]

TANISAKI Sigetosi: Microdamain Structure in Paraelectric Phase of $NaNO_2$ (S.N.)...... 579
TAUCHI Shoji: [SHOJI Masakazu (1253) S.N.]
TAYLOR G.O.: [cf. FORSTAT H. (128) S.N.]
TERANISHI Teruo [cf. OHNISHI Haruyuki (35)]
TOBISAWA Shōtarō: Temperature Dependence of Magnetic Susceptibilities of $KClO_3$, $KBrO_3$ and KIO_3 654
TOKITA Yasuo: Vibration of a Plate and Sound Radiation Generated by an Impulsive Force........1008
TOKUNAGA Masakatsu;
——— and K. SHONO: Forward Characteristics of Si *pπn*-Jnnctions (S.N.)....1029
TOMISHIMA Yasuo [cf. UMEDA KWAI (S.N.) (341)]
TOMITA Sadami: Effects of the Special Heat-treatment on Permalloys........ 393
TOMONO Masami: Regrowth of Germanium Single Crystal from Indium Melt........ 439
———: Regrowth of Germanium from Molten Indium or Lead........ 711
———: [cf. SHOJI Masafusa (1253) S.N.]
TOMONO Yuzo;
———, and H. NAGASAWA: Proton Resonance and Spin Quenching Effect in $NiSO_4 \cdot 7H_2O$ (S.N.)........ 123
TOSIMA Soitiro: Inelastic Scattering of Thermal Neutrons by Paramagnetic Ions 241
TSUBOKAWA Ichiro: Magnetic Anisotropy of Chromium Antimonide and its Manganese Substitutes........ 277
TSUBOYA Ichiro;
——— and Makoto SUGIHARA: On the New Magnetic Phase in Manganese-Aluminium-Copper System (S.N.)........ 571
———, and M. SUGIHARA: The New Magnetic Phase in Manganese-Aluminium-Nickel System (S.N.)........1257
TSUJIMURA Akira [cf. KŌI Yoshitaka (574, 1040) S.N.]
TSUKADA Kineo;
———, S. TANAKA and M. MARUYAMA: Inelastic Scattering of Neutrons by the Time-of-Flight Method........ 166
TSUZUKI Takuji: Quantum Statistics of surface Effect........ 377
TSUZUKU Takuro: Cavity Growth by Vacancy Condensation and Transformation to Dislocation Loop in the Graphite Structure........ 407
———: Cavity Growth by Vacancy Condensation and Transformation to Dislocation Loop in the Graphite Structure (Errata)........1042
TUBOTA Hirosi;
———, H. SUZUKI and K. HIRAKAWA: The Electrical Properties of Zinc Telluride (S.N.)........1038
UCHIDA Ichizo;
——— and K. SATAKE: Impedance Changes Induced by Light in ZnS Phosphors (S.N.)........ 573
UCHIDA Yoichi: [cf. FUKUDA Kuniya (1256); NAKAMURA Kaizo (1262) S.N.]
UEDA Hiroshi: Resistivity Striations in Germanium Single Crystals........ 61
UEDA Ichiro: [cf. IKEGAMI Seiji (572)]
UEDA Ikuhiko: The Crystal Structure of Chloroanil and Bromoanil........1185
UETA Masayasu;
———, M. HIRAI and M. IKEZAWA: Interaction of Exciton with Electron Trapping Centers in Alkali Halide Crystals 3. Exciton Induced Photoconductivity of *U* center........ 538
UMEDA Jun-ichi: Electrical Properties of Sb-Doped *n*-Type SnSe (S.N.)........ 124
UMEDA Kwai;
———, Y. TOMISHIMA and C. KAWABATA: The Inverse Solution of the TFD Equation (S.N.)........ 341
UYEDA Ryozi [cf. KAMIYA Yoshihiro (846) Errata]
WADA Yasaku: Mechanical Dispersions and Transition Phenomena in Semicrystalline Polymers........1226
WAKESHIMA Hiromu: On the Theory of the Fracture of Liquids........ 9
WAKU Shigeru;

———, K. MASUNO and T. TANAKA: Ferroelectricity in (K, NH), (K, Rb) and (K, Tl) Ferrocyanide Mixed Crystals 1158
WATANABE Denjiro: [cf. IWASAKI Hiroshi (132) Errata]
———: Study on the Ordered Alloys of Gold-Manganese System by Electron Diffraction, III. Lattice Modulation in the Ordered Au_3Mn 469
WATANABE Hiroshi: [cf. KOHRA Kazutake 580 S.N.]
———, Magnetic Properties of Perovskites Containing Strontium, II. Lanthanum-Strontium Manganites 433
———: Angular Distribution of Electrons Suffering Characteristic Energy Loss in Passage through Metal Films 912
———, M. FUKASE: Weak Ferromagnetism in β-$NaFeO_2$ 1181
WATANABE Kenji: *Mu*-Meson Component of Air Shower Below the Ground 855
WATANABE Takashi: The Magnetic Investigation of Mn^{++}, Co^{++}, Ni^{++} and Cu^{++} Ammine and Anhydrate Salts at Low Temperature 1131
———: [cf. KIDO Kiyoshi (353) Errata]
WATANABE Tsutomu: A Theory of Electron Impact on Some Polyatomic Molecules.. 510
———: On the Additivity Rule in the Ionization Cross Section of Molecules.. 529
WOLF W. P.: On the Ferrimagnetic Resonance of Europium Iron Garnet (Addendum) 582
YAMABE Shotaro: [cf. KONDO Michiya (1091)].......................................
YAMAGUCHI Hisashi: Angular Distributions of Protons from the Alpha Particle Bombardment of B^{10}, N^{14}, O^{16} and Ne^{20} 583
YAMAMOTO Hisao: [cf. HIRONE Tokutaro (455)]
YAMAMOTO Mikio: [cf. NAKAMICHI Takuro (126) S.N.]
———: [cf. SUMINO Kôji (131) S.N.]
——— and S. TANIGUCHI: Weak Field Behaviour of the ΔE Effect in Ferromagnetic Cubic Solid Solution Alloys (S.N.) 1035
YAMANOUCHI Hirokage: [cf. KURIYAMA Masao (701)]
YAMASHITA Jiro: Low-Temperature Electrical Breakdown in Germanium 720
YAMASHITA Toshio: [cf. KITAMURA Saburo (351) S.N.]
YAMAZAKI Sozaburo [cf. TAKEYAMA Mikio (1255) S.N.]
YAMAZAKI Takashi [cf. KONDO Michiya (1091)]
YAMAZAKI Toshimitsu [cf. SAKAI Mitsuo (148)]
YANAGI Taketoshi: [cf. NOMURA Shoichiro (706)]
YASUKŌCHI Kō: [cf. OHOYAMA Tetuo (352)]
———, K. KANEMATSU and T. OHOYAMA; Magnetic Properties of Intermetallic Compounds in Iron-Germanium System: $Fe_{1.67}Ge$ and $FeGe_2$ 429
———, K. KANEMATSU and T. OHOYAOA: Magnetic Properties of Intermetallic Compounds in Manganese-Tin System: $Mn_{3.67}Sn$, $Mn_{1.77}Sn$ and $MnSn_2$..1123
YOKOZAWA Yasaburo;
——— and Y. KAZUMATA: Paramagnetic Resonance of Mn^{++} Associated with Impurities in Alkali Chlorides.. 694
YONEDA Yasuharu;
——— and K. NISHIOKA: X-ray Small Angle Scattering from Precipitated Platelets in Al-Ag Alloy (S.N.) 578
YOSHIDA Masayuki: Distribution of Interstitials and Vacancies Produced by an Incident Fast Neutron 44
YOSHIDA Toshio: [cf. SUGANUMA Ryōji (676)]
———: [cf. SUGANUMA Ryōji (1042) Errata]
YUHARA Jiro [cf. SUZUKI Tatsusaburo (152)]